Chemistry for Bio-Circular-Green Economy

PACCON

Pure and Applied Chemistry International Conference 2024

Pure and Applied Chemistry International Conference 2024

PROCEEDINGS

Chemistry for Bio-Circular-Green Economy

BHIRAJ CONVENTION CENTRE, BITEC,

BANGKOK, THAILAND

JANUARY 26 - 27, 2024

www.paccon2024.kasetsart.org

IC-P-11

PROCEEDINGS

Pure and Applied Chemistry International Conference 2024 (PACCON 2024)

"Chemistry for Bio-Circular-Green Economy"

January 26-27, 2024

at

Bhiraj Convention Center,
BITEC, Bangkok, THAILAND

Organized by

The Chemical Society of Thailand under the Patronage of
Professor Dr. Her Royal Highness Princess Chulabhorn
Krom Phra Srisavangavadhana

In association with

The Department of Chemistry, Faculty of Science,
Kasetsart University

Pure and Applied Chemistry International Conference 2024 (PACCON 2024)

Proceedings

e-ISBN	978-616-278-829-1
1st Edition	April 2024 (available in PDF version only)
Published by	The Chemical Society of Thailand under the Patronage of Professor Dr. Her Royal Highness Princess Chulabhorn Krom Phra Srisavangavadhana in association with the Department of Chemistry, Faculty of Science, Kasetsart University

COMMITTEES

Professional Conference Organizers

1. Chemical Society of Thailand under the Patronage of Professor Dr. Her Royal Highness Princess Chulabhorn Krom Phra Srisavangavadhana

2. Kasetsart University

Conference Chair

Paiboon Ngernmeesri	Kasetsart University

International Advisory Committee

Javier García Martínez	IUPAC President, Spain
Mustafa Culha	FACS President, Turkey
Pimchai Chaiyen	VISTEC, Thailand
Andrew P. Dove	University of Birmingham, United Kingdom
Alexander Kuhn	University of Bordeaux, France
Supawan Tantayanont	CST Past-President, Chulalongkorn University, Thailand
Supa Hannongbua	CST Past-President, Kasetsart University, Thailand
Vudhichai Parasuk	CST President, Chulalongkorn University, Thailand

Scientific Committee

Günther Rupprechter	Technische Universität Wien, Austria
Shuangjun Lin	Shanghai Jiao Tong University, China
Qiuquan Wang	Xiamen University, China
Ryszard Lobinski	Université de Pau et des Pays de l'Adour, France
Christophe M. Thomas	Chimie ParisTech, PSL University, France
Jan J. Weigand	Technische Universität Dresden, Germany
Kazuo Akagi	Ritsumeikan University, Japan
Masashi Hasegawa	Kitasato University, Japan
Kowit Hengphasatporn	University of Tsukuba, Japan
Takashi Kaneta	Okayama University, Japan
Masaki Kuse	Kobe University, Japan
Seiji Mori	Ibaraki University, Japan
Yasuhiro Morisaki	Kwansei Gakuin University, Japan
Hirotomo Nishihara	Tohoku University, Japan
Hiroyuki Nishikawa	Ibaraki University, Japan
Shin-Ichi Ohira	Kumamoto University, Japan
Satoko Suzuki	JASCO Corporation, Japan
Siriporn Taokaew	Nagaoka University of Technology, Japan

COMMITTEES

Il Won Kim	Soongsil University, Korea
Mylene M. Uy	MSU–Iligan Institute of Technology, Philippines
Anna Kajetanowicz	University of Warsaw, Poland
Roderick W. Bates	Nanyang Technological University, Singapore
Cheng-Chau Chiu	National Sun Yat-Sen University, Taiwan
Takumi Konno	National Taiwan Normal University, Taiwan
Jeng-Yu Lin	Tunghai University, Taiwan
Kanoktip Boonkerd	Chulalongkorn University, Thailand
Metta Charoenpanich	Kasetsart University, Thailand
Natthawat Chuanopparat	Kasetsart University, Thailand
Chatree Faikhamta	Kasetsart University, Thailand
Pimpa Hormnirun	Kasetsart University, Thailand
Sirirat Jitkarnka	Chulalongkorn University, Thailand
Wirunya Keawwattana	Kasetsart University, Thailand
Sutasinee Kityakarn	Kasetsart University, Thailand
Utai Klinkesorn	Kasetsart University, Thailand
Patraporn Luksirikul	Kasetsart University, Thailand
Supawadee Namuangruk	National Nanotechnology Center, Thailand
Thitaphat Ngernsutivorakul	Kasetsart University, Thailand
Wanchai Pluempanupat	Kasetsart University, Thailand
Prapasiri Pongprayoon	Kasetsart University, Thailand
Chaiya Prasittichai	Kasetsart University, Thailand
Vinich Promarak	VISTEC, Thailand
Vatcharin Rukachaisirikul	Prince of Songkla University, Thailand
Atitaya Siripinyanond	Mahidol University, Thailand
Weekit Sirisaksoontorn	Kasetsart University, Thailand
Ekasith Somsook	Mahidol University, Thailand
Thawatchai Tuntulani	Chulalongkorn University, Thailand
Tirayut Vilaivan	Chulalongkorn University, Thailand
Pinsuda Viravathana	Kasetsart University, Thailand
Pakorn Wattana-Amorn	Kasetsart University, Thailand
Edman Tsang	University of Oxford, United Kingdom
T. Randall Lee	University of Houston, United States of America

COMMITTEES

■ Organizing Committee

Supakit Achiwawanich	Kasetsart University, Thailand
Khrongkhwan Akkarachaneeyakorn	Kasetsart University, Thailand
Sunisa Akkarasamiyo	Kasetsart University, Thailand
Orapin Chienthavorn	Kasetsart University, Thailand
Natthawat Chuanopparat	Kasetsart University, Thailand
Pitak Chuawong	Kasetsart University, Thailand
Tanwawan Duangthongyou	Kasetsart University, Thailand
Supa Hannongbua	Kasetsart University, Thailand
Panitat Hasin	Kasetsart University, Thailand
Wisit Hirunpinyopas	Kasetsart University, Thailand
Pimpa Hormnirun	Kasetsart University, Thailand
Witcha Imaram	Kasetsart University, Thailand
Junya Jattanasen	Kasetsart University, Thailand
Kannika Jeamjumnunja	Kasetsart University, Thailand
Thitinun Karpkird	Kasetsart University, Thailand
Wirunya Keawwattana	Kasetsart University, Thailand
Pipat Khongpracha	Kasetsart University, Thailand
Sutasinee Kityakarn	Kasetsart University, Thailand
Theerachart Leepasert	Kasetsart University, Thailand
Pongsak Lowmunkhong	Kasetsart University, Thailand
Patraporn Luksirikul	Kasetsart University, Thailand
Supatta Midpanon	Kasetsart University, Thailand
Tanin Nanok	Kasetsart University, Thailand
Paiboon Ngernmeesri	Kasetsart University, Thailand
Thitaphat Ngernsutivorakul	Kasetsart University, Thailand
Somkiat Nokbin	Kasetsart University, Thailand
Piboon Pantu	Kasetsart University, Thailand
Waraporn Parasuk	Kasetsart University, Thailand
Wanchai Pluempanupat	Kasetsart University, Thailand
Prapasiri Pongprayoon	Kasetsart University, Thailand
Chaiya Prasittichai	Kasetsart University, Thailand
Chadchalerm Raksakoon	Kasetsart University, Thailand
Montida Raoarun	Kasetsart University, Thailand

COMMITTEES

Ramida Rattanakam	Kasetsart University, Thailand
Tharinee Saleepoch	Kasetsart University, Thailand
Patchreenart Saparpakorn	Kasetsart University, Thailand
Jakkapan Sirijaraensre	Kasetsart University, Thailand
Weekit Sirisaksoontorn	Kasetsart University, Thailand
Wilai Siriwatcharapiboon	Kasetsart University, Thailand
Apisit Songsasen	Kasetsart University, Thailand
Bunyarithi Sookcharoenpinyo	Kasetsart University, Thailand
Pannaree Srinoi	Kasetsart University, Thailand
Wannisa Sukjee	Kasetsart University, Thailand
Songwut Suramitr	Kasetsart University, Thailand
Potjanart Suwanruji	Kasetsart University, Thailand
Siree Tangbunsuk	Kasetsart University, Thailand
Pinsuda Viravathana	Kasetsart University, Thailand
Boontana Wannalerse	Kasetsart University, Thailand
Chompunuch Warakulwit	Kasetsart University, Thailand
Pakorn Wattana-Amorn	Kasetsart University, Thailand
Kuntawit Witthayolankowit	Kasetsart University, Thailand
Peerada Yingyuad	Kasetsart University, Thailand
Wanlapa Aeungmaitrepirom	Chemical Society of Thailand
Chanat Aonbangkhen	Chemical Society of Thailand
Supakorn Boonyean	Chemical Society of Thailand
Suchada Chatrapromma	Chemical Society of Thailand
Ekarat Detsri	Chemical Society of Thailand
Narumol Kreua-ongarjnukool	Chemical Society of Thailand
Phoosak Hirunyatrakul	Chemical Society of Thailand
Surin Laosooksathit	Chemical Society of Thailand
Ladda Meesuk	Chemical Society of Thailand
Thanuttkhul Mongkolaussavarat	Chemical Society of Thailand
Orasa Onjun	Chemical Society of Thailand
Vudhichai Parasuk	Chemical Society of Thailand
Waraporn Parasuk	Chemical Society of Thailand
Buncha Pulpoka	Chemical Society of Thailand
Pumidech Puthongkham	Chemical Society of Thailand

COMMITTEES

Singto Sakulkhaemaruethai	Chemical Society of Thailand
Montip Srirattana	Chemical Society of Thailand
Boonnak Sukhummek	Chemical Society of Thailand
Supawan Tantayanon	Chemical Society of Thailand
Prapaipit C. Terni	Chemical Society of Thailand
Boonsom Watcharachanchai	Chemical Society of Thailand
Kanda Wongwailikhit	Chemical Society of Thailand

SCIENTIFIC SESSIONS

AC-Analytical Chemistry

Chair: Atitaya Siripinyanond

Co-Chair: Thitaphat Ngernsutivorakul

CC-Catalytic Chemistry

Chair: Metta Charoenpanich

Co-Chair: Patraporn Luksirikul

CE-Chemical Education

Chair: Chatree Faikhamta

Co-Chair: Sutasinee Kityakarn

EE-Environmental Chemistry and Renewable Energy

Chair: Ekasith Somsook

Co-Chair: Weekit Sirisaksoontorn

FA-Food, Agriculture and Cosmetics and Renewable Energy

Chair: Utai Klinkesorn

Co-Chair: Wanchai Pluempanupat

IC-Inorganic Chemistry

Chair: Thawatchai Tuntulani

Co-Chair: Pimpa Hormnirun

IE-Industrial and Engineering Chemistry

Chair: Sirirat Jitkarnka

Co-Chair: Pinsuda Viravathana

MN-Material Chemistry and Nanotechnology

Chair: Vinich Promarak

Co-Chair: Chaiya Prasittichai

SCIENTIFIC SESSIONS

NP-Natural Products, Biological Chemistry and Chemical Biology

Chair: Vatcharin Rukachaisirikul

Co-Chair: Pakorn Wattana-Amorn

OM- Organic Synthesis and Medicinal Chemistry

Chair: Tirayut Vilaivan

Co-Chair: Natthawat Chuanopparat

PC-Polymer Chemistry and Bio-Based Materials

Chair: Kanoktip Boonkerd

Co-Chair: Wirunya Keawattana

PT-Physical and Theoretical Chemistry

Chair: Supawadee Namuangruk

Co-Chair: Prapasiri Pongprayoon

TABLE OF CONTENTS

TABLE OF CONTENTS

TABLE OF CONTENTS

TABLE OF CONTENTS

TABLE OF CONTENTS

TABLE OF CONTENTS

TABLE OF CONTENTS

TABLE OF CONTENTS

TABLE OF CONTENTS

TABLE OF CONTENTS

TABLE OF CONTENTS

TABLE OF CONTENTS

TABLE OF CONTENTS

TABLE OF CONTENTS

Chemistry for Bio-Circular-Green Economy

www.paccon2024.kasetsart.org

Production and certification of certified reference material of andrographolide in *Andrographis Paniculata* powder by a network of competent laboratories approach

Ponhatai Kankaew*, Kittiya Shearman, Kanjana Hongthong, Cheerapa Boonyakong, and Charun Yafa

Organic Analysis Laboratory, Chemical Metrology and Biometry department, National Institute of Metrology (Thailand), Pathumthani 12120 Thailand

**E-mail: pornhatai@nimt.or.th*

Abstract:

Andrographis paniculata is in Thailand's official list of essential medicines (Herbal medicine list) from the Ministry of Public Health for the management of respiratory and gastrointestinal disorders, including COVID-19 treatment. It was recommended that the proper amount of active pharmaceutical ingredient (Andrographolide) for COVID-19 treatment is 180 mg/day. Accurate measurement of the amount of active ingredient in herbal medicine is, therefore, important, not only for the effectiveness of treatment, but also for minimizing potential for drug overdose. There were no certified reference materials available to allow laboratories to measure their analytical method performance. A matrix-matched Certified Reference Material (CRM), TRM-F-5011, was prepared at the National Institute of Metrology, Thailand (NIMT), from freeze dried, ground, Green Chiretta (*Andrographis Paniculata*) leaves. Homogeneity and stability of the material were rigorously assessed. Characterization of the reference material was carried out by a network of competence laboratories. The interlaboratory results were statistically analyzed, and median was calculated as assigned value of CRM. Measurement uncertainty of the certified value was evaluated from the between-unit inhomogeneity, long-term storage stability of the material at -20 °C, and laboratory biases from characterization by a network of competence laboratories. The results showed that TRM-F-5011 contained Andrographolide at (18.7 ± 1.3) mg/g.

1. Introduction

Andrographis paniculata is widely used as a Thai traditional medicine for treating colds, fevers, and sore throats. The fresh leaf juice extract of *Andrographis paniculata* was also effective in treating diarrhea, low appetite, and pain associated with muscle contractions including upper respiratory tract infections and gastrointestinal disorders.[1] During the COVID-19 pandemic, *Andrographis paniculata* was approved by Thailand's Health Ministry to treat COVID-19 patients who have minor symptoms.[2-4]Therefore, *Andrographis paniculata* is listed in Thailand's official list of essential medicines (Herbal medicine list) for the remedy of respiratory and gastrointestinal disorders including COVID-19 treatment.[1]

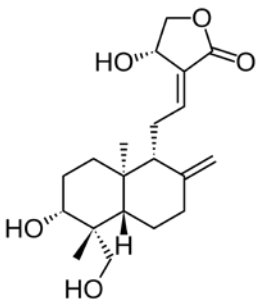

Figure 1. Structure of andrographolide

The main active ingredient in *Andrographis paniculata* is andrographolide, the structure is shown in Figure 1. It is recommended that the proper amount of andrographolide for COVID-19 treatment was 180 mg per day. Therefore, accurate measurement of the active ingredient content in herbal medicine is crucial for both treatment success and reducing the risk of drug overdose.

Reference materials (RMs) are the materials that contain one or more specified property values and those values are sufficiently stable and homogenous. Certified reference materials (CRMs) are RMs that provided the metrological traceability and measurement uncertainty of those values. CRMs are important tools in confidence building in measurement results performed by testing laboratories. CRMs are utilized for various purposes such as calibration of instruments, method validation, instrument performance evaluation, traceability of measurement results, and uncertainty assessment.[5-15] However, regarding the measurement of andrographolide in the *Andrographis paniculata*, there were no certified reference materials available to allow laboratories to access their analytical method performances. Thus, a matrix-matched CRM of andrographolide in *Andrographis paniculata* is an essential tool to reach the reliable results for the measurement of andrographolide in *Andrographis paniculata* medicine.

Reference materials (RMs) produced by the National Institute of Metrology, Thailand (NIMT) are registered under a tradename as Thailand reference material (TRM). This work aims to produce a matrix-matched CRM of andrographolide in *Andrographis paniculata*. The code of this CRM is TRM-F-5011.

This article describes CRM production including homogeneity, stability studies, and characterization by a network of competent laboratories. This CRM was produced in accordance with the international standard of ISO 17034 and ISO Guide 35. [16-17]

2. Materials and Methods

2.1 Chemicals and reagents

The high purity CRM of andrographolide used for calibration was supplied by NIMT (TRM-S-5047). Methanol was purchased from RCI Labscan. The *Andrographis paniculata* dried powder was purchased from a local market and stored in the dark at -20 ◦C until further processing.

2.2 Instruments

Measurement of andrographolide was performed by High-Performance Liquid Chromatography combined with Photo Diode Array Detector (HPLC-PDA). The HPLC system consists of the Waters 2998 photodiode array detector, 600 solvent pump, 600 controller, 717 autosampler, PC- with Empower software. Chromolith High Resolution RP-18 (4.6 × 150 mm, 3 µm) was used as an analytical column. All sample preparations and calibration solutions were gravimetrically prepared using a calibrated analytical balance, Mettler Toledo XP205.

2.3 Determination of andrographolide in RM

The andrographolide in the *Andrographis Paniculata* powder was determined using HPLC-PDA. An amount of 150 mg of *Andrographis paniculata* powder was accurately weighed and transferred into a 50 mL centrifuge tube, 40 mL of methanol was then added and sonicated for 60 min. The mixture was then centrifuged at 35.776 RCF for 10 mins. The supernatant was collected and filtered through a 0.22 µm PTFE syringe filter. The concentration of Andrographolide in the extract was then measured by applying an external calibration curve. The HPLC condition was illustrated in Table 1.

To quantify the mass fraction of andrographolide, a calibration curve was gravimetrically constructed using the pure CRM of andrographolide standard. The mass fraction is determined using Equation 1.

$$w_x = c_0 . \frac{m_0}{m_t} \qquad \text{Equation 1}$$

where w_x is mass fraction of andrographolide in *Andrographis Paniculata* powder (mg/g), c_0 is mass fraction of andrographolide obtained from the calibration curve (mg/g), m_0 is mass of andrographolide extract (g), and m_t is mass of *Andrographis Paniculata* powder (g)

Table 1. HPLC-PDA condition

HPLC column	Chromolith High Resolution RP-18 (150 mm long, 4.6 mm)
Mobile phase	Methanol:water (40:60)
Flow rate	1.0 mL/min
Oven temperature	40 °C
λ_{max}	220 nm

2.4 Production and Certification of Certified Reference Material

2.4.1 Material processing, packing and storage

Approximately 2 kg of dried *Andrographis paniculata* was cryodessicated using a freeze-dryer for 24 hours. The dried material was then blended and homogenised by using a V-mixer. Aliquots of 10 g of the dried powder were manually poured into 40 mL amber glass bottles. The bottles were closed with screw caps to protect from moisture during storage and transport. The candidate RMs were then stored at -20 ◦C.

2.4.2 Homogeneity study

The homogeneity study of TRM-F-5011 was performed according to the ISO 17034 and ISO Guide 35.[16-17] Eleven units of a candidate reference material were randomly selected using the systematic sampling strategy. Then, each sample was analyzed in duplicate by HPLC-PDA under repeatability conditions using basic homogeneity study design. Samples were analyzed in a random order to be able to distinguish any potential analytical drift from measurement and bottling trends. A statistical tool, Student's *t* – test trend analysis was applied to detect if there is any significant trend during the bottling process. One-way analysis of variance (ANOVA) was utilized to assess the homogeneity of the prepared reference material for both within-unit and between-unit variations.

The data sets were tested for outliers by use of Cochran-tests. The homogeneity of the batches was evaluated by one-way ANOVA approach with *F*-test in accordance with the requirements as stipulated in ISO Guide 35.

Additionally, linear regression functions were calculated according to filling, and analysis order. The slopes of the lines were tested for significance on a 95 % confidence level to check for significant trends.

The uncertainty of homogeneity (u_{bb}') study results can be calculated using the equation as follows.

$$u'_{bb} = \sqrt{\frac{MS_{within}}{n_0}} \cdot \sqrt[4]{\frac{2}{df_{within}}} \quad \text{Equation 2}$$

Where MS_{within} is mean square of within-group, n_o is number of replicates per unit or bottle. df_{within} is degree of freedom of within-group.

2.4.3 Short-term stability study

The short-term stability was studied using isochronous scheme to assess the transport condition. The candidate CRM was stored at 4 °C, 25 °C, and 40 °C for 4 weeks. The reference temperature was set at -20 °C. The studied samples were selected using a random statistical sampling scheme. For each studied temperature, samples were moved from the reference temperature to the corresponding temperature at different times (e.g. 0, 1, 2, 3, and 4 weeks). At the defined end time, all the samples were analyzed immediately or put back at the reference temperature before analysis. The mass fraction of andrographolide was analyzed by HPLC-PDA under repeatability condition. The data was evaluated by trend analysis using *t*-test.

2.4.4 Long-term stability study

For the long-term stability study, the samples were stored at -20 °C for 1, 3, 6 and 12 months. The samples were tested after each time point using the same protocol as used for the short-term stability study.

The uncertainty of stability during storage (u_{lts}) can be calculated as follow.

$$u_{lts} = s(b_1)(t_{m1} + t_{cert}) \quad \text{Equation 3}$$

Where u_{lts} is uncertainty of stability, s(b_1) is the standard error for the estimated slope, $t_{m1}$is time interval between value assignment and initial stability monitoring point, and t_{cert} is the period of validity of a certificate issued during that time.

2.4.5 Characterization

The material characterization was conducted based on a non-operationally-defined measurand using a network of competent laboratories.[16] Each laboratory obtained three bottles of candidate reference materials and analyzed in duplicate. The statistical approach used for assignment of property value of the material is the median, as shown in the following Equation 4.

$$med(x) = \begin{cases} \frac{1}{2}\left(x'_{\frac{m}{2}} + x'_{\frac{m}{2}+1}\right), meven \\ x'_{m+1/2}, modd \end{cases} \quad \text{Equation 4}$$

Where x'$_1$,….,x'$_m$ denote the participant values arranged in increasing order.

The measurement uncertainty of the characterizations (u_{chr}) was calculated as Equation 5.

$$u_{char} = \sqrt{u^2(med(x))} = \sqrt{\frac{\pi}{2m}\sigma^2} \quad \text{Equation 5}$$

Where σ^2 is a robust estimate of standard deviation, usually based on the median absolute deviation mad(x) multiplied by 1.483. This corrected estimate is sometimes called MAD_E, and m is a number of laboratories.

3. Results & Discussion

3.1 Homogeneity assessment and evaluation of uncertainty

The twenty-two results (11 bottles × duplicate analysis) of the mass fraction of andrographolide in candidate reference material were investigated for outliers by Cochran-tests. The result showed that there was no outlier. The trend analysis using Student's *t*-test showed that there was no significant trend for the measurement sequences and filling order of TRM0F-5011. ANOVA results provided between-unit and within-unit standard deviations. The results are summarized in Table 2. As shown in Table 2, the *P*-value from ANOVA analysis is 0.831, greater than 0.05, and the F_{cal} (0.5373) is less than $F_{critical}$ (2.854), therefore the andrographolide in TRM-F-5011 were sufficiently homogeneous.

The uncertainty of homogeneity (u_{bb}') was calculated by equation 2 and the result was 0.212 mg/g.

Table 2. Results of homogeneity test of andrographolide by ANOVA: Single Factor ANOVA

Source of Variation	*SS*	*df*	*MS*	*F*	*P-value*	*F crit*
Between Groups	1.1293	10	0.1129	0.5373	0.8313	2.854
Within Groups	2.3119	11	0.2102			
Total	3.44129	21				

3.2 Characterization of CRM

TRM-F-5011 was characterized by a network of competence laboratories approach. The competence of laboratories was demonstrated by the results of the first round of proficiency testing program with *z*-score of less than 2. There were six selected laboratories including NIMT. Thirty-six values obtained from the participants (6 labs × 3 bottles × 2 analysis in duplicate) were analyzed. The outlier was assessed by Cochran test. The results revealed that there was no outlier and the results were not significantly different form each other. The results of mean andrographolide concentration from each laboratory is shown in Table 3. However, there was a participant that did not report its measurement uncertainty. A weighted mean therefore cannot be employed to assign the certified valued of the TRM-F-5011. Therefore, the most statistically suitable tool for characterization of the TRM-F-5011 was median. The mean of andrographolide concentration form each laboratory and the median of laboratory's results including their uncertainties are shown in the Table 3.

Table 3. The median results of andrographolide

Laboratory ID	Mass fraction of andrographolide (mg/g)	Standard uncertainty (mg/g)
1	17.33	0.92
2	19.90	0.07
3	21.52	0.57
4	18.12	0.5
5	17.70	-
6	19.33	1.3
Median	**18.70**	**0.43**

3.3 Stability

3.3.1 Short-term stability

The short-term stability data was evaluated using trend analysis (Equation 6) for each temperature.

$$t_{cal} = \frac{b_1}{s(b_1)} \qquad \text{Equation 6}$$

Where b_1 is the slope and $s(b_1)$ is standard error of the slope.

As shown in Table 4, the stability testing result showed no significant trend (95% confidence level) at 4 °C and 25 °C. However, statistically significant trend was observed at 40°C. The material, therefore, should be dispatched under controlled conditions.

Table 4. Evaluation of short-term stability results of andrographolide in TRM-F-5011 stored at studied temperatures

Temp. (°C)	t_{cal}	t_{crit}	**Result**
4	0.736	2.306	$t_{cal} < t_{crit}$ stable
25	0.948	2.306	$t_{cal} < t_{crit}$ stable
40	6.531	2.306	$t_{cal} > t_{crit}$ Not stable

3.3.2 Long-term stability

The stability study of a candidate certified reference material was studied using the Student's *t*-test based on the regression parameters of the stability graphs. The statistical evaluation of the obtained results proves that the slope of the regression is not statistically different from zero (t_{cal} (1.10) <t_{crit} (2.306)). Therefore, the candidate certified reference material is stable at -20 °C throughout the study period. Based on these measurements, it can be concluded that the TRM-F-5011 can be stored at -20 °C for 12 months.

The uncertainty of stability study can be calculated as described in section 2.4.4. Therefore, u_{lts} of TRM-F-5011 is 0.42 mg/g.

3.4 Certified uncertainty

The uncertainty of TRM-F-5011 has contribution from three components, the material heterogeneity (u_{bb}'), material instability (u_{lts}) and the measurement uncertainty of the characterizations (u_{chr}). The uncertainty is calculated as the square root of the sum of squares of the individual contributions, according to Equation 7.

$$U_{CRM} = k \cdot \sqrt{u_{char}^2 + u'^2_{bb} + u_{lts}^2}$$ Equation 7

Therefore, the expanded uncertainty of TRM-F-5011 was 1.3 mg/g. Each component of the uncertainty is tabulated in Table 6.

Table 6. Source of uncertainty of TRM-F-5011

Components	standard uncertainty
u_{char}	0.43
u'_{bb}	0.21
u_{lts}	0.42
Certified value (mg/g)	18.70
Combined standard uncertainty, u_c (mg/g)	0.637
Expanded uncertainty (U), *k*=2 at 95% CI	1.30

4. Conclusion

A new matrix-match CRM of andrographolide was successfully developed by NIMT. The characterization was conducted by a network of competence laboratories approach. The measurement results were statistically analyzed and the certified value of andrographolide in *Andrographis paniculata* was assigned to be 18.7 mg/g with the associated expanded uncertainty of 1.3 mg/g. The homogeneity of TRM-F-5011 was assessed and the results showed that this CRM is sufficiently homogenous. The period of validity of CRM under the proposed storage condition of -20 °C is 1 year after the issuance of certificate. The CRM can be kept at temperatures of 4 ◦C and 25 ◦C for one month. The recommended temperature for transportation is lower than 25 ◦C. This new CRM is used for assessing method validation and quality control purposes. The produced CRM can be used for supporting quality system according to the ISO/IEC 17025 in testing laboratories and improving measurement capabilities.

Acknowledgements

This work was supported by the National Institute of Metrology (Thailand).

References

1. Siripongboonsitti, T.; Ungtrakul, T.; Tawinprai, K.; Auewarakul, C.; Chartisathian, W.; Jansala, T.; et al. Efficacy of Andrographis paniculata extract treatment in mild to moderate COVID-19 patients being treated with favipiravir: A double-blind, randomized, placebo-controlled study (APFaVi trial). *Phytomedicine* **2023**, 119.
2. Nutho, B.; Wilasluck, P.; Deetanya, P.; Wangkanont, K.; Arsakhant, P.; Saeeng, R.; et al. Discovery of C-12 dithiocarbamate andrographolide analogues as inhibitors of SARS-CoV-2 main protease: In vitro and in silico studies. *Computational and Structural Biotechnology Journal* **2022**, 20, 2784–2797.
3. Cui, J.; Gao, J.; Li, Y.; Fan, T.; Qu, J.; Sun, Y.; et al. Andrographolide sulfate inhibited NF-κB activation and alleviated pneumonia induced by poly I:C in mice. *Journal of Pharmacological Sciences* **2020**, 144(4), 189–196.
4. Shi, T. H.; Huang, Y. L.; Chen, C. C.; Pi, W. C.; Hsu, Y. L.; Lo, L. C.; et al. Andrographolide and its fluorescent derivative inhibit the main proteases of 2019-nCoV and SARS-CoV through covalent linkage. *Biochemical and Biophysical Research Communications* **2020**, 533(3), 467–473.
5. International Atomic Energy Agency. Development and Use of Reference Materials and Quality Control Materials; IAEA, 2003.
6. Padariya, C.; Rutkowska, M.; Konieczka, P. The accessibility, necessity, and significance of certified reference materials for total selenium content and its species to improve food laboratories' performance. *Food Chemistry* **2023**, *425*, 136460.
7. Olivares, I. R. B.; De Souza, G. B.; Nogueira, A. R.; De Toledo, G. T. K.; Marcki, D. C. Trends in developments of certified reference materials for chemical analysis - Focus on food, water, soil, and sediment matrices. *TrAC Trends in Analytical Chemistry* **2018**, *100*, 53–64.
8. Chen, W.; Zhang, Y.; Chen, H.; Jin, W.; Chen, X.; Huang, X.; et al. Development of a Pure Certified Reference Material of D-Mannitol. *Molecules* **2023**, 28(19). doi:10.3390/molecules28196794.
9. Lee, J.; Kim, B.-J.; Lee, S. Y.; Choi, J.-T.; Kang, D.; Lee, H.; Choi, K.; Lee, H.; Sim, H.; Baek, S.-Y.; Lee, H.; Hyung, S.; Ahn, S.; Seo, D.; Hwang, J.; Park, J.; Kwak, B.; Won, J. Development of an infant formula certified reference material for the analysis of organic nutrients. *Food Chemistry* **2019**, *298*, 125088.
10. Kline, M. C.; Duewer, D. L.; Travis, J. C.; Smith, M. V.; Redman, J. W.; Vallone, P. M.; Decker, A. E.; Butler, J. M. Production and certification of NIST Standard Reference

Material 2372 Human DNA Quantitation Standard. *Analytical and Bioanalytical Chemistry* **2009**, *394* (4), 1183–1192.
11. Ahmed, H. E.; Tahoun, I. F.; Zakel, S. Development of decahydronaphthalene reference material for low flash point measurements. *Egyptian Journal of Petroleum* **2021**, 30(1), 7–10.
12. Gab-Allah, M. A.; Lijalem, Y. G.; Yu, H.; Lee, S. Y.; Baek, S.-Y.; Han, J.; Choi, K.; Kim, B.-J. Development of a certified reference material for the accurate determination of type B trichothecenes in corn. *Food Chemistry* **2023**, *404*, 134542.
13. Caroli, S.; Forte, G.; Alessandrelli, M.; Cresti, R.; Spagnoli, M.; D'Ilio, S.; Pauwels, J.; Kramer, G. L. A pilot study for the production of a certified reference material for trace elements in honey. *Microchemical Journal* **2000**, *67* (1–3), 227–233.
14. Singh, S. C.; Khatri, D. K.; Singh, K.; Kanchupalli, V.; Madan, J.; Singh, S. B.; Singh, H. Molecular encapsulation of andrographolide in 2-hydroxypropyl-β-cyclodextrin cavity: synthesis, characterization, pharmacokinetic and in vitro antiviral activity analysis against SARS-CoV-2. *Heliyon* **2021**, *7* (8), e07741.
15. Josephs, R. D.; Koeber, R.; Linsinger, T. P. J.; Berndt, A.; Ulberth, F.; Schimmel, H. Production of certified reference materials for mycotoxins: IRMM?s view on the assessment of uncertainties. *Analytical and Bioanalytical Chemistry* **2004**, *378* (5), 1190–1197.
16. ISO 17034: 2016 General requirements for the competence of reference material producers.
17. ISO GUIDE 35:2017(E), Reference materials –Guidance for characterization and assessment of homogeneity and stability.

Development of an electrochemical DNA super-sandwich assay for porcine adulteration detection via one-step immobilization using a poly-adenine oligonucleotide approach

Vasita Lapee-e[1,2], Sudkate Chaiyo[2], and Abdulhadee Yakoh[2]*

[1]*Program in Biotechnology, Faculty of Science, Chulalongkorn University, Bangkok, 10330, Thailand*
[2]*The Institute of Biotechnology and Genetic Engineering, Chulalongkorn University, Bangkok 10330, Thailand*
**E-mail: Abdulhadee.y@chula.ac.th*

Abstract:

Amid rising meat consumption, concerns about meat adulteration and mislabeling have grown, eroding consumer trust, especially among those with cultural, religious, or allergic sensitivities. Traditional meat identification methods like PCR are time-consuming and inconvenient. In this study, we present an electrochemical DNA biosensor for detecting porcine mitochondrial DNA. This biosensor combines a gold nanoparticle-modified screen-printed graphene electrode (AuNPs/SPGE) with a one-step DNA probe immobilization using poly-adenine (poly-A) oligonucleotides. The detection mechanism employs a DNA super-sandwich assay, enhancing sensitivity without extensive sample amplification. This structure monitors the hybridization of target porcine DNA to the poly-A probe through labeled-ferrocene, using differential pulse voltammetry (DPV). The results show a distinct difference between positive and negative controls. The linear range spans 10^1 to 10^6 pM, with a limit of detection (LOD) of 2.2 pM. While most meat adulteration biosensors rely on optical techniques, our electrochemical DNA super-sandwich assay, along with the simple poly-A probe immobilization, provides an efficient, cost-effective, and user-friendly solution for detecting porcine adulteration throughout the meat industry and even by end consumers.

1. Introduction

Amid escalating meat consumption, especially in developing nations due to the raising population, has brought the issue of meat adulteration and mislabeling to the forefront. A notable instance is the 2020 “fake meat scandals” in Thailand, where counterfeit beef falsely presented as halal was discovered to be pork dipped in cattle blood, deceiving Muslim and halal markets for an extended period[1]. Consequently, consumers trust loses, especially among individual driven by culture, religious or allergic consideration, driving the need for a sensing device capable of identifying meat adulteration.

In the context of meat adulteration detection, nucleic acid detection holds greater promise than proteins detection in most immunoassays primarily due to the greater stability of nucleic acids during meat processing. Hence, significant efforts have been directed towards developing DNA biosensors for the simple detection of restricted meat contamination. Detecting pork or porcine DNA contamination is a common concern, often addressed through DNA extraction combined with conventional amplification methods like real-time polymerase chain reaction (PCR). The amplified DNA products are typically identified using techniques such as gel electrophoresis, colorimetric detection, and electrochemical detection.

Among the limited research available on meat adulteration detection, two primary types of biosensors have gained popularity: optical and electrochemical, with optical biosensors comprising the majority[2]. These optical biosensors often require additional amplification steps, necessitating the need for a compact, cost-effective, and user-friendly device. In contrast, electrochemical biosensors offer several advantages, including high sensitivity, selectivity, stability, rapid response, and ease of miniaturization. However, even with enhanced sensitivity achievable using electrochemical sensor, traditional electrochemical detection principle such as labeling (tagging) or label-free approaches may not always suffice to overcome the challenges posed by the low abundance and complex nature of real samples. Therefore, signal amplification becomes imperative to attain the desired sensitivity without the need for prior nucleic acid amplification

In this study, we present an autocatalytic DNA super-sandwiched assay for the detection of *S. scrofa* gene[3], indicating porcine adulteration in meat samples. In contrast to traditional DNA sandwich assays where a specific target sequence hybridizes with a single capturing probe and a redox-tagging probe, limiting the generated signal, our approach utilizes a redox tagging probe referred to as “DNA helper” in this study, designed to hybridize with two regions of a single DNA target. This results in the formation of an elongated hybridization structure, known as “super-sandwiched”, containing multiple tagging probe.

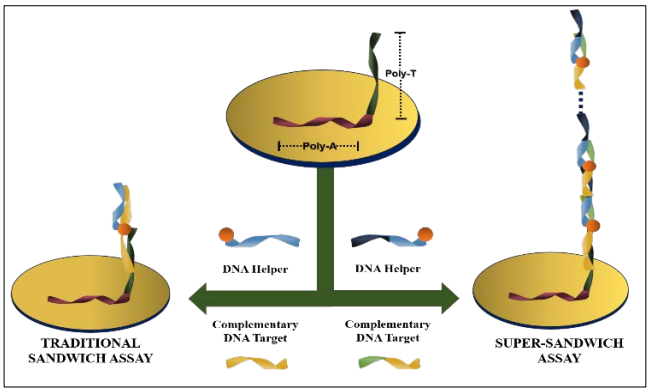

Figure 1. (A) A schematic illustration of the sandwich assay (left) and super-sandwich assay (right).

This autocatalytic signal generation can be self-activated rapidly, taking less than 30 mins surpassing the time requirements of most traditional DNA assays, which often take at least 30 mins or up to 1 hr.

Furthermore, we introduce an automated one-step DNA immobilization approach using a poly-adenine sequence. In this approach, a DNA capturing probe containing poly-thymines–poly-adenines (poly-T – poly-A) tail at its 5'-end is designed to biofunctionalize the gold metal surface, forming an L-shape upright orientation[9,10] (**Figure 1**). This direct immobilization allows for a controllable distribution and orientation, simplifying the process compared to traditional and complexed grafting methods, such as EDC/NHS covalent grafting, avidin-biotin affinity, chitosan-glutaraldehyde cross-linking, or thiol-metal self-assembled monolayer (SAM)[4].

2. Materials and Methods

2.1 Chemicals and Apparatus

Analytical grade reagents were used in this work. Ultrapure water, generated using a Millipore Milli-Q purified water system (with a resistivity of 18.2 MΩ cm) was used throughout the experiments. Additionally, 0.01M Phosphate buffered saline (PBS) containing 10mM $MgCl_2$ solution functioned as working buffer. $KAuCl_4$, 6-Mercapto-1-hexanol (MCH), Tris-HCl, EDTA, NaCl, H_2SO_4, $K[Fe(CN)_6^{3-/4-}]$ and Sodium dodecyl sulfate (SDS) were sourced from Sigma-Aldrich **(**MO, USA**).** The surface morphology of the electrodes underwent characterized via three distinct methods: a 3D measuring confocal laser scanning microscope (CLSM) model LEXT OL55000 (Olympus, Japan), an atomic force microscope (AFM) model SPI3800N / SPA400 (Seiko Instruments Japan), and a field-emission scanning electron microscopy (FESEM) model JSM-7610F (JEOL Ltd., Japan).

Three single strand DNA (ssDNA) sequences were synthesized by Pacific Science (Bangkok, Thailand). These sequences are summarized in **Table 1** below. Notably, the ferrocene redox indicator was tagged to the DNA helper structure to generate the electrochemical signal through ferrocene oxidation during DPV analysis.

All voltametric experiments, including cyclic voltammetry (CV) and differential pulse voltammetry (DPV), were performed using Palmsens Emstat 3+ Blue Potentiostat analyzer (PalmSens BV, Netherlands). For CV characterization, the potential scan range was set from –1.0 to 1.0 V (vs. graphene pseudoreference electrode (GPRE)) with potential step of 0.00244 V (vs. GPRE) and scan rate of 0.1 V/s. Electrochemical impedance spectroscopy (EIS) experiments were carried out using an Autolab electrochemical system with a potentiostat PGSTAT 128 N (EcoChemie, Utrecht, Netherlands). In EIS measurements, the EIS nyquist plot was monitored within the frequency range of 0.1 Hz to 100 kHz, applying AC potential of 0 V (vs GPRE) and a logarithmic scale of 10 points per decade.

Table 1. Sequences of oligonucleotides **(**written in the 5' to 3' direction**)**.

Poly-A capturing DNA probe	5'- AAA AAA AAA AAA AAA – TTT TTT TTT TTT TTT – CG ATA TAA GGG ATA GCT GAT -3'
Ferrocene-tagging DNA helper	5'- GTA GAT TTG TGA TGA CCG TAC CGA TAT AAG GGA TAG CTG AT – ferrocene -3'
Complementary DNA target	5'- TAC GGT CAT CAC AAA TCT ACT ATC AGC TAT CCC TTA TAT CG -3'

2.2 Fabrication of the gold nanoparticles-modified screen-printed graphene electrode (AuNPs/SPGE)

In the construction of the screen-printed graphene electrode (SPGE), three essential components were involved: working electrode (WE), counter electrode (CE) and reference

electrode (RE). These components were fabricated by depositing conductive carbon-graphene paste (SSG-1760A, Serve Science Co., Ltd., Bangkok, Thailand) onto a transparent PET sheet. Subsequently, the printed electrodes underwent a 30-minute curing process at 60 °C

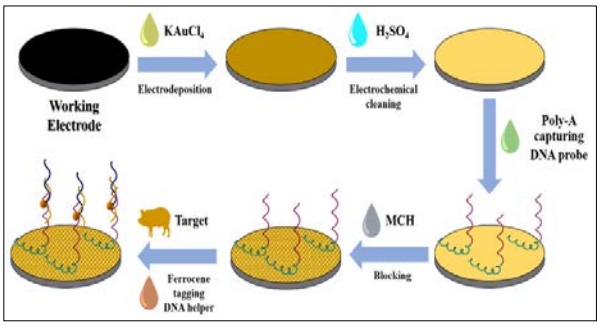

Figure 2. Schematic illustration of AuNPs-modified SPGE for biosensor of porcine adulteration detection

For the immobilization of poly-A DNA probe, an initial step was taken to enhance the SPGE by decorating it with gold nanoparticles (AuNPs), a process outlined in **Figure 2**. This involve the electrodeposition of AuNPs onto the SPGE surface through a chronoamperometric experiment conducted at a constant potential of –0.6 V for 60 s utilizing 5 mM $HAuCl_4$ aqueous solution in 0.5 M H_2SO_4.

Following this, the AuNPs-modified SPGE (abbreviated as AuNPs/SPGE) underwent a thorough rinsing with Milli-Q water and was subsequently air-dried at room temperature. The next phase involved an electrochemical cleaning procedure for the prepared AuNPs/SPGE. This entailed conducting a CV experiment, scanning the potential between –0.5 and 1.0 V (vs. GPRE) at scan rate of 1 V/s for a total of 20 cycles. The objective here was to ensure that the electrode was entirely free from impurities. Lastly, the cleaned AuNPs/SPGE was subjected to another round of rinsing with milli-Q water and then left to air-dry at room temperature, making it ready for subsequent experiments.

2.3 Poly-A immobilization procedure

As detailed in **Table 1**, the poly-A capturing DNA probe was meticulously designed to complement a specific region of the cytochrome b gene found in porcine (*Sus scrofa*) mitochondrial DNA, spanning approximately 16,569 base pairs. This probe was constructed with a distinctive feature at its 5' end –a poly-A tail containing 15 adenines[5]. This tail was strategically incorporated to facilitate the specific adsorption of adenine molecules on gold surfaces. The interaction occurs through the coordination of the metal with the N-atom of the amine group. Additionally, a spacer region, between consisting of 15 consecutive thymine (poly-T) sequences, was strategically placed between the functional group and the capturing region. This spacer served to enhance the accessibility of the target DNA[4]. To enable the immobilization of poly-A **DNA** probe onto the AuNPs/SPGE, a solution of poly-A capturing DNA probe was cast onto the working area of AuNPs/SPGE (see **Figure 2**). Subsequently, the electrode was left to incubation at 4°C overnight. Following this immobilization process, the electrode underwent a thorough washing step with PBS and was then air-dried at room temperature. To block possible active site, a 5 mM MCH solution was applied to the WE and incubated at room temperature for 30 min. Once again, the electrode was diligently rinsed with PBS and left to dry at room temperature. At this juncture, the electrode was deemed ready for use in the detection of porcine adulteration. These prepared, ready-to-use screen-printed graphene electrodes (SPGE) were stored at a temperature of 4°C in anticipation of their future application.

2.4 Meat sample preparation

Real meat samples (including beef and pork) were prepared according to literature reported by Flauzino et al[3]. Firstly, 5.0 g of meat sample underwent a 5-min soaking and blending process in 10 mL of an extraction buffer. This extraction buffer contained 0.2 M Tris-HCl, 0.01 M EDTA, 0.5 M NaCl, and 1% v/v SDS. After this step, which involved the disruption of cells and mitochondria, the sample was sonicated for 15 min at 80 °C to facilitate DNA fragmentation. Following sonication, the sample solution was centrifuged at 12,000 rpm for 15 min. Subsequently, the supernatant was collected and stored at -20 °C. The extracted samples were 5-times diluted to minimize interferent effects before analysis.

2.5 Detection of complementary targets and real meat samples

Differential pulse voltammetry (DPV) was employed to verify the DNA hybridization on working area. In Brief, a mixture comprising 5 µL of DNA target (or the extracted sample) and 2 µL of DNA helper was applied to the working area of ready-to-use electrode. This mixture was left to incubation at room temperature for 30 mins. After the hybridization process, the electrode underwent a thorough washing with PBS and was then subjected to air-drying. Next, 50 µL of working buffer (PBS/$MgCl_2$) was applied to the test area,

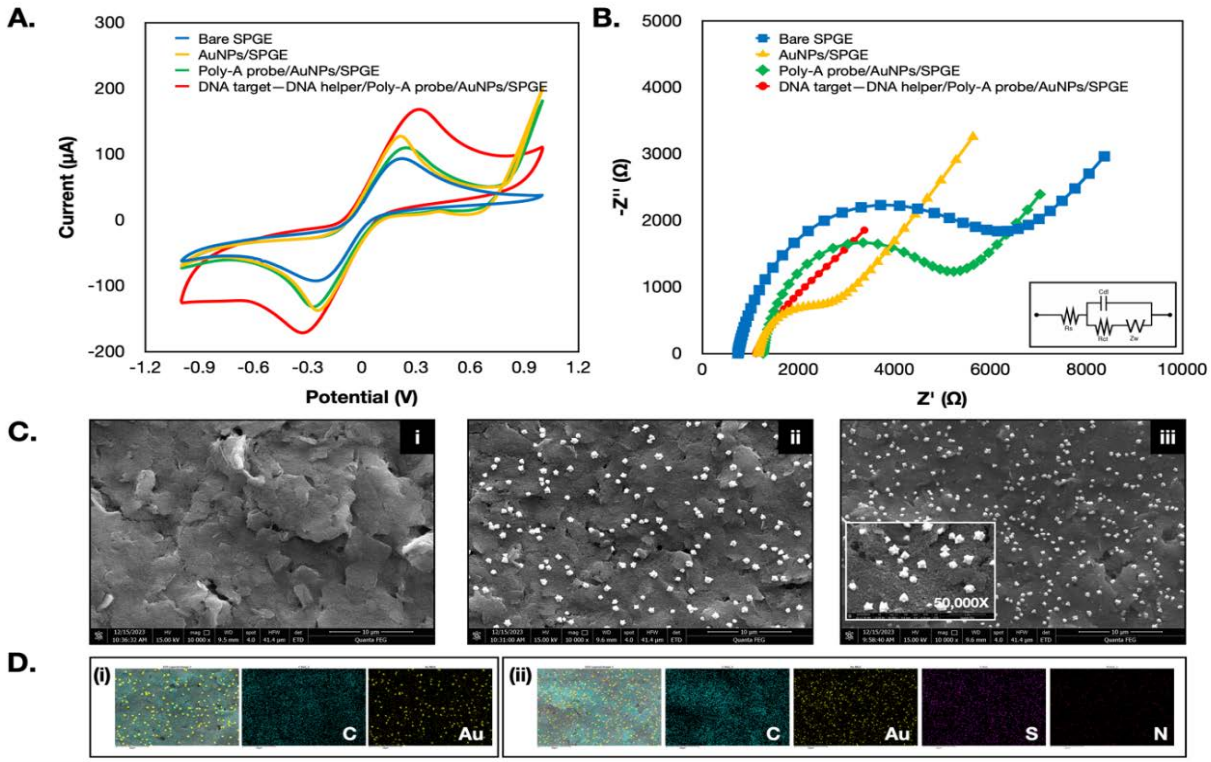

Figure 3. Characterization results of each fabrication step (A) Cyclic voltammogram of Bare SPGE, AuNPs/SPGE, and Poly-A/AuNPs/SPGE, and DNA helper/ target DNA/Poly-A/AuNPs/SPGE electrodes. Note that all EIS Nyquist plots were fitted with the Randles equivalent circuit. (B) Nyquist plot obtained by EIS analysis in each modified electrode. (C) SEM images at 10000X magnification of the bare SPGE (i), AuNPs/SPGE (ii), and poly-A probe/AuNPs/SPGE modified electrode(iii), respectively. (D) Elemental composition detected and EDX elemental mapping of (i) AuNPs/SPGE and (ii) Poly-A probe/AuNPs/SPGE.

encompassing the 3 electrodes required for DPV measurement. DPV measurements were configured with specific parameters, including a potential scan ranging from 0.0 V to +0.6 V, a step potential of 0.01 V, a pulse potential of 0.05 V, a pulse time of 0.1 s, and a scan rate of 0.05 V/s. It is noteworthy that the GPRE was used as the reference electrode throughout the electrochemical analysis.

3. Results & Discussion

3.1 Electrochemical and Morphological Characterization

In this study, both electrochemical characterizations using cyclic voltammetry (CV) and electrochemical impedance spectroscopy (EIS) techniques and employing 5 mM $Fe(CN)_6^{3-/4-}$] in 0.1 M KCl, as well as morphological characterization using field-emission scanning electron microscopy (FE-SEM), were employed.

The electrochemical behaviors of each electrode were initially verified using CV (**Figure3A**). For the bare SPGE, the peak current (including both anodic (Ip_a) and cathodic (Ip_c) currents) was the lowest. The cyclic voltammograms exhibited a significant increase in the peak current after the electrodeposition of metallic AuNPs. A reduction in peak current was observed on Poly-A/AuNPs/SPGE due to the decrease in electron transfer, caused by the inherent steric hindrance of the poly-A film that prevents the $Fe(CN)_6^{3-/4-}$ ions from reaching the electrode surface[6]. Another contributing factor was the repulsion between the negative charges of the phosphate backbone of poly-A capturing DNA probe and the negative charges of the redox mediator ($Fe(CN)_6^{3-/4-}$), leading to a lower peak current[7]. Upon the formation of the super-sandwiched hybridization structure between poly-A capturing DNA probe, the target DNA, and the ferrocene-tagging DNA helper, the peak current increased. This increase indicated the binding of complementary DNA target to the poly-A probe and the catalytic charge-transport properties provided by the ferrocene-tagging DNA helper[8].

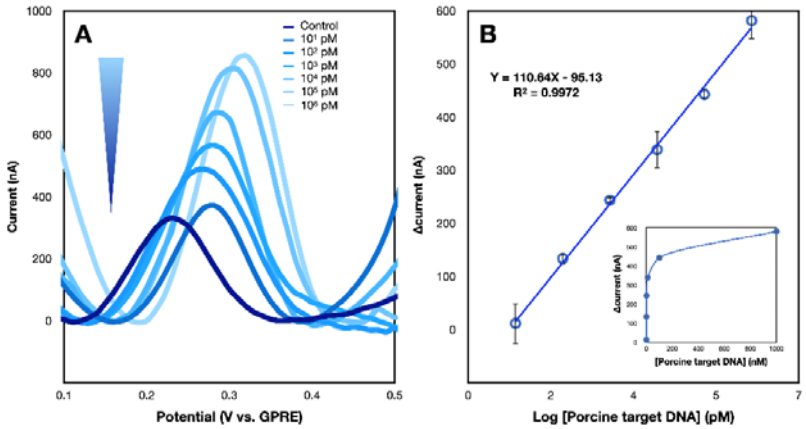

Figure 4. (A) DPV responses of the developed DNA sensor tested with different concentrations of complementary porcine DNA. (B) Relationship between current difference (Δcurrent) as a function of complementary target concentration and inset showing a linear calibration plot between Δcurrent vs logarithmic concentration of complementary target ranging from 10^1 to 10^6 pM**.**

The results collectively confirmed the successful immobilization of the probe and hybridization of the target DNA.

The electrochemical behavior of the electrode was further assessed by measuring the charge transfer resistance (R_{ct}) using the EIS technique. All EIS Nyquist plots were fitted with the Randles circuit. As shown in **Figure 3B**, the largest semicircle, representing the highest resistance to charge transfer, was observed for the bare SPGE. After Au electrodeposition, the R_{ct} decreased, indicating greatly enhanced electron transfer rates for AuNPs-modified electrode. However, upon the immobilization of poly-A probe onto AuNPs/SPGE, the R_{ct} increased due to the formation of poly-A capturing DNA, which impeded the electron transfer. Conversely, the application of complementary DNA with the DNA-helper decreased the R_{ct} value, offering lower resistance to charge transfer from the ferrocene tagging DNA helper[8].

Additionally, the analysis of the electrode morphology was also characterized via FE-SEM/EDX analysis. As demonstrated in **Figure 3**, a comparison between bare SPGE (**Figure 3 (i)**) and AuNPs/SPGE (**Figure 3 (ii)**) revealed the decoration of AuNPs on the SPGE surface. The electrodeposition of Au onto the electrode surface, with the sheet structure of graphene in the carbon-graphene paste, resulted in a homogenous distribution of AuNPs, supporting improved electrochemical signal. Besides, the surface morphology of the poly-A probe-immobilized SPGE (**Figure 3 (iii)**) was found to be smoother compared to that of AuNPs/SPGE. Also, the elemental composition difference and its elemental mapping obtained from EDX analysis between AuNPs/SPGE and poly-A/AuNPs/SPGE (shown in **Figure 3D (i)** and **(ii)**) conclusively confirmed the presence of additional components, specifically nitrogen (from the DNA structure) and sulfur (from the electrode blocking step with MCH). These results collectively validated the successful immobilization of poly-A probe and the target porcine hybridization using the modified electrode.

3.2 Analytical performance

The analytical performance of the system for detecting porcine DNA was evaluated under optimal conditions. To assess the sensitivity of the proposed method, the current signal as a function of complementary DNA target concentration was examined. **Figure 4A** demonstrates an increase in the current response at the higher target concentrations. In addition, the potential shift towards positive direction is observed. We hypothesized that a high concentration of target DNA, or a highly dense super-sandwich structure, might create a barrier to ferrocene oxidation, making it harder for electrons to transfer at these levels. This effect probably causes the potential to shift towards a higher, more positive value, suggesting that more energy is needed for the reaction to occur. Furthermore, the current difference signal ($\Delta current = I_{tested} - I_{control}$) exhibited a linear increase with increasing logarithmic concentration of target DNA (**Figure 4B**). A good linear relationship spanning from 10^1 pM to 10^6 pM, with a correlation coefficient (R^2) of 0.9972 was established. The limit of detection (LOD; calculated as $3.3(\sigma_{y\text{-intercept}}/s)$) and limit of quantitation (LOQ; calculated as $10(\sigma_{y\text{-intercept}}/s)$) were determined to be 2.2 pM and 10.6 pM, respectively. The sensing device also exhibited good reproducibility, with an RSD ranging from

3.87-9.76% across DNA target concentrations (10^1, 10^3, and 10^5 pM). These findings confirm that the developed sensor could promptly and sensitively detect porcine DNA (within 30 mins) over a wide dynamic range, spanning five orders of magnitude.

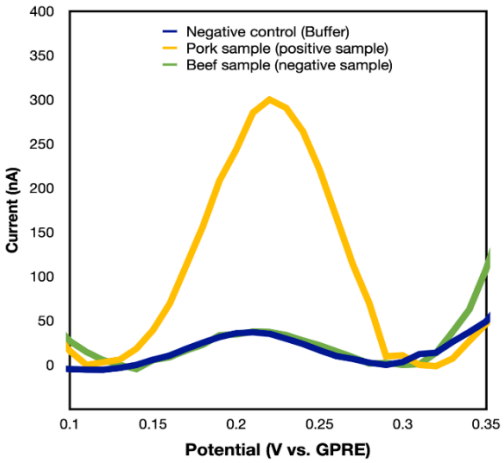

Figure 5. DPV response of the developed DNA sensor testing with real samples (including beef and pork) compared with the negative control.

3.3 Real sample analysis

To verify the applicability of the developed DNA sensor, real samples, including beef and pork, were investigated by DPV. In the absence of any target DNA (serving as the negative control), the curve displayed the lowest peak current. Similar values were recorded in the presence of beef as a negative sample (containing non-complementary target DNA). Conversely, when a pork sample containing complementary target DNA was applied, the peak current substantially increased. This enhancement can be attributed to the super-sandwiched hybridization of the complementary poly-A probe, DNA target, and DNA helper. The results from the real sample analysis strongly affirm the successful utilization of the proposed sensor in real-world samples with complex matrices.

4. Conclusion

In conclusion, we have successfully combined a gold nanoparticle-modified screen-printed graphene electrode (AuNPs/SPGE) with a one-step DNA probe immobilization, employing a DNA super-sandwich assay for the detection of porcine DNA. The primary objective was to introduce an amplification-free DNA sensor for meat adulteration detection. This innovative device exhibits an impressive limit of detection (2.2 pM) and limit of quantification (10.6 pM). Importantly, we have demonstrated the practicality of our approach by effectively differentiating real meat samples. By eliminating the need for complex techniques, our biosensing device is user-friendly, cost-effective, and reduces the overall operation time. This technique presents a viable alternative for detecting porcine adulteration, serving as a valuable tool across the meat industry supply chain, and even for consumers themselves.

References

1. Matichon online. https://www.matichon.co.th/news-monitor/news_2289163 (accessed January 01, 2024)
2. Flauzino, J. M.; Alves, L. M.; Rodovalho, V. R.; Madurro, J. M.; Madurro, A. G. B. Application of biosensors for detection of meat species: A short review. *Food Control* **2022**, 109214.
3. Flauzino, J. M.; Nguyen, E. P.; Yang, Q.; Rosati, G.; Panáček, D.; Brito-Madurro, A. G.; Madurro, J. M.; Bakandritsos, A.; Otyepka, M.; Merkoçi, A. Label-free and reagent less electrochemical genosensor based on graphene acid for meat adulteration detection. *Biosensors and Bioelectronics* **2022**, *195*, 113628.
4. Huertas, C. S.; Soler, M.; Estevez, M.-C.; Lechuga, L. M. One-step immobilization of antibodies and DNA on gold sensor surfaces via a poly-adenine oligonucleotide approach. *Analytical chemistry* **2020**, *92* (18), 12596-12604.
5. Garcia, I.; Jones, E.; Ramos, M.; Innis-Whitehouse, W.; Gilkerson, R. The little big genome: The organization of mitochondrial DNA. *Frontiers in bioscience (Landmark edition)* 2017, *22*, 710.
6. Srisomwat, C.; Yakoh, A.; Chuaypen, N.; Tangkijvanich, P.; Vilaivan, T.; Chailapakul, O. Amplification-free DNA sensor for the one-step detection of the hepatitis B virus using an automated paper-based lateral flow electrochemical device. *Analytical chemistry* **2020**, *93* (5), 2879-2887.
7. Srisomwat, C.; Teengam, P.; Chuaypen, N.; Tangkijvanich, P.; Vilaivan, T.; Chailapakul, O. Pop-up paper electrochemical device for label-free hepatitis B virus DNA detection. *Sensors and Actuators B: Chemical* **2020**, *316*, 128077.
8. Deenin, W.; Yakoh, A.; Kreangkaiwal, C.; Chailapakul, O.; Patarakul, K.; Chaiyo, S. Integrated lateral flow electrochemical strip for leptospirosis diagnosis. *Analytical Chemistry* **2022**, *94* (5), 2554-2560.

9. Schreiner, S. M., Hatch, A. L., Shudy, D. F., Howard, D. R., Howell, C., Zhao, J., Koelsch, P., Zharnikov, M., Petrovykh, D. Y., & Opdahl, A. Impact of DNA–surface interactions on the stability of DNA hybrids. *Analytical chemistry* **2011**, *83*(11), 4288-4295.
10. Schreiner, S. M., Shudy, D. F., Hatch, A. L., Opdahl, A., Whitman, L. J., & Petrovykh, D. Y. Controlled and efficient hybridization achieved with DNA probes immobilized solely through preferential DNA-substrate interactions. *Analytical chemistry* **2010**, *82*(7), 2803-2810.

Development of aptamer-based detection kit by electrochemistry for rapid assessment of vitamin D levels

Sattawat Boonchaleaw[1], Supaphorn Seetaha[2], and Kiattawee Choowongkomon[2]*

[1]*Genetic Engineering interdisciplinary program, Graduate school, Kasetsart University, Bangkok, 10900, Thailand*

[2]*Department of Biochemistry, Faculty of Science, Kasetsart University, Bangkok, 10900, Thailand*

**E-mail: Kiattawee.c@ku.th*

Abstract:

Vitamin D deficiency is a widespread health concern affecting both general populations and patients, exerting diverse effects beyond bone health, encompassing several vital organ systems. Prompt and accurate monitoring of vitamin D levels is imperative to ensure timely intervention and management of deficiencies. However, the existing methodologies for vitamin D detection often demand specialized expertise and present financial constraints. To address these challenges, we propose a novel detection kit employing a DNA aptamer immobilized on a screen-printed carbon electrode and an electrochemistry assay for precise measurement. Our investigation into DNA aptamers specific to vitamin D revealed the efficacy of VD2-VD3 aptamer in detecting both vitamin D2 and D3, and VD3 aptamer specifically targeting vitamin D3, with an optimal concentration of 20 µM. The resultant detection kit demonstrates the capability to identify both forms of vitamin D, exhibiting a detection limit of 10 ng/mL and a detection range spanning 10-100 ng/mL. This innovation holds promising implications for the efficient and cost-effective diagnosis and management of vitamin D deficiencies, thereby positively impacting public health outcomes.

1. Introduction

Vitamin D is classified as a steroid hormone, and its fat-soluble vitamins are necessary for the human body. Improves dental and skeletal strength. Enhances the assimilation of calcium and phosphorus in the gastrointestinal tract.[1] It regulates the concentrations of calcium and phosphorus in the bloodstream, particularly in the skeletal system and gastrointestinal tract. The body produces vitamin D on its own through solar exposure and ingesting nourishment. There are minimum of ten distinct variations of vitamin D. However, vitamin D and its principal metabolites are present in two separate nutritional forms: vitamin D2 is obtained from plants, fungus, and yeast, whereas vitamin D3 is derived from fish liver oil, egg yolks, and the process of sun-induced synthesis on human and animal skin.

Both the general population and patients suffering from chronic illnesses exhibit a shortage in vitamin D. Vitamin D insufficiency not only affects bone health, but also has an impact on several other physiological systems in the body. The presence of insufficient levels of Vitamin D initiates the activation of genes linked to cardiovascular disease, type 1 diabetes, infectious illnesses, asthma, colon cancer, depression, Alzheimer's disease, and hypertension.[2,3,4] Various factors that influence the immune system increase the probability of getting osteoporosis.[1]

Individuals diagnosed with cancer, diabetes, and high blood pressure can assess their vitamin D levels through blood samples, employing vitamin D assays for diagnostic and monitoring purposes. Timely management and continuous monitoring are crucial for patients grappling with rickets and osteoporosis. Two primary techniques for evaluating vitamin D levels include chromatographic tests, such as Liquid Chromatography Tandem Mass Spectrometry (LC MS/MS) and High-Performance Liquid Chromatography (HPLC), and immunoassays, such as Radioimmunoassay (RIA), Enzyme Immunoassay (EIA), Chemiluminescent Immunoassay (CLIA), and Chemiluminescent Microparticle Immunoassay (CMIA). Chromatographic assays demand meticulous examination over the long term, requiring a high level of analytical skill in a laboratory setting. Importantly, immunoassay requires professional expertise for thorough scrutiny and authentication, leading to elevated costs. The research team endeavors to develop a test kit utilizing a device capable of detecting electrical impulses generated by a DNA aptamer-binding vitamin D, aiming to assess serum vitamin D levels.

Given the significance of vitamin D and the prevalent issue of vitamin D insufficiency in Thailand, the research team hypothesizes that elevating vitamin D levels will yield positive outcomes for public health and vitamin D assessment. Conventional vitamin D tests are both costly and constrained. To mitigate the prevalence of vitamin D deficiency, the team endeavors to create a portable and cost-effective tool for testing vitamin D levels. The research goal is to develop a serum vitamin D test kit utilizing a chip that can detect electrical signals generated by DNA aptamer-binding vitamin D. This diagnostic test kit is characterized by its simplicity, speed, and capacity to swiftly provide results for ongoing diagnostic monitoring, facilitating prompt assessment of vitamin D deficiency by physicians. This approach aims to minimize the workload of patient treatment and reduce hospital expenses.

2. Materials and Methods

2.1 Materials

Gold nanoparticles (AuNPs) (Sigma-Aldrich; 20 nm), NaCl, electrolyte solution (KCl, $K_3Fe(CN)_6$, $K_4Fe(CN)_6$), ethanolamine, graphene oxide (Sigma-Aldrich). The sequences of VD2-VD3 and VD3 are 5'-ATACGGGAGCCAACA-CCATAGTGTTGGGCCAATACGGTAACGTG TCCTTGGAGAGCAGGGTGACGGAT-3' and [5′-AGCAGCACAGAGGTCATGGGGGGTGT-GACTTTGGTGTGCCTATGCGTGCTACGGA A-3′] respectively. In order to enhance their affinity for carbon particles present on the working electrode (WE), both aptamers are intentionally designed with an amino group ($-NH_2$).

2.2 Colorimetric assay

The aptamers were incubated at 95°C for 10 minutes before being placed on ice for 10 minutes and supplemented with vitamin D. Then, incubate at 37°C and shake at 200 rpm for 10 minutes, then add AuNPs and incubate at room temperature for 10 minutes before mixing AuNPs-Aptamer:NaCl at a 2:5 ratio.

2.3 Preparation of carbon screen-printed electrode

Homogenizing graphene oxide in an ultrasonic bath for 10 minutes. Then, mix it with aptamer at a 1:1 ratio and incubate it at room temperature for 5 minutes. Add 5 µL to the working electrode and incubate at room temperature, leave to dry (30-60 minutes). Drop 5 µL of 0.1 M ethanolamine solution. Incubate at room temperature for 10 minutes, then rinse with water.

2.4 Electrochemical detection of Vitamin D

Drop 5 µL of sample over the working electrode and incubate for 10 minutes. After that, blow air out to dry, then drop electrolyte solution over all three electrodes and measure the sample using square wave voltammetry (SWV) technique.

3. Results & Discussion

3.1 Confirmation of binding via colorimetric assay

Colorimetric analysis is employed to assess the interaction between an aptamer and vitamin D. The substance will undergo a color change from red to purple in the presence of an arrest, as indicated by the aggregation of AuNPs.[5] The test findings in the figure 1 indicated the VD2-VD3 aptamer ability to attach to both vitamin D2 and vitamin D3, whereas the VD3 aptamer specifically affected only vitamin D3. Both aptamers demonstrated the ability to bind to vitamin D. Consequently, it has been implemented in electrochemical methodologies.

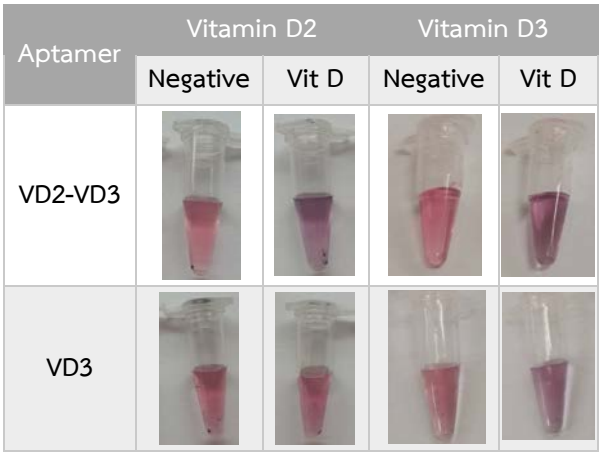

Figure 1. The aptamers VD2-VD3 and VD3 colorimetric analysis using vitamin D2 and D3, respectively. The amounts of aptamer, vitamin D, and NaCl were kept same amount for both tests.

3.2 Optimizing Graphene oxide concentration

The process involves applying each aptamer onto a carbon screen-printed electrode by combining Graphene oxide and aptamer in equal proportions (1:1 ratio). The mixture is then applied to a working electrode and blocked with 0.1 M Ethanolamine. The change in electric current (ΔI) is measured by adjusting the conditions to determine the optimal concentrations of Graphene oxide and aptamer. Capable of quantifying the change in current (ΔI) of vitamin D at concentrations as low as 10 ng/mL. Graphene oxide, a variant of graphene that possesses oxygen-containing functional groups on its surface. Its

enormous surface area, biocompatibility, and capacity to enable electron transfer reactions make it a highly promising material for biosensors.[7,8]

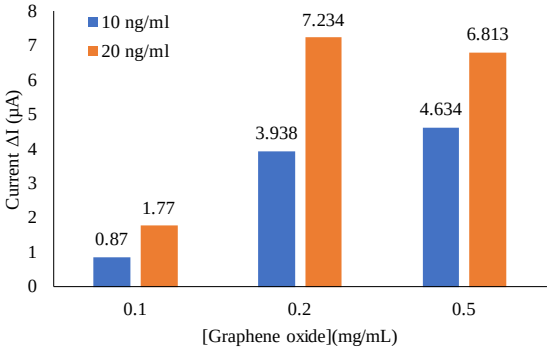

Figure 2. ΔI values of vitamin D samples were measured at concentrations of 10 ng/mL and 20 ng/mL, using graphene oxide concentrations of 0.1, 0.2, and 0.5 mg/mL.

The concentration of Graphene oxide was determined by conducting tests at 0.1, 0.2, and 0.5 mg/mL. It was observed that when the concentration of Graphene oxide was 0.2 mg/mL, the change in current (ΔI) of vitamin D at a concentration of 10 ng/mL could be quantified. The change in current (ΔI) is equivalent to that of graphene oxide when the concentration is 0.5 mg/mL (Figure 2). To achieve this objective, the screen-printed electrode is prepared using graphene oxide at a concentration of 0.2 mg/mL.

3.3 Electrochemical detection of Vitamin D

Therefore, once the appropriate concentration of aptamer and Graphene oxide (0.2 mg/mL) is achieved, the levels of vitamin D2 and vitamin D3 were determined at concentrations of 10, 20, 40, 80, and 100 ng/mL, as shown in Figure 3 and 4. It was demonstrated that by raising the concentration of vitamin D, the ΔI value increased correspondingly. With an increase in the content of vitamin D, there is a greater availability of molecules to attach to the aptamers that are fixed

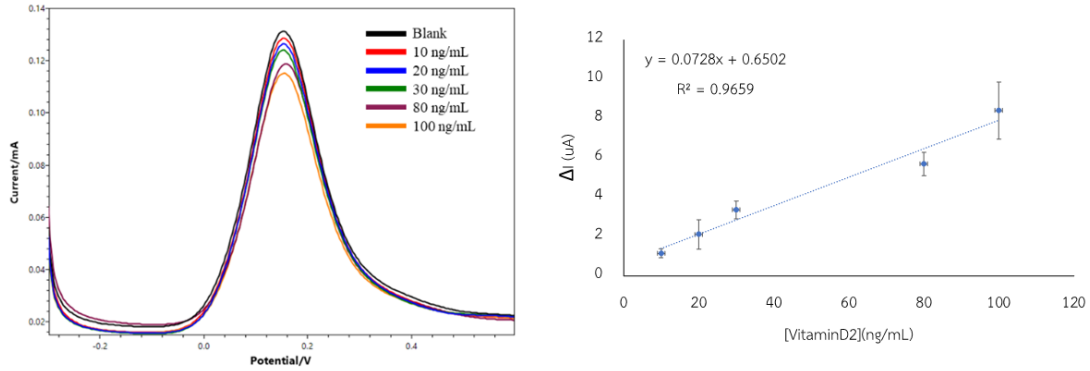

(A) (B)

Figure 3. (**A**) Square wave voltammetry signal approach by VD2-VD3 Aptamer to measure the concentration of vitamin D2 at 10, 20, 30, 80 and 100 ng/mL. (**B**) The ΔI value was obtained and plotted vs. vitamin D concentration (n=3).

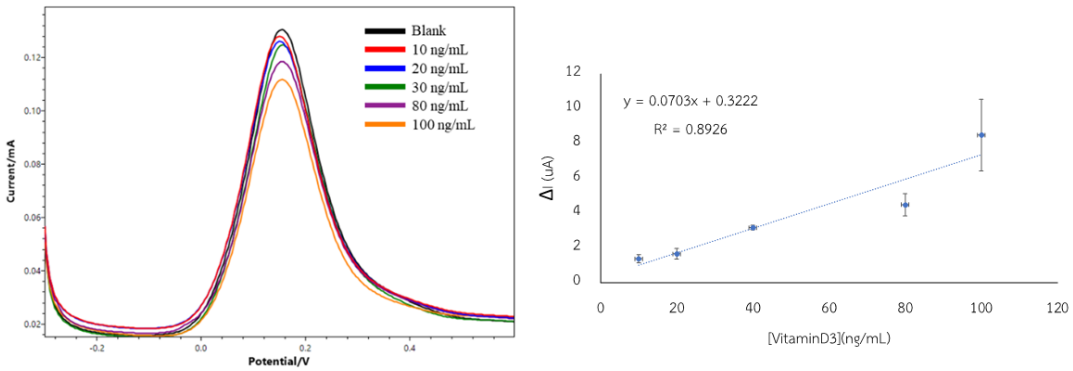

(A) (B)

Figure 4. (**A**) Square wave voltammetry signal approach by VD3 Aptamer to measure the concentration of vitamin D3 at 10, 20, 30, 80 and 100 ng/mL. (**B**) The ΔI value was obtained and plotted vs. vitamin D concentration (n=3).

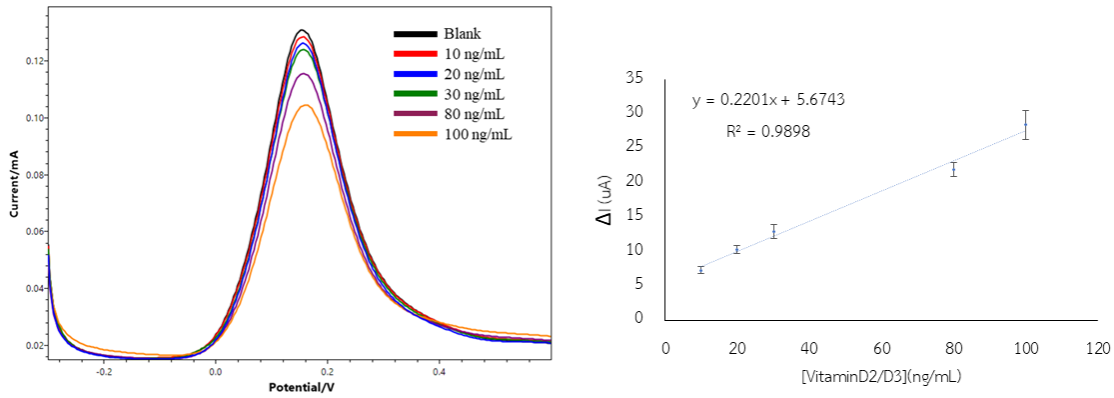

(A) (B)

Figure 5. (**A**) Square wave voltammetry signal approach by combined of VD2-VD3 with VD3 Aptamer to measure the concentration of mixing of vitamin D2 and D3 at 10, 20, 30, 80 and 100 ng/mL. (**B**) The ΔI value was obtained and plotted vs. vitamin D concentration (n=3).

on the surface of the electrode. The process of binding during this event modifies the electrical characteristics of the interface, resulting in a measurable alteration in the current, denoted as ΔI.[6] The binding of vitamin D may cause conformational alterations in the aptamer's structure. These modifications may impact the aptamer's interaction with the electrode surface, leading to changes in the pathways through which electrons are transferred and resulting in an increased ΔI value.

Table 1. The allocation of vitamin D levels compare to ΔI value of the test kit

Vitamin D2/D3		
Vitamin D status	**ng/mL**	**ΔI (μA)**
Deficiency	<20	<10
Insufficiency	20-30	11-15
Sufficiency	>30-80	16-20
Toxic level	>100	>25

VD2-VD3 and VD3 Aptamer were used to assess the combination of vitamin D2 and D3 as a standard vitamin D for electrochemical detection, assuming that both forms of vitamin D are present in the bloodstream. The curve depicted in Figure 5 illustrates that an increase in the concentration of vitamin D leads to an amplified ΔI in both models. Comparatively, the combination of both vitamins D2 and D3 has been observed to yield greater ΔI values when compared to their individual effects. This implies increased sensitivity and the impact of ΔI in comparison to the allocation of vitamin D levels based on blood vitamin D levels, as previously documented by the Endocrine Society of the United States (Table 1.). Consequently, this condition can serve as a means of monitoring vitamin D in medical diagnostic.

3.4 Specificity test

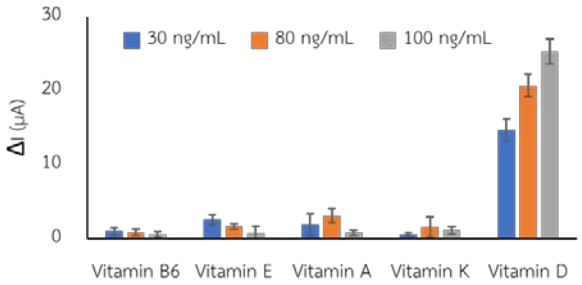

Figure 5. Show aptamer binding results specifically for vitamin D by measuring ΔI compared to vitamins B6, E, A, and K at concentrations of 30, 80 and 100 ng/mL (n=3).

The test confirmed the specificity of the vitamin D test kit, ensuring that it only detects vitamin D. In this study, a test set was utilized to assess the levels of vitamin D, similar to the evaluation of vitamin B6 (a water-soluble vitamin) and vitamins A, E, and K (fat-soluble vitamins), which belong to the same category as vitamin D. As a consequence, Figure 5, was found that when this specific test set is subjected to different vitamins, the ΔI values are significantly lower in comparison to the ΔI value of vitamin D, which is considerably greater. This demonstrated the precise nature of the test kit. Measurement is only possible for vitamin D.

4. Conclusion

In summary, this research introduces a promising approach for developing a portable and cost-effective vitamin D test kit using a chip-based electrochemical method. The colorimetric assay

confirms the aptamers ability to bind to both vitamin D2 and D3, while optimization of graphene oxide concentration at 0.2 mg/mL enables quantification of vitamin D at low concentrations. Electrochemical detection shows a correlation between increased vitamin D concentrations and ΔI values, demonstrating successful detection. The proposed method addresses the limitations of current testing techniques and holds potential for widespread use in diagnostic monitoring of vitamin D levels, particularly in resource-constrained settings. For further experiments, it is essential to validate the test kit's performance with a larger and diverse set of clinical samples, assess its accuracy against established methods, and explore potential applications in point-of-care settings. Additionally, long-term stability studies and optimization of the assay conditions for real-world scenarios would enhance the robustness and reliability of the developed test kit.

References

1. DeLuca, H. F. Overview of General Physiologic Features and Functions of Vitamin D. Am J Clin Nutr **2004**, 80(6 Suppl), 1689S–1696S.
2. Wang, L.; Song, Y.; Manson, J. E.; Pilz, S.; März, W.; Michaëlsson, K.; Lundqvist, A.; Jassal, S. K.; Barrett-Connor, E.; Zhang, C. Circulating 25-Hydroxy-Vitamin D and Risk of Cardiovascular Disease: A Meta-Analysis of Prospective Studies. Circulation: Cardiovascular Quality and Outcomes **2012**, 5, 819–829.
3. Cooper, J. D.; Smyth, D. J.; Walker, N. M.; Stevens, H.; Burren, O. S.; Wallace, C.; Greissl, C.; Ramos-Lopez, E.; Hyppönen, E.; Dunger, D. B.; Spector, T. D. Inherited Variation in Vitamin D Genes Is Associated with Predisposition to Autoimmune Disease Type 1 Diabetes. Diabetes **2011**, 60(5), 1624–1631.
4. McCullough, M. L.; Zoltick, E. S.; Weinstein, S. J.; Fedirko, V.; Wang, M.; Cook, N. R.; Eliassen, A. H.; Zeleniuch-Jacquotte, A.; Agnoli, C.; Albanes, D.; Barnett, M. J. Circulating Vitamin D and Colorectal Cancer Risk: An International Pooling Project of 17 Cohorts. JNCI: Journal of the National Cancer Institute **2019**, 111(2), 158–169.
5. Alsager, O. A.; Alotaibi, K. M.; Alswieleh, A. M.; Alyamani, B. J. Colorimetric Aptasensor of Vitamin D3: A Novel Approach to Eliminate Residual Adhesion between Aptamers and Gold Nanoparticles. Sci. Rep. **2018**, 8, 12947.
6. Yin, S.; Li, Y.; Hossain, M. N.; Sun, C.; Kraatz, H.-B. Electrochemical detection of 25-hydroxyvitamin D3 using an oligonucleotide aptasensor. Sens. Actuators B Chem. **2021**, 340, 129945.
7. Chen, D.; Feng, H.; Li, J. Graphene Oxide: Preparation, Functionalization, and Electrochemical Applications. Chem. Rev. **2012**, 112(11), 6027–6053.
8. Singh, D. P.; Herrera, C. E.; Singh, B.; Singh, S.; Kumar Singh, R.; Kumar, R. Graphene Oxide: An Efficient Material and Recent Approach for Biotechnological and Biomedical Applications. Mater. Sci. Eng. C **2018**, 86, 173–197.

Ecological risk assessment of heavy metals in sediment from Klong Luang Reservoir, Chonburi, Thailand

Sophit Buth[1], Lita Chheang[1,2], and Sudtida Pliankarom Thanasupsin[1,3]*

[1]*Department of Chemistry, Faculty of Science, King Mongkut's University of Technology Thonburi, Bangkok 10140, Thailand*

[2]*Department of Chemistry, Faculty of Science, Royal University of Phnom Penh, Phnom Penh 12150, Cambodia*

[3]*Chemistry for Green Society and Healthy Living Research Unit, Faculty of Science, King Mongkut's University of Technology Thonburi, Bangkok 10140, Thailand*

**E-mail: sudtida.tha@kmutt.ac.th*

Abstract:

Heavy metals (HMs) in the aquatic system are a global problem and environmental hazard. Sediment is widely recognized as the repository and sink pollutants of HMs. The increasing concentration of HMs in the Khlong Luang reservoir can be attributed to natural origin and anthropogenic, including discharge from various urbanization, industrialization, direct and indirect discharges from open dumping, vehicle emissions, agriculture, and road runoff can release HMs to the reservoir. The potential harm posed by HMs has emerged as a significant concern for human health and ecological risk. HMs, including arsenic (As), nickel (Ni), zinc (Zn), manganese (Mn), lead (Pb), and copper (Cu) were quantified in the sediment by using Inductively Coupled Plasma-Optical Emission Spectrometry (ICP-OES) technique. Resulting, Mn had the highest concentration 349.81 mg/kg. Data monitoring geo-accumulate index (Igeo) of As found in heavily contaminated (3.70). The Contamination factor (CF) of As, Pb, Zn, and Cu are in a high degree of contamination (CF≥6). Modified contamination degree (mCd) and potential ecological risk (PER) indicate Khlong Luang reservoir is in high-risk condition (8<mCd≤ 16), (PER>200). Considering environmental quality, the reservoir status is at a very high ecological risk. Hence, it is imperative to monitor pollution in the future.

1. Introduction

Heavy metal (HM) is defined as a toxic metal or metalloid with a density greater than water [1, 2]. Metals Cu and Zn are known as essential for biochemical and physiological functions; Cr is necessary for the [3]metabolism of fats, carbohydrates, and the synthesis of proteins, whereas Mn and Ni are required cofactors of enzymes, and hormonal activity, lipid metabolism, activation of some enzymes, and stabilization of DNA and RNA for human health, yet excess concentration will toxic to human as well as living organisms[3, 4]. HM is a significant environmental pollutant due to its long-term persistence, easy bio-accumulation, and unbreakability, which exist wildly in water, sediment, soil, and air[5, 6]. Regarding (Zhang Hua, 2017)[7], sediment accumulates heavy metals about 85%; through biological and chemical mechanisms that enhance their toxicity, these substances pose an increased ecological risk to aquatic organisms and human health. Hence, sediment serves as an essential repository of the HMs [5]. HM can be separated and released from the sediment to the water body; the water quality is degraded via this phenomenon [8]. The two primary sources of heavy metal are natural sedimentary rocks, volcanic eruptions, soil formation, and rock weathering, and anthropogenic known as an industry, agriculture, mining, domestic effluents, ore mining, metal-related factories, fertilizer, and pesticide usage in agriculture [9, 10]. Klong Luang Reservoir is an essential reservoir built to prevent floods and provide residents with water for consumption, supporting industrial and commercial development in the eastern coastal area and agriculture during the dry season[11].

In recent years, the rapid population, urban development, industrial, and artificial agriculture, have led to the massive contamination of the Klong Luang reservoir due to improper waste. It is vital for the future of the Klong Luang reservoir for sustainable development for sediment quality and the environment. Consequently, the purpose of this study is to measure the content of heavy metals, including As, Cu, Ni, Pb, Zn, and Mn, in the sediment of the Klong Luang reservoir and utilized the single and synergistic methods to provide perspective on the current state of heavy metal pollution in the Klong Luang reservoir.

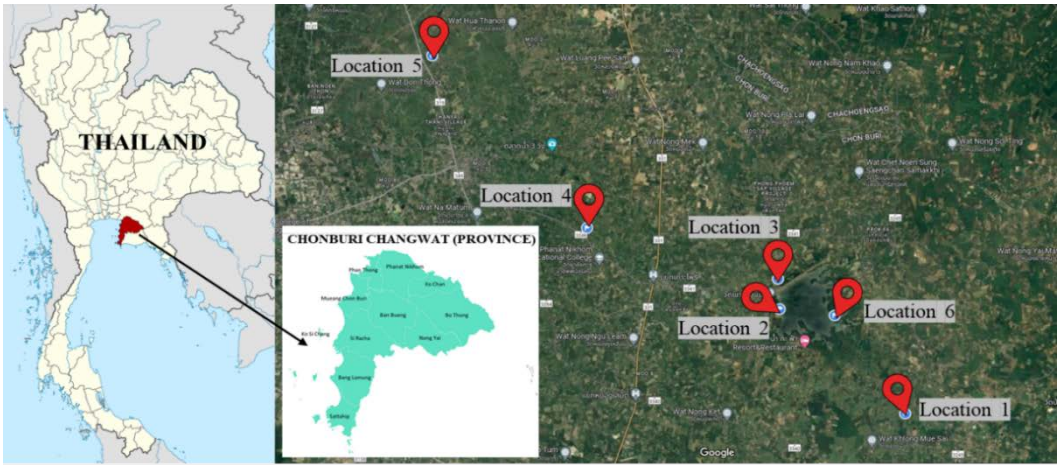

Figure 1. Study area and location of sediment

2. Methodology

2.1 Study Region

Klong Luang Reservoir is located in Ban Klong village, Koh Chann commune, Phanasnikom district, Chonburi province, with latitude 130-23'-00" N and latitude 1010-22'-40" E. The study region set up at Klong Luang was Wat Luang, Norng Breu, Rai Lak Thong, Norn Heang, Wang Hin, Ban Chang, Narerk, and Tha Bon Mi commune, in Phanasnikom and Bor Thong district, Chonburi province. A total of 6 locations of sediment samples were collected randomly around the Klong Luang reservoir in Chonburi Province, Thailand. L1; overflow weir next to Wat Suwan in Bor Thong district. L2; near the pumping tap water station in Phanat Nikhom district, L3; at the bridge across Khlong Luang which is the end of the dam, L4; overflow weir of Khlong Luang in Na Roek commune, L5; Ban Soun Tan, Rai Lak Thong commune, Phanat Nikhom district and L6 at the village 7, Koh Chan commune Koh Chan district in the middle of reservoir

2.2 Sampling, sample preparation, and analysis

During the wet season (September 2023), 18 sediment samples were gathered by using a grab sampler with 6 locations (L1 to L6). About 1 kg of samples were collected at a depth from 5 to 10 cm below the location site. All samples were stored at 3 to 4 °C. After collection, the sediment was dried at room temperature and kept until evaluated. All samples (sediment) were ground using an agate mortar and a sieve with 2 mm nylon mesh. 1 g of ground sediment was digested with 5 mL of 65% HNO_3, 15 mL of 37% HCl, and 10 mL of 30% H_2O_2 200 ◦C on a hotplate in a fume hood for 30 min [12, 13]. The liquid mixtures were filtered using Whatman filter paper (grade no. 42, diameter 70 mm), and they were then further filtered using a nylon membrane filter. The concentration of heavy metals (HMs) was determined by inductively coupled plasma optical emission spectrometry (ICP-OES, Perkin Elmer, Optima 8000 DV, Waltham, MA, USA). According to the heavy metal readings in the sediment samples, the following were the % recovery and R^2 values: As (114.65±0.002%, R^2=0.9998), Cu (98.11±0.002%, R^2=0.9999), Ni (88.69±0.003%, R^2=0.9998), Zn (99.46±0.003%, R^2=0.9991), Pb (98.41±0.002%, R^2=0.9999), and Mn (103.97±0.08%, R^2=0.9998). The relative standard deviation (RSD) was used to assess the method's precision. The value ranged from 1.05 to 15.42% (n=3).

2.3 Heavy Metals Evaluation Index

2.3.1 Geoaccumulate Index (Igeo)

The geo-accumulation index is utilized to quantify the level of pollution extent in the sediment[14]. To investigate the geo-accumulation is calculated by the given equation below:

$$I_{geo}=\log_2\left(\frac{C_n}{1.5B_n}\right)$$

C_n represents the concentration of study heavy metal "n", and B_n represents the concentration background of heavy metal "n". Factor 1.5 is applied for background matrix correction and lessening effects from lithogenic compositions. The background of heavy metals was selected from the study of Chonburi province, Thailand. The classification of Igeo is set to evaluate the level of extent pollution in the sediment as follows:

Table 1. Heavy metals concentration in the sediment of Klong Luang reservoir (mg/kg)

Locations	As	Cu	Ni	Pb	Zn	Mn
1	ND	12.95±0.57	8.56±0.98	5.51±0.19	20.27±0.88	255.68±5.21
2	3.58±0.31	111.30±10.46	7.63±0.90	12.69±0.62	86.92±3.87	316.78±6.53
3	0.21±0.02	2.62±0.29	5.48±0.14	2.61±0.08	4.82±0.14	146.49±2.59
4	ND	6.03±0.58	5.33±0.30	3.32±0.25	13.35±0.75	527.00±15.72
5	ND	19.97±0.31	8.12±0.43	137.77±1.77	34.55±2.23	660.83±6.97
6	7.67±0.66	11.52±1.19	4.40±0.30	16.13±2.49	10.51±1.03	192.07±3.83
Min	0.21	2.62	4.40	2.61	4.82	146.49
Max	7.67	111.30	8.56	137.77	86.92	660.83
Mean ± SD	3.82±3.74	27.40±41.54	6.59±1.73	29.67±53.23	28.40±30.43	349.81±202.14

ND: Not detected

uncontaminated (Igeo ≤ 0), slightly contaminated (0 < Igeo ≤ 1), moderately contaminated (1 < Igeo ≤ 2), moderately to heavily contaminated (2 < Igeo ≤ 3), heavily contaminated (3 < Igeo ≤ 4), heavily to significantly contaminated (4 < Igeo ≤ 5), and highly contaminated (Igeo ≥ 5).

2.3.2 Contamination Factor (CF)

Contamination Factor (CF) is the method used to evaluate the contamination factor of the concentration of individual metal to the background original or composition of earth crush [15, 16]. CF can be calculated by the given equation below

$$CF=\frac{C_i}{C_{xi}}$$

C_i is denoted by the study concentration of metal "i," and the concentration background of metal denotes C_{xi} "i". Location 3 was chosen as the background of heavy metals due to being out of the dam, and the sediment is new. To monitor the contamination level of a single metal, CF is classified into four groups: low degree of contamination (CF < 1), moderate degree of contamination (1≤ CF <3), considerable degree of contamination (3≤ CF <6) and (CF≥ 6) high degree of contamination.

2.3.3 Modified Contamination Degree (mCd)

The modified degree of contamination (mCd) is the parameter used to indicate the metal pollution level in the sediment containing all pollutants in the ecosystem [17]. mCd calculated using the equation;

$$mC_d=\frac{\sum_{i=1}^{i=n} CF_i}{n}$$

CF_i is the contamination factor of metal "i," and n is the number of metals. The value of mCd can estimate the contamination by grouping it as follows: uncontaminated to very low contamination grade (mCd ≤ 1.5), low contamination grade (1. 5 < mCd ≤ 2), moderate contamination grade (2 < mCd ≤ 4), high contamination grade (4 < mCd ≤ 8), very high contamination grade (8 < mCd ≤ 16), extremely high contamination grade (16 < mCd ≤ 32), and ultra-high contamination grade (mCd > 32) [17].

2.3.4 Potential Ecological Risk (PER)

Potential ecological risk (PER) is known as the parameter suit to evaluate the total ecological pollution in the environment results from HMs of the sediment[13]. The value of PER is the sum of ecological risk calculation. The equation of ER and PER are shown as follows:

$$PER=\sum_{i=1}^{n} E_r^i \qquad E_r=T_r^i \times CF_r^i$$

, where Tr represents the biological toxic factor of a single metal, and CF is the contamination factor of the individual HM. According to a previous study, T_r of each HMs is Cu = Pb= Ni = 5, Zn=Mn = 1, and As = 10. The classification of PER is as follows: low potential risk (PER < 50), moderate potential risk (50 ≤ PER < 100), considerable potential risk (100 ≤ PER < 200), and high-risk condition (PER > 200).

3. Result and Discussion

3.1 Heavy Metals in the Sediment

All the studied heavy metals were detected from the sediment of Klong Luang Reservoir with 6 heavy metals As, Cu, Ni, Pb, Zn, and Mn and 6 locations (L1 to L6) were shown in Table 1. The mean concentration of the studied heavy metals descended in the order of Mn > Pb > Zn > Cu > Ni > As. The concentration of all locations is higher at L5 and followed by L3 is the lowest. In comparison, the rainy season contains a greater concentration of HMs than the dry season. It may caused by the parent rock, runoff, and community

Table 2. Heavy metals pollution and ecological risk assessment of the Klong Luang reservoir

Metal	Parameters	Values	Interpreted
As	Igeo	3.70	Heavily Contamination
	CF	18.63	High degree of contamination
Cu	Igeo	2.91	Moderate to heavily contamination
	CF	10.45	High degree of contamination
Ni	Igeo	0.81	Slightly Contamination
	CF	6.59	High degree of contamination
Pb	Igeo	2.59	Moderate to heavily contamination
	CF	11.37	High degree of contamination
Zn	Igeo	2.53	Moderate to heavily contamination
	CF	5.89	Considerable degree of contamination
Mn	Igeo	1.64	Moderate contamination
	CF	2.39	Moderate degree of contamination
	mCd	8.32	Very high contamination grade
	PER	243.44	High-risk condition

waste from the catchment area and transports those HMs to deposit into the downstream[18]. Due to the L5 is downstream[19], where contaminants move from other locations and settle and sediment at location 3 (flood gate, 2021) being out of the reservoir and near the dam; thus, the sediment is new and less contaminated. Among of 6 HMs, Pb was found the highest concentration at L5, which is close to the arterial road (315). The tripartition of Pb demonstrates this via the vehicles from the runoff, and Mn is found naturally highly in the earth's crust [20].

Whereas, As was found, a high concentration at L6 where the agricultural land and contaminated by the pesticide. High concentrations of Cu and Zn were found in L2. Cu is naturally from the mineral and industry as well as in pesticide, fertilizer (agricultural) and domestic waste water[21], and Zn is from the industrial, which is used as raw material at L2 and is known as the farmland and also adjacent to metal and brass factory.

3.2 Sediment Contamination Assessments

Table 2 summarizes the proportion of contamination level of single pollution of the single heavy metal geo-accumulation index (Igeo) and contamination factor (CF) and integrated indices, including modified contamination degree (mCd) and potential ecological risk (PER).

The mean values of Igeo As, Cu, Ni, Pb, Zn, and Mn are 3.70, 291, 0.81, 2.59, 2.53, and 1.64, respectively. Fig. 2a shows Igeo value of each heavy metal with the different sampling locations. Most heavy metal had their highest value at L2, L5, and L6, except for L3 had the lowest. As had the highest Igeo value (3.70) demonstrated heavy metal contamination in L2 and L6. The agriculture activities that are practised near the L2 and L6 and the use of pesticides and fertilizers could be the agriculture activities that are practised near the L2 and L6, and the use of pesticides and fertilizers could be the reason for the high contamination of As [5].

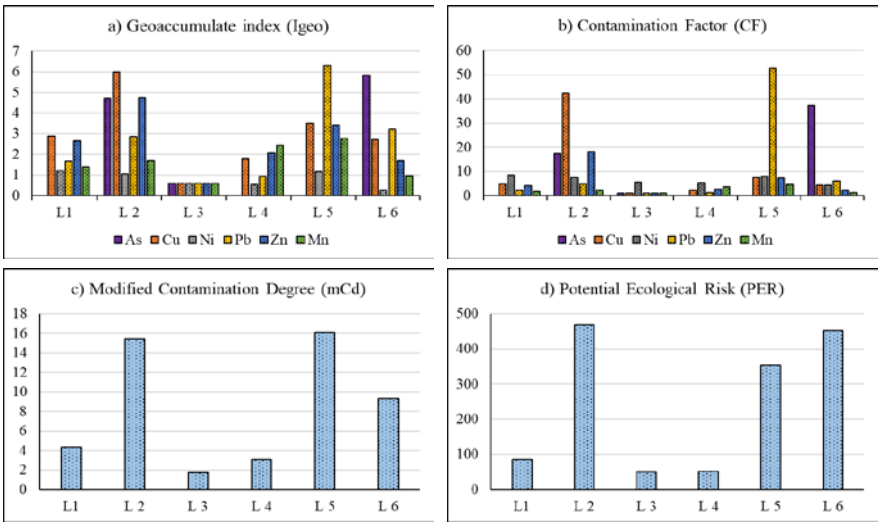

Figure 2. The value of a) Igeo, b) CF, c) mCd, d)PER of the Khlong Luang

The CF values is shown in Fig.2b result revealed that the most contaminants are Pb and As, Cu, and Zn at the Klong Luang reservoir, with a high degree of contamination (CF≥ 6). Those metals were found to have high-value at L2, L5, and L6 due to the location of downstream and agricultural land adjacent to the industrial. In contrast, Mn and Ni had the lowest value, indicating between of moderate degree of contamination (1≤ CF <3) and a considerable degree of contamination (3≤CF <6) moderate contamination. The mean CF decreases in order Mn < Zn < Ni < Cu < Pb <As shown in Table 2.

Modified contamination degree (mCd) was used to analyze the six heavy metals in the Klong Luang reservoir. Resulting for the mean value of mCd is 8.32 in Table 2, which demonstrates that the Klong Luang reservoir has a very high contamination grade. The mCd for the individual location is shown in Fig. 2c. Refer to the mCd value; anthropogenic activities polluted all locations.

Potential ecological risk (PER) is the combination of all heavy metals to evaluate the risk of biota in the Klong Luang reservoir. The result found that PER in L1, L3, and L4 are moderate potential risk (50 ≤ PER < 100) except for L2, L5, and L6 are high-risk condition (PER > 200) as shown in Fig.2d. The mean value of PER is 243.44 indicate the high-risk condition. The data of PER shows the significant ecological risk of the Klong Luang reservoir, probably from anthropogenic sources such as community wastewater, artificial agriculture, and various industrial waste.

4. Conclusion

Heavy metals As, Cu, Ni, Pb, Zn, and Mn were measured in the concentration in the sediment of the Klong Luang reservoir. Resulting, the concentration of Mn is the highest at 349.81 mg/kg. Location 5 had the highest concentration among all locations due to the endpoint point of the water flow as well as the downstream. The assessment of ecological risk Igeo, CF, mCd, and PER revealed the Igeo of As had the highest value at L2 and L6 were contaminated from As resulting from the agriculture land. At L5, Pb is the contaminant which had the highest value. The integrated indices demonstrate the Klong Luang reservoir is in high -risk condition. Hence, it is necessary to monitor and control the improper discharge to the Klong Luang reservoir. This study is a useful tool for a sustainable environment

Acknowledgements

The author is grateful to the Department of Chemistry, Faculty of Science, King Mongkut's University of Technology Thonburi, for financial support through the Greater Mekong Subregion (GMS) Scholarship. The author also expresses gratitude to the advisor, Asst. Prof. Dr. Sudtida Pliankarom Thanasupsin and co-advisor Dr. Chheang Lita for their priceless advice.

References

1. Singh, R.; Gautam N Fau - Mishra, A.; Mishra A Fau - Gupta, R.; Gupta, R., Heavy metals and living systems: An overview. (1998-3751 (Electronic)).
2. Tchounwou, P. B.; Yedjou Cg Fau - Patlolla, A. K.; Patlolla Ak Fau - Sutton, D. J.; Sutton, D. J., Heavy metal toxicity and the environment. (1664-431X (Print)).
3. Grembecka, M.; Szefer, P., Comparative assessment of essential and heavy metals in fruits from different geographical origins. *Environmental Monitoring and Assessment* **2013,** *185* (11), 9139-9160.
4. Chronopoulos, J.; Haidouti, C.; Chronopoulou-Sereli, A.; Massas, I., Variations in plant and soil lead and cadmium content in urban parks in Athens, Greece. *Science of The Total Environment* **1997,** *196*, 91-98.
5. Xiao, H.; Shahab, A.; Li, J.; Xi, B.; Sun, X.; He, H.; Yu, G., Distribution, ecological risk assessment and source identification of heavy metals in surface sediments of Huixian karst wetland, China. *Ecotoxicology and Environmental Safety* **2019,** *185*, 109700.
6. Zhao, X.; Gao, B.; Xu, D.; Gao, L.; Yin, S., Heavy metal pollution in sediments of the largest reservoir (Three Gorges Reservoir) in China: a review. *Environmental Science and Pollution Research* **2017,** *24* (26), 20844-20858.
7. Zhang, H.; Jiang, Y.; Ding, M.; Xie, Z., Level, source identification, and risk analysis of heavy metal in surface sediments from river-lake ecosystems in the Poyang Lake, China. *Environmental Science and Pollution Research* **2017,** *24* (27), 21902-21916.
8. Simpson, S. L.; Spadaro, D. A., Bioavailability and chronic toxicity of metal sulfide minerals to benthic marine invertebrates: implications for deep sea exploration, mining and tailings disposal. *Environmental science & technology* **2016,** *50* (7), 4061-4070.
9. Mohammadi, R. M.; Sobhan, A. S.; Karimi, H.; Sorooshnia, R., Natural and anthropogenic

source of heavy metals pollution in the soil samples of an industrial complex; a case study. **2015**.
10. Hoang, H.-G.; Lin, C.; Tran, H.-T.; Chiang, C.-F.; Bui, X.-T.; Cheruiyot, N. K.; Shern, C.-C.; Lee, C.-W., Heavy metal contamination trends in surface water and sediments of a river in a highly-industrialized region. *Environmental Technology & Innovation* **2020,** *20*, 101043.
11. Foundation, T. C. Sustainable Management of Natural Resources. https://www.chaipat.or.th/eng/our-work/water-and-natural-resources-management.html.
12. Peña-Icart, M.; Villanueva Tagle, M. E.; Alonso-Hernández, C.; Rodríguez Hernández, J.; Behar, M.; Pomares Alfonso, M. S., Comparative study of digestion methods EPA 3050B (HNO3–H2O2–HCl) and ISO 11466.3 (aqua regia) for Cu, Ni and Pb contamination assessment in marine sediments. *Marine Environmental Research* **2011,** *72* (1), 60-66.
13. Chheang, L.; Limsuwan, P.; Thongkon, N.; Sriwiriyarat, T.; Thanasupsin, S. P. Ecological Risk Assessment and Source Contributions of Heavy Metals in the Sediment of the Chan Thnal Reservoir, Kampong Speu, Cambodia *Water* [Online], 2023.
14. Muller, G., Index Of Geoaccumulation In Sediments Of The Rhine River. *GeoJournal* **1969,** *2*, 108-118.
15. Hakanson, L., An ecological risk index for aquatic pollution control.a sedimentological approach. *Water Research* **1980,** *14* (8), 975-1001.
16. Luo, W.; Lu Y Fau - Giesy, J. P.; Giesy Jp Fau - Wang, T.; Wang T Fau - Shi, Y.; Shi Y Fau - Wang, G.; Wang G Fau - Xing, Y.; Xing, Y., Effects of land use on concentrations of metals in surface soils and ecological risk around Guanting Reservoir, China. (0269-4042 (Print)).
17. Custodio, M.; Espinoza, C.; Orellana, E.; Chanamé, F.; Fow, A.; Peñaloza, R., Assessment of toxic metal contamination, distribution and risk in the sediments from lagoons used for fish farming in the central region of Peru. *Toxicology Reports* **2022,** *9*, 1603-1613.
18. Nguyen, B. T.; Do, D. D.; Nguyen, T. X.; Nguyen, V. N.; Phuc Nguyen, D. T.; Nguyen, M. H.; Thi Truong, H. T.; Dong, H. P.; Le, A. H.; Bach, Q.-V., Seasonal, spatial variation, and pollution sources of heavy metals in the sediment of the Saigon River, Vietnam. *Environmental Pollution* **2020,** *256*, 113412.
19. Shanbehzadeh, S.; Vahid Dastjerdi, M.; Hassanzadeh, A.; Kiyanizadeh, T., Heavy metals in water and sediment: a case study of Tembi River. (1687-9813 (Electronic)).
20. Algül, F.; Beyhan, M., Concentrations and sources of heavy metals in shallow sediments in Lake Bafa, Turkey. *Scientific Reports* **2020,** *10* (1), 11782.
21. Sfakianakis, D. G.; Renieri, E.; Kentouri, M.; Tsatsakis, A. M., Effect of heavy metals on fish larvae deformities: A review. (1096-0953 (Electronic)).

Development of distance-based paper device for measuring chloride ion in food

Ruj Samarnworakit[1], Buddhima Phrirojchaikul[1], Wiput Tienwanpen[1], Chaiyarerk Homsirikamol[2], Wijitar Dungchai[3], and Kamonchanok Phoonsawat[1]*

[1]*Engineering Science Classroom, Darunsikkhalai School, King Mongkut's University of Technology Thonburi, Bangkok, 10140, Thailand*
[2]*Department of Biotechnology, Faculty of Engineering and Industrial Technology, Silpakorn University, Nakorn Pathom, 73000, Thailand*
[3]*Department of Chemistry, Faculty of Science, King Mongkut's University of Technology Thonburi, Bangkok, 10140, Thailand*

**E-mail: kamonchanok.phoon@kmutt.ac.th*

Abstract:

Chloride (Cl^-) is a necessary mineral for humans, but the effect of an inappropriate amount of Cl^- can cause health problems. Cl^- in food is typically in form of table salt. A distance-based paper device (dPAD) for measuring Cl^- in food allowing people to control Cl^- intake is considered one of the easy-to-use, affordable, and portable; nevertheless, dPAD required sample dilution before analysis due to the limited measurement of Cl^-. For these reasons, the purpose of this research is to develop the dPAD to measure Cl^- in food with the most-reduced dilution ratio. The results showed that the concentration of $AgNO_3$ and $K_2Cr_2O_7$ reagents on the detection zone at 0.50 M and 0.25 M, respectively, provided a range of 0.5-20 g L^{-1} for 30 µL of Cl^- sample volume and the detection time of 20 minutes. The effects of pH, sediment, and anion interferences in food were insignificant. To develop the prototype test-kit, a plastic dropper with single drop of sample was used. The effect of viscosity in detection can be modified by using clear packing tape. In conclusion, this dPAD is reliable and should be tested to see its possibility in commercialization.

1. Introduction

Chloride (Cl^-) is an essential mineral for human health, but an improper Cl^- intake can lead to headaches, delirium, fatigue, slower perception, and hyperchloremic acidosis causing dehydration. The recommended daily Cl^- intake for adults has been reported 3,100 mg.[1] Normally, Cl^- is in the form of sodium chloride (NaCl) or table salt. Therefore, the correlation between Cl^- amount and sodium level is significant, and both factors impact health conditions. To prevent excessive Cl^- intake, it is important to determine and monitor the Cl^- content in food using analytical methods.

The standard method for measuring Cl^- is through the titration method, which involves high sample volumes, leading to waste and inaccuracies. To ensure precision, techniques like spectrophotometry and electrochemistry have been developed, however, these precise instruments can be costly and demand expertise.[2,3] Therefore, the development of affordable and portable chloride measurement devices for food is crucial, enabling consumers to limit chloride at a lower expense.

The Paper-based analytical device (PAD) is easy-to-use, affordable, and portable, making it appropriate to be applied as a rapid Cl^- analytical device to analyze chloride levels in food samples.[2] Mostly, the PAD was used to measure chloride levels by detecting color intensity. Conversely, this detection method approaches high levels of error and needs additional software to detect color intensity.[4,5] Accordingly, the distance paper-based analytical device (dPAD) is more convenient, but dPADs that has been developed to date still require to dilute the sample before the detection which results in more detection time.[2,6-8]

Therefore, the dPAD that is not required to dilute the sample or dilute at a smaller ratio has been developed in this work. This device is designed to be user-friendly and be able to detect a large amount of Cl^- while being economical. The optimal concentration of reagents for preparing dPAD was determined to improve the measurement range for the detection of chloride in food. Furthermore, the optimum conditions were analyzed, and the dPAD was developed for commercialization.

2. Materials and Methods

2.1 Chemicals and materials

Chemicals for the concentration reagent and optimum pH test ($AgNO_3$, $K_2Cr_2O_7$, KCl, HNO_3, KOH) were purchased from Poch, Merck, Univar, Qrec, and KAMAUS in order (AR Grade). Standard anions for assessing interference under optimum conditions (KI and $KHCO_3$) were purchased from Univar and KAMAUS in order (AR Grade). Standard anions (K_2SO_4, KNO_3, KBr, K_2HPO_4, Na_2S) were all purchased from Merck (AR grade). All of the solutions were prepared using pure Milli-Q water.

2.2 Instrumentation of dPAD

The dPAD is designed with a rectangular shape measuring 40×4 millimeters, and at the end, it includes a circular shape measuring 10 mm in diameter at the end, along with 1 millimeter of the line (Figure 1). The detection zone within the rectangle measures the distance of a reaction, while the sample zone within the circle is for dropping the sample solution. It is printed on filter paper No.1 (Whatman) using a wax printer (Xerox, ColorQube 8570), then heated at 120 °C for 2 minutes in a hot air oven. The black wax area is hydrophobic to prevent outflow. The back side of the dPAD was pasted with clear tape to prevent seepage. Subsequently, the detection zone turns red brick after coating the dPAD with $AgNO_3$ and $K_2Cr_2O_7$ at 7 µL, respectively.

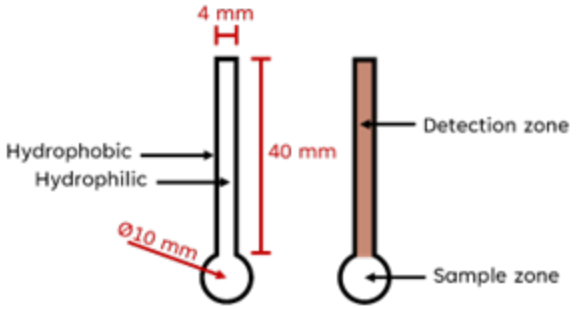

Figure 1. The size and component of dPAD.

2.3 The appropriate state for this dPAD

The standard of Cl^- (Concentration Cl^- 0.5 to 20 g L^{-1}) adjusts the pH value by adding HNO_3 or KOH for aspiring pH (Range 3 to 10 pH). The effects of time were studied in this section to confirm pH and time effect. For the second part, Cl^- solution was mixed with sugar (0, 20, 40, 60, and 80 % w/v) to studied the viscosity effect. For the third part, Cl^- solution was mixed with groundnut (0.5, 1, and 2 % w/v) to studied precipitate effect. Sugar and groundnut were purchased from a local supermarket.

2.4 Optimization for test kits

Micropipette was used for all processes in this study, however, that was not suitable outside of the laboratory. A plastic dropper could be used instead of micropipette. The tested of the plastic dropper are the volume per drop and each drop in the calibration curve of Cl^-.

2.5 Examination in food samples

The food samples were purchased from a restaurant in KMUTT Bangkhuntien's canteen. All the samples were diluted in pure water (ratio 1:1 v/v). In another set of experiments, the samples were mixed with standard Cl^- solutions at different concentrations (ratio 1:1 v/v).

3. Results & Discussion

3.1 Optimal concentration of silver nitrate and potassium dichromate

The study ensured the concentration of $AgNO_3$ solution by using 99.9% AR-grade $AgNO_3$, preparing the solution freshly, and assuring insignificant difference of white precipitate distance after testing with the same concentration of NaCl on the dPAD. Since K_{sp}, Ag_2CrO_4 < K_{sp}, AgCl < K_{sp}, $Ag_2Cr_2O_7$, the dichromate reagent has been preferred to the common chromate reagent in order to allow the white silver chloride sediment over the silver dichromate coat after dropping the sample containing Cl^-. $AgNO_3$ solution which has a concentration of 1 and 0.75 M when detecting Cl^- in a range of 0.25-0.50 g L^{-1} has a high standard deviation, thus, it cannot determine Cl^- at low concentrations. Figures 2a and 2b showed that in $AgNO_3$ solution at 0.25 M when detecting high Cl^- concentration the distance of the white precipitate has a small change, and the graph becomes saturated which implies that it cannot determine the high concentration of Cl^- precisely. Although, the linearity of the $AgNO_3$ solution at 0.50 M is the second highest, the graph was not saturated and had a wide range of Cl^- measurements. Therefore, $AgNO_3$ at the concentration of 0.50 M has been selected, and the linear equation was
y = 19.056x - 45.6, with the coefficient of determination (R^2) of 0.9735.

$$2AgNO_{3\,(aq)} + K_2Cr_2O_{7\,(aq)} \rightarrow Ag_2Cr_2O_{7\,(s)} + 2KNO_{3\,(aq)} \quad (1)$$

$$Ag_2Cr_2O_{7\,(s)} + 2Cl^-_{\,(aq)} \rightarrow 2AgCl_{\,(s)} + Cr_2O_7^{2-}{}_{(aq).} \quad (2)$$

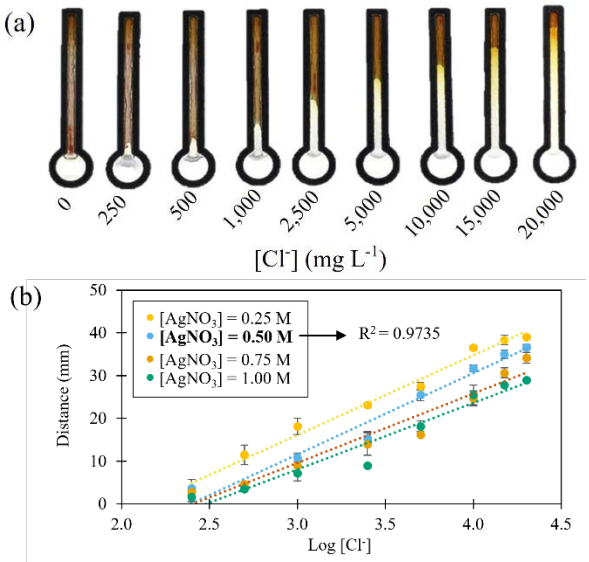

Figure 2. (a) Photograph of dPAD showing the distance of reaction from Cl^- by using $AgNO_3$ 0.50 M and $K_2Cr_2O_7$ 0.25 M reagents. And (b) Calibration curve for Cl^- concentration versus white precipitate distance of AgCl.

3.2 Optimal conditions for Cl^- measurement

3.2.1 Effect of interference

The results in Figure 3 demonstrated that interfering anions including Br^- (10 mg L^{-1}), I^- (10 mg L^{-1}), S^{2-} (10 mg L^{-1}), NO_3^- (500 mg L^{-1}), SO_4^{2-} (2,500 mg L^{-1}), and CO_3^{2-} (2,500 mg L^{-1}) have insignificant effects on the Cl^- detection. PO_4^{3-} at 500 mg L^{-1} has a statistically significant (p < 0.0001) effect on Cl^- measurement, but when the concentration of PO_4^{3-} is 250 mg L^{-1}, PO_4^{3-} did not cause any significant effect on Cl^- detection. This effect can be caused by the solubility product constant (K_{sp}) of Ag_3PO_4 ($K_{sp} = 1.8 \times 10^{-18}$) which is less than AgCl ($K_{sp} = 1.6 \times 10^{-10}$), so the ion Ag^+ from $Ag_2Cr_2O_7$ will react with anion PO_4^{3-} and form a precipitate of Ag_3PO_4 instead of AgCl.

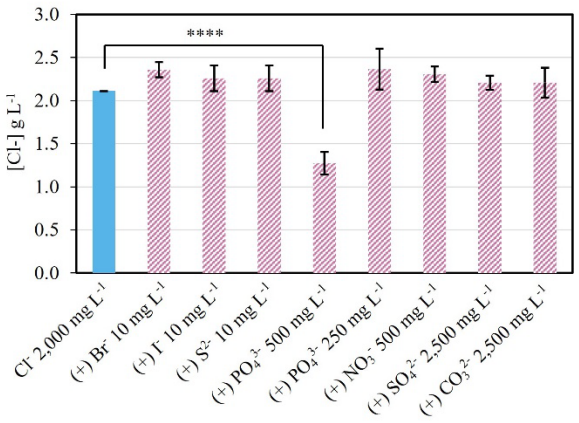

Figure 3. The response of AgCl precipitates without and with (+) interfering anions. Data are presented as mean ± standard deviation (n = 3). ****$p < 0.0001$ (ANOVA with Tukey's post hoc test).

3.2.2 Effect of pH

The pH value in food is generally in the pH range of 3-10, so the 5 g L^{-1} of the standard Cl^- was determined using a buffer solution in the pH range of 3-10. pH did not have a statistically significant effect on this dPAD to detect Cl^- (p-Value = 0.0758) (One-Way ANOVA) reference from Figure 4. This result is not a wonder because neither protons nor hydroxide anions from pH affect the precipitation of the reaction.

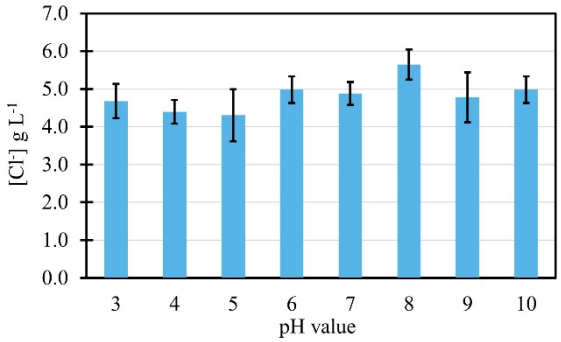

Figure 4. pH effect on a dPAD in the presence of Cl^- at 5 g L^{-1}.

3.2.3 Optimization drops of plastic dropper

The plastic droplets have an average volume of 26, 48, and 70 µL based on 1, 2, and 3 drops, respectively. As a result, 1 and 2 drops were applied in the linear calibration curve since it is close to 30 µL. The study revealed that the two drops of plastic dropper saturated at 15 and 20 g L^{-1} of Cl^- solution (Figure 5). Therefore, a single drop of the plastic dropper is appropriate for this device in the test kit, maintaining linearity in Cl^- measurement with minimal error and offering the quickest Cl^- measurement.

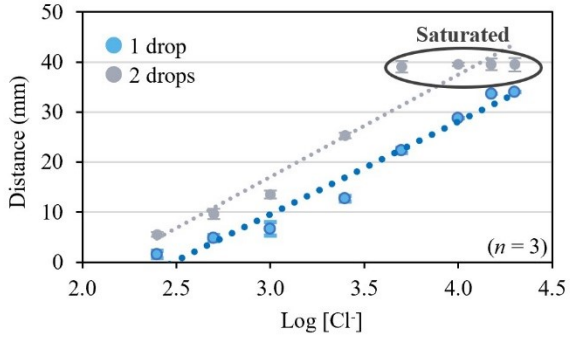

Figure 5. Applying dropper plastic at 1 and 2 drops on linear calibration curve, which Cl^- concentrations in range 0.25 – 2 g L^{-1}, between distance (mm) and log [Cl^-].

3.2.4 Effect of reaction times

The effect of reaction times was determined by adding the sample solution to the sample zone and waiting until the liquid flowed to the end of the detection zone. The dPAD required 20 minutes for a sufficient result, considering the white precipitate was stable during that time. Nonetheless, the prolonged measurement time can be mitigated by covering the dPAD with clear packing tape to prevent effects from the external environment.

3.2.5 Effect of viscosity

The high viscosity poses a significant obstacle to sample flow. The findings revealed that different concentrations of sugar, used as an indicator of varying viscosity (0%, 20%, 40%, 60%, and 80% w/v), significantly influenced the distance, as the *p*-Value was 0.0023 with a one-way ANOVA statistical test as shown in Figure 6. Due to the limitations imposed by viscosity, samples must inevitably diluted in a 1:1 ratio.

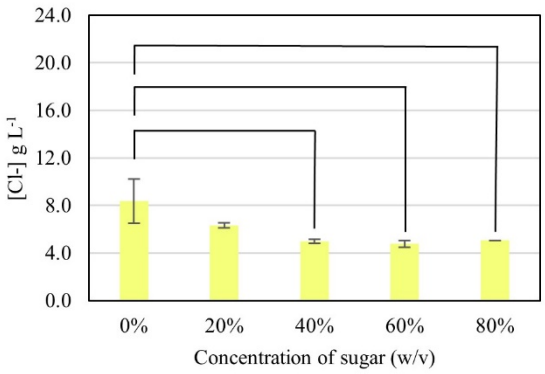

Figure 6. The response of AgCl precipitates in the absence and presence of various viscosities. Data are presented as mean ± standard deviation (n = 3). $^{**}p < 0.01$ (ANOVA with Tukey's post hoc test).

3.2.6 Effect of sediment

Small sediments are commonly present in foods and can potentially affect Cl^- measurement. However, the results indicated that different concentrations of groundnuts, representing varying sediment concentrations (0.5%, 1%, and 2% w/v), did not have an impact on the distance of white sediment.

3.3 Analytical performance

Using the optimized conditions of the reagent, a linear calibration curve between the color band length and log of Cl^- concentration was in the range of 0.5 to 20 g L^{-1} (R^2 = 0.9735) as shown in Figure 2b. The linear range showed that the dPAD was able to detect Cl^- 3.10 g for examining food where the maximum intake per day. The limit of detection (LOD) values of Cl^- in the distance-based device are 4.5 µg Cl^- by naked eyes (Figure 7). Recovery percentage was determined using spike (food samples mixed with Cl^- standard solution at 0.75 and 2 g L^{-1} at 1:1). The mean of recovery percentage of this dPAD is 81% and 83% based on 30 µL 0.75 and 2 g L^{-1}, respectively (as shown in Table 1). The mean of relative standard deviation percentage of this dPAD is 6.0%, 6.6%, and 8.8% based on 30 µL 0.75, 2, and 8 g L-1, respectively.

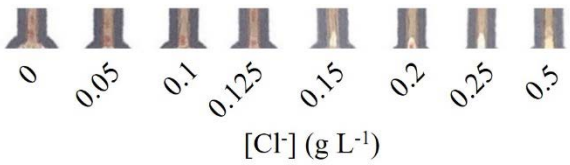

Figure 7. Photograph of dPAD showing measurements of Cl^- in a range of 0-0.5 g L^{-1} (n = 3).

Table 1. Mean measured Cl^- concentration and recorvery percentage.

Sample	[Cl^-] (mg L^{-1})	%Recorvery
Standard Solution	2,371.27 ± 221.26	-
0.75 g L^{-1} spiked	2,981.99 ± 578.71	81
2.00 g L^{-1} spiked	4,023.97 ± 713.95	83

3.4 Detection in food samples

The dPAD can detected at a high concentration of Cl^-. In contrast, food contains some sugar, viscosity affects the flow of the solution. Dilution of samples with water at 1:1 ratio and covering the detection zone with clear packing tape could reduce the effect of viscosity. The dPAD detector for chloride ion relies on the flow of the liquid sample. As the flow progresses, a portion of solvent undergoes evaporation, leading to a reduction in volume and an increase in viscosity. In certain instances, the sample may evaporate entirely before reaching the end of the dPAD. The use of clear packing tape proves effective in mitigating solvent evaporation during the detection. The study studied three food samples in a type of soup, as shown in Table 2.

Table 2. Mean measured Cl^- concentration and standard deviation of tested food samples.

Sample	[Cl^-] (mg L^{-1})
Sample 1	2,495.28 ± 280.25
Sample 2	3,445.94 ± 648.34
Sample 3	3,877.53 ± 408.98

4. Conclusion

The research aimed to enhance the Cl^- detection capability of the dPAD, which typically has limited sensitivity. The hypothesis posited that increasing the concentration of reagent ($Ag_2Cr_2O_7$) on the detection device would improve the measured chloride levels. The study found that utilizing a solution concentration of 0.50 M silver nitrate ($AgNO_3$) and 0.25 M potassium dichromate ($K_2Cr_2O_7$) allowed for the measurement of chloride ion concentrations ranging from 0.25 to 20 g L^{-1}. The sample volume was maintained at 30 µL, and the effect of pH between 3 to 10 did not

impact the measured Cl^- on this dPAD. Moreover, interference from anions such as Br^-, I^-, S^{2-}, NO_3^-, SO_4^{2-}, and CO_3^{2-} did not affect the accuracy of Cl^- measurements, except for PO_4^{3-} at 0.50 g L^{-1}. The study also discovered that using 1 drop of plastic dropper has a better R-square and it is not saturated on high Cl^- concentration when compared with 2 drops. The dPAD designed for the Cl^- detection, proved suitable for concentrations ranging from 0.50 to 20 g L^{-1}, and the limit of detection (LOD) was established at 0.15 g L^{-1} when employing one drop of plastic dropper. After testing the impact of sediment and viscosity on the measurement of Cl^- using this dPAD, it was found that sediment has no effect, but viscosity does. To address the challenge of highly viscous food samples, this dPAD is covered with clear packing tape, and food samples were diluted in a 1:1 ratio.

Acknowledgements

This project was supported by department of chemistry, faculty of science, King Mongkut's University of Technology Thonburi, and Science Classroom in University Affiliated School (SCiUS) under King Mongkut's University of Technology Thonburi and Darunsikkhalai Science School.

References

1. Turck D.; Castenmiller J.; de Henauw S.; Hirsch-Ernst, K.I.; Kearney J.; Knutsen, H.K.; Maciuk A.; Mangelsdorf I.; McArdle, H.J.; Pelaez C.; Pentieva K.; Siani A.; Thies F.; Tsabouri S.; Vinceti M.; Aggett P.; Fairweather-Tait S.; Martin A.; Przyrembel H.; de Sesmaisons-Lecarre A.; Naska A. Scientific Opinion on dietary reference values for chloride. *EFSA Journal* **2019**, *17*(9), 1831-4732.
2. Rahbar, M.; Paull, B.; Macka, M. Instrument-free argentometric determination of chloride via trapezoidal distance-based microfluidic paper devices. *Anal. Chim. Acta.* **2019**, *1063*, 1-8.
3. Abbas, Y.; de Graaf, D.B.; Olthuis, W.; van den Berg, A. Dynamic electrochemical measurement of chloride ions. *JoVE*. **2016**, *108*, e53312.
4. Nery, E.W.; Kubota, L.T. Sensing approaches on paper-based devices: a review. *Anal. Bioanal. Chem.* **2013**, *405*(24), 7573-7595.
5. Busa, Lori Shayne Alamo. Development of Microfluidic Paper-based Devices for Food Analysis. Ph.D. Dissertation, Hokkaido University, Sapporo, Hokkaido, 2016. http://hdl.handle.net/2115/67169 (accessed 2016-09-26).
6. Kamonchanok Phoonsawat; Nalin Ratnarathorn; Henry, C.S.; Wijitar Dungchai. A distance-based paper sensor for the determination of chloride ions using silver nanoparticles. *Analyst* **2018**, 143, 3867. DOI: 10.1039/c8an00670a
7. Longfei Cai; Zhuang Ouyang; Jiahong Song; Liye Yang. Indicator-Free Argentometric Titration for Distance-Based Detection of Chloride Using Microfluidic Paper-Based Analytical Devices. *ACS Omega* **2020**, 5 (30), 18935-18940. DOI: 10.1021/acsomega.0c02143
8. Abdulhadee Yakoh; Poomrat Rattanarat; Weena Siangproh; Orawon Chailapakul. Simple and selective paper-based colorimetric sensor for determination of chloride ion in environmental samples using label-free silver nanoprisms. *Talanta* **2017**, 2018 (178), 0039-9140. DOI: 10.1016/j.talanta.2017.09.013

Paper-based test strip for analysis of organophosphate pesticides

Wanchalearm Manchan[1,2] and Yupaporn Sameenoi[1,2]*

[1]*Department of Chemistry and Center of Excellence for Innovation in Chemistry, Faculty of Science, Burapha University, Chon Buri 20131, Thailand*
[2]*Research Unit for Sensor Innovation (RUSI), Burapha University, Chon Buri 20131, Thailand*

**E-mail: yupaporn@buu.ac.th*

Abstract:

A paper-based test strip for analysis of organophosphate pesticide using enzyme inhibition assay has been developed. The strip composed of two ends for control and sample test zones. Both zones were immobilized with the acetylcholinesterase enzyme (AChE) and Ellman's Reagent (DTNB). In the absence of pesticides, the enzyme AChE catalyzed the formation of thiocholine (TC) that reacts with DTNB to produce a yellow product (TNB^-). After incubation with organophosphate pesticide, the activity of AChE was inhibited and produced less TC, and hence, reduced yellow product. Color intensity was analyzed by scanning the paper-based test strip and measuring the intensity using ImageJ software. This developed assay is able to analyze organophosphate pesticides with the detection limits of organophosphate pesticides as low as 0.025 µg/mL of methyl-paraoxon. The developed method has been successfully applied to detect methyl-paraoxon in spiked cabbage and kale obtaining recovery values about 95% and 96%, respectively. Therefore, the developed method is promising for analysis of organophosphate pesticides in real samples.

1. Introduction

Vegetables, crucial for nutrition globally[1], face challenges from pests during cultivation. Pesticides such as organophosphates (OPs) are commonly used to ensure high yields and control vector-borne diseases.[2, 3] However, this practice results in pesticide residues in food, posing a serious health risk. The main concern is the acute toxicity mechanism of OPs, which inhibit acetylcholinesterase (AChE) activity, leading to the accumulation of acetylcholine (ACh) and potential organ failure, even death.[4, 5] This poses a significant food safety issue observed both in Thailand and worldwide.[6, 7]

Various methods are employed for the analysis of OP pesticides, including liquid chromatography-mass spectrometry (LC-MS) [8, 9], gas chromatography-mass spectrometry (GC-MS)[10, 11], and enzyme activity inhibition methods[12, 13]. While these techniques offer efficient analysis at low nanomolar concentrations with low limits of detection, they have drawbacks such as high cost, the need for specialized equipment and personnel, and the limitation of laboratory-based analysis. Paper-based devices is of interest as an alternative method for OP detection because of their portability, ease of use, and rapid analysis. The enzyme inhibition assay has been the most widely employed method for OP detection on paper-based devices, where the detection is based on the observation of a decreasing colorimetric signal in the presence of OPs compared to the control. By using different colorimetric detection agents such as nanoceria and Ellman's reagent, different analytical features were obtained.[14-16] However, previous paper-based enzyme inhibition assays for pesticides observed a decreasing signal in the presence of pesticides in different paper devices than that of the control where there is no pesticide added. This discrepancy can lead to errors in reading the test results due to being on different paper devices.

Here, a paper-based test strip was designed and developed for the determination of OP pesticides using enzyme inhibition assay, as shown in Figure 1. The device was designed in a pH strip-like format consisting of two ends: control (C) and test (T) ends on the same test strip. Under normal condition without OP pesticides, the enzyme catalyzes the hydrolysis reaction to convert acetylthiocholine (ATC) to thiocholine (TC). Then, when TC reacts with DTNB, it produces a yellow product (TNB^-) and the color intensity is observed at the C end of the strip. However, in the presence of OPs pesticide, AChE enzyme are inhibited by OP pesticide resulting in a reduction of yellow color intensity at the T end. The amount of OP pesticide in the sample can be monitored from the difference of yellow color intensity between the C and T ends. This readout format is easy to observe the presence of OPs in the sample in single paper-based test strip and hence reducing error readout without the need of complicated instruments.

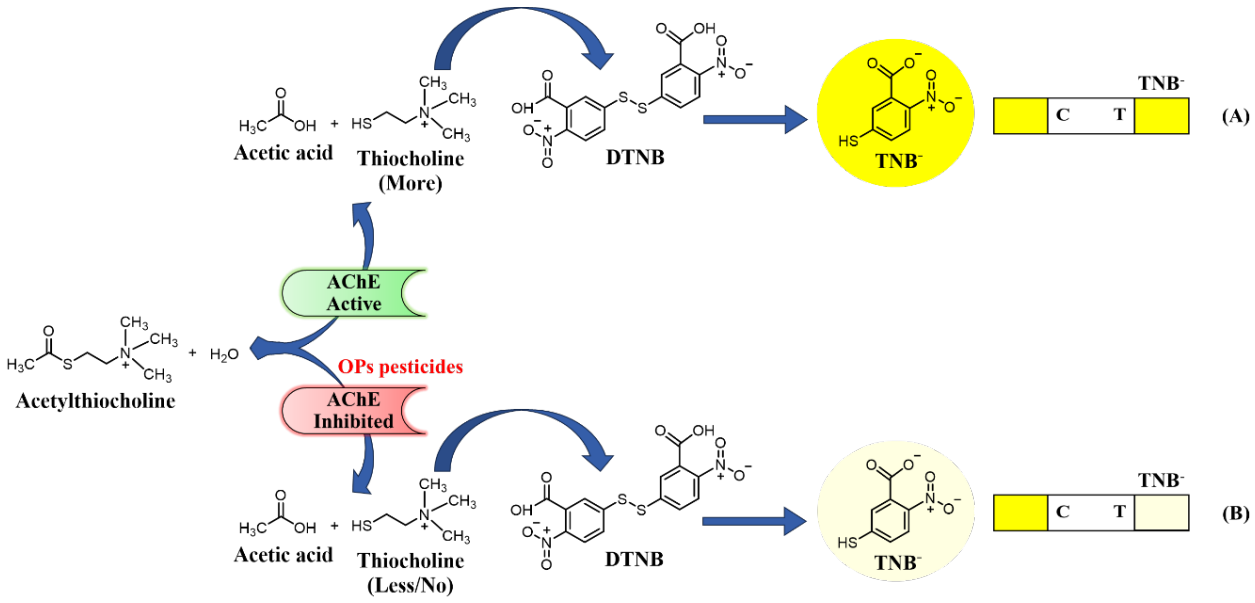

Figure 1. Assay reaction for OP pesticide analysis using enzyme inhibition assay on the paper-based test strip. (A) In the absence of OP pesticides, AChE activity is normally active, producing TC which then reacts with giving the yellow color products on the T zone that are comparable intensity to that of the C zones. (B) Upon the addition of OP pesticides, AChE activity is inhibited resulting in no/less TC and hence less yellow color developed on the T zone compared to the C zone.

2. Materials and Methods

2.1 Materials

Unless otherwise stated, all chemicals were obtained from Sigma-Aldrich (USA). Acetylthiocholine iodide (ATC) was achieved from Acros Organics (Belgium). Disodium hydrogen phosphate (Na_2HPO_4) and sodium dihydrogen phosphate (NaH_2PO_4) were purchased from Ajax Finechem (Austria). Cetyltrimethylammonium bromide (CTAB) and sodium carboxymethyl cellulose (NaCMC) were achieved from Loba Chemie (India). Polyethylene glycol (PEG) and bovine serum albumin (BSA) were purchased from Merck KGaA (Germany). Acetic acid and methanol were obtained from RCI Labscan (Thailand). Citric acid was obtained from Fisher Scientific (UK). Aluminium chloride ($AlCl_3$) was purchased from QRëC (New Zealand). Paper substrate, Whatman No.1 was obtained from GE Healthcare company (China).

2.2 Fabrication of the paper-based test strip

Paper-based test strips were designed to have a rectangular shape containing two detection zones indicated as C and T for the control zone and a test zone, respectively. Each detection zone has a dimension of 1cm x 1.5 cm. The wax-printed paper was then heated at 150°C in an oven for 30 seconds to allow the wax to melt through the paper to form a hydrophobic barrier and defined the test zones. Then, the 3M clear tape was adhered to the back of the paper strip to prevent the solution leakages. The fabricated paper-based strip was then employed for biopolymer assisted reagent immobilization for both C and T zones. Firstly, chitosan solution (2% w/v in a solution of 2% acetic acid and 5% w/v citric acid) was coated onto the paper-based strip using a paintbrush, and dry in oven at 35°C for 10 min. Next, a NaCMC-CTAB-DTNB solution, containing 5 mM DTNB in 0.1 M phosphate buffer pH 7.4, 0.5% (w/v) CTAB, 2.5% (w/v) NaCMC and 5% (w/w) citric acid, was coated onto the paper-based device using a paintbrush, and dry in oven at 35°C for 10 min. Next, 2.5% (w/v) NaCMC solution was coated to the paper-based device using a paintbrush, and dry in oven at 35°C for 10 min. The strip was next immersed in 0.25% (w/v) $AlCl_3$ solution for 10 min to form a hydrogel structure via chemical crosslinking and dried in oven at 35°C for 20 min. For the next layer, the detection zones were immersed in 1% (w/v) PEG solution for 10 min to increase their hydrophilicity and dried in oven at 35°C for 20 min. Finally, 20 µL of 1 U/mL AChE solution was added to the detection zones and dried in oven at 35°C for 10 min to create a ready-to-use paper-based test strip for OP analysis.

2.3 Procedure for detection OPs pesticides

First, 20 µL 4% methanol (blank solution) and the OP standards/sample dissolved in 4% methanol was dropped on the C and T zones of the paper-based test strip, respectively. The reaction

was allowed to take place for 5 min. Next, 20 µL 1 mM ATC solution was added onto both detection zones and the reaction was allowed to take place for another 5 min. The yellow color of the two zones was observed and the paper-based test strip was scanned and the color intensity was measured using ImageJ for quantitative analysis of OP pesticides.

2.4 Sample preparation

Firstly, the vegetables sample was cut and homogenized using a blender. Next, a 5 g of homogenized samples were then placed into a 50 mL centrifuge tube and spiked with methyl paraoxon (MPO) pesticides standard. The mixture was shaken for 1 min and left in the dark for 15 min. Next, 20 mL of methanol was added, and the mixture was vortexed for 30 min and then, centrifuged at 4000 rpm for 10 min. Then, 1 mL of supernatant was collected and dried under the hood. Finally, the extracted residue was reconstituted in 1 mL of 4% methanol for analysis of OP using the developed paper-based test strip according to the procedure mentioned above.

3. Results and Discussion

3.1 Optimization

All optimization experiments were conducted without the addition of OP pesticides. The AChE enzyme concentration was first optimized as it significantly influenced analytical sensitivity, allowing for the clear observation of the reduction in the initial signal after the addition of OPs pesticides, as AChE enzyme activity is inhibited. As shown in Figure 2A, the yellow intensity increased as the AChE concentration increased from 0.1 to 5 U/mL as a result of increasing enzyme activity. However, when AChE concentration was higher than 5 U/ mL, the color intensity became saturated. Therefore, the concentration of AChE in the range of 0.1–5 U/mL was considered as the optimal value to allow for sensitive-response analysis of OP pesticide. The result demonstrates that it is possible to measure AChE activity and thus OP pesticides that inhibit AChE activity in a dose-response manner. Therefore, in this study, the concentration of 1 U/mL AChE was chosen for further experiments to obtain sensitive response for OP detection and use small amount of enzyme.

The ATC concentration is then optimized as it serves as a substrate in the reaction and also affects assay sensitivity. The results showed that the color intensity increased with increasing in

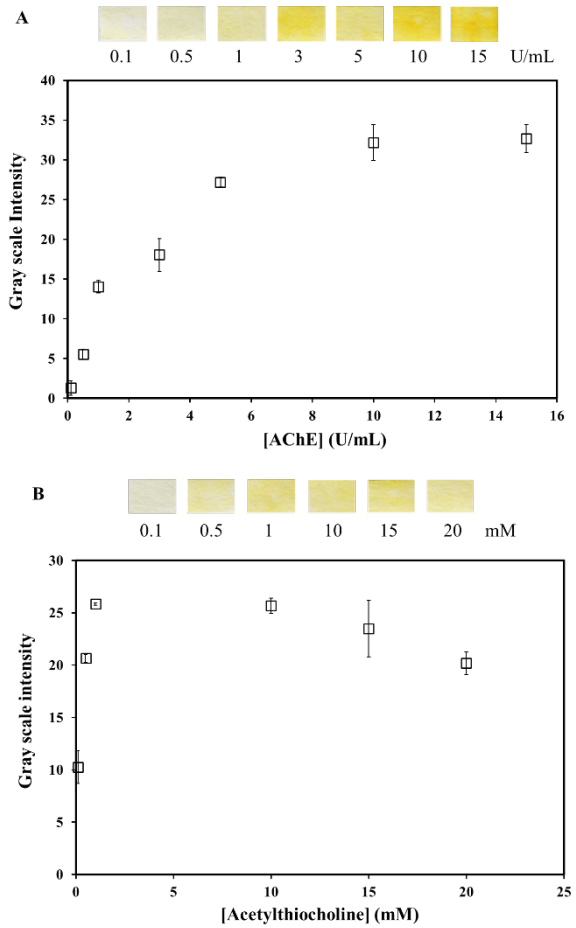

Figure 2. The graph shows the relationship between gray scale intensity with concentration of (A) AChE and (B) ATC (n=3).

ATC concentration and reached saturation at concentration of 1 mM (Figure 2B). Therefore, an ATC concentration of 1 mM was selected for further experiments. This concentration provided sufficient color intensity for the control, and a decrease in this color intensity can be expected when testing for pesticides.

In our current work, the interference study has not yet been carried out. However, we anticipate that the interference in the analysis is negligible. Heavy metals and organic solvents have been reported to affect the AChE inhibition assay.[17] In this case, the target samples are vegetable samples, which are reported to have very trace amounts of heavy metals.[18] As for organic solvents, methanol was used to dissolve the pesticide standard as well as extract the samples. In our previous work, we evaluated the methanol concentration that did not inhibit AChE activity but still dissolved the pesticide, which was a 4% (v/v) methanol solution.[14] Therefore, this methanol concentration was used as pesticide solvent throughout the experiment.

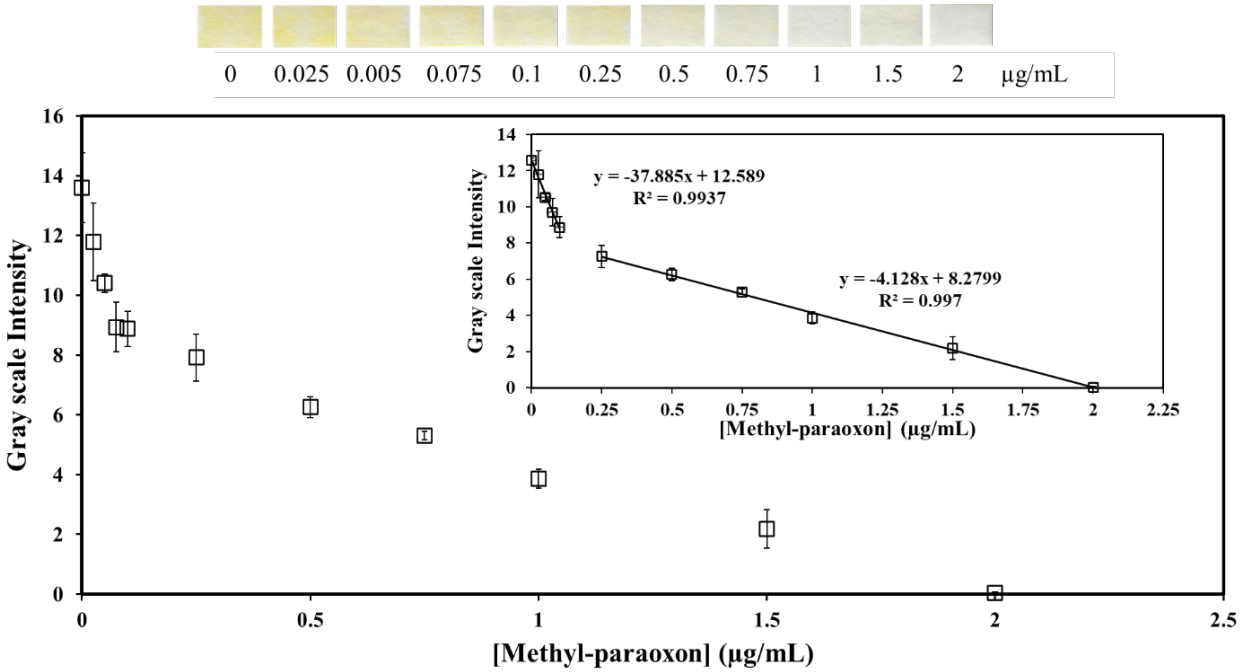

Figure 3. Graph showing the relationship between gray scale intensity with MPO concentration and calibration curve of MPO from the developed method (inset) (n=3).

3.2 OP pesticide analysis using paper-based test strip

Under the optimal conditions, the paper-based test strip was employed for analysis of methyl-paraoxon (MPO) as a proof-of-concept. The MPO was analyzed in the concentration range of 0-4 µg/mL. As shown in Figure 3, the yellow intensity decreased as the MPO concentration increased as a result of AChE inhibition by the pesticide. The linear ranges were found for two portion which are in the range of 0-0.1 µg/mL and 0.25-2 µg/mL. The lower range portion resulted from the highly sensitive response of the signal to the pesticide. On the other hand, the higher pesticide range portion provided lower sensitivity as the signal became saturated. These two linear ranges are useful for pesticide analysis from low level to high level concentration. The limit of detection (LOD), defined as defined as the pesticide concentration that causes a decrease in the signal three times the signal-to-noise ratio relative to the control, was 0.025 µg/mL. This LOD value is sufficient to detect MPO at toxic level in real samples where the toxicity of methyl-paraoxon when exposed to living cells, is 0.46 mM.[19] The repeatability study obtained from the replicate analysis of MPO at the concentration in the linear range giving the RSD in the range of 1.1-6.7% (n=3) indicated that the assay provided high repeatability for OP analysis.

3.3 Analysis of OP pesticides in real samples

To verify the efficiency of the developed paper-based test strip, the analysis of OPs in spiked vegetable samples, including cabbage and kale, was carried out. MPO at concentrations of 0 and 1 µg/mL was spiked into both samples, and the extracts were analyzed using the developed paper-based assay. The results showed that the measured MPO concentrations were comparable to the spiked values in both samples (Table 1). The calculated recoveries obtained from the analysis of both samples are in the acceptable range[20], indicating the high accuracy of the assay for OP analysis in complex matrix vegetable samples. Hence, the developed assay shows promise for serving as a screening analysis for OPs in real samples.

Table 1. Analysis of OP pesticides in samples by the developed method.

Samples	Spiked MPO (µg/mL)	Found (µg/mL) ± SD (n=3)	Recovery (%)
Cabbage	0	ND	-
	1	0.95 ± 0.07	95
Kale	0	ND	-
	1	0.96 ± 0.08	96

ND: not detected

4. Conclusion

In this work, the analysis of OP pesticides was achieved using the developed paper-based test strip. Various parameters including AChE enzymes and ATC substrates were optimized to provide highly sensitive detection of OP pesticides. Analytical performance for the measurement of standard MPO pesticides was observed with low limit of detection of 0.025 µg/mL and detection ranges of 0-0.1 and 0.25-2 µg/mL with high repeatability. The accuracy of the developed method was then verified by spiking MPO pesticide in cabbage and kale samples, with satisfactory test results. Finally, this paper-based test strip method is promising as an analytical tool for the rapid and low-cost screening of OPs pesticides.

Acknowledgements

This research was supported by (i) Fundamental Fund: Grant no.25/2566 and (ii) the Center of Excellence for Innovation in Chemistry (PERCH-CIC) and Department of Chemistry, Faculty of Science, Burapha University.

References

1. Soltani Firouz, M.; Sardari, H., Defect Detection in Fruit and Vegetables by Using Machine Vision Systems and Image Processing. *Food Engineering Reviews* **2022,** *14* (3), 353-379.
2. Sun, F.; Wong, S. S.; Li, G. C.; Chen, S. N., A preliminary assessment of consumer's exposure to pesticide residues in fisheries products. *Chemosphere* **2006,** *62* (4), 674-80.
3. Ngegba, P. M.; Cui, G.; Khalid, M. Z.; Zhong, G., Use of Botanical Pesticides in Agriculture as an Alternative to Synthetic Pesticides. *Agriculture* **2022,** *12* (5).
4. Chowdhary, S.; Bhattacharyya, R.; Banerjee, D., Acute organophosphorus poisoning. *Clin Chim Acta* **2014,** *431*, 66-76.
5. Sultatos, L. G., Mammalian toxicology of organophosphorus pesticides. *J Toxicol Environ Health* **1994,** *43* (3), 271-89.
6. Bhandari, G.; Zomer, P.; Atreya, K.; Mol, H. G.; Yang, X.; Geissen, V., Pesticide residues in Nepalese vegetables and potential health risks. *Environmental research* **2019,** *172*, 511-521.
7. Nisha, U. S.; Khan, M. S. I.; Prodhan, M. D. H.; Meftaul, I. M.; Begum, N.; Parven, A.; Shahriar, S.; Juraimi, A. S.; Hakim, M. A., Quantification of Pesticide Residues in Fresh Vegetables Available in Local Markets for Human Consumption and the Associated Health Risks. *Agronomy* **2021,** *11* (9).
8. Dzuman, Z.; Zachariasova, M.; Veprikova, Z.; Godula, M.; Hajslova, J., Multi-analyte high performance liquid chromatography coupled to high resolution tandem mass spectrometry method for control of pesticide residues, mycotoxins, and pyrrolizidine alkaloids. *Anal Chim Acta* **2015,** *863*, 29-40.
9. Seebunrueng, K.; Santaladchaiyakit, Y.; Srijaranai, S., Vortex-assisted low density solvent based demulsified dispersive liquid-liquid microextraction and high-performance liquid chromatography for the determination of organophosphorus pesticides in water samples. *Chemosphere* **2014,** *103*, 51-8.
10. Alder, L.; Greulich, K.; Kempe, G.; Vieth, B., Residue analysis of 500 high priority pesticides: better by GC-MS or LC-MS/MS *Mass Spectrom Rev* **2006,** *25* (6), 838-65.
11. Wong, J. W.; Hennessy, M. K.; Hayward, D. G.; Krynitsky, A. J.; Cassias, I.; Schenck, F. J., Analysis of organophosphorus pesticides in dried ground ginseng root by capillary gas chromatography− mass spectrometry and− flame photometric detection. *Journal of Agricultural and Food Chemistry* **2007,** *55* (4), 1117-1128.
12. Amine, A.; Mohammadi, H.; Bourais, I.; Palleschi, G., Enzyme inhibition-based biosensors for food safety and environmental monitoring. *Biosens Bioelectron* **2006,** *21* (8), 1405-23.
13. ekaya, N.; Saiapina, O.; Ben Ouada, H.; Lagarde, F.; Ben Ouada, H.; Jaffrezic-Renault, N., Ultra-sensitive conductometric detection of pesticides based on inhibition of esterase activity in Arthrospira platensis. *Environmental Pollution* **2013,** *178*, 182-188.
14. Nouanthavong, S.; Nacapricha, D.; Henry, C. S.; Sameenoi, Y., Pesticide analysis using nanoceria-coated paper-based devices as a detection platform. *Analyst* **2016,** *141* (5), 1837-46.
15. Badawy, M. E.; El-Aswad, A. F., Bioactive paper sensor based on the acetylcholinesterase for the rapid detection of organophosphate and carbamate pesticides. *International Journal of Analytical Chemistry* **2014,** *2014*.
16. Marques, F.; Mitra, S. K., Dip-and-Fold Device: A Paper-Based Testing Platform for Rapid Assessment of Insecticides in Water Samples. *ACS Applied Bio Materials* **2021,** *4* (12), 8456-8465.

17. Arduini, F.; Ricci, F.; Bourais, I.; Amine, A.; Moscone, D.; Palleschi, G., Extraction and detection of pesticides by cholinesterase inhibition in a two-phase system: a strategy to avoid heavy metal interference. *Analytical letters* **2005,** *38* (11), 1703-1719.
18. Manzoor, J.; Sharma, M.; Wani, K. A., Heavy metals in vegetables and their impact on the nutrient quality of vegetables: A review. *Journal of plant Nutrition* **2018,** *41* (13), 1744-1763.
19. Wang, Y.; Kim, B.; Walker, A.; Williams, S.; Meeks, A.; Lee, Y.-J.; Seo, S. S., Cytotoxic effects of parathion, paraoxon, and their methylated derivatives on a mouse neuroblastoma cell line NB41A3. *Fundamental Toxicological Sciences* **2019,** *6* (2), 45-56.
20. AOAC International Guidelines for Standard Method Performance Requirements AOAC Official Methods of Analysis. Appendix F. **2016,**1-18

Paper-based test strip for formaldehyde gas detection

Wannisa Sroisarika[1] and Yupaporn Sameenoi[1,2]*

[1]*Department of Chemistry and Center of Excellence for Innovation in Chemistry, Faculty of Science, Burapha University, Chon Buri 20131, Thailand*
[2]*Research Unit for Sensor Innovation (RUSI), Burapha University, Chon Buri, 20131, Thailand*

**E-mail: yupaporn@buu.ac.th*

Abstract:

This work aims to develop a novel, and one-step analysis method for formaldehyde gas using a paper-based test strip. The proposed method relies on the reaction between formaldehyde and acetylacetone in the presence of ammonium acetate (Nash's reagent), which yields a yellow-colored product of 3,5-diacetyl-1,4-dihydropyridine (DDL). The paper-based test strip has a rectangular shape, measuring 6 cm long and 1 cm wide. The test zone, which is 1 cm long and 1 cm wide, is located at one end of the strip. To prepare the test zone, the paper is dipped into Nash's reagent and then dried at 40°C. The formaldehyde test is performed by exposing the test strip to formaldehyde gas, and if formaldehyde is present in the sample, the test area will appear yellow. The intensity of the yellow color is directly proportional to the amount of formaldehyde in the sample being tested. The yellow that appeared on the test zone was measured for color intensity using a scanner and ImageJ software. It was found that the developed device was able to measure formaldehyde in the two-portion linear range of 0.25–1 ppmV and 3–40 ppmV, with the limit of detection of 0.15 ppmV, which is lower than the air quality threshold set by the Occupational Safety and Health Administration (OSHA). These preliminary results demonstrated that the developed paper-based test strip is promising for measuring formaldehyde in air samples.

1. Introduction

Formaldehyde (FA) is a colorless, flammable gas with disinfectant properties and a pungent odor. It exhibits high solubility in water and is commonly referred to as formalin, constituting a 37–40% formaldehyde solution in water.[1-2] It is a compound extensively employed in various fields, including medicine, cosmetics, agriculture, and industry.[3-6] Despite its widespread use, formaldehyde is categorized as a hazardous air pollutant and can pose health risks with prolonged exposure.[7] Moreover, the International Agency for Research on Cancer (IARC) designates it as a carcinogen.[8] The National Institute for Occupational Safety and Health (OSHA) has established a Permissible Exposure Limit (PEL) of 750 ppbV and an Immediately Harmful to Life or Health (IDLH) limit of 20 ppmV.[9]

Formaldehyde analysis can be performed using various methods, such as gas chromatography (GC), fluorescence spectrophotometry, and electrochemical techniques.[10-12] These methods offer high specificity, accuracy, precision, and sensitivity, allowing for the detection of formaldehyde at low concentrations in parts per billion. However, they have several drawbacks, including expensive instruments, well-trained personnel for operation, and time-consuming, laboratory-based analysis. Consequently, they are not suitable for on-site use.

The paper-based device is currently a popular technology that is used for chemical analysis. Paper-based devices refer to sensing platforms that utilize paper as a substrate to perform the test. These devices have gained increasing interest in recent years due to their numerous advantages, such as that they can be produced easily, the cost of production is low, and the paper test strips are portable.[13-14] Liao, C., et al. (2021) have developed a paper sensor for formaldehyde gas by employing paper towel as a substrate coated with the sulfuric acid salt of hydroxylamine ($(NH_2OH)_2 \cdot H_2SO_4$) and two pH indicators, bromophenol blue and thymol blue. Upon exposure to FA, the hydroxylamine reacts with the absorbed FA to form a Schiff base (H_2C=N-OH), releasing a stoichiometric amount of sulfuric acid. This reaction induces a color change in the pH indicators, correlating with the concentration of FA vapor. The sensor exhibits high sensitivity and selectivity, although its accuracy and precision have not been proven. Furthermore, the use of paper towels as the substrate may not provide sufficient mechanical strength, potentially causing inconvenience during the detection process.[15]

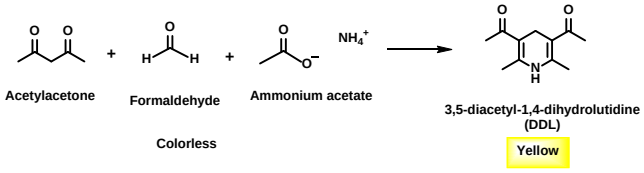

Figure 1. Hantzsch reaction for formaldehyde detection.

Therefore, this study aims to develop a novel, one-step analysis method for formaldehyde gas using a paper-based test strip. The analysis is based on the Hantzsch reaction involving the condensation of acetylacetone in ammonium acetate (Nash's reagent), and formaldehyde, which yields a yellow-colored product of 3,5-diacetyl-1,4-dihydrolutidine (DDL) (Figure 1).[16-18] Here, the Nash's reagent was deposited on the paper-based strip and used to expose to the formaldehyde gas giving the yellow color product whose color intensity was directly proportional to formaldehyde gas in the air.

2. Materials and Methods

2.1 Chemicals and Materials

Ammonium acetate and acetylacetone (Nash's reagent) were purchased from Loba Chemie (India). Acetic acid was purchased from RCI Labscan (Thailand). Formaldehyde solution (38% w/v) was purchased from BDH Laboratory Suppliers (UK). All chemicals were analytical grade and used without further purification. Filter paper Grade 1 was purchased from Whatman GE Healthcare Lifesciences (China).

2.2 Fabrication and immobilization of reagents onto paper-based devices

The paper-based test strip was designed to have a rectangular shape like the pH strip containing a clear PVC sheet with a paper test zones with the dimension as indicated in Figure 2A. Whatman No. 1 filter paper was used to create a test zone by taping 3M tape on the back of the filter paper. Nash's solution (a mixture of ammonium acetate (2 M), acetylacetone (3 M), and acetic acid (0.05 M)) was immobilized on a paper-based test strip by immersing the filter paper in the solution. The immobilized paper was then dried at a temperature of approximately 40 °C for 1 hr. Next, the reagent-immobilized filter paper was attached with double-sided membrane tape and cut into pieces measuring 1 cm long and 1 cm wide and adhered to a clear plastic sheet 6 cm in length and 1 cm in width to create a ready-to-use paper-based test strip for formaldehyde gas analysis, as shown in Figure 2A.

2.3 Assay for formaldehyde gas analysis

The formaldehyde gas was generated from formalin solution according to equation (1) reported by Dong and Dasgupta [19] where [HCHO (aq)] is molar concentration of formalin, [HCHO(g)] is formaldehyde gas in ppmV and T is temperature in Kelvin. The formaldehyde gas was

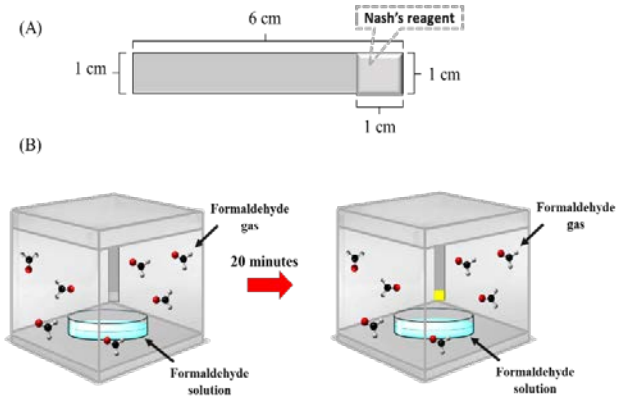

Figure 2. (A) Typical paper-based test strip (B) The process of formaldehyde gas detection using the developed paper-based test strip.

generated in a box (15 cm × 15 cm × 15 cm) and the gas was measured by affixing a paper-based test strip to the inside of the cap of the box. When exposed to formaldehyde gas, the paper-based test strip appeared yellow as the reaction between acetylacetone and formaldehyde occurred in the presence of ammonium acetate, as shown in Figure 2B. The paper-based test strip was scanned, and the picture was analyzed for the color intensity using ImageJ software for quantitative analysis of formaldehyde gas.

$$[\text{HCHO (aq)}] = 10^{[(4538/T) - 11.34]}[\text{HCHO (g)}]^{[(252.2/T + 0.2088]} \quad (1)$$

3. Results & Discussion

3.1 Optimization of the developed assay on paper-based test strip

3.1.1 Acetylacetone concentration

Acetylacetone concentration in Nash's reagent was first optimized as it acted as a key reagent to react with formaldehyde to generate yellow color product. The color intensity from

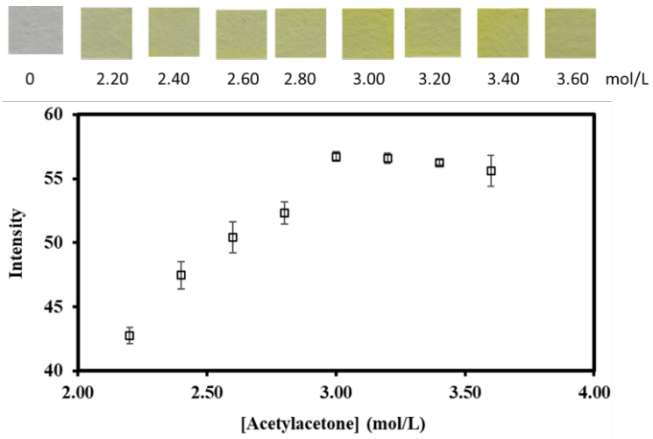

Figure 3. The optimization of acetylacetone for formaldehyde detection using paper-based test strip (n= 3).

analysis of 15 ppmV formaldehyde increased as the concentration of acetylacetone in Nash's reagent increased in the range of 2-3 M and became saturated above 3 M (Figure 3). As a result, we chose 3M acetylacetone as the optimal concentration and used for further experiments.

3.1.2 Reaction pH

To evaluate the effect of pH on the Hantzsch reaction, Nash's reagent at various pH levels was immobilized on the test zones for measuring formaldehyde gas at a concentration of 15 ppmV. The color intensity of the product was highest when the pH ranged from 5.5 to 6.5 (Figure 4). Hence, in this study, we adjusted the Nash's reagent solution to a pH of 5.5, considering it as the optimal pH for quantifying the amount of formaldehyde gas.

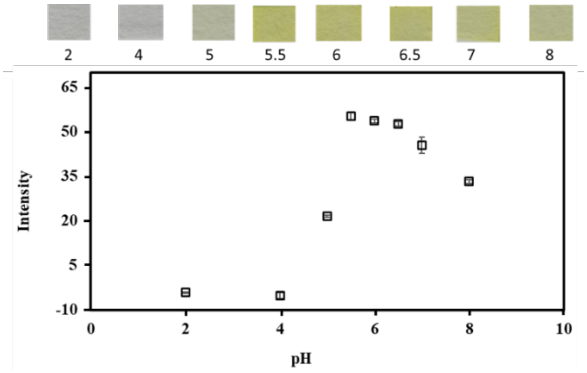

Figure 4. Optimization of Nash's reagent pH for the detection of formaldehyde gas using paper-based test strip (n=3).

3.1.3 Reaction time

The reaction time for 15 ppmV formaldehyde gas detection was evaluated in the range of 1–60 min. It was observed that at the reaction time increased the color intensity increased and reach the saturation in 20 min (Figure 5). Consequently, a reaction time of 20 min was used as optimal value for measuring formaldehyde gas using the developed paper-based test strip.

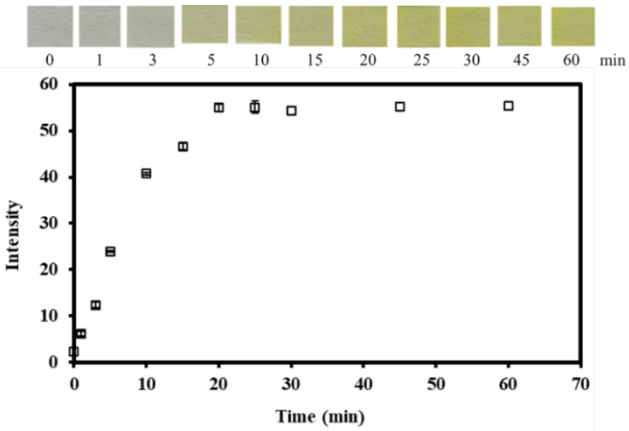

Figure 5. Study of reaction time for formaldehyde gas analysis (n=3).

3.4. Analysis of formaldehyde gas

Under optimal conditions, the paper-based test strip was employed for formaldehyde gas analysis. As the concentration of formalin increased, the color intensity increased. The plot of color intensity as a function of formaldehyde concentration was generated giving the linear range in two portions including 0.25–1 ppmV and 3–40 ppmV (n = 3), as shown in Figure 6. The limit of detection was determined to be 0.15 ppmV, calculated as three times the standard deviation of the 10-repeat blank signal divided by the slope of the calibration curve (3sd(blank)/slope). This value

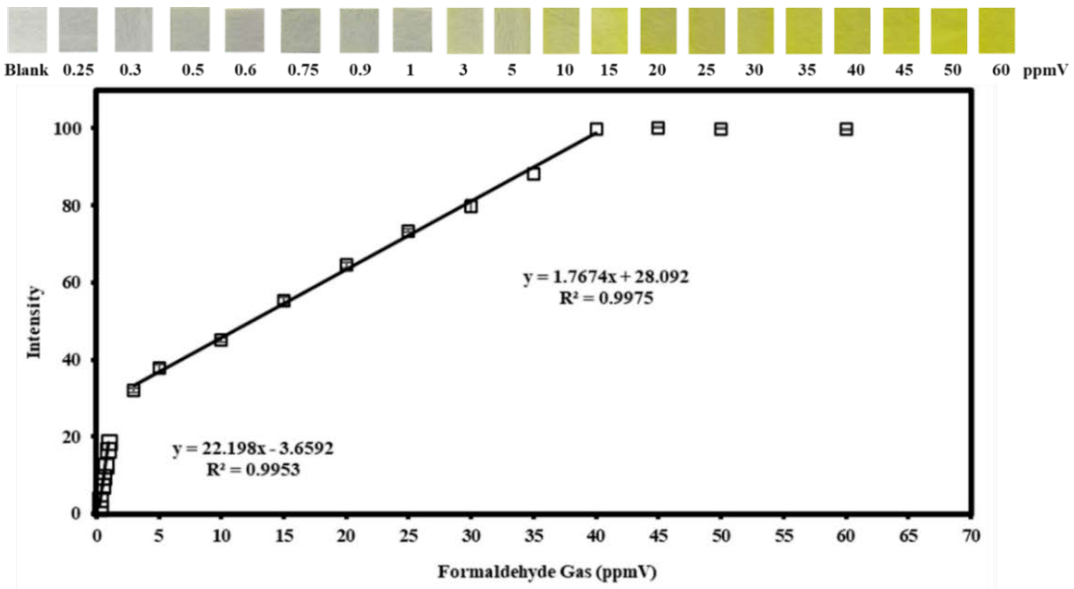

Figure 6. The relationship between the color intensity and the concentration of formaldehyde gas (n=3).

is lower than the air quality threshold set by the Occupational Safety and Health Administration (OSHA) indicating that the developed assay is promising for on-site use to determine formaldehyde gas.

4. Conclusion

The paper-based test strip has been developed for formaldehyde gas detection in one step. The analysis is based on Hantzsch reaction between formaldehyde and acetylacetone in ammonium acetate pH 5.5. Under optimal conditions, the developed device was able to measure formaldehyde in the two-portion linear range of 0.25–1 ppmV and 3–40 ppmV, with a limit of detection of 0.15 ppmV, which is lower than the air quality threshold set by the Occupational Safety and Health Administration (OSHA). The developed paper-based test strip required low-cost materials, low analysis time and cost and can be used for formaldehyde gas detection in one step. These preliminary results indicated that the developed paper-based test strip holds promise for measuring formaldehyde in air samples.

Acknowledgments

This research was supported by the Center of Excellence for Innovation in Chemistry (PERCH-CIC) and Department of Chemistry, Faculty of Science, Burapha University.

References

1. Kiernan, J. A., Formaldehyde, formalin, paraformaldehyde and glutaraldehyde: what they are and what they do. *Microscopy today* **2000,** *8* (1), 8-13.
2. Talaiekhozani, A.; Fulazzaky, M.; Ponraj, M.; Abd Majid, Z. In *Formaldehyde from production to application*, the 3th Conference of Application of Chemistry in Novel Technologies, 2013; pp 1-16.
3. Berton, F.; Di Novi, C., Occupational hazards of hospital personnel: assessment of a safe alternative to formaldehyde. *Journal of occupational health* **2012,** *54* (1), 74-78.
4. Brandão, P. F.; Ramos, R. M.; Rodrigues, J. A., GDME-based methodology for the determination of free formaldehyde in cosmetics and hygiene products containing formaldehyde releasers. *Analytical and bioanalytical chemistry* **2018,** *410*, 6873-6880.
5. Dorieh, A.; Mahmoodi, N.; Mamaghani, M.; Pizzi, A.; Mohammadi Zeydi, M., Comparison of the properties of urea-formaldehyde resins by the use of formalin or urea formaldehyde condensates. *Journal of Adhesion Science and Technology* **2018,** *32* (23), 2537-2551.
6. Liu, Y.; Li, J.; Ma, R.; Dong, Y.; Huang, S.; Sao, J.; Jiang, Y.; Ma, L.; Cheng, D., Determination of Residual Formaldehyde in Urea–Formaldehyde Fertilizer and Formaldehyde Release from Urea–Formaldehyde Fertilizer During Decomposition. *Journal of Polymers and the Environment* **2020,** *28*, 2191-2198.
7. Kim, K.-H.; Jahan, S. A.; Lee, J.-T., Exposure to formaldehyde and its potential human health hazards. *Journal of Environmental Science and Health, Part C* **2011,** *29* (4), 277-299.
8. Bosetti, C.; McLaughlin, J.; Tarone, R.; Pira, E.; La Vecchia, C., Formaldehyde and cancer risk: a quantitative review of cohort studies through 2006. *Annals of Oncology* **2008,** *19* (1), 29-43.
9. (OSHA), O. S. a. H. A., Fact Sheets Highlighting Program: Formaldehyde (29 CFR–1910.1048). Labor, U. S. D. o., Ed. 2002.
10. Kukkar, D.; Vellingiri, K.; Kaur, R.; Bhardwaj, S. K.; Deep, A.; Kim, K.-H., Nanomaterials for sensing of formaldehyde in air: Principles, applications, and performance evaluation. *Nano Research* **2019,** *12*, 225-246.
11. Wang, Y.-S.; Tan, X.; Xue, J.-H.; Li, G.-R.; Shi, L.-F.; Yang, H.-M.; Liu, L.; Zhou, B.; Xiao, X.-L., Determination of trace formaldehyde in blood plasma by resonance fluorescence technology. *Analytica chimica acta* **2011,** *690* (2), 234-239.
12. Yoo, M.-J.; Jo, S.-H.; Kim, K.-H., An advanced technique for rapid and accurate monitoring of gaseous formaldehyde using large-volume injection interfaced with gas chromatograph/barrier discharge ionization detector (LVI/GC/BID). *Microchemical Journal* **2019,** *147*, 806-812.
13. Nery, E. W.; Kubota, L. T., Sensing approaches on paper-based devices: a review. *Analytical and bioanalytical chemistry* **2013,** *405*, 7573-7595.
14. Sameenoi, Y.; Nongkai, P. N.; Nouanthavong, S.; Henry, C. S.; Nacapricha, D., One-step polymer screen-printing for microfluidic paper-based analytical device (μPAD) fabrication. *Analyst* **2014,** *139* (24), 6580-6588.
15. Liao, C.; Zhang, M.; Gao, N.; Tian, Q.; Shi, J.; Chen, S.; Wang, C.; Zang, L., Paper-Based Vapor Detection of Formaldehyde: Colorimetric Sensing with High Sensitivity. Chemosensors 2021, 9, 335. **2021**.

16. Belman, S., The fluorimetric determination of formaldehyde. *Analytica Chimica Acta* **1963,** *29*, 120-126.
17. Nash, T., The colorimetric estimation of formaldehyde by means of the Hantzsch reaction. *Biochemical journal* **1953,** *55* (3), 416.
18. Saini, A.; Kumar, S.; Sandhu, J. S., Hantzsch reaction: Recent advances in Hantzsch 1, 4-dihydropyridines. **2008**.
19. Dong, S.; Dasgupta, P. K., Solubility of gaseous formaldehyde in liquid water and generation of trace standard gaseous formaldehyde. *Environmental science & technology* **1986,** *20* (6), 637-640.

Paper-based devices for water hardness analysis

Alicha Marut[1] and Yupaporn Sameenoi[1,2]*

[1]*Department of Chemistry and Center of Excellence for Innovation in Chemistry, Faculty of Science, Burapha University, Chon Buri 20131, Thailand*
[2]*Research Unit for Sensor Innovation (RUSI), Burapha University, Chon Buri, 20131, Thailand*

**E-mail: yupaporn@buu.ac.th*

Abstract:

A diameter-based measurement paper device for analysis of water hardness has been developed. The device was designed to have a circular test zone with diameter of 3 cm and fabricated using wax-printing method. Eriochrome Black T (EBT) in glycine buffer (pH 10) was stored in the test zone and allowed to dry. The device was then laminated with plastic sheets where the top layer was hole-punched with 0.5 mm diameter at the center and used as sample inlet. The analysis of water hardness is based on the complex reaction of Ca^{2+} and Mg^{2+} with EBT at pH 10. As the sample solution containing Ca^{2+} and Mg^{2+} diffuses from sample inlet outward radially towards the edge of the test zone, the ions react with EBT and the magenta color is formed whose diameter measured by a ruler within 5 min is proportional to the ion concentration. The method provided limit of detection for total hardness as equivalent to $CaCO_3$ of 0.013 mM. The linear range of 0.20-10 mM was obtained using the developed device. The device was employed for hardness analysis in drinking water, tap water, and pond water giving the recovery in the range of 95-105% indicating the high accuracy of the developed device for water hardness analysis.

1. Introduction

Water is a crucial resource essential for various human activities, including consumption, agriculture, and industry.[1,2] Regulatory organizations implement water quality control measures to ensure human and environmental safety.[2] One of the important parameters in assessing water quality is hardness which is indicated by the concentration of calcium ions (Ca^{2+}) and magnesium ions (Mg^{2+}). These ions are naturally present in water at comparatively higher levels than other metal ions.[3-6] The World Health Organization (WHO) categorizes water hardness into four levels based on calcium carbonate concentration equivalents: soft (< 0.61 mM), moderately hard (0.61–1.20 mM), hard (1.21–1.80 mM), and very hard (>1.80 mM). [2]

Traditionally, water hardness is determined using EDTA titration at pH 10 using Eriochrome Black T (EBT) as an indicator.[7, 8] However, these methods are typically performed in a laboratory setting by trained personnel, requires large amount of reagent and samples and can be time-consuming and expensive making it challenging for the public to access.[9, 10]

This research therefore developed a paper-based device to analyze water hardness using diameter-based readout detection. The device was designed to have a circular test zone coated with Eriochrome Black T (EBT) acting as a complexing agent for calcium and magnesium complexes at pH 10 (equation 1).

$$EBT + M^{2+} \xleftrightarrow[pH = 10]{} [M\text{-}EBT] \quad .....(1)$$

When a solution containing these ions is added to the center of the device, it diffuses radially to the edge and reacts with EBT, simultaneously producing a magenta color whose diameter directly correlates to the concentration of calcium and magnesium ions in the solution. Therefore, the developed paper-based devices offer a titrant-free, rapid and low-cost analysis and can be further used as an alternative on-site method of water hardness to assess water quality.

2. Materials and Methods

2.1 Chemicals and Materials

All chemicals were analytical grade. Glycine (NH_2CH_2COOH) was purchased from Calbiochem®, Magnesium chloride ($MgCl_2$) was purchased from Merck KGaA, Zinc (Zn) was obtained from Ajax Finechem Pty Ltd, Copper (II) nitrate trihydrate ($Cu(NO_3)_2{\cdot}3H_2O$) and Nickel (II) nitrate hexahydrate ($Ni(NO_3)_2{\cdot}6H_2O$) were purchased from Applichem Panreac (Germany). Acetic acid (CH_3COOH) and methanol (CH_3OH) were purchased from RCI Labscan, and Aluminum chloride hexahydrate ($AlCl_3{\cdot}6H_2O$) was purchased from KEMAUS (Thailand). Sodium acetate anhydrous (CH_3COONa) was purchased from QRëC® (New Zealand). Eriochrome Black T ($C_{20}H_{12}N_3O_7SNa$) was obtained from Ajax Chemicals, Calcium chloride ($CaCl_2$) was purchased from Ajax Finechem, Potassium chloride (KCl) was obtained from APS Finechem, Lithium chloride (LiCl) and Mercury II Chloride ($HgCl_2$) was purchased from APS Ajax Finechem (Austria). Sodium chloride (NaCl) was obtained

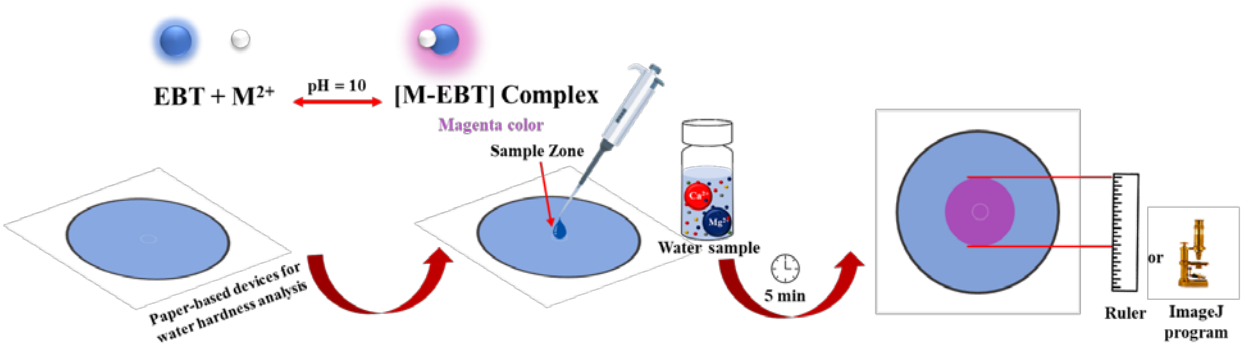

Figure 1. The measurement procedure of water hardness analysis using the developed paper-based device with diameter-based readout detection.

from Loba Chemie PVT.LTD., Sodium hydroxide (NaOH) was obtained from Loba Chemie (India). Wax printer (ColorQube 8870) was obtained frim Xerox, Flextronics Technology (Malaysia). Whatman No.1 filter paper was purchased from GE Healthcare (China).

2.2 Device fabrication and water hardness analysis

The paper-based sensor was fabricated using wax-printing method. Firstly, the device was designed using Microsoft Word to have a 3 cm diameter circular test zone. The design was transferred to the Whatman No. 1 filter paper using a wax printer. The printed paper was heated to allow the wax melt into paper to create 3D hydrophobic barrier.[11] The EBT solution (0.5 mM 150 µL in glycine buffer pH 10) was deposited onto the test zone and baked at 35°C for 30 min. Finally, the device was laminated and a 0.5 mm hole of the top film was drilled at the center of the test zone for use as a sample inlet.

The analysis of water hardness was carried out by adding 75 µL standard/sample solution into the sample inlet. After 5 min, the appeared magenta diameter was measured and used to quantify water hardness.

2.4 Real Samples

Samples used for analysis included tap water, pond water, and drinking water collected from the area of the Faculty of Science, Burapha University, Thailand. Drinking water and tap water were analyzed without further sample preparation. Pond water was prepared by filtering the samples using Whatman No. 1 filter paper before analysis.

3. Results & Discussion

3.1 Assay Principle

The analysis of water hardness relies on the complex reaction between Ca^{2+} and Mg^{2+} and EBT at pH10 (equation 1) giving a magenta color of Ca^{2+}/Mg^{2+}-EBT complex products. The product formed during the Ca^{2+}/Mg^{2+} sample flows outward radially. Upon flowing, the Ca2+ and Mg2+ adsorbed on the negatively charge cellulose filter paper at pH 10^{12} due to electrostatic interaction and simultaneously reacts with EBT to form the Ca/Mg-EBT products. The higher the cations, the more the adsorption distance and the diameter of the complex product was obtained. Therefore, the apparent diameter, reflecting cation amounts, is analyzed for water hardness by measuring with ImageJ or a ruler (Figure 1).

3.2 Optimization

EBT concentration was first optimized as it impacted on assay sensitivity. Different concentrations (0.5, 1.0, and 2 mM) of EBT gave different intensity of blue color when coated onto the test zones. The higher the EBT concentration, the darker the blue color was obtained (Figure 2A). These devices were then used to detect water hardness in tap water, obtaining the formation of Ca/Mg-EBT magenta complex in all devices. The diameter of the magenta complex product decreased as the EBT concentration increased (Figure 2B). This can be attributed to difference in EBT density on the paper test zone resulting from the use of different concentrations of EBT. The test zone with lower EBT density requires a larger area to completely react with Ca^{2+}/Mg^{2+} compared to the higher density of EBT. Therefore, 0.5 mM EBT concentration was chosen for the next experiment as it provided higher diameter signal than other conditions and gave sufficient magenta color intensity to observe.

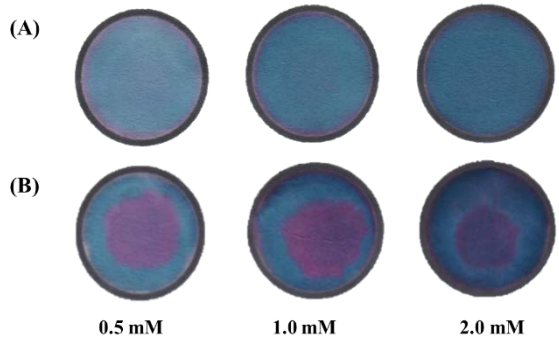

Figure 2. Optimization of Eriochrome Black T concentration (0.5, 1.0 and 2.0 mM) deposited on the detection zones (A) Before tap water testing (B) After tap water testing.

The glycine buffer concentration at pH 10 was then investigated to determine the optimal concentration that would effectively maintain the pH and facilitate the complex reaction between hardness ions and EBT. In the pH range of 7-11, free EBT exhibited a blue color, while outside this range, it showed red and blue colors for lower and higher pH values, respectively. Therefore, it is crucial to control the reaction's pH during the analysis to achieve the desired blue color for free EBT and the magenta color complex of Ca/Mg-EBT. The glycine buffer in the concentrations of 0.16 M, 0.40 M, and 1.04 M were investigated. The 0.16 M concentration proved insufficient to control the pH of EBT solution since the red color appeared all over the detection zones without the addition of harness ions. Conversely, at 1.04 M, the glycine concentration was too high, causing excessively dark colors both in the free EBT and after reacting with Ca^{2+} and Mg^{2+}, rendering this concentration unsuitable for accurate measurement. A glycine concentration of 0.40 M was determined as optimal since it provided a blue color for free EBT, and gave clear color changes when tested with tap water containing Ca^{2+} and Mg^{2+}.

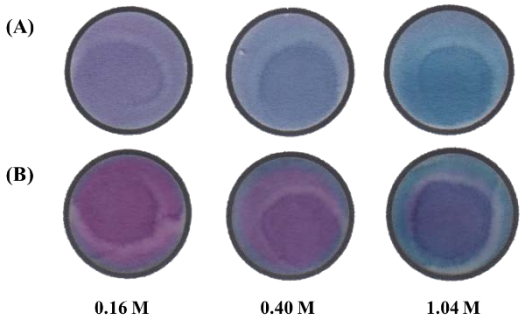

Figure 3. Optimization study of glycine buffer concentration range of 0.16-1.04 M (pH10) (A) Before tap water testing (B) After tap water testing.

3.2 Diameter-based readout paper device for total hardness

Under optimal condition, total hardness detection was carried out by analyzing the solution containing equal amount of Ca^{2+} and Mg^{2+} with a concentration range of 0.013-10 mM. When the solution was applied into the sample inlet, it diffused in a circular pattern towards the edge of detection zones giving a circular magenta color as displaced to the blue color of free EBT. The magenta diameter increased as the concentration of hardness ions increase as shown in Figure 4. The diameter was measured to create the plot of measured diameter as a function of hardness concentration in the range of 0.013-10 mM. The diameter signal obtained from ImageJ program and manual ruler by the two users were compared and the results showed that the obtained diameter by different measuring procedure were similar. The method provided the linear range of hardness analysis at 0.20-10 mM. The limit of detection (LOD) defined as a concentration that gives the signal 3x higher than the standard deviation of the blank is 0.013 mM. The repeatability obtained from replicate analysis of hardness ions with the concentration in the linear range are in the range of 0.30-6.10% (n=3) indicating that the high repeatability of the developed assay was obtained.

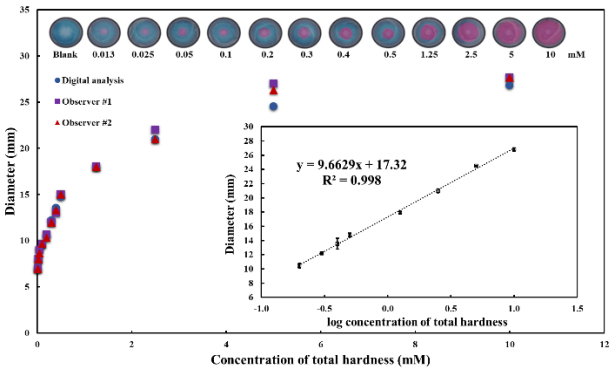

Figure 4. Analysis of total hardness using the diameter-based measurement paper devices. Quantitative calibration was generated for 0.013-10 mM. (n = 3), with a linear calibration range from 0.20-10 mM. (R^2 = 0.998).

3.3 Interferences

Since EBT can form complex reaction with various ions at different pH, the interfering ions were then investigated for their impacts on the hardness assay. These ions included Na^+, K^+, Li^+, Zn^{2+}, Cu^{2+}, Ni^{2+}, Hg^{2+}, and Al^{3+}. The solution of hardness ions with the concentration 0.1 mM was spiked with varying concentration of interfering ions. The mixture was tested on the developed paper-based devices. The interfering ion is

considered to affect the hardness assay if the observed diameter was significant difference from those obtained from the 0.1 mM hardness ion alone (Pool variance t-test at the 95% confidence level). Table 1 shows that the proposed method has high tolerance to alkaline ions (Na^+, K^+ and Li^+) but low tolerance with heavy metals (Zn^{2+}, Cu^{2+}, Ni^{2+}, Hg^{2+} and Al^{3+}) at the concentrations of 0.1-50 mM. This is because the heavy metals can form complex reaction with EBT at high pH. However, the heavy metals are presented in water samples such as drinking water, pond water or tap water at much lower concentrations than the hardness ions and tolerance level reported here.

Table 1. Tolerance levels for interfering cations.

Interfering ions	Tolerance [mM]	Interfering ions	Tolerance [mM]
Na^+	100	Cu^{2+}	0.05
K^+	100	Ni^{2+}	0.5
Li^+	100	Hg^{2+}	5
Zn^{2+}	0.1	Al^{3+}	50

3.4 Application in real water samples

The paper-based device was used to analyze water hardness in drinking water, tap water, and pond water. Calcium and magnesium standard were added to these samples at concentrations of 0.2 mM, and 0.3 mM. The results showed that the recovery for all three samples are in the range of 100-104% indicating that the acceptable accuracy of the developed device for hardness analysis in the investigated samples was obtained (Table 2). The method validation of the developed assay against the reference method in various water samples is current carried out.

Table 2. Hardness analysis of water samples using the developed paper-based assay. (n = 3)

Samples	Spiked $Ca^{2+}$and Mg^{2+}(mM)	Found (mM) ± SD	%Recovery
Drinking water	0	0.02 ± 0.00	-
	0.2	0.22 ± 0.01	100
	0.3	0.32 ± 0.02	103
Tap water	0	0.27 ± 0.03	-
	0.2	0.47 ± 0.01	104
	0.3	0.57 ± 0.01	101
Pond water	0	1.75 ± 0.03	-
	0.2	1.96 ± 0.03	104
	0.3	2.06 ± 0.01	103

4. Conclusion

The diameter-based readout paper device has been developed for total hardness analysis. The assay preliminary demonstrated that it can appropriately detect the total hardness of water quantitatively in accordance with the linear range of 0.20-10 mM, LOD of 0.013 mM with high repeatability (0.40 %). The recovery obtained from water sample analysis were found in the range of 100-104% indicating that the acceptable accuracy of the developed device for water hardness analysis. These preliminary results demonstrated that the developed paper-based assay is possible for use as on-site, rapid, low-cost analysis of total hardness in water in the future.

Acknowledgements

This research was supported by the Center of Excellence for Innovation in Chemistry (PERCH-CIC) and Department of Chemistry, Faculty of Science, Burapha University.

References

1. 1.Almeida, M.; Jayawardane, B. M.; Kolev, S. D.; McKelvie, I. D., Developments of microfluidic paper-based analytical devices (muPADs) for water analysis: A review. *Talanta* **2018,** *177*, 176-190.
2. 2.Oyewunmi, O. D.; Safiabadi-Tali, S. H.; Jahanshahi-Anbuhi, S., Dual-Modal Assay Kit for the Qualitative and Quantitative Determination of the Total Water Hardness Using a Permanent Marker Fabricated Microfluidic Paper-Based Analytical Device. *Chemosensors* **2020,** *8* (4).
3. 3.Abeliotis, K.; Candan, C.; Amberg, C.; Ferri, A.; Osset, M.; Owens, J.; Stamminger, R., Impact of water hardness on consumers' perception of laundry washing result in five European countries. *International Journal of Consumer Studies* **2014,** *39* (1), 60-66.
4. 4.Gaur, N.; Sarkar, A.; Dutta, D.; Gogoi, B. J.; Dubey, R.; Dwivedi, S. K., Evaluation of water quality index and geochemical characteristics of surfacewater from Tawang India. *Sci Rep* **2022,** *12* (1), 11698.
5. 5.Reyes-Toscano, C. A.; Alfaro-Cuevas-Villanueva, R.; Cortés-Martínez, R.; Morton-Bermea, O.; Hernández-Álvarez, E.; Buenrostro-Delgado, O.; Ávila-Olivera, J. A., Hydrogeochemical Characteristics and Assessment of Drinking Water Quality in the Urban Area of Zamora, Mexico. *Water* **2020,** *12* (2).
6. 6.Hinge, G.; Bharali, B.; Baruah, A.; Sharma, A., Integrated groundwater quality analysis using Water Quality Index, GIS and multivariate technique: a case study of Guwahati City. *Environmental Earth Sciences* **2022,** *81* (16).

7. 7.Kurniawati, P.; Jauharo, A. F.; Purbaningtias, T. E.; Wiyantoko, B., Comparison analysis of titrimetric and Spectrometry method for water hardness determination. In *The 4th International Seminar on Chemical Education (Isce) 2021*, 2022.
8. 8.Ward, R. E.; Legako, J., Traditional methods for mineral analysis. Ch. 21. In *Food analysis*, Nielsen, S. S., Ed. Springer: New York, 2017.
9. 9.Nouanthavong, S.; Nacapricha, D.; Henry, C. S.; Sameenoi, Y., Pesticide analysis using nanoceria-coated paper-based devices as a detection platform. *Analyst* **2016,** *141* (5), 1837-46.
10. 10.Aryal, P.; Brack, E.; Alexander, T.; Henry, C. S., Capillary Flow-Driven Microfluidics Combined with a Paper Device for Fast User-Friendly Detection of Heavy Metals in Water. *Anal Chem* **2023,** *95* (13), 5820-5827.
11. 11.Taprab, N.; Sameenoi, Y., Rapid screening of formaldehyde in food using paper-based titration. *Anal Chim Acta* **2019,** *1069*, 66-72.
12. 12.Yousefi, N.; Jones, M.; Bismarck, A.; Mautner, A., Fungal chitin-glucan nanopapers with heavy metal adsorption properties for ultrafiltration of organic solvents and water. *Carbohydr Polym* **2021,** *253*, 117273.

Pencil lead electrode discs with rubbed Prussian Blue particle modification as cheap and ecological hydrogen peroxide sensors

Thanakorn Hussana[1], Nattapol Ma[2], Sareeya Bureekaew[3], Satoshi Horike[2], and Albert Schulte[1]*

[1]School of Biomolecular Science and Engineering (BSE), Vidyasirimedhi Institute of Science and Technology (VISTEC), 21210 Rayong, Thailand, [2]Department of Chemistry, Graduate School of Science, Kyoto University, 606-8502 Kyoto, Japan and [3]School of Energy Science and Engineering (ESE), Vidyasirimedhi Institute of Science and Technology (VISTEC), 21210 Rayong, Thailand.

**E-mail: albert.s@vistec.ac.th*

Abstract:

Hydrogen peroxide (H_2O_2) is a valued compound with many applications ranging from medical to industrial processes and crucial in living organisms as a signaling molecule in important cellular pathways. H_2O_2 is for oxidase-based biosensors targeting an indirect quantification of the biocatalyst's substrates. Modern H_2O_2 electroanalysis exploits cathodic detection at the sensor with a Prussian blue (PB) modification that facilitates the reduction of the target upon surface contact. Standard methods for PB deposition on electrodes are electrochemically or chemically induced precipitation from customized aqueous ferric and ferricyanide solutions. Although the two procedures work, their execution requires experience, careful parameter optimization and significant time with potential problems of maintaining stability. This article presents a very simple and efficient alternative H_2O_2 sensor modification with PB and PB analogues (PBA) in a novel strategy for practical PB sensor adoption. A quick and easy rubbing method with just a few milligrams of PB or PBA powders appeared sufficient to produce a good H_2O_2 detection performance. The details of the pencil lead electrode fabrication, its PB modification and its application for H_2O_2 testing will be presented, and a model sample analysis with the proposed PB-PLEs shall be discussed.

1. Introduction

Hydrogen peroxide (H_2O_2) is a small, simple compound that provides highly valuable applications whether it is environmental, pharmaceutical, industrial or clinical, among many others.[1] Within the context of biology, hydrogen peroxide belongs to a class of intracellular signaling molecules called reactive oxygen species (ROS), involved in many regulating processes including programmed cell death, immune cell activation and vascularization.[2] In addition, hydrogen peroxide has also been widely used as a disinfecting agent for various surfaces and tools in clinics, and as a stain remover and bleaching agent within household.[3] Because of its value and utility, the accurate and reliable detection method of hydrogen peroxide is of great importance to analyses. Most commonly used H_2O_2 determination techniques like spectrophotometry, chemiluminescence and fluorescence are often expensive and time-consuming[1]. Electrochemistry techniques, namely amperometry and potentiometry, offer an alternative hydrogen peroxide detection method that is simpler, more rapid and cost-effective.[4]

Many materials have been immobilized onto an electrochemical sensing platform towards determination of H_2O_2.[4] Prussian blue (PB) and Prussian blue analogues (PBA), for instance, are a large subclass of metal-inorganic or -organic compounds which found applications for the task in sensing, biomedicine, batteries and water purification, to name a few.[5] The controllable atomic compositions, peculiar channel structures and the reversible insertion of metal centers of PB and PBAs make them exceptional choices for electrochemistry and battery developments.[6] Commercially available soluble Prussian blue, or ferric ferrocyanide ($Fe^{III}_4[Fe^{II}(CN)_6]_3$), is an electrocatalytic material that has been widely used in amperometric biosensors for hydrogen peroxide detection in glucose sensing platforms.[7] Their heavy use in research is due to an excellent H_2O_2 reduction at low potentials[7], leading to them being dubbed as "artificial peroxidase".[1] Back in 2022, in an article titled "Exploration of glassy states in Prussian Blue analogues", Nattapol Ma *et al.* discovered glass and recrystallized phases of PBAs via the smart process of mechanically-induced crystal-to-glass transformation.[8] These researchers found that recrystallization of PBA after mechanical milling enhances its porosity, generating local bypassing routes to improve the porous network.[8] While the initially synthesized, original PB has been used extensively in electrochemical sensing platforms,[1] the electrochemical performance of these novel recrystallized and glass-type PBAs has yet to be explored.

In modern electroanalysis, cathodic detection at the electrode surface via PB modification relies on two methods; chemical or electrochemical deposition.[9] Although these two procedures are deemed effective and have been widely used, they require a good level of laboratory experience, freshly made chemical mixtures, significant time for optimizing parameters and obtained yields are often short-lived in their stability and lifespan by nature.[9] To overcome and avoid these limitations, this study aims to develop an H_2O_2 amperometric biosensor through simple modification of a pencil-lead electrode with the earlier mentioned crystal-type, "homemade" PBAs for practical laboratory use.

2. Materials and Methods

2.1 Chemical and instrumentation

The chemicals used in the experiments of this study were from common suppliers, of analytical grade and used unadulterated. A Reference 600 Plus potentiostat from Gamry (Warminster, PA, USA) in standard three-electrode configuration was used in all the electrochemical experiments. The reference electrode (RE) was an Ag/AgCl system with a microporous frit to protect the 3M KCl filling from contamination, while a Pt plate served as a counter electrode (CE) and the working electrodes (WEs) were the pencil lead electrodes (PLEs) with the proposed PBA modification. Electrochemical data acquisition was controlled by the Gamry Framework and Analyst software, while OriginPro 2021 and Microsoft Excel and Inkscape were used for data analysis and graphics.

2.2 Fabrication of PLEs

The fabrication of the PLE-based WEs is described in Figure 1A. The graphite model is an HB-grade, 2.0 mm pencil lead, Mars carbon edition from STAEDTLER (Staedtler Mars GmbH & Co. KG, Nürnberg, Germany). First, the pencil lead is cut into smaller pieces, about 4.0 cm in length. The stick is then introduced into a glass capillary tube of 3 cm in length, and 3 mm in diameter. About 1 cm of the pencil lead is allowed to protrude out from one side of the capillary when fully inserted. An epoxy glue is utilized to fix the pencil lead into position within the glass capillary. After filling the capillary with epoxy glue, the electrode is left to set and dry at room temperature overnight.

Refinement of the disk electrode surface (non-protruding side of the PLE) is carried out after epoxy settles with sandpapers in descending levels of roughness, leaving a clean, flat surface of the pencil lead exposed. The electrode is then put through sonication for 10 minutes to remove residues of glass and loosen graphite pieces. The final step involves polishing with 0.40 μM alumina in DI water and cleansing the electrode surface for further use. In line with the goal of creating a user-friendly and affordable sensor platform, the modification step is simple, yet effective. On a suede-like microfiber inside a petri dish, take out barely a few milligrams of the Prussian blue analogue powder, in its original solid state, and drop it on. Then, for 25-30 seconds, in a slow, circular motion, rub the PLE surface on the powder gently. In a very quick and efficient manner, the modification is now complete, and the electrode with a PB modification is ready for detection. Due to the level of ease and quickness involved with the preparation step, we are choosing, for this methodology, to omit the considerations of stability and storage capability. This proposed procedure is remarkably simple and repeatable, meaning that the electrode modification can be done on a per-use basis.

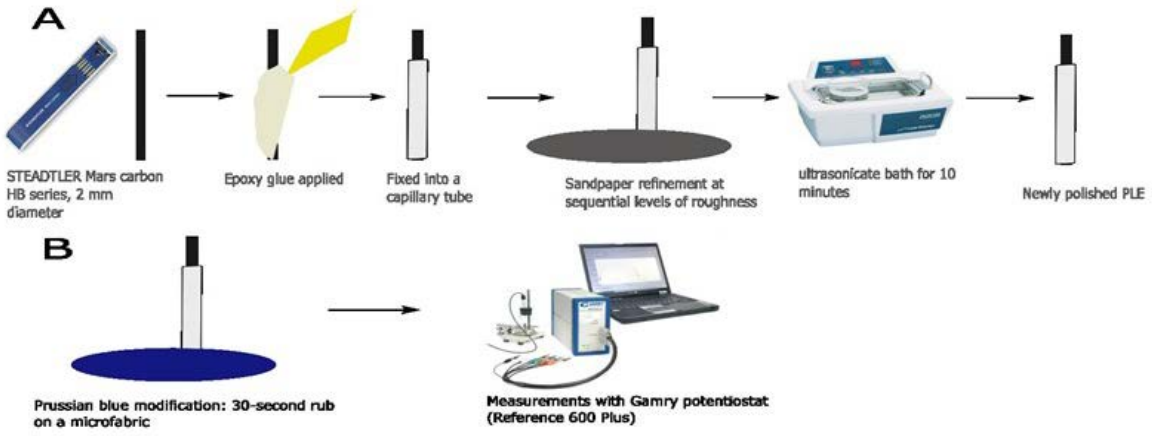

Figure 1. (A) The pencil-lead electrode (PLE) fabrication. The final product is a PLE disk electrode. (B) The simple "rubbing" method on a microfiber cloth for quick and instant PLE modification with PB material.

2.3 PLE performance determination

The electrochemical performance of bare and PBA-modified PLEs is verified using the physical electrochemistry techniques of cyclic voltammetry and chronoamperometry. Calibration of the H_2O_2 response of PBA-modified PLEs is conducted at a detection potential of - 0.20 V vs. Ag/AgCl RE in sodium phosphate buffer (Na-PB, pH 7.0).

3. Results & Discussion

3.1 PLE performance test

The cyclic voltammetry technique is deployed to determine the performance of the bare, untreated PLEs as functional WEs. With this common physicochemical method, the disk electrode's capability to facilitate electron exchange at surface-level contact with electrochemically active species is tested. The redox species identified for testing is dissolved ferricyanide, also known as hexacyanoferrate (III), which is commercially available as fine, soluble monoclinic crystals.[10] Figure 2 displays an overlay of ferricyanide cyclic voltammograms (CVs) at varying concentrations of 10, 5, 2.5, 1.25 and 0.625 mM. All the parameters are kept identical, at the scan rate of 50 mV s^{-1}. As evident from the CV plots, there is a proportional relationship between the concentration of ferricyanide and the redox peak currents; the higher the concentration, the higher the current response at both oxidation and reduction potentials of ferricyanide. These results demonstrate the competency of this cheap yet elegant electrode fabrication to be further used as a H_2O_2 sensor platform, which will be discussed in detail in this article.

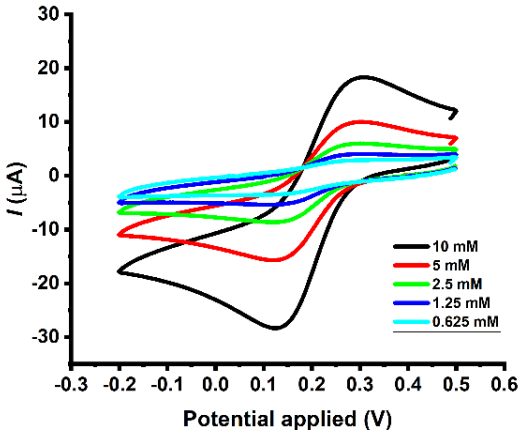

Figure 2. A collection of representative 50-mV s^{-1} cyclic voltammograms of a bare pencil-lead electrode with varying concentrations of ferricyanide (10, 5, 2.5, 1.25 and 0.625 mM).

3.2 PB & PBA H_2O_2 amperometry

With the effort to develop a H_2O_2 sensor platform from the pencil-lead electrode, three types of Prussian blue and its analogues are compared, in the hopes of picking out the best-performing redox mediator. The three types, as previously described, are the commercially synthesized PB, a newly synthesized glass-type PBA and the recrystallized PBA. A comparison between the H_2O_2 detection performance of these three electrode variants is done via amperometric measurements in response to increasing analyte levels. The calibration takes place in a Na-PB buffer of pH 7.0 and at a detection potential of -0.20 V vs RE. Typical examples of the calibration amperograms for the three tested electrodes are shown in Figure 3.

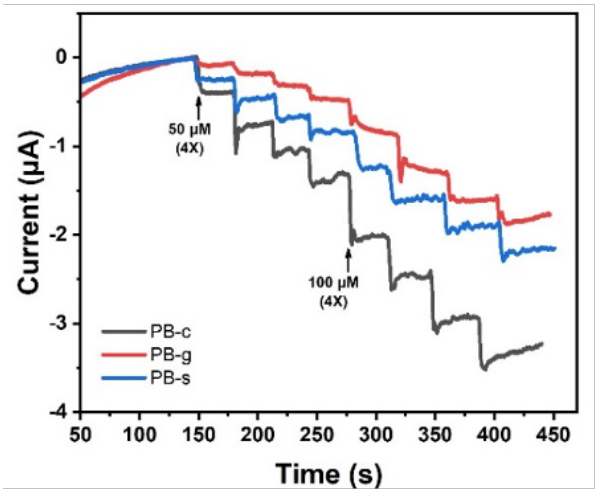

Figure 3. Typical data for the calibration of the cathodic H_2O_2 response of disk-shaped PLE with PB, glass-type and recrystallized surface modification. The recordings were taken at -0.20 V vs Ag/AgCl/3.0M KCl and monitored current steps for the sequential addition of H_2O_2 stock solution in small aliquots: 4 times 50 and four times 100 µM additions, from the left to the right.

As obvious from the three plots, for both the 50 and the 100 µM increments, all four additions lead to distinct current steps of similar magnitude corresponding to changes in the concentration. The three types of PB and PBAs all demonstrated good responses to H_2O_2, although to different degrees. The analysis of the amperometric data led to plots of current step heights vs, H_2O_2 levels (Figure 4) and verified that PLEs with a recrystallized PBA modification induced the highest sensitivity to H_2O_2 at 0.0054 µA $µM^{-1}$ cm^{-2}, while the glass-type PBA and PB worked with considerably lower sensitivities of 0.0033 µA $µM^{-1}$ cm^{-2} and 0.0032 µA $µM^{-1}$ cm^{-2}, respectively. Apparently, the PLE disk that got rubbed with

recrystallized PBA turned out to be best as a H_2O_2 sensing platform.

3.3 Model sample analysis

From the previous section, it is established that the recrystallized PBA is most promising in its response to H_2O_2, and it is therefore chosen to be experimented on further. The accuracy of H_2O_2 quantification by PB-PLE is derived from a set of triplicate standard addition trials with a model sample of 100 µM solutions of the analyte in Na-PB, pH 7.0. In Figure 5, a set of original amperograms as obtained from a standard addition measurement run is given, while Figure 6 depicts the corresponding standard addition plots. For a model sample with a 100 µM H_2O_2 adjustment the average measured concentration of the target is 108.6 ± 5.9 µM, which relates to a recovery rate of 108.6 ± 5.9 %. As mentioned in our methodology, the electrode modification is done on a per-use basis, with a quick cleaning and polishing step. The reasonable recovery rate performance is a sign of practicality of the procedure, allowing for an adequate H_2O_2 cathodic detection in a window of time, after the modification, that preserves and minimizes the decrease in sensitivity due to the loss of recrystallized PBA particles into the solution.

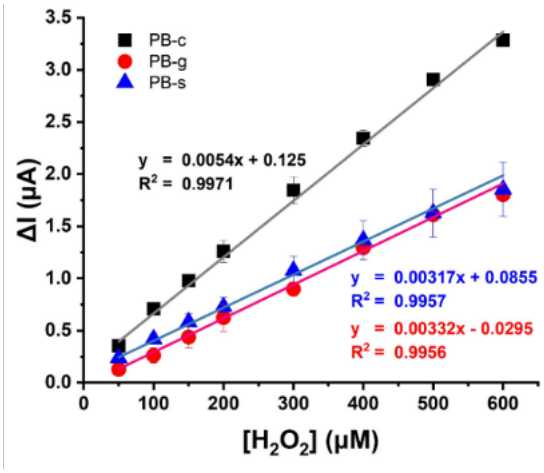

Figure 4. Calibration plots showing the magnitude of amperometric current steps in Figure 3 vs. the adjusted H_2O_2 concentration, interpreted from the three representative trials for the PB and PBAs variants. Data points are mean values and error bars illustrations of the standard deviations.

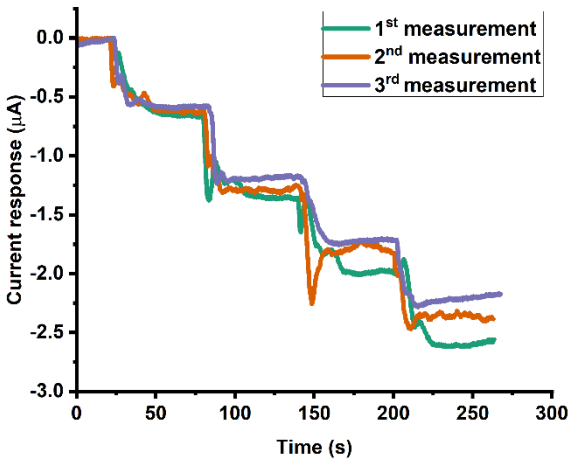

Figure 5. Display of the three original amperograms of a triplicate repetition of a H_2O_2 quantification with a disk-shaped PB-PLE that was worked with in the standard addition mode. The addition of an aliquot of a 100 µM sample was followed by three 100 µM standard additions.

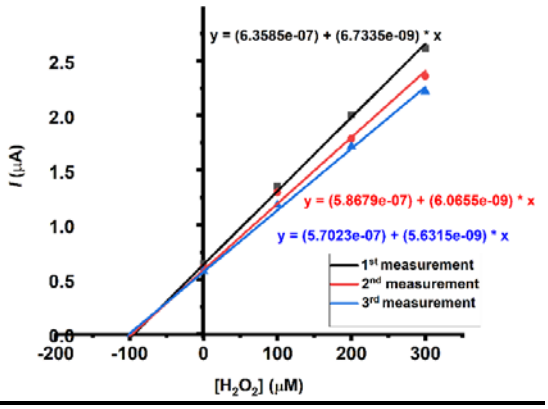

Figure 6. Standard addition plots as constructed with the data of the amperograms in Figure 5. The regression lines through the three sets of data points were extrapolated to obtain the x-axis intercepts, the absolute value of which is a measure of the quantity of the sample's H_2O_2.

4. Conclusion

This article describes a simple and sustainable fabrication of a pencil-lead disc electrode made from affordable graphite pencil leads, which gets modified with commercially synthesized PB and novel PB analogue materials in a remarkably simple but efficient method. Through conducting a cathodic H_2O_2 amperometry, PB-PLEs are shown to have adequate sensitivity to H_2O_2, accurate quantification in model sample analysis within an acceptable range, in addition to having a simple and easily repeatable preparation that justifies the single-use nature. This entails the practicality of this PB-PLE sensor as a simple and effective solution to H_2O_2 detection, certainly in

research laboratory settings with limited financial resources.

Acknowledgements

The authors thank VISTEC and its kind sponsors from the industry and business section for general laboratory support and the VISTEC M. (Eng. Scholarship for Thanakorn Hussana. Furthermore, the Thailand Science Research and Innovation public funding agency is acknowledged for supply of funding through a grant within the Global Partnership Program.

References

1. Chen, W.; Cai, S.; Ren, Q.-Q.; Wen, W.; Zhao, Y.-D. Recent advances in electrochemical sensing for hydrogen peroxide: a review. *Analyst* **2012**, *137* (1), 49-58, 10.1039/C1AN15738H.
2. Liu, J.-X.; Ding, S.-N. Non-enzymatic amperometric determination of cellular hydrogen peroxide using dendrimer-encapsulated Pt nanoclusters/carbon nanotubes hybrid composites modified glassy carbon electrode. *Sensors and Actuators B: Chemical* **2017**, *251*, 200-207.
3. Rutala, W. A.; Weber, D. J. Disinfection and Sterilization in Health Care Facilities: What Clinicians Need to Know. *Clinical Infectious Diseases* **2004**, *39* (5), 702-709.
4. Rad, A. S.; Mirabi, A.; Binaian, E.; Tayebi, H. A Review on Glucose and Hydrogen Peroxide Biosensor Based on Modified Electrode Included Silver Nanoparticles. *International Journal of Electrochemical Science* **2011**, *6* (8), 3671-3683.
5. Azhar, A.; Li, Y.; Cai, Z.; Zakaria, M. B.; Masud, M. K.; Hossain, M. S. A.; Kim, J.; Zhang, W.; Na, J.; Yamauchi, Y.; Hu, M. Nanoarchitectonics: A New Materials Horizon for Prussian Blue and Its Analogues. *Bulletin of the Chemical Society of Japan* **2019**, *92* (4), 875-904.
6. Wu, Z.; Xie, J.; Xu, Z. J.; Zhang, S.; Zhang, Q. Recent progress in metal–organic polymers as promising electrodes for lithium/sodium rechargeable batteries. *Journal of Materials Chemistry A* **2019**, *7* (9),
7. Chandra Sekar, N.; Mousavi Shaegh, S. A.; Ng, S. H.; Ge, L.; Tan, S. N. A paper-based amperometric glucose biosensor developed with Prussian Blue-modified screen-printed electrodes. *Sensors and Actuators B: Chemical* **2014**, *204*, 414-420.
8. Ma, N.; Ohtani, R.; Le, H. M.; Sørensen, S. S.; Ishikawa, R.; Kawata, S.; Bureekaew, S.; Kosasang, S.; Kawazoe, Y.; Ohara, K.; et al. Exploration of glassy state in Prussian blue analogues. *Nature Communications* **2022**, *13* (1), 4023.
9. Ding, Y.; Gu, G.; Xia, X.-H. Electrochemical deposition and mechanism investigation of Prussian blue on graphic carbon paste electrode from an acidic ferricyanide solution. *Journal of Solid State Electrochemistry* **2008**, *12* (5), 553-558.
10. Gail, E.; Gos, S.; Kulzer, R.; Lorösch, J.; Rubo, A.; Sauer, M.; Kellens, R.; Reddy, J.; Steier, N.; Hasenpusch, W. Cyano Compounds, Inorganic. In *Ullmann's Encyclopedia of Industrial Chemistry*.

Square wave voltammetry on a modified screen-printed electrode for selective detection of dopamine in the presence of uric acid

Tharaton Nooin [1,2]*, Thaneeya Hawiset[3], and Prachak Inkaew[1,2]

[1]*Center of Chemical Innovation for Sustainability (CIS), Mae Fah Luang University, Chiang Rai 57100, Thailand*
[2]*School of Science, Mae Fah Luang University, Chiang Rai 57100, Thailand*
[3]*School of Medicine, Mae Fah Luang University, Chiang Rai 57100, Thailand*

**E-mail: 6551102001@lamduan.mfu.ac.th*

Abstract:

Dopamine, a neurotransmitter compound, is associated with several important diseases of the nervous system such as Parkinson's disease, depression, and schizophrenia. Dopamine in the blood can be detected by several methods. The square-wave voltammetric analysis is one of the methods of choice for dopamine determination. However, this method of analysis of dopamine in the blood is hindered by interference from ascorbic acid and uric acid; the oxidation peak of dopamine on most solid electrodes appears at about the same potential as the aforementioned acids. In this study, a modified electrode based on activated carbon powder coated on a screen-printed gold electrode was prepared and used for dopamine detection. The prepared electrode enhanced the responses for dopamine and suppressed the interfering effect from uric acid. The modified electrode showed a good linear range of 0.50 – 800.0 μM (R^2 = 0.998) with a detection limit (S/N = 3) of 0.36 μM (scan rate of 100 mV/s, amplitude of 0.04 V, frequency of 50 Hz and e-step potential of 0.01 V). Analysis of dopamine in blood samples confirmed the ability of this modified electrode for dopamine detection. The concentrations of dopamine in blood samples obtained from square-wave voltammetric analysis were in good agreement with the values obtained from UV-visible spectroscopy.

1. Introduction

Dopamine (DA) is a neurotransmitter, a chemical messenger crucial to numerous bodily processes, including pleasure and motivation. It is associated with feelings of pleasure and satisfaction, and plays a role in regulating mood, attention, learning, and movement.[1] Dopamine levels have been linked to various illnesses such as addiction, schizophrenia, and Parkinson's disease. Some of these disorders are treated by either increasing or decreasing the activity in the brain.[2] Uric acid (UA) is a waste product formed during the breakdown of purines.[3] Purines break down into uric acid, which dissolves in the blood, gets filtered by the kidneys, and is eliminated from the body through urine. Elevated UA levels in human blood might elevate the risk of kidney disease, heart disease, hypertension, and gout. DA and UA serve as important indicators coexisting in human fluids, influencing physiological functions.
Therefore, it is imperative to develop an effective method for the highly sensitive and selective determination of DA and UA, their structures shown in Figure 1.

Capillary electrophoresis[4] and high-performance liquid chromatography (HPLC).[5] were used to determine dopamine in blood. These methods are challenging due to their complexity in preparing the sample, high cost, and the need for timely analysis. In comparison to other analytical methods, the electrochemical method stands out for its simplicity, low cost, rapidity, and high sensitivity. Electrochemical approaches are employed for the simultaneous detection of two or more target analytes. However, the presence of potential interferents can complicate the accurate detection of dopamine and uric acid. Consequently, there is a pressing need to modify sensors to enhance accuracy and specificity.

In this study, magnetic carbon from spent coffee grounds is utilized to modify electrodes, improving their performance in various aspects, including high conductivity, expanded surface area, and enhanced stability.

Spent coffee grounds, organic waste material generated from various sources including households and coffee shops, can be repurposed in several ways to reduce environmental impact. One such application involves utilizing carbon derived from spent coffee grounds to modify a screen-printed gold electrode.[6] The carbon prepared from spent coffee grounds is then coated onto the surface of the gold electrode. Characterization techniques such as scanning electron microscopy (SEM), cyclic voltammetry (CV), or electrochemical methods are employed to study the structure, morphology, and electrochemical properties. The modified screen-printed gold electrodes (MC/SPGE) were employed to determine dopamine concentration in the presence of uric acid.

2. Materials and Methods

2.1 Chemicals and Materials.

Activated carbon, dopamine, uric acid, ferric chloride, ferrous sulfate, sulfuric acid, Sodium hydroxide, nafion, ferricyanide, hexaammineruthenium(III)chloride, potassium chloride were purchased from Sigma-Aldrich (St. Louis, USA) and used without further purification. Solutions were prepared fresh each day using double distilled water.

Spent coffee grounds were obtained from a local café.

2.2 Apparatus and Instruments.

Electrochemical studies were performed using Emstat 3 controlled by a PStrace 5.8 software (PalmSens, Netherlands). The electrode was screen-printed gold electrode with gold as a working electrode, silver as a reference electrode, and gold as an auxiliary electrode (ItalSens Gold SPE, PalmSens).

X-ray diffraction analyzer (PAN analytical X'Pert Pro MPD) was used to characterize the crystalline properties of the magnetic carbon. The samples were tightly packed into the sample holder for analysis. The samples were scanned from 4.9° to 100.0° at a scan speed of 0.050 degree/s. Then, the XRD diffractogram patterns for AC and both magnetic-activated carbons were obtained from the system.

SEM (Tescan, Mira 4, Czech Republic) was used for imaging surface morphology. The magnifications used for the analysis of the samples were between 500 and 3,000 under the condition of 15.0 kV operating voltage.

UV-visible spectrophotometer (PerkinElmer) equipped with UV Win Lab Data Processor and Viewer Version 10.6.2 was used. The wavelength for dopamine was set at 290 nm.

2.3 Activation of Spent Coffee Grounds

The spent coffee grounds were pyrolyzed at 800 ℃ in a tube furnace for 1 hour and then filtered through a 75 µm sieve. Following this, they were immersed in 18 M sulfuric acid for 24 hours, and filtered through a Whatman No. 1 filter paper, and dried in an oven at 80 ℃ for 2 hours. Sulfuric acid treatment was employed to increase oxygen - containing species of the carbon. This treatment can modify surface functional groups, enhancing their ability to interact with various substances.[7]

2.4 Preparation of Magnetic Carbon

The synthesis of magnetic carbon involves utilizing ferric chloride ($FeCl_3$) and ferrous sulfate ($FeSO_4$) as precursors to introduce iron ions into the carbon structure. 0.5 g of activated carbon from spent coffee ground was mixed with 10 mL solution containing 2.0 g of $FeCl_3$ and 2.0 g of $FeSO_4$. The solution was stirred for 30 minutes. 4 M NaOH was then added to the mixture until reaching a pH of 12, and the mixture was stirred for 1 h under heat. The mixture was then filtered through a Whatman No. 1 filter paper and dried in an oven at 80 ℃ for 2 h.

2.5 Preparation of Modified Screen-Printed Gold Electrodes

A mixture of 0.1 g activated spent coffee ground carbon and 0.1 mL of nafion (5% in methanol) was prepared. 20.0 µL of the mixture was then dropped onto the screen-printed electrode and left to dry in the air at room temperature. The structure of nafion is shown in Figure 1.

2.6 Electrochemical Analysis

Square-wave voltammetry (SWV) was carried out with a modified electrode in 0.1 M phosphate buffer pH 7.3 (PBS). Current measurements were performed using SWV in the potential range between -0.5 and 0.80 V. The following instrumental parameters were used: scan rate of 100 mV/s, amplitude of 0.04 V, frequency of 50 Hz and e-step potential of 0.01V. All electroanalytical measurements were made at room temperature.

2.7 Sample Preparation

The preparation of human blood and rat blood involved collecting 3 mL from volunteers using a 5-mL syringes. The collected blood was immediately transferred into a vial containing ethylenediaminetetraacetic acid (EDTA) anticoagulant. Human and rat blood, collected using the same procedure, were then centrifuged at 1000 xg for 10 minutes to separate the serum from the red blood cells. The supernatant was pipetted into vials and stored in the freezer at 4 °C. The blood samples were warmed to room temperature before being used.

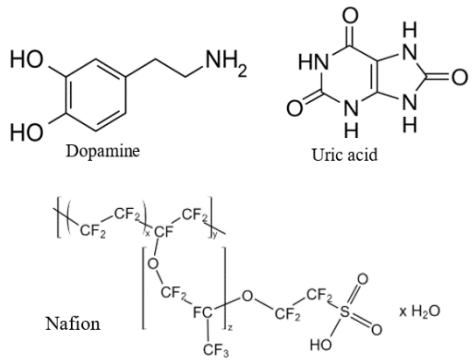

Figure 1. Chemical Structure of dopamine, uric acid and nafion.

3. Results & Discussion

3.1 Surface Morphology: SEM, EDX Mapping and XRD Analysis

The SEM images provide visual insights into the morphology of activated carbon. The surface morphology of commercially available activated carbon indicates a minimal porous surface. In contrast, the SEM image of magnetic carbon shows an increase in surface area, resulting from the activation treatment, as shown in Figure 2A. Figure 2B shows EDX results for the distribution of iron and oxide on the carbon surface. The absence of other elements indicates that the magnetic carbon is free of metal contaminants. Figure 2C shows the XRD pattern of the magnetic carbon, which consists of a series of peaks at 30.0822, 35.4433, 43.208, 52.6633, 57.0889, and 62.6699˚ (2 theta). The XRD pattern confirms the presence of magnetite (Fe_3O_4) on the carbon surface.

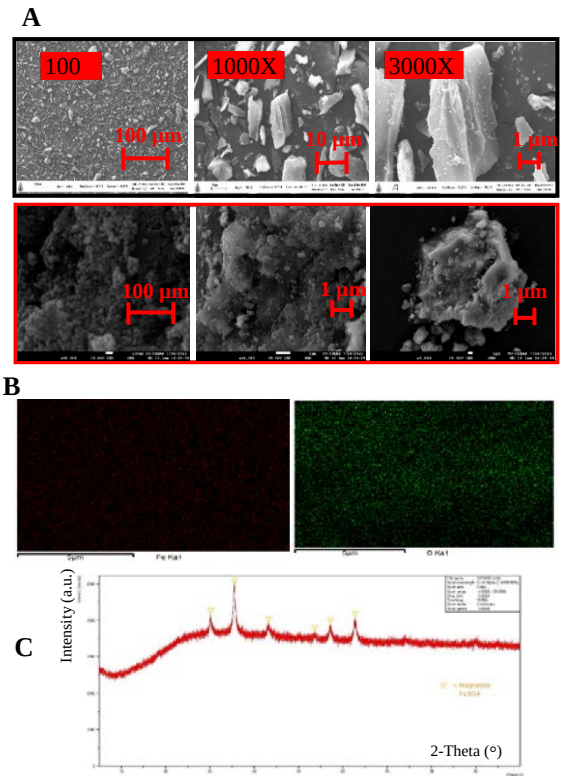

Figure 2. (A) SEM images of commercially available activated carbon (Top) and of Magnetic Carbon (bottom). (B) The energy dispersive (EDX) surface distributions confirmed the presence of Fe (left) and O (right). (C) Peak of XRD magnetic activated carbon.

3.2 The Electrochemical Behaviors

Figure 3A and 3C show cyclic voltammograms at various scan rates (10, 20, 30, 50, 100, 200, 300, and 500 mV/s) in 1.0 mM $[Fe(CN)_6]^{4-/3-}$ or 1.0 mM $[Ru(NH_3)_6]^{2+/3+}$. The current peak height was plotted against the square root of the scan rate. The resulting curve exhibited a linear behavior (Figures 3B and 3D) confirming diffusion control of the processes. The higher current response of $[Ru(NH_3)_6]^{2+/3+}$ compared to those of $[Fe(CN)_6]^{4-/3-}$ (Figure 3A and 3C) indicated the negative nature of the activated carbon surface.

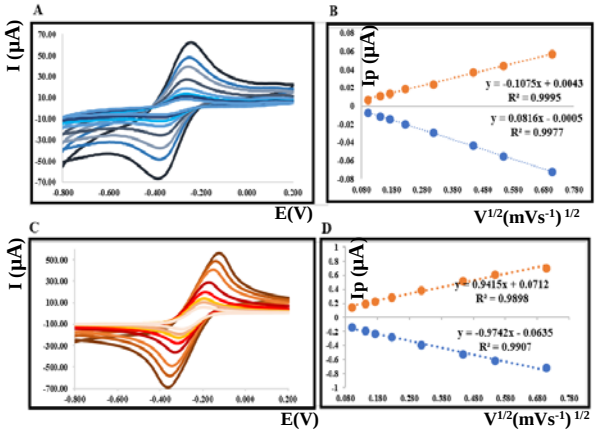

Figure 3. Cyclic voltammograms of MC/SPGE in $[Fe(CN)_6]^{4-/3-}$ (A) $[Ru(NH_3)_6]^{2+/3+}$ (C) and the linear regression reporting the current peak height plotted versus the square root of the scan rate (B) and (D) respectively in 0.10 M KCl. Experimental parameters: potential range from −800 to +200 mV; scan rates 10, 20, 30, 50, 100, 200, 300 and 500 mV/s.

Figure 4A shows cyclic voltammograms of commercially available carbon or CAC/SPGE (solid line) and magnetic carbon or MC/SPGE (dashed line). The capacitive envelope of MC/SPGE is larger than that of bare CAC/SPGE, indicating a larger surface area of the electrode. Figure 4B displays the cyclic voltammograms of 0.50 mM DA in PBS of pH 7.3 on the CAC/SPGE (blue line) and MC/SPGE (red line). DA oxidation peak was observed at 0.34 V.

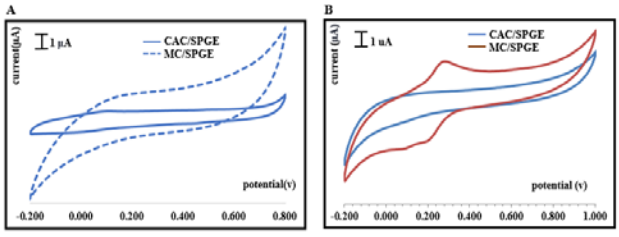

Figure 4. (A) Cyclic voltammograms of CAC/SPGE (solid line), MC/SPGE (dashed line). Scan rate 100 mV/s. 0.5 M H_2SO_4 and (B) of MC/SPGE of 0.50 mM DA in 0.10 M PBS of pH 7.3.

3.3 Electrochemical Detection of Interference

The oxidation potentials of DA and UA typically overlap on gold electrodes. In Figure 5A, square-wave voltammograms on MC/SPGE with 0.50 mM DA or 0.50 mM UA are presented. The yellow line represents the voltammogram of the blank, while the blue and orange lines depict the voltammograms after adding DA or UA separately to identify the positions of the oxidation peaks. The oxidation peaks of DA and UA occur at 0.18 and 0.42 V, respectively, on our modified electrode. Consequently, the UA peak should not interfere with DA determination. Figure 5B illustrates oxidation peaks when a solution of 1.0 mM DA and UA was introduced. Two well-separated peaks corresponding to the oxidation of DA and UA appear at the same positions as in Figure 5A, where DA and UA were added separately. However, the UA peak height was reduced in the presence of DA.

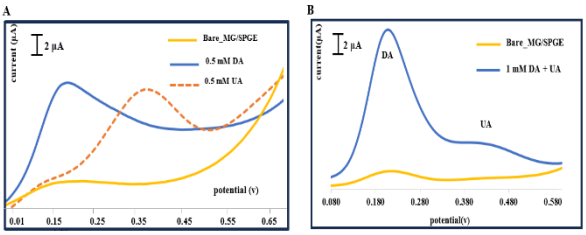

Figure 5. (A) Square-wave voltammograms of DA and UA using MC/SPGE and (B) electrochemical activated electrodes in the presence of UA and DA using MC/SPGE in 0.10 M PBS of pH 7.3. Scan rate 100 mV/s.

Figure 6A shows the SWV of MC/SPGE in 1.0 mM UA and various concentrations of DA (0.50-800 µM). The peak current corresponding to DA oxidation increased linearly with its concentration. UA peaks are scarcely observed at 0.42 V. Long decay tails of DA oxidation peaks are noticeable, attributed to the slow oxidation occurring on this modified electrode surface. This observation also occurs when oxidizing DA and UA separately, as shown in Figure 5A. Figure 6B shows the calibration curve of DA between 0.50-800 µM. A good linear curve was obtained (R^2 = 0.9983, Figure 6B). Compared to other electrodes, our modified electrode displayed a low detection limit, wide linear range, and good reproducibility (Table 1). The modified electrode was stored for 7 days at room temperature before the experiment. The result demonstrates a storage stability of MC/SPGE.

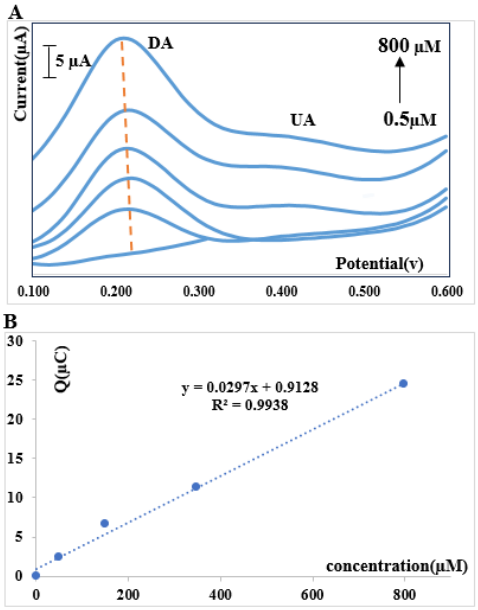

Figure 6. (A) SWV of the electrochemical modified electrode in the presence of various concentrations (0.50-800 µM) of DA and 1.0 µM UA. 0.10 M PBS pH 7.3. Scan rate 100 mV/s. Amplitude 40 mV, Step potential 4 mV, frequency 25 Hz. (B) Plot of oxidation peak current versus varying DA concentration

Table 1. summarizes the comparison of our fabricated MC/SPGE with earlier reported methods for dopamine detection

Electrodes	Detection limit (µM)	Linearity range (µM)	Ref
PEDOT-GO	2.0	6-200	8
NG/DMF/GCE	0.3	1-1000	9
rGO-SS	1.0	1-1000	10
Au-Cu_2O/rG	3.9	10-90	11
MG/SPGE	0.36	0.5-800	This work

3.6 Real Sample Analysis

Table 2 shows human serum and rat serum analysis using modified electrode. Good percent recovery and low RSD were obtained from both human and rat serum. DA concentration on one of human serum from SWV employing our modified electrode (44 ± 2 µM) is in good agreement with those of UV-vis spectroscopy (45 ± 2 µM). These results indicated that MC/SPGE has the potential application for determining DA in blood.

Table 2. Determination of DA in human and rat serum

Samples	Added (μM)	Detected (μM)	Recovery (%)	RSD (%)
Human serum	0	0.6	-	-
	5.0	5.4	107.92	1.95
	15.0	15.2	101.32	0.77
	26.0	25.7	98.83	0.69
Rat serum	0	0.8	-	-
	5.0	4.7	93.58	1.87
	15.0	16.5	109.68	1.76
	26.0	25.0	96.11	0.27

4. Conclusion

The MC/SPGE was prepared for the detection the dopamine by square-wave voltammetry. MC/SPGE exhibited a good response towards DA in the presence of UA. Separate peaks of DA and UA were observed. This modified electrode provided a low detection limit, high sensitivity and good linear range comparable with those reported on other electrodes.

Acknowledgements

Helps with operating SEM, UV-Vis spectrophotometer, and XRD from staff at Scientific & Technological Instruments Center, Mae Fah Luang University, and financial support from Mae Fah Luang University are greatly appreciated.

References

1. Speed, N. K.; Matthies, H. J. G.; Kennedy, J. P.; Vaughan, R. A.; Javitch, J. A.; Russo, S. J.; Lindsley, C. W.; Niswender, K.; Galli, A. Akt-Dependent and Isoform-Specific Regulation of Dopamine Transporter Cell Surface Expression. *ACS Chem Neurosci* **2010**, *1* (7), 476–481.
2. Shin, M.; Copeland, J. M.; Venton, B. J. Real-Time Measurement of Stimulated Dopamine Release in Compartments of the Adult Drosophila Melanogaster Mushroom Body. *Anal Chem* **2020**, *92* (21), 14398–14407.
3. Zen, J. M.; Hsu, C. T.; Hsu, Y. L.; Sue, J. W.; Conte, E. D. Voltammetric Peak Separation of Dopamine from Uric Acid in the Presence of Ascorbic Acid at Greater than Ambient Solution Temperatures. *Anal Chem* **2004**, *76* (14), 4251-5.
4. Voegel, P. D.; Zhou, W.; Baldwin, R. P. Integrated Capillary Electrophoresis/ Electrochemical Detection with Metal Film Electrodes Directly Deposited onto the Capillary Tip. *Anal Chem* **1997**, *69* (5) 951–957
5. Mishra, A.; Upadhyay, A.; Patra, A.; Chaudhury, S.; Chattopadhyay, P. Simultaneous Determination of Epinephrine and Norepinephrine by High Performance Liquid Chromatography. *Sci Pharm* **2009**, *77* (2). 367-374
6. Rosson, E.; Garbo, F.; Marangoni, G.; Bertani, R.; Lavagnolo, M. C.; Moretti, E.; Talon, A.; Mozzon, M.; Sgarbossa, P. Activated Carbon from Spent Coffee Grounds: A Good Competitor of Commercial Carbons for Water Decontamination. *Applied Sciences (Switzerland)* **2020**, *10* (16), 678.
7. Figueroa Campos, G. A.; Perez, J. P. H.; Block, I.; Sagu, S. T.; Saravia Celis, P.; Taubert, A.; Rawel, H. M. Preparation of Activated Carbons from Spent Coffee Grounds and Coffee Parchment and Assessment of Their Adsorbent Efficiency. *Processes* **2021**, *9* (8), 1396.
8. Li, D.; Luo, L.; Pang, Z.; Ding, L.; Wang, Q.; Ke, H.; Huang, F.; Wei, Q. Novel Phenolic Biosensor Based on a Magnetic Polydopamine-Laccase-Nickel Nanoparticle Loaded Carbon Nanofiber Composite. *ACS Appl Mater Interfaces* **2014**, *6* (7), 5144–5151. (9) Li, D.; Liu, M.; Zhan, Y.; Su, Q.; Zhang, Y.; Zhang, D. Electrodeposited Poly(3,4-Ethylenedioxythiophene) Doped with Graphene Oxide for the Simultaneous Voltammetric Determination of Ascorbic Acid, Dopamine and Uric Acid. *Microchimica Acta* **2020**, *187* (1), 94.
9. Jiang, J.; Ding, D.; Wang, J.; Lin, X.; Diao, G. Three-Dimensional Nitrogen-Doped Graphene-Based Metal-Free Electrochemical Sensors for Simultaneous Determination of Ascorbic Acid, Dopamine, Uric Acid, and Acetaminophen. *Analyst* **2021**, *146* (3), 964-970.
10. Farajikhah, S.; Innis, P. C.; Paull, B.; Wallace, G. G.; Harris, A. R. Facile Development of a Fiber-Based Electrode for Highly Selective and Sensitive Detection of Dopamine. *ACS Sens* **2019**, *4* (10), 2599-2604.
11. Zhang, N.; Zhao, W.; Xu, C. H.; Xu, J. J.; Chen, H. Y. Amperometric Monitoring of Vesicular Dopamine Release Using a Gold Electrode. *ChemicalCommunications* **2019**, *55* (24), 3461-3464.

Electrochemical microflow injection analysis on cloth-based device

Tanaporn Boonnikom[1] and Yupaporn Sameenoi[1,2]*

[1]*Department of Chemistry and Center of Excellence for Innovation in Chemistry, Faculty of Science, Burapha University, Chon Buri 20131, Thailand*
[2]*Research Unit for Sensor Innovation (RUSI), Burapha University, Chon Buri, 20131, Thailand*

**E-mail: yupaporn@buu.ac.th*

Abstract:

A microflow injection analysis (μFIA) system with integrated electrochemical detection has been developed on a cloth-based device (CAD). The CAD was designed to have a long channel to allow the capillary flow and fabricated by polymer screen-printing method using polystyrene as a hydrophobic material. The electrode was screen-printed on the CAD at the end of the channel using silver-silver chloride, carbon paste with Prussian blue, and carbon paste as reference, working, and auxiliary electrodes, respectively. A μFIA system is created by immersing the top end in a microtube containing the carrier solution. The area next to the electrode is inclined at an angle of 50 degrees to the plane and the end of the channel is dipped in the lower reservoir. The flow analysis was performed by injecting the H_2O_2 used as a model analyte for proof-of-concept at the sample injection zone which is located 0.4 cm away from the reference electrode. Using this system, the solution flowed on the CAD by the capillary wicking, and the gravitational force from the carrier's upper reservoir and pushed the analyte to pass through the electrodes to the lower reservoir. Under optimal conditions, the method provided a linear range of 0.5-30 mM (R^2 = 0.9933) for H_2O_2 analysis with the limit of detection as low as 0.33 mM, demonstrating that it could be used as a platform for chemical analysis in several areas.

1. Introduction

Microflow injection analysis system (μFIA) is a technology created by the combination of microfluidic technology and conventional flow injection analysis. The system can provide several advantages such as low reagent consumption and waste generation, small sample size, fast analysis, and portability. Traditional μFIA was created using silicon, glass, and polymer materials[1] with external forces or micropumps to drive the flow.[2] Therefore, it requires expensive microfluidic materials with complicated fabrication processes and the use of external micropumps, which have a high cost and difficult integration to drive the fluid flow in the microfluidic channels. Therefore, low-cost microfluidic substrates, such as paper and thread, that can provide for passive pumping to drive the flow in the μFIA system have been developed. However, the limitations of using paper and thread[3, 4] are that (i) paper has low mechanical strength when wet (ii) thread has higher mechanical strength but is unable to create small mechanically stable structures and hence, it difficult to fabricate the detection part into the system (such as electrodes) to create the integrated analysis system.

Recently, cloth has been employed as a material to create microfluidic devices called microfluidic cloth-based analytical devices (μCAD)[5] since it is affordable, low-cost, worldwide available, and has wicking properties by capillary forces to allow the solution flow during the analysis without the need of an external pump.[6] Major advantages of using cloth as a microfluidic substrate over existing alternative technology such as paper are that (i) cloth has better mechanical properties such as greater tensile strength, more flexibility, and higher durability (ii) more choices of fibers can be used to make cloth and (iii) cloth has more interstitial space to allow the solution flow faster.[7]

In this work, cloth was employed as a microfluidic substrate to develop a novel, low-cost, and simple analytical microflow system called continuous flow electrochemical cloth-based microfluidic analytical devices (CF-eμCADs). The proposed CF-eμCADs system uses a small amount of reagents and samples, and provides fast analysis time and low analysis cost with integrated electrochemical detection and flow analysis without an external pump.

2. Materials and Methods

2.1 Materials and Chemicals

Unless otherwise stated, all chemicals were obtained from Sigma Aldrich (USA) and all chemical reagents are analytical grade and used as received without any further purification. Toluene, acetone, and 37% (w/w) hydrochloric acid were purchased from RCI Labscan (Thailand). Polystyrene (Foam) was acquired from the stationery store (Chonburi, Thailand). Silver/silver

chloride paste and carbon graphite pastes were purchased from Sun Chemical (UK). 35% (w/w) Hydrogen peroxide (H_2O_2) and sodium carbonate were purchased from Merck KGaA (Germany). Potassium nitrate was purchased from Ajax Finechem (Australia).

Potentiostat (Model µStat400) was obtained from DropSens. The patterned screen was purchased from Nong Mon market (Chonburi, Thailand). PVC patterned film (Chonburi, Thailand). Cotton cloth was purchased from Pan Muslin brand (Chonburi, Thailand).

2.2 Fabrication of CF-eµCADs

The CF-eµCADs was fabricated using the following procedure. Firstly, cotton cloth was scoured by immersing the cloth in 1.0% Na_2CO_3 at 100˚C for 5 min followed by washing with water. Next, the µCAD was fabricated using a one-step polymer screen printing technique.[8] Briefly, the device was designed to have a hydrophilic flow channel of 3 mm. The design was transferred to the patterned screen to allow for polymer screen-printing process. The patterned screen was placed on top of the cloth and the polystyrene solution (35% w/v in toluene) was poured and squeegeed onto the patterned screen. The polystyrene passed through the patterned screen and penetrated though the cloth to form hydrophobic barrier in one step. The device was adhered with clear tape to prevent solution leakage during the analysis.

The electrodes were fabricated at the end of the channel using a stencil-printing method. The stencil PVC was put on a channel and silver-silver chloride paste, carbon paste mixed with Prussian blue (20%) and bare carbon paste was printed as a reference, working and auxiliary electrodes, respectively. The cloth-based device containing printed electrode was then baked at 45°C for 24 hours. After that, the electrodes are connected to the copper wires using silver ink as a connector and baked at 45°C for another hour. Finally, the device was cut into the dimension as shown in Figure 1B for use as a microflow system.

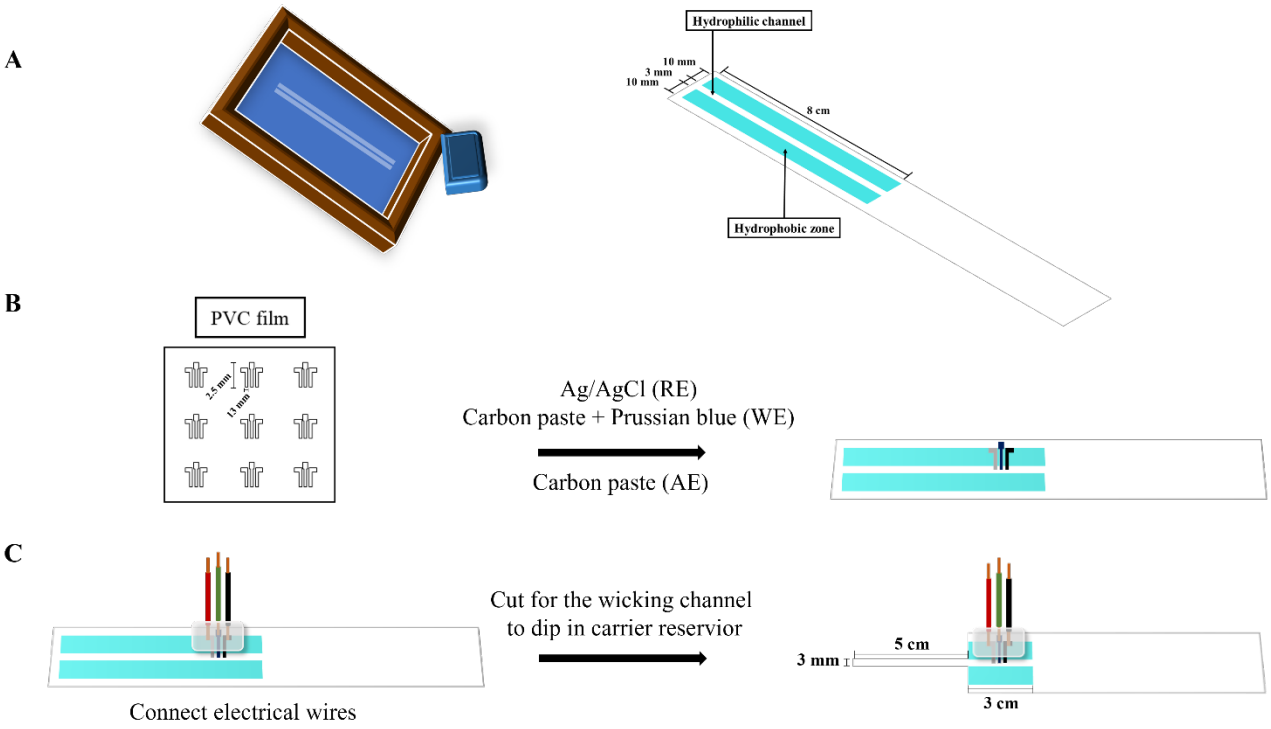

Figure 1. Procedure for fabrication of CF-eµCADs. (A) Fabrication of the CAD using polymer screen printing method. (B) Electrode fabrication using stencil printing method. (C) Wire connection and cutting

2.3 Microflow injection analysis on cloth-based devices.

The microflow injection analysis on a cloth-based device with electrochemical measurements was set as shown in Figure 2. The channel end was immersed in the carrier solution in the upper reservoir, and the other end is placed in the lower reservoir. The flow region containing channel and electrodes are tilted at an angle of 50 degrees to the plane and the last part of the device is put to the waste reservoir. The height of the upper reservoir and the lower reservoir is 12 cm. The flow injection analysis began with injecting 2.0 µL the sample into the channel containing the continuous flow of the carrier at the injection distance of 0.40 cm from the reference electrode. The carrier solution (1.0 M KNO_3) flowed and pushed the plug of the sample to flow through the electrode and to the waste reservoir. The amperometric detection was recorded. In this work, H_2O_2 was used as a model standard as a proof-of-concept. The detection potential was -0.30 V vs Ag/AgCl paste.

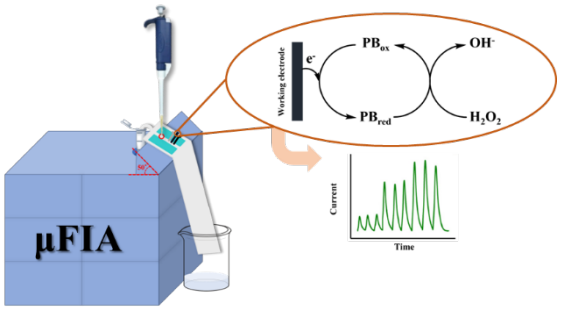

Figure 2. Microflow injection analysis system on a cloth device.

3. Results & Discussion

3.1 Characterization of the electrodes on cloth-based devices by cyclic voltammetry

To test the performance of the fabricated electrode, the cyclic voltammetry was performed with the static condition where the µCAD in the zone containing electrochemical detection zone was cut and the KNO_3 electrolyte and H_2O_2 was dropped on to the electrode. Using the experimental condition described in Figure 3, a well-defined response of the electrochemical signal of both supporting electrolyte (KNO_3) and H_2O_2 was observed. The cyclic voltammogram for KNO_3 solution (dash line) gave both oxidation current and reduction current as a result of the reaction of Prussian blue redox reaction in the working electrode.[9] In the present of H_2O_2 (solid line), higher reduction current was obtained indicating that the electrochemical detection can be performed using the fabricated method and materials and can be further used for the flow system.

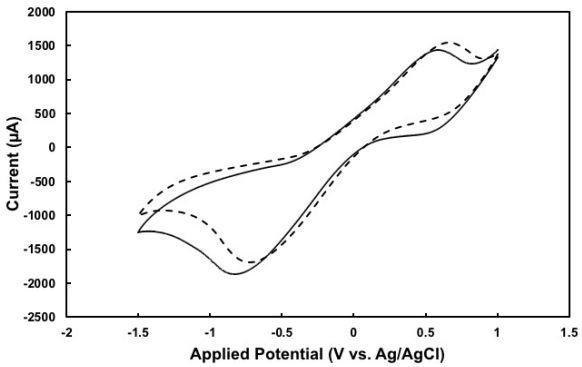

Figure 3. Cyclic voltammogram obtained from analysis of H_2O_2 (solid line) and KNO_3 (dash line) using the electrodes fabricated on cloth-based devices. Experimental conditions: Scanning potential: -1.2-1.0 V; Scan rate at 0.050 V/s; Step potential 0.0020 V; Supporting electrolyte is 1.0 M KNO_3.

3.2 Optimization of microflow injection analysis system

The sample injection volume was first investigated as it impacted on the flow profile and the analysis time. The injection volume of 1.0, 2.0, and 3.0 µL of 5.0 mM H_2O_2 was investigated. The results showed that as the injection volume increased, the peak height of reduction current and peak width increased. Since the peak width is considered as the time required for analysis of each sample, we selected 2.0 µL as an optimal injection volume and used for further experiments as it gave observable reduction current but provided a much narrower peak than that of 3.0 µL injection volume (Figure 4A).

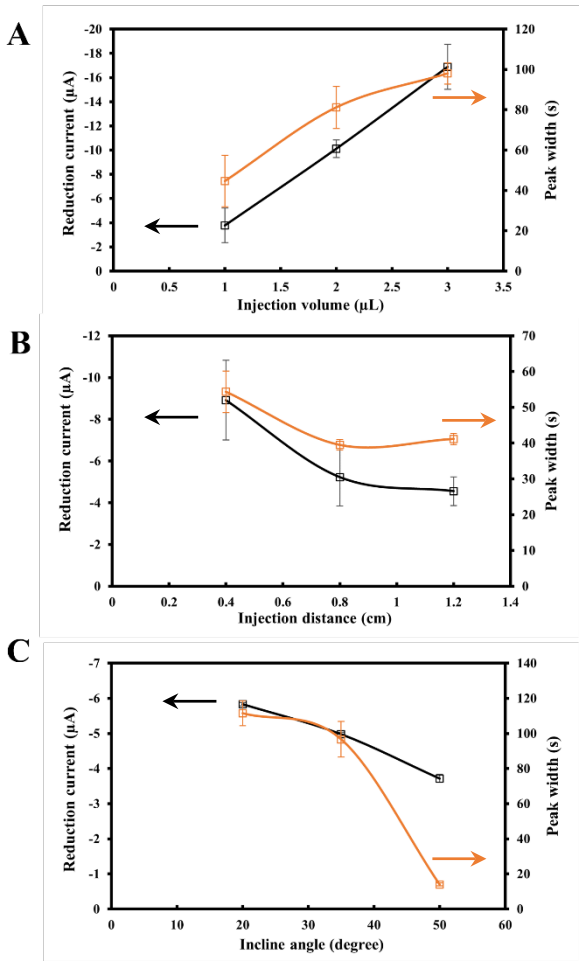

Figure 4. (A) the relationship between the reduction current (black) and peak width (orange) and the injection volume. (Applied potential: -0.30 V vs Ag/AgCl; H_2O_2: 5.0 mM; Injection distance: 0.80 cm; Incline angle: 35 degree) (B) plot of reduction current (black) and peak width (orange) as a function of sample injection distance (measured from reference electrode). (Applied potential: -0.30 V vs Ag/AgCl; H_2O_2: 1.0 mM; Injection volume: 2.0 µL; Incline angle: 35 degree) (C) Relationship between the reduction current (black) and peak width (orange) and the inclined angle of the µCAD. (Applied potential: -0.30 V vs Ag/AgCl; H_2O_2: 1.0 mM; Injection distance: 0.40 cm; Injection volume: 2.0 µL)

Next, the injection distance of the sample measured from the reference electrode was evaluated as it impacted on the peak width and height of the flow profile. The investigated distance was in the range of 0.40- 1.2 cm. From the analysis of 1.0 mM H_2O_2 (Figure 4B), the injection distance at 0.40 cm provided highest reduction current while its peak width was similar to other two injection distances. Shorter injection distance was found to give high noise. Therefore, the injection distance of 0.40 cm was considered as an optimal value and used in further experiments.

Study of optimal inclined angle of the µCAD was carried out. A solution of 1.0 mM H_2O_2 was injected into the sample injection area of the µCAD which was tilted at the angles of 20, 35, and 50 degrees. As shown in Figure 4C, the inclined angle of µCAD at 50 degrees gave a narrowest peak width and highest reduction current attributed to the sharper angle yielding a higher flow rate. Consequently, the optimal angle for tilting the µCAD was determined to be 50 degrees.

3.3 Analytical features for the analysis of H_2O_2 using the developed microflow injection analysis.

Under optimal conditions, the analysis of H_2O_2 was carried out using the developed CF-eµCADs as a proof-of-concept. As shown in Figure 5A, flow profiles for different concentration of H_2O_2 were obtained where the peak height of the flow profile increased as H_2O_2 concentration increased. Plot of reduction current as a function of H_2O_2 concentration gave a linear range of 0.50-30 mM.

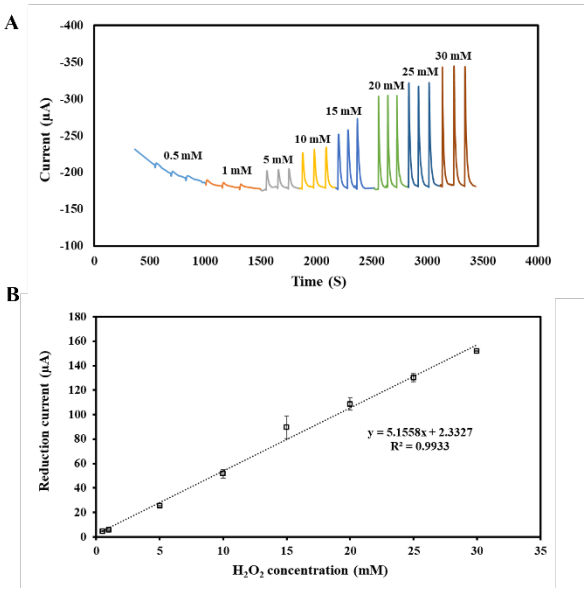

Figure 5. (A) The signal of hydrogen peroxide measured with amperometry. (B) Calibration curve of hydrogen peroxide on a cloth-based device with microflow injection analysis. Experimental conditions: Applied potential: -0.30 V vs. Ag/AgCl; Carrier solution: 1.0 M KNO_3; Injection volume:2.0 µL; Injection distance: 0.40 cm ; Inclined angle: 50 degree.

The limit of detection (LOD) and limit of quantification defined as the concentration that gave signal 3 and 10 times the noise (S/N = 3, 10) was found to be 0.33 mM and 2.16 mM respectively. The repeatability evaluated by

replicate analysis of H_2O_2 at the concentration in the linear range was found to have a relative standard deviation (RSD) in the range of 2.74-5.57% (n=3). The %RSD value obtained is within the accepted standard value.[10] These preliminary results indicated that the developed microflow system have been proven for analysis of chemical active species and promising for use as an analytical platform that provides for simple, low-cost, and continuous analysis with low sample and reagent consumption.

4. Conclusions

The CF-eμCADs was successfully developed and preliminary demonstrated for use as continuous microflow injection analysis with low sample and reagent consumptions. Optimal parameters affecting the flow analysis were investigated including injection volume, injection distance and inclined angle. Under optimal condition, analysis of H_2O_2 used as a model standard as a proof-of-concept was carried out. Well-defined flow profile was obtained as continuous injection of H_2O_2 was conducted. These preliminary results indicated that the developed microflow system is promising for use as flow injection platform for low-cost analysis with low sample and reagent consumption. Other experiments including real sample analysis as well as method validation are currently investigated.

References

1. Sam-ang SUPHAROEK, N. Y., and Jaroon JAKMUNEE. A Simple Microfluidic Integrated with an Optical Sensor for Micro Flow Injection Colorimetric Determination of Glutathione. *Analytical Sciences* **2012**, *28*.
2. Zhang, C.; Su, Y.; Liang, Y.; Lai, W. Microfluidic cloth-based analytical devices: Emerging technologies and applications. *Biosens Bioelectron* **2020**, *168*, 112391. DOI: 10.1016/j.bios.2020.112391.
3. Pradela-Filho, L. A.; Noviana, E.; Araujo, D. A. G.; Takeuchi, R. M.; Santos, A. L.; Henry, C. S. Rapid Analysis in Continuous-Flow Electrochemical Paper-Based Analytical Devices. *ACS Sens* **2020**, *5* (1), 274-281. DOI: 10.1021/acssensors.9b02298.
4. Agustini, D.; Bergamini, M. F.; Marcolino-Junior, L. H. Characterization and optimization of low cost microfluidic thread based electroanalytical device for micro flow injection analysis. *Anal Chim Acta* **2017**, *951*, 108-115. DOI: 10.1016/j.aca.2016.11.046.
5. Li, H.; Wang, D.; Liu, C.; Liu, R.; Zhang, C. Facile and sensitive chemiluminescence detection of H2O2 and glucose by a gravity/capillary flow and cloth-based low-cost platform. *RSC Advances* **2017**, *7* (68), 43245-43254. DOI: 10.1039/c7ra06721f.
6. Ferreira, T. A.; Guevara-Lara, A.; Paez-Hernandez, M. E.; Mondragon, A. C.; Rodriguez, J. A. Micro flow injection analysis of leucomalachite green in fish muscle using modified henequen fibers as microfluidic channels. *RSC Adv* **2021**, *11* (56), 35375-35382. DOI: 10.1039/d1ra06301d.
7. Nilghaz, A.; Wicaksono, D. H.; Gustiono, D.; Abdul Majid, F. A.; Supriyanto, E.; Abdul Kadir, M. R. Flexible microfluidic cloth-based analytical devices using a low-cost wax patterning technique. *Lab Chip* **2012**, *12* (1), 209-218. DOI: 10.1039/c1lc20764d.
8. Tasaengtong, B.; Sameenoi, Y. A one-step polymer screen-printing method for fabrication of microfluidic cloth-based analytical devices. *Microchemical Journal* **2020**, *158*. DOI: 10.1016/j.microc.2020.105078.
9. Wijitar Dungchai, O. C., and Charles S. Henry. Electrochemical Detection for Paper-Based Microfluidics. *Analytical Chemistry* **2009**, *81*.
10. Appendix F: Guidelines for Standard Method Performance Requirements. *AOAC Official Methods of Analysis* **2016**.

Preparation and evaluation of ammonium ion reference material in salt matrix

Thararat Tangjit[1,2], Duangjai Nacapricha[1], Kanchana Uraisin[1], Nongluck Tangpaisarnkul[2], and Phoonthawee Seatear[1]*

[1]*Department of Chemistry and Center of Excellence for Innovation in Chemistry, Faculty of Science, Mahidol University, Bangkok 10400, Thailand*
[2]*Chemical Metrology & Biometry Department, National Institute of Metrology (Thailand), Pathumthani 12120, Thailand*
**E-mail: phoonthawee.sae@mahidol.ac.th*

Abstract:

An ammonium ion (NH_4^+) plays a pivotal role in the nitrogen cycle within aquatic environments. Elevated NH_4^+ levels, reaching up to 1.0 mgN L^{-1}, poses health risks to shrimp and other aquatic organisms. Consequently, regulating ammonium concentration in shrimp farming water is crucial to mitigate potential health issues. As a result, the reliability and accuracy of NH_4^+ measurements are essential for addressing this matter effectively. Ensuring measurement accuracy requires the calibration and verification of instruments using ammonium ion reference material (NH_4^+- RM). While numerous commercial reference materials cater to freshwater, this work introduces the development of the NH_4^+-RM within a salt matrix (aquacultural water). This approach ensures the suitability of RMs for instrument validation before their application in measuring water in shrimp ponds. Potentiometric technique with ion selective electrode (ISE) is selected for selective determination of NH_4^+ in the developed RMs, prepared with ammonium chloride in artificial sea salt water. Salinity (0-10 psu) is observed as the effect of ionic strength. Magnesium sulfate solution as ionic strength adjuster (ISA) is also investigated. According to the preliminary results, the linearity range is 0.8 - 10 mgN L^{-1} with a limit of detection (LOD) of 0.25 mgN L^{-1} and limit of quantitation (LOQ) of 0.80 mgN L^{-1}. The NH_4^+ value slightly increases with increasing salinity. With increasing the amount of ISA, the NH_4^+ concentrations are then more reliable due to the reduction of ionic strength effect. Verification and its application of the developed NH_4^+-RM to aquacultural water for shrimp pond will be investigated and discussed. To address measurement issues, the potential of the salinity solution detecting on NH_4^+- ISE was identified; therefore, the correction factor value was employed in this method.

1. Introduction

Ammonia (NH_3) occurs naturally in water, arising from the decomposition of organic matter and human activities such as the manufacturing of fertilizers, plastics, pharmaceuticals, and petrochemicals. When ammonia dissolves in water, a portion of the ammonia molecules acquires a hydrogen ion, forming the positively charged species known as ammonium (NH_4^+). The chemical equation that drives the relationship between ammonia and ammonium is:

$$NH_3 + H_2O \rightleftharpoons NH_4^+ + OH^-$$

The ratio of NH_3 to NH_4^+ is dependent on the pH and temperature of the water. The lower the pH and the warmer the water, the higher the concentration of ammonium This is due to the increase of H^+ ions. In the water industry, it is important to know the concentrations of hydrogen bound nitrogen. Therefore, the terms of ammonia and ammonium are used interchangeably, depicted as NH_3-N or NH_4^+-N with typical notation in the units of mgN L^{-1} or ppmN. It is worth nothing that high concentrations of ammonia are harmful to aquatic organisms, especially in shrimps and fish.[1]

Besides, several factors i.e., temperature, salinity, total suspended solids (TSS), dissolved gases, and nutrients, have also either direct or indirect impact on water quality.[2] These factors ultimately determine the well-being and survival of organisms in the aquatic ecosystem. Therefore, water quality management is crucial for aquacultural water for shrimps. The optimal value of total ammonia nitrogen (TAN) that has been reported in the literature is 1.0 mgN L^{-1}. [2]

To ensure the accuracy and reliability of the analytical results of NH_4^+ measurement, the calibration and the verification of instruments through the use of ammonium ion reference material (NH_4^+−RM) is required. There are various commercial reference materials available for freshwater applications. The methodology employs appropriate reference materials for verification of instruments prior analysis of water sample in shrimp ponds.

Antunes G. *et.al* reviewed several methods used for the determination of ammonium ion in water samples, including spectroscopy (such as Nessler's reagent method and the indophenol blue method (phenate and salicylate), ion chromatography (IC), gas chromatography (GC)

and high-performance liquid chromatography (HPLC), potentiometry (ion selective electrode) and titration. However, spectroscopy, chromatography, and titration methods have more sample preparation steps. Furthermore, some of these methods have limitations for testing ammonium. For Nessler's reagent method, it is important to control a reaction condition, to avoid and to prevent the solution turbidity. The use of mercury solution in this method has been criticized due to waste disposal issues. For the indophenol blue method, some application of this method to directly determine ammonium ion in seawater is unsuccessful due to interference from magnesium and calcium. However, this interference can be addressed by distilling seawater and eliminating hydrogen sulfide with the addition of HCl. This method also involves highly toxic substances such as phenol and nitroprusside, necessitating pretreatment techniques.[3] Ion chromatography (IC) is an effective technique for separation and determination of ammonium ion at low concentration. However, the high concentration of sodium ion is the major interference in seawater sample. Sodium ion is difficult to eliminate due to a memory effect in column, background drift and flushing column after each run.[4] An ion selective electrode (ISE) technique has been considered as an effective analytical method for detecting NH_4^+ since it provides simple operation, excellent sensitivity, selectivity, and compatibility with straightforward instrumental setups.[5]

In this work, the development of the NH_4^+-RM within a salt matrix (aquacultural water) is introduced. This approach ensures the suitability of RMs for instrument validation before their application in measuring water in shrimp ponds. Potentiometric technique with ion selective electrode (ISE) is also selected for selective determination of NH_4^+ in the developed RMs, prepared with ammonium chloride in artificial sea salt water. Salinity is observed as the effect of ionic strength, as well as magnesium sulfate solution as ionic strength adjuster (ISA) is also investigated. Verification and its application of the developed NH_4^+-RM to aquacultural water for shrimp pond was also investigated. The NH_4^+ value slightly increases with increasing salinity. In order to address measurement issues, the potential of the salinity solution detecting on NH_4^+- ISE was identified; therefore, the correction factor value was employed in this method.

2. Materials and Methods

2.1 Chemicals

Magnesium sulfate ($MgSO_4$), Magnesium chloride ($MgCl_2 \cdot 6H_2O$), strontium chloride hexahydrous ($SrCl_2 \cdot 6H_2O$) potassium chloride (KCl), sodium bicarbonate ($NaHCO_3$), and ammonium chloride (NH_4Cl) were purchased from Sigma-Aldrich (Gillingham, UK). Sodium hydroxide (NaOH), Sodium sulfate (Na_2SO_4), Sodium chloride (NaCl), calcium chloride dihydrate anhydrous ($CaCl_2$), sodium fluoride (NaF), and boric acid (H_3BO_3) were purchased from Merck (Darmstadt, Germany). Potassium bromide (KBr) was purchased Kemaus (New South Wales, Australia). All compounds were dried at 100 ^oC in an electric furnace prior use. All chemical compounds were dissolved in deionized water for preparation of solutions by gravimetric method.

2.2 Commercial Standard Solutions

A 1000 mg $L^{-1}$of ammonium ion standard solution (Merck, Darmstadt, Germany) was used as a stock solution for preparation of working standard solutions.

Three secondary electrolytic conductivity solutions: (1) 1413 µScm^{-1} (0.01 mol L^{-1} KCl), (2) 12.88 mScm^{-1} (0.1 mol L^{-1} KCl), and (3) 111.3 mScm^{-1} (1 mol L^{-1} KCl) were purchased from National Institute of Metrology (Thailand) (NIMT) and was used to calibrate the conductivity probe in the conductivity measurement.

2.3 Preparation of Substitute Ocean Water (Artificial Seawater)

Salinity is determined by analyzing measurements of the conductivity ratio, taking into account the known temperature and pressure during the measurement process. The Practical Salinity Scale algorithm is then applied in this computation by Perkin and Lewis (1980).[6] The numeric unit is psu (practical salinity unit). This algorithm known as the Practical Salinity Scale 1978 (PSS-78) which provides practical salinity values by considering the ratio of the electrical conductivity of seawater at 15°C in relation to that of a standard potassium chloride solution (KCl) and the mass fraction of KCl is 32.4356 g.kg^{-1} at the same temperature and pressure, the K_{15} value exactly value to 1 corresponds, by definition, to the practical salinity exactly equal to 35. The Practical Salinity is defined in term of the ratio K_{15} by following the equation (1).[7]

$$S = \sum_{i=0}^{5} a_i (R_t)^{\frac{i}{2}} + \frac{(t-15)}{(1+k(t-15))} \sum_{i=0}^{5} b_i (R_t)^{\frac{i}{2}} \quad (1)$$

where S_p the salinity, R_t the conductivity ratio at temperature, a_i is the coefficient, b_j the coefficient, t is temperature.

Noted that; $R_t = \frac{K_s}{K_{ssw}} . K_{15}$

K_s is the electrolytic conductivity of sample.
K_{ssw} is the electrolytic conductivity of standard seawater (SSW), which defined to be equal to the conductivity of a reference solution of potassium chloride (KCl) at the same temperature and pressure (KCl mass fraction of 32.4356 g kg^{-1}).

Then, Salinity (S) can be calculated from R_T and t by following rewrite equation (1).

$$S = \left(a_0 + a_1(R_t)^{\frac{1}{2}} + a_2(R_t) + a_3(R_t)^{\frac{3}{2}} + a_4(R_t)^2 + a_5(R_t)^{\frac{5}{2}}\right) + \frac{(t-15)}{(1+k(t-15))}\left(b_0 + b_1(R_t)^{\frac{1}{2}} + b_2(R_t) + b_3(R_t)^{\frac{3}{2}} + b_4(R_t)^2 + b_5(R_t)^{\frac{5}{2}}\right) \quad (2)$$

where the value of a_i as given below;
a_0= 0.0080, a_1= -0.1692, a_2= 25.3851, a_3= 14.0941
a_4= -7.0261, a_5= 2.7081.
and the value of b_i as given below;
b_0= 0.0005, b_1= -0.0056, b_2= -0.0066, b_3= -0.0375,
b_4= 0.0636, b_5= -0.0144.
k = 0.0162 (constant).

The salinity of artificial seawater (K_s) was determined by the conductivity meter and calculated using secondary electrolytic conductivity value from NIMT. To measure IAPSO standard seawater bottles whose salinity and conductivity ratio at 15 ˚C or K15 (K_{ssw}), to calculate R_t.

The preparation procedure was adopted from the ASTM D1141-98 (2021).[8] A stock solution of 35 psu artificial seawater was made by dissolving 12.267 g of NaCl and 2.047 g of Na_2SO_4 in the mixture of 10 g of ***'Stock Solution No. I'*** and 5 g of ***'Stock Solution No.II'***. Deionized water was finally added to 500 g of artificial seawater solution. Then, the artificial seawater solution was adjusted the pH to 8.2 with 0.1 N sodium hydroxide. A series of working artificial seawater solutions (0, 1, 3, 5, 7 and 10 psu) was then prepared by dilution of the stock artificial seawater with a gravimetric method, in three different batches.

Noted:
Stock Solution no. I, weigh approximately 27.780 g of $MgCl_2 \cdot 6H_2O$, 2.895 g of $CaCl_2$ and 0.105 g of $SrCl_2 \cdot 6H_2O$**;** dissolve in deionized water to a total volume of 50 g. **Stock solution no. II,** weigh approximately 3.475 g of KCl, 1.005 g of $NaHCO_3$, 0.500 g of KBr, 0.135 g of H_3BO_3, 0.015 g of NaF; dissolve in deionized water to a total volume of 50 g.

2.4 Preparation of A Series of Working Standard Ammonium Ion

A working stock ammonium solution of 50 mgN L^{-1} was prepared by weighing 2.5 g of the 1000 mgN L^{-1} of commercial ammonium ion standard solution and diluting with deionized water to a total volume of 50 g. A series of working standard ammonium solutions (0.8, 1.0, 2.0, 5.0, 10 mgN L^{-1}) was prepared by appropriate diluting from the working stock 50 mgN L^{-1} by gravimetric method.

2.5 Apparatus

All apparatus were from Mettler Toledo AG, (Schwerzenbach, Switzerland).

A conductivity meter (model S230 SevenCompact (S/N B412416514)) with a conductivity probe (model Cond Sensor InLab® 710 (S/N C14103)) were employed to measure the salinity of the testing solutions.

An ammonium ion-selective electrode (NH_4^+-ISE) (S/N DX218 NH_4^+) with a SevenExcellence™ potentiometer, accompanying a Ag/AgCl reference electrode (model: Inlab reference plus (S/N 1133291) was used as potentiometric setup for ammonium measurements.

3. Results & Discussion

3.1 Analytical performance of ammonium measurement using ISE instrument

We first tested the ISE to measure the ammonium ion in artificial seawater and found the salinity affect to the decreasing of NH_4^+ concentration when increasing of the volume of ISA solution. Therefore, ISA was unnecessary to add to the sample for measuring the ammonium ion in artificials seawater according to the high matrix sample.

The validation data of the instrument shows the linearity range is 0.8 – 10 mgN L^{-1} with a limit of detection (LOD) of 0.25 mgN L^{-1} and limit of quantitation (LOQ) of 0.80 mgN L^{-1}. The assessment the Limit of detection and the Limit of quantification were estimated by regression parameter of standard solutions prepared in water.

3.2 Salinity Measurement

In this work, the artificial seawater solution was prepared to investigate the effects of salinity on the ammonium measurements. Prior use of the prepared 35 psu of artificial seawater, conductivity measurement was employed to confirm the reliable salinity of a series of working artificial seawater solutions (0, 1, 3, 5, 7 and 10 psu). After calibrating the conductivity probe with the secondary electrolytic conductivity solutions (mentioned in Section 2.2), a series of working artificial seawater was tested. With triplicate measurement of each solution and conversion of conductivity to salinity in psu unit (according to the official definition of the Practical salinity scale 1978), the salinity of nominal values of 1, 3, 5, 7, 10 and 35 psu were found to be 0.97±0.10, 3.07±0.05, 4.99±0.00, 7.06±0.06, 10.01±0.11 and 35.31±0.25 psu, respectively. The temperature was controlled at 25±1 ^{o}C. Under the statistic test using *t*-test, it shows no significant differences as compared to the nominal value (t_{stat} = 1.34, t_{crit} = 2.57, P = 0.05). Therefore, the prepared artificial seawater solution and its working standard solutions were reliable for further use in the experiment.

3.3 Effect of salinity

The effect of the salinity on the ammonium measurement was investigated. Experiment was carried out by measurement of ammonium concentrations in the presence of salinity as compared to in the salinity (deionized water). The ammonium solution at 1 mgN L^{-1} was added to the artificial seawater solution containing various salinity (1, 3, 5, 7 and 10 psu). Table 1 shows the ammonium concentrations found in each solution containing various salinity. It was found that higher salinity in artificial seawater, higher measurable ammonium concentrations. This may be due to the ionic strength of salinity affecting the cation-exchange property at the ion-selective membrane, leading to the false positive results in ammonium detection. Therefore, chemical ion suppression may be an alternative way to minimize the salinity effect in the ammonium measurement.

3.4 Effect of Ionic Strength Adjustment (ISA)

According to the results in Section 3.3, salinity affects the measurement of ammonium ion. In practical, there is a recommendation to use ionic strength adjustment (ISA) for suppression of the foreign ions in sample, leading to obtaining the accurate concentration of ammonium. In general, $MgSO_4$ was used as ISA when handling ammonium ISE. Hence, the addition of ISA was investigated. Results are tabulated in Table 2.

Table 1. Ammonium concentrations found in various artificial seawater.

Salinity in artificial seawater (psu)	Measurable ammonium concentration (mgN L^{-1}), n=3
0.00	0.90 ± 0.02
0.97	1.40 ± 0.04
3.07	2.80 ± 0.05
4.99	4.17 ± 0.06
7.06	5.70 ± 0.09
10.01	8.10 ± 0.10

Table 2. Ammonium concentrations found in various artificial seawater with and without addition of 0.40 mL of 0.5 mol L^{-1} ISA.

Salinity in artificial seawater (psu)	Measurable ammonium concentration (mgN L^{-1}), n=3	
	None ISA added	ISA added
0.00	0.90 ± 0.02	0.73 ± 0.06
0.97	1.40 ± 0.04	1.43 ± 0.07
3.07	2.80 ± 0.05	2.68 ± 0.04
4.99	4.17 ± 0.06	4.09 ± 0.06
7.06	5.70 ± 0.09	5.74 ± 0.10
10.01	8.10 ± 0.10	8.19 ± 0.12

It was found that addition of ISA cannot suppress salinity in artificial seawater solutions, as seen in the measurable ammonium concentrations. This is due to the concentration of dissolved salt in seawater is significantly higher than the concentration of ISA. Therefore, in this case of ammonium measurement in seawater solutions, ISA is not proper to solve the problem of salinity effect.

3.5 The Correction Factor for NH_4^+ Measurement in Artificial Seawater

Regarding Section 3.4, ISA cannot suppress the salinity in seawater solution. We then apply a correction factor to normalize the ammonium concentration to be more reliable concentration.

We considered the different value of ammonium concentration in various salinity and found that the difference is comparable (see Table 3). As seen in Table 3, correction factor per 1 unit of salinity was found to be 0.65 ± 0.10. Therefore, in the real application, the correction factor of 0.65 has to be corrected with the salinity contained in seawater sample for the reliable concentration of ammonium.

Table 3. Correction factor studies on the NH_4^+-ISE (1 mg L^{-1} NH_4^+ added under different various artificial seawater value with difference environment. Note: triplicate measurement with mean(±SD)).

Batch 1			Batch 2			Batch 3		
[Salinity] (psu)	Measured mg L^{-1} NH_4^+	Correction factor/1 unit of salinity	[Salinity] (psu)	Measured mg L^{-1} NH_4^+	Correction factor/1 unit of salinity	[Salinity] (psu)	Measured mg L^{-1} NH_4^+	Correction factor/ 1 unit of salinity
0.0	0.90 ± 0.06	-	0.0	0.91 ±0.01	-	0.0	1.10 ±0.00	-
1.0	1.43 ±0.05	0.52	1.0	1.39±0.01	0.49	1.1	1.59 ±0.09	0.47
3.1	2.98 ± 0.23	0.67	3.1	2.86 ±0.12	0.64	3.1	3.28±0.04	0.71
4.7	3.74 ± 0.07	0.61	5.0	4.09 ±0.12	0.64	5.1	5.12 ±0.23	0.79
7.1	5.18 ± 0.12	0.61	7.1	5.73 ±0.06	0.68	7.1	6.48 ±0.23	0.76
10.2	7.39± 0.04	0.64	10.0	7.97 ±0.12	0.70	10.2	8.80 ±0.10	0.76
Average of a correction factor / 1 unit of salinity					**0.65 ± 0.10**			

Estimated by F-test when F critical < F calculated (0.2 <3.9)

The Analysis of Variance (ANOVA) was performed to compare the average of the NH_4^+ analysis. The results are shown in table 1. the comparison was performed to verify if there was homogeneity between the variances. The F-calculated value by considering that it is smaller than, F-critical. There are no statistically significant differences between the variances for a confidence level of 95 %.

4. Conclusions

This work presents a development of NH_4^+-RM, the characterization process is an important step. For the good practice of ammonium concentration determination in artificial seawater, the salinity was measured first because of the salinity effected to the results. The measurement of ammonium ion in artificial seawater was done with correction value by 0.65 per 1 unit of salinity. Therefore, artificial seawater is a high matrix sample, high ionic strength solution so no need to add the ISA into the sample. In the future work, to determine the homogeneity, stability including the characterization value with uncertainty and optimizing for development the NH_4^+-RM.

Acknowledgements

This work was a financially supported by Thai government scholarship and the Laboratory at Electrochemical Analysis Laboratory, Chemical Metrology and Biometry Department, National Institute of Metrology (Thailand) (NIMT).

References

1. Zhao, M.; Yao, D.; Li, S.; Zhang, Y.; Aweya, J. J. Effects of ammonia on shrimp physiology and immunity: a review. *Reviews in Aquaculture* **2020**, *12* (4), 2194–2211.
2. Venkateswarlu, V.; Seshaiah, P.; Arun, P.; Behra, P. A study on water quality parameters in shrimp L. vannamei semi-intensive grow out culture farms in coastal districts of Andhra Pradesh, India. *International Journal of Fisheries and Aquatic Studies* **2019**, *7* (4), 394–397.
3. Galvão, J. A.; Matthiensen, A.; Oetterer, M.; Moliner-Martínez, Y.; González-Fuenzalida, R. A.; Muñoz-Ortuño, M.; Herráez-Hernández, R.; Verdú-Andrés, J.; Molins-Legua, C.; Falcó, P. C. - Determination of ammonia in water samples. In *CRC Press eBooks*; 2013; pp 266–299.
4. Tzollas, N. M.; Zachariadis, G. A.; Anthemidis, A. N.; Stratis, J. A. A new approach to indophenol blue method for determination of ammonium in geothermal waters with high mineral content. *International Journal of Environmental Analytical Chemistry* **2010**, *90* (2), 115–126.
5. Choosang, J.; Numnuam, A.; Thavarungkul, P.; Kanatharana, P.; Radu, T.; Ullah, S.; Radu, A. Simultaneous Detection of Ammonium and Nitrate in Environmental Samples Using on Ion-Selective Electrode and Comparison with Portable Colorimetric Assays. *Sensors* **2018**, *18* (10), 3555.
6. Lewis, E. L.; Perkin, R. G. The practical salinity scale 1978: conversion of existing

data. *Deep-sea Research* **1981**, *28* (4), 307–328.
7. Menn, M. L. About uncertainties in practical salinity calculations. *Ocean Science* **2011**, *7* (5), 651–659.
8. ASTM D1141-98, Standard Practice for Preparation of Substitute Ocean Water (reapproved 2021). ASTM International: West Conshohocken, PA, 2021.

Portable sensor for Dengue virus detection by modified screen-printed electrode

Wattanachai Boonprapha[1], Supaphorn Seetaha[2], Kiattawee Choowongkomon[2], and Chaiya Prasittichai[1,3*]

[1]*Department of Chemistry, Kasetsart University, Bangkok, Thailand*
[2]*Department of Biochemistry, Kasetsart University, Bangkok, Thailand*
[3]*Center of Excellence for Innovation in Chemistry, Faculty of Science, Kasetsart University, Bangkok, Thailand*

**E-mail: chaiya.pr@ku.th*

Abstract:

Dengue hemorrhagic fever (DHF), a severe disease transmitted by infected mosquitoes, can lead to circulatory system failure, shock, and even death. Traditional detection methods, such as immunoassays, polymerase chain reaction (PCR) test, enzyme-linked immunosorbent assay (ELISA) and mass spectroscopy, are commonly used for identifying the dengue virus. However, these methods may not be suitable for on-site testing. In this study, we developed portable electrochemical electrodes using gold nanoparticles (AuNPs) on screen-printed carbon electrodes (SPEs) for dengue virus detection. The AuNPs were carefully deposited on the electrodes through electrochemical reduction of chloroauric acid in a concentrated sulfuric solution. Following this modification, the SPEs were immersed in a specific protein receptor solution to accurately identify and quantify the dengue virus in a suitable solution. A correlation between the reduction in electrochemical signal and the concentration of the dengue virus was seen, enabling the detection of the virus at concentrations as low as 0.001 FFU/mL. Additional tests are currently performed in the real samples to verify the effects of interferences. These findings provide valuable insights for the development of electrodes for measuring pathogenic microorganisms, offering potential applications in the field of rapid and on-site virus detection.

1. Introduction

Dengue fever (DF) initially characterized by mild symptoms without causing fatalities, has been known for over 200 years. In 1954, the first outbreak of dengue hemorrhagic fever (DHF) occurred in the Philippines, marking it as an emerging disease. Subsequently, an outbreak was reported in Thailand in 1958, followed by various tropical countries in Asia. At that time, there were only nine countries with outbreaks of DHF. Currently, DHF is considered an epidemic in more than 100 countries across Asia, America, Africa, the Mediterranean, and the Western Pacific region. The World Health Organization estimates that each year there will be 50–100 million cases of dengue virus and approximately 22,000 deaths.[1,2] Dengue infection still pose a significant public health problem in tropical and sub-tropical regions, including Central and South America, Southeast Asia, and the Western Pacific.[3]

Dengue virus, a single-stranded RNA virus in the Flaviviridae family, has four serotypes (DENV 1, DENV 2, DENV 3, DENV 4). These serotypes share some common antigens, resulting in short-term cross protection when a patient is infected with one serotype.[4] Permanent immunity against one serotype is set, but immunity to other 3 serotypes last only 6–12 months. Subsequent infections with different serotypes can lead to secondary dengue infections, a crucial factor in dengue hemorrhagic fever (DHF) development.[5] In high-prevalence areas, individuals may potentially experience up to four infections. All four serotypes can cause either dengue fever (DF) or DHF, with factors such as age and immunity playing significant roles. Dengue fever is diagnosed based on clinical symptoms, and pathophysiological changes include variations in platelet levels and plasma leakage. In most cases, patients contracting DF for the first time display pretty mild symptoms.[6]

In suspected cases of DHF, laboratory tests can provide diagnostic support through various methods, such as, (1) Viral isolation via intracerebral inoculation, (2) Detection of dengue virus genetic material using molecular techniques like RT-PCR, real-time PCR, and NASBA, (3) Identification of specific viral antigens, including structural and non-structural proteins[7] or (4) Rapid Tests, a commercially available, user-friendly, portable, and don't require instruments. The Rapid test employ immune-chromatography principles to detect both antigens and antibodies. However, rapid testing has limitations in detectability and primarily provides qualitative results.[8] In contrast, biosensors offer quantitative responses by converting biochemical reactions into measurable electrical signals. Specifically, electrochemical biosensors utilizing screen printed electrodes have been developed as appropriate tools for point-of-care testing. The products provide numerous advantages, such as ease of mass production and versatility. Screen-printed electrodes (SPEs) can

combine good electrochemical properties and portability with easy and inexpensive production techniques, thus being a good strategy to accomplish safety, disposable, and quantitative immunosensors.[9,10]

A single chain fragment variable (ScFv) antibody is made up of variable regions of heavy (VH) and light (VL) chains that are joined together by a flexible peptide linker that can be easily expressed in functional terms. This makes it possible for protein engineering to improve the properties of ScFv, such as making it more specific and increasing its affinity.[11] Recent developments, both in our group and elsewhere, have shown the effectiveness of this ScFv in detecting fragmented DNA and viruses, including H1N1, CoV, and Dengue. Our work focuses on modifying and constructing screen-printed electrodes for the detection of Dengue virus (DENV) using this recent ScFV development. Additionally, we explore various electrochemical techniques to enhance sensitivity in DENV detection. We believe that this modified SPEs could be readily used as a point-of-care testing for DENV in the foreseeable future.

2. Materials and Methods

2.1 Apparatus and measurements

A Potentiostat / Galvanostat / Impedance Analyzer (PalmSens 4, PalmSens, Houten, Netherlands) was used to carry out the cyclic voltammetry, differential pulse voltammetry, chronoamperometry and impedance spectroscopy measurements. Screen-printed carbon electrodes (SPEs) from Quasense Co., Ltd. (Bangkok, Thailand) with two carbon electrodes were employed as the working electrode, the counter electrode, and silver/silver chloride (Ag/AgCl) as the reference electrode. The pH measurement for the buffer solution was done using a METTLER TOLEDO pH meter.

2.2 Materials and reagents

Sulfuric acid (H_2SO_4), Gold (III) chloride trihydrate ($HAuCl_4 \cdot 3H_2O$), Disodium phosphate (Na_2HPO_4), Potassium Dihydrogen phosphate (KH_2PO_4), Sodium chloride (NaCl), Potassium chloride (KCl), Cysteamine (Cys), Ethanolamine, 1-ethyl-3-(3′-dimethylaminopropyl) carbodiimide · HCl (EDC), N-hydroxysuccinimide (NHS), Potassium ferro-cyanide ($K_4Fe(CN)_6 \cdot 3H_2O$), protein receptor for dengue detection (ScFv-C9 , MW = 29 kDa) and dengue virus (DENV 1-4) from department of biochemistry, Kasetsart University.

2.3 Modified gold nanoparticles (AuNPs) on surface area of SPEs

SPEs were treated with 0.5 M sulfuric acid by cyclic voltammetry. The measured potential range was between -0.1 and 1.3 V, with a scan rate of 0.1 V/s. Then, 5 mM $HAuCl_4$ was added to 0.5 M H_2SO_4 to synthesize AuNPs by chronoamperometry. The constant potential in the range of -0.4 to -1.2 V was applied for 60 s.[12] SEM is used to characterize the as-synthesized AuNPs surfaces.

2.4 Modified protein receptor on surface area of SPEs

Ten µL of 2.5 mM linking reagent (cysteamine) was added to the working electrode and allowed to dry overnight at room temperature and in darkness. Next, a solution of protein receptor comprising 2.5 µL 400 µM (EDC), 2.5 µL 100 µM (NHS), and 5 µL with 50 ng/mL of protein receptor (ScFv-C9) was thoroughly mixed, dropped onto the surface area of the working electrode, and incubated for 30 minutes at room temperature. Next, the blocking agent (ethanolamine) of 10 µL 0.01 M was added to the working electrode and incubated for 10 minutes at room temperature. Then, activate the electrode with 0.05 M $K_4Fe(CN)_6$ in 0.1 M phosphate buffer saline (PBS) (Na_2HPO_4, KH_2PO_4, NaCl and KCl) at pH 7.4.[13] After that, dropped 10 µL of PBS (blank) and a series of 0.001 to 1,000 FFU/mL of dengue virus solution (DENT 1) onto the working electrode and incubated for 15 minutes at room temperature before electrochemical measurement.[14]

2.5 Electrochemistry measurement process

A solution of 0.05 M $K_4Fe(CN)_6$ in PBS pH 7.4 was used. Electrochemical techniques, such as cyclic voltammetry (CV) and differential pulse voltammetry (DPV) were applied to measure the electrical response as a function of the amount of deposited protein receptor on the electrode. For CV technique, the measured potential range was between -0.4 and 0.8 V, the potential step was 0.01 V, with a scan rate of 0.1 V/s, and the number of scans was 5 scans. In the DPV technique, the measured potential range, potential step, and scan rate were the same as in the CV technique, where the potential pulse and time pulse were 0.2 V and 0.02 second, respectively.

The general protocol of electrochemical biosensor development has been illustrated in Figure 1.

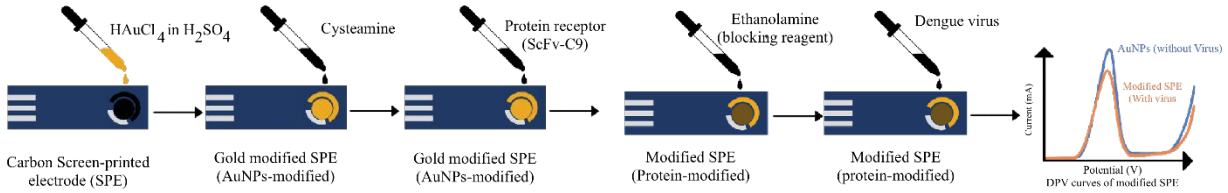

Figure 1. Graphical illustration of the modified biosensor for dengue detection.

3. Results & Discussion

3.1 Illustration of protein receptor specific (ScFV-C9) with dengue virus.[15]

Vasudevan has reported the route to separate DENV virions using SDS-PAGE and then run them through a Western blot to identify the viral structural protein that the Fabs recognized. All the Fab and the 4G2 control that binds to the fusion loop in EDII found a protein that was about 65 kDa (Figure 2a). This protein is the viral envelope protein. None of the Fabs detected the 25 kDa protein that corresponds to the precursor membrane (prM) protein seen with the 2H2 control. In terms of the reactivity of the unique antibody (C9) IgG with the DENV virion was further examined using immunofluorescence staining of DENV2 infected BHK 21 cells (Figure 2b). Both C9 IgG and the control antibody 4G2 produced clear fluorescence intensity in the cytoplasm of DENV2 infected cells 24 h post infection (panel II and IV), with no evidence of cross reactivity with other cellular components in the uninfected cells (panel I and III). This ScFV is used in our study for the detection of DENV in the SPE electrodes.

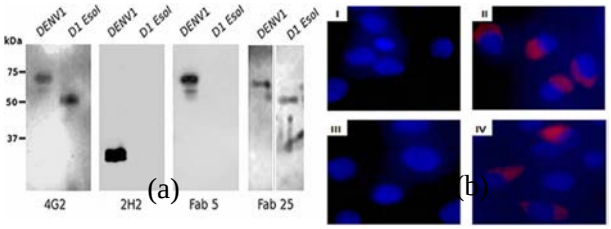

Figure 2. (a) A Western blot of selected Fab with whole virus and Esol from DENV1. 4G2 and 2H2 are control mouse mAbs, which bind E and prM proteins, (b) Immunofluorescence of uninfected BHK-21 cells (panel I and III) and cells infected with DENV2 (panel II and IV). Cells were incubated with C9 IgG (panel I and II) or 4G2 (3 nmol/L, panel III and IV) followed by goat anti-human or anti-mouse AF594 (Invitrogen) and mounted with ProLong Gold containing DAPI.[15]

3.2 Morphology of AuNPs onto surface area of SPEs

Figure 3 displays SEM images of AuNPs on the surface of working electrode SPEs. Electrodeposition at -0.4, -0.8, and -1.2 V for 60 seconds resulted in average AuNPs diameters of 164.79 nm, 82.54 nm, and 85.10 nm, respectively. At potentials of -0.8 V and -1.2 V, the AuNPs exhibited nearly spherical morphology. The working electrode composition consists of around 10.39% weight in Au elements, representing the AuNPs (Figure 4 and Table 1). In this study, we chose AuNPs that was electrodeposited at -0.8 V for a duration of 60 seconds. This choice was made because it yielded the smallest AuNP size, resulting in the largest surface area for the working electrode. Additionally, it exhibited the highest Au content percentage based on EDS analysis.

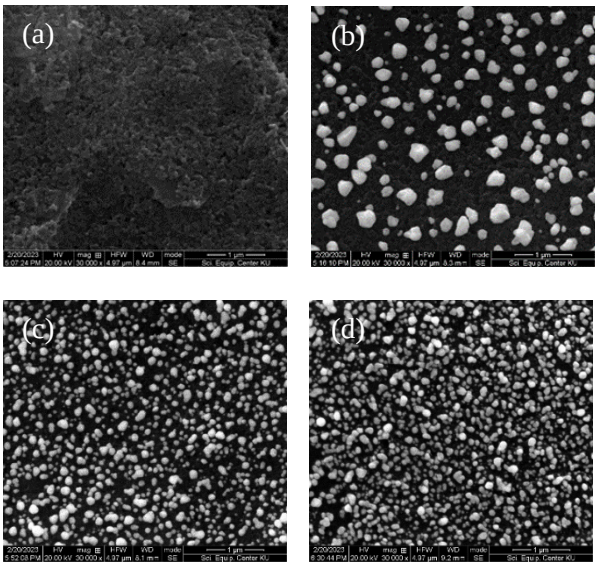

Figure 3. SEM images of (a) bare SPE, (b) AuNPs-SPE with potential -0.4 V , (c) AuNPs-SPE with potential -0.8 V and (d) AuNPs-SPE with potential -1.2 V, respectively.

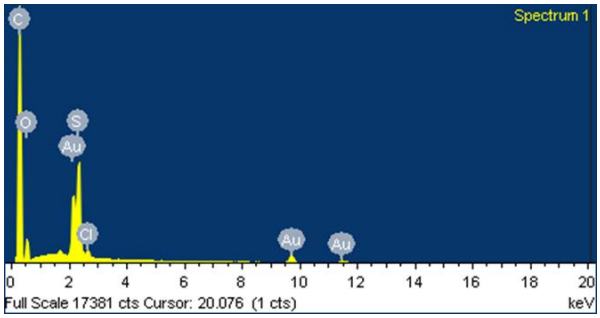

Figure 4. EDS spectra of the AuNPs size electrodeposited at potential -0.8 V for 60 s

Table 1. Composition element of modified AuNPs/ SPEs with potential -0.8 V on working electrode.

Element	Weight %	Atomic %
C	74.12	88.20
O	9.30	8.31
S	5.59	2.49
Cl	0.60	0.24
Au	10.39	0.75
Total	100.00	100.00

3.3 Electrochemical response to dengue virus

Figure 5 shows the DPV curves of modified SPEs for dengue detection. In comparison to the Bare-SPEs, the current observed with modified AuNPs-SPEs was higher when AuNPs were deposited onto the working electrode of SPEs, indicating that the addition of gold-based conductive materials enhanced the signal strength. However, upon W protein receptor binding with Au-decorated SPEs, a significant drop in current was seen. This also suggest a rather effective protein attachment on the gold surface. A further drop of current, though particularly small, was also observed when a certain concentration of dengue virus was applied to the electrode. The result proves a further interaction between the binding protein and the specific virus in the electrode. The behavior of the electrode current in response to varying virus concentrations, reaching as low as 0.01 FFU/mL and extend to almost 1,000 FFU/mL (for the serotypes DENV1), as determined through different concentration measurements. Current investigations are being explored to enhance sensitivity of the DENV detection through other types of electrochemical techniques, namely electrochemical impedance or cyclic voltammetry. A comprehensive report on these findings will be presented in the future.

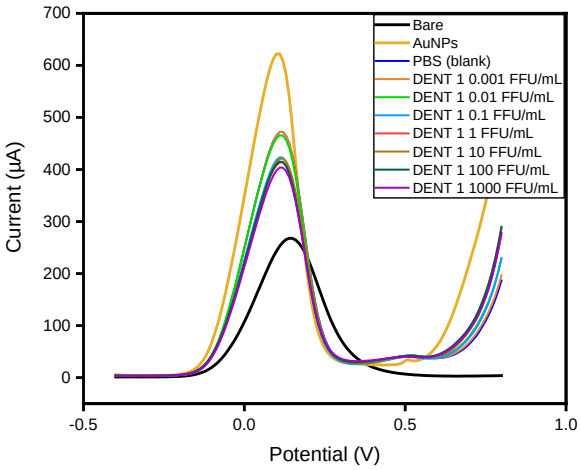

Figure 5. DPV spectra of bare, AuNPs-modified, and protein-modified with different concentrations of DENT 1 (0.01–1,000 FFU/mL).

3.4 Selectivity of each dengue virus species

In Figure 6, we present a comparative analysis of Dengue virus (DENV) detection for each serotype using our modified screen-printed electrodes (SPEs). Notably, our findings demonstrate that our modified SPEs exhibit their highest sensitivity when detecting DENV serotype 2 (the highest slope of linear calibration curve, show in Table 2), with a detection limit (LOD) reach below 0.001 FFU/mL. The good sensitivity can be attributed to the selective interaction between the single-chain variable fragment proteins (ScFV) toward DENV serotype 2, showcasing a clear preferential affinity. We are currently exploring the development of other ScFv variants tailored to detect other DENV serotypes. This ongoing research aims to expand our diagnostic capabilities and further optimize our detection methods. We also focuses on the practical application of these modified SPEs in real sample detection for Dengue virus. Such results will be presented elsewhere in the future.

4. Conclusion

We successfully developed single-chain variable fragment proteins (ScFV) designed for Dengue virus detection. These ScFVs were effectively integrated onto the surface of AuNPs in SPEs electrodes. Currently, our modified SPEs can detect Dengue virus at concentrations lower than 0.001 FFU/mL, particularly for DENV serotype 2. We acknowledge the potential for further sensitivity enhancements through additional electrode modifications. Nevertheless, our current results indicate the feasibility of a relatively straightforward Dengue virus detection method.

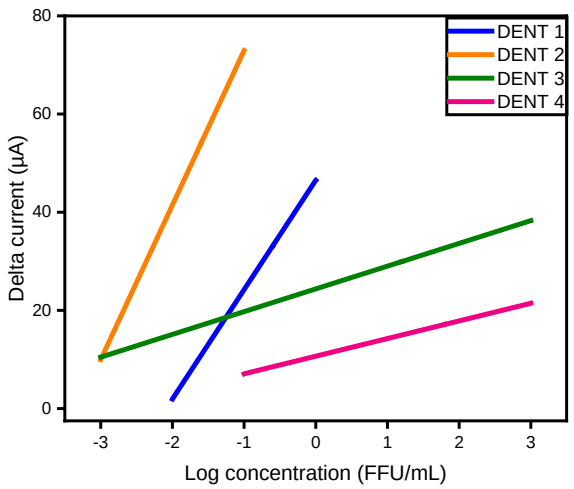

Figure 6. The trend line between the delta current of the PBS (blank) and dengue virus (DENT 1-4) with log concentrations of dengue virus 4 serotypes.

Table 2. Summary of the linear equation and R-square of the modified SPEs for dengue virus detection.

Serotypes	Linear equation	R^2
DENT 1	y = 22.17x + 46.39	(1)
DENT 2	y = 26.67x + 94.78	(2)
DENT 3	y = 3.046x + 24.38	(3)
DENT 4	y = 0.967x + 13.30	(4)

Notes: (1) = 0.9996, (2) = 0.8465, (3) = 0.6418 and (4) = 0.2220

Acknowledgements

The Kasetsart University Research and Development Institute (KURDI) has provided financial support for this work. The Center of Excellence for Innovation in Chemistry Scholarship (PERCH-CIC) and Kasetsart University Research and Development Institute (KURDI) have also provided some financing assistance for this work. The facilities are supported by the Department of Chemistry and Department of Biochemistry, Kasetsart University.

References

1. Kyle, J. L.; Harris, E., Global Spread and Persistence of Dengue. Annual Review of Microbiology **2008**, 62 (1), 71-92.
2. Asian, J.; Res; Nwalozie, R., Dengue Fever: Etiology, Diagnosis, Prevention and Treatment. Asian Journal of Research in Infectious Diseases **2023**, 14.
3. Kularatne SA; Dalugama C. Dengue infection: Global importance, immunopathology and management. Clin Med (Lond). **2022**, 9-13.
4. Rico-Hesse; R., Microevolution and virulence of dengue viruses. In *Advances in Virus Research*, Academic Press: 2003; Vol. 59, pp 315-341.
5. Vaughn, D. W.; Green, S.; Kalayanarooj, S.; Innis, B. L.; Nimmannitya, S.; Suntayakorn, S.; Endy, T. P.; Raengsakulrach, B.; Rothman, A. L.; Ennis, F. A.; Nisalak, A., Dengue Viremia Titer, Antibody Response Pattern, and Virus Serotype Correlate with Disease Severity. The Journal of Infectious Diseases **2000**, 181 (1), 2-9.
6. Zhang, H.; Zhou, Y. P.; Peng, H. J.; Zhang, X. H.; Zhou, F. Y.; Liu, Z. H.; Chen, X. G., Predictive Symptoms and Signs of Severe Dengue Disease for Patients with Dengue Fever: A Meta-Analysis. BioMed Research International **2014**, 359308.
7. Muller, D. A.; Depelsenaire, A. C. I.; Young, P. R., Clinical and Laboratory Diagnosis of Dengue Virus Infection. The Journal of Infectious Diseases **2017**, 215 (suppl_2), S89-S95.
8. Ricci, F.; Adornetto, G.; Palleschi, G., A review of experimental aspects of electroche-mical immunosensors. Electrochimica Acta **2012**, 84, 74-83.
9. V. Somerset; J. Leaner; R. Mason; E. Iwuoha; A. Morrin, Electrochim. Acta **2010**, 55, 4240–4246.
10. A.C.M.S. Dias; S.L.R. Gomes-Filho; M.M.S. Silva; R.F. Dutra, Biosens. Bioelectron. **2013**, 44, 216–221.
11. Ahmad ZA; Yeap SK; Ali AM; Ho WY; Alitheen NB; Hamid M., scFv antibody: principles and clinical application. Clin Dev Immunol. **2012**, 2012:980250.
12. Hassani, S.; Akmal, M. R.; Salek-Maghsoudi, A.; Rahmani, S.; Ganjali, M. R.; Norouzi, P.; Abdollahi, M., Novel label-free electro-chemical aptasensor for determination of Diazinon using gold nanoparticles-modified screen-printed gold electrode. Biosensors and Bioelectronics **2018**, 120, 122-128.
13. Gudić, S.; Vrsalović, L.; Kvrgić, D.; Nagode, A. Electrochemical Behaviour of Ti and Ti-6Al-4V Alloy in Phosphate Buffered Saline Solution Materials [Online], 2021.
14. Aiemderm, P.; Monkhang, K.; Wongjard, S.; Choowongkomon, K.; Swainson, N.; Prasittichai, C., Advantages of Electro-deposited Gold on Carbon Electrodes for NT-proBNP Immunosensor for Development of Heart Failure Test Kit. Applied Science and Engineering Progress 2023.
15. Moreland, N. J.; Susanto, P.; Lim, E.; Tay, M. Y. F.; Rajamanonmani, R.; Hanson, B. J.; Vasudevan, S. G. Phage Display Approaches for the Isolation of Monoclonal Antibodies Against Dengue Virus Envelope Domain III from Human and Mouse Derived Libraries International Journal of Molecular Sciences [Online], 2012, p. 2618-2635.

A highly sensitive colorimetric sensor for detection and speciation of arsenic in soil samples

Juthatip Ninlapan and Siriboon Mukdasai*

Materials Chemistry Research Center, Department of Chemistry and Center of Excellence for Innovation in Chemistry, Faculty of Science, Khon Kaen University, Khon Kaen, 40002, Thailand

**E-mail: sirimuk@kku.ac.th*

Abstract:

A colorimetric sensor based on amino silane modified on the surface of silica sol was developed for the determination and speciation of inorganic arsenic (As) species. The colorimetric probe was fabricated by loading ammonium molybdate (Mo) in amino silane/silica sol before As detection. The As(V) was performed the arsenomolybdenium blue complex on the colorimetric probe and was directly determined. The As(III) concentration was determined by subtracting As(V) from total As following oxidation of As(III) to As(V) by $K_2S_2O_8$ in acidic medium. The quantitative data is obtained by UV–Vis spectrophotometry and naked-eye detection based on the changing of color which is captured by smartphone in combination with Image J program. Under optimal conditions, the linear range was in the range of 0.04 - 0.10 mM with the correlation coefficient of 0.9949 and limit of detection (LOD) was 4.57 µM. Good precision was obtained with relative standard deviation (%RSD) less than 1.0% for intra-day and inter-day. The proposed colorimetric sensor was successfully applied for detection and speciation of arsenic in soil samples and the obtained results were comparable to those from inductively coupled plasma atomic emission spectroscopy (ICP-OES) method.

1. Introduction

Arsenic is a natural component of the earth's crust and is widely distributed throughout the environment in the air, water and land. It is highly toxic in its inorganic form which is rated in the top environmental health hazards leading to hyperpigmentation, keratosis, various types of cancer and vascular diseases.[1,2] The cause of arsenic contamination in nature is released from agriculture, mining and manufacturing which can affect to human.[3] Natural levels of arsenic in soil usually range from 1 to 40 mg/kg, with a mean of 5 mg/kg, although much higher levels may occur in the industrial sources.[4] It has many different chemical forms in nature, this element mainly exists in two oxidation states, including trivalent (arsenite, As(III)) and pentavalent (arsenate, As(V)). As(III) specie is more mobile and toxic than As(V), but As(III) is easily converted to As(V) depending on the redox condition of environment in the system. In the environments, the As(V) is present in the form of an anion including arsenate (AsO_4^{3-}), hydrogen arsenate ($HAsO_4^{2-}$), and dihydrogen arsenate ($H_2AsO_4^-$) ions, which constitute the most common forms of As(V) in contaminated soil and groundwater.[5,7] Therefore, detection of trace amounts of As species including As(III) and As(V) can provide meaningful information not only on the distribution and degree of contamination of As species in the environment but also on the potential risk to human health.

Several instrument methods such as the atomic absorption spectroscopy (AAS),[8] graphite furnace atomic absorption spectrophotometry (GFAAS),[9,10] atomic fluorescence spectroscopy (AFS),[11-14] hydride generation atomic absorption spectroscopy (HGAAS),[15-19] inductively coupled plasma mass spectrometry (ICP-MS)[11,13,14,16] and high performance liquid chromatography (HPLC)[20] have been performed for the arsenic detection. These techniques are high costs, expert user, time-consuming and complicated method. Among these detection techniques, the colorimetric detection was performed based on the principle of aggregation or anti-aggregation of nanoparticles such as gold,[21] silver,[22] copper[23] nanoparticles and carbon nanodots[24] because of its low cost, easy operation, high precision and accuracy, high selectivity and sensitivity.[25-27]

The silica nanoparticles are one of the materials that are widely employed due to its good characteristic including high porosity, high surface area and easy to modify surface. The interactions between silica and analytes are the result of hydrogen bonding, electrostatic attraction of the silanol groups and porosity. However, these strategies use silica particles obtained after their synthesis. The method widely used for the synthesis of silica particle is the Stöber method. This method is based on the hydrolysis and condensation of tetraethoxysilane (TEOS).[28-32] Similar to drying and calcination steps in the most of the methods for the preparation of nanoparticle sorbents are needed for the synthesis of silica particles. Therefore, the synthesized silica sol can reduce time and energy consumption. To improve the sensitivity and selectivity, silica sol is modified

with certain functional groups such as C_8, [33] C_{18}, [34] 2,6-diamino-4-phenil-1,3,5-triazine,[35] 3-amino-5-mercapto-1,2,4-triazol.[36] Therefore, the modification of silica sol surface is required with appropriate ligand including aminosilane[37-39] to enhanced the aggregation of silica sol.

This study is aimed to develop a simple colorimetric method for the detection and speciation of arsenic in the environmental samples. The colorimetric probe was fabricated by loading ammonium molybdate (Mo) in amino silane/silica sol before As detection. The As(V) was performed the arsenomolybdenium[40-44] blue complex on the colorimetric probe and was directly determined. The As(III) concentration was determined by subtracting As(V) from total As following oxidation of As(III) to As(V) by $K_2S_2O_8$ in acidic medium. The quantitative data is obtained by UV–Vis spectrophotometry and naked-eye detection based on the changing of color which is captured by the smartphone in combination with Image J program. The applicability of the proposed method is demonstrated for the trace determination and speciation of arsenic in environmental samples that is soil samples. The obtained results were comparable to those from inductively coupled plasma atomic emission spectroscopy (ICP-OES) method.

2. Materials and Methods

2.1 Chemicals and reagents

All the chemicals used the analytical grades except tetraethyl orthosilicate (TEOS) was GC grade and used without further purification. The aqueous solutions were prepared using Reverse Osmosis water (RO). (3-Aminopropyl) triethoxysilane (APTES), sodium (metal) arsenite ($AsNaO_2$), and sodium arsenate dibasic heptahydate ($AsHNa_2O_4{\cdot}7H_2O$) were obtained from Sigma-Aldrich (Spain). Aluminium chloride hexahydrate ($AlCl_3{\cdot}6H_2O$), L-ascorbic acid ($C_6H_8O_6$), sodium chloride (NaCl), and magnesium chloride ($MgCl_2$) were obtained from Ajax Finechem (Australia). Ammonium molybdate ($(NH_4)_6Mo_7O_{24}{\cdot}4H_2O$) was purchased from Carlo Erba reagent (France). Kaliumantimon-(III)-oxidtatrat Hydrat reinst ($K(SbO)C_4H_4O_6{\cdot}0.5H_2O$) was purchased from Merck (Germany). L(+)-Arinine (L-Arg) ($C_6H_{14}N_4O_2$) was obtained from ACROS (USA). Magnesium sulfate ($MgSO_4$) was obtained from QRëC (New Zealand). Potassium peroxodisulphate ($K_2S_2O_8$) was purchased from PanReac AppliChem (Germany).

2.2 The synthesis and modification of silica sol

Silica sol was prepared by using the hydrolysis and the condensation of TEOS and L-Arg[30] which the process was undergone the self-assembly and amino silane/silica sol were prepared by adding APTES into silica sol. Briefly, 0.09 g L-Arg was dissolved with 250 mL RO water and L-Arg solution was heated at 60°C in the oil bath for 30 min. Then, TEOS was slowly dropped into L-Arg solution to complete the reaction. The mixture of L-Arg and TEOS was stirred at 60°C for 26 h. Finally, silica sol was obtained and kept at the room temperature for the subsequent experiments.

The silica sol was modified using 3-aminopropyl triethoxysilane or APTES as the amino silane was used as a modifier. Firstly, APTES (3.5 g) was dissolved in 125 mL diluted H_2SO_4 (1.0 M) and APTES was added into silica sol (100 mL). Finally, the mixture was further stirred and heated at 60°C for 1 hour to modify the silica sol and then obtained APTES/silica sol.

2.3 Colorimetric probe for arsenic detection

The colorimetric probe (Mo/APTES/silica sol) was prepared as follow: 0.020 M ammonium molybdate (100 µL) and APTES/silica sol (50 µL) were added into a centrifuge tube. Then, 0.0160 M antimony (50 µL), 0.20 M ascorbic acid (300 µL) and 1 mM As(V) were added into the probe and then diluted up to 10 mL. The solution is mixed by manual shaking and centrifuged at 5000 rpm for 30 sec. After centrifugation, at the bottom of tube as precipitate phase was obtained using membrane filter and was taken a photo by smartphone analyzed with Image J program for evaluation and the upper supernatant phase was measured the absorbance at 895 nm. Finally, the adsorption of As(V) complex on the proposed probe was studied and expressed equation in the terms of %adsorption[32,45]:

$$\%\text{Adsorption} = [(A_0 - A_t)/A_0] \times 100$$

where A_0 is before the adsorption on colorimetric probe and A_t is after the adsorption on colorimetric probe.

For the speciation of inorganic arsenic, total As content was determined using the oxidation method based on the colorimetric probe (Mo/APTES/silica sol). As(V) and As(III) (0.04 mM each) were mixed in centrifuge tube, and 1.2 mL $K_2S_2O_8$ (0.024 M) were added to oxidize As(III) to As(V) in 2.5 M of H_2SO_4. Subsequently, the total As (in terms of As(V)) was obtained using the proposed method. Thus, the As(III) content was

obtained by subtracting the As(V) content from the total As.[46]

2.4 Sample analysis

The colorimetric sensor was fabricated to detect As(V) in soil samples that was collected from Khon Kaen and Saraburi province, Thailand. The preparation of sample was left to dry at room temperature and were filtered with the sieve (size 180 µm). The weight (20 g) of soil samples was adjusted into 150 mL with RO water and were shaken with the shaker at 250 rpm for 30 min and transferred into the centrifuge tubes to perform centrifugation at 5000 rpm for 3 min. Finally, the sample solution was obtained and then analyzed using the proposed colorimetric sensor.

3. Results & Discussion

3.1 Characterization of APTES/silica sol

To confirm the formation and morphology of the prepared APTES/silica sol, SEM and FT-IR techniques were employed. The functional group of silica particle (a), silica sol (b), and APTES/silica sol (c), FT-IR spectra of pure and modified silica sol as well as silica particle were recorded (Figure 1). There are similarities of peaks between 3200 -3750 cm^{-1} where the OH^- stretching of silanol, 1630 cm^{-1} where O-H deformation of H_2O, 1100 cm^{-1} where Si-O-Si stretching. Only the spectra of silica sol and APTES/silica sol showed a peak at 960 cm^{-1} for Si-OH stretching of silanol groups.[47] The characteristic peak of amino group of APTES (C-N stretching) at 1302 cm^{-1} from APTES/silica sol is absent from silica sol. Therefore, the characterization results can ensure successfully the modification of silica sol with APTES.

The shape and size of APTES/silica sol were characterized by SEM. The SEM images (Figure 2A and 2B) of (A) silica sol and (B) APTES/silica sol, are presented, respectively. The size of the silica sol and APTES/silica sol are 16.38 nm and 21.67 µm, respectively. Moreover, EDS and elemental mapping characterization were carried out to explore the composition of synthesized APTES/silica sol that consisted of Si (39.4%), O (30.5%), C (25.5%) and N (4.7%) atoms in inset at Figure 1B. It can be seen N emission peak was observed in the EDS of APTES/silica sol. The uniform distribution of N element was apparent in the EDS mapping data provided in Figure 2C. These results further well confirm the successfully modification of silica sol with APTES.

Zeta potential was evaluated to confirm the possible interaction on surface of silica sol. The

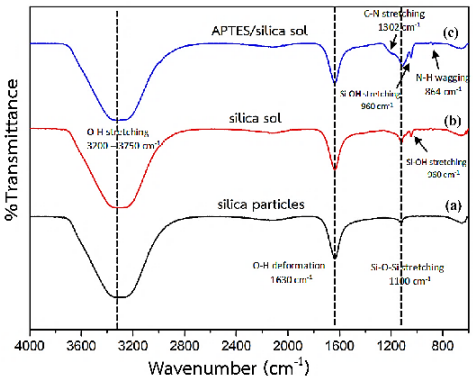

Figure 1. FT-IR spectra of silica particles (a), silica sol (b) and modified silica sol (c).

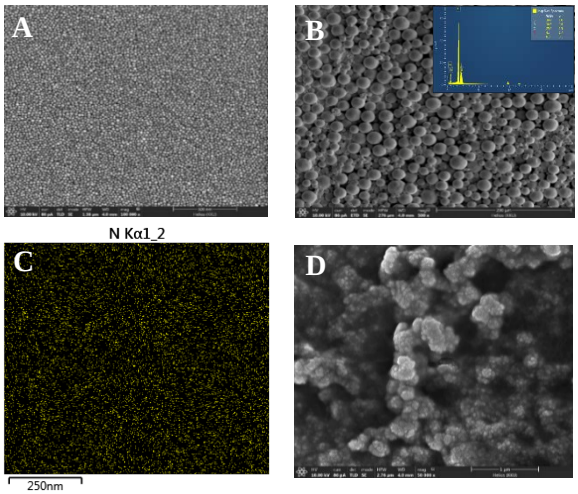

Figure 2. The SEM images of silica sol (A), modified silica sol (inset; EDS spectrum of APTES/silica sol) (B), EDS elemental map of N atom distribution on modified silica sol (C) and SEM image of the As(V) addition into the colorimetric probe (D).

silica sol showed a negative potential (-8.17 mV), after the addition of APTES which have a positive charge, the zeta potential was slightly increased to positive value (4.11 mV). In presence of As(V), it was changed to 0.64 mV. From these results, it can be confirmed the formation of As(V) complexes on APTES/silica sol surface and aggregated on APTES/silica sol.

3.2 Selectivity of colorimetric sensor for As(V)

The selectivity is another important parameter in sensor assay. Therefore, other ions should not respond under the same conditions. The other cations and anions which were possible contaminate in soil samples, including Na^+, K^+, Mg^{2+}, Al^{3+}, Cl^- and SO_4^{2-}. The tests were carried out in two systems: (i) Figure 3A shows the absorbance of As(V) complexes at 0.04 mM and all the individual ions expected to respond to the proposed colorimetric sensing were studied at 1.20 mmol L^{-1} or 30-fold. Only As(V) complexes was found to produce a blue

complex corresponding to the observed absorption intensity. (ii) The competitive experiments were performed by mixing 0.04 mM of As(V) with the other ions (30-fold). The results indicated in Figure 3B, Mo/APTES/silica sol formed complex with As(V) that showed the blue solution while the other ions did not significantly affect the intensity. Furthermore, the interfering ions had a negligible effect on the absorbance of the As(V) complex. Thus, the proposed colorimetric sensor exhibits excellent selectivity for the detection of As(V).

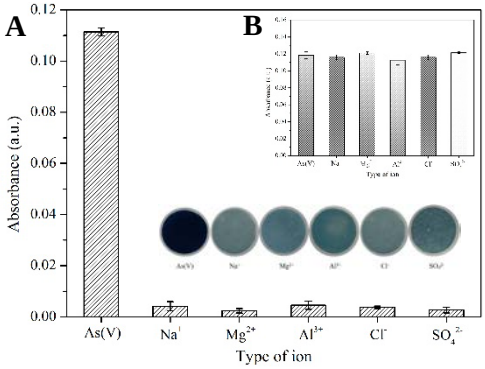

Figure 3. Selectivity of interference ions by spectrophotometric technique: (A) Absorption intensity and photographic images of colorimetric probe with various ions. (B) Absorption intensity of colorimetric probe with a mixture of different ions and As(V) and only As(V).

3.3 Analytical performance

Under the optimal conditions, the proposed colorimetric sensor demonstrated the analytical performance parameters that including the linear range, the limit of detection (LOD), the limit of quantification (LOQ) and precision (intra-day and inter-day) were evaluated by UV-Vis spectrophotometry and smartphone combined with Image J program. The spectra of upper supernatant phase in presence of the various concentration of As(V) and concentration of As(V) obtained in range from 0.04 to 0.1 mmol L^{-1} (Y = 631.59X – 118.63) with the determination coefficient (R^2) of 0.9949 (Figure 4). Furthermore, the gray intensity versus concentration of As(V) was evaluated with taking the photo and applying the Image J program based on the intensity values of color. The calibration curve was plotted between intensity ($I_0 - I/I_0$) and As(V) concentrations, where I and I_0 are value of the gray of the As(V) complex on the membrane and control, respectively, which gave the regression equation Y = 3.3827X + 0.0754 and R^2 of 0.9977. The results of the gray scale intensity of Image J program were corresponding with UV-Vis spectrophotometry. The LOD and LOQ were calculated follow by the equations: LOD = 3σ/S and LOQ = 10σ/S, where σ is the standard deviation of blank (n = 6) and S is the slope of the calibration plot. The obtained LOD and LOQ by using the colorimetric probe were found to be 4.57 and 40.0 µM, respectively. The obtained precision was 0.36% for intra-day (n=11) and 0.44% for inter-day (n=5x5). These results reveal that the proposed method has high sensitivity and precision.

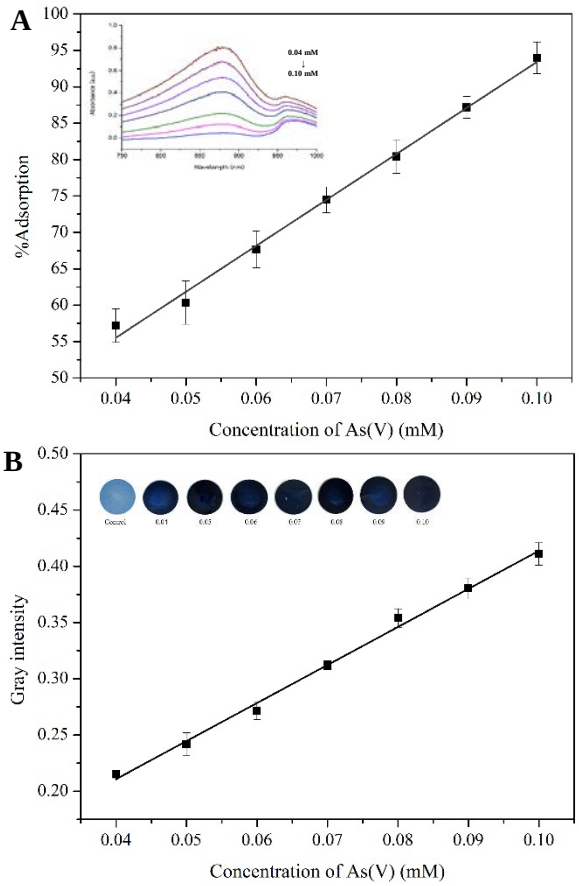

Figure 4. (A) The calibration plots obtained from the %adsorption versus concentration of As(V) and absorption spectra on colorimetric sensor (Mo/APTES/Silica sol) for the determination of As(V) at 895 nm. (B) The calibration plot obtained from the gray intensity ($I_0 - I/I_0$) versus As(V) concentration and the photographic images of As(V)–Mo/APTES/Silica sol.

3.4 Detection of As speciation and total As in soil samples

The proposed colorimetric method was evaluated by the determination of arsenic in soil samples. The total As (in term As(III) and As(V)) was calculated after the conversion of As(III) to As(V) was occurred by adding oxidizing agent with 0.02 M $K_2S_2O_8$ in 12.5 mM H_2SO_4 into samples for completely oxidation reaction of As(III). The As(III) content was calculated with following equation: As(III) = total As – As(V).

To determine the accuracy of the proposed colorimetric sensor in percentage recovery (Table 1), the soil samples were spiked with known amounts of As(V) and total As before the addition of colorimetric probe and analysis by UV-Vis spectrophotometer. The results show acceptable recoveries of soils in the ranges of 96.4-109.0% and 95.0–104.9 % were obtained for As(V) and total As, respectively. In addition, a t-test was indicated to compared the proposed colorimetric method with the standard method that was the inductively coupled plasma atomic emission spectroscopy (ICP-OES) based on the p-value of 0.10 (at the 90% confidence limit). The calculated t (t-cal, 1.27) was found to be lower than the tabulated t (t-table, 2.92). From the results were not significant difference between the proposed method and the standard ICP-OES method.

4. Conclusion

A simple colorimetric sensor has been developed for the detection and speciation of arsenic based on Mo/APTES/silica sol as a colorimetric probe. The proposed sensor is highly sensitive and selective for the determination of As(V) over interfering ions in soil samples. This method facilitates the study of the speciation of arsenic. The total As was determined after the oxidation of As(III) to As(V) by potassium persulfate as the reducing agent, and then the amount of As(III) specie was calculated as the difference between the total As and As(V) contents. The quantitative analysis was obtained using UV-Vis spectrophotometry. The naked-eye detection was performed by taking photos using the smartphone followed by the Image J program for the evaluation of color change. The LOD of the proposed colorimetric sensing was 4.57 µM, In addition, the colorimetric probe was applied for the detection and speciation of As in the soil samples with satisfactory results. The proposed colorimetric method offers outstanding advantages, such as ease to use, low cost, rapid analysis, high sensitivity and efficient preconcentration and detection techniques.

Table 1. The proposed colorimetric sensor for the As determination in the soil samples.

Sample	Proposed colorimetric sensor								
	As(V)				Total As				As(III)
	Spiked (mM)	Found (mM)	Recovery (%)	%RSD	Spiked (mM)	Found (mM)	Recovery (%)	%RSD	Found (mM)
Soil sample 1	-	-	-	-	-	-	-	-	
	0.04	0.040	99.7	0.37	0.04	0.039	95.1	2.1	0.001
	0.07	0.073	104.6	0.47	0.07	0.073	104.9	1.6	-
	0.10	0.096	96.4	0.06	0.10	0.098	98.0	4.6	-
Soil sample 2	-	-	-	-	-	-	-	-	
	0.04	0.040	100.1	0.52	0.04	0.041	104.6	2.5	0.001
	0.07	0.068	97.0	0.12	0.07	0.067	95.4	4.8	-
	0.10	0.103	103.8	0.75	0.10	0.102	101.9	7.2	-
Soil sample 3	-	-	-	-	-	-	-	-	
	0.04	0.040	99.3	0.53	0.04	0.041	103.5	2.4	0.001
	0.07	0.074	105.3	0.80	0.07	0.068	96.5	5.1	-
	0.10	0.096	96.4	0.42	0.10	0.101	101.4	1.3	0.005
Soil sample 4	-	-	-	-	-	-	-	-	
	0.04	0.039	97.7	1.80	0.04	0.042	105.0	4.6	0.003
	0.07	0.077	109.0	2.00	0.07	0.066	95.0	1.0	-
	0.10	0.100	99.8	0.10	0.10	0.102	102.0	2.2	0.001

Acknowledgements

Financial supports from Materials Chemistry Research Center (MCRC) and the Center of Excellence for Innovation in Chemistry (PERCH-CIC), Ministry of Higher Education, Science, Research and Innovative, Thailand are gratefully acknowledged.

References

1. Gibb, H.; Haver, C.; Gaylor D.; Ramasamy, S.; Lee, J.S.; Lobdell, D. *Environ Health Perspect*. **2011**, 119(3), 284–290.

2. Argos, M.; Kalra, T.; Rathouz, P.J.; Chen, Y.; Pierce, B.; Parvez, F. *Lancet*. **2020**, 76(9737), 252–258.

3. Rajkumar, M.; Thiagarajan, S.; Chen, S. *Int. J. Electrochem. Sci.* **2011**, 6, 3164 – 3177.
4. Sullivan, C.; Lu, D.; Brack, E.; Drew, C.; Kurup, P. *Anal. Chim. Acta*. **2020**, 1107, 63-73.
5. Gudlavalleti, R. H.; Bose, S. C.; Verma, S. K.; Khatri, P.; Scaria, J.; Dhewa, S.; Chaubey, V. K. *IEEE Sensors Journal*. **2017**, 17(17), 5391–5398.
6. Hong, S.; Park, S.; Lee, S.; Yang, Y.; Song, H.; Yi, J. *Anal. Chim. Acta*. **2011**, 694, 136–14.
7. Han, M.; Hao, J.; Xu, Z.; Meng, X. *Anal. Chim. Acta*. **2011**, 692, 96-102.
8. Liu, Z.; Li, G.; Xia, T.; Su, X. *Sensors Actuators, B Chem.* **2015**, 220, 1205-1211.
9. Holak, Walter. *Analytical Chemistry*. **1969**, 41(12), 1712–1713.
10. Sounderajan, S.; Udas, A.C.; Venkataramani, B. *Journal of Hazardous Materials*. **2007**, 149, 238–242.
11. Koesmawati, T. A.; Buchari, B.; Sulaeman, A.; Ibrahim, S. *Procedia Chemistry*. **2015**, 17, 200–206.
12. Sanchez-Rodas, D.; Corns, W. T.; Chenb, B.; Stockwell, P. B. *J. Anal. At. Spectrom*. **2010**, 25, 933–946
13. Go´mez-Ariza, J. L.; Lorenzo, F.; Garcı´a-Barrera, T. *Anal Bioanal Chem*. **2005**, 382, 485–492.
14. Gómez-Ariza, J.; Sánchez-Rodas, D.; Giráldez, I.; Morales, E. *Talanta*. **2000**, 51, 257–268.
15. Coelho, N. M. M.; da Silva, A. C.; da Silva, C. M. *Anal. Chim. Acta*. **2002**, 460, 227–233.
16. Nookabkaew, S.; Rangkadilok, N.; Satayavivad, J. *J. Agric. Food Chem.* **2006**, 54, 6939−6944.
17. Ng, J. C.; Johnson, D.; Imray, P.; Chiswell, B.; Moore, M. R. *Analyst*. **1998**, 123, 929–933.
18. Howard, A. G.; Salou, C. *Journal of Analytical Atomic Spectrometry*. **1998**, 13, 683–686.
19. Shraim, A.; Chiswell, B.; Olszowy, H. *Talanta*. **1999**, 50, 1109–1127.
20. Jeong, S.; Lee, H.; Kim, Y.; Yoon, H. *Microchemical Journal*. **2017**. 134, 295-300.
21. Keskin, B.; Üzer, A.; Apak, R. *Talanta*. **2020**, 206, 120240.
22. Pinyorospathum, C.; Rattanarat, P.; Chaiyo, S.; Siangproh, W.; Chailapakul, O. *Sensors and Actuators B: Chemical*. **2019**, 290, 226-232.
23. Aparna, R.S.; Anjali Devi, J.S.; Sachidanandan, P.; George, S. *Sensors and Actuators B: Chemical*. **2018**, 254, 811-819.
24. Liua, X.; Lia, T.; Wua, Q.; Yanb, X.; Wud, C.; Chena, X.; Zhang, G. *Talanta*. **2017**, 165, 216–222.
25. Ajay P. V.S.; Printo J.; Kiruba D. S.C.G.; Susithra, L.; Takatoshi, K.; Sivakumar M. *Materials Science and Engineering C*. **2017**, 78, 1231–1245.
26. Lin H.; S. Suslick, K. *J. AM. CHEM. SOC*. **2010**, 132, 15519–15521.
27. Feng, L.; J. Musto, C.; W. Kemling, J.; H. Lim, S.; Zhong, W.; S. Suslick, K. *Analytical Chemistry*, **2010**, 82, 9433–9440.
28. Takeda, Y.; Komori, Y.; Yoshitake, H. *Colloids and Surfaces A: Physicochemical and Engineering Aspects*. **2013**, 422, 68–74.
29. Bazuła, P. A.; Arnal, P. M.; Galeano, C.; Zibrowius, B.; Schmidt, W.; Schüth, F. *Microporous and Mesoporous Materials*. **2014**, 200, 317–325.
30. Metarwiwinit, S.; Mukdasai, S.; Poonsawat, C.; Srijaranai, S. *New Journal of Chemistry*. **2018**, 42, 3401–3408.
31. Liberman, A.; Mendez, N.; Trogler, W. C.; Kummel, A. C. *Surface Science Reports*. **2014**, 69(2-3), 132–158.
32. Charoensuk, J.; Thonglao, J.; Wichaiyo, B.; Mukdasai, K.; Santaladchaiyakit, Y.; Srijaranai, S.; Mukdasai, S. *Microchemical Journal*. **2021**, 160, 105666.
33. Liu, X.; Feng, J.; Sun, X.; Li, Y.; Duan, G. *Anal. Chim. Acta*. **2016**, 916, 102–111.
34. Ortiz-Villanueva, E.; Benavente, F.; Giménez, E.; Yilmaz, F.; Sanz-Nebot, V. *Anal. Chim. Acta*. **2014**, 846, 51–59.
35. Mendil, D.; Demirci, Z.; Uluozlu, O.D.; Tuzen, M.; Soylak, M. *Food Chemistry*. **2017**, 221, 1394-1399.
36. Fu, L.; Zhang, L.; Wang, S.; Peng, J.; Zhang, G. *Journal of Molecular Liquids*. **2017**, 241, 292–300.
37. Liu, X.; Xing, J.; Guan, Y.; Shan, G.; Liu, H. *Colloids and Surfaces A: Physicochemical and Engineering Aspects*. **2004**, 238, 127–131.
38. Soto-Cantu, E.; Cueto, R.; Koch, J.; Russo, P. S. *Langmuir*. **2012**, 28(13), 5562–5569.
39. Wu, K. H.; Chang, Y. C.; Tsai, W. Y.; Huang, M. Y.; Yang, C. C. *Polymer Degradation and Stability*. **2010**, 95(12), 2328–2333.
40. Tsang, S.; Phu, F.; Baum, M. M.; Poskrebyshev, G. A. *Talanta*. **2007**, 71(4), 1560–1568.
41. Crouch, S. R.; Malmstadt, H. V. *Analytical Chemistry*. **1967**, 39(10), 1084–1089.
42. Tomić, M.; Fohlerova, Z.; Gràcia, I.; Figueras, E.; Cané, C.; Vallejos, S. *Sensors and Actuators B: Chemical*. **2021**, 328, 129046.
43. Okazaki, T.; Kuramitz, H.; Hata, N.; Taguchi, S.; Murai, K.; Okauchi, K. *Analytical Methods*. **2015**, 7(6), 2794–2799.
44. Nayeem, K. I.; Carl, P. Tripp. *Talanta*. **2022**, 238, 123043.

45. Awual, M. R.; Yaita, T.; Suzuki, S.; Shiwaku, H. *Journal of Hazardous Materials*. **2015**, 291, 111–119.
46. Laosuwan, M.; Mukdasai, S.; Srijaranai, S. *Molecules*. **2020**, 25, 552.
47. Sven, C. F.; Fred, L. *Journal of Nanobiotechnology*. **2011**, 9(1), 59.

Detection of histamine based on gold nanoparticles using a UV-Vis spectrophotometer for analysis of histamine in seafood samples

Monticha Photin, Orawan Kanluang, Wijitar Dungchai, and Chacriya Malasuk*

Depatment of Chemistry, Faculty of Science, King Mongkut's University of Technology Thonburi, Bangkok, Thailand

**E-mail: Chacriya.mal@kmutt.ac.th*

Abstract:

This study sought to determine histamine content in seafood samples using gold nanoparticles (AuNPs) and an NaCl solution with a UV-Vis spectrophotometer. AuNPs were simply synthesized using citrate reduction. Optimization of the concentration of AuNPs and the concentration of NaCl were performed. Under the optimum condition using 0.25 mM AuNPs with 0.9%w/v of NaCl solution, histamine was successfully determined in a concentration range of 1-1,000 nM by monitoring decrease in absorbance at 520 nM. The limit of detection (LOD) and the limit of quantitation (LOQ) of the method were 0.9 and 1.3 nM, respectively. Selectivity of the method was investigated showing no effect of interferences. The developed method was applied to determine histamine in real samples during storage process at 10 °C. It was found that the histamine contents in tuna and salmon were not excess FDA limit (500 mg/kg) within 3 days, which was confirmed by HPLC method. The accuracy and precision of the method was confirmed by %recovery value of 93.2-97.5% and %RSD value of 2.4-5.3% in tuna and salmon samples, respectively. The results show that this developed method can be used to analyze histamine in real samples and is suitable for monitoring seafood spoilage to ensure food safety.

1. Introduction

Histamine (4-(2-aminoethyl)-1H-imidazole) is produced by histidine, an essential amino acid in organisms. When spoilage microorganisms grow in living organisms under unappreciated storage conditions, microbial organisms generate histidine decarboxylase enzyme which can change histidine to histamine.[1] Histamine is one of the most important biogenic amines (such as cadaverine, putrescine, and tyramine) and interest has grown in relation to decarboxylation of amino acids in high-protein foods, for example seafood, daily products, and meat products.[2] Histamine is known as a central neurotransmitter. Furthermore, it is the chemical mediator related to immune function and physiological functions (such as inflammatory response, vasodilation, sleep-wake regulation, and erection).[3-5] However, high level of histamine can damage respiratory and digestive functions, resulting food poisoning in humans.[6-7] Increased contamination of histamine in various foods is caused by unsuitable food processing, storage, and transportation. Thus, strict guidelines of histamine in foods were established because of its toxicity directly involved in food quality and safety. The maximum level of histamine in foods regulated by FDA (US Food and Drug Administration) is 500 mg/kg.[8] At present, the histamine level can globally indicate the freshness and spoilage of seafoods due to increases in histamine generated by improper storage time.[9] Hence, a simple, accurate, and sensitive sensor to monitor histamine in seafoods is essential to ensure food safety.

Previously, various analytical methods have been reported to detect histamine in aquatic products such as thin layer chromatography,[10] high-performance liquid chromatography (HPLC),[11-14] gas chromatography (GC),[15] capillary electrophoresis,[16-17] and electrochemical detection.[18-20] These methods are sensitive and reliable, yet they require expensive equipment, skilled operators, are time-consuming processes, and need sophisticated sample preparation. Thus, a simple and highly sensitive method is very challenging to analyze histamine in real seafood samples.

Nanosensors are gradually raised interest for monitoring histamine due to its cost-effective, effective, and sensitive method.[21-22] In those approaches, AuNPs were functionalized with specific ligands and histamine induced the aggregations of AuNPs by electrostatic exclusive force or steric hindrance. The aggregation of AuNPs remarkably changed the electrochemical properties achieving histamine determinization in real biological samples. However, a complex functionalization step is required and a monodispersity of AuNPs is difficult to control during this process. In addition, AuNPs are applicable for colorimetric detection, in which the absorption spectrum and the color of AuNPs alter due to the aggregation of AuNPs with analyte.[23] Colorimetric assays of AuNPs have been applied in environmental analysis and bioanalysis.

In 2020, Bi et. al. was reported AuNPs for colorimetric and fluorescence detection for histamine analysis in fresh salmon muscle.[24] 1.0 mM AuNPs with 0.9%w/v NaCl was employed to determine histamine in the salmon. Satisfied precision and accuracy were observed. However, high concentration of AuNPs was used for the determination of histamine in this method, which is expensive for the experiment. Moreover, only histamine content in fresh salmon was investigated. Herein, unmodified and low concentration AuNPs were developed for histamine analysis in seafoods. NaCl solution was used for histamine preparation to enhance the electrostatic interactions with AuNPs. The color of the AuNPs solution was changed by histamine and decreased the absorbance of AuNPs at 520 nm which is related to an increase in histamine concentration, as measured using a UV-Vis spectrophotometer. Analytical performance and selectivity of the developed method were performed. The method applied quantitative analysis of histamine in real samples, tuna and salmon during the storage process to confirm that their histamine contents met FDA standards and to ensure the method is useful for food safety applications. Moreover, the proposed method was compared results of histamine contents in real samples with HPLC method to confirm a reliability of the proposed method.

2. Materials and Methods

2.1 Materials

Gold (III) chloride trihydrate ($HAuCl_4.3H_2O$) and 2-5 dihydroxybenzoic acid was purchased from Sigma Aldrich (St. Louis, MO, USA). Histamine dihydrochloride, histidine, dopamine, putrescine dihydrochloride, cadaverine dihydrochloride, phenylethylamine hydrochloride, and tyramine hydrochloride were obtained from Tokyo chemical industry, TCI (Tokyo, Japan). Trisodium citrate, nitric acid, sodium chloride, and acetonitrile were from KEMAUS (Cherrybrook, NSW, Australia). Salmon and tuna samples were purchased from a local market. All samples and reagents were prepared using Milli-Q-purified water.

2.2 Synthesis of Au-NPs

Every piece of glassware was soaked in 10% nitric solution and entirely washed with purified water before use. 100 mL of 0.10 and 0.25 mM $HAuCl_4$ were heated and stirred at 100°C until the solution boiled. Then 1.5 mL of 1%w/v Trisodium citrate was rapidly added into the boiled $HAuCl_4$ solution. The reaction slowly occurred by continuous stirring and heating for 15 minutes. Finally, a red wine solution was observed showing complete synthesis of AuNPs. The AuNPs solution was cooled and stored at 4°C until use within 6 months.

2.3 Detection of histamine standard solution

1 mM stock solution of histamine was prepared in 0.5, 0.9, and 1.5%w/v of NaCl solution to achieve various final concentrations. Then, the standard solution was stored at 4°C for reserve within 6 months.

Detection of histamine was performed by vigorously mixing histamine with an AuNPs solution at 1:1 ratio for 2 minutes. The absorbances of the mixed solution were measured at 520 nm.

2.4 Detection of histamine in seafood samples

Tuna and salmon in storage process at 10 °C were sampling every 24 hr until 72 hr. 10 mL of a 0.9%w/v NaCl solution was added to 1 g of the sampled salmon or tuna and homogenized at high-speed for 2 minutes. Then, the sample solution was centrifuged at 5,000 rpm for 10 minutes. 2 mL of the supernatant was mixed with 2 mL of AuNPs solution (1:1 ratio) and absorbance was measured by UV-Vis spectrophotometer. Each sample was investigated three times.

The spike samples were prepared to evaluate precision and accuracy by adding 50 nM histamine standard into 1 g of the samples. Then, the prepared samples underwent the aforementioned steps.

2.5 Spectroscopic measurement

UV-vis absorption spectra from 300 to 800 nm were obtained via UV-Vis spectrophotometer (UV-1800, Shimadzu, Kyoto, Japan). The decrease in absorbances of AuNPs by histamine were measured at 520 nm.

2.6 Method comparison using High Performance Liquid Chromatography (HPLC)

The developed method was compared with HPLC method according to Xu et. al. method.[25] The samples during the storage process were analyzed using RP-HPLC (C18 column, 250 mm × 4.6 mm id × 5 µm particle diameter) with UV detector (LC-40 Series, Shimadzu, Kyoto, Japan). For determination of histamine, isocratic elution was used for separation of histamine in samples. Mobile phase composition was 50% of acetonitrile and 50% of 6 mM 2,5 dihydroxybenzoic acid at pH 2.5. The flow rate was set at 0.7 mL/min. The injection volume of the sample was 20 µL. The column temperature was controlled at 35 °C, and the UV detector was monitored at 205 nm for detection of histamine in samples. Each sample was investigated three times.

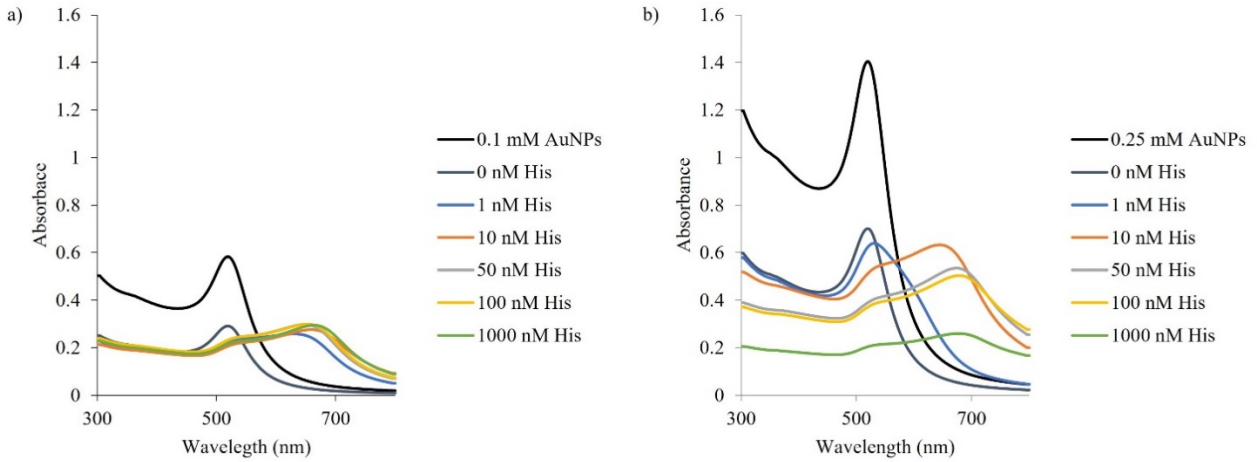

Figure 1. Absorbance spectrum of AuNPs and AuNPs aggregated with various concentrations of histamine under the condition of 0.9% NaCl with: a) 0.1 mM AuNPs and b) 0.25 mM AuNPs.

3. Results & Discussion

3.1 Optimization of AuNPs concentration

The synthesized AuNPs solution of 0.10 mM and 0.25 mM in 0.9%w/v NaCl solution were observed using absorption spectra ranging from 300-800 nm. The absorption spectra of 0.10 mM and 0.25 mM AuNPs in various histamine concentrations are presented in Figures 1a and 1b, respectively. The strong UV-Vis absorbance at 520 nm (λ_{max}) confirmed the forming of AuNPs with intense surface plasmon resonance absorption in both concentrations of AuNPs. Under the 0.10 mM AuNPs condition, the absorption spectra of various concentration of histamine decreased in absorbances at 520 nm and the color of the solution changed from red wine to dark blue, indicating that electrostatic interactions between histamine and AuNPs were performed. An increase in electron density and surface amino group content results in aggregation of AuNPs [23] showing a red shift of the AuNPs absorption peak. However, the decrease in absorbance at 520 nm was not significantly different in various concentration of histamine due to the limit of the AuNPs concentration. Small amounts of histamine (1 nM) caused complete aggregation of 0.10 mM AuNPs. Thus, the decrease in the absorbances were not directly related to the histamine concentrations (Figure 1a). Meanwhile, the absorbances at 520 nm of 0.25 mM AuNPs was higher than that of 0.10 nM of AuNPs and gradually decreased with increased histamine concentration (1–1,000 nM), as shown in Figure 1b. An increase in the concentration of AuNPs enhanced the absorbance of AuNPs shown in the darker red wine color of the solution. The electrostatic interactions of AuNPs with histamine was also increased which could further reduce the monodispersity and affected the surface plasmon resonance of AuNPs [23]. The forming of a histamine layer on the surface of Au-NPs resulted in the scattering of high-momentum surface plasmons, so the radiation intensity increased [24] which is shown in the color of the AuNPs solution, in which the solution was gradually changed into dark blue with increased histamine concentrations (Figure 1b). Hence, the 0.25 mM AuNPs was selected for further study.

3.2 Optimization of NaCl concentration

The concentration of NaCl varied from 0.5 to 1.5%w/v for preparation of standard histamine. 0.5, 0.9, and 1.5%w/v of NaCl were used to dissolve histamine before mixing with 0.25 mM of AuNPs in 1:1 ratio. The results show that the electrostatic interaction of AuNPs increased with higher NaCl concentration. NaCl could induce the interaction between AuNPs with histamine and caused the aggregation of AuNPs. Thus, at lower concentration of NaCl (0.5%w/v NaCl), the absorbances of AuNPs were slightly decreased which were not related to histamine concentration (Figure 2a). High concentrations of histamine (1,000 nm) could only observably change in color of the solution because of insufficient aggregation of AuNPs by histamine. In contrast, higher concentration of NaCl (1.5%w/v NaCl) resulted in remarkable decreases in absorbance at 520 nm despite a very low concentration of histamine (1 nM). Figure 2c shows the absorption spectra of 0.25 mM AuNPs with histamine in 1.5%w/v NaCl at various concentrations, in which the concentrations of histamine were not related to the absorbance at 520 nM due to excessive NaCl concentration. Compared to the condition of 0.9%w/v NaCl (Figure 2b), the decrease in the absorbance at 520 nm was most related to the increased histamine concentration. Thus, 0.9%w/v

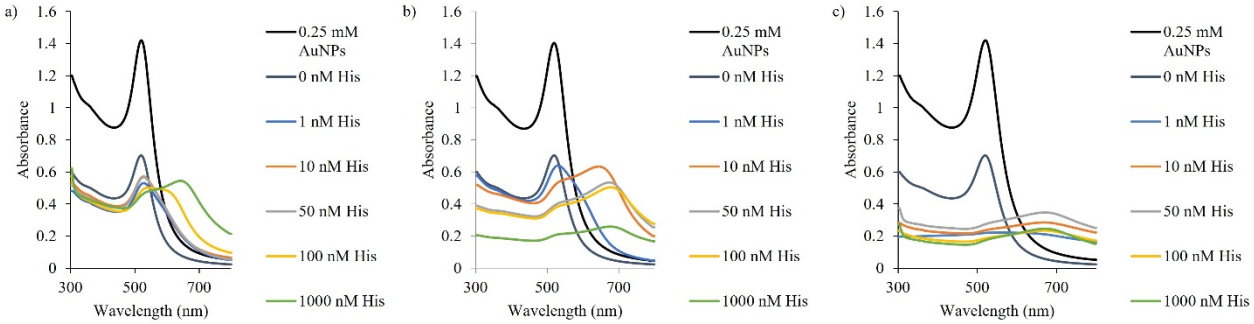

Figure 2. Absorbance spectrum of AuNPs and AuNPs aggregated with various concentration of histamine under the condition of 0.25 mM AuNPs with: a) 0.5%w/v NaCl; b) 0.9%w/v NaCl; and c) 1.5%w/v NaCl.

NaCl was the optimum concentration when used with 0.25 mM AuNPs for histamine analysis.

3.3 Analytical performances of the AuNPs method for histamine analysis

A calibration curve shows the relationship between the absorbance at 520 nm and the logarithm value of histamine concentration in the dynamic range from 1 nM to 1,000 nM which was performed under the optimized conditions. A degressively linear graph was observed with the regression equation y = -0.1407x + 0.637 and the correlation coefficient of the calibration curve was 0.9916 (Figure 3). This confirms that the method can determine histamine.

The limit of detection (LOD) and limit of quantitation (LOQ) were evaluated by measurement of absorbance at 520 nm of a blank solution which was repeated 10 times. The LOD and LOQ were calculated using the following equations

$$LOD = \bar{x} + 3SD$$
$$LOQ = \bar{x} + 10SD$$

where $\bar{x}$ is average concentration of the blank solution and SD is standard deviation of the blank solution. Hence, the LOD and LOQ of this method were 0.9 nM and 1.3 nM, respectively. Although using a lower AuNPs concentration, the method showed highly sensitive detection in which the LOD value was comparable or lower than other traditional methods [23, 24].

3.4 Selectivity of AuNPs method for histamine analysis

AuNPs method was investigated for selectivity with various biological substances containing amino groups including histamine, histidine, dopamine, putrescine, cadaverine, phenylethylamine, and tyramine, each with concentrations of 1,000 nM. It found that only histamine could be observed to change the color of the solution from red wine to dark blue. Figure 4 presents the results of %different absorbances of histamine with the other substances, which were not over 5%. This means that there was no interference effect from these substances. Because histamine has a relatively high polar surface area, the electrostatic interactions of histamine and AuNPs cause the aggregations of AuNPs, while the other biological substances cannot induce the interaction due to differences in their electron density and surface amino group content.

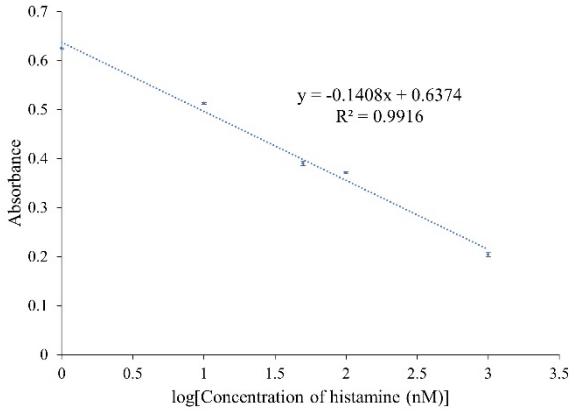

Figure 3. Calibration curve showing linear relationships between the absorbance at 520 nm and the logarithm value of histamine concentrations observed under the optimized conditions.

3.5 Analysis of histamine in real samples

The prepared sample solution was measured with absorbance at 520 nm to determine histamine concentrations in tuna and salmon samples. In addition, the precision and accuracy of the method were investigated by calculating %RSD and %recovery, respectively. The results show that the method was successfully applied to

the real samples with satisfactory %recovery value of 93.2-97.5% and excellent precision (%RSD<10) as shown in Table 1. The histamine contents in tuna and salmon were increased during the storage process (Table 1). The histamine contents showed increasing around 2 times per day (24 hr) when kept at 10 °C, however, for storage process within 72 hr, the seafoods do not exceed the FDA limit that may cause an allergic response in humans (500 mg/kg). This AuNPs method is capable for analysis of histamine in seafoods with respect to FDA requirements. Moreover, the developed method requires no sophisticated sample preparation, incurs no expensive experimental costs, and is a convenient and easy analysis method. Therefore, the method can be used to effectively monitor seafood freshness and spoilage to ensure food safety under FDA criteria.

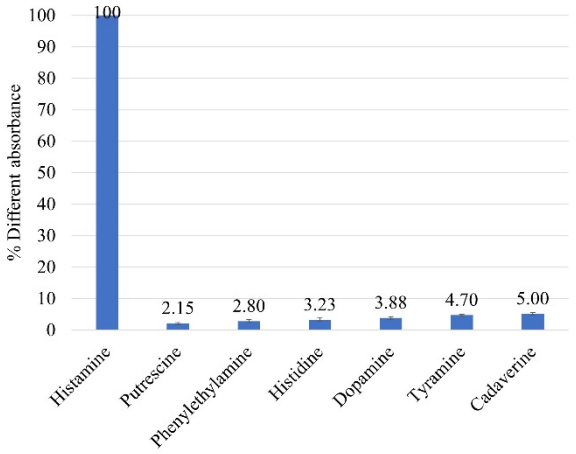

Figure 4. Selectivity results of various biological substances containing amino groups: histamine, histidine, dopamine, putrescine, cadaverine, phenylethylamine, and tyramine at concentrations of 1,000 nM each in comparison to the absorbances of histamine with the other substances.

2.6 Method comparison using High Performance Liquid Chromatography (HPLC)

The samples were evaluated by HPLC to compare results of histamine contents in real samples. The calibration curve of HPLC method was plotted between histamine concentration (10 nM-200 nM) and peak area (mAU*min), showed correlation coefficient ≥0.99, which is suitable for determination of histamine in real samples. The results of histamine contents in the samples and %difference of histamine contents investigated by the developed AuNPs method and HPLC method are presented in Table 2. It was observed that %difference of histamine contents investigated by those two methods was not over 10%. The comparison results can guarantee a reliability of the developed method for determination of histamine in real seafood samples.

4. Conclusion

The AuNPs method was developed to determine histamine in NaCl solution. Histamine induced the aggregation of the AuNPs by the specific electrostatic interactions resulting in a color change of the AuNPs solution from red wine to dark blue. The decrease in the absorbance of the solution related to increased histamine concentration was monitored at 520 nm due to red shift of AuNPs absorption peak. The 0.25 mM AuNPs and 0.9%w/v NaCl was the optimum condition achieved for quantitative measurement of histamine in a dynamic range of 1-1,000 nM. The degressive linear equation from the calibration curve of a relationship between the absorbance at 520 nm and logarithm of histamine concentration was -0.1407x + 0.637 with r^2 = 0.9916. Highly sensitive detection was guaranteed by the LOD value of 0.9 nM and the LOQ value of 1.3 nM with using low AuNPs concentration. The method was

Table 1. Summarized results of real sample analysis by the developed AuNPs method for histamine determination.

Sample (Storage at 10 °C)	Spiked concentration[a] (nM)	Found concentration[a] (nM)	Unspiked concentration[a] (nM)	Histamine content[a] (mg/kg)	%Recovery[a]	%RSD[a]
Tuna						
-Storage 0 hr	50	75.064	27.365	0.050	95.4	4.2
-Storage 24 hr	50	90.614	42.742	0.079	95.7	3.5
-Storage 48 hr	50	137.366	89.127	0.164	96.5	3.7
-Storage 72 hr	50	244.148	195.384	0.360	97.5	2.4
Salmon						
-Storage 0 hr	50	60.485	13.627	0.025	93.7	5.3
-Storage 24 hr	50	67.213	20.622	0.038	93.2	4.8
-Storage 48 hr	50	90.343	42.735	0.079	95.2	3.6
-Storage 72 hr	50	133.548	85.174	0.157	96.7	3.2

[a]Measurements repeated three times under optimum condition for each sample.

investigated for selectivity with various biological substances containing amino groups and shows high detection sensitivity with negligible interferences. The developed method was applied with real samples analysis for histamine determination. The results showed that histamine content in the tuna and salmon samples were not exceeded the FDA limit during the storage process at 10 °C within 3 days, with satisfactory accuracy (%recovery of 93.2-97.5%) and precision (%RSD of 2.4-5.3%). The developed method was confirmed a reliability of the results by using HPLC method, which the %difference of histamine contents investigated by the two methods was not over 10%. In conclusion, the developed method was achieved for histamine analysis in real samples with a simple process, low experimental costs, good stability, and excellent accuracy that is beneficial for food safety applications.

Table 2. Comparison of results of histamine determination in real samples by using AuNPs method and HPLC method

Sample (Storage at 10 °C)	Histamine content[a] (mg/kg) by AuNPs method	Histamine content[a] (mg/kg) by HPLC method	% Difference of histamine content
Tuna			
- 0 hr	0.050	0.047	6.38
- 24 hr	0.079	0.084	5.95
- 48 hr	0.164	0.155	5.80
- 72 hr	0.360	0.370	2.70
Salmon			
- 0 hr	0.025	0.023	8.70
- 24 hr	0.038	0.040	5.00
- 48 hr	0.079	0.082	3.65
- 72 hr	0.157	0.152	3.29

[a]Measurements repeated three times under optimum condition for each sample.

Acknowledgements

The authors gratefully acknowledge Thailand Science Research and Innovation for funding support (Fundamental Fund of King Mongkut's University of Technology Thonburi, Thailand) and laboratory colleagues for their assistance.

References

1. Sørensen, K.M.; Aru, V.; Khakimov, B.; Aunskjær, U.; Engelsen, S.B. Biogenic Amines: A key freshness parameter of animal protein products in the coming circular economy. *Curr. Opin. Food Sci.* **2018**, *22*, 167–173.
2. Heerthana, V.R.; Preetha, R. Biosensors: A potential tool for quality assurance and food safety pertaining to biogenic amines/volatile amines formation in aquaculture systems/products. *Rev. Aquacult.* **2019**, *11*, 220–233.
3. Brown, R.E.; Stevens, D.R.; Haas, H.L. The physiology of brain histamine. *Prog Neurobiol.* **2001**, *63*, 637–672.
4. Loesel, R.; Homberg, U. Anatomy and physiology of neurons with processes in the accessory medulla of the cockroach *Leucophaea maderae*. *J Comp Neurol.* **2001**, *439*, 193–207.
5. Yanai, K.; Tashiro, M. The physiological and pathophysiological roles of neuronal histamine: an insight from human positron emission tomography studies. *Aliment Pharm Therap*, **2007**, *113*, 1–15.
6. Veseli, A.; Vasjari, M.; Arbneshi, T.; Hajrizi, A.; Svorc, L.; Samphao, A.; Kalcher, K. Electrochemical determination of histamine in fish sauce using heterogeneous carbon electrodes modified with rhenium(IV) oxide. *Sensor Actuat B-Chem*. **2016**, *228*, 774–781.
7. Del, R.B.; Redruello, B.; Linares, D.M.; Ladero, V.; Fernandez, M.; Martin, M.C.; Ruas-Madiedo, P.; Alvarez, M.A. The dietary biogenic amines tyramine and histamine show synergistic toxicity towards intestinal cells in culture. *Food Chem.* **2017**, *218*, 249–255.
8. Yang, H.; Yoon, M.; Um, M.Y.; Lee, J.; Jung, J.; Lee, C.; Kim, Y.T.; Kwon, S.; Kim, B.; Cho, S. Sleep-Promoting Effects and Possible Mechanisms of Action Associated with a Standardized Rice Bran Supplement. *Nutrients.* **2017**, *9*, 512.
9. Adams, F.; Nolte, F.; Colton, J.; De, B.J.; Weddig, L. Precooking as a Control for Histamine Formation during the Processing of Tuna: An Industrial Process Validation. *J. Food Protect.* **2018**, *81*, 444–455.
10. Hui, Y.; Zhuang, D.; Hu, X.; Shuang, Z.; Zhiyong, H.E.; Zeng, M.; Fang, X.; Chen, J.; Chen, X. Rapid determination of histamine in fish by thin-layer chromatography-image analysis method using diazotized visualization reagent prepared with p-nitroaniline. *Anal. Methods-UK.* **2018**, *10*, 3386–3392.
11. Carralero, V.; Gonzalez-Cortes, A.; Yanez-Sedeno, P.; Pingarron, J.M. Pulsed amperometric detection of histamine at glassy carbon electrodes modified with gold nanoparticles. *Electroanalysis.* **2005**, *17*, 289–297.

12. Todoroki, K.; Ishii, Y.; Miyauchi, C.; Kitagawa, S.; Min, J.Z.; Inoue, K.; Yamanaka, T.; Suzuki, K.; Yoshikawa, Y.; Ohashi, N.; Toyo'oka, T. Simple and sensitive analysis of histamine and tyramine in Japanese soy sauces and their intermediates using the stable isotope dilution HILIC-MS/MS method. *J Agric Food Chem.* **2014**, *62*, 6206–6211.
13. Preti, R.; Antonelli, M.L.; Bernacchia, R.; Vinci, G. Fast determination of biogenic amines in beverages by a core-shell particle column. *Food Chem.* **2015**, *187*, 555–562.
14. Xinna, W.; Liang, Y.; Wang, Y.; Fan, M.; Sun, Y.; Liu, J.; Zhang, N. Simultaneous determination of ten kinds of biogenic amines in rat plasma using high-performance liquid chromatography coupled with fluorescence detection. *Biomed. Chromatogr.* **2018**, *32*, e4211.
15. Kamankesh, M.; Mohammadi, A.; Mollahosseini, A.; Seidi, S. Application of a novel electromembrane extraction and microextraction method followed by gas chromatography-mass spectrometry to determine biogenic amines in canned fish. *Anal. Methods-UK.* **2019**, *11*, 1898–1907.
16. Uzasci, S.; Baskan, S.; Erim, F.B. Biogenic amines in wines and pomegranate molasses-a non-ionic micellar electrokinetic chromatography assay with laser-induced fluorescence detection. *Food Anal Methods.* **2012**, *5*, 104–108.
17. Daniel, D.; dos Santos, V.B.; Vidal, D.T.R.; do Lago, C.L. Determination of biogenic amines in beer and wine by capillary electrophoresis-tandem mass spectrometry. *J Chromatogr A.* **2015**, *1416*, 121–128.
18. Basozabal, I.; Guerreiro, A.; Gomez-Caballero, A.; Goicolea, M.A.; Barrio, R.J. Direct potentiometric quantification of histamine using solid-phase imprinted nanoparticles as recognition elements. *Biosens. Bioelectron.* **2014**, *58*, 138–144.
19. Henao-Escobar, W.; del Torno-de Roman, L.; Dominguez-Renedo. O.; Alonso-Lomillo, M.A.; Arcos-Martinez, M.J. Dual enzymatic biosensor for simultaneous amperometric determination of histamine and putrescine. *Food Chem.* **2016**, *190*, 818–823.
20. Leonardo, S.; Campàs, M. Electrochemical enzyme sensor arrays for the detection of the biogenic amines histamine, putrescine and cadaverine using magnetic beads as immobilisation supports. *Microchim Acta.* **2016**, *183*, 1881–1890.
21. Rkr, G.; Palathedath, S.K. Cu@Pd core-shell nanostructures for highly sensitive and selective amperometric analysis of histamine. *Biosens. Bioelectron.* **2018**, *102*, 242–246.
22. Kumar, N.; Goyal, R.N. Silver nanoparticles decorated graphene nanoribbon modified pyrolytic graphite sensor for determination of Histamine. *Sens. Actuators B-Chem.* **2018**, *268*, 383–391.
23. Bi, J.; Tian, C.; Zhang, G.L.; Hao, H.; Hou, H.M. Detection of histamine based on gold nanoparticles with dual sensor system of colorimetric and fluorescence. *Foods.* **2020**, *9*, 316.
24. Huang, C.; Wang, S.; Zhao, W.; Zong, C.; Liang, A.; Zhang, Q.; Liu, X. Visual and photometric determination of histamine using unmodified gold nanoparticles. *Microchim Acta.* **2017**, *184*, 2249-2254.
25. Nadeem, M.; Naveed, T.; Rehmana, F.; Xu, Z. Determination of histamine in fish without derivatization by indirect reverse phase-HPLC method. *Microchem J.* **2019**, *144*, 209–214.

Aptamer-based lateral flow biosensor for the detection of cadmium

Vorawan Yurayart[1,2], Sirowan Ruantip[2], Abdulhadee Yakoh[2,3], and Sudkate Chaiyo[2,3]*

[1]*Program in Biotechnology, Faculty of Science, Chulalongkorn University, Bangkok 10330, Thailand*
[2]*The Institute of Biotechnology and Genetic Engineering, Chulalongkorn University, Bangkok 10330, Thailand*
[3]*Center of Excellence for Food and Water Risk Analysis (FAWRA), Department of Veterinary Public Health, Faculty of Veterinary Science, Chulalongkorn University, Bangkok, 10330, Thailand*

**E-mail: Sudkate.c@chula.ac.th*

Abstract:

Currently, chemical test kits are popular for detecting cadmium (Cd^{2+}) contamination in food and the environment. However, this device still has many steps of operation. Here, an aptamer-based lateral flow biosensor was developed for the rapid detection of Cd^{2+}. This sensor combines a flow test strip with an aptasensor not only to increase the specificity for Cd^{2+} detection but also to reduce the detection steps of the device. In the operating principle of this strip test, the Cd-aptamer probe was mixed with the sample before being applied to the sample pad. In the absence of Cd^{2+}, the Cd-aptamer probe was free, and then this solution continuously flowed into a conjugate pad coated with an AuNPs conjugated probe. This free Cd-aptamer probe was hybridized with the AuNPs conjugated probe so that the test line did not appear as a color band. The cadmium detection was interpreted as negative. In the case of positive, Cd^{2+} ions are specifically bound to the Cd-aptamer probe. Next, this solution continued to flow to the conjugate pad, which could not bind to the AuNPs conjugated probe. For this reason, the test line appears as a colored band from the binding of the AuNPs conjugated probe, and the aptamer sequences match the test line. This test strip has been shown to detect as low as 9 ppb of Cd^{2+}. As an additional suggestion, this test strip could potentially be applied to detect Cd^{2+} in tap water samples, demonstrating its ease of use, rapidity, and field readiness.

1. Introduction

Cadmium (Cd^{2+}) is a type of heavy metal that can be found in the environment. It is generally released in the form of industrial waste, mining, agriculture, etc. Cd^{2+} is classified as a heavy metal and is harmful to animals and humans.[1] When it enters the body through the food chain and consumes water, even low levels can lead to adverse effects on the respiratory system, heart system, reproductive immunity, and embryonic development.[2] The Department of Medical Sciences in Thailand has set a standard amount not exceeding 5 ppb of Cd^{2+} that can be found in drinking water. There are standard methods for measuring Cd^{2+}, including inductively coupled plasma mass spectrometry (ICP-MS), inductively coupled plasma mass spectrometry (ICP-MS), graphite furnace atomic absorption spectrometry (GF-AAS),[3] etc. These methods have the advantage of providing precision and highly accurate measurement results. However, the instrument's high cost and the sample preparation complexity are considered limitations in using this instrument, and importantly, the test requires only experts for laboratory analysis. Currently, test kits for testing Cd^{2+} are being developed for sale, but they are still only qualitatively detectable and are still expensive.

Based on these limitations, the idea was to develop an aptamer-based lateral flow test strip combined with colorimetric measurement as an alternative method for qualitative measurement of Cd^{2+}. The test strips developed combine the advantages of both techniques: Aptamer-based lateral flow assays are user-friendly, quick, and in situ, using knowledge aptamers[4] that are highly specific to the target DNA sample. It can specifically bind to various substance molecules, has high stability, and is easy to modify and conjugate with gold nanoparticles (AuNPs) with a sulfhydryl (-SH) group to use as a signal probe. The color of the test line (T-line) and control line (C-line) can be seen with the naked eye on the developed test strip. Therefore, the research focused on developing a lateral flow aptasensor test strip for Cd^{2+} detection. Finally, this test strip can measure Cd^{2+} in real samples such as drinking and tap water.

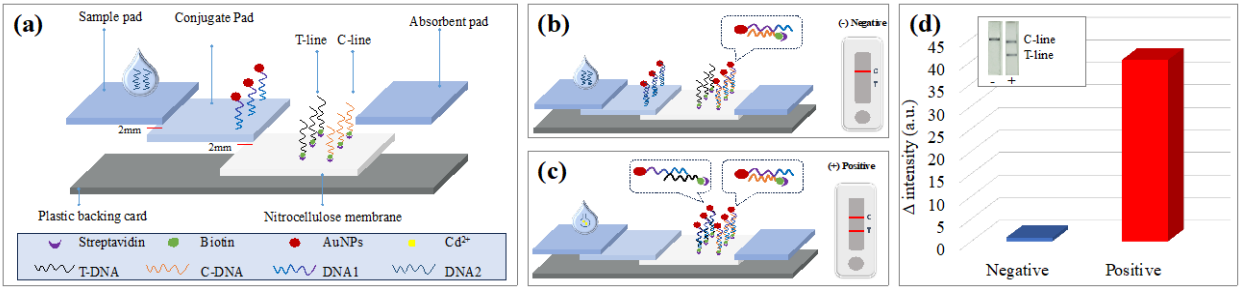

Figure 1. The design of the aptamer-based lateral flow assay for the detection of Cd^{2+}: (a) the composition of the test strip; (b) binding and colorimetric signal in the presence of Cd^{2+} (positive test); (c) binding and colorimetric signal in the absence of Cd^{2+} (negative test); and (d) the detection results: intensity of the test by the ImageJ program.

2. Materials and Methods

2.1 Chemicals and Materials

All elements of the lateral flow test strip included a sample pad, conjugated pad, nitrocellulose membrane, and absorbent pad (standard 17, GF33, UnisartCN140, and CF7 of Whatman), respectively, obtained from Cytiva (China). Potassium tetrachloroaurate (III) n-Hydrate ($KAuCl_4$), was purchased from Wako (Osaka, Japan). Magnesium chloride ($MgCl_2$) and Tris (2-carboxyethyl) phosphine (TCEP) were obtained from Sigma-Aldrich (USA). 6-Mercapto-1-hexanol (MCH) was obtained from TCL (Tokyo, Japan). Sodium chloride (NaCl) was obtained from Kemaus (Australia). All aqueous solutions were prepared with ultrapure water (18. 2mΩ, Milli-Q). The sequences of the DNA_1 capture probe or DNA1 (5'- CCGTCGTCCTGAGTTTTTTTTTTTTTTT TTTT-thiol-3'), DNA_2 cadmium-aptamer probe or DNA2 (5'- CTCAGGACGACGGGTTCACAGTCCGTT GTC-3'),[5] its complementary DNA1 or T-DNA (5'- CTCAGGACGACGG-biotin-3'), and complementary DNA1 or C-DNA or poly A probe (5'- AAAAAAAAAAAA AAAAAAAA-biotin-3') were synthesized by Pacific Science Co. Ltd. (Bangkok, Thailand).

2.2 Synthesis of AuNPs

Ultrapure water (18.2 mΩ) was boiled at 100°C, and condensation was observed. Subsequently, 1% (w/v) $KAuCl_4$ was added, and add 1% trisodium citrate (v/v) was introduced. When the solution boiled, the color of the liquid changed to wine red. The solution was moved out of the stove, allowed to cool down, and the pH was adjusted to 8.2 with 0.2 M NaH_2CO_3. The gold nanoparticles (AuNPs) were stored in sterile plastic bottles at 4°C to be attached to 5'-thiolate aptamer.[6]

2.3 Preparation of AuNPs conjugated probe

To activate the aptamer, 5'-Thiolate aptamer was mixed with folding buffer, then TCEP was added and incubated for 1 h at room temperature. After the time was up, AuNPs were added and incubated at 4°C for 24 h before adding and incubating NaCl (1 M), and then solutions were incubated at 4 °C overnight. To block the unmodified fraction and eliminate nonspecific adsorption on the AuNPs surface, MCH (28µM) was added to aged AuNP-aptamer solution and incubated for 1 h, Excess thiolated aptamer and MCH were removed by pulling out the supernatant after centrifugation at 25,000 rpm for 30 min and AuNPs conjugates were resuspended in 0.01 M Phosphate buffer (PB-T buffer) pH 7.4. Washing was then repeated for the final 3 rounds to obtain aptamers labeled with AuNPs (AuNPs conjugated probe). Finally, the final solution was kept at 4°C until it could be applied to studies.[7]

2.4 Preparation of Nitrocellulose Membrane

Fifty µM T-DNA (test line) and C-DNA (control line) were mixed with streptavidin at a ratio of 1:1 and shaken at room temperature for 1 h. After that, it was sprayed onto a 2.5 x 30 mm of nitrocellulose pad using dispenser (BIODOT xyz32100047, USA) at a speed of 2 µL/cm, and it was dried for 1 h at 37°C.

2.5 Fabrication of the lateral flow test strips

As shown in Figure 1a, the test kit is built on a 2.5 x 30 cm plastic backing consisting of the following components: a sample pad (treated with 0.01 M PB-T, 1% Tween 20 (v/v), and 3% sucrose (w/v), pH 7.4), a conjugate pad (coated with AuNPs - conjugated probe), a nitrocellulose pad, and a sub pad. Each plate is overlapped by 2 mm. The complete composed sheets were then cut using a cutting machine (Biodot, USA) to a strip test size of 4 mm.

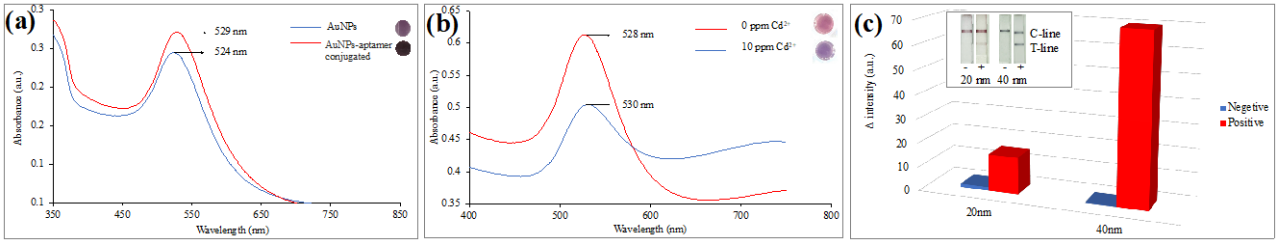

Figure 2. Ultraviolet-visible (UV-Vis) absorption spectra of AuNPs and AuNPs conjugated probe (a), UV-Vis of binding test between DNA2 and the presence (10 ppm) or absence of Cd^{2+}(b), and comparison sensitivity of Cd^{2+} detection between 20 and 40 nm of size AuNPs (c)

2.6 Detection process on test strips

The Cd^{2+} was dissolved in ultrapure water (18.2 mΩ) to create the stock solution. To prepare the droplet solution, 50 µL of PB buffer containing DNA2 were mixed with a 5 µL Cd^{2+} sample solution of different concentrations. After that, the mixture was dropped into the test kit. The color change could be observed after 15 min. After the photo was taken with a smartphone, the intensity of the color bands was checked using the Image J application.

3. Results & Discussion

3.1 Principle of aptamer-based later flow biosensor for Cd^{2+} detection

The principle of the aptamer-based lateral flow biosensor for detecting Cd^{2+} in this study is that the aptamer binds to protein targets by folding into a three-dimensional conformation. This aptamer was indicated that could form a stem-loop structure with Cd^{2+} by a coordinate bond forming.[4] For this study, the Cd^{2+}attached cadmium-aptamer probe (DNA2) complex can be unable to bind the AuNPs conjugate probe, which is free to bind the T-DNA; thus, the color T-line can be observed by the naked eye as the signal-on interpretation. In figure 1a, the sample solution is premixed with DNA2 for binding incubation before being added to the sample pad. Then solution flows by capillary action to the conjugate pad, which contained the AuNPs conjugated probe to bind the free DNA2. In the absence of Cd^{2+}, DNA2 in the premixed buffer is free and unchanged in structure by without Cd^{2+} complementary sequence, so that it can bind with AuNPs conjugated probe on the conjugate pad. Therefore, there are no free AuNPs conjugated probe for attaching to T-DNA on the test line for colored bands appearance. Hence, only PolyT part of DNA1 probe can bind the PolyA probe immobilized as C-line for a colored band appears on the control line, and then the result is read as negative shown in Figure 1b. On the other hand, in the presence of Cd^{2+}, Cd^{2+} molecule is complementary sequence to the DNA2 in the premixed buffer that leads to change its structure to form a loop. Thus, DNA2 strand lost its free property to bind DNA1 for presenting a colored band appearance on the test line. In parallel, PolyT part of DNA1 binds to PolyA probe immobilized as C-line, so the positive is seen two bands by the naked eye as shown in Figure 1c.

The results of the binding principal test on the preliminary test are shown in Figure 1d. It was found that the difference in color intensity was approximately 0.8 and 40 for negative and positive, respectively.

3.2 Characterization of AuNPs conjugated probe

As illustrated in Figure 2a, the AuNPs showed typical extinction spectra for such particles, with a maximum located at 524 nm due to the excitation of plasmons. After the conjugation process, the extinction maximum shifted slightly to around 529 nm, and this phenomenon revealed that the aptamer coated AuNPs were successfully formed. When the complex is coated, the color of the complex changes from purple before conjugating to dark purple, resulting in lower light absorbance, as shown in the inset of Figure 2a.

The binding test of the DNA2 and Cd^{2+} samples was tested by incubating Cd^{2+} with DNA2 before adding AuNPs bind the free DNA2 and then observing aggregation by salt induction. This procedure prepared according to the procedure reported in the literature with slight modifications.[8] Briefly, 10 µL of 50 µM DNA2 was heated to 90°C for 15 min and allowed to cool rapidly at room temperature. Mix 10 ppm Cd^{2+} 20 µL and incubate at room temperature for 10 min with blank ultrapure water. After that, add 160 µL of AuNPs and incubate for another 10 min, and finally add 10 µL of 10% NaCl and incubate for another several min or until a change in the color of the solution is seen. From the experiment as in the inset of Figure 2b, the color of the solution was noticed with the naked eye becoming darker, so it can be said that there is accumulation AuNPs by salt inducing apart from combining of Cd^{2+} and DNA2, which was

clearly observed when the salt was added in the last step. The shift in the higher wavelength with the higher Cd^{2+} sample occurred due to the aggregation of AuNPs after adding the salt, consistent with the value measured at 528 and 530 mm of negative and positive Cd^{2+} sample, respectively.

In the AuNP comparison experiment for aptamer conjugates between 20 and 40 nm in size, Figure 2c demonstrates that no test lines appear in the absence of Cd^{2+}; only control lines are observed for both sizes. If there is Cd^{2+} in the sample, it shows that the test and control lines appear. When comparing the color intensity deltas of Cd^{2+} detection, it was found that the AuNP size for the aptamer conjugate at 40 nm gave a higher color intensity than the 20 nm size. Therefore, 40 nm AuNP was chosen for the aptamer conjugate in this research for easier observing the color bands by naked eye.

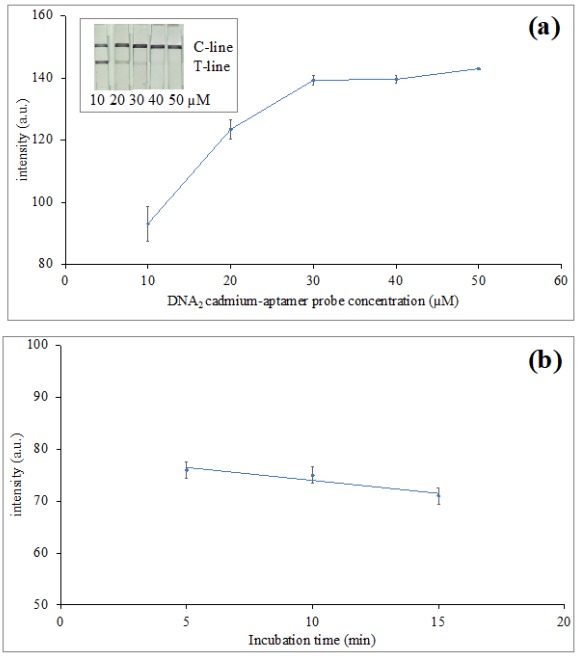

Figure 3. Optimization of DNA2 concentration range (10 to 50 µM) for premix with Cd^{2+} sample (a) and the incubation time of for premix step between the DNA2 and the Cd^{2+} sample (b).

3.3 Optimization of experiment condition

DNA2 majorly corresponds to the AuNPs conjugated probe. In this work, 2 5 µM AuNPs conjugated probe was used to study the DNA2 concentration. In figure 3a, it was found that when the DNA2 (10 and 20 uM) was lower than the concentration of AuNPs conjugated probe, the s test-line resulted in false positive because there were excess AuNPs conjugated probe that could bind to the test line. Therefore, the DNA2 concentration was increased enough to fully cover the AuNPs conjugated probe. It can be seen from the image inserted in Figure 3a that at 5 0 µM DNA2, no false positive appears, which corresponds to the measured intensity value. The higher concentration of DNA2, the higher the color intensity value occurred. Therefore, the optimal concentration of Cd^{2+} probe aptamer was 50 µM.

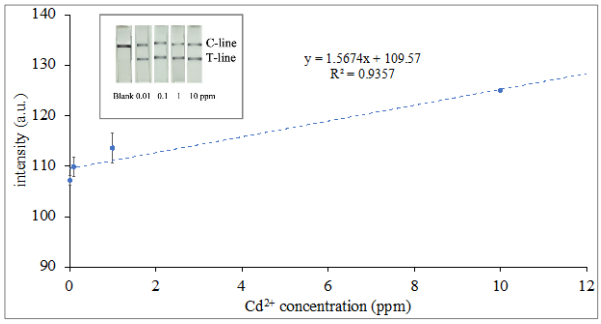

Figure 4. The linear relation of the aptasensor lateral flow for detection of Cd^{2+} with a concentration range from 0.01 to 10 ppm.

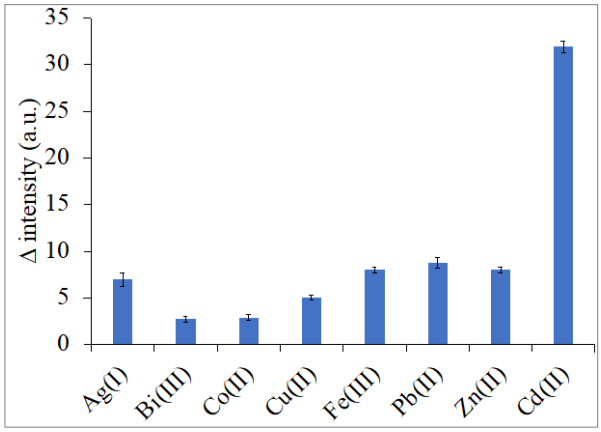

Figure 5. The selectivity of the aptasensor lateral flow for Cd^{2+} detection is compared with 10 times that of other interference. The error bars represent standard divisions for n = 3 replicates.

In Figure 3b, a study of the incubation time between the DNA_2 cadmium-aptamer probe and the Cd^{2+} sample at 5, 10, and 15 min found that the positive test line intensity was similar as well as no remarkable visual observation. Therefore, this device took only 5 min to incubate the solution of the DNA2 and the Cd^{2+} sample before dropping onto the sample pad.

3.4 Detection performance

After obtaining the appropriate conditions, testing for linear range detection of Cd^{2+} at concentrations of 0, 0.01, 0.1, 1, and 10 ppm showed a good linear relationship with an R^2 value of 0.9357. The limit of detection (LOD) is 0.009 ppm or 9 ppb by calculating 3SD/slope. Figure 4 shows that blank or negative gives a correct

negative result, and positive gives a strong test line from 0.01 to 10 ppm. This is related to the intensity value mentioned in Figure 4; the more concentrated the Cd^{2+} sample was, the higher the intensity value was found by visualization as well.

3.5 Reproducibility and Test of specificity

We evaluated the reproducibility of the proposed device by using three independent devices to detect Cd^{2+} at 0.1 ppm. The obtained intensity was calculated as the relative standard deviation (RSD) of 1.90%, which is acceptable according to the Association of Official Analytical Chemists (AOAC) guidelines.[9]

In addition, to ensure this test's specificity, seven metal ions were tested under the optimized experimental conditions above. The concentration of Cd^{2+} was 1 ppm, and the concentration of other ions was 10 ppm, as shown in Figure 5. After adding the disturbing heavy metal ions, the intensity value changed slightly compared to the blank. While the intensity value changed increasingly after adding Cd^{2+}, the developed test kit has good selectivity towards Cd^{2+} ions.

4. Conclusion

In this work, the aptamer-based lateral flow assay was successfully developed to detect Cd^{2+} ions. The developed assay was designed based on the aptamer's conformation changes under the target analyte's introduction. This step was performed before adding the test sample to the sample pad, which led to a more significant increase in binding between the DNA2 and target analyte. Then, the sample flowed to a conjugate pad with a maintained AuNPs conjugated probe, which could not bind to the AuNPs conjugated probe. The free conjugated probe subsequently flowed to bind with T-DNA aptamer on the test line and appeared as a colored band. This strategy can improve the sensitivity, selectivity, and reduce the detection steps of the device. Under optimization, the aptamer later flow provided LOD was 9 ppb for Cd^{2+} detection.

Acknowledgements

This study was supported by a Wittayabundit Fellowship from the Graduate School, Chulalongkorn University, and the Biotechnology Program in the Faculty of Science. Finally, we would like to thank the Institute of Biotechnology and Genetic Engineering, Chulalongkorn University, for generously providing its scientific laboratories.

1. Mezynska, M.; Brzóska, M. M. Environmental exposure to cadmium—A risk for health of the general population in industrialized countries and preventive strategies. *Environmental Science and Pollution Research* **2018**, *25*, 3211-3232.
2. Waalkes, M. P. Cadmium carcinogenesis. *Mutation Research/Fundamental and Molecular Mechanisms of Mutagenesis* **2003**, *533* (1-2), 107-120.
3. Lima, A. S.; Silva, D. G.; Teixeira, L. S. Determination of cadmium in biodiesel using microemulsion and electrothermal atomization atomic absorption spectrometry. *Environmental monitoring and assessment* **2015**, *187*, 1-8.
4. Chen, A.; Yang, S. Replacing antibodies with aptamers in lateral flow immunoassay. *Biosensors and bioelectronics* **2015**, *71*, 230-242.
5. Xu, L.; Liang, J.; Wang, Y.; Ren, S.; Wu, J.; Zhou, H.; Gao, Z. Highly selective, aptamer-based, ultrasensitive nanogold colorimetric smartphone readout for detection of Cd (II). *Molecules* **2019**, *24* (15), 2745.
6. Grabar, K. C.; Freeman, R. G.; Hommer, M. B.; Natan, M. J. Preparation and characterization of Au colloid monolayers. *Analytical chemistry* **1995**, *67* (4), 735-743.
7. Dalirirad, S.; Han, D.; Steckl, A. J. Aptamer-based lateral flow biosensor for rapid detection of salivary cortisol. *ACS omega* **2020**, *5* (51), 32890-32898.
8. Gan, Y.; Liang, T.; Hu, Q.; Zhong, L.; Wang, X.; Wan, H.; Wang, P. In-situ detection of cadmium with aptamer functionalized gold nanoparticles based on smartphone-based colorimetric system. *Talanta* **2020**, *208*, 120231.
9. Analysis, A. O. M. o. Appendix F: guidelines for standard method performance requirements. AOAC International Gaithersburg, MD: 2016.

Use of rice straw-cellulose nanofibril for determination of fluorescein injection medicine

Ratchanon Sangsriboonrueng[1]*, Panumart Thongyoo[2], Chutima Phechkrajang[3], Thanapat Intarawong[1], Chatdanai Sangson[1] and Nathawut Choengchan[1,4]*

[1]*Department of Chemistry and Applied Analytical Chemistry Research Unit, School of Science, King Mongkut's Institute of Technology Ladkrabang, Bangkok, 10520, Thailand*
[2]*Medicinal Chemistry Research Unit, Chemistry Department, Thammasat University, Pathumthani, 10210, Thailand*
[3]*Department of Pharmaceutical Chemistry, Faculty of Pharmacy, Mahidol University, Bangkok, 10400, Thailand*
[4]*Flow Innovation-Research for Science and Technology Laboratories (FIRST Labs), Bangkok, 10400 Thailand*

**E-mail: 64605094@kmitl.ac.th, nathawut.ch@kmitl.ac.th*

Abstract:

Cellulose nanofibrils (CNFs) has been attracting great attention due to their properties such as flexible, transparent, and biodegradable. Herein, we are interested in the fabrication of a colorimetric platform based on CNFs for the determination of the liquid fluorescein injection medicine which is used for diagnostic angioscopy of the retina. Excess of the injected fluorescein can result in optics and eyes damage. Quality control of commercially available fluorescein injection is therefore necessary. In this work, the CNFs was prepared from rice straw by chemical modification using TEMPO (2,2,6,6-Tetramethylpiperidine 1-oxyl)-mediated oxidation reaction. Later, the suspended rice straw was disintegrated by a household blender. The obtained CNFs suspension was spiked with different concentrations of standard fluorescein solution and dried at room temperature. For the colorimetric detection, these strips were image captured under UV irradiation by a smartphone's camera. The RGB color intensity of each image was evaluated by ImageJ™. The calibration was plotted between the green color intensity and the standard concentration. The calibration curves had high linearity in the concentration range of 10-50 %w/v ($r^2 > 0.99$) and high reproducibility (RSD = 0.45-1.43 %). The method detection limit (MDL) was 0.05 %w/v. The sample were spiked to the CNFs and were determined as the same protocol as the standard strip. The results were agreed very well with the labeled fluorescein concentration in sample (Relative error = 2.1-3.6 %).

1. Introduction

Fluorescein injection or fluorescein angiography is a common method used for diagnosing retinal and chloride layers abnormalities by intravenous injection of a fluorescein sodium solution.[1,2] Moreover, fluorescein injections are used to investigate other diseases such as diabetes,[3] root caries,[4] and oral cancer[5] including use in neurological surgery.[6] Fluorescein injection medicine is normally prepared from fluorescein sodium salt. Therefore, its commercial name has been assigned as "fluorescein sodium". However, it may cause some side effects such as nausea, vomiting, skin discoloration, allergies and seizures.[7-10] Leakage of fluorescein sodium in retinal after intravenous injection is particularly relevant to rhegmato-genous retinal detachment, cerebral malaria and brain swelling,[11,12] with depending on the concentration of sodium fluorescein.[13] Therefore, the quality control of commercial fluorescein sodium is important.

There are several techniques for quantitative analysis of fluorescein sodium such as high-performance liquid chromatography,[14] capillary electrophoresis[15] or atomic absorption spectrophotometry.[16] Apart from the quantitative analysis, there was the research reported the monitoring of leakage of fluorescein sodium by using the confocal scanning laser ophthalmoscopy technique.[13] All of the above-mentioned techniques provide the advantages of high sensitivity, high accuracy and selectivity. However, the instruments are bulky and their analytical process are complicated with time-consuming.

Therefore, this work is interested in development of the alternative portable device for the simple and rapid determination of fluorescein sodium based on using "Cellulose nanofibrils (CNFs)". The CNFs are flexible fiber-like materials which compose of amorphous and crystalline fractions of cellulose with nano-sized diameters.[17] They offer many benefits such as large surface area, biodegradable, flexible and high optical transparency.[18,19] There are many publications presenting use of the specific reagent-immobilized CNFs for the quantitative analyses of cholesterol,[20] mercury (II),[21] tetracycline,[22] ammonium,[23] hydrogen peroxide and glucose.[18] However, to the best of our literature reviews, the application of the CNFs for the colorimetric

detection of fluorescein injection has not been reported so far.

Herein, this work, we aim to develop the CNFs and adapt as the colorimetric analytical platform for the simple measurement of fluorescein injection sample for quality control. The CNFs was prepared from rice straw, one of the major agricultural biowaste materials in Thailand, based on the TEMPO-mediated oxidation reation.[24] The bare CNFs were further immobilized with both the fluorescein standard and sample solutions to obtain the "Fluorescein-immobilized CNFs (Fl-CNFs)" strip. The RGB color intensity of the Fl-CNFs were evaluated by ImageJ™ after capturing of the photographic image of the sensing strips via a mobile phone. Quantitative analysis was carried out by construction the calibration plot between the green channel intensity and the standard concentration.

2. Materials and Methods

2.1 Materials

All chemicals used were of analytical reagent grade and used as purchased. Fluorescein sodium salt and absolute ethanol were purchased from Carlo-Erba, France. TEMPO (2,2,6,6-tetramethylpiperidine 1-oxyl radical), sodium bromide (99.0 %, NaBr) and sodium hypochlorite (4.00-4.99 %, NaClO) were purchased from Sigma-Aldrich, USA. Sodium hydroxide (NaOH) was purchased from SDFCL, India. Deionized-distilled water (18.2 MΩ · cm) purified by Zeneer up 900 water purification unit (Human corporation, USA) and used throughout.

Rice straw was powdered by ball milling for 3 h, and treated with 3 % w/v NaOH 70 °C for 4 h, then washed with water to remove excess chemicals. After that, it was dried at 70 °C for 24 h before oxidized with TEMPO-mediated.[25]

The working standard solution of fluorescein (10 to 50 % w/v) were prepared. A stock standard solution of 50 % w/v (100.0 mL) was prepared by dissolving 0.0250 g of fluorescein sodium salt with water and this solution was kept at 4 °C before use. The standards of 10 to 40 % w/v fluorescein were daily prepared by appropriate dilution of the stock solution.

2.2 Preparation of the cellulose nanofibrils (CNFs)

CNFs were prepared from rice straw after treated with NaOH and subjected to TEMPO-mediated oxidation by applying previous methods with slightly modification.[19] Briefly, 1 g of grinded rice straw was dispersed in 100 mL of water and stirred for 30 min, then 0.033 g of TEMPO and 0.33 g of NaBr were added into the suspension solution. The oxidation reaction was initiated when aliquots of 15 mL of NaClO were dropped. The pH value was adjusted to around 10 by adding 1 % w/v of NaOH. When the pH value was constant for 15 min, the oxidation reaction was complete.[26] The oxidation reaction was terminated by adding 7 mL of absolute ethanol and stirred for 20 min. The TEMPO-oxidized product was washed until pH value was 7. Then, 50 mL of water was added and the solution was disintegrated by household blender for 20 min. Later, it was centrifuged at 9000 rpm for 15 min to obtain CNFs suspension.

2.3 Preparation of the fluorescein-immobilized Cellulose nanofibrils (Fl-CNFs)

The Fl-CNFs were prepared by silicone molds. At first, pipetting the aliquots of 0.75 mL of CNFs suspension and 0.75 mL of fluorescein with different concentrations (10, 20, 30, 40, and 50 % w/v) into the commercial available plastic silicone molds (1.5 × 1.5 × 1.0 cm^3). The mixture was sonicated for 20 min, and then it was drying at room temperature to obtain the Fl-CNFs.

2.4 Assay for fluorescence detection of fluorescein

To confirm that the fluorescein sodium was immobilized on CNF, fluorescence detection of fluorescein sodium was studied. The immobilized CNFs were directly put into the

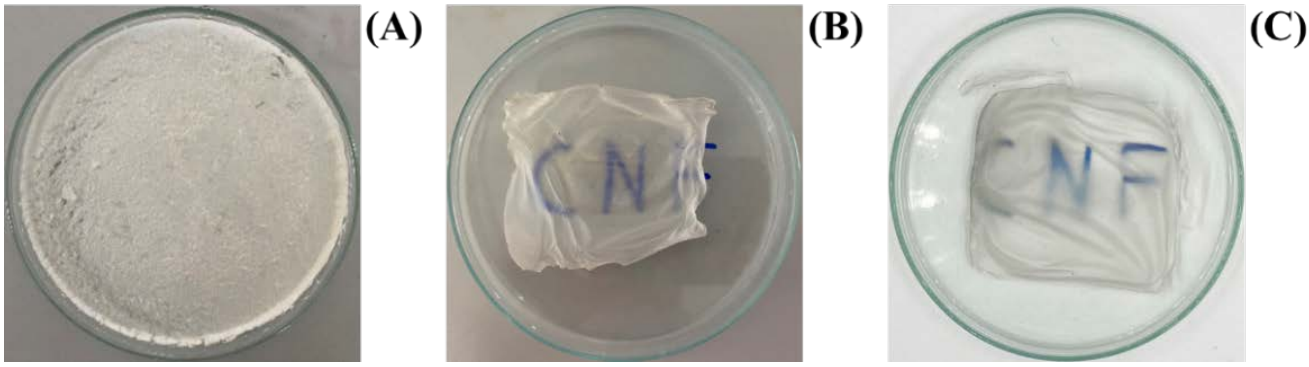

Figure 1. (A-C) Photographs images of CNFs obtained by oxidizing rice straw 1, 2, and 3 times, respectively.

'home-made' sample holder. Then, the holder was inserted into the sample compartment of a 630 JASCO spectrofluorometer (USA) for the fluorometric measurement.

2.5 Assay for colorimetric detection of fluorescein

For the colorimetric detection of fluorescein, we employed an "iPhone11"^{TM} for image capturing of the Fl-CNFs under UV irradiation using UV LED tube 8 W AC220V in a light-controlled studio. The RGB colored intensity were evaluated by "ImageJ"^{TM}. We constucted the linear equations of the plottings between three color intensities (red, green, and blue) and concentrations of the standard fluorescein immobilized-CNFs. It was found that green color intensity gave the best linearity. Therefore, the green color channel was selected for the quantitative analysis.

3. Results & Discussion

3.1 Effect of oxidation by TEMPO

Because the bare CNFs were synthesized from rice straw by oxidizing with TEMPO, the effect of the number of the oxidation cycle by TEMPO was studied. **Figure 1** are photographs images of the CNFs obtained after the TEMPO-mediated oxidization. When the CNFs were oxidized for the first time, it was not transparent (**Figure 1A**). While the rice straw was repeatedly oxidized for the second and the third times, the obtained CNFs become more transparent (**Figure 1B and 1C**). However, their appearances are not difference as investigated by naked eye. Therefore, the appropriate number for the oxidization cycle was selected at two cycles for minimizing reagents and time consumption.

3.2 Characterization

Scanning Electron Microscope (SEM) was employed for characterization of the morphology of the CNFs in this work. **Figure 2A** shows the SEM image of CNFs. It was found that the networking cellulose fibers with small dimensions were obtain. The CNFs in this work was transparent (**Figure 2B**).

3.3 Immobilization of fluorescein to rice straw-CNFs

The conditions for fluorescein immobilization on the CNFs were studied by measuring the fluorescence intensity under an excitation wavelength at 494 nm with a spectrofluorometer. From **Figure 3**, it was found that the fluorescence spectrum of CNFs after immobilizing the bare CNFs in standard fluorescein concentration at 10 %w/v for 72 hr. has a maximum emission intensity at the wavelength of 535 nm, and the inset photograph of **Figure 3** shows that the Fl-CNFs exhibits a bright emitted green color under UV irradiation which confirmed that the fluorescein was successfully immobilized on the CNFs.

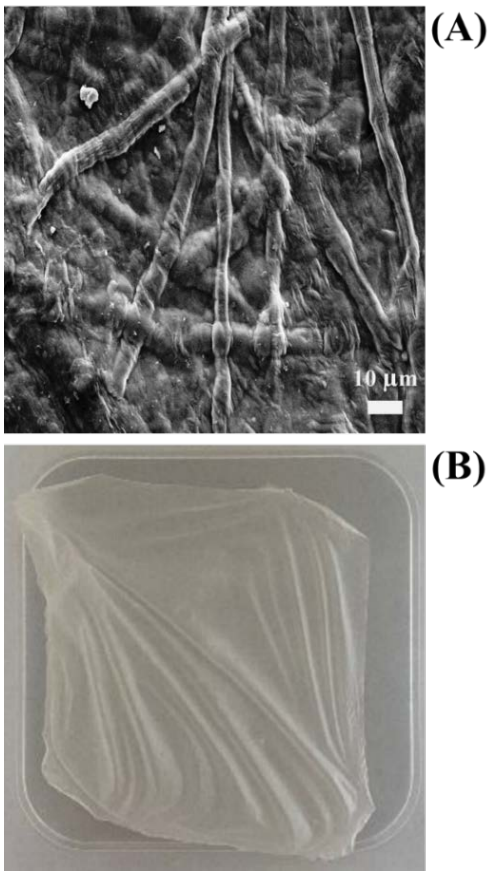

Figure 2. (A) SEM image of CNFs, (B) Photographs images of CNFs

3.4 Analytical performances

The analytical performance of the developed method namely, linear working range, relative standard deviation (RSD), and method detection limit (MDL) were studied.

Figure 4 shows the linear responses of the green-color intensity obtained when the immobilized Fl-CNFs was studied. It was found that as the concentration of the standard fluorescein increased from 10-50 %w/v, the green-color intensity decreased with satisfied linearity. The results show that although the uniformity of fluorescein on CNFs in this study is not the same in every piece (inset photographs), it can be used for quantitative analysis.

The calculated RSD values of the linear responses of colorimetric detection of Fl-CNFs are shown in **Table 1.** It was found that the RSDs were

relatively small, indicating that the methods have high reproducibility.

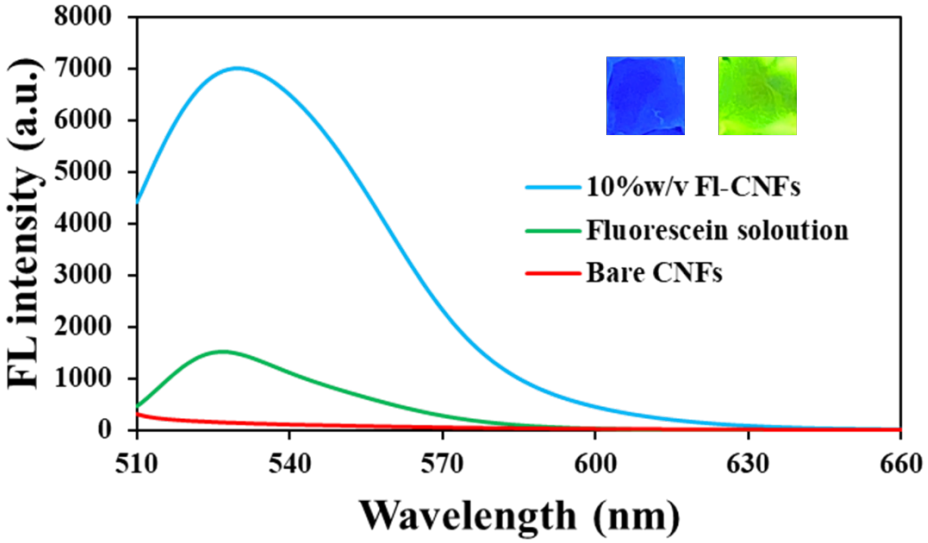

Figure 3. The Fluorescence spectra of bare CNFs and 10%w/v Fl-CNFs. Inset: photographs of Bare CNFs (left) and 10%w/v Fl-CNFs (right) under UV light.

Table 1. Relative standard deviation (RSD) of the developed Fl-CNFs method of the determination of fluorescein solution (n = 3)

Concentration of fluorescein solution (%w/v)	RSD from the colorimetric detection (%)
10	0.45
20	1.43
30	0.74
40	1.05
50	0.20

MDL was measured concentration can be observed. This work assessed the MDL by imaging the Fl-CNFs sensing platform with various concentrations of fluorescein immobilized and compared with bare-CNFs under UV light. The results are shown in **Figure 5.** It was found that at0.01 %w/t of fluorescein immobilized was no fluorescence and the fluorescence of Fl-CNFs was observed at the lowest concentration of 0.05 %w/v. Therefore, the MDL of the developed method was 0.05 %w/v.

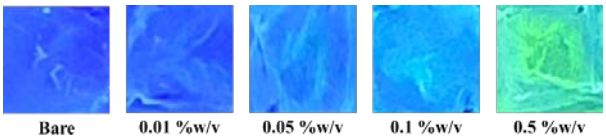

Figure 5. Photographs of bare CNFs and Fl-CNFs with various concentrations of fluorescein immobilized under UV light

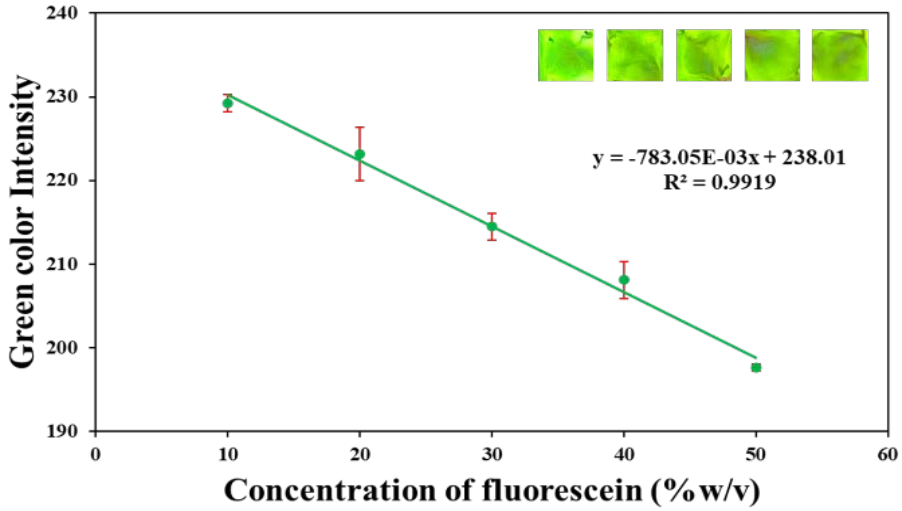

Figure 4. The linear responses of the color intensity of Fl-CNFs with various concentrations of fluorescein immobilized. Inset: photographs of Fl-CNFs with various concentrations of fluorescein immobilized under UV light.

3.5 Validation and application to fluorescein injection samples

To verify the practicability of the developed method, it was applied to measure the concentration of the fluorescein in the synthetic and the commercial samples. For the synthetic sample (S1-S5) the compared to the result obtained by spectrofluorometer **(Table 2).** The fluorescein contents were statistically compared using a Paired t-test,[27] it was found that there were no significant differences between the compared method and the developed method (t_{cal}: 1.27, t_{cri}: 2.78 at 95% confidence level). Advantages of using the Fl-CNFs as the colorimetric strips are their robustness and cost-effectiveness as the fragile fluorescence quart cell and the expensive and bulky spectrofluorometer are not necessary.

In addition, the developed method was applied to a commercial 10 %w/v fluorescein injection sample (S6-S7). As shown in **Table 3**, the results were consistent with the label values with a relative error of <5%. These results mean that our method is highly accurate.

Table 2. Comparison of the concentrations of fluorescein (%w/v), determined by this work and by spectrofluorometry.

Sample	Fluorescein concentration (Mean ± SD, n = 3)	
	This work	Fluorescence detection
S1	14.27 ± 0.51	15.58 ± 0.04
S2	22.81 ± 0.76	23.44 ± 0.09
S3	36.59 ± 0.85	36.89 ± 0.07
S4	44.24 ± 0.51	45.64 ± 0.03
S5	48.48 ± 0.34	47.53 ± 0.02

Table 3. Summary of the commercial fluorescein concentrations (%w/v), determined by this work.

Sample	Label	Concentration of fluorescein (Mean ± SD, n = 3)	% Relative error
S6	10	10.36 ± 0.41	3.6
S7	10	10.21 ± 0.38	2.1

Note: Relative error (%) = ((Calculated value – Label value)/Label value) ×100.

4. Conclusion

Transparent Fl-CNFs, synthesized by oxidizing rice straw with TEMPO were successfully applied as a colorimetric strip to quantify the fluorescein content in the fluorescein injection medicine. The calibration curves for working ranges of fluorescein (10-50%w/v) have high linearity with $r^2 > 0.99$, and also provide high reproducibility (RSD <5%). The method detection limit (MDL) of the developed method was 0.05 %w/v. No significantly different from the analytical results with the fluorescence detection. Therefore, it can be confirmed that the developed method is accurate. Moreover, it can be used for quantitative analysis with commercial fluorescein, providing highly accurate analytical results.

Acknowledgements

Financial support (Grant no. CW-2-2564-M-002) from the Faculty of Science, King Mongkut's Institute of Technology Ladkrabang (KMITL) to RS, is gratefully acknowledged. The authors also thank the Applied Analytical Chemistry Research Unit, Department of Chemistry, Faculty of Science, KMITL for instrumental support.

References

1. Din, A. A.; Hammerschmidt, M.; Maamri, A.; Munteanu, C.; Bernhard, H.; Michael, B.; Seitz, B.; Abdin, A. Chronic renal failure as predictive factor for acute elevation of systolic blood pressure after fluorescein angiography in patients with retinal diseases. *Heliyon*. **2023**, 9, E22700.
2. Ali, S. M.; Kozak, I. Fundus fluorescein angiography via percutaneous endoscopic gastrostomy: Description of technique. *Am. J. Ophthalmol. Case Rep*. **2023**, 30, 101832.
3. Sarici, K.; Yordi, S.; Martin, A.; Lunasco, L.; Mugnaini, C.; Chu, K.; Moini, H.; Vitti, R.; Srivastava, S. K.; Ehlers, J. P. Longitudinal Quantitative Ultrawide-field Fluorescein Angiography Dynamics in the RUBY Diabetic Macular Edema Study. *Ophthalmol. Retina*. **2023**, 7, 543-552.
4. Van Der Veen, M. H.; Tsuda, H.; Arends, J.; ten Bosch, J. J.; Evaluation of Sodium Fluorescein for Quantitative Diagnosis of Root Caries. *J. Dent. Res*. **1996**, 75, 588-593.
5. Thapa, P.; Bhatt, S.; Mishra, D.; Mehta, D. S. Effect of fluorescein dye concentration in oral cancer tissue: statistical and spectroscopic analysis. *Photodiagnosis Photodyn. Ther*. **2023**, 44, 103889.
6. Restelli, F.; Bonomo, G.; Monti, E.; Broggi, G.; Acerbi, F.; Broggi, M. Safeness of sodium fluorescein administration in neurosurgery: Case-report of an erroneous very high-dose administration and review of the literature. *Brain and Spine*. **2022**, 2, 101703.
7. Kvopka, M.; Chan, W.; Lake, S. R.; Durkin, S.; Taranath, D. Fundus fluorescein angiography imaging of retinopathy of prematurity in infants: A review. *Surv. Ophthalmol*. **2023**, 68, 849-860.
8. Musa, F.; Muen, W. J.; Hancock, R.; Clark, D. Adverse effects of fluorescein angiography

in hypertensive and elderly patients. *Acta Ophthalmol. Scand*. **2006**, 84, 740-742.
9. Bertani, R.; Ferrarez, C. E.; Perret, C. M.; Batista, S.; Koester, S. W.; Lovato, R. M.; Ribeiro de Oliveira, M. M. The Fluorescent Patient: An Unusual Effect of Fluorescein Angiography. *Cureus*. **2021**, 13, E15011.
10. Zgolli, H.; Mabrouk, S.; Chebbi, A.; Malek, I.; Nacef, L. Generalized pseudopsoriasis due to fluorescein injection. *J. Fr. Ophtalmol*. **2021**, 44, 922-923.
11. Rajeh, A.; Serhan, H. A.; Alfakir, A.; Askar, M.; Kassom, A. Leakage of Fluorescein Angiography Secondary to Rhegmatogenous Retinal Detachment: A Case Report. *Cureus*. **2022**, 14, E32763.
12. Zhao, Y.; MacCormick, I. J. C.; Parry, D. G.; Leach, S.; Beare, N. A. V.; Harding, S. P.; Zheng, Y. Automated Detection of Leakage in Fluorescein Angiography Images with Application to Malarial Retinopathy. *Sci Rep*. **2015**, 5, 10425.
13. Ossewaarde-Van Norel, J.; Van Den Biesen, P. R.; Van De Kraats, J.; Berendschot, T. T. J. M. Comparison of fluorescence of sodium fluorescein in retinal angiography with measurements in vitro. *J. Biomed. Opt*. **2002**, 7, 190-198.
14. Habib, A. A.; Mabrouk, M. M.; Hammad, S. F.; Megahed, S. M. Application of Chromatographic Response Function in Development of Stability Indicating HPLC Method for Determination of Benoxinate Hydrochloride and Fluorescein Sodium Mixture Using Factorial Design. *J. Adv. Med. Pharm. Res*. **2020**, 1, 1-8.
15. Sun, Y.; He, Y.; Wang, S.; Liang, S.; Zhu, G. Nonaqueous capillary electrophoresis in microchip: Influence of solvent properties on separation performance, In *2011 International Conference on Remote Sensing, Environment and Transportation Engineering*, Guangdong Pharmaceutical University, China, June 24-26, 2011, 8365-8368.
16. Mota, M. C.; Carvalho, P.; Ramalho, J.; Leite, E. Spectrophotometric analysis of sodium fluorescein aqueous solutions. Determination of molar absorption coefficient. *Int. Ophthalmol*. **1991**, 15, 321-326.
17. Garavand, F.; Nooshkam, M.; Khodaei, D.; Yousefi, S.; Cacciotti, I.; Ghasemlou, M. Recent advances in qualitative and quantitative characterization of nanocellulose-reinforced nanocomposites: A review. *Adv. Colloid Interface Sci*. **2023**, 318, 102961.
18. Bandi, R.; Alle, M.; Park, C. W.; Han, S. Y.; Kwon, G. J.; Kim, N. H.; Kim, J. C.; Lee, S. H. Cellulose nanofibrils/carbon dots composite nanopapers for the smartphone-based colorimetric detection of hydrogen peroxide and glucose. *Sens. Actuators B Chem*. **2021**, 330, 129330.
19. Fu, J.; Zhu, J.; Tian, Y.; He, K.; Yu, H.; Chen, L.; Fang, D.; Jia, D.; Xie, J.; Liu, H.; Wang, J.; Tang, F.; Tao J.; Liu, J. Green and transparent cellulose nanofiber substrate-supported luminescent gold nanoparticles: A stable and sensitive solid-state sensing membrane for Hg(II) detection. *Sens. Actuators B Chem*. **2020**, 319, 128295.
20. Alle, M.; Bandi, R.; Sharma, G.; Dadigala, R.; Lee, S. H.; Kim, J. C. Gold nanoparticles spontaneously grown on cellulose nanofibrils as a reusable nanozyme for colorimetric detection of cholesterol in human serum. *Int. J. Biol. Macromol*. **2022**, 201, 686-697.
21. Fu, J.; Zhu, J.; Tian, Y.; He, K.; Yu, H.; Chen, L.; Fang, D.; Jia, D.; Xie, J.; Liu, H.; Wang, J.; Tang, F.; Tao, J.; Liu, J. Green and transparent cellulose nanofiber substrate-supported luminescent gold nanoparticles: A stable and sensitive solid-state sensing membrane for Hg(II) detection. *Sens. Actuators B Chem*. **2020**, 319, 128295.
22. Zhang, X.; Peng, J.; Huang, H.; Qi, X.; Zhang, N.; Wang, Y.; Qiao, J.; Guo, X.; Wu, Y. Synthesis of cellulose nanofibrils modified with carbon dots-graft-polyacrylamide/ZIF-8 composite hydrogel for simultaneous adsorption and detection of tetracycline. *J. Chem. Eng*. **2023**, 470, 144087.
23. Khanjanzadeh, H.; Park, B. D.; Pirayesh, H. Intelligent pH- and ammonia-sensitive indicator films using neutral red immobilized onto cellulose nanofibrils. *Carbohydr. Polym*. **2022**, 296, 119910.
24. Isogai, A.; Saito, T.; Fukuzumi, H. TEMPO-oxidized cellulose nanofibers. *Nanoscale*, **2011**, 3, 71-85.
25. Miao, X.; Lin, J.; Bian, F. Utilization of discarded crop straw to produce cellulose nanofibrils and their assemblies. *J. Bioresour. Bioprod*. **2020**, 5, 26-36.
26. Zhang, P.; Wang, X.; Xue, B.; Huang, P.; Hao, Y.; Tang, J.; Maletić, S. P.; Rončević, S. D.; Sun, H. Preparation of graphite-like biochars derived from straw and newspaper based on ball-milling and TEMPO-mediated oxidation and their supersorption

performances to imidacloprid and sulfadiazine. *J. Chem. Eng.* **2021**, 411, 128502.

27. Miller, J. N.; Miller, J. C.; Miller, R. D. Statistics and Chemometrics for Analytical Chemistry, 7th edition, In *Pearson Education*, Loughborough University, England, April 26, 2018.

Preparation and evaluation of zeolite composite monoliths for micro-solid phase extraction

Manaphon Traswiman, Kesara Ar-sanork, Jatuporn Wittayakun, Sanchai Prayoonpokarach, and Patcharin Chaisuwan*

School of Chemistry, Institute of Science, Suranaree University of Technology, 111 University Avenue, Muang District, Nakhon Ratchasima 30000, Thailand

**E-mail: p.chaisuwan@sut.ac.th*

Abstract:

Currently, monoliths are garnering interest as excellent adsorbents for micro-solid phase extraction (µ-SPE) due to the high surface area and high permeability. In this work, we proposed a preparation method of zeolite composite monoliths for µ-SPE. The composite monoliths were synthesized through photo-assisted co-polymerization of methacrylic acid and ethylene glycol dimethacrylate (MAA-EDMA), which were not only used as a support but also functional monomers. Two different types of zeolites, NaX and NaY, were composited with the MAA-EDMA monolith to obtain NaX-MAA-EDMA and NaY-MAA-EDMA monoliths, respectively. The synthesized materials were characterized by scanning electron microscope and energy dispersive X-ray spectroscopy. To assess the capability of the sorbents, 8-hydroxyl-2'-deoxyguanosine (8-OHdG) was employed as the adsorbed model. The adsorption abilities were investigated by comparing % trapping of 8-OHdG on NaX-MAA-EDMA, NaY-MAA-EDMA and MAA-EDMA monoliths. The crucial extraction parameter, including zeolite contents, amount of sorbents, and pH of sample loading were examined. The results showed a maximum trapping of 69 % for adsorbing 8-OHdG on NaY-MAA-EDMA. Meanwhile, NaX-MAA-EDMA and MAA-EDMA exhibited % trapping of 31 % and 4 %, respectively.

1. Introduction

Micro-solid phase extraction (µ-SPE) has played a crucial role in sample preparation before the analysis, particularly for the determination of trace analytes in complex samples. The µ-SPE is employed to remove matrix interferences and enrich the target analyte(s).[1,2] Adsorbent-based µ-SPE is a popular method, offering simple operation, time-saving, relatively low organic solvent requirements compared to traditional liquid-liquid extraction, and high extraction efficiency.[3-5] Solid sorbents are commonly packed or synthesized in several housing such as cartridge,[6-8] syringe,[8,9] polyether ether ketone (PEEK) tubing,[10-12] and polypropylene (PP) pipette tip.[6-8,13]

In order to achieve effective sample clean up with high pre-concentration factor, selecting the adsorbent is an important parameter. Monolithic material is one of the most widely used adsorbents for µ-SPE method. Monolith is continuous single rod of porous material, providing two different pores, mesopores and macropores, which offer high surface area with high permeability.[14] However, their drawbacks include limitations in hydrophilic and ion-exchange applications due to their polymer-based nature.

Inorganic materials such as silica,[15,16] graphene,[15-17] graphene oxide,[15,16] carbon nanotubes, metal oxide,[15-18] and zeolite[17-19] have been widely employed as solid sorbents for extracting various target analytes and applications. Among these, zeolites, crystalline aluminosilicates with a dimensional network of aluminum and silicon tetrahedral linked by the sharing of oxygen atoms[20] (the structure is shown in Figure 1), possess a special property due to their well-defined microporous structure, ion exchange sites, and their hydrophilicity.[21] Zeolites have been applied as ion exchanger sorbent for adsorption processes.[22] Among the advantages of the zeolite-based materials, fabrication technologies are critical. Generally, particles-based sorbents for µ-SPE are packed between two frits to prevent the loss of sorbents. However, this packing is complicated and high-density packing leads to low permeability with high-flow resistance.

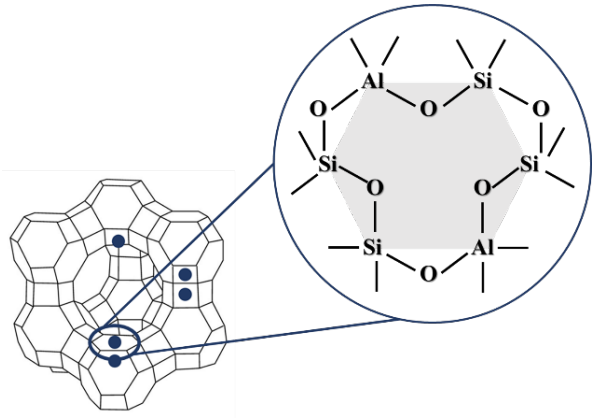

Figure 1. Structure of zeolite.

This work composited monolithic material with zeolites and investigated the potential of the composite materials for using as solid sorbent for the extraction of a DNA damage marker, 8-hydroxy-2'-deoxyguanosine (8-OHdG). The zeolite composite monoliths were synthesized by dispersing zeolitic particles in methacrylic acid-co-ethylene dimethacrylate (MAA-EDMA) monolith prior to *in situ* synthesis in PP pipette tips. The fabricated monolith composited zeolite in pipette tips were characterized by scanning electron microscope (SEM) and energy dispersive X-ray spectroscopy (EDS). Important extraction parameters, including zeolite content, pH of loading sample, and monolith amount, were investigated. Two types of zeolites, NaX and NaY were employed for the synthesis and compared for the 8-OHdG adsorption abilities.

2. Materials and Methods

2.1 Materials, reagents, and buffer preparation

PP pipette tips were acquired from Axygen (USA). MAA, EDMA, NaX, 8-OHdG, 2,2-dimethoxy-2-phynylacetophenone (DMPAP) and 1-decanol were purchased from Sigma-Aldrich (USA). Potassium dihydrogen phosphate (KH_2PO_4), and methanol (MeOH) were purchased from RCI Labscan (Thailand). NaY was purchased from Alfa Aesar (USA). Toluene was purchased from QRëCTM-Qchemical (New Zealand) and disodium hydrogen phosphate (Na_2HPO_4) was purchased from Merck (Germany).

A 20 mM phosphate buffer pH 7.0 was prepared by dissolving 0.6805 g of KH_2PO_4 in approximately 230 mL of RO water. The pH was adjusted using 1 M NaOH and then made up the volume with RO water in a 250 mL volumetric flask.

2.2 HPLC-UV method

The HPLC-UV method was performed on a C18 column (BDS Hypersil™, 150 mm x 4.6 mm, 5 µm, Thermo Fisher Scientific, USA) with mobile phase of 10:90 (v/v) MeOH:20 mM phosphate buffer at pH 7.0. The separation condition was carried out at 25 °C, 1.0 mL min^{-1} flow rate, 60 µL injection volume, and UV detection at 210 nm.

2.3 Synthesis of zeolite composite monolith and MAA-EDMA monolith in PP pipette tips

Pre-polymerization solutions of MAA-EDMA, NaX-MAA-EDMA, and NaY-MAA-EDMA were prepared by weighting monomers, porogen, and initiator in cleaned glass vials. The compositions and weights of the components are shown in Table 1.

To fabricate the monolith and composite monoliths in PP tips, the tips were cleaned with MeOH and dried before use. The ends of the cleaned tips were sealed with parafilm®. The pre-polymerization solutions were accurately transferred into the prepared tips, then sealed the top of the tips with parafilm® to prevent the solvent evaporation. The tips were irradiated under UV light (365 nm) to initiate the polymerization for 10 min. The polymerized monoliths in tips were washed with MeOH to eliminate the residual of monomers and porogen. Procedure for the fabrication of monolith and zeolite composite monolith in PP pipette tip is demonstrated in Figure 2.

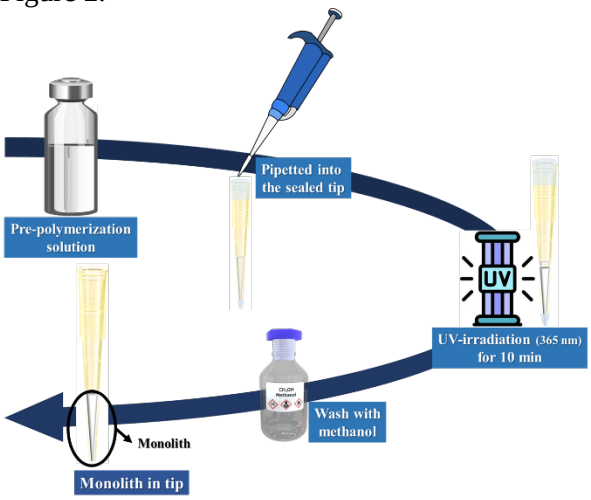

Figure 2. Procedure for the fabrication of monolith and zeolite composite monoliths in PP pipette tip.

2.4 Characterization of monoliths in tip

To visualize the morphology of the monolith in PP pipette tips, SEM technique was carried out. The fabricated monolith in tips were cross sectioned before investigated by SEM (Model Quanta450, Thermo Fisher Scientific, USA).

EDS mapping was carried out to observe the existence of zeolite in the monoliths. The synthesized monoliths were cross-sectioned at the middle and bottom of the tips before being investigated by EDS (XGT-5200, Horiba, Japan).

2.5 Trapping of 8-OHdG on the composite monoliths evaluation

The materials were activated with 200 µL MeOH and 50 µL water. An aliquot 200 µL of 8-OHdG (1 mg L^{-1}) was subsequently flowed through the activated sorbent. To assess the adsorption performance of the sorbent to 8-OHdG, the flowthrough solution was collected and then subjected to the HPLC-UV.

Table 1. Compositions of pre-polymerization solutions and weights of monomer, crosslinker, porogen and initiator for synthesis of MAA-EDMA, NaX-MAA-EDMA, and NaY-MAA-EDMA monoliths in pipette tips.

	Zeolite content	Weight (g)					
			Monomer		Porogen		Initiator
		Zeolite	MAA	EDMA	Toluene	1-Decanol	DMPAP
MAA-EDMA							
	0 %	-	0.1856	1.6304	0.9911	7.2359	0.0207
		Pre-polymerization of MAA-EDMA solution (g)					
NaX-MAA-EDMA							
	5 %	0.0516			0.9720		
	10 %	0.1025			0.9182		
	20 %	0.2013			0.8166		
		Pre-polymerization of MAA-EDMA solution (g)					
NaY-MAA-EDMA							
	20 %	0.2094			0.8072		

Percent trapping of 8-OHdG was calculated as followed.

$$\% \text{ Trapping} = \frac{C_{before} - C_{after}}{C_{before}} \times 100\%$$

Where: C_{before} = concentration of 8-OHdG before flowing through the monolith, C_{after} = concentration of 8-OHdG after flowing through the monolith.

3. Results & Discussion

3.1 Fabrication and characterization of monolith and zeolite composite monoliths in PP pipette tips

The monolithic sorbents were *in situ* synthesized in PP pipette tips via photo-assisted polymerization method. Rapid polymerization could be achieved within 10 min by UV irradiation at 365 nm. Bare monolith of MAA-EDMA and zeolite composite monoliths of NaX-MAA-EDMA and NaY-MAA-EDMA monoliths could be form in the PP pipette tips, as shown in Figure 3 (a). White rigids of a single rod materials are observed without cracking and detachment (see Figure 3 (a)).

Permeability of the synthesized monoliths were evaluated by flowing through the materials with MeOH. As summarized in Table 2, the bare MAA-EDMA monolith allowed the solvent percolate easily, presenting the highest permeability. Meanwhile, presenting of zeolite significantly decreased their permeabilities due to the higher flow resistance by the zeolite particles.

Morphologies of the zeolite composite monoliths were investigated by SEM technique. Well attachments of the monoliths against the PP tip wall were observed, as demonstrated in Figure 3 (b), left. There is no observation of void space. Moreover, the prepared monoliths provided good pore distribution which allows percolation of desired solvents and samples (see Figure 3 (b) right).

Table 2. Permeabilities comparison of in pipette tip monolith and zeolite composite monoliths.

Monolith	Zeolite content	Permeability
MAA-EDMA	-	+ + + +
NaX-MAA-EDMA	5 %	+++
	10 %	++
	20 %	+

++++ = Highest permeability; + = Lowest permeability.

To confirm the existing of zeolite in the synthesized monoliths, mappings of zeolite-based elements were investigated, including carbon (C) oxygen (O), aluminum (Al), and silicon (Si). EDS mapping in Figure 3 (c) demonstrated distribution of C in the material which is from polymer-based monolithic material. In addition, O, Si and Al elements could be clearly observed, indicating successful of the preparing zeolite composite monolith.

From the characterizations, the fabrication of in tip monolith and zeolite composite monoliths can be achieved which are ready to apply for µ-SPE.

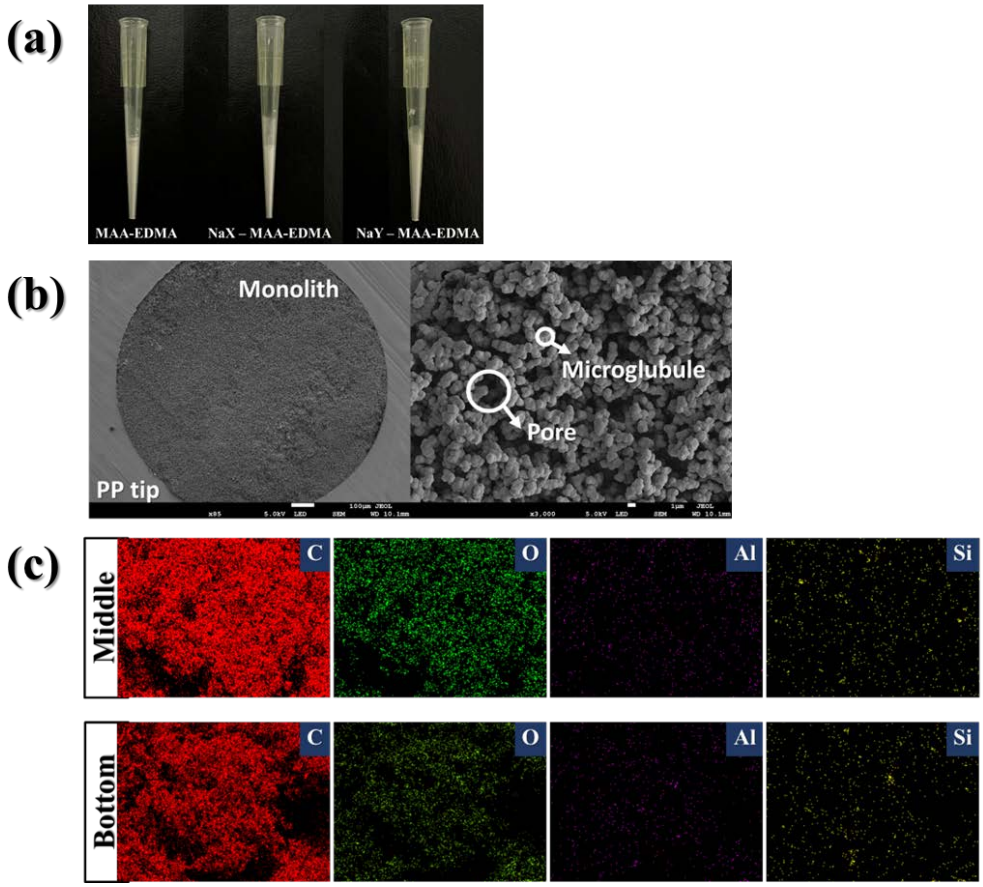

Figure 3. (a) Photographs of representative synthesized MAA-EDMA, NaX-MAA-EDMA, and NaY-MAA-EDMA monoliths in PP tips, (b) representative SEM images of zeolite composite monolith in PP tip (left) and pore and macroglobulin of the NaX-MAA-EDMA (right), and (c) representative elemental mappings of carbon, oxygen, aluminum, and silicon of the NaX-MAA-EDMA using EDS technique.

3.2 Optimization of µ-SPE condition for adsorption of 8-OHdG on the synthesized monoliths

8-OHdG is a biomarker for diseases associated with oxidative stress.[23] Extracting 8-OHdG faces a challenge as it contains amide, amine, and hydroxyl groups, contributing to its nature as a polar compound.[24] To evaluate the adsorption ability of the synthesized monoliths to 8-OHdG, several parameters were studied, including zeolite content, pH of sample loading, and monolith amount. The NaX-MAA-EDMA monolith was selected for the investigations.

3.2.1 Effect of zeolite content

The amount of zeolite in the composite materials was investigated in the range between 5 % to 20 %. As showed in Figure 4 (a), the existing of zeolite impressively increased % trapping of 8-OHdG. % Trapping could be improved from 3.1 % to 16.9 % by adding 5 % zeolite. % trapping of 8-OHdG was increased with increasing of zeolite contents, as indicated in Figure 4 (a). To obtain the highest % trapping, 20 % zeolite was therefore selected for further investigation.

3.2.2 Effect of pH

Sample loading pH was studied at 2.0, 7.0, and 10.0, as depicted in Figure 4 (b). Increasing of pH from 2.0 to 7.0 led to increase in % trapping from 25.6 % to 46.5 %. However, adsorption performance decreased to 3.2 % when pH 10.0 was used, which may be due to the change in properties of zeolite at the high pH.[25] The pH for sample loading was therefore recommended at pH 7.0.

3.3 Comparison of NaX-MAA-EDMA, NaY-MAA-EDMA, and MAA-EDMA monoliths and effect of sorbent amount for adsorption of 8-OHdG

Extraction of 8-OHdG on bare monolith (MAA-EDMA) and zeolite composite monolith with two different types of zeolites, NaX and NaY were preliminary investigated to study the potential of the composite materials for adsorption of polar compounds. As expected, zeolite composite monoliths, NaX-MAA-EDMA and NaY-MAA-EDMA provided higher ability to adsorb 8-OHdG compared to MAA-EDMA monolith (see Figure 5).

Surprisingly, increasing monolith amount by increasing pre-polymerization volume from 50 µL to 100 µL decreased % trapping of 8-OHdG for employing NaX-MAA-EDMA monolith. Meanwhile, increasing monolith amount in NaY-MAA-EDMA significantly improved % trapping of 8-OHdG, as demonstrated in Figure 5, blue graphs.

The highest %trapping of 69.1 % was observed by using 100 µL of NaY-MAA-EDMA monolith in pipette tip.

4. Conclusion

In this work, the zeolite composite monoliths, NaX-MAA-EDMA and NaY-MAA-EDMA have been successfully synthesized in PP pipette tips via photo-polymerization. The materials provided good morphology in terms of pore distributions with good permeability. EDS mapping demonstrated the existing and distribution of zeolite within the monolith pieces. A compound of 8-OHdG was used as the test compound for adsorption investigation in terms of % trapping. Zeolite content, pH of sample loading, amount of composite monolithic sorbent, as well as type of zeolites have been investigated. Compositing of zeolite in the monolithic materials significantly increased trapping of 8-OHdG. Under the optimized condition, 100 µL of pre-polymerization solution of NaY-MAA-EDMA provided the highest % trapping of 69 %, superior to NaX-MAA-EDMA (47 %) and MAA-EDMA (4 %). The investigations indicate that the proposed zeolite composite monoliths are promising as an alternative adsorbent for µ-SPE applications.

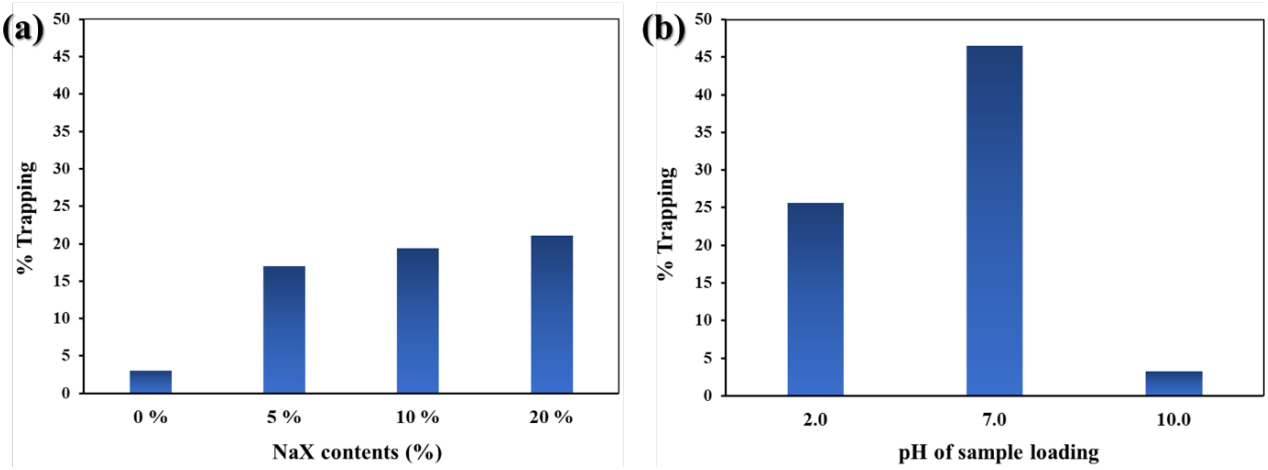

Figure 4. Effect of a) NaX content (%) and b) pH of sample on % trapping of 8-OHdG.

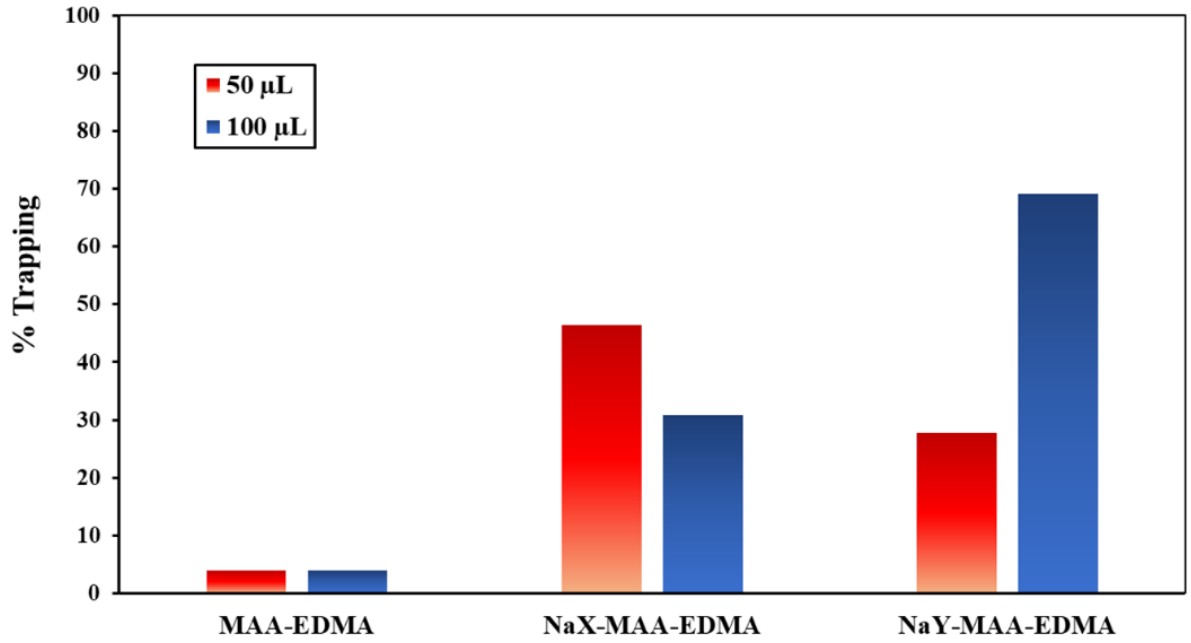

Figure 5. Influence of type of zeolites and amount of monolith on % trapping of 8-OHdG.

Acknowledgements

This work is also supported by Suranaree University of Technology (SUT), Thailand Science Research and Innovation (TSRI), and National Science, Research and Innovation Fund (NSRF; NRIIS number 179338).

References

1. Khezeli, T.; Daneshfar, A. *TrAC, Trends Anal. Chem*. **2017**, *89*, 99-118.
2. Arabi, M.; Ostovan, A.; Bagheri, A. R.; Guo, X.; Wang, L.; Li, J.; Wang, X.; Li, B.; Chen, L. *TrAC, Trends Anal. Chem*. **2020**, *128*, 115923.
3. Wen, S.; Zhu, X. *Food Anal. Methods*. **2014**, *7*, 291-297.
4. Fung, J.; Loussala, H. M.; Han, S.; Ji, X.; Li, C.; Sun, M. *TrAC, Trends Anal. Chem*. **2020**, *125*, 115833.
5. Zhang, J.; Li, W.; Zhu, W.; Qin, P.; Lu, M.; Zhang, X.; Miao, Y.; Cai, Z. *Chem. Commun*. **2019**, *55*, 10019-10022.
6. Płotka-Wasylka, J.; Szczepańska, N.; Guardia, M.; Namieśnik, J. *TrAC, Trends Anal. Chem*. **2016**, *77*, 23-43.
7. Badawy, M. E. I.; El-Nouby, M. A. M.; Kimani, P. K.; Lim, L. W.; Rabea, E. I. *Anal. Sci*. **2022**, *38*, 1457-1487.
8. Dugheri, S.; Marrubini, G.; Mucci, N.; Cappelli, G.; Bonari, A.; Pompilio, I.; Trevisani, L.; Arcangeli, G. *TrAC, Acta Chromatogr*. **2021**, *33*, 99-111.
9. Mehrani, Z.; Ebrahimzadeh, H.; Moradi, E. *Microchim. Acta*. **2020**, *187*, 401.
10. Maciel, E. V. S.; Toffoli, A. L. D.; Lanças, F. M. *J. Sep. Sci*. **2019**, *42*, 258-272.
11. Wang, C.; Zhou, W.; Liao, X.; Li, W.; Chen, Z. *Talata*. **2020**, *208*, 120442.
12. Nasrollahi, S. S.; Yamini, Y.; Shamsayei, M. *J. Sep. Sci*. **2021**, *44*, 1122-1129.
13. Sun, H.; Feng, J.; Han, S.; Ji, X.; Li, C.; Feng, J.; Sun M. *Microchim. Acta*. **2021**, *188*, 189.
14. Nema, T.; Chan, E. C.; Ho, P. C. *J. Pharm. Biomed. Anal*. **2014**, *87*, 130-141.
15. Azzouz, A.; Kailasa, S.; Lee, S. S.; Rascón, A. J.; Ballesteros, E.; Zhang M.; Kim K. H. *TrAC, Trends Anal. Chem*. **2018**, *108*, 347-369.
16. Jing, W.; Wang, J.; Kuipers, B.; Bi, W.; Chen, D. D. Y. *TrAC, Trends Anal. Chem*. **2021**, *137*, 116212.
17. Jalili, V.; Barkhordari, A.; Ghiasvand, A. *Microchem. J*. **2020**, *153*, 104386.
18. Sharma, H.; Dhir, A. *Environ. Chem. Lett*. **2021**, *19*, 851-873.
19. Baile, P.; Fernández, E.; Vidal, L.; Canals, A. *Analyst*. **2019**, *144*, 366-387.
20. Cao, J.; Liu, X. W.; Fu, R.; Tan, Z. *Sep. Purif. Technol*. **2008**, *63*, 92-100.
21. Mohammed, B. B.; Yamni, K.; Tijani, N.; Alrashdi, A. A.; Zouihri, H.; Dehmani, Y.; Chung, M.; Kim, S. H.; Lgaz, H. *J. Mol. Liq*. **2019**, *296*, 111997.
22. Gong-wei, W. *Sea-Lake Salt Chem. Ind*. **2004**, https://api.semanticscholar.org/CorpusID:132445353 (accessed December 28, 2023).
23. Ock, C. Y.; Kim, E. H.; Choi, D. J.; Lee, H. J.; Hahm, K. B.; Chung, M. H. *World. J. Gastroenterol*. **2012**, *18*, 302-308.
24. Sambiagio, N.; Sauvain, J. J.; Berthet, A.; Auer, R.; Schoeni, A.; Hopf, N. B. *Antioxidants*. **2021**, *10*, 38.
25. Buttersack, C.; König, A.; Gläser, R. *Microporous. Mesoporous. Mater*. **2019**, *281*, 148-160.

Laser-induced biochar for the solid-phase extraction of organophosphorus pesticides

Sherwin Hugo T. Lu and Puttaruksa Varanusupakul*

Department of Chemistry, Faculty of Science, Chulalongkorn University, Bangkok 10330, Thailand

**E-mail: puttaruksa.w@chula.ac.th*

Abstract:

Biochar is a carbon-rich material made from the combustion of biomass. It is a sustainable material that can be used as a solid-phase extraction (SPE) sorbent, but conventional research uses energy-intensive pyrolysis methods to produce this. A more energy-efficient approach, using a laser irradiation process, was explored to produce a biochar sorbent for the SPE of organophosphorous pesticides (OPPs). Various biomass materials, rich in lignin, were assessed to produce laser-induced biochar. From characterization data by Raman spectroscopy, cork sheet was the most consistent and, hence, selected as the main biomass material. A central composite design (CCD) was employed in optimizing the following lasing parameters: speed, power, and number of lase times. Lasing speed was best at high settings (200-250 mm/s), and number of times lased was optimal at 1 lase time. Power varied according to the physical properties and functionalities of the analyte. OPPs that were non-polar and aromatic favored high power (10.5-12 W), while OPPs that are non-aromatic favored low power (6-7.5 W). The optimized parameters that covered most OPPs were 9 W, 250 mm/s, and 1 lase time. This new application of laser-induced biochar shows the potential for low-energy production of a biochar sorbent for solid-phase extraction.

1. Introduction

Organophosphorous pesticides (OPPs) have been used since their invention in the 1900's. These chemicals can cause neurological damage as acetylcholinesterase inhibitors and have all been classified as either toxic to humans and/or to the environment.[1] The US banned the use of Chlorpyrifos since 2021.[2] As these analytes are found in trace or sub-ppb levels, sample preparation requires preconcentration methods, such as μ-SPE, prior to analysis by GC-MS.[3]

Several adsorbents were developed for extraction of OPPs by solid-phase extraction.[4,5] Recently, the use of biochar or biomass-derived carbon material has been gaining attention as an inexpensive, eco-friendly, and readily available porous carbon material.[3,6,7] The ability of biochar to adsorb various environmental analytes is from its carbon-rich nature and functional groups.[8,9] These properties are derived from both its biomass source and production process. Biochar can be made from various biomass, mostly carbon- or lignin-rich parts, that are heated to high temperatures (600-1000ºC) under N_2 atmosphere, in a process known as slow pyrolysis.[3,6] Many biochar studies optimize this temperature as an initial step.[3,9-11] Slow pyrolysis will use about 1000 W for 2 or more hours and a review article reported an average biochar yield of 35% for slow pyrolysis,[7]

Laser-induced graphene (LIG) has been reported for making flexible and organic electronics from plastic films, such as polyimide using a laser irradiation process.[12-15] Studies have also shown that fine-tuning laser parameters on polyimide films can be used to control LIG properties, such as oxygen content.[16-18] In addition, some studies have also investigated the lasing of biomass. Chyan *et al.* (2018) successfully produced LIG on raw coconut shell and cork.[14] As the laser irradiation method can apply to create a graphene-rich carbon material, it may be a promising energy-efficient process for small-scale production of biochar. Lasers can use as little as 4.5 W and take only 2.5 minutes to finish. This has the potential to use only 0.19 Wh for 1 run – lessening power consumption compared to pyrolysis methods.

The aim of this study is therefore to investigate the feasibility of biochar production by the laser irradiation method. The laser-induced biochar is then applied as a sorbent for extraction of OPPs in water as summarized in Figure 1.

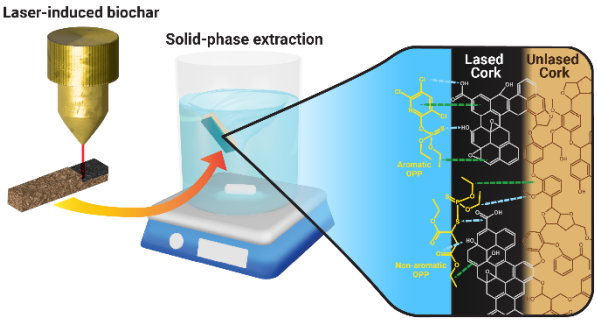

Figure 1. Production of laser-induced biochar for solid-phase extraction of OPPs.

2. Materials and Methods

2.1 Materials

All organophosphorous pesticides (dichlorvos, parathion-methyl, chlorpyrifos-methyl, pirimiphos-methyl, fenitrothion,

malathion, chlorpyrifos, profenofos, ethion, phosalone) were procured from LGC Standards (Dr. Ehrenstorfer). Ethyl acetate (AR grade, 99.9%) was from Carlo Erba. All OPP standards were prepared in ethyl acetate. Ethion was used as an internal standard at 10 mg/L.

Dried water hyacinth stems were bought from a local market as 2-3 cm long pre-cut pieces. Coconut fiber (coir) sheet and cork sheet were obtained from an online store (Lazada Thailand). The thickness of coir sheet and cork sheet were 12 mm 3 mm, respectively.

2.2 Production of laser-induced biochar

Biomasses were lased using a commercial laser engraver, Beamo Flux, equipped with a 30 W 10.6-µm CO_2 laser. Each studied biomass was prepared as follows: The dried water hyacinth stems were cut open to a 3 x 2 cm and had a thickness of 3 - 5 mm. The coir sheet was cut into 5 x 5 cm. In addition, the coir was also prepared as compressed coir pellet. First, coir sheet was soaked in water and shredded. After drying, about 0.05g was compressed using a hydraulic press in a 20 mm pellet mold. Lastly, the resulting pellet had a thickness of about 0.70 mm. Finally, the cork sheet was cut to 20 x 3 mm size.

Each material was held in place using double-sided tape on aluminum foil sheet and lased. The lasing parameters were power (4.5 to 12.0 W), speed (30 to 250 mm/s), and number of lased times (one to five) and varied per material.

2.3 Characterization of laser-induced biochar

The laser-induced biochar produced from all biomasses was characterized by Raman spectroscopy (Thermo Fisher Scientific DXR3 Raman Microscope), SEM-EDX (Jeol IT-100), N_2 adsorption (MicrotracBEL BELSORP-mini II), FT-IR spectroscopy (Nicolet iS50) and thermogravimetric analysis (Perkin-Elmer Pyris 1 TGA).

Raman spectroscopy was performed with a 532-nm laser at 10 mW. Prior to SEM-EDX analysis, samples were coated with gold. For N_2 adsorption study, samples were pretreated at 125 ºC for 20 hours. FT-IR spectroscopy was performed using the KBr pellet method. Lastly, TGA was done using the following temperature programming: 50 ºC for 2 minutes, then ramped to 800 ºC at a heating rate of 20 ºC/min.

2.4 Optimization of lasing parameters by central composite design (CCD)

The lasing parameters, specifically power (in Watts), speed (in mm/s), and number of lased times, were optimized using a five-level-three-factor central composite design (CCD). A circumscribed model with the values of 19.9 – 40.1% power, 99.32 – 250.68 mm/s, and 1 - 5 times were studied. The enrichment factor (EF) from the solid-phase extraction of 9 OPPs using the laser-induced biochar was used as a response of the experimental runs. A response surface was utilized for visualization.

2.5 Solid-phase extraction procedure

Prior to analysis, each sorbent was conditioned by soaking it in 400 µL of ethanol, vortexed for 5 minutes, then finally air dried.

Exactly 40-mL of 10 µg/L mixed OPPs in Milli-Q® water was applied as a water sample. The laser-induced biochar was floated on the surface of water sample with the lased side facing down, and the solution magnetically stirred. After 30 minutes, the sorbent was removed, placed onto a clean Kimwipe™ for water removal, and transferred to a 1.5-mL tube. Then, 400 µL of ethyl acetate was added for desorption, vortexed for 10 minutes, and was filtered through a 0.22-µm syringe filter. The filtrate was dried with nitrogen gas, reconstituted with 200 µL of ethyl acetate, and spiked with 10 µL of 10 ppm ethion as an internal standard prior to GC-MS analysis.

2.6 Analysis of OPPs by GC-MS

The analysis of organophosphorous pesticides was performed using an Agilent 8890 Gas Chromatography system coupled with an Agilent 5977B Series Mass Selective Detector (mass spectrometer). The HP-5ms UI (Agilent J&W, Thailand) fused-silica capillary column (30 m x 250 µm) coated with 0.25 µm bonded film of (5%-phenyl)-methylpolysiloxane. The GC column temperature program used was as follows: 50 ºC held for 2 mins, then ramped to 250 ºC at 15 ºC/min (held for 3 mins). A 1-µL sample volume was injected in a splitless mode with an inlet temperature of 260 ºC and an MSD transfer line temperature of 280 ºC. Helium was used as a carrier gas at a constant flow rate of 1.2 mL/min. The mass spectrometer was operated in the electron impact mode with an ion source temperature of 230 ºC, electron impact energy was tuned at 70 eV, and MS quad temperature of 150 ºC. For quantitative determination using selected ion monitoring (SIM), pesticides were identified by ions with the following m/z values and quantified by the ions 179 and 304 for diazinon; 246 and 263 for parathion-methyl; 286 and 288 for chlorpyrifos-methyl; 260 and 277 for fenitrothion; 290 and 305 for pirimiphos-methyl; 127 and 173 for malathion; 197 and 314 for chlorpyrifos; 337 and 339 for profenofos; 231 and 384 for ethion; 182 and 367 for phosalone.

3. Results & Discussion

3.1 Selection of biomass for laser-induced biochar

Various lignin-rich biomass materials which are dried water hyacinth, coconut fibers and cork were examined for laser-induced biochar production. As shown in Figure 2A and 2B, dried water hyacinth and coconut coir had ablation or produced embers, and no biochar was formed for these biomasses.

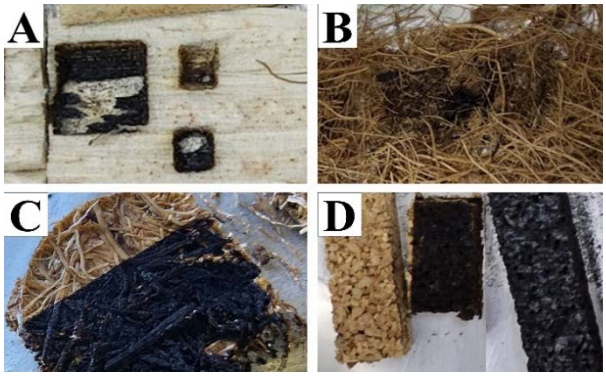

Figure 2. Laser-induced biochar from (A) water hyacinth stems, (B) coir sheet, (C) compressed coir pellet, and (D) cork sheet

The lasing of compressed coir pellet achieved some degree of biochar production, formed on the surface (Figure 2C). Unfortunately, this material was difficult to produce both procedurally and repeatably. Lastly, lased cork sheet resulted in good reproducibility of biochar formation (Figure 2D). As a result, only coir pellet and cork were able to produce laser-induced biochar.

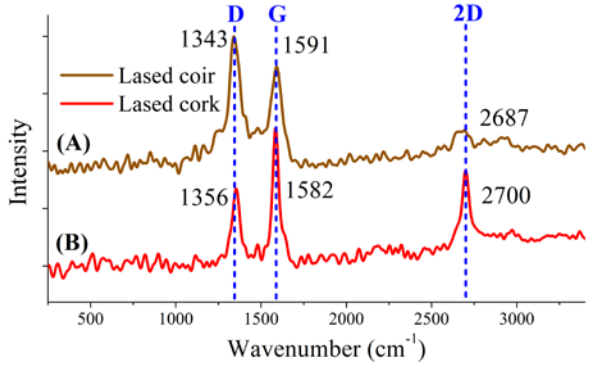

Figure 3. Raman spectra of (A) coir pellet and (B) cork.

Comparing the laser-induced biochar produced from coir pellet and cork sheet via Raman spectroscopy (Figure 3), the coir pellet did not achieve graphene quality as good as the cork did. We see that cork produces a clear 2D peak, while coir does not, which indicates greater quality of graphene. We also see the D peak of cork is lower than its G peak, also showing the graphene would have less defects, such as open rings or oxygen groups. This can be controlled by adjusting lasing parameters, but only until the material undergoes ablation. In this case, coir ablates before achieving good graphene. During lasing, it was also easier to replicate the Raman spectrum of cork using the same parameters compared to coir pellet. The laser-induced biochar from cork was, therefore, chosen for further characterization for its easier preparation and higher quality graphene produced.

3.2. Characterization of laser-induced biochar

Characterizing the laser-induced biochar from cork was done using TGA, FTIR, N_2 adsorption, and SEM-EDX.

TGA profile of cork and lased cork are nearly identical. Deviation from cork happens only at around 75 ºC. This is consistent as the laser irradiation method only affects the top-most layer of the cork piece, while the remaining bottom layer is still cork.

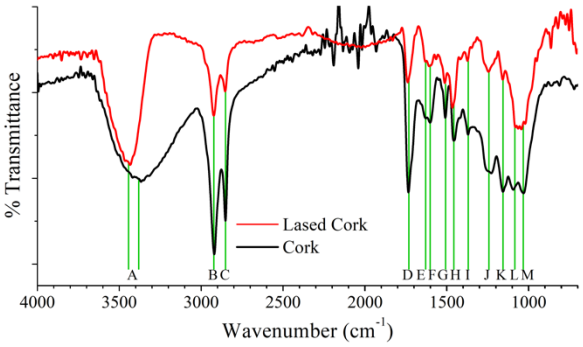

Figure 4. FTIR spectra of lased cork and cork

FTIR of cork and lased cork are shown in Figure 4, where 13 peaks, as listed in Table 1, were identified based on previous literatures of cork and biochar.[19-21]

Table 1. FTIR peak wavenumbers (cm^{-1}) of cork and lased cork with their corresponding bonds

Peak	Wavenumber		Bond
	Cork	Lased	
A	3368	3432	-OH stretch
B	2921	2921	C-H stretch (alkane)
C	2851	2853	C-H stretch (O-CH_3)
D	1734	1735	C=O stretch
E	1628	1624	C=O stretch (aromatic)
F	1604	1601	Skeletal aromatic vibrations
G	1509	1510	
H	1457	1462	C-H bend (methoxy)
I	1370	1373	O-H bend (phenolic)
J	1230	1243	C-O stretch (aromatic)
K	1159	1157	C-O stretch (ether)
L	1101	1080	
M	1033	1043	C-O stretch (ether/alcohol)

From FTIR spectra of cork and lased cork, peak A was decreased significantly and blue-shifted upon lasing. This can be from ablation or dehydration upon lasing and caused the OH groups that remain to be nearer to aromatic groups. In peak B and C, the hydrocarbon groups are maintained with decreased intensity. From peaks D to M, most peaks decreased drastically, as expected from the laser irradiation method, except for peaks G and H. These two peaks decreased less compared to the others and are assigned to the aromatic skeletal vibrations or methoxy group. This may show that the laser irradiation method decreases the oxygen and other functionalities to produce graphene material, while retaining most aromatic groups.

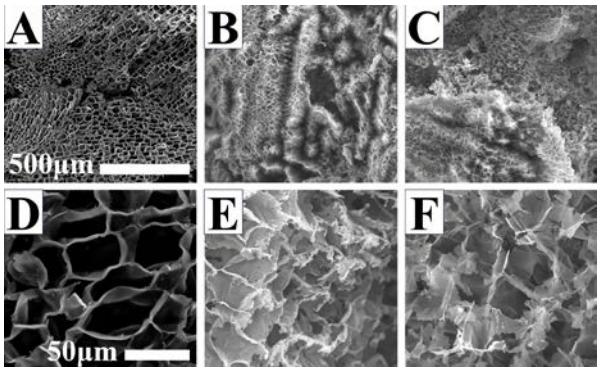

Figure 5. SEM images of cork (A, D), lased cork at 9 W, 175 mm/s, and 3 times (B, E), and lased cork at 10.8 W, 130 mm/s, and 4 times (C, F) at 100x (A-C) and 650x (D-F) zoom

The cork material was analyzed by SEM-EDX, and its images can be seen in Figures 5A & 5D. Its surface is even with many pores. This was also found to have 65.2 %C (carbon content) and 34.8 %O (oxygen content) by mass. Compared to the lased cork in Figures 5B, 5C, 5E, and 5F, the surface was more uneven, but the initial surface features were collapsed. Its surface was composed of about 93.5 %C and 6.5 %O by mass.

Additionally, the surface composition was investigated by changing laser parameters. This revealed minor changes in the composition. Most notably, one lase time produced the highest carbon content of 95.3%, while increasing to five lase times decreased this to 87.1 %. The cause was not investigated but could be from greater ablation amount as the cork layer below also became much thinner with more lase times.

N_2 adsorption showed the surface properties of lased cork by fitting the BET and BJH isotherms. BET isotherm fitting had a C of 12.97 and an estimated surface area of 2.873 $m^2 g^{-1}$. BJH isotherm fitting had an estimated mean pore diameter of 2.43 nm.

3.3. Optimization of lasing parameters by Central Composite Design (CCD)

As the laser irradiation method has not yet been previously applied to produce a biochar for solid-phase extraction of OPPs, it is necessary to optimize the laser parameters for extraction which involve laser power, speed, number of lase times, and defocus. For simplicity, the laser was set to 0 mm defocus (focused). These parameters were varied using a CCD and the enrichment factor (EF) from extraction was used as the response. The response surfaces are plotted in Figure 6.

Starting with lase times, all OPPs had the highest EF with only one lase time. This parameter was investigated as a previous work had studied on multiple lasing on biomass as a way to improve graphene quality under ambient conditions.[14] Laser power was optimal at 9.0 W for most OPPs, 10.8 W or higher for some, and 7.2 W or less for one. Malathion was the only OPP that did not favor higher power, which could be from to its lack of an aromatic ring, thereby removing π-π interactions between it and the biochar.[9] A lower power results in slightly more oxygen content that may improve analyte-sorbent interaction for malathion only. To accommodate all OPPs, a power of 9.0 W was chosen. Lastly, for speed, almost all OPPs favored speeds higher than 220 mm/s, except for diazinon. Although diazinon is the least non-polar but with

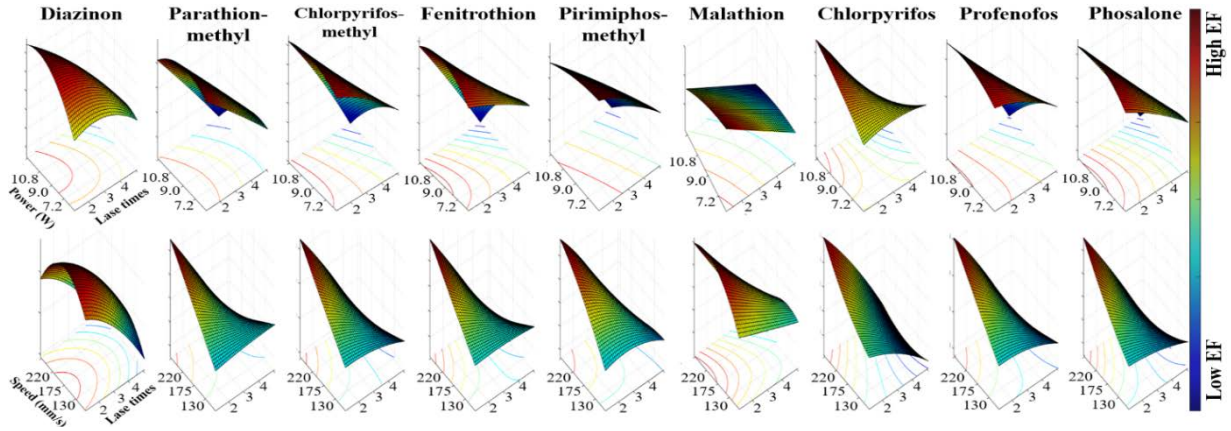

Figure 6. CCD response surfaces relating power with lase times (top graphs) and speed with lase times (bottom graphs) for 9 OPPs with enrichment factor (EF) as the response.

an aromatic ring, its aromatic ring is a pyrimidine with an isopropyl and methyl group. Other OPPs would have nitrate or halogens groups instead. This could be the cause, but it is uncertain without further investigations. For speed, 250 mm/s was chosen as this was the fastest speed of the laser engraving machine.

Using the center-point of the CCD, which had 4 trials, the concentrations, %RSDs, and Horwitz ratios (HorRat) were determined (Table 2). The HorRat values were found to be less than 2, with some values even below 0.5. This indicates good repeatability.[22] EF values ranged from 8.0 to 42.2 times of the original concentration of 10 µg/L. These EF values are from unoptimized lasing conditions and SPE procedure.

Table 2. Concentration, RSD, and HorRat for the extractions done at the center point (9 W, 175 mm/s, 3x)

OPP	Conc (µg/L)	%RSD	HorRat
Diazinon	153	11.9	0.56
Chlorpyrifos-methyl	206	11.6	0.57
Parathion-methyl	204	11.4	0.56
Fenitrothion	209	12.2	0.60
Pirimiphos-methyl	152	15.5	0.73
Malathion	56	16.5	0.67
Chlorpyrifos	240	8.7	0.44
Profenofos	210	8.7	0.43
Phosalone	298	8.3	0.43

Lastly, to evaluate the consistency of sorbent production, ten pieces of cork were lased at the optimized parameter (9.0 W, 250 mm/s, 1 lase time). After lasing, the I_D/I_G ratio (Intensity of D and G peak) ranged from 0.866 to 1.15 and had an RSD of 8.56% This low RSD of production combined with repeatability from the HorRat values of extraction shows the applicability of laser-induced biochar for the solid-phase extraction of OPPs.

4. Conclusion

From multiple biomasses, it was found that compressed coir pellets and cork were able to produce laser-induced biochar. From these two, cork was a better material due to easier material preparation and better graphene quality. Optimization of a laser-induced biochar by the laser irradiation method using a CCD on a response surface yielded optimal parameters of 9.0 W, 250 mm/s, and 1 lase time. Production was found to have good consistency from I_D/I_G ratios and extraction at the center-point had good repeatability from HorRat values.

Overall, the laser irradiation method for biochar sorbent production was successfully applied to the solid-phase extraction of OPPs. Further studies should optimize its extraction procedure and investigate its adsorption mechanism through pH, salt, and solvent effects.

Acknowledgements

This work was supported by the Department of Chemistry, Faculty of Science, Chulalongkorn University and the graduate scholarship program for ASEAN or Non-ASEAN Countries supported by Chulalongkorn University. I would also like to thank Dr. Pumidech Puthongkham for the laser engraver, Asst. Prof. Dr. Prompong Pienpinijtham and Mary Jane Balani for their assistance in Raman Spectrometer.

References

1. Manahan, S. E. *Toxicological chemistry and biology*; Lewis Publishers, 2003.
2. US-EPA. *Epa takes action to address risk from chlorpyrifos and protect children's health*. United States Environmental Protection Agency, 2021. https://www.epa.gov/newsreleases/epa-takes-action-address-risk-chlorpyrifos-and-protect-childrens-health (accessed April 30, 2023).
3. Zhang, S.; Hua, Z.; Yao, W.; Lü, T.; Chen, Y.; Fang, Z.; Zhao, H. *J. Chromatogr. A* **2021**, *1660*, 462673,
4. Jiang, Q.; Zhang, S.; Sun, M. *TrAC, Trends Anal. Chem.* **2023**, *168*, 117283,
5. Zang, X.; Jiang, R.; Zhu, H.-Y.; Wang, Q.; Fu, Y.-Q.; Zhao, D.-X.; Li, J.-B.; Liu, H. *Sep. Purif. Technol.* **2024**, *330*, 125521,
6. Das, S. K.; Ghosh, G. K.; Avasthe, R. *Environ. Technol. Innov.* **2021**, *21*, 101306,
7. Safarian, S. *Energy Reports* **2023**, *9*, 4574-4593,
8. Schwantes, D.; Gonçalves Jr, A. C.; Fuentealba, D.; Hornos Carneiro, M. F.; Tarley, C. R. T.; Prete, M. C. *Chem. Eng. Res. Des.* **2022**, *188*, 142-165,
9. Yin, Z.; Liu, Y.; Liu, S.; Jiang, L.; Tan, X.; Zeng, G.; Li, M.; Liu, S.; Tian, S.; Fang, Y. *Sci. Total Environ.* **2018**, *639*, 1530-1542,
10. Tan, Z.; Wang, Y.; Kasiulienė, A.; Huang, C.; Ai, P. *Clean Technol. Environ. Policy* **2017**, *19*, 761-774,
11. Wen, Q.; Chen, Y.; Rao, X.; Yang, R.; Zhao, Y.; Li, J.; Xu, S.; Liang, Z. *Bioresour. Technol.* **2022**, *350*, 126860,
12. Le, T.-S. D.; Phan, H.-P.; Kwon, S.; Park, S.; Jung, Y.; Min, J.; Chun, B. J.; Yoon, H.; Ko, S. H.; Kim, S.-W.; et al. *Adv. Funct. Mater.* **2022**, *32*, 2205158,

13. Le, T.-S. D.; Park, S.; An, J.; Lee, P. S.; Kim, Y.-J. *Adv. Funct. Mater.* **2019**, *29*, 1902771,
14. Chyan, Y.; Ye, R.; Li, Y.; Singh, S. P.; Arnusch, C. J.; Tour, J. M. *ACS Nano* **2018**, *12*, 2176-2183,
15. Carvalho, A. F.; Fernandes, A. J. S.; Martins, R.; Fortunato, E.; Costa, F. M. *Adv. Mater. Technol.* **2020**, *5*, 2000630,
16. Nasser, J.; Lin, J.; Zhang, L.; Sodano, H. A. *Carbon* **2020**, *162*, 570-578,
17. Duy, L. X.; Peng, Z.; Li, Y.; Zhang, J.; Ji, Y.; Tour, J. M. *Carbon* **2018**, *126*, 472-479,
18. Abdulhafez, M.; Tomaraei, G. N.; Bedewy, M. *ACS Appl. Nano Mater.* **2021**, *4*, 2973-2986,
19. Shi, Z.; Xu, G.; Deng, J.; Dong, M.; Murugadoss, V.; Liu, C.; Shao, Q.; Wu, S.; Guo, Z. *Green Chemistry Letters and Reviews* **2019**, *12*, 235-243,
20. Sigma-aldrich. *Ir spectrum table & chart*. https://www.sigmaaldrich.com/TH/en/technical-documents/technical-article/analytical-chemistry/photometry-and-reflectometry/ir-spectrum-table (accessed.
21. Zhao, J.; Xiuwen, W.; Hu, J.; Liu, Q.; Shen, D.; Xiao, R. *Polym. Degrad. Stab.* **2014**, *108*, 133-138,
22. Horwitz, W.; Albert, R. *J. AOAC Int.* **2019**, *89*, 1095-1109,

Vortex-assisted dispersive liquid-liquid microextraction for determination of organophosphate pesticides using gas chromatography

Andaman Thomthong[1], Anuwat Ratsamisomsi[2], and Warawut Tiyapongpattana[1,3]*

[1]*Department of Chemistry, Faculty of Science and Technology, Thammasat University,Pathumthani 12120, Thailand*
[2]*Center of Scientific Equipment for Advanced Research, Office of Advance Science and, Thammasat University, Pathumthani 12120, Thailand*
[3]*Flow Innovation Research for Science and Technology Laboratories (FIRST Labs) Thailand*

**E-mail: twarawut@tu.ac.th and twarawut@gmail.com*

Abstract:

A method for determining trace levels of organophosphate pesticides (chlorpyrifos and ethion) in mango, orange, and tomato juices was developed using a dispersive liquid-liquid microextraction coupled with a vortex agitation approach. In this method, hexane served as a low-density extraction solvent, and acetone was employed as the dispersive solvent. These solutions were added sequentially to the diluted sample solution, which was spiked with carbophenothion as the internal standard. After vortexing and centrifugation at room temperature, the solution was frozen at -25 ºC for 60 min, and hexane was subsequently decanted into a vial before injection into gas chromatography with flame ionization detection. Under optimal conditions, the analytical performance of chlorpyrifos and ethion was as follows: the linear ranges were 0.5 – 500 and 5 – 500 µg L^{-1}, the coefficients of determination (R^2) were 0.9994 and 0.9991, the limits of detection were 0.1 and 2.0 µg L^{-1}, and the limits of quantification were 0.5 and 5.0 µg L^{-1}, respectively. The recoveries were ranged from 85 to 110 % at the spiked concentration of 100 µg L^{-1}, with relative standard deviations (RSDs) below 3 %. The validated method successfully met the criteria outlined in SANTE 11312/2021. This proposed approach is characterized by its simplicity, cost-effectiveness, and demonstrated effectiveness in determining chlorpyrifos and ethion in fruit and vegetable juice samples.

1. Introduction

Pesticides are chemical compounds that protect crops from pests such as insects, fungi, and weeds and play a crucial role in increasing agricultural products. Organophosphorus pesticides (OPPs) are the most used pesticides in the world due to their efficacy against insects. Nevertheless, the residues of these compounds may persist in the environment and lead to the contamination of agricultural products.[1,2] In Thailand, the Thailand Pesticide Alert Network (ThaiPAN) has detected and reported the presence of OPPs, specifically chlorpyrifos and ethion, in fruits and vegetables.[3] The residues of these pesticides have been identified as harmful to human health, plants, aquatic animals, and the environment.[4] Hence, the Thai Agricultural Standard and the Codex Alimentarius Commission (CODEX) have established maximum residue limits (MRLs) for chlorpyrifos in fruits at 1 mg kg^{-1} and tomato at 10 mg kg^{-1},[5] and for ethion in fruits at 5 mg kg^{-1}.[5,6]

Gas chromatography (GC) is the preferred analytical method for OPPs pesticides analysis owing to their volatility. The use of diverse detectors, particularly the nitrogen phosphorus detector (NPD),[7-9] proves efficient in identifying nitrogen and phosphorus in OPPs, resulting in high selectivity. Nevertheless, challenges arise from its short material lifespan and the associated high maintenance costs.

The flame ionization detector (FID) is widely used in the instrumental laboratories. GC–FID offers simplicity, the ability to detect a wide range of compounds, and a more economical instrument maintenance cost.[10] However, it has low sensitivity in detecting OPPs. Although the GC method delivers high separation efficiency, the optimization of analytical performance for trace analysis, particularly for FID, necessitates applying sample clean-up and preconcentration methods for increasing detection performance.

Conventional sample preparation techniques such as solid phase extraction (SPE),[11,12] and liquid-liquid extraction (LLE)[13,14] are commonly used for pesticide residue analysis. However, these methods have specific limitations, such as consuming large volumes of organic solvents and being time-consuming.[15] Consequently, sample preparation techniques designed to minimize solvent usages, such as liquid-phase microextraction (LPME), solid-phase microextraction (SPME), single-drop micro-extraction (SDME), and hollow fibre liquid-phase microextraction (HF-LPME) have been developed.[16] Although most of these techniques consume less organic solvents than conventional

techniques, they require special materials or apparatus, laboratory expertise, and high cost. Therefore, a new microextraction technique, dispersive liquid-liquid microextraction (DLLME), was introduced by Rezaee *et al*. in 2006.[17] This technique is based on the dispersion of tiny extraction solvent droplets into an aqueous sample, forming a cloudy solution. Subsequently, centrifugation is employed for phase separation, dividing the mixture into aqueous and organic phases. Over the years, DLLME became a powerful sample preparation and preconcentration technique and gained widespread popularity owing to its advantages such as sensitivity, simplicity, rapidity, minimal extraction solvent usage, and cost-effectiveness.[18]

Various agitators were employed for promoting the dispersion of extraction solvent in DLLME, such as ultrasound-assisted DLLME (USA–DLLME), magnetic stirring-assisted dispersive liquid-liquid microextraction (MSA-DLLME), and vortex–assisted DLLME (VA–DLLME).[19] Among the methods, using a simple and rapid vigorous vortex mixer proves to be highly effective in achieving a high mass transfer between the analyte and the extraction solvent.[10]

This work developed a simple analytical approach for determining chlorpyrifos and ethion residue in fruit and vegetable juice using VA-DLLME coupled with GC-FID. In this method, a vortex mixer was employed to aid in the dispersion of the extraction solvent to improve extraction efficiency. After DLLME, the aqueous phase was frozen to facilitate easy phase collection, with only the organic phase containing the analyte being collected for subsequent analysis. The parameters affecting the extraction efficiency, such as type and volume of extraction solvent, type and volume of disperser solvent, and extraction time, were optimized.

2. Materials and Methods

2.1 Chemicals and reagents

All chemicals and reagents are pesticide and analytical reagent grades. Chlorpyrifos, ethion, and carbophenothion (as an internal standard) were obtained from Dr.Ehrenstroter (99%) (Augsburg, Germany). Sodium chloride (≥99%) was purchased from KemAus (New South Wales, Australia). Acetone, acetonitrile, ethanol, ethyl acetate, hexane, methanol, octanol, and toluene were obtained from RCI Lab Scan (Bangkok, Thailand). Distilled water (18.2 MΩ) was purified using an ultra-pure water purification system (Elgastat UHQ, Bucks, UK). Individual primary stock standard solutions (1,000 mg L^{-1}) were prepared by weighing and dissolving each standard in methanol and stored in a refrigerator at -20 ºC.

2.2 Instrumentation

A gas chromatograph (Shimadzu GC-2010 Plus, Japan) equipped with the FID. One microliter of the sample was injected in splitless conditions with a constant linear velocity of 30.0 cm sec^{-1} using ultrapure-grade helium as a carrier gas. The injector temperature was set at 260 ºC. Chromatographic separation was achieved on HP-5MS UI (5% phenyl, 95% Dimethylpolysiloxane; Agilent Technologies, USA) fused silica capillary column (30 m × 0.25 mm i.d., 0.25 µm film thickness). The column oven temperature was initially held at 120 ºC for 2 min, then raised to 250 ºC at 30 ºC min^{-1}, to 280 ºC at 10 ºC min^{-1}, and finally to 300 ºC at 50 ºC min^{-1} and held for 2 min. The detector temperature was set as 310 ºC.

2.3 Sample preparation

Packaged mango, orange, and tomato juices were bought from a local market in Phathumthani province, Thailand. 50.00 mL of each juice sample was centrifuged at 10,000 rpm for 30 min, and the supernatant was filtered through a 0.45 µm nylon membrane filter. All samples were diluted with deionization water at a ratio of 1:1 v/v and stored in a refrigerator at 4 ºC before analysis.

2.4 VA-DLLME procedure.

A 5.00 mL aliquot of a standard mixture or the diluted sample solution containing 100 µg L^{-1} of carbophenothion (internal standard) was transferred into a 10 mL centrifuge tube. Subsequently, 50 µL of hexane and 1,250 µL of acetone were added to the tube. The solution was further mixed using a vortex mixer for 1 min. After centrifugation at 5,000 rpm for 10 min, the aqueous solution was frozen at -25 ºC for 60 min. The upper organic layer was poured into a vial before being injected into GC-FID.

2.5 Method validation

The analytical performance of the developed VA-DLLME method was validated according to the SANTE 11312/2021 requirment.[20] The internal calibration curve was constructed by plotting between the peak area ratio of the analyte and the internal standard (Y-axis), and the concentration of the analyte (X-axis). The limit of detection (LOD) and the limit of quantitation (LOQ) were evaluated based on a signal-to-noise ratio (S/N) of three and a signal-to-noise ratio (S/N) of ten, respectively. The precision was reported in terms of relative standard deviations. The accuracy of the method was studied regarding

recovery by spiking the mixture of the standards at 100 µg L^{-1} into fruit and vegetable juice samples.

3. Results & Discussion

3.1 Optimization of VA-DLLME conditions

To investigate each parameter, the VA-DLLME efficiency was optimized using 100 µg L^{-1} of mixed standard solution. All optimization experiments were conducted with three replication analyses.

3.1.1 Effect of type of extraction solvent

The selection of extraction is a crucial step for achieving high extraction efficiency during the VA-DLLME process because the physical properties of a specific solvent influence its ability to extract targeted analytes. Generally, an appropriate extraction solvent should have good analyte extraction capability, low solubility in the aqueous phase, and excellent chromatographic behavior. Hence, four organic solvents with different polarity (polarity index),[21] such as ethyl acetate (4.4), octanol (3.4), toluene (2.4), and hexane (0.1), were studied. Figure 1 shows that the extraction efficiency of chlorpyrifos and ethion was increased when using the non-polar solvent. In the case of ethyl acetate, the organic layer cannot be collected efficiently due to its limited separation from the aqueous phase. Hexane, with its higher hydrophobicity compared to toluene, octanol, and ethyl acetate, not only yielded the highest peak area but also benefited from its low-density property, facilitating phase separation through freezing. Therefore, hexane was chosen as the extraction solvent.

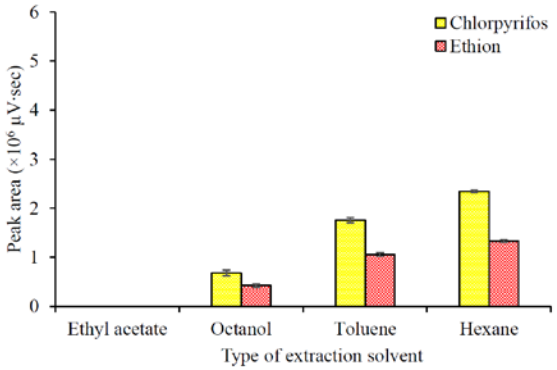

Figure 1. Effect of type of extraction solvent on extraction efficiency. Extraction conditions – volume of extraction solvent: 80 µL, disperser solvent: acetone, volume of disperser solvent: 500 µL, extraction time: 60 seconds.

3.1.2 Effect of volume of extraction solvent

The extraction solvent volume also plays an important role in the extraction procedure. The different volumes of hexane (40, 50, 60, 70, 80, 90,100, and 120 µL) were examined. The result showed that with the increase in the extraction solvent volume, the peak area of analytes responses gradually decreased due to the dilution effect (Figure 2). On the other hand, the difficulty of phase separation or collection was increased when using the lower volume of hexane resulting in the precision of the method. The organic phase cannot be collected practically using a volume less than 50 µL. Thus, 50 µL of hexane was selected to compromise sensitivity and precision.

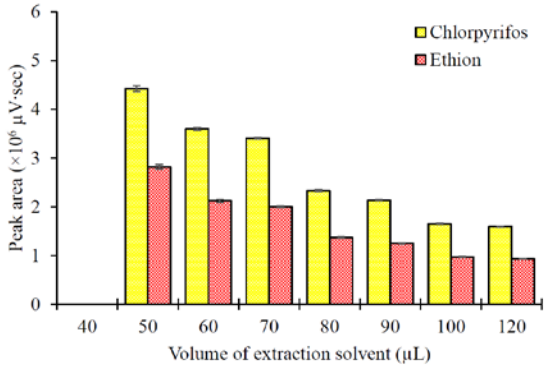

Figure 2. Effect of volume of extraction solvent on extraction efficiency. Extraction conditions – extraction solvent: hexane, disperser solvent: acetone, volume of disperser solvent: 500 µL, extraction time: 60 seconds.

3.1.3 Effect of type of disperser solvent

In VA-DLLME, the disperser solvent has the ability to initiate the fine droplet formation of the extraction solvent, inducing a cloudy solution through the dispersion of the extraction solvent into the aqueous phase. The appropriate disperser solvent is based on its miscible in both aqueous and organic phases. Furthermore, the type of disperser solvent has a direct impact on the binary solvent's viscosity therefore affecting the stability of the cloudy solution and the extraction efficiency.[22]

Three solvents with different relative polarity, including acetone (0.355), acetonitrile (0.460), and methanol (0.762),[23] were investigated. Among them, acetone demonstrated the highest peak area (Figure 3). This observation may be attributed to acetone's high compatibility with the aqueous solution, reducing its polarity compared to methanol and acetonitrile, resulting in an enhanced dispersion of hexane in the aqueous phase.[24,25] This effect can enhance the solubility of chlorpyrifos and ethion in hexane. Additionally, acetone has less toxicity and is less expensive. As a result, acetone was chosen as the disperser solvent for subsequent studies.

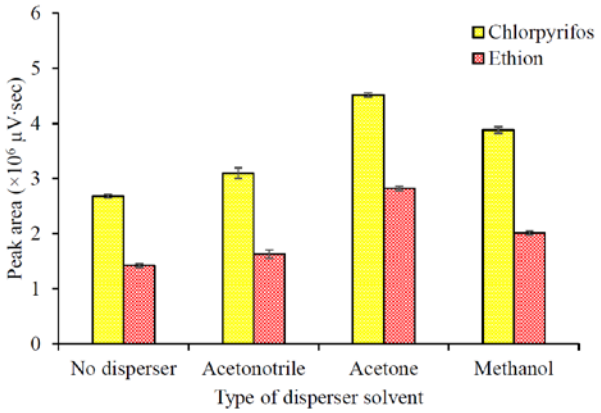

Figure 3. Effect of type of disperser solvent on extraction efficiency. Extraction conditions – extraction solvent: hexane, volume of extraction solvent: 50 µL, volume of disperser solvent: 500 µL, extraction time: 60 seconds.

3.1.4 Effect of volume of disperser solvent

The volume of the disperser solvent directly affected the formation of a cloudy solution. The various volumes of acetone (0, 750, 1000, 1250, and 1500 µL) were investigated. According to the result, at low volumes, the formation of a cloudy state in the solution was insufficient, resulting in incomplete extraction of the analyte. Contrastingly, a greater peak area was attained at a higher volume, with the increased volume of disperser solvent enhancing the dispersion effect of the extraction solvent in a sample. However, an excess volume may also increase the dilution effect. Figure 4 showed that the optimal volume of acetone was 1,250 µL.

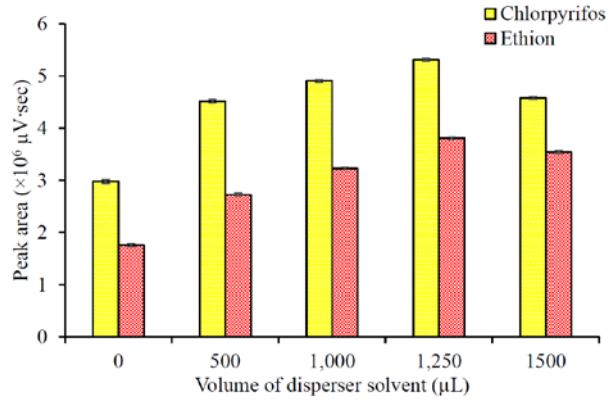

Figure 4. Effect of volume of disperser solvent on extraction efficiency. Extraction conditions – extraction solvent: hexane, volume of extraction solvent: 50 µL, type of disperser solvent: acetone, extraction time: 60 seconds.

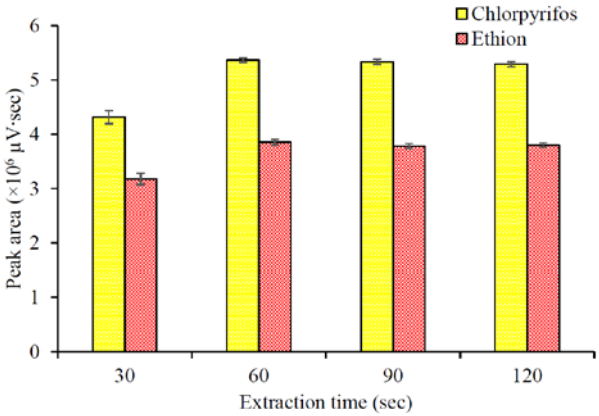

Figure 5. Effect of extraction time on extraction efficiency. Extraction conditions – extraction solvent: hexane, volume of extraction solvent: 50 µL, type of disperser solvent: acetone, volume of disperser solvent: 1,250 µL.

3.1.5 Effect of extraction time

Vortex agitation-assisted extraction was applied to promote the dispersion of the extraction solvent to the fine droplets, enhancing the interaction between the extraction solvent and the sample solution. Several extraction times of 30, 60, 90, and 120 seconds were studied. Figure 5 showed that the peak area increased when extending the vortex time and then remained constant after 60 seconds. Hence, 60 seconds was selected as the optimum extraction time.

3.2 Method validation

The analytical performance of the developed VA-DLLME method was validated per the requirements outlined in SANTE 11312/2021. The method validation results are presented in Table 1.

Table 1. Method validation of the developed method

Parameter	Criterion	Result	
		Chlorpyrifos	Ethion
Linearity			
- Working range[a]	-	0.5 – 500	5 – 500
- Equation		y = 310.27x + 498.74	y = 245.74x + 213.28
- R^2	-	0.9996	0.9995
LOD (3S/N)[a]	-	0.1	2.0
LOQ (10S/N)[a]	≤ MRL	0.5	5
Precision (%RSD)[b]	≤ 20 %	3	2

[a] µg L^{-1}
[b] Ten replicate analyses

The proposed method demonstrates a favorable linear range and high sensitivity in terms of LOQ, which is lower than the MRL specified by the Thai Agricultural Standard and the Codex

Alimentarius Commission (CODEX). Additionally, its achieved high precision is partly attributed to the incorporation of the internal standard. Validation results meet the SANTE 11312/2021 acceptability criteria for all the parameters.

3.3 Application to samples

The proposed method was applied for the analysis of chlorpyrifos and ethion in nine samples, including two fruits (mango and orange) and one vegetable (tomato) juice. No chlorpyrifos and ethion were found in all the samples. The accuracy of the method in terms of recovery was carried out by spiking 100 µg L^{-1} of chlorpyrifos and ethion in all the samples before the centrifugation step in section 2.3. The recoveries of the method were expressed as the mean percentage between the amounts found and those added, calculated following AOAC requirements.[26] The recoveries of chlorpyrifos and ethion are presented in Table 2 and Table 3, respectively. The method showed high accuracy in the range of 85 – 110 % and accepted in the criteria of 70 – 120 %.

Table 2. Recovery study of chlorpyrifos in juice samples.

Sample	Chlorpyrifos	
	% Recovery (Mean ± SD)	Found concentration
Mango A	91.8 ± 0.6	n.d.[a]
Mango B	89.7 ± 0.4	n.d.[a]
Mango C	91.2 ± 1.1	n.d.[a]
Orange A	103.4 ± 0.3	n.d.[a]
Orange B	100.1 ± 0.4	n.d.[a]
Orange C	99.8 ± 0.5	n.d.[a]
Tomato A	96.5 ± 1.1	n.d.[a]
Tomato B	92.3 ± 0.5	n.d.[a]
Tomato C	97.9 ± 0.3	n.d.[a]

[a] n.d.: not detected (three replicate analyses)

Table 3. Recovery study of ethion in juice samples.

Sample	Ethion	
	% Recovery (Mean ± SD)	Found concentration
Mango A	86.2 ± 0.4	n.d.[a]
Mango B	85.1 ± 0.3	n.d.[a]
Mango C	88.9 ± 1.0	n.d.[a]
Orange A	100.1 ± 0.4	n.d.[a]
Orange B	109.7 ± 0.4	n.d.[a]
Orange C	107.5 ± 0.5	n.d.[a]
Tomato A	92.2 ± 0.4	n.d.[a]
Tomato B	90.2 ± 0.8	n.d.[a]
Tomato C	91.5 ± 0.6	n.d.[a]

[a] n.d.: not detected (three replicate analyses)

The GC–FID chromatograms (Figure 6) illustrate the determination of target analytes in mango A samples. The analyte peaks were effectively separated from the matrix, achieving separation within 12 min.

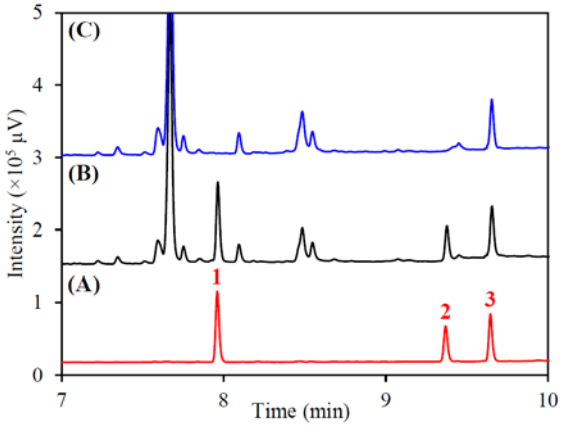

Figure 6. The GC-FID chromatograms of the standard chlorpyrifos and ethion (A), spiked mango A sample (B), and mango A sample (C). Peak identification 1. Chlorpyrifos; 2. Ethion; and 3. Carbophenothion (Internal standard).

4. Conclusion

The study accomplished the successful development of the VA-DLLME method coupled with GC-FID for the determination of chlorpyrifos and ethion in mango, orange, and tomato juices. The rapid dispersion of the extraction solvent in the DLLME operation was improved through vigorous vortex agitation. Phase collection was facilitated by freezing the aqueous phase after DLLME. The proposed method underwent validation and met the requirements outlined in SANTE 11312/2021. Beyond high accuracy and precision, this method also offers simplicity and environmental friendliness, and enhances the detection performance of GC-FID at trace levels for the organophosphate pesticide analysis.

Acknowledgements

This work was supported by the Thailand Science Research and Innovation Fundamental Fund, Contract No. TUFF 18/2565 and Thammasat University Research Fund, Contract No. TUFT-FF 14/2565. AT would like to thank a scholarship for talent student to study graduate program in Faculty of Science and Technology, Thammasat University, Contract No. TB 29/2565. The authors would like to thank the Department of Chemistry and Faculty of Science and Technology, Thammasat University for partial support and the instrument facility.

References

1. Tsoukali, H.; Theodoridis, G.; Raikos, N.; Grigoratou, I. *Journal of Chromatography B* **2005**, *822*, 194–200.
2. Farajzadeh, M. A.; Khorram, P.; Alizadeh Nabil, A. A. *Journal of Food Composition and Analysis* **2015**, *43*, 96–105.
3. *ThaiPAN*. https://thaipan.org/ (accessed 2023-12-05).
4. Laohaudomchok, W.; Nankongnab, N.; Siriruttanapruk, S.; Klaimala, P.; Lianchamroon, W.; Ousap, P.; Jatiket, M.; Kajitvichyanukul, P.; Kitana, N.; Siriwong, W.; Hemachudhah, T.; Satayavivad, J.; Robson, M.; Jaacks, L.; Barr, D. B.; Kongtip, P.; Woskie, S. *An International Journal* **2020**, *27* (5), 1147–1169.
5. *Pesticides CODEXALIMENTARIUS FAO-WHO*. https://www.fao.org/fao-who-codexalimentarius/codex-texts/dbs/pestres/pesticides/en/ (accessed 2023-12-05).
6. *Thai agricultural standard.* https://www.acfs.go.th/standard/download/maximum_residue_limits.pdf (accessed 2023-12-05).
7. Pagliuca, G.; Gazzotti, T.; Zironi, E.; Sticca, P. *Journal of Chromatography A* **2005**, *1071* (1-2), 67–70.
8. Ravelo-Pérez, L. M.; Hernández-Borges, J.; Miguel Ángel Rodríguez-Delgado. *Journal of Chromatography A* **2008**, *1211* (1-2), 33–42.
9. García de Llasera, M. P.; Reyes-Reyes, M. L. A. *Food Chemistry* **2009**, *114* (4), 1510–1516.
10. Hoisang, W.; Nacapricha, D.; Wilairat, P.; Tiyapongpattana, W. *Journal of Separation Science* **2019**, *42*, 2032–2043.
11. Bakırcı, G. T.; Yaman Acay, D. B.; Bakırcı, F.; Ötleş, S. *Food Chemistry* **2014**, *160*, 379–392.
12. Fan, S.; Zhao, P.; Yu, C.; Pan, C.; Li, X. *Food Additives & Contaminants: Part A* **2013**, *31*, 73–82.
13. Wang, P.; Yang, X.; Wang, J.; Cui, J.; Dong, A. J.; Zhao, H. T.; Zhang, L. W.; Wang, Z. Y.; Xu, R. B.; Li, W. J.; *et al*. *Food Chemistry* **2012**, *134*, 1691–1698.
14. Cho, S.-K.; Abd El-Aty, A. M.; Park, K. H.; Park, J.-H.; Assayed, M. E.; Jeong, Y.-M.; Park, Y.-S.; Shim, J.-H. *Food Chemistry* **2013**, *136*, 1414–1420.
15. Zhao, M.; Zhao, E.; Wu, J.; Li, Y.; Li, B. *Acta Chromatographica* **2021**, *34*, 53–60.
16. Carasek, E.; Merib, J.; Mafra, G.; Spudeit, D. *TrAC Trends in Analytical Chemistry* **2018**, *108*, 203–209.
17. Rezaee, M.; Assadi, Y.; Milani Hosseini, M.-R.; Aghaee, E.; Ahmadi, F.; Berijani, S. *Journal of Chromatography A* **2006**, *1116*, 1–9.
18. March, J. G.; Cerdà, V. *Talanta* **2016**, *156–157*, 204–208.
19. Ahmad, W.; Al-Sibaai, A. A.; Bashammakh, A. S.; Alwael, H.; El-Shahawi, M. S. Recent. *TrAC Trends in Analytical Chemistry* **2015**, *72*, 181–192.
20. *Guidance SANTE 11312/2021*. https://www.accredia.it/en/documento/guidance-sante-11312-2021-analytical-quality-control-and-method-validation-procedures-for-pesticide-residues-analysis-in-food-and-feed/ (accessed 2023-12-05).
21. Snyder, L. R. *Journal of Chromatography A* **1974**, *92* (2), 223–230.
22. Rahbar, N.; Hesami , M. M.; Ramezani , Z.; Savarizadeh, A. *Jundishapur J Health Sci* **2020**, *12* (4).
23. Reichardt, C. *Solvents and Solvent Effects in Organic Chemistry*; John Wiley & Sons, **2006**.
24. Gharehbaghi, M.; Shemirani, F.; Baghdadi, M. *International Journal of Environmental Analytical Chemistry* **2008**, *88* (7).
25. Rezaee, M.; Yamini, Y.; Faraji, M. *Journal of Chromatography A* **2010**, *1217* (16) , 2342-2357.
26. AOAC International. Official Methods of Analysis. *Appendix F: Guidelines for Standard Method Performance Requirements*; AOAC International: Maryland, **2019**; pp 1-18.

Optimization of ultrasonic extraction for the determination of PAHs in sediment by GC-MS

Apinya Navakhun* and Ausanee Saengin

Department of Chemistry, Faculty of Science, Burapha University, Chonburi, Thailand
**E-mail: apinyan@go.buu.ac.th*

Abstract:

The extraction of 6 polycyclic aromatic hydrocarbons (PAHs) including naphthalene, acenaphthylene, acenaphthene, fluorene, phenanthrene, and fluoranthene in sediment samples by ultrasonic extraction method was studied. The amounts of PAHs were analyzed by gas chromatography-mass spectrometry. The extracted solvent of 25 mL dichloromethane: hexane (1:1 v/v), ultrasonic extraction time of 30 minutes, drying temperature of 40°C, and addition of 2.50 g sodium chloride was achieved for good extraction efficiency. Under the optimum conditions, the limit of detection and the limit of quantification were in the range of 0.0008 – 0.2970 and 0.0024 – 0.9000 µg/kg, respectively. The correlation coefficients of the calibration curve were in the range of 0.9802 - 0.9960. For the precision study, repeatability of 0.83 - 5.83% and reproducibility of 16.42 – 25.46% were obtained.

1. Introduction

The polyaromatic hydrocarbon compounds, PAHs are hydrophobic compounds with very low water solubility. They contain several aromatic rings consisting only of carbon and hydrogen atoms. The sources of PAHs in the environment include both natural and anthropogenic. Natural sources are forest, oil seeps and volcanic eruptions whereas anthropogenic sources of PAHs include the burning of fossil fuel, coal tar, wood, garbage, refuse, used lubricating oil and oil filters, municipal solid waste incineration and petroleum spills and discharge.[1] They often occur at typically low levels in complicated and polluted aquatic environments[2], and tend to adsorb rapidly and accumulate on sediment.[3] PAHs have mutagenic, carcinogenic and toxic properties. There are sixteen PAHs placed in the priority-pollutant list by the United States Environmental Protection Agency (USEPA).[4] However, due to the low concentration of PAHs contaminated in the environment, improvement in analytical methods for sample preparation and determination has been needed for analytical chemists. In addition, the preconcentration process is usually important because the concentrations of target analytes in real samples are very low or the sample matrix is too complicated.[5-6] The Ultrasonic extraction method is a well-known technique for the extraction of solid samples.[7-9] This technique presents the advantage of speeding up and simplifying sample pretreatment. During extraction, ultrasonic energy imparts to the solution and causes acoustics cavitation, in which bubble formation and subsequent implosion occur. The collapse of bubbles created from the sonication of solution results in the generation of extremely high local temperature and pressure gradients. During the ultrasonic wave cavitation cycle, bubbles are produced that fill with the vapor of solvent. The bubbles and gas within them are also compressed resulting in a significant increase in temperature and pressure. This results in the collapse of the bubble with shockwave passing through the solvent and enhanced mixing occurring. Ultrasonic waves also exert a mechanical effect, allowing greater penetration of solvent into the solid sample. This is coupled with enhanced mass transfer via cavitation bubble collapse. In this work, the ultrasonic extraction method was used as an easy and quick extraction method for PAHs in sediment samples. The extracted PAHs were determined by GC-MS. The ultrasonic extraction parameters affecting the extraction efficiency were illustrated in this work. Finally, the proposed method was applied for the determination of PAHs in sediment samples collected from the eastern area of Thailand.

2. Materials and Methods

2.1 Chemicals, Reagents and Samples

The six PAHs (naphthalene, Nap; acenaphthylene, Acy; acenaphthene, Ace; fluorene, Fl; phenanthrene, Phe; and Fluoranthene, Fluo) were purchased from Supelco (Bellefonte, PA, USA). Analytical grade dichloromethane, methanol, hexane, and sodium chloride were purchased from VMR Chemical (France). A special grade florisil, 60-100 mesh, was from Carlo erba reagent (Germany). The stock solutions were prepared by dissolving PAHs standard in mixture of dichloromethane and methanol (50:50 v/v) to obtain a 1000 mg/L solution and stored in the refrigerator.

2.2 Instrumentation

A Hewlett Packard GC-MS (6890 series) coupled with a quadrupole mass spectrometer (5972 series) was used for separation and determination of PAHs. The PAHs separation was carried out on a HP-5MS capillary column (30 m x 0.25 mm) with a 0.25 µm stationary film thickness (Agilent, USA). The oven temperature was programmed as follows: initial 60 °C held for 2 min, increased to 290 °C at a rate of 10 °C/min, and held at 290 °C for 2 min. The injection temperature was set at 300 °C, and injection was performed in a splitless mode for 1 min. Helium gas flow rate was set at 1.0 mL/ min. Mass detector temperature was set at 250 °C. The mass spectra were acquired with a selected ion monitoring (SIM) mode.

2.3 Ultrasonic extraction method

The 5 g of sediment sample was accurately weighted into a 30 mL vial. The extraction solvent was added into the vial and immersed into the ultrasonic bath for appropriate temperature and time. After the extraction was completed, the solution was centrifuged at 2000 rpm for 5 minutes**.** The clear solution was transfer to clean vial and dried under N_2 flow at 40°C. The extraction solvent was added and then cleaned up by eluting through a small amount of florisil to eliminate organic matrix. The sample solution was analysis by GC-MS.

The parameters affected extraction efficiency including type of extraction solvent, extraction solvent volume, extraction time and temperature, and salt adding were carried out. In the optimization extraction study, the PAHs standard was spiked into sediment sample. The spiked sample has been extracted with three replicates analysis. The validation of the proposed method was performed under the standard AOAC method guidelines. Finally, PAHs contaminated in sediment sample was determined under the optimum conditions.

3. Results & Discussion

3.1 Optimization of ultrasonic extraction

Ultrasonic extraction was chosen to be an extraction technique in this work because it reduces the total extraction time for taking, extracting, and preparing samples. In addition, no conditioning is necessary for this extraction technique. First extraction parameter, type of extraction solvent was studied. The amount of PAHs extracted by 3 types of solvents including dichloromethane (DCM), DCM: hexane (1:1 v/v), and hexane was compared. The extraction efficiency was performed by peak area of PAHs that illustrated as the normalized peak area. Dichloromethane, medium – high polarity solvent, suits for extraction of polar solutes whereas hexane, non-polar solvent suits for non-polar solutes. In addition, mixture of DCM: hexane (1:1 v/v) shows wide range of polarity extractable property that should be suitable for extraction of PAHs that different size and polarity. The reasonable results in Figure 1 showed that the highest peak area of all PAHs obtained from DCM: hexane (1:1 v/v), thus this solvent was used for further studies.

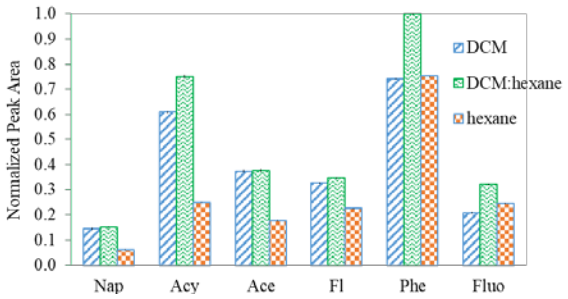

Figure 1. The effect of type of extraction solvent on the normalized peak area of 6 PAHs.

The next extraction parameter was extraction solvent volume. The effect of extraction solvent volumes of 15 and 25 mL on the peak area of PAHs were compared. The volume of solvent used for extraction affects the concentration and amount of extracted substances. In the case of the same amount of extracted substance, using a lower volume of solvent will result in an increase in concentration and peak area. This is consistent with the results of the study in Figure 2 which found that low molecular weight PAHs (Nap, Acy Ace, and Fl) preferred lower solvent volume (15 mL) due to being easily extracted into organic solvent and the peak areas of Naphthalene, Acenaphthylene, Acenaphthene and Fluorene were decreased with 25 mL of solvent used. Whereas high molecular weight PAHs (Phen and Flu) prefer to binding with sediment matrix resulting in difficult to extract into organic solvents. Therefore, when using a lower solvent volume, high molecular weight PAHs cannot be extracted completely. The results found that increasing the solvent volume (25 mL) leads to better extraction of high molecular weight PAHs (Phe and Fluo). To compromise the extraction efficiency in this work, 25 ml of solvent was chosen as the extraction solvent volume. The next parameter, the extraction time in the range of 10-60 minutes was carried out. Firstly, extraction time of 60 minutes showed high deviation results that may be the evaporation of extraction solvent from too long extraction time thus the 60 minutes extraction time was excluded in this study. The results in Figure 3 show that

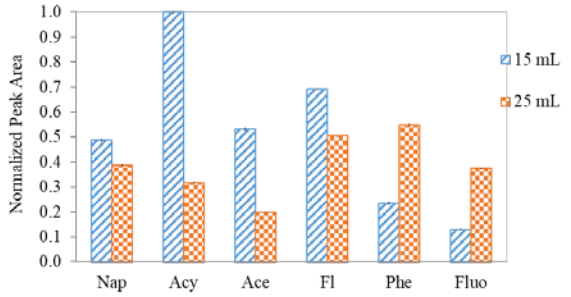

Figure 2. The effect of extraction solvent volume on the normalized peak area of 6 PAHs**.**

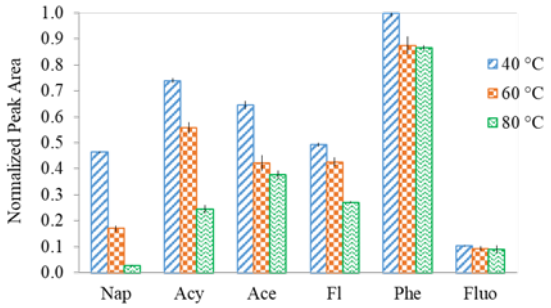

Figure 4. The effect of extraction temperature on the normalized peak area of 6 PAHs.

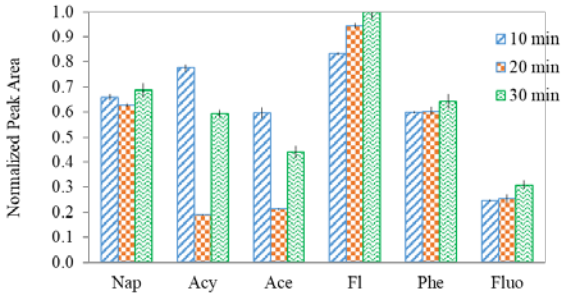

Figure 3. The effect of extraction time on the normalized peak area of 6 PAHs.

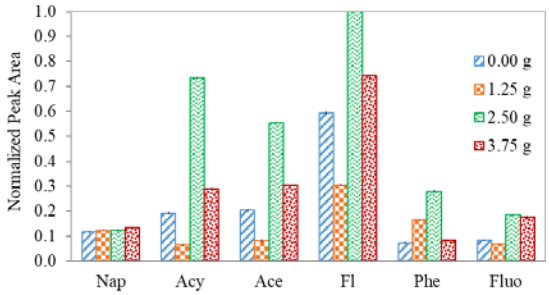

Figure 5. The effect of salting out on the normalized peak area of 6 PAHs.

increasing the extraction time will improve the extraction efficiency. The extraction of 30 minutes provided better PAHs extraction efficiency and was chosen as the optimum condition.

The extraction temperature also affects the extraction efficiency. Higher temperatures improve the solubility of PAHs from the sediment into the organic solvent phase, which results in better extraction efficiency. However, on the other hand, high temperatures cause the loss of organic solvent from evaporation during the extraction process. Figure 4 shows that the temperature increases from 40°C to 80°C, the extraction efficiency decreases which corresponds to the low boiling points of dichloromethane and hexane, which are 36.9°C and 68.7°C, respectively. Therefore, an optimum extraction temperature in this study was 40°C. Addition of sodium chloride salt is the final extraction parameter studied in this work. Salt adding can increase the ionic strength of the sample solution. It often improves the solubility of solutes from aqueous phase or solid phase to the organic phase due to the salting-out effect leading to increase in the extraction efficiency. To evaluate the effect of salting out on the extraction efficiency, different amounts of sodium chloride (0.00-3.75 g) were added. The result in Figure 5 found that naphthalene had the highest peak area when 3.75 g NaCl was added, while acenaphthylene, acenaphthene, fluorene, phenanthrene, and fluoranthene had the highest peak area when 2.5 g NaCl was added. However, high standard deviations of the peak area were found when 3.75 g NaCl was added. Therefore, the addition of 2.5 g NaCl was chosen as the optimum condition.

3.2 Validation of the proposed method

The validation of the ultrasonic extraction method was investigated in terms of limit of detection (LOD), limit of quantification (LOQ), calibration curve, precision, and accuracy under optimum extraction conditions, as summarized in Table 1. To evaluate LODs and LOQs, the six PAHs standard solutions, which concentration of 0.06 – 0.36, 1.29 – 2.77, 1.55 – 3.35, 0.45 – 0.98, 0.03 – 0.06, and 0.03 – 0.12 µg/kg for Naphthalene, Acenaphthylene, Acenaphthene, Fluorene Phenanthrene, and Fluoranthene, respectively were spiked into the sediment samples, then extracted using ultrasonic extraction under optimum conditions, and analyzed by GC-MS (n=10). The LODs and LOQs value were calculated from the equation,[10]

$$LOD = \frac{3.3SD}{m}$$

$$LOQ = \frac{10SD}{m}$$

Whereas SD was the standard deviation of peak area and m was the slope of calibration curve

For the calibration curves of PAHs, it was found that good linearity was provided. The R^2 greater than 0.992 were obtained for five PAHs, except for Naphthalene, which had the R^2 value of 0.9871. The accuracy of the method was evaluated in terms of relative standard deviation (%RSD) of peak area and retention time. The analysis of 10 replicates in one day and 4 replicates within consecutive 3 days were performed for repeatability and intermediate precision, respectively. The %RSD values shown in Table 1 indicate that this method has good reliability, as the %RSDs are lower than the acceptable AOAC value, which ranges from 26.50 to 49.22 %[11]. Finally, the accuracy of the method was investigated by spiking standard PAHs into sediment sample, then extract and analysis by GC-MS. The %recoveries of PAHs found were calculated. The recoveries in the range of 41.41-104.74%, falling within the acceptable value of 20-120%, were achieved. The method validation results indicated that the ultrasonic extraction and GC-MS in this work could be the reliable method for determination of PAHs contaminate in sediment samples.

Table 1. Analytical characteristics of the proposed method

Characteristics	Value
LOD	0.8-297 ng/kg
LOQ	2.4 - 900 ng/kg
Calibration curve	
R^2	0.9802-0.9960
Precision (%RSD, n=12)	
Repeatability	
Peak area	0.83-5.83
Retention time	0.00-0.07
Intermediate precision	
Peak area	16.42-25.46
Retention time	0.04 -0.08
Accuracy	
% Recovery	41.41- 104.74

3.3 Determination of PAHs in sediment samples

Two sediment samples were collected at Ao Phrao, Koh Samet, Rayong Province and at Wonnapha Beach. Chonburi Province. The samples were dried, extracted, and analyzed under optimum conditions. The chromatograms of the samples were illustrated in Figure 6. The amount of PAHs found in sediment samples were also shown in Table 2. The amount of PAHs found in sediments from Wonnapha Beach was higher than Ao Phrao. This may be because Wonnapha Beach is a fishing port. Oil from fishing boats may leak into seawater and accumulate in the sediment. In addition, PAHs are hydrophobic substances with high octane-water constant, thus PAHs can adsorb on sediment particles well. Although there was a crude oil spill in the Ao Phrao area in 2013 due to the additions of new sand, the contamination of PAHs found is not high. In addition, the contamination of PAHs in both areas was not more than the standard values for soil sediment from hazardous substances. Concentrations expected to have no adverse effects on benthic fauna for Napthalene, Acenaphthylene, Acenaphthene, Fluorene, Phenanthrene, and Fluoranthene are 160, 44, 16, 19, 240 and 600 µg/kg, respectively, as reported by the AUS/NZ (IISQG-L) standard.

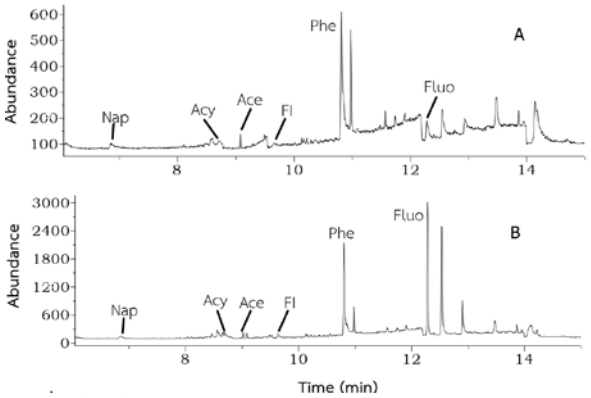

Figure 6. Chromatogram of sediment samples: A Ao Phrao, B Wonnapha Beach.

Table 2. The amount of 6 PAHs found in sediment samples.

PAHs	PAHs found in µg/kg (mean ±SD)	
	Ao Phrao, Rayong	Wonnapha Beach, Chonburi
Nap	0.18± 0.00	0.48± 0.01
Acy	3.53± 0.06	3.15± 0.10
Ace	2.49± 0.14	12.65± 0.44
FI	0.51± 0.01	3.95± 0.22
Phe	0.09± 0.00	0.23± 0.02
Fluo	0.09± 0.00	4.49± 3.20

4. Conclusion

This paper described an ultrasonic extraction for preparation and preconcentration of trace amount of polycyclic aromatic hydrocarbons contaminate in sediment samples. The 25 mL of dichloromethane: hexane (1:1 v/v), ultrasonic extraction time of 30 minutes, extraction temperature of 40°C, and 2.50 g of sodium chloride adding were performed as the optimum extraction condition. The 6 PAHs were completely separated and quantified by GC-MS within 13 minutes. The reliable validation results demonstrated that this method was acceptable to the international standard method. Finally, this method was also convenient, cost effective and sensitive, which can

be apply for the determination of PAHs in sediment samples collected from eastern area of Thailand.

Acknowledgements

The authors thank the Department of Chemistry, Faculty of Science, Burapha University for their research experience. The Center of Excellence on Environmental Health and Toxicology (EHT), OPS, MHESI, Thailand was also acknowledged.

References

1. Haritash. A. K.; Kaushik. C. P. *J. Hazard. Mater.* **2009**, *169*, 1–15.
2. Kursheva, A. V.; Litvinenko, I. V.; Petrova, V. I.; Galishev, M. A. *Mar. Chem.* **2009**, *49*, 655-662.
3. Puig, D.; Barceló, D. Analytical Methods for Monitoring Industrial Effluents and Waste 1996, 15, 362-375.
4. Li, Y.; Li, P.; Ma, W.; Song, Q.; Zhou, H.; Han, Q.; Diao, X. *Mar. Pollut. Bull.* **2015**, *92*, 244-251.
5. Camagong, C. T.; Honjo, T. *Anal. Bioanal. Chem.*, **2002**, 373, 856-862.
6. Arthur, C. L.; and Pawliszyn, *J. Anal. Chem.*, **1990**, 63, 2145-2148.
7. Joanna, L. H.; Richard, G. C. *Analyst*, **2001**, 126, 2025-2031.
8. Kevin, A.; Ronnee, N. A.; Laura, C.; Martine, D. *J. Anal. At. Spectrom.*, **2001**, 16, 1147-1153.
9. Kevin, A. *Trends Anal. Chem.*,**1998**, 17(6), 366-372.
10. ICH Q2 (R1) Guideline: Validation of Analytical Procedures: Text and Methodology; 2005.
11. AOAC International. AOAC® peer-verified method program: manual on policies and procedures. United States of America, 2012

Determination of the Δ9-tetrahydrocannabinol metabolite in urine by online-solid phase extraction coupled with liquid chromatography-mass spectrometry

Waranyu Nachiangtai[1,2], Ajjima Thongbo[2], Chuleeporn Jantarasena[2], Sittiporn Parnmem[3], and Kraingkrai Ponhong[1]*

[1]*Department of Chemistry, Faculty of Science, Mahasarakham University, Maha Sarakham 44150, Thailand*
[2]*Regional Medical Sciences Center 8 Udon Thani, Udon Thani 41330, Thailand*
[3]*National Institute of Health, Department of Medical Sciences, Ministry of Public Health, Nonthaburi 11000, Thailand*

**E-mail: kraingkrai.p@msu.ac.th*

Abstract:

Delta-9-tetrahydrocannabinol (THC), the bioactive compound in marijuana (*Cannabis sativa* L.), is used for medical purposes at low concentrations. THC is metabolized in the liver and transformed to 11-nor-Δ9-tetrahydrocannabinol-9-carboxylic acid (11-nor-Δ9-THC-COOH), which is excreted in the urine. This study developed a sensitive analytical method for the determination of the THC metabolite in urine at trace levels. Online-solid phase extraction (HyperSep Retain PEP Online-SPE column) was employed to extract 11-nor-Δ9-THC-COOH in urine before analysis by liquid chromatography-mass spectrometry (LC-MS). Online-SPE is a simple and rapid method that reduces preparation steps by passing the sample through an SPE cartridge and then eluting with an appropriate solvent before separating by LC-MS. This method achieved detection and quantification limits at 0.20 ng/mL and 1.00 ng/mL, respectively with linearity range 1.00–100.00 ng/mL. The accuracy value (%bias) and precision value of the developed method were within the SWGTOX guidelines (±20%), with percentage recovery 99.16–101.60%. Therefore, this method is accurate, precise, and appropriate for analyzing 11-nor-Δ9-THC-COOH metabolite in urine samples at low-level concentrations.

1. Introduction

Cannabis (*Cannabis sativa* L.), also known as marijuana, has many health benefits such as treating glaucoma, controlling epileptic seizures, and mitigating the spread of cancer.[1] Cannabis can be consumed by smoking, eating or mixing with food and has long been used in Thai traditional medicine. Some five hundred natural compounds have been identified in cannabis. One hundred compounds classified as cannabinoids are presented in unfertilized cannabis female flowers. Flowers are an important plant part for developing medical products. In cannabis, the major active substances with psychotropic properties found in the flowers are delta-9-tetrahydrocannabinol (THC) and cannabidiol (CBD). THC is the most psychologically active component,[2] whereas CBD is non-intoxicating and exerts other effects including anticonvulsive, anti-inflammatory, mildly sedative, and anxiolytic properties.[3] CBD in the body is mainly excreted through the feces in an unchanged form, whereas THC substances entering the body are broken down in the liver and changed to 11-Nor-delta 9-tetrahydrocannabinol-9-carboxylic acid (11-Nor-Δ9-THC-COOH), which is excreted in the urine in a conjugated form. THC accumulates with fat tissue in the body and is gradually excreted through the urine or feces as a free-form acid or conjugated glucuronide,[4,5] as shown in **Figure 1**.

The Narcotics Act of Thailand (No. 7) B.E. 2562 (2019) states that marijuana can be used for medicinal and research purposes, with cannabis extracts prescribed under the guidance of a licensed physician.[6] Cannabis has now been developed into a variety of therapeutic medicines or products for patients with different objectives.[7] Cannabis products are utilized to treat patients receiving palliative care, end-state cancer, Parkinson's disease, Alzheimer's disease, generalized anxiety disorders, and demyelinating diseases such as neuromyelitis optica and autoimmune encephalitis.[8] The Ministry of Public Health (B.E. 2565 (2022)) specified category 5 narcotics as extracts containing delta-9-tetrahydrocannabinol at not more than 0.2% by weight as not a drug of abuse.[9]

According to the announcement of the Narcotics Control Board B.E. 2565 has established a cannabis concentration, and/or active substances or cannabis (cannabinoids) or cannabis metabolites in the urine not exceeding 50 ng/mL to judge whether a person is a drug addict or has been prescribed cannabis for medical purposes.

Urine samples are easy to collect compared with other biomaterials. It can be sampled in large quantities resulting in sufficient samples to be used for analysis and drug residues in urine can be detected within 3-30 days.[11]

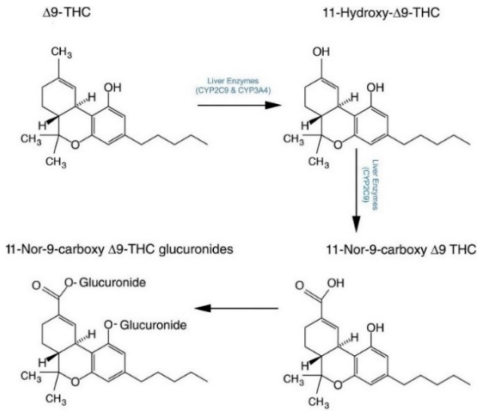

Figure 1. The metabolism of THC.[10]

11-Nor-Δ9-THC-COOH in human urine was commonly quantified by liquid-chromatography tandem spectrometry (LC-MS/MS)[12-14] and gas chromatography tandem spectrometry (GC-MS/MS).[2,3] However, the drawback of these method is the high cost of equipment acquisition and analysis.

Regional Medical Sciences Center 8 Udon Thani no the method currently exists for detecting of cannabis (cannabinoids) and/or cannabis metabolites at low levels than 20 ng/mL. Therefore, this research developed a method for the quantitative analysis of the Δ9-tetrahydrocannabinol metabolite in urine at trace concentrations using liquid chromatography-mass spectrometry (LC-MS). The LC-MS technique can separate and detect the Δ9-tetrahydrocan-nabinol metabolite at ng/mL. Moreover, this technique is also highly sensitive and specific. An online-solid phase extraction method was utilized to preconcentrate the 11-Nor-Δ9-THC-COOH before quantification by LC-MS. The proposed extraction method was rapid, simple, and cost-effective and provided high accuracy and precision.

2. Materials and Methods

2.1 Materials

2.1.1 Chemicals and reagents

Certified reference standards (1 mg/mL) of 11-Nor-Δ9-THC-COOH and the internal standard (IS) deuterated 11-Nor-Δ9-THC-COOH (11-Nor-Δ9-THC-COOH-*d3*) were purchased from Cerilliant Analytical Reference Standards (Round Rock, TX, USA). LC-MS grade acetonitrile, methanol, 99% formic acid, and 99% ammonium formate for the preparation of the mobile phase were obtained from Merck (Merck, Darmstadt, Germany). AR grade sodium hydroxide was obtained from Merck (Merck, Darmstadt, Germany). Blank human urine used for the preparation of quality control (QC) samples and calibrators was obtained from healthy volunteers with written informed consent. Ultrapure water (Type I) for the preparation of solutions and eluents was obtained with a Millipore-Q-plus system (Millipore, Milan, Italy).

2.1.2 Instrumentation

The liquid chromatography system consisted of a Thermo Scientific Vanquish™ UHPLC (USA) and an ISQ™ EC Single Quadrupole Mass Spectrometer. An Accucore™ C18 HPLC Column (2.1 × 150 mm, 2.6 µm) (Merck, Germany) was used as the analytical column carried out at room temperature. A HyperSep Online-SPE Retain PEP (2.1x20 mm) was employed as an online-SPE to enrich the analyte. The injection volume (10 µL) was transferred to an online-SPE with acetonitrile:0.2% formic acid in 10 mM ammonium formate (10:90) at a flow rate of 0.5 mL/min. Chromeleon™ chromatography data system (CDS) software was utilized for data acquisition and processing. The 11-Nor-Δ9-THC-COOH was separated using elution with acetonitrile:water (50:50) as the mobile phase at a flow rate of 0.3 mL/min.

A vortex mixer (50 Hz, Model Genie 2, Scientific Industries, USA), dry bath incubator (50 Hz, Model MK200-2, ALL SHENG, China), and centrifuge (Model 5430, Eppendorf, USA) were used to mix the solution and accelerate the phase separation, respectively.

2.1.3 Standard solutions and quality control preparation

Stock standard solution of 11-Nor-Δ9-THC-COOH was prepared at 10,000 mg/L and 1,000 mg/L in methanol. The standard and quality control solutions were diluted from the stock standard solution in drug-free human urine samples. A calibration curve was prepared at 1.0 – 100.0 ng/mL. Quality controls were prepared at 3.0, 40.0, and 80.0 ng/mL. The IS working solution was prepared in ultrapure water at a concentration of 1,000.00 ng/mL.

2.1.4 Urine samples

Urine samples are easy to collect in large quantities compared with other biomaterials, resulting in sufficient samples for analysis. Drug residues in urine can be detected within 3-30 days.[3,5] Urine samples were collected from volunteers at the Regional Medical Sciences Center 8 Udon Thani. Both male and female individuals were in good health, with ages ranging from 25 to 60 years. The subjects had not taken any medication for at least 7 days and provided a minimum urine volume of 200 mL.

2.2 Method

2.2.1 Sample pretreatment

The IS working solution (100 µL) was placed in a test tube (3 mL capacity). Then, 1 mL of standard or sample solution was added. The solution was vortexed for 10 s before adding 20 µL of 10 M sodium hydroxide. The solution was then mixed using a vortex for 10 s and incubated at 40 °C for 10 min before leaving to cool at room temperature. The mixing solution was then pipetted into a microcentrifuge tube (2 mL capacity) and centrifuged at 10,000 rpm for 10 min to complete the phase separation of the precipitant from the aqueous solution. Approximately 600 µL of the supernatant was then aspirated into a 1.8 mL vial for analysis by LC-MS. **Figure 2** shows the protein precipitation procedure.

2.2.2 Online-SPE

The online-SPE consisted of various automated steps. The loading and washing sample steps were initiated by injecting 10 µL of the sample by an autosampler into the HyperSep Retain PEP Online-SPE column. This step was operated for 1 min with a flow rate of 0.5 mL/min of a mixture of acetonitrile:0.2% formic acid in 10 mM ammonium formate (10:90). The injection step was followed with eluents of the analytes separated in the analytical column using acetonitrile:water (50:50) as the mobile phase at a flow rate of 0.3 mL/min. The analyte was entered to analytical column for separation and directly to the MS for detection.[15] Online-SPE system to preconcentration of analyte was demonstrated in **Figure 3**.

2.2.3 LC-MS parameters

An injection volume of 10 µL was chosen. The mobile phase for loading and washing the sample consisted of acetonitrile:0.2% formic acid in 10 mM ammonium formate (10:90). The mobile phase for eluting and separating the analytes was acetonitrile:water (50:50). The MS was equipped with an electrospray ionization (ESI) source, operating in negative ionization mode (Vaporizer temperature 450°C, ion transfer tube temperature 350°C, Dwell time 200 ms). The selected ion monitoring (SIM) mode was operated for quantitative analysis. The ions for confirmation were 343.5 m/z for 11-Nor-Δ9-THC-COOH and 346.5 m/z for 11-Nor-Δ9-THC-COOH-*d3*. Total run time was 10.0 min.

2.2.4 Method development

The effect of pH was studied by varying the NaOH concentration at 5.0, 10.0, and 15.0 M with speed and time of centrifugation investigated at 8,000-12,000 rpm and 5-15 min, respectively. Incubation time and temperature were optimized between 5 and 25 min and 40-70 °C, respectively.

2.2.5 Method validation

The proposed method was validated according to the U.S. Department of Health and Human Services, Food and Drug Administration and the Scientific Working Group for Forensic Toxicology (SWGTOX) guidelines.[16,17] The validation parameters were evaluated for specificity, carryover, limit of detection (LOD), limit of quantification (LOQ), linearity and range, accuracy, intra-day and inter-day precision, recovery and dilution integrity (for a routine practice within the laboratory). Standard solutions were prepared and the working solution was diluted in negative urine before injection into LC-MS under the optimal conditions.

3. Results and Discussion

The chromatogram and mass spectra of 11-Nor-Δ9-THC-COOH together with 11-Nor-Δ9-THC-COOH-*d3* is demonstrated in **Figure 4**. The analyte and IS provided retention time at 6.51 and 6.50 min, respectively. Mass of the analyte and IS was detected at 343.5 and 346.5 m/z, respectively.

3.1 Method optimization

A NaOH concentration of 10 M and 20 µL achieved the highest peak area. Centrifugation speed and centrifugation time were optimal at 10,000 rpm for 10 min, while incubation time and temperature of 10 min at 40 °C gave the highest peak area.

3.2 Method validations

3.2.1 Specificity - Interfering peaks were not observed from at least ten different batches of blank urine at the retention times of analytes and the internal standard. **Figure 5** shows chromatogram for 11-Nor-Δ9-THC-COOH and 11-Nor-Δ9-THC-COOH-*d3* with blank samples.

3.2.2 Carryover - Drug-free urine samples after injection of the highest concentration were tested at 100.00 ng/mL. Interfering peaks were not observed in blank urine after injecting 11-Nor-Δ9-THC-COOH at the ULOQ.

Table 1. Assay linearity of 11-Nor-Δ9-THC-COOH.

Concentration (ng/mL)	Response ratio	Determined Concentration (ng/mL)	Bias (%)
1.00	0.02	1.06	6.19
5.00	0.09	5.11	2.19
10.00	0.18	10.16	1.55
25.00	0.44	24.41	2.34
50.00	0.91	50.82	1.64
75.00	1.32	73.90	1.47
100.00	1.80	100.54	0.54

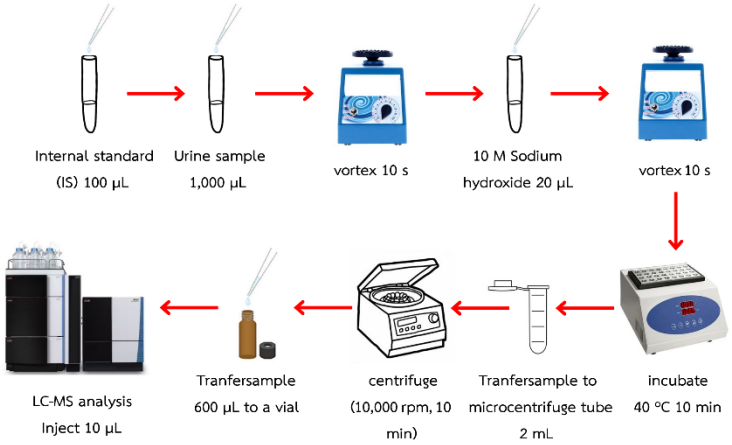

Figure 2. Simplified schematic of the procedure for preparing urine samples by hydrolysis.

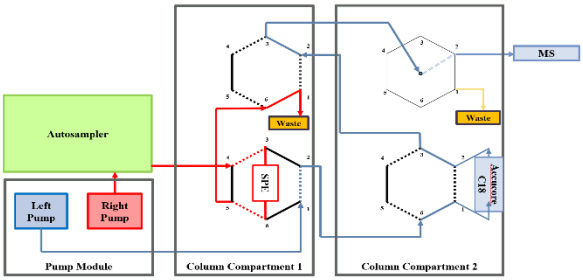

Figure 3. Schematic of the online-SPE LC-MS.

3.2.3 The LOD (3S/N) and LOQ (10S/N), where S = signal and N = noise, were estimated at 0.20 and 1.00 ng/mL, respectively, as shown in **Table 2**.

3.2.4 The linearity ranged from 1.00 to 100.00 ng/mL with correlation coefficients (r) better than 0.9990, while %bias (equation 1) did not exceed 15% at all concentration levels, as shown in **Tables 1 and 2**.

$$\%Bias = \frac{\text{Measured concentration-Nominal Concentration}}{\text{Nominal Concentration}} \times 100 \quad (1)$$

3.2.5 Accuracy, precision, and recovery (equation 2) were evaluated, with results shown in **Table 3**. The accuracy (%bias) varied between −0.93% and 3.69%, within the acceptable criteria (±20%). Precision (coefficient of variation; %CV (equation 3)) ranged from 0.30% to 4.74% (below the acceptable criteria (±15%), with percentage recovery 99.16–101.60%.

$$\%Recovery = \frac{\text{Measured Concentration}}{\text{Nominal Concentration}} \times 100 \quad (2)$$

$$\%CV = \frac{SD \times 100}{\bar{X}} \quad (3)$$

3.2.6 Dilution integrity (equation 4)

Sample dilution was determined at 1:1, 1:5, 1:10, and 1:20. A dilution factor of 20 showed a %bias of -6.24 to 2.74% with %CV between 0.26% and 1.17%, as shown in **Table 4**.

$$\text{Back-calculated concentration} = \frac{\text{ratio-intercept}}{\text{Slope}} \quad (4)$$

Table 2. Limits of detection (LOD) and quantification (LOQ), linear range and regression parameters.

Analyte	LOD (ng/mL)	LOQ (ng/mL)	Linearity range (ng/mL)	Regression parameters			
				Slope	Intercept	Correlation coefficient (r)	Coefficient of determination (R^2)
11-Nor-Δ9-THC-COOH	0.20	1.00	1.00-100.00	0.0179	0.0005	0.9999	0.9997
				0.0216	0.0005	0.9999	0.9998
				0.0212	0.0029	0.9998	0.9996

Table 3. Intra-day and inter-day precision, accuracy and recovery for each analyte at low, medium and high concentrations.

Analyte	Concentration (ng/mL)	Intra-day precision (%CV), (n = 7)	Intra-day precision (%CV), (n = 21)	Accuracy (%Bias), (n = 7)	Recovery (%) (n = 21)
11-Nor-Δ9-THC-COOH	3.00	3.32	2.17	0.40	101.09±0.066
	40.00	0.30	0.40	-0.87	99.16±0.159
	80.00	0.66	0.54	1.75	101.60±0.439

Table 4. Dilution integrity (n = 5).

Analyte	Concentration (ng/mL)	Mean back-calculated concentration (ng/mL)	Mean SD	%CV	%Bias
11-Nor-Δ9-THC-COOH	100.00 (1:1)	98.72	0.26	0.26	-1.28
	80.00 (1:5)	41.10	0.24	0.57	2.74
	20.00 (1:10)	18.75	0.13	0.68	-6.24
	10.00 (1:20)	9.52	0.11	1.17	-4.76

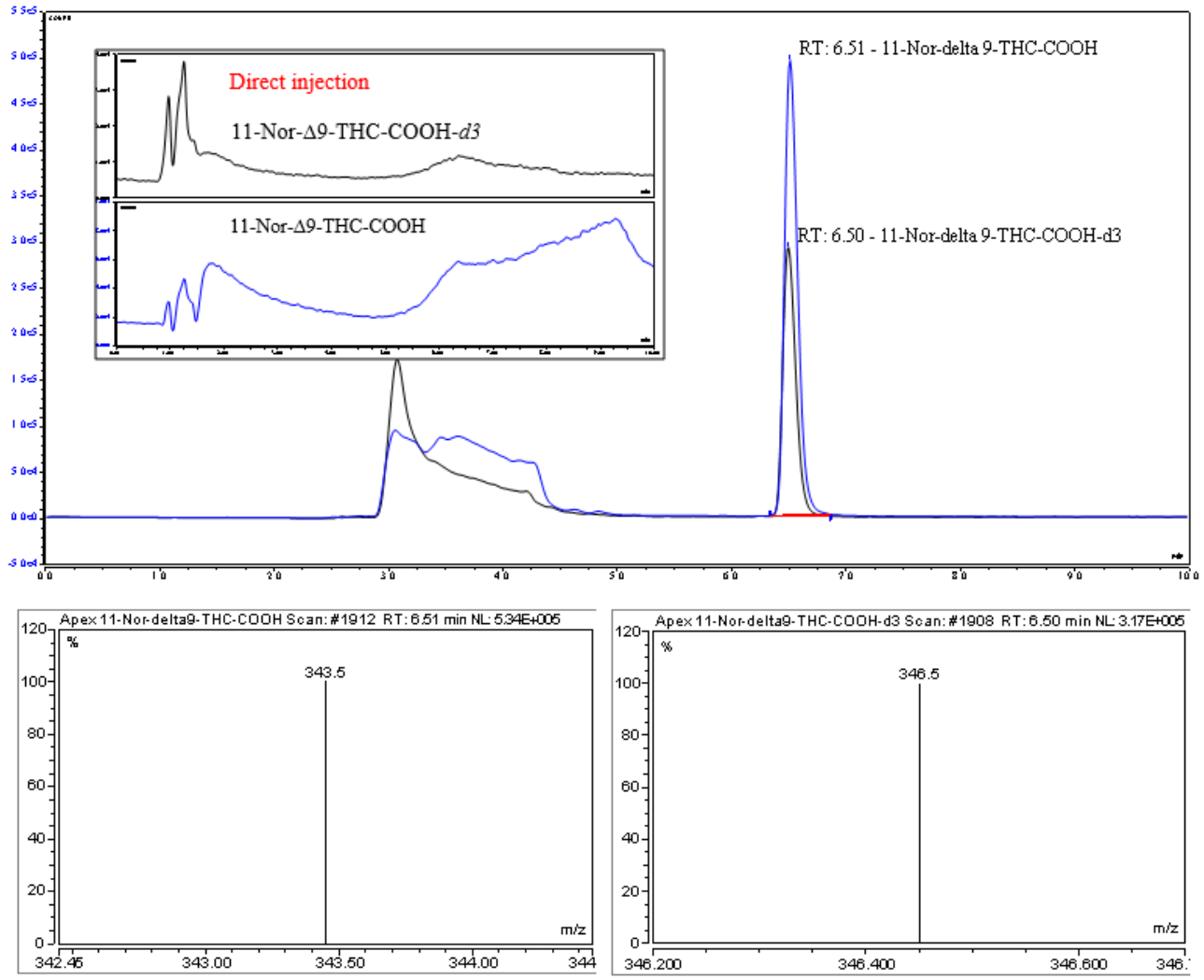

Figure 4. SIM chromatogram and mass spectra for 11-Nor-Δ9-THC-COOH at 100.00 ng/mL and 11-Nor-Δ9-THC-COOH-*d3* at 1,000.00 ng/mL.

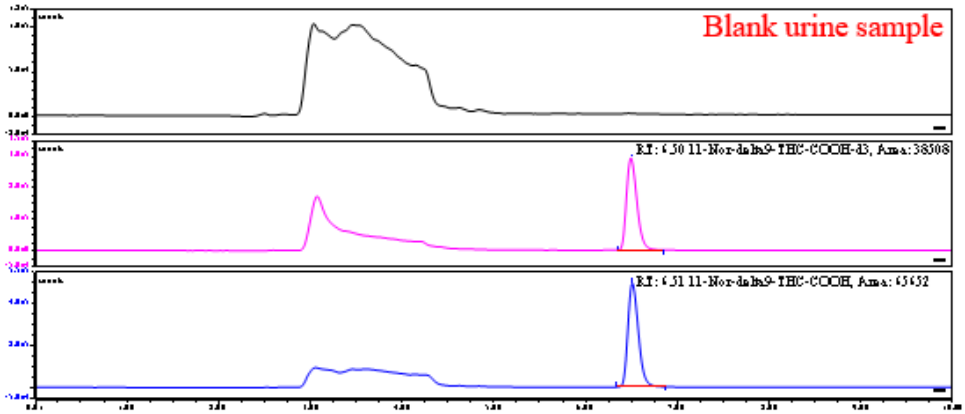

Figure 5. Representative chromatogram for 11-Nor-Δ9-THC-COOH and 11-Nor-Δ9-THC-COOH-*d3* with blank urine samples.

4. Conclusions

A detection method for the 11-Nor-Δ9-THC-COOH in urine was successfully developed and validated using online-solid phase extraction coupled with liquid chromatography-mass spectrometry. The developed method was specific for quantifying the 11-Nor-Δ9-THC-COOH in urine. This method achieved LOD and LOQ at 0.20 ng/mL and 1.00 ng/mL, respectively. This method was effective for analysis in the concentration range 1.00-100.00 ng/mL and no interfering peaks. Parameters for the characterization of the proposed method such as accuracy, precision, and recovery were within the accepted criteria. Dilution integrity was confirmed for analyzing samples with higher concentrations than the maximum value of the calibration curve. The developed analytical method is simple, with fast execution in preparing the urine sample. It is accurate, precise and appropriate for analyzing 11-nor-Δ9-THC-COOH in urine samples at trace concentrations.

Acknowledgements

The authors would like to express their gratitude to the Department of Chemistry, Faculty of Science, Mahasarakham University and the Regional Medical Sciences Center 8 Udon Thani for providing facilities and instrumental support.

Ethical approval

This study (number 320-270/2566) was approved by Mahasarakham University, Division of Research Facilitation and Dissemination on 25 August 2023**.**

References

1. Zhang, W.; Wang, J.; Mi, Z.; Su, J.; You, X.; Keceli, G.; Wang, Y.; Cao, R.; Lai, H. C. Extraction and Analysis of Tetrahydrocannabinol, A Cannabis Compound in Oral Fluid. *International Journal of Biology* **2016**, *9* (1). DOI: 10.5539/ijb.v9n1p30.
2. Korac, N.; Vidic, D.; Sutlovic, D. Modified QuEChERS extraction and GC-MS analysis of selected cannabinoids from human urine. *Bulletin of the Chemists and Technologists of Bosnia and Herzegovina* **2020**, (54). DOI: 10.35666/ghtbh.2020.54.07.
3. Frei, P.; Frauchiger, S.; Scheurer, E.; Mercer-Chalmers-Bender, K. Quantitative determination of five cannabinoids in blood and urine by gas chromatography tandem mass spectrometry applying automated on-line solid phase extraction. *Drug Test Anal* **2022**, *14* (7), 1223-1233. DOI: 10.1002/dta.3241 From NLM Medline.
4. Goncalves, J.; Rosado, T.; Soares, S.; Simao, A. Y.; Caramelo, D.; Luis, A.; Fernandez, N.; Barroso, M.; Gallardo, E.; Duarte, A. P. Cannabis and Its Secondary Metabolites: Their Use as Therapeutic Drugs, Toxicological Aspects, and Analytical Determination. *Medicines (Basel)* **2019**, *6* (1). DOI: 10.3390/medicines6010031 From NLM PubMed-not-MEDLINE.
5. BUREAU OF DRUG AND NARCOTIC. Department of Medical Sciences, M. o. P. H. *Standard Methods for Analysis of Narcotics in Urine*; 2015.
6. Srisubat, A.; Thanasithichai, S.; Thaiyakul, A.; Konlaeaid, S.; Arunratanachot, W.; Imsuwanasri, T.; Mongkol, C.; Phaisaltuntiwongs, W.; Sawetprawichkul, W. Outcomes of THC Enriched in Advanced Staged Cancer Patients. *Journal of the Department of Medical Services.* **2020**, *45*, 208-214.
7. Schep, L. J.; Slaughter, R. J.; Glue, P.; Gee, P. The clinical toxicology of cannabis. *N Z Med J* **2020**, *133* (1523), 96-103. From NLM Medline.
8. Narcotics Control Management Center, M. o. P. H. *Recommendation of Cannabis treatment and care in Thailand*; 2019.
9. Department of medical services, M. o. p. h. *Guidance on Cannabis for Medical Use*; 2022.
10. Allen, K. R. Screening for drugs of abuse: which matrix, oral fluid or urine? *Ann Clin Biochem* **2011**, *48* (Pt 6), 531-541. DOI: 10.1258/acb.2011.011116 From NLM Medline.
11. Brenneisen, R.; Meyer, P.; Chtioui, H.; Saugy, M.; Kamber, M. Plasma and urine profiles of Delta9-tetrahydrocannabinol and its metabolites 11-hydroxy-Delta9-tetrahydrocannabinol and 11-nor-9-carboxy-Delta9-tetrahydrocannabinol after cannabis smoking by male volunteers to estimate recent consumption by athletes. *Anal Bioanal Chem* **2010**, *396* (7), 2493-2502. DOI: 10.1007/s00216-009-3431-3 From NLM Medline.
12. Fernandez Mdel, M.; Wille, S. M.; Samyn, N.; Wood, M.; Lopez-Rivadulla, M.; De Boeck, G. On-line solid-phase extraction combined with liquid chromatography-tandem mass spectrometry for high throughput analysis of 11-nor-Delta9-tetrahydrocannabinol-9-carboxylic acid in urine. *J Chromatogr B Analyt Technol Biomed Life Sci* **2009**, *877* (22), 2153-2157. DOI: 10.1016/j.jchromb.2009.04.047 From NLM Medline.
13. Rumpler, M. J. Quantitative analysis of 11-nor-9-carboxy-tetrahydrocannbinol (THC-COOH) in

urine by LC-MS/MS following a simple filtration. *J Chromatogr B Analyt Technol Biomed Life Sci* **2014**, *957*, 77-83. DOI: 10.1016/j.jchromb.2014.02.056 From NLM Medline.

14. Montesano, C.; Sergi, M.; Odoardi, S.; Simeoni, M. C.; Compagnone, D.; Curini, R. A mu-SPE procedure for the determination of cannabinoids and their metabolites in urine by LC-MS/MS. *J Pharm Biomed Anal* **2014**, *91*, 169-175. DOI: 10.1016/j.jpba.2013.12.035 From NLM Medline.
15. Heuett, N. V.; Ramirez, C. E.; Fernandez, A.; Gardinali, P. R. Analysis of drugs of abuse by online SPE-LC high resolution mass spectrometry: communal assessment of consumption. *Science of the Total Environment* **2015**, *511*, 319-330.
16. Scientific Working Group for Forensic, T. Scientific Working Group for Forensic Toxicology (SWGTOX) standard practices for method validation in forensic toxicology. *J Anal Toxicol* **2013**, *37* (7), 452-474. DOI: 10.1093/jat/bkt054 From NLM Medline.
17. U.S. Department of Health and Human Services, F. a. D. A. *Bioanalytical Method Validation Guidance for Industry*; 2018.

Assessing the quality of alcohol-based hand sanitizers purchased from Thailand's online market using a GC-FID technique

Orapan Apirakkan, Chompoonoot Paimoolpiam, Chaweewan Peangpitak, and Neungrutai Saesaengseerung*

Department of Science Service (DSS), 75/7 Rama VI Road, Ratchathewi Bangkok 10400, Thailand

**E-mail: sneungrutai@dss.go.th*

Abstract:

Since the COVID-19 pandemic, the proliferation of online marketplaces has provided consumers with convenient access to a wide range of alcohol-based hand sanitizers. However, without rigorous post-marketing surveillance, the quality of these products remains a significant concern, given the potential risks associated with substandard or counterfeit formulations. This research conducted post-marketing surveillance for quality investigation of alcohol-based hand sanitizers purchased from Thailand online markets. The alcohol content and ingredient authenticity were examined for compliance with Thai industrial standards (TIS: 3302-2021) using gas chromatography-flame ionization detector (GC-FID) technique. Each of the non-gel hand sanitizer samples was diluted tenfold with deionized water; a small amount of hydrochloric acid was added to gel formulation samples to disrupt the polymer crosslinking before dilution. Isobutanol was added as an internal standard prior to the analysis. The results show that the random purchase during March to August 2023 of the 41 alcohol-based products bought from Thai online markets come in various formulations, 29 liquid forms, 8 gel forms and 4 wet wipe forms. Products that have alcohol content compliance with TIS: 3302-2021 ($\geq$ 70%v/v), were found to be 65.9% of all products. However, based on packaging labels, 27 products out of 41 found alcohol content label mismatch in either higher or lesser than the maximum acceptable deviation in the active substance content specified on label. 3 products found methanol content exceed the TIS: 3302-2021 limit, among of these, 1 product spotted as a counterfeit formulation of using methanol instead of ethanol/isopropanol. Methanol is harmful and hardly distinguishable by odor from ethanol. These results reveal that the post-marketing surveillance of alcohol-based hand sanitizers by laboratory testing is therefore very necessary to ensure safety for consumers.

1. Introduction

In Thailand, alcohol-based hand sanitizers are categorized as cosmetic products. As outlined in the Ministry of Public Health's notification regarding the specifications for manufacturing, importing, and selling alcohol-based hand sanitizers[1] and the Thai industrial standards on alcohol-based hand sanitizer (TIS:3302-2021),[2] these products are required to have a minimum volume of 70% ethyl alcohol, isopropyl alcohol, n-propyl alcohol, or a mixture of these compounds. Alcohols have been recommended by the World Health Organization (WHO) to be used as active ingredients in hand sanitizer products,[3] also they have a non-irritating effect on the skin. With a suitable concentration, germ-killing properties can be effectively demonstrated against a broad spectrum of microbes including SARS-CoV-2. It is assumed that their mode of action involved membrane damage and rapid denaturation of proteins.[4]

The COVID-19 pandemic has led to a surge in the popularity of online shopping, with hand sanitizers being a particularly sought-after product for online purchases due to the awareness of hygiene, convenience, improved formulations, availability and affordability.[5,6] E-commerce also offers manufacturing industries and retailers the advantage of easily expanding their target customer base and reducing service costs through the application of automation. However, with the convenience of launching an online shop, consumers often encounter issues like dealing with fraudulent sellers or receiving low-quality products. Therefore, purchasing items directly from the online store necessitates ensuring the quality and safety of the products. One of the approaches to be used to monitor the quality and safety of online products is post-marketing surveillance (PMS).[7] Implementing PMS is one of the strategies for risk management. It aims to ensure health-related issue of consumers following the launch of cosmetic and drug products into the market.[8] Thus, this research aims to conduct post-marketing surveillance of alcohol-based hand sanitizer products from Thailand's online market. To enhance consumer confidence in the quality of alcohol-based hand sanitizer products from the online market through post-market quality monitoring. The hand sanitizer products were interested in three preparations which were liquid, gel and wet wipe.

2. Materials and Methods

2.1 Materials

Alcohol-based hand sanitizer samples were test-purchased online from Thailand online market from March to August 2023. A total forty-one products, separated into twenty-nine liquid, eight gel, and four wet wipe preparations were obtained from online retailers. Some samples were labeled with the type of alcohol, the amounts, or the Thai FDA registration number but some were not. Samples were kept at room temperature before analysis. Sample descriptions and details are shown in Table 1.

Ethanol (>99.9% purity, for HPLC plus gradient grade) was from Carlo Erba (France). Methanol (>99.99% purity, HPLC grade) and isopropanol (>99.95% purity, HPLC grade) were from Fisher Scientific (UK). Isobutanol, for HPLC, was from Sigma-Aldrich (USA).

2.2 Analytical instruments

GC-FID: A TRACE 1300 GC equipped with a TriPlus RSH autosampler and a flame ionization detector (FID) was used. Chromeleon software version 7.2.10 was employed to control the equipment. A TG-624 SilMS column length 30 m × 0.32 mm i.d., film thickness 0.25 µm was purchased from ThermoScientific. Helium was used as a carrier gas at flow rate 2.5 mL/min. Split mode was set at flow rate 350 mL/min. Inlet temperature was 170 °C, detector temperature was 250 °C. Oven temperature was started at 40 °C, hold for 4 minutes, and ramping to 120 °C with 40 °C/min rate and hold for 2 minutes, then ramping to 250 °C with 35 °C/min rate and hold for 0.3 minutes. By comparing the retention times of alcohols in a standard solution with the alcohol peaks present in the samples, the quantities of alcohols were identified.

GC-MS: GC-MS was used to confirm methanol peak found in sample. A TRACE 1300 GC equipped with an AI/AS 1310 autosampler and a ISQ LT mass spectrometer was used. XCalibur software was employed to control the equipment. A TG-17 SilMS column length 30 m × 0.25 mm i.d., film thickness 0.25 µm was purchased from ThermoScientific. Helium was used as a carrier gas at flow rate 1 mL/min. Split mode was set at flow rate 50 mL/min. Inlet temperature was 250 °C. Oven temperature was started at 40 °C, hold for 5 minutes, and ramping to 240 °C with 30 °C/min rate and hold for 4 minutes. Transfer line temperature was 240 °C, and ion source temperature was 230 °C. Full scan MS mode detected mass at 28-80 m/z was set. By comparing mass spectra of methanol peaks in standard solution and in the samples with the library, methanol was confirmed.

Density meter: An Anton Paar DMA 4500 M density meter was used to determined density of standard alcohols and samples at 20 °C.

2.3 Sampling plan

Samples were not ordered only from the online shop in the capital city. Different geographical areas were chosen. Details of the online shops selected of each sample are shown in table 1.

2.4 Standard and sample preparations for alcohol content determination

Standard preparation: calibration curve of standard ethanol and standard isopropanol were prepared in six concentration levels from 1%w/v to 15%w/v in water. Calibration curve of standard methanol to quantify in trace level was prepared from 0.001%w/v to 1%w/v in water. Isobutanol was used as internal standard for all three alcohols determination.

Sample preparation: each sample 1 mL was pipetted and weight in 10 mL volumetric flask, then was diluted with deionized water. Five microliters of 37% hydrochloric acid was added to gel formulation samples to disrupt the polymer crosslinking before dilution. Wet wipe samples were analyzed by squeezing liquid from wipe sheet before dilution. Isobutanol was added at the same amount of calibration curve preparation prior to the analysis. Recovery sample was prepared by adding known amounts of standard alcohol to sample.

2.5 Standard and sample preparations for methanol confirmation using GC-MS

Standard methanol was prepared at 500 ppm in acetonitrile. Samples were prepared by pipetting 1 mL in a 100 mL volumetric flask and diluting with acetonitrile.

3. Results & Discussion

3.1 Determination of alcohol concentration by GC-FID

Forty-one samples of alcohol-based hand sanitizers randomly purchased from Thai online markets between March and August 2023, underwent quantification of alcohol type and content using gas chromatography-flame ionization detector (GC-FID). Regarding the previously mentioned GC system, the methanol, ethanol, isopropanol, and isobutanol peaks exhibit retention times of 1.98, 2.66, 3.32, and 5.91 minutes, respectively. Figure 1 displays chromatograms depicting standard alcohols and a

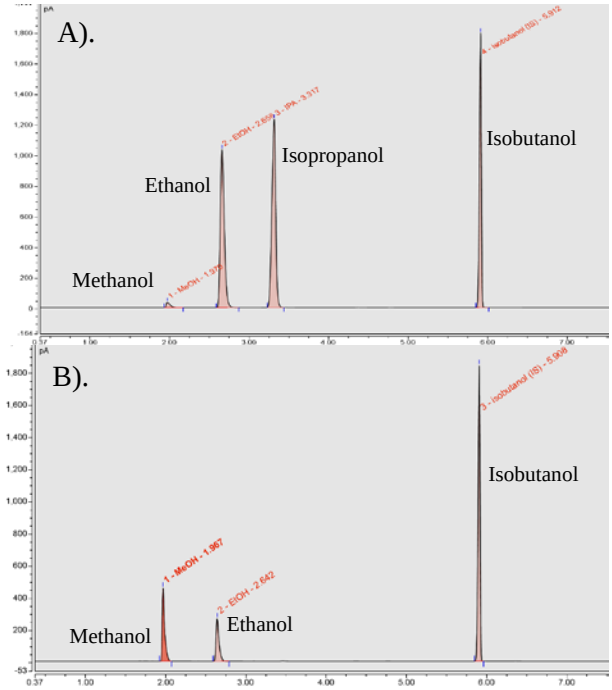

Figure 1. A). Chromatogram of standard alcohols **B).** Chromatogram of alcohol-based hand sanitizer containing methanol that exceeds the specification on TIS: 3302-2021 limit.

sample containing methanol that exceeds the specification on TIS: 3302-2021 limit.

Analysis based on the specifications outlined in TIS: 3302-2021 revealed that 27 out of 41 products met the compliance standards for ethanol/ isopropanol content (>70% v/v), accounting for 65.9% of the total samples. Conversely, 13 products exhibited alcohol contents below the 70%v/v threshold. Within these 13, two products exceeded the permissible limit for methanol content. Additionally, one product was identified as a counterfeit formulation, utilizing methanol instead of the recommended ethanol/isopropanol (Figure 2A.)

Based on packaging labels, every product except one (ES-26) displays the labeled alcohol content on its packaging. Among them, one product (ES-33) labeled as containing IPA 70%, was found to contain ethanol at 73.5% instead. Furthermore, another product (ES-18) was labeled as having 75% alcohol content but was identified as a counterfeit, containing 78.4% methanol as previously mentioned (Table 1).

Comparing the experimentally determined alcohol contents with the labeled information on the package, 27 out of 41 products found alcohol content label mismatch in either higher (10) or lesser (17) than the maximum acceptable deviation in the active substance content specified on the label as stipulated by the Ministry of Public Health's notification regarding criteria for deviations from specified quantities of the active ingredient in hazardous materials that responsible by the Thai Food and Drug Administration.[9] Among of these, 11 products found alcohol content outside the WHO recommended range (60-80% v/v).[3] Only 12 products exhibited alcohol contents that aligned with the specified value stated on their package (Figure 2B).

Interestingly, almost all products except one that was found issued with their Thai FDA registration numbers stated on the packaging (ES-7, ES-11, ES-12, ES-13, ES-18, ES-29, ES-33, ES-39). These issues ranged from the inability to locate the registration number on the Thai FDA website upon checking, encountering registration numbers printed too small or unclear, or the registration number was absent. These products were associated with one or more of the following: substandard quality, counterfeit production, or alcohol content labeling mismatch (Table 1 and Figure 2B).

There was a concern regarding the detection of methanol exceeding the TIS limit (not more than 200 ppm, 0.02% v/v) in two products (ES-3, ES-8), yet no irregularities were observed with their Thai FDA registration numbers. These registration numbers can even be verified on the Thai FDA website as checked.

The association between the geographical distribution of online shop locations (central versus other regions) and the quality of hand sanitizer products according to TIS: 3302-2021 specification was explored. Chi-square test of independence was employed and the findings indicate a p-value of 0.46, so that, there was no significant association between online shop locations (central versus other regions) and quality of alcohol-based hand sanitizer products. Hence, the quality of hand sanitizer products was not influenced by location of online shop ($p>0.05$) for this population.

Table 1. Sample descriptions, details, the labeled information on the package and the experimentally determined alcohol contents with GC-FID**.**

Sample No.	Description	Thai FDA registration no.	%Alcohol stated on the label (%v/v)	Online shop location	Region	%Alcohol found by GC-FID (%v/v)
ES-1	Clear light blue liquid	✓	Ethanol 75%	Bangkok	Central	Ethanol 74.9%
ES-2	Clear light blue liquid	✓	Ethanol 75%	Bangkok	Central	Ethanol 78.2%
ES-3	Clear light blue liquid	✓	Ethanol 75%	Korat	North East	Ethanol 16.0%, Methanol 33.3%
ES-4	Clear orange liquid	✓	Ethanol 75%	Nakhon Pathom	Central	Ethanol 75.9%
ES-5	Clear light blue liquid	✓	Ethanol 75%	Phetchaburi	South	Ethanol 72.3%
ES-6	Colorless gel	✓	Ethanol 70%	Bangkok	Central	Ethanol 73.4%
ES-7	White wet wipe	Not found	Ethanol 75%	Bangkok	Central	Ethanol 30.1%
ES-8	Light blue gel	✓	Ethanol 75%	Korat	North East	Ethanol 5.6%, Methanol 41.5%
ES-9	Light blue gel	✓	Ethanol 75%	Samut Prakan	Central	Ethanol 47.3%
ES-10	Light blue gel	✓	Ethanol 75%	Samut Prakan	Central	Ethanol 49.1%
ES-11	White wet wipe	Not found	Ethanol 75%	Bangkok	Central	Ethanol 15.7%
ES-12	White wet wipe	Not found	Ethanol 75%	Bangkok	Central	Ethanol 5.7%
ES-13	White wet wipe	Not found	Ethanol 75%	Bangkok	Central	Ethanol 4.0%
ES-14	Colorless gel	✓	Alcohol 70%	Bangkok	Central	Ethanol 72.5%
ES-15	Clear light blue liquid	✓	Alcohol 75%	Pathum Thani	Central	Ethanol 75.0%
ES-16	Clear light blue liquid	✓	Alcohol 75%	Pathum Thani	Central	Ethanol 73.6% Isopropanol 6.9%
ES-17	Colorless gel	✓	Alcohol 75%	Nonthaburi	Central	Ethanol 72.9%
ES-18	Clear light blue liquid	✓*	Alcohol 75%	Bangkok	Central	Methanol 78.4%
ES-19	Colorless liquid	✓	Alcohol 75%	Pathum Thani	Central	Ethanol 73.8%
ES-20	Colorless liquid	✓	Alcohol 77%	Bangkok	Central	Ethanol 76.9%
ES-21	Clear orange liquid	Not found	Alcohol 75%	Samut Prakan	Central	Ethanol 74.8%
ES-22	Clear light blue liquid	✓	Alcohol 75%	Chiang Mai	North	Ethanol 98.2%
ES-23	Clear light blue liquid	✓	Alcohol 75%	Chiang Rai	North	Ethanol 84.0%
ES-24	Greenish-blue liquid	✓	Alcohol 75%	Chiang Mai	North	Ethanol 80.6%
ES-25	Clear light blue liquid	✓	Alcohol 75%	Songkhla	South	Ethanol 72.3%
ES-26	Clear light blue liquid	✓	Not specified	Khon Kaen	North East	Ethanol 73.3%
ES-27	Clear light blue liquid	✓	Alcohol 75%	Surin	North East	Ethanol 76.2%
ES-28	Clear light blue liquid	✓	Alcohol 75%	Nonthaburi	Central	Ethanol 60.3%
ES-29	Clear light blue liquid	✓*	Ethanol 70%	Korat	North East	Ethanol 76.1%
ES-30	Clear pink liquid	✓	Alcohol 79%	Buri Ram	North East	Ethanol 18.4%
ES-31	Colorless liquid	✓	Alcohol 75%	Chon Buri	East	Ethanol 80.1%
ES-32	Clear light blue liquid	✓	Ethanol 75%	Chon Buri	East	Ethanol 69.1%
ES-33	Light blue gel	Not found	IPA 70%	Prachuap Khiri Khan	South	Ethanol 73.5%
ES-34	Colorless liquid	✓	Ethanol 75%	Kanchanaburi	West	Ethanol 72.0%
ES-35	Colorless liquid	✓	Ethanol 75%	Ratchaburi	West	Ethanol 47.2%
ES-36	Colorless liquid	✓	Ethanol 75%	Pathum Thani	Central	Ethanol 81.0%
ES-37	Colorless liquid	✓	Alcohol 75%	Bangkok	Central	Ethanol 71.6%
ES-38	Light blue gel	✓	Ethanol 75%	Samut Prakan	Central	Ethanol 75.6%
ES-39	Colorless liquid	✓**	Alcohol 75%	Bangkok	Central	Ethanol 55.5%
ES-40	Clear light blue liquid	✓	Ethanol 75%	Bangkok	Central	Ethanol 72.8%
ES-41	Clear light blue liquid	✓	Alcohol 75%	Bangkok	Central	Ethanol 74.5%

✓ = the Thai FDA registration number is stated on the package and also found on the Thai FDA website as checked.
✓* = stated the Thai FDA registration number on the package but could not find it on the Thai FDA website as checked.
✓** = stated the Thai FDA registration number on the package but it is very small and not clear.

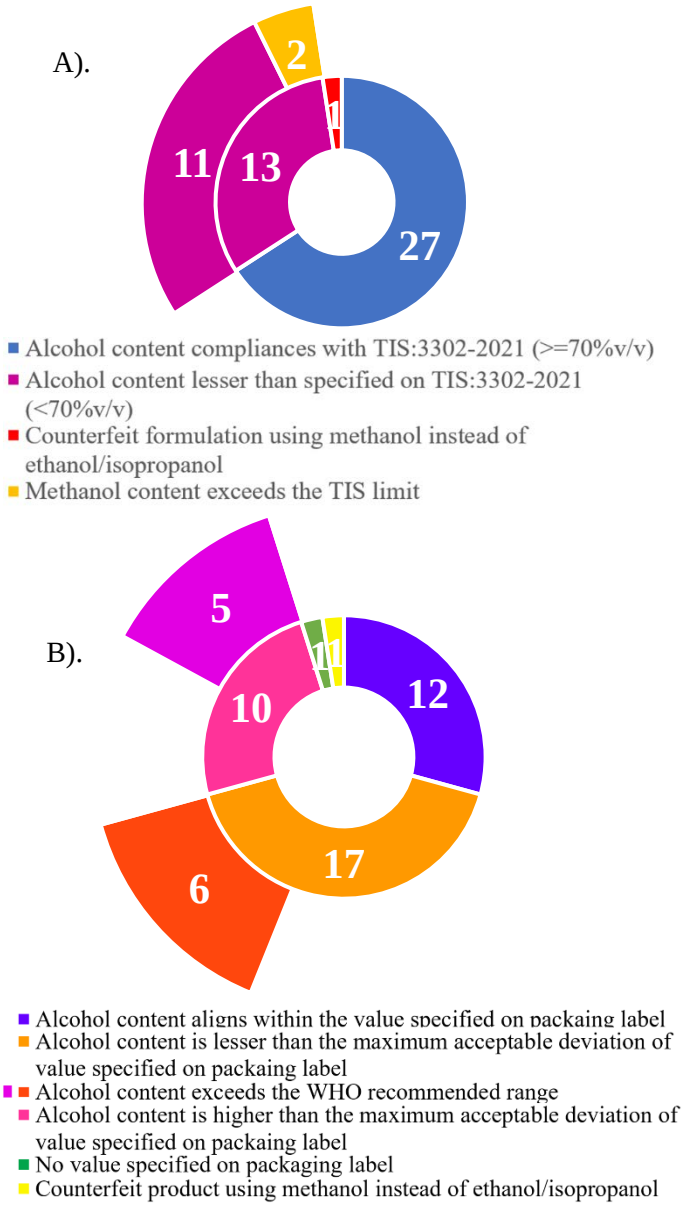

Figure 2. Pie charts represent **A).** Frequency of samples categorized by alcohol type and content according to the specifications outlined in TIS: 3302-2021 **B).** Frequency of samples categorized by alcohol type and content according to the labeled information on their packaging.

3.2 GC-MS confirmation

Methanol peaks identified in 3 samples (ES-3, ES-8, ES-18) were confirmed through a gas chromatography-mass spectrometry detector (GC-MS) utilizing the electron impact ionization (EI) technique. The chromatogram (Figure 3A, B) illustrates that the GC-MS method employed provided sufficient resolution to detect and confirm methanol in the samples with the methanol peak eluted at a retention time of 1.55 minutes. Comparing the mass spectra at the 1.55-minute retention time of both standard and sample (Figure 4A, B) revealed a similar pattern and matched the methanol library entry (Figure 4C).

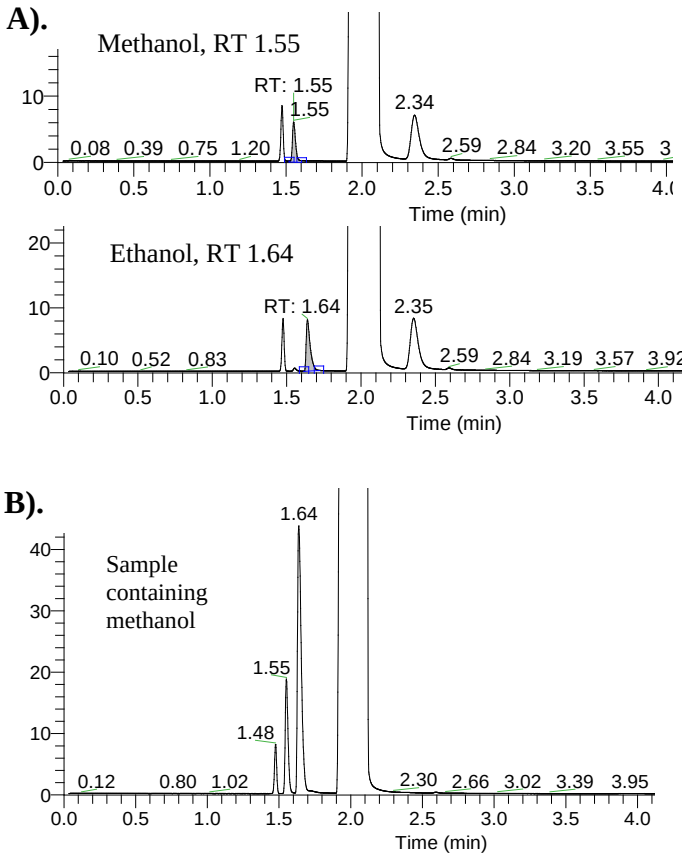

Figure 3. GC-MS chromatogram of **(A).** standard alcohol and **(B).** sample containing methanol

The mass spectral match quality between fragmentation pattern of methanol from library and from samples gives a high library matching score at 915-931, indicated as an excellent match as recommended by NIST library guidelines [10].
GC-MS fragmentation of methanol shows the base peak ion at m/z 31 represented CH_2OH^+, whereas a molecular ion, CH_3OH^+, presents at m/z 32. Other peaks at m/z 29 and 30 corresponded to CHO^+ and CH_2O^+ respectively. These fragmentations confirm the structure of methanol that is presented in samples, (Figure 4).

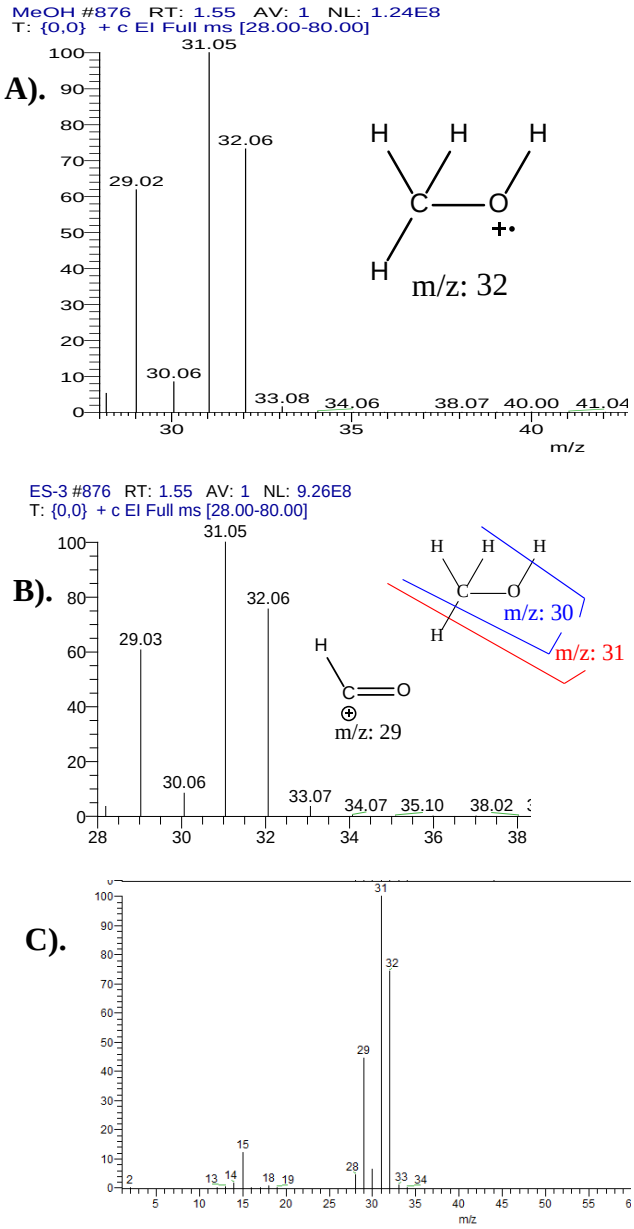

Figure 4. Mass spectrum corresponding to the peak with a retention time of 1.55 minutes (methanol peak) in **(A).** standard methanol, **(B).** sample (ES-3) and **(C).** mass spectrum of methanol from library searching (NIST MS searching library version 2.0)

Regarding the specifications outlined on TIS: 3302-2021, products are required to have ≥70% v/v of alcohol. The WHO recommends an alcohol content of approximately 60-80% v/v for hand sanitizer products.[3] In relation to the WHO guideline, excessive alcohol content can render hand sanitizers less effective as the insufficient water content may not adequately denature bacteria proteins. Conversely, insufficient alcohol content can result in an ineffective hand sanitizer.

Hand sanitizer products containing methanol that exceed the permitted limits or are counterfeited by substituting methanol for ethanol for any reasons such as reduced cost or improper manufacturing practices, pose severe risks to consumers' health. Methanol poses significant harm and is hardly distinguishable by odor from ethanol**.**

4. Conclusion

In this post-marketing surveillance (PMS) study, the investigation into alcohol-based hand sanitizer products obtained from various online retailers across diverse regions of Thailand uncovered that approximately 66% of these products complied with the quality standards specified in the TIS: 3302-2021 guidelines. However, several products exhibited alcohol contents that fell outside the WHO-recommended range of 60-80%, that potentially reducing their effectiveness. Furthermore, some of the inferior products displayed seemingly regular Thai FDA registration numbers on their packaging, making it challenging for consumers to identify and avoid these inadequate items.

Substandard or counterfeit hand sanitizers have the potential to harm consumers and prove ineffective for their intended purposes. Given that these products are directly applied to the skin and rapidly absorbed into the bloodstream, their quality is critical**.** Our post-marketing surveillance study highlights the hazards associated with randomly purchasing alcohol-based hand sanitizers online, indicating the need for consumer vigilance and careful selection.

Acknowledgements

This project was supported under the 2023 fundamental fund by Thailand Science Research and Innovation (TSRI).

References

1. Ministry of Public Health, Notification of the Ministry of Public Health Re: Specification of cosmetics containing alcohol for hand hygiene that are prohibited from manufacturing, importing, or selling. (No. 137-54) B.E. 2563, 2020.
2. Thai Industrial Standards Institute, Ministry of Industry, Alcohol-based hand sanitizer TIS: 3302-2021, 2021.
3. World Health Organization and WHO Patient Safety, WHO Guidelines on Hand Hygiene in Health Care, 2009.
4. McDonnell, G.; Russell, A.D. *Clinical Microbiology Reviews* **1999**, 12(1), 147-179.

5. Shen, H.; Namdarpour, F.; Lin, J. *Transportation Research Interdisciplinary Perspectives* **2022**, 14, 100580.
6. Vuppu, S.; Mishra, T.; Chinamgari, A. *Pharmacoepidemiology* **2023**, 2, 257–271.
7. Hendriksen, K. E-commerce and product safety-key challenges. European Commission.
8. Kingston, R.; Sioris, K.; Gualtieri, J.; Brutlag, A.; Droege, W.; Osimitz, T. G. *Regulatory Toxicology and Pharmacology* **2021**, 126, 105028.
9. Ministry of Public Health, Notification regarding criteria for deviations from specified quantities of active ingredient in hazardous materials, 2012.
10. NIST Standard Reference Database 1A, NIST/EPA/NIH Mass Spectral Library (NIST 08) and NIST Mass Spectral Search Program (Version 2.0f) user's guide.

COVID-19 Screening in sweat by volatile analysis using GC-MS and the relationship with military training dog results

Suriwipa Chuachaina[1], Isaya Thaveesangsakulthai[1], Jantima Traipattanakul[2], Pornpawit Sinsukudomchai[3], Sorrawit Songsathitmetha[4], Kaywalee Chatdarong[5], Chadin Kulsing[1,6]*, and Thumnoon Nhujak[1]*

[1]*Department of Chemistry, Faculty of Science, Chulalongkorn University, Bangkok, 10330, Thailand*
[2]*Division of Infectious Disease, Department of Medicine, Phramongkutklao Hospital, Bangkok, Thailand*
[3]*Department of Biomedical Engineering, Faculty of Engineering, Chulalongkorn University, Bangkok, 10330, Thailand*
[4]*Department of Pathology, Faculty of Veterinary Science, Chulalongkorn University, Bangkok, 10330, Thailand*
[5]*Department of Obstetrics, Gynaecology and Reproduction, Faculty of Veterinary Science, Chulalongkorn University, Bangkok, 10330, Thailand*
[6]*Electrochemistry and Optical Spectroscopy Center of Excellence (EOSCE), Department of Chemistry, Faculty of Science, Chulalongkorn University, Bangkok, 10330, Thailand*

**E-mail: thumnoon.n@chula.ac.th, ckulsing@gmail.com*

Abstract:

Several approaches have been recently developed as an alternative method for COVID-19 screening due to the pandemic of SARS-CoV-2 since 2019 based on rapid, non-invasive and cost- effectiveness. Sniffer dog is one of those alternative methods successfully developed with the performance results showing as > 90% of accuracy. Two military training dogs were trained to recognize unique smells of positive COVID-19 patients' sweat as well as smells of negative cases. Then, these training dogs could differentiate among patients who were infected and uninfected with COVID-19. We worked with gas chromatography – mass spectrometry (GC-MS) for volatile analysis in sweat samples of volunteer patients together with statistical analyses to clarify the potential markers of volatile organic compounds (VOCs) with the relationship of COVID-19 screening results obtained from military training dog. This work was under the collaboration of Phramongkutklao Hospital and Chulalongkorn University in Bangkok, Thailand. Two sets of sweat samples were collected from each volunteers using sterile cotton rods as an absorbent material. A set of sweat samples included two cotton rods after sweat absorption from both right and left sides of armpits. the first sample set was brought to military training dog and the second sample set was brought to GC-MS method for volatiles analysis. In addition, all results were validated by comparison with RT-PCR results. Finally, several volatile compounds were identified and reported as possible markers in human sweat that the canines recognized. This study is expected to provide a new insight into the area of dogs' odor recognition for improved screening of COVID-19 and the other related diseases in the future.

1. Introduction

Due to the SARS-CoV-2 pandemic, there were several techniques developed for COVID-19 diagnosis such as real time polymerase chain reaction **(**RT-PCR**)**, which was used worldwide as it provides high performances of accuracy, sensitivity, and specificity.[1] RT-PCR mainly detects the viral genome in respiratory secretion samples collected by swabbing.[1] Although this technique of RT-PCR provides many strengths, there are also some limitations as it requires medical specialists and time consuming.[2] Alternatively, several approaches were also developed based on rapid, effective, and non-invasive. For example, biological detection is one of the alternative techniques using trained dogs/sniffer dogs to differentiate between infected COVID-19 patients and non-infected COVID-19 patients.[3,4] Dogs were trained to recognize individual smells of COVID-19 from patient's samples such as in sweats as it was studied in previous work.[5] After that, dogs were then trained to respond to COVID-19 infected samples by responding in posture change such as sitting in front of the chamber of sample.[5] This technique of bio-detection provided fast and high-sensitivity results.[3,4] However, names of compounds suspected to be potential VOCs/Odor markers that training dogs recognized from sniffing had not been clarified enough. A challenge is to identify VOCs/Odor markers that dogs recognize and differentiate for COVID-19.

Previously, sweat was reported as a safe body secretion sample with no possibility of SARS-CoV-2 transmitting according to negative RT-PCR results in sweat sample from the infected COVID-19 patients.[6] In addition, since VOCs profiles in sweat significantly relate to changes in internal hormones, immunities, metabolic pathways, and skin bacteria activities,[7-9] then, different profiles of VOCs in sweat may be possibly observed after SARS-CoV-2 infection.

GC-MS has been widely used for VOCs identification together with the use of HS-SPME as an extraction method because of its ability to directly extract volatiles without solvent consumption.[10] Potential VOC markers can be obtained from data analysis using a statistic analysis program that can categorize all identified compounds into groups.

In this study, potential VOC/Odor markers that military training dogs recognize for COVID-19 screening in sweat samples were studied using HS-SPME-GC-MS. Samples were collected under the consent form of volunteers recruited from Phramongkutt Hospital and Chulalongkorn Hospital, Bangkok, Thailand.

2. Materials and Methods

2.1 Sample collection

This study's sample collection was approved by the Central Research Ethics Committee and the Institutional Review Boards at Phramongkutklao Hospital (897/63), and the Faculty of Medicine, Chulalongkorn University (COA-CREC103/2020) in Bangkok, Thailand.

Trained nurses collected ten sweat samples from volunteers, consisting of five positive and five negative cases confirmed by RT-PCR. These samples were collected in two sets, each with the direction shown in Figure 1. Each set of samples included two pieces of sterile cotton rods used as an adsorbent, a glass vial used as a container, and aluminum caps as a cover. Then, the vial was packed separately in a plastic zip-lock bag. After collecting all the samples, they were kept under the condition of biosafety laboratory level 2 (BSL2) and then transported to the laboratory room in the chemistry department. The samples are now ready to be used.

2.2 Dog training

Two military training dogs that participated in this project were Lopez and Hero. The dogs were trained to recognize the unique VOCs between positive and negative sweat samples.

Each of six sweat sample sets were placed in each of six separate chambers. One sweat sample among all was set as an infected COVID-19 case. These two military training dogs were trained to respond to the COVID-19 sweat sample in form of posture changing, which was to sit in front of the chamber containing the COVID-19 sample, indicating a positive result. Dogs in training would receive food as an award if they could sit correctly in front of the RT-PCR proven positive sweat sample. According to the correct response behavior to COVID-19 sweat samples, the labeled sample names were reported for further study in the next section of volatile analysis using GC-MS.

2.3 Volatile analysis of sweat sample

Headspace solid phase micro-extraction (HS-SPME) was used as the VOCs extraction method. The fiber was conditioned at 270 °C for 1 hour and was checked the background signals before use. A mixture of n-alkanes (C8-C20) was used as standard reference and for calculation of retention indices (*I*).

After equilibrating the sweat sample by leaving the vial at room temperature for at least 15 minutes, the SPME fiber was used to extract VOCs in the vial with the chosen method of extraction (70°C for 45 min). After that, extracted VOCs were injected into the injection port of the GC instrument, then separated and detected followed by GC-MS method under the proper conditions; GC oven temperature ramped from 40 to 240°C at a rate of 4°C per minute, using an HP-5 capillary column and helium as the carrier gas.

2.4 Data analysis

Peaks of separated VOCs in form of chromatograms were obtained from GC-MS. All of collected peaks were identified using a qualitative program by comparing their mass spectrum with NIST22 library database followed by the accepted criteria for identification (match score >650, within a 20-unit difference of *I*). After that, an in-house data alignment program was then used to categorize all identified compounds into groups of potential compounds that were suspected to be biomarkers for COVID-19 screening in sweat samples.

T-test, a type of statistical evaluation, was used to compare means of two independent sample groups by setting hypothesis. Null hypothesis (at p-value $\geq$ 0.05) was set as a statistically non-significant difference between two mean peak areas from two sample groups. On the other hand, at p-value < 0.05 was set as statistically significant difference between two mean peak areas from two independent groups.

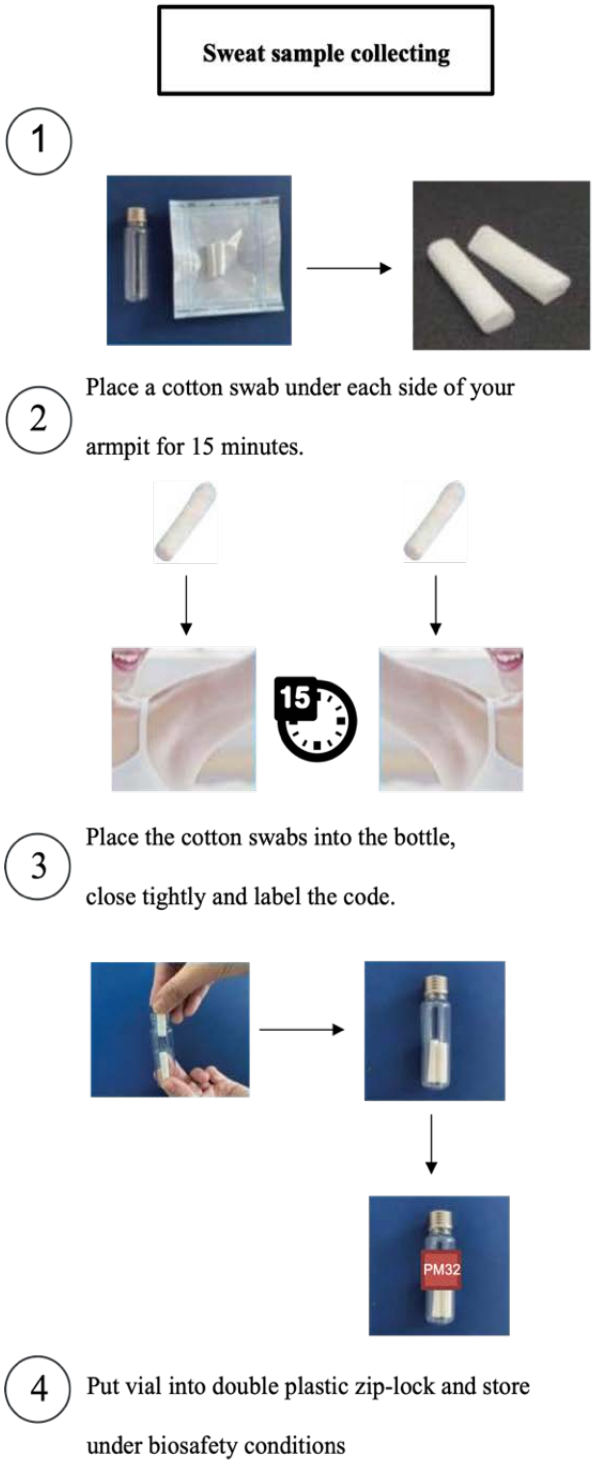

Figure 1. The process chart of sweat sample collecting showed the way to collect samples in one set. Volunteers were required to collect two sets each of samples (one set was for training dog screening and another one set was for volatile analysis by GC-MS

3. Results & Discussion

3.1 Volatile compound analysis

Volatile analysis in sweat samples was studied by the technique of HS-SPME-GC-MS to clarify potential VOCs markers, which might relate to the screening results obtained from military training dogs. Three positive and negative sweat samples proven by military training dogs were identified under proper conditions of separation methods, shown as chromatograms given in **Figure 2**. There were 40-65 of identified compounds found in positive and negative sweat samples. Aromatics, aldehydes, ketones, and alkanes were mainly found in sweat samples. An example of identified VOCs obtained from a qualitative program providing information on compound name, retention time, and peak area are shown in **Table 1**. Specific VOCs peaks in retention time ranges of 0 – 15 minutes were able to be observed as the difference of peak patterns between those in positive and negative samples.

A statistical method, t-test, was then performed and p-value was calculated to differentiate between VOCs found in COVID-19 sample and non-COVID-19 sample. There are 3 compounds found as < 0.05 of p-value; styrene ($1.2x10^{-6}$), 2,2,6-trimethyloctane ($3.8x10^{-4}$), and nonanal ($1.2x10^{-6}$) indicating selected compounds as potential markers.

Potential biomarkers in sweat samples for COVID-19 screening were shown in **Table 2** including compound names, retention time, and average peak area. It is obviously seen that the average peak areas of potential markers were significantly different between those in positives and negatives.

Sweat is composed of water, minerals, lipids, and amino acids mainly produced by skin glans.[11] Sweat originates smells known as body odors when contracting with skin bacteria and or elements in the environment.[12-15] Changes of internal hormones and immunities also relate to body smell production.[16] Then, VOCs in the human body could relate to COVID-19 infection due to changes of metabolic pathways occurring when a person contracted with SAR-CoV-2 infectious.[12] For this reason, it could affect changes in the growth and or colonization of microorganisms coinfecting with SARS-CoV-2.[8,9] In addition, possible sources of volatile markers production were studied as it was shown in **Table 3.**

Table 1. Example of VOCs data in sweat sample characterized by qualitative program

PM36	Time	Retention index		Peak Area	Match	R Match
		Exp	Lit			
Ethylbenzene	5.5	843.9	855	12421	676	683
p-xylene	5.7	852.4	865	15314	605	668
Styrene	6.2	875.7	893	199226	902	921
4-tert-Butylaniline, N-pentafluoropropionyl-	9.7	992.7	1440	9933	503	543
Neopentyl alcohol, TBDMS derivative	9.9	999.7	991	114455	447	505
Cyclopentane, (2-methylbutyl)-	10.6	1018.6	1000	6628	462	632
Nonanal	13.6	1107.6	1100	25440	740	801
Decane, 2,4-dimethyl-	14.0	1117.6	1106	21912	588	815
2-Amino-4-methylphenol, 2TMS derivative	15.2	1150.9	1501	641935	466	662
Undecane, 5-methyl-	15.5	1161.3	1156	6429	580	759
Naphthalene	15.8	1169.1	1182	12102	754	770
Benzoic acid, 3-methyl-, methyl ester	16.3	1182.2	1206	16668	631	660
(S)-(-)-1,2,4-Butanetriol, 2-acetate	19.4	1275.1	1247	955276	535	544
Octanoic acid, 3-hydroxy-, methyl ester	19.6	1278.7	1243	315205	518	837
1,3-Dioxolane, 2-hexyl-	19.9	1288.7	1144	16559	565	658
Glyceric acid, 3TMS derivative	21.0	1323.9	1344	1367077	439	532
Triacetin	22.7	1375.8	1344	143175174	850	853
Tetradecane	23.2	1390.7	1400	8970	657	784
:	:	:	:	:	:	:
:	:	:	:	:	:	:

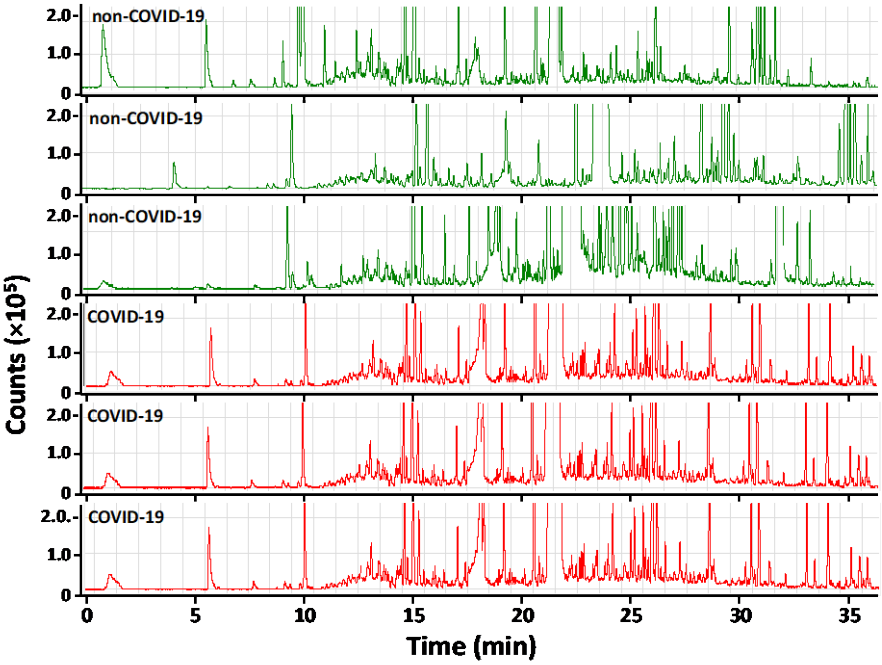

Figure 2. Chromatograms obtained from GC-MS analysis in sweat showed differences among three COVID-19 cases resulting from training dogs (labeled as Pos) and three non-COVID-19 cases (labeled as Neg)

Table 2. Potential marker compounds that canines recognize for COVID-19 in sweat samples

Compounds	CAS number	Retention time (min)	average peak area		p-value
			positive	negative	
Styrene	100-42-5	6.3	27,434	1,527	$1.2x10^{-6}$
2,2,6-trimethyloctane	62016-28-8	9.1	29,901	3,458	$3.8x10^{-4}$
Nonanal	124-19-6	13.1	30,263	4,604	$1.2x10^{-6}$

Table 3. Biomarkers production relating to microorganism in human body

Compound name	Microorganism relating to compound production	sources	References
styrene	*Pseudomonas aeruginosa*	breath, skin	[17], [21]
2,2,6-trimethyloctane	*Pseudomonas aeruginosa*	lung	[22]
nonanal	*Streptomyces griseovariabilis*	skin	[18], [19], [20]

After being infected with SARS-CoV-2, various metabolic pathways could change relating to different production of VOCs/Odor in sweat samples, which were suspected as COVID-19 biomarkers that military training dogs recognized. For example, when a person is infected with SARS-CoV-2, the metabolic pathway of relative bacteria such as *Pseudomonas aeruginosa*[17] may change leading to styrene and toxins production.[16] In addition, *Pseudomonas aeruginosa and Acinetobacter baumannii* play important roles in reduction reactions for nonanal production which is usually found in the respiratory system and on the skin.[18,20]

There might be a few parameters that influenced the performance of this work such as an ability to produce VOCs markers by local microorganisms in local environment of volunteer patients, which could lead to the existence of the same biomarker production as those observed from COVID-19 infection. For this reason, false positive results could then occur. On the other hand, false negative results might also occur due to a decrease in marker compounds when a patient had taken a shower or when they had used an odorant product before participating in the process of sample collection.

4. Conclusion

Volatile marker compounds that military training dogs recognize for COVID-19 in sweat were studied. Samples were collected under the consent of volunteers recruited from Phramongkutt Hospital and Chulalongkorn Hospital, Bangkok, Thailand. Two military training dogs were trained to recognize and respond to the unique VOCs patterns of COVID-19 patients' sweat samples. The Labeled sweat samples of positive and negative cases from dog sniffing results were then identified. Potential markers obtained from this study included styrene, nonanal, and 2,2,6 trimethyloctane. These biomarkers' production might relate to changes in metabolism pathways in the patient's body after COVID-19 infection. The researcher anticipated that this study would have practical implications for improving COVID-19 screening by training dogs in the future.

Acknowledgments

The Scholarship from the Graduate School, Chulalongkorn University to commemorate the 72nd anniversary of his Majesty King Bhumibol Adulyadej is gratefully acknowledged. Chevron Thailand Exploration and Production, Ltd. and Captain Lertchai Chaumrattanakul also fund this research project.

References

1. Vishakha, S.; Prince, A.; Amit, K.; Anil, K. B.; Kala, K. B., *Sens Int.* **2021**, *2*, 100098.
2. Yan, M.; Herman, K.; Muhammad, K.; Aaron, N.; Chuen-Yen, L. *Front. Med.* **2021**, *8*, 615099-615123.
3. Rania, S.; Cedra, G.; Celine, R.; Vanessa, L.; Rachelle, R.; Chadia, H.; Marouan, Z. *Postgrad Med J.* **2022**, *98*, 139410-139417.
4. Paula, J.; Claudia, S.; Friederike, T.; Sebastian, M.; Maren, K.-B.; Albertus, D. M. E. O.; Janek, E.; Veronika, P.; Isabell, P.; Tobias, W.; Michael, P. M.; Anahita, F.; Christiane, E.; Marylyn, M. A.; Esther, S.; Holger, A. V. *BMC Infectious Diseases*, **2020**, *20*, 536-542.
5. Federica, P.; Patrizia, P.; Massimo, G.; Roberto, G.; Aldo, L. S.; Lorenzo, S.; Mariangela, *A. Scientific Reports*, **2023**, *13*, 3679.
6. Hadis, F.; Sepehr, T.; Rohollah, S.; Saeid, S. K.; Bayaz, B.; Fatemeh, H.; Khudaverdi, G.; Silvano, E.; Elham, Z.; Sounkalo, D.; Şükran. K.; Hossein, S. K. *Microb Pathog*. **2020**, *149*, 104556-104561.
7. Niels, O. V.; Rob, A.; Ulrike, G.; Gabriella, B. K.; Stefan, S.; Willem, T.; Joop, J. A. L.; Gosse, S.; Renate, C. S. *PLoS One*. **2010**, *5*, 15829.
8. Charles, F.; Ronald, A. *Pneumonia (Nathan).* **2021**, *13*, 5.
9. Shinya, Y.; Makoto, S.; Azumi, T.; Diki, P.; Taketoshi, M.; Hiroshi, Y. *PLoS One*, **2021**, *16*, e0253293.
10. Pourya, B.; Amir, A. M. *IntechOpen*, **2012**, *10*, 30501-30531.
11. Yi-Lang, C.; Wen-Hui, K.; Chao-Lin, L. *Int J Environ Res Public Health*., **2020**, *17*, 3377.
12. Rachel, H.M.; Raechel, M. L.; Cheryl, A. W.; Brian, E. N.; Conor, M. D. *J. Soc. Cosmet. Chem*. **1982**, *34*, 193–202.
13. Niels, O. V.; Rob, A.; Ulrike, G.; Gabriella, B. K.; Stefan, S.; Willem, T.; Joop, J. A. L.; Gosse, S.; Renate, C. S. *PLoS One*. **2010**, *5*, 15829.
14. Charles, J. W.; George, P. *The Anatomical Record*, **2004**, *281A*, 1201-1211.
15. Johan, N. L.; Mats, J. O.; *Vitam Horm.*, **2010**, *83*, 1-23.
16. Mika, S.; Kazushige, T. *J Biochem.* **2011**, *150*, 257-266

17. Melissa, S. M.; Natalie, R. L.; Caitlin, E. B.; Kristina, N. V.; Nicholas, A. S.; W. Edward, S. *Microbiol Spectr*. **2023**, *14*, 11-1.
18. Moamen, M. E.; Birgit, P. *Front Neurosci.* **2020**,*14*, 257.
19. Mohammad, R. H.; Mohammed, S.; Andrés, P.-L. *Front. Genet.* **2021**, *12*, 721556.
20. ASEAN Microbial Data Center, Thailand bioresource research center, https://www.amibase.org (2018).
21. Microbewiki, Department of Biology of Kenyon college, https://microbewiki.kenyon.edu/index.php/Pseudomonas_putida (2006).
22. Pieter, C. G.; Thomas, V.; Johan, V. E.; Bart, M. N.; Maarten, L. H.; Lieven, J. D. *Respir. Res*. **2012**, *13*, 1-9.

Peptide mapping characterization analysis of monoclonal antibody (mAb) using liquid chromatography quadrupole time-of-flight mass spectrometer (LC/Q-TOF)

Ubonwan Chaiyo, Dalad Waropastrakul, and Ariya Chaisawadi*

Biopharmaceutical Characterization Laboratory, Nation Biopharmaceutical Faculty, King Mongkut's University of Technology Thonburi, Bangkok, Thailand

**E-mail: Ariya.cha@kmutt.ac.th*

Abstract:

A characterization of monoclonal antibody (mAb) by peptide mapping using liquid chromatography time-of-flight mass spectrometry (LC/QTOF) has been developed and validated. Sample preparation steps and gradient ratio of mobile phase were optimized to improve the protein coverage percentage. The Protein Metrics software was also used for analyzing the coverage percentage of peptide mapping. The samples were prepared by reduced disulfide bond of the mAb with dithiothreitol (DTT) and alkylated free thiol group with Iodoacetamide (IAA). The peptides were then digested with restriction enzyme, trypsin, which specifically cleaves C-terminal to Arginine (R) and Lysine (K). The digestion reaction was performed at 37 ºC and incubated overnight then stopped the reaction using formic acid. LC was performed by using C18 column and 0.1% formic acid and 0.01% TFA in water and 0.1% formic acid and 0.01%TFA in acetonitrile (ACN) as mobile phases. The QTOF was operated using positive mode electrospray ionization using data-dependent acquisition. The m/z values were selected for second fragmentation according to a priority list generated by the calculated m/z of the interested molecule. Other data acquisition processing was performed using an in-house method that can be adjusted for new molecules of interest. This method gives the coverage percentage over 90% in both heavy chain and light chain of the mAb molecule. The use of LC-MS/MS technique gives the highly efficient and robust approach to confirm the characteristics of the trastuzumab molecule in peptide mapping parameter which can be updated to use with other protein molecules for further characterization.

1. Introduction

Monoclonal antibodies (mAbs) have revolutionized medicine, spearheading targeted therapies against cancer, autoimmune diseases, and more. However, ensuring their precise structure and integrity is paramount for both efficacy and safety. This is where liquid chromatography-mass spectrometry with quadrupole time-of-flight (LC/QTOF) emerges as a powerful tool, to identify these complex molecules.

LC/QTOF is a unique combination of high mass accuracy, exceptional resolution, and sensitive detection, making it ideal for identifying protein structure. Unlike classical methods, LC/QTOF mass spectrometry provides a direct and label-free approach, allowing researchers to dissect proteins in their native state, preserving their delicate conformations and interactions.

2. Materials and Methods

2.1 Sample Preparation

Trastuzumab was prepared by diluted Trastuzumab lyophilized powder with 50 mM Ammonium bicarbonate solution (ABC solution) pH 6.0 to give final concentration of 1 mg/mL. The disulfide bond reduction step was carried by adding 100 mM dithiothreitol (DTT) solution to give the final DTT concentration of 5 mM then incubated the solution at 60ºC for 60 minutes. The alkylation step to alkylate the free thiol group was treated by adding freshly prepared 100 mM Iodoacetamide (IAA) solution to give the final IAA concentration of 10 mM and incubated the solution at room temperature, in the dark, for 60 minutes. Then digested the peptides with restriction enzyme, trypsin, which specifically cleaves C-terminal to Arginine (R) and Lysine (K) Trypsin enzyme was added to the solution to achieve a final protein: enzyme ratio of 50:1. The digestion reaction was performed at 37 ºC and incubated overnight then stop the reaction by using 20% formic acid. The sample was collected by vacuum drying to remove salt and liquid and re-suspend sample with 0.1%formic acid to give final concentration at 2 µg/µL. Carefully transfer sample without disturbing any possible sediment to LC sample vial for LCMS Q-TOF analysis.

2.2 Spectroscopic measurement

LCMS 9030, Shimadzu and Velox C18 column were used to analyze the sample. For the analytical analysis setting value, the Liquid Chromatography (LC) parameters, data Acquisition parameters, mass spectrometer (MS) parameters were set with the setting value shown in Table 1, Table 2, and Table 3 respectively. The priority list of peptide m/z was calculated and generated by the Protein Metrics software. The retention time of each peptide chain was recorded

Table 1. LC Parameters setting

Parameters	Settings
LC system:	Shimadzu Nexera UHPLC
Column:	Shim-pack GISS-HP C18 (150 mm x 3.0 mm I.D., 3 µm)
Column temp:	40 ºC
Flow rate:	0.5 mL/min
Mobile phase A:	0.1%FA + 0.01%TFA in water
Mobile phase B:	0.1%FA + 0.01%TFA in acetonitrile
Gradient program	B. conc. 0% (0-0.2 min) → 15% (10 min) → 35% (23 min) → 45% (30 min) → 75% (35-40 min) → 0% (40.1-45 min)
Injection Volume	20 µL

Table 2. Data Acquisition Parameters setting

Parameters	Settings
MS system:	Shimadzu LCMS-9030 (Q-TOF)
Start of data acquisition:	3 min → switch diverter valve to MS
End of data acquisition:	45 min → switch diverter valve to drain
Polarity:	Positive only
Acquisition type:	MS1 scan + MSMS (DDA)
MS1 mass range:	100-2000 *m/z*
MS1 event time:	0.1 s
MS1 threshold:	High
MSMS mass range:	200-1800 *m/z*
MSMS DDA:	15 dependent events, threshold 500, 0s delay time, 3s automatic exclusion, 5 iterative measurement, charge filter 2-4)
MSMS CE:	35 ± 17
MSMS event time:	0.00 s
MSMS Q1 resolution:	4
MSMS threshold	Low

by injection of sample by using the following instrument parameters.

2.3 Data Analysis

Data analysis was performed in Protein Metrics software using PTM workflow. The know sequence of Trastuzumab (FASTA format) was used as the reference peptide sequence for mapping analysis. Shimadzu LCMS-9030 raw data (*.lcd) can directly be loaded and analyzed in Protein Metrics software.

Table 3. MS Parameters setting

Parameters	Settings
MS system:	Shimadzu LCMS-9030 (Q-TOF)
Interface:	Heated ESI (+)
Interface voltage:	4.5 kV
Interface temperature:	300 ºC
Nebulizing gas:	N_2, 3 L/min
Heating gas flow:	Zero air, 10 L/min
DL temperature:	250 ºC
Drying gas flow:	N_2, 10 L/min
Heat block temperature:	400 ºC
MS scan:	100-2000 *m/z*

3. Results & Discussion

This method achieves the coverage percentage over 95% in both heavy chain and light chain of the mAb molecule. Sample preparation was the most important step in ensuring accurate results. An acidic pH is essential to minimize random shuffling of disulfide bonds during sample preparation. Since acidic pH was not ideal for most enzymatic reactions, the pH of ABC buffer solution should not be less than 6.0 unless the disulfide bond was not included in the analysis. Enzymatic digestion should be performed for a minimum of 15 hours to ensure complete digestion. During the vacuum drying process, the temperature should not exceed 45°C to preserve protein stability. After water removal from the peptide solution, it would become thick due to protein concentration. Adding 0.1% formic acid aided in maintaining protein solubility. However, sedimentation may occur, the protein solution resuspension step was required. The tryptic digest of trastuzumab was analyzed using Q-TOF for confirmation of the peptide sequences based on accurate mass matching, including two large peptides: LC7 from light chain and HC15 from heavy chain with masses of 1396.6441^+ and 1679.0841^+, respectively. The peptides listed in Table 4 and 5 were confirmed with high reliability by matching the spectrum within a 2-ppm mass accuracy and corresponding charge number. Achieving 100% sequence coverage for the trastuzumab sample (Figure 1), significantly enhances the reliability of peptide mapping. Method development for peptide mapping should include repeatability and reproducibility studies for further validation.

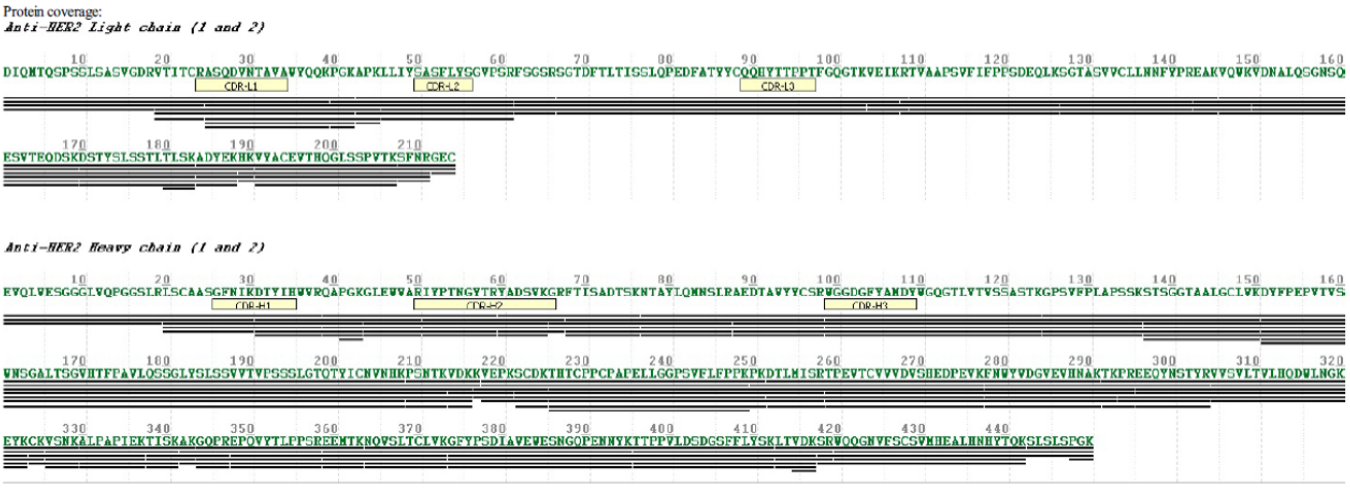

Figure 1. Summary of peptide coverage, fragmentation coverage and PTMs for trastuzumab biosimilar

Table 4. List of measured tryptic peptides of trastuzumab (light chain)

Peak no.	RT (min)	Peptide (amino acid numbers)	Peptide (m/z)	Adduct Ion
LC1	15.14	DIQMTQSPSSLSASVGDR	939.9467	$[M+2H]^{2+}$
LC2	10.46	VTITCR	375.2024	$[M+2H]^{2+}$
LC3	15.10	ASQDVNTAVAWYQQKPGK	664.3376	$[M+3H]^{3+}$
LC4	2.36	APK	315.2027	$[M+H]^{+}$
LC5	22.67	LLIYSASFLYSGVPSR	886.9827	$[M+2H]^{2+}$
LC6	7.32	FSGSR	277.1401	$[M+2H]^{2+}$
LC7	22.81	SGTDFTLTISSLQPEDFATYYCQQHYTTPPTFGQGTK	1396.6441	$[M+3H]^{3+}$
LC8	9.29	VEIK	488.3079	$[M+H]^{+}$
LC9	21.86	TVAAPSVFIFPPSDEQLK	973.5171	$[M+2H]^{2+}$
LC10	23.43	SGTASVVCLLNNFYPR	899.4513	$[M+2H]^{2+}$
LC11	2.02	EAK	347.1925	$[M+H]^{+}$
LC12	11.11	VQWK	560.3191	$[M+H]^{+}$
LC13	11.25	VDNALQSGNSQESVTEQDSK	712.6611	$[M+3H]^{3+}$
LC14	17.40	DSTYSLSSTLTLSK	751.8829	$[M+2H]^{2+}$
LC15	7.35	ADYEK	313.145	$[M+2H]^{2+}$
LC16	2.02	HK	284.1717	$[M+H]^{+}$
LC17	13.56	VYACEVTHQGLSSPVTK	625.9805	$[M+3H]^{3+}$
LC18	8.11	SFNR	523.2623	$[M+H]^{+}$
LC19	2.63	GEC	365.1125	$[M+H]^{+}$

Table 5. List of measured tryptic peptides of trastuzumab (heavy chain)

Peak no.	RT (min)	Peptide (amino acid numbers)	Peptide (m/z)	Adduct Ion
HC1	17.38	EVQLVESGGGLVQPGGSLR	941.5051	$[M+2H]^{2+}$
HC2	14.89	LSCAASGFNIK	584.295	$[M+2H]^{2+}$
HC3	16.20	DTYIHWVR	545.2774	$[M+2H]^{2+}$
HC4	4.13	QAPGK	500.2827	$[M+H]^{+}$
HC5	16.12	GLEWVAR	415.7296	$[M+2H]^{2+}$
HC6	11.98	IYPTNGYTR	542.7747	$[M+2H]^{2+}$
HC7	8.80	YADSVK	341.674	$[M+2H]^{2+}$
HC8	2.02	GR	232.1404	$[M+H]^{+}$
HC9	12.97	FTISADTSK	485.248	$[M+2H]^{2+}$
HC10	16.09	NTAYLQMNSLR	655.8297	$[M+2H]^{2+}$
HC11	12.30	AEDTAVYYCSR	667.7877	$[M+2H]^{2+}$
HC12	23.45	WGGDGFYAMDYWGQGTLVTVSSASTK	1392.6341	$[M+2H]^{2+}$
HC13	17.50	GPSVFPLAPSSK	593.827	$[M+2H]^{2+}$
HC14	15.88	STSGGTAALGCLVK	661.3427	$[M+2H]^{2+}$
HC15	25.13	DYFPEPVTVSWNSGALTSGVHTFPPAVLQSSGLYSL SSVVTVPSSSLGTQTYICNVNHKPSNTK	1679.0841	$[M+4H]^{4+}$
HC16	2.73	VDK	361.2082	$[M+H]^{+}$
HC17	6.29	VEPK	472.2766	$[M+H]^{+}$
HC18	2.16	SCDK	509.2024	$[M+H]^{+}$
HC19	22.20	THTCPPCPAPELLGGPSVFLFPPKPK	948.824	$[M+3H]^{3+}$
HC20	13.63	DTLMISR	418.2207	$[M+2H]^{2+}$
HC21	17.43	TPEVTCVVVDVSHEDPEVK	713.6807	$[M+3H]^{3+}$
HC22	17.93	FNWYVDGVEVHNAK	839.4046	$[M+2H]^{2+}$
HC23	2.55	TKPR	501.3144	$[M+H]^{+}$
HC24	14.89	EEQYNSTYR	595.2596	$[M+2H]^{2+}$
HC25	23.18	VVSVLTVLHQDWLNGK	603.3403	$[M+3H]^{3+}$
HC26	5.64	EYK	439.2187	$[M+H]^{+}$
HC27	2.02	CK	307.1435	$[M+H]^{+}$
HC28	2.34	VSNK	447.2562	$[M+H]^{+}$
HC29	13.37	ALPAPIEK	419.7553	$[M+2H]^{2+}$
HC30	6.28	TISK	448.2766	$[M+H]^{+}$
HC31	2.02	AK	218.1499	$[M+H]^{+}$
HC27	2.02	CK	307.1435	$[M+H]^{+}$
HC28	2.34	VSNK	447.2562	$[M+H]^{+}$
HC29	13.37	ALPAPIEK	419.7553	$[M+2H]^{2+}$
HC30	6.28	TISK	448.2766	$[M+H]^{+}$
HC31	2.02	AK	218.1499	$[M+H]^{+}$
HC32	3.98	GQPR	457.2518	[M+H]+
HC33	14.37	EPQVYTLPPSR	643.8406	$[M+2H]^{2+}$
HC34	7.02	EEMTK	319.1467	$[M+2H]^{2+}$
HC35	17.00	NQVSLTCLVK	581.3184	$[M+2H]^{2+}$
HC36	20.11	GFYPSDIAVEWESNGQPENNYK	848.7153	$[M+3H]^{3+}$
HC37	21.07	TTPPVLDSDGSFFLYSK	937.4645	$[M+2H]^{2+}$
HC38	9.42	LTVDK	288.1736	$[M+2H]^{2+}$
HC39	2.02	SR	262.151	$[M+H]^{+}$
HC40	17.24	WQQGNVFSCSVMHEALHNHYTQK	934.4272	$[M+3H]^{3+}$
HC41	11.54	SLSLSPGK	394.7293	$[M+2H]^{2+}$

4. Conclusion

The sample preparation for peptide mapping analysis is the most important first step to achieve highly yield of the protein. The parameter setting of the data acquisitions also another factor for efficient result of protein coverage percentage. A method for characterization on peptide mapping parameter using liquid chromatography time-of-flight mass spectrometry (LC/QTOF) is an alternative technique to give the highly efficient approach to confirm the characteristic of the Trastuzumab molecule in peptide mapping parameter which can be updates to use with other protein molecules for further characterization especially in early stage of drug discovery

research. This approach would help to confirm the characterization of the molecule.

References

1. Jumhawan, U.; Liw, W. T.; Xing J.; Zhan, Z. Peptide Mapping of Monoclonal Antibody (mAb) Using Nexera Bio with Q-TOF Mass Spectrometer for Full Sequence Confirmation., AD-0176, Application News, Shimadzu Excellence in Science Application Development & Centre, Shimadzu (Asia Pacific), Singapore
2. Lu Y.; Zhan, Z. Peptide Mapping of Monoclonal Antibody (mAb) Using LCMS™-9030 (Q-TOF) Mass Spectrometer with Shim-pack™ GISS-HP Column., AD-0212B, Application News, Shimadzu Excellence in Science Application Development & Centre, Shimadzu (Asia Pacific), Singapore.
3. Allen, D.R.; McWhinney B.C. Quadrupole time-of-flight mass spectrometry: a paradigm shift in toxicology screening applications. *The Clinical Biochemist Reviews.* 2019 Aug;40(3):135.
4. Qin, M.; Wang, W.; Thirumalai, D. Protein folding guides disulfide bond formation. *Proceedings of the National Academy of Sciences* 2015, 112(36):11241-6.
5. Wysocki VH, Resing KA, Zhang Q, Cheng G. Mass spectrometry of peptides and proteins. *Methods* 2005, 35(3):211-22

Development of analytical method for analysis of tetrahydrocannabinol and cannabidiol in tea infusion by High Performance Liquid Chromatography

Thoranin Yosbunruengsin[1]* Thitiphan Chimsook[1], Anakhaorn Srisaipech[1], and Supaporn Sangsrichan[1,2]*
[1]*Applied Chemistry Program, Faculty of Science, Maejo University, Chiang Mai 50290, Thailand*
[2]*Research Center of Agricultural and Environmental Innovation, Maejo University, Chiang Mai 50290, Thailand*
**E-mail: mju6404303001@mju.ac.th, supaporn-s@mju.ac.th*

Abstract:

In accordance with the Notification of Ministry of Public Health No. 427 (2021) issued under the Thai food act, the amount of tetrahydrocannabinol (THC) and cannabidiol (CBD) in food products containing certain parts of cannabis or hemp, shall not exceed 1.6 and 1.41 mg per package, respectively. This study aims to develop a simple analytical method to determine THC and CBD in tea infusion by High Performance Liquid Chromatography (HPLC). THC and CBD from tea samples were extracted by using solvent extraction then cleaned-up by SPE before HPLC quantitation. HPLC mobile phase consisted of 5 mM ammonium acetate and acetonitrile with gradient elution program operated at a flow rate of 1.0 mL/min. A Photodiode array detector (DAD) was set at a wavelength of 220 nm. The standard calibration curves of CBD and THC were linear in the concentration range of 0.5-10.0 mg/L and the correlation coefficient (r^2) were 0.9998 and 0.9992, respectively. The limits of detection and quantitation of this method for CBD were 0.21 and 0.51 mg/L and THC were 0.19 and 0.47 mg/L, respectively. The accuracy of the method was between 71% and 108%, with a precision of 10.75% to 11.72%RSD. This method required simple instrument, accurate enough for quantitative analysis of THC and CBD in tea and tea infusion to comply with the Thai law.

1. Introduction

The cannabis plant is a native plant that grows in the temperate regions of Asia. It is a plant that has been recorded in ancient documents as being grown for its use as a fiber plant and as an addictive plant since ancient times.[1]

Plant is *Cannabis sativa* L. It has many common names, such as hemp, marijuana, pot, gandia, etc. Generally, it can be divided into several subspecies, such as *C. sativa* subsp. *Sativa.*, *C. sativa* subsp. *Indica*, *C. sativa* subsp. *Ruderalis*, *C. sativa* subsp. *Spontanea*, *C. sativa* subsp. *Kafiristanca*. It is hard to clearly differentiate both morphology and the number of important substances of each subspecies because these characteristics change according to the environment. Therefore, the name *Cannabis sativa* is applied to all subspecies of cannabis plants. Differentiating cannabis plants from other plants can be done by a test for important substances in the cannabinoids group, which are only found in the cannabis plant[1].

Cannabinoids[2] are terpenophenolic compounds whose main structure is geranyl pyrophosphate. In plants, substances in the cannabinoids group are in the form of carboxylic acid or acid form, but when exposed to light and heat, they are decarboxylate to neutral form. The most important substance found is Delta-9-tetrahydrocannabinol (Δ^9-THC or THC) which is an important substance acting on the nervous system (psychotomimetic). Δ^8-THC is isomer of Δ^9-THC but approximately 5 times less effective than cannabidiol (CBD). CBD is one of the most important substances but is non-psychoactive, has a THC antagonist effect, found mainly in strains that produce fiber and seeds (industrial hemp). It also has the effect of reducing seizures, anti-inflammatory and reducing nausea. Cannabichromene (CBC) has anti-inflammatory effects, reduces pain, and has antimicrobial and antifungal effects. Cannabinol (CBN) is a decomposition of THC when exposed to heat and oxygen in the air. Oxidation is very rarely occurred in fresh plants but it increased when stored for a long time and has a mild effect on the nervous system.

The cannabis plant is one of the most interest herbal plants of many countries around the world, including Thailand. It has been used for medication because of its relaxing, refreshing effects, reducing tension and anxiety, as well as being able to relieve pain and help with sleep. These active substances are cannabinoids, which have more than 545 types.[3] They can be divided according to their nature of action into 2 groups: substances that are not psychotropic (non-psychotropic) compound such as tetrahydrocannabinolic acid (THCA), cannabidiol (CBD), cannabinol (CBN) and psychotropic compounds such as Δ^9-tetrahydrocannabinol (THC), which is the most effective substance. This substance acts like the endocannabinoid found in the bodies of animals and humans when it binds to specific receptors, which are the cannabinoid receptor type CB1 found mostly in the brain and

CB2 found in immune cells and peripheral nerves. This cannabinoid affects the cognitive part of the brain, causing feelings of happiness, anxiety, pain, control of body movement and the endocrine system. Therefore, the effects of receiving cannabinoids have symptoms like those receiving psychotropic drugs, causing sedation, sedation, and hallucinations. When they are used, they may cause both benefits and harm. This depends on the amount received and the physical condition of each person.[4]

Many countries have changed their laws regarding cannabis and hemp to allow for greater commercial use. Whereas it is the policy of the Thai government to promote and develop cannabis and hemp into commercial plants and as Thai traditional wisdom by issuing the notification of the Ministry of Public Health[5-9] on prescription of the list of category 5 narcotics to grant exemption for certain parts of cannabis and hemp which conform to the rules, procedures and conditions set forth in the notification of the Narcotics Control Committee to be used in the food industry and other industries, provided that their use as food must be in compliance with the law on food and must be for food purposes only. Food and beverage products that contain cannabis and hemp ingredients[7] shall not contained THC and CBD substances exceed 1.6 and 1.41 milligrams per package unit, respectively.

There have been reported for the analysis of cannabis plant extracts such as Gas Chromatography coupled with Flame ionization detector (FID) and Mass Spectrometer (MS) but encountered with the difficulty of analysis acidic cannabinoids which need to be derivatized. For analysis of neutral and acidic cannabinoids, High Performance Liquid Chromatography coupled with Mass Spectrometer (LC-MS), supercritical fluid chromatography-Mass Spectrometer (SFC-MS) have been reported.[10-13] Mass Spectrometers are expensive, and the running cost is high. Hence, the method for screening and analyzing of CBD and THC by using a reversed phase HPLC DAD with a simple, fast and accurate method was developed.

2. Materials and Methods

2.1 Standards, chemicals, and reagents

The standard solutions of (-)-trans-Δ^9-tetrahydrocannabinol (Dronabinol) solution (Δ^9-THC) 0.9303 ± 0.0792 mg/mL in ethanol (Lipomed Inc., Cambridge, USA) by DMSc reference standard control No. 01A65244. Each ampoule is intended for one-time use. For maximum stability store airtight at 2-8 °C in dark. The standard Cannabidiol (CBD) powder contained 993.8 ± 4.9 µg/mg of cannabidiol ($C_{21}H_{30}O_2$) obtained by DMSc reference standard control No. 02A64217. They were all analytical purity grade, and all the solvents and acids used were HPLC grade. HPLC grade water was produced using a MilliQ laboratory system (Millipore, Bedford, MA, USA).

Preparation of standard solutions of Δ^9-THC and CBD to a concentration of 10 µg/mL using methanol as the solvent. The mixed standard solution with 6 concentrations of Δ^9-THC and CBD for analysis and standard curves. The concentrations were 0.5, 0.9, 1.9, 3.7, 5.6, 7.4, 9.3 µg/mL for Δ^9-THC and the concentrations were 0.5,1.0,2.1,4.1,6.2,8.2,10.3 µg/mL for CBD.

2.2 Sample preparation and extraction

Sample approximately 0.5 grams was extracted with 10 mL of methanol, mixed for 30 seconds, shaken for 10-15 minutes and centrifuged at 4000 rpm per minute at 4 °C for 10 minutes. The supernatant was transferred to further cleaned up by solid phase extraction (SPE). [14]

SPE clean-up process was carried out by loading 2 mL of supernatant into a conditioned SPE cartridge with 5 mL methanol and 5 mL water, respectively. Interference was removed by 3 mL of 25% methanol, after that use 5 mL of 90:10 acetonitrile - methanol followed by 3 mL of 60:40 acetonitrile - methanol for eluting step. The extract solution was evaporated to dryness with a nitrogen evaporator under temperature below 40 °C and reconstructed to a volume with acetonitrile. The sample solution was filtered by a 0.45 µm syringe filter prior to analysis with a High Performance Liquid Chromatograph.

2.3 HPLC-DAD analysis

The analysis was performed by using a High Performance Liquid Chromatograph (HPLC) Agilent Model 1260 Infinity II employing an Eclipse XBD-C18 4.6 x 250 mm, 5 µm column, at 25°C.

Mobile phase composition studied were the amount of salt added and organic solvents.

Standard and sample solutions of 20 µL were injected in the HPLC system and the detection was made at a wavelength of 220 nm by using a diode array detector (DAD). CBD an THC mixture of 6 working standard solution were injected in the HPLC system under optimal conditions and constructed calibration curve.[15-18]

3. Results & Discussion

3.1 HPLC Optimization

The ammonium acetate concentrations of 5, 10 and 25mM in water **(**mobile phase A**)** and

methanol as mobile phase B were compared**.** The overlaid chromatogram obtained as shown in Figure 1**.** The higher concentration of the salt added, the higher the base line of the chromatogram obtained, hence 5 mM ammonium acetate was selected as mobile phase A**.**

The mobile phase B were compared between methanol and acetonitrile at the same concentration**.** The result showed that acetonitrile gave a shorter retention time as shown in Figure 2**.**

The mobile phase used was consisted of 5 mM ammonium acetate/0.025% glacial acetic acid in water (mobile phase A) and acetonitrile (mobile phase B) operated at a flow rate of 1.0 mL/min. Gradient elution was started from mobile phase B 70% to 85% in 17 minutes then increased to 95 %B within 1 minute and keep constant for 2 minutes. Total run time for separation of THC and CBD was 20 minutes.

3.2 Method validation

Verification of analytical method was validated according to Association of Official Analytical Chemists (AOAC)[19] and Eurachem Guide,[20] such as linearity, limit of detection (LOD), limit of quantitation (LOQ) measurement, also precision and accuracy.

From the chromatogram, the retention time (t_R) of the standard CBD and THC were 11.40 and 17.93 minutes, respectively as shown in Figure 3. The calibration curves were linear with the linear coefficient (r^2) for CBD and THC were 0.9998 and 0.9992, respectively as shown in Figure 4.

Limit of detection and limit of quantitation were studied by addition of CBD and THC standard into the blank sample without analytes. The concentrations added were 0.21 and 0.19 mg/L, respectively, the analytical limit of detection and the limit of quantitation were 0.51 and 0.47 mg/L, respectively. The chromatograms of CBD and THC standard at the LOD and LOQ were overlaid as shown Figure 5.

Analysis of the precision diagnose the %RSD and the accuracy diagnose the %recovery by addition CBD and THC standard to the samples without the substance to be analyzed to a concentration which at the LOQ of 0.51 and 0.47 mg/L, then analyzed the samples with the same the procedure as the standard. The %RSD were calculated to be 10.75 for CBD and 11.72 for THC. Percentage recoveries were 71-96% for CBD and 81-108% for THC, was reported in Table 1.

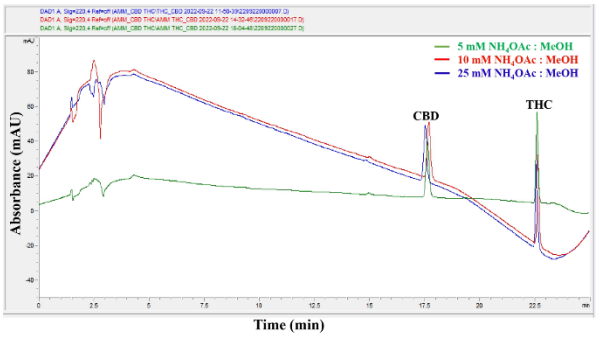

Figure 1. Effect of ammonium concentration.

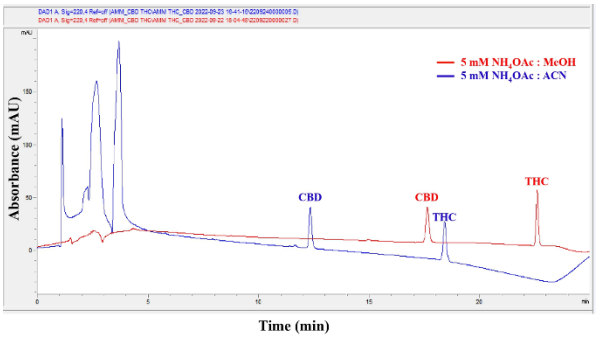

Figure 2. Overlaid chromatograms of standard mixed CBD and THC using methanol and acetonitrile as mobile phase B.

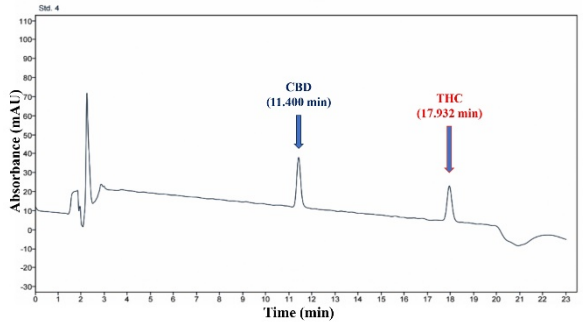

Figure 3. Chromatogram of standard mixed of CBD (4.1 mg/L) and THC (3.7 mg/L).

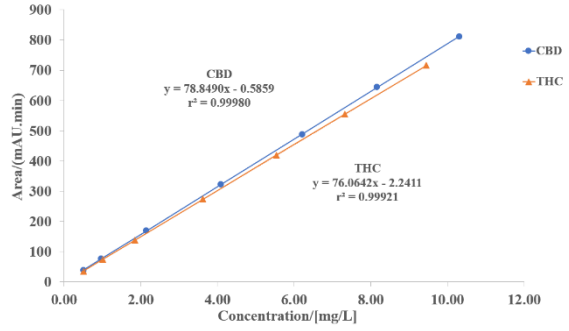

Figure 4. Standard calibration curves of CBD and THC.

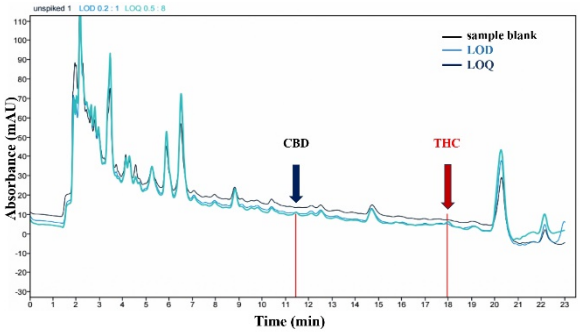

Figure 5. Overlaid chromatograms of sample blank, standard spiked at LOD and LOQ concentrations.

Table 1. The parameters obtained from the Methods Validation of CBD and THC

Parameter	CBD	THC
LOD (mg/L)	0.21	0.19
LOQ (mg/L)	0.51	0.47
Precision (%RSD)	10.75	11.72
Accuracy (%recovery)	71-96	81-108

4. Conclusion

The developed analytical method can be used to detect CBD and Δ^9-THC in tea infusion by HPLC-DAD technique. This method exhibited good precision, accuracy, sensitivity and specific to the substance to be tested in a complicated matrix sample. The developed method are suitable for analysis of food quality control in compliance of the announcement of the Thai Ministry of Public Health.

Acknowledgements

The authors would like to thank the Applied Chemistry Programs, Faculty of Science, Maejo University and Medical Science Center 1 Chiang Mai, Department of Medical Sciences Center that provides botanical information on the cannabis plant and facilities.

References

1. UNODC. *Recommended Methods for the Identification and Analysis of Cannabis and Cannabis Products*; United Nation, 2009.
2. Tipparat, P. *Cannabis Plant: General Knowledge and Examination of Important Substances*. 2019. https://www.oncb.go.th/ncsmi/cannabis4/Forms/AllItems.aspx (accessed Online).
3. Radapong, S.; Suppajariyawat, P.; Phadungkit, M. Pharmacological and Toxicological effects of Cannabis. *Journal of Department of Medical Scienes* **2021**, *63* (1), 219-323.
4. Metadilokkul, O. *Cannabinoid medicine & medical cannabis*. 2019. https://thaicam.go.th/%E0%B8%81%E0%B8%B2%E0%B8%A3%E0%B9%81%E0%B8%9E%E0%B8%97%E0%B8%A2%E0%B9%8C%E0%B9%81%E0%B8%84%E0%B8%99%E0%B8%99%E0%B8%B2%E0%B8%9A%E0%B8%B4%E0%B8%99%E0%B8%AD%E0%B8%A2%E0%B8%94%E0%B9%8C-%E0%B9%81%E0%B8%A5/ (accessed Online).
5. (Food Standards Australia and New Zealand. *Supporting Document 6 International Hemp Regulations*. 2009. https://www.foodstandards.gov.au/code/applications/Pages/applicationa1039lowt4708.aspx (accessed Online).
6. The Ministry of Public Health. Prescribing food prohibited from production, import, or sale. The Ministry of Public Health: Thailand, 2021; Vol. Notification of the ministry of public health (No. 424), B.E. 2564 (2021).
7. The Ministry of Public Health. Hemp seeds, hemp seed oil, hemp seed protein, and food products containing hemp seeds, hemp seed oil or hemp seed protein. The Ministry of Public Health: Thailand, 2021; Vol. Notification of the ministry of public health (No. 425), B.E. 2564 (2021).
8. The Ministry of Public Health. Food products containing certain parts of cannabis or hemp. The Ministry of Public Health: Thailand, 2021; Vol. Notification of the Ministry Of Public Health (No. 427), B.E. 2564 (2021), pp 22-24.
9. The Ministry of Public Health. Standards of food containing tetrahydrocannabinol and cannabidiol contaminants. The Ministry of Public Health: Thailand, 2021; Vol. Notification of the Ministry of Public Health (No. 428), B.E. 2564 (2021), pp 25-26.

10. Hewavitharana, A. K.; Gloerfelt-Tarp, F.; Nolan, M.; Barkla, B. J.; Purdy, S.; Kretzschmar, T. Simultaneous quantification of 17 cannabinoids in cannabis inflorescence by liquid chromatography-mass spectrometry. *Separations* **2022**, *9* (4). DOI: 10.3390/separations9040085.
11. Jambo, H.; Dispas, A.; Avohou, H. T.; André, S.; Hubert, C.; Lebrun, P.; Ziemons, É.; Hubert, P. Implementation of a generic SFC-MS method for the quality control of potentially counterfeited medicinal cannabis with synthetic cannabinoids. *J Chromatogr B Analyt Technol Biomed Life Sci* **2018**, *1092*, 332-342. DOI: 10.1016/j.jchromb.2018.05.049 From NLM Medline.
12. McRae, G.; Melanson, J. E. Quantitative determination and validation of 17 cannabinoids in cannabis and hemp using liquid chromatography-tandem mass spectrometry. *Anal Bioanal Chem* **2020**, *412* (27), 7381-7393. DOI: 10.1007/s00216-020-02862-8 From NLM Medline.
13. Wittayanan, W.; Chaimongkol, T. Determination of pesticides residue in cannabis, cannabis extract and cannabis oil by gas chromatography tandem mass spectrometry technique. *Pharmaceutical Sciences Asia* **2021**, *48* (4), 354-366. DOI: 10.29090/psa.2021.04.20.107.
14. Somsuntisuk, S.; Inkaew, A.; Wajasit, S.; Muadmah, S.; Chuakunchat, K.; Wangkaewhiran, W.; Payanan, T. The Development and Validation of Analysis Method for Cannabinoids in Coconut Juice using LC-MS/MS. *Journal of Department of Medical Scieces* **2021**, *63* (3), 556-570.
15. Backer, B. D.; Debrus, B.; Lebrun, P.; Theunis, L.; Dubois, N.; Decock, L.; Verstraete, A.; Hubert, P.; Charlier, C. Innovative development and validation of an HPLC/DAD method for the qualitative and quantitative determination of major cannabinoids in cannabis plant material. *Journal of Chromatography B* **2009**, *877* (32), 4115-4124. DOI: 10.1016/j.jchromb.2009.11.004 From NLM Medline.
16. Hädener, M.; König, S.; Weinmann, W. Quantitative determination of CBD and THC and their acid precursors in confiscated cannabis samples by HPLC-DAD. *Forensic Sci Int* **2019**, *299*, 142-150. DOI: 10.1016/j.forsciint.2019.03.046 From NLM Medline.
17. Mandrioli, M.; Tura, M.; Scotti, S.; Toschi, T. G. Fast Detection of 10 Cannabinoids by RP-HPLC-UV Method in Cannabis sativa L. *Molecules* **2019**, *24* (11). DOI: 10.3390/molecules24112113 From NLM Medline.
18. Patel, B.; Wene, D.; Fan, Z. T. Qualitative and quantitative measurement of cannabinoids in cannabis using modified HPLC/DAD method. *J Pharm Biomed Anal* **2017**, *146*, 15-23. DOI: 10.1016/j.jpba.2017.07.021 From NLM Medline.
19. Latimer, G. W. *Official Methods of Analysis of AOAC International*; AOAC International, 2023.
20. Eurachem. *The Fitness for Purpose of Analytical Methods*; Europe, 2014.

Chromatographic resolution of (+/-) -chabamide using modified silica with *N*-propylglutarimide chiral selectors

Varaporn Paradamit*, Watcharapol Wong-iam, Tinnapat Thongngen, Phongsathorn Khlongkhleao, Sasipa Booranamonthol, Jitanapa Sirirak, Nuttapon Yodsin, and Punlop Kuntiyong

Department of Chemistry, Faculty of Science, Silpakorn University, Sanamchandra Palace, Nakhon Pathom, 73000, Thailand

**E-mail: paradamit_v@silpakorn.edu*

Abstract:

Chiral resolution or the separation of enantiomers though can be performed by various techniques, the chromatographic resolution by chiral stationary phases (CSP) has proven to be the most attractive and applicable method for separating and acquiring pure enantiomer. Over the past few decades, huge numbers of CSPs have been widely studied and developed to be used in the HPLC system to give enantiomerically pure substrates which are of great importance in the early steps of medicinal synthesis. This can reduce overall cost of the synthesis process. Herein, we describe new chiral selectors for modification of the silica gel used for column chromatography. The chiral selectors are derivatives of *N*-propylglutarimide with different substituted amino group at C2 position. The chiral selectors **A** and **B** were synthesized in 1 step from L-N-CBz-glutamine and 2 steps from L-glutamic acid, respectively. They were coupled to the triethoxychloropropylsilane-modified silica gel to give NHCBz-chiral selector and NBn2-chiral selector. In order to prove chromatographic resolution of racemic mixture, the modified silica was used for separation of racemic (+/-) -chabamide, a bis-amide natural products which was synthesized from piperine via Diels-Alder reaction and resulted in partial resolution to give enantioenriched (-)-enantiomer using NCBz-chiral selector. Molecular Docking experiments were carried out to gain an insight into the mechanism of the separation. The results, conditions and hypothesis of the resolution based on three-point interaction between the analyte and a chiral selector approach that resulted in different polarity value from each eluted fraction will be discussed in the presentation.

1. Introduction

During last few decades, chiral drugs, agrochemicals, food additives and fragrances have become significant in potential and economics.[1] Synthesis of the specific enantiomer can be achieved by the asymmetric synthesis or by enantio-separation of the racemic products. Utilize of asymmetric synthesis is limited due to the high catalyst cost [2], poorly suited to mass production and allows for only specific enantio-selective reactions. Chiral resolution or enantio-separation is of great important since enantiomers are mirror images of chiral compound which react differently in a highly stereoselective or enantioselective biological environment. The art of enantio-separation has been developed and progress dramatically. Chiral resolution of racemic can be performed directly in the presence of chiral environment known as the chiral selector (CS). Though several models for the requirements to obtain chiral recognition, the most reliable model is the three-point contact model proposed by Dalgliesh, C.E in 1952.[3] The difference of the interactions between a chiral selector and two enantiomers is the significant role in this approach. Huge numbers of chiral stationary phase (CSPs) have been widely studied and developed to be used in chromatographic methods.

We have previously developed and studied chiral resolution by synthesis of a small molecule to be used as chiral selector equipped on the silica gel since 2018. The silica gel stationary phase modified with 3S-N-butenyl-dibenzylamino-succinimide had separated D/L-*N*,*N* dibenzylglutamic acid racemate and concluded that the racemate were partially resolved.[4] Herein, we describe new chiral selectors for modification of the silica gel used for column chromatography. The chiral selectors are derivatives of *N*-propylglutarimide with different substituted amino group at C2 position. The chiral selectors **A** and **B** were synthesized in 1 step from L-N-CBz-glutamine and 2 steps from L-glutamic acid, respectively. They were coupled to the triethoxychloropropylsilane-modified silica gel to give NHCBz-chiral selector and NBn2-chiral selector as shown in scheme 1 and 2. To test their ability to separate racemic mixture, a bisamide natural product chabamide was synthesized as a racemate from piperine and was used as the analyte for the chromatographic resolution.

2. Materials and Methods

2.1 Materials

Silica gel 60 (0.063- 0.200 nm, 70-230 mesh ASTM) for column chromatography was purchased from Merck (Germany). Sulfuric acid and Hydrogen peroxide (D 20°c 1.120) were purchased form Carlo Erba. Potassium carbonate (K_2CO_3) was from Riedel-de Haën. N, N-Dimethylformamide (DMF), Triethylamine (Et_3N) d = 0.726 g/mL, Toluene (0.87 kg/L) and Dimethylamineopyidine (DMAP) were purchased from Merck (Germany). 1,1'-Carbonyldiimidazole was from Thermo Scientific. (3- Chloropropyl)triethoxysilene were from Aldrich and Dichloromethane was from BDH. All chemicals were AR grade and used without further purification.

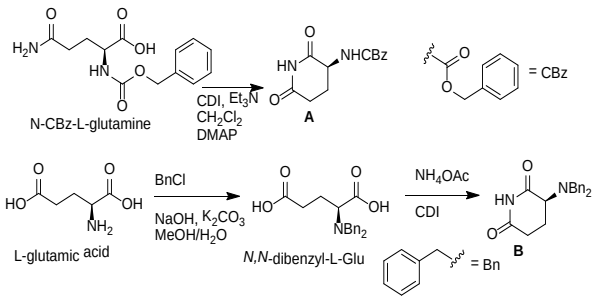

Scheme 1. Synthesis of chiral selectors A and B

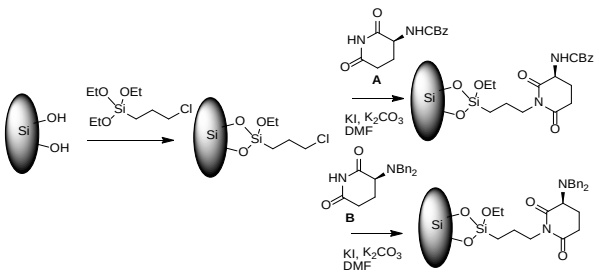

Scheme 2. Modification of the silica gel surface with N-propylglutarimide chiral selectors

2.2 Instrument

The BRUKER (ADVANCE-300) Nuclear magnetic resonance spectrometer was used to the confirmation. Optical rotation value of each separated fraction was measured and calculated from KRUSS (P3000series) digital polarimeters.

2.3 Modification the silica with chiral selector

2.3.1 Modification of silica gel by (3-chloropropyl)triethoxysilane

10.00 g of Silica gel was activated at 95 °C with piranha solution (98% H_2SO_4/ 30% H_2O_2 70:30 v/v) for 1 hour. Then the white precipitate was filtered and rinsed with distilled water. It was subsequently heated in an oven at 120 °C for 24 hours. Dry toluene (30 mL) and (3-chloropropyl) triethoxysilane (10 mL) were added to the silica gel. After the mixture was heated to reflux for 14 hours at 100 °C, the modified silica gel was filtered and washed with a portion of 30 mL toluene and CH_2Cl_2 twice.

2.3.2 Synthesis of chiral selector A

To a solution of L-NCBz-glutamine (32 mg, 0.07 mmol) in CH_2Cl_2 (10 mL) were added CDI (46 mg, 0.21 mmol), DMAP (2.0 mg) and Et_3N (39 mL, 0.21 mmol) and the mixture was stirred for 3 h. Water (10 mL) was added and the phases were separated. The aqueous phase was extracted with CH_2Cl_2 (2 × 5 mL) and the combined organic layers were dried (by anhydrous Na_2SO_4), filtered and concentrated under reduced pressure. The crude product was purified by flash chromatography (silica gel, 1:1 hexane/EtOAc) to give *N*-CBZ-glutarimide **A** (30 mg, 95%). The 1H NMR spectrum of L-NCBz-glutarimide clearly showed peaks of the glutarimide NH at 8.60 ppm, 5 benzene protons at 7.52-7.40 ppm, NH-C=O at 5.70 ppm, O-CH_2- at 5.12 ppm, CH-NCBz at 4.48 ppm, O=C-CH_2 at 2.90-2.60 ppm and CH_2 of C4 at 2.65 and 1.87 ppm (Figure 1).

Figure 1. 1H NMR spectrum of NCBz-chiral selector

2.3.3 Synthesis of chiral selector B

To a solution of N,N-dibenzylglutamic acid (60 mg, 0.14 mmol) in CH_2Cl_2 (10 mL) were added NH_4OAc (77 mg, 1.0 mmol), CDI (46 mg, 0.28 mmol), DMAP (2.0 mg) and Et_3N (39 mL, 0.21 mmol) and the mixture was stirred for 6 h. Water (10 mL) was added and the phases were separated. The aqueous phase was extracted with CH_2Cl_2 (2 x 5 mL) and the combined organic layers were dried (anhyd Na_2SO_4), filtered and concentrated under reduced pressure. The crude product was purified by flash chromatography (silica gel, 2:1 hexane/EtOAc) to give 3-N,N-dibenzylglutarimide **B** (48 mg, 80%). The 1H

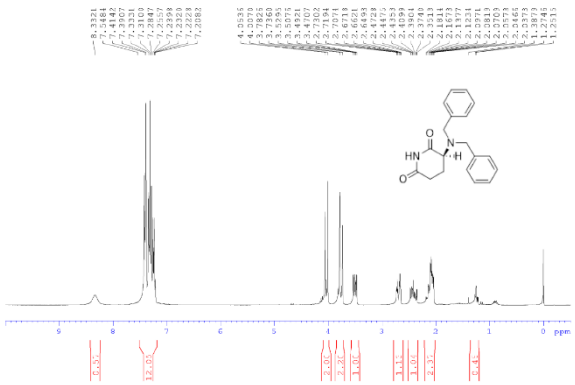

Figure 2. 1H NMR spectrum of NBn2-chiral selector

NMR spectrum of L-NBn_2-glutarimide clearly showed peaks of NH at 8.40 ppm, 10 benzene protons at 7.60-7.20 ppm, NCH_2 at 4.05 and 3.80 ppm, CH-NBn_2 at 3.50 ppm, O=C-CH_2 at 2.70 and 2.45 ppm, CH_2 (C4) at 2.21-2.00 ppm (Figure 2).

2.3.4 Application of the chiral selectors on the modified silica

To a suspension of the silica that was modified with triethoxypropylsilane (10.0 g) in DMF (10 mL) were added the chiral selector (50 mg), KI (10 mg) and K_2CO_3 (138 mg, 1.0 mmol) and the mixture was stirred for 12 h. The mixture was then filtered with reduced pressure and washed with water (5 × 10 mL) and CH_2Cl_2 (5 × 10 mL). The resulting modified silica was dried in an oven (105 ^oC) for 16 h.

2.4 Synthesis of chabamide

Piperine (285 mg, 1.0 mmol) was dissolved in ethanol (20 mL) and silica (10 g) was added to this solution. The mixture was heated in an open round-bottom flask at 160 ^oC for 24 h. To the resulting brown mixture was then added ethanol (50 mL). The mixture was filtered under reduced pressure and repeatedly washed with ethanol (5 ×1.0 mL). The ethanolic filtrate was concentrated under reduced pressure. The crude mixture was purified by column chromatography (silica, hexane/ethyl acetate:1:1) to give chabamide (128 mg, 45%). The 1H NMR spectrum in Figure 3 shows the peaks of the proton signals of chabamide; 6 aromatic protons at 6.90-6.60 ppm, ArCH= at 6.40 ppm, 4 protons of two O-CH_2-O units at 6.05-5.90 ppm, cyclohexene HC=CH at 5.90 and 5.75 ppm, =CH- at 6.22 ppm, 3 cyclohexene CH's at 4.12, 3.70 and 2.90 ppm, 8 N-CH_2 protons overlap with another chcylohexene CH at 3.60-3.15 ppm, 12 piperidine CH_2 protons at 1.80-1.10 ppm.

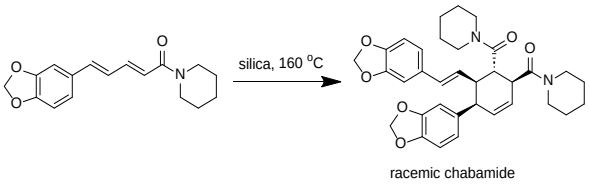

Scheme 3. Synthesis of racemic chabamide from piperine

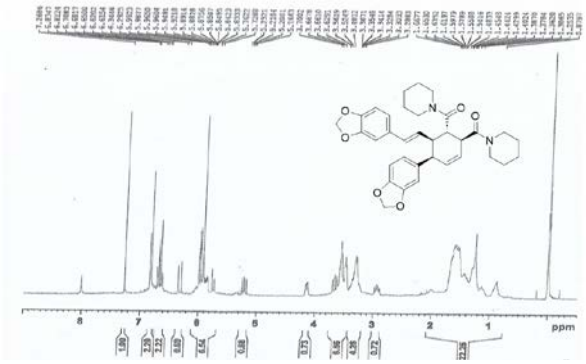

Figure 3. 1H NMR spectrum of Chabamide

2.4 Resolution of racemic chabamide using flash column chromatography with chiral-molecule-modified silica

In the separation, 5.0 g of modified silica was determined to contain 25 mg of chiral selector. The silica was packed into a glass column (2.60 cm diameter). The racemic mixture of chabamide 25 mg was loaded onto the top of the column. The eluent (hexane/ EtOAc 1:1) was passed through the column and the eluted compounds were received in test tubes (4 mL each) with the flow rate of 6.0 mL/minute for the chiral selector A column and 3.0 mL/minute for the chiral selector B column, respectively. The separation was carried out until it was determined by analytical TLC that chabamide had stopped passing through the column. The eluents were concentrated and the optical rotations were measured.

3. Results & Discussion

From the chromatographic resolution of racemic chabamide using NCBz-chiral selector modified silica, the compound was detected in fraction 4-6 and 12-14 with the retention time ($t_{r,A1}$) of 3.33 and ($t_{r,A2}$) 8.67 minutes. While resolution of racemic chabamide using NBn2-chiral selector modified silica column resulting in the compound coming through in fraction 9-10 and 13-19 with the retention time ($t_{r,B1}$) of 12.67 and ($t_{r,B2}$) 21.33 minutes. Retention factor can be calculated from

$$K' = (t_r - t_0)/t_0 \quad (1)$$

Where t_r = retention time of analyte and t_0 is the time of void volume takes to elute

The retention factors of two enantiomeric compounds separated by NCBz-chiral selector modified silica, the K'_{A1} (for the first eluted isomer) was (3.33-1.14)/1.14 = 1.92, the K'_{A2} (for the second isomer) was (8.67-1.14)/1.14 = 6.60. Selectivity factor was 3.44 and column resolution was 4.01. In the meantime, NBn2-chiral selector modified silica column has K'_{B1} = (12.67-1.14)/1.14 = 10.11 and the K'_{B2} = (21.33-1.14)/1.14 = 17.71. Selectivity factor was 1.75 and column resolution was 1.86

The solutions collected from both separations were concentrated to give the compounds with 2.7 and 2.6 mg weighs form the column modified by NCBz while 2.1 and 3.0 mg weighs were from the column modified by NBn2. After the two isomers of chabamide were determined the optical rotation value, the two enantiomers separated from NCBz- chiral selector have the optical rotation $[\alpha]_{25}^{D}$ of +133 and -158 (c 0.4, MeOH), respectively. While the optical rotation value $[\alpha]_{25}^{D}$ of the enantiomers were +71 and -241 (c 0.3, MeOH). This suggested that our chiral-selector -modified silica resulted in partial resolution and enantio-enrichment of the racemic mixture**.**

Computational Methods

To further investigate the binding between racemic chabamide (+,-) and NCBz, the geometry of chabamide bound with NCBz were designed and optimized at the DFT B3LYP/6-31g* level in 50% hexane in ethyl acetate using the polarizable continuum model (PCM) solvation model with Gaussian09. Their relative energy (ΔE) was then calculated and compared in kcal/mol.

The optimized structures of NCBz bound with chabamide (+, -) were displayed in Figure 4. It was found that carbonyl group of both chabamide (+/-) formed hydrogen bond with hydrogen on the carbamate nitrogen. Moreover, (-)-chabamide bound with NCBz more strongly (4.18 kcal/mol more stable) than that of (+)-chabamide bound with NCBz. This calculation results are in accord with the separation results that showed (+)-chabamide passing through the column more readily than (-)-chabamide.

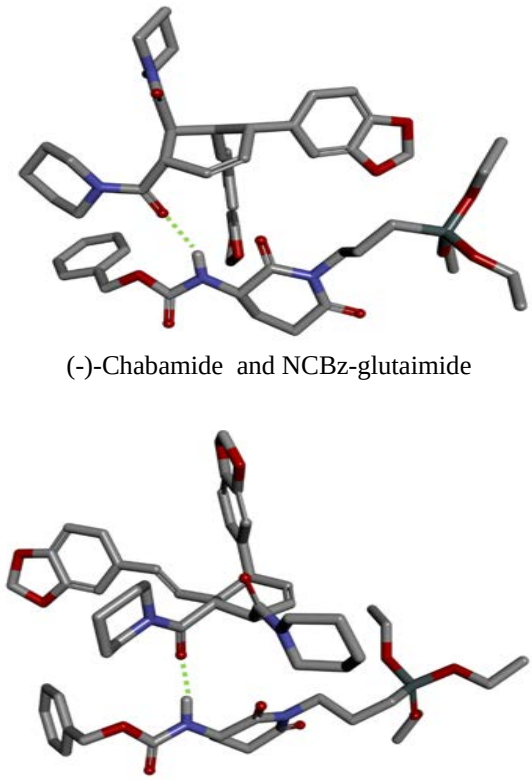

(-)-Chabamide and NCBz-glutaimide

(+)-Chabamide and NCBz-glutarimide

Figure 4. Optimized geometry of chabamide +/- bound with NCBz and their hydrogen bond interaction (green dash line).

4. Conclusion

We have developed new chiral selectors in the form of chiral glutarimides and they have shown the ability to partially resolve the racemic mixture of natural product chabamide which has been reported to have various medicinal properties. The mode of action of the chiral selector was studied using molecular docking experiments which showed hydrogen bonding between the NHCbz moiety and the carbonyl of chabamide to be vital in strong binding. Enantio-separation efficiencies of our columns, determined by the α 3.44 and Rs 4.01 (flow rate 6.0 mL/minute) for NCBz-chiral selector column and α 1.75 and Rs 1.86 (flow rate 3.0 mL/minute) for NBn2-chiral selector column. More detailed study of the chromatographic resolution of this alkaloids and other racemic compounds with various applications are ongoing in our laboratory.

Acknowledgements

Financial support for this research is provided by the Faculty of Science, Silpakorn University, Thailand.

References

1. Norbert M. Maier, Pilar Franco and Wolfgang Lindner, *J. of Chromatographic A* **2001**, 906, 3-33
2. Gogoi, A., Mazumder, N., Konwer, S., Ranawat, H., Chen, N. and Zhuo, G. *Molecules* **2019**, 24, 1007, doi: 10.3390/molecules24061007
3. Gübitz, G.; Schmid, M. G. *Methods in Molecular Biology (243) Chiral Reparations Methods and Protocals* **2004**, Humana Press, USA, 1-28
4. Taepakdee, K., Paradamit, V., Laiyangkoor, P., Kuntiyoug, P. *Proceeding of Pure and Applied Chemistry International Conference (PACCON)*, **2023**, pp AN89-AN94
5. Yuan, C.; Jia, W.; Yu, Z.; Li, Y.; Zi, M.; Yuan, l.; Cui, Y. *Journal of the American Chemical Society* **2022** *144* (2), 891-900 DOI: 10.1021/jacs.1c11051
6. Ong, C. S.; Oor, J. Z.; Tan, S. J.; Chew, J. W. *ACS Appl. Mater. Interfaces*. **2022**, 14, 10875-10885
7. Fernandes, C.; Phyo, Y. Z.; Silva, A. S.; Tiritan, M. E.; Kijjoa, A; Pinto, M. M. M. *Separation & Purification Reviews* **2017**, 1326939
9. Fernandes, C.; Teixeira, J.; Pinto, M.M.M.; Tiritan, M.E. *Molecules* **2021**, 26, 5477.

Derivatized alpha-cyclodextrin as gas chromatographic stationary phase for separation of chiral alcohols

Atiptiya Sriprasit, Pinyada Jungkanjana, and Aroonsiri Shitangkoon*

Department of Chemistry, Faculty of Science, Chulalongkorn University, Bangkok 10330 Thailand

**E-mail: aroonsiri.s@chula.ac.th*

Abstract:

Many chiral compounds are important in pharmaceutical industries. The use of pure single enantiomer is desired to avoid unwanted properties. Gas chromatography (GC) is a common technique used to analyze volatile organic compounds. Derivatized beta-cyclodextrins (CDs) were largely used as chiral GC stationary phases to separate enantiomers, while derivatized alpha-CDs were less reported. In this work, the small-size methylated alpha-CD mixed with polysiloxane was explored as a chiral stationary phase. A capillary column of 15 m long, 0.25 mm i.d., and 0.25 µm film of stationary phase was used. Underivatized chiral alcohols were examined including aliphatic alcohols and alcohols with aromatic and/or cyclic structure. Separations of all analytes were investigated by GC equipped with a split injector (250 °C) and a flame ionization detector (250 °C). Hydrogen was used as a carrier gas at a velocity of 50 cm/sec. Conditions for complete enantiomeric separation of all analytes were determined. It was found that all aliphatic alcohols could be separated into their enantiomers. Enantiomeric separations of alcohols with aromatic or cyclic structure depended on position of stereogenic center and type and position of substitution. While enantiomers of 1-phenylethanol could be completely separated (at 127 °C, k'_2 = 2.74, α = 1.04); enantiomers of 1-phenylpropan-2-ol could not be separated with this column. The influence of column temperature on enantioselectivity and retention were compared. This methylated alpha-CD showed good enantioselectivity towards chiral alcohols of different structures, including aliphatic alcohols. It can be an alternative supplement to other chiral columns.

1. Introduction

Many natural and synthetic chiral compounds are important in pharmaceutical industries. Two enantiomers of a chiral compound have identical physical and chemical properties. However, each enantiomer may display different pharmacological activity, biological property and toxicity. For chiral drugs, pharmacological activity of each enantiomer should be determined.[1] The use of pure single enantiomer is preferred to avoid unwanted properties. Therefore, fast and accurate analytical technique for determination of enantiomeric purity is essential.

Among several analytical techniques, capillary gas chromatography (GC) is a suitable technique used to analyze volatile and thermally stable organic compounds. Despite of the development of new chiral GC stationary phases, cyclodextrin (CD) derivatives are still useful and widely employed.[2,3] CDs are cyclic oligosaccharides with a cavity in their structures. Three common CDs contain 6, 7 and 8 glucose units and are called α-, β- and γ-CDs, respectively. A large number of CD derivatives were successfully synthesized and employed as GC stationary phases. They showed good selectivities towards many classes of chiral compounds.[4,5] Nevertheless, size of CD as well as type and position of substitution on derivatized CDs highly affected enantioseparation of analytes.[4] While derivatized β-CDs were commonly used as CD-based GC stationary phases, derivatized α- and γ-CDs were less reported.[5]

The objective of this work was to investigate the property of a smaller size, hexakis(2,3-di-*O*-methyl-6-*O*-*tert*-butyldimethylsilyl)-α-CD (Figure 1) as a chiral GC stationary phase. Sixteen chiral alcohols of different structures were examined including aliphatic alcohols and alcohols with aromatic and/or cyclic structure (Figure 2). The optimum condition for complete enantiomeric separation of each chiral alcohol was determined. The influence of alcohol structure on enantioselectivity was examined.

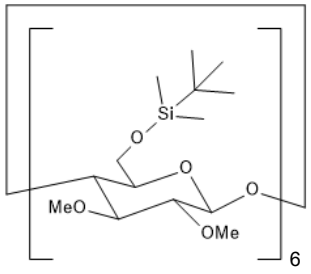

Figure 1. Structure of hexakis(2,3-di-*O*-methyl-6-*O*-*tert*-butyldimethylsilyl)-α-CD

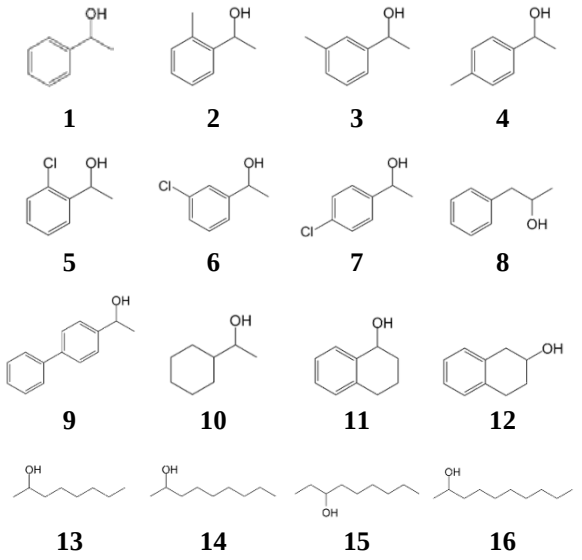

Figure 2. Structures of sixteen chiral alcohols

2. Materials and Methods

2.1 Chiral alcohols

Nine chiral alcohols and solvents were purchased from commercial vendors. Chiral alcohols are **1** (1-phenylethanol, 98%, Fluka); **7** (1-(4-chlorophenyl)ethanol, 98%, Aldrich); **8** (1-phenyl-2-propanol, 98%, Aldrich); **10** (1-cyclohexylethanol, 97%, Fluka); **11** (1,2,3,4-tetrahydro-1-naphthol, 97%, Aldrich); **13** (2-octanol, 98%, Fluka); **14** (2-nonanol, 99%, Aldrich); **15** (3-nonanol, 97%, Fluka) and **16** (2-decanol, 98%, Aldrich).

Other racemic alcohols were prepared from reduction of their corresponding ketones using sodium borohydride.[6] The structures of synthesized alcohols were characterized by ^{1}H NMR (Bruker AV-400 spectrometer) using $CDCl_3$ as a solvent. They are **2** (1-(2-methylphenyl)ethanol), **3** (1-(3-methylphenyl)-ethanol), **4** (1-(4-methylphenyl)ethanol), **5** (1-(2-chlorophenyl)ethanol), **6** (1-(3-chlorophenyl)ethanol), **9** (1-(4-biphenylyl)ethanol), and **12** (1,2,3,4-tetrahydro-2-naphthol).

2.2 GC analyses

All GC analyses were performed on an Agilent 7890B gas chromatograph equipped with a split injector (250 °C) and a flame ionization detector (250 °C). A split ratio was 100:1. Hydrogen was used as a carrier gas at a velocity of 50 cm/sec. A capillary column (15 m long, 0.25 mm i.d.) was coated with a 0.25 µm thick film of stationary phase by a static method.[7] The stationary phase was a mixture of hexakis(2,3-di-*O*-methyl-6-*O*-*tert*-butyldimethylsilyl)-α-CD in poly-siloxane. The efficiency of the coated column was tested using *n*-alkanes at various temperatures and was found to be greater than 3800 plates/m.

Each chiral alcohol was dissolved in dichloromethane and was analyzed by GC without derivatization. Each alcohol solution (approximately 0.2-0.4 µL) was individually injected at isothermal column temperature. The column temperature for each alcohol was adjusted until a complete separation of enantiomers was achieved (resolution of 1.5).

3. Results & Discussion

GC analyses of sixteen chiral alcohols were performed isothermally using hexakis(2,3-di-*O*-methyl-6-*O*-*tert*-butyldimethylsilyl)-α-CD as a chiral stationary phase. All analytes showed quite symmetric peak shapes. The column temperature for each alcohol was then adjusted until a resolution (Rs) between two enantiomers of at least 1.5 was achieved. The optimum column temperature, retention factor of the more retained enantiomers (k'_2) and enantioselectivity (α) for each alcohol were reported in Table 1. Among sixteen chiral alcohols tested, only alcohol **8** could not be separated into enantiomers by this column. Several analytes could be successfully separated into their enantiomers in short analysis times.

It was clear that analyte structure strongly affected enantioseparation as shown in Table 1. Alcohols **2**-**4** are positional isomers with methyl-substitution at different position of the aromatic ring. Alcohol **2** with *ortho*-substitution could be separated at high column temperature leading to shorter analysis time. The analysis time at their optimum temperatures increased from alcohols **2** < **3** < **4** corresponding to *ortho*- < *meta*- < *para*-substitution, respectively (Figure 3). However, an attempt to enantioseparate another positional isomer, alcohol **8**, was not successful. Only single peak was observed even at lower column temperature (80 °C). The results suggested the influence of the position of the stereogenic center. The stereogenic center of **8** was away from the aromatic ring, while alcohols **1**-**4** have their stereogenic centers next to the aromatic ring.

Table 1. Optimum column temperatures and other chromatographic parameters for complete enantiomeric separations of alcohols (Rs ≥ 1.5).

alcohol	column temperature (°C)	$t_{R,2}$ (min)	k'_2	α	Rs
1	127	2.010	2.74	1.04	1.55
2	156	1.369	1.56	1.05	1.56
3	138	2.196	3.10	1.03	1.50
4	100	9.576	16.93	1.03	1.52
5	176	1.124	1.10	1.05	1.56
6	130	7.178	12.39	1.03	1.55
7	120	9.943	17.28	1.03	1.52
8	80	17.766	32.27	1.00	[a]
9	150	26.529	48.68	1.02	1.00[b]
10	97	3.646	5.83	1.03	1.53
11	179	1.454	1.72	1.05	1.63
12	115	16.976	30.79	1.02	0.98[b]
13	90	4.275	7.01	1.03	1.52
14	100	5.328	8.98	1.03	1.52
15	112	2.851	4.34	1.03	1.61
16	103	8.210	14.37	1.03	1.53

[a] No separation of enantiomers.
[b] Incomplete separation of enantiomers (Rs < 1.5).

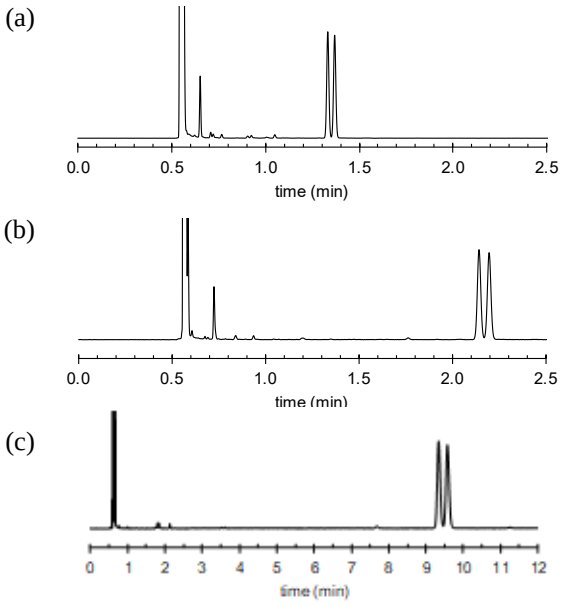

Figure 3. Chromatograms of alcohols (a) **2**, (b) **3**, and (c) **4** at their optimum temperatures.

The influence of column temperature on retention factor (k') and enantioselectivity (α) of alcohols **2-4** were further investigated. Generally, retention factors and enantioselectivity of analytes increased when the column temperature decreased. Plots of ln k' vs. 1/T of the more retained enantiomers were shown in Figure 4(a). At the same column temperature, alcohols **2-4** were closely retained, with a slight decrease in k' values from **2** > **3** > **4**. As the column temperature decreased, their k' values increased similarly (same slope). However, the enantioselectivity did not show the same trend. At the same column temperature, enantioselectivity of alcohol **2** was highest. In addition, the slope of ln α vs. 1/T plot for alcohol **2** was steepest. The slopes decreased in the order **2** > **3** > **4** as in Figure 4(b). Therefore, enantioselectivity of alcohol **2** could be markedly improved by decreasing the column temperature. For alcohols **3** and **4**, a decrease in temperature would result in longer analysis times with lesser improvement in enantioselectivities. Separations of alcohols **2-4** were compared at the same temperature (Figure 5). Their resolution decreased in the order **2** > **3** > **4**. At 130 °C, alcohol **4** was partially separated.

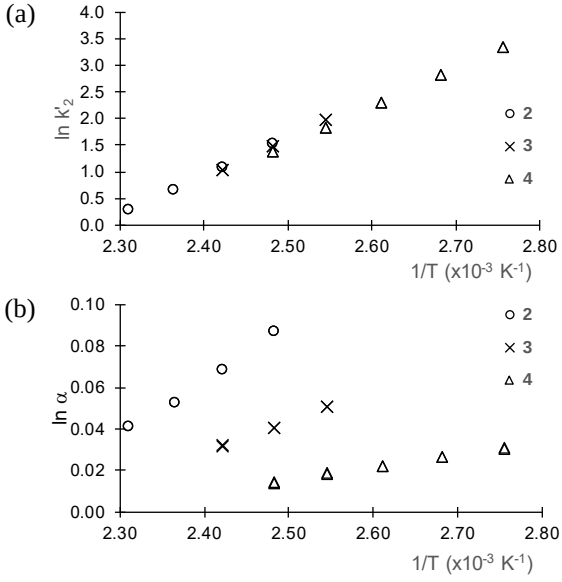

Figure 4. Plots of (a) ln k' vs. 1/T of the more retained enantiomers and (b) ln α vs. 1/T of alcohols **2**, **3**, and **4**.

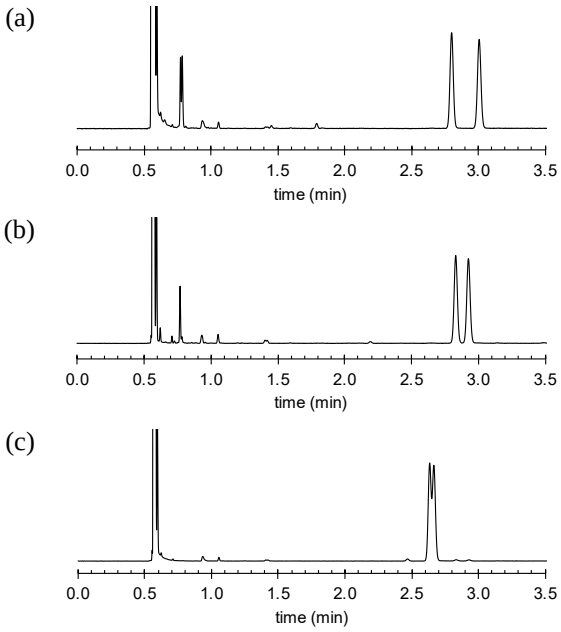

Figure 5. Chromatograms of alcohols (a) **2**, (b) **3**, and (c) **4** at 130 °C.

Similar trends were also observed for alcohols **5-7**. They are positional isomers with chloro-substitution at different position of the aromatic ring. Alcohol **5** with *ortho*-substitution could be completely separated in shorter analysis time compared to alcohols **6** and **7**, with *meta*- and *para*-substitutions, respectively (Table 1). Comparing at the same column temperature, α value of alcohol **5** was highest. In addition, the slope of ln α vs. 1/T plot for alcohol **5** was steepest (Figure 6). As a result, the separation of alcohol **5** could be completed in very short analysis time (less than 1.2 min). Previous study on ln α vs. 1/T plots of alcohols **5-7** using derivatized β-CD stationary phase showed similar trends as observed on derivatized α-CD stationary phase: alcohol **5** showed the steepest slope[6].

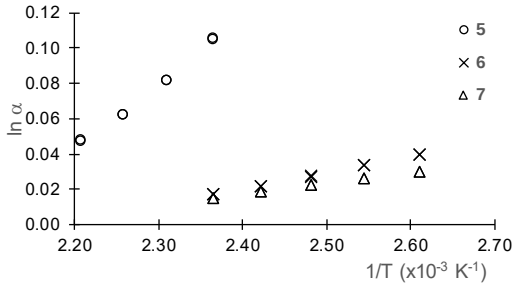

Figure 6. Plots of ln α vs. 1/T of alcohols **5**, **6**, and **7**.

When *para*-substitution is a large phenyl group as in alcohol **9** (compared to smaller methyl or chloro group), the α value was small. It could be explained that the small cavity of α-CD was not suitable for separation of large molecules. A decrease in column temperature resulted in a small increase of enantioselectivity but longer analysis time. An incomplete separation was observed at 150 °C (k'_2 = 48.68, Rs = 1.00). Further decrease in column temperature was not attempted as it led to broader peak shape and very long analysis time.

Enantiomeric separation of alcohols with different cyclic structure was also investigated with this derivatized α-CD stationary phase. When the analyte structure changed from an aromatic ring (alcohol **1**) to a cyclohexyl ring (alcohol **10**), the analysis time at optimum conditions increased slightly. Interesting results were found for alcohols **11** and **12**. Both analytes contained an aromatic ring and a cyclohexyl moiety in the structures, their separations significantly differed depending on the position of the stereogenic center. While alcohol **11** could be completely separated in less than 1.5 min, a complete separation could not be achieved with alcohol **12**.

Enantioseparation of alcohols with aliphatic structure was rarely reported. This derivatized α-CD stationary phase could separate enantiomers of all four aliphatic alcohols **13-16**. As the alkyl chain length increased from **13** < **14** < **16**, the analysis time at optimum conditions increased. Interestingly, alcohol **15** (3-nonanol) was separated in a much shorter analysis time than alcohol **14** (2-nonanol). This was clearly the effect of the position of the stereogenic center. Enantiomeric separations of alcohols **13**, **14**, and **15** were compared in Figure 7. Result obtained from alcohol **13** was compared to those from alcohols **1** and **10**, as they all have the same number of carbon atom. It was seen that alcohol **13** with more flexible structure was separated in longer analysis time.

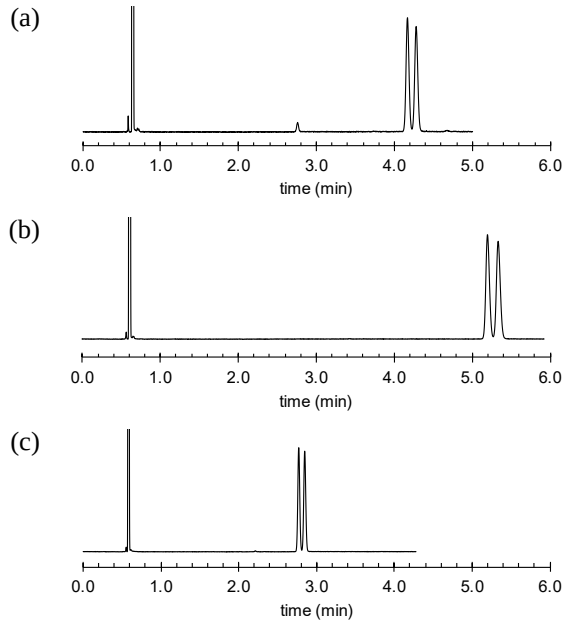

Figure 7. Chromatograms of alcohols (a) **13**, (b) **14**, and (c) **15** at their optimum temperatures.

4. Conclusion

The property of hexakis(2,3-di-*O*-methyl-6-*O*-*tert*-butyldimethylsilyl)-α-CD as a chiral GC stationary phase was investigated using sixteen underivatized chiral alcohols of different structures. All alcohols exhibited quite symmetrical peak shapes. All aliphatic alcohols could be successfully separated into their enantiomers. Enantiomeric separations of alcohols with aromatic and/or cyclic structure depended greatly on the size and position of substituent of analyte as well as the position of the stereogenic center. From this study, alcohols with substitution at the *ortho*-position of the aromatic ring and alcohols with the stereogenic center closed to the ring showed high enantioselectivity, thus could be separated in short analysis time. This α-CD derivative showed good enantioselectivity towards chiral alcohols of different structures, including aliphatic alcohols. It can be an alternative supplement to other chiral GC columns.

Acknowledgements

Professor Gyula Vigh is greatly appreciated for providing the cyclodextrin derivative for this study.

References

1. Blumenstein, J.J. Chiral Drugs: Regulatory Aspects. In *Chirality in Industry II*; Collins, A.N.; Sheldrake, G.N.; Crosby, J. Eds.; John Wiley & Sons; Chichester, 1997; pp 11-18.
2. Gus'kov, V. Yu.; Maistrenko, V.N. *J. Anal. Chem.* **2018**, *73*, 937-945.
3. Xie, S.M.; Yuan, L.M. *J. Sep. Sci.* **2017**, *40*, 124-137.
4. Shurig, V. *J. Chromatogr. A* **2001**, *906(1-2)*, 275-299.
5. Betzenbichler, G.; Huber, L.; Kräh, S.; Morkos, M.-L. K.; Siegle, A.F.; Trapp, O. *Chirality* **2022**, *34*, 732-759.
6. Iamsam-ang, W. Enantiomeric Separation of Aromatic Alcohols by Gas Chromatography Using Derivatized β-Cyclodextrins as Stationary Phases. M.Sc. Thesis, Chulalongkorn University, Bangkok, 2002.
7. Grob, K. *Making and Manipulating Capillary Columns for Gas Chromatography*, Hüthig, 1986.

Method validation for determination of lead and cadmium in paper for food contact using microwave digestion followed by inductively coupled plasma mass spectrometry

Netsirin Gissawong, Veerapat Ramanee, Warunrat Buranakul, Nootjarin Phonhong, and Weera Suanthaisong*

Metallic Products Group, Chemicals and Consumer Products Division, Department of Science Service, Bangkok 10400, Thailand

**E-mail: weera@dss.go.th*

Abstract:

Nowadays, paper-based materials are one of food contact materials (FCMs), extensively used worldwide to fulfill eco-friendly trend due to its degradation. However, paper is often treated with coating, additive, and adhesive materials to enhance its functional properties. Therefore, contaminants such as optical brightening agents, antimicrobial constituents and heavy metals can migrate from paper based FCMs to food. This work proposed the method validation for lead (Pb) and cadmium (Cd) analysis in the paper. It is necessary that the laboratory has to validate this testing method to evaluate whether the validated method is fit for intended use. The paper-based FCMs were digested using microwave digestion in acidic condition. All metals were then analyzed by inductively coupled plasma mass spectrometry (ICP-MS) which is used instead of European Standard (EN) 12498 method referred in Thai Industrial Standard (TIS) 2948-2019 standard due to unacceptable accuracy in adsorbent-paper. The results indicated that this method can detect the metals in the acceptable range of TIS criteria as Pb lower than 3.0 mg kg^{-1} and Cd lower than 0.50 mg kg^{-1}. The bias and precision studies showed that percentage of recovery and relative standard deviations of two elements were between 86-103% and less than 10%, respectively. Moreover, the expanded uncertainties of all elements were not more than ±20% at the confidence level of 95%. Thus, this test method for determination of two heavy metals in food contact paper by ICP-MS using microwave digestion was valid and fit for the intended use.

1. Introduction

Currently, bio-circular-green economy (BCG) is interesting because it focuses on reducing the problems of global warming using science, technology, and innovation to impel economy. Papers for food contact materials (FCMs) are one of innovation that involved Circular Economy. They are produced to alternatively use for foam and plastic container or non-biodegradable FCMs which papers based FCMs are widely used due to environmentally-friendly, biodegradable, direct food contact, and recyclable.[1,2] However, the substandard papers based FCMs may be contaminated heavy metals including lead (Pb) and cadmium (Cd) which can migrate to food. The heavy metals contamination in FCMs can occur for many reasons such as manufacturing process, printing ink residue, and recycling process.[2] Moreover, the contaminant in recycled papers is mostly higher than new paper based FCMs. It is occurred from incomplete elimination of heavy metals in recycling process. The residual Pb and Cd in FCMs result in various undesirable effects to the consumers including exhausted, anorexia, weight loss, abdominal cramp, and neurotoxin.[3] Therefore, industry guideline of the paper for food contact is important as same as food safety which many countries have strict standard or law of FCMs especially European Union covering 17 types of FCMs, including paper.

In Thailand now, there is a relevant law with FCMs; namely Thai Industrial Standards (TIS) that is set by the technical committee of the Thailand Industrial Standards Institute (TISI). The TIS of FCMs are consisted of TIS no. 2948-2019: Paper for food contact and TIS no. 3438-2022: Cooking paper which determined Pb and Cd migration to food of no more than 3.0 mg/kg and 0.5 mg/kg, respectively.[4,5] Generally, the standard test method of paper-based FCMs is BS EN 12498: Paper and board - Paper and board intended to come into contact with foodstuffs - Determination of cadmium, chromium and lead in an aqueous extract.[6] According to BS EN 12498, heavy metals migration in the paper are measured by an extraction with intermediate solvent depending on usage characteristics of FCMs. For example, the paper-based FCMs that contacted hot food are tested using hot water extraction followed in BS EN 647.[7] As for the paper with no contacting hot food are analyzed using cold water extraction followed in BS EN 645.[8] However, these methods have a limitation leading to error of the measurement (method bias) because some paper-

based FCMs have adsorption property. For this reason, the obtained bias of method was not acceptable criteria of BS EN 12498. Therefore, the development of paper-based FCMs test method is important for the analysis of all papers.

This work proposed the method validation for Pb and Cd analysis in the paper using microwave digestion followed by inductively coupled plasma mass spectrometry (ICP-MS). It focused on method development that is accurate, precise, valid and acceptable by criteria of BS EN 12498. The performance characteristics were studied including instrument working range, limit of detection (LOD), limit of quantitation (LOQ), bias, intermediate precision, matrix effect and measurement uncertainty according to the standard documents of Eurachem Guide and VAM Project 3.2.1.[9,10]

2. Materials and Methods

2.1 Materials

All of chemicals were analytical reagent grade and acquired from various suppliers including two reference standard solutions of lead and cadmium, 1000 mg L^{-1} from AccuStandard (USA) and High-Purity Standard (USA). Nitric acid, 65% w/v (HNO_3) was purchased from Merck (Germany). Deionized water produced from Milli-Q® Reference A+ System (Millipore water, USA) with a specific resistivity of 18.2 MΩ cm^{-1}, was used throughout.

The stock solution (10 mg L^{-1}) and the working standard solution of Pb and Cd were prepared into two groups by dilution an appropriate amount of the standard solution in 2%v/v HNO_3 and daily stepwise dilution of the stock solution with 2%v/v HNO_3, respectively. The first group, from AccuStandard, was used to study a calibration curve of Pb and Cd. Another group, from High-Purity Standard, was used to verify the calibration curve, and investigate bias and precision.

2.2 Instrumentation

Paper samples were digested using TOPWave microwave digestion, analytik jena, South Africa, which the digestion condition was displayed in Table 1. Inductively coupled plasma mass spectrophotometer (ICP-MS), PerkinElmer, NexION 350S, USA, was used to detect Pb and Cd which ICP-MS condition was showed in Table 2.

Table 1. Parameters of microwave digestion.

Step	Temperature (°C)	Pressure (bar)	Ramp	Time (min)	Power (%)
1	170	50	5	15	90
2	200	50	1	30	90
3	50	0	1	10	0
4	50	0	1	10	0
5	50	0	1	1	0

Table 2. ICP-MS parameters for Pb and Cd detection.

Parameter	Condition	
Analyte	Cd	Pb
Mass	110.904	207.977
Internal standard	In	Bi
Mass	114.904	208.98
Analysis mode	KED	
Reaction gas	He	
Reaction gas flow	3.5 mL min^{-1}	
RF power	1,550 W	
Nebulizer gas flow	0.96 mL min^{-1}	
Auxiliary gas flow	1.25 mL min^{-1}	
Plasma gas flow	18 mL min^{-1}	
Pump speed	20 rpm	
Delay time	45 s	

2.3 Pb and Cd analysis in paper sample

Figure 1 shown the schematic diagram of determination of Pb and Cd in food contact paper using microwave digestion followed by ICP-MS. Firstly, paper sample was cut into 1.0 x 1.0 cm^2. The obtained sample was weighted to 0.50 g into microwave vessels. Concentrated HNO_3, 10 mL was then added to the vessels. It was stand until no reaction between the sample and acid, approximately 1 h. After that, the sample was digested using microwave digestion. The obtained solution was adjusted to 100.00 mL with deionized water and then filtered through a Whatman 4 filter paper before Pb and Cd analysis by ICP-MS.

3. Results & Discussion

3.1 Instrument working range

To confirm linear range, standard solution of Pb and Cd at four concentration levels was analyzed. The calibration curve was then plotted between m/z (y axis) against concentration of solution (x axis). Consider correlation coefficient (r) shall be ≥ 0.995 or coefficient of determination (R^2) shall be ≥ 0.990.[11] It was found that the instrument working range of 2.0–20.0 µg L^{-1} for Pb and 0.20–2.0 µg L^{-1} for Cd was proper with the regression equation of y=0.0355x-0.0102 and y=0.0412x+0.0004, and the correlation coefficient (r) of 0.9999 and 0.9999, respectively.

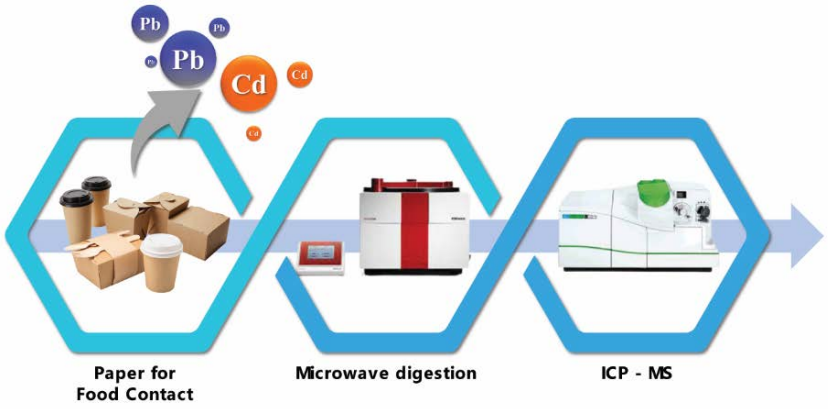

Figure1. Schematic diagram of determination of Pb and Cd in food contact paper using microwave digestion followed by ICP-MS.

3.2 Limit of detection (LOD) and limit of quantitation (LOQ)

To study the lowest concentration of analyte in a sample that can be detected (limit of detection, LOD) and determined with acceptable precision and accuracy (limit of quantitation, LOQ), Pb and Cd in the sample blank was analyzed at 10 batches. LOD and LOQ were calculated using the following equation:

$$LOD = 3SD \quad (1)$$
$$LOQ = 10SD \quad (2)$$

where SD is standard deviation at n = 10. It was founded that LOD of 0.043 and 0.0024 mg kg^{-1} was achieved for Pb and Cd, respectively. LOQ was 0.14 and 0.010 mg kg^{-1} for Pb and Cd, respectively.

To confirm the obtained LOQ, the standard solution at Pb 0.20 mg kg^{-1} and Cd 0.020 mg kg^{-1} was studied. Considering percentage of recovery and relative standard deviation (%RSD), criteria of %recovery is 80-110% and %RSD is ≤10%.[11] It was found that the two values were not accepted at Pb 0.20 mg kg^{-1} and Cd 0.020 mg kg^{-1}. Afterwards, studying the standard solution and spiked sample solution at Pb 0.40 mg kg^{-1} and Cd 0.040 mg kg^{-1}, the results were accepted providing %recovery of 103.2% for Pb and 92.1% for Cd with %RSD of ≤10% for spiked sample solution. Thus, LOQ of this work was 0.40 and 0.040 mg kg^{-1} for Pb and Cd, respectively, due to providing accuracy and precision.

3.3 Bias

The spiking paper sample at three concentrations (low, medium, and high concentrations of calibration curve) was detected to investigate bias which reported in term of %recovery. Bias is the difference between the expectation of the test results and an accepted reference value; estimate of a systematic measurement error.[9] As can be seen in Table 3, the obtained %recoveries were accepted confirming the accuracy of the proposed method.

Table 3. %Recovery of Pb and Cd in paper sample solution for bias study (n=10).

Analyte	Solution	%Recovery
Pb	sample + 0.40 mg kg^{-1} (2.0 µg L^{-1})	103.2
	sample + 2.0 mg kg^{-1} (10.0 µg L^{-1})	97.0
	sample + 4.0 mg kg^{-1} (20.0 µg L^{-1})	102.5
Cd	sample + 0.040 mg kg^{-1} (0.20 µg L^{-1})	92.1
	sample + 0.20 mg kg^{-1} (1.0 µg L^{-1})	86.5
	sample + 0.40 mg kg^{-1} (2.0 µg L^{-1})	90.9
Criteria: BS EN 12498 [6]		
	Pb at 15 µg L^{-1}	97-103%
	Cd at 4.5 µg L^{-1}	90-110%

3.4 Matrix effect

To study the effect of matrix in paper sample, the obtained data from bias was used to evaluate matrix effect. Graph between spiked concentration and found concentration in paper sample was plotted as displayed in Figure 2. The slope and y-intercept of the graph was evaluated which the values shall not significantly different from 1 and 0, respectively.[9] The results indicated that they were not different from criteria concluding there is no matrix effect.

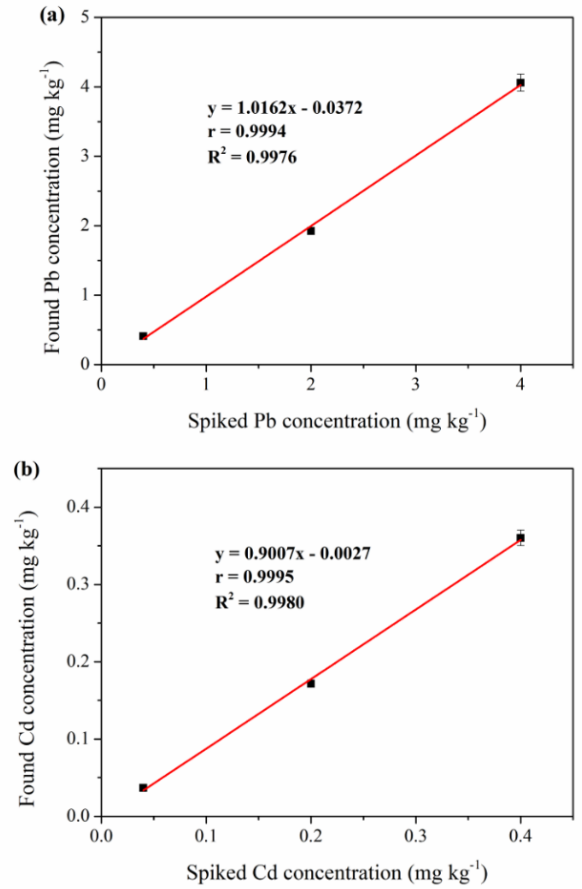

Figure 2. Curve of Pb (a) and Cd (b) between spiked concentration and found concentration in paper sample.

3.5 Intermediate precision

In this work, precision of the method was studied by replicate measurements on the same sample solution (n=10) under repeatability conditions at three concentration levels (low, medium, and high concentrations of calibration curve) in three days. It is reported in terms of relative standard deviation (RSD) (Table 4). The RSDs are less than 10%, indicating an acceptable reproducibility of the proposed method.

Table 4. %RSD of Pb and Cd in paper sample solution for precision study (n=10).

Analyte	Solution	%RSD
Pb	sample + 0.40 mg kg^{-1}	9.4
	sample + 2.0 mg kg^{-1}	5.2
	sample + 4.0 mg kg^{-1}	3.4
Cd	sample + 0.040 mg kg^{-1}	7.1
	sample + 0.20 mg kg^{-1}	5.2
	sample + 0.40 mg kg^{-1}	3.4
	Criteria [11]	≤10

3.6 Measurement uncertainty

The measurement uncertainty of the proposed method was calculated from data of bias (u(R)) and precision (u(P)/P) study according reference of VAM Project 3.2.1.[10] Combined uncertainty (u_c) was calculated using the following equation:

$$u_C = C \times \sqrt{\left(\frac{u(R)}{R}\right)^2 + \left(\frac{u(P)}{P}\right)^2} \qquad (3)$$

where C is concentration of the solution. Expanded uncertainty (U) was then calculated using the following equation:

$$U = k \times u_C \qquad (4)$$

where k is coverage factor, 2 at 95% confidence level. Table 5 concluded measurement uncertainty of Pb and Cd which the expanded uncertainties were not more than ±20%.

Table 5. Measurement uncertainty of Pb and Cd.

Uncertainty source	Pb	Cd
bias, u(R)/R	0.038	0.084
precision, u(P)/P	0.065	0.055
combined uncertainty, u_c	0.15	0.020
expanded uncertainty, U	0.30	0.040
concentration (mg kg^{-1})	2.0	0.2
% U	15.0	20.0

4. Conclusion

This work proposed method validation for Pb and Cd detection in paper based FCMs using microwave digestion followed by ICP-MS. The results of performance characteristics including linearity, LOD, LOQ, bias, precision, and target uncertainty were followed acceptable criteria of BS EN 12498; Paper and board - Paper and board intended to come into contact with foodstuffs - Determination of cadmium, chromium and lead in an aqueous extract.[6] It can be indicated that the proposed method; microwave digestion followed by ICP-MS, was valid and fit for the intended use. Therefore, the method that validated acceptance can be used to determine Pb and Cd in paper based FCMs for laboratory service. Moreover, this study can develop to further use as guideline for other metals detection in the FCMs.

Acknowledgements

We gratefully acknowledge the Metallic Products Group, Chemicals and Consumer Products Division, Department of Science Service, Ministry of Higher Education, Science, Research and Innovation, Thailand.

References

1. Salvatore, C.; Mélanie, D.M.; Séverine, G.; Els, V.H. *Foods.* **2023**, 12, 2737.
2. Gaurav, K.D.; Narender, R.P.; Tanweer, A. J *Food. Sci. Technol.* **2019**, 56, 4391-4403.
3. Dilek, B.; Yasemin, B.K.; Gokhan, U. *Food. Chem. Toxicol.* **2011**, 49, 202-207.
4. Thai Industrial Standards, *TIS no. 2948-2019: Paper for food contact*, Royal Thai Government Gazette, 2020; Vol. 137.
5. Thai Industrial Standards, *TIS no. 3438-2022: Cooking paper*, Royal Thai Government Gazette, 2022; Vol. 139.
6. European Committee for Standardization (CEN), *BS EN 12498: Paper and board - Paper and board intended to come into contact with foodstuffs - Determination of cadmium, chromium and lead in an aqueous extract*, British Standards, 2018.
7. European Committee for Standardization (CEN), *BS EN 647: Paper and board, intended to come into contact with foodstuffs - Preparation of a hot water extract*, British Standards, 1994.
8. European Committee for Standardization (CEN), *BS EN 645: Paper and board, intended to come into contact with foodstuffs - Preparation of a cold water extract*, British Standards, 1994.
9. Magnusson, B.; Örnemark, U. *Eurachem Guide: The Fitness for Purpose of Analytical Methods – A Laboratory Guide to Method Validation and Related Topics*, 2nd ed, 2014. http://www.eurachem.org (accessed October 15, 2014)
10. Barwick, V.J.; Ellison, S.L.R. *VAM Project 3.2.1 Development and Harmonisation of Measurement Uncertainty Principles. Part (d): Protocol for uncertainty evaluation from validation data*, LGC/VAM/1998/088, 2000.
11. AOAC International, *Appendix F: Guidelines for standard method performance requirements*, Official methods of analysis of AOAC International, 2016.

Method validation for determination of heavy metals in Alum (Aluminium sulphate) by Inductively Coupled Plasma Mass Spectrometer

Inthuon Sukkseam, Jirasa Krongkrod*, Sorada Khunhon, and Titiporn Wattanakul

Chemicals for Industrial Section, Chemicals and Consumer Products Division, Department of Science Service, Bangkok 10400, Thailand

**E-mail address: jirasa@dss.go.th*

Abstract:

Aluminium sulphate (Alum) is widely used in water purification and wastewater treatment. It can remove the suspended impurities by coagulating them into larger particles which will settle to the bottom of the container or will be filtered out easily. However, the presence of heavy metals like Manganese (Mn), Chromium (Cr), and Cadmium (Cd) in large amounts can negatively impact the water quality. At present, the analysis of heavy metal content in alum according to Thai Industrial Standard (TIS) 165 - 2011 uses the graphite furnace atomic absorption spectrophotometer. However, a limitation of this technique is a time-consuming and not suitable for routine work. The linearity range of these heavy metals was narrow. Therefore, the high-concentrated sample need to be diluted from the initial concentration. Additionally, the determination of Cd and Cr required to use standard addition techniques, due to a matrix interference effect, which was more tedious to prepare the calibration plot for each sample separately. In this work, the heavy metals in alum were tested by digesting the sample with 1:1 nitric acid and then quantifying the amount of Mn, Cr, and Cd simultaneously by using an Inductively Coupled Plasma Mass Spectrometer (ICP-MS). The linear range of three elements was 0 - 500 µg/L. LOD of 0.0270, 0.0030, and 0.0148 µg/Lwas achieved for Mn, Cd and Cr, respectively. LOQ was 0.0899, 0.0098, and 0.0492 µg/L for Mn, Cd and Cr, respectively. The bias and precision studies showed that the percentage of recovery and relative standard deviations of the three elements were between 89 - 101% and less than 10%, respectively. As a result, this developed method was suitable for routine work in the analysis of heavy metals in alum using ICP-MS.

1. Introduction

The water supply system is one of the most important basic utilities of all sectors of society, including households, services, and industries. The water supply system will have the duty to produce quality tap water and to supply enough tap water for human consumption. The tap water production system consists of various processes to make high-quality water. Firstly, raw water is pumped from surface water and is stored in reservoirs. Then, large particles are removed by pre-screening and/or pre-sedimentation. The remaining small and light particles are removed by coagulation and flocculation. Coagulants are added and stirred to bring the non-settling particles together into larger particles called floc which are eliminated by the sedimentation step.[1]

Aluminium sulphate (Alum) is a nontoxic liquid that is commonly used as an inorganic coagulant in water treatment to remove particles like dissolved organic carbon which may be suspended in the medium. After coagulation, the alum acts as a flocculant allowing particles to cling together and forming larger particles which in turn fall from suspension and settle in the bottom of sedimentation tanks. However, a large amount of heavy metals in alum can negatively impact the water quality.

Currently, Thailand has alum standards, namely Thai Industrial Standard (TIS) 165 - 2011. The standard specifies that the amounts of heavy metals, including manganese (Mn), cadmium (Cd), and chromium (Cr) are not more than 50, 4, and 20 mg/kg, respectively.[2] According to the above standards, the heavy metal analysis method uses Graphite furnace atomic absorption spectrophotometer. This technique is known to be time-consuming and not suitable for routine work because this technique can determine only one element at a time and the calibration curve must be prepared separately one by one. In addition, the determination of Cd and Cr according to the standard method uses standard addition techniques, due to a matrix interference effect, which was more tedious to prepare the calibration plot for each sample separately.

In this work, the researchers wanted to develop a method for the simultaneous determination of Mn, Cr, and Cd by an inductively coupled plasma mass spectrometer (ICP-MS). The performance characteristics were studied including instrument linear range, limit of detection (LOD), limit of quantitation (LOQ), bias, intermediate precision, and matrix effect according to the standard documents of Eurachem Guide.[3]

2. Materials and Methods

2.1 Materials

All of chemicals were analytical reagent grade and acquired from various suppliers including two reference standard solutions of ICP multi-element standard solution 1000 mg/L from AccuStandard and CPAChem. ICP- MS Internal standard (ISTD) (Bi, Ge, In, ^{6}Li, Lu, Rh, Sc and Tb) 100 mg/L from Agilent Technologies. Nitric acid, 65 % w/v (HNO_3) was suprapure grade for preparing calibration curve and purchased from Merck. Deionized water produced from Milli-Q® Reference A+ System (Millipore water, USA) with a specific resistivity of 18.2 MΩ/cm, was used throughout.

The stock solution (10 mg/L) and working standard solution of Mn, Cd, and Cr were prepared by using 1% v/v HNO_3 as a solvent. The stock solution and working standard solution are prepared into two groups. The first group from CPAChem was used to study a calibration curve. Another group from AccuStandard was used to verify the calibration curve and investigate bias and precision.

2.2 Instrumentation

Inductively coupled plasma mass spectrometer (ICP-MS), Agilent, 7900, was used to detect Mn, Cd and Cr in alum. ICP-MS condition shown in Table 1.

Table 1. ICP-MS parameters for determination of heavy metals in alum.

Parameter	Condition
Mass	52 for Cr 55 for Mn 111 for Cd
Oxide Ratio (CeO/Ce)	156/140
Doubly Charged Ratio (Ce^{2+}/Ce)	70/140
Reaction gas flow	He
RF Power	1550 W
RF Matching	1.10 V
Nebulizer Gas	0.85 L/min
Nebulizer Pump	0.1 rps
Dilution Gas	0.30 L/min
Auxiliary Gas	0.90 L/min
Plasma Gas	15.0 L/min

2.3 Sample preparation

Firstly, 2 g of liquid alum was dissolved in 40 mL of deionized water and added 2 mL of a 1:1 HNO_3 solution. Then, the solution was boiled for 2 – 3 min and made up to the volume in a 100 mL volumetric flask with deionized water. After that, the sample solution was filtered with Whatman filter paper No. 5 or equivalent.

3. Results & Discussion

3.1 Instrument linear range

To confirm the linear range, the standard solution of Mn, Cd, and Cr was analyzed. The calibration curve was then plotted between the ratio intensity of standard/ISTD (y-axis) against the concentration of solution (x-axis). The results were shown in Fig. 1. Coefficient of determination (R^2) shall be greater than or equal to 0.990. It was found that the instrument linear range of 0 - 500 µg/L for Mn, Cd and Cr.

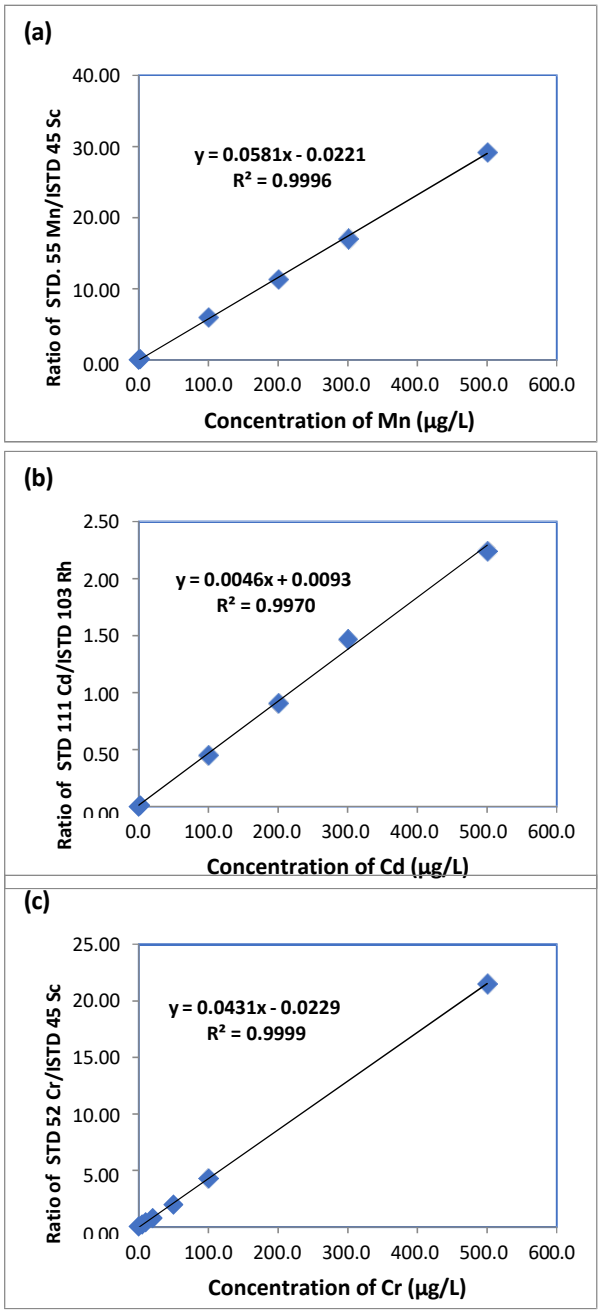

Figure 1. Calibration curve of (a) Mn, (b) Cd and (c) Cr.

3.2 Limit of Detection (LOD) and Limit of Quantitation (LOQ)

To study the lowest concentration of analyte in a sample that can be detected (Limit of detection, LOD) and determined with acceptable precision and accuracy (Limit of quantitation, LOQ). The sample blank measured 10 times and calculated according to following equation:

$$LOD = 3S'_0 \quad (1)$$

$$LOQ = 10S'_0 \quad (2)$$

S'_0 is calculated from:

$$S'_0 = S_0\sqrt{\frac{1}{n} + \frac{1}{n_b}} \quad (3)$$

when $\mathbf{S_0}$ is the estimated standard deviation of m single results at or near zero concentration. **n** is the number of replicate observations averaged when reporting results where each replicate is obtained following the entire measurement procedure.
$\mathbf{n_b}$ is the number of blank observations averaged when calculating the blank correction according to the measurement procedure.

The measurement procedure states that test sample should be measured triplicate (n = 3) and the results corrected by the result for a single sample blank sample (n_b = 1). It was found that LOD of 0.0270, 0.0030, and 0.0148 µg/L was achieved for Mn, Cd, and Cr, respectively. LOQ was 0.0899, 0.0098, and 0.0492 µg/L for Mn, Cd, and Cr, respectively.

3.3 Bias

Bias is the difference between the expectation of the test results and an accepted reference value; an estimate of a systematic measurement error.

The spiking sample at three concentrations (low, medium, and high concentrations of calibration curve) was detected to investigate bias which was reported in term of %recovery. As can be seen in Table 2, the obtained %recovery is within the accepted range (80-110%)[4] to confirm the correctness of the proposed method**.**

3.4 Intermediate precision

In this work, the precision of the method was studied by replicating measurements on the same sample solution (n = 10) under repeatability conditions at three concentration levels (low, medium, and high concentrations of the calibration curve) in ten days. It is reported in terms of relative standard deviation (RSD) (Table 3). The RSD is less than 10%[4], indicating an acceptable reproducibility of the proposed method.

Table 2. %Recovery of Mn, Cd, and Cr in alum sample for bias study (n = 10).

Analyte	Sample+ Spikes	%Recovery
Mn	Sample + 2.0 µg/L Sample + 100 µg/L Sample + 500 µg/L	99.9 95.6 90.9
Cd	Sample + 2.0 µg/L Sample + 100 µg/L Sample + 500 µg/L	89.4 90.7 94.8
Cr	Sample + 5.0 µg/L Sample + 100 µg/L Sample + 200 µg/L	99.4 95.0 100.5

Table 3. RSD of Mn, Cd, and Cr in alum sample for precision study (n = 10).

Analyte	Sample+ Spikes	RSD (%)
Mn	Sample + 2.0 µg/L Sample + 100 µg/L Sample + 500 µg/L	4.1 1.1 1.2
Cd	Sample + 2.0 µg/L Sample + 100 µg/L Sample + 500 µg/L	1.8 0.9 0.6
Cr	Sample + 5.0 µg/L Sample + 100 µg/L Sample + 200 µg/L	1.6 2.3 4.4

3.5 Metrix effect

To study the effect of the matrix in the sample, the obtained data from bias was used to evaluate the matrix effect. The graph between the matrix-free calibration plot (standard) and the matrix calibration plot (spike sample) was plotted as displayed in Figure 2. The slope of the graph was evaluated which the values shall not significantly different from 1.[3] The percentage of slope difference of Mn, Cd and Cr was calculated using the following equation:

$$\%\text{Difference of the slopes} = \frac{|S_{std} - S_{spk}| \times 100}{S_{std}} \quad (4)$$

when S_{std} is the slope of standard curve
S_{spk} is the slope of spiked sample

%Difference of the slopes was 1.17, 2.08 and 5.61 for Mn, Cd and Cr, respectively**.** The acceptance limit is less than 10**%.** The results indicated that they were not different from the criteria concluding three is no matrix effect**.**

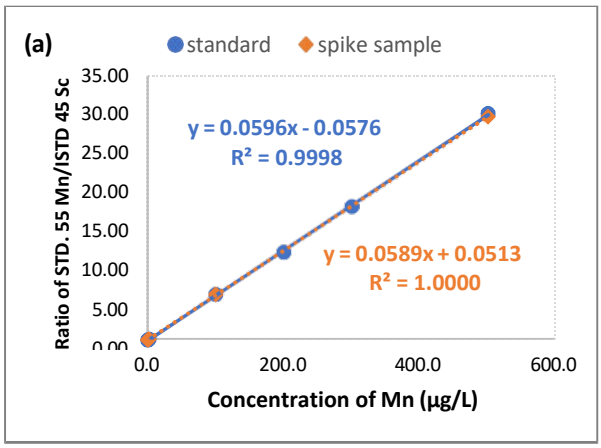

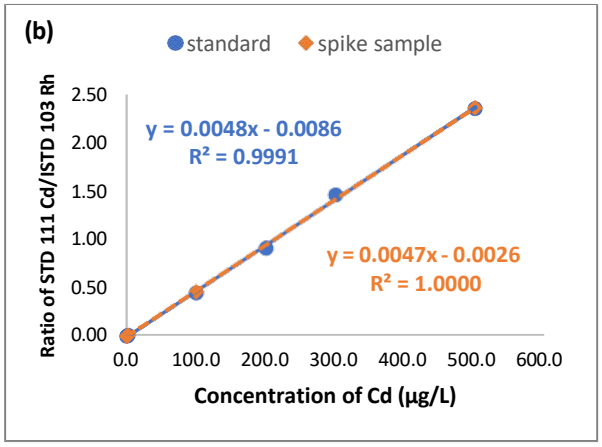

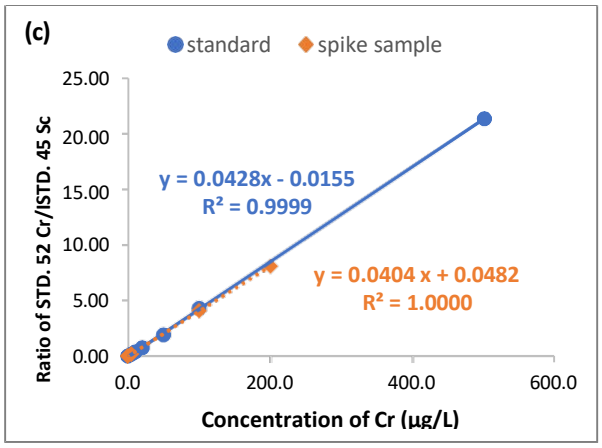

Figure 3. Matrix-free (standard) and matrix (spiked sample) calibration plot of (a) Mn, (b) Cd and (c) Cr.

4. Conclusion

This work proposed method validation for Mn, Cd, and Cr detection in alum by ICP-MS. The results of performance characteristics including linearity, LOD, LOQ, bias, precision and matrix effect followed acceptable criteria of TIS 165 - 2011. It can be determined that the proposed method is valid and suitable for use for routine work. The advantage of this method is less time- and chemical-consuming. However, the ICP-MS has a limitation, the percentage of total solids of the injected sample solution must be less than 3%, because that may clog the nebulizer. Therefore, the method that validated acceptance can be used to determine Mn, Cd, and Cr in alum for laboratory service. Moreover, this study can develop to further use as a guideline for other metals detection in alum.

Acknowledgements

We gratefully acknowledge the Chemicals for Industrial Section, Chemicals and Consumer Products Division, Department of Science Service.

References

1. R. Thamnoon. A comparative study of the efficiency of water supply production between the system using sedimentation and the system using dissolved air floatation. In *Research and development journal.* **2011**, Vol. 22.
2. Thai Industrial Standards, *TIS no. 165 – 2011:Alum*, Royal Thai Government Gazette,2011.
3. B. Magnusson and U. Örnemark. *Eurachem Guide: The Fitness for Purpose of Analytical Methods – A Laboratory Guide to Method Validation and Related Topics*, 2nd ed, 2014.
4. AOAC International, Appendix F: Guidelines for standard method performance requirements, Official methods of analysis of AOAC International, 2016.

Thailand reference material: TRM-F-2007 elements in turmeric powder

Pranee Phukphatthanachai, Nunnapus Laitip, and Usana Leekriangkrai

National Institute of Metrology (Thailand), Klong 5, Klong Luang, Pathumthani 12120 Thailand

**E-mail: pranee@nimt.or.th*

Abstract:

The application of certified reference material (CRM) in analytical chemistry for quality control purposes is recognized and recommended by international, national and professional organizations worldwide. Due to the unavailability of matrix matched CRMs in our country, TRM-F-2007: elements in turmeric powder (*Curcuma longa*) was initiated by National Institute of Metrology (Thailand) (NIMT) for the analysis of key elements. It was developed under the trade name of Thailand Reference Material (TRM).

Quantification of fifteen elements was performed by ICP-MS and ICP-OES using three analytical calibrations: isotope dilution mass spectrometry (IDMS), gravimetric standard addition (GSA) and external calibration. Homogeneity and short-term stability were studied using external calibration technique, while long-term stability was studied using IDMS or GSA. Statistical data shows that TRM-F-2007 is homogeneous and stable at temperature 45 ^{o}C for three weeks and it is stable at room temperature at least 3 years. Characterization of the elements requires at least two analytical methods. Eleven elements (As, Ca, Cd, Cu, Fe, K, Mg, Ni, P, Pb and Zn) were certified by weighting method from 2 – 6 analytical methods to provide accuracy and measurement uncertainty whereas 4 elements (Cr, Hg, Mn and Na) are mentioned as information value.

The entire process of production, measurement and the statistical models used are all performed according to the quality system ISO 17034, ISO/IEC 17025 and ISO Guide 35, respectively. TRM-F-2007, which is reliable and traceable to SI units demonstrating the unbroken chain, is suitable for quality control purposes such as method validation, and quality control sample.

1. Introduction

Turmeric (*Curcuma longa*) has been used in many industries such as food, cosmetic and medical supplement over centuries. For example, it is used as a natural coloring agent for some kinds of mustard, and it is an ingredient in curry powder. Thai government prioritized turmeric as product champion to ramp up to export in 2023-2027.[1]

Concerning parameter is heavy metal, namely cadmium (Cd) and lead (Pb), which are mentioned the maximum level to allow in EU. Commission Regulation (EU) 2021/1323: fresh herb max 0.2 mg/kg and food supplements max 1.0 mg/kg for Cd[2] and Commission Regulation (EU) 2021/1317: fresh turmeric max 0.8 mg/kg and Food supplements max 3.0 mg/kg for Pb.[3]

To support the trade of the country's herbal products, the quality assurance of the product is necessary especially quality control of the product. Since, "there is no quality without measurement" and "measured once, accepted everywhere", therefore, measure at any place, the results must be comparable. Certified reference material (CRM) in analytical chemistry plays a crucial role for quality control purposes. It is recognized and recommended by international, national and professional organizations worldwide.

TRM-F-2007 (elements in turmeric powder (*Curcuma longa*)) was initiated by National Institute of Metrology (Thailand) (NIMT) for the analysis of key elements. It was developed under the trade name of Thailand Reference Material (TRM) due to the unavailability of matrix matched CRMs in our country. ISO 17034, ISO Guide 35 and ISO/IEC 17025 quality systems are implemented to control quality of the TRM.

2. Materials and Methods

2.1 Materials

Material processing of turmeric (Curcuma longa) powder was purchase locally.

65 % Nitric acid suprapur grade was purchased from National Institute of Metrology (Thailand) and hydrofluoric acid, 40 % HF suprapur grade from Merck KgaA (Darmstadt, Germany) were used to digest the sample. Milli-Q water (from Millipore Water Purification System (Milli-Q IQ 7000) was used to prepare all solutions.

Primary standard solutions were from National Institute of Standards and Technology (Gaithersburg, USA), NIST standard solutions;

total arsenic (As, SRM3103a), calcium (Ca, SRM3109a), cadmium (Cd, SRM3108), copper (Cu, SRM3114), chromium (Cr, SRM3112a), iron (Fe, SRM3126a), mercury (Hg, SRM3133), potassium (K, SRM 3141a), magnesium (Mg, SRM3132), manganese (Mn, SRM3132), sodium (Na, SRM3152a), nickel (Ni, SRM3136), phosphorus (P, SRM3139a), lead (Pb, SRM3128), zinc (Zn, SRM3168a).
Plant-matrix CRMS, namely SRM1570a (spinach leave CRM) and SRM1575a (pine needles CRM) were used as QC sample to ensure validity of the measurements.

All plastic stuff such as amber bottle and sample tube were soaked in 10% HNO_3 then rinse with plenty of Mill-Q water before use.

2.2 Equipment

List of equipment is divided to material preparation and characterization in Table 1.

Table 1. Equipment list

Material preparation	Model/manufacturers
sieve shaker	AS 300 control, Retsch
sample divider	PT 100, Retsch
oven	KBF-S 240, Binder
Characterization	**Model/manufacturers**
ICP-SFMS	Element XR, Thermo Fisher Scientific
ICP-QMS	8800 Triple Quad, Agilent
ICP-OES	Avio500, PerkinElmer
microwave digestion	Multiwave 7000, AntonPaar
clean room	Class 10,000
analytical balance	XP205, Metter Toledo
oven	UF110, Memmert

2.3 Preparation of candidate reference material

Approximately 14 kg of fine turmeric powder was purchased to be used as a candidate reference material. Detail of the material preparation is described in Figure 1.
All bottles were labeled, cleaned and sealed with thermo-plastic seal. Finally, 339 bottles (~30 g each in 125-mL amber plastic) were obtained and called that “the candidate reference material”. The candidate reference materials were then irradiated by gamma radiation in order to minimize microbial activities for prolongs stability.

2.4 Sample preparation

Turmeric powder 0.25 g was accurately weighted into PTFE-TFM microwave vessels and carefully added 5 mL of concentrated HNO_3 and 0.2 mL of HF. After that, the sample was digested (ramping it up to 250 ^oC in 30 minutes and holding it for 15 minutes).

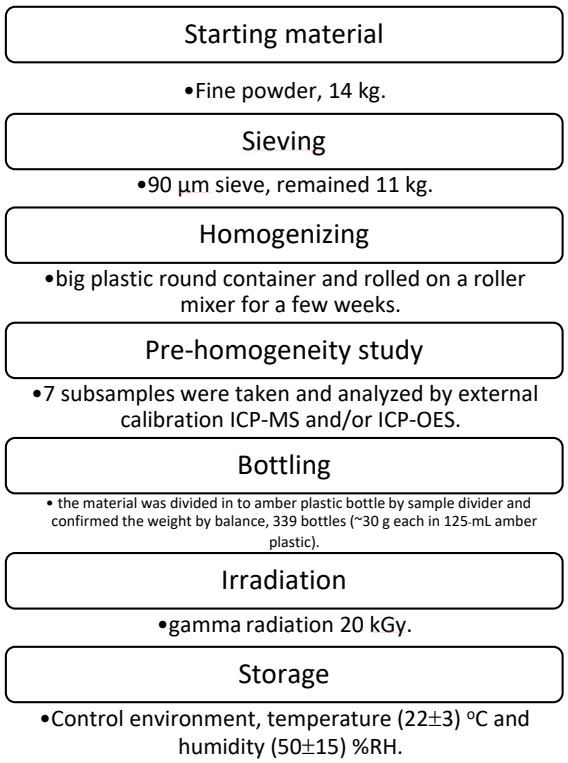

Figure 1. Flowchart of candidate reference material production.

When the digestion completed, the sample solutions were cold down to 40 ^oC before diluted with Milli-Q water under fume hood and control environment.

2.5 Homogeneity study

To be a representative number of packaged units of the substance, the number of 11 bottles was chosen for homogeneity study (see ISO Guide 35:2017, 7.4.1).[4]

Homogeneity testing for all element mass fraction in the candidate material was carried out in duplicate in a single measurement run by external calibration with internal standard. For total As, Cr, Cu, Ni, Pb, Zn were measured by ICP-MS, while Ca, Fe, K, Mg, Mn, Na, P, Zn were measured by ICP-OES.

2.6 Stability study

Short-term stability: Due to transportation, especially in summer time, temperatures up to 45°C can be reached and stability under these conditions must be demonstrated. Therefore, room temperature and 45 ^oC were selected to study short-term stability for three weeks. The selected bottles of the first two bottles were kept in reference temperature 4 ^oC. Six bottles represented for room temperature for 1, 2 and 3 weeks, respectively, while another six bottles represented 45 ^oC for the same period. Isochronous scheme was selected and at the end all the bottles were stored at 4 ^oC before measurement. After that period, all samples were

analyzed under repeatability condition, to minimize the parameters affecting from day-to-day variation.

Long-term stability: Candidate reference materials 12 bottles were chosen using a random stratified approach. The stability of the candidate reference material was tested by storing the candidate reference material at 25 °C for a period of 12 months. Two bottles were taken at every three months (0, 1, 3, 6, 9 and 12 months), all bottles were then stored in 4 °C. After that period, all samples are analyzed under repeatability condition by duplicate.

3. Results & Discussion

3.1 Homogeneity testing

Check for sufficient homogeneity, it need to be confirmed that the variation within and between units is sufficiently small for intended use of the material. The maximum heterogeneity, was determined the between-unit and within-unit standard deviation.

Between-unit variability (s_{bb}) expressed as a relative standard deviation is given by the following equation[1]:

$$s^2_{bb} = max(\frac{M_{between} - M_{within}}{n_0},\ 0) \quad \text{equation 1}$$

where $M_{between}$ = between group mean square
M_{within} = within group mean square
n_0 = replicate unit

Within-unit variability (s_{wb}), or method repeatability (s_r), expressed as a relative standard deviation can be computed as:

$$s_r = \sqrt{M_{within}} \quad \text{equation 2}$$

In conclusion, no outliers for all target elements was found and the distribution of them for certification can be considered as homogeneous within acceptable uncertainties, except Mn and Na. ANOVA with single factor test shows F_{cal} obtained for Mn and Na are larger than $F_{crit,}$, this can happen even pre-homogeneity was studied prior bottling. Therefore, Mn and Na are reported as information values instead of certified values.

3.2 Stability testing

Short-term stability: Mass fraction of all elements was measured with ICP-MS and ICP-OES in duplicate analysis. Grubbs test was performed to detect potentially outlying results. For the simple case, a student *t* test for slope significantly different from zero was performed using the *t* statistic in equation 3.

$$t_{b_1} = \frac{|b_1|}{s(b_1)} \quad \text{equation 3}$$

The calculated results were then compared with the critical value of Student's *t* for *n*-2 degrees of freedom at 95 % level of confidence. If the calculated test statistic (t_{b1}) exceeds the critical value, the slope is considered to be significantly different from zero.
For all elements, no outlying measurements and no significant degradation in mass fraction during dispatch even at 45 °C. Therefore, the material can be transported at ambient conditions without special precautions.

Long-term stability: Mass fraction of all elements was measured with ICP-MS and ICP-OES in duplicate analysis. No outlying data points were found. The *t*-test for slope significantly different from zero was used in the same manner as short term stability study. Evaluation results of long-term stability study found no trend observed in the period of 12 months as mentioned earlier.

Nevertheless, post-certification stability will be monitored out during the period in which the TRM is in service.

3.3 Moisture content

Dry mass correction is required when the material is analyzed. A minimum of three separate portions (about 0.5 g each) of the sample was placed in the oven at 95 °C for 16 hours. Each sample must be evenly spread (less than 1 cm thick) and immediately placed in a desiccator when it is done. Samples were then weighed after allowing a minimum of an hour to establish temperature equilibrium. The average observed moisture content was 9.59 %.

3.4 Certification

Characterization: Mass fraction of 15 elements in turmeric powder was quantified using 6 analytical methods. The analytical methods used for the RM characterization listed in Table 2.

Table 2. Analytical method performed characterization.

Analytical method*	Element
IDMS[5]with ICP-SFMS and / or ICP-QMS	Ca, Cd, Cu, Fe, Hg, Ni, Pb, Zn
GSA[6] with ICP-SFM or ICP-QMS	Total As, Cd, Cu, Fe, Mn, Ni, Pb, Zn
GSA with ICP-OES	Ca, Fe, K, Mg, Mn, Na, P, Zn
ExCal[7] with ICP-QMS	Total As, Cd, Cu, Fe, Mn, Ni, Pb, Zn
ExCal with ICP-OES	Ca, Fe, K, Mg, Mn, Na, P, Zn

**IDMS = isotope dilution mass spectrometry, GSA = gravimetric standard addition, ExCal = external calibration*

NIMT had consistently participated and showed the capabilities in international inter-laboratory comparisons with relevant scopes as follows;

- 2007 CCQM-P97 and APMP.QM-P10 Cadmium and lead in herb.
- 2008 APMP.QM-S3 Cd in rice powder.
- 2011 CCQM-K89 Trace and Essential Elements in *Herba Ecliptae*.
- 2015 CCQM-K108.2014 : Determination of arsenic species and total arsenic in brown rice flour.

Based on IDMS and GSA, satisfactory results were accepted for claiming calibration and measurement capability (CMC) on International Bureau of Weight and Measures (BIPM) website.[8]

This material was characterized by using several analytical methods. For example, Zn was characterized by 5 analytical methods and the measurement results show in Figure 2. All measurement results were compatible therefore, a weighting approach was employed and calculated based on equation 7.

$$y_{char} = \sum_{i=1}^{p} w_i x_i \Big/ \sum_{i=1}^{p} w_i \qquad \text{equation 7}$$

In equation 7, y_{char} is the weighted mean; w_i, the weight proportional to $(1/u_i)$, where u_i is the reported standard uncertainty for the value x_i; x_i, mean value obtained by method *i*. The value of y_{char} (Zn) is 21.7 mg/kg.

Measurement uncertainty: ISO Guide 35 was used to estimate measurement uncertainty. This is well known that homogeneity, stability and characterization are three crucial characteristics of any certified reference material. Therefore, the model used for evaluating the uncertainty is based on main components.

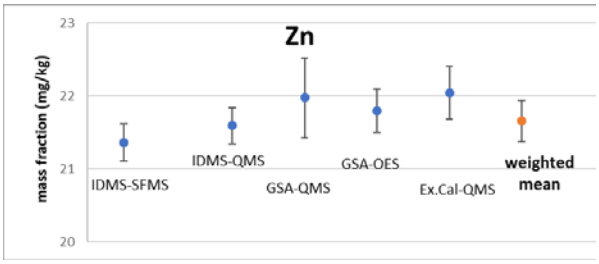

Figure 2. Characterization for Zn in turmeric powder reference material. The error bars are standard uncertainty.

The combined standard uncertainty of the certified value (u_{CRM}) includes contributions from the homogeneity (u_{bb}), long-term storage (u_{lts}) and the characterization (u_{char}) study. The relative combined standard uncertainty is calculated according to following equation:

$$u_{CRM} = \sqrt{u_{bb}^2 + u_{lts}^2 + u_{char}^2} \qquad \text{equation 5}$$

The expanded uncertainty (U) is given by equation below, where a coverage factor (*k*) is 2.

$$U_{CRM} = k * u_{cRM} \qquad \text{equation 6}$$

Table 3 summaries the individual standard uncertainty contributions and the resulting expanded uncertainties as well as the certified values and their uncertainties for turmeric powder TRM.

Four elements (Cr, Hg, Mn and Na) are reported information values as a predicted range due to inhomogeneity of the material and incompatibility of measurement results among analytical techniques.

Shelf life: Prediction of shelf life for estimation of storage lifetime ("shelf-life") could be predicted by confidence interval for the regression line. It also supported by experiences and literature publication. This TRM will be monitored throughout its lifetime. Therefore, the shelf-life of this material is more than 36 months based on the convergence of confidence interval and uncertainty.

3.5 Metrological traceability

Metrological traceability is property of a measurement result whereby the result can be linked to a reference through a documented, unbroken chain of calibrations, each contributing to the overall measurement uncertainty.[9] Regarding the reliability of measurement results metrological traceability is mandatory and must be illustrated clearly. When an unbroken chain of calibrations was established, and thus traceability

Table 3. Certified values and their measurement uncertainties. Data set is in mg/kg unit (k =2).

Elements	Property values	Standard uncertainty			Combined uncertainty	Expanded uncertainty	Certified values
		u_{homo}	u_{lts}	u_{char}			
As	0.398	0.009	0.013	0.007	0.017	0.040	0.398 ± 0.040
Ca	1,379	21.5	13.5	14.6	29.3	59	1,379 ± 59
Cd	0.170	0.002	0.001	0.002	0.003	0.006	0.170 ± 0.006
Cu	5.46	0.09	0.03	0.04	0.11	0.22	5.46 ± 0.22
Fe	534	10.9	1.2	4.0	11.63	24	534 ± 24
K	27,541	309	230	367	532	1,064	27,500 ± 1,100
Mg	2,444	9.9	18	22	30.3	61	2,444 ± 61
Ni	2.67	0.04	0.05	0.03	0.07	0.14	2.67 ± 0.14
P	2,914	16.2	56.8	48.7	76.5	154	2,910 ±160
Pb	0.903	0.016	0.018	0.007	0.025	0.060	0.903 ± 0.060
Zn	21.7	0.35	0.48	0.14	0.611	1.300	21.7 ± 1.3

to an international standard, preferably to the SI, the measurement result is considered reliable, acceptable and comparable.

The mass fractions of elements, w_x, in the TRM-F-2007 are established by an unbroken chain of comparisons, each accompanied by an uncertainty budget. Figure 3 showing the traceability from *kg*, down to the final mass fraction. In the boxes at the bottom line the mass fraction of element in the TRM and their measurement uncertainty are presented. Both are assigned by measurement procedure 3, 4 and 5 which employs gravimetrically prepared using calibrated analytical balances and quantified by IDMS, GSA and external calibration strategy by ICP-MS. External calibrators (NIST SRMs) are used to calibrate the instruments, which for this exact mass fraction of elements were obtained by primary measurement procedure 1 and 2 at NIST. With the same concept, other elements which are not characterize by IDMS or ICP-MS, it can be applied.

4. Conclusion

TRM-F-2007 is homogeneous and stable at temperature 45 ^{o}C for three weeks and it is stable at room temperature at least three years. Characterization of the elements requires at least two analytical methods. Eleven elements including; As, Ca, Cd, Cu, Fe, K, Mg, Ni, P, Pb and Zn are certified by weighting method from 2 – 5 analytical methods to provide accuracy and measurement uncertainty while four elements (Cr, Hg, Mn and Na) are mentioned as information value.

The entire production process is performed to comply with the quality system ISO 17034, ISO Guide 35 and ISO/IEC 17025. Therefore, TRM-F-2007 is reliable and traceable to SI units through unbroken chain. This TRM is suitable for quality control purposes such as method validation, and quality control sample.

References

1. National Master Plan Book Concerning the Development of Thai Herbs, Issue 1, 2017-2021, 2016.
2. Commission Regulation (EU) 2021/1323, 2021.
3. Commission Regulation (EU) 2021/1317, 2021.
4. SO Guide 35:2017 Reference Materials Guidance for Characterization and Assessment of Homogeneity and Stability, 2017.
5. Calibration Procedure: Isotope Dilution Mass Spectrometry Analysis, Inorganic Analysis Laboratory, NIMT, 2021.
6. Calibration Procedure: Gravimetric Standard Addition Analysis, Inorganic Analysis Laboratory, NIMT, 2021.
7. Calibration Procedure: External Calibration Analysis, Inorganic Analysis Laboratory, NIMT, 2021.
8. Calibration and Measurement Capabilities, 2023. https://www.bipm.org/kcdb/cmc (accessed 2023-12-22).
9. International Vocabulary of Metrology – Basic and General Concepts and Associated Terms (VIM), 2012.

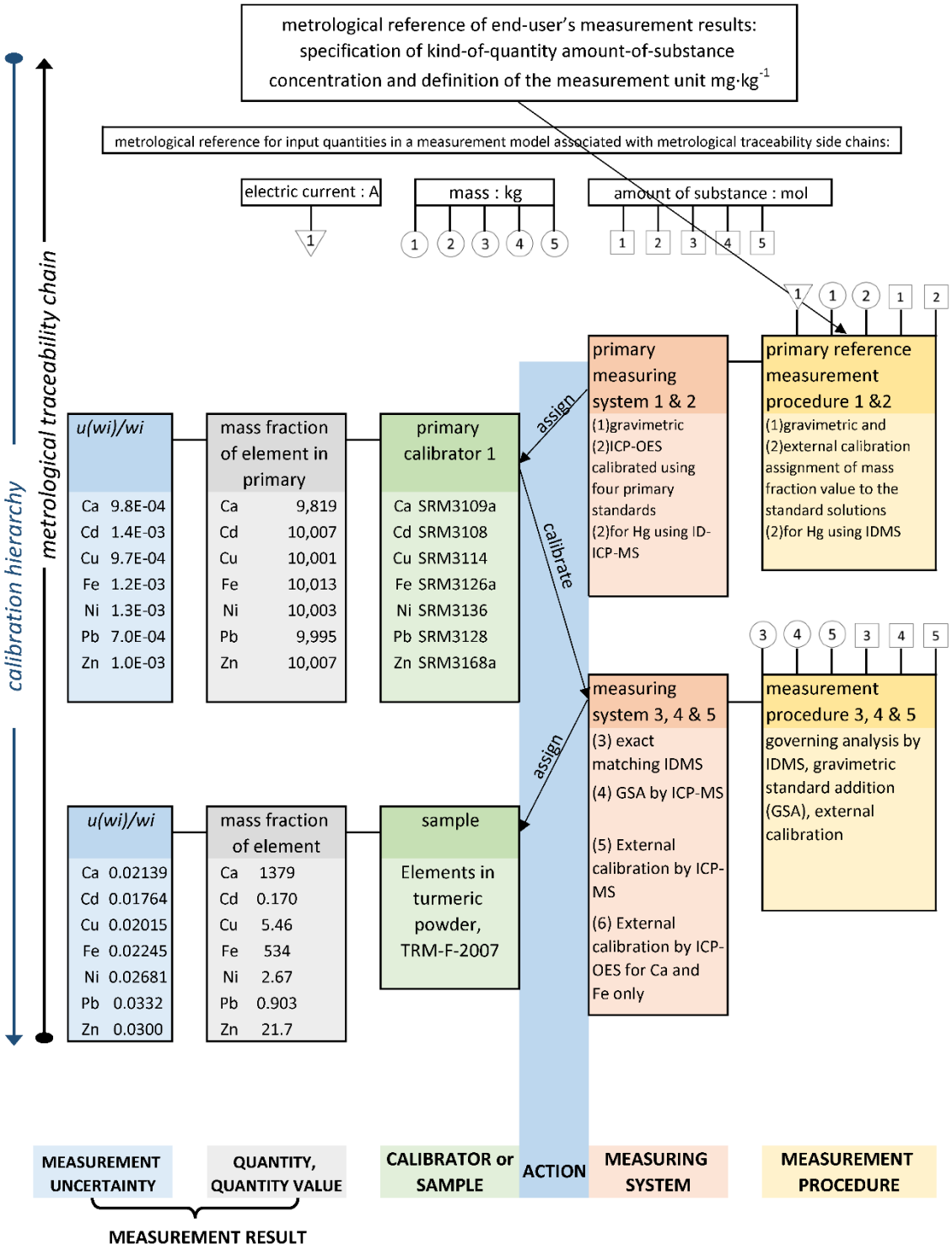

Figure 3. Metrological traceability chain for Ca, Cd, Cu, Fe, Ni, Pb and Zn.

The removal of green and red reactive dyes by photolysis, oxidation and photooxidation processes using a simple UV reactor

Orawan Kritsunankul[1]*, Piyatida Kamlueng[1], Wanwisa Jaisarn[1], Tamisa Maporn[1], and Chanyud Kritsunankul[2]

[1]*Department of Chemistry, Faculty of Science, Naresuan University, Phitsanulok 65000, Thailand*
[2]*Department of Natural Resources and Environment, Faculty of Agriculture Natural Resources and Environment, Naresuan University, Phitsanulok 65000, Thailand*

**E-mail: orawant@nu.ac.th*

Abstract:

This research investigates the efficiency of advanced oxidation processes for the removal of green and red reactive dyes. These processes are photolysis (with only UV lamp), oxidation (with only potassium persulfate) and photooxidation (with UV lamp plus potassium persulfate) processes. All processes were done in a simple UV reactor. Firstly, the absorption spectra and linear calibration graphs of both reactive dyes were carried out using UV-Visible spectrophotometer. After that the conditions of treatment processes were examined such as flow rates, types of tubing for roll round the UV lamp, sample volumes, UV lamp powers, potassium persulfate concentrations and dye concentrations. Under optimum conditions, a 1.13±0.06 mL/min of flow rate, a PTFE tubing (200 cm length, 0.86 mm i.d.), a 10 mL of sample volume, a 36 W of UV power, a 3.0 %w/v of potassium persulfate and a 350 mg/L of green and red dye were selected. From the results, the photolysis process of green and red dyes achieved 100% dye removal in 80 mins, respectively. For the oxidation process, a green dye was removed 35.95% of the dye in 90 min, while a red dye was removed 18.33% of the dye in 60 min. And for the photooxidation process, green and red dyes achieved 100% dye removal in 25 mins, respectively. Results also revealed that the photooxidation process was higher efficiency for green and red removals than the photolysis and oxidation processes, respectively.

1. Introduction

Generally, the formula structure of reactive dyes consists of four parts; solubilizing, chromogen, bridging and reactive groups.[1] This reactive group forms covalent bond with the cellulosic fiber, acting as an integral part of the fiber. The covalent bond is established between the dye molecules and the terminal –OH (hydroxyl) group of cellulosic fibers or between the dye molecules and the terminal $–NH_2$ (amino) group of nylon or wool fibers.[2] In contemporary chemistry, reactive dyes are extensively used for dyeing cellulosic fibers in the textile industry due to their favorable properties. These include good all-around characteristics such as water solubility, ease and variety of applications, availability of different shades, brightness of color shades, and excellent wash and light fastness.[2] Textile dyes, however, are toxic and often discharged as effluent into aquatic environments. To regulate wastewater quality, the Ministry of Industry in Thailand assigns and assesses the color discharge limit, set at less than 300 American Dye Manufacturers (ADMI) units. Non-pretreated effluent can have significant negative impacts on living microorganisms. Therefore, it is crucial to effectively treat dye-containing wastewater using eco-friendly methods.[3]

Various technologies and methodologies have been reported for the treatment of textile dye-containing wastewater, particularly reactive dyes. These processes involved both biological.[4,5] and chemical[6-8] systems. However, some of these processes are associated with disadvantages such as complexity and tedious techniques. Consequently, advanced oxidation processes (AOPs) like photolysis, oxidation, photooxidation, Fenton-based processes, and photocatalytic oxidation have been developed to overcome these challenges. Many AOPs attempt to utilize dissolved oxidants for the treatment of textile wastewater, including ozone (O_3), hydrogen peroxide (H_2O_2) and potassium persulfate ($K_2S_2O_8$). These AOPs, in conjunction with oxidants, can be accelerated to generate strong oxidizing hydroxyl radicals (•OH) with relatively high oxidation activity, facilitating the degradation of dyes.[6-10]

In this work, the photolysis (using only UV), oxidation (using only an oxidant) and photooxidation (using UV plus oxidant) processes were proposed to investigate the color removal of green and red reactive dyes in water samples using a simple UV reactor. This UV reactor ensure simple operation and safe equipment usage.

2. Materials and Methods

2.1 Materials

All chemicals used were of analytical reagent grade, excepted for the reactive dyes. Double distilled water (Elgastat Maxima, Elga, England) was employed to prepare all aqueous solutions. Stock standard solutions of a 10000 mg/L reactive green 19 dye (INDAFIX, KTB Textil) , a 10000 mg/L reactive red 195 dye (INDAFIX, KTB Textil), and a 5.0 %w/v potassium persulfate ($K_2S_2O_8$, Ajex Finechem) were prepared in water. Working standard solutions for the two dyes and $K_2S_2O_8$ were freshly prepared by diluting the stock solution with water.

A simple UV reactor system (Figure 1) consists of a vertically placed UV lamp (rolled round with Teflon or PTFE tubing (Cole Parmer 3/32" Natural PTFE Masterflex Tubing, USA) and housed in a light-tight with fan-vented box (35 cm width x 50 cm length x 15 cm height) and a peristaltic pump (Cole-Parmer Masterflex C/L 77120-62, USA). This UV rector was a homemade system and constructed by Chanyud Kritsunankul. Each dye solution was contained in a 50 mL centrifuge tube (polypropylene for the tube and HDPE for the cap). Two UV lamps of 10 and 36 W (emitted at 254 nm, Philips) were utilized in this work. A UV-Visible spectrophotometer (Specord Series, Analytik-Jena, Germany) was employed to study the absorption spectra, measure absorbance and analyze the color removal.

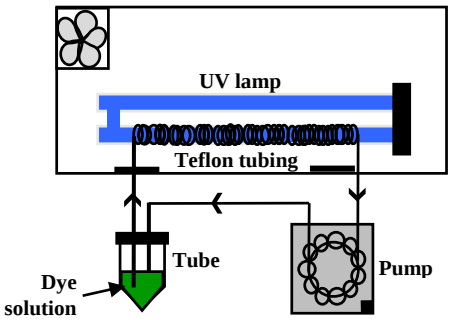

Figure 1. A simple UV reactor system.

2.2 Absorption spectra and linear calibration graph studies

The absorption spectra of the 200 mg/L green and red dyes, respectively, were recorded in the wavelength of 190-1100 nm with a scan rate of 50 nm/s. Standard solutions of 10, 20, 40, 60, 80, 100, 200, 400, 600, 800 and 1000 mg/L for both green and red dyes were prepared to study the linear range of calibration graphs.

2.3 Procedure of the treatment process

The photolysis (using only UV lamp), oxidation (using only $K_2S_2O_8$) and photooxidation (combining UV lamp with $K_2S_2O_8$) treatment processes were conducted in a simple UV reactor under a solution recirculation mode with a constant flowrate**.** For each treatment process, the UV lamp was turned on, excepted for the oxidation process. A 350 mg/L of both green and red dyes, along with 10 mL of each dye solution in centrifuge tube, was transferred to a Teflon tubing under a constant treatment time**.** After the desired treatment time, dye concentrations were measured spectro-photometrically at 620 nm and 540 nm for green and red dyes, respectively. The treatment efficiencies of dye color (%Dye removal) were calculated using the following equation**:**

$$\text{Dye removal (\%)} = [(C_o - C_t)/C_o] \times 100$$

Where C_o and C_t represent the dye color concentrations before and after the treatment processes, respectively**.**

3. Results & Discussion

3.1 The study of absorption spectra and linear calibration graphs

The absorption spectra (in the range of 400-800 nm) for green and red dyes are shown in Figure 2. It was evident that the maximum absorptions for green and red dyes occurred at 620 and 540 nm, respectively. The linear calibration graphs, summarized in Table 1, were established in the range of 10-400 mg/L for green dye and 10-600 mg/L for red dye.

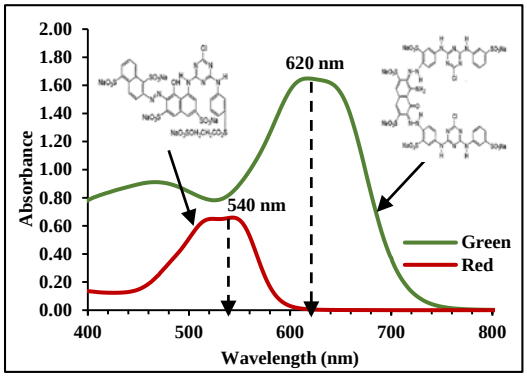

Figure 2. Absorption spectra of 200 mg/L solutions of green and red dyes.

Table 1. Calibration data for determining green and red dyes using the UV-Visible Spectrophotometric method.

Dyes	Range (mg/L)	Linear equation (y = ax + b)	r^2	LOD [a]	LOQ [a]
Green	10-400	y = 0.0074x+0.0570	0.9966	0.17	0.57
Red	10-600	y = 0.0031x+0.0129	0.9988	0.04	0.13

[a] LOD and LOQ were calculated as LOD (mg/L) = 3S and LOQ (mg/L) = 10S, respectively, where S represents the standard deviation of the y-intercept).

3.2 Effect of UV lamp power, flow rate, sample volume, and types of tubing using photooxidation process

To enhance and evaluate treatment efficiency by increasing hydroxy radical production using the designed UV reactor, the effects of UV lamp powers (10 and 36 W), flow rates (0.53±0.05, 1.13±0.06 and 1.67±0.05 mL/min), types of tubing (Teflon, Tygon and no tubing used), and dye sample volumes (10, 25 and 50 mL) in a centrifuge tube were initially investigated through the photooxidation process. For this investigation, a starting concentration of 350 mg/L for both green and red dyes, a 10 mL of dye solution in centrifuge tube, a 0.5 %w/v of $K_2S_2O_8$ and a 10 min of treatment time were selected throughout the experiment.

In Figure 3(a), after treatment process, it was resulted that the dye color reduction at 36 W was higher than at 10 W. At 10 W, the concentrations of green and red dyes were reduced to 138.7±0.1 and 125.1±0.2 mg/L, respectively. Meanwhile, at the 36 W, the concentrations of green and red dyes were reduced to 51.6±0.1 and 117.7±0.2 mg/L, respectively. The results indicate that at higher UV power levels, the expected production of hydroxyl radicals is higher, resulting in a greater extent of color reduction. Based on the obtained results, a power level of 36 W was selected for further experiments.

In Figure 3(b), it was observed that a flow rate of 1.67±0.05 mL/min was resulted in a higher and faster color reduction compared to 1.13±0.06 mL/min and 0.53±0.05 mL/min, respectively. This result can be attributed to the high homogenized solution and enhanced contact between color molecules and hydroxy radicals. The concentrations of green dye were found to be reduced to 137.8±0.3, 51.6±0.1 and 18.7±0.1 mg/L at flow rates of 0.53±0.05, 1.13±0.06 and 1.67±0.05 mL/min, respectively. Similarly, for the red dye, the concentrations were reduced to 163.6±0.3, 117.7±0.2 and 85.1±0.2 mg/L at flow rates of 0.53±0.05, 1.13±0.06, and 1.67±0.05 mL/min, respectively. Due to the convenience of an absorbance detection and achieving acceptable dye color reduction, a flow rate of 1.13±0.06 mL/min was chosen for further experiments.

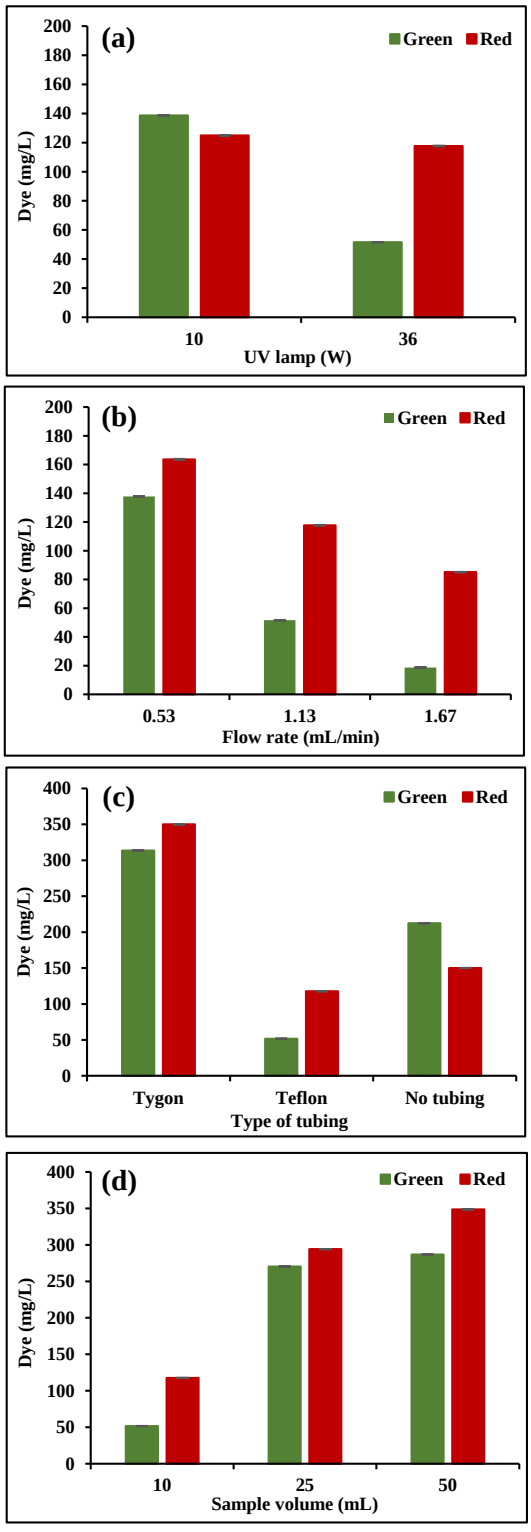

Figure 3. All results related to the effect of (a) UV lamp power, (b) flow rate, (c) tubing type and (d) sample volume in a centrifuge tube were recorded after treatment using the photooxidation process. Meanwhile, a 350 mg/L for both green and red dyes was used for all studies.

Figure 3(c) illustrates the impact of available tubing type on color reduction under varying thickness. It was observed that Teflon tubing (200 cm length, 0.86 mm i.d. and 0.2 mm thickness) resulted in a higher color reduction compared to Tygon tubing (200 cm length, 0.89 mm i.d. and 1.1 mm thickness) and no tubing (indicating a standing glass vessel placed next to a UV lamp). With Teflon tubing, the removal of green and red dyes was reduced to 51.6±0.1 and 117.7±0.2 mg/L, respectively. Under the no tubing condition, the concentrations of green and red dyes were reduced to 212.3±0.1 and 150.0±0.1 mg/L, respectively. In contrast, Tygon tubing was resulted in a lower color reduction, with values of 313.5±0.1 mg/L for the green dye and 350.1±0.1 mg/L for the red dye. Therefore, Teflon tubing was selected for its superior color reduction.

Figure 3(d) presents the results of the sample volume effect in a centrifuge tube. It was resulted that a sample volume of 10 mL (resulting in green and red dyes reduced to 51.6±0.1 and 117.7±0.2 mg/L, respectively) was exhibited a higher color reduction compared to 25 mL (with green and red dyes reduced to 270.4±0.1 and 294.1±0.2 mg/L) and 50 mL (with green and red dyes reduced to 286.7±0.1 and 348.6±0.2 mg/L), respectively. Therefore, a sample volume of 10 mL was selected for all further experiments.

3.3 Effect of treatment times using photolysis, oxidation and photooxidation processes

The photolysis, oxidation and photooxidation processes were employed to degrade 350 mg/L of green and 350 mg/L of red dye pollutants and determine dye removal efficiencies (%) in water samples. These processes primarily involve the generation of hydroxyl radicals to oxidize dye compounds. Consequently, the study necessitated an investigation into the effects of treatment times and $K_2S_2O_8$ concentrations (0.5, 1.0, 2.0, and 3.0 %w/v). The results are presented in Figure 4(a) for green dye and Figure 4(b) for red dye. In the photolysis process using only 36 W UV lamp, both green and red dyes were achieved 100% dye removal in 80 mins of treatment time, respectively. In the oxidation process using only 3.0 %w/v $K_2S_2O_8$, the removal efficiency was 35.95% for green dye in 90 mins and 18.33% for red dye in 60 mins. For the photooxidation process using 36 W UV lamp with different concentrations of $K_2S_2O_8$, both green and red dyes were achieved 100% dye removal in 40 mins for 0.5 %w/v $K_2S_2O_8$, 35 mins for 1.0 %w/v $K_2S_2O_8$, 30 mins for 2.0 %w/v $K_2S_2O_8$, and 25 mins for 3.0 %w/v $K_2S_2O_8$.

It could be concluded that a higher concentration of $K_2S_2O_8$ resulted in increased degradation of dye compounds under both the photolysis and photooxidation processes. Additionally, the results demonstrated that the photooxidation process exhibited faster treatment with reduced treatment time and higher efficiency for the removal of green and red dyes compared to the photolysis and oxidation processes, respectively.

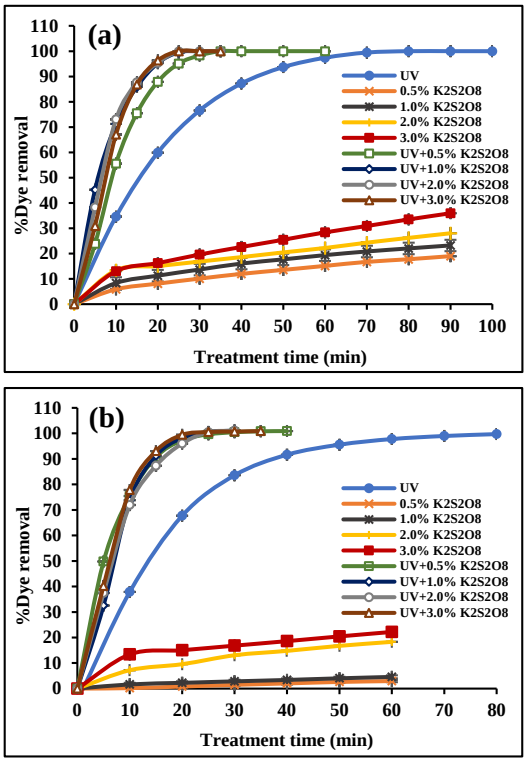

Figure 4. The effect of treatment times and $K_2S_2O_8$ concentrations on the treatment efficiency was represented as % dye removal for (a) 350 mg/L green dye and (b) 350 mg/L red dye.

3.4 Application of photooxidation process to synthetic samples

Under the condition of the highest %dye removal, the proposed photooxidation process (36 W UV + 3.0 %w/v $K_2S_2O_8$) was applied for the removal of 350 mg/L of green and red dyes prepared in filtered river water. The results were also compared with the preparation of two dyes in distilled water and are shown in Figure 5. For the two dyes in distilled water, both green and red dyes were achieved 100% dye removal in 25 mins, respectively. However, in filtered river water, both green and red dyes were achieved 100% dye removal in 50 mins, respectively. This difference may be attributed to higher concentrations of cations, anions, and other compounds found in the river, which could interfere with the degradation of

both green and red dyes. These factors will be investigated in further studies.

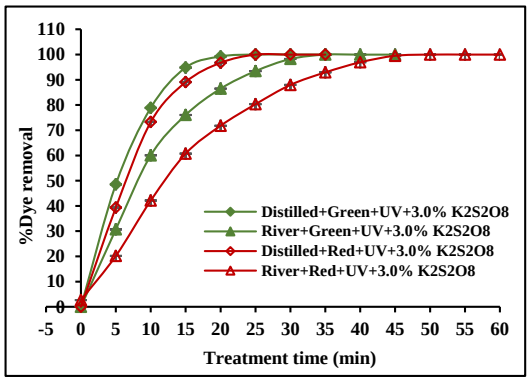

Figure 5. Comparison of the results for green and red dye removal in synthetic samples (spiked in distilled and filtered river water) using the proposed photooxidation process (36 W UV + 3.0 %w/v $K_2S_2O_8$).

4. Conclusion

This research aimed to investigate the photolysis, oxidation and photooxidation processes using a simple UV reactor for color removal from 350 mg/L green and 350 mg/L red reactive dyes in a synthetic sample. The UV reactor was demonstrated successful use, simple operation and safety in equipment usage. It can be concluded that the photooxidation process (using 36 W UV lamp + 3.0 %w/v $K_2S_2O_8$) exhibited the highest treatment efficiency and rapid color removal for both green and red reactive dyes compared to the photolysis process (using 36 W of UV lamp only) and the oxidation process (using 3.0 %w/v $K_2S_2O_8$), respectively. Despite these three proposed processes achieving 100% color removal with different treatment times, they could serve as alternative treatment processes for the degradation of green and red reactive dyes. Nevertheless, photolysis holds a distinct advantage as it is considered a chemical-free AOP (Advanced Oxidation Process) for the degradation of reactive dyes [3-7].

Acknowledgements

The authors would like to express their gratitude to the Department of Chemistry, Faculty of Science, Naresuan University for providing partial support for this research.

References

1. Chattopadhyay, D. P. Fundamental Principles of Reactive Dyeing, In *Handbook of Textile and Industrial Dyeing: Principles, Processes and Types of Dyes*; Clark M., Ed.; Volume 1 Woodhead Publishing Limited, 2011; pp 150-183.
2. Shang, S.M., Reactive Dye and Dyeing Technology, In *Process Control in Textile Manufacturing*; Majumdar A., Das A., Alagirusamy R., Kothari, V.K., Ed.; Woodhead Publishing Limited, 2013; pp 475-492.
3. Al-Tohamy, R.; Ali, S.S.; Li, F.; Okasha, K.M.; Mahmoud, Y.A.-G.; Elsamahy, T.; Jiao, H.; Fu, Y.; Sun, J. Ecotoxicology and Environmental Safety. **2022**, *231*, 113160, 1-17.
4. Aksu, Z. Process Biochem. **2005**, *40*, 997-1026.
5. Gül, U.D. Water SA. **2013**, *39(5)*, 593-598.
6. Xu, X.R.; Li, H.B.; Wang, W.H.; Gu, J.D. Chemosphere. **2005**, *59*, 893-898.
7. Bilgi, S.; Demir, C. Dyes Pigm. **2005**, *66*, 69-76.
8. Rezaee, A.; Ghaneian, M.T.; Khavanin, A.; Hashemian, S.J.; Moussavi, G.; Ghanizadeh, G.; Hajizadeh, E. Iran J Environ. Health. Sci. Eng. **2008**, *5(2)*, 95-100.
9. Haddad, F.A.; Moussavi, G.; Moradi, M.J. Water Process Engineering. **2019**, *27*, 120-125.
10. Ayare, S.D.; Gogate, P.R. Sep. Purif. Technol. **2020**, *233*, 1-10.

Ethanol steam reforming using Ni catalyst supported on ZrO_2 –doped Al_2O_3 with magnetic inducement

Marucheth Thongtheppairoj, Pattarika Tarawan, Sasimas Katanyutanon, and Pisanu Toochinda*

School of Bio-Chemical Engineering and Technology (BCET), Sirindhorn International Institute of Technology (SIIT), Thammasat University, Pathum Thani 12120, Thailand

**E-mail: pisanu@siit.tu.ac.th*

Abstract:

Nickel catalysts are used to enhance catalytic activity in ethanol steam reforming; however, they suffer from deactivation. It has been shown that partially doping alumina support with ZrO_2 can improve the stability, adjust the acidity, and influence catalyst adsorption. The dispersion of the dopant in the support is essential to ensure homogeneity of the dopant effect. The application of magnetic inducement has been shown to affect the dispersion of cerium in alumina support. Therefore, in this study, magnetic fields were used during the preparation of ZrO_2-doped-Al_2O_3 to influence ZrO_2 dopant in the support. It was found that the support prepared between same poles of magnets showed higher catalytic activity at 600 °C for ethanol steam reforming. This can be attributed to the decrease in the number of acid sites which affects catalyst deactivation due to coke formation. Further investigation on coke formation, the dispersion of ZrO_2, and the lattice structure of the alumina support will be required.

1. Introduction

The quest for clean and sustainable energy sources has ignited research and innovation in various fields. One of the main challenges in this game is hydrogen production, a clean energy carrier with huge potential.[1] Among the methods explored, ethanol steam reforming (ESR) is one of the promising ways for hydrogen production. ESR involves the conversion of ethanol, a renewable biofuel, into hydrogen and carbon dioxide through a catalytic process.[2] This approach offers the advantages of utilizing a sustainable feedstock while producing high-purity hydrogen for various applications, including fuel cells and industrial processes.[2] The reaction mechanism of ethanol steam reforming primarily involves the catalytic decomposition of ethanol in the presence of steam. The process takes place at elevated temperatures, typically ranging from 500°C to 700°C and is catalyzed by metal-based catalysts such as nickel or copper.[1-3] The catalyst facilitates the breaking of the carbon-carbon and carbon-hydrogen bonds present in ethanol, leading to the production of hydrogen and carbon monoxide as the primary products. The operating conditions, including temperature, pressure, and composition of the reactants, play an important role in the efficiency of ethanol steam reforming. Higher temperatures promote better ethanol conversion and higher hydrogen production rates. However, excessive temperatures can lead to catalyst deactivation and the formation of undesirable by-products. Similarly, the steam-to-ethanol ratio should be carefully controlled to maintain the optimal balance between water gas shift reactions and the steam reforming process. While ESR holds promise, it faces a difficult challenge due to the requirement for catalyst performance at very high temperatures. A catalyst, typically based on nickel supported on alumina. The alumina support, while enhancing catalytic activity, introduces acidic sites that promote coke formation.[2] Partial doping of the alumina support with elements like zirconium has shown potential in improving thermal stability and high adsorption-dissociation,[4] therefore dispersion of ZrO_2 on Al_2O_3 framework surface should affect Ni dispersion on the support. The literature review suggests that the application of an external magnetic field to an aqueous solution can alter the movement of paramagnetic ions.[5] Hence, in this study, magnetic inducement will be utilized to regulate the insertion of ZrO_2 within the Al_2O_3 framework in the sol-gel process, which may reflect in terms of specific surface area and surface acidity of the ZrO_2 -doped Al_2O_3 support.

2. Materials and Methods

2.1 Support Preparation

The preparation of ZrO_2-doped-Al_2O_3 supports involved obtaining 5% mol Zr from 30 g of ZrO_2-doped-Al_2O_3 through the sol-gel method. In this process, sol-gel supports were created by combining $ZrO(NO_3)_2$•$6H_2O$, $Al(NO_3)_3$•$9H_2O$, and deionized water to form an aqueous solution. The solution was stirred at room temperature until completely mixed. Ammonia was introduced to the solution to create a gel until reaching a pH of 9,[6] with and without the influence of a magnetic field. Magnetic field was created by placing 9 neodymium magnets in a 3×3 configuration onto

each side of an aluminum frame in 2 setups, namely between same magnetic poles (N-N) and between opposite magnetic poles (N-S).

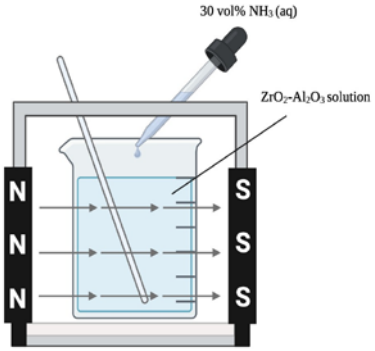

Figure 1. Magnetic setup for magnetic inducement (N-S)

The resulting gel was left at room temperature for 48 h. The gel was dried in an oven at 60°C until completely dehydrated. The sample was put in the oven at 110°C for 16 h and calcinated in a furnace at 800°C for 3 h. The ZrO_2-doped-Al_2O_3, ZrO_2-doped-Al_2O_3 (N-N), and ZrO_2-doped-Al_2O_3 (N-S) supports obtained were subsequently ground using a mortar and sieved with a 106um sieves.

2.2 Catalyst Preparation

The incipient wetness impregnation method was used for preparing catalysts containing 5% nickel on Al_2O_3. 1.25M nickel solution was obtained from dissolving Ni $(NO_3)_2$•$6H_2O$ in deionized water. These solutions were impregnated onto the supports by adding and mixing the solution drop-by-drop into the supports. Following the impregnation, the catalysts were left at room temperature and underwent a drying process at 110 °C for 16 h, then were followed by calcination at 600°C for 4 h. The calcined samples were then ground into powder.

2.3 Support and Catalyst Characterization

The total surface area of the supports prepared, and the loaded catalysts were evaluated using the Brunauer-Emmett-Teller (BET) method. It was also expected that the addition of ZrO_2 may affect the surface acidity of the supports. Surface acidity of the supports was characterized using NH_3 temperature-programmed desorption in the temperature range of 100 to 600°C.

2.4 Experimental Setup

The ethanol steam reforming procedure was carried out in a tubular reactor, utilizing a catalyst with a weight of 0.1 g mixed with 0.4 g quartz sand packed between layers of quartz wool. Ethanol and water were heated to their respective boiling points and introduced into the reactor with the flow of argon. The feed reactants were consistently set at a 1:3 molar ratio of ethanol to water. The ethanol steam reforming reaction operated at a temperature of 575°C and 600°C. The resulting gas composition was analyzed using gas chromatography.

3. Results & Discussion

3.1 Characterization of ZrO_2-Al_2O_3 Supports using NH_3 TPD and BET Method.

The ZrO_2-Al_2O_3 supports prepared under different magnetic environments, which are (1) under no magnetic field (no magnet); (2) prepared between north–north magnetic poles (N-N); and (3) between north–south magnetic poles (N-S), were characterized using NH_3 temperature-programmed desorption (TPD) and the Brunauer, Emmett and Teller (BET) method. Table 1 lists the physical properties of ZrO_2-doped Al_2O_3 with and without magnetic inducement including the surface area, pore volume and pore diameter calculated using the BET method. The (N-N) support shows the highest surface area of 162.91 m^2/g, in Al_2O_3 support, the (N-S) support shows the lowest surface area of 126.61 m^2/g, Coupled with a previous study on CeO_2-doped Al_2O_3,[6] it thus confirms that magnetic inducement affects the surface area of the doped supports; however, the mechanism of which must be further investigated.

Table 1. Physical properties of ZrO_2-doped-Al_2O_3 without magnetic inducement (No magnet), ZrO_2-doped Al_2O_3 (N-N), and ZrO_2-doped Al_2O_3 (N-S).

Support	Support surface area (m^2/g)	Pore volume (cm^3/g)	Average pore diameter (nm)
No magnet	140.84	0.3357	9.5332
N-N	162.91	0.3527	8.661
N-S	126.61	0.4423	13.973

3.2 Effect of ZrO_2-Al_2O_3 Supports Prepared under Magnetic Inducement on H_2 Production

A hydrogen production study from ESR was performed on Ni catalysts loaded without magnetic inducement on the prepared supports. Table 2 shows the hydrogen production rate from

ESR using Ni catalysts supported on ZrO_2 - Al_2O_3 prepared with and without magnetic inducement at 575 and 600 °C. The results show that the N-N support yields the highest hydrogen production both at 575 °C and 600°C, which corresponds with the results from previous on CeO_2- Al_2O_3 supports.[7]

Table 2. H_2 production rate of ZrO_2-doped-Al_2O_3 without magnetic inducement (No magnet), ZrO_2-doped-Al_2O_3 (N-N), and ZrO_2-doped-Al_2O_3 (N-S).

Magnetic Inducement	H_2 Production Rate (μmol/min)	
	575 °C	600 °C
No magnet	328.70	516.41
N-N	406.34	595.89
N-S	339.12	436.89

Figure 2 shows the results from NH_3 TPD which was used to analyze the acidity of the supports. It can be observed that no-magnet and (N-S) supports have a similar peak which corresponds to strong acid sites at 300–400°C and a peak for weak acid sites at 100–200°C.[8] The peaks, however, exhibit some shifts which indicate the effect of magnetic field on the strength of the acid sites due to the paramagnetic Zr atoms. On the other hand, N-N support does not show any observable peaks, so it can be inferred that the acidity of the support has been greatly affected by the N-N magnetic inducement. To understand the underlying cause of this change in the surface acidity, further characterizations are needed. However, inferring from our previous work on CeO_2-Al_2O_3 which has similar magnetic properties to the ZrO_2-Al_2O_3 used in this study, since Ce and Zr are both paramagnetic, this change in surface acidity is probably due to the influence of magnetic inducement on the insertion of Zr atoms in Al_2O_3 framework, as it has been shown that magnetic field could control the dispersion of Ce in Al_2O_3 framework.[6]

4. Conclusion

In this study, the properties of Al_2O_3 supports were modified through the addition of ZrO_2 coupled with the use of magnetic inducement. The application of magnetic inducement during the preparation stage of the supports affects the acidity of the support surface. Nickel catalysts loaded on these supports tested for H_2 production from ESR exhibit different productivity. As shown in Table 2, it can be observed that the N-N support exhibits the highest H_2 production among the prepared supports due to its lowest acidity compared to other supports in this study. These effects of magnetism the surface area, pore volume, pore diameter, and acid sites can be useful in other applications. Further investigation on the dispersion of ZrO_2 and the lattice structure of the doped supports will be required for a more in-depth understanding of the effect of magnetic inducement on ZrO_2 dopant in Al_2O_3

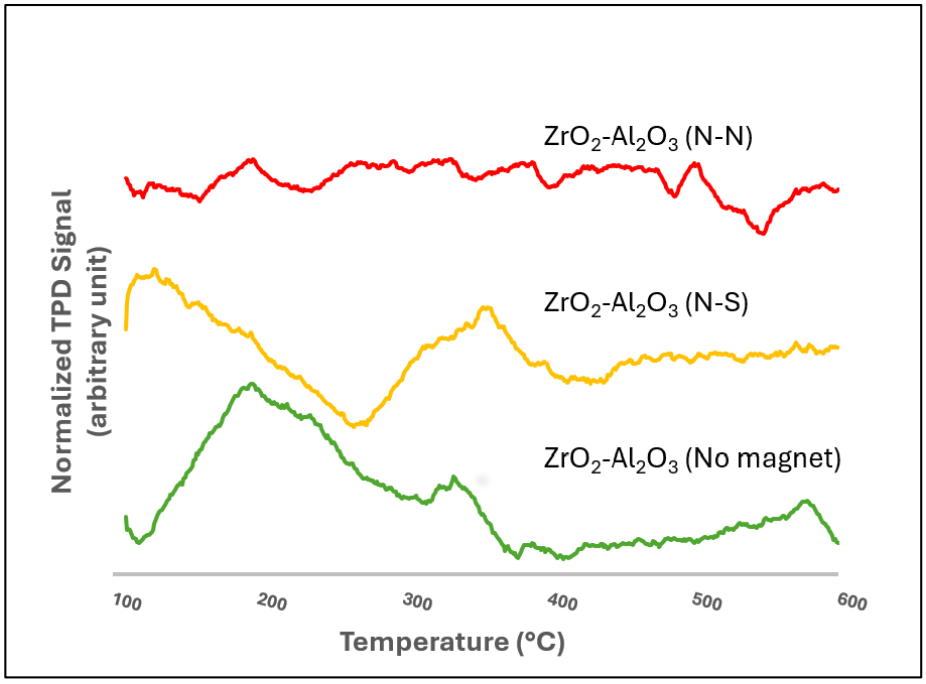

Figure 2. A Normalized NH_3TPD of ZrO_2-doped Al_2O_3 without magnetic inducement (No magnet), ZrO_2-doped Al_2O_3 (N-N), and ZrO_2-dopedAl_2O_3 (N-S).

References

1. Arslan, A., S. Gunduz, and T. Dogu, *Steam reforming of ethanol with zirconia incorporated mesoporous silicate supported catalysts.* International Journal of Hydrogen Energy, 2014. **39**(32): p. 18264-18272.
2. Shtyka, O., et al., *Correction to: Steam reforming of ethanol for hydrogen production: influence of catalyst composition (Ni/Al_2O_3, Ni/Al_2O_3–CeO_2, Ni/Al_2O_3–ZnO) and process conditions.* Reaction Kinetics, Mechanisms and Catalysis, 2021. **134**(2): p. 1089-1089.
3. Yakovlev, V.A., et al., *Development of new catalytic systems for upgraded bio-fuels production from bio-crude-oil and biodiesel.* Catalysis Today, 2009. **144**(3): p. 362-366.
4. Li, S., et al., *Steam reforming of ethanol over Ni/ZrO_2 catalysts: Effect of support on product distribution.* International Journal of Hydrogen Energy, 2012. **37**(3): p. 2940-2949.
5. Fujiwara, M., et al., *On the Movement of Paramagnetic Ions in an Inhomogeneous Magnetic Field.* The Journal of Physical Chemistry B, 2004. **108**(11): p. 3531-3534.
6. Vacharapong, P., et al., *Enhancement of Ni Catalyst Using CeO_2–Al_2O_3 Support Prepared with Magnetic Inducement for ESR.* Catalysts, 2020. **10**(11): p. 1357.
7. Katanyutanon, S., et al., *Catalytic Activity Enhancement of Cu-Zn-Based Catalyst for Methanol Steam Reforming with Magnetic Inducement.* Catalysts, 2021. **11**(9): p. 1110.
8. Turco, M., et al., *TPD study of NH_3 adsorbed by different phases of zirconium phosphate.* Journal of Catalysis, 1989. **117**(2): p. 355-361.

Role of incorporated metal/phosphorus acidity modification over low Si/Al ratio HZSM-5 catalysts in methanol-to-olefins process

Chotika Yoocham, and Pattaraporn Kim-Lohsoontorn*

Centre of Excellence on Catalysis and Catalytic Reaction Engineering, Department of Chemical Engineering, Faculty of Engineering, Chulalongkorn University, Bangkok, 10330, Thailand

**E-mail: pattaraporn.k@chula.ac.th*

Abstract:

Green methanol has garnered considerable attention as it can be derived from non-petroleum feedstocks such as CO_2-based products which can lead to a significant market volume in the future. Consequently, value-added products of green methanol can be produced through processes, such as methanol to olefins (MTO). In this current work, the MTO process was investigated under atmospheric pressure, maintaining a reaction temperature of 500°C. The primary focus of this research was on the modified low Si/Al ratio HZSM-5 zeolite catalyst, prepared through the co-impregnation of magnesium and phosphorus. The modification by adding magnesium and phosphorus (Mg-P) led to an increase in crystallinity, contributing to enhanced structural stability. The introduction of these promoters slightly increased the Si/Al ratio, resulting in a reduction in the acidic properties of both acid sites and strength. Catalytic performance tests revealed that the Mg-P modification can enhance olefin selectivity, specifically ethylene and propylene, reaching 18.8% and 35.7%, respectively. This improvement in selectivity was accompanied by an extended catalyst lifetime, attributed to a suppression in aromatization and a slowdown in the deactivation.

1. Introduction

Methanol to hydrocarbon is a broader process that involves the conversion of methanol into a range of hydrocarbons and undergoes a series of reactions. Methanol is preferable for the industrial sector based on various criteria to address global warming issues through breakthrough CO_2 conversion products.[1] Mainly, related to the degree of technology majority as well as the market size, both of which can be integrated into chemicals to fuel.

Methanol to olefins (MTO) specifically targets the production of olefins, such as ethylene and propylene, which are primarily produced using petroleum resources accomplished as the valuable building blocks for the petrochemical industry. The demand for olefins is continuously rising due to their necessity as starting materials in the modern chemical industry. However, alternative technologies are being widely researched to explore more feasible and competitive ways of producing olefins through sustainable processes based on renewable resources.[2-7]

The zeolite catalyst plays a crucial role in determining the selectivity and yield of the products. HZSM-5, a unique three-dimensional pore structure (intersecting zigzag channels (5.1 × 5.5 Å) and straight channels (5.3 × 5.6 Å)).[2, 5, 8] Its MFI-type topology with high silica/alumina (Si/Al) zeolite catalyst (the optimal Si/Al range of 200-280) is more suitable for the MTO process.

The MTO reaction is performed under hydrocarbon pool mechanism (HCP), where the HZSM-5 catalyst proposes the dual-cycle mechanism. The generation and evolution of HCP species have an ultimate influence on catalytic activity. According to its autocatalytic reaction, the dual cycle mechanism contains two cycles of active species, i.e., aromatic and alkene cycle. The initial hydrocarbon species within the pores and/or the surfaces are considered to be the reaction intermediate that polymethyl benzene,[5,9,10] and higher olefins can act as active HCP species. Depending on the acidity of the catalyst and reaction conditions can lead to different product distribution. In the aromatic cycle, aromatic intermediates are alkylated by the methanol feed that produces the initial product and/or intermediate of ethylene. In the alkene cycle, the methylation reaction then occurs to grow the longer chain of hydrocarbon, and alkenes, these formation results in isomerization, oligomerization, and cracking of higher olefins into ethylene, propylene, and aromatics. These multi-cyclized species are further transformed to coke formation.

2. Materials and Methods

2.1 Materials

The ammonium ZSM-5 commercial zeolite with SiO_2/Al_2O_3 of 40 was supplied by TOSOH Corp., Japan. Methanol was used as the feedstock, while magnesium nitrate hexahydrate,

and phosphoric acid, were used for impregnation of the modified catalyst, purchased from Sigma-Aldrich.

2.2 Catalyst Preparation

For parent HZSM-5, the Ammonium ZSM-5 were dried at 110°C overnight to remove the moisture content then calcined at 550°C with a heating rate of 10°C/min in air for 4 hours to remove the organic impurities, the ammonium ZSM-5 was then converted into HZSM-5.

For modified HZSM-5, the HZSM-5 were impregnated with 1 wt% of chemical(X) loading of Mg and P, denoted as X-HZ, either metal/phosphorus loading to approach total loading of 1 wt%, denoted as X-P-HZ. The modified catalysts were dried and calcined in the same conditions as mentioned above. The catalyst particles were crushed and sieved through a 180 mesh for catalytic study and characterization.

2.3 Methodology

In the experimental setup, the catalytic performance of MTO process was carried out under atmospheric pressure at the reaction temperature of 500°C. Initially, 100 mL/min of nitrogen was obtained as a carrier gas to remove moisture and activate the catalyst at the same reaction temperature for an hour. The vaporized methanol (≥99.9%) was introduced through the stainless-steel fixed bed reactor, packed with 0.2 grams of the parent or modified HZSM-5 catalyst. The weight hour space velocity (WHSV) was maintained at 2.0 h^{-1}, determined the time on stream (TOS) over 24 hours of reaction. At the outlet stream, the unconverted methanol and gas products were analyzed by online gas chromatography equipped with a flame ionization detector (FID) and thermal conductivity detector (TCD). Likewise, the deactivation of the catalyst was observed by collecting the catalytic activity data.

2.4 Catalyst Characterization

The surface topography and chemical composition of catalysts were evaluated by Scanning electron microscopy with energy dispersive X-ray spectroscopy (SEM-EDX), using JEOL mode JSM-5800LV equipped with Link Isis Series 300 program.

The powder was examined the crystallinity and bulk phase by using X-ray diffraction (XRD) patterns, 2θ recorded in the 5-60° of SIEMENS D5000 X-rays diffractometers containing CuKα radiation (40 kV, 30 mA, λ = 1.5406 Å) with a step of 0.021°. Peak detection was compared using the Joint Committee on Powder Diffraction Standards (JCPDS) database.

The temperature-programmed desorption of ammonia (NH_3-TPD) was carried out on Micromeritics chemisorb 2750 to analyze the acidity. The prepared samples of 0.05 grams were loaded into a quartz tube supported by quartz wool at the bottom, then heated to 300°C for degases in an hour at a heating rate of 10°C/min along with 30 mL/min of He. Consequently, the temperature was cooled down to 40°C before being treated with ammonia gas for an hour. Afterward, the constant thermal conductivity detector (TCD) signal monitored the ammonia desorption while the sample was then flushed with He stream with increasing temperature from 40 to 750°C.

3. Results & Discussion

3.1 Crystalline structure and textural properties

The surface morphology of unmodified/modified catalysts was analyzed through SEM as shown in Figure 1a-d, the catalysts have a similar morphological shape of hexagonal crystal. The morphology illustrated the uniform crystal distribution of parent HZSM-5 in Figure 1a. However, the modified HZSM-5 via impregnation method resulted in smoother hexagonal edges clearly seen in P-HZ and Mg-P-HZ modification. In addition, the agglomerated catalyst between the surface formed the larger particle of Mg-HZ, presented in Figure 1c-d, and 1b, respectively. Furthermore, Figure 1e shows the photograph of fresh HZSM-5, Mg-P modification, and spent HZSM-5 catalyst on the reaction time of 24 h. As briefly mentioned in the introduction, the multicycle reactions finally led to the formation of polymerized species and aromatic species that can be further condensed to form coke deposits on the catalyst. This phenomenon caused the coverage of active sites and partial blockage of the accessibility of gas feed and products, resulting in the retained hydrocarbon mainly attributed to the coke formation.[4, 11]

As mentioned above, EDX was equipped with SEM to analyze the average element composition on the external surface. Table 1 reveals for all the samples that the modification with a low element loading of 1 wt%, the Si/Al molar ratio increased. The results ensured that a reduction in the acidity of catalysts can be caused by the loss of Al framework in the dealumination. During the thermal treatment, calcination was obtained to remove the moisture and impurities in the zeolite. Si-O-Al bond gradually and partially

hydrolyzed where the Al and Si were evacuated and formed the extra framework silica-alumina.[8] The introduction of P partially caused the dealumination by breaking Si-O-Al bond[8,9,12] as well as the Mg incorporation of alkaline earth metal to decrease the number hydroxyl group.[13]

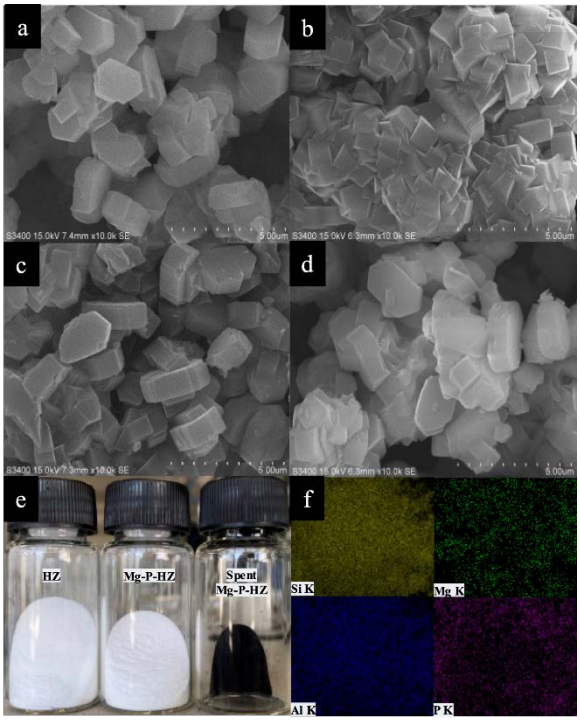

Figure 1. SEM images a) parent HZ b) Mg-HZ c) P-HZ d) 0.5Mg0.5P-HZ e) Photograph of catalyst before and after the reaction f) EDX images of Si, Al, Mg and P.

XRD patterns of the parent and modified HZSM-5 zeolite are shown in Figure 2, indicated a set of diffraction peaks at 2θ = 7.9°, 8.8°, 9.0°, 23.0°, 23.3°, 23.7°, 23.9°, and 24.3°, corresponding to the typical MFI structure of HZSM-5 by the agreement of JCPDS No. 44-0003.[11,14,5] The results showed that the metal/nonmetal impregnated catalyst had the same peak with different intensities, and none of impurities were presented.[15] The relative crystallinity and the average crystal size using Scherrer equation were calculated as shown in Table 1. It revealed that the structures were destroyed by the modification of Mg and P, leading to a reduction in diffraction peaks.[2,3,13] In contrast, the modified Mg-P-HZ(40) exhibited the highest crystallinity over the parent HZSM-5, attributed to the structural stability.[7] Furthermore, the change of the crystal size relates to the morphology of the catalysts. The presence of P promoted the self-annealing of external Si-OH group leading to the aggregation of catalyst.[8] The lower loading amount of each Mg-P catalyst may facilitate the formation of larger crystal sizes and more well-defined crystals due to the interaction of Mg and P, leading to higher crystallinity.

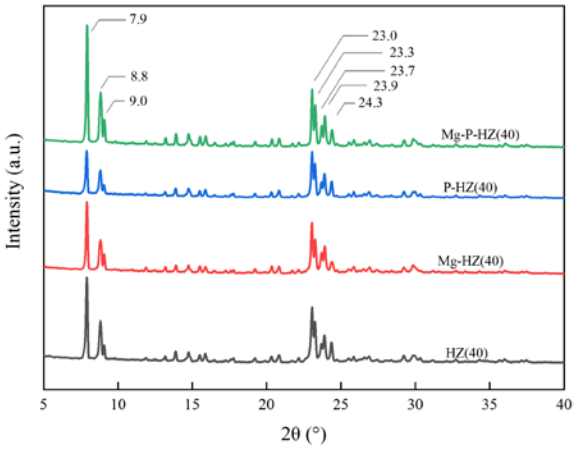

Figure 2. XRD pattern of the fresh MTO catalyst.

Table 1. Chemical composition, relative-crystallinity of MTO catalysts.

Sample	[a] Chemical composition			[b] R_c	[b] D
	Si/Al mol	Mg wt%	P wt%	%	nm
HZSM-5	16.27	-	-	100	52.55
Mg-HZ	17.18	1.06	-	89.23	52.54
P-HZ	16.47	-	1.44	73.97	54.27
Mg-P-HZ	19.56	0.74	0.27	115.7	58.63

[a] Si/Al molar ratio were determined by EDX.
[b] Relative crystallinity and average crystallite size were calculated using XRD data.

3.2 Catalyst acidity

Acidity is one of the limitations of solid acid catalyst. It represented the relationship between parent HZSM-5 and modified HZSM-5. Figure 3 indicated the NH_3-TPD results where it combined with 2 identical peaks of acid strength. The desorption peaks occurred in the range of low temperature (185-235°C) corresponding to the weak acid strength, in contrast to the higher temperature (400-450°C) represented of strong acid strength. The peak area is associated with the number of acid sites. In brief, the strong acid sites are formed by the protons present in framework bridging hydroxyl group, though the weak acids sites consisted of silanol and aluminol group.[8] The HZSM-5 showed the highest intensity of both weak and strong acid sites meanwhile the modified HZSM-5 similarly decreased the acid strength and acid sites. According to the quantitative data, the

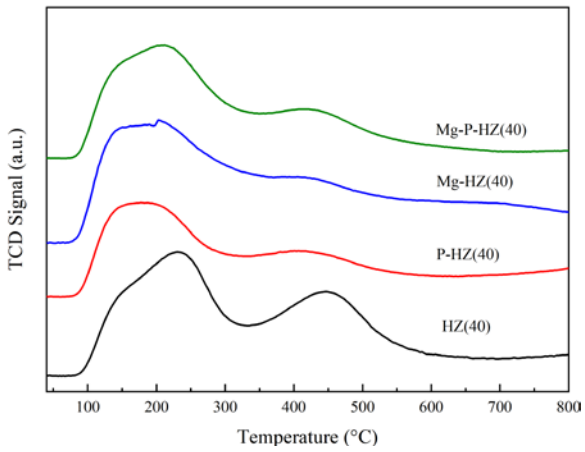

Figure 3. NH_3-TPD results of all catalysts.

Table 2. The acidity of MTO catalysts.

Sample	Acid strength °C		[c]Acid sites mmol/g		
	T_{Weak}	T_{Strong}	Weak	Strong	Total
HZSM-5	208.9	441.0	0.709	0.766	1.475
Mg-HZ	193.7	403.2	0.616	0.649	1.265
P-HZ	179.4	398.0	0.442	0.629	1.070
Mg-P-HZ	191.8	390.1	0.624	0.626	1.250

[c] The acid sites were approximately calculated by deconvolution technique using Gaussian function.

approximation of weak acid strength was in the following order: P-HZ < Mg-P-HZ < Mg-HZ < HZSM-5 while the strong acid strength were Mg-P-HZ < P-HZ < Mg-HZ < HZSM-5, respectively.

In addition, HZSM-5 showed the highest of total acid sites, then the decline expressed in the modified catalysts, reported in Table 2. The Mg modification might force the interaction to the zeolite which neutralized the surface acidity.[3] Both the weak and strong acid sites of Mg-HZ experienced a slight decrease, which contrasts with the acidity findings reported by Yuan, Sang, Xing, Wang, Miao and Sun,[15] where an increase in weak acid sites was observed. Likewise, P promoter significantly decreased the strong acid sites in agreement that protonation of phosphoric acid with bridging hydroxyl group. Phosphoric acid can coordinate with tetrahedrally coordinated zeolite framework aluminum (TFAl), inducing the octahedral coordination in aluminum. These studies suggested the reversible of hydrogen bonding between hydrogen atom in phosphoric acid and oxygen framework.[8,12] However, The interaction lead to the reduction of TFAl and a decreased in Brønsted acid sites[8]. It reacted with extra framework alumina to form the extra amorphous $AlPO_4$[7,8] located on the external surface.

In MTO process, solid acid catalyst was widely used to enhance the catalytic activity of methanol conversion to approach olefins products. The post-synthetic modification results in tuning of the acidity that MTO required to react in the low acidity zeolite. The strong acid strength led to rapid byproduct formation. Consequently, both strong and weak acid sites on HZSM-5 are essential for the MTO process. Weak acid sites are involved in the initial adsorption and dehydration while strong acid sites play a critical role in the subsequent dehydration and cracking reactions leading to the formation of light olefins. The balance between these two types of acid sites influences the selectivity and efficiency of the MTO catalyst.

3.3 Catalytic performance

The methodology of catalytic were mentioned above, the methanol conversion and hydrocarbon selectivity were defined as follows in Eq (1)-(2). The product distribution was investigated after 6 h on stream as given in Table 3. As expected, the olefins selectivity clearly seen that production of propylene was greater the other products, where the modification of Mg-P resulted the highest selectivity. According to the alkene cycle of hydrocarbon pool mechanism, co-impregnation of Mg-P showed the ability to crack the higher olefins e.g. butene, pentene to light olefins. Where, the abilities of Mg were to selectively produce olefins and suppress the formation of aromatics by olefins conversion.[6,15] Methanol dehydration still generated the dimethyl ether as an intermediate before converted to ethylene by methylation reaction. However, water was the byproduct during dehydration, presented as steam. The combination of steam and high reaction temperature promoted the dealumination of zeolite,[8] contributed the permanent loss of acid sites. The presence of Mg promoter was interesting in the capability to increase the catalyst lifetime.[6,15] The P modification mostly activated the methanol methylation to ethylene[8] and further produced propylene which partially oligomerized to higher olefins. For all catalysts, an increasing time-on stream, the olefins and hydrocarbon species assigned to polymerization, aromatization, and enduringly formed the near graphite carbon[4,6,10] known as carbon deposit. Consequently, the selectivity of products decreased due to the accumulation of coke on the external surface and pore channel caused the blocking the accessibility to active sites.[15,16] Mg-P modification tends to suppress the coke formation, slowing down the deactivation of catalysts including increasing the olefins selectivity.

$$X = \frac{n^{i}_{MeOH} - (n^{o}_{MeOH} + 2n^{o}_{DME})}{n^{i}_{MeOH}} \quad (1)$$

$$S = \frac{a \times n^{o}_{C_aH_b}}{n^{i}_{MeOH} - (n^{o}_{MeOH} + 2n^{o}_{DME})} \quad (2)$$

Table 3. The product distribution of MTO process over modified HZSM-5 catalysts[f].

Sample	Catalyst			
	HZ	Mg-HZ	P-HZ	Mg-P-HZ
%Conversion	95.7	94.1	87.9	89.4
%Selectivity				
CH_4	1.57	1.37	2.15	1.51
C_2H_4	20.5	10.1	18.1	18.8
C_3H_6	30.3	19.4	32.7	35.7
C_4H_8	11.9	8.88	13.8	9.47
DME	0.10	0.42	0.67	0.98

[f] Reaction condition: T 500°C, P 1 atm, WHSV 2 h^{-1}, TOS 6 h.

4. Conclusion

Methanol to olefins (MTO) process gained more attention these recent years, with the increased olefins demand especially propylene and ethylene. For the purpose of Carbon Capture and Utilization (CCU), methanol was produced through CO_2 conversion. Regarding a new sustainable route, HZSM-5 has achieved widespread use with excellent catalytic activity and stability. In this study, the modified HZSM-5 zeolite catalyst by co-impregnation of magnesium and phosphorus, resulted in a higher crystallinity in advance of structural stability. Furthermore, the interaction between magnesium and phosphorus during the thermal treatment likely damaged the Al framework due to the dealumination, compared with the parent HZSM-5. As described, these promoters slightly increased the Si/Al ratio of the catalyst. Consequently, the reduction of the acidic properties for both acid sites and strength was detected. The corresponding catalytic performance test showed that the Mg-P modification can enhance the olefins selectivity with increasing catalyst lifetime.

Acknowledgments

This work was supported by Malaysia Thailand Joint Autority (MTJA) Research Cess Fund and the NSRF via the Program Management Unit for Human Resources & Institutional Development, Research and Innovation [B16F640164].

References

1. Chauvy, R.; Meunier, N.; Thomas, D.; De Weireld, G. Selecting emerging CO2 utilization products for short- to mid-term deployment. Applied Energy 2019, 236, 662-680.
2. Bakare, I. A.; Muraza, O.; Yoshioka, M.; Yamani, Z. H.; Yokoi, T. Conversion of methanol to olefins over Al-rich ZSM-5 modified with alkaline earth metal oxides. Catalysis Science & Technology 2016, 6 (21), 7852-7859.
3. Chen, C.; Zhang, Q.; Meng, Z.; Li, C.; Shan, H. Effect of magnesium modification over H-ZSM-5 in methanol to propylene reaction. Applied Petrochemical Research 2015, 5 (4), 277-284.
4. Díaz, M.; Epelde, E.; Valecillos, J.; Izaddoust, S.; Aguayo, A. T.; Bilbao, J. Coke deactivation and regeneration of HZSM-5 zeolite catalysts in the oligomerization of 1-butene. Applied Catalysis B: Environmental 2021, 291.
5. Feng, R.; Yan, X.; Hu, X.; Zhang, Y.; Wu, J.; Yan, Z. The effect of co-feeding ethanol on a methanol to propylene (MTP) reaction over a commercial MTP catalyst. Applied Catalysis A: General 2020, 592.
6. Goetze, J.; Weckhuysen, B. M. Spatiotemporal coke formation over zeolite ZSM-5 during the methanol-to-olefins process as studied with operando UV-vis spectroscopy: a comparison between H-ZSM-5 and Mg-ZSM-5. Catalysis Science & Technology 2018, 8 (6), 1632-1644.
7. Gorzin, F.; Yaripour, F. Production of light olefins from methanol over modified H-ZSM-5: effect of metal impregnation in high-silica zeolite on product distribution. Research on Chemical Intermediates 2018, 45 (2), 261-285.
8. van der Bij, H. E.; Weckhuysen, B. M. Phosphorus promotion and poisoning in zeolite-based materials: synthesis, characterisation and catalysis. Chem Soc Rev 2015, 44 (20), 7406-7428.
9. Rostamizadeh, M.; Taeb, A. Highly selective Me-ZSM-5 catalyst for methanol to propylene (MTP). Journal of Industrial and Engineering Chemistry 2015, 27, 297-306.
10. Sang, Y.; Xing, A.; Wang, C.; Han, Z.; Wu, Y. Near-Graphite Coke Deposit on Nano-HZSM-5 Aggregates for Methanol to Propylene and Butylene Reaction. Catalysts 2017, 7 (6).
11. He, M.; Ali, M.-F.; Song, Y.-Q.; Zhou, X.-L.; Wang, J. A.; Nie, X.-Y.; Wang, Z. Study on the deactivation mechanism of HZSM-5 in the process of catalytic cracking of n-hexane. Chemical Engineering Journal 2023, 451.
12. Xia, W.; Huang, Y.; Ma, C.; Li, S.; Wang, X.; Chen, K.; Liu, D. Multiple important roles of phosphorus modification on the ZSM-5 in ethanol to olefin reaction: Acidity adjustment,

hydrothermal stability and anti-coking. Fuel 2023, 341.
13. Vu, D.; Hirota, Y.; Nishiyama, N.; Egashira, Y.; Ueyama, K. High Propylene Selectivity in Methanol-to-olefin Reaction over H-ZSM-5 Catalyst Treated with Phosphoric Acid. Journal of The Japan Petroleum Institute - J JPN PET INST 2010, 53, 232-238.
14. Chen, B. H.; Chao, Z. S.; He, H.; Huang, C.; Liu, Y. J.; Yi, W. J.; Wei, X. L.; An, J. F. Towards a full understanding of the nature of Ni(II) species and hydroxyl groups over highly siliceous HZSM-5 zeolite supported nickel catalysts prepared by a deposition-precipitation method. Dalton Trans 2016, 45 (6), 2720-2739.
15. Yuan, D.; Sang, Y.; Xing, A.; Wang, C.; Miao, P.; Sun, Q. Tuning of Magnesium Distribution in ZSM-5 via Different Impregnation Methods and Its Effect on Methanol to Propene Reaction. Industrial & Engineering Chemistry Research 2019, 58 (13), 5112-5120.
16. Sano, T. Production of Light Olefins from Methanol and Ethanol Using ZSM-5 Type Zeolite Catalysts. Journal of the Japan Petroleum Institute 2017, 60 (6), 263-276.

Effect of manganese and magnesium promoter on catalytic hydrogenation of CO_2 over cobalt-based catalyst

Saowaluk Intarasiri[1,2]*, Chutikan Tupmee [1], and Jakkarin Hongsawong[1]

[1]*Faculty of Science, Energy and Environment, King Mongkut's University of Technology North Bangkok, Thailand*
[2]*Research and Development of Chemical Engineering Unit Operation and Catalyst Design. King Mongkut's University of Technology North Bangkok, Thailand*

**E-mail: saowaluk.i@sciee.kmutnb.ac.th*

Abstract:

Concerning the problem of greenhouse gas, this attention has been focused on the conversion of CO_2 to value-added hydrocarbons via catalytic hydrogenation. This research aimed to improve the property of cobalt-based catalysts in CO_2 hydrogenation by adding the Mn and Mg as a promoter. A parent 20CS (20%Co/SiO_2) and promoted catalysts; 20CS1Mn and 20CS1Mg (20%Co/SiO_2-1%Mn and 20%Co/SiO_2-1%Mg) were synthesized and characterized by N_2-adsorption, XRD, H_2-TPR, H_2-TPD and CO_2 TPD techniques. The catalytic performance in CO_2 hydrogenation was investigated in a fixed-bed reactor at 220 ^oC under atmospheric pressure. The promoters influence the physical and chemical properties of the catalyst. A significant increase in pore size diameter and average crystallite size of promoted catalyst leads to the ease of catalyst reduction. The CO_2 hydrogenation over the promoted catalyst demonstrates the possibility of chain polymerization during the reaction time (2, 4 and 6 hrs.). The selectivity towards C_3 and C_4 light hydrocarbon gas might be due to the electronic and structural effect of promoter.

1. Introduction

Soaring of CO_2 emission from fuel combustion is a major cause of environmental problems. Concept of reduce and recycles of CO_2 by converting CO_2 as a source of carbon into chemicals and fuels is a crucial solving problem. Utilization of CO_2 based fuels essentially contributes to a net-zero CO_2 emission. Synthetic hydrocarbon fuels can be produced via CO_2 hydrogenation. This catalytic reaction normally takes place over metal supported catalyst, which a metal is supported on metal oxide.[1,2] Typically, transition metals such as, Pt, Pd, Ru, Rh, Cu, Ni, and Co, have been found to be potential active metal in hydrogenation.[2,3] Copper, nickel, and cobalt are common metals that provide extensive possibilities for various applications, mostly due to their notably low cost. Each of these three metals possesses distinct characteristics that facilitate CO_2 hydrogenation reactions: Copper-based catalysts are predominantly investigated for high-pressure methanol synthesis and low-pressure reverse water gas shift reactions. Nickel-based catalysts are recognized for their capability in CO_2 methanation.[4] Cobalt-based catalysts are primarily focused on the Fischer-Tropsch process. Despite the limited exploration of cobalt-based catalysts in CO_2 hydrogenation, they have been literatured to generate short-chain alkanes.

The hydrocarbon compound (light gas and liquid) can be produced by a direct FT reaction using CO_2 or by a sequential two-step reaction starting with the reverse water–gas shift reaction (RWGS) and followed by FT synthesis, as described by equations (1) and (2), respectively[5]:

$$CO_2 + H_2 \rightarrow CO + H_2O \quad (1)$$

$$CO + 2H_2 \rightarrow -(CH_2)_n- \quad (2)$$

Catalytic activity and product selectivity are greatly influenced not only the selection of active metal but also the presence of support material. The support plays a role in metal dispersion and improve the stability. In addition, the electrical interactions between metal particles and support can contribute the catalytic performance. Support materials that are being explored on CO_2 methanation include acidic oxides and basic oxides, such as Al_2O_3, TiO_2, SiO_2, ZrO_2, and CeO_2.[3] Mesoporous support is a good candidate to promote the dispersion of active species, therefore improving catalytic performance.[6] Mesoporous silica material is of great interest because of uniform shape and pore size, large specific surface area and thermal stability.

Additionally, the catalytic performance also depends on the promoter, which generally presents in a low content. Promoter can play a key role in reducibility and dispersion of catalyst. It can affect the textural and electronic properties of catalyst. Reducible metal oxide, alkaline and alkaline earth metal are effective promoters for hydrogenation reaction. They involve the changes

in the oxidation state of metal, the interaction of metal-metal or metal oxide. The hydrogenation of CO_2 is initially achieved by the adsorption of reactants over the catalyst surface. CO_2 is Lewis acid gas, which central carbon is electrophile. The active site of CO_2 adsorption is electropositive metal or oxygen vacancy site or Lewis basic site. Improvement in adsorption ability and catalytic performance can be modified by adding promoters such as ZnO_x, MnO_x, Cu, Ru, K, Na, Cs, Rb, Ca and Mg.[5]

MnO_x is an interesting transition metal oxide as Mn has variety of metal oxidation states. Its redox property can contribute the electronic promotion of the catalyst. Mn promoter was reported to enhance the synergy with the catalyst. This affects the ability of H_2 dissociation and improves the selectivity towards olefin product. The presence of Mn promoters has been verified, along with the strong adsorption of CO_2. The elevated concentration of Mn promoter enhances the capacity of H_2 adsorption on the surface, which improves the hydrogenation of intermediate compounds into paraffin and leads to a reduction in the proportion of olefins compared to paraffin.[7] However, literature regarding the use of MnO_x as a promoter in CO_2 hydrogenation is still confined.

The amount of adsorbed CO_2 also depends upon the physical and chemical properties of the support material, including its surface area and basicity. MgO was reported to increase the ability of converting CO_2, resulting in enhancement of activity and selectivity towards CO to produce higher hydrocarbons. The higher basicity of catalyst increases the adsorption behavior of CO_2, leading to the higher CO_2 conversion during the reaction.[8]

As mentioned, the adsorptive properties of the catalyst directly influence catalytic activity and selectivity. These catalytic properties depend on the catalyst compositions. Accordingly, this research work focuses on the effect of the acid–base and redox properties of the catalyst in CO_2 hydrogenation. Magnesium oxide and manganese oxide were used as promoters for cobalt supported mesoporous silica catalysts. The catalyst properties and catalytic performance were determined in CO_2 hydrogenation.

2. Materials and Methods

2.1 Materials

Mesoporous silica support was synthesized using tetraethyl orthosilicate (TEOS, Sigma Aldrich, Reagent grade) as a silica source and gelatin as organic template (Acros, Analysis grade). Cobalt (II) nitrate hexahydrate ($Co(NO_3)_2.6H_2O$, Sigma Aldrich, Reagent grade), manganese (II) nitrate hexahydrate ($Mn(NO_3)_2.6H_2O$, Sigma Aldrich, Reagent grade) and magnesium (II) nitrate hexahydrate ($Mg(NO_3)_2.6H_2O$, QReC™, AR grade) were used as precursors for catalyst preparation. Reactant gases (High pure grade) were supplied by Linde Public Company Limited (Thailand) and Thai Special Gas (Thailand).

2.2 Catalysts preparation

Mesoporous silica support was synthesized by solgel method using the organic template.[9] The mixture of support precursor was dropwise by 20 ml TEOS and stirred for 6 hrs. The white precipitate was washed with deionized water to reach the neutral pH. Finally, it was dried in air at 50 ˚C for 48 hrs. and calcined at 700 ˚C for 5 hrs. Before impregnation, the support was dried in an oven at 80 ˚C for 0.5 hrs. Then, 20%Co/SiO_2 (w/w) was prepared by incipient wetness impregnation method, using $Co(NO_3)_2.6H_2O$ as precursor. The portion of catalyst was dried at 60 ˚C for 48 hrs. and calcined at and 550 ˚C for 5 hrs. The promoted catalyst was prepared using the same method. Salt solutions of $Mn(NO_3)_2.6H_2O$ and $Mg(NO_3)_2.6H_2O$ were co-impregnated on 20%Co/SiO_2 (20CS) and thermal treated in the same manner with parent catalyst to obtain 20%Co-1%Mn/SiO_2 (w/w) (20CS1Mn) and 20%Co-1%Mg/SiO_2 (w/w) (20CS1Mg).

2.3 Catalyst characterization

Phase composition and crystalline structure of cobalt based catalyst were determined by X- ray Powder Diffractometer (Bruker, D8 ECO) with monochromatized Cu Kα radiation (40 kV, 40 mA) at $2\theta = 10 - 80^{o}$.

Total surface area, pore-volume and pore diameter (BET method) were determined using Quantachrome Autosorp iQ-MP analyzer (Anton Paar instrument) at -196 ºC. The catalysts were treated under vacuum at 300 °C for 2 h before the test.

Temperature programmed desorption was investigated using Quantachrome Autosorp iQ-C-XR analyzer (Anton Paar instrument). H_2- TPR was used to study the reduction behavior of all catalysts. 0.2 g of sample was pretreated at 220 ºC for 40 min by inert gas. Then, 5% H_2/ Ar gas mixture was switched through the catalyst, while the temperature was programmed from ambient temperature to 850 ºC. H_2-TPD was determined to calculate the metal dispersion, metal crystallite size and H_2 desorption behavior. Approximately, 0.2 g of catalyst was loaded into the sample cell then reduced at 500 ºC by H_2 gas before cooling to 100 ºC and hold about 40 min before cooling down

to ambient temperature. Inert gas was switched into the sample cell, then temperature programmed to 600 ºC with ramping at 10 ºC/min. The amount of desorbed H_2 was determined by TCD detector.

CO_2-TPD was also studied using the same chemisorption analyzer. 0.2 g of catalyst was loaded into the sample cell then reduced at 500 ºC by H_2 gas, after that cooled down under inert gas. CO_2 was switched into the sample cell to be adsorbed on the active surface at ambient temperature, then temperature programmed to 600 ºC with ramping at 10 ºC/min. The amount of desorbed CO_2 was determined by TCD detector.

2.3 Catalytic performance

The CO_2 hydrogenation reaction was investigated in a fixed-bed stainless steel reactor applied 1.0 g of catalyst. The catalyst was reduced in pure H_2 gas at 500 ºC for 20 hrs. After that, the catalyst bed was cooled down to 220 °C under the inert gas. Then, the CO_2 hydrogenation reaction was operated under atmospheric pressure in a flow of H_2/CO_2 at ratio of 3 for 6hrs.

The effluent gases were detected by the on-line gas chromatograph (Agilent 8890) using FID and TCD detector. The activity, selectivity and CO_2 conversion were calculated as follows:

$$CH_4 \text{ Acitivity} = \frac{\text{mol of } CH_4}{\text{Time-on-steam (sec) x 1g of catalyst}} \quad (3)$$

$$CH_4 \text{ selectivity} = \frac{\text{mol of methane}}{\text{Total mole of product}} \text{ x } 100 \quad (4)$$

$$CO_2 \text{ conversion} = \frac{\text{mol } CO_{2\,in} - \text{mol } CO_{2\,out}}{\text{mol } CO_{2\,in}} \text{ x } 100 \quad (5)$$

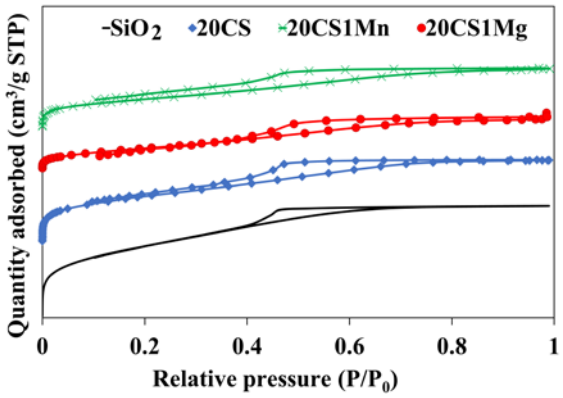

Figure 1. N_2 adsorption-desorption isotherm of support and catalysts.

3. Results & Discussion

3.1 Catalyst characterization

N_2 Adsorption and desorption isotherms of supports and catalysts are shown in Figure 1. According to the IUPAC classification, the isotherm obtained presents type IV with hysteresis loop of type H2, indicating the mesoporous material. The hysteresis effect occurs due to capillary condensation in the pores of support material.[12,13] This type of hysteresis is usually found in solids consisting of aggregates or agglomerates of particles forming slit shaped pores with no uniform size and/or shape.[14]

BET results are shown in Table 1. The cobalt-based catalyst presents the total surface area and total pore volume lower than SiO_2 support, while, the mean pore diameter increases due to the present of Co_3O_4, MnO_x and MgO on SiO_2 support. This can be the result of pore blocking effect.[10]

XRD patterns of SiO_2, 20CS, 20CS1Mg, and 20CS1Mn display in Figure 2. The XRD patterns of all catalysts illustrate the same pattern. The diffraction peaks of Co_3O_4 appear 2θ at 31.27°, 36.83°, 44.69°, 59.26° and 65.3°. Unfortunately, the diffraction peaks of MgO and MnO_x were not obviously observed due to low content of this promoter and the limit of apparatus.

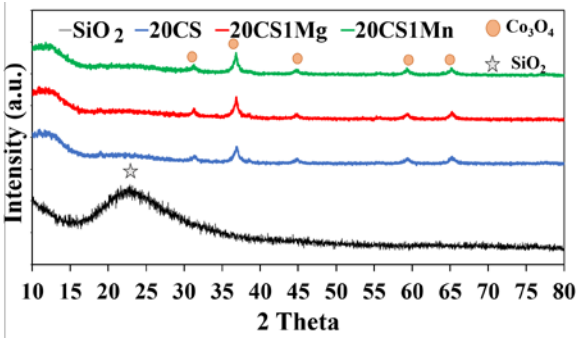

Figure 2. XRD pattern of a) silica support, b) 20CS, c) 20CS1Mg and d) 20CS1Mn catalyst

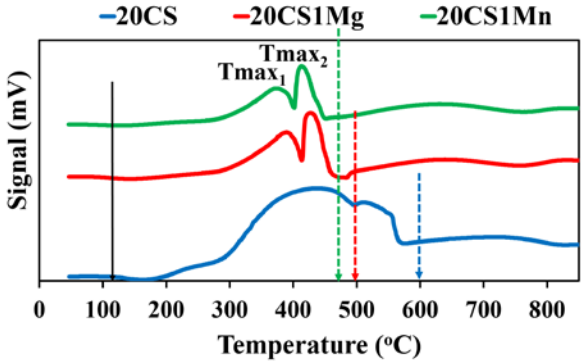

Figure 3. H_2-TPR profiles of catalyst

Table 1. Physical properties of cobalt-based catalysts

Sample	Surface area (m^2/g)*	Total pore volume (cm^3/g)*	Mean pore diameter (nm)*	Percent Metal Dispersion (%)**	Average Crystallite Size (nm)**	Monolayer Uptake (µmol/g)**
SiO_2	480.43	0.33	2.66	-	-	-
20CS	309.09	0.25	3.02	1.88	52.97	31.91
20CS1Mn	195.86	0.18	3.49	1.57	63.53	19.95
20CS1Mg	149.69	0.31	7.80	1.15	86.19	16.61

* Evaluated by N_2 adsorption technique

**Evaluated by H_2-TPD technique

Figure 3. presents the TPR profile of all calcined catalysts. The reducibility of cobalt oxide shows similar profile in temperature range from 150-570°C. At least two reduction peaks were observed for all catalysts. TPR profiles of 20CS1Mg and 20CS1Mn depict narrow peak compared to the 20CS catalyst, which has two distinct broaden peak and a shoulder peak at lower temperature. These indicate that the catalyst was reduced at least in two steps reduction. The first peak corresponds to the reduction of Co_3O_4 to CoO, while the second peak can be assigned to the reduction of CoO to Co.[11] Additionally, the reduction peak above 650 °C present the reduction of cobalt silicate species. The parent 20CS catalyst is completely reduced at temperatures 570 °C, while promoted catalysts are completely reduced at lower temperatures (approximately 480 °C). Profile of 20CS1Mn depicts lower $Tmax_1$ and $Tmax_2$ compared to 20CS1Mg catalyst. The shift to lower reduction temperature hints that Mn promoter might contribute to the electronic effect for the reduction. Moreover, large particle size of cobalt oxide, obtained when promoters were added, makes its ease for the reduction. The reducibility of catalyst is summarized in the order of 20CS1Mn > 20CS1Mg > 20CS. Mn and Mg promoter increase the reducibility of Co_3O_4. The property for the reduction behavior could be due to the electronic and structural effect of promoter.[12, 13]

The amount of H_2 chemisorption were used to calculated cobalt crystallite size and metal dispersion are reported in Table 1. The average crystallite size of the 20CS1Mn is 63.53 nm and metal dispersion is 1.57%, meanwhile the average crystallite size of the 20CS1Mg is 86.19 nm and metal dispersion is 1.15%. This result can indicate that the addition of Mn and Mg promoter decreases the dispersion of Co particles leading to larger Co crystallites. This is owing to the incorporation of MgO and MnO_x in the Co_3O_4 particle during co-impregnation of catalyst preparation step.

The CO_2-TPD experiment was carried out to study the basicity of the catalysts and the results are shown in Figure 4. CO_2-TPD profile of 20CS catalyst depicts the highest and broaden desorption peak centered around 140 °C, indicating the overlapping of weak and medium basic site of CO_2 adsorption. Large amount of CO_2 desorbed from the 20CS catalyst due to well dispersion of Co over high surface area of mesoporous silica. For the promoted catalyst, desorption peaks shift to higher temperature. Desorption was observed in temperature ranges of 50–135 °C and 150–500 °C, corresponding to weak and medium basic sites of adsorption, respectively. The addition of Mg and Mn promoter increases basicity of catalyst leading to stronger CO_2 adsorption. Obviously, large particle size of Co phase exists with promoter adding, leading to the less amount of CO_2 desorbed from the promoted catalyst. However, the basicity of the catalyst has a major influence on the catalytic performance due to the acidic nature of CO_2. Thus, strong basic sites can enhance catalytic activity and increase the chemisorption and reaction.[14,15]

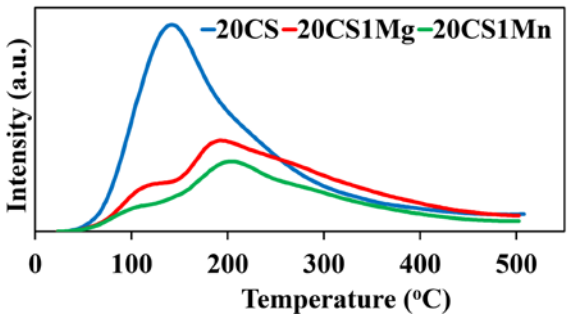

Figure 4. CO_2-TPD profiles of catalyst

Table 2. Catalytic performance of cobalt-based catalyst for 6 hrs. time-on-steams.

Catalysts	CO_2 Conversion (%)	Activity (mol/sec.g of catalyst)				Selectivity (%)			
		C_1	C_2	C_3	C_4	C_1	C_2	C_3	C_4
20CS	3.09	4.89E-06	4.17E-08	-	-	99.16	0.84	-	-
20CS1Mn	2.45	2.61E-06	2.78E-08	3.70E-09	3.38E-09	98.68	1.05	0.14	0.13
20CS1Mg	4.10	2.53E-06	2.95E-08	3.96E-09	3.41E-09	98.56	1.15	0.15	0.14

3.2 Catalytic performance

The catalytic performance of all catalysts was studied in CO_2 hydrogenation at 220°C for 6 hrs. Table 2 displays catalytic activity and product selectivity. %CO_2 conversion of all catalysts are not much different. The activity of 20CS1Mg is slightly higher than 20CS and 20CS1Mn catalyst. Product selectivity of all catalysts presents a decrease in methane along with time-on-stream (2, 4, and 6 hrs.). The promoted catalysts are selective toward C_3 and C_4 hydrocarbons. According to the physical properties and CO_2 TPD, CO_2 is moderately strong adsorbed over all catalyst surfaces. Large particle size of cobalt phase obtained for promoted catalyst assists the possibility for chain growth. The basicity and the redox properties of Mg and Mn may affect the strength of adsorbed CO intermediate from dissociative adsorbed CO_2 and H_2 to produce higher light hydrocarbons.

4. Conclusion

The Mn and Mg promoters influence the physical and chemical properties of cobalt support mesoporous silica catalyst. A significant increase in pore size diameter and average crystallite size of promoted catalyst leads to the ease of catalyst reduction. The CO_2 hydrogenation over the promoted catalyst demonstrates the possibility of chain polymerization during the reaction time (2, 4 and 6 hrs.). The selectivity towards C_3 and C_4 light hydrocarbon gas might be due to the electronic and structural effect of promoter.

Acknowledgements

The authors would like to thank the Research and Development Center for Chemical Engineering Unit Operation and Catalyst Design (RCC), King Mongkut's University of Technology of North Bangkok. This research was founded by Faculty of Science Energy and Environment, King Mongkut's University of Technology of North Bangkok, Rayong Campus (KMUTNB) with Contact No. SciEE-67-001

References

1. Ronda-Lloret, M.; Wang, Y.; Oulego, P.; Rothenberg, G.; Tu, X.; Shiju, N. R., CO2 Hydrogenation at Atmospheric Pressure and Low Temperature Using Plasma-Enhanced Catalysis over Supported Cobalt Oxide Catalysts. *ACS Sustainable Chemistry & Engineering* **2020,** *8* (47), 17397-17407.
2. Tawalbeh, M.; Javed, R. M. N.; Al-Othman, A.; Almomani, F.; Ajith, S., Unlocking the potential of CO2 hydrogenation into valuable products using noble metal catalysts: A comprehensive review. *Environmental Technology & Innovation* **2023,** *31*, 103217.
3. Albeladi, N.; Alsulami, Q. A.; Narasimharao, K., Recent Progress in Nickel and Silica Containing Catalysts for CO2 Hydrogenation to CH4. *Catalysts* **2023,** *13* (7), 1104.
4. Frontera, P.; Macario, A.; Ferraro, M.; Antonucci, P., Supported Catalysts for CO2 Methanation: A Review. *Catalysts* **2017,** *7* (2), 59.
5. Pawelec, B.; Guil-López, R.; Mota, N.; Fierro, J. L. G.; Navarro Yerga, R. M., Catalysts for the Conversion of CO2 to Low Molecular Weight Olefins—A Review. *Materials* **2021,** *14* (22), 6952.
6. Wang, X.; Zhu, L.; Zhuo, Y.; Zhu, Y.; Wang, S., Enhancement of CO2 Methanation over La-Modified Ni/SBA-15 Catalysts Prepared by Different Doping Methods. *ACS Sustainable Chemistry & Engineering* **2019,** *7* (17), 14647-14660.
7. Zhang, Z.; Wei, C.; Jia, L.; Liu, Y.; Sun, C.; Wang, P.; Tu, W., Insights into the regulation of FeNa catalysts modified by Mn promoter and their tuning effect on the hydrogenation of CO2 to light olefins. *Journal of Catalysis* **2020,** *390*, 12-22.
8. Sharma, S.; Paul, B.; Srivastava, A.; Pal, R. S.; Poddar, M.; Khan, T.; Samanta, C.; Bal, R., The role of MgO during CO2 hydrogenation to methanol over Pd/ZnO Catalyst. *Sustainable Chemistry for Climate Action* **2023,** *2*, 100019.

9. Intarasiri, S. Development of Cobalt-Based Catalyst for Synthetic Liquid Fuels via Fischer-Tropsch Reaction in Multichannel Reactor Fischer - Tropsch Reaction. Research, King Mongkut's University of Technology North Bangkok, King Mongkut's University of Technology North Bangkok, 2017.
10. Warayanon, W.; Tungkamani, S.; Sukkathanyawat, H.; Phongaksorn, M.; Ratana, T.; Sornchamni, T., Effect of Manganese Promoter on Cobalt Supported Magnesia Catalyst for Fischer-Tropsch Synthesis. *Energy Procedia* **2015,** *79*, 163-168.
11. Ehrhardt, C.; Gjikaj, M.; Brockner, W., Thermal decomposition of cobalt nitrato compounds: Preparation of anhydrous cobalt(II)nitrate and its characterisation by Infrared and Raman spectra. *Thermochimica Acta* **2005,** *432* (1), 36-40.
12. James R. Gallagher , P. B., Gary B. Combes , Don Ozkaya , Dan I. Enache , Peter R. Ellis , Gordon Kelly , John B. Claridge and Matthew J. Rosseinsky, The effect of Mg location on Co-Mg-Ru/γ-Al2O3 Fischer–Tropsch catalysts. *Philosophical Transactions of the Royal Society A: Mathematical, Physical and Engineering Sciences* **2016,** *374* (2061), 18.
13. Dalebout, R.; Barberis, L.; Visser, N. L.; van der Hoeven, J. E. S.; van der Eerden, A. M. J.; Stewart, J. A.; Meirer, F.; de Jong, K. P.; de Jongh, P. E., Manganese Oxide as a Promoter for Copper Catalysts in CO2 and CO Hydrogenation. *ChemCatChem* **2022,** *14* (19), e202200451.
14. Zhu, F.; Zhang, H.; Yan, X.; Yan, J.; Ni, M.; Li, X.; Tu, X., Plasma-catalytic reforming of CO2-rich biogas over Ni/γ-Al2O3 catalysts in a rotating gliding arc reactor. *Fuel* **2017,** *199*, 430-437.
15. Słoczyński, J.; Grabowski, R.; Kozłowska, A.; Olszewski, P.; Lachowska, M.; Skrzypek, J.; Stoch, J., Effect of Mg and Mn oxide additions on structural and adsorptive properties of Cu/ZnO/ZrO2 catalysts for the methanol synthesis from CO2. *Applied Catalysis A: General* **2003,** *249* (1), 129-138.
16. Liu, H.; Xu, S.; Zhou, G.; Xiong, K.; Jiao, Z.; Wang, S., CO2 hydrogenation to methane over Co/KIT-6 catalysts: Effect of Co content. *Fuel* **2018,** *217*, 570-576.

Photocatalytic activity of N- and S-heteroatoms co-doped on graphene quantum dots under visible irradiation for degradation of organic dye

Ilada Sanprasert[1], Okorn Mekasuwandumrong[2], and Joongjai Panpranot[1,*]

[1]*Center of Excellence on Catalysis and Catalytic Reaction Engineering, Department of Chemical Engineering, Faculty of Engineering, Chulalongkorn University, Bangkok 10330, Thailand*

[2]*Department of Chemical Engineering, Faculty of Engineering and Industrial Techonology, Silpakorn University, Nakorn Pathom 73000, Thailand.*

**E-mail: joongjai.p@chula.ac.th (J. Panpranot)*

Abstract:

The rapid industrialization and increased use of organic dyes for production in many industries have led to extensive environmental pollution concerns. In this research, we investigate the synthesis and applications of nitrogen and sulfur co-doped graphene quantum dots (N,S-GQDs) as photocatalysts for degradation of organic dyes. N,S-GQDs were prepared via hydrothermal method using glycine as the carbon precursor with incorporation of nitrogen and sulfur heteroatoms using ammonium sulfate as nitrogen and sulfur sources. The presence of carbon, oxygen, nitrogen, and sulfur on the prepared N,S-GQDs was confirmed by SEM-EDX analysis. The particle size of the N,S-GQDs is approximately 10 nm based on the TEM measurement. Methylene blue (10 ppm) is a representative of organic dye solution that was used to evaluate the photocatalytic performance under visible light source that was produced by xenon lamp with wavelengths from 100 to 1100 nm. The concentration of methylene blue was measured using UV-visible spectrophotometer at a wavelength of 665 nm, The results demonstrate that N,S-GQDs can contribute to highly efficient photodegradation of methylene blue at room temperature with 77 % conversion after 2 h reaction time

1. Introduction

Nowadays, the world is confronting a plentiful of pollution and one of the most essentially environmental problems is water pollutant, which due to diverse activities in human consisting of household and industries waste lead to lack of fresh water for living.[1] Mostly contaminant in wastewater is organic dye solutions from many industries such as textiles, leather, paint, paper, cosmetics, ceramic, ink and medication that are transferred to water bodies during products making process.[2-4] Dye are harmful to aquatic plants and animals cause it can cover entire surface of the water to create obstruction of the sunlight for photosynthesis of living organism underwater.[4,5] Water is the importantly necessary factor of human being and environment hence it is essential that the wastewater be treated with removal of organic dye contaminants.[6] Normally, degradation of organic pollutants is carried out by several methods for example adsorption, chemical precipitation, coagulation, photodegradation, membrane filtration, and ion-exchange etc.[7,8] However photodegradation using photocatalysts have attracted attention due to their alternative green methods and cost-effective for organic dye degradation.[9]

In recent years, graphene quantum dots (GQDs) have received considerable interest in a variety of applications, for instance catalysis, molecular imaging, drug delivery, and biosensors because of their unique properties exhibit excellent photostability, good biocompatibility, chemical stability, low toxicity, and water solubility.[10,11] Moreover, GQDs are commonly doped with heteroatoms such as nitrogen (N)[12], boron (B)[13], and sulfur (S)[4] etc. to improve their photocatalytic performance. In previous studies, researchers have prosperously prepared N and S co-doped on GQDs that showed excellent photocatalytic activity and small band-gap which, corresponds with visible light spectrum led to active under visible region.[2,14] The GQDs can be synthesized using different methods that are generally separated into two groups consisting of bottom-up and top-down approaches.[14] In the bottom-up method, it is usually prepared from carbon-containing small precursors via chemical reaction. [15] On the other hand, the top-down technique GQDs are synthesized by using physical or chemical approaches to transform larger carbon structures into smaller quantum dots.[16] GQDs can be synthesized by using bottom-up technique with various natural-based as carbon source including

citric acid, starch, plant, fruit, and hair etc. via hydrothermal method.[2]

In our study, we synthesized nitrogen and sulfur co-doped on GQDs and employed as a photocatalyst via bottom-up approach using hydrothermal reaction under relatively mild conditions with glycine as the carbon precursor along with ammonium sulfate as nitrogen and sulfur source. Methylene blue was used to represent the organic dye solution for photodegradation testing under visible irradiation.

2. Materials and Methods

2.1 Materials

The precursor for synthesis of graphene quantum dots i.e. glycine (KRUNGTHEPCHEMI CO.,LTD, Thailand.), ammonium sulfate ($(NH_4)_2SO_4$: KEMAUS, Australia.), hydrogen peroxide (H_2O_2 : NIPPON INTERTRADE CO.,LTD, Thailand), deionized water. Methylene blue as organic dye solution.

2.2 Synthesis of N, S co-doped graphene quantum dots (N,S-GQDs)

N,S-GQDs was prepared with 5.63 g of glycine and 2.64 g of ammonium sulfate were dissolved in 36.5 ml of deionized water and 13.5 ml of 35% hydrogen peroxide to obtained final volume of 50 ml after that the mixture was stirred under temperature of 300 °C and stirring rate of 390 rpm for 40 minutes (or until the mixture be similar to a black mud). Then the sample was dried in carbolite with temperature of 270 °C overnight and would get the black powder. The final product was washed by deionized water several times and dried in 110 °C oven overnight.

2.3 Characterization

The sample analyzation consisting of powder X-ray diffraction (XRD) measurement was carried out by a Siemens D5000 diffractometer with CuK_α radiation (λ = 1.5418 Å) in scanning range of 2θ between 10° to 80° to determine the crystalline of the photocatalyst. Transmission electron microscopy (TEM) images were obtained using a Talos F200X (STREC, Chulalongkorn university, Thailand). The elemental compositions analyses were determined using a scanning electron microscopy (SEM) and energy dispersive X-ray (EDX) with Hitachii mode S-3400N. The optical properties were analyzed by a Varian Cary 5000 UV-Vis-NIR UV-visible spectrophotometer.

2.4 Photocatalytic activity measurement

The organic dye solution that was used to estimate photocatalytic performance is methylene blue (MB) with concentration of 10 ppm (10 mg/L). 0.1 g of N,S-GQDs was dispersed into 50 ml of methylene blue solution. Before irradiation, the mixture was magnetically stirred at 500 rpm under ambient temperature in photoreactor without any light source for 30 minutes to ensure the establishment of adsorption-desorption equilibrium between methylene blue solution and photocatalyst surface. After that the solution was exposed to visible light irradiation using a 35 W, 12 V xenon lamp for 120 minutes and 5 ml of sample was withdrawn every 20 minutes for analysis of MB concentration. Prior to analysis, the samples were centrifuged to remove solid catalyst particles. The methylene blue concentration was determined by UV-visible spectrophotometer at wavelength 665 nm. The degradation efficiency of organic dye solutions was calculated using the following equation:

$$\text{Degradation (\%)} = \frac{C_0 - C}{C_0} \times 100 \qquad (1)$$

where C_0 and C represent the concentration of dye at the initial ((t) = 0 s) and time ((t) = t s), respectively.

3. Results & Discussion

3.1 Characteristics of the catalysts

The crystallinity of the synthesized N,S-GQDs was confirmed by the XRD results as shown in Figure 1. A sharp diffraction peak around 27° (2θ), corresponding to the (002) plane of graphite indicated the N,S-GQDs has a graphitic nature with some amorphous carbon.[2,6,17]

Raman spectroscopy technique was performed to determine defects, disorder, and structural imperfections in the carbon materials. The D band in the Raman spectrum is associated with defects and disorder, and its intensity can provide insights into the structural quality of the material. The Raman result of the prepared N,S-GQDs is shown in Figure 2. Two outstanding Raman peaks demonstrated disordered D-band

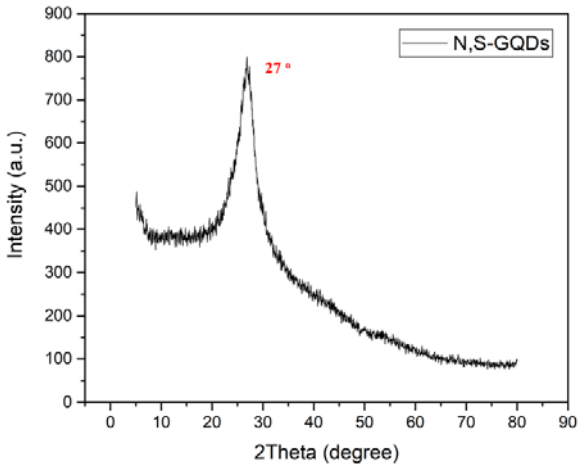

Figure 1. XRD pattern of N,S-GQDs.

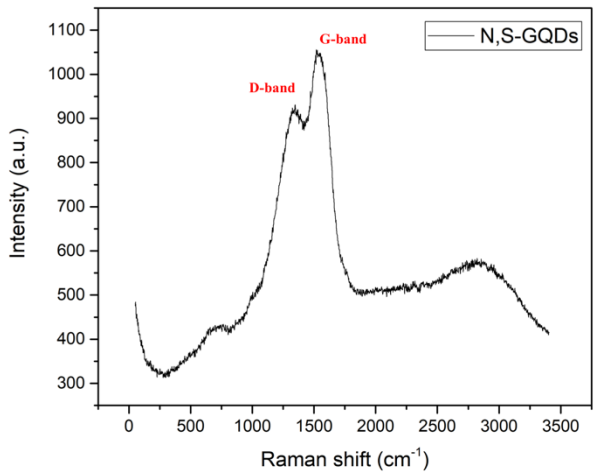

Figure 2. Raman spectra of N,S-GQDs.

around 1375 cm^{-1}, corresponding to presence of sp^3 hybridized carbon, and the crystalline G band which is associated to sp^2 carbon atoms display around 1550 cm^{-1}. Generally, the intensity ratio between D-band (I_D) and G-band (I_G) is used as a quantitative measure of the structural of graphene-based materials. In this spectrum, the intensity of G-band is higher than D-band and the calculated corresponding ratio (I_D/I_G) is 0.88, which is higher than the pristine graphene. Defects in the N,S-GQDs or a partially disordered crystal structure are proposed, to be stemming from the small size of sp^2 cluster.[14,18-20]

The TEM images of N,S-GQDs are shown in Figure 3. The N,S-GQDs are spherical with particle size around 10 nm with the lattice spacing approximately 0.205 nm, which is related to

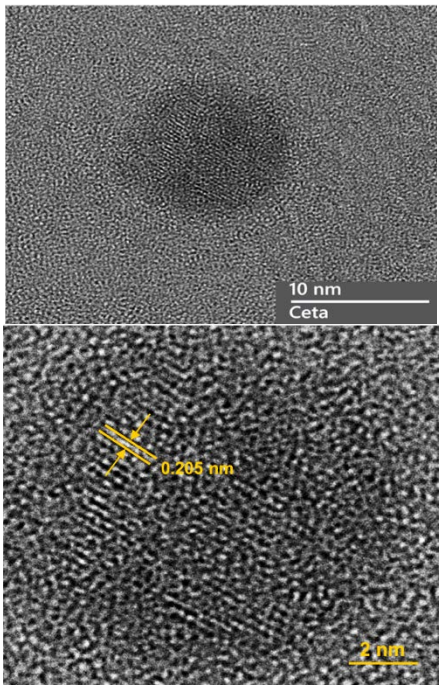

Figure 3. TEM image for N,S-GQDs.

graphitic carbon in the synthesized N,S-GQDs. In addition, the value of lattice spacing can be ascribed to (100) plane of sp^2 hybridized carbon nanostructures.[6,10,14,17,21]

The elemental distribution and elemental composition of the synthesized N,S-GQDs were indicated by SEM-EDX-Mapping result as shown in Figure 4a-b. and Table 1, respectively. Carbon, nitrogen, oxygen, and sulfur were detected in the

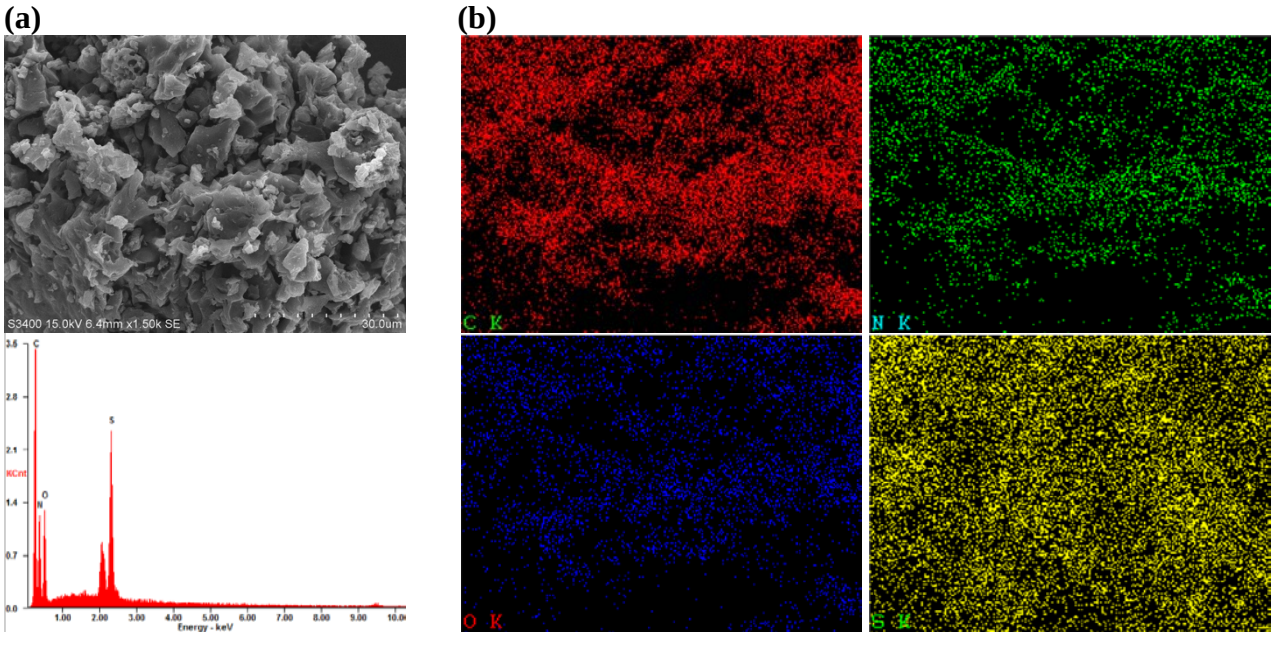

Figure 4. (a) SEM-EDX image and (b) SEM elemental mapping image of N,S-GQDs.

Table 1. Elemental weight and atomic percentages of N,S-GQDs.

Element	Line type	Wt %	At %
C	K series	40.57	48.89
N	K series	27.46	28.38
O	K series	18.32	16.58
S	K series	13.64	6.16
Matrix		Correction	ZAF

structure of the synthesized N,S-GQDs, confirming that nitrogen and sulfur were successfully incorporated into GQDs. From the atomic percentages of each element, carbon has the highest concentration at around 50 At.%, confirming that carbon is the predominant element in the graphitic structure.

The UV spectrum is shown in Figure 5. It was carried out to measure the optical properties of the N,S-GQDs in wavelength between 200 to 800 nm. In this region, we observed two major absorption peaks at ~232 nm and ~332 nm, which could be related to $\pi - \pi^*$ transitions of aromatic C=C and n $-$ π^* transition of C=O and C=N group on surfaces, respectively.[2,4,18,22]

3.2 Photocatalytic performance

The results of photocatalytic activity testing are shown in Figure 6 (a-b). The comparative between different doses of N,S-GQDs to degrade 10 ppm MB solution are observed in Figure 6a. It indicates that the degradation efficiencies of 50 mg of N,S-GQDs is ~35.53 % in 120 min, whereas the 100 mg of N,S-GQDs reveals around 77.99 % degradation. Higher photocatalytic activity was observed when increased the concentration of the photocatalyst due to the increasing of the number of active sites to react with MB solution in degradation process. Figure 6b presents the efficiency of N,S-GQDs when absorbing the MB dye solution without visible light illumination in 120 min. The result demonstrates that the activity of N,S-GQDs

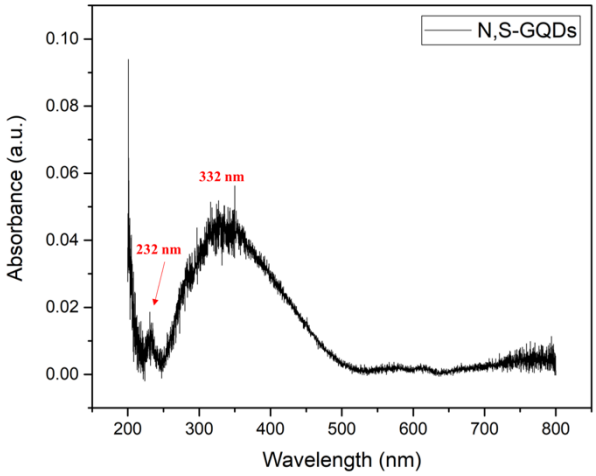

Figure 5. UV spectrum of N,S-GQDs.

in dye degradation was lower compared to their performance under visible light. Hence, to increase the performance of N,S-GQDs, it is necessary to work with visible irradiation. Because of light, the photocatalyst can generate the active sites to decompose organic dye solution.

3.3 Photodegradation mechanism

The possible mechanism pathway of photocatalytic degradation using N,S-GQDs is provided in Scheme 1. When photocatalyst is treated by visible light source, electrons (e^-) in valence band (VB) can be excited and transit to conduction band (CB), then hole (h^+) are generated and left on the valence band. At the same time, the electron-hole pairs (e^-/h^+) initiate redox reactions on the photocatalyst surface composing of e^- from valence band that can trap with O_2, which plays role in accepting electrons and is reduced to superoxide anion radicals ($\cdot O_2^-$), while h^+ on the valence band can react with water due to water provides protons to generate hydroxyl radicals ($\cdot OH^-$) during the redox reactions. Hence, these radicals including h^+, $\cdot O_2^-$, and $\cdot OH^-$ are the active species that attack and break down the MB dye solution to carbon dioxide and water.

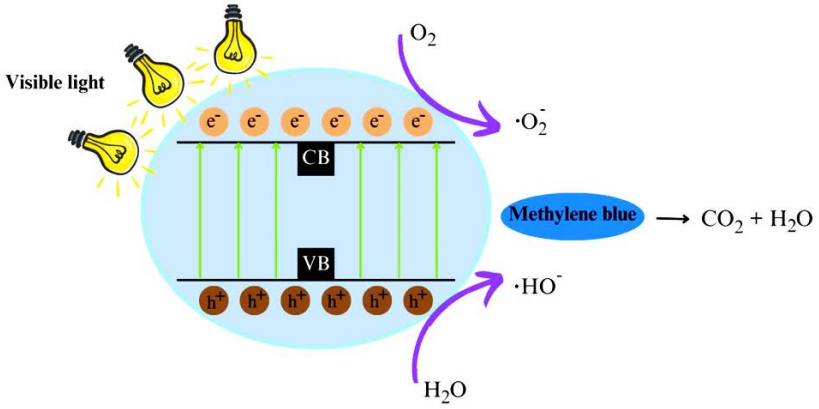

Scheme 1. Photocatalytic mechanism pathway of N,S-GQDs.

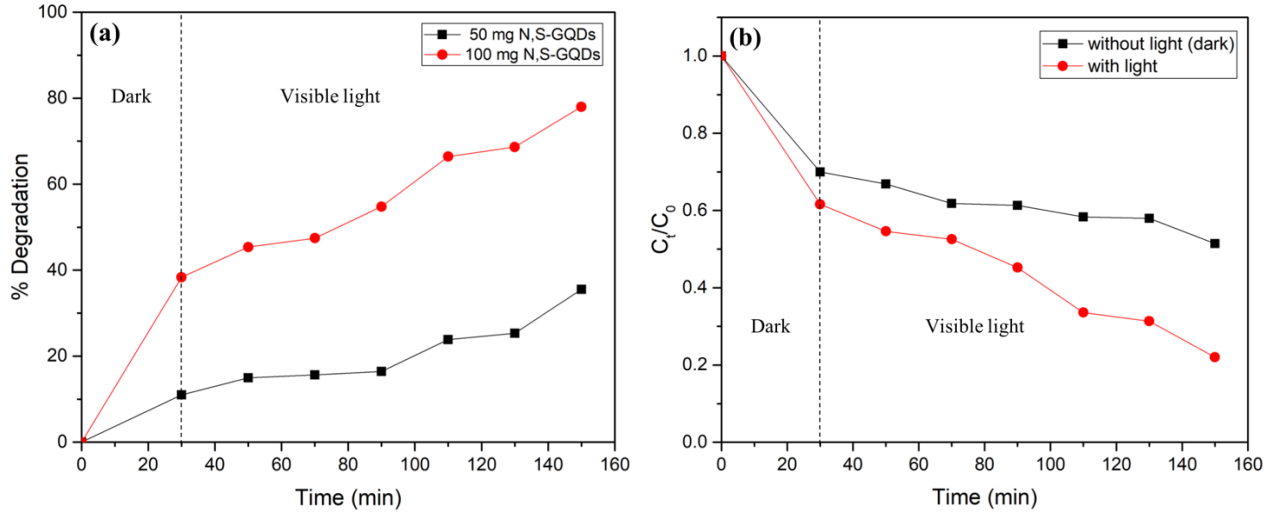

Figure 6. The comparison of degradation efficiency between (a) 50 mg and 100 mg of N,S-GQDs, (b) under visible irradiation and without visible irradiation with 100 mg of N,S-GQDs.

4. Conclusions

In this report, nitrogen and sulfur heteroatoms co-doped on graphene quantum dots were synthesized through a hydrothermal reaction of a natural-based compound under mild conditions using glycine as carbon precursor. The characteristics of N,S-GQDs were analyzed by XRD, Raman, TEM, SEM-EDX, and UV-vis techniques. The results indicate the successful synthesis of N,S-GQDs with a particle size approximately 10 nm. In addition, nitrogen and sulfur were successfully incorporated into GQDs in the synthesis step. The photocatalytic testing results reveal that 100 mg of N,S-GQDs give 77.99 % degradation after 2 h reaction time under visible light irradiation. The degradation process was described in the mechanism pathway.

Acknowledgements

The authors would like to thank Center of Excellence in Catalysis and Catalytic Reaction Engineering (CECC) and CrystalLyte Co., Ltd. Or supporting this research.

References

1. Mohammadnejad, M.; Nekoo, N. M.; Alizadeh, S.; Sadeghi, S.; Geranmayeh, S. Enhenced removal of organic dyes from aqueous solutions by new magnetic HKUST-1:facile strategy for synthesis. *Scientific reports*. **2023**, 13, 17981.
2. Selvakumar, T.; Rajaram, M.; Natarajan, A.; Harikrishnan, L.; Alwar, K.; Rajaram, A. Highly efficient sulfur and nitrogen codoped graphene quantum dots as a metal-free green photocatalyst for photocatalysis and fluorescent ink applications. *ACS Omega*. **2022**, 7, 12825-12834.
3. Shamsipur, M.; Rajabi, H. R. Study of photocatalytic activity of ZnS quantum dots as efficient nanoparticles for removal of methyl violet: Effect of ferric ion doping. *Spectrochimica Acta Part A: Molecular and Biomolecular Spectroscopy*. **2014**, 122, 260-267.
4. Rani, U. A.; Ng, L. Y.; Ng, C. Y.; Mahmoudi, E.; Hairom, N. H. H. Photocatalytic degradation of crystal violet dye using Sulphur-doped carbon quantum dots. *Materials Today: Proceeding*. **2021**, 46, 1934-1939.
5. Tammina, S. K.; Mandal, B. K.; Kadiyala, N. K. Photocatalytic degradation of methylene blue dye by nonconventional synthesized SnO_2 nanoparticles. *Environmental Nanotechnology, Monitoring & Management*. **2018**, 10, 339-350.
6. Atchudan, R.; Edison, T. N. J. I.; Perumal, S.; Muthuchamy, N.; Lee, Y. R. Hydrophilic nitrogen-doped carbon dots from biowaste using dwarf banana peel for environmental and biological applications. *Fuel*. **2020**, 275, 117821.
7. Rajabi, H. R.; Farsi, M. Study of capping agent effect on the structural, optical and photocatalytic properties of zinc sulfide quantum dots. *Materials Science in Semiconductor Processing*. **2016**, 48, 14-22.
8. Mukherjee, D.; Das, P.; Kundu, S.; Kundu, L. M.; Mandal, B. Graphene quantum dots decorated MIL-100(Fe) composites for dye degradation. *Journal of Photochemistry & Photobiology, A: Chemistry*. **2023**, 442, 114776.
9. Shamsipur, M.; Rajabi, H. R.; Khani, O. Pure and Fe^{3+}-doped ZnS quantum dots as novel and

efficient nanophotocatalyst: Synthesis, characterization and use for decolorization of Victoria blue R. *Materials Science in Semiconductor Processing*. **2013**, 16, 1154-1161.
10. Taymaz, B. H.; Kurukavak, C. K.; Kamis, H.; Kus, M. Improved visible light-driven photocatalytic degradation of methylene blue and methyl red by boron-doped carbon quantum dots. *Turkish Journal of Chemistry*. **2022**, 46, 1128-1136.
11. Kalluri, A.; Dharmadhikari, B.; Debnath, D.; Patra, P.; Kumar, C. V. Advance in structural modifications and properties of graphene quantum dots for biomedical applications. *ACS Omega*. **2023**, 8, 21358-21376.
12. Du, Y.; Guo, S. Chemically doped fluorescent carbon and graphene quantum dots for bioimaging, sensor, catalytic and photoelectronic applications. *Nanoscale*. **2016**, 8, 2532.
13. Tam, T. V.; Kang, S. G.; Babu, K. F.; Oh, E. S.; Lee, S. G.; Choi, W. M. Synthesis of B-doped graphene quantum dots as a metal-free delctrocatalyst for oxygen reduction reaction. *J. mater. Chem*. A. **2017**, 5, 10537.
14. Qu, D.; Zheng, M.; Du, P.; Zhou, Y.; Zhang, L.; Li, D.; Tan, H.; Zhao, Z.; Xie, Z.; Sun, Z. Highly luminescent S,N co-doped graphene quantum dots with broad visible absorption for visible light photocatalyst. *Nanoscale*. 2013, 5, 12272.
15. Ibarbia, A.; Grande, H. J.; Ruiz, V. On the factors behind the photocatalytic activity of graphene quantum dots for organic dye degradation. *Part. Part. Syst. Charact*. **2020**, 2000061.
16. Kang, H.; Kim, D.; Cho, J. Top-down fabrication of luminescent graphene quantum dots using self-assembled Au nanoparticles. *ACS Omega*. **2023**, 8, 5885-5892.
17. Atchudan, R.; Edison, N. J. I.; Aseer, K. R.; Perumal, S.; Lee, Y. R. Hydrothermal conversion of Magnolia liliiflora into nitrogen-doped carbon dots as an effective turn-off fluorescence sensing, multi-colour cell imaging and fluorescent ink. *Colloids and Surfaces B: Biointerfaces*. **2018**, 169, 321-328.
18. Tian, H.; Shen, K.; Hu, X.; Qiao, L.; Zheng, W. N,S co-doped graphene quantum dots-graphene-TiO2 nanotubes composite with enhanced photocatalytic activity. *Journal of Alloys and Compounds*. **2017**, 691, 369-377.
19. Zhang, M.; Bai, L.; Shang, W.; Xie, W.; Ma, H.; Fu.; Fang, D.; Sun, H.; Fan, L.; Han, M.; Liu, C.; Yang, S. Facile synthesis of water-soluble, highly fluorescent graphene quantum dots as a robust biological label for stem cells. *J. Mater. Chem*. **2012**, 22, 7461.
20. Kuo, N. J.; Chen, Y. S.; Wu, C. W.; Huang, C. Y.; Chan, Y. H.; Chen I. W. P. One-pot synthesis of hydrophilic and hydrophobic N-doped graphene quantum dots via exfoliating and disintegrating graphite flakes. *Scientific Report*, **2016**, 6, 30426.
21. Leong, K. H.; Fong, S. Y.; Lim, P. F.; Sim, L. C.; Saravanan, P. Physical mixing of N-doped graphene quantum dots functionalized TiO2 for sustainable degradation of methylene blue. *Materials Science and Engineering*. **2018**, 409, 012009.
22. Mondal, T. K.; Dinda, D.; Saha, S. K. Nitrogen, sulfur co-doped graphene quantum dot: An excellent sensor for nitroexplosives. *Sensors and Actuators B: Chemical*. **2018**, 257, 586-593.

Solid acid catalyst development from rubber tire waste for biofuel and biochemical production

Yanisa Doungkumchan[1] and Sarttrawut Tulaphol[2]*

Department of Chemistry, Faculty of Science, King Mongkut's University of Technology Thonburi, Bangkok, Thailand 10140

**E-mail: sarttrawut.tul@kmutt.ac.th*

Abstract:

The growth of vehicle industries increases the demand for rubber tires, resulting in high rubber tire waste affecting the environment. Using rubber tire waste is one of the methods to reduce environmental concerns as follows as Bio-Circular-Green-Economy (BCG). Many researchers have developed a way to utilize rubber tires in new applications, such as catalysts and adsorbents. To synthesize a rubber tire as a solid acid catalyst, the rubber tire is pyrolyzed at a high temperature to form carbon and further functionalized into a solid acid catalyst. Although this method seems promising, the process is complex and involves pyrolysis, leading to high energy consumption. This research aims to develop a solid acid catalyst from rubber tire waste using an uncomplex method and low energy consumption by the sulfonation reaction of rubber tires. The effects of catalyst synthesis were studied on the efficiency and stability through the esterification of levulinic acid and methanol as a probe reaction against a commercial solid acid catalyst (Amberlyst-15). The TW-SO_3H synthesized under 150 ^oC and 98% H_2SO_4 concentration showed higher catalyst performance than Amberlyst-15 up to 10% conversion with high product selectivity at 98% conversion and catalyst recyclability. This research approach addresses the environmental impact of waste tires and contributes to sustainable catalyst development, paving the way for an eco-friendly waste management strategy.

1. Introduction

Currently, the waste from car tires is a significant environmental concern. With the increasing production rate of tire rubber in tandem with the production of automobiles, data indicates a substantial rise in car production. One billion tires reach the end of their lifespan1 in one year alone,[1] highlighting a considerable volume of waste generated. The disposal of car tire waste presents challenges due to its slow decomposition and low economic value.[2] Traditional methods such as burial are unsustainable, as tire waste requires a long time to degrade and occupies significant space. Burning, used as fuel in cement production, represents a recycling method. Still, it releases toxic substances like carbon oxides (NOx), nitrogen oxides (COx), and sulfur oxides (SOx), directly impacting air pollution.

Recycling non-incinerated tire waste involves incorporating it into road construction, artificial turf, or as a component in various industries. Additionally, the waste can be activated for absorbing pollutants in water, such as methylene blue (MB), organic matter (MO), and trichloroethylene (TC), with absorption capacities reaching up to 833 mg/g for MB, 555 mg/g for MO, and 303 mg/g for TC.[3] Furthermore, tire waste is used as a substitute for positive electrodes in lithium batteries[4] showing a high coulombic efficiency of 71%. Pyrolysis technology is employed for tire reuse as a solid acid catalyst in biodiesel production. The process involves pyrolyzing tires without oxygen and sulfonation using sulfonic groups derived from sulfuric acid. This results in a solid acid catalyst with BrØnsted acidity sites, demonstrating high efficiency in transesterification and esterification reactions with up to 80% methyl ester yield.[5]

As exemplified by Amberlyst-15, solid acid catalysts are heterogeneous catalysts widely used in various industries, including esterification, etherification, cyclization, and electrophilic aromatic substitution reactions.[6] In esterification reactions for biodiesel production from organic acids and ethanol, Amberlyst-15 exhibits a high yield of up to 53%.[7]

This research aims to synthesize a solid acid catalyst from tire waste without pyrolysis. The catalyst will be tested in esterification of levulinic acid and methanol to assess its performance compared to Amberlyst-15. The goal is to find a catalyst that can be effectively applied to other reactions and studied for potential reuse.

2. Materials and Methods

2.1 Chemicals and Material

Sulfuric acid (purity, 98%), Methanol (purity, 99.9%), and Ethanol (purity, 99.9%) were purchased from Qrec (New Zealand). Levulinic Acid (purity,>97%) and Methyl Levulinate (purity, >99%) were purchased from TCL (Japan). Amberlyst-15 was purchased from Sigma-

Aldrich. All chemicals were analytical grade and used without further purification unless noted.

Tire waste provided by Union Commercial Development Company, Thailand. The size of tire waste was 20 mesh (850 µm), and the ASTM D5644 test method and the sieving standards followed ASTM E1. The samples were dried at a temperature of 80°C to eliminate moisture.

2.2 Synthesis of acid catalyst

A sample of 5.00 grams of tire waste was combined with 50 ml of concentrated sulfuric acid at a ratio of 1:10. The mixture underwent reflux at a temperature of 150°C for 1 h, with continuous stirring at a rotation rate of 400 rpm. After completion, the reaction mixture was allowed to cool to room temperature. Subsequently, 200 ml of cold deionized water. The solution was further diluted by adding 500 ml of deionized water 4 times, and the mixture was filtered until reaching a neutral pH of around 7. The filtrate was heated at 80°C until dry.

2.3 Titration acid-base of TW-SO_3H

The acidity of TW-SO_3H, which indicates the content of -SO_3H groups, was determined by the back titration method. 0.0085 M of NaOH was standardized with KHP. Then, 0.1 g of TW-SO_3H was stirred in 10 mL of 0.0085M of NaOH for 10 h. The solution was filtered the TW-SO_3H out. The filtrate was titrated with 0.0136 M of HCl using phenolphthalein as an indicator. The acidity of TW-SO_3H was calculated using the following equation:

$$\text{Total Acidity} = \frac{(\text{Mol initial NaOH - Mol remained NaOH})}{\text{grams of catalyst used}}$$

When Mol initial NaOH is initial mol NaOH of 10 ml 0.0085 M NaOH and Mol remained NaOH is NaOH mol titrated with 0.0136 M HCl.

2.4 Esterification of levulinic acid and methanol

Esterification of levulinic acid and methanol was conducted in a 10 ml headspace vial at a molar ratio of 1:25 (0.5g levulinic acid: 3.5g methanol), followed by the addition of a catalyst (10% loading). The solution was heated at 65 °C for 2 h at 400 rpm in a silicone bath, and samples were collected every 30 minutes. The reaction was halted by immersing the vial in an ice bath and adding 5.00 ml of ethanol to dissolve levulinic acid and methanol. The mixture was then shaken with a vortex mixer at 3600 rpm. Samples were collected and filtered before analysis using a GC-FID.

The efficiency of the catalyst was determined by measuring the concentration of reactants and products using a gas chromatograph (Nexis GC-2030, Shimadzu, Japan) equipped with a mass spectrometer and flame ionization detector (FID). The analytical conditions included an HP-INNOWAX column (30m x 0.25 mm x 0.25 µm) with an injection temperature of 250 °C and an FID detector temperature of 250°C. The split ratio was 1:100. The temperature program started at 80°C, increased to 170°C at a heating rate of 8 °C/min, and then further increased to 240°C at a heating rate of 15°C/min. Levulinic acid conversion (LA conversion), Methyl levulinate as product yield (ML yield), and product selectivity (ML selectivity) were calculated using the following formulas:

$$\text{LA conversion (\%)} = \frac{\text{reactant reacted (mol)}}{\text{initial reactant (mol)}} \times 100$$

$$\text{ML yield (\%)} = \frac{\text{product generated (mol)}}{\text{initial reactant (mol)}} \times 100$$

$$\text{ML selectivity (\%)} = \frac{\text{product yield}}{\text{reactant conversion}} \times 100$$

3. Results & Discussion

3.1 Characterize properties of sulfonated tire waste

As illustrated in Figure 1, the FTIR results revealed a significant peak in the wavenumber range of 1074-1038 cm^{-1}, indicating the attachment of the sulfonic group within the structure of the tire powder used in the reaction. This finding aligns with sulfonation[8]. A peak of the -OH group appeared at the wavenumber 3695 cm^{-1}, signifying increased hydrogen due to more sulfonic groups in the structure.

Additionally, the main structure of the tire waste sample displayed CH_2 bending at wavenumbers 1379 and 1430 cm^{-1}, attributed to the deformation from CH_2 stretching and CH_3 stretching observed at wavenumbers 2859 cm^{-1} and 2920 cm^{-1}, respectively.[8,9]

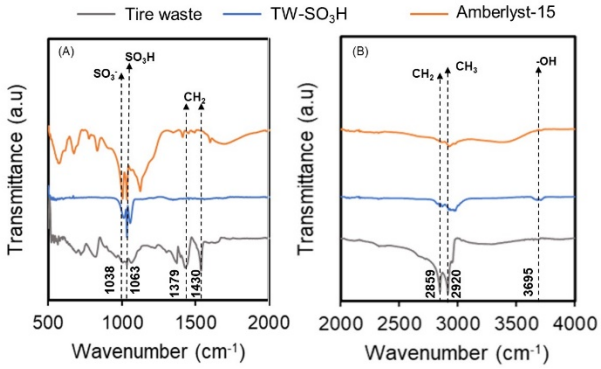

Figure 1. FTIR spectra of the sulfonated tire waste (TW-SO_3H), Tire waste, and Amberlyst-15

We utilized suspension and contact angle measurements to assess the hydrophilicity and density of the catalyst compared to water. The results, shown in Figure 2, indicated that the tire waste had a contact angle of 150° and was less dense than water, as observed by its floating on the surface. Amberlyst-15 and the sulfonated tire waste (TW-SO_3H) were hydrophilic and had a contact angle of 0°, demonstrating a higher density than water and indicating higher hydrophilicity than tire waste. This characteristic is considered beneficial for use in various reactions.

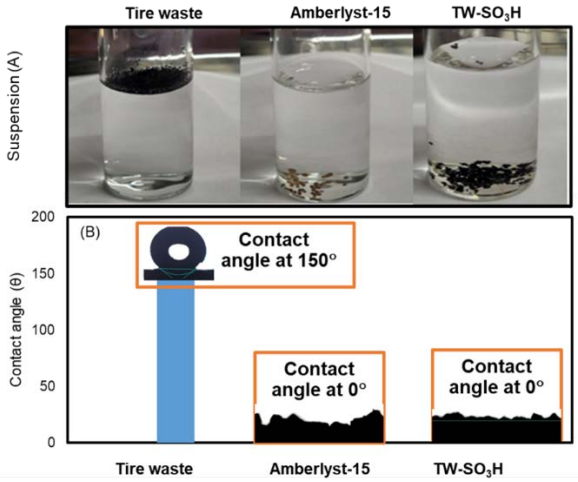

Figure 2. Physical characteristics of the sulfonated tire waste (TW-SO_3H), Tire waste, and Amberlyst-15 by suspension (A) and contact angle (B).

3.2 Effect of Reaction Parameters on Esterification

The efficiency of the catalyst is studied through the reaction. The esterification of levulinic acid with methanol has factors explored, including temperature, Molar ratio between levulinic acid and methanol, and Catalyst loading.

3.2.1 Effect of Molar Ratio

Figure 3 (A) shows a comparison of the molar ratio between levulinic acid (LA) and methanol at a temperature of 65°C, 10% catalyst loading, and a reaction time of 2 h. We found that the 1:10 molar ratio of LA with methanol had the lowest LA conversion, ML yield, and ML selectivity compared with the 1:25 and 1:50 molar ratio of LA with methanol. The result found that a 1:25 molar ratio of LA with methanol had the highest LA conversion, ML yield, and selectivity due to different moles of methanol at high methanol moles. The reactants can interact more efficiently at higher methanol concentrations.[10] However, the 1:50 molar ratio of LA with methanol had higher moles of methanol, but the results were not high. This is because having too much methanol can lead to lower product yield. As a result, Figure 3 (A) shows that ML yield does not increase when conversion increases.

3.2.2 Effect of temperature and catalyst loading

From Figure 3 (B), which illustrates a comparison of the temperatures used in the reaction, the study compared three temperature ranges: 50°C, 65°C, and 80°C, at a 1:25 molar ratio of levulinic acid with methanol over a 2 h reaction time and 10% catalyst loading. An increase in temperature from 50°C to 80°C improved LA conversion from 62% to 98% at 120 min. These results indicated a trend where temperature variations significantly influenced LA conversion. However, the reaction temperature at 65 °C led the highest ML yield at 98% for 120 min.[10,11] These results suggested that ML might be degraded at higher temperatures, leading to a drop in ML yield. Regarding the influence of catalyst loading, the study found that increasing the catalyst loading led to an upward trend in both LA conversion and ML yield[11].

3.3 Performance of TW-SO_3H and Amberlyst-15

The efficiency of TW-SO_3H and Amberlyst-15 in the esterification of levulinic acid with methanol was compared with two blanks: one involving levulinic acid mixed with methanol and two involving levulinic acid mixed with methanol containing 10% loading tire waste equal with catalyst, To compare the efficiency of employing a catalyst versus not employing one in a portion of tire waste, for studying the effects of sulfur groups in tire waste that the reaction could influence. The results, shown in Figure 4, at 2 h, demonstrate that TW-SO_3H exhibited the highest selectivity and conversion, reaching 98% conversion and 100% selectivity, compared to Amberlyst-15, which showed lower conversion (74%) and selectivity (53%). However, the conversion results of the two control blanks were high due to the decomposition of levulinic acid, which caused the emergence of undesired products.[12] The selectivity results, on the other hand, highlight the performance of the catalysts, indicating that TW-SO_3H has higher selectivity than Amberlyst-15. Even though the total acidity result obtained from titration, Amberlyst-15, had higher total acidity (4700 $\mu molg^{-1}$)[13] than TW-SO_3H (1118 $\mu molg^{-1}$). The yield of methyl levulinate also showed that TW-SO_3H had the highest yield compared to Amberlyst-15, Increased acid sites do not necessarily translate to higher product yield and selectivity for the catalyst.

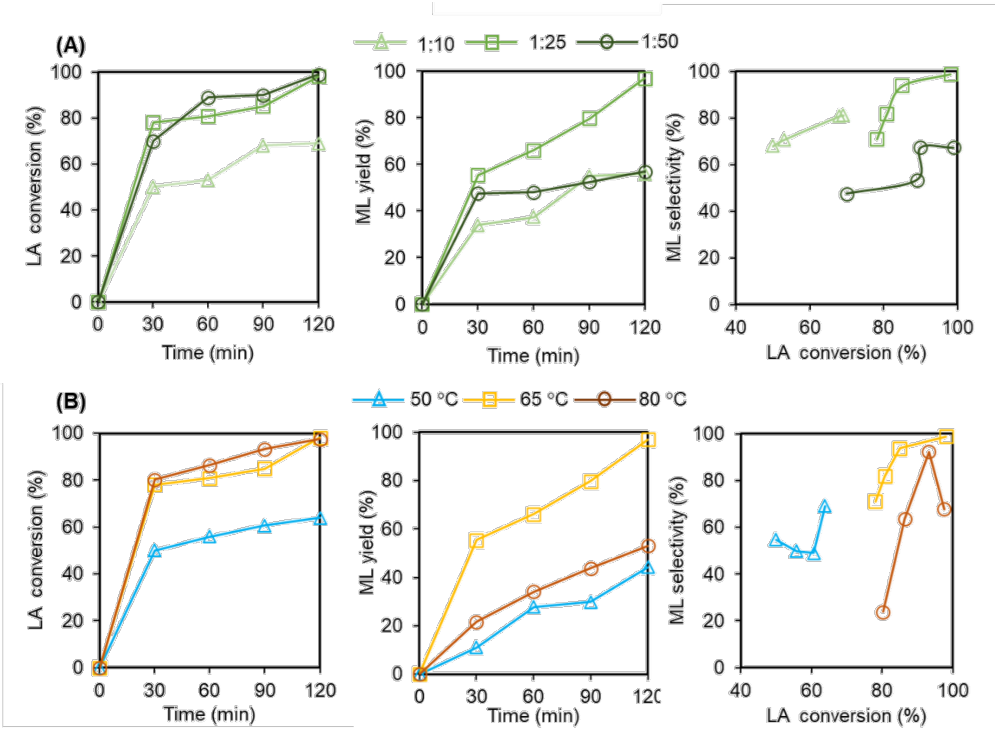

Figure 3. Effect of reaction parameters in esterification of levulinic acid (LA) and methanol at 1:25 (molar ratio), 10% catalyst loading, 65°C for 2 h. (A) Effect ratio between moles of LA and moles of methanol of 1:10,1:25, and 1:50 (B) Effect of temperature used in the reaction of 50°C, 65°C, and 80°C.

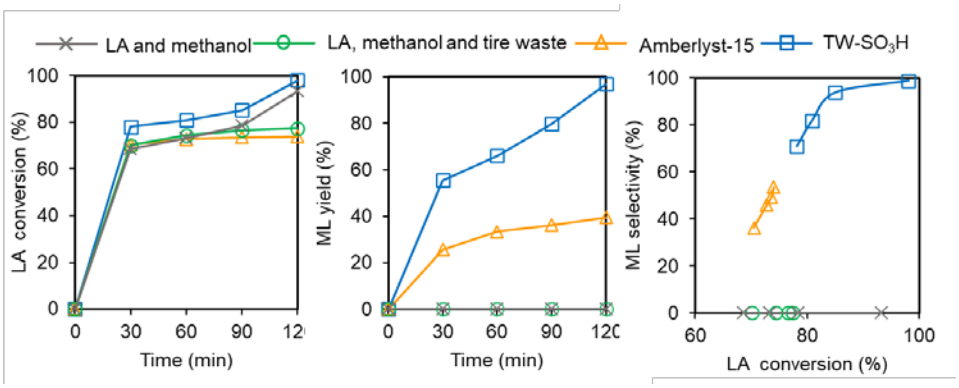

Figure 4. The efficiency of TW-SO3H in the esterification of levulinic acid (LA) and methanol at 1:25 (molar ratio), 10% catalyst loading, 65°C for 2 h of TW-SO_3H, Amberlyst-15, LA with methanol, and LA methanol and tire waste.

3.4 Reusability of TW-SO_3H

Reusing catalysts is another way to efficiently heterogeneous catalysts, as it can signify the strength of active sites. The same reaction was studied with 0.5 g levulinic acid: 3.5g methanol, 1:25 molar ratio, and 10% loading at 65°C for 2 h. After the run reaction (fresh), wash with deionized water and methanol, followed by overnight drying at 80°C. We found that the TW-SO_3H could be reused three times with a slight drop of LA conversion from 98% to 83% and ML selectivity from 98% to 80% (**Fig. 5**). A decrease in catalytic activity might be a leach of the acid site during recycle process.

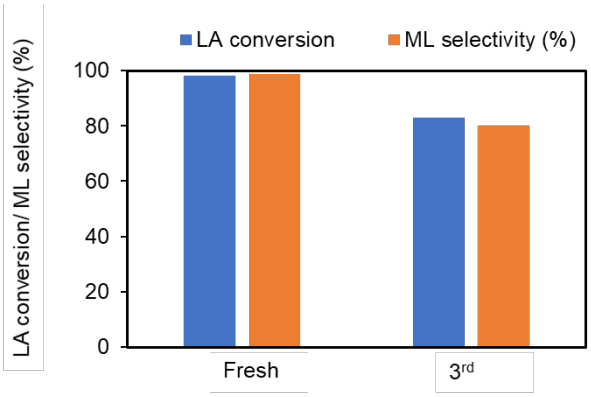

Figure 5. Reusability of TW-SO_3H for esterification of levulinic acid (LA) and methanol at 1:25 (molar ratio), 10% catalyst loading, 65°C for 2 h.

4. Conclusion

This work successfully sulfonated tire waste to synthesize a solid acid catalyst under 150 °C and 98% H_2SO_4 concentration. The FTIR results revealed a significant peak in the wave number range of 1074-1038 cm^{-1}, indicating the attachment of the sulfonic group. The suspension and contact angle results demonstrated the hydrophilic properties of TW-SO_3H, which exhibited higher hydrophilicity than tire waste, suggesting its suitability for various reactions. The esterification comparison between TW-SO_3H and Amberlyst-15 and control blanks yielded compelling results. At 65°C and after 2h, TW-SO_3H exhibited unparalleled performance, achieving 98% conversion and 100% selectivity, surpassing Amberlyst-15 (74% conversion, 53% selectivity). TW-SO3H showed high catalytic stability with a slight decrease in activity after three times recycling. These findings underscore the potential of TW-SO3H is a solid acid catalyst, particularly in environmentally friendly and sustainable catalytic processes.

Acknowledgements

This research was supported by research scholarship by the Chemistry department, faculty of Science, King Mongkut's University of Technology Thonburi.

References

1. Roychand, R.; Gravina, R. J.; Zhuge, Y.; Ma, X.; Youssf, O.; Mills, J. E. *Construction and Building Materials*. **2020**, 237, 117651.
2. Afash, H.; Ozarisoy, B.; Altan, H.; Budayan, C. *Sustainability*. **2023**, *15*, 14178.
3. Islam, M.T.; Saenz-Arana, R.; Hernandez, C.; Guinto, T.; Ahsan, M.A.; Bragg, D.T.; Wang, H.; Alvarado-Tenorio, B.; Noveron, J.C. *J. Environ. Chem. Eng*. **2018**, 6, 3070-3082.
4. Naskar, A.K.; Bi, Z.; Li, Y.; Akato, S.K.; Saha, D.; Chi, M.; Bridges, C.A.; Paranthaman, M.P. *RSC Adv*. **2014**, 4, 38213-38221.
5. Sánchez-Olmos, L.; Medina-Valtierra, J.; Sathish-Kumar, K.; Sánchez Cardenas, M. *Environ. Prog. Sustainable Energy*. **2017**, 36, 619-626.
6. El-Nassan, H.B. *J. Org. Chem*. **2021**, 57(7), 1109-1134.
7. Hykkerud, A.; Marchetti, J.M. *Biomass Bioenergy* **2016**, 175.
8. Sánchez-Olmos, L.; Sánchez-Cárdenas, M.; Sathish-Kumar, K.; Tirado-González, D.; Rodríguez-Valadez, F. *Revista Mexicana De Ingeniería Química*. **2020**, 19 (Sup. 1), 429-444.
9. Karabork, F., Pehlivan, E., Akdemir, A. *Journal of Polymer Engineering*. **2014**, 34.
10. Nandiwale, K. Y.; Bokade, V. V. *Chemical Engineering & Technology*. **2014**, 38 (2), 246–252.
11. Ramli, N. A. S.; Zaharudin, N. H.; Amin, N. A. S. *Jurnal Teknologi*. **2016**,79.
12. Bravo Fuchineco, D.A.; Heredia, A.C.; Mendoza, S.M.; Rodríguez-Castellón, E.; Crivello, M.E. *ChemEngineering*. **2022**, 6, 26.
13. Chaffey, D. R.; Bere, T.; Davies, T. E.; Apperley, D. C.; Taylor, S. H.; Graham, A. E. *Applied Catalysis B: Environmental*. **2021**, 293, 120219.

Enhancing carbon capture efficiency: Optimization of ZIF-8 synthesis and integration into advanced adsorbent systems

Kanoakwan Chanheeb[1] and Pattaraporn Kim-Lohsoontorn[2]
Centre of Excellence on Catalysis and Catalytic Reaction Engineering, Department of Chemical Engineering, Faculty of Engineering, Chulalongkorn University, Bangkok, 10330, Thailand

**E-mail: [1]kanoakwan13nw@gmail.com, [2]pattaraporn.k@chula.ac.th*

Abstract:

The quest for mitigating CO_2 emissions has fueled research into innovative carbon capture technologies. ZIF-8 (Zeolitic Imidazolate Framework-8) a type of metal-organic framework (MOF) is investigated as a CO_2 sorbent due to its anticipated qualities, including pore size, adjustable pore dimension, and high surface area. The synthesis methods are one of the processes for developing and improving ZIF-8 to make it more physically efficient including morphology. ZIF-8 has been prepared by solvothermal synthesis and impregnation using methanol as solvent, $Zn(NO_3)_2 \cdot 6H_2O$ as the metal source, and 2-methylimidazole as the organic linker. The reaction mixtures were transferred into a Teflon-lined autoclave for heating at various temperatures (130°C and 140°C) over distinct time intervals (14h, 24h, and 30h). The resultant material is then subjected to ethanol washing. Scanning electron microscopy (SEM), energy dispersive X-ray spectroscopy (EDX), and X-ray Diffractometer (XRD) are used to characterize prepared adsorbents for crystalline structure and morphological attributes. CO_2 capture and regeneration are carried out in a fixed bed reactor and CO_2 loading capacity including the adsorption behavior of the adsorbent is determined. Our findings provide an important addition to continuing efforts to improve ZIF-8 materials, making them more durable and efficient for practical applications in carbon capture.

1. Introduction

Carbon dioxide holds the distinction of being the predominant anthropogenic greenhouse gas, contributing to approximately 80% of all greenhouse gases (GHG).[1] The atmospheric concentration of carbon dioxide is measured at 404 parts per million (ppm), marking an increase of 120 ppm compared to pre-industrial levels.[2,3] Elevated concentrations of CO_2 contribute to the greenhouse effect, influencing the climatic environment and impacting people's lives.[4] CO_2 capture and storage/sequestration (CCS) technologies are deemed crucial as a short to mid-term solution for mitigating the impact of global warming, serving as an interim measure until renewable technologies attain the necessary maturity.[5] Extensive efforts have been dedicated to the advancement of novel technologies for CO_2 capture.[6, 7] The primary challenge associated with CO_2 capture technology is that the materials used for CO_2 capture should benefit the environment green and capable of regeneration. CO_2 capture is categorized into 3 kinds; pre-combustion capture, post-combustion capture, and oxy-fuel combustion.[8] However, in the post- combustion conventional method, amine treatment liquid strippers have a low absorption rate and require a large amount of energy resulting in a higher absorber column, high operating cost, and may cause human cancer due to their chemical hazard.[9]

Metal-organic frameworks (MOFs) are characterized by high pore volume, highly ordered pores, low density, large surface area, demonstrating suitable chemical and thermal stability. The ability to mix various metals and organic ligands to make a large number of materials varied with crystal structures and chemical compositions is their most appealing property.[8] As a major class of MOFs, Zeolitic imidazole frameworks (ZIFs) are highly ordered porous solids bridged by inorganic metal ions in a tetrahedral environment with imidazole ligands. Imidazole unit types can control their topological and porous structures.[10,11] ZIF-8, one of the most thoroughly studied zeolitic imidazole framework materials, has a sodalite structure. It is formed with transition metal cations (e.g., Zn^{2+}) and 2-methylimidazole (Hmim), which have been widely used as a CO_2 adsorbent.[2,12,13] MOFs are often synthesized using the solvothermal method, microwave-assisted method, ultrasonic chemistry method, ionothermal method, and mechano-chemical method.[14,15] Moreover, innovative methods for producing MOFs and crystalline inorganic-organic hybrid materials have emerged in recent year.[16, 17] These include the surfactant-thermal method[18,19] and the surfactant-introduction strategy.[20] Notably, ZIF-8 is frequently synthesized using the solvothermal method.

The impact of particle morphology and size on the physical and chemical properties of

crystals is widely recognized. Numerous studies reveal that the synthesis parameters of ZIF-8 have a significant impact on their shape and size.[21-23] While existing studies have extensively explored the effects of reaction parameters on the morphology and size of ZIF-8 during synthesis, the effects on CO_2 adsorption capacity are rarely examined. In this research, we not only examine the key operational parameters in the synthesis process but also provide comprehensive evidence linking these parameters to the CO_2 adsorption capacity.

2. Materials and Methods

2.1 Materials

All the purchased analytical grade chemicals were used without further purification. Zinc nitrate hexahydrate ($Zn(NO_3)_2 \cdot 6H_2O$, 98%), 2-methylimidazole (99%), methanol, and ethanol were purchased from Sigma Aldrich.

2.2 Synthesis of ZIF-8 by Solvothermal synthesis

In a typical solvothermal synthesis based on the method reported by Yueting Chen and the research group with modified synthesis parameters[21]. Initially, zinc nitrate hexahydrate 15.95 g and 3.52 g of 2-methylimidazole were dissolved in 150 mL of methanol. After stirring the reaction mixtures to generate a clear solution, they were placed in a Teflon-lined autoclave. The system was then heated for varying periods at 120°C, 130°C, and 140°C over distinct time intervals at 14h and 24h. The resultant material is then subjected to ethanol washing, centrifugation at 3,000 r/min for 5 min and overnight drying. The product was named ST-T(H), where T represents temperature (°C) and H is for reaction time (h). For example, ST-130(24) refers to the sample heated at 130°C for 24 h with solvothermal synthesis.

2.3 Synthesis of ZIF-8 by impregnation

ZIF-8 was synthesized based on the method reported by Siva and the research group[24]. In the rapid synthesis, 6.56 g of 2-methylimidazole was dissolved in 100 ml of methanol. A second solution consisting of 2.97 g of zinc nitrate hexahydrate was dissolved in 100 ml of methanol. Both the clear solutions were mixed and stirred for 2 h at room temperature under a constant speed of 240 rpm and then washed with methanol. After that, the product was dried at a temperature of 110°C for 4 h.

2.4 Characterization method

The morphology of adsorbents was investigated by scanning electron microscopy (SEM) and energy dispersive X-ray (EDX) was used to identify the surface composition of ZIF-8. The XRD peaks were obtained with a Bruker D-8 ADVANCE diffractometer using a CuKα-ray source (40 kV, 40 mA) with a scanning step of 0.02° in the range 5-50°.[2]

2.5 CO_2 adsorption measurement

Figure 1 shows the CO_2 adsorption-desorption experiment via a fixed bed reactor. ZIF-8 0.5 g with ceramic fiber as a supporter was packed into a stainless-tube reactor. The adsorbent was initially treated for 30 minutes at 200°C with N_2 gas at a flow rate of 30 mL/min. It was subsequently cooled to the required adsorption temperature of 75°C. The flow of gas was then altered in the N_2 balance to 15.0 vol% and CO_2 at a flow rate of 30 mL/min. The adsorption process was repeated until saturation was reached. For desorption, CO_2 feed was stopped while N_2 still flowed as a carrier gas, and the furnace was heated to the desorption temperature of 200°C. CO_2 gas was detected every 30 minutes with the CO_2 sensor (K33 BLG 30%CO_2+RH/T) to investigate adsorption behavior.

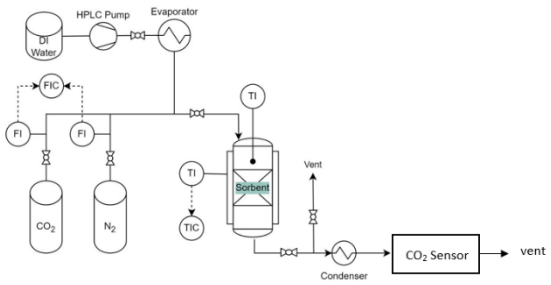

Figure 1. Schematic of the CO_2 adsorption experiment.

3. Results & Discussion

3.1 SEM

The morphology and weight percentage of samples were investigated. Figure 2 (a-e) shows the morphology of the specimen synthesized through solvothermal methods under varying conditions. Figure 2 (f) shows the morphology of the samples obtained by impregnation. Fig.2 (a) and (e) show porous hydrangea-like morphology.[21]

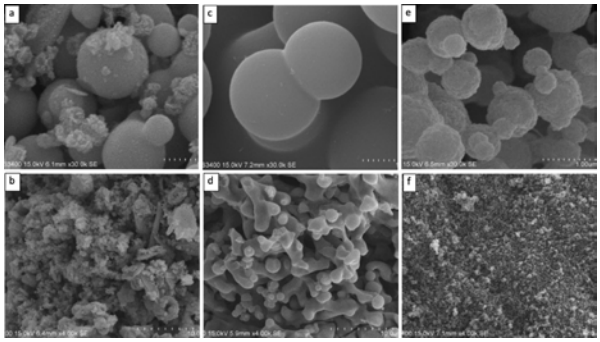

Figure 2. SEM images of ZIF-8. (a) ST-130(14), (b) ST-130(24), (c) ST-130(30), (d) ST-140(14), (e) ST-140(24) and (f) ZIF-8 by impregnation.

Table 1 presents the average weight percentage of all elements on the samples. ZIF-8 by solvothermal synthesis at 140°C 14h (ST-140(14)) had the most amount of zinc source (93.70%). ST-130(30) has a lower percentage of zinc source because it takes too much time to synthesize. During the synthesis process, zinc-containing species may be lost due to volatilization, side reactions, or incomplete precipitation. These losses might lead to a reduced zinc percentage in the finished product of ZIF-8 by impregnation.

Table 1. Element weight percentage (wt%) of samples.

Samples	Average weight percentage (wt%)			
	Carbon (C)	Nitrogen (N)	Oxygen (O)	Zinc (Zn)
ST-130(14)	0.68	0.25	5.61	93.45
ST-130(24)	1.30	0.26	6.08	92.36
ST-130(30)	26.17	13.05	8.71	52.06
ST-140(14)	0.76	0.21	5.33	93.70
ST-140(24)	1.03	0.22	6.46	92.29
ZIF-8	33.77	16.01	1.83	48.39

3.2 XRD analysis

Figure 3 shows XRD obtained by solvothermal synthesis and impregnation. The impregnation method has successfully produced ZIF-8 crystals characterized by a pure phase and high crystallinity. Conversely, when employing the solvothermal approach to achieve a hydrangea-like morphology, the resulting samples were found to be composed entirely of ZnO instead of ZIF-8. This discrepancy suggests a possible conversion of zinc nitrate to zinc oxide, and the energy provided under these solvothermal conditions was inadequate for the rapid transformation of ZnO into the desired ZIF-8 product.[21]

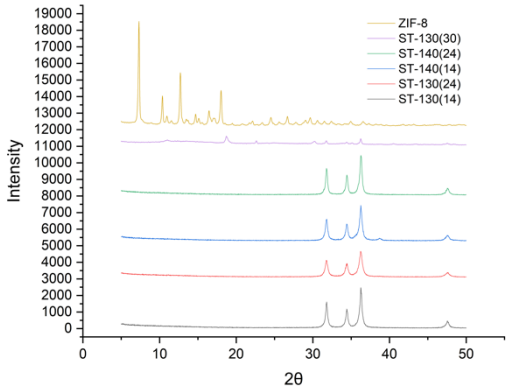

Figure 3. XRD of ZIF-8 by solvothermal synthesis and impregnation

3.3 CO_2 Adsorption

Table 3 illustrates the CO_2 loading capacity at 75°C, indicating an increase as the synthesis time extended from 14 to 30 hours. The CO_2 loading capacity of ZIF-8 at 14 hours initially rose from 5.27 mmol/g to 5.84 mmol/g. When synthesized at 130°C for 30 hours, the ZIF-8 samples exhibited the maximum CO_2 loading capacity of 5.84 mmol/g.

CO_2 adsorption behavior is shown in Figure 4. As shown in Figure 4 all ZIF-8 samples reached their equilibrium at almost the same time. It can be seen that, ST-130(30) and ST-140(14) provided highest CO_2 uptake.

Almost of samples by solvothermal synthesis have higher CO_2 loading capacity than sample by impregnation due to the chemical affinity of ZnO can chemically react with CO_2 to form carbonate species, which enhances its CO_2 capture capacity through chemisorption.

Table 3. CO_2 loading capacity at adsorption temperature of 75°C

Samples	CO_2 loading (mmol CO_2/g adsorbent)
ST-130(14)	5.27
ST-130(24)	5.77
ST-130(30)	5.84
ST-140(14)	5.80
ST-140(24)	5.27
ZIF-8	5.43

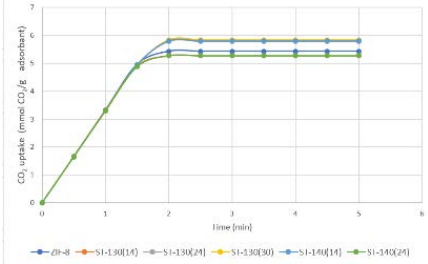

Figure 4. CO_2 adsorption at 75°C

4. Conclusion

In this study, we have synthesized ZIF-8 in solvothermal method and impregnation, and the influences of key operating parameters are investigated. As shown in SEM images, ST-130(14) and ST-140(24) have a uniform particle size distribution of porous hydrangea-like morphology. The XRD analysis reveals that ZIF-8 is formed in samples synthesized through impregnation, whereas samples synthesized through the solvothermal method result in the formation of ZnO. The CO_2 loading capacity shows that the samples from solvothermal synthesis have higher CO_2 loading capacity than the samples from impregnation. Meanwhile, the high CO_2 adsorption indicates that solvothermal synthesis and impregnation are promising ways for CO_2 capture.

Acknowledgments

This research was supported by Research Cess Fund, Malaysia-Thailand Joint Authority (MTJA) and the NSRF via the Program Management Unit for Human Resources & Institutional Development, Research, and Innovation [B16F640164].

References

1. Hussain, A. A Single Stage Membrane Process for CO2 Capture from Flue Gas by a Facilitated Transport Membrane. *Separation Science and Technology* **2012**, *47* (13), 1857-1865. DOI: 10.1080/01496395.2012.661013.
2. Shi, Z.; Yu, Y.; Fu, C.; Wang, L.; Li, X. Water-based synthesis of zeolitic imidazolate framework-8 for CO2 capture. *RSC Advances* **2017**, *7* (46), 29227-29232, 10.1039/C7RA04875K. DOI: 10.1039/C7RA04875K.
3. Schneider, T.; Teixeira, J.; Bretherton, C. S.; Brient, F.; Pressel, K. G.; Schär, C.; Siebesma, A. P. Climate goals and computing the future of clouds. *Nature Climate Change* **2017**, *7* (1), 3-5. DOI: 10.1038/nclimate3190.
4. Lenton, T. M. Climate Change to the End of the Millennium. *Climatic Change* **2006**, *76* (1), 7-29. DOI: 10.1007/s10584-005-9022-1.
5. Bae, Y.-S.; Snurr, R. Q. Development and Evaluation of Porous Materials for Carbon Dioxide Separation and Capture. *Angewandte Chemie International Edition* **2011**, *50* (49), 11586-11596. DOI: https://doi.org/10.1002/anie.201101891 (acccessed 2023/12/24).
6. Kenarsari, S. D.; Yang, D.; Jiang, G.; Zhang, S.; Wang, J.; Russell, A. G.; Wei, Q.; Fan, M. Review of recent advances in carbon dioxide separation and capture. *RSC Advances* **2013**, *3* (45), 22739-22773, 10.1039/C3RA43965H. DOI: 10.1039/C3RA43965H.
7. Sreenivasulu, B.; Sreedhar, I.; Suresh, P.; Raghavan, K. V. Development Trends in Porous Adsorbents for Carbon Capture. *Environmental Science & Technology* **2015**, *49* (21), 12641-12661. DOI: 10.1021/acs.est.5b03149.
8. Sabouni, R.; Kazemian, H.; Rohani, S. Carbon dioxide capturing technologies: a review focusing on metal organic framework materials (MOFs). *Environmental Science and Pollution Research* **2014**, *21* (8), 5427-5449. DOI: 10.1007/s11356-013-2406-2.
9. Onarheim, K.; Santos, S.; Kangas, P.; Hankalin, V. Performance and costs of CCS in the pulp and paper industry part 1: Performance of amine-based post-combustion CO2 capture. *International Journal of Greenhouse Gas Control* **2017**, *59*, 58-73. DOI: 10.1016/j.ijggc.2017.02.008.
10. Phan, A.; Doonan, C. J.; Uribe-Romo, F. J.; Knobler, C. B.; O'Keeffe, M.; Yaghi, O. M. Synthesis, Structure, and Carbon Dioxide Capture Properties of Zeolitic Imidazolate Frameworks. *Accounts of Chemical Research* **2010**, *43* (1), 58-67. DOI: 10.1021/ar900116g.
11. Chen, R.; Yao, J.; Gu, Q.; Smeets, S.; Baerlocher, C.; Gu, H.; Zhu, D.; Morris, W.; Yaghi, O. M.; Wang, H. A two-dimensional zeolitic imidazolate framework with a cushion-shaped cavity for CO2 adsorption. *Chemical Communications* **2013**, *49* (82), 9500-9502, 10.1039/C3CC44342F. DOI: 10.1039/C3CC44342F.
12. Duan, J.; Pan, Y.; Pacheco, F.; Litwiller, E.; Lai, Z.; Pinnau, I. High-performance polyamide thin-film-nanocomposite reverse osmosis membranes containing hydrophobic zeolitic imidazolate framework-8. *Journal of Membrane Science* **2015**, *476*, 303-310. DOI: https://doi.org/10.1016/j.memsci.2014.11.038.
13. Hu, Y.; Liu, Z.; Xu, J.; Huang, Y.; Song, Y. Evidence of Pressure Enhanced CO2 Storage in ZIF-8 Probed by FTIR Spectroscopy. *Journal of the American Chemical Society* **2013**, *135* (25), 9287-9290. DOI: 10.1021/ja403635b.
14. Xia, W.; Lau, S. K.; Yong, W. F. Comparative life cycle assessment on zeolitic imidazolate framework-8 (ZIF-8) production for CO2 capture. *Journal of Cleaner Production* **2022**, *370*, 133354. DOI: https://doi.org/10.1016/j.jclepro.2022.133354.

15. Li, P.; Cheng, F.-F.; Xiong, W.-W.; Zhang, Q. New synthetic strategies to prepare metal–organic frameworks. *Inorganic Chemistry Frontiers* **2018**, *5* (11), 2693-2708, 10.1039/C8QI00543E. DOI: 10.1039/C8QI00543E.
16. Qin, Z.-S.; Dong, W.-W.; Zhao, J.; Wu, Y.-P.; Zhang, Q.; Li, D.-S. A water-stable Tb(iii)-based metal–organic gel (MOG) for detection of antibiotics and explosives. *Inorganic Chemistry Frontiers* **2018**, *5* (1), 120-126, 10.1039/C7QI00495H. DOI: 10.1039/C7QI00495H.
17. Xiong, W.-W.; Zhang, Q. Surfactants as Promising Media for the Preparation of Crystalline Inorganic Materials. *Angewandte Chemie International Edition* **2015**, *54* (40), 11616-11623. DOI: https://doi.org/10.1002/anie.201502277 (acccessed 2023/12/26).
18. Xiong, W.-W.; Miao, J.; Ye, K.; Wang, Y.; Liu, B.; Zhang, Q. Threading Chalcogenide Layers with Polymer Chains. *Angewandte Chemie International Edition* **2015**, *54* (2), 546-550. DOI: https://doi.org/10.1002/anie.201409653 (acccessed 2023/12/26).
19. Xiong, W.-W.; Li, P.-Z.; Zhou, T.-H.; Tok, A. I. Y.; Xu, R.; Zhao, Y.; Zhang, Q. Kinetically Controlling Phase Transformations of Crystalline Mercury Selenidostannates through Surfactant Media. *Inorganic Chemistry* **2013**, *52* (8), 4148-4150. DOI: 10.1021/ic4002169.
20. Zhao, J.; Wang, Y.; Dong, W.; Wu, Y.; Li, D.; Liu, B.; Zhang, Q. A new surfactant-introduction strategy for separating the pure single-phase of metal–organic frameworks. *Chemical Communications* **2015**, *51* (46), 9479-9482, 10.1039/C5CC02043C. DOI: 10.1039/C5CC02043C.
21. Chen, Y.; Tang, S. Solvothermal synthesis of porous hydrangea-like zeolitic imidazole framework-8 (ZIF-8) crystals. *Journal of Solid State Chemistry* **2019**, *276*, 68-74. DOI: https://doi.org/10.1016/j.jssc.2019.04.034.
22. Wang, Q.; Bai, J.; Lu, Z.; Pan, Y.; You, X. Finely tuning MOFs towards high-performance post-combustion CO2 capture materials. *Chemical Communications* **2016**, *52* (3), 443-452, 10.1039/C5CC07751F. DOI: 10.1039/C5CC07751F.
23. Shieh, F.-K.; Wang, S.-C.; Leo, S.-Y.; Wu, K. C. W. Water-Based Synthesis of Zeolitic Imidazolate Framework-90 (ZIF-90) with a Controllable Particle Size. *Chemistry – A European Journal* **2013**, *19* (34), 11139-11142. DOI: https://doi.org/10.1002/chem.201301560 (acccessed 2023/12/26).
24. Siva, V.; Murugan, A.; Shameem, A.; Thangarasu, S.; Bahadur, S. A. A Simple Synthesis Method of Zeolitic Imidazolate Framework-8 (ZIF-8) Nanocrystals as Superior Electrode Material for Energy Storage Systems. *Journal of Inorganic and Organometallic Polymers and Materials* **2022**, *32* (12), 4707-4714. DOI: 10.1007/s10904-022-02475-x.

Tuning selectivity of Ni/Al_2O_3 catalysts in CO_2 Hydrogenation by incorporation of N, S-doped carbon

Nipitpon Jarumalai, Suthasinee Watmanee, and Joongjai Panpranot *

Center of Excellence on Catalysis and Catalytic Reaction Engineering, Department of Chemical Engineering, Faculty of Engineering, Chulalongkorn University, Bangkok 10330 Thailand

**E-mail: joongjai.p@chula.ac.th*

Abstract:

In recent years, the continuously rising levels of CO_2 have become a primary concern. CO_2 hydrogenation is considered a promising approach to reduce the impact of CO_2. CO is an interesting intermediate for the synthesis of higher value liquid hydrocarbon and oxygenate products but selective CO_2 hydrogenation towards CO over Ni catalysts is challenging . The objective of this study is to study the effect of N- and S-doped carbon (1%, 3%, and 5% by weight) on Ni/Al_2O_3 catalysts in the gas-phase CO_2 hydrogenation at 300-500 ^oC. All the catalysts were prepared by the incipient wetness impregnation method and then calcined at 550 ^oC for 5 h. The results show that increasing the N and S-doped carbon content significantly enhances the selectivity towards CO. The relationship between catalyst properties and activities was analyzed based on various characterization results including SEM, EDX, XRD, FTIR, and H_2-TPR. Among the various catalysts studied, the $15Ni5NSC/Al_2O_3$ (15wt% Ni and 5 wt% N and S-doped carbon) showed the best performances towards CO with 99 percent CO selectivity and 30 percent conversion at the reaction temperature 500 ^oC.

1. Introduction

A primary contemporary concern has been the persistent elevation of carbon dioxide (CO_2) levels. Carbon dioxide, a compound containing carbon, has garnered significant attention as a potential feedstock in recent decades.[1] The utilization of green technology for the hydrogenation of carbon dioxide, a prominent byproduct within the chemical industry, holds promise for fostering the emergence of more environmentally sustainable businesses and facilitating the transition towards a circular economy. CO_2 hydrogenation represents a noteworthy approach believed to have the potential to mitigate the adverse impacts of elevated CO_2 levels.[2] Carbon monoxide, a key product of this process, assumes vital significance within the chemical and petrochemical industries, serving as a foundational building block for the synthesis of higher-value products. The combination of hydrogen and carbon monoxide, commonly referred to as synthesis gas or syngas, can be strategically converted into various valuable outputs.[3] These include, but are not limited to, serving as a power generator, contributing to the production of naphtha, petrochemicals, wax, and diesel through Fischer-Tropsch synthesis, and facilitating the synthesis of chemical compounds such as methanol, ethylene, and polyolefin. This multi-faceted utilization underscores the potential of CO_2 hydrogenation to contribute meaningfully to both environmental sustainability and industrial efficiency.[4]

The hydrogenation of carbon dioxide (CO_2) typically engages in two distinct chemical pathways. One of these routes is exemplified by the reverse water gas shift (rWGS) reaction. This reaction constitutes an endothermic chemical process wherein carbon dioxide is transformed into carbon monoxide. Achieving economically acceptable conversion rates in this specific process necessitates the application of temperatures surpassing 700 °C. [5]Such elevated temperatures are requisite to activate the thermodynamically stable CO_2 molecule. Conversely, the exothermic nature of the Sabatier reaction becomes advantageous for methane synthesis when executed at lower temperatures. The favorable exothermic characteristics of the Sabatier reaction underscore its suitability for achieving methane synthesis under conditions where temperatures are comparatively lower.

The rWGS reaction plays a key role in the coupling of CO_2 conversion with renewable energy because it is an appealing approach to use H_2 from renewable energies with CO_2 to supply CO as a C_1 the production of methanol. Even in very moderate circumstances, the rWGS reaction may be catalyzed by heterogeneous catalysts at temperatures of around 200−600°C. Frequently heterogeneous catalysts systems being used are supported ceria or copper-based, such as Cu-Ni or $Cu-Zn/Al_2O_3$. Numerous innovative catalysts have

been documented; nevertheless, contrasting the various systems can be difficult because of disparate experimental setups and insufficient data on reaction speeds, conversions, or yields. Both noble- and non-noble-metal catalysts can be used for the rWGS reaction in the dry reforming of methane. Noble metals like platinum can withstand 500°C. [6-8]

Numerous studies have been conducted on the direct hydrogenation of carbon dioxide (CO_2) into methane (CH_4) using catalysts predominantly composed of nickel. Throughout the CO_2 hydrogenation process, carboxyls, carbonates, formates, and chemisorbed CO surface species are generated, displaying robust bonding characteristics and exhibiting chemisorbed modes responsive to various exposed nickel (Ni) sites.[9] The methanation of CO_2 on Ni single metal catalysts involves loading onto diverse supports, including alumina, ceria, a ceria–zirconia mixed oxide, and titania. The resultant metal-support interactions impart distinct behaviors in terms of both activity and selectivity.[10]

The variation in Ni particle size on different supports follows the order Ni/Al < Ni/Ce < Ni/ZrCe < Ni/Ti, with sizes ranging from 7.1 to 67 nm. Bimetallic Ni-x catalysts, explored over the past decade, involve the incorporation of a second transition metal (e.g., Fe, Co) [11] or a noble metal (e.g., Ru, Rh, Pt, Pd, and Re) [12-14]. The synergistic effect between the two metals in bimetallic catalysts has been observed to enhance overall catalytic performances significantly. As a strategy to mitigate the costs associated with noble and transition metals, metal-free catalysts have emerged, featuring carbon-based materials such as graphene, graphene oxide, carbon nanotubes (CNT), and carbon with functionalized groups (N, K, and S). However, a drawback of metal-free catalysts lies in their limited catalytic activity, resulting in low CO_2 conversion rates. To address this challenge, we propose the incorporation of carbon-modified catalysts aiming to reduce metal costs while concurrently augmenting the catalytic activity of metal-free catalysts. [6, 12]

Catalytic CO_2 methanation encompasses three fundamental chemical reactions, as elucidated in equations 1-3. These reactions, denoted as "overall reactions," may entail the involvement of the catalyst and multiple steps or intermediate molecules .

Direct CO2 methanation : $CO_2 + 4H_2 \leftrightarrow CH_4 + 2H_2O \quad \Delta H298\,°C = -165\ kJ\ mol^{-1}$ (eq.1)

Reverse water gas shift : $CO_2 + H_2 \leftrightarrow CO + H_2O \quad \Delta H298\,°C = +41.2\ kJ\ mol^{-1}$ (eq.2)

Direct CO methanation : $CO + 3H_2 \leftrightarrow CH_4 + H_2O \quad \Delta H298\,°C = -165\ kJ\ mol^{-1}$ (eq.3)

In order to expand the scope of catalyst design, non-metal modified carbon was examined and compared to that of Ni bimetallic catalysts in terms of both CO_2 conversion and selectivity towards CO. Although it is difficult to selectively hydrogenate CO_2 towards CO over Ni catalysts, CO is a useful intermediate for adjusting the selectivity towards CO over modified Ni-based catalysts on Al_2O_3 support, which serves as the main inspiration for this work. The focus of this work is to examine the relationship between catalyst performance and catalyst properties, as well as the effects of N- and S-doped carbon (1%, 3%, and 5% by weight) on Ni/Al_2O_3 catalysts during the gas-phase hydrogenation of CO_2 at temperatures ranging between 300 and 500 °C.

2. Experimental

2.1 Catalyst synthesis

2.1.1 Nikel catalyst preparation

For all xNi/Al_2O_3 catalysts (x=5%, 10%, and 15% wt), 1 g of commercial γ-Al_2O_3 support was utilized. An aqueous solution was prepared using nickel (II) nitrate hexahydrate as a Ni precursor and mixed with deionized (DI) water. The catalysts were synthesized through the incipient wetness impregnation method. Subsequently, water was removed at 110 °C for 12 h, followed by calcination under N_2 gas at 550 °C for 5 h to obtain the xNi/Al_2O_3 catalyst.

2.1.2 N,S-doped carbon on nickel catalyst preparation

The N, S-doped carbon solution was obtained from CrystalLyte Co., Ltd. (Thailand). For preparing N,S-doped carbon on Nickel catalysts, 1 g of commercial γ-Al_2O_3 support was used. An aqueous solution was prepared using nickel (II) nitrate hexahydrate as a Ni precursor and mixed with deionized (DI) water. The catalysts were synthesized through the incipient wetness impregnation method by adding the N,S-doped carbon solution (y = 1, 3, and 5 wt%) to the well-mixed nickel catalyst. Afterward, water was removed at 110 °C for 12 h, followed by calcination under N_2 gas at 600 °C for 5 h to obtain the xNiyNSC/Al_2O_3 catalyst.

2.2 Characterization of catalyst

2.2.1 Scanning Electron Microscopy--Energy Dispersive X-Ray spectroscopy (SEM-EDX)

SEM with Hitachi model S-3400N and EDX with Edex 2371 series 300 programs were used to observe the morphology of all catalyst, along with surface element.

2.2.2 X-ray Diffraction (XRD)

The Ni and Ni-N,S doped carbon catalysts were calcination at 600 °C under N_2. The crystallinities were performed by a Bruker D-8 advance X-ray diffractometer with CuK_α radiation (λ = 1.54439x10-10 m). Diffraction patterns were recorded in the reflection mode at room temperature with the scans from diffraction angle 2 θ = 20 to 80° with scan speed of 0.3 sec/step and a step size of 0.02.

2.2.3 Thermogravimetric Analyzer (TGA)

Thermogravimetric analysis is used to study the amount of carbon can be cooperated for tuning Nikel catalyst, using the SDT Q600, TA Instruments, under the nitrogen flow. It is analyzed at a room temperature of 800 °C at a temperature increase of 10 °C/min.

2.2.4 Hydrogen Temperature-programmed Reduction (H_2-TPR)

The reducibility of the catalyst was evaluated using hydrogen temperature-programmed reduction (H_2-TPR) measurements, using Micromeritics chemisorb 2750. In a typical experiment, 50 mg of the catalyst was placed in a U-shaped reactor and exposed to a flow of 25 ml/min of mixture H_2/Ar (10% H_2) from room temperature to 850°C with a heating rate of 10° C/min. The H_2 consumption was tracked using a thermal conductivity detector TCD.

2.3 Catalyst Activity test

To evaluate the activity of the produced catalysts, the CO_2 hydrogenation reaction was conducted in a fixed-bed reactor equipped with a heated jacket (length=390 mm, width=10 mm). Initially, 0.4 g of catalyst was packed in the middle of the tube. After sealing the reactor and ensuring no gas leakage, an in-situ reduction pretreatment was performed at 500 °C for 1 h with hydrogen gas flowing and Nitrogen gas flowing at H_2/N_2 ratio. The reduced catalysts were then cooled to 100 °C under a nitrogen stream. Each catalyst was maintained at the chosen temperature (300-500 °C) for 1 h before sampling the product for analysis using GC-TCD.

2.4 Calculation

CO_2 conversion (XCO_2), CH_4 selectivity (SCH_4), and CO selectivity (SCO) were calculated as functions of the corresponding inlet (F(in)) and outlet (F(out)) molar flow rates according to the following equations:

$$XCO_2(\%) = \frac{FCO_2(\text{in}) - FCO_2(\text{out})}{FCO_2(\text{in})} \cdot 100$$

$$SCO(\%) = \frac{FCO(out)}{FCO(\text{out}) + FCH_4(\text{out})} \cdot 100$$

$$SCH_4(\%) = \frac{FCH_4(out)}{FCO(\text{out}) + FCH_4(\text{out})} \cdot 100$$

3. Results & Discussion

3.1 Characterization of catalyst

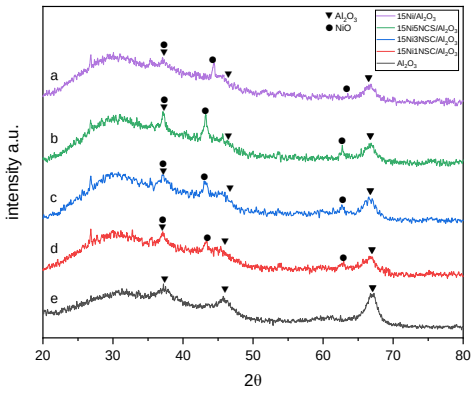

Figure 1. XRD of a) 15Ni/Al_2O_3 b) 15Ni5NSC/Al_2O_3 c) 15Ni3NSC/Al_2O_3 d)15Ni1NSC/Al_2O_3 e) Al_2O_3.

Figure 1 shows the XRD patterns of all catalysts. The XRD analysis reveals a broad peak of alumina at 37.5, 46, and 67 degrees. For all synthesized NiNSC/Al_2O_3, NiO peaks are observed around 37.3, 43, and 62.8 degrees, some peaks are similar to the alumina peaks. Carbon peaks cannot be observed in XRD patterns due to low percentages of carbon loading. The EDX analysis results confirm the incorporation of N and S-doped carbon on the Ni/Al_2O_3 catalysts.

All catalysts (Ni, NiNSC, and NSC) were synthesized under N_2 gas atmosphere instead of air, in order to prevent carbon loss. Thermogravimetric analysis (TGA) of the catalysts was conducted under N_2 atmosphere within a temperature range of 100-900 °C.

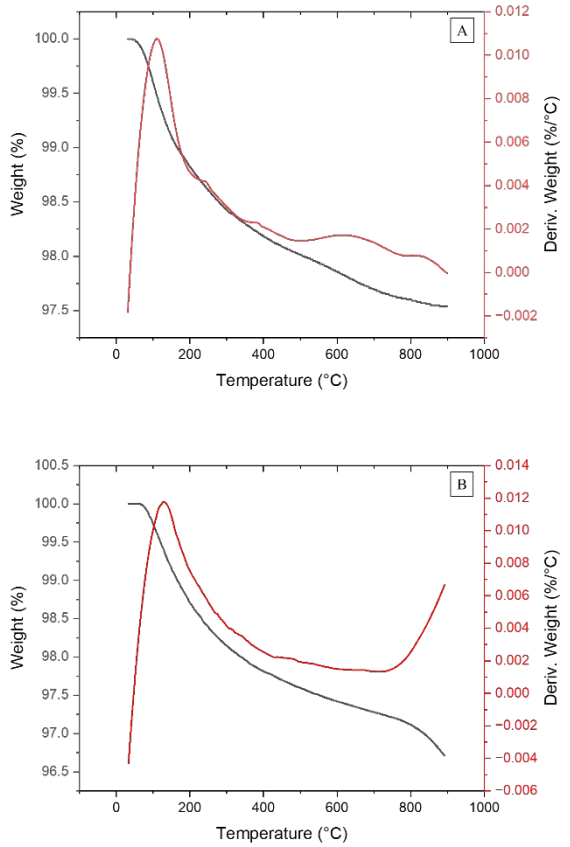

Figure 2. TGA of A. 15Ni/Al_2O_3 and B. 15Ni3NSC/Al_2O_3.

In Figure 2A, two major weight loss sections are observed at 100-200 °C. The initial weight loss at 100 °C is attributed to the dehydration through water evaporation, followed by lower weight losses at 260-300 °C and 360 - 410 °C due to the absence of nitrate. For 15Ni3NSC/Al_2O_3, three sections are evident, with the first two sections similar to those observed for the 15Ni/Al_2O_3 catalyst. At temperatures exceeding 800 °C, carbonation occurs, leading to weight loss.

Figure 3 illustrate the morphology of the 15Ni5NSC/Al_2O_3 catalyst synthesized via the incipient wetness impregnation method, demonstrating a successful and distribution of Ni, N, and S-doped carbon on the alumina support. The method's effectiveness ensures a homogeneous dispersion of active components, contributing to the catalyst's well-defined structural features and enhanced catalytic properties. Table 1. Shows atomic percentage of 15Ni5NSC/Al_2O_3. C, N, O, Al, S and Ni, which are major component of Ni doped N,S carbon on alumina support, as detected by EDX on the fresh catalysts.

Table 1. Atomic percentage of 15Ni5NSC/Al_2O_3.

Element	Line type	Wt %	At %
C	K series	2.09	4.21
N	K series	1.11	1.90
O	K series	26.86	40.52
Al	K series	50.48	45.15
S	K series	0.65	0.49
Ni	K series	18.81	7.73
Matrix		Correction	ZAF

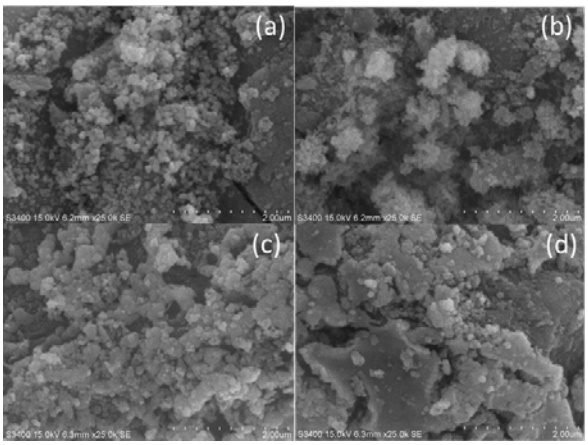

Figure 3. SEM images of 15Ni/Al_2O_3 (a), 15Ni1NSC/Al_2O_3 (b), 15Ni3NSC/Al_2O_3 (c), 15Ni5NSC/Al_2O_3 (d)

3.2 Catalytic performance CO_2 hydrogenation

The hydrogenation of CO_2 was conducted in a fixed-bed reactor with a gas composition of 1:4 (CO_2/H_2 vol/vol) at a flow rate of 100 mL/min and a temperature range of 300-500 °C. Various catalysts, including 15Ni/Al_2O_3, 15Ni1NSC/Al_2O_3 and pure NSC were tested. CO_2 conversion, as shown in Figure 4A, exhibited similar behavior for both 15Ni/Al_2O_3 and 15Ni1NSC, while pure Ni/Al_2O_3 without NSC doping demonstrated slightly better performance in terms of CO_2 conversion. The CO_2 conversion of 15Ni/Al_2O_3 and 15Ni1NSC/Al_2O_3 increased with temperature until reaching a maximum of 77.5%, after which it declined for the reaction temperature above 400 °C.

For N,S-doped carbon (pure NSC), a low CO_2 conversion rate of 2.2% at 500 °C was reported. The impact of increasing the percentage loading of NSC on 15Ni/Al_2O_3 CO_2 conversions showed a dramatic drop at 300-400 °C for 3 wt% and 5 wt% NSC loadings. However, the selectivity and total CO rate (Figure 4B and C) toward the reverse water-gas shift (rWGS) reaction to form CO increased to 99% and produced higher rates compared to pure Ni/Al_2O_3. The literature claims that because of the higher mobility of intermediate species on the Ni surface,[11] larger nanoparticles

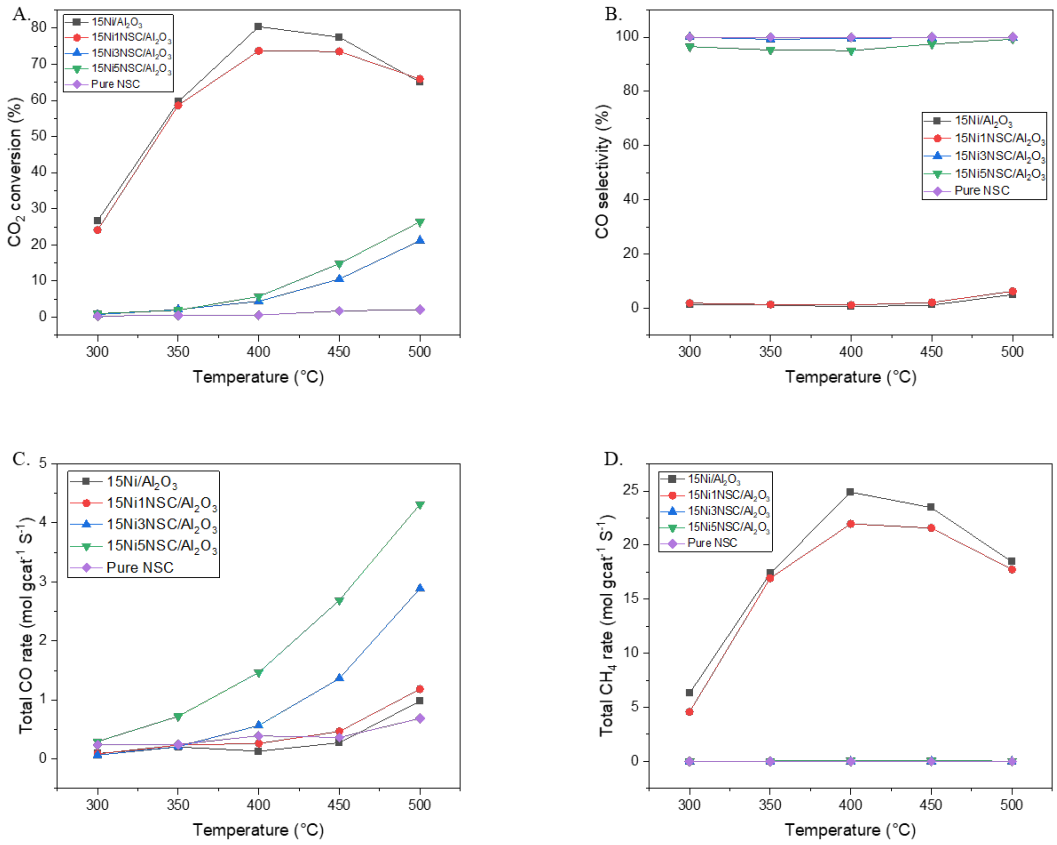

Figure 4. Catalytic performance of NiNSC/Al_2O_3 A. CO_2 conversion; B. CO selectivity; C. Total CO rate; D. Total CH_4 rate.

produce more CH_4 than smaller ones. The addition of NSC into the Ni catalyst induced changes in the formation of metal-support interactions, resulting in a reduction in the particle size of Ni. This decrease in particle size contributed to a decrease in CO_2 conversion and altered the selective hydrogenation pathway for CO_2. However, the selectivity and total CO rate (Figure 4B and 4C) toward the reverse water-gas shift (rWGS) reaction to form CO increased to 99% and produced higher rates compared to pure Ni/Al_2O_3. The highest reported rate was 4.3 mol. $gcat^{-1}$ s^{-1} for 15Ni5NSC/Al_2O_3 at 500 °C.

4. Conclusions

In this study, we successfully synthesized Ni/Al_2O_3 incorporated N,S-doped carbon to modulate the selectivity of CO_2 hydrogenation towards CO. A thorough characterization of all synthesized catalysts was performed, confirming the presence of metal and carbon-doped components through XRD, EDX, and TGA analyses. Subsequently, the catalyst's performance was evaluated for selectivity and CO production under atmospheric pressure and temperature range between 300-500 °C. Changes in the catalyst performances were attributed to the size reduction of Ni through the addition of N, S-doped carbon. This development paves the way for further investigation into achieving low-temperature CO production using Ni-based catalysts in future studies.

Acknowledgements

The authors would like to express their gratitude to Chulalongkorn University for supporting N.J. and extend their appreciation to CrystalLyte Co., Ltd., for providing the N-, S-doped carbon supports for this research.

References

1. Artz, J.; Muller, T. E.; Thenert, K.; Kleinekorte, J.; Meys, R.; Sternberg, A.; Bardow, A.; Leitner, W. Sustainable Conversion of Carbon Dioxide: An Integrated Review of Catalysis and Life Cycle Assessment. Chem Rev 2018, 118 (2), 434-504. DOI: 10.1021/acs.chemrev.7b00435 From NLM PubMed-not-MEDLINE.
2. Anderson, T. R.; Hawkins, E.; Jones, P. D. CO_2, the greenhouse effect and global warming: from the pioneering work of

Arrhenius and Callendar to today's Earth System Models. Endeavour 2016, 40 (3), 178-187. DOI: 10.1016/j.endeavour.2016.07.002 From NLM PubMed-not-MEDLINE.
3. Ye, R. P.; Ding, J.; Gong, W.; Argyle, M. D.; Zhong, Q.; Wang, Y.; Russell, C. K.; Xu, Z.; Russell, A. G.; Li, Q.; et al. CO_2 hydrogenation to high-value products via heterogeneous catalysis. Nat Commun 2019, 10 (1), 5698. DOI: 10.1038/s41467-019-13638-9 From NLM PubMed-not-MEDLINE.
4. Martínez-Vargas, D. X.; Sandoval-Rangel, L.; Campuzano-Calderon, O.; Romero-Flores, M.; Lozano, F. J.; Nigam, K. D. P.; Mendoza, A.; Montesinos-Castellanos, A. Recent Advances in Bifunctional Catalysts for the Fischer–Tropsch Process: One-Stage Production of Liquid Hydrocarbons from Syngas. Industrial & Engineering Chemistry Research 2019, 58 (35), 15872-15901. DOI: 10.1021/acs.iecr.9b01141.
5. Zhu, M.; Ge, Q.; Zhu, X. Catalytic Reduction of CO2 to CO via Reverse Water Gas Shift Reaction: Recent Advances in the Design of Active and Selective Supported Metal Catalysts. Transactions of Tianjin University 2020, 26 (3), 172-187. DOI: 10.1007/s12209-020-00246-8.
6. Galhardo, T. S.; Braga, A. H.; Arpini, B. H.; Szanyi, J.; Goncalves, R. V.; Zornio, B. F.; Miranda, C. R.; Rossi, L. M. Optimizing Active Sites for High CO Selectivity during CO(2) Hydrogenation over Supported Nickel Catalysts. J Am Chem Soc 2021, 143 (11), 4268-4280. DOI: 10.1021/jacs.0c12689 From NLM PubMed-not-MEDLINE.
7. Gioria, E.; Ingale, P.; Pohl, F.; Naumann d'Alnoncourt, R.; Thomas, A.; Rosowski, F. Boosting the performance of Ni/Al_2O_3 for the reverse water gas shift reaction through formation of CuNi nanoalloys. Catalysis Science & Technology 2022, 12 (2), 474-487. DOI: 10.1039/d1cy01585k.
8. Dias, Y. R.; Perez-Lopez, O. W. Carbon dioxide methanation over $Ni-Cu/SiO_2$ catalysts. Energy Conversion and Management 2020, 203. DOI: 10.1016/j.enconman.2019.112214.
9. Silaghi, M.-C.; Comas-Vives, A.; Copéret, C. CO2 Activation on $Ni/\gamma–Al_2O_3$ Catalysts by First-Principles Calculations: From Ideal Surfaces to Supported Nanoparticles. ACS Catalysis 2016, 6 (7), 4501-4505. DOI: 10.1021/acscatal.6b00822.
10. González-Rangulan, V. V.; Reyero, I.; Bimbela, F.; Romero-Sarria, F.; Daturi, M.; Gandía, L. M. CO2 Methanation over Nickel Catalysts: Support Effects Investigated through Specific Activity and Operando IR Spectroscopy Measurements. Catalysts 2023, 13 (2). DOI: 10.3390/catal13020448.
11. Meshkini Far, R.; Ischenko, O. V.; Dyachenko, A. G.; Bieda, O.; Gaidai, S. V.; Lisnyak, V. V. CO_2 hydrogenation into CH4 over Ni–Fe catalysts. Functional Materials Letters 2018, 11 (03). DOI: 10.1142/s1793604718500571.
12. Chein, R.-Y.; Wang, C.-C. Experimental Study on CO2 Methanation over Ni/Al2O3, Ru/Al2O3, and Ru-Ni/Al2O3 Catalysts. Catalysts 2020, 10 (10). DOI: 10.3390/catal10101112.
13. Quindimil, A.; De-La-Torre, U.; Pereda-Ayo, B.; Davó-Quiñonero, A.; Bailón-García, E.; Lozano-Castelló, D.; González-Marcos, J. A.; Bueno-López, A.; González-Velasco, J. R. Effect of metal loading on the CO2 methanation: A comparison between alumina supported Ni and Ru catalysts. Catalysis Today 2020, 356, 419-432. DOI: 10.1016/j.cattod.2019.06.027.
14. Jalama, K. Carbon dioxide hydrogenation over nickel-, ruthenium-, and copper-based catalysts: Review of kinetics and mechanism. Catalysis Reviews 2017, 59 (2), 95-164. DOI: 10.1080/01614940.2017.1316172.

Development of CaO promoted Ni/Al_2O_3 catalyst for direct methanation of biogas into biomethane

Jidapa Tatiyapantarak[1], Atthapon Srifa[1], Wanida Koo-Amornpattana[1], Choji Fukuhara[2] and Sakhon Ratchahat[1]*

[1]*Department of Chemical Engineering, Faculty of Engineering, Mahidol University, Nakhon Pathom, 73170, Thailand*

[2]*Department of Applied Chemistry and Biochemical Engineering, Graduate School of Engineering, Shizuoka University, Shizuoka 432-8561, Japan*

**E-mail: sakhon.rat@mahidol.edu*

Abstract:

The direct methanation of biogas to biomethane was performed via a CO_2 methanation reaction over Ni-based catalysts. The catalysts were prepared by a simple impregnation method. The catalytic enhancement of as-prepared catalysts in terms of CO_2 conversion and CH_4 yield was investigated in a fixed-bed reactor at 200-500°C, and atmospheric pressure. The CaO loading on Al_2O_3 support (10, 20, and 30 wt.%) was studied, while the Ni loading of 10 wt.% was fixed. The 10% Ni/(10% CaO)-Al_2O_3 catalyst exhibited the highest CO_2 conversion of 80.1% and CH_4 yield of 79.7% at 325°C. The nickel loading (10, 20, 30, and 40 wt.%) was optimized using the 10 wt.% CaO-Al_2O_3 support. The 30 wt.% Ni provided the highest CO_2 conversion of 86.3% and CH_4 yield of 86.2% at temperature of 275 °C. The sequence for loading Ni and CaO on Al_2O_3 was studied by using the 30% Ni/(10% CaO)-Al_2O_3 catalyst. It found that the loading sequence had a significant effect on the catalytic activity, especially at 225°C, the CO_2 conversions were 13.2% to 76.2% for sequential-impregnation method and co-impregnation method, respectively. The various characterization techniques were performed, and results revealed that the promotion of CO_2 adsorption and H_2 dissociation active sites is necessary to carry out CO_2 methanation.

1. Introduction

Converting organic waste into biogas emerges as a promising method for renewable energy production commonly employed in electricity generating engines. Traditional biogas upgrading techniques involve removing CO_2 through separations, yet this leads to residual CO_2 and potential emission issues. A more efficient alternative is the direct methanation of biogas, utilizing the entire content and minimizing CO_2 emissions. This approach optimally employs biomass feedstock for biogas production. The shift towards direct methanation aligns with sustainability goals, addressing CO_2 emission concerns while maximizing resource utilization.[1] An innovative solution known as Dual Function Materials (DFMs) has been proposed and patented for coupling carbon capture with carbon utilization[2,3] These materials aim to capture CO_2 and hydrogenate the captured CO_2 to generate fuel while regenerating the adsorbent. Specifically designed for selective CO_2 capture at higher temperatures (300–350°C), DFMs, after CO_2 adsorption, are exposed to a (renewable) H_2-containing stream. This process produces CH_4 while concurrently regenerating the adsorbent at the same elevated temperature.[4,5] The process aligns with CO_2 methanation, an exothermic reaction also well known as the Sabatier reaction, $CO_2 + 4H_2 \rightarrow CH_4 + 2H_2O$ ($\Delta H^o_{298} = -165$ kJ/mol), which typically takes place at temperatures in the range of 200-550°C.[6,7]

Ni is the most commonly used methanation catalyst for Power-to-Gas (PtG) applications.[8] According to Mills and Steffgen,[9] the important methanation catalysts are ordered by selectivity: Ni > Co > Fe > Ru, and activity: Ru > Fe > Ni > Co > Mo, respectively. The catalytic performance of a Ni-based catalyst over CO_2 methanation is dependent on various factors, such as Ni loading and support materials. Ni loading was found to affect both the interaction of Ni with the support and Ni dispersion on the support. Typical Ni loading is in the range of 1-20 wt.%.[10]

DFM is composed of a catalytic metal closely in contact with alkaline metal oxides, e.g., Na_2O, CaO, K_2O, and MgO, supported on high surface area carriers[3]. Researchers, Mills G.A. et al., Chang F.W. et al., and Belova A.A.G. et al., have found that dispersing CaO on γ-Al_2O_3 can improve the sorption capacity and minimize sintering.[11-13] Gruene P. et al. observed that dispersed CaO was an active sorbent at moderate temperature with a CO_2 capture capacity at 300°C to 1.7 times as efficient compared to bulk CaO powder. Moreover, the adsorbent can be regenerated when CO_2 is removed from the feed stream at lower temperatures (300-650°C).[12]

This work explores direct CO_2 methanation for biogas-to-biomethane conversion using the innovative concept of Dual Function Materials (DFMs) which adeptly absorb CO_2 and facilitate its reduction to CH_4. Work on using CaO as a CO_2 adsorbent to improve the performance of Ni/Al_2O_3 catalysts for methanation. All catalysts were synthesized by the wet impregnation method with the evaporation-to-dryness technique. The objective is to determine the optimal composition of Ni, CaO, and γ-Al_2O_3 for maximum methane production. The effect of the impregnation sequence is also studied.

2. Materials and Methods

2.1 Materials

Nickel nitrate hexahydrate ($Ni(NO_3)_2 \cdot 6H_2O$), Alumina (γ-Al_2O_3, <300 μm), Calcium nitrate tetrahydrate ($Ca(NO_3)_2 \cdot 4H_2O$), Calcium oxide (CaO, commercial grade), Distilled water, Hydrogen (H_2, 99.99% purity), and mixed gas (15% CO_2, 23% CH_4, and 62% H_2).

2.2 Synthesis of support materials

A series of catalyst supports consisting of 10, 20, and 30 wt.% of CaO was prepared by wet impregnation method to promote CO_2 adsorption on γ-Al_2O_3. A certain amount of $Ca(NO_3)_2 \cdot 4H_2O$ precursor was dissolved in distilled water. Then, a certain amount of γ-Al_2O_3 powder was mixed with the solution. The mixture was evaporated at 80°C to remove water and calcined at 700°C for 3 h.

2.3 Synthesis of catalysts

2.3.1 For the study of the effect of CaO addition, a series of catalysts (5 g) consisting of 10 wt.% of Ni as active phase and 90 wt.% of support material was prepared by wet impregnation method. Firstly, 2.4772 g of $Ni(NO_3)_2 \cdot 6H_2O$ was dissolved in distilled water. Then, 4.5 g of the support powder was mixed with the solution. The mixture was evaporated at 80°C to remove water prior to calcination at 500°C for 3 h.

2.3.2 For study effect of Ni loading, a catalyst support consisting of 10 wt.% of CaO was prepared using the same procedure as described in 2.2. A series of catalysts consisting of 10, 20, 30, and 40 wt.% of Ni was prepared by wet impregnation method using the same procedure as described in 2.3.1.

2.3.3 For study effect of the impregnation sequence, the catalyst containing the same composition as $30Ni/10CaO\_Al_2O_3$ was prepared by co-impregnation method by mixing both Ni and CaO precursors with γ-Al_2O_3 support. The mixture was evaporated and then calcined under the same calcination conditions as described in 2.3.1.

2.4 Characterization

The properties of the catalysts were characterized by the following techniques:

2.4.1 The specific surface area, total pore volume, and average pore size diameter of the sample were determined by adsorption-desorption isotherms of nitrogen at 77K using a Multipoint Surface Area Analyzer (Tristar II3020, Micromeritics) after degassing the sample under vacuum for 4 h at 150°C. The specific surface areas were calculated according to the Brunauer-Emmett-Teller (BET) method using the adsorption isotherm. The total pore volume was obtained from the maximum amount of adsorption at p/p_0 of 0.999. The pore size distribution was calculated by BJH method using the desorption branch.

2.4.2 The crystallinity was analyzed by X-ray diffraction (Bruker D2 Phaser) with CuKα radiation. The XRD patterns were collected in the 2θ range of 5–80° and a step size of 0.02 degree/step. The metal crystallite size was determined by the Scherrer equation.

2.4.3 The reducibility of the calcined catalyst was analyzed by the temperature-programmed reduction of hydrogen (H_2-TPR) using a chemisorption analyzer (BEL BELCAT-B) and the hydrogen consumed was detected by thermal conductivity detector (TCD). Pre-treatment of the examined sample was carried out at 500°C for 1 h under 10 % O_2/He with a flow rate of 30 mL/min. After 1 h, the temperature was cooled down to 50°C under Ar with a flow rate of 30 mL/min. Then, the reduction under the 10% H_2/Ar atmosphere with a flow rate of 30 mL/min was performed in a temperature range of 50-900°C with a heating rate of 10°C/min.

2.4.4 The metal (Ni) surface and metal (Ni) dispersion were analyzed by H_2-temperature-programmed-desorption (H_2-TPD) using a chemisorption analyzer (BEL BELCAT-B), and the H_2 consumed was detected by thermal conductivity detector (TCD). Prior to the H_2 chemisorption measurement, the examined sample was pre-treated at 200°C for 1 h under inert gas. Then it was reduced under 10% H_2/Ar from 200 to 500°C with a heating rate of 10 °C/min, followed by isothermal heating at 500°C for 1 h. And finally, it was cooled to the chemisorption temperature of 30°C under inert gas with a flow rate of 30 mL/min. H_2 was adsorbed by feeding 10% H_2/Ar at 30°C for 1 h. Then, it was purged with inert gas flow for 30 mins to remove excess H_2 and

physically adsorbed H_2. The desorption was performed under inert gas flow from 30 to 850°C with a heating rate of 10°C/min. All steps were performed using a constant gas flow rate of 30 mL/min.

2.4.5 The basic surface properties were analyzed by CO_2-temperature-programmed-desorption (CO_2-TPD) using a chemisorption analyzer (BEL BELCAT-B) and the CO_2 consumed was detected by thermal conductivity detector (TCD). Prior to the CO_2 chemisorption measurement, the examined sample was pre-treated at 200°C for 1 h under inert gas. Then it was reduced under 5% H_2/Ar from 200 to 500°C with a heating rate of 10 °C/min, followed by isothermal heating at 500°C for 1 h. And finally, it was cooled to the chemisorption temperature of 30°C under inert gas with a flow rate of 30 mL/min. CO_2 was adsorbed by feeding 10% CO_2/He at 30°C for 1 h. Then, it was purged with inert gas flow for 30 mins to remove excess CO_2 and physically adsorbed CO_2. The desorption was performed under inert gas flow from 30 to 850°C with a heating rate of 10°C/min. All steps were performed using a constant gas flow rate of 30 mL/min.

2.5 Catalytic activity test

The direct methanation of biogas was carried out in a horizontal fixed-bed tubular reactor made of quartz (ID: 8 mm and 600 mm long). Briefly, the catalyst (300 mg, granule: 0.85-1.18 mm) was packed and in situ reduced under a H_2 flow of 100 mL/min at 500°C for 1 h. Then, a mixture of biogas and H_2 was fed into the reactor at a total flow rate of 100 mL/min, corresponding to a weight hourly space velocity (WHSV) of 20,000 mL/g·h. The catalyst performances for direct CO_2 methanation of biogas were tested at temperatures of 200-500 °C and 1 atm. The feed used contains simulated biogas (40% CO_2 and 60% CH_4) with stoichiometric H_2 (H_2/CO_2 ratio = 4). The flow rates of feed and effluent were measured by soap film meter. The compositions of feed and effluent gases (CO, CO_2, and CH_4) were analyzed by GC-TCD (Shimadzu 8A). A detail of the experimental setup is shown in **Figure 1**. The CO_2 conversion and CH_4 yield were calculated according to Eqs. (1) and (2). The carbon balances were calculated (Eq. (3)). Only CO_2, CH_4, and CO were considered with an overall result of 100% and a deviation of less than ± 5%. All gases employed in this study are UHP grade (>99.999%).

$$\text{Eq. (1): } CO_2 \text{ Conv. (\%)} = \frac{[CO_2]_{in} \times F_{in} - [CO_2]_{out} \times F_{out}}{[CO_2]_{in} \times F_{in}} \times 100$$

$$\text{Eq. (2): } CH_4 \text{ Yield (\%)} = \frac{[CH_4]_{out} \times F_{out} - [CH_4]_{in} \times F_{in}}{[CO_2]_{in} \times F_{in}} \times 100$$

$$\text{Eq. (3): C bal. (\%)} = \frac{([CO_2]_{out} + [CH_4]_{out} + [CO]_{out}) \times F_{out}}{([CO_2]_{in} + [CH_4]_{in}) \times F_{in}} \times 100$$

When $[i]_{in}$ and $[i]_{out}$ represent the concentrations of reactants (i = CO_2) or products (i = CH_4 or CO) at the inlet and outlet of the reactor, respectively. F_{in} and F_{out} are the total flow rates (mL/min) at the inlet and outlet of the reactor, respectively.

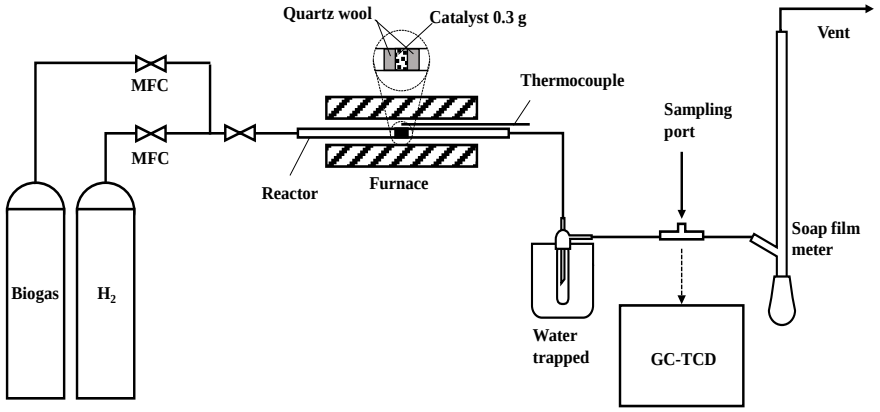

Figure 1. A schematic diagram of the experimental setup

3. Results & Discussion

3.1 Characterization

Characterization of catalysts was carried out employing various techniques. The details of the catalysts' characterization are presented in Table 1, providing a comprehensive overview of their key properties as revealed by the applied characterization methods.

3.2 Effect of CaO addition

The promotion of Ni-based catalysts involves the addition of CaO as the storage material onto alumina support. The study focused on varying the CaO loading (10, 20, and 30 wt.% based on the total support) while maintaining 10 wt.% of Ni and 90 wt.% of support for the catalyst. Figures 2 and 3 illustrate the CO_2 conversion and CH_4 yield of each catalyst.

A comparison was made with 10Ni/Al_2O_3 as 0% CaO and 10Ni/CaO as 100% CaO. The 10Ni/10CaO_Al_2O_3 catalyst demonstrated the highest CO_2 conversion among all catalysts in the temperature range of 275-375°C, achieving peak performance with a CO_2 conversion of 80.1% and a CH_4 yield of 79.7% at 325°C.

The addition of CaO improves catalytic performance, particularly at moderate to high temperatures (350-500°C). However, at lower temperatures (<350°C), the catalytic effectiveness decreases with CaO additions exceeding 10 wt.%, indicating that 10 wt.% CaO achieves optimal dispersion on Al_2O_3, promoting effective CaO dispersion. Contrary to higher CaO loadings, agglomeration reduces CaO dispersion. In line with Gruene P. and team's findings, well-dispersed CaO enhances CO_2 adsorption capacity and adsorbent regeneration at lower temperatures (300-650°C).[12] Despite a reduction in surface area with 10 wt.% CaO due to pore blocking, it enhances Ni dispersion on the catalyst support. This is evident in the smaller crystallite size of Ni, providing a higher Ni surface and effective area for H_2 dissociation and CO_2 reactions, ultimately enhancing catalyst activity. The observed CO_2-TPD results affirm that CaO addition improves the catalyst's ability to capture CO_2 effectively.

Consequently, the CaO 10 wt.% dispersed on Al_2O_3 configuration 10CaO_Al_2O_3 was employed as the support of the catalyst in further experiments.

Table 1. Characterization of catalysts

catalyst	S_{BET}[a] m^2/g_{cat}	$d_{Ni,111}$[b] nm	S_{metal}[c] m^2_{Ni}/g_{cat}	$S_{effective}$[d] m^2_{Ni}/m^2_{total}	Basicity[e] %	Reducibility[f] %
10Ni/Al_2O_3	161.5	4.56	32.12	0.20	0.30%	18.27%
10Ni/10CaO_Al_2O_3	117.7	2.50	32.51	0.28	0.67%	56.64%
30Ni/10CaO_Al_2O_3	94.02	12.10	41.88	0.45	0.66%	69.97%
30Ni/10CaO_Al_2O_3 (co-imp)	98.01	11.98	55.01	0.56	0.58%	66.94%

[a] The specific surface area (S_{BET}) was calculated by the Brunauer-Emmett-Teller (BET) method.
[b] The Ni crystallite size (111) plane ($d_{Ni,111}$) was determined by Scherrer equation.
[c] The metal (Ni) surface area (S_{metal}) was determined by H_2-TPD.
[d] The effective surface area; $S_{effective} = S_{metal}/S_{BET}$
[e] The basicity was determined by CO_2-TPD.
[f] The Reducibility was determined by H_2 consumption at 500°C from H_2-TPR

3.3 Effect of Ni loading

To optimize the Ni loading on the 10CaO_Al_2O_3 support, nickel loadings ranging from 10 to 40 wt.% were investigated. Figures 4 and 5 illustrate the CO_2 conversion and CH_4 yield of each catalyst.

It's noteworthy that all improvements occurred at temperatures lower than 350°C. For the specified support 10CaO_Al_2O_3, there was a substantial enhancement in performance from 10 to 20 wt.% Ni loading, followed by a slight improvement at 30 wt.% Ni loading.

The Ni loading significantly influences both Ni interaction with the support and Ni dispersion on the support. Higher Ni amounts diminish the interaction between Ni and support, in line with H_2-TPR results. Enhanced Ni content improves catalytic performance by providing more active sites and an increased effective area for H_2 dissociation and CO_2 reactions. However, at a 40 wt.% Ni loading, there is a slight decrease in catalytic performance due to Ni dispersion and a mass transfer limit resulting from the reduced catalyst surface area.

Importantly, the optimal outcome was achieved with a 30 wt.% Ni loading, demonstrating the highest performance with a CO_2 conversion of 86.3% and CH_4 yield of 86.2% at 275°C. Testing with the 10CaO_Al_2O_3 support reveals its ability to accommodate a higher maximum Ni loading compared to existing literature,[10] implying that CaO addition enhances Ni dispersion. This, in turn, increases active sites, enhancing overall performance. Interestingly, Ni loading shows no significant effect on basicity and CaO utilization, likely due to the consistent support materials.

Consequently, the 30Ni/10CaO_Al_2O_3 was employed as catalyst in further experiments.

3.4 Effect of the impregnation sequence

The sequential impregnation and co-impregnation preparation methods were compared. The primary advantages of co-impregnation include reduced energy utilization, simplified catalyst preparation, lower costs, and less time consumed. Figures 6 and 7 illustrate the CO_2 conversion and CH_4 yield obtained with

30Ni/10CaO_Al_2O_3 prepared from two different impregnation methods.

There was no significant effect on catalytic performance at moderate to high temperatures (>250°C). It was found that the preparation method had a significant effect on the catalytic activity at temperatures lower than 250°C. In addition, CO_2 conversion at 225°C drastically increased 5.8 times, from 13.2% for sequential-impregnation method to 76.2% for co-impregnation method. Also, a significant effect of the preparation method on the CH4 yield at a low temperature of 225°C was also observed. The CH_4 yield increased from 12.9% for sequential-impregnation method to 76.1%. for co-impregnation method.

Compared with the same composition of sequential impregnation catalyst, catalyst prepared by co-impregnation method show an increase in Ni surface, indicate more area for H_2 dissociation and CO_2 reactions, and facilitate greater mass transfer. A decrease in Ni crystallite size and a slight drop in reducibility are attributed to the enhanced Ni dispersion and interaction between Ni, CaO, and Al_2O_3. The decrease in basicity is observed, suggesting that Ni gradually covers and obstructs CO_2 accessibility to the adsorbent, leading to a decrease in CaO dispersion.[14]

Furthermore, suggest that the co-impregnation method provides more insertion of Ni-CaO, which leads to more interaction between Ni and support material and more Ni-CaO interfaces that facilitate the CO_2 dissociation on CaO to convert into CH_4 by reacting with H_2 dissociated on Ni.

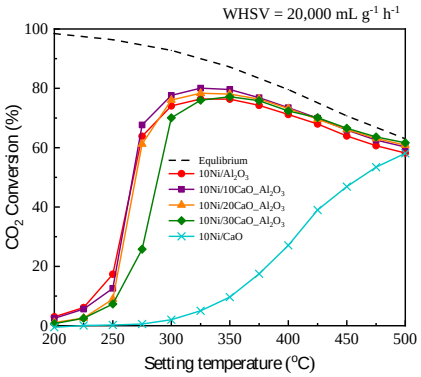

Figure 2. Effect of CaO addition: CO_2 conversion

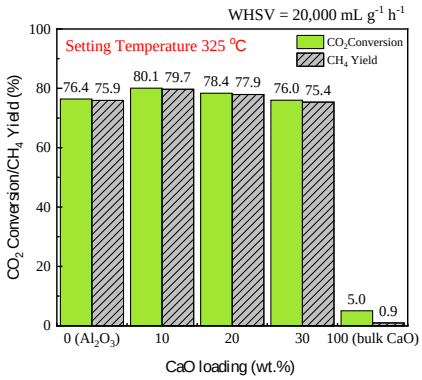

Figure 3. Effect of CaO addition: CO_2 conversion and CH_4 yield at 325°C.

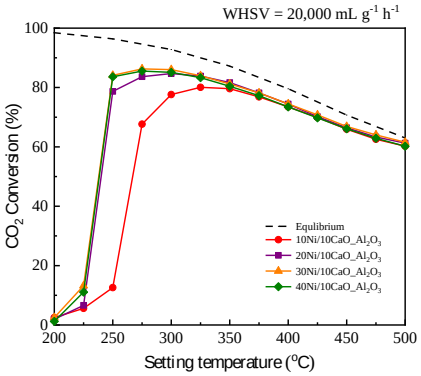

Figure 4. Effect of Ni loading: CO_2 conversion

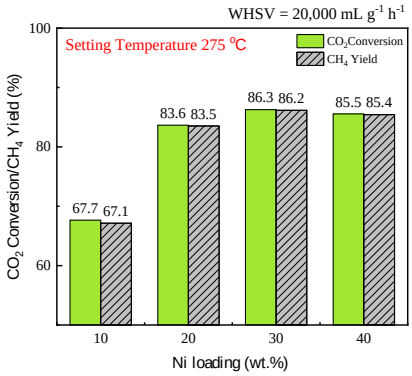

Figure 5. Effect of Ni loading: CO_2 conversion and CH_4 yield at 275°C.

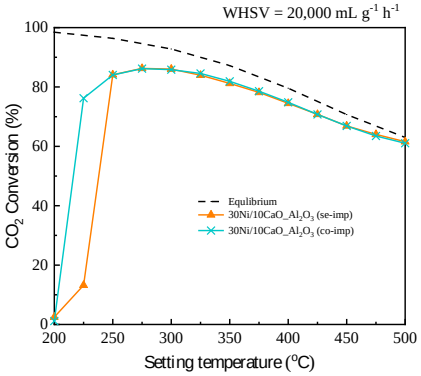

Figure 6. Effect of the impregnation sequence: CO_2 conversion

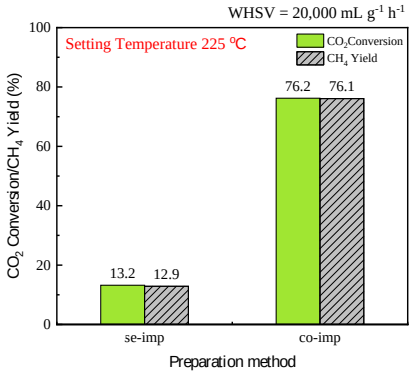

Figure 7. Effect of the impregnation sequence: CO_2 conversion and CH_4 yield at 225°C.

4. Conclusion

Introducing CaO on Ni/Al_2O_3 catalysts by using the "DFMs" concept further facilitates efficient CO_2 adsorption and improves catalyst active surface area for better catalyst activity in terms of CO_2 conversion and CH_4 yield.

Optimizing the catalyst composition revealed that $30Ni/10CaO\_Al_2O_3$, prepared using the co-impregnation method, and demonstrated the highest performance. The preparation method played a pivotal role, particularly at low temperature (225°C), showcasing a significant increase in CO_2 conversion from 13.2% to 76.2% for both sequential-impregnation and co-impregnation methods. Additionally, catalytic activity at the same low temperature witnessed a substantial rise in CH_4 purity from 25.3% to 60.2% for the sequential-impregnation and co-impregnation methods, respectively.

The highest performance of $30Ni/10CaO\_Al_2O_3$ (co-imp) direct methanation of biogas appears at 275 °C which 86.19% CO_2 conversion 70.1% CH_4 purity.

Based on all the experiments, to convert CO_2 into methane, the catalyst must have special spots where CO_2 can stick and H_2 can break apart. The best catalyst, $30Ni/10CaO\_Al_2O_3$, follows this idea, showing it can grab onto CO_2 well and has a big area where the reaction can happen. This area is important for how well the catalyst works.

Acknowledgment

This research work is financially supported by Mahidol University (Basic Research Fund: Fiscal Year 2021, BRF1-A12/2564).

References

1. Dadi, S.; Ebbe, M. P. Upgrading of Biogas to Biomethane with the Addition of Hydrogen from Electrolysis. https://futuregas.dk/wp-content/uploads/2018/06/FutureGas-WP1-Deliverable-1.1.1.- Technologies-and-status-of-methanation-of-biogas-2017_Final.pdf. (accessed September 18,2017)
2. Duyar, M. S.; Treviño, M. A. A.; Farrauto, R. J. Dual Function Materials for CO_2 Capture and Conversion Using Renewable H_2. *Appl. Catal., B* **2015**, *168–169*, 370– 376.
3. Farrauto, R. J.; Duyar, M. S.; Park, A. A. Methods, Systems and Materials for Capturing Carbon Dioxide and Converting It to a Chemical Product. WO 2016/007825 A1, 2016.
4. Melo Bravo, P.; Debecker, D. P. Combining CO_2 Capture and Catalytic Conversion to Methane. *Waste Dispos. Sustain. Energy* **2019**, *1* (1), 53– 65.
5. Tsiotsias, A. I.; Charisiou, N. D.; Yentekakis, I. V.; Goula, M. A. The Role of Alkali and Alkaline Earth Metals in the CO_2 Methanation Reaction and the Combined Capture and Methanation of CO_2. *Catalysts* **2020**, *10* (7), 812.
6. Schaaf, T.; Grünig, J.; Schuster, M.R.; Rothenfluh, T.; and Orth, A. Methanation of CO_2 - storage of renewable energy in a gas distribution system, *Energy, Sustainability and Society*, **2014**, *4(1)*, 2.
7. Ghaib, K.; Nitz, K.; and Ben-Fares, F.-Z. Chemical Methanation of CO_2: A Review, *ChemBioEng Reviews*, **2016**, *3(6)*, 266-275.
8. Rönsch, S.; Schneider, J.; Matthischke, S.; Schlüter, M.; Götz, M.; Lefebvre, J.; Prabhakaran, P.; Bajohr, S. Review on Methanation - From Fundamentals to Current Projects. *Fuel* **2016**, *166*, 276– 296.
9. Mills, G.A.; Steffgen, F.W.; Catalytic Methanation. *Catalysis Reviews* **1974**, *8(1)*, 159-210.
10. Chang, F.W.; Kuo, M.S.; Tsay, M.T.; Hsieh, M.C. Hydrogenation of CO_2 over nickel catalysts on rice husk ash-alumina prepared by incipient wetness impregnation. *Applied Catalysis A: General* **2003**, *247(2)*, 309-20.

11. Belova, A.A.G.; Yegulalp, T.M.; Yee, C.T.; Feasibility study of In Situ CO_2 capture on an integrated catalytic CO_2 sorbent for hydrogen production from methane. *Energy Procedia* **2009**, *1(1)*, 749-55.
12. Gruene, P.; Belova, A.G.; Yegulalp, T.M.; Farrauto, R. J.; Castaldi, M. J. Dispersed Calcium Oxide as a Reversible and Efficient CO_2−Sorbent at Intermediate Temperatures. Industrial & Engineering *Chemistry Research* **2011**, *50(7)*, 4042-9.
13. Duyar, M. S.; Farrauto, R. J.; Castaldi, M. J.; Yegulalp, T.M. In Situ CO_2 Capture Using CaO/γ-Al2O3 Washcoated Monoliths for Sorption Enhanced Water Gas Shift Reaction. *Industrial & Engineering Chemistry Research* **2014**, *53(3)*, 1064-72.
14. Bermejo-López, A.; Pereda-Ayo, B.; González-Marcos, J.A., González-Velasco, J.R. Ni loading effects on dual function materials for capture and in-situ conversion of CO_2 to CH_4 using CaO or Na_2CO_3, *Journal of CO_2 Utilization* **2019**, *34*, 576-587

Transesterification of refined palm oil with methanol catalyzed by anion-exchange resin in rotating packed bed reactor

Rawipa Choknumchaisiri and Palang Bumroongsakulsawat*

Center of Excellence on Catalysis and Catalytic Reaction Engineering, Department of Chemical Engineering, Faculty of Engineering, Chulalongkorn University, Bangkok 10330, Thailand.

**E-mail: palang.b@chula.ac.th*

Abstract:

Transesterification of palm oil with methanol was carried out with alkaline anion exchange resins: modified AmberLite™ IRA402 and AmberLyst™ A26 OH, yielding fatty acid methyl ester (FAME) in both conventional and rotating packed bed (RPB) setups. In a conventional setup at 60 °C and 4 h reaction time with a stirring speed of 750 rpm, modified IRA402 produced a FAME yield of about 5%, while the RPB rotating at 750 rpm achieved a higher yield of approximately 7.9%. This increase in the RPB setup was attributed to enhanced mass transfer between phases, facilitated by the rotational movement of the bed. For modified A26, the FAME yield remained consistent in both setups at 750 rpm due to the lack of external mass transfer limitations, highlighting internal limitations instead. The study also explored the use of n-hexane as a co-solvent in the RPB setup at 46 °C and 750 rpm to increase the solubility between oil and methanol and hence mass transfer. Lower yields of 1.25% to 3.23% were obtained. However, when the reaction temperature was increased to 56 °C, a significant increase in the FAME yield to 77.48% was observed, underscoring the effectiveness of n-hexane in enhancing the reaction rate.

1. Introduction

In recent decades, fossil fuels consumption has increased and resulted in air pollution and global warming. Biodiesel is an alternative fuel that can reduce dependence on fossil fuels. Biodiesel usually includes fatty acid methyl esters (FAMEs) formed by the transesterification of triacylglycerols (oils and fats) with methanol. The chemical reactions (1) to (4) show the transesterification of triglycerides with methanol, which involves three consecutives reversible reactions.[1]

Overall reaction: $TG + 3MeOH \rightleftharpoons 3FAME + G$ (1)
Step (1): $TG + MeOH \rightleftharpoons DG + FAME$ (2)
Step (2): $DG + MeOH \rightleftharpoons MG + FAME$ (3)
Step (3): $MG + MeOH \rightleftharpoons G + FAME$ (4)

where TG, DG, MG, G, FAME are triglycerides, diglyceride, monoglyceride, glycerol and fatty acid methyl ester, respectively.

Alkali catalysts including potassium hydroxide (KOH), sodium hydroxide (NaOH), sodium methoxide ($NaOCH_3$) and potassium methoxide ($KOCH_3$) are frequently used for production of biodiesel on commercial scale. However, these catalysts are difficult to remove from the reaction mixture. In general, homogeneous catalysts need to be neutralized into salts and removed as thick slurry. So, the consumption of acid and waste generation are unavoidable. A solution to this problem is using heterogeneous catalysts which can be separated more easily and recycled. Also, the use of heterogeneous catalysts generates fewer discharges and yields high purity glycerol.[2]

Ion exchange resins (IERs) are a class of heterogeneous catalysts, which are versatile materials possessing a modulable framework based on cross-linked copolymers bearing functional groups that can participate in ion exchange.[6] Ion exchange resins are categorized into two main types: anion-exchange and cation-exchange resins. Anion-exchange resins exhibit much higher catalytic activities than cation-exchange resins for transesterification. Moreover, anion-exchange resins with a lower cross-linking density and a smaller particle size gave higher reaction rates as well as high conversion.[4]

The insolubility of methanol in the oil phase hinders the progress of the transesterification reaction with both homogeneous and heterogeneous catalysts. Vigorous mixing is essential to create sufficient contact between the two immiscible phases for improving mass transfer. Co-solvents such as n-hexane, acetone, and tetrahydrofuran (THF) can be added to reaction mixture to increase the miscibility of oil and methanol or even to form a single liquid phase.[10] The conventional transesterification unit used in batch operation is considered slow, tedious, labor intensive, and not well-adapted to automation.[3]

Chen and coworker[7] did a research study on transesterification in a rotating packed bed

(RPB) using K/γ-Al_2O_3 solid catalyst. The RPB presents excellent micromixing ability for three immiscible phases (methanol, oil, solid catalyst).

Hung Chen and others[11] studied the continuous-flow transesterification of soybean oil with methanol using a rotating packed bed (RPB) to produce fatty acid methyl esters (biodiesel). In this study, biodiesel is synthesized via the methanolysis of soybean oil using potassium hydroxide as the catalyst. Due to its excellent micromixing characteristics, the RPB system shows satisfactory transesterification efficiency. A RPB is considered a practical transesterification reactor with high transesterification efficiency.

Research by Yanibiao and others[5] studied transesterification of soybean oil with methanol in a fixed bed reactor packed with D261 anion-exchange resin as a heterogeneous catalyst and the influences of four co-solvents namely MTBE, n-hexane, TBA, and THF. The results indicated that all four co-solvents demonstrated excellent compatibility with the soybean oil/methanol system, leading to high FAME production rates of 98.9% for THF, 98.4% for TBA, and 96.7% for n-hexane. However, THF caused resin swelling, while TBA, with a lower melting point of 328.15 K, exhibited reduced solubility in soybean oil. Consequently, n-hexane was deemed the most suitable co-solvent and was ultimately employed in the process.

In this research, we studied transesterification of refined palm oil with methanol catalyzed by anion-exchange resin in rotating packed bed reactor (RPB reactor). In some experiments, n-hexane was added as a co-solvent to increase the miscibility of oil and methanol. Two types of anion-exchange resin: modified AmberLite™ IRA402 Cl (dense) and modified AmberLyst™ A26 OH (porous) were used in this work. The results from using these two types of resin were compared and discussed in this work.

2. Materials and Methods

2.1 Rotating packed bed reactor (RPB reactor)

The frames of rotating packed bed reactors were made by additive manufacturing (3D printing) from polypropylene (Ultimaker) or carbon-fiber-reinforced nylon (Markforged's Onyx). Stainless steel mesh was inserted into the frames to form pockets for ion-exchange resin. A magnetic stir bar was inserted into a dedicated slot of an RPB so that the reactor could be spun by a magnetic stirrer. Figure 1 shows the RPBs made from both materials. Polypropylene RPBs were used in experiments without co-solvent because polypropylene is one of a few polymers that can withstand concentrated methanol. Nylon RPBs were used when hexane was added as a co-solvent as nylon is compatible with a wide range of solvents.

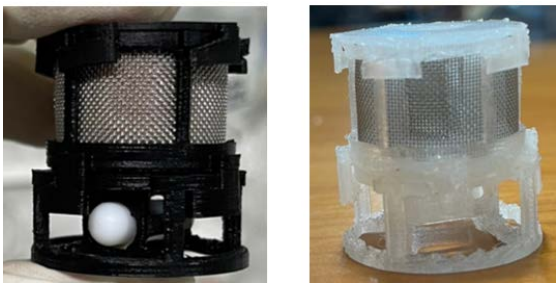

Figure 1. Nylon RPB (left) and Polypropylene RPB (right)

2.2 Resin preparation

Two types of anion-exchange resins were used in this experiment. AmberLite™ IRA402 and AmberLyst™ A26 were originally in the chloride and hydroxide forms, respectively. IRA402 resin was converted to hydroxide form by gently stirring 3 mL of resin in 32 mL of 1.5 M aqueous solution of sodium hydroxide for 30 minutes. Then, the resin was washed with methanol until the pH of methanol became stable to remove species adhering to resin surfaces but not adsorbed by ion exchange. Washing the resin in methanol also converted all hydroxide into methoxide which is the active catalytic species for transesterification with methanol. The A26 resin was originally in hydroxide form. So, the resin was only washed with methanol before use.

2.3 Transesterification without co-solvent

The reaction was conducted at 60 °C in a jacketed glass reactor with a Graham condenser. A thermometer was inserted inside a reactor to monitor the reaction temperature. The reactor was filled with 27.1 g of palm oil (Morakot). 3 mL of modified resin was used. In the conventional setup, the resin was poured directly into the oil. In the RPB setup, the resin was packed in a rotating packed bed reactor which in turn was lowered into the oil inside the reactor. The reaction mixture was preheated to 65 °C. After that, 12.3 mL of methanol (AR, Thermo Fisher) was poured into the reactor. This amount of methanol resulted in a methanol-to-oil molar ratio of 9.5 to 1 and a total mixture volume of ca. 42 mL which was kept constant to maintain the hydrodynamic characteristics of the reaction mixture during agitation. Timing and stirring with a magnetic stir bar (for conventional setup) or spinning the RPB (for RPB setup) were started when the reaction temperature reached 60 °C.

2.4 Transesterification with n-hexane added as co-solvent

The reaction was performed at 46 °C in the same jacket glass reactor used for the experiments without co-solvent. Only experiments in the RPB setup were carried out. 5.0 g of palm oil and 34.0 mL of n-hexane (AR, RCL Labscan Limited) were added in the reactor with an RPB inside. Then, the reaction mixture was preheated to 47 °C. Next, 2.266 mL of methanol was poured into the reactor. Timing and spinning were initiated when the temperature reached 46 °C. A lower temperature was required to keep the reaction mixture liquid because n-hexane form azeotropic mixture with methanol.

2.5 FAME analysis

At the end of transesterification, the agitation or spinning was stopped. 20 mL of reaction mixture was transferred to another jacket vessel for evaporation of methanol and n-hexane (if added) at 75 °C for 2 h. Gas Chromatography (GC) was used to evaluate the amount of fatty acid methyl ester (FAME). The GC system was equipped with a ZB-5HT column and a flame ionization detector (FID). 0.25 g of the sample was prepared and mixed with 0.050 g methyl heptadecanoate as an internal standard. The solution was diluted to 5 mL in n- heptane. The GC system was programmed to inject 1 µL of the diluted sample with the injector temperature of 250 °C. The temperature was then kept at 150 °C for 5 min before being raised at a rate of 3 °C min^{-1} to 190 °C and maintained at 220 °C for the following 5 min. A FAME yield was calculated by the following formula:

$$\text{FAME yield\%} = \left\{ \frac{A_{FAME}}{A_{IS}} \times \frac{m_{IS}}{m_s} \right\} \times 100\%$$

A_{FAME} is the total area of FAME peaks.
A_{IS} is the area of internal standard (methyl heptadecanoate) peak.
m_{IS} is the mass of internal standard (methyl heptadecanoate) in the diluted sample.
m_s is the mass of sample of oil phase which contain FAME.

3. Results & Discussion

3.1 Resin characterization

The methoxide resins of both modified IRA402 and A26 were examined by SEM (Hitachi S 3400N) and N_2 physisorption with BET isotherm.

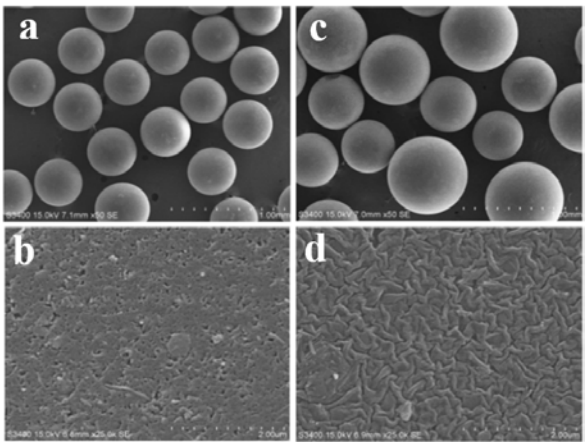

Figure 2. SEM micrographs a.) modified A26 at 50x magnifications b.) modified A26 at 25x magnifications c.) modified IRA402 at 50x magnifications d.) modified IRA402 at 25x magnifications.

Figure 2 presents SEM micrographs which show that the bead size of the modified IRA402 was larger than that of the modified A26. Moreover, the bead size of modified A26 was more uniform than that of modified IRA402. The outer surface of modified IRA402 appeared as folds while that of modified A26 seemed to form multiple elongated grains. Table 1 shows some properties of both resins.

Table 1. Properties of modified IRA402 and modified A26

Properties	modified IRA402	modified A26
BET surface area, m^2/g	5.33	28.3
Pore volume, cm^3/g	0.007	0.197
Average particles diameter, mm	0.55	0.44
S.D. of particle diameter, mm	0.012	0.008
Exchange capacity, eq/dm^3	0.57	0.73

The BET model was used to determine BET surface area and pore volume of both resins in Table 1.

3.2 Transesterification without co-solvent

Figure 3 shows that in the conventional transesterification with only a magnetic stir bar, two liquid phases persisted with large droplets of one phase in the other throughout and the resin beads agglomerated in lumps. In contrast, the reaction mixture during transesterification with resin packed in the RPB was transformed into a colloidal mixture, which significantly enhanced the yield compared to that from the conventional one.

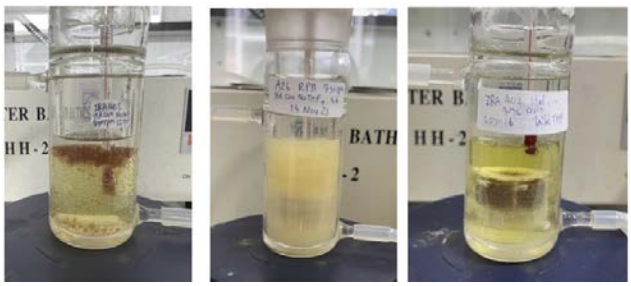

Figure 3. Photographs of the reaction mixture with modified IRA402: after reaction in the conventional setup (left), colloidal mixture during reaction in the RPB setup (middle), after reaction in the RPB setup (right).

Table 2. FAME yields obtained from modified IRA402 and modified A26 at 750 rpm and 200 rpm in the conventional and RPB setups at 4 h, 60 °C.

Mode	Agitation speed (rpm)	%FAME yield from modified IRA402		%FAME yield from modified A26	
		1st run	2nd run	1st run	2nd run
CONVEN*	750	5.03	5.57	9.45	10.05
CONVEN*	200	3.05	1.27	1.46	4.77
RPB**	750	7.34	7.90	9.66	9.50
RPB**	200	3.13	3.58	7.00	7.13

*Conventional setup
** Rotating packed bed setup

Table 2 shows %FAME yields obtained using both resins at 750 rpm and 200 rpm in different modes. For modified IRA402, in the conventional setup, the FAME yields obtained were 5.03% and 5.57% at 750 rpm, whereas in the RPB setup, higher FAME yields of 7.34% and 7.90% were achieved. The enhanced performance of the RPB setup could be attributed to improved inter-phase mass transfer. The rotational movement of the bed promoted better contact between the two phases, ultimately boosting the reaction rate. %FAME yields, when modified A26 was employed, were higher compared to those obtained when modified IRA402 was used in both setups. This activity enhancement could be ascribed to the porous nature of the modified A26 resin. Even though the particles size of A26 was slightly smaller than that of IRA402, the porous nature of the former was more likely to be the main factor contributing to an increase in the specific surface area and the number of active sites available for the reactant molecules to bind to and undergo chemical reactions, resulting in higher reaction rates and FAME yields from A26.

For both modified IRA402 and modified A26 in the conventional setup at 200 rpm, inconsistent %FAME yields were observed. These results were attributed to poor dispersion of both resin and the two liquid phases at this low agitation speed. These phenomena led to poor inter-phase mass transfer and also low liquid-catalyst contact, ultimately resulting in low and inconsistent yields (Table 2 and Figure 4). The inconsistent %FAME yields at the low agitation speed of 200 rpm were also consistent with the observed poor resin distribution, which led to the presented inconsistent results.

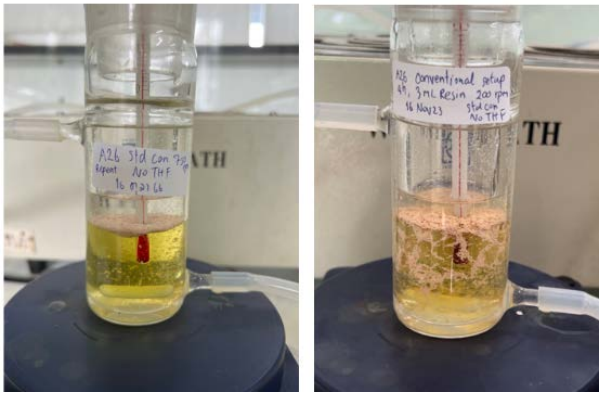

Figure 4. Transesterification with modified A26 in the conventional setup at 200 rpm. The resin agglomerated at the interface before agitation (left). The resin and the two liquid phases were poorly dispersed during 200 rpm agitation (right).

There are two types of mass transfer resistances involved in ion exchange catalysis: external mass resistance and internal mass transfer resistance[8]. For the catalytic systems with the modified A26 resin, there were largely unchanged %FAME yields obtained from both conventional and RPB setups at 750 rpm. This is due to the absence of external mass transfer limitation and thereby corroborated the internal mass transfer limitation. Because of secondary liquid phase creation within the modified A26 pores, prompted by the production and buildup of glycerol [9].

3.3 Kinetic profile without co-solvent

Figure 5 shows the FAME yields obtained from the RPB setup with the modified A26 resin catalyst at different reaction times at 200 rpm. The reaction rate was largely constant. The gradual drop in the rate was plausibly caused by the lower reactant concentrations over the course of the reaction.

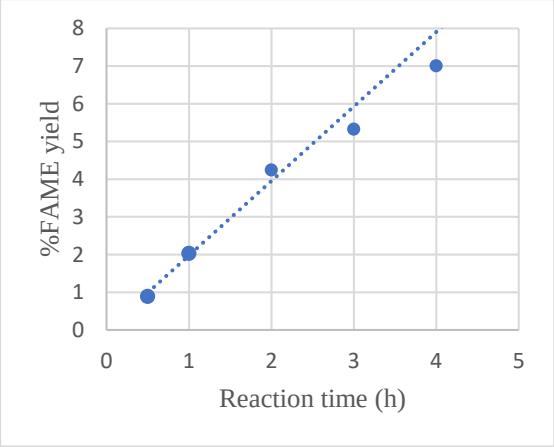

Figure 5. FAME yields obtained at different reaction times at 200 rpm in the RPB setup. The linear trend line extrapolates from the initial reaction rate and is added to highlight the gradual drop in the reaction rate.

3.4 Effect of n-hexane as co-solvent

Figure 6 shows the transesterification with modified A26 in the RPB setup at 46 °C and a spinning speed of 750 rpm. The amount of hexane added was enough for the mixture to form a single liquid phase, eliminating inter-phase mass transfer limitations. Nevertheless, Figure 7 shows that %FAME yields were only around 1.25% to 3.23%, which were lower than the yields without co-solvent at 60 °C. The much lower yields were very likely caused by the low reaction temperature. When the reaction was conducted at 56 °C for 4 h in the RPB setup, a FAME yield of 77.48% was achieved. This result clearly demonstrated that the use of n-hexane as a co-solvent significantly enhanced the reaction rate.

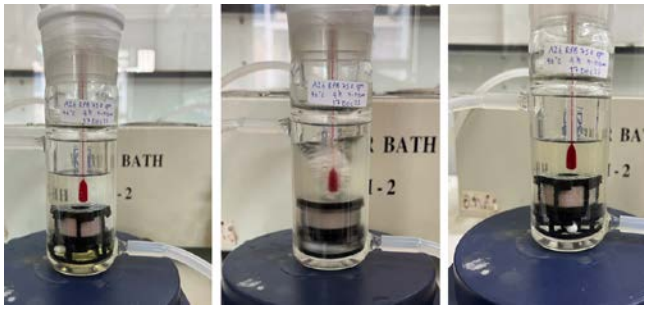

Figure 6. Photographs of the reaction mixture in the transesterification with modified A26 resin in the RPB setup: before the reaction started (left), during the reaction (middle), and after the reaction (right).

In addition, it can be seen in Figure 7 that the initial rate was slightly faster, before transitioning to a slower rate sometime between 0 h and 1 h. The rate suppression occurred plausibly

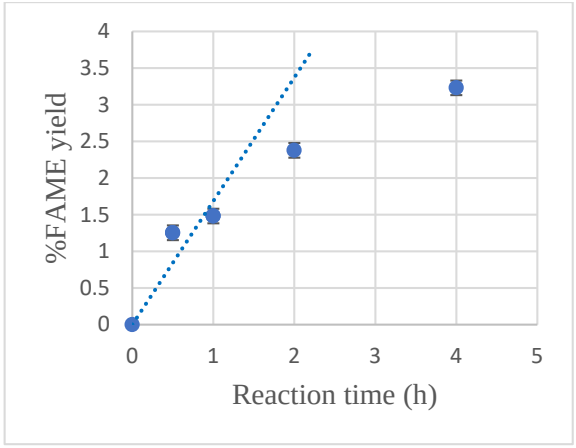

Figure 7. FAME yields obtained at different reaction times at 750 rpm, RPB setup with n-hexane as a co-solvent. The linear trend line projects the FAME yield that would be obtained were the first-stage fast reaction rate to continue.

because a secondary liquid phase was created within the modified A26 pores, prompted by the production and buildup of glycerol [9]. This secondary liquid phase would block the active sites in the pores of modified A26, leaving only the sites on the external surfaces of the resin beads for reaction.

4. Conclusion

The present research shows that the transesterification of palm oil with methanol could be carried out using alkaline anion exchange resins, specifically modified dense AmberLite™ IRA402 and modified porous AmberLyst™ A26, resulting in the production of FAME. The transesterification without co-solvent, two setups were studied: the conventional setup and the rotating packed bed (RPB) setup. After 4 h reaction in the conventional setup at 750 rpm, the FAME yield obtained was only around 5% with modified IRA402, whereas in the RPB setup, a higher FAME yield of around 7.9% was achieved. The enhanced performance of the RPB could be attributed to improved inter-phase mass transfer (resin-oil-methanol). The rotational movement of the bed promoted better contact between the two phases, ultimately boosting the reaction rate. For modified A26, there was a largely unchanged FAME yield obtained in both the conventional setup and RPB setup at 750 rpm because of the absence of external mass transfer limitation and thereby corroborated the internal mass transfer limitation. n-hexane was used as a co-solvent to aid single-phase formation of the reaction mixture. With the RPB setup at 56 °C and 750 rpm, a FAME yield of 77.48% was achieved from a reaction time of 4 h.

Acknowledgements

The work was successfully completed with the assistance of my professor, Asst. Prof. Palang Bumroongsakulsawat. I would like to express my sincere thanks for his invaluable help and constant encouragement throughout the course of this research.

References

1. Simonelli, G.; Ferreira Jr, J.; Pires, C.; Santos, L. Biodiesel production using co-solvents: a review. Research, Society and Development **2020**, 9, 99911672.
2. Atadashi, I. M.; Aroua, M. K.; Abdul Aziz, A. R.; Sulaiman, N. M. N. The effects of catalysts in biodiesel production: A review. Journal of Industrial and Engineering Chemistry **2013**, 19 (1), 14-26.
3. Chen, Y.-H.; Huang, Y.-H.; Lin, R.-H.; Shang, N.-C. A continuous-flow biodiesel production process using a rotating packed bed. Bioresource Technology **2010**, 101 (2), 668-673.
4. Shibasaki-Kitakawa, N.; Honda, H.; Kuribayashi, H.; Toda, T.; Fukumura, T.; Yonemoto, T. Biodiesel production using anionic ion-exchange resin as heterogeneous catalyst. Bioresource Technology **2007**, 98 (2), 416-421.
5. Ren, Y.; He, B.; Yan, F.; Wang, H.; Cheng, Y.; Lin, L.; Feng, Y.; Li, J. Continuous biodiesel production in a fixed bed reactor packed with anion-exchange resin as heterogeneous catalyst. Bioresource Technology **2012**, 113, 19-22.
6. Török, B.; Schäfer, C.; Kokel, A. Chapter 2 - Solid catalysts for environmentally benign synthesis. In Heterogeneous Catalysis in Sustainable Synthesis, Török, B., Schäfer, C., Kokel, A. Eds.; Elsevier, **2022**; pp 23-80.
7. Chen, Y.-H.; Huang, Y.-H.; Lin, R.-H.; Shang, et al, Biodiesel production in a rotating packed bed using K/γ-Al2O3 solid catalyst. Journal of the Taiwan Institute of Chemical Engineers **2011**, 42 (6), 937-944.
8. Abidin, S. Z.; Mohammed, M. L.; Saha, B. Two-Stage Conversion of Used Cooking Oil to Biodiesel Using Ion Exchange Resins as Catalysts. In Catalysts, **2023**; Vol. 13.
9. Juntuma, A.; Ammara, Z.; Methaapanon, R.; Bumroongsakulsawat, P. Two-stage reaction rates in transesterification of palm oil with methanol catalysed by anion-exchange resin with tetrahydrofuran as a co-solvent. Arabian Journal of Chemistry **2024**, 17 (1), 105449.
10. Díaz, L.; Horstmann, F.; Brito, A.; González, L. A. A comprehensive review of the influence of co-solvents on the catalysed methanolysis process to obtain biodiesel. Heliyon **2023**, 9 (1), e13006.
11. Chen, Y.-H.; Huang, Y.-H.; Lin, R.-H.; Shang, N.-C. A continuous-flow biodiesel production process using a rotating packed bed. Bioresource technology **2009**, 101, 668-673.

Effect of CH_4 impurity in flue gas feed on ethanol-assisted methanol synthesis from CO_2 hydrogenation over copper-based catalyst

Banthita Woraphan,[1,2] Wen-Yueh Yu,[2]* and Pattaraporn Kim-Lohsoontorn[1]*

[1]*Centre of Excellence on Catalysis and Catalytic Reaction Engineering, Department of Chemical Engineering, Faculty of Engineering, Chulalongkorn University, Bangkok, 10330, Thailand*
[2]*Department of Chemical Engineering, National Taiwan University, Taipei 10617, Taiwan*
**E-mail: pattaraporn.k@chula.ac.th*

Abstract:

The rising amount of CO_2 emission from flue gases into the atmosphere is one of the major issues leading to global warming. Applying CO_2 to produce methanol could potentially address the concerns of CO_2 emission. The flue gases from industries contain not only CO_2 but also impurities such as CH_4. Here, we present a study that examines the effect of CH_4 in CO_2 and H_2 feed for methanol production using Cu/ZnO catalyst. The results indicated that the optimal condition, with 1% CH_4 at 170°C, achieved 77% CO_2 conversion and a 34.67% methanol yield were achieved. Surprisingly, the systems with CH_4 impurity in feed consistently outperformed those without. The likely reason is the generation of CO, which leads to CO hydrogenation to methanol enhancement and improved reducing ability, facilitating the Cu^{2+} to Cu^0 transition in the catalyst, which is beneficial for methanol synthesis. Thus, the presence of a limited amount of CH_4, not exceeding 1%, proved advantageous in CO_2-to-methanol conversion in terms of both CO_2 Conversion and methanol yield.

1. Introduction

Addressing greenhouse gas emissions is a global imperative, and carbon dioxide (CO_2) stands out as a predominant greenhouse gas present in virtually every sector, including petrochemicals, human activities, and agriculture. Recognizing the urgency of this issue, Carbon Capture and Utilization (CCU) has emerged as a pivotal concept, extensively deliberated for its potential in mitigating CO_2 emissions. An intriguing approach involves repurposing CO_2 as a raw material to generate high-value products, with methanol chosen as the focal point in this research. Methanol holds significance as a primary precursor in various industries, spanning pharmaceuticals, polymers, and biodiesel production.[1] The conventional method for producing methanol from CO_2 involves hydrogenation using a $Cu/ZnO/Al_2O_3$ catalyst, as outlined in Equation (1). However, a drawback of this approach lies in its demand for elevated temperature (220-300 ˚C) and high pressure (50-100 bar).[2] Ongoing efforts aim to overcome these challenges, exploring alternative methodologies to enhance the efficiency and sustainability of CO_2 hydrogenation for methanol production.

$$CO_2 + 3H_2 \rightarrow CH_3OH + H_2O \quad (1)$$

The methanol synthesis from CO_2 is the exothermic reaction with $\Delta H_{25°C}$ = -49.5 kJ/mol. Methanol synthesis faces a significant challenge as conventional processes necessitate low temperatures and high pressures in line with Le Chatelier's principle. However, the kinetic constraints and chemical inertness of CO_2 impose a need for elevated reaction temperatures, creating a conflict between the reaction's thermodynamics and the pursuit of high methanol yield.[3] To surmount this challenge, a novel approach emerges, advocating the synthesis of methanol at lower temperatures from syngas.[3,4] This technique involves introducing alcohol into the reaction as a catalytic solvent, effectively mitigating thermodynamic limitations. By incorporating alcohol into the reaction pathway, the important part is when the formate species, which are stuck to a surface, react with alcohols to make ester species. This happens at low temperatures. Then, the ester is changed into methanol through hydrogenation with hydrogen atoms on metallic copper as demonstrated in Equations (2) to (5), The process undergoes a significant change, markedly lowering the required reaction temperature. This breakthrough enables the creation of methanol under more favorable and energy-efficient conditions, representing a significant advancement in the field.

$$CO_2 + 1/2\,H_2 + Cu \rightarrow HCOOCu \quad (2)$$
$$HCOOCu + ROH \rightarrow HCOOR + CuOH \quad (3)$$
$$HCOOR + 2H_2 \rightarrow ROH + CH_3OH \quad (4)$$
$$CuOH + 1/2\,H_2 \rightarrow H_2O + Cu \quad (5)$$

The novel alcohol-assisted methanol synthesis introduces a transformative approach which alcohol plays important roles as a solvent and a catalyst for the process, enabling the reaction

to occur under mild conditions, typically operating at temperatures between 150-170 °C and pressures ranging from 30-50 bar. [3] While this method holds the promise of reducing operational costs, a potential drawback is the formation of undesired ester by-products.[5] However, the focus of this study extends beyond addressing by-products. In the quest to produce methanol from CO_2, obtaining pure CO_2 gas as a precursor is crucial. Unfortunately, flue gas, a common source, contains a myriad of impurities, both toxic and non-toxic, necessitating an energy-intensive and wasteful CO_2 capture process.[6] To mitigate these costs, the incorporation of some impurities into the feed stream is considered. Of particular interest is CH_4, a prevalent impurity found in various waste gas sources. Refinery chemical industry data indicate that many production units generate a "dry-gas" by-product comprising CH_4 and H_2, constituting 3–6 wt.% of the products.[7] It is noteworthy that the presence of light hydrocarbons, such as CH_4, during the hydrogenation of CO_2 to methanol on $CuO/ZnO/Al_2O_3$, leads to a more than 50% decrease in methanol productivity.[6] Therefore, investigating the impact of CH_4 impurity in the gas stream on the catalyst and methanol productivity becomes a compelling and pivotal aspect of this study.

The primary aim of this study is to investigate the impact of CH_4 impurity at various operating temperatures on the efficiency of the Cu/ZnO catalyst concerning CO_2 conversion, methanol yield, and selectivity in the context of alcohol-assisted methanol production from CO_2 and H_2. This research is geared towards enhancing our understanding of how different operational conditions influence the overall performance of the catalyst, providing valuable insights for optimizing the methanol production process.

2. Materials and Methods

2.1 Catalyst preparation

The synthesis of 5 g of CuO/ZnO was done by the co-precipitation method between the metal precursor and precipitate agent. The metal precursor was composed by 1:1 molar ratio of aqueous solutions, copper nitrate ($Cu(NO_3)\cdot 3H_2O$, Sigma-Aldrich, 99.5%) and zinc nitrate ($Zn(NO_3)_2\cdot 6H_2O$, Sigma-Aldrich, 98%). The metal precursor was slowly dropped into 600 mL deionized water with 1.5 M sodium carbonate (Na_2CO_3, Sigma-Aldrich, 99.8%) as a precipitate agent to maintain a pH of 8. The precipitate was aged for 3 h with a constant stirring rate at 60°C and then washed until no basicity remained. The precipitated was separated by centrifugation, dried at 110°C for 24 h, and calcined at 350°C for 3 h. Eventually, the catalyst was reduced by 50%H_2 in N_2 using a fixed bed reactor at 300°C for 3 h to convert CuO/ZnO to Cu/ZnO.

2.2 The Ethanol-assisted Methanol production from CO_2 hydrogenation

3 g of reduced Cu/ZnO was placed into a stainless-steel autoclave reactor with a total volume of 360 mL, followed by 60 mL of ethanol filled as an alcohol catalytic solvent. The CH_4 was introduced into the reactor by varying composition from 0% to 2.5% of the total pressure, followed by the mixture of CO_2 and H_2 (ratio = 1:4.57) until the reactor reached pressures of 33.5, 36, and 38.3 bar for the operating temperature of 130, 150, and 170 °C, respectively. The temperature was increased to the target temperature along with the pressure increase to 50 bar. The reaction proceeded with a constant stirring rate at 600 rpm for 24 h. After the reaction, the gas and liquid phase compositions at the effluent were analyzed by FID gas chromatography (SHIMADZU Nexis GC-2030 with SH Rtx™-624 capillary columns). The catalyst's effectiveness was evaluated based on CO_2 conversion, methanol yield, and methanol selectivity, determined through the following equations,

$$\%CO_2\ \text{Conversion} = \frac{\text{mol of converted } CO_2 \times 100\%}{\text{mol of initial } CO_2} \quad (6)$$

$$\%\text{Methanol Yield} = \frac{\text{mol of methanol in product} \times 100\%}{\text{mol of initial } CO_2} \quad (7)$$

$$\%\text{Methanol Selectivity} = \frac{\text{mol of methanol in product} \times 100\%}{\text{mol of total product}} \quad (8)$$

2.3 Catalyst characterization

The characterization of physical properties includes X-ray diffraction (XRD, Bruker AXS, D8 Advance) for analyzing and identifying compound types, crystallized structures, along with crystallite sizes which were calculated by using Scherrer's equation,

$$d = \frac{K\lambda}{B\cos\theta} \quad (9)$$

where d = average crystallize size (nm)
K = Scherrer constant, 0.9 in this study
λ = x-ray wavelength, CuK_α = 1.5406 Å
B = full width at half maximum of peaks in radian located at any 2θ
θ = Bragg's angle (degree)

The calculation of the amount of coke deposited on the used catalyst surface was conducted using Thermal gravimetric analysis (TGA, TA Instruments, SDT Q600). Meanwhile,

the chemical analysis will employ the characterization technique of an In-situ infrared spectrometer (IR, Thermal Scientific, Nicolet iS50) with In-Situ Reaction Cell (Harrick Praying Mantis HVC-DRP-5) was employed to examine the reactions occurring at the catalyst's surface by determining the adsorbed molecules on the surface.

3. Results & Discussion

3.1 Methanol synthesis at different operating temperature

In the initial phase of the experiment, conducted in a CH_4-free system to determine the optimal operating temperature conditions, the findings depicted in Figure 1 revealed notable trends. It became evident that as the operating temperature increased, there was a corresponding rise in methanol yield, methanol selectivity, and CO_2 conversion in the range of high temperature. The methanol yield supposed to be higher than the result obtained theoretically. However, After the methanol product in the form of vapor has been obtained from the reaction, there is still some methanol vapor that has not completely condensed into liquid and remaining in the reactor. This occasion corresponds to some of the product to be purged with the final output gas. It is considered one of losses due to operation. The CO_2 conversion gave the direct variation from intermediate range of temperature to high temperature (150 °C to 170 °C) but inversely proportional at low temperature (130 °C). The exorbitant CO_2 conversion at low temperature might result from high CO_2 solubility in ethanol aqueous solution, which increased by decreasing the temperature.[8] In this point, it seems to be clear that higher temperature will give better production performance. This correlation is attributed to the accelerated kinetics of the system, showcasing the influence of temperature on the reaction rate. Furthermore, the hydrogenation of CO_2 to methanol, facilitated through formic acid and ethyl formate intermediates in liquid ethanol, exhibited a preference for temperatures ranging from 150 to 220 °C.[9] This preference for higher temperatures contributed to an increased production of methanol products. Consequently, for the subsequent phase of the experiment involving varying amounts of CH_4, an operating temperature of 170 °C was selected to further explore the impact of CH_4 on the overall reaction dynamics. This strategic choice aims to provide insights into the interplay between operating temperature and CH_4 presence in optimizing methanol production.

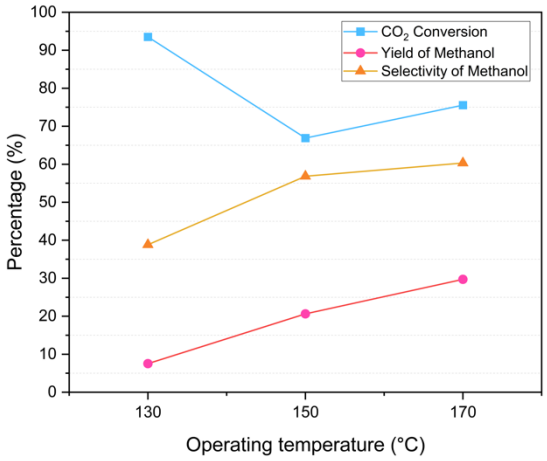

Figure 1. The percentages of CO_2 conversion, methanol yield, and methanol selectivity at various operating temperatures in the system containing 0% CH_4.

3.2 CO_2 conversion and methanol yield at different CH_4 composition

In Figure 2, CO_2 conversion, methanol yield and selectivity are presented. The CH_4 content was introduced in the feed gas at an operating temperature of 170 °C. Intriguingly, it was observed that the introduction of CH_4 at 1% of the total pressure resulted in an enhancement of CO_2 conversion, methanol yield, and CO yield compared to the system without CH_4. The peak methanol yield, reaching 34.67%, was achieved at this 1% CH_4 concentration, coupled with a remarkable CO_2 conversion of 77%. However, upon further increasing the CH_4 proportion to 2.5%, a nuanced pattern emerged. While CO_2 conversion continued to rise, both methanol yield and CO yield experienced a decline, along with a decreasing selectivity for methanol as the CH_4 concentration increased. This fascinating insight suggests that the presence of CH_4 may indeed bolster the efficiency of methanol production. One plausible mechanism for this improvement could be the promotion of CH_4 dry reforming to CO (Equation 10), subsequently facilitating the enhancement of CO hydrogenation to methanol (Equation 11). This subtle interaction between CH_4 concentration and methanol production efficiency adds a layer of complexity to our understanding of the reaction dynamics.

$$CH_4\,(g) + CO_2\,(g) \rightleftarrows 2CO\,(g) + H_2\,(g) \quad (10)$$

$$CO\,(g) + H_2\,(g) \rightleftarrows CH_3OH\,(g) \quad (11)$$

This phenomenon may lead to a reduction in methanol selectivity attributed to an elevated preference for CO. Furthermore, the CO_2 conversion rose due to a consequence of increased consumption in dry reforming reactions. However,

the continuity of increase in CH_4 more than 1% results in a decline in methanol selectivity, consequently compromising the efficiency of methanol formation. This decline was likely due to the degradation of the catalyst activity. It is noted that the presence of CH_4 in the system can contributes to heightened production of H_2 and CO, and both functioning as potent reducing agents.[10,11] This, in turn, triggers the reduction of the catalyst from CuO to Cu.

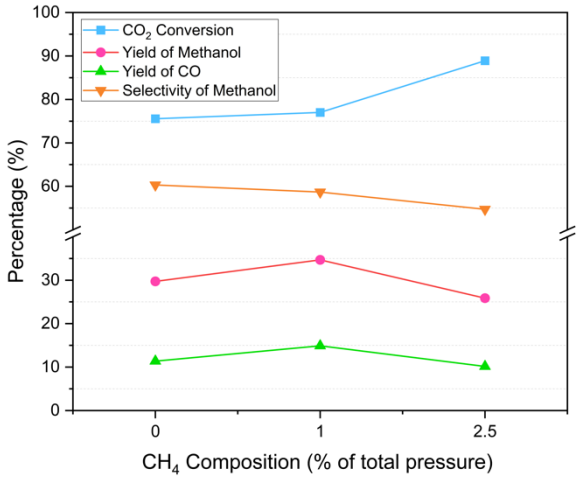

Figure 2. The percentages of CO_2 conversion, methanol yield, CO yield, and methanol selectivity at various CH_4 compositions at operating temperature of 170°C.

Hence, as the catalyst undergoes more reduction, an increased presence of carbon deposits on its surface ensues, disrupting the active sites. This disruption leads to a decline in effectiveness and the swift deactivation of the metallic catalyst.[10] This aspect will be elaborated upon in the subsequent discussion, specifically delving into the results of catalyst characterization.

3.3 Catalyst characterization results

As illustrated in Figure 3, the XRD results provide insights into the catalyst's transformation, encompassing its fresh catalyst after calcination and after reduction at 300 °C. Figure 4 display the used catalyst spent in the 0% CH_4 feed, and spent in the 1% and 2.5% CH_4 feed. Initially synthesized, the catalyst retained CuO peak, poised for conversion to the desired Cu form through a subsequent reduction process at 300 °C. Upon utilization in the CH_4-free system, the catalyst underwent reoxidation, and CuO peak reappeared due to the presence of oxide in the system. In contrast, the CH_4-containing system demonstrated a distinct behavior, acting as a reducing agent that facilitated the catalyst's reduction. As depicted in the figures, even a trace amount of CH_4 induced catalyst reduction, leaving carbon deposits on the surface. This scenario may contribute to a pronounced decline in catalyst activity.

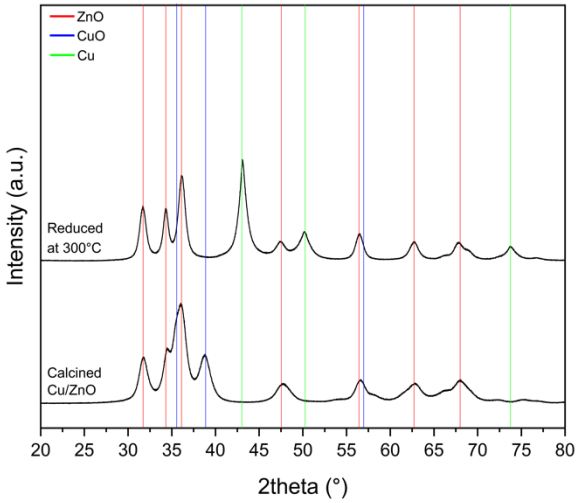

Figure 3. The XRD patterns of reduced and calcined catalyst.

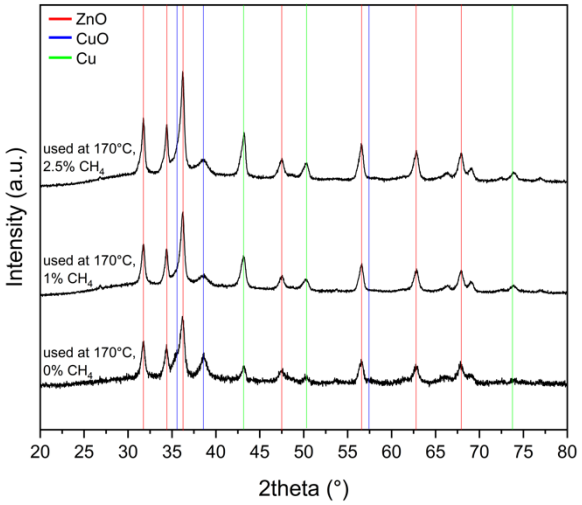

Figure 4. The XRD patterns of used catalysts at various CH_4 compositions at operating temperature of 170°C.

The catalyst's crystallize size is presented in Table 1. It is evident that adding 1% CH_4 reduces the size of Cu crystals compared to the CH_4-free system, which enhances surface area. However, the increase in crystallize size observed in the system containing 2.5% CH_4 may result from coke deposition on the catalyst surface, leading to additional catalyst deactivation.

In the assessment of coke formation on the catalytic surface, Table 2 highlights that a minimal CH_4 content of 1% correlated with a low level of coke deposition, similar to the system lacking CH_4. However, as the CH_4 content elevated to 2.5%, a substantial increase in surface coke became apparent. This aligned with the XRD results, reinforcing the notion that the presence of CH_4

contributes to catalyst reduction and subsequent coke formation on the surface.

Table 1. The crystallize size of fresh and used catalyst in different conditions.

Catalyst **conditions**	Crystallize size (nm)		
	Cu	CuO	ZnO
Fresh CuO/ZnO (calcined)	-	6.59	5.28
Fresh Cu/ZnO (reduced)	8.89	-	10.39
Used at 170 °C, 0% CH_4	17.6	10.39	11.86
Used at 170 °C, 1% CH_4	13.65	6.79	12.65
Used at 170 °C, 2.5% CH_4	16.44	4.54	12.33

Table 2. Amount of coke deposited on the used catalyst in the different condition from TGA characterization.

CH_4 composition (% of total pressure)	Coke formation (g coke/3 g cat.)
0	0.015
1	0.015
2.5	0.024

3.4 Preliminary In-situ IR result

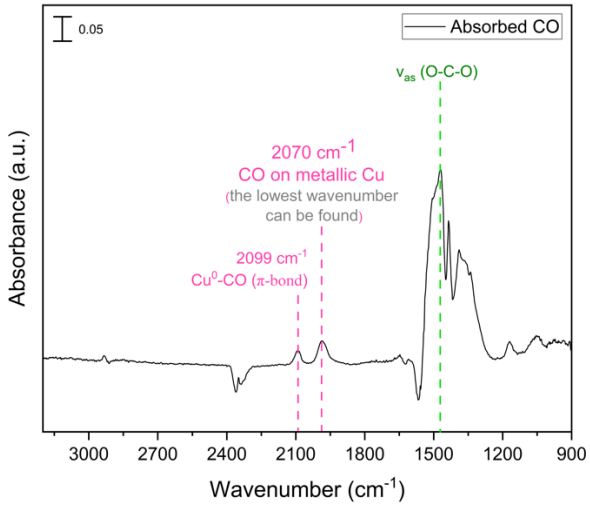

Figure 5. In-situ IR peak study on the adsorption of CO after adsorption for 20 min on Cu/ZnO at ambient pressure.

Comparing methanol production via CO_2 and CO hydrogenation methods reveals that CO hydrogenation yields more methanol products under equivalent operating temperatures.[12] To substantiate the finding that CH_4 presence enhances CO as a side product, promoting CO hydrogenation to methanol, Infrared Spectroscopy (IR) was employed to test this hypothesis. Figure 5 depicts the absorption peak of CO on a reduced catalyst for used as a background observation. The absorption peak of CO on Cu/ZnO is known to occur within a wavenumber range of approximately 2099-2070 cm^{-1}, aligning with literature indicating it at 2236-2070 cm^{-1}.[13] Experimental results, as shown in Figure 6, indicate that in the absence of CH_4 in the feed system, the absorption of CO on Cu/ZnO is not observed. To further validate this hypothesis, the future plan involves introducing CH_4 to observe reactions both with and without ethanol assistance.

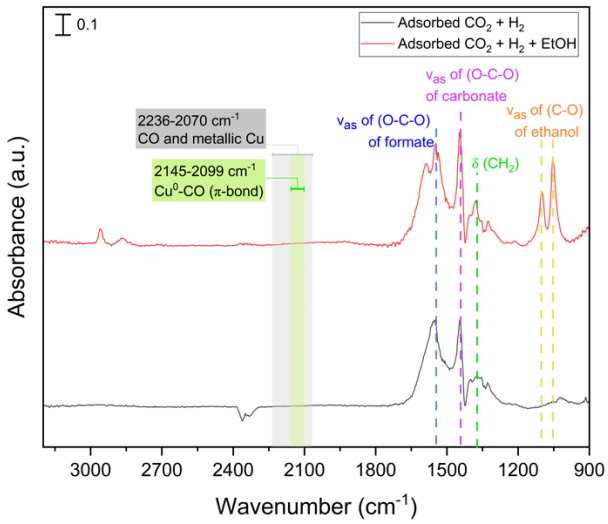

Figure 6. In-situ IR peak study on the adsorption of CO_2 + H_2 (black line) and CO_2 + H_2 + ethanol (red line) after adsorption for 20 min on Cu/ZnO at ambient pressure.

4. Conclusion

Methanol production was accomplished through ethanol-assisted CO_2 hydrogenation, incorporating varying trace amounts of CH_4 in the feed stream. Notably, the presence of CH_4 demonstrated the potential to induce CO formation via dry reforming reactions, consequently promoting CO hydrogenation to methanol. This scenario contributed to a heightened methanol yield, coupled with an increase in CO_2 conversion, as CO_2 was consumed in both CO_2 hydrogenation and dry reforming reactions. The optimal conditions, as determined from experimental observations, occurred at an operating temperature of 170°C with 1% CH_4 of the total pressure, resulting in an impressive 77% CO_2 conversion and a 34.67% methanol yield. The involvement of CH_4 in catalyst reduction, transitioning from CuO to Cu, possibly led to coke deposition from CH_4 on the catalyst surface, interfering with active sites—supporting evidence was obtained from XRD and TGA results. The inclination towards CO hydrogenation to methanol was further corroborated by an In-situ IR study. In the absence of CH_4 in the system during the early phases of experiments, the absence of a CO peak was noted. The forthcoming plan involves adsorbing CO_2, H_2, with and without ethanol assistance, to observe the

CO peak. Subsequent steps will ascertain whether the CO in the system can indeed contribute to increased methanol production.

Acknowledgements

This research was supported by Research Cess Fund, Malaysia-Thailand Joint Authority (MTJA) and the NSRF via the Program Management Unit for Human Resources & Institutional Development, Research and Innovation [B16F640164].

References

1. Bozzano, G.; Manenti, F. Efficient methanol synthesis: Perspectives, technologies and optimization strategies. *Prog. Energy Combust. Sci.* **2016**, *56*, 71-105.
2. Din, I. U.; Shaharun, M. S.; Naeem, A.; Tasleem, S.; Ahmad, P. Revalorization of CO_2 for methanol production via ZnO promoted carbon nanofibers-based Cu-ZrO_2 catalytic hydrogenation. *J. Energy Chem.* **2019**, *39*, 68-76.
3. Tsubaki, N.; Ito, M.; Fujimoto, K. A New Method of Low-Temperature Methanol Synthesis. *J. Catal.* **2001**, *197* (1), 224-227.
4. Shi, L.; Yang, G., Tao, K.; Yoshiharu, Y.; Tan, Y., Tsubaki, N. An Introduction of CO_2 Conversion by Dry Reforming with Methane and New Route of Low-Temperature Methanol Synthesis. *Acc. Chem. Res.* **2013**, *46* (8), 1838–1847.
5. Meesattham, S.; Kim-Lohsoontorn P. Low-temperature alcohol-assisted methanol synthesis from CO_2 and H_2: The effect of alcohol type. *Int. J. Hydrog. Energy* **2022**, *47* (54), 22691-22703.
6. Heracleous, E.; Koidi, V.; Lappas, A. A.; Hauser, A.; Haag, S. Valorization of steel-work off-gases: Influence of impurities on the performance of Cu-based methanol synthesis catalyst. *J. Chem. Eng.* **2022**, *444*, 136571
7. Ma, Q.; Chang, Y.; Yuan, B.; Song, Zh., Xue, J.; Jiang, Q. Utilizing carbon dioxide from refinery flue gas for methanol production: System design and assessment. *Energy* **2022**, *249*, 123602
8. Dalmolin, I.; Skovroinski, E.; Biasi, A.; Corazza, M. L.; Dariva, C.; Oliveira. J. V. Solubility of carbon dioxide in binary and ternary mixtures with ethanol and water. *Fluid Phase Equilib.* **2006**, *245* (2), 193-200.
9. Chen, Y.; Choi, S.; Thompson, L. T. Low-Temperature CO_2 Hydrogenation to Liquid Products via a Heterogeneous Cascade Catalytic System. *ACS Catal.* **2015**, *5* (3), 1717–1725.
10. Mirkarimi, S. M. R.; Bensaid, S.; Negro, V.; Chiaramonti, D. Review of methane cracking over carbon-based catalyst for energy and fuels. *Renew. Sustain. Energy Rev.* **2023**, *187*, 113747.
11. Haouas, A.; Nogier, J. Ph.; Fraissard, J. On the kinetics of the oxidation of traces of CO on CuO-SnO_2 catalysts. *Catal. Today* **1993**, *17* (1-2), 63-69.
12. Salahudeen, N.; Rasheed, A. A.; Babalola, A.; Moses, A. U. Review on technologies for conversion of natural gas to methanol. *J. Nat. Gas Sci. Eng.* **2022**, *108*, 104845.
13. Hadjiivanov, K.; Venkov, T.; Knözinger, H. FTIR Spectroscopic Study of CO Adsorption on Cu/SiO_2: Formation of New Types of Copper Carbonyls. *Catal. Lett.* **2001**, *75*, 55-59.

Conversion of amine-captured CO_2 to $CaCO_3$ by electrodialysis

Wongchanok Chewathum and Palang Bumroongsakulsawat*

Center of Excellence on Catalysis and Catalytic Reaction Engineering, Department of Chemical Engineering, Faculty of Engineering, Chulalongkorn University, Bangkok 10330, Thailand

**E-mail: palang.b@chula.ac.th*

Abstract:

The urgent need for efficient technology to reduce CO_2 emissions is increasingly highlighted to combat climate change. Currently, the most successfully commercialized technology for CO_2 capture is perhaps amine capture technology. CO_2-containing waste gas is passed through an absorber with amine solution as an absorbent. More than 90 % of CO_2 can be absorbed chemically in the amine solution. One of the commonly used absorbents is aqueous monoethanolamine (MEA) solution. If MEA is used, carbamate and ammonium ions form from the reaction between MEA and CO_2 after absorption. This spent absorbent is regenerated in a reboiled stripper, which requires heat to operate, to reclaim the absorbent and release high-concentration CO_2 gas. This project studies electrodialysis as an alternative means for absorbent regeneration with co-conversion of CO_2 into fine $CaCO_3$ particles, converting waste into a potential product. 30 wt% monoethanolamine (MEA) presaturated with 1 atm CO_2 was used to imitate industrial spent absorbent. $CaCl_2$ solution was used as a calcium source. In some experiments, NaCl was added to carbamate solution and/or HCl was added to $CaCl_2$ solution to study their effects. Our electrodialysis system offered a faradaic efficiency of 49% for $CaCO_3$ production at a current of 0.1 A. A key issue apart from this still low faradaic efficiency was precipitation of $CaCO_3$ directly on electrodialysis membrane. It was found that the addition of NaCl to carbamate solution minimized on-membrane precipitation of $CaCO_3$. This study aims to improve both the faradaic efficiency and the membrane-precipitation issue.

1. Introduction

Human activity has caused the atmospheric concentration of greenhouse gases such as carbon dioxide, methane, nitrous oxide, and chlorofluorocarbons to gradually increase over the last century. The main CO_2 source is the combustion of fossil fuels such as coal, oil, and gas in power plants for transportation and in homes, offices and industry, leading to global warming.[1] Therefore, the development of technologies for the capture and use of this gas is of great importance for the mitigation of greenhouse gases (GHG) and the reduction of their negative environmental effects.[2] Carbon capture and utilization (CCU) is known as an effective strategy to realize industrial carbon dioxide (CO_2) emission reduction. Moreover, efficient CO_2 capture, conversion and product purification driven by renewable energy have been regarded as one of the most promising options for reducing the atmospheric CO_2 concentration and achieving carbon neutrality.[3]

Solvent absorption is currently a favored method for capturing CO_2 for its low cost, strong adaptability, and technical feasibility.[4-6] A common CO_2 absorbent is aqueous solution of monoethanolamine (MEA), which absorbs CO_2 chemically according to the following net reactions:

$MEA + CO_2 + H_2O \leftrightarrow MEACOO^- + H_3O^+$ (carbamate formation)

$MEA + H_3O^+ \leftrightarrow MEA^+ + H_2O$ (amine protonation)

In other words, roughly 2 mol of MEA can absorb 1 mol of CO_2.

The spent absorbent is conventionally regenerated in a reboiled stripper to produce concentrated CO_2 gas stream and lean MEA solution with a heat requirement of about 3.6–4 GJ/ton-CO_2.[7] However, the elevated temperature led to absorbent degradation and high energy costs for amine regeneration.[8]

Using electrochemical approaches to capture CO_2 in various forms is gaining significant interest.[9] Following this trend, our research utilized electrodialysis to regenerate CO_2-rich MEA solution by injecting Ca^{2+} ion to the rich MEA solution and precipitating $CaCO_3$ as a product. Electrodialysis is a process by which ion exchange membranes in combination with an electrical potential difference are used to transfer ionic species between aqueous solutions. Ion exchange

membranes are the key components in electrodialysis. They consist of highly swollen gel-type polymer structures carrying fixed positive or negative charges.[10] Without the need for elevated temperature, this method may extend the life of MEA solution.

Two main issues were encountered in our process: precipitation of $CaCO_3$ directly on membrane surfaces and low faradaic efficiency.

. Various means of tackling these two problems have been explored and reported in this work.

2. Materials and Methods

Cation exchange membrane (FKE-50) and Anion exchange membrane (FAA-3-PK-130) were purchased from The Fuel Cell Store, USA. MEA (99%) was purchased from Sigma Aldrich. CO_2 (99.5 %) was obtained from Linde, Thailand. Sodium hydroxide (NaOH) and hydrochloric (HCl) were obtained from Quality Reagent Chemical Product (QREC Asia). Calcium chloride dehydrated (97%) was procured from Fluka chemicals. Sodium chloride (NaCl) was supplied by Merck.

2.1 Preparation of CO_2-rich absorbent (carbamate solution)

CO_2 gas was sparged into 5 M solution of monoethanolamine (MEA) in DI water. The solution was deemed saturated with CO_2 when its pH reached 8. In some experiments, NaCl was added to the MEA solution to achieve a concentration of 2 M before CO_2 sparging.

2.2 Electrodialysis

The electrodialysis cell used consisted of four chambers: acid chamber, calcium chamber, carbamate chamber, and base chamber (Fig. 1). Anion-exchange membranes (Fumatech's FAA-3-PK-130) were placed between the acid chamber and the calcium chamber and between the carbamate chamber and the base chamber. A cation-exchange membrane (Fumatech's FKE-50) was placed between the calcium chamber and the carbamate chamber. The cathode and anode were made of platinized titanium mesh and placed in the base chamber and acid chamber, respectively.

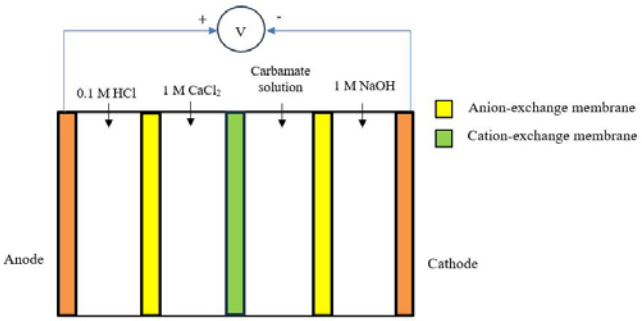

Figure 1. An illustration of an Electrodialysis cell.

Aqueous solutions of 0.1 M HCl, 1 M $CaCl_2$, and 1 M NaOH were added to the acid, calcium, and base chambers, respectively. The prepared carbamate solution was added to the carbamate chamber. A power supply (Tenma 72-2700) was connected to the cathode and anode to pass an electric current through the electrodialysis cell. After a set amount of time, the power supply was stopped. The mixture from the carbamate chamber was collected and filtered. The obtained precipitate was washed several times with DI water. The precipitate adhering to the cation-exchange membrane on the carbamate chamber side was also collected and washed several times with DI water. The precipitates from the two sources were weighed separately. In some experiments, HCl was also added to the $CaCl_2$ solution to achieve a pH of 1 in an attempt to minimize on-membrane precipitation.

The faradaic efficiency was calculated by dividing the electron equivalent of the total precipitates, assumed to consist of pure $CaCO_3$, from both sources by the electron equivalent of the electric current passed through the cell by the power supply. The Faradaic efficiency can be determined by the equation (1).

$$FE = \frac{\text{The number of moles of electrons that result in CaCO3}}{\text{The actual number of moles of electrons input}} \quad (1)$$

The morphology of the precipitate was analyzed with a scanning electron microscope (Hitachi S-3400N).

3. Results & Discussion

3.1 Surface Morphology of $CaCO_3$

After electrolysis, white precipitates were found both on the membrane and suspended in the MEA solution. Fig. 2 shows the precipitate on the membrane.

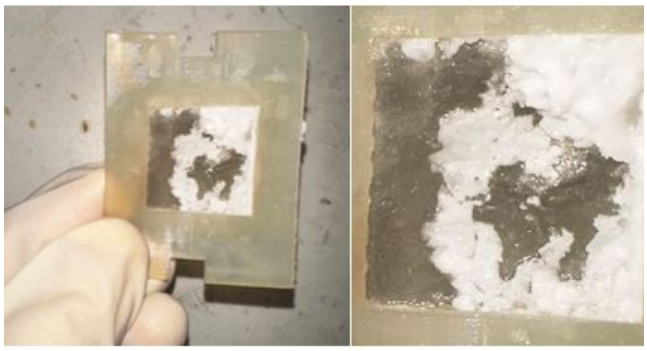

Figure 2. Digital image of $CaCO_3$ precipitated on the membrane.

The surface morphology of $CaCO_3$ precipitated on the membrane is shown in Fig. 3. The obtained $CaCO_3$ precipitates appeared largely spherical with irregular surfaces. An individual particle's diameter ranges from 1 to 5 μm.

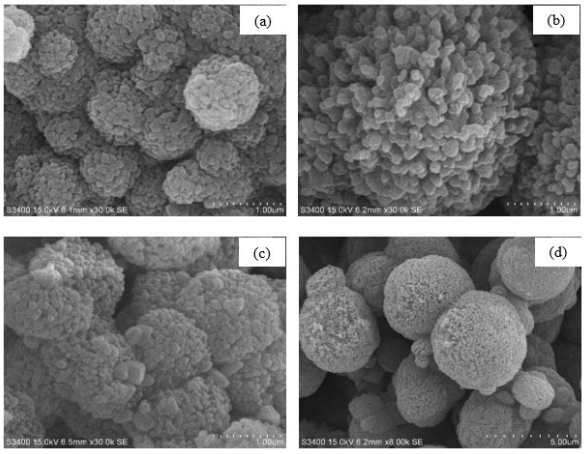

Figure 3. SEM image of $CaCO_3$ on the membrane; with HCl added to $CaCl_2$ solution and NaCl added to carbamate solution (a), with HCl added to $CaCl_2$ solution (b), with NaCl added to carbamate solution (c), without both HCl and NaCl added (d).

The surface morphology of $CaCO_3$ precipitated in the carbamate solution is shown in Fig. 4. The micrographs suggest that there was no obvious difference between $CaCO_3$ precipitates obtained from the two sources.

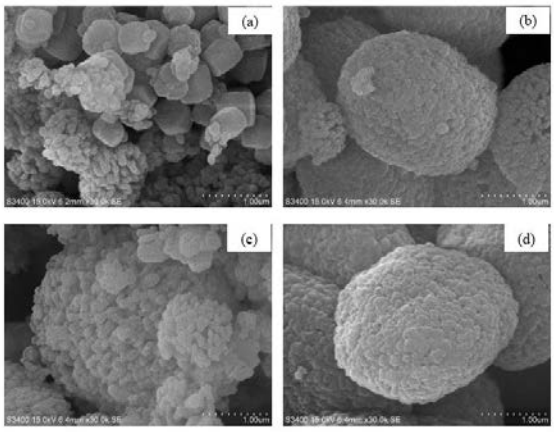

Figure 4. SEM image of $CaCO_3$ from carbamate solution; with HCl added to $CaCl_2$ solution and NaCl added to carbamate solution (a), with HCl added to $CaCl_2$ solution (b), with NaCl added to carbamate solution (c), without both HCl and NaCl added (d).

3.2 Effects of solution additives

Table 1 shows the amounts of $CaCO_3$ from electrodialysis experiments with and without additives added to the carbamate solution and $CaCl_2$ solution. The addition of NaCl to the carbamate solution minimized on-membrane precipitation of $CaCO_3$. This was done to increase the solution's ionic conductivity, which would also affect $CaCO_3$ precipitation behavior as will be discussed later. This was evident from the results in Experiments 3 and 4. The presence of NaCl increased the conductivity of the carbamate solution and decreased the electric field induced by the passing current in the carbamate solution. This would weaken the electromigration of ions; the transport of the carbamate ions to the surface of the cation-exchange membrane would have to rely on diffusion more to match the transport rate of Ca^{2+} through the membrane. This would necessitate a steeper concentration gradient, lower the local concentration of carbamate at the membrane surface, and ultimately minimize the on-membrane precipitation of $CaCO_3$. This effect of NaCl addition was also observed when HCl was added to the $CaCl_2$ solution (Experiments 1 and 2).

Table 1. Weight of $CaCO_3$ from 2 h electrodialysis experiments at 0.1 A with and without additives added to the carbamate solution and the $CaCl_2$ solution.

Experiment no.	Experiments	$CaCO_3$ weight on membrane (g)	$CaCO_3$ weight in solution (g)	Faradaic efficiency (%)
1	NaCl in carbamate sol. HCl in $CaCl_2$ sol.	0.046	0.104	40
2	No NaCl in carbamate sol. HCl in $CaCl_2$ sol.	0.059	0.065	33
3	NaCl in carbamate sol. No HCl in $CaCl_2$ sol.	0.0325	0.127	43
4	No NaCl in carbamate sol. No HCl in $CaCl_2$ sol.	0.1035	0.0535	42

HCl was also added to the $CaCl_2$ solution in some experiments (Experiments 1 and 2) in an attempt to minimize on-membrane precipitation by decomposing the $CaCO_3$ formed on the membrane into CO_2, H_2O, and $CaCl_2$. This had been expected to dislodge the precipitate from the membrane surface but this desired result was not achieved. The effect of HCl addition to the $CaCl_2$ solution on the amount of on-membrane precipitation was inconclusive but the addition of HCl appeared to consistently decrease the faradaic efficiency. The latter effect was plausibly caused by the decomposition of $CaCO_3$ after protons were transported to the carbamate solution.

3.4 Attempt to minimize on-membrane precipitation by switching the $CaCl_2$ solution to HCl solution

In an attempt to minimize or dislodge the precipitate adhering to the membrane, after a regular 2 h electrodialysis session, the $CaCl_2$ solution was replaced with 0.1 M HCl solution and 0.1 A was passed through the cell for another 30 min. The protons from the HCl solution had been expected to decompose some $CaCO_3$ on the membrane into Ca^{2+}, H_2O, and CO_2. Table 2 shows the results of these experiments. Comparing these results with the previous ones in Table 1, the amounts of $CaCO_3$ on the membrane did not decrease but those in the solution increased significantly. The faradaic efficiencies also increased following the increases in the $CaCO_3$ suspended in the MEA solution. The remarkably higher faradaic efficiency of the experiment with NaCl added to the MEA solution was attributed to additional precipitation during the 30 min electrodialysis session after the $CaCl_2$ solution was switched to HCl solution. In the pores of the $CaCO_3$ layer deposited on the membrane, significant amounts of Ca^{2+} were expected in the form of dissolved ions without forming $CaCO_3$. The chloride ions from NaCl added to the MEA solution would suppress the electromigration of the carbamate ions to the membrane surface by electromigrating themselves, leading to the depletion of the carbamate ions at the membrane surface. Without carbamate and carbon-dioxide-derived species, Ca^{2+} could exist in the pores of the $CaCO_3$ layer without precipitation. During the second electrodialysis session, these Ca^{2+} ions were driven out of the $CaCO_3$ layer deposited on the membrane into the solution, where they came into contact with carbamate ions and precipitated as $CaCO_3$. These phenomena could not happen without the addition of NaCl to the MEA solution.

4. Conclusion

Electrodialysis of MEA-captured CO_2 with $CaCl_2$ yielded $CaCO_3$ as a product. Near-spherical $CaCO_3$ particles were obtained. However, a major issue encountered in the process was the formation of $CaCO_3$ precipitates on the membrane. To address this, NaCl was added to the MEA solution and/or HCl was added to the $CaCl_2$ solution. The addition of NaCl appeared to be effective for reducing the amount of on-membrane $CaCO_3$.

Solution switching and conducting a second electrodialysis session did not decrease the amount of on-membrane $CaCO_3$ but significantly increased the faradaic efficiency, especially with NaCl added to the MEA solution. From the experiment, the addition of NaCl with solution switching resulted in an increase in the Faradaic efficiency to as high as 75%, compared to the original level of around 37%.

Table 2. Weight of $CaCO_3$ after switching experiments; after regular 2 h electrodialysis experiments, the $CaCl_2$ solution was replaced with 0.1 M HCl and 0.1 A was passed through the cell for another 30 min.

Experiments	$CaCO_3$ weight on membrane (g)	$CaCO_3$ weight in solution (g)	Faradaic efficiency (%)
NaCl in carbamate sol. No HCl in $CaCl_2$ sol.	0.042	0.240	75
No NaCl in carbamate sol. No HCl in $CaCl_2$ sol.	0.060	0.079	37

Acknowledgements

This work was conducted with the assistance of my professor, Asst. Prof. Palang Bumroongsakulsawat. I would like to express my sincere thanks for his invaluable help and constant encouragement throughout the course of this research.

References

1. Abu-Zahra, M. R. M.; Schneiders, L. H. J.; Niederer, J. P. M.; Feron, P. H. M.; Versteeg, G. F. CO2 Capture from Power Plants. *International Journal of Greenhouse Gas Control* 2007, *1* (1), 37–46.
2. Vaz, S.; Rodrigues de Souza, A. P.; Lobo Baeta, B. E. Technologies for Carbon Dioxide Capture: A Review Applied to Energy Sectors. *Cleaner Engineering and Technology* 2022, *8*, 100456.
3. Ghiat, I.; Al-Ansari, T. A Review of Carbon Capture and Utilisation as a CO2 Abatement Opportunity within the EWF Nexus. *Journal of CO2 Utilization* 2021, *45*, 101432.
4. Van der Spek, M.; Arendsen, R.; Ramirez, A.; Faaij, A. Model Development and Process Simulation of Postcombustion Carbon Capture Technology with Aqueous AMP/PZ Solvent. *International Journal of Greenhouse Gas Control* 2016, *47*, 176–199.
5. Nwaoha, C.; Smith, D. W.; Idem, R.; Tontiwachwuthikul, P. Process Simulation and Parametric Sensitivity Study of CO2 Capture from 115 MW Coal–Fired Power Plant Using MEA–DEA Blend. *International Journal of Greenhouse Gas Control* 2018, *76*, 1–11.
6. Osagie, E.; Biliyok, C.; Di Lorenzo, G.; Hanak, D. P.; Manovic, V. Techno-Economic Evaluation of the 2-Amino-2-Methyl-1-Propanol (AMP) Process for CO2 Capture from Natural Gas Combined Cycle Power Plant. *International Journal of Greenhouse Gas Control* 2018, *70*, 45–56.
7. Wang, Y.; Song, L.; Ma, K.; Liu, C.; Tang, S.; Yan, Z.; Yue, H.; Liang, B. An Integrated Absorption–Mineralization Process for CO_2 Capture and Sequestration: Reaction Mechanism, Recycling Stability, and Energy Evaluation. *ACS Sustainable Chemistry & Engineering* 2021, *9* (49), 16577–16587.
8. Rubin, E. S.; Mantripragada, H.; Marks, A.; Versteeg, P.; Kitchin, J. The Outlook for Improved Carbon Capture Technology. *Progress in Energy and Combustion Science* 2012, *38* (5), 630–671.
9. Renfrew, S. E.; Starr, D. E.; Strasser, P. Electrochemical Approaches toward CO_2 Capture and Concentration. *ACS Catalysis* 2020, *10* (21), 13058–13074.
10. Oloye, O.; O'Mullane, A. P. Electrochemical Capture and Storage of CO2 as Calcium Carbonate. *ChemSusChem* 2021, *14* (7), 1767–1775.
11. Landsman, M R.; Sintu Rongpipi; Guillaume Freychet; Gann, E.; Jaye, C.; Lawler, D.F.; Katz, L.E.; Su, G.M Linking Water uality, Fouling Layer Composition, and Performance of Reverse Osmosis Membranes. *Journal of Membrane Science 2023*, 680, 121717-121717.
12. Sedighi, M; Behvand Usefi, M M; Ismail, A.F.; Ghasemi, M Environmental Sustainability and Ions Removal through Electrodialysis Desalination: Operating Conditions and process Parameters. *Desalination 2023*, 549, 116319.

Using an esterification activity to enhance advanced placement (AP) chemistry students' competency in higher-order thinking (HOT)

Sonthi Phonchaiya[1]* and Sanikan Saneewong[2]

[1]*Chemistry and Biology Department* [2]*Compulsory Science Department*
The Institute for the Promotion of Teaching Science and Technology (IPST)
924 Sukhumvit rd., Prakanong, Klongtoei, Bangkok. 10110. Thailand

**E-mail: sopho@ipst.ac.th*

Abstract:

This work objective is to illustrate using an Esterification activity to Enhance Students' Competency in HOT which is one of the five students' key competencies, according to the Basic Education Core Curriculum. Participants were 17 ninth graders who enrolled in an AP chemistry subject. The activity comprises 2 parts: In part 1, students play a card game to practice writing the structures of organic compounds in esterification equations. Then, utilizing the information in the clue, the students investigated a mystery cube and discovered how an ester is structured on its blank face. Finally, they designed their mysterious cubes. In part 2, students synthesized an ester as their perfume through esterification. Various carboxylic acids and alcohols were provided. Then, they created infographics to present perfume in Padlet. By analyzing data from observation, scoring rubric of HOT competency (critical and creative thinking were emphasized in this work), students' works, and self-assessment (mean = 2.96, S.D. = 0.19), students were able to apply the clue information as evidence to find out the ester structure on the blank face of the cube. In addition, students could create their cubes and infographics well. This indicated that students could apply critical and creative thinking throughout the activity.

1. Introduction

A synthesis of an ester by employing an organic acid to react with an alcohol in a reaction is called esterification. In a reaction, the functional groups of a carboxylic acid (-COOH) and an alcohol (-OH) combine to form an ester (-COO) and this process is irreversible.[1] The general reaction of esterification is illustrated in Figure 1 where R and R' are alkyl or phenyl groups.

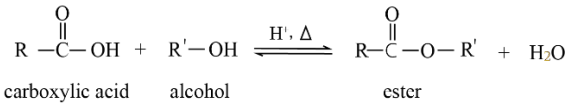

Figure 1. The general equation of esterification.

Many esters have pleasant odors; for example, methyl salicylate smells similar to a wintergreen whereas isoamyl acetate has a banana-like odor; therefore, esters are widely used in perfumes and artificial flavors.[2,3] The utilization of the distinctive odor of an ester allows us to detect the progression of a reaction without relying on sophisticated or expensive laboratory instruments, such as a spectrophotometer because the presence of an ester in a reaction mixture is readily observed by its odor. In the vital role of such physical property, esterification is favorable to teach as chemistry experiments for introductory university and high school students as an inquiry-based or evident-based laboratory, to introduce chemical reactions in organic chemistry.[4-6] Esterification is also included as a learning outcome in Thailand, according to the basic education core curriculum A.D. 2008; hence, this concept is necessary for high school students before pursuing a higher level of education.[7]

In the Academic year 2023, we were asked to develop the course syllabus along with learning activities of the Advanced Placement (AP) Chemistry program. The AP Chemistry program was aimed at introducing high school chemistry concepts to elite ninth-grade students through active learning[8] or inquiry-based activities.[9] Esterification was chosen to address the course syllabus for many reasons. First, it could help introduce students to the concepts of functional groups and chemical reactions in organic chemistry. Second, experimental esterification could be conducted in less than an hour when the used chemicals were available and acceptable for ninth-grade students. Also, the progression of the reaction was easily observed by just using physical properties such as odor. Last, the concept of esterification could be connected to the real world such as perfume synthesis which made the learning meaningful.

Thai students need to strengthen their competencies to meet the demands of the rapidly changing global economy and technological workplace and to become effective citizens of the twenty-first century. The importance of developing

students' competencies for the future is highlighted by both the research findings and the Tenth National Economic and Social Development (A.D. 2007–2011) statement.[10] To identify the habits that students need to develop, the Ministry of Education of Thailand examines the students' key competencies. Five key competencies in the basic education curriculum B.E. 2551 (A.D. 2008) are communication capability, thinking capability, problem-solving capability, capability in applying life skills, and capability in technological application.

Thinking capacity lays the groundwork for cognitive abilities, and Higher-Order Thinking (HOT) represents a more advanced and complex level of cognitive processing. Both concepts are interconnected and play crucial roles in intellectual development. Many studies discuss the components of HOT. According to Yen and Halili (2015), these skills go beyond basic memorization and involve critical analysis, problem-solving, creativity, and application of knowledge.[11] The components of HOT identified by Schraw et al. (2011) include critical thinking and problem solving abilities, reasoning skills, and argumentation abilities.[12] According to Bloom, high-order thinking skills are found in analysis, synthesis, and evaluation, whereas low-order thinking skills are found in knowledge and comprehension.[13] Furthermore, Anderson and Krathwohl (2001) categorized the cognitive domain of HOT as including analysis, evaluation, and creation.[14] HOT skills are crucial for students worldwide, including those in Thailand. Moreover, HOT lays the foundation for lifelong learning, enabling students to adapt to new technologies, industries, and information throughout their lives. Additionally, Thailand, like many countries, faces complex challenges, including environmental issues, social inequality, and economic disparities. HOT skills enable students to analyze challenges critically and contribute to sustainable solutions.[15]

Many concepts in chemistry are abstract as well as complex where students need to use their mental model to connect or explain the three levels of representations: symbolic, microscopic, and macroscopic.[16] Hence, learning chemistry is not just about memorizing or understanding but HOT is needed. Various active learning pedagogies such as inquiry-based learning, problem-based learning, game-based learning, questioning techniques, and worksheets, are utilized to promote HOT of students in chemistry.[17-21]

Different strategies are used to address the development of higher-order thinking abilities. One such strategy that has attracted more attention lately is game-based learning. Game-based learning has the potential to be a motivator, encouraging students to participate in specific activities.[22] Furthermore, students are frequently faced with obstacles or problems in game-based learning that call for analysis, critical thinking, and strategic decision-making. As students work through different scenarios and come up with solutions, this develops their HOT skills.

In this study, HOT refers to thinking abilities that entail critical thinking, analyzing, evaluating, and creating to provide a solution or justification for a problem. Two advanced cognitive processes: critical thinking and creative thinking were focused on in this study. Creative thinking involves the generation of new ideas and concepts that have value to the individual or others, and the development of these ideas and concepts from thought to reality.[23] While Critical thinking involves making judgments based on reasoning, students consider options, analyze these using specific criteria, draw conclusions, and make judgments.[24]

This research aimed to study the use of an esterification activity to enhance students' competency in HOT which is one of the five students' key competencies, according to the Basic Education Core Curriculum.

2. Materials and Methods

2.1 Materials

Teaching materials of esterification are divided into two parts. The theory part consists of activity sheets, worksheets, card games, a mysterious cube, and a blank cube.

Figure 2. Teaching materials for the theory part.

The experiment part comprises chemicals (various carboxylic acids and alcohols, and concentrated sulfuric acid), available glassware, and apparatuses in the school such as test tubes,

alcohol lamp sets, etc. Padlet,[25] a cloud-based software, is also a platform for students to share their synthesized esters.

2.2 Method

This work was studied under the conceptual framework as shown in Figure 3

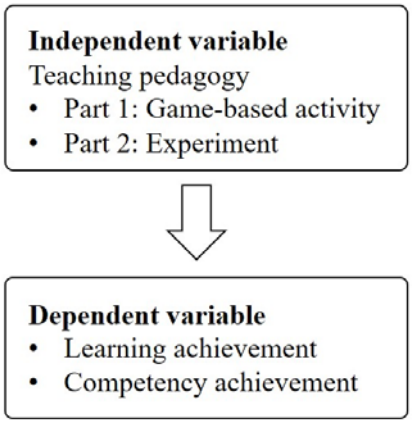

Figure 3. The conceptual framework of this study

Learning achievement provides the knowledge base and understanding necessary for students to develop competencies, while competency achievement reflects students' ability to effectively apply their learning in practical situations.

The population and participants of this study were 17 ninth graders, who enrolled in an AP chemistry subject, purposively sampling.

An esterification activity including worksheets and exercises, and data collection instruments such as students' evaluation, and performance task assessment forms were developed based on the rubric criteria of higher-order thinking (HOT), thinking capacity, which is one of the five students' key competencies[26,27] according to the basic education core curriculum B.E. 2551 (A.D. 2008). An index of congruence or IOC was also made to ensure whether the activities and data collection instruments were aligned with HOT suggested by the Ministry of Education. The activity consisted of two parts:

In Part 1, the theory part, students learned functional groups of some organic compounds, and chemical equations of esterification through game-based activities. This part required 1.5 hours. In this part, students read and discussed functional groups and esterification. Then, they played the esterification card game which allowed students to practice writing the chemical structures of alcohols, carboxylic acid, and esters along with esterification equations. The rule of a game was provided and discussed. Then, the students received the mysterious cube and explored a chemical structure, a number, and an alphabet in each face. They had to find out the missing chemical structure along with a number as well as an alphabet in the blank face of the cube. This mysterious cube was similar to the classic activity introducing students to the inquiry and the nature of science;[28] however, the esterification concept was essential to be used in this task besides merely logic. Finally, students applied their knowledge of esterification and the logic from the previous activities to design their mysterious cubes. The cube templates of the mysterious esterification game, developed by us, are available at https://bit.ly/3NYhUSD.

In Part 2, the experimental par which is required about 1.5 hours. Students explored the list of available carboxylic acids and alcohols and applied their knowledge of esterification to predict esters that can be possibly synthesized in the laboratory. They also used Google to search for odor information about each ester and selected the odor they liked. Then, Students designed an experimental method and selected a carboxylic acid and an alcohol for their reaction. Students discussed the safety issue before experimenting. After experimenting, students made a presentation. Finally, they created infographics to present their ester as a perfume product and shared them in the Padlet.

2.3 Data collection and analysis

Instruments for data collection were worksheets including exercise and laboratory reports, students' works such as mysterious cubes, and infographics, the scoring rubric of the HOT competency, and students' self-evaluation. Instructors' notes from the classroom observation while students undertook the activities, conducted an experiment, and made a presentation were also used to diagnose students' learning and competency achievement. Students' opinions regarding teaching pedagogy were also collected from the Padlet. Quantitative data were analyzed by using mean, and standard deviation (S.D.). Qualitative data were analyzed using content analysis.

3. Results & Discussion

3.1 Learning Achievement

The finding of the study showed that these activities enhanced the student's understanding of the chemistry content. According to the results of the analyst students' worksheets including exercises, students were able to respond to the esterification reaction question correctly. With this knowledge, students could use esterification to create an ester for their perfume. Moreover, many students believed they had learned more in-depth

content and enjoyed participating in activities. The supporting pieces of evidence from students' answers in the worksheets are shown below.

"We had learned about esterification and had applied the knowledge to solve the problem…. It was a lot of fun to do this. We enjoyed learning. Moreover, we had a chance to demonstrate what we have learned by creating the cube."

"It was not a lecture-based learning process… Good learning atmosphere encourages deep thinking. These hands-on activities help me to better understand the concept of esterification."

3.2 Competency Achievement

The research results showed that the students who participated in Esterification activities developed HOT: creative thinking and critical thinking skills while they planned, created, reflected, and presented their tasks. Additionally, the findings of the analyst students' self-assessment indicated that a large number of them thought they had developed thinking skills (mean=2.96, S.D.=0.19).

The evidence of students' learning showed that doing activities helped them think critically about their tasks. Students analyzed information, synthesized ideas, made expressions, and formulated an opinion or conclusion to determine the ester structure on the blank face of the cube by using the clue information as supporting documentation.

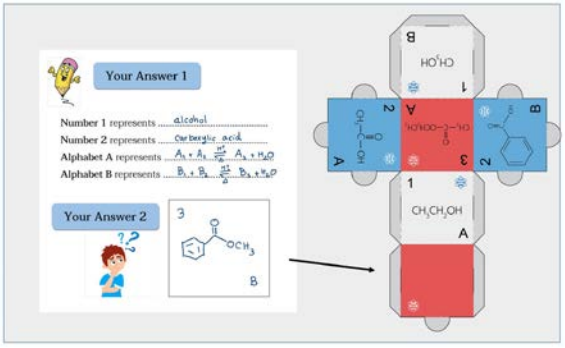

Figure 4. The students' response regarding the ester structure on the blank face of the cube

Additionally, students were able to make their mysterious cubes. In these situations, students' ability to think creatively was developed based on the activities that would transition from problem tasks to creative thinking.

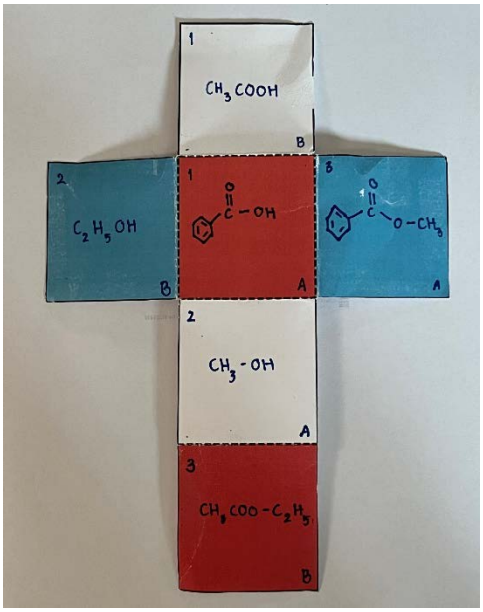

Figure 5. The students' mysterious cube

After obtaining an ester from a reaction and testing an odor, students synthesized their existing ideas to produce the outcome which were creative artifacts. They were able to organize and select media such as texts, and pictures involved in the content to create poster presenting their perfume. An example of the student's infographic presenting their perfume is illustrated in Figure 6.

Figure 6. The student's infographic in Padlet

4. Conclusion

This study intended to enhance students' key competency in thinking capability. According to those results, it could be concluded that the developed esterification activity could help contribute the development of both contents and HOT. Game-based learning has the potential to significantly increase student engagement.[29] Students played a card game to practice writing the structures of esters, carboxylic acids, and alcohols along with esterification equations. These direct experiences helped students developed concept of esterification. The cube activities allowed students to apply knowledge to solve problems in the new situation critically and creatively. This is because, to complete the activity tasks, students had to analyze information in the clue, synthesize the structures of ester on the blank face of cube, communicate their idea, and formulate conclusion of ester structure. Using these information, students could develop their own mysterious cubes. Moreover, creative thinking skill was developed by combining prior knowledge about theory and experimental esterification to generate a large number of ideas to create infographics to present their ester as a perfume product. In addition, Students were facing the problems which made them concentrate to complete their tasks. It helped students develop their thinking capacity in critical thinking skills.[30]

The Implication of This Study

The participants in this research were elite students who experienced inquiry-based learning and problem-based learning throughout the extra curriculum with us. Therefore, they conducted all activities and performance tasks very effectively within the time constant. If these activities were implemented for general students, teaching basic concepts of organic chemistry or spending more time for discussion might be needed to help students achieve learning objectives.

Pre and post-tests and also the learning progression of students are recommended for further research.

Acknowledgments

We would like to thank our students for actively participating. Also, we would like to thank the staff of the AP chemistry program for their help and support.

References

1. Byju's. Esterification. https://byjus.com/chemistry/esterification (accessed January 9, 2023).
2. Rio, A. C., French, G. *J. Chem. Educ.* **2011**. *88. 954*-959.
3. Gatta, F. L. Esterification. https://www.ccmr.cornell.edu/wp-content/uploads/sites/2/2015/11/Esterification.pdf (accessed January 9, 2023).
4. McCullagh, J. V. and Hirakis, S. P, *J. Chem. Educ.* **2017**. *94.* 1347-1351.
5. Logan, J. L. and Rumbaugh, C. F. *J. Chem. Educ.* **2012**. *89.* 613-619.
6. The Institute for the Promotion of Teaching Science and Technology. *Science and technology fundamental textbook (Chemistry 5), based on learning standards, science and technology learning group, according to the basic education core curriculum A.D. 2008.* Chulalongkorn University Press: Bangkok. 2019; pp 63.
7. Ministry of Education. *Indicators and cores learning content, Science learning group (Revised edition 2017)*, according to the basic education core curriculum A.D. 2008. Bangkok: Thailand Agricultural Cooperative Assembly Printing House Limited. 2017; pp 177.
8. Michael, J., *Adv Physiol Educ.* **2006.** *30.* 159-167.
9. Gholam, A., *Journal of Inquiry & Action in Education*, **2019**. *10.* 112-133.
10. The Ministry of Education (MoE). *The Basic Education Core Curriculum B.E. 2551 (A.D. 2008)*. The Ministry of Education, Thailand. 2008. pp 1-7.
11. Yen, T. S. and Halili, S. H, Effective Teaching of Higher-Order Thinking (HOT) in Education *The Online Journal of Distance Education and e-Learning*, **2015**, *3*. 41-47.
12. Schraw, G., McCrudden, M. T., Lehman, S., Hoffman, B. An Overview of Thinking Skills. In *Assessment of Higher Order Thinking Skills;* Robinson D. R. and Schraw G., Ed.; Information Age Publishing, Inc, USA, 2011; pp 23–62.
13. Zohar, A., *Teaching and Teacher Education*, **1999.** *15*. 413-429.
14. Anderson, L. W., Krathwohl, D. R. *A Taxonomy for Learning, Teaching, and Assessing: A Revision of Bloom's Taxonomy of Educational Objectives*. Addison Wesley Longman, Inc, USA, 2001.
15. Kammanee, T. Thinking. In *Encyclopedia of the teaching profession honor His Majesty the King On the auspicious occasion Celebrating His Majesty the King's 80th Birthday Anniversary*; Wisalaporn. S., Ed.; Bangkok;

Teachers Council Secretariat, 2009; pp 33 – 40.
16. Lansangan, R., Orleans, A. and Camacho, V., *Adv. Sci Lett.* **2018**. *24*. 7930 – 7934.
17. Hugerat M., and Kortam, N., *Eurasia Journal of Mathematics, Science & Technology Education.* **2014.** *10*. 447-454
18. Madhuri, V., Kantamreddi, N. and Prakash S. *European Journal of Engineering Education.* **2012.** *37*. 117-123.
19. Priyasmika. R, and Yuliana,I., *Journal of Chemistry Education Research.* **2021**. *5*. 70-76.
20. Fishovitz, J., Crawford, G. and Kloepper,K., *J. Chem. Educ.* **2020**. *97*. 681−688.
21. Verdina R., Gani, A., and Sulastri A., *Journal of Physics: Conf. Series 1088.* **2018.** 1-6
22. Tan, M., and Hew, K. H., *Australasian Journal of Educational Technology.* **2016.** *32*. 19–34.
23. Sternberg, R, J. Creative Thinking in the Classroom. *Scandinavian Journal of Educational Research*. **2003**. *47*. 325–338.
24. Paul, R. and Linda, E, *The Miniature Guide to Critical Thinking: Concepts and Tools. Foundation for Critical Thinking*, 2006.
25. Wikipedia, *Padlet*. https://en.wikipedia.org/wiki/Padlet (accessed January 11, 2023).
26. Ministry of Education. *Basic education core curriculumA.D.2008.* https://www.ipst.ac.th/wp-content/uploads/2020/10/CoreCurriculum2551-en.pdf (accessed January 11, 2023).
27. Bureau of Educational Testing, Office of the Basic Education Commission. *Handbook of a Competency Appraisal for Basic Education students based on the Basic Education Core Curriculum B.E. 2551 (A.D.2008), ninth graders*, National Office of Buddhism Printing House: Bangkok. 2019; pp 22-23.
28. National Academy of Sciences. *Introducing Inquiry and the Nature of Science.* http://eteamscc.com/wp-content/uploads/2014/05/Cube-Activity.pdf (accessed January 11, 2023).
29. da Rocha Seixas, L., Gomes, A. S., and de Melo Filho, I. J. *Computers in Human Behavior*. **2016**. *58*. 48–63.
30. Bourke, B. *Using Gamification to Engage Higher-Order Thinking Skills*, 2021.

The effect of STEAM BCG through natural tie dye activities

Tanchanok Poonsin[1], Thathiya Songklin[2], Atcharaporn Chuchuea[2], and Ninna Jansoon [3]*

[1]*Department of Science and Mathematics Teaching, Faculty of Education, Thaksin University, Thailand*
[2]*Wat Rom Muang School, Phatthalung, Thailand*
[3]*Department of Basic Science and Mathematics, Faculty of Science and Digital Innovation, Thaksin University*

**E-mail: ninna@tsu.ac.th*

Abstract:

STEAM would enable students to learn and integrate scientific knowledge to hone problems- solving skills. The BCG Model is holistic economic development in which it is not only developing the economy but also promotes social development and the conservation of the environment to be balanced, stable, and sustainable. Both seem essential to integrate students into learning processes until they could develop their knowledge and abilities. Therefore, this study took tie dye of *Ban Khao Khram Community* traditional culture as the carrier to carry out STEAM BCG activity design. The effect of STEAM BCG through natural traditional culture tie dye activities on the basis of inheriting and developing *Ban Khao Khram Community* for increasing students' 21st century skill and STEAM competencies were also studied. The target of the study was grade-5 students from a primary school under Phatthalung Educational Service Area. The STEAM BCG through natural traditional culture tie dye activities was designed with 2 phase as follow: (1) identification of suitable in students' local area context and (2) development of the tie dye fabric. The results revealed that STEAM BCG through natural traditional culture tie dye activities has been proven to help students develop their 21st century skills and STEAM competencies.

1. Introduction

STEM education is a learning approach widely used for developing students to become problem solvers and innovators. Its objectives are to empower students to be citizens prepared to live in the real world and have the competencies required for careers in the digital transformation era. Even though STEM education has played a significant role in Thailand education since 2012, it has been plagued by deep-seated problems, as the STEM curriculum and approach have failed to support students' performances in problem-solving and innovation in authentic contexts including the economy, society, and environment. In addition, Thai's government launches BCG (Bio-Circular-Green) economy model aiming at developing the country to a balanced economy, society, and environment with sustainable development.[1]

The STEM BCG model, which is an innovative framework for education. This framework is expected to raise the level of STEM education that follows the economic policy of the Thai government through empirical.[1] STEM BCG for education uses suitable in a local area context as STEM activities (teaching STEM knowledge-based society) to enhance students' learning process which lead to creative innovation of students from the resource in their community for solving and increasing income of the people in the community. The students improve their core competencies which are based on competency-based education through integrates cross-disciplinary knowledge, leading to well-being.

STEAM education is an educational model extending from STEM education. With the development of STEM education practice research, Arts (Art) courses have been added to STEM courses.[2] STEAM education is a new educational paradigm to cultivate students' problem-solving ability and innovation ability in a multi-disciplinary way. At present, countries all over the world pay attention to promoting the integration of disciplines and developing students' comprehensive abilities, emphasizing the use of multidisciplinary knowledge to solve problems in real situations. The scientific literacy, technical literacy, engineering literacy, artistic literacy and mathematical literacy it points to are regarded as the core literacy necessary for innovative talents in the new era. The philosophy of STEAM revolves around the concept that: STEAM = Science & Technology interpreted through Engineering & the art, all based in Mathematical elements.[3]

At the present, Thailand's local traditional culture education has jumped to the strategic height of "culture power". It has become the consensus of the domestic education circle to promote the local traditional culture to enter the school. Tie dyeing technology is a good carrier to infiltrate local cultural confidence education. Choosing traditional cultural tie dyeing technology as the activity content can not only stimulate learning enthusiasm and promote students to

transfer existing knowledge and skills to real problem situations to solve real-life problems by using suitable in a local area context, but also help students improve their cognitive ability and ability to efficiently solve real problem and develop their community.[2]

Based on mention above, this study took tie dye of *Ban Khao Khram Community* traditional culture as the carrier to carry out STEAM BCG activity design, connected traditional culture with the classroom. Moreover, the effect of STEAM BCG activity through natural traditional culture tie dye activities on the basis of inheriting and developing *Ban Khao Khram Community* for increasing students' 21st century skills and STEM competencies were also studied.

2. Methodology and Program Design

2.1 Participants

The participants were 30 grade-5 students selected by purposive sampling from a primary school under Phatthalung Educational Service Area.

2.2 STEAM BCG activity design

The main characteristics of STAEM BCG for education include: (1) use suitable in a local area context as STEM activities (2) create activities to stimulate active learning of learning for promote higher-order thinking skill and citizenship (3) enhance students' learning process which lead to creative innovation of students from the resource in their community for developing economic in the community and (4) develop students' 21st century skills.

This study designed **"STEAM BCG activity"** with 2 phases through natural traditional culture tie dye activities as follow below:

Phase 1: Identification of suitable in students' local area context

In, this step was integrated science process. The students analyzed the local plants and designed the unique pattern on the clothes by using scientific inquiry. Moreover, the students learned simple extraction and mathematics through design pattern on the clothes and how was the changing of color from plant after adding Mordant. The activities in phase 1 consisted of *"What is the plant" "Let's get to know the plant" "Plant extraction" "Tinting" and "Tie dye"*.

"What is the plant" the students had the task given by the teacher to explore colored plants in their community. After that, the students studied the colored plants with application *"Picture This"* (Figure 1). In this step, the students got the information of the colored plants in their community such as species, biochemical, characteristics and economic values etc.

Figure 1. The students learned the information about their colored plants with the application *"Picture This"*.

"Let's get to know the plant" the students searched the information and explained the properties of tie dye from the colored plants in their community using Canva. Then, the students chose only one colored plant for producing textile product by traditional culture dyeing techniques.

"Plant extraction" the teachers demonstrated the color extraction from mangosteen (economic plant in *Ban Khao Khram Community*) through their local wisdom (*Ban Khao Khram Community*). The dried mangosteen peels was extracted with water at a temperature between 60°C-80°C and alcohol at room temperature. Then, the students observed the color extraction from mangosteen at the different conditions.

"Tinting" and "Tie dye" in this step, the students learned and practiced natural traditional culture dyeing technique. After that, the teachers explained the effect of changing color by Mordant. Then, students added 4 Mordant (rust, ash, limewater and alum) to Kaen Fang *(Caesalpinia sappan* Linn) extract and observed the changing color of Kaen Fang extract.

Phase 2: Development of the tie dye fabric

In this step, students created and designed the tie dye fabric by using natural traditional culture tie dye process. Kaen Fang, Turmeric and Mangosteen were the local plants. Their color was used to development of the tie dye fabric (Figure 2).

Figure 2. The products of students' tie dye fabric by using natural traditional culture tie dye process.

2.3 Data collection and analysis

This study utilized qualitative method in the collection and analysis of data. The research tool assessments for evaluate S-T-E-M knowledge and skills couple with STEM competencies and 21st century skills as a follow below:

(1) Scientific knowledge and skills

The application of knowledge and skills/scientific processes through scientific inquiry refers to the student's behavior and expressions demonstrating knowledge, skills, and ability to search for scientific information through the inquiry process.[4]

(2) Technology literacy skills

Technological literacy refers to student behavior that shows knowledge, skills, and the ability to choose technology. The students can use technology to help them in solving problems i.e., process, equipment, tools, machines, materials etc. In addition, information sources can be selected with judgment and appropriateness to solve problem or develop things.[5,6]

(3) Engineering design process skills

Engineering design process skills are behavioral expressions of students demonstrating knowledge and ability to understand and analyze situations or problems. Students are able to plan and design to systematically solve problems. They can create innovation under limitations or various conditions such as time, finance support etc.[4]

(4) Mathematical thinking skills

Students exhibit behaviors that demonstrate their knowledge, skills, and ability to think rationally and structured.[7]

(5) STEAM competencies

STEM Competencies in the integration of knowledge of science, technology, engineering, mathematics and art refers to student behaviors which can express and demonstrate knowledge, skills, ability to understand and apply concepts, processes, attitudes, ways of thinking and nature of science, technology, engineering, mathematics and art to innovate.[8]

(6) The 21st century learning skills

21st century learning skills emphasize the ability to use cognitive and innovative skills for creativity and innovation, higher-order thinking to solve problems, communicate and collaborate with others[9]

S-T-E-M knowledge and skill couple with STEM competency and 21st century skill of students are graded on a 1 to 5 scale for each criterion. Scoring guide: Mean 4-5=excellent; 3-3.9=good; 2-2.9=pass; 0-1.9=lack.

3. Results and Discussion

After the completion of STEAM BCG through natural traditional culture tie dye activities, the students were evaluated based on the six dimensions of assessment.

3.1 Scientific knowledge and skills

The students' scientific knowledge and skills are presented in Table 1.

Table 1. The Students' scientific knowledge and skills

Scientific knowledge and skills	Average	Category
Systematically implementing the process of acquiring scientific knowledge	3.85	good
Contributions to relevant scientific questions	4.15	excellent
The emphasis on the scientific evidence	3.11	good
Creating a scientific explanation of the information exists	3.25	good
Connecting the description of their scientific knowledge with other subjects	4.22	excellent
Average score	**3.71**	**good**

As shown in Table 1, the average score of each students' scientific knowledge and skills dimension was 3.71 which categorized as good. The results suggested that the student's scientific knowledge and skills are sufficient to enhance comprehension and explanation for applying scientific knowledge to problem solving and create products.

3.2 Technology literacy skills

The students' technology literacy skills are depicted in Table 2. The ability to choose technology to solve problems or improve things to meet their need more effectively had the lowest average score of 3.55, while the ability to assess and manage technology appropriately had the highest average of 4.60. However, the average score of the students' technology literacy skills was 4.26. This indicated that the students have an excellent level for method selection and use of tools to solve problems. Moreover, the information

resources can be selected and used to manage and evaluate technology appropriately in order to solve problems, improve or develop things effectively.

Table 2. The Students' technology literacy skills

Technology literacy skills	Average	Category
Selection of technology (media, material, or method) with suitable properties	4.58	excellent
Selection of information sources critically and reliability	4.32	excellent
The ability to assess and manage technology appropriately	4.60	excellent
The ability to choose technology to solve problems or improve things to meet their need more effectively	3.55	good
Average score	**4.26**	**excellent**

3.3 Engineering design process skills

The evaluation results of engineering design concept, it represented skill, ability to understand and analyze the problem of the students (Table 3).

Table 3. The students' engineering design process skills

Engineering design process skills	Average	Category
An accurate and rational reflection on the situation or problem	3.85	good
Comprehensive analysis of the problem	3.77	good
Designing, planning, and applying knowledge to create new innovations under constraint or condition	4.22	excellent
The application of knowledge, skills and expertise in socio-economic sciences to design engineering	4.35	excellent
Creating innovation through a systematic engineering design process	4.24	excellent
Average score	**4.09**	**excellent**

The results found that students' engineering design process skills were assessed with an average score of more than 4 which categorized as excellent. This indicated that the students can apply their knowledge to solve problems associated with the real situation. Furthermore, they can create products/innovations under limitations such as time.

3.4 Mathematical thinking skills

Mathematical and statistical issues related to quantities and various formulas to assist in thinking and decision making in solving problems of students.[7]

Table 4. The students' mathematical thinking skills

Mathematical thinking skills	Average	Category
Use appropriate mathematical and statistical quantities	3.37	good
Choosing the right formula or mathematical knowledge	3.12	good
The ability to think rationally, systematically, with a plan, and be able to analyze problems carefully	3.86	good
Using mathematical thinking processes such as comparison, classification, geometry, etc., to simulate, apply in problem solving and create innovation	4.25	excellent
Average score	**3.65**	**good**

The results found that the students' mathematical thinking skills had the average score in each dimension at the level of 3.12 to 4.25 as presented in Table 4. This indicated that the students are able to apply their knowledge and mathematical thinking processes to create the design of processes and work.[7]

3.5 STEAM competencies

The STEAM Competencies of students are shown in Table 5.

Table 5. Students' STEAM Competencies

STEAM Competencies	Average	Category
The integrity of the use of knowledge : Science/ Technology/Engineering/ Mathematics and Art (STEAM)	3.12	good
The ability to understand and apply concepts, processes, attitudes, ways of thinking STEAM for innovation	3.55	good
Ability to clearly integrate all 5 disciplines	3.01	good
Average score	**3.23**	**good**

The average score of students' STEAM Competencies after the completion of STEAM BCG through natural traditional culture tie dye activities was 3.23 which categorized as good. This results suggested that the students should be motivated to solve integrated interdisciplinary sets of complex problems collaboratively using higher-order thinking and knowledge of STEAM disciplines. Furthermore, the teachers should be used suitable in a local area context as STEAM activities.

3.6 The 21st century learning skills

Upon the completion of STEAM BCG through natural traditional culture tie dye activities, the students were interviewed with researchers and teachers for evaluate 21st century learning skills of the students.

Table 6. The 21st century learning skills of students

21st century learning skill	Average	Category
Creation of workpieces or solutions that are diverse and appropriate to the situation	3.38	good
Higher-order thinking in using reasoning to make decisions about creating a workpieces or finding a solution	3.59	good
Teamwork skills to create items or find effective solutions	4.55	excellent
Communicating to present workpieces or solutions effectively	4.49	excellent
Average score	**4.00**	**excellent**

As shown in Table 6, the average score of students' 21st century learning skills obtained 4.16 which categorized as excellent. The resulted indicated that the 21st century learning skill of students was promoted by using STEAM BCG through natural traditional culture tie dye activities.

4. Conclusion

The STEM BGG through natural traditional culture tie dye activities enhanced the students to develop and create the new products (tie dye fabric) from the resource in their community (*Ban Khao Khram Community*) for solving and increasing income of the people in the community with awareness and social responsibility. Moreover, STEAM BCG through natural traditional culture tie dye activities has been proven to develop their 21st century skills and STEAM competencies through integrate cross-disciplinary knowledge, leading to well-being.

Acknowledgments

The success of this study was due to the support and cooperation of many people and organization. The authors greatly appreciate the support provided by Faculty of Education, Faculty of Science and Digital Innovation and Thaksin university.

References

1. Faikhamta, C,; Suknarusaithagul, N.; Yokyong, S.; Panyanukit, P.; Prasop;arb, T.; Muangsong, K.; Ninubon, J,; Nuamcharoen, N. *J. Res. Unit Sci. Technol. Environ. Learning.* **2022**, *13*, 344-362.
2. Yang, Y.; Yan, W.; Yang, Y. *Front. Educ. Res.* **2020**, *3*, 7-14.
3. Yakman, G.; Lee, H. J. *Korea Assoc. Sci. Edu.* **2012**, *32*, 1072-1086.
4. Kelley, T. R.; Knowles, J. G. *Int. J. STEM Educ.* **2016**, *11*, 2-11
5. Burghardt, M. D.; Hacker, M. *Tech. Teac.* **2004**, *64*, 6-8.
6. Herschbach, D. R. *J. STEM. Teac. Educ.* **2011**, *48*, 96-12.
7. Ruamcharoen, J.; Musor, H.; Loonjang, K. *SEA-STEM*. **2021**, *2*, *62-66.*
8. Moore, T.; Stohlmann, M.; Wang, H.; Tank, K.; Glancy, A.; Roehrig, G. Implementation and integration of engineering in K-12 STEM education. In *Engineering in Pre-College Settings: Synthesizing Research, Policy, and Practices*; Purzer, S.; Cardella, M., Eds; West Lafayette, Purdue University Press, 2014; pp 35-60.
9. Williams, D. *Math. Tech.* **2007**, *100*, 572-575.

Evaluating surface tension via smartphone-captured pendant drop method: Enhancing accuracy in simplified experimental designs

Pannaporn Omee, Jutamas Changkian, Kanoksak Saelee,
Akapong Suwattanamala, and Teeranan Nongnual*

Department of Chemistry, Faculty of Science, Burapha University, Chonburi, Thailand 20131

**E-mail: teeranan.no@buu.ac.th*

Abstract:

Surface tension is a fluid property that reflects the force minimizing a liquid surface area. This force is vital in industrial applications such as detergents, oil recovery, paints, foods, and pharmaceuticals. Traditional surface tension measurement methods, including the capillary tube, Wilhelmy plate, and Du Nouy Ring, tend to be expensive, complicated, and require specialized equipment. This research introduces a simplified and cost-effective alternative: the pendant drop method using a smartphone for capture, making it accessible for high school and higher education lab settings. Optimized experimental parameters indicated that videos should be recorded at approximately two drops per second, capturing on drops exceeding half their full size. The drop width and height are processed using image software like ImageJ or Microsoft Paint. These measurements are carefully taken at the drop edge to maintain a misplacement of fewer than two pixels, thereby suppressing pixelation errors under 10%. For pixel-to-metric conversion, the reference scale in the image must be more than 80 pixels per mm, achievable with a standard ruler or sticker label. A straightforward experimental approach, under optimized conditions and with proper data analysis, measured the surface tension of distilled water to be 67.817 mN/m (n = 10) at 27 °C, in accordance with the Young-Laplace equation. This closely matched the 69.790 mN/m (n = 10) obtained from the Wilhelmy plate method. These results support our experimental design and analysis as appropriate for intensive science programs and science projects, ensuring precise results. Additionally, this technique could help determine the critical micelle concentration of surfactants.

1. Introduction

Surface tension is a significant physical property of liquids caused by intermolecular attractive forces or cohesive forces between liquid molecules. It is a common effect where molecules on the surface are pulled inward due to cohesive forces of molecules on the bottom and sides, while the molecules on the top surface experience zero attraction. It reduces the surface area of the liquid making the surface of the liquid behave more like a film, which is constantly being pulled by forces (Kritsana Chutima, 2013: 314). For example, the ability of certain insects to walk on water surface, paper clips that float on the water surface, the use of surfactant-containing detergent soap, etc. There are numerous techniques available at current for determining surface tension of liquids, such as capillary rise, Wilhelmy plate, Du Nouy ring, dripping from a needle, and pendant drop methods. However, these techniques have certain limitations as they require expensive, specialized equipment and substantial amounts of materials.

The pendant drop method is probably the most practical, adaptable, and widely used method for measuring interfacial tension. The pendant drop method entails determining the profile of a drop of one liquid suspended in another at mechanical equilibrium. A drop of liquid suspended in another is given a profile by the balance between gravity and surface forces. Through a nonlinear differential equation, Laplace's equation connects the drop profile to the interfacial tension. It is frequently utilized in both research and industry applications where surface qualities are crucial, such as the creation of novel materials, medicines, and numerous fluid-related processes.

This research introduces an evaluation of surface tension using a smartphone-captured pendant drop for cost-effective, compact, and highly accurate surface tension measurements make it accessible for high school and higher education lab settings, which could help students understand the concept of surface tension through simple experiments and enhance accuracy in simplified experimental designs by studying the factors that affect the surface tension value, comparing the scale with a standard ruler, sticker label, and needle finding the appropriate range of water droplets to collect data for calculating the surface tension value and errors due to aberrations the image's pixilation. Subsequently, assess how accurate were in comparing liquids' surface tension with Sigma 700/701 force tensiometers.

2. Materials and Methods

2.1 Materials

Ultrapure water (Ultra-Pure System): Ultrapure water is water that is of high purity with lowest possible contamination content and it should be used immediately after production. This type of water has been utilized in analyses and tests that demand a high degree of precision and accuracy. The water system used in this study was Merck Milli-Q for producing Type I lab water with electrical resistivity of 18.2 MΩ.cm at 25 °C, electrical conductivity of < 2000 µs/cm and dissolved carbon content of < 30 ppm.

Smartphone: iPhone 13 smartphone with 12 MP rear camera, f/1.6 aperture, 4K video recording at 60 fps, 2x optical zoom and 3x digital zoom.

2.2 Experimental Setup

Design of an experimental setup for water surface tension determination based on the Pendant drop method using a smartphone for capture

An experimental setup consisting of a lamp as a light source covered with a sheet of A4 paper for light control was set up. The dropper with a blunt-tip syringe needle was connected to a 3-mL syringe and an extension tube was connected to a liquid container in order to keep the flow rate constant. iPhone 13 smartphone with 12 MP rear camera, f/1.6 aperture, 4K video recording at 60 fps and 3x digital zoom was used for capture. It was clamped onto the stand and clamp set with the camera positioned at the same level as the tip of the syringe needle. A standard ruler and sticker label were attached near the syringe needle for scale conversion.

The water temperature at the start of the experiment was recorded and the flow rate was fixed to 2 seconds per drop. The focus and resolution of video was adjusted to obtain clear, visible edges of droplets at 3x digital zoom. A video clip of 5 water droplets was recorded, the first droplet, however, was not accounted due to errors in video recording.

The average number of frames for each water droplet was calculated using the video clip of 5 water droplets. Every captured image from the video clip representing 5% of droplet size was selected. In this study, 0% is when the water droplet has not yet exited the needle tip, while 100% is when the water droplet is about to leave the needle tip and 100% of the first droplet is 0% of the next droplet.

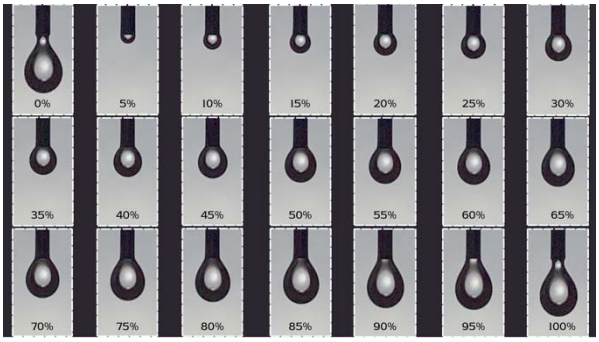

Figure 1. An example of capturing images of droplet size for determining surface tension involves suspending a liquid droplet from the end of a needle.

Images were imported into ImageJ software and the image solution was adjusted. The Straight icon was selected and used to measure D_E and D_S where D_E is defined as the diameter of the widest part of the droplet and D_S is defined as the diameter of the droplet at a distance D_E from the bottom of the droplet. The Analyze icon was selected. After that, Measure button was selected and D_E and D_S values were recorded.

D_E and D_S values of water droplets were used to calculate water surface tension (γ) using Young-Lapace equation describing the balance between surface tension and the gravitational force due to weight of water droplet. Numerical methods have been used to determine the optimum constant in many studies (Joseph et al., 2015; Stauffer C.E., 1965). In this study, the following equation (C. E. Stauffer, 1967) was used.

$$\gamma = \frac{\Delta\rho g D_E^2}{H} \qquad (1)$$

Where γ represents the surface tension, $\Delta\rho$ represents the density difference between water and air, g represents the Earth's gravitational acceleration (9.81 m/s^2), and 1/H is a function of the D_S/D_E ratio.

$$\frac{1}{H} = \alpha\left(\frac{D_S}{D_E}\right)^b \qquad (2)$$

1/H is a dimensionless function. The variables a and b are constants obtained from calculation in this study, which are equal to 0.345 and -2.54, respectively, based on a study by Nicolas-Alexandre Goy et.al (Nicolas A.G. et.al., 2017). These values were substituted into Equation (2) together with the D_S/D_E ratio in order to estimate 1/H. The data obtained were used to create a graph of the relationship between log(1/H) and log(D_S/D_E) as shown in Figure 1. This graph was used to determine the values of a and b for further use. From the graph, the values of a and b were 0.33 and -2.50, respectively.

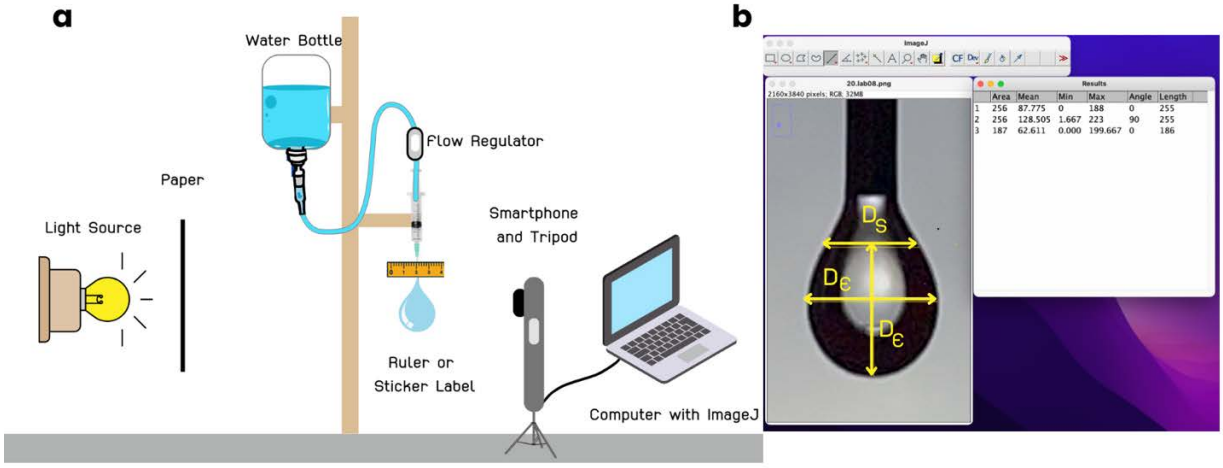

Figure 2. Design of an experimental setup
(a) experimental setup for water surface tension determination based on the pendant drop method using a smartphone for capture
(b) determine the dimensions of the droplet. Parameters such as the diameter D_E and D_S of the droplet are measured.

2.3 Methods

In order to develop an effective experimental setup and to reduce the error in surface tension measurement, the following factors were studied:

In experimental setups involving the study of water droplets, it is common to utilize photographs taken from a syringe needle. The analysis typically involves measuring parameters such as D_E and D_S. The recorded values are usually in pixel units.

For pixel-to-metric conversion the reference scale in the image is achievable with a standard ruler, sticker label or needle.

Conversion of D_E and D_S using standard ruler, sticker label, and needle scales

Images were imported into ImageJ software and D_E and D_S were measured in pixel unit. The unit was converted from pixels to millimeters using scales on the standard ruler, sticker label, and syringe. The conversion was performed by selecting the Straight icon then selecting the edge of the scale to be matched. The Analyze icon was then selected, followed by Set Scale button.

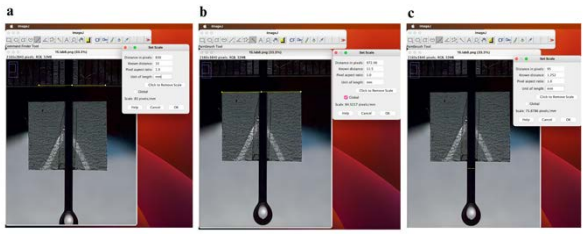

Figure 3. Scale settings in ImageJ software

The surface tension values obtained using standard ruler, sticker label, and needle were compared using Anova statistics in order to determine the best tool for scale conversion.

Optimal range of data set for determination of surface tension

The surface tension values were determined using the captured images and they were then used it to create a graph of surface tension–droplet shape. The time interval where the surface tension value was closest to the actual value and the standard deviation was low was selected.

Pixelation error

Since the calculation is based on photographic data, pixelation may cause error, the D_E value was therefore measured and used to estimate the standard D_S value. After that, pixelation-induced error was determined by increasing the D_E value obtained from the standard measurement by 1 pixel in order to estimate the new D_S value. The D_E value and new D_S value were recorded for calculation of error in surface tension.

3. Results & Discussion

Study water surface tension determination based on the pendant drop method using a smartphone for capture. The analysis typically involves measuring parameters such as D_E and D_S. The recorded values are usually in pixel units.

For pixel-to-metric conversion the reference scale in the image is achievable with a standard ruler, sticker label or needle.

The results of the experiment are as follows:

Data for calculating surface tension using the pendant drop method, pixel-to-metric conversion, the reference scale achievable with a Sticker Label.

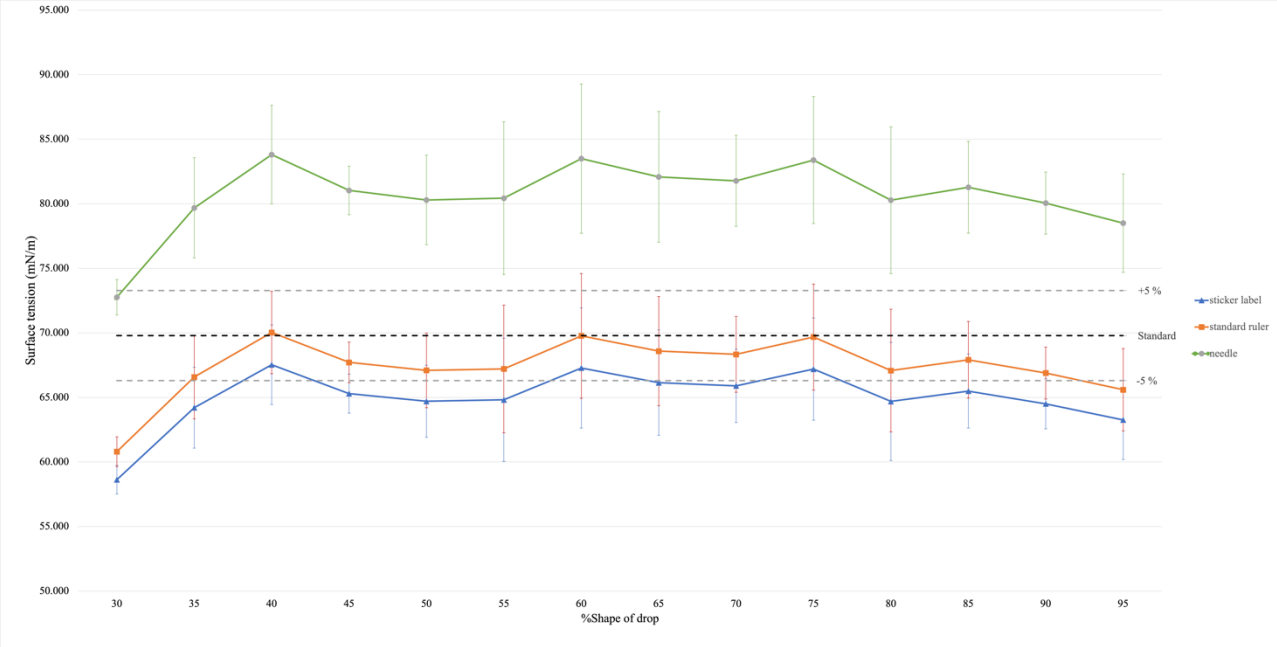

Figure 4. Compare for calculating surface tension using the pendant drop method, pixel-to-metric conversion, the reference scale achievable with a Sticker Label

Compare surface tension data resulting from pixel-to-metric conversion, utilizing three distinct reference variables: a sticker label, standard ruler and needle. The reference scale in the picture has the following sizes: 84.522, 83.000 and 75.871 pixel/mm respectively. The Young-Laplace equation was then applied to calculate surface tension based on the converted data. The results obtained are as follows: 64.974, 67.378 and 80.635 respectively.

the standard deviation (S.D.) of surface tension measurements of water droplets and the percentage error compared to the standard surface tension values obtained using the Wilhelm plate method, it is evident that using the Sticker Label and Standard Ruler scales results in lower standard deviations and percentage errors than using the Needle scale. Therefore, based on the presented table, it is apparent that for pixel-to-metric conversion, it is advisable to have more than 80 pixels per millimeter. This can be achieved using the Sticker Label and Standard Ruler scales, as comparing scales with smaller sizes may introduce higher standard deviations and errors due to the challenges associated with smaller scales.

Part 2. Pixelation error

Pixelation error is uncertainty in surface tension due to image pixel from measuring the distance D_E or D_S using ImageJ or Microsoft Paint program.

Table 1. Pixelation error arising from measuring the distance D_E using ImageJ or Microsoft Paint program.

Pixel error De (pixel)	De (pixel)	Ds (pixel)	γ (mN/m)	% error
-5	225.4	159.998	58.749	15.743
-4	226.4	159.218	60.692	12.992
-3	227.4	157.084	64.053	8.398
-2	228.4	156.450	65.967	5.449
-1	229.4	156.718	67.007	3.999
0	230.4	155.400	69.873	0.000
+1	231.4	152.648	74.430	6.616
+2	232.4	152.050	76.720	9.804
+3	233.4	150.591	80.096	14.676
+4	234.4	149.172	83.571	19.678
+5	235.4	147.230	88.061	26.087

Pixelation error arising from measuring the distance D_E using ImageJ or Microsoft Paint program. The measurement error arises from the image resolution. If students measure the distance D_E inaccurately, it will affect the values of D_S and surface tension. These measurements are carefully taken at the drop edge to maintain a misplacement of fewer than two pixels, thereby suppressing pixelation errors under 10%. As observed in the comparative table, when the D_E distance is greater than the standard D_E, it results in a 6.616% deviation in surface tension per pixel. Conversely, if the D_E distance is less than the standard D_E, it causes only a 3.999% deviation in surface tension per pixel. Therefore, for accuracy in determining surface tension, emphasis should be placed on precise measurements of D_E and D_S. It is crucial not to measure beyond the black edge of the water

droplet image, as it would lead to increased measurement errors.

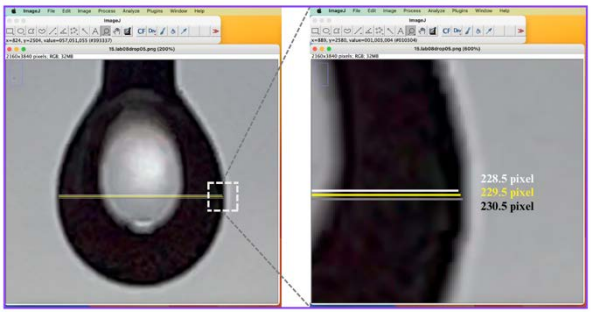

Table 2. Pixelation error arising from measuring the distance D_S using ImageJ or Microsoft Paint program.

pixelation	De (pixel)	Ds (pixel)	γ (mN/m)	% error
-5	230.4	145.330	82.438	8.824
-4	230.4	146.330	81.037	6.975
-3	230.4	147.330	79.669	5.248
-2	230.4	148.330	78.333	3.405
-1	230.4	149.330	77.028	1.683
0	230.4	150.330	75.753	0.000
+1	230.4	151.330	74.508	1.644
+2	230.4	152.330	73.291	3.250
+3	230.4	153.330	72.102	4.820
+4	230.4	154.330	70.940	6.354
+5	230.4	155.330	69.803	7.854

The measurement error resulting from measuring the D_S distance using ImageJ or Microsoft Paint is influenced by the image resolution. If students measure the D_S distance with a 2-pixel deviation, it will result in a surface tension deviation of no more than 3.5%. This illustrates that the D_S distance has a lesser impact on the deviation of surface tension compared to the D_E distance.

4. Conclusion

Optimized experimental parameters indicated that videos should be recorded at approximately two drops per second, capturing on drops exceeding half their full size. The drop width and height are processed using image software like ImageJ or Microsoft Paint. These measurements are carefully taken at the drop edge to maintain a misplacement of fewer than two pixels, thereby suppressing pixelation errors under 10%. For pixel-to-metric conversion, the reference scale in the image must be more than 80 pixel per mm, achievable with a standard ruler or sticker label. Straightforward experimental approach, under optimized conditions and with proper data analysis, measured the surface tension of distilled water to be 67.817 mN/m (n = 10) at 27 °C, in accordance with the Young-Laplace equation. This closely matched the 69.790 mN/m (n = 10) obtained from the Wilhelmy plate method. These results support our experimental design and analysis as appropriate for chemistry labs, ensuring precise results. Additionally, this technique could help determine the critical micelle concentration of surfactants.

Acknowledgements

The authors thank the Department of Chemistry, Faculty of Science, Burapha University, for Chemistry Laboratory for this experiment.

References

1. Berry, J. D., Neeson, M. J., Dagastine, R. R., Chan, D. Y., & Tabor, R. F. (2015). Measurement of surface and interfacial tension using pendant drop tensiometry. *J Colloid Interface Sci, 454*, 226-237. doi:10.1016/j.jcis.2015.05.012
2. Gascon, K. N., Weinstein, S. J., & Antoniades, M. G. (2019). Use of Simplified Surface Tension Measurements to Determine Surface Excess: An Undergraduate Experiment. *Journal of Chemical Education, 96*(2), 342-347. doi:10.1021/acs.jchemed.8b00667
3. Goy, N.-A., Denis, Z., Lavaud, M., Grolleau, A., Dufour, N., Deblais, A., & Delabre, U. (2017). Surface tension measurements with a smartphone. *The Physics Teacher, 55*(8), 498-499. doi:10.1119/1.5008349
4. Phan, C. M., Yusa, S. I., Honda, T., Sharker, K. K., Hyde, A. E., & Nguyen, C. V. (2018). Micelle and Surface Tension of Double-Chain Cationic Surfactants. *ACS Omega,3*(9), 10907-10911. doi:10.1021/acsomega.8b01667

Enhancing physical chemistry education: Active learning strategies, student engagement, and assessment alignment for successful learning outcomes

Wissawat Sakulsaknimitr

Department of Fundamental Science and Physical Education, Faculty of Science at Sriracha, Kasetsart University, Sriracha campus, Chonburi 20230, Thailand

E-mail: wissawat.s@ku.th

Abstract:

Teaching physical chemistry in line with curriculum learning outcomes involves utilizing active learning techniques such as Think-Pair-Share, collaborative learning, games, and video analysis. Students actively participate by creating tests, taking notes, and utilizing technology for learning through models and data analysis with Excel. This approach enhances the overall learning experience, promotes information-seeking, and encourages opinion expression. Results from these activities indicate improved understanding of physical chemistry principles among students. They exhibit a more assertive attitude, engaging in increased opinion exchange and demonstrating greater determination in presentations. Evaluation results, including exam scores, work pieces, and presentations, are consolidated into a score scale aligned with the program learning outcomes (PLO) of the curriculum, providing a clear reflection of each student's characteristics. This teaching information informs the organization of future teaching activities, ensuring alignment with curriculum goals and facilitating continuous improvement. The aim is to guarantee that students successfully achieve the curriculum's learning objectives.

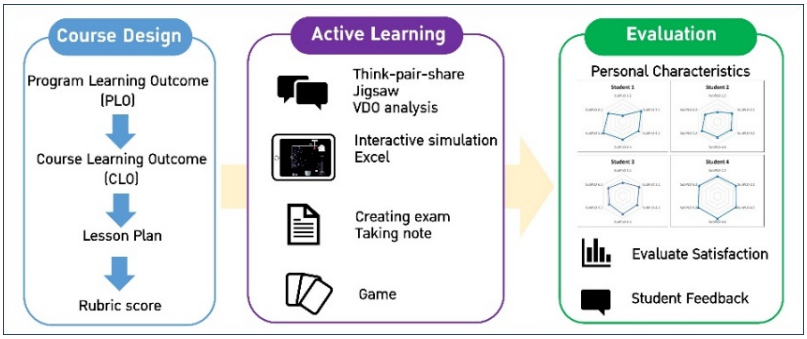

1. Introduction

The learning loss observed during the COVID-19 pandemic, particularly in online education, has significant implications for future workforce readiness.[1] To address this, integrating active learning methods into the curriculum is crucial. These methods, rooted in constructivism theory, emphasize learners' active engagement with new information, encouraging reflection, exploration, questioning, and interaction with peers. Active learning creates an enjoyable learning experience, improves student engagement, fosters a positive attitude toward the subject, and integrates technology to support students in gaining clarity in physical chemistry and effectively reducing learning loss.

This research aims to present a method for utilizing a variety of active learning methods to develop an understanding of physical chemistry concepts. The results will be collected through assessments such as satisfactions, worksheets, quizzes, and exams, using rubric scores. These results will be applied to create a mapping for individual student outcomes related to the curriculum. Moreover, exam scores will be compared to those of the last year's group to determine the efficiency of active learning.

2. Methods

2.1 Study participants

This study employed a quasi-experimental research design. A total of 22 the second-year students, enrolled in physical chemistry I classroom, at chemistry program, Faculty of Science at Sriracha, Kasetsart University, Sriracha campus, Thailand, participated in this study. They were 18 females (82%) and 4 males (18%) and they age between 19 and 20 years old. The students, who have an average grade of 2.59 in Basic Chemistry I and II, can be categorized into different learning levels: high (26%), moderate (63%), and low (11%).

2.2 Study Plan

The instructor devised teaching methods that integrate active learning and established

approaches to assess learning outcomes. The design of activities considers alignment with the contents, employing various formats to enhance knowledge, understanding, and communication skills.[2] This includes activities such as group idea exchange using the “Jigsaw” method,[3] games, simulations, students generating questions,[4] writing a learning journal, and presentation. Assessment utilizes a rubric score, and weight is assigned to the assessment across various learning outcomes, as illustrated in Table 1. The scores are applied to evaluate the individual characteristics of each student based on the Sub-Program Learning Outcomes (SubPLOs) aligned with Course Learning Outcomes (CLO) of the curriculum.

Table 1. The SubPLOs and the assessment weights

SubPLOs	Assessment weights
1.2 Correctly explains the principles and theories of physical chemistry.	Quiz and exam (10)
3.1 Applies foundational knowledge to systematically analyze and explain phenomena in the field of study.	Phet simulation (5) Excel (5)
4.2 Effectively communicates scientific and mathematical knowledge, including choosing appropriate communication formats.	Presentation (5) Jigsaw learning (5)
4.4 Efficiently uses information technology to research and collect scientific data in the field of chemistry.	Student generated question (8) Citations (2)
5.2 Demonstrates discipline, honesty, responsibility to society, and respect for regulations.	Timely Submission of Assignments (5)
6.2 Takes continuous responsibility and is committed to personal development.	Learning journal (7) Presentation (3)

3. Results & Discussion

3.1 Teaching Clarification and Knowledge Foundation Adjustment

The instructor developed a comprehensive teaching and assessment plan, providing students with information on teaching activities, assessment criteria, exam scores, assignments, presentations, and class participation. Additionally, SubPLOs were introduced to evaluate the outcomes of the activities.

Subsequently, an "ice-breaking" activity aimed to shift students' attitudes towards active learning, using questions to assess knowledge and foster idea exchange through pair discussions (Think-Pair-Share).[2]

Observing student behaviors, their initial silence and hesitation evolved into active participation during paired discussions. The gathered responses were then employed to collectively synthesize knowledge, significantly improving the interactive atmosphere of the classroom's question-and-answer sessions.

3.2 Gamified Learning

The instructor has designed a sequencing game to review the concepts of basic units, namely weights, volumes, densities, and moles. In this game, students receive cards with various units of measurement. Within a specified time, they arrange the cards to assess their understanding of measurement units. Participating in games keeps students engaged, focused, and provides opportunities for discussion. Kahoot is also utilized for both pretests and posttests, capturing attention, and offering an enjoyable opportunity for students to challenge their knowledge against their peers.

3.3 Interactive models

The instructor utilizes interactive models from the websites PhET[5] and LearnChemE,[6] accessible on iPads. These models demonstrate the continuous movement of gas particles and the pressure generated when colliding with container walls. Gas particles undergo energy changes based on temperature. The instructor guides students to adjust variables such as temperature, volume, and gas quantity to observe their impact on pressure. Subsequent activities involve discussions, summaries of knowledge, and quiz assessments.

Observing student behavior, it's evident that students enjoy experimenting with variables and learning from the models. The instructor uses questions to encourage thinking and find the answer by themselves. While most students can explain the relationship between temperature and gas velocity, they still struggle to elucidate the connection between the frequency of collisions with the walls and pressure. The results of the posttest indicate that engaging with the model helps students achieve a clearer understanding of the topic.[7]

3.4 Jigsaw learning

Jigsaw learning is a collaborative group activity wherein students rely on one another to attain a shared objective.[3] In the first step, each group is assigned a distinct topic, necessitating

members to acquire expertise as subject matter experts capable of explaining it to their peers. Subsequently, in the second step, a new group is formed consisting of subject matter experts. Here, each student is tasked with elucidating their respective topic to the group members, followed by the completion of a summary submitted as a worksheet.

The students behavior unequivocally indicates that the activity promotes active participation in the exchange of ideas, providing individuals with the opportunity to both articulate their thoughts and attentively listen to others. In certain topics, instructors observed that students still harbored some misunderstandings, yet these were addressed during the summary section of the activity.

3.5 Excel Graphing Activity

Proficiency in graphing and linear equations is crucial for the study and research of chemistry. In pairs, students were instructed to utilize the Excel program to generate a linear graph from provided sample data. Subsequently, they were tasked with creating a trend line and employing the linear equations to determine enthalpy (ΔH) and entropy (ΔS) using Equation 1.

$$\ln K = -\frac{\Delta H^o}{RT} + \frac{\Delta S^o}{R} \qquad (1)$$

During the practice of creating graphs, the instructor observed that students lacked basic knowledge about linear equations, making it challenging for them to understand how to find the slope value and the point of intersection from the resulting straight-line equation. In response, the instructor had to provide individualized instruction and subsequently led a class discussion to collectively solve problems.

3.6 Students generating questions.

The instructor assigns students to observe the physical properties of substances for designing the question that involve calculations based on real gas equations and pure substance equations. Students learn to identify reliable information sources and develop the skill of choosing pertinent details, such as selecting the appropriate temperature based on the state of the given substance, taking into consideration its melting point and boiling point.

Observing student behavior initially, it was noted that most students conducted searches in Thai, limiting their access to relevant information. In some instances, there were inaccuracies in temperature selection that did not correspond to the calculation equation. To address this, the instructor provided examples of effective search terms and demonstrated how to choose the temperature based on the state of the substance.

3.7 Phase Diagram

After explaining the simple phase diagram of the mixture, students were assigned the task of creating their own phase diagrams on the worksheet. They were required to identify the boiling point, components of the mixture, and its proportions at the specified point.

Assigning different problems to each person helps students take ownership of their thinking and problem-solving. This approach differs from merely completing exercises, where some students may lack enthusiasm or simply wait for the teacher's answers to copy without a genuine understanding of the problem.

3.8 Learning Journal

Students are tasked with maintaining learning journals and solving example calculations for each weekly topic for aiding knowledge organization.

Observing students' behavior reveals that those with a solid chemistry background can create a comprehensive and well-organized learning journal, often correlated with higher test scores. Conversely, individuals with a lower level of understanding tend to take incomplete or unclear learning notes, posing challenges in connecting and remembering information.

3.9 Presentations

Students are grouped to present on assigned topics related to apply physical chemistry knowledge to technology and everyday phenomena. Presenters are questioned and assessed by both the instructor and peers, using a rubric score.

This activity is organized in the last week of the course. The instructor observes that most students are proactive in preparing information and rehearsing for their presentations compared to students in previous years. Groups with higher scores exhibit well-structured content, eye-catching slides, clear presentation skills, and effective response to questions. The assessment scores from both the instructor and peers align in the same direction.

The instructor believes that the interactive learning process encourages students to think and express themselves more confidently through a relaxed learning atmosphere. It allows for making mistakes as a normal part of the learning process. One survey comment stated, "It feels enjoyable to see classmates engaging in question-and-answer interactions.

3. Learning Outcomes and Student Evaluations

3.1 Satisfaction Assessment of Active Learning Activities

The instructor conducted a survey to assess student satisfaction with the active learning activities. The results of the satisfaction assessment are presented in Tables 2 and Table 3, along with comments highlighting the advantages, disadvantages, and suggestions for improvement provided by students.

Table 2. Satisfaction Assessment Regarding the Overall Active Learning Activities (5=Strongly Agree/4=Agree/3=Neutral/2=Disagree/1=Strongly Disagree)

Assessment Criteria "Active learning …"	Average score
helps you learn better than lectures.	4.67
spends too much time on activities.	3.62
facilitates discussion and exchange of ideas.	4.81
keeps you engaged with the content until the end of the session.	4.60
improves your performance in quizzes and exams.	4.52
aids in better retention of the knowledge.	4.52
enhances your understanding of the course material.	4.62
should incorporate more in the other courses.	4.48

Table 3. Satisfaction Assessment of Active Learning Activities in Enhancing Understanding (5=Very Helpful / 4=Helpful / 3=Better than Lecture Alone / 2=Neutral, Optional / 1=Not Necessary, Better without)

Active Learning	Average score
Creating simple phase diagrams of mixtures	4.76
Kahoot	4.76
Games	4.67
Interactive Simulation	4.62
Using Excel to create graphs	4.48
Learning logs	4.38
Jigsaw learning	4.33
Presentations	4.33
Problem-solving design	4.25
Think-pair-share	4.24

The overall satisfaction assessment found that active learning activities effectively improved understanding of course content. Students show that these activities keep them engaged for longer periods of time. and would like to have additional courses to use active learning strategies. A notable challenge is the need for better time management during activity sessions. Some students felt that the time spent on the activities was relatively high compared to the content received. The instructor acknowledged this concern and aimed to improve time management for future sessions.

The activities encompass generating phase diagrams of ingredients, games, and interactive model-based discussions, receiving a high satisfaction score (>4.50). This suggests that hands-on practice significantly enhances students' comprehension of the content. While most students relish game-based activities as effective teaching tools, satisfaction slightly decreased for those involving discussions and knowledge sharing. This decline may stem from inadequate foundational knowledge and nervousness during presentations. To remedy this, the instructor intends to foster a supportive learning environment and enhance presentation skills in future sessions.

3.2 Response to Course SubPLOs

The scores for each section, depicted in Table 1, were adjusted on a 5-point scale to generate a radar chart illustrating individual student characteristics based on the SubPLOs, as presented in Figure 1. Examples in Figure 1 underscore noticeable inter-individual variation in SubPLOs 1.2, reflecting cognitive abilities assessed by test scores. Conversely, other SubPLOs scores exhibit a distribution in the 3-5 range, stemming from assessments involving hands-on learning activities that encompass evaluations of various components. These activities provide opportunities for students to revise their work in accordance with the instructor's feedback, resulting in commendable scores for the submitted assignments.

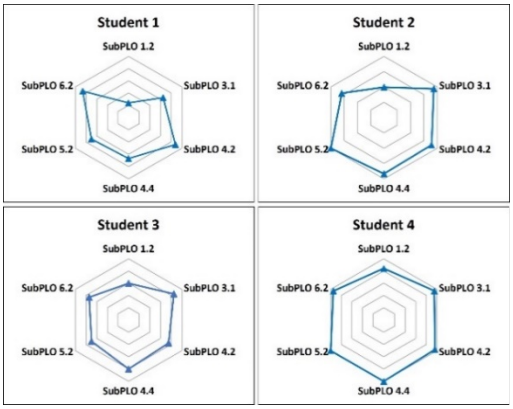

Figure 1. Radar chart illustrating the assessment of student characteristics aligned with Physical Chemistry I SubPLOs

3.3 Comparative Analysis of Average Scores with semester of 2022 Examination Results

The instructor employed a two-sample unequal variance T-test to examine the differences in mean scores between two distinct student

cohorts. The analysis utilized scores obtained from multiple-choice questions using the same test set. The distinguishing factor is the number of students in the 2022 academic year, which comprised 52 individuals undergoing lecture-based teaching. The results of the statistical analysis are presented in Table 4.

Table 4. t-test of the mean scores (%) for multiple-choice exams comparing students in Physical Chemistry I between the academic years 2022 (n=52) and 2023 (n=22)

	mean	sd	skewness	t	sig
Mid-66	46.82	15.51	1.043**	1.901*	0.066
Mid-65	39.76	12.17	0.139		
Final-66	55.32	15.41	0.136	3.547*	0.001
Final-65	42.47	10.81	0.008		

***Score of Mid-66 has an unequal mean-median and a skewness >0.5, which mean the data is not normal distribution.*

The mid-term exam results of students in the academic year 2023 show no significant difference compared to those in the academic year 2022. This lack of distinction is attributed to the non-normal distribution of scores among the 2023 student cohort. However, notable disparities are observed in the final exam scores for the academic year 2023, where there is a relatively wide distribution of scores.

In response to this distribution, the instructor initiated discussions with the students who scored lower, aiming to collectively reflect on challenges and explore strategies to enhance the effectiveness of their learning. The students conveyed that the active learning activities significantly improved their understanding, surpassing the benefits of traditional lectures. However, they also highlighted a deficiency in practice exercises and review the contents, leading to difficulties in performing well in exams.

Subsequent discussions revealed that the students in this group exhibited a positive attitude and increased collaboration in active learning activities. This is anticipated to result in higher average scores and the better of the normalized score distribution, facilitating the feasibility of statistical t-test analysis. In conclusion, it can be inferred that the incorporation of active learning activities has positively contributed to improving student learning outcomes.

4. Conclusion

Implementing active learning in Physical Chemistry 1 enhances self-expression and cooperation among students. Assessment through exams and assignments aligns with curriculum outcomes. Students prefer the active learning approach over traditional lectures, leading to increased engagement throughout the class. However, inadequate review affects some students' exam performance. Providing key takeaway notes and review exercises can alleviate this issue. This proactive teaching method allows instructors to identify challenges, gather feedback, and refine teaching and assessment strategies for improved learning outcomes.

Acknowledgements

This work was supported in part by Kasetsart University, Sriracha campus. All are gratefully acknowledged for the support.

References

1. Ignacio, A.; Arantxa, V.V.; Victoria, G.P.; Patricia, D.C. *RCR.* **2023**, *11*. 172-189.
2. Prayalaw, P. *JEIL*. **2022**, *2*, 87–96.
3. Soundariya, K.; Senthilvelou, M.; Shivayogappa S.; Teli, S.S.; Deepika, V.; Senthamil S.K.; Mangani, M.S. *Biomedicine.* **2021**, *41*, 654-659.
4. Aflalo, E. Students generating questions as a way of learning. *Active Learn. High. Educ.*, **2021**, *22*, 63-75.
5. PhET Interactive Simulation. https://phet.colorado.edu/ (accessed 2024-01-12).
6. LearnChemE. https://learncheme.com/ (accessed 2024-01-12).
7. Rayan, B.; Daher, W.; Diab, H.; Issa, N. *Educ. Sci.* **2023**, *13*, 884-901.

Developing the skill of applying exponential and logarithm function in the context of chemical kinetics for 11th grade students using the backward design teaching approach

Sittichoke Som-am[1], Monsikarn Jansrang[1], and Usa Jeenjenkit[2]*

[1]*Department of Mathematics and Computing Science, Mahidol Wittayanusorn School, Nakhon Pathom, 73170, Thailand*

[2]*Department of Chemistry, Mahidol Wittayanusorn School, Nakhon Pathom, 73170, Thailand*

**E-mail: usa.jjk@mwit.ac.th*

Abstract:

This study aims to enhance students' adeptness in utilizing exponential and logarithmic functions to comprehend and address challenges in chemical kinetics. The backward design approach is employed to efficiently structure the learning trajectory. The study involved a sample of 23 11th grade students of Mahidol Wittayanusorn School, selected through purposive sampling. A paired t-test was conducted to compare the math pretest and posttest. Additionally, a paired t-test was employed to compare the chemistry posttest with the 70% criterion. The relationship between the math posttest and chemistry posttest was analyzed to assess the effectiveness of math learning for chemistry. Furthermore, the sample was divided into two groups for interviews, one comprising students with high scores in both chemistry and math tests, and the other consisting of students with a high score in math but a low score in chemistry. The findings revealed the following: 1) After the learning process, the average math scores significantly exceeded the pre-learning scores and surpassed the 70% criterion at a significance level of 0.05. 2) The mean chemistry scores of the student sample after learning surpass the 70% criterion at a significance level of 0.05. And 3) A relationship between the math and chemistry scores was observed. In the interviews, it was observed that the high-scoring group comprehended and could demonstrate chemistry formulas, enabling them to tackle chemistry problems. Conversely, the low-scoring group only memorized the formulas without a deep understanding, hindering their ability to apply mathematical concepts to solve chemistry problems.

1. Introduction

In contemporary education, the synergy between mathematics and science is vital for a holistic understanding of scientific principles, particularly in chemistry where mathematical concepts like exponential and logarithmic functions are indispensable for unraveling the complexities of chemical kinetics (Hofstein & Mamlok-Naaman, 2007; Nakhleh & Krajcik, 1994). The ability to apply mathematical concepts to scientific domains is very important and necessary for students to explain the phenomena in mathematical terms (Hake, 1998). This study explores pedagogical strategies, specifically the backward design approach, aiming to enhance 11th-grade students' proficiency in applying exponential and logarithmic functions within the context of chemical kinetics. Researcher has indicated that students often encounter challenges in seamlessly seamlessly integrating mathematical principles into their understanding and application of chemical kinetics (Hofstein & Mamlok-Naaman, 2007; Nakhleh & Krajcik, 1994). Students' scores from the previous few years often had problems in applying mathematical knowledge to explain the relationship between concentration and reaction time in terms of mathematics as well as rate law in terms of integrated rate law (Nakhleh & Krajcik, 1994). They also continue to expand the rate law to show half-life of the reaction. To explain it, it is necessary to use mathematical knowledge. The backward design teaching approach (Jay McTighe & Grant Wiggins, 2011), provides a theoretical framework that emphasizes the importance of beginning curriculum design with clearly defined learning outcomes (Bybee et al., 2006). This approach advocates for aligning assessments with learning objectives, ensuring a purposeful and coherent instructional trajectory. By focusing on the desired end goals, researchers have more emphasis on facilitating student understanding and application of concepts (Bybee et al., 2006). To address this gap, our research undertakes a meticulous examination of the backward design teaching approach for enhancing students' proficiency in these mathematical functions, thus empowering them to tackle the complexities inherent in chemical kinetics.

2. Materials and Methods

This research adopts a quasi-experimental design employing a pretest-posttest methodology to measure the learning outcomes of 11th-grade students in exponential and logarithmic functions before and after the implementation of a specific pedagogical approach (Campbell, D.T., & Stanley,

J.C., 1963). The study focuses on a selected group consisting of 11th-grade students from a total of 23 participants. Among the total participants, 8 are female, while the remaining 15 are male (Hake, 1998).

2.1 Data collection

The study begins with a pretest to assess students' knowledge of exponential and logarithmic functions. Subsequently, the backward design method is implemented during the mathematics class, and a posttest is administered upon completion of the session. Finally, the same group of students engages in the study of chemical kinetics in chemistry class, specifically the law of integration, followed by a posttest to evaluate the impact of backward design approach on their understanding in this cross-disciplinary context. In addition, interviews are conducted with high - scoring math students, categorized into two groups based on their performance in chemistry. Group 1 consists of students with scores falling below the passing threshold in chemistry (n=1), while Group 2 comprises students scoring above the passing threshold (n=5). These interviews are designed to probe into similarities and differences in the application of acquired knowledge, with each group responding to 7 questions.

2.2 Methodology used in Math Class

Utilizing the backward design in our research, we crafted a final assessment and then structured our lessons to ensure that students could apply exponential and logarithmic functions, particularly in the context of applied problems, especially in chemical kinetics. In the math class, data were collected and analyzed using pretest and posttest assessments. The pretest includes three questions related to zero, first, and second-order reactions, topics that students will later study in their chemistry class. For each of these questions, students were provided with the differential forms of the reactions and subsequently tasked with deriving an equation that describes the concentration of the reactant at any time *t*. Furthermore, they were instructed to plot the graph of each equation and calculate the half-life. Although students have not previously encountered the context of chemical kinetics, we expect that, based on their knowledge of differentiation and integration from their grade 10 studies, they will be able to solve certain sections of the pretest. The result of the pretest shows that students can solve problems related to zero-order reactions more accurately than those pertaining to first and second-order reactions. While solving the first-order reaction, some students applied the power rule of integration to the reciprocal function 1/x, which is an incorrect method. Most of the students who got the right equation were able to draw its graph correctly. These findings guided us in creating lesson plans for the math class, integrating instructional strategies and instructional activities. The instructional strategies began with teacher-centered approaches, involving the presentation of definitions for exponential and logarithmic functions, graph plotting, and subsequent explanations of their characteristics. Additionally, the class explored the practical applications to solve real-world problems. Examples of real-world problems discussed in class included compound interest, exponential growth and decay models, and chemical kinetics. Following that, we utilized student-centered approaches such as peer discussion and inquiry-based learning. Two problems were selected from the worksheet involving logarithmic models and chemical kinetics for discussion. To enhance student's learning during instructional activities, we utilized videos posted on Google Sites and engaged in group presentations. At the end of the learning section, students evaluate their learning through a posttest consisting of three questions: one related to chemical kinetics and two related to math problems. The reason for selecting only one chemical kinetics problem is that there will also be a posttest in the chemistry class.

2.3 Data analysis

For data analysis, the paired t-test is employed to assess the scores obtained from both the math pretest and math posttest, as well as the scores derived from chemistry posttest and 70% criterion. Additionally, descriptive statistics were employed to explore the relationship between math and chemistry scores. As for the interview component, the recorded interviews are divided into two groups and then transcribed into textual format to facilitate subsequent analysis.

3. Results & Discussion

We divided the results into 4 subsection based on data analysis as follow

3.1 Math pretest and posttest

A paired t-test was used to assess the impact of the backward design approach on students' mathematical literacy, comparing the scores of a math pretest and posttest. The average math pretest score of 11.24 significantly increased to 26.30 ($p = 6.07\times 10^{-8}$), see Table 1, surpassing the 70% criterion ($p = 3.05\times 10^{-8}$). This substantial enhancement underscores the

positive impact of the backward design method on students' mathematical skills.

3.2 Chemistry posttest and 70% criterion

Comparing the learning outcomes of the chemistry posttest with the 70% criterion, using a paired t-test, it was found that there was a statistically significant difference ($p=0.0002$). This indicates that at a 95% confidence level, students' chemistry learning outcomes were higher than the 70% criterion. This may be attributed to students having good learning outcomes in mathematics.

3.3 Relationship between Math and Chemistry score

In Figure 1, it is depicted that 22 students have met the 70% criterion in mathematics, while 21 students have achieved the same criterion in chemistry. Remarkably, all students who passed the chemistry criterion also surpassed the math criterion. Notably, only one student who met the math criterion did not reach the chemistry criterion. This observation suggests that strong performance in mathematics significantly facilitates understanding the context of chemical kinetics for students.

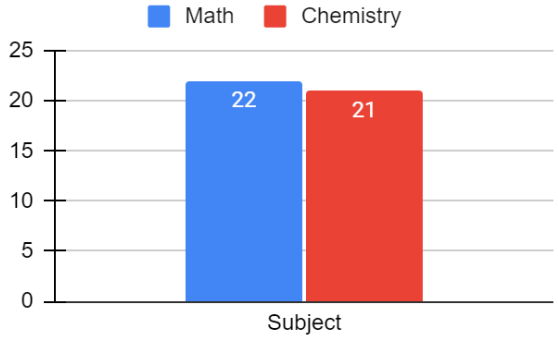

Figure 1. The graph illustrates the number of students who achieved the 70% criterion in mathematics and chemistry.

3.4 Interview results

Group 1 expresses challenges in memorizing and applying mathematical and chemical formulas, leading to difficulties in chemistry exams. Despite understanding integration and having a good understanding of mathematical fundamentals, the foundational understanding of chemistry is lacking. The preference is to avoid repetitive learning and to relate mathematics to chemistry for better comprehension. This group faces challenges in using calculators for logarithmic and exponential functions during exams. Additionally, difficulties arise in proving rate laws, comparing triatomic laws, unit conversions, and graphing log and expo functions. This group suggests incorporating more applied topics in math classes and including chemistry-related questions in exams. For chemistry, there is a desire for exams to include questions requiring the recall formulas, reviewing the process of solving certain problems, and clearer explanations during math-related topics.

Group 2 demonstrates a strong background in applying integration and successfully derived formulas for zero, first and second-order reactions in chemical kinetics. Students in this group express that a profound grasp of mathematical terms and content enhances their learning in chemical kinetics. Encountering applied problems in math class, such as those related to chemical reactions or acid-base concepts, can assist students in applying their knowledge to the chemistry class. However, the results from Group 1 still focus the researchers' attention on finding a more effective way to enhance students' learning in chemical kinetics. Additionally, they suggest having more practice problems.

4. Conclusion

Our investigation into the relationship between mathematics and chemistry scores highlights the profound impact of these disciplines on student performance. Through the application of a paired t-test, we observed significant enhancements in both mathematical literacy and chemistry learning outcomes among 11th-grade students. These findings are consistent with previous research demonstrating the importance of integrating mathematical concepts into science education (Hofstein & Mamlok-Naaman, 2007; Nakhleh & Krajcik, 1994). Notably, our results revealed a strong relationship between excellence in mathematics and superior performance in chemistry, echoing the findings of studies that have emphasized the interplay between mathematical proficiency and success in scientific domains (Hake, 1998). Moreover, the observation that all students who met the chemistry criterion also surpassed the math criterion aligns with the notion that mathematical skills are crucial for understanding complex scientific concepts such as chemical kinetics (Wiggins & McTighe, 2011; Bybee et al., 2006). Insights from Group 2's interviews underscores the benefits of encountering applied problems in math class, which resonates with previous research highlighting the importance of contextualizing mathematical concepts to enhance student understanding and application (Hofstein & Mamlok-Naaman, 2007; Nakhleh & Krajcik, 1994). However, the presence of a single student

Table 1. Results of the comparison of students' mathematical literacy scores before and after learning.[a]

Test	Number of students	Mean	S.D.	t	Sig.
Pretest	23	11.24	8.92	-16.39	0.00*
Posttest	23	26.30	3.19		

[a]Level of significance is 0.05

who excelled in mathematics but struggled in chemistry suggests that while mathematical skills are beneficial, they may not guarantee success in chemistry without a comprehensive understanding of chemical principles.

To address challenges in comprehending chemical kinetics using exponential and logarithmic functions, students are guided through a series of steps. They analyze various chemical reactions, determine reaction rates based on reactant concentration, and ascertain reaction orders using differential and integral methods. Integration of mathematical concepts becomes crucial at this stage, requiring students to apply their knowledge effectively. To enhance understanding, collaborative group activities are employed, allowing students to articulate their perspectives and support one another. Classroom instruction on determining reaction orders using integrated rate laws, followed by hands-on experimentation and comprehensive evaluation, further solidifies students' comprehension and application of both mathematical and chemical concepts.

Acknowledgements

We would like to thank Deaw Jaiboon, mathematics teacher at Mahidol Wittayanusorn School, for providing valuable assistance and expertise in the field of statistics.

References

1. Hofstein, A.; Mamlok-Naaman, R. The Laboratory in Science Education: The State of the Art. *Chem. Educ. Res. Pract.* **2007**, *8* (2), 105–107.
2. Nakhleh, M. B.; Krajcik, J. S. Influence of Levels of Information, Knowledge, and Complexity on Understanding Chemical Equilibrium. *J. Res. Sci. Teach.* **1994**, *31* (2), 129–142.
3. Hake, R. R. Interactive-Engagement versus Traditional Methods: A Six-Thousand-Student Survey of Mechanics Test Data for Introductory Physics Courses. *Am. J. Phys.* **1998**, *66* (1), 64–74.
4. Wiggins, G.; McTighe, J. *The Understanding by Design Guide to Creating High-Quality Units*; ASCD: Alexandria, VA, 2011.
5. Bybee, R. W.; Taylor, J. A.; Gardner, A.; Van Scotter, P.; Powell, J. C.; Westbrook, A.; Landes, N. *The BSCS 5E Instructional Model: Origins and Effectiveness*; BSCS: Colorado Springs, CO, 2006.
6. Campbell, D. T.; Stanley, J. C. Experimental and Quasi-Experimental Designs for Research on Teaching. In *Handbook of Research on Teaching;* Gage, N.L., Ed.; Rand McNally: Chicago, 1963; pp. 171–246.

Determination of ethanol content in disinfectant spray by color photo intensity measuring on mobile phone

Metinee Mektan, Sasitorn Muncharoen, Sarayut Watchasit, and Jaray Jaratjaroonphong*

Department of Chemistry, Faculty of Science, Burapha University, Chonburi, Thailand 20131

**E-mail: jaray@buu.ac.th*

Abstract:

In the context of the COVID-19 pandemic, ethanol-based disinfectant formulations with a mandated minimum concentration of 70% v/v ethanol are essential for the mitigation of pathogens. This study introduces a rapid and reliable colorimetric method for measuring ethanol levels, utilizing mobile phone technology for data collection. The method involves oxidizing ethanol with a $K_2Cr_2O_7$ solution for 5 minutes, then capturing color images of the reaction using a mobile phone camera. These images are subsequently analyzed using an application capable of measuring color intensity in the RGB system. The color intensity is then converted into absorbance values, enabling precise quantitative analysis. The method exhibits an impressive linear range with a commendable correlation coefficient (R^2 = 0.9933) for the relationship between absorbance values and ethanol concentration (50-90% v/v). Notably, results obtained from mobile phone cameras align well with established techniques such as nuclear magnetic resonance (NMR) and UV-visible spectrophotometry, highlighting their analytical usefulness. Furthermore, this approach provides educational benefits, especially for high school chemistry labs with limited resources, by integrating digital imaging technology into teaching practices. Emphasizing portability, affordability, and rapid analysis enriches the learning experience, fostering students' proficiency in quantitative analysis techniques while demonstrating the synergy between technology and modern chemical education.

1. Introduction

Given the current COVID-19 pandemic, it's crucial to implement effective disinfection protocols to curb the spread of viruses. Alcohol-based disinfectants, in the form of gels and handwashing sprays, are widely utilized for eliminating microorganisms and germs from different surfaces. This is due to the rapid evaporation of high-concentration alcohol, which enhances its disinfection capabilities. For these alcohol-based disinfection products to achieve optimal efficacy, they must contain a minimum ethanol concentration of 70% to ensure thorough disinfection.

The analysis of alcohol concentration in typical disinfectants mainly focuses on ethanol and isopropanol compounds. However, the presence of methanol, another type of alcohol, poses a significant health hazard due to its high toxicity to humans. Exposure to methanol can result in serious health issues, including damage to the optic nerve leading to blindness, and in severe instances, it can be fatal.[1-2]

Several methods are employed to measure alcohol concentration in disinfectant products, each with its strengths and weaknesses. These methods encompass Headspace Chromatography (HC), Gas Chromatography (GC), nuclear magnetic resonance spectroscopy (NMR), and UV-visible analysis tools such as the spectrophotometer. Although these methods provide accurate results, many schools face challenges in acquiring these instruments due to their high costs. As a result, secondary school students miss out on the opportunity to utilize these resources.[3-9]

Acknowledging the limitations of conventional methods, this study explores the integration of contemporary technology, specifically smartphones, owing to their widespread use among students nowadays. Researchers and developers have harnessed the capabilities of smartphones via mobile applications and software platforms, enabling the analysis of RGB color intensity from images. This approach, proven effective in numerous applications such as phenolic compounds analysis and measuring various ions and substances, is deemed appropriate for color analysis in field laboratories, general research laboratories, and diverse ions and substances, is considered suitable for color analysis in field laboratories, general research laboratories, and secondary school chemistry laboratories.[10-13]

This research endeavors to create a methodology for assessing ethanol content via color intensity analysis. It involves a direct chemical reaction between ethanol and a potassium dichromate ($K_2Cr_2O_7$) solution, resulting in a unique green color. The goal of the research is to establish a dependable approach for determining ethanol concentration in alcohol aerosol products using smartphone camera imaging. The advancement of these analytical techniques not

only improves the affordability and ease of evaluating ethanol concentrations in commercially sold alcohol aerosol products but also provides consumers with important information, fostering trust in the efficacy and safety of these products for infection prevention.

Furthermore, the proposed methodology shows potential for educational use, especially in high school chemistry labs that may not have advanced scientific equipment. Introducing students to this technique encourages them to delve into digital imaging technology for fundamental chemistry analysis, providing a practical and accessible pathway for learning science. This approach not only provides an understanding of ethanol content analysis in alcohol sprays but also fosters a hands-on and captivating educational experience.

2. Materials and Methods

2.1 Materials

Spray alcohols were purchased from the local market and analyzed for their alcohol content. Five different spray alcohol samples, namely A1, A2, A3, A4, and A5 were used. Potassium dichromate ($K_2Cr_2O_7$) and concentrated sulfuric acid (H_2SO_4) were obtained in AR grade from Quality Reagent Chemical. For this study, an iPhone SE 2020 mobile phone camera with a 12-megapixel resolution was employed to assess RGB intensity using the PANTONE application. The RGB color intensity analysis on the iPhone SE 2020 is notably accurate, although slight variations may occur due to factors like lighting conditions and white balance settings. To control the light intensity for photography, a studio box measuring 23 cm in width, 31 cm in length, and 21.5 cm in height was constructed. (Figure 1.)

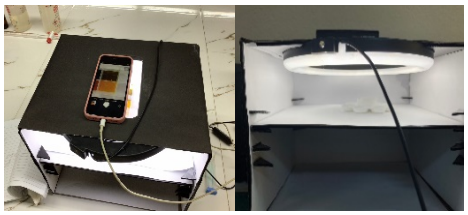

Figure 1. Studio Box

2.2 Qualitative analysis

Analysis of the type of alcohol in alcohol spray products aims to identify the specific alcohol present in these alcohol spray products. Four testing methods namely ceric ammonium nitrate reagent, Lucas test, Iodoform reaction, and NMR analysis, are employed for this purpose. The procedure involves sampling from all alcohol spray products.

For the first method, 5 samples of alcohol spray products are taken, each measuring 2.00 ml. To each sample, 1.00 ml of $(NH_4)_2Ce(NO_3)_6$ solution is added, and the mixture is left to stir for 5 minutes while observing the resulting color of the solution. Moving on to the Lucas test, 5 samples of the alcohol spray product are taken, each measuring 0.50 ml. These samples are then tested with 2.00 ml of Lucas reagent solution. The mixture is shaken well, and after 5 minutes, any changes are observed. For the Iodoform reaction test, 0.50 ml is taken from each of the five alcohol spray product samples, and they are tested with 1.00 ml of iodine solution. The mixture is allowed to sit for 5 minutes, and any resulting changes are observed.

2.3 Quantitative analysis

Determining the ethanol content in alcohol spray involves quantifying the ethanol present in samples of alcohol spray products. The chosen method entails analyzing absorbance values derived from examining the Red, Green, and Blue color (RGB) intensities in photographs. The results obtained through absorbance analysis using a mobile phone camera are subsequently compared with those obtained through the UV-Vis technique and the NMR technique.

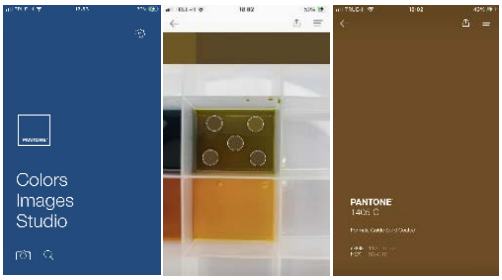

Figure 2. Color intensity analysis With the PANTONE application.

To analyze the ethanol content in samples of alcohol spray products, take 1.00 ml of 90%, 80%, 70%, 60%, and 50% ethanol solutions. Add 0.30 M concentrated $K_2Cr_2O_7$ solution (0.5 ml) to each solution. Allow the solutions to stand at room temperature for 300 seconds, then capture photos using a mobile phone camera. Use a photography light box (Studio Box) to ensure standardized lighting conditions. Subsequently, analyze the photos for R, G, and B color values using the PANTONE application (Figure 2). The obtained

color intensity values are then utilized to calculate the light absorption values using Equation 1.

$$A = -\log\frac{I}{I_0} \quad (1)$$

Where:

A is the absorbance,

I is the color intensity value of the sample solution, and

I_0 is the color intensity value of the blank solution.

Next, record the obtained light absorbance value and proceed to create a standard graph. Choose the RGB absorbance curve with the highest slope and the decision coefficient R^2 closest to 1; this will serve as the standard curve for measuring ethanol content. Following this, take a sample of the alcohol spray product and conduct a test with $K_2Cr_2O_7$ solution. Calculate the amount of ethanol in the alcohol spray sample using the formula for determining the total ethanol amount, as shown in Equation 2:

$$\text{EtOH content (\%v/v)} = [\ (A - B) / M\ ] \quad (2)$$

A represents the light absorption value from color intensity, B is the Y-intercept point of the ethanol standard curve, and M is the slope value of the ethanol standard curve. The results will be presented in concentration units %v/v for the alcohol spray sample product. The experiment was conducted three times, and the mean (± standard deviation) was calculated.

For ethanol content analysis in alcohol spray sample products using the UV-visible technique spectrophotometer, follow these steps:

1. Prepare a sample of the alcohol spray product, measuring 2.00 ml in volume. Add $K_2Cr_2O_7$ solution with a concentration of 0.30 M, measuring 1.00 ml in volume. Shake the solution thoroughly.
2. Prepare a sample of the alcohol spray product, measuring 2.00 ml in volume. Add $K_2Cr_2O_7$ solution with a concentration of 0.30 M, measuring 1.00 ml in volume. Shake the solution thoroughly.
3. Calculate the amount of ethanol in the alcohol spray sample product using Equation 3:

$$\text{EtOH content (\%v/v)} = [(A_{585} - B) / M] \quad (3)$$

Where A is the absorbance value at a wavelength of 585 nm, B is the Y-intercept point of the ethanol standard curve, and M is the slope value of the ethanol standard curve.

To analyze the sample, the Nuclear Magnetic Resonance Spectrometer (NMR) technique is employed, serving as an analytical tool to confirm the structure of the substance. This involves taking 50 µL of each alcohol spray sample product and combining it with 50 µL of ACN (CH_3CN), 60 µL of D_2O, and 490 µL of distilled water. Subsequently, the structure of the alcohol, an ingredient in the spray, is analyzed and quantified. The concentration of ethanol in the alcohol spray product sample is determined using Equation 4, outlined as follows:

$$\%\text{EtOH} = \frac{\text{Peak Area}(SMP)}{\text{Peak Area}(STD)} \times \frac{\text{N}\ (STD)}{\text{N}\ (SMP)} \times \frac{\text{V}\ (STD)}{\text{V}\ (SMP)} \times 100 \quad (4)$$

Where N is the number of hydrogen atoms and V is the volume.[4]

3. Results & Discussion

3.1 Analysis of the Type of Alcohol in Alcohol Spray Products

For qualitative analysis of alcohol types, the sample undergoes testing with ceric ammonium nitrate reagent to ascertain if it is an alcohol compound. The Lucas test and iodoform reaction are employed to analyze and categorize the type of alcohol in the sample before proceeding with the quantification of ethanol content.

Upon testing alcohol spray products with $(NH_4)_2Ce(NO_3)_6$, all five samples exhibited the presence of alcohol, as indicated by a color change to red. This reaction, triggered by the hydroxyl group's interaction with ceric ammonium nitrate, led to the formation of a red complex, which was confirmed by the Lucas test. Subsequent examination with $HCl/ZnCl_2$ showed no additional changes after 10 minutes, confirming the presence of primary alcohol types. Further analysis using the iodoform reaction (I_2/NaOH) resulted in the formation of a yellow precipitate in all samples, indicating the presence of ethanol in the alcohol spray products (Table 1).

3.2 Analysis of Ethanol Content in Disinfectant Spray

Part 1 : Ethanol Content Analysis in Sample disinfectant spray by color photo intensity measuring on a mobile phone.

This analysis involves determining the ethanol content in sample alcohol spray products utilizing a method that analyzes colors captured in

Table 1. Results of testing the type of alcohol in samples of alcohol spray products.

Type of substance/sample	A1	A2	A3	A4	A5
$(NH_4)_2Ce(NO_3)_6$	Dark red	Orange	Dark red	Reddish brown	Reddish brown
$HCl/ZnCl_2$	-	-	-	-	-
Iodine	Yellow precipitate	Yellow precipitate	Yellow precipitate	Yellow precipitate	Yellow precipitate

The "-" sign means no changes have occurred.

mobile phone photos. The data are presented in a table displaying the RGB color intensity values and the corresponding light absorbance values obtained from the RGB color intensity values of the solutions containing ethanol at various concentrations.

For the standard graph creation of a study analyzing ethanol content in disinfectant spray, this study explores methods for analyzing ethanol content in alcohol spray samples by assessing color intensity in mobile phone photos. Five different concentrations of ethanol solutions were reacted with $K_2Cr_2O_7$ solution, inducing an oxidation reaction that transformed Cr^{6+} from yellow to Cr^{3+}, exhibiting a green color.[8] After leaving the solution for 300 seconds, photographs were taken using a mobile phone. The photography method was validated by placing the solution in a clear container within a photography box, maintaining a suitable distance of approximately 10 cm from the camera lens**.** The photos were analyzed for color intensity using the PANTONE application on a mobile phone**.** Figure 1 illustrates the RGB color values used to calculate the light absorption value, serving as the basis for creating a standard graph**.**

Upon examining the graph illustrating the relationship between ethanol solution concentration and RGB color intensity absorbance, a linear relationship was observed when comparing absorbance values from R, G, and B. The graph depicting the relationship between light absorbance values from the R channel and ethanol concentration revealed a slope value (R^2) closest to 1, at 0.9933. This linear equation was selected as the standard graph. The linear equation derived from the R value's absorbance was used to calculate the ethanol intensity in the alcohol spray product sample.

Part 2: **Ethanol Content Analysis in Sample disinfectant spray by UV-visible technique**

Analysis of ethanol content in alcohol spray samples using the UV-visible technique spectrophotometer revealed a green solution when the ethanol solution reacted with $K_2Cr_2O_7$. Measurements at a wavelength of 585 nm showed a linear relationship between light absorption values and different ethanol concentrations, with a slope value (R^2) of 0.9971. The resulting linear equation was $y = 0.0568x - 2.3699$. In addition to color intensity analysis from mobile phone photos, this study employed UV-visible technique spectrophotometer and NMR techniques, generating data presented in Table 2.

Table 2. Comparison of Ethanol Concentration (%v/v) Estimated in Real Samples from Different Methods

Sample	Mobile Phone	UV-Vis	NMR
A1	73.38 ± 1.10	73.06 ± 1.07	68.82 ± 1.06
A2	68.06 ± 1.51	67.03 ± 1.20	62.21 ± 2.22
A3	65.53 ± 2.71	65.70 ± 2.02	60.91 ± 3.51
A4	71.58 ± 1.50	72.90 ± 1.65	73.63 ± 1.98
A5	71.60 ± 1.21	72.98 ± 1.18	69.51 ± 0.85

Upon analyzing ethanol levels using color intensity analysis from mobile phone photos, UV-visible technique spectrophotometer, and NMR techniques, it was determined that different ethanol concentrations could be accurately measured. The results of ethanol concentration analysis in all five alcohol spray samples, conducted through color intensity analysis from mobile phone photos, were consistent with the findings obtained through UV-visible analysis, spectrophotometer, and NMR techniques.

The complexation and oxidation reactions of ethanol were learned by the high school students, as well as the determination of the amount of ethanol in the analyzed samples, to increase interest and understanding of analytical chemistry content and its applications in daily life. Furthermore, the application of knowledge and analytical thinking skills with the scientific process gained from such activities can enable high school students to further develop new chemistry projects.

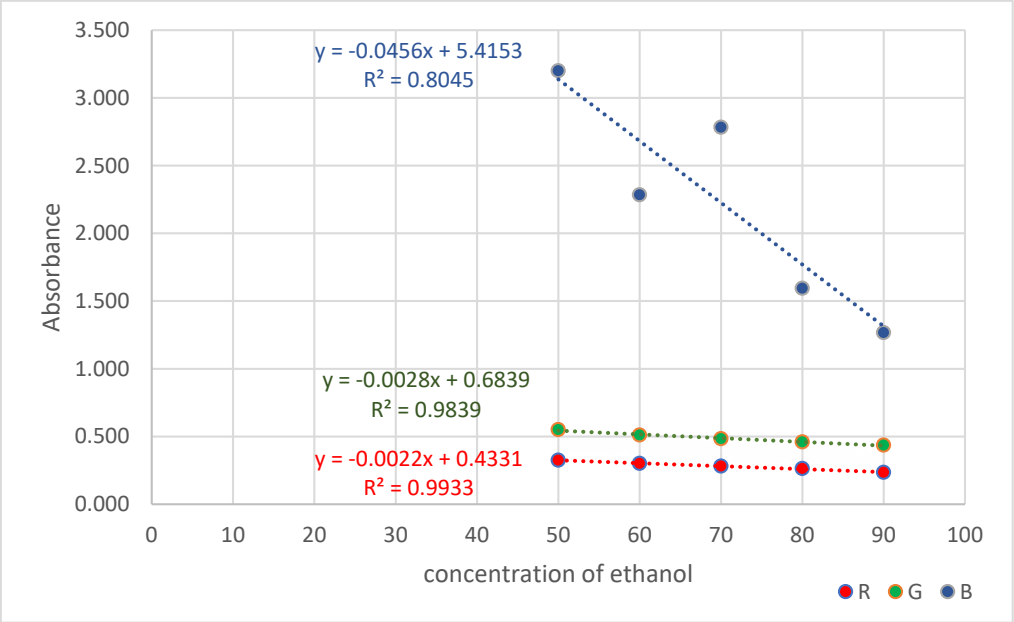

Figure 3. Graph plotted between absorbance and concentration of ethanol

4. Conclusion

The utilization of color intensity analysis to evaluate ethanol content was proven successful. By employing a 0.30 M concentration of potassium dichromate ($K_2Cr_2O_7$) solution for reacting with the ethanol solution, followed by a 300-second incubation period and subsequent imaging using a mobile phone camera, a linear correlation between the color intensity value represented by R and ethanol concentration was established, exhibiting an R^2 value of 0.9933. The determination of ethanol concentration in the five alcohol spray product samples validated that the outcomes obtained through color intensity analysis from mobile phone photographs concurred with those derived from UV-visible analysis and NMR techniques.

The effectiveness of the developed method was assessed through the analysis of ethanol content in the alcohol spray product samples. This was achieved by employing a technique that assessed the color intensity in mobile phone images, enabling easy quantitative analysis using a smartphone. This methodology diverges from conventional spectroscopy methods and can be implemented in high school classrooms. Students will be instructed on qualitative and analytical analysis, standard curve creation, concentration calculations, and utilization of the standard curve for sample quantification.

Moreover, this experiment fosters practical and analytical skills in quantitatively assessing ethanol levels in the disinfectant spray, thereby enriching students' learning journey. Tailored for high school chemistry laboratories with restricted equipment, it encourages students to delve into digital imaging technology for fundamental chemistry analysis. The focus is on portability, cost-effectiveness, and rapid analysis, providing a holistic learning encounter.

However, utilizing cell phone camera photos for color intensity measurement when analyzing ethanol content has its limitations. Variables such as lighting conditions can distort colors, while differences in camera resolutions can impact image clarity, potentially resulting in inaccuracies. Therefore, the selection of a high-resolution camera is vital to guarantee precise color analysis. It is recommended to capture photos within a studio box with appropriate lighting settings to preserve color accuracy. Students are encouraged to use smartphones equipped with high-resolution cameras to improve accuracy in their photography experiments.

Acknowledgments

The authors are highly thankful to the Department of Chemistry, Faculty of Science, Burapa University for supporting this project.

References

1. Ministry of Public Health., *Announcement of the Ministry of Public Health on specifying the characteristics of cosmetics containing alcohol for hand hygiene that are prohibited from production, import, or sale, 2020.* Royal Gazette 2020, 137.

2. Sirismuth., T., *Toxicology of ethyl alcohol and isopropyl alcohol*. Thai Journal of Hospital Pharmacy 2021, 31 (1), 14-23.
3. Wiwan, M., *Testing the accuracy of methods for analyzing alcohol content in products containing alcohol as a component for hand hygiene using gas chromatography*. The Bulletin of the Department of Medical Sciences 2020, 62 (3), 268-280.
4. Isaac-Lam, M. F., *Determination of Alcohol Content in Alcoholic Beverages Using 45 MHz Benchtop NMR Spectrometer*. International Journal of Spectroscopy 2016, 2016, 1-8.
5. Nunnapat Thitisaksakul, S. P., Issaree Parasindecha, Poowanarth Muenhong,; Rapee Jarungsirawat, S. D., Thanee Tessiri, *Analysis of Alcohol Content in Alcohol-based Hand Sanitizer Product from Khon Kaen Province*. Isan Journal of Phaemaceutical Sciences 2021, 17 (3), 59-73.
6. Yadav, P.; Laddha, H.; Agarwal, M.; Gupta, R., *Fun with Smartphones: Handy Solution for Quantification of Debilitating Fluoride Ions in Drinking Water*. Journal of Chemical Education 2022, 99 (7), 2677-2683.
7. Fletcher, P. J.; van Staden, J. F., *Determination of ethanol in distilled liquors using sequential injection analysis with spectrophotometric detection*. Analytica Chimica Acta 2003, 499 (1-2), 123-128.
8. Kotchabhakdi, N., *Using a Smart Phone Camera as a Color Detector for Ethanol Estimation based on Time Analysis in Mixed Alcoholic Drinks*. Science and Thecnology Nakhonsawan Rajabhat University Journal 2019, 11 (14), 77-86.
9. Moonrungsee, N.; Pencharee, S.; Jakmunee, J., *Colorimetric analyzer based on mobile phone camera for determination of available phosphorus in soil*. Talanta 2015, 136, 204-9.
10. Anh-Dao, L.-T.; Thanh-Nho, N.; Huu-Trung, B.; Tien-Giang, N.; Ut Dong, T.; Quoc-Duy, N.; Quang-Hieu, N.; Le-Vy, N.; Thanh-Dieu, N.-T.; To, D. V. T.; Minh-Huy, D.; Cong-Hau, N., *A portable colorimetric tool using a smartphone camera applied for determining total phenolic contents in coffee products*. Chinese Journal of Analytical Chemistry 2023, 51 (3).
11. Destino, J. F.; Cunningham, K., *At-Home Colorimetric and Absorbance-Based Analyses: An Opportunity for Inquiry-Based, Laboratory-Style Learning*. Journal of Chemical Education 2020, 97 (9), 2960-2966.
12. Doughan, S.; Shahmuradyan, A., *At-Home Real-Life Sample Preparation and Colorimetric-Based Analysis: A Practical Experience outside the Laboratory*. Journal of Chemical Education 2021, 98 (3), 1031-1036.
13. Kehoe, E.; Penn, R. L., *Introducing Colorimetric Analysis with Camera Phones and Digital Cameras: An Activity for High School or General Chemistry*. Journal of Chemical Education 2013, 90 (9), 1191-1195.

A simple electrochemical experiment kit made from electrolyte gels

Suchittra Channgan and Akapong Suwattanamala*

Department of Chemistry, Faculty of Science, Burapha University, Chonburi 20131, Thailand

**E-mail: akapong@go.buu.ac.th*

Abstract:

In this work, we investigate the effect of adding hydrocolloid substances to $CuSO_4$ and $ZnSO_4$ electrolytes and the use of zinc and copper electrodes to create electrolyte gels and gel batteries for electroplating experiments. Comparison of the permanent electric potential values of galvanic cells in 3 types of hydrocolloids mixed with 1.0 M electrolytes. The result showed that the potential of the galvanic cells in the electrolytes carrageenan, agar-carrageenan, and gelatin were initially 1.076 V, 1.093 V, and 1.095 V, respectively. The effect of four concentrations mixed with carrageenan. The electrical potential of the cell initially is 1.092 V, 1.089 V, 1.081 V, and 1.079 V, respectively. In addition, a new prototype 6-cell gel battery made of 0.10 M $CuSO_4$ and $ZnSO_4$ mixed with carrageenan with an electric potential of 6.433 V was used as a current source by electroplating an iron nail with zinc. This resulted in a higher percentage yield compared to a normal 6-volt battery. This study suggests that gel batteries offer a stable and long-lasting electrical potential for a considerable duration, comparable to or slightly below the standard value. Gel batteries can be produced from diluted waste solutions from other experiments, ensuring safety and cost efficiency, which emphasizes the green aspect of this approach.

1. Introduction

The basics of electrochemistry in upper secondary school deal with the complicated relationship between electricity and chemical processes.[1] Students explore the properties of electrodes, electrolytes, electrical conductivity, redox reactions, and the movement of electrons. The curriculum covers chemical cells, electrolysis, and theoretical principles such as Nernst's equations and Faraday's laws.[2-6] They require the skillful use of equations, the interpretation of data, and the mastery of laboratory techniques. The basic experiment to study electrochemistry is to experiment with the electron transfer reaction between a metal (electrode) and an electrolyte solution to understand the importance of a redox reaction.[7] An experiment was then carried out to measure the electrical potential of the cell $Zn(s)|Zn^{2+}(aq,1.0\ M)||Cu^{2+}(aq,1.0\ M)|Cu(s)$
A highly concentrated solution with an electrolyte concentration of 1.0 mol/L was required and a saturated potassium nitrate solution (KNO_3) was used as a salt bridge. Compare the experimental results with the standard potential of the cell. This leads to the deposition of copper metal and the formation of zinc ions in the solution. These materials may need to be properly disposed of or recycled. Similar to experiments with electrolytic cells, especially with batteries for electroplating, waste containing heavy metal is often generated and poses a challenge for disposal.[8] Hydrogels are proving to be a promising solution to replace liquid electrolytes, which tend to leak and are hazardous. Hydrogel electrolytes made from gelatine, agar, and carrageenan offer a biocompatible, semi-solid alternative that is biodegradable, cost-effective, and environmentally friendly. Hydrogels, made from gelatin, agar, and carrageenan have been used for electrochemistry experiments, including electrolysis of water,[9] properties of electrolyte gels that can store water molecules the transparent and stable properties of these hydrogels eliminate the need to use a saturated solution as a salt bridge in an electrochemical cell.[10] The hydrogels provide a matrix through which solution can diffuse, allowing ions to move between the two half-cells, and their thermoreversible gel properties allow easy handling in electrochemical experiments.[11, 12]

This work focuses on testing the properties of using hydrocolloids, agar, carrageenan, and gelatin in electrolyte solutions to form electrolyte gels. To create a prototype gel battery to use as a power source in electroplating experiments. To understand voltage, current, and their relationship in the context of a galvanic cell and electrolyte cells. In the future, battery design can be used as an assessment tool to measure students' abilities in electrochemical principles and as a visualization tool to identify misconceptions in electrochemistry. The structure of these devices is to help students understand the concept of electrical energy resulting from chemical reactions.[4, 7]

2. Materials and Methods

2.1 Materials

$CuSO_4 \cdot 5H_2O$, $ZnSO_4 \cdot 7H_2O$, *K*-carrageenan, Agar, Unflavored gelatin powder, Sandpaper sheet, Zinc sheet 1.5 x 5 cm, Copper sheet 1.5 x 5 cm, Alligator clip connectors, Silicone block 3 x 3 x 3 cm, Metal Stud Crimper, 6-cell plastic container, Iron nail Digital Multimeter.

2.2 Types of electrolyte gels that affect the stability of galvanic cells electric potential.

Gel electrolytes Preparation

From gelatin

- Placing the unflavored gelatin powder 3 g in the beaker; add the hot 1.0 M $ZnSO_4$ solution 100 ml (about 50 °C) and stir until the powder completely dissolves.

From carrageenan

- Placing the *K*-carrageenan powder 1.5 g in the beaker; add the hot 1.0 M $ZnSO_4$ solution 100 ml (about 70 °C) and stir until the powder completely dissolves.

From Agar-carrageenan

- Placing the *K*-carrageenan powder 1.5 g and Agar 1.5 g in the beaker; add the hot 1.0 M $ZnSO_4$ solution 100 ml (about 80 °C) and stir until the powder completely dissolves.

The same procedure can be applied to prepare the 1.0 M $CuSO_4$ half cell. Pour the solution into the silicon block, and place it into the refrigerator until it gels (around 2 h).

Galvanic Cell Assay

Detach the gel blocks from the silicon block and place them on a plastic box. Attach an alligator clip connector to the copper sheet and another one to the zinc sheet using alligator clip connectors at one end. Introduce the copper sheet into the $CuSO_4$ gel electrolyte and the zinc sheet into the $ZnSO_4$ gel electrolyte. Put the two gel electrolytes in contact, and connect the free ends of the two wires to the multimeter in **Figure 1.** Measure the electrical potential difference every 10 minutes for 360 minutes at 25°C.

2.3 Effect of concentration on the stability of galvanic cell electric potential.

Prepare electrolyte gel as in Section 2.2. Use solutions of 0.10, 0.25, 0.50, 1.00 M. Measure the electric potential difference every 10 minutes for 360 minutes at 25°C.

2.4 Creating a battery from gel electrolyte

Prepare carrageenan electrolyte gel using 0.10 M concentrated solutions of $ZnSO_4$ and $CuSO_4$. Pour the solutions into 6 silicon blocks of each type. Utilize crimping pliers to join the copper and zinc sheets securely in **Figure 4 (A)**. Arrange the electrolyte gel in pairs, forming a total of 6 channels. Insert the metal into the electrolyte gel and establish a series circuit. Attach the black alligator clip terminal to one end of the zinc sheet, connecting the other end to the negative terminal of the multimeter. Connect the red alligator clip terminal to one end of the copper sheet and link the other end to the positive terminal of the multimeter and measure the electrical potential difference every 10 minutes for 360 minutes at 25°C.

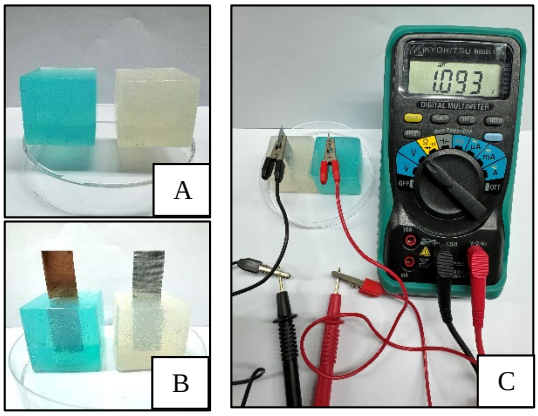

Figure 1. (A) Electrolyte gel of $CuSO_4$ (left) and $ZnSO_4$ (right). (B) Place the metal pieces into the electrolyte gel. (C) Connect the metal piece to the multimeter and measure the electrical potential difference.

2.5 Determine the performance of battery gel electroplating experiments.

Prepare battery gel according to Section 2.4. Scrub iron nails and zinc sheets with sandpaper. Wipe off metal scraps thoroughly and weigh before plating. Then dip it into 0.10 M $ZnSO_4$ solution to a depth of 3 cm. Connect the red wire of alligator pliers to the battery's copper sheet (anode), and the other end to the multimeter's positive terminal. Connect the black wire with alligator pliers to the battery's zinc sheet (cathode), and the other end to an iron nail. Connect the zinc sheet in the beaker to the negative terminal of the multimeter. Arrange the metal pieces so that they do not touch each other. Measure electric potential difference and electric current. After 5 minutes of plating, the iron nail and zinc were washed with distilled water, blotted dry with tissue paper and weighed after plating.

3. Results & Discussion

3.1 Results of testing of electrolyte gel properties in galvanic cells.

The investigation focused on evaluating the characteristics of the galvanic "gel" cell,

employing a combination of agar-carrageenan, carrageenan, and unflavored gelatin powder. These substances were mixed with 1.00 M $CuSO_4$ and $ZnSO_4$ solutions along with copper and zinc sheets. Each metal plate was embedded into its respective gels block, resembling the arrangement of a Daniel cell, allowing the measurement of potential difference using a multimeter. Electrical connectivity was established by positioning two gel blocks adjacent to each other, eliminating the necessity for a salt bridge. The absence of a salt bridge demonstrates the potential of the gel matrix to serve as an effective medium for ion transport, mitigating the need for traditional salt bridge arrangements. Redox reactions that occur in electrochemical cells are

$$Cu^{2+}(gel) + Zn(s) \leftrightarrow Cu(s) + Zn^{2+}(gel) \quad (1)$$

From Equation 1, the standard cell potential (E^0_{cell}) is equal to 1.100 V.[10] In this experiment, the initial electrical potential differences of the galvanic cells utilizing agar-carrageenan, carrageenan, and gelatin gel were determined to be 1.076 V, 1.093 V, and 1.095 V, respectively. After 6 hours, the electric potential difference decreased to 0.974 V, 0.989, and 0.954 V. in **Figure 2**.

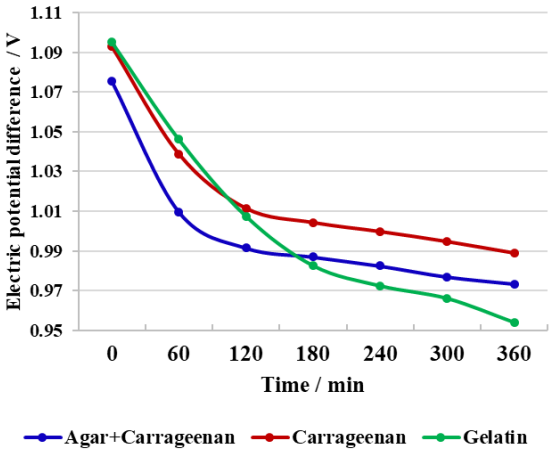

Figure 2. Representative electrical potential difference (V) curves vs time (minute) of the 3 electrolyte gels at concentration 1.00 M at 25°C

The observed electric potential difference in carrageenan closely resembled that of gelatin and exceeded that of agar-carrageenan. This is attributed to the superior formation of complexes with Zn^{2+} and Cu^{2+} in gelatin and carrageenan compared to gels with fewer functional groups, such as agar. The different complexes formed with metal ions have a notable impact on the movement of ions within the galvanic cell. It was also found that over time the electrolyte obtained from gelatin had a greater decrease in electrical potential than carrageenan. This is because the evaporation of water is greater when compared at the same temperature. In addition, the effect of the concentration of the electrolyte solution on the electric potential difference of the galvanic cell. Using electrolyte gel from carrageenan and $ZnSO_4$ and $CuSO_4$ solutions with concentrations of 1.00 M, 0.50 M, 0.25 M and 0.10 M. It was found that the electric potential difference at the beginning was 1.092 V, 1.089 V, 1.081 V and 1.079 V, respectively. After 6 hours, the electrical potential difference decreased by 0.987±0.030 V, 0.978 ± 0.030 V, 0.964±0.033 V, and 0.948± 0.035 V, respectively in **Figure 3.**

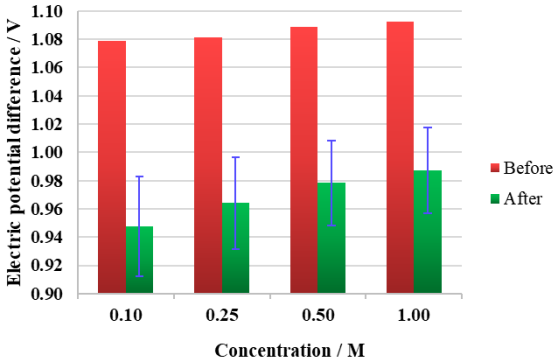

Figure 3. Electrical potential difference (V) values before and after 6 hours of 4 concentrations of electrolyte gel at 25 °C.

Therefore, the cell potential for a single cell can be calculated by applying the Nernst equation using concentrations and known half-cell reduction potential values at 25 °C.[10] Example calculation at a concentration of 0.10 M is as follows:

$$E_{cell} = E^0_{cell} - \frac{0.059}{n}\log Q \quad (2)$$

$$E_{cell} = E^0_{cell} - \frac{0.059}{2}\log\frac{[Zn^{2+}]}{[Cu^{2+}]} \quad (3)$$

$$E_{cell} = 1.100 - \frac{0.059}{2}\log\frac{[0.10]}{[0.10]} \quad (4)$$

If the concentration of reactants and products is the same (at equilibrium), Q/K becomes 1, and the natural logarithm term becomes zero. In this case, the Nernst equation simplifies to:

$$E_{cell} = E^0_{cell} = +1.100\ V \quad (5)$$

In equation 5. under equilibrium conditions (when the concentrations are the same and the reaction quotient is equal to the equilibrium constant), the cell potential is equal to the standard cell potential. Therefore, other concentrations have a value of E^0_{cell} 1.100 V as well.[4] the electric potential difference values for concentrations 1.00 M, 0.50 M, 0.25 M, and 0.10 M. seem comparable, with % relative errors of 0.697, 1.030, 1.727, and 1.909 respectively. This similarity is attributed to the water retention properties inherent in the carrageenan gel electrolyte. The outcomes of measuring the electric potential difference across various concentrations indicate that higher concentrations contribute to a prolonged duration of the electric potential difference. This is attributed to increased ions in the electrolyte gel at higher concentrations. From the results of the experiment, the researchers studied using a concentration of 0.10 M as the least concentration to create a prototype of a 6-volt gel battery, as shown in **Figure 4**.

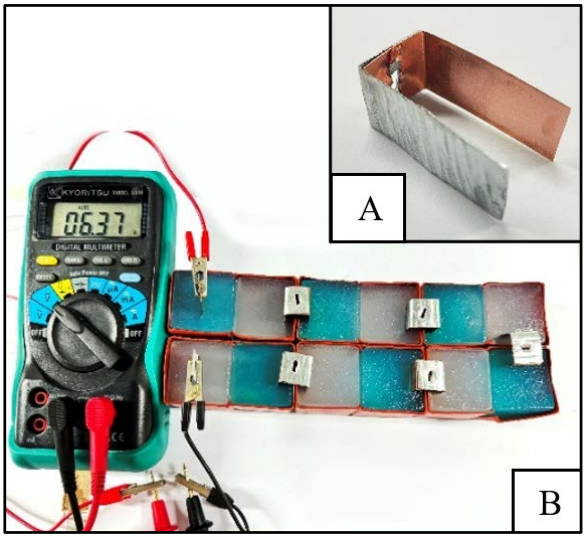

Figure 4. (A) Crimping pliers are designed for electrical connectivity between zinc and copper electrodes. (B) Representative for prototype 6-cell gel batteries circuited in series between Zn and Cu electrodes in a gel electrolyte and measured the electric potential difference using a multimeter.

The battery is constructed from galvanic cells made from carrageenan gel electrolyte. Connect the circuit in series with 6 cells. The initial electric potential difference is 6.433±0.055 V and continues to be measured every 10 minutes for 6 hours. The value decreases to 5.173±0.042 V in **Figure 5**. The durability of the electric potential difference aligns with the properties of the mentioned gel. The practical application of the battery will be tested in the following section obtained using a normal 6-vote battery in **Figure 6** (A).

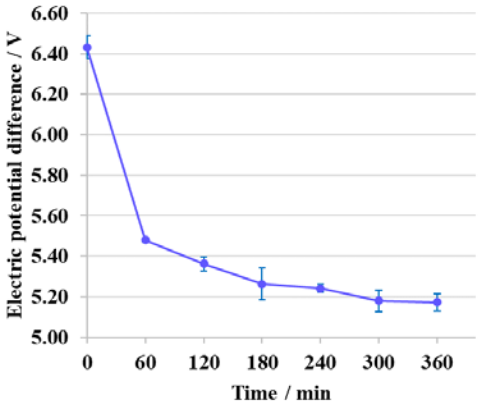

Figure 5. Representative electrical potential difference (V) vs time of a 6-cell gel battery after 6 hours of measurement at 25 °C.

3.2 Performance of battery gel electroplating experiments.

In this section, A comparative investigation into the efficiency of electroplating was conducted using two different power sources: a conventional a normal 6-volt battery and a 6-cell gel battery. The study focused on electroplating of an iron nail with zinc, subjected to the electroplating process for 5 minutes, as illustrated in Figure 6 (A-B). The reaction that occurs at the cathode (nail) causes zinc to adhere to the surface of the nail and corrosion of the zinc at the anode. As shown in Equations 6-7.

Anode : $Zn(s) \rightarrow Zn^{2+}(aq) + 2e^-$ (6)

Cathode: $Zn^{2+}(aq) + 2e^- \rightarrow Zn(s)$ (7)

In Table 1, it is the result of comparing the weight of iron nail before and after plating. By determining the theoretical weight of zinc deposited on the nail surface, it is possible to calculate the amount of metal (m) attached to the cathode. According to Faraday's law[4] in equation 8.

$$\frac{m}{A_r} = \frac{It}{nF} \quad (8)$$

Where $n = 2$, $F = 96{,}485$ C/mol, $A_r = 65.38$ g/mol, $t = 300$ s, and I (Current) in a normal 6-volt battery is 0.1527 A, and in a 6-cell gel battery is 0.027 A.

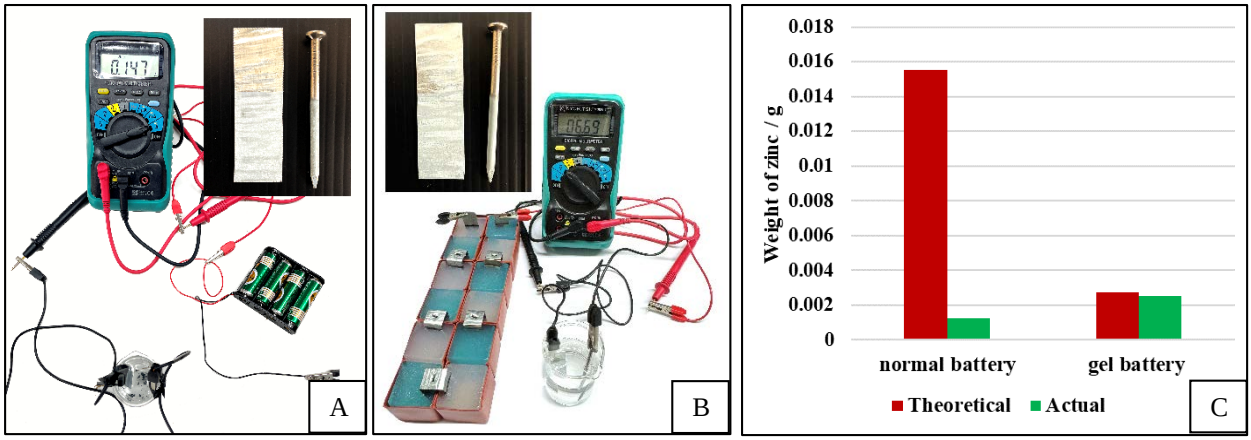

Figure 6. Compare the electroplating of an iron nail with zinc using a normal 6-volt battery in (A) and a 6-cell gel battery in (B)**.** (C) Shows the percentage yield of zinc weight that adheres to the iron nail surface after plating.

In the assessment of metal plating performance, iron nails of uniform size were employed. The estimated average surface area for plating was approximately 2.578 cm^2. Following a 5-minute plating duration, the results revealed that the experiment utilizing a normal 6-volt battery yielded a zinc weight of 0.0013 g. on the iron nail surface, while the 6-cell gel battery experiment resulted in 0.0025 g. The percentage yields are 8.2044 and 93.5965, respectively, as shown in the bar graph of Figure 6 (C). This variation can be attributed to the higher current influencing the current density ($J = \frac{I}{A}$) with values of 0.059 A/cm^2 and 0.010 A/cm^2, respectively. A higher current density accelerates the deposition rate, but practical limitations may arise, including issues such as poor adhesion and plating quality, particularly when the accumulation rate is excessively high.[13-16]

Table 1. Values obtained from the experiment of plating iron nails with zinc.

Iron nails[a]	normal 6-volt Battery	6-cell gel Battery
Surface Area (cm^2)	2.578	2.578
Initial Weight (g)	2.5215	2.5221
Final Weight (g)	2.5228	2.5246
Weight Gain (g)	0.0013	0.0025

[a]The value shown is from the average (n = 3)

4. Conclusion

Gel batteries made with hydrogel electrolytes, such as carrageenan, gelatin, and agar, offer a biocompatible and environmentally friendly alternative to liquid electrolytes.[9] They possess thermoreversible gel properties and can be easily handled and manipulated by students during experiments. In this study, carrageenan was the best choice. Although gelatin has a high electric potential and is close to theory, it melts easily at high temperatures[11] and is not suitable for making batteries. Agar will have a decrease in hardness as the concentration of the solution increases. Therefore, it must be mixed with other hydrocolloids, resulting in a higher cost. Gel batteries provide a stable and durable electric potential for a significant duration, making them suitable for conducting electroplating experiments that require a consistent power source.[11] The galvanic cell potential of gel batteries using hydrogel electrolytes is comparable to or slightly lower than the standard value, ensuring reliable results. Gel batteries can be fabricated using low-concentration electrolyte solutions, such as 0.10 M $CuSO_4$ and $ZnSO_4$, which are safer and more cost-effective for high school laboratories. These gel batteries have shown higher efficiency in electroplating experiments compared to normal 6-volt batteries, resulting in a higher percentage yield. By using gel batteries, high schools can promote the use of eco-friendly energy sources and teach students about waste reduction, reuse, and recycling, as gel batteries can be made from metal-contaminated waste diluted and turned into electrolyte gels. In the future, the authors aim to use the solution to be discarded after the students have experimented with galvanic cells under standard conditions (1 M) and dilute it to a lower concentration. Change to electrolyte gel for use in learning other topics, such as electroplating in gel electrolyte. Electrolysis of water in the hydrogel, metal purification, and battery design to understand the working principle and apply it in the laboratory.

Acknowledgements

The study was supported by the Graduate School and partially funded by a research grant from the Department of Chemistry, Faculty of Science, at Burapha University.

References

1. Intaraprasit, M.; Tawornparcha, P.; Veerapong, P.; Limpanuparb, T., Intuitive Small-Scale Electrochemistry on 24-Well Plate and 3D-Printed Cover Yielding Accurate Results. *Journal of Chemical Education* **2023,** *100* (8), 3144-3150.
2. Toma, H. E., Microscale Educational Kits for Learning Chemistry at Home. *Journal of Chemical Education* **2021,** *98* (12), 3841-3851.
3. Tan, S. Y.; Hölttä-Otto, K.; Anariba, F., Development and Implementation of Design-Based Learning Opportunities for Students To Apply Electrochemical Principles in a Designette. *Journal of Chemical Education* **2019,** *96* (2), 256-266.
4. Tan, S. Y.; Chia, V. Y. Y.; Hölttä-Otto, K.; Anariba, F., Teaching the Nernst Equation and Faradaic Current through the Use of a Designette: An Opportunity to Strengthen Key Electrochemical Concepts and Clarify Misconceptions. *Journal of Chemical Education* **2020,** *97* (8), 2238-2243.
5. O'Donoghue, J.; Domenech, N. G.; McArdle, F.; Connolly, M.; Lang, Y.; McGoldrick, N., Current Chemistry Investigators (CCI): Development and Evaluation of a Scientist in a Classroom Electrochemistry Workshop. *J Chem Educ* **2023,** *100* (10), 4138-4146.
6. Khalafi, L.; Nikzad, N.; Alhajeri, A.; Bacon, B.; Alvarado, K.; Rafiee, M., Electro-chemistry under Microscope: Observing the Diffusion Layer and Measuring Diffusion Coefficient. *Journal of Chemical Education* **2023,** *100* (10), 4056-4061.
7. Karpudewan, M.; Daman Huri, N. H., Interdisciplinary Electrochemistry STEM-Lab Activities Replacing the Single Disciplinary Electrochemistry Curriculum for Secondary Schools. *Journal of Chemical Education* **2022,** *100* (2), 998-1010.
8. Peng, X.; Xu, B.; Zeng, Y.; Xie, S.; Zhang, Z., Waste Iron Oxidation Reaction-Assisted Electrochemical Flocculation for Rhodamine B Extraction from Wastewater: A Hands-On Experiment for Undergraduates. *Journal of Chemical Education* **2023**.
9. Fogde, A.; Kurten, B.; Sandberg, T.; Huynh, T. P., Colorimetric Hydrogel from Natural Indicators: A Tool for Electrochemistry Education. *J Chem Educ* **2020,** *97* (10), 3702-3706.
10. Sosa, G. L.; Deluchi, G. E.; Ramírez, S. A.; Hamer, M., Jelly Potentiometry, Do It Yourself. *Journal of Chemical Education* **2023**.
11. Saha, D.; Bhattacharya, S., Hydrocolloids as thickening and gelling agents in food: a critical review. *J Food Sci Technol* **2010,** *47* (6), 587-97.
12. Robal, M.; Brenner, T.; Matsukawa, S.; Ogawa, H.; Truus, K.; Rudolph, B.; Tuvikene, R., Monocationic salts of carrageenans: Preparation and physico-chemical properties. *Food Hydrocolloids* **2017,** *63*, 656-667.
13. contributors, N. W. E. Electroplating. https://www.newworldencyclopedia.org/p/index.php?title=Electroplating&oldid=1062094 (accessed 29 December).
14. Kishi, Y.; Suzuki, T., Enhanced "Copper to Silver to Gold: The Alchemist's Dream" Demonstration Using Aluminum Foil and an Anionic Surfactant. *Journal of Chemical Education* **2022,** *99* (9), 3332-3336.
15. Liu, K.; Huang, S.; Jin, Y.; Lam, J. C.-H., Teaching Electrometallurgical Recycling of Metals from Waste Printed Circuit Boards via Slurry Electrolysis Using Benign Chemicals. *Journal of Chemical Education* **2022,** *100* (2), 782-790.
16. Moloney, J. G.; Campbell, C. D.; Worrall, A. F.; Stewart, M. I., Hands-on Inquiry-Based Qualitative Identification of Metals in Coins Utilizing Atmospheric Pressure Chemical Ionization Mass Spectrometry. *Journal of Chemical Education* **2022,** *99* (7), 2697-2703.

Minimize residual formaldehyde content in melamine-formaldehyde PCM microcapsules

Nichakorn Wangkajai, Apinan Soottitantawat, and Rungthiwa Methaapanon*

Center of Excellence in Material Processing and Particle Technology (CEPT), Department of Chemical Engineering, Faculty of Engineering, Chulalongkorn University, Bangkok, 10330, Thailand

**E-mail: Rungthiwa.M@chula.ac.th*

Abstract:

Phase change materials (PCM) can be used as latent heat thermal storage (LHTS) systems. Due to the phase transition, encapsulation of PCMs is normally required to avoid leakage of liquid PCM to the surroundings. The material commonly used for microencapsulation shells is melamine formaldehyde (MF) due to its good thermal and mechanical stability, and chemical resistance. However, formaldehyde, one of MF's raw materials, is a dangerous chemical compound that is hostile to human health. Therefore, the residual formaldehyde that might remain in the microencapsulated PCMs (microPCMs) should be minimized and removed. In this work, microPCMs were synthesized by in-situ polymerization using MF resin as a shell and *n*-Hexadecane as a PCM core. The MF prepolymer was prepared by varying the molar ratio of melamine (M) to formaldehyde (F). Residual formaldehyde content, which exists in a ppm concentration range, and properties of microPCMs were analyzed. Free formaldehyde in microPCMs is extracted with water and then derivatized by a 2,4-dinitrophenylhydrazine (DNPH) agent before being analyzed by high-performance liquid chromatography (HPLC). The MF shell from the M-F molar ratio of 1:3 appeared spherical in shape with slightly rough surfaces and showed the least residual formaldehyde content in microPCMs. The encapsulation efficiency and latent heat seemed unaffected by varying M-F molar ratios.

1. Introduction

Phase change materials (PCMs), e.g., fatty acid, *n*-alkane, and salt hydrates, in general, have a high heat of fusion and can absorb, store, and release a large amount of thermal energy during melting or solidifying process.[1] Due to their distinctive thermal properties, PCMs serve as well-suited candidates for energy storage applications. PCMs are widely applied in industries like textiles, and construction, including ceilings,[2] walls,[3] roofs,[4] and even house paint, etc.

In building applications, PCMs are typically designed to undergo a phase transition through a liquid phase. The direct use of these materials may result in leakage problems during the transition from solid to liquid, as well as problems with heat conduction and long-term deterioration. Therefore, encapsulation is required to reduce the problem of PCM leakage and avoid the reaction of the PCMs with the surrounding environment.[5]

The microencapsulated PCMs (microPCMs) involve the packing of PCM materials in capsules. The material used to encapsulate should not react with PCMs or deteriorate over time[4]. MicroPCMs therefore comprise 2 main parts: PCMs as a core and polymer or inorganic as a shell.[6]

In general, organic PCMs are widely favored for building applications due to their safety, non-corrosive, non-toxic, no phase segregation, and more importantly high latent heat, appropriate phase-transition temperature, and chemical stability.[4] As one of the typical organic PCMs, *n*-Hexadecane is an interesting organic PCM, featuring a high latent heat (236 kJ/kg) and a phase transition temperature of around 18-19°C.[7] This aligns with the suitable working temperature ranges of building applications is 19-26°C[8]. In addition, melamine formaldehyde (MF) is chosen as a shell material due to its versatile chemical crosslinking agent which offers low leakage, good chemical and thermal stability, mechanical strength, and resistance to acid-alkaline conditions. These qualities contribute to the popularity of MF in shell material applications.[9, 10]

However, formaldehyde, one of MF's raw materials, is a dangerous chemical compound, that adversely affects human health. After forming the shell through in-situ polymerization, residual formaldehyde that could cause environmental and health problems inevitably persists. Therefore, it is necessary to have a process to reduce formaldehyde content before use. Li, W., et al.[11] have successfully synthesized low remnant formaldehyde content in microPCMs using MF resin as a shell through the method of repeatedly adding melamine post encapsulation. The resulting free formaldehyde content in these microPCMs is 67.1 mg/kg. In addition, adding formaldehyde scavengers such as ammonia,[12] and ammonium chloride[9] during the microencapsulation process can reduce the free formaldehyde in microPCMs as well. However, generally, there is still little

information available on the free formaldehyde reduction for microPCMs.

In this study, microPCMs were synthesized by in-situ polymerization using MF resin as a shell and *n*-Hexadecane as a PCM core. The MF prepolymer was prepared by varying the molar ratio of melamine (M) to formaldehyde (F) The residual formaldehyde content and properties of microPCMs were analyzed.

2. Materials and Methods

2.1 Materials

Melamine (99 wt%, Sigma Aldrich) and formaldehyde (37% in methanol, Loba Chemie) were used as monomers; *n*-hexadecane (Verasuwan Co.,Ltd) was used as core material. SDBS (Sodium Dodecylbenzene Sulfonate, Sigma Aldrich) was employed as an emulsifier. Triethanolamine (Carlo Erba), citric acid, and sodium hydroxide, purchased from Loba Chemie were used for pH adjustments. DI water and toluene were used to extract formaldehyde from microPCMs.

2.2 Preparation of microcapsules

Oil in water emulsion preparation: 10 g *n*-hexadecane, 1 g SDBS, and 80 ml distilled water were added to a beaker. Then, the emulsion was continuously stirred at a rate of 8000 rpm for 3 min at 70°C. The emulsion was adjusted to pH 3.6 using a citric acid solution.

Prepolymer solution synthesis: 3 g melamine, 5.3 ml formaldehyde solution, and 50 ml distilled water were added into a flask. The pH of the mixture was adjusted to 8.5 with 10wt% triethanolamine solution. Then, the mixture was stirred at 600 rpm for 20 min at 70°C. The processes were repeated with the melamine content adjusted to 3.6 g, 3.8 g, and 4 g, respectively.

Microcapsules fabrication: the prepolymer solution was dropped into the emulsion at a rate of 0.6 ml/min and the solution was stirred at a rate of 2500 rpm at 70°C. After complete dropping, the emulsion was continuously stirred for an additional 2 h. The pH of the mixture was adjusted to 8.5 using 10wt% sodium hydroxide solution, which also terminated the reaction. The microcapsules were filtered and washed with hexane. The white powders were dried in an oven at 60°C until they were completely dry.

2.3 Standard derivatization and calibration

DNPH derivatization has been used for its effectiveness in the interaction with formaldehyde and produces a stable compound. The derivatization was prepared by 2 g of the DNPH derivatization agent was dissolved in 500 ml of acetonitrile and the pH of the mixture was adjusted by 10% phosphoric acid to the range of 5-6. This solution was used for the derivatization of formaldehyde standards and samples of interest.

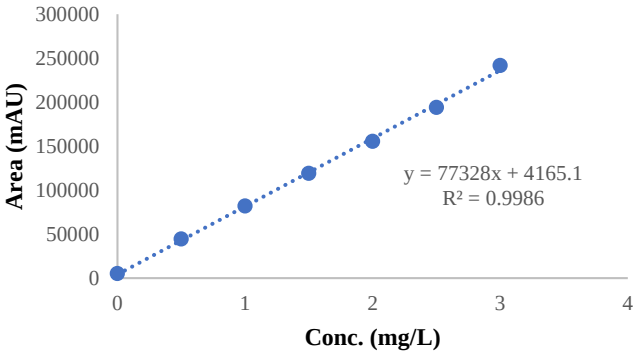

Figure 2. Calibration curve of formaldehyde concentration

Calibration was performed at 0, 0.5, 1, 1.5, 2, 2.5, and 3 mg formaldehyde/L in 50:50 v/v acetonitrile/water. 1 ml of DNPH solution was added to 5 ml of the standard formaldehyde solution. The mixture reacted at 60°C for 30 min. After filtering the mixture with a syringe filter (pore size = 0.45 µm). The limit of detection (LOD) was 0.144 mg/L.

The formaldehyde content was then measured using high-performance liquid chromatography (Shimadzu LC-20 HPLC) equipped with diode array detector with a Shim-pack GIST C18 column (5 µm, 4.0x250). The wavelength was set to 355 nm and the oven temperature at 40°C. The HPLC pump flow rate was at 0.8 ml/min and the injection volume was 25 µL. Acetonitrile/water (50:50, v/v) was used as a mobile phase. The total run time was 20 min.

2.4 Measurement of free formaldehyde content in the dried microcapsules

150 mg of dried microcapsules were immersed in 100 ml of distilled water and stirred at a rate of 600 rpm for 3 h at room temperature. An extracted solution was obtained. 1 ml DNPH solution was added to 5 ml of the extracted solution. The mixture reacted at 60°C for 30 min. After filtering the mixture with a syringe filter (pore size = 0.45 µm), the mixture was ready for injection into high-performance liquid chromatography (HPLC).

2.5 Measurement of free formaldehyde content in slurry

As the limit of detection (LOD) is 0.144 mg/L, the slurry should be diluted to achieve a measurable concentration, and this is accomplished by diluting the slurry to 20 mg/L. A 25 µL slurry of each condition (1:3, 1.2:3, 1.4:3 and 1.6:3) was prepared in a 50:50 v/v acetonitrile/water. Subsequently, 1 ml of DNPH solution was added to 5 ml of the solution. The mixture reacted at 60°C for 30 min. After filtering the mixture with a syringe filter (pore size = 0.45 µm), the mixture was ready for injection into HPLC.

2.6 Characterization of the microcapsules

The thermal properties of microcapsule and *n*-hexadecane were investigated using differential scanning calorimeter (DSC, DSC3+ module Mettle Toledo) in the range of 0-60°C at a heating or cooling rate of 4°C/min under a nitrogen atmosphere.

The microcapsules' morphologies were analyzed using a scanning electron microscope (SEM, JEOL JSM-IT500HR). Samples of microcapsule were coated with a thin coating of carbon, gold and platinum by high vacuum evaporation.

3. Results & Discussion

3.1 Thermal properties of microcapsules

The latent heat of the microPCMs were determined by the DSC. The thermal properties of *n*-hexadecane and microPCMs are listed in Table 1. The latent heat of the microPCMs remained unaffected by the increase in the amount of melamine during the synthesis, as the obtained latent heat values were similar across all cases. This observation indicates that the reaction was complete or similar in all cases. Therefore, irrespective of the quantity of melamine added, the latent heat of microPCMs remained consistent. Meanwhile, microcapsules cleaned with hexane show lower latent heat than those not subjected to hexane cleaning, indicating a possible removal of surface oil from the microcapsules during the cleaning process.

3.2 Morphology of microcapsules

The SEM images of the prepared microPCMs are shown in Figure 1. MicroPCMs with a M-F ratio of 1:3 (a,2a) exhibits a spherical shape with slightly rough surfaces. Exceeding this molar ratio, however, led to the breakage of microcapsules. All the microPCMs showed agglomeration.

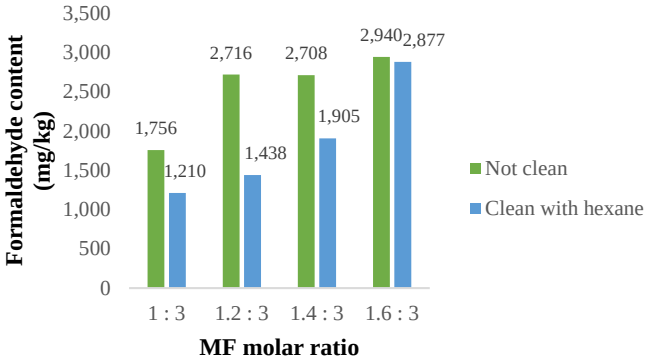

Figure 3. Correlation between Melamine-Formaldehyde ratio and residual formaldehyde content of the microcapsules

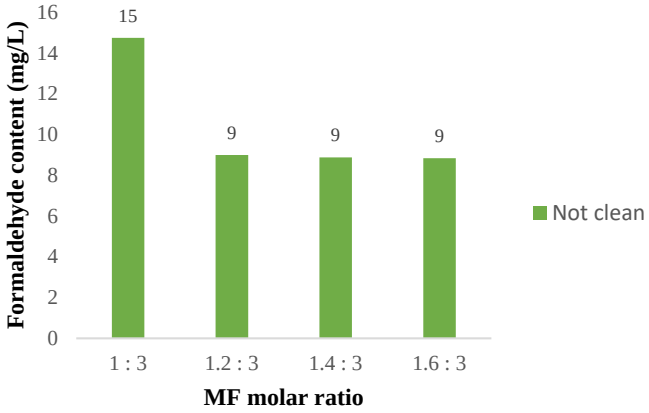

Figure 4. Correlation between Melamine-Formaldehyde ratio and residual formaldehyde content of the slurry

3.3 Free formaldehyde content of microcapsules

The formaldehyde calibration curve and equation can be derived from the data presented in Figure 2. The residual formaldehyde content of the microcapsules and slurry is presented in Figure 3 and Figure 4, respectively.

The microPCMs fabricated with a melamine-to-formaldehyde molar ratio of 1:3 show the lowest residual formaldehyde content across all cases. This is possibly caused by attributed to the formation of microcapsules, as illustrated in Figure 1. The microPCMs with a M-F ratio 1:3 exhibited a relatively complete shape compared to other ratios, where incomplete capsules with cracked shells might contribute to variations in the amount of free formaldehyde in the microPCMs. As shown in the Figure 3, the microPCMs with surface oil (not cleaned with hexane) exhibited a residual formaldehyde content of 1,756 mg/kg, while those without surface oil (cleaned with hexane) showed a 1,210 mg/kg residual formaldehyde. In compared to previous

work,[9,11,12] these values are still quite high. This may be influenced by the lack of formaldehyde scavengers as in previous studies. The use of formaldehyde scavengers may result in a lower free formaldehyde in the microcapsules. Generally, microPCMs cleaned with hexane displayed lower residual formaldehyde content compared to those not cleaned, regardless of the MF molar ratio. On the other hand, the slurry with M-F molar ratio of 1:3 has the highest residual formaldehyde compared to the other ratios. This is attributed to the fact that melamine and formaldehyde typically react in a 1:3 ratio. Therefore, increasing the amount of melamine beyond the 1:3 ratio results in a reduce of the remaining formaldehyde in the slurry.

Table 1. Thermal properties of the microPCMs

	M-F molar ratio								*n*-hexadecane
	1:3		1.2:3		1.4:3		1.6:3		
	With surface oil	Without surface oil	With surface oil	Without surface oil	With surface oil	Without surface oil	With surface oil	Without surface oil	
$\Delta H_{m,microPCMs}$ (J/g)	163	157	160	153	167	151	163	161	226
Encapsulation (%)	72	70	71	68	74	67	72	71	-

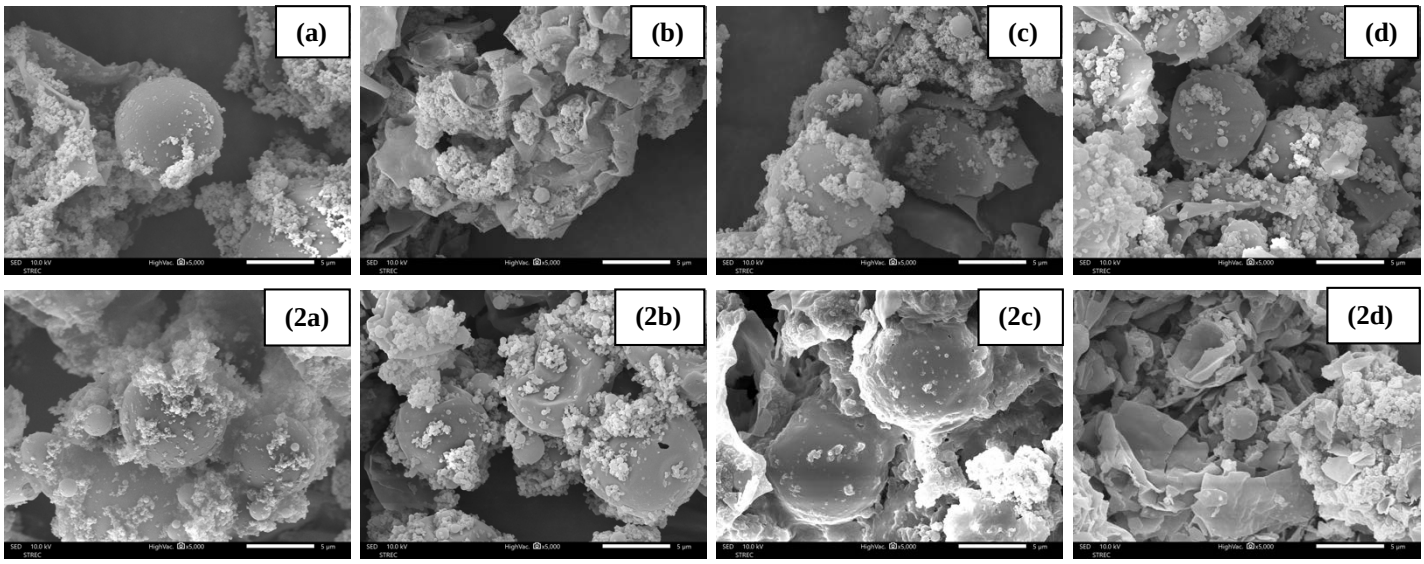

Figure 1. SEM micrographs of microPCMs: (a) 1:3 not cleaned with hexane, (2a) 1:3 cleaned with hexane, (b) 1.2:3 not cleaned with hexane, (2b) 1.2:3 cleaned with hexane, (c) 1.4:3 not cleaned with hexane, (2c) 1.4:3 cleaned with hexane, (d) 1.6:3 not cleaned with hexane, and (2d) 1.6:3 cleaned with hexane

4. Conclusion

MicroPCMs were synthesized by in-situ polymerization using melamine formaldehyde as shell and n-hexadecane as core and the employed melamine-formaldehyde prepolymer was prepared by varying the molar ratio of melamine to formaldehyde. As the amount of melamine increased, the reaction in each case showed no significant variation, as evidenced by the similarity in latent heat. Morphological analysis revealed that increasing melamine led to the broken of microPCMs. Microcapsules with a M-F ratio 1:3 exhibited the most favorable shape. Notably, microcapsules at this ratio exhibited the lowest free formaldehyde content, with the microPCMs with surface oil exhibited a residual formaldehyde content of 1,756 mg/kg, while those without surface oil showed a 1,210 mg/kg residual formaldehyde. However, this is still considered a relatively high amount, suggesting the need for further process development in the future.

Acknowledgements

This research was supported by the Center of Excellence in Material Processing and Particle Technology (CEPT), Faculty of Engineering, Chulalongkorn University.

References

1. Agyenim, F.; Hewitt, N.; Eames, P.; Smyth, M. A review of materials, heat transfer and phase change problem formulation for latent heat thermal energy storage systems (LHTESS). *Renewable and Sustainable Energy Reviews* **2010**, *14* (2), 615-628. DOI: 10.1016/j.rser.2009.10.015.
2. Abden, M. J.; Tao, Z.; Pan, Z.; George, L.; Wuhrer, R. Inclusion of methyl stearate/diatomite composite in gypsum board ceiling for building energy conservation. *Applied Energy* **2020**, *259*. DOI: 10.1016/j.apenergy.2019.114113.
3. Rashid, F. L.; Al-Obaidi, M. A.; Dulaimi, A.; Mahmood, D. M. N.; Sopian, K. A Review of Recent Improvements, Developments, and Effects of Using Phase-Change Materials in Buildings to Store Thermal Energy. *Designs* **2023**, *7* (4). DOI: 10.3390/designs7040090.
4. Kalnæs, S. E.; Jelle, B. P. Phase change materials and products for building applications: A state-of-the-art review and future research opportunities. *Energy and Buildings* **2015**, *94*, 150-176. DOI: 10.1016/j.enbuild.2015.02.023.
5. Jiang, X.; Luo, R.; Peng, F.; Fang, Y.; Akiyama, T.; Wang, S. Synthesis, characterization and thermal properties of paraffin microcapsules modified with nano-Al 2 O 3. *Applied Energy* **2015**, *137*, 731-737. DOI: 10.1016/j.apenergy.2014.09.028.
6. Peng, G.; Dou, G.; Hu, Y.; Sun, Y.; Chen, Z. Phase Change Material (PCM) Microcapsules for Thermal Energy Storage. *Advances in Polymer Technology* **2020**, *2020*, 1-20. DOI: 10.1155/2020/9490873.
7. Vélez, C.; Khayet, M.; Ortiz de Zárate, J. M. Temperature-dependent thermal properties of solid/liquid phase change even-numbered n-alkanes: n-Hexadecane, n-octadecane and n-eicosane. *Applied Energy* **2015**, *143*, 383-394. DOI: 10.1016/j.apenergy.2015.01.054.
8. Kahraman Döğüşcü, D.; Kızıl, Ç.; Biçer, A.; Sarı, A.; Alkan, C. Microencapsulated n - alkane eutectics in polystyrene for solar thermal applications. *Solar Energy* **2018**, *160*, 32-42. DOI: 10.1016/j.solener.2017.11.072.
9. Li, W.; Wang, J.; Wang, X.; Wu, S.; Zhang, X. Effects of ammonium chloride and heat treatment on residual formaldehyde contents of melamine-formaldehyde microcapsules. *Colloid and Polymer Science* **2007**, *285* (15), 1691-1697. DOI: 10.1007/s00396-007-1744-3.
10. Sui, C.; Preece, J. A.; Zhang, Z.; Yu, S.-H. Efficient encapsulation of water soluble inorganic and organic actives in melamine formaldehyde based microcapsules for control release into an aqueous environment. *Chemical Engineering Science* **2021**, *229*. DOI: 10.1016/j.ces.2020.116103.
11. Li, W.; Zhang, X.-X.; Wang, X.-C.; Niu, J.-J. Preparation and characterization of microencapsulated phase change material with low remnant formaldehyde content. *Materials Chemistry and Physics* **2007**, *106* (2-3), 437-442.DOI:10.1016/j.matchemphys.2007.06.030.
12. <Production of Melamine-Formaldehyde PCM Microcapsules with Ammonia.pdf>.

Conversion of fat and oil contaminant waste produced by stationary wastewater treatment plant into calcium soap for ruminant feed

Aung Thae Oo[1], Kitiyot Tungsudjawong[2], and Suchat Leungprasert[3]*

[1]*Master of Engineering Program in Sustainable Energy and Resources Engineering, Faculty of Engineering, Kasetsart University, 50 Ngam Wong Wan Rd, Ladyao Chatuchak, Bangkok 10900, Thailand*

[2]*Division of Environmental Science and Technology, Faculty of Science and Technology Phra Nakhon, Bangsue, Bangkok 10800, Thailand*

[3]*Department of Environmental Engineering, Faculty of Engineering, Kasetsart University, 50 Ngam Wong Wan Rd, Ladyao Chatuchak, Bangkok 10900, Thailand*

**E-mail: fengscl@ku.ac.th*

Abstract:

Urban wastewater containing fat, oil and grease often creates problems not only when collecting and transporting sewage to wastewater treatment plants (WWTPs) but also for their final management and treatment in WWTPs. Grease becomes a distinct waste when it undergoes a flotation process to separate it from the influent as an upper emulsion, defined as grease and oil mixture from oil/water separation (GOMOWS). This grease must be disposed of properly, or this can be a challenge, with the potential for environmental contamination. One efficient way to solve this problem is to transform this waste into a valuable product. In this research work, the utilization of this waste, GOMOWS, for the production of calcium soap was investigated. The reaction conditions relating to initial temperature, amount of calcium oxide and volume of water were optimized using response surface methodology (RSM) in order to achieve the maximum product yield within the acceptable acid value for commercialization purposes. Results showed that using 5g of brown grease, the optimized conditions were an initial temperature of 60°C, a stoichiometric mole ratio of CaO/g sample at 1.285, and water at 25%, resulting in a product yield of 6.63g with an acid value of 1 mgKOH/g sample.

1. Introduction

Fat, oil and grease contained in urban wastewater (UW-FOG) is an ever-growing environmental concern and it accounts for 25-35% of total chemical oxygen demand (COD) in raw wastewater flowing into municipal wastewater treatment plants (WWTPs).[1] The typical course of treating wastewater includes primary, secondary, and tertiary care. FOG removal is one of the principal treatments frequently carried out by gravity separators. Once separated, the upper layer (GOMOWS) contains FOG mixed with cellulosic waste and other light materials. This grease must be disposed of properly or this can be a challenge, and there is always the potential for environmental contamination.

An efficient valorization of GOMOWS turning it into valuable product would eliminate the cost to its disposal and additionally it would generate a net profit. GOMOWS consists of water, UW-FOG, and biosolids.[2] UW-FOG can be used as a source material for ruminant feed.[3] However, the presence of foreign materials, and high content of free fatty acid (FFA) causes the several concerns about the utilization of UW-FOG for animal supplement. Therefore, if grease waste is going to be used as animal feed, it need to be converted into protected fat.[4] Protected fat calcium soap also known as calcium salt of fatty acid can be produced through saponification and there are three common processes in the production of calcium soap: double decomposition, direct reaction and fusion process.[3] For the synthesis of calcium salts, the fusion process is typically chosen since it produces a purer and higher yield product with a faster reaction time.[3] During the fusion process saponification, the amount of calcium oxide, initial mixing temperature and volume of water significantly affects the physical and chemical properties.[5,6,7] Moreover, the optimum reaction condition for conversion of used cooking oil into calcium soap was reported by Mohamad Asrol (2023), which gave the acceptable level of free fatty acid and solidification score.[8] However, the optimum reaction conditions for achieving maximum product yield while maintaining an acceptable acid value still need to be identified. Optimizing the reaction conditions to achieve maximum product yield can attract the businessmen to invest in circular economy. Therefore, the objectives of the present work are to provide a new way for the utilization of GOMOWS and to optimize the fusion reaction conditions in order to get the maximum product yield while

maintaining acceptable acid value, employing response surface methodology.

2. Materials and Methods

2.1 Materials

Waste produced by oil/water separation (GOMOWS) were taken from Lotus Prachacheon wastewater treatment plant, Bangkok, Thailand. All chemicals, including calcium oxide, sodium hydroxide, ethyl alcohol, phenolphthalein, and distilled water, were of analytical grade.

2.2 Separation of UW-FOG from GOMOWS

Separation of fatty phase from GOMOWS was achieved by combining two distinct separation methods previously utilized by different researchers: Pastore (2014) and Kolet et al (2020).[2,9] GOMOWS were dewatered by keeping them into the separating funnel for 18 hours and then excess water was drained off.[2] After that, the decanted upper layer was preheated at 70°C and then centrifuged at 3200 rpm, 25°C for 5 minutes. The fraction of brown grease fatty phase obtained was 8.6% of the starting raw material. The percentage of free fatty acid in UW-FOG was measured using AOCS (1989), revealing an FFA content of 84.6%. The observation was ally with previous researches (Pastore, Lopez et al. 2014), > 82%, and (Kolet, Zerbib et al. 2020), 83-88%.

2.3 Production of calcium soap from brown grease (UW-FOG)

The possibility of production of calcium oxide from brown grease was examined by using fusion method reported by Pablos Perez (2008).[7] Brown grease was preheated until it reached the examined temperature. After that calcium oxide was added and then the mixture was vigorously stirred. When the mixture became homogeneity, water was added as the catalyst to initiate the saponification reaction.

2.4 Experimental design

Response surface methodology (RSM) with central composite design (CCD) was used to investigate the effect of independent variables, including initial mixing temperature (iTemp), the amount of calcium oxide (CaO) and volume of water on output variables, such as acid value and product yield. Twenty sets of experimental runs, including eight cube points, six axial points, and six replications of the central points were generated using Design Expert Software Version 6.0.4 (State Ease, Inc., Minnesota, United States). In the present work, the range of initial mixing temperature was between 60°C and 90°C. The lowest initial mixing temperature should be same with molten brown grease, which is 60°C.[6] The parameter of the amount of calcium oxide as the stoichiometry mole ratio of CaO/UW-FOG was set between 1 and 1.4. In the natural source of fat or oil to be saponified, at least the same number of moles of calcium oxide as fatty acid must be added and this amount should not be higher than the calcium requirement for dairy cattle (50.7 g/day).[7,10] The used water range was between 15 and 25% suggested by Handojo et al., (2017).[3]

A second order polynomial equation was used to indicate the predicted responses as a function of an independent variables as shown in **Eq. 1**:

$$Y=\beta_0+\sum_{i=1}^{k}\beta_i X_i+\sum_{i=1}^{k}\beta_{ii}X_{ii}^2+\sum_{i=1}^{k}\sum_{i^1j=1}^{k}\beta_{ij}X_i X_j+\varepsilon$$

(Eq. 1)

Where, Y= predicted response; $\beta_0,\beta_i,\beta_j,\beta_{ij}$ = regression constants corresponding to intercept, linear, quadratic, and interaction coefficients respectively; X_i,X_j = variables used as inputs, ε = random error.

The degree of freedom (DF), determination coefficient, adjusted determination coefficient, F-value, p-value, and other variables were all examined using the analysis of variance (ANOVA) to assess the statistical fitness of the CCD model and determine whether the second-order polynomial equation was adequate. In addition, the impact of combination factors on the product yield and acid value of calcium soap from brown grease was assessed using three-dimensional (3-D) graphical plots.

2.5 Acid value determination

The resulting calcium soap's acidity were assessed using the ((AOCS), 1989) standard procedure.[11] One gram of calcium soap was dissolved in 50ml of ethyl alcohol at 40 °C. The resulting mixture was titrated with 0.1 N potassium hydroxide using phenolphthalein as an indicator. The acid value in the product was calculated with the following equation.

$$\text{Acid value}=\frac{V\times N\times 56.1}{W}\ (\text{mgKOH/g})$$

Where, V= volume of Std. alkali, N= concentration of Std. alkali, W= mass of sample

2.6 Statistical analysis

Experimental data were statistically analyzed using Design Expert Software (Version 6.0.11). Statistical analysis with p-value less than 0.05 was considered statistically significant. All these experiments were performed in triplicate.

Table 1. Experimental design with a response of independent variables using response surface methodology (RSM)

Run	Space Type	A: CaO/UW-FOG stoichiometric ratio	B: Initial Temp	C: Water	Acid Value	Product Yield
			°C	%	mg KOH/ g sample	g
1	Factorial	1	60	15	2.8	6.24
2	Axial	0.86	75	20	2.57	6.06
3	Factorial	1	90	15	1.68	5.87
4	Factorial	1	90	25	0.74	6.24
5	Center	1.2	75	20	1.1	6.04
6	Center	1.2	75	20	1.08	6.37
7	Center	1.2	75	20	1.1	6.36
8	Factorial	1	60	25	2.43	6.5
9	Axial	1.2	49.77	20	2.12	6.45
10	Axial	1.2	75	28.41	0.6	6.8
11	Center	1.2	75	20	1.09	6.26
12	Axial	1.2	100.23	20	0.32	6.09
13	Factorial	1.4	90	25	0.08	6.78
14	Center	1.2	75	20	1.09	6.3
15	Axial	1.2	75	11.59	1.86	6.26
16	Center	1.2	75	20	1.3	6.25
17	Axial	1.54	75	20	0.05	6.92
18	Factorial	1.4	90	15	0.5	6.36
19	Factorial	1.4	60	15	1	6.9
20	Factorial	1.4	60	25	0.4	7.04

Table 2. Regression coefficients and the F-test value of the predicted second order polynomial models for acid value

Source	Sum of Squares	df	Mean Square	F-value	p-value	
Model	12.41	6	2.07	124.56	< 0.0001	significant
A-CaO/UW-FOG stoichiometric ratio	7.19	1	7.19	433.00	< 0.0001	
B-Initial Temp	3.25	1	3.25	195.48	< 0.0001	
C-Water	1.45	1	1.45	87.31	< 0.0001	
AB	0.4950	1	0.4950	29.82	0.0001	
AC	0.0105	1	0.0105	0.6332	0.0405	
BC	0.0190	1	0.0190	1.15	0.0304	
Residual	0.2158	13	0.0166			
Lack of Fit	0.1795	8	0.0224	3.09	0.1149	not significant
Pure Error	0.0363	5	0.0073			
Cor Total	12.62	19				

3. Results and Discussion

3.1 Fitting the model

Response Surface Methods (RSM) are designs and models for working with continuous treatments when finding the optima or describing the response is the goal.[12] The experimental results of product yield and acid value obtained from 20 different combinations of independent variables (initial mixing temperature, CaO, and water) are shown in Table 1.

Analysis of variance, regression, and coefficient of determination (R^2) for acid value and product yield were analyzed as shown in Table 2 and 3, respectively. According to statistical analysis (ANOVA) data, the experimental results of acid value and product yield may be well

Table 3. Regression coefficients and the F-test value of the predicted second order polynomial models for product yield

Source	Sum of Squares	df	Mean Square	F-value	p-value	
Model	1.89	6	0.3143	37.11	< 0.0001	significant
A-CaO/UW-FOG stoichiometric ratio	0.9896	1	0.9896	116.87	< 0.0001	
B-Initial Temp	0.3034	1	0.3034	35.82	< 0.0001	
C-Water	0.3224	1	0.3224	38.07	< 0.0001	
BC	0.0190	1	0.0190	2.25	0.0579	
A^2	0.1169	1	0.1169	13.81	0.0026	
C^2	0.1567	1	0.1567	18.51	0.0009	
Residual	0.1101	13	0.0085			
Lack of Fit	0.0380	8	0.0047	0.3288	0.9213	not significant
Pure Error	0.0721	5	0.0144			
Cor Total	2.00	19				

described by a 2FIvsQuadratic polynomial model, with a coefficient of determination (R^2) being 0.9829 and 0.9482 respectively. A closer value to unity for R^2 indicates a better fit between the model and the data.[13] Conversely, lower R^2 values suggest that the response variables were insufficient to account for the behavioral variation.[13] Therefore, the current study's closeness to unity R^2 indicates that the chosen model might provide an effective description of the effects of the initial mixing temperature, the volume of water, and the mole ratio of CaO on the response variables.

Moreover, p-values less than 0.05 indicate model terms are significant and values greater than 0.1 indicate the model terms are not significant. In this case, p-values for the selected model are less than 0.0001. For every variable, the lack of fit was not statistically significant ($p > 0.05$) in comparison to pure error, which indicates the statistical accuracy of our model. Therefore, the model was fit to be explored for optimization.

The predictive model equations for acid value and product yield are shown in Eq. 2 and 3 respectively. The fitness of equations can be assessed by checking the difference between adjusted R^2 and predicted R^2. In this case, the predicted R^2 is in reasonable agreement with the adjusted R^2; i.e. the difference is less than 0.2.

$$\text{Acid value} = 1.2 - 0.7255\,A - 0.4578\,B - 0.3258\,C + 0.2488\,AB + 0.0363\,AC - 0.0488\,BC \quad \text{(Eq. 2)}$$

$$\text{Product Yield} = 6.27 + 0.2692A - 0.149B + 0.1536C - 0.0213AB - 0.0088AC + 0.0488BC + 0.0896\,A^2 + 0.1038\,C^2 \quad \text{(Eq. 3)}$$

Where, A = CaO/UW-FOG stoichiometric ratio, B= initial temperature, C= water

3.2 Effect of independent variables on acid value

The suitability of calcium salt of fatty acid known as calcium soap to be used as a ruminant supplement can be assessed by acid value. Acid value can also be used to determine the amount of saponification process and it reflects the proportion of conversion reaction that has been taken place. The soap's lower acid value indicates that the reaction's conversion was higher. Higher value of acid value may disturb the fiber digestion in the rumen of ruminants.[14] RSM can help to investigate the effect of independent variables on the response by providing three-dimensional (3-D) images. According to ANOVA result, all independent variables have significant effect on acid value of calcium soap products.

The interaction between independent variables and acid value are shown in Figure 1(a-c). Figures 1a and 1b showed that mole ratio of CaO had significant effect on acid value of produced calcium oxide. Both figures pointed out that mole ratio of CaO was inversely proportion to acid vale: the more amount of CaO was added, the less value of acid value will be. Similar observation was reported by Handojo et al., (2019).[3] However, providing dairy cattle with too much calcium could interfere with their ability to absorb minerals.[10] Figure 1c provided the information that iTemp had the interaction effect with water but the prominent was less when they interacted with CaO. In the present work, the result showed that higher iTemp can give less value of acid value that we desired but it can lead to degradation of lipid.[15] Water was added as a catalyst to initiate the saponification reaction. According to the result, the amount of water can help to decrease acid value and this result was ally with Mohamad Asrol (2023).[8]

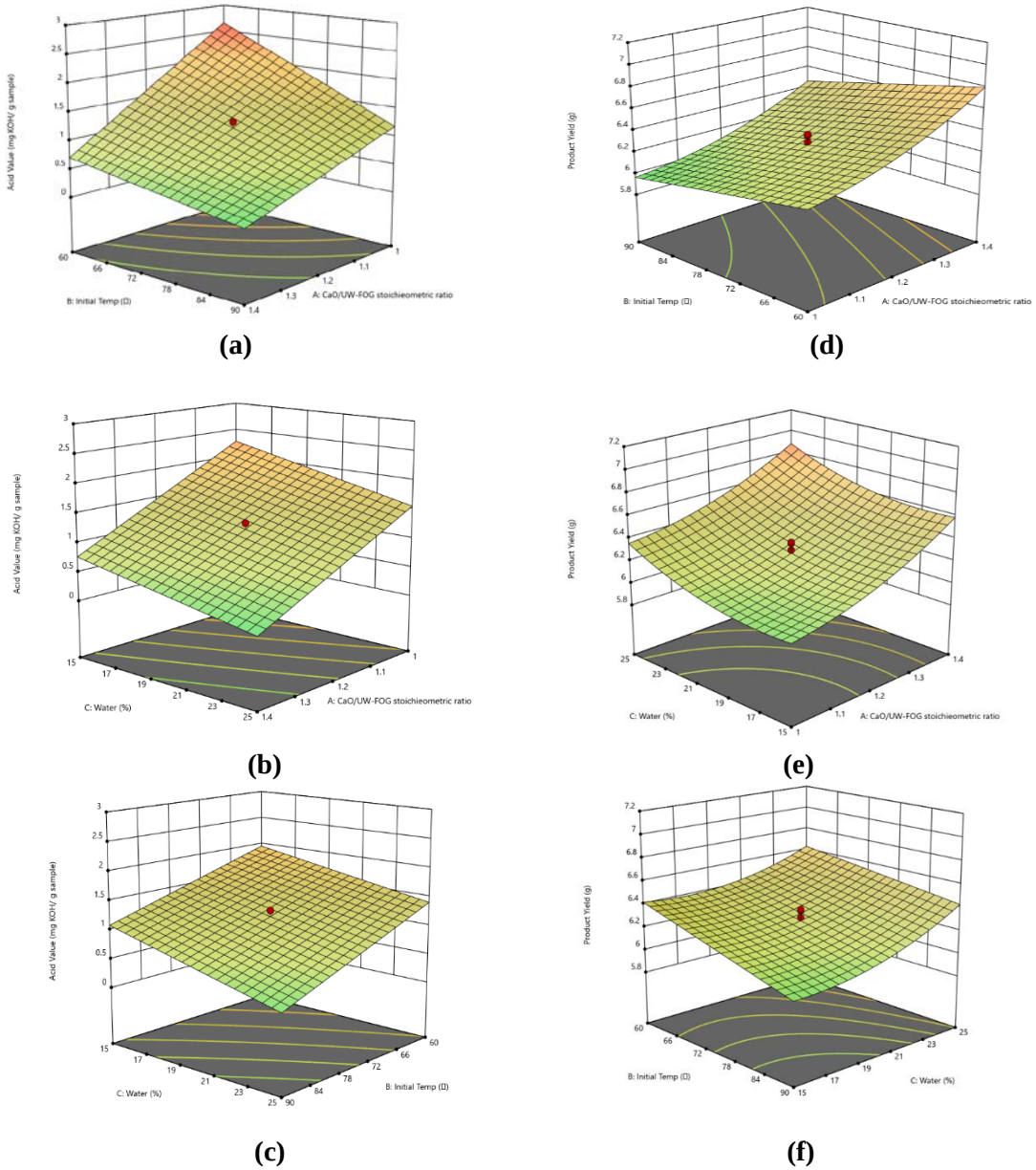

Figure 1. 3-D response surface plots for the interaction of studied variables on acid value (a - c), and product yield (d-f)

3.3 Effect of independent variables on product yield

In the present work, the reaction was optimized to achieve the maximum product yield and also the influence of independent variables on product yield was investigated. Figure 1(d-f) showed that the interaction between independent variables and product yield. According to the result, all independent variables had effect on the amount of product yield. The effect was more prominent when percentage of water interacted with CaO as compared to the other two when percentage of water interacted with iTemp and CaO interacted with iTemp. This is because mole ratio of CaO and percentage of water were directly proportional to product yield, whereas iTemp was inversely proportional to product yield. So, when CaO and water interacted with iTemp, one made to increase the product yield and the other made to decrease it again.

3.4 Optimization of independent variables

The advantage of RSM is that it can help to find out the best optimum point within the parameter that we set. RSM allows to set the important level of dependent responses to find out the best optimum point. In this study, achieving the low level of acid value was set as the first priority and achieving maximum product yield was set as the second. The best condition of the production of calcium soap from brown grease given by the system was CaO/UW-FOG stoichiometric mole ratio (1.285), iTemp (60°C) and water (25%). This

optimized condition can provide the acid vale (1 ± 0.15 mgKOH/g sample), and product yield (6.63 ± 0.05 g).

4. Conclusion

This study found the optimum reaction conditions–CaO mole ratio (1.285), iTemp (60°C) and water (25%)–to achieve the maximum product yield of calcium soap from brown grease while maintaining an acceptable acid value. Since the acid value of the calcium soap from brown grease at the optimum point was lower than permitted, it can be concluded that the produced calcium soap was safe for ruminant feed. However, vitro analysis should be carried out before commercialization.

Acknowledgements

The first author acknowledges the scholarship under the Thailand Advanced Institute of Science and Technology and Tokyo Institute of Technology (TAIST-Tokyo Tech) Program, awarded by Kasetsart University, funded by the National Research Council of Thailand (NRCT) and the National Science and Technology Development Agency (NSTDA).

References

1. Team, F. N. Removal of Fat, Oil and Grease https://www.fluencecorp.com/removal-of-fat-oil-and-grease-from-wastewater/.
2. Pastore, C.; Lopez, A.; Mascolo, G., Efficient conversion of brown grease produced by municipal wastewater treatment plant into biofuel using aluminium chloride hexahydrate under very mild conditions. *Bioresource Technology* **2014,** *155*, 91-97.
3. Handojo, L. A., Indarto, A., Pramudita, D., , Calcium soap from palm fatty acid distillate for ruminant feed: Reaction method. *International Journal of Engineering and Advanced Technology* **2019,** *8*, 422-425.
4. Suksombat, W., Improving the productivity of lactating dairy cows through supplementation. *Int Dairy Top* **2009,** *8* (1), 7-11.
5. Handojo, L. A.; Indarto, A.; Shofinita, D.; Meitha, A.; Nabila, R.; Triharyogi, H. In *Calcium soap from palm fatty acid distillate (PFAD) for ruminant feed: Quality of calcium source*, MATEC web of conferences, EDP Sciences: 2018; p 02007.
6. Handojo, L.; Indarto, A.; Shofinita, D.; Saadi, M.; Yulistia, D.; Hasyyati, F. In *Calcium Soap from Palm Fatty Acid Distillate for Ruminant Feed: The Influence of Initial Mixing Temperature*, IOP Conference Series: Materials Science and Engineering, IOP Publishing: **2019**; p 012017.
7. Perez, E. P., Method for producing calcium soaps for animal feed. Google Patents: 2009.
8. Mohamad Asrol, K.; Dek, P.; Suyub, I.; Sumita, S.; Jusoh, S., Production and optimisation of used cooking palm oil into protected fat calcium salts by fusion method using response surface methodology (RSM). *International Food Research Journal* **2023,** *30* (3).
9. Kolet, M.; Zerbib, D.; Nakonechny, F.; Nisnevitch, M., Production of biodiesel from brown grease. *Catalysts* **2020,** *10* (10), 1189.
10. NRC, Nutrient requirements of dairy cattle. Canada: NRC. **2001**.
11. (AOCS), A. O. C. S., Official methods and recommended practices of the American Oil Chemists' Society. 4th ed. United States: AOCS. **1989**.
12. Oexlert *Design and analysis of experiments: Response surface design*; New York: W.H. Freeman and Company: 2000.
13. Myers, R. H.; Montgomery, D. C.; Anderson-Cook, C., Process and product optimization using designed experiments. *Response surface methodology* **2002,** *2*, 328-335.
14. Jenkins, T. C.; Harvatine, K. J., Lipid feeding and milk fat depression. *Veterinary Clinics: Food Animal Practice* **2014,** *30* (3), 623-642.
15. Handojo, L. A.; Indarto, A.; Shofinita, D.; Meitha, A.; Nabila, R.; Triharyogi, H.; Kevin, L. In *Calcium soap from palm fatty acid distillate for ruminant feed: The influence of water temperature*, IOP Conference Series: Earth and Environmental Science, IOP Publishing: **2018**; p 012010.

Nanostructured $MoO_2/MoS_2/MoP$ heterojunction and N, S dual-doped reduced graphene oxide as high-performance electrode for supercapacitors

Kasira Kaewplod[1], Jeng-Yu Lin[2], Pimpa Limthongkul[3], and Panitat Hasin[1]*

[1]*Department of Chemistry, Faculty of Science, Kasetsart University, Bangkok, Thailand*
[2]*Department of Chemical and Materials Engineering, Tunghai University, Taichung, Taiwan*
[3]*National Energy Technology Center, Pathum Thani, Thailand*

**E-mail: fscipths@ku.ac.th*

Abstract:

Herein, a nitrogen, sulfur dual-doped reduced graphene oxide (N,S-rGO)-coated $MoO_2/MoS_2/MoP$ heterojunction ($MoO_2/MoS_2/MoP$/N,S-rGO) architecture was developed, which exhibited favorable diffusion kinetics of electrolyte through an internal electric field built at heterointerfaces and alleviated the volume change through the core-shell structure, resulting in a $MoO_2/MoS_2/MoP$/N,S-rGO with the high adsorption of redox species, excellent electrical conductivity, and high reaction kinetics. This $MoO_2/MoS_2/MoP$/N,S-rGO can be used directly as a supercapacitive electrode with a high specific capacity of 867.8 F g^{-1} at 1 A g^{-1} and an excellent rate capability of 487.18 F g^{-1} when the current density was increased to 16 A g^{-1}. The prepared $MoO_2/MoS_2/MoP$/N,S-rGO electrode exhibited excellent cycle stability with a coulombic efficiency of 99.30 % at 16 A g^{-1} after 3,000 cycles, highlighting the promising prospect of the electrode for supercapacitor application.

1. Introduction

As miniaturization of modern electronics has rapidly advanced in recent years, research on the development of electrochemical energy technologies has attracted widespread attention. Batteries and capacitors are two energy storage devices that are most frequently employed, and both have their individual advantages and disadvantages. However, batteries are characterized by long charging times and low power density. Thus, their use in some fields has been limited. Supercapacitors (SCs) are one of the most promising candidates because of their exceptional charge-discharge characteristics, high power density, and remarkable cycle stability. They are based on the charging and discharging processes at the electrode/electrolyte interface for energy storage. SCs employ a similar energy storage mechanism compared with traditional capacitors, but they require a much more shorter time to charge and release energy just as fast. Because of these benefits, SCs are anticipated to successfully replace current energy storage technologies. However, the low energy density hinders the further development of SCs. Their performance is determined directly by the selection of electrode materials.

SCs are grouped based on their storage mechanism namely electrochemical double-layer capacitors (EDLCs) and pseudocapacitors. While the redox-based techniques known as pseudocapacitors employ electrode materials, including metal oxide nanoparticles and polymers with conducting characteristics, EDLCs mainly employ carbon electrode materials, such as graphene, activated carbon, nano-architectured carbon, and carbon aerogels for the accumulation of charge via reversible adsorption/desorption of ions at the electrode/electrolyte interface. Nevertheless, there are also some intrinsic drawbacks facing these pseudocapacitive materials, such as poor electrical conductivity, low cycling stability, and limited rate capability. As a typical transition metal oxide, molybdenum dioxide (MoO_2) has also been applied in energy storage due to its high electrochemical activity, multiple valence state, and environmental friendliness.[3]

However, the modest reaction kinetic and poor cycling behavior of MoO_2 hinder its practical application for SCs. To solve this problem, a desirable material is desperately required to build MoO_2-based composites characterized by higher capacitive properties. Because of their excellent electrochemical capacitive properties, broad potential range, low cost, environmental friendliness, and distinctive structure-property relationships, graphene-like layered-structured molybdenum disulfide (MoS_2) has recently attracted great attention in energy storage, particularly in SCs. First, Van Der Waals force supports the lamellar structure consisting of S-Mo-S covalent bonds, providing additional ion-diffusion pathways to enhance structural stability in electrochemical charge-discharge cycles.[2] Moreover, S, the homologous of O of the same Mo

source, displays the internal electrical field guiding the electron transfer and ion diffusion from MoO_2 to MoS_2 at the interface, decreasing the ion adsorption energy and migration barrier. Therefore, MoO_2/MoS_2 nanoarchitecture becomes a key to overcome the obstacles of MoO_2.[3] However, due to the interlayer Van Der Waals interactions and high surface energy, the specific capacitance of bare MoS_2 is still far below the theoretical value. It may be because of poor electronic conductivity and 2D nanosheets MoS_2 restacking. Eventually, the cycling abilities of SCs substantially deteriorate. Relatively, molybdenum phosphide (MoP) has attracted a lot of attention to energy conversion and storage applications,[1] owing to its similar electronic structure like Pt, superior electrical conductivity, and specific electronic structure, which offer a great benefit to electrochemical application. Furthermore, it has demonstrated that MoP possesses higher stability than Mo-based oxide/sulfides in the electrochemical process. Therefore, $MoO_2/MoS_2/MoP$ heterostructure is used as an effective way to improve the capacitive properties of materials as it increases the surface area and enhances the active electrochemical sites in the superior heterostructure. This heterostructure with complementary properties exhibits enhanced properties that are not found in the individual materials. This architecture enables fast and reversible faradaic reactions taking place at the electrode/electrolyte interface and, to a certain extent, in the bulk of the material near the surface of the electrode. These contribute to increasing the capacitance and the energy density of SCs. Therefore, this challenge by leveraging the distinct properties of $MoO_2/MoS_2/MoP$ based heterostructure enhances the performance of SCs.

However, due to the semi-insulating nature of MoO_2, MoS_2, and MoP, it is not quite attractive electrode material for energy storage. To improve the electrochemical performance of $MoO_2/MoS_2/MOP$ based heterostructure and, to some part, overcome the aforementioned obstacles, one possible approach is to extend $MoO_2/MoS_2/MoP$ based heterostructure with a conductive network. Such conductive network encompasses an interface between MoO_2, MoS_2, and MoP offering improved electrochemical performance due to synergistic effects. Furthermore, the strategy of composite or hybrid with conductive network at the hetero-interface has proven effective in stabilizing electrochemical reactions/ion diffusion and preventing physical crushing of $MoO_2/MoS_2/MOP$ during electrochemical process. Hence, the synergistically coupled hybrid materials with 2D carbon networks are the promising energy storage materials for SC applications. 2D heterostructure can improve their electrochemical performances such as specific capacitances, rate capability, stability, and crystallinity due to the synergistic contribution of pseudo and/or electrochemical capacitance from the materials involved in the heterostructure. Graphene is regarded as a promising candidate material among these alternative network scaffolds due to its large surface area, high electrical conductivity, and exceptional mechanical capabilities. However, due to the lack of band gap, the conductivity of graphene cannot be completely controlled. From the chemical point of view of highly crystalline pristine graphene, graphene is smooth and chemically inert. In addition, the strong dynamic surface $\pi - \pi$ interaction between graphene layers causes a strong agglomeration of the graphene sheets.[2] These hinder the application of graphene. Developing graphene materials by using the heteroatoms is of great significance in terms of amplifying the spectrum of new electrocatalytic materials and their various applications. With this focus, it was found that nitrogen-doped graphene can deliver surprising electrocatalytic activity due to heteroatom-disturbed electroneutrality in the sp^2 lattice, subsequently destroying its structural uniformity and causing many defects in the crystal structure so as to improve the performance of graphene. Recently, more researchers have discovered that the electrocatalytic activity of carbon materials can be enhanced by dual-heteroatom (N, P, S, B, etc.) doping. Dual doping results in a greater number of carbon atom active sites through the redistribution of spin and charge densities than single-doped samples as revealed by density functional theory study. In addition, co-doping is also the method to offer more flexibility which can modify electronic/charge distribution on the carbon framework by optimizing doping sites, dopant ratio, and densities. Besides N, S atom, featuring *p* orbits in its outermost shell, possesses a close electronegativity to carbon, which can induce strain and stress in the graphene matrix. Although the electronegativity of S (2.58) is close to that of C (2.55), doping with S can induce the polarization of carbon atom neighboring to the S dopant, promoting ion adsorption. Therefore, a higher density of active sites can be created due to synergistic effects induced by unique electron distribution. Consequently, dual-element-doped carbon nanomaterials are demonstrated to be more efficient electrode materials than single-element-doped carbon nanomaterials.

In the present study, we designed and fabricated a nanostructured $MoO_2/MoS_2/MoP$ heterojunction/nitrogen, sulfur dual doped reduced graphene oxide composite ($MoO_2/MoS_2/MoP$/N,S-rGO) and utilized it directly as an electrode for SCs. Further, an electrochemical study was carried out by an asymmetric device where the composite was used as a cathode. The better electrochemical performance of the $MoO_2/MoS_2/MoP$/N,S-rGO composite electrode points toward its enormous application potential in energy storage for small and light electronic devices.

2. Materials and Methods

2.1 Materials

Natural graphite flake (99.9%), was bought from Alfa Aesar. Sodium nitrate ($NaNO_3$), sulfuric acid (H_2SO_4), potassium permanganate ($KMnO_4$), hydrogen peroxide (H_2O_2), ethanol (99.9%), thiourea (CH_4N_2S), and phytic acid ($C_6H_{18}O_{24}$) were supplied from J.T. Baker. L-cysteine hydrochloride monohydrate ($C_3H_{10}ClNO_3S$) and ammonium molybdate tetrahydrate ($(NH_4)_6Mo_7O_{24}.4H_2O$) were supplied from Sigma-Aldrich.

2.2 Synthesis of MoS_2, MoO_2, and MoP doped nitrogen, sulfur dual doped reduced graphene oxide ($MoO_2/MoS_2/MoP$/N,S-rGO)

Graphene oxide (GO) was prepared from natural graphite powder (325 mesh) by a modified Hummer's method. In concentrated sulfuric acid and concentrated nitric acid media, GO was oxidized to obtain many single-layer graphite by introduction of oxygen-containing functional groups between graphite layers. Thiourea (CN_2H_4S, 1 g) was added to the as- prepared GO aqueous dispersion (1 mg mL^{-1}, 70 mL) with vigorous stirring and ultrasonicating at room temperature for 30 min. Then, the mixture was transferred into the hydrothermal reactor and reacted at 180 °C for 12 h. The N,S-rGO was collected by centrifugation, washed with deionized water and ethanol, and further dried in an oven at 80 °C for 12 h. 74.15 mg of ammonium molybdate tetrahydrate ($(NH_4)_6Mo_7O_{24}.4H_2O$)), 1.580 g L-cysteine hydrochloride, and 604.5 mg of N,S/rGO were dispersed in 60 mL deionized water and stirred continuously for 60 min at room temperature followed by heating at 200 °C for 24 h in a Teflon-lined steel autoclave. After cooling to room temperature, the MoO_2/MoS_2/N,S-rGO was collected by centrifugation, washed with deionized water and ethanol several times, and subsequently dried at 60 °C for 12 h. 80 mg of MoO_2/MoS_2/N,S-rGO prepared above and 1.539 mL of phytic acid ($C_6H_{18}O_{24}P_6$) were placed in two separate alumina boats in an alumina tube with phytic acid on the upstream side of the tubular furnace. Then, the boats were heated and kept at a temperature of 800 °C for 2 h under N_2 atmosphere.

2.3 Characterizations

The composition and surface morphologies were characterized by scanning electron microscope (SEM) (JSM-7000F) equipped with an energy dispersive X-ray spectroscopy (EDS). The phase and structures of crystalline were examined by X-ray diffractometer (Brucker D8-CuK_α). The transformation of structure was characterized by Raman spectrometer (I HR550).

2.4 Electrochemical characterization of materials

In the three-electrode system, $MoO_2/MoS_2/MoP$/N,S-rGO was used as a working electrode, Pt sheet was used as a counter electrode, and Ag/AgCl was used as a reference electrode with 2.0 M KOH aqueous solution as an electrolyte. Using a N-methyl pyrrolidone (NMP), the sample, conductive carbon black, and polyvinylidene fluoride (PVDF) were combined at a mass ratio of 80:10:10 and stirred to uniform consistency. After drying, it was coated on nickel foam (3 mg cm^{-2}). The self-supported $MoO_2/MoS_2/MoP$/N,S/rGO and rGO were used as the positive and negative terminals of the asymmetric supercapacitor (ASC) (rGO// $MoO_2/MoS_2/MoP$/N,S-rGO), respectively. Cyclic voltammetry (CV), galvanostatic charge-discharge (GCD), and electrochemical impedance spectroscopy (EIS) measurements were conducted on a CHI 660B electrochemical workstation. In CV test, the potential windows of $MoO_2/MoS_2/MoP$/N,S-rGO and ASCs were set at 0-0.5 V and -1.0-0.55 V, respectively. GCD measurements were carried out at different current densities in the potential range of 0-0.5 V. EIS analyses were conducted in a frequency from 0.01 Hz-100 kHZ at the open circuit potential. Specific capacities of the electrodes were obtained based on the CV and GCD curves from the eq. (1) and (2), respectively:

$$C_m = \frac{\int I(V)dv}{mv\Delta V} \qquad (1)$$

where I(V) = current, ΔV = voltage window, v = scan rate, m = mass of the electroactive material

$$C_m = I\Delta t/m\Delta V \qquad (2)$$

where I = current density, Δt = discharge time

3. Results & Discussion

Microstructure of each sample was observed by SEM. The SEM images in Figure 1a-b show the morphology of pure rGO with the typical wrinkled and lamellar surfaces, which are randomly curled, forming a small number of irregular voids. In addition, the SEM images in Figure 1c-d reveal the evolution of wrinkled patterns and 3D interconnected network nanoarchitecture in comparison with rGO which can be ascribed to heteroatom doping in the rGO framework. As shown in Figure 1e-f, $MoO_2/MoS_2/MoP$ with good uniform both in the size (200 nm) and nanosphere structure is adhered onto N,S-rGO surface. Such a geometric confinement of $MoO_2/MoS_2/MoP$/N,S-rGO could effectively suppresses the aggregation of $MoO_2/MoS_2/MoP$ nanoparticles and enhances its electrochemical activity for high-performance SC application.

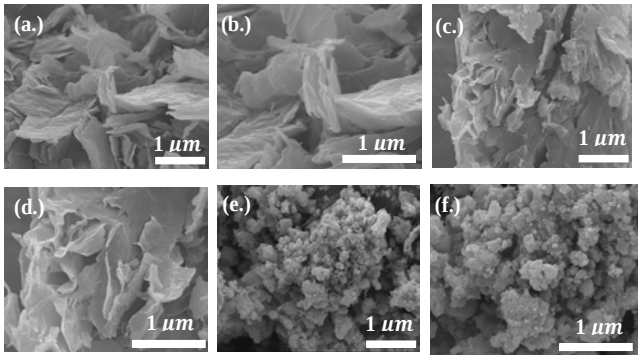

Figure 1. SEM imgaes of rGO (a-b), N,S-rGO (c-d), and $MoO_2/MoS_2/MoP$/N,S-rGO (e-f)

The chemical composition and crystal structure of the electrocatalyst were examined by XRD (Figure 2a). The XRD pattern of N,S-rGO shows a relatively wide characteristic peak at 2θ= 24.2°, corresponding to the (002) plane of graphene. The observed diffraction peaks at around 26.5°, 36.7°, 42.8°, and 60.2° are assigned to MoO_2 (JCPDS# 86-0135),[3] 14.3°, 25.4°, 37.2°, 39.4°, 53.9°, and 58.9° are well indexed to MoS_2 (JCPDS# 37-1492),[3] and 22.5°, 32.2°, and 43.9° are corresponded to MoP (JCPDS# 65-6024).[1] The peak at around 25° (reflection of the (002) plane of graphite carbon) in $MoO_2/MoS_2/MoP$/N,S-rGO sample is not detected. This is because the N,S-rGO is perfectly incorporated into the $MoO_2/MoS_2/MoP$ nanoparticles. These results confirm the complete conversion of different oxide, sulfide, and phosphide precursors into the desired $MoO_2/MOS_2/MoP$ heterojunction product, and also verify that the presence of N,S-rGO does not influence the crystalline structure of $MoO_2/MoS_2/MoP$.

In Figure 2b, peak G at 1598 cm^{-1} represents the complete sp^2 laminar structure, and peak D at 1351 cm^{-1} is induced by the laminar structural defects and disorder. The ratio (I_D/I_G) of the D to the G bands is commonly cited as a measurement of structural disorder in a graphitic structure. The I_D/I_G of N,S-rGO is determined to be about 1.53, suggesting that more defects and disordered structures exist in the as-prepared N,S-rGO network in comparison to rGO (I_D/I_G = 0.85) due to dual-doping by N,S. The disorder degree is further improved after N,S-rGO is combined with $MoO_2/MoS_2/MoP$ (I_D/I_G = 1.56). The new bands at ~282-403 cm^{-1} are seen in the $MoO_2/MoS_2/MoP$/N,S-rGO sample, which can be ascribed to the presence of $MoO_2/MoS_2/MoP$. However, the peaks attributed to $MoO_2/MoS_2/MoP$ are weakened, which also reflect that the defect density is improved after recombination.

In order to further study the chemical composition of $MoO_2/MoS_2/MoP$/N,S-rGO, SEM-EDX analysis was carried out. The EDS energy spectrum (Figure 2c) shows peaks which are attributed to C, O, N, S, P and Mo, indicating the successful synthesis of the nanostructured $MoO_2/MoS_2/MoP$ heterojunction and N,S-rGO composite.

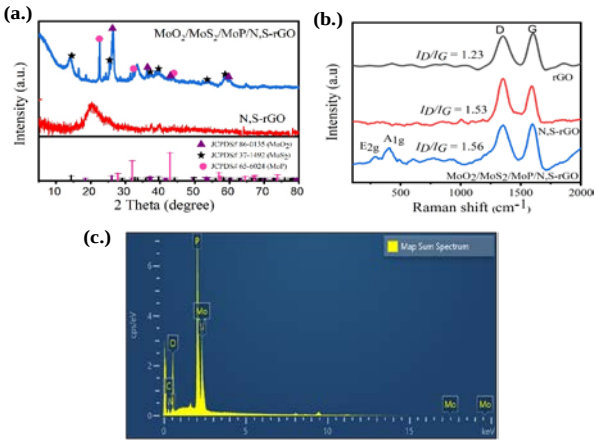

Figure 2. XRD patterns of N,S-rGO and $MoO_2/MoS_2/MoP$/N,S-rGO (a), Raman spectra of rGO, N,S-rGO and, $MoO_2/MoS_2/MoP$/N,S-rGO (b), and EDS elemental spectrum of $MoO_2/MoS_2/MoP$/N,S-rGO (c)

Figure 3a compares the CV curves of all electrodes at the same scan rate of 50 mV s^{-1}. The CV area of the $MoO_2/MoS_2/MoP$/N,S-rGO electrode is larger than other electrodes at this scan rate, which suggests its better electrochemical activity and enhanced energy storage capacity. The maximum capacity of 899 F g^{-1} was measured for $MoO_2/MoS_2/MoP$/N,S-rGO electrode at scan rate of 50 mV s^{-1} while for rGO and N,S-rGO, the values of 116 F g^{-1} and 24 F g^{-1} were calculated,

respectively. Notably, the current density of rGO is significantly affected by the dual N,S doping, where bared rGO has very limited specific capacitance. Impressively, $MoO_2/MoS_2/MoP$/N,S-rGO displays the strongest redox peaks, representing the reversible redox reaction between Mo^{3+} and Mo^{4+}. This indicates that the capacitance of $MoO_2/MoS_2/MoP$/N,S-rGO mainly comes from Faraday pseudo-capacitance, resulting in the largest specific capacitance. GCD measurements were recorded in the potential range between 0 and 0.4 V vs Ag/AgCl (Figure 3b). Interestingly, N,S-rGO (386 F g^{-1}) exhibits the higher specific capacitance than rGO (178 F g^{-1}) at a current density of 1 A g^{-1}, demonstrating that the charge and spin densities of N,S dual-doped rGO framework at different sites change, resulting in more active sites to store much more electrical energy. According to the GCD curves, the $MoO_2/MoS_2/MoP$/N,S-rGO electrode exhibits the highest specific capacitance (868 F g^{-1}). Through the construction of a $MoO_2/MoS_2/MoP$ heterogeneous structure, a $MoO_2/MoS_2/MoP$ heterogeneous interface can be created, the electronic structure can be optimized, and the active materials can cooperate with each other to obtain a higher specific capacitance. In order to understand the charge transfer kinetics of the hybrid SC electrochemical properties, EIS spectra of rGO, N,S-rGO, and $MoO_2/MoS_2/MoP$/N,S-rGO electrodes was measured within the frequency range from 0.01 Hz to 100 kHz in 2 M KOH (Figure 3c). It was found that, as the N and S are doped into the lattice of rGO, the defect density is increased, shortening the migration path of charge in the electrode material and weakening the electrochemical polarization in the electrochemical reaction; therefore, the charge transfer resistance of N,S-rGO is reduced. Additionally, after combining N,S-rGO with $MoO_2/MoS_2/MoP$ heterostructure, the charge transfer resistance is further reduced. Besides, the slope of the Nyquist plot at low frequency for the hybrid electrode is the steepest, indicating the rapid diffusion of electrolyte ions onto the inner surface of the electrode. This reflects the higher supercapacitive performance. These can be attributed to the synergistic effect between $MoO_2/MoS_2/MoP$ heterojunction and N,S dual-doped hybrids. In Figure 3d, the specific capacitance retention rate and coulombic efficiency of $MoO_2/MoS_2/MoP$/N,S-rGO sample are 81.3 and 93.2% after 3000 loops (at 16 A g^{-1}), respectively, showing prolonged cyclic stability. In order to verify the practicability of the $MoO_2/MoS_2/MoP$/N,S-rGO electrode, an ASC device was constructed with a positive electrode of $MoO_2/MoS_2/MoP$/N,S-rGO and a negative electrode of rGO with 2 M KOH as an electrolyte. Figure 3e shows the CV curves of both cathode and anode materials in separate potential windows of 0-0.55 and -1.0 to 0 V, respectively at a scan rate of 50 mV s^{-1} in a three-electrode configuration. Because of the different potential windows, such ASC device shows an expected operation voltage of 0-1.55 V. Furthermore, this observation is substantiated by the symmetrical GCD plots at various voltage windows (from 0 to 1.55 V) at a current density of 2 A g^{-1} illustrated in Figure 3f. The ASC shows fairly triangular-shaped charge-discharge profiles up to 1.55 V. However, a considerable increase in current density is observed beyond this voltage range due to the oxygen evolution reaction of electrolyte. Therefore, a stable working voltage of 1.55 V is suggested, which is an extremely wide for the aqueous-based SCs. The charge and discharge states of the ASC were evaluated using the GCD curves in Figure 3g, demonstrating symmetrical shape with small *iR* drop even as the current density increased from 1 to 16 A g^{-1}. This represents low internal resistance due to N,S dual doping and nanostructure $MoO_2/MoS_2/MoP$ heterojunction on the positive electrode. Owing to N,S dual doping and nanostructure $MoO_2/MoS_2/MoP$ heterojunction, solvated OH ions has an unusually high mobility. In addition, all GCD curves show almost linear discharge lines similar to their representing charge counterpart because of the excellent electrical conductivity and high electrochemical performance of rGO at the negative electrode. As calculated from the discharge profiles, the ASC delivers a specific capacitance of 102.11 F g^{-1} at a load-current density of 1 A g^{-1}.

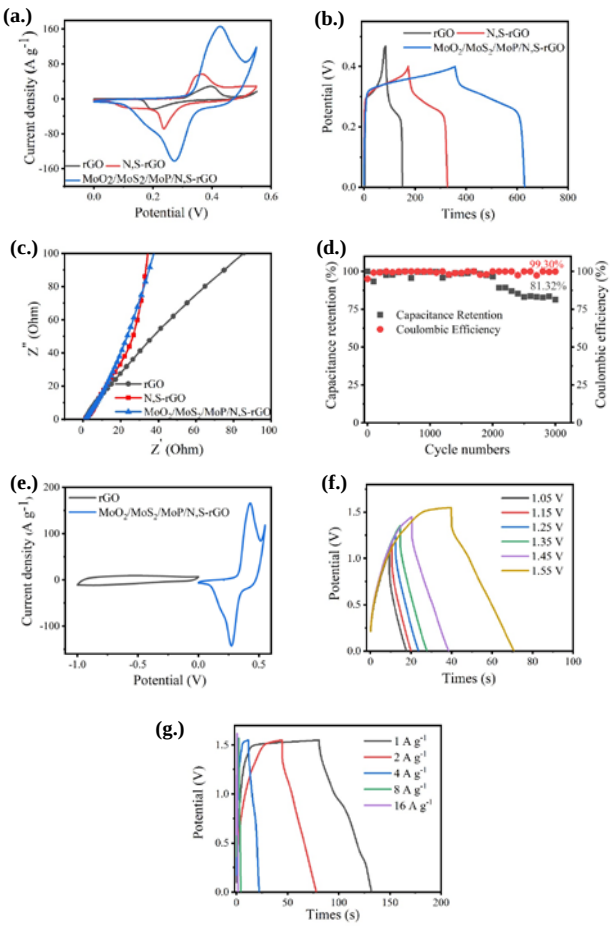

Figure 3. CV curves at scan rate 50 mV s^{-1} (a), GCD curves at current density of 1 A g^{-1} (b), EIS spectra (c) of rGO, N,S-rGO, and MoO_2/MoS_2/MoP/N,S-rGO, cycle life at a current density of 16 A g^{-1} of MoO_2/MoS_2/MoP/N,S-rGO (d), comparative CV curves of MoO_2/MoS_2/MoP/N,S-rGO and rGO (e), GCD curves at different potential windows at a current density of 2 A g^{-1} (f), and at different current densities (g) of rGO// MoO_2/MoS_2/MoP/N,S-rGO device

4. Conclusion

In summary, we have demonstrated a novel approach to building heterostructures by stacking MoO_2/MoS_2/MoP materials and N,S dual-doped reduced graphene oxide (N,S-rGO). The combination of N,S-rGO and MoO_2/MoS_2/MoP effectively inhibits the agglomeration of the graphene sheet layer as well as improves the defect density and electrochemical performance of the nanohybrids. Compared with bared rGO, MoO_2/MoS_2/MoP/N,S-rGO has a more significant effect on performance improvement. The potential use of the MoO_2/MoS_2/MoP/N,S-rGO hybrid film in a high-performance supercapacitor (SC) was also investigated. The hybrid film displays enhanced electrochemical performance, i.e., high specific capacitance and permanent cycle life, because the MoO_2/MoS_2/MoP exhibits excellent SC performance, and the high electrical conductivity is achieved by metal-metal oxide/sulfide/phosphide heterostructure. Moreover, this superior electrochemical performance can be attributed to the high hydrophilicity of N and S, high conductivity, and high amount of active sites in the N,S dual doped rGO framework. The optimized hybrid film is quite suitable as an electrode for an asymmetric supercapacitor (ASC). The results of this research suggest that our MoO_2/MoS_2/MoP/N,S-rGO heterostructure could be extended to other heterojunction materials for various applications in energy storage and electronics.

Acknowledgements

This work was financially supported by the National Research Council of Thailand (NRCT) and Kasetsart University: N42A650285, Center of Excellence for Innovation in Chemistry (PERCH-CIC); Department of Chemistry, Faculty of Science at Kasetsart University, National Energy Technology Center, Thailand Graduate Institute of Science and. Technology (TGIST) at National Science and Technology Development Agency (NSTDA), Thailand and the International Affairs Division at Kasetsart University. In addition, the authors gratefully thank to Taiwan Experience Education Program Internship in Taiwan (TEEP) and Department of Chemical and Materials Engineering, Tunghai University, Taiwan.

References

1. Ma, C.; Deng, C.; He, X.; He, Y.; Ma, Z.; Xiong, H. Urchin-like MoP Nanocrystals Embedded in N-Doped Carbon as High Rate Lithium Ion Battery Anode. *ACS Appl. Energy Mater*. **2018**, *1*, 7140–7145.
2. Li, Z.; Zhao, J.; Yin, Z.; Wang, X.; Liu, D.; Zhu, M.; Wang, A. Novel Robust Nanohybrids of Pompon-like MoS_2 and N/S Dual-Doped Graphene for High-Performance Asymmetric Supercapacitors. *Energy Fuels*. **2021**, *35*, *3*, 2692-2703.
3. Zhao, B.; Cong, Z.; Cheng, Z.; Sun, Z.; Yuan, B.; Shen, F.; Han, X. Facile Microwave-Impulse Synthesis of Multifunctional $rGO/MoS_2/MoO_2$ Composites as a Permselective Separator-Coating Layer for Li–S Batteries. *ACS Appl. Energy Mater*. **2021**, *4*, 10252–10262.

The fabrication of Ru_xP nanoparticle decorated P-doped vegetable root-derived hierarchical porous carbon for supercapacitors with ultrahigh capacitance

Sudarat Laihang[1], Jeng-Yu Lin[2], Pimpa Limthongkul[3], and Panitat Hasin[1]*

[1]*Department of Chemistry, Faculty of Science, Kasetsart University, Bangkok, Thailand*
[2]*Department of Chemical and Materials Engineering, Tunghai University, Taichung, Taiwan*
[3]*National Energy Technology Center, Pathum Thani, Thailand*

[*]*E-mail: fscipths@ku.ac.th*

Abstract:

The present work deals with the fabrication of electrode material, that is, ruthenium phosphide nanoparticle decorated phosphorous-rich hierarchical porous carbons (Ru_xP/P-PACs) with a three-dimensional (3D) architecture by the facile carbonization of celery root followed by chemical activation. Celery roots are used as the precursor to prepare PACs due to extensively cultivated worldwide as human food and an abundant 3D structure, which remain unused and produce enormous pressure on the environment. PACs serves as both a support and a current collector. The inclusion of Ru_xP into the P-PACs backbone, that is Ru_xP/P-PACs, serves as the electrochemically active species. Several spectroscopic and microscopic methods are used to characterize the fabricated electrode material. The prepared material possesses pore volume of 1.91 cm^3 g^{-1}. Scanning electron microscopy image of material shows a unique 3D hierarchical porosity. The formation of this 3D hierarchical morphology depicts stable architecture showing improved electrochemical performance. Cyclic voltammetry and galvanostatic charge-discharge measurement are used to evaluate the electrochemical performance of the prepared electrode material. The electrochemical study reveals a high specific capacitance of 2,433 F g^{-1} for Ru_xP/P-PACs. Finally, the strategy presented in this work provides valuable insights for designing electrode material for supercapacitors with tunable specific capacitance that could be one among the future developments in flexible energy-storage systems.

1. Introduction

Supercapacitors are considered as the potential energy storage devices due to the advantages of fast charge/discharge rate, high power density, and long life. Electrode material is a vital parameter, which can influence the electrochemical performance of a supercapacitor.[2] Typically, porous carbon materials are the primary candidates of supercapacitive energy storage materials because of their high chemical stability, large surface area, and excellent electrical conductivity contributing to rapid adsorption/desorption of ions via an electrical double-layer mechanism.[1] The raw materials for the preparation of carbon materials can be divided into two types: nonrenewable resources (coal, petroleum, etc.) and renewable resources (biomass).[2,5] From a viewpoint of sustainability, the pursuit of renewable carbon sources and exploration of facile yet economical synthesis processes are of particular importance in bringing the carbon-based analogues into real energy storage application. [10]

Recently, various crude biomass (cellulose, grape marcs, alginic acid, dumpling flour, sugar cane bagasse, fir sawdust, etc.) have been utilized to produce carbon materials through pyrolysis and/or activation processes.[2,5,8] Nevertheless, for most carbon from biomass materials without other dopants developed so far still cannot achieve high specific capacitance, thus limiting their broad applications in supercapacitors.[8] At present, the preparation of carbon materials from vegetable roots has been of great interest, due to their richness in honeycomb-like epidermal, vascular, and ground tissues. Thus, the vegetable roots may be transformed into 3D hierarchical porous carbon, which is an effective way to utilize this biomass waste.[2]

However, porosity and specific surface areas of biomass carbon compounds directly carbonized by pyrolysis are relatively low. One way to improve the performance of the carbon-based supercapacitors is to incorporate heteroatoms, such as boron (B), nitrogen (N), oxygen (O), phosphorus (P), etc.[5] into the carbon matrix to enhance the capacitive performance of supercapacitors by combining of the electrical double-layer and pseudocapacitive characteristics, thereby reducing the resistance and providing more ion active sites.[1] It has been found that the replacement of C atoms by impurity atoms like B, N, O, and P introduces defects inside the carbon chain and changes the electronic properties of the carbon samples by providing a single electron or a pair of electrons that facilitate electron donor/acceptor interactions.[5] For example, the P dopant has good electron-donating ability, the

electronegativity of the P atom is low, and the atomic size is relatively large, altering the local charge density to create structural defects, blocking the unstable redox-active sites, widening the potential window, and improving the stability of the active oxygen group on the surfacing of materials in the discharging process.[5]

To improve the energy density, which is an urgent task to develop efficient and novel supercapacitor electrode materials, the application of transition metal phosphides (TMPs) in supercapacitors has been widely studied because of the electronic and functional effects.[7] Previous studies have demonstrated that the electrons from the metal could be attracted by P atoms, and the negatively charged P could bring a positively charged ion near its surface during charge/discharge process. Among them, ruthenium-based transition metal phosphides (RuP, Ru_2P, and RuP_2) have been intensively evaluated as the promising electrocatalysts for electrocatalysis.[9] Ruthenium (Ru) is a 4d transition metal that is more abundant, less expensive, and high reactive due to the optimal D-band electronic structure.[6] Nevertheless, most of the currently reported ruthenium-based transition metal phosphide electrocatalysts only exhibited good electrocatalytic activity in a narrow pH range (e.g. in acid electrolyte) owing to a limited number of active sites and low conductivity.[10] Moreover, the high temperatures promote agglomeration, leading to the reduction of the active surface area and the electron transport. This can decrease the performance of supercapacitors. Therefore, the design of highly dispersed Ru_xP-based electrocatalysts is significant to drive the application of supercapacitor technologies. Dispersing electrocatalytic active Ru_xP nanoparticles on carbon nanomaterials is an effective strategy to increase the number of accessible electrocatalytic active sites.[8]

In this case, this paper uses Ru_xP/P-doped bioderived porous activated carbons (Ru_xP/P-PACs) prepared from vegetable roots via KOH activation as the supercapacitor electrodes (Figure 1). Bioderived porous activated carbon has the characteristics of a high specific surface area and rich pore structure, providing sufficient growth space for loaded Ru_xP. The results show that the electrochemical properties of Ru_xP/P-PAC composites are significantly improved compared with those of PACs.

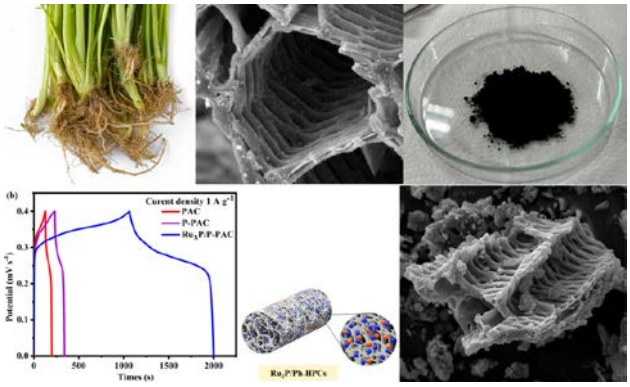

Figure 1. Schematic representation of this research

2. Materials and Methods

2.1 Materials

Celery roots were obtained from a local market in Bangkok, Thailand**.** Ethyl alcohol and n-propanol from RCI labscan limited, potassium hydroxide from Fisher chemical, hydrochloric acid 37 % from VWR chemicals, aniline (AN), sodium persulfate, sodium phosphates, and ruthenium (III) chloride from PaRreac, phytic acid 37 % from Practical grade, 1-methyl-2-pyrrolidinone (NMP) 99.0% from SIGMA-Aloric, nickel foam from ZOPIN, carbon black 45 (acetylene carbon black; model Li-400) from UBIQ, polyvinylidene fluoride (PVDF) from MERCK.

2.2 Synthesis of Ru_xP/P-doped bioderived porous activated carbons (Ru_xP/P-PACs)

The natural celery roots were first cut into small pieces and impurities were removed by washing with ethanol and water before being dried in an oven at 80 °C. The dried celery roots were carbonized for 2 h at 500 °C (heating rate: 5 °C min^{-1}) in a tube furnace under the protection of a N_2 atmosphere. Subsequently, the resulting char was mixed in KOH aqueous solution with KOH/char ratio of 4. Physical activation was done starting with heating biochar at 800 °C for 2 h (heating rate: 5 °C min^{-1}) in a N_2 atmosphere. To eliminate residue, the resulting carbon materials were washed with 6 M HCl and then thoroughly rinsed with deionized water until the filtrate was neutral, and the pure carbon products were dried at 80 °C for 12 h.[2] The obtained sample was name as PACs. The mixture of $Na_2S_2O_8$ (0.29 g) and phytic acid (0.92 mL) was slowly added dropwise into the prepared 2 g mL^{-1} PAC suspension in a solution of water and n-propanol (ratio = 1 to 3 by volume). After stirring for 24 h in an ice bath (0-5 °C), the purple gel-like substance was centrifuged with a high-speed of 10,000 rpm for precipitation. The resulting sludge was subjected to a pyrolytic carbonization process

at 800 °C for 2 h under a N_2 flow (heating rate: 5 °C min^{-1}) to obtain P-doped PACs (P-PACs).[3] 100 mg of P-PACs and 0.02 g of sodium dihydrogen phosphate (NaH_2PO_4) were dispersed in 8 mL of deionized water by vigorous stirring. 0.01 g of ruthenium (III) chloride ($RuCl_3$) was dissolved in 2 mL of deionized water. After that, the $RuCl_3$ solution was poured into the above P-PAC dispersion and then constantly stirred at 60 °C until the water evaporated completely. The as-prepared Ru_xP/P-PACs were kept in the central part of the tube furnace and calcined at 700 °C for 2 h with a heating rate of 5 °C min^{-1} under a continuous N_2 flow; then, the obtained microstructure electrode material was named Ru_xP/P-PACs.[4]

2.3 Structural and morphological characterizations

The morphology of carbon materials was characterized using a scanning electron microscopy (SEM) technique with an accelerating voltage of 5 kV by Quanta 450 (FEI) instrument. The Barrett-Joyner-Halenda (BJH) method and Brunauer-Emmett-Teller (BET) adsorption were used to calculate the pore size distribution and BET specific surface area (S_{BET}), respectively by Micromeritics 3Flex surface characterization with a nitrogen adsorption temperature of 77 K. The microstructure was examined using Raman spectroscopy. The Raman spectra with an excitation wavelength of 532 nm were captured using a Renishaw InVia micro-Raman system. X-ray diffraction (XRD) patterns were collected on X-ray diffractometer (Brucker D8 Advance instrument) with CuKα radiation operating at 40 kV and 20 mA as well as scanning speed of 10° min^{-1} between 10° and 80° to study microstructures of samples.

2.4 Electrochemical measurements and supercapacitor assembly

Electrochemical measurements were carried out with a 2 M KOH electrolyte in a CHI660B workstation. A three-electrode electrochemical cell was composed of the sample-coated Ni foam, which acted as a working electrode, a platinum wire, which functioned as a counter electrode, and a Ag/AgCI electrode as a reference electrode. The working electrode was fabricated by the following steps: 80 wt% Ru_xP/P-PAC, 10 wt% conductive carbon black, and 10 wt% polyvinylidene fluoride (PVDF) were fully mixed in N-methylpyrrolidone (NMP) to form a slurry, which was evenly coated on the foam nickel collector. For the standby, the prepared electrode was dried in a vacuum oven for 72 h at 80 °C. A working electrode with 0.24-0.32 mg of electroactive substance loading was obtained.

The potential range of cyclic voltammetry (CV) and galvanostatic charge-discharge (GCD) measurements was 0 to 0.6 V. Two different working electrodes were separated with a fiber separator and immersed in 2 M KOH aqueous electrolyte to obtain a pouch-type asymmetrical supercapacitor. The specific capacitance values of the samples from the GCD curves have been calculated from the following equation:

$$C_m = \frac{I\Delta t}{m\Delta V}$$

Herein, I = current in ampere (A), Δt = discharge time in seconds (s), m = mass of the active material on the working electrode in gram (g), and ΔV = change in discharge potential in volt (V).

3. Results & Discussion

3.1 Structural and morphological characterizations of Ru_xP/P-PACs

The pore structure of the PACs was explored through SEM, which exhibited a continuous 3D porous framework (Figure 2). The precarbonization of celery roots using the heat treatment at 500 °C can produce a highly porous carbon framework, which further evolved into interconnected polygonal channels (Figure 2a-b). The PACs after the activation of the precarbonized celery roots using KOH possessed a large number of pore structures on the surface of carbon at both low (Figure 2c) and high (Figure 2d) magnifications, indicating that the presence of KOH can etch the carbon to produce pore structures. The introduced KOH could react with the carbon material, which would then be decomposed into many kinds of volatile substances, such as CO, CO_2, and water vapor. This broke the polygonal channels along the length of the root and generated elongated blocks possessing interconnected porous networks on the channel walls. Moreover, the material with an increased specific surface was obtained after being activated by the KOH solution. In turn, the KOH activation can promote the electrochemical performance of PACs attributed to the acceleration of transport speed of ions. This makes PACs as the electrode materials for supercapacitors close to the commercialization. The Ru_xP/P-PACs shown in Figure 2d-e had the most abundant defect structure, and its collapsed structure was more obvious because Ru_xP electrocatalyst were likely to move and aggregate into larger particle with high calcination temperature of 700 °C. Obviously, the

Ru_xP nanoparticles were attached to the porous carbon substrate, indicating that Ru_xP/P-PACs had been successfully synthesized in the experiment. As shown in Figure 2d-e, the Ru_xP nanoparticles had a very high distribution density, which may cause the ease of storage and transportation of electrolyte ions thus affecting the electrochemical performance. Moreover, the porous structure provided more transport channels for electrolyte ions, so the electrochemical performance of Ru_xP/P-PACs was excellent.

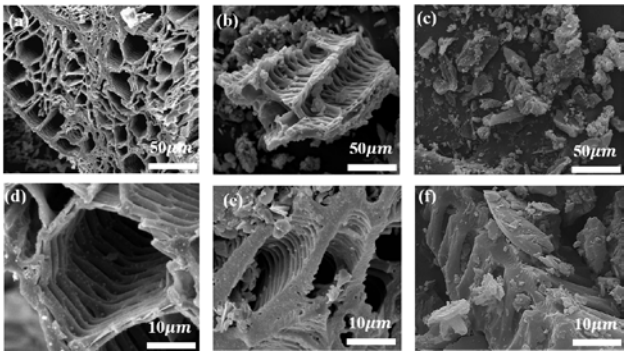

Figure 2. SEM images of carbon materials prepared from celery roots after annealing at 500 °C (a and d), PACs after being activated with potassium hydroxide and then annealed at 800 °C (b and e), and Ru_xP/P-PACs (c and f)

Figure 3a depicts the XRD patterns of PACs and Ru_xP/P-PACs. The diffraction peaks observed at 31 and 43° were attributed to the structured graphite stage (002) and (100) diffraction in the amorphous form of the PACs, respectively. Differently, several sharp peaks, which were appeared in the XRD patterns of Ru_xP/P-PACs; among them 19.8, 26.4, 32.9, 38.4, 47.1, and 58.7° corresponded to (101), (011), (201), (210), (020), and (221) crystal planes of Ru_2P, respectively (Joint Committee on Powder Diffraction Standards: 65-2382). Furthermore, the Ru_xP/P-PACs also had obvious characteristic peaks at 21.7, 29.2, 31.8, 32.4, 44.3, and 46.0° of 2θ, which were attributed to (101), (002), (011), (200), (112), and (211) of the RuP lattice planes (Joint Committee on Powder Diffraction Standards: 65-1863). In addition, the sharp XRD peaks of Ru_xP might cover the carbon reflections of (002) and (100).

The Raman spectra in Figure 3b show two obvious characteristic peaks at 1350 and 1590 cm^{-1} attributed to D (amorphous characteristics) and G (degree of graphitization) peaks, respectively. The relative intensity ratio of the D and G band (defined as I_D/I_G) was calculated according to the curves in Figure 3b, 1.38 for PACs and 1.69 for Ru_xP/P-PACs, proving that Ru_xP/P-PACs had the largest degree of defect structure. However, it is worth noting that Ru_xP/P-PACs retained the original graphite structure and lattice defects of PACs to a certain extent. The amounts of defect sites may activate the original sluggish carbon and generate positive influence on the electrochemical performance of Ru_xP/P-PACs.

To quantitatively study the influence of internal structure on the electrochemical properties of Ru_xP/P-PACs, the N_2 adsorption/desorption isotherm and pore size distribution were measured by the BET method. Figure 3c-d show the N_2 adsorption/desorption and pore size distribution curves of PACs and Ru_xP/P-PACs. Both PACs and Ru_xP/P-PACs exhibited a type I curve with high adsorption capacity, according to IUPAC in the low-pressure region, indicating that PACs and Ru_xP/P-PACs were mainly composed of microporous structure (0.5-2 nm). It was beneficial to improve the ion storage capacity of supercapacitors during charging and discharging. However, the curves exhibited small hysteresis loops (type H4) at the middle and high pressure, meaning that the coexistence of mesopores (2-50 nm) and macropores (>50 nm) on the carbon framework of PACs and Ru_xP/P-PACs was abundant. The specific surface area of Ru_xP/P-PACs calculated by BET was 3,643 $m^2\ g^{-1}$, showing that the specific surface area of Ru_xP/P-PACs can be improved compared with that of PACs (3,315 $m^2\ g^{-1}$) due to the existence of Ru_xP nanoparticles. The larger specific surface area in the Ru_xP/P-PACs improved the electric double-layer capacitance and accelerated the rate of ion diffusion. The pore size distribution curves presented in Figure 3d could potentially serve as an evidence of porous structures being present in the

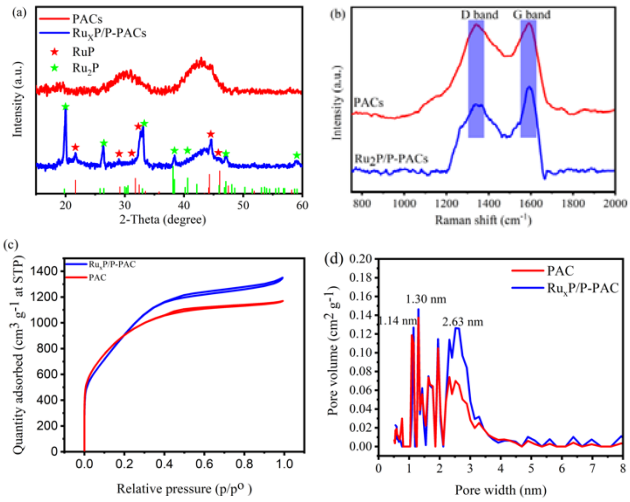

Figure 3. XRD patterns (a), Raman spectra (b), N_2 adsorption/desorption isotherms (c), and pore distribution curves (d) of PACs and Ru_xP/P-PACs

substances. The pore size of PACs and Ru_xP/P-PACs was mainly focused at 1-3 nm demonstrating that the pore consisted of an amount of micropores and a few mesopores. This can be observed from three sharp peaks at 1.1, 1.3, and 2.6 nm.

3.2 Electrochemical performance of Ru_XP/P-PACs

The electrical characteristics of the samples were examined in this investigation using three electrodes and a 2 M KOH solution as the electrolyte. To begin with, the cyclic voltammograms (CVs) of all samples have been studied at 50 mV s^{-1}, and the results are demonstrated in Figure 4a. The curve of PACs, whose capacitance was mainly provided by the pseudocapacitance, showed an obvious hump appearing between 0.2 and 0.3 V. This signified the participation of heteroatoms such as N and O atoms in the faradic charge-transfer process. The hump became broader and the area of CV was larger as the phosphorus atoms were doped into PACs. This indicated that the doping of P atoms promoted the enhanced electrochemical performance of PACs. The excellent electrochemical behavior imparted by P doping was attributed to a shift in the electronic states, leading to increased electrical conductivity with lower band gaps, surface polarity, and wettability, offering more accessible species. Moreover, it is obvious that CV curve of Ru_xP/P-PACs presented the strongest redox peaks (0.25 V/0.45 V) caused by Ru_xP. The Ru_xP/P-PACs additionally acquired pseudocapacitance through a redox reaction initiated by Ru atoms that occurred on the electrode surface. Alloying P with Ru optimized surface electronic structure and also introduced new electrocatalytic functions that could kinetically accelerate the redox reaction. According to Figure 4b, the GCD curves exhibited nearly symmetrical profiles, with plateau within the potential range of 0.2 to 0.3. This indicated that the dominant energy storage mechanism is pseudocapacitance, while a gradual decrease in the EDLC contribution is observed when P and Ru_xP are incorporated into PAC frameworks. The specific capacitances of PACs, P-PACs, and Ru_xP/P-PACs at 1.0 A g^{-1} current density were 171, 252, and 2,433 F g^{-1}, respectively. Therefore, the comparison curves of constant current charge/discharge curves revealed the successful incorporation of P and Ru_xP into the frameworks of PACs, paving a way to enhance charge transport in charge/discharge processes. Figure 4c shows that the capacitance retention rate of Ru_xP/P-PACs was 63.38 % and the Coulombic efficiency was 100 % after 1,000 cycles of charging and discharging. Nevertheless, the self-aggregation or the loss of Ru_xP nanoparticles during charge/discharge will lead to the poor cycling stability.

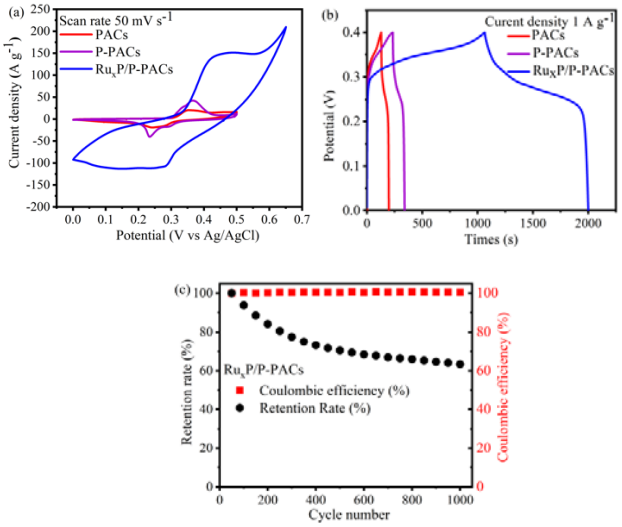

Figure 4. CV curves at a potential sweep rate of 50 mV s^{-1} (a), GCD curves at a current density (b) of 1 A g^{-1} of PACs, P-PACs, and Ru_xP/P-PACs, and Long-term cycling stability and the Coulombic efficiency of Ru_xP/P-PACs in 2 M KOH (c).

In a three-electrode configuration, the electrochemical behavior of Ru_xP/P-PACs and activated carbon (AC) was tested across positive (0-0.6) and negative potential windows (-1 to 0 V), respectively. CV at 50 mV s^{-1} depicted in Figure 5a demonstrates the electrochemical peak of Ru_xP/P-PACs at ~0.34 V, indicating the pseudonature, whereas the CV curve of AC shows a quasirectangular shape, indicating the behavior of dominant electrical double-layer nature with a minor pseudoeffect. The redox peak profile indicated that the Ru_xP/P-PAC electrode stores charges based on adsorption/desorption of the electrolyte ions at the electrode surface as well as the formation of functional groups and interaction of Ru ions with them, thus undergoing redox reactions. Our results suggested that the combination of these two electrodes for an asymmetrical supercapacitor (ASC) can afford an AC//Ru_xP/P-PACs device with a 1.6 V operation voltage, which was substantially broader than the reported PAC-based ASCs in aqueous electrolyte. Figure 5b displays the GCD curves of the ASC of the AC//Ru_xP/P-PAC measured at 1.0 A g^{-1}. As can be seen, the GCD curves still remain highly linear and symmetrical within all potential ranges due to good intrinsic cyclic reversibility of AC and Ru_xP/P-PACs. Furthermore, the working voltage

of this ASC can reach 1.3 V. In addition to this, the GCD profiles shown in Figure 5c also show a similar pseudonature of the device with negligible IR drop. The prepared ASC device displayed a high specific capacitance of 359.5 F g^{-1} at 1 A g^{-1} due to the dominating pseudonature of the device. The total specific capacitance of this ASC was found to be 192.3 F g^{-1} at 16 A g^{-1}, at least 53.51 % of its C_m value at 1 A g^{-1}.

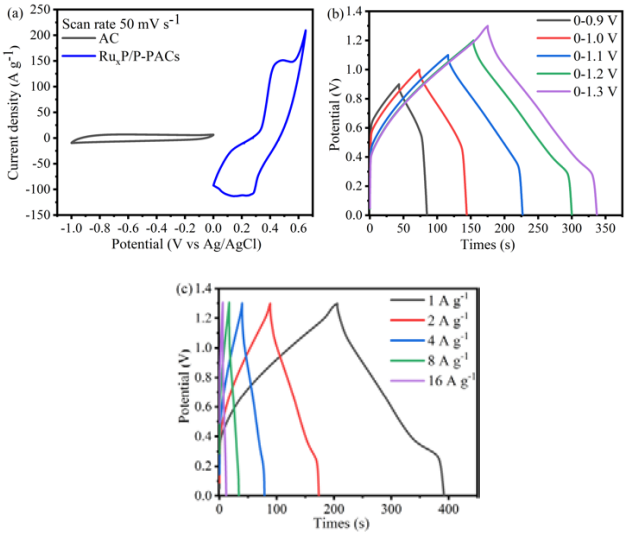

Figure 5. CV curves of Ru_xP/P-PACs and AC in a three-electrode system (a), GCD curves of the AC//Ru_xP/P-PACs at various potential windows measured at 1 A g^{-1} (b), and current densities (c) in 2 M KOH aqueous solution

4. Conclusion

To summarize, the bioderived porous activated carbons (PACs) was successfully prepared from vegetable roots via KOH activation, in which PACs incorporated by P and Ru_xP (Ru_xP/P- PACs) showed better electrochemical properties. In comparison with the electrode prepared from PACs, the electrode prepared from Ru_xP/P-PACs displayed a high specific capacitance of 2,433 F g^{-1} along with capacitance retention of 63.4 % after 1,000 cycles. An ultrahigh specific capacitance asymmetric supercapacitor (ASC) device was fabricated with Ru_xP/P-PAC as a cathode and activated carbon (AC) as an anode. The assembled AC//Ru_xP/P-PAC ASC device showed excellent performance with a C_{cell} of 359.5 F g^{-1} at 1 A g^{-1}. This superior electrochemical performance of AC//Ru_xP/P-PAC indicated that it could be an ideal choice for a low-cost and superior-performance supercapacitor to meet high specific capacity needs.

Acknowledgements

This work was financially supported by the Kasetsart University Research and Development Institute (KURDI), FF(KU)23.67, the Center of Excellence for Innovation in Chemistry (PERCH-CIC); Department of Chemistry, Faculty of Science at Kasetsart University; Graduate scholarship, and the International Affairs Division at Kasetsart University. In addition, the authors gratefully thank to Taiwan Experience Education Program Internship in Taiwan (TEEP) and Department of Chemical and Materials Engineering, Tunghai University, Taiwan.

References

1. Chang, C.; Simchi-Levi, D.; Zhang, Y.; Wang, S.; Liu, X.; Li, *L.* Fabrication of Hierarchical Porous Carbon Frameworks from Metal-Ion-Assisted Step-Activation of Biomass for Supercapacitors with Ultrahigh Capacitance. **2019**, *7* (12), 10763–10772.
2. Guo, N.; Li, M.; Wang, Y.; Sun, X.; Wang, F.; Yang, R. Soybean Root-Derived Hierarchical Porous Carbon as Electrode Material for High-Performance Supercapacitors in Ionic Liquids. *ACS Applied Materials & Interfaces* **2016**, *8* (49), 33626–33634.
3. Li, R.; Wei, Z.; Gou, X. Nitrogen and Phosphorus Dual-Doped Graphene/Carbon Nanosheets as Bifunctional Electrocatalysts for Oxygen Reduction and Evolution. *ACS Catalysis* **2015**, *5* (7), 4133–4142.
4. Yu, J.; Wu, X.; Zhang, H.; Ni, M.; Zhou, W.; Zhou, W. Core Effect on the Performance of N/P Codoped Carbon Encapsulating Noble-Metal Phosphide Nanostructures for Hydrogen Evolution Reaction. **2019**, *2* (4), 2645–2653.
5. Liu, S.; Hu, X.; Ma, J.; Li, M.; Lin, H.; Han, S. N/P Codoped Carbon Materials with an Ultrahigh Specific Surface Area and Hierarchical Porous Structure Derived from Durian Peel for High-Performance Super-capacitors. *Energy & Fuels* **2020**, *34* (11), 14948–14957.
6. Hu, C.-C.; Chang, K.-H.; Lin, M.-C.; Wu, Y.-T. Design and Tailoring of the Nanotubular Arrayed Architecture of Hydrous RuO_2 for next Generation Supercapacitors. *Nano Letters* **2006**, *6* (12), 2690–2695.
7. Zhang, N.; Li, Y.; Xu, J.; Li, J.; Wei, B.; Ding, Y.; Amorim, I.; Thomas, R.; Thalluri, S. M.; Liu, Y.; Yu, G.; Liu, L. High-Performance Flexible Solid-State Asymmetric Super-capacitors Based on Bimetallic Transition

Metal Phosphide Nanocrystals. *ACS Nano* **2019**, *13* (9), 10612–10621.

8. Zhang, J.; Duan, Y.; Zhao Hua Jiang; Chen, T.; Wang, K.; Wang, K.; Zhang, W.; Hu, J. Investigation of the Supercapacitance of Ruthenium-Based/ Hemp Stem Activated Carbon. *Journal of Physics and Chemistry of Solids* **2021**, *153*, 110019–110019.
9. Zhang, N.; Xu, J.; Wei, B.; Li, J.; Amorim, I.; Thomas, R.; Sitaramanjaneya Mouli Thalluri; Wang, Z.; Zhou, W.; Xie, S.; Liu, L. Mille-Crêpe-like Metal Phosphide Nanocrystals/ Carbon Nanotube Film Composites as High-Capacitance Negative Electrodes in Asymmetric Supercapacitors. *ACS Applied Energy Materials* **2020**, *3* (5), 4580–4588.
10. Ruiyi, L.; Keyang, H.; Yongqiang, Y.; Haiyan, Z.; Zaijun, L. Atomically Dispersed RuO2-Tryptophan Functionalized Graphene Quantum Dot-Graphene Hybrid with Double Schottky Heterojunctions for High Performance Flexible Supercapacitors. *Chemical Engineering Journal* **2021**, *426*, 130893.

Conversion of food waste to a valuable soil resource in a day

Apichat Junsod*, Patomporn Pulsawad, Parichat Yamsri, and Sukhontha Silaart

Expert Centre of Innovative Clean Energy and Environment, Thailand Institute of Scientific and Technological Research (TISTR), Khlong Luang, Pathum Thani 12120, THAILAND

**E-mail: Apichat@tistr.or.th*

Abstract:

Each year, more than 1,300 million tons of food must become wasted organic waste. The amount of organic waste is mostly from households, causing greenhouse gases, global warming, and environmental pollution. In addition, the cost and energy to dispose of organic waste is quite high. Composting is an effective and environmentally friendly alternative to change organic waste to use again. In this study, the researcher saw the importance of reducing organic waste by composting. The researcher therefore designed and developed a suitable composter for household composting machines that can replace 5 kg of organic waste per day, which the composter can digest organic waste without making an odor and can decompose within 48 hours. The researcher studied the factors as follows: aeration, temperature, microorganisms in the decomposition process, moisture content, pH, primary macronutrients, etc., before and after fermentation. The results of the pre-fermentation experiments using organic waste fermentation machines showed that the average moisture content was between 40-95%. The temperature during the process is in the range of 40-60 °C. After the experiment, the moisture content was decreased in the range of 1-10%, the pH was in the range of 6-8.5, the ratio of carbon to nitrogen (C: N) was 17:1, the value of organic matter (OM) was between 38-59 percent by weight, the total nitrogen content (total N) was in the range of 1-4%, the total phosphate content (total P_2O_5) was in the range of 0.5-1%, and the total potassium contents (total K_2O) was in the range of 0.7-1.6%, which meets the organic compost standard.

1. Introduction

Each year, organic waste is caused by food waste that is discarded from the beginning of production to the distribution destination. Greenhouse gas emissions are up to 8% and may increase as high as 10% from the amount of greenhouse gases that are emitted around the world. Because the amount of food waste is continuously increasing every year and is also the waste that everyone cares about the least. See that it is useless, low value, making no motivation to manage that waste 1 ton of organic waste emits greenhouse gases equal to 0.51 tons of carbon dioxide equivalent. The production rate per person is 1.14 kilograms per day but only 32% is sent to be disposed of correctly. More than 31% causing accumulated waste to be a pollution problem is a breeding source of germs and throws resources in vain due to the shortage of resources and for sustainability, it is pushing for a major change in organic waste management. Composting from organic waste has become the best option to convert organic waste into valuable materials such as fertilizer. It can be considered an effective and environmentally friendly alternative for organic management and is widely used around the world. Sustainability needs to see waste as a renewable resource, where food waste and organic waste can be recovered.

The purpose of this study is to design and developed a suitable composter for household that can replace 5 kg of organic waste per day, which the composter can digest organic waste without making an odor and can decompose within 48 hours.

2. Materials and Methods

2.1 Composting machine

The machine used in this study is designed to fully automatic and highly compact composting machine. The machine volume 15 L composting tank, controlled 3 factors, which are the moisture, air volume, and heating temperature**.**

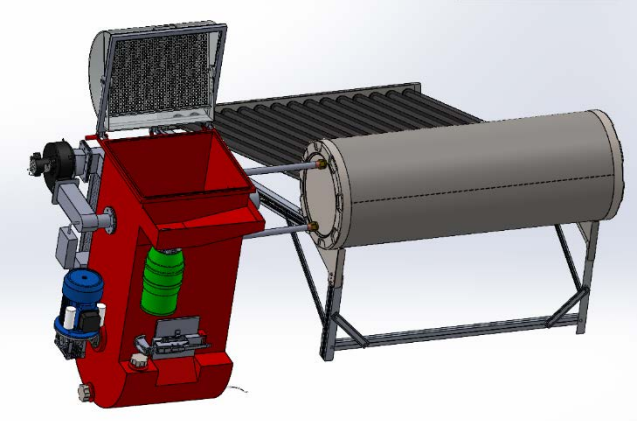

Figure 1. The machine used in this study.

2.2 Experimental conditions

This project is divided into two main parts. The first part is designing a machine that can convert 5 kilograms of organic waste per day. The second part is testing and analysis by operating the machine and checking its performance. This article focuses on the second part. Experiments using sludge from biogas digesters, cannabis scraps, and water hyacinth. The materials have controlled duration and temperatures are the same. The conditions tested are shown in Table 1.

Table 1. Various conditions and factors for the machine test.

Run	Condition
1	Sludge
2	Cannabis + Yogurt
3	Cannabis + Milk
4	Cannabis + Dry rain tree leaves + Moringa seeds
5	Water hyacinth + Cannabis + Dry rain tree leaves
6	Water hyacinth + Sludge + Dry rain tree leaves
7	Water hyacinth + Cannabis + Food waste

2.3 Analysis of compost

This study was conducted at the Thailand Institute of Scientific and Technological Research (TISTR) located in Thailand. The sludge from the biogas digester was obtained from a biogas improvement research project and received cannabis scraps from other projects that were no longer needed in order not to be a waste material the researcher therefore brought these two raw materials to experiment.

Pick out chicken bones, tissue paper, plastic, and inorganic substances from food scraps. After that, Mix the ingredients well and processed in various conditions. It takes 2 days to process each time. (Figure 2).

Figure 2. Cannabis scraps mixed with water hyacinth and food waste

Samples were removed from the composter after 48 hours to check for moisture, pH, organic matter, carbon-to-nitrogen ratio, electrical conductivity, total nitrogen, total phosphate, and total potassium. Analytical methods are shown in Table 2.

Table 2. Analytical methods

Characteristics	Unit	Analytical methods
pH	-	pH meter
Moisture content	%	Oven Drying
Nitrogen (N)	%	Kjeldahl method
Phosphate (P)	%	ICP-OES
Potassium (K)	%	ICP-OES
C/N ratio	%	Calculation
Organic Matter (OM)	%	Wet Oxidation
Electrical Conductivity (EC)	dS/m	EC meter

3. Results & Discussion

The result is shown in Table 3. The moisture content after the experiment ranged between 2.5-10.9%. The temperature during the experimental process is in the range of 45-60℃ to keep the humidity after fermentation below 35%. After 2 days at the end of every experiment, pH was found in the range of 6-8.5, the carbon to nitrogen (C/N) ratio is one of the important factors affecting the composting process as well as the properties of the end-product. In general, the optimal C/N ratios in the standard composting of most materials have been reported as not more than 20:1 to ensure the carbon energy intake while enabling the rapid growth of microorganisms. In this study the best condition C/N ratio is 17:1. The Electrical Conductivity is in the range of 2.29 the compost without animal manure should have a value not exceeding 3 dS/m. which run 2-7 have higher values than the standard. The Organic Matter was in the range of 38.5-76.4% by weight, the total nitrogen content (total N) was in the range of 1.48-4.02%, the total phosphate content (total P_2O_5) was in the range of 0.49-1.22%, the total potassium contents (total K_2O) were in the range of 0.74-1.89%. By considering the aeration patterns, the 48 hrs. operated aerator was considered the best condition. For this study, it was shown that experiments using cannabis scraps as the main ingredient produced the best results in response to the standard composition.

Table 3. Experimental results of organic waste composting, 48 hours per experiment.

Run	pH	Moisture content (%)	C: N ratio	OM (%)	EC (dS/m)	Total N (%)	Total P_2O_3 (%)	Total K_2O (%)
1	7.7	9.0	16:1	50.74	2.29	1.88	1.5	0.74
2	8.5	10.9	16:1	62.08	5.53	2.29	0.63	1.89
3	8	10.8	17:1	76.4	6.58	2.64	0.57	1.88
4	6.1	3	8:1	57.99	6.03	4.02	1.22	1.65
5	6.1	2.5	17:1	59.01	4.63	2.01	0.49	1.53
6	6	2.5	15:1	53.28	4.82	2.06	0.58	1.47
7	6.2	2.5	15:1	38.5	3.66	1.48	0.76	1.03

4. Conclusion

Composting food waste has become the best choice for turning organic waste into valuable materials as fertilizer. These processes are an efficient and environmentally friendly alternative for managing food waste and are used extensively worldwide. It can be regarded as an alternative to food waste management to replace traditional the disposed by landfill. The composting machine prototype was able to decompose organic waste in a time frame of 2 days with no added special microorganisms only using natural microorganisms to break down all kinds of organic food waste into compost. This machine had an advantage because automatic easy to control, highly compact composting machine, noiseless, odorless and reduce time to turning food waste into fertilizer from 60 to 2 day compare with pile compost. The disadvantage of the machine is that it cannot put large food scraps such as pork bones and chicken bones. This study is only the first part and, in the future, will further study try to reduce the time to turn food waste into fertilizer from 2 to 1 day by adding a unit to reduce food waste sizes because in this study the food waste was different sizes which could also affect the processing time.

Acknowledgements

A part of this study was supported by the Thailand Science Research and Innovation.

References

1. Dume, B.; Hanc, A.; Svehla, P.; Michal, P.; Chane, A.D.; Nigussie, A. *Ecotoxicol. Environ. Saf.* **2023**, *263*, 115255.
2. Jiang, Y.; Ju, M.; Li, W.; Ren, Q.; Liu, L.; Chen, Y.; Yang, Q.; Hou, Q.; Liu, Y. *Bioresour. Technol.* **2015**, *197*, 7-14.
3. Li, Y.; Sun, B.; Deng, T.; Lian, P.; Chen, J.; Peng, X. *Ecotoxicol. Environ. Saf.* **2021**, *222*, 112497.

Comparative study of torrefaction and pyrolysis behavior on rice straw using thermogravimetry-mass spectrometry (TG-MS) technique

Chakrya Theap[1], Penjit Srinophakun[1], Jatuporn Parnthong[2], Channarith Be[2], and Sanchai Kuboon[2]*

[1]*Faculty of Engineering, Kasetsart University, 50 Ngamwongwan Rd, Chatuchak Bangkok,10900, Thailand*
[2]*National Nanotechnology Center National Science and Technology Development Agency, Thailand Science Park, Pahonyolthin Road, Khlong Nueng, Khlong Luang, Pathum Thani 12120, Thailand*

**E-mail: sanchai@nanotec.or.th*

Abstract:

Rice straw is regarded as one of the most abundant agricultural biomass resources in many rice-producing regions worldwide. Although it is a potential feedstock for biocoal production, selecting an efficient conversion method must be considered to get a better quality of biocoal. It is shown that rice straw has a carbon content of around 39.73% and a high heating value (HHV) of about 15.28MJ/Kg. Torrefaction is a thermal treatment technique that involves heating biomass at 200-300°C in an inert environment to enhance its properties as a fuel or feedstock in various applications such as power generation and other industrial processes. Pyrolysis is another technique requiring higher temperatures above 600°C in an oxygen-free condition. This study paid particular attention to both qualitative and quantitative generation of gases throughout the thermal treatment process, utilizing the TG-MS technique for evaluating rice straw biomass's torrefaction and pyrolysis behavior. The amounts of gas-forming products of pyrolysis condition upon weight loss decomposition was in the order of H_2<CH_4<CO<CO_2, whereas torrefaction produced only minor gases of CO and CO_2, according to the findings of this research, torrefaction, and pyrolysis. It has provided varied solid, liquid, and gas yields of 79.30%, 16.95%, 4.04%, 29.63%, 48.87, and 21.50%, respectively.

1. Introduction

The promise of biomass to reduce climate change and supply sustainable energy has made it a more popular and adaptable renewable energy source in recent years.[1] A sustainable alternative to fossil fuels, biomass feedstocks can be burned or converted into biofuels, biogas, or other renewable energy sources.[2, 3]

Utilizing biomass for energy may assist in handling and lowering the amount of organic waste, such as agricultural residues, forest residues, and food waste, which could otherwise end up in landfills or contribute to pollution.[4] Biomass is a typical renewable energy source that most commonly occurs in Asian countries.[5] The rapid expansion of rice straw residues can be attributed to the high demand for human intake, making it a readily accessible and renewable resource.[6] Regarding energy density, stability, transportation, handling, and environmental benefits, turning biomass into biocoal provides various advantages.[4] However, the higher moisture content could cause storage issues such as decay and a substantial reduction in heating value.[7] These factors can cause an unfavorable effect on the energy conversion.

Multiple approaches have been established to mitigate these negative aspects and improve fuel volumetric energy density. Torrefaction is typically performed in an inert atmosphere at temperatures ranging from 200 to 300°C and a relative residence time (30-60mn).[8, 9] The goal of this technique is mainly focused on improving biomass handling, storage, and combustion qualities by reducing moisture content and increasing energy density.[8] In addition, pyrolysis is one of the thermochemical processes involving heating biomass in a low oxygen or inert atmosphere to produce various products, such as syngas, biochar, and bio-oil.[10] The products of the torrefaction and pyrolysis process consist of biochar, liquid components (water and tar), and gasses (mainly CO_2 and CO).[11]

Thermogravimetry-mass spectrometry (TG-MS) is an analytical technique that combines mass spectrometry and thermogravimetry, two distinct approaches. This combination makes it possible to analyze the evolved gases (mass spectrometry) as a function of temperature or time and detect changes in a material's mass simultaneously (thermogravimetric analysis).[12]

Thermal and chemical properties of substances are studied using TG-MS in various domains, such as environmental analysis, materials science, and chemistry. TG-MS is a helpful method for thoroughly investigating compounds' degradation, decomposition, and gas release features, offering insights into their thermal and chemical behavior.[12]

Based on the literature, the differences in the weight-decreasing profiles and gas generation rates were discovered to be attributable to fluctuations in hemicellulose, cellulose, and lignin content.[13] Also, the TG-MS study revealed that an increased temperature affected the structure of biomass feedstock, and a cross-linking reaction occurred during thermochemical treatment, resulting in an increase in char yields and a decrease in tar yields.[7]

Thus, this study aims to characterize the physicochemical properties of rice straw biomass, which is potentially a solid fuel. Moreover, rice straw biomass and its volatile species and solid biochar are also investigated through thermochemical treatment of torrefaction and pyrolysis techniques.

2. Materials and Methods

2.1 Sample preparation

Rice straw (RS) was selected as biomass feedstock in this study. It was obtained from local farms in Thailand. They were cut and dried under sunlight for 2-3 days to remove surface moisture. They were then ground, put through a standard sieve to control the particle size in the 1-2mm range, and stored in a dry, closed container.

2.2 Biomass properties characterization

The elemental composition as the ultimate analysis was determined by the elements such as carbon (C), hydrogen (H), and nitrogen (N) via CHN analyzer (CHN628, LECO). Proximate analysis was analyzed via the Thermogravimetry technique (no. TA-129). High heating value (HHV) was analyzed via bomb calorimeter (AC500 series, LECO).

2.3. Lignocellulosic composition analysis

Lignocellulosic components such as hemicellulose, cellulose, and lignin were analyzed via NREL standard (NREL/TP-510-42618). 0.3g of rice straw was put into a tared pressure tube and 3ml of 72% acid sulfuric H_2SO_4 was added. It was then mixed for 2h at room temperature using vortex.

Upon the completion, the sample and acid were well mixed and diluted with 84ml of DI water and then transferred to autoclave at 121℃ for 1h. It was allowed to cool down at room temperature hereafter. The 12ml liquid sample was transferred into a sample storage bottle to analyze cellulose and hemicellulose inform of sugar composition using HPLC and analyze acid soluble lignin (ASL) using UV-visible. For the remaining solid was transferred out of the pressure tube and put into filtering crucible and rinse with DI water until pH reaches 5-6 to analyze acid insoluble lignin (AIL).

2.4 Gas forming via TG-MS

Thermobalance (Perkin-Elmer, Pyris1TGA) was used to quantify the weight loss profile during torrefaction and pyrolysis at a heating rate of 10°C/min and a helium flow rate of 120ml/min. A quadrupole mass spectrometer (Perkin-Elmer, Clarus 500 MS) coupled to a thermobalance was used for evolving gas analysis. To avoid subsequent reaction and condensation of the gaseous product, the gas was passed between TGA and MS at 200°C. MS continually detected signals with 2, 15, 28, and 44 mass numbers corresponding to H_2, CH_4, CO, and CO_2. The mass number will then be converted into concentration using the calibration curve created with standard gas and detected using micro-GC (Agilent 490 micro-GC). The total mass balance of solid, liquid, and gas is illustrated in Equation 1:

Solid yield (%) +condensable (Tar+H_2O) (%) +gases (H_2+CH_4+CO+CO_2) (%) =100% (1)

3. Results & Discussion

3.1. Raw material characterization

The results of ultimate/ proximate analysis, colorific value (HHV), and lignocellulosic components of raw rice straw are given in Table 1. Based on the ultimate analysis, RS has high carbon and oxygen content, about 39.73% and 42.65%, respectively. Meanwhile, the sulfur content has the least amount at only 0.11%. Moreover, proximate analysis indicates that RS has a moisture content of 8.56%, fixed carbon (FC) of 21.97%, volatile matter (VM) of 67.16%, and high ash content of about 11.26%. The calorific value HHV is 15.28MJ/Kg.

Additionally, lignocellulosic components in RS, including cellulose, hemicellulose, and lignin, are 33.20%, 19.60%, and 16.87%, respectively. This value is in good agreement with the previous report.[14]

Table 1. Ultimate, proximate analysis, HHV and lignocellulosic composition of rice straw.

Biomass properties analysis	**Rice straw**
Ultimate analysis (wt%, d.b.)	
C	39.73±0.33
H	5.14±0.12
N	1.10±0.08
O	42.76±1.21
Proximate analysis (wt%, a.r.)	
Moisture	8.56±0.03
FC	21.97
VM	67.16
Ash*	11.26±0.86
Higher heating value HHV (MJ/Kg)	15.28±0.19
Lignocellulosic components (%)	
Cellulose	33.20±0.22
Hemicellulose	19.60±0.05
Lignin	16.87±1.22
Other	19.07±0.67

*Ash was analyzed using the NREL method.
d.b. Dry basis.
a.r. As received.

3.2. Biochar properties from torrefaction and pyrolysis

Table 2 illustrates RS biochar's ultimate and proximate analysis during torrefaction and pyrolysis. For ultimate analysis, It was found that, with temperature increases, the proportion of carbon content increased, which agreed well with the literature.[15-17] However, due to deoxygenation, dehydration, and decarboxylation, biochar's hydrogen and oxygen content dramatically decreased.[18] Interestingly, the proximate analysis proved that fixed carbon was also improved with increased temperature, whereas the volatile matter decreased, as shown in Table 2. Devolatilization and thermal cross-link reactions were the leading cause of the change in FC and VM.[19-21]

Table 2. Ultimate/ proximate analysis of biochar during torrefaction and pyrolysis process.

Biochar properties analysis	**TR-RS (250°C,30mn)**	**PY-RS (900°C)**
Ultimate analysis (wt%, d.b.)		
C	42.48±1.29	54.80±0.23
H	4.97±0.14	1.05±0.13
N	1.13±0.33	1.31±0.00
O	27.49±1.77	17.77±0.26
Proximate analysis (wt%, a.r.)		
Moisture	2.58	6.65
FC	38.81	50.63
VM	34.68	17.63
Ash	23.93	25.08

The elemental analysis of biochar revealed that the temperature at which torrefaction and pyrolysis substantially affected the elemental composition of the biochar. The H/C and O/C atomic ratios were observed and disclosed in Table 3. It illustrates that the atomic ratio gradually reduced as the temperature rose, suggesting that the biochar became more aromatic and carbonaceous.[19, 22]

Table 3. Atomic ratio H/C and O/C of Raw RS, TR-RS, and PY-RS in the study and literature.

Sample	Atomic ratio		Ref.
	H/C	O/C	
Raw-RS	1.55	0.81	This study
TR-RS-200°C, 30mn	1.50	0.86	[23]
TR-RS-250°C, 30mn	1.40	0.49	This study
TR-RS-300°C, 30mn	0.72	0.20	[15]
PY-RS-500°C, 8mn	0.69	0.23	[24]
PY-RS-700°C	0.36	0.17	[17]
PY-RS-900°C	0.23	0.24	This study

The Van-Krevelen diagram is a graphical plot for interpreting solid fuel capabilities based on the H/C and O/C atomic ratios. Figure 1 displays how the rising temperatures influence the properties of biochar. Torrefied rice straw (TR-RS-250°C, 30mn) had H/C and O/C atomic ratios of 1.40 and 0.49, respectively, and it was close to peat, confirming that it can be utilized as peat. Furthermore, PY-RS (900°C) has proven that RS biochar can be classified as a sub-bituminous coal, with H/C and O/C atomic ratios of 0.23 and 0.24, respectively.

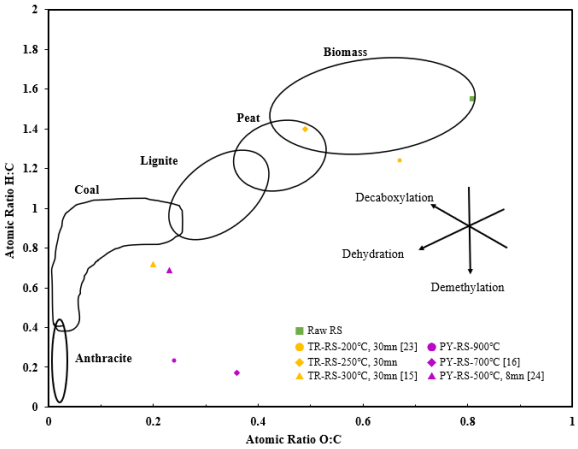

Figure 1. This study's van-Krevelen diagram of RS under different temperatures is linked to the literature.

3.2 Gas-forming products

The weight loss from the TG curve against the gas formation rate during the torrefaction process of rice straw operated at 250°C with 30 minutes of holding was depicted in Figure 2(a).

The weight of the rice straw began to decrease at a temperature above 150°C, suggesting that the biomass's surface moisture had been removed, followed by inherent moisture. Subsequently, the weight loss dropped rapidly at temperatures between 220°C and 250°C, indicating the significant loss of the lignocellulosic composition. The char yield from the designed torrefaction setup (250°C, 30mn) is approximately 80%.

The gas evolving formation rate illustrates that CO_2 has a firm release of 1.4×10^{-4} mol/min g-sample, where the CO product was the least at 0.7×10^{-4}mol/min g-sample. The release product of CO_2 is highly partly caused by hemicellulose and small portion of cellulose decomposition at low temperatures (<500°C), described as the breaking and reforming of carbonyl (C-O-C) and COOH[13, 25, 26], while CO products caused by cracking of the carbonyl (C-O-C) and carboxyl (C=C) groups, originating from the hemicellulose decomposition.[26, 27] The CH_4 and H_2 gases monitoring was undetectable during this process, suggesting no cracking of methoxyl (–O–CH_3) groups to form CH_4 and no identical H_2 at lower temperatures.[26]

The yield of condensable volatile products, known as condensable, was approximately 17% during the torrefaction at 250°C. This result is neatly consistent with the previous study.[7]

It is also interesting to observe the gas formation during the pyrolysis system. Figure 2(b) illustrates the gas generation rates and weight loss against the temperature range of 100-900°C. It was observed that the initial weight loss started at a temperature above 100°C, which is close to the torrefaction system.

The products of CO and CO_2 were also found to have stronger release than those of torrefaction systems. The formation rate of CO and CO_2 are 5.9×10^{-4} mol/min g-sample and 5.4×10^{-4} mol/min g-sample, respectively. Interestingly, the formation rate of CH_4 during pyrolysis released at 1.5×10^{-4}mol/min g-sample, while products of H_2 were relatively low in the pyrolysis system.

The yield of condensable during pyrolysis at 900°C was as high as 48%. It was suggested that increasing temperature increases condensable yield,[7] resulting in tar and H_2O formation during pyrolysis.

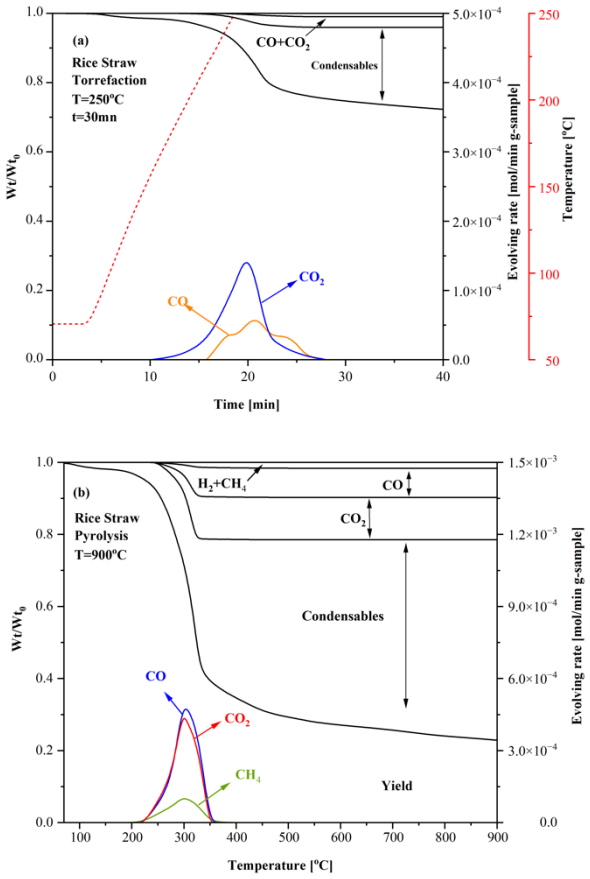

Figure 2. TG-MS curve and gas formation rate during (a) torrefaction and (b) pyrolysis process.

3.3. Yield of products during torrefaction and pyrolysis

Three critical products of torrefaction and pyrolysis, liquid, solid, and gases, offered additional details to classify the product distribution. Figure 3 represents the product of the torrefaction and pyrolysis systems. Torrefaction (250°C, 30mn) produced 79% of solid biochar, whereas the pyrolysis system (900°C) produced only 29.63%.

For incondensable gases, H_2 and CH_4 yields were absent during torrefaction, yet a modest fraction of 0.43% and 1.2% could be seen during pyrolysis, respectively. Beyond that, the yields of CO and CO_2 in torrefaction were relatively low, only 0.97% and 3.07%, compared to 8.11% and 11.76% in pyrolysis.

On top of that, the condensable yields during torrefaction at 250°C and pyrolysis at 900°C were substantially different, at 16.65% and 48.87%, respectively.

This study's results follow the previous studies.[7, 13]

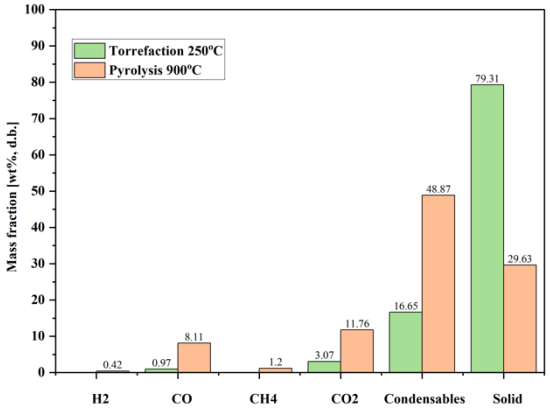

Figure 3. Product distribution through torrefaction and pyrolysis processes of the rice straw.

4. Conclusion

The torrefaction and pyrolysis behavior of rice straw was compared with the TG-MS technique, which focused explicitly on the gas formation at different temperatures. The carbon and fixed carbon increased with temperature; meanwhile, the oxygen content and volatile matter dramatically decreased due to deoxygenation, dehydration, decarboxylation, and devolatilization. The solid yield was the primary product formed during torrefaction, followed by condensable, CO_2, and CO. However, the condensable was dramatically increased, indicating the primary product, whereas the solid yield gradually decreased. Furthermore, among incondensable gases such as H_2, CH_4, CO, and CO_2, it has been identified that CO and CO_2 are the dominating gas products during pyrolysis, despite H_2 and CH_4 being insignificant products. Given the gas formation and product yield, it can be concluded that further research on condensable compounds such as H_2O and acid compounds is desirable for observing reaction pathways during thermal treatment. Investigating the torrefaction and pyrolysis behaviors of merged biomass feedstocks is also suggested for a higher level of comprehension.

Acknowledgment

This work is supported by the Nanomaterial for Energy and Catalyst Laboratory, National Nanotechnology Center (NANOTEC), National Science and Technology Development Agency (NSTDA), and King Mongkut's University of Technology Thonburi (KMUTT).

References

1. IEA World Energy Outlook 2022 shows the global energy crisis can be a historic turning point towards a cleaner and more secure future. https://www.iea.org/news/world-energy-outlook-2022-shows-the-global-energy-crisis-can-be-a-historic-turning-point-towards-a-cleaner-and-more-secure-future.
2. de Albuquerque, T. L.; Silva, J. d. S.; de Macedo, A. C.; Gonçalves, L. R. B.; Rocha, M. V. P., Biotechnological Strategies for the Lignin-Based Biorefinery Valorization. In *Reference Module in Chemistry, Molecular Sciences and Chemical Engineering*, 2019.
3. Hingsamer, M.; Jungmeier, G., Biorefineries. In *The Role of Bioenergy in the Bioeconomy*, 2019; pp 179-222.
4. Kalak, T., Potential Use of Industrial Biomass Waste as a Sustainable Energy Source in the Future. *Energies* **2023,** *16* (4).
5. Tun, M. M., ASEAN STRATEGY ON SUSTAINABLE BIOMASS ENERGY FOR AGRICULTURE COMMUNITIES AND RURAL DEVELOPMENT IN 2020-2030. 2015.
6. Matsumura, Y.; Minowa, T.; Yamamoto, H., Amount, availability, and potential use of rice straw (agricultural residue) biomass as an energy resource in Japan. *Biomass and Bioenergy* **2005,** *29* (5), 347-354.
7. Wannapeera, J.; Fungtammasan, B.; Worasuwannarak, N., Effects of temperature and holding time during torrefaction on the pyrolysis behaviors of woody biomass. *Journal of Analytical and Applied Pyrolysis* **2011,** *92* (1), 99-105.
8. Wang, L.; Barta-Rajnai, E.; Skreiberg, Ø.; Khalil, R.; Czégény, Z.; Jakab, E.; Barta, Z.; Grønli, M., Impact of Torrefaction on Woody Biomass Properties. *Energy Procedia* **2017,** *105*, 1149-1154.
9. Mohammed Umar Garba; James Moritiwon Oloruntoba; Abubakar Garba Isah; Alhassan, M., Production of Solid Fuel From Rice Straw Through Torrefaction Process. **2014**.
10. Cai, W.; Wang, X.; Zhu, Z.; Kumar, R.; Nana Amaniampong, P.; Zhao, J.; Hu, Z.-T., Synergetic effects in the co-pyrolysis of lignocellulosic biomass and plastic waste for renewable fuels and chemicals. *Fuel* **2023,** *353*.

11. Wang, G.; Luo, Y.; Deng, J.; Kuang, J.; Zhang, Y., Pretreatment of biomass by torrefaction. *Chinese Science Bulletin* **2011,** *56* (14), 1442-1448.
12. Li, R.; Huang, Q.; Wei, K.; Xia, H., Quantitative Analysis by Thermogravimetry-Mass Spectrum Analysis for Reactions with Evolved Gases. *J Vis Exp* **2018,** (140).
13. Worasuwannarak, N.; Sonobe, T.; Tanthapanichakoon, W., Pyrolysis behaviors of rice straw, rice husk, and corncob by TG-MS technique. *Journal of Analytical and Applied Pyrolysis* **2007,** *78* (2), 265-271.
14. Isikgor, F. H.; Becer, C. R., Lignocellulosic biomass: a sustainable platform for the production of bio-based chemicals and polymers. *Polymer Chemistry* **2015,** *6* (25), 4497-4559.
15. Tu, P.; Zhang, G.; Wei, G.; Li, J.; Li, Y.; Deng, L.; Yuan, H., Influence of pyrolysis temperature on the physicochemical properties of biochars obtained from herbaceous and woody plants. *Bioresources and Bioprocessing* **2022,** *9* (1).
16. Jindo, K.; Mizumoto, H.; Sawada, Y.; Sanchez-Monedero, M. A.; Sonoki, T., Physical and chemical characterizations of biochars derived from different agricultural residues. **2014**.
17. Nakason, K.; Khemthong, P.; Kraithong, W.; Chukaew, P.; Panyapinyopol, B.; Kitkaew, D.; Pavasant, P., Upgrading properties of biochar fuel derived from cassava rhizome via torrefaction: Effect of sweeping gas atmospheres and its economic feasibility. *Case Studies in Thermal Engineering* **2021,** *23*.
18. Chen, Y.-C.; Chen, W.-H.; Lin, B.-J.; Chang, J.-S.; Ong, H. C., Impact of torrefaction on the composition, structure and reactivity of a microalga residue. *Applied Energy* **2016,** *181*, 110-119.
19. Phuong, H. T.; Uddin, M. A.; Kato, Y., Characterization of Biochar from Pyrolysis of Rice Husk and Rice Straw. *Journal of Biobased Materials and Bioenergy* **2015,** *9* (4), 439-446.
20. Chen, W.-H.; Peng, J.; Bi, X. T., A state-of-the-art review of biomass torrefaction, densification and applications. *Renewable and Sustainable Energy Reviews* **2015,** *44*, 847-866.
21. Chen, W.-H.; Lin, B.-J.; Colin, B.; Chang, J.-S.; Pétrissans, A.; Bi, X.; Pétrissans, M., Hygroscopic transformation of woody biomass torrefaction for carbon storage. *Applied Energy* **2018,** *231*, 768-776.
22. Wu, W.; Yang, M.; Feng, Q.; McGrouther, K.; Wang, H.; Lu, H.; Chen, Y., Chemical characterization of rice straw-derived biochar for soil amendment. *Biomass and Bioenergy* **2012,** *47*, 268-276.
23. Seithtanabutara, V.; Kaewmahawong, S.; Polvongsri, S.; Wang, J.; Wongwuttanasatian, T., Impact of positive and negative pressure on rice straw torrefaction: Optimization using response surface methodology. *Case Studies in Chemical and Environmental Engineering* **2023,** *7*.
24. Tsai, W. T.; Lee, M. K.; Chang, Y. M., Fast pyrolysis of rice straw, sugarcane bagasse and coconut shell in an induction-heating reactor. *Journal of Analytical and Applied Pyrolysis* **2006,** *76* (1-2), 230-237.
25. <Di Blasi et al. - 1999 - Product distribution from pyrolysis of wood and agricultural residues-annotated.pdf>.
26. Yang, H.; Yan, R.; Chen, H.; Lee, D. H.; Zheng, C., Characteristics of hemicellulose, cellulose and lignin pyrolysis. *Fuel* **2007,** *86* (12-13), 1781-1788.
27. Zhang, C.; Yang, W.; Chen, W.-H.; Ho, S.-H.; Pétrissans, A.; Pétrissans, M., Effect of torrefaction on the structure and reactivity of rice straw as well as life cycle assessment of torrefaction process. *Energy* **2022,** *240*.

Copper calcium hydroxide nitrate derived from chicken eggshell and their catalytic activity in the removal of aqueous methyl orange

Yiping Han[1], Taweechai Amornsakchai[1,2], Supakorn Boonyuen[3], and Siwaporn Meejoo Smith[1,2]*

[1]*Natural Resources and Waste Module, Department of Chemistry, Faculty of Science, Mahidol University, Rama VI Rd, Rajathewi, 10400, Thailand*
[2]*Center of Sustainable Energy and Green Materials, Faculty of Science, Mahidol University, Salaya, Nakorn Pathom, 73170, Thailand*
[3]*Department of Chemistry, Faculty of Science and Technology, Thammasat University, Paholyothin, Klong-Luang, Pathumthani 12120, Thailand*

**E-mail: siwaporn.smi@mahidol.edu*

Abstract:

In this work, waste chicken eggshell was applied as precursors for the preparation of copper-calcium hydroxide nitrate (CuCa HN), a wet air oxidation catalyst, in the degradation of methyl orange (MO) dye from water. Chicken eggshell was calcined for 4 hours at varying temperatures, 750 ℃-1050 ℃, to obtain bio-CaO. The CuCa HN catalysts were hydrothermally heated in 30 minutes assisted with metal oxide method, at the control molar ratio of Cu: Ca as 4:1. The physicochemical, structural and surface properties of bio-CaO and catalysts were investigated. The catalytic performance of the catalysts was evaluated in degradation of MO, through catalytic wet air oxidation process under ambient conditions, using 500 ppm of MO, and 2 g/L of catalyst loading. The results showed that the optimum calcination temperature of 900 ℃ gave a relatively high specific surface area of bio-CaO (21.10 m^2g^{-1}) and relatively smaller particle size (747 nm). All CuCa HN materials showed ~100% color removal efficiencies of MO and >90% COD removal efficiencies within 5 minutes. The waste chicken eggshell is of high potential to be utilized as a raw material to produce effective and reusable CuCa HN catalysts for the treatment of wastewater.

1. Introduction

The increasing global population results in a rapid development of industrialization. It leads to the scarcity of fossil fuels, increased environmental problems, and the production of waste. Researchers have attempted to develop renewable flues, sustainable waste management, and advanced treatments for environmental pollution.[1] Concerning sustainable development, wastes should be recycled, repurposed, and reused to produce value-added products. It has, therefore, led many researchers and scholars to a constant investigation on transforming and converting waste from daily domestic use and the food processing industries into value-added materials for further use. The egg industry is one of the key food sources throughout the world. A large number of eggs are supplied to several industries for production like dairy products, confectionery, drinking, salad dressing, and sauces, which results in an estimated 6.82 million tons of eggshell waste generated annually all over the world.[2] Eggshell wastes have been used on a small scale as ceramic wall tile, fertilizer, nutritional supplement, animal feed, and soil amendment due to their rich in calcium, magnesium, and phosphorus.[2-7] The application of eggshell wastes varies based on the purpose and chemical composition selected from waste eggshells. Other researchers reported that eggshells mainly contain calcium carbonate (94%), with small composition of calcium phosphate (1%), magnesium carbonate (1%), and 4% of organic matter. $CaCO_3$ obtained in eggshells could be transformed into CaO by the calcination process, which has been widely used in the production of bio-diesel as a low-cost heterogeneous catalyst.[8]

The catalytic wet air oxidation (CWAO) process as one of the chemical treatment methods for azo dye removal in wastewater, is effective in breaking down double-bonded azo dye molecules. The CWAO process involves the oxidation of organic matter dissolved in wastewater, which uses air or oxygen over a catalyst to either destroy the organic compounds into carbon dioxide and water or convert them into biodegradable intermediates. The oxidative process does not require energy input (higher temperature or pressure) and gives a high oxidation rate and short reaction time, which is due to the usage of catalysts. Copper hydroxyl salts, a class of hydroxyl double salts that have a brucite-like layered structure, have been less reported as effective heterogeneous catalysts in the removal of azo dyes or phenol in the presence of H_2O_2.[9-11] Our previous work focused on the synthesis of copper-containing hydroxyl double salts via a one-step hydrothermally metal oxide assisted-method, using different metal oxides, such

as ZnO, CaO, TiO_2, Al_2O_3 and so on, with the aim of removal of methyl orange (MO) in water under ambient conditions through wet air oxidation process. Among these metal oxides, CaO was prepared by chicken eggshell calcined at 900 ℃ for 6 h, the as-synthesized catalyst was reported to have high MO removal efficiency.[12] Hence, in order to recycle and reuse eggshell waste and explore the possibility of the application of copper-containing hydroxyl double salts derived from waste chicken eggshell, the aim of this work includes the preparation of bio-CaO from waste chicken eggshell as precursors in the synthesis of copper-containing hydroxide nitrate catalysts by 30-min hydrothermal treatment assisted with metal oxide method and investigation of the catalytic performance of as-synthesized catalysts (denoted as CuCa HN) for degradation of MO through catalytic wet air oxidation process under mild conditions. The catalytic performance was evaluated by color removal of MO, chemical oxygen demand (COD), and reusability.

2. Materials and Methods

2.1 Materials

Copper nitrate trihydrate ($Cu(NO_3)_2 \cdot 3H_2O$) was purchased from Univar, Methyl orange ($C_{14}H_{14}N_3NaO_3S$) was purchased from Fischer Scientific. Commercial CaO was purchased from KemAus-1350. The chemicals used were analytical grade of reagents and were used without further purification. Water used in this work was deionized (DI) water.

2.2 Preparation of bio-CaO

Waste chicken eggshells (CES) were collected from canteens at the Salaya campus, Mahidol University, Thailand. Chicken eggshells were first washed with tap water, and dried in an oven at 100 °C for 24 hours. Then, the dried eggshells were ground up and sieved with 400 mesh. The fine powder was calcined at designed temperatures (750 ℃, 850 ℃, 900 ℃, 950 ℃, 1050 ℃) for 4 hours in a muffle furnace. (Heating rate: 10 $^oC \cdot min^{-1}$).

2.3 Synthesis of CuCa HN

Copper calcium hydroxide nitrate (CuCa HN) was obtained by weighing 1 g of calcined eggshell products or commercial CaO in an aqueous copper nitrate solution, the molar ratio of Cu: Ca was controlled of 4:1, undergoing 30 minutes sonication in an ultrasonic bath, and then the suspension was transferred into Teflon-lined stainless-steel autoclave and hydrothermally treated in oven at 100 °C for 30 minutes. The treated suspension, after cooling down, was washed by vacuum filtration with DI water to collect precipitation, then the precipitation was dried at 65 °C for 24 hours for further use.

2.3 Spectroscopic measurement

A thermogravimetric analyzer (PerkinElmer TGA4000) was used to evaluate the thermal property of fine CES powder under gas flow of air zero. MicroActive (ASAP 2460) was used to analyze the specific surface area of CES powder and calcined eggshell products, based on nitrogen adsorption at 77.3 K. Particle size and zeta potential of CES and calcined products were evaluated by Litesizer 500. To characterize the crystal structure of uncalcined and calcined CES, and as-prepared catalysts, the powdered X-ray diffraction (PXRD, Bruker AXS model D8 Advance) was carried out with CuKα radiation (λ= 1.540 Å) operating at 40 kV and 35 mA. The PXRD patterns were recorded from 10^o to 70^o. Attenuated total reflectance-Fourier transform infrared (ATR-FTIR, PerkinElmer) was performed to analyze IR spectra between 400 cm^{-1} and 4000 cm^{-1} for precursors and catalysts. Elemental compositions of uncalcined and calcined eggshells were analyzed by FAAS analysis (Perkin Elmer PinAAcle 900T) and MP-AES (Agilent MPAES 4200). SEM-EDX analysis (FE-SEM HITACHI SU8010), was used to investigate the chemical composition of fresh CuCa HN catalysts.

2.4 Catalytic activity of catalysts

Methyl orange (MO) dye was used as the target compound for catalytic degradation experiments. All catalytic reaction was performed by adding 20 mg of each catalyst with 10 mL methyl orange solution (500 ppm) in a test tube, magnetic stirring with time under ambient temperature. Then the treated MO solution was collected by syringe filtration and was monitored by the measurement of absorbance using the UV-vis spectrophotometer with the absorbance recorded at 464 nm (GENESYS 10s UV-Vis Spectrophotometer). The concentration of treated MO solution was calculated following previous work.[12,13]

The removal efficiency of chemical oxygen demand (COD) in treated MO solutions after the reaction at specific times, was assessed by a standard closed reflux / colorimetric method, followed by previous work.[12,13]

The catalytic reusability test followed the MO removal experiment. After the first run, the used catalyst was kept in the test tube, and the treated dye solution was syringe filtered for UV-vis analysis to calculate MO removal efficiency. The used catalyst was continuously tested with

MO solution for the next run. Once the MO removal efficiency was calculated below 50 %, the experiment was stopped.

3. Results & Discussion

3.1 Characterization of eggshells and catalysts

The thermalgravimetric (TGA/DTG) profiles of the dried chicken eggshell (CES) are shown in Figure 1, which illustrates three steps of mass loss for the CES decomposition when heated in a controlled environment. Slightly weight loss (1.28 wt.%) in the first step for raw chicken eggshell powder with temperature raised from 30 ℃ to 250 ℃, is attributed to the release of moisture absorbed on the sample surface and the loss of low molecule weight of organic compounds. The second mass loss (7.36 wt.%) between 250 ℃ and 650 ℃ is due to the degradation of organic matter. The main weight loss (40.86 wt.%) that occurred from around 650 ℃ to 850 ℃ is related to the decomposition of calcium carbonate and the release of carbon dioxide, yielding around 50.34 wt.% of CaO similar to other reported researches.[14,15] The amount of $CaCO_3$ or Ca was calculated as 93.3 wt%, 37.32 wt% respectively according to the loss of CO_2. Further heating above 832 ℃ brought negligible change to the sample, the temperature of 900 ℃ was available for the calcination temperature to produce CaO completely converted from $CaCO_3$.

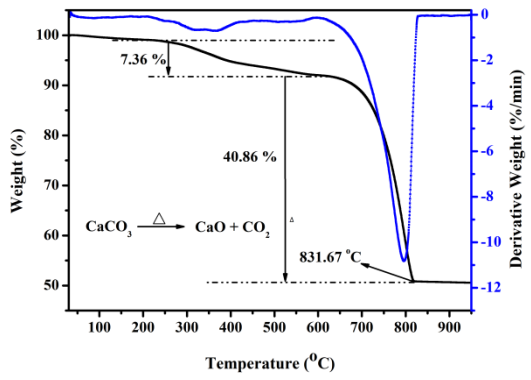

Figure 1. TGA profile of CES.

The thermal treatment resulted in a modification in the XRD profile due to the elimination of CO_2 from CES. In Figure 2(a), the diffraction pattern of the CES powder showed characteristic patterns of $CaCO_3$ with the major peak occurring at 2θ = 29.5°, confirmed by the standard diffraction pattern of COD No. 1010962. A similar trend associated with calcium carbonate was reported by other researchers.[16,17] The intensity of the characteristic peak of $CaCO_3$ became lower or even disappeared in calcined eggshell samples. For each calcined product, it showed similar peaks associated with CaO with the main peak obtained at 2θ = 37.6°, and other peaks appeared at 2θ = 32.4°, 54.2°, 64.5°, and 67.7°, matching the standard COD No. 1011095. It contributed to the conclusion that the formation of bio-CaO from chicken eggshell was completely crystallized during the calcination process and was stable up to temperature 1050 ℃. The mean crystallite size of CaO derived from calcined eggshell was calculated based on the Scherrer's equation and shown in Table 1. It was found that the crystallite size of calcined eggshells was increased with calcination temperature increased, with the order as CES_950 > CES_900 > CES_1050 > CES_850 > CES_750. This indicates the CaO crystal can be well grown at higher calcination temperatures, however, a slight decrease in crystallite size of CaO at 1050 ℃ might be due to the interconnected units of particles. Hence, to obtain pure CaO from waste eggshell, 900 ℃ is the optimal calcination temperature as it requires less energy input, compared to calcination temperature of 950 ℃ and 1050 ℃.

Figure 2(b) shows the diffraction patterns of CuCa HN samples derived from commercial CaO and CES, it could be observed that the structural characteristics of $Cu_2(OH)_3NO_3$ for the as-synthesized catalysts are evident by the highly intense peaks at 2θ=12.9°, 25.9°, well agreement with the COD No. 9012715, which correspond to (001) and (002) basal planes and match well with other researchers.[18-20] In addition, the CaO peak in the catalysts could not be observed, which suggests that the impurity of calcium carbonate and calcium oxide was absent in the as-prepared catalysts.

Table 1. Crystallite size of CES series.

Sample	2θ	FWHM	Crystallite size (nm)
CES_750	37.53	0.131	63.91
CES_850	37.62	0.125	67.20
CES_900	37.63	0.115	73.18
CES_950	37.54	0.123	78.23
CES_1050	37.47	0.119	70.79

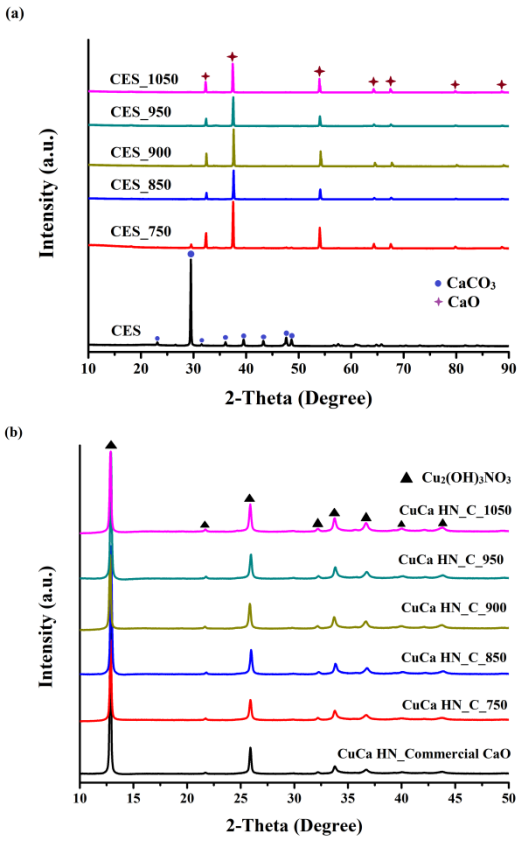

Figure 2. XRD patterns of (a) CES series, and (b) CuCa HN catalysts.

Figure 3(a) shows the FTIR spectra of CES and its corresponding calcined products. The spectra of CES gave a broadband at 1391 cm^{-1}, assigned to carbonate-based asymmetric stretching mode, and two sharp bands occurring at 872 cm^{-1} and 712 cm^{-1} are associated with out-of-plane and in-plane bending mode respectively of CO_3^{2-} groups. The absorption band of the carbonate group for calcined eggshell samples became weak from 750 ℃ up to 1050 ℃, which correlates with the loss of carbonate and functional group attached to the carbonate ion. And calcined eggshell sample showed an absorption peak at 3640 cm^{-1}, which is due to the O-H bond in $Ca(OH)_2$ formed from water absorbed on the surface of the sample.[21,22] IR spectra of catalysts derived from calcined eggshell and commercial CaO further confirmed the formation of $Cu_2(OH)_3NO_3$ and was given in Figure 3(b). The absorption peak in Figure 3(b) was centered at around 3541 cm^{-1} and 3400 cm^{-1}, which was indexed to OH group stretching. The IR bands at 1417 cm^{-1}, and 1310 cm^{-1} were due to the vibration of the NO_3^- group, a sharp peak at 1047 cm^{-1} was associated with N-O stretching from monodentate O-NO groups. The bands at 876 cm^{-1}, 769 cm^{-1}, and 666 cm^{-1}, were Cu-OH bending vibrations, IR bands at 507 cm^{-1} and 420 cm^{-1} might be due to the presence of metal-oxygen bonds[12,13,23,24].

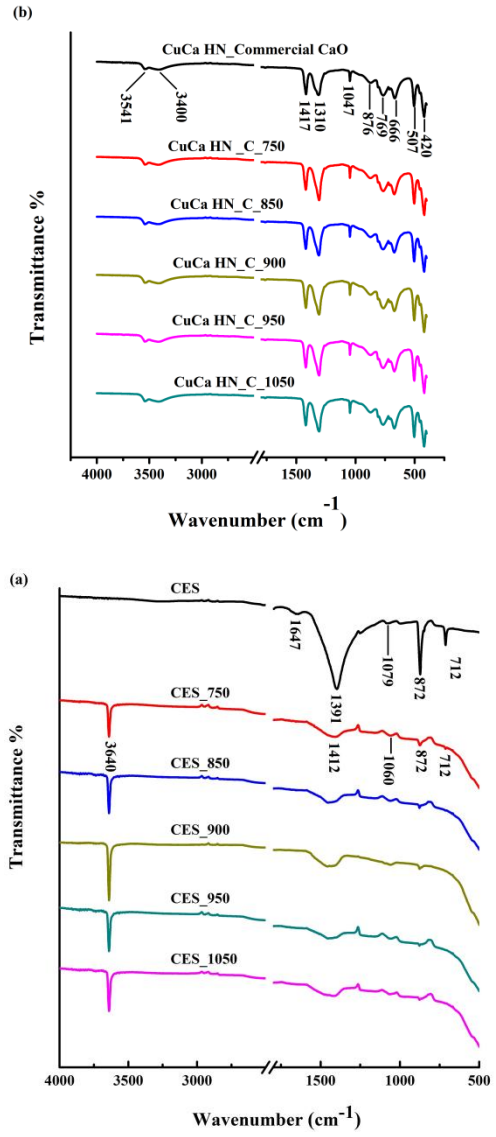

Figure 3. FTIR of (a) CES series, and (b) CuCa HN catalysts.

The cumulative particle size distribution of each bio-CaO sample and the characteristic diameter of D_{50} for each sample are shown in Figure 4. The order of particle size was CES_950 (1216 nm) > CES_1050 (1034 nm) > CES_750 (1034 nm) > CES_850 (953 nm) > CES_900 (747 nm). It suggests that higher calcination temperature from 750 ℃ to 900 ℃ can reduce the particle size of a hen eggshell. The particle size of calcined chicken eggshell would be directly proportional to the surface area.

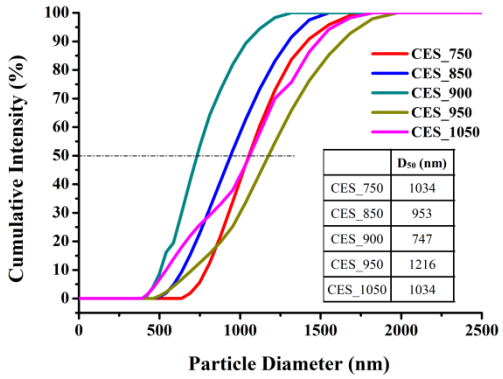

Figure 4. Particle size of calcined chicken eggshells.

The specific surface area of CES and bio-CaO samples was determined by BET surface area measurement (MicroActive ASAP 2460) based on N_2 adsorption, and listed in Table 2. It showed that the specific surface area of CES_750 is 7.22 m^2g^{-1} which is higher than that of CES (4.10 m^2g^{-1}). The increase of BET surface area with heating temperature correlates with weight loss in the TGA curves, which is related to a modification of the sample composition during calcination. At a calcination temperature of 900 ℃, the BET surface area of CES_900 increased significantly to 21.10 m^2g^{-1}, due to the crystal growth of calcium oxide as nearly complete decomposition of $CaCO_3$ to CaO at above 850 ℃, supported by TGA and XRD results. When calcination temperature was up to 950 ℃ and 1050 ℃, the specific surface area of CES_950 and CES_1050 was 4.5 m^2g^{-1} and 6.61 m^2g^{-1} respectively, slightly higher than that of CES, however less than that of CES_900, which might relate to the sintering effect brought on by extended heating at a higher temperature. In addition, the particle size of CES_900 (747 nm) was smaller than that of CES_750 (1034 nm) and CES_950 (1216 nm), indicating that the higher surface area of a sample contained from the smaller particle size of calcined eggshell. However, the BET surface area of the CES_850 sample (4.09 m^2g^{-1}) wasn't developed which might be due to the agglomeration of particles. The specific surface area of commercial CaO was 13.24 m^2g^{-1}, higher than calcined chicken eggshell excluded CES_900. It was reported that having a high specific surface area for CaO enhances the catalytic activity of CaO as a heterogeneous catalyst.[17,25,26]

The zeta potential of dried eggshell powder and its calcined products is listed in Table 2. It is noted that the zeta potential of raw chicken eggshells is negative (-22.32 mV) due to the formation of CO_3^{2-} ion in water. After calcination,

Table 2. The specific surface area of CES series and commercial CaO, and zeta potential of CES series.

Sample	Specific surface area (m^2g^{-1})	Zeta potential (mV)
CES	4.10	-22.32
CES_750	7.22	20.96
CES_850	4.09	24.32
CES_900	21.10	25.19
CES_950	5.00	21.48
CES_1050	6.61	21.50
Commercial CaO	13.24	-

the zeta potential of each calcined eggshell changed to positive and with a value similar to each other, suggesting the as-prepared eggshell calcined at 900 ℃ is relatively more stable in water than others and particle size is relatively smaller than others.

The elemental composition of CES and calcined eggshells is listed in Table 3. The detection of Ca was done by using FAAS (Perkin Elmer PinAAcle 900T) and trace elements were monitored by MP-AES (Agilent MPAES 4200). The data showed that Ca has 37.88 wt% obtained in raw chicken eggshell, the value was similar to the result from TGA (37.32 wt%). A small amount of Co, Mg, K, and Cd was also found in raw chicken eggshells. When calcined at different temperatures, the amount of Ca, Co, and Mg was slightly different. The Ca content in calcined chicken eggshells was higher than in raw eggshells. Hence, hen eggshell can be considered as a potential natural carbonate-based material.[22] The elemental compositions of CuCa HN catalysts were evaluated by EDX analysis, listed in Table 4. The elemental composition of as-prepared catalysts derived from chicken eggshell calcined at different calcination temperatures showed slight differences from each other, and a little higher than catalyst derived from commercial CaO.

Table 3. The elemental composition (% w/w) of CES series via FAAS analysis and MP-AES analysis.

Sample	[a]Ca	[b]Mg	[b]Co	[b]Cd	[b]K
CES	37.88	0.38	0.82	0.01	0.02
CES_750	47.88	0.68	1.78	0.02	0.03
CES_850	51.27	0.69	1.58	0.02	0.02
CES_900	48.51	0.67	1.62	0.01	0.02
CES_950	53.97	0.75	1.30	0.01	0.03
CES_1050	50.77	0.72	0.79	n.d	0.02

[a]Ca was evaluated via FAAS analysis, the standard deviation is within 1.7%, [b] (Mg, Co, Cd, K) was evaluated via MP-AES, the standard deviation is within 0.25%).

Table 4. The elemental composition (% w/w) of CuCa HN catalysts via SEM-EDX analysis. The standard deviation is within 2.65%.

Sample	Cu	Ca	O	N
CuCa HN_C_750	46.49	0.15	36.74	7.26
CuCa HN_C_850	45.42	0.11	41.46	8.36
CuCa HN_C_900	45.66	0.35	40.43	6.67
CuCa HN_C_950	51.12	0.24	37.22	6.73
CuCa HN_C_1050	51.73	0.20	36.06	4.91
CuCa HN_Commercial CaO	43.13	0.11	42.46	8.96

Figure 5 illustrates the particle size distribution of CuCa HN derived from calcined chicken eggshells and commercial CaO, it showed similar particle sizes of each other catalyst. Therefore, the chemical-physical properties of calcined chicken eggshells at different temperatures do not affect the properties of as-synthesized CuCa HN catalysts.

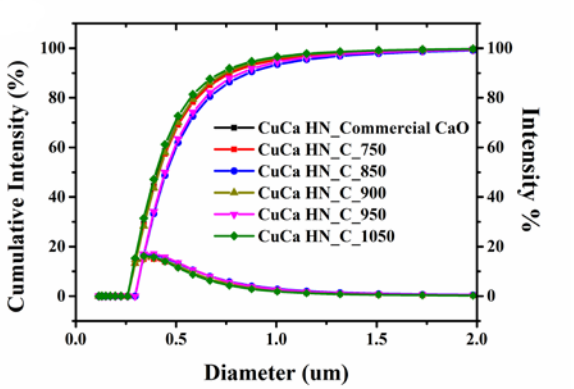

Figure 5. Particle size of CuCa HN catalysts.

3.2 Decolorization of methyl orange

The catalytic performance of the CuCa HN catalysts in the removal of MO solution was evaluated, as shown in Figure 6(a). It was found that the MO removal was nearly complete for 5 min for all catalysts, indicating the as-prepared CuCa HN materials are highly efficient CWAO catalysts in the degradation of MO. The amount of oxygen needed to oxidize the organic compound in water can be measured by the chemical oxygen demand (COD) method. Figure 6 (b) shows that more than 90 % COD removal efficiency was achieved in a 5-minute reaction for MO removal undergoing the CWAO process for all CuCa HN catalysts. It indicates effective mineralization of MO to produce carbon dioxide and water and intermediates having less chemical oxygen demand by using the catalysts. None of the catalysts give complete COD removal efficiency which might be due to the highly oxidation-resistant degradation products that could occur during the process.[12]

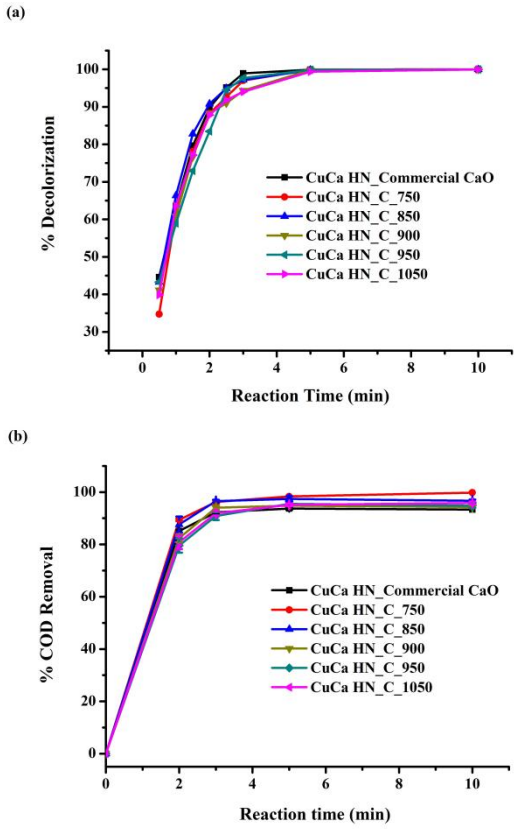

Figure 6. (a) MO removal efficiency, and (b), COD removal efficiency of CuCa HN catalysts.

The reusability of as-synthesized catalysts was studied by observing the continuous color removal efficiency of MO using 2 g/L catalysts under ambient conditions. The results from Figure 7 showed that color removal efficiencies for MO degradation using as-synthesized catalysts were more than 90 % for 3 consecutive cycles without purification in a 5-minute reaction. When the catalysts were further reused in the 4th run of the reaction, the MO removal efficiency using these catalysts was found to drop dramatically to around 50%, one of the reasons might be the loss of the catalyst when separating the treated MO supernatant and used catalyst. In order to obtain the catalytic activity by using these catalysts for further use in MO removal through the CWAO process. The catalysts after 3rd reaction cycle should be properly regenerated, such as rinsing with ethanol[27] or acetone,[28] a combination of rinsing in HCl and calcination,[29] a combination of pure water and calcination,[30] etc.

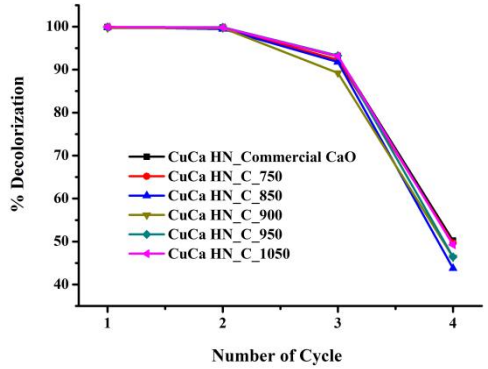

Figure 7. Reusability of CuCa HN catalysts.

4. Conclusion

The results from this work highlight the possibility of the economic preparation of CuCa HN derived from chicken eggshell waste, and an effective operational CWAO process for the degradation of concentrated MO dye in water using CuCa HN catalysts, which could be carried out under ambient conditions. Catalytic activity in MO removal and COD removal using CuCa HN derived from chicken eggshell in the CWAO system is comparable to the catalyst derived from commercial CaO. Bio-CaO can be completely converted from $CaCO_3$ and was found to be obtained in chicken eggshell calcined at a temperature above 850 ℃. The specific surface area of bio-CaO was different in calcination temperatures. The optimum calcination temperatures of 900 ℃ gave a relatively higher specific surface area of bio-CaO derived from chicken eggshell (21.10 m^2g^{-1}), and a relatively smaller particle size (747 nm). Continuously heating the eggshell samples to 950 ℃ and 1050 ℃, the surface area of bio-CaO decreased owing to sintering effects. Since eggshell waste is largely generated from egg processing industries, the utilization of the wastes could help reduce the cost of waste management for egg processing industries and help some wastewater treatment industries to reduce the expenditure on starting material to prepare catalysts in the degradation of organic pollutants in water.

Acknowledgements

YH received partial scholarship from Mahidol University. We thank Mahidol University-Frontier Research Facility (MU-FRF) for instrument supports, and the MU-FRF scientists, Nawapol Udpuay, and Dr. Suwilai Chaveanghong for their kind assistance in sample analyses.

References

1. Kavitha, V.; Geetha, V.; Jennita Jacqueline, P. *Process Safety and Environmental Protection*. **2019**, *125*, 279-287.
2. Faridi, H.; Arabhosseini, A. *Research in Agricultural Engineering*, **2018**, *64(2)*, 104-114.
3. Oliveira, D. A.; Benelli, P.; Amante, E. R. *Journal of Cleaner Production*. **2013**, *46*, 42-47.
4. Freire, M.; Holanda, J. *Cerâmica*, **2006**, *52 (324)*, 240-244.
5. Gaonkar, M.; Chakraborty, A. *Agricultural and Food Science*, **2016**, *5(3)*, 3520-3525.
6. Schaafsma, A.; Pakan, I.; Hofstede, G.; Muskiet, F.; Van Der Veer, E.; De Vries, P. J. P. s. *Poult Sci*, **2000**, *79 (12)*, 1833-1838.
7. Sharath, B.; Tiwari, R.; Mal, S. S.; Dutta, S. J. M. T. P. *Materials Today: Proceedings*, **2019**, *17*, 77-84.
8. Rivera, E. M.; Araiza, M.; Brostow, W.; Castano, V. M.; Dıaz-Estrada, J.; Hernández, R.; Rodrıguez, J. R. *Materials Letters*, **1999**, *41(3)*, 128-134.
9. Zhan, Y.; Zhou, X.; Fu, B.; Chen, Y. *Journal of Hazardous Materials*, **2011**, *187(1-3)*, 348-354.
10. Huang, K.; Wang, J.; Wu, D.; Lin, S. *RSC Advances*, **2015**, *5 (11)*, 8455-8462.
11. Zhan, Y.; Li, H.; Chen, Y. *J Hazard Mater*, **2010**, *180 (1-3)*, 481-5.
12. Weeramonkhonlert, V.; Srikhaow, A.; Smith, S. M. *Ceramics International*, **2019**, *45(1)*, 993-1000.
13. Srikhaow, A.; Smith, S. M. *Applied Catalysis B: Environmental*, **2013**, *130-131*, 84-92.
14. Muliwa, A. M.; Leswifi, T. Y.; Onyango, M. S. *Minerals Engineering*, **2018**, *122*, 241-250.
15. Ferraz, E.; Gamelas, J. A. F.; Coroado, J.; Monteiro, C.; Rocha, F. *Materials and Structures*, **2018**, 51 (5).
16. Park, H. J.; Jeong, S. W.; Yang, J. K.; Kim, B. G.; Lee, S. M. *Journal of Environmental Sciences*, **2007**, *19(12)*, 1436-1441.
17. Ferraz, E.; Gamelas, J. A. F.; Coroado, J.; Monteiro, C.; Rocha, F. *Materials and Structures*, **2018**, 51 (5).
18. Thomas, N. *Materials Research Bulletin*, **2012**, *47(11)*, 3568-3572.
19. Aguirre, J. M.; Gutiérrez, A.; Giraldo, O. *Journal of the Brazilian Chemical Society*, **2011**, *22 (3)*, 546-551.

20. Biswick, T.; Jones, W.; Pacuła, A.; Serwicka, E. *Journal of Solid State Chemistry*, **2006**, *179 (1)*, 49-55.
21. Correia, L. M.; Saboya, R. M. A.; de Sousa Campelo, N.; Cecilia, J. A.; Rodríguez-Castellón, E.; Cavalcante Jr, C. L.; Vieira, R. S. J. B. t. *Bioresource Technology*, **2014**, *151*, 207-213.
22. Boro, J.; Thakur, A. J.; Deka, D. *Fuel Processing Technology*, **2011**, *92 (10)*, 2061-2067.
23. Liu, B., One-dimensional copper hydroxide nitrate nanorods and nanobelts for radiochemical applications. Nanoscale 2012, 4 (22), 7194-8.
24. Wang, S.; Zhang, X.; Pan, L.; Zhao, F.-M.; Zou, J.-J.; Zhang, T.; Wang, L. *Applied Catalysis B: Environmental*, **2015**, *164*, 234-240.
25. Risso, R.; Ferraz, P.; Meireles, S.; Fonseca, I.; Vital, J. *Applied Catalysis A: General*, **2018**, *567*, 56-64.
26. Tan, Y. H.; Abdullah, M. O.; Nolasco-Hipolito, C.; Taufiq-Yap, Y. H. *Applied Energy*, **2015**, *160*, 58-70.
27. Zhang, Y.; Li, D.; Chen, Y.; Wang, X.; Wang, S. *Applied Catalysis B: Environmental*, **2009**, *86 (3-4)*, 182-189.
28. Najafi, M.; Abbasi, A.; Masteri-Farahani, M.; Janczak, J. *Polyhedron*, **2015**, *93*, 76-83.
29. Liu, Y.; Sun, D. *Applied Catalysis B: Environmental*, **2007**, *72 (3-4)*, 205-211.
30. Zheng, Y.; Jensen, A. D.; Johnsson, J. E. *Industrial & Engineering Chemistry Research*, **2004**, *43 (4)*, 941-947.

Performance evaluation of Phase Change Materials (PCMs) to improve energy-saving potential for buildings

Kanyamon Ausaman, Apinan soottitantawat, and Rungthiwa Methaapanon*

Center of Excellence in Material Processing and Particle Technology (CEPT), Department of Chemical Engineering, Faculty of Engineering, Chulalongkorn University, Bangkok 10330, Thailand

**E-mail: Rungthiwa.m@chula.ac.th*

Abstract:

Phase change materials (PCMs) have the potential to be used in building construction to reduce temperature fluctuations and reduce energy consumption, which helps to promote sustainability in the building sector. This research investigates the thermal performance and energy efficiency of PCMs integrated in a residential building located in Bangkok through an energy transfer simulation. DesignBuilder software was used to model typical residential buildings and numerically analyze the efficiency of indoor temperature reduction and annual energy savings. Buildings with the integration of a 2.5 cm-thick PCM layer in the wall were compared to those without PCM installation. PCMs with melting points ranging from 27 ˚C to 34 ˚C were studied. The energy-saving potential was studied for a building that operates its HVAC air conditioning system 24 hours a day. The results found that PCM with a melting point of 29 ˚C was the most suitable for use in buildings located in Bangkok due to the highest efficiency in annual energy savings of 167.0 kWh which translates to 738 baht saving in annual electricity bills. It was found to be the most effective to use in buildings during the summer. It potentially reduces the energy consumption for cooling by up to 35.9 kWh, which could save as much as 158 baht in March on electricity bills.

1. Introduction

Energy is crucial for the existence and development of humanity. The rapid progress of the economy and technology has brought the energy problem to the core of global attention.[1] For the past century, the globe has been faced with the issue of escalating energy requirements in residential buildings. This is mostly due to the growing global population and the expansion of urban societies, which has led to an increase in the number of buildings.[2] Hence, we are becoming apprehensive about potential energy issues that may arise in the future due to the escalating electricity demand (Energy Consumption), particularly in major urban areas.[3] According to reports from The International Energy Agency (IEA), building energy consumption has increased by 30% from 2010 to 2021. Additionally, the IEA discovered that heating and cooling systems accounted for up to 30% of the total energy used in buildings.[4] From 2020 to 2021, the energy consumption of the cooling system has increased by 6.5%, while the energy usage of the refrigeration unit has climbed by an average of 4% per year, which is twice the energy needed for indoor lighting.[5] Therefore, for a sustainable future, energy-saving technology should be used in buildings to reduce energy use within buildings in the future.

The introduction of thermal energy storage (TES) technology, which can retain heat energy during the phase change of the medium, is considered an interesting alternative. The medium materials, such as Phase Change Materials (PCMs), store heat energy from the environment as latent heat when the temperature of the environment is higher than the melting temperature of the material, and release it when the temperature of the environment is lower than the melting temperature. PCMs may help maintain a consistent temperature within the structure throughout the day. Consequently, the cooling load of electrical equipment in buildings is decreased. Currently, researchers extensively acknowledge the potential of Phase Change Material (PCM), particularly in its use for building constructions such as ceilings, floors, walls, and others.[6]

Energy simulation software tools are beneficial for energy-efficient building design. The energy simulation program allows accurate calculation of factors that could assist designers in making decisions about the optimum measures to take for buildings. About one-third of the energy utilized in buildings is put towards improving the performance of cooling systems and lights.[7]

This research investigated the effectiveness of using Organic Phase Change Materials with a melting temperature between 27 °C and 34 °C to reduce indoor temperatures and energy consumption in buildings by considering the weather conditions of Bangkok, a city located in the tropical savanna climate zone (Aw) according to Koppen-Geiger climate classification. Using DesignBuilder software and EnergyPlus,

numerical calculations can be made using modeling methods. Simulations utilizing the PCM can be performed at any location on the surface layout. Illustrations show the effects of incorporating PCMs within a wall structure, along with examples of the annual changes in energy efficiency resulting from the utilization of PCMs.[8]

2. Materials and Methods

2.1 Building reference

The building model as shown in Figure 1 was used to represent a typical residential building used for the study. The front of the residential building faces east. The dimensions of the building model are 9.0 x 9.0 x 3.5 m, with a 0.40 m pitched roof extending from the house and a roof slope of 30 degrees. The thermal and energy performance analysis includes the wall with and without PCM installation, as shown in Figure 2.

Figure 1. Typical building with PCM and without PCM

PCMs with melting points ranging from 27 °C to 34°C were investigated. The 2-digit suffix (PCMxx) refers to the melting point of PCM, for example, PCM27 has a melting point of 27 °C. As shown in the enthalpy-temperature curve, Figure 3, all PCMs are considered to have a specific heat of 2000 J/Kg-K and the same phase transition temperature range of 3.9 °C. PCM27 starts melting at 24.5 °C and completes the phase transition at 28.4 °C. Once the temperature of the environment increases and drives the PCM temperature to reach the melting point, PCM begins to melt, transitioning from a solid to a liquid state. The temperature remains relatively constant during the phase transition, shielding the inside from further temperature increase. During nighttime, when the temperature dropped below 27 °C, the PCM began to solidify by releasing the stored heat, leading to a slight rise in the surrounding ambient temperature.[9]

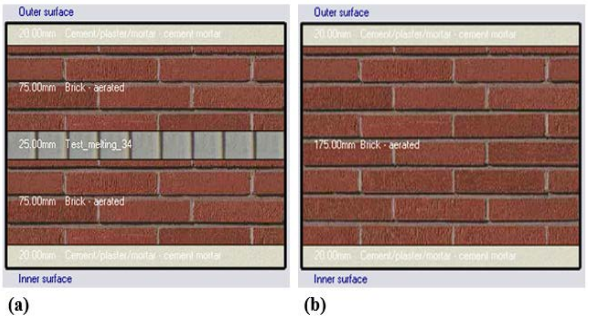

Figure 2. Details of (a) wall with PCM and (b) wall without PCM

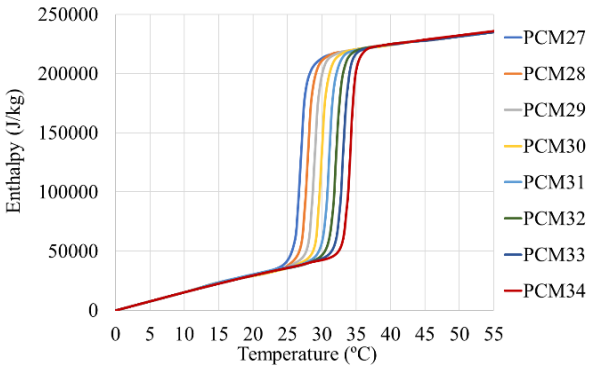

Figure 3. Enthalpy-temperature graph for PCM27 - PCM34

2.2 Weather data

The simulations used International Weather for Energy Calculation (IWEC-2) weather data files, recommended by the American Society of Heating, Refrigerating, and Air-Conditioning (ASHRAE). The climatic data from 'climatic.OneBuilding.Org', representing Typical Meteorological Years (TMY) was used. The location of the building under investigation is Bangkok.

2.3 Energy simulation

To evaluate the energy-saving potential of PCMs in buildings, this study utilized DesignBuilder V7.0.2.006, which uses the open-source code of EnergyPlus V9.4.0.002 to simulate indoor building climate and energy use for a detailed energy simulation. DesignBuilder software is widely acknowledged as the most extensive and proficient graphical user interface for EnergyPlus.[10] The software's capabilities including modeling construction materials, heating and cooling loads, cooling systems, lighting, ventilation, air conditioning, and energy flow, were leveraged to assess the impact of PCM integration on overall building energy performance.[11]

The EnergyPlus, a dynamic software for building energy simulation, was used to conduct numerical simulations of Phase Change Materials (PCMs). The Conduction Finite Difference (CondFD) solution algorithm was used to simulate PCMs, dividing the building envelope into nodes and solving heat transfer equations numerically using a finite difference method (FDM). The study used the fully implicit discretization method, which integrated the CondFD method with an enthalpy-temperature function to account for specific heat changes.[12] Subsequently, the enthalpies in each node are updated during each iteration, and subsequently utilized to derive an equivalent specific heat Cp at each time step.[13]

A finite difference algorithm was used to simulate phase change materials via enthalpy inputs at different temperatures. The phase change energy was considered by using the following equation:

$$\rho C_p \Delta x\left(\frac{T_{i,new}-T_{i,old}}{\Delta t}\right) = \frac{k_{int}(T_{i-1,new}-T_{i,new})}{\Delta x} + \frac{k_{ext}(T_{i+1,new}-T_{i,new})}{\Delta x} \quad (1)$$

$$k_{int} = \frac{k_{i+1,new}+k_{i,new}}{2} \quad (2)$$

$$k_{ext} = \frac{k_{i+1,new}+k_{i,new}}{2} \quad (3)$$

Where ρ is density (kg/m^3), C_p is specific heat capacity (kJ/kg K), Δx is layer thickness (m), T is node temperature (k), i is the node being modeled, $i+1$ is the node adjacent node to the interior of a construction, $i-1$ is the adjacent node to the exterior of construction, k is thermal conductivity (kW/m K), Δt is calculation time step (s), and h is enthalpy (kJ/kg)

For PCM, the specific heat capacity in each iteration is updated by using the following equation[14]:

$$C_p = \frac{h_{i,new}-h_{i,old}}{T_{i,new}-T_{i,old}} \quad (4)$$

Where h is a specific enthalpy (kJ/kg)

The annual energy saving (ES) along with energy consumption reduction (%ECR) calculated by using Eq. (5) and Eq. (6) for all PCMs melting points are shown in Table 1.

$$Es = EC(no\ PCM) - EC(PCM) \quad (5)$$

$$\%ECR = \frac{EC(no\ PCM)-EC(PCM)}{EC(no\ PCM)} \times 100\% \quad (6)$$

where EC = energy consumption (kWh), ECR = energy consumption reduction.[10]

The approximate annual electricity bill saving was calculated by using Eq. (7).

Annual electricity saving = ES (kWh) × Electricity rate (4.42Bath/kWh)[15] (7)

2.4 HVAC system

The heating and cooling energy demands were determined using the optimal load air module. The HVAC system operates continuously for 24 hours. The heating and cooling set points for residential buildings were set at 24°C and 26°C respectively.

3. Results & Discussion

3.1 Impact of Phase Change Materials on monthly energy savings

In Figure 4, the monthly energy-saving results of a building using PCM with a melting temperature between 27°C and 34°C are compared to a building without PCM in the walls. In March, PCM29 achieved a maximum energy saving of 35.9 kWh, and PCM30 saved 31.9 kWh in April, respectively. In this section, the monthly energy-saving efficiency of PCM at each melting point is related to the outside temperature of the environment. It was found that March had an average temperature of 29 °C and April had an average temperature of 30 °C, which corresponds to the melting points of effective PCM in March and April.

Meanwhile, it can be observed that PCM had higher energy-saving efficiency in March than compared to April. Figure 5 shows the daily energy-saving results for both months during the summer. This is the period when the use of cooling energy is the highest in the year. It shows that the year's highest outdoor temperatures occur in April, with this month having increased fluctuations in maximum temperatures and the trend of the minimum temperature fluctuating less than the highest temperature, as shown in Figure 5. The temperature fluctuation during the day is not enough to cause the PCM to cause a melting-freezing cycle, resulting in the PCM still solidifying at night. So thus, there were some days when the use of PCM in building walls required more energy for the cooling system than in the case of buildings without PCM in April. In addition, the cloud cover level in March was 52%–70% and the humidity comfort level was 92%, less than in April with 70–83% and 98%, respectively.[16] As a result,

the use of PCM in building walls in April had more negative energy-saving than in March. Consistent with research that has said that PCM is effective in reducing energy use in clear skies and dry air.[17]

In conclusion, PCM can effectively reduce the energy consumption of the cooling system during summer, which corresponds to the highest outside temperatures. Moreover, PCM with different melting temperatures exhibits different levels of energy-saving efficiency at different times of the year. It is evident that energy-saving efficiency gradually declines from August to December, which is during the rainy and winter seasons.

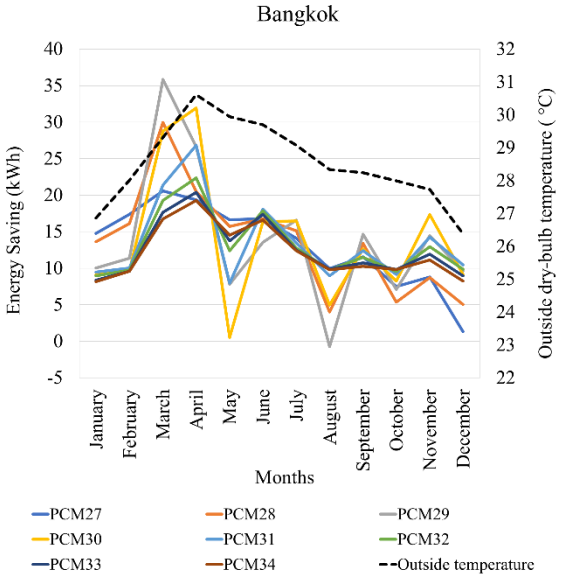

Figure 4. Monthly energy saving for cooling with PCM installation into a building.

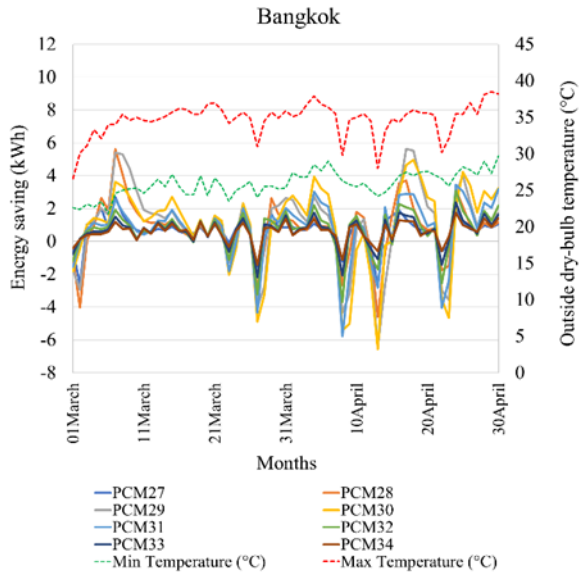

Figure 5. Daily energy saving (March – April) for the cooling system in a building.

3.2 Impact of PCMs on annual energy savings

The purpose of this section is to present a comparison between buildings that use PCM with a melting point of 27°C to 34°C compared to buildings without PCM in terms of annual energy savings, energy consumption reduction percentage, and electricity bill savings to determine the optimum melting point of PCM for use in Bangkok.

Figure 6 shows the annual energy savings and annual electricity bill savings for different melting point PCMs. As well as the %ECR calculated as the percentage energy consumption reduction for the cooling system compared to without PCM, as shown in Table 1. PCM29 shows its highest annual energy savings capability, reaching 167.0 kWh. This results in a cost reduction of up to 738 baht per year in electricity bills, with an energy consumption reduction (%ECR) of 0.385% per year when compared to buildings without PCM. This can be seen as consistent with the highest monthly energy-saving performance of PCM29, which attained the best energy savings in March.

Although PCM29 showed the most performance in this simulation, the %ECR values still fell short of the desired levels when compared to cities that were previously reported.[18] This depends on many factors such as the location of the PCM in the building wall, the thickness of the PCM layer, and the addition of the PCM layer.[10, 19]

Additionally, it has been suggested that PCM will be most efficient in situations where there is an average temperature fluctuation of 10 °C per day. If there is consideration for a city with a tropical climate, such as Bangkok, it becomes evident that nighttime temperatures are high. The effective cycle of PCM solidification and melting is impeded.[20]

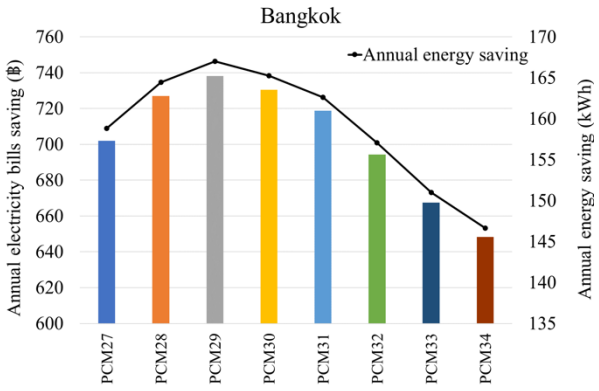

Figure 6. Annual electricity bill saving and annual energy saving for buildings in Bangkok.

Table 1. Annual Energy savings and Energy consumption reduction for all PCMs melting point.

PCM	ES (kWh)	Electricity bill saving (฿)	%ECR
PCM27	158.8	702	0.366
PCM28	164.5	727	0.379
PCM29	167.0	738	0.385
PCM30	165.3	731	0.381
PCM31	162.6	719	0.375
PCM32	157.1	694	0.362
PCM33	151.0	667	0.348
PCM34	146.7	648	0.338

4. Conclusion

The study investigates the monthly energy-saving results for a building that uses PCMs with a melting temperature ranging from 27°C to 34°C, compared to a building without PCM. PCM29 achieved the highest energy-savings of 35.9 kWh in March, which is related to the average temperature of 29°C in March. In April, May, and June, energy savings decreased. Meanwhile, the lowest energy-saving recorded in December was associated with the lowest outside temperature of the year.

Considering the annual energy-saving potential, PCM 29 has the highest annual energy-saving. It has annual energy savings of 167.0 kWh per year, while PCM30 and PCM28 have similar energy savings of 165.3 kWh and 164.5 kWh, respectively. The utilization of PCM in conjunction with the building cooling system results in significant savings in annual electricity bills. PCM29 proves to be the most effective, leading to a reduction of roughly 738 baht per year in electricity bills.

Acknowledgments

This research was supported by the Center of Excellence in Material Processing and Particle Technology (CEPT), Faculty of Engineering, Chulalongkorn University.

References

1. Wang, K. W.; Yan, T.; Pan, W. G. Optimization strategies of microencapsulated phase change materials for thermal energy storage. *Journal of Energy Storage* **2023**, *68*, 107844. DOI:https://doi.org/10.1016/j.est.2023.107844
2. Rahi, M. F.; Arıcı, M.; Abdulateef, A. M.; Niyas, H. Numerical investigation and optimization of macro-encapsulated phase change material capsules in building roof slab. *Journal of Energy Storage* **2023**, *68*. DOI: 10.1016/j.est.2023.107806.
3. Ascione, F.; Bianco, N.; Mauro, G. M.; Napolitano, D. F. Effects of global warming on energy retrofit planning of neighborhoods under stochastic human behavior. *Energy and Buildings* **2021**, *250*, 111306. DOI: https://doi.org/10.1016/j.enbuild.2021.111306.
4. Energy Statistics Data Browser. *IEA*. https://www.iea.org/data-and-statistics/data-tools/energy-statistics-data-browser (accessed.
5. Ürge-Vorsatz, D.; Cabeza, L. F.; Serrano, S.; Barreneche, C.; Petrichenko, K. Heating and cooling energy trends and drivers in buildings. *Renewable and Sustainable Energy Reviews* **2015**, *41*, 85-98. DOI: https://doi.org/10.1016/j.rser.2014.08.039.
6. Kant, K.; Anand, A.; Shukla, A.; Sharma, A. Heat transfer study of building integrated photovoltaic (BIPV) with nano-enhanced phase change materials. *Journal of Energy Storage* **2020**, *30*, 101563. DOI: https://doi.org/ 10.1016/j.est.2020.101563.
7. Sousa, J. R. B. Energy Simulation Software for Buildings : Review and Comparison. 2012.
8. Yang, S.; Oliver Gao, H.; You, F. Model predictive control in phase-change-material-wallboard-enhanced building energy management considering electricity price dynamics. *Applied Energy* **2022**, *326*, 120023. DOI: https://doi.org/10.1016/j.apenergy.2022.120023.
9. Alam, M.; Jamil, H.; Sanjayan, J.; Wilson, J. Energy saving potential of phase change materials in major Australian cities. *Energy and Buildings* **2014**, *78*, 192-201. DOI: https://doi.org/10.1016/j.enbuild.2014.04.027.
10. Sovetova, M.; Memon, S. A.; Kim, J. Thermal performance and energy efficiency of building integrated with PCMs in hot desert climate region. *Solar Energy* **2019**, *189*, 357-371. DOI: 10.1016/j.solener.2019.07.067.
11. Sousa, J. Energy simulation software for buildings: review and comparison. In *International Workshop on Information Technology for Energy Applicatons-IT4Energy, Lisabon*, 2012; Citeseer: pp 1-12.
12. Yang, T.; Ding, Y.; Li, B.; Athienitis, A. K. A review of climate adaptation of phase change material incorporated in building envelopes for passive energy conservation. *Building and Environment* **2023**, *244*. DOI: 10.1016/j.buildenv.2023.110711.
13. Tabares-Velasco, P. C.; Christensen, C.; Bianchi, M. Verification and validation of EnergyPlus phase change material model for

opaque wall assemblies. *Building and Environment* **2012**, *54*, 186-196. DOI: https://doi.org/10.1016/j.buildenv.2012.02.019.
14. Nazir, K.; Memon, S. A.; Saurbayeva, A.; Ahmad, A. Energy consumption predictions by genetic programming methods for PCM integrated building in the tropical savanna climate zone. *Journal of Building Engineering* **2023**, *68*, 106115. DOI: https://doi.org/10.1016/j.jobe.2023.106115.
15. Household electricity prices worldwide in June 2023, by select country.https://www.statista.com/statistics/263492/electricity-prices-in-selected-countries (accessed).
16. Spring Weather in Bangkok Thailand. https://weatherspark.com/s/113416/0/Average-Spring-Weather-in-Bangkok-Thailand#Figures-CloudCover (accessed.
17. Solgi, E.; Fayaz, R.; Kari, B. M. Cooling load reduction in office buildings of hot-arid climate, combining phase change materials and night purge ventilation. *Renewable Energy* **2016**, *85*, 725-731. DOI: https://doi.org/10.1016/j.renene.2015.07.028.
18. Ascione, F.; De Masi, R. F.; de Rossi, F.; Ruggiero, S.; Vanoli, G. P. Optimization of building envelope design for nZEBs in Mediterranean climate: Performance analysis of residential case study. *Applied Energy* **2016**, *183*, 938-957. DOI: https://doi.org/10.1016/j.apenergy.2016.09.02.
19. Zhu, N.; Liu, F.; Liu, P.; Hu, P.; Wu, M. Energy saving potential of a novel phase change material wallboard in typical climate regions of China. *Energy and Buildings* **2016**, *128*, 360-369. DOI: https://doi.org/10.1016/j.enbuild.2016.06.093.
20. Sadineni, S. B.; Madala, S.; Boehm, R. F. Passive building energy savings: A review of building envelope components. *Renewable and Sustainable Energy Reviews* **2011**, *15* (8), 3617-3631. DOI:https://doi.org/10.1016/j.rser.2011.07.014.

Simulation of hydrogen production from water-hyacinth with equilibrium reactors

Sirikul Boonterm and Deacha Chatsiriwech*

Chemical Engineering Department, Faculty of Engineering Chulalongkorn University 254 PhayaThai Road, Wang Mai, Pathumwan District, Bangkok 10330

E-mail: deacha.c@chula.ac.th

Abstract:

The dependency on non-renewable resources, particularly fossil fuels, to produce chemical and energy to support daily needs has resulted in growing negative environmental impacts. Climate change is one of the most significant impacts of greenhouse gas emissions, especially carbon dioxide (CO_2) from the combustion of fossil fuels. Currently, using renewable energy sources, hydrogen fuel (H_2) is a more interesting way to reduce the effects of climate change. Utilizing biomass conversion is one of sustainable renewable methods for producing H_2. A potential process that combines steam reforming (SR), CO_2 reforming (DR), and water gas shift (WS) reactions is called bi-reforming (BR). This process can be utilized for the generation of H_2 while capturing CO_2. The process has been simulated with a series of equilibrium reactors on Aspen plus process simulator for hydrogen production from Water-Hyacinth. The bi-reforming process has been investigated on a single equilibrium reactor (SR+DR+WS), 2 equilibrium reactors in series (SR+WS separate DR), and 3 equilibrium reactors in series (SR to WS to DR, DR to SR to WS, and SR to DR to WS). The investigated results have revealed that the equilibrium concentration of H_2 and CO products could be 0.48% and 0.52% respectively, at 950 ^oC 1 bar. Consequently, equilibrium reactor models could be employed for predicting equilibrium product distribution for well-defined catalytic reactions.

1. Introduction

Energy is an essential agent for meeting the energy needs of the humanity from turning on lights and faucets, to driving cars and riding in airplanes, to growing and cooking our food. With the growth of the world's population and the development of industries and technology, there is an increasing demand for energy.[1] In Thailand, Fossil fuels account for the greatest share of the country's annual primary energy consumption is 93.82 percent in 2019.[2] Using fossil fuels for energy has exacted an enormous toll on humanity and the environment. Fossil fuel combustion is a major source of carbon dioxide emissions (CO_2), an important element to increase the natural effects from water and air pollution to climate change and global warming.[3] Thus, one intriguing alternative is to look for alternative clean energy sources instead of fossil fuels.

Among the various alternative energy sources, Hydrogen fuel (H_2) is considered an important energy source for the future. It can be used as a vehicle fuel, an energy storage medium, a raw material for the chemical industry, and to generate electrical energy. Since H_2 is a highly efficient combustion fuel with the highest energy content per unit mass of any fuel (between 120 and 142 MJ/kg) and be the clean energy source produces only water as a by-product. The utilization of H_2 can significantly contribute to the reduction of greenhouse gas emissions and mitigate the impact of climate change. As a highly efficient and eco-friendly fuel, H_2 fuel is a highly attractive renewable source for conventional fossil fuels.[4]

H_2 can be produced using various methods, each with its own set of advantages and limitations. The most process in Thailand that is widely used commercially include methane reforming, gasification, and water electrolysis. Recent developments methane reforming process is bi-reforming (BR), involves the reaction of steam reforming (SR), CO_2 reforming (DR), and water gas shift (WS) to produce H_2-rich syngas (H_2 + CO). This process can be utilized for the generation of H_2 while capturing CO_2.[5]

The major reforming reactions taking place in methane bi-reforming are as follows:

Methane CO_2 reforming (DR):

$$CH_4 + CO_2 \leftrightarrow 2CO + 2H_2 \quad (1)$$

Methane steam reforming (SR):

$$CH_4 + H_2O \leftrightarrow CO + 3H_2 \quad (2)$$

Water gas shift (WS):

$$CO + H_2O \leftrightarrow CO_2 + H_2 \quad (3)$$

Terrell *et al.* (2019) have studied BR process through thermodynamic simulation compared with lab-scale experimentation at 950^oC. Experimentally showed 80-90% conversion with 1.48 maximum H_2:CO ratio. Simulation with Gibbs reactor (RGibbs), 100% conversion with

1.75 maximum H_2:CO ratio. H_2 and CO are the only major products formed at high temperatures and there is no significant improvement in conversions at temperatures in excess of 800 °C.[6]

The thermodynamic technique uses the RGibbs to minimize a system's Gibbs free energy, which eliminates the need for the reaction system's kinetic constants and yields the equilibrium composition for all chemical reactions between the components of the incoming streams. In this case, the experimental results in RGibbs are likewise not explained by the reaction stoichiometry. Use an additional reactor, such as an equilibrium reactor (REquil), to identify the possible reaction products in order to provide more specific verification.[7]

Otherwise, utilizing biomass conversion is one of sustainable renewable methods for producing H_2. The process has been simulated with a series of equilibrium reactors on Aspen plus process simulator for H_2 production from biomass such as Water-Hyacinth.

Water-hyacinth (*Eichhornia crassipes*) is a free-floating aquatic weed, which is a widely prevalent aquatic weed in Thailand, constitutes a potential biomass resource for various uses. Average water-hyacinth biomass productivity is 0.26 ton of dry biomass per hectare in all seasons. Due to its fast growth and the robustness of its seeds, water-hyacinth has caused many problems in the whole river area, i.e. a reduction of fish, physical interference with fishing. Water-hyacinth consists of three main fractions i.e., cellulose, hemicellulose and lignin. It has a high content of hemicellulose (30-55% of dry weight), which further pretreated and obtained hemicellulosic sugars as a by-product.[8]

Therefore, this research is interested in studying the simulation of H_2 production from water-hyacinth with equilibrium reactors by using the Aspen plus V.12 program to find the most suitable conditions for producing H_2-rich syngas. The variables that the study focuses on include temperature, pressure, concentration of reactants used in the H_2 production process, and series in reactor for predicting equilibrium product distribution for well-defined catalytic reactions.

2. Simulation research

2.1 Biomass extraction by RGibbs

Aspen Plus V.12 program was utilized to generate simulations for biomass bi-reforming with Gibbs reactor in a very simple flow process (Figure 1) with based solely on thermodynamic equilibrium and reaction kinetics are not necessary to reach a solution to find overall product in biomass extraction.

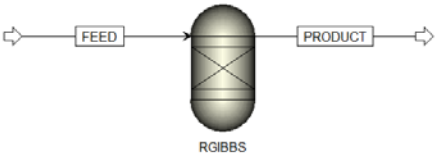

Figure 1. ASPEN flow schematic with RGibbs used in simulation.

Cellulose, hemicellulose, and lignin are represented (Figure 2), respectively, by the biomass characteristics created in Aspen with feed of LEVOGLUCOSAN ($C_6H_{10}O_5$-N1), BETA-D-XYLO PYRANOSE ($C_5H_{10}O_5$-D3), and 4-ALLYL-2-METHO XYPHENOL ($C_{10}H_{12}O_2$-N3).

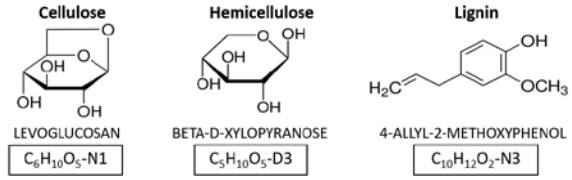

Figure 2. Representative biomass extraction feed input in Aspen.

The thermochemical biomass conversion can be further dehydrated and decomposed biomass to form a series of the unstable compounds (e.g., phenols, aldehydes, and ketones) and converted into light hydrocarbons (C_2-C_5) and aromatics as well as syngas (CO and H_2) as the allowed chemical species for products included.[9]

2.2 Methane Bi-reforming in REquil

The methane bi-reforming simulations with Equilibrium reactor process (Figure 3) were carried out for input in Table 1 and feeds in Table 2 with flowrate ratios of CH_4:H_2O:CO_2 in Table 3 The CO_2 in the reactant stream comes from a biomass gasifier inlet, along with appropriate amounts of CO, H_2, CH_4 and N_2 that are expected in the gasifier syngas. The CH_4 and H_2O streams were included to reach the desired inlet reactant ratios. The pressure for the process was set at 1 to 10 bar and temperature ranged from 600 to 1000 °C. The three inlet streams (gasifier, steam, and methane) were fed into a mixer and then into a Gibbs reactor. The allowed chemical species for products included H_2, N_2(inert), H_2O, CO, CO_2, and CH_4. Additionally, the series reactor type in Table 4 are observed in this study.

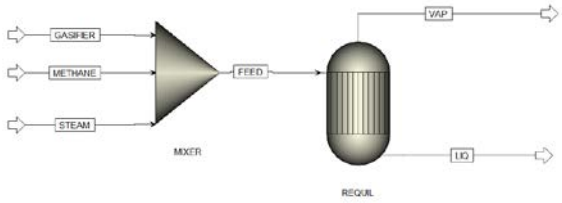

Figure 3. ASPEN flow schematic with REquil used in simulation (Type1).

Table 1. Attributes input in Aspen Plus.

Operating conditions and thermodynamic properties	
Temperature, °C	600–1000
Pressure, bar	1-10
Thermodynamic packages	Peng-Robinson
Input mode	Isothermal
Phase system	Vapor-liquid

Table 2. Mole fraction of each gas in inlet flow streams.

Inlet streams	H_2	N_2	H_2O	CO	CO_2	CH_4
GASIFIER[a]	0.18	0.48	0	0.18	0.14	0.02
METHANE[a]	0	0	0	0	0	1
STEAM[a]	0	0	1	0	0	0
CO_2	0	0	0	0	1	0

Table 3. Flow rate (mol h^{-1}) of inlet streams with excess H_2O and CO_2.

Inlet streams (CH_4:H_2O:CO_2)	GASIFIER	METHANE	STEAM	CO_2
3 : 1 : 1	64.90	26.01	9.09	–
3 : 2 : 1	59.49	23.86	16.65	–
3 : 3 : 1	59.49	23.86	25.05	–
3 : 4 : 1	59.49	23.86	34.00	–
3 : 5 : 1	59.49	23.86	42.00	–
3 : 6 : 1	59.49	23.86	50.00	–
3 : 7 : 1	59.49	23.86	59.00	–
3 : 2 : 2	59.49	23.86	16.65	8.33
3 : 2 : 3	59.49	23.86	16.65	16.72
3 : 2 : 4	59.49	23.86	16.65	24.97
3 : 2 : 5	59.49	23.86	16.65	33.30

Table 4. Series reactors type in simulation.

Types	Reactor1	Reactor2	Reactor3
1.	SR,DR,WS	–	–
2.	SR,DR	WS	–
3.	WS	SR,DR	–
4.	SR,WS	DR	–
5.	DR	SR,WS	–
6.	DR,WS	SR	–
7.	SR	DR,WS	–
8.	SR	WS	DR
9.	DR	SR	WS
10.	SR	DR	WS

2.3 Water-hyacinth bi-reforming in REquil

In this study, the simulations for Water-Hyacinth bi-reforming with Aspen's Equilibrium reactor are focuses on stuitable condition of series reactor type1 at 950 °C 1 bar adapting with Water-Hyacinth feed as Table 5 for predicted product.

Table 5. Characteristics of whole water hyacinth plant.

Water content (%.wt)	Organic component (%.wt)[a]			
	Cellulose	Hemi-cellulose	Lignin	Other
95.3	16.2	55.5	6.1	22.8

a; on a dry basis.

2.4 Performance bi-reforming in REquil

In the present study, Aspen Plus simulations were conducted at various operating conditions including Water-Hyacinth bi-reforming and methane bi-reforming process. The influence of the operating temperature, pressure and feed concentration are observed.

All results for product composition are determined in term of conversions (A), yield (B), selectivity (C), and enthalpy (D) were calculated based on the simulation results and plotted appropriately by equations below, where F represents flow rate, R represents reactant, and P represent product:

$$Conversion\ R_i = \frac{F_{R_i in} - F_{R_i out}}{F_{R_i in}} = 1 - \frac{F_{R_i out}}{F_{R_i in}} \quad \text{(A)}$$

; $i = CH_4, CO_2, H_2O$ or Biomass

$$Yield\ P_i = \frac{F_{P_i in}}{F_{R_j in}} \quad \text{(B)}$$

; $i = H_2$ or CO, $j = CH_4$ or Biomass

$$Sensitivity\ R_i = Conversion\ R_i \times \frac{F_{R_i in}}{F_{R_j in}} \quad \text{(C)}$$

; $i = H_2O$ or CO_2, $j = CH_4$ or Biomass

$$Enthalpy\ per\ H_2 = \frac{\Sigma(\Delta Enthalpy_{inlet} + \Delta Heat\ duty)}{\Delta F_{H_2 out}} \quad \text{(D)}$$

3. Results & Discussion

3.1 Biomass bi-reforming equation

After extracting biomass in RGibbs, the result of simulation showed the final product compound in Table 6 is the most product concentration is syngas (CO, H_2) than other compound. It seems that we can create biomass bi-reforming equation as in Table 7.

Table 6. Biomass extraction product compound.

Biomass extraction product compound	Mole fraction
H_2	0.3345
CO	0.4900
Alkane,Alkene (C_2H_2,C_2H_4,C_3H_4,C_3H_6)	0.1743
Phenols,Aldehydes,Ketones (C_6H_5OH,CH_2O,C_3H_6O)	0.0013

The major biomass bi-reforming reactions are as follows:

Biomass CO_2 reforming (BDR):

$$C_6H_{10}O_5 + H_2O \leftrightarrow 6CO + 6H_2 \quad (4)$$

$$C_{10}H_{12}O_2 + 8H_2O \leftrightarrow 10CO + 14H_2 \quad (5)$$

Biomass steam reforming (BSR):

$$C_6H_{10}O_5 + CO_2 \leftrightarrow 7CO + 5H_2 \quad (6)$$

$$C_{10}H_{12}O_2 + 8CO_2 \leftrightarrow 18CO + 6H_2 \quad (7)$$

The hemicellulose can be extracting by them-self with Hemicellulose thermal cracking (HTC) reaction as follows:

$$C_5H_{10}O_5 \leftrightarrow 5CO + 5H_2 \quad (8)$$

Table 7. Summary of the methane and biomass reforming reactions.

		Reaction in reactor
Eq1.	DR:	$CH_4 + CO_2 \leftrightarrow 2CO + 2H_2$
Eq2.	SR:	$CH_4 + H_2O \leftrightarrow CO + 3H_2$
Eq3.	WS:	$CO + H_2O \leftrightarrow CO_2 + H_2$
Eq4.	CDR:	$C_6H_{10}O_5 + CO_2 \leftrightarrow 7CO + 5H_2$
Eq5.	CSR:	$C_6H_{10}O_5 + H_2O \leftrightarrow 6CO + 6H_2$
Eq6.	LDR:	$C_{10}H_{12}O_2 + 8CO_2 \leftrightarrow 18CO + 6H_2$
Eq7.	LSR:	$C_{10}H_{12}O_2 + 8H_2O \leftrightarrow 10CO + 14H_2$
Eq8.	HTC:	$C_5H_{10}O_5 \leftrightarrow 5CO + 5H_2$

3.2 Methane bi-reforming in REquil

The methane bi-reforming is performed by comparing the predicted syngas composition between model experiment data, Rgibbs and REquil models with ratios of CH_4:H_2O:CO_2, namely, 3:1:1 and 3:2:1. The result of syngas composition as mole fraction in Table 9. REquil type 1,2,3,5,6,and7 are in the same result data and nearly RGibbs result. The other REquil types 4,8,9, and 10 have a little different result data.

3.3 Water-hyacinth bi-reforming in REquil

The prediction of Water-Hyacinth bi-reforming from Aspen plus showed the in same condition with methane, the H_2 and CO concentration have mirrored. The H_2 concentration is less than CO but the reactant consumption is fully.

3.4 Performance of bi-reforming in REquil

The discussion of the influence of operating conditions is presented herein.

A. Effect of temperature

Based on the data showed in these graphs (Figure 4), it can be observed that the simulation the varies temperature in $CH_4 : H_2O : CO_2$ inlet 3 : 2: 1 with increasing temperature appear to contribute to increasing H_2 production. While increasing from 600 °C to a reactor temperature roughly 800 °C, the mole fraction of H_2 concentration rises steadily at this temperature. Types 1,2,3,5,6, and 7 are also in the same result data, but different with Type4, Type8, Type9, and Type10, respectively, while decreasing temperature.

Table 8. Comparison of Methane and Water-Hyacinth bi-reforming product composition.

Product composition	Methane	Water-Hyacinth
CH_4	0.0476	-
CELLULOSE	-	0.0000
HEMICELLULOSE	-	0.0000
LIGNIN	-	0.0000
H_2O	0.0004	0.0000
CO_2	0.0002	0.0000
H_2	0.5948	0.4773
CO	0.3571	0.5227

B. Effect of pressure

The varies pressure in $CH_4 : H_2O : CO_2$ inlet 3 : 2: 1 by series reactor type (Figure 5), while the pressure has less effect on H_2 concentration as increasing pressure from 1 to 10 bar. The increasing pressure appear to contribute to decrease H_2 production. Types 1,2,3,5,6, and 7 are also in the same result data, but different with Type4, Type8, Type9, and Type10, respectively, while increasing pressure.

Table 9. Methane reforming reaction type in simulation.

Reactor	Ratio	CH_4	CO_2	H_2O	CO	H_2
Experimental*	3:1:1	0.0700	n/a	n/a	0.2500	0.3100
Experimental*	3:2:1	0.0400	n/a	n/a	0.2500	0.3700
RGibbs	3:1:1	0.0671	0.0000	0.0001	0.2855	0.4187
RGibbs	3:2:1	0.0040	0.0010	0.0025	0.2911	0.5096
REquil (Type1,2,3,5,6,7)	3:1:1	0.0671	0.0000	0.0001	0.2855	0.4187
REquil (Type1,2,3,5,6,7)	3:2:1	0.0040	0.0010	0.0025	0.2911	0.5096
REquil (Type4)	3:1:1	0.0670	0.0000	0.0000	0.2856	0.4189
REquil (Type4)	3:2:1	0.0023	0.0018	0.0001	0.2910	0.5137
REquil (Type8)	3:1:1	0.0670	0.0000	0.0000	0.2856	0.4189
REquil (Type8)	3:2:1	0.0023	0.0018	0.0001	0.2910	0.5137
REquil (Type9)	3:1:1	0.0671	0.0000	0.0001	0.2855	0.4188
REquil (Type9)	3:2:1	0.0034	0.0008	0.0021	0.2914	0.5106
REquil (Type10)	3:1:1	0.0670	0.0000	0.0000	0.2856	0.4189
REquil (Type10)	3:2:1	0.0023	0.0005	0.0013	0.2922	0.5125

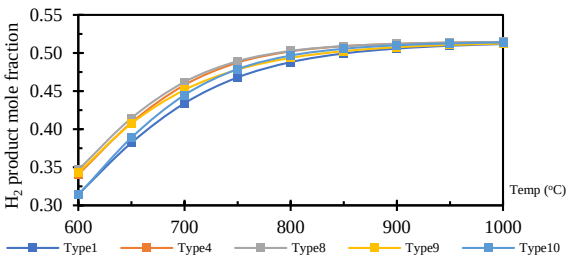

Figure 4. Simulated temperature reactor products CH_4:H_2O:CO_2 ratio inlet 3:2:1; Type1, Type4, Type8, Type9, and Type10.

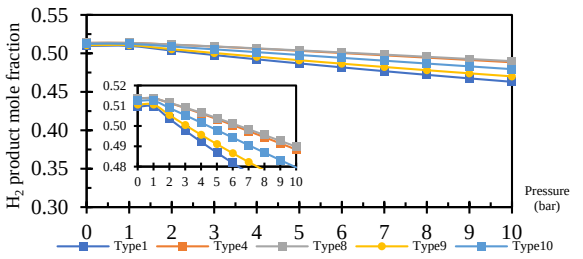

Figure 5. Simulated pressure reactor products CH_4:H_2O:CO_2 inlet 3:2:1; Type1, Type4, Type8, Type9, and Type10.

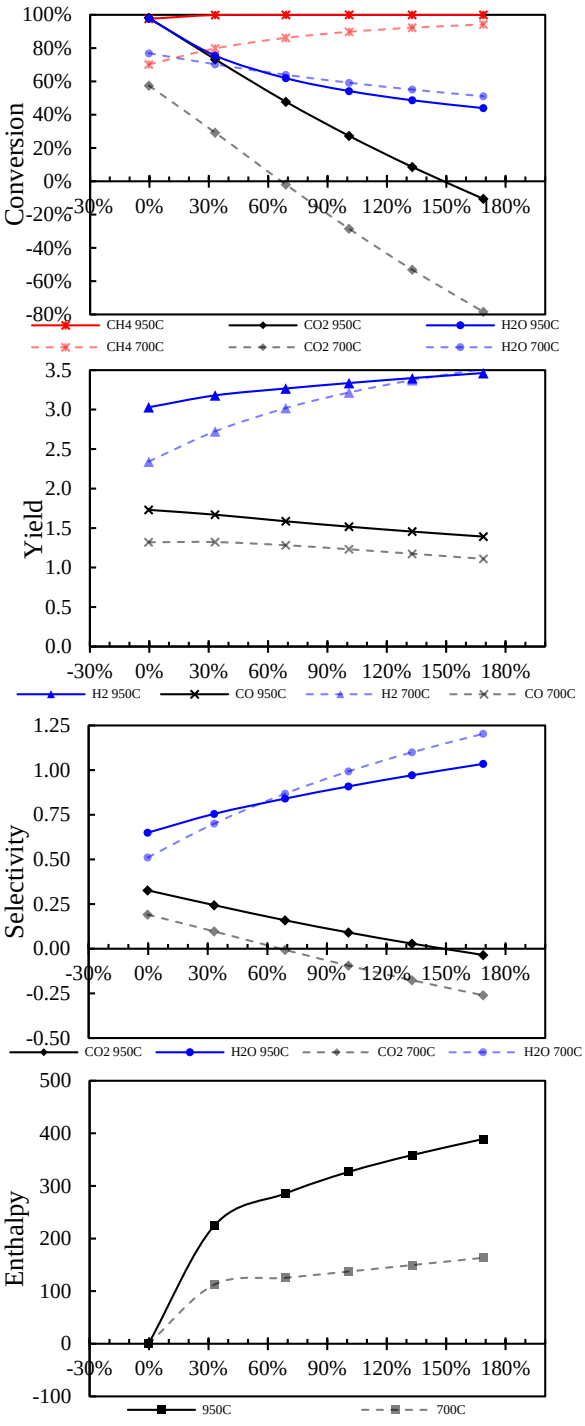

Figure 6. Performance of methane bi-reforming in REquil with excess H_2O feed ; Conversion, Yield, Selectivity, and Enthalpy.

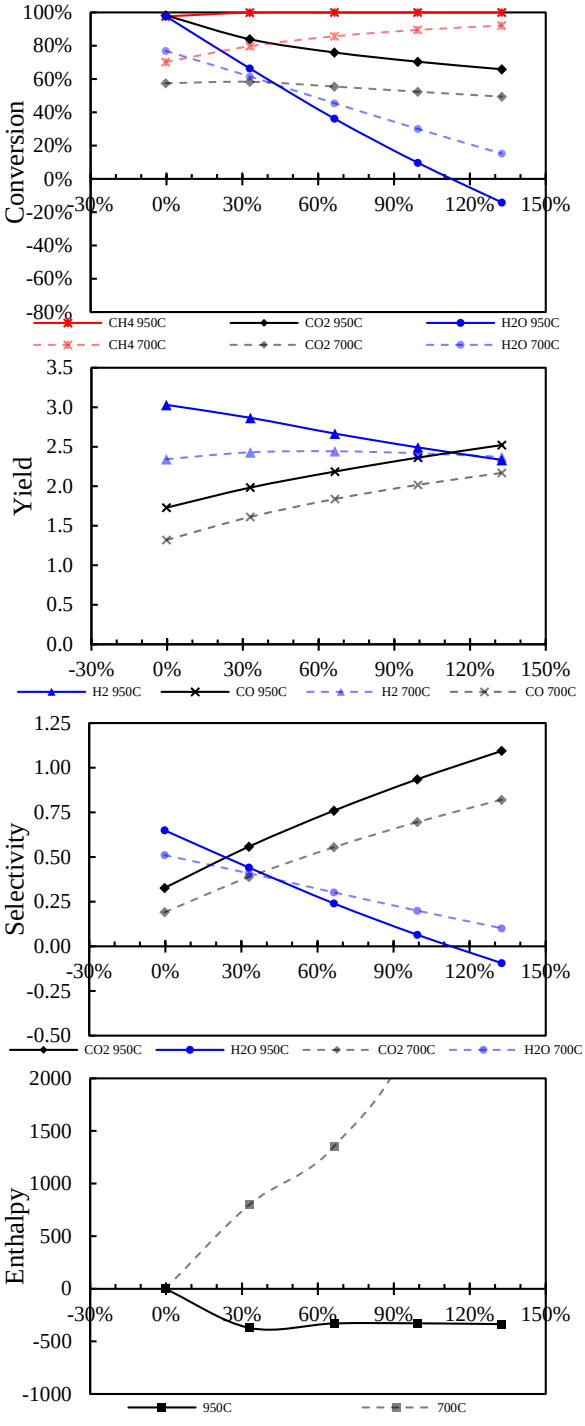

Figure 7. Performance of methane bi-reforming in REquil with excess CO_2 feed ; Conversion, Yield, Selectivity, and Enthalpy.

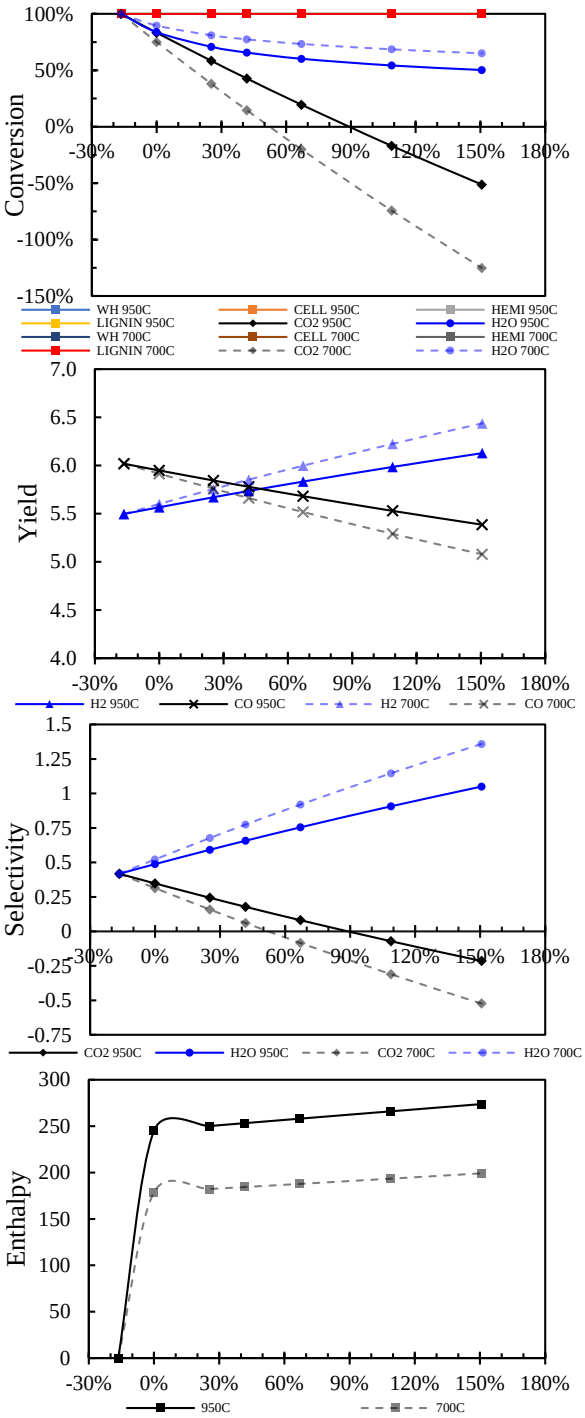

Figure 8. Performance of Water-Hyacinth bi-reforming in REquil with excess H_2O feed ; Conversion, Yield, Selectivity, and Enthalpy.

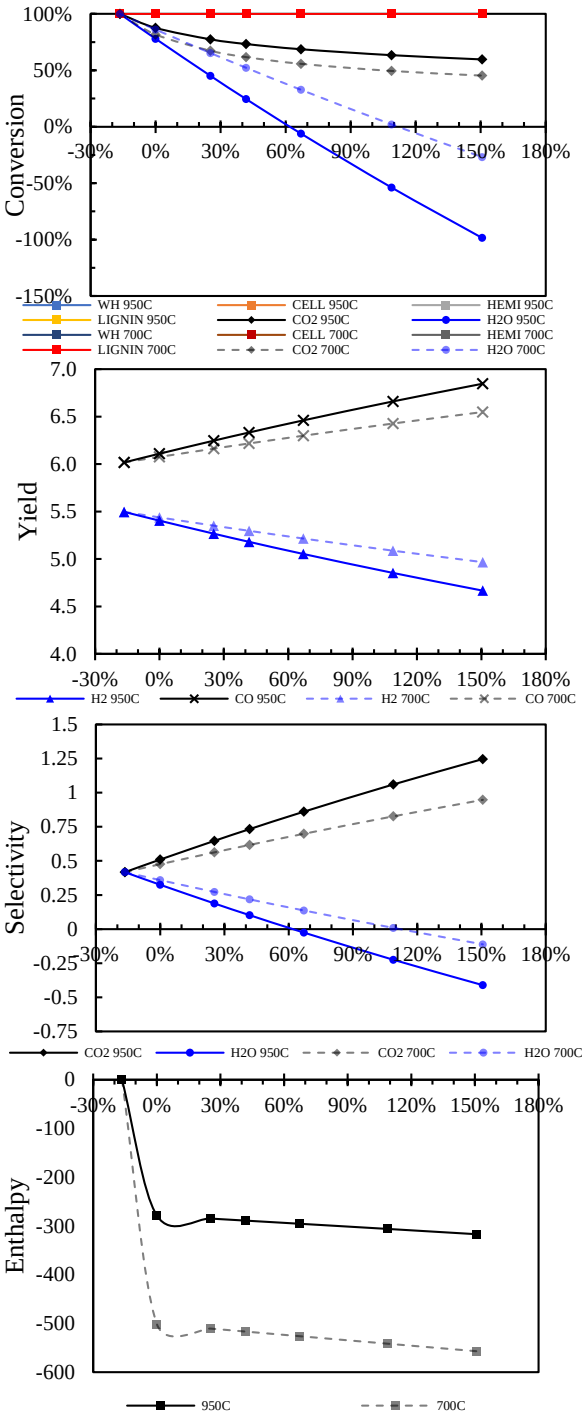

Figure 9. Performance of Water-Hyacinth bi-reforming in REquil with excess CO_2 feed; Conversion, Yield, Selectivity, and Enthalpy.

C. Concentration in feed

The excess H_2O concentration feed in methane bi-reforming at 700 and 950 °C, 1 bar (Figure 6) showed increasing CH_4 conversion close to 100% with decreasing H_2O and CO_2 conversion. The CO_2 conversion more decreases than H_2O. At 169% excess H_2O, the increasing H_2 yield are along increasing and finally meet in 3.5 yield. The increase H_2O and decrease CO_2 selectivity are resulted when excess H_2O. The CO_2 selectivity stop produce on 70% and 150% excess. With high CH_4 and H_2O conversion, high H_2 yield and high H_2O selectivity are need the enthalpy at 750 and 950 °C totally 165.55 and 389.25 btu per ton H_2, respectively. The result that seems the increasing excess H_2O concentration at 750 °C are used less enthalpy for H_2 production.

The excess CO_2 concentration feed in methane bi-reforming (Figure 6) are also showed the H_2O conversion more decreases than CO_2 and stop converse on 110% excess at 950 °C. The increases CO yield max at 2.521 and decrease H_2 yield are present in this concentration. The higher CO_2 selectivity and lower H_2O selectivity is stopped with 110% excess at 950 °C. The H_2 production at 700 °C with excess CO_2 more than 90% excess are over enthalpy to 2,000 btu per ton H_2 and at 950 °C showed that excess CO_2 no suitable for H_2 production.

The excess H_2O and CO_2 concentration feed in water-hyacinth bi-reforming at 700 and 950 °C, 1 bar (Figure 8 and 9) showed the conversion, yield, selectivity and enthalpy results same as the methane bi-reforming results concepted. The result in this study showed that the suitable condition for H_2 production from water-hyacinth bi-reforming is while excess H_2O at 700 °C, this condition used the less enthalpy only 200 btu per ton H_2 and more H_2:CO ratio with 1.28, while 150% excess H_2O. The CO_2 selectivity in water-hyacinth bi-reforming reaction stop produce at 90% excess H_2O.

4. Conclusion

In this study, the equilibrium results in the H_2 and CO products may be 0.48% and 0.52%, respectively, at 950 °C 1 bar, according to the simulation of hydrogen production from Water-Hyacinth with equilibrium reactors by Aspen plus researched results. Based on the analyzed results, the following conclusions could be addressed: The increase H_2 concentration temperature had a positive effected by the increase temperature and decrease pressure. The H_2O excess feed led to the formation of H_2 concentration, mirrored the CO_2 excess feed led to formation CO concentration. The H_2:CO yield ratio more than 1.28, while >150% excess H_2O at 700C. The Water-Hyacinth bi-reforming process was able to enhance the H_2 yield and enthalpy efficiency. The present work could give an idea of the conceptual process design of Water-Hyacinth Bi-reforming processes for more improvement.

Acknowledgements

The authors would like to thank Assoc. Prof. Deacha Chatsiriwech for assistance with this research. The commercial Aspen Plus software was used to simulate the thermodynamic modeling which is licensed and fully supported by Chemical Engineering, Chulalongkorn University.

References

1. Kabeyi MJB., Olanrewaju OA. Sustainable Energy Transition for Renewable and Low Carbon Grid Electricity Generation and Supply. Frontiers energy research: Vol. 9, 2021; pp 1-45.
2. Ritchie H, Roser M. Thailand: Energy Country Profile. https://ourworldindata.org/energy/country/thailand. (accessed August 30, 2023).
3. Lindsey R., Dlugokencky ED. Climate Change: Atmospheric Carbon Dioxide. https://www.climate.gov/news-features/understanding-climate/climate-change-atmospheric-carbon-dioxide (accessed December 30, 2023)
4. Hantoko D., Su H. Thermodynamic study on the integrated supercritical water gasification with reforming process for hydrogen production: Effects of operating parameters. International Journal of Hydrogen Energy. Vol. 43, 2018; pp 17620-7632.
5. Somchit S., Talhakulthorn S., Mungkalasiri W. Simulation analysis of hydrogen production from biogas via tri-reforming. Thammasat engineering journal: Vol. 4 No. 2, 2018; pp 5-12.
6. Terrell E., Theegala CS. Thermodynamic simulation of syngas production through combined biomass gasification and methane reformation. Sustainable Energy Fuels: Vol.3, 2019, pp 1562-1572.
7. Gibbs vs. Equilibrium Reactor. https://www.owlnet.rice.edu/~ceng403/hysys/gibbs.html (accessed December 30, 2023)
8. Pattra S.,Sittijunda S. Optimization of Factors Affecting Acid Hydrolysis of Water Hyacinth Stem (Eichhornia Crassipes) for Bio-Hydrogen Production. Energy Procedia: Vol. 79, 2015; pp 833-837.
9. Liu WJ., Yu HQ. Thermochemical Conversion of Lignocellulosic Biomass into Mass-Producible Fuels: Emerging Technology Progress and Environmental Sustainability Evaluation. ACS Environmental. 2022; 98-114.

Study of the content of particulate matter in the office and working unit of Muban Chombueng Rajabhat University

Paitoon Mueanpetch*, Juntima Donjuntai, and Khanatthapan Parnnarong

Department of Occupational Health and Safety, Faculty of Industrial Technology
Muban Chombueng Rajabhat University, Ratchaburi

**E-mail: paitoonmue@mcru.ac.th*

Abstract:

The purpose of this study is to determine the particulate content and size measured in the office or working unit of Muban Chombueng Rajabhat University (MCRU), Rachaburi. The particulate matter measurement was done from February to March 2023 which is the high $PM_{2.5}$ content and brought to the different content of each particle. Aerocet 381 is an automatic particle measuring that measures 5 types of particulate matter TSP, PM_{10}, PM_4, $PM_{2.5,}$ and PM_1. The working units were divided into educational units; the office of the Dean, including the office of the director of the demonstrate school; and supporting working units that were separated as 1) working units on stand-alone buildings and 2) working units on office buildings with boundaries. The tool was installed and collected particles during working hours (8 h.) in each working unit. The results show that $PM_{2.5}$ is higher than the Thai Air Quality Standard (TQAS) in 10 working units. These working units are stand-alone buildings with there are wind-received or there are no buffer trees against the wind. Moreover, from 10 working units, 3 working units are PM_{10} raised over the TQAS. Another thing worth noting, some working units had PM_1 raised abnormally, however, the standard of PM_1 does not control the content of PM_1 in air quality. From this study, the different areas an important for finding the prevention and control the PM problems in the office for risk or danger health reduction from particulate for officers.

1. Introduction

The cause of PM2.5 ultimately affects humans in changing health problems and diseases related to winter transportation in Thailand along the route, problems with the amount of dust that has reached a critical level and there is still a period for the dust to occur continuously throughout the winter. The amount of dust and the weather conditions that occur in which the dust can be released or dispersed, the dust will move from the outside into the interior works through various routes, such as, for example, closing the office door. Dust comes from everyone entering and leaving the workplace and openings in buildings, and most importantly, there will be dust everywhere. Workplaces or closed areas, according to a study by Nezis I.[1] and colleagues in 2019 to investigate and survey, found that PM2.5 results in health problems. (Investigation of eyes, dry cough, runny nose can be found at Very tired, headache and reducing the intoxication that confuses again directly, which will result in PM2.5 as a consequence of the efficiency and noise that has not yet reached this stage and is often found in part of people Offices that must be exposed to PM2.5 at the same time and the study of Yu Y. et al.[2] (2023) studied the phenomenon of forest fires and were able to produce PM2.5 that could detect PM2.5 in the event of a forest fire emergency. Affects the symptoms of chronic illness, even if it occurs in an open area, it still occurs in a survey of the physiology of the metabolic system. The reason for being off work and still being important at work, which may be an important reason apart from the general symptoms of the case study of Nezis I. et al. in the area where the forest incident occurred, it was found that A study of the case of exposure to PM2.5 dust and known health effects of people in garbage collection areas in New Zealand[3] PM2.5 concentration in the amount of 87.5 - 1080 micrograms per sip. m. The health check was at the level of 1.61 and 3.02. Sometimes work and various symptoms may be caused by cough, headache, or eye. Needless to say, special vigilance is required to find a solution to the dust problem.

The amount of PM that occurs in that building will have a further impact on the health and working conditions of workers, especially in workplaces that are not cleaned or have improper ventilation. The dust level set by the Pollution Control Department (2023)[4] is currently the $PM_{2.5}$ level in 24 hours not to exceed 37.5 $\mu g/m^3$ and not to exceed 15 $\mu g/m^3$ in a year. However, PM and various things are still able to enter the workplace. The grip on various objects in the office is still a problem that requires consideration of the health of workers in the workplace and the amount of various dust particles present in the office. Another thing is that the office building is considered a barrier to prevent dust from entering the work area.

Entrance and exit design ventilation characteristics, including the outside landscape will affect the amount of dust that can enter.

In addition, the amount of dust inside the home was studied using air quality measuring devices available on the market. together with considering movement-related routines to study exposure to $PM_{2.5}$ within the home,[5] it was concluded that If you are not interested in human movement and spatial changes then Solving the $PM_{2.5}$ dust problem with a dynamic approach will help to plan and create policies to solve the $PM_{2.5}$ problem in a way that is not caused by normal human movement or exposure. In the study, Kellnerova' E. et al. (2018)[6] studied and evaluated PM exposure in fire rescue operations. The amount of dust in the conditioning room and chemistry laboratory was found to be $1.02x10^4$ and $2.51x10^4$ respectively, similar to the study by Yurtseven E. et al (2012)[7] who studied the amount of $PM_{2.5}$ dust inside the faculty building. Medicine in Istanbul, Turkey, found that during 8 working hours, the highest amount was 388.5 $\mu g/m^3$ at the faculty office building and the highest average was 160.1 $\mu g/m^3$ in the waiting room in the operations center. This is significantly higher than the value set by the World Health Organization. The next danger, besides the high amount of PM2.5, is things that are attached to PM2.5 dust, such as a study by Niu Y. et al.[8] in 2021 that analyzed the composition of heavy metals in dust measured from factories. It was found that from dust analysis, very high levels of As, Mn, and Cd were found, and all three of these types were dangerous and had serious health effects on humans. They further studied the sources and found that 34.7% came from cooking for As, while Mn and Cd came from rock fragments from earthquakes and the movement of kitchen equipment, etc. In addition to heavy metals, there is also a study of the PAHs group of substances that are on PM2.5. Abdull N. et al.[9] (2021) studied the concentration of PAHs and metals that come with PM2.5 in Industrial areas of Malaysia It was found that the ratio of the inside and outside areas of the measurement It was found the number of PAHs was found to be greater in the area of the production unit, while PM2.5 and heavy metals were found more in areas outside than in areas inside the production unit. However, all these studies the study has not yet focused on the characteristics of the office structure or many agencies that will be affected by PM2.5, including landscape design that will reduce the problem of $PM_{2.5}$

In this study, we measured and analyzed dust with an automatic dust reader for 8 working hours in various locations of the agency, including units that were independent buildings or agencies located on various floors of the President's Office building with clear agency boundaries to measure the amount of dust of various sizes, including the total dust amount (TSP), the amount of dust not exceeding 10, 4, 2.5, and 1 micrometer. The results are analyzed against the standard values of government agencies and propose guidelines for adjusting the amount of dust from landscape design features to reduce the agency's PM2.5 problem. In this study, we measured and analyzed dust with an automatic dust reader for 8 working hours in various locations of the agency, including units that were stand-alone buildings or agencies located on various floors of the President's Office building with boundaries to measure the amount of dust of various sizes, including the total dust amount (TSP), and the amount of dust not exceeding 10, 4, 2.5, and 1 micrometer. The results are analyzed against the standard values of government agencies and propose guidelines for adjusting the amount of dust from landscape design features to reduce the agency's PM2.5 problem.

2. Materials and Methods

2.1 Materials

In this study, an automatic dust measuring instrument, model Aerocet 381, was used, which can measure dust of various sizes, including PM_{10} and $PM_{2.5}$, mounted on a tripod high from the floor at the breathing level of the operator. In various agencies, collect for a period of 8 hours per agency during March - April 2023 and transfer the data into the computer.

2.2 Analysis and determine PM

The dust quantity analysis results are reported in terms of the average dust quantity throughout the 8 hours of PM collection and compare with the standard values of the Pollution Control Department in Thailand to assess exposure and danger of exposure in the workplace and propose ways to reduce PM problems further.

3. Results & Discussion

3.1 PM Quantity analysis and comparison with standard values

From the results of measuring the amount of dust of all 5 sizes, focusing on PM_{10} and $PM_{2.5}$, the Pollution Control Department has determined the values of all 3 types of dust according to Table 1

Table 1. Thai Air Quality Standard (PCD)

PM	PM2.5	PM10	TSP
24-hours (μg/m^3)	37.5	120	330
Yearly (μg/m^3)	15	50	100

by the first group in the analysis. It is a group of offices of the dean or director's office that is the educational organization of the university. All of them are single buildings. No other agencies were present in the building. This group can also be divided into 2 parts: the part in Chom Bueng District, 6 units, and the part in Mueang District. (Center in the city) totaling 2 agencies. When measuring all 8 agencies, it was found that there were 3 agencies with PM2.5 dust levels higher than the 24-hour average, with values between 37.7 - and 98.7 μg/m^3, and in the other faculties, the $PM_{2.5}$ values were less than the specified standards, including the PM_{10} and TSP amounts were also lower than the values set by the Pollution Control Department, all of which are shown in the Table 2. As for the support agencies, they are divided into two subgroups: Agencies that have their buildings, it was found that the amount of PM2.5 was high, except for the food processing building, which did not exceed the specified value. Three other agencies had PM_{10} values higher than the specified standard, with $PM_{2.5}$ in the range of 36.4 - 98.7 μg/m^3 while PM_{10} exceeds the standard at 130.8 - 174.6 μg/m^3. As for units that live in buildings together, it was found that 3 units had PM2.5 values. Exceeds the standard between 41.2 - 56.8 μg/m^3, all shown in the table 3

3.2 Characteristics and landscape of the measured building on the effect of $PM_{2.5}$ concentration and other PM.

From the location of the building in the faculty or educational area, it was found that they are all isolated buildings. But the difference is that the building is obscured by trees or other buildings that affect the flow of $PM_{2.5}$ into the area of the dean's office of each faculty. From the measurement results, it was found that the nature of the Dean's office, which is a room in the building, is not open like a canteen (Niu Y. et al. (2021)) or even the Dean's office area itself is closed, so the amount of dust that comes in is low. This contradicts the results of the study of Yurtseven E. et al (2012) which had a $PM_{2.5}$ amount much higher than the maximum value measured in this study. There may be factors of other origins that may occur in the office. However, the measurement of PM in the study is to consider PM which may come from the flow of air currents. Agencies with high levels of $PM_{2.5}$ are characterized by the nature of the building's area being a wind ridge area. Air circulates easily into the school building and various rooms, thus causing a higher amount of PM to enter the office space than a building that is obscured by planting trees, gardening, or having other buildings help block the wind that blows $PM_{2.5}$ in. You can come. As for the building that is a single unit, it has a similar appearance in that it is a building with no shelter from anything or even a garden or tree It is in the direction where the wind blows directly. The shape of the building is also a groove that supports wind, allowing dust to flow in and accumulate in the area. As a result, the amount of $PM_{2.5}$ in this group of buildings is high. But for the departments that are in the building, it is found that the volume is low, except for work in front of the building that receives direct wind. The amount of PM is not high and results from ventilation and the use of air conditioners within the unit, causing airflow and reducing the amount of PM. In the study by Jones. E.R. et al (2021)[10] have shown the results of ventilation and air filtration to reduce $PM_{2.5}$ in buildings in 4 countries, concluding that ventilation and $PM_{2.5}$ filtration affect the exposure of workers in the area. There is a shorter period of exposure to PM and less quantity. Compared with this study, there are air conditioning systems in buildings in universities, especially units that live together in a single building and are not directly affected by wind currents. The air conditioning system can vent and filter $PM_{2.5}$ from the work area and has values that meet standards.

4. Conclusion

From measuring the amount of $PM_{2.5}$ and other forms of PM, it was found that the amount of $PM_{2.5}$ and PM_{10} were higher than the standards in 10 agencies, and in 3 agencies the PM_{10} values were higher. In addition, it was found that There is one agency that has measured abnormally high levels of PM_1, but since Thailand does not yet have a standard for controlling the amount of PM_1, there is no standard comparison at all. When considering the nature of the building's location, it was found that a building or agency that is a single building in the middle of the wind direction. It also has a concave shape or a hole that allows the wind to blow, which will lead to the accumulation of $PM_{2.5}$ and other PM. Other buildings that have a low amount of PM will come from being a unit within the building. Some buildings have protection against air currents by using gardens or trees, which reduces PM entering the unit and affect the health of workers from reduced exposure and according to the standard values of the Pollution Control Department. Therefore, there are

guidelines for preventing or reducing the problem of PM dust within the agency. In addition to cleaning the area and reducing the source of dust. There should be good ventilation and adjust the landscape by planting trees or arranging a garden to reduce the blowing of PM by air currents. This reduces the exposure to PM of workers within the office and reduce the risk of health hazards from exposure during work. There is also an interesting approach from the study of Azarov A.V. et al. (2017)[11] in reducing the impact of PM by using a water spray system in the form of an aerosol. In the work area of the building, construction machinery, it was found that the amount of dust could be reduced. Agencies that may be open-air agencies or have gardening areas and are empty areas should use this method to reduce the amount of PM blown into the agency. But, wastefulness must be considered in other matters.

Acknowledgments

This study was supported by the sustainable university unit of Muban Chombueng Rajabhat University that funds for this study in the green university project.

Table 2. PM concentration in the Dean's or Director's office

Office of the Dean of Director	PM concentration (μg/m^3)				
	TSP	PM1	$PM_{2.5}$	PM_4	PM_{10}
In Mueang District					
Demonstrate school	33.6	20.5	23.8	27.3	31.2
College of Muaythai and Thai Traditional Medicine	168.3	73.5	98.7	122.9	174.6
In Chombueng District					
Faculty of Humanity and Social Science	19.5	12.8	14.8	19.6	18.9
Faculty of Science and Technology	67.0	31.1	37.7	45.2	67.2
Faculty of Management Science	86.0	50.4	65.3	74.9	84.3
Faculty of Industrial Technology	84.3	34.9	21.2	71.3	58.4
Faculty of Education	64.2	44.3	25.3	42.5	54.3
Graduated School	80.8	21.9	28.4	36.5	53.8

Table 3. PM concentration in the support unit

Office or working unit	PM concentration (μg/m^3)				
	TSP	PM1	$PM_{2.5}$	PM_4	PM_{10}
Stand-alone					
Dormitory office	168.3	73.5	98.7	122.9	174.6
NARIT	135.6	57.6	74.6	92.7	131.7
Food production building	68.4	34.3	36.4	40.2	65.5
Logistic and transport division	145.6	52.2	65	85	130.8
Thai Art and Traditional office	106.8	40	55.5	70.5	94.5
Student development office	110.5	49.9	61.3	73.1	98.2
Co-building					
Language centre	68.8	48.8	56.5	61.1	67.7
Computer centre	82.2	30.8	35.5	46.8	91.1
Office of the President	68.6	48.1	56.8	63.1	68.6
Research and Development Institute	39.2	20.9	24.3	27.7	34.4
Academic Promotion and Registered Office	68.9	25.5	33.7	42.7	60.9
Documentary centre	34.4	21.8	25.7	29.1	33.8
Science centre	126.8	130.4	41.2	57.5	100.9
Agricultural Testing centre	35.2	14	16.3	18.8	25.4

References

1. Nezis, I.; Biskos, G.; Eleftheriadis, K.; Kalantzi, O. *J. Build. Env.* **2019**, *156*, 62-73.
2. Yu, Y.; Zou, W.; Jerrett, M.; Meng, Y. *J. Env. Advs.* **2023**, *12*, 1-16.
3. Abidin, A.U.; Maziya, F.B.; Susetyo, S.H,; Yoneda, M.; Matsui, Y. *J. Envc.* **2023**, *13*, 1-8.
4. Pollution Control Department. Announcement of Thai Air Quality Index 2566 B.E. https://www.pcd.go.th/pcd_news/30028 (accessed November 3, 2023)
5. Lu, Y. *J. Env. Res.* **2021**, *201*, 1-13.
6. Kellnerová, E.; Kellner, J.; Navrátil, J.; Paulus, F. *En. Proc.* **2018**, *153*, 315-319.
7. Yurtseven, E.; Erdogan, M.S.; Ulus, T.; Sahin, U.A.; Onat, B.; Erginoz, E.; Vehid, S.; Koksal, S. *Env. Protec. Eng.* **2012**, *38*, 115-127.
8. Niu, Y.; Wang, F.; Liu, S.; Zhang, W. *J. Atm. Env.* **2021**, *244*, 1-12.
9. Abdull, N.; Shaari, Z.; Suhaimi, N.S.; Zahaba, M. *Healt. Build*. **2021**, *n.d*, 182-187.
10. Jones, E.R.; Laurent, J.G.C.; Young, A.S.; MacNaughton, P.; Coull, B.A.; Spengler, J.D.; Allen, J.G. *J. Build. Env.* **2021**, *200*, 1-11.
11. Azarov, A.V.; Zhukova, N.S.; Antonov, F.G. *Proc. Eng.* **2017**, *206*, 1407 – 1414.

Synthesis of zeolite from industrial-waste coal fly ash for amine solution regeneration in CO_2 capture

Natthawan Prasongthum[1], Kritakorn Janna[2], Darunee Sukchit[3], Amornrat Suemanotham[1], Lalita Attanatho[1], Pornpan Pungpo[3], and Yoothana Thanmongkhon[1]*

[1]*Expert Centre of Innovative Clean Energy and Environment Thailand Institute of Scientific and Technological Research (TISTR), Khlong Luang, Pathum Thani 12120, Thailand*
[2]*Department of Chemistry, Faculty of Science and Technology, Thammasat University, Pathum Thani 12120, Thailand*
[3]*Department of Chemistry, Faculty of Science, Ubon Ratchathani University, Ubon Ratchathani 34190, Thailand*

**E-mail: yoothana_t@tistr.or.th*

Abstract:

Post-combustion CO_2 capture using amine solution has a great potential to reduce anthropogenic CO_2 emissions, but this process has the disadvantage of consuming a lot of energy for CO_2 stripping during solvent regeneration. To overcome this limitation, adding a solid acid catalyst such as zeolite to amine regeneration process has been investigated to decrease the energy requirement. However, the development of abundant and cost-effective materials is essential. In this work, the zeolite catalyst was synthesized by the hydrothermal method using an industrial-waste coal fly ash as a raw material and investigated its catalytic performance in the process of amine regeneration at a temperature of 100 °C. The experimental results showed that the prepared catalyst showed highly effective in amine regeneration process and could significantly improve the CO_2 desorption performance. Catalyst characterization results showed that the prepared catalyst possessed a high acidity, which increased the CO_2 desorption rate to ultimately reduce the amount of heat required for amine regeneration by approximately 30%. The use of zeolite in the amine regeneration process improved the desorption performance by 2 times in comparison with the blank run. Results manifested that the low-cost zeolite catalyst showed high potential to be used in a stripper column for energy-efficient CO_2 capture processes.

1. Introduction

Absorption-based post-combustion carbon capture is considered a crucial technology for mitigating climate change by capturing CO_2 emissions after combustion process of fossil fuel in power plant generation. This process involves the utilization of solvents to selectively capture CO_2 from flue gas before releasing it into the atmosphere. Monoethanolamine (MEA) is a very common type of amine used in CO_2 post-combustion capture due to its low price, fast CO_2 absorption rate, and wide research.[1] However, the biggest challenge of this process is the high energy requirement for CO_2 stripping during solvent regeneration, commonly conducted at elevated temperatures e.g., 120-150 °C. This process accounts for about 70-80% of the operating cost for CO_2 capture process. Due to this, the amount of heat needed to regenerate the solvent has become a very important factor to consider when evaluating a CO_2 capture process. To decrease the amount of heat needed, the temperature for solvent regeneration should be lowered to 100 °C or less.[2] Recently, the addition of a solid acid catalyst into an amine regeneration process has been reported to be one of the promising ways to increase the rate of CO_2 desorption at lower temperatures (< 100 °C), leading to reduce a significant portion of solvent regeneration energy. Liang et al. conducted a study on the addition of Al_2O_3 and HZSM-5 into the regeneration process of 5M MEA at 105 °C. The results showed a noticeable heat duty reduction with 22% for Al_2O_3 and 18% for HZSM-5. Al_2O_3 helped with a type of acidity called Lewis acidity, while HZSM-5 helped with another type called Brønsted acidity. Both Lewis and Brønsted acids acted as active sites to make the CO_2-amined bond cleavage process easier.[3] Subsequent to these developments, numerous researchers have investigated the catalytic CO_2 desorption of MEA solvent employing a range of acid catalysts, including Hβ, HY, H-mordenite, MCM-41, SO_4^{2-}/ZrO_2 and $Ce(SO_4)_2/ZrO_2$.[4,5] Their findings indicated that the utilization of solid acid catalysts in the CO_2 desorption of MEA solvent contributed to a reduction in the operating temperature to the range of 96 – 105 °C. However, to date, these catalysts have faced challenges related to high production costs and low efficiency when deployed on a large scale. Therefore, there is a need to develop abundant and cost-effective catalysts.

With that in mind, in this work, coal fly ash waste generated from coal combustion process was used as raw material to synthesize zeolite A and study its catalytic performance in the desorption of

MEA 5M solvent at temperature 100 °C. Catalytic performance was evaluated through the CO_2 desorption rate, the amount of CO_2 desorption and the amount of heat consumed to regenerate the MEA.

2. Materials and Methods

2.1 Materials

Coal fly ash (CFA) used in this study was generously supplied by BLCP Power Limited (Thailand). Ethanolamine (MEA, ≥99% purity), sodium aluminum oxide ($NaAlO_2$), sodium hydroxide (NaOH, ≥99% purity), 1 N hydrochloric acid (HCl) and methyl orange (indicator for titration) were purchased from Sigma Aldrich. Commercial-grade zeolite 4A (Zeolite A_Com) was delivered by Tosoh Corporation. CO_2 (15 vol% purity) was obtained from Thai Special Gas. Co. Ltd.

2.2 Synthesis of zeolite A

Zeolite A was synthesized from CFA via fusion followed by hydrothermal. First, CFA and NaOH were blended using a mortar, with a CFA:NaOH mass ratio of 1:1. The mixture was then subjected to calcination at 500 °C for 90 min to activate the silicon and aluminum elements. After calcination, the fused material was further ground, mixed with 12 g of $NaAlO_2$ and transferred to a polypropylene bottle. Subsequently, deionized water was added to the solid mixture to dissolve at the solid-liquid mass ratio of 4.5. The suspension was stirred at ambient temperature for 30 min and then placed in an oven at 80 °C for 720 min. Following this, the obtained product was filtered, washed with deionized water several times until pH reached 7, and subsequently dried at 80 °C. The obtained zeolite product was identified as Zeolite A_CFA

2.3 Characterization

Both CFA and zeolitic products were characterized by X-ray fluorescence spectrometer (XRF, S8-Tiger Bruker AXS) and X-Ray diffractometer (XRD, SmartLab Rigaku), Scanning electron microscopy (SEM, Hitachi SU-8230), N_2 adsorption-desorption technique involving Brunauer–Emmett–Teller (BET, Micromeristics ASAP 2020), NH_3-temperature-programmed desorption technique (NH_3-TPD, Bel-Cat B).

2.4 CO_2 absorption and desorption experiments

CO_2 absorption experiment was performed on a round bottom flask with a reflux condenser at temperature of 40 °C, 5 M MEA and 15 vol% CO_2. For all experiments, the initial CO_2 loading was consistently set within the range of 0.59 − 0.61 mol CO_2/mol amine. In each run, 100 mL MEA was added into the flask and placed into a hotplate. The solution was stirred at 500 rpm and heated to 40 °C. Once the reaction temperature reached 40 °C, CO_2 at a flow rate of 200 mL/min was introduced into the MEA solution. The samples were taken every 10 min for the first hour then, 30 min until reaction time reached 480 min. The CO_2 loading was determined by titrating with 1.0 N HCl solution.

For CO_2 desorption experiment, 10 g of the catalyst was placed in a bag and attached to the central neck of the flask to ensure that the catalyst was completely immersed in the MEA solution. The solution was stirred at 500 rpm and heated to 100 °C. The MEA solution temperature of 100 °C was maintained using an oil bath heater for approximately 480 min. Samples were collected at intervals of 2 min during the initial 20 min and then at 30 min intervals until the reaction time reached 480 min. CO_2 loading was assessed by titration through the Chittick apparatus (Horwitz et al.).[5]

2.5 Calculations

Catalytic performance was assessed by CO_2 loading, CO_2 desorption rate, cyclic capacity, and heat duty. These parameters were calculated using Eq. (1), (2) and (3), respectively.

$$\text{CO}_2 \text{ loading} = \alpha = \frac{n_{CO2}}{n_{amine}} \quad (1)$$

$$\text{Desorption rate} = (\alpha_{rich} - \alpha_{lean}) x\ CV \quad (2)$$

$$\text{Heat duty} = \frac{heat\ input/time}{amount\ CO2/time} = \frac{Electricity\ (kJ)}{nCO2} \quad (3)$$

where, α_{rich} and α_{lean} represent the initial and final amine-CO_2 loading, respectively. C and V refer to amine concentration and amine volume solutions.

3. Results & Discussion

3.1 Characterization of catalysts

The chemical compositions of CFA and zeolite A_CFA are shown in Table 1. The results indicated that CFA predominantly consists of SiO_2 (63.36%) and Al_2O_3 (21.92%) with low content of Na_2O (0.33%), and it exhibits a Si/Al molar ratio of 2.45. After fusion and hydrothermal treatment, the amount of Na_2O increased to 8.65% indicating the Na^+ in the extra framework of zeolite. The Si/Al molar ratio was found to be 1, aligning with the theoretical molar ratio of Zeolite A.[6]

Table 1. Chemical compositions of CFA and zeolite (wt.%)

Composition	SiO_2	Al_2O_3	Na_2O	Si/Al
CFA	63.36	21.92	0.33	2.45
Zeolite_A CFA	41.10	35.00	8.65	1.00

XRD pattern of CFA is depicted in Figure 1, revealing the presence of amorphous phases such as quartz and mullite. This observation aligns with the composition of CFA reported by Belviso et al. After the synthesis of zeolite, the characteristic peaks associated with mullite and quartz disappeared, and new diffraction peaks emerged, aligning with the diffraction pattern of zeolite A according to the JCPDS No. 01-073-6285.

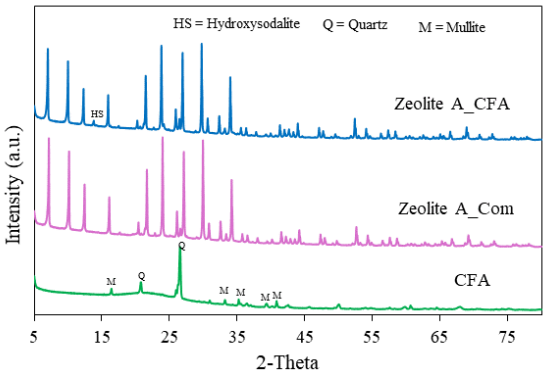

Figure 1. XRD patterns of CFA and Zeolite.

The structures of CFA and zeolite product were further examined through SEM, as illustrated in Figure 2. The CFA consisted of predominantly spherical structures with an average size of 6.3 µm. After undergoing fusion and hydrothermal treatment, the spherical structures transformed into cubic crystal structures with a smaller size (1.79 µm), as illustrated in Figure 2(b). This observation confirms the successful formation of Zeolite A. It has been reported that during the synthesis of zeolite, NaOH served as a co-solvent, participating in reactions with mullite and quartz in CFA to generate soluble silicate and aluminate species that can dissolve in water. Additionally, NaOH interacts with silicate and aluminate molecules to form a gel during hydrothermal process. This gel, serving as nuclei, subsequently undergoes crystallization to produce Zeolite A.[6]

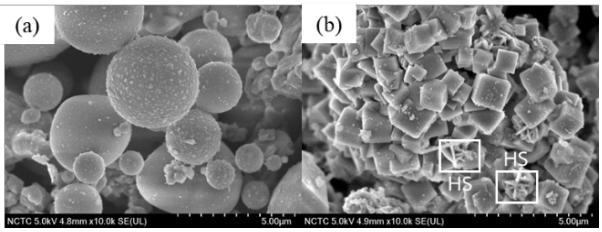

Figure 2. SEM images of (a) CFA and (b) Zeolite.

The physicochemical properties of CFA and zeolite are displayed in Table 2. The surface area of CFA is 5.50 m^2/g, while after the synthesis of zeolite its surface area increases to 23.92 m^2/g. These findings are in accordance with the SEM results.

Table 2. Physicochemical properties of CFA and zeolite

	BET (m^2/g)	Acidity by strength (mmol/g)		
		Weak	Strong	Total acidity
CFA	5.50	-	-	-
Zeolite_ A CFA	23.92	1.298	0.508	1.806

Acid strength plays a crucial role in CO_2 desorption. Figure 3 shows the NH_3-TPD profiles of CFA and zeolite A. The results showed that CFA had no peak, while zeolite product showed two desorption peaks observed around 200 °C and 400 °C corresponding to weak and strong acid sites, respectively. In Table 2, the amount of total acid sites is 1.806 mmol/g.

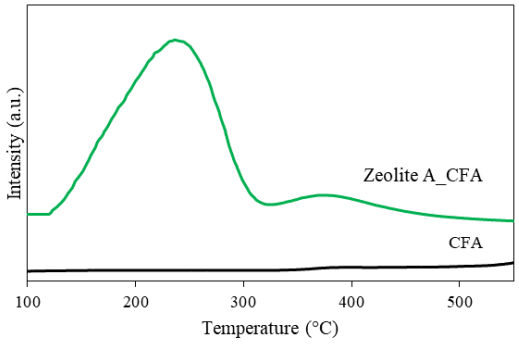

Figure 3. NH_3-TPD profiles of CFA and Zeolite.

3.2 CO_2 desorption performance

In this study, catalyst performance for CO_2 desorption was determined by CO_2 desorption rate, cyclic capacity, and heat duty. Prior to desorption test, the CO_2 was loaded to MEA amine at 40 °C for 420 min to obtain CO_2 loading of 0.59 − 0.61 mol CO_2/mol amine. The CO_2 loading was evaluated by titration through the Chittick apparatus (Horwitz et al.)[5] presented in Figure 4. The results show that after approximately 300 min, these solutions reached equilibrium. And later on, CO_2 is absorbed very slowly because the MEA solution becomes saturated.

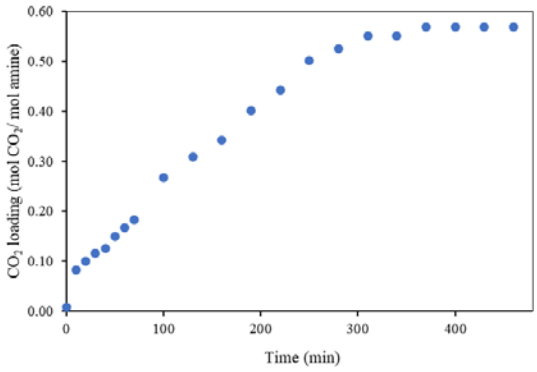

Figure 4. CO_2 absorption profile of 5 M MEA

In the context of absorption reactions, monoethanolamine (MEA) undergoes a reaction with CO_2 to form carbamate according to Eq. (4) and (5). The process takes place as the absorption reaction is progressing, and the absorption of CO_2 is increasing as the absorption reaction proceeds and CO_2 loading increases. In addition, CO_2 hydration reactions occur, leading to the formation of bicarbonate (HCO_3^-) and carbonate (CO_3^{2-}) according to Eq. (6) and (7).

$$MEA + CO_2 \leftrightarrow MEA^+COO^-_{(zwitterion)} \quad (4)$$
$$MEA + COO^- + MEA \leftrightarrow MEACOO^- + MEAH^+ \quad (5)$$
$$CO_2 + H_2O \leftrightarrow H^+ + HCO_3^- \quad (6)$$
$$CO_2 + H_2O \leftrightarrow 2H^+ + CO_3^{2-} \quad (7)$$
$$MEACOO^- + H_3O^+ \leftrightarrow zwitterion \leftrightarrow MEA + CO_2 \quad (8)$$
$$MEAH^+ + H_2O \leftrightarrow MEA + H_3O^+ \quad (9)$$
$$H^+ + HCO_3^- \leftrightarrow CO_2 + H_2O \quad (10)$$
$$2H^+ + CO_3^{2-} \leftrightarrow CO_2 + H_2O \quad (11)$$

For the CO_2 desorption process, this can be divided into two parts: carbamate breakdown as shown in Eq. (8) and $MEAH^+$ deprotonation as shown by Eq. (9). However, $MEAH^+$ deprotonation demands a significant amount of energy and is thermodynamically unfavorable in basic conditions, resulting in a limited availability of protons for the regeneration of MEA. Consequently, the traditional amine regeneration process often occurs at elevated temperatures.[3,4]

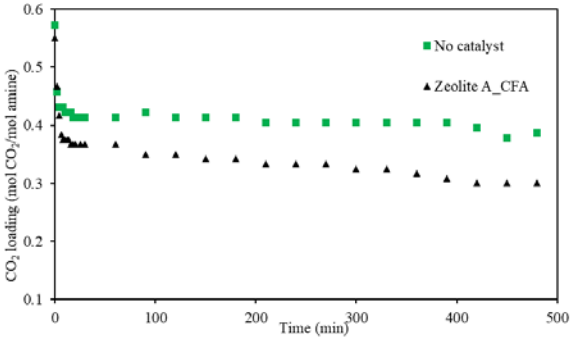

Figure 5. CO_2 desorption profiles of 5 M MEA at 100 °C with and without catalyst.

CO_2 desorption test was conducted at 100 °C, as illustrated in Figure. 5 The findings indicate a rapid decrease in CO_2 loading within the initial 10 min, implying swift release of CO_2. However, the rate of decrease in CO_2 loading became less pronounced as time advanced. Furthermore, it is evident that the incorporation of catalysts in the regeneration of the solvent facilitated the release of CO_2 and improved the overall performance of CO_2 desorption, consequently.

Table 3. CO_2 desorption amount and desorption rate of 5 M MEA at 100 C with and without catalyst based on 90 min

	CO_2 desorption amount (mol)	CO_2 desorption rate (mmol/min)
No catalyst	0.13	1.44
Zeolite_A CFA	0.20	2.22

Table 3 displays the CO_2 desorption amount and desorption rate findings. The results show that under non-catalytic condition, the CO_2 desorption amount and initial desorption rate were 0.13 mmol/min and 1.44 mmol/min, respectively, aligning with values reported in previous literature.[3] Upon introducing catalysts to the desorber, a notable enhancement in desorption rate was observed the catalysts exhibited an initial desorption rate of 2.22 mmol/min, marking a 54% increase compared to the non-catalytic condition. The catalysts facilitated the provision of protons (H^+) or metal atoms (Al) to initiate an attack on the N atom of the MEA^-COO^-, inducing a transformation in configuration from sp^2 to sp^3 consequently, the N-C bond experienced stretching, leading to the cleavage of carbamate into MEA and CO_2.[3,4]

Table 4. Heat duty and relative heat duty of 5 M MEA at 100 °C with and without catalyst based on 90 min

	Heat duty (MJ/kg mol CO_2)	Relative heat duty (%)
No catalyst	12.14	100
Zeolite_A CFA	7.89	65

Apart from improving the CO_2 desorption rate, the catalytic solutions also resulted in the release of larger quantities of CO_2, providing a positive advantage in reducing the heat duty required for amine solution regeneration. The heat duty in amine solvent regeneration is defined as the

energy needed for desorption of one unit of CO_2, typically expressed in term of MJ/kgCO_2. The enhancement in reducing the solvent regeneration heat duty is detailed in Table 4 evidently, the introduction of catalysts led to a substantial decrease in heat duty. The catalytic process demanded less energy as it supplied protons (H^+) or metal atoms (Al) to facilitate CO_2 desorption. The heat duty could be decreased from 12.14 to 7.89 MJ/mol CO_2 with the introduction of the zeolite catalyst, resulting in a reduction in energy consumption by up to 37%. The results highlight the exceptional effectiveness of zeolite A derived from CFA in minimizing the energy requirements for amine regeneration.[3]

4. Conclusion

In summary, zeolite A was prepared from an industrial-waste coal fly ash and used as a catalyst in MEA regeneration process. XRD and SEM analyses unveiled the characteristic crystalline structure of zeolite A. The BET surface area analysis determined a value of 23.92 m^2/g. Furthermore, the analysis of acidic property using NH_3-TPD technique revealed an overall acid strength was 1.806 mmol/g. The performance of zeolite A in MEA regeneration presented that the introduction of zeolite A notably improved both the CO_2 desorption amount and desorption rate. Moreover, the addition of catalyst led to a substantial reduction in the heat duty, decreasing from 12.14 to 7.89 MJ/kg mol CO_2.

Acknowledgements

The authors acknowledge the financial support of Program Management Unit for Competitiveness Enhancement (PMU-C) and BLCP Power Limited on Contract No. C04F660071.

References

1. Appiah, F.A.; Nugloze, D.; SaiObodai, L. S.; Natewong, P.; Idem, R. *ACS Omega.* **2023**, *8*, 9346−9355.
2. Shi, H.; Zheng, L.; Huang, M.; Zuo, Y.; Kang, S.; Huang, Y. Idem, R.; Tontiwachwuthikul, P. *Ind. Eng. Chem. Res.* **2018**, *57*, 11505−11516.
3. Liang, Z.; Idem, R.; Tontiwachwuthikul, P. *AIChE Journal*. **2016**, *62*, 753–765.
4. Prasongthum, N.; Natewong, P.; Reubroycharoen, P; Idem, R. *Energy Fuels* **2019**, *33*, 1334−1343.
5. Horwitz, W.; Senzel, A.; Reynolds, H.; Park, D. *Gaithersburg MD: George Bant.* **1975**.
6. Bairq, Z.A.S.; Gao, H.; Huang, Y.; Zhang, H.; Liang, Z. Appl. Energy. **2019**, *252*, 113440.
7. Cui, Y.; Zheng, Y.; Wang, W. *Minerals.* **2018**, *8*, 338.

A prepared biosorbent from corn husk for the removal of crystal violet dye from aqueous solution

Ornanong Aekkaphong[1], Chutima Yoothong[1], Ratiwun Suwattanamala[2], and Akapong Suwattanamala[1]*

[1]*Department of Chemistry, Faculty of Science, Burapha University, Chonburi 20131, Thailand*
[2]*Division of Environmental Health, Faculty of Public Health, Burapha University, Chonburi 20131, Thailand*

**E-mail: akapong@go.buu.ac.th*

Abstract:

In this work, the potential and efficiency of usage corn husks, obtained as an agricultural waste by-product from harvesting, as an affordable biosorbent for the removal of crystal violet (CV), a cationic dye used in dyeing of cotton, wood, and silk, from aqueous solution has been studied. The pre-treated biosorbents were prepared under the presence of three different concentration of sulfuric acid (98%, 75% and 50% by weight) and compared with untreated biosorbents as a reference. To investigate the surface morphology and potential interaction between the biosorbent and CV dye, the biosorbents were characterized by SEM and FT-IR spectroscopy techniques. The effects of contact time, initial dye concentration (10-50 mg/L) and biosorbent dosage (0.10-0.30 g) on dye sorption tests were systemically carried out to determine the optimal conditions by batch experiments. The result showed that as the contact time and initial dye concentration increased, the adsorption capacity also increased, whereas an increasing in adsorbent dosage resulted to a decrease in adsorption capacity. The adsorption process could be well fitted by the pseudo-second-order kinetic model with r^2 value of 0.999, reaching the equilibrium at 120 min, and the calculated activation energy was 46.45 kJ/mol. The isotherm of the adsorption equilibrium data was found to be best followed by the Langmuir model. This research indicated that corn husk waste is an effective, low-cost, eco-friendly biological adsorbent, presenting a new sustainable alternative for crystal violet removal in industrial wastewater treatment.

1. Introduction

The expansion of the textile industry has led to the discharge of wastewater contaminated with dyes into water sources. Among these dyes, crystal violet, a commonly used cationic dye in the textile sector, causes a significant threat. Upon entering water sources, it exhibits toxicity by interacting with negatively charged cell membrane surfaces, enabling penetration into cells. This adversely affects mammalian cells,[1] and exposure to such pollution can result in severe health consequences, including nausea, vomiting, diarrhea, gastritis, and respiratory complications. Prolonged exposure to crystal violet can lead to kidney damage and permanent blindness.[1,2] To address these issues, it is crucial to reduce or eliminate the presence of dyes in wastewater before its release into waterways.

In solving wastewater treatment from the textile industry, various methods are available to apply, including coagulation and flocculation membrane filtration, chemical sedimentation, electrochemical treatment, photocatalytic degradation, ion-exchange and more. However, challenges have persisted due to high investment requirements, time consuming, energy intensive and the need for specialized knowledge. The adsorption method frequently stands out for its popularity owing to its convenience, minimal time consumption, cost-effectiveness, performing in natural condition and efficiency. Nowadays, biosorbents (untreated and treated forms) derived from natural materials like rice straw, rice husk, bean husks, and other agricultural wastes have been considerable interested because these materials not only offer cost-effective solutions but also possess biodegradable capabilities, streamlining both steps and production time.[1]

The global issue of air pollution stems from combustion processes that emit carbon dioxide and other greenhouse gases, intensifying the impacts of global climate change. Biomass combustion is a primary contributor, posing significant health risks associated with cardiovascular disease and respiratory problems.[3] To address these extensive and sustainable challenges, minimizing harmful impacts on the environment and public health, the utilization of agricultural waste emerges as a promising avenue for biosorbent development. In this work, the corn husk is proposed a low-cost natural agricultural waste developed an alternative biosorbent for the removal of hazardous crystal violet dye in aqueous solution. Besides, the usage such biosorbent can significantly prevent open burning corn husk in waste disposal. This approach not only provides economic benefits but is also in alignment with the concept of zero waste within the circular economy framework. It integrates seamlessly with the Bio-Green Economy (BCG) model, propelling

Thailand 4.0 and contributing to the achievement of the Sustainable Development Goals (SDGs).

2. Materials and Methods

2.1 Materials

All used chemicals were of Analytical Grade without further purification. Sulfuric acid (98% H_2SO_4) was supplied by QRëC™ and crystal violet (CV) and sodium bicarbonate ($NaHCO_3$) were supplied by Ajax Finechem. A stock solution of CV dye of 100 mg/L was prepared by accurate weight dissolving in double -distilled water. The further solution with desired concentration was prepared by prior dilution the stock solution to use.

2.2 Biosorbent preparation

Corn husks (CH) were collected from agricultural farm around Kanchanaburi Province of Thailand. They were washed by tap water to remove dust and dirt and dried under sunlight. After complete drying, the corn husks were cut into a small piece, it is ground and sieved to a size of approximately 0.30 mm (50 mesh).

About 20 g of dried powder of CH was mixed with 20 g of H_2SO_4 solutions of three different concentrations (50%, 75%, and 98% by weight) separately (mixing ratio 1:1). After mixing the ingredients well and then kept in an oven at 200°C for 24 hours. The acidic residues were removed by washing the pre-treated biosorbents with boiling distilled water and neutralized by treating with 1% $NaHCO_3$ solution for 24 hours and then filtered. After filtering the treated biosorbents, they were washed again with deionize water and finally, they were applied after drying in the oven at 105 °C for 24 hours. The three pre-treated biosorbents were coded as TCH-50, TCH-75, and TCH-98 for produced with 50%, 75% and 98 % H_2SO_4, respectively.

2.3 Characterization techniques

Attenuated Total Reflectance Fourier Transform Infrared Spectroscopy (PerkinElmer, ATR-FTIR -2000 type) in the wavenumber range of 400-4000 cm^{-1} was applied to identify functional group of CH and TCHs biosorbents. Scanning Electron Microscope (LEO, SEM-LEO 1450 VP type) was used to determine of porous surface morphology of CH and TCHs biosorbents. UV-VIS Spectrophotometer (Agilent, UV-VIS-Agilent Cary 3500 type) was applied to determine of CV dye concentration after adsorption.

2.4 Batch adsorption study

In this study, three different adsorbents were obtained by treatment the corn husk with sulfuric acid at different concentrations. The adsorption performance of a total of four adsorbents from aqueous solution together with the original corn husk was tested. As the adsorbate, crystal violet (CV), a basic cationic dye, was used to represent the total dyes in the adsorption studies.

The efficiency adsorption of pre-treated and untreated bio-sorbents for the removal of hazardous CV dye from aqueous solutions was carried out by batch method. Batch adsorption studies were performed by the series of 125 mL conical flasks containing desired bio-sorbent dosage and 30 mL of CV dye solution, using a shaker water bath keeping constant 30 °C. Optimum conditions were determined by performing batch adsorption experiments in the adsorbent dosage range of 0.10-0.30 g, in the concentration range of 10-50 mg/L, and in the contact time range of 0–180 min. The adsorption isotherms, and kinetics were performed in the temperature range of 25-35°C to obtained the parameters. After the desired contact time, the solutions were filtered by filter paper and the residual dye concentration in the supernatant part was analyzed by absorbance measurements at 584 nm in a UV-VIS Spectrophotometer. After verifying Beer-Lambert 's law via standard curve, the starting and residual dye concentrations (before and after adsorptions) were used to calculate the amount of adsorbed material and the percentage of removal ability. The adsorption capacities of CV dye at time t (q_t, mg g^{-1}) and at equilibrium (q_e, mg g^{-1}) and the percentage of CV dye removal (% removal) were determined by the following Eq. (1), (2), and (3), respectively:

$$q_t = \frac{C_o - C_t}{m} \times V \quad (1)$$

$$q_e = \frac{C_o - C_e}{m} \times V \quad (2)$$

$$\%removal = \frac{C_o - C_e}{C_o} \times 100\% \quad (3)$$

where C_o, C_t, and C_e (mgL^{-1}) are the concentrations of dye at initial, at time t and at equilibrium, respectively; V (L) is the volume of the reaction solutions; m (g) is the mass of the bio-sorbent used.

3. Results & Discussion

3.1 Characterization of biosorbent

The SEM image of CH and TCHs under a magnification of 10,000x are presented in Figure 1. The surface of TCH-50 was very irregular surfaces and porous structures (Figure 1b), as compared to the disappearance in untreated corn husk (CH), TCH-75 and TCH-98. These characteristics contributed to be useful for effective CV adsorption.

FTIR analysis was applied to investigate the presence of functional groups on the CH and

TCHs surface, as shown in Figure 2. The intense broadband between 3200-3400 cm $^{-1}$ and peak at 2919 cm^{-1} in untreated corn husks (CH) is attributed to –O-H stretching in alcohols, phenols, and carboxylic acids and –C-H stretching, respectively while TCHs was observed to reduce intensity and to shift to 2970 cm^{-1}.[4,5] The appeared peak at 897 cm^{-1} in CH may be caused by the β-glycosidic linkage between glucose unit in cellulose which disappeared in TCHs.[5] The fundamental peaks at 1735 cm^{-1},1630 (1598) cm^{-1} and 1032 cm^{-1} could be attributed to the − C = O stretching in aldehydes, ketones, carboxylic acids, esters and − C − O − C – stretching in ethers. These oxygen-containing functional groups could play an important role in enhancing CV adsorption efficiency.

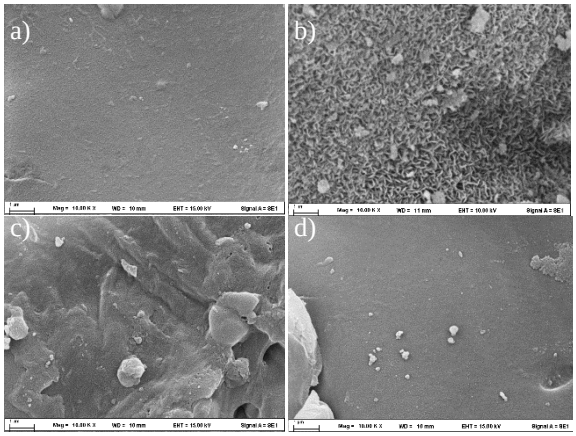

Figure 1. SEM images of a) untreated corn husk (CH), b**)** corn husk treated with 50% H_2SO_4 (TCH-50), c**)** corn husk treated with 75% H_2SO_4 (TCH-75), and d**)** corn husk treated with 98% H_2SO_4 (TCH-98)

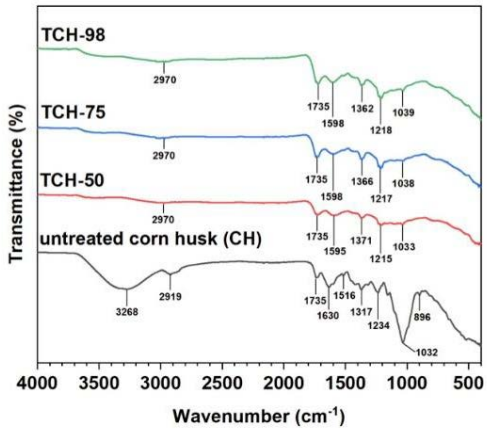

Figure 2. FTIR spectra of CH and TCHs

3.2 Effect of contact time

The effect of contact time on the adsorption process was investigated by different contact times from 0 to 180 min as represented in Figure 3, while the other parameters such as 0.15 g of biosorbent dosage, 30 ^{o}C were kept constant at each initial dye concentration. As contact time period increases the adsorption capacity is heightened rapidly in first 10 min, which may be due to abundance of available vacancies on the adsorbent surface. Consequently, the number of vacancies is almost completely occupied the adsorption rate is slow down and finally reaches to a completely saturation as equilibrium state within 120 min.[4] This phenomenon was observed for all initial dye concentrations. It might suggest that the optimal contact time period for adsorption equilibrium was obtained as 120 min for all further experiments.

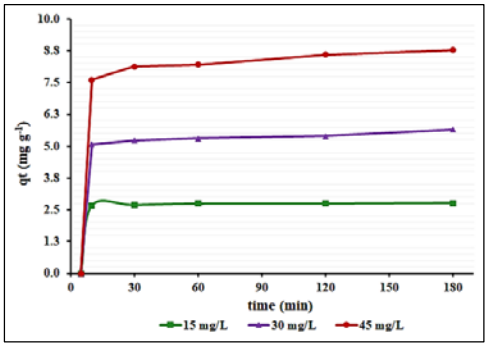

Figure 3. Effect of contact time on the adsorption of CV dye on TCH-50 at different initial concentrations

3.3 Effect of biosorbent dosage

The behavior of biosorbent dosage against percentage of dye removal is presented in Figure 4. The other parameters including C_o = 30 mg/L, 30 ^{o}C, 120 min were kept constant.

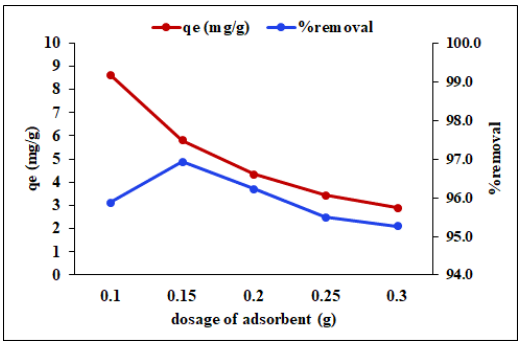

Figure 4. Effect of biosorbent dosage on the adsorption of CV dye on TCH-50

An increase in the percentage of removable ability could be attributed to a greater surface area of biosorbent and more accessibility of available adsorption sites. On the other hand, a further increase in the adsorbent dosage might cause aggregation of biosorbent surface area

accessible for dye molecule and could decrease the available adsorption sites.[4] The 0.15 g of adsorbent dosage was selected as the optimum dose for all further experiments in this study, which presented high acceptable level of adsorption capacity.

3.4 Effect of initial dye concentration

The impact of the initial concentration of CV dye ranging from 10 to 50 mg/L on efficiency of dye removal is depicted in Figure 5. The other parameters including 0.15 g of biosorbent dosage, 30 °C, 120 min were controlled. An increasing of initial dye concentration leads to an increase in the adsorption capacity, which might be likely attributed to enhancement in the driving force of a concentration gradient to overcome the mass transfer resistance of the CV dye between the liquid-solid phases resulting more dye molecules attached to more adsorption sites.[6]

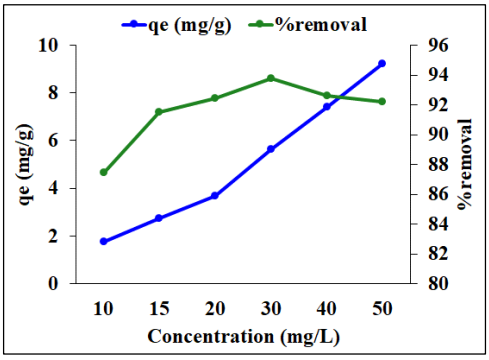

Figure 5. Effect of initial dye concentration on the adsorption of CV dye on TCH-50

3.5 Effect of different pre-treated biosorbents

The effect of difference biosorbents using three different concentrations of H_2SO_4 (50%, 75% and 98% by weight) in pretreatment corn husk for ratio 1:1 as symbolized TCH-50, TCH-75, TCH-98, respectively on the dye adsorption are presented in Figure 6 while the other parameters such as 0.15 g of biosorbent dosage, 120 min contact time, 30 °C were controlled. Within the initial dye concentration was increased in the range of 10-50 mg/L the adsorption capacity of CV rose from 1.90 to 9.86 mg/L for TCH-50 biosorbent. As seen in Figure 6, the different pre-treated biosorbents seems to not affect to the adsorption capacity whereas the percentage removal ability seems to significantly change in order TCH-98 < TCH-75 < TCH-50. These results showed a good agreement with the prior study on SEM morphology. Then TCH-50 was selected to be a good choice for all further kinetic and equilibrium adsorption studies.

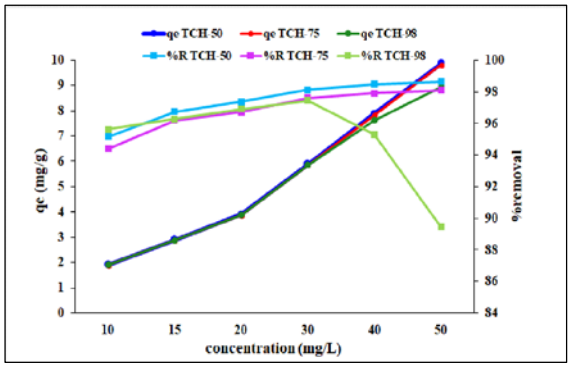

Figure 6. Effect of different pre-treated biosorbents (TCH-50, TCH-75, TCH-98) for the adsorption of CV dye

3.6 Kinetic of adsorption

Two well-known kinetic models (pseudo-first-order and pseudo-second-order) are applied to investigate the behavior dynamics of adsorption process of CV dye on to TCH-50. The pseudo-first-order kinetic model can be represented by the following Lagergren equation:

$$ln(q_{e,obs} - q_t) = lnq_{e,cal} - k_1 t \qquad (4)$$

where $q_{e,obs}$ (observed values), q_t are the amounts of CV dye removed by TCH-50 (mg/g) at equilibrium and at contact time t (min), respectively and k_1 is the pseudo-first-order rate constant (min^{-1}). The $q_{e,cal}$ (calculated values), and k_1 are calculated from the intercepts and the slopes of a linear plot of ln (q_e - q_t) versus t, as presented in Table1. The results showed that the $q_{e,obs}$ did not agree with the $q_{e,cal}$. It suggests that the adsorption kinetics for CV were not in a good corresponding to the pseudo-first-order kinetic model.

The pseudo-second-order kinetic model was also applied to describe adsorption kinetics of CV dye on TCH-50. This model is expressed as:

$$\frac{t}{q_t} = \frac{1}{k_2 q_e^2} + \frac{t}{q_e} \qquad (5)$$

where k_2 is the pseudo-second-order rate constant (g mg^{-1} min^{-1}). The linear plot of t/q_t versus t are shown in Figure 7. The values of k_2 and q_e are calculated from the slopes and intercepts of the graph, as summarized in Table 1. This plot exhibits that the $q_{e,cal}$ closely matched the $q_{e,obs}$. The corresponding correlation coefficient (r^2) values for the pseudo-second-order kinetic model were higher than 0.999 for all CV initial concentrations and temperature, as shown in Table1 and Table 2. Thus, the adsorption of CV onto the TCH-50 followed well by the pseudo-second-order kinetic model. These results showed a good agreement with the previous similarity study on CV

adsorption onto bio-sorbent.[4, 5, 7] Activation energy (E_a) for removal CV by TCH-50 was obtained from a plot of ln*k* versus 1/T in Arrheneius 's equation, where *k* is the pseudo-second-order rate constant. At the low value of E_a in the range of 5-40 kJ/mol the adsorption mechanism might be controlled by physical adsorption, while for the high value of E_a between 40 and 800 kJ/mol the adsorption mechanism might be determined by chemical adsorption.[8] As shown in Table 2, E_a value was less high than 40 kJ/mol indicating a physical mechanism for adsorption should be dominant.

Table 1. Kinetic parameters of pseudo-first and pseudo-second-order models for the adsorption of CV dye onto TCH-50 at various concentration

Concentration (mg/L)	15	30	45
Pseudo-first-order			
k_1 (min^{-1})	1.9976	0.2766	-0.1092
$q_{e,cal}$ (mg/g)	0.14	0.76	1.12
$q_{e,obs}$ (mg/g)	2.80	5.85	8.79
r^2	0.8384	0.9613	0.9597
Pseudo-second-order			
k_2 (g mg^{-1} min^{-1})	0.8584	0.1250	0.0812
$q_{e,cal}$ (mg/g)	2.77	5.68	8.86
r^2	1	0.9994	0.9999

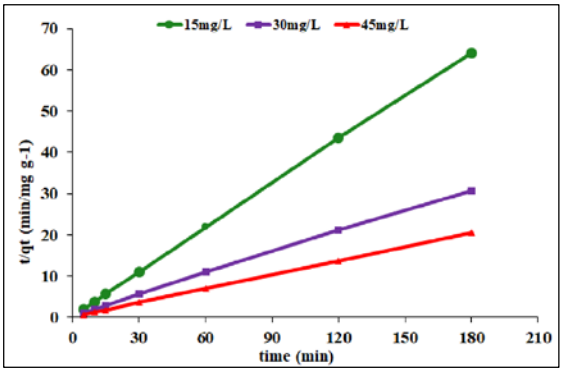

Figure 7. Pseudo-second-order kinetic plots for the adsorption of CV onto derived TCH-50

Table 2. Kinetic parameters of pseudo-second-order models for the adsorption of CV on TCH-50 at various temperature

Temperature (°C)	25	30	35
Pseudo-second-order			
k_2 (g mg^{-1} min^{-1})	0.3428	0.4206	0.6310
$q_{e,\,cal}$ (mg/g)	2.82	2.83	2.85
$q_{e,exp}$ (mg/g)	2.81	2.83	2.85
r^2	0.9999	0.9999	0.9999
1/T (K^{-1})	0.0034	0.0033	0.0032
lnk_2	-1.0707	-0.8662	-0.4605
E_a (kJ/mol)		46.45	
r^2		0.9641	

3.7 Equilibrium adsorption isotherms

To study of relation between the residual concentrations of CV dye in aqueous solution and the adsorption capacities of TCH-50 at a various temperature, the Langmuir and Freundlich isotherm models were applied to check the validity of the experimental data obtained for CV adsorption onto TCH-50. The Langmuir isotherm model is given by the following linear equation:

$$\frac{C_e}{q_e} = \frac{1}{q_m K_L} + \frac{C_e}{q_m} \qquad (6)$$

where C_e (mg/L) is the equilibrium CV concentration in solution; q_e (mg/g) is the equilibrium amount of CV absorbed per unit mass of bio-sorbent; q_m (mg/g) is the maximum adsorption capacity at saturation, and K_L (L/mg) is Langmuir constant related to the energy of adsorption. The Freundlich isotherm model is expressed by the following linear equation:

$$ln\ ln\ q_e = ln\ ln\ K_F + \frac{1}{n} ln\ ln\ c_e \qquad (7)$$

where *n* and K_F are Freundlich parameters. The value of *n* shows the favorable adsorption ability and K_F (mg$^{1-1/n}$ g^{-1} L$^{1/n}$) relates to the adsorption capacity.

Langmuir and Freundlich isotherm plots in linear forms of CV adsorption are established in Figure 8. The slope and the intercept of each linear plot in Figure were used to obtain Langmuir and Freundlich parameters, as listed in Table 3. The results indicated that Langmuir model with r^2 values up to ~ 0.995 is the best fitting curve for the adsorption of CV than Freundlich model. As an increasing temperature led to a rising of K_L, which might suggest the endothermic adsorption of CV dye on TCH-50.

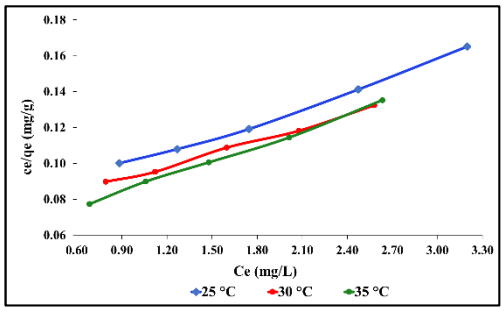

Figure 8. Langmuir plots for the adsorption of CV onto derived TCH-50

Additionally, one essential parameter of the Langmuir isotherm equation can be confirmed in terms of the R_L (dimensionless) as known the

Hall separation factor or equilibrium factor, which is calculated using the following equation:

$$R_L = 1/(1 + K_L C_O) \quad (8)$$

where K_L (L/mg) is the Langmuir constant and C_o (mg/L) is the initial concentration of CV in the liquid phase. The value of R_L shows the type of the isotherm shape and predicts whether a sorption system is favorable ($0 < R_L < 1$), unfavorable ($R_L > 1$), linear ($R_L = 1$) or irreversible ($R_L = 0$). In this study, the obtained R_L values for the adsorption of CV onto the TCH-50 were found to be in a range of 0.0239 - 0.0302. These R_L values indicates that TCH-50 is favorable for adsorption CV from water under the conditions used in this study. The Langmuir model is based on the assumption that there is no interaction between the CV adsorbate molecules. Therefore, TCH-50 shows great potential to be a good bio-sorbent for the removal of CV in water treatment.

Table 3. Isotherm parameters for the adsorption of CV dye on TCH-50

Temperature (°C)	25	30	35
Langmuir model			
q_m (mg/g)	19.36	19.48	19.47
K_L (L/mg)	0.7124	0.7417	0.9057
R_L	0.0302	0.0291	0.0293
r^2	0.9948	0.9955	0.9963
Freundlich model			
K_F	1.2210	10.827 6	11.379 3
n	1.42	1.88	1.94
r^2	0.9981	0.9761	0.9787

4. Conclusion

In this work, corn husks, treated with varying concentrations of sulfuric acid, proved to be an efficient biosorbents for adsorption crystal violet dye from aqueous solutions. The highest percentage removal ability of CV was obtained by the biosorbent produced with 50% H_2SO_4 (TCH-50) as compared to those produced with 75% and 98 % H_2SO_4 (TCH-75, TCH-98). The adsorption capacity of TCH-50 increased with longer contact times and higher initial dye concentrations, but decreased with an increase in adsorbent dosage. The optimal condition of parameters such as 0.15 g of TCH-50 biosorbent, 120 min contact time, 30°C yielded the highest percentage removal ability of CV dye as 95%-98% in the initial dye concentration range of 10-50 mg/L. The adsorption process adhered to the pseudo-second-order kinetic model, attaining equilibrium within 120 minutes, with a calculated activation energy of 46.45 kJ/mol. The Langmuir model was found to best fit the adsorption equilibrium data and maximum adsorption capacity was obtained as 19.36 mg/g for CV at 25°C. This work highlights the potential of corn husk waste, as a cost-effective and environmentally friendly alternative, to be applied for crystal violet dye removal in industrial wastewater treatment.

Acknowledgements

This work was partially funded by research grant from Department of Chemistry, Faculty of Science, Burapha University.

References

1. Gemici, B. T.; Ozel, H. U.; Ozel, H. B., Adsorption property and mechanism of forest wastes based naturel adsorbent for removal of dye from aqueous media. *Biomass Conversion and Biorefnery* **2023,** *13*, 13653-13665.
2. Georgin, J.; Franco, D. S. P.; Netto, M. S.; Allasia, D.; Oliveira, M. L. S.; Dotto, G. L., Evaluation of Ocotea puberula bark powder (OPBP) as an effective adsorbent to uptake crystal violet from colored effluents: alternative kinetic approaches. *Environmental Science and Pollution Research* **2020,** *27*, 25727-25739.
3. Suriyawong, P.; Chuetor, S.; Samae, H.; Piriyakarnsakul, S.; Amin, M.; Furuuchi, M.; Hata, M.; Inerb, M.; Phairuang, W., Airborne particulate matter from biomass burning in Thailand:Recent issues, challenges, and options. *Heliyon* **2023,** *9* (3).
4. Isik, B.; Avci, S.; Cakar, F.; Cankurtaran, O., Adsorptive removal of hazardous dye (crystal violet)using bay leaves (Laurus nobilis L.): surface characterization, batch adsorption studies,and statistical analysis. *Environmental Science and Pollution Research* **2023,** *30*, 1333-1356.
5. Omer, A. s.; Naeem, G. A. E.; Abd-Elhamid, A. I.; Farahat, O. O. M.; El-Bardan, A. A.; Soliman, H. M.A.; Nayl, A. A., Adsorption of crystal violet and methylene blue dyes using a cellulose-based adsorbent from sugercane bagasse: characterization, kinetic and isotherm studies. *Journal of Materials Research and Technology* **2022,** *19*, 3241-3254.
6. Patil, S. A.; Kumbhar, P. D.; Satvekar, B. S.; Harale, N. S.; Bhise, S. C.; Patil, S. K.; Sartape, A. S.; Kolekar, S. S.; Anuse, M. A., Adsorption of toxic crystal violet dye from aqueous solution by using waste sugarcane leaf-based activated carbon: isotherm, kinetic and thermodynamic study. *Journal of the*

Iranian Chemical Society **2022,** *19*, 2891-2906.

7. Homagai, P. L.; Poudel, R.; Poudel, S.; Bhattarai, A., Adsorption and removal of crystal violet dye from aqueous solution by modified rice husk. *Heliyon* **2022,** *8* (4), e09261.
8. Alfrhana, M. A.; Hammuda, H. H.; Al-Omaira, M. A.; El-Sonbati, M. A., Uptake of crystal violet from water by modified Khalas dates residues. *Desalination and Water Treatment* **2020,** *174*, 361-375.

Microplastic contamination in selected carbonated drinks in Thailand

Napaphat Taechapattraporn, Panisara Suwannagate, Rattanaporn Suwansawang, Anh Tuan Ta, and Sandhya Babel*

School of Biochemical Engineering and Technology, Sirindhorn International Institute of Technology, Thammasat University, P.O. Box 22, Pathum Thani 12121, Thailand

**E-mail: sandhya@siit.tu.ac.th*

Abstract:

Microplastics (MPs) contamination in human food is an emerging issue. Recent studies have indicated that MPs have been found in various human tissues and organs, including the placenta, lungs, liver, and blood. This highlights the importance of investigating the presence and quantity of MPs in human food. This study investigates the number and characteristics of MP contamination in commercially available soft drinks in Thailand. Three soft drink brands in Thailand, namely S, F, and C, with different packing types, including plastic bottles, aluminum cans, and glass bottles, were investigated in this study. The soft drinks were filtered through cellulose nitrate (0.45 µm) membrane filters. For each brand, the filters were separated into two groups for analysis using fluorescent microscopy and Micro-FTIR analysis. Results indicated that all investigated soft drink brands, irrespective of packaging material, were contaminated with MPs, with MP concentrations varying from 16 ± 2 to 86 ± 14 particles/liter. Fragments were predominant, accounting for more than 93. PE and PET were mainly found in the three soft drink brands. The presence of MPs in soft drinks raises concerns about potential impacts on human health due to their direct consumption.

1. Introduction

Nowadays, a significant portion of plastic production is geared towards single-use applications. Despite efforts to reduce and reuse plastic, these measures prove inadequate in addressing the escalating global plastic pollution crisis. Currently, around 79% of the world's plastic waste has found its way into natural ecosystems, including rivers, oceans, and land.[1] This alarming trend underscores the urgent need for more sustainable and comprehensive solutions to mitigate the environmental impact of plastic consumption. Furthermore, the breakdown of larger plastics into microplastics exacerbates the issue, posing additional threats to ecosystems and wildlife. Microplastics (MPs) are small pieces of plastic that vary in size from 1 µm to 5 mm and are constantly breaking down due to natural forces, including wind, sun radiation, and currents. Due to the small size of MPs, biota is at risk of accidental ingestion. Recent investigations have discovered MPs in drinking water, milk, and beer.[2] Among various types of plastics, polyethylene terephthalate (PET), polyethylene (PE), and polypropylene (PP) are commonly used for the body and cap of bottled water, making them potential significant sources of MP contamination in drinking water.[3] A study on MP contamination in single-use PET-bottled water in Thailand found that the presence of MPs ranged from 8 to 2600 particles per liter of water, with sizes ranging from 1 to 20 µm.[4] Due to the small size of these particles, there is a concern that they can be ingested into the human body through consumption and accumulate in organs such as the liver, lungs, or kidneys, which might negatively impact health.[5] Previous studies from other regions have found the contamination of MPs in many bottled beverages,[5] such as carbonated drinks, energy drinks, and milk.[6] However, MPs' knowledge of bottled beverages in Thailand is still insufficient. Therefore, there is a crucial need for studies to investigate the presence of MPs in bottled beverages in Thailand.

This study focuses on the analysis of the quantity of MP contamination in three soft drink brands in Thailand, each packaged in different materials: aluminum cans, glass bottles, and plastic bottles. Additionally, the study aims to determine the characteristics of MPs, including their size, shape, and polymer types.

2. Materials and Methods

2.1 Sampling

This study selected three best-selling soft drink brands in Thailand for the investigation of MPs. The soft drink brands are denoted as C, F, and S and labeled to maintain the confidentiality of brand names. A total of 120 soft drinks from the three brands were purchased, comprising 45 aluminum cans, 45 single-use plastic bottles, and 30 glass bottles from supermarkets in Pathum Thani, Thailand. Since glass bottles of the S brand were not available on the market, they were not included in the investigation. All samples had a shelf life from October to November 2023 to ensure consistency.

2.2 Sample Analysis

2.2.1 Filtration

MPs were filtered by passing soft drinks through filter paper and using a vacuum pump to enhance the fast flow of those soft drinks. Due to 2 analytical methods (i.e., fluorescence microscope and micro-FTIR), 2 filter papers were used, including glass fiber filters with a pore size of 1.2 µm and cellulose nitrate membrane filters with a pore size of 0.45 µm. Each soft drink batch underwent a filtration process wherein approximately 900 to 1,100 milliliters passed through the filter paper. Subsequently, the results were normalized to the number of MPs per liter of samples to ensure uniformity across all tests.

After filtration, the filters were placed on Petri dishes and sealed with foil to prevent contamination. These dishes were then subjected to an oven drying phase at 60 degrees Celsius for 24 hours, ensuring thorough drying and eliminating residual moisture.

2.2.2 Fluorescence microscope and micro-FTIR analysis

Before the analysis of samples with a fluorescence microscope, the Nile Red staining process was needed.[11] The Nile red solution was prepared by dissolving Nile red with chloroform to a concentration of 5 mg/L. After drying the filter samples separately, Nile red solution was applied onto each glass fiber filter using a glass dropper. Samples were covered with aluminum foils to avoid contamination.[12] Then, the filter papers were stored in the darkness for 5 – 6 hours before scanning by the fluorescence microscope (GE Healthcare, DeltaVision Elite) using an excitation DAPI of 390/18 nm and an emission DAPI of 435/48 nm. The particles observed by the microscope were counted and classified into fibers and fragments. The number of MPs found in the soft drinks was reported as particles per liter (p/L).[13]

The micro-FTIR spectroscope (Nicolet iN10 model, Thermo Scientific, USA) was utilized to investigate polymer types of MPs. The analysis was conducted in the ATR mode by analyzing 5 particles in each sample. The condition requirements for collecting data included 25 seconds, employing 128 scans for each measurement. The spectral resolution was set to 8 cm^{-1}. The aperture dimensions for the ATR mode were configured with a width and height range of 50-300 µm. Thermo Scientific OMNIC™ Picta™ software was used to control and operate the complete experimental apparatus. Results were presented as unknown spectra. Then, sample spectra were compared with the reference spectra of polymer types. A matching rate of 70% or higher was utilized to confirm the polymer type.

Researchers took precautions to minimize contamination risks, such as wearing cotton lab coats and latex gloves. Sampling and analysis utilized solely metal or glass apparatus, thoroughly cleaned with deionized water before use. Experiments were conducted within a fume hood to mitigate airborne contamination, and all glassware and equipment were shielded with aluminum foil. To ensure quality control, blank samples (composed of deionized water) were concurrently analyzed with river samples. The identified MP number in the blank samples was then subtracted from the quantity detected in the soft drink sample.

3. Results & Discussion

3.1 Number of microplastics

Figure 1 shows the mean MP numbers of three soft drink brands with different packaging. MPs were found in all soft drink samples, ranging from 16 ±2 to 86±14 particles/L. Notable variations emerge when examining individual brands within each container type. The F brand records the highest concentration of MPs in glass bottles (86 ± 14 particles/L). However, regarding cans, the F brand exhibits the lowest number of MPs (16 ± 2 particles/L). Similarly, within the C brands, the highest number of MPs is observed in glass bottles at (44 ± 3 particles/L), while the lowest count is associated with cans (29 ± 4 particles/L). For the S brand, since glass bottles are not available on the market, only cans and plastic bottles were investigated. The results indicate a higher concentration of MPs in plastic bottles (73 ± 12 particles/L) than in cans (45 ± 23 particles/L), aligning with the observed trend in other brands. The observed variation in MP number among the three brands underscores the importance of material selection and manufacturing processes in influencing MP contamination. Glass bottles tend to show higher microplastic counts, potentially stemming from production, transportation, or glass recycling.

This research represents one of the limited inquiries into MP contamination in soft drinks. A study from Mexico identified a total of 40 MPs (average: 7 ± 3.21), equivalent to two MPs per sample across the 19 examined bottles[7]. Another study conducted in Ecuador revealed an average of 32 particles/ L of soft drinks.[25]

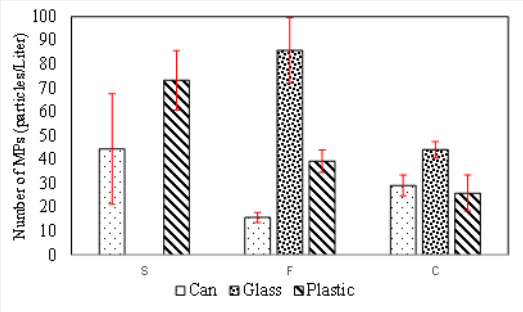

Figure 1. Number of microplastics in the three soft drink brands with different packaging

3.2 Characteristics of microplastics

3.2.1 Size of microplastics

The size variation of MPs in different soft drink brands is depicted in Figure 2. As illustrated, MPs within the size range of 0.1-0.5 mm were predominant in all samples, accounting for 67-96%. In contrast, the 1-2 mm size range was only found in the S brand can, constituting 7% of the total. The present study's findings align with those of Shruti et al. (2020)[7] and Abdullah (2023),[17] indicating that most soft drink particles typically range in size from 0.1 to 1 mm.

The size of MPs is particularly noteworthy due to its potential impact on human health. The predominance of small-sized MPs in Thai soft drinks suggests a heightened potential for adverse effects on human health since they can penetrate deeper into the human body.

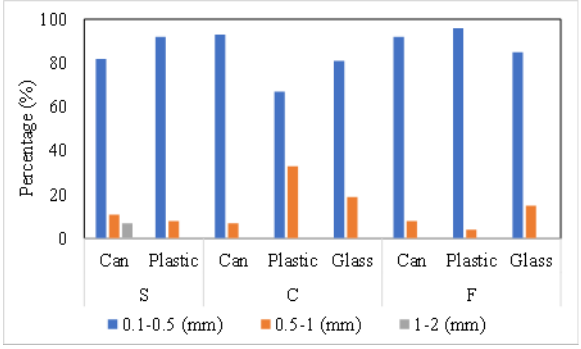

Figure 2. Variability of microplastic sizes in the three soft drinks

3.2.2 Morphologies of microplastics

Fragments and fibers are the most common morphologies of MPs identified in this study. As shown in Table 1, over 90% of the MPs identified were fragments, with fibers being the second most prevalent morphology. Previous studies have also reported the predominance of fragments in soft drinks and water bottles.[22-24] Mason et al. (2018)[24] hypothesized that using industrial lubricants in the water bottling process may be the origin of these particles.

Table 1. Percentage of MPs shape (%)

Brand	Packaging	Shape (%)	
		Fiber	Fragment
S	Can	3.45	96.55
	Plastic	3.31	96.69
C	Can	3.17	96.83
	Glass	5.28	94.72
	Plastic	7.37	92.63
F	Can	5.56	94.44
	Glass	6.58	93.42
	Plastic	4.02	95.98

3.2.3 Polymer types

Figure 3 illustrates the variations in polymer types across three soft drink brands. As depicted, PE was prevalent in the majority of soft drink brands. PE was the primary polymer for all brands in plastic bottles, followed by polyethylene terephthalate (PET). Soft drinks in cans were predominantly composed of PE and phenoxy. The trend continued in glass bottles, where PE and copolymer were the primary constituents.

In comparison with other studies, Shruti et al. (2020)[7] reported that polyamide (PA) was the most common type of microplastics (MPs) found in the soft drinks they analyzed. Other polymers identified in their study included PET and Acrylonitrile-butadiene-styrene (ABS). On the contrary, Diaz-Basantes et al. (2020)[25] found that polypropylene (PP) and polyacrylamide (PAM) were prevalent polymers in various foodstuffs such as soft drinks, honey, milk, and beer. Meanwhile, a study by Schymanski et al. (2018)[18] revealed that in German packaged water, PET accounted for 84% and PP for 7% of the identified polymers. Furthermore, polystyrene (PS) was detected in mineral waters in Iran, as reported by Makhdoumi et al. (2021).[19]

According to the research cited,[21,26] the production of PET for bottles and PE for caps is a significant factor contributing to the prevalence of PET and PE in plastic bottles. Additionally, insights into the origin of plastics in water suggested that mechanical characteristics and the manufacturing procedure influence how plastics break down and disperse.[22]

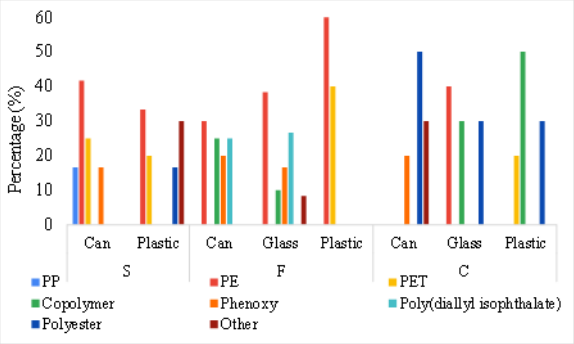

Figure 3. Polymer types of MPs in three soft drink brands

4. Conclusion

This study investigates MP contamination in three popular soft drink brands in Thailand, analyzing various packaging types. Microplastics were found in all samples, ranging from 16 ± 2 to 86 ± 14 particles per liter. Glass bottles had the highest number of microplastics, followed by plastic bottles. Microplastics were predominantly 0.1-0.5 mm in size, with the most common shapes being fragments and fibers. Polymer analysis revealed that polyethylene (PE), polyethylene terephthalate (PET), and polypropylene (PP) were the dominant types. The presence of microplastics in Thai soft drinks, particularly those with small sizes, raises concerns about potential effects on human health upon consumption.

Reference

1. Hernández-Delgado, E. A. (2015). The emerging threats of climate change on tropical coastal ecosystem services, public health, local economies and livelihood sustainability of small islands: Cumulative impacts and synergies. Marine Pollution Bulletin, 101(1), 5–28.
2. Kosuth, M., Mason, S. A., & Wattenberg, E. V. (2018). Anthropogenic contamination of tap water, beer, and sea salt. PLOS ONE, 13(4), e0194970.
3. Napper, I. E., & Thompson, R. C. (2016a). Release of synthetic microplastic plastic fibres from domestic washing machines: Effects of fabric type and washing conditions. Marine Pollution Bulletin, 112(1–2), 39–45.
4. Kankanige, D., & Babel, S. (2020). Smaller-sized micro-plastics (MPs) contamination in single-use PET-bottled water in Thailand. Science of The Total Environment, 717, 137232.
5. Blackburn, K., & Green, D. (2022). The potential effects of microplastics on human health: What is known and what is unknown. Ambio, 51(3), 518–530.
6. Liu, P., Zhan, X., Wu, X., Li, J., Wang, H., & Gao, S. (2020). Effect of weathering on environmental behavior of microplastics: Properties, sorption and potential risks. Chemosphere, 242, 125193.
7. Shruti, V. C., Pérez-Guevara, F., Elizalde-Martínez, I., & Kutralam-Muniasamy, G. (2020). First study of its kind on the microplastic contamination of soft drinks, cold tea and energy drinks - Future research and environmental considerations. Science of The Total Environment, 726, 138580.
8. Vartanian, L. R., Schwartz, M. B., & Brownell, K. D. (2007). Effects of Soft Drink Consumption on Nutrition and Health: A Systematic Review and Meta-Analysis. American Journal of Public Health, 97(4), 667–675.
9. Grimm, G. C., Harnack, L., & Story, M. (2004). Factors associated with soft drink consumption in school-aged children. Journal of the American Dietetic Association, 104(8), 1244–1249.
10. Nel, H. A., & Froneman, P. W. (2017). A Quantitative Analysis of Microplastic Pollution Along the South-eastern Coastline of South Africa. In Fate and Impact of Microplastics in Marine Ecosystems (p. 11). Elsevier.
11. Erni-Cassola, G., Gibson, M. I., Thompson, R. C., & Christie-Oleza, J. A. (2017). Lost, but Found with Nile Red: A Novel Method for Detecting and Quantifying Small Microplastics (1 mm to 20 μm) in Environmental Samples. Environmental Science & Technology, 51(23), 13641–13648.
12. Bradbury, S., & Evennett, P. (2020). Contrast Techniques in Light Microscopy. Garland Science.
13. Shim, W. J., Song, Y. K., Hong, S. H., & Jang, M. (2016). Identification and quantification of microplastics using Nile Red staining. Marine Pollution Bulletin, 113(1–2), 469–476.
14. Käppler, A., Fischer, M., Scholz-Böttcher, B. M., Oberbeckmann, S., Labrenz, M., Fischer, D., Eichhorn, K.-J., & Voit, B. (2018). Comparison of μ-ATR-FTIR spectroscopy and py-GCMS as identification tools for microplastic particles and fibers isolated from river sediments. Analytical and Bioanalytical Chemistry, 410(21), 5313–5327.
15. Primpke, S., Lorenz, C., Rascher-Friesenhausen, R., & Gerdts, G. (2017). An automated approach for microplastics analysis using focal plane array (FPA) FTIR

microscopy and image analysis. Analytical Methods, 9(9), 1499–1511.
16. Mohammed Raffic, N., Mohammed Khondoker, A., Mohammed Ali Kaabi, A., Ali Hamad Majrashi, A., Yhaya Mohammed Qusadi, I., Ibrahim Mohamed Moawad, F., Hadidi, H., Tharwan, M., & Saminathan, R. (2023). Utilization of ANOVA analysis identifying the effects of various parameters on the corrosion behaviour of 7021 Al alloys in simulated RED SEA conditions. Materials Today: Proceeding
17. Altunışık, A. (2023). Prevalence of microplastics in commercially sold soft drinks and human risk assessment. Journal of Environmental Management, 336.
18. Schymanski, D., Goldbeck, C., Humpf, H.-U., & Fürst, P. (2018). Analysis of microplastics in water by micro-Raman spectroscopy: Release of plastic particles from different packaging into mineral water. Water Research, 129, 154–162.
19. Makhdoumi, P., Amin, A. A., Karimi, H., Pirsaheb, M., Kim, H., & Hossini, H. (2021). Occurrence of microplastic particles in the most popular Iranian bottled mineral water brands and an assessment of human exposure. Journal of Water Process Engineering, 39, 101708.
20. Julienne, F., Lagarde, F., & Delorme, N. (2019). Influence of the crystalline structure on the fragmentation of weathered polyolefines. Polymer Degradation and Stability, 170, 109012.
21. Enfrin, M., Lee, J., Le-Clech, P., & Dumée, L. F. (2020). Kinetic and mechanistic aspects of ultrafiltration membrane fouling by nano- and microplastics. Journal of Membrane Science, 601, 117890.
22. Ibeto, C.N., Enyoh, C.E., Ofomatah, A.C., Oguejiofor, L.A., Okafocha, T., Okanya, V., 2021. Microplastics pollution indices of bottled water from South Eastern Nigeria. Int. J. Environ. Anal. Chem. 1–20.
23. Makhdoumi, P., Amin, A.A., Karimi, H., Pirsaheb, M., Kim, H., Hossini, H., 2021. Occurrence of microplastic particles in the most popular Iranian bottled mineral water brands and an assessment of human exposure. J. Water Process Eng. 39, 101708.
24. Mason, S.A., Welch, V.G., Neratko, J., 2018. Synthetic polymer contamination in bottled water. Front. Chem. 6.
25. Diaz-Basantes, M.F., Conesa, J.A., Fullana, A., 2020. Microplastics in honey, beer, milk and refreshments in Ecuador as emerging contaminants. Sustainability 12 (14), 5514.
26. Singh, Nisha & ArijitMondal, & AmarjeetBagri, & Tiwari, Ekta & Khandelwal, Nitin & Abdolahpur Monikh, Fazel & Darbha, Gopala. (2021). Characteristics and spatial distribution of microplastics in the lower Ganga River water and sediment. Marine Pollution Bulletin.

Removal of chloride ions from wastewater through Friedel's salt chemical precipitation method

Abhi Shrestha, Prakaidaw Panichvattana, Anh Tuan Ta, and Sandhya Babel*

School of Bio-Chemical Engineering and Technology, Sirindhorn International Institute of Technology, Thammasat University, Pathum Thani 12120, Thailand

**E-mail: sandhya@siit.tu.ac.th*

Abstract:

Numerous industries, such as pickling and water washing treatment for bottom ash, generate wastewater with elevated chloride ion levels. Discharging this wastewater into the environment can lead to problems, including pipeline corrosion, soil salinization, and harmful effects on plant growth and aquatic life. Consequently, there is a critical demand for developing cost-effective technologies to remove or control chloride ions before discharge. This study focuses on removing chloride ions from wastewater through chemical precipitation, forming insoluble Friedel's salt ($Ca_2Al(OH)_2 \cdot H_2O$). A comparative analysis assessed the chloride removal efficiency by comparing the combination of $Al(OH)_3$ and Al_2O_3 reagents with CaO. Optimum reaction time was also investigated in this study. Sodium chloride at a concentration of 2600 g/L served as a synthetic wastewater sample. Batch experiments were performed with varying molar ratios of Ca:Al:Cl, using $Al(OH)_3$ and Al_2O_3 as reagents to determine the optimal parameters for chloride removal. The results indicated that the combination of $Al(OH)_3$ and CaO was more effective than Al_2O_3. The highest chloride removal efficiency, reaching 47%, was achieved at a Ca:Al:Cl ratio of 2.5:1:1 at room temperature. The optimum reaction time for chloride removal at the same Ca:Al:Cl ratio was determined to be 20 minutes.

1. Introduction

Wastewater, an inescapable byproduct of industrial and domestic activities, plays a pivotal role in our modern world. While significant strides in wastewater management have led to improved treatment processes, concerns about wastewater quality, especially in chloride contamination, remain paramount. Chlorine has many uses in various industries and applications, such as disinfection of drinking water,[1] swimming pools, and wastewater. It helps killing harmful bacteria, viruses, and other microorganisms.[2] This makes the water safe for human consumption. However, excess chloride may form trihalomethane, which causes cancer[3,4] and can negatively affect the taste of water.

The main sources of chloride in water are industrial effluents, which contain high chlorine concentrations, flue gas desulfurization,[3] chloralkali industries, paper and pulp mills, and leather tanning.[4] In the case of leather tanning, the production of chloride ions is primarily attributed to the use of chloride-based chemicals and processes across various tanning stages, including pre-tanning, the utilization of chloride-containing tanning agents, neutralization, retaining, and dyeing.[5,6,8] These chloride ions are introduced into the tanning process through specific chemicals, such as sodium chloride, a common salt used during curing for preservation and leather pickling to prevent excessive acidic swelling, and finally discharged into wastewater after processing. The water washing treatment for bottom ash also generates a high chloride ion wastewater.[9] These byproducts often lead to acid rain and corrosion.[10] Chlorine released from various sources and waste has the potential to pollute surface water, groundwater, and soils, can inhibit effective use, and increase the process's cost[11] affecting both the environment and human well-being. Therefore, removing chloride from wastewater is mandatory. Friedel's salt ($Ca_4Al_2(OH)_{12}Cl_2(H_2O)_4$), an insoluble chloride salt with an intricate crystal structure consisting of alternating layers of positively charged metal hydroxides and negatively charged water molecules. Embedded within this structure are chloride ions, which play a crucial role in maintaining electrical neutrality. This unique crystal arrangement facilitates the adsorption of chloride ions from aqueous solutions. Friedel's salt possesses strong anion-exchange properties, which can attract and retain chloride ions within its structure, effectively removing them from the solution. This property makes Friedel's salt a valuable adsorbent in wastewater treatment, where it is employed to purify and desalinate water.[9,12]

Therefore, this study aims to remove chloride ions from wastewater through chemical precipitation, forming insoluble Friedel's salt ($Ca_2Al(OH)_4 \cdot H_2O$). Batch experiments were conducted to compare the chloride removal efficiency of combinations of $Al(OH)_3$ and Al_2O_3 reagents with that of CaO. The suitable Ca:Al:Cl molar ratio and reaction time were also determined in this study.

2. Materials and Methods

2.1 Materials

The synthetic wastewater was prepared by dissolving sodium chloride (NaCl) in distilled water to achieve a chloride ion concentration of 2600 mg/L, representing the concentration level present in wastewater from bottom ash washing. In this study, calcium oxide (CaO) was utilized as the calcium reagent, and aluminum hydroxide ($Al(OH)_3$) along with aluminum oxide (Al_2O_3) served as the aluminum reagents to form the insoluble Friedel's salt. These chemicals were added to the synthetic wastewater in powder form. The dosages of CaO, $Al(OH)_3$, and Al_2O_3 are expressed in the Ca:Al:Cl molar ratio. The specific amounts of CaO, $Al(OH)_3$, and Al_2O_3 added are determined based on the chloride ion concentration.

2.2. Determination of optimal conditions for chloride removal.

Batch experiments were conducted in this study. In each experiment, a 1000 mL chloride ion solution was poured into a 1000 mL beaker with a stainless-steel magnetic stirrer. CaO was added in dosages corresponding to two reagents, Al_2O_3 and $Al(OH)_3$, at varying multiples of the theoretical molar ratio (e.g., Al:Cl = 0.5, 1, 1.5, 2, 2.5, 3, and Ca:Cl = 2). Subsequently, the influence of the Ca:Cl ratio on chloride removal was investigated by adjusting the Ca/Cl ratio to 2, 2.5, 3, 3.5, 4, and 4.5, with the optimum ratio of Al. All tests were conducted at room temperature with a stirring speed of 150 rpm for 60 minutes. Then, the supernatant was filtered using filter paper (Whatman No. 1001-110) and sampled to determine remaining chloride concentration. After determining the suitable aluminum reagent and the Ca:Al:Cl molar ratio, the ratio was used to investigate the impact of reaction time on chloride removal. The experiment was conducted for 1 hour, and samples were collected every 20 minutes to analyze chloride concentration.

2.3. Analysis techniques

Mohr's method is employed to determine the concentration of chloride ions in the liquid fraction. The Mohr's method is a precipitation titration method that uses silver nitrate to titrate chloride ions in aqueous solutions.[13] The chloride removal efficiency is calculated using the following equation based on the initial and residual chloride ion concentration difference.

$$RE\ (\%) = \left(\frac{A-B}{A}\right) \times 100 \quad (1)$$

Where:
A: Initial concentration (in grams per liter)
B: Final concentration - the concentration of chloride ions remaining in the aqueous solution after removal (in grams per liter).

3. Results & Discussion

3.1 Effect of $Al(OH)_3$ and Al_2O_3 reagents and Al:Cl molar ratios on chloride removal

Figure 1 illustrates the removal efficiency of the combination of $Al(OH)_3$ and Al_2O_3 with CaO at different molar ratios of Al:Cl. The results indicate that $Al(OH)_3$ exhibits higher removal efficiencies than Al_2O_3 at most Al/Cl molar ratios. At a ratio of 0.5:1, the two reagents' removal efficiency is similar. However, as the ratio increases, the chloride removal efficiency of $Al(OH)_3$ significantly surpasses that of Al_2O_3, ranging from 50% to 73%. Therefore, $Al(OH)_3$ was selected as the preferred reagent for aluminum.
Figure 1 also indicates that when using $Al(OH)_3$ as the aluminum reagent, as the Al:Cl molar ratio increases from 0.5 to 1, the chloride removal efficiency increases to 78%. However, the chloride removal efficiency decreases when the Al:Cl ratio exceeds 1. Similar results were found with Al_2O_3, where the chloride removal efficiency increased as the Al:Cl ratio increased from 0.5 to 1 but decreased as the ratio exceeded 1.5. This can be explained by the formation of $Al(OH)_4^-$ through the hydrolysis of AlO_2^- (Eq. (2)), which further precipitates as katoite (Eq. (3)) and Friedel's salt (Eq. (4)). Therefore, the decrease in the chloride removal could be attributed to the overdose of $Al(OH)_3$ and Al_2O_3, leading to the reaction between Friedel's salt and newly generated $Al(OH)_4^-$, resulting in the formation of katoite and the release of chloride (Eq. (5)).[14,15] Based on these results, using $Al(OH)_3$ with an Al:Cl ratio of 1 is optimal for chloride removal.

$$AlO_2^- + 2H_2O \rightarrow Al(OH)_4^- \ (2)$$

$$3Ca^{2+} + 2Al(OH)_4^- + 4OH^- \rightarrow Ca_3Al(OH)_{12} \downarrow (3)$$

$$2Ca^{2+} + Al(OH)_4^- + Cl^- + 2OH^- + 2H_2O \rightarrow Ca_2Al(OH)_6Cl \cdot 2H_2O \downarrow (4)$$

$$3Ca_2Al(OH)_6Cl \cdot 2H_2O \downarrow + Al(OH)_4^- + 2OH^- \rightarrow 2Ca_3Al_2(OH)_{12} \downarrow + 3Cl^- + 2H_2O \ (5)$$

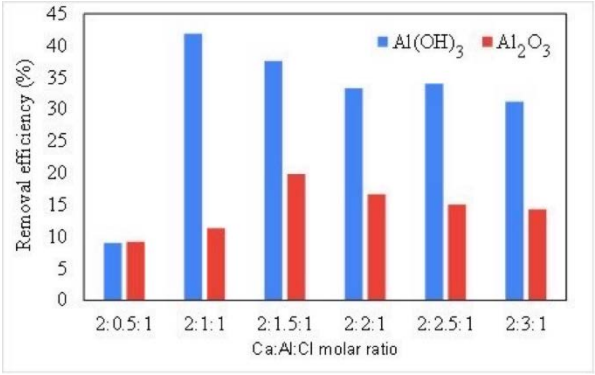

Figure 1. Effect of Al:Cl malor ratio with $Al(OH)_3$ and Al_2O_3 reagents on chloride removal.

3.2 Effect of Ca:Cl ratio on the chloride removal

The effect of Ca:Cl was investigated after determining the suitable Al reagent (i.e., $Al(OH)_3$) and optimal Al:Cl molar ratio (at 1). Figure 2 demonstrates the chloride removal efficiencies at different Ca:Cl ratios. As the ratio increases from 2 to 2.5, the chloride removal efficiency increases from 40% to 47%. However, when the ratio exceeds 2.5, the removal efficiency significantly decreases. Thus, the highest chloride removal efficiency was achieved at a ratio of 2.5:1, and when the molar ratio was higher than 2.5:1, the chloride removal efficiency couldn't be further improved.

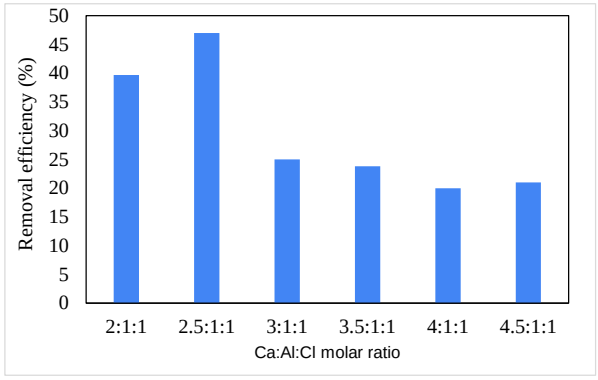

Figure 2. Effect of Ca:Cl molar ratio on chloride removal

3.3 Effect of reaction time on the chloride removal

Reaction time is essential when assessing the effectiveness of Fridel's salt in removing chloride. This aspect holds particular significance in real-scale wastewater treatment plants, as it is used to calculate wastewater retention time in the treatment unit. If the optimum reaction time is determined, it can contribute to cost-effectiveness in the construction and operation of wastewater treatment plants.

Figure 3 illustrates how the duration of the reaction impacts chloride removal efficiency. Keeping the molar ratio at 2.5:1:1 for Ca:Al:Cl, the findings revealed a swift rise in chloride removal efficiency within the initial 20 minutes. Then, the efficiency reached equilibrium after 1 h. This indicates that chloride ion is rapidly removed through the formation of Friedel's salt.

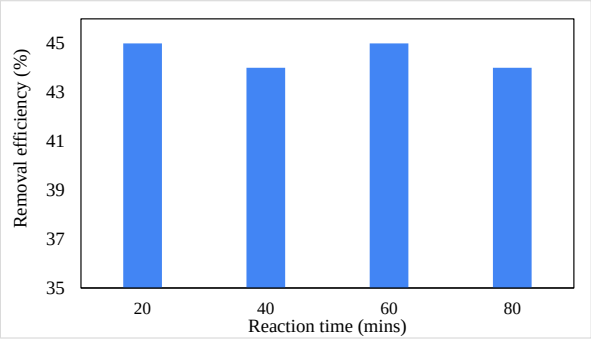

Figure 3. Effect of reaction time on chloride removal with the ratio of Ca:Al:Cl at 2.5:1:1

4. Conclusion

This study focused on efficiently removing chloride ions from wastewater, addressing environmental concerns associated with elevated chloride levels. Chemical precipitation, specifically forming Friedel's salt ($Ca_2Al(OH)_4 \cdot H_2O$), is a promising method. Comparative analysis favored $Al(OH)_3$ and CaO as superior reagents, with an optimal Ca:Al:Cl ratio of 2.5:1:1 and a 20-minute reaction time, achieving a peak chloride removal efficiency of 47%. This underscores the importance of selecting reagents and optimizing ratios for effective chloride precipitation. The obtained results demonstrate that the formation of Friedel's salt is effective for chloride removal and can potentially serve as a valuable adsorbent in wastewater treatment. Further experiments are required to determine the effects of other factors on chloride removal efficiency, such as reaction temperature, initial chloride concentration, and UV oxidation.

Acknowledgments

This research was supported by the Matching Fund between Thammasat University and the National Taipei University of Technology. This study was also supported by the Kurita Water and Research Foundation (KWEF202315).

References

1. Cai, M.-Q.; Feng, L.; Zhang, L.-Q. Transformation of Aminopyrine in the Presence of Free Available Chlorine: Kinetics, Products, and Reaction Pathways. *Journal of Chemosphere* **2017**, *171*, 625–634.
2. Sorlini, S.; Collivignarelli, C. Chlorite Removal with Ferrous Ions. *Journal of Desalination* **2005**, *176* (1-3), 267–271.
3. Hsu, C.-H.; Jeng, W.-L.; Chang, R.-M.; Chien, L.-C.; Han, B.-C. Estimation of Potential Lifetime Cancer Risks for Trihalomethanes from Consuming Chlorinated Drinking Water in Taiwan. *Journal of Environmental Research* **2001**, 85 (2), 77–82.
4. Li, J. W.; Yu, Z.; Cai, X.; Gao, M.; Chao, F. Trihalomethanes formation in water treated with chlorine dioxide. *Journal of Water* Research **1996**, 30(10), 2371-2376.
5. Appala, V. G.; Pandhare, N. N.; Bajpai, S. Biorefining of leather solid waste to harness energy and materials—a review. *Biomass Conversion and Biorefinery* **2022**, 1-18.
6. Jian, Z.; Shuxiang, H.; Ya-Nan, W.; Qiang, H.; Xueping, L.; Wenhua, Z.; Bi, S. Release of Chrome in Chrome Tanning and Post Tanning Processes. *Journal of the Society of Leather Technologists and Chemists* **2012**, 96(4), 157.
7. Sundar, V. J.; Muralidharan, C.; Mandal, A. B. A Novel Chrome Tanning Process for Minimization of Total Dissolved Solids and Chromium in Effluents. *Journal of Cleaner Production* **2013**, 59, 239–244.
8. Xu, Y.; Zhang, Y.; Shu, Y.; Song, H.; Shu, X.; Ma, Y.; Hao, L.; Zhang, X.; Ren, X.; Wang, Z.; Zhang, X. Composition and Leaching Toxicity of Hydrochloric Acid Pickling Sludge Generated from the Hot-Dip Galvanized Steel Industry. *ACS Omega* **2022**, 7 (16), 13826–13840.
9. Wang, L. P.; Lee, W. H.; Man Tseng, S.; Cheng, T. W. Removal of Chloride Ions from an Aqueous Solution Containing a High Chloride Concentration through the Chemical Precipitation of Friedel's Salt. *Materials Transactions* **2018**, 59 (2), 297–302.
10. Gołda, M.; Janas, A.; Olszewska, D. The Leaching of Chlorine from Hard Coal: Part I. Relationship between the Process Parameters and Its Effectivity. *Journal of Fuel Processing Technology* **2011**, 92 (6), 1230–1235.
11. Man, K.; Zhu, Q.; Guo, Z.; Xing, Z. Fe-Ti/Fe (II)-Loading on Ceramic Filter Materials for Residual Chlorine Removal from Drinking Water. *Journal of Chemosphere* **2018**, 200, 405–411.
12. Zahir, Md. H.; Irshad, K.; Rahman, M. M.; Shaikh, M. N.; Rahman, M. M. Efficient Capture of Heavy Metal Ions and Arsenic with a CaY–Carbonate Layered Double-Hydroxide Nanosheet. *ACS Omega* **2021**, 6 (35), 22909–22921.
13. Hazen, A. On the Determination of Chlorine in Water. *The Analyst* **1889**, 14, 229.
14. Barzgar, S.; Lothenbach, B.; Tarik, M.; Di Giacomo, A.; Ludwig, C. The Effect of Sodium Hydroxide on al Uptake by Calcium Silicate Hydrates (c S H). *Journal of Colloid and Interface Science* **2020**, 572, 246–256.
15. Jiménez, A.; Misol, A.; Morato, A.; Rives, V.; Vicente, M. Á.; Gil, A. Synthesis of Pollucite and Analcime Zeolites by Recovering Aluminum from a Saline Slag. *Journal of Cleaner Production* **2021**, 297, 126667–126667.

Decolorization and detoxification of Solvent Red 24 by Bacillus sp. FN1 producing laccase and lignin peroxidase

Peraya Buapho and SinthuwatRitthitham*

Department of Biotechnology, Faculty of Engineering and Industrial Technology, Silpakorn University, Nakhon Pathom 73000, Thailand

**E-mail: sinthuwat@hotmail.com*

Abstract:

Bacillus sp. FN1 isolated from textile effluent could efficiently degrade and decolorize the Solvent Red 24, a water-insoluble dye from textile industrial dying process. In this study, the microorganism was cultivated at 37 °C under shaking condition in the medium containing 1% (w/v) sucrose, 0.3% (w/v) peptone, and 50 mg/L of dye dissolved in DMSO. The decolorization efficiency of 66.01% was achieved after 96 h of incubation. The laccase and lignin peroxidase continuously produced with the maximum activities of 48.35 U/L and 5.34 U/L: respectively. The FTIR spectrum of the dye after treated with Bacillus sp. FN1 showed the degradation of the azo bond and the aromatic rings. The biodegraded products metabolized by *Bacillus* sp. FN1 did not adversely affect the growth of *Oryza sativa* L.

1. Introduction

Solvent Red 24 ($C_{24}H_{20}N_4O$) is the solvent soluble diazo synthetic dye used for coloring various non-polar hydrocarbon products including fabric dying industry.[1] As the azo dye in wastewater is the most polluting contaminant among all industrial sectors because of its volume and composition of the effluents,[2] the degradation processing of the effluent before its release into the environment becomes essential.[3]

The decolorization and degradation of azo-synthetic dye from the effluent by microorganisms is considered as a biological system-assisted transformation protocol that has been proven to be very effective experimentally[4] and also eco-friendly and cost-effective as compared with conventional treatment methods such as photodegradation, electrolysis, adsorption, precipitation, and chemical oxidation.[5] As some microorganisms produce the enzyme involving in dye degradation like azoreductase, laccase, lignin peroxidase, and manganese peroxidase, the decolorization of azo dyes by biological process has been found to be applied in textile wastewater treatment effectively.[6]

The objective of this study was to investigate the potential capability of Bacillus sp. FN1 for degrading and decolorizing of Solvent Red 24. The effects of aeration and carbon sources on decolorization efficiency were evaluated and the laccase and lignin peroxidase activities in the decolorization processes were determined. Furthermore, the phytotoxicity of the biodegraded products was also investigated.

2. Materials and Methods

2.1 Chemicals and dye stock preparation

Solvent Red 24 used in this study was supplied by Nobletex Dyeing Co., Ltd. (Nakhon Pathom, Thailand). The dye (50 mg/L) was dissolved in DMSO under aseptic condition. All chemicals were from Sigma Aldrich and were analytical grade with the highest purity available.

2.2 Microorganism and culture condition

Bacillus sp. FN1 previously isolated from textile effluent stored 4 °C was cultivated on the medium containing (g/L): glucose (10), peptone (3), KH_2PO_4 (0.6), K_2HPO_4 (0.4), $MgSO_4{\cdot}7H_2O$ (0.5), $MnSO_4.H_2O$ (0.05), $FeSO_4{\cdot}7H_2O$ (0.0005), $ZnSO_4{\cdot}7H_2O$ (0.001) and 0.2% (v/v) Guaiacol. The pH was adjusted to 7.0 before sterilization at 121 °C for 15 min. The culture was incubated at 37 °C for 72 h with a shaking speed of 150 rpm.

2.3 Effect of aeration on Solvent Red 24 decolorization

The effect of aeration on decolorization of Solvent Red 24 was investigated by cultivation the microorganism under incubator shaker and controlled incubator chamber. The decolorization studies were performed in an Erlenmeyer flask (250 ml) containing 80 ml of a sterilized medium (pH 7.0) and 10 ml of 50 mg/L Solvent Red 24 dissolved in DMSO and 10 ml inoculums. The aeration was provided by shaking speed of 150 rpm while the static condition was performed by incubating the culture at 37 °C. The sample (5 ml) was then aspetically collected at time intervals and centrifuged at 6,000 rpm for 20 min. The cell pellets were washed twice with 20% (v/v) acetone to remove the dye absorbed on cells and

resuspended in distilled water before measuring the cell growth at 600 nm. The supernatant was scanned the UV-Vis spectra from 200-800 nm with the maximum visible wavelength of 509 nm. The supernatant was also analyzed for laccase and lignin peroxidase activity.

2.4 Effect of carbon source on Solvent Red 24 decolorization

The effect of carbon source on the dye decolorization was investigated by separately substitution of glucose (1% w/v) with sucrose and starch in the basal medium containing 0.3% (w/v) peptone as a nitrogen source and 50 mg/L Solvent Red 24 dissolved in DMSO. The culture incubated at 37 °C, 150 rpm for 96 h was then periodically collected and subsequently centrifuged at 6,000 rpm for 20 min. The cell pellets were washed twice with 20% (v/v) acetone to remove the dye absorbed on cells and resuspended in distilled water before measuring the cell growth at 600 nm. The cell free supernatant was scanned the UV-Vis spectra from 200-800 nm and measured the absorbance of 509 nm for decolorization efficiency. The laccase and lignin peroxidase activities in the supernatant were also analyzed.

2.5 Decolorization efficiency

After bacterial cells were separated by centrifugation, the supernatant was analyzed for the extent decolorization efficiency by UV-Vis spectrophotometry at 509 nm. The decolorization percentage was calculated by the following formula: Decolorization (%) = $[(A_0-A_t)/ A_0] \times 100$, where A_0 and A_t were the initial absorbance and the absorbance at a specific time, respectively.

2.5 Quantification of enzyme activities

Lignin peroxidase (LiP) activity was quantified by using 3,4-Dimethoxybenzyl alcohol (veratryl alcohol) as a substrate [7]. The reaction mixture containing 200 µl of 10 mM veratryl alcohol dissolved in 25mM Glycine-NaOH buffer (pH 10.0), 400 µl of 25mM Glycine-NaOH buffer, 200 µl of 2 mM H_2O_2, and 200 µl of the sample was incubated at 60 °C for 30 min. The absorbance at 310 nm was then measured (ε = 9,300 M^{-1} cm^{-1}). One unit of lignin peroxidase activity was defined as the amount of enzyme required to oxidize one µmol of veratryl alcohol per minute.[8]

Laccase activity was assayed by the method as described by Wariishi *et al*. (1992) using 2,6-dimethoxyphenol (DMP) as a substrate.[9] The reaction mixture containing 200 µl of 2 mM DMP (dissolved in 10% (v/v) absolute ethanol) in 25 mM Tris-HCl buffer (pH 9.0) and 50 µl of sample was incubated at 60 °C for 30 min and measured the absorbance at 468 nm (ε = 14,800 M^{-1} cm^{-1}). One unit of laccase activity was defined as the amount of enzyme causing an increase of one µmol of the 3,3′,5,5′-tetramethoxy-1,1′biphenyl-4,4′-diol (TMBP) per minute.[10]

2.6 FT-IR analysis

FTIR analysis was performed by Frontier FTIR Spectrometer (Perkin - Elmer, England) with high sensitivity in the scan range of 400 - 4,000 cm^{-1} at a resolution of 4 cm^{-1}. The supernatant at 96 h was extracted twice by two volumes of ethyl acetate. The organic phase was then evaporated by rotary evaporator and dried in desiccator. The Solvent Red 24 powder was used as a control.

2.7 Phytotoxicity assay

The phytotoxicity assay of the Solvent Red 24 decolorized by *Bacillus* sp. FN1 was performed by observing the germination of *Oryza sativa* L. To perform the germination, 10 seeds of each plant were placed in a sterile petri dish with 15 ml of the treated textile effluent.[11] After 5 d, the differences in shoot length (cm), root length (cm), and relative seed germination percentage were recorded and compared with the control.[12] The germination percentage was calculated as the following formula: Germination (%) = (The number of seed germination / Total number of seeds) x 100.

3. Results and Discussion

3.1 Effect of aeration on Solvent Red 24 decolorization

The effect of aeration on Solvent Red 24 decolorization efficiency by *Bacillus* sp. FN1 was evaluated at 37 °C under shaking (150 rpm) and static condition. The results presented in Figure 1 showed 25.05% decolorization of Solvent Red 24 (50 mg/L) was obtained within 96 h under shaking condition. However, under static condition, the decolorization percentage of 14.02 was achieved, which might indicate that the shaking has a positive effect on the decolorization process. As showed in Figure 1, the laccase and lignin peroxidase activities under shaking was higher than under static condition. The laccase activity under shaking and static conditions was 21.27 and 20.45 U/L at 48 h while the lignin peroxidase activity was 5.96 and 3.60 U/L: respectively. The higher decolorization percentage under shaking condition might be due to the increase in oxygen transfer between the cells and the medium, thus effecting on the biomass production. In addition, the dye degradation and decolorization may have occurred because of the action of the ligninolytic enzymes produced during the decolorization process.[13] For *Pseudomonas* sp. SUK1 showed

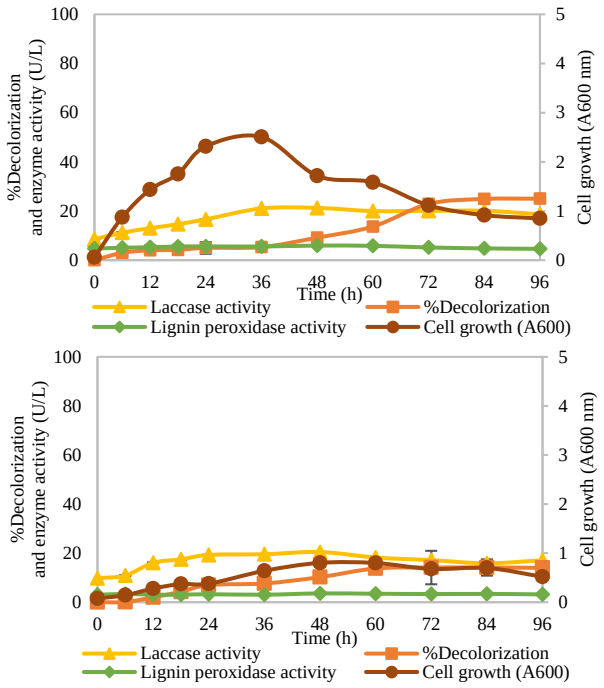

Figure 1. Effect of shaking (A) and static (B) conditions on cell growth, enzymes production and decolorization of Solvent Red 24 by *Bacillus* sp. FN1

96% decolorization of 300 mg/L Reactive Red 2 within 24 h under shaking condition[14] *Alternaria alternata* CMERI F6 also showed a 99.99% decolorization percentage in 48 h for 600 mg/L of Congo Red with a shaking speed of 150 rpm[15] and *Bacillus subtilis* could completely decolorize the Reactive Blue 160 (500 mg/L) in 48 h under shaking condition with 150 rpm.[16]

3.2 Effects of carbon sources on Solvent Red 24 decolorization

The effect of carbon sources on the decolorization of Solvent Red 24 by *Bacillus* sp. FN1 was investigated by cultivation the microorganism at 37 °C with a shaking speed of 150 rpm. As showed in Figure 2, the decolorization percentage of 66.01 was obtained at 96 h when sucrose was used as a carbon source. The medium with glucose and starch as a carbon source yielded the decolorization percentage of 25.05% and 58.52%; respectively. The production of laccase and lignin peroxidase in the condition with sucrose as a carbon source was as high as 48.35 U/L at 60 h and 5.34 U/L at 48 h: respectively (Figure 2B). In the presence of 1% (w/v) sucrose as a carbon source, the highest decolorization of methyl orange by *Aeromonas* sp. DH-6 was also obtained.[17] *Aeromonas hydrophila* showed 94% decolorization of methyl orange within 120 h in the medium containing 1% (w/v) sucrose as a carbon source.[18]

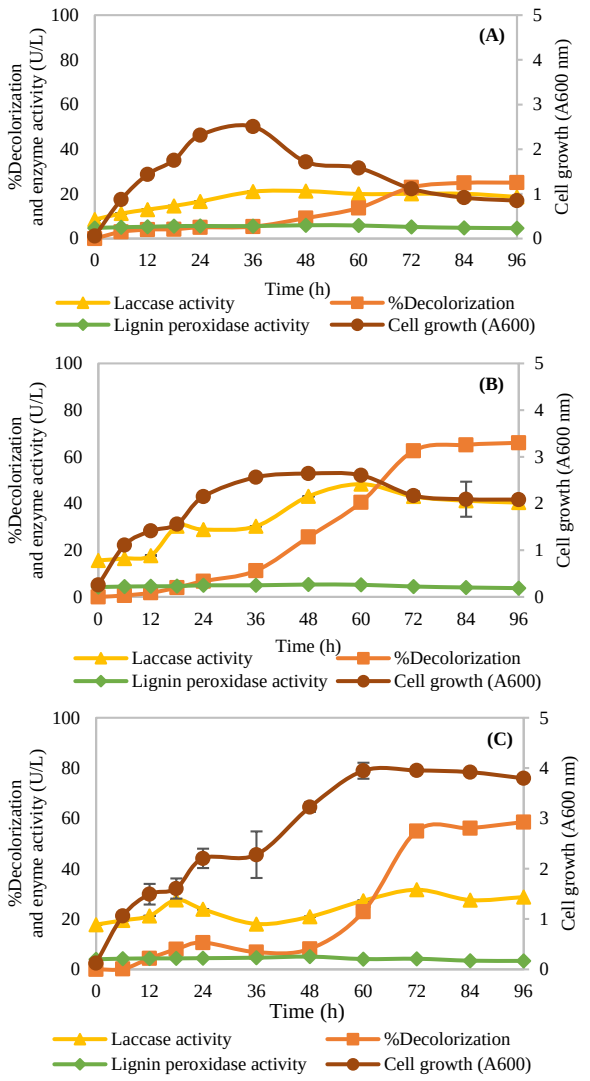

Figure 2. Effect of glucose (A), sucrose (B), and starch (C) on cell growth, enzyme activities, and decolorization of Solvent Red 24 by *Bacillus* sp. FN1.

3.3 UV-Vis spectra of Solvent Red 24 before and after decolorization by *Bacillus* sp. FN1

The UV-VIS spectra of the dye after decolorized by *Bacillus* sp. FN1 for 36 h showed the decreasing of the absorbance at the wavelength of 509 nm, as compared with the initial time. However, the increase in absorbance at a wavelength of 200 to 400 nm with the incubation time was observed, which might indicate that the chemical structure of degraded dyes could probably be the aromatic compounds. This observation was also reported by Parshetti *et al.* (2010) for the decolorization of methyl orange by *Kocuria rosea* MTCC 1532.[19] The similar results of the increasing in absorbance at the wavelength of 200 to 300 nm after the decolorization process was found when the methyl orange was decolorized by *Bacillus stratosphericus* SCA1007.[5]

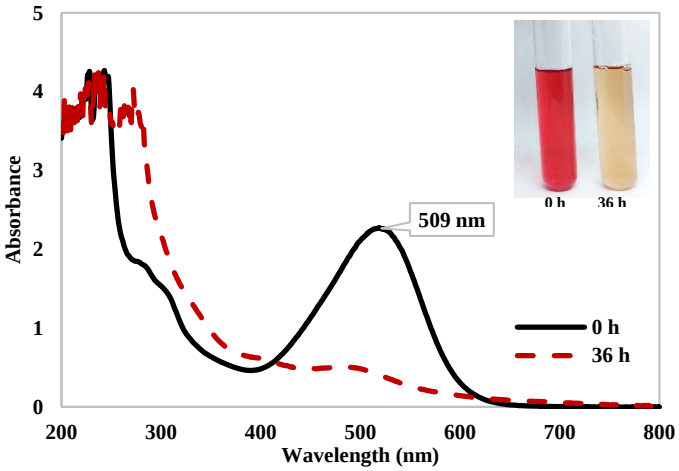

Figure 3. UV-Vis spectra of Solvent Red 24 before (black) and after decolorization (red) by *Bacillus* sp. FN1

3.4 FT-IR analysis

The functional groups and chemical bonds of treated Solvent Red 24 and its powder (control) Solvent Red 24 were identified by FTIR. As showed in Figure 4. The spectrum of the dye powder (black curve) showed the peak at 1754 cm^{-1} which agrees with the -C-H bending vibration and the peak at 1558 cm^{-1} corresponds to the stretching of the azo group (-N=N-).[20] The peak at 1042 cm^{-1} represents N-H bonds[21] and the peak at 847 cm^{-1} corresponds to the ring vibration, which confirms the benzene ring structure.[22] The spectrum of the Solvent Red 24 after degradation and decolorization by *Bacillus* sp. FN1 (red curve), showed the peaks at 3326 cm^{-1} corresponds to the -OH group, while the peaks at 2920, 1650, and 1013 cm^{-1} corresponds to the C-H bending, C=C bonding, and N-H bonding, respectively.[23] The peaks at 600-800 cm-1 disappeared indicating the loss of benzene derivatives. FN1. Similar work[13,24] has also been reported by Saratale *et al.*, (2013) and Bharagava *et al.*, (2018).

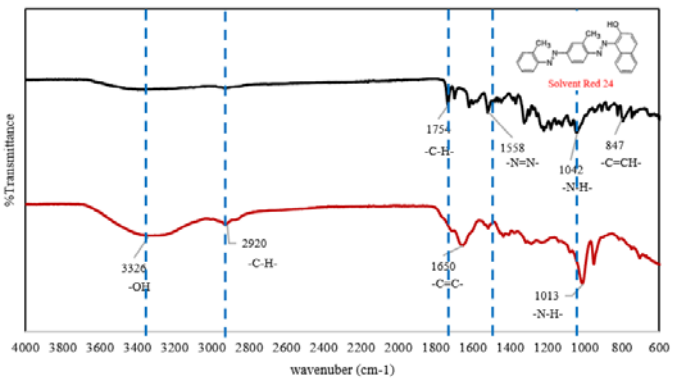

Figure 4. FTIR spectra of Solvent Red 24 before (black) and after decolorization (red) by *Bacillus* sp. FN1

Table 1. Phytotoxicity test of Solvent Red 24

Parameters studied	*Oryza sativa* L	
	Distilled water	Solvent Red 24
%Germination	100%	80%
shoot length (cm)	5.48±0.45	4.27±0.40
root length (cm)	3.71±1.02	0.84±0.09

3.5 Phytotoxicity assay

The phytotoxicity test on *Oryza sativa* L indicated that the degraded Solvent Red 24 had a negligible effect on germination percentage, shoot length, and root length (Figure 5.). The germination percentage, shoot length, and root length after 5 d were showed in Table 1. As previously reported by Barathi *et al.* (2020), *Bacillus subtilis* was capable of decolorizing the Reactive Blue 160 (800 mg/L) into non-toxic metabolites as tested for phytotoxicity with *Zea mays* and *Vigna radiate.*[16] Telke *et al.* (2008) also reported the phytotoxicity test of the Reactive Red (50 mg/L) with *Triticum aestivum* and *Oryza sativa.*[25]

Figure 5. The phytotoxicity test on *Oryza sativa* L in Solvent Red 24 after treated by *Bacillus* sp. FN1

4. Conclusion

In the present study, the *Bacillus* sp. FN1 isolated from textile effluent demonstrated the ability to decolorize and degrade the Solvent Red 24. A high decolorization efficiency and the production of the enzymes involving in dye degradation process were achieved in the medium containing sucrose as a carbon source under shaking condition. The FTIR spectrum of the dye treated with *Bacillus* sp. FN1 indicated that the azo bonds and the aromatic hydrocarbon compounds were enzymatically degraded. Thus, the isolated *Bacillus* sp. FN1 is considered as a potential microorganism for environmentally friendly decolorization of solvent soluble synthetic dyes.

Acknowledgements

This work was supported by Silpakorn University Research, Innovation and Creative Fund Biotechnology, Faculty of Engineering and Industrial Technology, Silpakorn University.

References

1. Zhang, H.-M.; Wang, Y.-Q.; Jiang, M.-L., A fluorimetric study of the interaction of CI Solvent Red 24 with haemoglobin. *Dyes and Pigments* **2009,***82* (2), 156-163.
2. Karatay, S. E.; Kılıç, N. K.; Dönmez, G., Removal of Remazol Blue by azoreductase from newly isolated bacteria. *Ecological Engineering* **2015,***84*, 301-304.
3. Singh, A. L.; Chaudhary, S.; Kumar, S.; Kumar, A.; Singh, A.; Yadav, A., Biodegradation of Reactive Yellow-145 azo dye using bacterial consortium: A deterministic analysis based on degradable Metabolite, phytotoxicity and genotoxicity study. *Chemosphere* **2022,***300*, 134504.
4. Saratale, G.; Kalme, S.; Bhosale, S.; Govindwar, S., Biodegradation of kerosene by *Aspergillus ochraceus* NCIM-1146. *Journal of Basic Microbiology* **2007,***47* (5), 400-405.
5. Akansha, K.; Chakraborty, D.; Sachan, S. G., Decolorization and degradation of methyl orange by *Bacillus stratosphericus* SCA1007. *Biocatalysis and Agricultural Biotechnology* **2019,** *18*, 101044.
6. Mustafa, G.; Zahid, M. T.; Kurade, M. B.; Patil, S. M.; Shakoori, F. R.; Shafiq, Z.; Ihsan, S.; Ahn, Y.; Khan, A. A.; Gacem, A., Molecular characterization of azoreductase and its potential for the decolorization of Remazol Red R and Acid Blue 29. *Environmental Pollution* **2023,** *335*, 122253.
7. Tien, M.; Kirk, T. K., Lignin peroxidase of *Phanerochaete chrysosporium*. In *Methods in enzymology*, Elsevier: **1988**; Vol. 161, pp 238-249.
8. Oliveira, S. F.; da Luz, J. M. R.; Kasuya, M. C. M.; Ladeira, L. O.; Junior, A. C., Enzymatic extract containing lignin peroxidase immobilized on carbon nanotubes: Potential biocatalyst in dye decolourization. *Saudi Journal of Biological Sciences* **2018,** *25* (4), 651-659.
9. Wariishi, H.; Valli, K.; Gold, M. H., Manganese (II) oxidation by manganese peroxidase from the basidiomycete *Phanerochaete chrysosporium*. Kinetic mechanism and role of chelators. *Journal of Biological Chemistry* **1992,** *267* (33), 23688-23695.
10. Wan, Y.; Du, Y.; Miyakoshi, T., Enzymatic catalysis of 2, 6-dimethoxyphenol by laccases and products characterization in organic solutions. *Science in China Series B: Chemistry* **2008,** *51* (7), 669-676.
11. Sudha, M.; Bakiyaraj, G.; Saranya, A.; Sivakumar, N.; Selvakumar, G., Prospective assessment of the *Enterobacter aerogenes* PP002 in decolorization and degradation of azo dyes DB 71 and DG 28. *Journal of environmental chemical engineering* **2018,** *6* (1), 95-109.
12. Chen, Y.; Feng, L.; Li, H.; Wang, Y.; Chen, G.; Zhang, Q., Biodegradation and detoxification of Direct Black G textile dye by a newly isolated thermophilic microflora. *Bioresource technology* **2018,** *250*, 650-657.
13. Bharagava, R. N.; Mani, S.; Mulla, S. I.; Saratale, G. D., Degradation and decolorization potential of a ligninolytic enzyme producing *Aeromonas hydrophila* for crystal violet dye and its phytotoxicity evaluation. *Ecotoxicology and environmental safety* **2018,** *156*, 166-175.
14. Kalyani, D.; Telke, A.; Dhanve, R.; Jadhav, J., Ecofriendly biodegradation and detoxification of Reactive Red 2 textile dye by newly isolated *Pseudomonas* sp. SUK1. *Journal of hazardous materials* **2009,** *163* (2-3), 735-742.
15. Chakraborty, S.; Basak, B.; Dutta, S.; Bhunia, B.; Dey, A., Decolorization and biodegradation of congo red dye by a novel white rot fungus *Alternaria alternata* CMERI F6. *Bioresource technology* **2013,** *147*, 662-666.
16. Barathi, S.; Aruljothi, K.; Karthik, C.; Padikasan, I. A., Optimization for enhanced ecofriendly decolorization and detoxification of Reactive Blue160 textile dye by *Bacillus subtilis*. *Biotechnology Reports* **2020,** *28*, e00522.
17. Du, L.-N.; Li, G.; Zhao, Y.-H.; Xu, H.-K.; Wang, Y.; Zhou, Y.; Wang, L., Efficient metabolism of the azo dye methyl orange by *Aeromonas* sp. strain DH-6: characteristics and partial mechanism. *International Biodeterioration & Biodegradation* **2015,** *105*, 66-72.
18. Velusamy, K.; Periyasamy, S.; Kumar, P. S.; Jayaraj, T.; Gokulakrishnan, M.; Keerthana, P., Transformation of aqueous methyl orange to green metabolites using bacterial strains isolated from textile industry effluent. *Environmental Technology & Innovation* **2022,** *25*, 102126.

19. Parshetti, G.; Telke, A.; Kalyani, D.; Govindwar, S., Decolorization and detoxification of sulfonated azo dye methyl orange by *Kocuria rosea* MTCC 1532. *Journal of Hazardous Materials* **2010,** *176* (1-3), 503-509.
20. Mishra, A. K.; Arockiadoss, T.; Ramaprabhu, S., Study of removal of azo dye by functionalized multi walled carbon nanotubes. *Chemical engineering journal* **2010,** *162* (3), 1026-1034.
21. Kishor, R.; Purchase, D.; Saratale, G. D.; Ferreira, L. F. R.; Bilal, M.; Iqbal, H. M.; Bharagava, R. N., Environment friendly degradation and detoxification of Congo red dye and textile industry wastewater by a newly isolated *Bacillus cohnni* (RKS9). *Environmental Technology & Innovation* **2021,***22*, 101425.
22. Quan, L.; Huang, J.; Qi, J.; Zhu, Y., Isolation of Different Azo Dye Decolorizing Bacteria and Their Decolorization Mechanisms. *Nature Environment and Pollution Technology* **2018,** *17* (3), 981-986.
23. Kishor, R.; Purchase, D.; Saratale, G. D.; Ferreira, L. F. R.; Hussain, C. M.; Mulla, S. I.; Bharagava, R. N., Degradation mechanism and toxicity reduction of methyl orange dye by a newly isolated bacterium *Pseudomonas aeruginosa* MZ520730. *Journal of Water Process Engineering* **2021,** *43*, 102300.
24. Saratale, R. G.; Gandhi, S. S.; Purankar, M. V.; Kurade, M. B.; Govindwar, S. P.; Oh, S. E.; Saratale, G. D., Decolorization and detoxification of sulfonated azo dye CI Remazol Red and textile effluent by isolated *Lysinibacillus* sp. RGS. *Journal of bioscience and bioengineering* **2013,** *115* (6), 658-667.
25. Telke, A.; Kalyani, D.; Jadhav, J.; Govindwar, S., Kinetics and Mechanism of Reactive Red 141 Degradation by a Bacterial Isolate *Rhizobium radiobacter* MTCC 8161. *Acta Chimica Slovenica* **2008,** *55* (2).

Greenhouse gas-certified reference materials for tackling climate change in Thailand

Kanokrat Charoenpornpukdee*, Bunthoon Laongsri, Arnuttachai Wongjuk, Soponrat Rattanasombat, and Ratirat Sinweeruthai

Gas Analysis Group, Chemical Metrology and Biometry Department, National Institute of Metrology (Thailand), Pathum Thani, Thailand, 12120

**E-mail: kanokrat@nimt.or.th*

Abstract:

Climate change, driven primarily by the increasing concentrations of greenhouse gases (GHG) in the Earth's atmosphere, poses a significant threat to the global environment. The National Institute of Metrology (NIMT) aims to produce reference materials crucial for enhancing the accuracy and reliability of GHG measurements. NIMT has developed a production method for reference materials of key GHGs; carbon dioxide (CO_2), methane (CH_4), and nitrous oxide (N_2O) using gravimetric preparation which is widely recognized as a primary method for standard gas mixture preparation. The outcome of this research is several fit-for-purpose certified reference materials (CRMs) for GHGs. CRMs produced by NIMT, known as Thailand Reference Material (TRMs), have been published on the International Bureau of Weights and Measures (BIPM) key comparison database (KCDB), established on Calibration and Measurement Capabilities (CMCs). Currently, NIMT has the capabilities to produce certified gas reference materials in nitrogen balance (amount fraction range, % U_{rel}); 1.6 µmol/mol - 50 cmol/mol (0.2 %) CO_2; 500 µmol/mol - 50 cmol/mol (0.4 %) CH_4; and 100 µmol/mol - 50 cmol/mol (0.4 %) N_2O. These TRMs can improve the accuracy and reliability of the GHG measurements in Thailand, enabling the assessment of the effectiveness of mitigation strategies, and making informed policy decisions.

1. Introduction

Climate change severely affects all countries and has had an unprecedented impact worldwide. Carbon dioxide (CO_2), methane (CH_4), and nitrous oxide (N_2O) are the top three potent greenhouse gases (GHG).[1] The United Nations Framework Convention on Climate Change (UNFCCC) is an international environmental treaty to combat "dangerous human interference with the climate system", to some extent by stabilizing greenhouse gas concentrations in the atmosphere, which is incorporated with the World Meteorological Organization (WMO). WMO has long-standing GHG activities such as monitoring, research, and provision of related services. The Global Atmosphere Watch (GAW) program of WMO focuses on building a single coordinated global entity for high-quality atmospheric composition observations and impact science, which helps to improve the understanding of atmospheric composition, its change and the interaction between the atmosphere, the oceans and the biosphere.[2] In 2015 the Paris Agreement was adopted by the UNFCCC. Thailand later ratified the Paris Agreement in 2016. At the 28th Conference of the Parties (COP28) Thailand has committed to carbon neutrality by 2050 and net-zero greenhouse gas emissions by 2065. Successful implementation of the Paris Agreement of the UNFCCC will require sustained, near-real-time monitoring of GHG fluxes and concentrations to assess the impact and overall effectiveness of mitigation efforts undertaken by the parties to the agreement. To effectively address the challenges posed by the climate crisis, it is important to implement GHG measurements with minimal uncertainty and accepted traceability. This approach ensures that observed trends are accurately accounted for and helps us tackle the climate crisis more effectively.

Metrological traceability is a property of a measurement result whereby the result can be related to a reference through a documented unbroken chain of calibrations, each contributing to the measurement uncertainty, according to the definition by the International Vocabulary of Metrology (VIM).[3] In practice, traceability of measurement standards and instruments to the SI units is established through an unbroken chain of calibrations or comparisons linking them to relevant primary standards of the SI units of measurements as shown in Figure 1. The individual National Metrology Institutes (NMIs) are responsible for maintaining their local scales, disseminating gas reference materials traceable to the SI unit, and providing uncertainties. Ensuring measurement traceability is a crucial responsibility within the atmospheric monitoring community, as it allows for internationally recognized field measurement techniques. Advances in the state of the art gas reference materials and measurement techniques have provided the framework for underpinning global observations, ensuring

consistency across monitoring networks and long-term stability of data.[4,5,6]

The Gas Analysis Group, Chemical Metrology and Biometry department, NIMT has consistently demonstrated competence in the Consultative Committee for Amount of Substance: Metrology in Chemistry and Biology (CCQM) Key Comparison programs. The measurement capabilities of NIMT will then be listed in the BIPM Key Comparison Data Base (KCDB) with its Calibration and Measurement Capability (CMC) indicated in Appendix C.[7] TRM (Thailand Reference Material) is a certified reference material issued by NIMT, TRMs are produced according to ISO 17034, ensuring their consistent quality. TRMs are produced with a well-defined traceability linkage to the SI unit. The traceability of property value is established using metrologically valid procedures for the certification of reference material given by NIMT.[8] We prepared SI-traceable certified reference materials of CO_2, CH_4, and N_2O using gravimetric method. Our work, the primary reference material produced by NIMT establishes national traceability and supports the quality control of greenhouse gas measurement.

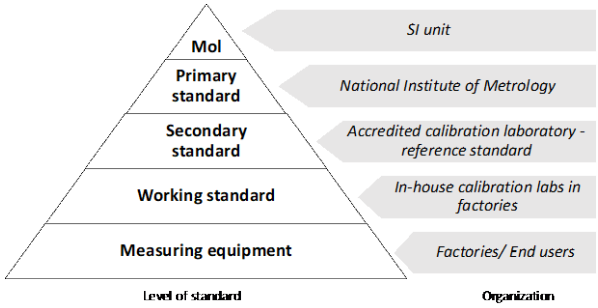

Figure 1. Metrological traceability chain of the certified value to the SI traceability unit.

2. Materials and Methods

This study adheres to the guidelines set forth by ISO 6142-1 Gas Analysis,[9] which pertains to the gravimetric preparation of calibration gas mixtures for Class I applications. The gravimetric preparation process involves transferring substances such as pure gases, pure liquids, or pre-mixed gases into a controlled cylinder. ISO 6142-1 provides a comprehensive framework for gravimetric preparation, including the concept, scheme, and level of uncertainty associated with the preparation of calibration gas mixtures.[9]

The scope of the gravimetric preparation process mentioned initially creates a preparation hierarchy plan (section 2.2) which considers the target composition, associated uncertainty, and any alternative preparation options. Also, a purity assessment of the gas mixture (section 2.1) is conducted to ensure compliance with SI traceability requirements. The filling process follows the preparation recipe and the weighing is performed carefully. Finally, the homogenized process is undertaken before performing a verification approach. The propagation of uncertainty marks the completion of the gravimetric preparation process. This preparation of primary gas reference material is followed by our in-house method under a controlled environment (temperature 23±2 °C, humidity 50±15 % RH). In this work, 10 litre aluminium cylinders with CGA 580 brass valves were used for this preparation. The primary gas reference material after preparation completion is stored at a temperature of 20 °C - 28 °C and relative humidity of 20 %RH - 80 %RH, kept away from direct sunlight, and protected from physical damage.

2.1. High-purity gases

Purity analysis of the gas mixture is a critical step to identify the amount of impurity contained. Purity assessment and the treatment of purity data were encountered following the guidelines of ISO 19229.[10] In our approach, the presence of significant impurities in the parent materials is minimized by using sufficient high-quality grades of pure gases. The impurities of pure gas such as N_2, CO, CO_2 and CH_4 are determined by gas chromatography (GC) (Agilent Technologies, USA) with several detectors such as pulsed discharge helium ionization detector (PDHID) and flame ionization detector (FID). Assessment of the amount fraction of target gas purity (X_{pure}) was performed by subtracting a sum of impurity gas (x_i) as indicated in equation 1.

$$X_{pure} = 1 - \sum_{i=1}^{N} x_i \qquad (1)$$

2.2 Gravimetric preparation

To prepare an accurate and precise gravimetric mixture, a preparation plan with adequate weighing mass is needed. These diagrams show the hierarchy of the primary gas standard which requires two sets of similar gas mixtures to verify against each other. The pure gas was used in the first step, and it was further diluted to the target amount fractions with N_2. reveals the preparation recipe of the gas mixture CO_2 at 0.1 - 20 mmol/mol, CH_4 at 0.1 - 6 mmol/mol, and N_2O at 1000 µmol/mol in nitrogen.

The cylinder used for preparing the primary reference material was cleaned to eliminate impurity which appears as a significant source of uncertainty. Firstly, external dirt was removed, and the internal cylinder was completely

cleaned using a scroll pump (ULVAC, Japan) and a turbo pump (Pfeiffer, USA) to evacuate the cylinder until the pressure obtained below 10^{-5} Pa, meanwhile, the cylinder was heated up at 60 °C using a heating jacket for 6 hours. An automatic weighing machine (Lannice, Thailand) with analytical balance (Mettler Toledo, USA) was deployed to weigh the cylinder, the identical cylinder was used as a reference and alternately weighed against the sample cylinder for the entire process. At the beginning of the preparation, a weighing measurement of an emptied cylinder was taken place and then the weighing was repeated after filling each component; the different mass was calculated and referred to as the mass of the added compound. At the last step of the filling process, nitrogen gas (balance gas) was filled up, which can improve the blending tolerance. After the filling process was completed, the gas mixture was homogenized using a rolling machine (Lannice, Thailand) for approximately 12 hours. The cylinder was left at room temperature for at least three days before being verified or used.

Equation *2* shows the calculation of amount fractions of each component X_i of the final gas mixture, which is diluted from parent gas (the upper amount fraction level of the preparation hierarchy), converting the mass composition to molar composition.

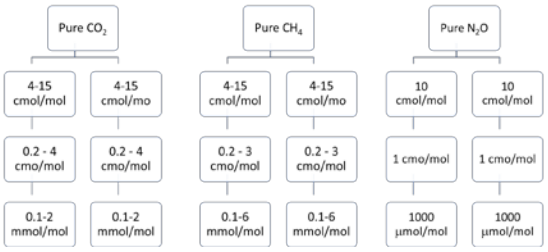

Figure 2. Preparation hierarchy of CO_2, CH_4 and N_2O

$$X_i = \frac{\sum_{j=1}^{r}\left\{\frac{x_{(i,j)}.m_j}{\sum_{i=1}^{q} x_{(i,j)}.M_i}\right\}}{\sum_{j=1}^{r}\left\{\frac{m_j}{\sum_{i=1}^{q} x_{(i,j)}.M_i}\right\}} \qquad (2)$$

Where;
i = 1, 2, 3,…., q denoted the components (including quantified impurities) of the final calibration gas mixture
j = 1, 2, 3,…., r denoted the parent gases used in the preparation.
X_i = amount fraction of component i
m_j = mass taken from parent cylinder j
$x_{(i,j)}$ = amount fraction of component i in parent cylinder j
M_i = Molar mass of component i
$i_{(i,j)}$ = indices of those components in parent cylinder j

2.3 Verification method

Although the gas component is assigned by gravimetrical preparation, the verification of the chemical composition was required to identify the bias between the gravimetric value and analytical measurement [9]. Gas chromatography was deployed in these cases; GC-TCD was used to perform analysis at high levels of CO_2, CH_4 and N_2O. While GC-FID was used to analysis of CH_4 and GC-FID equipped with a methanizer was used for low levels of CO_2. The measurement conditions are listed as shown in Table 1. After sufficiently mixing, the gas mixture was allowed to equilibrate in the analysis room for three days before performing a measurement. The measurement procedure was based on our in-house method of calibration of the gas mixture using a one-point calibration method according to ISO 12963[11]. A primary standard with the closest or similar amount fraction and matrix gas was selected as a reference standard. Using the bracketing technique, analyses were arranged interspersing a reference standard between each gas mixture and the respective ratio, gas mixture vs reference standard was considered to adjust the gravimetric amount fraction. The assigning of an analytical amount fraction of the gas mixture, X_S was shown in equation 3, where the average response of standard gas mixture, Y_S. Average measurement response of standard gas mixture, Y_{ref} and the standard gas mixture contents, X_k.

$$X_S = \frac{Y_S}{Y_{ref}} \times X_{ref} \qquad (3)$$

Table 1. GC conditions for the verification process

Gas		**CO_2**
Range	0.05 - 50 cmol/mol	50 -5,000 µmol/mol
Detector	TCD	FID/Methanizer
Detector Temp.	200 °C	250 °C
Column	Heysep Q	Shin-Carbon
Oven Temp.	60 °C	90 °C
sample flow rate	45 mL/min	45 mL/min
Gas		**CH_4**
Range	1-15 cmol/mol	1-10 mmol/mol
Detector	TCD	FID
Detector Temp.	200 °C	200 °C
Column	Molecular Sieve 13X	Molecular Sieve 13X
Oven Temp.	30 °C	30 °C
sample flow rate	5 mL/min	30 mL/min

Gas	N_2O
Range	1-15 cmol/mol and 50 -10,000 µmol/mol
Detector	TCD
Detector Temp.	200 ℃
Column	HeySep Q 80/100 µm
Oven Temp.	90 ℃
sample flow rate	30 mL/min

3. Results & Discussion

3.1 Characterization of Gravimetric Standard

Our gas mixture was assigned an amount fraction by gravimetrical preparation, considering the high-purity gas component. Quality control of specification of gas components is essential (Table 2), meaning that high purity is required ≥ 99.99 %, as well as amount fractions of impurity. Additionally, verification was performed to quantify the measurement bias of the gravimetric amount fraction against the analytical amount fraction with less than 0.05 % measurement bias.

Table 2. Gas component purity is used in the gas mixture preparation and the specification.

High pure gas	Component	Specification
CO_2	Carbon dioxide	> 99.995 %
	Nitrogen	< 20 ppm
	Oxygen	< 5 ppm
	Carbon monoxide	< 0.5 ppm
	Methane	< 0.2 ppm
CH_4	Methane	> 99.995 %
	Nitrogen	< 20 ppm
	Oxygen	< 1 ppm
N_2O	Nitrous oxide	> 99.999 %
	Moisture	< 1 ppm
	Nitrogen	< 2 ppm
	Oxygen	< 1 ppm
	Carbon dioxide	< 1 ppm
	Carbon monoxide	< 0.1 ppm
	Methane	< 0.1 ppm
Nitrogen	Nitrogen	> 99.9995 %
	Moisture	< 0.5 ppm
	Carbon dioxide	< 0.2 ppm
	Carbon monoxide	< 0.1 ppm
	Methane	< 0.1 ppm
	Oxygen	< 1.5 ppm

3.2 Measurement uncertainty

Evaluation of uncertainty is a key element of the SI traceability chain. The JCGM GUM[12] and ISO6142[9] provide a guideline for estimating uncertainty. In this study, the standard uncertainty $u(x)$ of the primary gas reference material is calculated from the following equation 4.

$$u(x) = \sqrt{u^2(X_i) + u^2(X_S) + u^2(X_{Stab}) + u^2(X_B) + u^2(X_D)} \quad (4)$$

The first component of the uncertainty budget is the standard uncertainty $u(X_i)$ of the gravimetric standard. This contribution considered the uncertainty in molar mass calculated from atomic weights of the elements in IUPAC technical report.[13] The standard uncertainty is the combination of uncertainty from weight and pure gas standards, which are the sum of individual impurities. $u(X_s)$ is the uncertainty of verification from equation 3. Additionally, the values of unity were uncertainties contributed while they carry a specific uncertainty which corresponds to the individual sources that were also taken into account; the uncertainty of stability $u(X_{stab})$, which is a characterization of the stability of a primary gas reference material; the uncertainty of bias, $u(X_B)$ was identified from the measurement bias between the gravimetric amount fraction and the verified amount fraction. In addition, the uncertainty of lab bias, $u(X_D)$ is the difference between the reference value obtained from the international comparison programs.

Finally, in reporting uncertainty, the expanded uncertainty (U) was used, which reported at a 95 % confidence level with coverage factor (k) equals 2.

$$U(x) = k.u(x) \quad (5)$$

As a result, the uncertainty budget of the primary gas reference materials is shown in Figure 3, reporting the expanded uncertainty of CO_2 is 0.3 % relative and CH_4 and N_2O are at 0.4 % relative. The largest uncertainty contribution appeared from the stability of the reference material.

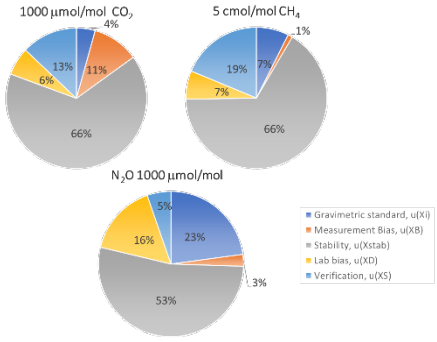

Figure 3. Uncertainty budget of the primary gas reference materials

3.3 Inter-laboratory comparison programs

To establish, maintain and assure the measurement capabilities, the Gas Analysis Group of NIMT has actively participated in several interlaboratory comparisons. We have been successful in participating in international key comparisons such as EURO.QM-S5/1166 (2012): Carbon dioxide mixtures in nitrogen,[14] APMP; APMP.QM-S15 (2017): Carbon dioxide mixtures in nitrogen[15], APMP.QM-S7 (2014): Methane in nitrogen[16]; and APMP.QM-S13 (2018): N_2O in nitrogen[17]. In Figure 4 the degree of equivalence (Di, Δx), identified the comparison bias and SI

traceability chain. These comparisons were applied to support CMC claims for CO_2, CH_4 and N_2O, respectively and will be further explained in section 3.4.

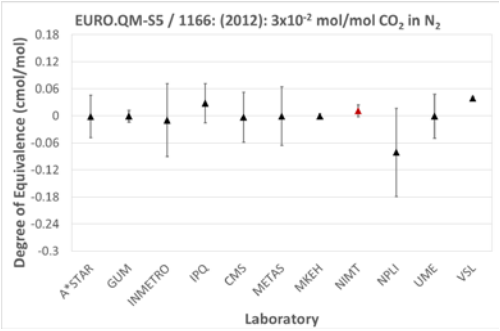

EURO.QM-S5/1166 (2012): $3x10^{-2}$ mol/mol CO_2 in N_2 [14]

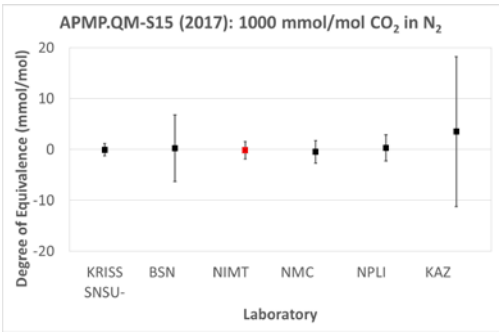

APMP.QM-S15 (2017):1000 mmol/mol CO_2 in N_2 [15]

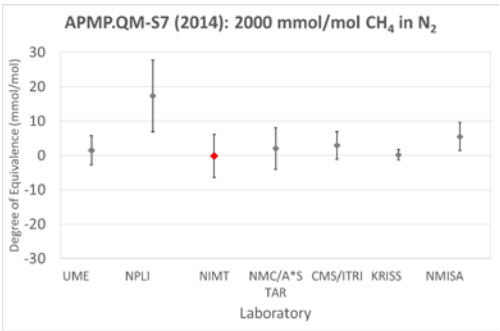

APMP.QM-S7 (2014): 2000 mmol/mol CH_4 in N_2 [16]

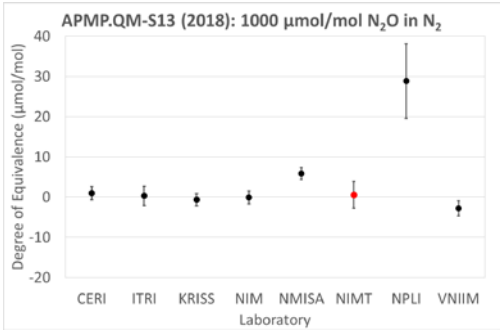

APMP.QM-S13 (2018): 1000 µmol/mol N_2O in N_2 [17]

Figure 4. International comparison programs of CO_2, CH_4 and N_2O

3.4 Calibration and measurement capabilities (CMCs)

NIMT primary gas reference materials for GHGs comply with international standards and have been published in the BIPM (the international organization related to measurement science and measurement standards) key comparison database (KCDB**).** These established CMCs, listed in the KCDB have been reviewed and approved within the CIPM Mutual Recognition Arrangement (MRA).[7] The current CMCs list of NIMT capabilities for producing certified gas reference material is shown in Table 3.

Table 3. The CMCs of primary gas reference materials under the quality system following pathway C[7]

Measurand	Matrix	Range (mol/mol)	Expanded Uncertainty (k = 2) (% rel)
CO_2	N_2	$10x10^{-6}$– $50x10^{-2}$	≥ 0.20
CH_4	N_2	$500x10^{-6}$– $50x10^{-2}$	≥ 0.40
N_2O	N_2/Air	$100x10^{-6}$– 50 $x10^{-2}$	≥ 0.40

4. Conclusions

NIMT prepared a variety of certified reference materials of CO_2, CH_4, and N_2O using the gravimetric method, traceable to SI unit and established the capability of CMC on KCDB. These CRMs can be used to strengthen the metrology of greenhouse gases, allow measurement compatibility and make it comparable. With the advance of measurement technology, the high accuracy and precision measurement of GHG can improve the ability to discriminate source emissions and understand emission rates. Additionally, the benefit of long-term monitoring of atmospheric greenhouse gases can provide support for the verification of the national greenhouse gas inventory which is presently based on estimated calculations.

References

1. United States Environmental Protection Agency. EnviroAtlas. Greenhouse Gas Emissions-Overview of Greenhouse Gases. https://www.epa.gov/ghgemissions/overview-greenhouse-gases (accessed 2023-12-01).
2. World Meteorological Organization (WMO). Global Atmosphere Watch Programme (GAW), 2020. https://community.wmo.int/en/activity-areas/gaw (accessed 2023-12-01).
3. Joint Committee for Guides in Metrology (JCGM). International Vocabulary of Metrology – Basic and General Concepts and Associated Terms (VIM) 3rd Edition 2008 Version with Minor Corrections, 2012. https://www.bipm.org/en/committees/jc/jcgm/publications (accessed 2022-09-27).
4. Brewer, P. J.; Brown, R. J. C.; Tarasova, O. A.; Hall, B.; Rhoderick, G. C.; Wielgosz, R. I. SI Traceability and Scales for Underpinning Atmospheric Monitoring of Greenhouse Gases. *Metrologia* **2018**, *55* (5), S174–S181.
5. Brewer, P. J.; Kim, J. S.; Lee, S.; Tarasova, O. A.; Viallon, J.; Flores, E.; Wielgosz, R. I.; Shimosaka, T.; Assonov, S.; Allison, C. E.; van der Veen, A. M. H.; Hall, B.; Crotwell, A. M.; Rhoderick, G. C.; Hodges, J. T.; Mohn, J.; Zellweger, C.; Moossen, H.; Ebert, V.; Griffith, D. W. T. Advances in Reference Materials and Measurement Techniques for Greenhouse Gas Atmospheric Observations. *Metrologia* **2019**, *56* (3), 034006.
6. Charoenpornpukdee, K.; O'Doherty, S.; Webber, E. M.; Hill-Pearce, R.; Hillier, A.; Worton, D. R.; Arnold, T.; Rennick, C.; Safi, E.; Brewer, P. Step Change in Improving the Accuracy of Nitrous Oxide Reference Materials for Underpinning Atmospheric Composition Measurements. *Anal. Chem.* **2023**, *95* (34), 12867–12874.
7. The BIPM (the international organization related to measurement science and measurement standards) k. The CIPM MRA Database (KCDB), 2023. https://www.bipm.org/kcdb/.
8. National Institute of Metrology (Thailand), NIMT. TRM (Thailand Reference Material). https://www.nimt.or.th/etrm/ (accessed 2023-12-01).
9. International Organisation for Standardization. ISO 6142-1:2015 2015 Gas Analysis—Preparation of Calibration Gas Mixtures—Part 1: Gravimetric Method Metrologia 55 (2018) S17 P J Brewer et al S181 for Class I Mixtures, 2015.
10. International Organization for Standardization. ISO 19229:2019 Gas Analysis — Purity Analysis and the Treatment of Purity Data, 2019.
11. International Organization for Standardization. ISO 12963, Gas Analysis – Comparison Methods for the Determination of the Composition of Gas Mixtures Based on One-and Two-Point Calibration, 1st.
12. JCGM member organizations. JCGM 100:2008 GUM 1995 with Minor Corrections Evaluation of Measurement Data — Guide to the Expression of Uncertainty in Measurement, 2008. https://www.bipm.org/documents/20126/2071204/JCGM_100_2008_E.pdf/cb0ef43f-baa5-11cf-3f85-4dcd86f77bd6.
13. Berglund, M.; Wieser, M. E. Isotopic Compositions of the Elements 2009 (IUPAC Technical Report). *Pure Appl. Chem.* **2011**, *83* (2), 397–410.
14. Dias, F. A.; Baptista, G.; Rakowska, A.; Chye, T. C.; Keat, T. B.; Cieciora, D.; Augusto, C.; Lin, T.-Y.; Niederhauser, B.; Fükö, J.; Sinweeruthai, R.; Johri, P.; Akcadag, F.; Tarhan, T.; Veen, A. M. H. van der; Wijk, J. van. Final Report on International Comparison EURO.QM-S5/1166: Carbon Dioxide Mixtures in Nitrogen. *Metrologia* **2013**, *50* (1A), 08017.
15. Lee, J.; Lee, J.; Lim, J.; Moon, D.; Aggarwal, S. G.; Johri, P.; Soni, D.; Hui, L.; Ming, K. F.; Sinweeruthai, R.; Rattanasombat, S.; Zuas, O.; Budiman, H.; Mulyana, M. R.; Alexandrov, V. Final Report for Supplementary Comparison APMP.QM-S15: Carbon Dioxide in Nitrogen at 1000 Mmol/Mol. *Metrologia* **2021**, *58* (1A), 08014.
16. Hong, K.; Kim, B. M.; Bae, H. K.; Lee, S.; Tshilongo, J.; Mogale, D.; Seemane, P.; Mphamo, T.; Kadir, H. A.; Ahmad, M. F.; Nasir, N. H. A.; Baharom, N.; Soni, D.; Singh, K.; Bhat, S.; Aggarwal, S. G.; Johri, P. Final Report of Supplementary Comparison for APMP.QM-S7.1: Methane in Nitrogen at 2000 Mmol/Mol. *Metrologia* **2020**, *57* (1A), 08021.
17. Hai Wu; Haomiao Ma; Defa Wang, Jeongsik Lim; Jinbok Lee; Dongmin Moon; Dai; Akima; Midori Kobayashi; Shinji Uehara; Hsin-Wang Liu; Chiung-Kun Huang; Tsai-Yin; Lin; James Tshilongo; David Mogale; Silindile Lushozi; Bunthoon Laongsri; Arnuttachai; Wongjuk; Daya Soni; Prabha Johri; Shankar G Aggarwal; Khem Singh; , Sulakshina Bhat; L.A. Konopelko; Y.A. Kustikov; A.V. Kolobova; V.V. Pankratov; B.V. Ivakhnenko; O.V. Efremova. *Comparison APMP.QM-S13 Nitrous Oxide in Nitrogen (1000µmol/Mol): Final Report.*

A demonstration process of high quality biomass pellet produced from sugarcane wastes

Yoothana Thanmongkhon[1], Tosporn Phetyim[2], Pathumrat Butniam[1], Natthawan Prasongthum[1], Amornrat Suemanotham[1], Apichat Junsod[1], Wanchana Sisuthog[2], Chaiyan Chaiya[2] and Lalita Attanatho[1]*

[1]*Expert Centre of Innovative Clean Energy and Environment, Thailand Institute of Scientific and Technological Research (TISTR), Khlong Luang, Pathum Thani 12120, Thailand*

[2]*Department of Chemical and Materials Engineering, Faculty of Engineering, Rajamangala University of Technology Thanyaburi, Pathum Thani 12110, Thailand*

**E-mail: lalita@tistr.or.th*

Abstract:

This research aims to develop the production of high-quality biomass pellets from sugarcane leaves, employing a torrefaction technique. The 2-step processes are investigated. The first is conversion of sugarcane leaves and scraps into biomass pellets via pelletization, with and without a binder. The sugarcane leaves are prepared to achieve the appropriate size and moisture content. The feed is well-suited for the pelletization, resulting in a yield of 93-98%wt, while its properties consistently meet established standards. Notably, incorporating tapioca flour of 3.5%wt ratio as a binder, along with approximately 30%wt moisture content prior to process, yields pellets of superior quality in terms of bulk density and pellet durability. The second investigates into the production of high-quality biomass pellets by utilizing the sugarcane leaf-based pellets as feedstock. The torrefaction process is explored using a reactor of 5-kg capacity. The vessel, heated by LPG burners, is maintained a reaction temperature of around 260°C, for producing black pellet. The product derived from sugarcane wastes attains a yield of 70%wt, approximately. This study significantly contributes to the valorization of sugarcane leaves, presenting a sustainable solution for alleviating PM 2.5 emissions from the burning of sugarcane fields and potentially serving as biofuel for fossil fuels substitution.

1. Introduction

Sugarcane is one of the most important industrial crops and, also, sugar industries have played a crucial role in Thai economy. In 2023, Thailand has sugarcane plantation area about 11.4 million rai and its production is about 113 million tons which is the fourth leading producer, 8.1%, of the world sugar production.[1,2] During the harvesting season, sugarcane leaves (SCL) is the major residues of sugarcane waste leftover in the fields. Generally, farmers eliminate such biomass wastes in the field by burning which is much easier and cheaper. However, this probably causes of anthropogenic pollution, particularly fine particulate matter (PM2.5) and greenhouse gas emissions. The higher sugarcane plantation has been done, the more environmental harm has been aware.[3] Such sugarcane residues have a potential to be used as biomass resources for renewable energy. By the ways, its physical properties, i.e., highly bulky, low heating value, high oxygen content and hygroscopic behaviour, etc., limit its directed applications as commercial fuel.

Pre-treatments can enhance its physiochemical properties. Pelletization is a densifying method usually applied for increasing in the utilization of agricultural residues, i.e., saw dust, pine wood, eucalyptus bark, rice straw, switchgrass, etc., which widely promoted as a renewable energy for substitution of fossil fuels.[1,3] Torrefaction is a thermochemical treatment, in which biomass is reacted at temperature of 200-300 °C in an inert ambience and reaction time of 1 min - 1 h. During torrefaction, the decomposition of lingo-cellulosic components has been occurred to eliminate some volatiles via several reactions, i.e., dehydration, decarboxylation and dehydrogenation, generating a solid product with higher energy, higher carbon, and lower moisture contents, better grindability and hydrophobicity.[4] Torrefaction of different kinds of agriculture residues has been studied intensively such as, wheat straw, rapeseed husk, eucalypus bark, pine sawdust and palm kernel shell. Pimchuai et al, investigated the effect of temperature and residence time on characteristics of products and reported that physicochemical properties of torrefied biomass were affected by torrefaction temperature, residence time and types of feedstock.[5] Prasongthum et al, reported that torrefaction allowed the removal of hydroxy group in biomass due to the release of CO_2, CO, H_2O, and oxygen-containing organic compounds which resulted to improve hydrophobicity.[4,5] Khempila et al, torrefied SCL at 225 – 300 °C for 30 min and reported that torrefaction significantly improved the fuel ratio of SCL, reaching up to 0.62 at torrefaction temperature of 300 °C. The calorific of SCL before processing was 17.69 MJ/kg, while that of SCL after torrefaction was 22.07 MJ/kg.[1]

As aforementioned, the previous investigation mostly focused on the impacts of torrefaction on physicochemical analyses of different agriculture residues in the laboratory scales. Therefore, in this study, a prototype of high quality biomass pellet derived from sugarcane residues for community-based unit has been demonstrated for exploration and evaluation the possibility for promoting its application as solid biofuel in order to encourage the farmers on the mitigation of sugarcane burning during the harvesting season.

2. Materials and Methods

2.1 Materials

Dried sugarcane leaves (SCL) were obtained from plantation areas in the northeastern region of Thailand. Prior to the experiments, raw material was shredded into small size less than 3 mm, as seen in Figure 1, by a shredder, motor of 3.7 kW. Commercial grade of tapioca flour was available supplied from the market.

Figure 1. Preparation of sugarcane leaves

2.2 Pelletization of sugarcane leaves

Before pelletization, the sugarcane leaf-based feedstock was mixed with tapioca flour at any ratios, 0.86-10 %wt of biomass, then added water to maintain about 30%wt of moisture content. Pelletization was performed using an electric pellet mill, motor of 22 kW, as shown in Figure 2 (a) and (b) to produce the pellet products and check performance to investigate their overall properties.

(a)

(b)

Figure 2. Pelletized machine (a), Processing of sugarcane leaf-based pellets (b)

(a)

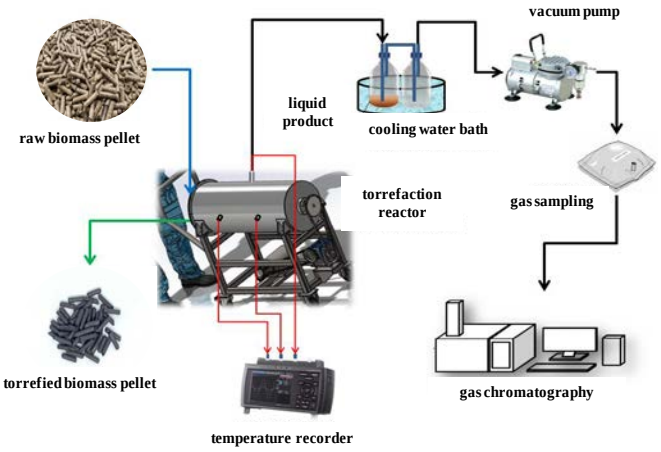

(b)

Figure 3. Torrefaction reactor with control panel (a), diagram of demonstration setup for biomass torrefaction process (b)

2.3 Torrefaction of sugarcane leaf-based pellets

Torrefaction was proceeded using a cylindrical reactor with an internal spiral-typed agitator as presented in Figure 3 (a). The capacity of reactor is about 5 kg a batch and the overall dimension of vessel is 30 cm of diameter with 80 cm long. The agitator is periodical and reversible driven by a 0.37 kW of motor with timer in the control panel for uniformly spreading torrefied biomass in the reactor. The heating is externally supplied by 2 sets of LPG burners located under the vessel. The reaction temperature is uniformly maintained around 260 °C. The experimental

procedure was run following shown in Figure 3 (b). For each batch, 5 kg of the sugarcane leaf-based pellets was loaded into the reactor. The reactor was slightly purged with N_2 at 100 mL/min to eliminate oxygen inside for about 20 min then, heated up from the ambience to the desired temperature within 40 min, about 5-6 °C/min of heating rate. The reaction was kept at a uniform temperature for different holding periods of 20, 30 and 40 min. After reactions, the burners are turned off to cool down the vessel. Finally, the torrefied products are unloaded from the reactor to determine the mass and energy yields using Eq. (1), (2) and (3), respectively, and then, kept solid products in plastic bags for further analyses.[6]

$$Mass\ yield\ (WP) = \frac{m_{white\ pellet}}{m_{raw\ material}} \quad (1)$$

$$Mass\ yield\ (TP) = \frac{m_{torrefied\ pellet}}{m_{white\ pellet}} \quad (2)$$

$$Energy\ yield\ = mass\ yield\ x\ \frac{HHV_{torr}}{HHV_{raw}} \quad (3)$$

3. Results & Discussion

3.1 Properties of sugarcane leaf-based pellets

The physical characteristics of SCL pellet using any mixed ratio of tapioca flour as a binder was determined. It was found that the average diameter, length, moisture content and bulk density of biomass pellet were in the range of 5.97-6.15 mm, 23.09- 27.83 mm, 2.78-5.35 %wt and 550-682 kg/m^3, respectively, as seen in Figure 4 (a) - (d). Besides, the examination reported that mechanical durability index and high heating value of SCL pellet, as shown in Figure 4 (e) - (f), were in the range of 97.32-98.84 %wt and 4,339-4,378 kcal/kg, respectively, when 0.86-10 %wt of tapioca flour was blended in the raw SCL feedstock.

Hence, the appropriate biomass pellet derived from SCL, in this study, is the feedstock of 3.53 %wt of tapioca flour blended in SCL with the moisture content of 30%wt. It could provide the pellet with the proper bulk density of 682.20 kg/m^3, HHV of 4,350 kcal/kg (20.72 MJ/kg) and pellet mass yield of 93.42 %wt, as exhibited in Figure 4 and 5.

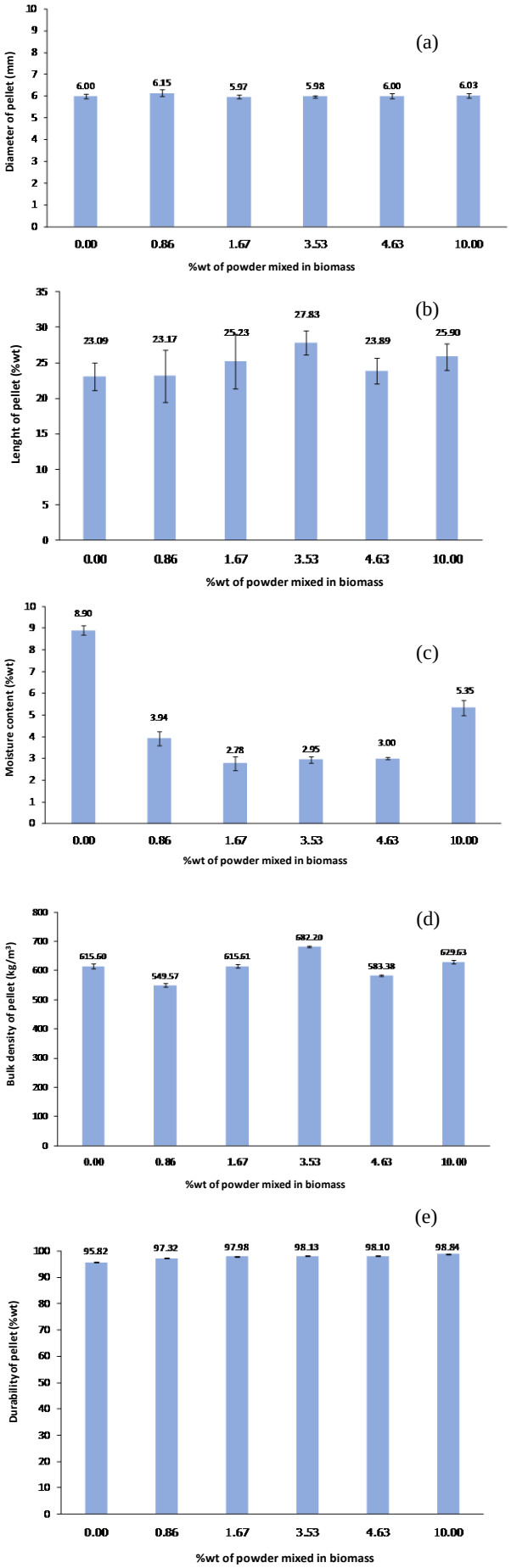

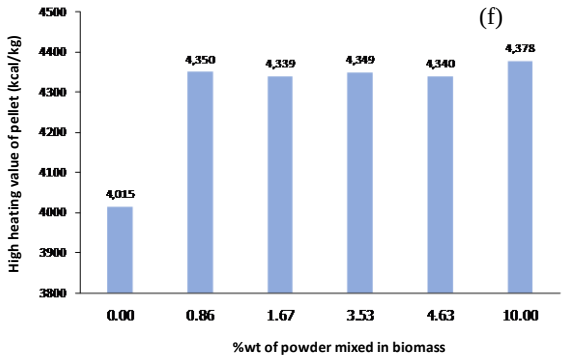

Figure 4. Physical properties of sugarcane leaf-based pellets at different mixing ratio with 30%wt of moisture; diameter (a), length (b), moisture (c), bulk density (d), durability (e), heating value (f)

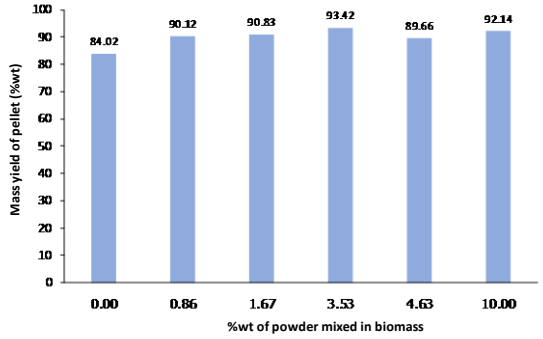

Figure 5. Mass yield from sugarcane leaf-based pellets at different mixing ratio with 30%wt of moisture

3.2 Properties of torrefied pellets

The SCL pellet was fed to torrefy in the reactor when its temperature was elevated to 260 ^{o}C. The torrefaction temperature was slightly fluctuated in the range of 250 - 275 ^{o}C during the process. The reaction was tested within 20 - 40 min and pellet was uniformly roasted by an internal agitator. The torrefied products at different period are shown in Figure 6. The longer time of reaction, the darker pellet has been obtained.

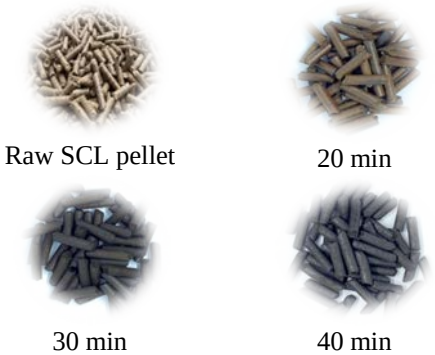

Figure 6. Physical appearance of torrefied products at 260 ^{o}C at different reaction time

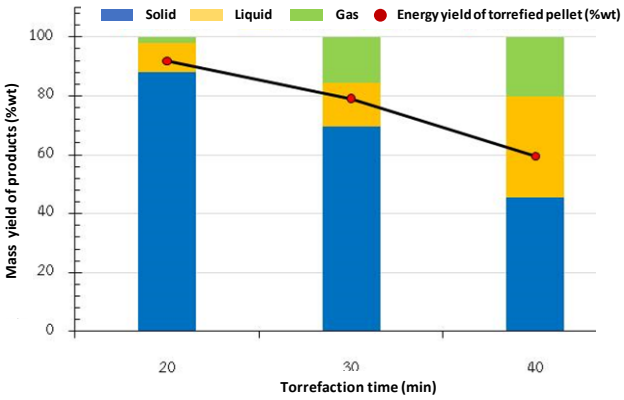

Figure 7. Mass and energy yields of products obtained from torrefaction at 260 ^{o}C at different reaction time

In Figure 7, the mass yield of pellets after the torrefaction is 45 - 88% and the energy yield is 59-90% by weight. The mass and energy yields of biomass in torrefaction process for period of 20 min had the highest values of 88 and 91 %wt, respectively. The mass gain and energy gain of the biomass pellets at torrefaction period of 30 min decreased to 70 and 79 %wt, respectively. However, when its residence time was increased to 40 min, the quantity of solid product was definitely reduced. Mass and energy yields are, also, lowered to 45 and 59 %wt, respectively.

The physiochemical properties of torrefied SCL pellet reacted at temperature of 260 ^{o}C at different time, 20, 30 and 40 min, are reported in Table 1 and 2. The volatile and oxygen contents in SCL pellet are decreased while the fixed carbon and ash contents are increased when torrefaction time is longer. The calorific value is also enhanced from 18.27 to 23.93 MJ/kg as dry basis.

Table 1. Ultimate analysis of solid products

Torrefaction time (min)	Component (%wt)			HHV (MJ/kg)
	VM	FC	Ash	
0	81.71	11.94	6.35	18.27
20	79.02	14.31	6.68	19.04
30	71.48	20.31	8.20	20.72
40	53.77	34.85	11.39	23.93

Table 2. Proximate analysis of solid products

Torrefaction time (min)	Elemental composition (%wt)				
	H	C	N	O	S
0	5.94	48.11	0.39	39.14	0.08
20	5.88	47.14	0.45	39.77	0.08
30	5.84	52.53	0.73	32.66	0.04
40	4.95	58.56	0.76	24.18	0.15

The characteristics of SCL pellet and torrefied SCL pellet, 260 °C and 30 min, are entirely listed in Table 3. The mechanical durability of the final product is slightly dropped from the raw SCL pellet after torrefaction process. However, its diameter and bulk density are vastly decreased because the lingo-cellulosic components in raw material is decomposed due to heat from reaction.

Table 3. Physiochemical properties of products

Properties	Dried sugarcane leaves	Sugarcane leaf-based pellet	Torrefied sugarcane leaf-based pellet
Bulk density (kg/m^3)	NA	682.2 ± 2.7	521.7 ± 7.5
Average diameter (mm)	NA	5.98 ± 0.1	5.73 ± 0.1
Durability index (%)	NA	98.13 ± 0.1	97.54 ± 0.1
Proximate analysis (%wt, dry basis)			
Moisture	20.22*	2.95**	1.60**
Volatile matter	83.56	81.71	71.48
Fixed carbon	11.25	11.94	20.31
Ash	5.19	6.35	8.20
Ultimate analysis (%wt, dry basis)			
Carbon	49.98	48.11	52.53
Hydrogen	5.8	5.9	5.8
Nitrogen	0.04	0.38	0.73
Sulfur	0.04	0.08	0.04
Oxygen **	38.94	39.14	32.66
High heating value (MJ/kg)	18.41**	18.27**	20.72**

*as received, **air dried

3.3 Cost of torrefied products from the demonstration unit

The production cost of torrefied sugarcane leaf-based pellet was roughly breakdown to estimate and evaluate the possibility of community-based manufacture. In Table 4, the common expense for only pelletization is about 5.27 baht/kg and the sum up will be increased to 14.09 baht/kg when torrefaction is allowed.

Table 4. Estimated cost breakdown of torrefied pellet derived from sugarcane leaves

Description	Amount (Baht/kg)
Cost of dried sugarcane leaves	1.00
Energy cost for shredding	0.33
Energy cost for pelletization	0.35
Energy cost for torrefaction	4.38
Labor cost for shredding	0.59
Labor cost for pelletization	3.00
Labor cost for torrefaction	4.44
Estimated production cost	14.09

4. Conclusion

This study demonstrated the feasibility to produce high quality solid biofuel from SCL using a community-based unit of pelletization and torrefaction processes. The production of sugarcane leaf-based pellet was conditioned by mixed 3.5 %wt of tapioca powder and 30 %wt of moisture content. The pellet was introduced to torrefy via a 5-kg batched-type reactor in 30 min of residence time to upgrade such a fuel which increasing the heating value from 18.27 to 20.72 MJ/kg and about 70%wt of solid mass yield. The properties revealed that the longer period of torrefaction, the higher of carbon content and HHV of torrefied product were received. However, the energy yield was likely declined. Therefore, pelletization and torrefaction are interesting pathways to upgrade sugarcane residues into carbon-enriched solid fuel, sometimes named biocoal, could potentially be an alternatively non-fossil for heat and power generations. Moreover, the farmers can consider as an extra income and support the environmental policy on reduction of PM 2.5 caused of the agricultural residues burning.

Acknowledgements

The authors would like to thank Thailand Science Research and Innovation (TSRI) for financial support and BLCP Power Limited for providing biomass.

References

1. Khempila, J.; Kongto, P.; Meena, P. *Bioenergy Res.* **2022**, *15*, 1265–1280.
2. Report of cane area and yield 2022-2023. https://www.ocsb.go.th/report_area_yield/ (accessed January 5, 2024).
3. Kaia, X.; Meng, Y.; Yang, T.; Li, B.; Xing, W. *Bioresour. Technol.* **2019**, *278*, 1–8.
4. Prasongthum, N.; Duangwongsa, N.; Khowattana, P.; Suemanotham, A.; Wongharn, P.; Thanmongkhon, Y.; Reubroycharoen, P.; Attanatho, L. *J. Phys. Conf. Ser.* **2022**, *2175*, 012027.
5. Pimchua, A.; Dutta, A.; Basu, P. *Energy Fuels.* **2010**, *24(9)*, 4638–4645.
6. Suemanotham, A.; Attanatho, L.; Prasongthum, N.; Sisuthog, W.; Laosombut T.; Thanmongkhon, Y. *J. Phys. Conf. Ser.* **2022**, *2175*, 012031.

A machine learning approach to gasification process model for environmental sustainability

Kritsana Suwanamad and Phuet Prasertcharoensuk

Department of Chemical Engineering, Chulalongkorn University, 254 Phayathai Road, Wang Mai Subdistrict, Pathumwan District, Bangkok 10330

**E-mail: Phuet.p@chula.ac.th*

Abstract:

Concerns about greenhouse gas emissions can be alleviated by investigating biomass/waste residue usage for sustainable biofuels, a viable alternative to petroleum in transportation. Gasification, a low-cost way of converting biomass, lacks adequate simulation tools. Using Aspen Plus, the study evaluates the effect of operating parameters on biomass gasification. The findings emphasize the importance of temperature, ER ratio, and pressure in molding syngas quality. Artificial Neural Networks (ANN) and multiple linear regression (MLR) models were used to improve simulation accuracy. The study reveals that ANN outperforms MLR with a high accuracy exceeding 0.95 because of its capacity to capture non-linear process patterns. The simulation demonstrates promise as a design tool for estimating syngas composition under different gasifier conditions. The use of this paradigm in scaling up processes can result in cost and time savings in engineering and development, easing the transfer from laboratory to industrial stages.

1. Introduction

Among other important global challenges, immediate action to prevent climate change is required due to continued greenhouse gas emissions, the majority of which are caused by human activities such as fossil fuel combustion.[17] Climate models forecast a temperature increase of 1.1 to 6.4 ℃ this century, underlining the crucial importance of shifting to renewable and sustainable energy sources.[1]

Lignocellulosic materials, notably biomass/waste residues, appear as possible biofuel sources in the field of renewable resources. They provide a clean, limitless energy source, seeking to reduce reliance on fossil fuels while mitigating environmental consequences.[2] Biomass gasification, which converts varied biomass feedstocks into multipurpose products, stands out as an effective and environmentally benign technology. This establishes it as a promising clean energy source with the potential to minimize energy dependence and greenhouse gas emissions.[3]

The gasification process, which occurs at temperatures ranging from 600 to 1500 °C, is a critical stage in biomass utilization. Carbon-based molecules in biomass feedstocks are thermochemically converted into syngas, a flexible combination of combustible gases. The composition of syngas, which includes hydrogen (H_2), carbon monoxide (CO), carbon dioxide (CO_2), methane (CH_4), nitrogen (N_2), water vapor (H_2O), and other hydrocarbons, varies depending on the type of biomass and gasification process parameters.[5] Drying, pyrolysis, oxidation, and reduction are the four steps of the gasification process.[4]

Given the complexities of biomass gasification, modeling is critical for scale-up, industrial management, and performance evaluation under a variety of scenarios.[3] Aspen Plus stands out among simulation tools, identifying biomass as "non-conventional" due to its variety. To mimic equilibrium, biomass is broken down into constituent molecules using methods such as PENG-ROB and RKS, while density and enthalpy are computed using models such as "DCOALIGT" and "HCOALGEN".[5] Significant research has been conducted on the performance analysis of biomass gasification systems, with variables such as biomass properties, reactor design, and operating parameters being considered.[6-8]

Machine learning, which is a collection of algorithms that use mathematical and statistical methodologies, includes well-known solutions such as linear regression and artificial neural networks. Machine learning has been used in research to build models for biomass gasification, with artificial neural networks proving usefulness in forecasting syngas yield, work, LHV, and HHV based on operational factors and biomass type.[9-11]

This research analyzes linear regression and artificial neural networks to improve data analysis in biomass gasification, thus contributing to long-term energy solutions. This method of scaling up operations can save time and money in engineering, facilitating the transfer from lab to industrial stages.

2. Methodology

2.1 Simulation

Using ASPEN Plus, an equilibrium simulation model for biomass gasification is created.[12] Penge Robinson's equation of state is applied to calculate the physical properties of the conventional components in the gasification process.[12] The HCOALGEN and DCOALIGT models are also used to calculate the enthalpy and density of nonconventional components such as biomass and ash.[6] The MCINCPSD stream, which consists of three substreams of the MIXED, CIPSD, and NCPSD classes, is also used to describe the biomass structure and ash streams, which are not included in the Aspen Plus component database.[6]

The modeling technique of the system is a two-zone gasification model in which the moisture decrease of feed during drying is not taken into account, and the pyrolysis zone is represented using ASPEN's RYield reactor. Figure 1 depicts the modeling of the two-zone simulation model. RYield is an ASPEN reactor model that can accept multiple input material streams and output a single material stream. Because pyrolysis is a basic thermal breakdown process, a single input of solid biomass feed is taken into account. The chemical stoichiometry of the pyrolysis process is quite complicated, and there has been no previous research on the pyrolysis yield of OPF. As a result, the yield distribution is estimated using the final analysis data. Thus, the ASPEN RYield reactor model, which runs solely with a specific yield distribution and ignores reaction stoichiometry and kinetics, is used to describe the pyrolysis zone of gasification. As indicated in Figure 1, the oxidation and reduction zones of gasification are merged and modeled using a single RGibbs reactor. ASPEN's Gibbs reactor is an equilibrium modeling block that operates on the premise of minimizing Gibbs free energy.[7]

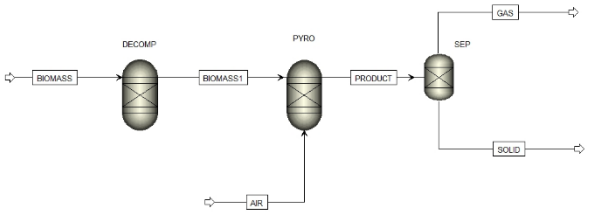

Figure 1. Gasification simulation on ASPEN plus

2.2 Validation

The simulation is validated against the experiments of Striūgas, Nerijus, et al.[13] The fuel used to validate is Sewage sludge sawdust pellets with proximate and ultimate analysis as shown in Table 1.[13] The input data for the model are input fuel stream mass flow 28 kg/h, temperature 750 ℃, pressure 1 atm, and equivalent ratio 0.39.[13]

Table 1. Proximate and Ultimate Analysis of Sewage sludge sawdust pellets[13]

Proximate Analysis	Wt.%
Moisture	4.4
Fixed carbon	14.3
Volatile matter	59.5
Ash	21.8
Ultimate Analysis	**Wt.% (dry basis)**
Carbon (C)	41.08
Hydrogen (H)	5.51
Nitrogen (N)	3.77
Chlorine (Cl)	0
Sulfur (S)	0.94
Oxygen (O)	26.9

2.3 Data analysis

The mean and standard deviation (SD) of variables were calculated as an initial examination of the raw data. The monotonic link between data pairs was then measured using Spearman's correlation coefficients (SCC) for the continuous predictor data. Because the data was not known to follow a Gaussian distribution, SCC was utilized instead of the more widely used Pearson correlation coefficient, and SCC is less impacted by outliers.[14] SCC was calculated using Eq. (1):

$$SCC = \frac{\sum_{i=1}^{N}(X_i - X_{mean})(Y_i - Y_{mean})}{\sqrt{\sum_{i=1}^{N}(X_i - X_{mean})^2 \sum_{i=1}^{N}(Y_i - Y_{mean})^2}} \quad (1)$$

Where X_i and Y_i are individual data points, and X_{mean} and Y_{mean} are the means of variables X and Y, respectively.

A SCC of 0 indicates that two parameters are unrelated. The monotonic relationship grows stronger as one gets closer to 1.[14] In this investigation, an SCC of 0.6 was selected to signify a substantial connection.[14] Figure 2 depicts the SCC matrix of all continuous predictors.

2.4 Developed machine learning model (multiple linear regression and artificial neural network)

The machine learning model is developed by Python. In this work, there are 12 input variables, which include temperature (T), pressure (P), equivalent ratio (ER), carbon element (C), hydrogen element (H), nitrogen element (N), sulfur element (S), oxygen element (O), moisture (M), fixed carbon (FC), volatile matter (VM) and ash, and 4 outputs, which include hydrogen (H_2), carbon monoxide (CO), carbon dioxide (CO_2) and

methane (CH_4). Characteristics of input and output variables in the model for gasifier are shown in Table 2 which is obtained from the simulation model results. From collecting the result of the simulation, this research focuses on machine learning between multiple linear regression (MLR) and artificial neural network (ANN) to create a model from simulation results.

MLR is the study of the linear relationship between two or more variables. The features will be correlated with the target that can be shown in Eq. (2)

$$y_{output} = Tx_T + Px_P + ERx_{ER} + Cx_c + Hx_H + Nx_N + Sx_S + Ox_O + Mx_M + FCx_{FC} + VMx_{VM} + ashx_{ash} \quad (2)$$

Where output are mole fraction of syngas (H_2, CO, CO_2, and CH_4)

ANN is an architecture composed of a large number of neurons organized in different layers, with neurons from one layer connected to those from another layer via weights, and it can be trained to perform a specific task by adjusting its connecting weights, bias, and architecture.[15] ANN can be shown in the architecture in Figure 3.

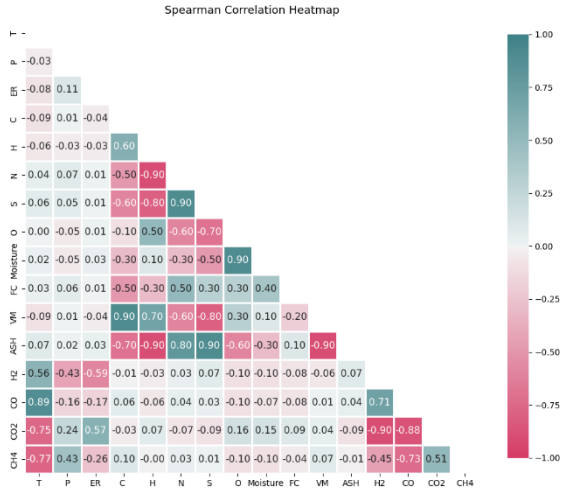

Figure 2. Spearman Correlation Coefficient matrix

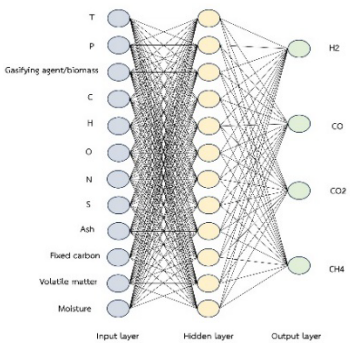

Figure 3. Architecture of ANN

Table 2. Characteristics of input and output variables in the model for gasifier

Input of model	Range
T	400 - 1300 °C
P	0.1 - 100 bar
ER	0.01 - 0.50
C	39.60 - 49.20
H	5.16 - 6.20
N	0.05 - 4.63
S	0.01 - 0.94
O	26.90 - 48.54
M	4.40 - 14.90
FC	12.80 - 17.20
VM	59.50 - 79.20
Ash	0.40 - 21.80
Output of model	**Range**
H_2	0.02 - 0.59
CO	0 - 0.55
CO_2	0 - 0.85
CH_4	0 - 0.55

2.5 Train and test model by k-fold cross-validation

The difficulty with training the neural network is that the variation is considerable owing to the unevenness of the training and testing data. This may lead to model misunderstanding. As a result, the idea of K-fold cross-validation exists. The network is repeated K times throughout development, and with each K turn, the network is further developed using a different set of training and validation data. The choice of K value is critical since a higher K value minimizes variation but requires a long calculation time.[16] This allows us to average the evaluation values and use them to represent the performance of the model that is reliable in the performance of the model. In this research, the data will be divided into 10 times, which is called 10-fold cross-validation. 10-fold cross-validation can be shown in Figure 4.

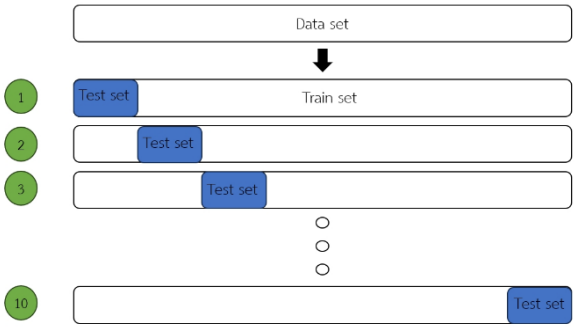

Figure 4. 10-fold cross-validation

2.6 Evaluation model

In a feed-forward neural network, values of instances progress proportionally from input to output across layers. Errors are then retroactively conveyed, forcing the preceding layer's weights

and biases to be adjusted to reduce these errors. This iterative procedure improves the generalization performance of the ANN model, resulting in more exact predictions for new examples. The inaccuracy of the network is calculated by comparing estimated and real values. The estimated error exhibits significant variance at first, but as the number of repetitions increases, it converges to a minimum value and remains generally steady thereafter.[10] The Mean Square Error (MSE) in Eq. (3), The Mean Absolute Error (MAE) in Eq. (4) and the coefficient of determination R^2 in Eq. (5) are typically used to assess the predictive accuracy of the ANN model. The following are the Eq. (3) – (5):

$$MSE = \frac{1}{N}\sum_i^N (y_{actual}-y_{predict})^2 \quad (3)$$

$$MAE = \frac{1}{N}\sum_i^N \left|y_{actual}-y_{predict}\right| \quad (4)$$

$$R^2 = 1 - \frac{\sum_i^N (y_{actual}-y_{predict})^2}{\sum_i^N (y_{actual}-y_{mean})^2} \quad (5)$$

Where N is the number of observation values, y_{actual} is the target value, $y_{predict}$ is the model predicted value and y_{mean} is the mean of the target value.

3. Results & Discussion

3.1 Validation

The simulation model was validated by using gasification data from the studies conducted by Strigas, Nerijus, et al.[13] Figure 5 depicts the validation procedure, which shows a clear agreement between the model's predictions and the experimental data. This regularity lends credence to the model's dependability. It is crucial to highlight that, this research has neglected hydrocarbon in this simulation.

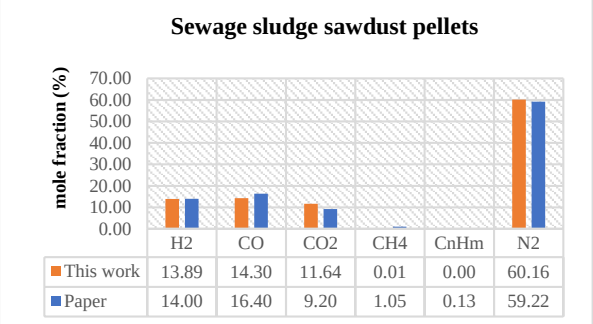

	H2	CO	CO2	CH4	CnHm	N2
This work	13.89	14.30	11.64	0.01	0.00	60.16
Paper	14.00	16.40	9.20	1.05	0.13	59.22

Figure 5. Comparison model and Strigas, Nerijus, et al[13]

3.2 Data analysis

Figure 2 depicts the interplay of variables during the gasification process. The dataset under consideration has 12 input variables (T, P, ER, C, H, N, S, O, M, FC, VM, and ash), and four output variables (H_2, CO, CO_2, and CH_4). According to the data, Temperature has the most substantial positive influence on H_2 and CO, as demonstrated by the highest positive Spearman's rank correlation coefficient (SCC). The equivalent ratio, on the other hand, has the most significant negative influence, as evidenced by its greatest negative SCC. Furthermore, given their largest positive SCC values, the input factors with the most beneficial impact on CO_2 and CH_4 are equivalent ratio and pressure, respectively. Temperature, on the other hand, emerges as the most negatively influencing variable. This conformity with reality corresponds to the desired outcome of the gasification process of syngas, which consists of H_2, CO, CO_2, and CH_4. Notably, H_2 and CO are prioritized due to their high heat energy content per unit, making them attractive fuels for generating power in gas turbines or producing value-added compounds such as methanol and ethanol. High CO_2 concentrations, on the other hand, are undesirable due to their potential environmental impact as a greenhouse gas. Modern preferences favor running the gasification process at high temperatures, moderate equivalent ratio, and ambient pressure. This deliberate approach promotes the overall endothermic gas transformation reaction, resulting in syngas rich in H_2 and CO. The type of biomass used in the process has an impact on the composition of the resulting syngas.

3.3 Compare model performance between multiple linear regression and neural network

Figure 6 depicts a thorough examination of model performance using a rigorous 10-fold cross-validation method targeted at reducing answer variation across various linear regression and neural network models. Figures 7 and 8 go deeper into the comparison by displaying the projected results vs the actual target values as well as the residual analysis. The multiple linear regression model has an average efficiency of 0.7398, as shown in Figure 6. The neural network model, on the other hand, has a substantially better average efficiency of 0.9593. Figures 7 and 8 show a visual representation of the model's prediction ability, showing the neural network's advantage in capturing the underlying patterns in the test dataset. The neural network's predictions closely match the model line, indicating its precision when compared to the multiple linear regression model.

The evaluation of error/residual values in Figures 7 and 8 demonstrates the neural network model's superior performance even further. This improved proficiency is due to the non-linear character of the gas transformation process. Multiple linear regression, which is based on linear relationships, is less capable of effectively describing such sophisticated non-linear processes. Neural network models, on the other hand, excel at dealing with non-linear complexities by exploiting the power of iterative alterations in weight and bias values via backpropagation learning. The flexibility of neural networks enables them to learn efficiently from training data, gradually improving their predictions until they closely match target values. As a result, the neural network model emerges as a formidable tool for forecasting non-linear features, surpassing multiple linear regression in this context. This observation highlights neural networks' potential as a more robust and versatile option for predictive modeling in circumstances characterized by detailed non-linearity.

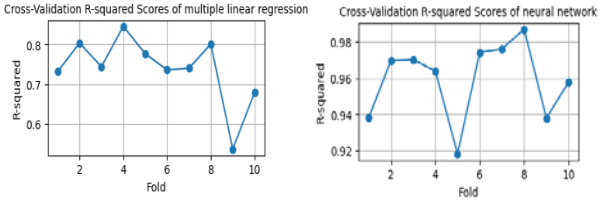

Figure 6. Evaluation of model using 10-fold cross-validation

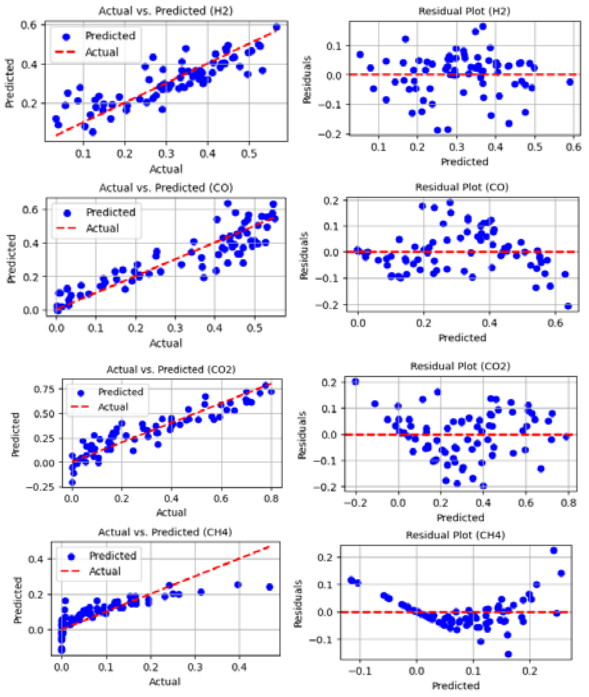

Figure 7. The predicted and residual compared multiple linear regression model and the actual target

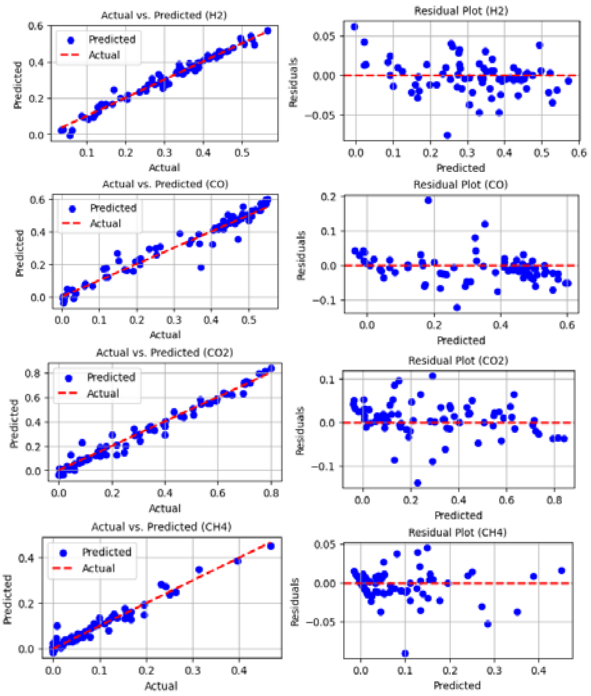

Figure 8. The predicted and residual compared neural network model and the actual target

4. Conclusions

Concerns regarding greenhouse gas emissions can be mitigated by researching the use of biomass/waste residue for sustainable biofuels, which can be used as a viable alternative to petroleum in transportation. Gasification, a low-cost method of converting biomass, is not well-supported by simulation tools. Thus, this research focuses on data analysis and creating efficient models by machine learning between multiple linear regression and neural networks. As a result, the gasification process data analysis demonstrated that input factors had a considerable impact on syngas composition, with temperature (T) positively increasing H_2 and CO generation. The neural network outperformed multiple linear regression in terms of model performance, with 0.9593 over 0.7398. The neural network's accuracy in capturing non-linear patterns during the gas transformation process demonstrated its potential as a more robust and versatile predictive modeling tool, particularly in environments marked by detailed non-linearity. This shows that neural networks outperform classic linear regression methods in terms of accuracy and adaptability for forecasting gasification processes.

Acknowledgements

I am grateful to my professors for their helpful advice and to my family for their continuous support. Thank you all for contributing to the success of this research.

References

1. Constantin, F.A. and I. Loredana, The causes and effects of global warming. International Multidisciplinary Scientific GeoConference: SGEM, **2009**. 1: p. 147.
2. Amponsah, N.Y., et al., Greenhouse gas emissions from renewable energy sources: A review of lifecycle considerations. *Renewable and Sustainable Energy Reviews*, **2014**. 39: p. 461-475.
3. Puig-Arnavat, M., et al., Artificial neural network models for biomass gasification in fluidized bed gasifiers. *Biomass and Bioenergy*, **2013**. 49: p. 279-289.
4. Koido, K. and T. Iwasaki, Biomass gasification: a review of its technology, gas cleaning applications, and total system life cycle analysis. *Lignin: Trends and Applications*, **2018**: p. 161.
5. Mutlu, Ö.Ç. and T. Zeng, Challenges and opportunities of modeling biomass gasification in Aspen Plus: A review. *Chemical Engineering & Technology*, **2020**. 43(9): p. 1674-1689.
6. Saleh, A., et al. Modeling of oil palm frond gasification process in a multistage downdraft gasifier using aspen plus. *Journal of Physics: Conference Series*. **2020**. 1517: p. 012036.
7. Atnaw, S.M., S.A. Sulaiman, and M.R.T. Ahmad. Prediction of biomass conversion process for oil palm fronds in a downdraft gasifier. *AIP Conference Proceedings*. **2012**. 1440: p. 981-990.
8. Begum, S., et al., Performance analysis of an integrated fixed bed gasifier model for different biomass feedstocks. *Energies*, **2013**. 6(12): p. 6508-6524.
9. Safarian, S., et al., Artificial neural network integrated with thermodynamic equilibrium modeling of downdraft biomass gasification-power production plant. *Energy*, **2020**. 213: p. 118800.
10. Kartal, F. and U. Özveren, A deep learning approach for prediction of syngas lower heating value from CFB gasifier in Aspen plus. *Energy*, **2020**. 209: p. 118457.
11. Yucel, O., E.S. Aydin, and H. Sadikoglu, Comparison of the different artificial neural networks in prediction of biomass gasification products. *International Journal of Energy Research*, **2019**. 43(11): p. 5992-6003.
12. Gagliano, A., et al., Development of an equilibrium-based model of gasification of biomass by Aspen plus. *Energy Procedia*, **2017**. 111: p. 1010-1019.
13. Striūgas, N., et al., An evaluation of performance of automatically operated multi-fuel downdraft gasifier for energy production. *Applied Thermal Engineering*, **2014**. 73(1): p. 1151-1159.
14. Ascher, S., et al., A comprehensive artificial neural network model for gasification process prediction. *Applied Energy*, **2022**. 320: p. 119289.
15. Safarian, S., et al., Modeling of hydrogen production by applying biomass gasification: Artificial neural network modeling approach. *Fermentation*, **2021**. 7(2): p. 71.
16. Ming, J.L.K., et al. Artificial neural network topology optimization using k-fold cross validation for spray drying of coconut milk. *IOP Conference Series: Materials Science and Engineering*. **2020**. 778: p. 012094.
17. Kumar, S., S. Himanshu, and K. Gupta, Effect of global warming on mankind-a review. *International Research Journal of Environmental Sciences*, **2012**. 1(4): p. 56-59.

Effect of fuel type on the characteristics and photocatalytic activity of ZnO nanoparticles synthesized via solution combustion method

Shabnam Purmahammad Abdollahi[1], Wuttichai Reainthippayasakul[1,2], and Karn Serivalsatit[1,2]*

[1]*Department of Materials Science, Faculty of Science, Chulalongkorn University, Bangkok 10330, Thailand*
[2]*Photocatalysts for Clean Environment and Energy Research Unit, Faculty of Science, Chulalongkorn University, Bangkok 10330, Thailand*

**E-mail*: *karn.s@chula.ac.th*

Abstract:

This research investigates the influence of organic fuels, including urea, citric acid, and agar, on the synthesis and photocatalytic performance of zinc oxide (ZnO) nanoparticles through the solution combustion method. Various analytical techniques, including X-ray diffraction (XRD), N_2 adsorption-desorption isotherms, scanning electron microscopy (SEM), UV-VIS diffuse reflectance spectroscopy (DRS), and photoluminescence spectroscopy (PL), were employed to characterize the synthesized ZnO nanoparticles. The photocatalytic activity of the synthesized nanoparticles was evaluated by degrading methyl orange under ultraviolet irradiation at ambient temperature. The results revealed that single-phase and well-crystalline ZnO nanoparticles with a wurtzite structure were formed regardless of fuel type. The ZnO nanopowders prepared with agar as a fuel had a foamy microstructure with the highest specific surface area of 8.58 m^2/g compared to the others. The highest photodegradation of methyl orange under ultraviolet irradiation was also achieved by the ZnO powders prepared with agar due to their good crystallinity and higher specific surface area.

1. Introduction

Photocatalysts are materials that accelerate the rate of a chemical reaction that takes place under the influence of light. The use of photocatalysts has gained significant attention in recent years due to their potential applications in clean energy generation, environmental remediation, and chemical synthesis.

Zinc oxide (ZnO) is widely recognized as one of the most important semiconductors, possessing a direct wide band gap (3.37 eV) and high exciton energy (~60 meV). It has attracted considerable attention as semiconductor photocatalysts in environmental remediation through the degradation of organic pollutants.[1, 2]

ZnO nanoparticles can be synthesized by various techniques, including precipitation,[3] sol-gel,[4] hydrothermal,[5] and solution combustion.[6] Among these techniques, the solution combustion method is known as a simple and inexpensive method to synthesize nanoparticles with a large surface area. Nanoparticles are synthesized through the redox reaction between an oxidizer containing metal cation and organic fuel at a relatively low temperature of around 400-600 °C. The type of organic fuel plays a significant role in the characteristics of the combustion reaction and the flame temperature which influences the microstructure, defects, and specific surface area of the synthesized nanoparticles.

In this study, ZnO nanoparticles were synthesized by the solution combustion method. The effects of organic fuels, including urea, citric acid, and agar, on the characteristics and photocatalytic activity of the synthesized zinc oxide were investigated.

2. Materials and Methods

2.1 Preparation of ZnO Nanoparticles

Zinc oxide (ZnO) nanoparticles were synthesized using the solution combustion method. Zinc nitrate hexahydrate ($Zn(NO_3)_2{\cdot}6H_2O$) was employed as an oxidizer, while a variety of organic fuels, namely agar, urea, and citric acid, served as fuels. Stoichiometric amounts of oxidizer (O) and fuel (F) were taken based on the condition that the valence of F/O to be unity. The combustion reactions for the different fuels used were as following:

Urea;

$$Zn(NO_3)_2+\frac{10}{6}CH_4N_2O\rightarrow ZnO+\frac{10}{6}CO_2+\frac{10}{3}H_2O+N_2$$

Citric acid;

$$Zn(NO_3)_2+\frac{10}{17}C_6H_8O_7\rightarrow ZnO+\frac{90}{17}CO_2+\frac{80}{17}H_2O+\frac{20}{17}N_2$$

Agar;

$$Zn(NO_3)_2+\frac{10}{62}C_{14}H_{24}O_9+Zn(NO_3)\rightarrow ZnO+\frac{100}{62}CO_2+\frac{120}{62}H_2O+\frac{15}{62}N_2$$

The synthesis process began by carefully weighing and mixing specific ratios of $Zn(NO_3)_2{\cdot}6H_2O$ and the selected organic fuels according to the above equations. In each photocatalyst preparation, the amount of fuels,

agar, urea, citric acid mixed with 2.97 grams of $Zn(NO_3)_2 \cdot 6H_2O$ were 0.53, 1.00, 1.17 grams, respectively. These stoichiometric amounts of starting materials were dissolved in 30 ml of distilled water. After thorough mixing, the resulting solution was transferred into a crucible and subsequently subjected to a drying process in an oven at a temperature of 100 °C. Subsequently, the dried precursor was subjected to the combustion process. This involved heating the samples in a furnace at a temperature of 600°C for a duration of 4 hours. During this combustion reaction, the fuel source underwent combustion, facilitating the formation of ZnO nanoparticles. The combustion process was critical in ensuring the conversion of the precursor into ZnO nanoparticles with desired characteristics. Then, the obtained ZnO nanoparticles were ground to a fine powder using a porcelain mortar and pestle.

2.2 Characterization Methods

The crystalline structure of the ZnO nanoparticles was characterized by X-ray diffractometer (Bruker AXS, Model D8 Discover) operating at 40 kV and 25 mA, with Cu Kα radiation (λ = 0.15406 nm). The average crystallite size of the nanoparticles was calculated using the Scherer formula.

$$D = \frac{K\lambda}{\beta cos(\theta)}$$

where

D is the mean size of the ordered (crystalline) domains

K is a dimensionless shape factor

λ is the X-ray wavelength

β is the line broadening at half is the maximum intensity (FWHM)

θ is the Bragg angle.

The morphology of the synthesized ZnO nanoparticles were observed by scanning electron microscope (JEOL, JSM-6480LV). N_2 adsorption-desorption isotherms were analyzed by Micromeritics 3Flex adsorption analyzer. The specific surface area and pore volume were calculated from the Brunauer-Emmett-Teller (BET) equation and Barrett-Joyner-Halenda (BJH) method. The band gap of the synthesized powders was analyzed by a diffused reflectance spectrophotometer (Perkin Elmer, Lambda 950). The photoluminescence spectra of the ZnO nanoparticles were measured at the excitation wavelength of 320 nm by a Perkin Elmer LS55 fluorescence spectrometer.

2.3 Photocatalytic Activity Measurements

The photocatalytic activity of the synthesized ZnO nanoparticles was estimated by monitoring the degradation of methyl orange (MO) under 85W blacklight irradiation. 0.2 grams of the synthesized ZnO nanoparticles were added to 200 ml of the 10 ppm MO solution. This suspension was magnetically stirred in the dark for an hour to establish the adsorption/desorption equilibrium. Then the suspension was exposed to blacklight irradiation. The suspension was collected at the time interval of 60 min. The MO dye solution was separated from the ZnO nanoparticles using syringe filter. The residual concentration of MO dye in the solution was used to measure the photocatalytic activity of the synthesized ZnO nanoparticles. The absorbance spectra of MO solution were recorded by UV-VIS NIR spectrometer (Agilent, Cary 7000).

3. Results & Discussion

3.1 X-ray Diffraction (XRD)

The XRD patterns of the synthesized ZnO nanoparticles are shown in Figure 1. The diffraction peaks (100), (002), (101), (102), (110), (103), and (112) demonstrate the formation of hexagonal wurtzite structure with P63mc space group (JCPDS PDF no 00-003-0888).[7]

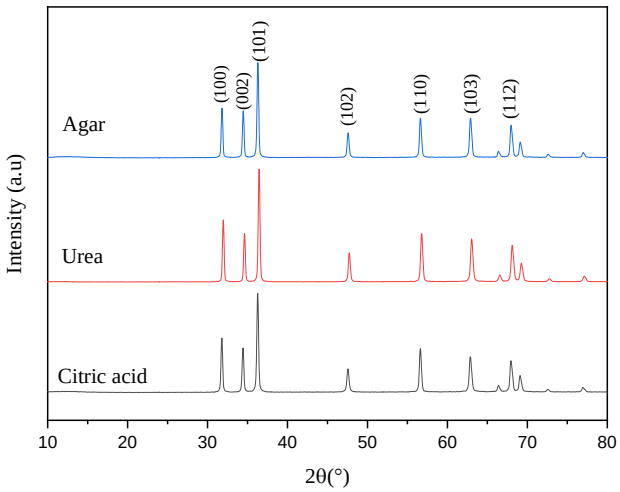

Figure 1. XRD patterns of the ZnO powders prepared with different fuels

Upon examination of the XRD patterns, it is evident that there are variations in peak intensities, indicating differences in crystallinity among the synthesized nanoparticles. Crystallite size calculated using the Scherrer equation is shown in Table 1. ZnO nanoparticles prepared using agar as a fuel exhibit minimum crystallite size of 23 nm in comparison to the other samples.

Table 1. The Crystallite size (D_{XRD}), BET surface area, pore volume, and pore size of ZnO powders prepared with different fuels

Fuels	Crystallite size (D_{XRD})	BET surface area (m^2/g)	Pore volume (cm^3/g)	Pore size (Å)
Agar	23	8.58	0.0129	60.478
Citric acid	30	3.98	0.0057	57.517
Urea	27	0.48	0.0006	51.009

3.2 Morphology Observation

The samples exhibit different characteristics in their structure after drying in the oven. While using urea as a fuel favors the precipitation of metal cations in the dried sample, leading to the agglomeration of the particles after combustion.[8] For the use of citric acid, the dried precursor became a dry gel. The dried precursor prepared with agar has a foamy structure. The structure of the dried precursor serves as a template during the combustion reaction.[9]

SEM micrographs of ZnO powders synthesized with different fuels after calcining at 600 °C for 4 hours are shown in Figure 2. The morphological investigation through SEM images of ZnO synthesized using agar, citric acid, and urea as fuels revealed distinctive characteristics, elucidating their template contributions. Even though all powder exhibited porous structures due to the release of gases during combustion reaction. The ZnO powder prepared with agar exhibited significantly less agglomeration and a more uniform structure in comparison to those prepared with urea and citric acid. This may be resulted from the foamy template of the dried precursor. This phenomenon helps to maintain the porous structure of the resulting powder.

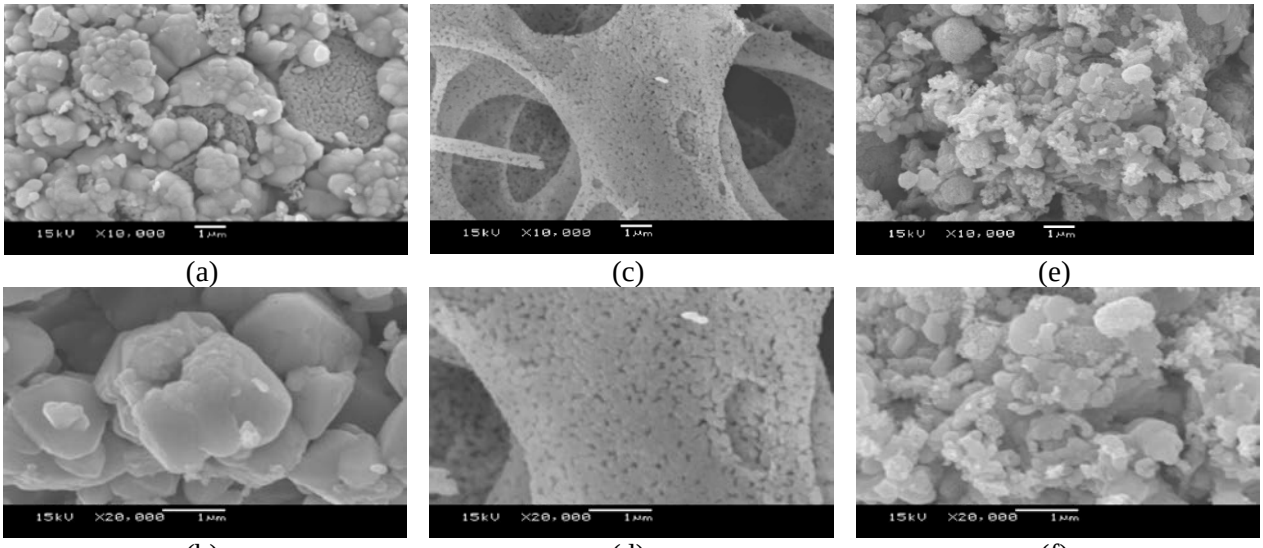

(a) (c) (e)

(b) (d) (f)

Figure 2. SEM images of ZnO powders prepared with (a,b) urea, (c,d) citric acid, and (e,f) agar

3.3 Textural Analysis

Figure 3 illustrates the N_2 adsorption-desorption isotherms of the samples. Following the IUPAC classification, it is observed that the isotherms exhibit characteristics of type IV, accompanied by a H3 hysteresis loop. These findings suggest the presence of particle agglomeration with a three-dimensional pore network. A summary of BET specific surface area and pore volumes can be found in Table 1. The ZnO powder prepared with agar has the highest specific area of 8.58 m^2/g and the largest pore volume of 0.0129 cm^3/g. The high specific surface area and pore volume may arise due to the porous structure of the dried precursor. During the combustion process, the liberation of gaseous products led to an increase of pore volume and specific surface area of the porous structure.

3.4 Optical Studies

Figure 4 shows the UV-VIS diffuse reflectance spectra of the ZnO powders prepared with different fuel types. The absorption edge at around 400 nm is due to the inherent band structure of ZnO. By means of the Tauc's equation, the band gap energy (E_g) can be calculated as follows;

$$(\alpha h\nu)^2 = A(h\nu - E_g)$$

where hν is the photon energy in eV, α is the absorption coefficient, and A is a material constant. The band gap energy values are determined by the extrapolating the straight line to $(\alpha h\nu)^2 = 0$. As shown in Figure 5, the E_g for the powders prepared with agar, citric acid and urea were 3.25 eV, 3.25 eV and 3.21 eV, respectively. The dependence of band gap on the type of fuel was negligible.

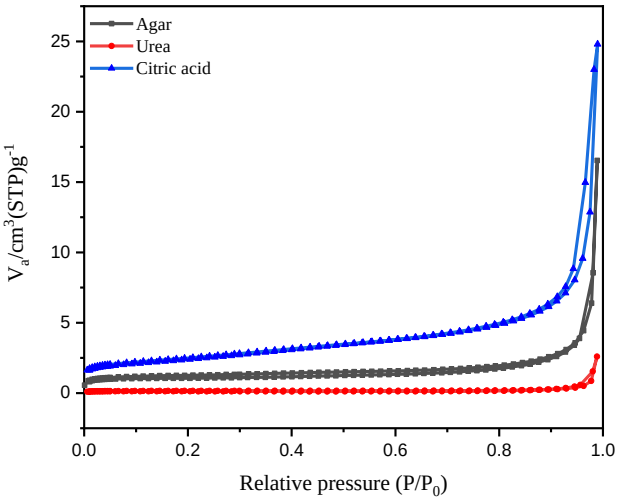

Figure 3. Adsorption and desorption isotherms of the ZnO powders prepared with different fuels

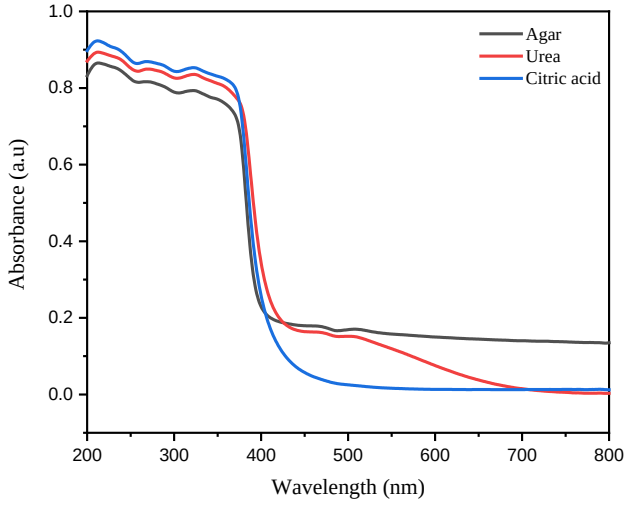

Figure 4. Diffuse reflectance spectra of the ZnO powders prepared with different fuels

3.5 Photoluminescence Analysis

Photoluminescence (PL) studies were used to investigate the defects in the samples. Figure 8 shows the PL spectra of ZnO powders prepared with different fuels using an excitation of 320 nm. The PL spectra of ZnO powder with different fuels exhibit emission peaks at about 409, 429, 487, and 533 nm. A green light emission at a wavelength of 487 nm indicates that the green light is produced due to an electron transition from the ionized oxygen vacancies level to the valence band.[10] A peak located at 533 nm can be linked with an electronic transition from the lower state of the conduction band to the interstitial oxygen (Oi) state.[11] The peaks at 409, 427 nm are likely due to an electronic transition involving the band structure of the material. This transition could involve energy levels related to defects, impurities, or specific electronic states within the structure of materials.[7] The variations in peak intensities could be attributed to the presence of defects or impurities introduced by different fuel sources.

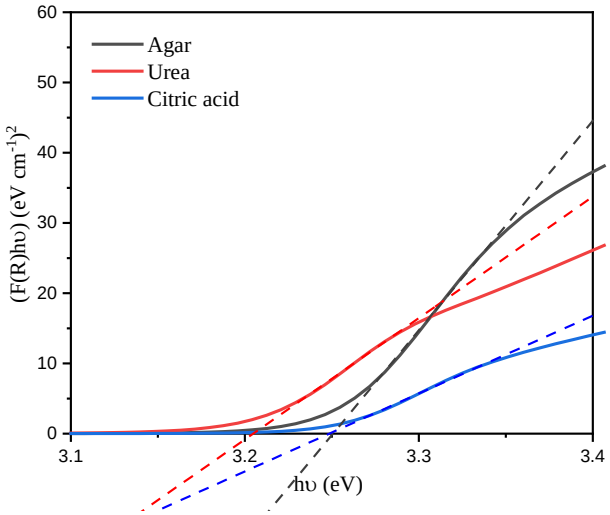

Figure 5. Tauc plots of the ZnO powders prepared with different fuels

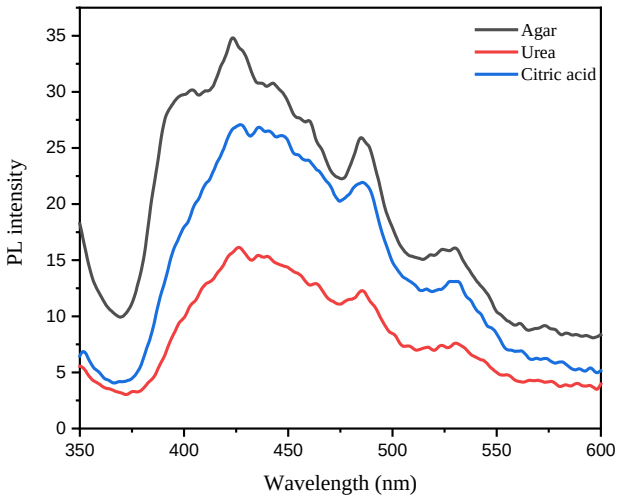

Figure 6. PL spectra of the ZnO powders prepared with different fuels

3.6 Photocatalytic Activity

The photocatalytic degradation of MO dye under blacklight irradiation was employed to assess the performance of the ZnO powders prepared using different fuels, including agar, citric acid, and urea, with zinc nitrate serving as the oxidizer. The temporal evolution of C/C_0, representing the normalized concentration of MO dye where C represents dye concentration after irradiation time and C_0 represents initial concentration of MO dye, was monitored to evaluate the efficiency of these photocatalysts as shown in Figure 7. Notably, the initial decolorization rate at time zero signifies the adsorption behavior of the samples under dark conditions. The photodegradation efficiency of ZnO nanoparticles prepared with agar reached 81% after 180 minutes under blacklight irradiation, whilst the photodegradation efficiency of those prepared with citric acid and urea reached only 69% and 41%, respectively. The higher photodegradation efficiency of the ZnO nanoparticles prepared with agar can be attributed to the larger specific surface area and pore volume, as well as, the smaller crystallite size, providing the higher active site.[12]

The type of organic fuel for ZnO nanoparticles preparation by solution combustion significantly impacts the morphology and photocatalytic performance. The morphology of the catalysts, especially their porosity and uniformity, plays a pivotal role in determining their photocatalytic efficiency. The exceptional photodegradation efficiency of ZnO nanoparticles prepared with agar can be attributed to their small crystallite size, uniform distribution, and pronounced porosity, which provide an increased surface area and pore volume. The obtained results underscore the complex interplay between fuel sources, morphology, and photocatalytic activity, offering valuable insights for the development of efficient photocatalytic materials.

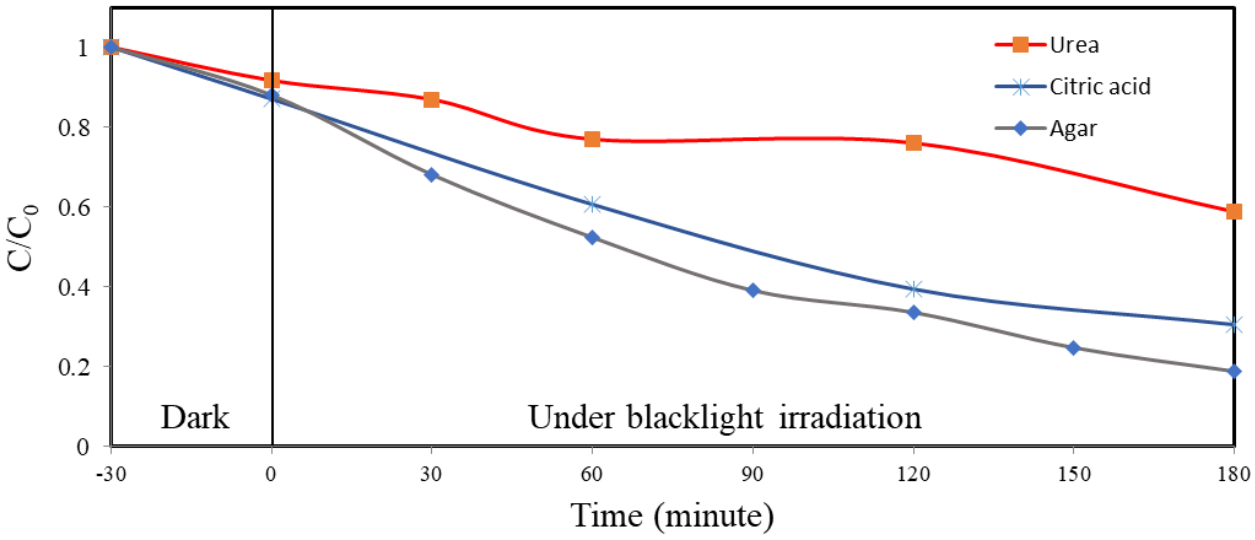

Figure 7. Photocatalytic degradation of MO dye by ZnO nanoparticles prepared with different fuels under blacklight irradiation for 180 minutes

4. Conclusion

ZnO nanoparticles were successfully synthesized by the combustion method using different fuels including agar, citric acid, and urea. The XRD patterns of all samples were consistent with hexagonal wurtzite structure. The crystallite size of ZnO nanoparticles changed for different fuels with minimum size obtained by using agar as a fuel. Furthermore, the ZnO nanoparticles prepared with agar as a fuel exhibit the porous and foamy microstructure and the highest specific surface area of 8.58 m^2/g due to the porous structure of the dried precursor, which serves as a template during the combustion process. The use of agar as a fuel lead to a significantly higher photodegradation efficiency of the ZnO nanoparticles, as compared to other fuels. The photodegradation efficiency of ZnO nanoparticles prepared with agar reached 81% after 180 minutes under blacklight irradiation.

Acknowledgements

This work was supported by Photocatalysts for Clean Environment and Energy Research Unit, Faculty of Science, Chulalongkorn University.

References

1. K.M. Lee, C. W. L., K.S. Ngai, J.C., Recent developments of zinc oxide based photocatalyst in water treatment technology: a review. *Water Res.* **2016,** *88*, 428-448.
2. C.B. Ong, L. Y. N., A.W. Mohammad A review of ZnO nanoparticles as solar photocatalysts: synthesis, mechanisms and applications. *Renew. Sustain. Energy Rev.* **2018,** *81*, 536–551.
3. Rania E. Adam a, G. P. b., Magnus Willander a, Omer Nur a, Synthesis of ZnO nanoparticles by co-precipitation method for solar driven photodegradation of Congo red dye at different pH. *Photonics Nanostructures: Fundam. Appl.* **2018,** *32*, 11-18.
4. J.N. Hasnidawani, H. N. A., H. Norita, N.N. Bonnia, S. Ratim, E.S. Ali, Synthesis of ZnO Nanostructures Using Sol-Gel Method. *Procedia Chem.* **2016,** *Volume 19*, 211-216.
5. Gerbreders, V.; Krasovska, M.; Sledevskis, E.; Gerbreders, A.; Mihailova, I.; Tamanis, E.; Ogurcovs, A., Hydrothermal synthesis of ZnO nanostructures with controllable morphology change. *CrystEngComm* **2020,** *22* (8), 1346-1358.
6. Abebe, B.; Tsegaye, D.; Sori, C.; Renuka Prasad, R. C. k.; Murthy, H. C. A., Cu/CuO-Doped ZnO Nanocomposites via Solution Combustion Synthesis for Catalytic 4-Nitrophenol Reduction. *ACS Omega* **2023,** *8* (10), 9597-9606.
7. Lutukurthi, D. N. V. V. K.; Dutta, S.; Behara, D. K., Effect of ignition temperature and fuel amount on photocatalytic activity of solution combustion synthesized ZnO. *Ceram. Int.* **2020,** *46* (14), 22419-22428.
8. H. Fathi, S. M. M., S. Alamolhoda, H. Parnianfar Effect of fuel type on the microstructure and magnetic properties of solution combusted Fe3O4 powders,. *Ceram. Int. 43* **2017,** *7448–7453*.
9. H. Vahdat Vasei, S. M. M., V. Kamrani Pouya, Photocatalytic activity of solution combustion synthesized ZnO powders by using a mixture of DTAB and citric acid fuels. *J. Phys. Chem. Solids* **2021,** *151* (0022-3697).
10. García Pérez, U. M.; Sepúlveda-Guzmán, S.; Martínez-de la Cruz, A.; Ortiz Méndez, U., Photocatalytic activity of $BiVO_4$ nanospheres obtained by solution combustion synthesis using sodium carboxymethylcellulose. *J. Mol. Catal. A Chem.* **2011,** *335* (1), 169-175.
11. X.M. Fan, J. S. L., Z.X. Guo, H.J. Lu Applied Surface Science Microstructure and photoluminescence properties of ZnO thin films grown by PLD on Si(1 1 1) substrates. *Appl. Surf. Sci.* **2005,** *239*, 176–181.
12. S. Ekambaram, Y. I., A. Kudo, Combustion synthesis and photocatalytic properties of transition metal-incorporated ZnO,. *J. Alloys Compd.* **2007,** *433*, 237-240.

Purification of biomethanol synthesized from biogas by three stages distillation

Rujira Jitrwung[1], Kuntima Krekkeitsakul [2]*, Nattawee Treerananont[2], Hiran Jinda[2], Parinya Thongyindee[2], Sunisa Luadlai[3], and Boonsita Jantapoon[3]

[1]*Research and Development Group for Sustainable Development, Thailand Institute of Scientific and Technological Research (TISTR), Khlong Luang, Pathum thani 12120, Thailand*
[2]*Expert Center of Innovative Clean Energy and Environment, Thailand Institute of Scientific and Technological Research (TISTR), Khlong Luang, Pathum thani 12120, Thailand*
[3]*Department of Chemical Engineering, College of Engineering, Rangsit University, Lak Hok, Mueang Pathum Thani, Pathum thani 12120, Thailand*

**E-mail: kuntima22@gmail.com*

Abstract:

Crude biomethanol obtained by varied ratio of CH_4 and CO_2 (30/70, 50/50, 70/30) was methanol purity 95.98, 96.50 and 96.95 percent, contaminants (ppm) of water 50,500, 48,150 and 44,870, ethanol 2,000, 1,882 and 1,676, acetone 260, 183 and 120 and isopropanol 115, 103 and 80 respectively. Simulation crude biomethanol contained in ppm unit of water 58,919, ethanol 1,098, acetone 100 and Isopropanol 635 was representative for the purification study. A 2-meter height of sieve column was tested in 5 steps that showed the decreasing of amount of water (ppm). The water impurities were dropped 5 times at the first step, and slightly decreasing then stable at the last step. A 2-meter packed column filled with glass cylindrical Raschig Ring was compared feeding methanol contaminated with 12,403 ppm of water, the result showed water (ppm) and reduction (%) 1,496 (12.06%), 5,600 (45.15 %) and 7,200 (58.05%). The packed column worked the best in low water contaminant. As a result, the 3 stages distillation combined column with the 2-meter sieve (1^{st}) and the 2-meter packed column (2^{nd}) and the 2-meter packed column (3^{rd}) was able to reduce contaminants (ppm) of water, ethanol, acetone and isopropanol 476 (58,919), 43(1,098), 30 (100) and 0 (635) respectively.

1. Introduction

Methanol is known as a major chemical in industrial for producing chemicals such as formaldehyde, acetic acid, MTBE, DME, biodiesel, solvent, and gasoline blending. It is produced from steaming of coal and natural gas. Methanol demand is growing every year as shown in Figure 1. The demand of Global methanol is rising in each year by 79.2 MMT (2015), 104.3 MMT (2020), 145.2 MMT (2025) and it is forecasted over 363.4 MMT (2035).[1] Methanol in Thailand is 100% importing and growing in the same as the Global demand and evaluated around 1% of the global methanol usage such as 0.78 MMT (2016), 0.88 MMT (2018), 0.81 MMT (2020) and 1.7 MMT (predicted 2036) (Hazardous Substance Report, 2021).

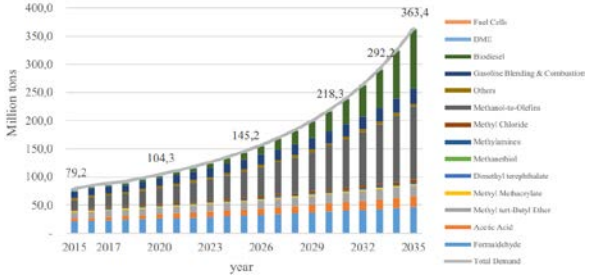

Figure 1. World methanol demand (million tons) according to industry users, 2015-2019 (realization) and 2020-2035 (forecast).

However, a global trend of bio circular and green economy (BCG), Substitution of commercial methanol by biomethanol are researched. Biomethanol can be obtained from biomass and renewable sources such as biogas.

Normally, Biogas comprise of 50-55% of Methane (CH_4) and 45-50% of Carbon dioxide (CO_2) and contained small amount of water and contaminated with hydrogen sulfide (H_2S).[2] According to methane is an important composition in biogas, it is interested for using biogas as a raw material for producing biomethanol. As a result, substituting commercial methanol by biomethanol is the utilization of biogas for methanol direct using or its downstream will be reducing petroleum dependence. Transforming of biogas is not only solving waste treatment of agricultural sector but also adding multi purposes of economic of biogas industry. Comparison of commercial methanol and biomethanol obtained from biogas is drawn as shown in Figure 2.

Using biogas as raw material for methanol production, it was required H_2S treatment before sending biogas combined with steam in reforming process. CO_2 and CH_4 is reacted with water under steam reforming and dry reforming by following equation (1) and (2) respectively. However, in the reforming stage, there are two major side reactions: 1) CO with H_2O shifting to CO_2 and H_2 called Water Gas Shift (WGS) by equation (3) and 2) CO_2 with H_2 reversing to CO and H_2O called Reverse Water Gas Shift (RWGS) by equation (4). These two side reactions would affect to varied ratios of syngas containing CO, CO_2 and H_2. The syngas is an intermediate for producing methanol. However, the appropriate ratio of $CO/CO_2/H_2$ is significant to obtain high yield methanol.[3] There are two principle of methanol synthesis by hydrogenation on CO or CO_2 shown in equation (5) and (6) respectively. The first concept, CO is the primary reactant to produce methanol which is reinforced by several researchers: Natta et al.,[4] and Chen et al.[5] They proposed that hydrogenation on CO was better than CO_2 and obtained more purity methanol contaminated with small amount of water. The last concept is stressed on CO_2 hydrogenation for methanol synthesis which is advocated by several researchers: Liu et al.,[6] Chinchen et al.,[7] Takagawa and Ohsugi[8], McNeil et al.,[9] Rozovskii et al.,[10] Lim et al.[11], and Fujitani et al,[12]

However, in the methanol synthesis process, not only water is major contaminant, but also it can transform to other contaminants. Methanol is continuously associated itself to an intermediate as DME (Dimethyl Ether) (7) then it is generated ethanol (8), acetone (9) and Isopropanol (10).

Steam Reforming (SR)

$CH_4 + H_2O \rightarrow CO + 3H_2$ ΔH= 206.0 kJ/mol (1)

Dry Reforming (DR)

$CH_4 + CO_2 \rightarrow 2CO + 2H_2$ ΔH= 274.7 kJ/mol (2)

Water Gas Shift (WGS)

$CO + H_2O \leftrightharpoons CO_2 + H_2$ ΔH= -41.12 kJ/mol (3)

Reverse Water Gas Shift (RWGS)

$CO_2 + H_2 \leftrightharpoons CO + H_2O$ ΔH= 41.12 kJ/mol (4)

Methanol Synthesis (MS)

$CO + 2H_2 \leftrightharpoons CH_3OH$ ΔH=-90.55 kJ/mol (5)

$CO_2+3H_2 \leftrightharpoons CH_3OH+H_2O$ ΔH =- 49.43 kJ/mol (6)

By products formation

DME formation

$CH_3OH \leftrightharpoons CH_3OCH_3 + H_2O$ (7)

Ethanol formation

$CH_3OCH_3 \leftrightharpoons CH_3CH_2OH$ (8)

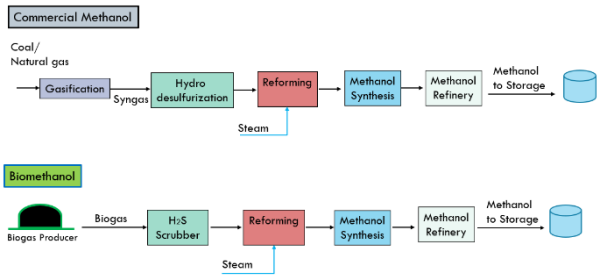

Acetone formation

$CH_3OCH_3+CH_3OH \leftrightharpoons CH_3COCH_3+2H_2O$ (9)

Isopropanol formation

$CH_3OCH_3+CH_3OH \leftrightharpoons CH_3CHCH_3OH+H_2O$ (10)

Figure 2. Comparison process of methanol production by commercial methanol and biomethanol from biogas.

Crude methanol produced by catalytic synthesis usually contaminates with water and small amounts of organic compounds such as ethanol, acetone and isopropanol. Hence, the impurities would be removed by a refinery technique to obtain pure methanol which has normal specification as anhydrous methanol which is contained minimum 99.85% methanol and accepted contaminants with minimum 1,000 ppm of water, 50 ppm of ethanol, 30 ppm of Isopropanol and 30 ppm of acetone. The components of feed items are different in boiling points which water (100 °C), Isopropanol (82.3 °C), ethanol (78.3 °C), methanol (64.7 °C) and acetone (56 °C). The relationship of ethanol and water solution is azeotrope, but methanol and water are not. However, ethanol and other alcohols are well soluble in methanol. This situation is related to the process of anhydrous ethanol which have been used/suggested. These include: (i) chemical dehydration process, (ii) dehydration by vacuum distillation process, (iii) azeotropic distillation process, (iv) extractive distillation processes, (v) membrane processes, (vi) adsorption processes and (vii) diffusion distillation process. These processes of manufacturing anhydrous ethanol can be applied for producing anhydrous methanol.[13] However, distillation is preferred because it is practical and low-cost maintenance comparing with others. Delzenne A. (1958) reported vapor liquid equilibrium data for ternary system methanol-ethanol-water by studying varying mole fractions and temperatures range 60 °C to 80 °C. [14] Roger Hardiman Scott and et.al. patented a process for purifying methanol by distillation[15] by using three columns distillation in series with feed composition of 83%methanol,

17% water and 660 ppm ethanol, the product was qualified 100% methanol, 0% water and 0.001 ppm ethanol. The purpose of this article is to give guidance for transforming biogas to biomethanol and refinery its which contained small quantities of impurities: water, ethanol, isopropanol and acetone by combination technique of sieve distillation and packed bed with Raschig Ring distillation.

2. Materials and Methods

2.1 Raw Materials

2.1.1 Biogas obtained from RE Power Company.

2.1.2 Simulation mixed CH_4 and CO_2 gas obtained from Thai Special Gas Co., Ltd.

2.1.3 Methanol (analytical grade) obtained from RCI Lab scan

2.1.4 Ethanol (analytical grade) obtained from RCI Lab scan

2.1.5 Deionized water obtained from RCI Lab scan

2.1.6 Isopropanol (analytical grade) obtained from RCI Lab scan

2.1.7 Acetone (analytical grade) obtained from RCI Lab scan

2.1.8 Catalyst A. (Ni/Al_2O_3) obtained from Hutong Global Co., Ltd.

2.1.9 Catalyst B. ($Cu/ZnO/Al_2O_3$) obtained Xi' an Sunward Aeromat Co.,ltd.

2.2 Apparatus

2.2.1 The 2 steps of fixed bed reactors containing 5 kg of Catalyst A then Catalyst B used for methanol synthesis supplied by Owner Food Machinery Co., Ltd. as shown in Figure 3.

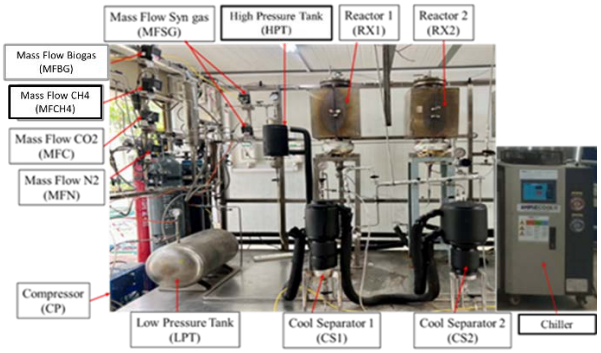

Figure 3. The scheme of two steps Methanol Synthesis from biogas.

2.2.2 The gas product amount was measured by a gas rotameter.

2.2.3 The gas composition was measured by gas analyzer obtained from MRU model Vario luxx and Gas chromatography obtained from Agilent model 7890 B.

2.2.4 The liquid product was measured by weighting balance.

2.2.5 Water content was measured by Karl Fischer Titrator from Metrohm Siam Co.,Ltd.

2.2.6 The liquid composition was measured by Gas chromatography obtained from Agilent 7890B

2.2.7 The 3 columns distillation in series contained sieve, 10 cm .X 12 cm .Raschig Ring and 10 cm .X 12 cm .Raschig Ring under copy right TISTR as shown in Figure 4.

Figure 4. The 3 Columns distillation process.

2.3 Experimental Conditions

2.3.1 Methanol synthesis: Variation ratio of mixed CH_4/CO_2 gas by 30/70, 50/50 and 70/30 were studied for Methanol Synthesis (MS) with two main reactions: 1) Reforming reaction is starting by total gas feed 5 kg/day with water 1 kg/day under condition of 5 kg of catalyst A, 600 °C and 1 to 2 barg. Products was syngas composing CO, H_2 and CO_2. The syngas is compressed by a compressor and stored at high pressure tank with 40 barg for feeding to the next step. 2) Methanol synthesis (MS) reaction is operated by the syngas from the first step under condition of 5 kg of catalyst B, 200 °C and 40 barg.

2.3.2 Methanol refinery: Feed composition contained methanol 95% and contaminants with 58,919 ppm of water, 1,098 ppm of ethanol, 635 ppm of isopropanol and 100 ppm of acetone was prepared and used a representative of crude methanol.

2.3.2.1 Number of steps of distillation was tested by 2-meter sieve column.

2.3.2.2 Comparison of sieve distillation was tested by 2-meter and 3-meter sieve column. Comparison of sieve distillation and packed be with Raschig Ring distillation was tested in 2-meter column.

2.3.2.3 Combination of sieve distillation and Raschig Ring distillation was tested with 2-meter column.

3. Results & Discussion

3.1 Methanol synthesis experiments

Biogas is normally composed of 50% CH_4 and 50% CO_2. Therefore, this research simulated mixed ratio of CH_4 and CO_2 by varying three concentrations of CH_4 in high (70%), medium (50%) and low (30%) biogas component in three compositions to cover all feasible ratio of biogas production. Three ratios of CH_4 mixed with CO_2 are processed in the methanol synthesis process by using TISTR technology. The qualities of methanol products were shown in Table 1.

Methanol synthesis by 2 steps process: Reforming and Methanol synthesis. The simulated mixed ratios of CH_4/CO_2 30/70, 50/50, 70/30 was fed to the methanol synthesis process. The raw methanol was generated by 2.45, 4.35, and 5.60 kg/day contained 95.98, 96.50, and 96.95% of methanol and contaminated with water 50,500, 48,150 and 44,870 ppm, ethanol 2,000, 1,882 and 1,676 ppm, acetone 260, 183, and 120 and isopropanol 115,103, and 80 ppm. It was found that increasing higher ratio of CH_4 resulting to higher quality of methanol and lower in all contaminants. However, all ratios yielded methanol qualities which were lower commercial methanol requirement shown in Table 1. Therefore, a refinery process was required to improve the methanol quality.

3.2 Methanol refinery experiments

3.2.1 Biomethanol refinery in 5 steps of 2-meter height by 7.5 cm. of diameter of sieve column.

A representative simulated biomethanol contained of 95% methanol and others in ppm unit of water 58,919, ethanol 1,098, acetone 100 and Isopropanol 635 was used for the purification study. A 2-meter height by 7.5 cm. of diameter of sieve column was tested in 5 steps that showed the decreasing of amount of water (ppm) from 58,919 to 12,403, 7200, 4,300, 2,700 and 2,600 and ethanol reduction (ppm) following with water decreasing from 977 to 694, 599, 531, 516 and 384 shown in Table 2. The water impurities were approximately dropped 5 times at the first step, and slightly decreasing then stable at the last step, but ethanol was slightly decreased step by step as shown in Figure 5. This result can be summarized that the number of steps would not solve for removing water and ethanol contaminated which are not met with the commercial methanol specification except acetone and isopropanol.

Therefore, the first stage of distillation by 2-meter height of sieve column is appropriate and the product composition from the first stage will be used as the feed in the second stage distillation in section 3.2.2.

Table 2. Contaminants in distillate (ppm).

Stage	H_2O	EtOH	Acetone	Iso propanol
0	58.919	977	15	0
1	12.403	694	13	0
2	7,200	599	14	0
3	4,300	531	16	0
4	2,700	516	19	0
5	2,600	384	22	0

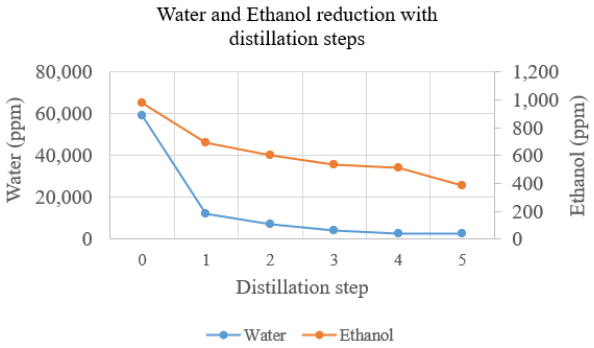

Figure 5. The reduction of impurities from 5 steps distillation.

3.2.2 Biomethanol refinery in 2 steps of 2-meter height by 7.5 cm. of diameter with Raschig ring in packed column.

A representative simulated biomethanol followed the product composition from the first stage contained of water 12,403 ppm, ethanol 694 ppm, acetone 13 ppm, and isopropanol 0 ppm was used as the feed to compare the distillation efficiency of different types of distillations: Sieve 2 meter-height (S_2M), Sieve 3 meter-height (S_3M) and Raschig Ring 2 meter-height (RR_2M).

Figure 6. showed the distillation product obtained from the stage 2 by comparing S_2M, S_3M and RR_3M. Increasing Column height from 2 M to 3M in sieve distillation improved water contaminant from 7,200 to 5,600 ppm and RR_2M yielded the lowest water contaminant as 1,496 ppm. Applying packed bed column by Raschig Ring reduced water contaminant over 8 times but increasing column height from 2 to 3 meter resulting from 1.72 to 2.2 times.

Table 1. Methanol synthesis and its quality by varying CH_4 ratio: 30, 50, and 70 % (v/v)

CH_4 ratio	MeOH (% wt.)	Water (ppm)	Ethanol (ppm)	Acetone (ppm)	Isopropanol (ppm)
30	95.98	50,500	2,000	260	115
50	96.50	48,150	1,882	183	103
70	96.95	44,870	1,676	120	80
Specification	99.95	< 1,000	< 50	< 30	< 30

As a result, replacing sieve column in the 2nd stage with Raschig Ring would be the better solution to deal with low level contaminations of water and ethanol and the contaminants were closed value of commercial requirement. So, the third stage of distillation would be added by Raschig Ring distillation to expect the value of contaminants for passing the commercial methanol specification.

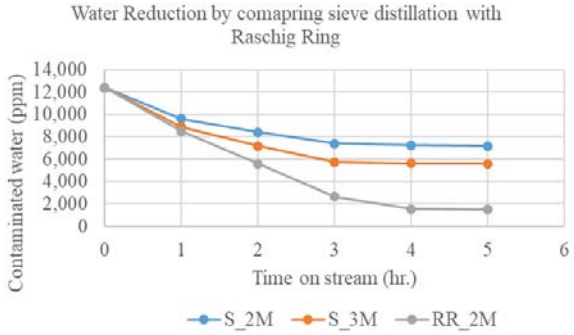

Figure 6. Distillation product obtained from the stage 2 by comparing S_2M, S_3M and RR_3M.

3.2.3 Biomethanol refinery in 3 steps of the 1st 2-meter height by 7.5 cm. of diameter with 4 mm. sieve column, the 2nd Raschig ring in packed column and the 3rd Raschig ring in packed column.

Three distillation columns are connected in series to minimize contaminants as shown in Figure 7. The process was started by feeding 20 ml/min of simulation methanol contained water 58,919, ethanol 1,098, Isopropanol 635 and acetone 100 ppm at the bottom of the first column, the first top product coming out and obtaining nearly steady and continuous feed to the second column, the second top product coming out until obtaining closely steady then sending to the third column, the product of the third column was measured until steady. All column were control the top column temperature at 64 °C. It was found that the first stage distillation taking 6 hours for steady and minimized contaminants of water 11,403, ethanol 694, isopropanol 42 and acetone 30 ppm. The second column consumed 4 hours to reach the unchanged value of contaminants of water 1,550, ethanol 150, isopropanol 30 and acetone 30 ppm. Finally, the third column spent 6 hours to reach the required commercial value by minimizing water 476, ethanol 43, isopropanol 0 and acetone 30 ppm. Isopropanol was completely removed at the third stage of distillation and acetone was unchanged after obtaining value 30 ppm. Water and ethanol were the primary contaminants which were relationship by hydrogen bond to methanol resulting that was difficult to remove all contaminants from methanol. Figure 8. showed the reduction of water and ethanol in 3 stages distillation. The data showed when lower amount of water and ethanol were diluted in methanol, it was hardly to remove theses contaminants.

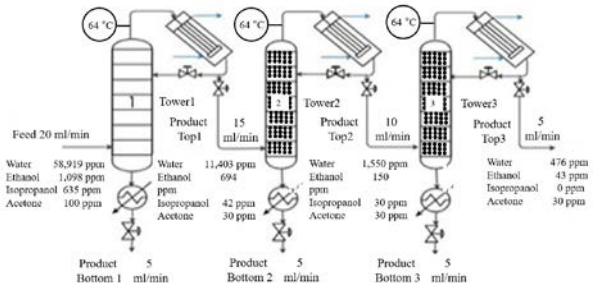

Figure 7. The composition of top products by series of the 1st, 2nd and 3rd column.

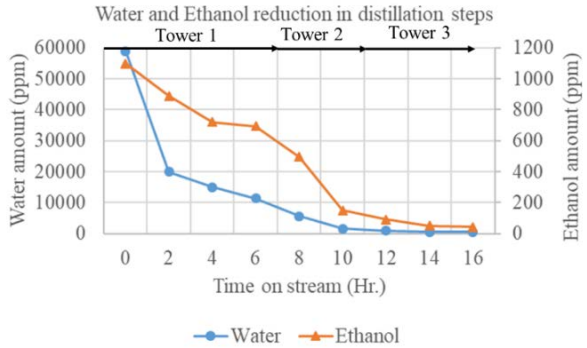

Figure 8. The reduction of water and ethanol in 3 stages distillation.

4. Conclusions

Crude methanol was produced by two steps catalytic synthesis of variation ratio of biogas which was contained CO_2 and CH_4. The more methane ratio was introduced the more quality of methanol and lower contaminants. Crude methanol

Table 3. The impurities in product (ppm).

Product Location	Time (hr.)	Water	Ethanol	Iso propanol	Acetone
Feed Tower 1	0	58,919	1,098	635	100
Product T1	2	20,000	890	45	30
Product T1	4	15,000	720	43	30
Product T1	6	11,403	694	42	30
Product T2	8	5,600	495	38	30
Product T2	10	1,550	150	30	30
Product T3	12	968	90	0	28
Product T3	14	500	50	0	29
Product T3	16	476	43	0	30
Commercial Methanol		Max 1,000	Max 50	Max 30	Max 30

contained maximum value of contamination of water 58,919 ethanol 1,098, isopropanol 635 and acetone 100 ppm was a representative for studying the refinery process. The three stages distillation by optimizing each stage with 2-meter columns height with sieve column, Raschig Ring and Raschig Ring respectively was fitted to remove all contaminants in the requirement level by continuous feed and maintained all top column temperature at 64 °C. The refinery product was obtained methanol purity over 99.85% with contaminants of water 476 ppm, ethanol 43 ppm and acetone 30 ppm without isopropanol.

Acknowledgements

The authors would like to acknowledge the Thailand Science Research and Innovation for approval and financial support and RE Power CO., Ltd. for support biogas data for this research.

References

1. Suseno, T.; Umar, D F. Prospect of coal-based methanol market in Indonesia International Seminar on Mineral and Coal Technology. *IOP Conf. Series: Earth and Environmental Science*. **2021**, *882*, 1-11.
2. Chaiprasert P. Biogas Production from Agricultural Wastes in Thailand. *JGSEE*. **2011**, 63-65.
3. Jitrwung, R.; Krekkeitsakul, K.; Kumpidet, C.; Tepkeaw, J.; Jaikengdee, K.; Wannajampa, A.; Pathaveekongka, W. Restored CO_2 from flue gas and utilization by converting to methanol by 3 step processes: Steam reforming, Reverse water gas shift, and Hydrogenation. *Int. j. sci. res.* **2022** ,18-23. (Conference Proceedings, Bangkok Thailand March 03-04, 2022).
4. Natta, G. Direct Catalytic Synthesis of Higher Alcohols from CO and H_2. *J. Catal.* **1955**, *349*, 131-114.
5. Chen, K.; Yu, J.; Liu, B. Si. C. Simple strategy synthesizing stable CuZnO/SiO_2 methanol synthesis catalyst. *J. Catal.* **2019**,*372*,163-173.
6. Liu, G.; Willcox, D.; Garland, M.; Kung, H.H. The role of CO_2 in methanol synthesis on Cu Zn oxide: An isotope labeling study. *J. Catal.* **1985**, *96*, 251-260.
7. Chinchen, G.C. Mechanism of methanol synthesis from CO_2/CO/H_2 mixtures over copper/zinc oxide/alumina catalysts: use of 14C-labelled reactants. *Appl. Catal.* **1987**, *30*, 333-338.
8. Takagawa, M.; Ohsugi, M. Study on reaction rates for methanol synthesis from carbon monoxide, carbon dioxide, and hydrogen. *J. Catal.* **1987**, *107*, 161-172.
9. McNeil, M.A.; Schack, C.J.; Rinker, R.G. Methanol synthesis from hydrogen, carbon monoxide and carbon dioxide over a CuO/ZnO/Al_2O_3 catalyst: II Development of a phenomenological rate expression. *Appl. Catal.* **1989**, *50*, 265-285.
10. Rozovskii, A.Y.; Lin, G.I. Fundamentals of Methanol Synthesis and Decomposition. *Top Catal.* **2003**, *22*, 137-150.
11. Lim, H.W.; Park, M.J.; Kang, S.H.; Chae, H.J.; Bae, J.W.; Jun, K.W. Modeling of the Kinetics for Methanol Synthesis using Cu/ZnO/Al_2O_3/ZrO_2 Catalyst: Influence of Carbon Dioxide during Hydrogenation. *Ind. Eng. Chem. Res*. **2009**, *48*, 10448-10455.
12. Fujitani, T.; Nakamura, I.; Watanabe, T.; Uchijma, T.; Nakamura, J. Methanol synthesis by hydrogenation of CO_2 over a Zn deposited Cu (111): formate intermediate. *Appl. Surf. Sci.* **1997**, *121-122*, 583-586.
13. Santosh, K.; Neetu, S.; Ram, P. Anhydrous ethanol: A renewable source of energy. *Renew. Sust. Energ. Rev*. **2010**, *14*, 1830-1844.
14. Delzenne, A. Vapor Liquid Equilibrim Data for Ternary System Methanol-Ethanol-Water. *Ind. Eng. Chem. Chem. Eng. Data Series.* **1958**, *3*, 224–230 (Publication October 1, 1958).
15. Roger H.S. Process for purifying methanol by distillation. Imperial Chemical Industries Limited, London, England Filed. **1975**.

High performance photodegradation of methyl orange with AgCl/Ag - impregnated glutaraldehyde-crosslinked alginate beads under sunlight irradiation

Katananipa Wanchai*and Chaiwat Aiamsaard

Department of Chemistry, Faculty of Science and Technology, Phranakhon Si Ayutthaya Rajabhat University, Phranakhon Si Ayutthaya, 13000, Thailand

**E-mail:Katnanipa@aru.ac.th*

Abstract:

In this paper, an AgCl/Ag photocatalyst was synthesized by a simple precipitation method, follow by impregnation with glutaraldehyde-crosslinked alginate to form beads (AGAB). The synthesized catalysts were characterized by XRD, FTIR and SEM-EDX. Their adsorption and photocatalytic activities were also investigated by the photodegradation of a methyl orange (MO) solution under sunlight irradiation. The results showed that AGAB exhibited excellent performance for the degradation of MO (99.4%) in 25 min, with activity higher than AgCl/Ag. It was shown that glutaraldehyde-crosslinked alginate could improve the photocatalytic activity by enabling more rapid and increased adsorption of MO. As a result, the photodegradation of AGAB increased. The kinetic analysis of AgCl/Ag and AGAB could be fitted with a first-order kinetic model. Moreover, The AGAB can maintain full photodegradation activity for at least four cycles. Consequently, AGAB is a promising material for the photocatalytic of dyes and similar organic contaminants in environmental pollution cleanup.

1. Introduction

Photocatalytic technology has been considered an excellent green environment and eco-friendly technology for hazardous pollutants, which can accumulate in living organisms and result in negative effects such as carcinogenicity. Titania (TiO_2) has been extensively exploited and investigated as a photocatalyst for the degradation of organic waste due to its nontoxicity, chemical stability and inexpensive. Unfortunately, TiO_2 can only be photoexcited by UV light, as a result, a tremendous effort has been made to explore visible light-driven photocatalysts.[1,2,3] Recently, many researchers have reported that AgCl/Ag showed excellent photocatalytic activity under visible light. Due to the surface plasmon resonance (SPR) of AgCl which is mainly caused by nanometallic Ag under light irradiation and is widely used for enhancing the photocatalytic activity.[4,5,6] However, nanoparticles of AgCl/Ag are easy to aggregate which always causes decreased photocatalytic activity.[7] In addition, photocatalysts used to degrade organic wastes are often used in suspended form, which difficult to separate the catalyst after the reaction. Therefore, another advantage of a supported catalyst is easy separation after the process and catalyst recycling can be investigated. Alginate salt is a natural polymer. It is cheap, non-toxic, biodegradable and forms stable hydrogel, which can be used as catalyst support. The most abundant function group in alginate polymer is the carboxylic group.[8,9,10] In the presence of divalent cations, it can form stable hydrogels. However, as divalent cations are removed by chelating agent or high concentration of ions such as Na^+ or Mg^{2+}, the crosslinking in gel decreases and the gel are destabilized.[11] Some cross-linking agent such as glutaraldehyde is widely used to bind alginate polymer to enhance gel stability. The feasibility of using alginate as the support photocatalyst in degradation organic wastes has been reported. A promising strategy is to couple the adsorption with a photocatalytic technique such as Sakar et al.[12] and Liu et al.[11] used glutaraldehyde-crosslinked alginate-supported TiO_2 nanoparticle for the degradation of pharmaceutical waste and Cr(VI), Zhao et al.[13] has revealed that a composite of TiO_2-calcium alginate beads has high removal efficiency of MO and Mohamed et al.[14] synthesized grafted sodium alginate/ZnO/graphene oxide composite for coupled adsorption photocatalytic degradation of crystal violet.

In this study, we want to demonstrate that AgCl/Ag can be effectively immobilized in glutaraldehyde-crosslinked alginate beads (AGAB) for photocatalytic degradation MO under sunlight irradiation. The effects of the initial concentration of MO, catalyst amount, kinetic of degradation and recyclability of AGAB were investigated.

2. Materials and Methods

2.1 Materials

The main chemicals used were: Silver nitrate ($AgNO_3$, BDH), sodium hydrogen carbonate ($NaHCO_3$, KEMAUS), ethylene glycol

(EG, Q Rëc), sodium alginate (Sigma-Aldrich), calcium chloride dihydrate ($CaCl_2 \cdot 2H_2O$, KEMAUS), glutaraldehyde (PanReac Applichem) and methyl orange (MO, Riedel-de Haen).

2.2 Preparation of photocatalytic

The AgCl/Ag was prepared using one pot precipitation method.[15] Typically, 20 mL of 0.1 M $NaHCO_3$ was dropwise into 20 mL of 0.1 M $AgNO_3$ under magnetic stirring. The clear aqueous solution gradually became milky white of Ag_2CO_3 after stirring for 20 min. Subsequently, the suspension was incubated at 60°C for 5 min, 0.5 mL of ethylene glycol was added and further incubated for another 5 min. After that, 2 mL of 0.1 M HCl was added with stirring for 30 min. The color of the suspension was observed to change into dark gray of AgCl/Ag. The precipitate was collected by filtration, washed with deionized water and dried at 60°C in oven.

The AGAB was prepared by entrapping AgCl/Ag in calcium alginate beads. About 100 mL of the precursor solution was prepared by mixing 1.5 g of sodium alginate and 1.5 g of AgCl/Ag powder in DI water and stirring until a homogenous solution was achieved. The mixture was injected dropwise into 400 mL of 4% (w/v) $CaCl_2$ using a syringe to form AgCl/Ag alginate beads and then cured in $CaCl_2$ solution for 4 h. After that the beads were washed with DI water several times. The AgCl/Ag alginate beads were cross-linked with 1%(v/v) glutaraldehyde and 0.1 M HCl at 40°C under magnetic stirring for 4 h. After that, AGAB was occurred, washed with DI water several times and kept in 4% $CaCl_2$ solution. The AGAB was stored at room temperature for use. The blank beads (glutaraldehyde-crosslinked alginate beads, GAB) were prepared by the same method without AgCl/Ag addition.

The crystal structure of the photocatalyst were examined by X-ray diffraction (XRD) patterns using a Bruker D8 Discover diffractometer. The patterns were collected using CuK_α radiation at 40 kV and 30 mA. Fourier transform infrared (FT-IR) spectra were recorded on FT-IR spectroscopy (Perkin Elmer spectrum one), using KBr pellets in the range of 4000–400 cm^{-1}. A Scanning electron microscope (SEM; JEOL JSM-5410LV) coupled with EDX was used to analyze the microstructure of the materials.

2.3 Photocatalytic activity

The batch photocatalytic experiment was performed in 200 mL of methyl orange (MO) under sunlight irradiation. 10 g of wet AGAB (10 g of AGAB contained 0.279 g AgCl/Ag) were introduced into 10 mg/L MO solution. The mixture was stirred in the dark for 30 min to attain adsorption-desorption equilibrium between the catalyst and dye. The mixture was then irradiated under sunlight in sunny condition, May- June 2022 between 11.00 am and 14.00 pm. At certain time intervals during both the dark adsorption and the light irradiation processes, 3 mL of the reaction solution was collected to remove the photocatalyst for analysis. The initial concentration (C_0) and the concentration (C_t) of MO at different irradiation times were determined by measuring the absorbance of the solutions at 464 nm with UV-vis spectroscopy (UNICO^{R}1205).

The photodegradation efficiency was calculated by the following formula:

$$\% \text{ degradation of MO} = ((C_0-C_t)/C_0) \times 100$$

All experiments in this paper had been repeated two times and average values of data were used.

3. Results & Discussion

3.1 Characterization of photocatalyst

The structure of AgCl/Ag and AGAB were characterized by XRD. As shown in Figure 1, the peaks at 2θ of 27.76°, 32.28°, 46.24°, 54.84°, 67.52°, 74.56° and 76.72° could be indexed to (111), (200), (311), (222), (400), (331) and (420) planes of cubic phase AgCl (JCPDS No. 31-1238), suggesting that AgCl was contained in all catalyst. Furthermore, the weak diffraction peaks at 2θ of 38.12° and 44.28° could be found, which is ascribed to the cubic phase of Ag (JCPDS No. 65-2871).[4,15,16,17] This result indicated that AgCl had transformed to Ag and content in these two catalysts is rather low.

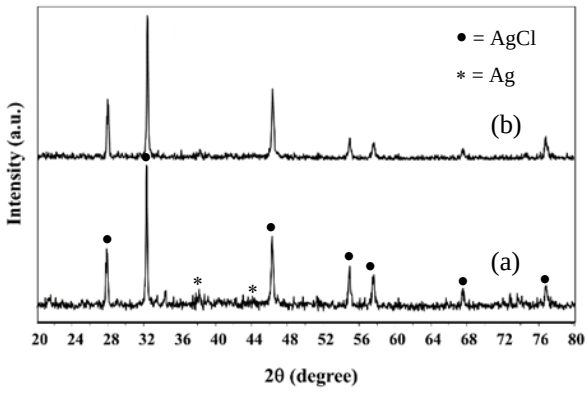

Figure 1. The XRD pattern of (a) AgCl/Ag powder and (b) AGAB.

The FTIR spectra of GAB and AGAB (Figure 2) show the characteristic peak of alginate at 3356 cm^{-1} (O-H), 1595 cm^{-1} (asymmetric stretching of COO^-), 1411 cm^{-1} (asymmetric stretching of COO^-) and 1022 cm^{-1} (C-O-C).[18,19,20]

The characteristic peak of glutaraldehyde at 1736 cm^{-1} (C=O), 1230 cm^{-1} (C-OH) and 1017 cm^{-1} (C-CH_2).[21] It can be observed that the glutaraldehyde actually crosslinks with alginate. Moreover, AGAB shows the spectrum peak at 800 cm^{-1} attributed to C-Cl group due to AgCl/Ag was impregnated with glutaraldehyde-crosslinked alginate.

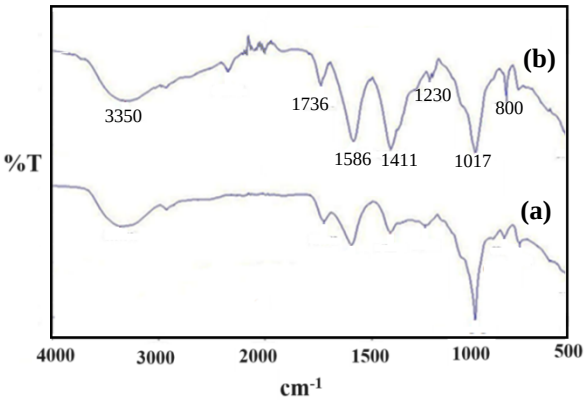

Figure 2. The FTIR spectra of (a) glutaraldehyde-crosslinked alginate beads and (b) AGAB.

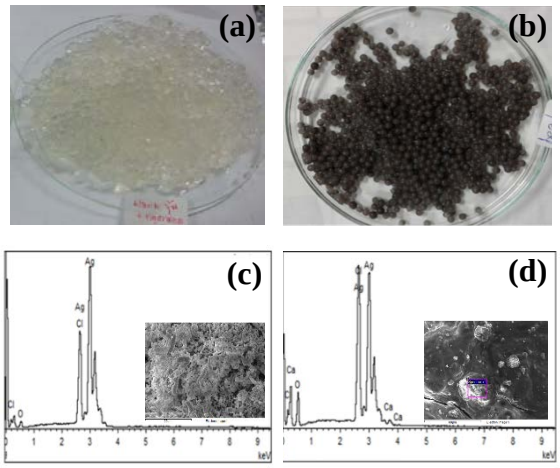

Figure 3. The digital photo of (a) wet GAB (blank beads) (b) wet AGAB (c) SEM/EDX of AgCl/Ag powder and (d) AGAB.

The digital photos of blank beads and AGAB are shown in Figure 3 (a) and (b). It was found that all of the beads presented a spherical shape, and the diameter of the wet beads was about 2 mm. The GAB appeared clear beads, whereas the AGAB was dark gray. Figure 3 (c) and (d) show the EDX spectrum of the AgCl/Ag and AGAB. It can be observed that the atomic ratio between Ag and Cl element in AgCl/Ag is approximately 1.56:1 while AGAB is 1.49:1. The value is higher than the theoretic stoichiometric atomic ratio in AgCl, 1:1, indicating that AgCl is reduced to Ag during the preparation process. The result suggests that the AgCl/Ag and AGAB consist of AgCl and Ag.

3.1 Photocatalytic activity

The photocatalytic activity of AgCl/Ag (1.39 g/L) and AGAB (50 g/L) was evaluated with the photodegradation of the MO under sunlight irradiation (Figure 4). It can be seen that the photodegradation of the AGAB was higher than AgCl/Ag. Furthermore, AGAB exhibited the highest photodegradation almost 100% in 25 min and the best adsorption performance. Whereas, the degradation of MO with AgCl/Ag, GAB and pure MO solution were only 79.2%, 4.2% and 1.2%, respectively. The photograph of MO solution (inset in Figure 4) shows that AGAB photocatalyst can degrade MO rapidly under sunlight irradiation. After 25 min, the MO solution became nearly colorless. The result shows that glutaraldehyde-crosslinked alginate could improve the photocatalytic activity by enabling more rapid and increased adsorption of MO solution.

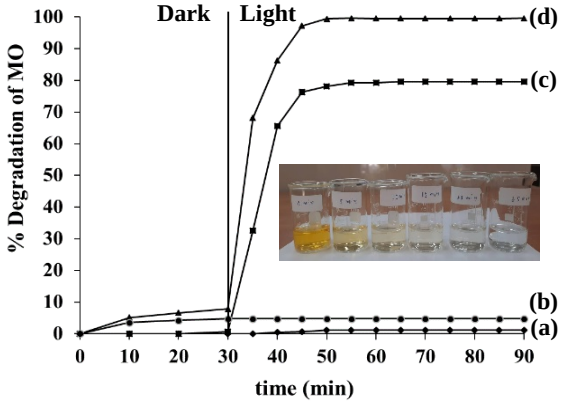

Figure 4. Comparison of photodegradation MO of (a) without catalyst (b) GAB (c) AgCl/Ag (d) AGAB and the color change photograph of MO solution (inset) in the presence of AGAB under sunlight irradiation.

The structure of AGAB and MO are shown in Figure 5.

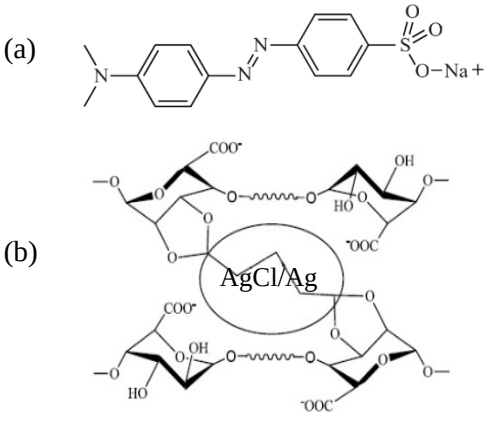

Figure 5. Structure of (a) MO and (b) AGAB.

To explain the photocatalytic activity of AGAB on MO under sunlight irradiation is proposed. In the first step, the MO diffused from the bulk solution to the external surface of the AGAB. It was postulated that the adsorption of MO onto the beads was controlled by ligand exchange between MO (anionic dye) and OH^- on the surface of the alginate beads, (equation 1).[22] While the second step, when a photon (sunlight irradiation) with sufficient energy on the AGAB surface, Ag on the surface of AgCl undergoes SPR, and hence, visible light gets absorbed on the surface of Ag. Due to the SPR effect, photogenerated electrons and holes (h^+), (equation 2). The electrons will be trapped by adsorbed O_2 to form superoxide radicals ($O_2^{\cdot-}$), (equation 3). Furthermore, holes were transferred to the surface of AgCl because of the high oxidation ability of the Cl^- to form Cl^0 atom (radicals), (equation 4). Both Cl^0 and $O_2^{\cdot-}$ are reactive radicals responsible for the degradation of MO. After MO is oxidized Cl^0 returns to Cl^- form again. The strong SPR effect of Ag led to the enhancement of the photocatalytic activity of AgCl/Ag.[1,8,15,17] The photodegradation mechanism of MO can be presented by the following mechanism.

$$\text{Alg-OH} + \text{MO} \rightarrow \text{Alg-MO} + OH^- \quad (1)$$
$$\text{AgCl/Ag} + h\upsilon \rightarrow h^+ + e^- \quad (2)$$
$$e^- + O_2 \rightarrow O_2^{\cdot-} \quad (3)$$
$$h^+ + Cl^- \rightarrow Cl^0 \quad (4)$$
$$O_2^{\cdot-} + \text{MO} \rightarrow \text{degradation products} \quad (5)$$
$$Cl^0 + \text{MO} \rightarrow Cl^- + \text{degradation products} \quad (6)$$

The degradation kinetic behavior of AGAB is displayed in Figure 6. The photodegradation of MO over AGAB can be well confirmed that the photodegradation of MO follows the Langmuir-Hinshelwood first-order kinetic model, as shown in the following equation: [3, 22, 23]

$$\ln \frac{C_0}{C_t} = kt$$

Where C_0 and C_t are the concentration of MO at initial time and t (irradiation time), respectively, k is rate constant. The kinetic plots of photodegradation of AGAB with different concentrations of MO.

Table 1. The kinetic parameters of the photodegradation of MO.

C_0 (mg/L)	k (min^{-1})	R^2
5	0.2836	0.9956
10	0.2209	0.9977
15	0.1367	0.9933
20	0.0916	0.9951
25	0.0446	0.9932

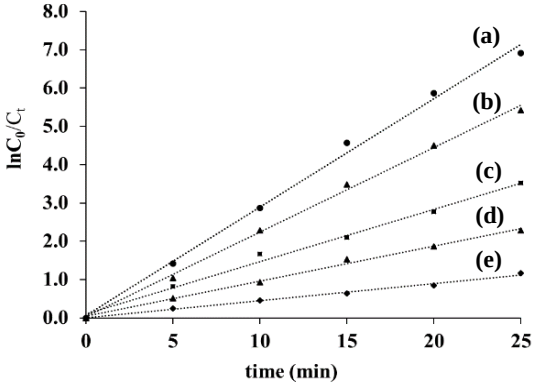

Figure 6. Plots of $\ln C_0/C_t$ vs irradiation time for the photodegradation of MO by AGAB at various initial concentration (a) 5 mg/L, (b) 10 mg/L, (c) 15 mg/L, (d) 20 mg/L and (e) 25 mg/L (50 g/L dosage of AGAB).

The relationship between $\ln C_0/C_t$ and t were all linear. Furthermore, the correlation coefficients (R^2) in Table 1 which show higher than 0.99, thus confirming the first-order kinetic model for the photodegradation of MO. The slope of the fitted regression lines showed the photodegradation rate constant of AGAB as 0.2836, 0.2209, 0.1367, 0.0916 and 9.0446 min^{-1}, respectively. The results show that the photodegradation efficiency decreases with increasing initial concentration of MO. The photodegradation efficiency of MO is lowered from 99.8% to 48.5% when the initial concentration increases from 5 to 25 mg/L. The adsorption of dye molecules on the catalyst surface influences the resulting active sites on the catalyst efficiency. Therefore, it is crucial to fix the concentration of dye molecules for adsorption.[24,25]

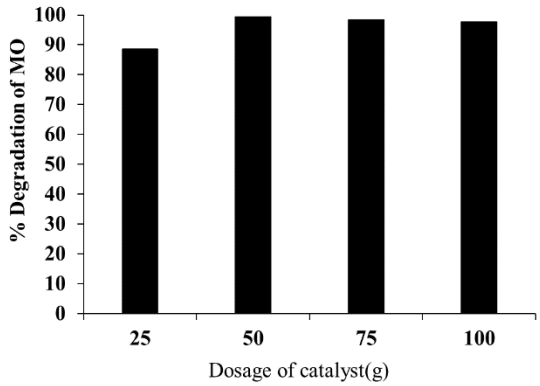

Figure 7. The effect of AGAB dosage on photodegradation activity of MO (10 mg/L) under sunlight irradiation for 30 min

Photocatalyst dosage is a key factor for evaluating photocatalytic efficiency.[26] The effect of photocatalyst dosage on the photodegradation of

MO was investigated in the range of 25 g/L to 100 g/L. As can be seen in Figure 7, the photocatalytic activity is increased with the increase in catalyst amount, due to the increase in surface area which multiplies the number of active sites.[27] However, the photodegradation activity was not enhanced significantly above 75 g/L, due to the scatter reflection will result in a low utilization of irradiation and due to an overdose of catalyst.[28] The dosage of 50 g/L is used in the next experiment.

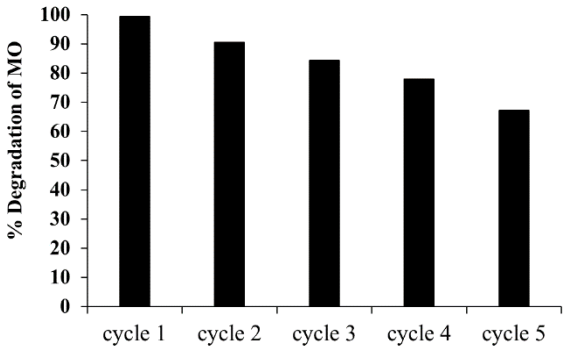

Figure 8. Recycle stable usability test of AGAB on photodegradation of MO.

The stability of AGAB was evaluated using five cycling runs. In this study, at the end of each cycle (initial MO concentration; 10 mg/L; amount of wet AGAB, 50 g/L; irradiation time; 30 min), the AGAB were separated from the solution by filtration and then rinsed several times with DI water and kept in 4% $CaCl_2$ for 2 h. After regeneration, the AGAB was used in the next cycle. The results are shown in Figure 8, the photodegradation efficiency of AGAB continuously decreased to 99.4%, 90.6%, 84.3%, 77.9% and 67.1% in the five cycles. This was probably due to the fouling of the AGAB catalyst porous surface and loss of catalyst during the recycling process.

4. Conclusion

In summary, the AGAB has been successfully synthesized. Most importantly, the AGAB photocatalyst displayed excellent photocatalytic activity over the degradation of MO under sunlight irradiation, which was greatly improved in comparison with AgCl/Ag. The alginate crosslinked, the superoxide radicals and the holes were suggested to play a dominant role in the photodegradation of MO. Besides these important results, the easy separation and good stability property of AGAB further make it a promising application in wastewater treatment.

Acknowledgements

This work was partially supported by Department of Chemistry, Faculty of Science and Technology, Phranakhon Si Ayutthaya Rajabhat University.

References

1. Yao, X; Liu, X; Zhu, D; Zhao, C; Lu, L. *Catal. Commun*. **2015**, *59*, 151-155.
2. Chakhtouna, H; Benzeid, H; Zari1, N; Qaiss, A.el kacem; Bouhfid, R. *Environ. Sci. Pollut. Res.* **2021**, *28*, 44638-44666.
3. Ma, Y-z; Cheng, W-s; Liu, W-s; Wang, J; Wang, Y-k. *Trans, Nonferrous Met. Soc. China*. **2015**, *25*, 112-121.
4. Feng, Z; Sun, J; Wang, T. *J. Colloid Interface Sci.* **2016**, *480*, 184-190.
5. Zhu, Y; Zhu, R; Xi, Y; Xu, T; Yan, L; Zhu, J. *Chem. Eng*. J. **2018**, *346*, 567-577.
6. Yang, Y; Zhang, Y; Dong, M; Yan, T; Zhang, M. *J. Hazard. Matter*. **2017**, *335*, 92-99.
7. Zhao, X; Wu, p; Lei, Y; Chen, F; Yu, Ze; Fang, P. *Appl. Surf. Sci.* **2020**,*52*, 147010-147021.
8. Lin, S; Huang, R; Cheng, Y; Liu, J; Wiesner, M.R. *Water Res.* **2013**, *47*, 3959-3965.
9. Gao, X; Guo, C; Hao, J; Zhao, Z, Long, H; Li, M. *Int. J. Biol. Intermol*. **2020**, *164*, 4423-4334.
10. Peretz, S; Cinteza, O; *Colliods Surf*. **2020**, *318*, 165-172.
11. Liu, Y-g; Hu, X-j; Wang, H; Chen, A-w; Liu, S-m; Guo, Y-n; He, Y; Hu,Xx; Li, J; Liu, S-h; Wang, Y-q; Zhou, L. *J. Chem. Eng*. **2013**, *226*, 131-138.
12. Sakar, S; Chakrabortg, S; Bhattacharjee, C. *Ecotoxico. Environ. Saf.* **2015**, *121*, 263-270.
13. Zhao, K; Feng, L; Lin, H; Fu, Y; Lin, B; Cui, W; Li, S; Wei, J. *Catal. Today*. **2014**, *236*, 127-134.
14. Mohamed, S.K; Hegazy, S; Abdelwahab, N.A; Ramadan, A.M. *Int. J. Biol. Macromol*. **2018**, *108*, 1185-1198.
15. Shu, J; Wang, Z; Xia, G; Zheng, Y. *Chem. Eng. J*. **2014**, *252*, 374-381.
16. Zheng, Y; Shu, J; Wang, Z. *Mater. Lett*. **2015**, *158*, 339-342.
17. Devi, Th.B; Begum, M; Amaruzzaman, M. *J. Photochem. Photobiol. B, Biol*. **2016**, *160*, 260-270.
18. Asadi, S; Eris, S; Azizian, S. *ACS Omega*. **2018**, *3*, 1540-15148.
19. Qian, D; Bai, L; Wang, Y-S; Song, F; Wang, X-L; Wang, Y-Z. *Ind. Eng. Chem. Res*. **2019**, *58*, 13133-13144.
20. Wanchai, K. *Key Eng. Mater*. **2017**, *751*, 689-694.

21. Andreas, A; Winata, Z. G; Ismadji, S; Hsu, H-Y, Go, A.W; Ju, Y-H. *J. Mol. Liq.* **2021**, *329*, 115579.
22. Eltaweil, A.S; El-Monaem, E.M.A; Elshishini, H.M; El-Aqapa, H.G; Hosny, M; Abdelfatah, A.M; Ahmed, M.S; Hammad, E.N; El-Subruiti, G.M; Fawzyc, M; Omer, A.M. *RSC Adv.* **2022**, *12*, 8228-8247.
23. Yao, X; Liu, X. *J. hazard. Mater*. **2014**, *280*, 260-268.
24. Song, L; Li, Y; Tian, H; Wu, X; Fang, S; Zhang, S. *Mater. Sci. Eng. B.* 2014, *189*, 70-75.
25. Wu, Y; Song, L; Zhang, S; Wu, X; Zhang, S; Tian, H; Ye, J. *Catal. Commun*. **2013**, *37*, 14-18.
26. Wang, H; Shi, H; Li, H; Tian, X; Wu, Z. *Solid Sci.* **2020**, *102*, 106159
27. Shinger, M; Idris, A.M; Devaramani, S; Qin, D.D; Baballa, H; Zhang, S-T; Shan, D-L; Lu, X. *J. Environ. Chem. Eng*. **2017**, *5*,1526-1535.
28. Wang, K; Xu, J; Li, N; Chen, M; Teng, F. *J. Mol. Catal. A Chem.* **2014**, *393*, 302-308.

Activated carbon derived from hemp core biowaste with a doped heteroatoms and large specific surface area for supercapacitor applications

Pattaramon Meefang, Thanapat Jorn-am, Preeyanuch Supchocksoonthorn, and Peerasak Paoprasert*

Department of Chemistry, Faculty of Science and Technology, Thammasat University, Pathum thani 12120, Thailand

**E-mail: peerasak@tu.ac.th*

Abstract:

The increasing energy consumption necessitates the development of energy storage systems. This study focuses on the synthesis of heteroatom-doped activated carbon from hemp cores for high-performance supercapacitors. The process involves converting hemp core biomass into activated carbon using thiourea as the sulfur source. Various thiourea ratios (wt%) were studied in both hydrothermal and activation methods. The resulting carbon has a high surface area of 2529 m^2 g^{-1}, 1.6 times higher than undoped activated carbon (1547 m^2 g^{-1}). The electrochemical properties of the activated carbon were examined using cyclic voltammetry. The resulting carbon showed outstanding electrochemical performance, providing a specific capacitance of 262 F g^{-1}, high energy density of 36 Wh kg^{-1}, and power density of 3935 W kg^{-1}. The electrochemical performance suggests that activated carbon from hemp cores could be a promising electrode material in electrochemical energy storage supercapacitors. The cost-effectiveness, availability, and simple chemical activation process make it feasible for commercial use in supercapacitors.

1. Introduction

The increasing emphasis on environmental sustainability has driven a rapid expansion in creating and using renewable energy sources. Consequently, the significance of energy storage devices has amplified. This rise in importance is linked to concerns regarding climate change, pollution, and the limited availability of fossil fuels. Energy storage plays a crucial role in addressing intermittency issues by storing excess energy generated during peak periods and supplying it during times of high demand or low generation.

Storing energy is a multifaceted procedure encompassing a range of forms and technologies such as battery energy storage, mechanical energy storage, and supercapacitors. Biological waste, which includes agricultural residues, wood waste, food waste, and industrial waste, has the potential to be converted into diverse carbon materials like biochar, activated carbon, or carbon nanomaterials.

Supercapacitors are appealing due to characteristics, such as high-power density, longer cycle life, fast charging and discharging capabilities, greater efficiency, compared to batteries, and a wide operating temperature range. These devices store energy using electrostatic storage, which differs from traditional batteries. When a voltage is applied, they form an electric field, causing ions from the electrolyte to congregate on the electrodes. Supercapacitors (SCs) are divided into three types based on their energy storage mechanisms: (I) Electrochemical Double-Layer Capacitors (EDLCs), (II) Pseudocapacitors, and (III) Hybrid capacitors.[1] EDLCs consist of an electrolyte, carbon-based electrodes, and a separator, storing charges electrostatically or through a non-faradaic process. Pseudocapacitors use metal oxides or conducting polymers with high electrochemical pseudocapacitance material, storing charges through a faradaic process. Hybrid Capacitors combine features from pseudocapacitors and EDLCs.

Hemp, a classification within the Cannabis sativa plant, is utilized for industrial or medicinal purposes. The level of tetrahydrocannabinol (THC) present in hemp differs significantly from that in marijuana. Legal hemp or hemp-derived products must contain less than 0.2-0.3% THC. Thailand has recently legalized the production, import, export, distribution, and possession of hemp for medical purposes and research. Although various parts of the hemp plant, such as seeds for food and personal hygiene, and stalks for fiber used in clothing, are currently being utilized, the hemp core remains largely unused, leading to its designation as biological waste.[2] Hence, this research aims to maximize the benefits by repurposing hemp cores to synthesize activated carbon, thereby reducing environmental waste.

In this work focuses on maximizing the use of hemp's underutilized waste components to reduce environmental impact. The waste materials from hemp were utilized as primary sources for synthesizing electrode materials, and thiourea was utilized as a source of sulfur to incorporate these elements into the activated carbon. The incorporation of sulfur atoms is aimed at

enhancing electrochemical activity by inducing structural defects in the carbon framework, leading to an increased number of active sites for charge localization. Additionally, sulfur doping is anticipated to improve electrode polarization, electron spin densities on the carbon surface, consequently enhancing the charge distribution within the electrode material. The introduction of sulfur enhances electronic conductivity and broadens the band gap of the activated carbon due to its electron-withdrawing characteristics. Moreover, S-doping plays a role in influencing the pore size,[3] aiming for optimal utilization of biological waste as shown in Figure 1.

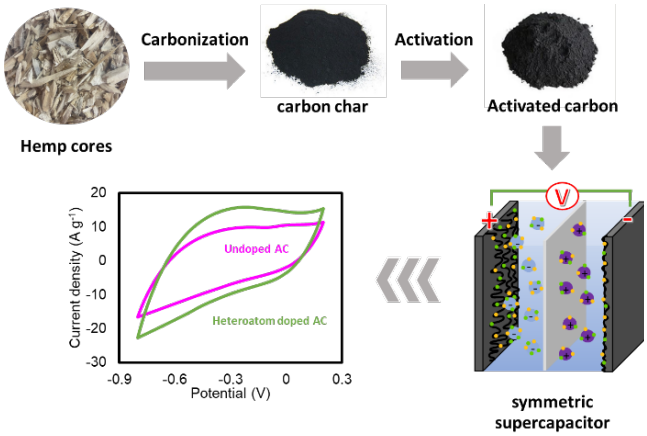

Figure 1. Schematic representation of this research

2. Materials and Methods

2.1 Materials

The hemp cores were obtained from a hemp plantation in Thailand. All compounds of analytical quality were sourced from Sigma-Aldrich, while the chemical solvents of analytical grade were obtained from Carlo Erba Reagents.

2.2 Synthesis of hemp-derived activated carbon

The dried hemp cores underwent a fine powdering process. Subsequently, in a Teflon-lined autoclave, 5 g of hemp cores were mixed with 100 mL of 1 M phosphoric acid and subjected to a hydrothermal process at 200°C for 5 hours. The resulting mixture was then cooled to room temperature, rinsed repeatedly with distilled water until reaching a neutral pH, filtered to obtain the carbon char (CC), and finally dried overnight. This CC was used in the production of activated carbon.

For the activation process, the CC was immersed in deionized water (60 mL) and impregnated with potassium hydroxide, functioning as an activating agent, in a 1:1 ratio. The mixture was heated to 80°C while continuously stirring until it formed a slurry. This slurry was activated within a tube furnace under nitrogen gas conditions and gradually heated at a rate of 10°C/min until reaching 800°C over a duration of 2 hours. Following the activation, the material was washed multiple times with 1 M hydrochloric acid and hot deionized water until achieving a neutral pH. Thereafter, it was dried in an oven at 80°C for 24 hours to yield the activated carbon (AC). The synthesis for classifying AC by adding thiourea via the hydrothermal and activation processes in various ratios is shown in Table 1.

2.3 Characterizations

A nitrogen adsorption-desorption experiment was conducted using a Belsorp Max Analyzer to determine specific surface area, pore size, and pore volume. The specific surface area was calculated using the Brunauer-Emmett-Teller (BET) technique, while the pore volume and pore size distribution were estimated utilizing the Barret-Joner-Halenda (BJH) method. To assess crystallinity and amorphous characteristics, an X-ray diffraction (XRD) analysis was performed using the RigakuD/max2550VL/PC system. Furthermore, the chemical state of the elements and material composition were investigated using X-ray photoelectron spectroscopy (XPS) from AXIS ULTRADLD, Kratos analytical.

2.4 Fabrication of electrodes

The AC, carbon black, and poly(vinylidene fluoride) (PVDF) served as the active components, conducting agent, and binder, respectively. They were blended in a weight ratio of 80:15:5% along with N-methyl pyrrolidone (NMP) solvent. This mixture was then applied onto carbon paper, which served as the current collector, and dried overnight at 50°C.

2.5 Electrochemical measurements

The electrochemical assessments were conducted using a potentiostat/galvanostat (μAutolab, PGSTAT204). A three-electrode cell setup was utilized, comprising the prepared electrode as the working electrode, platinum as the counter electrode, and an Ag/AgCl reference electrode. This three-electrode cell configuration was employed in cyclic voltammetry (CV) and galvanostatic charge-discharge (GCD) measurements. The experiments were conducted in a 3 M potassium hydroxide (KOH) electrolyte within a potential range of -0.8 to 0.2 V. Scan rates varied from 10 to 100 mV s^{-1} for CV, while current densities ranged from 4 to 10 A g^{-1} for GCD measurements. The specific capacitance (C_{sp}), energy density (E), and power density (P) can calculate from the equation below;

Table 1. Different types of activated carbon

Type	Hydrothermal process	Activation process	Specific surface area (m^2 g^{-1})	Pore volume (cm^3 g^{-1})	Pore diameter (nm)	Atomic concentration (%)			Specific capacitance (F g^{-1})
						C	O	S	
AC1	undoped		1547	0.39	1.75	87.25	11.05	-	175
AC2	-	10%wt thiourea doped	1574	0.53	1.71	83.55	14.68	-	157
AC3	-	20%wt thiourea doped	1853	0.60	1.60	90.19	9.11	-	164
AC4	10%wt thiourea doped	-	1673	0.49	1.65	90.02	9.30	-	189
AC5	20%wt thiourea doped	-	2380	0.97	1.47	89.96	8.78	0.35	262
AC6	5%wt thiourea doped	5%wt thiourea doped	2099	0.60	1.59	89.25	9.59	0.18	171
AC7	10%wt thiourea doped	10%wt thiourea doped	2529	0.99	1.65	90.01	9.37	0.39	217

$$C_{sp} = \frac{\int ivdv}{2\mu m \Delta V} \quad \text{(Eq.1)}$$

$$E = \frac{C_{sp}(\Delta V)^2}{2} \quad \text{(Eq.2)}$$

$$P = \frac{E}{t} \quad \text{(Eq.3)}$$

From Eq.1 C_{sp} is the specific capacitance (F g^{-1}), i and v are the current and potential in the CV test (A and V), μ is the scan rate (V/s), m is the mass of active materials (g), ΔV is the potential window of discharge. In Eq.2 and 3, E is energy density (Wh kg^{-1}), P is power density in (W kg^{-1}), and t is the discharge time (h).

3. Results & Discussion

3.1 Synthesis and characterization of AC

In this study, activated carbon derived from hemp cores was employed as an electrode material in conjunction with a 3 M KOH electrolyte for assembling supercapacitors. Different content of thiourea, incorporated during both the hydrothermal and activation processes, resulted in the creation of 7 types of AC. KOH was utilized as the activating agent to enhance surface properties like surface area, porosity, pore volume, and pore diameter.

The specific surface area (S_{BET}) and pore size distribution were determined through N_2 adsorption and desorption analysis. Figure 1(a) shows the N_2 sorption isotherm results for the samples, highlighting that AC5 and AC7 exhibit a high surface area of 2380 and 2529 m^2 g^{-1} and a pore volume of 0.97 and 0.99 cm^3 g^{-1} respectively. The isotherm observed in Figure 1(a) demonstrates characteristics of type I and IV adsorption isotherms. This classification indicates the presence of mesopores, which play a significant role in enhancing charged ion transport and improving electrochemical properties[4]. Furthermore, Figure 1(b) illustrates the associated pore size distributions investigated using the BJH system. The XRD pattern shows in Figure 1(c) obtained from the generated all AC represents its structural composition and degree of graphitization. The pattern reveals an amorphous phase, noticeable through a prominent peak between 2θ = 18–29°, and a faint, broad peak at 41–45°, corresponding to the (002) and (100) planes respectively. The existence of the (100) plane signifies the amorphous nature of the carbon, while the intensity of the (002) peak serves as an indicator of the extent of graphitization[3].

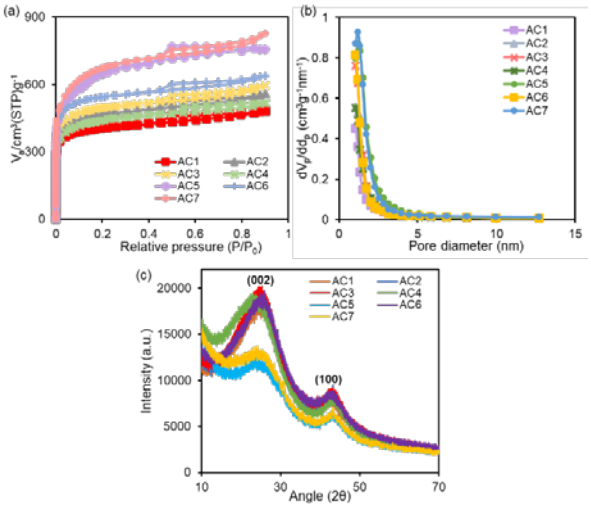

Figure 1. (a) N_2 adsorption-desorption isotherm and (b) pore-size distributions (c) XRD patterns of the various AC

In the study of heteroatom doping, oxygen came from self-doping and sulfur came from thiourea-doping. The AC5 sample underwent elemental composition analysis using X-ray photoelectron spectroscopy (XPS). The survey XPS spectrum (Figure 2(a)) revealed strong signals at 285, 533, and 169 eV, corresponding to C_{1s}, O_{1s}, and S_{2p}, with atomic concentrations of 89.96%, 8.78%, and 0.35%, respectively. The high-resolution of C_{1s} spectrum (Figure 2(b)) indicated distinct peaks attributed to C=C (285), C–S (286), C=O (287), and O-C=O (289) functional groups, indicating their respective doping. High-resolution O_{1s} (Figure 2(c)) exhibited peaks related to C=O (531), O-C-O (532), C-OH (534), and C=O aromatic (535) groups, discernible upon deconvolution. The S_{2p} high-resolution spectrum (Figure 2(d)) was characterized by doublets within the $S_{2p3/2}$ (168) to $S_{2p1/2}$ (170) region, denoting the presence of sulfide and thioul groups[5-6].

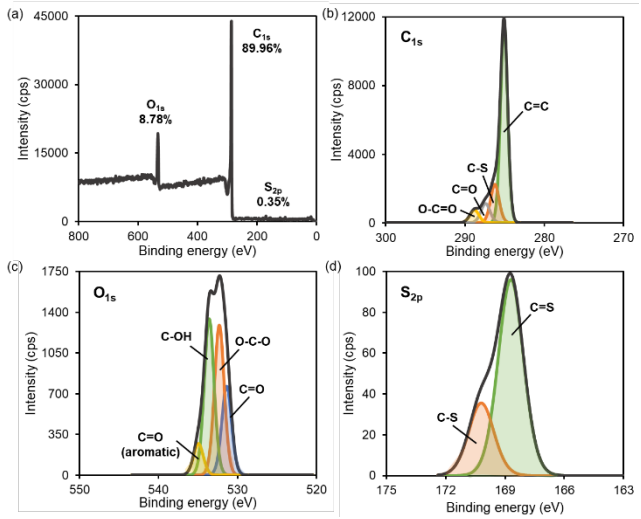

Figure 2. (a) Survey XPS spectra of AC5, (b) high-resolution spectra of C_{1s}, (c) high-resolution spectra of O_{1s}, and high-resolution spectra of S_{2p}.

3.2 Electrochemical performance

The CV was used to examine the electrochemical characterization of hemp core-derived activated carbon. The cyclic voltammograms were obtained for a comparison of the types of electrodes using a standard 3 M KOH solution as the electrolyte. Figure 3(a) illustrated that AC5 displayed the largest area under the curve, resulting in the highest specific capacitance recorded at 262 F g^{-1} at scan rate of 30 mV s^{-1} within a potential range of -0.8 to 0.2 V. This is due to its high surface area.

This observation underscores that the introduction of heteroatoms into the activated carbon structure significantly enhances its electrochemical performance. This improvement can be attributed to an enhancement in specific surface area and morphology, leading to increased wettability. The refined morphology contributes to the presence of highly active sites within the structure. Furthermore, CV curves in Figure 3(b) shows the performance of the AC5 electrode which exhibits an escalating current trend with rising scan rates up to 100 mV s^{-1}. This pattern indicates the diffusion of electrolyte ions, signifying low internal resistance and expedited kinetics. Additionally, the electrode's distinctive quasi-rectangular shape signifies characteristics ideal EDLC.

Moreover, GCD performed at a current density of 4 to 10 A g^{-1} shows the symmetric curves observed for the AC5 electrodes suggest an ideal capacitive behavior as shown in Figure 3(c). This behavior can be attributed to the favorable adsorption and desorption of electrolyte ions occurring at the electrode surface[5].

The supercapacitor electrode presented outstanding rate performance throughout several scan rate cycles, demonstrating its high-rate capabilities. This increased performance is due to the combination of a large specific surface area and the introduction of heteroatom doping, both of which significantly contribute to improved capacitive behavior and rate performance. Figure 3(d) depicts the electrode's rate capacity, which was calculated using specific capacitance calculations and the applied current density in this study.

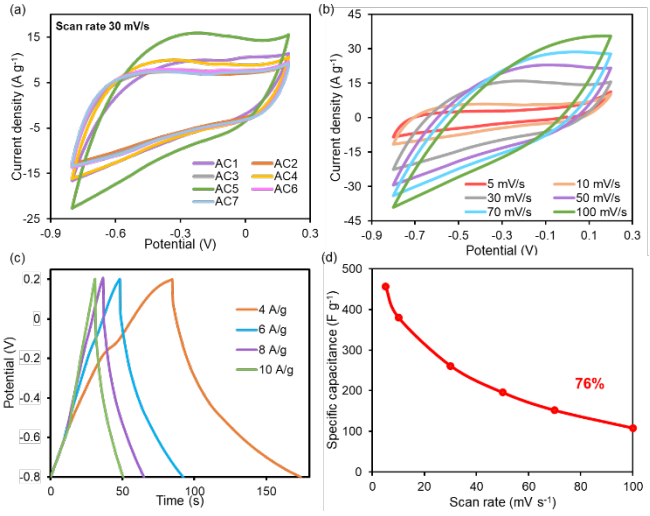

Figure 3. (a) CV curves comparison of various electrode at scan rate 30 mV s^{-1}, (b) CV curves of AC5 electrode at different scan rates (5, 10, 30, 50, 70 and 100 mV s^{-1}), (c) GCD curve of AC5 electrode at different current densities (4,6,8 and 10 A g^{-1}), and (d) rate performance of AC5

4. Conclusion

The symmetric supercapacitor was fabricated using hemp core-derived activated carbon as an active material and improved the performance using thiourea as a sulfur source for heteroatom doping. The AC5 electrode demonstrated a notable specific capacitance of 262 F g^{-1} in a 3 M KOH electrolyte at a scan rate of 30 mV s^{-1} due to its high surface area. This resulted in a high energy density of 36 Wh kg^{-1} and a power density of 3935 W kg^{-1}. Because the incorporation of heteroatom doping played a crucial role in improving the electrochemical properties, sulfur-doped activated carbon can undergo reversible redox reactions with electrolyte ions, forming sulfide and thiol groups. These groups participate in redox reactions, allowing sulfur to change its oxidation state during charge and discharge processes, resulting in electrical energy storage[7]. Contributing to a significant specific surface area of 2529 m^2 g^{-1}, which is 1.6 times greater than that of undoped activated carbon. Furthermore, this research presents an innovative approach leveraging renewable biomass sources to create high-performance supercapacitors, emphasizing improved functionality and practical application prospects.

Acknowledgements

This work was supported by Faculty of Science and Technology, Thammasat University, the Thailand Science Research and Innovation Fundamental Fund, Contract No. TUFF 13/2565, and Thammasat University Research Fund, Contract No. TUFT-FF 9/2565.

References

1. Jalal, N. I., Ibrahim, R. I., & Oudah, M. K. (**2021**, August). A review on Supercapacitors: Types and components. In Journal of physics: conference series (Vol. 1973, No. 1, p. 012015). IOP Publishing.
2. Chaiwat, S. Hemp: A new cash crop that brings both challenges and opportunities. https://www.krungsri.com/en/research/research-intelligence/hemp-2021 (accessed January 1, 2024)
3. Raj, F. R. M. S., Boopathi, G., Kalpana, D., Jaya, N. V., & Pandurangan, A. (**2022**). Sustainable development through restoration of Prosopis juliflora species into activated carbon as electrode material for supercapacitors. Diamond and Related Materials, 121, 108767.
4. Raj, F. R. M. S., Jaya, N. V., Boopathi, G., Kalpana, D., & Pandurangan, A. (**2020**). S-doped activated mesoporous carbon derived from the Borassus flabellifer flower as active electrodes for supercapacitors. Materials Chemistry and Physics, 240, 122151.
5. Dai, Z., Ren, P. G., Guo, Z., He, W., Hou, X., & Jin, Y. (**2021**). Three-dimensional porous carbon materials derived from locust for efficient N O S co-doped supercapacitors by facile self-template and in-situ doping method. Fuel Processing Technology, 213, 106677.
6. Muthuraj, D., Ghosh, A., Kumar, A., & Mitra, S. (**2019**). Nitrogen and sulfur doped carbon cloth as current collector and polysulfide immobilizer for magnesium-sulfur batteries. ChemElectroChem, 6(3), 684-689.
7. Shaheen Shah, S., Abu Nayem, S. M., Sultana, N., Saleh Ahammad, A. J., & Abdul Aziz, M. (**2022**). Preparation of sulfur-doped carbon for supercapacitor applications: a review. ChemSusChem, 15(1), e202101282.

Development of pouch-cell Zn-ion battery using MnO_2 synthesized from spent alkaline battery as cathode material

Budsayamas Kanthawong[1], Kamonpan Manowilaikun[1], Keeratipron Yoaharee[1], Kittima Lolupima[2], and Rojana Pornprasertsuk [1,3,4,5]*

[1]*Department of Materials Science, Faculty of Science, Chulalongkorn University, Thailand*
[2]*The Nanoscience and Technology program, Graduate School, Chulalongkorn University*
[3]*Center of Excellence in Petrochemical and Materials Technology, Chulalongkorn University, Thailand*
[4]*Center of Excellence on Advanced Materials for Energy Storage, Chulalongkorn University, Thailand*
[5]*Department of Materials Science and Bioengineering, Nagaoka University of Technology, Japan*

**E-mail: rojana.p@chula.ac.th*

Abstract:

This work focuses on the Mn recovery from the electrode powder of spent alkaline batteries to form δ-MnO_2 as a final recycled product. The first step was the leaching process of spent electrode powder using 2 M sulfuric acid with the addition of 12 vol% hydrogen peroxide as a reducing agent. The leaching solution was then mixed with potassium permanganate solution as precursors and produce δ-MnO_2 by the hydrothermal process at 160°C for 24 h. The recycled δ-MnO_2 was subsequently used as an active cathode material in the CR2025 and pouch-cell of Zn-ion batteries (ZIB), which consisted of Zn foil as anode, filter paper as a separator and three types of electrolytes: 2 M zinc sulfate solution, 1 M zinc sulfate solution with 0.01M polyethylene glycol (PEG) and 0.25 M zinc triflate in dimethyl sulfoxide (DMSO). The CR2025 ZIBs using the recycled δ-MnO_2 cathode exhibited the discharge capacities of 150.51 and 244.49 mAh/g, while pouch-cell ZIBs exhibited the highest specific capacity at 303.23 and 231.11 mAh/g at the current density of 0.2 A/g using the above electrolytes, respectively. The result thus suggests ZIBs using zinc sulfate electrolyte show higher initial specific capacity but much lower stability than zinc triflate in DMSO electrolyte.

1. Introduction

Alkaline batteries are primary batteries commonly use in electronic devices and cannot be recharged after used. The spent alkaline batteries mostly end up as electronic waste in landfills. Spent alkaline electrode powder contains carbon, zinc oxide, zinc manganese oxide ($Zn_xMn_{3-x}O_4$) and potassium hydroxide (an electrolyte). The Mn recycle process begins with the leaching of manganese ions from the electrode powder of spent alkaline batteries. According to Buzatu et al. [1], sulfuric acid was effectively used in the leaching process of spent electrode powder with the addition of hydrogen peroxide as a reducing agent. One of the optimal leaching conditions was reported to be 2 mol/L of H_2SO_4, 20 ml/g, 25°C, and H_2O_2 6 % by volume for 2 hours, the manganese leaching efficiency could be increased from 30.1% (with no reducing agent) to 97 % , resulting in a leaching solution containing manganese sulfate and zinc sulfate as the main components.

Mn could be recovered from the leaching solution in the form of MnO_2 using various synthesis methods such as chemical precipitation with sodium hydroxide. However, it was discovered that this technique may result in Zn contamination, which caused the formation of $ZnMn_2O_4$ phase in the calcination process [2]. Another alternative method is the hydrothermal process, which has been commonly used for synthesizing manganese dioxide nanoparticles. Manowilaikun [3], Wongthaipadung and Punpeng [4] synthesized α-, β-, γ-MnO_2 from the leaching solution of spent alkaline-battery cathode powder using the hydrothermal process. By varying precursor and hydrothermal temperature, the MnO_2 nanoparticles with the various phases above were obtained with the Mn recovery efficiencies of 87, 64, 59, and 100 %, respectively.

Zinc ion batteries (ZIBs) contain the following components: zinc sheet or zinc powder as the anode, a transition metal oxide mixed with carbon as the cathode and electrolyte, which typically use an aqueous-based electrolyte such as $ZnSO_4$ solution. The advantages of ZIBs are their high gravimetric capacity, high efficiency, simple manufacturing, and inexpensive components [5]. However, the use of aqueous-based electrolytes causes instability issues due to hydrogen evolution ($Zn + 2H^+ \rightarrow Zn^{2+} + H_2$) and Zn dendrite formation, which reduces the performance of ZIBs. To address these issues, various methods have been proposed such as the addition of polyethylene glycol (PEG) to prevent dissolution of zinc, particle size and surface area manipulation to improve electrochemical performance [6].

Furthermore, the use of a non- aqueous-based electrolyte such as dimethyl sulfoxide (DMSO), which is an aprotic solvent could be an alternative solution to reduce Zn corrosion and

HER. Corpuz et al. [7] compared the performance of ZIBs using zinc triflate ($Zn(OTf)_2$) aqueous solution and $Zn(OTf)_2$ in dimethyl sulfoxide (DMSO) as an electrolyte and compare α-MnO_2 as a cathode. The results showed that using $Zn(OTf)_2$ in DMSO prolonged the recharging cycles up to 2000 cycles but with the highest specific capacity of only 60 mAh/g. When compared to the research of Kao-ian et al. [8], it was discovered that when δ-MnO_2 was used as the cathode and $Zn(OTf)_2$ in DMSO was used as the electrolyte, at over 1000th cycle, the capacity could still reach 159 mAh/g, which was higher than that of the α-MnO_2 cathode. The latter study thus confirmed that the use of DMSO-based electrolyte together with δ-MnO_2 cathode resulted in better battery stability than aqueous-based electrolyte.

Therefore, in this research, δ-MnO_2 was synthesized by hydrothermal process using the spent-alkaline-battery leaching solution as a precursor. The recycled δ-MnO_2 was then used as an active cathode material in CR2025 and pouch-cell ZIBs which used three types of electrolytes: (i) 2 M $ZnSO_4$ solution, (ii) 1 M $ZnSO_4$ solution with 0.01 M PEG addition and (iii) 0.25 M $Zn(OTf)_2$ in DMSO with 5 wt% of deionized water addition.

2. Materials and Methods

2.1 Materials

Materials for leaching and δ-MnO_2 recycled process were sulfuric acid (H_2SO_4) 98% hydrogen peroxide (H_2O_2), and potassium permanganate ($KMnO_4$). Materials for ZIB fabrication were $ZnSO_4$, $Zn(OTf)_2$, polyethylene glycol (M_w= 3600–4400 g/mol, PEG), dimethyl sulfoxide (DMSO), polyvinylidene fluoride (M_w = 660,00–700,000 g/mol, PVDF), carbon black (BP2000), Whatman filter paper No.1, 0.2-mm thick graphite foil (Shenzhen 3KS Electronic Material Co. Ltd.) and 0.1-mm thick Zn sheet (99.99%, Sirikul Engineering, Ltd.).

2.2 Synthesis of δ-MnO_2 from spent alkaline electrode powder.

In this study, δ-MnO_2 was prepared by a modified method of Liu et al [9]. δ-MnO_2 precursor solutions were first prepared by leaching 5 g of spent alkaline electrode powder in 2 M sulfuric acid (H_2SO_4) with the addition of 12 vol% hydrogen peroxide (H_2O_2) and stirring for 1 h. After that, the mixture was filtered to remove any undissolved residue. 0.58 ml of leaching solution was then mixed with the solution of 0.984 g of potassium permanganate ($KMnO_4$) in 35 ml of deionized water (DI water). The obtained precursor solution was stirred using the magnetic bar for 1 h to ensure homogeneity, transferred into Teflon autoclave and heated at 160 °C for 24 h in an oil bath. After cooling to room temperature, the obtained samples were filtered, washed 3 times with 500 mL of DI water and once with 500 mL of ethanol and dried at 60 °C overnight.

2.3 CR2025 and pouch-cell ZIB fabrication

The cathode mixture is composed of recycled δ-MnO_2, carbon black (BP2000) and PVDF at the mass ratios of 75:15:10, respectively. The cathode was prepared by (i) coating the cathode mixture on graphite foil by the doctor blade technique with the controlled thickness of 120 μm, (ii) heating at 90 °C for 24 h in a vacuum furnace, and (iii) cutting to 14-mm diameter circles for CR2025 cells and 55 mm x 42 mm rectangles with extended electrodes for pouch cells. Zn sheets as anodes were cut with the same size as cathodes. CR2025 and pouch-cell ZIBs were prepared using the above components and 3 types of electrolyte: (i) 2 M $ZnSO_4$ solution, (ii) 1 M $ZnSO_4$ solution with 0.01 M PEG addition and (iii) 0.25 M $Zn(OTf)_2$ in DMSO with 5 wt% of deionized water addition. The glass microfiber separators with a slightly larger size than the electrodes were impregnated in the electrolytes for 20 minutes prior to the assembling process.

CR2025 ZIBs were assembled starting with the cathode case, 50-μL electrolyte, glass microfiber, anode, spring support, anode case and pressed at 1000 psi. Pouch cells were prepared by placing the prepared electrodes, separators and 1.5 mL electrolyte into the aluminum laminated bags and sealed at 190 °C under vacuum.

2.3 Materials characterization and electro-chemical measurement

2.3.1 Materials characterization

The morphology and phase of the obtained MnO_2 particles were observed using scanning electron microscopy (SEM, JEOL JSM-7610F) and X-ray diffraction techniques (XRD, Bruker AXS Model D8 Discover) carried out with Cu Kα radiation at a scanning range of 5–80°, respectively.

2.3.2 Electrochemical measurements

Galvanostatic charge–discharge (GCD) tests were performed within the potential window of 1.0–1.75 V vs. Zn^{2+}/Zn at 0.05-0.5 A/g for 1000 cycles. The cyclic voltammogram (CV) tests were conducted in the potential range of 1.0 V-1.80 V vs. Zn^{2+}/Zn at a scanning rate of 0.1, 0.2, 0.5, 1.0, 2.0 mVs^{-1} for 3 times. All tests were carried out at room temperature.

3. Results & Discussion

XRD pattern of the obtained δ-MnO_2 is shown in Fig. 1. The diffraction peak at 12.3°, 25.4°, 37.7° and 66.9°, which are indexed to (001), (002), (-111) and (-312) planes of layered δ-MnO_2 (JCPDS no.80-1098), which has a two-dimensional (2D) layered structure with an interlayer spacing of about 0.69 nm. The microstructure and surface morphology of the prepared samples were investigated by SEM (Fig. 2). The results reveal the δ-MnO_2 nanoflower morphology which are expected to enhance Zn^{2+} ion extraction/ intercalation during the charge/discharge process [10].

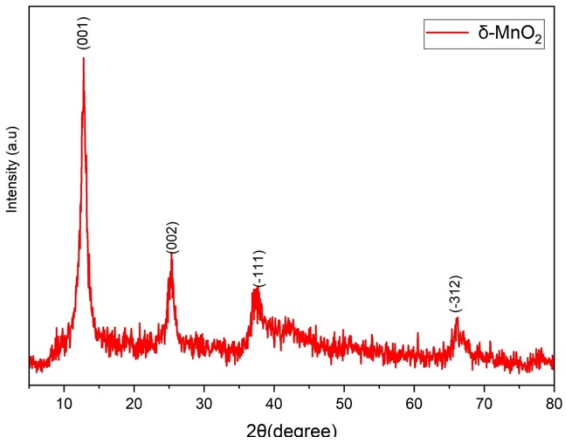

Figure 1. XRD pattern of the recycled δ-MnO_2.

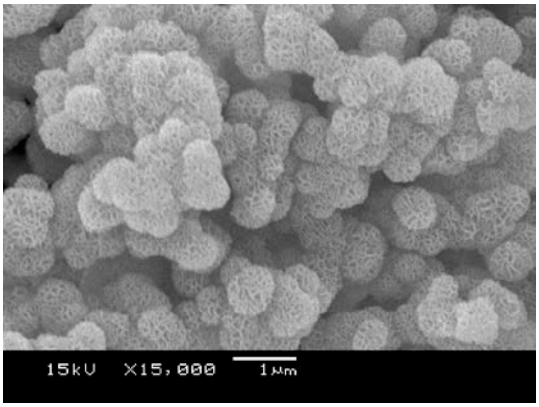

Figure 2. FESEM image of the recycled δ-MnO_2.

The CV curves of CR2025 cells with three different types of electrolytes are shown in Fig. 3a. For both aqueous electrolytes, each CV curve exhibited an anodic peak around 1.5 V and two distinct cathodic peaks around 1.18 V and 1.34 V. The two cathodic peaks indicated the two-step reduction process, which corresponds to the insertion of H^+ and Zn^{2+}, or the insertion of Zn^{2+} into different sites in the MnO_2 structure[3] .The higher anode/cathode peaks of ZIB with $ZnSO_4$ with PEG electrolyte indicated that the high electrical conductivity of electrolyte and more uniform ion distribution led to the higher electrochemical activities.

For the ZIB with DMSO electrolyte, only one anodic and one cathodic peak were observed because there was no H^+ insertion due to the aprotic electrolyte. Therefore, the CV results show broad oxidation and reduction peaks with low electrochemical current. The solvate ions surrounding Zn^{2+} were also different from the aqueous electrolyte resulting in different onset potentials compared to those of the aqueous electrolyte. According to these CV results, HER on the DMSO cells was expected to be reduced, indicating improved long-term electrochemical performance.

GCD was carried out to analyze the cyclability and long-term stability of CR2025 and pouch cells. As shown in Fig. 3b-c, the highest specific capacities of 384.84, 278.69 and 259.03 mAh/g at 0.2 A/g, respectively for CR2025 cells and at 209.15, 166.56 and 151.69 mAh/g at 0.2 A/g for pouch cells using $Zn(OTF)_2$ in DMSO, $ZnSO_4$ with PEG, and $ZnSO_4$ electrolytes, respectively. At the initial cycles (<10 cycles), the specific capacity of both CR2025 and pouch-cell ZIB using $ZnSO_4$ with PEG electrolyte was higher than those used $ZnSO_4$ aqueous solution and $Zn(OTF)_2$ in DMSO. This corresponds well with CV results, which indicate that the highest anodic/cathodic peaks were observed in $ZnSO_4$ with PEG electrolyte. However, after prolonging cycles (>30 cycles), the combination of electrode degradation and the built-up hydrogen gas may reduce the interface between electrode and electrolytes and the overall electrode active area, which in turn reduces the electrochemical activity and specific capacities of ZIBs using aqueous electrolytes. Interestingly, ZIBs using DMSO-based electrolytes showed a much lower capacity degradation rate likely due to the lower hydrogen generation, in good agreement with previous work by Kao-ian et al. [11].

For pouch-cell ZIBs, more swelling of the pouch cell was clearly observed in the aqueous-based electrolyte compared to that used DMSO electrolyte, which was likely caused by the higher HER in the aqueous electrolyte. Therefore, the stability test was only performed on pouch-cell ZIBs using DMSO-based electrolyte for 300 cycles (Fig. 3d). The result shows that the specific capacity of DMSO increases after the first 30 cycles could be maintained at a relatively high specific capacity up to 300 cycles. This suggests that DMSO can reduce the occurrence of HER,

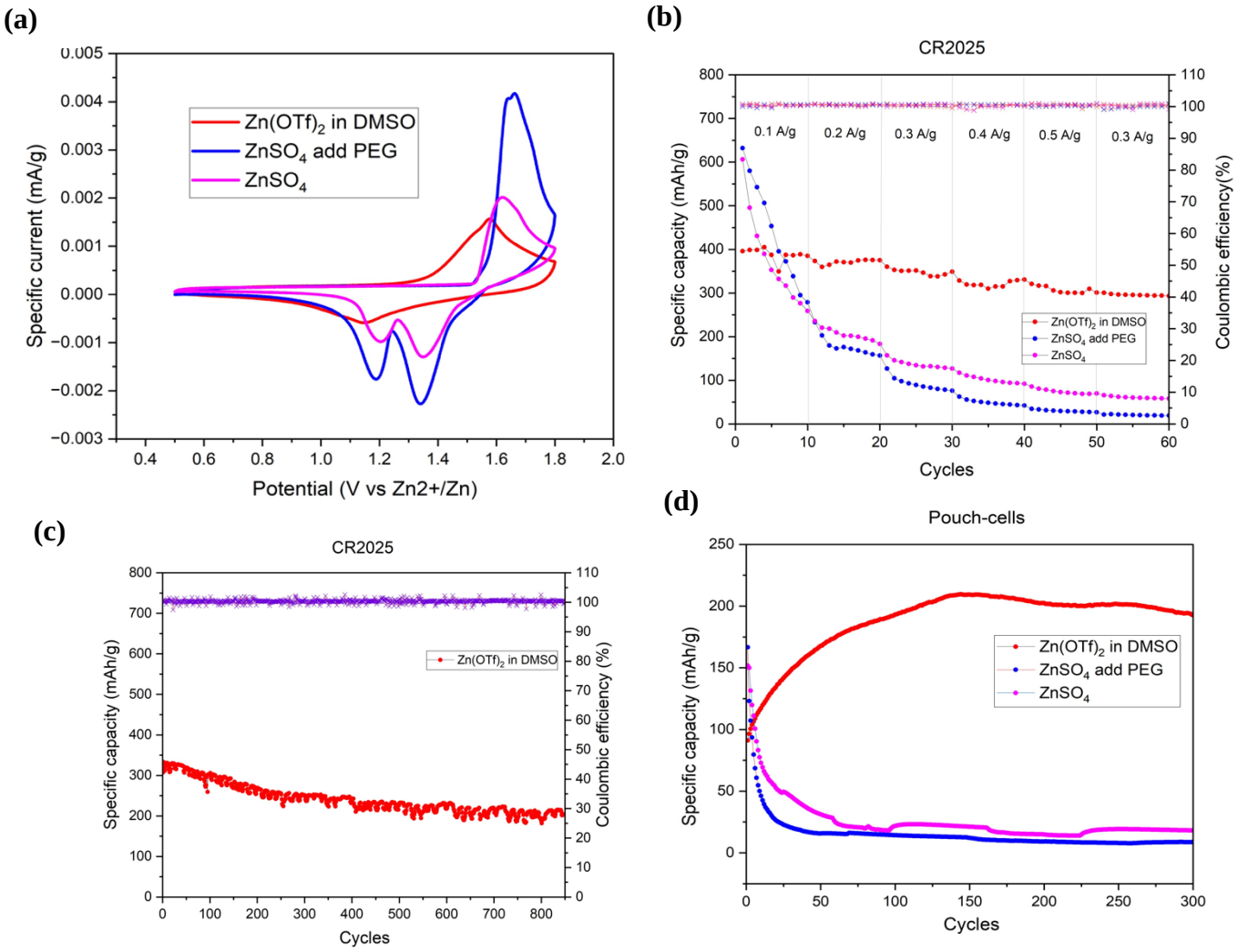

Figure 3. (a) CV curves of CR2025 ZIB using recycled δ-MnO_2 as cathode and three different types of electrolyte, (b) Specific capacities of CR2025 ZIBs using three types of electrolytes at various rates from 0.1 to 0.5 A/g for 60 cycles, (c) GCD of δ-MnO_2 in CR2025 using 0.25 M $Zn(OTf)_2$ in DMSO for from 0.3 A/g for 900 cycles and at 0.3 A/g and (d) Specific capacities of pouch-cell ZIBs at rate of 0.2 A/g.

thereby reducing the battery swelling problem. As well as enhance battery performance.

4. Conclusion

In summary, recycled δ-MnO_2 was successfully synthesized from spent alkaline battery powder, using a leaching solution as a precursor by hydrothermal process. By utilizing the recycled δ-MnO_2 as cathode in ZIBs with different types of electrolytes, ZIBs with non-aqueous electrolytes show much higher stability than that with aqueous base electrolytes but with a lower specific capacity in the initial cycles. However, after prolonged test (>30 cycles), the performance of ZIB with DMSO-based electrolyte shows much higher stability and eventually higher specific capacity. The CR2025 and pouch-cell ZIBs using recycled δ-MnO_2 were eventually achieved using $Zn(OTF)_2$ in DMSO electrolyte with the stability of at least 1000 and 300 cycles, respectively.

Acknowledgements

The alkaline battery waste was collected by Faculty of Science, Chulalongkorn University under Chula Zero Waste project. This research was financially supported by Thailand Energy Conservation Promotion Fund (ENCON Fund), This work was support by Chulalongkorn University of Thailand, Metallurgy and Materials Science Research Institute (MMRI).

Reference

1. Buzatu, M.; Săceanu, S.; Petrescu, M.I.; Ghica, G.V.; Buzatu, T. *J. Power Sources*. 2014, 247, 612–617.

2. จุฬามณี วชิรเดชา, สุทธิดา ชอุ่มเกต. (2018) "การเตรียมแมงกานีสไดออกไซด์จากแบตเตอรี่แอลคาไลน์ที่ผ่านการใช้งานแล้วเพื่อใช้ในแบตเตอรี่สังกะสี-อากาศ" โครงการเสริม สร้างประสบการณ์ภาควิชาวัสดุศาสตร์ คณะวิทยาศาสตร์ จุฬาลงกรณ์มหาวิทยาลัย
3. กมลพรรณ มโนวิไลกุล. (2020) "การสังเคราะห์แมงกานีสไดออกไซด์จากแบตเตอรี่แอลคาไลน์ที่ผ่านการใช้งานแล้วสำหรับการใช้งานในแบตเตอรี่สังกะสีไอออน." ภาควิชาวัสดุศาสตร์ คณะวิทยาศาสตร์ จุฬาลงกรณ์มหาวิทยาลัย, 23-24.
4. ธนัสพร วงษ์ไทยผดุง และ สิทธาพันธุ์ พันธุ์เพ็ง. (2022). "การสังเคราะห์ δ-MnO_2 จากแบตเตอรี่แอลคาไลน์ที่ผ่านการใช้งานแล้วเพื่อนำมาใช้ในแบตเตอรี่สังกะสีไอออนที่สามารถอัดประจุซ้ำได้." ภาควิชาวัสดุศาสตร์ คณะวิทยาศาสตร์ จุฬาลงกรณ์มหาวิทยาลัย, 19-20.
5. Li, X.; Qu, J.; Xu, J.; Zhang, S.; Wang, X.; Wang, X.; et al. *J. Electroanal. Chem.* 2021, 895, 115529.
6. Mitha, A.; Yazdi, A.Z.; Ahmed, M.; Chen, P. *J. Chem. Eur*. 2018, 5, 2409–18.
7. Corpuz, R.D.; De Juan-Corpuz, L.M.; Nguyen, M.T.; Yonezawa, T.; Wu, H-.L.; Somwangthanaroj, A.; et al. *Int. J. Mol. Sci.* 2020, 21, 3113.
8. Kao-ian, W.; Sangsawang, J.; Kidkhunthod, P.; et al. *J. Mater. Chem. A.* 2023, 11, 10584–1059.
9. Liu, H.; Wang, J-.G.; You, Z.; Wei, C.; Kang, F.; Wei, B. *Mater. Today*. 2021, 42, 73–98.
10. Khamsanga, S.; Pornprasertsuk, R.; Yonezawa, T.; Mohamad, A.A.; Kheawhom, S. *Sci. Rep*. 2019, 9.
11. Kao-ian, W.; Nguyen, M.T.; Yonezawa, T.; Pornprasertsuk, R.; Qin, J.; Siwamogsatham, S.; et al. *Mater. Today Energy*. 2021, 21, 100738.

Preparation of composite polymer electrolytes based on poly (ethylene oxide) and cellulose nanofiber for solid-state zinc-ion batteries

Weeraporn Treerittiwittaya[1] and Jitti Kasemchainan[1,2]*

[1]*International Graduate Program of Nanoscience & Technology, Chulalongkorn University, Bangkok 10330, Thailand*
[2]*Department of Chemical Technology, Faculty of Science, Chulalongkorn University, Bangkok 10330, Thailand*

**E-mail: jitti.k@chula.ac.th*

Abstract:

Recently, solid-state zinc-ion batteries (SSZIBs) based on polymer electrolytes have attracted increasing attention. Herein, composite solid polymer electrolytes (SPEs) are developed by incorporating polyethylene oxide (PEO) and zinc trifluoromethanesulfonate ($Zn(OTf)_2$) into a cellulose nanofiber (CNF) matrix derived from biological sources, acting as reinforcing phase. The PEO/$Zn(OTf)_2$/CNF composite with a 10 wt% CNF filling gave a high mechanical strength as evidenced by the Young's modulus of 601.39 MPa and the tensile strength of 36.22 MPa, which could be attributed to the continuous nanofiber network of CNF. Furthermore, the organic additive consisting of 0.5 M $Zn(OTf)_2$ and fume silica was introduced onto the PEO/$Zn(OTf)_2$/10%CNF electrolyte to enhance the ionic conductivity of 2.12×10^{-4} $S \cdot cm^{-1}$. After assembly of the symmetrical Zn/Zn cells using the composite polymer electrolyte, the constant-current cycling was performed and the resulting performance indicated that no short-circuiting was present as well as the zinc anode was favorable, ensuring sustained long-term stability (over 400 h) at a current density of 0.5 $mA \cdot cm^{-2}$. As for the full-cell testing: Zn | PEO/$Zn(OTf)_2$/10%CNF | δ-MnO_2, it was achievable for a high reversible capacity of 142 $mAh \cdot g^{-1}$ at a current density of 10 $mA \cdot g^{-1}$ and a high coulombic efficiency of 97% after 50 cycles.

1. Introduction

Rechargeable aqueous zinc-ion batteries (AZIBs) have become increasingly attractive as a potential energy storage technology in recent years. This is because of their high theoretical capacity (819 $mAh \cdot g^{-1}$) and volumetric energy density (5855 $mAh \cdot cm^{-3}$)[1]. Furthermore, there are a lot of advantages, including the abundance of Zinc in natural reservoirs, non-toxicity, non-flammability, stability, safety, and environmental friendliness. Nevertheless, the presence of water in the batteries poses several challenges such as corrosion and passivation at the Zn electrode, evolution of hydrogen gas, and dissolution of electrode species.

Solid-state Zn-ion batteries (SSZBs) employing solid electrolytes are widely recognized as the future battery due to their inherent safety, no leakage, non-corrosive behavior, and ability to inhibit dendrite growth. Accordingly, it is believed that the SSZBs can mitigate the issues of AZIBs. Extensive research indicates that solid polymer electrolytes (SPEs), typically composed of a
polymer and a metal salt, provides favorable technical characteristics, including high ionic conductivity, electrochemical stability, and thermal stability.

Polyethylene oxide (PEO) is one of the most selected polymers for polymer electrolytes[2]. General solid polymer electrolytes have a high degree of crystallinity that can hinder ionic conductivity. The polymer's low mechanical strength additionally leads to a risk of breaking when during the processes of cell assembly or operation. Incorporation of nano-sized fillers into the polymer matrix can improve both the ionic conductivity and mechanical strength of PEO at room temperature.

This research aims to develop high-performance composite polymer electrolytes (CPEs) by combining cellulose nanofiber (CNF) with a PEO matrix. CNF is derived from natural materials and is known for its superior thermal and chemical stability. Also, the use of an organic compound as a modifier in the composite polymer electrolyte is possible to complement the ionic conductivity, the mechanical characteristics, and the interfacial stability. To evaluate the battery-related function of CPEs and elucidate the fundamental reaction mechanisms in solid-state zinc ion batteries, a layered δ-MnO_2 as an active material for Zn-ion storage is utilized to prepare a composite electrode.

2. Materials and Methods

2.1 Materials

Poly (ethylene oxide) (PEO, Mw = 100,000), Zinc trifluoromethanesulfonate ($Zn(OTf)_2$, 98%) and Silica fumed (SiO_2, Mw = 60.08) were purchased from Sigma-Aldrich. Cellulose nanofiber from Pheedoo.Co.Ltd.

Anhydrous acetonitrile (CH_3CN, 99.99% HPLC Grade) was purchased from Fisher ChemAlert Guide. Super P Carbon black C65 was purchased from MSE Supplies. Zn foil thickness 0.1 mm was purchased from Advance Linear Co., Ltd. Tetrahydrofuran (THF, 99.5% AR Grade) was purchased from QRec.

2.2 Preparation of composite polymer electrolytes (CPEs)

The composite polymer electrolytes based on poly (ethylene oxide) and cellulose nanofiber were prepared via a conventional solution casting technique. The nanofiber cellulose dispersion was dissolved in deionized water at different concentrations (1, 5, 10, and 20 wt%). After 30 min stirring, the dispersion was coated onto a Teflon mold with a diameter of 5 cm and then dried overnight at 40 °C. The homogenous solution of 85 wt% PEO and 15 wt% $Zn(OTf)_2$ in anhydrous acetonitrile was added to cellulose membranes and then allowed to dry under vacuum. Finally, the composite polymer electrolytes were obtained.

2.3 Physical characterization

2.3.1 Physical characterization

The X-ray diffraction (XRD) patterns were achieved using an Aeris Benchtop X-ray Diffractometer (Malvern Panalytical) and Cu K-α radiation of wavelength (1.5418 Å). Scanning electron microscopy (SEM, JEOL-JEM-6480LV) was employed to investigate the microstructure of the materials. The mechanical properties of polymer membranes were measured on a universal testing machine (UTM (H10 KM)) equipped with a 1-ton load cell under ASTM D882.

2.3.2 Electrochemical characterizations

The assessment of ionic conductivity was conducted by placing a composite polymer electrolyte between two stainless steel plates at ambient temperature. Electrochemical impedance spectroscopy (EIS) measurements were conducted using a potentiostat (Gamry Instruments-Interface 101E, USA) within a frequency range of 1 MHz to 0.1 Hz, applying a voltage perturbation of 10 mV. The electrochemical stability of composite polymer electrolytes in the presence of a Zn metal electrode was measured by symmetric Zn|Zn cells to galvanostatic cycling at a current density of 0.2 and 0.5 $mA \cdot cm^{-2}$. Electrochemical cycling of solid-state Zn|δ-MnO_2 cells based on PEO/$Zn(OTf)_2$/CNF as the solid electrolytes were measured by using a pouch cell. The composite positive electrode was prepared by mixing δ-MnO_2, Super P Carbon black C65, and PEO binder with a ratio of 70:20:10 in anhydrous acetonitrile solvent to obtain a homogeneous slurry, which was then coated onto a graphite sheet. After vacuum drying at 60 °C, the composite cathode was obtained for use and the mass loading was about 1.5 $mg \cdot cm^{-2}$. Here, the minimized 0.5 M $Zn(OTf)_2$ and SiO_2 in THF viscous electrolyte amount of 5 µL was dropped to both sides of the CPEs in the cell assembly. The charge-discharge cycling was performed on a Neware-BTS4000-5V10mA and carried out at room temperature between 1 and 1.8 V.

3. Results & Discussion

3.1 Physicochemical properties of CPEs

X-ray diffraction (XRD) patterns of PEO, CNF, and PEO/ $Zn(OTf)_2$/CNF with different CNF contents are shown in Figure 1. The pristine PEO film indicates a crystalline structure characterized by two distinct peaks approximately 19.3° and 23.3° 2θ[3]. The addition of $Zn(OTf)_2$ causes a notable decrease in the intensity of the distinctive PEO peaks, implying an increase in the amount of the amorphous component. The pure CNF exhibits a disordered structure defined by a broad peak in the XRD pattern. The addition of CNF to the solid-state polymer electrolyte leads to a decrease in the intensity of the particular peak of PEO/$Zn(OTf)_2$, indicating an increase in the fraction of the amorphous component. When a concentration of 20 wt% CNF, the major peak 23.3° 2θ exhibits broadening, which confirms a high degree of pure CNF and an excess of CNF due to aggregation. This occurrence could affect the structural characteristics and electrochemical performance of solid-state polymer electrolytes further.

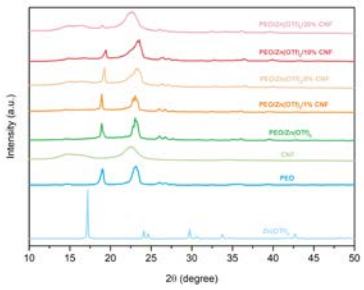

Figure 1. XRD patterns for PEO/ $Zn(OTf)_2$, CNF, and PEO/$Zn(OTf)_2$/CNF at different CNF contents.

Scanning electron microscopy images of composite polymer electrolytes in cross-section are included in Figure 2. (c-f). A significant increase in the fraction of the CNF reinforcement results in a highly porous distribution. The

enhanced quality of high-density CNF (1 to 10 wt%) is attributed to the evolution of pore density and interconnectivity. When the content of CNF exceeds 20 wt%, the membrane morphology becomes like that of pure CNF. This eliminates the transport pathway of Zn^{2+} in the host polymer. The CPE holds an outstanding standard of mechanical strength due to the compressed structure of the CNF.

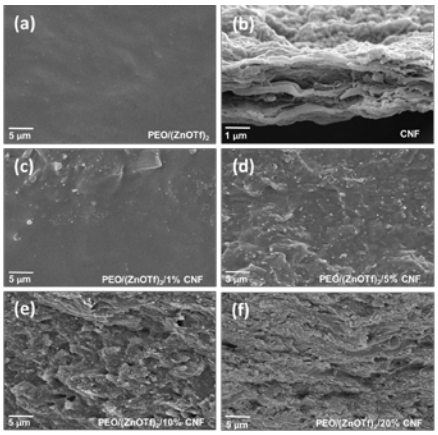

Figure 2. SEM images of (a) PEO/Zn(OTf)$_2$ (b) CNF (c-f) PEO/Zn(OTf)$_2$/CNF composite polymer electrolytes with the respective 1, 5, 10, and 20 wt% CNF.

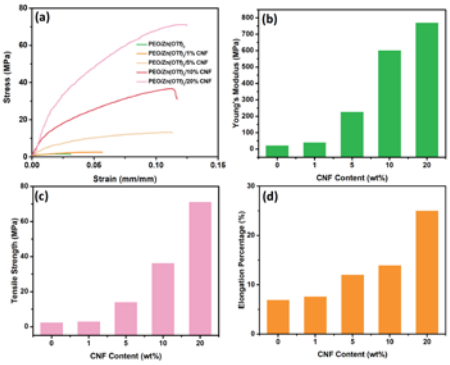

Figure 3. (a) Stress-strain curves for CPEs (b) Young's modulus (c) Histograms of the tensile strength (d) and Elongation percentage depending on different CNF contents.

3.2 Mechanical properties of the CPEs

The mechanical properties of the solid-state electrolyte are critical for its durability, as they allow it to resist the pressures that occur during battery reactions and prevent the formation or growth of dendrite structures. Figure 3. shows the Young's modulus, tensile strength, and elongation percentage of the CPE at different nanocellulose ratios. Mechanical properties were greatly enhanced with the addition of further CNF, resulting in values of 769 MPa of Young's modulus, 71 MPa of tensile strength, and 25% of elongation percentage when the electrolyte contained a 20 wt% CNF. The incorporation of cellulose nanofibers (CNF) significantly enhances the mechanical robustness of the polymer electrolyte. CNF enlarges the surface area over which force is received, hence improving the transmission of force in polymer electrolytes. As a result, this increases the material resistance to tensile strength.

3.3 Conductivity properties of the CPEs

Table 1 shows the ionic conductivity of electrolytes containing PEO/Zn(OTf)$_2$/CNF with different content of CNF (ranging from 1 to 20 wt%). The ionic conductivity of PEO/Zn(OTf)$_2$/CNF decreases as the weight fraction of CNF increases. It reaches its lowest value at 20 wt% CNF due to the influence of the pore structure of the electrolyte-containing fiber. The ionic conductivity of CNF content of 1, 5, and 10 wt% is comparable because the small pores are consistently interconnected, providing a homogeneous pathway for the transport of Zn^{2+}. The notable decrease of ionic conductivity observed in the 20 wt% CNF can be attributed to poor interactions between the polymer components and excessive CNF in the mixture.

Table 1. The ionic resistances and conductivities of PEO-SPE and PEO/Zn(OTf)$_2$/CNF with CNF at different contents.

Sample	Resistance (Ω)	Ionic conductivity (S·cm^{-1})
PEO/Zn(OTf)$_2$	29.5	5.29×10^{-4}
PEO/Zn(OTf)$_2$/1%CNF	31.9	4.44×10^{-4}
PEO/Zn(OTf)$_2$/5%CNF	37.2	4.09×10^{-4}
PEO/Zn(OTf)$_2$/10%CNF	76.1	2.12×10^{-4}
PEO/Zn(OTf)$_2$/20%CNF	660.0	2.88×10^{-5}

3.4 Stability of CPEs with Zn metal and electrochemical mechanism

The cycling performance of polymer composite electrolytes was thoroughly measured using Zn| PEO/Zn(OTf)$_2$/CNF |Zn symmetrical cells. Figure 4 (a) shows the galvanostatic cycling performed at a current density of 0.2 mA·cm^{-2}, The PEO/Zn(OTf)$_2$ without CNF and with 1 wt% CNF have a limited working lifecycles around 6 h and 250 h, respectively. As can be seen, the voltage polarization decreased before facing a short circuit, mostly caused by the large growth of Zn dendrites and the fragility of the membrane. The voltage polarization of the PEO/Zn(OTf)$_2$ /20% CNF system notably exceeds 0.2 V and early short circuit after 50 h, indicating an unstable interface between the electrolyte and the zinc anode. Conversely, the Zn|PEO/ Zn(OTf)$_2$/10% CNF|Zn cell demonstrates continuous cycling for at least 500 h without any short circuits or degradation in polarization. Also, it achieves a higher current density (0.5 mA·cm^{-2}), as shown in Figure 4 (b) while the voltage polarization noticed fluctuations of PEO/Zn(OTf)$_2$/5% CNF and eventually short-circuited after 200 h. Hence, it has been proven that the PEO/Zn(OTf)$_2$/10%CNF membrane exhibits remarkable improvements in electrochemical stability and mechanical strength, while also preventing the penetration of Zn dendrites.

Rate performance of PEO/Zn(OTf)$_2$/ 10%CNF|δ-MnO$_2$ solid-state batteries can be measured within the range of 10 mA·g^{-1} to 100 mA·g^{-1}. The δ-MnO$_2$ electrode has a discharge capacity of 145 mAh·g^{-1} at 10 mA·g^{-1}, as shown in Figure 5 (a). The discharge capacity was found to be 100 mAh·g^{-1} at 20 mA·g^{-1}, 75 mAh·g^{-1} at 50 mA·g^{-1}, and 60 mAh·g^{-1} at 100 mA·g^{-1}. The reversible capacity of the battery from 100 to 10 mA·g^{-1} recovers to 80% of the initial capacity (106 mAh·g^{-1}). The efficiency of the cell cycling is shown in Figure 5 (c) at a current rate of 10 mA·g^{-1}. The solid-state cell of Zn|PEO/ Zn(OTf)$_2$/10% CNF|δ-MnO$_2$ exhibited a discharge capacity of 142 mAh·g^{-1} and 65 % capacity retention after 50 cycles. Our hypothesis suggests that the gradual degradation in capacity while cycling is caused by the Mn dissolving into the electrolyte and the deformation of the structural layer, which decreases its Zn^{2+} storage capability[4]. This includes the complete evaporation of THF solvent in the viscous electrolyte that was dropped on the composite polymer electrolyte.

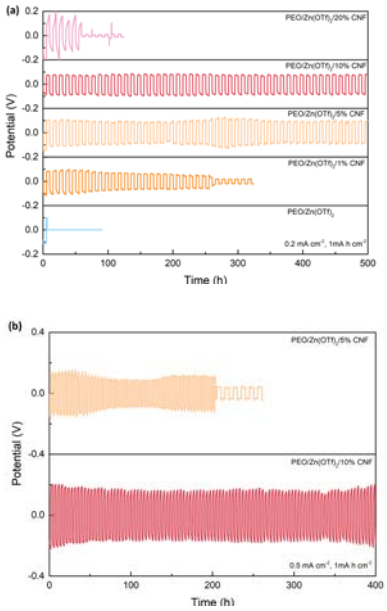

Figure 4. Galvanostatic cycling of Zn| PEO/Zn(OTf)$_2$/CNF |Zn symmetrical cells at (a) 0.2 mA·cm^{-2} and (b) 0.5 mA·cm^{-2}.

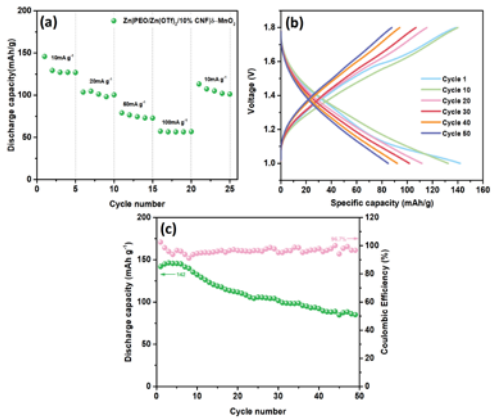

Figure 5. (a) Rate capability of Zn| PEO/Zn(OTf)$_2$/10%CNF |δ-MnO$_2$ cells from 10, 20, 50 and 100 mA·g^{-1} (b) Charge–discharge curves and (c) cycling performance of Zn| PEO/Zn(OTf)$_2$/10% CNF |δ-MnO$_2$ cell at 10 mA·g^{-1}.

4. Conclusion

In conclusion, we successfully prepared a flexible solid-state polymer electrolyte reinforced by the CNF filler with a facile solution casting method. The optimal PEO/Zn(OTf)$_2$/10% CNF membrane exhibited high mechanical strength as evidenced by Young's modulus of 601.39 MPa and the tensile strength of 36.22 MPa. This composite polymer electrolyte offers higher ionic conductivity of 2.12 × 10^{-4} S·cm^{-1} and good compatibility with Zn metal, allowing for steady plating and stripping with a small voltage polarization of 0.2 V for over 400 h without any

short circuits in symmetrical batteries at a current density of 0.5 $mA \cdot cm^{-2}$. In addition, the rechargeable solid-state ZIB was produced using a δ-MnO_2 as the active material. The solid-state zinc-ion battery cell of Zn|PEO/$Zn(OTf)_2$/ 10%CNF|δ-MnO_2 was achieved for a high reversible capacity of 142 $mAh \cdot g^{-1}$ at a current density of 10 $mA \cdot g^{-1}$, along with a coulombic efficiency of 97 %. Also, it maintained 65 % of the initial capacity after 50 cycles.

References

1. He, W.; Zuo, S.; Xu, X.; Zeng, L.; Liu, L.; Zhao, W.; Liu, J. *Mater. Chem. Front.* **2021,** *5* (5), 2201-2217.
2. Xue, Z.; He, D.; Xie, X., *J. Mater. Chem. A.* **2015,** *3* (38), 19218-19253.
3. Karan, S.; Sahu, T. B.; Sahu, M.; Mahipal, Y. K.; Agrawal, R. C. *Ionics* **2017,** *23* (10), 2721-2726.
4. Alfaruqi, M. H.; Gim, J.; Kim, S.; Song, J.; Pham, D. T.; Jo, J.; Xiu, Z.; Mathew, V.; Kim, J., *Electrochem. Commun.* **2015,** *60*, 121-125.

Fabrication of $Sr_2Fe_{0.9}Ni_{0.1}MoO_6$ anode-supported solid oxide fuel cell by powder injection molding

Kulanis Supprasert [1], Nutthita Chuankrerkkul[2], and Soamwadee Chianansutcharit[3]*

[1]*Department of Petrochemistry, Faculty of Science, Chulalongkorn University, Bangkok, 10330, Thailand*
[2]*Metallurgy and Materials Science Research Institute, Chulalongkorn University, Patumwan, Bangkok, 10330, Thailand*
[3]*Department of Chemistry, Faculty of Science, Chulalongkorn University, Bangkok, 10330, Thailand*

*****E-mail : Soamwadee.c@chula.ac.th*

Abstract:

This study aimed to fabricate and study the effects of anode fabrication parameters, e.g. feedstock composition on moldability, sintering temperature on microstructure and porosity, of $Sr_2Fe_{0.9}Ni_{0.1}MoO_6$ ($SFNi_{0.1}M$) phase. $SFNi_{0.1}M$ is prepared by a solid-state reaction and fabricated into anode-supported cells by powder injection molding (PIM) application using environmentally friendly chemicals. The mixture of polyethylene glycol (PEG) and polyvinyl butyral (PVB) is used as a binder for feedstock preparation and the feedstock ratio between the $SFNi_{0.1}M$ powder and binder are 45:55, 50:50, and 55:45 vol%. The sintering temperatures are 1250 °C and 1300 °C. A porous anode support in SOFC could be successfully fabricated. The results show that the optimal condition for PIM of anode support, of which the adequate strength and porosity achieved ensure gas transport on a fuel side, is the volume ratio of $SFNi_{0.1}M$ powder to binder at 45:55, and the sintering temperature of 1250 °C. The mechanical properties and microstructure of components could be controlled by adjusting processing parameters. The obtained anode support cell already shows the potential PIM fabrication method for future upscale and cost-effective SOFC production.

1. Introduction

Solid oxide fuel cells (SOFC) are a well-known alternative power generator that can transform chemicals into highly efficient electricity without pollution. Currently, the large-scale application of SOFC is hindered by its high working temperature (~1000 °C). A high operating temperature is usually required to achieve sufficient ionic and electronic conductivities in the cell components. However, the high operating temperature has several negative impacts such as faster material degradation and high operating cost. One of the ways to solve this problem is to reduce the operating temperature to intermediate temperature (IT-SOFC, 600-800 °C) by developing material with high electrochemical catalytic activity and employing a more complex cell design.[1,2]

In recent years, perovskite-type oxides have gathered enormous research attention for applying anode in SOFC operating in IT-SOFC. The double perovskite strontium iron molybdenum oxide, Sr_2FeMoO_6 (SFMO), has gained increasing attention as an electrode due to its high structural stability in both reducing and oxidation atmosphere, good electronic conductivity, and excellent oxide-ion conductivity.[3] Our research group has reported the substitution of Fe with Ni in double perovskites SFMO exhibiting good performance as anode materials for IT-SOFC. $Sr_2Fe_{1-x}Ni_xMoO_6$ with Ni (X=0.1), $SFNi_{0.1}M$, showed a high power density of 834 $mW.cm^{-2}$ at 800 °C for the electrolyte-supported fabricated of single fuel cells $SFMO|La_{0.9}Sr_{0.1}Ga_{0.8}Mg_{0.2}O_3|Sr_{0.5}Sm_{0.5}CoO_3$.[4]

However the electrolyte-supported SOFC is not widely commercially used because there is a disadvantage associated with the electrolyte thickness, which reduces efficiency and exhibits low power density due to higher ohmic resistance. This can be overcome by lowering the electrolyte resistance and improving flexibility in cell design anode supported.

Anode-supported solid oxide fuel cells are receiving considerable interest in design and use suited for operation at low temperatures.[5] It is advantageous that the ohmic resistance is lower than that of the electrolyte-supported cell because much thinner electrolyte films can be employed.

Powder injection molding (PIM) technique has been applied in the field of SOFC to produce anode support, PIM can be a solution to reduce the costs of SOFC. It allows the production of complex 3D designs with near-net shapes at an industrial rate.

During the PIM process, the raw powder is mixed with polymer binders to produce a feedstock, which is then processed with an injection molding press. The green parts (as-injected) can be handled and adjusted if needed before chemical and thermal debinding to remove

the polymers. The brown part (after debinding) is sintered to obtain final dimension and properties. The homogeneity of injection molded parts is higher than for uniaxial pressing, and their final dimensions after sintering shrinkage are well controlled.[6]

In this work, the fabrication of $Sr_2Fe_{0.9}Ni_{0.1}MoO_6$ as anode support for forming an electrolyte thin film is investigated. The anode support was prepared from $SFNi_{0.1}M$ with water-soluble binders using PIM technique. In this method, to avoid organic solvents, the binders are removed from the molded sample using water, which is an environmentally friendly debinding step developed by Chuankrerkkul et al.[7] We also present the effects of anode support fabrication parameters, e.g. feedstock composition on moldability, injection process, sintering temperature on microstructure, shrinkage, and porosity.

2. Materials and Methods

2.1 Materials

The powder of $Sr_2Fe_{0.9}Ni_{0.1}MoO_6$ anode was synthesized by a solid-state reaction method. The raw materials are $SrCO_3$ (Aldrich, 99.9+%), Fe_2O_3 (Labchem, 81%), MoO_3 (Univar, 99.5%), and NiO (Aldrich, 99%). In the first step, Fe_2O_3 and MoO_3 were used as the starting materials to synthesize the $Fe_2Mo_3O_{12}$ as described in Ref.[8] Next step, a stoichiometric ratio of $SrCO_3$, Fe_2O_3, $Fe_2Mo_3O_{12}$, and NiO was thoroughly ground with a ball mill for 1 hour and calcined in air at 1000 °C, for 12 hours and sintered in air at 1300 °C for 12 hours.

2.2. Anode-supported fabrication procedure

$SFNi_{0.1}M$ anode support was fabricated by PIM technique**.** $SFNi_{0.1}M$ powder was prepared as starting materials. Feedstocks having solid loading in range of 45 to 55 vol% were formulated and shown in Table 1.

Table 1. Feedstock compositions

Formula	Solid loading (vol% $SFNi_{0.1}M$)	PEG (wt%)	PVB (wt%)
F-55	55	80	20
F-50	50	80	20
F-45	45	80	20

The feedstocks were prepared using a composite binder, containing a major fraction of polyethylene glycol (PEG), which can be removed rapidly by water leaching, and a minor fraction of polyvinyl butyrate (PVB). PIM was performed using a simple plunger-type machine. The feedstock was then injected into a disc-shaped mold with a diameter of 2.0 cm and a thickness of 1.5 mm. After the PIM process, the anode supported was soaked in water for 24 hours to remove PEG binder and dried at 100 °C for 24 h. After that, the brown anode supports were sintered at 1250 °C and 1300 °C for 1 hour.

2.3 Characterization

X-ray diffraction (XRD, Rigaku D-max 2002 Ultima Plus) was applied to verify the phase structure of the $SFNi_{0.1}M$ anode in the procession of sample preparation. XRD diffractometer equipped with Cu-Kα radiation (λ = 0.154 nm) operating at 40 kV and 20 mA in 2 theta range of 20-80 degrees.

Particle size distribution of $SFNi_{0.1}M$ powder was analyzed by Laser Light Scattering (Particle Size Analyzer, Mastersizer 2000, Malvem)

Debinding Process After the PIM process, the anode supports were soaked in RO water for 24 hours to remove PEG binder and dried at 100 °C for 24 h. Rate of binder removal was studied by comparing the weight loss of samples after soaking in water.

The open porosity and density of anode support after sintering at 1250 °C and 1300 °C were determined by Archimedes method and shrinkage was calculated from the percentage of change in sample diameter before and after sintering process.

The microstructure of $SFNi_{0.1}M$ powder and anode supported after sintering at 1250 °C and 1300 °C were observed with a scanning electron microscope (SEM, JEOL IT-100, operating at 15 kV)

3. Results & Discussion

3.1. XRD analysis

X-ray powder diffraction patterns of $SFNi_{0.1}M$ powders from 20 ° to 80 ° are shown in Figure 1. The main diffraction peaks were assigned to the double-perovskite phase with the tetragonal structure and a *I*4/m space group and minor diffraction peaks of $SrMoO_4$ (JCPDS no. 08-0482) were observed as an impurity. The $SrMoO_4$ impurity could be formed during the preparation process of Sr_2FeMoO_6 in air as explained by Nakamura et al.[9] In air, an oxygen stoichiometry of 6 is attained when the Mo solubility limit is 17% ($Sr_2Fe_{1.34}Mo_{0.68}O_6$) and then the extra oxygen is accommodated in the $SrMoO_4$ phase as described by Rager et al.[10]

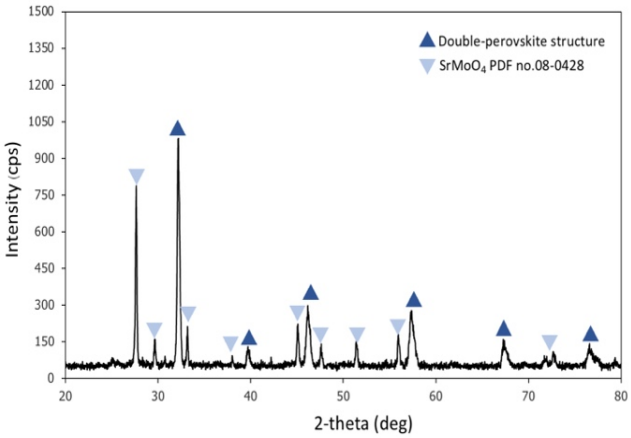

Figure 1. XRD patterns of $Sr_2Fe_{0.9}Ni_{0.1}MoO_6$ sintered in air at 1300 °C for 12 h.

3.2. Particle size distribution and $SFNi_{0.1}M$ powder microstructure

Before the PIM process, the particle size distribution was evaluated to observe the $SFNi_{0.1}M$ powder particle size. The results reveal a relatively uniform particle size distribution of approximately 6.72 µm, as depicted in Figure 2 and Figure 3. The microstructure of $SFNi_{0.1}M$ powder shows that $SFNi_{0.1}M$ powder exhibits an irregular shape with small particles clustered together. The presence of small-sized particles contributes to the preparation of composites with a relatively modest powder loading.

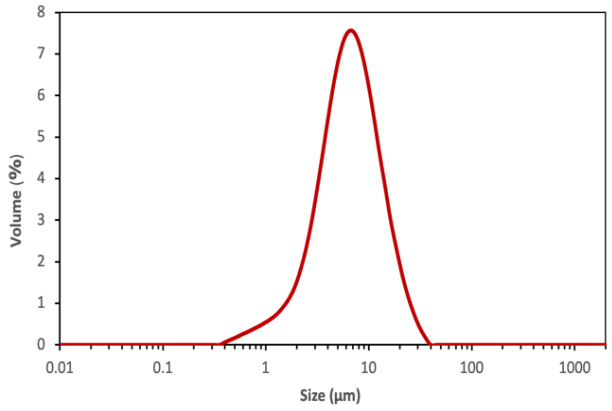

Figure 2. Particle size distribution of $SFNi_{0.1}M$ powder

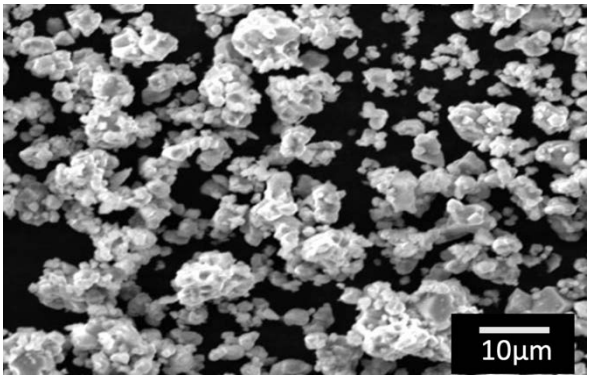

Figure 3. SEM micrographs of $SFNi_{0.1}M$ powder

3.3. Powder injection molding

The molding process involves injecting material using a Plunger-type machine to form the substrate for $SFNi_{0.1}M$ anodes. With a powder-to-binder ratio in the range of 45-55 by volume, it's observed that exceeding a volume ratio of 50 % for $SFNi_{0.1}M$ renders molding impractical. This limitation persists even at the maximum injection molding temperature of 200 °C due to excessive particle size and viscosity, stemming from a high powder content, the formula ratio of the binder used was insufficient for injection molding. The PIM compositions and moldability parameters are presented in Table 2.

Table 2. PIM compositions and moldability parameters

Formula	powder: binder (vol%)	Injection temperature (°C)	Mold ability
F-55	55:45	220	✗[a]
F-50	50:50	190	✓[b]
F-45	45:55	170	✓

[a]Injection molding is not possible.
[b]Injection molding is feasible.

3.4. Debinding PEG

Solvent debinding tests were carried out to investigate the time required for removal of the PEG, at room temperature. The results are presented in Figure 4. It can be observed that the sample with a 45:55 vol% ratio has a higher PEG removal efficiency than the sample with a 50:50 vol% ratio. After 8 hours, almost 80% of PEG has been removed, while other components in the specimen remain insoluble. The mass loss in the specimen aligns with the PEG mass, as the PEG removal rate is initially high. This is because the eliminated PEG at this stage is located on the surface, facilitating rapid reaction with water and

immediate dissolution. As time progresses, the PEG removal rate decreases due to increased difficulty in the reaction between water and PEG embedded within the specimen, requiring water infiltration to dissolve the internally inserted PEG. After conducting tests to assess the removal rate of PEG, the specimens were soaked in water for an additional 24 hours. Following this step, it was observed that there was very little remaining PEG in the specimens.

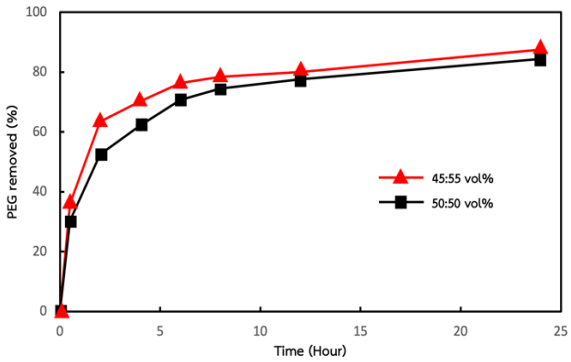

Figure 4. Water leaching specimen 45:55 vol% and 50:50 vol% (Various times and temperature)

3.5 Sintered properties and microstructure

The sintered properties are present in Table 3. Sintering at high temperatures also resulted in high shrinkage and less porosity. This is because the samples after sintering at high temperatures have a higher density.

Table 3. Sintered properties of specimens sintered at 1250 ºC and 1300 ºC for 1 h.

sample	Sintered at 1250 ºC		Sintered at 1300 ºC	
	Porosity (%)	Shrinkage (%)	Porosity (%)	Shrinkage (%)
F-45	42.08	10.25	27.55	16.18
F-50	37.86	13.43	22.20	20.05

The percentages of porosity in sample $SFNi_{0.1}M$(45:55 vol%), and $SFNi_{0.1}M$(50:50 vol%) anode support obtained from Archimedes' method were 42.08% and 37.86%, respectively. However, the porosity of $SFNi_{0.1}M$(45:55 vol%) was slightly higher than that of $SFNi_{0.1}M$(50:50 vol%) and difference became more significant after sintering (PVB removal). The results thus suggested that the pore channels were likely created around $SFNi_{0.1}M$ powders. More pore channels were created during PIM process. For brown samples, these channels were first partially filled with PVB leading to only slight difference in the porosity. In contrast, after PVB removal, the difference in porosity between $SFNi_{0.1}M$(45:55 vol%) and $SFNi_{0.1}M$(50:50 vol%) is due to the high binder ratio and the higher density that occurs at higher sintering temperatures. From this work, the suggested temperature is 1250 ºC which gives specimens having high porosity, suitable to use as porous anode support in SOFC. The SEM micrograph of $SFNi_{0.1}M$45:55 vol% specimens' microstructure of component sintered at 1250 ºC shown in Figure 5(a). It was observed that there were pore spaces resulting from the removal of the binder. The cross-section SEM images between the anode support and the GDC electrolyte are shown in Figure 5(b). $SFNi_{0.1}M$ anode support. It is observed that there are no cracks along the interface between the anodes and electrolytes, suggesting a good contact between the two materials.

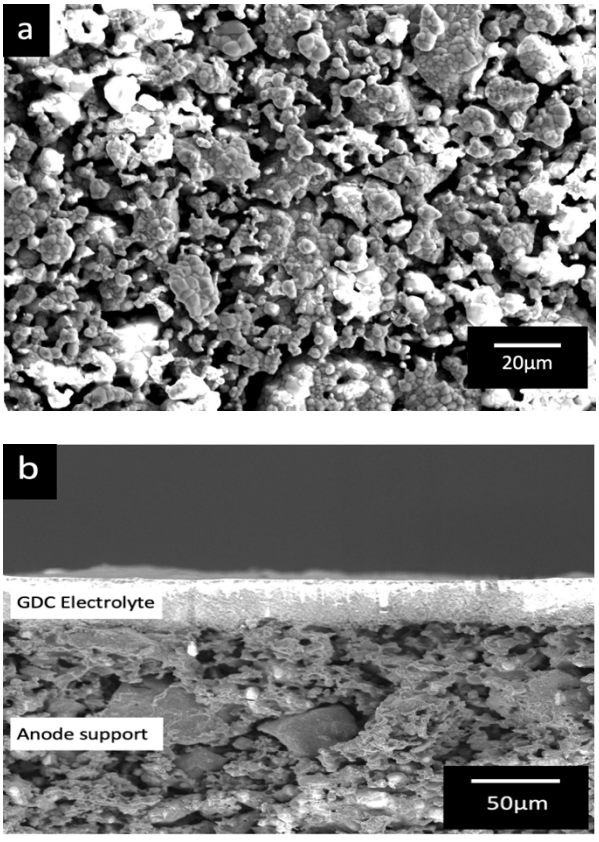

Figure 5. SEM micrographs of (a) surface and (b) cross-sectional microstructures of $SFNi_{0.1}M$ (45:55 vol%) sintered at 1250 °C for 1 h.

4. Conclusion

A porous $SFNi_{0.1}M$ anode support is successfully fabricated by PIM technique. The water-soluble system enables the process to be environmentally friendly by using a binder ratio of 80:20 wt% between PEG and PVB to create pore spaces. The samples with a solid loading ratio of 45-50 vol% can be injection moldable. Specimens 45:55 vol% sintered at 1250 ºC have a high

porosity of up to 42.08% as required by the SOFC system and can be used as porous anode support in SOFC for forming an electrolyte thin film to evaluate cell performance. The mechanical properties and microstructure of components could be controlled by adjusting processing parameters.

References

1. Mahano, N.; Banerjee, A.; Gupta, A.; Omar, S.; Balani, K. *Prog. Mater. Sci.* **2015**, *72*, 141-337.
2. Zakaria, Z.; Awangmat, Z.; Abu Hassan, S.H.; Boon Kar, Y. *Int. J. Energy Res.* **2020**, *44*, 594-611.
3. Bhattacharyya, R.; Das, S.; Omar, S. *Acta materialia*. **2018**, *159*, 8-15.
4. Ung-arphorn, Y. Thesis, Chulalongkorn University, 2558.
5. Yakabe, H.; Hishinuma, M.; Uratani, M.; Matsuzaki, Y.; Yasuda I. *J. Power Source*. **2000**, *86(1-2)*, 423–431.
6. Faes, A.; Girard, H.; Zryd, A.; Wuillemin, A.; Van Herle, J. *J. Power Sources*. **2023**, *227*, 35-40.
7. Chuankrerkkul, N.; Chauoon, S.; Meepho, M.; Pornprasertsuk, R. *Key Eng. Mater.* **2017**, *751*, 467-470.
8. Muñoz-García, A.B.; et al. *J. Am. Chem. Soc.* **2012**, *134*, 6826-6833.
9. Nakamura, T.; Kunihara, K.; Hirose, Y. *Mater Res Bull*. **1981**; *16*, 321-326.
10. Rager, J.; Zipperle, M.; Sharma, A.; MacManus-Driscoll L. *J. Am. Ceram. Soc.* **2004**, *87*, 1330-1335.

Biodiesel production via the electrocatalytic process from Pinari oil (*Sterculia foetida* L.)

Namfon Baothongkam[1], Chaturong Suparpprome[1], and Anusorn Vorasingha[1, 2]*

[1]*Department of Chemistry, Faculty of Science, Naresuan University, Maung, Phitsanulok, 65000 Thailand*
[2]*Research Center for Academic Excellence in Petroleum, Petrochemical and Advanced Materials, Phitsanulok, 65000 Thailand*

**E-mail: anusornv@nu.ac.th*

Abstract:

The conventional transesterification reaction of Pinari seed oil (*Sterculia foetida*) with methanol using natural fiber heterogeneous catalyst via electrocatalytic reactor was investigated. However, the cost is one of the main obstacles in commercializing in this process. Due to the multifaceted adversities of many of the catalysts, there is active consideration for an electrolysis process that does not require elevated temperature. In addition, an electrolysis by used heterogeneous catalyst is carried out the presence or absence of a catalyst or co-solvent. In this research, a various parameter such as electrolysis voltage, stirring rate, electrode type, water content, co-solvent, reaction temperature, molar ratio of oil to methanol and concentration of electrolyte. The chemical structure of biodiesel products was analyzed by nuclear magnetic resonance spectroscopy (NMR) and Fourier transform infrared Spectrometry (FT-IR) techniques. The result showed our heterogeneous catalyst from natural fiber could be used as electrolysis transesterification catalyst to give a fatty acid methyl ester (FAMEs) from Pinari and several seed oil in good yields.

1. Introduction

Renewable fuels have come to play an important role in meeting the world's energy requirement. There is a need to find out an alternative fuel to fulfill the energy demand. The use of bio oil as alternative fuels has increased due to the diminishing oil reserves and environmental consequences of exhaust gases from petroleum fuel dengines. Biodiesel (fatty acid methyl eater, FAME) are liquid or gaseous fuels made from biomass materials such as agricultural crops, municipal wastes, and agricultural and forestry by products via biochemical or thermos chemical processes. They can replace conventional fuels in vehicle engines, either totally or partially in a blend.[1] Vegetable oil methyl esters, commonly referred to as "biodiesel", are prominent candidates as alternative diesel fuels. The name biodiesel has been given to transesterified vegetable oil to describe its use as a diesel fuel.[2] Vegetable oil fuels have not been acceptable because they are more expensive than petroleum fuels. However, with recent increases in petroleum prices and uncertainties surrounding petroleum availability, vegetable oils have become more attractive recently because of their environmental benefits and the fact that they are made from renewable resources.[3,4]

Recently, the reactions for direct transformation of vegetable oils into ethyl esters and glycerol have been known more than a century. The reactions of interest today, mainly those producing methyl esters from palm, rapeseed, soybean and sunflower oils, have been studied and optimized in order to manufacture the high quality cosmetic material known as bioester. Several commercial processes to produce fatty acid ethyl esters from vegetable oils have been developed and are available today. These processes consume heterogeneous basic catalysts such as metal oxide which from unrecyclable waste products. This proceeding provides a general description of a new process using a heterogeneous basic catalytic system.

Transesterification is the reaction of vegetable natural oil with an alcohol to form esters and glycerol. A catalyst is used to improve the reaction rate and yield. Since the reaction is reversible, excess alcohol used to shift the equilibrium to the products information.[14] The liquid acid catalysed transesterification process does not enjoy the same popularity in commercial applications as its counterpart, the acid catalysed process. The fact that the homogeneous acid catalysed reaction is about 40 times slower than the homogeneous acid catalysed reaction has been one of the main reasons. However, acid catalysed transesterifications hold an important advantage with respect to base catalysed ones. The performance of the acid catalyst is not strongly affected by the presence of fatty acid ethyl ester (FAME) in the feedstock. In fact, acid catalysts can simultaneously catalysed both esterification and transesterification. Thus, a great advantage with acid catalysts is that they can directly produce biodiesel from low-cost lipid feed stocks, generally associated with high FAEE concentrations (low-cost feed stocks, such as used cooking oil.

Several biodiesel experiment methods have been developed. Electrolysis method can be used potentially to overcome global problems like warming and energy crisis through utilizing electrochemical reaction to convert waste organic matter into biofuel.18 In electrolysis method, a direct electric current passes between electrodes through an ionic substance that is either dissolved in a suitable product. The prepared biodiesel is reacted with methanol in present of base catalyst to result in fatty acid methyl ester and glycerol. A catalyst is employed to increase the presence of organic compounds, which modify and improve bio-oil as a precursor for fuel. Heterogeneous catalyst has the advantages of being environmentally goods because of easily recovered, reproduced and reused. However, the heterogeneous base catalyst has been proved to be and effective way for biodiesel production, they have the limitation of being sensitive to high free fatty acid (FFA). Particularly in solid state, they are not mixed with the alcohols in the trans-esterification process causing cellulose and zeolite to be the promising materials in the homogeneous catalyst.

Recently, the reactions for direct trans formation of vegetable oils into methyl esters and glycerol have been known for more than a century. The reactions of interest today, mainly those producing methyl esters from palm, rapeseed, soybean and sunflower oils, have been studied and optimized in order to manufacture the high quality diesel fuel known as biodiesel.

With over ten years of development and commercial use in Europe, booster has now proved its value as a fuel for diesel engines **[5-7]**. The product is free of sulfur and aromatics, and, as it is obtained from renewable sources, it reduces the lifecycle of carbon dioxide emissions by almost 70% compared to conventional diesel fuel. Moreover, recent European regulation have restricted sulfur content in fuel to no more than 50 ppm in year 2005. Sulfur is known to provide diesel fuels with a lubricity that will disappear as the regulations take effect. Boester addition at levels of one to two percent in diesel blends has the beneficial impact of restoring lubricity through an antiwear action on engine injection systems.

Sterculia Foetida (Pinari) is a native plant of Thailand that can reach 20 m in length. It can find from north of Thailand to the southeast of Myanmar. It is cultivated as an ornamental plant for shade and is suitable for use in reclamation. Samrong species have a pan tropical occurrence, with approximately 300 species distributed throughout tropical forests areas of Southeast Asia. *Sterculia Foetida* seeds are consumed by both wild life and humans, albeit raw, cooked or roasted by the latter. The seeds are tasty and rich in nutrients. The image of *Sterculia Foetida* as shown in Figure 1.

Figure 1. *Sterculia Foetida* (Pinari) seeds and tree

Several commercial processes to produce fatty acid methyl esters from vegetable oils have been developed and are available today. These processes consume heterogeneous basic catalysts such as metasilicate which from unrecyclable waste products. This proceeding provides a general description of a new process using a heterogeneous basic catalytic system.

2. Materials and Methods

2.1 Materials and Processes

The transesterification of triglycerides to ethyl esters with ethanol reaction was illustrated in Fig. 2. An excess of methanol is required to obtain a high degree of conversion.

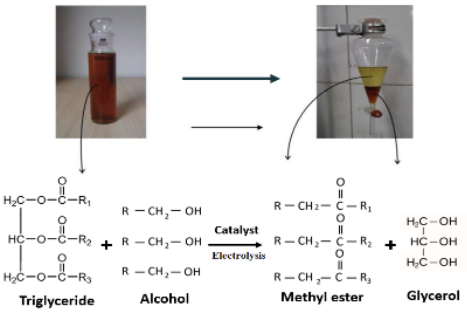

Figure 2. Over all of transesterification reactions for natural oil metanalysis

The conventional catalysts in natural oil transesterification processes are selected among bases such as alkaline or alkoxides. However transesterification could also be performed using acid catalysts, such as hydrochloric acid, sulfuric acid and sulfonic acid, or using metallic base catalysts such as oxides of calcium, tin, magnesium, or zinc. All these catalysts act as homogeneous catalysts and need to be removed from the product after the transesterification

process. The biodiesel product was % yield analysed with ^{1}H NMR spectrometer was shown in Figure 3.

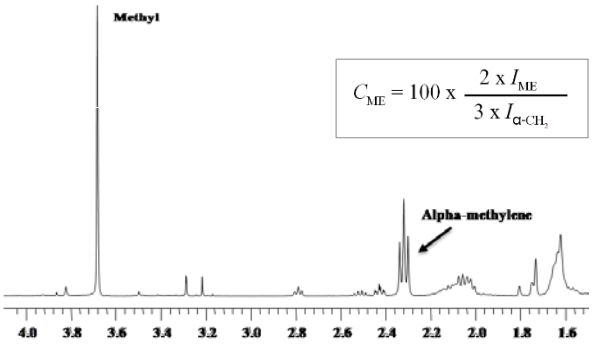

Figure 3. ^{1}H NMR Spectra of % conversion ofmethyl ester from natural oil

2.2 Homogeneous Catalyzed Processes

In conventional industrial booster processes, the ethanol transesterification of natural vegetable oils is achieved using a homogeneous catalyst system operated in either batch or continuous mode. In most cases the catalyst is acid. It is recovered after the trans-esterification reaction as sodium glycerate, sodium methylate and sodium soaps in the glycerol phase. An acidic neutralization step with, for example, aqueous hydrochloric acid is required to neutralize these salts. In that case glycerol is obtained as an aqueous solution containing salt. Depending on the process, the final glycerol purity is about 70% to 80%. When we used sulfuric as acid catalyst, side reactions forming salt generally occur. This type of reaction is also observed when acid is employed and traces of water are present. The salt was soluble in the glycerol phase and must be isolated after neutralization by decantation as fatty acids. The loss of esters converted to fatty acids can reach as high as 1% of the biodiesel production. Recently, a large variety of solid acid catalysts have been investigated for the synthesis of biodiesel over the past decade, including among them the use of solid acid with mesoporous acid. Several studies identified acid as a promising catalyst palm and other natural vegetable oil transesterification. The homogeneous trans-esterification reactor was shown in Fig. 4

Figure 4. Homogeneous transesterification reactor

2.3 Conventional Heterogeneous Catalyzed Electrolysis Processes

In the present of in this investigation, a small concentration of zeolite/cellulose/KOH heterogeneous catalyst (1, 3, 5 and 7 wt%, base on oil weight) was used. An electrolysis cell containing stainless steel plate electrode (2 cm x 4 cm x .01 cm) at a distance of 3 cm, 100 mL of reaction mixture containing methanol, natural oil (triglyceride), acetone, water and catalyst was used in the electrolysis process. The methanol/oil molar ratios were set at 1:3, 1:6 and 1:9. Different ratio of acetone (5% 10 % and 15%) were examined. 2 wt% of deionized water was also added to the electrolysis cell. This set electrolysis cell voltages ranged from 10 to 30 Volt. The heterogeneous electrolysis cell reactor was shown in Figure 5.

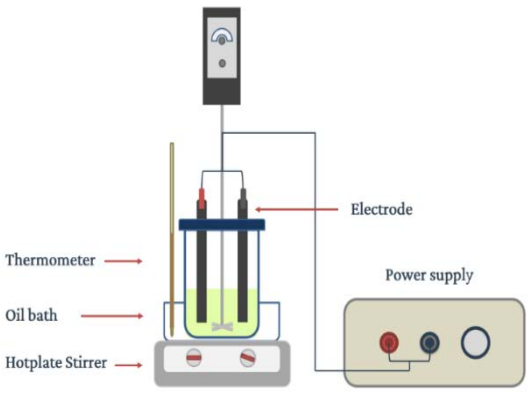

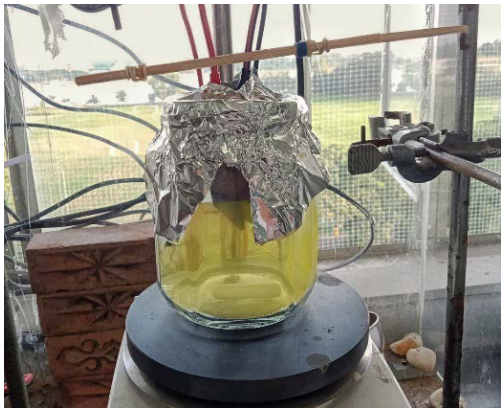

Figure 5. Heterogeneous electrolysis cell reactor

2.4 Catalyst preparation

The cellulose material with -SO_3H groups was prepared from dried bagasse fiber (Fig. 5) in laboratory at department of chemistry, faculty of science, Naresuan university. The starting material (20 g) was heated for different temperatures (300-550 ^oC) and carbonize times (15 h) under N_2 flow to produce a black solid, which was then ground by ball mill for 6 h (particle size, <90 µm). The powder (5 g) was then boiled in 50 ml of sulfuric acid (H_2SO_4) at 150 ^oC under N_2. After heating time for 18 h and then cooling to room temperature, the suspension was filtered to yield a black precipitate, with was washed repeatedly with distilled water until impurities such as sulfate ions were no longer detected in the wash water (detect pH by universal indicator). Dry and determine all acids content by back titration.

Figure 6. Heterogeneous catalyst

2.5 Spectroscopic measurement

The procedures of transesterification were designed to 1, 3, 5 and 7 wt% catalyst concentration (Catalyst ,%wt, is relative to the total weight of oils) at the reaction times 1, 2 and 3 h and 1:3, 1:6, 1:9 and 1:12 molar ratio of oil to methanol at temperature 35-40 ^oC. After time over, the reaction mixture was filtrated for cleave solid catalyst then poured into a collecting flask, which resulted in the phase separation of the methyl esters and the glycerol. The glycerol phase (bottom layer) was removed, and the methyl esters bioester phase (top layer) was evaporated with a thermostatic bath at 40 ^oC to remove the methanol. Then the biodiesel product was analyzed % conversion with ^1H NMR spectrometer.

^1H NMR of FAMEs

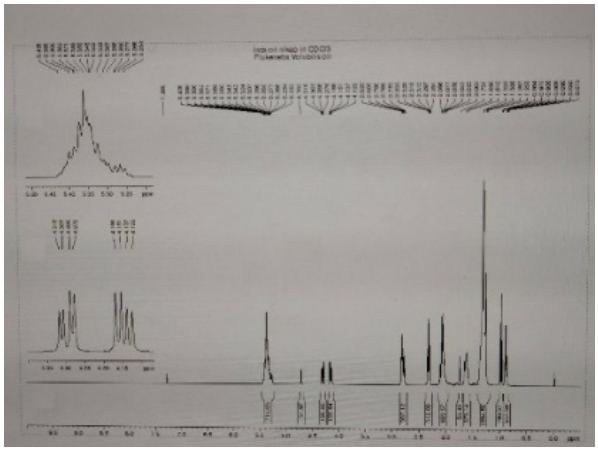

Figure 6. ^1H NMR spectra of methyl ester

In the ^1H NMR spectrum of methyl esters is shown in Figure 6, methyl groups were observed singlet spectra at δ 3.721 and triplet spectra of alpha-methylene at δ 2.352. The conversion percentage of methyl ester were determined by ratio of intrigration value between methyl and alpha-methylene spectra.

FT-IR of FAMEs

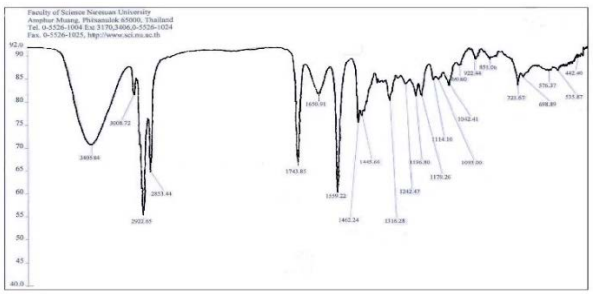

Figure 7. FT-IR spectra of methyl ester

The typical peak of the methyl ester (O-CH_3) at 1472 cm^{-1} (Fig. 7) is very narrow and moves along the natural oil peak. However, it has been observed that the peak measurement to give a direct indication of the attachment of the alkyl group of

the alcohol with the fatty acids of the triglycerides is not influenced by the alkyl group (-CH_3).

3. Results and Discussion

3.1 Methyl ester properties

^{1}H NMR analysis showed no artifact formation when acid catalyzed process was used. ^{1}H NMR spectra of the methyl esters obtained in basic catalyzed process showed no signals for triacylglycerols (δ 4.1–4.3) indicating that the transesterification was quantitative. These spectra showed an additional signal at δ 3.721, characteristic for methyl esters proton. Thus, peaks at δ 3.721 (-OCH_3) and at δ 0.920 (terminal -CH_3 groups) showed the same area indicating a complete methylation.

3.2 Heterogenous catalyst properties

The FTIR spectra of the carbon catalyst before and after sulfonation showed the vibration bands at 3400 cm^{-1} (OH stretching), 1713 cm^{-1} (C=O bending), 1615 cm^{-1} (OH stretching), 1040 cm^{-1} (SO_3- stretching) and 1365 cm^{-1} (O=S=O stretching in SO_3H) (Fig. 8). The material is carbonization at 300 ^{o}C, 5 h

.

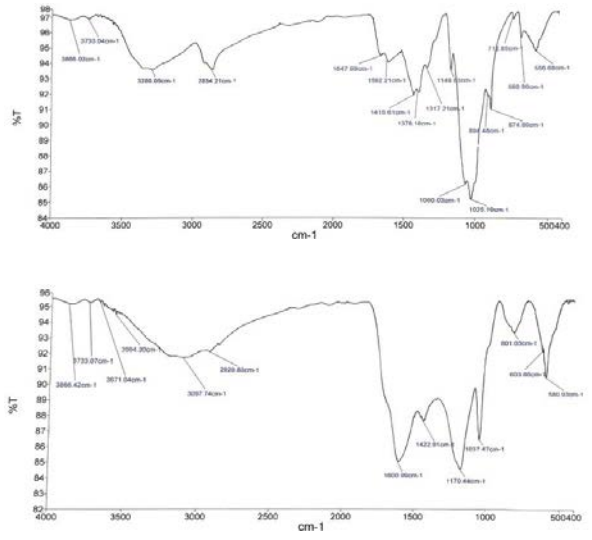

Figure 8. FTIR spectrum label : (up) Carbonized material, (down) Sulfonated material

The sample carbonized at lower temperatures presented smaller carbon sheets and therefore have hight acids densities because the -SO_3H groups are attached only to the edges of the carbon sheets (Polycyclic Aromatic Hydrocarbon). The all acid value have shown in Table 1.

Table 1. Determination of acid value on solid catalyst

Carbonization Temperatures (^{o}C)	All acid contents (mmol/g)
300	7.8562
400	5.7324
450	4.3267
500	3.6348
550	3.4326

3.3 Effect of catalyst concentration

The concentration of trifluoro acetic acid catalyst used in the process was varied as 1, 3, 5 and 7 % wt based on the volume of the reaction solution. An appropriate concentration of solid acid catalyst was 5% wt as it gave the higher amount of the methyl ester content after 1 h of reaction time. Therefore, 5%wt catalyst concentration was suggested in the acidic transesterification catalyzed by solid acid catalyst. The changes of the product specific gravity and the methyl ester content with reaction time under the conditions of 1:12 M ratio of oil to methanol and 40 ^{o}C temperature were further investigated.

4. Conclusion

The present study introduced a process for biodiesel production through high effective acidic transesterification catalysed by cellulose sulfonic acid and electrolysis process. A range of methanol to oil ratios, heterogeneous acid catalyst concentrations, reaction temperatures and reaction times were established. The research indicated that the oil could be converted to biodiesel directly by one-step natural fiber sulfonic acid catalyse process without extreme temperature and pressure conditions. The best process combination was 5 %wt catalyst content with 1:9 M ratio of oil to methanol at temperature of 40 ^{o}C. The conversion rates were as high as 79 % for the stainless steel sheet electrode. The present procedure represents a simple and mild method for bioester production in short reaction time and with high conversion rate, which would offer potential for an industrial process.

5. Acknowledgements

We are grateful for the financial support of the Faculty of Science, Naresuan University Research Grant 2022. Thank to Dr. Poolsak Sahakitpichan for his kind discussions. Special thanks to Associate. Prof. Dr. Wipharat Chuachuad Chaiyasith from department of chemistry, faculty of science, Naresuan university for her ingenious

suggestions. Thanks to Dr Sutthichat Kerdphon and Dr. Supanimit Chiampanichayakul from department of chemistry, faculty of science, Naresuan university for their insightful suggestions. Thanks also to Dr. Vichai Jaivisuthunsa for his helpful advice.

References:

1. E. C. (European Commistion), **(**2004**)** Proting Biofuels in Europe, Directorate General for Energy and Transport, B-1049 Brussels, Belgium.
2. P. N. Giannelos, F. Zannikos, S. Stournas, E. Lois and G. Anastopoulos, *Ind Crop Prod* **16** (2002) 1–9.
3. S. Aued-Pimentel, J.H.G. Lago, M.H. Chaves and E.E. Kumagai, *J. Chromatogr. A.* **1054** (2004) 235-239.
4. N.E. Pawlowsky, J.E. Nixon and R.O. Sinnhuber, *J. Am. Oil Chem. Soc.* **49** (1972) 387.
5. J. Miralles, E. Bassene and E.M. Gaydou, *J. Am. Oil Chem. Soc.* **70** (1993) 205.
6. J. Salaun and M.S. Baird, *Curr. Med. Chem.* 2 (1995) 511.
7. J. Salaun, *Top. Curr. Chem.* **207** (2000) 1.
8. R.O. Feuge, L.P. Codifer and H.J. Zeringue, *J. Am. Oil Chem. Soc.* **58** (1981) 718.
9. N.E. Pawlowski, J.D. Hendricks, M.L. Bailey, J.E. Nixon and G.S. Bailey, *J. Agric. Food Chem.* **33** (1985) 767.
10. S.W. Park and K.C. Rhee, *J. Food Sci.* **53** (1988) 1497.
11. P.M. Dewick, *Medicinal Natural Products*: A Biosyn-thetic Approach, second ed., John Wiley and Sons, New York (2001) 48–50.
12. A. Demirbas, *Energy Conv. Manage.* **47** (2006) 2271-2282.
13. L. Edgar, L. Yijun, E.L. Dora, S. Kaewta, A.B. David and G.G. James, *Ind. Eng. Chem. Res.* **44** (2005) 5353-5363.
14. K. Aninidita, K. Subrata and M. Souti, *Bioresource Technology* **101** (2010) 7201-7210.
15. E.C. (European Commistion), **(**2004**)** Proting Biofuels in Europe, Directorate General for Energy and Transport, B-1049 Brussels, Belgium.
16. D.Y.C. Leung, X. Wu and M.K.H. Leung, *Appl. Energy*, **87** (2010) 1083–1095.
17. M.J.Goff, N.S. Bauer, S. Lopes, and W.R. Sutterlin, *J. Am. Oil Chem. Soc.*, **81** (2004) 415-420.
18. R.S. Putraa, P. Hartonoa and T.S. Julianto, *Energy Procedia*, **65** (2015) 309-316.
19. L. Fereidooni and M. Mehrpooya, *Energy Convers. Manag.* **147** (2017) 145-154.
20. L. Fereidooni, K. Tahvildari and M. Mehrpooya, *Renew. Energy*, **116** (2018) 183-193.

Improved hydrogen electrolysis in sodium hydroxide solution by stainless steel electrodes optimization

Rujira Jitrwung[1]*, Kuntima Krekkeitsakul[2], Hiran Jinda[2], and Parinya Thongyindee[2]

[1]*Research and Development Group for Sustainable Development, Thailand Institute of Scientific and Technological Research (TISTR), Khlong Luang, Pathum thani 12120, Thailand*
[2]*Expert Center of Innovative Clean Energy and Environment, Thailand Institute of Scientific and Technological Research (TISTR), Khlong Luang, Pathum thani 12120, Thailand*

**E-mail: rujira_j@tistr.or.th*

Abstract:

Optimum resistance by gas bubbles, size and type of stainless electrodes in Alkali Hydrogen Electrolysis (AHE) effected to power consumption. The resistance of gas bubbles was studied by varying numbers of Anodes (A) and Cathodes (C) (A × C) by 4 × 4, 8 × 8 and 12 × 12 of Stainless steel SS304 operated in 20 % by weight of Sodium hydroxide solution. The hydrogen was increased relating numbers of electrodes 4 × 4, 8 × 8 and 12 × 12 which resulted rate of H_2 (ml/min) 35.00, 66.22 and 88.33, and required energy consumption (kW.h/kg.H_2) 132.09, 224.21 and 366.50 respectively. Increasing numbers of electrodes per AHE volume raising density of gas bubbles produced and reflected to increasing bubble resistance that effected to electron transferring from anodes to cathodes which caused of much power consumption. The resistance was minimized by reducing size of electrodes by varying diameters 9.5, 8 and 4 mm., the result showed rate of H_2 (ml/min) 29.10, 35.00 and 39.36 which consumed less energy (kW.h/kg.H_2) 141.48, 132.09 and 107.37 respectively. The thinnest diameter of electrodes showed the lowest resistance and reflected to the least energy consumption. SS316 generated lower 4.48 % in energy consumption (kW.h/kg.H_2) of 102.56 (107.37 for SS304) because it has lower resistance than SS304.

1. Introduction

The intensive of global warming and climate change has been a topic of concerning situation. There are scientific evidences which show that Carbon dioxide emissions is a major factor of the high-risk of the global weather situation. The highly contaminant of Carbon dioxide is related with the enormous consumption of fossil fuel particularly coal. Therefore, to minimize Carbon dioxide emission, transforming of using fossil to renewable or clean energy is forced by raising of many international regulations. Hydrogen is a valid alternative fuel which can replace fossil fuels. Hydrogen is classified as clean energy because it is released only water after it using. However, hydrogen is well known and used as a raw material in industrial sectors such as petroleum refining and ammonia production. Commercial hydrogen was produced from several sources such as reforming of natural gas or coal and called grey hydrogen. By the way, green hydrogen is in an interesting because it is produced from water electrolysis.[1] However, green hydrogen price is expensive cost comparing with grey hydrogen price, a significant advantage of hydrogen from water electrolysis is product of pure hydrogen (>99.9%) which is appropriated for high value usage such as fuel cell and using in manufacture of electronic components.[2] Commercial hydrogen major obtained from grey hydrogen which is mostly derived from natural gas, rather than electrolysis. Overseas, prices for this conventional hydrogen have touched of 10 USD/kg. The hydrogen price is corresponded to the availability and cost of natural gas. However green hydrogen which is derived from electrolyzer which was reported that shot up to 16.80 USD/kg in July 2022 by S&P Global Commodity Insights.[3] A report exhibited that hydrogen electrolyzer would connect with renewable energy such as wind and solar generators. It will reduce the cost of hydrogen production. As a result, the median price of H_2 in US will decrease from 10.61 USD/kg to 5.97USD/kg. and the median price of H_2 in Europe will decrease from 19.23 USD /kg to 10.02/ USD kg in 2020-2050.[4] The hydrogen price in the stock market was collected by Nasdaq as shown in Figure 1. Hydrogen price was lowering year by year and touching around 6 USD/kg.[5]

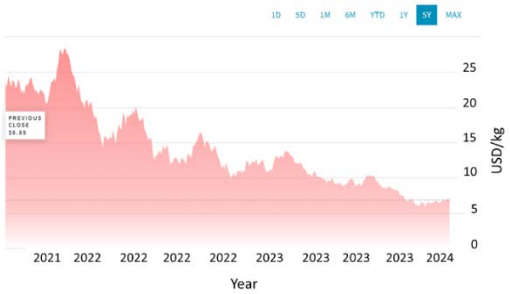

Figure 1. The statistical of hydrogen price in the market within 4 years.

Due to the lowering in commercial gray hydrogen price, the competition of green hydrogen in the hydrogen market is in trouble situation. Although the green hydrogen producer faced to the hard track, the alkali electrolysis technology is still in the right way of the competition. To minimize the cost of hydrogen electrolysis technology, researchers focused on the reduction of resistance by improving electrode materials[6], optimizing alkali solution[7] and electrode dimensions[8] and spaces,[9] in addition the reduction in electricity cost by integrating solar, wind or nuclear energy with electrolysis process which will support to levelized cost of CO_2 mitigation.[10] However, There were widely researches which focused on compatible materials and commonly utilized for water electrolysis that is required in stability and not fast corrosion. Normally the materials are based on Raney Nickel and alloys, but these materials are expensive. However, it is known that a material with nickel presence, more economic and abundance like stainless steel. The experiment studied on various type of stainless steel: 304, 316 and 430 and compared two types of alkali solutions: NaOH and KOH. The electrochemical analysis of the stainless-steel shows that the 316 steel is the best material as cathodic electrode since it has the highest nickel content. On the other hand, the results show that the electrical conductivity is similar in NaOH and KOH electrolyte solution.[11]

The water electrolysis technique is interested because it can be developed by reducing energy consumption, cost and maintenance and to increase reliability, durability and safety. The fundamentals of alkaline water electrolysis are known that the efficiency of H_2 production relying on an electrical circuit analogy of resistances in the electrolysis system. The resistances are classified into three categories, namely the electrical resistances, the reaction resistances and the transport resistances. Based on the thermodynamic and kinetic analyses of the alkaline water electrolysis, a number of resistances hindering the efficiency of the alkaline water electrolysis process. All resistances are exhibited in term of bubble resistances. The bubble resistances caused high density of current resulting to reduce in ionic transfer and electrical resistance in the circuit. In addition, the greater number of bubbles caused the void in the alkaline solution and effected to increase resistance.

To reduce the bubble resistances, electrode modification and electrolyte additives would decrease reaction overpotential and electrolyte circulation.[12] A novel work is introduced by installing capillary-induced transport along a porous inter-electrode separator which is produced by PES Porous materials in alkaline electrolyzer for leading to inherently bubble-free operation at the electrodes. The H_2 experiment was demonstrated in 27% KOH and obtained ionic resistance around 46 $m\Omega\ cm^2$ which applied a cell voltage at 0.5 A cm-2 and 85 °C of only 1.51 V, equating to 98% energy efficiency, with an energy consumption of 40.4 kWh/kg hydrogen.[13] However, the CAPEX of using PES would be required an economic evaluation.

The aim of this work was to minimize resistance by finding out the optimum condition of number of electrodes, electrode diameters, and electrode type by comparing SS304 with SS316. The H_2 production experiments were collected in one hour and replicated with continuous, and the power consumption was calculated in term of kW.h per volume and mass of H_2 then the resistance was obtained by calculation.

2. Materials and Methods

2.1 Chemicals and Materials

Deionized water is produced from an equipment of deionized water system of Thai water store. NaOH is obtained from Merck.

Power supply is provided by NICE-POWER. Screw stainless steel electrodes type SS304 and SS316 by 4, 8- and 12-mm. diameter which 140 mm in length are obtained from a general metal store.

2.2 Apparatus for Synthesis H_2 gas by Alkaline Electrolyzer (AE)

One cell of the Alkali Electrolyzer contained 12 equally electrodes installed in anode and cathode side. One group contained 4 electrodes, thereby there are 3 groups of anodes and cathodes installed in the electrolysis cell. Each group is installed in varying Anode-Cathode distance: Inner (20 mm.), Middle (55 mm.) and Outer (90 mm.). The alkali water electrolysis cell is used in this experiment shown in Figure 2.

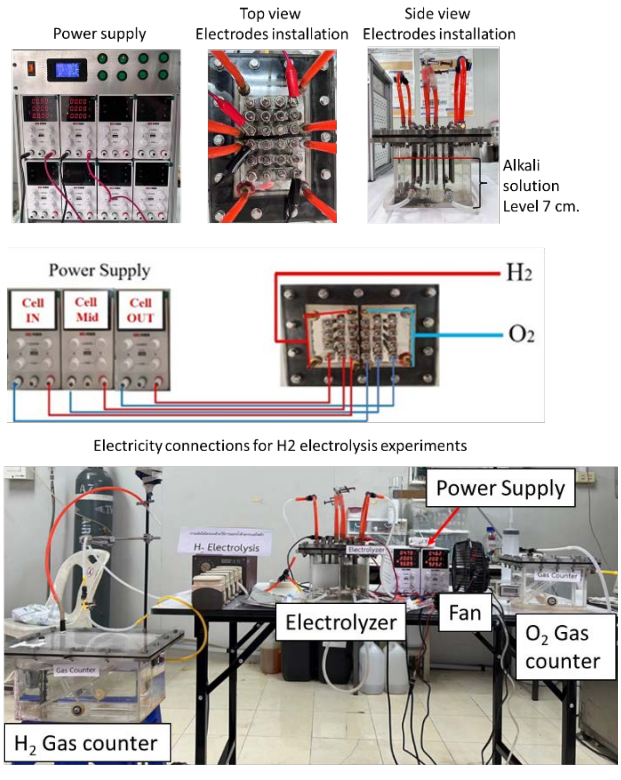

Figure 2. Alkali Electrolysis Cell system

2.3 Preparation of Alkali Electrolyzer

Alkali solution is prepared by 20% (w/w) NaOH solution contained 200 g of NaOH and 800 g of deionized water. Then the solution is filled in cell for 10 cm. height contacted with 7 cm. electrode height. The distance of electrodes is 3 cm. far from the bottom container. The electrolysis reactions under alkali solution are shown in Equation (1) and (2).

Anodes: $2OH^- \blacktriangledown H_2O + 2e^- + 1/2O_2$ (1)

Cathodes: $2H_2O + 2e^- \blacktriangledown H_2 + 2OH^-$ (2)

Electrolyzer is connected with Power supply unit to maintain current and a Fan to blow air around the electrolyzer for maintaining temperature around 50 to 60 ºC, H_2 and O_2 gas were separated by the reactions at Cathode and Anode side then measured by H_2 gas counter and O_2 gas counter as shown in Figure 2.

2.4 Calculation

$$Power\ (P)(kW) = \frac{[Current\ (A)\ \times\ Volt\ (V)]}{1000}$$

$$Power\ Usage\ (kW.h) = [Power\ (kW)]\ \times time\ (h)$$

$$Resistance\ (Ohm) = \frac{P\ (W.h)}{I^2\ (Amp^2)}$$

$$\frac{Electricity}{volume\ H_2} = [\frac{P\ (kW)}{H_2\ \left(\frac{m^3}{h}\right)}]$$

$$H_2\ Gas\ density\ (DenH_2) = 0.0899(\frac{kg}{m^3})\ \text{at NTP}$$

$$Electricity\ per\ mass\ \ H_2\ = [\frac{P\ (kW.h)}{H_2\ (kg)}]$$

3. Results & Discussion

3.1 Effect of Number of Electrodes (in Figure 3)

The H_2 production was started with using 8 mm. of SS304 electrode diameter and fixing current at 1 amp (A) per 1 electrode by increasing number of electrodes 4, 8, 12 electrodes. The result showed that H_2 production was rising of 2,100, 3,973 and 5,300 ml/h as shown in Table 1. If it considered only H_2 production, it meant that more electrodes were better than less electrodes.

However, power consumptions were rising by according with 1.50, 6.31 and 10.48 kW.h respectively. Thereby the efficiencies were calculated in terms of electrical powers per mass of H_2 are 132.09, 224.21 and 366.50 kW.h /kg.H_2 as shown in Table 1. Those results showed that increasing number of electrodes resulted to requiring more power which affected to the higher cost per unit of H_2 production. The more power consumption caused by boosting of resistance from more gas bubbles when increasing number of electrodes by 1.56, 6.57 and 10.91 ohm respectively as shown in Table 1. The number of electrodes against with H_2 rate, resistance and power consumption was shown in the same tendency by the greater number of electrodes the more resistance and higher power consumption. Therefore, the 4 × 4 of A × C electrodes was performed in the next section.

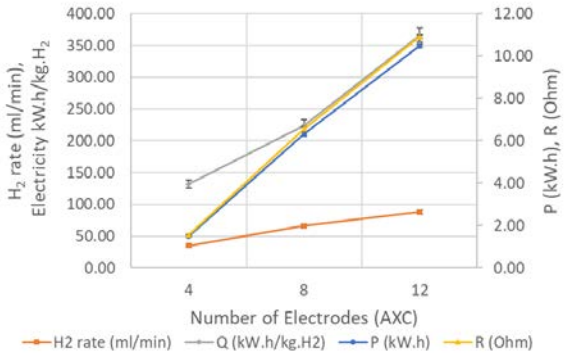

Figure 3. Number of Electrodes affected to H_2 rate, Resistance and Power Consumption.

Table 1. Comparison by adding electrodes for 4, 8, and 12 electrodes to H_2 production with fixed current

Electrode		Current	Power	Resistance	Total Gas	H_2	Electricity	Electricity
Diameters (mm.)	Numbers A × C	A/Cell	P(kW.h) Avg.(SD)	R (ohm) Avg.(SD)	ml/h Avg.(SD)	ml/h Avg(SD)	kW.h/M^3 Avg.(SD)	Q (kW.h/kg.H_2) Avg.(SD)
8	4 × 4	4.00	1.50 (0.03)	1.56 (0.03)	3,150 (194)	2,100 (143)	11.88 (0.55)	132.09 (6.09)
8	8 × 8	8.00	6.31 (0.11)	6.57 (0.11)	5,941 (271)	3,973 (186)	20.16 (0.78)	224.21 (8.66)
8	12 × 12	12.00	10.48 (0.08)	10.91 (0.08)	7,950 (300)	5,300 (200)	32.96 (1.01)	366.50 (11.22)

Table 2. Comparison electrode diameters to H_2 production with fixed current.

Electrode		Current	Power	Resistance	Total Gas	H_2	Electricity	Electricity
Diameters (mm.)	Numbers A × C	A/Cell	P(kW.h) Avg.(SD)	R (ohm) Avg.(SD)	ml/h Avg.(SD)	ml/h Avg(SD)	kW.h/M^3 Avg.(SD)	Q (kW.h/kg.H_2) Avg.(SD)
4	4 × 4	4.00	1.37 (0.10)	1.43 (0.10)	3,523 (259)	2,362 (183)	9.66 (0.55)	107.37 (6.09)
8	4 × 4	4.00	1.50 (0.03)	1.56 (0.03)	3,150 (194)	2,100 (143)	11.88 (0.55)	132.09 (6.09)
9.5	4 × 4	4.00	1.65 (0.08)	1.72 (0.08)	2,568 (282)	1,746 (180)	12.72 (0.93)	141.48 (10.29)

3.2 Effect of Electrode Diameters

By the way, the experiment of applying the less number 4 × 4 electrodes were studied by varying electrode diameters, the result showed in Table 2. The electrode diameters were varied from 4 mm. (Thin), 8 mm. (Medium) and 9.5 mm. (large). The diameters affected to resistances by increasing 1.43, 1.56 and 1.72 ohm and reducing hydrogen production 2,362, 2,100 and 1,746 ml/h which reflected to increasing power consumption 107.37, 132.09 and 141.48 kW.h/kg.H_2 respectively as shown in Table 2. The best in power consumption of 107.37 kW.h/kg.H_2 by using the thin electrode with 4 mm. diameter. The effect of larger electrode was seen when increasing diameter from thin to medium diameter affected to increasing power consumption by 23% or 5.75 % per 1 mm. diameter. (107.37 to 132.09 kW.h/kg.H_2), comparing with medium to large diameter, it resulted by increasing only 7% or 4.73 % per 1 mm. The trend showed that applying larger diameter would drop or unchanged after increasing electrode diameter as shown in Figure 4.

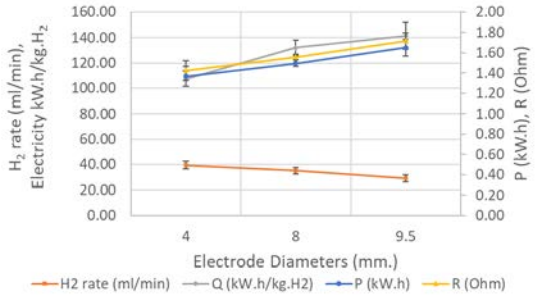

Figure 4. Electrode diameters affected to H_2 rate, Resistance and Power Consumption.

The thin electrode provided the lower in resistance, but the wider distance which related to the resistance from the distance of ion exchange[6] between anode and cathode. So that the data proved that the resistance was more effect than wider gap of electrode. The appropriate of electrode diameter was realized. This result, the thinnest of 4 mm. diameter was the best for minimizing bubble resistance and would perform in the next experiment.

3.3 Effect of Electrode Types

Additionally, the comparison of stainless-steel electrode types was investigated by 4 mm. diameter of SS304 and SS316 as shown in Table 3. The result showed that substitution of SS316 on SS304 reduced power consumption from 107.37 to 102.56 kW.h/kg.H_2 or 4.47% caused by reduction of resistance which SS316 contains more Ni than SS304 as described by previous research[5]. In addition, H_2 generation was increased by 3.3% comparing 2,362 ml/h by SS304 with 2,440 ml/h by SS316). As a result, the SS316 electrode type which was thinner (4 mm.) and appropriate number (4A × 4C) was an optimized condition which yielded the lowest power consumption about 102.56 kW.h/kg.H_2 and generated H_2 2,440 ml/h. The H_2 price was around 256.4 THB/kg.H_2 in case of supplying green electricity from Solar panel (2.50 THB/kW.h) and converting to 7.32 USD/kg.H_2 (Exchange rate 35 THB per 1 USD). The H_2 price is according to S&P Global Commodity Insights, as of August 2022, green hydrogen costs roughly 5.5- 9.5 USD/Kg.

Table 3. Comparison 4x4 electrodes by varying electrodes distances to H_2 production with fixed mild current

Type	Diameters (mm.)	Numbers A × C	A/Cell	P(kW.h) Avg.(SD)	R (ohm) Avg.(SD)	ml/h Avg.(SD)	ml/h Avg.(SD)	kW.h/M^3 Avg.(SD)	Q (kW.h/kg.H_2) Avg.(SD)
SS 304	4	4 × 4	4.00	1.37 (0.10)	1.43 (0.10)	3,523 (259)	2,362 (183)	9.66 (0.55)	107.37 (6.09)
SS 316	4	4 × 4	4.00	1.35 (0.08)	1.41 (0.09)	3,639 (250)	2,440 (175)	9.22 (0.54)	102.56 (6.00)

4. Conclusion

The Alkali Hydrogen Electrolyzer was optimized by reducing the resistance which comprised the number of electrodes, electrode diameter and stainless-steel electrode type. The maximum resistance was 10.91 ohm obtained by using 8 mm. of 12Anodes × 12Cathodes of SS304 electrodes which yielded H_2 rate about 5,300 ml/h and consumed power 366.50 kW.h/kg.H_2. On the opposite, the minimum resistance was 1.41 ohm derived from using 4 mm. of 4Anodes × 4 Cathodes of SS316 electrodes which generated H_2 rate about 2,440 ml/h and consumed power only 102.56 kW.h/kg.H_2. Comparing the maximum and minimum point, the optimum resistance advocated to reduce resistance and power consumption by 7.76 times and 3.57 times respectively which financed the reduction cost of H_2 generation by 3.57 times

Acknowledgements

The authors would like to acknowledge the Thailand Science Research and Innovation for approval and financial support. The authors also appreciate the Expert Centre of Innovative Clean Energy and Environment, Thailand Institute of Scientific and Technological Research (TISTR) to provide every assistance and support for this research.

References

1. Marchant, N. *World Economic Forum, Grey, blue, green - why are there so many colours of hydrogen.* https://www.weforum.org/agenda/2021/07/clean-energy-green-hydrogen/ (accessed 2022-12- 27).
2. Santos, D.M.F.; Sequeira, C.A.C.; Figueiredo, J.L. *Quim. Nova*. **2013**, *36*(8), 1176-1193.
3. Penrod, E. Green Hydrogen Prices have Nearly Tripled as Energy Costs Climb: S&P.https://www.utilitydive.com/news/green-hydrogen-prices-global report/627776 (accessed 2022-12-27).
4. Christensen; A., Assessment of Hydrogen Production Costs from Electrolysis: United States and Europe. https://theicct.org/publication/assessment-of-hydrogen-production-costs-from-electrolysis-united-states-and-europe/ (accessed 2022-12-27).
5. https://www.nasdaq.com/market-activity/etf/hydr.
6. Ming, R.; Zhu, Y.; Deng, L.; Zhang, A.; Wang, J.; Han, Y.; Ren, Z. *New J Chem*. **2018**, *42*, 12143-12151.
7. Munoz, D.S.L; Bergel, A.; Féron, D.; Basséguy, R. *Int. J. Hydrogen Energy*. **2010**, 8561-8568.
8. Jitrwung, R.; Krekkeitsakul, K.; Jinda, H.; Thongyindee, P.; Patthaveekongka, W.; Thongmee, N.; Deenan, S. Optimum stainless electrodes on hydrogen production by alkali electrolysis. *The 2023 Pure and Applied Chemistry International Conference (PACCON2023)* , 368-371.
9. Nagai, N.; Takeuchi, M.; Kimura, T., Oka, T. *Int. J. Hydrogen Energy*. **2003**, *28* (1), 35-41.
10. Parkinson, B.; Balcombe, P.; Speirs, J.F.; Hawkes, A.D.; Hellgardt, K. Levelized cost of CO_2 mitigation from hydrogen production routes. *Energy Environ. Sci*. **2019**, *12*, 19-40.
11. Olivares-Ramirez, J.M.; Campos-Cornelio, M.I.; Uribe-Godinez, J.; Borja-Arco,E.; Castellanos, R.H. *Int. J. Hydrog. Energy*. **2007**, *32* (15), 3170-3173.
12. Zeng, K.; Zhang, D. *Int. J. Hydrog. Energy*. **2010**, *36*(3), 307-326.
13. Hodges, A.; Hoan, A.L.; Tsekouras, G.; Wagner, K.; Lee, C.Y.; Swiegers, G.F.; Wallace, G.G. *Nat. Commun*. **2022**, *13*(1304).

Development of coffee silver skin into food beverage and testing antioxidant activity

Kimsuy Vang[1], Assama Jewto[1], Wannika Jaipit[1], and Sudtida Pliankarom Thanasupsin[1,2]*

[1]*Department of Chemistry, Faculty of Science, King Mongkut's University of Technology, Bangkok 10140, Thailand*
[2]*Chemistry for Green Society and Healthy Living Research Unit, Faculty of Science, King Mongkut's University of Technology Thonburi, Bangkok 10140, Thailand*

**E-mail: sudtida.tha@kmutt.ac.th*

Abstract

Coffee silver skin (CS) is an outer layer of coffee beans. The conversion of CS into a higher-value product offers a promising approach to managing waste because of its rich antioxidant contents. Cinnamon powder (CP) is abundant in antioxidants but does not contribute to a pleasant aroma, whereas Bael powder possesses a sweet scent. This study aims to optimize the combination of CS with Bael powder (BP) and cinnamon powder and assess their antioxidant capacity using brewing (100 mL of water) and tea bags (100 mL, 100°C, 3 min). Combinations ranging from 100%, 75%, 50%, and 25% of CS were studied. The results of the sensory evaluation show that the most favorable ratio was 25% CS with 75% BP, yielding a total phenolic content (TPC) of 43.85 mg GAE/100 mL and antioxidants of 14.39 mgAAE/100 mL for brewing, while 41.45 mg GAE/100 mL with antioxidant at 10.82 mgAAE/100 mL for tea bags. The highest sensory scores are optimal for CS and CP combination, with a ratio of 75% CS and 25% CP for brewing and 50% CS and 50% CP for tea bags. The results revealed a TPC of 17.81 mgGAE/100 mL with antioxidants of 19.39 mgAAE/100 mL for brewing and a TPC of 16.82 mgGAE/100 mL with antioxidants of 17.60 mgAAE/100 mL for teabag. The study highlights that blending CS with BP or CP at specific ratios produces antioxidant-rich beverages with maintained sensory acceptability. A combination of CS below 50% shows promise for developing a sustainable beverage for waste management.

1. Introduction

Coffee is a trendy global beverage. It is consumed by a large number of people around the world [1]. Additionally, it holds a prominent position in the global trading market, making it one of the most traded commodities[2]. Prior to roasting, coffee production generates by-products like coffee silver skin (CS)[3]. CS is a standout layer, constituting approximately 4.2% (w/w) of the total weight of coffee seeds. Prospectively, for every 120 tons of roasted coffee, about 1 ton of CS is generated[4]. Improper disposing of this by-product can have negative impacts on the environment. Burning CS is not a proper disposal option because it can release greenhouse gases into the atmosphere[5]. Despite being a relatively scarce coffee by-product, CS has gathered attention due to its potential applications in various sectors beyond food. CS contains 85% insoluble fiber and bioactive compounds, which are capable of lowering the high risk of oxidative stress diseases[6].

Bael powder is rich in vitamin C and minerals. It has a good flavor but is high in carbohydrates[7]. Furthermore, cinnamon powder also contains bioactive compounds that can lower inflammation, but it is objectionable to most consumers because of its tangy aroma[8]. This study aims to optimize CS with bael powder or cinnamon powder by brewing and tea bag methods and testing their antioxidant properties.

2. Materials and Methods

2.1 Materials

Coffee silver skin (CS) samples were prepared by blending to a smaller size and sieved by using a sizer of 500 µm. Sodium carbonate anhydrous (Na_2CO_3), Qrec Chemical Co. Ltd., New Zealand. Folin-Ciocalteu's phenol (2 N, analytical grade, Loba Chemie Pvt. Ltd., India). 1,1-Diphenyl-2-picryhydrazyl Free Radica (DPPH, HPLC, >97% assay, Tokyo Chemical Industry Co., Ltd, Japan.

2.2 Sample Preparations

Coffee silver skin was mixed with bael power or cinnamon in ratios of 100/0, 75/25, 50/50, 25/75, and 0/100 by hand mixing. Two grams of sample were used for the tea bag and brewing in 100 mL water.

2.3 Total phenolic Contents

The total phenolic contents (TPC) were analyzed following a previously established method[9]. 0.5mL of 5 times diluted sample or a standard solution was combined with 2.5mL Folin-coculture reagent (diluted ten times) and allowed to react without light for 3 minutes. Subsequently, 2mL of sodium carbonate (Na_2CO_3) solution at a concentration of 75g/L was added. The reaction was maintained in the dark for 30 minutes. The total phenolic content was assessed using a UV-visible spectrometer with a wavelength set at 765

nm. Gallic acid was used as the reference standard for standardization and calibration. The results were expressed as milligrams of Gallic Acid Equivalents per 100 milliliters of the sample (mgGAE/100 mL).

2.4 Antioxidant Assay

DPPH, a free radical, was employed as a reagent in the experiment, following the outlined in the previous method[1]. 0.2mL of sample or a standard solution was placed in a test tube. Subsequently, 2mL of ethanol was added, followed by 1.6mL of DPPH solution at a concentration of 0.6mM. The reaction mixture was then kept in the dark for 30 minutes. The antioxidants were analyzed using a UV-visible spectrometer set to a wavelength of 517 nm. Ascorbic acid was utilized as a reference standard. The results were expressed as milligrams of ascorbic acid equivalents per 100 milliliters of the sample. (mgAAE/100 mL sample)

The percentage of DDPH scavenging activity is calculated as follows:

$$\%\text{RSA} = \frac{A_{\text{control}} - A_{\text{sample}}}{A_{\text{control}}}$$

2.5 Sensory Evaluation

Thirty-five untrained panelists carried out the sensory analyses. The samples were presented in random order occasionally labelled with three-digit numbers. Drinks were evaluated in terms of color, texture, flavor taste, and general acceptance. A 9-point hedonic scale with 9-like extremely, 8-like very much, 7-like moderately,6-like slightly, 5-neither like or dislike, 4-dislike slightly, 3-dislike moderately, 2-dislike very much, and 1-dislike extremely was used. Final evaluation was calculated mean value of the individual scores given by all panelist.

2.6 Statistical analysis

The data of antioxidant activity and total phenolic contents were the average of triplicate. The data were recorded as mean ± SD and analyzed by One-way ANOVA (Microsoft offices version 16 excel.exe). Significant differences between means were determined by Duncanes multiple range test.

3. Results & Discussion

3.1 Total phenolic contents in the drink

Figure 1 compares total phenolic compounds between the brewing and tea bag methods. The study involved different ratios of CS and Bael Powder (CS: BP), ranging from 100/0, 75/25, 50/50, 25/75, to 0/100 for both brewing and teabag methods. For brewing, TPC values were found as 23.53, 22.74, 21.14, 43.85, 38.22 mgGAE/100 mL, respectively, while from teabag, the TPC values were as 21.77, 29.08, 20.68, 41.45, 44.88 mgGAE/100 mL, respectively. The highest concentrations of TPC were found in combination with 25% CS and 75% bael powder for brewing and teabag. Furthermore, brewing yields were higher than that observed from teabags. This result may be attributed to the water passing directly through the sample, enhancing the extraction process[10]. Figure 2 shows CS with cinnamon powder (CS:CP) combined in ratios 100/0, 75/25, 50/50, 25/75, and 0/100 for both brewing and teabag methods. It was observed in 23.53, 17.81, 17.17, 16.07, and 20.44 mgGAE/100 mL, respectively, for brewing, while in teabag has displayed TPC content 21.77, 18.44, 16.82, 19.42, 23.33 mgGAE/100 mL, respectively. The result from brewing was significantly not different from teabag. It was noted that for teabag, the extraction process of phenolic compounds relies on slowing mass transfer, leading to a decreased diffusion rate [11]. Phenolic compound yielded was found higher in a mixture of 75% CS and 25% CP 17.81 GAE/100 mL from brewing, while a blend of 25% CS and 75% CP yielded a higher concentration of 19.42 mg GAE/100 mL of the sample. Adding CS to the blends may not significantly boost the phenolic compound content. However, it positively impacts the flavor of drinks, particularly in enhancing the taste of bael and cinnamon-infused beverages. According to report of **Nzekoue et al.** (2020) CS from water extraction display most abundant of alkaloid group is caffeine and chlorogenic acid group showed 3-CQA>5-CQA>3,5-CQA. Those compounds are play importand for lowering chronic disease as antioxidant[12].

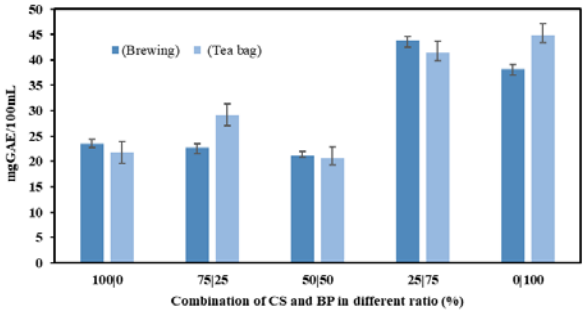

Figure 1. Total phenolic compounds contents in difference ratio of CS and BP in difference ratio using brewing and tea bag method for extraction.

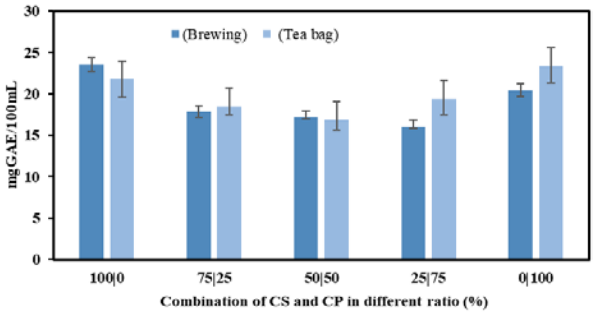

Figure 2: Total phenolic contents in different ratios of CS and CP using brewing and tea bag methods for extraction.

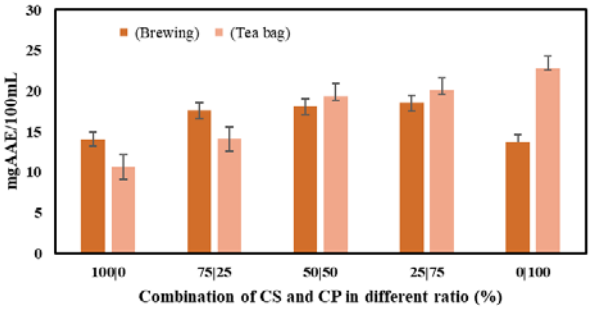

Figure 3: Antioxidant contents in different ratios of CS and BP in different ratios using brewing and tea bag methods for extraction.
*mg ascorbic acid equivalent per 100 mL (mgAAE/100 mL)

3.2 Antioxidant Assay

The antioxidant properties were observed in various combinations of CS ranging from 100%, 75%, 50%, 25%, to 0%, along with Bael powder. The result from the CS with bael powder mixture in brewing display 14.06, 14.22, 16.26, 14.39, and 9.09 mgAAE/100 mL, respectively. The results for teabag revealed 10.63, 10.63, 12.71, 10.82, and 16.69 mgAAE/100 mL, respectively. The mix of 50% CS and 50% bael powder among these combinations exhibited the highest antioxidant content. Specifically, when brewed, this combination yielded 16.26mg AAE/100 mL, whereas when used in a teabag, it resulted in 12.71 mgAAE/100 mL. Results obtained from brewing were better than those of teabag due to the brewing water flow through the sample, which increases the process of extracting by increasing diffusion rate[13]. Combination greater than both controls. This result can be explained as CS and bael powders also contain antioxidants. Another mixture was CS 100%, 75%, 50%, 25%, and 0%, along with cinnamon powder. The brewing method has shown antioxidant contents of 14.06, 17.6, 18.1, 18.56, and 13.76 mgAAE/100 mL, respectively. In comparison, the antioxidant contents of teabag showed 10.63, 14.08, 19.39, 20.11, and 22.8 mgAAE/100 mL, respectively. The combination of CS with cinnamon has shown the highest antioxidant activity, specifically with a composition of 25% CS and 75% cinnamon powder, yielding values of 18.56 mg AAE/100 mL for brewing and 20 mg AAE/100 mL for teabags. However, the antioxidant contents from brewing and teabag were not significantly different in each combination ratio. During extraction, it was observed that some blended ratios produced a gel-like appearance, which may disturb the phenolic compound extraction from the powder matrix[14].

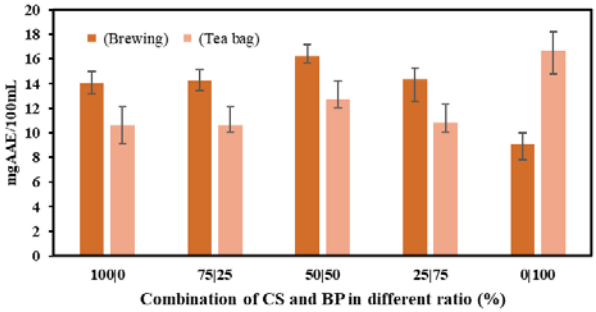

Figure 4: Antioxidant contents in different ratios of CS and CP using brewing and tea bag methods for extraction

3.3 Sensory Evaluation

Table 1 presents the sensory evaluation of CS combined with bael powder using both brewing and teabag methods. The combination in the brewing method displayed similar overall scores with bael powder compositions at 25%, 50%, and 75%, scoring 7.3, 7.7, and 7.2, respectively. The highest-rated combination was 50% coffee CS and 50% Bael powder, demonstrating the highest color, aroma, and taste scores. For teabag, the different ratios of bael with CS revealed overall scores of 7.9, 8.6, and 8, respectively. The combination of CS with bael powder at 50% and CS at 50% showed the highest score (8.6 out of 10). In addition, CS 50% mixed with bael powder 50% achieved the highest antioxidant with a better sensory evaluation for both brewing and teabag.

Table 1: Sensory evaluation from a combination of CS with bael powder in brewing and teabag method.

sample	Ratio %	Evaluation			Overall score
		Color	Smell	Taste	
CS:BP Brewing	100|0	9.2	8.8	8.8	8.9
	75|25	7.8	8.2	5.8	7.3
	50|50	7.4	8.0	7.6	7.7
	25|75	7.2	7.4	7.0	7.2
	0|100	6.6	6.2	6.4	6.4
CS:BP Teabag	100|0	7.4	7.6	7.4	7.5
	75|25	8.4	8.6	6.8	7.9
	50|50	8.4	8.6	8.8	8.6
	25|75	8.2	8.2	7.6	8.0
	0|100	6.4	7.8	6.6	6.9

Table 2: Sensory evaluation from a combination of CS with Cinnamon powder in brewing and teabag method.

sample	Ratio %	Evaluation			Overall score
		Color	Smell	Taste	
CS:CP Brewing	100|0	9.2	8.8	8.8	8.9
	75|25	8.4	7.0	7.6	7.7
	50|50	7.8	6.4	6.8	7.0
	25|75	7.2	4.8	4.8	5.6
	0|100	5.6	4.4	4.8	4.9
CS:CP Teabag	100|0	7.4	7.6	7.4	7.5
	75|25	7.0	5.4	5.8	6.1
	50|50	7.2	7.8	6.6	7.2
	25|75	6.6	6.4	6.4	6.5
	0|100	5.4	5.4	5.0	5.3

Table 2 presents the sensory evaluation of CS combined with cinnamon using both brewing and teabag methods. The combination from the brewing method displayed similar overall scores with cinnamon powder compositions at 25%, 50%, and 75%, scoring 7.7, 7.0, and 5.6, respectively. Teabag also reveal in different composition of cinnamon with overall score 6.1, 7.2 and 6.5, respectively. The highest-rated combination was 75% coffee CS and 25% Cinnamon powder, which demonstrated the highest overall score 7.7 from brewing. Teabag also reveal the highest score in combination of cinnamon powder 50% and CS 50% which is 7.2. Since cinnamon alone does not yield a high score in sensory evaluation, the addition of CS might enhance its pungent smell. Consequently, a mixture of 75% CS and 25% cinnamon powder was proposed for developing brewing and teabag products. Although this blend may not possess the highest antioxidant content, it gained better sensory evaluation scores.

4. Conclusion

When mixed with 50% Bael powder, using coffee silver skin can achieve an optimal level of antioxidant capacity, leading to higher scores in sensory evaluations when used in brewing or teabag drink products. Additionally, incorporating 25% cinnamon powder with coffee silver further enhances sensory evaluation and antioxidant capacity in brewing or teabag. However, using a teabag is not recommended because it might release microplastics when making the drinks, which could potentially cause cancer [15]. Moreover, additional of CS could be used to improve new product with higher nutritional composition with lower bad impact from coffee residual to environments.

Acknowledgements

The author would like to grant a Multi-intellectual Scholarship for funding support. Also, thank the Department of chemistry, faculty of science, KMUTT, Bangkok, for equipment support.

References

1. Nzekoue, F. K.; Angeloni, S.; Navarini, L.; Angeloni, C.; Freschi, M.; Hrelia, S.; Vitali, L. A.; Sagratini, G.; Vittori, S.; Caprioli, G. *Food Res. Int.* **2020**, *133*.
2. Cantele, C.; Tedesco, M.; Ghirardello, D.; Zeppa, G.; Bertolino, M. *Foods* **2022**, *11* (5).
3. Costa, A. S. G.; Alves, R. C.; Vinha, A. F.; Costa, E.; Costa, C. S. G.; Nunes, M. A.; Almeida, A. A.; Santos-Silva, A.; Oliveira, M. B. P. P. *Food Chem.* **2018**, *267*,28–35.
4. Beltrán-Medina, E. A.; Guatemala-Morales, G. M.; Padilla-Camberos, E.; Corona-González, R. I.; Mondragón-Cortez, P. M.; Arriola-Guevara, E. *Foods.* **2020**, *9* (8).
5. Sarasini, F.; Tirillò, J.; Zuorro, A.; Maffei, G.; Lavecchia, R.; Puglia, D.; Dominici, F.; Luzi, F.; Valente, T.; Torre, L. Matrix. *Ind Crops Prod.* **2018**, *118*, 311–320.
6. Martinez-Saez, N.; Ullate, M.; Martin-Cabrejas, M. A.; Martorell, P.; Genovés, S.; Ramon, D.; Del Castillo, M. D. *Food Chem.* **2014**, *150*, 227–234.
7. Singh Chauhan, E.; Banarasi, B.; Sharma, K.; Chauhan, E. S. Nutritional and Phytochemical Evaluation of Fruit Pulp Powder of Aegle Marmelos (Bael), 2023.

8. Jakhetia, V.; Patel, R.; Khatri, P.; Pahuja, N.; Garg, S.; Pandey, A.; Sharma, S. *J. Adv. Sci. Res.* **2010**, *1* (2),19-23.
9. Vázquez-Sánchez, K.; Martinez-Saez, N.; Rebollo-Hernanz, M.; del Castillo, M. D.; Gaytán-Martínez, M.; Campos-Vega, R. *Food Chem.* **2018**, *261*,253–259.
10. Etti, C. J.; Alonge, A. F.; Oladejo, A. O.; Akpan, M. G.; Okoko, J. U.; Etuk, N. I. *EJFOOD.* **2022**, *4* (4).
11. Alara, O. R.; Abdurahman, N. H.; Ukaegbu, C. I. *CRFS.* **2021**, 200-214.
12. Nzekoue, F. K.; Angeloni, S.; Navarini, L.; Angeloni, C.; Freschi, M.; Hrelia, S.; Vitali, L. A.; Sagratini, G.; Vittori, S.; Caprioli, G. *Food Res. Int.* **2020**, *133*.
13. Idham, Z.; Zaini, A. S.; Putra, N. R.; Rusli, N. M.; Mahat, N. S.; Yian, L. N.; Che Yunus, M. A. *IOP Conf. Ser.: Mater. Sci. Eng.* **2020**, *932*.
14. Chanioti, S.; Katsouli, M.; Tzia, C. *Molecules.* **2021**, *26* (6).
15. Bach, C.; Dauchy, X.; Severin, I.; Munoz, J. F.; Etienne, S.; Chagnon, M. C. *Food Chem.* **2013**, *139* (1–4), 672–680.

The application of coffee silver skin extract in pomegranate juice and study for its bioactivities

Thavy Kit[1], Punnanee Sumpavapol[3], and Sudtida Pliankarom Thanasupsin[1,2,*]

[1]*Department of Chemistry, Faculty of Science, King Mongkut's University of Technology Thonburi, Bangkok 10140, Thailand*
[2]*Chemistry for Green Society and Healthy Living Research Unit, Faculty of Science, King Mongkut's University of Technology Thonburi, Bangkok 10140, Thailand*
[3]*Department of Food Technology, Faculty of Agro-Industry, Prince of Songkla University, Hat Yai, Songkhla 90112, Thailand*

**E-mail*: *sudtida.tha@kmutt.ac.th*

Abstract:

Coffee silver skin (CS) is the main by-product of coffee roasting production. It consists of various valuable chemical compositions such as phenolic acids, polyphenols, flavonoid, and so on; therefore, it is highly interesting to valorize and study for its bioactivity and potential application. Then CS was extracted by a subcritical water extraction process and freeze-dried to obtain the coffee silver skin crude extract powder (CSE). This study aimed to propose an extra beneficial drink which is a CSE-pomegranate juice and quantify the bioactive compounds in the juice. The Pomegranate juice was made from pomegranate powder and pomegranate syrup. The total phenolic content (TPC), antioxidant activity (AA), total caffeoquinic acid (T-CQA), caffeine, anti-hyaluronidase, and anti-glucosidase were studied to confirm the beneficial bioactivities of the combined juice. It was found that the CSE-pomegranate juice contained TPC=439.20 mg GAE/100 mL, AA=62.22 (mg TE/100 mL), T-CQA=12.63 (mg/100 mL), and caffeine=30.49 (mg/100 mL). The percent inhibition of hyaluronidase was 52.73%, and the percent inhibition of glucosidase was 58.15%. These results indicate that coffee silver skin dried crude extract adds more benefits to the pomegranate juice. Therefore, coffee silver skin Extract (CSE) is a valuable industrial ingredient source of antioxidative materials.

1. Introduction

Coffee silver skin possesses many essential compounds including protein, polyphenols, caffeine, and phenolic acids. Subcritical water extraction method is used to extract herbal samples to maintain their bioavailability. The extract is potentially an ingredient of food and cosmetic products. Coffee silver skin and its extract were proven to have no cytotoxic effect [1,2] for food and cosmetic ingredients. The CS extract was found to have a great number of phytochemicals that possess radical scavenging activities (antioxidants). The phenolic acids, chlorogenic acids, and quinic acids exhibit high scavenging activities against free oxygen radicals, HAase, and alpha-glucosidase. Recently, pomegranate has become an emerging ingredient in both cosmetic and food products[3]. Pomegranate plant parts were found to have a high content of phenolic acid, flavonoids, tannins, amino acids, and alkaloids[4]. The recent development of healthy functional food [5]. It comes to attention that adding CSE to the fruit juice could add more health value to the juice. In this study, CSE power was added to the pomegranate juice for the extra healthy function of the juice. Several in-vitro tests such as total phenolic content test, radical scavenging test (DPPH), and hyaluronidase and alpha-glucosidase inhibition assays were performed to support the claim.

2. Materials and Methods

2.1 Materials

Coffee silver skin (CS) generated from roasting coffee beans, approximately 80% *Coffeea arabica* and 20% *Coffeea robusta*, was provided by Coffee Passion Co.Ltd., Samut Sangkaran, Thailand. Upon arrival, the CS samples were blended by a home blender and sieved to sizes ranging from 150 to 500 µm. Then, the samples were kept in a dry and cold place and avoided sunlight. The moisture content of the CS sample was analyzed by a moisture analyzer (Sartorius MA35, Göttingen, Germany) and found to be 9.45 ± 0.52% throughout the study.

Chlorogenic acid (3-(3,4-Dihydroxy cinnamoyl) quinic acid), trans-5-O-Caffeoyl quinic acid, 4-O-(3,4-Dihydroxycinnamoyl)-D-quinic acid, α-D-Glucosidase from yeast, *p*-Nitrophenyl α-D-glucopyranoside $C_{12}H_{15}NO_8$, (±)6-hydroxy-2,5,7,8-tetra-methylchromane-2-carboxylic acid (Trolox), 4-(dimethylamino) benzaldehyde, 5-methyl phenazinium methyl sulfate, and 7,8-dimethyl-10-[(2S,3S,4R)-2,3,4,5-tetrahydroxyphethl]benzo[g]pteridine-2,4-dione (ribo-flavin), 1,3,7-Trimethylxanthine (Caffeine),

Hyaluronic acid sodium salt from rooster comb, Hyaluronidase from bovine testes TypeI-S, ~55 kDa400-100 units/mg solid, and Nitro tetrazolium blue chloride HPLC grade, ≥90.0% assay were purchased from Sigma Aldrich, Singapore. 1,1-Diphenyl-2-picryhydrazyl Free Radica (DPPH) was purchased from Tokyo Chemical Industry, Japan. Other chemicals were analytical grade.

2.2 Sample Preparation

2.2.1 Coffee Silver skin Extraction by Subcritical Water

Subcritical water extraction was carried out in a 450 mL high-pressure autoclave reactor (AMAR EQUIPMENTS PVT.LTD, India). 25g of coffee silver skin and 250 mL of DI water were put in the reactor and the temperature was set to 147.8 ºC for 10 min[6]. Throughout the experiment, the sample mixture was constantly mixed using the impeller at 600 rpm. CS's aqueous extracts were obtained from the separation method using a Büchner funnel 250 mL with Whatman No. 1 filter paper under a vacuum. The liquid extracts were then concentrated using a rotary evaporator (45 ºC). Finally, the extracts were freeze-dried and stored at –20 ºC.

2.2.2 Pomegranate Juice Preparation

Pomegranate juice was made from 5 g of pomegranate powder and 3 g of pomegranate syrup in 90 g of water. Then, the mixture was stirred until homogeneous. 500 mg of CSE was added to the pomegranate juice for additional bioactivities.

2.3 UV Spectroscopic Measurement

2.3.1 Total Phenolic Content Measurement

The total phenolic content was determined by the Folin-Ciocalteu analytical method [7]. The test was started by pipette 400 µL sample into the test tube. Then, 6 mL of DI water and 1 mL of Folin-Ciocalteu (diluted 10x) were added to the test tube, and the mixture was incubated in the dark at room temperature for 3 min. After that, 4 mL of 20% (w/v) of sodium carbonate was added and incubated in the dark for 60 min. The mixture turned dark blue color and was measured by UV-Vis at 650 nm. The total phenolic (TPC) was expressed as mg of gallic acid equivalent per 100 mL. TPC can be calculated as follows:
TPC = Sample absorbance/slope.

2.3.2 Total Antioxidant Activities Measurement

The radical scavenging activity of the extract was tested by 2,2-diphenyl-1-picrydraxyl (DPPH). 0.2 mL of extract solution (1 mg/mL in DI water) is mixed with 3.8 mL DPPH reagent (0.6 mM in ethanol) in the 15 mL test tube. Then the mixture was incubated in the dark at room temperature for 30 min. For control, the DPPH reagent alone was used. The mixture was measured against blank (50% ethanol) by Perkin Elmer Lambda UV-Vis spectrophotometer at 517 nm[7]. The percentage of DDPH scavenging is calculated as follows:

$$\text{Antioxidant activties} = \frac{(A_C - A_S)}{A_S} \times 100$$

Where A_S is the absorbance of the tested sample, and A_C is the absorbance of the control.

2.3.3 Enzyme Hyaluronidase Inhibition

The hyaluronidase enzyme inhibitory activity of CS crude extract is assessed by determining the amount of N-acetylglucosamine formed from sodium hyaluronate. Prepare the six 15mL test tubes for 50 µL of different crude extract concentrations (1, 2, 3, 4, 5, and 6 mg/mL). Each test tube follows the same procedure. Add 50 µL of 1-S bovine (4.8 mg hyaluronidase dissolved in 0.6 mL of 0.1 mol/L acetate buffer, pH 3.5) then incubate in a water bath at 37 ℃ for 20 min. Add 100 µL of 12.5 mmol/L calcium chloride and incubate the mixture in a water bath at 37 ℃ for 20 min. The reaction is started by adding 250 µL of sodium hyaluronate (1.2 mg/mL) and incubating in a water bath at 37 ℃ for 40 min. Then 100 µL of 0.4 mol/L sodium hydroxide and 100 µL of 0.4 mol/L potassium borate are added to the mixture and incubated in a water bath at 100 ºC for 3 min. The last step is to cool down the mixture then add 3 mL of dimethyl benzaldehyde solution (4 g of p-dimethyl-amino-benzaldehyde dissolved in 350 mL of 100% acetic acid and 50 mL of 10 M HCl) and incubate in a water bath at 37 ℃ for 20 min. Absorbance was measured at 585 nm by Perkin Elmer Lambda UV-Vis spectrophotometer [2].

$$\%\,I = \frac{(A_C - A_{CB}) - (A_S - A_{SB})}{(A_C - A_{CB})} \times 100$$

Where AC is the absorbance of the control; AS is the absorbance of different concentrations of sample; A_{CB} is the blank of control; A_{SB} is the blank of an individual sample.

Table 1. TPC, AA, T-CQA, and Caffeine content in the CSE, CSE-pomegranate, and pomegranate juice

Parameters	Calibration equation	CSE	CSE-Po	Po
TPC (mg GAE/100 mL)	y =3.4826x R^2 = 0.9999	459.57	439.20	65.37
AA (mg TE/100 mL)	y = 0.5034x R^2 = 0.999	106.70	62.22	21.24
T-CQA (mg/100 mL)	3-CQA (y = 5793.5x) R^2 = 0.9994 4-CQA (y = 5515.8x) R^2 = 0.999 5-CQA (y = 6798.1x) R^2 = 0.9999	8.98	12.63	ND
Caff (mg/100 mL)	y = 25871x R^2 =0.9999	47.21	30.49	ND

ND*: not detected. Where TPC content was expressed in mg GAE/100 mL; AA was expressed in mg TE/100 mL; T-CQA was expressed in mg/100 mL; Caffeine was expressed in mg/100 mL.

2.3.4 Enzyme Alpha-glucosidase Inhibition

The α-glucosidase inhibition assay is conducted to determine the anti-diabetes activity of the crude extract. The assay was assessed according to the method described by [8,9]. Prepare 7 test tubes for each sample concentration (2, 5, 10, 15, 20, and 25 mg/mL) and control, and each test has its blank. Pipette 0.9 mL of 67 mM phosphate buffer (pH=6.8) into each test tube and add 0.9 mL of each sample into the individual test tube. Then add 0.9 mL of glucosidase enzyme (0.57 unit/mL prepare fresh in cold phosphate buffer pH=6.8) to each test tube except the control tube (for control replace enzyme with DI water). Then incubate the mixture in the water bath at 37 ºC for 10 min. After 10 min of incubation, add 0.9 mL of 5 mM *p*-Nitrophenyl α-Glucoside to every tube. Then incubate all the mixture in the water bath at 37 ºC for 20 min. For blanks, prepare a new set of test tubes (7) and follow the same steps except replace the enzyme with buffer. Then the mixture is measured by Perkin Elmer Lambda UV-Vis spectrophotometer at 405 nm. The inhibition of the enzyme is calculated as follows:

$$\%\,I = \frac{(A_C - A_{CB}) - (A_S - A_{SB})}{(A_C - A_{CB})} \times 100$$

Where A_C is the absorbance of the control; A_S is the absorbance of different concentrations of sample; A_{CB} is the blank of control; A_{SB} is the blank of an individual sample.

2.4 Total Chlorogenic Acids Measurement by HPLC-UV

The liquid samples were diluted with 5 dilution factors in 50% methanol solution, filtered with a 0.20 µm syringe filter, and injected and analyzed

according to the following chromatographic conditions. Chromatographic conditions: C18-AR column (25 cm × 4.6 mm i.d, particle size 5 µm), temperature 25 °C, mobile phase Acetonitrile: trifluoroacetic acid 0.1% (v/v) (10:90), injection volume 20 µL, and the flow rate 1 mL/min. The read channel was set to 325 nm for chlorogenic acid and 272 nm for caffeine.

3. Results & Discussion

3.1 Quantification of Total Phenolic Content (TPC), Antioxidant Activities (AA), Caffeine, and Total Caffeoylquinic Acids (T-CQA)

The screening of coffee silver skin crude extract powder shows a good number of phytochemicals-polyphenols. The CSE was found to have a wide range of phenolic acids including hydroxybenzoic acids (gallic acid, ellagic acid, vanillic acid) and hydroxycinnamic acids [6] (caffeic acid, chlorogenic acid, cinnamic acid, ferulic acid), and flavonoid (epicatechin, hyperoxide, quercetin dihydrate, and rutin hydrate), and alkaloids (caffeine and quinine) [10]. This study also found some phytochemicals such as chlorogenic acids and caffeine as shown in **Table 1**.

Other bioactive compounds were also found in CSE, pomegranate + CSE juice, and pomegranate juice by conducting total phenolic contents (TPC), and it displayed reactive oxygen species (ROS) radical scavenging activity, **Table 1**. All three samples presented with TPC and antioxidant activities (AA); however, pomegranate juice presents the lowest TPC and AA. By adding CSE to the pomegranate juice, the TPC and AA contents of the juice tragically increase. Regarding the T-CQA and caffeine contents, there are

significant changes in the pomegranate juice after adding CSE from no trace to 12.63 mg/100mL and 30.49 mg/mL, respectively.

3.2 Enzyme Inhibition Activities

3.2.1 Hyaluronidase Inhibition Activities

Table 2. Percent inhibition of enzyme hyaluronidase in the testing samples

Sample	% Inhibition	SD*
CSE (6mg/mL)	57.74	0.10
CSE-Pomegranate juice (5mg/mL)	58.20	0.77
Pomegranate juice	71.47	0.10

In this study, the hyaluronidase inhibition activity was done to determine how the CSE with pomegranate capacity against aging. The smaller IC_{50} indicates stronger enzyme inhibition which means that a small amount of extract of inhibitor is used in the test. **Table 2.** the result indicated the possibility of developing CSE as a supplementary anti-aging beverage for daily consumption. 500 mg of CSE was mixed with pomegranate juice and its hyaluronidase inhibition activity was 58.20%. Pomegranate alone showed significantly high inhibition of hyaluronidase enzyme activity. After mixing pomegranate with CSE, the inhibition remained around 50% which suggested that pomegranate preserves the bioactivity of CSE.

3.2.2 Alpha-glucosidase Inhibition Activities

Alpha-glucosidase enzymes such as Lactase, maltase, and sucrase are key agents in the disaccharide degrading mechanism into monosaccharide[11]. The inhibition of the α-glucosidase enzyme can slow the carbohydrate digestion process. The result from **Table 3.** shows that CSE alone exhibits high enzyme inhibition activity, 54.65% at the concentration of 10 mg/mL, and pomegranate juice alone exhibits lower inhibitory activities, 23.49 %. By adding CSE to the pomegranate juice, the percent inhibition was increased which directed that the antioxidants from both CSE and pomegranate are working in a synergic manner.

Table 3. Percent inhibition of enzyme α-glucosidase in the testing samples

Sample	% Inhibition	SD*
CSE 10mg/mL)	54.65	0.13
CSE-Pomegr[12]anate juice (9mg/mL)	58.15	0.81
Pomegranate juice	23.49	0.10

4. Conclusion

This study revealed that coffee silver skin crude extract can be a potential ingredient in pomegranate juice. The phytochemical of CSE remains significantly high after introducing it to the pomegranate juice. CSE not only contains health-beneficial bioactivities but also various bound phenolic acids and flavonoids. Most importantly, the combined juice (pomegranate-CSE) exhibits high enzyme inhibition activities including hyaluronidase and alpha-glucosidase. The inhibition of hyaluronidase results in a lower aging process of the cell[3], and the inhibition of alpha-glucosidase slows the disaccharide digestion mechanism which can lower the sugar content in the bloodstream[13]. These bioactivities are a great component in our daily consumption, and the test results suggested that CSE-pomegranate juice could inhibit hyaluronidase and alpha-glucosidase enzyme activities. This study could enable the development of healthy drinks. Further research should include the safety parameter tests regarding the food industry regulations to put this product on the market.

Acknowledgments

The first author (TK) expresses her sincere thanks to the Faculty of Science, Department of Chemistry of King Mongkut's University of Technology Thonburi, Thailand (KMUTT). This work was supported by the Petchra Prajom Klao Scholarship program for a master's degree.

Reference

1. Nolasco, A.; Squillante, J.; Esposito, F.; Velotto, S.; Romano, R.; Aponte, M.; Giarra, A.; Toscanesi, M.; Montella, E.; Cirillo, T. *Foods* **2022**, *11* (18).
2. Rodrigues, F.; Gaspar, C.; Palmeira-De-Oliveira, A.; Sarmento, B.; Amaral, M. H.; Oliveira, M. B. P. P. *Drug Dev. Ind. Pharm.* **2016**, *42* (1), 99–106.
3. Juncan, A. M.; Moisă, D. G.; Santini, A.; Morgovan, C.; Rus, L. L.; Vonica-țincu, A. L.; Loghin, F. *Molecules* **2021**, *26* (15), 1–43.
4. Yu, M.; Gouvinhas, I.; Rocha, J.; Barros, A. I. R. N. A. *Sci. Rep.* **2021**, *11* (1), 1–14.
5. Cheng, Y.; Xue, F.; Yu, S.; Du, S.; Yang, Y. *Molecules* **2021**, *26* (13), 1–38.
6. Ginting, A. R.; Kit, T.; Mingvanish, W.; Thanasupsin, S. P. *Sustain.* **2022**, *14* (14).
7. Castaldo, L.; Narváez, A.; Izzo, L.; Graziani, G.; Ritieni, A. *Molecules* **2020**, *25* (9).

8. Prommaban, A.; Kheawfu, K.; Chittasupho, C.; Sirilun, S.; Hemsuwimon, K.; Chaiyana, W. *Evidence-based Complement. Altern. Med.* **2022**, *2022*.
9. Madan, K.; Nanda, S. *Bioorg. Chem.* **2018**, *77*, 159–167.
10. Nzekoue, F. K.; Angeloni, S.; Navarini, L.; Angeloni, C.; Freschi, M.; Hrelia, S.; Vitali, L. A.; Sagratini, G.; Vittori, S.; Caprioli, G. *Food Res. Int.* **2020**, *133*, 109128.
11. Gutierrez, A. S. A.; Guo, J.; Feng, J.; Tan, L.; Kong, L. *Food Hydrocoll.* **2020**, *102* (November 2019), 105603.
12. Bessada, S. M. F.; Alves, R. C.; Oliveira, M. B. P. P. *Cosmetics* **2018**, *5* (1).
13. Carpentieri, S.; Soltanipour, F.; Ferrari, G.; Pataro, G.; Donsì, F. *Antioxidants* **2021**, *10* (9).

Effect of solutions on retrogradation of cooked sticky rice

On-ong Chanprasartsuk[1], Kamolwan Jantranon[2], and Pornpen Atorngitjawat[2]*

[1]*Department of Food Science, Faculty of Science, Burapha University, Chonburi 20131, Thailand*
[2]*Department of Chemistry, Faculty of Science, Burapha University, Chonburi 20131, Thailand*

**E-mail: pornpena@go.buu.ac.th*

Abstract:

To increase the shelf life and preserve texture of Khao Tom Mud (cooked sticky rice mixed with coconut milk), the effect of solutions on retrogradation of cooked sticky rice was studied. The sticky rice was soaked in sodium chloride (6 %*w/v*) and glycerol (1 %*v/v*) solutions compared with filtered water for 8 hours at a room temperature. The ratio of sticky rice and soaking solutions was 1:10 (*w/v*). The cooked sticky rice was blended with coconut milk, packed with banana leaves and vacuum plastic bags. All samples were stored in the refrigerator at 4 ºC for 7, 21 and 28 days. The percentage of retaining water content was studied. The chemical structure of sticky rice was studied by Fourier transform infrared spectroscopy (FTIR). The hardness was studied by texture analyzer technique. The result showed that the highest rate of water content percentage was found for sticky rice soaked in sodium chloride solution. The chemical structure of all samples, observed from FTIR spectra, was similar and no significant changes in amylose and amylopectin structure. The short-range order of amylose and amylopectin, examined from the ratio of absorbance at 1047 and 1022 cm^{-1}, indicated that the retrogradation was started at storage time for 7 days and the lowest retrogradation rate was found for sticky rice soaked in sodium chloride solution. The lowest rate of retrogradation from the hardness property was found for sticky rice soaked in sodium chloride and highest for that soaked in glycerol solutions. Sodium chloride solution can delay the rate of retrogradation.

1. Introduction

Sticky rice (*Oryza sativa*) also called waxy or glutinous rice, is one of widely consumed all over regions of Thailand and most Asian countries. They can be used as the main ingredient in instant and semi-finished foods or consumed directly. There are many Thai desserts that have sticky rice as the main ingredient, such as Khao Tom Mud (cooked sticky rice mixed with coconut milk), Khao Neow Mamuang (coconut stick rice with mango), Khao Lam (sticky rice cooked in bamboo). These desserts are commercial products of Thailand that make a profit for Thai people. However, the shelf life of these desserts is relatively short, changing taste and texture, due to the retrogradation or recovery of starch in sticky rice during storage. The chemical composition of the sticky rice grain generally varies depending on the environment of cultivation, soil, planting, and rice varieties. The rice's appearance is a milky white color. The main chemical component of sticky rice grains is carbohydrates, mainly containing of amylopectin (> 98%). An adhesive texture is found for cooked sticky rice and has longer shelf life than other normal rice.[1-2] As seen in Figure 1, amylose is a polymer with a straight chain structure, consisting of about 200 – 2,000 units of glucoses connected by α-(1, 4) glucosidic linkages. Amylopectin is a branched polymer that consists of a straight chain of glucoses connected by α-(1, 4) glucosidic linkages. Its branched chain is a short-chain glucose polymer, connected by α-(1,6) glucosidic linkages.[3-5]

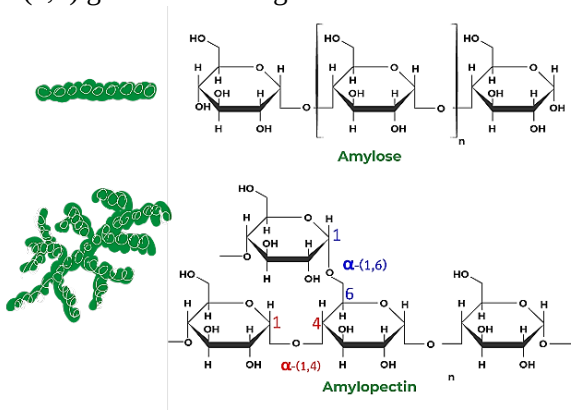

Figure 1. Amylose and amylopectin structure.

When the starch is dispersed in water and heated to a gelatinization temperature, the small molecules of amylose and amylopectin will scatter and burst. After cooling, amylose molecules that are close to each other will form hydrogen bonds between molecules and three-dimensional networks, which reduces the ability to hold water. Amylopectin can be rearranged and crystallized from the short-range order, but this is possible more slowly than the crystallization of the rearrangement of amylose chains[3-8] as shown in Figure 2.[8] This phenomenon is called retrogradation and the resulting sediment is called retrograded starch. Retrogradation can be divided into 2 phases. First, the short-term phase, retrogradation is observed in one or two days of storage at low temperatures. This phase, the starch

retains its amorphous arrangement. Second, the longer storage time, the retrogradation occurs from increasing order and crystallinity of starch.[8]

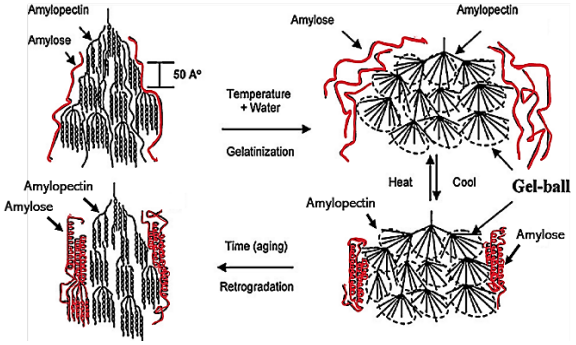

Figure 2. Schematics of gelatinization and retrogradation process of starch.

Therefore, the aim of this work is to increase the shelf life and preserve the texture of the cooked sticky rice in Khao Tom Mud. This research focused on the effect of soaking solutions, sodium chloride and glycerol solutions compared to filtered water, on the retrogradation of cooked sticky rice.

2. Materials and Methods

2.1 Materials

Sticky rice (Kaijaerice®) and coconut milk (Brand Aroy-D) were purchased from Nongmon market in Chonburi province, Thailand. Sodium chloride (NaCl) and glycerol were purchased from QRëCTM.

2.2 Preparation of cooked sticky rice

Prepare three clean plastic containers. 100 g of raw sticky rice was put in each container and rinsed out water for couple times. The sticky rice was soaked in 1,000 mL of 6 *%w/v* NaCl solution, 1 *%v/v* glycerol solution and filter water (H_2O) for 8 h, respectively. The sticky rice was steamed in a rice cooker for 25 min. Then 60 mL of coconut milk was added and blended thoroughly and restreamed for 15 min. The cooked sticky rice was at room temperature for 1 h before wrapped with banana leaves and put in vacuum plastic bags. All samples were stored in the refrigerator at 4 ºC for 7, 21 and 28 days. The sticky rice soaked in filter water, sodium chloride and glycerol solutions were referred to as H_2O, NaCl and Gly, respectively.

2.3 Characterization

The retaining water content of cooked sticky rice samples was determined by the oven-drying method. The sample was weighted before placing in an oven at 105 ºC for 2.5 hours, then let it cool in desiccator for 1 hour. The water content (*WC*) was calculated according to equation:

$$WC\ (\%) = \frac{w_0 - w_1}{w_0} \times 100$$

When w_0 and w_1 are the weight of wet and dried samples, respectively.

The structure characteristic of raw and cooked sticky rice was examined by using a PerkinElmer Frontier system, ATR-FTIR spectrometer in a range of 400 to 4,000 cm^{-1}, signal accumulation 4 scans at a resolution of 4 cm^{-1}.

The hardness properties of all samples were measured using a TA-XT plus texture analyzer, pressure probe code P/75 in a compression mode. The sample was molded in a cylindrical shape with a height of 2.0 cm.[1]

3. Results & Discussion

3.1 Water content

As seen in Figure 3, the water content of H_2O and NaCl increased during refrigerated storage. The water content of Gly increased with stored times up to 21 days. However, compared with samples before refrigerated storage, NaCl provided the highest rate of water content at 28 days (27.5 %). This indicated that NaCl can hold water in the rice structure after retrogradation.

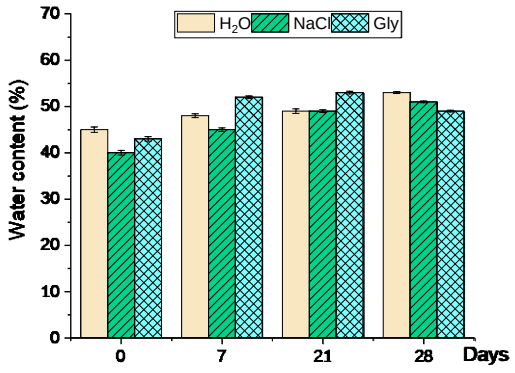

Figure 3. The water content of all samples during storage.

3.2 Structure characteristics

The FTIR spectra of all samples before and after retrogradation (used 28 days as examples) were shown in Figure 4. There are no significant different spectra of before and after retrogradation for all cooked sticky rice. All samples show the band at 3700-3100 cm^{-1}, attributed to the O-H stretching of intermolecular hydrogen bonds. The band at ~2923 and 2854 cm^{-1} is related to -C-H stretching of CH_2 in the starch. The band at 2854 cm^{-1} was absent in raw sticky rice (see Figure 4a) but clearly observed for all cooked and retrogradation sticky rice, which was reported

that it was due to the overlapping the vibration of -CH_2 stretching between protein and starch structures. The band at 1744 cm^{-1} was allocated to vibration of O-H bonds due to water, which absent for a raw sticky rice. The bands in the region around 1637- 1367 cm^{-1} were assigned to C-H bending. Peaks at 1150 - 996 cm^{-1} were related to the vibration of C-O, C-O-C glycosidic and C-O-H bonds.[9-12]

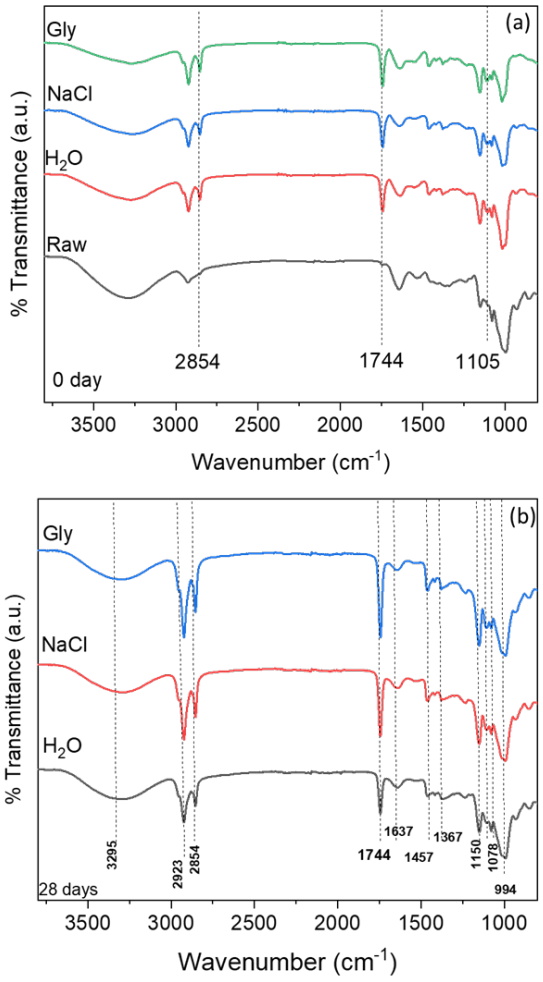

Figure 4. FTIR spectra of before (a) and after (b) retrogradation for 28 days of all samples.

Figure 5 displayed the short-range order before and after retrogradation, which was calculated by the intensity ratio between the absorbance bands at 1047/1022 cm^{-1}. The absorbance at 1047, and 1022 cm^{-1} is related to the order and disorder area of starches, respectively.[8,10-11] As seen in Figure 5, NaCl provided the lower rate of the short-range order during storage. Moreover, this result also showed that all samples started retrograding at storage time for 7 days. According to the amount of amylopectin in sticky rice gains, this retrogradation of cooked sticky rice is mainly due to slow rearrangement of the short amylopectin chains.[3,8-9]

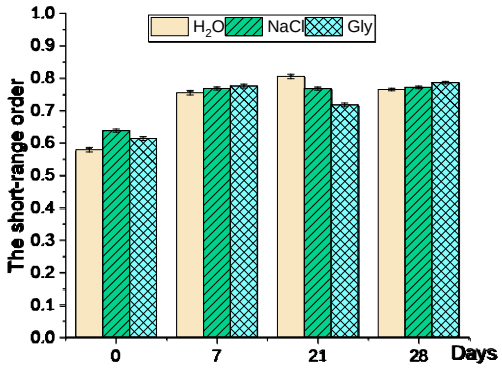

Figure 5. The short-range order ($R_{1047/1022}$) of starches during storage.

3.3 Texture Analysis

The hardness obtained from texture analysis of all samples was shown in Figure 6. The hardness values were inversely proportional to retrogradation. The hardness of all samples decreased during refrigerated storage due to water evaporation from the cooked sticky rice gel, yielding a weaker gelling texture and making a rice ball crumble. As seen in Figure 6, the order hardness reduction rate was Gly > H_2O > NaCl. This also presents that NaCl has the least retrogradation. The mechanisms of NaCl solution on starch retrogradation remain unclear. However, this study proposed that NaCl promoted the gelatinization temperature and water absorption of starch granules due to the strong polarity of Na^+ and Cl^- ions. This ion could inhibit the hydrogen bonds between the starch molecules and retard the recrystallization of amylopectin.[13]

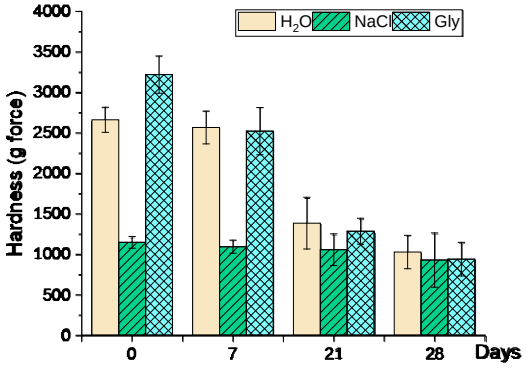

Figure 6. The hardness of all samples during storage.

4. Conclusion

This primary study on retrogradation of cooked sticky rice, using different soaking solutions demonstrated that sticky rice soaking

with NaCl solution provided the least retrogradation rate during 28 days at low temperatures and soaking in glycerol provided the highest. The highest rate of retaining water content, the lowest rate of crystallinity and the lowest rate of hardness during refrigerated storage were observed for the sticky rice soaking with NaCl. The information from this study can be further applied to solve the problem of starch retrogradation in Khao Tom Mud and other desserts that have cooked sticky rice mixed with coconut milk as ingredients.

Acknowledgements

This work was supported by project fundings from the Department of Chemistry, Faculty of Science, Burapha University.

References

1. Qui, S.; Abbaspourrad, A.; Padilla-Zakour, Q.I. *Foods* **2022**, *11*, 1306-1320.
2. Qui, S.; Punzalan, M.E.; Abbaspourrad, A.; Padilla-Zakour, Q.I. *Foods* **2020**, *98*, 10524-10535.
3. Xu, J.; Wang, Q.; Bashari, M.; Chen, F.; Wang, P.; Cui, L.; Yuan, J.; Xu, X.; Fan, X. *Food Hydrocolloids*. **2014**, *39*, 136-143.
4. Li, J.; Yuan, Y.; Zhang, H.; Zou, F.; Tao, H.; Wang, N.; Guo, L.; Cui, B. *Food Chemistry*. **2022**, *380*, 13226-1095.
5. Lian, X.; Wang, C.; Zhang, K.; Li, L. *Int. J. Biol. Macromol*. **2014**, *64*, 288–293.
6. Lu, W.; Lakonishok, M.; Gelfand, V.I. *Current Biology*. **2021**, *31*, 3207-3220.
7. Tako, M.; Hizukuri, S. *J. Carbohydr. Chem*., **1995**, 14, 613-622.
8. Lu, H.; Ma, R.; Chang, R.; Tian, Y. Food Hydrocolloids. **2021**, *120*, 106975-8.
9. Yu, L.; Christie, G. *J. Mater. Sci*. **2005**, *40*, 111- 6.
10. Pourfarzad, A.; Yousefi, A.; Ako, K. *Food Hydrocolloids*. **2021**, *111*, 106380-10.
11. Parikh, H.; Prajapati, B.; Petel, M.; Dave, G. *J. Food Meas. Charact*. **2023**, *17*, 3568-3578.
12. Rao, D.F.; Santagapita, P.R.; Buera, M.P.; Tolaba, M.P. *Food Bioprocess Technol*. **2014**, *7*, 2723-2731.
13. Wang, W.; Zhou, H.; Yang, H.; Zhao, S.; Liu, Y.; Liu, R. *Food Chemistry*. **2017**, *214*, 319-327.

Antioxidant activity of spent coffee ground and its extracts from solvent with varying polarity

Chitinsee Paidech and Chaleeda Borompichaichartkul*

Department of Food Technology, Faculty of Science, Chulalongkorn University, Payathai, Bangkok, 10330, Thailand

**E-mail: Chaleeda.B@chula.ac.th*

Abstract:

Spent coffee ground (SCG) is a by-product from coffee brewing process. SCG contains a considerable amount of organic compounds and is a great source of antioxidants. The objectives of this work were to evaluate the antioxidant activity of SCG and SCG extracts by different solvents and concentrations (ethanol (60 - 90% w/w) and hexane), as well as to determine oxidative stability by peroxide value, conjugated diene value, iodine value and acid value. The results showed that total phenolic content (TPC) of SCG was 16.49 mg GAE/g. The 2, 2-diphenyl1-1-picrylhydrazyl (DPPH) radical scavenging activity and ferric reducing antioxidant power (FRAP) were 32.57 µmol TE/g and 140.9 µmol Fe(II)/g, respectively. For SCG extracts, 60% w/w ethanol extract contained the highest TPC and the strongest DPPH radical scavenging activity. The 80% ethanol extract had the highest FRAP value. The chlorogenic acid and 3,4-dihydroxybenzoic acid were the antioxidative compound found in all extracts except the hexane extract. This study shows that the 60%w/w ethanol extract had the strongest antioxidant activity. Therefore, spent coffee ground can be considered as an antioxidant source for use in food products and SCG extract can be great interested for applying to vegetable oils.

1. Introduction

Coffee is one of the world's most popular beverage and one of the largest traded commodities.[1] Recently, cold brew coffee is increasing in its popularity. Cold brew coffee is prepared at low temperature over a longer period of time[2]. Coffee processing generates residues from coffee fruit and spent coffee ground (SCG) is one of the by-products produced during the brewing process. By-products of coffee fruit and coffee brewing can be considered as potential functional ingredients for the food industry.[1]

SCG contains large amounts of organic compounds (i.e. fatty acid, protein, lignin, cellulose and other polysaccharides) and it contains a great source of antioxidants (i.e. chlorogenic acid)[1]. The main phenolic compound in SCG is chlorogenic acid and the SCG contains a great source of tocopherols that liposoluble antioxidant vitamin The antioxidant compounds from SCG have been extracted by solid-liquid solvent extraction using a range of solvents and maceration.[3-4] Incorporation of antioxidants retards lipid oxidation by interfering with the propagation of this reaction by accepting free radicals and forming stable free radicals before they can attack unsaturated fatty acids.[5]

Therefore, this study aimed at evaluating the antioxidant activities of SCG from cold brewing, together with determining the antioxidant activities of SCG extracts by comparing different solvents (hexane and 60-90% ethanol) extraction to obtain both aqueous and oil soluble compounds.

2. Materials and Methods

2.1 Materials and Sample Preparation

Medium-roasted coffee robusta bean was supplied from local enterprise in Chiang Rai, Thailand. All chemical reagents, hexane and ethanol were laboratory grade. SCG was generated from cold brew coffee processing. The cold brewing process was carried out at refrigerator temperature (4˚C) and used the ground coffee/water ratio (1:10). SCG was dried in a hot-air oven at 45 ˚C until the moisture content as below 4% (w.b.). Then, the color of the dried SCG was evaluated using the Konica Minota CR-400 chroma meter. The moisture content was determined using the Mettler MJ33 moisture analyzer.

2.2 Spent Coffee Ground Extract

The extraction was carried out by maceration method. The dried SCG was mixed with solvent (hexane and 60-90% ethanol) at a SCG/solvent ration of 1:10 w/v and was shaken at room temperature (25 ˚C) for 24 hr. The mixture was filtered by using a Whatman No.1 filter paper and a vacuum pump to obtain the clear solution. Filtrate was concentrated in a rotary evaporator at 50 ˚C and dried at 50 ˚C for 1 hr. All Extracts were stored at -20 ˚C until analyses within 2 weeks.

2.3 Chemical Properties

2.3.1 Free Fatty Acid Content

Free fatty acids content (FFA) was determined by titration described by Meerasri and Sothornsri.[6] Each sample (0.25 g) was dissolved in 50 mL hot neutralized ethanol (99.9%) and was titrated against standardized 0.25 N NaOH solution using phenolphthalein as an indicator. The results were expressed as %FFA calculated using Eq. (1).

$$\%FFA = \frac{N \times V \times 26.75}{m} \quad (1)$$

Where N and V are the normality and volume of the titrant used, respectively, m is the mass of sample.

2.4 Determination of Polyphenols and Antioxidant Activity

2.4.1 Total Phenolic Content

Total phenolic content (TPC) was determined by using method of Waterhouse[9] using Folin-Ciocalteu reagent and standard curve was prepared using gallic acid. Each sample (0.1 mL) was dissolved with distilled water (7.9 mL) and mixed with 0.5 mL of Folin-Ciocalteu reagent, Then, the solution was kept in the dark at room temperature for 30 min. The absorbance was determined at 765 nm. The results were expressed as milligrams of gallic acid equivalents/g of sample.

2.4.2 Antioxidant Activity

The DPPH radical scavenging activity was determined following the method described by Shimada et al.[7] and calibration curve determined from Trolox. Each sample (0.5 mL) was mixed with 5 mL of 0.1 mM DPPH solution and kept in the dark at room temperature (27-29˚C) for 30 min. The DPPH radical scavenging activity was calculated as the percentage of the decrease of the absorbance at 515 nm relative to a blank. The results were expressed as micromoles of Trolox equivalent/g of sample.

The ferric reducing antioxidant power (FRAP) assay was determined by using the method of Benzie and Strain.[8] Each sample (0.5 mL) was mixed with FRAP reagent (7.5 mL) and kept in the dark at room temperature for 30 min. After that, the absorbance was determined at 593 nm. The FRAP values were expressed as micromoles of ferrous equivalent /g of sample.

2.4.3 Analysis of Antioxidative Compounds

Antioxidant compounds were analyzed using a high-performance liquid chromatography (HPLC) equipped with a diode array detector at 280 nm. Antioxidant compounds were eluted using a gradient mobile phase consisting of 1% formic acid (solvent A) and methanol (solvent B) through a Zorbax SB-C18 5 µm (4.6 x 150 mm) column at a flow rate of 1 ml/min. The injector volume was 20 µl. The gradient was programmed as follows: 100%B at 30 min, 0%B at 31-35 min. Authentic standards (3,4-dihydroxybenzoic acid, gallic acid, chlorogenic acid and caffeic acid) were used to verify the retention time.

Tocopherols were analyzed by using the HPLC equipped with a diode array detector at 292 nm. The mobile phase was 100% methanol pump at 1 ml/min. Sample were eluted with Eclipse Plus-C18 3.5 µm column. The injector volume was 20 µl. Standard tocopherols were used to identify the peak and amount of tocopherols presented in the sample.

2.5 Oxidative Stability

2.5.1 Peroxide Value

Peroxide value (PV) was determined using a modified International Dairy Federation standard method described by Dermis et al.[10] Each sample (0.01 g) was diluted with methanol/isopropanol (2:1 v/v, 3.0 mL). After adding ammonium thiocyanate solution (0.015 mL) and ferrous chloride solution (0.015 mL), the mixture was then kept for 20 min at room temperature. The absorbance was determined at 510 nm. The PV was calculated using Eq. (2).

$$PV = \frac{(As - Ab) \times m}{55.84 \times m_0 \times 2} \quad (2)$$

Where As is the absorbance of the sample, Ab is the absorbance of the blank, m is the slope of the standard cure and m_0 is the mass of sample.

2.5.2 Acid Value

Acid value (AV) was determined using AOCS Official Method Cd 3d-63[11] with a slight modification. Each sample (5 g) was dissolved in neutralized toluene-isopropyl alcohol (1:1 v/v, 125 mL) and titrated with 0.1 M KOH solution using phenolphthalein as an indicator. The AV was calculated using Eq. (3).

$$AV = \frac{V \times C \times 56.1}{w} \quad (3)$$

Where V is the volume of the titrant used, C is the concentration of KOH and W is the mass of sample.

2.5.3 Iodine Value

Iodine value (IV) was determined by using AOAC Official Method 993.20.[12] Each sample (0.25 g) was dissolved in cyclohexane-acetic acid solvent (1:1 v/v, 15 mL) and mixed with Wij's

iodine solution. After the solution was kept in the dark for 30min and then mixed with 15% w/w KI (20 mL) and distilled water (150 mL). The solution was titrated using 0.1 M sodium thiosulfate solution with starch solution as an indicator. The IV was calculated as following formula in equation (4).

$$IV = \frac{V \times M \times 12.69}{mass\ of\ sample\ (g)} \qquad (4)$$

Where V is the volume of the titrant used and M is the molarity of sodium thiosulfate.

2.5.4 Conjugated Dienes Value

Conjugated dienes value (CD) was determined by using method of Ronald.[13] Each sample (0.01-0.03 g) was dissolved with isooctane. The absorbance was determined at 233 nm. The CD value was calculated using the equation. (5).

$$CV\ value = \frac{\left(c_{CD} x (2.5 x 10^4)\right)}{W}\ , c_{CD} = \frac{A_{233}}{\varepsilon x l} \qquad (5)$$

Where c_{CD} is the concentration of conjugated dienes, W is the mass of the sample, A_{233} is the absorbance at 233 nm of the sample, ε is the molar absorptivity of linoleic acid hydroperoxide and *l* is the path length of cuvette.

2.6 Statistical Analysis

All analytical determinations were carried out in triplicate. Data were analyzed by the one-way ANOVA and performed using the SPSS statistic. All means of data were compared by Duncan's multiple range test with statistical significance at $P < 0.05$.

3. Results & Discussion

3.1 Spent Coffee Ground Properties

The total phenolic content of SCG was 16.49 mg GAE/g (Table 1). This value was lower than the result of Choi and Koh[14] who had reported that TPC of Arabica and blend comprising various species spent coffee ground ranged between 19.3-25.5 mg GAE/g. The DPPH radical scavenging activity and the FRAP value were 32.57 µmol TE/g and 0.141 mmol Fe(II)/g, respectively. These were higher than the result studied by Ballesteros et al.,[15] who reported that SCG from mixtures of Arabica and Robusta coffee produced 20.04 µmol TE/g of the DPPH value and 0.102 mmol Fe(II)/g of the FRAP value. The different results might be due to the differences in coffee species, storage condition, the extraction method and the solvent type used for extraction.[16]

The FFA content of SCG was 2.53%. This was lower than the result of Meerasri and Sothornvit[6] who had reported that robusta SCG oil produced 5.56% of the FFA content. The peroxides are the main primary oxidation products.[17] The peroxide value (PV) of oil in SCG (2.397 meq/kg) was lower than that described by Böger et al.,[18] who reported that PV of Arabica coffee oil was 3.208 meq/kg. This value is not over than the recommended value of the Ministry of Public Health, who reported that PV of Arabica coffee oil was 3.208 meq/kg. This value is not over than the recommended value of the Ministry of Public Health, that mentioned that PV of oil should not exceeded a maximum of 10 meq/kg of peroxide value for oil. Moreover, it is recommended that the acid value should be less than 4 mgKOH/g for oil from natural process and less than 0.6 mgKOH/g for oil from processing process.[19]

Table 1. Chemical properties and antioxidant activities of robusta spent coffee ground.[a]

Property	Spent coffee ground
Moisture (%)	3.9 ±0.4
Color	L* = 45.39 ±1.60, a* = 2.87 ±0.09, b* = 2.91 ±0.11
Free fatty acid (%)	2.5 ±0.1
FRAP (µmol Fe(II)/g)	140.9 ±10.3
DPPH (µmol TE/g)	32.57 ±0.60
TPC (mg GAE/g)	16.49 ±0.48
Peroxide value (meq/kg)	2.397 ±0.357
Acid value (mg KOH/g)	0.055 ±0.002
Iodine value (g I_2/100 g)	3.822 ±0.370
Conjugated diene value (µmol CD/g)	0.088 ±0.016

[a]Results were expressed as means ±SD

The acid value (AV) is an important parameter indicating free fatty acid content. The high free fatty acid content increases susceptibility to oxidation.[20] So, the AV of oil in SCG (0.055 mgKOH/g) was lower than that recommended by the Ministry of Public Health.[19] The iodine value (IV) indicates the degree of unsaturation in oil.[21] The IV of oil in SCG (3.822 gI_2/100g) was lower than that reported by Bijla et al.,[22] who found that IV of SCG oil from mixtures of Arabica and Robusta coffee was 92 g I_2/100 g. The conjugated dienes are the primary products of lipid oxidation, as well as peroxides.[23] The conjugated diene (CD) value of oil in SCG (0.088 µmolCD/g) was lower than that described by Ribeiro et al., who reported that CD value of roasted coffee oil was 1.2 µmolCD/g.[24] These results suggested that SCG had a good oxidative stability.

The antioxidant compounds were analyzed. SCG contained 3,4-Dihydroxybenzoic acid (0.02243 mg/g), gallic acid (0.1380 mg/g), caffeic acid (0.05746 mg/g), chlorogenic acid (3.229 mg/g), alpha-tocopherol (2.098 µg/g) and

beta-tocopherol (23.10 µg/g). Therefore, the major antioxidative compound was chlorogenic acid. Similarly to the results from Belščak-Cvitanović and Komes[4] who reported that chlorogenic acid was the main polyphenolic compounds of coffee processing by-products. However, the different

Table 2. Chemical properties, antioxidant activity, antioxidant compounds and oxidative stability of SCG extracts.[a),b)]

	Hexane extract	90% Ethanol extract	80% Ethanol extract	70% Ethanol extract	60% Ethanol extract
Free fatty acid (%)	7.164^{a} ±0.702	7.521^{a} ±0.811	6.752^{ab} ±0.038	5.746^{b} ±0.704	2.662^{c} ±0.014
FRAP (µmol Fe(II)/g)	2.923^{e} ±0.189	304.3^{d} ±2.9	683.6^{c} ±2.5	812.9^{b} ±16.1	1291^{a} ±5
DPPH (µmol TE/g)	4.312^{e} ±0.891	56.37^{d} ±0.78	493.2^{a} ±0.9	488.4^{b} ±1.4	457.2^{c} ±2.9
TPC (mg GAE/g)	4.113^{d} ±0.465	36.22^{c} ±6.76	91.56^{b} ±5.01	93.96^{b} ±2.41	116.4^{a} ±4.8
PV (meq/kg)	9.510^{a} ±2.115	1.270^{c} ±0.234	2.397^{bc} ±1.080	4.187^{b} ±0.269	3.439^{bc} ±1.029
AV (mg KOH/g)	1.850^{d} ±0.056	18.21^{c} ±0.37	31.64^{b} ±7.22	41.81a ±3.14	30.64^{b} ±4.69
IV (g I2/100 g)	46.48^{a} ±4.43	15.84^{b} ±2.19	14.12^{b} ±2.68	12.20^{b} ±0.93	4.569^{c} ±1.375
CD (µmol CD/g)	12.80^{a} ±2.38	13.54^{a} ±2.60	6.168^{b} ±1.24	11.77^{a} ±0.45	11.28^{a} ±1.82
3,4-Dihydroxybenzoic acid (mg/g)	ND[c)]	0.5644^{a} ±0.018	0.3819^{d} ±0.0063	0.4724^{c} ±0.0104	0.5061^{b} ±0.0238
Gallic acid (mg/g)	ND	ND	ND	ND	ND
Caffeic acid (mg/g)	ND	ND	ND	ND	ND
Chlorogenic acid (mg/g)	ND	38.99^{c} ±1.86	64.48^{a} ±3.28	60.97^{a} ±3.46	45.19^{b} ±4.50
Alpha-tocopherol (µg/g)	93.39^{a} ±5.02	36.68^{b} ±2.33	ND	ND	ND
Beta-tocopherol (µg/g)	2005^{a} ±65	580.4^{b} ±7.1	ND	ND	ND

[a)] Results are expressed as means ±SD;
[b)] Different letters in the sa6me column indicate a significate difference at $p<0.05$
[c)] Not detected

amount found could be due to the type of coffee and technological factors, such as, roasting degree and extraction method.

3.2 Antioxidant Activity and antioxidant compounds of SCG Extracts

In general, antioxidant activity of SCG extracts has the synergism and antagonism of individual compounds.[25] It is difficult to evaluate a single compound. So, antioxidant activity of SCG extracts are needed to analyze by the contribution of each compound. Therefore, in the current study, antioxidant activity and antioxidative compounds were determined by TPC, FRAP value and DPPH radical scavenging activity. As shown in Table 2. The 60% ethanol extract had the highest TPC (116.4±4.8 mgGAE/g) followed by the 70% ethanol extract (93.96±2.4 mgGAE/g) and the 80% ethanol extract (91.5±5.0 mgGAE/g). This result was well correlated with FRAP value. The 60% ethanol extract had the highest FRAP value (1291±5.2 Fe(II)/g) followed by the 70% ethanol extract (812.9±16 Fe(II)/g) and then the 80% ethanol extract (683.6±2.5 Fe(II)/g). However, these results were different with DPPH assay that showed the 80% ethanol extract had the highest DPPH value (493.2±0.92 µmol TE/g). This indicates that the major compounds contributing to FRAP and DPPH were different. The FRAP assay measures the ability of antioxidants to reduce ferric ion. But the DPPH assay evaluates the antioxidant potential through free radical scavenging by the samples by donated a hydrogen atom to DPPH.[26] Polyphenolic compounds are easily solubilized in polar solvents for solvent extraction method, resulting to different obtained by concentration based on polarity.[4] Overall, the 60% ethanol extract showed higher antioxidant activity than the hexane extract and 70-90% ethanol extracts.

These antioxidative compounds of SCG extracts were determined (Table 2). The chlorogenic acid and 3,4-dihydroxybenzoic acid were the antioxidative compound found in all extracts except the hexane extract, so the chlorogenic acid was the major compound found in SCG extract by ethanol. The hexane extract and 90% ethanol extract contained alpha- and beta-tocopherols and the amount of beta-tocopherol was found to be more than alpha-tocopherol. Tocopherols are lipid-soluble amphipathic compounds.[27]

3.3 Chemical properties and oxidative stability of SCG extracts

The unsaturated fatty acid will decompose during lipid oxidation to form small and produce volatile molecules associated with oxidative rancidity.[5] Therefore, this study was determined free fatty acid (FFA) content. The FFA content is defined as the percentage by weight of free acid groups in sample. The high FFA content increases susceptibility to oxidation.[20] The hexane extract, 90% and 80% ethanol extract had the highest FFA content (7.164±0.70, 7.521±0.81 and 6.752

±0.038%, respectively). Lipid oxidation is affected by unsaturated fatty acids which are susceptible to chemical reactions.[28] Generally, oxidative stability is commonly evaluated by the peroxide value, acid value, iodine value and conjugated diene value. As shown in Table 2. The CV and PV show the degree of lipid oxidation. The conjugated dienes are the primary products of polyunsaturated fatty acid oxidation produced from the double bond displacement.[21] The CD value showed that the 80% ethanol extract had the lowest CD value (6.168 ±1.2 µmol CD/g). The PV measures the amounts of total peroxides resulting from primary oxidation. Polyunsaturated fatty acid oxidation arises during the formation of hydroperoxides and the double bond displacement.[21] So, the higher peroxide value consists of the lower oxidative stability.[17] The PV showed that the 90% ethanol extract had the lowest PV (1.270 ±0.23 meq/kg) followed by 60% ethanol extract (3.439 ±1.0 meq/kg) and 80% ethanol extract (2.397 ±1.1 meq/kg), with similar values. The AV is considered the amount of free fatty acid by defined as the weight of potassium hydroxide required to neutralize the free acid groups.[28] The hexane extract had the lowest AV. The IV is considered the degree of unsaturated fatty acid in oil.[21] The lower IV, indicating the higher oxidative stability and longer shelf life.[29] The IV showed that the 60% ethanol extract had the lowest IV (4.567 ±1.375 gI_2/100g).

4. Conclusion

SCG contained certain amount of antioxidative compounds and had high level of antioxidant activity comparing with reference reported. The different value obtained from literature may due to type of coffee, brewing method and other factor, which affected the amount of antioxidative compound extracted. Among the extracts investigated, it was found that the 60% ethanol extract of cold-brewing SCG showed significantly higher in antioxidant activity than hexane extract and 70-90% ethanol extracts. So, this result correlated with the previous report revealed[4] that polarity of solvent may affect to antioxidative compounds. Thus, SCG extract had the potential as a natural antioxidant for applying to vegetable oils. Nevertheless, the PV, CV, IV and AV may be used for an approximate prediction of the oxidative stability of SCG extracts, so the oxidative stability analysis must be evaluated by applied into the target oil under similar conditions. In conclusion, SCG extract could be of great interest for demonstrating its application as a natural antioxidant in vegetable oils.

Acknowledgements

This research was supported by funding from Chulalongkorn University, Bangkok, Thailand.

References

1. Campos-Vega, R.; Loarca-Pina, G.; Vergara-Castañeda, H. A.; Oomah, B. D. *Trends Food Sci*. **2015**, *45* (1), 24-36.
2. Rao, N. Z.; Fuller, M. *Sci. Rep*. **2018,** *8* (1), 16030.
3. Alves, R. C.; Rodrigues, F.; Nunes, M. A.; Vinha, A. F.; Oliveira, M. B. P. State of the art in coffee processing by-products. Handbook of coffee processing by-products 2017; pp 1-26.
4. Belščak-Cvitanović, A.; Komes, D. Extraction and formulation of bioactive compounds. In Handbook of coffee processing by-products, Elsevier, 2017; pp 93-140.
5. Chaiyasit, W.; Elias, R. J.; McClements, D. J.; Decker, E. A. *Crit. Rev. Food Sci. Nutr*. **2007**, *47* (3), 299-317.
6. Meerasri, J.; Sothornvit, R. *J. Food Process. Preserv*. **2022**, *46* (7), e16687.
7. Shimada, K.; Fujikawa, K.; Yahara, K.; Nakamura, T. *J. Agric. Food Chem.* **1992**, *40* (6), 945-948.
8. Benzie, I. F.; Strain, J. J. Anal. Biochem. **1996**, *239* (1), 70-76.
9. Waterhouse, A. L. Determination of total phenolics. Current protocols in food analytical chemistry 2002, 6 (1), I1. 1.1-I1. 1.8.
10. Dermiş, S.; Can, S.; Doğru, B. *Spectrosc. Lett*. **2012**, *45* (5), 359-363.
11. AOCS. Official method cd 3d-63, Sampling and analysis of commercial fats and oils: Acid value, 2009.
12. AOCS. Iodine value of fats and oils (Wijs method), AOCS Press Champaign, 1999.
13. Ronald, R. Measurment of primary lipid oxidation products. Current Protocols in Food Analytical chemistry. D2-1 2001.
14. Choi, B.; Koh, E. *Food Sci. Biotechnol*. **2017**, *26*, 921-927.
15. Ballesteros, L. F.; Teixeira, J. A.; Mussatto, S. I. *Food bioprocess tech.* **2014**, *7*, 3493-3503.
16. Kovalcik, A.; Obruca, S.; Marova, I. *Food and Bioproducts Processing*. **2018**, *110*, 104-119.
17. Yang, Y.; Song, X.; Sui, X.; Qi, B.; Wang, Z.; Li, Y.; Jiang, L. *Ind Crops Prod.* **2016**, *80*, 141-147.
18. Böger, B.; Mori, A.; Viegas, M.; Benassi, M. *Grasas Aceites.* **2021**, *72* (1), e394-e394.
19. The Ministry of Public Health. Notification of the Ministry of Public Health, Re: oil and fat

(Issue 205) 2000. https://fic.nfi.or.th/law/upload/file1/TH_95.pdf (accessed December 3, 2023).
20. Al-Hamamre, Z.; Foerster, S.; Hartmann, F.; Kröger, M.; Kaltschmitt, M. *Fuel.* **2012**, *96*, 70-76.
21. Acevedo, F.; Rubilar, M.; Scheuermann, E.; Cancino, B.; Uquiche, E.; Garcés, M.; Inostroza, K.; Shene, C. Journal of Biobased Materials and Bioenergy **2013**, *7* (3), 420-428.
22. Bijla, L.; Aissa, R.; Bouzid, H. A.; Sakar, E. H.; Ibourki, M.; Gharby, S. *Biointerface Res Appl Chem.* **2021**, *12*, 6308-6320.
23. Ribeiro, E. F.; Jorge, N. *Food Science and Technology* **2017**, *37*, 5-10.
24. Ribeiro, E. F.; Polachini, T. C.; Locali-Pereira, A. R.; Janzantti, N. S.; Quiles, A.; Hernando, I.; Nicoletti, V. R. Storage Stability of Spray- and Freeze-Dried Chitosan-Based Pickering Emulsions Containing Roasted Coffee Oil: Color Evaluation, Lipid Oxidation, and Volatile Compounds. Processes 2023, 11 (4), 1048.
25. Yen, W.J.; Wang, B.S.; Chang, L.W.; Duh, P.D. *J. Agric. Food Chem.* **2005**, *53* (7), 2658-2663.
26. Alam, M. N.; Bristi, N. J.; Rafiquzzaman, M. *Saudi Pharm J.* **2013**, *21* (2), 143-152.
27. Alves, R. C.; Casal, S.; Oliveira, M. B. P. Tocopherols in coffee brews: Influence of coffee species, roast degree and brewing procedure. *J. Food Compos. Anal.* **2010**, *23* (8), 802-808.
28. Wrolstad, R. E.; Acree, T. E.; Decker, E. A.; Penner, M. H.; Reid, D. S.; Schwartz, S. J.; Shoemaker, C. F.; Smith, D. M.; Sporns, P. Handbook of food analytical chemistry, volume 1: Water, proteins, enzymes, lipids, and carbohydrates; John Wiley & Sons, 2005.
29. Panpraneecharoen, S.; Chumanee, S. *Sci. Technol. Asia.* **2020**, 12-19.

Pesticide residues in chilies collected from chili farms in southern Thailand

Sujanya Jitlang[1]*, Panwadee Wattanasin[2], Kwanruthai Tadpetch[2], Thitima Rujiralai[2,3]*

[1]*Office of Scientific Instrument and Testing, Prince of Songkla University, Songkhla, 90110, Thailand*
[2]*Center of Excellence for Innovation in Chemistry and Division of Physical Science, Faculty of Science, Prince of Songkla University, Songkhla, 90110, Thailand*
[3]*Analytical Chemistry and Environment Research Unit, Division of Science, Faculty of Science and Technology,Prince of Songkla University, Pattani, 94000, Thailand*

**E-mail: sujanya.j@psu.ac.th, thitima.r@psu.ac.th*

Abstract:

The major chili production areas in southern Thailand are found in Songkhla, Phatthalung and Nakhon Si Thammarat provinces. In these areas, pesticides are applied to chili plants to control pests such as chili thrips and cotton bollworm, and viral or bacterial diseases such as anthracnose disease, powdery mildew, and leaf roll. Information on pesticide contamination of chilies from these provinces is limited. Therefore, this study will focus on the determination of pesticide residues in chilies (*Capsicum annuum* L.) collected from farms in Ranot district of Songkhla province (32 samples), Lampam district of Phatthalung province (18 samples), and Hau Sai district of Nakhon Si Thammarat province (20 samples). These sampling sites have been chosen since they are in main chili production areas where 3500–11000 chili plants are planted per area of about 2–5 rai. Some pesticides, *e.g.* chlorpyrifos, carbaryl, carbofuran, cypermethrin, λ-cyhalothrin and deltamethrin are of interest due to being the pesticide frequently used by farmers in the last 15 years. Chilies were extracted with hexane/acetone (1:1, v/v), and dichloromethane for testing (i) chlorpyrifos, carbaryl, carbofuran and (ii) cypermethrin, λ-cyhalothrin and deltamethrin contaminations, respectively. The extracts were purified using Florisil and C_{18} solid phase extraction (SPE). After concentrating the extracts, final residues were analyzed in solution by gas chromatography (GC). Differences in the mean value were analyzed by one-way ANOVA. Most samples were not contaminated with the pesticides of interest. Two samples collected from Hau Sai district contained λ-cyhalothrin concentrations at 4.39 and 3.57 μg/kg which do not exceed the maximum residue limit (MRL) of 10 μg/kg for spices and 300 μg/kg for chilies established by the Commission Regulation (EU) and the Thai Agricultural Standard, respectively.

1. Introduction

Chili (*Capsicum annuum* L.) is one of high valuable crops in Thailand. Fresh chili and chili products including dried chili, chili powder, chili paste and chili sauce are widely used as food ingredients and exported to many countries across the world, *e.g.*, Malaysia, the Netherlands, Spain, and Singapore.[1] During cultivation, chili always suffers from pests such as chili thrips and cotton bollworm and viral or bacterial diseases such as anthracnose disease, powdery mildew, and leaf roll.[2] Thus, farmers have used pesticides intensively to control these insects and diseases. Pesticides are applied at different stages of growth. For example, seeds are soaked with pesticides before sowing and crops are sprayed with pesticides. Without the application of pesticides, yields of chili could be reduced by more than 50%.[3]

Pesticides are an integral part of agriculture in Thailand. Imports of herbicides, insecticides, and fungicides have been increasing. During the period 2017–2021 pesticide imports increased from 98,254 to 197,646 tons.[4] As well as the known heavy pesticide usage, inappropriate or illegal use of pesticides poses a threat to consumer health and the environment. Pesticides accumulate in the human body through diet, contaminated water, and polluted air. Frequent exposure to pesticides has provoked various conditions among farm workers.[5] Adverse effects caused by organophosphate and carbamate pesticides are related to cholinesterase depression and plasma cholinesterase.[5] Thus, to guarantee safety from pesticides, maximum residue limits (MRLs) of pesticides were established by many organizations, *e.g.* Commission Regulation (EU) and Thai Agricultural Standard (TAS).[6,7]

The standard tightly restricts pesticide contamination, but in the past few years, pesticides have still been detected in fruits, vegetables and the environment in Thailand, and several assessments of pesticide exposure have been made. In 2020, 3,067 Thais suffered from pesticide-related health effects and 407 deaths were reported to have been caused by pesticides.[8] Chilies collected from Songkhla province in the south were found to contain organophosphate concentrations from 0.01 to 0.81 mg/kg, but the hazard quotient ratio (HQ) of organophosphates in the chili samples were low, ranging from 0.0002 to 0.0375.[3] Also in southern Thailand, Khemvong and Suksawat[9] found

concentrations of chlorpyrifos, profenofos, ethion, dicofol and cypermethrin in chilies that ranged from 0.01 to 0.59 mg/ kg.

The production areas of chilies in southern Thailand contribute ~2.5% of the total chili production areas of the country[10] but very few studies have assessed levels of pesticides in chilies from these provinces.[9,11] Thus, the aim of this study is to determine pesticide residues in chilies collected from Songkhla, Phatthalung and Nakhon Si Thammarat provinces. Chlorpyrifos, carbaryl, carbofuran in chilies were extracted with hexane/acetone (1:1, v/v) whereas cypermethrin, λ-cyhalothrin and deltamethrin were extracted with dichloromethane. Further, the extracts were purified using Florisil and C_{18} solid phase extraction (SPE). After concentrating the extracts, final residues in solution were determined by means of gas chromatography (GC) with different detector, *i.e.*, flame photometric detector (FPD) for chlorpyrifos, flame ionization detector (FID) for carbaryl and carbofuran and electron capture detector (ECD) for λ-cyhalothrin, cypermethrin and deltamethrin. This study will provide data about the concentration of pesticides in chilies grown in the study areas.

2. Materials and Methods

2.1 Materials

Carbaryl, carbofuran, λ-cyhalothrin, cypermethrin and deltamethrin were purchased from the National Institute of Metrology (Thailand). Chlorpyrifos was obtained from AccuStandard (USA). HPLC-grade reagents, *i.e.*, hexane, dichloromethane, acetone, acetonitrile, isooctane, methanol, and toluene were purchased from LabScan (Thailand). A Waters Sep-Pak Florisil column (6 mL, 500 mg, Ireland) and an Agilent Technologies Bond Elut C_{18} column (6 mL, 1 g, USA) with an SPE vacuum manifold (Agilent Technologies, USA) were used for sample clean-up. Glassware was furnaced at 450°C at least 1 h before use to remove any pesticide residues. Working standard solutions of chlorpyrifos, carbaryl and carbofuran were prepared in hexane/acetone (1:1, v/v) while those of λ-cyhalothrin, cypermethrin and deltamethrin were prepared in hexane/toluene (1:1, v/v). The Florisil column was pre-conditioned with 4 mL of isooctane for 5 min whereas the C_{18} column was pre-conditioned with 4 mL of methanol for 5 min, followed by 4 mL of acetonitrile for 5 min.

2.2 Sample areas and collection

Chilies were collected from nine sampling sites across three provinces (Figure 1). Four sampling sites were located in Ranot district, Songkhla province. They were in Wat Son sub-district (S1 and S2: 7°38'54.4"N 100°23'04.3"E), Ranot sub-district (S3: 7°38'46.9"N 100°22'26.8"E) and Daen Sa-nguan sub-district (S4). Two sampling sites (P1: 7°39'23.9"N 100°06'57.6"E and P2: 7°39'08.0"N 100°07'25.1"E) were in the Lampam sub-district, Lampam district, Phatthalung province. Three sampling sites (N1: 8°02'16.6"N 100°14'11.8"E, N2: 8°08'16.5"N 100°07'30.7"E and N3: 8°08'10.2"N 100°07'31.1"E) were in Khao Phang Krai sub-district of Hau Sai district, in Nakhon Si Thammarat province. These sampling sites were chosen because they are in main chili production areas where 3500–11000 chili plants are planted per area of about 2–5 rai.[10] The chili variety grown in Songkhla and Nakhon Si Thammarat is Duangmanee cultivar while the variety grown in Phatthalung is the Yod-son cultivar. The Duangmanee cultivar is more for export to Malaysia since it is a bigger, shinier chili and less spicy than the Yod-son cultivar.[10] Similar pesticide types were applied in the studied areas, but we observed that the farmers in Songkhla and Nakhon Si Thammarat utilized natural substances such as a mixture of chicken waste, fish waste and eggshells more than in Phatthalung.

Sampling was undertaken every month during harvest season from May to September 2017. It is noted that samplings were not conducted at N3 in July and August and at S1-S4, N1-N2 and P2 in September because chili seedlings were being cultivated. Insufficient samples were collected from S3 in July and were not analyzed. Approximately 1 kg of chilies were collected at each sampling site and sealed in plastic bags. Latex surgical gloves were worn during collection. All samples were kept in a cool box during transportation to the laboratory and stored at -20°C before pesticide extraction and analysis.

2.3 Sample pretreatment, extraction and clean-up procedure

Chilies were taken from the refrigerator, allowed to warm to room temperature, cut into small pieces with a table knife and blended in a blender. To extract the chilies from each site, 10 g of blended sample were weighed in a 250 mL brown glass bottle. Each sample was prepared in duplicate. Overall extraction and clean-up methods are summarized in Figure 2. Pesticides were extracted in the amble bottle according to a reported method[12] with modifications. The obtained extract was cleaned up by SPE before analysis by GC.

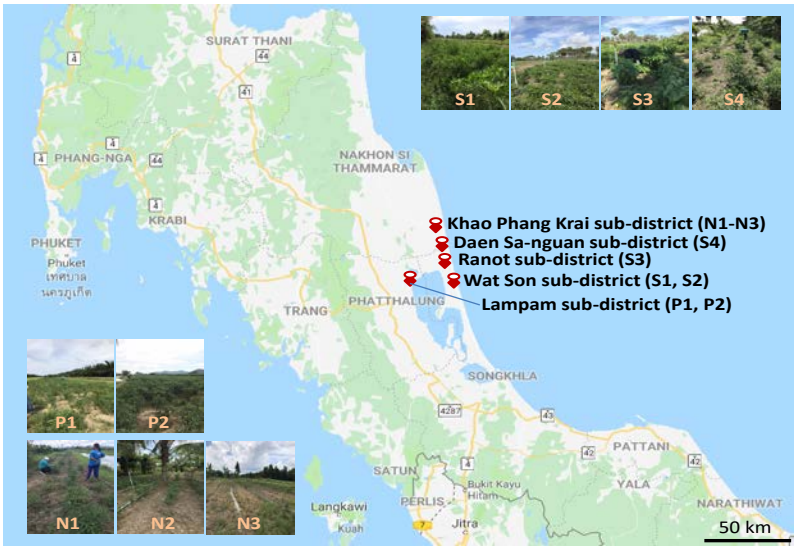

Figure 1. Chili sampling sites: Four sampling sites (S1-S4) were in Ranot district, Songkhla province. Two sampling sites (P1 and P2) were in Lampam district, Phatthalung province. Three sampling sites (N1-N3) were in Hau Sai district, Nakhon Si Thammarat province. The map was cited from https://maps.google.com (accessed December 2, 2023).

2.4 Gas chromatography (GC) analysis

The GC analysis of pesticides was performed using a Hewlett-Packard GC series 6890 coupled with different detectors (Table 1). The GC separation was performed using a DB-35 (30 m × 0.32 μm × 0.25 μm) capillary column in splitless mode. Analytical conditions of GC analysis are listed in Table 1. The identification of pesticides was confirmed by comparing the retention time of each analyte in the sample extract with that of the pesticide standard. The retention times of the analyte should not differ by more than ± 0.1 min from the retention time of the standard.[12] Concentrations of residues were quantified by the standard calibration curve method, for which analyte peak areas were plotted against five concentrations of each pesticide. All calibration plots were linear with R^2 greater than 0.9900. Based on a signal-to-noise ratio of 10, the limit of quantitation (LOQ) of the tested pyrethroids (λ-cyhalothrin, cypermethrin and deltamethrin), chlorpyrifos and carbamates (carbaryl, carbofuran) were 1.0, 25.0 and 2.0 μg/kg, respectively, which were much lower than the MRLs of TAS.[7,13] Concentration of pesticides lower than LOQ was reported as "not detected"

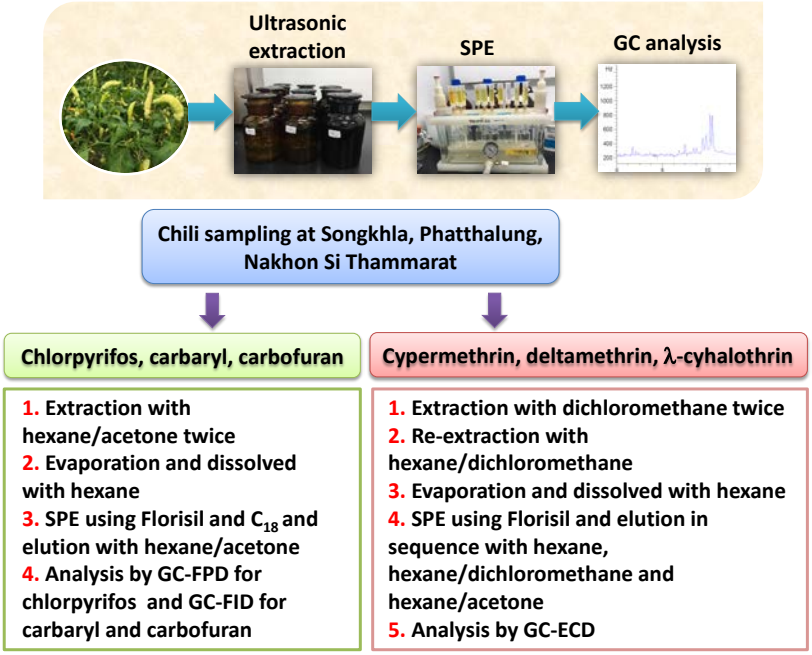

Figure 2. The workflow describes the overall methods of analysis used in

(ND). Two replicate injections of each sample were determined, and the detected concentrations were reported as means ± SD. Differences in the mean value were analyzed by one-way ANOVA at 95% confident limit.

3. Results & Discussion

3.1 Determination of pesticides in chilies

Pesticides can be divided into four main types based on their chemical structures: organophosphates, carbamates, organochlorines and pyrethroids.[5,14] Organophosphates and carbamates predominate and are highly toxic to humans and other organisms.[5] Chlorpyrifos has been the pesticide most frequently used by farmers in the last 15 years, followed by cypermethrin.[9,11,15] According to the Thai statistics from 2012 to 2022,[4] chlorpyrifos was the most valuable imported pesticide, but imports have significantly decreased since 2021, when it was banned. Deltamethrin and λ-cyhalothrin were imported more than other pesticides in 2022. Very small quantities of carbofuran (36 kg, cost 1266 $) were imported in 2012, and this pesticide has been banned since 2013. We also found that the trade names on empty pesticide containers abandoned around the sampling areas indicated the use of chlorpyrifos, cypermethrin and cyhalothrin. Other pesticides of interest in this work included carbaryl and carbofuran.

Table 2 shows the concentrations of pesticides measured in chilies sampled during May to September 2017. Chlorpyrifos, carbofuran and carbaryl were not found. Samples were also analyzed for the presence of the pyrethroid pesticides λ-cyhalothrin, cypermethrin and deltamethrin. Most of the samples were not contaminated with pyrethroids, except two samples collected in July at the N1 and N2 sites. The respective samples contained λ-cyhalothrin residues at 4.39 ± 2.56 μg/kg and 3.57 ± 0.00 μg/kg. The concentrations of λ-cyhalothrin were detected possibly due to low water solubility which cannot be rinsed by rain compared to other studied compounds. However, these concentrations are much lower than MRL of 10 μg/kg for spices and 300 μg/kg for chilies established by EU and TAS, respectively.[6,7]

3.2 Pesticide Toxicity Index (PTI)

Since two samples contained λ-cyhalothrin, the Pesticide Toxicity Index (PTI) was estimated. The PTI, like the HQ, is calculated to screen for pesticide toxicity and presents the effect of multiple pesticide residues on the quality of samples. When the PTI is less than 1.00, the sample poses no risk to human health.[16] The PTI was modified and calculated as follows:

$$\mathrm{PTI} = \sum \mathrm{TQ} = \sum_{i=1}^{n} \frac{C_i}{\mathrm{MRL}_{x,i}}$$

where TQ is the ratio between individual pesticide concentration and MRL, C_i is the individual pesticide concentration (mg/kg), and $\mathrm{MRL}_{x,i}$ is the EU MRL (mg/kg).[16]

The TQs of the samples from N1 and N2 were 0.439 and 0.357, respectively (Table 3). The PTI was estimated to be 0.796, indicating that these samples were safe to consume. Even though chlorpyrifos, cypermethrin and cyhalothrin have been used in the study areas, overall, they were not detected in this work. It is possibly because they are weakly persistent in the environment.[17] Compared to organochlorines, their half-lives are much shorter, from 3–15 days, depending on temperature and sunlight.

We collected samples during cropping season in May 2017 (summer) and June to September 2017 (rainy season). Duration of the chili harvest is ~5 months per year (May to September), and all chili plants in studied areas had been removed after the harvest since September to prepare agriculture land for cultivating chili seedling. It was reported that pesticide concentrations decreased in rainy seasons likely from leaching of pesticides to the soil. A previous report supported that soil can be a sink for pesticides, where they absorb into the surface of soils.[18] However, further study would be needed to investigate the contamination of soil at the sampling sites.

The undetectable or low found concentrations may also be a result of our sampling of chilies after spraying. Most farmers in the study areas know the right time to harvest chilies. It was mentioned that exposure to pesticide residues could be minimized by harvesting at the appropriate time. Harvesting of chilies was recommended on the 9th day after the last spraying of chlorpyrifos and on the 15th day for cypermetrin.[11] We also notice that some farmers are not using synthetic pesticides, instead using natural substances such as fertilizer made from a mixture of chicken waste, fish waste and eggshells, or compost made from garlic and Cassia leaves. Thus, these were the reasons that pesticides were hardly found in this work.

Table 1. Analytical conditions of GC coupled with different detectors for pesticide determination.

Condition	Pyrethroid	Organophosphate	Carbamate
Detector	ECD	FPD	FID
Injection volume (µL)	2.00	1.00	1.00
Flow rate of He (mL/min)	1.00	1.20	1.00
Inlet temperature (°C)	280	270	250°C
Inlet flow rate (mL/min)	75 (0.5 min)	-	75 (0.5 min)
Temperature program	100°C; increased to 270°C by 30°C/min, to 280°C by 10°C/min (20 min)	70°C (2 min); increased to 250°C by 9°C/min, to 300°C by 2°C/min (2.5 min)	100°C (1 min); increased to 200°C by 20°C/min; to 210°C by 2°C/min, to 224°C by 1°C/min (7 min)
Post run (°C)	320 (2 min)	-	280 (2 min)
Detector temperature (°C)	250	250	300
Flow rate of N_2/H_2/Air (mL/min)	60/-/-	15/75/100	25/30/300

Table 2. Pesticide concentrations detected in chilies from Songkhla, Phatthalung and Nakhon Si Thammarat provinces collected during May to September 2017.

Compound	Concentration of pesticides at each area (µg/kg) (n = 2)								
	S1	S2	S3	S4	P1	P2	N1	N2	N3
					May 2017				
Chlorpyrifos	ND	ND	ND	ND	ND	ND	ND	ND	ND
Carbaryl	ND	ND	ND	ND	ND	ND	ND	ND	ND
Carbofuran	ND	ND	ND	ND	ND	ND	ND	ND	ND
Cypermethrin	ND	ND	ND	ND	ND	ND	ND	ND	ND
λ-Cyhalothrin	ND	ND	ND	ND	ND	ND	ND	ND	ND
Deltamethrin	ND	ND	ND	ND	ND	ND	ND	ND	ND
					June 2017				
Chlorpyrifos	ND	ND	ND	ND	ND	ND	ND	ND	ND
Carbaryl	ND	ND	ND	ND	ND	ND	ND	ND	ND
Carbofuran	ND	ND	ND	ND	ND	ND	ND	ND	ND
Cypermethrin	ND	ND	ND	ND	ND	ND	ND	ND	ND
λ-Cyhalothrin	ND	ND	ND	ND	ND	ND	ND	ND	ND
Deltamethrin	ND	ND	ND	ND	ND	ND	ND	ND	ND
					July 2017				
Chlorpyrifos	ND	ND	ND	ND	ND	ND	ND	ND	-[a]
Carbaryl	ND	ND	ND	ND	ND	ND	ND	ND	-[a]
Carbofuran	ND	ND	ND	ND	ND	ND	ND	ND	-[a]
Cypermethrin	ND	ND	-	ND	ND	ND	ND	ND	-[a]
λ-Cyhalothrin	ND	ND	-	ND	ND	ND	4.39 ± 2.56	3.57 ± 0.00	-[a]
Deltamethrin	ND	ND	-	ND	ND	ND	ND	ND	-[a]
					August 2017				
Chlorpyrifos	ND	ND	ND	ND	ND	ND	ND	ND	-[a]
Carbaryl	ND	ND	ND	ND	ND	ND	ND	ND	-[a]
Carbofuran	ND	ND	ND	ND	ND	ND	ND	ND	-[a]
Cypermethrin	ND	ND	ND	ND	ND	ND	ND	ND	-[a]
λ-Cyhalothrin	ND	ND	ND	ND	ND	ND	ND	ND	-[a]
Deltamethrin	ND	ND	ND	ND	ND	ND	ND	ND	-[a]
					September 2017				
Chlorpyrifos	-[a]	-[a]	-[a]	-[a]	ND	-[a]	-[a]	-[a]	-[a]
Carbaryl	-[a]	-[a]	-[a]	-[a]	ND	-[a]	-[a]	-[a]	-[a]
Carbofuran	-[a]	-[a]	-[a]	-[a]	ND	-[a]	-[a]	-[a]	-[a]
Cypermethrin	-[a]	-[a]	-[a]	-[a]	ND	-[a]	-[a]	-[a]	-[a]
λ-Cyhalothrin	-[a]	-[a]	-[a]	-[a]	ND	-[a]	-[a]	-[a]	-[a]
Deltamethrin	-[a]	-[a]	-[a]	-[a]	ND	-[a]	-[a]	-[a]	-[a]

ND = not detected. [a] No sampling was conducted at this site since chili plants were removed for the planting of new chili seedlings.

Table 3. Pesticide Toxicity Index (PTI) for samples containing contained λ-cyhalothrin.

Sampling site	Concentration (mg/kg)	EU MRL (mg/kg)[17]	TQ	PTI
N1	0.00439	0.01	0.439	0.796
N2	0.00357	0.01	0.357	

4. Conclusion

The study determined pesticide residues in chilies collected from the Thai provinces of Songkhla, Phatthalung and Nakhon Si Thammarat. The pesticides chlorpyrifos, carbaryl, carbofuran, cypermethrin, deltamethrin and λ-cyhalothrin were determined by gas chromatography. Only λ-cyhalothrin was detected in this work. The Pesticide Toxicity Index of the detected λ-cyhalothrin (0.796) was lower than 1.000, implying that chilies produced in the study areas are safe.

Acknowledgements

The authors thank the Food Innovation and Research Institute (Grant number 2559/003) for financial support. The Division of Physical Science, the Center of Excellence for Innovation in Chemistry (PERCH-CIC), Ministry of Higher Education, Science, Research and Innovation, Faculty of Science, Prince of Songkla University, and the Office of Scientific Instrument and Testing, Prince of Songkla University are acknowledged.

References

1. Wongsakoonkan, W.; Nguiyai, S.; Phomngam, P.; Deelap, S. *VRU Research and Development Journal Science and Technology* **2016**, *11*, 75-83.
2. Manond, T.; Jomduang, J.; Varamit A. *Thaksin University Journal* **2011**, *14*, 30-39.
3. Lunliu P. Pre-risk Management of Organophosphate in Chili Consumers from Amphoe Sadao, Changwat Songkhla. Master Thesis, Prince of Songkla University, Songkhla, 2005.
4. The office of Agricultural Regulation, Department of Agriculture. Statistics of Thai Pesticide Imports. https://www.doa.go.th/ard/?page_id=386 (accessed December 22, 2023).
5. Kachaiyaphum, P.; Howteerakul, N.; Sujirarat, D.; Siri, S.; Suwannapong, N. *J. Occup. Health* **2010**, *52*, 89-98.
6. EU, European Union. COMMISSION REGULATION (EU) 2018/960 of 5 July 2018, Official Journal of the European Union 2018; pp L169/27-L169/50.
7. TAS 9002-2016, Thai Agricultural Standard. Pesticide Residues: Maximum Residue Limits, National Bureau of Agricultural Commodity and Food Standards, Ministry of Agriculture and Cooperatives, Thailand, 2016; pp 1-55.
8. TCIJ, Thai Civil Rights and Investigative Journalism. https://www.tcijthai.com/news/2019/10/scoop/9456 (accessed December 20, 2023).
9. Khemvong, S.; Suksawat, A. Study of Types and Amount of Pesticide Residues in Vegetables and Fruits from Lower Southern Part of Thailand After Certified Good Agricultural Practice (GAP). http://www.doa.go.th/oard8/wp-content/uploads/2019/08/v5805-03.pdf(accessed December 20, 2023).
10. Phuangkaew, L.; Sae-Yang, R.; Lerslerwong, L. *Songklanakarin J. Pl. Sci.* **2018**, *5*, 69-76.
11. Khemvong, S.; Sankaew, N. Duration of Harvest After Spraying Pesticide for Safety of Residues in Chilli, Report of Office of Agricultural Research and Development Region 8, Songkhla, Thailand, 2013.
12. Sante, Guidance Document on Analytical Quality Control and Validation Procedures for Pesticide Residues Analysis in Food and Feed, European Commission, 2017.
13. TAS 9003-2004, Thai Agricultural Standard. Pesticide Residues: Extraneous Maximum Residue Limits, National Bureau of Agricultural Commodity and Food Standards, Ministry of Agriculture and Cooperatives, Thailand, 2004; pp 1-5.
14. Tadeo, J. L.; Brunete, C. S.; González, L. Pesticide: Classification and Properties. In *Analysis of Pesticides in Food and Environmental Samples*; Tadeo, J. L., Ed.; New York; CRC Press, 2008.
15. Plianbangchang, P.; Jetiyanon, K.; Wittaya-areekul, S. *Southeast Asian J. Trop. Med. Public Health* **2009**, *40*, 401-410.
16. Chaikasem, S.; Na Roi-et, V. *App. Envi. Res.* **2020**, *42*, 46-61.
17. Barr, D. B.; Panuwet, P.; Nguyen, J. V.; Udunka, S.; Needham, L. L. *Environ. Health Perspect.* **2007**, *115*, 1474-1478.
18. Ungsoongnern, S. *EAU Heritage Journal Science and Technology* **2015**, *9*, 50-56.

Sensomic approach characterization of odorants in fried chicken

Nattapon Deesom[1], Preecha Phuwapraisirisan[1], Suwimon Keeratipiboon[2], Aphiniharn Phewpan[3]*

[1]*Center of Excellence in Natural Products, Department of Chemistry, Faculty of Science, Chulalongkorn University, Bangkok 10330, Thailand,* [2]*Chula Unisearch,* [3]*CPF Food Research & Development Center C.*

**E-mail: apiniharn33@gmail.com*

Abstract:

Herein. The odorants in fried chicken (thigh) was studied for quality control in food industry using sensomic approach. In this work, fried chicken was orthonasally evaluated using olfactory profiling to generate odor profiles of fried chicken for process follow-up. Fried chicken was initially extracted by dichloromethane, in which the volatile components were isolated by solvent associated flavor extraction (SAFE) and concentrated by fractional distillate. Analysis of volatile components by gas chromatography-olfactometry resulted in identification of odorants mainly responsible for meaty, oily and steam (cooked) perception. Moreover, 65 odorants detected by trained panelists were mainly categorized into pyrazine, hydrocarbon, and thiazole classes. This is the first report using sensomic approach to identify active odorants that can represent their perception, through aroma extract dilution analysis (AEDA), in fried chicken.

1. Introduction

Thailand is a top exporter of chicken meat and chicken in the world[1]. Over the past years, the consumption of chicken products in Thailand has been raised annually, resulting in the expansion of numerous fast-food chains, especially fried chicken. The crispiness of the fried chicken skin and the flavor of the cooked chicken meat as well as the unique aroma led to the popularity in the market. Therefore, the quality control of aroma as an opening perception of the consumer is crucial. However, the lack of information on aroma-active compounds in previous reports causes quality control of aroma could not be adopted. To circumvent this problem, the sensomic approach, which combines the separation technique of gas chromatography (GC) along with the olfactory sensory detection function of humans, will be applied. The olfactory profiling of the fried chicken is first constructed by trained panelists after sensory evaluation. Then, solvent extraction is applied to liberate aromas that are embedded in chicken meat texture, in which the volatile compounds are isolated from non-volatile components by solvent-assisted flavor evaporation (SAFE). The fractional distillation is operated to concentrate the volatile compounds and authenticate a model of olfactory profiling of a distilled volatile by trained panelists. Identification of aroma-active compounds in a distilled volatile is finally achieved through gas chromatography spectrometry (GC-MS) and confirmed by comparison with authentic compounds through gas chromatography-olfactory/flame ionization detector (GC-O/FID). The compounds truthfully contributed to fried chicken can be identified based on the sensomics approach and further applied as biomarkers for quality control. Over the past decade, a wide range of 'omics' technologies have grown exponentially, including metabolomics, lipidomics, proteomics, genomics, and transcriptomics. In the field of food science, metabolomics for food and beverages are classified as foodomics, flavoromics, and sensomics[2]. Sensomics is a field study of compounds using sensory perception of food as a guidance to identify the active components essentially responsible for the perception in association with a multistage analytical process[3-5].

Studies on the presence of aroma compounds in our daily diet have been carried out since the late 1950s through the use of GC in analysis[6]. In the early 1960s, GC studies were conducted in which experiments assumed that the whole batch of volatile compounds formed in food, body aroma, or environmental aromas contribute to the specific smell of the chemosensory entity[3]. Approximately 10,000 volatile compounds have been reported in foods and are responsible for their aroma, resulting in the investigation of aromas present in foods known as the "sensory approach". Initially, the coupled gas chromatography-electroantenno graphy (GC-EAG) was used by detecting voltage changes between the tip and base of the insect antennae that occur when the insect antenna is exposed to the insect's biologically significant aroma[7]. GC-EAG was subsequently replaced by gas chromatography-olfactometry (GC-O), which is the technique that integrates separation of volatile compounds using GC with the detection of aroma using an olfactometer (human assessor). Due to the most sensitivity and selectivity in biological detection of human nose, GC-O has been broadly applied to analyze substances with different aroma strengths by

various methods such as comparative aroma extract dilution analysis (cAEDA)[8]. However, only the GC-O technique could not confirm the exact substance found in the food. Therefore, gas chromatography-mass spectrometry (GC-MS), infrared spectroscopy (IR), nuclear magnetic resonance (NMR), and other techniques have helped to confirm the identity of the substances[9]. For quantitative accuracy, stable isotope dilution analysis (SIDA) is often used, which is an internal standards method, where stable isotope (^{13}C, ^{2}H)-labeled twin molecules are added to the substance that has been confirmed[3].

Once both the amount and type of compounds present in the food are known, odour activity values (OAVs) are calculated to predict the tendency of the substances to be the active substances in the food's aroma prior to the addition of the compounds. High OAVs are mixed in order to verify the authenticity of the smell to match the flavor of the food, a process known as "aroma reconstitution". In fact, active aroma with low OAVs should be further extracted from the reconstitution model to evaluate the smell of the mixture is whether different from that of real food.

Aroma compounds in meat and meat products have been studied in the plentiful previous reports[10-19]. They varied in chemical structures and quantity due mainly to the cooking process applied for meats[10-19]. As for chicken meat, the research on aroma compounds mainly focuses on boiled chicken[10,12-17], smoked chicken[12-19], and fried chicken[11,14-17]. A variety of extraction and isolation techniques such as steam distillation (SD), headspace solid phase microextraction (HS-SPME), and simultaneous distillation extraction (SDE)[10-18], were applied together with GC-MS[11-19] to identify the aroma compounds.

In 1983, Jian Tang and coworkers studied fried chicken using specially designed apparatus followed by a fractionation technique. The aroma compounds were identified using gas chromatography-mass spectrometry (GC–MS). They found 130 compounds including hydrocarbons alcohols, aldehydes, ketones, acids, esters, pyrazines, pyridines, thiazoles, thiazolines, oxazoles, oxazolines, thiophenes, pyrroles, furans, a trithiolane, a trithiane, and thialdine[11]. Of the identified aroma compounds, pyrazines (21 compounds) and hydrocarbons (21 compounds) were major components in fried chicken flavor. The presence of hydrocarbons were possibly stemmed from cooking oil, fat content in chicken meat and herb seasoning while the occurrence of pyrazines was potentially derived from Maillard reaction from chicken protein. However, the lack of sensomic approach applied to this study, the aroma-active compounds and key aroma compounds remains unidentified.

2. Materials and Methods

2.1 Materials

Fried chickens. Hot and spicy fried chickens were purchased from KFC at samyan mirtown, Bankok, Thailand, in April 2023.

Reference odorants. 2-methyl-3-furanthiol, 2-furanmethanethiol, trans-2,4-decadienal, trans-2,4-decadienal, ethane-d_5-thiol, butyric acid, 2,5-dimethyl pyrazine, white pepper powder, 4-ethyl phenol were supported from CPF Food Research and Development Center.

Chemical and reagents. Dicholrometane and sodium sulfate, ethanol, and *n*-alkanes were from Merck (Germany).

2.2 Olfactory profiling of fried chicken

Fried chicken (thigh) (20g) was cut into small pieces and kept in 25-mL glass vials. The sample was evaluated by 10 trained panelists, who were trained in odor recognition from reference odorants with FEMA number, odor distinguishing from mixture compounds, and odor intensity scoring from difference concentration of reference odorants, using free-choice attributes with the closed odor profile to be the descriptors used in the olfactory profiling for rating intensity with reference odorants. Panelists rated by panelists on a scale from 0 to 5 with 5.0 = strong, 3 = medium, 1.0 = low, and 0 = not detectable.

2.3 Isolation of fried chicken volatile

Fried chicken (thigh) meat and skin were frozen in liquid nitrogen and ground into a powder (100 g) with a laboratory grinder. Fried chicken powder was extracted with dichloromethane (1 × 300, 1 × 200). Then extract was filtered through filter paper and dehydrated with anhydrous Na_2SO_4. The volatile components in the dehydrated extract were isolated from non-volatile residues using the solvent-assisted flavor evaporation (SAFE) technique. The volatile components were concentrated in fractional distillation using Vigreux column and micro-distillation column, respectively, to obtain a final volume of 1 mL.

2.3 Screening of odorants using gas chromato-graphy-olfactometry (GC-O)

The concentrated volatile components were injected into the GC-O/FID with a cold-on column into DB-FFAP-capillary as a column (each 30 m, 0.32 mm, 0.25 μm film thickness) (Agilent). The flow rate was set to 3.0 mL/min. After 1 min

at 30 °C, the oven temperature was increased at 60 °C/min to 60 °C and held for 5 minutes, then increased at 6 °C/min to 230 °C, and held for 10 minutes. The effluent was split into a ratio of 1:1 (v/v) at the end of the capillary by using a Y-type splitter. One section is directed to the flame ionization detector (FID) held at 250 °C and the other part to a heated sniffing port held at 180 °C. The panelist evaluated the aroma of the effluent throughout during GC-O/FID analysis. Once an aroma is detected, the retention time, aroma quality, and aroma strength are recorded. Retention indices (RI) are calculated from these retention times of adjacent n-alkanes by linear interpolation.

2.4 Screening of active-odorants using aroma extract dilution factor (AEDA)

The AEDA is also performed using the above protocol with serial dilutions (1:2, 1:4, 1:8, ... and 1:2048) of volatile components. The Dilutions were analyzed using GC-O with the FFAP column, FD factor of each component was identified by highest dilution that was detectable.

2.5 Identification of active-odorants

Volatile isolate was injected into a GC with FFAP as a column (each 30 m, 0.32 mm, 0.25 µm film thickness) (Agilent) and was coupled via heated (250 °C) transfer line to Shimadzu QP-2021 mass spectrometer detector. Potential volatile components are identified based on RI value, aroma quality and MS data. In addition, individual components are finally confirmed by comparison with authentic compounds.

3. Results & Discussion

3.1 Olfactory characteristic of fried chicken.

Fried chicken was evaluated by trained panelists using free-choice attributes with the closed odor profile of reference odorants and food (Table 1) and thereafter a olfactory profiling (Figure 1).

Table 1. Olfactory characterization of fried chicken using orthonasal free-choice attribute (8 trained Panelists)

No	Odor discription	Reference odorant
1	Meaty	2-methyl-3-furanthiol
2	Sweet	2-furanmethanethiol
3	Oily	trans-2,4-decadienal
4	Sulfury	ethane-d_5-thiol
5	Steam	butyric acid
6	Bread (bakery)	2,5-dimethyl pyrazine
7	Pepper	white pepper powder
8	Burnt	4-ethyl phenol

Result showed the odor of fried chicken with strong oily and meaty. The moderate of cooked, burned and sulfury were represented in odor profile.

Figure 1. Olfactory profile of fried chicken. The intensity of each attribute was rated by panelists on a scale from 0 to 5 with 5.0 = strong, 3 = medium, 1.0 = low, and 0 = not detectable.

The bottom of sweet, pepper, and bready showed in odor profile of fried chicken.

3.2 Screening of odorants using gas chromatography-olfactometry (GC-O)

The concentrated volatile were submitted to a the GC-O/FID and deteded the odor of odorants by 3 trained panelists that were trained by sniffing mixture compounds with GC-O/FID trained panelist. As a result, 78 odorants of concentrated volatile with 17 odorants represented oily (fatty, or deep fried), 16 odorants represented roasted (or burned), 7 odorants represented pungent (or musty or drain).

3.3 Screening of active-odorants using aroma extract dilution factor (AEDA).

The concentrated volatiles were submitted to AEDA[8] which results in 65 active odorants in the FD factor range from 2 to 2048 (Table 2). For 9 odorants (**7, 17, 25, 39, 45, 48, 52, 54, and 58**) showed higest FD factor value (2048). For a odorant **36** showed 1024 for FD factor value. The 512 and 256 showed in 3 odorants (**1, 2, and 4**), and 7 odorants (**3, 4, 6, 10, 23, 41, and 60**) Figure 2 which exhibite an FD factor ≥ 256 as a most potent active odorants.

Table 2. Active odorants (FD ≥ 2) in the volatile isolates obtained from fried chicken.

No.[a]	Odorant[b]	Odor quality[c]	RI[d]	FD factor[e]
1	ethyl acetate	yeast	885	512
2	2-hexanethiol	mushroom/rancid	1052	256
3	hexanal	fatty green	1074	256
4	2-heptanone	Sweet	1190	128
5	1-pentanol	musty/fruity	1246	256
6	1-octen-3-one	mushroom	1290	2048
7	2,5-dimethylpyrazine	nutty/cooked meat	1310	128
8	2-acetyl-1-pyrroline	cooked rice	1324	32
9	2,3-dimethylpyrazine	nutty	1342	32
10	1-hexanol	herbal (siam weed)	1347	256
11	1-heptanol	citrus	1366	64
12	3-octanol	rubber/sweet	1371	4
13	nonanal	fatty green	1390	64
14	2-propionyl-1-pyrroline	roasted coffee	1405	64
15	2,6-diethylpyrazine	cooked rice	1408	32
16	(E)-2-octenal	deep fried	1416	16
17	2-furanmethanethiol	roasted coffee	1422	2048
18	2-ethyl-3,6-dimethylpyrazine	burnt	1433	128
19	3-(methylthio)propanal	fatty	1446	32
20	(E,Z)-2,4-heptadienal	fatty	1457	64
21	4-mercapto-2-decanol	burned	1459	128
22	furfural	floral	1464	4
23	2-pentylpyridine	herbal/fatty	1477	256
24	(E,E)-2,4-heptadienal	fatty	1485	128
25	1-decen-3-one	herbal	1507	2048
26	(E)-3-nonen-2-one	fatty/oily/herbal	1515	128
27	(E)-2-nonenal	fatty green	1522	8
28	propanoic acid	burnt/musty	1535	4
29	1-octanol	fecal/fatty	1551	128
30	2-acetyl-1,4,5,6-tetrahydropyridin	roasted onion	1563	128
31	fenchol	green/musty/fatty	1569	8
32	(2-furanyl)propanethiol	nutty/roasted oinion	1597	8
33	(Z)-2-decenal	deep fired/rubber	1600	16
34	2-acetylpyrazine	popcorn-like, roasty	1613	128
35	butanoic acid	sweaty	1617	4
36	(E)-2-decenal	deep fried	1622	1024
37	2-phenylethanethiol	roasted chilli	1645	16
38	2-methyl-3-(methyldithio)furan	musty (drain)/pungent	1654	128
39	4-acetyl-3-thiazoline	dried rice	1664	2048
40	(E,E)-2,4-nonadienal	pungent	1700	2
41	cyclohexanepentanethiol	cooked rice	1729	256
42	2-((pentylthio)methyl)furan	fatty green	1735	32
43	(E,Z)-2,4-decadienal	fatty	1751	128
44	1,6-hexanedithiol	roasted chilli/sour	1774	2
45	(E,E)-2,4-decadienal	fatty	1795	2048
46	1-tridecen-3-one	seasoning	1820	16
47	hexanoic acid	sweaty	1830	512
48	1-dodecen-3-ol	oily/herbal	1852	2048
49	1,7-heptanedithiol	burned	1895	128
50	heptanoic acid	Sweaty	1938	32
51	maltol	Sweet/caramel	1962	4
52	4-hydroxy-2,5-dimethyl-3(2H)-furanone	Sweet/caramel	2023	2048
53	2-pyrrolidone	Sweet/caramel	2069	16
54	2-ethyl-3-mercapto-1-heptanol	roasted coffee	2070	2048
55	2-methoxy-4-propylphenol	drain	2102	128
56	3-((2-methyl-3-furanyl)disulfaneyl)-2-pentanone	drain	2148	128
57	2-methoxy-5-vinylphenol	roasted coffee/burned	2229	32
58	5-propionyl-2,3-dihydro-1,4-thiazine	roasted coffee/burned	2249	2048
59	δ-undecalactone	caramel	2291	128
60	1-(2-hydroxyethyl)hexyl ethanethioate	caramel	2309	256

61	3-((2-furanylmethyl)dithio)-2-butanone	burned	2347	128
62	δ-(Z)-6-dodecenolactone	burned/sweet	2397	128
63	3-methyl-1H-indole	musty (drain)/pungent	2448	128
64	3'-hydroxyacetophenone	drain	2876	16
65	syringaldehyde	dried rice/burned	2886	16

[a]Odorants number ranked according to retention time on FFAP cloumn. [b]Identified by RIs, odor quality, and mass spectra. [c]Odor quality was detected during GC-O. [d]Retention index. [e]Flavor dilution factor.

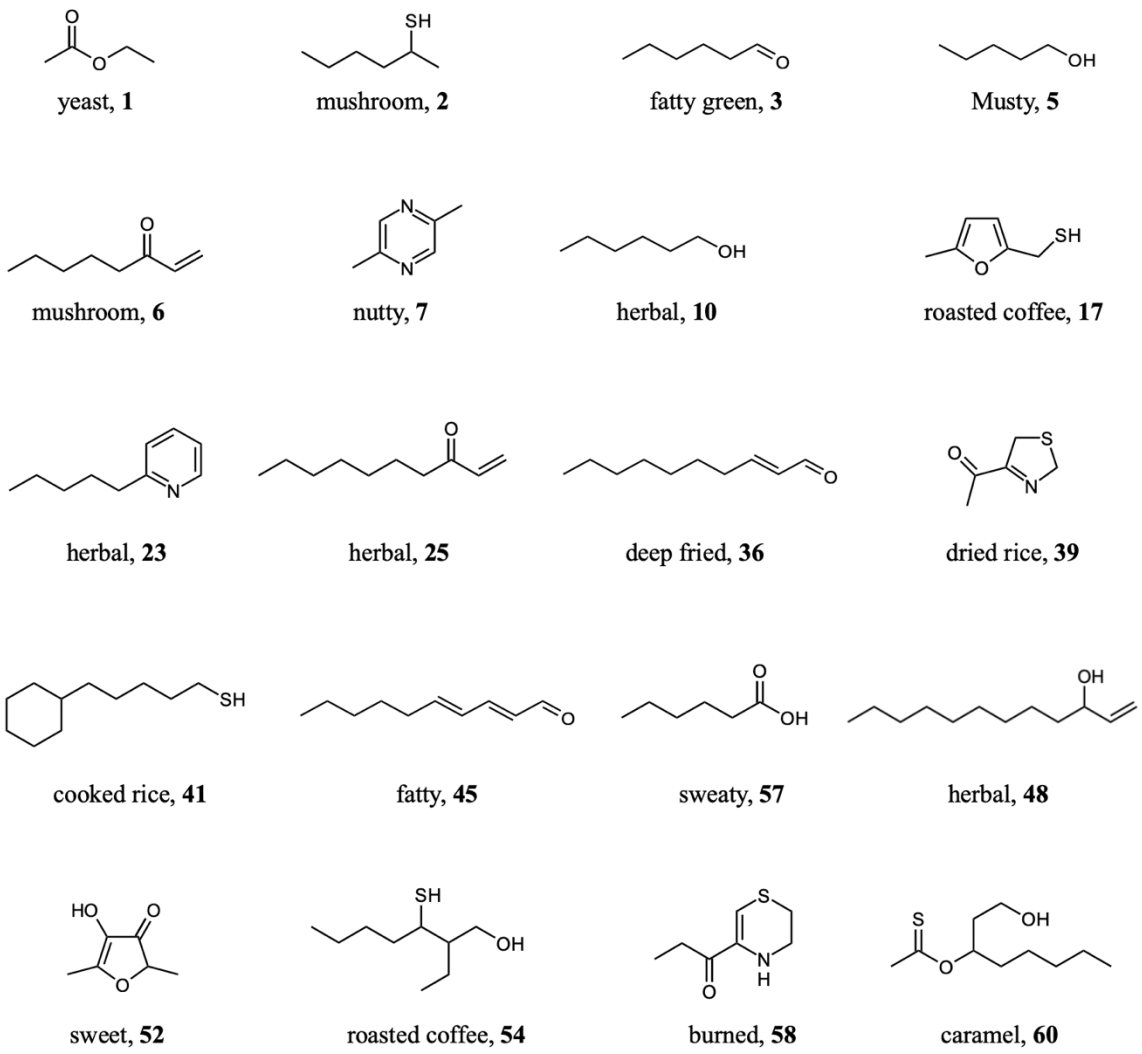

Figure 2. Active odorants with an FD factor ≥ 256.

3.4 Identification of active-odorants

The structure of active odorants were assigned based on their RIs, odor quality, and mass spectra. the identify of each active odorant was finaly comfirmed by GC compared authentic compounds. The identification experiments results that was combined with FD factors reveald the 20 active odorants in Figure 2. According to AEDA result, active odorants FD factor ≥ 2048 included 2,5-dimethyl pyrazine(**7**), 2-furanmethanethiol(**17**), 1-decen-3-one(**25**), 4-acetyl-3-thiazoline(**39**), (E,E)-2,4-decadienal(**45**), 1-dodecen-3-ol(**48**), 4-hydroxy-2,5-dimethyl-3(2H)-furanone(**52**), 2-ethyl-3-mer capto-1-heptanol(**54**), and 5-propionyl-2,3-dihy dro-1,4-thiazine(**58**). On the other hand, there was only one active odorant with FD factor ≥1024, named (E)-2-decenal(**36**). Three active odorants with ≥ 512 comprised ethyla cetate(**1**),2-hexanethiol(**2**), and hexanoic acid(**47**). Seven active odorants with ≥ 256 composed hexanal(**3**), 2-heptanone(**4**), 1-octen-3-one(**6**), 1-heptanol(**10**), 2-pentylpyridine (**23**), cyclohexanepentanethiol(**41**), and 1-(2-hydroxy ethyl)hexyl ethanethioate(**60**).

Of active odorants (Table 2), pyrazines (4 compounds), thiols (7 compounds), and

carbonyl compounds (22 compounds) constituted the major odorants of fried chicken. Pyrazines generally show nutty and dried rice odor. They were probably formed in fried chicken via Millard reaction between amino acids and carbohydrate at high temperature of frying[11,13]. Thiols are probably formed via Millard reaction from sulfur-containing amino acid, where the product odorant represent roasted, burned, and cooked rice flavor[11]. Carbonyl compounds, which included aldehydes and ketones are probably developed by lipid oxidation of fatty acid during frying process to exhibit deep fried, fatty, and sweaty odor[20].

4. Conclusion

Sixty five active odorants were identified in fried chicken using sensomic approach. Their RIs, odor quality, and mass spectra were used to assign the structure of each odorant and confirm with authentic compounds. Pyrazines, thiols, and carbonyls constituted major odorants in fried chicken. Twenty identified odorants with high FD factor (≥ 256) were potentially to be key odorants, which were constituted as biomarkers used in industry for quality control and food development.

Acknowledgements

We thank the department of chemistry, faculty of science, Chulalongkorn University, and Chula Unisearch for the equipment. CPF food research & development center for ingredients and compounds.

References

1. Office of Agricultural Economics, chicken meat and products. https://www.dtn.go.th/th/file/get/file/1.20220401b13d85e0b079b00bffc227a7e327b460091515.pdf (accessed Oct 10, 2023).
2. Mondello, L. *J. Sep. Sci*. **2013**, *36* (11), 1869–1869.
3. Dunkel, A.; Steinhaus, M.; Kotthoff, M.; Nowak, B.; Krautwurst, D.; Schieberle, P.; Hofmann, T. *GDch*. **2014**, *53*, 7124-7143.
4. Vrzal, T.; Olšovská, J. *KVASNY PRUMYSL*. **2019**, *65* (5), 166-173.
5. Lasekan, O.; Dabaj, F.; Muniandy, M.; Juhari, N. H.; Lasekan, A. *BMC Chemistry*. **2021**, *15*, 1-13.
6. Weurman, C.; Dhont, J. *Nature*. **1959**, *184*, 1480-1481.
7. Cork, A.; Beevor, P. S.; Gough, A. J. E.; Hall, D. R. *BMC Chemistry*. **2021**, *15*, 1-13.
8. Munafo, J. P.; Didzbalis, J.; Schnell, R. J.; Schieberle, P.; Steinhaus, M. *J. Agrie. Food Chem*. **2014**, *62*, 4544-4551.
9. Song, H.; Liu, J. *Food Res. Int*. **2018**, *114*, 187-198.
10. Lewis, J. M.; Amber, M. P.; Les, E. D.; Bernard, S. S. *J. Agrie. Food Chem*. **1965**, *13*, 298-300.
11. Jian, T.; Qi, Z.; Gouhui, S.; ChiTang, H.; Stephen, S. C. *J. Agric. Food Chem*. **1983**, *31*, 1287-1292.
12. Ang, C.Y.W.; Liu, F. *J. Muscle Foods*. **1996**, *7*, 291-302.
13. Donald, S. M. *J. Food Chem*. **1998**, *62* (4), 415-424.
14. John. S. E.; Don S. Flavour development in meat. *Improving the Sensory and Nutritional Quality of Fresh Meat*, 2009; pp. 111-146
15. Dawson, P. L.; Spinelli, N. Poultry Meat Flavor. *Handbook of Meat, Poultry and Seafood Quality*; Second Edition, 2012; pp. 341–359
16. Dinesh, D. J.; Dong, U. A.; Ki, C. N.; Cheorun, J. *J. Anim. Sc*. **2013**, *26*, 732-742
17. Monika, K.; Małgorzata, A. M.; Teresa, F. *J. Food Sci*. **2017** *37* (1), 1-7
18. Yuxi, J.; Huanxian, C.; Xiaoya, Y.; Lu, L.; Xiaojing, L.; Yongli, W.; Jiqiang, D.; Hai, X.; Xinxiao, Z.; Jianfeng, L.; Hua, Li; Guiping, Z.; Jie, W. *j. Food Chem*. **2021**, *359*, 129930
19. Cong, Y.; Zhinan, Z.; Yufeng, Z.; Shuangyu, M.; Jun, Q.; Dengyong, L. *J. Food*, **2021**, *19* (1), 163–173
20. Chang, C.; Wu, G.; Zhang, H.; Jin, Q.; Wang, X. *Crit. Rev. Food Sci. Nutr*. **2019**, *60* (9), 1496–1514.

Sensory attributes and antioxidant capacity of tomato meal extracts: A comparative analysis of enzymatic and ultrasonic extraction methods

Pacharaporn Putthangkul[1], Phawinee Srinuan[3], Orrapun Selamassakul[3], Natta Laohakunjit[3,4] and Chanikan Sonklin[1,2]*

[1]*Department of Industrial Chemistry, Faculty of Applied Science, and King Mongkut's University of Technology North Bangkok, 1518 Pracharat 1 Rd., Wongsawang, Bangsue, Bangkok, 10800, Thailand*
[2]*Food and Agro-Industry Research Center, King Mongkut's University of Technology North Bangkok, 1518 Pracharat 1 Rd., Wongsawang, Bangsue, Bangkok, 10800, Thailand*
[3]*Pilot Plant Development and Training Institute, King Mongkut's University of Technology Thonburi, 49 Tientalay Rd.,Thakam, Bangkhuntien, Bangkok, 10150, Thailand*
[4]*School of Bioresources and Technology, King Mongkut's University of Technology Thonburi, 49 Teintalay 25 Rd.,Thakam, Bangkhuntein, Bangkok 10150, Thailand*

**E-mail: chanikan.s@sci.kmutnb.ac.th*

Abstract:

This research explored the sensory and antioxidant properties of tomato meal extracts by enzymatic and ultrasonic extraction based on sensory attributes and antioxidant activity. Tomato meal was treated with bromelain at 0, 5, 10 and 15% (w/w) for 0, 15, 30 and 45 min which compared to ultrasonic extraction at 50 °C for 0, 15, 30 and 45 min. Results showed that 15% of bromelain for 45 min was the optimum condition for enzymatic extraction while 30 min with ultrasonic wave was the optimum condition for ultrasonic extraction. The sensory scores were measured by semi-trained panelists using quantitative descriptive analysis with a 5-point scoring test (0-4). The umami and overall acceptance of tomato meal extract derived from 15% of bromelain for 45 min were higher than tomato meal while ultrasonic extraction played a crucial role in imparting distinct characteristics, demonstrating a significant increase in sourness. In addition, tomato meal extracts from enzymatic extraction exhibited DPPH and ABTS radical scavenging activity with 55.12 and 73.78 mmol trolox equivalents/100g, respectively. Ultrasonic extraction could enhance DPPH and ABTS radical scavenging activity as well which were 52.04 and 79.26 mmol trolox equivalents/100g, respectively. The chemical structure of glutamic acid was detected by Fourier Transform Infrared Spectroscopy (FTIR). The observed peaks at 1407 cm^{-1} and 1622 cm^{-1}, which were assigned to amino group structure and carboxylic group were detected. The tomato meal extracts exhibited a significant potential as a functional flavor enhancer with different characteristics which could be a viable alternative to synthetic flavor enhancers.

1. Introduction

Tomatoes, the fruit of the species *Solanum lycopersicum* Roma (Tor), is a good source of both nutrients and bioactive compounds[1]. Every year, more than 30 million tonnes of tomatoes are processed globally to create a variety of goods, including sauce, ketchup, canned tomatoes, and tomato juice. Since tomato pomace has little market value, it is either fed to animals or disposed away as solid waste. On closer inspection, though, this substance turns out to be a rich source of essential nutrients and phytochemicals. Tomato seeds, in particular, have a highly nutritious oil[2]. Tomato pomace composition (in dry weight basis) is as follows: 59.03% of fiber, 25.73% of total sugars, 19.27% of protein, 7.55% of pectins, 5.85% of total fat and 3.92% of minerals[3]. Amino acids, flavanols, and phenolic acids were also present in tomato pomace. Interestingly, tomato pomace contained high content of protein which was explore to various function in food. In term of flavor chemistry, amino acid or peptide which are the hydrolyzed protein. They could play an important role in flavor or taste in food stuff, but the original protein could not provide umami flavour or any sensory attributes. Thus, the process of obtaining umami flavor from a protein's free amino acid or short peptide chain formation is known as enzyme hydrolysis. Based on their specialised cleavage, which produces desired products, proteases including flavoenzyme, alcalase, papain, and bromelain were selected as enzymes for cleaving peptide bonds in protein. Bromelain was a bord-specific enzyme and products after bromelain hydrolysis contained a plenty of glutamic acid (Glu)[4]. The optimum condition to extract umami taste amino acid was 10% papain, pH 3, 40°C, and hydrolysis time for 6 h, which resulted in 727.6 mg/mL of Glu and 149.9 mg/mL of aspartic acid (Asp) which these amino acid predominantly contributed to umami perception[5]. Previous work discovered that Glu was extracted from mushrooms by protease enzyme possessed a high score of umami[6]. Moreover, Glu plays an important role in the antioxidant activity[7]. In addition, ultrasonic

extraction is another method of extraction. The ultrasonic cavitation effect is based on the cavitation phenomena and describes how ultrasonic waves cause small bubbles to form in liquid. Furthermore, the superior performance of ultrasonic extraction in comparison to conventional extraction permits the use of controlled equipment and less solvent amounts[8]. Therefore, this study was to investigate a comparative analysis of enzyme and ultrasonic extraction methods in order to explore the sensory attributes and antioxidant capacity of tomato meal extracts.

2. Materials and Methods

2.1 Materials

Tomato purchased from Makro, CP Axtra Public Co., Ltd., Thailand. Bromelain (enzymatic activity = 97,540 CDU) was provided by K-Much-Industry Co., Ltd. (Bangkok, Thailand)[4]. All other chemical reagents were of analytical grade and purchased from Thermo Fisher Scientific (Waltham, MA, USA) or Sigma Aldrich (St. Louis, MO, USA).

2.2 Preparation of tomato pomace

The ripening stage of tomato (red stage 6)[9] was washed and separated pomace by fruit pulp separator according to the mimic method from Doi Kham Food Products Company, Limited, Thailand. The tomato pomace was freeze-dried (FreeZone 4.5 Liter Benchtop Freeze Dryers, LABCONCO, Germany), grounded to powder which was called tomato meal power (TMP). The TMP was kept in -20°C until used.

2.3 Extraction of tomato extract by enzymatic extraction method

The influence of enzyme concentration and extraction time by bromelain enzyme on sensory characteristics and antioxidant activity of tomato extract were determined, and the experiments were designed in a 4x4 factorial in complete randomization design. Ten grams of tomato meal pomace was mixed in 100 mL of distilled water and acidified to pH 6.0 for the pH optimum of bromelain enzyme in 100 mL of distilled water. Then bromelain was added into the tomato pomace with various concentrations at 0, 5, 10, and 15% (w/w) and extraction time for 0, 15, 30, and 45 minutes at 50°C. The enzyme reaction in each sample was stopped by heating at 95°C for 15 mins, cooling down, centrifuging at 7500 rpm for 10 mins, filtering, and freeze dried, and storing in the freezer at -20°C.

2.4 Extraction of tomato extract by ultrasonic extraction method

Tomato meal extracts were performed by adding 10 g of Tomato meal pomace in 100 mL of distilled water. The samples were extracted by ultrasonic bath 400 watt for 0, 15, 30 and 45 mins at 50±5 °C. The temperature was continuously detected by thermometer and controlled by adding ice cube. After the finished reaction, each sample was cool-downed in a cooling bath, centrifuged at 7500 rpm for 10 mins, filtrated, freeze-dried, and kept at -20°C before analysis.

2.5 Sensory analysis

Tomato meal extracts from all extraction conditions were evaluated for the sensory profile by different qualitative tests with a 5-point scoring test. Tomato odor, sour odor, salty odor, sweet odor, umami taste, sweet taste, salty, sour, and overall acceptances were scored by 15 semi-trained panelists, which were scaled from 1 (the lowest instance) to 5 (the highest instance). All samples were statistically analyzed by randomized completely blocked design (RCBD) using the SPSS program Version 20.0.0 (IBM, 2011, USA).

2.6 Determination of antioxidant activity

DPPH radical scavenging activity

DPPH activity of tomato extracts was carried out with slightly modification[10]. Tomato extracts were dissolved in methanol to a concentration 2 mg/mL. Samples (100 µL) were pipetted into 96-well plate, added 100 µL of DPPH solution and incubated at room temperature for 30 min in the dark. The blank (Ab) and samples (As) absorbance values were measured at 517 nm. Deionized water (DI water) was added to replace sample as a blank control. Trolox was used as the standard. The DPPH antioxidant was expressed as mmol of trolox equivalents/100 g of tomato dry weight [11].

ABTS radical scavenging activity

The ABTS solution was composed of two stock solutions; the ABTS stock solution was 7.4 mM 2,2'-azino-bis (3-ethylbenzthiazoline-6-sulfonic acid) and 2.6 mM potassium persulfate. The working solution was mixed stock solutions in similar quantities and left to react for 12 h at room temperature in the dark. After that, the solution was diluted by mixing 1 mL ABTS solution with 50 mL ethanol to obtain an absorbance of 1.1±0.02 at 734 nm. The 950 µL ABTS solution was mixed with 50 µL of sample and reacted at room temperature for

ethanol to obtain an absorbance of 1.1±0.02 at 734 nm. The 950 µL ABTS solution was mixed with 50 µL of sample and reacted at room temperature for 2 min in the dark. Blank was used DI water instead of sample. Trolox was used as the standard. The ABTS antioxidant was expressed as mmol of trolox equivalents per 100 g of tomato dry weight. The absorbance of sample was measured at 734[11].

2.7 Fourier Transform Infrared Spectrometer (FT-IR)

The chemical composition of tomato extracts was characterized by FTIR. Tomato extracts were mixed with KBr before analysis at IR ranges of 400 and 4000 cm^{-1} and 200 resolutions with a scan rate of 16 scan/ min by Fourier Transform Infrared Spectroscope (PerkinElmer, Spectrum 100, USA).

2.8 Statistical analysis

All assays were performed in triplicate and means (n-3) of data were analysed by the analysis of variance while Duncan's multiple range test of variables was used to separate the means using the IP program Version 6.0 (1997, USA); significant differences were accepted at $p < 0.05$ by SPSS statistic program Version 20.0.0 (IBM, 2011, USA)

3. Results & Discussion

3.1 Sensory profile of tomato meal extracts

The influences of enzyme concentration and extraction time on sensory profile of tomato meal extracts were determined and compared to the without enzyme condition. The tomato extracts derived from extraction without enzyme conditions still had a highly intense tomato odor and low umami and overall acceptance despite extending the extraction time to 45 min (Figure 1a). After treatment with enzymes at different concentrations, tomato meal extracts contributed to higher scores of umami and overall acceptance with low tomato odor (Figure 1a-d). The umami and overall acceptance increased with increasing enzyme concentration and extraction time. The tomato extracts from 15% enzyme of every extraction time possessed the higher score of umami and overall acceptance when compared to 0, 5 and 10% enzyme for any extraction time. Especially the 15% enzyme for 45 min can obviously increase the umami taste of tomato extract. The umami and overall acceptance scores of the 15% enzyme for 45 min were 1.5 and 2.2, while these scores of the without enzyme at the same extraction time were 1.0 and 1.3, respectively. The results could suggest that the

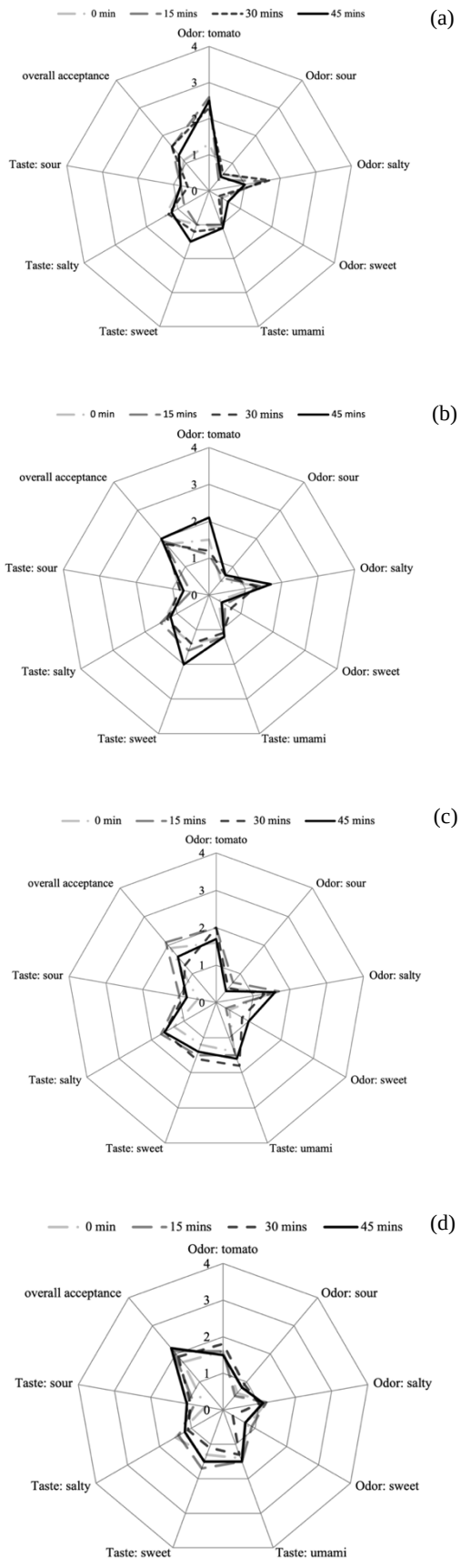

Figure 1. Sensory profile of tomato meal extracts derived from 0% enzyme (a), 5% enzyme, (b), 10% enzyme, (c), and 15% enzyme (d).

umami taste may derive from the released glutamic acid from tomato protein because the umami increased with the increase of bromelain and time for extraction. Bromelain enzyme can cleave peptide bonds in protein chains and become short peptides or free amino acids[4]. The glutamic acid, which is rich in tomato protein, can be cleaved and explored into the extract, resulting in increasing umami intensity in the tomato meal extracts.

The sensory profile of tomato meal extracts from ultrafiltration contributed to noticeable differences from bromelain extraction. A sour taste was detected in extracts from every ultrasonic condition, particularly for the longest time (Figure 2). The sour taste of tomato extracts from ultrasonic extraction for 0, 15, 30, and 45 mins were 1.9, 1.9, 2.2, and 2.3, respectively. Moreover, a salty taste was also found with longer extraction times which was 0.2, 0.2, 0.6, and 0.8, respectively. In contrast, the umami score was decreased when the ultrasonic extraction time was increased. The overall acceptance was slightly higher after ultrasonic extraction from 0 min, followed by 15 min, 30 min and slightly decreased after 45 min which the scores were 2.1, 2.2, 2.5, and 2.2. This might be a cause of some particles related to sourness, such as phenolic compounds or lycopene, organic acid that could be released after ultrasonic treatment. Citric and malic acid which is organic acid is responsible for sour taste in tomato fruits consists mainly of citric and malic acid. The acid content varies from 0.3% to 0.6%[12]. Tomatoes also contain salts such as potassium which can make them taste salty if the concentration is high enough. Researchers has found that fresh tomatoes have a potassium amount 1868-3211 mg/100g[13]. Analysis of classification and amount of phenolic acid compounds in the extracts are going to be investigated in the further study to achieve this issue.

3.2 Antioxidant activity of tomato meal extracts

DPPH radical scavenging activity

The DPPH inhibition was observed in tomato meal extracts from enzyme extraction. Results showed that fifteen percentages of bromelain enzyme and extraction time for 45 min was the maximum inhibition of the DPPH radical with 56.08 mmol TE/100g sample, followed by 15% enzyme for 30 min inhibited the DPPH radical as 55.12 mmol TE/100g sample (Figure 3). The tomato meal extracts from ultrasonic extraction also inhibited the DPPH radicals. The maximum percentage of DPPH inhibition as 52.04 mmol TE/100g sample was observed at 45 min and followed by 30 min. The DPPH scavenging

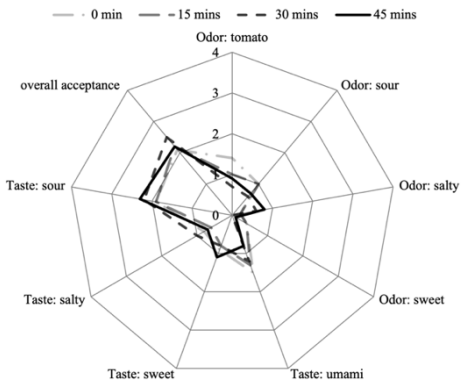

Figure 2. Sensory profile of tomato meal extracts derived from ultrasonic extraction for 0, 15, 30 and 45 min.

activity was 51.48 mmol TE/100g sample. The antioxidant activity of extracts may be obtained from the amino acid[4, 14], phenolic compounds, or carotenoids that are released during extraction, such as glutamic acid, lycopene, phenols, flavonoids, and vitamins in tomatoes. These compounds are mainly responsible for the antioxidant capacity because they can quench free radicals and are responsible for oxidative changes in the human body[15].

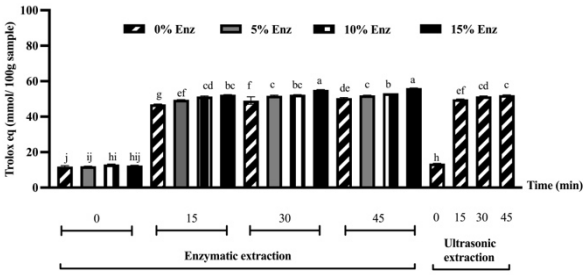

Figure 3. DPPH scavenging activity of tomato meal extracts using enzyme concentration and ultrasonic extraction.

ABTS radical scavenging activity

The tomato meal extracts by bromelain enzyme and ultrasonic extraction were analyzed for ABTS radical scavenging activity and compared to the trolox standard. For the enzyme extraction, the enzyme concentration and extraction time had a significant influence on ABTS activity (Figure 4). The ABTS activity of the extracts was stronger when using higher enzyme concentrations. A extract from 15% enzyme for 30 min showed the highest potential to promote the ABTS activity which was 73.78 mmol TE/100g sample. However, its activity was not significantly different from 45 min with the 15% enzyme. Similarly, the tomato meal extracts from ultrasonic extraction displayed the ABTS radical scavenging activity after extracting by ultrasonic

wave. The ultrasonic extraction could release compounds that contributed to antioxidant activity after 15 min and time-independent of extraction. The extracts from the longest extraction time, which was 45 min, showed the ABTS activity 79.26 mmol TE/100g sample, whereas the activity of extracts using the shorter time was not significantly different. This indicated that at 15 min of ultrasonic method is proper time for extraction because of the limited bioactive substances in the tomato pomace.

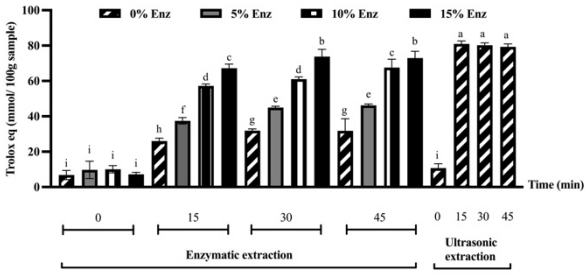

Figure 4. ABTS radical scavenging activity of tomato meal extracts using enzyme concentration and ultrasonic extraction.

3.3 Fourier Transform Infrared Spectrometer (FT-IR)

The tomato meal extract by 15% of bromelain for 45 min (E) was the optimum condition for enzymatic extraction and 30 min with ultrasonic wave (U) was the optimum condition for ultrasonic extraction because these extracts contributed to high desired sensory perception with low tomato odor and high DPPH and ABTS antioxidant activity. Then these two extracts were analyzed the chemical composition by FT-IR compared to the tomato meal (TM) before extraction. Tomato meal (TM) showed an absorption peak ranging from 3600-3300 cm^{-1} (Figure 5). The observed peak was linked to O-H and phenolic compounds, which may indicate that alcohols, quercetin, and phenolic compounds were presented. Alkanes (C-H stretching) could be responsible for the bands at ~2900 while peaks at 1640 cm^{-1} show conjugated carbonyl bonds that could be from flavonoids[16]. The tomato meal extract from enzymatic extraction (E) showed an absorption peak ranging from 3600-3300 cm^{-1} (O-H), 2900-2800 cm^{-1} (N-H), and 1750-1680 cm^{-1} (C=O). However, ultrasonic extraction (U) showed a similar pattern to TM, but transmittance was a higher percentage than TM. The absorption peak ranges from 3600-3300 cm^{-1} (O-H). The frequencies of 1407 and 1622 cm^{-1} are related to amino group structure and carboxylic group[17]. For Glu spectrum, an absorption peak ranging of from 3111-2871 cm^{-1} linked to N-H, 1682 was linked to C=O, and 1161-1272 was linked to C-O, which are primary IR spectrum of Glu. Obviously, glutamic acid was found in all samples. In addition, other important substances such as lycopene, phenolic compounds, and flavonoids[18]. These compounds, which are found with functional groups appearing in the FTIR diagram, could be referred to as the antioxidant activity of the tomato meal extract.

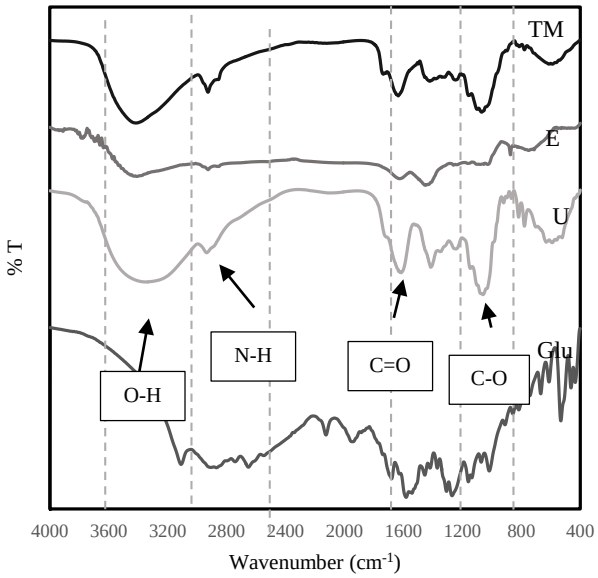

Figure 5. FTIR diagram of the tomato meal (TM), tomato extract by enzymatic extraction (E), and tomato extract by ultrasonic extraction (U)

4. Conclusion

Tomato meal extract 15% of bromelain for 45 min was the optimum condition for enzymatic extraction while 30 min with ultrasonic wave was the optimum condition for ultrasonic extraction for the sensory scores Tomato meal extract derived from 15% of bromelain for 45 min were higher than tomato meal while ultrasonic extraction played a crucial role in imparting distinct characteristics, demonstrating increase in sourness. In addition, tomato meal extracts from enzymatic and ultrasonic extraction exhibited DPPH and ABTS radical scavenging activity and confirmed structure of amino glutamic acid by FT-IR and the tomato meal extracts exhibited a significant potential as a functional flavor enhancer with different characteristics which could be a viable alternative to synthetic flavor enhancers.

Acknowledgements

This research was funded by National Science, Research and Innovation Fund (NSRF),

King Mongkut's University of Technology North Bangkok with Contract no. KMUTNB-PP-65-12.

References

1. Choi, S. H.; Kim, D. S.; Kozukue, N.; Kim, H. J.; Nishitani, Y.; Mizuno, M.; Levin, C. E.; Friedman, M. *J. Food Compos. Anal.* **2014,** *34* (2), 115-127.
2. Zuorro, A.; Lavecchia, R.; Medici, F.; Piga, L. *Food Bioprocess Technol.* **2013,** *6* (12), 3499-3509.
3. Valle, M.; Cámara, M.; Torija, M. E. *J. Sci. Food Agric.* **2006,** *86*, 1232-1236.
4. Sonklin, C.; Laohakunjit, N.; Kerdchoechuen, O.; Ratanakhanokchai, K. *J Food Sci Technol.* **2018,** *55*, 265–277.
5. Zhang, Y.; Pan, Z.; Venkitasamy, C.; Ma, H.; Li, Y. *LWT-Food Sci. Technol.* **2015,** *62* (2), 1154-1161.
6. Poojary, M. M.; Orlien, V.; Passamonti, P.; Olsen, K. *Food Chem.* **2017,** *234*, 236-244.
7. Sonklin, C.; Alashi, A. M.; Laohakunjit, N.; Aluko, R. E. *Molecules.* **2021,** *26* (6), 1515.
8. Li, J.; Pettinato, M.; Casazza, A. A.; Perego, P. A Comprehensive Optimization of Ultrasound-Assisted Extraction for Lycopene Recovery from Tomato Waste and Encapsulation by Spray Drying *Processes* [Online], 2022.
9. Garcia, M.; Ambat, S.; Adao, R., *Tomayto, Tomahto: A Machine Learning Approach for Tomato Ripening Stage Identification Using Pixel-Based Color Image Classification*. 2019.
10. Sonklin, C.; Laohakunjit, N.; Kerdchoechuen, O. *PeerJ.* **2018,** *6*, e5337.
11. A, P.; Barracosa, P.; Guiné, R.; Gonçalves, F. *Effect of drying on the phenolic content and antioxidant activity of thistle flower*. 2013.
12. Felföldi, Z.; Ranga, F.; Socaci, S. A.; Farcas, A.; Plazas, M.; Sestras, A. F.; Vodnar, D. C.; Prohens, J.; Sestras, R. E. *Plants (Basel).* **2021,** *10* (11).
13. Kumar, S.; Shree, B.; Sharma, S.; Sharma, A.; Priyanka. *Sci. Hortic.* **2024,** *327*, 112867.
14. Xu, N.; Chen, G.; Liu, H. *Molecules.* **2017,** *22* (12).
15. Bianchi, A. R.; Vitale, E.; Guerretti, V.; Palumbo, G.; De Clemente, I. M.; Vitale, L.; Arena, C.; De Maio, A. *Antioxidants (Basel).* **2023,** *12* (3).
16. Animashaun, O. H.; Sobowale, S. S. Microwave exposure of tomato varieties before catalytic oven drying and its effect on physicochemical and bioactive components studied by Fourier transform infrared (FTIR) spectroscopy. *Food and Humanity.* **2024,** *2*, 100197.
17. Vorobyova, V.; Skiba, M.; Vasyliev, G. Extraction of phenolic compounds from tomato pomace using choline chloride–based deep eutectic solvents. *J. Food Meas. Charact.* **2022**, *16*.
18. Kumcuoglu, S.; Yilmaz, T.; Tavman, S. *J. Food Sci. Technol.* **2014,** *51* (12), 4102-7.

Improvement of sensory attribute and antioxidant property of mung bean peptides by Maillard reaction

Sarocha Sapcharoen[1], Nachomkamon Saengsuk[3], Natta Laohakunjit[4], and Chanikan Sonklin[1, 2]*

[1]*Department of Industrial Chemistry, Faculty of Applied Science, King Mongkut's University of Technology North Bangkok, 1518 Pracharat 1 Rd., Wongsawang, Bangsue, Bangkok, 10800, Thailand*
[2]*Food and Agro-industrial Research Center, King Mongkut's University of Technology North Bangkok, 1518 Pracharat 1 Rd., Wongsawang, Bangsue, Bangkok, 10800, Thailand*
[3]*School of Food Industry, King Mongkut's Institute of Technology Ladkrabang, 1, Lat Krabang, Bangkok 10520, Thailand*
[4]*School of Bioresources and Technology, King Mongkut's University of Technology Thonburi, 49 Teintalay 25 Rd., Thakam, Bangkhuntein, Bangkok 10150, Thailand*

**E-mail: chanikan.s@sci.kmutnb.ac.th*

Abstract:

At present, plant-based proteins are rising in popularity in food protein consumption. The high protein content of 70% in mungbean meal renders it a compelling protein source for a flavoring agent. This study aimed to improve sensory attributes and antioxidant activity of mungbean peptides. Mungbean peptides were separated based on different molecular weights (P1 = >10 kDa, P2 = 5-10 kDa, P3 = 1-5 kDa, and P4 = <1 kDa) and were reacted with reducing sugar as glucose and ribose under a thermal process (Maillard reaction). The sensory characteristics of all samples were determined by quantitative descriptive analysis (QDA) with 5-point scoring (1-5). Results showed that Maillard reaction products from P4 peptides reacting with ribose (R-P4) contributed to a higher score of sensory perception than its original peptides and all peptides reacting with glucose. The flavor characteristics of R-P4 possessed a high intensity of overall acceptance (3.6), meaty flavor (3.4), sweet flavor (4.2), and umami (3.2). In addition, R-P4 inhibited DPPH and hydroxyl radical scavenging activity with 290 μmol TE/g and 79.80%, respectively. The chemical structure change of Maillard reaction products was explored by Fourier Transform Infrared Spectroscopy (FTIR). The functional group of ribose and amino acid bonding was detected after the reaction. The absorption peak of the amino groups of peptides bound to the carbonyl groups of reducing sugar was found in the observed peak at 1646 cm^{-1}. Therefore, the Maillard reaction product of mung bean meal peptide might be an alternative to a plant-based flavoring agent.

1. Introduction

Plant-based proteins are very interesting for food industry applications because the source is inexpensive and more sustainable source when compared to animal proteins. Mung bean meal is a waste product of mung bean noodle processing which has a high protein content 70 % dry weight and contains high levels of hydrophobic amino acid. These amino acids contributed to antioxidant activity[1]. Mung bean meal contains important amino acids that possess desired flavor. Especially, glutamic acid, and aspartic acid had umami taste. Cysteine was also found in high content which was important for meat flavor[2]. Therefore, protein from mung bean meal is suitable to add value by producing protein hydrolysate to be used as a flavor enhancer in food.

Protein hydrolysate is produced by enzymatic hydrolysis of plant proteins such soybean, corn, and mung bean, which yields free amino acids and short peptides. According to earlier research, a protein hydrolysate made from mung bean meal hydrolyzed by bromelain may be used as a flavoring agent with strong antioxidant properties[3]. Mung bean protein hydrolysate showed DPPH and hydroxyl radical scavenging activity with EC_{50} 0.53 mg/mL and 54.50%, respectively[4]. However, the flavor characteristics of protein hydrolysate obtained were unclear. Its flavor characteristics could be modified to the specific flavor, such as pork flavor, chicken flavor or seafood flavor via Maillard reaction.

Maillard reaction (MR) is a non-enzymatic reaction between a carbonyl group of reducing sugar and amino group in terminal end of free amino acid, peptide or protein by heating and resulting in aroma, color, and taste compounds which are called Maillard reaction products (MRPs)[5,6]. MRPs are composed of volatile compounds heterocyclic compounds such as pyrrole, furan, thiophene, and pyrazine, which play an important role in flavoring properties. MR has been reported to enhance the aroma and sensory characteristics of different food proteins or peptides[7,8] and the bioactive properties, e.g. antioxidant activity. A previous study reported that MRPs from sesame seed meal contributed to DPPH radical scavenging activity of 51% and hydroxyl radical scavenging activity of 80%[9]. However, sensory attributes and antioxidant

activity from MRPs from mung bean meal protein hydrolysis has been limited. Therefore, the objective of this study was to determine the sensory attributes and antioxidant activity of mung bean peptides by Maillard reaction.

2. Materials and Methods

2.1 Materials

Mung bean meal obtained from Sittinan Co. Ltd., Lat Lum Kaeo District, Pathum Thani, Thailand. Bromelain (enzymatic activity = 97,540 CDU) was provided by K-Much-Industry Co., Ltd. (Bangkok, Thailand). Mung bean meal defatted (DMM) was extracted twice using hexane. The proximate composition of DMM 76.34% protein, 1.05% fat, 3.16% ash, 0.96% fiber and 18.49% carbohydrate (dry weight). Chemical reagents were of analytical grade from Thermo Fisher Scientific (Waltham, MA, USA) or Sigma Aldrich (St. Louis, MO, USA).

2.2 Preparation of peptide fraction

DMM 10 g in 100 mL of deionized water was hydrolysate using 15% (w/w) bromelain for 12 h according to the method[3]. The reaction was stopped by heating at 95 °C for 15 minutes. The supernatant was collected after centrifugation (7000 × g, 15 min, 4 °C) and filtration, respectively. The supernatant was collected as the mung bean meal protein hydrolysate (MMPH) or (Crude-MMPH). The MMPH was fractionated by ultrafiltration with molecular weight cut-off (MWCO) of 10, 5 and 1 kDa (Millipore, Germany). This process four fractions: P1 (MW > 10 kDa), P2 (MW 5-10 kDa), P3 (MW 1-5 kDa) and P4 (MW < 1 kDa). The protein hydrolysate fractions were then freeze-dried and store at -20 °C.

2.3 Preparation of Maillard rection products (MRPs)

For preparation of MRPs was modified from the method[9]. Mung bean peptides (Crude, P1, P2, P3 and P4) were reacted with reducing sugar as glucose and ribose. Each mixture of sample (1.2 g) with glucose (1.2 g) was separately dissolved in 40 mL Milli-Q water. The mixture was adjusted to pH 9.0 with 6 M NaOH. The solutions were heated at 99 °C for 120 minutes in a water bath. After heating, the solutions were rapidly cooled in an ice bath to stop the reaction, freeze-dried, and stored at -20 °C. The Maillard product reactions with ribose were similarly prepared. The control of reaction was reaction without glucose and ribose and was prepared the same manner.

2.4 Fourier transform infrared (FTIR) analysis.

Original peptides and MRPs were investigated in the chemical composition by FTIR. Each sample was mixed with KBr before detecting with the FTIR spectra at IR ranges of 400 and 4000 cm^{-1} by Fourier Transform Infrared Spectroscope (PerkinElmer, Spectrum 100, USA).

2.5 Sensory analysis

Quantitative descriptive analysis (QDA) of peptide fractions was obtained by using 15 semi-trained panelists. All semi-trained panelists had previously received training in descriptive sensory analysis with more than 20 h of experience in sensory analysis of various food samples. Sample paste (1 mL) was prepared by dissolving in 10 mL of water at room temperature. Scores of samples were quantitative descriptive, with a 5-point scoring test (1-5), where 1-point score means none, 2-point score means slight, 3-point score means moderate, 4-point score means strong and 5-point score means very strong of meaty flavor, salty flavor, sour flavor, sweet flavor, bouillon flavor, smoky flavor, bitter taste, salty taste, sweet taste, sour taste, pungency, umami and overall acceptance. Sensory analysis was conducted based on a randomized complete block design (RCBD) with three replications.

2.6 Antioxidant activities

2.6.1 DPPH radical scavenging activity

The DPPH radical-scavenging activity of the hydrolysate according to the method [10]. Sample 50 µL were mixed with 150 µL of a 0.1 mM DPPH solution. The mixtures were incubated for 30 min in the dark at room temperature and the absorbance was measured at 517 nm using a microplate spectrophotometer (MOLECULAR DEVICES, SpectraMax iD3, USA). The blank was conducted in the same manner, except distilled water was used instead of the sample. Trolox was used as a positive standard. DPPH radical-scavenging activity was calculated as:

$$\text{DPPH activity (\%)} = \frac{(A_b - A_s)}{A_b} \times 100$$

where Ab is the absorbance of blank

As is the absorbance of sample

2.6.2 Hydroxyl radical scavenging activity

The hydroxyl radical scavenging assay was modified using the method[11]. Samples were dissolved in 0.1 M sodium phosphate buffer (pH 7.4) to a final concentration of 2 mg/mL. The reactions were carried out in a microplate well plate. Fifty microliters of samples or buffer (Blank) was mixed with 50 µL of 3 mM 1, 10-phenanthroline in 0.1 M sodium phosphate buffer

(pH 7.4) and 50 µL of 3 mM $FeSO_4$. To initiate the Fenton reaction, 50 µL of 0.01% hydrogen peroxide (H_2O_2) was added and absorbance read at 536 nm using a microplate spectrophotometer (MOLECULAR DEVICES, SpectraMax iD3, USA) every 10 min for 1 h while incubating at 37 °C with continuous shaking. The percentage hydroxyl radical scavenging activity was calculated using the following equation:

$$\text{Hydroxyl activity (\%)} = \frac{(A_b - A_s)}{A_b} \times 100$$

where Ab is the absorbance of blank
As is the absorbance of sample

2.7 Statistical analysis

The experimental data was analyzed using the SPSS statistics program Version 20 (SPSS Institute, USA). The statistical significance of differences between samples was accepted with confidence at 95%.

3. Results & Discussion

3.1 Sensory analysis

The sensory of MRPs and their original peptide fractions (C, P1, P2, P3 and P4) were analyzed. The MRPs which prepared by glucose were called G-C, G-P1, G-P2, G-P3 and G-F4, respectively. The MRPs from ribose were called R-C, R-P1, R-P2, R-P3, R-P4 and compared to MPRs without sugar (H-C, H-P1, H-P2, H-P3, H-P4). The assessors also described characteristics such as meaty flavor, salty flavor, sour flavor, sweet flavor, bouillon flavor, smoky flavor, bitter taste, salty taste, sweet taste, sour taste, pungency, umami, and overall acceptance by quantitative descriptive analysis (QDA) with a 5-point scoring test (from 1 to 5). Results showed that all peptide fractions before the Maillard reaction, including C, P1, P2, P3, and P4, possessed a meaty flavor, sweet flavor, and moderately bouillon flavor, slightly umami, moderately bitter taste and sour taste (Figure 1A). Particularly, P4 (< 1 kDa) provides higher intensity of umami and overall acceptance than other original peptide fractions. The flavor characteristics of P4 possessed a meaty flavor (2), salty flavor (1.8), sour flavor (1.6), sweet flavor (3.2), bouillon flavor (2.8), smoky flavor (1.6), bitter taste (2.4), salty taste (1.6), sweet taste (1.6), sour taste (3.4), pungency (1.4), umami (2.2), and overall acceptance (2). As well as, peptides were heated without sugar (Figure 1B), including H-C, H-P1, H-P2, H-P3, and H-P4. These fractions contributed to good flavor and test. Especially, H-P4 provides umami, bouillon flavor and higher overall acceptance. H-P4 possessed a meaty flavor (2.2), salty flavor (1.4), sour flavor (2), sweet flavor (3), bouillon flavor (2.8), smoky flavor (1.2), bitter taste (2), salty taste (2.2), sweet taste (2), sour taste (3.2), pungency (1.2), umami (2.6), and overall acceptance (2.6). Maillard reaction products that derived from the reaction of peptides with glucose and ribose explored stronger instances of sensory characteristics than their original peptides. MRPs from glucose reaction (Figure 1C) contributed to lower score of sensory attributes than meat flavor, sweet flavor, umami, and a high score of overall acceptance from the panelists than MRPs derived from ribose reaction. The MRPs from the ribose reaction, which were R-C, R-P1, R-P2, R-P3, and R-P4, provided strong instances of meaty flavor, sweet flavor, and umami taste but low scores of bitter tastes (Figure 1D). Considering The R-P4, which was peptides fraction less than 1 kDa reacted with ribose, it had a better score for meat flavor, sweet flavor, umami, and overall acceptance than other flavors when compared with glucose and unreacted. It might be low molecular weight and peptides as a result of crosslink during heating. Thus, the crosslinking of less than 1000 Da peptides enhances the umami[12]. Moreover, The peptides < 1 kDa composed of low MW peptides could be crosslinked with ribose easier than higher MW peptides, resulted in providing higher amount of meat like flavor molecule. Ribose is five carbon atom which is easier to open rings than glucose[13]. The flavor characteristics of R-P4 possessed a meaty flavor (3.4), salty flavor (2.8), sour flavor (1.4), sweet flavor (4.2), bouillon flavor (2.4), smoky flavor (2.8), bitter taste (1.2), salty taste (2), sweet taste (2.6), sour taste (1.6), pungency (1), umami (3.2), and overall acceptance (3.6). Similarly, a previous study reported that Maillard reaction from soybean meal reacted with ribose sugar presented strong umami, caramel aroma, nutty flavor, and grilled meat flavor because there are furan, pyrazine, ketone, and aldehyde[8] or mushroom showed meat flavor and umami[7]. MR contributed to good flavor because reducing sugar reacted with amino or peptides by heating to generate compounds such as thiazoles, 2-methylthiophene, 2-methyl-5-ethylthiophene and sulfur compounds, which led to meat-like flavor and umami taste[14]. Moreover, the original peptide MW less than 1000 Da showed cysteine provides sulfur compounds, which exhibited meaty and umami taste[13]. The Maillard reaction process can improve the flavor characteristics of the product.

3.2 Antioxidant activities

3.2.1 DPPH radical scavenging activity

The activity of mung bean meal peptides before Maillard reaction, peptides was heating without sugar and after Maillard reaction with glucose and ribose. The results are shown in (Figure 2A). It was found that the Maillard reaction products were obtained from mung bean meal peptides reacted with ribose and glucose, which contributed to DPPH antioxidant activity. Especially, R-P4 (< 1 kDa) using ribose had the highest DPPH radical scavenging activity with 290 μmol TE/g. R-P4 was a low molecular weight peptides of less than 1 kDa, which makes this fraction easier to scavenge the radicals and it original peptides (F4) consisted of hydrophobic amino acid[4]. Low molecular weight peptides, peptides of less than 1 kDa, which makes this fraction easier to scavenge the radicals and it original peptides (F4) consisted of hydrophobic amino acid[4]. Low molecular weight peptides, which contained hydrophobic amino acids in chain, expressed high antioxidant potentials[11]. Another reason was the generated heterocyclic compounds by Maillard reaction of R-P4. Similarly, a previous study reported that the Maillard reaction from cabbage leaves, exhibited DPPH antioxidant activity with a DPPH value of 76% because there are compounds containing heterocyclic compounds and a thiol group that contributed to antioxidant activities[16].

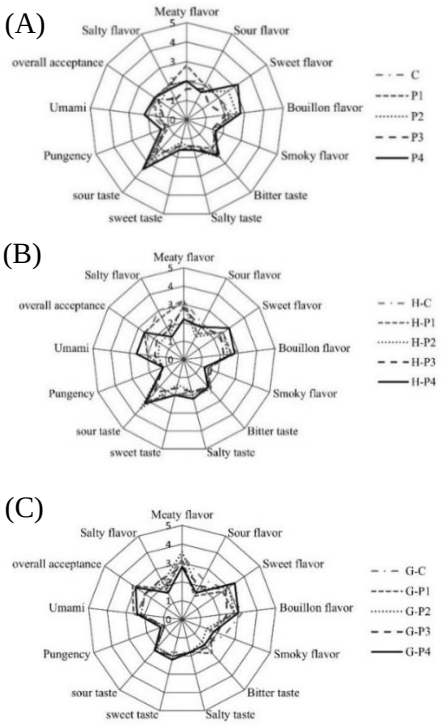

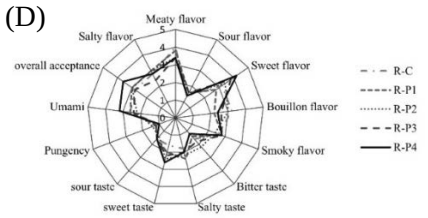

Figure 1. Sensory characteristics of mung bean meal peptides before Maillard reaction (A) and after Maillard reaction without sugar (B), with glucose (C) and with ribose (D).

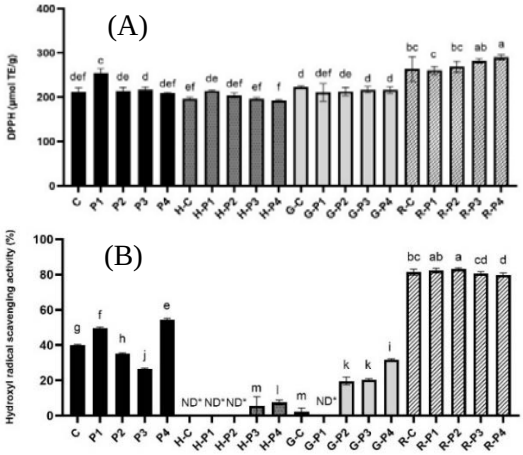

Figure 2. DPPH radical scavenging activity (A) and Hydroxyl radical scavenging activity (B) of mung bean meal peptides before Maillard reaction and after Maillard reaction without sugar, with glucose, and with ribose.

3.2.2 Hydroxyl radical scavenging activity

Hydroxyl radical scavenging activity of mung bean meal peptides before Maillard reaction, peptides was heating without sugar and peptides reacted with glucose and ribose. MRPs from ribose sugar have a stronger antioxidant capacity than peptides with glucose, heating without sugar, and original peptides (Figure 2B). The peptides reacted with ribose sugar, Ri-F2 had the highest hydroxyl radical antioxidant efficiency with 83.14 %, which is different from Ri-C, Ri- F1, Ri-F3, and Ri-F4 were 81.47, 82.27, 80.60, and 79.80 %, respectively. So, these results are not the same DPPH trend because it could be the peptides fraction < 1 kDa contributed to the highest DPPH because influence of low MW and high content of hydrophobic amino acid in peptide chain. Results from this study indicated that MMPH peptides donate protons to free radicals because they had significantly high DPPH value compared to hydroxyl, which reaction were electron donation [4]. All samples from ribose reaction dramatically explored the enhancement of antioxidant capacity

because ribose is a pentose sugar with a long carbon core of 5 atoms while glucose is hexose sugar with 6 carbon atoms. Ribose sugar is easier and quicker to open rings and will react with other atoms[17], resulting in high generating of heterocyclic compounds. The heterocyclic compounds such as thiophenes, furans, pyrazine, pyrroles, and sulfur-containing, which were generated after the Maillard reaction, caused the increased inhibition of hydroxyl activity[9].

3.3 FTIR spectroscopy analysis

Mung bean meal peptides and MRPs are an important component in protein, which consists of peptides, carbonyl group, amino group, and carbohydrates[3]. R-P4 has the highest sensory characteristics and antioxidant activity. R-P4 was chosen for analysis of chemical composition by FTIR. Results showed the absorption peak ranging from 3000-2800 cm^{-1} (N-H), 1710-1600 cm^{-1} (C=O), and 1400-1300 cm-1 (C-H) of the P4 (Figure 3). The absorption peaks ranging from 3550-3200 cm^{-1}, 3000-2800 cm^{-1}, 1710-1600 cm^{-1}, 1590-1470 cm^{-1}, 1300-1400 cm^{-1}, and 1250-1020 cm^{-1} were detected in R-F4 which indicated the characteristics of the O-H, N-H, amide (C=O), C=C (aromatic ring), C-H, and C-N, respectively. From R-P4 FTIR spectrum could be explained that the consumption of amino group reacted with ribose in the Maillard reaction and generated of novel functional group, amadori compound (C=O) as well as *N*-containing compounds (C-N)[18, 19]. This might be due to the crosslink of an amino group and a carbonyl group. The absorption peak of the amino groups of peptides bound to the carbonyl groups of reducing sugar was found in the observed peak at 1646 cm^{-1}.

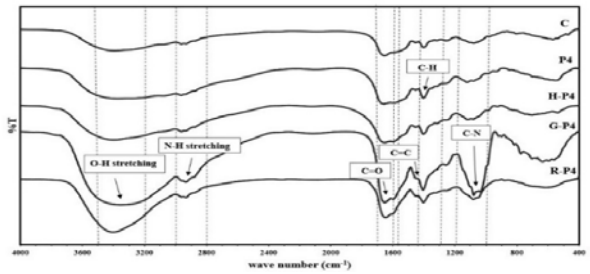

Figure 3. FTIR of mung bean meal peptides before and after Maillard reaction of P4 (< 1 kDa).

4. Conclusion

Maillard reaction product (MRP) obtained from peptide less than 1 kDa which was reacted with ribose (R-P4) contributed to great sensory characteristics (meaty flavor, sweet flavor, smoky flavor, umami, and high score of overall acceptance) and antioxidant efficiency when compared to glucose and non-reacted peptides. Therefore, mung bean meal peptides from Maillard reaction have great potential as flavor enhancers and antioxidants. It will be developed to an alternative to a plant-based flavoring agent and food application.

Acknowledgements

This research budget was allocated by National Science, Research and Innovation Fund (NSRF), and King Mongkut's University of Technology North Bangkok (Project no. KMUTNB-FF-67-B-53).

References

1. Wattanasiritham, L.; Theerakulkait, C.; Wickramasekara, S.; Maier, C. S.; Stevens, J. F. *Food Chem.* **2016,** *192*, 156-62.
2. Sonklin, C.; Laohakunjit, N.; Kerdchoechuen, O. *J. Agric. Food Chem.* **2011,** *59* (15), 8475-83.
3. Sonklin, C.; Laohakunjit, N.; Kerdchoechuen, O.; Ratanakhanokchai, K. *J. Food Sci. Technol.* **2018,** *55* (1), 265-277.
4. Sonklin, C.; Laohakunjit, N.; Kerdchoechuen, O. *PeerJ*. **2018,** *6*, e5337.
5. Yu, M.; He, S.; Tang, M.; Zhang, Z.; Zhu, Y.; Sun, H. *Food Chem.* **2018,** *243*, 249-257.
6. Siewe, F. B.; Kudre, T. G.; Bettadaiah, B. K.; Narayan, B. *Ultrason. Sonochem.* **2020,** *65*, 105055.
7. Chen, X.; Yu, J.; Cui, H.; Xia, S.; Zhang, X.; Yang, B. *Molecules*. **2018,** *23* (2), 247.
8. Sun, L.; Wang, D.; Huang, Z.; Elfalleh, W.; Qin, L.; Yu, D. *LWT*. **2023,** *185*, 115097.
9. Shen, Y.; Hu, L. T.; Xia, B.; Ni, Z. J.; Elam, E.; Thakur, K.; Zhang, J. G.; Wei, Z. J. *Food Chem.* **2021,** *365*, 130463.
10. Bersuder, P.; Hole, M.; Smith, G. *J. Am. Oil Chem.' Soc.* **1998,** *75* (2), 181-187.
11. Ajibola, C. F.; Fashakin, J. B.; Fagbemi, T. N.; Aluko, R. E. *Int. J. Mol. Sci.* **2011,** *12* (10), 6685-702.
12. Habinshuti, I.; Mu, T.-H.; Zhang, M. *Food chem.* **2021,** *361*, 130090.
13. Ni, Z.-J.; Liu, X.; Xia, B.; Hu, L.-T.; Thakur, K.; Wei, Z.-J. *Food Chem.: X.* **2021,** *11*, 100127.
14. Eric, K.; Habimana, J. D. D.; YuJingyang; NicoleMurekatete; XiaomingZhang; KingsleyMasamba; Emmanuel, D.; Bertrand, M.; Masamba, K. *Int. J. Food Eng.* **2017,** *13*.
15. Habinshuti, I.; Chen, X.; Yu, J.; Mukeshimana, O.; Duhoranimana, E.; Karangwa, E.; Muhoza, B.; Zhang, M.; Xia, S.; Zhang, X. *LWT*. **2019,** *101*, 694-702.

16. Fadel, H. H. M.; Lotfy, S. N.; Asker, M. M. S.; Mahmoud, M. G.; Abd El-Aleem, F. S.; Ahmed, M. Y. S.; Saad, R. *Appl. Food Res.* **2023,** *3* (2), 100327.
17. Jiang, Z.; Wang, L.; Wu, W.; Wang, Y. *Food chem.* **2013,** *141* (4), 3837-45.
18. Madadlou, A. *Food chem.* **2016,** *192*, 831-836.
19. Chen, W.; Ma, X.; Wang, W.; Lv, R.; Guo, M.; Ding, T.; Ye, X.; Miao, S.; Liu, D. *Food Hydrocoll.* **2019,** *95*, 298-30.

Immobilization of transglucosidase enzyme via polymer-inorganic hybrid for isomaltooligosaccharide production

Phassorn Khumfu[1], Areeya Phakpachai[1], and Yupin Phuphuak[1,2,*]

[1]*Department of Chemistry, Faculty of Science, Naresuan University, Phitsanulok 65000, Thailand*
[2]*Center of Excellence in Biomaterials, Faculty of Science, Naresuan University, Phitsanulok 65000, Thailand*

**E-mail: yupinp@nu.ac.th*

Abstract:

Isomaltooligosaccharides (IMOs) are relatively new functional foods as prebiotic ingredients and have been utilized as dietary fibers that can be produced from carbohydrate raw materials by transglycosylation using transglucosidase enzyme (TGE). Normally, using free enzymes in the process of IMOs always denatured enzymes by the high temperature of heating wasted time and could not be reused or recycled enzymes. Thus, immobilized TGE is interesting for IMOs production because of many advantages such as high production efficiency and reusability. This work proposes to use cationic biopolymers hybridization with $Ca_3(PO_4)_2$ nanoparticles (CP-NPs) for immobilization of transglucosidase at concentrations of 10% and 25% w/v that were fabricated by beads gelation of alginate (SA) and chitosan (CS) under salt solution for formatting CP-NPs and adding PEG to improve pore density and hydrophilicity of the immobilized enzyme. All samples were analyzed by scanning electron microscopy (SEM), X-ray diffraction (XRD), Fourier transform infrared (FTIR), DC (detergent compatible) protein assay, and thin layer chromatography (TLC). The results showed that the optimized ratio of SA/CS is 1:2 and the concentration of salts was at 100 mM for completing spherical beads as an increase of salts affected on breaking bead surface. The addition of PEG enhanced the immobilization efficiency of SA/CS/CP-NPs transglucosidase due to surface roughness and reduction of CP particle sizes. Hydrogen bonds form between PEG and SA and the addition of CS can form polyelectrolytic wall beads which support the reducing the decomposition and improving the stability of the beads. Moreover, the TLC analysis revealed that using 10% TGE-SA/CS/PEG/CP-NPs could produce IMOs better than that using 25%TGE immobilized beads.

1. Introduction

Nowadays, Prebiotics additives in foods are widely used around the world which has increasingly developed new functional food, producing, and studying new technology or knowledge that promotes increase the high efficiency of industrial production and also reduces production costs as well.[1]

Isomaltooligosaccharide (IMOs) is one of the functional oligosaccharides that can be produced by enzymatic hydrolysis using starch as substrates. IMOs can stimulate beneficial bacteria or probiotics in the gut as prebiotics affecting to promote immune system and health.[2] Probiotic-microorganisms beneficial to the body such as *Lactobacillus* spp. and *Bifidobacterium* spp. can inhibit the growth of pathogenic microorganisms in the intestines, reducing the occurrence of diarrhea, inflammation, bloating, distension, preventing colon cancer, and promoting nutrient absorption for immunity. Production processe of IMOs is usually via a free enzymatic hydrolyzation system for 3 steps including liquefaction, saccharification, and transglycosylation. In transglycosylation step, transglucosidase or α-glucosidase, is an important enzyme in the production of Isomaltooligosaccharide. It is obtained from the extraction of *Aspergillus niger* that induce a trans-type of bonding on sugar molecule from 1,4-glycosidic bond to 1,6-glycosidic bond in the oligosaccharide molecule containing DP 2-20 of 1,6-glycosidic bond.[3]

However, transglucosidase enzyme still needs a solution to improve some enzyme limitations: reusability or recovery, enzyme performance, enzyme purity, stability, possibility of enzyme reactivation, activity, specificity, selectivity, or reducing enzyme inhibition.

Enzyme immobilization is a widely used approach that permits an easy recovery of both the used enzymes and their support materials. Immobilized enzymes possess much higher stability and are also easier to handle when compared to their free forms.[4] The immobilization of enzyme can be prepared in various techniques,[5] such as covalent attachment, organic methods, inorganic-organic hybrid encapsulation, magnetic particles, polymer-superparamagnetic hybrid, electrospun nanofiber, polymer-inorganic hybrid, etc.[3, 6-9] This enzyme immobilization bounds to solid support materials which can be removed easily from the reaction mixture of substrates of bioreactor by minimized contamination of the final products with enzymes. Polymer-Inorganic hybrid

method is interested in immobilized enzyme. Therefore, it was fabricated by the polymer reaction and inorganic particles during preparation in the gel beads format for example, using chitosan and alginate hybrid with calcium carbonate of phosphate or silicate and Iron oxide, ete. And the chitosan gel also can remove some ions in the aqueous solution because they present a larger contact surface by electrostatic attraction.

This work aims to develop immobilization of transglucosidase via a polymer-inorganic hybrid forming spherical gel beads by using alginate, chitosan, and polyethylene glycol containing calcium phosphate. The physical and chemical properties of the immobilized enzyme were analyzed by Fourier Transform Infrared (FTIR), X-ray Diffraction (XRD), and Scanning Electron Microscopy (SEM) techniques. Homnin rice starch was used as raw material for producing IMOs prebiotics in order to investigate the performances of immobilized and free transglucocidase enzymes. Finally, TLC was used for preliminary test of IMOs formations.

2. Materials and Methods

2.1 Materials

Transglucosidase L "Amano" (activity 300,000 U/ml from Amano Co, Ltd) was immobilized on substrates in this methodology by using polymers and salts including sodium alginate (SA) from Vejichemicals, Chitosan (CS) from Sin Udom, polyethylene glycol (PEG) (Mw = 4000) from Sigma Aldrich, disodium hydrogen phosphate (Na_2HPO_4) from Kemaus, Calcium chloride ($CaCl_2$) from Vejichemicals. Homnin rice starch (HN) was purchased from Bangyai supple Co. Ltd, α-amylase (activity 200,000 U/g and activated pH 6.5, 95℃) and β-amylase (activity 40,000 U/ml and activated pH 5.5, 55℃) were obtained from iknow, Reach Biotechnology.

2.2 Preparation of sodium alginate/chitosan calcium phosphate (SA/CS/CP) spherical gel beads via polymer-inorganic hybrid

The SA/CS/CP spherical gel beads were prepared based on the previous report.[3] In the first step, sodium alginate (SA) was dissolved in deionized water in a concentration of 2% w/w with disodium hydrogen phosphate concentration of 10-200 mM called SA solution. Chitosan (CS) was dissolved in deionized water in a concentration of 1%w/v with calcium chloride 10-200 mM called CS solution.

In the second step, CS solution was stirred in a beaker and SA solution was contained in a syringe using a diameter tip of 0.7 cm then CS solution was dropped into SA solution by ratios of 1:1, 1:2, and 1:3 (v/v) and held on stirring for 30 min to form gel beads. In the final step, spherical gel beads were filtrated by white filtered fabric. After that, it was washed with DI water for 3 times to remove salts and was dried in an oven at 50℃ for 3 h called samples within calcium phosphate (CP).

All samples were characterized by X-ray diffraction (XRD), Field Emission Scanning Electron Microscopy (FE-SEM), and Fourier Transform Infrared (FTIR), and then the best condition of SA/CS/CP was selected to prepare the enzyme immobilization with adding PEG4000 in the next step.

2.3 Preparation of transglucosidase immobilization

Transglucosidase and PEG were dissolved in SA solution (prepared in 2.2) at a concentration of TGE 10 and 25% v/v and PEG 1, 3, and 5% w/v.

CS solution was stirred in a beaker, meanwhile, SA with TGE and PEG solution were contained in a syringe using a diameter tip of 0.7 cm then SA solution was dropped into CS solution stirring for 30 min. The spherical gel beads were filtrated by white filtered fabric. After that, it was washed with DI water 3 times to remove salts and was dried in an oven at 50℃ for 3 h. The immobilized enzyme was kept at 4℃ until used.

2.4 Preparation of IMOs syrup by transglycosylation of Homnin rice using TGE immobilized gel beads

Homnin rice starch (HN) was liquidized by α-amylase 0.1% w/w for liquefaction (L) of HN. The optimized condition should have maltodextrin at 12 dextrose equivalents (DE)[7] for suitable maltose syrup production obtained from the conditions of 1% (w/w) of α-amylase (activity 200,000 U/g and activated pH 6.5, 95℃) of 30% (w/v) HN for 20 min. Sample L was optimized maltose syrup by β-amylase saccharification (S) which is 1.5% w/w β-amylase (activity 40,000 U/ml and activated pH 5.5, 55℃). Finally, sample S has added with TGE immobilized gel beads 5-10 beads/ml for the reaction time of 30 min, 1 h, and 2 h. The qualitative test of sugar was performed by thin layer chromatography (TLC).

2.5 X-ray diffraction (XRD)

All samples were detected at 5-25˚ on the rotator in a chamber of the X-ray Diffractometry (XRD) Bruker, D2 Phaser.

2.6 Field Emission Scanning Electron Microscopy (FE-SEM)

All samples were prepared on the carbon taps on FE-SEM stubs which dried at 50°C in the oven over time before testing in the FE-SEM instrument using high voltage mode 15 kV.

2.7 Fourier Transform Infrared (FTIR)

All samples were analyzed at the range of wavenumber of 400-4000 cm^{-1} using ATR mode (Spectum GX, Perkin Elmer).

2.8 Thin Layer Chromatography (TLC)

The sugar types in IMOs samples after being treated by TGE immobilized gel beads were analyzed using TLC technique with the mobile phase containing propanal-1-ol, ethyl acetate, and water in a ratio of 6:1:3, v/v/v. Then, the samples were spotted onto the TLC plate (TLC silica gel 60 F_{254} Merck KGaA, Germany) and then dipped in the prepared mobile phase, dried and sprayed α-naphthol with 0.5%v/v sulfuric acid solution on TLC plate after that incubated at 110°C to colorize the samples.

3. Results & Discussion

3.1 Effect of SA/CS ratios on spherical gel beads

The SA/CS spherical gel beads were prepared by using the salt concentration of 10 mM to study the effect of sustainable gel formation. The ratios of SA/CS spherical gel beads were varied into 1:1, 1:2, and 1:3 v/v. Figure 1 shows that spherical beads of 1:1 could not form spherical gel beads completely. When the ratio was adjusted to 1:2, spherical gel beads were formed as the electrostatic and metal ions interaction between alginate (cationic polymer) and chitosan (anionic polymer) can be cross-linked and blended into the gelation form (insoluble gel). Additionally, the sizes of the beads depend on the sizes of the droplets generated from the needle tip used in the preparation process.

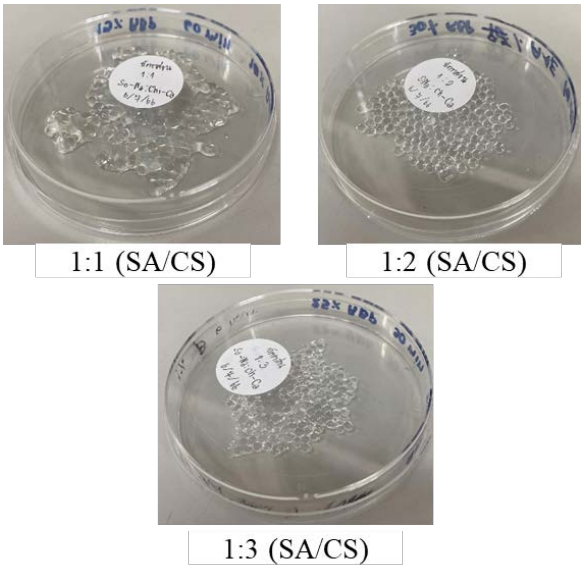

Figure 1. Photos of SA/CS spherical gel beads with various ratios of 1:1, 1:2 and 1:3.

When the ratio was adjusted to 1:3, spherical gel beads were not completely round compared to the 1:2 ratio. This could be noticed that the proportion in the welding of polymers with the salt solution between sodium hydrogen phosphate and calcium chloride affects the gelation of alginate and chitosan. Therefore, the most appropriate ratio of SA/CS for creating perfectly spherical gel beads was at 1:2 which also affects the surface area of the beads observed from the SEM image in Figure 2.

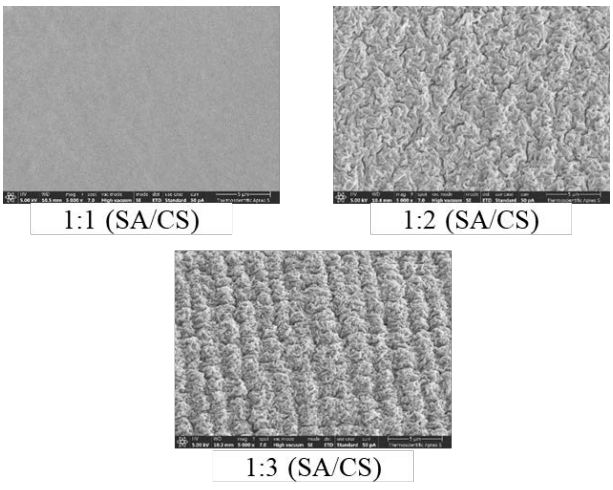

Figure 2. SEM images (5kX) of various ratios of 1:1, 1:2, and 1:3 (SA/CS).

The results of SEM images (5kX) displayed the surface morphology of spherical gel beads that were dried at 50°C for 24 h. The 1:1 (SA/CS) was a smooth surface and calcium phosphate particles were scattered within the surface. At the ratio of 1:2, it appeared rough surface leading to the high surface area. This

contributes to a good contact with the molecule of sugar and a fine distribution of calcium phosphate ($Ca_3(PO_4)_2$) nanoparticles (CP-NPs). Thus, this surface type tends to support the contact between the enzyme with the substrate in IMOs production. In the case of the 1:3 ratio, it shows a roughness clearly and it can be noticed that CP-NPs possess good arrangement.

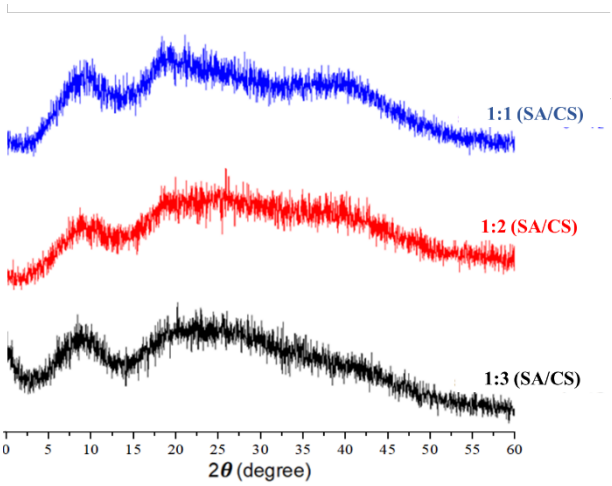

Figure 3. XRD patterns of various ratio of 1:1, 1:2, and 1:3 (SA/CS) adding 10 mM of salts.

XRD pattern shows the crystal structure of alginate chitosan calcium phosphate beads in various ratios which was found that there were peaks corresponding to the polymer mixture at 13˚ and 24˚ (Figure 3). These was also found in all 3 ratios and characteristics of peaks showing CP-NPs occurring in the beads depicted at peaks of approximately 31˚ to 35˚ which is relatively low peak consistent with the previous report.[10] In addition, the ratio of 1:1 prepared with a salt concentration of 10 mM, have less clear peaks than that of the higher concentration of salts. However, the ratio of 1:2 shows the CP-NPs peaks at approximately 31˚ to 35˚ and the chitosan peak occurs in the range of 11-13˚ and 20-23˚ which corresponds to the previous work.[11] Thus, it can be noted that the ratio 1:2 is the most suitable condition because a CP-NPs peak was clearer than 1:1 and 1:3, and greatly spherical beads with a rough surface were formed. Nevertheless, characteristic peaks of CP-NPs of all samples are not clear by XRD patterns using the concentration of 10 mM salt in a polymer solution. For this reason, the higher concentrations of salt for the reaction of CP-NPs in any form such as $Ca_3(PO_4)_2$ should be further studied.

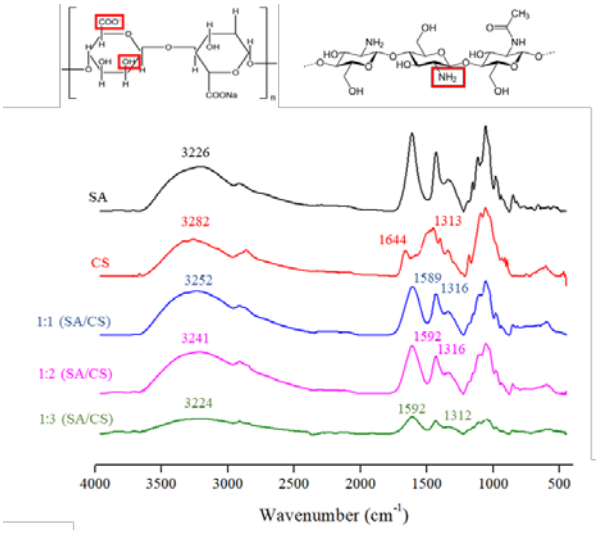

Figure 4. FTIR spectra of SA, CA, 1:1, 1:2, and 1:3 SA/CS.

FTIR was utilized to study the functional groups on the beads to confirm the chemical components at ratios of 1:1, 1:2, and 1:3 (SA/CS), respectively. In Figure 4, it was found that the characteristic peak of chitosan (CS) depicted the amide I group occurring at 1644 cm^{-1}, amide II at the peak at 1312 cm^{-1}, respectively. The characteristic peak of Sodium alginate (SA) depicted O-H stretching at the wavenumber range of 3200-3500 cm^{-1} and -COO at 1650-1850 cm^{-1}. The ratio was increased as seen from the high peak of chitosan. In the 1:3 (SA/CS), the alginate peak was decreased as chitosan increased. And there is also a shift of the -COO peak in the 1:1 and 1:2 samples due to the interaction between the chitosan molecule with alginate and CP-NPs according to the previous report.[9] This can be concluded that 1:2 is the most suitable ratio of SA/CS to form spherical gel beads and CP-NPs are uniformly distributed on the surface. Thus, it was selected to be further developed by varying the salt concentration in the solution into 100, and 200 mM in the next part.

3.2 Effect of concentration of salts (10, 100, and 200mM) on spherical gel beads of 1:2 (SA/CS)

Figure 5 represents that the appearance of 1:2 (SA/CS) at 10 mM show clearer and smoother beads than that of 100 mM and 200 mM indicating that when increase concentration of salts, it affects the morphology of calcium phosphate particles on the surface of gel beads. This was also confirmed by SEM measurements as shown in Figure 6.

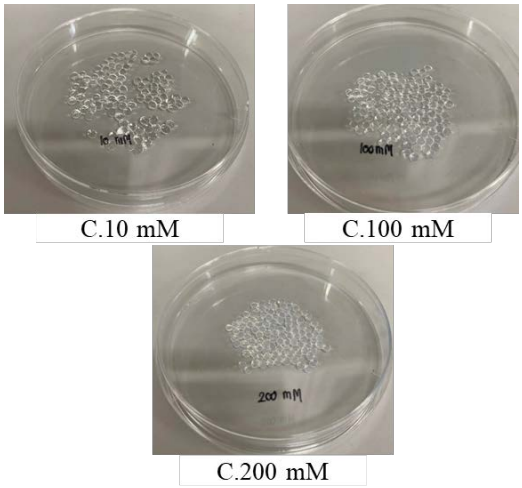

Figure 5. Photos of spherical gel beads of with various concentrations of salts 10, 100, and 200 mM in 1:2 (SA/CS).

SEM images (Figure 6) show that at 10 mM of salts possesses a relatively smooth surface while at 100 mM displays rough surface and small clear. Moreover, it can be noticed that concentration of salt at 200 mM shows the large particles with disorganized and rough surface of calcium phosphate particles. From this evidence, it can be pointed out that at the 100 mM concentration of salts is the most appropriate condition because CP-NPs are distributed regularly and have the most complete physical characteristics compared to 10 mM and 200 mM concentrations. Thus, it was suggested that adding PEG in gel beads at 200 mM of salts improved the surface and inhibited the reaction between the disodium hydrogen phosphate and calcium phosphate for the large-size particles.

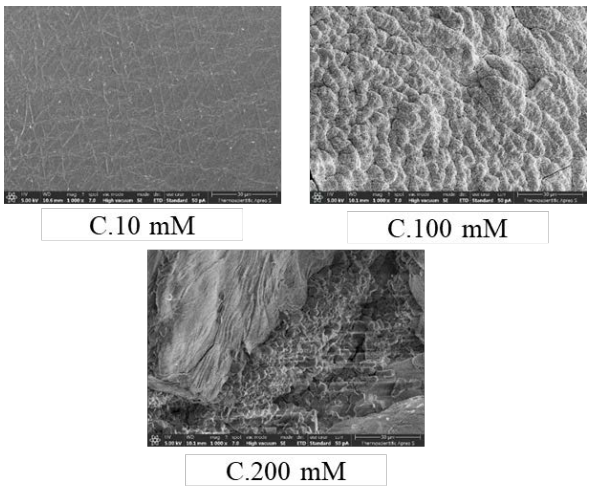

Figure 6. SEM illustrations (5kX) of various concentrations of salts 10, 100, and 200 mM in 1:2 (SA/CS).

In Figure 7, XRD patterns display the crystallization of $Ca_3(PO_4)_2$ of beads at each concentration of salt precursors in a polymer solution at various concentrations of 10 mM, 100 mM, and 200 mM respectively. It was found that a $Ca_3(PO_4)_2$ characteristic peaks at a concentration of 100mM occur at approximately 31˚ to 35˚, whereas at 200 mM, a $Ca_3(PO_4)_2$ peak gives relatively high signal indicating to the excess amount of $Ca_3(PO_4)_2$. Hence, the 100mM is the optimum concentration for further study by adding PEG.

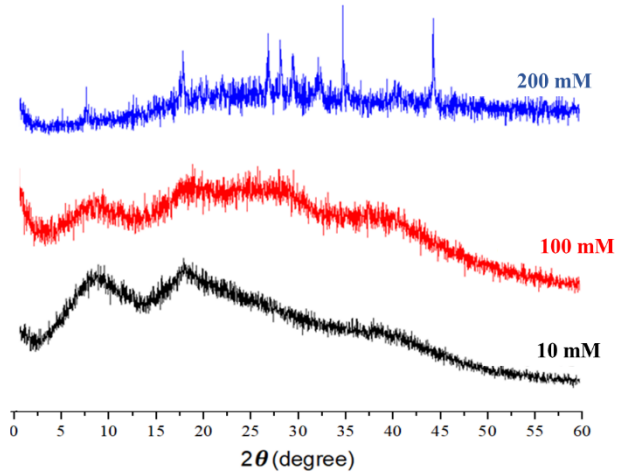

Figure 7. XRD patterns of various concentrations of salts 10, 100, and 200 mM for the reaction of CP-NPs in 1:2 (SA/CS).

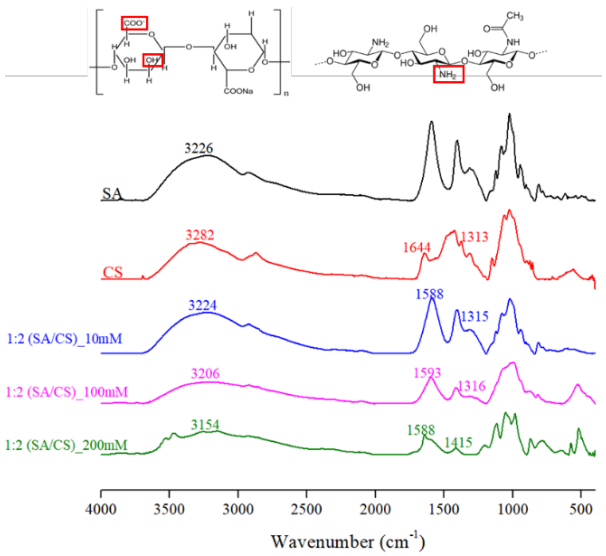

Figure 8. FTIR spectra of various concentrations of salts 10, 100, and 200 mM for the reaction of CP-NPs in 1:2 (SA/CS).

FTIR spectra showed the functional group of polymers and $Ca_3(PO_4)_2$ reaction at the concentrations of 10, 100, and 200 mM as shown in Figure 8. It was found that at the concentrations of 10, 100, and 200 mM, the characteristic peak of

chitosan (CS) of the amide I group occurred at 1644 cm^{-1}, and amide II occurred at 1312 cm^{-1}. The O-H stretching of alginate (SA) appears in the range of 3200-3500 cm^{-1} and -COO occurs in the range of 1650-1850 cm^{-1}. When increasing the intensity of $Ca_3(PO_4)_2$ salts, the peaks of O-H stretching occurred and amide I decreased, but amide II increases due to the interaction between the polymers.[9]

3.3 Effect of concentration of PEG4000 (1, 3, and 5% w/v) on spherical gel beads

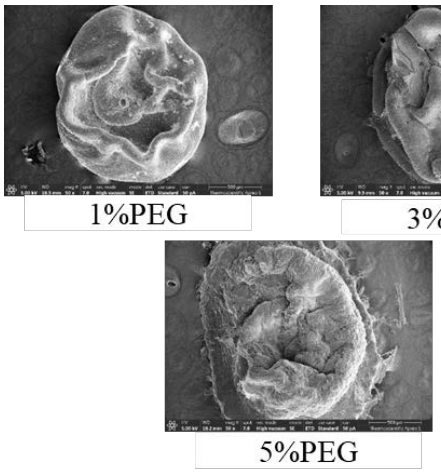

Figure 9. SEM illustrations (50X) of various concentrations of PEG 1, 3, and 5% w/v in 1:2 (SA/CS).

Figure 9 shows the shape and surface of the beads after adding PEG4000 at concentrations of 1%, 3%, and 5% w/v at a magnification of 50X. It reveals that the exterior of the beads would collapse breakdown at a concentration of 1% and a slight collapse of the surface. When the concentration was increased to 3%, it shows more collapsed surface, and the surface area of the beads increases. Particularly, the most collapse of the beads was found in the case of 5% w/v PEG resulting in the highest surface area. Figure 10 showed that when adding PEG at 1% w/v in 1:2 (SA/CS) with adding 200 mM salts, the agglomeration of $Ca_3(PO_4)_2$ particles in a certain area of the surface could be clearly observed. At 3% w/v PEG, $Ca_3(PO_4)_2$ nanoparticles were found to be uniformly distributed on the surface. And at a concentration of 5% w/v PEG, $Ca_3(PO_4)_2$ nanoparticles shows good distribution on the surface.

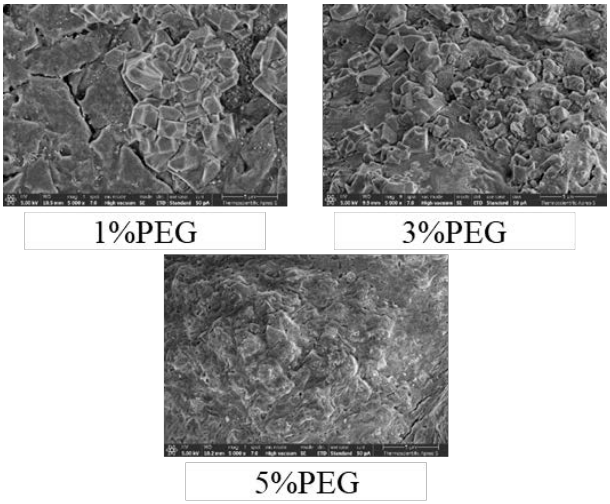

Figure 10. SEM illustrations (5kX) of various concentrations of PEG 1, 3, and 5% w/v in 1:2 (SA/CS) with adding 200 mM salts.

The functional structure of the polymer with polyethylene glycol of 1%, 3%, and 5% w/v in 1:2(SA/CS) gel beads was analyzed by FTIR technique. From Figure 11, it was found that when adding 1%w/v PEG, there was a shift of the O-H stretching signal of alginate (SA) from 3,226-3,252 cm^{-1} and a shift from 1591-1600 cm^{-1} due to asymmetric stretching of C=O and from 1403-1409 cm^{-1} due to symmetric stretching of C=O. For the concentration of 3% w/v PEG, there was a shift of the O-H stretching relative to alginate (SA) from 3,226-3,265 cm^{-1}, while a shift from 1591-1614 cm^{-1} as asymmetric stretching and C=O stretching

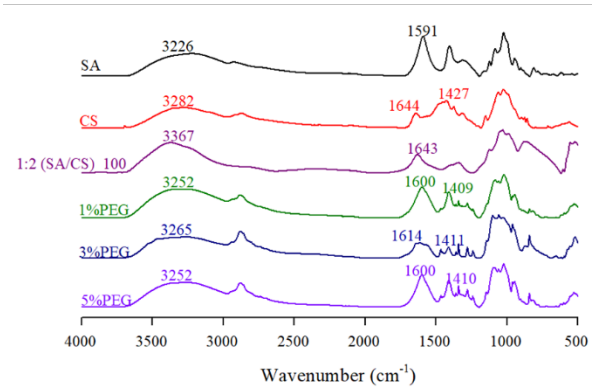

Figure 11. FTIR spectra of various concentrations of PEG 1, 3, and 5% w/v in 1:2 (SA/CS) with adding 100 mM salts.

from 1403-1411 cm^{-1} due to symmetric stretching. In addition, PEG 5% w/v, there was a shift of O-H stretching of alginate (SA) from 3226-3252 cm^{-1} while there was a shift from 1591-1600 cm^{-1} as C=O asymmetric stretching and from 1403-1410 cm^{-1} as C=O symmetric stretching. Therefore, it

can be concluded that after adding PEG4000 at concentrations of 1%, 3%, and 5% w/v. It implied that the O-H and -COO groups in alginate are cross-linked with Ca^{2+} and the peak of 1:2 (SA/CS) with 100 mM salts for CP-NPs reaction compared to the peak after adding PEG. It was found that there was a shift of O-H groups at all concentrations indicating hydrogen bonds between PEG with sodium alginate. With the addition of chitosan, the amide III peak was shifted in all concentrations resulting from the electrostatic attraction occurred after adding chitosan. This is in agreement with the previous report.[9]

3.4 Effect of concentration of TGE (10% and 25%) on spherical gel beads

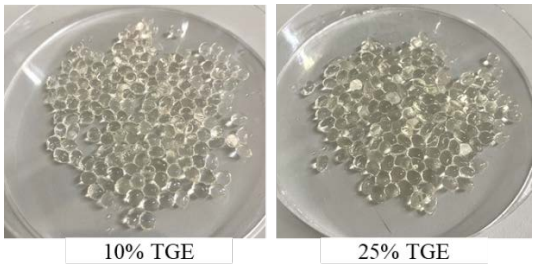

Figure 12. Photos of tranglucosidase immobilized gel beads with 10% and 25% TGE v/v.

Transglucosidase (TGE) immobilizations were studied by adding TGE at the concentration of 10% and 25% v/v. Figure 12 depicts completely spherical beads with 10% TGE while adding 25% TGE shows the imperfect beads.

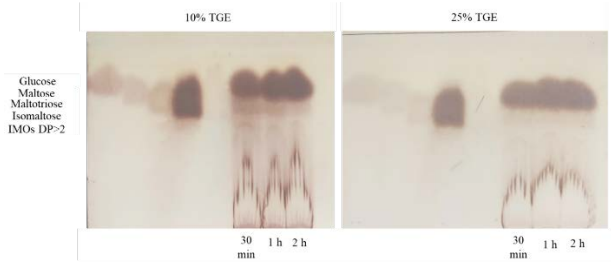

Figure 13. TLC images of sugar analysis from transglycosylation of Homnin rice starch using 10%TGE and 25%TGE gel beads to produce IMO at 30 min, 1 h and 2 h.

In Figure 13, the TLC images show RF of sugar standards including glucose, maltose, maltotriose, isomaltose, and IMOs DP >2 of IMO solution treated by 10%TGE gel beads and 25%TGE gel beads at 30 min, 1 and 2 h. For the preliminary test of the TGE immobilized gel beads on producing IMOs, it was found that the production of IMOs with TGE immobilized gel beads of 10% and 25% concentrations adding in homnin rice maltose solution of approximately 5-10 beads/ml at reaction time 30 min, 1 h, and 2 h at 55℃ pH 5.5. It was found that the band of the oligomers or Isomaltooligosaccharides (IMOs) is lower than that of glucose, maltose, maltotriose, isomaltose, and panose bands. Isomaltooligosaccharides obtained from using immobilized enzymes 10%TGE was clearly higher than that of using 25%TGE. It can be noticed that 25% of TGE beads gave high levels of glucose, maltose, and maltotriose. The TLC provides the limitation of the addition of Transglucosidase loaded in gel beads which should be less than 25% v/v. Furthermore, IMOs production using transglucosidase 10% have good physical characteristics of beads. However, the activity, stability, efficiency and repeatability need to be studied as well as the amount of IMOs production both before and after treated with TGE immobilized gel beads must be further analyzed by high performance liquid chromatography (HPLC). Now, it is on going to be done to compare the influences of free enzyme and enzyme immobilization on synthesis of IMOs for further publication.

4. Conclusion

Biopolymer-inorganic hybrid materials can be used to improve manufacturing processes of IMO production from homnin rice starch. It can be concluded that the polymers are 2% (w/v) alginate, 1% (w/v) chitosan successfully spherical gel bead as 1:2 (SA/CS) combining with disodium hydrogen phosphate and calcium chloride for the reaction of calcium phosphate nanoparticles to a final concentration of 100-200 mM in solution and 5% polyethylene glycol (MW=4000) which showed the perfectly spherical gel beads, good surface roughness, good CP-NPs distribution. The optimized conditions of transglucosidase enzyme immobilization on biopolymer-inorganic hybrid materials were studied to improve the production process of prebiotics from homnin rice maltose syrup. It was found that at 10%TGE gel bead is seem to be better than that at 25% TGE gel beads to produce IMOs. However, the system is being improved and studied further on entrapment efficiency, reusability, and thermal properties in progress.

Acknowledgements

Thank you for the facilities from Naresuan University and financial supported from Fundamental Funds (FF66).

References

1. Gibson, G. R.; Probert, H. M.; Loo, J. V.; Rastall, R. A.; Roberfroid, M. B. *Nutr. Res. Rev.* **2004**, *17* (2), 259-275.
2. Chow, J.J *Ren Nutr* **2002**, *12* (2), 76-86.
3. Zhang, L.; Jiang, Y.; Jiang, Z.; Sun, X.; Shi, J.; Cheng, W.; Sun, Q. *Biochem. Eng. J.* **2009**, *46* (2), 186-192.
4. Liu, X.; Chen, X.; Li, Y.; Wang, X.; Peng, X.; Zhu, W. *ACS Appl. Mater. Interfaces.* **2012**, *4* (10), 5169-5178.
5. Weng, Y.; Ranaweera, S.; Zou, D.; Cameron, A. P.; Chen, X.; Song, H.; Zhao, C.-X. *Food Hydrocoll.* **2023**, *137*, 108385.
6. Liga, B.-C.; Natalija, B. Research of Calcium Phosphates Using Fourier Transform Infrared Spectroscopy. In *Infrared Spectroscopy*, Theophile, T. Ed.; IntechOpen, 2012; p Ch. 6.
7. Wang, J.; Li, W.; Niu, D.; Singh, S.; Lu, F.; Liu, X. *Food Sci. Biotechnol.* **2017**, *26* (3), 731-738.
8. Chen, X.; Fan, M.; Tan, H.; Ren, B.; Yuan, G.; Jia, Y.; Li, J.; Xiong, D.; Xing, X.; Niu, X.; Hu, X. *Mater. Sci. Eng. C.* **2019**, *101*, 619-629.
9. Wang, Y.; Feng, C.; Guo, R.; Ma, Y.; Yuan, Y.; Liu, Y. *Process Biochem.* **2021**, *107*, 38-47.
10. Murata, Y.; Kodama, Y.; Isobe, T.; Kofuji, K.; Kawashima, S. *Int. J. Polym. Sci.* **2009**, *2009*, 729057.
11. Wang, G.; Wang, X.; Huang, L. *Biotechnol. Biotechnol. Equip.* **2017**, *31* (4), 766-773.

Encapsulation of turmeric extracts via complex emulsion-coacervation for active ingredients in dietary supplement foods

Benjakarn Phungphian[1], Phassorn Khumfu[1], Phattaraphon Jampen[1], Waranya Rachayotha[1], and Yupin Phuphuak[1,2,*]

[1]*Department of Chemistry, Faculty of Science, Naresuan University, Phitsanulok 65000, Thailand*
[2]*Center of Excellence in Biomaterials, Faculty of Science, Naresuan University, Phitsanulok 65000, Thailand*

**E-mail: yupinp@nu.ac.th*

Abstract:

Turmeric extract (TME) contains more than 95% curcuminoids, commonly used in foods, beverages, nutraceuticals, and functional foods. In the food industry, Turmeric extract is added to dry powder dietary supplements. However, it tends to be difficult to dissolve in water and has low bioavailability. The objective of this research is to develop a turmeric extract delivery system using emulsion coacervation that has better permeability than free extract for healthy food and nutraceuticals. Research has shown that the ternary phase diagram of the emulsion displays the best conditions: 50% water, 20%-30% coconut oil, and a 1:1 mixture of lecithin and Tween80 resulted in smooth droplet with a size of approximately 399 nm and less than 3 μm. The particles were coacervated with a core emulsion. The optimal formulation, 70/30EMCT/1%wall comprised 50% \water, 30% lecithin and Tween80, and 20% oil. Functional group confirmation of the samples by Fourier Transform Infrared (FTIR) on coacervate particles incorporated with turmeric extract emulsion revealed that the CH stretching, CH stretching, CH stretching, NH and OH stretching peaks confirmed the effectiveness of 70/30EMCT/1%wall formula. This represents an optimized Turmeric extract encapsulation due to the particle size of 378 nm.

1. Introduction

Recently, there has been a growing demand for turmeric herbs in health supplement products, commonly used in powder and capsule forms. However, the issue lies in the poor water solubility and instability of curcumin, a key component of turmeric extracts, particularly in herbal powder formulations. Therefore, it is of great interest to address this challenge by developing innovative nanocapsules for turmeric extract, enhancing its properties for easy absorption into the body.[1, 2]

Turmeric (Curcuma longa L.) possesses pharmacological properties attributed to three bioactives: curcumin (Cur), demethoxycurcumin. (Dmc) and bisdemethoxycurcumin (Bdmc).[3] These curcuminoids exhibit antioxidant activity, anti-inflammatory antimicrobial, anticancer, anti-protozoan, and antienzyme activities with relevance to Alzheimer's disease prevention (anti-Alzheimer activity).[1] In general, curcuminoids are hydrophobic drugs with liposoluble properties, consequently, they exhibit low soluble in the aqueous environment of the human body, which is predominantly composed of water. This characteristic results in limited absorption of curcumin. Therefore, there is a need to develop a drug delivery system capable of effectively delivering active ingredients to cells or organs while controlling their release.

Several strategies have been proposed to address the challenge of incorporating curcumin into food recipes, as outlined earlier. Encapsulation and nanotechnologies have emerged as promising approaches to enhance stability and facilitate the controlled release of active ingredients. Nanocapsules, in particular, offer a means to encapsulate important substances within an inner core, surrounded by a wall made from biopolymers such as lipids, proteins, or polysaccharides.[4] Various methods can be employed for the preparation of these nanocapsules, including precipitation, sol-gel, emulsion, and coacervation. Each method offers unique advantages and can be tailored to achieve a controlled release of curcumin from turmeric extracts through the development of an efficient delivery system, ultimately producing nanoparticles..[5-7]

The purpose of this study is to enhance the delivery properties of turmeric extract by preparing nanoparticles using the nanocomplex emulsion-coacervation method. The appropriation of this preparation method will be assessed through analysis using an optical microscope (OM), dynamic light scattering (DLS), and Fourier Transform Infrared (FTIR).

2. Materials and Methods

2.1 Materials

Turmeric extract (TME) 95% was obtained from Quinn Chem Co Ltd (Q1-FD-CQ8007) Thailand. Virgin coconut oil, extra virgin olive oil, soy lecithin, tween 80 (polysorbate 80), pectin (food additive), whey protein (concentrate), and citric acid (food additive) were purchased from Krungthepchemi. Ethanol 95% was purchased from RCI Labscan.

2.2 Preparation of dissolved turmeric extracts with coconut oil and olive oil

Turmeric extract powder was dissolved in both coconut oil and olive oil at concentrations of 0.01% (5 mg), and 0.03% (15 mg) w/v at room temperature. The solution was then centrifuged at a speed of 3,000 rpm for 5 min to separate the supernatant from the non-dissolved precipitants.

2.3 Emulsion formulations

2.3.1 Simple emulsion preparation

In this study, lecithin (Lc) and Tween 80 (Tw80) were utilized as surfactants to prepare a basic emulsion. The system was investigated under three conditions: lecithin-Tween 80 mixture alone, a 1:1 lecithin-Tween 80 mixture, and solely lecithin as a surfactant. Initially, the surfactant was dissolved in oil phase and thoroughly stirred using stirring rod. Subsequently, the surfactant-dissolved oil was added deionized water contained in a glass flask. The mixture was then stirred vigorously at 1500 rpm using a hot plate magnetic stirrer. Over time, the oil phase gradually dispersed into the water phase. The stirring process continued for 15 minutes, as illustrated in Figure 1(a).

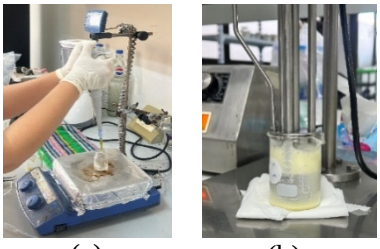

(a) (b)

Figure 1. Pictures of: (a) simple emulsion preparation, (b) emulsion preparation and coacervation with a homogenizer.

2.3.2 Preparing emulsions with a homogenizer

The optimal plain emulsion for each formula was prepared using a Homogenizer at Beauty Cosmetics Co., Ltd., a company specializing in the manufacture and sale of health supplements and cosmetic products. This process, as depicted in Figure 1(b), was selected from Section 2.3.1 and subsequently homogenized. The homogenization process involved adjusting the high speed to 30% kb (approximately 3,000 rpm) for 2 minutes followed by 50% kb (approximately 5,000 rpm) for an additional 2 minutes. Samples were then analyzed by adding 95% ethanol to 10% wt/wt water to compare the effect of co-surfactants on droplet size.

2.3.3 Preparation of complex coacervation (CCT) and complex emulsion-coacervation (EMCT) of turmeric extracts

2.3.3.1 Preparation of stock solution

Polymer mixture solution was prepared as follows:

1) Whey protein was mixed with pectin at a ratio of 4:1 in various concentrations of 2 and 2.5% w/v, and then dissolved in deionized water. The mixture was stirred until fully dissolved, which typically took about 2 h and then refrigerated overnight for hydration. This allowed water to penetrate into the polymer chains before using it as a stock solution for the preparation of the complex coacervation process. This part of the process is referred to as the “wall” of microencapsulation.[8]

2) Turmeric extract was dissolved in coconut oil at a concentration of 0.03% w/v (15 mg), and this solution was incorporated into the emulsion. The emulsion sample chosen for preparation consisted of 50% water, 30% surfactant (Le+Tw80), and 20% oil (EMh-CCO6). This mixture was then homogenized at high speed (approximately 5,000 rpm) following the method outlined in section 2.3.2 referred to as the “core” of microencapsulation.

2.3.3.2 Preparation of complex emulsion-coacervation

The complex emulsion-coacervated samples (EMCT) were prepared by mixing the core and wall solutions in ratios of 60:40 and 70:30 w/w. The mixed solution was then homogenized at a high speed of 30% kb or approximately 3,000 rpm for 2 min and 50% kb or approximately 5,000 rpm for an additional 2 min. Subsequently, the pH of EMCT samples was adjusted to 3 using 0.1 M citric acid, and then the mixture was homogenized again at 50% kb for 2 min. Finally, the samples were centrifuged at a speed of 3,000 rpm to separate the supernatant from the precipitant.

2.3.4 Characterizations of physical and chemical properties

Particle size was analyzed using a zeta-sizer employing dynamic light scattering (DLS) technique to determine the average particle size and particle size distribution in liquids, with a size not exceeding 1,000 nm. It important to note that the particle size obtained from the DLS technique

represents the equivalent particle size of spherical particles. The morphologies of all samples were characterized by an OM or Optical Microscope (Olympus, model DP72). It is a magnifying glass used to look at the surface of a sample at the micrometer level. Look at the physical characteristics on the surface. Look at the crystallinity of the particles. (polarization lens) by looking at size 5 um, while chemical structures were measured by FTIR within the wave number region of 4000-400 cm^{-1}.

3. Results & Discussion

3.1 Physical characterizations of simple emulsion in Pseudo ternary phase diagrams

3.1.1 Simple emulsion preparation using lecithin as a surfactant

Emulsion formulations were investigated using two types of surfactants, lecithin and Tween 80, to create self-emulsions based on surfactant principles and the ratio of water and oil phase. Lecithin and Tween 80 are phospholipids that dissolve better in oil than in water. Therefore, the preparation involved slowly dropping oil in water, which typically results in the formation of small nanoscale micelle droplets with the appropriate composition in emulsion. The crucial factor is the ratio of the three components, which impacts the stability, particle size, and homogeneity of the emulsion formulation.

Through experimentation, it was observed that lecithin was added at a concentration of 10%, the ratios between water, lecithin, and oil at 80:10:10, 70:10:20, and 60:10:30 exhibited clearly separation into water and oil phases. This separation occurred due to an excessive amount of water phase, resulting in low distribution of lecithin micelles and poor dissolution of lecithin. In the ratio of 50:10:40, there was a slight separation of the water phase because the amount of water and oil phase was equal, while the surfactant concentration was lower. This imbalance affected surface tension and micelle formation of emulsion, as illustrated in the pseudo tertiary phase diagram in Figure 2.

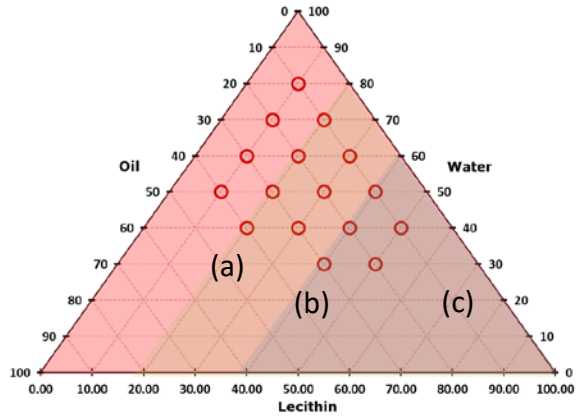

Figure 2. Pseudo ternary phase diagram of the stages of emulsion formation with lecithin: (a) two phases, (b) homogeneous one phase, and (c) three phases separation between water, oil, and lecithin.

3.1.2 Recipe with Tween 80 added to olive oil and coconut oil

Emulsions supplemented with Tween 80 at concentration of 10% and 20% displayed water and oil phase separation, likely due to the insufficient amount of surfactant. Conversely, emulsion containing higher percentages of Tween 80 exhibited a single phase, albeit requiring a significantly larger proportion of Tween 80 compared to the addition of lecithin at low quantities. Observation of the emulsion texture of the revealed homogeneity without phase separation when Tween 80 was added in excess of 30% as depicted in Figure 3.

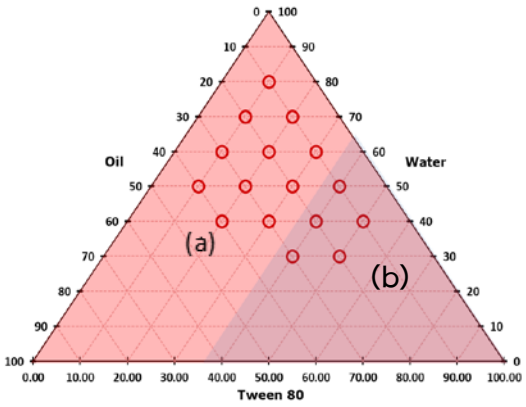

Figure 3. Pseudo ternary phase diagram representing the phases of the Tween 80 emulsion: (a) two phases, and (b) one phase.

3.1.3 Recipe with lecithin mixed with Tween 80 at 1:1 ratio w/w in olive oil and coconut oil

When incorporating lecithin mixed with Tween 80 at concentration of 10% and 20%, separation occurred, mirroring the outcomes observed formulations containing only lecithin, as depicted in Figure 4. Moreover, formulations with

higher proportions of Tween 80 exhibited a smoother texture in the emulsion. However, when an increase in the amount of oil, the emulsion became more viscous, which was deemed undesirable.

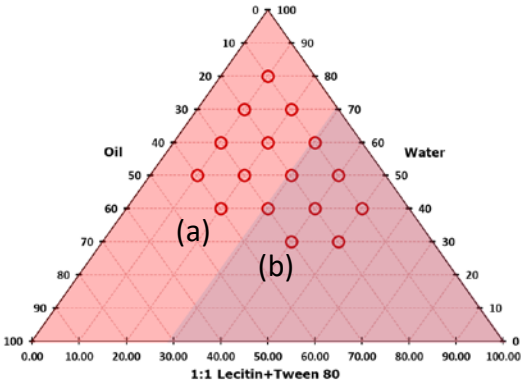

Figure 4. Pseudo ternary phase diagram of the emulsions containing Tween 80 and lecithin: (a) two phases and (b) one phase.

3.2 Emulsion preparation using a homogenizer

As a result of simple emulsion preparation, it was discovered that high proportions of surfactants, particularly Tween 80 and lecithin, hindered the formation of a homogeneous emulsion using homogenizer. Therefore, it became evident that a recipe with lower amount of surfactant was necessary. However, a blend of lecithin and Tween 80 surfactants in specific proportions could still be prepared using high-speed blending as illustrated in Figure 5 (a).

(a) (b)

Figure 5. Characteristics of emulsions with a high concentration of surfactant.

The formula that meets the requirements consists of 50% water phase, 30% Lc + Tw80, and 20% oil w/w. During the emulsion preparation using a homogenizer, 95% ethanol is added as a co-surfactant. As depicted in Figure 5 (b), it was observed that the texture of the emulsion became smoother. This improvement can be attributed to ethanol acting as a potential reducing agent. By dissolving in water, ethanol reduces surface tension, facilitating better blending with the oil and resulting in the greater uniformity in the emulsion.

3.3 Emulsion particle sizes

The particle size of emulsion prepared with both coconut oil and olive oil in the same proportion, along with 95% ethanol co-surfactant, was analyzed using zeta sizer technique (ZS). The results revealed that the emulsion prepared with coconut oil without adding extract (EMh-CCO6) had an average particle size of 389.49 nm and a PDI (polydispersity index) of 0.422 with the addition of extract (EMh-CCO6/TME), the average particle size slightly increased to 399.27 nm, with a PDI of 0.462.

Upon adding co-surfactants to the coconut oil emulsion without extracts (EMh-CCO6/EtOH), the average particle size increased significantly to 562.97 nm, with PDI of 0.454. This indicates that the size increased further with the addition of extracts and co-surfactants (EMh-CCO6/TME/EtOH), lead to an average particle size of 868.462 nm and a PDI of 0.481. Additionally, it was observed that the emulsion prepared with olive oil exhibited larger particle sizes compared to the emulsion prepared with coconut oil as detailed in Table 1.

Table 1. The average particle sizes of emulsions in coconut oil and olive oil.

Entries	Average size (nm)	PDI	SD
EMh-CCO6	389.49	0.422	1.249
EMh-CCO6/TME	399.27	0.467	2.762
EMh_2CCO6/EtOH	562.97	0.454	0.903
EMh-CCO6/TME/EtOH	868.46	0.418	0.753
EMh_OLO6	1631.67	0.602	6.127
EMh_OLO6/TME	798.51	0.570	3.504
EMh_OLO6/EtOH	798.51	0.563	1.717
EMh_OLO6/TME/EtOH	1012.62	0.603	1.625

3.4 Chemical analysis using FTIR

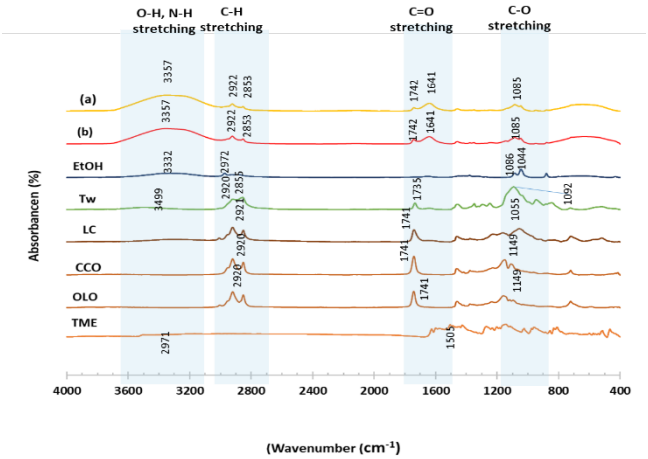

Figure 6. FTIR of emulsion (a) EMh- OLO6/ TME/EtOH, (b) EMh-CCO6/TME/EtOH.

From the results of the FTIR analysis presented in Figure 6 (a-b), the O-H stretching peak appears at 3357 cm^{-1}, indicating the presence of water as a component in the preparation process. The characteristic peaks of C-H stretching, C=O stretching, and C-H stretching are observed at 2922, 1742-1641, and 1085 cm^{-1}, respectively. However, it was observed that the peak corresponding to TME was not visible, which probably attributed to its overlap with another peak. This could be owing to the tiny amount of the extract present in the sample.

3.3 Complex emulsion-coacervation

In this study, whey protein and pectin were utilized as biopolymers to prepare emulsion-coacervation complexes. The process involved pH adjustment to facilitate protein complexation with polysaccharides. It was observed that when the emulsion was added to the water phase system containing a mixture of protein and pectin, high-speed blending was required, often resulting in the generation of excessive bubbles. However, the addition of surfactants to the emulsion led to a decrease in the formation of bubbles. Furthermore, when the pH was adjusted to 3 using 0.1 M citric acid, an increase in the volume of water was noticed. Conversely, when the pH was lowered below 3, the volume of the water phase increased. These findings suggest that complex coacervation occurred at pH 3 as can be seen in Figure 7 (a-b).

(a) **(b)**

Figure 7. Pictures of emulsion-coacervation complexes: (a) after adjusted pH=3 and (b) coacervation precipitate.

Figure 7 (a) depited the color of the emulsion, which appears cloudy. This could be attributed to an improper proportion between the wall and the emulsion, resulting in an overload of the emulsion. Consequently, centrifugation is required to separate the coacervation precipitate, as illustrated in Figure 7 (b).

3.4 Morphology and size of turmeric extract microcapsules

From the characteristics of the turmeric extract microcapsules shown in Figure 8 (c)-(k), it was observed that coacervation occurred at pH 3. The particles appeared to be enveloped with protein and polysaccharides. Compared to the emulsion characteristics depicted in Figure 8 (a)-(b), the coacervation characteristics appeared larger. This observation corresponds to the average size of the coacervation particles.

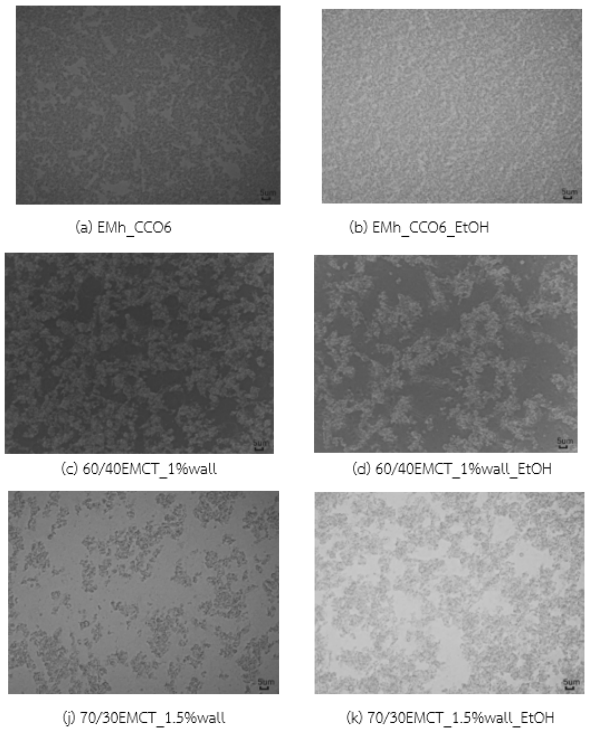

Figure 8. Images of optical microscope of all turmeric extract microcapsules.

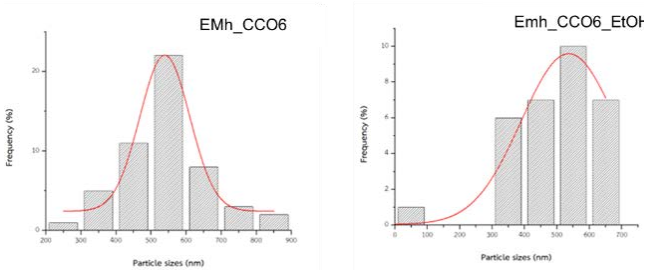

Figure 9. Particle distributions of EMh-CC06 and EMh-CC06/EtOH.

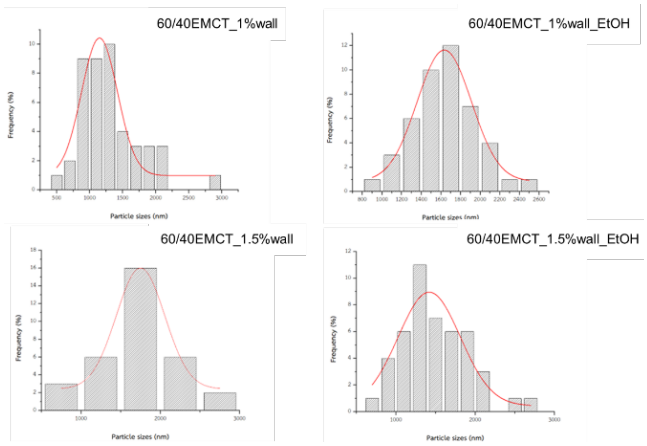

Figure 10. Particle distributions of all turmeric extract microcapsules.

3.5 Particle sizes of complex Emulsion-coacervation

From the results of particle size analysis using the zeta potential analyzer (ZS), which measures the size of particles dispersed in a suspension, it was observed that the microcapsule particles were dispersed in water based on the scattering principle. Interestingly, it was found that the particle size increased when 95% ethanol was added as co-surfactant. This increases in size can be attributed to the insertion of ethanol as a surfactant into the walls of the microcapsule, resulting in a wider area for the capture of substances and an increased ratio of mixing substances in the entire system. Furthermore, it was noted that the emulsions and coacervations at a ratio of 70:30 with a concentration of whey protein mixed with pectin of 1%PT/WP exhibited smaller size compared to those with a concentration of 1.5%PT/WP. Conversely, at a ratio of 60:40 with a concentration of 1% PT/WP, larger particle sizes were observed compared to 1.5%PT/WP, as shown in Table 2.

Table 2. Average particle sizes of emulsions in coconut oil and olive oil.

Entries	Average size (nm)	PDI	SD
6040_1PT/WP_CCO/TME	482.83	0.573	0.419
6040_1PT/WP_CCO/TME_ 10%EtOH	559.16	0.505	0.485
6040_1.5PT/WP_CCO/TME	437.79	0.460	0.381
6040_1.5PT/WP_CCO/TME _10%EtOH	574.53	0.557	1.620
7030_1PT/WP_CCO/TME	378.04	0.529	0.31
7030_1PT/WP_CCO/TME_ 10%EtOH	441.10	0.501	0.78
7030_1.5PT/WP_CCO/TME	665.35	0.541	1.876
7030_1.5PT/WP_CCO/TME 10%EtOH	657.10	0.956	1.625

3.6 FTIR analysis of complexes Emulsion-Coacervation

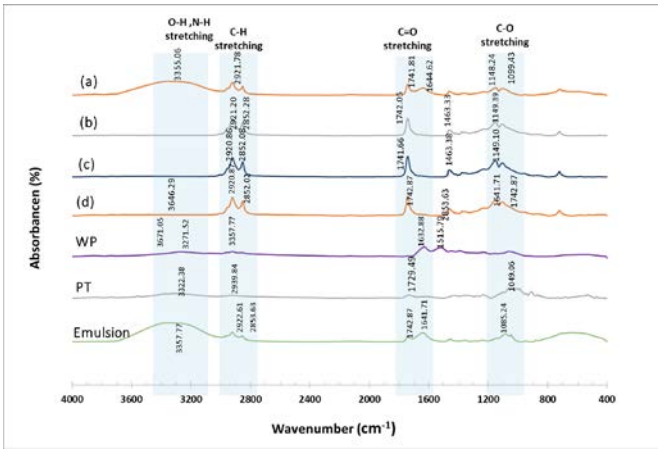

Figure 11. FTIR of coacervation (a) 60/40EMCT/ 1%wall/EtOH, (b)70/30/1%wall/EtOH, (c) 60/ EMCT/1.5%wall/EtOH, (d) 70/30EMCT/ 1.5%wall/EtOH.

From the analysis using the FTIR technique, it was found that in Figure 11 (a), a peak corresponding to O-H stretching appears at the position of 3355 cm^{-1}. This peak indicates the presence of water residue in the preparation process. In addition, signals corresponding to C-H stretching, C=O stretching, and C-O stretching are identified at the position of 2921, 1741, and 1148 cm^{-1}, respectively. Figure 11 (b)-(d) exhibit similar peak positions as they consist of the same compound. However, peaks corresponding to TME are not visible due to overlap with other peaks.

4. Conclusion

The optimum condition for preparing emulsion via a simple method involve a composition of 50% water, 20% coconut oil, and a mixture of lecithin and Tween 80 (1:1) at 30% w/w. This decision was based on achieving a smooth texture and small droplet size of approximately 399 nm, with droplets less than 3 microns in size. The best complex Emulsion-coacervation formulation involved dissolving TME in coconut oil and prepared it with a core-to-wall ratio of 70:30 w/w, adjusted to pH 3. This resulted in particle sizes of approximately 378 nm, smaller than those of other EMCT samples. FTIR analysis of the emulsion-coacervated of TME revealed the peaks corresponding to O-H stretching, C=O stretching, C-O stretching, and NH, indicating successful encapsulation. However, further studies are needed to assess encapsulation efficiency, stability, solubility, and biological activities in future research endeavors.

Acknowledgements

Thank you for the facility from Naresuan University and supporting research fund from Agricultural Research Development Agency (Public Organization) (ARDA), 2023.

References

1. Carpenter, J.; George, S.; Saharan, V. K.*Langmuir* **2019**, *35* (33), 10866-10876.
2. Aditya, N. P.; Aditya, S.; Yang, H.-J.; Kim, H. W.; Park, S. O.; Lee, J.; Ko, S.*Journal of Functional Foods* **2015**, *15*, 35-43.
3. Ang, L. F.; Darwis, Y.; Por, L. Y.; Yam, M. F.*Pharmaceutics* **2019**, *11* (9),
4. Chawda, P. J.; Shi, J.; Xue, S.; Young Quek, S.*Food Quality and Safety* **2017**, *1* (4), 302-309.
5. Mohammadian, M.; Waly, M. I.; Moghadam, M.; Emam-Djomeh, Z.; Salami, M.; Moosavi-Movahedi, A. A.*Food Science and Human Wellness* **2020**, *9* (3), 199-213.
6. Shaddel, R.; Hesari, J.; Azadmard-Damirchi, S.; Hamishehkar, H.; Fathi-Achachlouei, B.; Huang, Q.*Food Hydrocolloids* **2018**, *77*, 803-816.
7. Yadava, S. K.; Basu, S. M.; Valsalakumari, R.; Chauhan, M.; Singhania, M.; Giri, J.*ACS Applied Bio Materials* **2020**, *3* (10), 6811-6822.
8. Reichert, C. L.; Salminen, H.; Badolato Bönisch, G.; Schäfer, C.; Weiss, J.*Colloids and Surfaces A: Physicochemical and Engineering Aspects* **2019**, *561*, 267-274.

Evaluation of total phenolic contents and *in-vitro* antioxidant activity of hemp leaves extracts for its application in cosmetic product

Nutlada Nusontra[1], Chakree Wattanasiri[2], Naphatsorn Ditthawutthikul[3], and Acharavadee Bunkoom[1]*

[1]*School of Science, Mae Fah Luang University, Chiang Rai, Thailand*
[2]*School of Integrative Medicine, Mae Fah Luang University, Chiang Rai, Thailand*
[3]*School of cosmetic science, Mae Fah Luang University, Chiang Rai, Thailand*

**E-mail: acharavadee.pan@mfu.ac.th*

Abstract:

Hemp (*Cannabis sativa L.*) contains cannabidiol (CBD) with lower amount of Δ9-tetrahydrocannabinol compared to cannabis. It also contains terpenoid, flavonoids, and other. These phytochemical compounds have therapeutic effects. Hemp has been utilized for various purposes, including ingredients in cosmetics formulations. Hemp leaves are the main waste of industrial hemp plantation. This study aimed to produce ethanolic extract of hemp leaves using a plant to solvent ratio of 1:10. Ethanolic extract of hemp leaves was investigated and evaluated for it *in-vitro* biological activity focusing on antioxidant activity using 1,1-diphenyl-2-picrylhydrazyl (DPPH) radical-scavenging capacity and hydrogen peroxide (H_2O_2) scavenging method. In addition, total phenolic content expressed as total flavonoids (TFC) content and total tannin content (TTC) of the extracts were studied. The flavonoids total and total tannin amount were analyzed by Folin-Ciocalteu's assay and aluminum chloride colorimetry, respectively. The result showed that hemp extract showed antioxidant activity with the IC_{50} value in DPPH scavenging assay at 0.32±0.05 mg/mL, while Trolox (standard) showed at IC_{50} 3.04±0.05 µg/mL. The H_2O_2 scavenging method showed the hemp extracts IC_{50} value at 0.258±0.034 mg/mL while ascorbic acid (standard) showed 0.131±0.006 mg/mL. Flavonoids content and tannic content were found at 129.90±14.73 mg quercetin equivalent/g and 65.12±9.89 mg tannic acid equivalent/g extract, respectively. Phenolic compounds influence antioxidant activity that can minimize damages of skin cells from oxidative stress. All these results suggested that ethanolic hemp leaves extract can be used as active ingredients in skin care products and use as an alternative source of antioxidant compounds in the cosmetics industry.

1. Introduction

Cosmetics are any product and substance used to improve or enhance the physical appearance of the external part of the human body (skin, hair, nail, etc.) without changing its basic structure. Cosmetics are a mixture of chemical compounds derived from either synthetic and natural source. Nowadays, global market is rapidly changing in natural demand and efficient ingredients for skin care developing[1,2], then interest in herbal cosmetics is increased.

Several Thai herbs are used as an ingredient in cosmetic. For example, kaffir lime, aloe vera, turmeric, and etc.,[3–6]. Hemp (*cannabis sativa L.*) also found as an ingredient in cosmetic product, hemp is used for benefit the skin as a moisturizing, repairing, brightening, and acne treatment[7].

In 2018, Thailand legalized medicinal cannabis, allowing for the controlled cultivation and use for cannabis medicinal purpose, including hemp plant. Hemp belongs to Cannabaceae family, it is known for its abundance in cannabidiol (CBD) with small amount of tetrahydrocannabinol (THC) compares to cannabis[8].

Hemp leaves extracts contain cannabinoids, they are a class of the chemical compound that has various therapeutic effect[9]. Cannabinoids have potential to use as an active ingredient applied in cosmetic product due to antioxidant activity which can provide various benefit to the skin. Moreover, natural extracts also found common secondary metabolite compounds which are flavonoids and tannin. These compounds are well known as antioxidant agents. Natural antioxidant mixture found in hemp leaves extracts would have synergic effect that can show better antioxidant activity and less harmful effect. Skin cell components can be damage by interaction with reactive oxygen species (ROS) and free radical. These can affect internal and external skin, leading increase skin aging, appear wrinkle, dryness of the skin. Antioxidants compound found in hemp leaves extracts might have ability to minimize cell damage from ROS and free radical that can improve skin appearance and reduce the sign of skin aging.

This study aims to extract hemp leaves and investigate cannabinoids, flavonoids, and tannin contents in hemp extracts, and evaluate antioxidant properties to use hemp extracts as an active

ingredient loaded into skin care product. This can increase the value of hemp leaves and use as alternative source in cosmetic industry.

2. Materials and Methods

2.1 Materials

Leaves of *cannabis sativa L.* were harvested on August, 2023 from Rungreungkunpanit co., LTD., Thailand. 95% ethanol were purchase from L PURE (Chiang Mai, Thailand). Tannic acid was from Tokyo Chemical Industry. Sodium Nitrite and Folin-Ciocaltue's reagent were derived from LOBO CHEMIE PVT. LTD. Aluminium chloride hexahydrate and 2,2-Diphenyl-1-picrylhydrazyl were from Sigma-Aldrich company.

2.2 Extraction of *cannabis sativa L.* leaves

Fine dried hemp leaves were used to prepare hemp leaves extracts. Ethanol is used as a solvent for extraction. The plant materials were maceration in ethanol in 1:10 ratio for 24 hours, 3 days. The extracted were collect by the filtration and concentrated.

2.3 Determination of chemical composition of *cannabis sativa L.* leaves extracts by LC-MS

Hemp extracts were transferred to a glass vial with a syringe and 0.45 µM nylon syringe filter before liquid chromatography–triple quadrupole mass spectrometry (LC-QqQ) analysis. The method was conducted following[10]. Injection volume uses 20 µL. C18 column was used, the column temperature was maintained at 35◦C. Flow rate was using 0.5 mL/min at 35◦C. Mobile phase: The mobile phases were water (phase A) and methanol (phase B); both contained 0.1% formic acid and 2 mM ammonium formate. The method running by gradient elution: 60% - 90% (B) from 0 to 7.00 min. 90% (B) from 7.00 to 9.00 min. 90% - 60% (B) from 9.00 to 9.50 min. 60% (B) from 9.50 to 13.00 min. Total running time is 13 min.

2.4 Evaluation of polyphenolic content

2.4.1 Total flavonoid content

Total flavonoid content (TFC) was analyzed by aluminum chloride colorimetry followed by the modified method[11]. A solution of 15% w/w sodium nitrite ($NaNO_2$) was introduced by adding 15 µL to 100 µL of diluted plant extracts, and the mixture was left to incubated for 6 mins at room temperature. Following this, 15 µL of 15% w/w aluminum chloride ($AlCl_3$) solution was added to the mixture, and the reaction was allowed to proceed for another 6 mins at room temperature. Subsequently, 70 µL of 8% w/w sodium hydroxide (NaOH) solution was introduced into the reaction, and the mixture was further incubated in the dark room for 15 minutes. The absorbance of solution was measured at 510 nm. Quercetin is used as standard (0.01-3.0 mg/mL) TFC of each sample was quantified and expressed as milligrams quercetin equivalent per gram extracts (mg QE/g extracts).

2.4.2 Total tannin content

The determination of Total tannin content (TTC) followed a modified method based on a previous study that utilized Folin-Ciocalteu phenol reagent[12]. In this process, 20 µL of diluted plant extracts was combines with 100 µL of 0.2 N Folin-Ciocalteu phenol reagent in 96-well plate and the mixture allowed to incubated for 4 mins at room temperature. Following this, 80 µL of 7.5% sodium carbonate (Na_2CO_3) solution was added. The reactions mixtures were then incubated in a dark place for 2 hours. The absorbance of each sample was measured at a wavelength 725 nm. Tannic acid is us as standard (0.01-1.0 mg/mL). TTC of each sample was quantified expressed as milligrams tannic acid equivalent per gram extracts (mg TAE/g extracts).

2.5 Analysis of antioxidant activities

2.5.1 DPPH-radical scavenging activity

2,2-Diphenyl-1-picrylhydrazyl (DPPH) scavenging of hemp extracts was determined by modified following[13]. 100 µL of 1.0 mg/mL of sample hemp leaves extracts in ethanol was mixed with 100 µL of 60 µM DPPH solution in 96-well plate and incubate in the dark place for 30 min. Then, the absorbance was measure at 517 nm. All measures were done in triplicate. Trolox is used as a standard (0.0003-0.0075 mg/mL). All test were done triplicate. DPPH activity of hemp leaves extracts was calculation following equation:

$$Inhibition\ (\%) = \frac{ABScontrol - ABSsample}{ABScontrol} \times 100 \quad \text{(eq.1)}$$

2.5.2 Hydrogen peroxide Scavenging activity

Hydrogen peroxide (H_2O_2) scavenging activity was investigated by a modified method described in the previous study[14]. A solution 40 mM hydrogen peroxide was prepared in deionized (DI) water then mixed with 1 mL of diluted hemp extracts in ethanol. Reaction was incubated in a dark place for 10 mins. The absorbance of the solution was measured at 230 nm. Ascorbic acid is used as standard (0.005-0.25 mg/mL) and DI water as a control. All test were done triplicate. Percentage inhibition can calculate as equation 1 (eq.1).

3. Results & Discussion

3.1 Chemical composition of cannabis sativa L. leaves extracts

Hemp extract was analyzed chemical constituents by liquid chromatography-mass spectrometry quadrupole triples quad (LC-QqQ). The result summarized in **Table 1.** The main chemical compound found in hemp extracts are cannabinoids group. There is cannabinol (CBD) and cannabigerol (CBG) also known as non-psychoactive compound. Moreover, they also founded the psychoactive contents which are tetrahydrocannabinol (THC), tetrahydrocannabi-nollic acid (THCA-A), and tetrahydrocannabivarin (THCV). The quantification of hemp extract will further study.

3.2 Polyphenol content of hemp extracts

Total flavonoids and tannin content of hemp extracts are 129±14.73 mg QE/g extracts and 65.12±9.89 mg TAE/g extracts. Flavonoids and tannin categorized as secondary metabolites commonly found in plant that potent antioxidant activity due to the presence of one or more hydroxyl group on their aromatic ring confer scavenging ability[15]. These natural antioxidant agents help to promote positive effect to human health, non-harmful, and being used in the cosmetic industrial because they retard oxidative stress and improve skin appearance. From this result, the antioxidant activities were used to study the biological activities of hemp extracts.

3.3 Antioxidant Activities

DPPH radical scavenging refer to the ability of substance to neutralize DPPH radical. Hemp extracts has antioxidant properties, it can donate electron or hydrogen atom to DPPH radical and convert them in to non-radical form. The percentage inhibition of Trolox and hemp extracts shown in **Figure 1**. Standard Trolox shown IC_{50} at 3.04±0.05 µg/mL while hemp extract shown at IC_{50} 0.32±0.05 mg/mL.

Table 1. Qualification of chemical composition of 0.1 mg/mL hemp extracts.

No.	Structure	Name	Molecular Weight (g/mol)	Appearing (m/z)	Area	Height
1	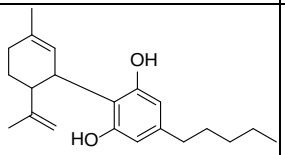	Cannabidiol (CBD)	314.47	315.0>193.05	271953063	19971418
2	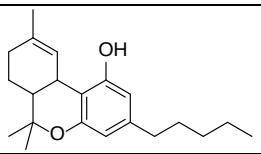	Tetrahydrocannabinol (THC)	314.45	315.10>193.05	265868939	19971462
3	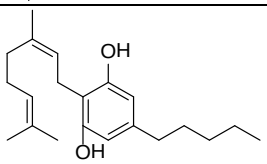	Cannabigerol (CBG)	316.48	317.10>123.05	14427702	1484381
4	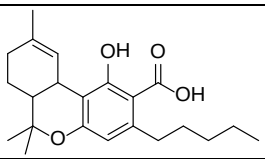	Tetrahydrocannabi-nolic acid (THCA-A)	358.478	359.10>341.15	3597085	386351
5	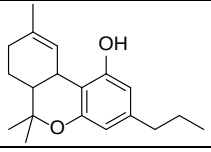	Tetrahydrocannabiva-rin (THCV)	286.4	287.05>231.05	6847554	764240

H_2O_2 is a reactive oxygen species that can produce in the body and it involves in oxidative stress that can lead to damage of cell and tissues. Antioxidant agent help to neutralize and eliminate H_2O_2. Hemp extracts able to scavenge hydrogen peroxide which can prevent oxidative stress-related damage. Hydrogen peroxide scavenging activity of ascorbic (standard) shown IC_{50} 0.131±0.006 mg/mL and hemp extract at IC_{50} 0.258±0.034 mg/mL as shown in **Figure 2**.

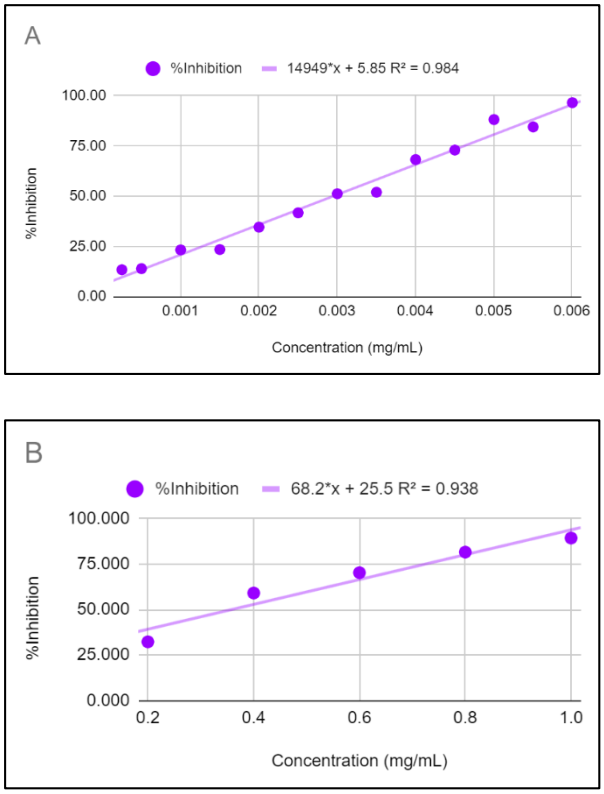

Figure 1. Antioxidant activity of *cannabis sativa L.* leaves extracts on DPPH radical scavenging activity of Trolox (A) and extracts (B).

Hemp extracts has antioxidant activity due to they contain abundant of cannabinoids chemical compound, the primary cannabinoids are THC and CBD. Phyto-cannabinoids has potential antioxidant properties because presence of phenolic structure which is resonance structure and has hydroxyl group of phenyl rings[16]. In addition, flavonoids and tannin group also effect on antioxidant activity of hemp extracts. Extracts contain a mixture of natural antioxidant compound that could have synergic effect, so they would show better pharmacological activity and less toxicity[17].

Imbalance of redox reaction leading oxidative stress condition that cause injury of cellular components such as protein, lipid, DNA, and lead to cell death. The most importance processes are lipid peroxidation, it directly affects both functional and structural of cell membrane, resulting in disorder of cell and cause many diseases[18].

Human skin cell has its own defense mechanism. But under imbalance of oxidant and antioxidant, ROS/free radicals can affect skin cell, the interact of ROS/free radical and skin cell would be generate biochemical transformation in collagen, elastin, and connective tissue. Theses transformation can affect skin elasticity and firmness, appear wrinkle and fine line, cause acne, and making the skin dry. Hemp extract contained antioxidant compound that can reduce the level of oxidants level to balance the redox reaction by delay or minimize propagation and initiation of chain reaction, capture or transform radical into less active form, which can benefit to the skin cell by improve the appearance of skin, reduce the wrinkle, and etc.

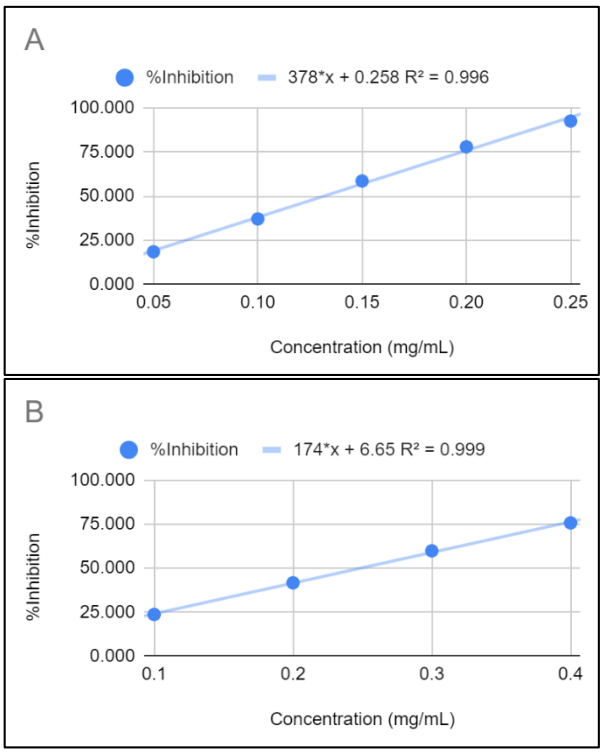

Figure 2. Antioxidant activity of *cannabis sativa L.* leaves extracts on hydrogen peroxide scavenging activity of ascorbic acid (A) and extracts (B).

Hemp extracts could be using as natural active ingredient in cosmetic product which can benefit to the skin due to its potential antioxidant activity. The formulation of cosmetic product with hemp extracts loaded will further study.

4. Conclusion

As a conclusion, ethanolic extracts of *cannabis sativa L.* leaves showed potential antioxidant on DPPH radical and hydrogen peroxide scavenging activity. Extracts contain cannabinoids, flavonoids, and tannin as the active phytochemical. The results of the study demonstrated that the *cannabis sativa L.* leaves extracts can be use as alternative source of natural antioxidant in cosmetics industry.

Acknowledgements

The author would like to thank Mae Fah Luang University and School of Science for support chemical, material, and instruments used in this study. Moreover, we would like to thank Rungreungkunpanit co., LTD. For supporting the plant materials.

References

1. Pimentel, F. B.; Alves, R. C.; Rodrigues, F.; Oliveira, M. B. P. P. *Cosmetics.* **2018**, *5*, 2.
2. Resende, D. I. S. P.; Ferreira, M.; Magalhães, C.; Sousa Lobo, J. M.; Sousa, E.; Almeida, I. F. *Algal Res.* **2021**, *55*.
3. Fortin, H.; Vigor, C.; Lohézic-Le Dévéhat, F.; Robin, V.; Le Bossé, B.; Boustie, J.; Amoros, M. *Fitoterapia*. **2002**, *73* (4).
4. Rafiq, S.; Kaul, R.; Sofi, S. A.; Bashir, N.; Nazir, F.; Ahmad Nayik, G. *Saudi Soc. Agric. Sci.* **2018**, *17*, 351-358.
5. Tunjung, W. A. S.; Cinatl, J.; Michaelis, M.; Smales, C. M. *Procedia Chem.* **2015**, *14*.
6. Heng, M. C. Y. *Int. J. Dermatol.* **2010**, *49*, 608–622.
7. Martins, A. M.; Gomes, A. L.; Boas, I. V.; Marto, J.; Ribeiro, H. M. *Pharmaceuticals*. **2022**, *15* (2), 210.
8. Morales, P.; Reggio, P. H.; Jagerovic, N. *Front. Pharmacol.* **2017**, *8*, 422.
9. Iffland, K.; Grotenhermen, F. *Cannabis Cannabinoid Res.* **2017**, *2* (1), 139–154.
10. Galant, N.; Czarny, J.; Powierska-Czarny, J.; Piotrowska-Cyplik, A. *Molecules.* **2022**, *27* (23).
11. Ardestani, A.; Yazdanparast, R. *Food Chem.* **2007**, *104* (1).
12. Son, D. H.; Nam, M. H.; Hong, C. O.; Seol, H. M.; Yang, J. E.; Kim, Y. B.; Kim, C. T.; Lee, K. W. *Biosci. Biotechnol. Biochem.* **2013**, *77* (4).
13. Molyneux, P. *SJST.* **2004**, *26* (2).
14. Gülçin, I.; Alici, H. A.; Cesur, M. *Chem Pharm Bull*. **2005**, *53* (3).
15. Hässig, A.; Linag, W. X.; Schwabl, H.; Stampfli, K. *Med. Hypotheses*. **1999**, *52* (5).
16. Borges, R. S.; Batista, J.; Viana, R. B.; Baetas, A. C.; Orestes, E.; Andrade, M. A.; Honório, K. M.; Da Silva, A. B. F. *Molecules*. **2013**, *18* (10), 12663-12674.
17. Chermahini, S. H.; Adibah, F.; Majid, A.; Sarmidi, M. R. J. *Med. Plant Res.* **2011**, *5* (14).
18. Gaschler, M. M.; Stockwell, B. R. *Biochem Biophys Res Commun.* **2017** *482*, 419-425.

Evaluate the green tea quality through post-fermentation utilizing *Eurotium cristatum*

Daria Hayesalea[1], Antikan Klomchit[1], Phattharasaya Rattanawongkun[2], Nattakan Soykeabkaew[2], and Siraprapa Brooks[1]*

[1]*School of Science, Mae Fah Luang University, Chiang Rai 57100 Thailand*
[2]*Center of Innovative Materials for Sustainability (iMatS), School of Science, Mae Fah Luang University, Chiang Rai 57100 Thailand*

**E-mail: siraprapa.bro@mfu.ac.th*

Abstract:

Green tea is known for its rich content of polyphenols such as catechin and gallic acid. Epigallocatechin-3-gallate (EGCG) is the most common group of catechin found in green tea and is associated with numerous health benefits. However, EGCG is considered to increase the bitterness and astringency of green tea. *Eurotium cristatum* is commonly used in Fuzhuan brick tea and plays a significant role in the post-fermentation process of dark tea. Thus, this study aims to improve the flavor and aroma of green tea through post-fermentation of green tea with *E. cristatum*. The *E. cristatum*, was isolated from a briquette of Fuzhuan brick tea. The species identification was done based on morphological and molecular phylogenetic analysis. Green tea was packed into a brick shape with a density of 0.25 and 0.35 g/cm^3 using a compression molding technique before being sprayed with a spore suspension of *E. cristatum*. The quality of tea was evaluated after two weeks of incubation at 28°C. The caffeine levels increased in both treatments inoculated with fungi while the levels of catechin and gallic acid were decreased. In BT01, catechin content measured at 2.44±0.35, compared to 3.49±0.35 in control1. The gallic acid content was 10.77±0.16 and 15.58±1.59 mg/kg in BT02 and Control2, respectively. Moreover, the principal component analysis revealed a significant difference in overall organic and volatile compounds between the two treatments. The sensory test also confirmed that *E. cristatum* had a beneficial effect on the quality of green tea as less bitterness and strong honey test notes were present in tea that was post-fermented with this fungus strain.

1. Introduction

Besides water, another frequently consumed beverage worldwide is tea. As an extract made from the leaves of the tea plant, *Camellia sinensis* has high concentrations of flavonoids and other antioxidants with posited beneficial properties.[6] The biological property of tea is closely linked to its polyphenol content, including flavonoids, catechins, and tannins, as well as caffeine. Phenolic compounds exert various health-promoting properties, ranging from free radical scavenging to antivirus and anticancer effects.[7] The different processes of drying and fermentation determine its chemical composition.

In general, there are four types of tea based on processing or harvested leaf development including black (fermented), green (non-fermented), oolong (semifermented) and Fuzhuan brick tea (FBT) (post-fermented).[6] FBT a type of microbial fermented and unique brick-shaped tea. FBT is raw black matured tea leaves. The general steps for manufacturing this kind of tea include panning, rapid pile-fermentation, rolling, drying, softening with steam, piling, partitioning, tea-brick pressing, fungal fermentation, drying, and packing.[13] The health-promoting functions of this tea, such as its anti-obesity, hypolipidemic, and antiproliferation could be attributed to the participation of microorganisms found in solid-state fermentation. Several microorganisms such as *Candida albicans*, *Candida famata*, *Eurotium cristatum*, *Aspergillus niger*, and *Aspergillus sydowii* have the potential to reduce caffeine content through inoculated and converting caffeine to theophylline.[14]

The *Eurotium cristatum*, a fungus commonly found in FBT, plays a significant role in the fermentation process of post-fermented dark tea. This fungus secretes extracellular enzymes during fermentation, which influence the metabolism of chemical compounds in tea leaves and, consequently, impact the quality of FBT).[13] Moreover, the fungus secretes various extracellular enzymes e.g. Polyphenol oxidase (PPO), cellulase, pectinase, and proteinase to degrade and transform polysaccharides, polyphenols, protein, and cellulose which results in producing aroma, taste, and health-benefit compound.[11]

The bitterness and astringency of green tea are closely associated with the catechin content. To enhance the taste of autumn green tea, efforts have been made to reduce catechin levels.[12] improved the sweetness and overall acceptability of green tea infusion by hydrolyzing EGCG and ECG with tannase. These methods effectively reduced bitterness and astringency in autumn green tea, and there's a need for further development of techniques to enhance its overall quality, encompassing taste and aroma. Since, *E. cristatum* shows promise in altering phenolic compounds and

decreasing catechin levels, indicating its ability to mitigate the bitterness and astringency of autumn green tea potentially.

Therefore, this study aims to utilize *E. cristatum* in fermenting Chiang Rai's local green tea. In addition, the tea's quality particularly chemical composition and sensory test were evaluated in this study.

2. Materials and Methods

2.1 Isolation of fungi

Compressed FBT tea samples were loosened with the help of a mortar and pestle. FBT tea sample was placed on the Potato Dextrose Agar (PDA), and the agar plates were incubated at 25–28°C for 3 days. Mycelium growing from tea leaves was transferred to a new Sabouraud Dextrose Agar (SGA) plate until a pure strain was obtained.

2.2 Identification of new fungal strain

Morphological and molecular identification: isolated strains were cultured on PDA and Czapek's agar (CA) using a two-point inoculation method and were also cultured in an incubator at 28°C to observe whether they could grow at this temperature. The reproductive structures were examined by a compound microscope and a stereo microscope.

The extraction of total DNA from fungal biomass was performed using the Genomic DNA Isolation Kit (BIO-HELEX CO., LTD., Taiwan). Polymerase chain reaction (PCR) was carried out using a set of PCR master mix reagents (Promega Go Taq™, USA). The final volume of the 25 µl PCR mix included 12.5 µl of 2X PCR Master Mix, 9.5 µl of nuclease-free water, 1 µl of each of the primers (ITS1/4, β-tub and RPB2) and 1.0 µl of DNA template. Fungal primer sets and thermocycling programs as described in Efimenko, T. A., et al., (2021).[5] The amplification products were purified by PCR clean-up and gel extraction kit (BIO-HELEX CO., LTD., Taiwan) and visualized on a 1% agarose gel at 100V for 30 min. Samples were submitted for Sanger sequencing at SolGent Co., Ltd. (Daejeon, Korea).

The sequences were searched by Basic Local Alignment Search Tool (BLAST) in the National Center for Biotechnology Information (NCBI) database. Sequences were inspected and assembled in BioEdit v.7.1.8, sequence alignments were performed using the FFT-NSi strategy implemented in MAFFT v.7 and maximum likelihood (ML) trees were constructed with FigTree v.1.4.4.[2]

2.3 Microbial culture

Selected strains were sub-cultured in PDA medium at 28ºC for 10 days and then inoculated ten pieces (0.5 x 0.5 cm^2) of mycelia agar plugs in 500 mL Erlenmeyer flasks containing 300 mL potato dextrose broth (PDB) medium. Broth cultures were incubated at 28ºC for 2 weeks under static conditions. After that fungal mycelium was separated by using sheet cloths then pre-freeze by storing in a -80ºC refrigerator for 1-2 h and then freeze-dried. The temperature of the condenser was approximately -80ºC and the chamber pressure and approximately 1 mbar. After 24 h, the fungal samples were ground by mortar and pestle.

2.4 Fuzhuan brick tea processing

The primary processing process was done by mixing fresh tea leaves with shoot (appropriate ratio: leave 80% and shoot 20%). A conventional tea process was performed following enzyme inactivation, first rolling, file fermentation, and second rolling. The reprocessing process was done following the step of steam pilling (102ºC for 35 min), and pile fermentation (80-88ºC for more than 2 h). Tea was compacted shaped and pressed into moderate tightness brick with two different densities, BT02 (0.25 g/cm^3) and BT01 (0.35 g/cm^3) into moderate tightness brick. Fungus fermentation was done by spraying a spore of fungal suspension ($6x10^5$ CFU/mL) into tea brick and was incubated at 28ºC for 16 days. Control treatment was done with a spray of sterile water.[8]

2.5 Determination of tea quality

2.5.1 Analysis of caffeine, catechins, and gallic acid by high-performance liquid chromatography (HPLC).

A ground tea sample (0.5 g) was extracted with 5 mL of 70% methanol by Sonicator bath at room temperature for 30 min. The sample solution was filtered through a 0.22-µm nylon membrane and analyzed by a Thermo Ultimate 3000 HPLC system with an Ultimate 3000 diode array detector (Thermo Fisher Scientific, Waltham, MA, USA) and an Inertsil ODS-4 column (4.6 mm × 250 mm × 5 µm; GL-science Inc., Tokyo, Japan). The gradients using eluent A (ultrapure water-0.1% formic acid) and eluent B (methanol) were programmed as follows: 5–22% B at 0–5 min, 22% B at 5–20 min, 22–24% B at 20–35 min, 24–25% B at 35–45 min, 25–40% B at 45–50 min and 40–45% B at 50–60 min. The UV detection wavelength was 280 nm and the column temperature was 30ºC. The flow rate was 0.8 mL min^{-1}, and the injection volume was 1.0 µl, 15 min.[13]

2.5.2 Analysis of volatile compounds by gas chromatography mass spectrometry (GCMS)

A ground tea sample (2.0 g) was brewed with 5 mL of boiling water in a 20 mL headspace vial and equilibrated at 60ºC for 30 min. Volatile compounds were then extracted at 60 ºC for 30 min using a 50 µm solid-phase microextraction (SPME) fiber coated with divinylbenzene/car boxen/poly-dimethylsiloxane (DVB/CAR/PDMS) (Supel co, Sigma Aldrich, St Louis, MO, USA). The GC-MS analysis was performed by a GCMS-QP2010 SE instrument (Shimadzu, Kyoto, Japan) operated at 70 eV over 35 to 400 amu. Volatiles were desorbed into the gas chromatography (GC) injector at 325ºC for 5 min, and were separated with an RTX-5Sil MS capillary column (30 m × 0.25 mm × 0.25 µm) at the programmed temperatures: an initial temperature of 40ºC for 3 min; raised to 85ºC at 3ºC min^{-1}, and held for 3 min; then increased to 160ºC at 3ºC min^{-1}; and finally increased at 10 ºC min^{-1} to 240ºC and held for 5 min. The temperatures of the interface port from GC to MS and iron source were 280ºC and 230ºC, respectively. Helium (>99.99%) was used as carrier gas at 1.0 mL min^{-1}. The identification of volatiles was performed by searching the National Institute of Standards and Technology MS data library (NIST14s). The relative proportions of volatiles were obtained by peak area normalization and the results were expressed as the ratio of a single constituent area to the total.[13]

2.5.3 Analysis of organic acid by liquid chromatography mass spectrometry (LCMS).

A ground tea sample of 0.5 g was extracted with 5 mL of 50% methanol by Sonicator bath at room temperature, 30 min, and the sample solution was filtered through a 0.22-µm nylon membrane and analyzed by using the LCMS-9030 or LCMS-9050 quadrupole time-of-flight (Q-TOF) mass spectrometer (Shimadu Corporation, Japan) and an Inertsil ODS-4 column (4.6 mm × 250 mm × 5 µm; GL-science Inc., Tokyo, Japan). The gradients using eluent A (ultrapure water-0.1% formic acid) and eluent B (methanol) were programmed as follows: 5–22% B at 0–5 min, 22% B at 5–20 min, 22–24% B at 20–35 min, 24–25% B at 35–45 min, 25–40% B at 45–50 min and 40–45% B at 50–60 min. The UV detection wavelength was 280 nm and the column temperature was 30ºC. The flow rate was 0.8 mL min^{-1}, and the injection volume was 1.0 µl.[13]

2.6 Sensory analysis

Tea leave was washed with water for 40 mins. One gram of tea leave was sieved in 100 mL of RO water (TDS10, 95ºC) for 3 mins. Sensory evaluation in for fragrance, flavor, and color was conducted with the use of the ranking test. The tea quality was estimated and scored by five professional tea tasters, from Chiang Rai provinces.

2.7 Statistical analysis

Data presentation and statistical analysis of tea quality showed all results are expressed as means ± standard deviations. The statistical significance was analyzed by a one-way ANOVA and was evaluated by Duncan's test ($P < 0.05$) using SPSS 20.0 software (SPSS Inc., Chicago, IL, USA). Orthogonal principal components analysis (PCA), partial least squares discriminant analysis (PLS-DA), dendogram and heatmap were performed with Statistical Analysis by MetaboAnalyst (R:https://github.com/xia-lab/MetaboAnalystR). Hierarchical clustering analysis (HCA) was performed with an environment (http://www.r-project.org/) using the heatmap package.[13]

3. Results & Discussion

3.1 Morphological and molecular identification

The phylogenetic tree shows that the fungus strain *E. cristatum* was clustered in the same group of *Eurotium* sp. and *Aspergillus cristatus*. The complexity between this group was also reported in Xiao, Y., et al., (2020).[13] based on morphological and molecular characteristics was identified as *E. cristatum*. In particular, the genus *Eurotium* is the teleomorph of *Aspergillus*, and the nomenclature of *E. cristatum* (*A. cristatus*) is more widely accepted nowadays to avoid nomenclatural confusion. Figure 2 shows the morphology of *E. cristatum*, after incubation in media for 3 days, colonies grown on CA and PDA had diameters of 16 and 14 mm, respectively. At 17 days, the diameters of colonies on CA and PDA reached 28 and 24 mm, respectively. The morphology of the colonies on both media was similar. They had a sub-circular shape with a central bulge and were granular-shaped due to the abundant production of ascomata. They were slightly sulcate, with a gold-yellow color, then changed to sand color when mature. Yellow pigments were produced and abundant, no exudates were seen and colonies on PDA had a coarser surface than those on CA. Micromorphological observation of a fungus revealed unique features of *Eurotium* species. The fungus displayed smooth conidiophore stalks, translucent and divided hyphae with asymmetric branching, round to slightly round vesicles that were fertile, and flask-shaped phialides arranged in a single layer. Conidia were observed budding from mature phialides, with some forming chains.

Although, the DNA data was perplexed between two species but the morphology of fungal strain shows similarity to *E. cristatum* compared to *A. cristatus*. Thus, we identified this strain as *E. cristatum*.

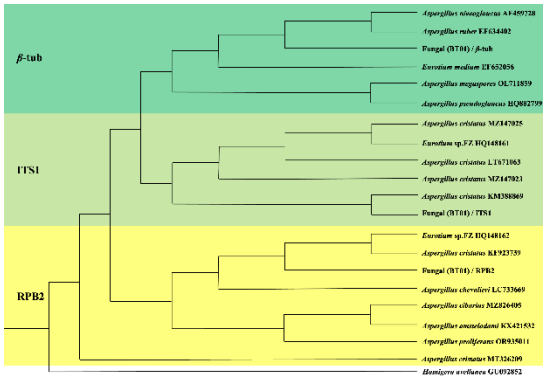

Figure 1. Phylogenetic tree of *E. cristatum* isolated from Pingwu Fuzhuan brick. The tree is rooted with *Hamigera avellanea* NRRL 1938^{T}

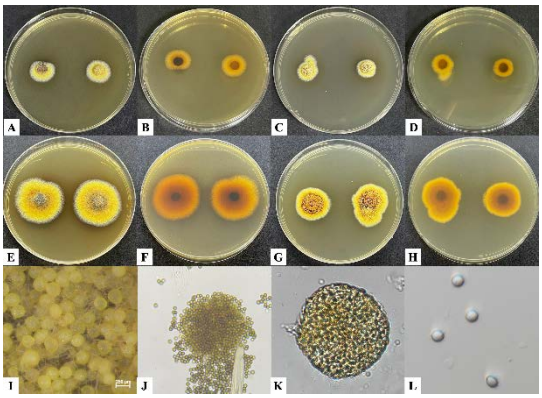

Figure 2. Morphological features of fungus strain *E. cristatum*; (A, B, C, D): colonies after 3 days at 28°C on CA and PDA and (E, F, G, H): colonies after 7 days at 28°C on CA and PDA. (I): Ascomata under stereo microscope. (J, K, L): Conidia, Ascomata and Ascospore under compound microscope.

3.2 Sensory and chemical composition of fermented brick tea

Two tea bricks BT01 and BT02 were successfully inoculated with *E. cristatum* (Fig. 3). Brew tea of BT01 and BT02 was clear and gold color with test notes of honey, mushroom, seaweed, earthy, and caramel. Honey-like flavor and long sweet aftertaste are the predominant characteristics of these post-fermented teas. The content of catechin and gallic acid slightly decreased after 16 days of fermentation (Table 1). This is consistence with a previous report that *E. cristatum* lowered the level of GA in post-fermented Pingwu Fuzhuan brick tea.[11] Interestingly, the content of caffeine was increased approximately 1.5 times in two tea bricks BT01 and BT01 compared to un-inoculated tea (control1; Table 1). These data suggested that the decrease of catechin and gallic acid and the increase in caffeine content were due to the activity of *E. cristatum*.

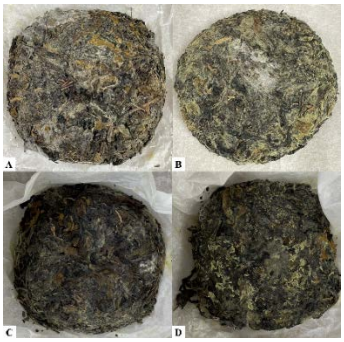

Figure 3. Tea bricks after incubated for 16 days, A) High density brick with sterile water [Control1]; High density brick with *E. cristatum* [BT01]; C) Low density brick with sterile water [Control2]; D) Low density brick with *E. cristatum* [BT02].

An analysis using GCMS-SPME identified 88 volatiles in tea across all treatments. The volatile compounds of both tea bricks that were inoculated with *E. cristatum* were clustered under the negative value while volatile compounds in control treatments were grouped in the positive value of companent1 (Fig. 4). This data suggested that post-fermentation with *E. cristatum* led to distinct variations in overall volatile compounds. Notably, linalool and methyl salicylate were identified as key volatiles present in the tea sample inoculated with *E. cristatum* but absent in the control. Previously, linalool was reported to be an important contributor to tea aroma.[6] Similar to volatile compounds, post-fermentation by *E. cristatum* resulted in a change of amino acids in both BT01 and BT02. As shown in Fig 5, the overall amino acids in tea inoculated with *E. cristatum* and control exhibited at positive and negative values in PC2, respectively. Organic acids, particularly malic acid, lactic acid, and citric acid, constitute a primary category of components influencing the sour taste of tea broth. An appropriate concentration of these sour compounds enhances the richness of the taste, while an excessive amount may contribute to a decline in overall quality. Moreover, Chen, H. et al., (2023)[3] reported that fumaric acid significantly contributes to the "mellow and fresh" taste characteristic of black tea. Thus, the reduced levels of malic acid and citric acid, coupled with elevated concentrations of fumaric acid, contribute positively to the flavor profile of post-fermented tea with *E. cristatum.*

Table 1. The contents of caffeine, catechins and gallic acid in tea samples after fermented with fungal *E. cristatum* by HPLC at different fermentation stages.

Tea	Concentration (mg/kg)		
	Caffeine**	Catechins*	Gallic acid*
Control1	5.60 ± 0.22[a]	3.83 ± 0.14[c]	11.58 ± 0.17[a]
BT01	8.31 ± 0.61[b]	3.02 ± 0.29[b]	10.88 ± 0.82[a]
Control2	5.57 ± 0.41[a]	3.49 ± 0.35[c]	15.58 ± 1.59[b]
BT02	8.22 ± 0.40[b]	2.44 ± 0.08[a]	10.77 ± 0.16[a]

Control1 = High density brick with sterile water, BT01 = High density brick with *E. cristatum*, Control2 = Low density brick with sterile water), BT02 = Low density brick with *E. cristatum*. Each value is expressed as the mean SD. The results were statistically analyzed with a one-way ANOVA. [a, b, c] The correlation coefficients between the variables used in constructed and the constituents that were correlated with the total quality were listed. *and** indicate significantly different values $P < 0.05$ (*$P < 0.05$, **$P < 0.01$).

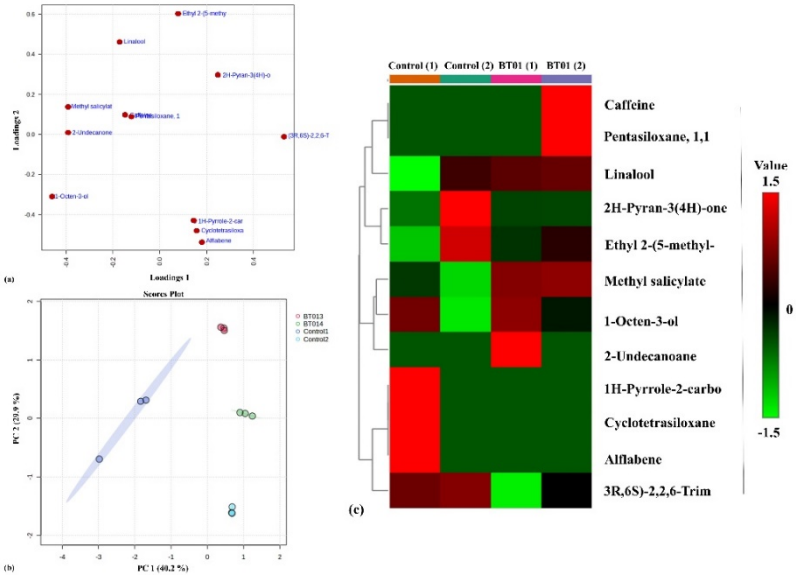

Figure 4. Orthogonal partial least squares discriminant analysis (OPLS-DA) of different fermented tea samples based on volatile compounds; A) PLS-DA loading plot; B) OPLS-DA score plot; C) heatmap.

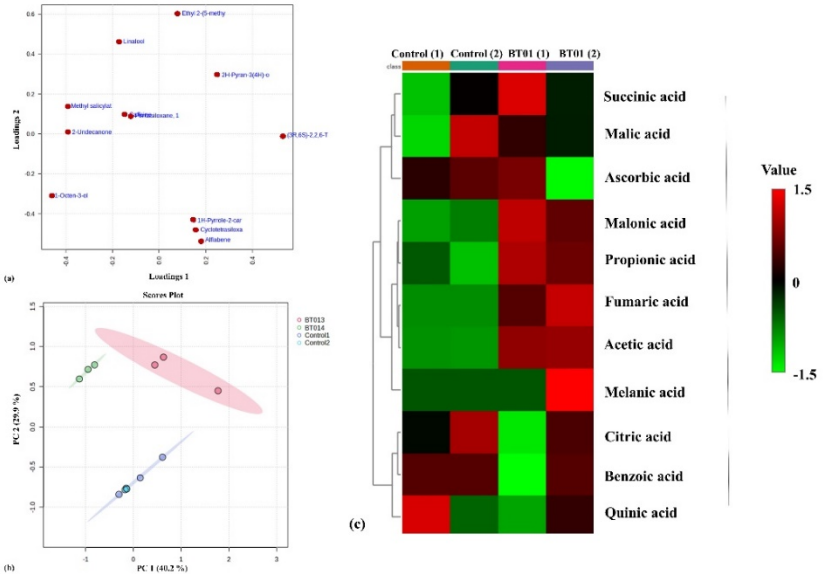

Figure 5. Orthogonal partial least squares discriminant analysis (OPLS-DA) of different fermented tea samples based on organic acid. (a) OPLS-DA loading plot. (b) OPLS-DA score plot. (c) heatmap.

4. Conclusion

The utilization of *E. cristatum* was successfully improved the chemical components of the green tea, leading to potential changes in flavor, aroma, and overall sensory attributes.

Acknowledgments

This work was supported by grants from pre-talent mobility from the Ministry of Higher Education, Science, Research and Innovation.

References

1. Agriopoulou, S.; Stamatelopoulou, E.; Varzakas, T. *Foods*. **2020**, *9* (4), 518.
2. Chen, A. J.; Hubka, V.; Frisvad, J. C.; Visagie, C. M.; Houbraken, J.; Meijer, M.; Varga, J.; Demirel, R.; Jurjevic, Z.; Kubatova, A.; Sklenar, F.; Zhou, Y. G.; Samson, R. *Stud. Mycol.* **2017**, *88* (1), 37–135.
3. Chen, H.; Yu, F.; Kang, J.; Li, Q.; Warusawitharana, H. K.; Li, B. *Molecules*. **2023**, *28* (5), 2339.
4. Chinwong, D.; Charaj, P.; Panitsupakamol, P.; Chankaew, T.; Chinwong, S.; Saenjum, C. *Sustainability*. **2021**, *13* (13), 7381.
5. Efimenko, T. A.; Shanenko, E. F.; Mukhamedzhanova, T. G.; Efremenkova, O. V.; Nikolayev, Y. A.; Bilanenko, E. N.; Gernet, M. V.; Grishin, A. G.; Serykh, I. N.; Shevelev, S. V.; Vasilyeva, B. F.; Filippova, S. N. *Int. J. Food. Sci.* **2021**, *2021*.
6. Khan, N.; Mukhtar, H. *Curr. Pharm. Des* **2013**, *19* (34) 2013, 6141–7.
7. LIczbiński, P.; Bukowska, B. *Ind. Crop. Prod.* **2022**, *175*, 114265.
8. Liu, G.; Duan, Z.; Wang, P.; Fan, D.; Zhu, C. *RSC advances*. **2020**, *10* (37), 22234-22241.
9. Muhammad Adnan, M. A.; Asif Ahmad, A. A.; Anwaar Ahmed, A. A.; Khalid, N.; Imran Hayat, I. H.; Iftikhar Ahmed, I. A. *Pak. J. Bot.* **2013**, *45*, 901-907.
10. Office of Agricultural Economics. (2023). Table showing details of coffee. https://www.oae.go.th/view/1/ Table showing details of coffee/TH-TH (accessed September 5, 2023).
11. Rui, Y.; Wan, P.; Chen, G.; Xie, M.; Sun, Y.; Zeng, X.; Liu, Z. *LWT*. **2019**, *110*, 168–174.
12. Xiao, Y.; Li, M.; Liu, Y.; Xu, S.; Zhong, K.; Wu, Y.; Gao, H. *Food Chem*. **2021**, *358*, 129848.
13. Xiao, Y.; Zhong, K.; Bai, J. R.; Wu, Y. P.; Gao, H. *J. Sci. Food Agric.* **2020**, *100* (9), 3598-3607.
14. Zhou, B.; Ma, C.; Ren, X.; Xia, T.; Li, X.; Wu, Y. *BMC Microbiology*. **2019**, *19* (1), 1-1

Development and optimization of spray-dried kaffir lime peel essential oil microparticles using emulsion stabilized by modified cassava starch

Nipaporn Rungjitvaranont[1], Rattiya Tangratniyom[1], Sirapat Jitanawasan[1] and Suthida Boonsith[1]*

Department of Chemical Engineering, Faculty of Engineering, Mahidol University, Nakhon Pathom 73170, Thailand

**E-mail: suthida.bos@mahidol.edu*

Abstract:

Thailand is recognized as the world leader in cassava production and there has been a campaign to encourage the use of cassava in a range of industries in order to increase the value of cassava starch. Consequently, in this work, cassava starch was modified and stabilized with kaffir lime peel essential oil through pickering emulsification for use in personal care products. Modified cassava starch, as a pickering emulsion stabilizer, was developed by using 1.58 M sulfuric acid and hydrophobic modification, which was altered by chemical and physical methods. Octenyl succinic anhydride was employed in the chemical process, while tetrafluoroethane and helium gas were used in the physical process (cold plasma process). To archive the dried powder, the emulsion was dried by a spray dryer with an inlet temperature of 160 °C, a sample flow rate of 9 ml/min, and an air flow rate of 600 L/h. The hydrophobic properties and encapsulation efficiencies were analyzed by contact angle measurements and gas chromatography flame ionization detector (GC-FID). The results demonstrated that essential oil was successfully encapsulated in both chemically and physically modified casava starch, with the chemical technique being more effective (3.71±0.78% encapsulation efficiency). However, the modified casava starch using the physical technique effectively eliminated bacteria (*Staphylococcus epidermidis*) and fungus (*Candida albicans*). Though both procedures still cause skin irritation. Therefore, more research is required to establish the dose that may be applied without affecting consumer safety.

1. Introduction

Thailand is regarded as the leader in cassava production. Currently, Thailand produces about 2 million tons of cassava starch per year. Cassava is a plant that is easy to grow, and the budget for investments is not particularly high. Thus, mass production has resulted in a lower price for cassava, leading to a campaign to encourage its use in various industries to increase the value of cassava starch. One alternative way to increase its value is by using it in cosmetic products such as dry shampoo. Dry shampoo, typically made with a base of starch and available in a spray bottle, absorbs dirt, oil, and grease from the scalp without water. It is suitable for individuals who want to freshen their hair during the day or those who have difficulty taking showers without assistance.

Essential oils can enhance the benefits of dry shampoo, beautiful-looking and fragrant hair. One notable essential oil commonly used with shampoo is kaffir lime peel extract. Kaffir lime peel essential oil is a popular addition to high-quality organic soaps, hair products, natural shampoos, and conditioners. In addition to its pleasant fragrance, it can moisturize the scalp, preventing dandruff and promoting overall hair health, growth, strength, and shine. The primary chemical constituents in kaffir lime peel include limonene, β-pinene, and sabinene. Furthermore, inhaling its aroma can effectively reduce stress and anxiety, providing a sense of relaxation (Sreepian et al., 2021)

Pickering emulsions are increasingly employed in various fields, including food, cosmetics, paints, coatings, pharmaceutics, and drug delivery. In a Pickering emulsion, solid particles accumulate at the interface between two immiscible phases, creating a physical barrier that reduces the likelihood of coalescence. These solid particles can be derived from natural sources such as starch or cellulose, which are modified to adjust particle size or hydrophobicity, making them suitable for emulsion systems (Cossu et al., 2015). Contact angle measurements are utilized to predict hydrophilicity or hydrophobicity. In the range of 15°–90°, solid particles exhibit better stability in water than in oil, while in the range of 90°–165°, solid particles demonstrate better stability in oil than in water (Wang et al., 2022).

The most predominant method for synthesizing starch nanocrystals is acid hydrolysis. Starch nanocrystals produced through this method typically exhibit a platelet-like shape and possess a high degree of crystallinity. In the process, starch is mixed with a diluted acid, such as sulfuric acid or hydrochloric acid, under constant agitation at a controlled temperature for a specific period. Subsequently, the nanocrystals formed during acid hydrolysis are subjected to centrifugation and

washed with distilled water to neutralize the eluent. Finally, the suspension underwent mechanical stirring to achieve a homogeneous suspension (Lu et al., 2021)

Cold plasma treatment involves creating a partially ionized gas by applying energy, such as thermal, electromagnetic, electric, microwave, and radio frequencies, to a neutral gas at low or atmospheric pressure. This process can be utilized in the food industry to deactivate bacteria, germs, fungi, and even multi-resistant pathogens. Additionally, cold plasma treatment promotes cell growth, blood circulation, and cell metabolism, thereby stimulating wound healing. Moreover, cold plasma treatment can enhance the hydrophobicity of starch surfaces by facilitating the adhesion of fluorine element. (Thirumdas et al., 2017)

The aims of this study were to investigate the production of spray-dried kaffir lime peel essential oil microparticles using emulsion stabilized by hydrophobically modified cassava starch. The hydrophobicity ofcassava starch was altered by chemical and physical methods. Octenyl succinic anhydride was employed in the chemical process, while tetrafluoroethane and helium gas were used in the physical process (cold plasma process). The studies of encapsulation efficiency, antimicrobial activity, and skin irritation test were conducted in order to compare between two methods and suitability as cosmetic ingredient.

2. Materials and Methods

2.1 Materials

Commercial cassava starch was purchased from Charoenworrakit Co. Ltd, Thailand. Kaffir lime peel essential oil was purchased from Asian Bioplex, Thailand. Helium gas (He) purity 99.99% was purchased from Charoenchai oxygen, Nakhon Pathom, Thailand. Tetrafluoroethane (R-134a) (Freezing®) was purchased from SW intertrade Co. Ltd, Thailand. All chemicals were of the highest grade available and purchased from local suppliers, Thailand.

2.2 Hydrolysis of cassava starch using sulfuric acid (H_2SO_4)

Starch nanocrystals were obtained by adding 35 g of cassava starch in 40 ml of 1.58 M H_2SO_4 and constant stirring at 300 rpm, 40°C for 5 days. Upon completion, the suspension was centrifuged at 10,000 rpm for 10 minutes to recover the starch granules. Starch granules were washed with deionized (DI) water until the pH reached 6.5. The starch granules were then placed into an oven at 40°C overnight and grounded to obtain starch nanocrystals (SNC) (Adeyeye et al., 2023).

2.3 Modify of cassava starch with Octenyl Succinic Anhydride (OSA)

Octenyl succinic anhydride modified starch nanocrystals (OSNC) were obtained by dissolving 30 g of SNC in 100 mL of DI water. The pH of the mixture was adjusted to 8.5 using sodium hydroxide. The OSA solution was prepared according to the desired concentration in isopropanol. The OSA solution was dripped into the starch mixture, and the mixture was stirred at 35°C (maintaining a pH of 8.5 throughout) for 4 hours. Afterward, the pH was neutralized using hydrochloric acid. Starch granules were washed with DI water twice, ethanol twice. and were then dried in an oven at 40°C overnight (Zhao et al., 2018).

2.4 Cold plasma treatment

Cassava starch 500 mg was placed on a petri dish in the box, helium and tetrafluoroethane gas were circulated into the system with a 40-watt continuous electrical discharge for 5 or 10 minutes at atmospheric condition, as shown in Figure 1. The volume flow rate of helium gas was 0.5, 1, and 2 L/min, while for tetrafluoroethane gas was 0, 0.5, and 1 L/min (Samanta et al., 2021). Repeated experiments were conducted with 500 mg of SNC thus, cold plasma-modified starch nanocrystals were obtained (CP-SNC).

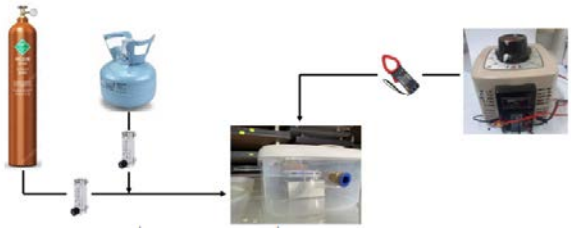

Figure 1. Diagram of cold plasma treatment

2.5 Preparation of encapsulated kaffir lime peel essential oil

Emulsion was prepared by mixing 1 g of modified starch sample with 9 ml of deionized water and 1 ml of kaffir lime peel essential oil using a sonicator probe with a 35% amplitude for 4 minutes. The emulsion was then dried by a spray dryer (Buchi Model B190, Switzerland) with an inlet temperature of 160 °C, a sample flow rate of 9 ml/min, and an air flow rate of 600 L/h. Encapsulated oil powders were obtained.

2.6 Physical characterization

Contact angle measurement was conducted with the Optical Contact Angle (OCA) (Kino, SL200KS, USA). 100 mg of the sample was pelleted using a hydraulic pump. The glass syringe created a small droplet and the drop was then slowly brought into contact with the solid surface. The image of contact angle measurements was taken and calculated using software. The micro morphology was observed using a scanning electron microscope (SEM) (JEOL, JSM 5600LV, Japan) scanning operated at 5 kV. The optical properties of cassava starch, modified cassava starch was obtained with Fourier-transform infrared spectroscopy (FTIR) (FT-IR-6700, Nikon, Japan) that employed a wavenumber interval of 4000-400 cm^{-1}. The grounded sample was mixed uniformly with potassium bromide (KBr) and pelleted using a hydraulic pump. The thermal decomposition of starch was studied by TGA. The temperature was raised from 20 °C to 600 °C at a 10 °C/min under a nitrogen atmosphere (flow rate 50 ml/min). The chemical composition of the starch surface was analyzed by X-ray photoelectron spectroscopy (XPS) (Kratos, Axis Ultra DLD,UK).

2.7 Chemical composition of kaffir lime peel essential oil and quantification of limonene

Components of kaffir lime peel essential oil and the quantification of limonene were analyzed with a gas chromatography flame ionization detector (GC-FID) (PerkinElmer, Clarus 680, USA). 100 mg of encapsulated oil powders were dissolved in 1 ml of hexane and sonicated for 30 minutes. After being left overnight, the sample was sonicated for an additional 30 minutes and then centrifuged for 10 minutes. The supernatant was filtered with a 0.45 µm syringe filter and analyzed with GC-FID. The GC was equipped with a PE-5 capillary column (60 m length × 0.25 mm i.d. × 0.25 µm film thickness). Nitrogen was used as the carrier gas at a flow rate of 1.0 ml/min, and the sample volume was 1 µl using split mode at a flow rate of 5 ml/min. The initial oven temperature was 45 °C (maintained for 2 min) and increased to 230°C (maintained for 5 min) at a rate of 5°C/min. The injector and detector temperatures were 270°C and 280°C, respectively.

2.8 Antimicrobial Activity

The antimicrobial activity of all samples was determined using disc diffusion method. All the tests were performed by Thailand institute of scientific and technological research (TISTR). Staphylococcus epidermidis (ATCC 14990), a Gram-positive bacterium primarily found on the skin, contributing to issues like hair loss, and Candida albicans (ATCC 10231), a fungus responsible for causing dandruff were chosen as a model. The preparation of test inoculum was direct colony suspension method using a loop to touch the test organism from the working stock tube and streak it onto the surface of nutrient agar (NA) for bacteria and yeast malt Agar (YM agar) for yeast. Incubated at 37°C for 24 h. Selected individual colonies for 2-3 colonies and placed them into normal saline solution (0.85% NaCl), shook well to ensure uniform mixing. Prepared the test inoculum by adjusting the turbidity of the culture with normal saline to match the turbidity of the McFarland No. 0.5 standard solution (Biomerieux). The test medium was prepared by pouring NA or YM agar nutrient medium, which has been melted and cooled to approximately 45°C, into petri dishes (90 mm diameter) to a volume of 20 mL/dish. Allowed the medium to solidify and used a cotton swab to touch the microorganism and streak onto the surface of the test medium evenly. The sterile forcep was used to pick up a test sample disc and place it onto the surface of the test medium. Gently pressed the test sample disc with the forceps tip to ensure full contact with the test medium. Incubated the test plates under appropriate conditions. After the appropriate incubation period, measure the diameter of the inhibition zone around the discs. Calculated the average size and recorded the measurements in millimeters.

2.9 Skin Irritation Test

The powder samples were applied topically to a 3-dimensional reconstructed human epidermis model (LabCyte EPI-MODEL), produced by culturing normal human epidermal cells to become multilayered. After the samples were incubated in the assay medium for 24 h, 3-[4,5-dimethylthiazol-2-yl]-2,5-diphenyl tetrazolium bromide assay (MTT assay) was performed to measure cellular metabolic activity as an indicator of cell viability, proliferation, and cytotoxicity. Absorbance was read at 570 and 650 nm with a Microplate reader, using isopropanol as the blank.

3. Results & Discussion

3.1 Physical characterization

From Figure 2, it was found that the modification of cassava starch with Octenyl succinic anhydride resulted in the substitution of OSA groups for hydroxyl groups (-OH) in cassava starch. This substitution contributed to enhancing the hydrophobic properties of the modified starch and was reflected in the characteristic absorption peaks observed at 1725 cm^{-1} (-COOH) and 1570 cm^{-1} ($RCOO^-$), indicating the interaction between the starch structure and OSA. These results from OSNC showed that the hydroxyl groups in the starch were replaced with ester carbonyl and carboxyl groups from OSA (Wang et al., 2009).

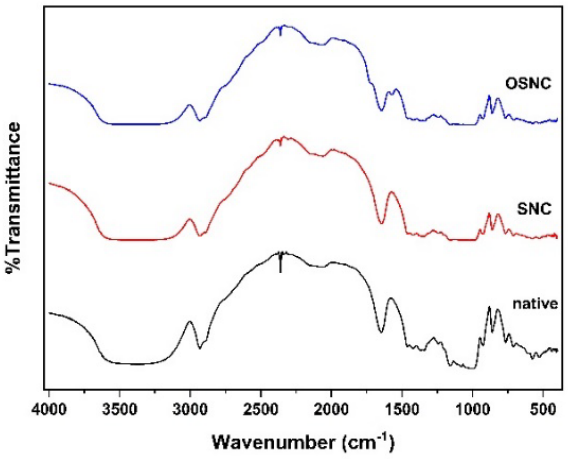

Figure 2. Spectrum of cassava starch and cassava starch nanocrystals analyzed by FTIR

The morphology of the starch granules before and after modification were investigated using a scanning electron microscope, as shown in Figure 3. The micrographs revealed that starch granules had irregular, hexagonal, and polyhedral shapes with few or no holes on the surface. This could be attributed to etching caused by the plasma reactive species. The formation of fissures on the surface allowed plasma ions to penetrate into the molecular level, resulting in the depolymerization and crosslinking of starch granules (Thirumdas et al., 2017).

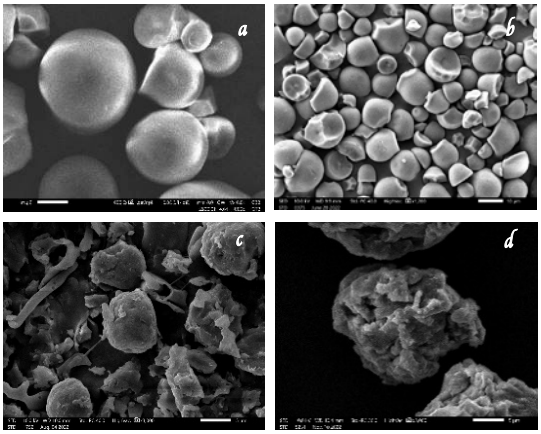

Figure 3. Morphology of (a) native starch, (b) cold plasma treated native starch, (c) starch nanocrystal, and (d) cold plasma treated starch nanocrystal using a scanning electron microscope

The elemental composition of cold plasma modified starch nanocrystal is presented in Figure 4. Surface modification with helium gas in combination with tetrafluoroethane resulted in the presence of fluorine elements clinging to the surface, which had a significant influence on hydrophobic properties of cassava starch (Resnik et al., 2018), (Samanta et al., 2021).

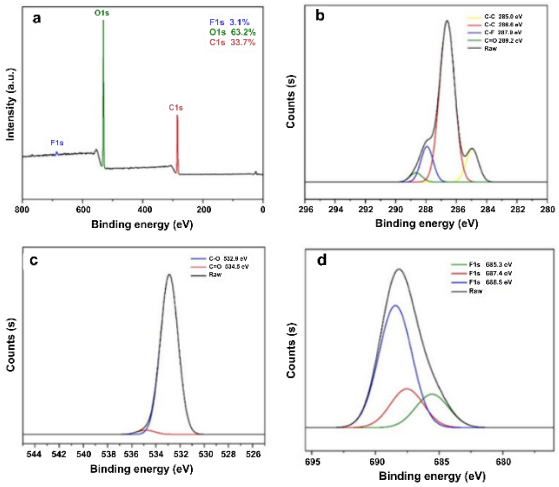

Figure 4. Surface chemistry analysis of cold plasma modified starch nanocrystal

The modification of cassava starch with cold plasma significantly impacted the starch structure. Specifically, when the starch was subjected to heat, there was a notable change in weight at temperatures lower than those for regular cassava starch. This resulted in a two-phase weight change. In contrast, starch modified using the chemical method (OSNC) exhibited a weight change pattern similar to regular cassava starch but occurred at slightly lower temperature. This difference was attributed to the enzymatic

breakdown process reducing the length of the chains in the structure as shown in Figure 5.

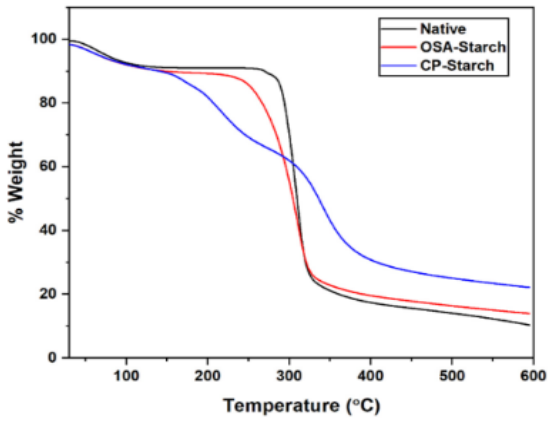

Figure 5. Thermal gravimetric analysis of native starch compared to Octenyl succinic anhydride-modified starch nanocrystals (OSNC) and Cold plasma-modified starch nanocrystals (CPSNC)

3.2 Contact angle and hydrophobic properties

Contact angle measurement was used to observed a trend in hydrophobic properties when optimizing conditions of cold plasma with native starch. Subsequently, SNC were modified under optimal cold plasma conditions because SNC, which are native starch modified with acid hydrolysis, can encapsulate oil better than native starch. According to the value of water contact angle shown in Table 1, cold plasma increased hydrophobic properties of cassava starch. The flow rate of helium had a greater effect on increasing the contact angle value compared to tetrafluoroethane. Helium primarily cleaned the surface through physical bombardment, potentially increasing hydrophilicity, while tetrafluoroethane could introduce fluorine atoms to the surface, decreasing surface energy and increasing the contact angle (Samanta et al., 2021). Exposure times for the cold plasma process were 5 minutes and 10 minutes, and there was no significant difference in results. SNC had a contact angle around 53 and did not increase even with changes in the flow of tetrafluoroethane or an increase in irradiation time. Therefore, a ratio of helium to tetrafluoroethane at 2:0.5 L/min for a period of 5 minutes was found to be the most suitable for increasing starch hydrophobicity.

Table 1. The water contact angle of modified cassava starch

Sample	He (L/min)	R-134a (L/min)	Time (min)	Contact Angle
Native starch	-	-	-	45.70±1.40
	0.5	1	10	53.60±3.50
	1	1	10	60.70±6.20
	2	1	10	70.00±3.80
	2	0	10	62.70±6.80
	2	0.5	10	71.00±2.00
	2	0.5	5	88.80±0.15
SNC	2	0.5	5	54.32±1.87
	2	1	5	53.25±6.42
	2	1	10	53.61±2.58

3.3 Encapsulation efficiency and loading content of kaffir lime peel essential oil

The results in Table 2 demonstrated that the essential oil was successfully encapsulated in the emulsion stabilized with the chemical technique (OSNC) better than the physical technique (CPSNC) which is 3.71±0.78% and 2.50±0.07%, respectively. The structure of SNC affected oil encapsulation as cold plasma-modified native cassava starch (CP-CS) had a lower encapsulation efficiency even though showed a higher water contact angle than cold plasma-modified SNC (CPSNC). Moreover, the OSA coating on the starch granules provided hydrophobic interactions with the essential oil, promoting efficient oil encapsulation within the nanochannels. While cold plasma treatment introduced hydroxyl groups onto the starch surface, which rendered it somewhat hydrophilic and less suitable for interacting with the hydrophobic essential oil. Encapsulation efficiency (%EE) was calculated with the following formula, when O_t was total amount of oil incorporated into microparticles and O_i was amount of oil added initially during preparation (El-Messery et al., 2020)

$$\%EE = \frac{O_t}{O_i} \times 100\%$$

Table 2. Effect of modified cassava starch on encapsulation efficiency

Sample	He (L/min)	R-134a (L/min)	Time (min)	%EE
CP-CS	2	1	10	0.23±0.47
CPSNC	2	0.5	5	2.50±0.07
OSNC	-	-	-	3.71±0.78

3.4 Antimicrobial activity

The antimicrobial activity of the modification cassava starch was tested against *S. epidermidis* ATCC 14990 and *C. albicans* ATCC 10231. The diameters of inhibition zones are shown in Table 3. No inhibition zone in cassava starch for all microorganisms tested, cold plasma modified starch nanocrystal (CPSNC) demonstrated the highest zone of inhibition for *S. epidermidis* ATCC 14990 and Oil encapsulated CPSNC (EO-CPSNC) had the highest zone of inhibition for *C. albicans* ATCC 10231. Interestingly, cold plasma modified cassava starch exhibited the ability to inhibit microorganisms without having Kaffir lime peel essential oil as presented in Table 3 and Figure 6.

Table 3. Inhibition zone diameter (mm) for antimicrobial activity of individual samples

Sample	*S. epidermidis* ATCC 14990	*C. albicans* ATCC 10231
1. Native cassava starch (CS)	0	0
2. Cold plasma modified starch nanocrystal (CPSNC)	19.6	14.3
3. EO encapsulated CPSNC (EO-CPSNC)	18.6	17.6
4. OSA modified starch nanocrystal (OSNC)	0	0
5. EO encapsulated OSNC (EO-OSNC)	18.3	21

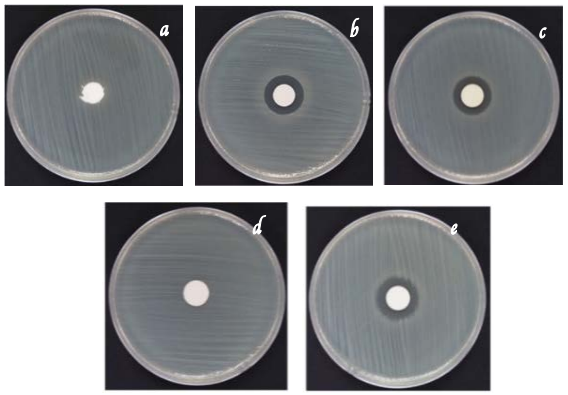

Figure 6. Antibacterial activity of *S. epidermidis* ATCC 14990 (a) Native cassava starch (CS), (b) Cold plasma modified starch nanocrystal (CPSNC) and (c) EO encapsulated CPSNC (EO-CPSNC) (d) OSA modified starch nanocrystal (OSNC) (e) EO encapsulated OSNC (EO-OSNC)

3.5 Skin irritation

OSNC encapsulating kaffir lime peel essential oil (EO-OSNC) and CPSNC encapsulating kaffir lime peel essential oil (EO-CPSNC) exhibited cell viability lower than 50% as presented in Table 4, indicated that both products adversely affected skin cell, with EO-CPSNC showing a bit higher cytotoxicity than EO-OSNC. However, it is necessary to find the optimum amount of the modified starch to be added in the final product. And it could not be inferred whether cytotoxicity occurred from the starch or the kaffir lime peel essential oil.

Table 4. Skin irritation test using LabCyte EPI-MODEL24

Sample	% Cell viability
Positive (5%SLS) (15 min)	4.13±0.61
Negative (water) (24 hr)	100.00±3.74
EO encapsulated OSNC (EO-OSNC) (24 hours)	7.92±0.35
EO encapsulated CPSNC (EO-CPSNC) (24 hours)	4.47±0.56

4. Conclusion

Modified cassava starch as a Pickering emulsion stabilizer was achieved through chemical and physical modifications. The chemical modification involved using 1.58 M sulfuric acid and octenyl succinic anhydride, resulting in the successful encapsulation of essential oil with an encapsulation efficiency of 3.71±0.78%. On the other hand, the physical modification, utilizing tetrafluoroethane and helium gas in a cold plasma process, demonstrated effective antibacterial and antifungal properties against *Staphylococcus epidermidis* ATCC 14990 and *Candida albicans* ATCC 10231, respectively. However, both methods were found to cause skin irritation. Overall, the study highlights the potential of modified cassava starch for diverse applications, showcasing its ability to encapsulate essential oils and exhibit antimicrobial properties, albeit with some associated skin irritation concerns.

Acknowledgements

The project was funded by the National Research Council of Thailand (NRCT). We also appreciate Mahidol University-Frontier Research Facility (MU-FRF), the department of Chemical Engineering, Mahidol University, and Professor Mohammad Naghi Eshtiaghi for instruments support.

References

1. Sreepian, A.; Sreepian, P. M.; Chanthong, C.; Mingkhwancheep, T.; Prathit, P. *Trop. Biomed*. **2019**, *36* (2), 531–541.
2. Cossu, A.; Wang, M. S.; Chaudhari, A.; Nitin, N. *Int. J. Pharm*. **2015**, *493* (1–2), 233–242.
3. Wang, W.; Liu, C.; Zhang, H.; Zhu, X.; Wang, L.; Zhang, N.; Yu, D. *Food Res Int* **2022**, *161*, 111845.
4. Lu, H.; Tian, Y. *J Agric Food Chem* **2021**, *69* (25), 6929-6942.
5. Thirumdas, R.; Kadam, D.; Annapure, U. S. *Food Biophys*. **2017**, *12* (1), 129–139.
6. Adeyeye, S. A. O.; Surendra Babu, A.; Guruprasath, N.; Sankar Ganesh, P. *Current Research in Nutrition and Food Science Journal* **2023**, *11* (1), 01–21
7. Zhao, S.; Tian, G.; Zhao, C.; Lu, C.; Bao, Y.; Liu, X.; Zheng, J. *Food Hydrocoll*. **2018**, *85*, 248–256.
8. Samanta, K. K.; Joshi, A. G.; Jassal, M.; Agrawal, A. K. *Carbohydr. Polym.* **2021**, *253*, 117272.
9. Wang, J.; Su, L.; Wang, S. *Journal of the Science of Food and Agriculture* **2009**, *90* (3), 424–429.
10. Resnik, M.; Zaplotnik, R.; Mozetic, M.; Vesel, A. *Materials (Basel)* **2018**, *11* (2), 311.
11. El-Messery, T. M.; Altuntas, U.; Altin, G.; Özçelik, B. *Food Hydrocoll*. **2020**, *106* (105890),

Method validation of a QuEChERS-GC-µECD method for the pesticide analysis of pyrethroids in mango

Padungrat Toopmuang, Pattama Prangchan, and Juthathip Thepsit

Plant Standard and Certification Division, Department of Agriculture, 50 Phaholyothin Road, Ladyao, Chatuchak, Bangkok 10900, Thailand

**E-mail: kaipadungrat@gmail.com*

Abstract:

Method validation for the analysis of pyrethroid pesticides in mango using GC-µECD is essential for laboratories to ensure accurate and reliable test results. Laboratories are required to validate parameters and criteria in accordance with SANTE/11312/2021, including linearity of analytical curves, instrument and method limits of detection and quantification, accuracy, and precision. The QuEChERS method (Quick, Easy, Cheap, Effective, Rugged, and Safe) was used to extract pyrethroid pesticides. The Calibration curves for the pesticides were linear in the range of 10–180 µg/kg, with correlation coefficients (r) exceeding 0.995. The limits of detection (LOD) and quantification (LOQ) were 5 µg/kg and 10 µg/kg, respectively. Recovery and precision were evaluated by spiking blank mango samples with 10, 50, and 100 µg/kg of each pesticide, with five replicates at each concentration level plus a blank sample. The average recovery rates obtained for each pesticide ranged from 74.55% to 113.17%, with relative standard deviations ranging from 2.77% to 13.55% for all evaluated concentrations. This demonstrates the excellent repeatability of the method. Overall, the method validation results demonstrate that the GC-µECD method can be used to analyze pyrethroid pesticides remaining in mango.

1. Introduction

Mango (*Mangifera indica* L.) is classified as a vital economic fruit for the country due to its easy cultivation and maintenance, thriving in various soil conditions. Additionally, mangoes can be grown off-season for year-round sales. The resulting harvest is utilized for both domestic consumption and export. Before exporting mangoes abroad, it is essential to analyze pesticide residues resulting from insecticides to meet the required standards.

Presently, insecticides play a crucial role in the cultivation of agricultural products, particularly fruits and vegetables, driven by the growing demand both within the country and on the international market. Consumer preferences for visually appealing and well-shaped produce incentivize farmers to increase their use of insecticides, resulting in expedited harvests compared to the timelines achievable without these chemicals.

Among the insecticides commonly employed by farmers for the eradication of borer insects is pyrethroid. Although these compounds naturally undergo degradation in sunlight, their resistance persists when associated with sediment or tissue. Pyrethroids pose a threat to the well-being of both animals and humans.[1]

The drive for higher yields and reduced crop losses often results in an increased use of insecticides, raising concerns about the safety of users. In recognition of this issue, Thailand has implemented the TAS 9002-2016 standard[2], which establishes stringent maximum residue limits for pesticides in agricultural products. This comprehensive standard not only governs domestic production but also guides international trade and quality control, placing a strong emphasis on consumer safety through rigorous regulation of pesticide residues. Therefore, it is essential to analyze pesticides to ensure agricultural products are free from these pesticide residues.

Ensuring the quality and reliability of data is paramount, and the validation of analytical methods plays a crucial role in achieving this goal.[3] This study focuses on the validation of the pesticide analysis of pyrethroids in mango, following the guidelines outlined in SANTE/11312/2021.[4] The chosen instrument for this analysis is gas chromatography (GC) with a micro electron capture detector (µECD).

The extraction method employed in this study is QuEChERS (quick, easy, cheap, effective, rugged, and safe), a well-regarded technique known for its efficiency, accuracy, suitability, speed, and cost-effectiveness. Notably, this method minimizes the use of chemical substances, thereby saving time and ensuring the safety of both laboratory personnel and the environment.

Furthermore, the QuEChERS method is adept at detecting pesticide residues at low concentrations, with the lowest detectable concentration being equal to or less than the maximum residue limits (MRLs) permitted in agricultural products. These MRLs, typically established by trading partners like the European Union or Japan, often specify a limit of 0.01 milligrams per kilogram.

The validation process encompassed several key parameters, including selectivity, linearity, the limit of detection (LOD), the limit of quantification (LOQ), precision, accuracy, and working range. Each of these parameters was rigorously tested to ensure the robustness and reliability of the analytical method used in the pesticide analysis of pyrethroids in mango.

2. Materials and Methods

2.1 Standards and solvents

Analytical standards of pyrethroids (Cyfluthrin, Cypermethrin, lambda-Cyhalothrin, Deltamethrin, Fenvalerate, Permethrin) were purchased from Dr. Ehrenstorfer (Augsburg, Germany). Individual stock standard solution of pesticide was prepared by dissolving 10 mg of each compound in 10 mL of acetone: toluene (1:1) and stored in amber bottles at -18^{o}C. A mixed standard solution was prepared in ethyl acetate from the stock solutions with a concentration of 10 mg/L.

Acetonitrile and toluene were purchased from JT baker (Radnor, USA), ethyl acetate and hexane from Labscan (Bangkok, Thailand), sodium chloride (NaCl), trisodium citrate dehydrate from Merck (Darmstadt, Germany). magnesium sulphate ($MgSO_4$) from Panrac (Barcelona, Spain), disodium hydrogencitrate sesquihydrate from Sigma (Darmstadt, Germany)and the clean-up QuEChERS from Agilent Technology were used for sample extraction and preparation.

2.2 Sample preparation[5]

The mango fruit used for the method validation of pyrethroids pesticide was obtained from an organic supermarket in Bangkok, Thailand.

A representative portion of 1 kg mango was chopped and ground in a blender, immediately placed into a zip-lock plastic bag and stored in a freezer until analysis.

2.3 QuEChERS extraction method[6]

Mango was extracted and cleaned up by the QuEChERS method as follows: 10 g sample was mixed with 10 ml acetonitrile, salt extraction ($MgSO_4$, NaCl, Trisodium, Disodium) in a centrifuge tube and shaken for 1 min. The extract was centrifuged at 4,000 rpm for 5 min. For the clean-up step, 6 ml supernatant of extract was cleaned up with a mixture of 900 mg PSA, 150 mg anhydrous $MgSO_4$ and 15 mg activated charcoal (application of activated charcoal in the stage of clean up to remove pigments from matrix). The extract was again shaken for 1 min and centrifuged for 5 min at 4,000 rpm. The supernatant was taken and diluted with ethyl acetate and hexane (3:1) in a GC vial for the GC-µECD analysis.

2.4 GC-analysis

Pesticide analysis was done on Agilent model 7890 Gas-Chromatography with HP-5 column (30 m x 0.32 mm x 0.25 µm) using micro-electron capture (GC-µECD). General operating conditions were as follows; injector port temperature: 250^{o}C; detector temperature 320^{o}C; helium was used as a carrier gas at flow rate of 2 ml/min and make up gas is 60 ml/min. Column temperature program: initially 80^{o}C hold 1 min, increase at 20^{o}C/min to 190^{o}C hold 0 min, then increase at 2^{o}C/min to 215^{o}C hold 0 min, increase at 10^{o}C/min to 265^{o}C hold 5 min and increase at 20^{o}C/min to 280^{o}C hold 5 min; injection volume: 2 µl spitless mode. The total run time was 35 minutes, and Agilent ChemStation GC Solution software was used for instrument control and data analysis.

2.5 Method validation

The validation of the analytical method was performed by the linearity, limit of detection (LOD), quantification (LOQ), accuracy, precision and working range. All the analysis was carried out using the same blank samples of mango . Accuracy and precision data were obtained with recovery studies by spiking samples with pesticide standards at levels of 10, 50, and 100 µg/kg. The spiked and control samples were analyzed in five replicates. Precision of the method was evaluated through the relative standard deviations (%RSD) associated with pesticides measurements during recovery.

Table 1. The retention time and peak area of pyrethroid pesticides standard at 10 µg/L. (n=7)

Pesticides	RT(min)	%RSD	Peak area	%RSD
L-cyhalothrin	22.29	0.01	1198.92	1.92
Permethrin 1	23.29	0.00	135.37	1.08
Permethrin 2	23.50	0.01	107.36	3.95
Cyfluthrin 1	24.21	0.01	248.29	0.85
Cyfluthrin 2	24.36	0.01	290.72	0.91
Cyfluthrin 3	24.46	0.01	157.48	4.45
Cyfluthrin 4	24.54	0.01	178.17	1.45
Cypermethrin 1	24.64	0.00	232.64	1.05
Cypermethrin 2	24.82	0.01	245.79	1.05
Cypermethrin 3	24.92	0.01	154.56	2.04
Cypermethrin 4	24.99	0.01	182.34	2.23
Fenvalerate 1	25.86	2.92	732.34	0.85
Fenvalerate 2	26.57	0.01	266.16	2.43
Deltamethrin	27.74	0.01	1068.26	1.85

3. Results & Discussion

3.1 GC-µECD condition

The conditions for analyzing pyrethroid pesticides of mango sample using a GC-µECD must be adjusted, specifically the temperature and temperature ramp rate of the column, to allow for the analysis of all six pyrethroid pesticides.

The chromatographic resolution obtained with the conditions described in Section 2.4 was considered satisfactory. It was found that a chromatogram was showed in Figure 1(b) and Table 1 as shown RT and peak area standard at 10 µg/L.

When standards were prepared in solutions, higher peak areas were obtained. Therefore, this method is used in the analysis.

3.2 Method validation of QuEChERS

The specific analysis of the six pyrethroid pesticides using the GC-µECD is characterized by the ability to differentiate each pesticide based on their retention times, as shown in Table 1. When comparing the chromatograms of the solvent blank, standard solution, and sample solution in Figure 1, it was observed that there was no interference with the detection signals of the standard pesticides.[7] This indicates the capability of the analysis method to separate the pesticides of interest from other substances, including impurities, degradation products, and matrix.[8]

The detector response exhibited a linear relationship for six pyrethroid pesticides studied. A calibration curve was constructed using external standard solutions in ethyl acetate: hexane (3:1) at eight concentration levels (10–180 µg/L). Each concentration level was analyzed in triplicate. High determination correlation coefficients (r) were obtained for all the pesticides as shown in Table 2.

The limits of detection (LOD) and limits of quantification (LOQ) were calculated according

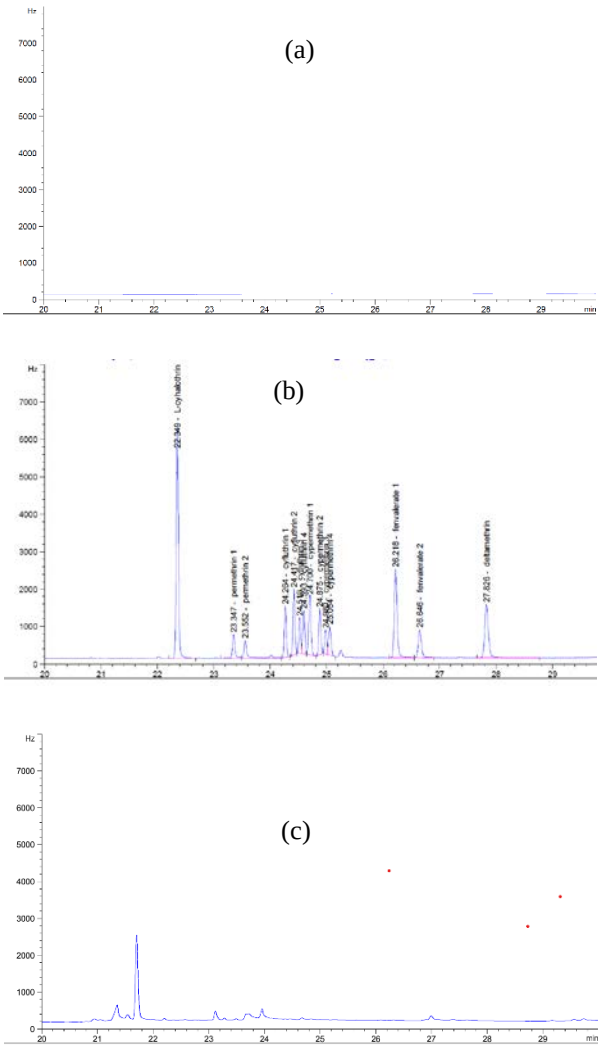

Figure 1. The chromatograms of the solvent blank (a), pyrethroid pesticides standard solution (b), and sample solution (c) with GC-µECD

Table 2. The linearity of pyrethroid pesticides standard at eight concentration levels (10–180 µg/L

Pesticides	slope	intercept	r
L-cyhalothrin	379.83	-1036.99	0.9994
Permethrin (sum)	64.03	382.79	0.9981
Cyfluthrin (sum)	331.77	-1115.67	0.9992
Cypermethrin (sum)	293.92	-449.15	0.9993
Fenvalerate (sum)	287.35	-527.16	0.9994
Deltamethrin	444.53	-2003.76	0.9993

to standard guidelines.[4,9-10] The LOD was calculated at the spiking level of 5 µg/kg as shown signal to noise ranged from 4.38-102.86, and LOQ at the spiking level of 10 µg/kg as shown ranged the relative standard deviation (RSDr) of precision from 5.31-13.55% and ranged the recovery of accuracy from 74.55-113.17%. And the LOQ for six pyrethroid pesticides were much lower than the maximum residue limit (MRLs) recommended by the EU, Japan.[11]

The proposed method's performance was assessed through precision and accuracy, following the SANTE/11312/2021[4] standard guidelines. Blank mango samples were artificially enriched at three different spike levels (10, 50, and 100 µg/kg). Precision was quantified using the relative standard deviation (RSDr), while accuracy was measured through mean recovery, as detailed in Table 3. For a spiked level of 10 µg/kg, the precision (RSDr) exhibited an acceptable range of 5.31-13.55%, and the recovery spanned from 74.55% to 113.17% across six pyrethroid pesticides. At the 50 µg/kg spike level, precision (RSDr) ranged from 6.66% to 11.58%, with recovery values ranging between 75.16% and 90.03%. Finally, at the 100 µg/kg spike level, precision (RSDr) demonstrated a range of 2.77-11.90%, and recovery spanned from 77.35% to 113.04%.

To confirm the method's reliable performance over its intended concentration range, validation was conducted, encompassing both method linearity and calibration procedures.[12] The working range was evaluated between the LOQ and the instrument's upper limit, using six spiked mango samples (10-100 µg/kg) to establish a concentration-response relationship. Each level was analyzed in triplicate, yielding high determination correlation coefficients (r) for all pesticides (Table 4).

4. Conclusion

Method validation of pyrethroids pesticide in mango obtained; the LOD was 5 µg/kg, LOQ was 10 µg/kg, and the average recovery rates obtained for each pesticide ranged from 74.55% to 113.17%, with relative standard deviations ranging from 2.77% to 13.55% for all evaluated concentrations. Overall, the method validation results demonstrate that the GC-µECD and QuEChERS method can be used to analyze pyrethroid pesticides remaining in mango.

Table 3. The summary of mean-percent recoveries of spiked levels and relative standard deviations (RSDr) for pyrethroid pesticides in mango sample. (n=5)

Pesticides	Spike levels (µg/kg)	Mean recovery	RSDr
L-cyhalothrin	10	93.89	7.50
	50	75.48	7.43
	100	113.04	2.77
Permethrin	10	97.23	13.02
	50	75.16	6.66
	100	107.32	4.22
Cyfluthrin	10	108.07	13.55
	50	90.03	10.91
	100	77.35	9.53
Cypermethrin	10	97.43	7.82
	50	87.98	9.69
	100	90.40	11.90
Fenvalerate	10	113.17	5.31
	50	83.41	8.44
	100	87.86	8.67
Deltamethrin	10	74.55	6.84
	50	87.14	11.58
	100	80.08	8.88

Table 4. The working range of pyrethroid pesticides by six different spike levels (10-100 µg/kg) in mango sample

Pesticides	slope	intercept	r
L-cyhalothrin	379830.37	-1036.99	0.9994
Permethrin (sum)	64029.60	382.79	0.9981
Cyfluthrin (sum)	331768.95	-1115.67	0.9992
Cypermethrin (sum)	293918.77	-449.15	0.9993
Fenvalerate (sum)	287351.86	-527.16	0.9994
Deltamethrin	444528.06	-2003.76	0.9993

Acknowledgements

We are deeply grateful to the dedicated staff of the Pesticides Laboratory for their invaluable contributions to this research. Their careful preparation and skilled analysis of samples using advanced GC technology were instrumental in obtaining accurate and reliable data. We also express our heartfelt thanks to Quality Control for Plant and Plant Products Group, Plant Standard and Certification Division, Department of Agriculture for generously providing the essential

research facilities that enabled this project to come to fruition.

References

1. Soderlund, D.M., *Chapter 77 - Toxicology and Mode of Action of Pyrethroid Insecticides*, Hayes' Handbook of Pesticide Toxicology (Third Edition); Elsevier: New York, 2010; pp 1665-1686.
2. National Bureau of Agricultural Commodity and Food Standards Ministry of Agriculture and Cooperatives, Pesticide Residues: Maximum Residue Limits, Thai Agricultural Standard TAS 9002-2016, 2016.
3. Yusuf, M.; Idroes, R.; Saiful; Lelifajri; Bakri, T. K.; Satria, M.; Nufus, H.; Yuswandi1, I.; Helwani, Z.; Muslem; Marlina, *IOP Conf. Ser.: Earth Environ. Sci.* **2021,** *667*; *012039*.
4. European Commission Directorate General for Health and Food Safety, Guidance Document on Analytical Quality Control and Method Validation Procedures for Pesticide Residues Analysis in Food and Feed. SANTE/11312/2021, 2021.
5. National Bureau of Agricultural Commodity and Food Standards Ministry of Agriculture and Cooperatives, Classification of Agricultural Commodities: Crop, Thai Agricultural Standard TAS 9045-2016, 2016.
6. European Committee for Standardization, Foods of plant origin - Multimethod for the determination of pesticide residues using GC- and LC- based analysis following acetonitrile extraction/ partitioning and clean up by dispersive SPE - Modular QuEChERS-method. EN 15662:2018, 2018.
7. Ashutos, K. S.; Satyajeet, R.; Srivastava, M. K.; Lohani, M.; Mudiam, M. K. R.; Srivastava, L. P., *PLoS ONE*. **2014**, *9(5)*; e96493.
8. Belouafa, S.; Habti, F.; Benhar, S.; Belafkih, B.; Tayane, S.; Hamdouch, S.; Bennamara A.; Abourriche, A., *Int. J. Metrol. Qual. Eng.* **2017**, *8(9)*; 10.1051/ijmqe/2016030.
9. Srivastava, A.; Singh, G.P.; Srivastava P.C., *PLoS ONE*. **2021**, *16(12)*; e0260851.
10. Konieczka, P.; Namiesnik, J., Quality Assurance and Quality Control in the Analytical Laboratory- A Practical Approach, Taylor&Francis Group, 2009.
11. Tian, F.; Qiao, C.; Luo, J.; Guo, L.; Pang, T.; Pang, R.; Li, J.; Wang, C.; Wang, R.; Xie H., *Scientific Reports.* **2020**, *10*: 7042; https://doi.org/10.1038/s41598-020-64056-7.
12. Magnusson, B.; Örnemark, U. (eds.), Eurachem Guide: The Fitness for Purpose of Analytical Methods – A Laboratory Guide to Method Validation and Related Topics, 2nd ed, 2014.

An exploratory approach to differentiate Khao Dawk Mali 105 rice located in the northern and northeastern region of Thailand based on Rb, Sr, Mo, Mg, P, K analyzed by ICP-MS

Piriya Kaeopookum, Nantanat Chailanggar, and Wiranee Sriwiang*

Nuclear Technology Research and Development Center,
Thailand Institute of Nuclear Technology (Public Organization) Nakhon Nayok, 26120, Thailand

**E-mail: wiranee@tint.or.th*

Abstract:

A high value of Thai Hom Mali rice in the global trade caused a potential problem of adulteration by suppliers mislabeling or adding inferior rice to make more profit. To reduce this risk, an indication of the geographical origin of rice packaging has been initiated. In this study, identification of the authentic geographical origin of rice has been investigated using its compositional elements which were transferred from the soil in which the rice is grown. To create the composition database of Khao Dawk Mali 105, samples of rice cultivated in the northern and northeastern regions of Thailand (144 samples) were collected. Six elemental data (Rb, Sr, Mo, Mg, P, K) were measured using inductively coupled plasma mass spectrometry (ICP-MS). The Analyse-it program was used for statistical analyses. The strongest correlation was found in Mg-P (0.868) and the most negative correlation was K-Rb (-0.394). Scatter plots among elemental compositions at 90% density matrix revealed both negative and positive correlation patterns. The 2D correlation monoplot from principles component analysis (PCA), which showed the relationship of the six variables, accounts for 64.0% of the total variance. The commonality and uniqueness factors of the three loading factors were visualized with exploratory factor analysis (EFA). Spearman's rank correlation coefficient, *Rs* value, calculated from the scatter plot showed a significance correlated in all elemental pairs of Rb-Mo, Mg-P, Mg-K, and P-K with a *p*-value less than 0.0001 at 95% CI. Extraction of the latent variables for three loading factors by EFA revealed common factors that probably be discriminating of this elemental data set are Rb, Mo, Mg, P, and K with communality correlation coefficients are 0.995, 0.995, 0.995, 0.776, and 0.652, respectively. This correlation analysis by scatter plotting and FA model showed a possible approach to discriminate rice cultivated in different areas based on elemental composition, such as in this study, comparisons the north and northeast regions. The elemental composition combined with multivariate analysis is a possible method to indicate the geographical origin of Thai Hom Mali rice.

1. Introduction

Thai Hom Mali rice (THMR) or Thai Jasmine rice is a premium rice that is known for its special fragrance. Thai Jasmine rice was distributed to farmers in 1959 by the Bureau of Rice Research and Development after accomplished online selection and has officially been named Khao Dawk Mali 105 or KDML 105[1]. THMR has mainly been cultivated in the northeast region of Thailand and three provinces of the region (Chiangmai, Chiang Rai, and Phayao). In world trade, THMR, especially, KDML 105 grown in the Tung Kula Rong Hai area located in the northeastern region, is recognized as high-quality rice for consumers. The high value of THMR may be an occurrence of fraudulent activities such as mislabeling of lower quality grains of different varieties or geographical origin. To reduce this risk of adulteration, the analytical techniques that indicated the authentication of origin should be developed. Trace elements composition in rice reflects the location of soil where it is grown and has been investigated to discriminate the geographical origin of rice and food products. Kelly[2] et al (2002) determined the elemental concentration of B, Mg, Se, Rb, Gd, Ho, and W in rice cultivated in the USA, Europe, and Basmati region with ICP-MS. They found a high level of B in rice from America, while Europe rice samples contained a high level of Mg. Spiros A. and co author[3] (2012) reviewed the articles involving discriminating food and beverage according to geographical origin by several techniques such as principal component analysis (PCA), cluster analysis (CA), analysis of variance (ANOVA), and linear discriminant analysis (LDA). Li and Kelly (2015)[4] analyzed the multi-elements in rice samples obtained from various countries including Australia, China P.R. France, India, Italy, Japan, Korea, Malaysia, Myanmar, Pakistan, Taiwan, and Thailand. The data were processed by canonical discriminant analysis (CDA). The corrected classification of this model was 90.7%. The example of previous studies[5-8] indicated the awareness of food safety and food authentication. Therefore, an authentication origin database of KDML 105 based on elemental composition according to cultivation region should be created.

In this study, KDML 105 rice samples collected from the paddy field in Thailand, were analyzed by ICP-MS to establish the elemental fingerprint of rice located in the north and northeast. The elemental composition of this authentic sample set was evaluated if it is feasible to differentiate THMR according to geographical origin.

2. Materials and Methods

2.1 Materials

2.1.1 Rice samples

One hundred and forty-four total paddy rice samples were available from farmers in Dec 2020, in 9 provinces;116 samples from the northeast, (Kalasin 10, Mahasarakham 14, Roi Et 20, Sri Sa Ket 35, Surin 7, Burirum 10, Nakorn Ratchasima 10, and Chaiyaphum 10). In the north region, samples were collected from Phayao and Chiang Rai (18 and 10 samples respectively). The rice samples were air-dried at room temperature. All samples were dehulled to be polished rice or white rice and were ground by a mortar to obtain a fine powder. The rice powders were dried again in an oven at 60 ± 2 °C until constant weight, kept in polyethylene containers, and stored in a desiccator until analysis.

2.1.2 Standard and Reagent

A multielement calibration standard 2A (10 mg L^{-1}) in 5% HNO_3 and Instrument check standard (10 mg mL^{-1}) of Mo, Sn, Sr, Ti in 2% HNO_3 were purchased from Agilent Technology, Thailand. Internal standard Mix (100 mg L^{-1} of Bi, Ge, In, Li-6, Lu, Rh, Sc, and Tb) and tunning solution (1 µg mL^{-1}) for ICP-MS were also purchased from Agilent (Thailand). Phosphorus standard (1000 µg mL^{-1}) was purchased from AccuStandard (AccuTrace™ Reference Standard, New Haven, USA). Nitric acid, 65% Suparpur®, and 30% H_2O_2 were available from Merck (Merck KGaA, Darmstadt, Germany). Standard reference material (SRM) rice flour 1568b was purchased from the National Institute of Standard and Technology, NIST (Gaithersburg, MD, USA). Type I ultra purification water was obtained from the Milli-Q® purification system (Merck Millipore, Bedford, MA, USA). Conical polypropylene centrifuge tubes 15-mL and 50-mL were purchased from Nunc, Thermo Fischer Scientific Inc Singapore). Nalgene Polypropylene wide mouth, 30-mL was available from Thermo Scientific™ Nalgene™, USA.

2.2 Instrument and Method

2.2.1 ICP-MS setting

All rice was analyzed for elemental composition with Agilent 7900 (Agilent Technologies, Santa Clara, CA, USA). The operating conditions were as follows: RF power, 1500 W; RF matching 1.5 V; carrier gas flow rate, 0.85 L min^{-1}; makeup gas flow rate, 0.3 L min^{-1}; nebulizer pump, 0.1 rpm; nebulizer, Mira Mist; spray chamber, Scott type; Sampling cone and skimmer cone, Nickel.

2.2.2 Elemental analysis by ICP-MS

All powdered rice samples (0.5 g) were digested in PTFE vessels with 4 mL of 65% w/w on a hot plate at 120 °C for 5 h. After digestion, the samples were evaporated to dryness and the residues were dissolved in 65% w/w HNO_3 and 30% w/w H_2O_2. After drying, the residues were dissolved with 2% v/v HNO_3. Finally, the dissolution samples were diluted to an appropriate concentration for ICP-MS analysis. All sample digestions were completed in triplicate. The standard reference material of rice flour (NIST 1568b) was used to check the procedure's accuracy. The elemental concentrations (Rb, Mo, Sr, Mg, P, and K) in rice samples were determined by ICP-MS. The calibration standard was prepared by dilution of a multi-element 2A calibration standard (Agilent Technology, Thailand) and mixed with an Indium (In) internal standard to compensate for any changes in analytical signals during the operation of ICP-MS. Standard calibration was constructed with a minimum of 5 points.

2.3 Statistical analysis

Analyse-it add-in software for Microsoft Excel was used for calculating its correlation among the variables and extracting the underlying factors that could differentiate THMR rice according to cultivation area. The statistical analysis of Microsoft Office Excel 2019 was used to calculate the mean, standard deviation (SD), minimum, and maximum of the elemental concentration. The difference between the means of the two data sets was evaluated using the student's *t*-test at the 95% confidence interval (*t*-test; $p < 0.05$).

3. Results & Discussion

3.1 Recovery and detection limit of the analysis

According to the IUPAC recommendation[9], the limit of detection (LOD) for all elements determined by ICP-MS was estimated from three times the standard deviation of the blank measurements. The limit of detection (in mg kg^{-1}) calculated from the method blank multiplied with dilution factor was as follows: Rb (0.0002), Sr (0.005), Mo (0.00005), Mg (0.028), P (0.012), and K (0.023) which is adequate for the determination of these elements in rice sample. The standard reference material of rice flour (NIST

1568b) was used to validate the analytical procedure. The result of the analyzed value showed good agreement with the certified value. The recoveries ranged between 89% to 112%, which is within the acceptance recovery yield (60-125% of the AOAC Official Method 2015.01: Heavy Metals in Food Inductively Coupled Plasma–Mass Spectrometry).

3.2 Elemental composition in rice

The trace element composition of rice is reflected to some extent in the soil where rice is grown. Different characteristic soil compositions as well as contributions from surrounding environmental pollution of each cultivation region result in a unique fingerprint elements profile of rice. Alkali metals, especially rubidium (Rb) and cesium (Cs) being labile in the soil and easily transported into the plant, are good indicators of geographical origin (S. Kelly 2002). Therefore, the elements of Rb, Mo, Sr, Mg, P, and K were chosen to test for a discriminating model of this data set. The summary statistics of elemental concentrations (mg kg^{-1}) of rice samples according to their cultivation region are shown in Table 1. Notice the wide range between the minimum and maximum value of Rb concentration in rice of the north was from the high value of Chiang Rai province. Rice samples in Chiang Rai province were also collected and measured in 2021 and found a high level of Rb content compared with other provinces. This event indicated the uniqueness of the soil in Chiang Rai province. A scatter plot matrix in Figure 1 showed an association between all variable pairs positively and negatively. Pearson's correlation parameter describes the linear correlation of the two variables with its strength shown in a color map matrix, blue for the positive correlation, and red for the negative correlation. The intensity of the color represents the magnitude of the correlated value, the darker more extreme. The most positive value of association is Mg-P and Mg-K with correlation coefficients of 0.868 and 0.761 respectively. The most negative coefficient value is -0.394 for Rb-K. When the association is not linear, such as an association of Sr-P, Sr-K, Mo-Mg, and Mo-P which is explained by the smaller coefficient values; 0.060, 0.038, 0.068, and -0.013, respectively; rank correlation is more suitable for account of the association.

Spearman's *Rs* correlation coefficient was calculated to represent the rank correlation at a 95% confidence interval (95% CI) with a *p*-value as shown in Figure 2. The *p*-value of Rb-Mo, Mg-P, Mg-K, and P-K was smaller than 0.0001, indicating the strongest correlation between variables. Interestingly, the small Pearson's correlation value of Sr-P and Mo-Mg revealed significance ($p<0.05$) in Spearman's parameter. This suggested that the association of the variables could be also estimated with a non-linear relationship. A PCA monoplot in Figure 3., represents elements as variables in a vector pattern. From the plot, elements of P, Mg, K, and Mo are suitable to describe the behavior of this data set, due to explain most of their total variance. Consideration on association of the elements; Mg is positively correlated with P and K and negatively correlated with Rb. This association trend was parallel with Pearson's correlation. Mo is more positively correlated with Sr greater than Rb.

By comparing the scatter plot of this studied model with the PCA model of Cheajesadagul et al. (2013), this work distinguished rice grown in the north and northeast, indicated by a *p*-value of 0.01. The PCA model of Cheajesadagul et al. found only partially separated THMR collected in central Thailand from the north and northeast, whereas rice in the north and northeast was still difficult to separate. Kongsri et al. (2021) used radar plots and multivariate analysis to distinguish THMR in three contiguous provinces based on the elemental composition of

Table 1. Summary of statistical of elemental composition in rice according to their cultivation region.

Location	Rb	Sr	Mo	Mg	P	K
Northeast (n= 116)						
Min	0.74	0.03	0.42	477	1527	1183
Max	4.96	0.20	0.96	600	2298	1721
Avg	3.25	0.09	0.59	538	1759	1520
SD	1.32	0.05	0.22	42	235.7	197
North (n=28)						
Min	0.79	0.01	0.33	409	1299	810
Max	26.7	0.04	0.50	427	1411	975
Avg	13.7	0.03	0.41	418	1356	892
SD	18.3	0.01	0.12	12	79	116

The value of all elemental concentrations is the mean of triplicate digested samples in mg kg^{-1} unit.

Mn, Rb, Co, and Mo. Most previous studies successfully separated rice according to country region or variety and obtained only elemental fingerprinting. In addition, our work needs to infer their association and explore the underlying factors that influence for discrimination of the dataset.

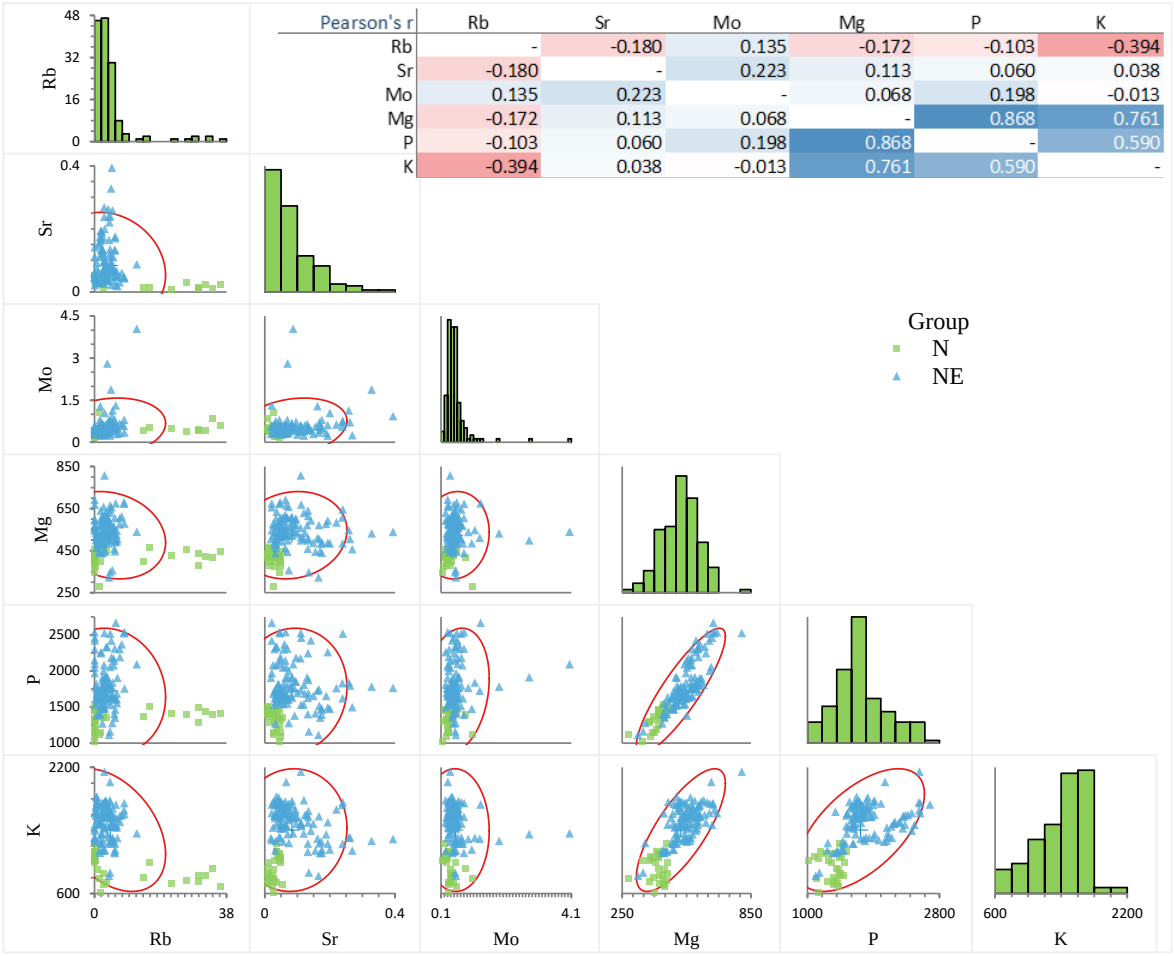

Figure 1. A scatter plot and color map matrix of correlation coefficient pattern (in the subset) of K, P, Mg, Mo, Sr, and Rb in rice cultivated in the north and northeast of Thailand. In case the association is a linear relationship, a bivariate normal density ellipse summarizes the correlation between variables. The narrower the ellipse with increasing together, the more positively correlated while the ellipse with decreasing together is negatively correlated. The wider and more round indicated no correlation of the variables.

Correlation

Pair	Spearman's rs	95% CI	0	p-value
Rb, Sr	0.003	-0.166 to 0.171		0.9737 ₂
Rb, Mo	0.396	0.244 to 0.529		<0.0001 ₁
Rb, Mg	0.113	-0.056 to 0.276		0.1775 ₂
Rb, P	0.106	-0.063 to 0.270		0.2058 ₂
Rb, K	-0.025	-0.193 to 0.144		0.7623 ₂
Sr, Mo	0.261	0.097 to 0.411		0.0016 ₁
Sr, Mg	0.233	0.067 to 0.386		0.0049 ₁
Sr, P	0.169	0.000 to 0.328		0.0433 ₁
Sr, K	0.112	-0.058 to 0.275		0.1826 ₂
Mo, Mg	0.207	0.040 to 0.363		0.0128 ₁
Mo, P	0.266	0.102 to 0.415		0.0013 ₁
Mo, K	0.054	-0.116 to 0.220		0.5217 ₂
Mg, P	0.888	0.846 to 0.919		<0.0001 ₁
Mg, K	0.706	0.610 to 0.781		<0.0001 ₁
P, K	0.612	0.495 to 0.708		<0.0001 ₁

H0: The variables are independent.
H1: The variables are not independent.
₁ Reject the null hypothesis in favour of the alternative hypothesis at the 5% significance level.
₂ Do not reject the null hypothesis at the 5% significance level.

Figure 2. A Spearman's correlation coefficient chart with *p*-value of elemental variable pairs.

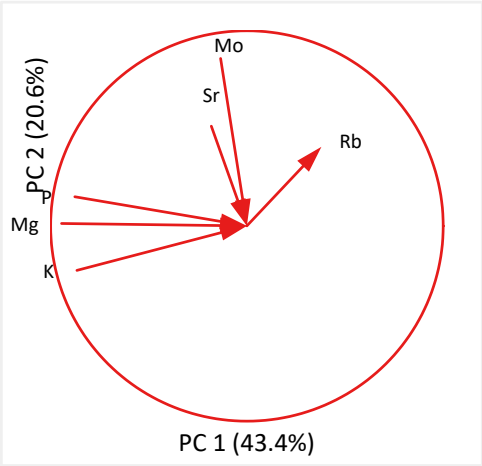

Figure 3. The correlation monoplot of six variables in two principle components (PC1 and PC2) represented as vectors point away from the origin. The length of the line and its closeness to the circle indicate how well the plot represents the variable. The angle between the vectors is an approximation of the correlation between the variables. A small angle indicates the variables are positively correlated, an angle of 90 degrees indicates the variables are not correlated, and an angle close to 180 degrees indicates the variables are negatively correlated.

Table 2. Common factor model is a combination of the common factors and unique factors.

Common factors	Uniqueness	Communality
Rb	0.005	0.995
Sr	0.901	0.099
Mo	0.005	0.995
Mg	0.005	0.995
P	0.224	0.776
K	0.348	0.625

Table 3. Factor correlation matrix of loading variables.

	Factor		
Elemental	1	2	3
Rb	0.801	-0.173	-0.569
Sr	-0.130	-0.208	0.197
Mo	0.299	-0.844	0.440
Mg	-0.672	-0.565	-0.473
P	-0.520	-0.609	-0.367
K	-0.706	-0.338	-0.198

Table 2 and Table 3 show the common factors and structure of matrix loading extracted by the exploratory factor analysis (EFA) model. All elementals explained an association among each other, except Sr with maximum strength on Rb, Mo, and Mg (communality = 0.995).

The factors that have an impact on the association of all variables extracted by EFA have been categorized into three groups, as displayed in Table 3. Variables with a coefficient greater than 0.5 have been taken into consideration. The first factor, which is represented by Rb, has shown results that are opposite to those of Mg, P, and K. The second factor was contributed by Mo, Mg, and P. Additionally, the third factor was an effect of elements of Rb, Mo, and Mg. The relationship of these elements with a common factor loading may be described as follows: the first factor may be correlated with the extent of alkaline earth metal existing in the soil (Rb) and major nutrients (Mg, P, K) that the farmer added to the soil and was then taken up by the rice. For the second group, the rice samples are grouped based on their high levels of Mo, Mg, and P. The third group is composed of rice samples that are high in Mo but low in Rb, Mg, and P.

Rice, grown in northern and northeastern Thailand may be differentiated by analyzing its elemental composition using scatter plots, PCA, and EFA statistical models. This study revealed that variation in elemental concentration in rice is from the nature of the soil and cultivation management system. The major nutrients of P, Mg, K, and Mo and the alkaline metal (Rb and Sr) in different soil areas are adsorbed by rice resulting in different seed grains, indicated by the p-value of Sperman's *Rs* < 0.0001. This accuracy of discrimination results between north and northeast was confirmed by the linear discrimination analysis (LDA) model and found to be greater than 90%.

4. Conclusion

The elemental composition combined with multivariate analysis (PCA and EFA) is a possible method to indicate the geographical origin of the THMR. This method is a promising analytical method to reduce the problem of mislabeling and adulteration.

Acknowledgments

We would like to thank the staff of the Agricultural Extension Office for their assistance in cooperation with the farmers. We wish to express our thanks to the farmers for providing their rice samples. This work has been financially supported by the International Atomic Energy Agency (Research Contract No.16523).

References

1. Vanavichi, A.; Kamolsukyeunyong, W.; Siangliw, M.; Siangliw, J. L.; Traprab, S.; Ruengphayak, S.; Chaichoompu, E.; Saensuk, C.; Phuvanartnarubal, E.; Toojinda, T.; Tragoonrung, S. *Rice*. **2018**, *11* (1), 20.
2. Kelly, S.; Baxter, M.; Chapman, S.; Rhodes, C.; Dennis, J.; Brereton, P. *Eur. Food. Res. Technol*. **2002**, *214*, 72-78.
3. Spiros, A. D.; and Constantinos, A.G. *Trends. Anal. Chem*. **2012**, *40*, 38-51.
4. Li, A.; Keely, B.; Chan, S. H.; Baxter, M.; Rees, G.; Kelly, S. *Qual. Assur. Saf. Crops Foods*. **2015**, *7* (3), 343-354.
5. Cheajesadagul, P.; Arnaudguihem, C.; Shitowatana, J.; Siripinyanond, A.; Szpunar, *J. Food Chem*. **2013**, *141*, 3504-3509.
6. Chung, I. M.; Kim, J. K.; Lee, K. J.; Park, S. K.; Lee, J. H.; Son, N. Y.; Jin, Y. I.; Kim, S. H. *Food Chem*. **2017**, *240*, 840-849.
7. Qiana, L.; Zhanga, C.; Zuoa, F.; Zhenga, L.; Lia, D.; Zhanga, A.; Zhanga, D. *J. Food Compos. Anal*. **2019**, *83*, 103276.
8. Arif, M.; Chilvers, G.; Day, S.; Naveed, S. A.; Woolfe, M.; Rodionova, O. Y.; Pomerantsev, A. L.; Kracht, O.; Brodie, C.; Mihailov, A.; Abrahim, A.; Cannavan, A.; Kelly, S. D. *Food Control*. **2021**, *123*, 107827.
9. McNaught, A. D.; Wilkinson, A. *IUPAC Compendium of Chemical Terminology*, 2nd Ed.; Blackwell Science Publications, Oxford, **1997**.
10. Kongsri, S.; Sricharoen, P.; Limchoowong, N.; Kukusamude, C. *Foods*. **2021**, *10*, 2349.

Optimization of nanostructured lipid carrier using box-behnken design and its potential use as lignin carrier system

Krittin Intaraopart, Suthida Boonsith, and Warangkana Pornputtapitak*

Department of Chemical Engineering, Faculty of Engineering, Mahidol University Nakhon Pathom, 73170, Thailand.

**E-mail: Warangkana.por@mahidol.edu*

Abstract:

Lignin is a natural polymer that has UV protection potential for sunscreen. However, lignin can cause irritation to the skin if applied at high concentration. Therefore, nanostructured lipid carriers (NLCs) were used in this work to reduce the irritation and prolong the UV protection efficiency. This study focuses on the optimization of lignin-loaded NLCs by using experimental designs including Plackett–Burman (PBD) and Box-Behnken design (BBD). PBD was studied first to investigate three significant variables among five variables in which affected the quality of NLCs. Then, BBD was applied to find the optimum condition for producing NLCs formulation. The results showed that the most affected variables were sonication time, amplitude of sonication, and lipid concentration, whereas surfactant to lipid and solid to liquid lipid ratio had less effect on the particle size of the NLCs compared to the others. These three variables were used as independent variables for BBD. A 50:50 ratio of cetyl palmitate and caprylic/capric triglyceride and a 50:50 ratio of tween 80 and span 40 were used as solid to liquid lipid ratio and co-surfactants, respectively. The optimum condition showed the smallest NLCs particle size of 95.9 ± 1.3 nm at time of 5 min 48 seconds, amplitude of 56%, and lipid concentration of 1.2%. The size was slightly decreased to 85.3 ± 0.86 nm after loading lignin in the NLCs. In conclusion, PBD and BBD are significant tools for the experimental design to find the optimal condition by reducing the number of experiments.

1. Introduction

The damaging effects of ultraviolet (UV) radiation are becoming more dangerous as the UV index increases over the year. During summer of 2021, the data from Thailand Meteorological Department (TMD) showed the averages UV index in Thailand was between 11- 13 which was extremely at high level[1,2].

Nanostructured lipid carriers (NLCs) are used widely as carrier in pharmaceutical applications, especially for topical drug delivery systems. NLCs compose of solid lipid, liquid lipid, surfactant, and active ingredient (carried substance). NLCs have the advantage potentials to be used in pharmaceuticals and cosmetics because they are safety, have good biological compatibility, and are small in particle size. Moreover, they can increase skin hydration. Some researchers claimed that they can protect hair damage from UV radiation[3].

Lignin, a natural phenolic bio-polymer, is one of renewable resources. Not only does it support the tissues of plants but also used as UV light protection. The phenolic group in lignin strongly affects the UV-shielding properties.

Packett-Burman design (PBD) and Box-Behnken design (BBD) are significant tools for the experimental design to find the optimal condition by reducing the number of experiments.

This study aims to optimize the condition for producing lignin-loaded NLCs with small particle size, and high lignin loading efficiency (%EE).

2. Materials and Methods

2.1 Materials

Cetyl palmitate, caprylic/capric triglycerides, tween80 and span40 were purchased from Chemipan Corporation Co., Ltd. Nakhon Pathom, Thailand. Lignin (alkaline) was purchased from TCI Co., Ltd. Tokyo, Japan.

2.2 NLCs Preparetion

For the preparation of NLCs using ultrasonic sonicator technique, lipid phase and aqueous phases were separately prepared. The lipid phase contained liquid lipid, solid lipid, and span40, while the aqueous phase contained distilled water and tween80. Tween80 and span40 were used as surfactant at the ratio of 1:1. Both phases were heated separately to 80 °C. Then, the aqueous phase was added to the lipid phase and then mixed using a homogenizer with 8000 rpm for 1 min. After that, the mixing of lipid and aqueous phase were sonicated by sonicate plobe.

2.3 Packett-burman design

Five variables studied by using the Packett–Burman design (PBD) were sonication time, amplitude, surfactant to lipid ratio, solid to liquid lipid ratio, and lipid concentration. The three effective variables that affect particle size and quality of NLCs were used for Box-Behnken Design (BBD). The Packett-Berman design experiments were shown in Table 1

Table 1. Packett-berman experiment for NLCs.

No	Time	Amplitude	Solid: liquid Lipid ratio	Surfactant: lipid ratio	Lipid concentration
1	5	50	90:10	1:4	10
2	1	50	90:10	1:1	2
3	1	10	90:10	1:1	10
4	5	10	50:50	1:1	10
5	1	50	50:50	1:4	10
6	5	10	90:10	1:4	2
7	5	50	50:50	1:1	2
8	1	10	50:50	1:4	2

2.4 Box Behnken Design

Three significant variables from PBD that affected to quality of NLCs the most were used as independent variables in BBD. The BBD is composed of 3-factors, 3-levels, and 15 runs for optimization as shown in Table 2. Sonication time (X1), amplitude (X2), and lipid concentration (X3) were selected as independent variables while particle size (Y1) and zeta potential (Y2) were dependent variables for optimization of NLCs. Constant variables were solid to liquid lipid ratio was 50:50 and surfactant to lipid ratio was 1:1. So the total surfactant concentration was 1% to 5%. From solid lipid to liquid lipid ratio was 1:1. So the concentration of total lipid was 1% to 5% according to Table 2.

The formulation was selected at minimum particle size which had small PDI, and zeta potential was more than ±30 mV. The quadratic model included polynomial equations, interaction factor, and main effect was used to investigate the optimum condition. 3-dimensional response surface plots were created by using MatLab R2022a The MathWorks, Inc.

Table 2. Independent variables (factor) and dependent variable (response) for BBD.

Variables	Low(-1)	Medium(0)	High(1)
Independent variables			
X1	2min	4min	6min
X2	30%	50%	70%
X3	1%	3%	5%
Dependent varibles			
Y1		Minimize	
Y2		Maximize	

2.5 Encapsulation lignin in NLCs

Lignin (alkali) was loaded in NLCs formulation by using ultrasonic sonicator. The lipid and aqueous phase were heated to 80 **℃.** Then, 1**%** of lignin was added to the aqueous phase before mixing both phases with homogenizer at 8000 rpm for 1 min**.** After that, the mixing of lipid and aqueous phase were sonicated at optimum condition according to BBD by using sonicate plobe.

2.6 Particle size measurement

The particle size of the NLCs and lignin-NLCs were measured at 25 **℃** using Zetasizer **(**from HOBITA. nanoPartica SZ-100V2 Series, Japan). NLCs and lignin-NLCs were measured after dilution with deionized (DI) water at the ratio of 1:200. The measurement results were reported as z-average size and polydispersity index (PDI).

2.7 Zeta-potential measurement

The zeta-potential of the NLCs and lignin-NLCs were measured at 25 **℃** using Zetasizer **(**from HOBITA. nanoPartica SZ-100V2 Series, Japan). 0.2 ml of samples were diluted with 4 ml of deionized water (DI). The measurement results were reported as zeta potential.

2.8 Encapsulation Efficiency

Lignin-loaded NLCs were diluted 10 times with distilled water**.** Then, the diluted samples were passed through a 0**.**22-micron syringe filter and then diluted 25 times with distilled water**.** After that, the samples were measured for absorbance by using a UV spectrometer at 278 nm. Encapsulation efficiency **(%**EE**)** of lignin-loaded NLCs was calculated by the following equation**:**

%EE **=** **(**lignin in NLCs ÷ total lignin**)** ×100

3. Results & Discussion

3.1 Packett-burman

From Figure 1, the most three significant factors of NLCs preparation were sonication time, amplitude of sonication, and lipid concentration**.** Meanwhile, surfactant to lipid and solid to liquid lipid ratio had less effect on the particle size of the NLCs compared to the others**.** From the standardized effect, time and amplitude were negative value which meant if the time and the amplitude of sonication were increased the particle size would be decreased**.**

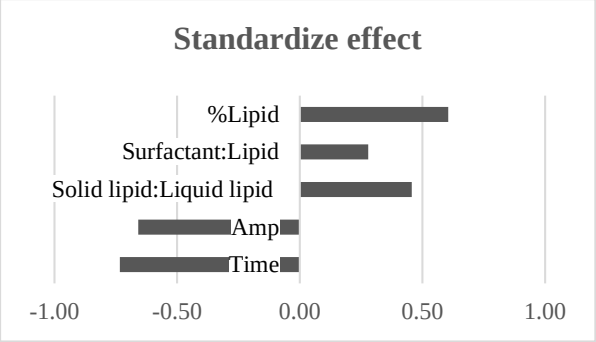

Figure 1. Standardize effect of independent variables with tween80 and span 40 as surfactant of NLCs.

3. 2 Optimization of NLCs by Box-Behnken Design

The most independent factors on particle size from PBD including sonication time (X1), amplitude (X2), and lipid concentration (X3) were selected as independent factors for BBD experiment. Moreover, conditions were slightly adjusted to sonicated time of 2-6 min, amplitude of 30-70%, and lipid content of 1-5%. The constant variables were solid to liquid lipid ratio (50:50) and surfactant to lipid ratio (1:1). The result from 15 experimental runs of BBD were shown in Table 3. The response surface plots (RSM) shown in Figure 2 were used to analyze the interactions of two independent variables on the dependent variables. The following equation were calculated by regression in Excel with quadratic model.

Particle size = $110.2 - 13.97X1 - 3.88X2 + 28.78X3 + 7.29X1X2 + 3.18X1X3 + 12.05X2X3 + 8.16X1^2 + 13.51X2^2 + 19.9X3^2$

Zeta potential = $-49.80 + 7.78X1 + 0.55X2 + 5.14X3 - 2.69X1X2 - 11.58X1X3 - 7.21X2X3 - 11.28X1^2 - 17.00X2^2 + 15.72X3^2$

From the above quadratic equation from the BBD experiment, the R^2 of equation was 0.9623. Positive coefficient refers to direct relationship between factors and responses, whereas negative coefficient indicates the inverse relationship. Thus, if sonication time and amplitude increased, the particle size would be decreased because ultrasonic wave causes the breakage of NLCs particles into smaller particle with monodisperse due to high shear forces[5]. On the other hand, the particle size of NLCs increased when lipid concentration increased due to an increase in particle agglomeration [6].

The optimum condition from BBD was at sonication time of 5 min 48 seconds, amplitude of 56%, and lipid concentration of 1.2%. The optimum particle size from equation (predicted) and actual value were 90.31 nm and 95.9 ± 1.3 nm with zeta potential of -34.40 mV and -38.33 ± 0.25 mV, respectively.

Table 3. Box-Behnken Design for NLCs.

Entries	Time(min) (X1)	Amplitude (X2)	%lipid concentration (X3)	Particle size(nm) (Y1)	Zeta potential(mV) (Y2)
1	2	30	3	156.8	-84.9
2	2	70	3	128.4	-82.8
3	6	30	3	120.8	-68.0
4	6	70	3	121.5	-76.6
5	2	50	1	134.6	-74.3
6	2	50	5	175.6	-36.0
7	2	50	1	93.8	-31.6
8	6	50	5	147.5	-39.6
9	4	30	1	122.2	-63.7
10	4	30	5	165.9	-43.9
11	4	70	1	96.4	-43.9
12	4	70	5	188.3	-52.8
13	4	50	3	116.4	-51.4
14	4	50	3	109.8	-48.0
15	4	50	3	104.5	-50.0

Solid to liquid lipid ratio **(**50**:**50**)** and Surfactant to lipid ratio **(**1**:**1**)** were constant variables**.**

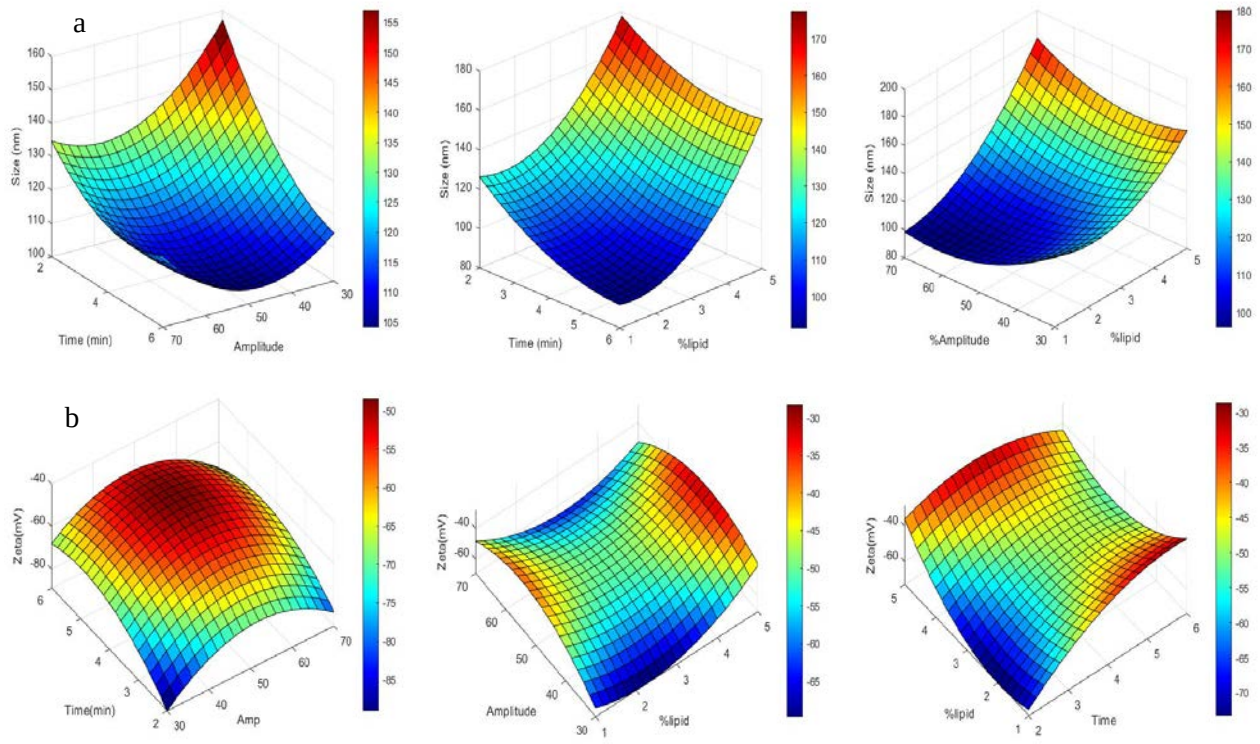

Figure 2. 3-D Response Surface plot showing the effect of significant variables on (a) particle size and (b) zeta potential.

3.3 Encapsulation lignin-NLCs

1% of alkali lignin by total weight was loaded in NLCs formulation according to optimum condition from BBD. The particle size after lignin loading was decreased to 85.3 ± 0.86 nm with zeta potential that increased to -92.43 ± 0.45 mV. Since lignin contains a phenolic group, the zeta-potential showed negative charge on NLCs. This strongly affects the UV- shielding properties[7]. % EE for lignin-loaded NLCs was 14.61 ± 0.28%.

4. Conclusion

PBD and BBD are significant tools for the experimental design to find the optimal condition by reducing the number of experiments. The particle size of NLCs and lignin-loaded NLCs at optimum conditions at sonication time of 5 min 48 seconds, amplitude of 56%, and lipid concentration of 1.2% were 95.9 ± 1.3 nm and 85.3 ± 0.86 nm respectively. It showed a small particle size when lignin was loaded in NLCs.

Acknowledgements

This research was funded by Ministry of science and technology. The authors are thankful to Mahidol University-Frontier Research Facility (MU-FRF) and department of Chemical Engineering, Faculty of Engineering, Mahidol University for facilities.

References

1. Punyaphat Sirithanabadeekul M.D., Thailand UV Index Rating and the Risk of Sunburn. https://www.samitivejhospitals.com/article/detail/uv-index (accessed May 15, 2021).
2. Thai Meteorological Department, UV index http: / / ozone. tmd. go. th/ UV_index. htm (accessed May 16,2021).
3. Miao, L.; Daozhou, L.; Ying, C.; Qibing, M.; Siyuan, Z. *Colloids and Surfaces B: Biointerfaces* **2021**, *204*, 111786.
4. Sadeghifar, H.; Ragauskas, A. Lignin as a UV Light Blocker—a Review. *Polymers* **2020**, *12* (5), 1134.
5. Alam, T.; Khan, S.; Gaba, B.; Haider, Md. F.; Baboota, S. ; Ali, J. *Journal of Pharmaceutical Sciences* **2018**, *107* (11), 2914–2926.
6. Subedi, R. K.; Kang, K. W.; Choi, H.-K. *European Journal of Pharmaceutical Sciences* **2009**, *37* (3-4), 508–513.
7. Zhang, Y.; Naebe, M. Lignin: *ACS Sustaina* **2021**, 9 (4), 1427–1442.

Preparation and properties of wet wipes from water hyacinth

Worakrit Chanai[1], Jamecharun Srikeaw[1], Ketsak Trerawaranun[1], and Sa-ad Riyajan[2]*

[1]*SCIUS TU-SKR, Suankularbwittayalai Rangsit School, Khlong Si, Khlong Luang, Pathum Thani, 12120, Thailand*
[2]*Department of Chemistry, Faculty of Science and Technology, Thammasat University, 99 Moo 18 Paholyothin Road, Klong-Luang, Pathumthani, 12120, Thailand*

**E-mail: saadriyajan@hotmail.com*

Abstract:

Wet wipes, or what Thai people like to call wet tissues, contain synthetic plastic fibers, making them unable to biodegrade naturally. If left untreated, it will become excess waste that remains in nature, directly affecting nature and the environment in that area, and cannot decompose naturally, including causing microplastics. Therefore, operators' research is interested in applying agricultural waste into wet wipe products to solve the problem and make it friendly to the natural environment by using cellulose fibers from water hyacinth. It is resistant to synthetic plastic fibers and reinforces the structure of cellulose fibers with silica from rice husks and pectin from rice husks in various ratios. Then, it will be experimented to compare and find the appropriate ratio formula with similar characteristics. It can be replaced with wet wipes that contain synthetic plastic fibers.

1. Introduction

Currently, we can observe that wet wipes, or "กระดาษทิชชู่เปียก" in Thai, are considered essential due to their convenience in various cleaning applications. They are commonly used for personal hygiene, replacing handwashing, facial cleansing, and even body cleaning as an alternative to bathing. Additionally, wet wipes are employed for discreetly cleaning hidden spots after completing heavy or light tasks.

However, it may not be widely known that the used wet wipes, if not disposed of properly or classified correctly for disposal, can pose hazards and create significant environmental problems. Wet wipes, often composed of synthetic plastic fibers, are non-biodegradable by nature. Improper disposal leads to environmental pollution, contributing to the persistence of excess waste in natural environments. Furthermore, their flammability increases the risk of forest fires, and their resistance to natural decomposition results in the generation of microplastics.

Cellulose fibers from Tapioca plants, strengthened with silica from rice husks and enriched with pectin from jackfruit rinds, offer a potential solution. Tapioca-derived fibers are a type of cellulose fiber found in plants or fruits, characterized by long-chain molecules with a high degree of intertwining, providing good flexibility and low elongation. Silica, derived from rice husks, enhances the strength of cellulose fibers, and pectin from jackfruit rinds contributes to their cohesion. Cellulose fibers are bio-based and exhibit good water and moisture absorption, efficient heat conduction, low thermal recovery, strong adhesion, and excellent electrical conductivity. Additionally, they are resistant to mold and insects, biodegradable in nature, and tolerant to sunlight.

The research team aims to repurpose agricultural residues to create environmentally friendly wet wipes. By using cellulose fibers from Tapioca plants to replace synthetic plastic fibers, the study seeks to address environmental concerns associated with conventional wet wipes. Using agricultural residues aligns with principles of natural degradation and environmental sustainability. The study involves testing cellulose fibers against synthetic plastic fibers to determine their suitability as an alternative in wet wipe production. The research team is particularly interested in utilizing Tapioca plant fiber

2. Materials and Methods

2.1 Materials

2.1.2 Eichhornia crassipes
2.1.2 Rice husk
2.1.3 Durian peel
2.1.4 Sodium hydroxide
2.1.5 Hydrochloric acid
2.1.6 Nitric acid
2.1.7 Sulfuric acid
2.1.8 Phosphoric acid

All materials and equipment used in the experiment are available in the Thammasat University laboratory.

2.2 Preparation of Substances

2.2.1 Preparation of Cellulose Fiber from Eichhornia crassipes

Grind or crush the Water hyacinth into small pieces then bake or sun-dry until they dry. Soak the dried Eichhornia crassipes in sodium hydroxide solution at a ratio of 100 grams per liter of water for 3-7 days. Wash the soaked Eichhornia crassipes with sodium hydroxide solution using distilled water until the pH value becomes neutral, then bake it at a temperature of 100 degrees Celsius for 24 hours. Soak the obtained Eichhornia crassipes in sulfuric acid for 3-7 days.

2.2.2 Preparation of Silica from Rice Husk

Clean the Rice husks with distilled water and place them on a Hotplate Stirrer. Immerse them in HCl, HNO_2, H_2SO_2, and H_3PO_6 (20% concentration in water, approximately 20 milliliters per gram of husk) at 100 degrees Celsius for 1 hour. Wash the Rice husks with distilled water until the pH value becomes neutral. Then, bake them at 70 degrees Celsius for 12 hours. Take the washed Rice husks and incinerate them in an electric furnace at 600 degrees Celsius for 6 hours, maintaining a temperature gradient of 2 degrees Celsius per minute.

2.2.3 Preparation of Pectin from Durian peel

Take the dried and ground Durian peel prepared in advance and place them in a beaker, 10 grams per beaker. Then, add the solvent used for extraction, which is hydrochloric acid (HCl) with a pH of 3, using a ratio of dried rinds to the solvent at 1:12 (w/v). Extract the mixture in a temperature-controlled water bath at 80 degrees Celsius for 60 minutes. Filter through a thin layer of white cloth once and take the filtered rinds to refill with the solvent, maintaining the same ratio as before (1:12 w/v). Extract again and, after completion, filter through a thin layer of white cloth. Combine the obtained solutions from both extractions. Precipitate Pectin by adding concentrated ethanol (ethanol 95%) in a ratio of 1:1 (v/v) to the Pectin solution. Mix vigorously using a glass rod, then let it stand at room temperature for 15 hours. Filter and separate the Pectin precipitate through a thin layer of two pieces of fine white cloth. Additionally, the Pectin precipitate was obtained three times with 95% ethanol and three times with acetone (50% concentration).

Take the Pectin precipitate obtained, dry it at 60 degrees Celsius, weigh it, and grind it into powder.

2.3 Experiment Method

2.3.1 Molding process for shaping pieces or Wet wipes.

Take cellulose fibers, disperse them in water, and mix them with pectin and silica in ratios of 20:2:0, 20:2:0.25, 20:2:0.5, 20:2:1, and 20:2:1.5 grams respectively. Then, mold the mixture into the desired shape using a mold and let it stand for 1-3 days.

2.3.2 Testing water absorption and ethanol absorption content percentage.

Take the Cellulose fibers reinforced with silica and pectin to test the percentage of moisture absorption in the air (Moisture). For each formula, cut the sample into 10 pieces, each sample measuring approximately 1 x 3 centimeters. Record the weight before baking using a digital scale with four decimal places and bake in a Hot Air Oven at 100 degrees Celsius for 1 hour. Record the weight after baking. Then, calculate the percentage of moisture absorption in the air by using the weight before and after baking. Test the percentage of water absorption after soaking for 1 hour for Cellulose fibers reinforced with silica and pectin. For each formula, cut the sample into 10 pieces, each sample measuring approximately 1 x 3 centimeters. Soak them in water for 1 hour. Record the weight after soaking using a digital scale with four decimal places and then bake them in a Hot Air Oven at 100 degrees Celsius for 1 hour. Record the weight after baking. Then, calculate the percentage of water absorption in the air using the weight after soaking and after baking. Test the percentage of water absorption in ethanol 90% after soaking in ethanol 90% for 1 hour for Cellulose fibers reinforced with silica and pectin. For each formula, cut the sample into 10 pieces, each sample measuring approximately 1 x 3 centimeters. Soak them in ethanol 90% for 1 hour. Record the weight after soaking using a digital scale with four decimal places and then bake them in a Hot Air Oven at 100 degrees Celsius for 1 hour. Record the weight after baking. Then, calculate the percentage of water absorption in the air using the weight after soaking and after baking.

2.3.3 Testing for Dissolution Rate

Take the Cellulose fiber after structural reinforcement with silica and pectin to test the dissolution. In each experimental formula, cut three sample pieces, each with dimensions of approximately 1 x 3 centimeters. Place the samples in a bottle filled with sterilized soil. Insert the cellulose fibers after structural reinforcement into the soil and cover them with soil to make it

compact. Then, bury the bottle in the soil. Take pictures and observe the results.

2.3.4 Testing the tensile strength value

Testing the tensile strength value of Cellulose fibers reinforced with silica and pectin. In each formula, a sample piece (1 piece per formula) is taken for testing using a dumbbell-shaped tensile testing machine, and the test results are recorded.

2.3.5 Test for Flexural Strength, Elasticity, and Modulus

Test Flexural Strength of Cellulose Fibers Reinforced with Silica and Pectin using the Three-Point Bending Test

2.3.6 Morphological Examination

Examine the Morphological Characteristics of Cellulose Fibers Reinforced with Silica and Pectin, including attributes such as color, structure, size, shape, and pattern, using histological methods.

2.3.7 Antimicrobial Activity Test

Testing the antimicrobial properties of cellulose fibers reinforced with silica and pectin against bacteria.

2.3.8 Incorporating Substance

When obtaining the reinforced cellulose fibers in the desired ratio, the next step is to fill or incorporate internal substances to achieve properties similar to wet wipes.

3. Results & Discussion

3.1 Density detection

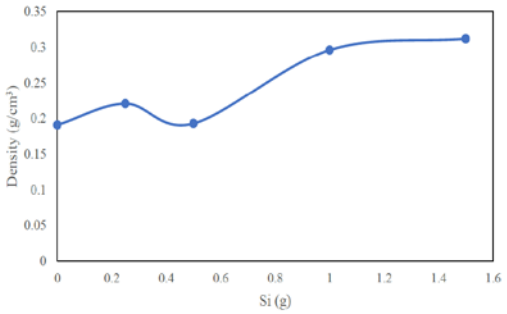

Figure 1. The density values of cellulose fiber strands after structural reinforcement with varying amounts of silica.

3.2 Testing water absorption and ethanol absorption content percentage.

3.2.1 Average percentage of water absorption in the air

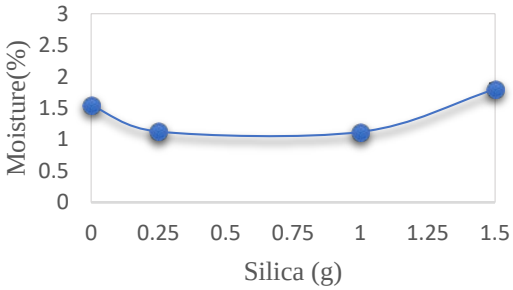

Figure 2. The average percentage of water absorption in the air for cellulose fiber-reinforced structures with varying amounts of silica.

3.2.2 Average percentage of water absorption after immersion in water

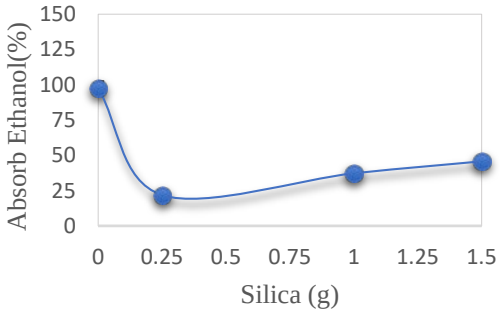

Figure 3. The average water absorption percentage after soaking for 1 hour for cellulose fibers reinforced with varying amounts of silica.

3.2.3 Average percentage of ethanol absorption after immersion in ethanol

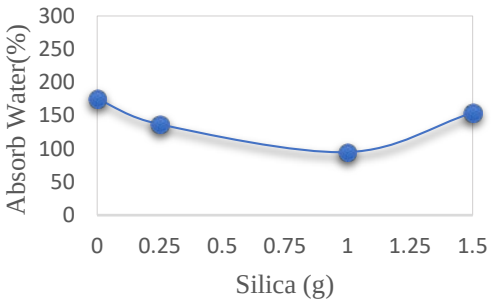

Figure 4. The average ethanol absorption percentage after soaking in ethanol for 1 hour for cellulose fibers reinforced with varying amounts of silica.

3.3 Testing for Dissolution Rate

Based on the observations recorded after the experiment on the 10th day, it was found that there were no remaining test specimens, indicating that the specimens had completely degraded into the soil within 10 days.

Figure 5. Depicts wet wipes after 10 days of biodegradation.

4. Conclusion

It is possible to manufacture wet wipes products from agricultural by-products that have similar characteristics to conventional wet wipes. These wet wipes are composed of synthetic plastic fibers, and the products are biodegradable, causing no harm to the natural environment. It reduces the amount of natural waste that does not degrade on its own or takes a long time to decompose from wet wipes, which consist of synthetic plastic fibers. We expect that we will expand product development to be widely accepted domestically and internationally, making it suitable for everyday use.

Acknowledgment

The authors would like to thank the Department of Chemistry, Faculty of Science and Technology, Thammasat University, for providing access to their excellent laboratory facilities and equipment and the SciUS Program (TU-SKR) for their generous financial support. These contributions have been crucial to the success of our research.

References

1. Allison, T.; Ward, B. D.; Harbottle, M.; Durance, I. *Sci. Total Environ.* **2023,** *894*, 164912.
2. Zhang, Y.; Xu, Y.; Zhao, Y.; Huang, C.; Jin, X. *Eur. J. Wood Wood Prod*. **2019**, *77*, 33-43.
3. Ramya, K.; Amutha, K. Eco-Friendly Wet Wipes-A Review, **2021**.
4. Hamouda, T.; Ibrahim, H. M.; Kafafy, H. H.; Mashaly, H. H.; Mohamed, N. H.; Aly, N. M. *Int. J. Biol. Macromol.* **2021**, *181*, 990-1002.
5. Zhang, Y.; Wen, Z.; Hu, Y.; Zhang, T. *J. Clean. Prod.* **2022**, *364*, 132684.
6. Zhang, Y.; Wen, Z.; Lin, W.; Hu, Y.; Kosajan, V.; Zhang, T. *Resour. Conserv. Recycl.* **2021**, *174*, 195803

α-Glucosidase inhibitory activity of *Cyperus rotundus* rhizome extracts

Lalita Pimsawang[1], Vasakorn Bullangpoti[2], and Wanchai Pleumpanpat[1]*

[1]*Department of Chemistry and Center of Excellence for Innovation in Chemistry, Special Research Unit for Advanced Magnetic Resonance, Faculty of Science, Kasetsart University, Bangkok 10900, Thailand*
[2]*Animal Toxicology and Physiology Specialty Research Unit, Department of Zoology, Faculty of Science, Kasetsart University, Bangkok 10900*

**E-mail: fsciwcp@ku.ac.th*

Abstract:

Cyperus rotundus L. or Ya Haew Moo is commonly named nutgrass and belongs to the Cyperaceae family. This plant displays various biological activities such as antidiabetic, antibacterial, antioxidant, and anti-inflammatory. Therefore, the present study extended to assess its utility for the enzyme inhibitory potential against *α*-glucosidase, tyrosinase, and acetylcholinesterase. The dried powder of *C. rotundus* rhizomes was produced using sequential extraction over 7 days with hexane, dichloromethane, ethyl acetate, and methanol, respectively, by maceration at room temperature. The extracts were preliminarily screened for their potential to inhibit enzymes at a concentration of 500 ppm. The results found that the methanol extract exhibited the highest *α*-glucosidase inhibition with 93.36 ± 0.62%. This extract has an IC_{50} value of 4.49 ± 0.56 ppm and was more potent than acarbose as a positive control, which has an IC_{50} value of 97.55 ± 7.67 ppm. However, the extracts of *C. rotundus* rhizomes showed no inhibition against tyrosinase and acetylcholinesterase.

1. Introduction

Diabetes is a chronic disease when the body produces insufficient amounts of insulin or cannot use the insulin that the pancreas produces. Insulin is one hormone that regulates blood sugar levels. Uncontrolled type 2 diabetes frequently results in hyperglycemia, which eventually damages the body's several systems, particularly the blood vessels and the neurons. *α*-glucosidase, an enzyme involved in carbohydrate metabolism, is present in the small intestines. Its role is to hydrolyze terminal nonreducing 1,4-linked *α*-glucose residues released into the bloodstream.[1] Consequently, inhibitors of *α*-glucosidase can effectively reduce blood glucose levels by inhibiting the hydrolysis of dietary carbohydrates in the small intestine. However, currently available *α*-glucosidase inhibitors, such as acarbose, come with undesirable gastrointestinal side effects. These include abdominal bloating, cramping, increased flatulence, and diarrhea.[2] Consequently, there is an urgent need for novel *α*-glucosidase inhibitory drugs that are selective and exhibit reduced side effects.

Tyrosinase is a type of oxidoreductase enzyme that is involved in the oxidation and reduction of epidermal cells. The melanogenesis process mainly depends on these chemical processes that the enzyme catalyzes.[3] Tyrosinase is a common target for pharmacological drugs because it catalyzes the first two rate-limiting steps in the biosynthesis of melanin pigment: the hydroxylation of L-tyrosine to L-DOPA, the oxidation of L-DOPA to dopaquinone, and synthesized to melanin pigments.[4] Consequently, tyrosinase inhibitors are now commonly used as "skin tone lighteners" for decreasing hyperpigmentation.[5]

The neurotransmitter acetylcholine, essential for memory and cognition, is hydrolyzed by acetylcholinesterase (AChE), one of the most important enzymes in the family of serine hydrolases.[6] Cholinergic transmission is improved by this enzyme's inhibitors, such as rivastigmine and galantamine, which increase the amount of acetylcholine. These compounds are used to treat Alzheimer's disease symptoms, which are associated with cholinergic neuron degeneration and impaired transmission.[7] Several synthetic and natural cholinesterase inhibitors are on the drug market. However, their limited medicinal application because of side effects and relatively low bioavailability leads to an urgent demand to discover novel cholinesterase inhibitors.

Cyperus rotundus L. or Ya Haew Moo is commonly named nutgrass and belongs to the Cyperaceae family. It is distinguished by having a perennial life cycle comparable to grasses, plants that can grow up to 40 cm tall, and rhizomes and tubers with significant medicinal benefits. Inflorescences of the *C. rotundus* have 2-4 bracts and 2–10 narrow, flat spikelets, while the leaves of the plant are linear. This species subsurface system, composed of tubers, bulbs, and rhizomes, ensures it can survive even under in unfavorable environments.[8]

Rhizomes of this plant have been reported for various biological activities including antidiabetic, antibacterial, antiapoptotic, anti-inflammatory, and anti-oxidative activities.[9,10] The chemical compositions of *C. rotundus* rhizomes consist of sesquiterpenes, iridoid glycosides and phenolic, phenolic compounds, flavonoids, saponins, phenylpropanoids, and alkaloids that should have the potential for enzyme inhibitory activity.[1,11,12,13] Consequently, the rhizome of *C. rotundus* was selected to evaluate its *α*-glucosidase, tyrosinase, and acetylcholinesterase inhibitory activities. This investigation aims to identify alternative plants for disease treatment, concurrently enhancing the medicinal properties and overall value of *C. rotundus* rhizomes.

2. Materials and Methods

2.1 Materials

All solvents used in this study were purified previously used by standard methodology. *α*-Glucosidase from *Saccharomyces cerevisiae*, tyrosinase from mushroom, acetylcholinesterase from *Electrophorus electricus* (electric eel), 3,4-dihydroxy-L-phenylalanine (L-DOPA), 5,5′-dithiobis(2-nitrobenzoic acid) (DTNB), acetylthiocholine iodine (ATCI), and 9-Amino-1,2,3,4-tetrahydroacridine hydrochloride hydrate (tacrine) were purchased from Sigma-Aldrich (USA). 4-Nitrophenyl-*α*-D-gluco-pyranoside (PNP-G), acarbose hydrate, and kojic acid were purchased from TCI (Japan). Sodium carbonate (Na_2CO_3) was purchased from Kemaus (Australia). And dimethylsulfoxide (DMSO) was purchased from Carlo Erba (France).

2.2 Plant materials

The dried rhizomes of *C. rotundus* (3.6 kg) were purchased in December 2020 from Chao Krom Poe Dispensary Pharmacy, Bangkok, Thailand.

2.3 Extraction

The dried rhizomes of *C. rotundus* were ground into a powder and sequentially extracted at room temperature over seven days for each solvent using hexane, dichloromethane, ethyl acetate, and methanol, respectively. Subsequently, all extracts were evaporated under reduced pressure in a rotary evaporator. Finally, all extracts were stored at 4°C in a refrigerator.

2.4 Enzyme inhibitory activity

2.4.1 *α*-Glucosidase inhibitory activity

The *α*-glucosidase inhibitory activity of the extracts of *C. rotundus* rhizomes was evaluated in a reaction of the solution, 50 µL 0.1 M phosphate buffer at pH 6.8, 10 µL of the crude sample (final concentration of 500 ppm containing 1% v/v DMSO), and 20 µL of 0.2 U/mL of *α*-glucosidase from *Saccharomyces cerevisiae*. After incubation at 37ºC for 5 minutes, 20 µL of 2.5 mM of PNP-G was added as a substrate. The incubation continued at 37ºC for 15 minutes, 50 µL of 0.4 M of Na_2CO_3 was added to stop the reaction. Then, the absorbance of 400 nm in each well was measured using a microplate reader (MPR, Spark™ 10M). Acarbose was used as a positive control. All experiments were performed in three replicates for each sample, and data were expressed as mean ± standard deviation (SD). The percentage inhibition and IC_{50} values of *α*-glucosidase activity were calculated using GraphPad Prism 6.[14] Sample concentrations in the range of 0.5-125.0 ppm were prepared in 1% v/v DMSO.

2.4.2 Tyrosinase inhibitory activity

The tyrosinase inhibitory activity of the extracts of *C. rotundus* rhizomes was evaluated by a dopachrome method using L-DOPA as a substrate. In a reaction mixture of the solution, 80 µL of 0.02 M phosphate buffer at pH 6.8, 40 µL of the crude sample (final concentration of 500 ppm containing 1% v/v DMSO), 20 µL of 100 U/mL of tyrosinase from the mushroom. After incubation at 23ºC for 10 minutes, 40 µL of 0.3 mM L-DOPA solution was added as a substrate. Then, the reaction was incubated for 5 minutes at 23°C and measured the absorbance of 475 nm in each well using a microplate reader (MPR, Spark™ 10M). Kojic acid was used as a positive control. All experiments were performed in three replicates for each sample, and data were expressed as mean ± standard deviation (SD). The percentage inhibition and IC_{50} values of tyrosinase activity were calculated using GraphPad Prism 6.[15]

2.4.3 Acetylcholinesterase inhibitory activity

The acetylcholinesterase inhibitory activity of the extracts of *C. rotundus* rhizomes was evaluated in a reaction of the solution, 90 µL of 0.1 M phosphate buffer at pH 8.0, 10 µL of the sample (the inhibitor) containing 20% DMSO (final concentration 500 ppm), 20 µL of 0.4 U/mL of acetylcholinesterase from *Electrophorus electricus* (electric eel), and 40 µL of 0.6 mM of DTNB were added. After incubation at 37ºC for 10 minutes, 40 µL of 0.6 mM of ATCI was added as a substrate. Then, the reaction was incubated for 20 minutes at 37°C, and measured the absorbance of 412 nm in each well using a microplate reader (MPR, Spark™ 10M). Tacrine was used as a positive control. All experiments were performed in three replicates for each sample, and data were

Table 1. Characteristics and amounts of extracts of *C. rotundus* rhizomes

Extract	Weight (g)	Yield[a] (%wt/wt)	Characteristics
Hexane	6.55	0.18	Dark brown oil
Dichloromethane	13.91	0.39	Dark brown gum
Ethyl acetate	43.52	1.21	Dark brown gum
Methanol	157.47	4.37	Dark brown gum

[a](weight of crude extract/weight of dried plant) × 100

Table 2. Enzyme inhibitory activity of the extracts of *C. rotundus* rhizomes at a concentration of 500 ppm

Extract	%Inhibition (%)		
	α-Glucosidase	Tyrosinase	Acetylcholinesterase
Hexane	87.94 ± 0.45	NI	NI
Dichloromethane	51.60 ± 2.15	NI	NI
Ethyl acetate	NI	NI	NI
Methanol	93.36 ± 0.62	NI	NI
Acarbose (1.60 mM)	89.12 ± 0.40	-	-
Kojic acid (1.00 mM)	-	98.59 ± 0.35	-
Tacrine (10.00 μM)	-	-	99.03 ± 0.24

NI = No inhibition

expressed as mean ± standard deviation (SD). The percentage inhibition and IC_{50} values of acetylcholinesterase activity were calculated using GraphPad Prism 6.[16]

3. Results & Discussion

3.1 Extraction

From the sequential extraction of *C. rotundus* rhizomes, the methanol extract was found at the highest yield (4.37%), whereas the hexane extract was obtained at the lowest yield (0.18%). The characteristic of hexane extract was dark brown oil and the other crude extracts were dark brown gum, as shown in Table 1.

3.2 Enzyme inhibitory activity

In enzyme inhibitory activity, the four crude extracts of *C. rotundus* rhizomes were preliminarily screened for their potential to inhibit the enzymes, *α*-glucosidase, tyrosinase, and acetylcholinesterase at a concentration of 500 ppm compared to standard acarbose, kojic acid, and tacrine, respectively.

Regarding *α*-glucosidase inhibitory activity, the results found that the methanol extract exhibited the highest inhibition with 93.36 ± 0.62%, followed by the hexane extract with 87.94 ± 0.45%. Meanwhile, the dichloromethane and ethyl acetate extracts showed moderate and no inhibition, respectively (Table 2). The IC_{50} value of the most active methanol extract was 4.49 ± 0.56 ppm, which was more potent than acarbose as a positive control approximately 22-fold (Table 3).

Unfortunately, all extracts of *C. rotundus* rhizomes had no inhibition against tyrosinase and acetylcholinesterase at a concentration of 500 ppm (Table 2).

Table 3. IC_{50} values of *α*-glucosidase inhibitory activity of *C. rotundus* rhizome extracts

Extract	IC_{50} ± SD (ppm)
Hexane	30.14 ± 11.39
Dichloromethane	>500
Ethyl acetate	>500
Methanol	4.49 ± 0.56
Acarbose	97.55 ± 7.67

IC_{50} = half maximal inhibitory concentration

4. Conclusion

This present study is the first report regarding the inhibition against *α*-glucosidase, tyrosinase, and acetylcholinesterase of *C. rotundus* rhizomes. It is important to note that the methanol extract of *C. rotundus* rhizomes was the first identified as the most active against *α*-glucosidase and could serve as a promising source of botanical medicine for the development of a new potential antidiabetic drug. Further studies are focused on the identification of active ingredients from the methanol extract of *C. rotundus* rhizomes and the mechanism of *α*-glucosidase inhibition.

Acknowledgements

This work was supported by the Center of Excellence for Innovation in Chemistry (PERCH-CIC), Ministry of Higher Education, Science, Research and Innovation; the Kasetsart University Research and Development Institute (KURDI); the Department of Chemistry, Department of Zoology, Faculty of Science, Kasetsart University.

References

1. Zeng, L.; Zhang, G.; Lin, S.; Gong, D. *J. Agric. Food Chem.* **2016**, *64* (37), 6939-6949.
2. Li, T.; Kongstad, K. T.; Staerk, D. *J. Nat. Prod.* **2019**, *82* (2), 249-258.
3. Wang, G.; Xia, Y.; Sui, W.; Si, C. *ACS Sustainable Chem. Eng.* **2018**, *6* (7), 9510-9518.
4. Jeong, S. H.; Ryu, Y. B.; Curtis-Long, M. J.; Ryu, H. W.; Baek, Y. S.; Kang, J. E.; Lee, W. S.; Park, K. H. *J. Agric. Food Chem.* **2009**, *57* (4), 1195-1203.
5. Mayr, F.; Sturm, S.; Ganzera, M.; Waltenberger, B.; Martens, S.; Schwaiger, S.; Schuster, D.; Stuppner, H. *J. Nat. Prod.* **2019**, *82* (1), 136-147.
6. Alarcón, J.; Cespedes, C. L.; Muñoz, E.; Balbontin, C.; Valdes, F.; Gutierrez, M.; Astudillo, L.; Seigler, D. S. *J. Agric. Food Chem.* **2015**, *63* (47), 10250-10256.
7. Ohlendorf, B.; Schulz, D.; Erhard, A.; Nagel, K.; Imhoff, J. F. *J. Nat. Prod.* **2012**, 75 (7), 1400-1404.
8. Bezerra, J. J. L.; Pinheiro, A. A. V. *S. Afr. J. Bot.* **2022**, *144*, 175-186.
9. Sim, Y.; Choi, J. G.; Gu, P. S.; Ryu, B.; Kim, J. H.; Kang, I.; Jang, D. S.; Oh, M. S. *Biomol. & Ther.* **2016**, *24* (4), 438-445.
10. Zhang, L.-L.; Chen, Y.; Li, Z.-J.; Fan, G.; Li, X. *J. Agric. Food Chem.* **2023**, *71* (1), 121-142.
11. Cui, C.; Wu, S.-L.; Chen, J.-J.; Gongpan, P.; Guan, M.; Geng, C.-A. *J. Agric. Food Chem.* **2023**, *71* (43), 16148-16159.
12. Alvi, K. A.; Diaz, M. C.; Crews, P.; Slate, D. L.; Lee, R. H.; Moretti, R. *J.Org.Chem.* **1992**, *57* (24), 6604-6607.
13. Ryu, H. W.; Lee, B. W.; Curtis-Long, M. J.; Jung, S.; Ryu, Y. B.; Lee, W. S.; Park, K. H. *J. Agric. Food Chem.* **2010**, *58* (1), 202-208.
14. Pluempanupat, W.; Adisakwattana, S.; Yibchok-Anun, S.; Chavasiri, W. *Arch. Pharmacal Res.* **2007**, *30* (12), 1501-1506.
15. Mutschlechner, B.; Rainer, B.; Schwaiger, S.; Stuppner, H. *Chem. Biodivers.* **2018**, *15* (4), e1800014.
16. Ellman, G. L.; Courtney, K. D.; Andres, V.; Featherstone, R. M. *Biochem. Pharmacol.* **1961**, *7* (2), 88-95.

Evaluation of enzyme inhibitory activity of *Ganoderma lucidum* (antler shaped lingzhi fruiting body) extracts

Apisara Bungarat[1], Prapassorn Rugthaworn[2], Udomlak Sukatta[2]*, and Wanchai Pluempanupat[1,3]*

[1]*Department of Chemistry, Faculty of Science, Kasetsart University, Bangkok, Thailand, 10900*
[2]*Kasetsart Agricultural and Agro-Industrial Product Improvement Institute, Kasetsart University, Bangkok, 10900, Thailand*
[3]*Center of Excellence for Innovation in Chemistry, Special Research Unit for Advanced Magnetic Resonance, Kasetsart University, Bangkok 10900, Thailand*

**E-mail: aapuls@ku.ac.th, fsciwcp@ku.ac.th*

Abstract:

In recent times, there has been a rising demand for supplementary food made from natural extracts and organic cosmetic items that contain bioactive compounds as part of their ingredients. Consequently, the extracts and bioactive compounds from Lingzhi (*G. lucidum*) stand out as particularly interesting ingredients due to their rich bioactive profile. In the present work, dried *G. lucidum* (antler shaped lingzhi fruiting body) was sequentially extracted using hexane, dichloromethane, ethyl acetate, and ethanol. All extracts were examined effectiveness for their α-glucosidase, tyrosinase, and acetylcholinesterase inhibitory activities. As a result, the ethanol extract possessed good potential both for tyrosinase with 302.03 ± 15.62 µg/mL and α-glucosidase 105.46 ± 3.21 µg/mL. However, no inhibition of the extracts was obtained for acetylcholinesterase. The results indicated that the mushroom extracts could be incorporated into the future development of skincare and dietary supplements.

1. Introduction

In recent times, consumers have become more conscious about the safety and effectiveness of processed products. Therefore, there is an increasing demand for supplementary food for maintaining or improving health from natural extracts and organic cosmetic items that contain bioactive compounds as part of their ingredients. Consequently, mushrooms have been known to exhibit a variety of biologically active compounds.[1] The extract and bioactive compound from *Ganoderma lucidum* are great interesting ingredients due to their rich bioactive profile with potential therapeutic benefits such as antioxidant, neuroprotective[2], antidiabetic, antitumor[3]. Additionally, they have been reported to effectively inhibit tyrosinase as an ezyme that involve in the synthesis of melanin pigment, as well as they also inhibit elastase and collagenase, enzymes that contribute to the degradation of the skin's extracellular matrix (ECM)[12].

Ganoderma lucidum Karst, commonly known as “Lingzhi” in Chinese or “Reishi” in Japanese, is a member of the *Ganoderma* genus and has been traditionally used for several thousand years in Asian countries. This mushroom is widely recognized as a popular folk medicine for the promotion of longevity and treatment of various human diseases.[4] *G. lucidum* contains a variety of chemical constituents, such as polysaccharides and triterpenes. Triterpenes are one of the significant compositions, and more than one hundred triterpenes have been reported from this mushroom in recent years. Ganoderic acid and lucidenic acid are reported to be the majority. Furthermore, there have been various studies for their significant bioactivities, such as reducing blood fat, decreasing blood pressure, regulating liver functions, and showing significant promise in promoting apoptosis.[2]

Furthermore, previous studies found that the ethanolic and water *G. lucidum* extracts showed α-glucosidase and tyrosinase inhibitory activities.[1,5,6] However, there has been no report on the inhibition against acetylcholinesterase of extracts. The present study has extended to investigate the bioefficacy of the fruiting body of *G. lucidum* extracts, which were produced by sequential extraction using hexane, dichloromethane, ethyl acetate and ethanol, on enzyme inhibitory activity, including α-glucosidase, tyrosinase, and acetylcholinesterase. This information may be helpful for the identification of active ingredients in further work.

2. Materials and Methods

2.1 Materials

The fresh fruiting body of *Ganoderma lucidum* mushroom was collected in September 2021 and obtained from Kasetsart Agricultural and Agro-industrial Product Improvement Institute (KAPI), Kasetsart University, Bangkok, Thailand.

Acetylcholinesterase from *Electrophorus electricus* (electric eel), α-Glucosidase from *Saccharomyces cerevisiae*, Tyrosinase from mushroom, 4-Nitrophenyl α-D-glucopyranoside

(PNPG), 3,4-Dihydroxy-L-phenylalanine (L-DOPA), Acetylthiocholine iodide (ATCI), 5,5′ Dithiobis(2-nitrobenzoic acid) (DTNB) and 9-Amino-1,2,3,4-tetrahydroacridine hydrochloride hydrate (Tacrine) were purchased from Sigma Aldrich (USA). Acarbose was purchased from Carbosynth Limited (China). Kojic acid was purchased from TCI (Japan).

2.2 Preparation and Extraction

The fresh mushrooms were dried in a hot air oven at 40-50 °C and ground in a blender. Then, the dried powders were sequentially extracted with four different solvents in the increasing polarity order, including hexane, dichloromethane, ethyl acetate, and ethanol, for seven days/solvent at room temperature. The extract was then filtrated through Whatman No. 4 filter paper and evaporated under a vacuum to obtain the crude extracts. All mushroom extracts were stored at 4°C before evaluating their enzyme inhibitory activity.

2.3 Determination of inhibitory effect on enzyme activity of the *G. lucidum* extracts

2.3.1 α-Glucosidase inhibitory assay

The α-glucosidase inhibitory activity of *G. lucidum* extracts were evaluated using a spectrophotometric method following the methods described by Feng *et al.*, (2011)[7] and Kazeem et al., (2013).[8] The α-glucosidase solution was diluted to a working concentration of 0.05 units/mL with 0.1 M phosphate-buffered saline (PBS) (containing 2% of bovine serum albumin (BSA) and 0.2% of sodium azide (NaN_3)). To initiate the assay, 500 µL of 0.1 M PBS (pH 6.8), 100 µL of the test sample, and 500 µL of the enzyme solution were mixed and incubated at 37 ºC for 10 minutes. Subsequently, a solution containing 5 mM PNPG in 0.1 M PBS (500 µL) was added, and then the mixture was incubated for an additional 30 minutes. The reaction was stopped by adding 2,000 µL of 0.2 M sodium carbonate (Na_2CO_3). Acarbose, a known α-glucosidase inhibitor, was used as a reference compound in this assay.

The absorbent of a yellow-colored product was measured at 405 nm using a spectrophotometer, and the percentage inhibition of enzyme activity was calculated. All experiments were performed in triplicate, and data were expressed as mean ± standard deviation (SD). The IC_{50} values were estimated by non-linear regression using GraphPad Prism 6 software.

2.3.2 Acetylcholinesterase inhibitory assay

The acetylcholinesterase inhibitory activity of *G. lucidum* extracts was evaluated using a spectrophotometric method following the methods described by Ellman *et al.*, (1961).[9] The acetylcholinesterase enzyme (AChE) solution was prepared in 0.1 M phosphate-buffered saline (PBS) at a pH of 8 and diluted to a working concentration of 0.4 units/mL. The assay was initiated by mixing 20 µL of the enzyme solution and 10 µL of the test sample in 90 µL of 0.01 M PBS (pH 8). Subsequently, 40 µL of 0.6 mM DTNB was added to measure cholinesterase inhibitory activity. The mixture was then incubated at 37 ºC for 10 minutes. After the initial incubation, 0.06 mM ATCI (40 µL) was added to the mixture and incubated for 20 minutes. Tacrine was used as a reference compound in this assay.

The absorbent of a yellow-colored product was measured at 412 nm using a microplate reader and the percentage inhibition of enzyme activity was calculated. All experiments were performed in triplicate, and data were expressed as mean ± standard deviation (SD). The IC_{50} values were estimated by non-linear regression using GraphPad Prism 6 software.

2.3.3 Tyrosinase inhibitory assay

The tyrosinase inhibitory activity of *G. lucidum* extracts was evaluated using a spectrophotometric method following the methods described by Mutschlechner *et al.*, (2018).[10] The tyrosinase enzyme solution was prepared in 0.02 M phosphate-buffered saline (PBS) at a pH of 6.8 and diluted to a working concentration of 100 units/mL. To initiate the assay, 2 µL of the test sample and 40 µL of the enzyme solution were mixed in 120 µL of 0.02 M PBS (pH 6.8) and incubated at 37 ºC for 10 minutes. Subsequently, a solution containing 0.3 mM L-DOPA in 0.02 M PBS (40 µL) was added, and the mixture was incubated for an additional 11 minutes. Kojic acid, a well-known depigmenting agent and tyrosinase inhibitor, was used as a reference compound in this assay.

The absorbent of an orange-red-colored product was measured at 475 nm using a microplate reader, and the percentage inhibition of enzyme activity was calculated. All experiments were performed in triplicate, and data were expressed as mean ± standard deviation (SD). The IC_{50} values were estimated by non-linear regression using GraphPad Prism 6 software.

3. Results & Discussion

3.1 Extraction

The results from sequential extraction of *G. lucidum* fruiting bodies showed that yields varied over a wide range of 0.27–1.09% (based on dry weight mushroom) among the solvents the production of the higher percentage of yield by

solvent was ethanol (1.09%) followed by dichloromethane (0.73%), ethyl acetate (0.63%) and hexane (0.27%), respectively (Table 1).

Table 1. The percentage of yield in sequential extraction of *G. lucidum*.

Solvent	Yield (%)
Hexane	0.27
Dichloromethane	0.73
Ethyl acetate	0.63
Ethanol	1.09

3.2 Determination of inhibitory effect on enzyme

All *G. lucidum* extracts obtained from sequential extraction were preliminarily evaluated for their enzyme inhibitory activity against α-glucosidase, tyrosinase, and acetylcholinesterase at a concentration of 50 µg/mL. The results found that all mushroom extracts had an inhibitory effect on tyrosinase and α-glucosidase (Table 2). Otherwise, they had no inhibitory effect on acetylcholinesterase.

3.2.1 α-Glucosidase inhibitory activity

The α-glucosidase inhibitory assay is one of the methods used in research and drug development to identify and evaluate potential inhibitors for the treatment of diabetes and metabolic syndrome.[11] In the present study, the inhibitory effects on α-glucosidase activity using the mushroom extracts were examined and expressed as IC_{50} value (Table 3). The results found that the ethanol extract exhibited the highest inhibition on α-glucosidase with an IC_{50} value of 105.46 ± 3.21 µg/mL, followed by the ethyl acetate, hexane, and dichloromethane extracts, respectively. Moreover, all mushroom extracts possessed potential against α-glucosidase better than acarbose, which was used as a reference compound, with an IC_{50} value of 638.64 ± 5.62 µg/mL.

Table 3. α-Glucosidase inhibitory activity of *G. lucidum* extracts

Extract	IC_{50} (µg/mL)
Hexane	170.54 ± 5.85^{c}
Dichloromethane	203.09 ± 1.56^{d}
Ethyl acetate	153.41 ± 4.05^{b}
Ethanol	105.46 ± 3.21^{a}
Acarbose	638.64 ± 5.62

Each value is expressed as IC_{50} ± SD, µg/mL (n = 3). Values with different superscripts within the same column are significantly at $p < 0.05$. Acarbose was used as a reference compound.

3.2.2 Tyrosinase inhibitory activity

The tyrosinase inhibitory assay is used to research and develop skin-whitening agents to identify and evaluate potential inhibitors for skin-whitening cosmetics.[5] The results found that the ethanol extract also exhibited the highest inhibition on tyrosinase compared to the other extracts, with an IC_{50} value of 302.03 ± 15.62 µg/mL (Table 4).

Table 4. Tyrosinase inhibitory activity of *G. lucidum* extracts

Extract	IC_{50} (µg/mL)
Hexane	>350
Dichloromethane	>350
Ethyl acetate	>350
Ethanol	302.03 ± 15.62
Kojic acid	5.28 ± 0.03

Each value is expressed as IC_{50} ± SD, µg/mL (n = 3). Kojic acid was used as a reference compound.

4. Conclusion

The increasing polarity of solvents in the sequential extraction method significantly influenced enzyme inhibitory activity. The ethanol extract demonstrated notable potential for α-glucosidase and tyrosinase inhibitory activities compared to the other extracts, which have lower polarity. These results could indicate that the bioactive inhibitors against both enzymes in *G. lucidum* may be highly polar compounds. Therefore, the ethanol extract of *G. lucidum* is an alternative active ingredient for developing supplementary foods, pharmaceuticals, and cosmetic products. Our ongoing studies are focused on identifying the active ingredients and their mode of inhibition.

Table 2. Inhibitory effects of *G. lucidum* extracts against α-glucosidase, tyrosinase, and acetylcholinesterase at a concentration of 50 µL/mL.

Extract	α-Glucosidase	Tyrosinase	Acetylcholinesterase
Hexane	17.93 ± 2.67	37.09 ± 0.43	NI
Dichloromethane	22.41 ± 0.65	17.82 ± 0.00	NI
Ethyl acetate	20.32 ± 2.21	12.79 ± 6.43	NI
Ethanol	24.45 ± 1.65	21.22 ± 0.57	NI

Each value is expressed as percentage inhibition of enzyme activity (n = 3), NI = No inhibition.

Acknowledgements

The research described herein was supported by the Kasetsart University Research and Development Institute (KURDI), Grant Number FF(KU)33.66; the Kasetsart Agricultural and Agro-Industrial Product Improvement Institute (KAPI); the Center of Excellence for Innovation in Chemistry (PERCH-CIC), Ministry of Higher Education, Science, Research and Innovation; the Department of Chemistry, Faculty of Science, Kasetsart University.

References

1. Abd Razak, D.L.; Jamaluddin, A.; Abd Rashid, N.Y.; Sani, N.A.; Abdul Manan, M. Assessment of Cosmeceutical Potentials of Selected Mushroom Fruitbody Extracts Through Evaluation of Antioxidant, Anti-Hyaluronidase and Anti-Tyrosinase Activity. *J* **2020**, *3*, 329-342.
2. Wang, C.; Liu, X.; Lian C.; Ke, J.; Liu, J. *Molecules.* **2019**, 24.
3. Ahmad, M.F.; Wahab, S.; Ahmad, F.A.; Ashraf, S.A.; Abullais, S.S.; Saad, H.H. *Fungal Biology Reviews.* **2022**, 39, 100-125.
4. Huie, C.W.; Di, X. 2004. *J Chromatogr B Analyt Technol Biomed Life.* **2004**, 812, 241-257.
5. Chien, C.C.; Tsai, M.L.; Chen, C.C.; Chang S.J.; Tseng, C.H.; *Mycopathologia*. **2008**, 166, 117-120.
6. Wińska, K.; Mączka, W.; Gabryelska, K.; Grabarczyk, M. *Molecules*. **2019**, 24(22), 4075.
7. Feng, J.; Yang, X.W.; Wang, R.F. *Phytochem.* **2011**, 72, 242–247.
8. Kazeem, M. I.; Adamson, J. O.; Ogunwande, I. A. Biomed. Res. Int. **2013**, 2013(3), 1–6.
9. Ellman, G.L.; Courtney, K.D.; Andres Jr., V.; FeatherStone, R.M. Biochemical *Pharmacology*. **1961**, 72, 242–247.
10. Mutschlechner, B.; Rainer, B., Schwaiger, S.; Stuppner, H. *Chem. Biodiversity*. **2018**, 15, e1800014.
11. Chen, B.; Tian, J.; Zhang, J.; Wang, K.; Liu, L.; Yang, B.; Bao L.; Liu, H. *Fitoterapia*. **2017**, 120, 6- 16.
12. Kozarski, M.; Klaus, A.; Jakovljević, D.; Todorović, N.; Wan-Mohtar Wan, A.A.Q.; Nikšić, M. *Arch Biol Sci.* **2019**; 71(2), 253-264

The effect of ethanol and water ratios of star fruit (*Averrohoa carambola*) extract on total phenolic, total flavonoid, tartaric acid contents and an inhibition of tyrosinase activity

Arunrat Sunthitikawinsakul[1]*, Rapeepan Kongtoom[2], and Wanpen Saengthongpinit[3]

[1]*Division of Chemistry, Faculty of Science and Technology, Nakhon Pathom Rajabhat University, Thailand*
[2]*Division of Chemistry, Faculty of Science and Technology, Muban Chombueng Rajabhat University, Thailan*
[3]*Division of Food Science and Technology, Faculty of Science and Technology, Nakhon Pathom Rajabhat University, Thailand*

**E-mail: arunrat28@webmail.npru.ac.th*

Abstract:

The research aimed to investigate the effects of different ethanol and water ratios on extracting phenolic, flavonoid compounds, as well as tartaric acid from star fruit, evaluating their inhibitory effect on tyrosinase activity. The ripe star fruit (*Averrohoa carambola)* puree was macerated for eight hours with various ethanol and water ratios of 0:100, 20:80, 50:50, 80:20, and 100:0. Different ratios yielded varied contents of total phenolic (TPC), flavonoid (TFC), and tartaric acid (TAC). The results showed contents of 8.48-101.50 mg GAE/g FW, 2.33-45.66 mg CE/g FW and 0.0490-0.0939 mg/g FW, respectively. The 50:50 ratio showed the highest TPC and TFC, whereas the 0:100 ratio had the highest TAC. The efficacy of the extracts on tyrosinase inhibition, using L-DOPA as a substrate, yielded the IC_{50} value (54.90-210.37 mg/L). All extracts exhibited a significant IC_{50} value ($p \leq .05$). The 80:20 ratio demonstrated the most significant inhibitory activity, showing moderate inhibition of tyrosinase activity. These findings suggest *A. carambola* extracts could be valuable in cosmeceuticals ingredient.

1. Introduction

Averrhoa carambola L., belonging to the Oxalidaceae family, was widely cultivated in Southeast Asia, including Thailand. Its fruit, commonly called 'Ma-Fueng' in Thai, 'carambola' or 'star fruit' in English, was popular in tropical and subtropical regions. Traditionally, in Asian medicine, it has been used for thousands of years to treat various conditions such as diabetes and diabetic nephropathy, arthralgia, vomiting, lithangiuria, coughing, chickenpox, intestinal parasites, hangovers, and chronic paroxysmal headache.[1,2]

Star fruit is characterized by its fleshy, crunchy, and juicy texture, offering a taste profile that a blend is slightly tart, acidic, and sweet. Generally regarded as an abundant source of nutrients such as minerals, proteins, and vitamins, it is notably rich in L-ascorbic acid, ranging from 8-1426 mg per gram of fresh weight.[1] Furthermore, being a natural reservoir of various phytochemicals, star fruit, particularly due to its rich phenolic and flavonoid contents, has been reported for its antioxidant activity[3,4,5,6] and inhibition of tyrosinase activity.[7] In addition to, tartaric acid, identified in citrus fruits and star fruits, is categorized as alpha-hydroxy acid (AHA),[1,8] contributing to the acceleration of epidermal turnover and desquamation.

Tyrosinase, a copper-containing enzyme found in both plant and animal tissues, plays a crucial role in catalyzing the production of a melanin and other pigments from L-tyrosine, which is converted into another compound called DOPA (dihydroxyphenylalanine) through the action of tyrosinase.[7,9] The melanin, divided into black to brown eumelanin and yellow to reddish-brown pheomelanin, was served a widespread natural pigment responsible for coloration of hair, skin, and eyes.[10] Melanogenesis, the intricate process through which melanin is produced in melanosomes by melanocytes, is essential for determining skin tone. Imbalances in melanin production, whether excessive or insufficient, can lead to various skin issues, including blemishes, freckles, fleckless, and dark or white spots.

Numerous tyrosinase inhibitors have been identified from various sources, including the natural and synthetic compounds. Examples include ellagic acid, kojic acid, azelaic acid, 4-hydroxyanisole, 4-S-cysteaminyl phenol, arbutin, chalcones, and coumarins. Additionally, polyphenol compounds and flavonoids have been recognized as effective tyrosinase inhibitors.[7]

This study explored the impact of various ethanol and water ratios on extraction of phenolic and flavonoid compounds, along with tartaric acid, from star fruit. The inhibitory effects of these extracts on tyrosinase activity were evaluated. We anticipate that the insights gained from this research will contribute to advancing the development of more efficient cosmeceuticals for treating blemishes and formulating skin-lightening products.

2. Materials and Methods

2.1 Materials

Mushroom tyrosinase (EC 1.14.18.1) with activity ≥1000 units/mg was purchased from Sigma-Aldrich (Darmstadt, Germany). L-DOPA or 3,4-dihydroxy-L-phenylalanine (purity >98%), ellagic acid (purity >99.5%), and L-tartaric acid (purity >99.5%) were acquired from Alfa Aesar (Thermo Fisher Scientific, England), Sigma-Aldrich (Darmstadt, Germany), and Rankem (Avantor Performance Materials, India), respectively. Phosphate buffer pH 6.8 was obtained from Alfa Aesar (Thermo Fisher Scientific, UK). Dimethyl sulfoxide (DMSO) was procured from Fischer Chemical (UK). Folin-Ciocalteu reagent 28% was sourced from Sigma (Darmstadt, Germany).

For chromatographic analysis, ethanol (HPLC grade) and sulfuric acid (H_2SO_4) were procured from Merck (Darmstadt, Germany). A standard (+)-L-tartaric acid (purity >99.5%) was obtained from Ajax Finechem Pty Ltd. (New South Wales, Australia). The Milli-Q water purification system, of research grade, was utilized without further purification.

2.2 Sample extraction

Fresh ripe star fruits at the edible stage were collected in Mabkae district, Amphur Muang, Nakhon Pathom Province, Thailand. The fruits, approximately 5-7 cm in diameter and 10-12 cm in length, were cut into small pieces for extraction. Ethanol and water were used in ratios of 0:100, 20:80, 50:50, 80:20, and 100:0. The extracted flesh (approximately 80 g) was mixed with 1000 mL of the solvent, finely ground into a puree using a food blender, and macerated at room temperature for 8 hrs. Each extract was then filtered and concentrated using a rotary evaporator until dry. The crude extracts were stored in amber bottles or covered with aluminum foil at 4°C until further analysis.

2.3 Total phenolic content (TPC)

Total phenolic content (TPC) of crude extracts was determined with Folin-Ciocalteu reagent, according to the method of Singleton et al. (1999).[11] A 0.5-mL sample aliquot was added to 2.5 mL Folin-Ciocalteu reagent and mixed thoroughly. After 3 min, 2.0 mL of 7.5% sodium carbonate solution was added and again mixed thoroughly. The control contained all the reaction reagents except the sample. After 30-min incubation at room temperature, the absorbance was measured using a UV-VIS spectrophotometer at 746 nm and compared to a standard curve [y = 0.0036x - 0.0017 with R^2 = 0.9982], with the Y-axis representing absorbance and the X-axis concentration, of prepared gallic acid solutions in the range of 0-10 mg/L. Results, obtained in triplicate, expressed as mg gallic acid equivalents (GAE) per gram of the fresh sample.

2.4 Total flavonoid content (TFC)

Total flavonoid content (TFC) of samples was assessed using the aluminum chloride colorimetric assay, referring to the method described by Wolfe et al. (2003).[12] A 1.0 mL of a diluted extract was added to a test tube containing 5.0 mL of distilled water. To the mixture was added 0.3 mL of 5% sodium nitrite solution, and this allowed to stand for 5 min. Then, 0.6 mL of 10% aluminum chloride was added. After 6 min, 2.0 mL of 1 M sodium hydroxide was added, and the mixture was diluted with another 1.1 mL of distilled water. The control contained all the reaction reagents except the sample. The absorbance of mixture at 510 nm was measured immediately using a UV-VIS spectrophotometer and compared to a standard curve [y = 0.0036x - 0.0017 with R^2 = 0.9982], with the Y-axis representing absorbance and the X-axis concentration, of prepared catechin solutions in the range of 0-10 mg/L. Results, obtained in triplicate, expressed as mg catechin equivalents (CE) per gram of the fresh sample.

2.5 Tartaric acid content (TAC)

Tartaric acid analysis using HPLC (KNAUER AZURA®, Germany) was modified from Wirod Chaipornpokin (2008).[13] Chromatographic separation was performed on a polymer Vertex plus column Eurokat H (10 µm, 300 mm x 8 mm i.d., KNAUER, Germany) at a column temperature of 60°C, eluted with 0.01 N H_2SO_4, and a flow rate of 0.6 mL/min. Detection was conducted by a refractive index (RI) detector with a run time of 30 min. All samples (20 µL) were injected into the column to obtain a retention time (RT).

The sample solution (0.05 g crude in 5 mL of 0.01 N H_2SO_4) was filtered through a 0.45 µm cellulose acetate membrane and transferred into a 1.5 mm vial. A stock tartaric acid solution (100 mg/L), used as a standard, was prepared by dissolving 100 mg tartaric acid in 100 mL Milli-Q water and stored at 4°C until analyzed. The mobile phase for chromatography was 0.01 N H_2SO_4, filtered through a 0.45 µm cellulose acetate membrane. Standard tartaric acid concentrations (0, 1, 5, 10, 15, and 20 mg/L) were used to create a calibration curve [y = 0.3012x - 0.0994, R^2 = 0.9987], with the Y-axis representing peak area and the X-axis concentration. Results, obtained in triplicate, expressed as mg per gram of the fresh sample.

Table 1. The series of reaction mixture used for mushroom tyrosinase inhibitory assay

Testing set	0.2 M Phosphate buffer pH 6.8	DMSO	Sample	Tyrosinase solution (250 U/mL)
A (control)	2 mL	0.1 mL	-	0.1 mL
B (blank control)	2 mL	0.1 mL	-	-
C (sample)	2 mL	-	0.1 mL	0.1 mL
D (sample control)	2 mL	-	0.1 mL	-

2.6 Mushroom tyrosinase inhibitory assay

Tyrosinase inhibition assay was conducted following the procedures outlined by Kubo et al. (2000).[14] The assay involved using L-DOPA as a substrate. A sample solution (0.001 g crude in 2 mL DMSO) was diluted ranging from 0-250 mg/L. Each of sample dilutions mixed with reagents is shown in Table 1. The mixtures were further incubated at 25°C for 10 min, and absorbance (Abs) was immediately measured using a UV-VIS spectrophotometer at 475 nm to detect dopachrome formation in the reaction mixture. Ellagic and tartaric acids, used as a standard, were evaluated for tyrosinase inhibition using the same method described above.

The percentage inhibition of tyrosinase was calculated using the following formula:

$$\% \text{ tyrosinase inhibition} = [Abs_{(A-B)} - Abs_{(C-D)}] / Abs_{(A-B)} \times 100$$

Half maximal inhibitory concentration (IC_{50}) values derived from the ln(x) equation, with the Y-axis representing % tyrosinase inhibition and the X-axis representing concentration. Activity levels were categorized as follows: $IC_{50} < 50$ mg/L (active), 50-250 mg/L (moderately active), and >250 mg/L (inactive).[14] The assay was performed in triplicate.

2.7 Statistical analysis

The experiments were designed in complete random. Each experiment was conducted in triplicate. The data were analyzed using the analysis of variance (ANOVA). Duncan's multirange test was used for establishing differences between mean values at a confidence level of 95% ($p \leq 0.05$).

3 Results & Discussion

3.1 Total phenolic content (TPC)

Total phenolic content (TPC) of all extracts of star fruit in various ratios provided TPC in the range of 8.48-101.50 mg GAE/g FW in significantly ($p \leq 0.05$) (Table 2). Notably, the TPC observed in this study is consistent with the findings of Pang et al. (2016),[15] who reported a range of 1.75-2.93 mg GAE/g FW for four cultivars of star fruit. It might be that the TPC content of star fruit depends on the varieties, maturity, and cultivation. The ethanol and water ratio of 50:50 exhibited the highest TPC at 101.50 ± 0.00 mg GAE/g FW. Most polyphenols in plants are water-insoluble, and the ethanol mixture aids in dissolving low or non-polar compounds.[16] Furthermore, previously reported phenolic compounds from star fruits include carambolasides K and L, (+)-isolariciresinol 9-O-β-D-glucoside, 1-O-feruloyl-β-D-glucose, protocatechuic acid, (+)-lyoniresinol 9-O-β-D-glucoside, (-)-lyoniresinol 9-O-β-D-glucoside, 1-O-vanilloyl-β-D-glucose, and koaburaside,[3] and others.

3.2 Total flavonoids content (TFC)

In the analysis of total flavonoid content (TFC), the results ranged from 2.33-45.66 mg CE/g FW in significantly ($p \leq 0.05$) (Table 2), Interestingly, all extracts exhibited TFC lower than TPC, aligning with the findings of Pang et al. (2016).[15] This result could be attributed to the composition of phenolic compounds in the star fruit extracts, encompassing different subclasses. Notably, flavonoids, a specific subgroup of phenolic compounds, contribute to this observation. Similarly to the results for the TPC, the varying ethanol mixture resulted in differences in TFC, highlighting the importance of the approximate polarity between the solvent and flavonoids. Furthermore, the ethanol and water ratio of 50:50 exhibited the highest TFC with a value of 45.66 ± 0.00 mg CE/g FW. Noteworthy flavonoids reported in previous studies include carambolasides A-D,[5] E-J,[6] M-Q,[4] R1-R3, S1-S2, T1-T3[17] pinobanksin 3-O-β-D-glucoside,[4] carambolaflavone, isovitexin 2''-O-α-L-rhamnopyranoside, hovertichoside C,5 3-hydroxycarambolaside P, T1,[17] and others.

3.3 Tartaric acid content (TAC)

The star fruit extracts were determined by HPLC analysis to identify the tartaric acid peak, which appeared at a retention time (RT) of 13.3 min (Figure 1). In quantitative analysis, various ratios of the ethanol and water extracts were assessed for tartaric acid content (TAC) significantly ($p \leq .05$), ranging from 0.0490-0.0939 mg/g FW (Table 2). Nuanjan Yangnisarapant (2003) found 0.05% w/w tartaric acid in dried star fruit methanol extract using column chromatography.[8]

The star fruit extract in the ratio of 0:100 exhibited the highest TAC with a value of 0.0939

± 0.0050 mg/g FW. When a decreasing polarity of the ethanol and water ratios as a solvent system resulted in sequentially lower tartaric acid content. This attributes to the nature of tartaric acid, an alpha-hydroxy dicarboxylic acid, which means it has two carboxyl and hydroxyl groups in the structure, making it more polar and easily soluble in water (139 g/100 mL).[18] The key factor contributing to the water solubility of tartaric acid is intramolecular hydrogen bond, as illustrated in Figure 2. The hydroxyl (-OH) groups can form hydrogen bonds with water, taking advantage of the highly polar nature of water molecules, where the hydrogen atom is partially positively charged, and the oxygen atom is partially negatively charged.

3.4 Mushroom tyrosinase inhibitory assay

In assessing the inhibitory effect of compounds on tyrosinase activity, the results were reported as IC_{50}, defined as the concentration of the sample causing a 50% loss of tyrosinase activity. All extracts exhibited moderate activity, with IC_{50} values ranging from 54.90-210.37 mg/L, and these differences were statistically significant ($p \leq 0.05$) (Table 2). Notably, the ethanol and water ratio of 80:20 demonstrated the strongest activity, with an IC_{50} value of 54.90 ± 0.04 mg/L. This activity was compared with ellagic and tartaric acids, which showed IC_{50} values of 6.00 ± 0.00 and 50.81 ± 0.05 mg/L, respectively.

Additionally, the result indicated that the compounds in the extracts with various ratios exhibited significant tyrosinase inhibition in a dose-dependent manner. Observingly, the highest tartaric acid content (TAC) in the ethanol and water ratio of 0:100, as well as the highest total phenolic content (TPC) and total flavonoid content (TFC) in the 50:50 ratio, displayed moderate tyrosinase inhibition (IC_{50} value of 210.37 ± 0.30 mg/L), which was less than the inhibition observed with the 80:20 ratio. A high ratio of ethanol decreased solvent polarity, which could extract non-polar substances, which displayed tyrosinase inhibition activity.

Furthermore, the composition of phenolic compound, extracted by low polarity solvent, had more phenol units or non-polar side chains than high polar extracts. This finding is interesting for several reasons. Importantly, our results align with previous studies on tyrosinase inhibitors, such as those indicating that natural compounds, including ellagic acid, exhibit tyrosinase inhibition through similar non-competitive mechanisms.[7] These suggests that phenolic compounds and flavonoids in star fruits may share common characteristics with other known tyrosinase inhibitors, potentially leading to a synergistic effect.

Table 2. The total phenolic (TPC), flavonoid (TFC), and tartaric acid (TAC) contents of the star fruit extracts

Extracts (ethanol:water)	TPC (mg GAE/g FW)	TFC (mg CE/g FW)	TAC (mg/g FW)	IC_{50} (mg/L)
0:100	8.48 ± 0.21^{d}	2.33 ± 0.19^{c}	0.0939 ± 0.0050^{a}	210.37 ± 0.30^{a}
20:80	31.28 ± 0.63^{c}	12.26 ± 0.80^{b}	0.0640 ± 0.0005^{b}	140.21 ± 0.19^{b}
50:50	101.50 ± 0.00^{a}	45.66 ± 0.00^{a}	0.0529 ± 0.0004^{c}	89.13 ± 0.06^{c}
80:20	66.98 ± 0.78^{b}	10.28 ± 0.27^{b}	0.0513 ± 0.0074^{c}	54.90 ± 0.04^{e}
100:0	23.26 ± 0.63^{c}	12.39 ± 0.26^{c}	0.0490 ± 0.0009^{d}	73.93 ± 0.10^{d}

All data were expressed as mean ±SD for 3 replications.
^{a,b,c,d,e}Different letters in the same column are significantly different ($p \leq .05$).

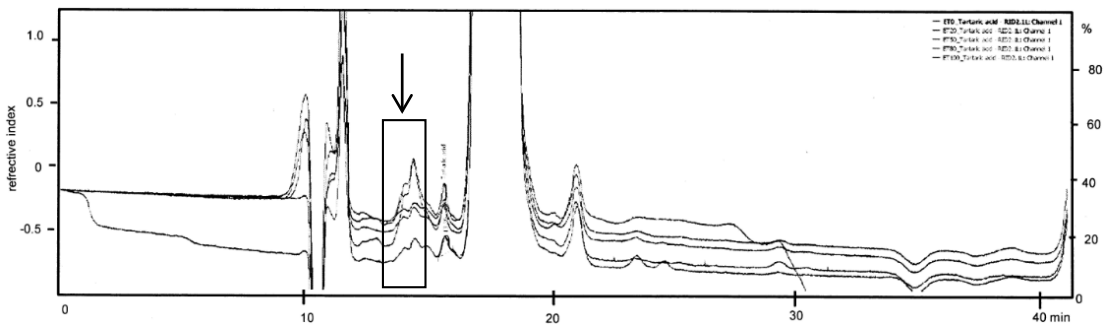

Figure 1. HPLC chromatogram showing tartaric acid peaks in various ratios of star fruit ethanol and water extracts, with a retention time (RT) of 13.3 min

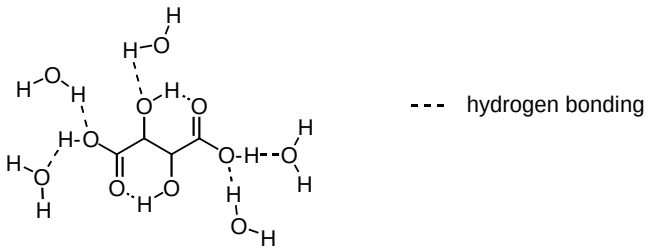

Figure 2. Intermolecular hydrogen bond between tartaric acid and water

4. Conclusion

The ethanol and water ratios demonstrated different polarity of the solvent. Therefore, solvent affected the composition of star fruit extracts. High polarity solvent (0:100) exhibited high tartaric acid content, and moderate polarity (50:50) revealed high contents of total phenolic and flavonoid. The extracts from 80:20 showed the highest inhibition of tyrosinase activity. However, all extracts exhibited moderate inhibition of tyrosinase activity. In conclusion, our study provided evidence of the inhibitory effect of those active constituents in star fruits on tyrosinase activity, positioning it as a possibility for development in skin-lightening and anti-pigmentation products. Also, further research is warranted to assess its safety, efficacy, and potential applications in cosmeceuticals.

References

1. Luan, F.; Peng, L.; Lei, Z.; Jia, X.; Zou, J.; Yang, Y.; He, X.; Zeng, N. *Front. Pharmacol.* **2021**, *12*, 699899.
2. Zhang, X.; Liu, X.; Qin, L.; Tang, C.; Huo, Y.; Wei, J.; Chen, M.; Gao, Y.; Zhang, X.; Wu, Y.; Zhao, Y.; Huang, R.; Zhong, L.; Wang, B. *Chin. Chem. Lett.*, **2023**, *34*, 107618.
3. Jia, X.; Yang, D.; Xie, H.; Jiang, Y.; Wei, X. *J. Funct. Foods*. **2017**, *32*, 419-425.
4. Jia, X.; Xie, H.; Jiang, Y.; Wei, X. *Phytochemistry*. **2018**, *153*, 156-162.
5. Yang, D.; Xie, H.; Jia, X.; Wei, X. *J. Funct. Foods*. **2015**, *16*, 204-220.
6. Yang, D.; Jia, X.; Xie, H.; Wei, X. *LWT-Food Sci. Technol*. **2016**, *65*, 604-609.
7. Chang, T.S. *Int. J. Mol. Sci*. **2009**, *10*, 2440-2475.
8. Yangnisarapant, N. Extraction and Isolation of AHA from *Phyllanthus acidus*, *Mangifera indica*, *Mangifera indica* and *Averrohoa carambola* Fruits. Master's degree, Chaing Mai University, Chiang Mai Province, Thailand, 2003. [in Thai]
9. Pillaiyar, T.; Manicham, M.; Namasivayam, V. *J. Enzym. Inhib. Med. Chem*. **2017**, *32*, 403-425.
10. Opperman, L.J.; Kock, M.; Klaasen, J.; Rahiman, F. *Cosmetics*. **2020**, *7*, 60.
11. Singleton, V.L.; Orthofer, R.; Lamuela-Raventós, R.M. *J. Cereal Sci*. **1999**, *299*, 152-178.
12. Wolfe, K.; Wu, X.; Liu, R.H. *J. Agric. Food Chem*. **2003**, *51*, 609-614.
13. Chaipornpokin, W. Quantitative Analysis of Organic Acids in Aqueous Extracts of *Tamarindus indica* Pulp and Preparation of Tamarind Power. Master's Degree, Chulalongkorn University, Bangkok, Thailand, 2008.
14. Kubo, I.; Kinst-Hori, I.; Chaudhuri, S.K.; Kubo, Y.; Sanchea, Y.; Ogura, T. *Bioorgan. Med. Chem*. **2000**, *8*, 1749-1755.
15. Pang, D.R.; You, L.J.; Zhou, L.; Sun-Waterhouse, D.X.; Liu, R.B. *RSC Advances*. **2016**, *6*, 90646-90653.
16. Rattanabhorn, J.; Amornlerdpison, D.; Chimsook, T. *Adv. Materials Res*. **2013**, *699*, 693-697.
17. Yang, Y.; Jia, X.; Xie, H.; Wei, X. *Phytochemistry*. **2020**, *74*, 112364.
18. Dalman L.H. *J. Am. Chem. Soc*. **1937**, *59*, 2547-2549.

Efficiency of commercial tea against *Escherichia coli* and *Staphylococcus aureus*

Mantana Boonnucht, Paweena Kumpai, Kotchapon Martpaijit, Rawinan Chanthabut, Siriporn Pranee, Jiravich Methewiroon, Sirapan Sukontasing, Patamaporn Umnahanant, and Sirinit Tharntada*

Department of Veterinary Technology, Faculty of Veterinary Technology, Kasetsart University, Bangkok, Thailand

**E-mail: Sirinit.t@ku.th*

Abstract:

Commercial tea has been consumed widely because of its flavor and unique fragrance. The phenolic compounds in tea, especially catechin, are known as antibacterial substances. The chemical substances of tea differ in manufacturing processes. The research aims to extract one commercial tea with ethyl acetate and determine the antimicrobial effect of crude extract against *Escherichia coli* and *Staphylococcus aureus*. The ethyl acetate, the medium polar solvent, is suitable for extracting phenolic compounds by liquid-liquid extraction. The yield of crude tea extract was approximately 1.49% (w/w). The crude tea extract dissolved in ethyl acetate to a concentration of 0.2 g/mL was minimized the insoluble substances and only the soluble fraction was evaluated for antimicrobial properties by the agar well diffusion technique. The results showed that the inhibition zone diameter was 27.5 ± 1.3 mm against *S. aureus*, whereas no inhibition zone was found against *E. coli*. The ethyl acetate was used as a negative control, and no inhibition zone was found against both bacteria. The soluble fraction was also performed two-fold dilution with ethyl acetate before testing against *S. aureus* by liquid growth inhibition. The 50% (v/v) soluble fraction showed growth inhibition and killing of *S. aureus.* The results showed that the crude extract from this commercial tea has an antibacterial effect against *S. aureus*. However, the amount of phenolic compound must be further determined, and the different commercial products must be tested more.

1. Introduction

Tea (*Camellia sinensis*) was first discovered in southern China and consumed over two-thirds of the world's population. The quality and chemical components of tea leaves differ when they come from different cultivated sources.[1] Tea is made from the leaves of young shoots or stalks and harvested by skilled people.[2] Then, tea was brought through different processing methods to obtain various kinds of tea, such as green tea, white tea, oolong tea, and black tea. Tea can be divided into three kinds that depend on the fermentation process. Green and white teas are not fermented, oolong tea is partially fermented, and black tea is fully fermented.[3] Tea has many chemical compositions, such as carbohydrates, amino acids, alkaloids, and polyphenols. Polyphenols are found in plants and are classified by the number of phenol rings. They are divided into four classes: phenolic acids, flavonoids, stilbenes, and lignans.[4] Tea flavonoids, polyphenolic compounds, were reported as chemical compounds with biological activity. Catechins are the important flavonoids in tea and comprise four major kinds: (-)-epicatechin (EC), (-)-epicatechin-3-gallate (ECG), (-)-epigallocatechin (EGC), and (-)-epigallocatechin-3-gallate (EGCG).[1,5] The catechin and the other polyphenols exhibit antibacterial activity against microorganisms such as Gram-positive bacteria like *Staphylococcus aureus* ATCC 29213 and *Streptococcus pyogenes* 308A and Gram-negative bacteria like *Escherichia coli* ATCC 25922, *E. coli* 078, *Enterobacter cloacae* 1321E, and *Pseudomonas aeruginosa* 9027.[1] There are many commercial tea products that have different chemical compositions, particularly polyphenolic compounds, and different antibacterial properties. This study aims to test the antibacterial activities of a commercial tea extract against *S. aureus* and *E. coli*, which are food-borne microorganisms.

2. Materials and Methods

2.1 Preparation of commercial tea extract

The 45-g dried commercial tea leaf sample in 600 mL of distilled water was placed in a 1000-mL round bottom flask, and 15 g of calcium carbonate ($CaCO_3$) was added. The mixture was then stirred and refluxed for 20 min and cooled down to room temperature. The tea leaves were filtered out by reduced pressure filtration. The filtrated solution was concentrated to 80 mL by reduced pressure evaporation and then transferred into the 250-mL separating funnel. Then, 20 drops of 5% HCl were added into the brownish solution; the solution was extracted with 80 mL ethyl acetate three times. After that, the ethyl acetate solvent was removed, and the solid was obtained. The 0.2 g of solid extract was dissolved in 1 mL of ethyl acetate with vortex shaking. The insoluble substances were

minimized by leaving the crude solution at room temperature for 30 min; then, the soluble fraction was explored for antimicrobial properties.

2.2 Microbial strains

The antimicrobial activity of tea extract was tested against two different microorganisms that might cause gastrointestinal illness in humans and other animals. Two microorganisms in this study were *E. coli* (Gram-negative bacterium) isolated from the ice and *S. aureus* ATCC25923 (Gram-positive bacterium).

2.3 Agar well diffusion method

The antibacterial activities against *S. aureus* and *E. coli* were screened by using the agar well diffusion. Two bacteria were cultured in Luria-Bertani (LB) broth at 37°C with shaking at 250 rpm for 16 hr. Both bacteria were diluted to 0.5 McFarland; each bacteria suspension was then spread on LB agar containing two wells with a 0.9 mm diameter. The 50 µL of soluble substance was pipetted into one well, and the 50 µL of ethyl acetate was also tested as a negative control. The plate was incubated at 37°C. The inhibition zones were observed and measured at 16 and 24 hr. Each experiment was performed four times.

2.4 Minimum inhibitory concentration (MIC) determination

The liquid growth inhibition assay modified from a previous method was used to determine the minimum inhibitory concentration.[6] A colony of *S. aureus* was cultured in LB broth at 37°C for 16 hr, and then the bacteria culture was inoculated in LB broth to obtain a fresh culture. The fresh culture was diluted to A_{600} of 0.001 with a poor broth (PB) medium. The soluble substance of commercial tea extract was performed 2-fold dilution with ethyl acetate. The 96-well plate assay was divided into three parts: blank control consisting of 2 µL of ethyl acetate mixed with 98 µL of PB medium; sample test consisting of 2 µL of soluble substance of various concentrations mixed with 98 µL of bacterial suspension; and negative control consisting of 2 µL of ethyl acetate mixed with 98 µL of bacterial suspension. The bacterial growth was measured absorbance at 595 nm (A_{595}) after incubation at 37 °C with shaking at 120 rpm for 16 hr. The experiment was performed in triplicate. The A_{595} of each test was calculated for percent bacterial growth relative to the average A_{595} of negative control.

2.5 Minimum bactericidal concentration (MBC) determination

The overnight culture of bacteria from MIC determination was streaked on an LB agar plate and incubated at 37°C for 16 hr. MBC was defined as the lowest concentration of commercial tea extract, in which the bacteria could not grow on an LB agar plate. The experiment was carried out in triplicate.

2.6 Statistical analysis

The MIC determination was carried out in triplicate. Then, the independent sample t-test was used to analyze data using IBM SPSS statistics version 29.0.2.0 (20). Data differences were considered significant at $P<0.05$.

3. Results & Discussion

3.1 Yield of commercial tea extraction by ethyl acetate

A commercial tea sample was extracted with ethyl acetate, suitable for extracting phenolic compounds. The yield percentage of tea extract was calculated relative to the leaves' weight. The yield percentage was approximately 1.49% (w/w), as shown in Table 1.

Table 1. Yield percentage of Commercial tea extraction

Solvent	Leaves weight (g)	Extract weight (g)	% yield[a]
Ethyl acetate	45	0.6693	1.4873

[a]Dried weight of extract /Dried weight of leaves ×100

3.2 Agar well diffusion

The soluble substance prepared from 0.2 g/mL of commercial tea extract was monitored for its antibacterial properties by agar well diffusion

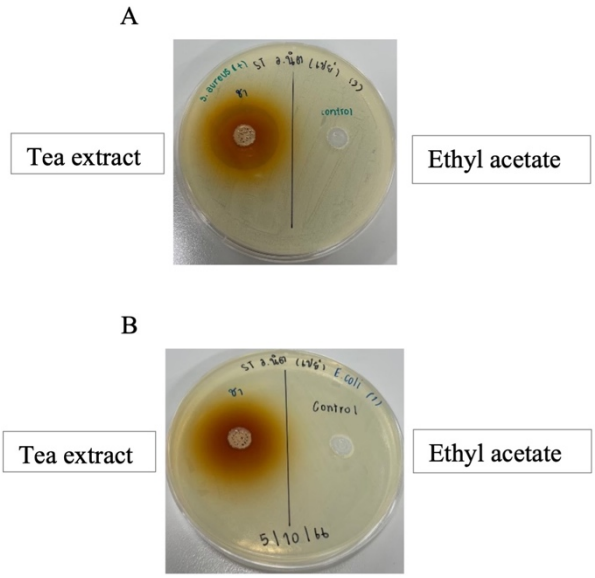

Figure 1. Agar well diffusion test of commercial tea extract against *S. aureus* (A) and *E. coli* (B). The ethyl acetate was used as negative control.

Table 2. Inhibition zone of commercial tea extract against bacteria at 16 and 24 hr

Bacteria	Plate	Inhibitor zone (mm)			
		Tea extract		Ethyl acetate	
		16 hr	24 hr	16 hr	24 hr
Staphylococcus aureus	1	28	28	0	0
	2	27	27	0	0
	3	26	26	0	0
	4	29	29	0	0
	Diameter (average)	27.5±1.3	27.5±1.3	0	0
Escherichia coli	1	0	0	0	0
	2	0	0	0	0
	3	0	0	0	0
	4	0	0	0	0
	Diameter (average)	0	0	0	0

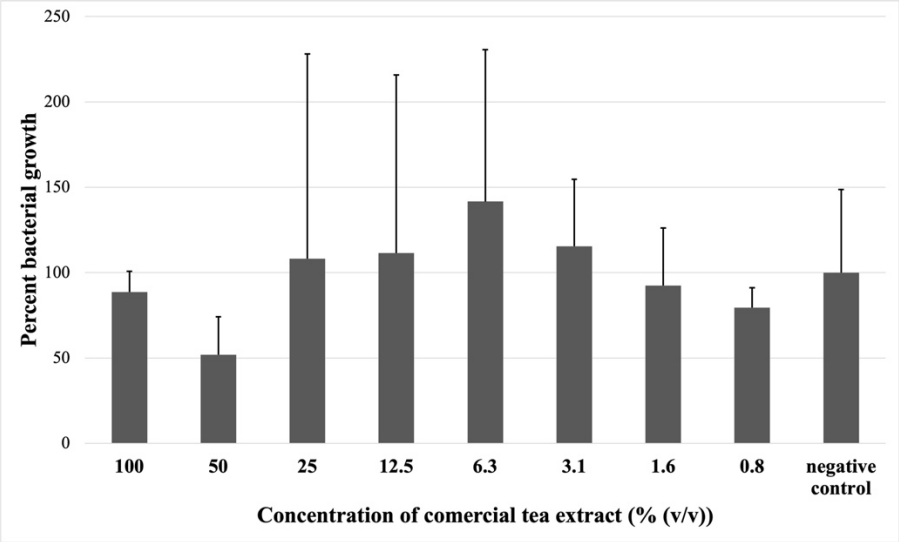

Figure 2. The effect of commercial tea extract at various concentrations on the growth of *S. aureus*. The values are means ± standard deviation. A *P* value of <0.05 was considered statistically significant.

method. The bacteria chosen for this study were *S. aureus*, a Gram-positive bacterium, and *E. coli*, a Gram-negative bacterium. After 16 hr incubation, the commercial tea extract showed the bacterial inhibition zone against *S. aureus* but not *E. coli* (Figure 1). The tea extract showing the inhibition zone was 27.50±1.3 mm against *S. aureus* (Table 2). In contrast, no inhibition zone was observed against *E. coli*. The incubation was continued until 24 hr to confirm bacterial inhibition, and the inhibition zone was measured again. The results showed that the inhibition zones had unchanged. The diameter of the inhibition zone did not decrease with increasing incubation time. The ethyl acetate was used as a negative control, and no inhibition zone was found against both bacteria. Thus, the commercial tea extract exhibited an antibacterial effect against *S. aureus* but not *E. coli*. However, the previous reports showed the antibacterial activities of tea extract against *S. aureus* and *E. coli*.[7]

3.3 Minimum inhibitory concentration

The agar well diffusion results showed the soluble substance of tea crude extract only inhibits *S. aureus*. Thus, the soluble substance was diluted two-fold serially and used to determine the MIC against *S. aureus*. Bacteria growth was measured as absorbance at 595 nm. However, the

precipitation of tea extract in the medium broth interferes with the optical density. Therefore, the MIC against *S. aureus* could not be determined. The percent bacterial growth in each concentration of tea crude extract was calculated related to the growth without tea crude extract (Figure 2). The 50% (v/v) soluble substance reduced the growth percentage to 52%, while the bacteria suspension with 100% (v/v) soluble substance showed a higher growth percentage. The high concentration of tea extract could be precipitated in the medium broth; thus, its pellet interferes with the high optical density. However, there was no significant between each concentration of tea extract and negative control (P <0.05).

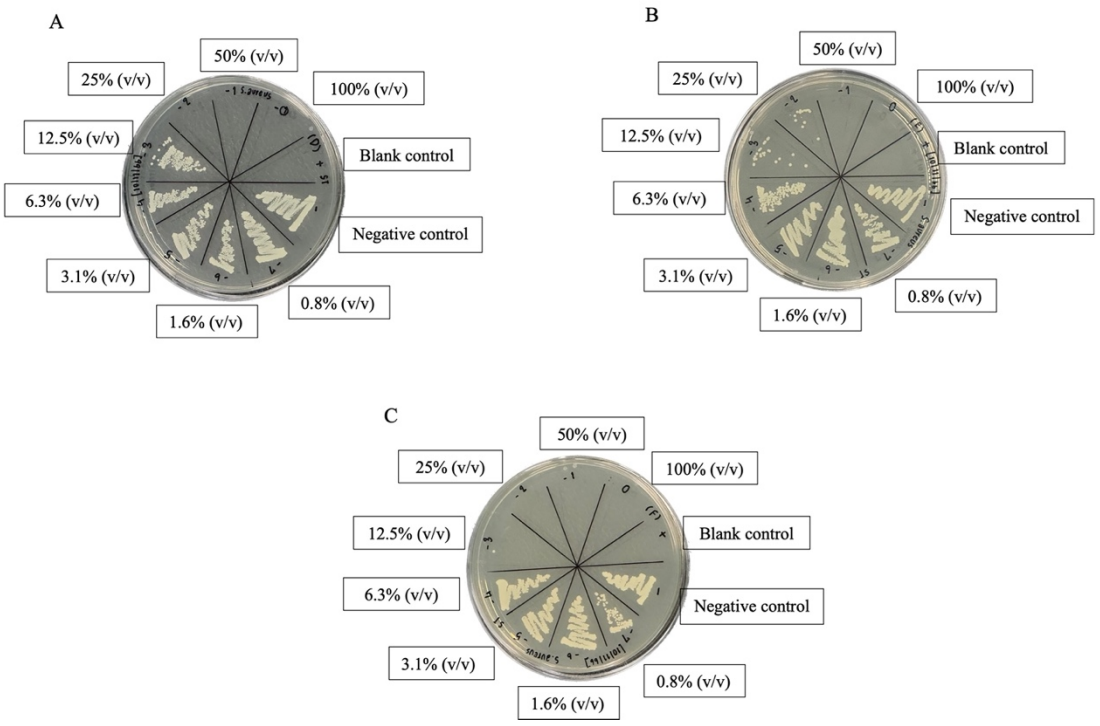

Figure 3. The bactericidal activity against *S. aureus* of commercial tea extract at various concentrations. A-C shows triplicate.

3.4 Minimum bactericidal concentration

To explore the bactericidal property of tea extract, the overnight culture from the above experiment was grown again on the medium plate. The results show in Figure 3 that the culture bacteria containing either 50% (v/v) or 100% (v/v) soluble substance of tea extract cannot grow after overnight incubation. The culture bacteria with the other concentration still grow at least one medium plate. Thus, the 50% (v/v) soluble substance of tea extract is MBC value because this concentration not only inhibited *S. aureus* but also killed the microbe. The 100% (v/v) soluble substance showed bactericidal properties, which confirmed that the high optical density in the above results was not bacteria growth.

4. Conclusion

Tea has been a worldwide flavor drink for a long time, and commercial tea is also a popular beverage. The polyphenols such as catechins and flavonoids are the active compounds in tea reported to be good for human health.[8] A commercial tea extract was observed to have antibacterial properties in this study. The tea polyphenols were extracted by ethyl acetate, the medium polar solvent, and it was previously reported that it is appropriate for extracting catechins.[9] The commercial tea extract revealed an antibacterial effect against *S. aureus* but not *E. coli* by agar well diffusion assay. After that, the liquid growth inhibition assay was done for the commercial tea extract against *S. aureus*, and the results showed that the 50% (v/v) soluble substance of extract can decrease the growth of *S. aureus* to about 50%. However, there was no significant at P <0.05. The bactericidal property of the extract was assayed against *S. aureus*. The results showed that the extract can kill this microbe at 100% (v/v) and 50% (v/v) soluble substance of extract. More commercial teas need further testing, and the Folin-Ciocalteu assay needs to be performed to measure the phenolic compound in products.

Acknowledgements

The authors would like to thank the Faculty of Veterinary Technology, Kasetsart University, and Department of Industrial Chemistry, the Faculty of Applied Science, King Mongkut's University of Technology North Bangkok for support in this work.

References

1. Bansal, S.; Choudhary, S.; Sharma, M.; Kumar, S. S.; Lohan, S.; Bhardwaj, V.; Syan, N.; Jyoti, S. Tea: A Native Source of Antimicrobial Agents. Food Res. Int. **2013**, *53* (2), 568-584.
2. Aaqil, M.; Peng, C.; Kamal, A.; Nawaz, T.; Zhang, F.; Gong, J. Tea Harvesting and Processing Techniques and Its Effect on Phytochemical Profile and Final Quality of Black Tea: A Review. Foods. **2023**, *12* (24), 1-28.
3. Almajano, M. P.; Carbó, R.; Jose Angel, L.; Gordon, M. Antioxidant and Antimicrobial Activities of Tea Infusions. Food Chem. **2008**, *108*, 55-63.
4. Pandey, K. B.; Rizvi, S. I. Plant Polyphenols as Dietary Antioxidants in Human Health and Disease. Oxid. Med. Cell. Longev. **2009**, *2* (5), 270-278.
5. Reygaert, W. C. The Antimicrobial Possibilities of Green Tea. Front. Microbiol. **2014**, *5*, 1-8.
6. Shafer, W. M. *Antibacterial Peptide Protocols*; Humana Press, 1997.
7. Liu, S.; Zhang, Q.; Li, H.; Qiu, Z.; Yu, Y. Comparative Assessment of the Antibacterial Efficacies and Mechanisms of Different Tea Extracts. Foods. **2022**, *11* (4), 1-11.
8. Sharangi, A. Medicinal and Therapeutic Potentialities of Tea (*Camellia sinensis* L.) – A review. Food Res. Int. **2009**, *42*, 529-535.
9. Dong, J.-J.; Ye, J.-H.; Lu, J.-L.; Zheng, X.-Q.; Liang, Y.-R. Isolation of antioxidant catechins from green tea and its decaffeination. Food Bioprod. Process. **2011**, *89* (1), 62-66.

A study of N-heterocyclic imidazolium-functionalized cage-like silsesquioxane on transition metals as a catalyst

Wannipa Phansuwan and Vuthichai Ervithayasuporn*

Department of Chemistry, Mahidol University, Rama VI Road, Ratchathewi, Bangkok 10400, Thailand

**E-mail: Vuthichai.erv@mahidol.edu*

Abstract:

Cage-like silsesquioxanes (SQ) or polyhedral oligomeric silsesquioxanes (POSS) have been played attention in wide-range of applications (e.g. catalysis, sensing, electronics, etc.) because cage-like SQ show properties like organic-inorganic hybrid compounds. In other words, cage-like SQ bearing organic functional groups show the ability to develop chemical compounds with various properties such as nano size, chemical inertness, and high thermal stability. One class of interesting organic functional groups is N-heterocyclic carbenes (NHC), which have been highly modified as support in particular transition metals to serve as catalysts. Interestingly, in earlier work, our group successfully investigated that cage-like SQ bearing NHC/imidazolium salt on palladium nanoparticles show as a highly active catalyst. However, palladium element provides some drawbacks such as toxicity, high price, and low abundance. Therefore, in this work, we are inspired to investigate the compound of copper(II)acetate and 1-methylimidazole-functionalized octakis(3-chloropropyl)octasilsesquioxane to directly catalyze alkyne-azide cycloaddition (CuAAC) reactions with follow on recent trends, including green and sustainable materials processing and catalytic performance.

1. Introduction

Recent works have shown that transition metals which are Mn, Co, Ni, and Cu have been widely utilized as catalysts in modern organic synthesis chemistry due to increasing environmental concerns in term of using toxic heavy metals and producing waste products.[1, 2] The green chemistry has grown along with the development of designing supporting ligands of catalysts. The compounds should be reactive and strongly coordinated with transition metals by using low toxicity, low cost and high abundance materials. In this context, hybrid organic-inorganic like silsesquioxanes cage is one of the key roles to gain sustainable catalyst.

Cage-like silsesquioxanes (SQ) or polyhedral oligomeric silsesquioxanes (POSS), based on the nature of cage-like SQ features have inorganic properties at an inner core which consists of silicone and oxygen (Si−O−Si) with general formulas $(RSiO_{3/2})_n$ where n is commonly 6,8, or 10. These inorganic core can provide symmetry and highly thermal material and can be further functionalized with organic substituents (R) (e.g. aryl, vinyl) at the outer core.[3] Consequently, its functional substituent surrounding silica core is compatible with other materials or transition elements. In other words, the outer core of cage-like SQ shows the ability to be catalytic sites with high surface area to occur reaction chemical process. Accordingly, cage-like SQ have get attention in various fields such as sensors, polymer pours materials, and especially in catalysts.[4]

N-heterocyclic carbenes (NHCs) are organic functional groups which serve as a strong σ-donor supporting ligand for transition metals.[5, 6] Moreover, NHC ligands have the capacity for activity of the catalyst toward many chemical reactions such as C-C coupling reactions, carbon dioxide fixation reactions, and ring closing metathesis.[7-9] For example, previously our reported, SQ nanocage functionalized with NHC/imidazolium for support Pd(II) species as highly efficient homogenous and heterogeneous catalysts for Suzuki-Miyaura cross-coupling reaction and Heck reaction.[10-12] However, based on the sustainable material concept, transition metals besides heavy metals like Pd are being explored to investigate new and promising SQ functionalized NHC as effective catalyst support. Therefore, in this work, a copper nanoparticle stabilized on imidazolium-functionalized SQ (Cu-IMSQ) is synthesized to use as a heterogeneous transition metal catalyst for “Click rection” in terms of alkyne-azide cycloaddition (CuAAC) reactions. For the CuAAC reaction, the catalyst is not only process in simple procedures with short time reaction, but also easily remove solvent (e.g. H_2O) and purified with high reaction product yield.[13, 14]

2. Materials and Methods

2.1 Materials

Octa(3-chloropropyl)octasilsesquioxane (T_8-Cl) was prepare according to the literature,[15] while of imidazolium-based SQ (IM-SQ) was synthesized following the earlier literature.[16]

Almost of the substrates were purchased from Sigma Aldrich and used without additional purification. Tetraethylammonium bromide was purchased from Alfa Aesar. The solvents of tetrahydrofuran, ethanol and methanol were used all commercial grade and distilled prior to use. Deionized (DI) water was obtained from Ultra Clear SIEMENS with ASTM type 2.

2.2 Measurements and instrumentations

The FT-IR spectra were collected using an attenuated total reflectance (ATR) technique with Bruker model Alpha spectrometer. Power X-ray diffraction (XRD) measurement on dried power were performed by Bruker D8 Advance with a monochromatic Cu K_α radiation at l = 0.154 nm. Applied voltage and current were used at 30 kV and 10 mA, respectively. The mode of recorded system was operated with 2θ=5.00-90.00 (scan rate = 0.005° s^{-1}). Inductively Coupled Plasma Mass (ICP-MS) Spectra were recorded by the inductively coupled plasma mass spectrometer, Perkin Elmer SCIEX ELAN 6000 and the samples were analyzed in diluted aqua regia (nitric acid/hydrochloric acid).

2.3 Synthesis of Cu-IMSQ catalyst

In 10 ml vial, (27.25 mg, 0.15 mmol) copper acetate was dissolved in 5 ml of MeOH. Then add (51.95 mg, 0.03 mmol) IM-SQ while vigorously stirring. After the remaining reaction 3 days, the green solid product was filtered and washed unreacted material with several amounts of MeOH (24.2 mg, 76% yield based on T_8-Cl).

2.4 Catalytic Testing for CuAAC

In thick wall, a solution of (1.0 mmol) terminal alkyne, (1.1 mmol) aryl azide, and the (0.42 mol% Cu) copper catalyst in 2 ml mixed solution of H_2O: EtOH (1:1 v/v) was stirred at 50 °C for appropriated time. The reaction was monitored by thin-layer chromatography. The complete reaction solution was extracted with EtOAc and water to remove catalyst. The organic layer was removed to centrifuge tube for remove residue and centrifuged for 10 min at 3,300 rpm. Then, the 1,2,3-triazole product was afforded from solution after centrifuging by recrystallization in EtOAc and methanol.

3. Results & Discussion

3.1 Preparation of Cu-IMSQ catalysts

The synthesis of Cu-IMSQ catalyst is shown in Scheme 1. Firstly, a mixture of octa(3-chloropropyl)octasilsesquioxane (T_8-Cl) and an excess methyl-imidazole was heated at 60 °C in toluene to produce IM-SQ. Then, mixing IM-SQ with $Cu(OAc)_2$ (OAc = CH_3COO^-) in MeOH

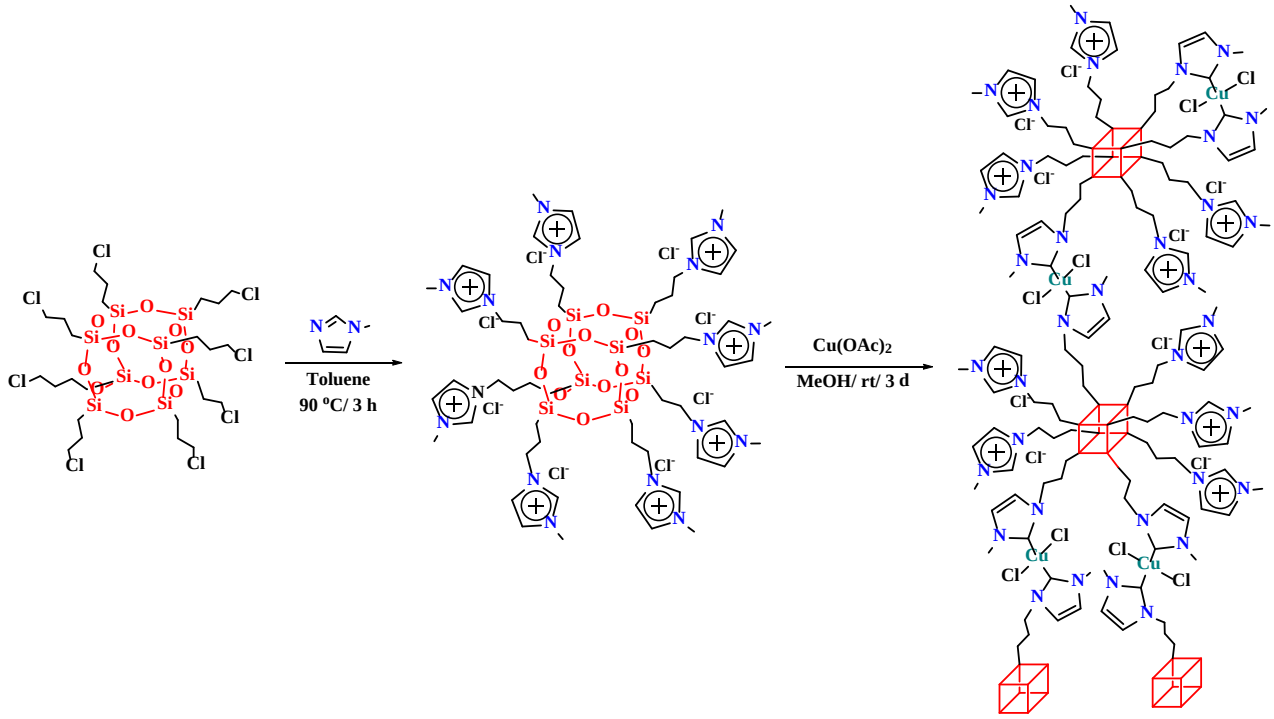

Scheme 1. Synthesis of Cu-IMSQ.

afforded the Cu-IMSQ, as a green solid, in 76% yield after 72 hours. Notably, this synthesis is simple to produce the catalyst materials, requiring only filtration since the product is insoluble both in polar and non-polar solvents.

3.2 Catalyst Characterizations

The formation of IM-SQ-Cu as a catalyst was confirmed by IR, XRD, and ICP methods. According to our previous reported, we can predict that two NHC ligand coordinating to each Cu(II), noted that a 1:5 mole ratio of IM-SQ:$Cu(OAc)_2$, should result in *ca.* 80% of unreacted imidazolium groups. The ICP-MS result show that 5.3%wt of Cu content or 1.5 Cu(II) per POSS unit which be proposed structure in Scheme 1. According to transition metal salt ($Cu^{2+}(OAc)_2^-$), acetate ion can act as base to abstract proton at C-2 of methylimidazolium surrounding cage-like SQ to be carbene, as the result, it able to occur coordination of NHC of methylimidazole to Cu^{2+}.[6,17,18] In other words, σ donor ability of lone pair electron of carbene able to donate into σ accepting orbital of copper.

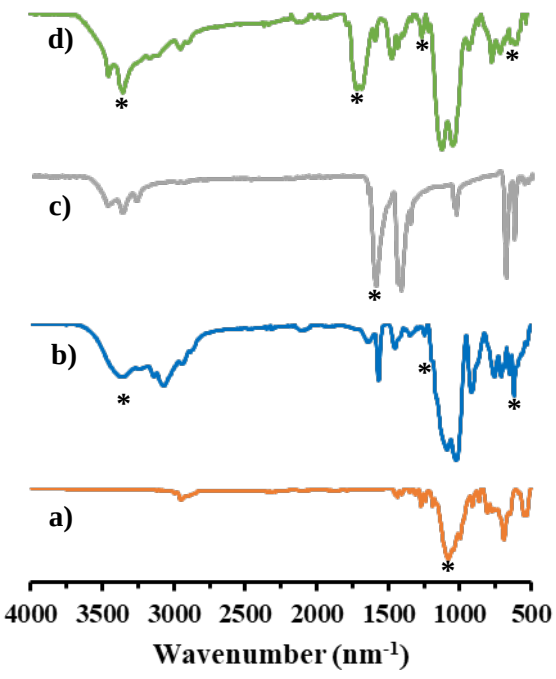

Figure 1. FT-IR spectra of a) T_8-Cl, b) IM-SQ c) copper(II)acetate, and d) Cu-IMSQ.

The FT-IR spectra of Cu-IMSQ (Figure 1) show that IM-SQ exhibits new C-N stretching bands of imidazole at 1180 and 619 cm^{-1} corresponding to presence of imidazole that nearly asymmetrical Si-O-Si stretching vibration at 1100 and 1020 cm^{-1},[19,20] as a result, disordered polyhedral SQ cages which sightly show broad band of O-H unit at 3000-3700 cm^{-1} when compared to perfect cage of T_8-Cl cage with strong band at 1080 cm^{-1} as shown in Figure 1a,[21] conforming occur some cage-degradation or open siliceous structures with silanol groups. The reason for the open cage could be explained by strong nucleophilicity of sp^2 nitrogen on imidazole, which one of possibility to occur the cleavage of Si-O bond at a SQ core.[22]

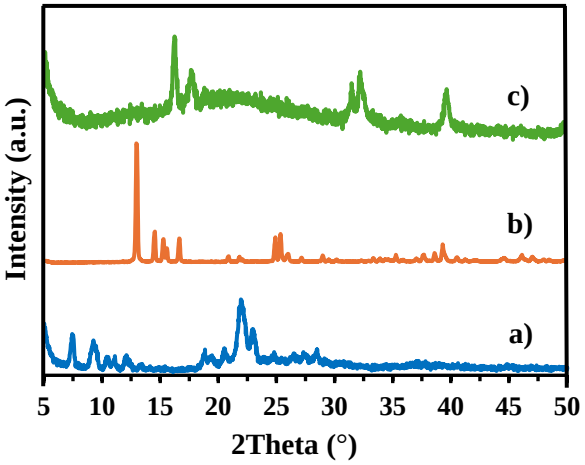

Figure 2. XRD spectra of a) $Cu(OAc)_2$, b) T_8-Cl, and c) Cu-IMSQ.

After adding copper(II)acetate, in IR of Cu-IMSQ reveal disappearance of ν(COO) at 1600 cm^{-1} that confirm removal of OAc^-.[23] Moreover, the intensity of imidazole band is sharply reduced suggest that NHC of imidazole occur forming with Cu. The XRD spectra of Cu-IMSQ catalyst in Figure 2c suggest a mixture of different crystalline phases mixed with an amorphous phase within the materials. In addition, a broad diffraction at 2θ = 22° indicates the existence of a cage-like SQ (Si-O-Si) of the solid materials with the d-value (spacing) of 0.41 nm.[24] The diffraction patterns observed in Figure 2c contain a new set of peaks, which are different from those of the T_8-Cl cage and $Cu(OAc)_2$ (Figures 2a and 2b). This is indicative that the new Cu-IMSQ product was generated.

Table 1. Alkyne-azide cycloaddition (CuAAC) reactions of benzyl azide and propagyl bromide[a]

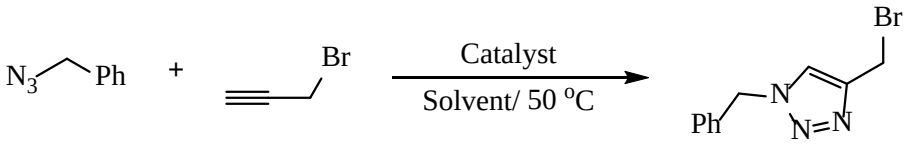

Entry	Catalyst	mol% Cu	Solvent	Time (min)	Yield[b] (%)
1	-	-	Ethanol/water	60	Traces
2	$Cu(OAc)_2$	2.5	Ethanol/water	60	40
3	Cu-IMSQ	0.4	Ethanol/water	15	73

[a]Benzyl alkyne (1.1 mmol), propargyl bromide (1.0 mmol) and (0.42 mol% Cu) Cu-IMSQ catalyst, in 2 mL of H_2O: EtOH (1:1 v/v) at 50 °C for 15 min.
[b]Isolated yields.

3.3 Catalytic Testing for CuAAC

The catalytic activity of Cu-IMSQ toward alkyne-azide cycloaddition (CuAAC) reactions between benzyl azide and propargyl bromide, used as model substrates, were performed in ethanol/water at 50 °C without added base, resulting in the triazole product in 73% yield after 15 min, as shown in entry 3, Table 1. In the absence of the catalyst, no reaction occurred under the same conditions after 1 h (entry 1). Interestingly, the use of $Cu(OAc)_2$ as a catalyst afforded the triazole product in 40% product yield at 1 h (entry 2).

4. Conclusion

The hybrid organic-inorganic material of cage like SQ functionalize NHC/imidazolium support copper as a catalyst was successfully synthesized though simple process to afford the Cu-IMSQ catalyst and was characterized by ICP, IR, and XRD. The catalyst exhibits the ability to catalyze toward CuAAC reaction of benzyl azide and propargyl bromide as starting materials within short time reaction in mild condition reaction. In the future, we plan to more explore efficiency catalyze CuAAC either electron-donating or electron withdrawing group of starting materials by simultaneously investigate recyclability and reusability.

Acknowledgements

This work is financially supported by the Mahidol University under the National Research Universities Initiative, Center of Excellence for Innovation in Chemistry (PERCH-CIC). Authors are also thankful to Assoc. Prof. Dr. Preeyanuch Sangtrirutnugul for help and support.

References

1. Yorimitsu, H.; Kotora, M.; Patil, N. T. *Chem. Rec.* **2021,** *21* , 3335-3337.
2. Obligacion, J. V.; Chirik, P. J. *Nat. Rev. Chem.* **2018,** *2*, 15-34.
3. Calabrese, C.; Aprile, C.; Gruttadauria, M.; Giacalone, F. *Catal. Sci. Technol.* **2020,** *10*, 7415-7447.
4. Du, Y.; Liu, H. *Dalton Trans.* **2020,** *49*, 5396-5405.
5. Koy, M.; Bellotti, P.; Das, M.; Glorius, F. *Nat. Cat.* **2021,** *4*, 352-363.
6. Hopkinson, M. N.; Richter, C.; Schedler, M.; Glorius, F. *Nature* **2014,** *510*, 485-496.
7. Bivona, L. A.; Giacalone, F.; Carbonell, E.; Gruttadauria, M.; Aprile, C. *ChemCatChem* **2016,** *8*, 1685-1691.
8. Zhang, Y.; Liu, K.; Wu, L.; Huang, H.; Xu, Z.; Long, Z.; Tong, M.; Gu, Y.; Qin, Z.;nChen, G. *Dalton Trans.* **2021,** *50*, 11878-11888.
9. Falk, A.; Dreimann, J. M.; Vogt. *ACS Sustain. Chem. Eng.* **2018,** *6*, 7221-7226.
10. Mohapatra, S.; Chaiprasert, T.; Sodkhomkhum, R.; Kunthom, R.; Hanprasit, S.; Sangtrirutnugul, P.; Ervithayasuporn, V. *ChemistrySelect* **2016,** *1*, 5353-5357.
11. Somjit, V.; Wong Chi Man, M.; Ouali, A.; Sangtrirutnugul, P.; Ervithayasuporn, V. *ChemistrySelect* **2018,** *3*, 753-759.
12. Ervithayasuporn, V.; Kwanplod, K.; Boonmak, J.; Youngme, S.; Sangtrirutnugul, P. *J. Catal.* **2015,** *332*, 62-69.
13. Takaya, J. *Chem. Sci.* **2021,** *12*, 1964-1981.
14. Tiwari, V. K.; Mishra, B. B.; Mishra, K. B.; Mishra, N.; Singh, A. S.; Chen, X. *Chem. Rev.* **2016,** *116*, 3086-3240.

15. Marciniec, B.; Dutkiewicz, M.; Maciejewski, H.; Kubicki, M. *Organometallics* **2008,** *27*, 793-794.
16. Tan, J.; Ma, D.; Sun, X.; Feng, S.; Zhang, C. *Dalton Trans.* **2013,** *42* (13), 4337-4339.
17. Ségaud, N.; McMaster, J.; van Koten, G.; Albrecht, M. *Inorg. Chem.* **2019,** *58*, 16047-16058.
18. Lake, B. R. M.; Willans, C. E. *Chem. Eur. J.* **2013,** *19*, 16780-16790.
19. He, Y.; Cai, C. *Chem. Comm.* **2011,** *47*, 12319-12321.
20. Sakka, S., The Outline of Applications of the Sol–Gel Method. In *Handbook of Sol-Gel Science and Technology*, Klein, L.; Aparicio, M.; Jitianu, A., Eds. Springer International Publishing: Cham, 2016; pp 1-33.
21. Park, E. S.; Ro, H. W.; Nguyen, C. V.; Jaffe, R. L.; Yoon, D. Y. *Chem. Mater.* **2008,** *20*, 1548-1554.
22. Jaroentomeechai, T.; Yingsukkamol, P. K.; Phurat, C.; Somsook, E.; Osotchan, T.; Ervithayasuporn, V. *Inorg. Chem.* **2012,** *51*, 12266-72.
23. Kragten, D. D.; van Santen, R. A.; Crawford, M. K.; Provine, W. D.; Lerou, J. J. *Inorg. Chem.* **1999,** *38*, 331-339.
24. Kim, J.; Kim, S. Y.; Yang, C.-M.; Lee, G. W. *Sci. Rep.* **2019,** *9*, 13313.

Facile synthesis of silsesquioxane appended with 1,8-naphthalimide benzo-15-crown-5 chemosensor

Boonsita Chanyong, Pattara Siripanich, and Vuthichai Ervithayasuporn*

Department of Chemistry, Mahidol University, RamaVI Road, Ratchathewi, Thailand 10400

**E-mail: vuthichai.erv@mahidol.edu*

Abstract:

Polyhedral oligomeric silsesquioxane (POSS) is a hybrid inorganic-organic material, which is utilized across various applications, particularly as functional materials for sensors. This work designed and synthesized a novel POSS chemosensor employing a heteroditopic concept. The incorporation of cation receptor, benzo-15-crown-5, within the POSS structure was achieved using low-cost catalysts and the reactions were conducted at low temperatures. In particular, the synthesis involved the use of copper-catalyzed azide-alkyne cycloaddition (CuAAC) to construct a silsesquioxane chemosensor based on 1,8-naphthalimide benzo crown ether. The "click" reaction allowed the reaction to proceed at room temperature while providing an acceptable product yield. The resulting product was characterized by ^{1}H, ^{13}C, ^{29}Si, COSY, HMQC nuclear magnetic resonance spectroscopy (NMR), and mass spectrometry to confirm that the substituent *N*-(benzo-15-crown-5)-4-(1,2,3-triazole)-1,8-naphthalimide (**PNC**) was incorporated into the POSS structure.

1. Introduction

Polyhedral oligomeric silsesquioxanes (POSS) are hybrid organic-inorganic materials. The structure of POSS consists of hybrid silicon-oxygen with the empirical formula $RSiO_{1.5}$, where R is hydrogen or organic moieties. Nanostructured cage-like POSS have been used in several applications such as light-emitting diode materials (OLED), catalysis, aerospace, adsorption materials, coating.[1] In recent years, POSS motifs have been used as main scaffolds in molecularly sensory agents for detections of charged species such as fluoride (F^-), cyanide (CN^-), and hydroxide (OH^-) at ppm levels.[2] In 2022, Siripanich *et. al.* demonstrated that F^- can form strong Si–F bonds with the Si atoms of POSS and induces quenching of fluorescence signals at the fluorophore reporting units, confirming electropositive characters of the Si binding site that capable of interacting with anions.[3]

Macrocycles are cyclic molecules consisting of more than 12 atoms and generally have specific cavity to accommodate guest species ranging from ions, small molecules, or complex structures with high affinity and selectivity.[4,5] Crown ethers are among the most versatile supramolecular hosts for cation recognition. By integrating the fluorescence reporter group such as 1,8-naphthalimide into the cation host, the receptors can exhibit fluorescence properties via photoinduced electron transfer (PET) or photoinduced charge transfer (ICT) mechanisms. The fluorescence phenomena depend on the intramolecular interactions of guest cations prescribed PET or ICT mechanism, resulting in either fluorescence enhancement or quenching.[6]

Fedorova et. al. designed a 4-acetamido substituent naphthalimide with *N*-benzo-15-crown-5, which yielded fluorescence signal from PET mechanism when crown ether selectively detected Mg^{2+} and Ba^{2+} led to fluorescence enhancement.[7] The receptor containing methoxy group displayed fluorescence enhancement under PET mechanism upon binding of Mg^{2+} and Ca^{2+}.[8] Additionally, metal ions could induce the fluorescence enhancement of 1,8 naphthalimide motifs through PET pathway. The 4-amino-1,8-naphthalimide, NIDPA, displayed enhancement of fluorescence signals when binding to Zn^{2+}.[9] The 4-*N*-(methylpiperazine)-substituted naphthalimide gave strong PET with the highest fluorescent intensity after adding Zn^{2+}.[10] The 1,8-naphthalimide connected to triazole at the 4-position is another potent fluorescence sensor motifs.[11] In particular, high 1,8-naphthalimide selectivity to metal ions is often achieved in the presence of an electron-donating substituent at the C4 position of the 1,8-naphthalimide.[10, 12, 13] Hence, the C4 position is an important part of naphthalimide ability to increase binding affinity with multiple metals. In general, the Heck coupling reaction was used to synthesize silsesquioxane chemosensors.[2] However, due to low product yields and expensive catalyst as well as high temperatures required, we were interested in using the click-cross coupling reaction, which is cheaper, greener, and affords high product yields.[14] In this study, we designed a dual responsive cations and anions silsesquioxane chemosensor based on 1,8-naphthalimide benzo-15-crown-5 with a triazole linker, which was synthesized via the copper-catalyzed azide alkyne cycloaddition

(CuAAC) at room temperature to incorporate the triazole moiety at the C4 position, linking the silsesquioxane and 1,8-naphthalimide benzo-15-crown-5. In general, the molecular design was presented in a receptor$_1$-spacer$_1$-fluorophore-spacer$_2$-receptor$_2$ format, as shown in **Figure 1**.

Figure 1. A diagram of a concept design for the molecular sensor.

2. Materials and Methods

2.1 Materials

The chemicals were purchased from the following sources: sodium azide (NaN_3), tris(benzyltriazolylmethyl)amine, copper iodide (CuI), and all analytes were purchased form Tokyo Chemical Industry. Alkyne-PIBPOSS **(1)**,[15] 6-Bromo-2-(2,3,5,6,8,9,11,12-octahydrobenzo[b][1,4,7,10,13] penta oxacyclopentadecin-15-yl)-1H-benzo[de]-isoquinoline-1,3(2H)-dione **(2)**,[16] were prepared following previous literature methods. Dichloromethane, acetone, hexane, and methanol were distilled before use. AR grade acetonitrile (ACN), ethanol, tetrahydrofuran (THF), ethyl acetate (EtOAc), dimethylformamide (DMF) and toluene were used without further purification.

2.2 Characterisation

^{1}H, ^{13}C{^{1}H}, and ^{29}Si{^{1}H} NMR spectra were recorded on a Bruker-AV 400 high-resolution magnetic resonance spectrometer. Fluorescence spectra were recorded by a spectrofluorometer (Horiba FluoroMax4+, integration time 0.1 s, slit width 3 nm). UV–vis spectrophotometer (Shimadzu UV2600) was used to perform the UV–vis spectrometry method. High-resolution electrospray ionization mass spectrometry (HR ESI-MS) spectra (positive mode) were recorded on a microTOF instrument. The FT-IR spectra were recorded by using attenuated total reflectance (ATR) technique on a Bruker model Alpha spectrometer.

2.3 Synthesis of 6-azido-2-(2,3,5,6,8,9,11,12) octahydrobenzo[b][1,4,7,10,13] pentaoxacyclopentadecin-15-yl)-1H-benzo[de]isoquinoline-1,3(2H)-dione (3)

Compound **2** (340 mg, 0.63 mmol) was dissolved in 10 mL of DMF along with NaN_3 (410 mg, 6.30 mmol). The mixture was stirred at 80°C overnight. Afterward, the solvent was evaporated under vacuum, and the residue was redissolved in THF. Upon filtration, the resulting solution was evaporated, yielding a dark red-brown solid. This solid was washed with water and dried in air, ultimately providing the product in a yield of 48%. (153 mg, 0.30 mmol). ^{1}H NMR (400 MHz, $CDCl_3$) δ (ppm): 3.76-3.78 (d, *J* = 6.3 Hz, 8H), 3.79-3.94 (m, 4H), 4.13-4.20 (m, 4H), 6.81 (d, *J* = 1.8 Hz,1H), 6.84-6.86 (dd, *J* = 8.4 Hz, 2.0 Hz, 1H), 6.99-7.01 (d, *J* = 8.4 Hz, 1H), 7.47-7.49 (d, *J* = 8.0 Hz, 1H), 7.74-7.78 (t, *J* = 7.8 Hz, 1H), 8.46-8.49 (d, *J* = 8.3 Hz, 1H), 8.58-8.60 (d, *J* = 8.0 Hz, 1H), 8.64-8.66 (d, *J* = 7.2 Hz, 1H). ^{13}C{^{1}H} NMR (100 MHz, $CDCl_3$) δ (ppm): 69.22, 69.39, 69.68, 69.78, 70.78, 71.35, 71.39, 114.15, 114.44, 114.90, 119.34, 121.38, 122.93, 124.62, 127.10, 128.47, 129.34, 129.64, 132.24, 132.76, 143.90, 149.43, 149.80, 164.00, 164.43. HRMS (ESI): calced for $[C_{26}H_{24}N_4O_7+Na]^+$: m/z 527.1537 $[M+Na]^+$. Found: m/z 527.1568. FT-IR (cm^{-1}): 2106 (N_3).

2.4 Synthesis of mono-substituted polyhedral oligomeric silsesquioxane by N-(benzo-15-crown-5)-4-(1,2,3-triazole)-1,8-naphthalimide (PNC; 4)

The product was synthesized according to **scheme 1.** Compound **3** (303 mg, 0.6 mmol) was dissolved in 8 mL of THF/ACN (8:2) along with tris(benzyltriazolylmethyl)amine (69 mg, 0.13 mmol), and CuI (25 mg, 0.13 mmol), in a 25-mL round-bottom flask. Alkyne-PIBPOSS (559 mg, 0.6 mmol) was then added to the mixture. The reaction was stirred at room temperature for 48 hours. After completion, the solvent was removed by rotary evaporation to yield a solid residue. This residue was dissolved in EtOAc and filtered. The desired product was obtained by filtration and subsequent washing with methanol, followed by hexane. The resulting brown solid obtained in 44% yield (340 mg, 0.24 mmol). ^{1}H NMR (400 MHz, $CDCl_3$) δ: 0.60-0.61 (m,16H, Si-CH_2), 0.74 (m, 2H, Si-CH_2), 0.95-0.96 (dd, 42H, CH_3), 1.79 (m,2H, CH_2), 1.86 (m,7H, C**H**—$CH_3)_2$), 3.52-3.54 (q,2H, CH_2-NH), 3.76 (d, *J* = 5.2 Hz, 8H), 3.89-3.94 (m, 4H), 4.13-4.20 (m, 4H), 6.83 (s, 1H), 6.86-6.88 (d, *J* = 8.0 Hz, 1H), 7.00-7.02 (d, *J* = 8.0 Hz, 1H), 7.36 (s, 1H, NH), 7.87-7.89 (m, 2H), 8.17-8.19 (d, *J* = 8.0 Hz, 1H), 8.59 (s, 1H), 8.74 (m, 2H). ^{13}C{^{1}H} NMR (100 MHz, $CDCl_3$) δ: 9.59

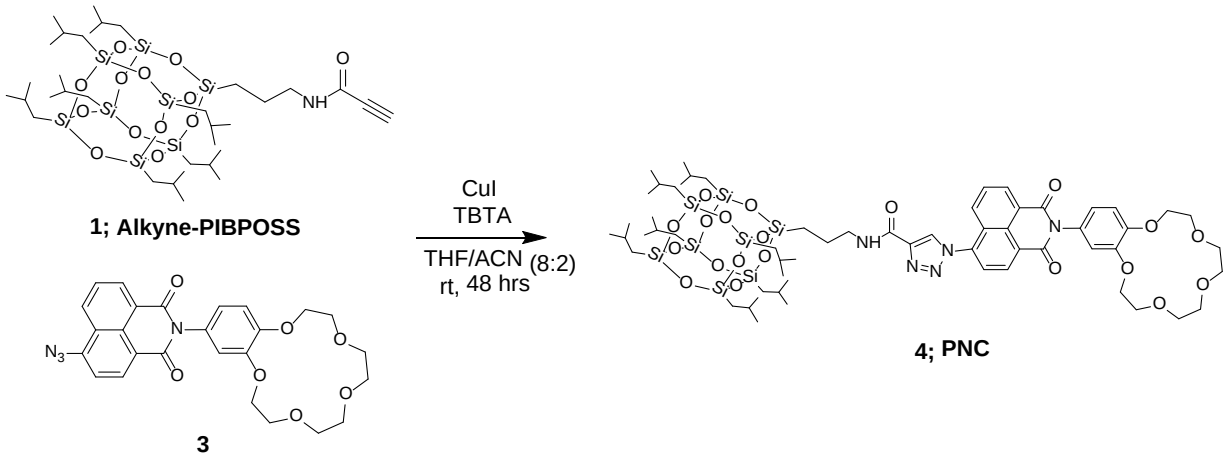

Scheme 1. Synthesis of **PNC** via CuAAC reaction.

(1C, Si-CH_2), 22.53-22.56 (7C, Si-CH_2), 23.20 (1C, CH_2), 23.93-23.99 (7C, **C**H-$(CH_3)_2$), 25.76 (14C, CH_3), 41.73 (1C, CH_2-NH), 69.11, 69.19, 69.52, 69.60, 70.61 (2C, CH_2), 71.19 (2C, CH_2), 113.96, 114.20, 121.26, 123.38, 124.10, 124.72, 126.56, 127.82, 127.87, 129.08, 129.18, 129.44, 131.12, 132.84, 137.80, 144.19, 149.52, 149.74, 159.42 (1C, **C**O-NH), 163.36, 163.89. $^{29}Si\{^1H\}$ NMR (79 MHz, $CDCl_3$) δ: -67.90, -67.83, -67.55. HRMS (ESI): calcd for $[C_{60}H_{95}N_5O_{20}Si_8+Na]^+$: m/z 1452.4647 $[M+Na]^+$. Found: m/z 1453.4644. FT-IR (cm^{-1}): 1090 (Si-O-Si), and azido stretching disappear.

2.5 Photophysical characterization of PNC in different organic solvents

The different polarity of organic solvent gives the slightly different absorption intensity. The maxima absorption showed λ_{max} = 342 nm, 335 nm, 344 nm in DMF, THF and EtOAc, respectively. The emitted fluorescence decreased when increasing the polarity of the solvent. Moreover, the increasing dielectronic constant of solvent was shifted to a higher wavelength from a bathochromic effect (red shift) in fluorescence measurement. The red-shift of increasing polarity could be an intramolecular charge transfer (ICT) from 1,2,3-triazole substituent into the aromatic of fluorophore.[13]

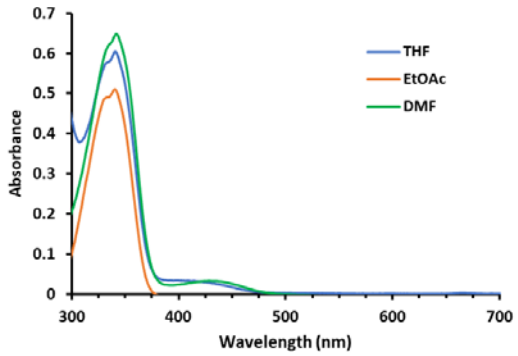

Figure 2. UV-Vis absorption of PNC sensor 3×10^{-5} M without guest cation in different polarity of solvents include tetrahydrofuran (THF), ethyl acetate (EtOAc), dimethylformamide (DMF).

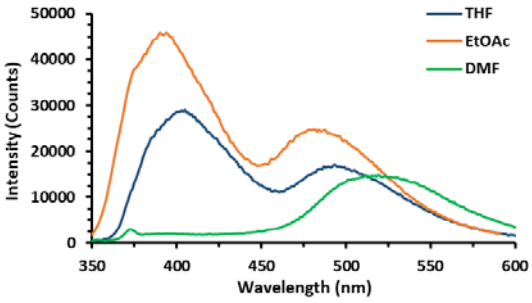

Figure 3. Fluorescence spectra of PNC sensor 5×10^{-5} M without guest cation in different polarity of solvents include tetrahydrofuran (THF), ethyl acetate (EtOAc), dimethylformamide (DMF).

3. Results & Discussion

3.1 PNC with guest cation sensing in different organic solvent

Solutions of PNC in EtOAc exhibited strong fluorescence emission signals in the presence of transition metal cations including Zn^{2+}, Fe^{2+}, Co^{2+}, Cu^{2+}, and Hg^{2+} with different degree of enhancement.

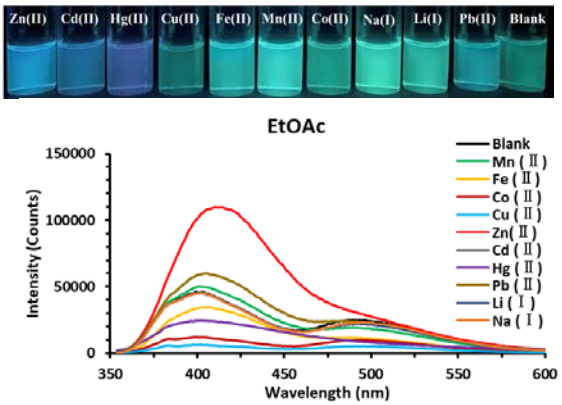

Figure 4. Photograph and fluorescence spectra PNC $5x10^{-5}$ M in ethyl acetate (EtOAc) after addition of various metals at 50 equiv. The reaction time equilibrium reaches at 24 h.

The fluorescence emission signals were significantly enhanced after adding Zn^{2+} (50 equiv.). The emission spectra of PNC exhibited a red shift of the maximum emission wavelength from 399 nm to 411 nm upon complexation with Zn^{2+}, resulting in a color change from light green to light blue presumably due to electron transfer (ET) from the binding site to the fluorophore.[17] Otherwise, the other metals (Fe^{2+}, Co^{2+}, Cu^{2+}, Hg^{2+}) displayed dramatic quench in the fluorescent emission.

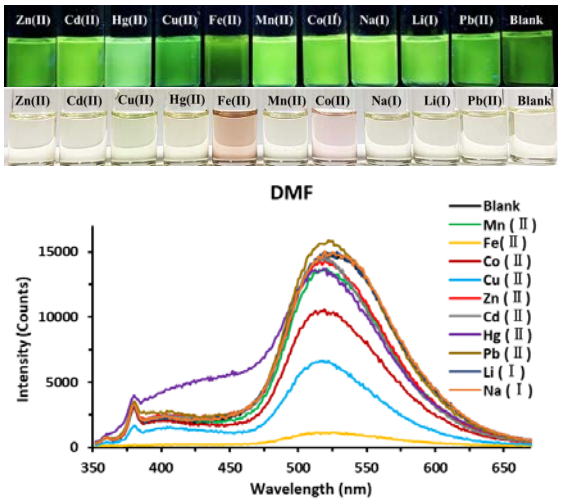

Figure 5. Photograph and fluorescence spectra PNC $5x10^{-5}$ M in dimethylformamide (DMF) after addition of various metals at 50 equiv. The reaction time equilibrium reaches at 24 h.

Cation titration experiments were carried out in DMF, a higher polarity solvent, reveal stark contrast results compared to in EtOAc. The maximum emission wavelength is centered at 526 nm, being red shift the spectra measured in EtOAc.The fluorescence emission exhibited quenching of signals upon additions of Fe^{2+}, Co^{2+}, and Cu^{2+} (Figure 5). Fluorescent spectra of PNC exhibited the highest degree of fluorescence quenching (92.4%) upon adding Fe^{2+} and showed about 57.6% quenching when adding Cu^{2+}. The color observed by naked eye changed from light yellow to orange-brown, and light green for Fe^{2+} and Cu^{2+}, respectively. The fluorescence enhancement observed in EtOAc solutions upon additions of Zn^{2+} suggested inhibitions of electron transfer from the 15-crown-5 receptor to the naphthalimide fluorophore. In contrast, the fluoresecence quenching in the presence of Fe^{2+}, Co^{2+}, and Cu^{2+} was observed in DMF solutions, indicating different sensing mechanisms. We propose that complexation of M^{2+} ions (M = Fe^{2+}, Co^{2+}, Cu^{2+}) lead to the emission quenching of a nearby fluorophore via electron transfer to suppress the reverse photoinduced electron transfer (PET) mechanism.

4. Conclusion

The mono-substituted polyhedral oligomeric silsesquioxane with N-(benzo-15-crown-5)-4-azido-1,8-naphthalimide (PNC) was successfully synthesized through a copper-catalyzed azide alkyne cycloaddition (CuAAC) reaction. The sensitivity of the PNC sensor was influenced by the characteristics of the solvent. The PNC sensor demonstrates excellent solubility in polar aprotic solvents, particularly as the dielectric constant of the solvent increases. This interaction between the PNC and the solvent can initiate an Intramolecular Charge Transfer (ICT) process, transitioning from a triazole moiety to a fluorophore, exhibiting solvatochromic characteristics. PNC was utilized as a sensor with excellent selectivity for Zn^{2+} in EtOAc, displaying a color change from light green to light blue and fluorescence enhancement through a PET mechanism. Conversely, reversed PET was observed in DMF solutions for Fe^{2+}. This chemosensor will be further studied for its anion sensing properties in the future.[2, 3]

Acknowledgements

This research project was supported by the Thailand Research Fund (RSA6280049 and RTA6180007), Mahidol University (Basic Research Fund: fiscal year 2022), and the Center

of Excellence for Innovation in Chemistry (PERCH-CIC).

References

1. Du, Y.; Liu, H., Cage-like silsesquioxanes-based hybrid materials. *Dalton Trans.* **2020,** *49* (17), 5396-5405.
2. Chanmungkalakul, S.; Ervithayasuporn, V.; Boonkitti, P.; Phuekphong, A.; Prigyai, N.; Kladsomboon, S.; Kiatkamjornwong, S., Anion identification using silsesquioxane cages. *Chem. Sci.* **2018,** *9* (40), 7753-7765.
3. Siripanich, P.; Bureerug, T.; Chanmungkalakul, S.; Sukwattanasinitt, M.; Ervithayasuporn, V., Mono and Dumbbell Silsesquioxane Cages as Dual-Response Fluorescent Chemosensors for Fluoride and Polycyclic Aromatic Hydrocarbons. *Organometallics* **2022,** *41* (3), 201-210.
4. Yudin, A. K., Macrocycles: lessons from the distant past, recent developments, and future directions. *Chem. Sci.* **2015,** *6* (1), 30-49.
5. Robert, D. H., Chelate, Macrocyclic, and Macrobicyclic Effects. In *Encyclopedia of Supramolecular Chemistry*, CRC Press: 2004.
6. Wang, H.; Wu, H.; Xue, L.; Shi, Y.; Li, X., A naphthalimide fluorophore with efficient intramolecular PET and ICT Processes: Application in molecular logic. *Org. Biomol. Chem.* **2011,** *9* (15), 5436-5444.
7. Panchenko, P. A.; Fedorov, Y. V.; Perevalov, V. P.; Jonusauskas, G.; Fedorova, O. A., Cation-Dependent Fluorescent Properties of Naphthalimide Derivatives with N-Benzocrown Ether Fragment. *J. Phys. Chem. A.* **2010,** *114* (12), 4118-4122.
8. Panchenko, P. A.; Leichu, N. V.; Fedorov, Y. V.; Fedorova, O. A., Crown-Containing 4-Methoxy-1, 8-naphthalimide Derivatives as a Basis for the Construction of Fluorescent PET Chemosensors for Metal Cations. *Macroheterocycles* **2019,** *12* (3), 319-323.
9. Fan, J.; Peng, X.; Wu, Y.; Lu, E.; Hou, J.; Zhang, H.; Zhang, R.; Fu, X., A new PET fluorescent sensor for Zn^{2+}. *J. Lumin.* **2005,** *114* (2), 125-130.
10. Staneva, D.; Vasileva-Tonkova, E.; Bosch, P.; Grabchev, I., A new green fluorescent tripod based on 1,8-naphthalimide. Detection ability for metal cations and protons and antimicrobial activity. *J. Photochem. Photobio A: Chem.* **2017,** *344*, 143-148.
11. Ast, S.; Kuke, S.; Rutledge, P. J.; Todd, M. H., Using Click Chemistry to Tune the Properties and the Fluorescence Response Mechanism of Structurally Similar Probes for Metal Ions. *Eur. J. Inorg. Chem.* **2015,** *2015* (1), 58-66.
12. Tian, Y.; Li, M.; Liu, Y. Detection Sensitivity Enhancement of Naphthalimide PET Fluorescent Probes by 4-Methoxy-Substitution *Molecules* [Online], 2020.
13. Gauci, G.; Magri, D. C., Solvent-polarity reconfigurable fluorescent 4-piperazino-N-aryl-1,8-naphthalimide crown ether logic gates. *RSC Adv.* **2022,** *12* (54), 35270-35278.
14. Beletskaya, I. P.; Averin, A. D., New trends in the cross-coupling and other catalytic reactions. *Catalytic cross-coupling* **2017,** *89* (10), 1413-1428.
15. Fernández, M. J.; Fernández, M. D.; Cobos, M., Synthesis, characterization and properties of telechelic hybrid biodegradable polymers containing polyhedral oligomeric silsesquioxane (POSS). *RSC Adv.* **2014,** *4* (41), 21435-21449.
16. Diacono, A.; Aquilina, M. C.; Calleja, A.; Agius, G.; Gauci, G.; Szaciłowski, K.; Magri, D. C., Enhanced ion binding by the benzocrown receptor and a carbonyl of the aminonaphthalimide fluorophore in water-soluble logic gates. *Org. Biomol. Chem.* **2020,** *18* (25), 4773-4782.
17. Mohan, B.; Noushija, M. K.; Shanmugaraju, S., Amino-1,8-naphthalimide-based fluorescent chemosensors for Zn(II) ion. *Tetrahedron Lett.* **2022,** *109*, 154155.

Electrochemical self-coupling of benzyl halides catalyzed by cobalt complex with pincer based ligand

Pornwimon Kongkiatkrai and Teera Chantarojsiri*

Department of Chemistry and Center of Excellence for Innovation in Chemistry, Faculty of Science, Mahidol University, Bangkok, Thailand

**E-mail: teera.cha@mahidol.edu*

Abstract:

The synthetic pathway for C—C bond formation has been highly of interest. In this report, we described a cobalt complex supported by pyridine diimine pincer which exhibited its ability in the electrochemical homo-coupling of organohalides. According to the cyclic voltammetry results, the addition of benzyl halides to the cobalt complex under argon atmosphere resulted in the current enhancement, leading to the presence of the homo-coupling reaction. The reactions proceeded through radical intermediates, generated by electricity. This reaction can be further developed as a greener methodology, as it reduces the by-product from the chemical reductant which is harmful to both humans and the environment. Benzyl halides were electrolyzed under argon to demonstrate the formation of C—C bond between the radical intermediates, providing bibenzyl as a desirable product.

1. Introduction

Metal-catalyzed cross-coupling is a key reaction to access valuable organic molecules by C—C bond formations. Several transition metals have been utilized to catalyze the cross-coupling reaction, particularly the second and third-row transition metals, which are costly and less abundant. Methodologies for C—C bond coupling reactions catalyzed by first-row transition metal are being developed. Particularly, the methodologies for the formation of C—C linkages are the challenges in the organic synthesis providing important products in pharmaceutical and medicinal chemistry.[1] In the past decades, there have been a variety development of C—C bond formation bond formation of alkynes[2] and aryl halides[3] with different efficient methodologies with a variety of transition metal catalysts. The dimerization of aryl halides was previously reported using the zero-valent nickel as a catalyst and providing biaryls as a product.[4] The synthesis of biaryls was also reported by utilizing the nickel(II) complex with a requirement of Zn as a reducing agent in the homocoupling of organic halides.[5] Moreover, Co(II) complex was previously exhibited an ability to perform homocoupling of terminal alkynes as dicobalt octacarbonyl in the hydroformylation reaction.[6, 7] The C—C bond formation was also developed in the process of Co-catalyzed dimer synthesis from alkyl chloride with manganese as a reductant.[8] The substrate scope of transition metal-catalyzed reactions is expanded as benzyl chloride homocoupling was investigated to demonstrate the Csp^3— Csp^3 bond formation catalyzed by Rhodium[9] and Nickel[10] with Zn reductant required. To avoid utilization of stoichiometric reductant, electrosynthesis was established in the reaction of electrochemical Nickel-catalyzed homocoupling of 2-bromomethylpyridine in an undivided cell in order to generate bipyridines as products.[11]

In this report, we investigated the electrochemical self-coupling of benzyl halides using cobalt complexes with a pincer ligand to generate C—C linkages between two radical intermediates producing bibenzyl as a product.

2. Synthesis and characterization

2.1 Synthesis of PDI(^{i}Pr)

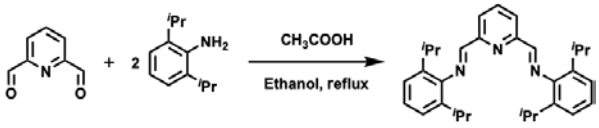

Scheme 1. Synthetic scheme of 2,6-bis(2,6-diisopropylphenyl imino)methyl pyridine, (PDI ^{i}Pr).

2,6-Pyridine dicarboxaldehyde (0.3337 g, 2.5 mmol, 1 equiv.) was dissolved in ethanol (10 mL). After the addition of 2,6-diisopropylaniline (0.9246 g, 5 mmol, 2 equiv.), 2-3 drops of glacial acetic acid were added dropwise. The reaction was refluxed for 4-5 hours at 85 °C. The mixture was filtered hot. The product was obtained as a yellow-green solid (1.0786 g, 96.0%).

^{1}H NMR ($CDCl_3$): δ 8.40 (2H, d), 8.36 (2H, s), 8.00 (1H, t), 7.15 (6H, m), 2.99 (4H, m), 1.19 (24H, d)

2.2 Synthesis of Co(II)-PDI(^{i}Pr)

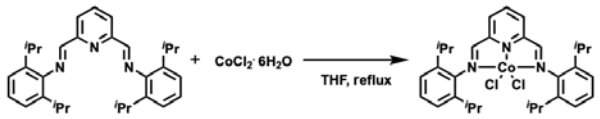

Scheme 2. Synthetic scheme of Cobalt(II)- 2,6-bis(2,6-diisopropylphenyl imino)methyl pyridine PDI(^{i}Pr), Co(II)-PDI(^{i}Pr).

PDI(^{i}Pr) (0.5146 g, 1.13 mmol, 1 equiv.) was dissolved in THF (5 mL). $CoCl_2.6H_2O$ (0.2823 g, 1.13 mmol, 1 equiv.) was separately dissolved in THF (5 mL). Two solutions were mixed. The reaction was stirred at room temperature for 1.5 hours. The solvent was removed under reduced pressure. The solid was redissolved in DCM and diethyl ether was added to the solution to precipitate out the products. The complex was obtained as a dark green solid (0.6527 g., 98.4%). The product is recrystallized by vapor diffusion of THF/Et_2O.

2.3 Characterization

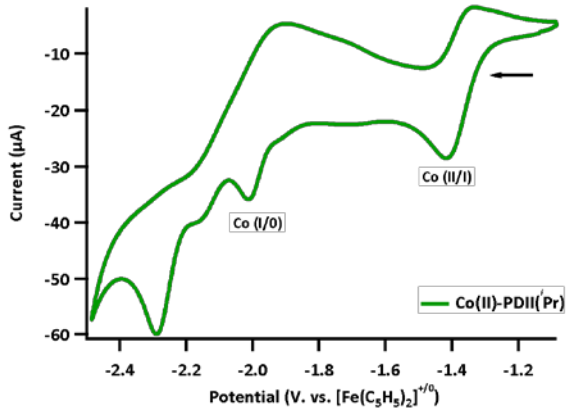

Figure 1. Cyclic voltammogram of Co(II)-PDI(^{i}Pr) with scan rate 100 mV. Conditions: working electrode, glassy carbon; counter electrode, Pt; reference electrode Ag/Ag^+ in 0.1 M $TBAPF_6$ in MeCN under Argon atmosphere, with ferrocene as an external standard.

Table 1. Electrochemical data for Co(II)-PDI(^{i}Pr)

Species	$E_{1/2}$ (V vs $[Fe(C_5H_5)_2]^{+/0}$)
Co(II/I)	-1.378

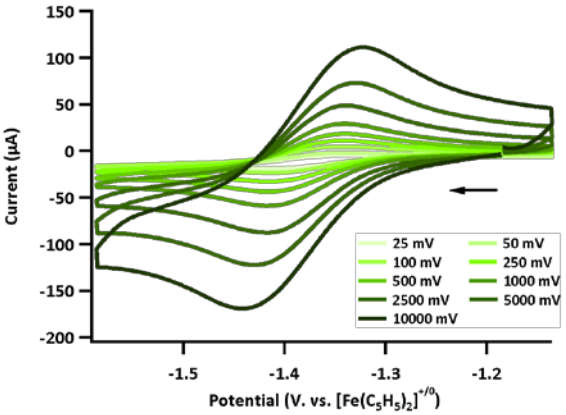

Figure 2. Scan rate-dependent cyclic voltammogram of Co(II)-PDI(^{i}Pr) with scan rate of 25mV/s (light green) to 10,000 mV/s (dark green). Conditions: working electrode, glassy carbon; counter electrode, Pt; reference electrode Ag/Ag^+ in 0.1 M $TBAPF_6$ in MeCN under Argon atmosphere, with ferrocene as an external standard.

Cyclic voltammetry was used to study their redox couples. Cyclic voltammogram of Co(II)-PDI(^{i}Pr) shows reversible Co(II/I) redox couple of at $E_{1/2}$ = -1.378 V vs $[Fe(C_5H_5)_2]^{+/0}$ (**Figure 1 and Table 1**). There is also a reduction of Co(I/0) at approximately -2.0 V vs $[Fe(C_5H_5)_2]^{+/0}$. The CV demonstrated the reduction of PDI(^{i}Pr) ligand at around -2.25 V vs $[Fe(C_5H_5)_2]^{+/0}$.

2.4 Method for Electrolysis

In a 50 mL two-necked cell with carbon cloth (1 cm x 2 cm), benzyl halides (0.5 mmol), Co(II)-PDI(^{i}Pr) (0.05 mmol), $TBAPF_6$ (0.5 mmol) were loaded. Then, the mixture was degassed under Argon for 5 times. After that, 5 mL of MeCN was injected into the cell by syringe. Constant current of 8 mA was passed for 4 hours at room temperature. After the electrolysis, the mixture was quenched with 2 M HCl (25 mL). The solution was extracted with Et_2O (3x50 mL), washed with brine. The organic layer was dried over $NaSO_4$, filtered and removed solvent under vacuum.

3. Electrochemical activity

3.1 Catalytic activity with substrates

The first substrate in the catalytic activity investigation is benzyl chloride. After the addition of 10 equiv benzyl chloride to the solution of Co(II)-PDI(^{i}Pr), the reductive peak current intensity was dramatically increased at

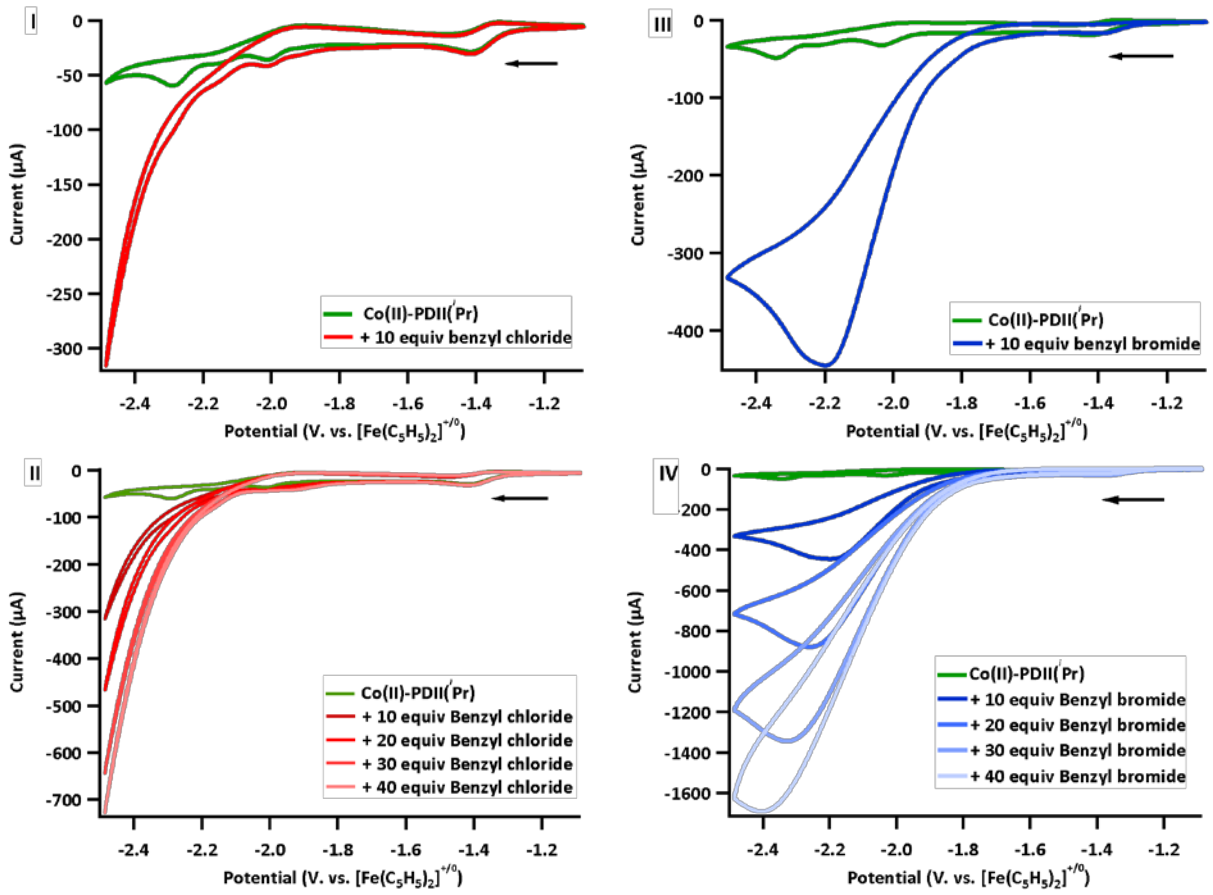

Figure 3. I) Cyclic voltammogram of Co(II)-PDI(^{i}Pr) with scan rate 100 mV (green), addition of 10 equivalent of benzyl chloride (red). **II**) Cyclic voltammogram of Co(II)-PDI(^{i}Pr) with scan rate 100 mV (green), benzyl chloride titration from 10 equivalent of benzyl chloride (dark red) to 40 equivalent of benzyl chloride (light red). **III**) Cyclic voltammogram of Co(II)-PDI(^{i}Pr) with scan rate 100 mV (green), addition of 10 equivalent of benzyl bromide (blue). **IV**) Cyclic voltammogram of Co(II)-PDI(^{i}Pr) with scan rate 100 mV (green), benzyl bromide titration from 10 equivalent of benzyl bromide (dark blue) to 40 equivalent of benzyl bromide (light blue). Conditions: working electrode, glassy carbon; counter electrode, Pt; reference electrode Ag/Ag^{+} in 0.1 M $TBAPF_6$ in MeCN under Argon atmosphere, with ferrocene as an external standard.

approximately -2.10 V vs $[Fe(C_5H_5)_2]^{+/0}$ which could be corresponding to the oxidative addition of benzyl chloride to Co(0) intermediates (**Figure 3I**). To further investigate the catalytic activities, the substrate titration was carried out by cyclic voltammetry. As shown in **Figure 3II**, the addition of 10-40 equivalents of benzyl chloride demonstrated an increase in the reduction catalytic peak. Benzyl bromide is the second substrate in the catalytic activity investigation. Similarly, the addition of 10 equiv benzyl bromide to the solution of Co(II)-PDI(^{i}Pr) resulted in a linear increase in reductive peak current at -1.80 V vs $[Fe(C_5H_5)_2]^{+/0}$ (**Figure 3III**), predicted to be the oxidative addition of benzyl bromide to the Co intermediate after the reduction of the cobalt complex. The cyclic voltammetry with benzyl bromide titration was also shown in **Figure 3IV**. After the addition of 10-40 equivalents of benzyl bromide was performed, the catalytic reductive peaks were increased, and the return peaks were reduced.

In comparison, benzyl bromide provides a larger increase in the catalytic reductive peak current than benzyl chloride. Additionally, the onset potential of the catalytic peak when benzyl bromide was used as a substrate appeared at a more positive potential, possibly suggesting an oxidative addition at Co(I) center. Therefore, the oxidative addition of benzyl bromide to the Cobalt intermediates may occur more easily than benzyl chloride. (**Figure 4**)

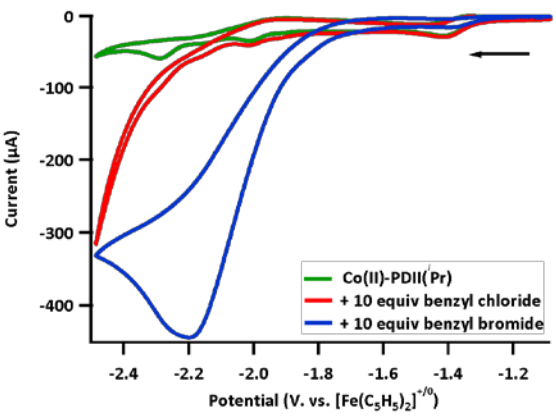

Figure 4. Cyclic voltammogram of Co(II)-PDI(^{i}Pr) with scan rate 100 mV (green), addition of 10 equivalent of benzyl chloride (red), addition of 10 equivalent of benzyl bromide (blue). Conditions: working electrode, glassy carbon; counter electrode, Pt; reference electrode Ag/Ag^+ in 0.1 M $TBAPF_6$ in MeCN under Argon atmosphere, with ferrocene as an external standard.

3.2 Proposed mechanism

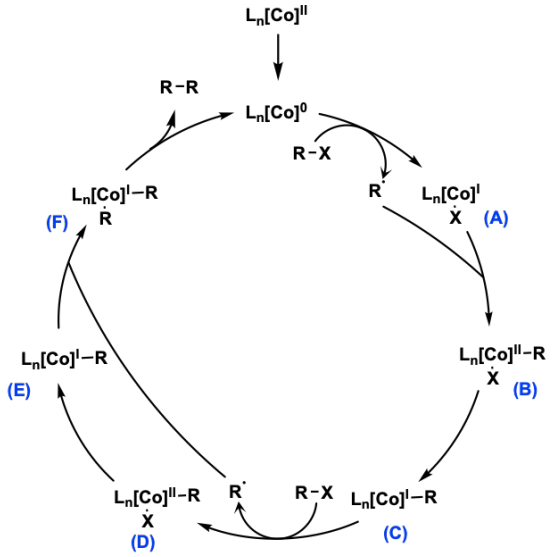

Scheme 3. Proposed mechanism of benzyl halide homocoupling.

In **scheme 3**, we proposed a mechanism of the electrochemical benzyl halides homocoupling reaction catalyzed by the cobalt complex. Firstly, cobalt(II) is electrochemically reduced to form cobalt(I) species (A) while benzyl radical is generated from benzyl halides. Cobalt(I), species A, reacts with the benzyl radical to form a cobalt(II) species B. Cobalt(II), species B, undergoes a reduction by an electron from electric current, generating cobalt(I) species C. Then, a similar procedure result in the cobalt-bibenzyl complex F. Finally, a reductive elimination gives the product of bibenzyl and regenerates the catalyst.

3.3 Electrolysis

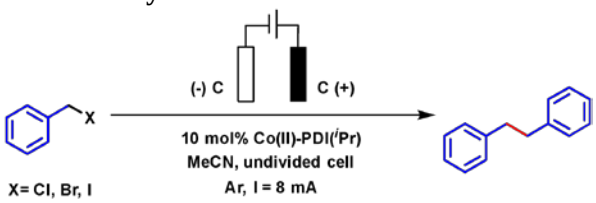

Scheme 4. electrochemical self-coupling of benzyl halides catalyzed by Co(II)-PDI(^{i}Pr).

Table 2. Result of homocoupling catalyzed by Co(II)-PDI(^{i}Pr)

Entry	Substrate	Conversion[a] (%)	GC Yield[b] (%)
1	**Benzyl bromide**	66	21
2	**Benzyl chloride**	97	0

[a]Conversions were calculated from the amount of substrate consumed in the reaction, compared to the starting amount

[b] GC yields were calculated from the amount of bibenzyl detected by Gas Chromatography in comparison to the theoretical yield.

The homocoupling of benzyl halides were performed under Argon atmosphere for 4 hours using electric current as a reductant. In entry 1 (**Table 2**). The result shows the homocoupling of benzyl bromide catalyzed by Co(II)-PDI(^{i}Pr) in MeCN provided 21% yield of bibenzyl while there is a high conversion of benzyl chloride but no bibenzyl detected from the homocoupling of benzyl chloride. A trace amount of benzyl alcohol was detected while the majority of benzyl chloride possibly decomposed. Benzyl alcohol could be generated from the hydrolysis of benzyl chloride with water. The result suggested the potential of our Co complex to act as a catalyst in the reaction of benzyl bromide self-coupling. Benzyl bromide, as a substrate, is more competent in forming radicals and, therefore, yields more bibenzyl than benzyl chloride.

3.4 Quantitative characterization of products

After working up the reaction, 100 µL of 50 mM 1,3,5-trimethoxybenzene was added to the reaction products with MeCN in 2 mL volumetric flask. The solution was filtered through a syringe filter into GC-vial. The samples were characterized using GC-FID. After obtaining the signals of each compound, the concentration of products were

calculated using the equation from the calibration curves.

[Bibenzyl] = [(signal/TMB) + 2.0595]/0.8462
[Benzyl Br] = [(signal/TMB) + 0.681]/0.4852
[Benzyl Cl] = [(signal/TMB) + 2.02]/0.165

Then, the concentration in mM was used to calculate the mmol of each product to finally obtain the GC yield. The conversion was shown by the amount of substrate consumed/ the amount of starting substrate.

4. Conclusion

In conclusion, we successfully synthesized and characterized the Co(II)-PDI(^{i}Pr) complex. The cyclic voltammetry of the complex was investigated in MeCN to demonstrate the potential catalytic activity of benzyl halide self-coupling catalyzed by our Co complex. The homocoupling of benzyl halides could occur by forming a C—C bond between the radical intermediates, resulting in the production of bibenzyl as a product.

Acknowledgements

We thank the Department of Chemistry, the Center of Excellence for Innovation in Chemistry, and the Central Instrument Facility, Faculty of Science, Mahidol University for facilitating this project. Also, we thank the Faculty of Graduate Studies, Mahidol University for supporting the project presentation.

References

1. Rayadurgam, J.; Sana, S.; Sasikumar, M.; Gu, Q., Palladium catalyzed C–C and C–N bond forming reactions: An update on the synthesis of pharmaceuticals from 2015–2020. *Org. Chem. Front.* **2021,** *8* (2), 384-414.
2. Batsanov, A. S.; Collings, J. C.; Fairlamb, I. J.; Holland, J. P.; Howard, J. A.; Lin, Z.; Marder, T. B.; Parsons, A. C.; Ward, R. M.; Zhu, J., Requirement for an oxidant in Pd/Cu co-catalyzed terminal alkyne homocoupling to give symmetrical 1,4-disubstituted 1,3-diynes. *J. Org. Chem.* **2005,** *70* (2), 703-6.
3. Contreras-Celedón, C. A.; Rincón-Medina, J. A.; Mendoza-Rayo, D.; Chacón-García, L., Oxidative homocoupling of arylboronic acids catalyzed by a 4-aminoantipyrine–Pd (II) complex. *Appl. Organomet. Chem.* **2015,** *29* (7), 439-442.
4. Semmelhack, M.; Helquist, P.; Jones, L.; Keller, L.; Mendelson, L.; Ryono, L. S.; Gorzynski Smith, J.; Stauffer, R., Reaction of aryl and vinyl halides with zerovalent nickel-preparative aspects and the synthesis of alnusone. *J. Am. Chem. Soc.* **1981,** *103* (21), 6460-6471.
5. Iyoda, M.; Otsuka, H.; Sato, K.; Nisato, N.; Oda, M., Homocoupling of aryl halides using nickel (II) complex and zinc in the presence of Et_4NI. An efficient method for the synthesis of biaryls and bipyridines. *Bull. Chem. Soc. Jpn.* **1990,** *63* (1), 80-87.
6. Krafft, M.; Hirosawa, C.; Dalal, N.; Ramsey, C.; Stiegman, A., Cobalt-catalyzed homocoupling of terminal alkynes: synthesis of 1, 3-diynes. *Tetrahedron Lett.* **2001,** *42* (44), 7733-7736.
7. Yamanaka, M.; Nakamura, E., Density functional studies on the Pauson− Khand reaction. *J. Am. Chem. Soc.* **2001,** *123* (8), 1703-1708.
8. Cai, Y.; Qian, X.; Gosmini, C., Cobalt-Catalyzed C− C Homocoupling. *Adv. Synth. Catal.* **2016,** *358* (15), 2427-2430.
9. Sato, K.; Inoue, Y.; Mori, T.; Sakaue, A.; Tarui, A.; Omote, M.; Kumadaki, I.; Ando, A., Csp^3–Csp^3 homocoupling reaction of benzyl halides catalyzed by rhodium. *Org. Lett.* **2014,** *16* (14), 3756-3759.
10. Chen, T.; Yang, L.; Li, L.; Huang, K.-W., Homocoupling of benzyl halides catalyzed by POCOP–nickel pincer complexes. *Tetrahedron* **2012,** *68* (31), 6152-6157.
11. de França, K. W.; Navarro, M.; Léonel, É.; Durandetti, M.; Nédélec, J.-Y., Electrochemical homocoupling of 2-bromomethylpyridines catalyzed by nickel complexes. *J. Org. Chem.* **2002,** *67* (6), 1838-1842.

The effect of polyethylene glycol chain length of nickel bis(aminomythyl)pyridine on hydrogen evolution reaction

Kanrawee Dechdang and Teera Chantarojsiri*

Department of Chemistry and Center of Excellence for Innovation in Chemistry, Faculty of Science, Mahidol University, Bangkok, Thailand

**E-mail: teera.cha@mahidol.edu*

Abstract:

The proximal charge as the secondary coordination sphere in enzyme cofactor shows a crucial role for small molecule activation. This concept has been used to design various chemical catalysts by incorporating pendent polyether chain for hosting redox-inactive cation as a second coordination sphere. Herein, we report the Ni complexes with different chain lengths of polyethylene glycol ($NiBAP_n$). The $NiBAP_n$ complexes were characterized by IR, UV-vis spectroscopy and their electronic properties were studied by cyclic voltammetry. The synthesized Ni complexes are able to perform electrochemical hydrogen evolution in organic media. The addition of redox-inactive cation to $NiBAP_n$ complexes, to generate heterobimetallic Ni complexes *in situ*, shows the enhancement of hydrogen production, showing that the binding of redox-inactive cation to the polyethylene glycol chain can affect the reactivity of the catalyst. The different chain length also imparted different binding ability and therefore, exhibited different hydrogen evolution reaction reactivity.

1. Introduction

Hydrogen (H_2) is considered a clean energy source due to the highest specific energy content among the fuel and the generation of a green product, water.[1] As a result, H_2 production has gained interest from chemists recently. H_2 generation from the combination of two protons ($2H^+ + 2e^- \rightarrow H_2$) or hydrogen evolution reaction (HER) requires chemical catalyst and the most efficient catalyst is the platinum metal,[2] which is not economical on the industrial-scale. The designing of HER chemical catalyst composed of earth-abundant metals with the same performance is still challenging.

HER in nature was reversible by hydrogenases enzymes. The [NiFe] hydrogenase, with Ni and Fe ions in the active site, inspired various Ni-based chemical catalysts.[3, 4] Also, the interactions within the enzyme, including the proximal charge as a secondary coordination sphere, have been investigated for catalyst improvement.[5] Many studies have shown the enhancement of chemical catalyst due to the addition of redox-inactive cation for various chemical catalyses.[6,7,8] Previous works reported that the bio-inspired catalysts with attached macrocycle or polyethylene glycol moieties to support the cation during the catalysis showed excellent performance.[9,10] In addition, some reports also studied the polyethylene glycol size and the cation size and found that the appropriate matching size between the polyether and cation gave the highest performance.[11] The investigation of the effect of polyether size effect toward HER catalysis has few examples.

Herein, the Ni(II) Bis(aminomethyl)pyridine complexes decorated with different chain lengths of polyethylene glycol ($NiBAP_n$; n=2 and 3) were used to study the effect of polyethylene glycol chain length with various redox-inactive cation, by forming Ni heterobimetallic complexes *in situ*, on HER catalysis. The redox-inactive cations studied in this work are triflate salts of Na^+, K^+, Cs^+, Ca^{2+}, and Ba^{2+}. The electronic properties and HER catalysis performance of $NiBAP_n$ in the presence and absence of the cations were investigated by cyclic voltammetry.

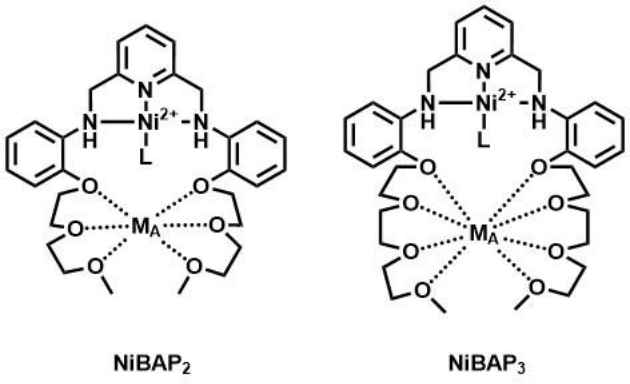

Figure 1. The chemical structure of $NiBAP_2$ (left) and $NiBAP_3$ (right), M_A = Na^+, K^+, Cs^+, Ca^{2+} or Ba^{2+}.

2. Materials and Methods

2.1 Methods

2-(2-methoxyethoxy)aniline (BAP_2-NH_2), Bis(aminomethyl)pyridine decorated with polyethylene glycol-3 (BAP_3) and Ni(II) Bis (aminomethyl)pyridine decorated with polyethylene glycol-3 ($NiBAP_3$) (figure 1) were synthesized according to the previous report.[12] Unless otherwise noted, chemicals were purchased from Tokyo Chemical Industry Co., Ltd. All solvents were distilled before use.

2.2 Synthesis of Bis(aminomethyl)pyridine decorated with ethylene glycol-2 (BAP_2)

Pyridine-2,6-dicarbaldehyde (1 equiv, 0.5 mmol, 67.7 mg) and BAP_2-NH_2 (7.6 equiv, 3.8 mmol, 797.3 mg) were dissolved in 10 mL of dried ethanol and heated at reflux overnight. $NaBH_4$ (10 equiv, 5.1 mmol, 192.4 mg) was slowly added into the reaction mixture as a solid and it was left at reflux for 2 hours. The residue was quenched with K_2CO_3, extracted with 50 mL of CH_2Cl_2 (3 times). The organic layers were combined and dried with anhydrous Na_2SO_4. The solvent was removed under reduced pressure to obtain brown oil. The product was purified by column chromatography (1% triethylamine in 50% EtOAc/Hexane solution) to obtain dark-orange oil as product (36.4 mg, 54%yield). ^{1}H NMR (400 MHz, $CDCl_3$) δ 7.54 (dd, *J* = 14.2, 6.5 Hz, 1H), 7.22 (d, *J* = 7.7 Hz, 2H), 6.86 – 6.78 (m, 4H), 6.64 (td, *J* = 7.8, 1.4 Hz, 2H), 6.55 – 6.49 (m, 2H), 5.32 (s, 1H), 4.52 (s, 4H), 4.25 – 4.17 (m, 4H), 3.93 – 3.85 (m, 4H), 3.75 – 3.67 (m, 4H), 3.58 – 3.51 (m, 4H), 3.35 (s, 6H). UV−vis in acetronitrile, λ, nm (ε, M^{-1} cm^{-1}): 246 (18781), 291 (8697). ATR-FT-IR (ν_{NH}, cm^{-1}): 3390.46

2.3 Synthesis of Ni(II) Bis(aminomethyl)pyridine decorated with ethylene glycol-2 ($NiBAP_2$)

$Ni(OTF)_2$ (1 equiv, 0.66 mmol, 232.8 mg) and BAP_2 (1 equiv, 0.66 mmol, 346.2 mg) was heated at reflux in 5 mL of acetonitrile at 85 °C for 16 hours. The solvent was removed under reduced pressure and the crude oil was washed with diethyl ether to obtain dark brown oil as the product (478.1 mg, 82% yield). UV−vis in acetronitrile, λ, nm (ε, M^{-1} cm^{-1}): 264 (8535), 270 (8233). ATR-FT-IR (ν_{NH}, cm^{-1}): 3352.10

2.4 Synthesis of Ni(II) Bis(aminomethyl)pyridine decorated with ethylene glycol-3 ($NiBAP_3$)

$Ni(OTF)_2$ (1 equiv, 0.82 mmol, 292.0 mg) and BAP_2 (1 equiv, 0.82 mmol, 360.3 mg) was heated at reflux in 5 mL of acetonitrile at 85 °C for 16 hours. The solvent was removed under reduced pressure and the crude oil was washed with diethyl ether to obtain dark brown oil as the product (610.4 mg, 76% yield). UV−vis in acetronitrile, λ, nm (ε, M^{-1} cm^{-1}): 264 (5956), 270 (5725). ATR-FT-IR (ν_{NH}, cm^{-1}): 3355.41

2.5 Spectroscopic measurement

NMR data was collected on 400 MHz of Bruker Ascend high-resolution magnetic resonance. All UV-Vis spectrophotometry experiments were performed on a Shimadzu UV-2600 UV-vis spectrophotometer. Infrared spectroscopy (ATR-FT-IR) was performed on Bruker Alpha II. All cyclic voltammetry experiment was done in CH_3CN using 0.1 M tetrabutylammonium hexafluorophosphate (NBu_4PF_6) as an electrolyte, with a glassy carbon working electrode, a Pt counter electrode, a Ag^0/Ag^+ pseudo-reference electrode, $Fe(C_5H_5)_2^{+/0}$ as the external reference, under an Ar atmosphere.

3. Results & Discussion

3.1 Characterization of $NiBAP_n$

After the Ni metal reacted with both BAP_2 and BAP_3 ligands, the resulting product was characterized using UV-vis spectroscopy and ATR-FTIR spectroscopy. UV-vis spectroscopy

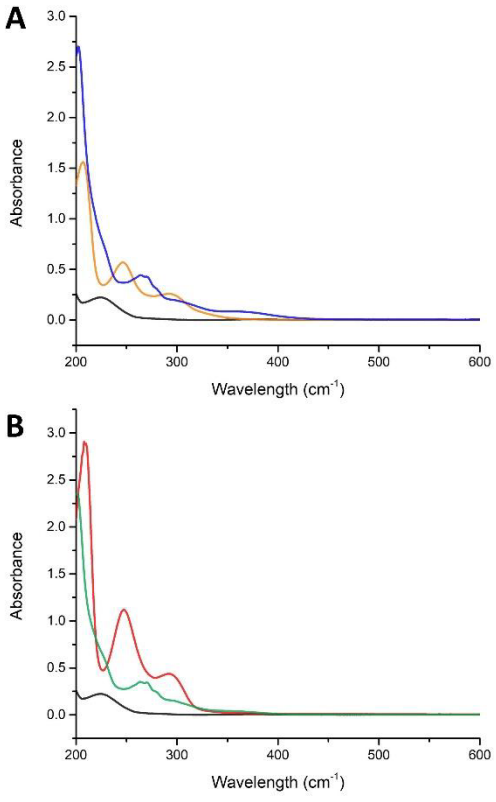

Figure 2. The comparison UV-vis spectra of A.) $Ni(OTf)_2$ (black), BAP_2 (orange) and $NiBAP_2$ (blue) and B.) $Ni(OTf)_2$ (black), BAP_3 (red) and $NiBAP_3$ (green).

was employed to investigate the changes in absorption following the formation of $Ni(OTf)_2$ with the BAP_n ligands. The λ_{max} of $Ni(OTf)_2$ was at 236 nm, BAP_n was at 246 and 291 nm, while those of $NiBAP_2$ and $NiBAP_3$ were found at 264 and 270 nm. This result illustrates the red shift of $NiBAP_2$ and $NiBAP_3$ compared to $Ni(OTf)_2$. Thus, UV-vis data can confirm the formation of $NiBAP_2$ and $NiBAP_3$. (Figure 2)

To confirm the position where Ni binds to the BAP_n ligand, ATR-FT-IR spectroscopy was employed to investigate the changes in N-H stretching at the amine position on the BAP_n ligand. The N-H stretching peaks for BAP_2 and BAP_3 were observed at 3390.46 cm^{-1} and 3393.90 cm^{-1}, respectively (Figure 3, Table 1). In comparison, the ATR-FT-IR spectra demonstrated a negative shift in N-H stretching after the metalation process, attributed to electron donation from the Ni center to the N-H bond. The changes in N-H stretching indicate the binding of the Ni center to the BAP_n ligand at the *NNN*-site.

Both the UV-vis and ATR-FTIR data confirm the successful formation of $NiBAP_2$ and $NiBAP_3$ complexes.

Table 1. The ATR-FT-IR data of the bare BAP_n ligand were compared with those of the $NiBAP_n$ complexes

Wavenumber (cm^{-1})	BAP_n	$NiBAP_n$	ΔWavenumber (cm^{-1})
n = 2	3390.46	3352.10	38.36
n = 3	3393.90	3355.41	38.49

3.2 Electronic properties of $NiBAP_n$

The redox properties of $NiBAP_2$ and $NiBAP_3$ were investigated in acetonitrile under an inert atmosphere. The cyclic voltammograms of $NiBAP_2$ and $NiBAP_3$ showed quasi-reversible redox-couple peaks at -1.21 and -1.30 V respectively, indicating the Ni(II/I) redox couple (Figure 4). The current and the square root of the scan rate also exhibited a linear correlation, suggesting that electron transfer from the Ni complex was diffusion-controlled.

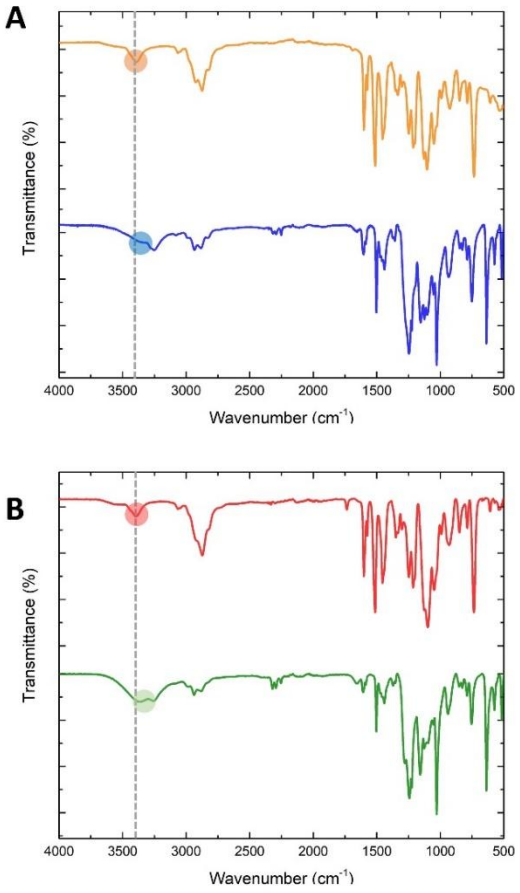

Figure 3. ATR-FT-IR spectra of A.) bare BAP_2 (orange), $NiBAP_2$ (blue) and B.) bare BAP_3 (red), $NiBAP_3$ (green).

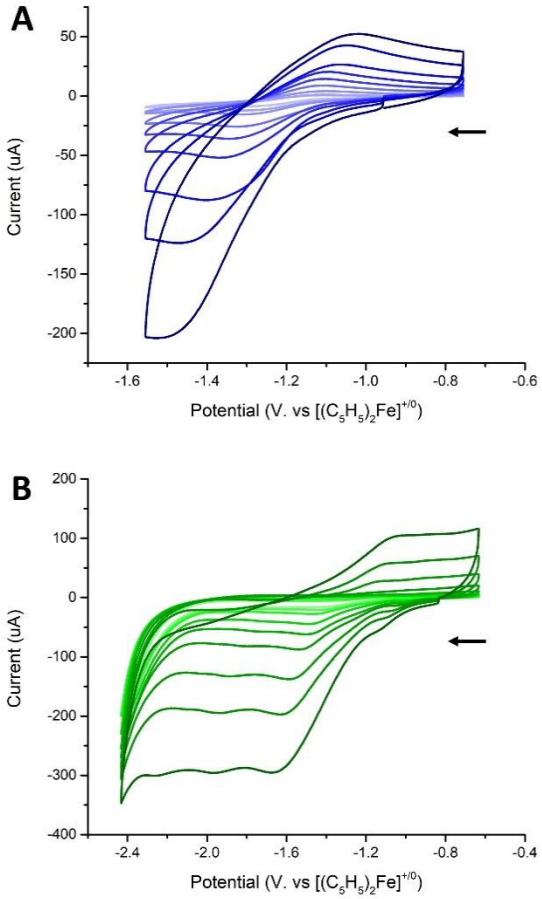

Figure 4. Cyclic voltammogram of A.) $NiBAP_2$ (blue) and B.) $NiBAP_3$ (green) 25 $mV \cdot s^{-1}$(light) to 10000 $mV \cdot s^{-1}$ (dark).

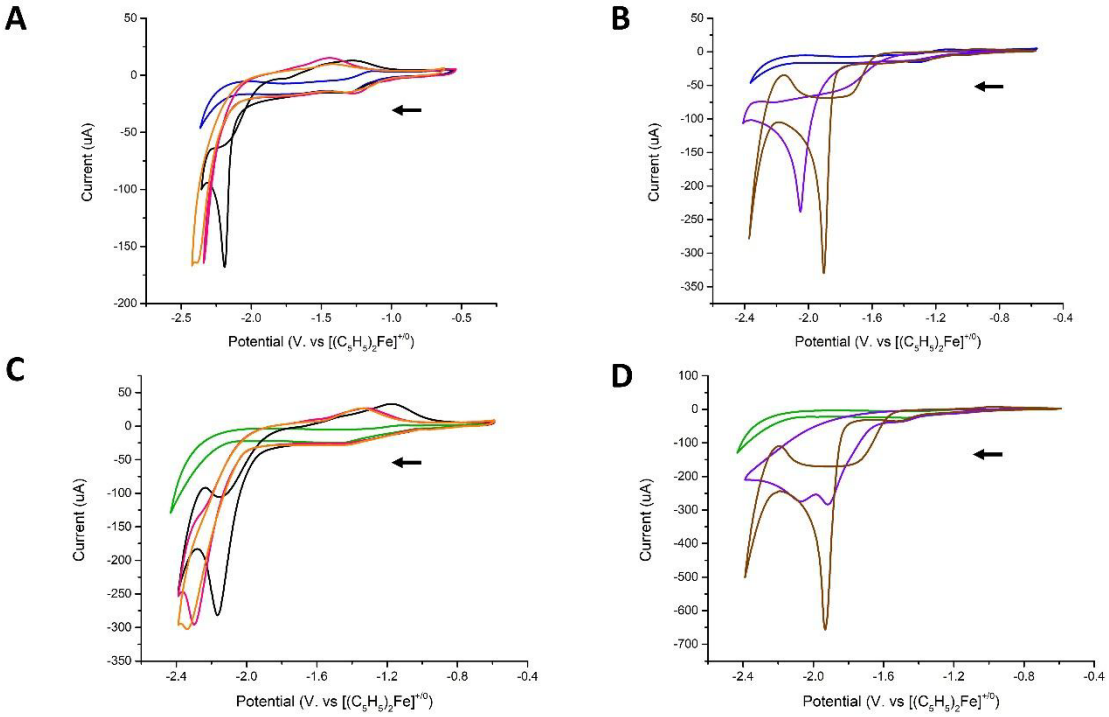

Figure 5. Cyclic voltammogram of $NiBAP_2$ (A-B, blue) and $NiBAP_3$ (C-D, green) in the presence of 5 equivalents of Na^+ (A, C, black), K^+ (A, C, pink), Cs^+ (A, C, orange), Ca^{2+} (C, D, purple) and Ba^{2+} (C, D, brown).

The addition of a redox-inactive cation to $NiBAP_n$ was also carried out in acetonitrile under an inert atmosphere. The changes in the voltammograms after the addition of the cation implied the *in situ* binding of the cation to the Ni complex. For group I cations such as Na^+, K^+, and Cs^+, an enhancement in current around -2.40 V was observed. Similarly, the addition of group 2 cations, Ca^{2+} or Ba^{2+}, also resulted in a current enhancement of -2.40 V. Indeed, the crossing of spectra was observed, indicating the heterogeneous behavior of $NiBAP_n$ when redox-inactive cations were added. (Figure 5)

3.3 Hydrogen evolution reaction reactivity

To investigate the hydrogen evolution reaction (HER) performance of $NiBAP_n$ complexes, anilinium triflate (AN) was utilized as a proton source in the solution, and the catalyst performance was assessed through cyclic voltammetry. The addition of AN to Ni complexes resulted in two reduction peaks, with HER catalytic waves observed around -1.53 and -2.40 V, respectively. The increased concentration of AN for both $NiBAP_2$ and $NiBAP_3$ showed an enhanced current around -1.53 and -2.40 V, suggesting catalysis in H_2 production (Figure 6).[4, 13]

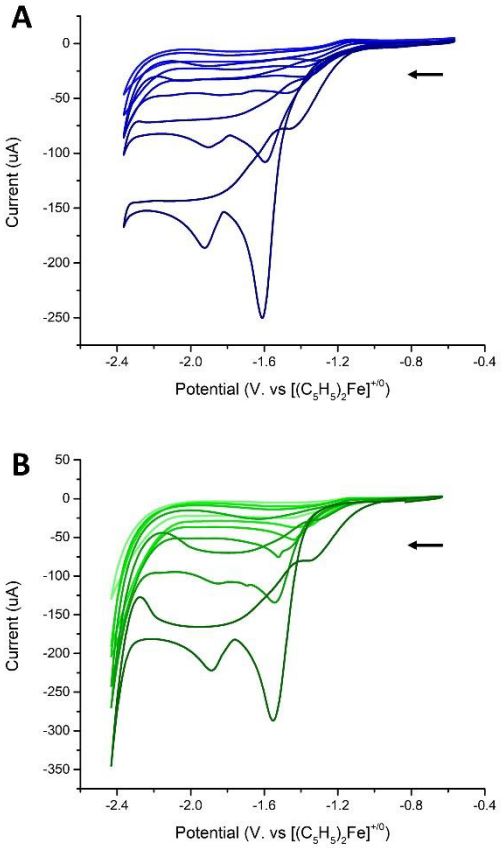

Figure 6. Cyclic voltammogram of A.) $NiBAP_2$ (blue) and B.) $NiBAP_3$ (green) in the increasing of AN 0 equivalent (light) to 10 equivalents (dark).

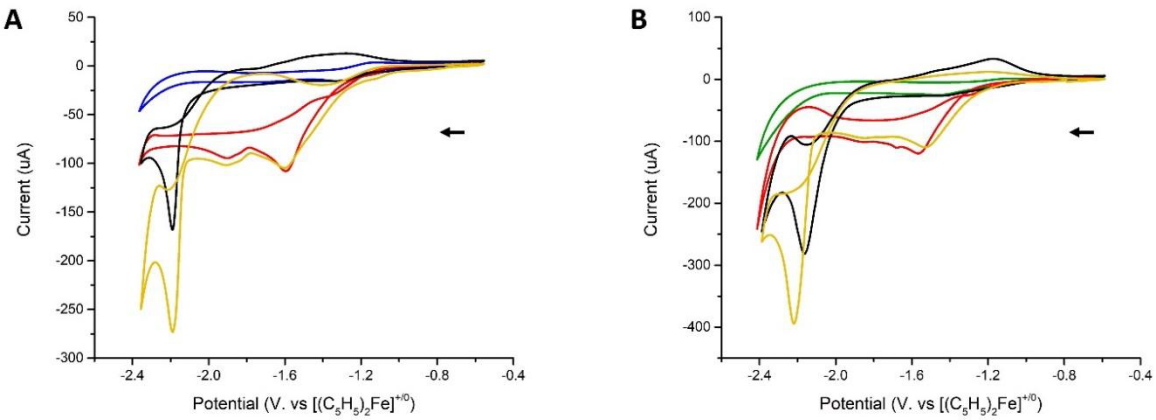

Figure 7. Cyclic voltammogram of $NiBAP_2$ (A, blue) and $NiBAP_3$ (B, green) in the presence 5 equivalents of AN (red), Na^+ (black) and the presence of both AN and Na^+ (yellow).

Table 2. The summary of the HER catalytic peak current around -2.40 V of $NiBAP_n$ in the presence of the redox-inactive cation [a]

Current (μA)	No cation	Na^+	K^+	Cs^+	Ca^{2+}	Ba^{2+}
n = 2	100.5	249.6	231.7	313.3	182.3	223.7
n = 3	241.7	245.7	330.4	419.8	282.8	670.2

[a] The data was achieved in the present of 5 equivalents of AN.

Subsequently, Na^+ was introduced to investigate the changes in the redox events of $NiBAP_2$ and $NiBAP_3$ in the presence of AN. For $NiBAP_2$, the protonation peak exhibited a similar potential and current to the condition without Na^+, while the current at -2.40 V increased. For $NiBAP_3$, a slight positive shift in the protonation wave ($\Delta E_{1/2}$ = 45 mV) was observed, along with an increase in the current at -2.40 V. These results demonstrate that the incorporation of a redox-inactive cation can enhance the HER reactivity of Ni complexes and possibly induce other mechanisms which will be further investigated (Figure 7).[4, 13]

In the presence of other redox-inactive cations, the current at -2.40 V was also improved for both $NiBAP_2$ and $NiBAP_3$. Cs^+ addition to $NiBAP_2$ yielded the highest peak current, while Ba^{2+} addition resulted in the highest current enhancement for $NiBAP_3$. Additionally, the addition of Ca^{2+} to $NiBAP_2$ and Na^+ to $NiBAP_3$ showed the lowest current improvement for HER reactivity (Table 2). The observed variations in current, which is dependent on the cation and polyethylene glycol chain length, align with our assumption that appropriate cations on the polyethylene glycol chain, yield different HER catalytic activities.[10] The shorter chain in BAP_2 fits Cs^+, which is the biggest cation, better while BAP_3 with a more steric and long chain fits Ba^{2+} better. These results highlight the tunable effects of redox-inactive cations and polyethylene glycol chain lengths on current enhancement.

4. Conclusion

$NiBAP_n$ complexes were successfully synthesized and characterized by UV-vis, ATR-FT-IR spectroscopy. The redox property study of both Ni complexes indicates the quasi-reversible redox couple. The presence of anilinium triflate (AN) as a proton source indicated HER catalysis which also showed that increasing AN amount also enhances the current. The incorporation of redox-inactive cation and Ni complexes in the presence of AN was confirmed by cyclic voltammogram which yielded the increasing peak current. Moreover, the addition of Na^+ gave slightly positive shift of protonation wave for $NiBAP_3$ while $NiBAP_2$ gave similar protonation peak. The different chain lengths of polyethylene glycol were shown to appropriately fit different cations that gave the highest catalytic peak current, Cs^+ for $NiBAP_2$ and Ba^{2+} for $NiBAP_3$. The controlled potential electrolyses will be performed to further investigate the HER catalytic reactivity of $NiBAP_n$, with the presence of redox-inactive cation.

Acknowledgements

The authors would like to thank the Department of Chemistry, the Center of Excellence for Innovation in Chemistry, and the Central Instrument Facility, Faculty of Science, Mahidol University for research funding. K.D. would like to acknowledge research assistantship from the Center of Excellence for Innovation in Chemistry.

References

1. Campen, A.; Mondal, K.; Wiltowski, T., Separation of hydrogen from syngas using a regenerative system. *Int. J. Hydrogen Energy.* **2008,** *33* (1), 332-339.
2. Monteiro, M. C. O.; Goyal, A.; Moerland, P.; Koper, M. T. M., Understanding Cation Trends for Hydrogen Evolution on Platinum and Gold Electrodes in Alkaline Media. *ACS Catal.* **2021,** *11* (23), 14328-14335.
3. Brazzolotto, D.; Gennari, M.; Queyriaux, N.; Simmons, T. R.; Pécaut, J.; Demeshko, S.; Meyer, F.; Orio, M.; Artero, V.; Duboc, C., Nickel-centred proton reduction catalysis in a model of [NiFe] hydrogenase. *Nat. Chem.* **2016,** *8* (11), 1054-1060.
4. Tang, H. M.; Fan, W. Y., Transition Metal Pyrithione Complexes (Ni, Mn, Fe, and Co) as Electrocatalysts for Proton Reduction of Acetic Acid. *ACS Omega* **2023,** *8* (7), 7234-7241.
5. de Visser, S. P., Second-Coordination Sphere Effects on Selectivity and Specificity of Heme and Nonheme Iron Enzymes. *Chem. Eur. J.* **2020,** *26* (24), 5308-5327.
6. Fukuzumi, S.; Ohkubo, K.; Lee, Y.-M.; Nam, W., Lewis Acid Coupled Electron Transfer of Metal–Oxygen Intermediates. *Chem. Eur. J.* **2015,** *21* (49), 17548-17559.
7. Karmalkar, D. G.; Seo, M. S.; Lee, Y.-M.; Kim, Y.; Lee, E.; Sarangi, R.; Fukuzumi, S.; Nam, W., Deeper Understanding of Mononuclear Manganese(IV)–Oxo Binding Brønsted and Lewis Acids and the Manganese(IV)–Hydroxide Complex. *Inorg. Chem.* **2021,** *60* (22), 16996-17007.
8. Sankaralingam, M.; Lee, Y.-M.; Pineda-Galvan, Y.; Karmalkar, D. G.; Seo, M. S.; Jeon, S. H.; Pushkar, Y.; Fukuzumi, S.; Nam, W., Redox Reactivity of a Mononuclear Manganese-Oxo Complex Binding Calcium Ion and Other Redox-Inactive Metal Ions. *J. Am. Chem. Soc.* **2019,** *141* (3), 1324-1336.
9. Cai, Z.; Xiao, D.; Do, L. H., Fine-Tuning Nickel Phenoxyimine Olefin Polymerization Catalysts: Performance Boosting by Alkali Cations. *J. Am. Chem. Soc.* **2015,** *137* (49), 15501-15510.
10. Rovira, L.; Fernández-Pérez, H.; Vidal-Ferran, A., Palladium-based supramolecularly regulated catalysts for asymmetric allylic substitutions. *Organometallics* **2016,** *35* (4), 528-533.
11. Vidal-Ferran, A.; Mon, I.; Bauzá, A.; Frontera, A.; Rovira, L., Supramolecularly regulated ligands for asymmetric hydroformylations and hydrogenations. *Chem. Eur. J.* **2015,** *21* (32), 11417-11426.
12. Sukchit, S.; Chantarojsiri, T., Synthesis and Characterization of heterobimetallic Complexes Supported by Polyethylene Glycol Chains-appended 2,6-Pyridinedimethanamine. In *The 47th International Congress on Science, Technology and Technology-based Innovation (STT47)* 2021; pp 559-566.
13. Tang, H. M.; Fan, W. Y., Dithiolato-Bridged Nickel(II) Salicylcysteamine Complexes as Robust Proton Reduction Electrocatalysts: Cyclic Voltammetry and Computational Studies. *Inorg. Chem.* **2021,** *60* (23), 17933-17941.

Synthesis of silicon carbide by using rice husk ash from power plant wastes

Benchanaree Singrattanaphan* and Anurak Petiraksakul

Department of Chemical Engineering, Faculty of Engineering, King Mongkut's University of Technology North Bangkok, 1518 Pracharat 1 Road, Wongsawang, Bangsue, Bangkok 10800, Thailand

**E-mail: bella.brunhilda1995@gmail.com*

Abstract:

This research aimed to investigate the synthesis of silicon carbide (SiC) using silica extracted from rice husk ash and carbon black as the reactants. Magnesium was used as a catalyst during the synthesis process. The reactions were carried out in an alumina crucible, encapsulated in an Argon atmosphere at a temperature of 1200 ◦C. The research focused on exploring various molecular ratios between SiO_2 and Mg to determine their impact on the formation and composition of SiC. To characterize the resulting structures and compositions, X-ray fluorescence (XRF), X-ray diffraction (XRD), and scanning electron microscopy (SEM) were utilized.

1. Introduction

Nowadays, the demand for energy is increasing significantly and making alternative energy sources more important. One of the popular options is to use agricultural waste as biomass fuel, such as rice husks. As Thailand is a major producer and exporter of rice, there is a large amount of rice husks generated each year.

Rice husks are used as biomass fuel in power plants to generate electricity. However, a significant amount of rice husk ash is often disposed of without further utilization, leading to issues with waste disposal and transportation costs. Therefore, there is a need to add value to rice husk ash by converting them into useful products. One of the interesting applications is carbon and silica extracted from rice husk ash to produce silicon carbide (SiC).

Silicon carbide (SiC) is a composite material with silicon and carbon as main components. It has unique properties such as good thermal and electrical conductivity, high strength at high temperatures, low density, excellent resistance to abrasion and corrosion, and high resistance to oxidation (Niyomwas, S. 2009), etc. These properties make SiC widely used in various industries, including engineering and manufacturing.

However, the most common method to synthesize SiC nowadays is still carbothermal reduction according to equation (1), which is based on the Acheson process.

$$SiO_{2\,(s)} + 3C_{(s)} \text{----> } SiC_{(s)} + 2CO_{(g)} \quad \text{--- (1)}$$

This method is complex and energy intensive. Therefore, many researchers have been focusing on finding alternative and more efficient methods. Some of the methods include combustion synthesis (Niyomwas, S. 2009; Mukasyan, A. S. 2011), sol-gel synthesis (Yasser and Said, 2009), synthesis with thermal plasma methods (Singh et al., 1993; Czosnek et al., 2015), microwave synthesis (Satapathy et al., 2005), etc.

Among these methods, the researcher has chosen combustion synthesis that is the straightforward method for synthesizing SiC, with simple steps and equipment. It also has relatively low energy requirements, contributing to cost reduction in production. By utilizing rice husks and optimizing the synthesis process, it is possible to produce SiC with lower costs and higher production capacity, meeting the increasing demand for this material in the future.

2. Materials and Methods

2.1 Materials

The chemicals and materials used in this research included sodium hydroxide (Merck, Germany), hydrochloric acid (35.0-37.0%, J.T.Baker, Taiwan), magnesium powder (purity 99%, KemAus, Australia), analytical grade carbon black (METRA, Thailand), and rice husk ash, which was a waste product from the electricity production factory, used as a source of silica and carbon ash.

The measurement and analysis of various elemental components of the rice husk ash were performed by using the X-ray fluorescence technique (XRF). The detailed results are shown in Table 1.

Table 1. Elemental percentage of rice husk ash.

Element	Mass [%]	Atomic [%]	Intensity [cps/mA]
Mg	33.95	39.11	3.93
Si	53.97	53.81	38.51
Ca	5.16	3.61	24.70
Cr	0.00	0.00	0.00
Fe	6.92	3.47	39.43

2.2 Sample preparation

The rice husk ash was grinded and washed with distilled water to clean any soil particles and impurities. Then, it was dried at a temperature of 105 °C until the weight remained constant and stored in a tightly closed container to prevent moisture from outside. The rice husk ash weighed 10 grams and reacted with sodium hydroxide (NaOH) solution with a concentration of approximately 4.5 M in a volume of 100 milliliters with constant stirring at a temperature of 70 °C for 6 hours in an opened system and let the solution cool down to ambient temperature for 18 hours. Then, the black-colored solution was filtered and washed with distilled water. The residue on the filter paper would be the ash sludge mainly composed of carbon and was dried in oven at 105 °C, while the yellowish-brown filtrate would be the sodium silicate (Na_2SiO_4) solution.

The sodium silicate solution was reacted with hydrochloric acid (HCl) solution with a concentration of 4 M in a volume of 100 milliliters on a hot plate and stirring under heating at a constant speed of 1150 rpm and a temperature of approximately 50 °C in a closed system for 24 hours. The resulting solution would have a gel-like white or grayish-white appearance. Then, the solution was filtered and washed to remove sodium chloride (NaCl) and other dissolved impurities and dried the white residue at 105 °C for 6 hours or until the weight remains constant. The white silica (SiO_2) residue was grinded into a fine powder and stored all the obtained silica samples in a desiccator to prevent contamination and moisture.

Silica powder and carbon extracted from rice husk ash were mixed with magnesium metal (Fuad et al., 2019; Tan et al., 2017), as the carbon was an excess reagent. The proportion of Silica to magnesium metal by moles was 3:1, 5:1, 10:1, 15:1, and 20:1. Then, the samples were burned in a closed alumina crucibles under argon atmosphere. The heating rate was 5 °C per minute, and the temperature was maintained at 1,200 °C (Morito et al., 2013; Gubernat et al., 2017) for 5 hours and 10 hours.

2.3 Characterization

Analysis of composition and crystal structure of samples were recorded by using X-ray diffraction (XRD) measurements on the Rigaku SmartLab intelligent multipurpose X-ray diffractometer, which was equipped with Kβ filter for Cu, scan mode 1D (scan), scan range 10 –80°, and D/teX Ultra 250 detector.

Scanning electron micrography (SEM) was performed on FEI Quanta 450 Field Emission scanning electron microscope.

3. Results & Discussion

3.1 Synthesized silicon dioxide

Silicon dioxide extracted from rice husk ash was in the form of amorphous structure cristobalite. From the XRD graph in Figure 1, it was observed that the main peak of cristobalite at 2θ was 22.26246 degrees. The extracted silicon dioxide was shown in the SEM image in Figure 2.

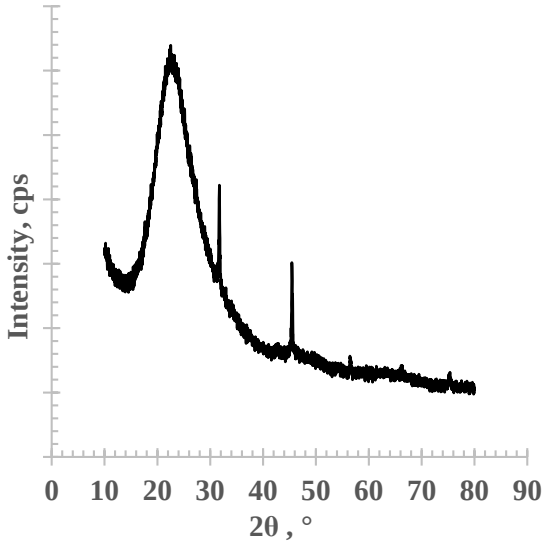

Figure 1. XRD graph of synthetic silicon dioxide (SiO_2) from rice husk ash.

3.2 Silicon carbide synthesis

After the initial samples with different molar ratios were burned at a temperature of 1,200 °C for a controlled period of 5 hours, the small peaks that were observed at 2θ approximately 35.9-37.8° and 60.4-63.9°. This might be indicated by silicon carbide (SiC). The main peak also observed at 2θ approximately 22 was silica in the form of cristobalite, as shown in Figure 3. A large amount of silica was still found in samples due to the internal temperature of the system not being sufficiently high and the duration of burning being too short (Odior et al., 2011; Park et al., 2019).

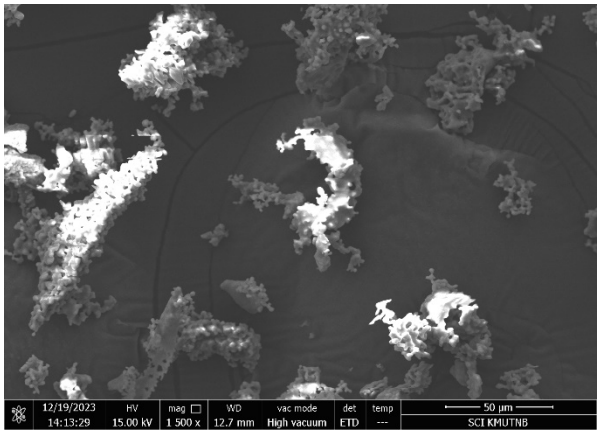

Figure 2. SEM image of synthetic silicon dioxide (SiO_2) from rice husk ash.

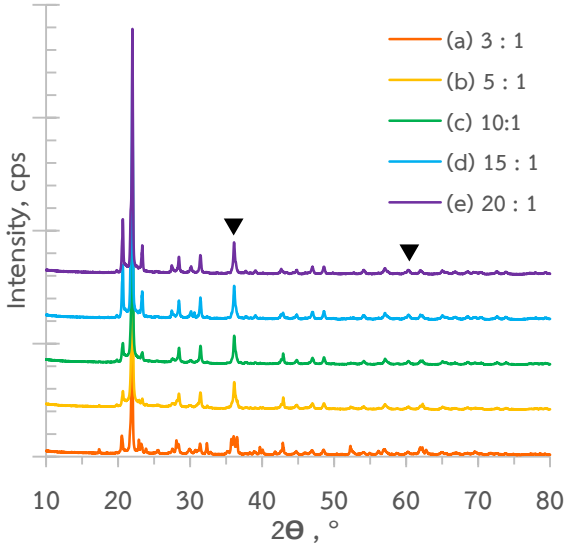

Figure 3. XRD graphs of synthetic samples burned at 1,200 °C for 5 hours at various silicon dioxide to magnesium metal mole ratio: (a) 3:1, (b) 5:1, (c) 10:1, (d) 15:1, and (e) 20:1.

In Table 2 and Figure 4, the XRD graph focused specifically on the main peak observed for SiC. The graph illustrated that the change in molar ratio between silica and magnesium could affect the height of the SiC peak, as clearly seen. The maximum peak observed was the result of burning silica with carbon, using a molar ratio of silica to magnesium of 15:1.

Table 2. The highest values of the intensity by using XRD from different samples that were burned at 1,200 °C for 5 hours.

SiO_2 : Mg ratio	2Θ , °	Intensity, cps
3:1	36.08	8787.5
5:1	36.14	12995
10:1	36.14	13483.33
15:1	36.12	15587.5
20:1	36.12	14820.83

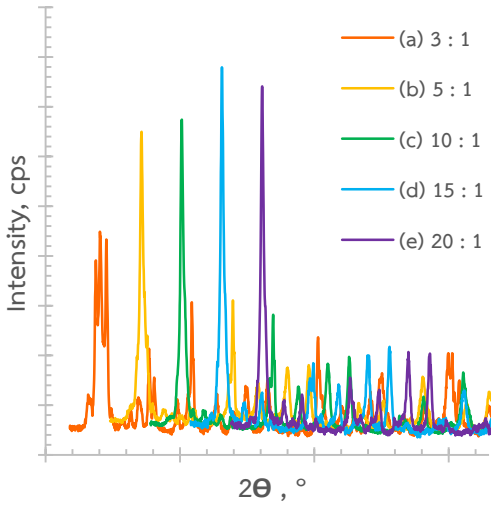

Figure 4. XRD graphs of synthetic samples compared only main peaks respectively, of SiC. The samples were burned at 1,200 °C for 5 hours at various silicon dioxide to magnesium metal mole ratio: (a) 3:1, (b) 5:1, (c) 10:1, (d) 15:1, and (e) 20:1.

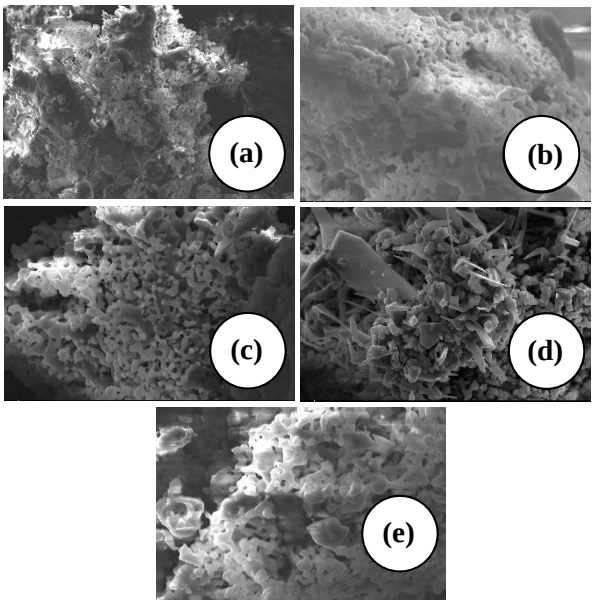

Figure 5. SEM images of synthetic samples burned at 1,200 °C for 5 hours at various silicon dioxide to magnesium metal mole ratio: (a) 3:1, (b) 5:1, (c) 10:1, (d) 15:1, and (e) 20:1.

Figure 5 has shown the SEM images of samples with different ratios of silica to magnesium metal after being annealed at a temperature of 1,200 °C for 5 hours. From the image, the formation of silicon carbide precipitates started to occur at a silica to magnesium molar ratio was 15:1 as shown in Figure 5(d). However, when the amount of magnesium introduced into the system was too high or too low as shown in Figure 5(a), 5(b), 5(c), 5(e), the sample did not exhibit

visible silicon carbide precipitate formation (Park et al., 2019).

According to this research, the molar ratio between silica and magnesium that produced the highest yield of silicon carbide has been determined. To achieve the desired form of silicon carbide, the duration of burning process was increased to 10 hours while maintaining a constant temperature of 1,200 °C and the result is shown in Figure 6, and in Table 3 and Figure 7, the XRD graph focused specifically on the main peak observed for SiC. By increasing the burning period, the peak of SiC formation significantly increased.

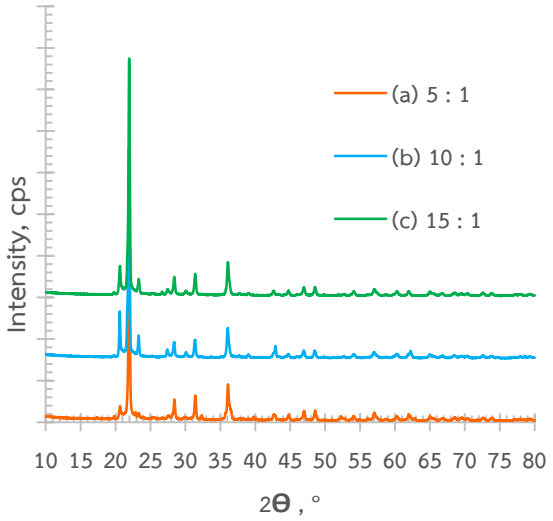

Figure 6. XRD graphs of synthetic samples burned at 1,200 °C with silicon dioxide to magnesium metal mole ratio 15:1 for: (a) 5:1, (b) 10:1, (c) 15:1.

Table 3.
The highest values of the intensity by using XRD from different samples that were burned at 1,200 °C for 10 hours.

SiO_2 : Mg ratio	2Θ , °	Intensity, cps
5:1	36.12	18204.17
10:1	36.06	15333.33
15:1	36.10	16937.5

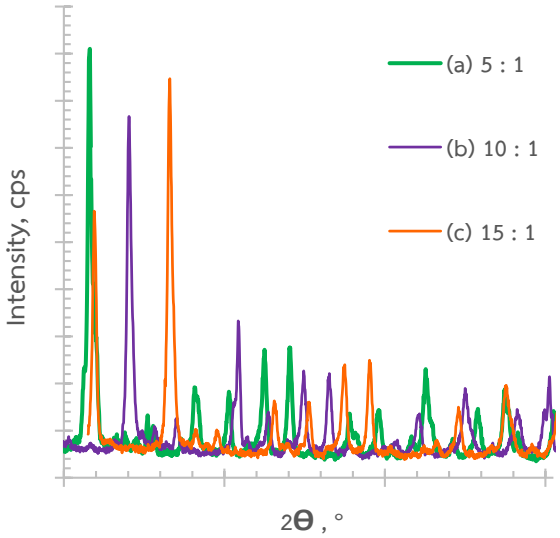

Figure 7. XRD graphs of synthetic samples compared only main peaks respectively, of SiC. The samples were burned at 1,200 °C for 10 hours at various silicon dioxide to magnesium metal mole ratio: (a) 5:1, (b) 10:1, (c) 15:1.

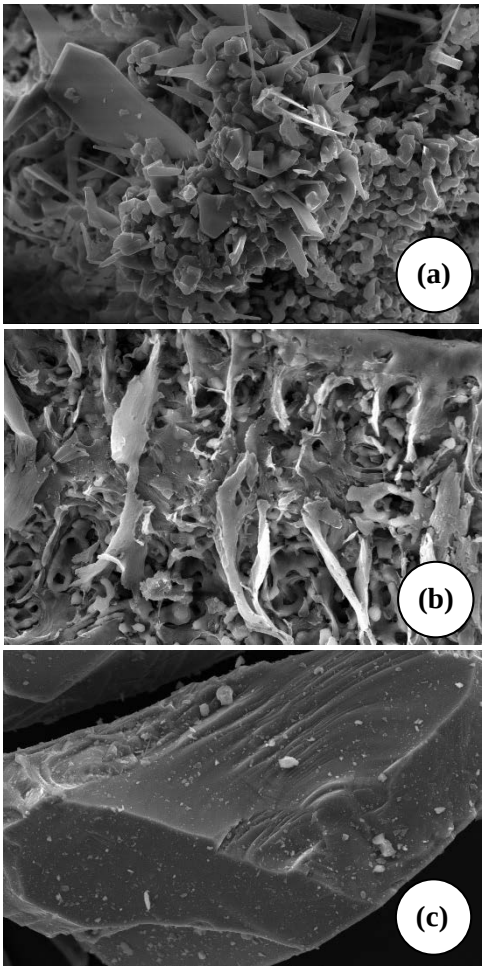

Figure 8. (a) SEM images of synthetic samples burned at 1,200 °C at silicon dioxide to magnesium metal mole ratio was 15:1 for 5 hours. (b) SEM images of synthetic samples burned at 1,200 °C at

silicon dioxide to magnesium metal mole ratio was 5:1 for 10 hours. (c) SEM images of commercial SiC powder

The clear formation of SiC could also be observed in the SEM image in Figure 8.

However, when comparing the silicon carbide synthesized in the research with the one produced in industrial factories, it was found that the resulting silicon carbide particles were much smaller and had an unstable structure. This is because the commercial silicon carbide powder was produced using a temperature of over 2,500 °C and required several days to complete the burning process.

4. Conclusion

This research aimed to produce silicon carbide with the synthesis of combustible substances from silica and carbon obtained from rice husk ash extraction by adjusting the ratio and reaction conditions appropriately as well as finding binder to produce silicon carbide.

Silicon carbide (SiC) was synthesized using raw materials consisting of silica and carbon extracted from rice husk ash. The reaction took place at a constant temperature of 1,200 °C. It was found that the peak intensity of SiC in the XRD graph was highest when magnesium metal was added to the reaction mixture at a mole ratio of 5:1 (silica to magnesium) and the reaction was carried out for a duration of 10 hours. The intensity of this sample was 18204.17 cps.

Acknowledgements

This research was funded by the department of chemical engineering, KMUTNB and thanks to graduate school, KMUTNB for a part of financial support.

References

1. Czosnek, C.; Bucko, M. M.; Janik, J. F.; Olejniczak, Z.; Bystrzejewski, M.; Labedz, O.; Huczko, A. Preparation of silicon carbide SiC-based nanopowders by the aerosol-assisted synthesis and the DC thermal plasma synthesis methods. *Mater. Res. Bull*. **2015**, *63*, 164–172.
2. Fuad, A.; Kultsum, U.; Taufiq, A.; Hartatiek. Low-temperature synthesis of α-SiC (6H-SiC) nanoparticles with magnesium catalyst. *Mater. Today: Proc*. **2019**, *17* (4), 1451-1457.
3. Gubernat, A.; Pichor, W.; Lach, R.; Zientara, D.; Sitarz, M.; Springwald, M. Low-temperature synthesis of silicon carbide powder using shungite. *Bol. Soc. Esp. Ceram. Vidrio*. **2017**, *56* (1), 39-46.
4. Morito, H.; Yamane, H. Synthesis of SiC via low-temperature heating of graphite and Si with Na flux. *J. Ceram. Soc. Jpn*. **2013**, *121* (11), 930-933.
5. Mukasyan, A. S. Combustion Synthesis of Silicon Carbide. In *Properties and Applications of Silicon Carbide*, Vol. 17; University of Notre Dame, 2011; pp 389-409. DOI: 10.5772/15620
6. Niyomwas, S. Synthesis and Characterization of Silicon-Silicon Carbide Composites from Rice Husk Ash via Self-Propagating High Temperature Synthesis. *J. Met., Mater. Miner*. **2009**, *19* (2), 21-25.
7. Satapathy, L.N.; Ramesh, P.D.; Agrawal, D.; Roy, R. Microwave synthesis of phase-pure, fine silicon carbide powder. *Mater. Res. Bull*. **2005**, *40* (10), 1871–1882.
8. Odior, A. O.; Oyawale, F. A. Formulation of Silicon Carbide Abrasives from Locally Sourced Raw Materials in Nigeria. *Proc. World Congr. Eng*. **2011**, 1.
9. Park, K. W.; Joo, E. R.; Kwon, O. Y. Synthesis of SiC from kenyaite-carbon nanocomposite using cobalt catalyst. *Appl. Clay Sci*. **2019**, *183*.
10. Singh, S. K.; Stachowicz, L.; Girshick, S. L.; Pfender, E. Thermal plasma synthesis of SiC from rice hull (husk). *J. Mater. Sci. Lett*. **1993**, *12*, 659-660.
11. Tan, C.; Liu, J.; Zhang, H.; Wang, J.; Li, S.; Song, J.; Zhang, Y. Low temperature synthesis of 2H-SiC powders via molten-salt-mediated magnesiothermic reduction. *Ceram. Int*. **2017**, *43* (2), 2431-2437.
12. Yasser, A.; Said E. S. Influence of the pH on the Morphology of Sol–Gel-Derived Nanostructured SiC. *J. Am. Ceram. Soc*. **2009**, *92* (11), 2724–2730

Heat transfer analysis of a microwave reactor using computational fluid dynamics for polymer recycling

Aung Khant Zaw[1], Issadaporn Wongwanichkangwarn[2], Hidetoshi Sekiguchi[3], Somboon Otarawanna[4], and Tanyakarn Treeratanaphitak[1]*

[1] *School of Integrated Science and Innovation, Sirindhorn International Institute of Technology (SIIT), Thammasat University, Pathum Thani 12121, Thailand*
[2] *Center of Excellence in Functional Advanced Materials Engineering, Thammasat University, Pathum Thani 12121, Thailand*
[3] *Department of Chemical Engineering, Tokyo Institute of Technology, Tokyo 152-8550, Japan*
[4] *National Metal and Materials Technology Center (MTEC), National Science and Technology Development Agency (NSTDA), Pathum Thani, 12120, Thailand*

**E-mail: tanyakarn@siit.tu.ac.th*

Abstract:

Microwave heating has emerged as an attractive heat source for polymer recycling processes such as alcoholysis. The rapid localized heating allows the reaction time for alcoholysis to be decreased from hours to minutes. Despite this, microwave heating does suffer from a shortcoming which is also present in conventional heating i.e., nonuniformity of the temperature distribution. In order to optimize the design of the microwave reactor for large-scale polymer recycling via alcoholysis, it is essential to understand and predict the temperature distribution inside the reactor. This can be achieved through numerical simulations of microwave heating and the hydrodynamics of the system. This study develops a microwave heating model by one-way coupling high-frequency electromagnetism, heat transfer, and fluid dynamics utilizing the finite element and finite volume methods by conducting two commercial packages i.e., ANSYS HFSS, and Fluent. The focus will be on analyzing the heat transfer mechanisms within the reactor using computational fluid dynamics simulations to capture temperature distribution accurately. Different operating conditions will be used to assess their impact on the temperature uniformity given a microwave heat source.

1. Introduction

Microwave heating has gained significant popularity in material processing due to its advantages over traditional heating methods. Microwave radiation is absorbed by taking advantage of the specific dielectric properties of molecules, which causes molecular vibrations and heat generation. This localized and rapid heating method significantly accelerates polymer degradation, eliminating the need for an intermediary heat transfer medium. This characteristic leads to improved energy efficiency and reduced heating time[1].

Microwave reactors have been extensively studied on a small scale, yielding insights into rapid and efficient chemical processes. Extensive research on simulating microwave heat transfer has been conducted, incorporating the solution of various equations including Maxwell's equations for electromagnetism, Navier-Stokes equations for fluid flow, and the heat transfer equation. For example, numerical simulations were used to analyze temperature changes in water flowing through a circular channel inside a microwave cavity, accounting for different flow rates[3,4]. Another study used COMSOL Multiphysics to investigate the temperature profile in a carboxymethyl cellulose solution and tap water flowing at two distinct flow rates while being heated continuously in a focused microwave system[5]. A comparative analysis of the modeling techniques in ANSYS and COMSOL Multiphysics was performed to understand the heating of Newtonian liquids during continuous microwave processes[6]. The electromagnetic power generation and power loss in fluids predicted by both models were compared. The models showed close agreement with a 5-13% variation.

Other studies have focused on heat transfer in flowing liquids in circular channels continuously heated with microwaves[9]. The research investigated temperature-dependent dielectric properties of the liquids and analyzed the waveguide design parameters. Furthermore, rectangular waveguides were used to analyze the heating process of water and NaCl-water solutions numerically and experimentally in layers and to study the influence of electrical conductivity and microwave power on the heating results[10]. These studies extended their scope to different liquids and analyzed sample volume, placement, and microwave power levels[11].

Simulation-driven optimization and control approaches in microwave reactors can boost process efficiency and product yield. However, optimizing microwave reactor design is

challenging due to interactions between electromagnetic fields, heat transmission, and chemical processes. Accurate multiphysics models are important to represent these interactions and their impact on reaction kinetics.

This study aims to address the need to optimize microwave-assisted chemical processes by exploring the importance of microwave power and reactor design. This will improve the overall understanding of microwave heating processes and the interaction with the hydrothermal behavior of the system under different operating conditions.

This paper is structured as follows: section 2 – model development, section 3 – results and discussion, and section 4 – conclusion.

2. Model Development

2.1 Model Governing Equations

The electric field ($\vec{E}$) can be described using Maxwell's equations[3],

$$\nabla.\vec{D} = q \quad (1)$$

$$\nabla.\vec{B} = 0 \quad (2)$$

$$\nabla \times \vec{E} = -\frac{\partial \vec{B}}{\partial t} \quad (3)$$

$$\nabla \times \vec{H} = \vec{J} + \frac{\partial \vec{D}}{\partial t} \quad (4)$$

where $\vec{E}$ and $\vec{H}$ denote the electric field in (V/m) and magnetic fields in (A/m), respectively, and $\vec{J}$ represents the current density in (A/m^2). $\vec{D}$ is the flux density in (C/m^2), q represents the electric charge density in (C/m^3), and $\vec{B}$ represents the magnetic flux density in (Wb/m^2). The material's dielectric properties determine its ability to absorb microwaves, which can be described mathematically using the equation below[1]:

$$tan\,\delta = \frac{\varepsilon''}{\varepsilon'} \quad (5)$$

where the dielectric constant, ε', estimates a material's ability to store heat energy, and the loss factor, ε'', is related to the amount of heat that a dielectric material can dissipate. The loss tangent, tan δ, is the dielectric constant ratio.

When a material is exposed to microwave radiation, its temperature increase is affected by both the electromagnetic properties and dielectric characteristics of material[1]. The effect of microwave heating on these materials can be summarized as follows[6]:

$$Q_{gen} = \sigma\left|\vec{E}\right|^2 = 2\pi\varepsilon_0\varepsilon'' f\left|\vec{E}\right|^2 \quad (6)$$

where σ is the electric conductivity of the material (S/m), ε_0= 8.854 x 10^{-12} (F/m) is the free space permittivity, $\varepsilon''$is relative dielectric loss, and f is frequency (Hz). Q_{gen} represents volumetric heat generation due to the microwave energy (W/m^3). The microwave interacts with the material on the molecular level and leads to bulk heating as power is absorbed within the lossy material, this is also known as the volume loss density Q_{gen} (W/m^3) [7,8]. This heat generation term is utilized as the energy source term in solving Fourier's energy balance equation to determine the temperature distribution[12].

$$\rho c_p\left(\frac{\partial T}{\partial t} + \vec{u}\cdot\nabla T\right) = k\nabla^2 T + \bar{\bar{\tau}}\cdot\nabla\vec{u} + Q_{gen} \quad (7)$$

where ρ is the density of the fluid in (kg/m^3), c_p is the constant pressure specific heat capacity (J/kg·K), t is time (s), $\vec{u}$ is the velocity vector of the fluid (m/s), k is the thermal conductivity of the fluid in (W/m·K), T is the temperature (K), $\bar{\bar{\tau}}$ is the stress tensor in (Pa).

The hydrodynamics of the fluid are described using the Navier-Stokes equations[13].

$$\frac{\partial}{\partial t}(\rho\vec{u}) + \nabla\cdot(\rho\vec{u}\vec{u}) = -\nabla P + \nabla\cdot(\bar{\bar{\tau}}) + \rho\vec{g} \quad (8)$$

where $\bar{\bar{\tau}}$ is the stress tensor expressed as:

$$\bar{\bar{\tau}} = \eta\left[(\nabla\vec{u} + \nabla\vec{u}^T) - \frac{2}{3}\nabla.\vec{u}I\right] \quad (9)$$

The continuity equation is given by:

$$\nabla\cdot(\vec{u}) = 0 \quad (10)$$

where η is the viscosity (Pa·s), P is the pressure force on the element per unit volume (N/m^2), and $\vec{g}$ is the acceleration due to gravity in (m/s^2). Turbulence is modeled using the realizable k-ϵ model, which has been found in the literature to perform best in microwave heating systems[14].

2.2 Simulation Conditions

A three-dimensional model of a small-scale batch microwave reactor has been developed. The microwave source is a 2.45 GHz single-mode magnetron. The 2-L batch reactor modeled in this work is in Figure 1, where the shaded region denotes the liquid level of the alcohol.

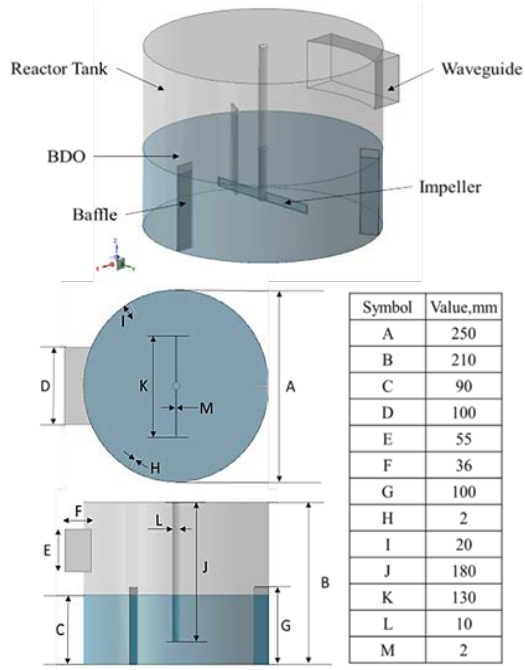

Symbol	Value,mm
A	250
B	210
C	90
D	100
E	55
F	36
G	100
H	2
I	20
J	180
K	130
L	10
M	2

Figure 1. Schematic of microwave geometry

Table 1. Boundary conditions [10,11,12]

	Domain	Boundaries
HFSS	Waveguide	Perfect electric conductor
	Reactor tank	
Fluent	Contact region	Interface
	Impeller	Wall
	Reactor tank	Wall
	Shaft	Wall
	Upper surface	Symmetry

Table 2. Simulation conditions

Microwave input power	1.2 kW
Frequency	2.45 GHz
Agitation speed	100-200 rpm

The boundary conditions for both simulations are given in Table 1. The simulation conditions are given in Table 2. In this study, the electric field is determined using ANSYS HFSS (version 2023 R1), and the hydrodynamics are resolved using ANSYS FLUENT (version 2023 R1). The electric field is converted into a heat source via Equation (6) in the subsequent FLUENT simulation. The workflow of the ANSYS R1 program is visually depicted in Figure 2. In this investigation, the simulations are carried out using an HP Core (TM) i5-4570 3.20 GHz desktop with 32.0 GB RAM.

2.3 Model Assumptions

To simplify the problem's complexity, the proposed model is based on the following assumptions:

1. The alcohol is assumed to be a Newtonian fluid.
2. The rectangular waveguide and cavity, including the air inside it, undergo negligible absorption of microwave energy.
3. Adiabatic conditions are considered at the cavity wall.
4. The influence of the reactor cavity on the electromagnetic field is omitted.
5. No phase change will be considered.

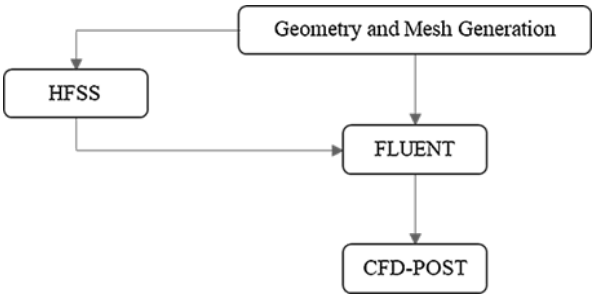

Figure 2. Workflow of ANSYS R1 program

Table 3. Dielectric and Thermo-Physical Properties of 1-4 Butanediol at Room Temperature

Parameter	Value
Dielectric constant ε' at 2.45 GHz	4.9 [15]
Dielectric loss ε'' at 2.45 GHz	3.75 [15]
Density ρ (kg/m^3)	1016.11[16]
Thermal conductivity k (W/m·K)	0.22 [17]
Viscosity η (kg/ms)	0.065 [17]
Specific heat capacity c_p (J/kg·K)	2210 [17]

2.4 Material Properties

The working fluid in this study was chosen to be 1,4-butanediol (BDO), one of the reactants in the alcoholysis process. In this work, the physical properties of BDO (Table 3) are assumed to be constant.

2.5 Mesh Independence

To ensure a converged solution, mesh independence studies are carried out for both the HFSS and Fluent simulations. For the electromagnetic simulations with HFSS, the chosen convergence variable is the average magnitude of the electric field. For the hydrodynamics simulations, the chosen convergence variable is the torque at the impeller blades. The mesh independence tolerance is set at 10^{-4}. Figure 3 shows the convergence behavior of the HFSS simulation with respect to the average magnitude of the electric field. The green line represents the average magnitude while the blue line represents the percent deviation from the

previous refinement level. After 13372 elements, the average magnitude only changes marginally, with a percent deviation of less than 0.25%. This small deviation indicates that the solution is mesh-independent within an acceptable tolerance.

Figure 4 shows the mesh convergence of the hydrodynamics simulation. The torque at the impeller blades is calculated from the simulation results using the following [18]:

$$\Gamma = \sum_i (\Delta P)_i A_i r_i \qquad (11)$$

where i is the index of the mesh element on the blade, Γ is the torque (Nm), ΔP is the pressure difference around the impeller at the surface element i (N/m^2) and r_i is the radial distance from the axis of the shaft on which the impeller is mounted (m). The impeller power is calculated using the following equation [19]:

$$p = 2\pi N\Gamma/60 \qquad (12)$$

where p is the power consumption (W) and N is the revolutions per minute (RPM). From Figure 4, the torque and power are shown to have converged after 307,195 elements.

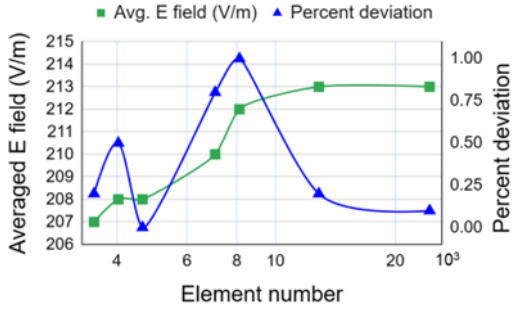

Figure 3. Mesh independence with average electromagnetic field at 2.45 GHz

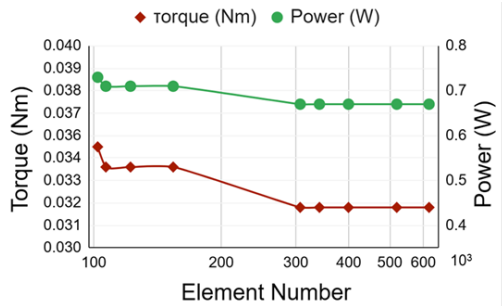

Figure 4. Mesh independence with torque at the impeller operating at 200 RPM

3. Results and Discussion

Numerical simulations are carried out based on the workflow in Figure 2 with simulation conditions as per Table 2. In this section, the electromagnetic and cold-flow hydrodynamical behaviors of the reactor are first studied independently. Then, the effect of microwave heating on the reactor is studied.

3.1 Electromagnetic Behavior

The input power to an electromagnetic system affects the intensity of the electric field generated within that system. Figure 5 shows the plots of microwave power versus the averaged electric field. From Figure 5, the effect of microwave power on the average electric field is observed to be linear. This relationship can be described using the equation $y = 0.124x + 70.2$.

In microwave systems, the interaction between microwave power and the electric field is crucial, as it directly affects heat generation. Subsequently, higher input power is expected to result in higher energy densities within the electric field. Figure 6 shows the electric field at different cross-sections. The uneven distribution of microwave energy arises from interactions between the electromagnetic wave and the reactor wall and internals, resulting in the generation of contrasting temperature zones, leading to the emergence of distinct hot spots and cold spots within the reactor. Significantly higher energy levels were observed in a concentrated hot region, particularly at the initial surface contact point between the fluid and air. A progressive transition from the hot zones toward colder regions is observed as one moves downward along the axial direction of the reactor.

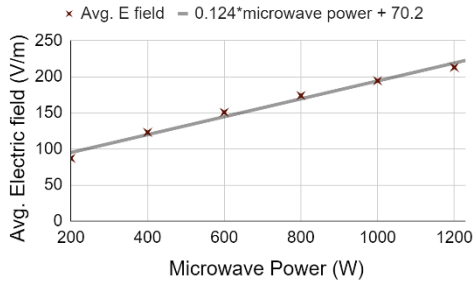

Figure 5. Comparison of the electric field within the BDO at various microwave power

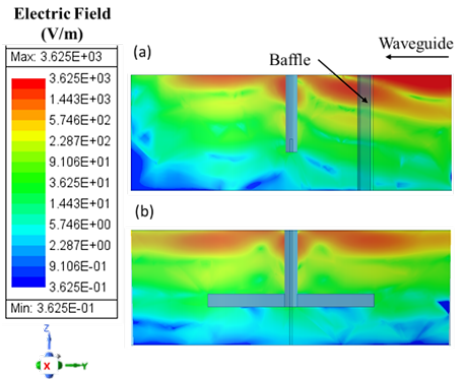

Figure 6. Electric field distribution of BDO phase at 2.45 GHz (a) xz-plane (b) xy-plane

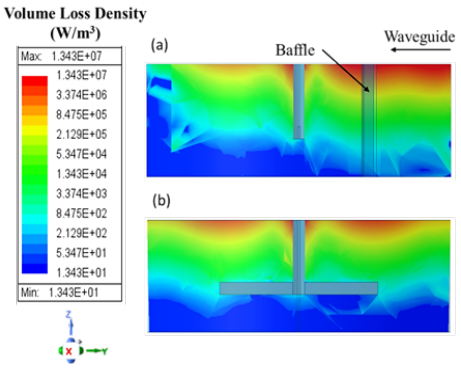

Figure 7. Distribution of volume loss density in BDO phase at 2.45 GHz (a) xz-plane (b) xy-plane

When the electromagnetic field passes through a material (solid or melted polymer and solvent), its intensity decreases exponentially from the free surface of the material until the transmitted power becomes too weak to cause heating due to the effect of skin depth [1]. The electric field distribution directly governs the magnitude of the heat source in the fluid. The dielectric power loss, which provides heat to the fluid, is calculated from the electric field by Eq. (6). The gradual shift in the magnitude of the electric field signifies a change in heating dynamics and temperature gradients within the system. At higher frequencies, particularly at 2.45 GHz, limited penetration capabilities are exhibited by electromagnetic waves, which predominantly interact with surface layers [1]. As a result, heating is concentrated closer to the surface due to the relatively shallow penetration of electromagnetic waves.

Figure 7 shows the volume loss density, which is converted into the heat source to the fluid, at an input power of 1.2 kW. The results show a substantial range in microwave loss density, ranging from 1.34×10^{1} to 1.34×10^{7} W/m³. This variation is attributed to dielectric losses within the fluid medium and the shallow penetration of electromagnetic waves in BDO. This extensive variation underscores the disparate energy concentrations within the reactor, contributing significantly to the observed hot spots and cold spots and underscores the need for sufficient mixing to ensure temperature uniformity in the reactor.

3.2 Flow Field

To understand the mixing behavior and energy requirements of mixing, steady-state cold-flow simulations of the reactor were carried out. The torque and power of the impeller are computed using Eqs. (11) and (12), respectively. The torque acting on the shaft is negligible in comparison to the torque at the blades and is thus neglected. In Figure 8, the relationship between impeller power number [20]:

$$N_p = \frac{p}{\rho N^3 D^5} \quad (13)$$

where N_p is the power number (-), D is the outer diameter of the impeller (m) and ρ is the density of the liquid (kg/m³), and the Reynolds number [20]:

$$N_{Re} = \frac{\rho N D^2}{\mu} \quad (14)$$

is shown. At a lower Reynolds number, fluctuations can dramatically affect the power number, showing that flow regime and features strongly influence mixing power. As Reynolds number increases, the power number stabilizes, showing that agitation power becomes less dependent on Reynolds in the turbulent flow regime [20]. As depicted in Figure 9, the presence of the baffle creates turbulent flow and therefore, it subsequently enhances the mixing effect in the flow field. It was discovered that there was a specific observation concerning the severity of the turbulence near the impeller tip. Notably, the turbulent flow displayed heightened intensity and vigor notably at the impeller tip. This observation implies a limited zone of heightened turbulence, suggesting a concentration of dynamic fluid forces and revealing the impeller's strong influence on fluid agitation within the reactor system.

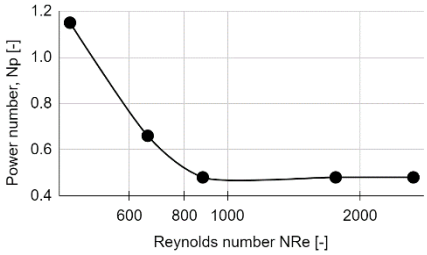

Figure 8. Relationship between power number and Reynolds number

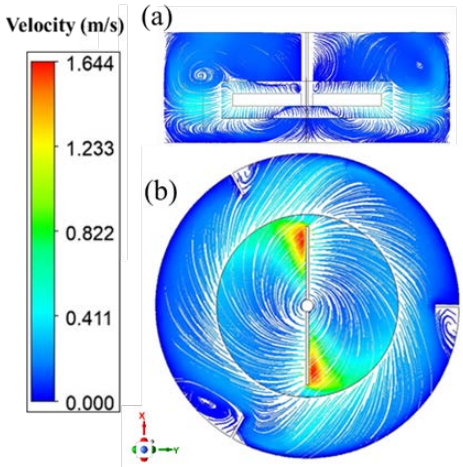

Figure 9. Velocity distribution of BDO at agitator speed of 200 rpm (a) yz-plane (b) xy-plane

3.3 Temperature Profile

The temperature profile variations over time are depicted in Figure 10. These profiles show a temperature gradient from indicated that the temperature was distributed from the liquid's surface, where it received microwave irradiation, resulting in heating. Conversely, the colder temperature distribution is observed near the wall. This occurred because of the decrease in volume density caused by the distribution of electric and electromagnetic fields, with the greatest intensity being observed near the surface of the BDO. These simulated results reflect the response of the reactor to the applied conditions, where the temperature increased progressively with extended reaction times. The results support the need for agitation to ensure temperature uniformity in the reactor. Therefore, the application of microwave irradiation selectively heats the reaction media within the reactor, thereby accelerating the reaction in comparison to traditional heating methods. Figure 11 shows the time evolution of the average temperature. For a 2 L reactor, the temperature is expected to increase by 150 ºC within the span of 25 minutes. This rapid heating greatly decreases the reaction time for alcoholysis.

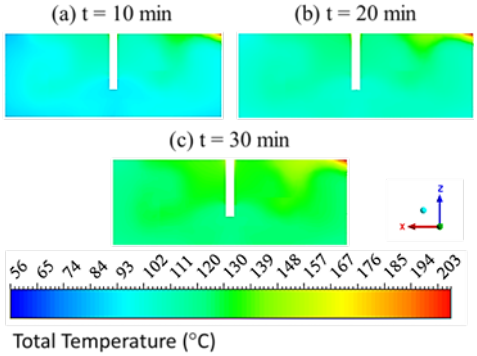

Figure 10. Cross-sectional temperature (xz-plane)

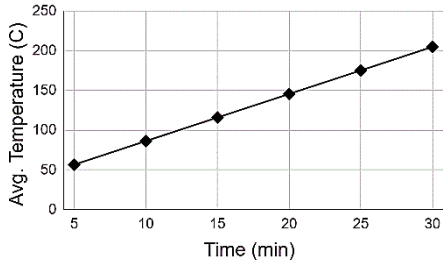

Figure 11. Average temperature against time

4. Conclusion

In this study, the coupling of electromagnetism with fluid dynamics and heat transfer of a microwave-assisted batch reactor was investigated using Computational Fluid Dynamics (CFD) simulation. Microwave heating and mechanical agitation within the batch reactor were studied independently and were later coupled to simulate microwave heating of the batch reactor. Simulation results show that microwave heating is limited to near the surface of the liquid. Good mechanical agitation is thus required to ensure temperature uniformity. The coupled simulation shows that microwave heating was able to rapidly increase the temperature of the fluid and with agitation, the temperature variation within the reactor is reduced. These results indicate that microwave heating is a viable heat source for larger-scale polymer recycling through alcoholysis.

Acknowledgments

AKZ acknowledges the scholarship under the Thailand Advanced Institute of Science and Technology and Tokyo Institute of Technology Program, awarded by Sirindhorn International Institute of Technology, Thammasat University, funded by the National Research Council of Thailand and the National Science and Technology Development Agency. IW and TT are partially supported by the Center of Excellence in Functional Advanced Materials Engineering, Thammasat University.

References

1. Belkhir, K.; Riquet, G.; Becquart, F.. *Adv. Polym. Tech.* **2022**, 3961233.
2. Vencels, J.; Birjukovs, M.; Kataja, J.; Raback, P. *Case Stud. Therm. Eng*. **2019**, *15*, 100530.
3. Sabliov, C. M.; Salvi, D. A.; Boldor, D. *J. Microw. Power Electromagn. Energy* **2016**, *41*, 5–17.
4. Yousefi, T.; Mousavi, S.A.; Saghir, M.Z.; Farahbakhsh, B. *Int. J. Therm. Sci.* **2013**, *71*, 118–127.
5. Salvi, D.; Boldor, D.; Aita, G. M.; Sabliov, C. M. *J. Food Eng.* **2011**, *104*, 422–429.
6. Salvi, D.; Boldor, D.; Ortego, J.; Aita, G. M.; Sabliov, C. M. *J. Microw. Power Electromagn. Energy* **2010**, *44*, 187–197.
7. EL Sabbagh, M., **2011**, Electrical Engineering and Computer Science - Technical Reports. 46.
8. Cherbanski, R.; Rudniak, L. *Int. J. Therm. Sci.* **2013**, *74*, 214–229.
9. Zhu, J.; Kuznetsov, A. V.; Sandeep, K. P. *Int. J. Therm. Sci.* **2007**, *46*, 328–341.
10. Ratanadecho, P.; Aoki, K.; Akahori, M. *Appl. Math. Model.*, **2002**, *26*, 449–472.
11. Klinbun, W.; Rattanadecho, P. *Appl. Math. Model*. **2012**, *36*, 813–828.
12. Muhtadin, A. F.; Wanking, P.; Kangsadan, T. *Int. J. Smart Grid Clean Energy* **2021**, *10*, 21-32.

13. Patel, H.; Ein-Mozaffari, F.; Dhib,. R. *Comput. Chem. Eng.* **2010**, *34*, 421–429.
14. Santos-Moreau, V.; Brunet-Errard, L.; Rolland, M. *Chem. Eng. J.* **2012**, *207–208*, 596-606.
15. Kadam, S. S.; Kanse, K. S.; Joshi, Y. S.; Rander, D. N.; Kumbharkhane, A. C. *Indian Journal of Physics* **2018.**
16. Zemankova, K.; Troncoso, J.; Romani, L. *Fluid Phase Equilibria* **2013**, *356*, 1-10.
17. Mitsubishi Chemical Corporation, https://www.m_chemical.co.jp/en/products/field/chemicals/index.html
18. R. Zadghaffari, J.S. Moghaddas, J. Revstedt, *Computers & Fluids* **2010**, 39, *7*, 1183-1190.
19. Xie, M.-H.; Zhou, G.-Z.; Xia, J.-Y.; Zou, C.; Yu, P.-Q.; Zhang, S.-L. *J. Chem. Eng. Japan* **2011**, *44*, 840–844.
20. I. Torotwa, C. S. Okinda , M. S. Memona, C. Jia. *International Agricultural Engineering Journal* **2018,** Vol. *27*, No. 2.

Development of dual-phase dyeing process for polyester fabric

Praifon Puangsing[1], Potjanart Suwanruji[1]*, and Jantip Setthayanond[2]

[1]*Department of Chemistry, Faculty of Science, Kasetsart University, Bangkok 10900, Thailand*
[2]*Department of Textile Science, Faculty of Agro-Industry, Kasetsart University, Bangkok 10900, Thailand*

**E-mail: fscipjs@ku.ac.th*

Abstract:

This study aims to investigate the dyeing of polyester with disperse dyes in an oil/water dual-phase system. Typically, conventional exhaust dyeing occurs in an aqueous medium at 130°C for 30 minutes, using a dispersing agent as a dyeing auxiliary. In this dual-phase system, palm oil serves as a non-aqueous phase with various oil-to-water ratios, and no dispersing agent is added. Two disperse dyes, Dianix Rubine S-2G 150% and Palanil Rubine SE-FG, were employed in dyebaths prepared at pH 4. Polyester was dyed with 1% on the weight of fabric (%owf) of disperse dyes at 110, 120, and 130°C for 30 minutes. The results demonstrate that dyeing polyester in a dual-phase system with both dyes, even at 120°C, yields similar K/S values compared to the conventional dyeing process. The optimal oil-to-water ratios are found to be 1:30 for Dianix Rubine S-2G 150% and 1:90 for Palanil Rubine SE-FG. Color yield could also be built up in the dual-phase system. Furthermore, the fastness to washing and rubbing were similar for both dyeing systems. Hence, an oil/water dual-phase dyeing system was successfully applied for polyester dyeing at lower temperatures without the need for a dispersing agent in the dyebath for both disperse dyes.

1. Introduction

Polyester fiber, commonly known in the textile industry as polyethylene terephthalate (PET), is considered the most frequently used type of polyester[1]. PET is a condensation polymer, or step-growth polymer, synthesized through esterification or transesterification reactions involving terepthalic acid or dimethyl terephthalate with ethylene glycol[2]. PET fibers possess desirable properties for textile applications, including excellent dimensional stability, excellent wear resistance, excellent chemical resistance, and very good heat resistance. However, PET fiber is inherently hydrophobic and exhibits relatively high crystallinity. Dyeing PET at temperatures below its glass transition temperature poses challenges due to its hydrophobic nature and high crystallinity[3].

Disperse dyes are commonly used for polyester, characterized by their non-ionic nature and extremely low water solubility due to the absence of water-solubilizing groups in their structures[4]. Consequently, dyeing temperature, pH and the presence of a dispersing agent are crucial factors for disperse dyes to efficiently diffuse into PET fabric[5]. Conventional aqueous disperse dyeing of polyester necessitates a significant quantity of chemicals, such as acid and dispersing agents, to achieve uniform dispersion in water. Additionally, the dyeing process requires high temperatures, typically around 130°C, to ensure proper dyeing[6]. Consequently, the conventional dyeing process for polyester fabric generates wastewater contaminated with chemicals, posing environment concerns. Moreover, the high energy requirements for the dyeing process further contribute to its environmental impact.

Various approaches have been proposed to minimize water and chemical usage in the dyeing process, such as non-aqueous dyeing and supercritical dyeing. A study was conducted on a modified decamethyl-cyclopentasiloxane (D5) and liquid paraffin non-aqueous medium dyeing system that incorporated a small amount of water. The results demonstrated a significant improvement in the dye uptake of disperse dyes on polyester fabric, attributed to a plasticization effect. The dyed fabric exhibited high color strength, excellent levelness, and superior colorfastness[7]. It is worth noting that these solvents, however, are toxic and pose risks to human health. Supercritical dyeing emerges as an intriguing alternative to conventional polyester fabric dyeing, utilizing a clean solvent that can be easily recovered and separated from excess dye at the end of the process. The dyeing results demonstrated good reproducibility, along with consistent dye uniformity and fastness comparable to that of the conventional process. Despite these advantages, it is important to acknowledge that this process is costly and requires a substantial initial investment[8].

Hence, a dual-phase dyeing process has been developed in this study as an alternative to conventional aqueous-based dyeing. This innovative approach involves transitioning from water to water and oil applications for dyeing, eliminating the need for a dispersing agent. The study focuses on polyester dyeing with dispersed

dyes using the palm oil/water dual-phase dyeing system, and the results are compared with those obtained from the conventional aqueous dyeing system. Two types of disperse dyes, specifically Dianix Rubine S-2G 150% and Palanil Rubine SE-FG, categorized as medium- and high-energy dyes, were utilized in the investigation. The study delves into understanding the impact of ratios between palm oil and water, as well as dyeing temperatures, on the color yield of the dyes on polyester. Additionally, the build-up properties of disperse dyes on polyester within this dyeing system were examined. To assess the practicality of the process, the colorfastness to washing and rubbing of the dyed fabrics is also evaluated.

2. Materials and Methods

2.1 Materials

Two monoazo disperse dyes, Dianix Rubine S-2G 150% and Palanil Rubine SE-FG, were supplied from DyStar, Singapore. The wetting agent (Sera Wash) and dispersing agent (Sera Sperse M-IS liq.03) were provided by DyStar, Thailand. Palm cooking oil was purchase from a local store. All chemicals used are of reagent grade. Polyester fabric (Mesh Syntrel Syn Set Wick, Yarn count: DTY75/72/1) was supplied by Nan Yang Textile Co.,Ltd, Thailand.

2.2 Methods

A Conventional dyeing process: Polyester fabric was scoured before use with a solution containing 1 g/L sodium carbonate (Na_2CO_3) and 1 g/L wetting agent at a liquor ratio of 30:1 at 60°C for 15 min. A dyebath was prepared with 1%owf disperse dyes and 5 mL dispersing agent at a liquor ratio of 20:1, and the pH was adjusted to 4 with acetic acid. Polyester fabric (5 g) was dyed at 130°C for 30 min using a Daelim Starlet infrared dyeing machine. The dyeing profile is illustrated in Figure 1. Subsequently, the dyed fabrics were rinsed with running water and subjected to reduction clearing at 70°C for 30 min using 1 g/L sodium hydrosulfite ($Na_2S_2O_4$) and 1g/L Na_2CO_3. The dyeing process was replicated three times. The color yields (K/S values) of dyed fabrics were measured with Datacolor 550 spectrophotometer and calculated by Kubelka-Munk Equation (1).

$$K/S = (1-R)^2/2R \quad (1)$$

Where; R is the reflection of all dyed polyester fabrics samples.

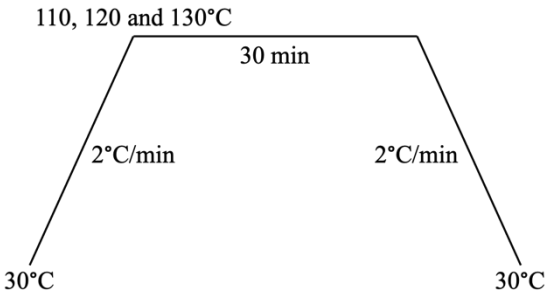

Figure 1. Dyeing profile of conventional and dual-phase dyeing process.

A dual-phase dyeing process: In the first experiment, dyebaths were prepared using five different volume ratios of palm oil to water (1:1, 1:10, 1:20, 1:30, 1:50 and 1:90) at a liquor ratio of 20:1 and pH 4. Scoured polyester fabric (5 g) was dyed with 1%owf disperse dye at 130°C for 30 min, following the same dyeing profile as the conventional dyeing process. The dyed fabric was rinsed, subjected to reduction clearing, and dried before evaluating K/S values. Next, the fabrics were also dyed at 120°C and 110°C for 30 min using the optimal ratios between palm oil and water for each dye determined in the first experiment to investigate the optimal dyeing temperature.

Build-up properties of the disperse dyes: Disperse dyes were applied to polyester fabrics by both conventional dyeing process and dual-phase dyeing process, employing the optimal oil to water ratio and dyeing temperature. The concentrations of dyes used were 0.5, 1.0, 2.0, 3.0 and 5.0%owf. K/S values were plotted against dye concentrations to evaluate the build-up properties of the disperse dyes.

Color fastness properties: The dyed fabric samples were investigated for their wash and rub fastness. Wash fastness was conducted following the ISO 105-C06 standard method No.06/B25. The color change of the dyed fabric samples and staining on PET fabric were assessed by a grey scale for color change and staining, respectively. Rub fastness, both dry and wet, was evaluated in accordance with the BS 1006 × 12 105 test method and assessed using a grey scale for staining. The grey scale ratings range from 1 to 5 with level 1 indicating the highest degree of shade change or staining, and level 5 indicating no shade change or staining.

3. Results & Discussion

Conventional dyeing process: The K/S values of the polyester fabrics dyed with Dianix Rubine S-2G 150% and Palanil Rubine SE-FG in a conventional aqueous-based dyeing system are

presented in Table 1. Despite applying both disperse dyes at the same concentration (1%owf), the K/S value of Dianix Rubine S-2G 150% was notably lower than of Palanil Rubine SE-FG, as anticipated. Dianix Rubine S-2G 150% is categorized as a high-energy disperse dye, typically having a larger molecular mass than that of Palanil Rubine SE-FG in a medium energy group, leading to more difficult penetration into fiber. Consequently, the amount of Dianix Rubine S-2G 150% fixed on the polyester fiber was less than that of Palanil Rubine SE-FG.

Table 1. K/S values of the dyed polyesters from a conventional dyeing system at 130°C

Disperse dyes	K/S
Dianix Rubine S-2G	8.33
Palanil Rubine SE-FG	16.64

Dual-phase dyeing process: The K/S values of the polyester fabrics dyed with Dianix Rubine S-2G 150% and Palanil Rubine SE-FG in palm oil/water dual-phase disperse dyeing systems at 130°C are shown in Table 2. Notably, at an oil/water ratio of 1:30, the K/S value of Dianix Rubine S-2G 150% was the highest at 8.94, while Palanil Rubine SE-FG, at an oil/water ratio of 1:90, exhibited the highest value at 19.21. The values are higher than the K/S values obtained from the conventional dyeing methods. In the work reported by Seemork et al., they used the coconut oil/water dual-phase dyeing system in different ratios of oil to water for reactive dyeing process of cotton and compared to conventional aqueous dyeing.[9] The results also showed that the dual-phase dyeing system imparted higher K/S values than the conventional aqueous dyeing which is similar to this work.

Table 2. K/S values of the dyed polyester from a dual-phase dyeing system with different oil/water ratios at 130°C

Oil/water ratio	K/S	
	Dianix Rubine S-2G	Palanil Rubine SE-FG
1:1	1.26	4.70
1:10	3.28	12.58
1:20	5.00	14.01
1:30	8.94	15.48
1:50	5.89	15.32
1:90	5.76	19.21

Applying the optimal oil/water ratio from Table 2, Dianix Rubine S-2G 150% and Palanil Rubine SE-FG were dyed on polyester fabrics at temperatures of 110 and 120°C using the same dyeing profile. The results presented in Table 3 suggested that decreasing dyeing temperatures in the dual-phase dyeing system led to a decrease in color strength for both dyes on polyester. In the case of Dianix Rubine S-2G 150%, the K/S value at 130°C in the dual-phase dyeing system showed an insignificantly improvement compared from the conventional method. However, when dyeing Palanil Rubine SE-FG at 120°C in the dual-phase system, it yielded a K/S value comparable to conventional dyeing at 130°C, and even exhibited a greater K/S value at 130°C without the use of a dispersing agent. The effectiveness of the dual-phase dyeing system for disperse dying was more pronounced for smaller dyes.

Table 3. K/S values of the dyed polyester from a dual-phase dyeing system at different temperatures and optimal oil to water ratios of Dianix Rubine S-2G 150% and Palanil Rubine SE-FG was 1:30 and 1:90 respectively.

Disperse dyes	Temperature (°C)		
	130	120	110
Dianix Rubine S-2G	8.94	7.86	5.98
Palanil Rubine SE-FG	19.21	16.39	14.12

Build-up properties of the disperse dyes: Figures 2 and 3 depict the build-up curves of Dianix Rubine S-2G 150% and Palanil Rubine SE-FG in both conventional aqueous-based and dual-phase dyeing systems, respectively. The optimal oil/water ratios and dyeing temperatures were applied for Dianix Rubine S-2G 150% and Palanil Rubine SE-FG in the dual-phase dyeing system, which were 1:30 and 1:90, and 130 and 120°C, respectively. The results indicate that both dyes can be built-up in the dual-phase system similarly to the conventional one. The K/S values increase as the dye concentration rises up to 5%owf, confirming that the dual-phase dyeing system can be applied at higher dye concentration as well. Moreover, Palanil Rubine SE-FG yielded slightly higher K/S values in the dual-phase dyeing system, especially at higher dye concentrations, compared to the conventional dyeing, even the dyeing was performed at a lower temperature without a dispersing agent.

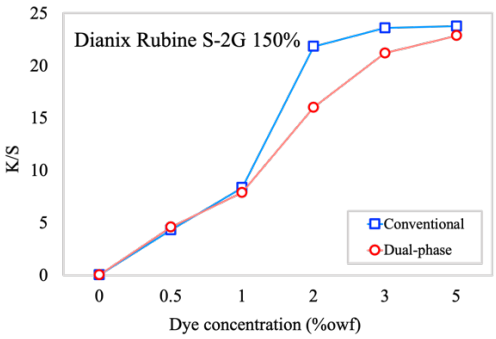

Figure 2. Build-up curves of the Dianix Rubine S-2G 150% on polyester fabric under onventional and dual-phase process at 1:30 and 130°C.

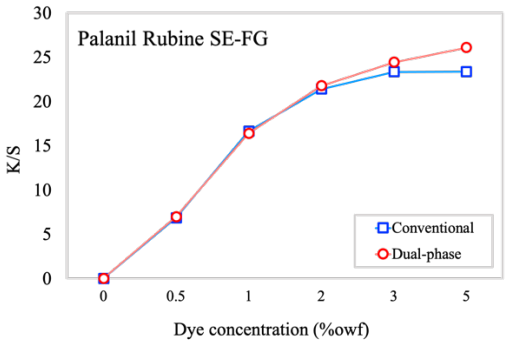

Figure 3. Build-up curves of the Palanil Rubine SE-FG on polyester fabric under conventional and dual-phase process at 1:90 and 120°C.

Color fastness properties: The result of wash fastness and rub fastness, both dry and wet, are presented in Table 4. For wash fastness, no color change was observed on the tested fabric samples for both the conventional and dual-phase dyeing processes of both dyes. However, there was slight staining on polyester fabric samples using the dual-phase dyeing. Similarly, rub fastness results were quite similar for both dyeing system, with only slight color loss observed in the case of Palanil Rubine SE-FG samples using the dual-phase dyeing in both dry and wet rub fastness tests. The results suggests that reduction clearing of surface dyes need to be a bit more of a concern when applying the dual-phase dyeing system.

4. Conclusion

The palm oil/water dual-phase dyeing system was successfully applied for disperse dyeing on polyester without the need of a dispersing agent. Both medium and high energy disperse dyes, Dianix Rubine S-2G 150% and Palanil Rubine SE-FG, could give comparable K/S values on polyester fabric using the dual-phase dyeing system compared to the conventional aqueous dyeing process. The optimal oil to water ratios and dyeing temperatures in dual-phase system of Dianix Rubine S-2G 150% and Palanil Rubine SE-FG was 1:30 and 1:90, and 130 and 120°C, respectively. The dyes demonstrated effective build-up on polyester in the dual-phase dyeing system similar to the conventional system. In the case of Palanil Rubine SE-FG which is a smaller dye, it achieved the same K/S value as the conventional dyeing system at a lower temperature, contributing to energy consumption reduction. Color fastness to wash and rubbing was also similar for both dyeing system. These results suggest that the palm oil/water dual-phase system might be an alternative for disperse dyeing of polyester fabrics.

Acknowledgements

This work is supported by the Department of Chemistry, Faculty of Science, Kasetsart University, Bangkok, Thailand.

Table 4. Color fastness of the dyed polyester from the conventional at 130°C compared to the dual-phase dyeing process of Dianix Rubine S-2G 150% and Palanil Rubine SE-FG was 1:30 and 1:90, and 130 and 120°C, respectively.

Dyeing process	Wash fastness				Rub fastness			
	Color change		Staining on PET		Dry		Wet	
	Dianix Rubine S-2G	Palanil Rubine SE-FG	Dianix Rubine S-2G	Palanil Rubine SE-FG	Dianix Rubine S-2G	Palanil Rubine SE-FG	Dianix Rubine S-2G	Palanil Rubine SE-FG
Conventional	5	5	5	5	5	5	5	5
Dual-phase	5	5	4/5	4/5	5	4/5	5	4/5

References

1. Lin, C. A. Manufacture of polyester fibers. *Polyesters and Polyamides*. **2008**, 62-96.
2. Khan, Z. et al. Current Developments in Esterification Reaction: A Review on Process and Parameters. *Journal of Industrial and Engineering Chemistry*. **2021**, *103*(10), 80-101.
3. Brown, E. A.; Reinhart, A. K. Polyester Fiber: From Its Invention to Its Present Position. *Science*. **1971**, *3994*(173), 287-293.

4. Koh, J. Dyeing with Disperse Dyes. *Textile Dyeing*. **2011**, 195-220.
5. Aspland, R. J. The Structure and Properties of Disperse Dyes And Related Topic. *Disperse Dyes*. **1993**, *25*(1).
6. Bone, J. A. et al. One-bath dyeing of polyester/cotton with disperse and bis-3-carboxypyridinium-s-triazine reactive dyes. *Coloration Technology*. **2007**, *123*(3), 152-162.
7. An, Y. et al. High-efficiency dispersant-free polyester dyeing using D5 non-aqueous medium. *Dyes and Pigments*. **2021**, *190*(1).
8. Banchero, M. et al. Supercritical Dyeing of Textiles – From the Laboratory Apparatus to the Pilot Plant. *Textile Research Journal*. **2008**, *78*(3), 217-223.
9. Seemork, K. et al. Optimization of Salt-Free Reactive Dyeing Process for Cotton with Coconut Oil/Water Dual-Phase Dyeing System. *Asian Journal of Chemistry*, **2021** *33*(9), 2099-2104.

Effect of fly ash to alkali activator ratios on pore properties of porous fly ash-based geopolymer under curing by microwave irradiation

Komchan Meecharoen[1], Khanthima Hemra[2], Sitthisak Prasanpan[2], and Sirithan Jiemsirilers[1]*

[1]*Department of Material Science, Chulalongkorn University, Bangkok 10330, Thailand*
[2]*National Metal and Materials Technology Center (MTEC), Klong Luang, Phathumthani 12120, Thailand*

**E-mail: Sirithan.j@chula.ac.th*

Abstract:

This study investigates the synthesis of porous geopolymers from fly ash using microwave irradiation. Microwave heating is a rapid and energy-efficient method for curing geopolymers to achieve pore structures. Porous geopolymers were prepared by mixing different weight percentages of fly ash (40%, 50%, and 60%) with sodium silicate solution and 10M sodium hydroxide solutions, with the weight ratio of $Na2SiO_3$ to NaOH solution fixed at 2.5. Then, the geopolymer pastes were cured in a microwave oven at 800 W for 10 minutes. The resulting porous geopolymers were characterized using XRD, FT-IR, SEM, BET method, and their physical properties. The fly ash content significantly affected the physical properties, which are bulk density, apparent density, porosity, pore properties, and specific surface area. The porosity and specific surface area decreased with the increase in fly ash content, while the pore size and pore volume increased. The XRD result presented the characteristic broad hump of geopolymer that confirmed the presence of geopolymer gel formation. The FT-IR spectra confirmed the geopolymerization. SEM micrographs showed partially reacted fly ash particles and a dense geopolymer structure resulting from the microwave irradiation enhanced dissolution. This study successfully synthesized porous geopolymers from fly ash using microwave irradiation. The microwave foaming technique proved to be efficient in creating porous structures. Fly ash content significantly influenced the specific surface area and pore characteristics of the porous geopolymers.

1. Introduction

Geopolymers are recognized as sustainable materials due to their eco-friendly nature and cost-effectiveness. They are typically synthesized at ambient or elevated temperatures via alkaline activation, employing readily available natural resources and waste products as primary raw materials. This process results in an amorphous material with a three-dimensional aluminosilicate network structure, contributing to their superior properties.[1,2] fly ash is a by-product from coal or lignite power plants which is a valuable resource for the production of eco-friendly geopolymer materials. It is used in a geopolymer process offering a long-term solution for handling the significant waste that generated from the power generation sector.[3] Initially, fly ash reacted with strong alkaline activators. Subsequently, geopolymerization occurred through oligomerization, polymerization, and condensation.[6,7] Geopolymers derived from fly ash exhibit excellent mechanical properties including minimal creep and remarkable resistance to both sulfate and acid attacks.[4,5] Additionally, they provide a superior compressive strength when implemented as conventional cement replacements. The superior characteristics of dense geopolymers make them highly suitable for construction applications. Meanwhile, porous geopolymers exhibit the versatility in synthesis, allowing for preparation under both high- and low-temperature conditions. This versatility leads to a wide variety of applications, including adsorbents, catalysts, thermal insulators, sensors, hot gas filters, and solid-liquid separation processes.[8,9,10,11,12] These applications are facilitated by the unique and complex properties of porous geopolymers, such as their low thermal conductivity, low density, incombustibility, and thermal and chemical stability.[13] Notably, recent research has shown that porous geopolymers could be used to absorb CO_2 during the production of hydrogen, which would help clean up the gas. However, further investigations of porous geopolymers are required to optimize the conventional synthesis process. Although, the porous geopolymer provides interesting characteristics, it has limitations in practical application due to its long curing time of 24-48 hours, which is necessary for pore formation and is mainly controlled by the use of a foaming agent.[14,15] In response to this challenge, many researchers have focused on developing advanced synthesis techniques aimed to achieve porous geopolymer structures with significantly reduced curing times. In recent years, microwave energy has emerged as an alternative power source for accelerating heating and facilitating chemical reactions, owing to its unique ability to penetrate materials and induce selective microwave

absorption.[16] Microwave heating offers distinct advantages for the synthesis of polymeric foams, including instantaneous heat-up, rapid processing, and precise control due to its direct interaction with materials at the molecular level. Its penetrative nature enables volumetric heating, making it particularly advantageous for polymers with low thermal conductivity. Utilization of the electromagnetic properties, microwave technology rapidly elevates the temperature throughout the material, leading to the swift vaporization of water and the formation of pores.[17,18] Notably, this method has also demonstrated its effectiveness in the microwave synthesis of geopolymers derived from fly ash. Several studies have explored the use of microwave irradiation for the synthesis of foam geopolymers. Ul Haq et al.[19] reported the utilization of a microwave heating product the thermally insulating foam from bottom ash, employing varying amounts of sodium silicate. In a different study, Onutai et al.[5] revealed that the amount of alkali activator strongly affected the porous fly ash-based geopolymer properties under microwave irradiation. Therefore, the present study aims to synthesize porous geopolymers from fly ash using microwave irradiation. The effect of microwave heating on various fly ash and alkaline activator compositions are investigated. Moreover, the pore properties, specific surface area by BET, phase analysis by XRD, chemical bonding by FT-IR, microstructure by SEM, and physical properties of the synthesized geopolymers will be evaluated.

2. Materials and Methods

2.1 Materials

Fly ash was the primary raw material which obtained from a power plant located in Rayong, Thailand. X-ray Fluorescence (XRF) analysis revealed the chemical compositions of the fly ash was 44.50% SiO_2, 25.18% Al_2O_3, 14.34% Fe_2O_3, 7.05% CaO, 2.58% MgO, 1.70% K_2O, 1.23% Na_2O, 1.20% SO_3, and 2.22% LOI. Figure 1 presents the XRD pattern of fly ash which indicates that the major crystalline phases are quartz, mullite and hematite. The alkali activator was prepared by mixing sodium silicate solution (Na_2SiO_3) and 10 M sodium hydroxide solution (NaOH) which the ratio of Na_2SiO_3 to NaOH solution was maintained at a constant weight ratio of 2.5.

2.2 Synthesis of porous geopolymers

Table 1 presents all geopolymer compositions with the investigated material precursors. These samples were subsequently designated FA40, FA50, and FA60, corresponding to their fly ash weight percentages of 40%, 50%, and 60%, respectively. Fly ash and alkali activator was mixed thoroughly for 10 minutes via a Hobart mixer. The resulting slurry was then cast into a silicone mold, 50x50x50mm. Then, the silicone mold was placed to cure in a microwave oven at 800 W for 10 minutes to achieve the desired pore formation.

2.3 Spectroscopic measurement

The resulting porous geopolymers were verified the occurrence of geopolymerization using Fourier Transform Infrared spectroscopy (FT-IR, PERKIN ELMER Spectrum One instrument) which scanned the samples across a wavenumber range of 500-4000 cm^{-1}. The phase composition was characterized by X-ray diffractometer (XRD), which observed at 10-80° 2θ. The morphology and microstructure were investigated by scanning electron microscopy (SEM, JEOL JSM-6480LV instrument). The specific surface area, pore volume, and pore size were determined by the Brunauer-Emmet-Teller method (BET, 3Flex version 5.02) using nitrogen adsorption at a temperature of 77 K. The apparent and bulk densities were measured by the test method of ASTM C373-88. The percentage porosity was calculated by the following equation:

$$\% \text{ Porosity} = \left[1 - \left(\frac{\text{Bulk density}}{\text{Apparent density}}\right)\right] \times 100$$

Table 1. Compositions of porous samples.

Sample name	Fly ash (wt.%)	Na_2SiO_3/10M NaOH 2.5:1 (wt.%)
FA40	40	60
FA50	50	50
FA60	60	40

3. Results & Discussion

3.1 XRD analysis of fly ash and porous geopolymers

XRD patterns of fly ash and porous fly ash-based geopolymers, which were cured using microwave irradiation, are shown in Figure 1. A prominent characteristic broad hump of geopolymer presented at 20° to 40° 2θ, which the center was located at around 30° 2θ. The broad peak of porous geopolymers was obviously

different from fly ash indicating a higher degree of geopolymerization. In addition, the XRD patterns also showed the remained crystalline peaks in porous geopolymer including quartz, mullite, and hematite. The lower peak intensity, the higher fly ash content. The existence of these crystalline phases suggests the transformation of fly ash into geopolymeric gel.[3,5]

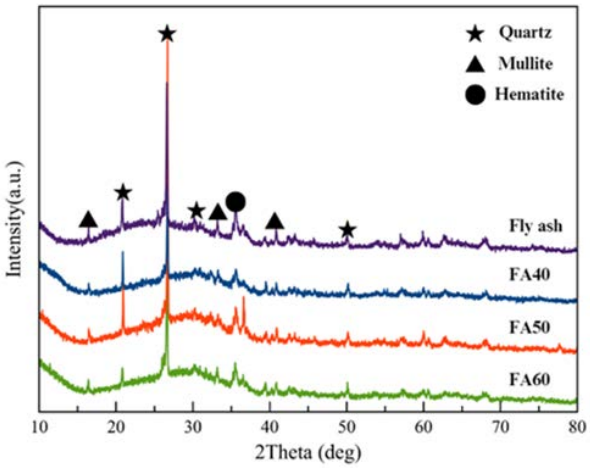

Figure 1. X-ray diffraction pattern of fly ash and porous geopolymers.

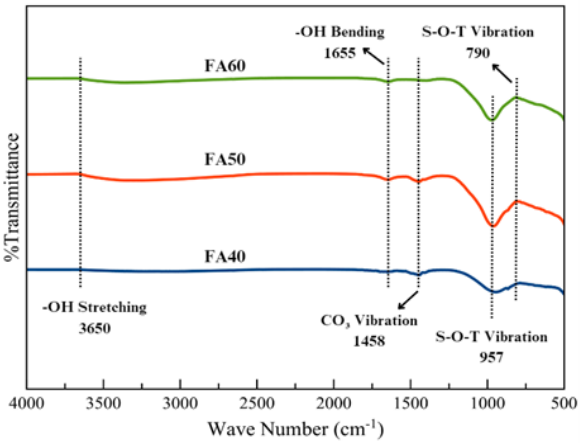

Figure 2. FTIR spectra of porous samples

3.2 FTIR analysis of porous geopolymer samples

FTIR analysis of the porous geopolymers reveals in Figure 2. The broad bands were observed at 3650 cm^{-1} and 1655 cm^{-1} corresponding to the bending and stretching vibrations of -OH groups, respectively.[18] A band at 1458 cm^{-1} assigned to carbonate groups which likely formed by the absorption of atmospheric CO_2 gas into the sodium silicate solution during synthesis.[19] Additionally, a band at 957 cm^{-1} attributed to the asymmetric stretching vibration of Si-O-T bonds (where T represents tetrahedral Si or Al)[3] which was the major fingerprint for geopolymer materials. As seen in Figure 2, the center of this broad band shifted to a higher wavenumber when the fly ash content was increased. It implies that more Si ion cooperated in geopolymerization which enhances the geopolymer structure. Finally, a band at the lower wavenumber of 790 cm^{-1} further supports the presence of Si-O-T bonds.[18]

3.3 SEM analysis of porous geopolymer samples

The SEM micrographs of all the porous samples are shown in Figure 3. The SEM analysis revealed that all porous geopolymer samples showed partially reacted fly ash particles and unreacted spherical fly ash embedded in the geopolymer matrix. Moreover, the dense geopolymer structure resulted from fly ash particles underwent dissolution in the alkaline solution. The microwave accelerated the reaction affected the reaction products and microstructure. The dissolution was significantly enhanced by microwave irradiation as evidenced by the formation of numerous gels on the fly ash particle surfaces, Figure 3 (a)-(c). The rapid heating of the aqueous solution by microwave irradiation promoted the release of Si and Al species from the fly ash facilitating the observed gel formation.[20] As a result, a denser structure was observed with small cracks. These cracks attributed to the removal of moisture during heat curing. The microstructure of FA60, Figure 3 (c), shows denser structure than FA40 and FA50, Figure 3 (a) and (b), respectively. It results from the high amount of fly ash in the composition of FA60 which is promoting the geopolymerization. Accordingly, FA60 presented lower porosity than FA40 and FA50.

3.4 Bulk density, apparent density and porosity of porous geopolymer samples

Table 2 shows bulk density, apparent density and porosity of porous geopolymers. The bulk density increased progressively from 0.91 g/cm^3 to 1.22 g/cm^3 when the fly ash content was increased from FA40 to FA60. This was confirmed by the dense geopolymer structure as shown in Figure 3. The apparent density showed a opposite trend to bulk density. It was reduced from 3.12 g/cm^3 to 2.24 g/cm^3 with the increase of fly ash content. The porosity exhibited an inverse relationship[21] with fly ash content. It decreased from 71% to 46% when increased the fly ash content from FA40 to FA60. As a result, the solid content increased and the alkali activator content decreased resulting in increased bulk density and decreased porosity. The pores and voids in geopolymer structure are created by the evaporation of water during microwave irradiation which the high amount of alkali activator would

lead to generate the large number of pores. Furthermore, the high temperature of microwave heating contributes to the dissolution and promotes geopolymerization and solidification. Therefore, the resultant porous geopolymer will set faster during curing within minutes.

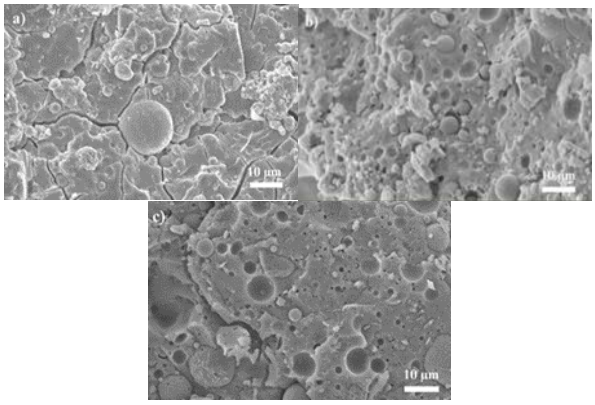

Figure 3. SEM micrographs of porous samples a) FA40, b) FA50, c) FA60

3.5 Specific surface area, pore volume, pore size of porous geopolymer samples

Table 3 presents the specific surface area of porous geopolymers. The specific surface area declined with the increase of fly ash content. These were 85.72 m^2/g, 66.68 m^2/g, and 42.46 m^2/g which the fly ash contents were FA40, FA50, and FA60, respectively. Conversely, the pore volume increased from 0.03463 cm^3/g to 0.08741 cm^3/g when the fly ash content was increased from FA40 to FA60. Additionally, the pore size is enlarged with the amount of fly ash which are 1.958 nm, 3.612 nm, and 8.234 nm. It was expected that the pore structure characteristics reflected the geopolymer microstructure. While microwave curing, an internal temperature gradient occurred, and the local overheating of the liquid took place inside the geopolymer samples causing numerous pores. Therefore, the high alkali activator content created a bigger number of pores after the moisture was removed that resulted in high porosity and high specific surface area as aforementioned. However, the pore volume and pore size exhibit the reversed results which would be caused from the heated internal liquid during microwave curing. The liquid in the geopolymer structure was repelled and attempted to evaporate by microwave heating, but the gas release could not come out to the surface easily because of the high content of fly ash in the composition and a viscous mixture. Thus, the pores coalesced into a large pore and were trapped in the geopolymer structure.

3.6 Comparison of porous geopolymers synthesized with conventional curing and microwave irradiation.

Microwave irradiation curing offers significantly faster processing times for geopolymer synthesis, typically achieving completion within minutes. This method eliminates the need for foaming agents, potentially reducing both cost and process complexity. Additionally, microwave curing provides greater control over pore characteristics through variations in fly ash content and the duration of microwave power application.

In contrast, conventional curing methods typically involve curing at ambient or elevated temperatures for extended periods, ranging from 24 to 48 hours.[14.15] These methods rely on the use of foaming agents to create pores, which can add cost and complexity to the process. Furthermore, conventional methods offer limited control over pore characteristics such as size and volume. Microwave curing achieves significantly higher porosities compared to conventional methods. Microwave-cured geopolymers have exhibited porosities up to 71%, exceeding the typical range of 50-60% achieved through conventional methods. Specific surface area is also significantly enhanced with microwave curing, reaching up to 85.72 m^2/g compared to conventional methods in the range of 20–50 m^2/g.[12] Moreover, microwave curing enables precise control over pore size. For example, FA40 exhibited micropores with an average diameter of 1.96 nm, while those prepared with FA60 displayed larger mesopores with an average diameter of 8.234 nm. Conventional methods often lack such control over pore size distribution. Ultimately, microwave irradiation curing emerges as a promising technique for synthesizing porous geopolymers with superior properties and significantly faster processing times compared to conventional methods. This technique offers greater control over pore characteristics, eliminates the need for foaming agents, and leads to geopolymers with higher porosity and specific surface area.

Table 2. physical properties of porous samples.

Sample name	Bulk density (g/cm^3)	Apparent density (g/cm^3)	Porosity (%)
FA40	0.91	3.12	71
FA50	1.07	2.50	58
FA60	1.22	2.24	46

Table 3. specific surface area and pore properties of porous samples.

Sample name	S_{BET} (m^2/g)	Pore volume (cm^3/g)	Pore size (nm)
FA40	85.72	0.03463	1.958
FA50	66.68	0.06021	3.612
FA60	42.46	0.08741	8.234

4. Conclusion

In this study, porous geopolymers were successfully synthesized from fly ash using microwave irradiation with varying fly ash to alkali activator ratios. Microwave irradiation is the effective method to create porous structures in geopolymers without pore former. The porous properties of fly ash-based geopolymers were strongly affected by the solid and liquid content under microwave irradiation. The high content of the alkali activator which was the low fly ash content significantly affected the porosity, specific surface area, and pore size. FA40 exhibited the max. porosity of 71%, the max. specific surface area of 85.72 m^2/g and the smallest pore size of 1.96 nm, which was predominantly micropores (pores with diameters less than 2 nm), whereas the pore volume was diminished of 0.035 cm^3/g. The best condition is FA40 due to its highest specific surface area, which, consisting of numerous micropores, could be ideal for use as adsorbent materials. The porous fly ash-based geopolymer is a sustainable and efficient material approaching for diverse utilizations. The high-performance adsorbent materials are the interesting application, particularly CO_2 absorbing in the hydrogen production.

Acknowledgements

The authors would like to acknowledge Chulalongkorn University and Thailand Science Research and Innovation Fund, Chulalongkorn University (BCG66230013) for financial support.

References

1. Provis, J. L.; Duxson, P.; Van Deventer, J. S. J.; Lukey, G. C. The role of mathematical modelling and gel chemistry in advancing geopolymer technology. *Chem. Eng. Res. Des.* **2005**, 83 (7), 853–860.
2. Gao, Y.; Yang, J. Preparation of geopolymer composites based on alkali excitation. *Arab. J. Geosci.* **2021**, *14* (7).
3. Böke, N.; Birch, G. D.; Nyale, S. M.; Petrik, L. New synthesis method for the production of coal fly ash-based foamed geopolymers. *Constr. Build. Mater.* **2015**, *75*, 189–199.
4. Nematollahi, B.; Sanjayan, J.; Shaikh, F. U. A. Synthesis of heat and ambient cured one-part geopolymer mixes with different grades of sodium silicate. *Ceram. Int.* **2015**, *41* (4), 5696–5704.
5. Onutai, S.; Jiemsirilers, S.; Thavorniti, P.; Kobayashi, T. Aluminium hydroxide waste based geopolymer composed of fly ash for sustainable cement. *Constr. Build. Mater.* **2015**, *101*, 298–308.
6. Duxson, P.; Fernández-Jiménez, A.; Provis, J. L.; Lukey, G. C.; Palomo, A.; Van Deventer, J. S. J. Geopolymer technology: the current state of the art. *J. Mater. Sci.* **2006**, *42* (9), 2917–2933.
7. Andini, S.; Cioffi, R.; Colangelo, F.; Grieco, T.; Montagnaro, F.; Santoro, L. Coal fly ash as raw material for the manufacture of geopolymer-based products. *Waste Manag. Res.* **2008**, *28* (2), 416–423.
8. Wang, H.; Li, H.; Wang, Y.; Yan, F. Preparation of macroporous ceramic from metakaolinite-based geopolymer by calcination. *Ceram. Int.* **2015**, *41* (9), 11177–11183.
9. Cilla, M. S.; Morelli, M. R.; Colombo, P. Effect of process parameters on the physical properties of porous geopolymers obtained by gelcasting. *Ceram. Int.* **2014**, *40* (8), 13585–13590.
10. Studart, A. R.; Gonzenbach, U. T.; Tervoort, E.; Gauckler, L. J. Processing Routes to Macroporous Ceramics: A review. *J. Am. Ceram. Soc.* **2006**, *89* (6), 1771–1789.
11. López, F. J.; Sugita, S.; Kobayashi, T. Cesium-adsorbent Geopolymer Foams Based on Silica from Rice Husk and Metakaolin. *Chem. Lett.* **2014**, *43* (1), 128–130.
12. Bai, C.; Colombo, P. Processing, properties and applications of highly porous geopolymers: A review. *Ceram. Int.* **2018**, *44* (14), 16103–16118.

13. Zhang, X.; Bai, C.; Qiao, Y.; Wang, X.; Jia, D.; Li, H.; Colombo, P. Porous geopolymer composites: A review. *Composites Part A: Appl. Sci. Manuf.* **2021**, *150*, 106629.
14. Somaratna, J.; Ravikumar, D.; Neithalath, N. Response of alkali activated fly ash mortars to microwave curing. *Cem. Concr. Res.* **2010**, *40* (12), 1688–1696.
15. Masi, G.; Rickard, W. D. A.; Vickers, L.; Bignozzi, M. C.; Van Riessen, A. A comparison between different foaming methods for the synthesis of light weight geopolymers. *Ceram. Int.* **2014**, *40* (9), 13891–13902.
16. Kuhnert, N. Microwave-Assisted reactions in Organic Synthesis—Are there any nonthermal microwave effects. *Angew. Chem. Int. Ed.* **2002**, *41* (11), 1863.
17. Stadler, A.; Pichler, S.; Horeis, G.; Kappe, C. O. Microwave-enhanced reactions under open and closed vessel conditions. A case study. *Tetrahedron* **2002**, *58* (16), 3177–3183.
18. Zaidi, S. F. A.; Haq, E. U.; Nur, K.; Ejaz, N.; Anis-Ur-Rehman, M.; Zubair, M.; Naveed, M. Synthesis & characterization of natural soil based inorganic polymer foam for thermal insulations. *Constr. Build. Mater.* **2017**, *157*, 994–1000.
19. Haq, E. U.; Padmanabhan, S. K.; Licciulli, A. Synthesis and characteristics of fly ash and bottom ash based geopolymers–A comparative study *Ceram. Int* **2014**, *40* (2), 2965–2971.
20. Inada, M.; Tsujimoto, H.; Eguchi, Y.; Enomoto, N.; Hojo, J. Microwave-assisted zeolite synthesis from coal fly ash in hydrothermal process. *Fuel* **2005**.
21. Vaou, V.; Panias, D. Thermal insulating foamy geopolymers from perlite. *Miner. Eng.* **2010**, *23* (14), 1146–1151. 151.

Amino acid fertilizer derived from poultry bio-waste

Natdanai Supawongchuwinit and Supakit Achiwawanich*

Department of Chemistry, Faculty of Science, Kasetsart University, Bangkok, THAILAND

**E-mail: supakit.a@ku.th*

Abstract:

Rapid growth in food industry has resulted in increasing bio-waste causing problem to surrounding environment. One of the bio-wastes are chicken feathers from poultry processing industries which are generally disposal in landfills. In this study, chicken feathers were hydrolyzed with 6M H_2SO_4 for 5 hours in order to produce amino acid fertilizer. The amino acid analyzer is employed to identify amino acid in the chicken feather hydrolysate. The result show cystine, glutamic, serine, proline and leucine are major amino acids with concentration higher than 5%by wt by weight in the chicken feathers. After hydrolysis, significant amount of amino acids are reduced due to strong hydrolysis conditions.Tomato, as test plants, is given 10ppm and 5 ppm hydrolysate solution to study its effect on plant growth. This liquid fertilizer may be used to generate valued added product from bio-waste, promoting zero waste economy.

1. Introduction

In recent years, the rapid growth of the commercial poultry industry has played an important role in solving issues related to unemployment, hunger, and poverty, and also contributing as a major global food production. However, the consequential growth in poultry farming has given rise to environmental issues such as the production of substantial amounts of waste, including feathers, packing materials, leftover feed, deceased poultry and broken eggs, for example. Chicken feathers alone generally weigh upto 10% of a chicken's total weight, contributing to a global solid waste in the billions of kilograms[1].

There are many methods employed to manage poultry waste, particularly feathers, which mostly associated with resource-intensive and time consuming methods. High-pressure and high-temperature treatments, followed by grinding into powder for use as feed supplements, have proven effective but come with a significant economic cost. Disposal methods such as burning or depositing waste in landfills may contributes to air pollution and water pollution, especially bacterial and microorganisms leaching to natural water reservoirs[2] . These conventional approaches suffer from limitations in terms of product quality, cost efficiency, environmental pollution, and long-term sustainability. Consequently, there is an urgent need for environmentally friendly and cost-effective methods to manage chicken feather waste. Chemical treatment or steam processing techniques are utilized in the conversion of chicken feathers into value-added feather fertilizer, owing to their dominant composition of approximately 92% of keratin[3].

Keratin is a natural source of essential amino acids, peptides, and micronutrients which can be used in animal feed supplements, and as biofertilizer[4, 5]. Keratin is fibrous protein with high degree of cross-linking of the poly-peptide using disulfide bonds[6]. As a result, keratin is usually insoluble and undegradable by most proteolytic enzymes[6]. Several studies employed strong alkaline and strong acid in order to hydrolyze chicken feather into small amino acid soluble proteins for animal food[7].

In agriculture, the chicken feathers hydrolysate (CH) has interests as alternative biostimulant and/or biofertilizer due to its ability to boost plant growth, yield, and quality[8, 9]. The performance of CH in promoting crop growth is depended on the method of application, dosage, frequency and plant species/cultivar type, for example. In this research, preliminary strong acid hydrolysis using 6M H_2SO_4 with various weight ratio were investigated. The produced CH were then analyzed using amino acid analyzer. The highest amino acid content CH was diluted and given to cherry tomatoes, *Solanum lycopersicum var. cerasiforme*, for 4 weeks in order to study its effect on plant growth stimulation.

2. Materials and Methods

2.1 Preparation of chicken hydrolysate (CH)

Chicken feathers, provided by the Department of Animal Science, Faculty of Agriculture, Kasetsart University, Thailand, were cleaned with distilled water and air dried before use. Subsequently, they were cut into small pieces with approximately 4-5 cm in length. Hydrolysis procedures were conducted using 6M H_2SO_4 with

varying ratios of chicken feathers (g) to acid (ml), specifically at ratios of 1:5 and 1:1.5. The reaction was carried out for 5 hours at temperature of 150 ^{o}C. Subsequently, the resultant chicken feathers hydrolysate (CH) underwent centrifugation at 6000 rpm for 5 minutes to eliminate precipitates, followed by neutralization with 6M KOH. In preparation for amino acid analyzer studies, the CH was subjected to freeze-drying to remove excess solvent.

2.2 Amino acid analysis

The amino acid composition of chicken feather hydrolysate (CH) was assessed at the Food Quality Assurance Service Center (FQA) within the Institute of Food Research and Product Development at Kasetsart University. High-Performance Liquid Chromatography (HPLC) using an Agilent 1260 instrument equipped with a fluorescence detector and an AdvanceBio AAA column (ID 4.6 mm x 100mm) was employed for the analysis. The CH underwent pre-column derivatization with o-phthalaldehyde in the presence of 3-mercaptopropionic acid, resulting in the formation of fluorescent derivatives. Fluorescence measurements were conducted with an excitation wavelength of 340 nm and emission wavelengths of 455 nm. Detailed information on the HPLC conditions can be found in the work of Dai *et al.* (2014)[9].

2.3 Effect of amino acid fertilizer on cherry tomato growth

Cherry tomatoes, (*Solanum lycopersicum var. cerasiforme)* were utilized in their purchased state from a nursery. Planting procedures ensured a consistent surrounding environment for all specimens. The study employed five conditions, as outlined in Table 1. All conditions were investigated using two test plants.

Table 1. Details of conditions

Condition	Detail
Control	No fertilizer
NPK	2g of NPK/ week
NPK10CH	2g of NPK/ week with 2ml of 10ppm CH spray on the leaves
NPK5CH	2g of NPK/ week with 2ml of 5ppm CH spray on the leaves
10CH	2ml of 10ppm CH spray on the leaves/1 week
5CH	2ml of 5ppm CH spray on the leaves/1 week

The height of tomato plants was measured weekly to assess the impact of chicken feather hydrolysate (CH) on tomato growth.

3. Results & Discussion

3.1 Amino acid in chicken hydrolysate

Table 2. Amino acid profiles in chicken feathers, CH1:1.5 and CH1:5 (mg/100g)

Amino acid	Feathers	CH1:1.5	CH1:5
Aspartic acid (ASP)	5,564	216.35	245.74
Glutamic acid (GLU)	9,504	100.29	102.56
Serine (SER)	12,334	258.23	426.20
Histidine (HIS)	317.99	Not detected	Not detected
Glycine (GLY)	6,704	337.82	397.58
Threonine (THR)	4,340	61.03	88.08
Arginine (ARG)	6,181	59.38	64.38
Alanine (ALA)	3748	98.67	109.15
Tyrosine (TYR)	2,075	22.30	41.66
Cystine (CYS)	10,595	395.08	504.74
Valine (VAL)	6,077	22.63	28.37
Methionine (MET)	330.53	18.48	28.08
Phenylalanine (PHE)	4,222	101.11	123.63
Isoleucine (ISO)	4,271	32.50	37.77
Leucine (LEU)	7,053	108.69	127.95
Lysine (LYS)	1,107	36.92	68.70
Tryptophan (TRY)	217.11	-	-
Proline (PRO)	11,053	148.56	160.26

Figure 1. Chicken feathers (A) and chicken hydrolysate (B)

amino acid concentrations were significantly reduced due to the strong acid hydrolysis conditions employed[10]. In comparing CH1:1.5 and CH1:5, the amino acid concentration in CH1:5 was found to be higher than that in CH1:1.5. This difference may be attributed to a higher volume of acid available to react with the feathers, facilitating hydrolysis reaction. In contrast, in CH1:1.5, some feather residues were left in the reaction flask, potentially influencing the lower amino acid concentration. It is noted that the amino acid content obtained through acid hydrolysis was found to be lower compared to alternative techniques, such as the hydrothermal method[11].

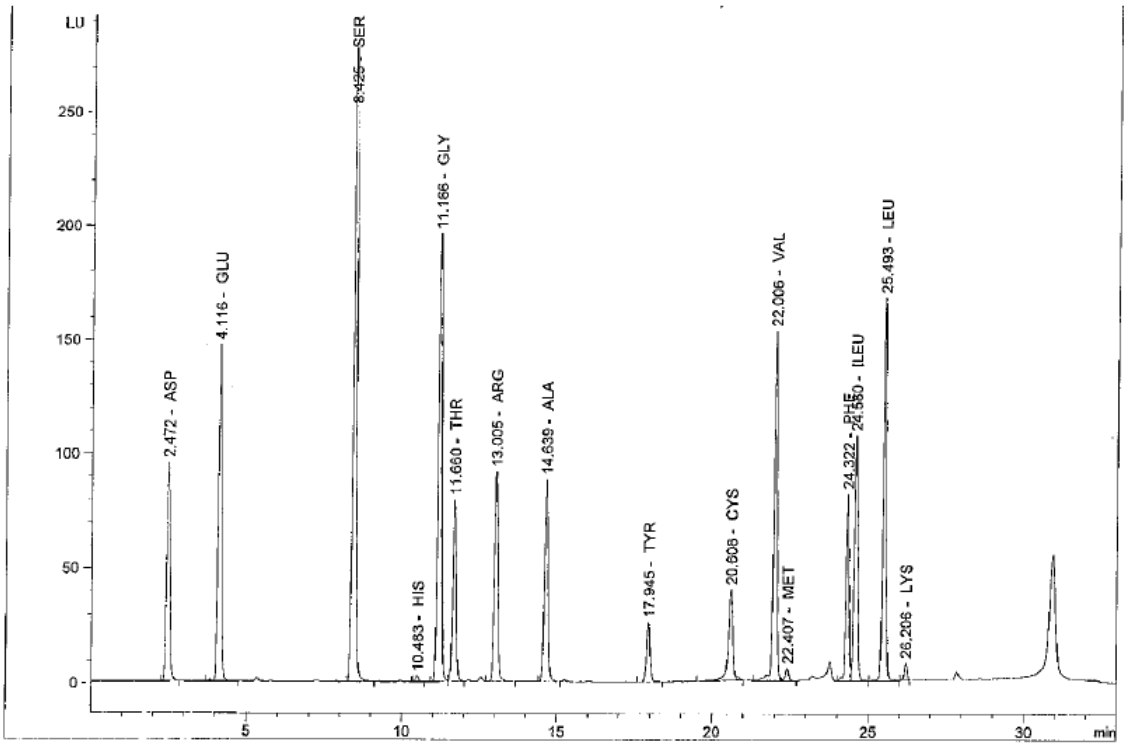

Figure 2. Representative HPLC chromatogram exhibiting separation and identification amino acid in chicken feathers

It can be seen that all feathers were hydrolysed both in 1:5 and 1:1.5 ratios (Fig. 1) , however, the 1:5 ratio giving higher hydrolysate conversion than that of the 1:1.5 ratio.

The amino acid compositions of CH1:5 and CH1:1.5 were contrasted with those of chicken feathers, as illustrated in Table 2. Notably, SER, GLU, CYS, VAL, PRO, and ARG emerged as prominent amino acids in chicken feathers hydrolysate. These specific amino acids play a crucial role in stimulating chlorophyll synthesis and enhancing mechanisms of resistance against viruses and bacteria, among other functions. The others acts as anti-stress agents, regulate biotic and anti-biotics in plants[2]. Following hydrolysis, all

3.2 Effect of amino acid fertilizer on cherry tomato growth

The test cherry tomatoes were plated and nursed for one week without fertilization. After week 1, plant height was measured every week. The weekly plant height increment is exhibited in Fig 3.

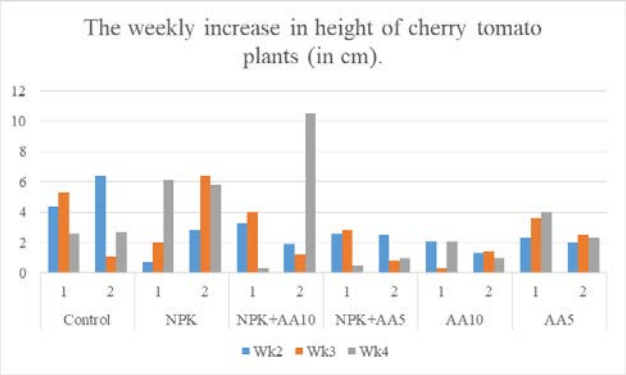

Figure 3. The weekly height increment of cherry tomatoes

It can be seen that height increment of control in week 2 and week 3 was higher than other conditions potentially influenced by various factors like the root system and overall plant strength. However, the growth was decreased after week 3. NPK fertilizer has been known for their essential elements for plant growth which exhibited significant growth between week 2-4. Test plants with different CH concentration showed insignificant increment in height. This might due to low concentration of CH or other application of CH should be employed. Interestingly, when CH was used in conjunction with NPK fertilizer, test plants with NPK and 10 ppm CH demonstrated a noticeable height increment after week 3. While the study remains inconclusive, CH appears to exhibit a stimulating effect on plant growth. Further study must be carried out with high CH concentration.

4. Conclusion

Chicken feather hydrolysate, comprising amino acids, can be synthesized through treatment with 6M H_2SO_4 with feathers (g) -to-acid (ml) ratio of 1:5 at 150 ^oC for 5 hours. Although the amino acid content exhibits a significant reduction compared to that found in the feathers, essential nutrients persist in the hydrolysate. Experimental trials with cherry tomato plants demonstrated that, by the 3rd to 4th week, NPK fertilizer effectively increased plant height. The combination of 10 ppm hydrolysate and NPK resulted in a noticeable height increment in test plants after the third week. Further investigations are necessary to validate the impact of amino acid on plant growth. This could involve exploring higher concentrations of amino acid fertilizer, among other variables, to ascertain the optimal conditions for plant growth development.

Acknowledgements

Authors would like to acknowledge Faculty of Science, Kasetsart University for funding.

References

1. Li, Z.; Reimer, C.; Picard, M.; Mohanty, A. K.; Misra, M. *Front. Mater.* **2020**, *7*, DOI. 10.3389/fmats.2020.00003.
2. Bhari, R.; Kaur, M.; Sarup Singh, R. *Curr. Microbiol.* **2021**, *78* (6), 2212-2230.
3. Kurien, R. A.; Biju, A.; Raj, K. A.; Chacko, A.; Joseph, B.; Koshy, C. P. *Mater. Today: Proc.* **2022**, *58*, 862-866.
4. Jagadeesan, Y.; Meenakshisundaram, S.; Raja, K.; Balaiah, A. *Process Saf. Environ. Prot.* **2023**, *170*, 573-583.
5. Zul, S. M.; Iwamoto, K.; Mohd Rahim, M. A.; Abdullah, N.; Mohamad, S. E.; Shimizu, K.; Hara, H. *IOP Conf. Ser: Earth Environl. Sci.* **2020**, *479* (1), 012033.
6. Onifade, A. A.; Al-Sane, N. A.; Al-Musallam, A. A.; Al-Zarban, S. *Bioresour. Technol.* **1998**, *66* (1), 1-11.
7. Cheong, C. W.; Lee, Y. S.; Ahmad, S. A.; Ooi, P. T.; Phang, L. Y. *Waste Manage.* **2018**, *79*, 658-666.
8. Ertani, A.; Cavani, L.; Pizzeghello, D.; Brandellero, E.; Altissimo, A.; Ciavatta, C.; Nardi, S. *J. Plant Nutr. Soil Sci.* **2009**, *172* (2), 237-244.
9. Cristiano, G.; De Lucia, B. *Front. Plant Sci.* **2021**, *12*, DOI. 10.3389/fpls.2021.640608.
10. Weiss, M.; Manneberg, M.; Juranville, J. F.; Lahm, H. W.; Fountoulakis, M. *J Chromatogr A* **1998**, *795* (2), 263-275.
11. Nurdiawati, A.; Nakhshiniev, B.; Zaini, I. N.; Saidov, N.; Takahashi, F.; Yoshikawa, K. *Environ. Prog. Sustain. Energy.* **2018**, *37* (1), 375-382.

Ion exchange capacity and ionic conductivity of polyvinyl alcohol and nanocellulose based anion exchange membranes

Piyamad Kaewkoon[1], Supatta Midpanon[1] and Pinsuda Viravathana[1,2]*

[1]*Department of Chemistry, Faculty of Science, Kasetsart University, Bangkok, 10900, Thailand*
[2]*Center of Excellence-Oil Palm, Kasetsart University, Bangkok, 10900, Thailand*

**E-mail: fscipdv@ku.ac.th*

Abstract:

This research is focused on a facile way of preparing anion exchange membranes (AEMs) based on polyvinyl alcohol (PVA) and nanocellulose (NC) from oil palm empty fruit bunch (OPEFB) for anion exchange membrane fuel cells (AEMFCs). Both PVA and NC were modified by the addition of poly (propylene glycol) diglycidyl ether (PPGDGE) (at 30%PPGDGE). Then, the modified PVA and NC were mixed and casted to form a modified PVA/NC composited membrane. By increasing NC in the composited membrane, degree of swelling and water uptake properties were investigated. Besides, for the transport properties, ion exchange capacity (IEC) was determined using Mohr's titration method and ionic conductivity (IC) was measured using two-probe alternative current electrochemical impedance spectroscopy.

1. Introduction

Rapid increase in global population, global urbanization and global economy are main reasons resulting in the shortage of fossil fuels energy and various environmental pollutions including greenhouse effects. Therefore, several countries need new energy supply technologies with eco-friendly, renewability and sustainability. Fuel cells are among the most dependable, effective, and clean energy production technologies that directly convert chemical energy to electric energy. Types of fuel cell are classified based on types of electrolytes such as polymer exchange membrane fuel, alkaline fuel cells, molten carbonate fuel cells and solid oxide fuel cells. With the exception of the electrolyte and the operating temperature the fuel cells described above have similar general designs.

Low temperature fuel cells are fuel cells with a polymer exchange membrane are divided into two types; proton exchange membrane fuel cells (PEMFCs) and anion exchange membrane fuel cells (AEMFCs). Technically, AEMFCs are similar to PEMFCs, with the main difference being the solid AEM instead of an acidic PEM in PEMFCs. [2,13]

While polymer exchange membrane is the main component in fuel cell technologies, the cost of DAFCs is the limitation for global commercialization because of the high-cost production of cell component such as Nafion membrane and platinum-based catalysts, for commercialization in most markers.[17]

In the development of AEMs, it was based on various aromatic polymers such as polysulfide, poly (arylene ether ketone), poly (phenylene oxide), and poly (ether ketone) with functionalization in several routes. However, aliphatic polymer as polyvinyl alcohol (PVA) are a serious candidate for AEM due to its low-cost, eco-friendly, renewability and sustainability.[3] PVA composites are widely used in different applications including PVA nanocellulose composite membranes due to its properties excellent film formation with high swelling degree and the addition of reinforcing agents.

Nanocellulose (NC) is used as bio-based materials for the manufacture of the key components parts of fuel cell, namely the ion exchange membranes and the catalyst electrodes, to minimize the impact of production and to make environmental friendly products. Besides, NC has many advantages including low density, high crystallinity, low cost, high specific strength, renewability, biocompatibility and biodegradability.[8,14]

In this research the focus is on a facile way of composting AEM based on PVA and NC from oil palm empty fruit bunch, for anion exchange membrane fuel cells (AEMFCs). Both PVA and NC were modified by poly (propylene glycol) diglycidyl ether (PPGDGE). The PVA and NC with poly(propylene glycol) diglycidyl ether (PPGDGE), respectively, and then mixed together to form a composite solution, cross-linked and cast to form quaternized polyvinyl alcohol nanocellulose (QPVA/QNC) membrane. By varying weight %NC, the properties of QPVA/QNC membranes were investigated by looking at degree of swelling and water uptake properties. For the transport properties, ion exchange capacity (IEC) was determined using Mohr's titration method and ionic conductivity (IC) was measured using two-probe alternative current electrochemical impedance spectroscopy.

2. Materials and Methods

2.1 Materials

Polyvinyl alcohol (hydrolysis degree >98.0%, Acros Organics), poly(propylene glycol) diglycidyl ether (PPGDGE, Sigma Aldrich), potassium hydroxide (KOH, >85.0%, Carlo Erba Reagents), silver nitrate ($AgNO_3$, ≥99.9%, Fisher Scientific), sodium chlorite ($NaClO_2$, 80.0%, DC Fine Chemicals), sodium chloride (NaCl, >99.5%, Carlo Erba Reagents), sodium hydroxide (NaOH, >97.0%, Carlo Erba Reagents), sodium sulfate (Na_2SO_4,≥99.0%, Carlo Erba Reagents), potassium chromate (K_2CrO_4,>98.5%, Daejung, Korea), and ethanol (C_2H_6O, 99.8%, Carlo Erba Reagents) were used as received from suppliers. Alpha cellulose was synthesized from OPEFB.

2.2 Synthesis of compound

2.2.1 Preparation of NC and modified NC

NC was prepared from alpha cellulose synthesized from Oil Palm Mesocarp Fiber (OPMF) with acid hydrolysis. Under vigorous stirring, 0.25 g of alpha cellulose was dissolved in 3.5 ml of 32.5% w/v H_2SO_4 at 45 ˚C for 2 h. To stop the hydrolysis, the reaction mixture was put into a container with ten times of water inorder to stop the reaction. The sulfate groups on the cellulose were eliminated from the suspension by centrifuging, dialyzing in deionized water, and centrifuging for 15 minutes. After removing the centrifugate, the NC precipitate was dried at 60˚C in a hot air oven for 24 h.

To synthesize the modified NC, 10% w/w NC was dissolved in 4.0 %w/v KOH solution and then added 30%w/w poly (propylene glycol) diglycidyl ether with respect to NC content. The modified NC mixture was vigorously stirred at room temperature for 24 h. The modified NC was filtrated, rinsed by deionized water until neutral, and dried at 50 ˚C for 24 h.

2.2.2 Preparation of modified PVA-NC membranes

Modified PVA-NC membranes were prepared via blending two mixtures; a modified PVA mixture and a modified NC mixture, before casting. The steps of preparation are shown in Figure 1.

First, 5 %w/v PVA solution was prepared by dissolving PVA in deionized water at room temperature for 2 h, 60˚ C for 1 h, and 95˚ C for 2 h, and then cooled down to room temperature. To modify PVA, the 5%w/v PVA solution was vigorously stirred before adding 4 %w/w KOH with respect to PVA content. Then, 30%w/w poly (propylene glycol) diglycidyl ether with respect to PVA content was added into the mixture. The modified PVA mixture was continuously stirred at 80 ˚C for 24 h.

Second, the modified NC was prepared as described in section 2.2.1.

Third, the modified PVA was mixed with the various contents of the modified NC (0.0, 5.0, 10.0, 15.0 and 20.0 %w/w of modified NC with respect to modified PVA), as presented in Table 1. The mixtures were blended together under vigorous stirring for 60 min before casting. The casted membrane was dried at room temperature for 2-4 days, and then peeled off. These membranes were dried in a hot air oven at 80 ˚C for 15 h for thermal crosslinking.

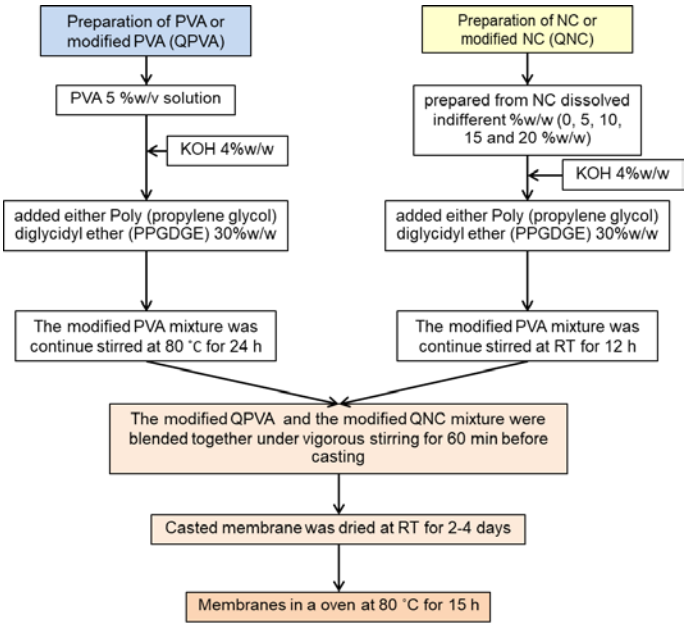

Figure 1. Preparation of modified PVA and NC to membrane.

2.3 Spectroscopic measurement

2.3.1 Water uptake and swelling degree

Water uptake (WU) was accessed in order to observe the hydrophilicity of the prepared membranes. The dried membrane sample was immersed in deionized water at room temperature for 24 h. Subsequently, the membrane was taken out, wiped surface water carefully with a filter paper, and weighed. Weight of the membrane before and after soaking in deionized water for 24 h was defined in term of W_{dry} and W_{wet},[15] respectively. The WU was evaluated using the following relation,

Table 1. Composition of the QPVA/QNC nanocomposite membranes by varying NC content

Membrane	QPVA solution (ml)	GE w.r.t. PVA (%w/w)	QNC		
			NC w.r.t. PVA (%w/w)	4%w/v KOH (ml)	GE w.r.t. NC (%w/w)
PVA	15.0	30.0	no NC	n/a	n/a
$PVA_{NC\ 5\%}$	15.0	30.0	5.0	0.006	30.0
$PVA_{NC\ 10\%}$	15.0	30.0	10.0	0.012	30.0
$PVA_{NC\ 15\%}$	15.0	30.0	15.0	0.018	30.0
$PVA_{NC\ 20\%}$	15.0	30.0	20.0	0.024	30.0

$$WU(\%) = \frac{W_{wet} - W_{dry}}{W_{dry}} \times 100$$

To study the dimensional stability[15], the swelling degree (SD) was investigated by measuring the membrane volume before and after immersing in deionized water for 24 hours, denoted as V_{dry} and V_{wet}, respectively. SD was calculated from the following equation,

$$SD(\%) = \frac{V_{wet} - V_{dry}}{V_{dry}} \times 100$$

2.3.2 Ion exchange capacity and ionic conductivity

IEC of the prepared membrane was determined using the Mohr's titration.[15] The membrane was weighed and converted to Cl^- form by immersing in 1.0 M NaCl for 48 hours. After that, the membrane was washed with deionized water in order to remove the excess Cl^-. Then, the membrane was immersed in 0.5 M Na_2SO_4 for 8 hours for Cl^- removal. The released Cl^- was titrated with 0.1 M $AgNO_3$ using a 0.25 M K_2CrO_4 solution as an indicator. From the amount of $AgNO_3$ used in the titration, the quantity of exchangeable Cl^- presented in the membrane was determined. The IEC value was determined by the following equation,[1]

$$IEC\ (mmol/g) = \frac{Volume\ of\ AgNO_3 \times Molarity\ of\ AgNO_3}{Weight\ of\ the\ dry\ membrane}$$

The ionic conductivity of the polymer electrolyte membrane under fully alkaline operation was evaluated by using two-probe alternative current electrochemical impedance spectroscopy (Autolab PGSTAT 302N, Metrohm Autolab B.V.) in the frequency range of 1.0 Hz to 1.0 MHz at the amplitude current of 10 mV. The conductivity cell containing two stainless-steel electrodes, each with 20 mm diameter, was applied to this measurement. Before the measurements, the membranes were equilibrated in 0.1 %w/v of NaCl for 24 h, sandwiched between two stainless-steel electrodes, fixed to a plastic block and placed in a sealed chamber containing NaCl for 100 % relative humidity. The ionic conductivity (σ, mS/cm) was defined from Nyquist plot, through the following equation and the point where the real axis and the high-frequency intercept cross.,[1]

$$\sigma = \frac{L}{R \times A}$$

where, L is the thickness of the membrane, R is the resistance of in membrane in Ω and A is the contact area of the membrane.

Figure 2. The prepared QPVA/QNC membranes

3. Results & Discussion

The pictures of the prepared QPVA/QNC membranes are shown in Fig.2. The membrane color becomes brownish as increasing the percentage of NC.

3.1 Water uptake and swelling degree

Water has an effect on the membrane properties, especially the mechanical strength and the ionic conductivity. With insufficient water, the membranes could become brittle. With the appropriate amount of WU, IC can be improved. However, excessive water uptake could cause the loss of mechanical characteristics. Excessive

water degrades the membrane's functionality and causes a dilution of the concentration of the ionic groups (OH^-).[11] The transportation and diffusion of hydroxide ions in the AEM are presented by the well-known concepts, Grotthuss mechanism.[16] The values of WU and SD could be related to the hydrophilicity and crystallinity, affecting the mechanical properties of the membranes[11]. From Figure 3, WU and SD of QPVA/QNC membranes altered when increasing the NC content while the PVA and GE contents were fixed. SD of QPVA/QNC membranes were decreased with the increase of %NC showing that NC addition enhanced the ether group of QNC, therefore decreasing the value of SD. For WU, the results showed that the QPVA/QNC membrane tended to have higher WU compared to the QPVA (without QNC) membrane. This could be from the increase of %GE in the membrane, which enhanced the stability and the membrane's crystallinity[6].

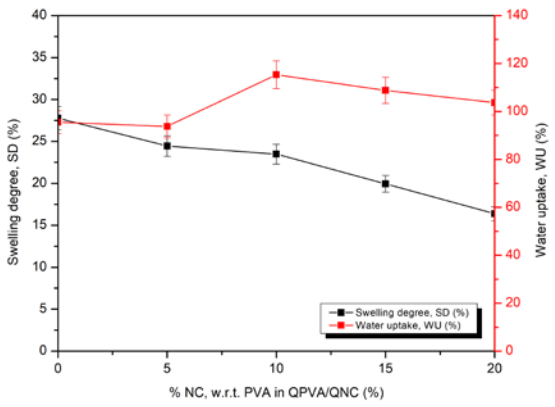

Figure 3. Swelling degree and Water uptake of QPVA/ QNC membranes as a function of %NC

3.2 Ion exchange capacity and ionic conductivity

IC is an important parameter for the fuel-cell performance, which depends on the ion concentration, water absorption capacity and charge carrier density as an ether group integrated into the membrane [9,10]. As shown in Figure 4 by repeating the measurements three times per sample and varying %NC in the QPVA/QNC membranes, the obtained IEC and IC increased with the increase of QNC percentage to 10% and then dropped at 15%. This behavior could be explained by two phenomena. One explanation is that the polymer crosslinker (GE) behaved as a plasticizer, which made the polymer chains in the membrane become more flexible and enhanced the ion transport[6,12]. Another explanation could be that the crosslinker increased the quantity of ethylene oxide groups, which were charge carriers in the membrane. As a result, both IC and the number of salt interactions raised. However, ionic transport was reduced when the polymer crosslinker content was further increased. This limitation of ionic transport was from the restriction in the polymer chain mobility in the polymer matrix with high crosslink densities[12].

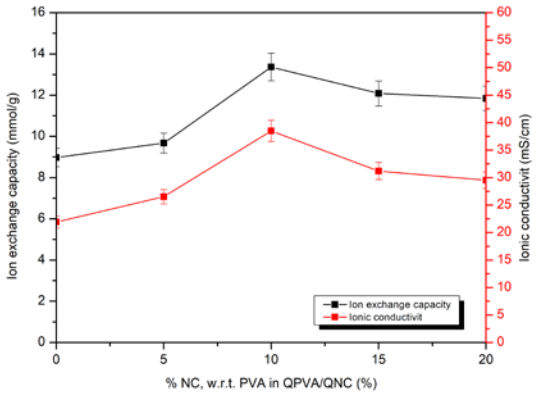

Figure 4. IEC and IC of QPVA/QNC membranes as a function of %NC

4. Conclusion

A facile route for anion exchange membrane preparation was developed. AEMs were prepared from PVA and NC from OPEFB via chemical and thermal cross-linking. The preparation of QPVA/QNC membranes was quite easily to proceed. With this approach, KOH was responsible for ion conduction inside the polymer matrix and avoided the previous problems linked to the use of liquid electrolyte. These properties make these membranes very attractive candidates for alkaline fuel cell applications. The QPVA/QNC ($PVA_{NC\ 10\%}$) membrane showed the highest IC of 38.49±0.02 mS/cm at room temperature with the highest IEC of 13.36±0.04 mmol/g. The prepared nanocomposite membranes will be fabricated in the DAHPFC and evaluated their performance in the further studies.

Acknowledgements

This work was supported by Department of Chemistry, Kasetsart University.

References

1. Dai, Z., Deng ,J. Fabrication and Evaluation of Bio-Based Nanocomposite TFC Hollow Fiber Membranes for Enhanced CO2 Capture, *ACS Appl. Mater. Interfaces.* **2019**, *11*, 10874−10882.
2. Hren, M., Božič, M., Fakin, D., Kleinschek, K. S., & Gorgieva, S. Alkaline membrane fuel cells: anion exchange membranes and fuels. *Sustainable Energy & Fuels.* **2021**, *5*(3), 604-637.

3. Tafete, G. A., Abera, M. K., & Thothadri, G. Review on nanocellulose-based materials for supercapacitors applications. *J. Energy Storage* **2022**, 48.
4. Jahan, Z., Niazi, M. B. K., & Gregersen, Ø. W. Mechanical, thermal and swelling properties of cellulose nanocrystals/PVA nanocomposites membranes. *J. Ind. Eng. Chem.* **2018**, *57*, 113-124.
5. Samsudin, A. M., Bodner, M., & Hacker, V. A Brief Review of Poly(Vinyl Alcohol)-Based Anion Exchange Membranes for Alkaline Fuel Cells. *Polymers (Basel)* **2022**, *14*(17).
6. Yunphuttha, C., Midpanon, S., Marr, D.W.M., Viravathana, P. Polyvinyl alcohol/ nanocellulose nanocomposites from oil palm empty fruit bunch as anion exchange membranes for direct alcohol-hydrogen peroxide fuel cells. *Cellulose* **2024**.
7. Vijayakumar, V., & Khastgir, D. Polymeric composite membranes for anion exchange membrane fuel cells. In Synthetic Polymeric Membranes for Advanced Water Treatment, Gas Separation, and Energy Sustainability. 2020; pp. 365-381.
8. Vilela, C., Silvestre, A. J. D., Figueiredo, F. M. L., & Freire, C. S. R. Nanocellulose-based materials as components of polymer electrolyte fuel cells. *J. Mater. Chem. A* **2019,** *7*(35), 20045-20074.
9. Msomi, P., Nonjola, P. Quaternized poly (2,6 dimethyl–1,4 phenylene oxide)/polysulfone blended anion exchange membrane for alkaline fuel cells application. *Materials Today: Proceedings*, *2018*, 10496–10504.
10. Muhamad Samsudin, A., Hacker, V. Preparation and Characterization of PVA/PDDA/Nano-Zirconia Composite Anion Exchange Membranes for Fuel Cells. *Polymers (Basel)* **2019**, *11*, 1399.
11. Merle, G., Wessling, M., Nijmeijer, K. Anion exchange membranes for alkaline fuel cells: A review. *J. Membrane Sci.* **2011**, *377*, 1–35.
12. Fu, J., Qiao, j. Alkali doped poly(vinyl alcohol) (PVA) for anion-exchange membrane fuel cells Ionic conductivity, chemical stability and FT-IR characterizations. *ECS Transaction* **2010**, *25*, 15-23.
13. Yu, E. H., Krewer, U., & Scott, K. Principles and Materials Aspects of Direct Alkaline Alcohol Fuel Cells. *Energies* **2010**, *3*(8), 1499-1528.
14. Mandal, A., Chakrabarty, D. Studies on the mechanical, thermal, morphological and barrier properties of nanocomposites based on poly(vinyl alcohol) and nanocellulose from sugarcane bagasse. *J. Ind. Eng. Chem.* **2014**, *20*, 462-473.
15. Hari Gopi, K., Dhavale, VM., Bhat, SD. Development of polyvinyl alcohol/chitosan blend anion exchange membrane with mono and di quaternizing agents for application in alkaline polymer electrolyte fuel cells. *Mater. Sci. Energy Technol.* **2019**, *2*, 194–202.
16. Zhou, T., Wang, M., He, X., Qiao, J. Poly (vinyl alcohol)/Poly(diallyldimethylammonium chloride) anion-exchange membrane modified with multiwalled carbon nanotubes for alkaline fuel cells. *J. Mater.* **2019**, *5*, 286–295.
17. Zakaria, Z., Kamarudin, SK. A review of quaternized polyvinyl alcohol as an alternative polymeric membrane in DMFCs and DEFCs. *Int J Energy Res.* **2020**, 1–17.

Synthesis of biphasic calcium phosphate porous ceramic from fish scales

Laksana Wangmooklang*, Parawee Pumwongpitak, Saengdoen Doungdaw, Siriporn Tong-On, and Siriporn Larpkiattaworn

Expert Centre of Innovative Materials, Thailand Institute of Scientific and Technological Research, Khlong Luang, Pathum Thani, 12120, Thailand

**E-mail: laksana@tistr.or.th*

Abstract:

Recently, the circular economy model concept has gained increasing attention for sustainable ecosystems. This model aims to reduce waste and promote reusing and recycling materials to make a new product. Fish scales are seafood industrial waste that has been used as natural raw material for synthesized hydroxyapatite (HA) in many applications. In this research, fish scales were utilized as natural raw material for fabricating biphasic ceramics of hydroxyapatite (HA) and tricalcium phosphate (TCP). Biphasic calcium phosphate powders were synthesized from fish scales via acidic treatment and calcination at 1000 and 1200°C. X-ray diffraction (XRD) and X-ray fluorescence (XRF) techniques were used to investigate the crystallinity and chemical composition of synthesized materials respectively. Then, the biphasic calcium phosphate was fabricated to porous granule and sintered at 1300°C. The morphology of biphasic calcium phosphate granule was observed by scanning electron microscope (SEM). The characterization of the pore size and their porosity was also investigated by the mercury porosimeter technique. The biphasic calcium phosphate fabricated from fish scales presents a porous structure with approximately 60 % porosity.

1. Introduction

Fish production is one of the seafood industries with the enhancement of production volume. The typical fish processing involves beheading, gutting and filleting etc. These methods generate enormous amount of waste. The waste from the filleting process was approximately 57% of total fish weight. It was composed of muscle-trimmings (15–20%), skin and fins (1–3%), bones (9–15%), heads (9–12%), viscera (12–18%) and scales (5%).[1] In recent years, there have been the development of novel products from the filleting waste to increase the value of waste and to gain the sustainable ecosystems.

Fish scales are the fish processing waste interested to be the value added due to their useful compositions. The three main components of fish scales are organic compounds (collagen, fat, lecithin, sclerotin, vitamins, etc.), inorganic compounds (calcium-deficient hydroxyapatite, calcium phosphate, etc.) and trace elements (magnesium, iron, zinc, strontium, etc.).[2-4] Many researches have extensively reported the methods used for the extraction of these compounds. The HA extraction from fish scales has been utilized in many applications such as fillers for polymers, absorbents for wastewater treatment, and bone substitute materials for medical applications[4-8].

As the compositions of fish scales are similar to the synthetic bone substitute or bone fillers, containing HA ($Ca_{10}(PO_4)_6(OH)_2$), and TCP ($Ca_3(PO_4)_2$), the fish scales have been developed and applied for the orthopedic and dental surgery. The advantages of HA and TCP were the excellent biocompatibility, bioactivity and osteoconduction. Furthermore, another type of calcium phosphate is called biphasic calcium phosphate, which is the mixture of HA and TCP, used in the synthetic bone fillers. The biphasic calcium phosphate can control the balance of resorption/solubilization better than pure HA and TCP. Therefore, it is largely used in clinical situations.[9-10]

This research aims to fabricate of porous ceramic containing biphasic calcium phosphate which was synthesized from the fish scales via alkaline treatment and calcination process. The necessary properties of synthesized materials, namely, crystallinity, chemical compositions and porous ceramic were observed. Furthermore, the morphology, pore size and porosity of granules were investigated.

2. Materials and methods

2.1 Materials

Sea bass fish scales were used as raw material. Hydrochloric acid (HCl; Merck, Germany) was used to deproteinize fish scales. Hydroxyapatite (HA; Sigma-Aldrich, Germany) was added to adjust the appropriated biphasic calcium phosphate ratio of porous granules.

2.2 Synthesis of biphasic calcium phosphate from fish scales

Fish scales were cleaned with water to remove any grease and dirt. After that, the cleaned fish scales were soaked in 1N HCl solution for 6 h at

room temperature for deproteinization. Then the deproteinated fish scales were washed with distilled water and dried in the oven at 60°C. The cleaned fish scales and deproteinated fish scales were calcined at 1000 and 1200°C for 2 h. The calcined fish scales were ground to obtain the powder.

2.3 Preparation of porous ceramic

Biphasic calcium phosphate from fish scales which was deproteinized with HCl and calcined at 1200°C was selected to fabricate porous granules. Biphasic calcium phosphate and HA were blended by a ball mill for 2 h. The blended mixture was sprayed with the distilled water at 3-6% to control its moisture. To form the porous granules, the moist mixture was sieved with an opening size of 28-35 mesh. Then the granules were dried at 105°C and subsequently sintered at 1300°C for 1 h.

2.4 Characterizations

The crystalline phases of HA and TCP from the fish scales and the porous granules were investigated by a XRD (Smartlab, Rigaku) at the scanning range of 2θ = 5-80 deg with the scan step of 0.02 deg. The phase contents were calculated by the relative intensities ratio (RIR) of the three main diffraction peaks of HA and TCP. The main XRD peak positions of HA were at 31.77, 32.90, and 32.197 deg, whereas the main XRD peak positions of TCP were at 31.027, 34.37, and 27.80 deg.[11]

$$\mathrm{RIR_{TCP}} = \left(\frac{I_{TCP}}{I_{TCP} + I_{HA}}\right) \times 100$$

The chemical compositions of biphasic calcium phosphate from the fish scales and the porous granules were also determined using a XRF (S8 Tiger, Bruker). SEM (Prisma E, Thermo Scientific) was used to observe the morphology of porous granule. A mercury intrusion porosimeter (MIP; Auto pore V, Micromeritics, USA) was used to characterize the pore size and the porosity of porous granules with Hg at a pressure level of 0.50-60,000 psi.

3. Results & discussion

3.1 Biphasic calcium phosphate from fish scales

The crystalline phases of synthesized materials from the fish scales are shown in Figure 1. All of the synthesized materials presented biphasic calcium phosphate phases of HA and TCP. The XRD peaks were more intense with an increase of the calcination temperature. The peak intensities of fish scales after cleaned and calcined at 1000°C (cleaned-1000°C) and 1200°C (cleaned-1200°C) were lower than the peaks of HCl-deproteinized and calcined fish scales at the same calcination temperature (HCl-1000°C and HCl-1200°C).

The main components of synthesized materials were calcium (Ca), phosphorus (P) and oxygen (O). Magnesium (Mg), strontium (Sr), iron (Fe), silicon (Si), sulfur (S), chlorine (Cl) and zinc (Zn) were also appeared as the trace elements.

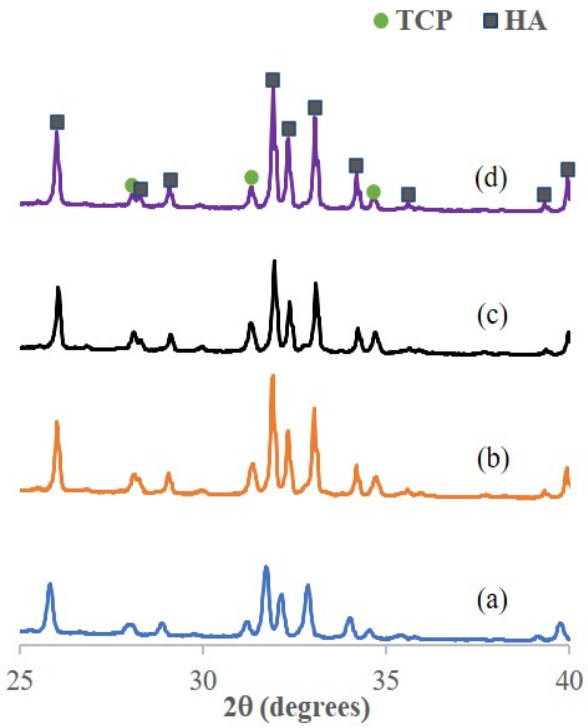

Figure 1. XRD patterns of synthesized materials: (a) cleaned-1000°C, (b) HCl-1000°C, (C) cleaned-1200°C and (d) HCl-1200°C.

The major compositions of synthesized materials are presented in Table 1. The Ca contents of cleaned fish scales after calcined at 1000°C and 1200°C and deproteinized fish scales after calcined at 1000°C and 1200°C were 42.1, 48.4, 44.1 and 50.3%, respectively. The Ca content of cleaned fish scales was less than that of deproteinized fish scales, which was opposite to the O and P contents. In addition, the amount of Ca increased with elevating calcination temperature, while the amount of P and O decreased with decreasing calcination temperature.

Table 1. The major compositions of synthesized materials from XRF

Sample	Component (%)		
	Ca	P	O
cleaned-1000°C	42.1	16.3	39.2
cleaned-1200°C	48.4	13	36.9
HCl- 1000°C	44.1	15.7	38.9
HCl-1200°C	50.3	12.1	36.3

3.2 Porous Ceramic

The XRD patterns of porous ceramic in the granule shape and biphasic calcium phosphate from fish scales (HCl-1200°C) are presented in Figure 2. Considering the peak intensities of TCP crystalline, the porous granules were higher than the biphasic calcium phosphate from fish scales. This result related to the calculated crystalline phase contents, as showed in Table 2. The percentage ratio of HA:TCP of biphasic calcium phosphate from the fish scales and porous granules were 75:25 and 70:30, respectively. The HA:TCP ratio of granules was similar to the commercial bone filler which content of HA:TCP ratio is 70:30.

From the XRF results, it presented that the porous granules contained the amount of Ca, P and O were 42.3, 16.8 and 39.4%, respectively. The Ca content of granules was less than that of biphasic calcium phosphate from fish scales (HCl-1200°C), which was opposite to the O and P contents.

Figure 3 presents the microstructures of porous granules. The rough surface with small pore sizes could be observed at both low and high magnitudes. Considering the high magnitude, macropores (>100 µm) and micropores (< 10 µm) were observed.

The pore size and porosity of porous granule are displayed in Figure 4 and Table 3. The result revealed distribution with pore size in the range of 0.02-5 µm, 5-60 µm and 60–300 µm. The average pore diameter and median pore diameter of porous granules were 11.47 µm and 47.64 µm, respectively. The porosity of granules was 58.91% (approximate 60 %). These results can be related to their microstructures

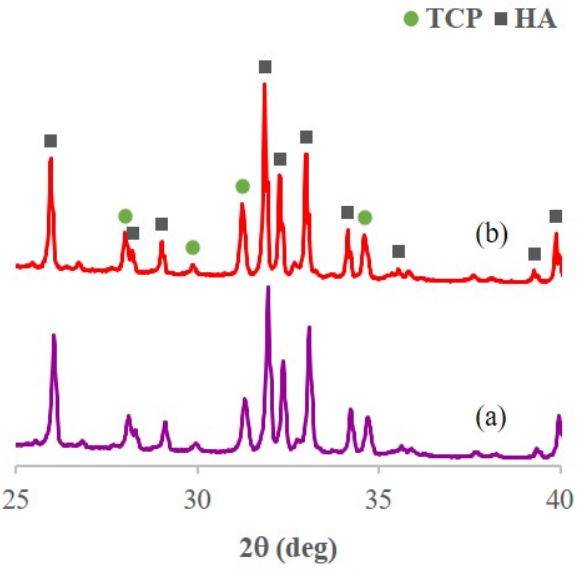

Figure 2. XRD patterns of (a) biphasic calcium phosphate from fish scales and (b) porous granules.

Table 2. The crystalline phase contents of biphasic calcium phosphate from the fish scales and the porous granules.

Sample	Phase ratio (%)	
	HA	TCP
HCl-1200°C	75	25
Porous granules	70	30
Commercial bone filler	70	30

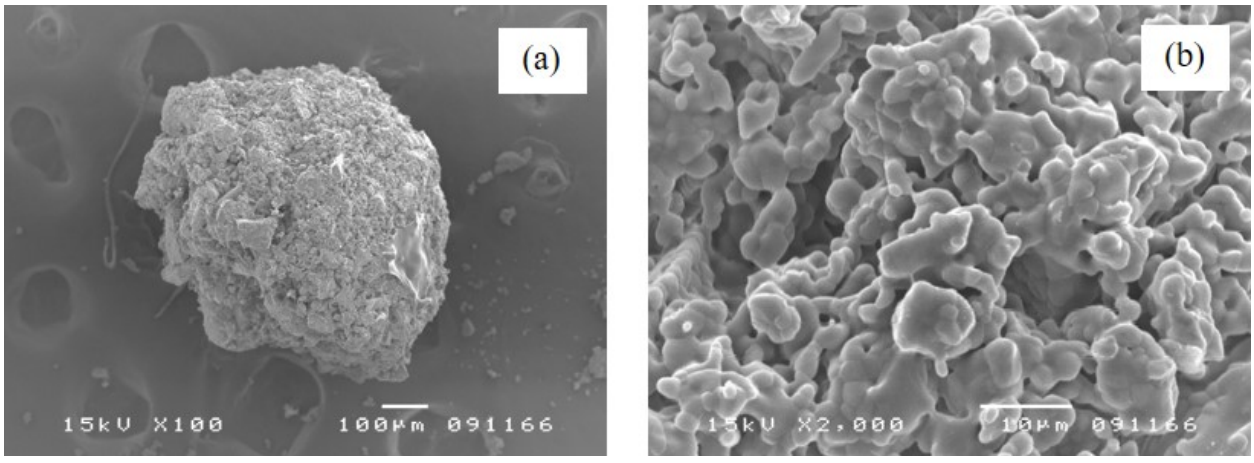

Figure 3. The morphologies of porous granules: (a) x100 and (b) x2000.

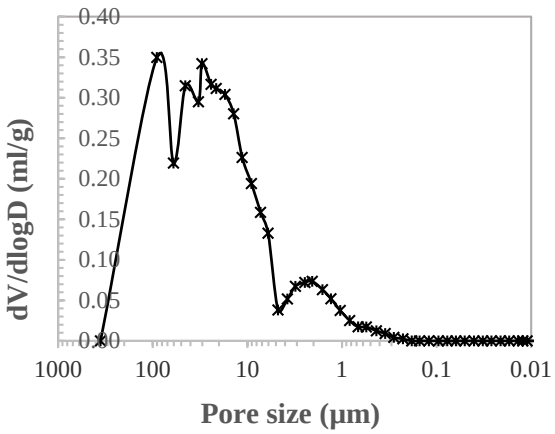

Figure 4. Pore size distribution of porous granules from MIP.

Table 3. The pore size and porosity of porous granules.

Porosity (%)	Mean Pore size (µm)	Median pore size (µm)
58.91	11.47	47.64

4. Conclusion

The biphasic calcium phosphate of HA and TCP which was synthesized from the fish scales with the acidic treatment and calcination was used to fabricate porous granules. Their percentage ratio of HA:TCP was 70:30. The biphasic granule appeared the micropores and macropore structure with approximately 60 % porosity. The components and porous structure of biphasic calcium phosphate porous ceramic were similar to the commercial bone filler. Additionally, both the HA and TCP, contained in the biphasic calcium phosphate porous ceramic, were the bioactive materials with the excellent biocompatibility. Hence, there has been a possibility to use the biphasic calcium phosphate porous ceramic from fish scales as bone filler or bone substitute for medical applications.

Acknowledgements

The authors would like to acknowledge National Research Council of Thailand (NRCT) and Thailand Institute of Scientific and Technological Research (TISTR) for financial support.

References

1. Martinez-Alvarez, O.; Chamorro, S.; Brenes, A. Protein Hydrolysates from Animal Processing By-products as A Source of Bioactive Molecules with Interest in Animal Feeding: A Review. *Food Res. Int.* **2015**, *73*, 204-212.
2. Chinh, N.T.; Manh, V.Q.; Trung, V. Q.; Lam, T. D.; Huyn, M.D; Tung, N.Q.; Trinh, N.D; Hoang, T. Characterization of Collagen Derived from Tropical Freshwater Carp Fish Scale Wastes and Its Amino Acid. *Nat. Prod. Common.* **2019**, *14* (7), 1934578–1986628.
3. Hola, M.; Kalvoda, J.; Skoda, R.; Kanicky, V. Possibilities of LA-ICP-MS Technique for The Spatial Elemental Analysis of The Recent Fish Scales: Line Scan vs. Depth Profiling. *Appl. Surf. Sci.* **2011**, *257*, 1932–1940.
4. Qin, D.; Bi, S.; You, X.; Wang, M.; Cong, X.; Yuan. C.; Yu, M.; Cheng, X.; Chen, X.G. Development and Application of Fish Scale Wastes as Versatile Natural Biomaterials. *Chem. Eng. J.* **2022**, *428*, 131102.
5. Majhool, A.A.; Zainol, I.; Jaafar, C.N.A.; Mudhafar, M.; Alsailawi H. A., Asaad. A.; Mezaal, F.W. Preparation of Fish Scales Hydroxyapatite (FsHAp) for Potential Use as Fillers in Polymer. *J. Chem. Eng.* **2019**, 97–104.
6. Hamzah, S.; Yatim,N.I.; Alias, M.; Ali, A.; Rasit, N.; Abuhabib., A. Extraction of Hydroxyapatite from Fish Scales and Its Integration with Rice Husk for Ammonia Removal in Aquaculture Wastewater. *Indones J. chem.* **2019**, *19*(4), 1019-1030.
7. Pon-On, W.; Suntornsaratoon, P.; Charoenphandhu, N.; Thongbunchoo, J.; Krishnamra, N.; Tang, I.M. Hydroxyapatite from Fish Scale for Potential Use as Bone Scaffold or Regenerative Material. *Mater. Sci. Eng.* **2016**, C *62*, 183–189.
8. Mondal, S.; Mondal, A., Mandal, N.; Mondal, B.; Mukhopadhyay, S.S.; Dey, A.; Singh, S. Physico-chemical characterization and biological response of Labeo rohita-derived hydroxyapatite scaffold. *Bioprocess. Biosyst. Eng.* **2014**, *37*(7):1233-1240.
9. Jeong, J.; Kim, J.H.; Shim, J.H.; Hwang, N.S.; Heo, C.Y. Bioactive Calcium Phosphate Materials and Applications in Bone Regeneration. *Biomater. Res.* **2019**, *23*:4, 2-11
10. Lobo, S.E.; Arinzeh, T.L. Biphasic Calcium Phosphate Ceramics for Bone Regeneration and Tissue Engineering Applications. *Mater.* **2010**, *3*, 815–826.
11. Toibah, A.R.; Misran, F.; Mustafa, Z.; Shaaban, A.; Shamsuri, S.R. Calcium Phosphate from Waste Animal Bones: Phase Identification Analysis. *J. Adv. Manuf. Technol.* **2018**, *12*, 99-110.

Preparation and characterization of oil palm fibers from oil palm trunks for industrial applications

Parawee Pumwongpitak*, Sureeporn Kumneadklang, Busarin Noikaew,
Laksana Wangmooklang, Saengdoen Daungdaw and Siriporn Larpkiattaworn

Expert Centre of Innovative Materials, Thailand Institute of Scientific and Technological Research, Khlong Luang, Pathum Thani, 12120, Thailand

**E-mail: parawee@tistr.or.th*

Abstract:

Thailand is the third-place country in the world that exports palm oil, even though it was only 3.8% of the global total of palm oil producers in 2021. The country's palm oil production is mainly in the southern area. However, the central, northeastern, and northern regions also find harvested oil palm areas. Usually, the commercial lifespan of the oil palm tree is 25 years after decreasing its fruit production. Then, the new palms are planted for the next cycle of cultivation, leaving a large amount of oil palm trunks as biomass waste on the plantation. However, these oil palm fibers have value and can be utilized as raw materials in the paper and construction industries. Therefore, this work focuses on the chemical, physical, and mechanical properties of the oil palm trunk fibers treated under various conditions. The fibers were treated with 0% to 5% sodium hydroxide (NaOH) solutions for different reaction times. Then, the TAPPI standard was used to investigate the chemical components of treated fibers, including cellulose, hemicellulose, lignin, and ash contents. The crystallinity of the fibers was measured using X-ray diffraction (XRD). Fibers' length, morphology, and microstructure were analyzed using an optical microscope and a Scanning Electron Microscope (SEM). Furthermore, the mechanical properties of the treated fibers, such as tensile strength, tear resistance, and burst strength, were determined.

1. Introduction

More than 6,000,000 rai of oil palm trees are planted in the plantation in Thailand in 2023[1]. For commercial harvest, the average economic life of an oil palm plantation is 25-30 years. After that, the trees are burned on farms or landfilled, causing environmental pollution. Therefore, the waste of oil palm trees, especially oil palm trunks (OPT), a large proportion of total oil palm waste compared to fronds and leaves, are abandoned as biomass in the plantation to be used for soil enrichment purposes[2]. In general, at the oil palm plantation 2,500 rai, there will be 48,000 trunks[3]. Therefore, there will be approximately 115,200,000 trunks as biomass in the future. This leads to the utilization of OPT to produce value-added products as alternative raw materials such as pulp, paper, and chipboard[4].

The OPT is composed of fibers and parenchyma cells, the main parts of the tissue of oil palm wood. The fiber cells are usually stiffer and more robust than the parenchyma cells, which is related to the physical and mechanical properties of oil palm wood[5]. There are various methods, such as mechanical, chemical, and chemo-mechanical, have been used to extract the OPT fibers. A chemical treatment using alkali solutions such as sodium hydroxide (NaOH), potassium hydroxide (KOH), and calcium hydroxide ($Ca(OH)_2$) provides cellulose crystallization. It decreases the hemicellulose and lignin content of the fiber. This results in rigid fibers and increases the mechanical properties of fibers[6-7]. Latip et al. studied oil palm empty fruit bunch fiber for composite products using 15% (w/v) NaOH and KOH as alkali pretreatment solutions at 130°C for 40 minutes. The results showed that both NaOH and KOH solutions improved the surface and cellulose structure of the fibers[8]. Noikaew et al. found that the 5% (w/v) NaOH treatment at 150°C for 1 hour can be performed for extracting the oil palm fibers[9]. The OPT fibers are composed of 42.67-82.99% α-cellulose, 6.16-34.00% hemicelluloses, and 5.06-22.90% total lignin[9-10].

This study aimed to produce oil palm fiber at a commercial scale using the chemical treatment method. Therefore, it was necessary to carefully consider the alkali solution concentration and the reaction time as they played a significant role in the production and waste treatment processes, which can affect the operation costs. The OPT from an approximately 25-year-old oil palm tree from a plantation was used as raw materials to extract the oil palm fibers. The 0% to 5% NaOH solutions at different reaction times were performed. Then, the physical and chemical properties of obtained fibers were investigated to determine the potential of OPT fiber for use on the commercial scale, especially in pulp and construction materials industries.

2. Materials and Methods

2.1 Materials

The oil palm trunk (OPT) was used as raw material to produce oil palm fibers. The sodium hydroxide (98% NaOH) was used in the alkali treatment process. In the chemical composition extraction, sodium chlorite ($NaClO_2$), sulfuric acid (H_2SO_4) 98%, acetic acid 98%, Toluene 99%, ethanol 95%, and acetone were used.

2.2 Alkaline treatment

In the pre-treatment process, the fresh OPT was chopped into small size and then dried to reduce the moisture. Then, the chopped OPT was treated in alkaline treatment at a temperature of 150°C using 0% NaOH solution for 1 h, 1% NaOH solution for 4 h, 2% NaOH solution for 4 h, 3% NaOH solution for 2 h, 4% NaOH solution for 2 h, 5% NaOH solution for 2 h, and 5% NaOH solution for 1 h. Then, the treated samples were neutralized by washing with water. Lastly, the treated fibers were dried in an oven at 80°C to remove any remaining moisture.

2.3 Characterization

The fiber length and width were analyzed using an optical microscope measurement by pulp morphology analyzer (Techpap, morfi neo) with a software analyzer.

The chemical composition of treated samples was performed using the standard methods of the Technical Association of the Pulp and Paper Industry (TAPPI). To determine the α-Cellulose, lignin, and ash content, the TAPPI T203, T222, and T211 were used as the standard methods[9,10], respectively.

The phase and crystalline of untreated and treated OPT were examined by X-ray diffraction (XRD) using Smartlab, Rigaku, with the range 10°-60° 2θ.

The crystallinity index was calculated using the following equation[11].

$$\text{Crystallinity index} = \frac{I_{200} - I_{am}}{I_{200}} \times 100$$

Where I_{200} = maximum Intensity of the diffraction peak and I_{am} = intensity of the amorphous peak.

The microstructure of the obtained fiber was investigated using a Scanning Electron Microscope (SEM, JEOL (JSM-5410LV)).

The mechanical properties of the selected fiber were determined according to the ASTM standards.

3. Results & Discussion

3.1 Physical property

The morphologies of treated OPT samples for the concentrations of 0%, 1%, 2%, 3%, 4%, and 5% NaOH at various treatment times are illustrated in Figure 1. It was shown that the isolated fibers could not be obtained when the OPT samples were treated with 0% NaOH for 1 h, 1% NaOH for 4 h, and 2% NaOH for 4 h. However, after treating the samples with NaOH at concentrations of 3%, 4%, and 5% for 2 h and 5% for 1 h, it was found that small and thin fibers could be successfully produced. The morphology of the isolated fibers observed from the optical microscope illustrates that the fibers contain flake-like and nearly cylindrical geometry.

The fiber length of isolated fibers from treated samples is shown in Table 1. It can be seen that the length of treated fibers after being treated with NaOH for 2 hours was 879-918 microns. The average width of the treated fibers using 2%, 3%, and 5% NaOH for 2 h were 31.9, 29.7, and 29.2 microns, respectively. Thus, the isolated fibers tended to be thinner when the concentration of NaOH increased. A study by Mamtaz et al. found that increasing chemical concentration in the treatment of natural fiber-epoxy composite leads to a reduction in fiber diameter[12].

In addition, the fibers' length and width also are affected by the treatment time. When the sample was treated with 5% NaOH for 1 h, the fiber length and average width were 1095 and 30.3 microns, respectively. It suggests that the longer the treatment time, the more effective the reaction is in isolating the OPT fibers.

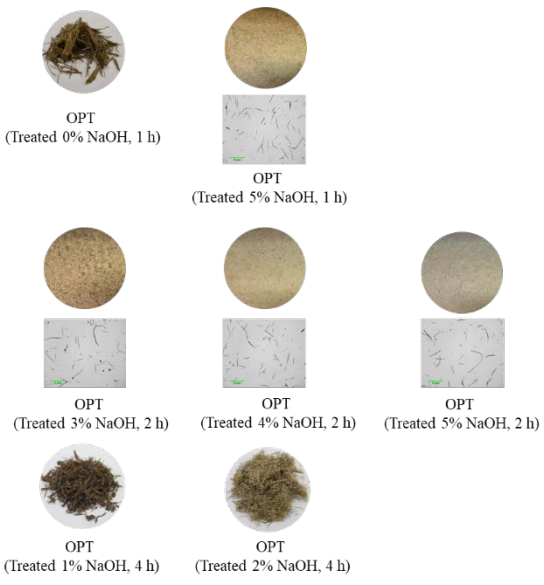

Figure 1. The morphology of treated samples.

Table 1. Length and width of fibers

	Mean length-weighted length (micron)	Average width (micron)
OPT Treated 3% NaOH 2h	881	31.9
OPT Treated 4% NaOH 2h	918	29.7
OPT Treated 5% NaOH 2h	879	29.2
OPT Treated 5% NaOH 1h	1095	30.3

The moisture of the raw OPT was 12.38%. After the treatment processes, the moisture of the treated samples was approximately 4-5%, as shown in Table 2.

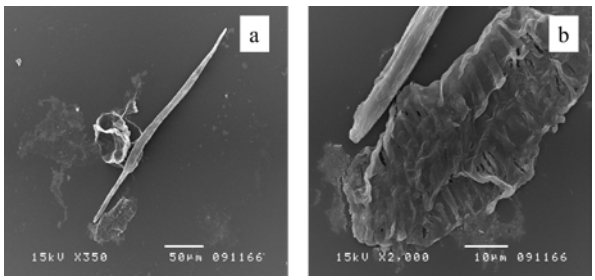

Figure 2. The microstructure of treated OPT sample with 5% NaOH for 2 h.

The microstructure of OPT treated with 5% NaOH for 2 h was illustrated in Figure 2. The samples revealed the rod-like and flake structures (Figure 2 (a)). It can be seen that the porous structure was observed due to the removal of lignin from biomass, leaving the cellulose and hemicellulose exposed on the surface[13] (Figure 2 (b)).

3.2 Chemical compositions

The treated OPT samples were prepared with different NaOH concentrations and reaction times. Table 2 shows the composition of the untreated and treated OPT under different conditions. The study showed that the cellulose content increased from 34.80% in untreated oil palm trunks to a range between 74.26-86.14% in the treated samples with 5% NaOH. The highest cellulose content was 86.14%, which was observed when the oil palm trunk was treated with 5% NaOH for 2 h. Moreover, the samples' hemicellulose and lignin content decreased after the NaOH treatment. The hemicellulose in the untreated sample was 40.93%, then the treated samples varied from 9.08 to 3.94% due to the higher concentration of NaOH and longer treatment time. The lignin content of OPT after treatment also decreased with increasing NaOH concentration and treatment time. The sample treated with 5% NaOH for 2 h period exhibited the lowest lignin content at 1.96%. The ash content of the treated samples was 1.59- 4.95%. Based on the results, the treatment processes with 3-5% NaOH have successfully delignified the OPT, as proven by reducing lignin and increasing cellulose contents.

3.3 XRD

The XRD patterns of OPT, which are untreated and treated at different concentrations of NaOH, are shown in Figure 3. The prominent characteristic peaks of cellulose (JCPDS No. 00-056-1718) at around 16° and 22° of 2θ were observed in the OPT samples, which corresponded to the crystallographic plane (200) and (110), respectively[8]. The intensity of the (200) plane increased with increasing the concentration of NaOH from 1-5%. This indicates that the higher concentration of NaOH can improve the crystallinity of cellulose content. The calculated crystallinity index of the samples is shown in Table 3. The highest crystallinity index was found in the sample prepared using 5% NaOH for 2 h. Then, with the lower concentration of NaOH and treatment time, the crystallinity index was reduced, suggesting that the treated samples exhibit a more ordered crystalline structure than the untreated sample[10]. However, by treating with 5% NaOH for 1 h, the crystallinity index of the fiber was only 34.43%. This may be due to incomplete removal of lignin, hemicellulose, and other non-crystalline components.

The high-value index of fibers can be beneficial for increasing the mechanical properties of the fibers, such as tensile strength modulus, toughness, and melting point[11].

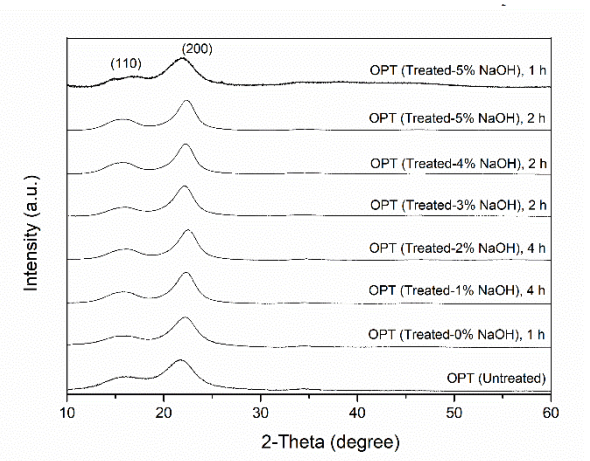

Figure 3. XRD patterns of untreated and treated samples at various conditions.

Table 2. Composition of treated samples

Component	Oil palm trunk Composition, % (Dry weight basis)				
	Untreated	Treated 3% NaOH, 2 h	Treated 4% NaOH, 2 h	Treated 5% NaOH, 2 h	Treated 5% NaOH, 1 h
% Cellulose	34.80	74.26	80.58	86.14	82.99
% Hemicellulose	40.93	9.08	6.03	3.94	6.16
% Lignin	22.90	4.76	2.91	1.96	1.98
% Ash	-	4.95	2.97	2.00	1.59
% Moisture	12.38	4.55	4.66	4.75	4.81

3.4 Mechanical properties

The OPT treated with 5% NaOH for 2 h. was selected for mechanical testing. The test results are shown in Table 4. The tensile and tear indexes of the samples were 5.37 mNm^2/g and 2.78 Nm/g, respectively. However, the burst index could not be determined due to the lower number of fibers and hardwood in the sample. The results from the physical properties of the sample using a pulp morphology analyzer indicated that the treated sample with 5% NaOH for 2 h was composed of 75.8% softwood and 24.2% hardwood.

Table 3. The crystallinity index of pulps at different treatment conditions.

Sample	Crystallinity Index (%)
OPT Untreated	51.92
OPT Treated 0% NaOH, 1 h	60.14
OPT Treated 1% NaOH, 4 h	79.84
OPT Treated 2% NaOH, 4 h	79.88
OPT Treated 3% NaOH, 2 h	79.99
OPT Treated 4% NaOH, 2 h	81.58
OPT Treated 5% NaOH, 2 h	82.55
OPT Treated 5% NaOH, 1 h	34.43

Table 4. Mechanical properties of treated sample with 5% NaOH for 2 h

	Mechanical properties
Tensile index (Nm/g)	5.37 ± 0.61
Tear index (mNm^2/g)	2.78 ± 0.16
Burst index ($kPa.m^2/g$)	-

4. Conclusion

The oil palm trunk can be treated with NaOH solution to produce isolated oil palm fibers. The obtained fibers are composed of cellulose, hemicellulose, lignin, and ash. The treatment process with 5% NaOH for 2 h, provides fine fibers and a high crystalline index compared to other conditions. Thus, the obtained fibers can be utilized as eco-friendly alternative materials for composite production. It can be used instead of traditional wood products for construction products such as particleboard, medium-density fiberboard, and plywood. Moreover, it can be applied for automotive industries as biocomposites with polymer.

Acknowledgments

We are thankful for the financial support provided by the Thailand National Research Council (NRCT). The Thailand Institute of Scientific and Technological Research (TISTR) is greatly appreciated.

References

1. Office of Agricultural Economics. 2023. https://www.oae.go.th. (accessed January 2024)
2. Pulingam, T.; Lakshmanan, M.; Chuah, J.-A.; Surendran, A.; Zainab-L, I.; Foroozandeh, P.; Uke, A.; Kosugi, A.; Sudesh, K., Oil palm trunk waste: Environmental impacts and management strategies. *Ind. Crop. Prod.* **2022**, *189*, 115827.
3. Siswati, L.; Insusanty, E.; Susi, N. In Oil palm trunk replanting as brown sugar raw materials, IOP Conference Series: Earth and Environmental Science, IOP Publishing: 2022; p 012054.
4. Awang, R.; Wahab, N. A.; Ibrahim, Z.; Aziz, A. A., Medium density fibreboard (MDF) from oil palm fibre: a review. *Malaysian J. Anal. Sci.* **2023**, *27* (3), 626-640.
5. Srivaro, S.; Matan, N.; Lam, F., Property gradients in oil palm trunk (Elaeis guineensis). *J. Wood Sci.* **2018**, *64* (6), 709-719.

6. N H Sari1 and Y A Padang1., The characterization tensile and thermal properties of hibiscus tiliaceus cellulose fibers. IOP Conf. Series: Materials Science and Engineering 2019, 539
7. Pan Z.; Meng J.; Wang Y., Effect of alkalis on deacetylation of konjac glucomannan in mechanochemical treatment. Particuology **2001**, *9*, 265–269.
8. N.A. Latip.; A.H. Sofian.; M.F. Ali.; S.N. Ismail.; D.M.N.D. Idris., Structural and morphological studies on alkaline pre-treatment of oil palm empty fruit bunch (OPEFB) fiber for composite production. Materials Today: Proceedings, 2018, 17
9. Noikaew B.; Pumwongpitak P.; Wangmooklang K.; Daungdaw S.; and Larpkiattaworn S., Chemical components and fiber properties from different parts of oil palm fiber. The 2022 Pure and Applied Chemistry International Conference (PACCON 2022) 2022, 678-682
10. Kumneadklang, S.; O-Thong, S.; Larpkiattaworn, S., Characterization of cellulose fiber isolated from oil palm frond biomass. Materials Today: Proceedings 2019, 17, 1995-2001.
11. Gond, R. K.; Gupta, M. K., A novel approach for isolation of nanofibers from sugarcane bagasse and its characterization for packaging applications. *Polym. Composite* **2020**, *41* (12), 5216-5226.
12. Mamtaz, H.; Fouladi, M.H.; Al-Atabi M.; Namasivayam S. N., Acoustic Absorption of Natural Fiber Composites, Journal of Engineering 2016.
13. Hermansyah, H.; Putri, D. N.; Prasetyanto, A.; Chairuddin, Z. B.; Perdani, M. S.; Sahlan, M.; Yohda, M., Delignification of oil palm empty fruit bunch using peracetic acid and alkaline peroxide combined with the ultrasound. International Journal of Technology **2019,** *10* (8).
14. Šoštarić, T.; Petrović, M.; Stojanović, J.; Marković, M.; Avdalović, J.; Hosseini-Bandegharaei, A.; Lopičić, Z., Structural changes of waste biomass induced by alkaline treatment: the effect on crystallinity and thermal properties. Biomass Conversion and Biorefinery **2022**, *12* (7), 2377-2387.

Effect of grog and cement on physical and mechanical properties for unfired brick production

Soravich Mulinta

Department of Production Innovation and Ceramics Design, Faculty of Industrial Technology, Lampang Rajabhat University, Lampang, 52100, Thailand.

E-mail:soravich@lpru.ac.th

Abstract:

The objective of this study was to crush fired brick waste, known as grog, which is used in mixtures with clayey bodies and cement for unfired brick production. The study evaluated the effects of the grog addition up to 50-90 wt.% and 10 - 50 wt.% cement on the compression forming on the physical and mechanical properties of clayey bricks after being fired at 900 – 1000 °C. Unfired clay brick consisting of 70% grog and 30% cement powder had a shrinkage volume of 6.5% and bulk density of 1.9 g/cm^2. The unfired clay brick is resistant to bending at 92 kg/cm^2 and has compressive strength at 18 MPa. These physical and mechanical properties of unfired clay bricks achieved Thai industrial standards' requirements (TIS 77-2545). The results indicate that adding grog did not impair the compression formation of the unfired clayey body. Reserves above 15wt% decreased the mechanical strength of the mixing process and the dry body. That is associated with increased porosity during the drying stage due to the grog behavior.

1. Introduction

In data collection of Small and Micro Enterprise Communities in Clay Brick Making Group San Bun Reung Village. There is an excellent production of red brick, mainly perforated brick, estimated at 200,000 units/month. Bricks are generally fired at around 900 °C in a draft kiln-type furnace, using firewood as fuel and a firing time of 2 days. Considering only the firing stage, the community generates 23.5 tons of fired brick waste every month. Quantity damage of clay brick from drying and firing sections, respectively [1], as shown in Figure 1.

Figure 1. The amount of damage caused in the processing of clay bricks.

In previous works, crushed-fired brick waste, known as grog, was used in mixtures with clayey bodies to make typical red ceramics for bricks. The effect of the grog addition up to 20 wt.% on the extrusion stage and the properties and microstructure of bricks fired at 700 °C were evaluated. The results indicate that the grog addition did not impair the extrusion of the unfired clayey body additions above 5 wt.% decreased the mechanical strength of the dry body and the fired ceramic pieces. This is associated with increased porosity during the firing stage due to the grog behavior [2, 3]. Crushed-fired brick waste, known as grog, screened at two different particle sizes, 840 (20 mesh) and 420 µm (80 mesh), was used in mixtures with clayey bodies to make typical red ceramics for bricks. The effect of the grog addition up to 20 wt.% on the properties and microstructure of bricks fired at 700°C was evaluated. The results indicated that the particle size and the amount of grog addition changed the fired properties of the clayey body. Additions above five wt.% of grog with a coarser particle size decreased the mechanical strength of the dry body and the fired ceramic pieces. On the other hand, grog with a finer particle size may be used up to 10% wt. Without deteriorating the properties and corresponding microstructure of the clayey body [4].

The present study aimed to determine the effects of grog and cement, with the objective of investigating the result corresponding to unfired clay brick production. In practice, traditional industries that produce waste bricks at 950°C could provide the grog; in this work, the physical and mechanical properties of the unfired clay bricks were correlated with the grog addition.

2. Materials and Methods

2.1 Characterization analysis of raw material

The particle size of the materials used was analyzed by laser diffraction (Mastersizer S, Malvern, USA). X-ray fluorescence (XRF, Megix Pro MUA/USEP T84005, Philips, USA) analyzed the chemical composition of the material used.

The mineralogical composition was identified by X-ray diffraction (XRF, D500, Siemens, Germany).

2.2 Raw materials for unfired clay brick.

The raw material used in the study is from local sources. They are pong san tong red clay in Lampang province. The binder used was Cement. The red clay passes through a 100-mesh sieve, generating a powder material. The grog materials used were waste bricks produced at 950 °C in the Small and Micro-Community Enterprise of Clay Brick Making Group in Son Bun Reung Village. The brick waste was an edge runner and passed through a 40-mesh sieve (particles smaller than 0.42 mm.), generating a powder material, which is here known as the grog. The cement selected for this study was Portland cement. The compositions produced, including that of the red clay, grog, and cement, are shown in Table 1. All compositions were wet, mixed, drained in a stainless mold size 5×5×5 inch, and cured for 7 days.

Table 1. The composition of the clay mixture in this study

Formula	Material	
	grog	Cement
1	90	10
2	85	15
3	80	20
4	75	25
5	70	30
6	65	35

2.3 Properties measurement of unfired clay brick.

Tests were carried out to obtain volume shrinkage. Linear shrinkage was assessed as the difference between the dry and fired specimens' diameter divided by the dry specimen's diameter.

The bulk density of a specimen has been defined as the relationship between the mass (weight) divided by the volume.

The compressive strength for unfired clay brick was determined by the universal testing machine, represented by the modulus of rupture equation:

$$MOR = \frac{3LD}{2bd^2} \quad (1)$$

where L is the breaking load
D is the distance between support
b is the breadth of the rectangular rod
and d is the depth of the rod [3]

The universal testing machine tested the fractural strength test is the equation that gives the compressive strength:

$$S_c = \frac{P}{A} \quad (2)$$

where P is the load of fracture
A is the cross-sectional area of the test specimen [4]

3. Results & Discussion

3.1 Characterization of Grog

The grog is controlled by grinding and passing through a 40 mesh, with an average particle size of 29.7 μm. The particle size of cement is crushing, and the particle size is average at 11.13 μm., as shown in Fig 2.

The chemical composition of grog analyzed by X-ray fluorescence is shown in Table 2. The major components included silicon oxide (SiO_2), aluminum oxide(Al_2O_3), and ferric oxide (Fe_2O_3). The amount of SiO_2 is much lower than Al_2O_3 and Fe_2O_3, respectively. CaO, K_2O, BaO MnO, ZrO_2, TiO_2, P_2O_5, MgO, Y_2O_3 and Rb_2O in small quantities. The grog using clay brick produces a large amount of Ferric oxide, up to 8.096wt%.

The significant components of cement included 66.320wt% Silicon oxide, 20.640% Calcium oxide, and 5.914% ferric oxide, which will mostly affect the color of the fired product (Fe_2O_3, MnO, TiO_2). Others (MgO, K_2O, Na_2O) will act as fluxes and may have a strong effect during sintering [7].

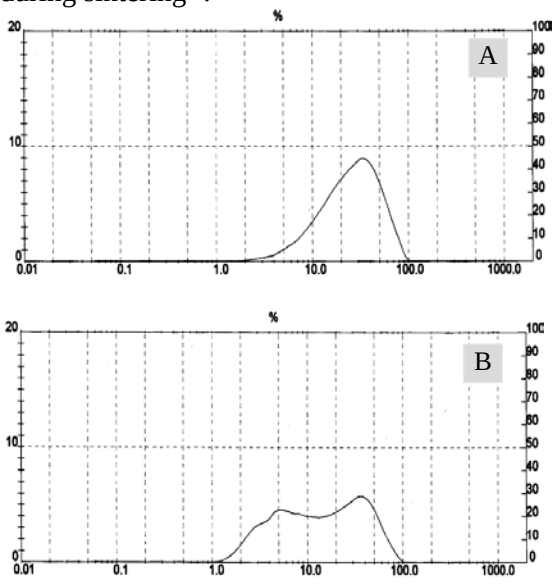

Figure 2. The particle size of raw materials is A; grog and B; cement.

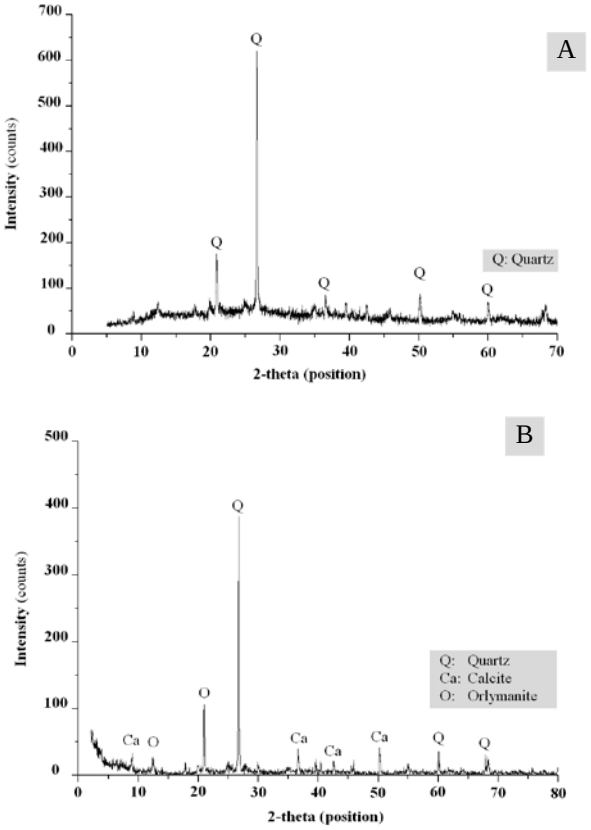

Figure 3. Mineralogical composition of raw materials, A; grog and B; cement.

The mineralogical composition of the grog was analyzed by X-ray diffraction. The results of the mineralogical analysis of Fig.2(A) show the XRD pattern of grog. The predominant peaks are associated with Quartz (Q). Fig. 3(B) indicates the XRD pattern of the grog. The predominant peaks are associated with Quartz (Q), while secondary peaks identify the crystalline mineral phases of Calcite (Ca) and Orlymanite (O).

Table 2. Chemical Composition of raw materials.

Element	Chemical composition (wt %)	
	Grog	Cement
SiO_2	68.886	66.320
Al_2O_3	14.351	0.127
Fe_2O_3	8.096	5.914
K_2O	3.518	2.131
CaO	0.894	20.640
MgO	0.922	0.008
MnO	< 0.01	0.523
Na_2O	< 0.01	0.375
P_2O_5	1.101	0.826
TiO_2	1.232	0.071
Loss on Ignition (LOI)	1.20	6.39
Total	**100.20**	**99.76**

3.2 Properties of Unfired Clay Bricks.

The grog and grog in formula 1 – 6; the addition of cement 10 – 20% lower volume shrinkage at 4.25 – 4.2%, and the addition of cement 20 % increase the volume shrinkage at 5.2, 6.5 and 6.9%, respectively, are shown in Fig 4.

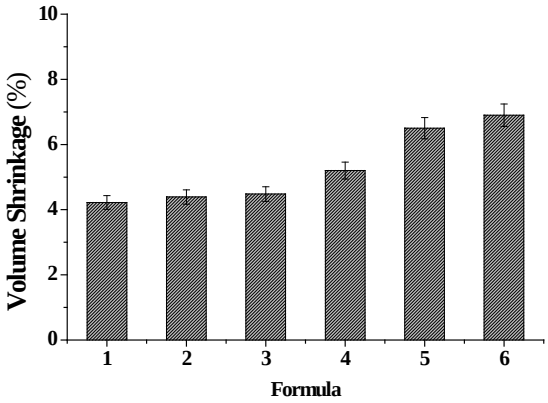

Figure 4. Volume Shrinkage of unfired clay brick.

Bulk density of the unfired clay brick**.** The formula 1-6 addition cement 10 – 15% had a lower bulk density of 2.25 – 2.15 g/cm^2, and addition cement 15 – 35% decreased the bulk density by 1.45 – 1.85g/cm^2**,** the bulk density increased, giving evidence for densification. C-S-H phases increased with the cement and curing time, and C-S-H density is almost 2.0 g/cm3. These formed phases may fill the void spaces and blind the materials in the stabilized clay specimens, leading to a decrease in volume shrinkage and an increase in bulk density[8]. The unfired clay bricks 30% had an optimum bulk density of 1.9 g/cm^2, as shown in Fig. 5.

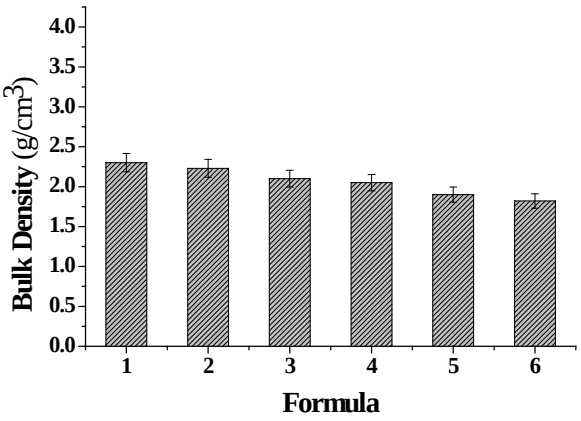

Figure 5. Bulk density of unfired clay brick.

The mechanical properties of the unfired clay brick. The results showed the unfired clay brick of the formula 1-6 addition cement 10 – 15% was lower resistant to fractural strength at 7.25 –7.64 MPa, and the additional cement of 25% increased the resistant fractural strength at 81 kg/cm^2. The addition of 30% cement was highly resistant to fractural strength at 92 and 96 kg/cm^2, as shown in Fig 6. A 30% Cement addition improved the compressive strength. Formula 5 composite was resistant to compressive at 18 MPa. The addition of cement to the unfired clay brick had a positive effect on its strength. This is attributed to the continuous hydration forming more C-S-H as the binding agent. It was discussed that grog has no cementing properties compared to Portland cement. Also, the results explained that the loss of strength increased with the grog content. This is due to the grog's slow setting time, which gains its strength over time[9]. In terms of comparing the strength development, cement is a more effective stabilizing agent than grog, as shown in Fig 7.

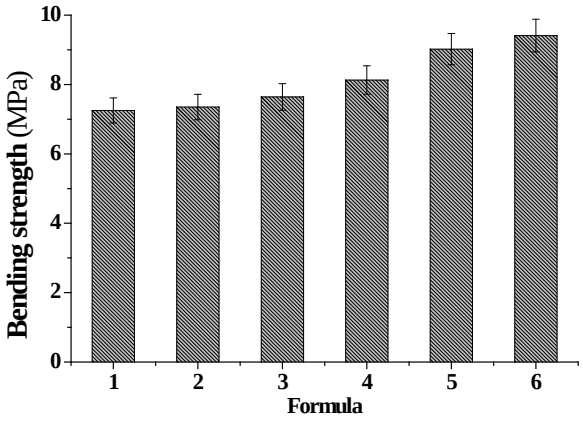

Figure 6. Fractural strength of unfired clay brick.

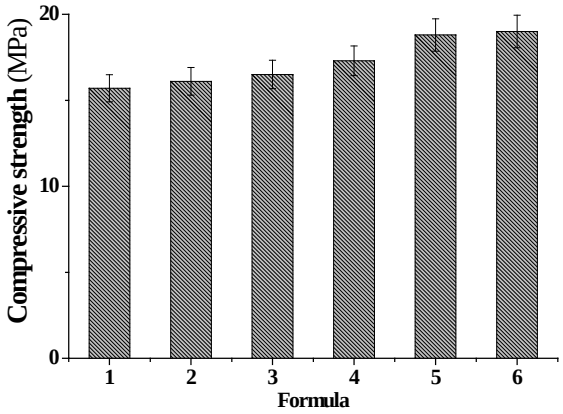

Figure 7. Compressive strength of unfired clay brick.

4. Conclusion

The result concluded that the unfired clay brick had optimum properties when adding cement. The physical properties of unfired clay brick consisting of 70% grog and 30% cement powder had a shrinkage volume of 6.5% and bulk density of 1.9 g/cm^2. The unfired clay brick is resistant to bending at 92 kg/cm^2 and has compressive strength at 18 MPa. The unfired clay bricks were not slaking.

The properties of unfired clay bricks produced by the community approved the requirements of Thai industrial standards (TIS 77-2545).

Acknowledgements

The authors would like to thank Lampang Rajabhat University for the experiment and support for the research.

References

1. I. Johari.; Ramadhansyah P.J.; Zainal A.A. Badorul Hisham A.B., Syamsuhaili S., *J. Constr. Build. Mater.* **2011**, *21*, 141 – 174.
2. Scripta T. The technology of ceramics and refractories. Massachusetts Institute of technology Cambrige, Massachusetts (1964).
3. C.M.F. Vieira.; S.N. Monteiro. *J. Cons.* **2007**, *21*(8), 1754-1759
4. C. M. F. Vieira.; J. Alexandre; S. N. Monteiro. *J. Mater. Sci. Forum.* **2006**, *531*, 438-443
5. W.Ray and C.Radford, Whitewares : Production, Testing and quality Control, Pergamon press, London, (1987)
6. J.T.Jone.; M.F. Berard. Ceramics Industrial Processing and Testing, second ed., Ames, Iowa, (1993).
7. Mohanad S. Eid; Hosam M. Saleh. Sustainability of Concrete with Synthetic and Recycled Aggregates. Intech Open; 2022
8. J.E. Oti; J.M. Kinuthia. *J. Appl. Clay. Sci.* **2012**, *58*, 52–59
9. Medhat S. El-Mahllawy; Ayman M. Kandeel. *J. HBRC.* **2014**, *10*, 82–91

Facile synthesis of highly active and durable carbon composite as a non-precious metal oxygen reduction reaction electrocatalyst in alkaline media

Kittimaporn Nernprom[1], Apichat Saejio[2], Nattawan Pitipuech[2], Narong Chanlek[3], Chedthawut Poompipatpong[4,5], Noppavan Chanunpanich[6,7], and Kriangsak Ketpang[1]*

[1]*Faculty of Science, Energy and Environment, King Mongkut's University of Technology North Bangkok, Rayong Campus, Rayong, Thailand*
[2]*Faculty of Engineering and Technology, King Mongkut's University of Technology North Bangkok, Rayong Campus, Rayong, Thailand*
[3]*Synchrotron Light Research Institute (Public Organization), Nakhon Ratchasima, Thailand*
[4]*Automotive Eco-Energy and Industrial Product Standard Research Center, Science and Technology Research Institute, King Mongkut's University of Technology North Bangkok, Bangkok, Thailand*
[5]*College of Industrial Technology, King Mongkut's University of Technology North Bangkok, Bangkok, Thailand*
[6]*Integrated Chemistry Research Center for Sustainable Technology (IRCT), Science and Technology Research Institute, King Mongkut's University of Technology North Bangkok, Bangkok, Thailand*
[7]*Department of Industrial Chemistry, Faculty of Applied Science, King Mongkut's University of Technology North Bangkok, Bangkok, Thailand*

**E-mail: kriangsak.k@sciee.kmutnb.ac.th*

Abstract:

Designing high performance and durable non-precious metal oxygen reduction reaction (ORR) catalyst is the key strategy to push the high efficiency and zero-carbon dioxide emission fuel cell and metal-air battery technologies to the global market. The Fe based carbon composite (FeImC_HT) electrocatalyst is simply fabricated by pyrolyzing the solid mixture of iron (II) acetate, 2-methyl imidazole, and carbon powder at 900 °C under N_2 atmosphere. The ORR performance for the synthesized non-precious catalyst against the precious Pt/C catalyst is electrochemically investigated using linear sweep voltammetry (LSV) technique under alkaline solution. The maximum ORR kinetic parameter ($E_{1/2}$) for the non-precious FeImC_HT catalyst is found to be 854 mV vs RHE, while the Pt/C catalyst generates $E_{1/2}$ value of 850 mV vs RHE at the same condition. The fabricated non-precious FeImC_HT catalyst facilitates ORR performance under alkaline media as efficient as the precious Pt/C catalyst. The outstanding ORR performance for the non-precious FeImC_HT sample is significantly contributed to the synergistic coupling effect of N doped C framework, Fe_2O_3, Fe_3C and Fe components. Furthermore, the synthesized FeImC_HT catalyst is extremely durable to operate ORR for 5000 cycles under alkaline media.

1. Introduction

An electrochemical oxygen reduction reaction (ORR) is the core reaction responsible for the drastic performance degradation for the high efficiency and zero-carbon dioxide greenhouse gas emission fuel cells and metal-air batteries technologies[1]. Because the ORR is rather complex and it must gain four electrons transfer number, thus relatively high overpotential must be applied to overcome the activation energy of the ORR process[1]. Several noble metals candidates have been intensively investigated as an ORR electrocatalyst to mitigate the ORR overpotential and the maximum ORR performance is attained when the precious nanosized Pt and/or Pt alloys supported on carbon nanostructures is contributed at the cathode electrode[2,3]. Despite the best ORR activity, the Pt nanostructures suffer from several serious issues: high cost, Pt aggregation, Pt dissolution, carbon oxidation during ORR operation that notoriously hinder the commercialization of the fuel cells and metal-air battery technologies to the global market[4,5]. Thus, an alternative nanomaterial with extraordinary functions of comparable ORR performance, lower cost, and more durable to that of the noble Pt/C nanomaterial is an ideal approach to push the fuel cell and metal-air battery technology in coming market soon.

Recently, nitrogen doped carbon nanomaterials (NC) have been widely recognized as an alternative Pt-free ORR electrocatalyst thanks to their competitive ORR electrocatalytic activity, lower price, more durable than the noble Pt/C nanomaterial[6-10]. The comparable ORR performance for the synthesized NC nanomaterial relative to Pt/C catalyst is a result of the formation of the positive charge on the carbon atoms located next to the nitrogen atom in the carbon framework where oxygen molecules effectively adsorb and facilitate electrochemical reduction reaction, yielding high ORR performance[6]. However, fabrication of NC catalyst employing various kinds

of nitrogen and carbon raw materials results in unpredictable ORR performance and the ORR catalytic activity for the fabricated NC electrocatalyst was mostly not superior to that of the expensive Pt/C catalyst[10-12]. It has been demonstrated that Fe-based materials in the forms of Fe_2O_3, Fe-N_x, Fe_3C and Fe have benefit in improving the ORR kinetic in alkaline media[13-15]. Nanosized Fe_2O_3 and Fe-N_x species are proficiently accepted as an ORR active site due to the reversible redox Fe^{3+}/Fe^{2+} capability[13]. On the other hand, Fe_3C phase can sufficiently activate oxygen bonding due to the carbon composition in the trigonal prismatic interstices[13]. Furthermore, metallic Fe has profit in increasing the electron conductivity of the ORR catalyst[13]. Thus, Cheng et al fabricated Fe_2O_3/Fe_3C nanoparticles supported on NC nanostructures by heat treatment a product derived from the chemical reaction of $FeCl_3.6H_2O$ and leucine at 800 ^oC for 2 hr under N_2 atmosphere[14]. The acid treated catalyst exhibited half-wave potential value as high as 0.82 V vs RHE under alkaline media[14]. In addition, Feng et al. successfully enhanced ORR performance of non-precious metal electrocatalyst to be as powerful as the noble Pt/C catalyst by constructing well-defined Fe, Fe_2O_3, Fe_3C on carbon black[13]. The excellent ORR performance promoted by the fabricated catalyst was mainly attributed to the synergistic effect of the Fe_2O_3, Fe-N_x, Fe_3C and NC components[13-15]. However, the Fe-base ORR electrocatalyst fabrication is solvent assistance, time consuming, and multi steps synthetic routes[13-15]. Development of the simple and cost-effective innovative methods to synthesize Fe based nanomaterial is highly desirable for the green technology application.

Herewith, we have proposed the high performance and excellent durability Fe-based carbon composite electrocatalyst that was fabricated using a very simple, economic, solvent free and scalable approach. This was accomplished by a one-step heat treatment of the solid mixture of 2-methylimidazole, iron acetate and commercial carbon black at 900 ^oC under N_2 atmosphere. The electrochemical ORR catalytic activity was investigated using cyclic voltammetry (CV) and linear sweep voltammetry (LSV) under 0.1 M KOH solution. It was found that the synthesized catalyst exhibited superior ORR performance and excellent durability against the noble Pt/C electrocatalyst under basic solution.

2. Materials and Methods

2.1 Preparation of ORR catalyst

2-Methylimidazole (Im) precursor with amount of 450.0 mg was physically pulverized using an agate mortar and a pestle. Commerical carbon nanopowder (VXC72R, C) with amount of 200.0 mg and iron (II) acetate (Fe) with amount of 200.0 mg were carefully transferred into agate mortar containing Im powder and all chemicals were ground homogeneously under ambient conditions. After that the solid mixture was delivered into a combustion boat and it was placed at the center position of the horizontally tubular furnace. High purity nitrogen gas with content of 100 ml/min was flowed into the furnace using a mass flow controller. The sample was heated at 900 ^oC for 60 min at a constant ramp rate of 10 ^oC/min under nitrogen atmosphere. Once the carbonization process was over, the finely black powder was obtained, and it was named FeImC_HT. The preparation of ImC_HT catalyst was similar to FeImC_HT catalyst synthesis procedure excepted Fe raw material was discarded.

2.2 Electrochemical ORR performance evaluation of catalyst

The electrochemical ORR catalytic activity for the prepared catalyst was undertaken by firstly ultrasonic dispersion of the mixture of 2 mg catalyst in the liquid of 10 µL DI-water, 200 µL isopropyl alcohol and 2.5% Nafion solution. A rotating ring disk electrode (RRDE) with an active area of 0.19 cm^2 was used as a working electrode and it was perfectly clean using diamond and alumina solution. Catalyst ink with solid content of 0.4 mg/cm^2 was uniformly loaded on the active area of the RRDE working electrode and let it naturally dry under ambient conditions[16,17]. A catalyst coated working electrode was locked into a rotating controller and it was put into a glass cell containing 0.1 M KOH electrolyte solution. A coiled platinum and a mercury/mercurous oxide (Hg/HgO) were put into the electrochemical cell as a counter electrode and a reference electrode, respectively. The electrochemical ORR performance was carried out using potentiostat (Solartron analytical, AMETEK) with techniques of cyclic voltammetry (CV) and Linear sweep voltammogram (LSV) at a potential range of 1.2 – 0.1 V vs RHE under O_2-saturated 0.1 M KOH solution. LSV experiment was performed at rotating speed of 800 to 2400 rpm, while CV measurement was conducted using a static working electrode.

2.3 Physical characterization of catalyst

The phase of the prepared catalysts was determined using a powder X-ray diffraction

analysis (XRD, Bruker). The XRD results were obtained using XRD experimental conditions of 40 kV generator voltage and 25 mA tube current. The presence of elemental carbon and nitrogen composition in the sample was investigated using X-ray photoelectron spectroscope (XPS, Thermo Fisher Scientific).

3. Results & Discussion

A series of Fe based carbon composite ORR catalysts (FeImC_HT, ImC_HT and C) were carefully fabricated by pyrolyzing the solid powder of C, Im and Fe raw materials at 900 °C for 60 minutes under N_2 atmosphere. The as-synthesized products were subsequently made catalyst ink and the black ink was uniformly coated on the active area of a clean RRDE working electrode. The fabricated working electrode was then assembled into an electrochemical cell equipped with counter and reference electrodes under 0.1 M KOH electrolyte solution. Cyclic voltammetry technique (CV) was first employed to investigate the possibility of the C, ImC_HT and FeImC_HT active materials to promote ORR in the potential range of 0.2 – 1.2 V vs RHE under N_2 and O_2-saturated KOH solution and the CV result is shown in Figure 1. It was found that the ORR peak potential for C, ImC_HT and FeImC_HT catalysts was found to be 773, 773 and 823 mV vs RHE, respectively. The FeImC_HT exhibited the highest ORR peak potential value, suggesting the most ORR active under alkaline environment.

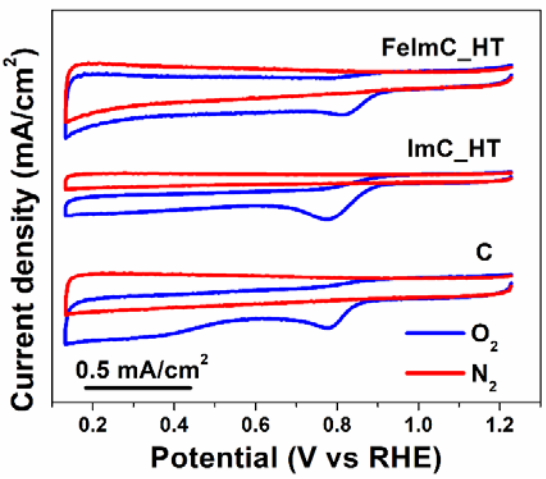

Figure 1. Cyclic voltammogram for C, ImC_HT and FeImC_HT catalysts under N_2 and O_2-saturated 0.1 M KOH solution.

However, CV result highlight only the possibility of the active material to undergo ORR process but was not capable of estimating the ORR kinetic and the number of electron transfer. For this reason, LSV technique was secondly selected to evaluate the ORR kinetic for the C, ImC_HT and FeImC_HT catalyst at working electrode rotation speed of 800 – 2400 rpm under O_2-saturated 0.1 M

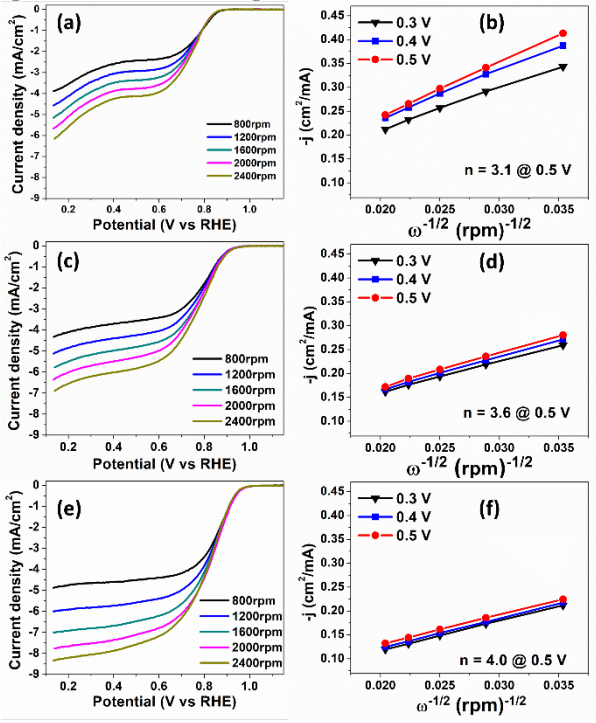

Figure 2. ORR polarization plots at various rotation speed for C (a), ImC_HT (c) and FeImC_HT (e) catalysts conducted by linear sweep voltammograms (LSV) in 0.1 M KOH at scan rate of 10 mV s^{-1}. Corresponding Koutecky-Levich (K-L) plots at different electrode potential for C (b), ImC_HT (d) and FeImC_HT (f) catalysts.

KOH solution and LSV polarization plots are displayed in Figure 2. The ORR current density generating from C (Figure 2a), ImC_HT (Figure 2c) and FeImC_HT (Figure 2e) catalysts was apparently larger as the rotation speed of RRDE working electrode was increased from 800 to 2400 rpm under O_2-saturated KOH solution. This phenomenon was a result of the large O_2 content entering the catalyst active site at high rotation speed, leading to higher value of ORR current density. To verify the ORR kinetic for C, ImC_HT and FeImC_HT catalyst, inversion of ORR current density ($-j^{-1}$) at potential of 0.3, 0.4 and 0.5 V vs RHE and rotation speed ($\omega^{-0.5}$) was graphically plotted, and it was known as Koutecky-Levich (K-L) plot. Figure 2 (b, d and f) depicts K-L plots at potential of 0.3, 0.4 and 0.5 V vs RHE at rotation speed of 800 to 2400 rpm under O_2-saturated KOH solution for C (Figure 2b), ImC_HT (Figure 2d) and FeImC_HT (Figure 2f) catalyst. It was found that the value of $-j^{-1}$ for all catalysts increased linearly with $\omega^{-0.5}$, demonstrating first order ORR kinetic. On the other hand, the K-L plots for C, ImC_HT and FeImC_HT catalysts at potential of

0.3, 0.4 and 0.5 V vs RHE were parallel, implying the electron transfer number at that potential was same. The calculated electron transfer number for C, ImC_HT and FeImC_HT catalysts at 0.5 V was found to be 3.1, 3.6 and 4.0, respectively. It has been reported that the noble Pt/C catalyst undergoes ORR process with a direct four electrons transfer number[8,10]. Thus, The FeImC_HT catalyst was able to boost up ORR process as sufficient as the precious Pt/C electrocatalyst under alkaline environment. Figure 3a represents the comparison of the ORR polarization for C, ImC_HT and FeImC_HT electrocatalysts with that of the standard Pt/C electrocatalyst using LSV technique at rotation speed of 1600 rpm under O_2-saturated 0.1 M KOH solution. Please note that the amount of all prepared electrocatalyst on working electrode was kept constant as 400 μg/cm^2, while the content of the precious Pt/C catalyst dispersed on RRDE electrode was 30 μg/cm^2. There are 3 crucial parameters directly responsible for the electrochemical ORR performance, can be extracted from the LSV plots: onset potential (E_{on}), half-wave potential ($E_{1/2}$) and limiting current density (j_L). The E_{on} value is the potential determining how efficient the electrocatalyst can boost up the ORR process. The C, ImC_HT and FeImC_HT electrocatalysts generated E_{on} values of 878, 950 and 1003 mV vs RHE (Table 1), respectively under basic conditions. The FeImC_HT electrocatalyst exhibited 125 and 53 mV greater E_{on} value than that of the C and ImC_HT catalysts. The highest number of E_{on} values for the FeImC_HT catalyst against C and ImC_HT catalysts indicated the FeImC_HT catalyst was the most efficient to facilitate ORR against the C and ImC_HT samples. On the other hand, the value of E_{on} for the noble Pt/C catalyst was 1008 mV vs RHE (Table 1) at the same environment. The non-precious metal FeImC_HT catalyst had the comparable E_{on} value as the precious Pt/C catalyst under alkaline solution. In addition to E_{on} factor, the $E_{1/2}$ parameter is the potential accounting for the ORR kinetic rate usually extracted at -3 mA/cm^2 from the LSV polarization at rotation speed of 1600 rpm. The number of $E_{1/2}$ for C, ImC_HT and FeImC_HT catalysts at -3 mA/cm^2 was 664, 750 and 854 mV vs RHE, (Table 1) respectively. The expensive Pt/C catalyst delivered $E_{1/2}$ value of 850 mV vs RHE (Table 1). Under alkaline environment, the FeImC_HT electrocatalyst facilitated ORR performance 190 and 104 mV faster than the C and ImC_HT catalysts. Eventually, the FeImC_HT catalyst accelerated the ORR process as fast as the noble Pt/C catalyst at rotation speed of 1600 rpm under basic solution. Beside E_{on} and $E_{1/2}$ parameters, the limiting current density (j_L) is the current independent to the potential corresponding to the rate of the reactant O_2 molecules transporting into the catalyst active site as well as the ORR product diffusing out from the catalyst surface. The larger value of j_L means high capacity of O_2 reactant electrochemically reducing into the OH^- product at the active site of catalyst material. The content of j_L value at 0.5 V vs RHE for C, ImC_HT, FeImC_HT and Pt/C catalysts was found to be -3.45, -4.80, -6.48 and -6.27 mA/cm^2, (Table 1) respectively. The FeImC_HT catalyst outperformed ORR performance relative to C, and ImC_HT catalysts under alkaline media. Figure 3b represents Tafel plots and its Tafel slope for C, ImC_HT, FeImC_HT in comparison with that of the noble Pt/C catalysts at rotation speed of 1600 rpm under KOH media. The value of Tafel slope extracted from C, ImC_HT and FeImC_HT samples was calculated to be 142, 118 and 84 mV/dec, (Table 1) respectively. The expensive Pt/C generated the number of Tafel slope of 85 mV/dec (Table 1). The FeImC_HT catalyst exhibited the lowest Tafel slope. Tafel slope is an important parameter directly corresponding to the electrochemical ORR kinetic. The small number of Tafel slope suggests the catalyst promoted ORR process under alkaline media with a less content of activation energy, yielding fast ORR kinetic. Therefore, the FeImC_HT catalyst facilitated the ORR process faster than that of the C and ImC_HT catalysts under KOH media. Furthermore, the non-precious FeImC_HT catalyst promoted ORR as efficient kinetic rate as the precious Pt/C catalyst.

To clarify the outstanding ORR performance for the FeImC_HT catalyst over the C and ImC_HT catalysts, XRD analysis was utilized to overview the phase of the samples under

Table 1. ORR kinetic parameters obtained from E_{on}, $E_{1/2}$, j_L and Tafel slope for different catalysts.

Catalysts	E_{on} (mV)	$E_{1/2}$ (mV)	j_L (mA/cm^2)	Tafel slope (mV/dec)
C	878	664	-3.45	142
ImC_HT	950	750	-4.80	118
FeImC_HT	1003	854	-6.49	84
Pt/C	1008	850	-6.27	85

room temperature and the XRD pattern for the C, ImC_HT and FeImC_HT samples are shown in Figure 4a. XRD pattern for C sample (red color) exhibited the symmetry peaks at the 2θ of 25 and 44 degree, that were perfectly matched to the

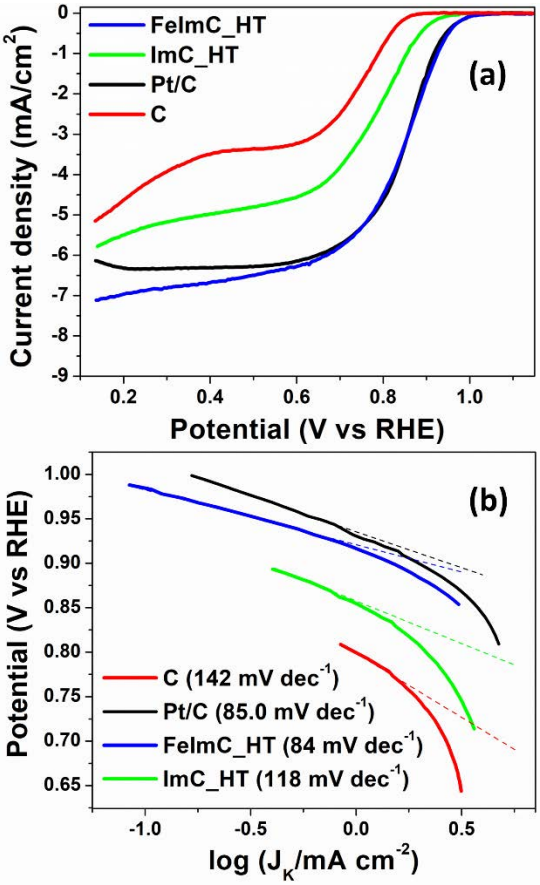

Figure 3. (a) comparison of ORR performance using LSV technique at 1600 rpm and (b) Tafel plots and its corresponding Tafel slopes for C, ImC_HT, FeImC_HT and Pt/C catalysts in 0.1 M KOH.

graphitic C(002) and C(100) planes of the turbostratic carbon structure. On the other hand, the peak at 2θ of 25 degree for the ImC_HT sample (green color) was not symmetrical as the XRD pattern for C sample. The C(002) plane in XRD pattern for ImC_HT was slightly shifted to 2θ lower than 25 degree. It was demonstrated that incorporating the N or/and S atom into carbon framework led to an increment of the interlayer spacing due to an increase in the d-spacing[8,16]. Obviously, the C(002) plane was apparently observed at the 2θ of 22 degree for the FeImC_HT sample (blue color). In addition, phases Fe, Fe_2O_3 and Fe_3C clearly appeared in the XRD pattern of FeImC_HT sample. It should be highlighted that heat treatment of Im mixed C precursors at 900 °C for 60 minutes under N_2 atmosphere significantly improved E_{on}, $E_{1/2}$ and j_L value in comparison with the untreated carbon sample. The superior ORR performance under basic media for ImC_HT catalyst over the pristine C was majorly due to increasing ORR active site by doping nitrogen atom into the carbon frameworks[6-10]. Furthermore, the ORR catalytic activity of the carbon based electrocatalyst greatly enhanced by introducing iron compound into the mixture of imidazole and carbon in the catalyst preparation procedure. Pyrolysis of the compounds containing Fe, N and C atoms under inert conditions resulted in not only the formation of Fe-N_x, Fe, iron oxide, and Fe_3C but the presence of N doped carbon as well[14,15]. Figure 4b depicts the deconvoluted N1s XPS spectra for the FeImC_HT sample. The quantity of C, N, O and Fe verified by XPS measurement was found to be 94.62, 1.31, 3.01 and 1.06 atom%. The N1s XPS spectra for FeImC_HT sample could be deconvoluted into 3 peaks: pyridinic N, graphitic N and pyridinic-N^+-O^-. The functional pyridinic N is reported to be an active site for ORR while the graphitic N has benefit in increasing the electrical conductivity of the catalysts[6-10]. On the other hand, it was reported that the sample contained Fe-N_x function group into carbon lattice effectively outperform the ORR performance against the noble Pt/C catalyst because the Fe-N_x specie was responsible for the major active site for ORR process in alkaline media[14]. On the other hand, the existence of Fe, Fe_2O_3 and Fe_3C phases were helpful for promoting the ORR process under KOH media as well[13]. Fe_2O_3 component was proficiently capable of gaining electron from the carbon support and transfer to the active Fe_3C through O-Fe-C-Fe-C bonds, facilitating ORR process in alkaline solution[13]. The presence of metallic Fe was helpful for improvement of the catalyst conductivity[13]. For this reason, the outstanding ORR performance for FeImC_HT sample in alkaline media was contributed to the synergistic coupling effect of doping N into C, Fe-N_x, Fe_2O_3, Fe_3C and Fe.

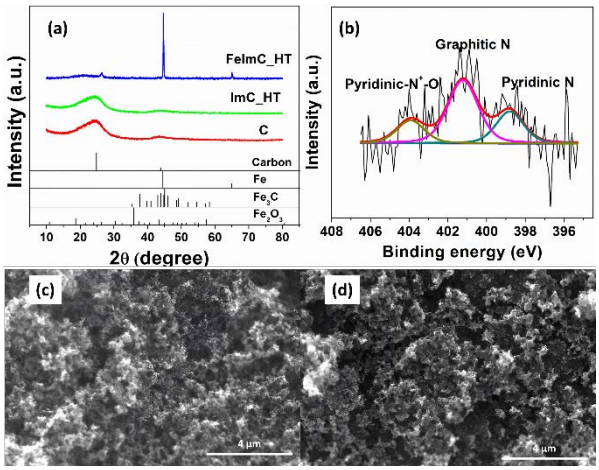

Figure 4. (a) XRD diffraction pattern for C, ImC_HT, FeImC_HT catalysts, (b) deconvoluted N1s XPS spectra for FeImC_HT catalyst and SEM images of (c) ImC_HT and (d) FeImC_HT catalysts.

Figure 4c-d presents the surface morphology for the ImC_HT (Figure 4c) and FeImC_HT (Figure 4d) samples using SEM technique. The surface of ImC_HT sample composed of nanosized particles joined together and the porosity was clearly observed. On the other hand, SEM image for the FeImC_HT sample (Figure 4d) was more clearly than that of the ImC_HT image, mainly due to the presence of Fe, Fe_2O_3 and Fe_3C phases leading to higher electron conductivity. In addition, aggregation of small particles was obviously visualized for the FeImC_HT sample (Figure 4d). The catalyst durability is an essential factor determining how much the ORR performance deterioration during ORR operation. Excellent electrocatalyst should not possesses only high ORR activity but the durability must be stable as well. Figure 5 displays the ORR polarization for the inexpensive FeImC_HT electrocatalyst at initial cycle and after 5000 ORR cycling test at the potential of 0.6-1.0 V vs RHE with scan rate of 50 mV/s in KOH media. It was found that the value of $E_{1/2}$ for the FeImC_HT catalyst at initial cycle and after 5000 cycles cycling test was found to be 0.854 and 0.853 V vs RHE at current density of -3 mA/cm^2. The negligible change in $E_{1/2}$ value after 5000 ORR cycling test indicated the FeImC_HT catalyst was durable to promote ORR in basic media. It has been demonstrating that the $E_{1/2}$ value for the expensive Pt/C catalyst decreased by 40 mV after 5000 accelerated durability study in KOH solution[10]. The ORR performance degradation for the noble Pt/C catalyst was severely attributed to the aggregation of the nanosized Pt particle into larger size[4,5,10]. The big particle size significantly led to the reduction of catalyst surface area, decreasing ORR active site and low ORR

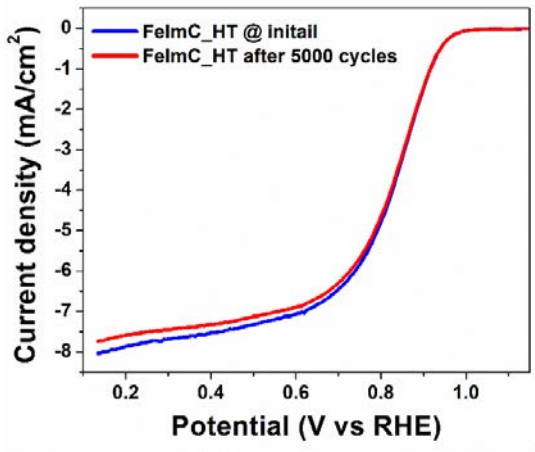

Figure 5. Polarization curves for the non-precious FeImC_HT catalyst during cycling durability test in O_2-saturated at 1,600 rpm (cycling test were carried out in potential range 0.6 - 1.0V vs RHE with 50 mV s^{-1} in 0.1 M KOH)

performance eventually[4,5,10]. On the other hand, Pt dissolution and carbon oxidation during ORR cycling test were also noticeably a result of the ORR performance deterioration for the noble Pt/C catalyst[4,5,10].

4. Conclusion

We succeeded in fabricating the non-precious metal incorporated carbon composite ORR electrocatalyst using a simple, economic, solvent free and scalable method at 900 ^oC under N_2 atmosphere The Fe functional groups with species of Fe-Nx, Fe_2O_3, Fe_3C and Fe incorporating to N doped carbon sample exhibited the ORR kinetic as efficient as the precious Pt/C electrocatalyst under alkaline media. The non-precious Fe based carbon composite catalyst, on the other hand, extremely durable to promote ORR process over 5000 cycles under alkaline conditions.

Acknowledgements

Authors gratefully acknowledged Faculty of Science, Energy and Environment (SciEE) and Faculty of Engineering and Technology (EAT) for providing laboratory facility, equipment, and analytical instruments.

References

1. Kulkarni, A.; Siahrostami, S.; Patel, A.; Norshov, J. K. *Chem. Rev.* **2018**, *118*, 2302-2312.
2. Shao, M.; Chang, Q.; Dodelet, J.P.; Chenitz, R. *Chem. Rev.* **2016**, *116*, 3594-3657.
3. Wang, Y. J.; Zhao, N.; Fang, B.; Li, H.; Bi, X. T.; Wang, H. *Chem. Rev.* **2015**, *115*, 3433 – 3467.
4. Yano, H.; Watanabe, M.; Iiyama, A.; Uchida, H. *Nano Energy* **2016**, *29*, 323-333.
5. Cherevko, S.; Kulyk, N.; Mayrhofer, K. J.J.; *Nano Energy*. **2016**, *29*, 275-298.
6. Gong, K.; Du, F.; Xia, Z.; Durstock, M.; Dai, L. *Science.* **2009**, *323*, 760-764.
7. Wang, S.; Iyyamperumal, E.; Roy, A.; Xue, Y.; Yu, D.; Dai, L. *Angew Chem Int Ed.* **2011**, *50*, 11756-11760.
8. Saejio, A.; Kongpunyo, K.; Buntao, N.; Nernprom, K.; Boonkor, K.; Wichienwat, K.; Chanunpanich, N.; Chanlek, N.; Shanmugam, S.; Ketpang, K. *E3S Web of Conferences.* **2022**, *355*, 01006.

9. Qu, L.; Liu, Y.; Baek, JB.; Dai, L. *ACS Nano*. **2010**, *4*, 1321-1326.
10. Nernprom, K.; Sanetuntikul, J.; Saejio, A.; Pitipuech. N.; Wichienwat, K.; Chanlek N.; Poompipatpong, C.; Chanunpanich, N.; Ketpang, K. *Int. J. hydrogen Energy*. **2024**, *50*, 1549-1558.
11. Liu, X.; Dai, L. *Nat. Rev. Mater*. **2016**, *1*, 16064-16076.
12. Wang, DW.; Su, D. *Energy Environ. Sci*. **2014**, *7*, 576-591.
13. Feng, W.; Liu, M.; Liu, J.; Song, Y.; Wang, F. *Catal. Sci. Technol*. **2018**, *8*, 4900-4906.
14. Tian, Y.; Xu, L.; Qian, J.; Bao, J.; Yan, C.; Li, H.; Li, H.; Zhang, S. *Carbon*. **2019**, *146*, 763-771.
15. Cheng, J.; Wu, D.; Wang, T. Inorg. Chem. Commun. **2020**, *117*, 107952.
16. Ketpang, K.; Boonkitkoson, A.; Pitipuech, N.; Poompipatpong, C.; Sanetuntikul, J.; Shanmugam, S. *E3S Web of Conferences*. **2019**, *141*, 01005.
17. Ketpang, K.; Prathum, J.; Juprasat, P.; Junla, W.; Wichianwat, K.; Saejio, A.; Poompipatpong, C.; Chanunpanich, N. *E3S Web of Conferences*. 2019, *141*, 01004.

Preparation and characterization of MoS_2/lignin-based carbon nanocomposite fibers for supercapacitor electrodes

Kamonluk Sirikarint [1], Autchara Pangon [2], and Thitirat Inprasit [1]*

[1]*Division of Materials and Textile, Faculty of Science and Technology, Thammasat University, Phathumthani 12121 Thailand*
[2]*National Nanotechnology Center, National Science and Technology Development Agency, Pathumthani 12120 Thailand*

**E-mail: thi_inp@tu.ac.th*

Abstract:

Carbon nanofibers derived from renewable sources, such as lignin, have garnered considerable attention for their potential application as supercapacitor electrodes. This is attributed to their outstanding properties, including a high specific surface area, excellent porosity, robust chemical and thermal stability, and superior electrical conductivity. Despite these merits, practical applications reveal that carbon materials alone do not sufficiently meet the growing demand for high specific capacitance. To improve their capacitive performance, the integration of the carbon nanofibers with transition metal sulfide is proposed. This study specifically explored the molybdenum disulfide/lignin-based carbon nanocomposite fibers (MoS_2/CNFs) as free-standing supercapacitor electrodes. Lignin-based carbon nanofibers were prepared through a straightforward electrospinning technique, while MoS_2 was synthesized via a hydrothermal process. The electrochemical performance of the MoS_2/CNFs electrodes was examined by cyclic voltammetry (CV), galvanostatic charge-discharge (GCD), and electrochemical impedance spectroscopy (EIS). Comparative analysis with CNFs electrodes reveals that the introduction of MoS_2 significantly enhances the specific capacitance of the carbon nanofibers up to 228.18 F/g. Moreover, the MoS_2/CNFs have the highest energy density of 31.69 Wh/kg and a power density of 211.07 W/kg. This notable improvement positions MoS_2/CNFs as a promising material for supercapacitor electrodes, showcasing its potential for addressing the rising need for advanced energy storage solutions.

1. Introduction

Recent concerns about energy security and environmental sustainability have notably heightened interest in generating electricity from renewable sources. The variability and unreliability inherent in these sources necessitate the development of electrical energy storage (EES) systems like batteries and supercapacitors. While batteries are compact and have a high energy density, they are limited by their lifespan and rechargeability. Supercapacitors, in contrast, offer enhanced power output and longer lifespans due to their large electrode surface areas, facilitating rapid and efficient energy release.[1,2] Supercapacitors, a crucial EES technology, are distinguished by their high-power density and specific capacitance, thanks to their expansive electrode surface areas.[3] Capable of releasing energy at high density over short durations,[4] they are classified into three main types based on their charge storage mechanisms: electric double-layer capacitors (EDLCs) that store charge electrostatically, pseudo capacitors that employ redox reactions and material intercalation, and hybrid capacitors that combine both mechanisms. In EDLCs, carbonaceous materials such as graphene, activated carbon, carbon nanotubes, and carbon nanofibers are commonly used because of their high surface area and porosity. Pseudo capacitors prefer redox-active materials, including transition metal oxides and conducting polymers. Hybrid capacitors merge these material types to maximize performance. This diverse range of materials and mechanisms underscores the adaptability and efficiency of supercapacitors as a solution to the challenges posed by the intermittent nature of renewable energy sources.[5]

Carbon-based materials are proposed for EDLC electrodes because of their high conductivity, large surface area, and significant porosity. Lignin, a bio-renewable precursor found in lignocellulosic plants, is a promising alternative for producing carbon-based electrodes, offering high carbon content, environmental benefits, and cost-effectiveness. However, carbonaceous materials, while advantageous, are constrained by their low capacitance and energy density.[6-8] To overcome these limitations, transition metal dichalcogenides (TMDs), particularly molybdenum disulfide (MoS_2), have garnered attention in the energy storage field due to their unique electronic, mechanical, and optical properties. MoS_2, with a structure like graphene, offers high theoretical specific capacitance and a range of oxidation states (+2 to +6). Its structure

features a Mo atom covalently bonded between two S atoms, with layers stacked via weak Van der Waals forces, creating a large interlayer spacing of 0.65 nm. The graphene-like structure of MoS_2 provides several benefits, including a large surface area contributing to double-layer capacitance and various oxidation states facilitating redox reactions, known as pseudo capacitance behavior. The charge storage in MoS_2 involves non-faradaic and faradaic reactions: [9]

$MoS_{2surface} + K^+ + e^- \leftrightarrow (MoS2^- - K^+)_{surface}$ (i)
$MoS_2 + K^+ + e^- \leftrightarrow MoS–SK$ (ii)

Electrospinning is a distinguished technique in biomass processing that specializes in producing freestanding electrodes from nonwoven carbon fibers.[6-8] This study emphasizes the development of lignin-based carbon nanofiber (CNF) electrodes using electrospinning, further enhanced by the hydrothermal synthesis of MoS_2 nanoparticles on the CNF surface, resulting in MoS_2/CNF composites. This unique method leads to electrodes with elevated specific capacitance, rendering them ideal for use in supercapacitors. The synthesized material underwent extensive physiochemical characterization to assess its quality. Additionally, its electrochemical performance was rigorously evaluated in a two-electrode system, using 1 M H_2SO_4 as the liquid electrolyte, to establish its efficacy and potential application in energy storage devices.

2. Materials and Methods

2.1 Materials

Organosolv lignin was obtained from ChemicalPoint. Polyvinylpyrrolidone (PVP) and L-cysteine (97%) were purchased from Sigma Aldrich. Sodium molybdate (VI) dihydrate ($Na_2MoO_4 \cdot 2H_2O$) was purchased from Thermo Scientific. *N*,*N*-dimethylformamide (DMF) and hydrochloric acid (HCl, 37%) were purchased from Carlo Erba. Distilled (DI) water and ethanol (95%) were used through the experiments, and all chemicals were used as received without further purification.

2.2 Preparation of lignin-based carbon nanofibers (CNFs)

Typically, to obtain an electrospinning solution, a mixed solution of lignin and PVP at a weight ratio of 80:20 was prepared by dissolving lignin and PVP in DMF by stirring at 80 °C until the mixed solution was homogenous. The mixed solution was transferred into a plastic syringe equipped with a 0.8 mm diameter needle. The as-spun nanofibers were collected at the electrospinning condition as follows; a working distance of 15 cm, an applied voltage of 15 kV, and a flow rate of 0.2 ml/h. The as-spun nanofibers were stabilized in air at 250 °C for 2 h with a heating rate of 1 °C/min. To prepare lignin-based carbon nanofibers (CNFs), the stabilized nanofibers were carbonized at 900 °C for 2 h with a heating rate of 10 °C/min under nitrogen atmosphere.

2.3 Synthesis of MoS_2 on CNFs (MoS_2/CNFs nanocomposite)

The MoS_2/CNFs composite was attained by the hydrothermal method. Illustrations of the preparation of MoS_2/CNFs nanocomposite are displayed in Scheme 1. Sodium molybdate (VI) dihydrate (0.15 g) and L-cysteine (0.4 g) were mixed in DI water (40 ml). With vigorous stirring for 1 h, the pH of the solution was adjusted to 6.5 by using 12 M HCl. The mixed solution and a piece of CNFs were transferred into a Teflon-lined stainless-steel autoclave and heated at 180 °C for 24 h. After cooling, the MoS_2/CNFs were washed with DI water for several times before rinsing with ethanol and drying in an oven at 70 °C for 12 h.

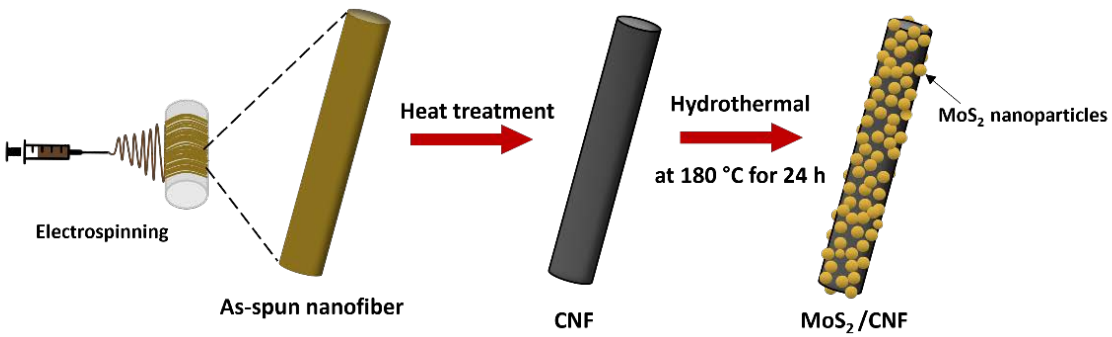

Scheme 1. Illustrations of the preparation of MoS_2/CNFs nanocomposite.

2.4 Electrochemical Measurements

To study electrochemical performance of the MoS_2/CNFs as electrode materials, cyclic voltammetry (CV), galvanostatic charge/ discharge (GCD), and electrochemical impedance spectroscopy (EIS) were measured on an Autolab PGSTAT12 potentiostat/galvanostat using two symmetric electrode cells in a 1 M H_2SO_4 electrolyte solution, an electrolyte suitable for Swagelok® cells. The MoS_2/CNFs electrodes were cut by hole-punching with a diameter of 5 mm and assembled with a separator using Whatman No.1. The CV measurements were operated at different scan rates (5, 10, 20, 50, 100, and 200 mV/s). The GCD data were recorded at various current densities (from 0.1 to 5 A/g). The EIS characterization was run in the frequency range from 100 kHz to 0.1 Hz at an AC amplitude of 10 mV. The specific capacitance was calculated from the GCD curve using eq. (1)[10]

$$C_s = \frac{4I\ x\ \Delta t}{m\ x\ \Delta V} \qquad (1)$$

where, Cs is specific capacitance (F/g), I is the discharge current (A), Δt is the discharge time (s), m is the total mass of two electrode materials (g), and ΔV is the maximum potential window to discharge the cell (V)

The energy density and power density of the materials were calculated using eq. (2) and (3), respectively.[10]

$$E = \frac{Cs \times \Delta V^2}{2 \times 3.6} \qquad (2)$$

$$P = \frac{E \times 3600}{\Delta t} \qquad (3)$$

where E is the energy density (Wh/kg) and P is the power density (W/kg).

2.5 Characterization

Scanning electron microscopic (SEM) measurement was conducted on a Hitachi S-3400N. The samples were sputtered with Au before SEM imaging at 15 kV. X-ray diffraction (XRD) patterns of the CNFs, MoS_2, and MoS_2/CNFs composite were examined using a Rigaku MiniFlex 600. The XRD scan was run at acceleration voltage and current of 40 kV and 15 mA, respectively with a resolution of 0.02º 2θ and a scan speed of 2.5 º/min. The surface elemental compositions of the CNFs, MoS_2, and MoS_2/CNFs composites were verified by using a PHI5000 Versa Probe II, ULVAC-PHI, (Japan) X-ray photoelectron spectroscope (XPS) at the SUT-NANOTEC-SLRI Joint Research Facility, Synchrotron Light Research Institute, Thailand.

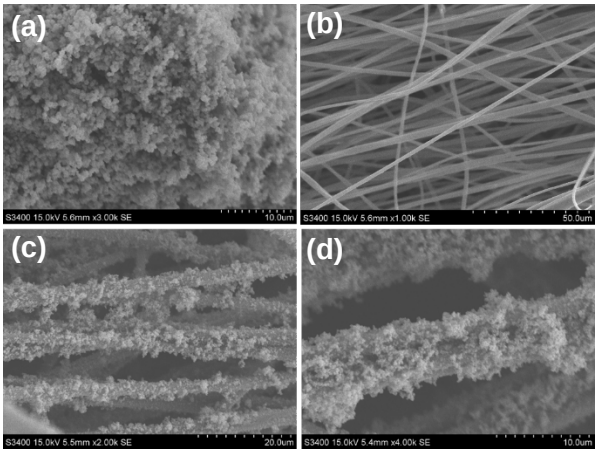

Figure 1. SEM images of (a) MoS_2 nanoparticles, (b) CNFs, and (c-d) MoS_2/CNFs nanocomposite at magnifications of x2k and x4k.

3. Results & Discussion

3.1 Morphological analysis

Surface morphologies of the CNFs, MoS_2, and MoS_2/CNFs were characterized by scanning electron microscopy (SEM). Figure 1(a) shows SEM image of the hydrothermally synthesized nanostructures of MoS_2 that exhibit the formation of nearly spherical-shape nanoparticles that are composed of self-assembly from MoS_2 nanosheets[11] with a diameter of 142.7 ± 8.8 nm. The CNFs display nonwoven fiber-like structure with a smooth surface with an average diameter of 152.9 ±3.5nm (Figure 1(b)). Figures 2(c) and 2(d) display SEM images of the MoS_2/CNFs composite. After hydrothermal process of CNFs in the presence of $Na_2MoO_4.2H_2O$ and L-cysteine, the small particles grew and evenly distributed on the CNFs, resulting in rough fiber surface.

3.2 X-ray diffraction (XRD) spectroscopy

Figure 2 shows XRD patterns of the pristine CNFs, MoS_2, and MoS_2/CNFs. The XRD pattern of CNFs exhibits two broad diffraction peaks centered at 24.7° and 43.6° 2θ, corresponding to (002) and (100) planes of graphitic carbon, respectively.[6] According to Bragg's law in eq. 4, the interlayer d-spacing calculated from the dominant (002) peak of CNFs is approximately 0.36 nm. In Figure 2(b), the major peaks appeared at 2θ of 9.2°, 17.0°,

Table 1. Atomic concentrations of different elements on the surface of CNFs, MoS_2, and MoS_2/CNFs determined by XPS analysis.

Sample	Atomic concentration (%)				
	C	N	O	Mo	S
MoS_2	-	-	-	36.4	63.6
CNFs	95.9	0.5	3.6	-	-
MoS_2/CNFs	26.5	24.1	27.4	9.4	12.6

32.1°, 33.9°, and 57.0° are attributed to (002), (004), (100), (102), and (110) crystal planes of MoS_2, respectively.[12] It should be noted that the existence of the peak at lower angle (9.2° 2θ) demonstrated the enlargement of interlayer spacing of MoS_2 is 0.96 nm, due to the growth of MoS_2 at relatively low temperatures (below 200 °C).[13] In addition, the broad diffraction peaks revealed disordered layer with small crystal size.[14] After hydrothermal treatment of the CNFs, the appearance of the peaks at 9.16°, 16.98°, 32.14°, 33.86°, and 56.98° 2θ confirmed the presence of MoS_2 on the CNFs.

$$d = \frac{n\lambda}{2sin\theta} \qquad (4)$$

where, d is interlayer spacing of the crystals, n is the integer, λ is the wavelength, and θ is the incident angle.

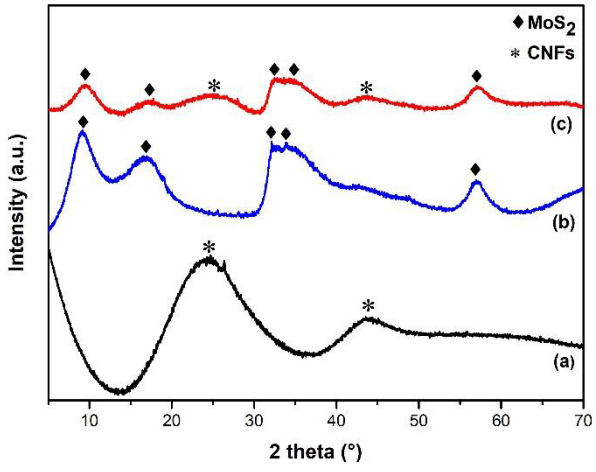

Figure 2. XRD patterns of (a) pristine CNFs, (b) MoS_2, and (c) MoS_2/CNFs.

3.3 Surface elemental composition analysis by XPS

The survey XPS spectra of MoS_2, MoS_2/CNFs, and pristine CNFs are depicted in Figure 3. The resulting surface elemental compositions verified by XPS are summarized in Table 1. As expected, MoS_2 contains molybdenum (Mo) and sulfur (S) while CNFs contain carbon (C), oxygen (O), and nitrogen (N) with the highest carbon content of >95%. The elements presented in the MoS_2/CNFs are C, N, O, Mo, and S.

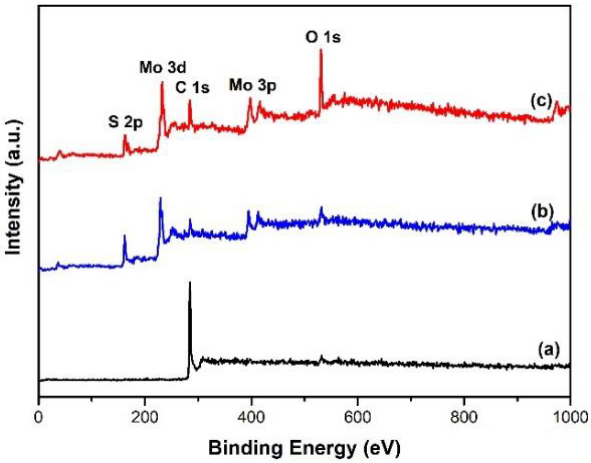

Figure 3. XPS survey spectra of (a) pristine CNFs, (b) MoS_2, and (c) MoS_2/CNFs.

3.4 Electrochemical performance

The electrochemical performance of the pristine CNFs and MoS_2/CNFs as electrodes materials was measured in a two-electrode system using 1 M H_2SO_4 as an electrolyte. In Figure 4(a), The pristine CNFs show deviation of CV curves from the rectangular shape, indicating non-ideal supercapacitor. This might be due to their relatively low surface area and conductivity, resulting in limited accessibility of the electrolyte ions to the electrodes. The absence of redox peak in the CV curve of CNFs suggested electrical double-layer capacitance behavior. Differently, the CV curves of the MoS_2/CNFs in Figure 4(b) appear redox reactions, revealing pseudo-capacitive behavior.[15] Figure 4(c) shows CV curves of the pristine CNFs and MoS_2/CNFs at low scan rate of 5 mV/s. The higher current density response and larger area of the CV curve demonstrated the higher specific capacitance of the MoS_2/CNFs than that of the pristine CNFs. The CV curve of the MoS_2/CNFs exhibits two obvious pairs of redox peaks, which correspond to anodic peaks at 0.946, 0.436 V, and cathodic peaks at 0.684, 0.403 V. The anodic and cathodic peaks arose from the insertion and desertion of proton from the acidic electrolyte

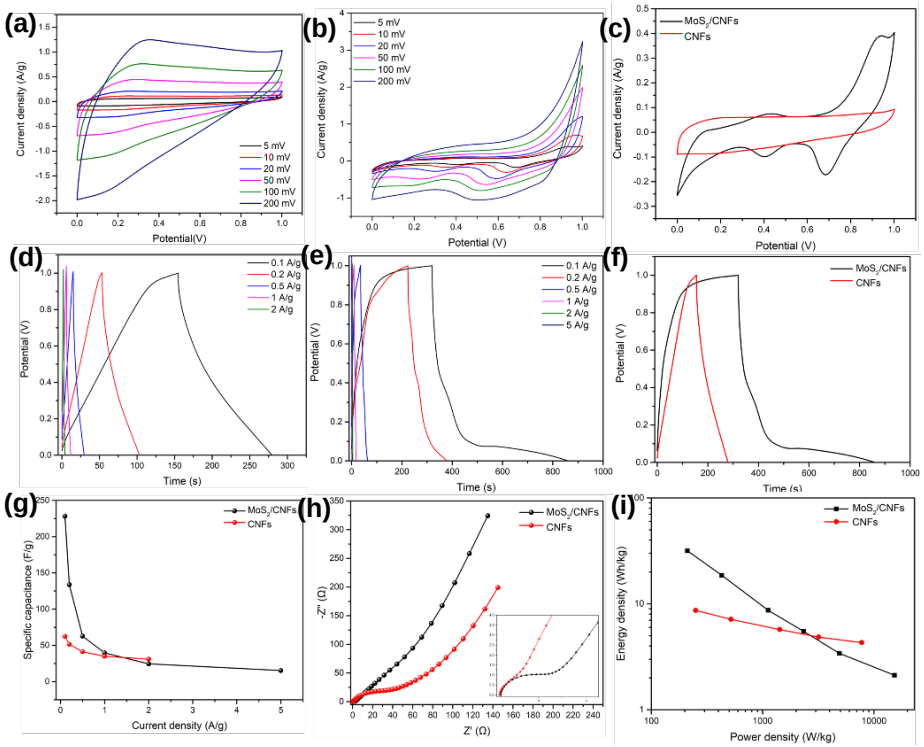

Figure 4. (a) CV curves of pristine CNFs at different scan rates, (b) CV curves of MoS_2/CNFs at different scan rates, (c) CV curves of CNFs and MoS_2/CNFs at a scan rate of 5 mV/s, (d) GCD curves of pristine CNFs at different current densities, (e) GCD curves of MoS_2/CNFs at different current densities, (f) GCD curves of CNFs and MoS_2/CNFs at a current density of 0.1 A/g, (g) plot of specific capacitance as a function of current density, and (h) Nyquist plot of CNFs and MoS_2/CNFs in the frequency range from 100 kHz to 0.1 Hz, (i) Ragone plot.

to the interlayer of MoS_2.[16] At low scan rate, the presence of MoS_2 allowed ions to diffuse into interlayers, where there were more redox charge transfer sites. The high density of Mo and S at the edge of MoS_2/CNFs offered an increased accessible site for protons to diffuse between layers through the intercalation mechanism followed by reduction of MoS_2 and deintercalation followed by oxidation of MoS_2, as demonstrated in reaction (iii);[17, 18]

$$MoS_2 + H^+ + e^- \leftrightarrow MoS–SH \qquad \text{(iii)}$$

The galvanostatic charge-discharge (GCD) analysis was done to determine charge storage efficiency of the CNFs and MoS_2/CNFs composite electrodes for supercapacitor at various current densities, i.e., 0.1, 0.2, 0.5, 1, 2, and 5 A/g. The GCD curves of the pristine CNFs display a nearly linear symmetrical triangular shape, indicating reversible charge/discharge behavior of electrical double layer (Figure 4(d)). In Figure 4(e), the GCD curves of MoS_2/CNFs are non-linear with an asymmetric triangle shape, suggesting pseudo capacitive behavior. Consistent with the CV analysis results, the GCD curve of MoS_2/CNFs shows longer charge-discharge times than CNFs (Figure 4(f)), indicating that the hybridization of MoS_2 with CNFs significantly increases the specific capacitance of the CNFs.[15] The highest specific capacitance of MoS_2/CNFs and CNFs was 228.18 and 62.5 F/g, respectively at a current density of 0.1 A/g. The Ragone plots displaying the energy density and power density of the MoS_2/CNFs and CNFs are shown in Fig 4(i). The MoS_2/CNFs exhibited the highest energy density of 31.69 Wh/kg and a power density of 211.07 W/kg, while the CNFs displayed the highest energy density of 8.68 Wh/kg and a power density of 250 W/kg. Due to the double-layer capacitive behavior of CNF, it results in a higher power density than the pseudocapacitive behavior of MoS_2/CNFs.[19]EIS was studied to understand capacitive behavior, ion diffusion kinetics, and internal resistance between the electrodes and electrolyte. The Nyquist plots of MoS_2/CNFs and CNFs are shown in Figure 4(g). The semicircle in the high-frequency region represents charge transfer resistance (R_{ct}) between electrode-electrolyte, and the straight line along the imaginary axis in the low-frequency region represents electrolyte ions diffusion, known as Warburg-impedance.[5,20] The MoS_2/CNFs present a

smaller semicircle loop in the high frequency region than the CNFs, as shown in Figure 4(g), revealing a lower charge transfer resistance. This might result in an improved electrochemical performance of the MoS_2/CNFs as electrodes in supercapacitor, compared to the pristine CNFs.

4. Conclusion

In summary, we successfully synthesized MoS_2/CNFs nanocomposite using electrospinning and hydrothermal methods as confirmed by SEM, XRD, and XPS. The enlargement of the MoS_2 interlayer was observed from the XRD analysis. With a large number of active sites for ion accessibility, the growth of MoS_2 on the surface of CNFs significantly improved the electrochemical performance of the electrode. By using 1 M H_2SO_4 as an electrolyte, the MoS_2/CNFs composite exhibited superior electrochemical performance with a specific capacitance of 228.18 F/g at a current density of 0.1 A/g. This work presents a simple approach to enhance the energy storage performance of MoS_2/CNFs for high-performance supercapacitor electrodes.

Acknowledgements

This work is funded by Faculty of Science and Technology, Thammasat University [grant number TB 3/2565], National Research Council of Thailand (NRCT) [grant number N41A640172] and NSRF via the Program Management Unit for Human Resources & Institutional Development, Research, and Innovation [grant number 40G660033]. The authors would like to acknowledge Faculty of Science and Technology, Thammasat University, Thailand, National Nanotechnology Center, National Science and Technology Development Agency, (NSTDA), Thailand, and Synchrotron Light Research Institute, Thailand for research facilities.

References

1. Andrew Burke, Z. L., Hengbing Zhao Review of the Present and Future Applications of Supercapacitors in Electric and Hybrid Vehicles.
2. Yang, Z.; Zhang, J.; Kintner-Meyer, M. C. W.; Lu, X.; Choi, D.; Lemmon, J. P.; Liu, J., Electrochemical Energy Storage for Green Grid. *Chemical Reviews* **2011,** *111* (5), 3577-3613.
3. Sarno, M., Chapter 22 - Nanotechnology in energy storage: the supercapacitors. In *Studies in Surface Science and Catalysis*, Basile, A.; Centi, G.; Falco, M. D.; Iaquaniello, G., Eds. Elsevier: 2020; Vol. 179, pp 431-458.
4. Keçili, R.; Arli, G.; Hussain, C. M., Chapter Fourteen - Future of analytical chemistry with graphene. In *Comprehensive Analytical Chemistry*, Hussain, C. M., Ed. Elsevier: 2020; Vol. 91, pp 355-389.
5. Sharma, S.; Chand, P., Supercapacitor and electrochemical techniques: A brief review. *Results in Chemistry* **2023,** *5*, 100885.
6. Zhu, M.; Liu, H.; Cao, Q.; Zheng, H.; Xu, D.; Guo, H.; Wang, S.; Li, Y.; Zhou, J., Electrospun Lignin-Based Carbon Nanofibers as Supercapacitor Electrodes. *ACS Sustainable Chemistry & Engineering* **2020,** *8* (34), 12831-12841.
7. Thielke, M. W.; Lopez Guzman, S.; Victoria Tafoya, J. P.; García Tamayo, E.; Castro Herazo, C. I.; Hosseinaei, O.; Sobrido, A. J., Full Lignin-Derived Electrospun Carbon Materials as Electrodes for Supercapacitors. *Frontiers in Materials* **2022,** *9*.
8. Yadav, R.; Zabihi, O.; Fakhrhoseini, S.; Nazarloo, H. A.; Kiziltas, A.; Blanchard, P.; Naebe, M., Lignin derived carbon fiber and nanofiber: Manufacturing and applications. *Composites Part B: Engineering* **2023,** *255*, 110613.
9. Mohan, M.; Shetti, N. P.; Aminabhavi, T. M., Phase dependent performance of MoS_2 for supercapacitor applications. *Journal of Energy Storage* **2023,** *58*, 106321.
10. Khamnantha, P.; Homla-or, C.; Suttisintong, K.; Manyam, J.; Raita, M.; Champreda, V.; Intasanta, V.; Butt, H.-J.; Berger, R.; Pangon, A., Stable Lignin-Rich Nanofibers for Binder-Free Carbon Electrodes in Supercapacitors. *ACS Applied Nano Materials* **2021,** *4* (12), 13099-13111.
11. Liu, X.; Wang, T.; Hu, G.; Xu, C.; Xiong, Y.; Wang, Y., Controllable synthesis of self-assembled MoS_2 hollow spheres for photocatalytic application. *Journal of Materials Science: Materials in Electronics* **2018,** *29* (1), 753-761.
12. Kour, P.; Deeksha; Kour, S.; Sharma, A. L.; Yadav, K., Mixed-phase MoS_2 nanosheets anchored carbon nanofibers for high energy symmetric supercapacitors. *Journal of Energy Storage* **2023,** *63*, 107054.
13. Hasmin, H.; Imawan, C.; Fauzia, V., The Role of Temperature in the Hydrothermal Synthesis on the Structural and Morphological Properties of MoS 2. *Journal of Physics: Conference Series* **2021,** *1951*, 012014.
14. Ungár, T., Microstructural parameters from X-ray diffraction peak broadening. *Scripta Materialia* **2004,** *51* (8), 777-781.

15. Liu, Q.; Zhu, H.; Ma, Q.; Liu, M.; Wang, B.; Tang, C.; Wang, Y.; Wu, Q.; Wang, X.; Hu, Z., Ultrathin MoS_2 nanosheets hybridizing with reduced graphene oxide for high-performance pseudocapacitors. *FlatChem* **2021,** *26*, 100212.
16. Xie, Y.; Sun, P., Electrochemical performance of interspace-expanded molybdenum disulfide few-layer. *Journal of Nanoparticle Research* **2018,** *20* (7), 183.
17. Koroteev, V. O.; Kuznetsova, I. V.; Kurenya, A. G.; Kanygin, M. A.; Fedorovskaya, E. O.; Mikhlin, Y. L.; Chuvilin, A. L.; Bulusheva, L. G.; Okotrub, A. V., Enhanced supercapacitance of vertically aligned multi-wall carbon nanotube array covered by MoS_2 nanoparticles. *physica status solidi (b)* **2016,** *253* (12), 2451-2456.
18. Soon, J. M.; Loh, K. P., Electrochemical Double-Layer Capacitance of MoS_2 Nanowall Films. *Electrochemical and Solid-State Letters* **2007,** *10* (11), A250.
19. Zhou, L.; Li, C.; Liu, X.; Zhu, Y.; Wu, Y.; van Ree, T., 7 - Metal oxides in supercapacitors. In *Metal Oxides in Energy Technologies*, Wu, Y., Ed. Elsevier: 2018; pp 169-203.
20. Rajapriya, A.; Keerthana, S.; Viswanathan, C.; Ponpandian, N., Direct growth of MoS_2 hierarchical nanoflowers on electrospun carbon nanofibers as an electrode material for high-performance supercapacitors. *Journal of Alloys and Compounds* **2021,** *859*, 157771.

Preparation and characterization of silver nanowires/cellulose nanofibrils-based conductive paper

Noppamas Thongsiri[1], Saowaluk Inpaeng[1], Chaisak Issro[2], and Karaked Tedsree[1]*

[1]*Department of Chemistry, Faculty of Science, Burapha University, Chonburi 20131, Thailand*
[2]*Department of Physics, Faculty of Science, Burapha University, Chonburi 20131, Thailand*

**E-mail: karaked@go.buu.ac.th*

Abstract:
Nanocellulose serves as an eco-friendly substrate for producing conductive paper by incorporating metal nanoparticles, particularly silver nanowires (AgNWs), into cellulose nanofibrils (CNFs) matrices. The synthesis process involves pretreating durian peel waste to obtain CNFs, controlling the synthesis of AgNWs using a polyol method, and blending these components to create composite paper. Material characterization entails Scanning electron microscopy (SEM), Transmission electron microscopy (TEM), and Fourier-transform infrared (FTIR) spectroscopy to assess the morphologies and surface properties of CNFs, AgNWs and composite paper. Additionally, X-ray diffraction (XRD) analysis is employed to examine the crystalline structures of CNFs, AgNWs, and composite paper. The resulting paper has a thickness of approximately 90 µm. Its electrical conductivity varies with different AgNWs loading percentages (ranging from 15% to 60% w/w). The optimal combination is achieved with 50% w/w AgNWs, resulting in conductive paper exhibiting low sheet resistance (0.033 Ω.m) and surface conductivity (30.52 S/m). Furthermore, these papers effectively shield electromagnetic signals in the context of mobile phone communication.

1. Introduction

The world of modern human beings is filled with electronics, including computers, mobile phones, and a variety of sensors. However, a significant challenge of these devices is the issue of electronic waste (e-waste) such as silicon wafers, glass, and polymers which belong to non-renewable resources.[1] Thus, developing a renewable, low-cost, and easy electronic substrate is necessary and has attracted lots of interest.

Conductive nanofiber paper has gained attention for its potential use in flexible and foldable electronics, sensors, and other emerging technologies.[2] Silver and copper nanowires are excellent candidates for one-directional electrodes. The unique characteristics of silver nanowires (AgNWs), such as high electrical conductivity and flexibility, make them an attractive choice for enhancing the conductivity of materials.[3] Additionally, nanocellulose, derived from renewable and abundant cellulose sources, exhibits excellent mechanical strength, low weight, biodegradability, and a fibrous structure ideal for paper production.[4] The synergistic combination of these two components presents an intriguing avenue for the creation of conductive paper that not only addresses the demand for efficient electronic materials but also aligns with the principles of green and sustainable technology.

Extracting nanocellulose from agricultural products such as rice straw, sugarcane bagasse, and corn cobs has become a recent research focus.[5] The process is initially a treatment process involving acids, bases, and bleaching agents to eliminate lignin, cellulose, and hemicellulose constituents. Subsequently, nanocellulose is achieved through hydrolysis, employing acids such as H_2SO_4, H_3PO_4, and organic acids.[6] The morphology, size, and other characteristics of nanocellulose depend on the cellulose origin, the extraction and processing conditions, as well as the pre- or post-treatment methods. Penjumras and co-workers[5] reported extracting cellulose from durian rind through a delignification process using acidic sodium chlorite and mercerization with 17.5% w/v sodium hydroxide. The cellulose extract exhibited a diameter and aspect ratio predominantly within the ranges of 100-150 µm and 20-25, respectively. In the study by Agung and co-workers[6], the synthesis and characterization of cellulose and nanocellulose derived from durian peel waste were studied. The durian peel was pretreated by various chemical processes, including alkaline and bleaching treatments, aimed at eliminating hemicellulose and lignin. Subsequently, acid hydrolysis using 45% H_2SO_4 solution at 45°C was employed to extract nanocellulose, followed by its isolation through centrifugation and ultra-sonication. The resulting nanocellulose manifested as micro to nano-sized granules, with an average particle size ranging from 13 nm to 1.15 µm. Ghazy and co-worker[7] extracted nanocellulose derived from sugarcane bagasse using 60 %wt H_2SO_4 acid hydrolysis at 45°C. This process yielded needle-like structures, and as hydrolysis

time increased, the degree of crystallinity rose from 38.22% to 65.37%.

In recent years, there has been a growing interest in utilizing nanocellulose for the development of conductive films with the aim of serving as effective electromagnetic interference (EMI) shielding materials. Chen and colleagues[8] reported a novel CNFs/AgNWs conductive paper. The paper, approximately 40 μm thick, tensile strength (~49.1 MPa), and sustained electrical conductivity after 2000 bends. The synergy of green CNFs and AgNWs resulted in high EMI shielding effectiveness (39.3 dB in X band), effectively shielding electromagnetic signals for practical mobile phone communication.

This study focuses on the synthesis, characterization, and application of conductive paper based on AgNWs and CNFs, on its potential as a proficient EMI blocking solution. Durian peel is selected as the source of CNFs because it is usually thrown away as waste. Additionally, durian peels have a high cellulose content (50-60%).[9] Using durian peels could boost the value of durian peels and help create valuable materials.

2. Materials and Methods

2.1 Chemicals and Materials

Durian peel was bought from Nong Mon Market, Saen Suk Subdistrict, Chonburi, Thailand. All chemicals were analytical grade and were used without any further purification. Acetone (C_3H_6O) ethanol (C_6H_6O) was purchased from LABSOLV, Thailand. Silver nitrate ($AgNO_3$) was purchased from POCH, Poland S.A. Nitric acid (HNO_3) and sulfuric acid (H_2SO_4) were purchased from QRëC, New Zealand. Ethylene glycol (EG, $C_2H_6O_2$) was purchased from KEMAUS, Australia. Hydrogen peroxide (H_2O_2) and sodium hydroxide (NaOH) were purchased from LOBA Chemie, India. Polyvinylpyrrolidone (PVP, $(C_6H_9NO)_n$ was purchased from Sigma Aldrich, Germany. Distilled water was used in all the experiments.

2.2 Synthesis of Nanocellulose

2.2.1 Durian Powder Preparation

Initially, durian peel (only white part inside) was first cleaned and cut into small pieces. Subsequently, it was allowed to dry in the sun to remove any moisture and dried in an oven at 70°C for approximately 24 h until it achieved a crispy texture. Once completely dried, the durian peel was pulverized for one minute using a blender; this step was repeated three times. Afterward, the ground durian peel was sifted through a 50-mesh sieve. The powder was stored in a plastic container with a lid.

2.2.2 Durian Peel Treatment

The durian peel was treated with an acid, base, and oxidizer to remove hemicellulose and lignin. In Step 1, 300 mL of a 6 %w/v HNO_3 solution was introduced into 30 g of durian powder within a 1L three-necked flask. The resulting suspension underwent heating at 80 ºC while being continuously stirred for 2 h. The residue was vacuum filtered and washed with distilled water several times until the pH of the filtrate becomes neutral. In step 2, a 300 mL of 1 %w/v NaOH solution was introduced to the product obtained from step 1 within a 1L three-necked flask. The mixture was then heated at 80°C and continuously stirred for 2 h. The suspension was then filtered, and washed with distilled water until it reached neutral. In step 3, the fibers obtained from step 2 were further bleached with an oxidizing agent. A 300 mL of 1 %w/v H_2O_2 solution was added to a 1L three-necked flask and stirred at room temperature for 2 h. The suspension was washed several times with distilled water until the pH was neutral. The obtained cellulose microfibers (CMFs) were dried at room temperature.

2.2.3 Extraction of Nanocellulose

The 4 g of CMFs were hydrolyzed with 100 mL of 32 %w/v H_2SO_4 solution under continuous stirring at room temperature for 24 h. The product was filtered and washed several times with distilled water until the pH was neutral. The obtained CNFs were kept in a plastic bottle and stored in a refrigerator.

2.3 Synthesis of Silver Nanowires (AgNWs)

The experimental method employed in this study was adapted from the procedure outlined in the Cao L, et al. report[10]. Typically, in a 250 mL three-necked flask, 1.187 g of PVP was dissolved in 38 mL of EG. Then, 1.189 g of $AgNO_3$, 1.2 mL of a 0.01 M NaCl solution, and 3.2 mL of 0.005 M NaBr solution in EG were added to the solution under magnetic stirring. The mix solution was heated in an oil bath at 175°C for 30 min. After completing the reaction, the suspension was centrifuged at 8000 rpm for 5 min, and washed until the supernatant became colorless. The synthesized silver nanowires were redispersed in ethanol with a concentration of 12.57 mg/mL for further utilization.

2.4 Preparation of AgNWs/CNFs Paper

The 2.0 g of CNFs were dispersed in 30 mL distilled water by stirring for 30 min. Then, different percentages of AgNWs dispersed in ethanol, ranging from 15 to 60 % wt, were added to the CNFs suspension and stirred for 30 min. The

mix suspension was filtered through a membrane under vacuum. The resulting filter paper was air-dried at room temperature and carefully peeled off from the filter, yielding an AgNWs/CNFs paper.

2.5 Characterization

The size, shape, and morphologies of CNFs, AgNWs, and the composite paper were examined using Transmission electron microscopy (TEM; model LEO 145 VP (LEO, England) and a Scanning electron microscopy (SEM; model LEO 145 VP LEO, England). Fourier transform infrared (FTIR) spectra of CNFs and the AgNWs/CNF paper were obtained in the range of 500-4000 cm^{-1} using ATR-FTIR spectrometer; model 2000 (Perkin Elmer, USA). The crystalline structural features of CNFs, AgNWs and AgNWs/CNFs paper were recorded by an X-ray diffraction (XRD; Model Panalytical/Expert. The crystallinity index (CI) was determined by the ratio of the maximum peak intensity at lattice diffraction of (200) to the intensity of the amorphous region between the (200) and (110) peaks.

2.6 Electrical conductivity

The electrical conductivity (σ) of the AgNWs/ CNFs paper was measured by a four-point probe method, performed with a digital multimeter at room temperature using copper electrode pads.

The surface resistivity (ρv) was calculated using equation (1). The corresponding surface conductivity (σv) was calculated in the following equation (2).

$$\rho_v = \frac{A}{T} \times R_v \qquad (1)$$

where A = (a + g) (b + g)

R_v = measured surface resistance (Ω),

A = the electrode surface area (cm^2),

T = the average thickness (cm),

g = the dimension of the digital multimeter probe (cm),

a, b = the length of the rectangular electrode (cm)

$$\sigma = \frac{1}{\rho} \qquad (2)$$

where ρ and σ are the resistivity (Ω·m) and the electrical conductivity (S/m), respectively.

2.7 Electromagnetic Wave Shielding Model

The electromagnetic shielding model was tested using a mobile phone connection in an iron box. Firstly, the phone was placed inside a box with a size of 11.5 cm. x 20.0 cm x 5.5 cm and covered with an iron cover. Another phone was then used to call the phone inside the box. Next, the phone was placed inside the box and covered with an iron cover that had a hole with a hole with diameter of 1 cm. Then, another mobile phone was used to call the phone inside the box. The performance of electromagnetic shielding was tested by covering the hole with AgNWs/CNTs paper and mobile phone connection.

3. Results & Discussion

3.1 Control synthesis of silver nanowires

Polyol method is accepted as an efficient approach for the control synthesis and growth of nanowires under high temperature.[11]In this work, $AgNO_3$ was used as a precursor, polyethylene glycol serves as reducing agent and solvent, while PVP acts as a capping agent. A small quantity of NaCl and NaBr was employed to modulate the wire shape.

Initially, Ag^+ ions were reduced to Ag^0 in ethylene glycol, subsequently forming clusters through a nucleation process. In the controlled growth process, the synergistic mechanism of Br^- and Cl^- was determined by the adsorption energy of the surface crystal plane. The length increase of the AgNWs depends on the growth of the Ag(111) crystal plane, while the diameter increase from the growth of the Ag(100) plane.[12] The co-adsorption of Br^- and Cl^- on the surface results in the more adsorption of the halides on the Ag(111) crystal plane compared to that on Ag(100), thereby promoting a faster increase in length than in diameter.

SEM images in Fig. 1a and 1b verify the wire morphology of the synthesized nano silver. These images demonstrate the existence of long and uniform one-dimensional nanowires. The particle size distribution curve of the nanowires indicates a diameter of 233±17 nm and a length of 3.4±0.1 µm.

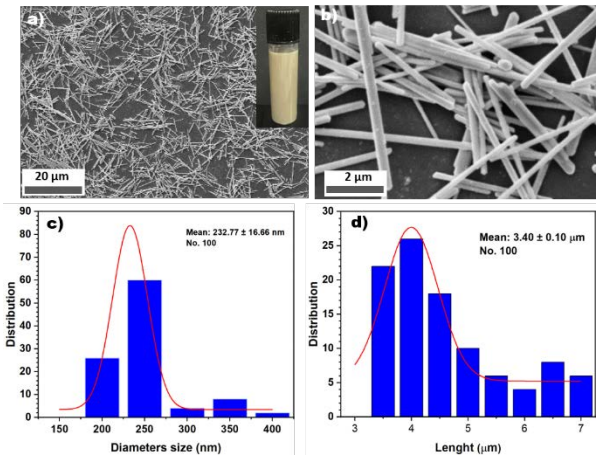

Figure 1. a) SEM image of AgNWs, with an inset photograph of their colloidal nature; b) a high-magnification image c) the width distribution curve and d) the length distribution curve.

3.2 Morphology and Structure of Nanocellulose

Nanocellulose is extracted from the white part inside the durian peel (Fig. 2a) through hydrolysis treatment with H_2SO_4 at 80°C. The resulting nanocellulose appears as a white, opaque, viscous liquid, as depicted in Fig. 2b. The morphology and diameter distribution of the extracted celluloses was examined using SEM and TEM (Fig. 2c and 2d), respectively. It is shown that the nanofibrils were delaminated from the fibers, forming a highly entangled network. The average diameter measures 9.8 ± 0.5 nm, with a length extending to several microns.

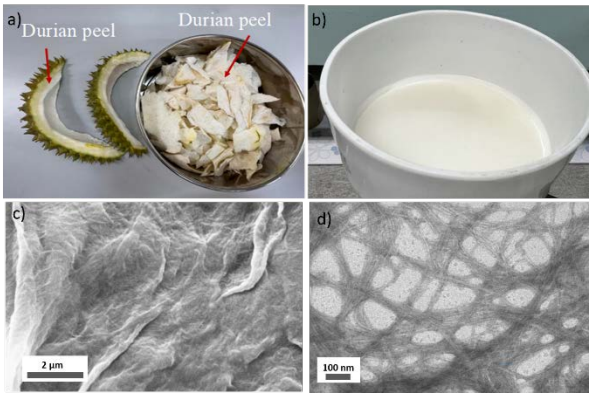

Figure 2. photograph of a) durian peel b) extracted nanocellulose from durian peel c) SEM d) and TEM image of the obtained CNFs.

The functional groups present in durian peel powder were compared with those in the CMFs obtained after treatments and CNFs from hydrolysis with H_2SO_4. Analysis was conducted using ATR-FTIR. The spectra are illustrated in Fig. 3.

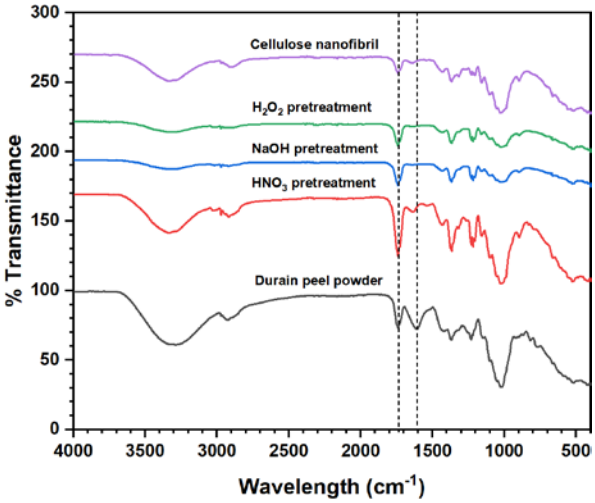

Figure 3. ATR-FTIR spectra of durian peel powder, cellulose microfibrils after pretreatment using HNO_3 (after step 1), HNO_3 and NaOH (after step 2), HNO_3, NaOH and H_2O_2 (after step 3) and nanocellulose after hydrolysis with H_2SO_4.

The peak at 3500-3200 cm^{-1} indicates that the stretching of intramolecular hydrogen bonds of O-H groups of cellulose became narrower after the different treatments due to the removal of part of the amorphous components. The peak around 2852-2942 cm^{-1} corresponds to the C–H stretching of methyl and methylene groups in cellulose, which was found to decrease after NaOH and H_2O_2 bleaching. The another peak located at 1725 cm^{-1} shows the presence of acetyl and ester groups of the hemicellulose or the ester linkage of the carboxylic group of ferulic and p-coumaric acids of lignin and hemicelluloses.[13] This peak was reduced and practically disappeared after the treatment process. The small peak located at 1612 cm^{-1} of durian peel powder is due to aromatic C=C ring stretching, which disappeared in cellulose and nanocellulose, which shows the absence or reduction of lignin and hemicelluloses after NaOH treatment and H_2O_2 bleaching. This shows the effectiveness of chemical treatments to remove lignin and hemicellulose.

3.3 Morphology of AgNWs/CNFs Paper

The fabrication of the AgNWs/CNFs paper involved suction filtration. The AgNWs/CNFs suspension was introduced into a vacuum filtration device, efficiently removing most of the free water. This process led to the creation of a densely packed layer of AgNWs at the bottom, with CNFs forming the top layer of the paper. Subsequently, the wet paper was carefully peeled off from the filter and allowed to dry at room temperature. The morphology of the obtained AgNWs/CNFs paper characterized by SEM is shown in Fig. 4.

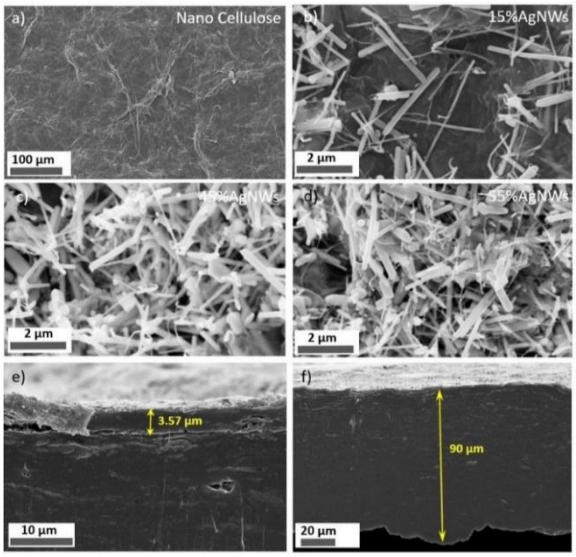

Figure 4. SEM images of a) CNFs b) 15 c) 45 d) 55 %wt AgNWs/CNFs paper and cross-sectional image of 45 %wt sample present e) the thickness layer of AgNWs and f) CNFs

It is evident that the cellulose nanofibril layer exhibits a tightly packed structure after the drying process. Notably, an increased density of wires is observed when a higher percentage of AgNWs is incorporated, as illustrated in Fig. 4b-4d. Fig. 4d and f shows that the paper has thickness of a CNFs layer of 90 µm, and the AgNWs conductive layer of 3.57 µm. The thickness of nanocellulose conductive paper is generally in the nanometer to micrometer range and can be influenced by factors such as the concentration of nanocellulose in the solution and the method of paper production.

3.4 X-ray Diffraction Analysis

The crystal structures of CNFs, AgNWs and AgNWs/CNFs composites were characterized by X-ray diffraction. The XRD pattern of CNFs (Fig. 5a) shows two diffraction peaks at 2θ = 16.2° and 22.5°, corresponding to the (101) and (200) crystal planes, respectively. These peaks are indicative of the characteristic crystalline structures associated with cellulose.[10] The crystallinity index of the obtained CNFs calculated following equation (3) is 88.77%.

$$\mathrm{CI} = \frac{I_{200} - I_{am}}{I_{200}} \qquad (3)$$

where I_{200} is the area of peak from 200 lattice planes and I_{am} is the area of an amorphous phase at 2θ ~18.9°

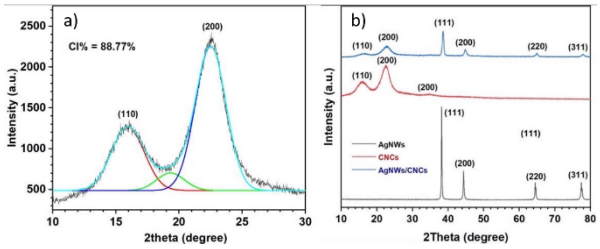

Figure 5. a) X-ray pattern a) with deconvolution of CNFs b) phase comparison between CNFs, AgNWs, and AgNWs/CNFs paper.

XRD pattern of AgNWs is shown in Fig. 5b, the main diffraction peaks at 2θ = 38.2° and 44.4° were assigned to the (111) and (200) crystal forms of silver, respectively.[8] Notably, the growth rate along the (111) crystal plane of AgNWs was significantly faster than other planes, indicating the successful fabrication of one-dimensional AgNWs.[8] The XRD patterns of AgNWs/CNFs paper reveal peaks corresponding to positions identified for both CNFs and AgNWs. No new peaks emerged, indicating that the paper consists of a composite of CNFs and AgNWs.

3.4 Electrical Conductivity Testing

To validate the electrical properties of the prepared composite paper, experiments were conducted involving its connection to a circuit consisting of an LED and two button batteries (Fig. 6a). Notably, the LED illuminated effortlessly, and there were no changes in brightness despite variations in blending. The four-probe apparatus was designed and fabricated as shown in Fig. 6b)

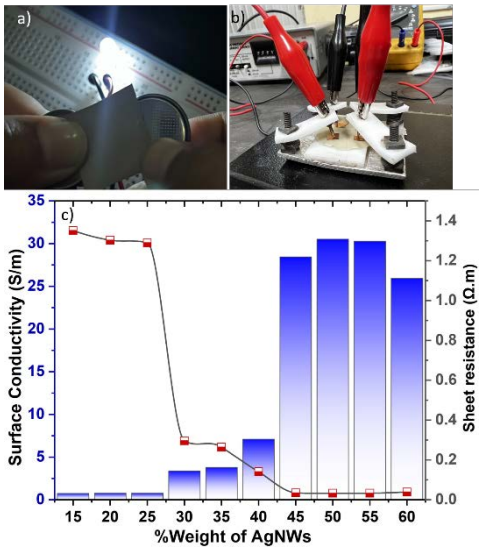

Figure 6. a) An electric circuit consisting of a LED, two button batteries (3V) and 45%wt the AgNWs/CNFs paper b) four-point-probe system c) electrical resistance (σ) and conductivity of the AgNWs/CNFs paper as a function of AgNWs contents.

The influence of % AgNWs content on electrical resistance and conductivity is depicted in Fig. 6c. In the range of 15-40 %wt AgNWs content, only a limited number of nanowires had a marginal impact on the paper, resulting in low electrical conductivity ranging from 0.74 to 7.11 S/m. However, as the % AgNWs content increased to 45 %wt, the sheet resistance decreased to 0.035 Ω·m, and surface conductivity increased significantly to 28.44 S/m. This was attributed to the formation of a continuous conductive pathway within the paper facilitated by the abundance of AgNWs. Beyond this threshold, in the range of 50-55%, the improvement in electrical conductivity gradually plateaued. The decrease in electrical conductivity at much higher AgNWs content may result from their aggregation. Thus, it is possible that the initial conductive network had been established, and the excess AgNWs contributed to the formation of repeated conductive networks, although their impact on the existing framework was limited.

3.5 Communication shielding demonstration.

To demonstrate the electromagnetic interference (EMI) shielding properties of AgNW/CNFs paper, we conducted a practical application following the methodology reported by Chen et al. (2020). The photograph in Fig. 7 illustrates the impact of AgNW/CNFs paper on EMI in mobile phone communication.

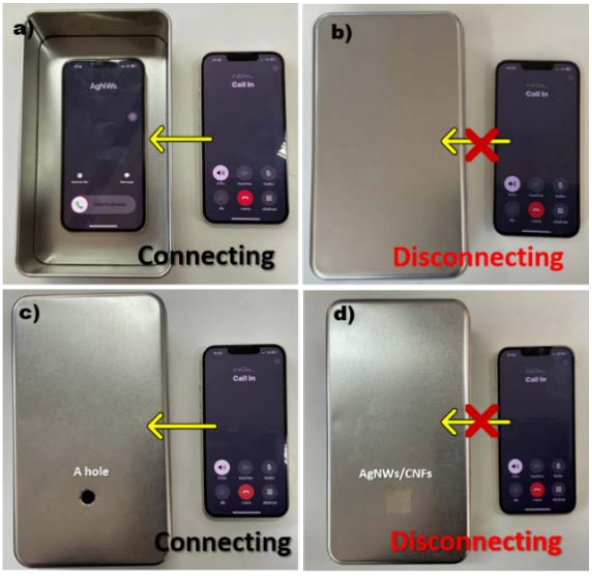

Figure 7. The realistic application simulation of EMI shielding for mobile phone communication involves an iron box tested under different conditions: a) open box, b) closed box, c) closed box with a hole, and d) closed box with a hole covered with AgNWs/CNFs paper.

In the absence of any EMI shielding materials, two mobile phones could establish a connection smoothly. However, when one of the phones was covered with a solid iron casing, the signal was obstructed, rendering the phone unable to make calls. Conversely, when a gap was introduced in the iron cover, electromagnetic waves leaked through, enabling the connected mobile phone to receive signals. By utilizing a piece of AgNWs/CNFs paper to seal the hole, this material effectively shielded all electromagnetic signals, preventing external communication. Therefore, it is believed that this AgNWs/CNFs conductive paper will exhibit great application prospects in the future as effective EMI shielding materials.

4. Conclusion

The successful synthesis of conductive paper involves the utilization of AgNWs and CNFs derived from durian peel. Morphological analysis verifies the formation of long and uniform AgNWs, complemented by a network of entangled nanofibril cellulose. The AgNWs/CNFs paper shows remarkable electrical conductivity, and CNFs, appreciated for their sustainable and renewable nature, presents a promising solution for applications in flexible electronics and EMI shielding.

Acknowledgement

Financial support for this research was provided by the Department of Chemistry, Faculty of Science, Burapha University.

References

1. Nandan, A.; Suresh, A. C.; Saole, P.; Jeevanasai, S. A.; Chandrasekaran, R.; Meili, L.; Wan Azelee, N. I.; Selvasembian, R., *Sustainability* **2023,** *15* (24), 16946.
2. Zhang, H.; Zhu, X.; Tai, Y.; Zhou, J.; Li, H.; Li, Z.; Wang, R.; Zhang, J.; Zhang, Y.; Ge, W., *International Journal of Extreme Manufacturing* **2023**.
3. Langley, D.; Giusti, G.; Mayousse, C.; Celle, C.; Bellet, D.; Simonato, J.-P., *Nanotechnology* **2013,** *24* (45), 452001.
4. Spagnuolo, L.; D'Orsi, R.; Operamolla, A., *ChemPlusChem* **2022,** *87* (8), e202200204.
5. Penjumras, P.; Rahman, R. B. A.; Talib, R. A.; Abdan, K., *Agriculture and Agricultural Science Procedia* **2014,** *2*, 237-243.
6. Pratama, A.; Noer, Z.; Akbar, G.; Annisa, R. D.; Misran, E.; Karolina, R.; Ikhwanuddin, I. AIP Conference Proceedings, AIP Publishing: 2023.
7. Pula, B.; Ramesh, S.; Pamidipati, S.; Doddipatla, P., *Bioresources and Bioprocessing* **2021,** *8*, 1-18.
8. Chen, Y.; Pang, L.; Li, Y.; Luo, H.; Duan, G.;Mei, C.; Xu, W.; Zhou, W.; Liu, K.; Jiang, S., *Composites Part A: Applied Science and Manufacturing* **2020,** *135*, 105960.
9. Lubis, R.; Wirjosentono, B.; Eddyanto, E.; Septevani, A. AIP Conference Proceedings, AIP Publishing: 2020.
10. Cao, L.; Huang, Q.; Cui, J.; Lin, H.; Li, W.; Lin, Z.; Zhang, P., *Nanomaterials* **2020,** *10* (6), 1139.
11. Hemmati, S.; Harris, M. T.; Barkey, D. P., *Journal of Nanomaterials* **2020,** *2020*, 1-25.
12. Xiao, N.; Chen, Y.; Weng, W.; Chi, X.; Chen, H.; Tang, D.; Zhong, S., *Nanomaterials* **2022,** *12* (15), 2681.
13. Shi, Z. J.; Xiao, L. P.; Xu, F.; Sun, R. C., *Journal of applied polymer science* **2012,** *125* (4), 3290-3301.

Plasmon enhancement of photodetectors based on $CsPbBr_3$ quantum dots

Zar Ni Thein Htay[1], Chaturika Madhuwanthi [1], Sakoolkan Boonruang [2], and Shu-Han Hsu[1]*

[1]*School of Integrated Science and Innovation, Sirindhorn International Institute of Technology, Thammasat University, Pathum Thani 12121, Thailand*
[2]*Spectroscopic and Sensing Devices Research Group (SSDRG), Opto-Electrochemical Sensing Research Team (OEC), National Electronic and Computer Technology Center (NECTEC), Pathum Thani 12120, Thailand*
**E-mail: shuhanhsu@siit.tu.ac.th*

Abstract:

Inorganic perovskite quantum dots ($CsPbBr_3$) show great potential for optical sensing applications that have excellent optic properties such as high carrier mobility, long carrier diffusion length, and excellent visible light absorption. The absorption spectrum well overlaps with localized surface plasma resonance (LSPR) of noble Au nanocrystals (Au NCs). Currently, the state-of-the-art photocurrent of $CsPbBr_3$ is within the nanoampere range, limiting further practical application. Therefore, we would like to enhance the photocurrent of $CsPbBr_3$ quantum dots and improve the device's stability. With the nature of energy level alignment between Au nanoparticle and $CsPbBr_3$ quantum dots significant photocurrent enhancement was demonstrated. In this study, $CsPbBr_3$ perovskite quantum dots have been synthesized and used to fabricate the photodetector onto the gold finger electrode. Under laser excitement with wavelength at 520 nm, it has been observed that $CsPbBr_3$ quantum dots alone could obtain the photocurrent to 100 nA. By introducing Au Nanoparticles, the net photocurrent has been increased nearly 1µA. Therefore, it could be said that Au nanoparticles can assist the photocurrent generation of $CsPbBr_3$ quantum dot more sufficiently with better stability. This allows the further device system integration of such $CsPbBr_3$ quantum dots with Au nanoparticles.

1. Introduction

Today, photodetectors can be used for a wide range of applications, such as environmental sensing, missile guidance, optical communications, optical imaging and biological analysis[1]. And, the application of PDs is becoming more and more common.

Nano-perovskite materials are considered the most promising for PD integration because of their properties like Diffusion length, Low defect density, and Tune direct band gap. However, it has been discovered that all inorganic CsPbX3 materials have all of these advantages and are more stable in humid environments than their hybrid organic-inorganic halide counterparts. However, the primary factor limiting perovskite NCs from being widely used is their ionic architectures, which naturally contribute to their poor stability. As a result, exposure to moisture, oxygen, high temperatures, or UV radiation can cause rapid material deterioration in perovskite NCs, which makes material storage, fabrication, and device functioning extremely unpredictable. The two main external elements affecting the environmental stability of perovskite nanoclusters are oxygen and moisture. In particular, hydration (or solvation in other polar solvents) can cause perovskite NCs to lose their structural integrity in the presence of water or even in a wet atmosphere. As a result, these stability problems restrict their use in aqueous medium-based processes like photocatalysis, photoelectric catalysis, and biological detection. Furthermore, because perovskites are inherently ionic, mixing different halide perovskite NCs to lose their structural integrity in the presence of water or even in a wet atmosphere. Furthermore, because perovskites are inherently ionic, mixing different halide perovskite NCs may cause anion exchange, homogenizing the composition. As a result, achieving environmental stability for perovskite NCs is essential for their use in real-world applications[9]. Thus, it has been proposed to integrate these with other materials for better efficiency and one recent solution is decorating these with metals such as Au and Ag and plasmonic nature can help the materials to overcome the challenges of QDs, making these more compatible for PD applications.

For fabricating perovskite-based photodetectors, enhanced localized surface plasmon resonance (LSPR) effect caused by local electric field on plasmonic nanoparticles' surface, is highly applied and it has been carried out to prove the plasmonic modulation on photodetectors. And, based on our results, it was found that plasmonic PDs have more photocurrent efficiency than the bare QD-based PDs and LSPR effect was well-demonstrated throughout our work.

2. Materials and Methods

2.1 Materials

Materials such as Lead bromide ($PbBr_2$), Cesium bromide (CsBr), dimethylformamide (DMF), Oleic acid (OA), Oleylamine (OAm), Toluene were purchased from Italmar Thailand Co.Ltd. 5mm Gold Interdigitated Finger Electrodes were fabricated by sputtering Cr-30 nm as adhesion layer and then, Au-80 nm with the help of shadow mask in National Science and Technology Development Agency. Au Nanoparticles were also purchased from Italmar Thailand Co.;Ltd.

2.2 Synthesis of $CsPbBr_3$ QDs

The precursor solution was prepared by dissolving 0.1428 g of $PbBr_2$ (0.4 mmol) and 0.0425 g of CsBr(0.2 mmol) in 5 ml of DMF. 0.5 ml of OA and 0.25 ml of OAm were added to the precursor solution to stabilization. Then 1 ml of precursor solution was added to 10 ml of toluene under vigorous stirring (800 rpm) for 30 seconds. The formed QDs were separated by centrifugation at 6000 rpm for 10 minutes. At first, $CsPbBr_3$ Quantum Dots were formed and the supernatant from Quantum Dots were separated by centrifugation at 6000 rpm for 10 minutes. The supernatant was kept for 2-3 days and yellow color $CsPbBr_3$ quantum dots were formed and separated by centrifuging at 6000 rpm for 10 minutes[15].

2.3 Device Fabrication

To fabricate the photodetector with bare Pe QDs/Au Nanoparticles, as shown in Figure 1, 0.01 mg of Au nanoparticles were mixed with Toluene and deposited onto the interdigitated electrode in stepwise manner. After being dried, around 1mg of $CsPbBr_3$ QDs, also mixed in Toluene form, was poured onto the existing Au Layer.

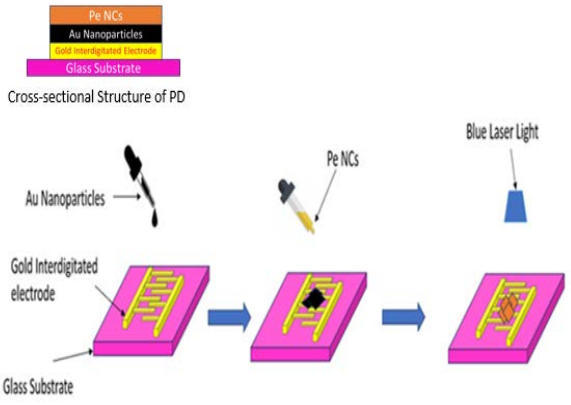

Figure 1. Photodetector Fabrication of Pe NCs with Au Nanoparticles

2.4 Spectroscopic measurement

$CsPbBr_3$ QDs were characterized for measurement of their absorption spectrum and PL emission spectrum. The former test was measured by UV-Vis Spectrophotometer while the latter was characterized by Spectrometer, using 520 nm as the excitation source. In both measurements, the samples were dispersed in Toluene. After that, to see the photo response of Pe NCs, a measurement of the I-t curve was performed. Besides, these took XRD and TEM tests too as in Figure 2. For TEM characterization, samples were placed as the film on the ultra-thin carbon film. For the $CsPbBr_3$ /Au composite structure, an I-t test was also done to see the photocurrent increase, response by the nanostructure based on the time. All tests above were carried out in ambient conditions.

3. Results & Discussion

3.1 Characterization Results of QDs

Throughout the synthesis method as mentioned in section 2.2, all inorganic perovskite NCs were prepared. From Figure 2, it can be seen that the particle size of $CsPbBr_3$ QDs were around 6 nm and measured by High-Resolution Transmission Electroscope Measurement. From the Figure, The XRD Pattern of $CsPbBr_3$ QDs verified the perovskite crystal structure and these are in the orthorhombic phase. As shown in Figure 3(a), the solution sample of NCs was measured by absorption spectra. One of the advantages of Perovskite QDs is having excellent absorption capacity and it can be known through, showing its peak around 502 nm which again verifies its applicability for future optoelectronic applications such as photodetector. The organic ligands on NCs' surfaces let the NCs to be able to well disperse in Toluene and for more than 6 months, the colloid is stable.

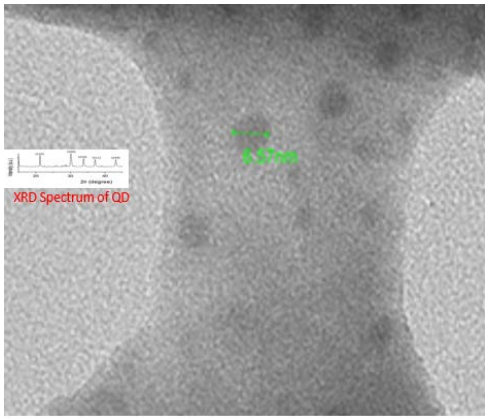

Figure 2. TEM Image of Quantum Dots

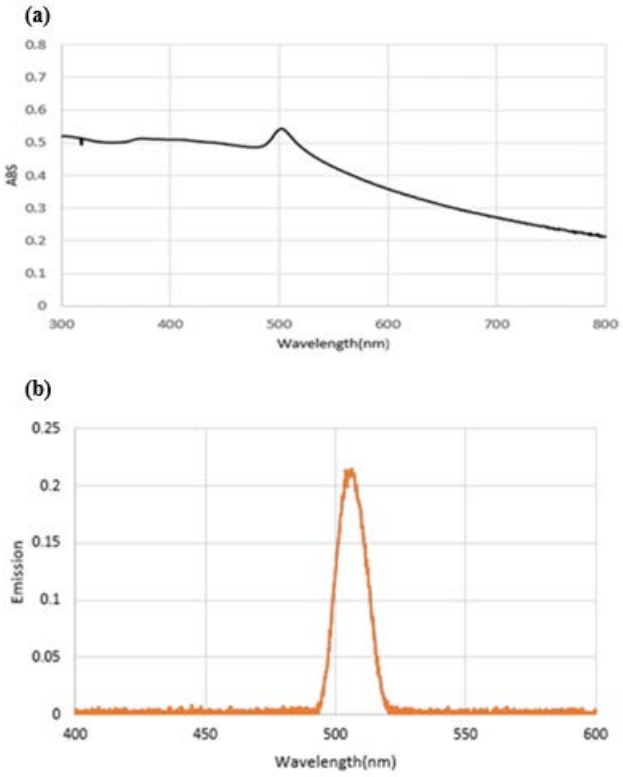

Figure 3. (a)Absorbance and (b) PL Emission Spectrum of Quantum Dots

The PL Emission Spectra of $CsPbBr_3$ QD is shown in Figure 3(b). Under the illumination of wavelength 520 nm, there was a slight red-shift being observed in the PL Intensity of Pe NS and the emission wavelength was around 505 nm.

The performance of PDs fabricated without and with Au NCs has been shown in Figure 4. From there, it can be known that the Dark Current was around 5 nA, and under the illumination of 520nm Laser Power at the bias voltage of 5, there was a photocurrent increase to around 100 nA. The Dark Current of PD with Au NCs was around 0.01 µA(10nA) and under the same conditions, the photocurrent has been increased to 1µA(1000nA).

3.2 Performance Results of PDs

Previously, the enhancement factor was around 100. For instance, Lin and colleagues combined an InAs quantum dot with a gold 2D hole array (2DHA) structure to produce a 130% improvement of photo response. Tang and colleagues compounded PbS NCs with Ag NCs as the active layer, resulting in photocurrent increase of 110%. By using Al nanoparticles to build the GaN PD, Ozbay and colleagues were able to increase photo response by 50%. Zhou and colleagues demonstrated CdSe nanoribbons with hollow gold nanoparticles applied to the surface; the photocurrent rose by 75%, from 84 to 147 µA. In contrast, our study shows a 900% rise. This is because carriers have a large capacity for light absorption and photogeneration, and their strong ability to separate into individual photocarriers is what causes the strong separation. Photocurrent Enhancement by the high light absorption and photogeneration ability of carriers, and the strong separation ability of photocarriers induced by the plasmonic effect could increase the performance of the photodetectors and therefore, should be explored more for better applications in optoelectronic devices[2]. It also has been observed that plasmonic effects can fill the gap of those in bare PDs without the fabrication and it can contribute to developing more flexible optical tools in the future. To be able to claim the better performance of Plasmonic PDs decorated with Au NPs in our work, enhancement factor has been calculated and along with the same parameter of different existing plasmonic photodetectors, the obtained value was compared in Table 1.

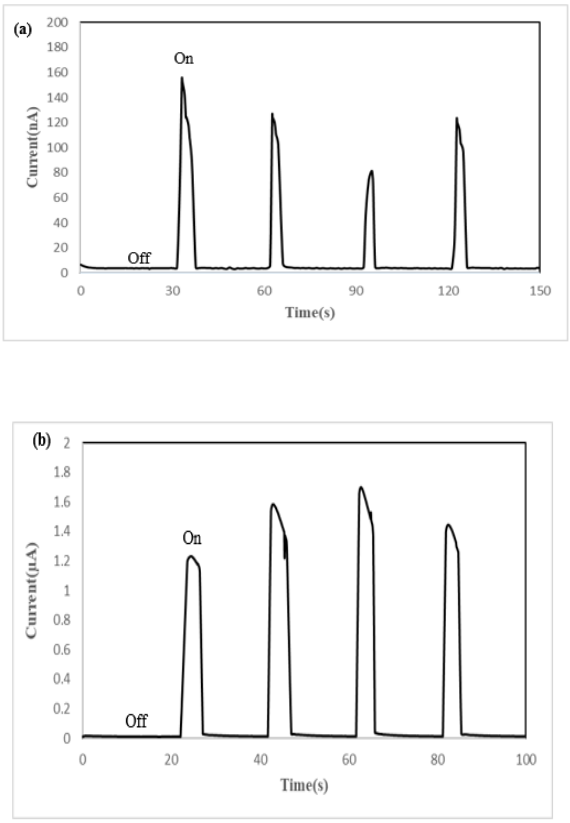

Figure 4. I-t Curves of (a) bare Pe QDs and (b) Pe QDs/Au Nanoparticles under 520 nm at 5V respectively

Table 1. Summary of Performance of Plasmonic PDs

Device	I_p	Enhanced I_p	Enhancement Factor
PbS+ Ag[16]	3.1 nA	6.5 nA	110%
$CsPbBr_3$+Au[2]	245.6μA	831.1μA	238%
$CsPbBr_3$+ Au[3]	0.25μA	1.5μA	500%
InAs+ Au[19]	1 a.u	3.1 a.u	130%
GaN+ Al[17]	1 a.u	1.5 a.u	50%
CdSe+ Au[18]	84	147	75%
Our Work	0.1μA	1μA	900%

Table 2. The Comparison of Device Performance without or with Au NPs

Device	I_{dark}(μA)	I_p(μA)	I_p/I_{dark}	Responsivity (mA/W)	Detectivity (J)	EQE(%)
Without Au	0.005	0.1	20	3.8×10^{-3}	11×10^{7}	9×10^{-12}
With Au	0.01	1	100	39×10^{-3}	37.7×10^{7}	9.3×10^{-11}

The enhancement factor of the device shown in Table 1 was calculated by the equation below-

$$i = \frac{I_{p^2} - I_{p^1}}{I_{p^1}}$$

where I_{p^2} is enhanced photocurrent, and I_{p^1} is the initial photocurrent. Therefore, the enhancement factor for the PD in this work is 900%.

For Table 2, some parameters of PDs with or without Au NPs have been calculated. Specific Detectivity(D^*) is regarded as the key parameter and it can be calculated as-

$$D^* = \sqrt{\frac{A}{2e\times I_{dark}}} \times R$$

For R, it can also be calculated as –

$$R = \frac{I_p - I_{dark}}{P_{inc} \times A_{active\ cross\ section}}$$

where, A= Area of the active region and R= responsivity of the device.

And, since = 8.3 W/cm^2, the Laser Power Density, values can be defined as 3.8×10^{-3} mA/W for bare QD PD and 39×10^{-3} mA/W for PD with Au NPs. Then, from the equation as above, D^* can be defined as 11×10^{7} and 37.7×10^{7} Jones for the Photodetector without or with Au NPs respectively. As the detectivity has been increased, the plasmonic effect can be proved well. Besides, the value of EQE (External Quantum Efficiency) has been calculated with the equation-

$$EQE = \frac{h \times c \times R}{e \times \lambda}$$

where, λ=wavelength and after that, PDs fabricated with only QDs could produce 9×10^{-12}(%) while those with Au NPs have 9.3×10^{-11}(%).

4. Conclusion

To summarize, photocurrent increase from $CsPbBr_3$ QDs by Au Nanoparticles have been demonstrated. Before applying with gold particles, the illuminated current produced from bare Pe NSs was about 100nA but after using a different method, stepwise layering, the current itself reached 1μA(1000nA) with the same parameters. It means that the Plasmonic effect could boost the performance of photodetectors and the enhancement factor is about 900%. Besides, as above-mentioned, the unique method could be interesting to study more and proved to be working. So, it is a fact that could be promising in fabricating optoelectronic applications such as flexible photodetectors.

Acknowledgments

The authors gratefully acknowledge the support from the School of Integrated Science and Innovation(ISI), Center of Excellence in Functional Advanced Materials Engineering, Sirindhorn International Institute of Technology (SIIT), Thammasat University, through the scholarship under the Thailand Advanced Institute of Science and Technology and Tokyo Institute of Technology (TAIST-TokyoTech) Program, funded by the National Research Council of Thailand(NRCT) and the National Science and Technology Development Agency(NSTDA).

References

1. Yang, Z.; Jiang, M.; Guo, L.; Hu, G.; Gu, Y.; Xi, J.; Huo, Z.-Y.; Li, F.; Wang, S.; Pan, C. A High Performance $CsPbBr_3$ Microwire Based Photodetector Boosted by Coupling Plasmonic and Piezo-Phototronic Effects. Nano Energy 2021, 85,105951–105951.
2. Dong, Y.; Gu, Y.; Zou, Y.; Song, J.; Xu, L.; Li, J.; Xue, J.; Li, X.; Zeng, H. Improving All-Inorganic Perovskite Photodetectors by Preferred Orientation and Plasmonic Effect. Small 2016, 12 (40), 5622–5632.
3. Dong, Y.; Xu, L.; Zhao, Y.; Wang, S.; Song, J.; Zou, Y.; Zeng, H. The Synergy of Plasmonic Enhancement and Hot-Electron Effect on $CsPbBr_3$ Nanosheets Photodetector. *Advanced Materials Interfaces* **2021**, *8* (6).
4. Li, M.; Shen, K.; Xu, H.; Ren, A.; Lee, J.; Sundar Kunwar; Liu, S.; Wu, J. Enhanced Spatial Light Confinement of All Inorganic Perovskite Photodetectors Based on Hybrid Plasmonic Nanostructures. *Small* **2020**, *16* (46).
5. Gao, Y.; Zhao, L.; Shang, Q.; Zhong, Y.; Liu, Z.; Chen, J.; Zhang, Z.; Shi, J.; Du, W.; Zhang, Y.; Chen, S.; Gao, P.; Liu, X.; Wang, X.; Zhang, Q. Ultrathin $CsPbX_3$ Nanowire Arrays with Strong Emission Anisotropy. Advanced Materials 2018, 30 (31).
6. Kagan, C. R.; Lifshitz, E.; Sargent, E. H.; Talapin, D. V. Building Devices from Colloidal Quantum Dots. Science 2016, 353 (6302), aac5523–aac5523.
7. Chen, H.; Wang, Y.; Wang, J.; Liu, W. Thermal Stability of $CsPbBr_3$ Perovskite Quantum Dots Assembled with SBA-15. Coatings 2021, 11 (8), 953.
8. Li, Z.; Hofman, E.; Li, J.; Davis, A. H.; Tung, C.; Wu, L.; Zheng, W. Photoelectrochemically Active and Environmentally Stable $CsPbBr_3/TiO_2$ Core/Shell Nanocrystals. Advanced Functional Materials 2017, 28 (1), 1704288.
9. Li, G.; Wisnivesky, F.; Nathaniel; Bai, S.; Jellicoe, T. C.; Ayala, F.; Hou, S.; Ducati, C.; Gao, F.; Friend, R. H.; Greenham, N. C.; Tan, Z.-K. Highly Efficient Perovskite Nanocrystal Light-Emitting Diodes Enabled by a Universal Crosslinking Method. Advanced Materials 2016, 28 (18), 3528–3534.
10. Vishaka, H. V.; Jesna, G. K.; Pasha, A.; Sarina, K.; R. Geetha Balakrishna. Lattice Constriction and Trapped Excitons: A Structure–Property Relationship Unveiled in $CsPbBr_3$ Perovskite QDs. Journal of Materials Chemistry C 2020, 8 (47), 17090–17098.
11. Zhou, B.; Liu, M.; Wen, Y.; Li, Y.; Chen, R. Atomic Layer Deposition for Quantum Dots Based Devices. Opto-Electronic Advances 2020, 3 (9), 19004301–19004314.
12. Chen, H.; Li, R.; Guo, A.; Xia, Y. Highly Fluorescent $CsPbBr_3$ /TiO_2 Core/Shell Perovskite Nanocrystals with Excellent Stability. SN Applied Sciences 2021, 3 (6).
13. Xu, F.; Meng, K.; Cheng, B.; Wang, S.; Xu, J.; Yu, J. Unique S-Scheme Heterojunctions in Self-Assembled $TiO_2/CsPbBr_3$ Hybrids for CO_2 Photoreduction. Nature Communications 2020, 11 (1).
14. Harmon, D. M.; Chen, C.; Halford, J. H. Portable Fluorescence Detection Platform with Integrating Sphere. PubMed 2018.
15. Xie, Y.; Yu, Y.; Gong, J.; Yang, C.; Zeng, P.; Dong, Y.; Yang, B.; Liang, R.; Ou, Q.; Zhang, S. Encapsulated Room-Temperature Synthesized $CsPbX_3$ Perovskite Quantum Dots with High Stability and Wide Color Gamut for Display. *Optical Materials*

Express **2018**, *8* (11), 3494–3494.https://doi.org/10.1364/ome.8.003494.
16. He, J.; Qiao, K.; Gao, L.; Song, H.; Hu, L.; Jiang, S.; Zhong, J.; Tang, J. Synergetic Effect of Silver Nanocrystals Applied in PbS Colloidal Quantum Dots for High-Performance Infrared Photodetectors. ACS Photonics 2014, 1 (10), 936–943.
17. Butun, S.; Cinel, N. A.; Ozbay, E. LSPR Enhanced MSM UV Photodetectors. Nanotechnology 2012, 23 (44), 444010.
18. Luo, L.-B.; Xie, W.-J.; Zou, Y.-F.; Yu, Y.-Q.; Liang, F.-X.; Huang, Z.-J.; Zhou, K.-Y. Surface Plasmon Propelled High-Performance CdSe Nanoribbons Photodetector. Optics Express 2015, 23 (10), 12979
19. Chun Chieh Chang; Sharma, Y. D.; Yong Sung Kim; Bur, J.; Shenoi, R. V.; Krishna, S.; Huang, D.; Lin, S.-Y. A Surface Plasmon Enhanced Infrared Photodetector Based on InAs Quantum Dots. 2010, 10 (5), 1704–1709.

Bio-$CaCO_3$ from *Perna viridis* shells for plant coating

Orakanya Kumphon[1], Chutiparn Lertvachirapaiboon[2], Sanong Ekgasit[3], and Tewarak Parnklang[1]*

[1]*Department of Industrial Chemistry, Faculty of Applied Science, King Mongkut's University of Technology North Bangkok, Bangkok 10800, Thailand*
[2]*National Nanotechnology Center, National Science and Technology Development Agency, Pathum Thani 12120, Thailand*
[3]*Sensor Research Unit, Department of Chemistry, Faculty of Science, Chulalongkorn University, Bangkok 10330, Thailand*
**E-mail: tewarak.p@sci.kmutnb.ac.th*

Abstract:

This study focuses on upcycling calcium carbonate ($CaCO_3$) extracted from green mussel shell waste as plant sunscreen for protecting sun damage. Based on the thermal gravimetric analysis, a green mussel shell is composed of 95–97% (w/w) $CaCO_3$ and 3–5% (w/w) organic matrix. The $CaCO_3$ extraction process mainly consists of two steps, including eco-friendly process of eliminating the organic matrix and physically disintegrating the hierarchical $CaCO_3$ structures. The extracted $CaCO_3$ has plate shapes with a bisector length of 3–5 microns and a thickness of 200–500 nm as observed in optical and SEM micrographs. Molecular information of the extracted $CaCO_3$ is investigated by FT-IR and Raman spectroscopies. Primary aragonite $CaCO_3$ platelets are stacked into layer structures that selectively reflect UV radiation with wavelengths ranging from 290 to 400 nm as revealed by UV-visible absorption test. The extracted $CaCO_3$ could be dispersed in aqueous media containing cellulose nanocrystals (CNCs), cellulose nanofibers (CNFs), and gelatin. The $CaCO_3$-CNC-CNF-gelatin aqueous mixture could be sprayed on various parts of plants and the resulting $CaCO_3$-CNC-CNF-gelatin composite film could prevent water loss and sun damage. The applications of the extracted $CaCO_3$ as plant sunscreen effectively address seafood waste upcycling, fresh produce quality, and food sustainability.

1. Introduction

Sunburn or solar injury creates important financial losses in numerous fruit species such as apples, mangoes, grapevines, pomegranates, and olives.[1] Solar damage in plant tissues caused by excessively high temperatures and light irradiation, generates photo-oxidative stress due to the high accumulation of reactive oxygen species (ROS) and manifests typical sunburn symptoms.

Ground, softwoods, and hardwoods are examples of lignocellulosic biomasses that may be processed into neolignanes and nanocelluloses, such as lignin nanoparticles (LNPs), cellulose nanocrystals (CNCs) and cellulose nanofibrils (CNFs). While CNFs are flexible filaments with a semicrystalline structure, CNCs are stiff, highly crystalline, needle-like nanoparticles. Both CNCs and CNFs present an average width of less than 10 nm.[2] The inherent characteristics of the cellulosic nanostructures, such as their high tensile strength, stiffness, biocompatibility, high optical transparency, and gas barrier, enable CNCs and CNFs for a broad spectrum of applications.[3]

Thailand generates approximately 42,000 tons of green mussel (*Perna viridis*) shell waste due to its extensive consumption. According to data on sea shellfish production in 2020, Samut Songkhram province produced 17,045.87 tons of mussels or 14.33% of the total amount produced. Currently, the local community has been dealing with the problem of mussel shell waste build up. Nevertheless, no government agency has taken the issue seriously.

Recently, researchers has developed a method for extracting calcium based on the high aragonite allotrope from mussel shells.[4] High purity Bio-calcium carbonate or Bio-$CaCO_3$ extracted from mussel shells is different from regular shellfish meals in that contaminant, such as shellfish meat and proteins, were removed by a chemical treatment. The extracted Bio-$CaCO_3$ particles contain a constant percentage of calcium carbonate. The Bio-$CaCO_3$ particles possess good physical properties, including heat resistance and water insolubilities. Nano-calcium and colloidal calcium carbonate could be employed as a biopesticide for various plants. In addition, nano-calcium and colloidal calcium could be utilized as a fertilizer, plant protection and monitoring control.[5] In addition, the Bio-$CaCO_3$extracted from green mussel shell is in the aragonite form possessing a good biocompatibility. The development of environmentally friendly coating is crucial for reducing the pesticide usage and improving the quality of agricultural goods. The Bio-$CaCO_3$ could be formulated as a sprayable coating forming a protective layer on various plant parts including stems, bases, leaves, and fruits of the plants. The formed coating could lower the rate of transpiration from the plant's surface by giving

the physical barrier. Furthermore, the Bio-$CaCO_3$ coating might prevent plant microbial infection and control insect and pest infestation.

Therefore, it is the main purpose of this research to develop a renewable coating based on Bio-$CaCO_3$ to prevent possible damages on plants. *Manihot esculenta* (L.) *Crantz* leaves were selected as a model plant parts to investigate the effectiveness of the developed coating. The Bio-$CaCO_3$ were analyzed by sieve analysis, laser diffraction, and microscopy. The effectiveness of the developed coatings was analyzed by optical microscopy and FT-IR spectroscopy.

2. Materials and Methods

2.1 Materials

The green mussel shells *(Perna viridis*) were obtained from Laem Yai community in Samut Songkhram, Thailand. The cellulose nanofibers (CNFs) and cellulose nanocrystals (CNCs) were analytical grades. Gelatin is a food-grade product. Organic, accessible surfactants were industry-grade.

2.2 Preparation of calcium carbonate ($CaCO_3$) from green mussel shell waste

$CaCO_3$ was extracted from green mussel shells. The dried green mussel shells (10 kg) were soaked in 1 M potassium hydroxide for 7 days under room temperature. Afterward, the shells were rinsed with clean water until the water's pH approaches a neutral value. After that, the mussel shells were dried under ambient conditions. The dried shells were pulverized using a pin mill. The crushed shells were finally immersed in a 30–50% hydrogen peroxide (H_2O_2) solution and dried under the sunlight.

Table 1. Preparation of plant coating solutions.

Sample	CNCs (28%) + CNFs (57%) in water (mL)	6% (w/w) Gelatin (mL)	$CaCO_3$ (powder) (g)	Organic surfactants (mL/1L)	Total (mL)
Control	0	0	0	0	0
Sample1	100	100	0.15	-	200
Sample2	0	0	2	0.5	1000

2.3 Preparation of film coating

The coating solutions were prepared by mixing various components listed in **Table 1** until the homogeneous solutions were obtained. Gelatin, CNCs, and CNFs and were employed as a film forming agent in the Sample-1 coating formula. The commercial organic surfactants employed in the Sample-2 coating formula are substances enhancing the adhesion of Bio-$CaCO_3$ to the substrates without forming the film. The effectiveness of the Bio-$CaCO_3$ coating formula were evaluated by the distribution and adhesion of Bio-$CaCO_3$ to the substrates.

2.4 Particle size distribution analysis

The extracted Bio-$CaCO_3$ were sieved with a sieve shaker. The particles retained on and passed through the 200-mesh sieve were subsequently analyzed using a laser particle size distribution analyzer (MALVERN Mastersizer 3000), the particle size distribution for each sample was measured in the range of 0.01–3,500 micrometers.

2.5 Morphology analysis

Microstructure and morphology of the sample Bio-$CaCO_3$ were analyzed using an optical microscope (AxioCam HRc coupled with CCD camera, Carl Zeiss Co., Ltd, Bangkok, Thailand). and a JEOL JSM-6510A scanning electron microscope (JEOL Ltd, Tokyo, Japan). The SEM microscope operates at an accelerating voltage of 10–15 kV.

2.6 Molecular information

Attenuated total reflection Fourier transform infrared (ATR FT-IR) spectroscopy was employed to investigate the functional groups of the starting extracted $CaCO_3$ powder. The ATR FT-IR spectra were acquired using a Nicolet iS5 FT-IR spectrophotometer (Thermo Scientific, Mas-

sachets, United States) equipped with a fast recovery deuterated triglycine sulfate (DTGS) detector. An iD5 single-bounce ATR accessory with a laminate-diamond crystal was employed as a sampling probe. To obtain the infrared spectrum, the dried specimen was placed on a flat diamond crystal IRE with a sampling diameter of 1.5 mm. The specimen was pressed against the flat diamond crystal with a pressure device until the maximum allowable pressure was obtained. All ATR FT-IR spectra were collected at a resolution of 4 cm^{-1}. The number of co-addition scans was 32.

3. Results & Discussion

3.1 Sieve analysis of Bio-$CaCO_3$

The extracted calcium carbonate powder is shown in **Figure 2**.

Figure 2. Calcium carbonate ($CaCO_3$) powder.

The weight distribution of the extracted Bio-$CaCO_3$ was analyzed by sieve analysis technique. Sixty percent of Bio-$CaCO_3$ can pass through a 40-mesh sieve. The proportion of finer particles passing through 4-, 10-, 20-, 40-, 100-, and 200-mesh sieves were 100 ± 0 %, 99.33 ± 0.31 %, 92.33 ± 0.94 %, 58.26 ± 2.60 %, 16.80 ± 1.05 %, and 1.73 ± 0.31%, respectively, as shown in **Table 2**. Only the extracted calcium carbonate particles with the size less than or equal to 200 mesh, i.e. the particles with diameters less than or equal to 0.075 mm, were employed for the film coating solution preparation to maximize the surface coverage and particle retention on the substrate.

Table 2. Sieve analysis of Bio-$CaCO_3$.

Sieve No.	Sieve Opening (mm)	Percent Finer
		Bio-$CaCO_3$ treated with H_2O_2
#4	4.750	100 ± 0
#10	2.00	99.33 ± 0.31
#20	0.850	92.33 ± 0.94
#40	0.425	58.26 ± 2.60
#100	0.150	16.80 ± 1.05
#200	0.075	1.73 ± 0.31
PAN (>#200)	-	-

3.2 Particle size distribution of Bio-$CaCO_3$

The laser diffraction spectra of the extracted Bio-$CaCO_3$ retained on and passing through a 200-mesh sieve are shown in **Figure 3**. The uniformity, span, and the Sauter diameter (D[3,2]) of a particle collection could be calculated by the following equations:[6]

$$\text{Uniformity} = \frac{\sigma}{\overline{D}_{mean}}$$

$$\text{Span} = \frac{D_{90} - D_{10}}{D_{50}}$$

$$D[3,2] = \frac{\sum D_i^3 v_i}{\sum D_i^2 v_i}$$

Where, σ is the standard deviation of the particle diameter, $\overline{D}_{mean}$ is the mean particle diameter, D_{90}, D_{50}, and D_{10} are the particle size at 90%, 50%, and 10% quantity, respectively, D_i is the mean size class of the particles, and v_i is the volume of particles in each size class. The uniformity values of the Bio-$CaCO_3$ particles were 0.802 ± 0.007 and 0.815 ± 0.004 for #200 and PAN samples, respectively. The particles formed from Bio-$CaCO_3$ are classified to be uniform-grade particles as they were specifically sieved through specified mesh and possessed the uniformity values less than 1. The span values of #200 and PAN samples were 2.460 ± 0.022 and 2.484 ± 0.011 respectively. The Sauter diameters or D [3,2] of #200 and PAN samples were 7.25 ± 0.15 and 5.51 ± 0.02 μm, respectively. The Sauter diameter, or surface-area averaged diameter is directly related to the coating application of Bio-$CaCO_3$. On average, a Bio-$CaCO_3$ particle could cover an area equivalent to the circular particles with diameter of 5–7 μm.

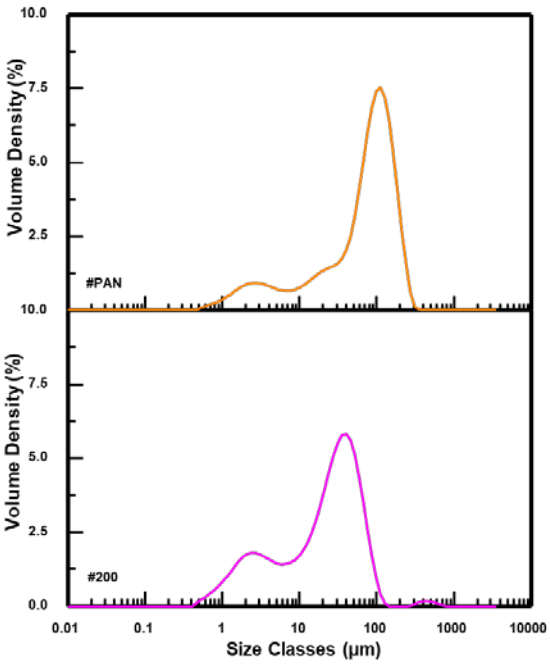

Figure 3. Laser light scattering spectra of Bio-$CaCO_3$ on 200-mesh sieve (#200) and the finer Bio-$CaCO_3$ particles (#PAN).

3.3 Morphology analysis

Figure 4 and **Figure 5** display the optical micrographs and scanning electron micrographs of Bio-$CaCO_3$ powder, respectively. The results revealed that Bio-$CaCO_3$ particles were a stacked polygonal sheet with smooth surfaces. A plate-like morphology of Bio-$CaCO_3$ particles has the potential to facilitate the particle connection on a flat surface and generate a strong interparticle force during coating.

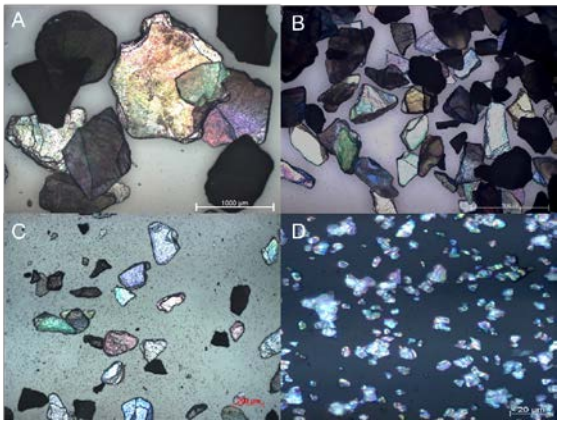

Figure 4. Optical micrographs of H_2O_2-treated Bio-$CaCO_3$ particles. The scale bars in A, B, C, and D are 1000 μm, 1000 μm, 200 μm, and 20 μm, respectively.

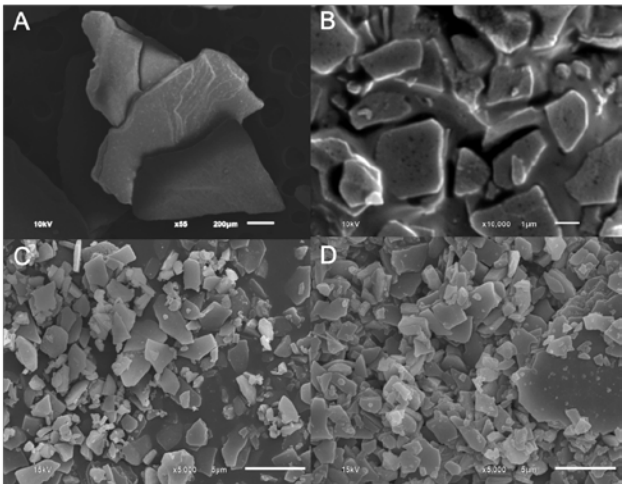

Figure 5. Scanning electron micrographs of H_2O_2-treated Bio-$CaCO_3$ particles. The magnifications in A, B, C, and D are 55X, 10000X, 5000X, and 5000X, respectively.

3.4 Plant coating

Sample-1-coating comprising CNCs, CNFs, gelatin, and 15% $CaCO_3$ was able to extend the water loss period of *Manihot esculenta* (L.) *Crantz* leaves when compared to control (deionized water) and Sample-2-coating with organic surfactants (**Figure 6**). Bio-$CaCO_3$ particles could be uniformly distributed on the entire coated leaf samples. The Bio-$CaCO_3$ might be distinguished from the coated surface by their light reflection (**Figure 7**).

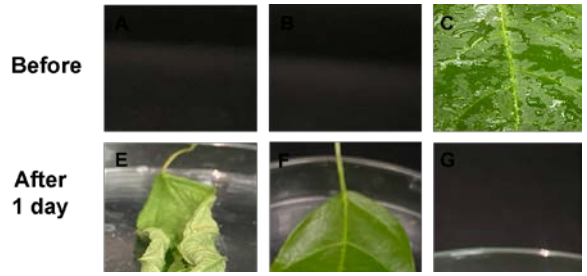

Figure 6. Film coating on *Manihot esculenta* (L.) *Crantz* leaves by control coating (A), Sample-1 coating (B), and Sample-2 coating (C). Film coating on leave samples after 1day for control coating, Sample-1 coating, and Sample-2 coating are shown in E, F, and G, respectively.

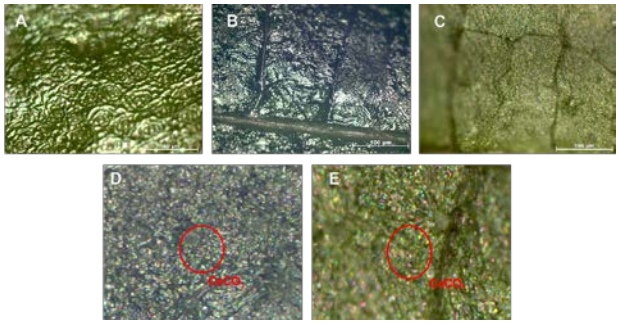

Figure 7. Surfaces of *Manihot esculenta* (L.) *Crantz* leave before (A) and after coating with Bio-$CaCO_3$ using Sample-1 coating (B and D) and Sample-2 coating (C and E).

3.5 FT-IR analysis

FT-IR spectroscopy was employed to confirm the presence of Bio-$CaCO_3$ on *Manihot esculenta* (L.) *Crantz* leaves. O—H stretching at 3329 cm^{-1}, CO_3^{2-} asymmetric stretching, ν_1, at 1425 cm^{-1} and carbonyl stretching of acidic proteins peak 1632 and 1591 cm^{-1} were only observed in Sample-1 coating (**Figure 8**). These results indicated the successful coating formulation that rendered Bio-$CaCO_3$ on *Manihot esculenta* (L.) *Crantz* leave surfaces.

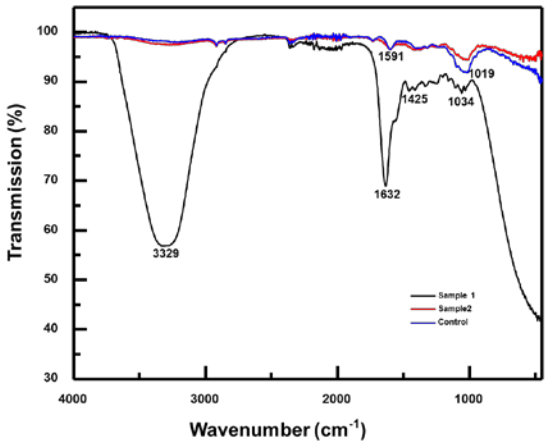

Figure 8. FT-IR spectra of control coating, Sample-1 coating, and Sample-2 coating.

4. Conclusions

We have successfully demonstrated that calcium carbonate extracted from green mussel shells could be employed as a coating for plants. The extracted $CaCO_3$ could be dispersed in aqueous media containing cellulose nanocrystals (CNCs), cellulose nanofibers (CNFs), and gelatin. The $CaCO_3$-CNC-CNF-gelatin aqueous mixture could be sprayed on various parts of plants and the resulting $CaCO_3$-CNC-CNF-gelatin composite film could prevent water loss and sun damage. The applications of the extracted $CaCO_3$ as plant sunscreen effectively address seafood waste upcycling, fresh produce quality, and food sustainability.

Acknowledgements

This research was funded by King Mongkut's University of Technology North Bangkok and National Science and Technology Development Agency, Thailand. Contract no. ๖๑.016/2565. The research supports from Department of Industrial Chemistry, Faculty of Applied Science, King Mongkut's University of Technology North Bangkok is greatly appreciated.

References

1. Schrader, L.; Zhang, J.; Sun, J., Environmental stresses that cause sunburn of apple. *Acta Hort* **2003,** *618*, 397-405.
2. Nuruddin, M.; Chowdhury, R. A.; Szeto, R.; Howarter, J. A.; Erk, K. A.; Szczepanski, C. R.; Youngblood, J. P., Structure–property relationship of cellulose nanocrystal–polyvinyl alcohol thin films for high barrier coating applications. *ACS applied materials & interfaces* **2021,** *13* (10), 12472-12482.
3. Camargos, C. H.; Poggi, G.; Chelazzi, D.; Baglioni, P.; Rezende, C. A., Protective coatings based on cellulose nanofibrils, cellulose nanocrystals, and lignin nanoparticles for the conservation of cellulosic artifacts. *ACS Applied Nano Materials* **2022,** *5* (9), 13245-13259.
4. Lertvachirapaiboon, C.; Parnklang, T.; Pienpinijtham, P.; Wongravee, K.; Thammacharoen, C.; Ekgasit, S., Selective colors reflection from stratified aragonite calcium carbonate plates of mollusk shells. *Journal of Structural Biology* **2015,** *191* (2), 184-189.
5. Hua, K.-H.; Wang, H.-C.; Chung, R.-S.; Hsu, J.-C., Calcium carbonate nanoparticles can enhance plant nutrition and insect pest tolerance. *Journal of Pesticide Science* **2015,** *40* (4), 208-213.

Microstructural modification of nickel aluminium bronze against erosion corrosion

Methawat Keereerakwattana and Napachat Tareelap*

Materials Technology Program, School of Energy, Environment and Materials, King Mongkut's University of Technology Thonburi, Bangkok, 10140, Thailand

**E-mail: napachat.tar@kmutt.ac.th*

Abstract:

Nickel aluminum bronze (NAB) used in marine applications usually undergoes erosion and corrosion from hard particle impingement and seawater corrosion. In materials viewpoint, the deterioration is caused by microstructural features, e.g. phases, and interfaces between phases. This work achieved heat treatment by hardening at 900 and 1000°C for 2 hours then water quenching to homogenize microstructure for lifetime extension of the alloy. An erosion corrosion test was performed in 3.5 wt.% NaCl solution containing 30 g/L of 300-500 μm SiO_2 sand particles at a rotational speed of 1500 rpm for 6 hours. The results suggested that heat treatment could improve microstructural uniformity by dissolving | phases, hence reducing corrosion initiation sites, interfaces between ⟨/| , reduced. Furthermore, hardness was enhanced by the formation of new phases, Al_3Cu, Al_7Cu_4Ni and Al_5FeNi, including changes in microstructure. The HT-1000 showed a superior hardness value because all of | precipitates dissolved and fine needle-shaped ⟨ phases formed. While HT-900 $|_{III}$, $|_{IV}$ dissolved, and ⟨ phase remained in the as-received condition. SEM micrographs indicated the least damage in the hardest HT-1000, whereas the most severe damage was found in the as-received sample. Heat treatment in this work not only improved hardness against impingement of SiO_2 but reduced corrosion initiation sites; therefore, erosion corrosion resistance was enhanced.

1. Introduction

Nickel Aluminium Bronze (NAB), a copper-based alloy, is typically used for marine applications such as impellers and ship propellers. During service, not only seawater is involved in the system, but also hard particles, e.g., sand. Corrosive seawater and the impact of hard particles on deteriorated metal are called slurry corrosion, which is a subtype of erosion corrosion. The damage is a synergy between mechanical attack from solid particle impingement and electrochemical reaction (corrosion) from corrosive electrolyte. Nickel-aluminum bronze is composed of a copper-rich α phase and various κ precipitates (κ_I, κ_{II}, κ_{III} and κ_{IV}) which transformed from a high temperature β phase. The $|_I$, $|_{II}$ and $|_{IV}$ were iron-rich phases; while, $|_{III}$ was a nickel-rich phase. The formation of κ phases depends on cooling temperature, according to the Cu-Al equilibrium phase diagram in Figure 1. The $|_I$ and $|_{II}$ phases form first at a temperature range of 900-920°C. The $|_{III}$ phase, a network lamella structure, forms at temperature range of 840-870°C and $|_{IV}$ forms at temperature lower than 840°C. In some case, the high temperature β phase could not completely decompose to κ precipitates; so, the retained β (β′) was observed in the microstructure as found in this work. Heat treatment is one of the most promising methods to homogenize the microstructure for property improvement. The previous document [1] stated that cavitation corrosion, another subtype of erosion and corrosion, caused by the non-uniformity of the microstructure, at which the damages are usually found at the interface between α/κ_{III} phases. For slurry corrosion, there are few documents that report a correlation between heat treatment and slurry corrosion. Wu et al. [2], carried out heat treatments at various temperatures and cooling means, stated that slurry corrosion resistance can be improved by increasing hard phases that are aligned with hardness. This work therefore used the hardening method by heat-treating the sample at 900°C and 1000°C then quenching it in water at room temperature to dissolve phases and homogenize microstructure for slurry corrosion resistance improvement of the alloy.

2. Materials and Methods

2.1 Materials

The cylindrical-shaped NAB samples were prepared by sand casting and machining to a diameter of 10 mm and a length of 75 mm. Its composition, analyzed by X-ray Fluorescence technique (XRF) is shown in Table 1. This sample is called "as-received" sample.

Table 1. Chemical composition of as-received NAB

Sample	Chemical composition (%wt.)				
	Al	Ni	Fe	Mn	Cu
As-received	9.48	5.49	5.44	0.48	Balance

To homogenize the microstructure by dissolving phases and hardening the specimens, heat treatment at temperatures of 900°C and 1000°C for 2 hours and then rapid cooling (quenching) in water at room temperature were achieved. These samples are named "HT-900" and "HT-1000" respectively. Heat treatment at 900°C was expected to dissolve β_{III} and β_{IV} according to the phase diagram in Figure 1; while, the disappearance of all β or the remaining of only α and β phases was presumed for heat treatment at 1000°C.

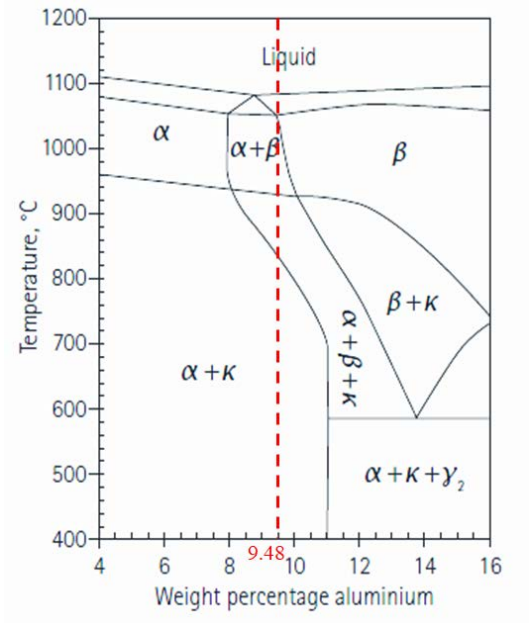

Figure 1. Phase diagram of CuAl10Ni5Fe5 [3]

2.2 Microstructure examination

The as-received and HT samples were cross-sectionally cut at the middle of the rod then cold-mounted. It was metallographically prepared by grinding with sand paper No. 180 to 4000 then polishing with diamond sticks of 3 and 1 µm, respectively. Next, it was cleaned with DI water, ethanol and dried with hot air. To reveal the microstructure, it was etched in a mixture solution of 5 g $FeCl_3$, 15 ml HCl and 60 ml of deionized water for 3 seconds. They were then examined microstructure with an optical microscope (SOPTOP-IE200M).

2.3 Hardness measurement

Vickers hardness measurements were performed on polished surface (non-etched) of as-received and HT samples. Load used was 30 Kgf. for 30 seconds. The measurements were achieved at least 3 times, the average and standard deviation of hardness values were reported.

2.4 Phase analysis by X ray diffraction (XRD)

Phase identification was investigated for as-received and HT samples using the X-ray diffractometer (Bruker Model D8 Discover) by scanning 2theta from an angle of 30° to 100°. The signals (peaks) obtained from X-ray diffractograms were identified by matching with the JCPDS-ICDD database.

2.5 Erosion corrosion test and investigation

The samples were tested with equipment shown in Figure 2. The test chamber contained 30 g/L of 300-500 µm SiO_2 sand particles suspended in 3.5 wt.% NaCl solution. The samples were surface finished by sand paper No.2000, then cleaned with DI water, ethanol and dried. They were then fitted with a sample holder. The test was run at a rotational speed of 1500 rpm for 6 hours. This test method allowed sand particles to erode and NaCl solution corroded the samples simultaneously. After testing, the surface of samples was examined by visual inspection, optical microscope (SOPTOP-IE200M), scanning electron microscope (FEI- Model Nova Nano SEM450**)** and Confocal laser scanning microscope (ZEISS LSM 900). Imaging was performed with a diode laser (405 nm wavelength). Zen imaging software and ConfoMap software were used to collect and analyze topography data.

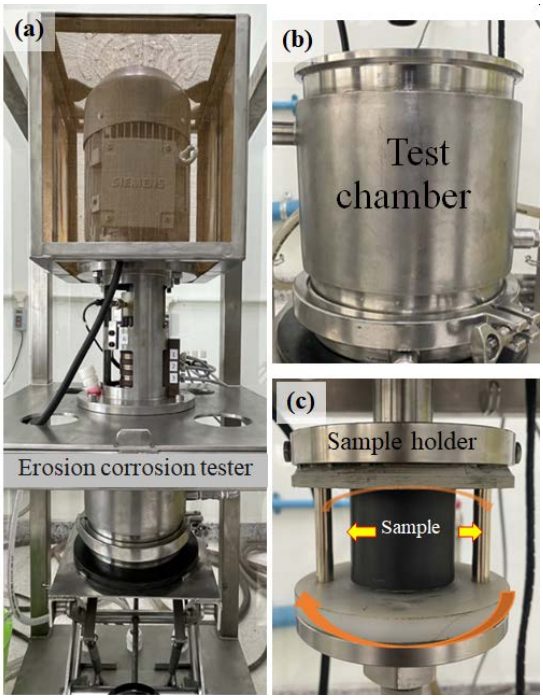

Figure 2. (a) erosion corrosion tester; (b) test chamber and (c) sample holder used in this work

3. Results & Discussion

3.1 Microstructure and hardness

The microstructure of the as-received sample is shown in Figure3(a). It mainly consisted of α phase (bright area) and Kappa (κ) precipitates or phases. The κ phases found in this research were κ_{II}, κ_{III} and κ_{IV}. The κ_{II}, Fe_3Al, was a flower-like structure smaller than 10 μm. The network lamella structure κ_{III} was NiAl; while, κ_{IV} was a fine circular Fe_3Al phase located within the α phase. The retained beta phase (β′) was also observed in this work as it could not be completely decomposed to κ precipitates during manufacturing.

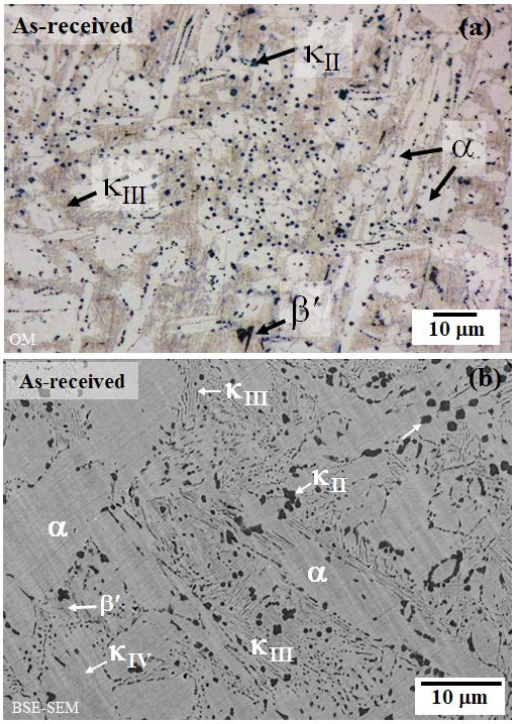

Figure 3. (a) optical and (b) BSE-SEM micrographs of as-received sample

After heat treatment, the microstructure of alloy altered significantly, as shown in Figure 4. The microstructure of HT-900 (Figure 4(a)) consisted of α, κ_{II} and β matrix phases, while, κ_{III} and κ_{IV} disappeared as expected. Note that the α phase remained α (α_{remain}) because its shape was similar to that of as-received sample and the heat treatment temperature was not high enough to dissolve the α phase. During heat treatment, κ phases dissolve back to be β phases. In β phase, there was martensite-like or martensitic structure, which usually occurs in hardened specimens [3-5] For the HT-1000 sample (Figure 4(b)), all of the κ phases were dissolved, and great amounts of needle-shaped α phase in the β matrix were observed. It is as expected and corresponds to the phase diagram in Figure 1. The needle-shaped α phase, or Widmanstätten structure, occurred in the former high-temperature ® grains, as reported in the previous literature [4].

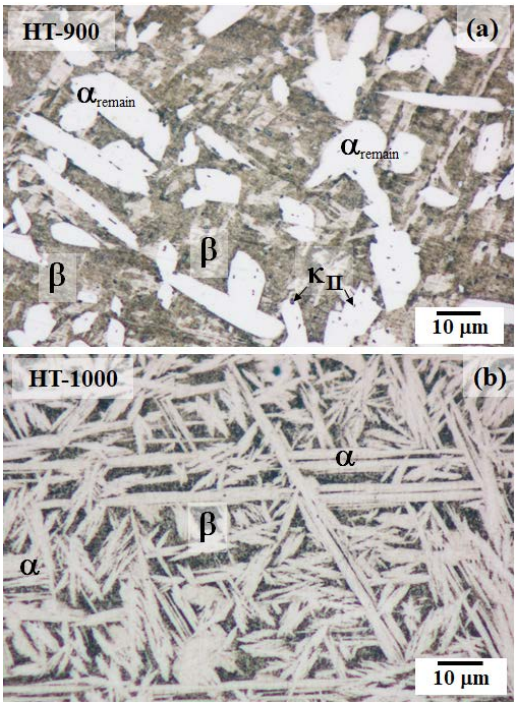

Figure 4. Optical micrographs of (a) HT-900 and (b) HT-1000

Among all of the samples, the HT-1000 showed the highest hardness value of 248.9 ± 2.6 HV30; whereas the HT-900 and as-received samples had hardness values of 182.5 ± 3.1 HV30 and 153.6 ± 2.5 HV30 respectively. The increase in hardness after heat treatment was possibly caused by the formation of hard phases and microstructures, e.g., martensitic and Widmanstätten structures, as aforementioned.

3.3 X-ray diffraction, XRD

The XRD patterns of as-received and heat-treated samples are shown in Figure 5.

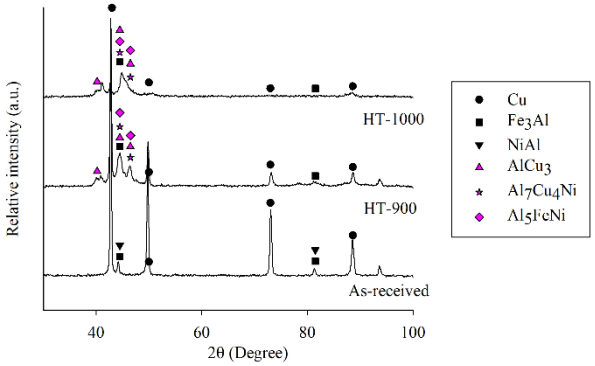

Figure 5. X-ray diffractograms of as-received and heat-treated NABs

The as-received sample showed 2θ peaks at 42.78°, 49.78°, 73.06°, 88.56° and 93.92° corresponding to copper (Cu) solid solution. The 2θ peaks appeared at 44.01°, 63.99°, 80.93° and 97.07° was Fe_3Al, 2θ peaks positions at 30.95°, 44.34°, 64.49° and 81.60° was NiAl. The Fe_3Al corresponded to κ_{II} and κ_{IV} phases; whereas, NiAl related to κ_{III} phase. Phases found from the XRD technique agreed with the microstructure of as-received in Figure 3. For heat-treated samples, HT-900 and HT-1000, the 2θ peaks positions of NiAl or κ_{III} disappeared, which corresponded to their microstructures in Figure 4(a) and (b) respectively. Not only the disappearance of NiAl in heat-treated samples but also the appearance of new peaks were recognized. The 2θ peaks positions at 40.28°, 44.81°, 46.61° can be identified as Al_3Cu. The 2θ peaks appeared at 44.28°, 46.26° and 44.69°, 47.23° were Al_7Cu_4Ni and Al_5FeNi respectively. The formation of new phases Al_3Cu, Al_7Cu_4Ni and Al_5FeNi probably resulted from dissolving of NiAl (κ_{III}) and Fe_3Al (κ_{II}, κ_{IV}) during heat treatment. The formation of new phases in heat-treated samples improved hardness in this work.

3. Erosion corrosion test

The typical appearance of the sample before and after testing is illustrated in Figure 6(a). The tested area turned dark due to erosion and corrosive damage after testing. Optical micrograph (Figure 6(b)) and SEM micrograph (Figure6(c)) showed non-tested area compared with tested area. It confirmed that the tested area was damaged, which was indicated by surface roughening.

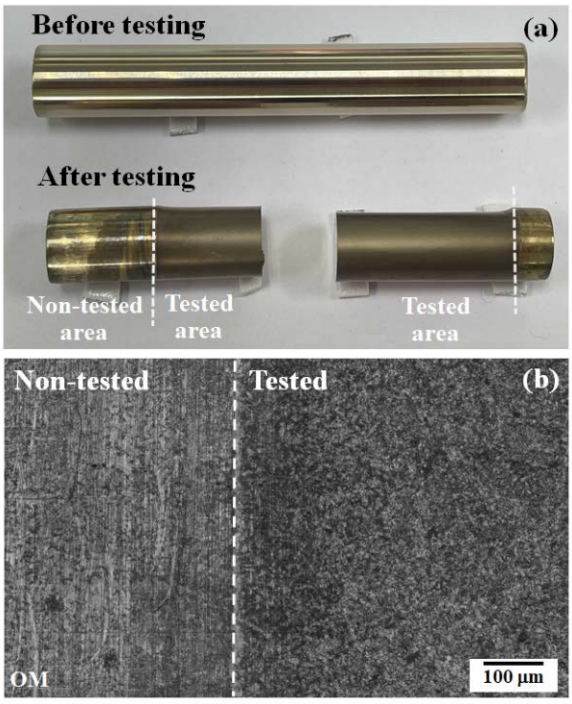

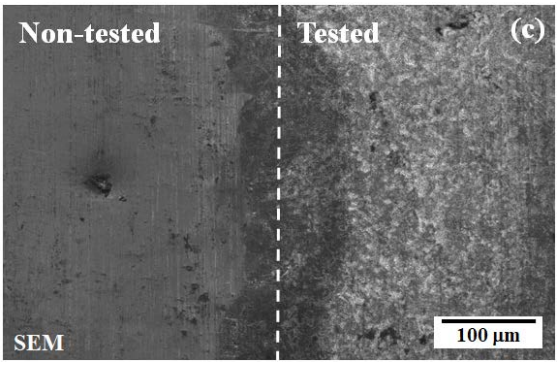

Figure 6. (a) typical appearance of sample before and after testing (b) optical micrograph and (c) SEM micrograph of non-tested area compared with tested area

The 2D- and 3D-surface profiles (Figure 7 (a) and (b)) analyzed by a confocal laser scanning microscope also showed a lower level at the tested area in comparison to the non-tested area. It is an implied loss of materials after testing. However, the depth of attacks analyzed by this technique for all samples was similar. It is probably due to the fact that the test period was not long enough to obtain attack depth differences among them.

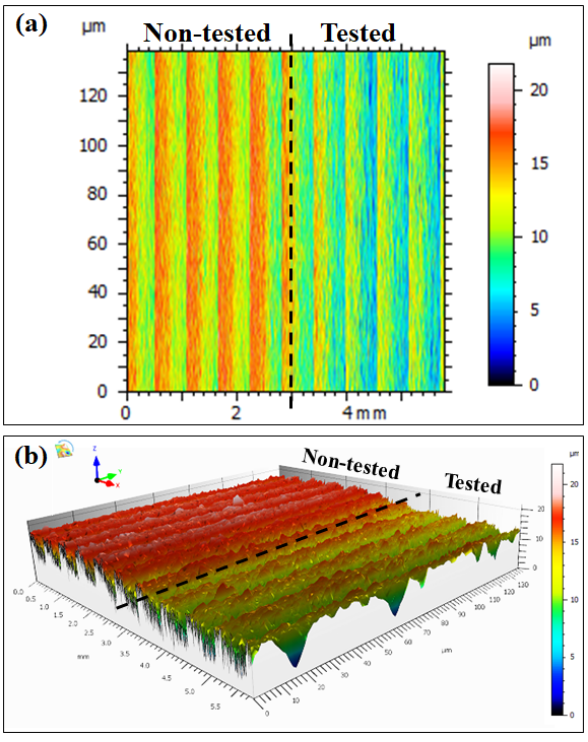

Figure 7. (a) Typical 2D- and (b) 3D- surface profiles of tested and non-tested area

For further investigation, SEM was used to analyze the damages as shown in Figure 8. The image in Figure 8(a) shows severe damage in the as-received sample. High magnification in Figure

8(b) reveals the remaining hard phases e.g. lamella κ_{III} (arrow); whereas, soft α was damaged. Related to microstructure of as-received NAB in Figure 3, there were large numbers of α/κ interfaces, as it chiefly composed of α and κ (| II, | III, | IV) phases. Once α soft phase was impinged by SiO_2 hard particles, it deformed. During deformation, the dislocation moved from the soft ⟨ phase to hard | phases; consequently, dislocation piling up at the α/κ interface occurred [6]. This phenomenon induced the formation of void or crack at α/κ interface [1]. Micro-galvanic effect between α and κ phases was a possible factor causing preferential corrosion at α/κ interface [7]. Both dislocation piling up and micro-galvanic corrosion were synergistic factors causing harsh damage in this specimen.

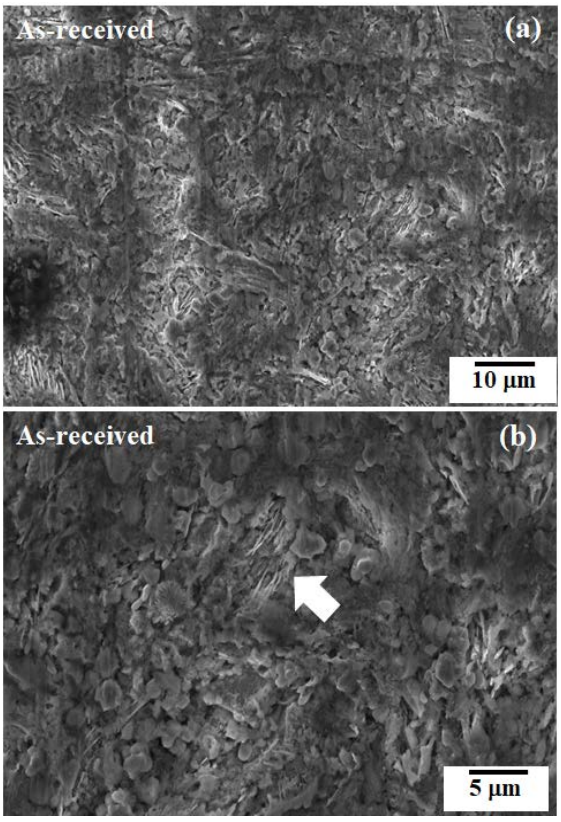

Figure 8. SEM surface images of as-received sample after testing

In contrast to as-received samples, the heat-treated specimens showed slighter damages. It is not only because of hardness enhancement but also the reduction of preferential sites of damages, α/κ interfaces. Between heat-treated samples, HT-900 showed greater amounts of displaced material, the material that have been moved or shifted from original location due to force from particle impingement (erosion), than that of HT-1000. It is due to HT-900 being softer than HT-1000; so, the impact of hard particles could wear off the alloy easier. The HT-900 was not as hard as HT-1000 because it was composed of soft α (α_{remain}) and hard β phase; therefore, α_{remain} preferred to deform and loss. Dislocation piling up at soft α_{remain} and hard β phase together with micro-galvanic effect is believed to still occur, but less than in as-received condition. The hardest sample, HT-1000, revealed a small amount of displaced materials. The least damage is not caused only from the dissolving of all | phases, but also from the formation of needle-shaped α phase or Widmanstätten structure. High density of needle-shaped α phase benefited for prohibiting deformation; therefore, loss of materials in this condition was mitigated. [2,8-10]

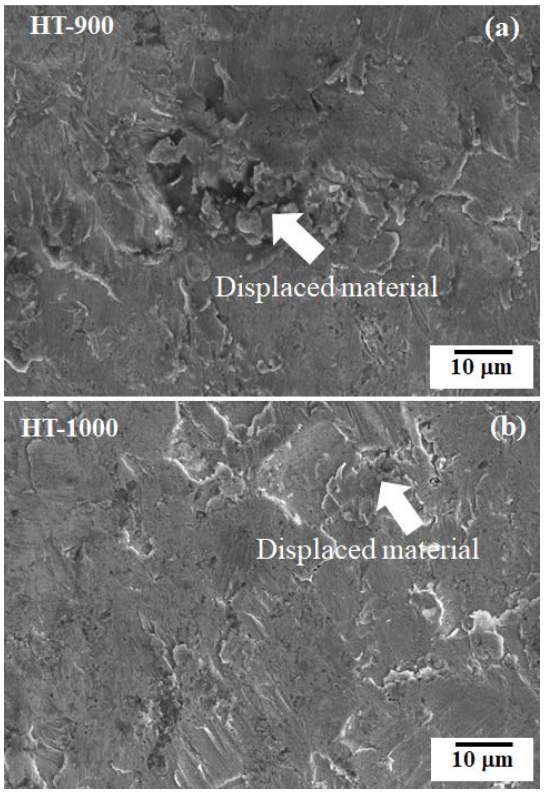

Figure 9. SEM surface images of (a) HT-900 and (b) HT-1000 after testing

4. Conclusion

Heat treatment by hardening in this work could improve hardness and reduce ⟨/κ interfaces, the initiation sites of deterioration. Enhancement of hardness in heat-treated samples resulted from formation of hard phases as well as changing in microstructure. The as-received sample showed the most severely attacked because of soft ⟨ and many types of hard | phases in its microstructure. The damages found in HT-900 was more severe

than that of HT-1000, but less than as-received, because it still had soft ⟨$_{remain}$ and some of ⏐ phase. The smallest amount of damage was observed in the hardest HT-1000 as it mostly consisted of a needle-shaped ⟨ phase.

Acknowledgements

This research project is supported by King- Mongkut's University of Technology Thonburi (KMUTT), Thailand Science Research and Innovation (TSRI), and National Science, Research and Innovation Fund (NSRF) Fiscal year 2024.

References

1. Basumatary, J.; Wood, R. J. K. *Different Methods of Measuring Synergy between Cavitation Erosion and Corrosion for Nickel Aluminium Bronze in 3.5% NaCl Solution*. Tribology International 2020, 147, 104843.
2. Wu, Z.; Cheng, Y.; Liu, L.; Weijie Lv; Hu, W. *Effect of Heat Treatment on Microstructure Evolution and Erosion–Corrosion Behavior of a Nickel–Aluminum Bronze Alloy in Chloride Solution*. 2015, 98, 260–270.
3. Richardson, I., *Guide to Nickel Aluminium Bronze for Engineer*. Powell, C. Copper Development Association, 2016. Vol. 222: p. 22.
4. Meigh, H. *Cast and Wrought Aluminium Bronzes*; CRC Press, 2018.
5. Orzolek, S. M.; Semple, J. K.; Fisher, C. R. *Influence of Processing on the Microstructure of Nickel Aluminum Bronze (NAB)*. Additive Manufacturing 2022, 56, 102859.
6. Qin, Z.; Zhang, Q.; Luo, Q.; Wu, Z.; Shen, B.; Liu, L.; Hu, W. *Microstructure Design to Improve the Corrosion and Cavitation Corrosion Resistance of a Nickel-Aluminum Bronze*. Corrosion Science 2018, 139, 255–266.
7. Zhang, L. M.; Ma, A.; Yu, H.; Aniefiok Joseph Umoh; Zheng, Y. *Correlation of Microstructure with Cavitation Erosion Behaviour of a Nickel-Aluminum Bronze in Simulated Seawater*. Tribology International 2019, 136, 250–258.
8. Rajahram, S. S.; Harvey, T. J.; Wood, R. J. K. *Electrochemical Investigation of Erosion–Corrosion Using a Slurry Pot Erosion Tester*. Tribology International 2011, 44 (3), 232–240.
9. Lakshminarayanan, A. K.; Rao, S. R. K.; Sridhar, K.; Vignesh, A. *On the Microstructure and Erosion Corrosion Behavior of Laser Processed Nickel Aluminium Bronze*. Materials Science Forum 2020, 979, 157–161.
10. Rajakumar, S.; Balasubramanian, V.; Balakrishnan, M. *Friction Surfacing for Enhanced Surface Protection of Marine Engineering Components: Erosion-Corrosion Study*. Journal of the Mechanical Behavior of Materials 2016, 25 (3-4), 111–119.

Synthesis of MnO_2/C composite from spent alkaline battery by one-step hydrothermal process for rechargeable Zn-ion battery application

Auscha Thongsri[1], Kamonpan Manowilaikun[1], Keeratipron Yoaharee[1] and Rojana Pornprasertsuk[1,2,3,4]*

[1]*Department of Materials Science, Faculty of Science, Chulalongkorn University, Thailand*
[2]*Center of Excellence in Petrochemical and Materials Technology, Chulalongkorn University, Thailand*
[3]*Center of Excellence on Advanced Materials for Energy Storage, Chulalongkorn University, Thailand*
[4]*Department of Materials Science and Bioengineering, Nagaoka University of Technology, Japan*

**E-mail: rojana.p@chula.ac.th*

Abstract:

Alkaline battery is one type of single-use energy storage devices that pose a significant waste issue and have a negative impact on the environment. Therefore, this research aims to recover Mn and C from the spent alkaline electrode powder in form of MnO_2/C composites and to utilize the recycled materials in the rechargeable zinc-ion battery (ZIB) application. The process began with the dismantling and sieving of spent alkaline batteries to obtain spent electrode powder. The spent electrode powder, $(NH_4)S_2O_8$, $(NH_4)_2SO_4$, and 0.0-0.5 M H_2SO_4 were then used as precursors to synthesize MnO_2/C composite through a one-step hydrothermal process. The XRD and SEM results confirm the presence of α-MnO_2/C (nanofiber) mixed with β-MnO_2 (nanorod). The XRF techniques were utilized to detect the chemical composition and to estimate the Mn recovery efficiencies. The results show that α-MnO_2/C synthesized with 0.125 H_2SO_4 addition has the highest Mn recovery efficiency of 62.79%. The recycled MnO_2/C was subsequently utilized as active cathode materials in ZIB. The galvanostatic charge-discharge analysis at 0.1-0.5 A/g was performed to demonstrate the electrochemical performance of CR2025 ZIBs. The results show that the recycled MnO_2/C cathode can achieve the highest specific capacity of 162.67 mAh/g at 0.1 A/g, which is comparable to the commercial MnO_2-based cathode.

1. Introduction

Alkaline battery is a type of battery that cannot be recharged after use. Alkaline batteries are widely used in home and personal electronic devices such as radios, watches, remotes, and digital doors because of their high energy density and cost-effectiveness. However, once used, they become electronic waste and are typically disposed of by landfill. Therefore, this study aims to reduce the amount of spent alkaline battery waste and minimize resource loss by the recycling process.

An unused alkaline battery consists of manganese dioxide (MnO_2) mixed with carbon (graphite) cathode, Zn powder anode, potassium hydroxide (KOH) as an electrolyte, a separator, current collectors, and a metal case. Once used, the battery undergoes discharge reactions as follows:
Anode:

$$Zn + 4OH^- \rightarrow [Zn(OH)_4]^{2-} + 2e^- \quad (1)$$

$$Zn + 2OH^- \rightarrow ZnO + H_2O + 2e^- \quad (2)$$

Cathode:

$$2MnO_2 + H_2O + 2e^- \rightarrow Mn_2O_3 + 2OH^- \quad (3)$$

$$3MnO_2 + 2H^+ + 2e^- \rightarrow 2MnOOH \quad (4)$$

$$[Zn(OH)_4]^{2-} + 2MnOOH \rightarrow ZnMn_2O_4 + H_2O + 2OH^- \quad (5)$$

Thus, net reactions could be several routes as examples below: [1, 2]

$$Zn + 2MnO_2 + H_2O + 2OH^- \rightarrow [Zn(OH)_4]^{2-} + Mn_2O_3 \quad (6)$$

$$2Zn + 3MnO_2 \rightarrow 2ZnO + Mn_3O_4 \quad (7)$$

$$Zn + 2MnO_2 \rightarrow ZnMn_2O_4 \quad (8)$$

Previous research revealed that the electrode powder of the spent alkaline batteries comprised major chemical components of Mn, Zn, and C at 51.2, 14.0, and 2.51 wt%, respectively, with the primary phases of $ZnMn_2O_4$ and Mn_3O_4, graphite and ZnO. [3]

Manowilaikun [4] leached the cathode powder of the spent alkaline batteries using 0.5-1.5 M sulfuric acid (H_2SO_4) and 6 vol% of hydrogen peroxide (H_2O_2) for 15-180 minutes at room temperature. The obtained leaching solution containing manganese sulfate ($MnSO_4$) was utilized as Mn precursor to synthesize α-, β- and γ-MnO_2 phases via the hydrothermal process adapting the procedures of Liu et al. [5] and Wang et al. [6] The results showed that high-purity α-, β-

and γ-MnO_2 nanoparticles were obtained with the Mn recovery efficiency of 87%, 64%, and 59%, respectively. The physical and chemical properties of the recycled MnO_2 were equivalent to those synthesized from commercial $MnSO_4$ solution.

Yoaharee[3] prepared MnO_2/C composites from the spent alkaline-battery electrode powders using acid leaching and hydrothermal processes. The starting precursors for the MnO_2/C composite synthesis were the leaching solution, residual carbon at the C:(expected) MnO_2 weight ratios of 0:75, 1:75, 5:75, and 15:75 together with $(NH_4)_2S_2O_8$ and $(NH_4)_2SO_4$ solutions. The composites were referred to as MnC0, MnC1, MnC5, and McC15, respectively. The results revealed that MnC1 could enhance the Mn recovery efficiency to 90.01%, 68.53%, and 69.02% for α-, β- and γ-MnO_2/C, respectively. However, this process still requires the leaching process, which involves the utilization of high concentration of acid and reducing agent. Thus, this research aims to simplify the MnO_2/C synthesis technique from spent alkaline-battery electrodes using one-step hydrothermal process without the leaching process.

The Zn-ion battery (ZIB) is a rechargeable battery that includes key components which are Zn anode, a cathode (such as manganese dioxide or other transition oxides mixed with C), an electrolyte (such as zinc sulfate solution), and a separator. [7] MnO_2, consisting of tetrahedral units (MnO_6) arranged differently in each phase [8, 9, 10], possesses a suitable cathode structure that can accommodate or release Zn^{2+} ions during discharging and charging. Therefore, MnO_2 becomes a common material for the ZIB cathode.

Using MnO_2/C composites as ZIB cathodes could further enhance the ZIB capacity and stability. Cao et al.[11] synthesized MnO_2/C composite materials by ball-milling nanosized graphite powder with MnO_2 at a weight ratio of 1:9. The results showed that the addition of graphite increased the surface area, pore size, water absorption capacity, and electrical conductivity, and improved the dispersion of MnO_2. This enhancement led to the increase in the specific capacity of ZIBs. Therefore, this research aims to recycle Mn and C from the spent alkaline batteries in the form of MnO_2/C and to utilize them as a cathode material for rechargeable ZIB batteries.

2. Materials and Methods

2.1 Preparation of spent alkaline electrode powders

Spent electrode powder was collected by dismantling the black mass from spent alkaline batteries (Panasonic, size AA). The powder was then ground with a high-speed planetary ball mill at 700 rpm for 3 h and dried at 60 °C for 48 h.

2.2 Synthesis of the recycled MnO_2/C using one-step hydrothermal process

The recycled MnO_2/C was prepared by one-step hydrothermal process as follows. First, spent electrode powder (1 g), $(NH_4)_2S_2O_8$ (1.826 g, analytical grade, KemAus), and $(NH_4)_2SO_4$ (1.982 g, analytical grade, KemAus) were mixed in 35 mL of de-ionized (DI) water at room temperature and stirred to form a homogeneous suspension. To investigate the effect of acid addition on the microstructure, phase, and Mn recovery efficiency, the precursor suspensions were prepared by replacing DI water with 0.125, 0.25, or 0.5 M H_2SO_4 solution and following the same preparation steps. The mixtures were subsequently placed in Teflon-lined stainless-steel autoclaves and heated at 140 °C for 24 h. After the autoclave cooled down to room temperature, the product was obtained by filtering, washing several times with DI water and ethanol, and drying at 60 °C for 24 h.

2.3 Materials characterizations

Phase and morphology of the obtained samples were analyzed by X-ray diffraction (XRD, Malvern Panalytical Aeris) and scanning electron microscopy techniques (SEM, JEOL JSM-6480LV), respectively. The chemical composition was investigated using an elemental analyzer (EA-CHNS, THERMO FLASH 2000) and an X-ray fluorescence spectrometer (XRF, BRUKER S8 TIGER). The Mn recovery efficiency was subsequently evaluated by calculating the weight ratio of Mn in the obtained MnO_2/C to that of black mass in the precursor suspension.

2.4 Electrochemical measurement

The electrochemical performance of the cathode materials was evaluated by assembling the CR2025 ZIB using 0.2-mm thick Zn foil (16-mm diameter) as an anode, 40 µL of 2M $ZnSO_4$ solution as an electrolyte, and glass fiber separator which was soaked in the electrolyte for 15 min. The cathode was prepared by mixing the recycled MnO_2/C, conductive carbon black (BP2000), and polyvinylidene fluoride (PVDF) at the mass ratio of 75:15:10, coating on 0.1-mm thick graphite foil (Shenzhen 3KS Electronic Material CO. Ltd.) with the mass loading of the active materials in a range

of 1.5-2.0 mg. After drying under vacuum at 60 °C for 24 h, the cathode was cut in a circle shape with a diameter of 16 mm. The No-BP cathode mixture was prepared by mixing the recycled MnO_2/C and PVDF at the mass ratio of 90:10 to explore the effect of reducing commercial carbon in the cathode on the battery performance. All components were assembled into CR2025 cells for galvanostatic charge/ discharge (GCD) test (BTS-4000 Series, Neware, China) under the potential of 1-1.75 V and the current loadings of 0.1, 0.2, 0.3, 0.4 and 0.5 A/g for 10 cycle each. The battery stability test was performed at the current loading of 0.3 A/g for 1,000 cycles.

3. Results & Discussion

3.1 Phase and microstructures of the recycled MnO_2/C

Phase of the MnO_2/C composites was analyzed by XRD technique as shown in Figure 1. The XRD patterns of all samples matched the α-MnO_2 (JCPDS: 00-044-0141) and β-MnO_2 phases (JCPDS: 00-024-0735). The XRD peaks at 12.78°, 18.11°, 28.84°, and 37.52° were corresponded to the (110), (200), (310) and (211) planes of α-MnO_2, while the peaks at 28.68°, 37.33°, 42.82°, and 56.65° were related to the (110), (101), (111) and (211) planes of β-MnO_2. The peak of graphite (JCPDS: 01-089-7213) was located at 26.54°. According to Fig. 1, MnO_2/C without H_2SO_4 addition showed α-MnO_2 and graphite phases, while MnO_2/C with 0.5 M H_2SO_4 addition showed mainly β-MnO_2 and graphite phases. For samples with 0.125-0.5 M addition, the fraction of β-MnO_2 was gradually increased with the increasing H_2SO_4 concentrations.

To observe the influence of H_2SO_4 addition on the morphology of the obtained MnO_2/C, SEM investigation was performed as shown in Figure 2. Clearly, without H_2SO_4 addition, the MnO_2/C contained highly uniform nanofibers on the graphite sheet. The nanofibers had diameters of 10-20 nm and lengths of 2-5 µm, which was the typical morphology of α-MnO_2. By adding 0.5 M H_2SO_4, the MnO_2/C became nanorods on the graphite sheets, with diameters of 100-300 nm and lengths of 1-2 µm, which was the typical morphology of β-MnO_2. Therefore, with the increasing H_2SO_4 concentration, the aspect ratio of MnO_2 was decreased (Figure 3). The XRD and SEM results thus confirm the morphological change due to the MnO_2 phase change from α-MnO_2 to β-MnO_2 at higher H_2SO_4 concentration. Zhou et al. [12] observed the similar effect of pH of the precursors on the morphology of MnO_2 synthesized by the hydrothermal process. The results reveal that the rod-like morphology became longer with decreasing H_2SO_4 concentration or increasing pH value. Kumar et al. [13] also observed the transition of α-MnO_2 to β-MnO_2 phase with increasing H_2SO_4 concentration from 0.3 M to 0.4 M H_2SO_4. Under low acid concentration, α-MnO_2 was favorable compared to β-MnO_2, which was more stable and had faster growth along (110) plane.

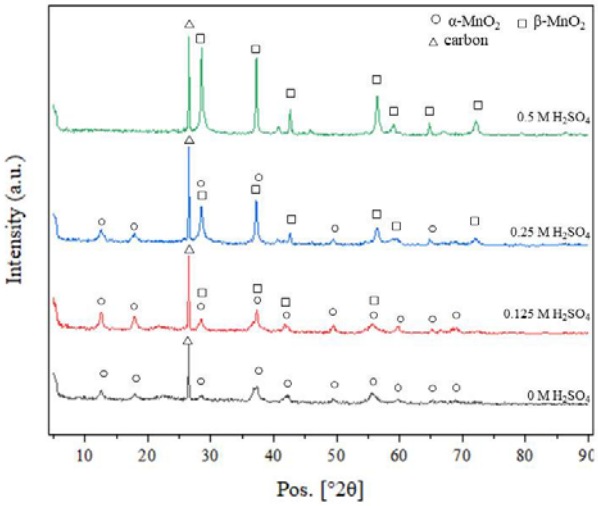

Figure 1. XRD patterns of the MnO_2/C composites: the concentrations of H_2SO_4 at 0.0-0.5 M.

3.2 Chemical composition of spent alkaline electrode powder and the recycled MnO_2/C

Chemical compositions of the spent electrode powder of alkaline battery [6] and the recycled MnO_2/C are summarized in Table 1. The main components of spent electrode powder were Mn, C, Zn, and K at 51.20, 2.51, 14.00, and 4.33 wt%, respectively. The recycled MnO_2/C composite contained 56.40 wt% Mn and 9.93 wt% C and traces of Zn, K, Ti, and S, indicating the relatively high purity MnO_2/C was obtained.

The Mn recovery efficiencies (MnRE%) of MnO_2/C synthesized under various concentrations of H_2SO_4 are compared in Figure 4. The highest MnRE% was MnO_2/C with 0.125 M H_2SO_4, while the lowest MnRE% was MnO_2/C without H_2SO_4 addition. The higher recovery efficiency may arise from the additional reaction of H_2SO_4 with the spent alkaline-battery electrode powder to form $MnSO_4$, which then reacted with $(NH_4)_2S_2O_8$ to become MnO_2 as shown in following steps (Eq. 9-11):

$$Mn_2O_3 + H_2SO_4 \rightarrow MnSO_4 + MnO_2 + H_2O \quad (9)$$

$$Mn_3O_4 + H_2SO_4 \rightarrow 2MnSO_4 + MnO_2 + H_2O \quad (10)$$

$$MnSO_4 + [(NH_4)]_2S_2O_8 + 2H_2O \rightarrow MnO_2 + [(NH_4)]_2SO_4 + 2H_2SO_4 \quad (11)$$

However, by adding too high H_2SO_4 concentration, phase of MnO_2 was gradually changed to β-MnO_2 with lower MnRE% as previously reported by Yoaharee[3] and Manowilaikun.[4] Moreover, Andak et al.[14] observed the effect of pH on metals extraction yields. Over pH 1.5, the concentration of other metal increases so the ratio of Mn decreses.

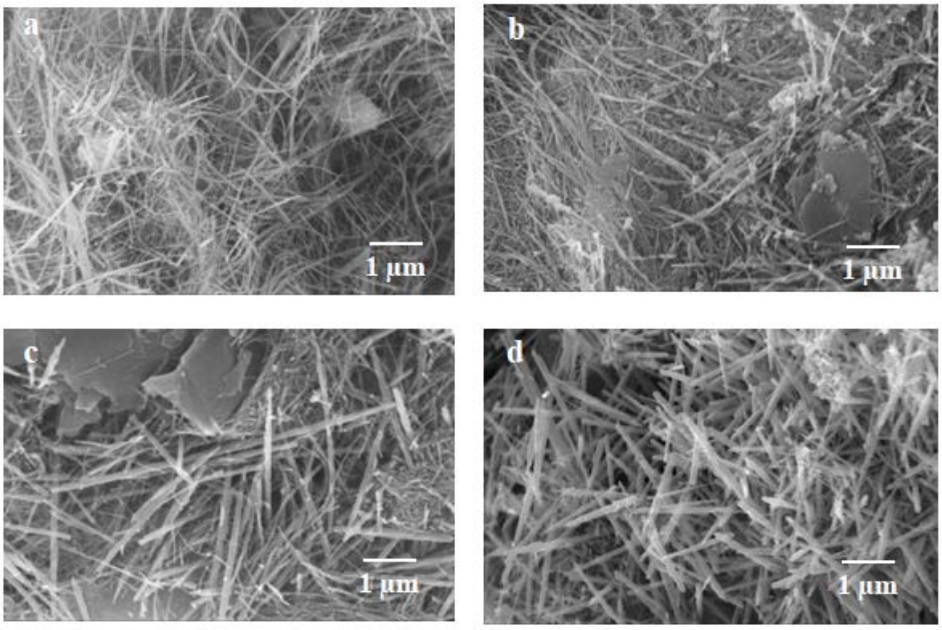

Figure 2. SEM images of MnO_2/C composites: the concentrations of H_2SO_4 at (a) 0 M, (b) 0.125 M, (c) 0.25 M and (d) 0.5 M

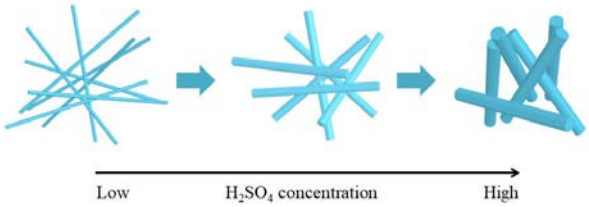

Figure 3. Schematic illustration of morphologic evolution simulation as synthesized MnO_2/C samples at different concentration of H_2SO_4

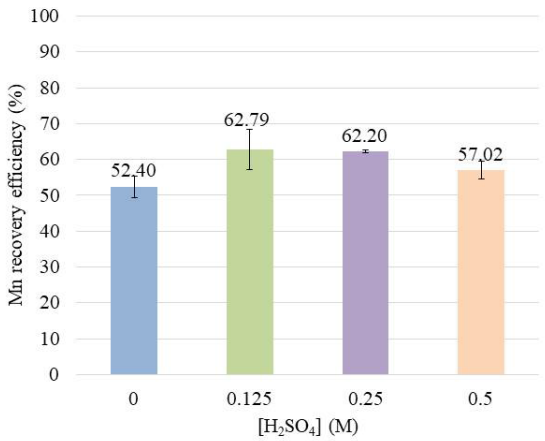

Figure 4. The Mn recovery efficiencies of the recycled MnO_2/C

Table 1. Chemical compositions of spent electrode powder of alkaline battery and MnO_2/C analyzed by XRF and elemental analytical techniques

	Element composition %					
	Mn	Zn	K	C	Ti	S
Spent electrode powders	51.20	14.00	4.33	2.51	0.20	0.18
MnO_2/C	56.40	0.71	0.39	9.93	0.31	0.31

3.3 Electrochemical performance

MnO_2/C sample synthesized with 0.125M H_2SO_4 addition was subsequently chosen as a cathode active material in ZIBs due to the highest MnRE%. The performances of two CR2025 ZIBs were compared: (i) CR2025 cell with MnO_2/C cathode (0.125 M H_2SO_4 addition) and (ii) CR2025 cell with MnO_2/C cathode without BP2000, referred to as No-BP cell. The specific capacities of CR2025 cells at various current rates ranging from 0.1-0.5 A/g are shown in Figure 5. The discharge specific capacity of MnO_2/C was much higher than the No-BP cell as expected. The highest average specific capacity of the MnO_2/C at 0.125 M H_2SO_4 was 162.7 mAh/g at the current loading of 0.1 A/g, and the capacity became ~85 mAh/g at the current density of 0.5 A/g.

Table 2. The discharge specific capacity of various cathode materials in ZIBs

Cathode material	Synthesis process	Discharge specific capacity (mAh/g)	Current density (A/g)	Electrolyte	Testing voltage (V)
Recycled α-MnO_2 [3]	leaching and hydrothermal	247	0.12	2 M $ZnSO_4$	1-1.75
Recycled α-MnO_2/C (at the weight ratio of MnO_2:C at 75:5) [3]	leaching, and hydrothermal	~200	0.12		
Commercial α-MnO_2 [4]	-	230	0.1		
Recycled α-MnO_2 [4]	leaching and hydrothermal	213	0.1		
Commercial α-MnO_2 [11]	-	113	0.1	2 M $ZnSO_4$ with 0.5 $MnSO_4$	1-1.8
α-MnO_2/C (at the weight ratio of MnO_2:C at 9:1) [11]	ball milling	230	0.1		1-1.8
MnO_2/C (this work)	one-step hydrothermal	162.7	0.1	2 M $ZnSO_4$	1-1.75

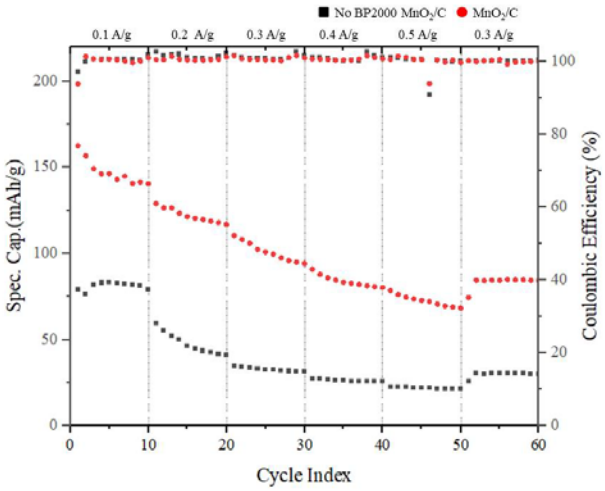

Figure 5. The specific capacity of CR2025 cell using MnO_2/C at 0.125 M H_2SO_4 and No-BP cell

The discharge specific capacities of various cathode materials in ZIBs are summarized in Table 2. The electrochemical performance of our recycled MnO_2/C was higher than those used commercial MnO_2 [11] and slightly lower than those with MnO_2/C [3, 11] that was synthesized from pure chemical with hydrothermal and ball milling processes. The mixture of MnO_2 and graphite plays a critical role in enhancing battery performance by improving charge transfer and ion diffusion. [3, 11] However, the graphite in the composite was not sufficient to replace the carbon black in the cathode mixture. The specific capacity of No-BP cell was much lower likely due to the lower carbon fractions leading to lower electronic conductivity and active surface area. [15]

4. Conclusion

The recycled MnO_2/C were synthesized by one-step hydrothermal process from spent alkaline-electrode powders, $(NH_4)_2S_2O_8$ and $(NH_4)_2SO_4$ solution with the addition of H_2SO_4 at various concentrations. The XRD and SEM results of MnO_2 show morphological and phase changes from α-MnO_2 (nanofiber) to β-MnO_2 (nanorod) with increasing H_2SO_4 concentration. The MnRE% of recycled MnO_2/C samples was above 50%, and the highest MnRE% of 62.79% was achieved with 0.125 M H_2SO_4 addition. The electrochemical performance of ZIBs with MnO_2/C cathode shows the highest specific capacity 162.7 mAh/g at 0.1 A/g, which is comparable to those of previously reported ZIBs using the commercial MnO_2.

Acknowledgements

The alkaline battery waste was collected by Faculty of Science, Chulalongkorn University under Chula Zero Waste project. This research was financially supported by Thailand Energy Conservation Promotion Fund (ENCON Fund), and the scholarship of Ms. Auscha Thongsri has been supported by the Development and Promotion of Science and Technology Talents Project (DPST). The authors would like to thank Department of Materials Science, Faculty of Science, Chulalongkorn University and Mr. Wirapong Kornpanom, Ms. Kamonpan Manowilaikun, and Ms. Keeratipron Yoaharee for their support with material characterization and suggestions.

References

1. Linden, D.; Reddy, T. B. *Alkaline-Manganese Dioxide Batteries.* In Handbook of Batteries; New York: McGraw-Hill; 2002, pp 245–247.
2. Belardi, G.; Ballirano, P.; Ferrini, M.; Lavecchia, R.; Medici, F.; Piga, L.; Scoppettuolo, *Thermochimica Acta* 2011, 526 (1-2), 169–177.
3. Yoaharee K. Preparation of Manganese dioxide/carbon Composites from Spent Alkaline Batteries for Zinc-ion Battery Application. M.S. Thesis, Chulalongkorn University, Bangkok, Thailand, 2022.
4. Manowilaikun K. Synthesis of Manganese dioxide from Spent Alkaline Batteries for Zinc-ion Battery Application. M.S. Thesis, Chulalongkorn University, Bangkok, Thailand, 2020.
5. Liu, Y.; Wei, J.; Tian, Y.; Yan, S. *Journal of Materials Chemistry A.* 2015, 3(37), 19000-19010.
6. Wang, X.; Li, Y. *Chemistry - A European Journal*. 2002, 9(1), 300-306.
7. Fang, G.; Zhou, J.; Pan, A.; Liang, S. *ACS Energy Letters.* 2018, 3(10), 2480-2501.
8. Sun, W.; Wang, F.; Hou, S.; Yang, C.; Fan, X.; Ma, Z.; Gao, T.; Han, F.; Hu, R.; Zhu, M.; Wang, C. *Journal of the American Chemical Society*. 2017, 139 (29), 9775–9778.
9. Alfaruqi, M. H.; Mathew, V.; Gim, J.; Kim, S.; Song, J.; Baboo, J. P.; Choi, S. H.; Kim, J. Chemistry of Materials. 2015, 27 (10), 3609–3620.
10. Shin, J.; Seo, J. K.; Yaylian, R.; Huang, A.; Meng, Y. S. International Materials Reviews. 2019, 65 (6), 356–387.
11. Cao, J.; Zhang, D.; Zhang, X.; Wang, S.; Han, J.; Zhao, Y.; Huang, Y.; Qin, J. Applied Surface Science. 2020, 534, 147630.
12. Zhou, L.; Zhang, J.; He, J.; Hu, Y.; Tian, H. Mater. Res. Bull. 2011, 46 (10), 1714–1722.
13. Kumar, N.; Sen, A.; Rajendran, K.; R. Rameshbabu; Jeevani Ragupathi; Helen Annal Therese; Thandavarayan Maiyalagan. RSC Advances. 2017, 7 (40), 25041–25053.
14. Andak, B.; Özduğan, E.; Türdü, S.; Bulutçu, A. N. Journal of Environmental Chemical Engineering 2019, 7 (5), 103372.
15. Wissler, M. Journal of Power Sources 2006, 156 (2), 142–150.

Improving photocatalytic efficiency of zinc oxide immobilized on glass slides by using plasma surface modification

Pamika Na-Ranong[1], Yuttida Sangsri[1], Watis Kongchanpat[1], Darapond Triampo[2], and Duangkhae Srikun[1]*

[1]*Mahidol Wittayanusorn School, Nakhon Pathom, Thailand*
[2]*Department of Chemistry, Faculty of Science, Mahidol University, Bangkok, Thailand*

**E-mail: duangkhae.sri@mwit.ac.th*

Abstract:

Photocatalytic oxidation is an effective method for removing organic pollution from wastewater. However, the transition from bench-scale operation to large-scale operation requires the development of heterogeneous catalysts that allow repeated use with low-cost recovery. This study aims to improve the efficiency of zinc oxide (ZnO) coated glass slides for photocatalytic oxidation by using air plasma to activate the glass surface. The low-pressure plasma treatment increased the wettability of the surface, facilitating the spreading and deposition of ZnO precursor onto the rough surface of sandblasted glass slides. Scanning electron microscopy (SEM) images showed that the plasma-treated glass surface had a more uniform distribution and better coverage of zinc oxide nanoparticles compared to the acid-treated glass surface. Under UV-C germicidal lamp illumination, the ZnO catalyst on plasma-treated glass slide led to an 86% degradation of methylene blue in 60 minutes which was higher than the 73% degradation when using the acid-treated glass slide. The plasma-treated glass slide exhibited high durability and could be reused more than five times without the decrease in catalytic efficiency. Higher photocatalytic activity was achieved by extending plasma treatment time from 30 seconds to 180 seconds.

1. Introduction

Photocatalytic oxidation is one of the advanced oxidation processes used for removing organic pollutants from wastewater. It involves the use of photocatalysts, typically semiconductors such as titanium dioxide (TiO_2) or zinc oxide (ZnO), which, when exposed to light, generate electron-hole pairs. These electron-hole pairs participate in redox reactions to generate reactive oxygen species like hydroxyl radical and superoxide radical that can break down organic pollutants into carbon dioxide and other less toxic byproducts.[1]

Since it does not require the addition of chemicals, photocatalysis is considered an environmentally friendly process. However, in practice, photocatalysis requires high energy consumption for the light source and the catalyst recovery.[2] Although slurry reactors, utilizing semiconductor nanoparticles as photocatalysts, can achieve high treatment efficiency, the removal of the catalyst requires a laborious separation process involving ultrafiltration or centrifugation. This issue in catalyst recovery can be addressed by employing heterogeneous catalysts, which involve immobilizing the photocatalytic nanoparticles onto a support such as a glass surface, membrane, or porous material. For example, a simple drop-coating of ZnO precursor on a glass slide before calcination resulted in a ZnO coated glass slide exhibiting excellent photocatalytic activity for up to five reuse cycles in the degradation of methylene blue.[3] A similar dip-coating method of sol-gel ZnO precursor was applied for fabricating ZnO coated glass spheres for a continuous flow photoreactor.[4]

The preparation of the glass surface before coating typically involves successive washing with acids, organic solvents, or calcination. Plasma surface modification can help avoid the use of corrosive or toxic chemicals for cleaning glass surface before applying adhesive coating. Two factors contributing to the increased hydrophilicity and wettability of the glass surface after plasma treatment are the removal of organic contaminants and the formation of polar functional groups.[5]

This study aims to investigate the application of air plasma treatment for the fabrication of ZnO coated glass slides for wastewater treatment. The glass surface was cleaned either through conventional acid bath or plasma treatment. The efficiency and durability of the catalyst were demonstrated in the photodegradation of methylene blue.

2. Materials and Methods

2.1 Materials

Zinc acetate dihydrate was purchased from Ajax Fine Chemical. Urea and methylene blue were purchased from KemAus. Nitric acid and ethanol were purchased from Quality Reagent Chemical (QREC).

2.2 Preparation of glass slides

Standard glass slides were abraded using a sand blasting machine (THC-90, Tochu Thailand Co., Ltd.). This study compared two methods for preparing a clean glass surface. In the first conventional method, the glass slides were cleaned by submerging in 30% w/v HNO_3 and ethanol, respectively. In the second method, the glass slides were cleaned with ethanol and then subjected to a low-pressure plasma treatment using a plasma cleaner (PE-50, Plasma Etch, USA) operating at the power of 20W for 30 seconds.

2.3 Preparation of ZnO-coated glass slides

N-doped ZnO precursor was a mixture of 0.73 g zinc acetate dihydrate, 0.4 mL triethylamine, 9.6 mL of anhydrous ethanol, and 28 mg urea. The mixture was sonicated for 30 minutes until a transparent sol was obtained. The ZnO precursor was deposited on glass slides by a DIY dip-coating equipment assembled from a linear actuator and a plastic holder (Figure 1B). The DIY dip-coating equipment was programmed to pull the slide at a speed of 2.5 mm/s. Then, the coated glass slides were dried in an oven at 80°C for 20 minutes and calcined at 500 °C for 2 hours in a muffle furnace (LT 5/12, Nabertherm, Germany). The glass slides were cut into 1x1 cm pieces for surface analysis using X-ray diffraction (XRD, Empyrean, Malvern Panalytical, UK) and scanning electron microscopy (SEM, SU8010, Hitachi, Japan). The size of zinc oxide nanoparticles was determined using ImageJ software.

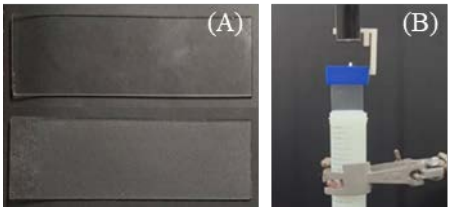

Figure 1. (A) Glass slides before and after sand abrasion. (B) DIY dip-coating device.

2.4 Photodegradation of methylene blue

The photocatalytic efficiency of ZnO-coated glass slides was evaluated by the photodegradation of 25 mL methylene blue solution. The glass petri-dish containing the methylene blue solution was placed under UV-C light illumination (Philips, TUV 8W, T5) at a distance of 5 cm from the light source. The absorbance of the methylene blue solution at 668 nm was measured every 15 minutes using a portable UV-Vis spectrometer (LabQuest2 with SpectroVisPlus, Vernier Science Education, USA). The degradation efficiency was calculated using the following equation: Degradation efficiency (%) = $(C_0–C_t)/C_0 \times 100$, where C_0 and C_t represent the initial and the absorbance at time t of methylene blue solution. The pseudo-first order rate constant (k_{obs}) was obtained from the plot of ln (C_t/C_0) versus irradiation time.

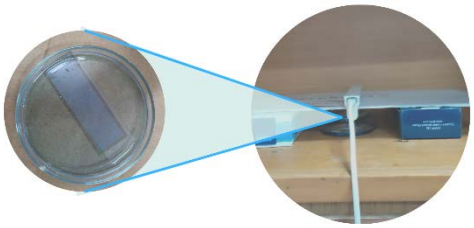

Figure 2. Experimental set up for photocatalytic degradation.

3. Results & Discussion

3.1 Characterization of ZnO-coated glass slides

The deposition of N-doped ZnO on the glass slides was verified by the XRD pattern of the hexagonal wurtzite ZnO. Similar to the values reported in the literature,[3,4] the peaks centered at an angle (2θ) of 31.9°, 34.6°, 36.6°, 47.8°, 56.9°, and 63.1°are corresponding to (100), (002), (101), (102), (110), and (103) planes, respectively (Figure 2). The XRD spectra had a poor signal-to-noise because the scanning was done directly on the glass surface.

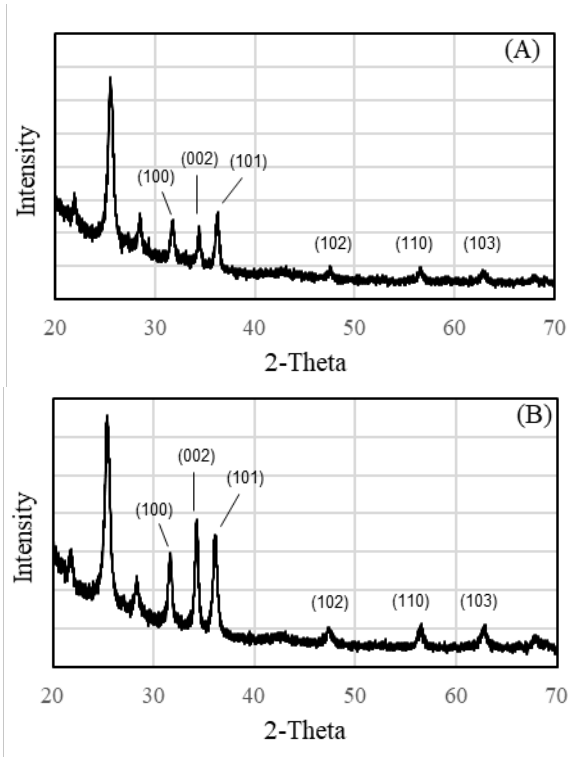

Figure 2. XRD patterns of ZnO nanoparticles on (A) plasma-treated glass slide (B) acid-treated glass slide.

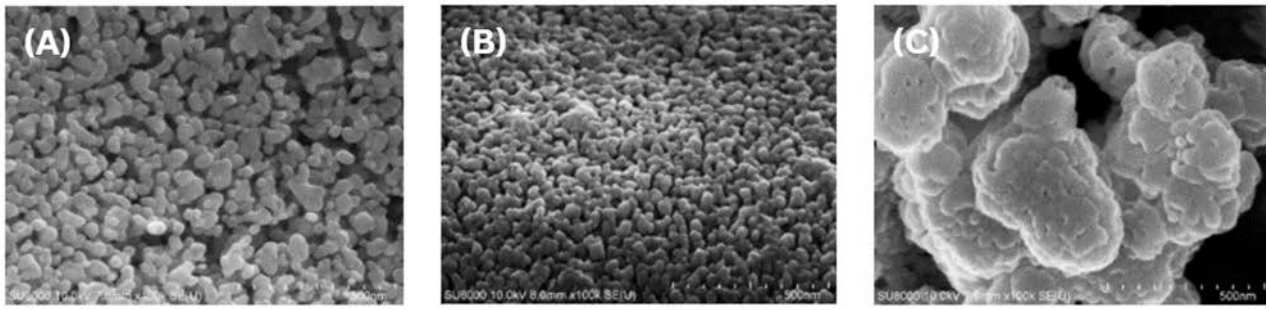

Figure 3. SEM images of N-doped ZnO on the glass surface: (A) Acid-treated glass slides, (B) Plasma-treated slides, (C) Plasma-treated slides with double dip-coating of ZnO precursor before calcination.

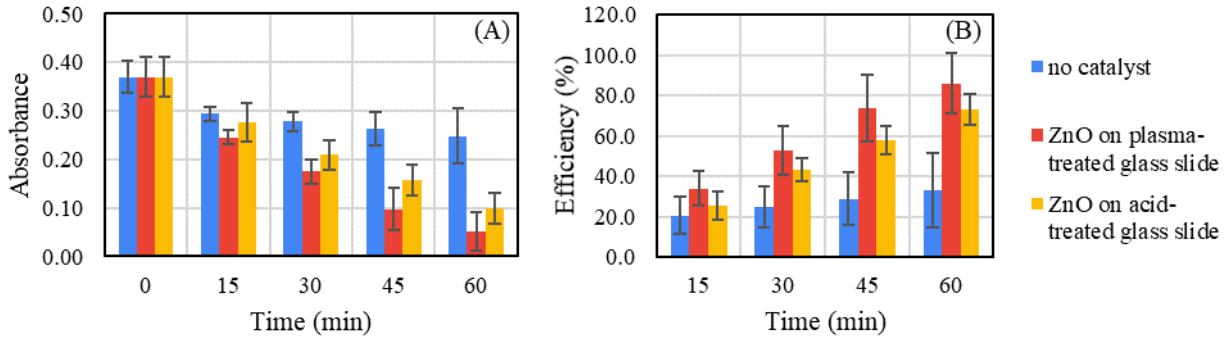

Figure 4. Photocatalytic activity of ZnO coated on plasma-treated glass slides: (A) Absorbance at 668 nm, (B) Degradation efficiency.

SEM images revealed the surface morphology and microstructure of ZnO nanoparticles on the glass slide. The SEM images indicated that plasma surface modification led to a more uniform nucleation site; ZnO nanoparticles on acid-treated slides exhibited an average diameter of 70 nm (Figure 3A), while those on plasma-treated slides showed a more homogenous distribution with an average diameter of 48 nm (Figure 3B). Consequently, the plasma-treated glass slide was expected to have higher photocatalytic efficiency than the acid-treated glass slide. In line with the finding by Vaiano and Lervolino,[4] the second dip-coating of ZnO precursor before calcination induced aggregation, resulting in thicker layers and larger clusters of ZnO (Figure 3C).

3.2 Photocatalytic activity

The UV-C germicidal lamp alone caused a 33% degradation of methylene blue in 60 minutes. The addition of ZnO photocatalyst coated on a plasma-treated glass slide resulted in a higher degradation efficiency of 86% (Figure 4). Plasma treatment emerges as a superior option for glass surface cleaning as it reduces the use of corrosive chemicals and enhances the coating of nanomaterials. ZnO coated on plasma-treated glass slides exhibited higher photocatalytic efficiency than ZnO coated on acid-treated glass slides. This higher catalytic efficiency of the plasma-treated glass slide is supported by the SEM images, showing a more regular microstructure with a higher catalytic surface. For this reason, the aggregation of nanoparticles in the glass slide with double coating of ZnO precursor exhibited slightly lower efficiency than the single coated glass slide.[4] The degradation of methylene blue followed the pseudo-first-order kinetic (Figure 5). In this study, the rate constant was about five to six times higher than those reported by Elias et al.[3] These differences could be influenced by the light source, light intensity, and catalyst loading (Table 1).

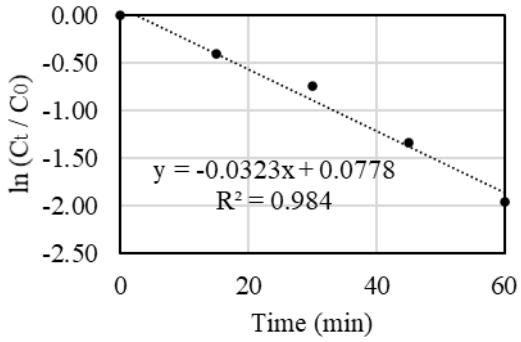

Figure 5. Pseudo-first-order kinetics of methylene blue photodegradation catalyzed by ZnO on plasma-treated glass slide.

Table 1. Pseudo-first-order rate constant of methylene blue photodegradation.

Photocatalyst	Rate constant (k_{obs}, min^{-1})	Correlation coefficient (r^2)
no catalyst	0.0081	0.9913
ZnO on acid-treated glass slide	0.0242	0.9886
ZnO on plasma-treated glass slide	0.0323	0.9840
Double layer of ZnO on plasma treated glass slide	0.0322	0.9777
N-doped ZnO on glass slide (Ref. 3)	0.0060	0.9778
ZnO nanoparticles (Ref. 7)	0.0158	0.9950

To investigate the reusability of ZnO coated on plasma-treated glass slides, five consecutive cycles were performed. The photocatalytic activity of ZnO on plasma-treated glass slides remained almost constant, with no significant changes observed in the degradation efficiency (Figure 6). The error bars, indicating the standard deviation (n=5), showed a relatively large distribution, possibly resulting from various factors such as the temperature of the UV lamp, variation in light intensity at each position, and the alignment of a glass slide and the UV lamp. Increasing the plasma treatment time from 30 to 180 seconds resulted in higher photocatalytic efficiency. Therefore, the photocatalytic efficiency and reusability of the immobilized catalyst can be further improved by optimizing plasma treatment parameters, such as the power of plasma generator and the duration of plasma treatment. Furthermore, it is essential to test the durability of the catalyst in a continuous flow reactor, simulating real-world conditions and providing insights into its long-term performance under continuous operation.[5,6]

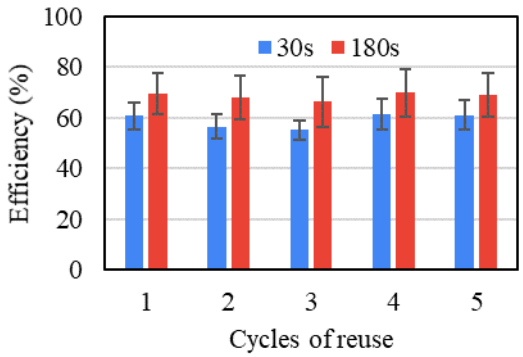

Figure 6. Reuse of ZnO coated on plasma-treated glass slides for methylene blue degradation using 45 mins irradiation time. The glass slides were obtained from different plasma treatment duration of 30 and 180 seconds.

4. Conclusion

This study demonstrated that plasma treatment can enhance the photocatalytic efficiency and reusability of immobilized ZnO, attributing the improvements to the better adhesive properties of the glass surface. ZnO coated on plasma-treated glass slides achieved an 86% degradation of a methylene blue solution in 60 minutes and displayed the ability to be reused at least five times. Further optimizing of the parameters of the air plasma treatment could potentially lead to even better performance.

Acknowledgements

We are deeply grateful to Mr. Wittawas Phunmunee and Mr. Chakrit Smanrak for their help in troubleshooting the DIY dip-coating machine. In addition, we would like to thank scientists and laboratory technicians at the Faculty of Science, Mahidol University, for their support in XRD and SEM operation.

References

1. Amakiri, K., T.; Angelis-Dimakis, A.; Canon, A. R. *Water Sci. Technol.*, **2022**, *85(3)*, 769-788.
2. Cates, E. L. *Environ. Sci. Technol.*, **2017**, *51*, 757-758.
3. Elias, M.; Uddin, M. N.; Saha, J. K.; Hossain, M. A.; Sarker, D. R.; Akter, S.; Siddiquey, I. A.; Uddin, J. *Molecules*, **2021**, *26(5)*, 1470.
4. Vaiano, V.; Lervolino, G. *J. Colloid Interface Sci.*, **2018**, *518*, 192–199.
5. Terpilowski, K.; Rymuszka, D. *Glass Phys. Chem.*, **2016**, 42, 535-541/
6. Ramos, B.; Silva, A. O.; Teixeira, A. C. *Braz. J. Chem. Eng.*, **2021**, *39(2)*, 403–414.
7. Spoiala, A.; Ilie, C.; Trusca, R.; Oprea, O.; Surdu, V.; Vasile, B.; Fical, A.; Andronescu, E.; Ditu, L. *Materials*, **2021**, *14*, 4747.

Wireless preparation of Ni-Ag alloyed Janus objects using bipolar electrochemistry

Oranit Phuakkong*and Suttisuk Plongnui

Division of Chemistry, Faculty of Science and Technology, Suratthani Rajabhat University, Surat Thani , THAILAND

**E-mail: oranit.phu@sru.ac.th*

Abstract:

The preparation of Ni-Ag Alloyed Janus particles by Bipolar Electrochemistry was studied. This technique allowed the development of new methods for controlling surface modification at the micro- and nanoscale. The optimum conditions for Ni deposition on 900 µm of carbon rods were investigated with 0.01 M $NiSO_4$ and electric field at 7 V/cm. Deposition time was 1 minute. While the optimum conditions for Ag deposition on carbon rods were determined by 0.005 M $AgNO_3$, electric field at 5 V/cm and deposition time of 1 minute. Furthermore, the alloyed deposition of Ni-Ag on 10 µm of carbon microfiber (CMF) was created with this technique and characterized by SEM and EDS. The modified objects can be created with bipolar electrochemistry that could find applications as key components for drug delivery.

1. Introduction

Bipolar electrochemistry is a type of electrochemical system where two different electrochemical cells or half-cells share a common electrode. It is widely used to trigger electrochemical reactions at the extremities of a conductive object, without physical contact with the feeder electrodes. The feeder electrodes are connected by an electrolyte, allowing for the flow of ions and the generation of an electric current. The bipolar electrode is immersed in solution under a strong electric field between two feeder electrodes. This arrangement allows for the generation of electrical potential differences across each individual cell. Bipolar electrochemical systems find applications in various fields, including electrochemical synthesis[1], water treatment[2], and sensor[3]. Furthermore, it has been shown that surface modification can be achieved by bipolar electrochemistry such as the asymmetric deposition of organic[4], polymer[5] and metal layers[6].

The synthesis of Ni-Ag alloy particles and their properties have been studied widely in recent years[7,8]. Bimetallic particles like Ni-Ag are particularly attractive due to their magnetic and catalytic properties depending on the structure of the alloy. There are various methods for preparing Ni-Ag alloy objects, such as laser ablation[9] radiolysis[10,11] and reduction method in organic or aqueous medium[7,8] In particular, the synthesis of Au-Ag alloy particles were synthesized by bipolar electrochemistry[12] and their composition is dependent on the applied potential. In this work, we study the optimum condition for bipolar electrodeposition and characterization of Ni-Ag alloy on carbon.

2. Materials and Methods

2.1 Materials

Silver nitrate ($AgNO_3$, 98.5%) and acetone (C_3H_6O, 99.5%) were purchased from RCL Labscan and used as received. Nickel sulphate Hexahydrate ($NiSO_4 \cdot 6H_2O$, 96.0%) was purchased from Unilab and used as received. Two graphite rods with a diameter of 2.0 mm were purchased from Rotring and used as feeder electrodes. Carbon fibers (Grade P100, Goodfellow) with a diameter of 10 µm and Graphite rods with a diameter of 0.9 mm (Pentel Stein) were employed as bipolar electrodes for asymmetric electrodeposition.

2.2 Bipolar electrodeposition of Ni-Ag on graphite

In order to study the Ni-Ag deposition by bipolar electrochemistry, graphite rods were used in the first proof-of-principle bipolar experiment.

To carry out a bipolar electrodeposition experiment, The bipolar electrochemical cell was made from plastic, containing feeder electrodes (graphite rods), as shown in Figure 1. A bipolar electrode was placed in the middle of the cell. The distance between two feeder electrodes was 2 cm while the bipolar electrodes were graphite rod with 0.9 mm and carbon fiber with 10 ⌈m in diameter. The length of the bipolar electrode was 10 mm. A potential difference (E_{app}) = E_a − E_c is applied between the two feeder electrodes, where E_a and E_c are the potentials of the anode and cathode, respectively. The electric field (ε) is given by the following equation

$$\varepsilon = \frac{E_{app}}{d} \qquad (1)$$

where d is the distance between the two feeder electrodes. The potential difference (ΔV) between the two ends of the bipolar electrode is given by

$$\Delta V = \varepsilon \cdot l \qquad (2)$$

where l is the length of the bipolar electrode. To carry out the two reactions at the opposite ends of the bipolar electrodes, ΔV has to be at least equal to the standard potential difference of the two redox reactions.

After the deposition, the sample was removed from the cell and was rinsed thoroughly with deionized water.

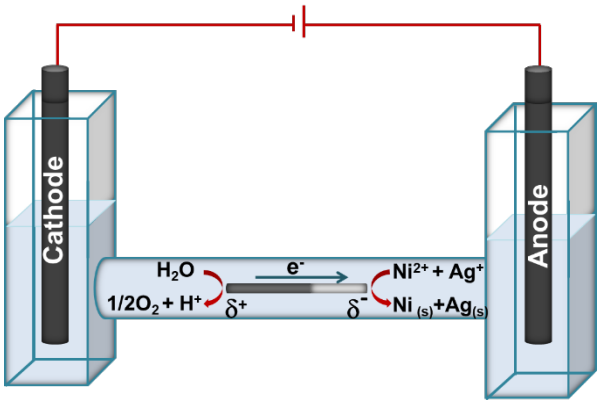

Figure 1. Experimental setup for the deposition of Ni-Ag on bipolar electrode.

2.3 Characterization

SEM observation was carried out with a JEOL (JSM-IT200) instrument to study the surface morphology of Ni and Ag on the bipolar electrode. It was also equipped with energy dispersive X-ray analysis for obtaining the elemental composition of the samples.

3. Results & Discussion

3.1 Bipolar electrodeposition of Ni and Ag on graphite rod

During the first screening experiments, Ni was electrodeposited on graphite rods by bipolar experiment in a solution containing 0.01 M $NiSO_4$ with varying electric fields and deposition times. To achieve Ni^{2+} reduction at the cathodic side and water oxidation at the anodic side of the bipolar electrode, the minimum potential value (ΔV) needed to induce reactions at both sides of the object was E2 − E1 = 1.0 V. As a consequence, for a bipolar electrode with a length of 1 cm, an electric field of at least 1.0 V cm^{-1} has to be applied between the feeder electrodes. In this experiment, the distance between the feeder electrodes was 2.3 cm; therefore, a minimum voltage of 2.3 V needs to be applied to observe the Ni deposition. The area of modification was evaluated as a function of the value of the electric field and the deposition time as shown in Figure 2a and 2b. However, it is clearly observed that the area of Ni deposit on the graphite rod is increased at long deposition time. But the destruction of the anodic end of the bipolar electrode is increasing. The optimum conditions for Ni deposition on graphite rods were investigated with 0.01 M $NiSO_4$ and electric field at 7 V/cm. Deposition time was 1 minute. The presence of Ni particles on cathodic side of the graphite rod is indicated by SEM (Figure 3b).

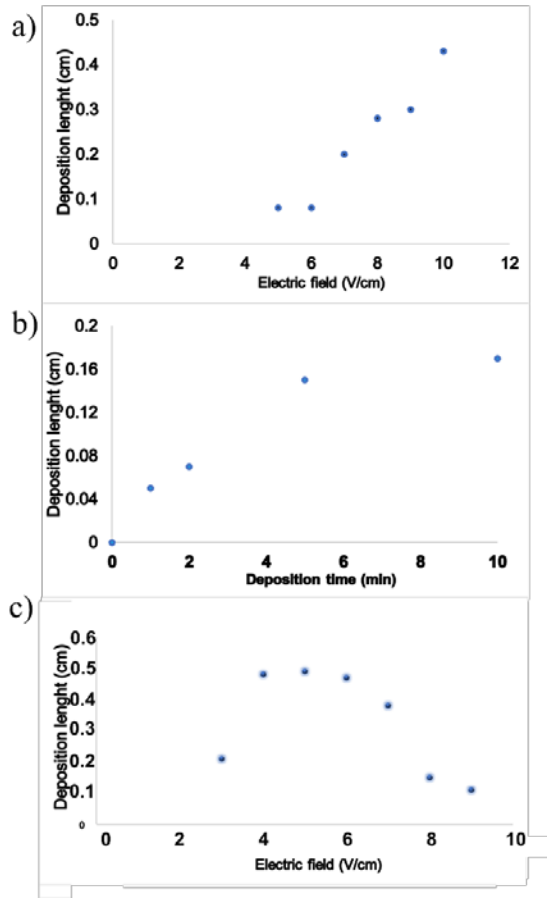

Figure 2. Variation of the distance between the end of the graphite rod and area of a) Ni deposition in the function of electric field b) Ni deposition in the function of deposition time and c) Ag deposition in the function of electric field**.**

For Ag electrodeposition, 0.005 M $AgNO_3$ with varying electric fields and deposition times were studied. To achieve Ag^+ reduction at the cathodic side and water oxidation at the anodic side of the bipolar electrode, the minimum potential value (ΔV) needed to induce reactions at both sides of the object was E2 − E1 = 2.03 V. To observe Ag deposition, a minimum voltage of 4.67 V needs to be applied. The area of deposition was evaluated as a function of the value of the electric field as shown in Figure 2c. Unfortunately, the electromigration was observed for long deposition time. The optimum conditions for Ag deposition on graphite rods were investigated with 0.005 M $AgNO_3$ and electric field at 5 V/cm.

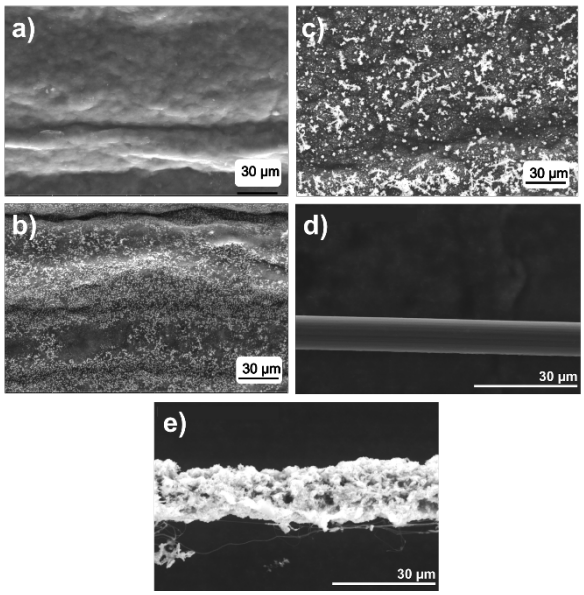

Figure 3. SEM images of the surface of a) bare graphite rod b) Ni@graphite rod c) Ag@graphite rod d) bare carbon fiber and e) Ni-Ag@carbon fiber.

3.2 Bipolar electrodeposition of Ni-Ag alloy on carbon fiber

The alloyed deposition of Ni-Ag on bipolar electrode was studied with 0.01 M $NiSO_4$ and 0.005 M $AgNO_3$ at electric field of 7 V/cm for 1 minute. The surface of bipolar electrode was characterized by SEM. At cathodic side of carbon fiber (Figure 3e) shows the surface modification of Ni-Ag alloy compared to the surface of anodic side (Figure 3d). Furthermore, EDX measurement evidenced the deposition of Ni-Ag on carbon microfiber as shown in Figure 4. Thus, it is demonstrated that Janus structure obtained by modifying a carbon fiber with Ni-Ag alloy, using an electric field of 71 $V \cdot cm^{-1}$.

4. Conclusion

In summary, we have described a route to prepare Ni-Ag alloyed Janus objects by bipolar electrochemistry. The concept is based on electrochemically induced co-reduction of Ni^{2+} and Ag^{+} in a wireless manner. Varying the electric field and the deposition time allows controlling the length of the deposit. Furthermore, the asymmetric carbon microfiber modified with Ni-Ag was characterized by SEM and EDS. This approach opens the route for the development of the structure of Ni-Ag alloy with Ni/Ag ratio. Modifying only one side of the fiber offers the possibility to develop in the future systems with two different types of materials on each side of micro objects with different properties.

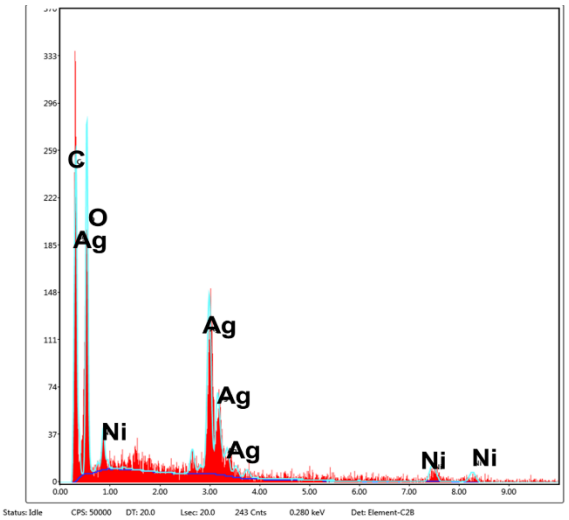

Figure 4. Energy dispersive X-ray analysis (EDX) spectrum of Ni-Ag alloy deposited on carbon fiber.

References

1. Crooks, R. M. *ChemElectroChem* **2016**, 3, 357−359
2. Fattah, Z. A. *ChemistryOpen* **2022**, *11*, *e202200231*.
3. Chow, K.-F.; Mavre, F.; Crooks, R. M. *J. Am. Chem. Soc.* **2008**, 130, 7544−7545
4. Shida, N.; Koizumi, Y.; Nishiyama, H.; Tomita, I.; Inagi, S. *Angew. Chem., Int. Ed.* **2015**,54, 3922−3926.
5. Kumsapaya, W.; Bakaï, M.-F.; Loget, G.; Goudeau, B.; Warakulwit, C.; Limtrakul, J.; Kuhn, A.; Zigah, D. *Chem. - Eur. J.* **2013**, 19, 1577−1580
6. Srivastava, C.; Chithra, S.; Malviya, K.D.; Sinha, S.K.; Chattopadhyay, K. *Acta Mater.* **2011**, 59,6501-6509.
7. Kumar, M.; Deka, S. *ACS Appl. Mater. Interfaces.* **2014**, 6, 16071-16081.
8. Van Ingen, R.P.; Fastenau, R.H.J.; Mittemeijer E.J. *J. Appl. Phys.***1994**, 76, 1871-1883.
9. Zhang, Z.; Nenoff, T.M.; Leung, K.; Ferreira, S.R.; Huang, J.Y.; Berry, D.;T. Provencio, P.P.; R. Stumpf, *J. Phys. Chem. C.* **2010**, 114, 14309-14318.
10. Zhang, Z.; Nenoff, T.M.; Huang, J.Y.; Berry, D.T.; Provencio, P.P.; *J. Phys. Chem. C.* **2009**, 113, 1155-1159.
11. Ramaswamy, R.; Shannon, C. Langmuir **2011**, 27, 878−881

Fabrication of high surface area electrode for potential use in direct CO_2 separation in gas mixtures

Theeratorn Treeintong[1,2] and Chaiya Prasittichai[1,2]*

[1]*Department of Chemistry, Faculty of Science, Kasetsart University, Bangkok 10900, Thailand*
[2]*Center of Excellence for Innovation in Chemistry (PERCH-CIC), Kasetsart University*

**E-mail: chaiya.pr@ku.th*

Abstract:

Swing Adsorption technology for capturing carbon dioxide (CO_2) in mixed gases, is a popular method for reducing CO_2 emissions. Continuous development is required to address issues related to excess energy consumption and to improve efficiency. Electro Swing Adsorption (ESA) employs redox molecule capable of CO_2 adsorption and releasing upon a change in applied potential. This technology offer a promising solution for cost-effective CO_2 capture and holds potential for practical field applications. In this study, we focus on enhancing the stability of redox molecules, which play pivotal roles in ESA. Routes to synthesize polymeric nanoparticles made from glycidyl methacrylate, designed to efficiently attach the redox molecule 2-amino anthraquinone (2-AAQ), were explored. Through 2-AAQ loading efficiency by colorimetric measurement, the optimum synthesis path for producing polymeric nanoparticles encapsulating redox molecules was achieved. This could provide the possibility of incorporating other redox molecules, capable of CO_2 adsorption, even when susceptible to oxidation by other gases for the ESA process.

1. Introduction

The volume of CO_2 produced by human activity such as motors or power plants, to the atmosphere at a frighteningly high pace right now. Global CO_2 emissions are predicted to rise by 1.5 billion tons this year, most likely as a result of increased human activity following the pandemic. Two thirds of the world's CO_2 emissions are currently produced by developing nations like Thailand. The present prediction states that if this trend continues and no significant effort is taken to reduce CO_2 emissions, the global temperature would likely increase by more than 4°C within this century[1]. One hundred and ninety-five territories, including Thailand, consented to join the agreements known as the Paris Accords, intending to cut CO_2 emissions significantly by 2050.[2] This agreement has led to the proposal of several strategies for either capturing CO_2 in the atmosphere or sequestering or using CO_2 emissions from power plants to create other useful products.

One particular method that could potentially capture CO_2 in the mix gas is called Electro Swing Adsorption, ESA. ESA is a technique that employs electric fields to promote the adsorption and desorption of CO_2 from the mix gases. This method utilizes materials called electrosorbents, which have the ability to both capture and release carbon dioxide when an electric potential is introduced or reversed. The primary advantage of ESA is its low-energy requirement compared to other CO_2 capture methods[3] and it may be used with renewable energy.

The heart of the ESA is the electrosorbents that are made from the redox molecules attached on the High-surface-area electrodes.[4] These redox molecules must undergo the CO_2 adsorption.[5] or releasing after the change in potentials. Examples of redox molecules that can be used in ESA and other related works include molecules, such as, quinones or dibenzylsulfane.

However, redox molecules do have some restrictions on their application, particularly in ESA. One significant limitation is their instability and sensitivity to some gaseous molecules, namely oxygen or moisture. This can result in low retention and service life, as the molecules could break down or interact with these oxidative gaseous in the gas mixtures. This would greatly affect the efficiency and longevity of ESA.

In the past decade, there have been significant advancements in the developments and applications of porous polymer networks. These networks, also known as covalent organic frameworks,[6] hyper cross-linked polymers,[7] conjugated micro-porous polymers,[8] polymer of internal micropores or porous aromatic frameworks have gained attention in both research and various industries. The comparatively strong endurance of polymer networks to temperature and air stability is one of the main advantages that could be used in various fields without sacrificing durability or performance.

Currently, continuous research and development are being done to create polymeric

compounds with increased specificity and CO_2 binding capacity,[9] due to the low inherent ability of polymers to capture CO_2. These polymers have been modified and supplemented with redox molecules capable of adsorb and desorb CO_2. The composite materials have been further developed into high-surface area electrodes and could be subsequently employed for ESA application.

In this report, we will preliminarily assess the potential use of redox-decorated modified porous polymeric network as the electrosorbent for CO_2 capture and release in ESA applications. Poly(methyl methacrylate) and poly(glycidyl methacrylate-*co*-ethylene glycol dimethacrylate) core-shell polymeric nanoparticles are synthesized and subsequently surface-decorated with 2-aminoanthraquinone. The strategic approaches for creating an efficient core-shell polymeric network, aimed at enhancing the binding of redox molecules (specifically anthraquinone) for optimal CO_2 adsorption and desorption, are presented.

2. Materials and Methods

2.1 Materials

2-aminoanthraquinone (2-AAQ, 98%), ethylene glycol dimethacrylate (EGDMA), 4-(4-nitrobenzyl)pyridine (NBP, 98%) and glycidyl methacrylate (GMA) were purchased from Tokyo Chemical Industry Co., Ltd. Methyl methacrylate (MMA) and sodium dihydrogen phosphate (NaH_2PO_4, 99%) were purchased from Sigma-Aldrich, Inc. Ethanol (EtOH, 98%) was purchased from Apex Chemicals Co., Ltd. Sodium hydrogen carbonate ($NaHCO_3$) and potassium persulfate (KPS) were purchased from Supelco, Inc. Carbon Cloth - 1071 HCB from AvCarb Material Solutions

2.2 Synthesis of MMA

The synthesis was initiated by polymerizing the core polymer using a combination of methyl methacrylate (MMA) and potassium persulfate. The reaction was performed in a 250 mL glass reactor equipped with a reflux condenser, a temperature probe, and a nitrogen inlet. The initial reaction was conducted at a temperature of 85 °C for a duration of 4 hours. The resulting MMA particles were collected, wash with solvents and stored for further uses.

2.3 Synthesis of MMA(GMA-co-EGDMA)

An appropriate amount of mixture of glycidyl methacrylate and ethylene glycol dimethacrylate was added to poly MMA suspensions. The mixture was stirred and maintained at 85°C for 4 hours. Afterward, the system was cooled to room temperature, a mixture solution of sodium hydrogen carbonate or sodium dihydrogen phosphate was added to the suspensions to adjust the pH. The final products appear as white suspension in solution.

2.4 Surface decoration of polymeric nanoparticles of MMA(GMA-co- EGDMA) by 2-AAQ

2-aminoanthraquinone (2-AAQ) was dissolved in ethanol until it reached saturation.[10] The precipitate was subsequently filtered out, and a saturated solution of 2-AAQ was transferred to a round-bottom flask. The MMA(GMA-co-EGDMA) core shell particles dispersions were then added dropwise to the 2-AAQ/EtOH solution. The reaction mixture was heated at 100 ^oC to reflux for a duration of 36 hours. Following the reaction, the resulting product was purified by centrifugation (6000 rpm and 20 mins) with ethanol until the supernatant become visibly clear.

2.5 Fabrication of 2-AAQ surface decorated polymeric nanoparticles of MMA(GMA-co-EGDMA) electrode

The conductive carbon cloth was immersed in nitric acid for a period of 10 minutes, followed by rinsing with distilled water for 10 minutes, and subsequently dried at a temperature of 100 °C for 30 minutes. This process was done to ensure the cleanliness of the cloth prior to applying nanoparticles onto the electrode. A cleaned carbon cloth was then soaked in the MMA(GMA-co-EGDMA) core shell particles dispersions at room temperature[11,12] for a duration of 1 day, and subsequently dried[13]in dry atmosphere.

3. Results & Discussion

3.1 Synthesis and Characterization of core-shell nanoparticles

The emulsion polymerization technique was employed to synthesize polymer-based nanoparticles with a core-shell structure. In order to ensure precise control over the particle size, structural modulations were implemented. To examine the particle sizes, both SEM and DLS analyses were conducted. The scanning electron micrographs depicting the stepwise synthesis are presented in Figure 1, while Table 1 provides a compilation of the average diameters obtained.

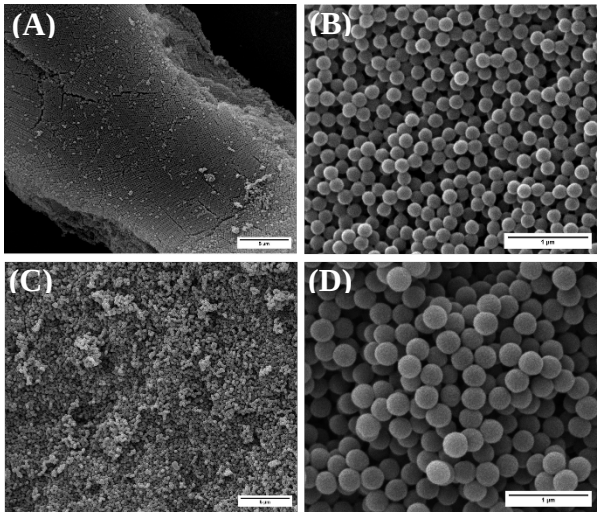

Figure 1. The SEM images of the nanoparticle of (A) MMA, (B) same sample of A with enhanced magnification and (C) MMA(GMA-co-EGDMA), (D) same sample of C with enhanced magnification.

Table 1. Comparison of the average diameters of the synthesized particles determined by SEM and DLS measurements.

Sample	SEM (nm)	DLS (nm)
core	177 ± 7	210 ± 3
core-shell	289 ± 15	303 ± 2

From the SEM measurement, the average sizes were measured at 177 ± 7 nm for the core particles and 289 ± 15 nm for the core-shell particles, respectively. The hydrodynamic diameter measured by DLS results in slightly larger average diameter values. Specifically, the average diameter values for the core and shell particles are 210 ± 3 nm and 303 ± 2 nm, respectively. This difference may be attributed to particle swelling in the solvent during DLS measurements. Nevertheless, both techniques confirm the precise control of the polymerization process in our synthesis.

3.2 Modification of GMA active functional group on MMA(GMA-co-EGDMA) particles

After successfully synthesizing monodisperse core-shell particles, we investigated the activity of the epoxy moieties present on the particle surfaces. These functional groups are essential prerequisites for the subsequent post-functionalization of polymeric particles with the redox shuttle of 2-AAQ. To test this, the *Preussmann reagent*, 4-(4-nitrobenzyl)pyridine, NBP, which is known to undergo an effective ring reaction,[14] was utilized.

Figure 2 illustrates the ring-opening reaction of the epoxy functional group on GMA and NBP, resulting in a distinct purple complex formation. This serves as a qualitative indicator, providing evidence for the presence of active epoxy moieties in the MMA(GMA-co-EGDMA) particles. The images in Figure 2 clearly demonstrate the successful incorporation of active GMA into the polymer shell, opening up the opportunity for further surface functionalization of the synthesized polymeric nanoparticles with 2-AAQ.

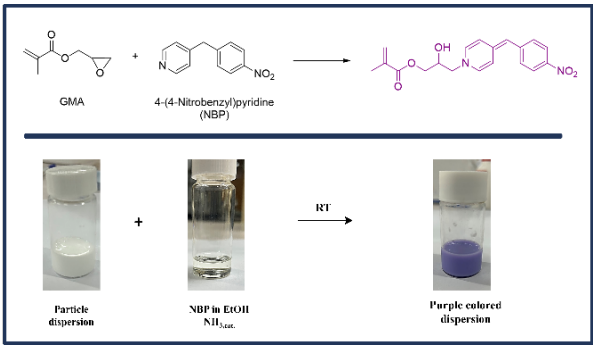

Figure 2. (Top) Reaction of GMA with the *Preussmann Reagent*, 4-(4-nitrobenzyl)Pyridine, NBP, forming a purple colored complex. (Bottom) Photographs of the pure MMA(GMA-co-EGDMA) dispersion particles, an ethanoic solution of NBP with a catalytic amount of ammonia, and the resulting dispersion at room temperature.

Upon verifying the presence of active GMA functional groups on the surface of the MMA(GMA-co-EGDMA) core-shell particles, we proceeded to attach 2-AAQ to these particles. Figure 3 showcases the color changes observed at each modification stage, starting from the core particle to the surface-decorated core-shell particles with 2-AAQ. The successful surface decoration of 2-AAQ is evidenced by the transformation of the polymer's color from white to a vibrant orange due to the presence of 2-AAQ. We also conducted similar polymer synthesis experiments with varying conditions to control the size and ratio of active functional groups of GMA, noting variations in color intensity (detailed data not shown here). A comprehensive report on these findings will be presented in the future.

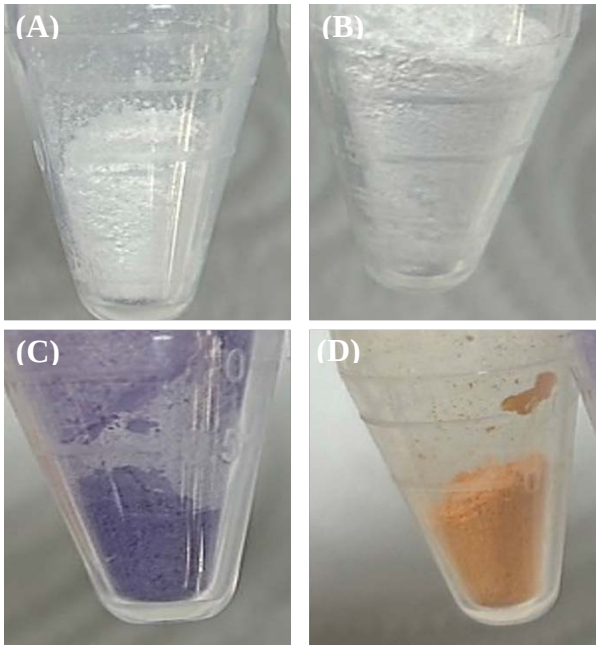

Figure 3. The photographs of dried powder after washing (A) MMA and (B) MMA(GMA-co-EGDMA) and (C) MMA(GMA-co-EGDMA) with NBP and (D) MMA(GMA-co-EGDMA) with 2-AAQ.

3.3 Coating 2-AAQ surface modified MMA(GMA-co-EGDMA) particles on high-surface-area conductive materials

To explore the possibility of using 2-AAQ surface modified MMA(GMA-co-EGDMA) core-shell particles as the electro-adsorbents in the ESA system, the polymeric nanoparticles were coated onto carbon cloth using a dip-coating method.[15]

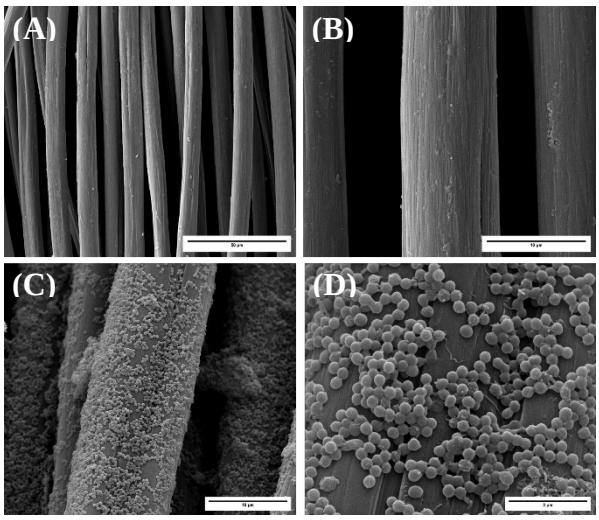

Figure 4. The SEM images of (A) an overview of a carbon cloth after chemically activated in nitric acid and (B) an enhanced magnification of A (C) an overview of a carbon felt coated with 2-AAQ-modified core shell particles and (D) same sample of C with enhanced magnification.

An appropriate quantity of core-shell particles modified with 2-AAQ and multiwall carbon nanotubes, was mixed in a polar solvent. The cleaned carbon cloth was then immersed in this solution and allowed to dry. Figure 4 visually depicts the contrast between the bare carbon cloth and the coated surface with core-shell particles containing 2-AAQ. The evident adherence of polymeric particles indicates the successful creation of a high surface area electrode decorated with redox shuttle capable of adsorb and desorb CO_2, paving the way for potential applications in the ESA field. Our ongoing research is currently investigating the ESA process of this polymer containing 2-AAQ, along with other similar systems, and the results will be reported separately in the future.

4. Conclusion

We have successfully established a pathway for the production of polymeric nanoparticles encapsulating redox molecules, designed for the Electrochemical Swing Adsorption (ESA) process. These polymeric particles have been effectively integrated onto high-surface-area electrodes, making them readily applicable for ESA in the near future. We anticipate that this synthetic approach opens up the potential for incorporating other redox molecules, even those vulnerable to oxidation by other gases, into the ESA process. We also believe that similar strategy (encapsulating redox molecule in a robust complex structure) would offer an alternative avenue for CO_2 adsorption capabilities.

Acknowledgements

This work receives financial support from Kasetsart University Research and Development Institute (KURDI) and a partial funding support from the Center of Excellence for Innovation in Chemistry Scholarship (PERCH- CIC). The facilities are supported by the Department of Chemistry, Faculty of Science, Kasetsart University, Bangkok, Thailand

References

1. New, M.; Liverman, D.; Schroeder, H.; Anderson, K., Four degrees and beyond: the potential for a global temperature increase of four degrees and its implications. *Philos Trans A Math Phys Eng Sci* **2011,** *369* (1934), 6-19.
2. Langevin, J.; Harris, C. B.; Reyna, J. L., Assessing the Potential to Reduce U.S. Building CO2 Emissions 80% by 2050. *Joule* **2019,** *3* (10), 2403-2424.

3. Voskian, S.; Hatton, T. A., Faradaic electro-swing reactive adsorption for CO2 capture. *Energy & Environmental Science* **2019,** *12* (12), 3530-3547.
4. Mano, N., Recent advances in high surface area electrodes for bioelectrochemical applications. *Current Opinion in Electrochemistry* **2020,** *19*, 8-13.
5. Qiao, X.; Li, D.; Cheng, L.; Jin, B., Mechanism of electrochemical capture of CO2 via redox cycle of chlorinated 1,4-naphthoquinone in BMIMBF4: An in-situ FT-IR spectroelectrochemical approach. *Journal of Electroanalytical Chemistry* **2019,** *845*, 126-136.
6. Baddeley, C. J., On Surface Polymerization With Amines. In *Encyclopedia of Interfacial Chemistry*, Wandelt, K., Ed. Elsevier: Oxford, 2018; pp 316-323.
7. Tan, L.; Tan, B., Hypercrosslinked porous polymer materials: design, synthesis, and applications. *Chemical Society Reviews* **2017,** *46* (11), 3322-3356.
8. Lee, J.-S. M.; Cooper, A. I., Advances in Conjugated Microporous Polymers. *Chemical Reviews* **2020,** *120* (4), 2171-2214.
9. Hoang, T.-D.; Bandh, S. A.; Malla, F. A.; Qayoom, I.; Bashir, S.; Peer, S. B.; Halog, A., Carbon-Based Synthesized Materials for CO2 Adsorption and Conversion: Its Potential for Carbon Recycling. *Recycling* **2023,** *8* (4).
10. Wu, Q.; Sun, Y.; Bai, H.; Shi, G., High-performance supercapacitor electrodes based on graphene hydrogels modified with 2-aminoanthraquinone moieties. *Phys Chem Chem Phys* **2011,** *13* (23), 11193-8.
11. Schäfer, C. G.; Viel, B.; Hellmann, G. P.; Rehahn, M.; Gallei, M., Thermo-cross-linked Elastomeric Opal Films. *ACS Applied Materials & Interfaces* **2013,** *5* (21), 10623-10632.
12. Lovell, P. A.; Schork, F. J., Fundamentals of Emulsion Polymerization. *Biomacromolecules* **2020,** *21* (11), 4396-4441.
13. Kredel, J.; Gallei, M., Ozone-Degradable Fluoropolymers on Textile Surfaces for Water and Oil Repellency. *ACS Applied Polymer Materials* **2020,** *2* (7), 2867-2879.
14. Winter, T.; Bitsch, M.; Müller, F.; Voskian, S.; Hatton, T. A.; Jacobs, K.; Presser, V.; Gallei, M., Redox-Responsive 2-Aminoanthraquinone Core–Shell Particles for Structural Colors and Carbon Capture. *ACS Applied Polymer Materials* **2021,** *3* (9), 4651-4660.
15. Schlander, A. M. B.; Gallei, M., Temperature-Induced Coloration and Interface Shell Cross-Linking for the Preparation of Polymer-Based Opal Films. *ACS Applied Materials & Interfaces* **2019,** *11* (47), 44764-44773.

Surface modification of titanium with poly(amidoamine) dendrimer and its impact on bacterial adhesion and biofilm formation

Wanida Wattanakaroon*, Kidtiya Boonkasam, Rossanee Fordsoongnern, Yanisa Jongrakwit, Nareenart Sripho-on

Department of Biotechnology, Faculty of Engineering and Industrial Technology, Silpakorn University, Sanamchandra Palace Campus, Nakhon Pathom 73000, Thailand

**E-mail: watanakaroon_w@su.ac.th*

Abstract:

Titanium-based materials have been widely used as implants in various applications. However, bacterial infections associated with titanium implants remain a serious clinical problem. Development of functional materials to improve efficacy and prevent infection is a promising solution. Thus, the use of poly(amidoamine) (PAMAM) dendrimer for coating was proposed as an effective strategy to control bacterial infection and colonization on the device surface. In this study, we performed the surface coating or functionalization of titanium with PAMAM dendrimer at a concentration of 1.0 mM. The effects of incubation period and the number of coatings (layer-by-layer) with PAMAM dendrimer were evaluated for optimization of surface modification. Additionally, the coated titanium surface was tested its properties regarding bacterial adhesion and biofilm formation. Results showed that the PAMAM dendrimer adsorbed on the titanium, and the coated surface exhibited functionality. No noticeable discrimination was observed between the incubation of 1 hour with double coating (bilayers) and of 2 hours with single coating (a monolayer). Titanium coated with PAMAM dendrimer showed a reduction in the number of *Enterococcus faecalis* TISTR 379 attached to the surface of the material compared to non-coated titanium. The antimicrobial test of the treated surfaces indicated the log reduction value of 0.157 ± 0.049 for 1-hour incubation and coating as bilayers and 0.072 ± 0.026 for 2-hour incubation and coating as a monolayer. This alternative coating method has great potential for the preparation of titanium implants and prevention of infections.

1. Introduction

Bacterial infection and colonization on implanted biomaterials remain a critical factor in the failure of implant procedures. Clinically, implant-associated infections are mainly caused by bacterial biofilm. Biofilms are aggregations of microorganisms that are embedded in a self-produced matrix composed of extracellular polymeric substances (EPS). Among different methods that have been reported to solve this problem, chemical modification and functionalization on material surface is regarded as one of the most preventive strategies. Poly(amidoamine) (PAMAM) dendrimer, a synthetic polymer, is a highly branched macromolecule consisting of three structural components: a core, interior branches, and terminal (or surface) groups. PAMAM dendrimer is recognized as unique properties such as nanoscale features, controlled size, low dispersivity and flexibility of modifying the terminal functional groups on their surface.[1,2] Thus, the purpose of this research was to study the biocompatible surface coating for medical titanium with PAMAM dendrimer, as our material of choice, in order to improve potential antibacterial properties. The effects of incubation period and the number of coatings (layer-by-layer) with PAMAM dendrimer were evaluated for optimization of surface modification. The ability of *Enterococcus faecalis* TISTR 379 to adhere and develop biofilms on the treated titanium surfaces was then investigated.

2. Materials and Methods

2.1 Chemicals

Commercially pure titanium foil (99.5% metals basis) with a thickness of 0.25 mm was purchased from Alfa Aesar (Tewksbury, MA, USA). Poly(amidoamine) (PAMAM) dendrimer, with an ethylenediamine core, generation 4.5 (-COOH) (5% wt in methanol, molecular weight = 26,258 g/mole, 128 carboxyl end groups) was obtained from Aldrich (St. Louis, MO, USA). All commercially available regents used were of analytical grade and no further purifications were made.

2.2 Surface coating of titanium

Titanium substrates were prepared according to the procedures of Liu et al. and Souza et al.[3,4] Briefly, the titanium foils (10 x 10 mm square) were polished using 400-, 600-, 800-, and 1,200-grit sandpaper sequentially in order to standardize the surfaces. Then, they were ultrasonically cleaned with acetone and 70% (v/v) ethanol for 20 minutes, followed by deionized

water twice for 10 minutes. After that, the titanium samples were dried in an oven at 80 °C for 15 minutes. The resulting titanium was further processed for PAMAM dendrimer coating. The titanium samples were modified with PAMAM dendrimer at a concentration of 1.0 mM. The effects of incubation period (i.e., 1 and 2 hours) and the number of coatings (layer-by-layer) (i.e., single and double coatings) with PAMAM dendrimer were investigated for optimization. Each titanium sample was immersed into the PAMAM dendrimer solution, and incubated with shaking, then immersed into phosphate buffered saline (PBS) for 1 minute and air drying under a laminar flow hood for 30 minutes.

2.3 Surface characterization

The surface structure of the titanium samples was observed using a field emission scanning electron microscopy (FESEM) (Tescan, Czech Republic) with accelerating voltage of 20 kV. The magnifications used were 1,000 x and 50,000 x.

2.4 Cell viability and biofilm formation

Colony biofilms were prepared by growing bacteria on the titanium surface according to the previous reports.[5,6] In brief, *E. faecalis* TISTR 379 was grown in brain heart infusion (BHI) broth at 37 °C for 24 hours. Titanium prepared as described above was placed into a tube containing 9.99 ml of BHI broth, and seeded with 0.01 ml of 24-hour *E. faecalis* TISTR 379, which was adjusted to 0.3-0.4 MacFarland. Samples were incubated at 37 °C for 24 hours. At the end of the treatment period, the biofilms were sampled by placing a titanium and associated bacteria into a sterile 5-ml tube containing 3 ml of 0.85% (w/v) NaCl solution and sonicated in an ultrasonic bath. The biofilms were then dispersed by vortexing and serial dilutions, and viable bacterial numbers were determined by drop-plating on BHI agar. Colony forming units (cfu) were counted after incubating plates at 37 °C for 16-18 hours. Biofilm areal cell density (cfu/cm^2) was calculated by dividing the total number of viable bacteria on the sample titanium by the surface area of the titanium. Antimicrobial activity was also reported as a log reduction. Furthermore, a scanning electron microscopy was used to visualize the morphology of the *E. faecalis* TISTR 379 biofilm on titanium surfaces. The samples were fixed in 2.5% glutaraldehyde in 0.1 M phosphate buffer pH 7.0 at 4 °C for 1 hour, and rinsed with 0.1 M phosphate buffer pH 7.0 three times for 15 minutes at each interval. The fixed specimens were dehydrated using 25, 50, 75, and 100% (v/v) graded ethanol twice for 15 minutes, followed by air drying under a laminar flow hood for 10-20 minutes. The samples were then fixed on aluminum stubs and coated with gold using a sputter coater (Cressington, UK) for observation using FESEM with accelerating voltage of 15 kV. The magnification used were 2,000 x and 10,000 x.

3. Results and Discussion

3.1 Surface modification and characterization

The surface and internal morphology of the non-coated titanium and titanium coated with PAMAM dendrimer were characterized using FESEM with the results presented in Figure 1.

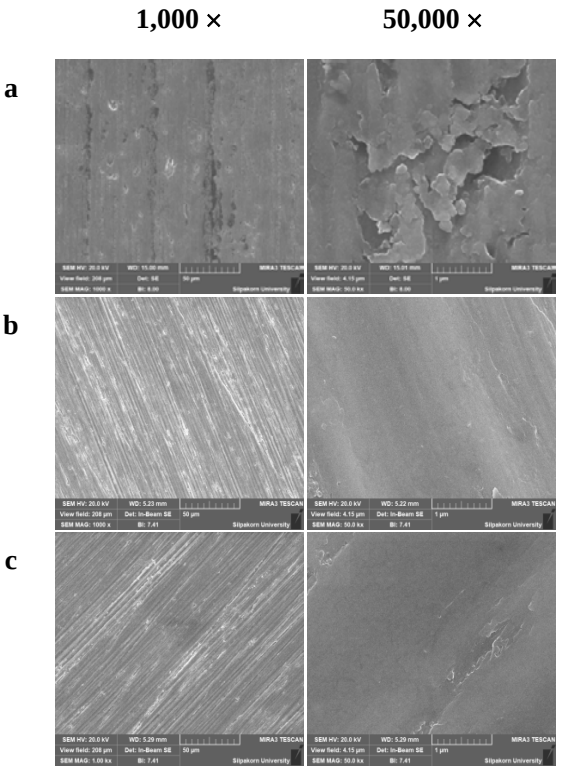

Figure 1. Scanning electron micrographs of the surface and internal morphology of (a) pure Ti, (b) PAMAM dendrimer-coated Ti (1-hour incubation/bilayers) and (c) PAMAM dendrimer-coated Ti (2-hour incubation/monolayer). A symbol denotes titanium (Ti). (left-hand side, Scale bar = 50 µm and right-hand side, Scale bar = 1 µm).

Figure 1a represents surface and internal morphology of unpolished pure titanium, which contained the oil stains. After cleaning, as shown in Figure 1b and 1c, the titanium surface exhibited scratches during polishing. Compared with a pure titanium substrate, the PAMAM dendrimer adsorbed on the titanium, and the coated surface exhibited functionality. No noticeable

discrimination was observed between the incubation of 1 hour with double coating (bilayers) and of 2 hours with single coating (a monolayer).

3.2 Cell viability and biofilm formation

The total number of bacterial colonies attached to various titanium substrates after 24 hours was illustrated in Table 1. As seen, titanium coated with PAMAM dendrimer showed a reduction in the number of *E. faecalis* TISTR 379 attached to the surface of the material compared to both non-coated titanium and PBS-coated titanium.

Table 1. Comparison of the effects of various treatments on the biofilm areal cell density (cfu/cm^2). Symbols denote titanium (Ti) and phosphate buffered saline (PBS).

Treatment	cfu/cm^2
Non-coated Ti	7.42 x 10^8
PBS-coated Ti (1-hour incubation/bilayers)	7.42 x 10^8
Dendrimer-coated Ti (1-hour incubation/bilayers)	6.21 x 10^8
Dendrimer-coated Ti (2-hour incubation/monolayer)	7.24 x 10^8

Corroborating these results, the data in Table 2 illustrate that the antimicrobial test of the treated surfaces indicated the log reduction value of 0.157 ± 0.049 for 1-hour incubation and coating as bilayers and 0.072 ± 0.026 for 2-hour incubation and coating as a monolayer. Apparently, as shown in the FESEM images (Figure 2a and 2b), the clusters of cells, where present, are seen and have much less substrate coverage than those grown on the non-coated titanium. With this, the PAMAM dendrimer coating had effects in preventing *E. faecalis* TISTR 379 adhesion and biofilm formation over a time span of 24 hours. Since an implant is susceptible to bacteria attack during the initial 6-hour post-implantation, this time period is thus critical for preventing bacterial adhesion.[7] The one plausible explanation revealed by our previous study was the wettability property of surfaces. Wettability is an important mediator of microbial adhesion. The coating of PAMAM dendrimer significantly reduced contact angles of titanium surface indicating more hydrophilic surfaces. Moreover, the PAMAM dendrimer films, especially as bilayers, exhibited antimicrobial activity against *E. faecalis* TISTR 379 and inhibited its colonization on the titanium. Our data are in agreement with the finding of Wang et al.[8]

Table 2. Comparison of log reduction on the coating. The mean ± SD are presented. *n*, in the third column, denotes the number of replicates. A symbol denotes titanium (Ti).

Treatment	Log reduction	*n*
Dendrimer-coated Ti (1-hour incubation/bilayers)	0.157 ± 0.049	3
Dendrimer-coated Ti (2-hour incubation/monolayer)	0.072 ± 0.026	5

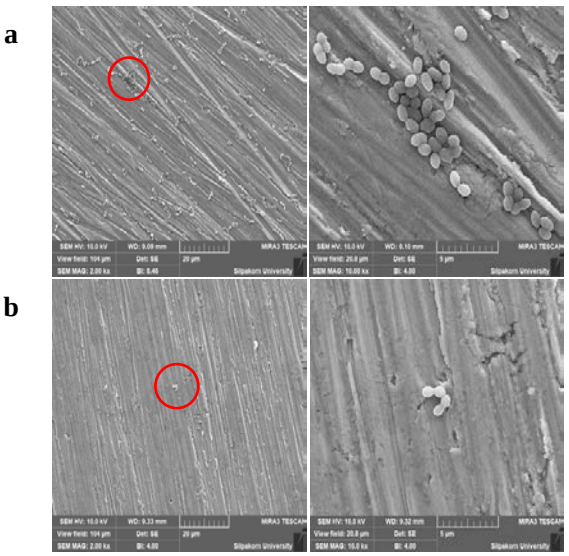

Figure 2. Representative scanning electron micrographs of *E. faecalis* TISTR 379 adhesion and biofilm formation on the titanium surface of (a) control (non-coated Ti) and (b) PAMAM dendrimer-coated Ti (1-hour incubation/bilayers). A symbol denotes titanium (Ti). (left-hand side, Scale bar = 20 µm and right-hand side, Scale bar = 5 µm).

4. Conclusion

This work demonstrated the simple modification of titanium substrates with PAMAM dendrimer possessing antibacterial activity and reduction of biofilm formation. This alternative coating method has great potential for the preparation of titanium implants and prevention of infections.

Acknowledgments

This research was financially supported by Silpakorn University Research, Innovation and Creative Fund. The authors are indebted to Witoon

Wattananit at the Scientific and Technological Equipment Centre in Silpakorn University for performing the scanning electron microscopy.

References

1. Esfand, R.; Tomalia, D. A. *Drug Discov. Today* **2001**, *6*, 427-436.
2. Tomalia, D. A. *Prog. Polym. Sci.* **2005**, *30*, 294-324.
3. Liu, Z.; Ma, S.; Duan, S.; Xuliang, D.; Sun, Y.; Zhang, X.; Xu, X.; Guan, B.; Wang, C.; Hu, M.; Qi, X.; Zhang, X.; Gao, P. *ACS Appl. Mater. Interfaces* **2016**, *8*, 5124-5136.
4. Souza, J. G. S.; Bertolini, M.; Costa, R. C.; Cordeiro, J. M.; Nagay, B. E.; de Almeida, A. B.; Retamal-Valdes, B.; Nociti, F. H.; Feres, M.; Rangel, E. C.; Barão, V. A. R. *ACS Appl. Mater. Interfaces* **2020**, *12*, 10118-10129.
5. Phoudee, W.; Wattanakaroon, W. *Adv. Mat. Res.* **2013**, *747*, 107-110.
6. Wattanakaroon, W.; Chonpracha, J.; Subsomboon, T. *Key Eng. Mater.* **2022**, *914*, 81-85.
7. Poelstra, K. A.; Barekzi, N. A.; Rediske, A. M.; Felts, A. G.; Slunt, J. B.; Grainger, D. W. *J. Biomed. Mater. Res.* **2002**, *60*, 206-215.
8. Wang, L.; Erasquin, U. J.; Zhao, M.; Ren, L.; Zhang, M. Y.; Cheng, G. J.; Wang, Y.; Cai, C. *ACS Appl. Mater. Interfaces* **2011**, *3*, 2885-2894.

Green preparation method of silver nanoparticles for cosmetic applications

Nakadech Youngwilai* and Suttinun Phongtamrug

Department of Industrial Chemistry, Faculty of Applied Sciences, King Mongkut's University of Technology North Bangkok, Bangkok, 10800, Thailand

**E-mail: nakadech.y@sci.kmutnb.ac.th*

Abstract:

This study aimed on investigating the environmental-friendly method involving the generation of suspensions of silver nanoparticles (AgNPs) with the antibacterial activity suitable for the use in cosmetic applications such as antibacterial pads and sanitary napkins. The colloidal suspension of AgNPs was successfully synthesized via green synthesis routes using Gac fruit (Momordica cochinchinensis Spreng) as a reducing agent. The size of the obtained AgNPs determined via the dynamic light scattering (DLS) technique was found to be in the average of 44 nm. The presence of metallic nanoparticles was also observed and confirmed using UV–Visible spectroscopy (UV-Vis) and transmission electron microscopy (TEM). The results illustrated the formation of the uniform, well-dispersed spherical AgNPs. The prepared AgNPs were found to be effective against both gram-positive and negative bacteria. The antibacterial effect of nano-sized silver solution was preliminary tested in the form of sanitary napkins. The personal satisfaction survey revealed the beneficial effect of the AgNPs on human skin after applying for 3 days.

1. Introduction

Synthesis of metallic nanoparticles has caught many attentions in research studies due to their unique mechanical, electrical, and magnetic properties that can be applied in many areas such as electrochemical, medical, environmental and energy sciences, and cosmetic.[1] Among the various metal nanoparticles, silver nanoparticles (AgNPs) have wide range of uses such as antiviral, anti-fungal and anti-inflammatory applications.[2,3] The nanoparticle morphology such as size, size distribution, shape and agglomeration are factors that affect the effectiveness of AgNPs.[4]

Different synthesis methods have been investigated and reported in the literature for the synthesis of AgNPs that produced particles of the desired characteristics.[3-5] Most of the synthesis routes was found to employ chemicals in the form of reducing agent that could be potentially harmful to the environment and living organisms.[2-4] In order to overcome these drawbacks, the biological and environmental-friendly approach has been employed to synthesize the AgNPs. Among the biological resources, plant extracts have been used as successful alternatives to synthesize the nanoparticles.[6,7] In this present study, Gac Fruit (Momordica cochinchinensis Spreng) was found to be a potential candidate for AgNPs synthesis due to its ease of growth in Thailand and ability to survive in the extreme conditions.

The "Green" biological synthesis of AgNPs from various plant materials have been carried out and reported for many years.[8-10] The presence of phytochemical in plants could successfully reduce Ag^+ ions to AgNPs. The presence of plant constituents such as sugars, polyphenols, phenolic acids, terpenoids and alkaloids has demonstrated the important role in reducing metal ions into nanoparticles.[9,10]

In this study, the synthesis of AgNPs was conducted by the use of Gac fruit extracts, consisting of various phytochemical constituents for the reduction of the silver. The synthesized AgNPs were characterized by using UV–Visible spectroscopy (UV-Vis), Dynamic Light scattering (DLS) technique and Scanning Electron Microscopy (SEM). The antibacterial activity of the synthesized AgNPs was evaluated and the antibacterial effect of nanosized silver solution was tested in the form of sanitary napkins.

2. Materials and Methods

2.1 Materials

Red Gac fruits (ripe) were obtained from an organic farm in Nakhon Ratchasima, Thailand. Silver nitrate, sodium hydroxide, acetone, and methanol were purchased from Sigma-Aldrich. All chemicals were used as received. Distilled water was used for all the solution prepared throughout this study.

2.2 Gac Fruit Extract Preparation

Gac fruits were cleaned and separated into pulp, peel, seed, and aril of the ripe fruit. Each part was cut and dried in hot air oven at 50 °C for 2 days, ground as powder, and kept in container prior to solvent extraction.

One gram of the dried aril part was mixed with 30 mL of methanol. The mixture was shaken

using an orbital shaker at 180 rpm for 30 min, then cooled and filtered.

2.3 Synthesis of AgNPs

The AgNPs were prepared by adding 20 mL of 0.01 M silver nitrate solution to the Gac fruit extract solution in a drop-wise manner. The mixture was then added with 5 mL of 0.1 M NaOH. The yield of AgNPs was further increased by heating the solution at 50 ^{o}C for 30 min. The resulting AgNPs were then centrifuged at 5000 rpm and washed with acetone and allowed to dry at room temperature.

2.4 Characterization of AgNPs

UV–Visible spectroscopy (UV-Vis) was employed to ascertain the formation of AgNPs in the solution after the reduction with Gac fruit extract. Transmission electron microscopy (TEM) was employed to characterize the morphology and particle size of AgNPs obtained in this study. Dynamic light scattering (DLS) technique was used to obtain the average size of AgNPs along with the SEM technique.

2.5 Evaluation of Antimicrobial Activity

Antibacterial activity of the AgNPs was tested by inhibition of bacterial growth against Gram-positive bacteria (*Staphylococcus aureus ATCC 25923*) and Gram-negative bacteria (*Escherichia coli ATCC 25922*) by agar diffusion test. The diameters of the inhibition zones were measured after the plates were incubated at 37 ^{o}C for 24 hours.

2.6 Preliminary Testing of Ag-Sanitary Napkins

The Ag-Sanitary Napkins were prepared by soaking the dried bamboo fabric into the AgNPs solution for 6 hours and allow the excess solution to drip off in order to prepare the moist napkins.

The customer satisfaction survey was carried out on 40 volunteers for 3 days in order to test the beneficial effect of the Ag-Sanitary Napkin.

3. Results & Discussion

3.1 UV spectroscopy

The UV-Vis spectroscopy was used to confirm the reduction of silver ions to AgNPs. The physical appearance of the colloidal solution, which appeared cloudy and brownish, along with its UV spectrum of AgNPs are shown in Figure 1.

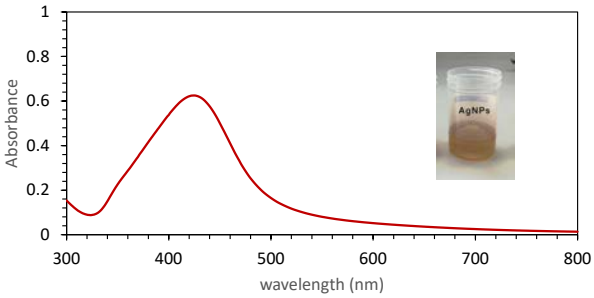

Figure. 1 UV-Visible spectrum and physical appearance of the AgNPs colloidal solution.

The surface plasmon resonance phenomena of metallic AgNPs observed at 430 nm is in good agreement with the result obtained from the literatures.[9]

3.2 TEM Analysis

The morphology and particle size of AgNPs was reveal by TEM analysis. A TEM micrograph of metallic AgNPs after being reduced with Gac fruit extract is displayed in Figure 2. The nanoparticles were found to exhibit nearly spherical shape with the size around 30-50 nm. The size distribution visibly appeared under an acceptable level.

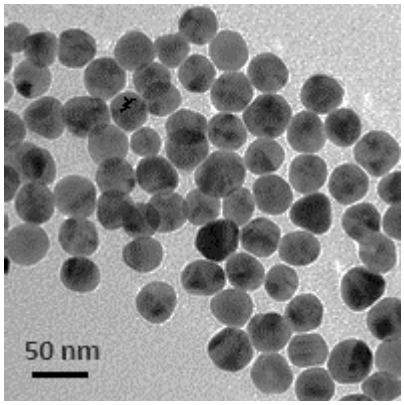

Figure 2. Transmission Electron Micrograph of AgNPs upon reduction with Gac fruit extract.

3.3 DLS Analysis

DLS technique was employed to determine particle size and size distributions of AgNPs along with the TEM analysis. It was found that the AgNPs prepared by Gac extract reduction exhibited a DLS signal indicating the sizes ranging from 20-200 nm as shown in Figure 3.

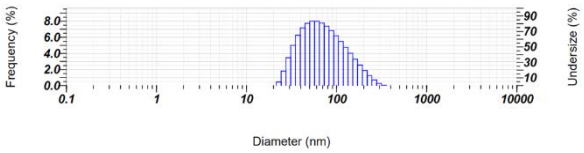

Figure 3. Particle size and size distribution of the synthesized AgNPs.

The DLS measurements of AgNPs were performed in triplicates with the average diameter of 44.2 ± 1.50 nm. The average size of the metallic nanoparticles is in good agreement with that obtained from TEM analysis shown in Figure 2.

3.4 Evaluation of Antimicrobial Activity

The AgNPs concentration of 500 ppm was tested against *Staphylococcus aureus* and *Escherichia coli*. As shown in Figure 4a-b. The AgNPs was found to exhibit moderate activity against the tested bacteria with inhibition zone in the average of 10.25 mm for *Staphylococcus aureus* and 8.75 mm for *Escherichia coli*.

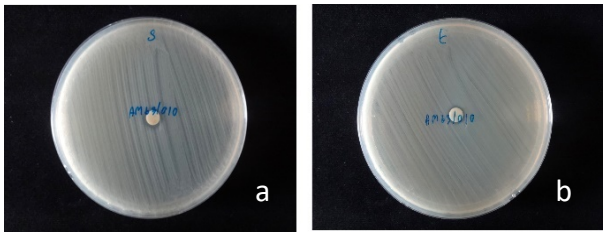

Figure 4. Inhibition zone of the AgNPs against a) *Staphylococcus aureus* and b) *Escherichia coli*.

Various mechanisms have been proposed to account for bacteria inhibition by silver nanoparticles[10-12]. Some of the mechanisms include disturbing the permeability of the cell membrane, and generating free radicals which are harmful to bacteria membrane. The effectiveness of inhibition has been found to be affected by the concentration of AgNPs with the higher the concentration having the higher activity against the tested bacteria.

3.5 Preliminary Testing of Ag-Sanitary Napkins

The antibacterial effect of AgNPs was preliminary tested in the form of sanitary napkins. The thin bamboo fabric was selected and cut into small pads with the size of 15 x 20 cm. The pads were dipped into the 500 ppm AgNPs solution until fully soaked as shown in Figure 5a-b. The prepared AgNPs sanitary pads were kept in the closed container prior to use.

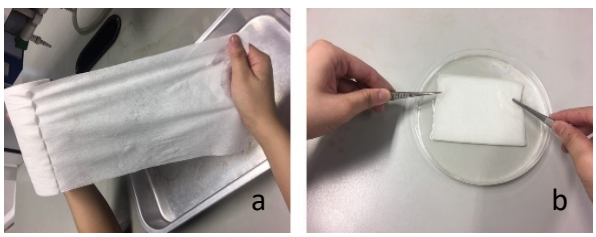

Figure 5. Preparation of sanitary napkin by soaking a) bamboo fabric in b) AgNPs solution.

The personal satisfaction survey on 40 volunteers for 3 consecutive days revealed the beneficial effect of the AgNPs on human skin in many aspects such as appearance, attractiveness of the product, cleanliness, odor, texture and any irritation it may cause (Figure 6). The beneficial effect was found to be evident with exceptional customer satisfaction in all aspects with the overall average score of 3.6 after the AgNPs sanitary pads were continuously applied on skin.

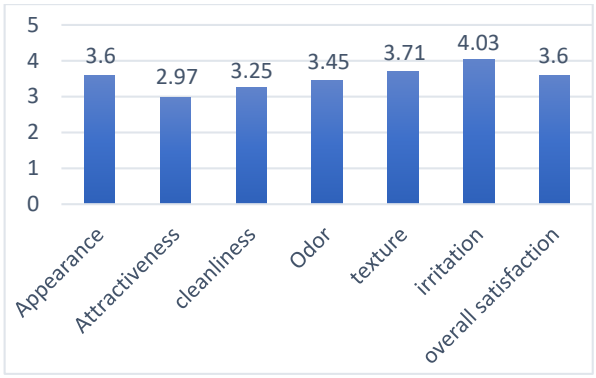

Figure 6. The personal satisfaction survey of the AgNPs napkin on human skin.

4. Conclusion

The synthesized silver nanoparticles were successfully prepared by the green reduction method using Gac fruit extract as a reducing agent. The characterization of the AgNPs by UV-Vis, TEM, and DLS analysis revealed the average particle size of AgNPs of 44 nm with nearly spherical and mono-dispersed characteristic. The synthesized AgNPs revealed the antimicrobial activity against Gram-positive and Gram-negative bacterial species.

The AgNPs were infused into the sanitary napkin and preliminary tested on 40 volunteers for its antibacterial effect. The results appeared to be beneficial on human volunteer skin after applying the sanitary napkins for 3 consecutive days.

Acknowledgements

The authors would like to acknowledge Faculty of Applied Science, King Mongkut's University of Technology North Bangkok for the full funding of chemicals and materials support for this research.

References

1. Ahmed, S.; Ahmad, M.; Swami B.; Ikram, S. *J. Adv. Res.* **2016**, *7(1)*, 17–28.
2. Kumar, V.; Anthony, S. *Surf. Chem. Nanobiomater*. **2016**, 265–300.

3. Rai, M.; Ingle, A.; Birla, S.; Yadav, A.; Santos, C. *Crit. Rev. Microbiol.*, **2015**, *42*, 1–24.
4. Zhang, X.; Huang, F.; Zhang, G.; Bai, D.; Massimo, D. *Int. J. Nanomed.* **2017**, *12*, 7551–7575.
5. Kim, M.; Osone, S.; Kim, T.; Higashi, H.; Seto, T. *KONA Powder Part. J.* **2017**, *34*, 80–90.
6. Govarthanan, M.; Cho, M.; Park, J. H.; Jang, J. S.; Yi, Y. J.; Kamala-Kannan, S.; Oh, B. T. *J. Nanomater.* **2016**, *2016*, 1–6.
7. Govarthanan, M.; Seo, Y. S.; Lee, K. J.; Jung, I. B.; Ju, H. J.; Kim, J. S.; Cho, M.; Kamala-Kannan, S.; Oh, B. T. *Artif. Cells, Nanomed., Biotechnol.* **2016**, *44(8)*, 1878–1882.
8. Ameen, F.; AlYahya, S.; Govarthanan, M.; ALjahdali, N.; Al-Enazi, N.; Alsamhary, K.; Alshehri, W. A.; Alwakeel, S. S.; Alharbi, S. A. *J. Mol. Struct.* **2020**, *1202*, 127233.
9. Kumar, D. A.; Palanichamy, V.; Roopan, S. M. *Spectrochim. Acta, Part A* **2014**, *127*, 168–171.
10. Dhand, V.; Soumya, L.; Bharadwaj, S.; Chakra, S.; Bhatt, D.; Sreedhar, B. *Mater. Sci. Eng.*, C **2016**, *58*, 36–43.
11. Tang, S.; Zheng, J. *Adv. Healthcare Mater.* **2018**, *7(13)*,1701503.
12. Keshari, A. K.; Srivastava, R.; Singh, P., Yadav, V. B.; Nath, G. *J. Ayurveda Integr. Med.* **2020**, *11(1)*, 37–44.

Preparation of silver nanoparticles (AgNPs) by orange peel extract for antibacterial paper packaging

Warisara Petphisit[1], Piyada Sailen[1], Pitt Supaphol[2,3], Narumol Kreua-ongarjnukool[1], and Saowapa Thumsing Niyomthai[1]*

[1]*Department of Industrial Chemistry, Faculty of Applied Science, King Mongkut's University of Technology North Bangkok*

1518, Pracharat I Road, Wongsawang, Bangsue, Bangkok 10800, Thailand

[2]*The Petroleum and Petrochemical College, Chulalongkorn University, Phyathai Road, Pathumwan, Bangkok 10330, Thailand*
[3]*The Center of Excellence on Petrochemical and Materials Technology, Chulalongkorn University, Phyathai Road, Pathumwan, Bangkok 10330, Thailand*

**E-mail*: *saowapa.t@sci.kmutnb.ac.th*

Abstract:

Fruits typically have a short shelf life after harvest, making them susceptible to spoilage, especially during transportation. The purpose of this research was to create antibacterial packaging to extend the shelf life of fruits by coating paper packaging with silver nanoparticles (AgNPs). These AgNPs were synthesized using a green method that utilized orange peel extract as a reducing agent. The results from absorbance, particle size, and morphology analysis revealed that the AgNPs exhibited maximum absorption at 425 nm and had an average size of 128.1 ± 26.6 nm, and showing good dispersion with spherical shape. Paper packaging coated with AgNPs effectively inhibited the growth of both gram-positive and gram-negative microorganisms, thereby reducing the risk of fruit spoilage. Furthermore, this research investigated the physical characteristics. The findings indicated that AgNPs-coated paper packaging extended the shelf life of tomatoes in comparison to uncoated paper packaging. This implies that the antibacterial properties of the AgNPs contributed to preserving the quality of tomatoes for a longer duration. In conclusion, the development of antibacterial packaging by coating paper with silver nanoparticles synthesized using green synthesized orange peel extract as a reducing agent has the potential to inhibit bacterial growth and prolong the fruit's shelf life.

1. Introduction

Most of Thailand has a tropical wet and dry climate which boasts a rich biodiversity of various fruit types. The country is a significant exporter of fruits but faces challenges due to the short shelf life of fresh fruits and vegetables after harvesting, which particularly impacts the export process.

Transportation duration is lengthy, leading to spoilage of these perishable goods, especially agricultural products with high humidity that require proper storage. The primary causes of spoilage in fresh fruits and vegetables are bacteria, yeasts, and molds.[1] Although preservation methods are utilized, such as canning, freezing, and drying, they often result in a loss of nutritional value and quality of these products. To address this issue and extend the shelf life of fruits and vegetables, it is crucial to explore new methods of food preservation. One promising approach involves adopting environmentally-friendly packaging by enhancing existing packaging through the incorporation of metal nanoparticles onto paper packaging to inhibit bacterial growth.[2]

Paper is often used in the production of packaging[2] because it is light, cheap, easy to design, made from renewable material, biodegradable, and environmentally safe. Coated nanoparticles on packaging materials can improve the preservation of perishable food[3], especially silver nanoparticles, which have antibacterial properties. Anti-fungal, anti-yeast, and anti-virus properties can be obtained from silver nanoparticles prepared by mandarin peel extract (*Citrus reticulata*).[4]

Nanoparticles are increasingly playing a significant role in various aspects of daily human activity, including use as catalysts in industries, such as chemical, biomedical, cosmetic, pharmaceutical, healthcare, electronics, and gene transfer, among others.[5] Among nanoparticles, silver nanoparticles and other metal nanoparticles have gained considerable attention. Typically ranging in size from 1 to 100 nm, silver nanoparticles are particularly renowned for their remarkable antibacterial properties.[6,7] The small particle size and high surface area of silver nanoparticles result in distinct chemical and physical properties that differ from larger particles, and their excellent surface reactivity makes them well-suited for antimicrobial coatings in packaging.[8] Consequently, silver nanoparticles

are employed to maintain fruit freshness, extend shelf life, and prevent or slow the rate of fruit decay.[9]

Various methods exist for synthesizing nanoparticles, including reduction, chemical, reactions, and photochemical reactions. Although these methods can quickly yield high-quality nanoparticles, the associated reducing agents are often expensive and toxic.[10] However, a green synthesis method utilizing medicinal plants offers a simple and environmentally-friendly alternative for producing highly efficient silver nanoparticles (AgNPs). Moreover, medicinal plants contain numerous beneficial elements, including antimicrobial, anti-cancer, and antioxidant properties, making them an attractive choice for coating paper packaging with antibacterial activity.[11]

Oranges, one of the most popular fruit crops in the world, contain phytochemicals that provide health benefits. They are abundant in vitamin C, folic acid, and pectin.[5] Citrus fruits, such as oranges, are well-known for their high concentration of flavonoids, which are essential secondary compounds predominantly found in plant tissues in the form of sugars.[12] These compounds possess diverse functional groups, including C=O, –OH, CHO, and COOH, which contribute significantly to their antioxidant potential. Moreover, they have a strong affinity for noble metals, aiding the stabilization of formed nanoparticles.[13]

This research focuses on the synthesis of silver nanoparticles using a biological approach that involves orange peel extract (*Citrus reticulata*) as a reducing agent and stabilizer. The presence of flavonoids in the extract enables them to act as reducing agents, converting positively-charged silver ions (Ag^{+}) into neutral silver (Ag^{0}) nanoparticles.

One of the advantages of this biosynthesis method is the reduced usage of chemicals compared to chemical and physical methods. Additionally, stabilizers are employed to maintain the stability of the particles over time. The resulting AgNPs have a spherical shape, which contributes to their effective inhibition of both gram-positive and gram-negative bacteria. This ability stems from the nanoparticles capacity to penetrate cell membranes, interfere with DNA replication, and disrupt bacterial proteins. Moreover, the reduction of silver ions within bacteria leads to an increased production of reactive oxygen species in fungal cells, ultimately causing their demise.[14] As a result, packaging coated with these AgNPs exhibits strong antibacterial properties, making it suitable for the transportation of perishable fruits.

2. Materials and Methods

2.1 Materials

Orange peel extract was purchased from *Skherbstore* and silver nitrate from *Sigma-Aldrich* (USA). All other chemical agents were of analytical grade.

2.2 Biological synthesis of silver nanoparticles

A solution was prepared by dissolving silver nitrate ($AgNO_3$) at a concentration of 1.00 mM in a three-neck round-bottom flask. The solution was continuously stirred with a magnetic bar until complete dissolution. Throughout the process, the temperature of the silver nitrate solution was maintained within the range of 88-90°C. Then, 4.00 mL of orange peel extract was added to the solution. After allowing the mixture to stand for approximately 15 minutes, a noticeable color change occurred. which represents AgNPs (The particle concentration based on $AgNO_3$ concentration). Finally, the prepared solution was utilized to measure its absorbance using a UV-Visible spectrophotometer.

2.3 Preparation of silver nanoparticles coated paper packaging

Begin preparing silver nanoparticles with a concentration of 1 mM, by filling a 10 mL spray bottle. Then, take the paper packaging and apply a coating of the silver nanoparticles on all sides, both inside and outside.

Allow the coated paper packaging to dry naturally at room temperature for a duration of 24 hours.

2.4 Characterization

2.4.1 FTIR analysis

To analyze the orange peel extract, begin by preparing a liquid sample for analysis. This can be done using FTIR spectroscopy (*PerkinElmer* Spectrum One) by dropping the extract onto a KBr sheet and then sandwiching it with another KBr sheet. Once the sample is prepared, place it in a holder and insert it into the FTIR instrument for analyzing the infrared spectrum of the orange peel extract. This analysis will allow for a comparison with the dissolution of rutin, which is a compound belonging to the standard flavonoid group.

2.4.2 UV-Visible Spectrophotometer and nano-particles analysis

Biosynthesize at a concentration of 1.00 mM, using deionized water as a blank, and study the absorbance with a UV-Vis spectrophotometer (C-7200).

2.4.3 Morphological observation by TEM

The silver nanoparticles solution, with a concentration of 1.00 mM, was sonicated for approximately 15 minutes to ensure proper dispersion. After sonication, the solution was transferred onto a sample backing plate (grid) and allowed to dry. The dried samples were then analyzed using a Transmission Electron Microscope (TEM). The microscope settings were adjusted to a pre-photograph scale of 100 nm, and images were captured using the appropriate software program.

2.5 Study of optimal concentration of silver nanoparticles with antibacterial effect by Minimum Inhibitory Concentration (MIC), Minimum Bactericidal Concentration (MBC) and Disc Diffusion Method (ASTM E1054-08)

S. aureus (ATCC 25923) and *E. coli* (ATCC 25922) were used as representative strains of gram-positive and gram-negative bacteria, respectively.

The bacteria were cultured in Trypticase Soy Broth (TSB) medium at 37°C for 24 hours, resulting in a cell density of approximately 10^8 cells/mL.

The bacterial solution was prepared using saline (0.85% sodium chloride) as a solvent. For the disc diffusion method, the bacterial solution was adjusted to a concentration of 1.5 x 10^8 CFU/mL, and the bacteria were spread onto a culture medium.

A circular filter paper with a diameter of approximately one centimeter was punctured, and 20 µL of the sample substance was then dropped onto it. The culture dish was incubated at 37°C for 24 hours.

For the determination of Minimum Inhibitory Concentration (MIC) and Minimum Bactericidal Concentration (MBC), the bacterial solution was adjusted to a concentration of 1.5 x 10^6 CFU/mL.

In a 96-well plate, 50 µL of TSB agar medium, 100 µL of the sample, and 50 µL of the bacteria were added.

The 96-well plates were placed in a shaker incubator at 250 rpm and 37°C for 24 hours. The results were observed and recorded by examining the color of each well in the 96-well plate.

After the MIC testing, samples were taken from each well and dropped onto agar medium. The agar plates were then incubated at 37°C for 24 hours.

2.6 Study on the simulation of packing fruits into paper packaging coated with silver nanoparticles

Tomatoes were packed in two types of packaging: one coated with silver nanoparticles and the other without silver nanoparticles (used as a control). The packaging was sealed and the physical appearance of the tomatoes was observed weekly for a month to assess any changes.

3. Results & Discussion

3.1 Orange peel extract (*Citrus reticulata*)

3.1.1 FTIR

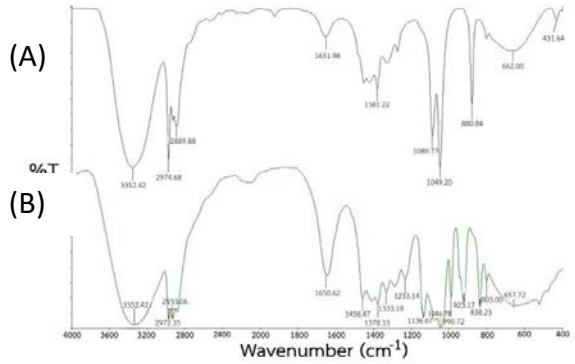

Figure 1. FTIR spectrum of (A) Rutin (B) *Citrus reticulata* peel extract

The orange peel extract was analyzed to identify the presence of biomolecules. In comparison to a rutin solution, which serves as a standard flavonoid compound, [7] similar functional groups were observed in the orange peel extract. Specifically, the O-H stretching function group was detected in the wavelength range of 3352-3340 cm^{-1}, the C-H stretching function group in the range of 2974-2972 cm^{-1}, the C=O stretching function group in the range of 1651-1650 cm^{-1}, and the C-O-C and C-O stretching functional groups in the ranges of 1333-1233 cm^{-1} and 1089-1049 cm^{-1}, respectively. These findings indicate that the orange peel extract shares functional groups with the flavonoid standard rutin solution.

3.1.2 UV-Visible Spectroscopy

The objective of this study was to determine the Total Flavonoid Content (TFC) in orange peel extract. This was calculated by comparing the absorbance curve of the extract to a rutin calibration curve (rutin calibration curve plot from the maximum absorption wavelength of rutin is 509 nm) see Figure 2, which was obtained through absorbance measurements. The calibration curve equation was y = 5.4578x + 0.0147, showing a high linearity with an R^2 = 0.9987. The TFC of the orange peel extract that can be calculated from

equation 1 expressed in rutin equivalents, reached a maximum value of 12.5 mg/g.

$$TFC = \frac{C \times V \times DF}{m} \quad \ldots\ldots\ldots (1)$$

Where C=concentration from the standard curve, V=the volume of the sample solution, DF=Dilution factor, m=mass of the extract[15]

This indicates a significantly higher flavonoid content compared to other citrus species and suggests a potential inhibitory effect on enzyme groups responsible for fruit spoilage.

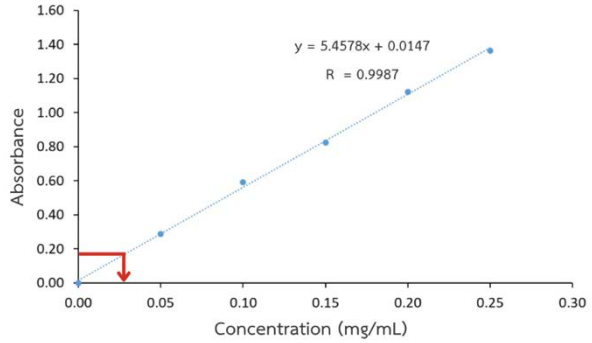

Figure 2. Rutin standard calibration curve

3.2 Biological synthesis of silver nanoparticles

3.2.1 UV-Visible Spectroscopy

The analysis of the experimental results (see Figure 3), depicting the relationship between absorbance and wavelength, revealed that the spectrum of the solution exhibited an absorbance value within the range of 400-450 nm. This observation aligns with the characteristic surface plasmon resonance phenomenon, typically associated with AgNPs.[16] The occurrence of this optical phenomenon serves as evidence for the presence of silver nanoparticles in the experimental setup, which confirmed the reduction in this synthesis facilitated by the orange peel extract acting as both a reducing agent and stabilizer.[5] The reducing agent plays a pivotal role in the reduction of Ag^{+} to Ag^{0}, ultimately leading to the formation of AgNPs.[5]

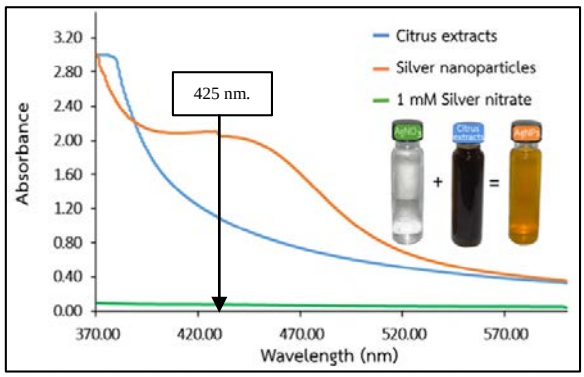

Figure 3. UV-Vis absorbance spectra of the silver nanoparticles synthesis using an extract of *Citrus reticulata* peel extract

The stability of silver nanoparticles was examined over a span of three months using a UV-Visible Spectrophotometer. The experimental findings (see Figure 4) demonstrate the enduring stability of silver nanoparticles at a concentration of 1 mM. The peak wavelength was identified to lie between 421 and 428 nm, indicating the involvement of a reduction reaction between the silver ions.

Notably, throughout the 3-month duration, no alterations were detected in the solution's spectral characteristics or color. This observation strongly implies the robust stability of the silver nanoparticles synthesized utilizing orange peel extract.[4]

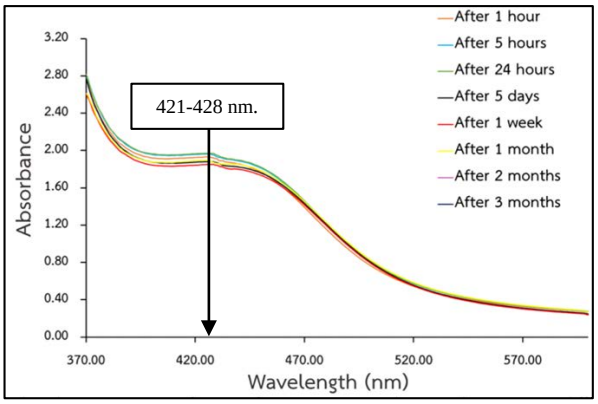

Figure 4. UV-Vis absorbance spectra of silver nanoparticles from *Citrus reticulata* peel extract at different storage time

3.2.2 TEM

The average diameter of the AgNPs, with a concentration of 1.00 mM, was determined to be 128.8±26.6 nm. (average diameter verified by Nanoparticle analyzer). The morphological analysis of these nanoparticles is presented in Figure 5, illustrating the experimental findings. It was observed that the silver nanoparticles, obtained through biosynthesis, demonstrated a spherical shape with good dispersion.

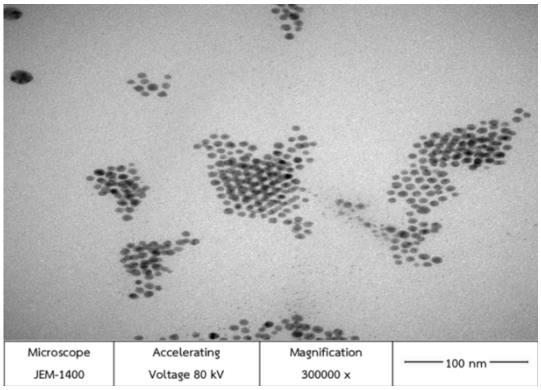

Figure 5. TEM images of silver nanoparticles from *Citrus reticulata* peel extract

3.2.3 FESEM-EDS

The analysis of the photographic morphology of silver nanoparticles synthesized using *Citrus reticulata* peel extract was conducted through Field Emission Scanning Electron Microscopy-Energy Dispersive Spectroscopy (FESEM-EDS), as depicted in Figure 6. The analysis revealed a prominent signal peak at 3 keV, which was attributed to the presence of silver (Ag) as the primary constituent in the silver nanoparticles. This signal peak originated from the interaction between the electron beam and the studied silver nanoparticles, resulting in ionization and the repulsion of electrons from the nanoparticles. Consequently, the atoms maintained stability by replacing electrons in the subsequent orbital layer, thereby releasing energy in the form of X-rays.

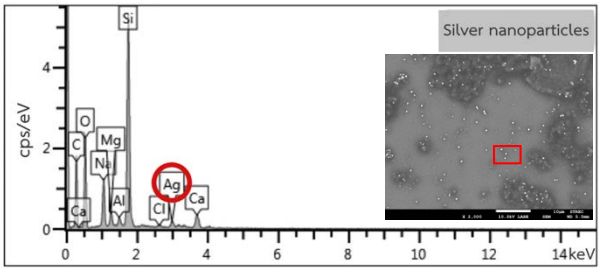

Figure 6. FESEM-EDS analysis of AgNPs from *Citrus reticulata* peel extract

3.3 Antibacterial activities

3.3.1 Silver nanoparticles affecting the bacterial resistance by disc diffusion method (ASTM E1054-08)

The study analyzed antibacterial resistance using the disc diffusion method, based on the results presented in Figure 7. It was observed that when silver nanoparticles were used at a concentration of 1 mM, they resulted in a clear zone of inhibition with a diameter of 18.60 ± 0.115 mm for gram-negative bacteria (*E. coli*) and 15.00 ± 0.057 mm for gram-positive bacteria (*S. aureus*). These findings indicate that the 1 mM concentration of silver nanoparticles effectively inhibited the growth of both gram-negative and gram-positive bacteria.

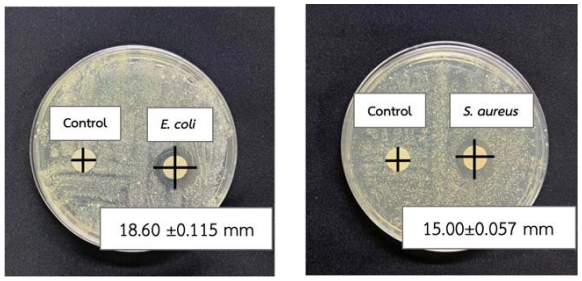

Figure 7. Clear zone of AgNPs (n=3)

3.3.2 Minimum Inhibitory Concentration (MIC) and Minimum Bactericidal Concentration (MBC)

The results obtained from the Minimum Inhibitory Concentration (MIC) and Minimum Bactericidal Concentration (MBC) tests clearly indicated that a concentration of 1 mM of silver nanoparticles was the minimum required to effectively inhibit and kill microorganisms. (When the experiment tested AgNPs with a concentration lower than 1 mM, they were unable to effectively inhibit and kill microorganisms. which is shown in picture 8 In channels 2-10, microbial growth will be found)

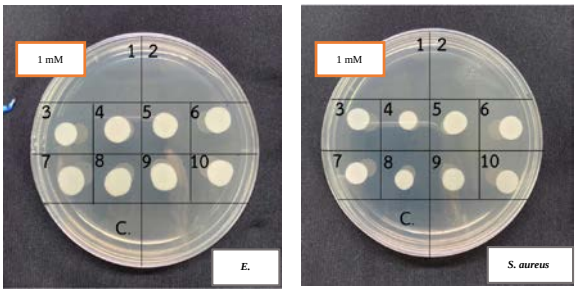

Figure 8. Minimum Bactericidal Concentration of AgNPs (n=3)

3.4 Simulate packing tomatoes into packaging coated with silver nanoparticles

The study conducted a life extension test on tomatoes using coated and uncoated AgNPs. The results revealed that tomatoes packed in containers without AgNPs coating experienced skin bruising within the first week. In contrast, tomatoes packaged with AgNPs showed only slight bruising after four weeks.

Based on these findings, it was concluded that paper packaging coated with AgNPs demonstrated effective antibacterial properties, leading to an extended shelf life for fruits. This conclusion was derived from the fact that AgNPs possess strong antibacterial efficacy against both gram-positive bacteria, such as *S. aureus*, and gram-negative bacteria, like *E. coli*, both of which are known to contribute to fruit decay.

Moreover, the AgNPs used are not harmful to humans because human cells are eukaryotic cells which have a large size and complex structure, and possess more functional subunits than bacterial cells that are prokaryotic cells. Therefore, human cells are not damaged when small amounts of AgNPs are used to inhibit bacterial cells.[17]

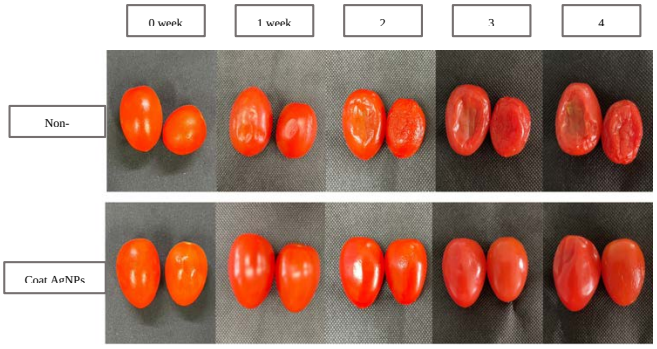

Figure 9. Simulate packing tomatoes into packaging (n=3)

4. Conclusion

This study successfully prepared silver nanoparticles using orange peel extract for antibacterial paper packaging. The analysis of absorbance, particle size, and morphology revealed that the silver nanoparticles showed maximum absorption at 425 nm. They had an average size of 128.1 ± 26.6 nm, exhibiting a spherical shape and good dispersion. Furthermore, the paper packaging coated with these silver nanoparticles demonstrated effective inhibition of both gram-positive (*S. aureus*) and gram-negative (*E. coli*) microorganisms. Additionally, the study found that the silver-coated paper packaging extended the shelf life of tomatoes compared to uncoated paper packaging. This conclusion was drawn based on the observed physical properties of the tomatoes. Consequently, the silver-coated paper packaging could be a suitable option for transporting perishable fruits.

Acknowledgments

The authors would like to acknowledge the partial support received from (a) The Center of Excellence on Petrochemical and Materials Technology, Thailand; (b) PPC, Chulalongkorn University, Thailand; (c) Grant for International Research Integration, Thailand: Research Pyramid, Ratchadaphiseksomphot Endowment Fund and (d) The Department of Industrial Chemistry, Faculty of Applied Science, KMUTNB, Thailand; (e) Grant from King Mongkut's University of Technology North Bangkok, Thailand. Contract no. KMUTNB-66-BASIC-08.

References

1. Kornkanok Ubolchollakhat; Samakphong, P., Synthesis of silver particles using white sugar for shelf-life extension of banana and tomato. 2016, 2067-2074.
2. Ravindra V. Gadhave; Chaitali R. Gadhave; Dhawale, P. V., Plastic-Free Bioactive Paper Coatings, Way to Next-Generation Sustainable Paper Packaging Application: A Review. Green and Sustainable Chemistry 2022, 12 (2), 9-27
3. Kumari SC, P. P., Anuradha K. , Green Silver Nanoparticles Embedded in Cellulosic Network for Fresh Food Packaging. 15 2021, 3, 1236-1244.
4. Niluxsshun, M. C. D.; Masilamani, K.; Mathiventhan, U., Green Synthesis of Silver Nanoparticles from the Extracts of Fruit Peel of Citrus tangerina, Citrus sinensis, and Citrus limon for Antibacterial Activities. Bioinorg Chem Appl 2021, 2021, 6695734.
5. Karnpimon Krorakai; Patramanon, R., Plant Extract Synthesized Silver Nanoparticles and their Antimicrobial Activity. KKU Science Journal 2022, 45 (1), 34-52.
6. Poadang, S., Synthesis of silver nanoparticle from fruit peels. 2014.
7. Gundo, S.; Parauha, Y.; Singh, N.; Dhoble, S. J., Eco-friendly synthesis route of silver nanoparticle: A review. Journal of Physics: Conference Series 2021, 1913, 012052.
8. Wutthichai Songsiriloedwatthana; Sukhan, P., GREEN SYNTHESIS OF SILVER NANOPARTICLES USING LONGAN SEED EXTRACT.
9. Motlagh, N. V.; Aliabadi, M.; Rahmani, E.; Ghorbanpour, S. In The Effect of Nano-Silver Packaging on Quality Maintenance of Fresh Strawberry, 2020.
10. Paweena Porrawatkul; Montakarn Thongsom; Pornpailin Khaosuk; Dolohmi, T., Green Synthesis of Silver Nanoparticles UsingGarcinia mangostanaLinn. for Antibacterial. Wichcha Journal, 35 2016, 1, 26-40.
11. Devanesan, S.; AlSalhi, M. S., Green Synthesis of Silver Nanoparticles Using the Flower Extract of Abelmoschus esculentus for Cytotoxicity and Antimicrobial Studies. Int J Nanomedicine 2021, 16, 3343-3356.
12. Rafiq, S.; Kaul, R.; Sofi, S. A.; Bashir, N.; Nazir, F.; Ahmad Nayik, G., Citrus peel as a source of functional ingredient: A review. Journal of the Saudi Society of Agricultural Sciences 2018, 17 (4), 351-358.
13. Kawaii, S.; Tomono, Y.; Katase, E.; Ogawa, K.; Yano, M., Quantitation of flavonoid constituents in citrus fruits. J Agric Food Chem 1999, 47 (9), 3565-71.

14. Alsakhawy, S.; Baghdadi, H.; El-Shenawy, M.; El-Hosseiny, L., Antibacterial Activity of Silver Nanoparticles Phytosynthesized by Citrus Fruit Peel Extracts. BioNanoScience 2022, 12.
15. Aderaw AntenehBelew, et al., *Evaluation of Total Phenolic, Total Flavonoid Content And Antioxidant Activity of Rhus Vulgaris.* 2021.
16. Geethalakshmi, R.; Sarada, D. V. L., Gold and silver nanoparticles from Trianthema decandra: synthesis, characterization, and antimicrobial properties. International Journal of Nanomedicine 2012, 7, 5375-5384.
17. Alt, V., et al., *An in vitro assessment of the antibacterial properties and cytotoxicity of nanoparticulate silver bone cement.* Biomaterials, 2004. 25(18): p. 4383-91.

Development of the cellulose microcrystalline as a potential carrier of biologics delivery

Phatheera Kachai[1,2] and Chaiya Prasittichai[1,2*]

[1]*Department of Chemistry, Faculty of Science, Kasetsart University, Bangkok 10900, Thailand*
[2]*Center of Excellence for Innovation in Chemistry (PERCH-CIC), Kasetsart University*

[*]*E-mail address: chaiya.pr@ku.th*

Abstract:

Cellulose-based microscale materials could be used as biocarriers for biologics and drug delivery systems due to their biocompatible, biodegradable, and low-toxicity properties. Preparation of cellulose microcrystalline (CMC) from cotton through an acid hydrolysis process with two different durations (1 hour 30 minutes and 4 hours), followed by a 2,2,6,6-tetramethylpiperidine-1-oxyl (TEMPO) oxidation process. The results showed that the hydrolysis duration affected the size and morphology of CMC, with longer hydrolysis times resulting in smaller CMC with a short fibrous structure. TEMPO oxidation process introduced numerous carboxyl groups on the surface of CMC, rendering it more hydrophilic and allowing for easy conversion to other functional groups. In this study, chitosan was selected for surface modification of CMC due to its hydrophobic nature, compatibility, and efficient binding capabilities with biologics. To assess their effectiveness as carriers, we examined biologic loading using bovine serum albumin (BSA) as a representative protein. The chitosan-modified CMC (CMC/CHI) demonstrated superior BSA loading, measuring around 10.40-11.44% by weight. We also demonstrated that pattern of BSA releasing between the CMC and CMC/CHI appeared differently under various pH levels (3.4, 7.4, and 9) in a standard phosphate buffer and standard buffer without phosphate.

1. Introduction

The development of innovative materials or carrier systems that may effectively transport drugs to their intended target is the main goal of the field of drug delivery. The release mechanisms of these drug delivery systems, such as targeted, regulated, and steady delivery, can be used to classify them. Guyue Cheng et al.[1] displayed the successful utilization of biologics as therapeutic agents in the treatment of disease. Additionally, there has been an important improvement in the development and usage of biologics for therapeutic purposes in humans.[2, 3] as well as animal culture, including the aquaculture sector.[4] Furthermore, research has demonstrated the potential utility of microparticles and nanoparticles developed specifically to carry and protect biologics and immune-stimulating. Natural materials such as alginate and chitosan, as well as synthetic materials like carbon nanotubes and poly-lactic-co-glycolic acid (PLGA), have shown encouraging potential as delivery systems in aquaculture and animal culture.[5]

The most abundant biopolymeric material on Earth is cellulose, classified as a polysaccharide and prominently present in plant cell walls. Structurally complex, cellulose consists of numerous glucose units linked by β-1,4-glycosidic bonds, establishing a robust foundational framework. Its versatile applications span various fields, with notable contributions in the textile and pharmaceutical industries. Due to their inherent biocompatibility, micro-cellulose is gaining interest as a biodegradable carrier in the development of biologic carriers.[6] However, there are certain disadvantages to cellulose, such as low barrier qualities and poor thermal stability.[7] To enhance these limitations, research has focused on novel synthetic methods that improve mechanical, optical, thermal stability, and barrier qualities through physical, chemical, and biosynthetic processes.[8] In this sense, cellulose microcrystalline (CMC), which is an unique derivative of micro-cellulose, stands out due to its large surface area.

In recent times, researchers have been generating cellulose microcrystalline, known as CMC or cellulose nanocrystal (CNC), through the acid hydrolysis of cellulose.[9-12] This process primarily removes the amorphous region while preserving the crystalline region, resulting in the production of nanocellulose. The morphology and size of micro-cellulose are importantly controlled by factors such as the duration of the reaction, temperature, the type of acid used, and its concentration during the acid hydrolysis process.[11,13]

Furthermore, the chemical pretreatment of cellulose using 2,2,6,6-tetramethylpiperidine-1-oxyl (TEMPO)-mediated oxidation has emerged as a straightforward and effective process for CMC production. The utilization of TEMPO as a catalyst during oxidation with NaOCl/NaBr selectively

converts the C_6 primary hydroxyl alcohol groups on cellulose into a C_6 aldehyde intermediate, which is then transformed into the C_6 carboxyl group. In this process, NaOCl serves as the main oxidant, while NaBr acts as a co-catalyst. In an aqueous alkaline medium with a pH near 10, NaBr enhances the reaction, and the co-catalyst BrO^- proves to be a more potent oxidizing agent than OCl^-.[14, 15] Moreover, the surface of TEMPO-oxidized CMC is enriched with numerous carboxyl groups, presenting a pivotal role due to their easy conversion into other functional groups.[16] This nanoscale structure, coupled with an expansive specific surface area, favorable colloidal properties, and impressive machinability, endows TEMPO-oxidized CMC with unique characteristics. These attributes position it as a highly sought-after material across various sectors, with notable applications gaining relevance in fields such as food processing and biomedicine.[6] The versatility of this material holds promise for the development of innovative products and valuable solutions.

In this work, we prepared CMC from cotton through TEMPO-mediated oxidation. Further, we also modified surface of CMC with chitosan, resulting in a composite labeled CMC/CHI. We chose chitosan to modify the surface because it is a biocompatible material, hydrophobic, low cost, insoluble and low toxicity.[17] In addition, in the aqueous medium, chitosan display positively charge, offering the possibility to bind a negatively charge protein or other substances.[18] An example of using CMC as biologics carriers were shown by employing bovine serum albumin (BSA) as a representative protein. Comprehensive characterization of both CMC and CMC/CHI was undertaken, focusing on aspects such as morphology, hydrophobicity, surface charge, as well as the loading and release capabilities of CMC.

2. Materials and Methods

2.1 Materials

Cotton roll as a starting material and deionized (DI) water were supplied by Kasetsart University. Hydrogen peroxide (H_2O_2) was sourced from Sigma-Aldeich. Sulphuric acid (H_2SO_4) was sourced from QRëC. Bovine serum albumin (BSA), and BCA protein assay kit were purchased from Merck KGaA. Acetic acid (CH_3COOH), sodium hydroxide (NaOH), and sodium hypochlorite (NaClO) were obtained from Carlo Erba. Sodium bromide (NaBr) was received from TCI. TEMPO was obtained from Alfa Aesar. Chitosan (Food grade) from received from Bona Fides Marketing Co., Ltd.

2.2 Preparation of pretreated cotton (chemical pretreatment)

A 5 L beaker was filled with a 1% v/v NaOH solution (2700 mL), and heating process was started. 20 g of cotton was added to the beaker and stirred continuously for an hour, or until the temperature reached 70-80 °C. Following that, the mixture was heated for an additional hour while constantly stirring and adding 300 mL of a 10% v/v H_2O_2 solution. After then, the mixture was allowed to cool until it reached room temperature. The product was then cleaned with DI water until the supernatant's pH reached 7 and filtered out the product. The pretreated cotton was dried for 24 hours at 50 °C.

2.3 Synthetic of cotton linter with acid hydrolysis

The round-bottom flask was filled with a 50% v/v piranha solution (H_2SO_4:H_2O_2, 3:1), and it was heated in an oil bath at 50°C with constantly stirring. After, the round bottom flask was filled with pretreated cotton (1 g: 40 mL; cotton: 50% v/v piranha solution), and the mixture was incubated at 50°C for 1.5 or 4 hours. Subsequently, the mixture was centrifuged for 15 minutes at 6000 rpm and then washed with DI water and 2% v/v NaOH. The mixture was sonicated for 10 minutes before centrifugation and washing with copious amount of water. After freeze-drying, the finished product was labeled as “cotton linter 1.5 h” or “cotton linter 4 h”.

2.4 Synthetic of cellulose microcrystalline (CMC) with TEMPO-mediated oxidation

A 250 mL beaker containing 100 mL of DI water, 1 g of cotton linter (either 1.5 h or 4 h), 0.0156 g of TEMPO, and 0.1029 g of NaBr was used to proceed with the synthesis of CMC. The mixture was stirred until TEMPO was dissolved completely. After that, the mixture was stirred for 5 minutes and 0.5 M NaOH was added until the pH reached 10. The TEMPO-mediated oxidation was initiated by adding 10.6343 g of NaOCl to the mixture, followed by continuous stirring at room temperature for 3 hours. The mixture was centrifuged for 15 minutes at 6000 rpm, and the supernatant was rinsed with DI water until its pH was nearly that of the DI water. The mixture was sonicated for 10 minutes before centrifugation and washing with copious amount of water. Finally, the product was collected, freeze-dried, and labeled as "CMC 1.5 h" or "CMC 4 h."

2.5 Modification of cellulose crystalline with chitosan (CMC/CHI)

Chitosan was dissolved in a 1% v/v CH_3COOH (chitosan: 1% v/v CH_3COOH, 1 g: 200 mL) at 45°C for 15 minutes in order to prepare CMC modified with chitosan. The chitosan solution was mixed with CMC at a 1:1 (CMC:chitosan) ratio, and the mixture continued to stir for 20 hours at 45°C. The mixture was later collected after finish heating process and provided a 10 minutes sonication. It was centrifuged at 6000 rpm for 15 minutes and washed with DI water. The finished product was collected, freeze-dried, and labeled as "CMC/CHI".

2.6 Cellulose microcrystalline loading with biologic

In 1 mL of 0.1 M PBS (pH 7.4), 10 mg of CMC or CMC/CHI were suspended and stirred for 5 minutes. After that, the mixture was loaded with 0.6 mg of BSA and was stirred at room temperature for 2 hours. For 1 minute, the mixture was centrifuged at 12,000 rpm. Supernatant and solid were separated and used to evaluate the BSA loading of CMC-BSA or CMC/CHI-BSA.

2.7 Release test

The release pattern of BSA under phosphate buffer (PBS) and standard buffer without phosphate (non-PBS) conditions was investigated through release analysis. Initially, CMC-BSA or CMC/CHI-BSA was suspended in 1 mL of 0.1 M PBS or non-PBS solution (at pH 3.4, 7.4, and 9). Subsequently, the samples underwent incubation at room temperature for various durations (0, 0.5, 1, 2, and 3 hours). Throughout the incubation, 50 µL of the supernatant was collected at different intervals and subjected to centrifugation at 12,000 rpm for 1 minute. Following centrifugation, 25 µL of the supernatant was transferred to a microplate. Further, 200 µL of the BCA protein assay kit (comprising BCA solution and 4% cupric sulfate at a ratio of 1 mL:20 µL) was added to the microplate and incubated at 60°C for 15 minutes. Finally, the resulting mixture was measured using a microplate reader at 562 nm

2.8 Morphology and characterization

Scanning electron microscopy (SEM; Quanta 450 - FEI) was utilized to observe the morphology of cotton linter samples (1.5 h and 4 h) as well as CMC samples (1.5 h and 4 h). SEM analysis was conducted using a 15 kV beam energy, a working distance of 10 mm, and magnifications of 150x and 500x. Zeta potential measurements (Zetasizer Nano-ZS90, Malvern) were carried out to assess the surface charge of CMC, CMC/CHI, CMC-BSA, CMC/CHI-BSA, and BSA. These samples were suspended in DI water. Microplate Reader (MPR; SparkTM 10M) was used to measure absorption and examine the loading and releasing of BSA on CMC and CMC/CHI. MPR analysis was conducted in absorbance mode with a measurement wavelength of 562 nm.

3. Results & Discussion

3.1 Morphology and characterization

Table 1. Zeta potential of cellulose microcrystalline.

Samples	Zeta potential (mV)
CMC 4 h	-27.07
CMC-BSA 4 h	-39.37
CMC/CHI 4 h	12.87
CMC/CHI-BSA 4 h	-37.57
BSA	-39.23

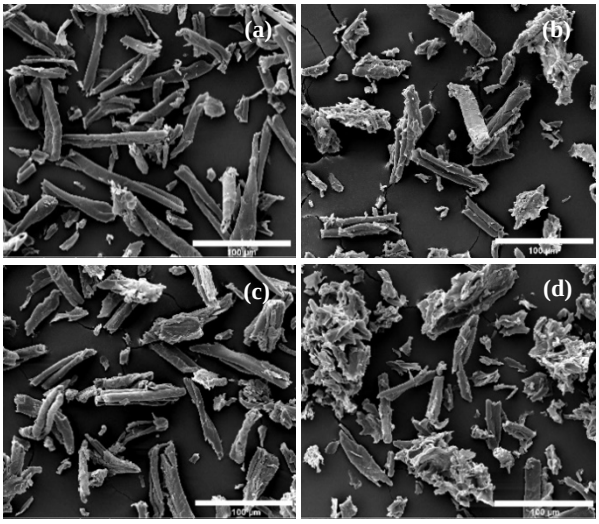

Figure 1. SEM image of (a) cotton linter 1.5 h, (b) cotton linter 4 h, (c) CMC 1.5 h, and (d) CMC 4 h with magnifications of 500x.

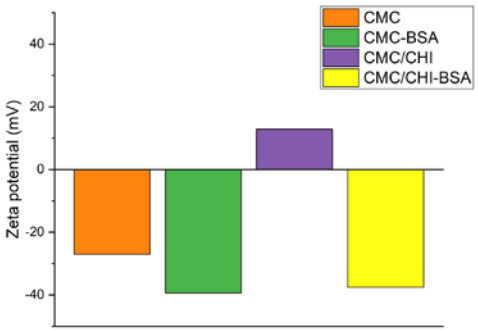

Figure 2. Zeta potential of CMC, CMC-BSA, CMC/CHI, and CMC/CHI-BSA (acid hydrolysis 4 hours).

Figure 1a-b presents the SEM image of cotton linter prepared by acid hydrolysis. The

results show that the size of cotton linter is affected by the duration of acid hydrolysis, with longer acid hydrolysis periods resulting in smaller cotton linter. Specifically, the diameters of cotton linter were 11.26 µm and 8.82 µm after 1.5 and 4 hours of acid hydrolysis, respectively, while their lengths were 104.16 µm and 73.15 µm, respectively, and the morphology exhibits a short fibrous structure. Micro-cellulose is composed of crystalline regions (highly ordered domains) and amorphous regions (disordered domains). During the acid hydrolysis process, acid molecules will preferentially penetrate the amorphous areas and assist in breaking the glycosidic bonds within cellulose molecular chains.[9] Consequently, the amorphous regions undergo degradation, resulting in a reduction in length.

From Figure 1c-d, the diameters of CMC 1.5 h and CMC 4 h that were obtained by TEMPO oxidation were smaller than those that were produced by the acid hydrolysis method. In particular, CMC 1.5 h and CMC 4 h had diameters of 10.80 µm and 8.67 µm, respectively, and lengths of 94.20 µm and 55.01 µm, respectively. The CMC surface, prepared through the TEMPO oxidation process, features a significant number of carboxyl groups, which can be readily converted into other functional groups.

The zeta potential of samples from acid hydrolysis for 4 hours are shown in Table 1 and Figure 2. The zeta potential of BSA, CMC 4 h, CMC/CHI 4 h, CMC-BSA 4 h, and CMC/CHI-BSA 4 h were -39.23, -27.07, 12.87, -39.37, and -37.57, respectively. The results showed that both the BSA and the CMC are negatively charge. The CMC may bind with BSA, possibly with BSA adhering only to the surface of CMC. However, after the modification of CMC with chitosan, it acquires a positive charge, enabling potential binding with negatively charged BSA through electrostatic forces.

3.2 Cellulose microcrystalline loading with biologic

Table 2. The % BSA loading of CNF-BSA and CNF/CHI-BSA by MPR.

Samples	% BSA loading
CMC-BSA 1.5 h	6.86
CMC-BSA 4 h	8.38
CMC/CHI-BSA 1.5 h	10.40
CMC/CHI-BSA 4 h	11.44

The % BSA loading on the CMC-BSA and CMC/CHI-BSA are approximately 6.86-8.38 and 10.40-11.44, respectively, as shown in Table 2. The results showed that CMC/CHI-BSA 4 h has the highest BSA loading, attributed to greater active site interactions with BSA.

3.3 Release test

In this study, the release of CMC-BSA and CMC/CHI-BSA under conditions with and without phosphate was investigated at various pH levels of 3.4, 7.4, and 9. The release was studied over a 3-hour period, and the 1-hour time point was selected as it represents a critical moment of sudden release. From Figure 3, in non-PBS conditions at pH 3.4, BSA release percentages for CMC-BSA at 1.5 h,

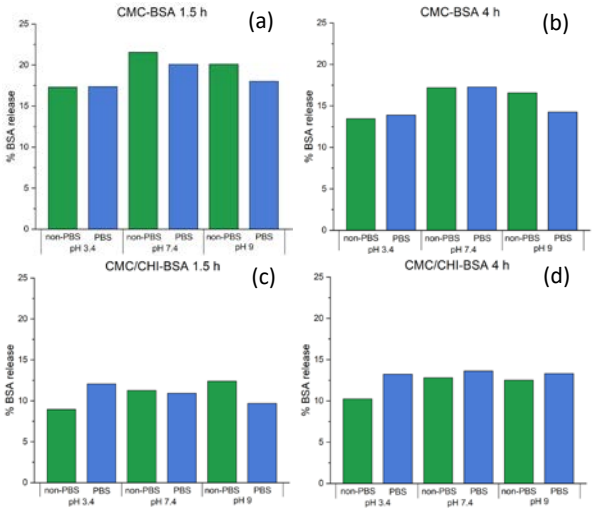

Figure 3. The release test of (a) CMC-BSA 1.5 h, (b) CMC-BSA 4 h, (c) CMC/CHI-BSA 1.5 h, and (d) CMC/CHI-BSA 4 h with under PBS and non-PBS conditions at pH levels of 3.4, 7.4, and 9 at 1 hour (green is non-PBS and blue is PBS).

CMC-BSA at 4 h, CMC/CHI-BSA at 1.5 h, and CMC/CHI-BSA at 4 h were 17.3, 13.4, 8.9, and 10.2, respectively. Meanwhile, in PBS at pH 3.4, these percentages were 17.4, 13.9, 12.1, and 13.2, respectively. At non-PBS pH 7.4, the percentages were 21.5, 17.2, 11.2, and 12.8, respectively, and in PBS, they were 20.1, 17.3, 10.9, and 13.6, respectively. Finally, at non-PBS pH 9, the percentages were 20.1, 16.6, 12.4, and 12.5, and in PBS, they were 18.0, 14.3, 9.7, and 13.3, respectively. Analyzing Figure 3a-b, it was observed that CMC-BSA, in both PBS and non-PBS conditions, exhibited a similar tendency in BSA release. In both conditions, the BSA release tendency of CMC-BSA increased, especially when comparing pH 3.4 with pH 7 or pH 3.4 with 9. In contrast, CMC/CHI, as shown in Figure 3c-d, exhibited opposite trends. In non-PBS conditions, the BSA release of CMC/CHI-BSA continued to increase from pH 3.4 to 7 or pH 3.4 to 9. However, in PBS, the BSA release of CMC/CHI-BSA trend decreased or showed minimal difference. This observation was consistent for both samples subjected to acid hydrolysis for 1.5 and 4 hours.

The results indicate that the release test of CMC-BSA is unaffected by phosphate, while CMC/CHI-BSA demonstrates a notable impact of phosphate on BSA release. This difference may be attributed to the influence of hydrophilic surfaces (CMC) and hydrophobic surfaces (CMC/CHI) on the binding of BSA to the surface. Furthermore, variations in pH lead to distinct BSA release patterns. Notably, the release of BSA at pH 7.4 yields the highest release value. This observation underscores the influence of pH on the BSA release process.

4. Conclusion

Cellulose-based materials on a microscale are considered interesting carriers for biologics delivery due to their favorable properties, including biocompatibility, biodegradability, and low toxicity. The preparation of CMC involves two key steps: 1. The acid hydrolysis process duration, which influences the size and length of the sample. 2. The TEMPO oxidation process, generating a significant number of carboxyl groups on the CMC surface. These carboxyl groups play a pivotal role as they can be easily converted to other functional groups. This study aimed to enhance CMC by transforming its hydrophilic carboxyl groups into a hydrophobic surface using chitosan. Leveraging chitosan's hydrophobic nature and compatibility, CMC/CHI-BSA 4 h exhibited the highest BSA adhesion at 11.44%. Additionally, BSA release testing indicated that the phosphate effect only affected CMC/CHI-BSA.

Acknowledgements

This work receives financial support from Kasetsart University Research and Development Institute (KURDI) and a partial funding support from the Center of Excellence for Innovation in Chemistry (PERCH-CIC). The facilities are supported from the Department of Chemistry, Faculty of Science, Kasetsart University, Bangkok.

References

1. Cheng, G.; Hao, H.; Xie, S.; Wang, X.; Dai, M.; Huang, L.; Yuan, Z., Antibiotic alternatives: the substitution of antibiotics in animal husbandry? *Front Microbiol* **2014,** *5*, 217.
2. Chung, S. W.; Hil-lal, T. A.; Byun, Y., Strategies for non-invasive delivery of biologics. *J Drug Target* **2012,** *20* (6), 481-501.
3. Maniadakis, N.; Toth, E.; Schiff, M.; Wang, X.; Nassim, M.; Szegvari, B.; Mountian, I.; Curtis, J. R., A Targeted Literature Review Examining Biologic Therapy Compliance and Persistence in Chronic Inflammatory Diseases to Identify the Associated Unmet Needs, Driving Factors, and Consequences. *Adv Ther* **2018,** *35* (9), 1333-1355.
4. Pumchan, A.; Cheycharoen, O.; Unajak, S.; Prasittichai, C., An oral biologics carrier from modified halloysite nanotubes. *New Journal of Chemistry* **2021,** *45* (20), 9130-9136.
5. Tafalla, C.; Bogwald, J.; Dalmo, R. A., Adjuvants and immunostimulants in fish vaccines: current knowledge and future perspectives. *Fish Shellfish Immunol* **2013,** *35* (6), 1740-50.
6. Wang, L.; Zhu, H.; Xu, G.; Hou, X.; He, H.; Wang, S., A biocompatible cellulose-nanofiber-based multifunctional material for Fe3+ detection and drug delivery. *Journal of Materials Chemistry C* **2020,** *8* (34), 11796-11804.
7. Ghaderi, M.; Mousavi, M.; Yousefi, H.; Labbafi, M., All-cellulose nanocomposite film made from bagasse cellulose nanofibers for food packaging application. *Carbohydr Polym* **2014,** *104*, 59-65.
8. Alila, S.; Aloulou, F.; Thielemans, W.; Boufi, S., Sorption potential of modified nanocrystals for the removal of aromatic organic pollutant from aqueous solution. *Industrial Crops and Products* **2011,** *33* (2), 350-357.
9. Cheng, M.; Qin, Z.; Hu, J.; Liu, Q.; Wei, T.; Li, W.; Ling, Y.; Liu, B., Facile and rapid one-step extraction of carboxylated cellulose nanocrystals by H(2)SO(4)/HNO(3) mixed acid hydrolysis. *Carbohydr Polym* **2020,** *231*, 115701.
10. Rajinipriya, M.; Nagalakshmaiah, M.; Robert, M.; Elkoun, S., Importance of Agricultural and Industrial Waste in the Field of Nanocellulose and Recent Industrial Developments of Wood Based Nanocellulose: A Review. *ACS Sustainable Chemistry & Engineering* **2018,** *6* (3), 2807-2828.
11. Kusmono; Listyanda, R. F.; Wildan, M. W.; Ilman, M. N., Preparation and characterization of cellulose nanocrystal extracted from ramie fibers by sulfuric acid hydrolysis. *Heliyon* **2020,** *6* (11), e05486.
12. Ruiz-Caldas, M.-X.; Carlsson, J.; Sadiktsis, I.; Jaworski, A.; Nilsson, U.; Mathew, A. P., Cellulose Nanocrystals from Postconsumer Cotton and Blended Fabrics: A Study on Their Properties, Chemical Composition, and Process Efficiency. *ACS Sustainable*

Chemistry & Engineering **2022,** *10* (11), 3787-3798.
13. Mhlongo, J. T.; Nuapia, Y.; Motsa, M. M.; Mahlangu, T. O.; Etale, A., Green chemistry approaches for extraction of cellulose nanofibers (CNFs): A comparison of mineral and organic acids. *Materials Today: Proceedings* **2022,** *62*, S57-S62.
14. Lal, S. S.; Mhaske, S. T., TEMPO-oxidized cellulose nanofiber/kafirin protein thin film crosslinked by Maillard reaction. *Cellulose* **2019,** *26* (10), 6099-6118.
15. Paquin, M.; Loranger, E.; Hannaux, V.; Chabot, B.; Daneault, C., The use of Weissler method for scale-up a Kraft pulp oxidation by TEMPO-mediated system from a batch mode to a continuous flow-through sonoreactor. *Ultrason Sonochem* **2013,** *20* (1), 103-8.
16. Tang, R.; Yu, Z.; Renneckar, S.; Zhang, Y., Coupling chitosan and TEMPO-oxidized nanofibrilliated cellulose by electrostatic attraction and chemical reaction. *Carbohydr Polym* **2018,** *202*, 84-90.
17. Manna, S.; Seth, A.; Gupta, P.; Nandi, G.; Dutta, R.; Jana, S.; Jana, S., Chitosan Derivatives as Carriers for Drug Delivery and Biomedical Applications. *ACS Biomater Sci Eng* **2023,** *9* (5), 2181-2202.
18. Bernkop-Schnurch, A.; Dunnhaupt, S., Chitosan-based drug delivery systems. *Eur J Pharm Biopharm* **2012,** *81* (3), 463-9.

Carbon dots from rubber latex using microwave-assisted pyrolysis for tyrosine detection

Thanathip Sitthichot [1]* and Sirilux Poompradub [2,3,4]

[1]*Program in Petrochemistry and Polymer Science, Chulalongkorn University, Bangkok 10330*
[2]*Department of Chemical Technology, Faculty of Science, Chulalongkorn University, Bangkok 10330*
[3]*Center of Excellence on Petrochemical and Materials Technology, Chulalongkorn University, Bangkok 10330*
[4]*Center of Excellence in Green Materials for Industrial Application, Faculty of Science, Chulalongkorn University, Bangkok 10330*

**E-mail: sirilux.p@chula.ac.th*

Abstract:

In this study, the carbon dots (CDs) were prepared from the rubber latex (Hevea brasiliensis) as the carbon source and ammonium persulphate as the nitrogen source using "microwave-assisted pyrolysis". Various instrumental techniques such as transmission electron microscopy, UV-visible spectrophotometer, fluorescent spectrophotometer and fourier-transform infrared spectroscopy were employed to characterize CDs. The particle size of synthesized CDs was less than 5 nm in size and CDs showed good optical properties and solubility in water. The optical properties of CDs were strongly influenced by several functional groups (-OH, –CHO, –COOH, –CO, –COO) formed on the CDs surface. Finally, the CDs were applied as a fluorescent probe for the selective and sensitive detection for tyrosine. The CD-based sensor showed an excellent applicability for the tyrosine detection.

1. Introduction

The evolution of fluorescent carbon nanoparticles took place in 2004 through the experimental by Chinese researcher (Xu et al., 2004). Carbon dots (CDs) are nanomaterials that show the strong fluorescence from light emitting, even though the materials itself are opaque (Li et al., 2019). Recently, the improved CDs exhibit the low cytotoxicity and high compatibility with living cells compared to the previous studies (Xu et al., 2004). CDs possess a strong ability to bind with organic and inorganic molecules because they contain many functional groups on the surface. Therefore, CDs have been applied to a variety of applications such as photocatalysts, chemical sensing, biosensing, bioimaging, and medical nanotechnology (Liu et al., 2019). Generally, the synthesis of CDs involves two processes: top-down approach, in which macromolecular precursors are degraded to smaller molecules and bottom-up approach which is continuous coalescence of small carbon particles to larger particles (Xia et al., 2019).

Here, the vital task is selecting precursors that are renewable and easily available to use for CDs synthesis. Thailand is considered one of the top natural rubber latex (*Hevea brasiliensis*) exporting countries in the world. Therefore, natural rubber latex can be used as a carbon source for CDs synthesis. It is because the structure of natural rubber mainly consists of 94 percent by weight of cis-1,4- polyisoprene $(C_5H_8)_n$ and the rest are proteins, fats and inorganic salts such as ashes, metal radicals etc. (Woo et al., 2008).

Tyrosine is a type of amino acid, which is commonly used to improve learning memory, alertness and attention. It creates the significant brain chemicals that facilitate nerve cells to communicate and may even regulate mood. However, the high accumulation of tyrosine causes Parkinson's disease or dementia. In humans, tyrosine is synthesized from phenylalanine, that comes from milk and food. Tyrosine analysis can be detected by a variety of techniques such as capillary electrophoresis, gas chromatography, Ion-exchange chromatography, etc. However, these techniques require the sophisticated instrumentation, long-time consuming and high cost. Therefore, it leds to the development technique with cost-saving for the tyrosine detection.

The aim of this study is to prepare CDs from natural latex as a carbon source by using ammonium persulfate and polyethylenimine as a nitrogen source via a microwave-assisted pyrolysis. The advantage of microwave-assisted pyrolysis is simple technique and requires a amount of raw materials. Then, CDs are characterized by transmission electron microscopy (TEM), UV-visible spectrophotometer, fluorescent spectrophotometer and fourier-transform infrared spectroscopy (FT-IR). Finally, the prepared CDs have been utilized for the sensitive detection of tyrosine.

2. Materials and Methods

2.1 Materials

The natural rubber latex of *Hevea brasiliensis* was obtained from rubber plantation, Phetchabun, Thailand. Ammonium persulphate was purchased from Sinopharm Chemical Reagent Co., Ltd. Polyethyleneimine was purchased from Sigma Aldrich, USA. Tyrosine was purchased from Himedia, India

2.2 Synthesis of CDs

2 mL natural rubber latex, 30 mL deionized water, 1 mL of polyethyleneimine and 1 g ammonium persulphate were mixed in the flask. Then, the solution was sonicated for 15 min. After that, the solution was heated with a microwave at a power of 750 watts for 5 min to get a viscous brown suspension. The obtained brown color viscous was dissolved in 30 ml of deionized water and centrifuged by centrifugation 8,000 rpm for 5 min. The supernatant was then filtered with 0.22 µm filter paper and stored in the refrigerator for further analysis.

2.3 Quantum yield measurement

The relative quantum yield of CDs was calculated based on Equation (1) (Wang et al., 2019).

$$QY_{sam} = QY_{ref}\frac{I_{ref}A_{sam}\eta_{sam}^2}{I_{sam}A_{ref}\eta_{ref}^2} \quad (1)$$

where "QY_{sam}" is quantum yield of sample. "QY_{ref}" is quantum yield of reference. "I" is emission intensity. "A" is UV-vis absorption intensity. "η" is the solution's refractive index with 1.33 as the default for both reference and sample. 0.1 M H_2SO_4 was used as the reference by using QY of 54%. The fluorescent spectra were recorded in the range of 200-800 nm at the excitation wavelength of 350 nm (Wang et al., 2019).

2.4 Characterization

The ultraviolet visible absorption spectrum was obtained by a (EVO-LUTION 201, Thermo Scientific) spectrophotometer at wavelength 200–800 nm. The fluorescent spectra were obtained by using fluorescent spectrophotometer at the excitation wavelength and emission wavelength at 190-440 nm and 360-700 nm, respectively. The morphology of CDs was carried out by TEM, TECHNAI 20 G2 at an accelerating voltage of 200 kV. The FT-IR spectrum was recorded on PerkinElmer with KBr pellets in transmittance mode in the wavenumber range from 400 to 4000 cm^{-1}.

2.5 Detection of tyrosine

The tyrosine detection procedures were measured as follows: 70 mg CDs powder was dispersed in 1000 mL of deionized water to form a 70 mg/L suspension. Then, 50 µl of the tyrosine with different concentrations (0, 20, 40, 60, 80 and 100 µM) was mixed with 50 µl of the above CD suspension. After 1 min, the fluorescence emission spectrum of the mixture was recorded under the excitation wavelength of 360 nm. The schematic illustration of the microwave-assisted pyrolysis synthesis of CDs from latex was represented in Fig. 1.

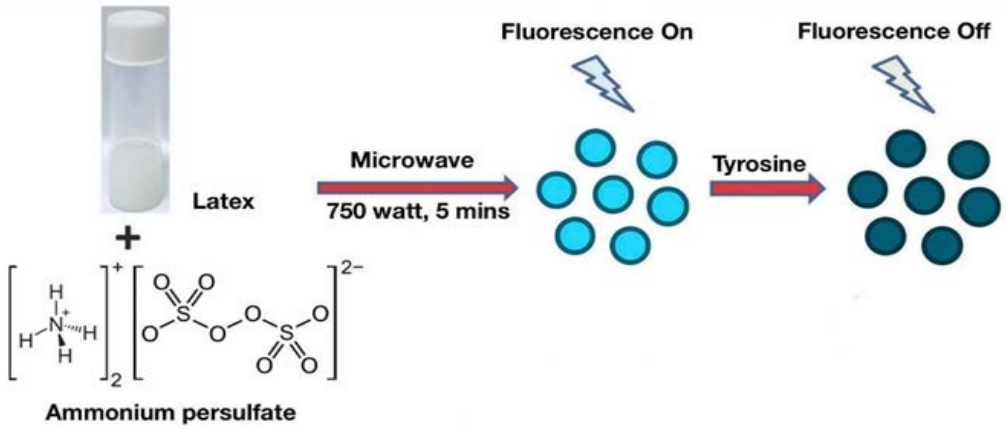

Figure 1. Schematic illustration of the microwave-assisted pyrolysis synthesis of CDs from latex.

3. Results & Discussion

3.1. Formation of CDs

The synthesis CDs were prepared by the microwave-assisted pyrolysis method using natural rubber latex as a precursor. It is because natural rubber latex mainly contains carbon and hydrogen (Woo et al., 2008). The obtained CDs after the microwave-assisted pyrolysis showed the dark viscous liquid under daylight and cyan blue fluorescence under ultraviolet (UV) light as seen in Fig. 2. The pH of CD suspension was about 2-4 and the quantum yield of CDs was 15.7 %. No precipitation was obtained when CDs were kept in refrigerator for one month. This result indicated that the obtained CDs showed the long-term stability.

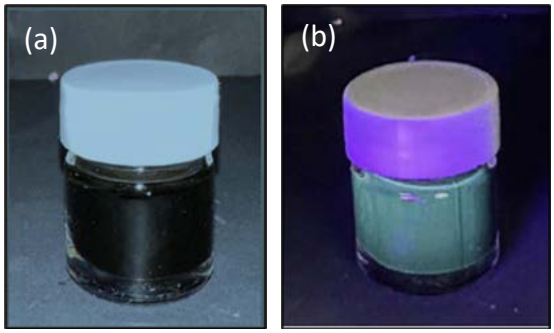

Figure 2. Suspension of CDs under (a) daylight and (b) UV light.

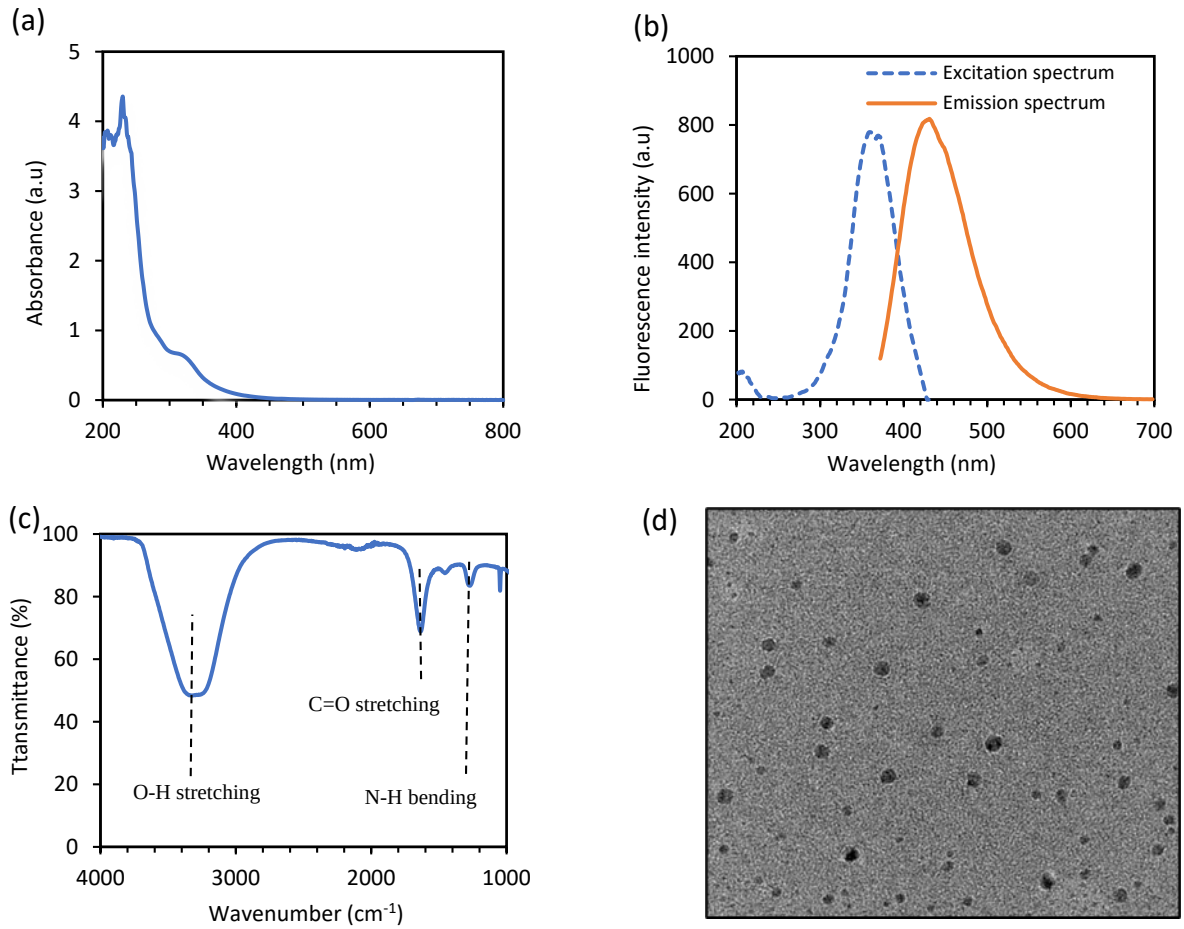

Figure 3. (a) UV-visible spectra (b) Fluorescent spectra (c) FTIR spectrum and (d) TEM image of CDs.

3.2. Characterization of CDs

The optical properties of CDs were examined by UV–visible and fluorescence spectroscopy. The UV–visible spectra in Fig. 3a showed the peaks at 233 and 335 nm corresponding to π to π* transition of conjugated skeletons and n to π* transitions of a heteroatom-containing bond belong to carbon-carbon double bond and carbonyl bond respectively. Figure 3b presents the maximum emission wavelength of CDs observed at 468 nm under the excitation wavelength of 350 nm, corresponding to the cyan blue fluorescence. Figure 3c shows FTIR spectra of CDs. It was found that the board band peak of O–H stretching appeared at the wavelength of 3320 cm^{-1}. A sharp peak at 1630 cm^{-1} was evident for the presence of the C=O stretching. The sharp peak at 1375 was N-H bending (Hu et al., 2020). Accordingly, the obtained CDs were successfully prepared. The size and shape of CDs were characterized by TEM as shown in Fig.3d. It was found that CDs were in the spherical shape with the average particle size in the range of 2-4 nm.

3.3 Detection of tyrosine

The sensitivity experiment of CDs fluorescent probe towards tyrosine detection was performed using a maximum excitation wavelength of 350 nm upon gradual addition of 50 µl of tyrosine (0, 20, 40, 60, 80, 100 µM) into the CDs suspension (30 mg/mL). The cyan blue fluorescence of CDs continuously decreased with increasing concentrations of tyrosine as seen in Fig. 4. It was referred that the strong interaction between CDs and tyrosine was obtained.

Figure 5(a) shows the fluorescent emission intensity of CDs after adding tyrosine solution (0, 20, 40, 60, 80 and 100 µM). It was found that the maximum emission intensity at 408 nm continuously decreased with the increase of tyrosine concentrations under the excitation wavelength of 350 nm. The selectivity of CDs might be due to the specific affinity between the carboxyl groups on the CDs and amino groups of tyrosine. It is interesting to note that there was no overlapped quenching peak before and after adding tyrosine, revealing the non-occurrence of the inner filter effect which is a loss of observed fluorescence intensity caused by absorption of light by the sample. This effect is closely linked to the path that the light takes through the sample before it reaches the detector (Conceicao et al., 2023).

The dynamic quenching or static quenching were confirmed by adding fluorophore (CDs) and quencher (tyrosine). The fluorescent quenching effectiveness was calculated based on Stern–Volmer Plot in Equation (2) (Yadav et al., 2021).

$$F_0/F = 1 + k_{sv}[Q] \qquad (2)$$

where "F_0" is fluorescent intensity of CDs. "F" is the fluorescent intensity of CDs in the presence of quencher (tyrosine). "Q" is the concentration of quencher, and "k_{sv}" is quenching constant.

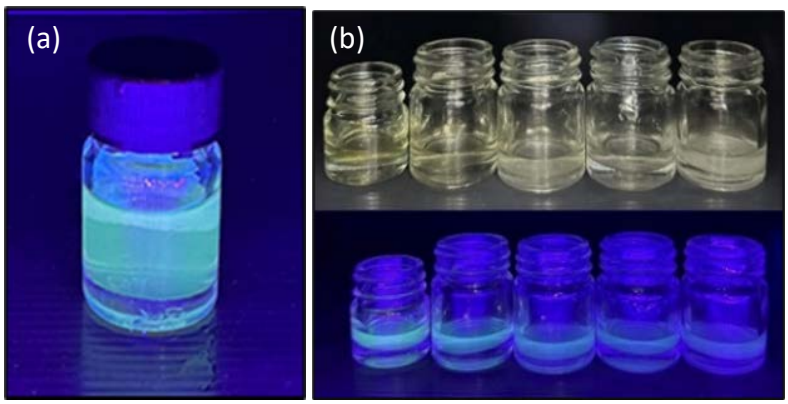

Figure 4. (a) Fluorescence of pure CDs and (b) Fluorescence of CDs upon addition of different concentrations of tyrosine (From left to right: 20, 40, 60, 80, and 100 µM)

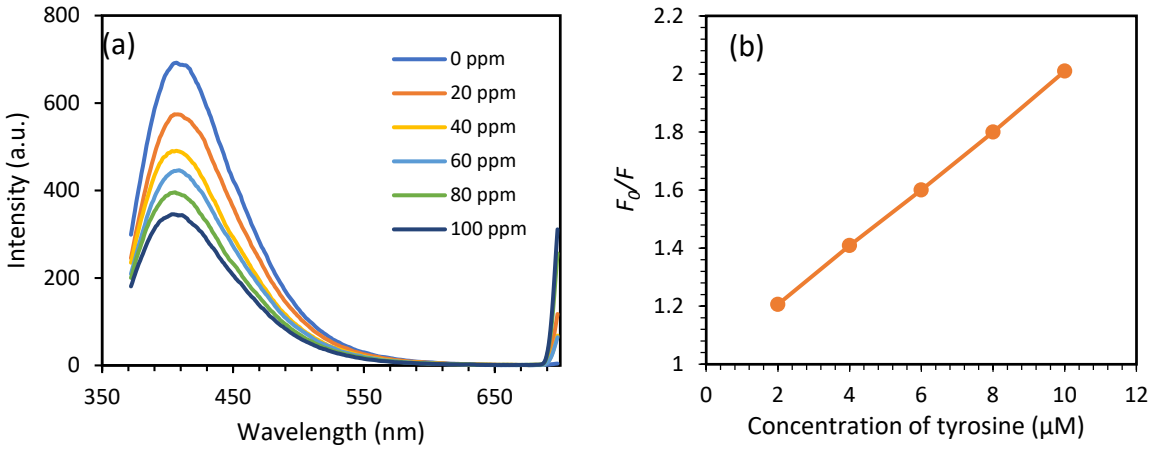

Figure 5. (a) Fluorescent emission spectra of CDs at 350 nm excitation upon the various tyrosine concentrations and (b) the Stern-Volmer plot.

Figure 5(b) shows the linear relationship between F_0/F and tyrosine concentration in the range of 2 to 10 μM. The correlation coefficient (R^2) was estimated to be 0.9956. The graph was constant straight line without deviation, responding to the static quenching. This result concluded that the CDs and tyrosine created a non-fluorescent complex in the ground state before the excitation occurs (Yadav et al., 2021). Furthermore, the k_{sv} value of the as-synthesized CDs was estimated to be 0.21105 $(\mu M)^{-1}$. Normally, tyrosine has a k_{sv} value about 0.18-0.22 $(\mu M)^{-1}$ (Woo et al., 2015). This indicates that the quencher (tyrosine) is well dispersed in fluorophore (CDs).

4. Conclusion

In summary, the fluorescent CDs were synthesized via the microwave-assisted pyrolysis method using the latex of *Hevea brasiliensis*. The synthesized CDs were in spherical shape with the particle size about 2-4 nm and exhibited cyan blue fluorescence under UV lamp. For tyrosine detection, CDs showed quenching with tyrosine as a static quenching. Accordingly, this study can be applied for tyrosine detection such as milk, yogurt, cheese, peanuts, banana, etc.

Acknowledgements

The authors gratefully acknowledge the financial support from Program in Petrochemistry and Polymer Science, Department of Chemical Technology and Center of Excellence in Green Materials for Industrial Application, Faculty of Science, Chulalongkorn University.

References

1. Xia, C., Zhu, S., Feng, T., Yang, M., & Yang, B. Evolution and Synthesis of Carbon Dots: From Carbon Dots to Carbonized Polymer Dots. *Advanced Science*. **2019**, 6(23), 1-23.
2. Woo, C.S., Kim, W.D., Kwon, J.D. A study on the material properties and fatigue life prediction of natural rubber component. *Materials Science and Engineering: A*. **2008**, 483, 376-381.
3. Dong, W., Zhou, S., Dong, Y., Wang, J., Ge, X., & Sui, L. The preparation of ethylenediamine-modified fluorescent carbon dots and their use in imaging of cells. *Luminescence*. **2015**, 30(6), 867-871.
4. Lim, S.Y., Shen, W. and Gao, Z. Carbon Quantum Dots and their Applications. *Chemical Society Reviews*. **2015**, 44(1), 362 - 381.
5. Hu, Y., and Gao, Z. Sensitive detection of Sudan dyes using tire-derived carbon dots as a fluorescent sensor. *Spectrochimica Acta Part A: Molecular and Biomolecular Spectroscopy*. **2020**, 239, 856-864.
6. Li, M., Chen, T., Gooding, J. J., & Liu, J. Review of carbon and graphene quantum dots for sensing. *ACS Sensors*. **2019**, 4(7), 1732-1748.
7. Wang, X., Feng, Y., Dong, P., Huang, J. A mini review on carbon quantum dots: preparation, properties, and electrocatalytic

application. *Frontiers in Chemistry*. **2019**, 7, 151-154.
8. Conceicao, P., Barata, J.F.B., Lacerda, P.S.S., Neves, M.G.P.M.S., Carlos, L.D., Trindade, T. Ratiometric nanothermometry via porphyrin inner filter effect applied to colloidal ZnS quantum dots. *Sensors and Actuators A: Physical*. **2023**, 357-365.
9. Zhang, Z., Hao, J., Zhang, J., Zhang, B. and Tang, J. Protein as the Source for Synthesizing Fluorescent Carbon Quantum Dots by a One-Pot Hydrothermal Route. *RSC Advances*. **2012**, 2(23), 8599 - 8601.
10. Yadav, P.K., Upadhyay, R.K., Kumar, D., Bano, D., Chandra, S., Jit, S. and Hasan, S.H. Synthesis of green fluorescent carbon quantum dots from the latex of Ficus benghalensis for the detection of tyrosine and fabrication of Schottky barrier diode. *New J. Chem*. **2021**, 45, 12549-12556.
11. Liu, M. L., Chen, B. B., Li, C. M., & Huang, C. Z. Carbon dots: synthesis, formation mechanism, fluorescence origin and sensing applications. *Green Chemistry*. **2019**, 21(3), 449-471.
12. Xu, X., Ray, R., Gu, Y., Ploehn, H. J., Gearheart, L., Raker, K., & Scrivens, W. A. Electrophoretic analysis and purification of fluorescent single-walled carbon nanotube fragments. *Journal of the American Chemical Society*. **2004**, 126(40), 12736-12737.
13. Zhang, Y., Wang, Y., Feng, X., Zhang, F., Yang, Y. and Liu, X. Effect of Reaction Temperature on Structure and Fluorescence Properties of Nitrogen-Doped Carbon Quantum Dots. *Applied Surface Science*. **2016**, 387, 1236 - 1246.
14. Reyes, D., Camacho, M., Camacho, M., Mayorga, M., Weathers, D., Salamo, G., Wang, Z.,and Neogi, A. Laser ablated carbon nanodots for light emission. *Nanoscale Research Letters*. **2016**, 424, 1-11
15. Woo, J. K., Tran, L. H., Jang, S. H., Lee. C. H., Kang, T, J. Molecular Interactions of Graphene Oxide with Aromatic Amino Acids Tyrosine and Tryptophan. *Bulletin of the Korean Chemica*

Microwave synthesis of nitrogen and boron co-doped carbon dots from ascorbic acid

Antika Boonruanganan[1], Karn Serivalsatit[1,2], and Wuttichai Reainthippayasakul[1,2]*

[1]*Department of Materials Science, Faculty of Science, Chulalongkorn University, Bangkok, Thailand*
[2]*Photocatalysts for Clean Environment and Energy Research Unit, Faculty of Science, Chulalongkorn University, Bangkok, Thailand*

**E-mail: Wuttichai.re@chula.ac.th*

Abstract:

In order to enhance optical performances and expand range of applications of carbon dots, doping with heteroatoms is one of the most interesting and effective approaches. In this work, nitrogen-doped carbon dots (N-CDs) and nitrogen/boron co-doped carbon dots (N/B-CDs) were successfully synthesized by facile microwave-assisted synthesis using ascorbic acid, urea, and boric acid as carbon, nitrogen, and boron sources, respectively. This method provides simplicity, rapid reaction rates, high efficiency in heating, environmental friendliness, and energy savings. Optical properties of the synthesized N-CDs and N/B-CDs were characterized by UV-Visible spectroscopy, and fluorescence spectroscopy. The N-CDs showed maximum fluorescence emission at wavelength of 412 nm with an excitation wavelength of 338 nm, while the N/B-CDs showed maximum fluorescence emission at wavelength of 413 nm with an excitation at wavelength of 324 nm. Both of carbon dots exhibited blue fluorescence under blacklight irradiation at wavelength of 365 nm. These materials potentially offer excellent performances in sensing and imaging applications.

1. Introduction

Carbon dots (CDs) are tiny spherical carbon nanoparticles with an extremely fine particle size, exhibiting an average diameter of less than 10 nanometers. Presently, carbon dots have been extensively interested owing to their excellent physical, optical, and chemical attributes, such as photoluminescence, photo-stability, low toxicity, biocompatibility, environmental friendliness and ease of preparation.[1] Thus, carbon dots find applications in a range of uses, including delivery systems, photocatalysis, sensors, and light-emitting devices.[2] With the ongoing advancement of research on CDs, the scope extends beyond the exploration of synthesis strategies; it also presents opportunities and challenges for achieving synthesis methods that are more scientifically rigorous, environmentally sustainable, and systematically controllable. For example, the facile microwave-assisted synthesis method offers many advantages such as simplicity, rapid reaction rates, high heating efficiency, energy savings, and environmental friendliness.[3] Carbon dots can be synthesized by employing precursors rich in carbon content.[4] Ascorbic acid is standing out as a fascinating source due to its carbon ring chemical structure. This characteristic is anticipated to contribute to the formation of the core structure of carbon dots effectively. Furthermore, ascorbic acid boasts numerous functional groups relative to its carbon count, enhancing its water solubility and presenting an opportunity for utilization as a sensor for the detection of various metal ions.[5-6] In recent years, researchers have used various heteroatoms as doping agents to enhance the physicochemical characteristics of carbon dots. Doping modifies the intrinsic properties of carbon dots by altering their structure and adding specific types of functional groups to the surface, subsequently influencing their fluorescence performance.[7-8] The optical and electronic properties can be tuned by selecting specific types and quantities of doping atoms, thereby improving the electronic structure. The energy gap, which determines the photophysical characteristics of carbon dots, may be influenced by varying the types and amounts of dopants inserted. To further tailor the properties of carbon dots, heterogeneous doping with other elements (nitrogen and boron) presents a promising functionalization strategy to modify the surface morphology of the carbon dots.[9-10] In this work, nitrogen-doped carbon dots (N-CDs) and nitrogen/boron co-doped carbon dots (N/B-CDs) were synthesized by a facile microwave-assisted synthesis using ascorbic acid, urea, and boric acid as carbon, nitrogen, and boron sources, respectively. The study aims to explore the characteristics and optical properties of these synthesized CDs.

2. Materials and Methods

2.1 Materials

L(+)-ascorbic acid, urea and boric acid were utilized as the precursors for the synthesis. All chemicals were purchased in analytical quality grade and were utilized without any additional purification. De-ionized (DI) water was utilized as a solvent in all the experiments.

2.2 Synthesis of Doped CDs

The synthesis of N-doped carbon dots (N-CDs) involved dissolving 1 g of ascorbic acid and 1 g of urea in a glass beaker containing 5 mL of DI water. Subsequently, the resultant mixture underwent sonication for 10 minutes in an ultrasonic bath, followed by heating in a household microwave oven (operating at a power of 700 W) for 4 minutes. This process led to a discernible transformation of the initially transparent solution into a dark brown color, indicative of the carbonization of the reactants. After cooling to room temperature, the solid product underwent grinding. Subsequently, 5 mL of DI water were added and the resulting mixture was subjected to centrifugation at 9000 rpm for 10 minutes. The obtained supernatant liquid was then filtered via a 0.22 mm membrane filter to separate larger particles. To remove water, the solution underwent freeze-drying for 24 hours, then the powder of N-CDs was kept for further investigation. The nitrogen/boron co-doped carbon dots (N/B-CDs) were synthesized by the same procedure used for N-CDs with the precursor composition containing 1 g of ascorbic acid, 0.5 g of urea, and 0.5 g of boric acid.

2.3 Characterizations

The optical properties were characterized by UV-Visible spectroscopy (Agilent, Carry 7000 UV-Vis-NIR) and fluorescence spectroscopy (PerkinElmer, LS 55). In addition, the absorbance and fluorescence intensity of the CDs were used to calculate their fluorescence quantum yield (QY) using Quinine sulfate in 0.1 M H_2SO_4 as a reference solution. Chemical structures of the synthesized CDs were studied by Raman spectroscopy (HORIBA, XploRA PLUS Confocal Raman Microscope) using an excitation wavelength at 532 nm.

3. Results & Discussion

3.1 Optical Properties

Both of carbon dots are well dispersed in water and exhibit a brownish-yellow color under visible light. Furthermore, they demonstrate blue-colored fluorescence emission under blacklight irradiation at a wavelength of 365 nm (**Figure 1**). The absorption spectra of N-CDs in **Figure 2a** reveal two peaks with shoulder at approximately 270 nm and 330 nm, which may be ascribed to the π-π* transition of C=N bonds and the n-π* transitions in carbonyl bond (C=O), respectively. On the other hand, the N/B-CDs exhibit a sharp absorption peak at 265 nm, corresponding to the π-π* transition of C=N bonds (**Figure 2b**).

The prepared N-CDs show maximum fluorescence emission at wavelength of 412 nm with an excitation wavelength of 338 nm (**Figure 2c**), while the N/B-CDs show maximum fluorescence emission at wavelength of 413 nm with an excitation at wavelength of 324 nm (**Figure 2d**). These results indicate that co-doping of nitrogen and boron atoms into the CDs do not affect their fluorescence emission.

3.2 Quantum Yield Calculation

Fluorescence quantum yield is denoted as the efficiency of converting absorbed light into emitted light, typically in the form of fluorescence, representing a characteristic property of a fluorescent species. Fluorophores with high quantum yield often exhibit strong fluorescence, even at low concentrations. This property reduces the quantity of fluorophores required for a given application, thereby cutting financial costs. It is noteworthy that the generally reported quantum yield for bare carbon dots (CDs) is below 10%. However, through the process of doping CDs and surface functionalization could affect their quantum yields.[11-12] Theoretically, the quantum yield was calculated by

$$Q_s = Q_r \left(\frac{A_r}{A_s}\right)\left(\frac{E_s}{E_r}\right)\left(\frac{\mathrm{n}_s}{\mathrm{n}_r}\right)^2$$

where Q, A, E and n are the quantum yield, absorbance of the solution, integrated fluorescence intensity of the emitted light and refractive index of the solvent. Subscripts 's' and 'r' stand for the sample and reference used.[12-13] Here, quinine sulfate dissolved in H_2SO_4 0.1 mol/L was used as a reference, while CDs solution was prepared in DI water. The quantum yields of N-CDs and N/B-CDs were calculated to be 5.9% and 2.0%, respectively. These suggest that co-doping of nitrogen and boron atoms can decrease the quantum yield of the CDs.

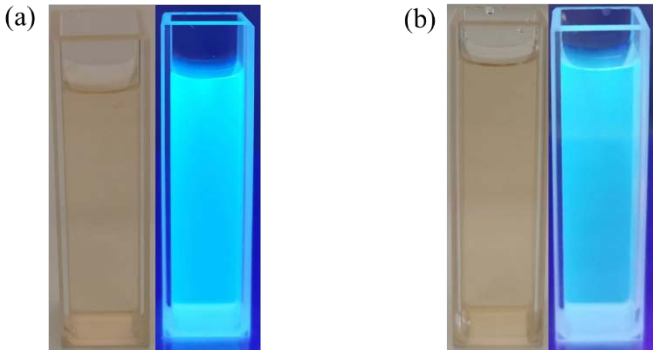

Figure 1. (a) The photographic images of N-CDs under the daylight and the UV light. (b) The photographic images of N/B-CDs under the daylight and the UV light.

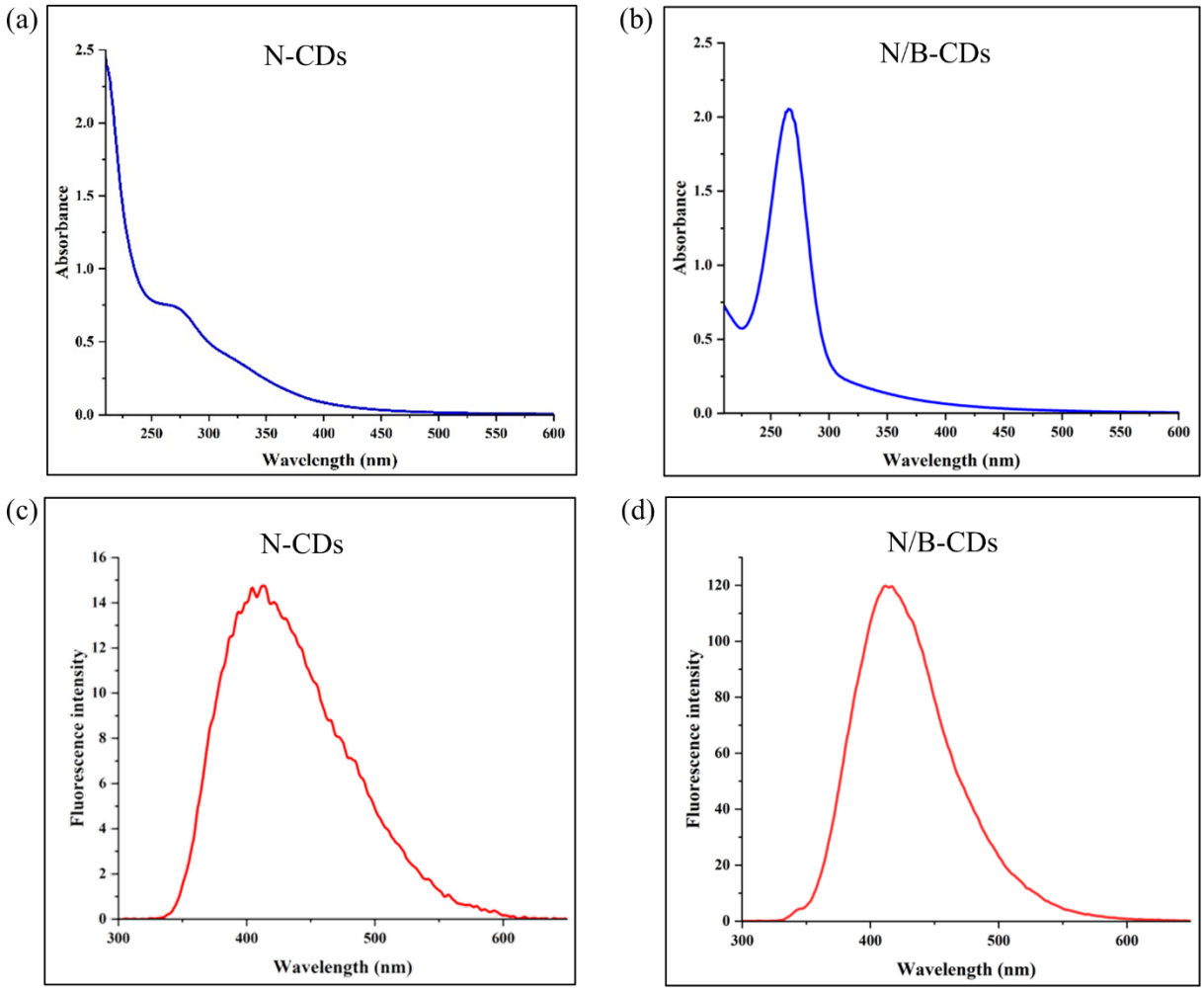

Figure 2. (a),(b) UV–Vis spectra of N-CDs and N/B-CDs and (c),(d) fluorescence emission spectra of N-CDs and N/B-CDs.

3.3 Structural Characterizations

The carbonization technique enables the conversion of organic material into carbon under conditions of extreme heat or pressure. The confirmation of carbonization was established through Raman spectroscopy, as illustrated in **Figure 3**. The spectrum of N-CDs exhibits a broad D band centered at about 1330 cm^{-1} and shoulder G band at about 1560 cm^{-1}, and a similar pattern is observed in the spectrum of N/B-CDs, with the broad D band centered at about 1335 cm^{-1} and shoulder G band at about 1570 cm^{-1}. The D (disorder) band originates from the vibrations of carbon atoms with dangling bonds in the termination plane of disordered graphite or glassy

carbon, while the G (graphitic) band corresponds to the first-order scattering of the stretching vibration mode E_{2g} observed for sp^2 carbon domains.[14-15]

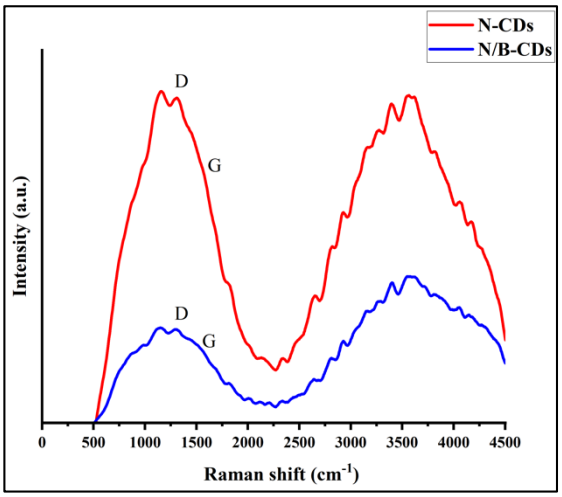

Figure 3. Raman spectra of N-CDs and N/B-CDs with excitation wavelength of 532 nm.

4. Conclusion

The nitrogen-doped carbon dots (N-CDs) and nitrogen/boron co-doped carbon dots (N/B-CDs) were successfully synthesized by facile microwave-assisted synthesis using ascorbic acid, urea, and boric acid as precursors. Both of carbon dots are well dispersed in water and exhibit a brownish-yellow color under visible light and blue fluorescence under blacklight irradiation. The N-CDs exhibit excitation/emission maximum at 338/412 nm, with a quantum yield of 5.9%., while the N/B-CDs show excitation/emission maximum at 324/413 nm, with a quantum yield of 2.0%. These materials potentially offer excellent performances in sensing and imaging applications.

Acknowledgements

This research was partially supported by Office of the Permanent Secretary, Ministry of Higher Education, Science, Research and Innovation. The author also would like to thank Department of Materials Science, Faculty of Science, Chulalongkorn University for the research facilities.

References

1. Bao, L.; Liu, C.; Zhang, Z.; Pang, D. Photoluminescence-tunable Carbon Nanodots: Surface-state Energy-gap Tuning. *Advanced Materials* **2015**, 27, 1663–1667.
2. Chahal, S.; Macairan, J.-R.; Yousefi, N.; Tufenkji, N.; Naccache, R. Green Synthesis of Carbon Dots and Their Applications. *RSC Advances* **2021**, 11 (41), 25354–25363.
3. Adeola, A. O.; Duarte, M. P.; Naccache, R. Microwave-Assisted Synthesis of Carbon-Based Nanomaterials from Biobased Resources for Water Treatment Applications: Emerging Trends and Prospects. *Frontiers in Carbon* **2023**, 2.
4. Meng, W.; Bai, X.; Wang, B.; Liu, Z.; Lu, S.; Yang, B. Biomass-derived Carbon Dots and Their Applications. *Energy & Environmental Materials* **2019**, *2* (3), 172–192.
5. M. Yussif, N. Vitamin C. *Vitamin C - an Update on Current Uses and Functions* **2019**.
6. Gayen, B.; Palchoudhury, S.; Chowdhury, J. Carbon Dots: A Mystic Star in the World of Nanoscience. *Journal of Nanomaterials* **2019**, *2019*, 1–19.
7. Miao, S.; Liang, K.; Zhu, J.; Yang, B.; Zhao, D.; Kong, B. Hetero-Atom-Doped Carbon Dots: Doping Strategies, Properties and Applications. *Nano Today* **2020**, *33*, 100879.
8. Xu, Q.; Kuang, T.; Liu, Y.; Cai, L.; Peng, X.; Sreenivasan Sreeprasad, T.; Zhao, P.; Yu, Z.; Li, N. Heteroatom-Doped Carbon Dots: Synthesis, Characterization, Properties, Photoluminescence Mechanism and Biological Applications. *Journal of Materials Chemistry B* **2016**, *4* (45), 7204–7219.
9. Zhang, Q.; Wang, R.; Feng, B.; Zhong, X.; Ostrikov, K. Photoluminescence Mechanism of Carbon Dots: Triggering High-Color-Purity Red Fluorescence Emission through Edge Amino Protonation. *Nature Communications* **2021**, *12* (1).
10. Liu, M. Optical Properties of Carbon Dots: A Review. *Nanoarchitectonics* **2020**, *1* (1), 1–12.
11. Fong, J. F. Y.; Ng, Y. H.; Ng, S. M. Carbon Dots as a New Class of Light Emitters for Biomedical Diagnostics and Therapeutic Applications. *Fullerens, Graphenes and Nanotubes* **2018**, 227–295.
12. Williams, A. T.; Winfield, S. A.; Miller, J. N. Relative Fluorescence Quantum Yields Using a Computer-Controlled Luminescence Spectrometer. *The Analyst* **1983**, *108* (1290), 1067.
13. Lawson-Wood, K.; Upstone, S.; Evans, K. Determination of Relative Fluorescence Quantum Yields Using the FL6500 Fluorescence Spectrometer. *PerkinElmer, Inc.* **2018**, 1–5.
14. Ma, X.; Li, S.; Hessel, V.; Lin, L.; Meskers, S.; Gallucci, F. Synthesis of Luminescent Carbon Quantum Dots by Microplasma Process.

Chemical Engineering and Processing - Process Intensification **2019**, *140*, 29–35.

15. Liu, F.; Sun, Y.; Zheng, Y.; Tang, N.; Li, M.; Zhong, W.; Du, Y. Gram-Scale Synthesis of High-Purity Graphene Quantum Dots with Multicolor Photoluminescence. *RSC Advances* **2015**, 5 (125), 103428–103432.

Effect of graphene quantum dots in enhancing plant growth and anti-oxidant activity of mung bean

Warawut Kongseangchai[1,*a], Kunat Suktham[2], Artiwan Shotipruk[2], and Joongjai Panpranot[1,*b]

[1]*Center of Excellence in Catalysis and Catalytic Reaction Engineering (CECC), Department of Chemical Engineering, Faculty of Engineering, Chulalongkorn University, Phayathai Road, Patumwan, Bangkok 10330, Thailand*
[2]*Bio-Circular-Green-economy Technology & Engineering Center, BCGeTEC, Department of Chemical Engineering, Faculty of Engineering, Chulalongkorn University, Phayathai Road, Patumwan, Bangkok 10330, Thailand*

**E-mail: [a]Warawut.ko@hotmail.com, [b]joongjai.p@chula.ac.th*

Abstract:

Graphene quantum dots (GQDs) are carbon nanomaterials with excellent fluorescent properties resulting from quantum confinement effects. They also exhibit relatively high biocompatibility with living cells and low toxicity. [1] In this research, mung beans were grown by incorporating GQDs through three different methods. The first method involved soaking the mung bean seeds in GQDs for one night before planting. The second method included adding GQDs as a form of fertilizer. The third method combined the first and the second approaches. It was found that all the methods enhanced the antioxidant activity of mung bean plants compared to conventional cultivation without GQDs. On the other hand, the addition of GQDs decreased the growth of mung bean in term of the total height. The best condition to obtain the highest antioxidant activity is using GQDs as fertilizer (0.3 mg/mL, F0.3QD), in which it enhances the activity by 32.3% compared to the one growing under water.

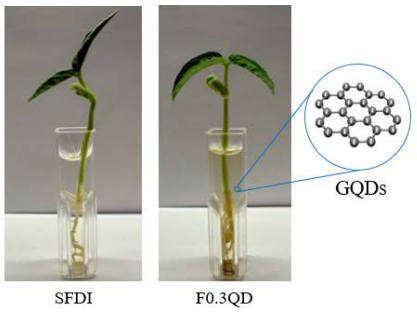

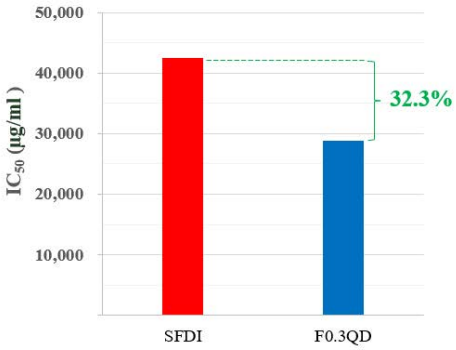

1. Introduction

Currently, we are in the era of nanotechnology, a period characterized by intense competition and high consumption of resources.[2] Mung bean themselves have become part of health foods due to their nutritional content, which includes protein, carbohydrates, and various biochemical components. Over the past decade, carbon-based nanomaterials have rapidly developed and played a significant role in human daily life.

Graphene was derived from graphite and was first discovered in 2003 by Dr. Andre Geim, Dr. Konstantin Novoselov, and their team at the University of Manchester.[3] They used scotch tape to extract graphene layers from graphite, resulting in a single layer hexagonal structure known as "graphene." Due to its unique honeycomb-like structure, graphene possesses remarkable properties such as high mechanical strength, excellent flexibility, thermal stability, and good electrical conductivity.[4]

In 2008, "graphene quantum dots" were developed using nanolithography techniques. These dots, which are about 30 nm thick and made from silicon coated with polymethylmethacrylate (PMMA), exhibit unique optical properties due to the quantum confinement effect.[5] They have shown compatibility with high-life forms and relatively low toxicity to lower life forms.[6] As a result, they have been applied in various fields, including fluorescence sensors, solar cells,[7] and biomedical applications.

Prior research has shown that graphene family nanomaterials (GFNs), such as graphite, graphene oxide, and amine-functionalized graphene oxide, can promote plant growth in crops like rice, wheat, tomatoes, garlic, and spinach. They particularly aid in seed germination and root development.[8]

In this research, mung beans were grown by incorporating GQDs through three different methods. The first method involved soaking the mung bean seeds in GQDs for one night before planting. The second method included adding GQDs as a form of fertilizer. The third method combined the first and the second approaches.

This study aims to track the absorption of GQDs into mung beans and their subsequent synthesis processes within the seeds. Mung beans are chosen as they are fast-growing leguminous plants, making them ideal for studying the phytotoxic impacts of GQDs. Additionally, the research explored the relationship between light synthesis processes in the beans and the antioxidant properties conferred by GQDs.

For this experiment, GQDs are prepared using a hydrothermal synthesis technique involving amino acid derivatives, a method known for producing high-quality GQDs with environmental friendliness in mind.

2. Materials and Methods

2.1 Chemicals

2,2-Diphenyl-1-picrylhydrazyl (DPPH) was procured from Sigma-Aldrich (Steinheim, Germany). L-ascorbic acid (Vitamin C) and methanol were obtained from Merck (Darmstadt, Germany). GQDs synthesized through the hydrothermal technique using amino acid-based precursors were prepared with deionized water (Bangkok, Thailand). All other reagents used were of analytical grade and obtained from usual suppliers.

2.2 Materials

A UV-Visible Spectrophotometer with Silicon Photodiode Detector (Jenway 6700, wavelength 320-1100 nm) with UV (quartz) semi-micro (1 mL) cuvette was employed for Antioxidant activity.

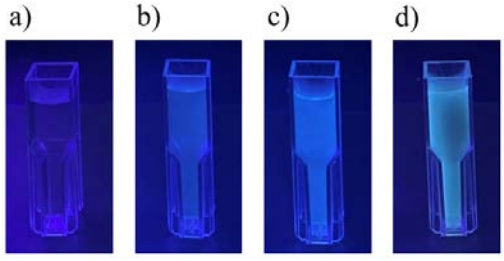

Figure 1. Photographs of DI water and GQDs under black light a) DI water, b) 0.01 mg/mL of GQDs, c) 0.05 mg/mL of GQDs d) 0.3 mg/mL of GQDs.

2.3 Stock standard solutions

Stock standard solution of L-ascorbic acid concentration 10 mg/mL was prepared by dissolving 10 mg of L-ascorbic acid in 1 mL of methanol solvent.

Table 1. Standard L-ascorbic acid concentrations were 1 5 10 15 20 25 50 and 100 µg/mL, respectively.

Concentration (µg/mL)	Stock of standard solution (µL) [a]	Methanol (µL) [b]
100	1,000	-
50	500	500
25	250	750
20	200	800
15	150	850
10	100	900
5	50	950
1	10	990

[a] L-ascorbic acid concentration 10 mg/mL
[b] Methanol solvent

2.4 Sample preparation

Weigh 160 mg of sample, then grind it thoroughly with a grinder and dissolve it with 4 mL of methanol solvent (to get a stock of sample solution concentration of 40 mg/mL or 40,000 µg/mL).

Table 2. Sample concentrations were 1,250 2,500 5,000 10,000 20,000 and 40,000 µg/mL, respectively.

Concentration (µg/mL)	Stock of sample solution (µL) [a]	Methanol (µL) [b]
40,000	1,500	-
20,000	750	750
10,000	375	1,125
5,000	188	1,312
2,500	94	1,406
1,250	47	1,453

[a] Stock of sample solution concentration 40 mg/mL
[b] Methanol solvent

2.5 Determination of antioxidant activity

The DPPH assay is another widely-used method to determine antioxidant properties. It employs the reagent 2,2-Diphenyl-1-picrylhydrazyl, which is convenient, quick, easy to analyze, and provides high accuracy and precision.

The initial step involves preparing a stock solution of DPPH at a concentration of 400 µM. From this stock, a working solution is prepared at a concentration of 200 µM. Following this, a calibration curve is constructed using L-ascorbic acid at concentrations of 1, 5, 10, 25, 50, and 100 µg/mL respectively (Figure 2.)

After obtaining the calibration curve, sample extracts are prepared by weighing the extract sample to achieve a concentration of 40 mg/mL Subsequently, sample solutions are prepared to have concentrations of 1,250 2,500 5,000 10,000 20,000 and 40,000 µg/mL

The testing procedure involves mixing the sample solutions with the DPPH working reagent in a 1:2 ratio (sample: DPPH). The mixture is then gently shaken and left in the dark for 30 minutes. After incubation, the absorbance is measured using a UV-vis spectrophotometer at 517 nm. The DPPH• scavenging activity was calculated based on the following equation:

$$\text{DPPH} \bullet \text{ scavenging activity (\%)} = \frac{(A_{control} - A_{sample})}{A_{control}} \times 100$$

were $A_{control}$ is the absorbance of DPPH• standard solution, and A_{sample} is the absorbance of the DPPH• solution incubated with mung bean sprouts extracts.[9]

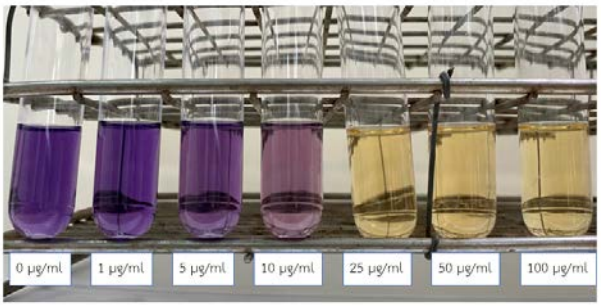

Figure 2. Discoloration of DPPH under the influence of L-ascorbic acid at difference concentration (0 – 100 µg/mL).

Table 3. Experimental conditions in this study

No.	Nomenclature	Soaking	Fertilizer
1	SFDI	DI water	DI water
2	S0.01QD	0.01 mg/mL GQDs	DI water
3	S0.05QD	0.05 mg/mL GQDs	DI water
4	S0.3QD	0.3 mg/mL GQDs	DI water
5	F0.01QD	DI water	0.01 mg/mL GQDs
6	F0.05QD	DI water	0.05 mg/mL GQDs
7	F0.3QD	DI water	0.3 mg/mL GQDs
8	SF0.01QD	0.01 mg/mL GQDs	0.01 mg/mL GQDs
9	SF0.05QD	0.05 mg/mL GQDs	0.05 mg/mL GQDs
10	SF0.3QD	0.3 mg/mL GQDs	0.3 mg/mL GQDs

S = Soaking, F = Fertilizer, QD = Graphene Quantum Dots

3. Results & Discussion

3.1 Effect of GQDs on plant growth

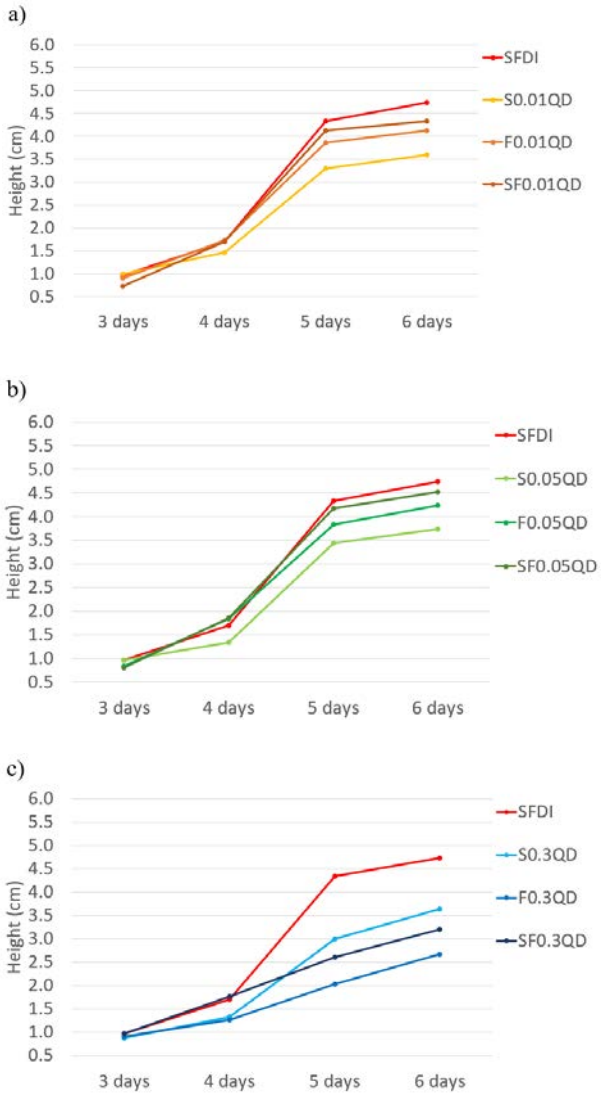

Figure 3. Growth in height of mung bean plants from day 3 to day 6 a) DI water compared to 0.01 mg/mL GQDs b) DI water compared to 0.05 mg/mL GQDs and c) DI water compared to 0.3 mg/mL GQDs.

When comparing among 10 testing conditions, it was found that in the SFDI, 0.01 mg/mL GQDs, and 0.05 mg/mL GQDs treatments, the mung bean plants exhibited good growth between days 4-6. However, for the 0.3 mg/mL GQDs treatment, it was observed that the growth rate of the mung bean plants was significantly lower (Figure 3).[10-13] The inhibition of plant growth could be attributed to the accumulation of GQDs around the root region in significant amounts, which hindered water absorption subsequently.[14]

3.2 Antioxidant activity of the mung beans

Figure 4. Comparison of IC_{50} of mung bean plants grown under water, 0.01 mg/mL GQDs, 0.05 mg/mL GQDs and 0.3 mg/mL GQDs.

From Figure 4, it was observed that treating mung bean plants with GQDs, whether by soaking the seeds or applying them as a fertilizer, resulted in plants with higher antioxidant properties compared to those grown using DI water. An increased in antioxidant activity of the mung beans with GQDs addition during plant growth is suggested to be due to GQDs enhancing the efficiency of electron transfer mechanisms in the photosynthesis process, specifically in the rates of photosystem I (PSI) and photosystem II (PSII). Additionally, GQDs themselves can also act as "electron donors" in this context.[15-16]

4. Conclusions

From the experimental results and previous research reviews [10, 11, 12, 13], it was evident that the amount of GQDs introduced to the mung bean plants directly influenced their growth. When treated with 0.3 mg/mL GQDs, the growth rate decreased due probably to blocking of water adsorption near roots. However, the introduction of 0.3 mg/mL GQDs led to enhanced antioxidant properties. The optimal condition to achieve the highest antioxidant activity is the use of GQDs as a fertilizer at a concentration of 0.3 mg/mL (F0.3QD). This condition enhanced the antioxidant activity by 32.3% compared to the one growing under water.

Acknowledgements

This research would have been impossible without the support of Chulalongkorn University, faculty of Engineering under CU Research Center of Excellence in Catalysis and Catalytic Reaction Engineering (CECC).

References

1. H.B. Wang, M.L. Zhang, Y. Song, H. Li, H. Huang, M.W. Shao, Y. Liu, Z.H. Kang, *"Carbon dots promote the growth and photosynthesis of mung bean sprouts"*, Carbon Volume 136, September, 2018; pp. 94-102
2. K.M. Ganesan, B.J. Xu, *"A critical review on phytochemical profile and health promoting effects of mung bean (Vigna radiata)"*, Food Science and Human Wellness, Volume 7, Issue 1, March 2018, pp. 11-33
3. K. S. Novoselov, A. K. Geim, S. V. Morozov, D. Jiang, Y. Zhang, S. V. Dubonos, I. V. Grigorieva, A. A. Firsov, *"Electric Field Effect in Atomically Thin Carbon Films"*, Nature Materials, 2004, pp. 666-669
4. M.C. Inagaki, F.Y. Kang, M.S.H.R. Toyoda, H.D.T.K. Konno, *"Chapter 3 - Graphene: Synthesis and Preparation"*, Advanced Materials Science and Engineering of Carbon, 2014, pp. 41-65
5. Zheng, X. T., Ananthanarayanan, A., Luo, K. Q., and Chen, P., *"Glowing graphene quantum dots and carbon dots: properties, syntheses, and biological applications."*, Small Volume 11, Issue 14, 2015, PP. 1620–1636
6. M.N. Gaur, C.R. Misra, A.W. Bihari Yadav, S. Swaroop, F. Maolmhuaidh, M.H. Bechelany and A.M. Barhoum, *"Biomedical Applications of Carbon Nanomaterials: Fullerenes, Quantum Dots, Nanotubes, Nanofibers, and Graphene"*, Materials 2021, 14, 5978
7. Sharma, V., and Jha, P. K., *"Enhancement in power conversion efficiency of edge-functionalized graphene quantum dot through adatoms for solar cell applications."*, Solar Energy Materials and Solar Cells 200, 2019, pp. 109908-109915
8. X. Zhang, H.F. Cao, H.Y. Wang, J.U. Zhao, K. Gao, J. Qiao, J.W. Li, and S. Ge, *"The Effects of Graphene-Family Nanomaterials on Plant Growth: A Review"*, Nanomaterials 12, 2022, pp. 936
9. Y. Tiana, A.N. Puganena, H.N.-L.N. Alakomib, A.L. Uusitupaa, M.R. Saarelab, B.R. Yang, *"Antioxidative and antibacterial activities of aqueous ethanol extracts of berries, leaves, and branches of berry plants"*, Food Research International 106, 2018; pp. 291–303
10. Begum, P., Ikhtiari, R., Fugetsu, B., *"Graphene phytotoxicity in the seedling stage of cabbage, tomato, red spinach, and lettuce."*, Carbon, 49, 2011; pp. 3907–3919
11. Anjum, N.A., Singh, N., Singh, M.K., Sayeed, I., Duarte, A.C., Pereira, E., Ahmad, I. *"Single bilayer graphene oxide sheet impacts and underlying potential mechanism assessment in*

germinating faba bean (Vicia faba L.).”, Sci. Total Environ.472, 2014; pp. 834–841

12. Chen, J., Yang, L., Li, S., Ding, W., *“Various physiological response to graphene oxide and amine-functionalized graphene oxide in wheat (Triticum aestivum).”*, Molecules, 23, 2018; pp. 1104
13. Li, F., Sun, C., Li, X., Yu, X., Luo, C., Shen, Y., Qu, S., *“The effect of graphene oxide on adventitious root formation and growth in apple.”*, Plant Physiol. Bioch., 129, 2018; pp. 122–129
14. W. Li, Y.J. Zheng, H.R. Zhang, Z.L. Liu, W. Su, S. Chen, Y.L. Liu, J.N. Zhuang, and B.F. Lei, *“Phytotoxicity, Uptake, and Translocation of Fluorescent Carbon Dots in Mung Bean Plants”*, ACS Appl. Mater. Interfaces 2016, 8; pp. 19939−19945
15. E.F. Kou, W. Li, H.R. Zhang, X. Yang, Y.Y. Kang, M.T. Zheng, S.N. Qu, and B.F. Lei, *“Nitrogen and Sulfur Co-doped Carbon Dots Enhance Drought Resistance in Tomato and Mung Beans”*, ACS Appl. Bio Mater. 2021, 4; pp. 6093−6102
16. Y.M.N. Chowmasundaram, T.L. Tan, R.S.M. Nulit, M.S.T. Jusoh and S.R.Y. Abdul Rashid, *“Recent developments, applications and challenges for carbon quantum dots as a photosynthesis enhancer in agriculture”*, RSC Adv., 2023, 13; pp. 25093–25117

One-pot synthesis of magnetic activated carbon by consecutive hydrothermal pretreatment and pyrolysis of cassava rhizome for methylene blue adsorption

Jenjira Phuriragpitikhon[1]*, Warinda Fuangchoonuch[1], Kittiya Pluamjai[2], and Laemthong Chuenchom[3]

[1]*Divison of Chemicals and Consumer Products, Department of science service, Ministry of Higher Education, Science, Research and Innovation, Bangkok, 10400, Thailand*

[2]*Division of Engineering Materials, Department of science service, Ministry of Higher Education, Science, Research and Innovation, Bangkok, 10400, Thailand*

[3]*Division of Physical Science, Faculty of Science, Prince of Songkla University, Songkla, 90112, Thailand*

**E-mail: Jenjira@dss.go.th*

Abstract:

Biomass derived magnetic activated carbons (MCs) have been widely studied as adsorbents to remove pollutants from water due to various carbon precursors, eco-friendly materials, variable textural properties, and magnetic separation capability. Conventional preparation methods of MCs involve multiple steps and the attachment of magnetic particles generated during the preparation process often leads to the pore clogging. Herein, MCs were prepared through one-step activation, magnetization, and pyrolysis process of hydrothermally treated cassava rhizome (CR). $ZnCl_2$ and $FeCl_3$ were added into the reaction mixture as the activator and the magnetizer, respectively. As-prepared CR-MC endows the highest S_{BET} (554 m^2/g) with 77% mesoporosity when addition of $FeCl_3$ into the mixture with the weight ratio of $FeCl_3$:$ZnCl_2$ of 1(CR-1MC). CR-1MC was tested as the adsorbent to investigate the adsorption efficiency of methylene blue (MB). The adsorption behavior of CR-1MC towards MB was monolayer adsorption based on Langmuir isotherm model with R^2 of 0.9953 exhibiting a maximum adsorption capacity of 102 mg/g. Moreover, CR-1MC with a saturation magnetization value of 3.34 emu/g could be easily separated from water by a magnet. The findings show that CR-MC can be successfully synthesized from biomass and simply functionalized the magnetic particles into the carbon enabling manipulations in industrial operations.

1. Introduction

Various dyes have been widely applied to textile, dyeing, printing, papermaking, and other industries. The discharge of dye wastewater into water bodies has caused severe public health issue and water pollution even at low concentrations[1]. The continuous attempts have been taken for the elimination of dye from water and reduction of the dye concentration to below the discharge threshold the limits. Therefore, it is needed to search for efficient, simple, eco-friendly ways to treat dye wastewater before releasing into public water. Currently, there are numerous methods employed to remove dyes from wastewater such as adsorption[2,3], advanced oxidation [4,5] and membrane filtration[6,7]. Among them, adsorption is generally considered as a simple, effective, low cost and environmental-friendly technique for water treatment[8,9].

Activated carbons (ACs) are the most widely used adsorbents for wastewater treatment due to large surface area, high pore volume, tunable pore structure and a rich in the surface functional groups[10-11]. In addition, ACs can be produced from various carbon precursors such as carbon containing polymers and agricultural wastes. The latter type of precursors is intriguing because of natural abundance, low-cost materials, renewability and environmental friendliness. So far, a board range of biomass materials such as corn stalk, saw dust, coconut shell and poultry litter have been successfully used as alternative carbon precursors for the preparation of ACs [12-15]. However, it is challenging to recover ACs from water stream upon the treatment. The traditional separation technique is filtration. By this way, the filter blockage and loss of ACs are major drawbacks deterring its economic feasibility. While, centrifugation is less practical due to high energy consumption led to incurring high operational and maintenance costs[16].

Magnetic ACs have substantial functions using as efficient adsorbents for water treatment. It is not only attributed to good adsorption properties but also making its recovery more rapid and easier. In recent years, magnetic ACs have been extensively studied for the removal of contaminants from water[17-18]. The conventional preparation method of magnetic ACs often involves multiple steps; namely, the carbon precursor is first converted to ACs by the activation process. Then, magnetic particles are introduced into ACs either via co-precipitation or

impregnation at high temperature[19]. By this way, magnetic particles formed during the process that usually leads to the pore clogging in ACs, resulting in poor adsorption performance[18,20].

In this work, one-pot synthesis method of biomass derived magnetic ACs has been proposed; namely, the activation, magnetization, and pyrolysis of the hydrothermally treated cassava rhizome (CR) were combined into one- step. $ZnCl_2$ and $FeCl_3$ were directly added into the reaction mixture as the in-situ activating agent and magnetizer during the hydrothermal treatment of CR. The resulting magnetic ACs prepared from CR (CR-MC) were applied as adsorbents to remove methylene blue (MB), which is toxic and carcinogenic compound, from aqueous solutions. The adsorption performance of CR-MC on MB was studied using batch-adsorption techniques.

2. Materials and Methods

2.1 Materials

Cassava rhizome (CR) obtained from Sapthip Co., Ltd., was used as the carbon precursor. Methylene blue hydrate (≥95%, calc. to the dried substance), ferric chloride hexahydrate (ACS grade) and zinc chloride (Reagent grade, ≥98%) were purchased from Sigma Aldrich. Hydrochloric acid fuming 37% (ACS grade) was acquired from Merck. N_2 gas (HP, ≥ 99.99 %) was supplied by Linde (Thailand) Public Company Limited. Deionized water (DI water) was used in all experiments.

2.2 Synthesis of magnetic activated carbons from CR (CR-MC)

Crude cassava rhizome (CR) was thoroughly rinse off impurities with distilled water, and then dried at 105 °C for 48 h in an oven. The dried CR was cut into finer pieces by cutting mill machine. In this study, CR was first pretreated by the hydrothermal treatment in the presence of $ZnCl_2$ and $FeCl_3$ as the activating agent and magnetizer respectively. Then the obtained pretreated CRs were subjected to one-step activation, magnetization and pyrolysis process; namely, 5 g of CR, 15 g of $ZnCl_2$ and varying amounts of $FeCl_3$ (15 g, 30 g, and 45 g) were added into 50 mL of DI water. The resulting mixture was stirred for 2 h at room temperature and then sealed in Teflon-lined autoclaves and hold 24 h at 150 °C under a static condition. After that, the solid product was separated from the mixture, washed several times with DI water and heated in an oven at 80 °C for drying, followed by the pyrolysis of resulting products under flowing nitrogen at 350 °C at a rate of 1°C /min for 1 h and subsequent heating to 800 °C at a rate of 5 °C /min for 1 h. The resulting samples was washed with 0.1 N of HCl until neutral pH and dried in an oven at 70 ∘C. The final magnetic ACs were designated as “CR-xMC”, where “x” refers to the weight ratio of $FeCl_3$ to $ZnCl_2$ in the synthesis mixture. For example, x = 1, 2 and 3 refer to 15 g, 30 g and 45 g of $FeCl_3$ added, respectively.

For the purpose of comparison, one magnetic AC sample was prepared by the conventional impregnation-pyrolysis method. The resultant material was labelled as nCR-xMC, where “x” indicates the weight ratio of $FeCl_3$ to $ZnCl_2$ in the synthesis mixture of the selected condition. The designation and formulation of as -prepared CR-MCs are summarized in Table 1.

Table 1. Formulation of as- prepared samples

No.	Sample	Preparation method	$FeCl_3$ to $ZnCl_2$ weight ratio[a]
1	CR-1MC	The proposed preparation method	1
2	CR-2MC		2
3	CR-3MC		3
4	nCR-1MC	The conventional method	1

[a]All carbon samples were prepared from 5 g of CR as a carbon precursor and 15 g of $ZnCl_2$ as the activating agent.

2.3 Characterization

Nitrogen adsorption–desorption isotherms were carried out at -196 °C on ASAP2460 volumetric analyzers (Micromeritics, Inc., Norcross, GA). All samples were degassed under vacuum for 15 h at 200°C prior to the adsorption measurements to remove adsorbed moisture and other contaminants. X-ray diffraction (XRD) analysis was performed on Bruker D8 Advance X-Ray diffractometer with a Cu anode operated at voltage and current of 40 kV and 40 mA, respectively. The scanning was conducted in a continuous mode with a step size of 0.020°. Scanning electron microscopy - Energy dispersive spectroscopy (SEM-EDS) analysis was conducted on a JEOL JSM-6610 LV operated at 20 kV of accelerating voltage to investigate the surface morphology and the surface elemental composition of the samples. The measurement of absorbance of all solution was performed on Shimadzu UV-2700 Spectrophotometer with a wavelength of 664 nm for methylene blue (MB). The magnetic property of as-prepared adsorbents was observed by vibrating sample magnetometer (VSM), Lakeshore Model 7404.

2.4 Batch adsorption experiments

In this work, methylene blue (MB) was chosen as a target contaminant to investigate the

adsorption performance of as-prepared adsorbents. The adsorption experiments were carried out by adding 0.07 g of the CR-MC in 250 mL of different concentrations of MB solutions (20, 50, 100, 150 and 200 mg/L) in 500 mL Erlenmeyer flasks. The mixture was shaken with a speed of 250 rpm at 298 K to reach equilibrium without any pH adjustment. At certain time intervals, the aqueous solution was taken out, followed by centrifugation.

The residue concentration of MB in the left supernatant solution was immediately determined using UV-Vis spectrophotometer to monitor the absorbance changes at wavelength of 664 nm. The adsorption study was conducted twice to check the reproducibility of the results[21]. The reported values are the means of duplicate experimental results. The amount of adsorbed MB on carbon adsorbents at equilibrium (qe, mg/g) was calculated according to Eq. (1):

$$q_e = \frac{(C_0 - C_e)}{m} \times V \qquad (1)$$

Where C_0(mg/L) and C_e(mg/L) were the initial and equilibrium concentrations of MB, respectively; V(L) stands for the total volume of MB solution; m(g) is the mass of adsorbent.

Two common isotherms equations including Langmuir and Freundlich isotherm models were adapted to the experimental data to understand the adsorption behaviors. The appropriate isotherms were determined by means of the following Eq. (2) and (3):
Langmuir isotherm:

$$\frac{C_e}{q_e} = \frac{1}{q_m K_L} + \frac{C_e}{q_m} \qquad (2)$$

where K_L is Langmuir constant and q_m is the maximum adsorption capacity of the adsorbent.
Freundlich isotherm:

$$\log q_e = \log K_f + \frac{1}{n_F} \log C_e \qquad (3)$$

where K_f is Freundlich constant and n_F is the constant presenting the adsorption intensity.

3. Results & Discussion

3.1 Characterization of CR-MCs

The characteristics of CR-MC were discussed based on textural properties, SEM-EDS analysis and XRD measurement.

The nitrogen adsorption-desorption isotherms and textural parameters of the obtained CR- MC are presented in Figure 1 and Table 2. As presented in Figure 1a, all nitrogen adsorption-desorption isotherms display type IV with hysteresis loops according to IUPAC classification indicating the existence of mesopores in all CR-MCs. This observation can be clearly confirmed by the presence of visible peaks on the pore size distribution (PSDs) curve in the range of mesopores (2-50 nm) for all samples as seen in Figure 1b. Besides, all CR-MCs also possess micropores as seen in Table 2. The values of S_{BET} of magnetic ACs range from 409 to 554 m^2/g, V_t values range from 0.51 to 0.62 cm^3/g, V_{mi} and V_{me} values range from 0.09 to 0.14 cm^3/g and 0.41 to 0.51 cm^3/g, respectively.

nCR-1MC herein has a lower S_{BET} (409 m^2/g) than all CR-MC prepared by the proposed synthesis method (440 – 554 m^2/g). It may be due to the pore clogging by the magnetic particles formed during the traditional synthesis method leading to reducing in specific surface area of carbon samples [16,22]. This finding indicates that the combining pyrolysis, activation, and magnetization of hydrothermally treated carbon precursors into one-step could overcome the limitation of the conventional preparation method. This may be because the hydrothermal pretreatment of CR before its conversion into CR-MC not only improves the access of the activators and magnetizers to the precursor structure, but also facilitates the full contact of the precursors with these agents resulting in a greater increase in pore generation and surface areas as reported by Wang and coworkers[23]. This fact can be confirmed by larger values of V_t and S_{BET} of all CR-MCs in comparison with those of nCR-MC. Moreover, the acquired textural properties reveal that the combining activation, magnetization and pyrolysis of hydrothermally treated CR into one-step allows for the preservation of the mesoporous structure of CR-MCs (V_{me}: 77 - 84% of V_t) the same as that obtained from the traditional preparation method. In addition, when the weight ratio of $FeCl_3$ to $ZnCl_2$ increased from 1 to 3, a reduction of S_{BET} and V_t values of CR-MC was observed as seen in Table 2. These findings may be possibly explained by several mechanisms including an excessive amount of $FeCl_3$ can intensely catalyze the activation reaction leading to pore merging.

It was found that higher amounts of $FeCl_3$ can result in bigger particles of iron oxide consequently acting as a mesopore template [24]. Herein, CR-1MC was selected for the further dye adsorption studies due to the relatively high values of S_{BET} and V_{mi} in addition to the presence of mesoporous structure which are important structural parameters for dye.

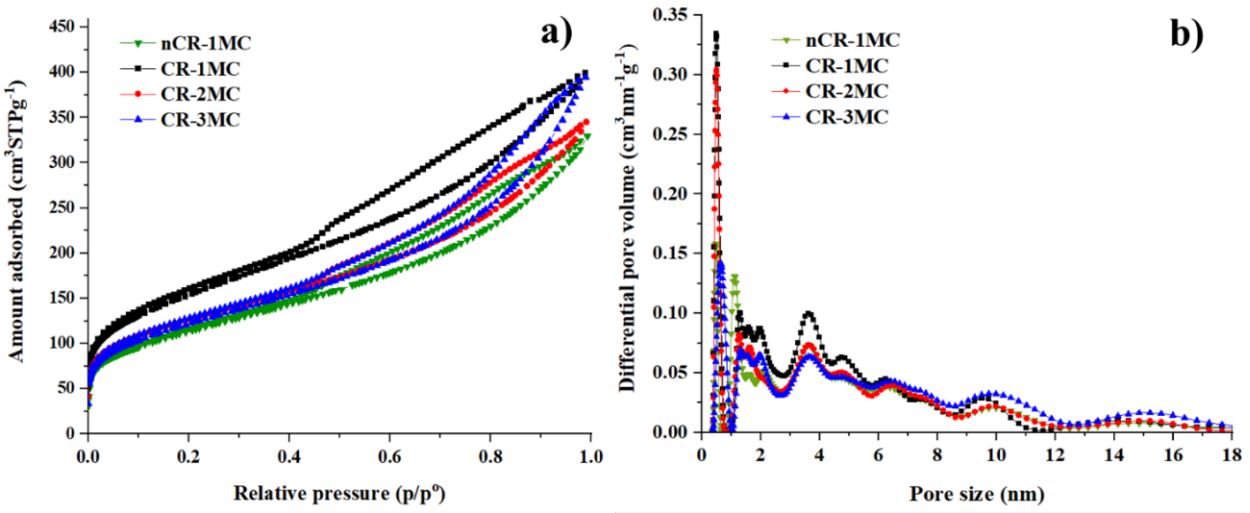

Figure 1. (a) Nitrogen adsorption isotherms for nCR-1MC, CR-1MC, CR-2MC and CR-3MC and (b) their differential pore size distributions (PSDs) up to 18 nm calculated using the 2D-NLDFT method

Table 2. Adsorption parameters for all carbon samples[b]

Sample	S_{BET} (m^2/g)	V_t (cm^3/g)	V_{mi} (cm^3/g)	V_{me} (cm^3/g)	Mesoporosity (%)
nCR-1MC	409	0.51	0.09	0.42	82
CR-1MC	554	0.62	0.14	0.48	77
CR-2MC	454	0.53	0.12	0.41	77
CR-3MC	440	0.61	0.10	0.51	84

[b] Notation: S_{BET} = specific surface area; V_t = total pore volume; V_{mi} were obtained from the cumulative pore volume calculated using the 2D-NLDFT method for pores smaller than 2 nm; and V_{me} represents the volume of mesopores (pore size between 2 and 50 nm) calculated by V_t - V_{mi}; mesoporosity – percentage of the volume of mesopores in the total pore volume.

The surface morphologies and its elemental compositions of CR-1MC was examined by SEM-EDS. As shown in Figure 2, the SEM image of CR-1MC shows the random distribution of small particles on the carbon surface. Those tiny particles probably are iron oxides formed during the preparation process.

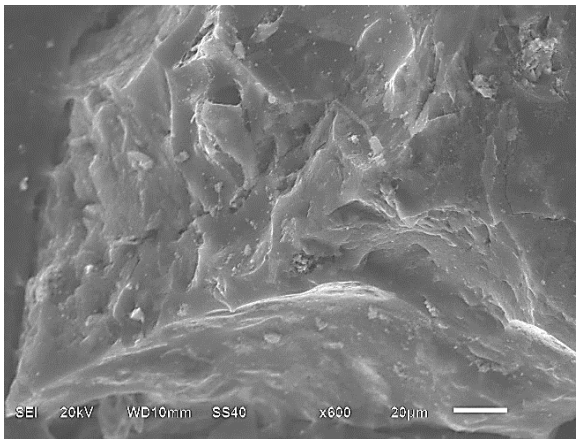

Figure 2. SEM image of CR-1MC (x600)

This observation is consistent with the EDS result presented in Figure 3. It shows that 9.79% of Fe was found on the carbon surface of CR-1MC. While, the presence of Zn and Cl in CR-1MC was attributed to the use of $ZnCl_2$ as the activator and the peaks of Al, S and K found in the EDS spectrums may be directly from CR precursor.

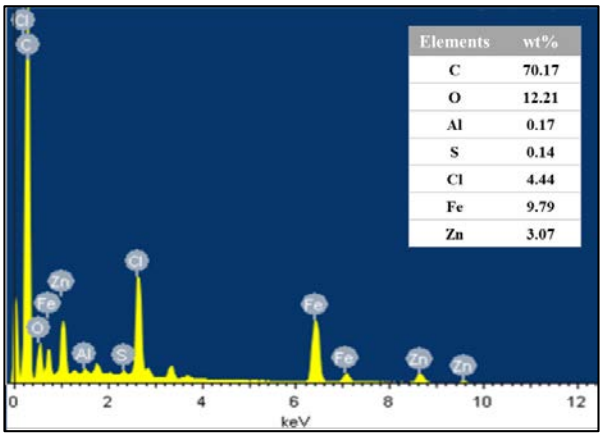

Figure 3. The EDS spectrum lines of CR-1MC

The successful incorporation of magnetic particles into the carbon structure of CR-1MC was clearly proved by the XRD analysis. As seen in Figure 4, the XRD spectrum of CR-1MC shows four peaks at 2θ = 35.1°, 42.6°, 56.3° and 62.5° corresponding to the (311), (400), (511), and (440) reflections, respectively which are the characteristic peaks for magnetite particles (Fe_3O_4). This finding presents a successful

conversion of Fe salt into iron oxide by one-step activation, magnetization, and pyrolysis of hydrothermally treated CR. However, the characteristic peaks for AC were not obvious for the XRD pattern of CR-1MC due to the influence of Fe_3O_4 with a high absorption peak and a high crystallinity[25]

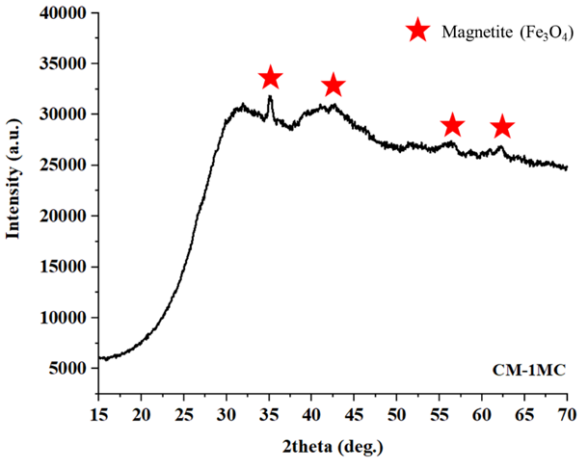

Figure 4. XRD spectrum of CR-1MC

3.2 Adsorption experiment

3.2.1 Effect of contact time

The contact time between adsorbent and adsorbate is an essential parameter for the assessment of adsorption ability in the adsorption process[26]. The effect of contact time on the MB adsorption process by CR-1MC is provided in Figure 5. The amount of the adsorbed MB was calculated at the initial concentration of 100 ppm MB solution (pH 8, without any pH adjustment).

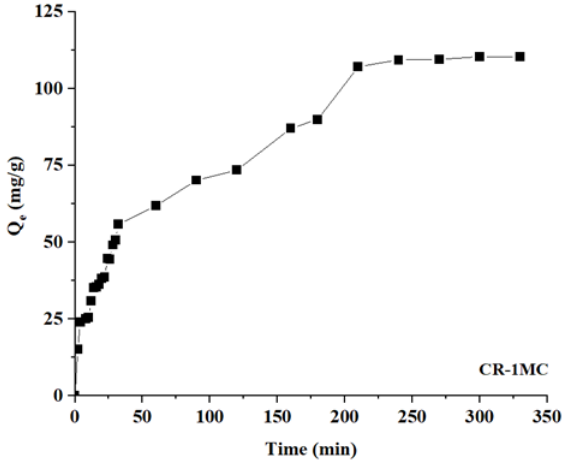

Figure 5. Adsorption of MB onto CR-1MC at different time (The experimental conditions: initial concentration 100 mg/L, temperature 25 °C, the solution pH 8 and adsorbent dosage 0.07 g, 250 rpm)

The adsorption experiment was approximately carried out for 6 h to determine the equilibrium time of adsorption. As seen in Figure 5, the amount of the adsorbed MB onto CR-1MC quickly increased with the contact time in the first 35 min and it reached equilibrium in 240 min. The fast initial adsorption of dye molecules is because many vacant sites on the surface were available for adsorption at the initial stage. Subsequently, the rate of adsorption slowly increased due to the accumulation of dye molecules in the vacant sites and their diffusion into the pores of adsorbent [27,28].

Interestingly, the time required for CR-1MC to reach adsorption equilibrium (240 min) was shorter than that of the commercial AC (Com-PAC, 270 min) reported in our previous work, although the S_{BET} value of CR-1MC is significantly smaller than that of Com-PAC[29]. It may be explained by the fact that a much higher fraction of mesopores in CR-1MC ($\%V_{me}$=77) than that of Com-PAC ($\%V_{me}$=8) facilitates the diffusion rate of MB from the external surface to porous structure in carbon materials.

3.2.2 Adsorption isotherm study

To acquire a better understanding of the adsorption behavior of CR-1MC towards MB, two adsorption nonlinear isotherm models were used to investigate the equilibrium adsorption behavior including Langmuir and Freundlich adsorption models as shown in Figure 6a and 6b, respectively. With respect to correlation coefficients (R^2) as presented in Table 3, it indicates that the isothermal data of CR-1MC was better fit the Langmuir model with R^2 of 0.9953. Based on this result, the adsorption behavior of MB on CR-1MC was monolayer adsorption. The maximum monolayer adsorption capacity (q_m) calculated according to the Langmuir adsorption model of CR-1MC is 102 mg/g.

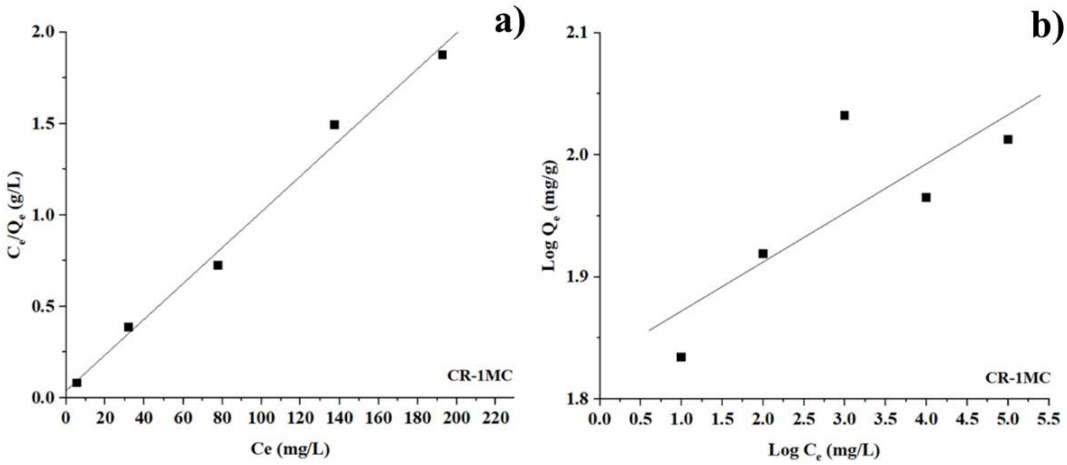

Figure 6. The linear regression by fitting the equilibrium adsorption data with (a) the Langmuir adsorption isotherm model and (b) Freundlich adsorption isotherm model of MB adsorption on CR-1MC

Table 3. Adsorption isotherm parameters and correlation coefficients of MB onto CR-1MC

Isotherms	Parameter	CR-1MC
Langmuir	K_L (L/mg)	0.247
	q_m (mg/g)	102
	R^2	0.9953
Freundlich	K_F (mg/g)	56.92
	1/n	0.1152
	R^2	0.8948

3.3 Magnetic Features

The magnetic hysteresis curve evaluated by the vibrating sample magnetometer (VSM) at room temperature and magnetic behavior of CR-1MC are presented in Figure 7 and 8, respectively. According to the results, CR-1MC possessed the saturation magnetization of 3.34 emu/g which is consistent with the existence of magnetite particles in materials. As illustrated in Figure 8, CR-1MC was easily attracted by an external magnet after MB adsorption which would be beneficial for removal of pollutants and recovery of adsorbents by magnets.

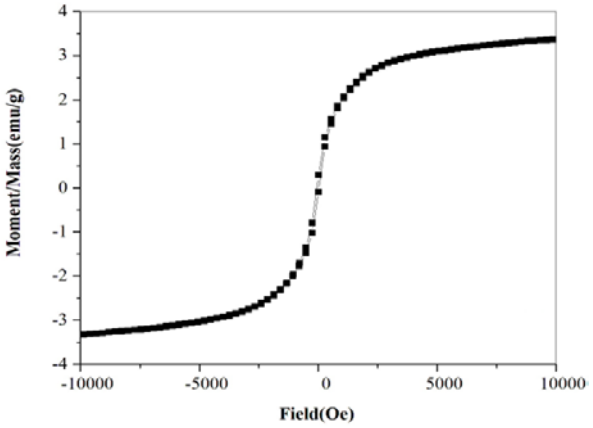

Figure 7. Magnetization curves of CR-1MC obtained by VSM at room temperature

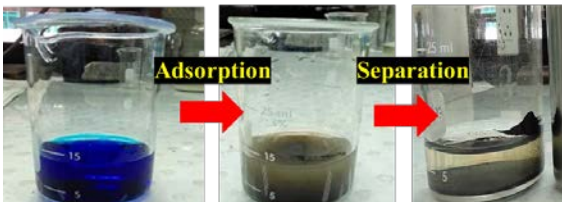

Figure 8. MB adsorption and the magnetic separation of CR-1MC by a magnet

4. Conclusion

Biomass derived magnetic carbon adsorbents were successfully prepared by one-step activation, magnetization, and pyrolysis of the hydrothermally treated cassava rhizome (CR) using $ZnCl_2$ and $FeCl_3$ as the activator and the magnetizer, respectively. As-synthesized CR-MC endows the highest S_{BET} (554 m^2/g) with 77% mesoporosity when addition of $FeCl_3$ into the reaction mixture with the weight ratio of $FeCl_3$:$ZnCl_2$ of 1(CR-1MC). CR-1MC was tested as the adsorbent to study the adsorption efficiency of MB dye in water. CR-1MC can adsorb MB from aqueous solution with adsorption capacity of 102 mg/g. In addition, such a magnetic ACs possesses a saturation magnetization value of 3.343 emu/g that can be attracted by magnets. The carbon adsorbents with magnetic property would be beneficial for removal of pollutants from the treatment media and adsorbent reusability. The results demonstrated that CR-MC can be regarded as the potential adsorbent for the removal of dyes in the future.

Acknowledgements

This work was financially supported by division of chemicals and consumer products, department of science service, Ministry of Higher Education Science, Research, and Innovation.

References

1. Dutta, S.; Gupta, B.; Srivastava, S. K.; Gupta, A. K., *Mater. Adv.* **2021,** *2* (14), 4497-4531.
2. Hambisa, A. A.; Regasa, M. B.; Ejigu, H. G.; Senbeto, C. B., *Appl. Water Sci.* **2022**, *13* (1), 24.
3. Wong, S.; Ghafar, N. A.; Ngadi, N.; Razmi, F. A.; Inuwa, I. M.; Mat, R.; Amin, N. A. S., *Sci. Rep.* **2020,** *10* (1), 2928.
4. Ledakowicz, S.; Paździor, K., *Molecules* **2021,** *26* (4), 870.
5. Hassaan, M. A.; El Nemr, A.; Madkour, F. F., *Egypt. J. Aquat. Res.* **2017**, *43* (1), 11-19.
6. Marszałek, J.; Żyłła, R., *Processes* **2021**, *9* (10), 1833.
7. Karisma, D.; Febrianto, G.; Mangindaan, D., *IOP Conference Series: Earth Environ. Sci* **2017**, *109* (1), 012012.
8. Singh, N. B.; Nagpal, G.; Agrawal, S.; Rachna, *Environ. Technol. Innov.* **2018,** *11*, 187-240.
9. Busetty, S., In *Handbook of Environmental Materials Management*, Hussain, C. M., Ed. Springer International Publishing: Cham, 2019; pp 1367-1397.
10. Kumar, N.; Pandey, A.; Rosy; Sharma, Y. C., *J. Water Proc. engineering.* **2023**, *54*, 104054.
11. Reljic, S.; Cuadrado-Collados, C.; Oliveira Jardim, E.; Farrando-Perez, J.; Martinez-Escandell, M.; Silvestre-Albero, J., *Fluid Phase Equilib.* **2022,** *558*, 113446.
12. Kang, C.; Shang, D.; Yang, T.; Zhu, L.; Liu, F.; Wang, N.; Tian, T., *Chem. Res. Chin. Univ.* **2018,** *34* (6), 1014-1019.
13. Pan, H.; Zhao, J.; Lin, Q.; Cao, J.; Liu, F.; Zheng, B., *Energy Fuel* **2016,** *30* (12), 10730-10738.
14. Sujiono, E. H.; Zabrian, D.; Zurnansyah; Mulyati; Zharvan, V.; Samnur; Humairah, N. A., *Results Chem.* **2022,** *4*, 100291.
15. Pontiroli, D.; Scaravonati, S.; Magnani, G.; Fornasini, L.; Bersani, D.; Bertoni, G.; Milanese, C.; Girella, A.; Ridi, F.; Verucchi, R.; Mantovani, L.; Malcevschi, A.; Riccò, M., *Microporous Mesoporous Mater.* **2019,** *285*, 161-169.
16. Lee, L. Z.; Ahmad Zaini, M. A., *Toxin Rev.* **2022,** *41* (1), 64-81.
17. Mehta, D.; Mazumdar, S.; Singh, S. K., *J. Water Proc.engineering* **2015**, *7*, 244-265.
18. Moosavi, S.; Lai, C. W.; Gan, S.; Zamiri, G.; Akbarzadeh Pivehzhani, O.; Johan, M. R., *ACS Omega* **2020,** *5* (33), 20684-20697.
19. Thue, P. S.; Umpierres, C. S.; Lima, E. C.; Lima, D. R.; Machado, F. M.; dos Reis, G. S.; da Silva, R. S.; Pavan, F. A.; Tran, H. N., *J. Hazard. Mater.* **2020**, *398*, 122903.
20. Phouthavong, V.; Yan, R.; Nijpanich, S.; Hagio, T.; Ichino, R.; Kong, L.; Li, L., *Materials* **2022**, *15* (3), 1053.
21. Phuriragpitikhon, J.; Ghimire, P.; Jaroniec, M., *J. Colloid Interface Sci.* **2020,** *558*, 55-67.
22. Anyika, C.; Asri, N. A. M.; Majid, Z. A.; Yahya, A.; Jaafar, J., *Nanotechnol. Environ. Eng.* **2017**, *2* (1), 16.
23. Wang, B.; Zhai, Y.; Wang, T.; Li, S.; Peng, C.; Wang, Z.; Li, C.; Xu, B., *Bioresour. Technol.* **2019**, *274*, 525-532.
24. Bedia, J.; Peñas-Garzón, M.; Gómez-Avilés, A.; Rodriguez, J. J.; Belver, C., *C* **2020**, *6* (2), 21.
25. Chen, C.; Mi, S.; Lao, D.; Shi, P.; Tong, Z.; Li, Z.; Hu, H., *RSC Adv.* **2019**, *9* (39), 22248-22262.
26. Ouachtak, H.; El Guerdaoui, A.; El Haouti, R.; Haounati, R.; Ighnih, H.; Toubi, Y.; Alakhras, F.; Rehman, R.; Hafid, N.; Addi, A. A.; Taha, M. L., *RSC Adv.* **2023**, *13* (8), 5027-5044.
27. Adeyemo, A. A.; Adeoye, I. O.; Bello, O. S., *Appl. Water Sci.* **2017**, *7* (2), 543-568.
28. Salunkhe, B.; Schuman, T. P., *Macromol* **2021,** *1* (4), 256-275.
29. Phuriragpitikhon, J.; Pluamjai, K.; Fuangchoonuch, W.; Chuenchom, L., *bull appl sc.i* **2022**, *11*, 45-56.

Synthesis and characterization of cellulose aerogel composite from pineapple leaves and polyvinyl alcohol

Arisa Jaiyu*, Julaluk Phunnoi, Passakorn Sueprasit, and Niphaporn Yawongsa

Expert Centre of Innovative Materials, Thailand Institute of Scientific and Technological Research, Khlong Luang, Pathum Thani, 12120, Thailand

**E-mail: arisa@tistr.or.th*

Abstract:

There are massive amounts of agricultural waste from discarded pineapple leaves after pineapple harvesting, which can cause environmental problems. To maximize agricultural waste utilization, pineapple leaves were used to synthesize the cellulose aerogel composite in this study. First, dry pineapple leaves were pretreated and bleached to obtain the pineapple leaf fiber (PF) and enrich the cellulose content. From the determination of the composition of PF, it was found that the cellulose content rose to 88%. Polyvinyl alcohol was used as a binder and cross-linker to synthesize the cellulose aerogel composite from PF via the freeze-dry method. The surface area and average pore diameter of the synthesized aerogels were characterized by nitrogen adsorption-desorption (BET) analysis. The density, thermal properties, morphologies, and chemical structure of the cellulose aerogels were investigated. The BET surface areas were between 188-207 m^2g^{-1} with an average pore diameter of 4.4-9.4 nm. The cellulose aerogels have low density and thermal conductivity of 0.03-0.04 $g.cm^{-3}$ and 0.056-0.067 $Wm^{-1}K^{-1}$. The cellulose aerogel composites from PF can be further developed as a good candidate for thermal insulation due to their low thermal conductivity.

1. Introduction

Pineapple is a highly popular crop in Thailand's economy, largely due to its resilience to environmental conditions. The country dedicates around 500,000 acres to pineapple cultivation, with an estimated production exceeding 1.96 million tons in 2023. Most of this output is used for consumption and processing into canned goods. In each production cycle, pineapple fields generate significant by-products, including discarded leaves and stems totaling between 8,000 to 10,000 kilograms per acre or approximately 4 million tons in total.[1-3] Unfortunately, a substantial portion of this waste is not put to beneficial use and is often disposed of through burning, contributing to air pollution issues. The burning of pineapple waste presents environmental challenges, particularly in the release of carbon dioxide, a major contributor to the greenhouse gas effect, leading to greenhouse gas emissions and particulate matter (PM 2.5) pollution.[4-7] These issues have become significant concerns in contemporary times. In response to these challenges, the strategic development of products to augment the value of pineapple waste emerges as a sustainable and enduring solution to address the ongoing issue.

Cellulose aerogels derived from natural sources have gained attention as prospective candidates for a broad spectrum of applications, owing to their lightweight nature, high surface area, and impressive mechanical properties.[8-14] The pineapple leaves, discarded after harvest, are of particular interest due to their elevated cellulose content. The abundant cellulose in pineapple leaves holds promise as a valuable resource for extracting cellulose, with the ultimate objective of synthesizing aerogels.[15-16]

Polyvinyl alcohol (PVA) was chosen to be used as a binder and cross-linker in the synthesis process of cellulose aerogels because it is a low-cost, environmentally friendly polymer known for its non-toxic and biodegradable properties.[17]

In this paper, the cellulose aerogel composites from PF and PVA were successfully synthesized via freeze-dry method. The effect of content of PVA used as binder and cross-linker on the aerogel properties were also studied. The density, porosity, average pore size, surface area, morphology, thermal stability, and thermal conductivity were investigated. The cellulose aerogel composites from PF can be further developed as a potential candidate for thermal insulation.

2. Materials and Methods

2.1 Materials

Pineapple leaves were obtained from commercial market. Polyvinyl alcohol (PVA) with a molecular weight of 86,000 was purchased from Sigma-Aldrich. Sodium hydroxide (NaOH) was supplied from KEAMUS, while hydrogen peroxide (H_2O_2) solutions were provided by Q RëC™. All chemicals were used without further purification.

2.2 Preparation of PF

The 50 grams of dried pineapple leaves were boiled in a 10% NaOH solution by weight, maintaining a weight-to-volume ratio of pineapple leaves to the solution at 1:10. The process was conducted at a constant temperature of 80 degrees Celsius for a duration of 3 hours. Subsequently, the extracted fibers were thoroughly rinsed with water until all traces of alkali were removed. The fibers were then dried at 60 degrees Celsius for 24 hours.

A 3-gram sample of the dried pineapple fiber obtained from the extraction process was utilized. The sample was immersed in a NaOH solution with a pH of 11, maintaining a weight-to-volume ratio of pineapple fiber to the solution at 1:10. The process was carried out at a constant temperature of 80 degrees Celsius with continuous stirring for even dispersion. Hydrogen peroxide with a concentration of 35%, equivalent to 5% by weight of the sample, was introduced. The mixture was allowed to stand for 3 hours. Subsequently, the bleached fibers were thoroughly rinsed with clean water until all discoloration was eliminated. The fibers were then dried at 60 degrees Celsius for 24 hours.

2.3 Synthesis of cellulose aerogel composites

The synthesis process of cellulose aerogel composites is depicted in Figure 1, while the composition of the aerogel composites is presented in Table 1. Initially, PVA is dissolved in 100 mL of water, and the solution is heated until complete dissolution. Subsequently, finely ground pineapple fibers, reduced in size, are introduced into the resulting solution. The mixture undergoes ultrasonic homogenization for a duration of 5 minutes. Following this, the mixture is placed in an oven at 80 degrees Celsius for 2 hours, facilitating the establishment of cross-linkages between the polyvinyl alcohol and hydroxy groups on the surface of the pineapple fibers.

After the thermal treatment, the sample is cooled and solidified at approximately -4 degrees Celsius for a period of 24 hours, enabling the formation of a gel network. After gelation, the sample undergoes freeze-drying for 50 hours at approximately -50 degrees Celsius while maintaining a pressure of 0.1 bar.

2.4 Characterization of PF and cellulose aerogel composites

Alfa-cellulose content in PF was tested following TAPPI I 203 cm-09. The chemical structure of PF, PVA, all cellulose composite aerogels were characterized by FTIR analysis using IRPrestige-21, Shimadzu in ATR mode. All samples were analyzed in the range of 750-4000 cm^{-1}, 45 scans and a resolution of 4 cm^{-1}. BET surface area, and average pore size of the aerogel composites were analyzed using a multipoint Brunauer-Emmett-Teller (BET) surface analyzer (Quantachrome autosorb iQ Station 1). The thermal stability of the samples was determined by thermogravimetric analysis (TGA) using STA 449 F3 Jupiter, Netzsch at temperature range of room temperature to 600°C. The heating rate was 10°C/min under nitrogen purge with a rate of 50 mL/min. The morphology of the core of aerogel composites were characterized by a Scanning Electron Microscope (SEM; Thermo Scientific model Prisma E). The density of the samples was calculated based on their mass to volume ratio.

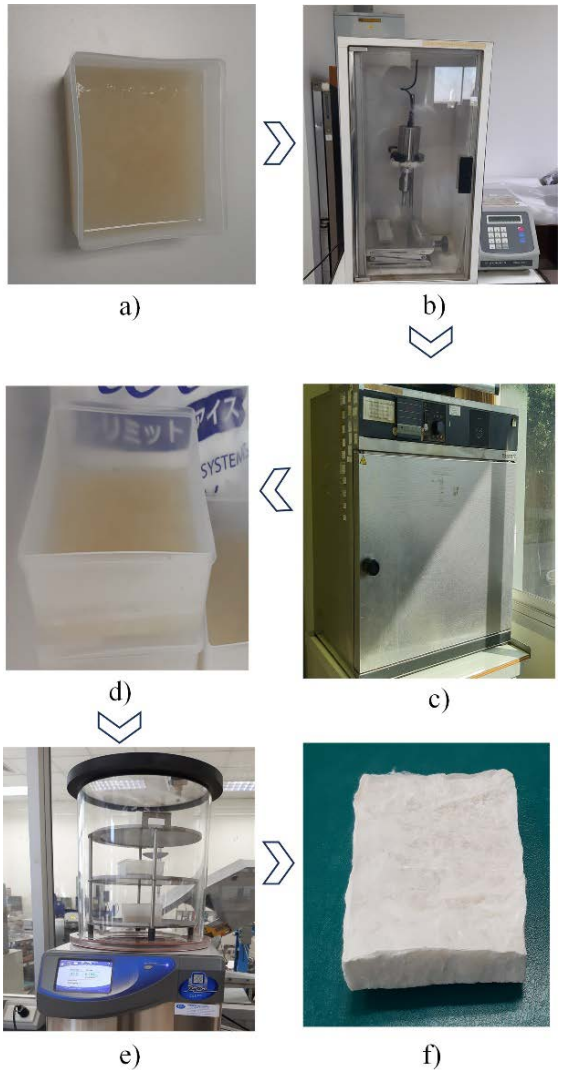

Figure 1. The synthesis process of cellulose aerogel composites a) PF and PVA Mix b) Ultrasonic homogenizer c) Oven d) Chill to solidification e) Freeze-drying f) cellulose aerogel composite

Porosity of the aerogel composites were calculated according to the eq $(1 - \rho^*/\rho) \times 100\%$, where ρ^* was the density of the aerogel composites and ρ was theoretical density of cellulose.[9,18] The thermal conductivity was measured using the hot disk thermal constant analysis (Hot Disk AB) with thermal constant analysis technique.

Table 1. Composition of cellulose aerogel composites

Code	Composition (% weight)	
	PF	PVA
PF_PVA0.5	2	0.5
PF_PVA1.0	2	1
PF_PVA1.5	2	1.5

3. Results & Discussion

After the extraction of fibers from pineapple leaves and the successive bleaching procedure employing sodium hydroxide and hydrogen peroxide treatments, pineapple fibers were obtained. These fibers underwent mechanical grinding to achieve size reduction, facilitating their incorporation into cellulose aerogel composites. An analysis of the resultant pineapple fibers disclosed an alpha-cellulose content of 88%. These fibers were then blended with polyvinyl alcohol (PVA) and homogenized using an ultrasonicate homogenizer. The resulting mixture underwent thermal treatment at 80 degrees Celsius, instigating cross-linking between PVA and the hydroxyl groups of pineapple fibers. Then, the mixture undergoes a chilling phase to achieve solidification, subsequently transitioning to a freeze-drying procedure for dehydration. In the synthesis of cellulose aerogel composites presented in this paper, the PF concentration was maintained at a constant 2%, while the PVA concentration varied at 0.5, 1 and 1.5%. After the synthesis, a thorough analysis of the cellulose aerogel composites was conducted to evaluate their inherent properties.

3.1 FTIR Analysis

The FTIR spectra of all samples were analyzed in ATR mode. Figure 2.a shows the FTIR spectrum of PF. The region of the spectrum around 890 cm^{-1} reveals the presence of the glycosidic linkage in cellulose, as indicated by vibrations associated with the C-O-C glycosidic linkage. The spectral band between 3200 and 3600 cm^{-1} reflects the existence of hydroxyl (OH) groups in cellulose, evidenced by a wide absorption band attributed to the stretching vibrations of O-H bonds. The 1000-1150 cm^{-1} spectral range is significant for cellulose, marked by a strong band at approximately 1030 cm^{-1}, representing the C-O stretching vibrations of the glycosidic linkage in cellulose. The region spanning 2800-3000 cm^{-1} exhibits absorption bands related to C-H stretching vibrations, while the bands in the 1400-1470 cm^{-1} range are linked to C-H bending vibrations of cellulose. The band at 1640 cm^{-1} corresponds to the H-O-H bending of water, which represents the moisture content in the PF.[19-20] The FTIR spectra of PF and PVA (Figure. 2b) share some common characteristics; however, PVA exhibits a strong band at 1085 cm^{-1} corresponding to the abundant C-O bonds present in PVA. The FTIR spectra of the cellulose aerogel composite show a combination band of PF and PVA. The intensity of FTIR band at 1085 cm^{-1}, corresponding to the C-O band of PVA, increases with the higher PVA content in the aerogel composition.

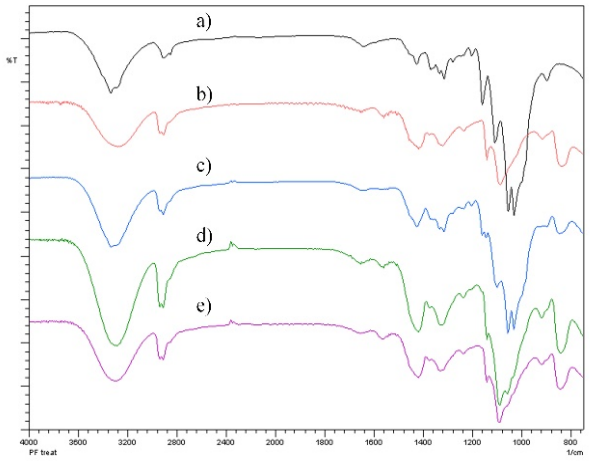

Figure 2. FTIR spectrum of a) PF b) PVA c) PF_PVA0.5 d) PF_PVA1.0 e) PF_PVA1.5

3.2 Density and Porosity

The density and porosity of cellulose aerogel composites are presented in Figure 3. The cellulose aerogels exhibit a low density of 0.03-0.04 g/cm^3 and a high porosity of 97.1-97.9%, indicating the lightweight and porous nature of the aerogel composites. The density of cellulose aerogel composites increases from 0.032 g/cm^3 to 0.040 g/cm^3 with an increase in PVA content from 0.5% to 1-1.5%. The reduction in porosity is evident with an increase in the quantity of PVA. The behavior of porosity is inversely correlated with density, as porosity is calculated based on the aerogel 's density.[9,18]

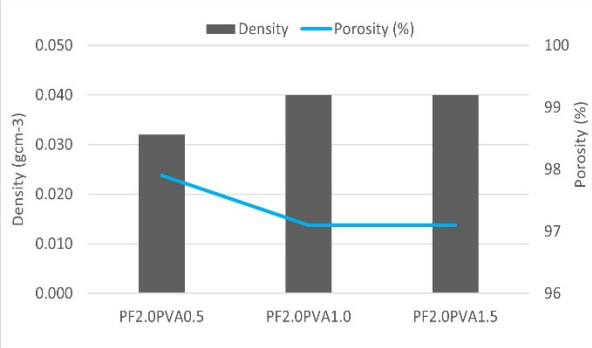

Figure 3. Density and Porosity of cellulose aerogel composites

3.3 Morphology

The SEM image of the core of the cellulose aerogel composites is revealed in Figure 4. All aerogels exhibit an interconnected, highly porous structure. Upon observation, it was noted that increasing the amount of PVA led to a reduction in the size of the pores, and the structure appeared denser.

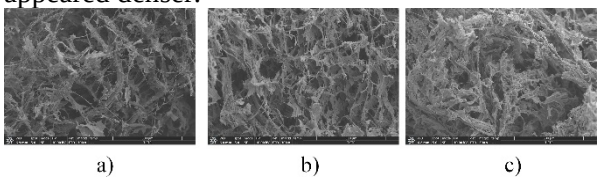

Figure 4. SEM image of the core of the cellulose aerogel composite a)PF_PVA0.5 b) PF_PVA1.0 c) PF_PVA1.5

3.4 BET surface area and average pore size

The BET surface areas of the cellulose aerogel composite ranged from 188 to 207 m^2g^{-1}, with an average pore diameter of 4.4 to 9.4 nm.(Table 2.) When increasing the quantity of PVA, it was observed that the BET surface area increased slightly, while the average pore size decreased significantly.

Table 2. BET surface area and average pore size

Code	BET surface area (m^2/g)	average pore size (nm)
PF2.0PVA0.5	188±2	9.4
PF2.0PVA1.0	201±2	5.0
PF2.0PVA1.5	207±4	4.4

3.5 Thermal stability and thermal conductivity

In the context of thermal insulation, crucial factors include thermal stability and thermal conductivity. Figure 5. illustrates the results of TGA analysis conducted on cellulose aerogel composites with varying proportions of PVA. The aerogel composite initiates decomposition at 272-301 degrees Celsius. Thermal stability experiences a slight decline with the increasing PVA content.

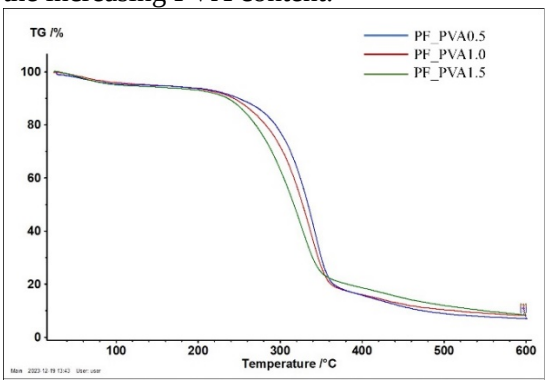

Figure 5. The TGA thermogram of cellulose aerogel composites

Figure 6. illustrates the thermal conductivity of cellulose aerogel composites. The synthesized aerogel composites exhibit a noteworthy thermal insulation property, characterized by a low thermal conductivity range of 0.056-0.067 $Wm^{-1}K^{-1}$. Upon increasing the PVA content from 0.5% to 1-1.5%, a slight elevation in thermal conductivity was noted. This suggests that when utilizing 2% PF, the most optimal PVA content is 0.5%, yielding the lowest thermal conductivity and the highest insulating properties.

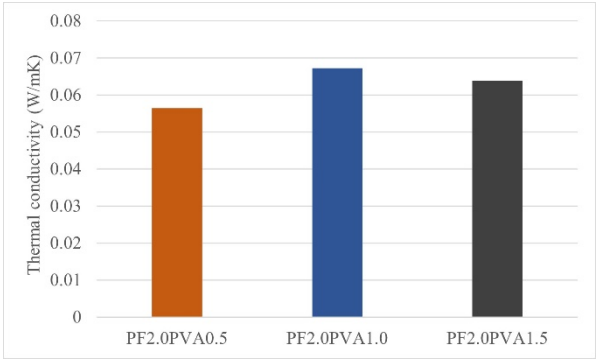

Figure 6. The thermal conductivity of the cellulose aerogel composites

4. Conclusion

In conclusion, this study successfully employed the freeze-dry method to synthesize cellulose aerogel composites using PF and PVA, with varying PVA concentrations as a binder and cross-linker while maintaining a constant PF content. The resulting aerogels demonstrated notable characteristics, including BET surface areas within the range of 188 to 207 m^2g^{-1} and an average pore diameter spanning 4.4 to 9.4 nm. Significantly, these cellulose aerogels exhibited low density (0.03-0.04 $g.cm^{-3}$) and thermal conductivity values (0.056-0.067 $Wm^{-1}K^{-1}$). Our findings indicate that, when incorporating 2% PF, an optimal PVA content of 0.5% led to the lowest

thermal conductivity and superior insulation properties. This highlights a synergistic interaction between PF and PVA, showcasing a composition with enhanced thermal insulation capabilities. Therefore, cellulose aerogel composites derived from PF demonstrate considerable promise as prospective materials for thermal insulation applications, owing to their low thermal conductivity. Furthermore, the results revealed a correlation between the reduction in the quantity of PVA and a subsequent decrease in thermal conductivity. Future experimental inquiries will systematically investigate the controlled reduction of PVA content while preserving the structural integrity of the cellulose aerogel composites. This pursuit aims to further elucidate and quantify the thermal conductivity properties, providing valuable insights for optimizing these materials in thermal insulation applications.

Acknowledgments

The authors gratefully acknowledge the Thailand Institute of Scientific and Technological Research (TISTR) and Thailand Science Research and Innovation (TSRI) for financial, material, and instrument support**.**

References

1. Pojanthon, S. Utilizing pineapple cores as nutrition for cattle and dairy. https://pvlo-uta.dld.go.th/webnew/images/stories/reprot/pine_ap.pdf (accessed June 15, 2023)
2. Anupunt, P.; Chairidchai, P.; Kongswat, A.; Isawilanon, S.; Subhadrabhandu, S.; Vasunun, S.; Siripat, S. *Acta Hortic.* **2000**, *529*, 99-110.
3. Daud, Z.; Mohd Hatta, M. Z.; Mohd Kassim, A. S.; Awang, H.; Mohd Aripin, A. *Bioresour.* **2014**, *9*, 872-878.
4. Luu, T. P.; Do N. H. N.; Chau, N. D. Q.; Lai, D. Q.; Nguyen, S. T.; Le, D. K.; Thai, Q. B.; Le, P. T. K.; Duong, H. M. *Chem. Eng. Trans.* **2020**, *78*, 433-438.
5. Norazreen, A. J.; Norfhairna, B.; Zurina, M.; Muhammad, M.; Siti, H. C. M. *Chem. Eng. Trans.* **2018**, *63*, 373-378.
6. Nguyen, L.; Tu, G. C.; Le, T. P.; Do, N. H. N.; Tran, V. T.; Mai, T. P.; Le, T. V.; Le, K. A.; Le, P. T. K. *Chem. Eng. Trans.* **2022**, *97*, 61-66.
7. Thai, Q. B.; Nguyen, S. T.; Ho, D. K.; Tran, T. D.; Huynh, D. M.; Do, N. H. N.; Luu, T. P.; Le, P. K.; Le, D. K.; Phan-Thien, N.; Duong, H. M. *Carbohydr. Polym.* **2020**, *228*, 115365.
8. Long, L. Y.; Weng, Y. X.; Wang, Y. Z.; *Polymers (Basel).* **2018**, *10*, 623-632.
9. Han, Y.; Zhang, X.; Wu, X.; Lu, C. *ACS Sustain. Chem. Eng.* **2015**, *3*, 1853–1859.
10. Aerogel. https://en.wikipedia.org/wiki/Aerogel (accessed June 20, 2023)
11. Correa, D. Aerogel market outlook, growth, application, raw materials, trend analysis, region, and forecasts 2021-2027. https://www.openpr.com/news/2785044/aerogel-market-outlook-growth-application-raw-materials. (accessed June 20, 2023)
12. Budtova, T. *Cellulose.* **2019**, *26*, 81–121.
13. Wang, L.; Soto, M. S. *RSC Adv.* **2015**, *5*, 31384-31391.
14. Zaman, A.; Huang, F.; Jiang, M.; Wei, W.; Zhou, Z. *Energy Built Environ.* **2020**, *1*, 60-76.
15. Sufian, M.; Azan, A. *Int. J. Eng. Adv. Res.* **2020**, *1*, 1-6.
16. Vu, P. V.; Doan, T. D.; Tu, G. C. *J. Porous. Mater.* **2022**, *29*, 1137–1147.
17. Rahman, L.; Goswami, J. *J Package Technol Res.* **2023**, *7*, 1–10.
18. Fan, B.; Chen, S.; Yao, Q.; Sun, Q.; Jin, C. *Mater.* **2017**, *10*, 311.
19. Hospodarova, V.; Singovszka, E.; Stevulova, N. *Am. J. Anal. Chem.* **2018**, *9*, 303-310.
20. Atykyan, N.; Revin, V.; Shutova, V. *AMB Express.* **2020**, *10*, 84-94.

The study of rheological properties of silk fibroin in ionic liquids

Tanissara Pinijmontree[1]*, Surassawadee Paliphot[1], Sathish K. Sukumaran[2], Masataka Sugimoto[2], Adisak Takhulee[3], and Yoshiaki Takahashi[4]

[1]Department of Chemistry, Faculty of Science and Agricultural Technology, Rajamangala University of Technology Lanna, Tak 63000, Thailand, [2]Department of Polymer Science and Engineering, Faculty of Engineering, Yamagata University, Yonezawa, Yamagata 992-8510, Japan, [3]Department of Chemistry, Faculty of Science, Udon Thani Rajabhat University, Udon Thani 41000, Thailand, [4]Evaluation Office of Materials Properties and Function, Institute for Materials Chemistry and Engineering, Kyushu University, Kasuga, Fukuoka 816-8580, Japan

**E-mail: arassinat@gmail.com*

Abstract:

The *Bombyx mori* silk fibroin (SF) which obtained from different degumming processes was prepared and dissolved in Ionic liquids (ILs) (AmimCl, BmimCl) with 0.1-15.0 %wt at 90 ˚C for 2 hrs and 60 ˚C for 1 hr, respectively, and kept in an oven until get uniform solution. The rheological properties of this sample were measured with Rheometer. The oscillatory shear measurement was performed under a stain-control model with the frequency, ω, in a range of 0.1-100 rad/s at various temperatures. The steady shearing behavior suggested that ILs is a good solvent for SF molecules. The modulus of SF/ILs obtained from precipitation procedure shows higher modulus than both SFs obtained by conventional procedure and regenerated SF with Ajisawa's reagent. These results corresponding to the degradation of SF from those methods. The viscosity of SF/ILs solutions were increased with concentrations increasing and showed a typical plastic flow behavior which observed by the increasing of the moduli with ω and tended to cross at high ω except at the highest temperature, which is similar to the dynamic viscoelastic behavior of the native silk spinning dope at low temperature. The existence of plateau like behavior denotes the weak network in the solution.

1. Introduction

The *Bombyx mori* silk fibroin (SF) materials are usually prepared from aqueous solutions. Generally, silk fibroin can be dissolved in Ajisawa's reagent, LiBr or LiSCN.[1] Then, salt ions can be removed by dialysis method and the solution can be lyophilized to obtain regenerated silk fibroin. The process is time-consuming more than one week and shows an unstable solution. During the past decade, Ionic Liquids (ILs) have attracted increasing attention as efficient, novel solvents for dissolving natural fibers. They are considered as green solvents with wide range attractive properties including chemical and thermal stability, excellent dissolution ability and non-flammability. It has been used to successfully dissolve silk fibroin by disruption hydrogen bonding in silk fibroin.[2] Ionic liquid, such as 1-Butyl-3-methylimidazolium chloride (BmimCl) can be used to dissolve silk fibroin for film casting and spinning but there is a little study of ionic liquid for dissolving silk fibroin. In addition, the effect of coagulant after spun can induce β-sheet crystallite formation.[2, 3]

Up to now, 1-Allyl-3-methylimidazolium chloride (AmimCl) and 1-Ethyl-3-methylimidazolium acetate (EmimAc) are used to carry out silk fibroin. It can be classified as good solvent for silk fibroin.

Certainly, the rheological properties measurement of silk fibroin in Ionic Liquids involves analyzing how the material behaves under different flow and deformation conditions. This process helps to understand the viscosity, elasticity, and overall flow characteristics in the presence of the ionic liquids.

Furthermore, optimizing processing conditions based on rheological data is essential for developing various industries such as 3D printing techniques, contributing to advancements in tissue engineering and other biomedical applications. Beyond these, the rheological data of SF/ILs also holds significance in various other fields. For example, Textile Industry, Coating and Films, Smart Materials, 3D-Printing, Hydrogels and Scaffolds, Drug Delivery, Membrane Technology Food Industry, Polymer Blend and so on.

Hence, further understanding of the rheological properties is a key for the high-performance processing of materials. Here, ILs was used to investigate the rheological behavior of SF/ILs by oscillatory shear measurement.

2. Materials and Methods

2.1 Materials

Raw silk (*B. mori*) warm gland, cocoons and fibers were obtained from the local silk plant in Thailand. Ionic liquid (ILs), AmimCl and BmimCl were synthesized in Takahashi's Lab,

Kyushu University. $CaCl_2$, Na_2CO_3 and Acetronitrile were supplied by Sigma-Aldrich. All chemicals were used without further treatment.

2.2 SF preparation by a precipitation method

Silk fibroin was extracted from silk warm gland and washed with de-ionized water. Then it was dissolved in BmimCl in a vacuum oven with the concentration at about 4.8 %wt. The rheological properties of this sample were measured with Physica MCR-300 Rheometer. For all oscillatory shear measurement, 50 mm diameter cone-plate measuring geometry was used under the stain-control mode. The frequency, ω, ranging from 0.1-100 rad/s and the measuring temperatures are at 10, 25 and 40 °C. The silk fibroin was precipitated by using acetronitrile as precipitation agent and recovered sample was dissolved in AmimCl to prepare the lower concentration (0.8 and 2.0 %wt) solutions. Then, the rheology test was performed by the similar method.

2.3 SF preparation by a conventional method

Raw silk was immersed in an aqueous solution containing 0.05 %w/v Na_2CO_3 with 1:30 of the material-to-liquor and then heated to 90°C for 30 mins and repeated 2 times.[4, 5] Then, fibers were washed with hot distilled water several times and then washed with room temperature distilled water to remove sericin from fibers. The sample was dried in a hot air oven at 60°C for 24 hrs and kept in desiccators over silica gel.

2.4 Regenerated SF preparation by Ajisawa's reagent

Degummed silk was dissolved in Ajisawa's reagent which can be prepared by mixing of the Calcium chloride, water and EtOH in mole ratio of 1:8:2, respectively, at 80 °C for 40 minutes until the solution was clear.[6] Then, this solution was filtered to remove solidified silk fibroin and small fibers and followed by dialyzing against water for 3-4 days in a cellulose tube with the molecular weight cut off (MWCO) 12-14 kDa to remove salt ions from silk fibroin. The dialysis tubes were soaked in water and changed every day. After that, pure fibroin solution was lyophilized at -20 °C for 24 hrs to obtain silk fibroin sponge.

Then SF/BmimCl solutions were prepared by dissolving SF sponge in BmimCl at 130 ºC for 2 hrs in the vacuum oven with concentration range of 10-18 %wt. Then, the rheological behaviors were measured by Rheometer, Physical MCR301 (Anton Paar). The measurement geometry was a cone plate with a diameter of 25 mm under Nitrogen atmosphere. All measurements were carried out with 0.05 mm gap.

On the other hand, the SF/AmimCl solutions were prepared at 1-15 %wt by dissolving SF sponge in AmimCl at 90 °C for 2 hrs under vacuum. The rheology test was performed on Physical MCR-301 Rheometer. For all oscillatory shear measurement, 25 mm diameter cone-plate measuring geometry was used under the stain-control model. The frequency, ω, ranging from 0.1-100 rad/s at 30 °C. The Time-Temperature Superposition (TTS) was achieved at a temperature ranging from 0 °C to 180 °C.

2.5 The rheological property of various SF

Precipitated SF was obtained by precipitating in acetonitrile. For **conventional degumming** method, silk fiber were boiled twice with 0.5 %wt Na_2CO_3 at 90 ˚C for 30 mins and washed with DI water. On the other hand, **regenerated silk fibroin** was obtained by dissolving degummed SF in Ajisawa's reagent. Then, all SF/ILs samples were dissolved in AmimCl with 0.1-1.0 %wt at 90 ˚C for 2 hrs and 60 ˚C for 1 hr, respectively, and kept in the oven until get uniform solution. The rheological property of all samples and viscosity measurement was carried out to investigate intrinsic viscosity of various SF.

3. Results and Discussion

3.1 Rheological properties of SF solution by the precipitation method

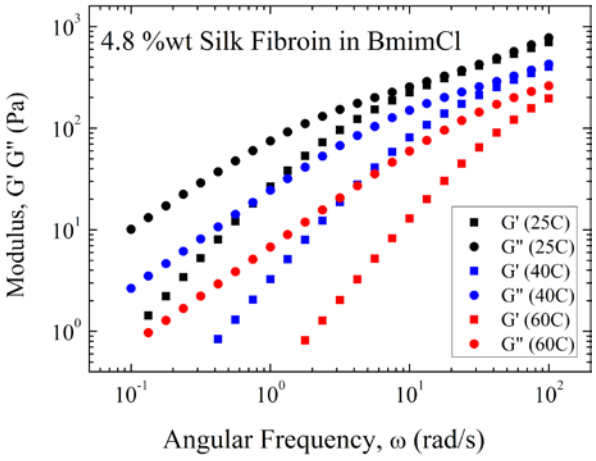

Figure 1. Storage (G') and loss (G") modulus as a function of ω increasing with concentration of 4.8 %wt SF in BmimCl solutions.

Figures 1-3 show the angular frequency dependences of storage (G') and loss (G'') moduli for SF/BmimCl and SF/AmimCl solutions with different concentrations and temperatures. The moduli showed the typical plastic flow behavior. That is, the moduli increased with ω and tended to cross at high ω except at the highest temperature,

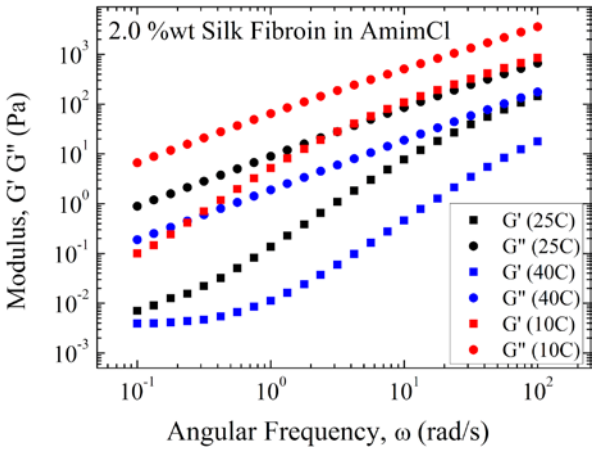

Figure 2. Storage (G') and loss (G") modulus as a function of ω increasing with concentration of 2.0 %wt SF in AmimCl solutions.

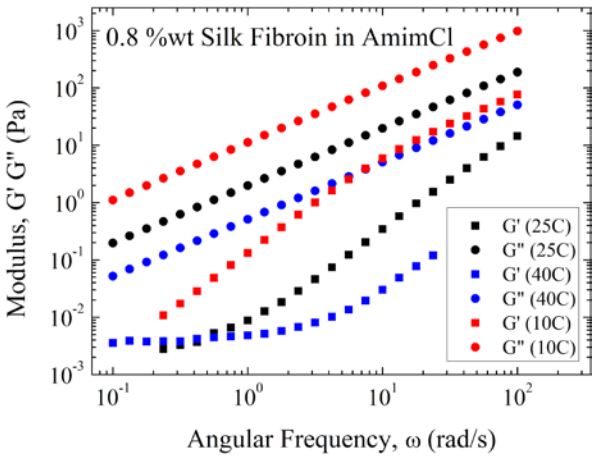

Figure 3. Storage (G') and loss (G") modulus as a function of ω increasing with concentration of 0.8 %wt SF in AmimCl solutions.

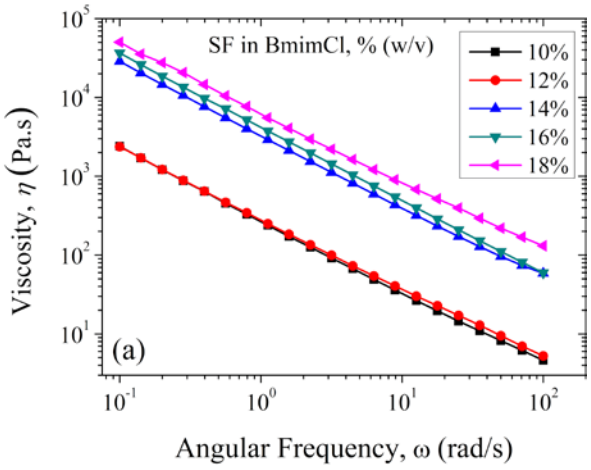

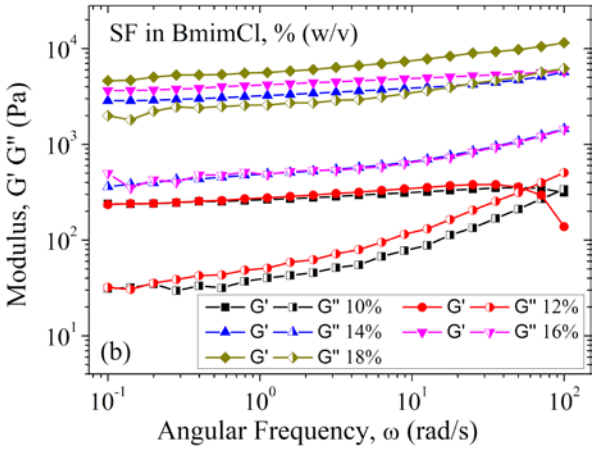

Figure 4. (a) viscosity and (b) rheological behaviors of silk fibroin in BmimCl with various concentrations.

which is similar to the dynamic viscoelastic behavior of the native silk dope at low temperature. The existence of plateau like behavior denotes the weak network in the solution.

3.2 Rheological properties of Regenerated SF by Ajisawa's reagent

3.2.1 SF/BmimCl solution

It was found that the viscosity of the solution was increased with concentration of silk fibroin increasing as shown in Figure 4.

At low concentration, 10-12 %w/v, silk fibroin molecules were random coil conformation with less molecular entanglement. At higher concentration, 14-18 %w/v of silk fibroin was higher viscosity with sufficient molecular entanglements. The rheological behaviors of these solutions were also investigated, it was found that at concentration of 10 %w/v and 12 %w/v, the G'' dominated G' at high shear rate and the crossover point was observed in both solutions which indicate the gelation behavior.

For concentration at 18 %w/v, the solution was observed as the network-like structure or there was sufficient chain entanglement of silk fibroin molecules. The viscosity of silk solution increased with silk fibroin concentration increasing. The rheological behavior of the solution exhibited a transition from Newtonian to non-Newtonian fluid and it formed the gelation at high concentration.

3.2.2 SF/AmimCl solution

Generally, the viscosity of SF/AmimCl solution increased with the amount of SF increasing (Figure 5). However, the dependence of viscosity on shear rate (that is, lower shear thinning at lower shear rate, Newtonian flow at intermediate shear rate, and greater shear rate thinning at higher shear rate) exhibited different trends in the range of concentrations investigated.

Flow curve of SF/AmimCl solution with low concentration showed lower shear thinning, followed by Newtonian flow in the subsequent shear rate range, which is similar to that of pure AmimCl solution.

As the concentration of SF increased, the region of lower shear thinning become less evident or even disappeared, meanwhile a higher rate shear thinning region emerged. It was apparent that pseudo-plastic flow occurred for SF/AmimCl solutions with high concentrations, which were the Newtonian region, followed by the higher rate shear thinning region, which was similar to that of typical polymer solutions.

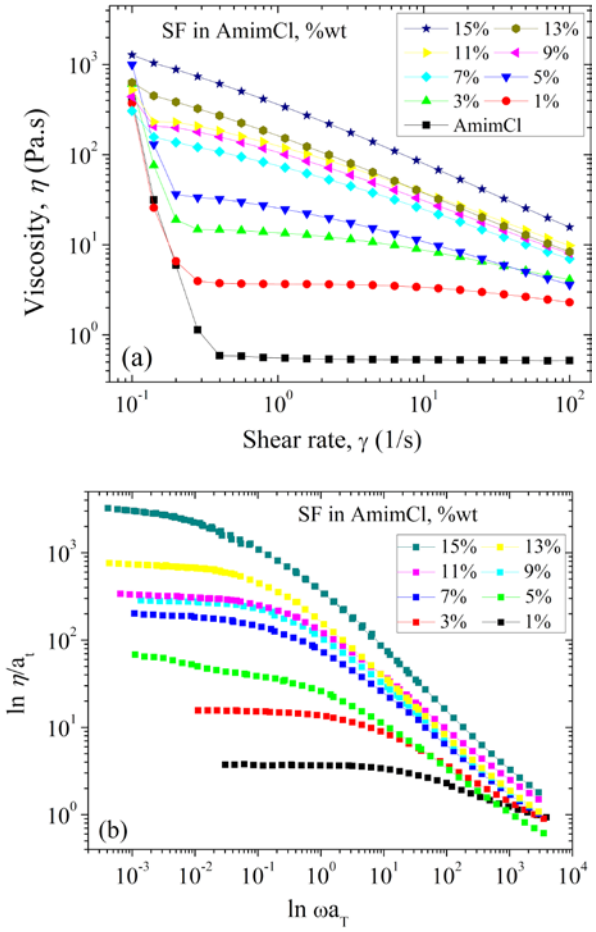

Figure 5. Flow curves of pure AmimCl and SF/AmimCl solution with various concentrations of SF at 30 °C.

Figure 6 showed the angular frequency dependences of storage (G') and loss (G'') for all SF/AmimCl solution varied with the concentration. The moduli showed the typical plastic flow behavior, which moduli increased with ω and was found it tended to cross at high ω, which is similar to the dynamic viscoelastic behavior of the native silk dope.[7, 8]

The plateau of moduli which denotes the weak network in the solution, can only be found in pure AmimCl suggesting the physical interaction network between molecules in the solution. SF molecules also tended to overlap and associate with each other.

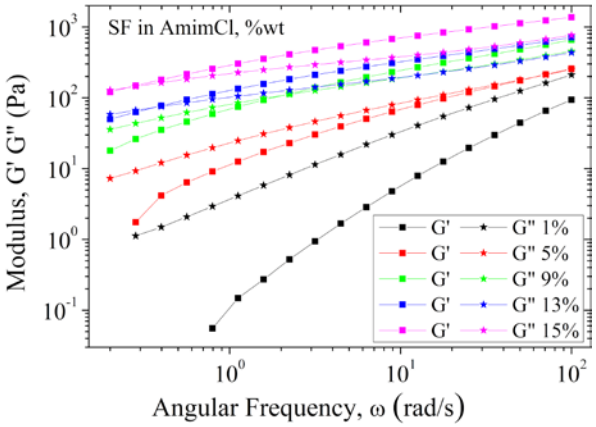

Figure 6. Storage (G') and loss (G") modulus as a function of ω increasing with concentration for SF/AmimCl solutions

The Time-Temperature Superposition (TTS) principle was introduced to overcome the limitations of the rheometer of measuring dynamic information at high frequency (ω larger than 100 rad/s). The master curve of storage (G') and loss (G") at various temperatures (with reference temperature T_f = 30 °C) for SF/AmimCl solution were shown in Figure 7.

To estimate the feasibility of TTS, the curve of horizontal shift factor (a_T) versus the inverse of the temperature is calculated. The linear form of the plot indicated that the temperature dependence of a_T could be described by Arrhenius-type equation. Therefore, the linear relationship of *ln* a_T again 1/*T* and the overlapping of the master curve proved that TTS hold well for the viscoelastic data of the SF/AmimCl solution, and the homogeneity of the solution under this experimental condition was also indicated.

$$a_T = \frac{\eta(T)T_0}{\eta(T_0)T} \quad (1)$$

As the master curve in Figure 8 (on the logarithmic scales), the moduli increased with frequency which behaving like a viscoelastic behavior of the native *Bombyx mori* dope.[8]

It could be supposed that AmimCl is the good solvent for SF. This frequency dependence of modulus confirmed that 5 %wt SF/AmimCl was in entanglement regime. Then showed the obvious crossover between G' and G" and a pseudo-plateau

modulus at high angular frequency, like the typical entangled polymer solution or melts.[9]

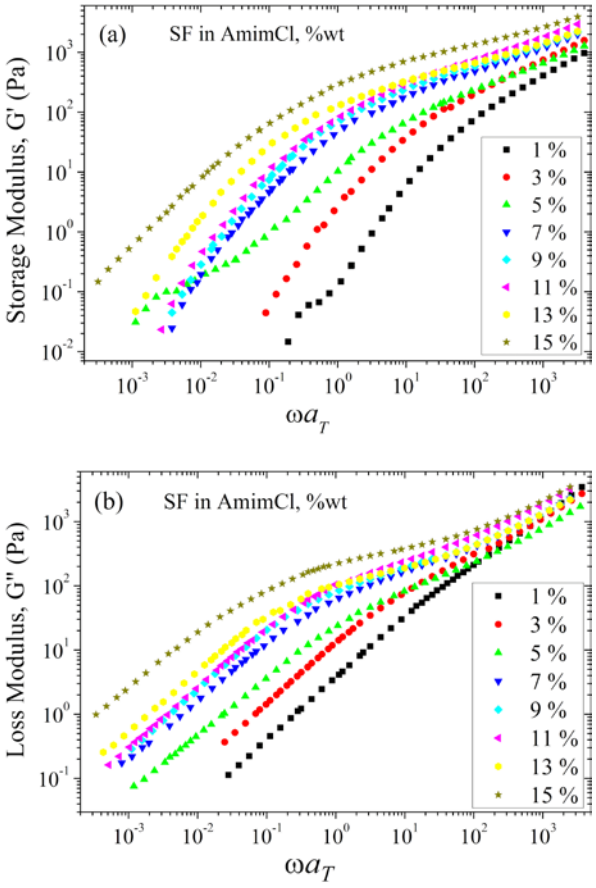

Figure 7 The master curve of (a) storage (G') and (b) loss (G") modulus at various temperatures (T_f = 30 °C).

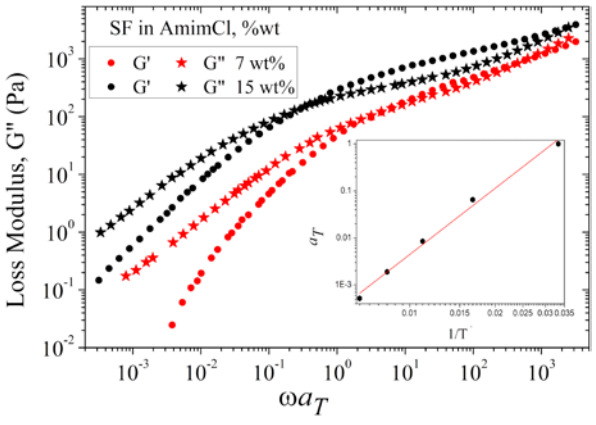

Figure 8 Time-temperature superposition for 7 %wt and 15 %wt SF/AmimCl solution (T_f = 30 °C). The inset shows the shift factor (a_T) with different temperatures.

3.3 Rheological properties of various SF

It was found that the modulus (Figure 9) of SF/ILs obtained from precipitation procedure showed higher modulus than both SFs obtained by the conventional procedure and regenerated SF with Ajisawa's reagent. These results corresponded to the degradation of SF from those methods. The viscosity of SF/ILs solutions increased with concentrations increasing and SF/EmimAc solution (data not show here) also exhibits lower viscosity than SF/AmimCl with each concentration

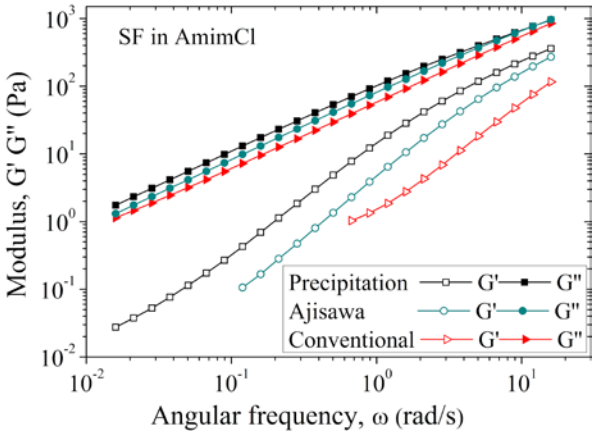

Figure 9 Modulus as a function of ω for various SF/ILs solutions.

4. Conclusion

Raw silk (*B. mori*) warm gland, cocoons and fibers were degummed and regenerated silk fibroin, RSF, sponge by dissolving in Ajisawa's reagent. Then, dissolved in Ionic liquids (ILs) (AmimCl, BmimCl) with 0.1-15.0 %wt at 90 ˚C for 2 hrs and 60 ˚C for 1 hr, respectively, and kept in the oven until get uniform solution. The rheological properties were measured with Rheometer under the stain-control model in the frequency, ω, range 0.1-100 rad/s at various temperatures.

The steady shearing behavior suggested that ILs is the good solvent for SF molecules. At low concentration, silk fibroin molecules were random coil conformation with less molecular entanglement which indicated the gelation behavior. At high concentration of silk fibroin, the viscosity was higher with sufficient molecular entanglements and the network-like structure or chain entanglement was observed. For SF/BmimCl, the viscosity of silk solution increased when increasing silk fibroin concentration. The rheological behavior of the solution exhibited a transition from Newtonian to non-Newtonian fluid and it formed the gelation at high concentration. On the other hand, the SF/AmimCl solutions showed a typical plastic flow behavior which similar to the dynamic viscoelastic behavior of the native silk dope. AmimCl and SF molecules showed the physical

network interaction in the solution. The entanglement regime is at 5 %wt SF/AmimCl solution. Moreover, the master curve from the time-temperature superposition (TTS) principle also described a viscoelastic behavior of the native *Bombyx mori* dope.

Acknowledgements

Authors would like to thanks the collaborative research project supported by The Network Joint Research Center for Materials and Devices (IMCE) for partial financial supported and the Research Institute for Applied Mechanics, Kyushu University, Japan, for partial facility supports on sample characterization.

References

1. Yamada H.; Nakao H.; Takasu Y.; Tsubouchi K. *Mater. Sci. Eng. C.* **2001**, 14, 41–46.
2. Phillips D.M.; Drummy L.F.; Conrady D.G.; Fox D.M.; Naik R.R.; Stone M.O.; Trulove P.C.; de Long Hugh C.; Mantz R.A. *J. Am. Chem. Soc.* **2004**, 126, 14350–14351.
3. Swatloski, R. P.; Spear, S. K.; Holbrey, J. D.; Rogers, R. D. *J. Am. Chem. Soc.*, **2002**, 124, 4974-4975.
4. Prachayawarakorn, J.; Boonsawat, K. *J. Appl. Polym. Sci.*, 2007, 106, 1526-1534.
5. Sofia, S.; McCarthy, M.B.; Gronowicz, G.; Kaplan, D.L. *J. Biomed. Mater. Res.* **2001**, 54, 139–148.
6. Ajisawa, A. *J. Sericultural Sci. Jpn.*, **1998**, 67, 91–94.
7. Holland.C.; Terry. A.E.; Porter, D.; Vollrath, F. *Polymer*, **2007**, 48, 3388-3392.
8. Holland.C.; Terry. A.E.; Porter, D.; Vollrath, F. *Nat. Mater.*, **2006**, 5, 870-874.
9. Colby, R. H. *Rheol. Acta.*, **2010,** 49, 425-442.

Fabrication and characterization of MOF-808/PVDF films

Nathakrit Trianreal and Jonggol Tantirungrotechai*

Department of Chemistry and Center for Innovation in Chemistry (PERCH-CIC), Faculty of Science, Mahidol University, Rama VI Road, Bangkok, 10400, Thailand

**E-mail: jonggol.jar@mahidol.ac.th*

Abstract:

Recently, metal-organic frameworks (MOFs) have attracted tremendous interest in preparing a MOF film, which could help expand their uses in a variety of technological applications such as catalysis or adsorption. Particularly, by employing MOFs as modifying agents, due to the benefits from their excellent functional designability, good compatibility with polymers, and customizable and regular pore structure, the film performance could be enhanced. In this study, MOF-808 film was created by anchoring MOF-808 within polyvinylidene fluoride (PVDF). The crystallinity, thermal stability, morphology, and functionality of MOF-808/PVDF films with varying MOF-808 content (10, 20, 30, and 40% by weight of MOF-808) were then thoroughly assessed. The MOF-808/PVDF films possessed good mechanical strength and flexibility. The films were characterized by FT-IR spectroscopy, XRD, and TGA measurement. Characterization of the films showed MOF-808/PVDF films still have the crystallinity of MOF-808 while retained the flexibility and elasticity of PVDF.

1. Introduction

Metal-organic frameworks (MOFs) or porous coordination polymers are highly desired ordered crystalline materials prepared using organic linkers to coordinate with metal ions or cluster of metal ions. These materials are attractive prospects for a range of applications due to their incredible surface areas (1000-1200 m^2g^{-1}), tunable functional groups, high thermal stability, high acidity and well-defined structure.[1]Therefore, MOFs have been used for storage, separation, sensing, proton conduction, and drug delivery.[2]

Among these, Zr-based MOFs have garnered significant interest due to their innate chemical, mechanical, and hydrothermal stabilities, which provide exceptional qualities for their extensive use in many catalytic processes. There are many Zr-based MOFs, but the most well-known are UiO-66, UiO-67, and MOF-808.[3] MOF-808 is constructed from zirconium secondary building units (SBUs), $Zr_6OH_4(CO_2)_6(HCOO)_6$,[3] and coordinated to 6 organic linkers to form a three-dimensional framework structure. The catalytic activity of MOF-808 is better than that of UiO-66 and UiO-67 because the coordination of the Zr sites in UiO-MOFs is fully saturated by linkers while that in MOF-808 is not.

Like the other MOFs, MOF-808 is frequently employed in small-scale processes. Due to operational issues including dirtiness and mass loss, MOFs in the form of powders are not appropriate for large-scale industrial applications. The molding of MOFs with polymer in the form of beads or films is very popular.

The widely used polymers are polyvinylidene fluoride(PVDF), polymethyl-methacrylate(PMMA) and poly(ether-sulfone) (PSF) because of their potential to form a tight junction with MOFs.[4] PVDF is an inert polymer that has high thermal stability, and is also easy to mold, which compatible with a variety of MOFs (MOF-808, UiO-66, MIL-53, HKUST-1).[4] Given its great mechanical and chemical resilience in harsh environments, PVDF is a desirable embedding polymer.[5] Therefore, this research focuses on the fabrication and characterization of MOF-808 embedded PVDF with various percentage of MOF-808. The resulting MOF-808/PVDF films retained the crystallinity of MOF-808 while still possessed the flexibility and elasticity of PVDF.

2. Materials and Methods

2.1 Materials

Poly (vinylidene fluoride) (PVDF), zirconium oxychloride octahydrate ($ZrOCl_2$•$8H_2O$, 98%) were purchased from Sigma-Aldrich. 1,3,5-benzene tricarboxylic acid (BTC, >98%) and formic acid were purchased from Tokyo Chemical Industry. *N*,*N*-dimethylformamide (DMF) was purchased from Quality Reagent Chemical Product. Ethanol and acetone were purchased from RCI Labscan.

2.2.1 Synthesis of MOF-808

1.67 mmol of $ZrOCl_2$• $8H_2O$ and 0.55 mmol of H_3BTC were dissolved in 25 mL DMF and 25 mL formic acid solution. The solution was placed in a Teflon-lined stainless-steel reactor and heated at 130 °C for 48 h. After cooling down to room temperature, the powder product was recovered by centrifugation.The white solid was

washed three times with DMF and soaked in DMF/acetone/water (1:1:1 by volume) solution for three days. Finally, the solid was vacuum dried at 160 °C overnight (0.154 g).[6]

2.2.2 Fabrication of MOF-808/PVDF films

The preparation of MOF film began by dissolving 0.6 g PVDF in 5 mL DMF at 60 °C followed by the addition of MOF-808 dispersed in 5 mL acetone. The amount of PVDF added was kept constant at 0.6 g, whereas the amounts of MOF-808 were varied at 0.068, 0.15, 0.23, 0.30, and 0.36 g for 10, 20, 30, and 40%MOF films, respectively. Then, the mixed solution was poured into the mold and dried at 100 °C for 15 min. After that, MOF film was soaked in acetone for 5 min and dried at room temperature.[7] (Figure 1)

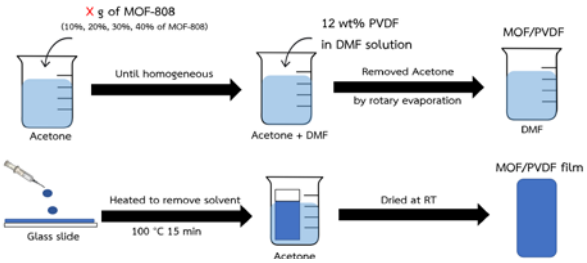

Figure 1. Fabrication of MOF-808/PVDF films.

2.3 Spectroscopic measurements

All MOF films were characterized by using the following techniques. The crystal structure was determined by x-ray diffraction (XRD) using a Bruker D2 Phaser X-ray diffractometer in a 2θ range of 0.5-40°. The functional groups were determined by Fourier-transform infrared (FT-IR) spectrophotometer (PerkinElmer), using a ATR technique between 400-4500 cm^{-1}. The thermal stability was determined by thermogravimetric analysis (TGA) using TA Instrument SDT2960.

3. Results & Discussion

3.1 Morphology and crystal structure

Figure 2 shows images of MOF-808/PVDF films with different MOF loadings fabricated by the technique described above. The higher MOF loading resulted in less flexible films. 40% MOF is the highest content of MOF for the film to maintain the shape without cracking as shown in Figure 3. MOF-808/PVDF films still possess the mechanical stability and flexibility of PVDF as illustrated in Figure 4.

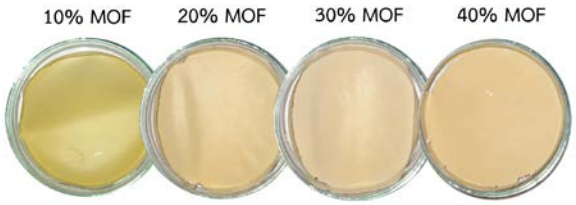

Figure 2. MOF-808/PVDF films with different MOF loading.

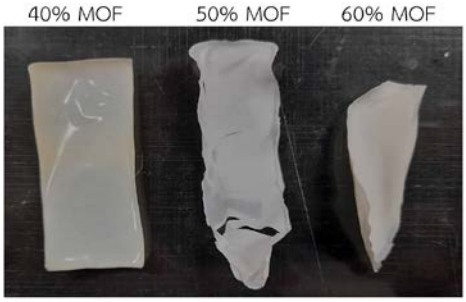

Figure 3. 40, 50 and 60% MOF-808/PVDF films

Figure 4. Image showcasing the ease of handling and the resilience of 30% MOF-808/PVDF film in terms of mechanical stability and flexibility.

XRD patterns of all materials, shown in Figure 5, reveal the characteristic peaks corresponding to the (331), (400), (222) and (311) reflections of MOF-808, confirming that the crystallinity of MOF-808 was maintained during the fabrication.[8] PVDF has characteristic peaks of (100), (020) and (110).[9] These distinctive peaks can be found in the MOF-808/PVDF films. In addition, the intensity of these peaks decreased as the content of MOF-808 in the film increased. From this result, we can conclude that the addition of PVDF did not damage the crystal structure of MOF-808.

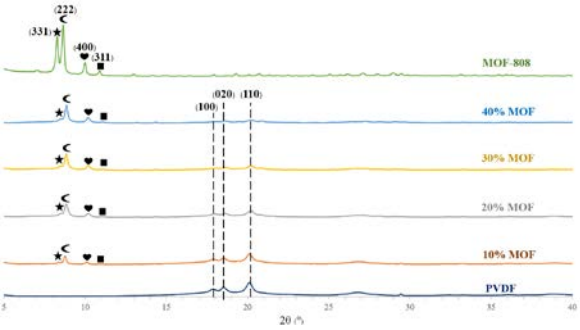

Figure 5. XRD patterns of MOF-808 and MOF-808/PVDF films

One thing to consider is the BET surface of MOF-808/PVDF film because PVDF has a very low surface area (3.76 m^2g^{-1}).[14] Mixing MOF with PVDF causes the surface areas to be significantly lower. Surface area of all samples will be measured to confirm this hypothesis.

3.2 Functional groups and thermal stability

Figure 6 shows the FT-IR spectra of MOF-808 and MOF-808/PVDF films. The peaks at 1624, 1377 and 1440 cm^{-1} were due to the BTC linker in MOF-808, the strong peak at 650 cm^{-1} represented the Zr–O vibration suggesting the coordination between the linkers and metal clusters.[10] The peaks at 489, 612, 769 and 971 cm^{-1} were the characteristic peaks of α-crystal shape of PVDF. The peaks at 863, 1378, 1395 cm^{-1} were the characteristic peaks of β-crystal shape of PVDF.[11] These characteristic bands are present in the MOF-808/PVDF films but not present in the MOF-808, demonstrating the successful fabrication of MOF-808/PVDF films.

Observably, as the amount of MOF increases in the MOF/PVDF film, the intensity of the bands belonging to MOF increases while the intensity of the peaks relating to PVDF decreases as the amount of PVDF decreases.

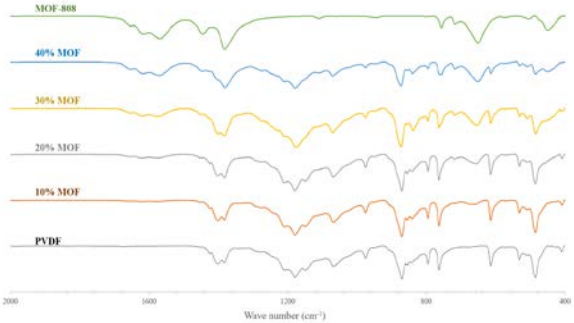

Figure 6. FT-IR spectra of MOF-808 and MOF-808/PVDF films.

For additional assessment of the fabricated MOF-808/PVDF films, TGA analyses were carried out as shown in Figures 7-9. MOF-808 and MOF-808/PVDF films show three-step weight losses. The first one for MOF-808 in the temperature range of 50-100 °C was due to the loss of adsorbed water. The second loss in the temperature range of 100-200 °C was related to the evaporation of formic acid, which was adsorbed to the surface of MOF-808. The final step in the temperature range of 200-600 °C was related to the breakdown of the organic linker. The remain of ZrO_2 residue was 44.4 wt% higher than the theoretical value of 38.5 wt%, possibly due to the presence of water and formic acid coordinated to the secondary building units.[12] TGA curve of PVDF revealed the decomposition of the polymer matrix at 400-600 °C, as shown in Figure 8.[13] The TGA curve of MOF-808/PVDF displayed a similar nature to that of MOF-808 as shown in Figure 9. The ZrO_2 residue of 18.4 wt% was close to the theoretical value of 17.7 wt% which confirmed the MOF content film in the film. The quantity of PVDF in MOF/PVDF film cannot be calculated because the mass loss range of PVDF overlaps with the linker of MOFs. This result confirms that MOF-808 embedded PVDF still maintained the thermal stability of MOF-808 and PVDF.

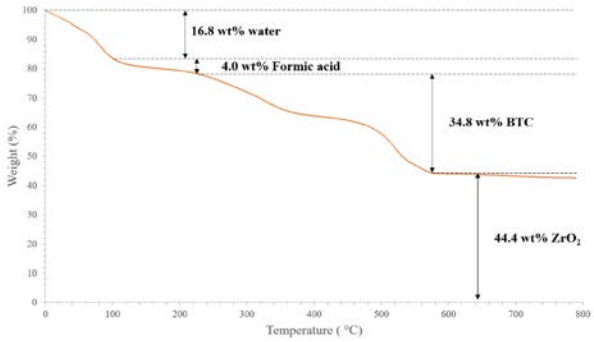

Figure 7. TGA curve of MOF-808

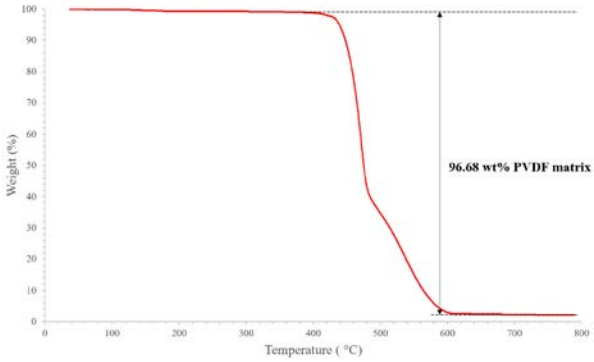

Figure 8. TGA curve of PVDF

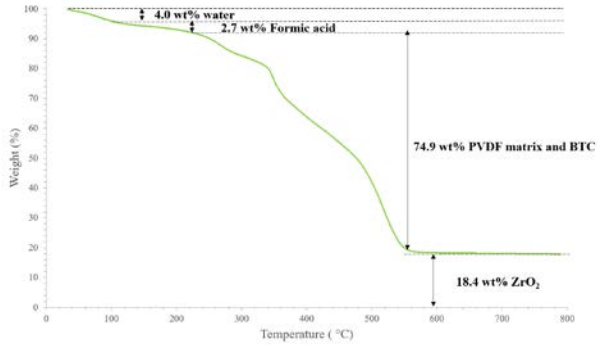

Figure 9. TGA curve of MOF-808/PVDF film (40%)

4. Conclusion

MOF-808/PVDF films were successfully fabricated by casting method. All characterization of MOF-808/PVD films confirmed that the films still have the crystallinity of MOF-808 while retained the flexibility and elasticity of PVDF.

Acknowledgement

The Center of Excellence for Innovation in Chemistry (PERCH-CIC), the Ministry of Higher Education, Science, Research and Innovation, the Faculty of Graduate Studies, and the Faculty of Science at Mahidol University have provided financial support, for which the authors are thankful.

References

1. Wang, j.; Liu, j.; Yu, X.; Zhang, W.; Zhang, G.; Liu, M.; Shen, J.; Yang.; Jin, X. *Mater. Today Energy*. **2020**, *18*, 100501-100531.
2. Ortuno, M.; Pineiro, M.; Luque, R. *ACS Sustain. Chem. Eng.* **2022**, *10*, 3567-3573.
3. Li, J.; Zhao, S.; Li, Z.; Lui, D.; Chi, Y.; Hu, C. *Inorg. Chem.* **2021**, *60*, 7785 -7793.
4. Denny, M.S., Jr.; Cohen, S. M. *Angew. Chem., Int. Ed*. **2015**, *54*, 9029-9032.
5. Wang, L.; Chen, P.; Dong, X.; Zhang, W.; Zhao, S.; Xiao, S.; Ouyang, Y. *RSC Adv.*, **2020**, *10*, 44679-44687.
6. Guarinos, J.; Cirujano, F.; Rapeko, A.; Xamena, F. *J. Mol. Catal*. **2021**, *515*, 111925-111936.
7. Kalai, M.; Bentz, k.; Ayala, S.; Palomba, J.; Barcus, k.; Katayama, Y.; Seth, C. *Chem. Rev.* **2020**, *120*, 8267-8302.
8. Nguyen, D. K.; Vo, T. N.; Le, M. T. K.; Vo, K.; Phan, N.; Ho, H.; Le, H. *New J. Chem.*, **2023**, *47*, 6433.
9. Lotfian, S.; Giraudmaillet, C.; Yoosefinejad, A.; Thakur, V.; Nezhad, H. *ACS Omega*, **2018**, *3*, 8, 8891-8902.
10. Parl, B.; Jung, Y.; Kim, S. *J. Inorg. Organomet. Polym. Mater.* **2021**, *31*, 1931-1938.
11. Cai, X.; Lei, T.; Sun, D.; Lin, L. *RSC Adv.*, 2017,**7**, 15382-15389.
12. Hu, Z.; Kundu, T.; Wang, Y.; Sun, Y.; Zeng, K.; Zhao, D. *ACS Sustain. Chem. Eng*. **2020**, *8*, 17042-17053.
13. Dhand, V.; Hong, S.; Li, L.; Kim, J.; Kim, S.; Rhee, K.; Lee, H. *Compos. B. Eng*. **2019**, *160*, 632-643.
14. Rosman, N.; Salleh, W.; Awang, N.; Ismail, F. A.; Jaafar, J.; Harun, Z. *Mater. Today: Proc.* **2019**, *19*, 1413-1419.

ZIF-8 synthesis for oil removal from water surface

Wachirapun Punkrawee*, Nimit Palee, and Amornpon Changsuphan

Green Innovation group, Chemicals and Consumer Products Division, Department of Science Service, Ministry of Higher Education, Science, Research and Innovation, Bangkok, 10400, Thailand
**E-mail: wachirapun@dss.go.th*

Abstract:

ZIF-8 (Zeolite imidazole framework) has excellent properties that are useful in oil/water separator applications, such as thermal and chemical stability, a high surface area, and reusable and hydrophobic properties. One-pot hydrothermal synthesis of ZIF-8 was prepared using TEA as a modulating agent for controlling the particle size. The reaction was conducted in a temperature range of 25 °C to 140 °C. The synthesized ZIF-8 is considered a hydrophobic material,whose contact angle (CA) is 113°. This result confirms the capability of oil-water separation. According to the XRD, FT-IR, SEM-EDS, and adsorption capacity, ZIF8-80°C is a suitable condition for synthesis due to its high crystallinity, small particle size, and well dispersion. It also shows the highest adsorption efficiency (2.5 g/g). For practical application, ZIF-8 was made as a pellet and directly adsorbed oil from the water surface. The results show that oil has been completely removed. Therefore, lab-synthesized ZIF-8 can be used for oil/water separation. However, compared with the oil adsorption capacity of other commercial products, the efficiency of ZIF-8 is in the average range of other products. On the contrary, ZIF-8 has some advantages, such as one-pot synthesis, which is suitable for large-scale production, high purity, and reusability. Therefore, ZIF-8 will be further studied for oil adsorption improvement.

1. Introduction

Environmental disasters caused by oil spills have been of interest. In the present time, there have been accidental spillages on water, leading to problems for aquatic and marine life[1]. In general, some techniques for cleaning oil spillage are oil boom, skimmer, oil dispersant, adsorbent, and suit burning. Among them, adsorbents, especially porous materials, have been investigated for removing oil from the water surface because of their lack of environmental impact, treatment efficiency, and ease of use [2,3]. Many porous sorbent materials have been used such as zeolite[4], synthetic polymer[4], organoclay[5], and natural fiber[6]. However, these materials have to develop their recirculation and regeneration to meet a user requirement[7].

Metal organic frameworks (MOF) has been interested as sorbent materials due to their porous structure, hydrophobicity, low cost and large scale production. More importantly, MOF has a metal ion inside its structure, which increases its active site[8]. Zeolitic imidazolate frameworks (ZIFs) are the group of MOFs composed of the M-Im-M structure (where M stands for metal cation, i.e., Zn or Co and Im represents the imidazole linkage). The angles of M-Im-M are closed to 145°. Hence, ZIFs structure are related to zeolite structure[9]. ZIFs have been widely applied in many fields, including H_2 storage material[10], CO_2 adsorption[11] and catalyst[12]. One of outstanding ZIFs is ZIF-8, with a sodalite (SOD) topology consisting of Zn and a five-member ring of 2-methyl imidazole (2Im)[13], has high mechanical strength and excellent chemical and thermal stability[14].Moreover, ZIF-8 has an excellent hydrophobic property due to its chemical composition, i.e., methyl in the 2Im linker and the coordinately saturated metal ion[15]. Therefore, ZIF-8 has been applied to oil spill cleanup, i.e., ZIF-8/teabag[16], ZIF-8-melamine sponge composite[17], ZIF-modified PLA (poly lactic acid) material[18], ZIF-PDA (polydopamine)- melamine sponge[19].

ZIF-8 has been synthesized by many methods including solvothermal[20], hydrothermal[21], solvent minimization[22] and mechanochemical[23].For particle size modification, increasing the ligand/metal ratio significantly reduced the particle size. An excess ligand will cover the crystal seed and restrict it to link to metal ion[24]. Another way is the addition of a modulating agent during the synthesis step. The modulating agent will act as a buffer for ligand promoting ligand-metal interaction. Hence, fast ligand-metal interaction will occur, resulting in a small crystal size[25]. Among these moderating agents, triethylamine (TEA) has been widely studied for controlling the particle size of ZIF-8[26].

The aim of this work is to study the synthesization of small particle ZIF-8 using high

ligand/metal ratio (8:1) and TEA as a modulating agent and varying synthesis temperature. The synthesized ZIF-8 will be investigated by XRD, FT-IR, SEM, TEM. The hydrophobicity will be confirmed by water contact angle. Oil adsorption capacity and oil mop up will be analyzed as well.

2. Materials and Methods

2.1 Materials

Zinc nitrate hexahydrate (Zn(NO$_3$)$_2$.6H$_2$O, 98%) 2-Methylimidazole (2IM ; C$_4$H$_6$N$_2$, 99%) and Triethylamine (TEA ; (C$_2$H$_5$)$_3$N , 95%) and standard ZIF-8 (ZIF8-std; Basolite® Z1200) were obtained from Sigma-Aldrich. All chemicals were used without further purification.

2.2 Synthesis

The solutions of Zn^{2+} salt (solution A) and 2-IM (solution B) were prepared separately. The molar ratio of Zn^{2+}: 2IM: TEA: H_2O = 1: 8: 2.57: 1240. For solution A, 0.334 g (1.12 mmol) of Zn(NO$_3$)$_2$.6H$_2$O was dissolved in 25 ml (694.4 mmol) deionized water. In the case of solution B, 0.7307 g (8.9 mmol) of 2-IM was dissolved in 25 ml (694.4 mmol) deionized water. Then 0.4 ml (2.89 mmol) of TEA was slowly added in this solution. Solution B was added into solution A under stirring at room temperature for 1 hr. Then the solution was poured into a Teflon liner and heated at 25, 80, 100, 120, 140 °C for 4 hrs. The resulting white solid was separated by centrifugation, washed 3 times with deionized water, and dried at 80 °C for 24 hrs. The synthesized ZIF-8 was defined as the symbol ZIF8-xxC, where xx is the synthesizing temperature.

2.3 Characterization

Structure and morphology of samples were studied by x-ray diffraction (XRD, Bruker, D8 advance), Fourier-transform infrared spectroscopy (FT-IR, Bruker, tensor 27), transmission electron microscope (TEM, JOEL, JEM2100) and scanning electron microscope (SEM, JEOL, JSM-5800 LV). Water contact angle was performed by optical contact angle (Dataphysics instruments, OCA25Q).

2.4 Oil sorption capacity

30 ml of soybean oil (100% purity, density@15 °C = 0.9223 g/cm^3, kinematic viscosity of 31.94 mm^2/s) was placed in a 100 ml glass bottle. A curtained amount of ZIF8-25C (0.1g) was then added to the bottle and completely mixed at 0.5, 1 ,1.5, 2, 2.5 and 3 hrs. Removed ZIF-8 by filtration and dried at 105 °C for 1 hr. Keep samples in the desiccator until they cool to room temperature. The adsorption capacity of ZIF-8 was calculated according to (1). Plotted graph adsorption capacity versus time and calculated equilibrium adsorption.

$$adsorption\ capacity\ \left(\frac{g}{g}\right) = \frac{m_2 - m_1}{m_1} \quad (1)$$

Where m_1 and m_2 are the masses of the sample before and after oil adsorption. Test oil adsorption for other samples using equilibrium adsorption time.

2.5 Oil-water separation

Soybean oil (100% purity, density@15 °C = 0.9223 g/cm^3, kinematic viscosity 31.94 mm^2/s) and lubricant oil (Omala S2 GX-150, density@15 °C = 0.8963 g/cm^3, kinematic viscosity 151.8 mm^2/s) were represented oil from household and industry, respectively.

The synthesized ZIF-8 powder was pressed into a pellet with a diameter of 13 mm by hydraulic press. 0.1 ml of oil was added to 10 ml distilled water in the petri dish. The pellet was placed on surface of oil on petri dish. The oil will be mopped up by ZIF-8 pellet.

3. Results & Discussion

3.1 Characterization of as synthesized ZIF-8.

In this research, ZIF-8 was synthesized from Zn(NO$_3$)$_2$.6H$_2$O and 2-methyl imidazole in aqueous solutions at different temperatures. Trimethylamine was used as a modulating agent. Figure 1 depicts the XRD spectra of different ZIF-8 samples. The characteristic diffraction peaks of ZIF-8 at 7.4°, 10.4°, 12.8°, 14.7°, 16.5°, 18.1°, 22.2°, 24.6°, 26.7°, 29.7°, 30.7°, 31.6° and 32.5° with corresponding to planes of (001), (002), (112), (022), (013), 18.1° (222), (114), (233), (134), (044), (334), (244) and (235), respectively[14]. However, ZIF8-25C and ZIF8-140C had other peaks at 13.5°, 15.5°, 18.8° and 21° which indicated an incomplete reaction at low temperature (ZIF8-25C) and high temperature (ZIF8-140C). Therefore, the suitable reaction's temperature of ZIF-8 is in range of 80 – 120 °C.

The FT-IR spectra of ZIF-8 samples prepared at
a different temperature is shown in figure 2. The main broad band at 3550 – 3200 cm^{-1} refer to existence of -OH stretching which indicates to water physisorption in ZIF-8 structure[27].

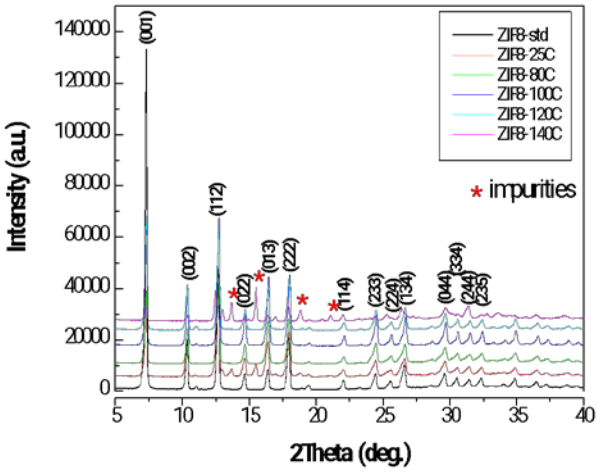

Figure 1. XRD patterns of ZIF-8 powder prepared at different temperatures.

The bands at 3135, 2929, 1678, 1586, 1470 and 1231 cm^{-1} are associated which C–H stretching of aromatic C–H[28], C–H stretching of aliphatic C–H bonds[29], N-H bending, N-H stretching[30], C=N stretching[31] and C-N[32] in imidazole ring. The band at 1530 - 1350 cm^{-1} and 1350 - 800 cm^{-1} were assigned to in-plane bending and stretching of imidazole ring[2]. In addition, the bands at 420 cm^{-1} confirmed the bond between Zn ion and methylimidazole (Zn-N stretching) which guaranteed the ZIF-8 structure[2]. There are no significant differences on chemical function groups of ZIF-8 samples at different temperatures.

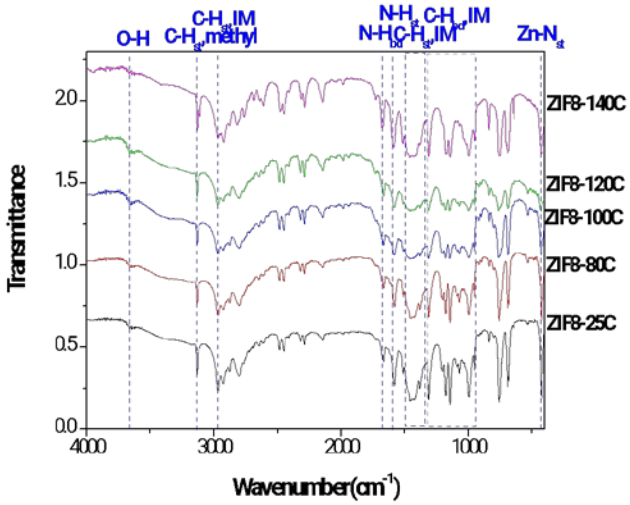

Figure 2. FT-IR spectra of the different ZIF-8 samples prepared at different temperatures.

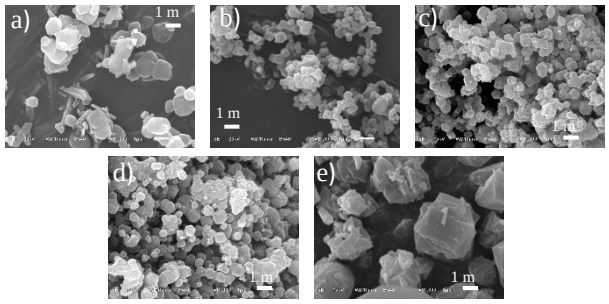

Figure 3. SEM images of ZIF-8 samples prepared at different temperatures: (a) 25 °C, (b) 80 °C, (c) 100 °C, (d) 120 °C, (e) 140 °C.

Figure 3 displays the morphology of prepared ZIF-8 at different temperatures. ZIF-8 has a plate-like shape. The size is about 1 ⌠m. When increasing the synthesis temperature from 25°C to 120 °C, the size of ZIF-8 particles increases while particle size distribution decreases. At 120 °C, ZIF-8 particles were agglomerated, and their size increased to more than 3 ⌠m.

From the results of XRD, FT-IR and SEM, ZIF8-80C is the most suitable preparation condition due to its high purity and size distribution. Therefore, ZIF8-80C will be used for further study.

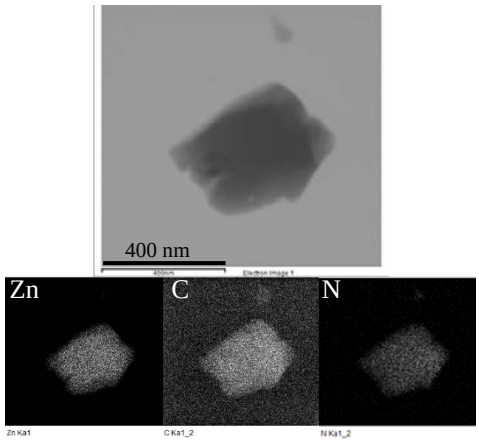

Figure 4. TEM image of ZIF8-80C (a) with energy-dispersive X-ray (EDX) mapping for different elements (Zn, C, and N).

Figure 4 shows a TEM image of ZIF8-80C, illustrating the plate-like shape of the obtained ZIF-8. The element mapping demonstrated a homogeneous distribution of Zn, C, N elements in ZIF-8. To further confirm the hydrophobicity, the water contact angle of ZIF8-80C will be measured. The result is shown in Figure 5. It was found that ZIF-8 is hydrophobic with a water (3⌠L) of 113°. The reason for its hydrophobicity comes from the hydrophobic

composition of conjugated imidazolate rings. Therefore, ZIF-8 exhibits the potential for oil/water removal.

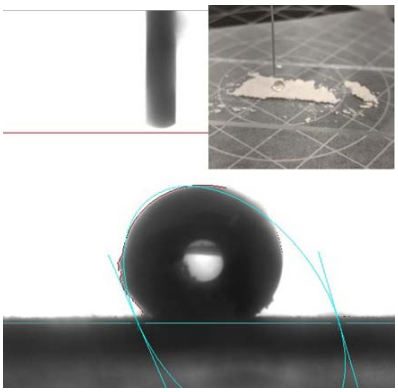

Figure 5. Contact angle measurement of ZIF8-80C after dropping water (3 μL) onto the sample. Insert show digital photograph.

3.2 Absorption of an oil

ZIF8-80C powder was tested to identify the oil adsorption capacity. In this study, soybean oil, with good water mixing, was used for oil adsorption because of its low kinematic viscosity. The results are shown in Figure 6. The kinetic adsorption of oil adsorption was reached to equilibrium adsorption (2.5 g/g) after 1.5 hr. Therefore, the equilibrium adsorption time (1.5h) will be applied to the rest of ZIF-8 samples.

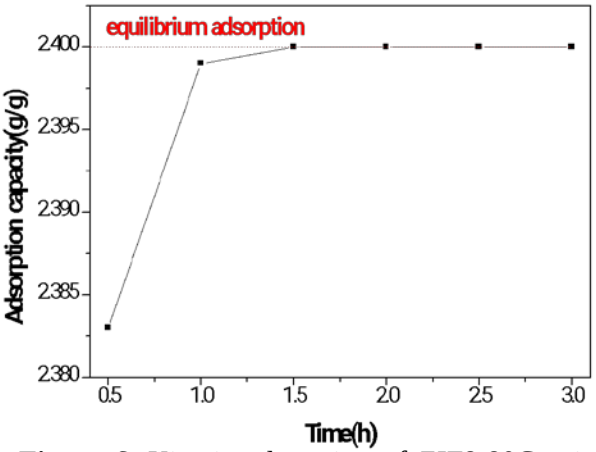

Figure 6. Kinetic adsorption of ZIF8-80C using soybean oil. (red dot line show the equilibrium adsorption capacity)

The adsorption capacity of ZIF-8 samples and comparison with standard ZIF-8 (ZIF8-std, Basolite® Z1200, Sigma-Aldrich) using soybean oil are shown in figure 7. The reuse of ZIF-8 was presented as well. Recorded adsorption values were in the range of 1.9 – 3.5 g/g (calculated using equation 1). The capacities were ordered as follows: ZIF8-std > ZIF8-120C H ZIF8-80C > ZIF8-100C > ZIF8-25C > ZIF8-140C. ZIF8-80C has the highest adsorption capacity of ZIF-8 samples (2.5 g/g). Although this capacity is slightly smaller than that of standard ZIF-8 (ZIF8-std, 3.5 g/g), it is still higher than 100%.

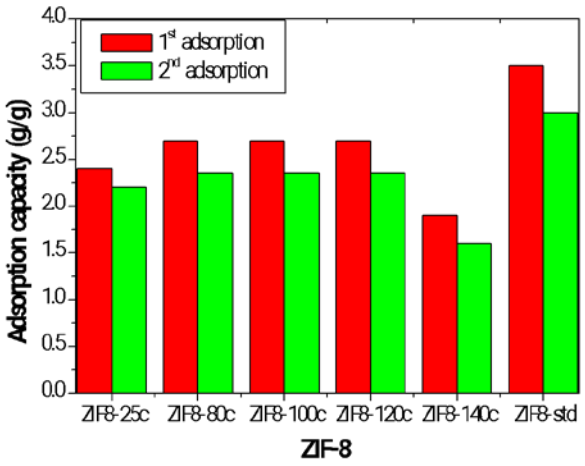

Figure 7. Adsorption capacities of ZIF-8 prepared at different temperatures after two cycles. (calculated using eq. 1).

In practical use, the reusability will be evaluated. Before the reusable experiment, oil trapping was removed by soaking in a nonpolar solvent (toluene). The results are illustrated in figure 7. It was confirmed that ZIF-8 samples were usable. The adsorption capacities decreased by about 11.8 – 20.4%. However, these capacities are still higher than 100%. Hence, it was confirmed that the ZIF-8 samples were usable. According to all the results mentioned above, ZIF8-80C will be selected for testing in the next step.

3.3 Oil removal from oil-water mixture

According to hydrophobicity (contact angle > 90°) and high adsorption capacity (2.5 g/g), ZIF8-80C was chosen to absorb oil spills on water surfaces. The sample was tested on volumetric oil/water (0.1:10) separation. ZIF-8 pellets were used for oil mobs over the water surface. To simulate an oil spill, lubricant oil and soy bean oil were used to represent oil contamination from industry and housing, respectively. The result is illustrated in Figure 8. The sample pellet can be placed over an oil spill spot and totally absorb all of the oil. In addition, the quality of water has not changed between before and after experiments, which confirms that ZIF-8 pellet absorb only oil on water surface

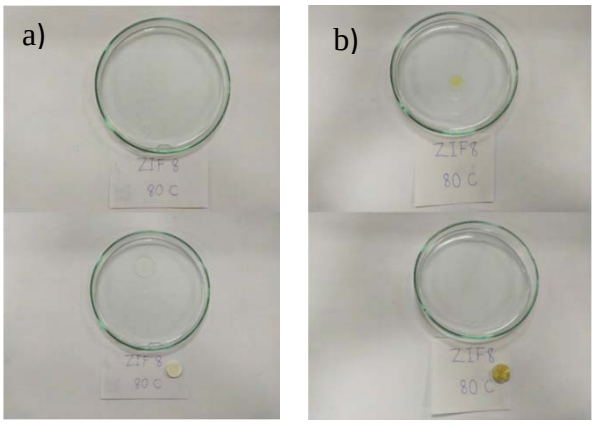

Figure 8. Oil removal by synthesized ZIF8-80C pellet**: (**a**)** Soybean oil, **(**b**)** Lubricant oil**.**

Table 1. Comparison of oil removal efficiency of synthesized ZIF-8 and commercial products

Name	Oil removal efficiency (g/g)
Synthesized ZIF-8	2.5
Absorb Pro clean	0.68
ZEP O-ZORB	1.15
BS-BOS-PULP	16.0
LITE-DRI	3.0
Absorb Pro clean	0.68

Table 1 shows oil adsorption capacities of synthesized ZIF-8 and commercial products**.** The adsorption capacities were ordered as follows: BS-BOS-PULP > LITE-DRI > ZIF-8 > ZEP O-ZORB > Absorb Pro Clean**.** Unfortunately, synthesized ZIF-8 does not have the highest capacity**.** Therefore, structure modification of ZIF-8 and large-scale production will be further investigated to gain higher adsorption capacity**.**

4. Conclusion

The successful ZIF-8 synthesized by hydrothermal method using TEA as a modulating agent is demonstrated. The hydrophobic property (water contact angle = 113°) indicated the oil adsorption capacity. Data from XRD, FT-IR, SEM, TEM and oil adsorption capacity suggested that ZIF8-80C is a suitable condition because of its high crystallinity, small and highly dispersed particle, and high oil adsorption capacity. For oil spill cleanup simulation, ZIF-8 pellets show high efficiency to mop up oil over water. However, synthesized ZIF-8 has the highest oil removal capacity compared with other commercial products. Therefore, ZIF-8 will further study oil adsorption improvement.

Acknowledgements

This work was financially supported by the division of chemicals and consumer products, department of science service, Ministry of Higher Education, Science, Research and Innovation.

References

1. Asif Z.; Chen Z.; An C.;Dong, J. *J. Mar. Sci. Eng.*, 2022, 10,6,762.
2. Pintor A.M.A.; Vilar V.J.P.; Botelho C.M.S.; et.al., *Chem.Eng.J.*,2016,297,229-255.
3. Akpomie K.G; Onyeabor C.F.; Ezeofor C.C.; et.al. *J. African Earth Sci*., 2019, 155, 118-123.
4. Adebajo M.O.; Fros R.L.; Kloprogge J.T.; et al., *J. Porous. Mater.*, 2003, 10, 159-170.
5. Sayari A.; Hamoudi S.; ; Yang Y., *Chem. Mater.*, 2005, 17, 212-216.
6. Deschamps G.; Caruel H.; Borredon M.E.; et.al., *Environ. Sci. Technol.* 2003, 37, 5, 1013–1015.
7. Zhu Q.; Pan Q.; Liu F., *J. Phys. Chem. C*, 2011, 115, 35, 17464–17470.
8. Schlichte K.; Kratzke T.;Kaskel S., *Microporous Mesoporous Mater.*, 2004, 73, 81–88.
9. Moggach S. A.; Bennett T. D.; Cheetham A. K., *Angew.Chem.*, 2009, 121, 7221–7223.
10. Li Y.S.; Liang F.Y.; Bux H.; et.al., *Angew. Chem. Int. Ed.*, 2010, 49, 548–551.
11. Morris W.; Leung B.; Furukawa H.; et.al., *J. Am. Chem. Soc.*, 2010, 132, 11006–11008.
12. Zhou X.; Zhang H.P.; Wang G.Y.; et.al., *J. Mol. Catal. A: Chem.*,2013, 366, 43–47.
13. Trung T. B.; Nguyen D. C.; Yong S. K.; et.al., *Mater. Lett.*, 2018,212,69-72.
14. Park S.K.;Ni.Z; Cote.A.P.; et.al., *PNAS*., 2006, 103, 27, 10186 – 10191.
15. Zhang K.; Lively R. P.; Dose M. E.; et.al., *Chem. Comm.*,2013,49,3245-3247.
16. Sann E.E.; Pan Y.; Gao Z.; et.al., *Sep. Purif. Technol.*,2018,206,186-191.
17. Zhu H.; Zhang Q.; Li B.G.; et.al., *Adv. Mater. Interfaces*., 2017,4,20,1700560.
18. Shen L.; Wang X.; Zhang Z.; et.al., *ACS Appl. Mater. Interfaces*., 2021, 13, 12, 14653–14661.
19. Zhang Y.; Hou S.; Song H.; et.al., J. *Hazard. Mater.*,2023,451,131064.
20. Nune S. K.; Thallapally P. K.; Dohnalkova A.;et.al., *Chem. Commun.*, 2010, 46, 4878–4880.
21. Tanaka S.; Kida K.; Okita M.; et.al., *Chem. Lett.*, 2012, 41, 1337–1339.

22. Lin. J.B.; Lin R. B.; Cheng X. N.; et.al., *Chen, Chem. Commun.*, 2011, 47, 9185–9187.
23. Cao S.; Bennett T. D.; Keen D. A.; et.al., *Chem. Commun.*, 2012, 48, 7805–7807.
24. Yamamoto D.; Maki T.; Watanabe S.; et.al., *J. Chem. Eng.*, 2013,227, 145-150.
25. Biemmi E.; Christian S.; Stock N.;et.al., *Microporous Mesoporous Mater.* 2009, 117, ,1–2, 111-117.
26. Ordoñez M. J. C.; Balkus K. J.; Ferraris J. P.; et.al., *J. Membr. Sci.*, 2010, 361,1–2, 28-37.
27. Yahia M.; Le Q. N. P.; Ismail N.; et.al. *Microporous Mesoporous Mater.*, 2021, 312, 110761.
28. Butova V.V.; Budnyk A.P.; Bulanova E.A.; et.al., *Solid State Sci*, 2017, 69, 13-21
29. Zhang Y.; Jai Y.; Li M.; Hou L., *Sci. Rep.*, 2018, 8, 9597.
30. Moggach S. A.; Bennett T. D.; Cheetham A. K., *Angew. Chem.*, 2009, 121, 7221–7223.
31. Goyal S.; Shaharun M.S.; Kait C.F.; et.al., *J. Phys. Conf. Ser.*, 2018, 123, 012062.
32. Santoso E.; Ediati R.; Istiqomah Z.; et.al., *Microporous Mesoporous Mater.*, 2021, 310, 110620.

Preparation of activated carbon from spent coffee grounds by radiation processing for methylene blue adsorption

Phunkamon Khantiakarapat[1], Jariyaporn Sangkaworn[1], Threeraphat Chutimasakul[2], and Jonggol Tantirungrotechai[1]*

[1]*Department of Chemistry, Faculty of Science, Mahidol University, Bangkok 10400, Thailand*
[2]*Thailand Institute of Nuclear Technology, Nakhon Nayok 26120, Thailand*

**E-mail address: jonggol.jar@mahidol.edu*

Abstract:

Activated carbon is commonly used in water purification systems due to its high surface area and non-toxicity. One of the promising precursors for the preparation of activated carbon is spent coffee grounds because of their high carbon and low inorganic contents. In addition, pre-treatment of the carbon source is an important step to improve the properties of the activated carbon. Therefore, in this work, we proposed a pre-treatment method for the activated carbon using e-beam irradiation to decompose the lignocellulose chains of the spent coffee grounds. The samples pre-treated with e-beam irradiation were compared to those without pre-treatment. The physical characteristics of all activated carbon were investigated using x-ray powder diffraction (XRD), scanning electron microscopy (SEM), Fourier-transform infrared (FT-IR) spectroscopy, and specific surface area measurements. Furthermore, we tested all samples in the adsorption of methylene blue (MB). The results showed that the activated carbon pre-treated with e-beam exhibited porous surface and a larger surface area. Compared to the sample without pre-treatment, the surface area improved from 117.82 to 1,064.1 m^2/g. Moreover, it demonstrated an adsorption capacity of 150 mg/g. The results illustrated that e-beam irradiation is an effective pre-treatment method for the preparation of activated carbon.

1. Introduction

Water pollution, a global issue, is primarily caused by dyes in industry, such as methylene blue, methyl orange, and neutral red, which directly impact the environment and human health.[1] Generally, numerous techniques have been used to remove these dyes from water, including physical, chemical, and biological methods.[2] The adsorption with porous materials is commonly used to remove dyes, owing to its simplicity, cost-effectiveness, and rapidity. One example of porous materials commonly used for dye removal is activated carbon (AC) because of its high porosity, surface area, and reactivity. Currently, biomass is the precursor used in producing activated carbon due to its low cost, high abundance, and carbon source. There are many types of biomasses, such as wood, rubber trees, paper, fruit peels, and spent coffee grounds.[2,3] Among these biomasses, spent coffee grounds are very interesting for preparing ACs. It is reported that each year spent coffee grounds continuously increased, from 8.82 million tons in 2012 to 10 million tons in 2020, in response to consumption.[4] Thus, exploring application for spent coffee grounds is attractive and can decrease waste.

The activated carbons can be prepared in two processes: pre-treatment and activation methods to enhance their porosity, surface area, and reactivity. The pre-treatment involves removing contaminants and shortening the biomass basic polymeric composites (cellulose, hemicellulose, and lignin) before activation to reduce the use of chemicals and energy. There are several pre-treatments, including physical processing (e.g., grinding/milling and washing), chemical processing (e.g., acid washing and oxidation), and radiation processing (e.g., plasma, gamma ray, and e-beam). This study focuses on radiation processing due to its advantageous features, such as time efficiency, eco-friendliness, minimal energy usage, and potential for extensive production.[5] In recent years, the radiation processing with electron beam (e-beam) has been applied for preparing ACs. In 2020, Sarosi et al. studied the effects of e-beam on cellulose pulps' properties with different lignin and hemicellulose contents. The results showed that e-beam can effectively break down cellulose chains, reduce the degree of polymerization, and increase the crystallinity of the cellulose.[6] Furthermore, Karthika et al. reported the combined treatment of acid and alkali pre-soaking with e-beam irradiation (EBI). They described that the use of EBI could help to decrease the crystallinity of the biomass, which also made it more susceptible to enzymatic hydrolysis.[7]

The chemical activation integrates the carbonization and activation processes into a single step, facilitated by the presence of activation agents such as KOH, $ZnCl_2$, H_2SO_4, and K_2CO_3. Among these activating agents, KOH emerges as a commonly employed substance because of its relatively moderate activation temperature,

increased biochar yields, and the creation of a highly developed microporous structure characterized by an exceptionally high specific surface area.[8] Several studies have explored the preparation of activated carbon by KOH activation. Their primary focus has been examining the chemical reactions between carbon and KOH, given that carbon constitutes the predominant component in these carbon-enriched feedstocks.[3,8-9.]

This work aimed to prepare the activated carbons from spent coffee grounds using an electron beam pre-treatment before the chemical activation to increase the efficiency of activated carbons in adsorbing methylene blue solutions.

2. Materials and Methods

2.1 Collection of spent coffee grounds

Spent coffee grounds from coffee shops in Bangkok city were selected to prepare activated carbon. To remove the mud and other impurities on their surface, spent coffee grounds were washed with hot deionized water (DI water) at 80 °C, dried at 120 °C overnight, sieved to 100-meth, and then stored in a sealed bottle for use in the future carbonizatio and activation processes. The obtained spent coffee grounds after washing were denoted as SCG.

2.2 Pre-treatment of SCG using electron beam irradiation (e-beam)

To improve the properties of activated carbon, the pre-treatment method using e-beam was used to decompose the lignocellulose chains of the spent coffee grounds. For the process, 100 g of SCG were irradiated by e-beam with different doses (100, 200, 300, and 400 kGy) using a linear accelerator (LINAC) at Thailand Institute of Nuclear Technology (TINT). The obtained samples pre-treated with e-beam at different doses were denoted SCG-E100, SCG-E200, SCG-E300, and SCG-E400, respectively.

2.3 Preparation of activated carbons (ACs) derived from SCG and pre-treated spent coffee grounds.

All samples (SCG and samples pre-treated with e-beam) were chemically activated by potassium hydroxide (KOH, 85%, AR grade, Loba) as the activating agent at the ratio of 1:2. The mixtures were impregnated for 3 days at 80 °C to ensure thorough penetration of KOH throughout the samples. Then, the impregnated samples were placed in a high-temperature tube furnace to be calcined under nitrogen gas. They were calcined at 800 °C with a heating rate of 5 °C/min for 5 h and then cooled to room temperature. After calcination, they were washed with 0.1 M sulfuric acid (H_2SO_4, 98%, AR grade, RCI) and DI water until obtaining a neutral pH, dried in a convection oven at 120 °C overnight, grounded, sieved to 100-meth, and then stored in a desiccator for use. The activated carbon derived from SCG was denoted SCG-AC, while the activated carbons derived from pre-treated spent coffee grounds were denoted SCG-ACs-EX, indicating which pre-treatment dose (X). For example, SCG-ACs-E100 is activated carbon pre-treated with e-beam at 100 kGy. However, the untreated spent coffee ground without chemical activation was denoted as SCG-Cs.

2.4 Characterization of ACs

All pre-treated ACs with e-beam irradiation and untreated ACs were characterized by using following techniques. The Fourier-transform infrared spectrophotometer (FTIR, KBr technique, 400-4000 cm^{-1}, PerkinElmer) was performed to determine the functional groups. X-ray power diffraction (XRD, 2θ = 10-80°, Bruker, D2 Phaser) was employed to investigate the crystallinity of materials. Field emission scanning electron microscopy (FE-SEM, 10 kV, HITACHI, SU-8010) was used to study the morphology of materials. Brunauer-Emmett-Teller (BET, Anton Paar/Autosorb IQ-MP, 3 STAT) was used to determine the specific surface area of the activated carbon and to obtain nitrogen adsorption-desorption isotherms.

2.5 Adsorptive characteristics of ACs

Adsorptive characteristics of the activated carbon derived from the spent coffee grounds were tested by removing methylene blue (MB) a textile dye model. In general, 20 mg of AC were added into 40 ml of MB solution to find the best condition study. The mixture was stirred continuously at 350 rpm at room temperature (33-35 °C) at 100 ppm of initial concentration. The solutions were collected at contact time (10-240 min) using 0.22 μm Teflon filter membrane in filtration to remove the solid particles. Then, the absorbance of MB filtrate solutions was measured at a wavelength of 665 nm using a UV–vis spectroscopy (UV–vis, Shimadzu, UV-2600). Finally, the adsorption capacity (Q_e, mg/g) was calculated according to Equation 1.

$$Q_e = \frac{(C_0 - C_e)}{m} V \quad (1)$$

Where Q_e (mg/g) is the equilibrium adsorption capacity, C_0 and C_e (ppm) are the initial and equilibrium dye concentrations of the adsorption experiment, m (g) is the adsorbent amount, and V (L) is the volume of the dye solution.

3. Results & Discussion

3.1 Characterization of ACs

FTIR spectra of untreated and pre-treated spent coffee grounds with e-beam irradiation before and after calcination are shown in Figure 1. For samples before calcination, shown in Figure 1(a), all pre-treated spent coffee grounds with e-beam irradiation (SCG-E100, SCG-E200, SCG-E300, and SCG-E400) and untreated spent coffee grounds (SCG) show similar FTIR spectra. All samples before calcination showed a broad adsorption band at 3200-3600 cm^{-1}, representing the stretching vibration of the hydroxyl group (–OH). The adsorption band at 2920 cm^{-1} indicates the presence of –C–H stretching.[10] In addition, the absorption band in the region of 1000-1200 cm^{-1} was the C–C vibrations in the cellulose structure. Moreover, the adsorption band at 1600-1700 cm^{-1} was the band of C=O stretching.[11] The pretreatment method may only break down the structure of cellulose or hemicellulose in spent coffee grounds to smaller molecules. For FTIR spectra of chemically activated carbons obtained from samples pre-treated with e-beam irradiation, shown in Figure 1(b), they showed the vibrations of C=C (aromatic ring) at 1620 cm^{-1}, indicating the aromatic linkage's stability.[12] And they showed a peak of C–O stretching at 1113 cm^{-1} and a weak peak of –OH stretching because high temperatures reduce the hydroxyl functional group and water content in cellulose fiber during calcination.[13] These FTIR results confirm the successful preparation of activated carbons by chemical activation.

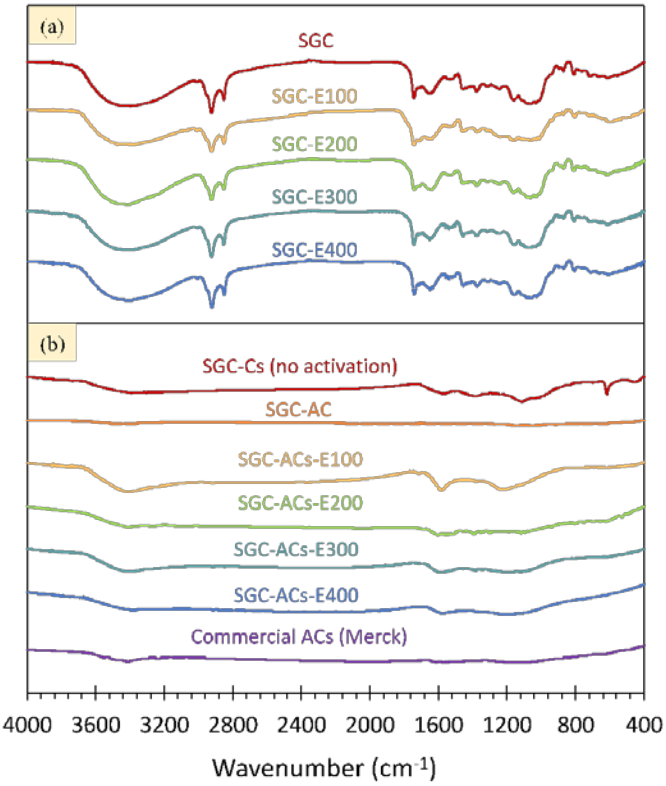

Figure 1. FTIR spectra of untreated and pretreated samples with e-beam irradiation (a) before and (b) after calcination.

X-ray diffractometer (XRD) was employed to study the crystallinity and graphitization degree of activated carbons. The XRD patterns of all chemically activated carbons were compared with untreated spent coffee ground without chemical activation (SCG-Cs) as shown in Figure 2. XRD pattern of SCG-Cs show two strong peaks near 2θ = 23.98° and 43.57° belonging to (002) and (10l) band, which represented of amorphous carbon nanomaterial that associate with hexagonal graphite lattice.[14] For XRD patterns of all chemically activated carbons, the weak diffraction maximum of 43.57° appears in disorder in the activated carbon.[15]

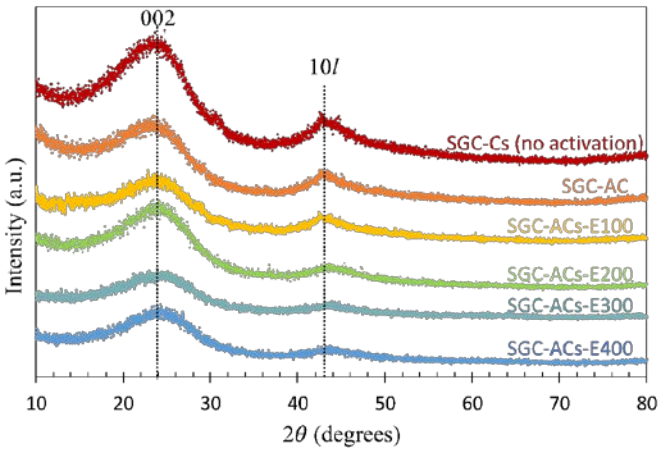

Figure 2. XRD patterns of activated carbons from spent coffee grounds.

SEM images were used to investigate the morphology changes of the chemically activated carbons as shown in Figure 3. All chemically activated carbons derived from samples pre-treated with e-beam irradiation show a porous-like appearance similar to a sponge and rough surfaces compared to those without pre-treatment (SCG-Cs).

N_2 adsorption-desorption isotherms of ACs are shown in Figure 4. They showed an adsorption behavior similar to the type I isotherm, suggesting the existence of micropores. Details of porous characteristics and surface area of all ACs are described in Table 1. The chemically activated carbon derived from samples pre-treated with 400 kGy of e-beam irradiation (SCG-ACs-E400) has the largest specific surface area of 1,064.1 m^2/g and total pore volume of 0.35 cm^3/g. High-treatment energy of e-beam can break down and remove surface contaminants present in the raw

carbon.[16] Moreover, in chemical activation, KOH, as an activation agent, introduces oxygen-containing functional groups like carboxylic acids onto the activated carbon surface during activation.[17] These groups can contribute to the surface area and provide additional binding sites for specific molecules, enhancing adsorption performances as shown in Figure 5.

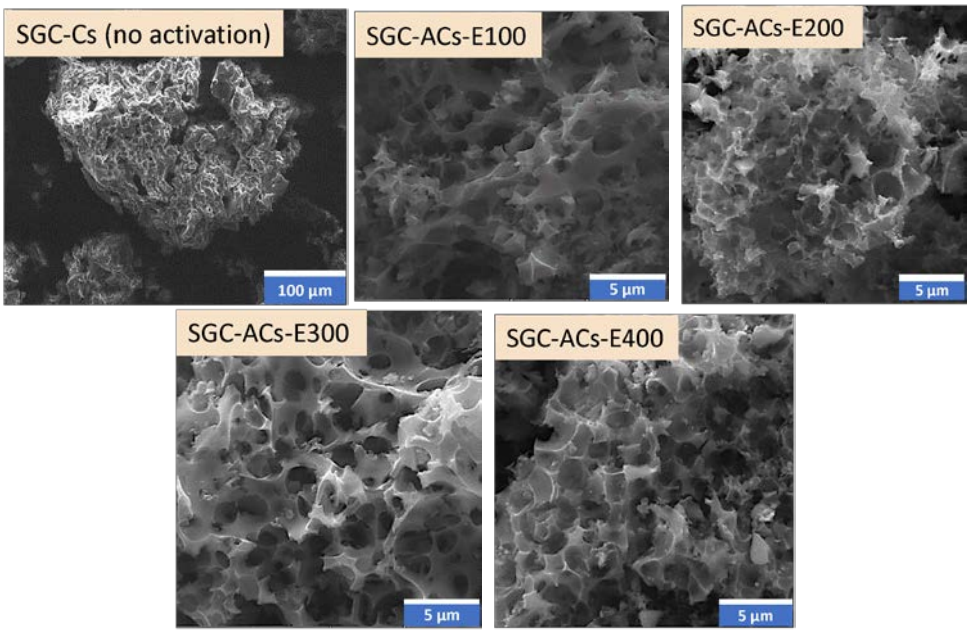

Figure 3. SEM images of untreated sample (SCG-Cs) and pretreated samples with e-beam irradiation; SCG-ACs-E100, SCG-ACs-E200, SCG-ACs-E300, and SCG-ACs-E400.

Table 1. Specific surface area and porosity of activated carbons.

Activated carbons	S_{BET}[a] (m^2g^{-1})	V_{TP}[b] (cm^3g^{-1})	$V_{\mu P}$[c] (cm^3g^{-1})	D_{AP}[d] (nm)
SCG-Cs (no activation)	9.3	0	-	0.06
SCG-AC	117.8	0.05	0.05	1.64
SCG-ACs-E400	1,064.1	0.35	0.24	1.33
Commercial ACs (Merck)	716.6	0.28	0.21	1.56

[a] BET Specific Surface Area
[b] Single point adsorption total pore volume of pores less than 9.384 Å width at p/p° = 0.01
[c] Total micropore volume
[d] Adsorption average pore diameter (4V/A by BET)

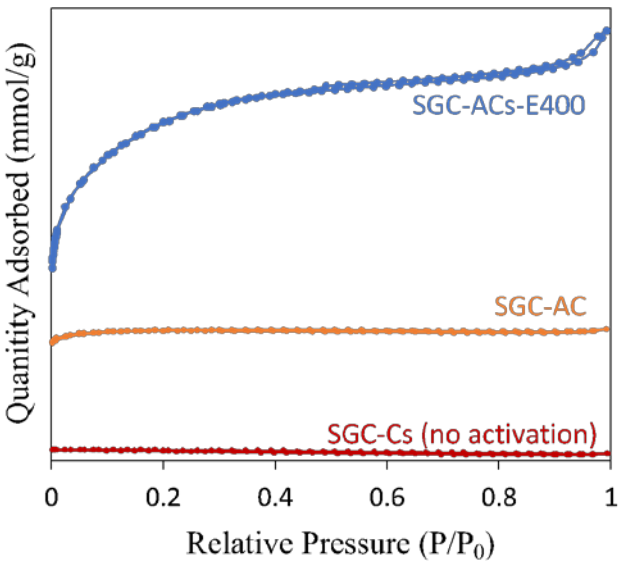

Figure 4. N_2 adsorption–desorption isotherms of activated carbons.

3.2 Adsorptive characteristics of ACs

The adsorption capacities of MB on the activated carbons at an initial concentration of 100 mg/L are shown in Figure 5. The adsorption reached its maximum capacity within a short time period. The equilibrium contact time for all activated carbons was 60 min. The adsorption rates increased during the initial period because of the external surface of the activated carbon. Before adsorption, there were no dye molecules attached to the surface.[18] So, it can absorb the dye on the external surface easily and quickly. After a period of time, the external surface of the activated charcoal is covered with a dye. This caused the slow down diffusion of dye molecules into the interior surface. As a result, the adsorption rate of the dye molecules slows down. Moreover, the dye adsorption capacities of the irradiated activated carbons were higher than those without irradiation. SCG-ACs-E400 has the highest adsorption capacity of 150 mg/g due to its surface area and porosity.

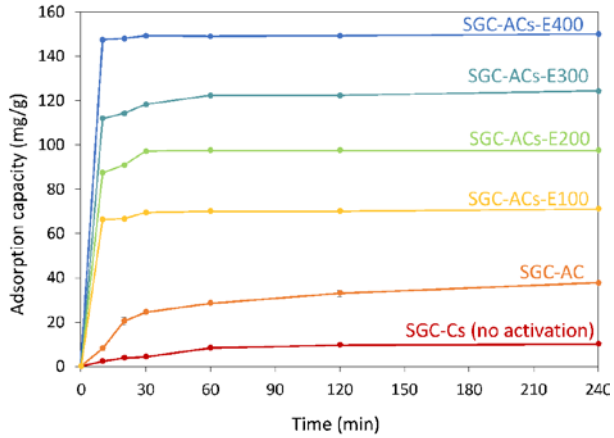

Figure 5. Adsorption capacity of activated carbon for MB vs. contact time. Adsorption condition: 10 mg activated carbon, 150 ml of 100 ppm dye.

4. Conclusions

This study has successfully prepared activated carbons (SGC-ACs-E400) from spent coffee grounds through radiation processing. SCG-ACs-E400 exhibited a specific surface area of 1,064.1 m^2/g and a total pore volume of 0.35 cm^3/g. The obtained high surface area suggests that the radiation processing method effectively created a structure to enhance adsorption properties. In MB adsorption, SGC-ACs-E400 demonstrated an outstanding maximum adsorption capacity (Q_m) of 150 mg/g. This high adsorption capacity highlights their potential for applications in wastewater treatment.

Furthermore, comparing activated carbons derived from spent coffee grounds with and without e-beam pre-treatment reveals that the pre-treated method (SGC-ACs-E400) exhibits superior properties. This finding suggests that the e-beam pre-treatment plays a crucial role in enhancing the overall performance of activated carbons, making them more effective adsorbents.

Acknowledgements

The authors are grateful to financial support from Center of Excellence for Innovation in Chemistry (PERCH-CIC), Faculty of Graduate Studies and Faculty of Science of Mahidol University and Thailand Institute of Nuclear Technology (Public Organization).

References

1. Vandevivere, P. C.; Bianchi, R.; & Verstraete, W. *J. Chem. Technol. Biotechnol.* **1998**, *72*, 289–302.
2. Chuah, T. G.; Jumasiah, A.; Azni, I.; Katayon, S.; Thomas Choong, S. Y. *Desalination.* **2005**, *175*, 305.
3. Wu, F.-C.; Tseng, R.-L.; Hu, C.-C. *Microporous Mesoporous Mater.* **2005**, *80*, 95.
4. Global coffee consumption 2021/21 https://www.statista.com/statistics/292595/global-coffee-consumption/ (accessed Dec 22, 2023).
5. Numee, P.; Sangtawesin, T.; Yilmaz, M.; Kanjana, K. *Carbon Resour. Convers.* **2023**, https://doi.org/10.1016/j.crcon.2023.07.001.
6. Sarosi, O. P.; Bischof, R. H.; Potthast, A. *ACS Sustain. Chem. Eng.* **2020**, *8*, 7235.
7. Karthika, K.; Arun, A. B.; Melo, J. S.; Mittal, K. C.; Kumar, M.; Rekha, P. D. *Bioresour. Technol.* **2013**, *129*, 646.
8. Chen, W.; Gong, M.; Li, K.; Xia, M.; Chen, Z.; Xiao, H.; Fang, Y.; Chen, Y.; Yang, H.; Chen, H. *Appl. Energy.* **2020**, *278*, 115730.
9. Bag, O.; Tekin, K.; Karagoz, S. *Fullerenes Nanotubes Carbon Nanostruct.* **2020**, *28*, 1030.
10. Mukherjee, A.; Borugadda, V. B.; Dynes, J. J.; Niu, C.; Dalai, A. K. *J. Environ. Chem. Eng.* **2021**, *9*, 106049.
11. Davarnejad, R.; Afshar, S.; Etehadfar, P. *Arab. J. Chem.* **2020**, *13*, 5463.
12. Guo, X.; Zhang, T.; Shu, S.; Zheng, W.; Gao, M. *ACS Sustain. Chem. Eng.* **2017**, *5*, 420.
13. Baquero, M. *J. Anal. Appl. Pyrolysis.* **2003**, *70*, 779.
14. Lee, S.-M.; Lee, S.-H.; Roh, J.-S. *Crystals (Basel)* .**2021**, *11*, 153.
15. Wang, B.; Li, S.; Tan, W. *Mater. Sci. Appl.* **2021**, *12*, 417.

16. Börrnert, F.; Avdoshenko, S. M.; Bachmatiuk, A.; Ibrahim, I.; Büchner, B.; Cuniberti, G.; Rümmeli, M. H. *Adv. Mater.* **2012**, *24*, 5630.
17. Zubrik, A.; Matik, M.; Hredzák, S.; Lovás, M.; Danková, Z.; Kováčová, M.; Briančin, J. *J. Clean. Prod.* **2017**, *143*, 643.
18. Jarvis, M. W.; Daily, J. W.; Carstensen, H.-H.; Dean, A. M.; Sharma, S.; Dayton, D. C.; Robichaud, D. J.; Nimlos, M. R. *J. Phys. Chem. A.* **2011**, *115*, 428.

The effect of calcination temperatures on NIR reflection of lateritic soil pigments

Chumphol Busabok[1]*, Wasana Khongwong[1], Sittichai Kanchanasutha[2], Yotin Kallayalert[3], and Pannraphat Takolpuckdee[3]

[1]*Expert Centre of Innovative Materials, Thailand Institute of Scientific and Technological Research, Pathum Thani 12120, Thailand*

[2]*Expert Centre of Innovative Industrial Robotics and Automation, Thailand Institute of Scientific and Technological Research, Pathum Thani 12120, Thailand*

[3]*Faculty of Science and Technology, Valaya Alongkorn Ratjabhat University under the Royal Patronage, Pathum Thani 13180, Thailand*

**E-mail: chumphol@tistr.or.th*

Abstract:

The objective of this research is to investigate the effect of calcination temperatures on the near-infrared (NIR) reflection of lateritic soil pigments. The lateritic soils from Pha Khao district, Loei province, Thailand, were used as raw materials. The raw lateritic soils were ground to reduce their size less than 45 µm and were then calcined at 900-1300℃ for 1 h. The calcined pigments were characterized by an X-ray diffractometer (XRD), a scanning electron microscope (SEM), and a UV-Vis-NIR spectrophotometer. The experimental results showed that quartz and $FeAl_2O_4$ were the two compositions of all calcined powders. $FeAl_2O_4$ spinel was a new phase that was formed by the gradual substitution of Fe^{3+} in the hematite structure (Fe_2O_3) into Al^{3+} in the kaolinite structure ($Al_2O_3{\cdot}2SiO_2{\cdot}2H_2O$). The intensity of $FeAl_2O_4$ was affected by the calcination temperature, the higher it was, the higher the intensity. The highest NIR reflective pigments from lateritic soil occupied a particle size in the range of 1-10 µm which could reflect more than 98% (at a wavelength of 1000 nm) of infrared radiation that was prepared through a calcined firing temperature of 1300℃ for 1 h.

1. Introduction

The world confronts disruptive global climate change from greenhouse gas emissions and extreme energy supplies.[1-3] Cool pigments that absorb near-infrared (NIR) reflecting radiation provide several advantages. Inorganic colored pigments with high near-infrared (NIR) reflectance are widely used in various fields for decorative and protective coatings (e.g. rooftop coverings, vehicle coatings, ceramics or glass coloring, natural fiber dying) due to their high chemical and thermal stability, more importantly, protective capability against solar heat radiation of these NIR reflective materials.[4] Solar spectrum possesses 5% UV (200-400 nm), 43% visible (400-700 nm), and 52% NIR (700-2500 nm) radiation, where the heat-producing area is in the NIR region.[5] This is because infrared (IR) radiation excites the molecules, atoms vibrating and position-changing, resulting in heat up inside those molecules.[6] Solar radiation is a key factor that has an impact not only on the appearance, condition, and rate of skin aging but also on the general health of the human body. Each of the solar radiation ranges has a different wavelength as well as the associated depth of penetration into the skin. Some part of IR (approximately 1/3) is reflected, after contact with the skin, the remaining part penetrates deep into the tissues. Penetration ability depends on the wavelength, the longer it is, the shallower the penetration.[7] IR radiation can be divided into 3 ranges as conventional types: 1) short-wave radiation, the so-called near (IR-A), with a wavelength of 770-1500 nm (penetrates about 30 mm deep into the tissues and is absorbed mainly at a depth of 10 mm), 2) medium-wave radiation (IR-B) with a wavelength of 1500-4000 nm (penetrates about 10 mm deep into the tissues; it is absorbed mainly at a depth of 3-5 mm) and 3) long-wave radiation (IR-C) with a wavelength of 4000-15,000 nm (penetrates about 0.5-3 mm deep into the skin).[8] The exposed skin for a long period can accumulate heat radiation, which has adverse effects on the skin, including deep wrinkles, aging skin, lost skin elasticity, skin dullness, freckles or dark spots, and the most frightening being skin cancer. Thus, inorganic pigments with high NIR reflectance can be employed as cool pigments and applied to textile dying, improving internal thermal comfort levels to save cooling energy in hot seasons.[9,10] Many NIR reflective pigments have been developed. Still, numerous of these pigments mainly contain toxic heavy metal elements such as Co, Pb, Cd, and Cr.[11-13] Therefore, there is a strong attempt to prepare excellent NIR reflective pigments that are less hazardous, durable, and could serve as superior alternatives for replacing

traditional toxic and heavy metal-based pigments. Among others, spinel-type oxides are an important group of compounds with the general formula AB_2O_4.[14] Fe_2O_3 brown pigments have been used as coating materials for many kinds of roofs to reduce the roof temperature and also simultaneously improve the roof's appearance. Moreover, lateritic soils have been used for traditional fiber dying as folk wisdom.

Lateritic soils are extensively used in tropical areas, including traditional construction materials, local road materials, and traditional natural fiber dying pigments. Lateritic soils consist mainly of kaolinite ($Al_2Si_2O_5(OH)_4$), goethite (α-FeO(OH)), hematite (Fe_2O_3), and gibbsite (γ-$Al(OH)_3$), and are rich in silica (SiO_2), alumina (Al_2O_3), and iron oxides (hematite and goethite).[15] Thus, the development of dying pigments using lateritic soils is reasonable.

Many processes for preparing Fe_2O_3 brown pigments have been developed by researchers.[16,17] Very few studies have reported on spinel red-brown pigments. Also recently, pigments based on rare earth compounds have been extensively studied.[18-20] However, the cost of the rare earth compounds used for synthesizing pigments is rather expensive and, therefore, is not economically available. In the present work, cost-effective new red-brown pigments based on a $FeAl_2O_4$ spinel were prepared and investigated to determine the effect of calcination temperatures on the NIR reflective ability of lateritic soil pigments.

2. Materials and Methods

2.1 Materials

The lateritic soil from the Northeast of Thailand, Pha Khao district, Loei province, was used as raw materials. The apparent color of the soil is quite red.

2.2 Preparation of lateritic soil pigments

The raw powder preparation procedure to develop the reflective near-infrared (NIR) radiation property was as follows. The received lateritic soils were first ground using the hammer mill and then sieved at 100 mesh. The passed-through particles were mixed and dispersed by a ball mill for 24 h. After ball milling, the soils were precipitated to separate the particles smaller than 45 µm by performing according to Stokes law. Next, the selected particles were calcined at 900-1300°C for 1 h. Finally, the calcined samples were ground into fine powder and then characterized.

2.3 Characterization of lateritic soil pigments

After the calcination process, all the calcined powders were detected as crystal structures by an X-ray Diffractometer (Shimazu 6000, Cu target, λ =1.54°A, Japan). Scanning Electron Microscopy (SEM, Prisma E, Thermo Scientific, United States) was used to measure soil particle morphology. The chemical composition of calcined lateritic soil pigments was analyzed by an Energy Dispersive Spectrometer (EDS-SEM, Prisma E, Thermo Scientific, United States). Infrared reflectance and color of pigments were measured by a UV-Vis-NIR spectrophotometer (AVANTES Avalight-DHS; Detector AvaSpec-2048L). The particle size distribution of soil pigment powders was characterized by a Particle Size Analyzer (Hydro 2000s, MALVERN, England). To study the effect of calcination temperatures on the infrared reflection of pigments, the calcined pigments at different temperatures of 900-1300°C were compared.

3. Results & Discussion

3.1 Properties of the lateritic soils from Pha Khao district, Loei province.

The morphology of the raw lateritic soil is shown in Figure 1. The lateritic soil had a flake structure along with tiny round grains. The tiny primary particles seemed to form agglomerate particles with particle sizes in the range of 1-15 µm. The chemical compositions in Table 1 show that the lateritic soil was composed of silica (SiO_2) and alumina (Al_2O_3) as two major components with 44.81% and 31.28%, respectively. The minor compositions were ferric oxide (Fe_2O_3) with 11.17% in conjunction with titanium dioxide (TiO_2) with 3.01% and ignition loss was approximately 9.73%.

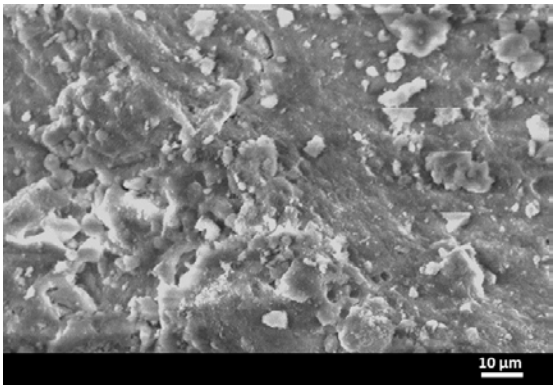

Figure 1. SEM photograph of the lateritic soil from Pha Khao district, Loei province.

Table 1. Chemical composition of the lateritic soil from Pha Khao district, Loei province.

Chemical composition	Amount (%)
SiO_2	44.81
Al_2O_3	31.28
Fe_2O_3	11.17
TiO_2	3.01
Loss on ignition (LOI)	9.73
Sum	100

Figure 2 shows the XRD pattern of the lateritic soil. From the main diffraction peaks, it could be identified that quartz (SiO_2, JCPDS card No. 46-1045) was a major phase, as clearly observed by the sharp peaks and narrow FWHM of SiO_2. Hematite (Fe_2O_3, JCPDS card No. 84-0311, as is well known in the name "red rust") and kaolinite ($Al_2Si_2O_5(OH_4)$, JCPDS card No. 05-0143) were two minor phases.

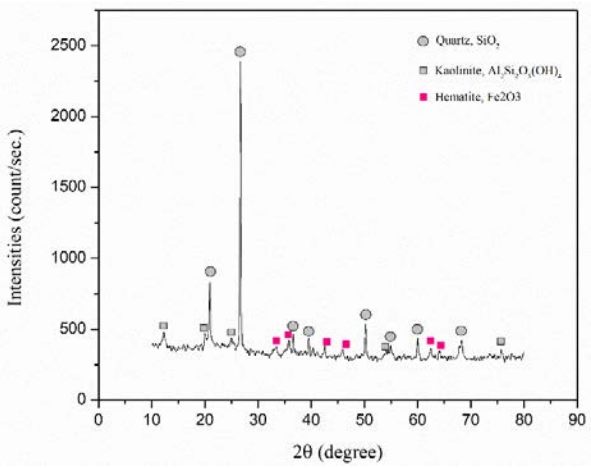

Figure 2. XRD pattern of the lateritic soil from Pha Khao district, Loei province.

3.2 The effect of calcination temperatures on the properties of lateritic soil pigments

Figure 3 shows XRD patterns of the lateritic soils calcined at various temperatures of 900-1300°C. At calcined temperatures of 900-1000°C, only sharp peaks of quartz (SiO_2) were measured. It seemed when the temperature was increased to 1100°C, a new phase as $FeAl_2O_4$ spinel (JCPDS card No. 34-0192) was detected with low intensities. The intensities of $FeAl_2O_4$ peaks increased with increasing temperature.

Thus, the intensities of $FeAl_2O_4$ peaks at 1300°C were higher than the intensities of $FeAl_2O_4$ peaks at 1200°C and 1100°C, respectively. From this result, it can be implied that Al^{3+} in the kaolinite structure ($Al_2O_3{\cdot}2SiO_2{\cdot}2H_2O$) was gradually substituted by Fe^{3+} in hematite structure (Fe_2O_3) at high temperatures. The happening new phase at low temperatures (900-1000°C) might be covered with quartz, or another reason was that the $FeAl_2O_4$ spinel crystal was still incomplete, resulting in it not being detected by XRD.

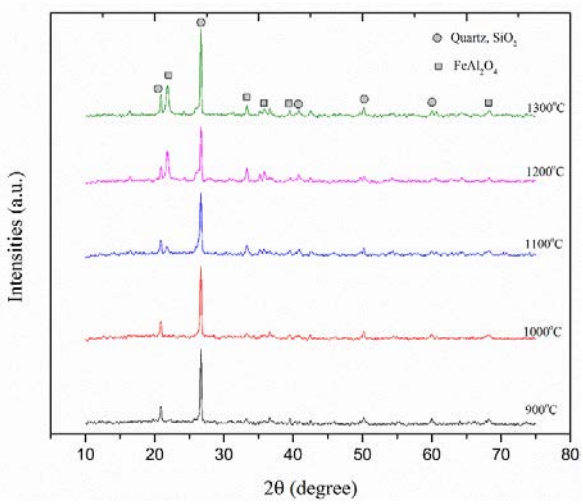

Figure 3. XRD patterns of the calcined lateritic soil at 900-1300°C.

The morphologies of the calcined lateritic soil pigments at 900-1300°C are shown as SEM photographs in Figure 4. Obviously, the particles of all calcined samples at 900-1200°C (see Figure 4 (a)-(d)) showed miniature round grains, not sharp edges. However, the sharp grains lightly appeared in calcined soil pigments at 1300°C (see Figure 4 (e). This was because quartz was the main composition of the calcined lateritic soil pigments. The morphology of quartz particles is quite spherical while $FeAl_2O_4$ is an incisive particle. All particles were distributed in agglomerate form, with particle sizes in the range of 1-10 µm.

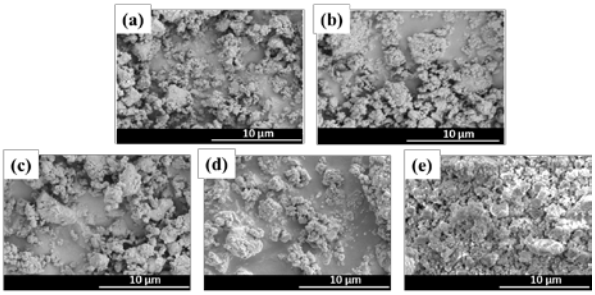

Figure 4. SEM photographs of the calcined lateritic soils at different temperatures; (a) 900°C, (b) 1000°C, (c) 1100°C, (d) 1200°C, and (e) 1300°C.

The NIR reflectance spectra of the calcined lateritic soils were investigated using a UV-Vis-NIR spectrophotometer as the results are shown in Figure 5. Considering at 700-1100 nm, which is the wavelength in the range of NIR spectra, the tendency of NIR reflectance of calcined soil pigments at 900°C and 1000°C

resembled that the value of NIR reflectance was around 87% at 1000 nm. At 1100°C and 1200°C, NIR reflectance gradually decreased, respectively. However, the NIR reflectance of calcined soil pigments at 1300°C becomes the highest of those with an NIR reflectance of approximately 100%. It was because the $FeAl_2O_4$ spinel crystals appeared in this sample.

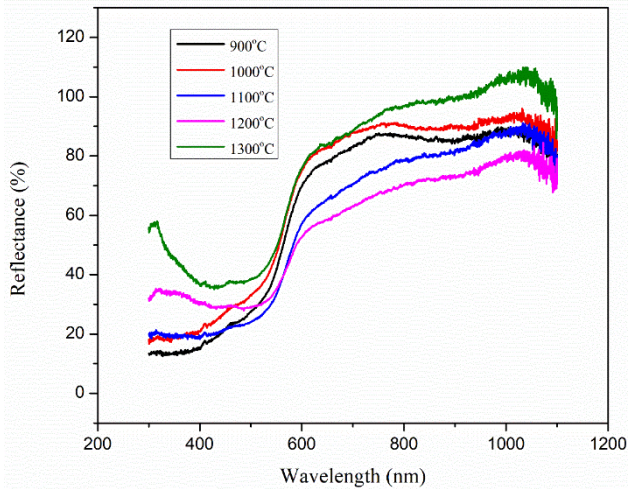

Figure 5. NIR reflectance of the calcined lateritic soils at 900-1300°C.

Figure 6 exhibits the color of the calcined lateritic soils at different temperatures in the range of 900-1300°C. The result presented that the lightness (L^*), redness (a^*) and yellowness (b^*) of the calcined lateritic soils at low temperatures (900°C and 1000°C) were equivalent, with values of 82.82, 19.87, and 35.87, respectively. Increasing the calcination temperatures from 1000°C to 1100°C and 1100°C to 1200°C show gradual descent in lightness, respectively. The calcined pigments at 1100°C, L^*, a^* and b^* were 71.09, 18.63, and 25.10, respectively, which were slightly lower than the calcined pigments at 900°C-1000°C. The values of L^*, a^* and b^* of the calcined pigments at 1200°C were 69.57, 15.50, and 12.11, respectively, which were slightly lower than the calcined pigments at 1100°C. However, increasing the calcination temperature to 1300°C resulted in a lighter pigment than at 1200°C. The values of L^*, a^* and b^* of the calcined pigments at 1300°C were 76.08, 16.50, and 18.31, respectively.

Considering together with XRD and NIR reflectance measurements, it can be confirmed that changing from Fe^{3+} to Fe^{2+} caused more darkness (at 1100-1200°C). However, when the

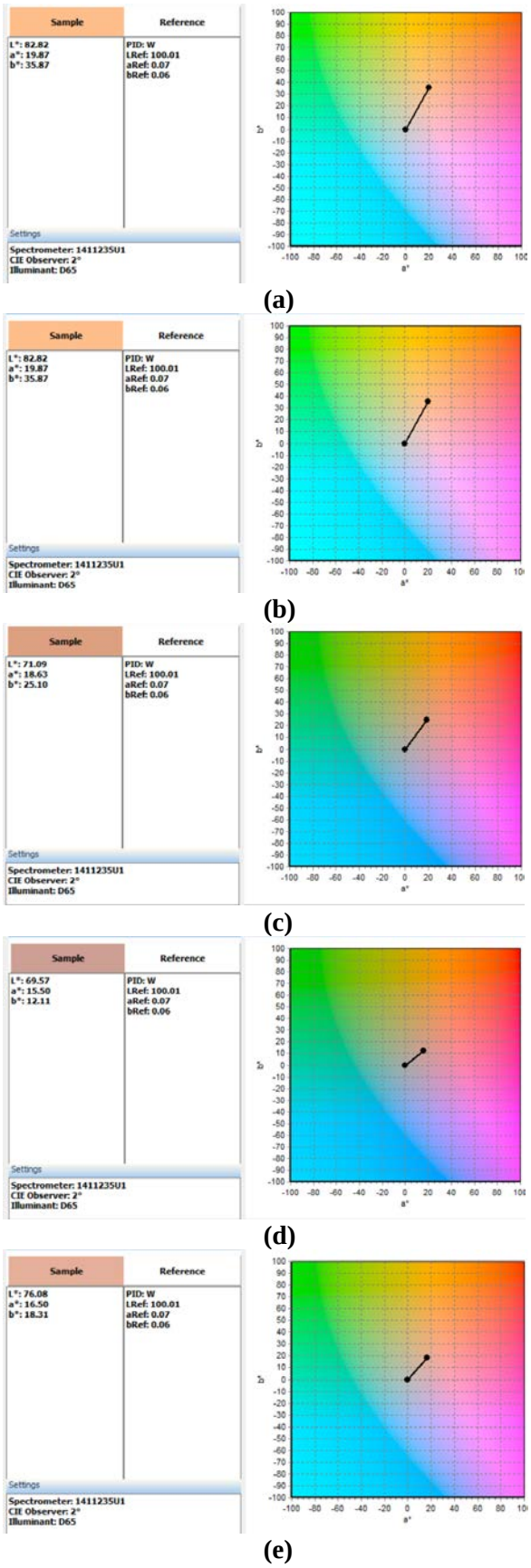

Figure 6. The color of the calcined lateritic soils at different temperatures; (a) 900°C, (b) 1000°C, (c) 1100°C, (d) 1200°C and (e) 1300°C.

$FeAl_2O_4$ spinel new phase was completed (at 1300°C) resulted in more lightness and more NIR reflectance.

Through this work, it was found that using lateritic soils under reasonable conditions can potentially act as alternative NIR reflective pigments for natural fiber dying, exterior paint, and so on. There are various purposes for using NIR reflective pigments, such as decorative and protective coatings, and the potential for reducing solar heat radiation and improving thermal comfort levels. These emphasize the importance of the continuous development of pigments with high NIR reflectance for efficiency application in many fields. Synthetic pigments such as $ZnFe_2O_4$, $TiZn_2O_4$, $SrTBO_3$, $CaCr_2O_4$, etc. can be replaced by low-cost lateritic soil pigments. Moreover, the use of lateritic soil pigments in the above activities is not only for value-added but also for cost reduction in the process and for career encouragement in the local community as well.

4. Conclusion

In this study, the low-cost $FeAl_2O_4$ spinel red-brown pigments with NIR reflectance employing lateritic soil from Pha Khao district, Loei province, Thailand, were prepared using the simple method. The effect of calcination at different temperatures in the 900-1300°C range was investigated. The lateritic soil pigments at higher calcination temperatures possessed sharper peaks of $FeAl_2O_4$ spinel than those pigments prepared at lower calcination temperatures. The Al^{3+} in Al_2O_3 which exists in raw powder, was substituted by Fe^{3+} and changed to Fe^{2+} to form the $FeAl_2O_4$ spinel structure at higher temperatures. The calcined lateritic soil pigments at 1300°C for 1 h occupied the highest NIR reflective pigments of more than 98% at 1000 nm, along with particle size in the 1-10 µm range. Therefore, the developed lateritic soil pigment from this experiment can be used in various applications to reduce the heat from solar energy.

References

1. Santamouris, M.; Cartalis, C.; Synnefa, A.; Kolokotsa, D. *Energy Build*. **2015**, *98*, 119–124.
2. Jabbar, H.K.; Hamood, M.N.; Al-Hameedawi, A.N. *IOP Conf. Ser.: Earth Environ. Sci.* **2023**, *1129*, 012038.
3. Rajagopal, P.; Shanthi Priya; R.; Senthil, R. *Sustain. Cities Soc*. **2023**, *88*, 104279.
4. Schildhammer, D.; Fuhrmann, G.; Petschnig, L.; Weinberger, N.; Schottenberger, H.; Huppertz, H. *Dyes and Pigments*. **2017**,*138*, 90-99.
5. Levinson, R.; Berdahl, P.; Akbari, H. *Sol. Energ. Mat. Sol. Cells*. **2005**, *89(4)*, 319-49.
6. Song, D.Y.; Sprague, R.; Macleod, H.A.; Jacobson, M.R. *Applied optics*. **1985**, *24(8)*, 1164-1170.
7. Anna, S.-W.; Sławomir, W.; Agnieszka, P.;Agata, L.; Łukasz C.; Zuzanna, N. *Clinical, Cosmetic and Investigational Dermatology*. **2023**, *I6*, 2663-2675.
8. Ash, C.; Dubec, M.; Donne, K.; Bashford, T. *Lasers Med Sci*. **2017**, *32(8)*, 1909-1918.
9. Pisello, A.L.; Cotana, F. *Energy and Buildings*. **2014**, *69*, 154-164.
10. Cozza, E.S.; Alloisio, M.; Comite, A.; Di Tanna, G.; Vicini, S. *Solar Energy*. **2015**, *116*, 108-116.
11. Saengsui, W.; Tangkittimasak, T.; Suwan, M.; Sangwong, N.; Tangon, C.; Chanlek, N.; Rakkwamsuk, P., Supothina, S.; Meevasana, W. *J. Alloys Compd*. **2023**, *939*, 168695.
12. Bai, M.; Li, W.; Hong, Y.; Wang, S.; Wang, Y.; Chang, Q. *Sol. Energy*. **2022**, *234*, 240-250.
13. Chen, C.; Han, A.; Ye, M.; Chen, X.; Wang, J. *J. Solid State Chem*. **2022**, *307*, 122873.
14. Alvarez-Docio, C.M.; Reinosa, J.J.; Camp, A. del.; Fernánolez, J.E. *Dyes and Pigments*. **2017**,*137*, 1-11.
15. Soea, M.; Won-Inb, K.; Takashima, I.; Charusirid, P. *Science Asia*. **2008**, *34*, 307-316.
16. Somayeh, S.-N.; Behrooz, G.; Ali, H.; Ebrahim, G.; Mehdi, G. *Materials Science and Engineering: B*. **2022**, *262*, 114752.
17. Yotin, K.; Pannraphat, T.; Sasamol, P.; Chumphol, B. *Prog Appl Sci Tech*. **2023**, *13(1)*, 19-25.
18. Sreeram, K.J.; Srinivasan, R.; Aby, C.P.; Nair, B.U.; Ramasami, T. *Sol. Energy Mat. Sol. C.* **2008**, *92*, 1462-1467.
19. Wang, J.; Han, A.; Ye, M.; Chen, C. *Sol. Energy*. **2022**, *244*, 218-226.
20. Zheng, J.; Li, Z.; Zheng, Y.; Zhao, W.; Tan, F.; Yang, F.; Chen, H.; Xue, L. *Ceram. Int*. **2023**, 49, 558-564.

Hydrogels containing liquid crystal droplets for stretchable display applications

Teerapat Lapsirivatkul, Daniel Crespy, and Pichaya Pattanasattayavong*

Department of Materials Science and Engineering, School of Molecular Science and Engineering, Vidyasirimedhi Institute of Science and Technology, Rayong 21210, Thailand

**E-mail: pichaya.p@vistec. ac.th*

Abstract:

This study explores the incorporation of liquid crystals (LCs) into hydrogels while addressing challenges associated with the inherent incompatibility between hydrophobic LCs and hydrophilic hydrogels. Utilizing direct oil-in-water miniemulsions,[1] non-polar LC droplets were first dispersed in an aqueous medium, overcoming issues of coalescence and Ostwald ripening, followed by the addition of a solution of hydrogel's precursor. The LC-embedded hydrogels exhibited an electro-optical response, manifested as an increase in the optical transmittance (lower turbidity) upon the application of an external bias. This change was ascribed to the positive dielectric anisotropy of LCs confined in the droplets. Differential scanning calorimetry revealed a shift in the nematic-isotropic phase transition towards lower temperatures in the miniemulsion and LC/hydrogel, suggesting a reduced anchoring energy due to confinement in the droplets. In addition, rheological characterization showed that LC-embedded hydrogels retained the mechanical properties of the gel state but with both the storage and loss moduli becoming higher. This work presents a route towards making electro-optically switchable hydrogels that can be developed into stretchable displays.

1. Introduction

Producing flexible and stretchable liquid crystal displays (LCDs) is an important challenge. Non-emissive LCDs have been made flexible through the use of polymer-dispersed liquid crystal (PDLC).[2,3] However, such displays are generally not stretchable and hence not suitable for emerging applications, such as wearable electronics. Hydrogels on the other hand can be designed to be stretchable and compatible with wearable devices. Combining LCs with hydrogels remains a key issue due to the inherent incompatibility between hydrophobic LCs and hydrophilic hydrogel structures. Thus, only a low amount of LCs, ~ 2 – 4 wt%, could be directly dispersed and stabilized in hydrogels.[4–7]

Herein, we present a new strategy for embedding LC emulsion droplets into a hydrogel matrix with LC content of up to 20 wt%, i.e. five times higher than previous reports. Droplets of a LC, *N*-(4-methoxybenzylidene)-4-butylaniline (MBBA), with sizes ranging from 670 to 840 nm were prepared via the miniemulsion technique, utilizing either a non-ionic surfactant (NS) or a cationic surfactant (CS). The droplets were incorporated into polyacrylamide hydrogels, and our LC-embedded hydrogel samples showed variable optical transmittance, controlled by an external alternating current (AC) electric field.

2. Materials and Methods

2.1 Materials

Acrylamide (AAm, 98.5%, ACROS Organics), di(ethylene glycol) diacrylate (DEGDA, 75%, Aldrich), ammonium persulfate (APS, >95%, Carlo Erba), *N,N,N',N'*-tetramethylethylene-diamine (TEMED, 99%, ACROS Organics), hexadecyltrimethylammonium chloride (CTMA-Cl, >95%, TCI), Lutensol AT 50 Pulver (Lutensol AT50, BASF), *n*-hexadecane (99%, ACROS Organics), 2-hydroxy-4′-(2-hydroxy-ethoxy)-2-methylpro-piophenone (Irgacure 2959, 98%, Aldrich), *N,N′*-methylenebis-(acrylamide) (MBAAm, 99%, Aldrich), and *N*-(4-methoxy-benzylidene)-4-butylaniline (MBBA, >98%, TCI) were used as received. Deionized water was used throughout this work.

2.2 Preparation of oil-in-water miniemulsions

MBBA (3 g) was added to 12.5 mg n-hexadecane. Subsequently, an aqueous solution of either Lutensol AT50 or CTMA-Cl (12 g, 0.30 wt%) was added to this mixture under stirring at 1000 rpm at ~25 °C for 1 h. Lutensol AT50 [oligoethylene-*block*-oligo(ethylene glycol)] is a non-ionic surfactant while CTMA-Cl is a cationic surfactant. The resulting emulsions underwent ultrasonication using a Branson Digital Sonifier SFX 550 with 3/400 tip at 40% amplitude in a pulsed mode for 3 min (1 s of sonication with 1 s pause) to form miniemulsion droplets. Then, the dispersions were heated at 60 °C under stirring to evaporate some of the water and obtain LC concentrations between 20 and 40 wt% (monitored by weighing the miniemulsions). The sizes of the nanodroplets in water were measured by dynamic light scattering (DLS) (Zetasizer Lab, Malvern).

Table 1. Compositions of hydrogels.

Using non-ionic surfactant (NS)	AAm (mg)	DEGDA (mg)	TEMED/APS (mg)/(mg)	MBBA LC/Lutensol AT50 emulsion at 25 wt% (mg)	Water (mg)
PAAm_NS1	180	10	120/120	0	1200
PAAm_NS2	180	5	120/120	0	1200
PAAm_NS3	180	2.5	120/120	0	1200
PAAm_NS4	90	5	120/120	0	1200
PAAm_NS4_5p	90	5	120/120	320	880
PAAm_NS4_20p	90	5	120/120	1200	-
Using cationic surfactant (CS)	AAm (mg)	MBAAm (mg)	Irgacure 2959 (mg)	MBBA LC/CTMA-Cl emulsion at 25 wt% (mg)	Water (mg)
PAAm_CS1	250	7.2	12.6	0	2000
PAAm_CS2	250	3.6	12.6	0	2000
PAAm_CS3	250	1.8	12.6	0	2000
PAAm_CS4	125	3.6	12.6	0	2000
PAAm_CS4_5p	125	3.6	12.6	450	1550
PAAm_CS4_20p	125	3.6	12.6	1800	200

2.3 Embedding LCs emulsion droplets in hydrogels

Emulsions stabilized by the non-ionic surfactant Lutensol AT50 were prepared as follows. Varying amounts of MBBA miniemulsions were added to a mixture containing AAm (monomer), DEGDA (crosslinker), and water (see **Table 1**). Note that no MBBA was added during the optimization of the hydrogel fabrication (conditions NS1 to NS4 in **Table 1**). This mixture was then added to 0.12 g of a 0.2 M aqueous solution of TEMED and stirred at 250 rpm for 5 min. Finally, 0.12 g of a 0.2 M aqueous APS solution was added to obtain a hydrogel precursor solution. The resulting solution was quickly deposited onto a fluorine-doped tin oxide (FTO) substrate (resistivity ~15 Ω/sq) with a square aperture made of Kapton serving as a spacer with a thickness of 125 µm. Another FTO was used as the top electrode. The cell was then assembled using a binder clip. The polymerization reaction took place within the cell.

Emulsions stabilized by the cationic surfactant CTMA-Cl were prepared via photopolymerization by substituting the crosslinker and initiator with MBAAm and Irgacure 2959 (see **Table 1**). Subsequently, the cells filled with the LC/hydrogel precursor were irradiated by UV (400 watt, AS01-M260, Awellcure) for 5 min.

2.4 Scanning electron microscopy (SEM)

SEM was employed to determine the pore size of the pure hydrogels without LCs by replacing the LC emulsions in the LC/hydrogel with water. The sample preparation for SEM involved the following steps. Firstly, the hydrogel precursor was mixed according to **Section 2.3** and left to polymerize in a vial (dia. = 28 mm, ht. = 61 mm) overnight. After completing the polymerizations, the hydrogels were cut into pieces and frozen in liquid N_2 for 10 min. Subsequently, the samples underwent freeze-drying (Martin Christ Gefriertrocknungsanlagen) at −55 °C for 24 h. The resulting dried samples were sectioned for cross-sectional micrographs using a Jeol JSM-7610F field-emission scanning electron microscope.

2.5 Electro-optical properties

Optical transmittance measurements of the samples were conducted at room temperature (~ 25 °C) using a USB4000 Fiber Optic Spectrometer (Oceanview) with a spectral range covering 200 to 1100 nm as a detector and a Thorlabs M455L2 light-emitting diode (LED) with an emission spectrum range of 420 to 500 nm (dominant wavelength at 455 nm) as a light source. Due to the limited sensitivity and saturation of the detector, each measured spectrum was normalized to a reference sample for the comparison. Specifically, the transmittance T_0 for each sample was recorded without any applied bias and set as the baseline transmittance. Then, the transmittance T_m was recorded under an applied bias to modulate the optical properties of the sample (bias held for 3 s before each measurement to ensure the state of the sample had already changed). The reference transmittance T_r for each condition was then recorded using the sample with the lowest transmittance which was the miniemulsion with 40 wt% MBBA in CTMA-Cl. The relative transmittance for each sample was calculated by Eq. (1), and the change in the relative transmittance due to the electro-optical response was calculated by Eq. (2):

$$Relative\ transmittance = \frac{T_0}{T_r} \quad (1)$$

$$Change\ in\ relative\ transmittance = \Delta T_m/T_r = \frac{T_m}{T_r} - \frac{T_0}{T_r} \quad (2)$$

2.6 Differential scanning calorimetry (DSC)

DSC measurements were performed by a PerkinElmer DSC 8500. The data were obtained in the temperature range of 4−80 °C at a heating rate of 20 °C min^{-1}.

2.7 Rheological characterization

Rheological analysis of the hydrogels was performed on a TA Instruments Discovery HR-20 rheometer, using a 20 mm steel plate-plate geometry. Measurements of the storage modulus (G′) and loss modulus (G″) as a function of frequency were performed over a range of 0.1−100 rad s^{-1} at 1% strain. We note that only samples prepared with NS could be made thick enough for the rheology analysis.

3. Results & Discussion

3.1 Pore structures of hydrogels

SEM was used to study the pore structures in the hydrogels. Comparing **Figure 1a-c**, the pore size was greatly reduced with the decreasing crosslinker concentration. At the lowest amount (**Figure 1c**), we observed that parts of the hydrogel collapsed to form dense regions. Between **Figure 1b** and **1d**, reducing the monomer concentration also decreased the pore size. We note that only micrographs of hydrogels prepared using CS are shown here for conciseness; the samples prepared with NS showed the same trend.

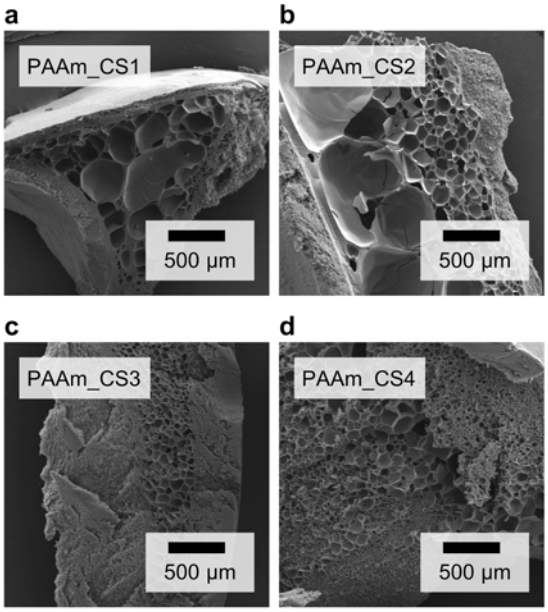

Figure 1. SEM images of hydrogels: (a) PAAm_CS1, (b) PAAm_CS2, (c) PAAm_CS3, and (d) PAAm_CS4 (see **Table 1** for sample conditions).

During the preliminary work, in fact we added the LC emulsions into all hydrogel conditions and found that only PAAm_NS4 and PAAm_CS4 conditions yielded some electro-optical response. This was likely due to the optimal pore size (small, yet non-collapsed pores). On the other hand, the larger pores (NS1-NS2 and CS1-CS2) could lead to the coalescence of the LC droplets whereas the dense structures due to the collapsed pores (NS3 and CS3) could not retain the emulsions in the hydrogels. As a result, only the above mentioned two conditions (NS4 and CS4) were selected for further study as discussed below.

3.2 Electro-optical response

Neat MBBA LC is reported to have a negative dielectric anisotropy ($\Delta\varepsilon < 0$),[8–10] meaning that the molecules tend to align with the short axis parallel to the electric field direction (and the long axis perpendicular to the field). This alignment results in a transition from transparent to opaque (decreasing transmittance) when a bias voltage is applied. In contrast, when MBBA is dispersed in a PDLC system, the molecules exhibit a positive dielectric anisotropy ($\Delta\varepsilon > 0$),[8] i.e., the long axis of the molecules tend to align parallel to the direction of electric field. Consequently, the electro-optical properties of dispersed MBBA change in the reverse direction: opaque to transparent, under an applied bias.

Herein, we also observed the same behavior. Pure MBBA showed a decrease in the transmittance whereas the MBBA miniemulsions and LC/hydrogel samples exhibited an increase in the transmittance as discussed below. We note that the bias AC voltage was adjusted to a minimum value required to achieve an electro-optical switching at 40 or 60 V. The driving frequency was selected at 1 MHz which is close to the maximum dielectric loss peak for the relaxation of the LC molecules along the short axis.[8,9,11] The bias conditions helped prevented the degradation of LCs in our samples by reducing heat accumulation.[12,13]

We found that the relative transmittance of the miniemulsions (without bias) decreased with increasing LC concentration. The emulsions with the highest concentration, 40 wt% of LC, using either CTMA-Cl or Lutensol AT50 as surfactant, appeared the most turbid. This turbidity can be attributed to the concentration of the dispersed phase (number of scattering objects) and the droplet size of the organic LC phase, with a hydrodynamic diameter of 831 nm (polydispersity index or PDI = 0.32) and 672 nm (PDI = 0.45) when stabilized by Lutensol AT50 and CTMA-Cl, respectively. The sizes were within the range of

Mie scattering.[14] To determine the appropriate LC concentration for embedding into the hydrogel, we evaluated the change in the relative transmittance [$\Delta T_m/T_r$, see **Eq. (2)**] of the miniemulsions under an applied bias as shown in **Figure 2a-f**. The LC concentration was 5, 10, 20, and 40 wt%, and we found that the emulsions with 40 wt% LCs (with

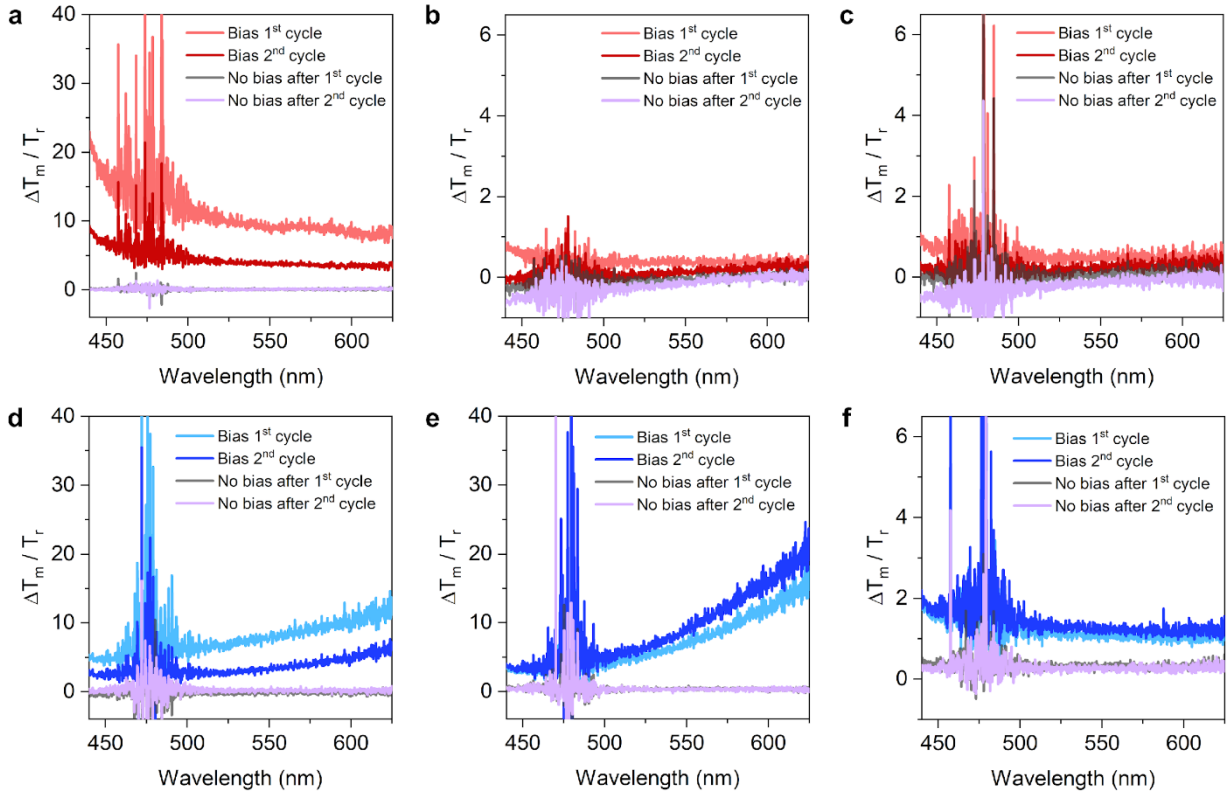

Figure 2. Change in the relative transmittance during an applied bias voltage (40 V, 1 MHz) for: (a) 5 wt%, (b) 10 wt%, and (c) 20 wt%, of MBBA miniemulsions stabilized by Lutensol AT50; and (d) 5 wt%, (e) 10 wt%, and (f) 20 wt% of MBBA miniemulsions stabilized by CTMA-Cl. Data from two cycles under bias and the recovery of the baseline after removing the bias are shown.

both types of surfactants) resulted in fast degradation, i.e., the baseline transmittance was not recovered when the bias was removed (data not shown for conciseness).

Thus, two concentrations of 5 wt% (low) and 20 wt% (high) were selected for the fabrication of LC-embedded hydrogels. As mentioned in **Section 2.3**, hydrogels were prepared with either NS or CS. For the hydrogel recipe, NS4 and CS4 conditions were selected due to the stable porous structures with a small pore size as mentioned in the previous section. It was found that only the 20 wt% LC CS hydrogel (PAAm_CS4 _20p condition in **Table 1**) displayed significant changes in $\Delta T_m/T_r$ under an applied bias as shown in **Figure 3a**

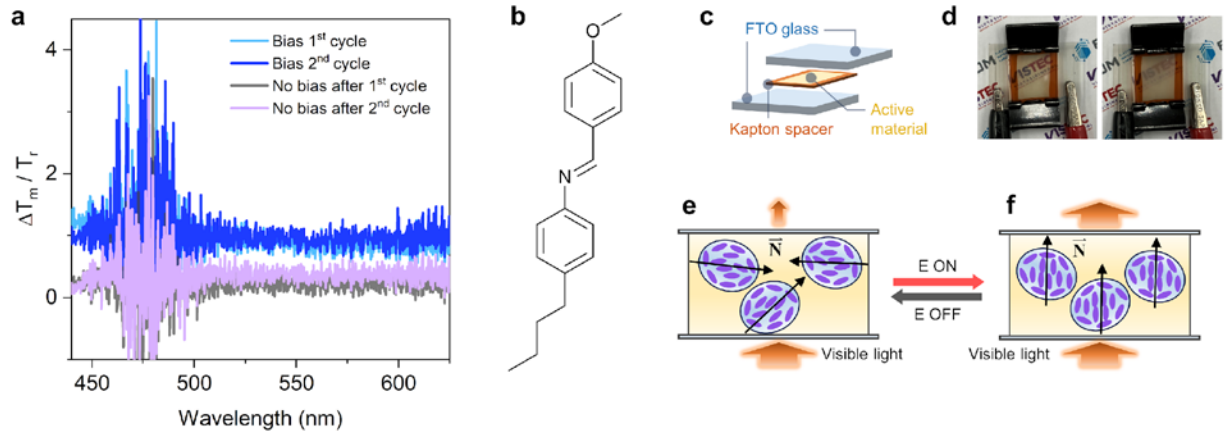

Figure 3. (a) Change in the relative transmittance during an applied bias (60 V, 1 MHz) for the hydrogel embedded with MBBA: PAAm_CS4_20p. (b) Molecular structure of MBBA. (c) Schematic diagram showing the cell structure. (d) Example of the electro-optical response of the cell (neat MBBA shown). (e-f) Orientation of MBBA confined in droplets that are embedded in a hydrogel (positive dielectric anisotropy) without bias and with bias, respectively.

To summarize, the neat MBBA molecules (**Figure 3b**) aligned themselves with the electric field along the short axis due to the negative dielectric anisotropy, resulting in a decrease in the transmittance under bias (**Figure 3c-d**). However, when MBBA was formed as droplets and embedded into the hydrogel network, the confinement turned the dielectric anisotropy to a positive value; the LC/hydrogel was initially turbid (due to Mie scattering) and appeared less turbid (higher relative transmittance) when the molecules aligned with the field along their long axis (**Figure 3e-f**).

3.3 Thermal and mechanical properties

The nematic-isotropic transition temperature (T_{N-I}) of MBBA in the miniemulsion droplets was determined using DSC. For the bulk phase, T_{N-I} was found at 43.2 °C as shown in **Figure 4a** while for the MBBA miniemulsions, this transition occurred around 24 to 27 °C. The decrease of the nematic-isotropic phase transition temperature indicates a lower anchoring energy,[15] related to the interactions between the LC molecules and the confining structure.[16,17]

For the LC/hydrogel samples, only the PAAm_CS4_20p condition exhibited an observable nematic-isotropic endotherm at 32.4 °C. Note that this was also the only condition that showed a distinct change in the relative transmittance as mentioned in the previous section. Therefore, we surmised that the environments of the LC droplets in other hydrogel conditions did not allow the realignment of the LC molecules, hence prohibiting the electro-optical switching behavior. In addition, the nematic-isotropic transition temperature was found to vary in the same trend as the minimum bias voltage required to change the optical transmittance as: (1) pure MBBA (highest T_{N-I} and voltage of 100 V), (2) LC/hydrogel (intermediate T_{N-I} and voltage of 60 V), and (3) LC emulsion (lowest T_{N-I} and voltage of 40 V).

Rheological measurements were conducted to investigate the influence of the presence of LC droplets on the mechanical properties of the hydrogels. Interestingly, **Figure 4b** reveals that the storage modulus (G') was higher than the loss modulus (G'') at 1% strain for PAAm hydrogels (with 0, 5, and 20 wt% of MBBA), confirming their gel-like behavior. The increase in G' and G'' appeared to correlate directly with the increasing MBBA concentration. Given the same total weights of all samples, the higher modulus could result from the incorporation of LC droplets into the gel structure, thereby reinforcing the network.[18]

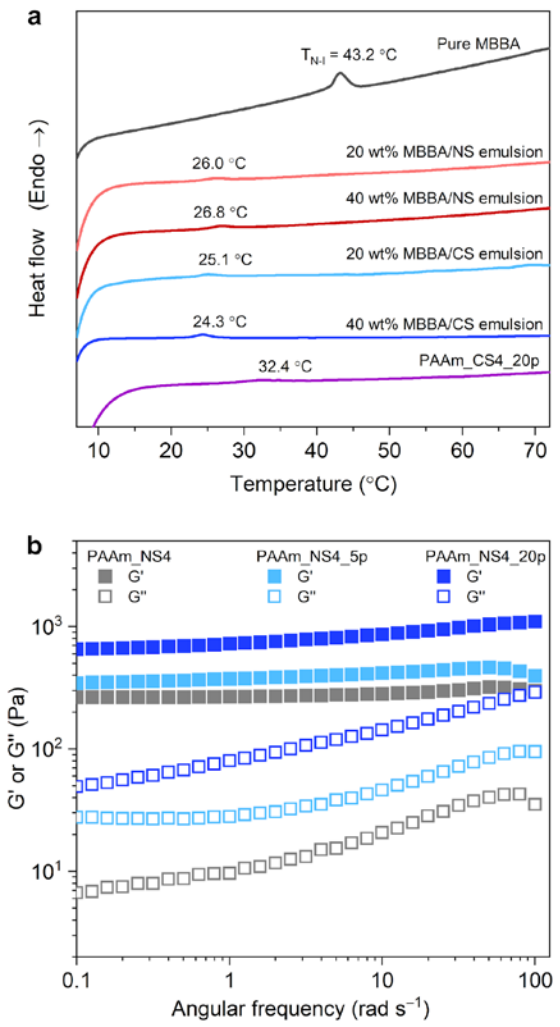

Figure 4. (a) DSC thermograms of bulk MBBA, MBBA miniemulsions, and MBBA-embedded hydrogel. (b) Frequency sweep measurements of G' and G'' for MBBA-embedded hydrogels.

4. Conclusions

In summary, we demonstrated one possible technique to incorporate LCs into hydrogels via the miniemulsion route. The optimal condition, which showed an observable change in the relative transmittance, contained a high amount of MBBA LCs: 20 wt%, significantly larger than previous reports of PDLC. This work can serve as a basis for the development of stretchable displays for wearable devices. Important aspects for further studies include the understanding of the effects of the interactions between LCs and the hydrogel pores and pore geometry on the electro-optical response.

Acknowledgements

T.L. and P.P. would like to acknowledge funding from VISTEC and support of transmittance measurements from Dr. Taweesak Sudyoadsuk.

References

1. Crespy, D.; Landfester, K. Miniemulsion Polymerization as a Versatile Tool for the Synthesis of Functionalized Polymers. *Beilstein J. Org. Chem.* **2010**, *6*, 1132–1148.
2. Büyüktanir, E. A.; Mitrokhin, M.; Holter, B.; Glushchenko, A.; West, J. L. Flexible Bistable Smectic-A Polymer Dispersed Liquid Crystal Display. *Jpn. J. Appl. Phys.* **2006**, *45* (5A), 4146–4151.
3. Doane, J. W.; Vaz, N. A.; Wu, B. -G.; Žumer, S. Field Controlled Light Scattering from Nematic Microdroplets. *Appl. Phys. Lett.* **1986**, *48* (4), 269–271.
4. Zhang, G.; Zhu, A.; Wang, S.; Chen, Q.; Liu, B.; Zhou, J.; Wu, Z. Stabilizing Liquid Crystal Droplets with Hydrogel Films and Its Application in Monitoring Adenosine Triphosphate. *Colloids Surfaces A Physicochem. Eng. Asp.* **2022**, *654*, 130122.
5. Deng, J.; Liang, W.; Fang, J. Liquid Crystal Droplet-Embedded Biopolymer Hydrogel Sheets for Biosensor Applications. *ACS Appl. Mater. Interfaces* **2016**, *8* (6), 3928–3932.
6. Deng, J.; Liang, W.; Rhodes, S.; Fang, J. Influence of Polymer Networks on the Sensor Properties of Hydrogel Dispersed Liquid Crystal Droplets. *Colloids Surfaces A Physicochem. Eng. Asp.* **2019**, *570*, 438–443.
7. Aouada, F. A.; de Moura, M. R.; Fernandes, P. R. G.; Rubira, A. F.; Muniz, E. C. Optical and Morphological Characterization of Polyacrylamide Hydrogel and Liquid Crystal Systems. *Eur. Polym. J.* **2005**, *41* (9), 2134–2141.
8. Tripathi, P. K.; Pande, M.; Singh, S. Dielectric and Electro-Optical Properties of Polymer-Stabilized Liquid Crystal. II. Polymer PiBMA Dispersed in MBBA. *Appl. Phys. A* **2016**, *122* (9), 847.
9. Theodoridis, T.; Kraemer, J. *Introduction to Liquid Crystals*; Priestley, E. B., Wojtowicz, P. J., Sheng, P., Eds.; Springer US: Boston, MA, 1975.
10. Andrienko, D. Introduction to Liquid Crystals. *J. Mol. Liq.* **2018**, *267*, 520–541.
11. Fernandes, P. R. G.; da Silva, K. A.; Mukai, H.; Muniz, E. C. Optical, Morphological and Dielectric Characterization of MBBA Liquid Crystal-Doped Hydrogels. *J. Mol. Liq.* **2017**, *229* (January), 319–329.
12. Dadivanyan, A. K.; Noah, O. V.; Pashinina, Y. M.; Belyaev, V. V.; Chigrinov, V. G.; Chausov, D. N. Anchoring Energy of Liquid Crystals. *Mol. Cryst. Liq. Cryst.* **2012**, *560* (1), 108–114.

13. Torres, J.; Vergaz, R.; Barrios, D.; Sánchez-Pena, J.; Viñuales, A.; Grande, H.; Cabañero, G. Frequency and Temperature Dependence of Fabrication Parameters in Polymer Dispersed Liquid Crystal Devices. *Materials.* **2014**, *7* (5), 3512–3521.
14. Born, M.; Wolf, E.; Bhatia, A. B.; Clemmow, P. C.; Gabor, D.; Stokes, A. R.; Taylor, A. M.; Wayman, P. A.; Wilcock, W. L. *Principles of Optics*; Cambridge University Press, 1999.
15. Tongcher, O.; Sigel, R.; Landfester, K. Liquid Crystal Nanoparticles Prepared as Miniemulsions. *Langmuir* **2006**, *22* (10), 4504–4511.
16. Dunmur, D. A.; de la Fuente, M. R.; Perez Jubindo, M. A.; Diez, S. Dielectric Studies of Liquid Crystals: The Influence of Molecular Shape. *Liq. Cryst.* **2010**, *37* (6–7), 723–736.
17. Ryu, S. H.; Yoon, D. K. Liquid Crystal Phases in Confined Geometries. *Liq. Cryst.* **2016**, *43* (13–15), 1951–1972.
18. Mcclements, D. J.; Monahan, F. J.; Kinsella, J. E. Effect of Emulsion Droplets on the Rheology of Whey Protein Isolate Gels. *J. Texture Stud.* **1993**, *24* (4), 411–422.

Encapsulation of *Mitragyna speciosa* (Roxb.) Korth. using coaxial electrospray technique

Chutatip Tongped, Prapatsorn Pansawat, Natchaya Sawatdirak, and Nisalak Trongsiriwat*

Department of Industrial Chemistry, Faculty of Applied Science, King Mongkut's University of Technology North Bangkok, 10800, Thailand

**E-mail: Nisalak.t@sci.kmutnb.ac.th*

Abstract:

Kratom is an herbal plant found mainly in Southeast Asia. Generally, people consume its leaves in order to be more productive at work and to be resistant under the hot weather. It is usually consumed in the form of an energy drink or by chewing fresh leaves. In the kratom plant, there are more than 25 kinds of alkaloids, such as Mitragynine, Speciogynine, Speciociliatine and Mitraciliatine, etc. However, alkaloids have low solubility in water. They are also unstable under light and heat. It's reported that there is good pharmacological activity when used at an optimized dosage. Overdosing should be avoided due to its unwanted side effects. To solve these problems, control the dosage, and prevent alkaloids' decomposition, the researchers are using the Coaxial Electrospray Technique to encapsulate kratom extracts in boba form. This study is focusing on optimization to demonstrate conditions for preparing boba capsules of crude kratom extract. Encapsulation of crude kratom extract mixed with gelatin in sodium alginate with core-shell structures was conducted. The effects of parameters such as the applied electric voltages and the flow rates were studied. The identity of the boba capsules was investigated using FT-IR spectroscopy. It was found that crude kratom extract was encapsulated inside the capsule particles. Physical characteristics were studied by imaging and measuring the size of the boba capsule particles. The result showed that the boba capsules formed using volt revealed more consistent capsules than the boba capsules formed without volt. Notably, the size of both conditions is slightly different. This research could be applied in food and medical industries.

1. Introduction

Kratom (*Mitragyna speciosa* (Roxb.) Korth.) is a plant from the Rubiaceous family found in Southeast Asia, especially in Malaysia and Thailand. Kratom is an herbal alternative that has been used as medicine for centuries. People typically consume its leaves to enhance work productivity and withstand heat and sun exposure. Usually, it is consumed by chewing fresh leaves or as an energy drink. Additionally, Kratom leaves are used for the treatment of intestinal infections, diarrhea, muscle pain, fever, coughing, and to induce sleep. Currently in Thailand, Kratom has been removed from the Thai Narcotics Act (No. 8), Schedule 5, since August 24, 2022, changing its status from a narcotic to a normal plant that could legally be planted, traded, and consumed.

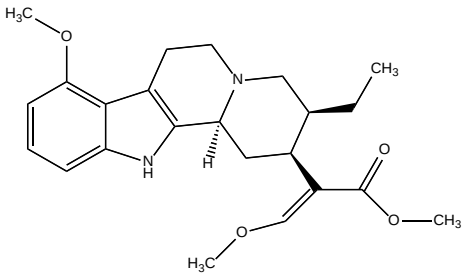

Figure 1. Mitragynine **(1)** is main ingredient of kratom extract.

In the kratom leaves, there are more than 25 kinds of alkaloids, such as Mitragynine **(1)**, Speciogynine **(2)**, Speciociliatine **(3)**, Mitraciliatine **(4)**, 7-Hydroxymitragynine **(5)**, Paynantheine **(6)**, Isomitraphyline **(7)**, etc. Their structures are shown in **Figure 2.** In 1996, Beckett reported the separation of at least 22 alkaloids from Mitragyna speciosa; the amount of all the separated compounds depended on time and cultivation area[1].

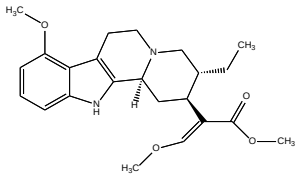

Speciogynine **(2)**

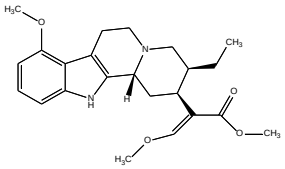

Speciociliatine **(3)**

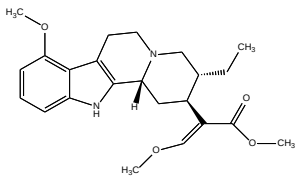

Mitraciliatine **(4)**

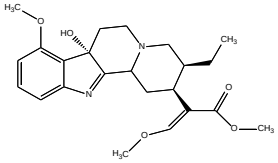

7-Hydroxymitragynine **(5)**

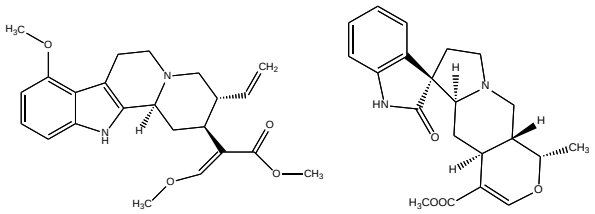

Paynantheine **(6)** Isomitraphyline **(7)**

Figure 2. Alkaloid compounds in kratom leaves extract.

Several studies in the past decade have exhibited that Kratom extract and mitragynine, major components in Kratom extract, show advantages in pharmaceutical and medicinal applications, including analgesic effects and antidepressant properties. The use of mitrgynine as a pain-relieving drug was reported in 2002. Takayama and coworkers demonstrated that mitragynine inhibited guinea pigs' electrically induced duodenal contractions[2]. Furthermore, mitragynine could inhibit the central serotonin neurotransmitter system in rats, affecting depression or serotonin syndrome[3]. It is obvious that mitragynine and kratom extracts are promising ingredients for therapeutic and medicinal applications. However, there are still some limitations, such as its low aqueous solubility and easy decomposition under light and heat, which could confine the use of mitragynine in the medical and pharmaceutical industries. Dosage-intake control is also a crucial part to consider when mitragynine or kratom extracts are used. As of right now, the FDA in Thailand has imposed a daily maximum for the quantity of mitragynine that could be consumed at 0.2 mg[4]. Consumption of mitragynine in a higher amount might cause nausea, a fast heart rate, hypertension, and seizures[5], so control of dosage consumption is required. To solve these problems, the encapsulation of kratom leaves extract in boba form using the coaxial electrospray technique was developed in this work. The advantages of coaxial electrospray are preventing active ingredient degradation, inhibiting unpleasant odors, and controlling dosage consumption. It is also commonly used in the medical, food, and cosmetic industries. Nowadays, many natural extracts have been encapsulated in nanocapsules and microcapsules using the coaxial electrospray process. Baspinar and colleagues studied the encapsulation of curcumin utilizing zein and chitosan as the outer shell biopolymers[6]. In 2021, Hu et al. encapsulated omega 6, or arachidonic acid, with zein as a shell part using coaxial electrospray to avoid oxidation and unpleasant odors[7].

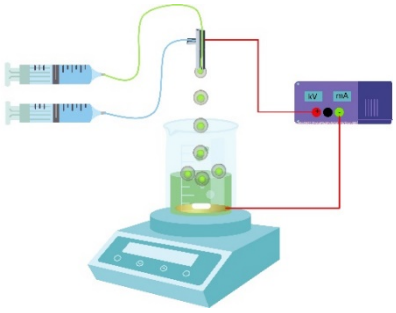

Figure 3. Coaxial electrospray technique**.**

The coaxial electrospray is a microencapsulation/nanoencapsulation process based on applying voltage using a DC power supply to provide electrical current to the needle and collector. When the voltage is applied, the liquid at the needle will combine into lumps and drop onto the collector. The flow rates of the outer shell, inner core, voltages, and properties of materials used in the process are the parameters that affect encapsulation efficiency, droplet size, and other performance characteristics of process[8]. In general, the size and shape of the droplet could be controlled by adjusting the voltage and flow rate of both the core and shell structure[9].

In this work, coaxial electrospray is first utilized to prepare encapsulated kratom extract in the application, using low voltages with a core-shell structure in one step to form boba capsules applied as a food product, utilizing sodium alginate as the shell and calcium chloride solution as the collector solution. Various parameters of the coaxial electrospray technique were investigated to identify the suitable conditions for preparing boba capsules from Kratom extract. In addition, the physical and chemical properties of the prepared boba capsules were characterized.

2. Materials and Methods

2.1 Materials

Kratom leaves (*Mitragyna speciosa* (Roxb.) Korth.) were obtained from southern Thailand, Ranong Province. 95% ethyl alcohol (food grade), gelatin, sodium alginate, and calcium chloride solution were also of food grade and ultra-pure water. Potassium bromide was of analytical grade for Fourier transform infrared spectroscopy (FT-IR).

2.2 Extraction of kratom extracts from kratom leaves

Crude kratom was extracted from kratom leaves. The dried kratom leaves (1.26 kg) were macerated with ethanol (12 L) for 3 days. After the third cycle, the ethanol extract was combined and evaporated under reduced pressure by rotavapor (BUCHI, R-300). The evaporator was operated under vacuum conditions with pressure at 200 mbar and 100 rpm, a heating bath at 50 °C, and a chiller at 5 °C, yielding the sticky green gel as shown below in **Figure 4.**

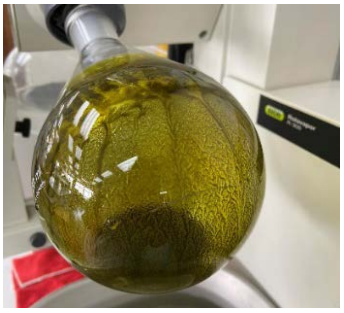

Figure 4. Crude extract of kratom leaves.

2.3 Coaxial electrospray process

Boba capsules were prepared through coaxial electrospray with a core-shell structure comprising an inner needle nested inside an outer needle. The inner needle contained crude kratom extract and gelatin to improve viscosity. The outer needle was sodium alginate, and the collector was calcium chloride solution. Crude kratom extract was mixed with gelatin in ratios of 1:1.5 and 1:4 in 100 mL of ultra-pure water as a core solution, and 1 g of sodium alginate was dissolved in 100 mL of ultra-pure water as a shell solution. The core and shell were poured into plastic syringes held on the electrospray equipment, and the 2% w/v calcium chloride solution was used on the collector basin. In two systems, with 400 volts and without voltage, the flow rates of the core were conducted at 9, 18, 25, and 30 mL/h, while the flow rates of the shell solution were 40, 45, 50, and 55 mL/h.

2.4 Optical microscope

The morphology of boba capsules was characterized by an optical microscope (Olympus model BX60). The boba capsules were placed on a slide, then examined at 5X magnification values.

2.5 Fourier transform infrared spectroscopy

Fourier transform infrared (FT-IR) spectra were obtained using the PerkinElmer Spectrum 100 FT-IR Spectrometer, analyzing the chemical composition of the prepared boba capsules. The samples were tested by using potassium bromide mixed with sample substances. Notably, the prepared boba capsules probably absorb moisture in the air. Therefore, a drying process was required by placing them in a desiccator before grinding and compressing them into transparent pellets. The pellets were scanned at a frequency of 4000 - 400 cm^{-1} for a total of sixteen scans.

2.6 Particle sizes of the boba capsules

The particle sizes of prepared boba capsules through coaxial electrospray were characterized by taking photographs and measuring the average size of the capsules via ImageJ software.

3. Results & Discussion

3.1 Suitable conditions for preparing boba capsules

The voltages, flow rates, and ratios of concentration of core in the coaxial electrospray technique have a vital influence on the formation of boba capsules.

Initial experiments were conducted without voltage by changing the flow rates of the inner shell at 9, 18, 25, and 30 mL/h and outer the shell at 40, 45, 50, and 55 mL/h. The result showed that the most constant flow rate for encapsulating boba capsules to be able to control the dosage of the active ingredient was the flow rate of the inner core at 30 mL/h and the outer shell at 50 mL/h. After that, the ratios of concentration of kratom extract mixed with gelatin varied between 1:1.5 and 1:4 at a constant flow rate, with the inner core at 30 mL/h and the outer shell at 50 mL/h. We found that the ratio of concentration of kratom extract : gelatin at 1:4, small amount of kratom extract was partially encapsulated **(a)** in **Figure 5**. When using the ratio of concentration of kratom extract : gelatin at 1:1.5, the mixture performed an appropriate viscosity in order to form boba capsules, resulting in the perfection of the shape of boba capsules **(b)**, In addition, with 400 volts applied and using the ratio of concentration of kratom extract : gelatin at 1:1.5 at the flow rate inner core at 30 mL/h and outer shell at 50 mL/h, The shape of the prepared boba was more consistent and perfectly round **(c)**.

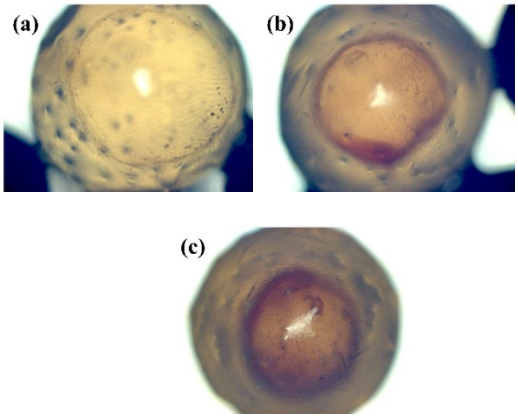

Figure 5. The morphology of boba capsules used a flow rate of 30:50 mL/h. Without voltage, kratom extract : gelatin ratio at 1:4 **(a)**. Kratom extract : gelatin ratio at 1:1.5 **(b)**. and kratom extract : gelatin ratio at 1:1.5 with voltage **(c)**.

3.2 Fourier transform infrared spectroscopy

The compositions of the boba capsules were characterized using FT-IR spectroscopy. The FT-IR spectra of crude kratom extract **(a)**, sodium alginate **(b)**, and prepared boba capsules **(c)** were displayed in **Figure 6**. The characteristic peaks of crude kratom extract **(a)** were N-H_2 amine group at frequencies of 3391.40 cm^{-1} and 2926.06 cm^{-1} and the 1070.37 cm^{-1} band of C-O. Sodium alginate, used as a shell structure **(b)**, demonstrated the functional groups at a frequency of 3435.71 cm^{-1} indicating the hydroxyl group, C=C at a frequency of 1615.07 cm^{-1} and 1028.50 cm^{-1} band of C-O. When the prepared boba capsules were characterized **(c)**, the characteristic peaks of the boba capsules at frequencies of 3425.15 cm^{-1} and 1637.10 cm^{-1} were found confirming the successful encapsulation of crude kratom extract with sodium alginate.

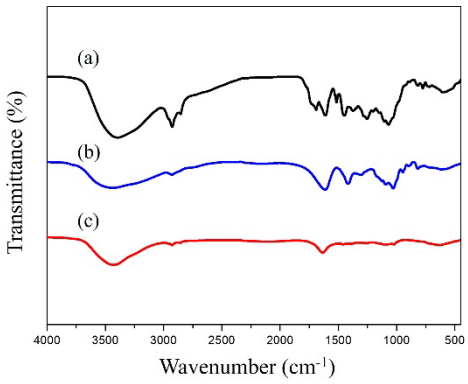

Figure 6. The FT-IR spectra of crude kratom extract **(a)**, sodium alginate **(b)** and prepared boba capsules **(c)**.

3.3 Particle size of the boba capsule

To investigate the size of the boba capsule, the mixture ratio of the core part and the applied voltage were examined. Changing the amount of gelatin in the core structure demonstrated no significant difference in the sizes of the prepared boba capsules measured by ImageJ software, as shown in **Figure 7.** However, increasing amounts of gelatin produced a core part with higher viscosity and homogeneity, generating the spherical boba capsule. Notably, when voltage was applied in the process, the larger size of the prepared boba was obtained, 3.9547 mm, because larger amount of core part was well encapsulated in spherical form whereas without voltage, smaller boba capsules was collected in 3.0508 mm due to their partial encapsulation, as shown in **Figure 8.**

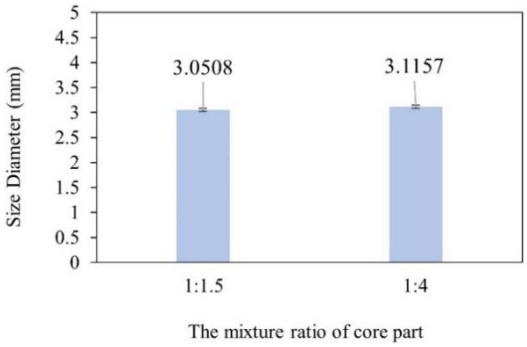

Figure 7. Effect of crude kratom extract : gelatin ratios at 1:1.5 and 1:4 with flow rate inner : outer shell at 30:50 mL/h on the boba capsule size.

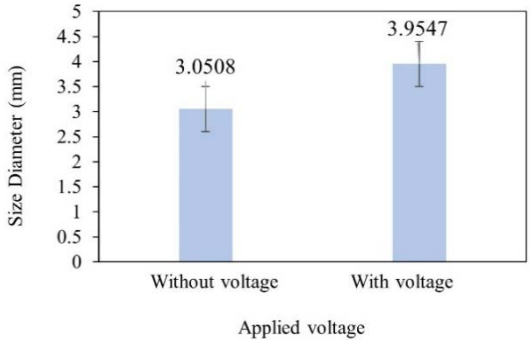

Figure 8. Effect of applied voltage with flow rate inner : outer shell at 30:50 mL/h on the boba capsule size.

4. Conclusion

The boba capsules of crude kratom extract were prepared through coaxial electrospray. The voltage, flow rate, and ratio of concentration of core in the coaxial electrospray technique have a vital influence on the formation of the boba capsules. The most suitable conditions for preparing boba capsules were the flow rate of the

inner core at 30 mL/h and the outer shell at 50 mL/h. In addition, using the ratio of concentration of kratom extract: gelatin at 1:1.5 applied with voltage can achieve excellent formation in the shape of boba capsules, and the sizes of the boba capsules that were prepared with voltage and without voltage were 3.9547 mm and 3.0508 mm, respectively. The sizes of both conditions are significantly different. The size of the prepared boba without voltage was smaller because of the improper encapsulation. Moreover, the quantity of kratom extract encapsulated in a capsule is in progress. These informations are beneficial basic knowledge for food and medical industry applications.

Acknowledgements

This research was supported by the Department of Industrial Chemistry, Faculty of Applied Science, King Mongkut's University of Technology North Bangkok.

References

1. Beckett, A. H., Shellard, E. J., Phillipson, J. D., and Lee, C. M. , The Mitragyna species of Asia. VII. Indole alkaloids from the leaves of Mitragyna speciosa Korth. *Plunta Medica* **1966,** *14*, 266 - 276.
2. Takayama, H.; Ishikawa, H.; Kurihara, M.; Kitajima, M.; Aimi, N.; Ponglux, D.; Koyama, F.; Matsumoto, K.; Moriyama, T.; Yamamoto, L. T., Studies on the synthesis and opioid agonistic activities of mitragynine-related indole alkaloids: discovery of opioid agonists structurally different from other opioid ligands. *Journal of medicinal chemistry* **2002,** *45* (9), 1949-1956.
3. Matsumoto, K.; Mizowaki, M.; Takayama, H.; Sakai, S.-I.; Aimi, N.; Watanabe, H., Suppressive effect of mitragynine on the 5-methoxy-N, N-dimethyltryptamine-induced head-twitch response in mice. *Pharmacology Biochemistry and Behavior* **1997,** *57* (1-2), 319-323.
4. Food and Drug Administration, T. How to Apply for Herbal Products Permission? https://herbal.fda.moph.go.th/media.php?id=511747726631903232.
5. Stanciu, C. N.; Gnanasegaram, S. A.; Rader III, G. L.; Sharma, A.; McCurdy, C. R., What Is the Kratom Overdose Risk? A Systematic Literature Review. *Current Addiction Reports* **2023,** *10* (1), 9-28.
6. Baspinar, Y.; Üstündas, M.; Bayraktar, O.; Sezgin, C., Curcumin and piperine loaded zein-chitosan nanoparticles: Development and in-vitro characterisation. *Saudi pharmaceutical journal* **2018,** *26* (3), 323-334.
7. Hu, M. X.; Chen, X. L.; Song, L. J.; He, F., Arachidonic acid-encapsulated microcapsules with core-shell structure prepared by coaxial electrospray. *Journal of Applied Polymer Science* **2021,** *138* (19), 50403.
8. Zhang, L.; Huang, J.; Si, T.; Xu, R. X., Coaxial electrospray of microparticles and nanoparticles for biomedical applications. *Expert review of medical devices* **2012,** *9* (6), 595-612.
9. Chen, X.; Jia, L.; Yin, X.; Cheng, J.; Lu, J., Spraying modes in coaxial jet electrospray with outer driving liquid. *Physics of fluids* **2005,** *17* (3).

Effect of flux treatment process on photocatalytic dye degradation of aluminium-doped strontium titanate

Natruja Towiratkit[1], Thanakorn Wasanapiarnpong[1], Wuttichai Reainthippayasakul[1,2], Noppakhate Jiraborvornpongsa[4], and Pornapa Sujaridworakun[1,2,3]*

[1]*Department of Materials Science, Faculty of Science, Chulalongkorn University, Bangkok, Thailand*
[2]*Photocatalysts for Clean Environment and Energy Research Unit, Faculty of Science, Chulalongkorn University, Bangkok, Thailand*
[3]*Center of Excellence on Petrochemical and Materials Technology, Chulalongkorn University, Bangkok, Thailand*
[4]*Metallurgy and Materials Science Research Institute, Chulalongkorn University, Bangkok, Thailand*

**E-mail: pornapa.s@chula.ac.th*

Abstract:

This study aimed to investigate the photocatalytic efficiency for organic dye degradation of aluminum-doped strontium titanate (Al-doped $SrTiO_3$) synthesized by the flux treatment method. The preparation process involves the solid-state synthesis of $SrTiO_3$ using $SrCO_3$ and TiO_2 as precursors at 900–1300 °C, followed by flux treatment with $SrCl_2$ in an alumina crucible at 1150 °C for 10 hours. Al doping was performed by adding Al_2O_3 powder during flux treatment process. To investigate the effect of flux-treatment, Al-doped $SrTiO_3$ was also prepared by solid state without fluxing process. The obtained products were characterized for phase, morphology, chemical composition, surface area and optical property using X-ray diffraction (XRD), Scanning electron microscopy (SEM), Energy-dispersive X-ray spectroscopy (EDS), Brunauer-Emmett-Teller (BET) analysis, and Fluorescence spectroscopy, respectively. It was found that the pure $SrTiO_3$ phase was formed after solid-state synthesis at 1300 °C and remained unchanged after treatment with $SrCl_2$ flux. SEM images obviously showed that the morphology of $SrTiO_3$ particles changed from a fine irregular shape to a cubic shape (1–2.5 μm) when it was treated with $SrCl_2$ flux. Additionally, the particle size of cubic $SrTiO_3$ was drastically decreased (200–500 nm) after Al-doping. The photocatalytic efficiency was evaluated by photodegradation of rhodamine B solution under UV light irradiation for 60 minutes. The results showed that flux-treated Al-doped $SrTiO_3$ sample could degrade rhodamine B up to 21.66%, more efficient than flux-treated $SrTiO_3$ (10.24%), solid-stated $SrTiO_3$ (3.10%) and solid-stated Al-doped $SrTiO_3$ (0.64%), respectively. It can be suggested that flux treatment using $SrCl_2$ and Al doping played an essential role in enhancing photocatalytic activity for dye degradation of $SrTiO_3$ under UV light.

1. Introduction

The increasing prevalence of organic contaminants in global water sources, driven by population growth and industrial/agricultural expansion, emphasizes the urgency for effective wastewater treatment. While biological processes address high-concentration biodegradable pollutants, challenges persist in decomposing complex pollutant structures.[1] The pioneering discovery of photoelectrochemical water splitting in 1972 by Fujishima and Honda introduced an environmentally friendly and energy-saving technology.[2] This approach, leveraging semiconductors, shows promise for treating wastewater with low biodegradability, high complexity, and elevated pollutant concentrations. Photocatalysts play a crucial role in utilizing solar energy for pollutant degradation, enhancing the economic viability of photocatalysis treatment.[1]

In recent times, metal oxide-based semiconductors, particularly titanium dioxide (TiO_2), have been extensively studied for breaking down organic pollutants in wastewater.[3] However, perovskite alkaline earth titanate, commonly known as $SrTiO_3$, has gained prominence due to its cost-effectiveness, high chemical stability, and biocompatibility. Unlike simple binary oxides, the physical and chemical properties of multi-cation oxide $SrTiO_3$ can be effectively tailored by adjusting its compositions. Numerous endeavors have focused on enhancing the chemical and physical properties of $SrTiO_3$, achieved through methods like introducing additional oxygen vacancies and employing element doping.[4,5]

Addressing the environmental challenges linked to organic dye pollutants is crucial, given their hazardous and carcinogenic nature. Synthetic dyes, prevalent in wastewater from diverse industries, obstruct sunlight penetration into water bodies, disrupting crucial aquatic activities. Noteworthy examples of dyes studied in photocatalysis include rhodamine B, methylene blue, and methyl orange. The intricate chemical structure of organic dyes can result in the production of toxic aromatic amines, posing a threat to aquatic life. Traditional wastewater

treatment methods prove ineffective against these non-biodegradable and persistent dyes. The proposed solution involves leveraging the photocatalytic process to efficiently degrade and eliminate synthetic dyes.[1]

Efficient photocatalytic materials are essential to address environmental challenges. Traditional materials face limitations in their photocatalytic performance due to a high band gap (UV range) and rapid recombination of photogenerated electron–hole pairs.[3] Aluminum-doped strontium titanate (Al-doped $SrTiO_3$) has shown promise in enhancing photocatalytic activity, as evidenced by previous studies.[6-8] Ham et al. explored the effects of $SrCl_2$ flux treatments and Al doping on the photocatalytic properties of $SrTiO_3$, revealing that flux-treated $SrTiO_3$ exhibited a notable apparent quantum efficiency of 30% at 360 nm in overall water splitting. This study explores the impact of $SrCl_2$ flux treatment on $SrTiO_3$, paving the way for our investigation into the synthesis of Al-doped $SrTiO_3$.[6] In a related study, Takata and Domen examined the impact of aliovalent metal cation doping on $SrTiO_3$ for overall water splitting. Lower-valence cation doping, intentionally introducing oxygen vacancies and reducing Ti^{3+}, significantly enhanced photocatalytic activity. The study demonstrated that defects, particularly Ti^{3+} rather than oxygen vacancies, played a crucial role in suppressing photocatalysis. This concept of defect engineering through aliovalent doping provides a strategic approach to designing active photocatalysts.[9]

Thus, this study aims to address an effect of flux treatment method and Al doping on physical and photocatalytic properties for organic dye degradation of aluminum-doped strontium titanate (Al-doped $SrTiO_3$).

2. Materials and Methods

2.1 Materials

In the synthesis of $SrTiO_3$ via the solid-state method, strontium carbonate ($SrCO_3$, Sigma-Aldrich, >98%), titanium dioxide (TiO_2, Fluka Chemika, >99%), and ethanol (C_2H_5OH, Merck, >99.9%) were employed. Strontium chloride hexahydrate ($SrCl_2 \cdot 6H_2O$, 99% AR Grade, KemAus) was used as the flux medium in the flux treatment process, and aluminum oxide (Al_2O_3, particle size 0.3μm, Taimei Chemicals) powder was used as the source for aluminum doping. In the assessment of the photocatalytic efficiency for dye degradation, Rhodamine B (RhB, Loba Chemie) was employed as the chosen dye.

2.2 Synthesis of $SrTiO_3$

The solid-state synthesis of $SrTiO_3$ involved the combination of $SrCO_3$ and TiO_2 in a 1:1 mole ratio. Specifically, 4.4288 g of $SrCO_3$ and 2.3958 g of TiO_2 were mixed with 10 ml of ethanol. The mixture was meticulously ground in a mortar until the ethanol completely evaporated. Subsequently, the resulting powder was transferred to an alumina crucible. The crucible was then subjected to a two-step heating process: first, heating at 600 °C for 15 minutes, followed by heating to 900-1300 °C for 12 hours, with a heating rate of $5°C \cdot min^{-1}$. The reaction equation is shown below in Equation (1)[10]:

$$SrCO_3 + TiO_2 \rightarrow SrTiO_3 + CO_2 \quad (1)$$

The resulting material is referred to as $SrTiO_3$(solid-state). Additionally, samples with 2% by mole Al_2O_3 addition are denoted as Al-$SrTiO_3$(solid-state).

2.3 Flux–treated $SrTiO_3$

In the flux treatment process, the $SrTiO_3$ powder obtained from the solid-state synthesis at 1300 °C was further heat-treated by utilizing $SrCl_2 \cdot 6H_2O$ as the flux medium. The mole ratio of $SrCl_2 \cdot 6H_2O$ to $SrTiO_3$ was maintained at 10:1, with 14.5308 g of $SrCl_2 \cdot 6H_2O$ and 1.0000 g of $SrTiO_3$ being mixed. The mixture was ground in a mortar and then heated to 1150 °C for 10 hours with a heating rate of 5 °C/min in an alumina crucible. After cooling to room temperature, $SrTiO_3$ was separated by washing the solidified mass with deionized water through centrifugation until no white AgCl precipitate formed in rinse solutions with $AgNO_3$[6, 7] The obtained product is referred to as $SrTiO_3$(flux). Additionally, during the grinding process of $SrTiO_3$ with $SrCl_2$ flux, samples with 2% by mole Al_2O_3 addition were prepared and denoted as Al-$SrTiO_3$(flux).

2.4 Characterizations

The crystal structures of the products were characterized using X-ray diffractometry (XRD; Bruker AXS Model D8 Discover, Germany) with Cu Kα radiation at 40 kV and 40 mA (λ=1.5406 Å). The crystallite size was determined employing the Scherrer equation in Equation (2):

$$D = \frac{k\lambda}{\beta cos\theta} \quad (2)$$

Here, D denotes the average crystallite size (nm), k is the shape factor (k = 0.90 used for spherical crystallites), λ is the X-ray wavelength (=0.15406 nm), β is the full width at half maximum (FWHM)

of the peak (radians), and θ is the Bragg-diffraction angle (radians). [11]

The morphology and chemical composition of the powder were observed by a Scanning Electron Microscope (JEOL JSM-6480LV) at an accelera-tion voltage of 15.0 kV, and energy-dispersive X-ray analyzer (Horiba EMAX X-MaxN).

The specific surface area of the samples was analyzed using a surface area analyzer (Micromeritics 3Flex 3500) measured by N_2 adsorption at 77 K. Before analysis, sample preparation involved degassing at 400°C for 12 hours through heating and evacuation. The specific surface area was determined using the Brunauer-Emmett-Teller (BET) method.

Photoluminescence (PL) spectra were examined at ambient temperature using a fluorescence spectrometer (PerkinElmer LS-55) with an excitation wavelength of 325 nm.

2.5 Photocatalytic efficiency evaluation

Photocatalytic dye degradation efficiency was assessed through rhodamine B degradation under a UV light source (300 W Xe lamp with visible light cutoff filter) positioned 15 cm away. A 0.05 g photocatalyst was ultrasonicated in 10 ppm rhodamine B solution (120 mL) for 5 minutes. Preceding light irradiation, the suspension was stirred with a magnetic stirrer in the dark for 30 minutes to attain adsorption-desorption equilibrium. UV light exposure followed for 1 hour, with 5 mL solution samples collected every 10 minutes during both dark and light conditions. After centrifugation to remove the catalyst, concentration analysis was conducted using a UV–Vis–NIR spectrophotometer (Agilent Cary 7000 UMS) at the maximum absorbance wavelength of 554 nm. The dye degradation efficiency of the samples was determined using Equation (3):

$$\textit{Dye degradation efficiency (\%)} = \frac{C_D - C}{C_D} \times 100 \quad (3)$$

where C_D is the dye concentration after being kept in the dark (mg·L^{-1}), and C is the dye concentration at each irradiated time (mg·L^{-1}).

3. Results & Discussion

3.1 Effect of calcination temperature on solid state synthesis of $SrTiO_3$

The XRD patterns of $SrTiO_3$ powders prepared at temperatures of 900, 1100, and 1300 °C are presented in Figure 1. The diffraction patterns of the samples calcined at 1300 °C exhibited a desired single phase, revealing a well-indexed perovskite cubic structure of $SrTiO_3$ with the *pm*-3*m* space group. This indicated the successful formation of $SrTiO_3$ through the solid-state reaction between $SrCO_3$ and TiO_2. However, the samples calcined at 900 and 1100 °C showed the presence of a second phase identified as $Sr_3Ti_2O_7$. In addition, TiO_2 in anatase phase was observed in the sample calcined at 900 °C. The average crystallite size of $SrTiO_3$ was determined by the Scherrer equation, increased with increasing calcination temperatures which are 46.58, 80.99 and 92.88 nm at 900 , 1100 , and 1300 °C, respectively.

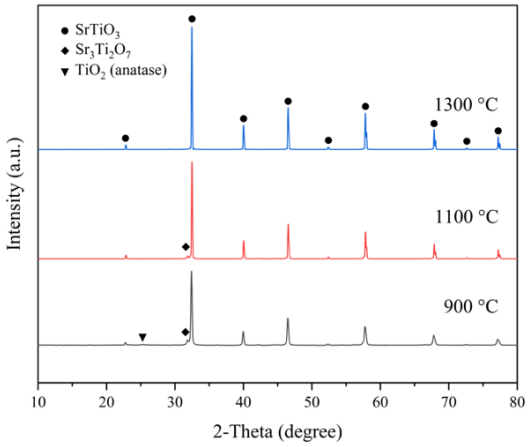

Figure 1. XRD patterns of $SrTiO_3$ solid-state synthesis at different temperatures

3.2 Effect of flux treatment and Al doping

Figure 2 illustrated the XRD patterns of $SrTiO_3$(solid-state), Al-$SrTiO_3$(solid-state), $SrTiO_3$(flux), and Al-$SrTiO_3$(flux). All samples exhibited a predominant $SrTiO_3$ phase, as evidenced by the peaks corresponding to $SrTiO_3$ in their respective XRD patterns, indicating that the $SrTiO_3$ phase remains unchanged after flux treatment. However, the presence of aluminum was not detectable through XRD, possibly due to the low concentration of Al ions and their incorporation within the $SrTiO_3$ lattice structure. The average crystallite sizes were calculated from these XRD patterns, with values of 92.88 nm for $SrTiO_3$(solid-state), 87.16 nm for Al-$SrTiO_3$(solid-state), 75.06 nm for $SrTiO_3$(flux), and 50.98 nm for Al-$SrTiO_3$(flux).

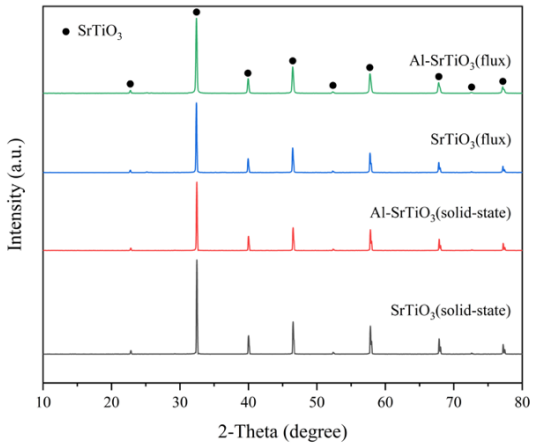

Figure 2. XRD patterns of $SrTiO_3$(solid-state), Al-$SrTiO_3$(solid-state), $SrTiO_3$(flux), and Al-$SrTiO_3$ (flux)

The BET surface area results, as presented in Table 1, provided insights into the surface area of the synthesized $SrTiO_3$ samples under different treatments. $SrTiO_3$(solid-state) exhibited a surface area of 0.6459 m^2/g, while the introduction of aluminum in Al-$SrTiO_3$(solid-state) resulted in an increased surface area to 0.9875 m^2/g. In the case of $SrTiO_3$(flux), the surface area was measured at 0.6087 m^2/g, indicating a comparable surface characteristic to $SrTiO_3$(solid-state). Notably, flux treatment with $SrCl_2$ led to a significant enhancement in the surface area for Al-$SrTiO_3$(flux), reaching 2.2856 m^2/g. This marked increase suggested that flux treatment, particularly with aluminum doping, played a crucial role in modifying the surface areas of $SrTiO_3$, a key factor influencing its photocatalytic activity.

Table 1. BET surface areas.

Sample	BET surface area (m^2/g)
$SrTiO_3$(solid-state)	0.6459
Al-$SrTiO_3$(solid-state)	0.9875
$SrTiO_3$(flux)	0.6087
Al-$SrTiO_3$(flux)	2.2856

The SEM images from Figure 3(a-c) clearly revealed the morphological transformations of $SrTiO_3$ particles under different synthesis conditions. Denoted as (a) $SrTiO_3$(solid-state), these particles exhibited fine irregular shapes. In the case of (b) $SrTiO_3$(flux), the particles adopted a cubic shape within the range of 1 to 2.5 µm. Lastly, (c) Al-$SrTiO_3$(flux) presented fine particles with sizes ranging from 200 to 500 nm. Notably, the cubic shape and size of $SrTiO_3$ particles were significantly altered after treatment with $SrCl_2$ flux. The introduction of Al further led to a decrease in particle size. Figure 3(d) displayed the Energy-dispersive X-ray spectroscopy (EDS) spectra of Al-$SrTiO_3$(flux), confirming the elemental composition of Sr, Ti, O, and Al without any detectable impurity peaks.

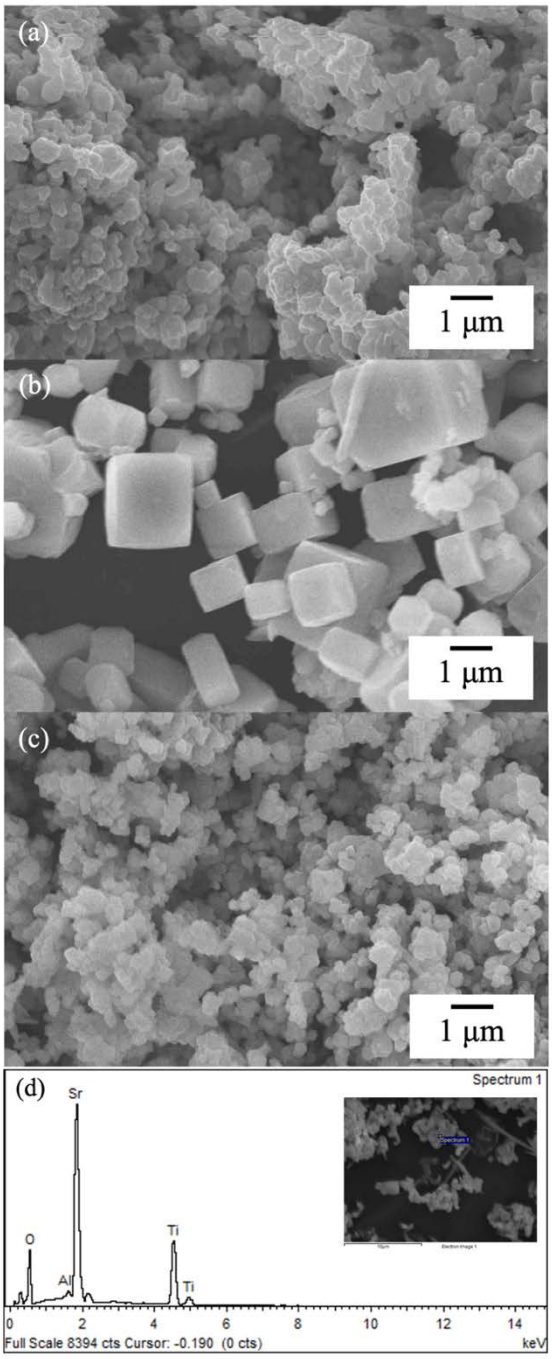

Figure 3. SEM images of (a) $SrTiO_3$(solid-state), (b) $SrTiO_3$(flux), and (c) Al-$SrTiO_3$(flux), and (d) Energy-dispersive X-ray spectroscopy (EDS) spectra of Al-$SrTiO_3$(flux)

Comparing the synthesis of $SrTiO_3$ in the solid-state at 1300 °C with and without the addition of Al, it was observed that the introduction of Al led to a decrease in the average crystallite size and an increase in surface area. Furthermore, a

comparison between $SrTiO_3$ before and after treatment with $SrCl_2$ flux revealed that flux treatment influenced a reduction in crystallite size, with surface areas showing slight change. Additionally, the introduction of Al in the flux treatment process further contributed to a reduction in crystallite size, as seen in Al-$SrTiO_3$(flux), and a significant increase in surface area. Additionally, SEM images depicted a decrease in particle size after the introduction of Al in the flux treatment process, aligning with the observed trends of increasing surface areas.

In Figure 4, the photoluminescence (PL) spectra exhibited distinctive intensity patterns among the $SrTiO_3$ samples subjected to different treatments. Notably, $SrTiO_3$(solid-state) displayed the highest intensity peak, indicative of a comparatively higher recombination rate of charge carriers. Conversely, Al-$SrTiO_3$(solid-state), $SrTiO_3$(flux), and Al-$SrTiO_3$(flux) demonstrated similar intensities, suggesting comparable recombination rates for these samples. The introduction of $SrCl_2$ flux, observed in $SrTiO_3$(flux), led to a noticeable reduction in intensity compared to $SrTiO_3$(solid-state), indicating a lower recombination rate. Furthermore, aluminum doping resulted in even lower recombination rate. This observed effect of flux treatment, particularly in the presence of aluminum doping, signified a potential enhancement in photocatalytic activity, as aluminium doping in $SrTiO_3$ effectively suppresses the generation of Ti^{3+} recombination centers which is a crucial factor for improved photocatalysis efficiency.[12]

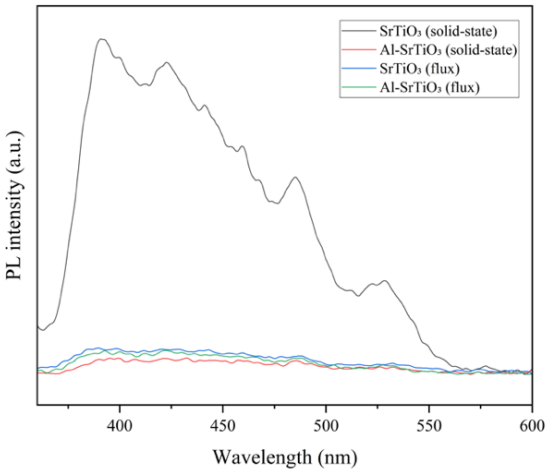

Figure 4. PL spectra of $SrTiO_3$(solid-state), Al-$SrTiO_3$(solid-state), $SrTiO_3$(flux), and Al-$SrTiO_3$ (flux)

3.3 Photocatalytic efficiency

In Figure 5, the dye degradation efficiency percentages for various $SrTiO_3$ samples were presented. $SrTiO_3$(solid-state) exhibited a degradation efficiency of 3.10%, while Al-$SrTiO_3$(solid-state) showed a lower efficiency of 0.64%. Interestingly, $SrTiO_3$(flux) demonstrated a higher degradation efficiency of 10.24%, and Al-$SrTiO_3$ (flux) surpassed the others with an efficiency of 21.66%. These results indicated a significant improvement in dye degradation efficiency, especially with the introduction of flux treatment and aluminum doping.

The $SrCl_2$ flux treatment plays a crucial role in modifying the morphology, as evidenced by the shift from irregular-shaped particles to well-defined cubic structures. Moreover, the observed reduction in photoluminescence intensity in $SrTiO_3$(flux) suggests a decrease in the recombination rate of charge carriers, contributing to improved photocatalytic efficiency.

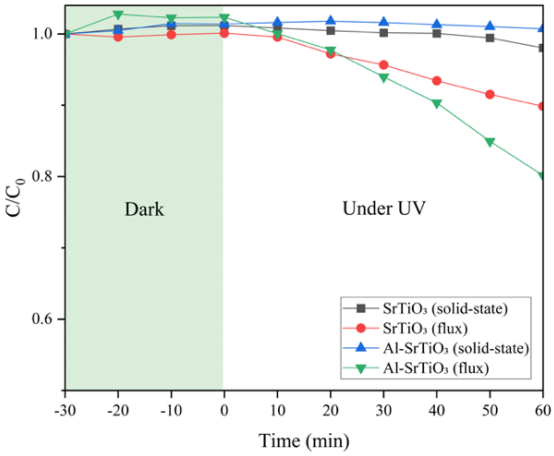

Figure 5. The correlation between C/C₀ and the irradiation time of photocatalysts under UV light for 60 minutes

Doping $SrTiO_3$ with lower-valence cations, such as Al, has been reported to boost its photocatalytic activity.[9] Aluminum doping significantly enhanced the photocatalytic performance of $SrTiO_3$, particularly when $SrCl_2$ was present during heating. In the absence of $SrCl_2$, effective Al doping during the solid-state reaction was not effective, as Al had to diffuse from the outer surface of the particles. Conversely, in the presence of $SrCl_2$ flux, a substantial portion of $SrTiO_3$ particles dissolved and recrystallized, facilitating improved Al doping.[6] This was evidenced by the distinct increase in dye degradation efficiencies of Al-$SrTiO_3$(flux) comparing with Al-$SrTiO_3$(solid-state). Furthermore, the increased surface area of Al-$SrTiO_3$(flux), attributed to flux treatment, provided more active sites for the adsorption of organic

dyes. As the results, the synergistic effects of flux treatment and aluminum doping collectively resulted in a more efficient degradation of organic dyes under UV light irradiation.

4. Conclusion

$SrTiO_3$ was successfully synthesized via solid-state method at 1300 °C. $SrCl_2$ flux treatment had affected on morphological transformations of $SrTiO_3$ particles, while aluminum doping resulted in a reduction in particle size, an increase in surface area, and lower recombination rates of charge carriers. Remarkably, Al-$SrTiO_3$(flux) exhibited the highest dye degradation efficiency at 21.66%, surpassing $SrTiO_3$ (flux), $SrTiO_3$ (solid-state) and Al-$SrTiO_3$(solid-state). These findings highlighted the synergistic effect of $SrCl_2$ flux treatment and aluminum doping, offering potential applications in advanced photocatalysis for environmental remediation.

Acknowledgements

This research is funded by Thailand Science Research and Innovation Fund Chulalongkorn University.

References

1. Koe, W. S.; Lee, J. W.; Chong, W. C.; Pang, Y. L.; Sim, L. C. An overview of photocatalytic degradation: photocatalysts, mechanisms, and development of photocatalytic membrane. *Environmental Science and Pollution Research* **2020**, *27* (3), 2522-2565. DOI: 10.1007/s11356-019-07193-5.
2. Fujishima, A.; Honda, K. Electrochemical Photolysis of Water at a Semiconductor Electrode. *Nature* **1972**, *238* (5358), 37-38. DOI: 10.1038/238037a0.
3. Kumari, H.; Sonia; Suman; Ranga, R.; Chahal, S.; Devi, S.; Sharma, S.; Kumar, S.; Kumar, P.; Kumar, S.; et al. A Review on Photocatalysis Used For Wastewater Treatment: Dye Degradation. *Water, Air, & Soil Pollution* **2023**, *234* (6), 349. DOI: 10.1007/s11270-023-06359-9.
4. Aravinthkumar, K.; Praveen, E.; Jacquline Regina Mary, A.; Raja Mohan, C. Investigation on $SrTiO_3$ nanoparticles as a photocatalyst for enhanced photocatalytic activity and photovoltaic applications. *Inorganic Chemistry Communications* **2022**, *140*, 109451. DOI: 10.1016/j.inoche.2022.109451.
5. Wei, H.; Cai, J.; Zhang, Y.; Zhang, X.; Baranova, E. A.; Cui, J.; Wang, Y.; Shu, X.; Qin, Y.; Liu, J.; et al. Synthesis of $SrTiO_3$ submicron cubes with simultaneous and competitive photocatalytic activity for H_2O splitting and CO_2 reduction. *RSC Advances* **2020**, *10* (70), 42619-42627. DOI: 10.1039/D0RA08246E.
6. Ham, Y.; Hisatomi, T.; Goto, Y.; Moriya, Y.; Sakata, Y.; Yamakata, A.; Kubota, J.; Domen, K. Flux-mediated doping of $SrTiO_3$ photocatalysts for efficient overall water splitting. *Journal of Materials Chemistry A* **2016**, *4* (8), 3027-3033. DOI: 10.1039/C5TA04843E.
7. Yamakata, A.; Yeilin, H.; Kawaguchi, M.; Hisatomi, T.; Kubota, J.; Sakata, Y.; Domen, K. Morphology-sensitive trapping states of photogenerated charge carriers on $SrTiO_3$ particles studied by time-resolved visible to Mid-IR absorption spectroscopy: The effects of molten salt flux treatments. *Journal of Photochemistry and Photobiology A: Chemistry* **2015**, *313*, 168-175. DOI: 10.1016/j.jphotochem.2015.05.016.
8. Wang, S.; Teramura, K.; Hisatomi, T.; Domen, K.; Asakura, H.; Hosokawa, S.; Tanaka, T. Effective Driving of Ag-Loaded and Al-Doped $SrTiO_3$ under Irradiation at $\lambda > 300$ nm for the Photocatalytic Conversion of CO_2 by H_2O. *ACS Applied Energy Materials* **2020**, *3* (2), 1468-1475. DOI: 10.1021/acsaem.9b01927.
9. Takata, T.; Domen, K. Defect Engineering of Photocatalysts by Doping of Aliovalent Metal Cations for Efficient Water Splitting. *The Journal of Physical Chemistry C* **2009**, *113* (45), 19386-19388. DOI: 10.1021/jp908621e.
10. Coonrod, S. S. Solid State Synthesis of the $SrTiO_3$ Nano-particle. Mechanical Engineering Undergraduate Honors Theses, University of Arkansas, Fayetteville, 2014. https://scholarworks.uark.edu/meeguht/39.
11. Uvarov, V.; Popov, I. Metrological characterization of X-ray diffraction methods for determination of crystallite size in nano-scale materials. *Materials Characterization* **2007**, *58* (10), 883-891. DOI: 10.1016/j.matchar.2006.09.002.
12. Li, R.; Takata, T.; Zhang, B.; Feng, C.; Wu, Q.; Cui, C.; Zhang, Z.; Domen, K.; Li, Y. Criteria for Efficient Photocatalytic Water Splitting Revealed by Studying Carrier Dynamics in a Model Al-doped SrTiO3 Photocatalyst. *Angewandte Chemie International Edition* **2023**, *62* (49), e202313537. DOI: 10.1002/anie.202313537.

Corrosion Inhibition Studies of Tamarind Shell Tannins on Mild Steel in Acidic Medium

Abdulmajid Abdullahi[1] and M. Hazwan Hussin[2]*

[1]*Department of Basic and Applied Sciences, College of Science and Technology, Hassan Usman Katsina Polytechnic, P.M.B 2052, Katsina State, Nigeria*
[2]*Materials Technology Research Group (MaTReC), School of Chemical Sciences, Universiti Sains Malaysia, 11800 Minden, Penang, Malaysia*

**E-mail: mhh.usm@gmail.com*

Abstract:

The tamarind shell tannins was characterized and studied for possible use in corrosion inhibition. Fourier-transform infrared spectroscopy (FTIR), nuclear magnetic resonance (NMR), and thermal gravimetric analysis (TGA), were applied to study tamarind shell tannins. The extraction yield (15.56%) of tamarind water extract (TWE) was rich in condensed tannins. Also, the FTIR and NMR studies established the occurrence of tannins. The inhibition studies on corrosion mitigation were observed using electrochemical impedance spectroscopy (EIS), potentiodynamic polarisation (PD), and electrochemical noise measurement (ENM) analysis. The inhibition efficiency was due to the increase in concentration of the extract up to 1000 ppm. The inhibition efficiency was 83.57%. Potentiodynamic polarization analysis revealed that (TWE) extract was mixed type corrosion inhibitor with major influence at cathodic sites. Nyquist plots presented that there was an increase in the resistance of charge transfer values as well as the decrease in constant phase element (CPE) as the concentrations of extract increases. The extracts study on adsorption followed Langmuir isotherm. The extract molecules were adsorbed on the mild steel surface physically with a free energy absorption of ΔG_{ads} TWE = −20.03 kJ mol^{-1}. Furthermore, the surface morphology and elemental composition studies using SEM and EDX, confirmed the adsorption of the extracts.

1. Introduction

Alloys and metals are exposed temporarily with acids in industrial processes, such as acid pickling, oil well acidizing, and acid descaling [1] Usually corrosion inhibitors are added to such acid solutions to stop or slow down the loss of metal and acid depletion rate [2–4]. Though, certain of these corrosion inhibitors are environmentally toxic and this has encouraged for finding eco-friendly inhibitors of corrosion for substrate in acid medium [5]. Diverse inorganic and organic compounds have been presented as efficient corrosion inhibitors to shield metals and alloys from corrosion occurrence. Typically, organic compounds were used as effective inhibitor of corrosion due to a significant influence of adsorption on the metal surface. The mitigation influence of various organic corrosion inhibitors is most likely to the existence of heteroatoms *i.e* . N, S, O, and π- electrons as well as heterocyclic compounds in their structures. The reaction center usually regarded as polar function is responsible for establishment of the adsorption process [6–8]. Organic molecules adsorption on the surface of the metal occurs by four different mechanisms: (a) the charged molecules electrostatic attraction with charged metal, (b) molecules uncharged electron pairs interaction with metal, (c) π-electrons interaction with metal and (d) (a) and (c) combination [8] . In present years the attention of researchers has been reacted toward eco-friendly green corrosion inhibitors from plant origin. These compounds are readily available, low-cost as well as renewable sources of materials [5]. It has been discovered that the, barks, leaves, fruits, seeds, and roots of plants extracts contains organic compounds mixtures with O, S, and N atoms are active compounds that inhibit corrosion in aggressive environment [4,7,9–12] .

Several authors reported the inhibition effect of green products extracted from plant materials [2,3,6,10,12,13]. Odewunmi et al. reported water melon rind extract (WMRE) as an active inhibitor for mild steel corrosion in HCl medium. They also establish that WMRE can be adsorbed on the mild steel surface physically in a HCl solution resulting in a Temkin isotherm [4]. Satapathy et al. considered justicia gendarussa plant extract (JGPE) as a corrosion inhibitor in HCl solution. In which JGPE acts as mixed type corrosion inhibitor upon polarization studies and 93% inhibition efficiency at 25 °C was achieved using 150 ppm [12]. Deng et al. studied the Ginkgo leaves extract (GLE) corrosion inhibition properties of mild steel substrate in sulfuric acid and hydrochloric medium. And disclosed that GLE is an effective inhibitor of corrosion, with enhanced effect in 1.0 M hydrochloric than 0.5 M sulphuric acid. The isotherm of adsorption on steel surface followed a Langmuir. GLE performed as a mixed-type corrosion inhibitor in 1.0 M hydrochloric acid medium, then with main

influence on the cathodic site in 0.5 M sulphuric acid medium [2]. *Tamarindus indica* or locally known as 'tsamiya' in Nigeria is a leguminous tree (family Fabaceae) bearing edible fruit that is indigenous to tropical Africa. The fruit is an indehiscent legume, sometimes called a pod, 12 to 15 cm in length, with a hard, brown shell [14]. Previous studies have revealed that the *Tamarindus indica* shell contains fiber, tannin, tartaric acid and calcium [15]. The tannin compounds can be extracted from *Tamarindus indica* shell to be utilised as corrosion inhibitor of mild steel. Thus the aim of this study is to investigate the effect of Tamarind shell tannin water extract as a new green corrosion inhibitor for mild steel in 0.5M HCl medium. The inhibition action was investigated by electrochemical techniques and Surface characterizations via SEM.

2. Materials and Methods

2.1 Materials and sample preparation

The Tamarind shell used in this study was collected from Nigeria and dried upon use. The dried fresh sample was made into powdered form using blander and extracted continuously using distilled water. During the extraction process, 10 g of powdered shells were mixed with 100 ml distilled water using a magnetic stirrer at room temperature for overnight. Next, the solution was filtered using whatman filter paper and the extraction process was carried out for 3 days at the same temperature to get a concentrated solution. Lastly, the dark brown extract was acquired using freeze drier. The obtained extract was used as corrosion inhibitor in the study. Mild steel (Mn: 0.15 %, S 0.16 %, P 0.01% and C 0.01%, Al 0.06 %, Na 0.02 %, Mg 0.03 %) and the balance Fe with 6 cm × 3 cm × 0.1 cm proportions were prepared for electrochemical measurement and surface characterization analysis. The steel sheets specimens were abraded using 200 to 1000 emery papers and formerly degreased with acetone and washed thoroughly with distilled and dried. A proper concentration of HCl 37% acid (0.5 M) was prepared in distilled water. Also, the concentration range was varied from 1 to 1000 ppm.

2.2 FT-IR, NMR and TGA

The chemical composition of the extract was studied by FT-IR (Perkin Elmer System 2000 (Waltham, MA, USA), with a wavelength range of 4000 to 400 cm^{-1} at 4 cm^{-1} resolutions and 16 scans. The potassium bromide technique (KBr) was applied to the samples with the proportion of 1:20 (w/w).

NMR studies, **a**pproximately 150 mg of the samples were dissolved in 0.4 mL of deteurated d_6 dimethyl sulfoxide (DMSO-d6) and injected into an NMR tube. A Bruker Avance 500 MHz spectrometer (Fallanden, Switzerland) was used to perform the analysis at 50°C overnight, at 7.0 kHz spinning speed, 4000 scans with 12s pulse delay. The spectra were processed using Bruker Top Spin software 3.5 (Oxford, U.K).

TGA Analysis was performed using Thermogravimetric analyzer A Perkin Elmer TGA 7 (Waltham, MA, USA) recorded the thermal degr**a**dation of 5 mg samples of the tamarind shell extract from 30 °C to 900 °C under nitrogen atmosphere with a 10 °C min^{-1} heating rate.

2.3 Electrochemical measurements

The inhibition actions of the ex**t**ract in 0.5 M HCl solution on the steel substrate was examined through electrochemical impedance spectroscopy (EIS) and polarization techniques. The experiment was carried out using Potentiostat/Galvanostat Gamry reference 600 (Gamry USA Instruments)**.** Both analys**e**s were conducted via a conventional three electrode cell comprising mild steel sheets 6 cm × 3 cm × 0.1 cm as working electrode (WE), a Platinum rod as counter electrode (CE) and a saturated calomel electrode as reference electrode (RE). The measurements were conducted in 50 ml of 0.5 M HCl solutions without and with 1, 10, 50, 100, 500 and 1000 ppm TWE at room temperature. The experiments were performed at open circuit potential (OCP) after 15 min immersion to steady state condition. Potentiodynamic measurements were carried out from cathodic to the anodic direction at ±250 mV around OCP with 0.5 mV/s scanning rate. The calculation of inhibition efficiency (IE) was done via the following equation 1

$$\text{IE } \% = \frac{R_{ct(i)} - R_{ct}}{R_{ct(i)}} \times 100$$

Besides, the EIS measurements were conducted at frequencies ranging from 10000 kHz to 0.01 Hz and amplitudes of ±5 mV. EIS data were fitted to some equivalent electrical circuit models using Gamry Echem analytical software. Equation 2 was used to calculate the percentage inhibition (IE) efficiency values.

$$\text{IE } \% = \frac{i_{corr} - i_{corr\,(i)}}{i_{corr}} \times 100$$

2.4 Electrochemical noise (EN)

Electrochemical noise measurements were carried out using (Gamry Reference 600) in the

presence of 1000 ppm inhibitor solution in an electrolyte of 0.5 M HCl. A total of 1 h of duration was employed for the E_{ocp} to reach a steady rate potential stability. After which the electrochemical current and potential noise were simultaneously acquired at a period of 1 h, a block time of 4 s and at 0.05 s sample period. Zero resistance ammeters, ZRA mode was used to record the noise generated during the mild steel corrosion process. Equation 3 was used to calculate the percentage inhibition efficiency values.

$$IE\ \% = \frac{R_{n\,(i)} - R_n}{R_n} \times 100$$

2.5 Surface Analysis

The surface morphology of mild steel substrate upon exposure to 0.5 M HCl in the absence and presence of TWE extract was examined by (SEM) (FEI Quanta FEG 650).

3. Results & Discussion

3.1. Characterization of TWE

According to the FTIR analysis, Figure 1 the spectra show similar transmission bands to that of *Aleppo pine* tannin [16] and Tannin [17]. Bands at ~3400 cm^{-1} are assigned to O-H stretching vibrations [18]. Bands located at ~2900 cm^{-1} are owing to CH and CH_2 aliphatic hydrocarbon vibrations [19]. FTIR bands at ~1600 cm^{-1} are attributed to C=C aromatic ring stretching vibrations. The bands at 1050 - 1284 are assigned to C-O-C stretching vibration [20]. The bands at ~1370 cm^{-1} are attributed to phenolic O-H stretching vibrations [21]. The presence of condensed tannin was evident by bands at ~1260 and~1050 cm^{-1} are attributed to the CO asymmetric stretching vibration from the pyran derived condensed tannin ring structure [16].

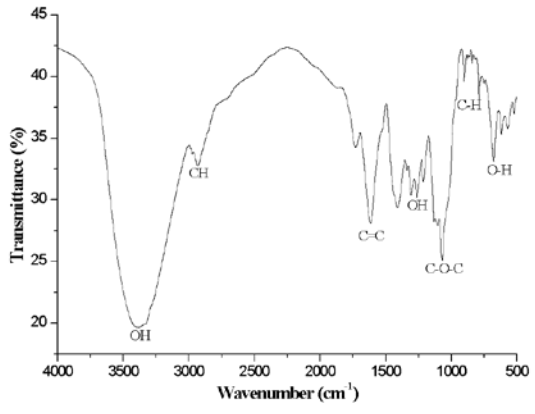

Figure 1. FT-IR spectrum of TWE

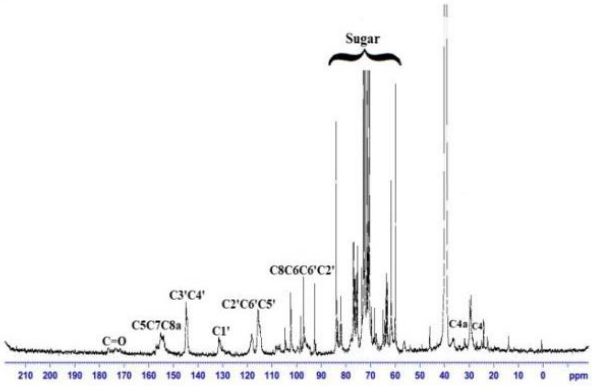

Figure 2. NMR spectrum of TWE

3.2. The ^{13}C NMR spectra

^{13}CNMR depicted in Figure 2 show tannin spectra that portrayed conventional signals of prodelphinidin (PD) and procyanidin (PC) entities, with the majority of PC units. The peaks between 115 ppm and 120 ppm signify C2′, C6′, and C5′ carbons of procyanidin entities. The NMR signals present from 142 ppm to 145 ppm symbolize C3′ and C4′ carbons of procyanidin entities. It can be deduced that the NMR peaks of C5, C7, and C8a carbons in procyanidin entities lie between 150 ppm and 160 ppm. Prodelphinidin entities were identified from the chemical shift of C4 positioned at 130.8 ppm, which overlays with the signal representing C1' carbon. Signals present between 90 ppm and 110 ppm were denoted as C8, C6, C6′, and C2′ of procyanidin entities. The C4 extension entities demonstrated a wide band at 36.6 ppm, but terminal C4 showed a distinctive signal at 29.4 ppm. Presence of carbohydrates in the extracts was represented by the bands between 60 ppm and 85 ppm [22, 23, and 24]. A signal at 170-182 ppm is observed suggesting the traces of galloyl groups which could be rationalized by the unpurified tannins [25].

3.3 TGA Analysis

Two distinct mass loss peaks can be seen at around 150 – 200 ℃ Figure 3 which corresponded to the first degradation of the TWE sample, due to the thermal reforming, preliminary oxidation steps and elimination of volatile fractions. The second degradation is sharper and more pronounced and it is found at around 200 - 300 °C, where the degradation of tannins begins, and it could be as a result of the breakdown of the intermolecular bonding [26, 16]. Finally, after 900 °C were remains of carbonized residue of TWE 28.10%. Meanwhile, established in the present study, the thermal stability of TWE could be attributed to high degree of polymerization.

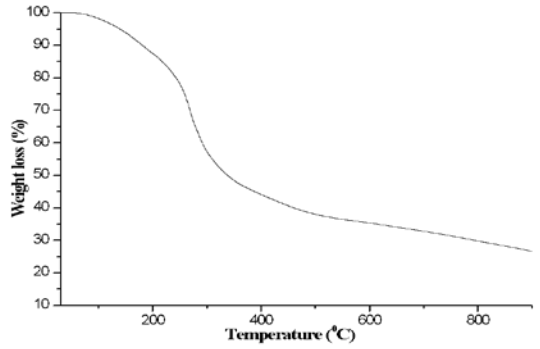

Figure 3. TGA of spectrum TWE

3.4 Electrochemical impedance spectroscopy measurements

The deterioration actions of mild steel in 0.5 M HCl solution in the absence and presence of TWE was examined by EIS technique. The Nyquist and Bode plots are displayed in Figures 5-6. From the Nyquist plots clearly show the distinct semicircles, thus, showing the inhomogeneity of the mild steel surface. Equivalent electrical circuit Figure 4 was employed to designate the electrochemical actions arisen on the blank sample and TWE in 0.5 M HCl solutions containing 1, 10, 50, 100, 500 and 1000 ppm TWE. Thus, the plot shows that the electrochemical actions on these samples are generally managed by charge transfer process. Still, Nyquist and Bode plots Figures 5-6 of the extracts in 0.5 M HCl solutions comprising various concentrations of TWE were well fitted by the constant electrical model. The results attained presented in Tables 1 Thus, in absence and presence of the inhibitors. The increase in inhibitor concentration caused the increase of *R*ct. The rise of *R*ct is in line to the adsorption of inhibitor molecules on the metal surface. The inhibitor adsorption on the active sites of mild steel surface is responsible for the hindering of destructive species contact to the metal surface [10]. The *C*PE values decreases with the increase of inhibitor concentration indicating the increase of inhibitor molecules adsorption on the mild steel surface at high concentrations [9]. A maximum inhibition efficiency of 82.43% was achieved for the sample immersed in the solution with 1000 ppm inhibitor.

3.5 Polarization measurements

Anodic and cathodic polarization curves for the mild steel substrate immersed in 0.5 M HCl solution in the presence and absence of various concentrations (1, 10, 50 100, 500 and 1000 ppm) of TWE are shown in Figure 7. Electrochemical factors comprising corrosion potential (E_{corr}), corrosion current density (I_{corr}), corrosion rate (CR), cathodic Tafel slope (-βc) anodic Tafel slope (βa) and inhibition efficiency (IE %) are attained from polarization plots and the effects are listed in Tables 2. It is well clear from Figure 7. That addition of even low concentration of TWE to the 0.5 M HCl medium leads to the shift of both cathodic and anodic sites toward lesser current densities and a small change of corrosion potential values. Thus, it is clear from the results that corrosion current density decreases and the inhibition efficiency 83.57% increases with the increase in concentration of TWE. The increase of TWE concentration also results in the major decrease in cathodic Tafel slope and a small increase of corrosion potential to less negative values. However, the result shows that TWE affected the nature of cathodic sites greater than anodic sites [13]. Consequently, these interpretations designate that TWE performed as a mixed-type inhibitor with major effect on cathodic sites.

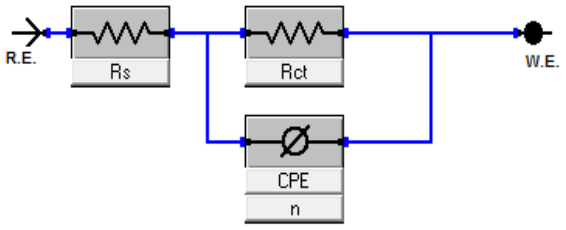

Figure 4. The equivalent circuit of Randles-CPE to fit EIS result of mild steel in 0.5 M HCl at different concentration of TWE at 303K

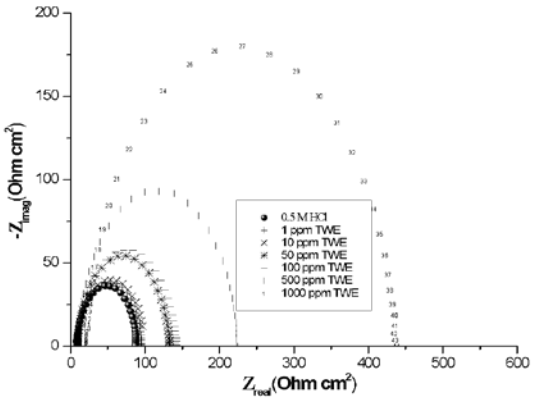

Figure 5. The Niquist impedence curves of mild steel in 0.5 M HCl solution at different concentration of TWE at 303K

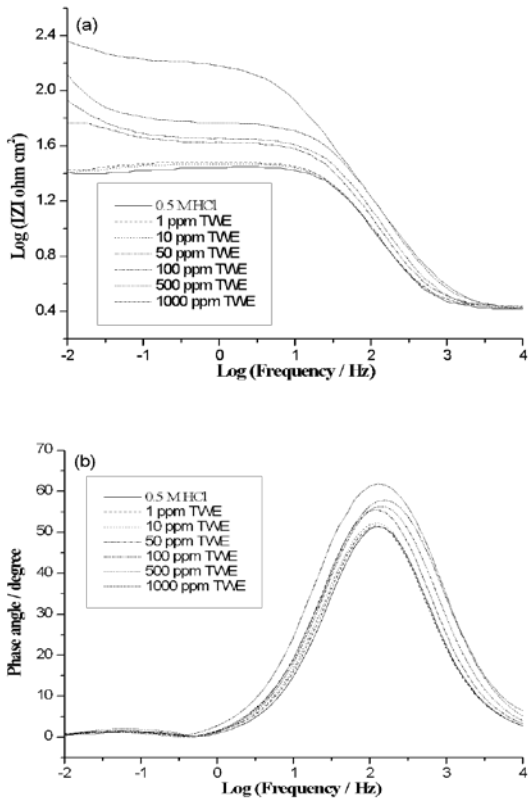

Figure 6. Bode impedence (a) and (b) phase angle plots obtained for the mild steel in 0.5 M HCl solution at different concentration of TWE at 303K

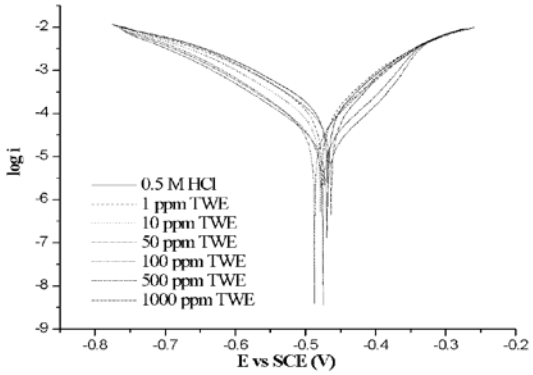

Figure 7. Tafel polarization curves of mild steel specimen in 0.5 M HCl solution at different concentration of TWE at 303K

Table 1. The Nyquist impedance parameters at different concentrations of TWE at 303 K

Concentrations (ppm)	R_{ct} (cm^2)	CPE (Fcm^{-2})	n	IE (%)
0.5 M HCl	76.51	273	0.9495	-
1 ppm TWE	83.92	236	0.9012	8.83
10 ppm TWE	92.84	273	0.9397	17.58
50 ppm TWE	134.3	267	0.9195	42.92
100 ppm TWE	145.78	254	0.9115	47.52
500 ppm TWE	226.50	231	0.9028	66.23
1000 ppm TWE	435.63	207	0.9039	82.43

Table 2. Electrochemical polarization parameters for mild steel in 0.5M HCl solution in the absence and presence of TWE at 303 K

Concentration (ppm)	E_{corr} (mV)	i_{corr} (mA cm^{-2})	β_a (mV $decade^{-1}$)	$-\beta_c$ (mV $decade^{-1}$)	IE (%)	CR (mpy)
0.5 M HCl	-468	0.1260	85	114	-	57.31
1 ppm TWE	-476	0.0981	84	100	22.14	44.70
10 ppm TWE	-479	0.0755	76	109	40.07	35.31
50 ppm TWE	-464	0.0659	70	93	47.69	30.06
100 ppm TWE	-487	0.0388	74	85	69.20	17.69
500 ppm TWE	-475	0.0269	81	84	78.65	12.26
1000 ppm TWE	-470	0.0207	71	70	83.57	9.44

3.6 Electrochemical Noise

The EN statistical data analyses are presented in Table 3. And Figure 8 shows fluctuation against the current noise per time for the inhibited and 0.5 M HCl solution. The mean resistance values of noise increased by 1000 ppm concentration of the extract in relation with the blank solution, besides the transient amounts are increased in 0.5 M HCl. Also, the transient's amplitude could be recognized as a speedy decrease and increase in current values, which are attributed to the activation process, *ie*, metastable pitting [27,28].

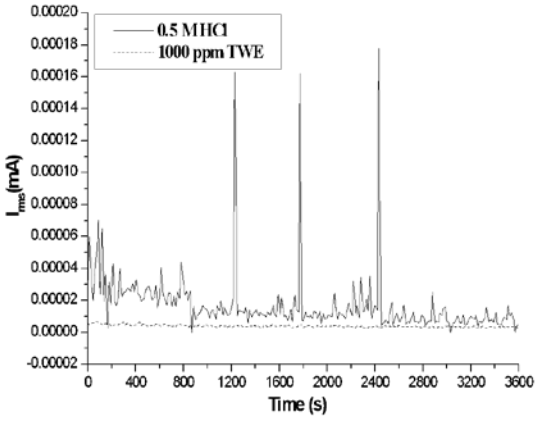

Figure 8. The electrochemical current noise plots after 1h immersion in 0.5 M HCl

Table 3. The noise resistance parameters for 1000 ppm of TWE extracts at 303K

Samples	R_n (Ω cm^2)	% IE
0.5 M HCl	21.97	-
1000ppm TWE	81.44	73.02

3.7 Adsorption isotherm

The corrosion inhibition mechanism on the steel surface in 0.5 M HCl solution can be examined by the assessment of adsorption isotherm. The Langmuir adsorption isotherm is the utmost and was tested. Langmuir adsorption isotherms were used to fit surface coverage (θ) values obtained from potentiodynamic polarization measurement at varying concentrations of TWE inhibitor. Equation 5 was used to calculate the surface coverage (θ).

$$\theta = \frac{i_{corr} - i_{corr\,(i)}}{i_{corr}}$$

where i_{corr} and $i_{corr(i)}$ denote corrosion current densities (mA cm^{-2}) with and without TWE inhibitor

From this adsorption study, the straight line of C / θ vs C with regression coefficient near toward 1 Figure 9, explains that all TWE extracts adsorption is sound to fit the model of Langmuir isotherm on the surface of the substrate; it also states that TWE adsorption on the substrate surface is a single layer molecular adsorption. Organic simple molecules possess two types of behaviour of adsorption to form a film, ***i.e.***, the chemical adsorption as well as physical adsorption [29]. The equilibrium constants of adsorption (K_{ads}) were acquired from the straight lines' intercepts. Similarly, K_{ads} is also related to the standard free energy of adsorption (ΔG_{ads}) [30]. Using the following equation 6, the equilibrium constant value (*K*) was calculated from the interception of the straight line in Figure 9. According to Table 4 the ΔG_{ads} value around 20 kJ/mol indicates that the TWE adsorption on the mild steel surface belongs to physical (physisorption) mechanisms [7].

$$\Delta G_{ads} = -RT \ln (K_{ads} \times 1000)$$

3.8 Inhibition mechanism of TWE

The FT-IR results of the TWE showed the presence of heteroatom *i.e.* O that might come

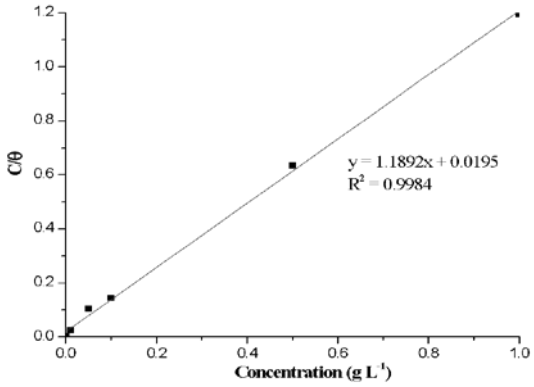

Figure 9. Adsorption isotherm plots using Langmuir equations upon potentiodynamic polarization measurements at different concentrations of TWE at 303K

Table 4. The adsorption parameters upon potentiodynamic polarization measurement at different concentrations of TWE at 303K

Concentrations (ppm)	θ	K_{ads} (L g^{-1})	ΔG_{ads} (kJ mol^{-1})
0.5 M HCl	-	-	-
1 ppm TWE	0.2214	51.28	-20.03
10 ppm TWE	0.3849		
50 ppm TWE	0.4769		
100 ppm TWE	0.6920		
500 ppm TWE	0.7864		
1000 ppm TWE	0.8361		

from the aromatic rings of the extracts. The anode and cathode site on the mild steel surface are in contact with destructive species resulting in the major dissolution of steel. The surface of the mild steel Figure 10 can be blocked by the adsorption of inhibitor molecules presented in the extracts against mass transfer and charge, hindering in corrosion process. Adsorption is usually measured in two ways. The extracts' neutral molecular constituents may be adsorbed on the metal surface by chemisorption mechanism consist of sharing of electrons between N and O atom and Fe, leading to the displacement of the water molecules from the metal steel surface. However, the molecules components of the extract might adsorb on the mild steel surface by vacant d-orbital of iron and π electrons of the fused benzene rings. Also, the protonated constituents of the extracted molecules may be physically adsorbed by electrostatic interactions between the adsorbed chloride ions and inhibitor cations. Thus, it suggested the kind of adsorption of the extract constituents on the mild steel surface [2, 10].

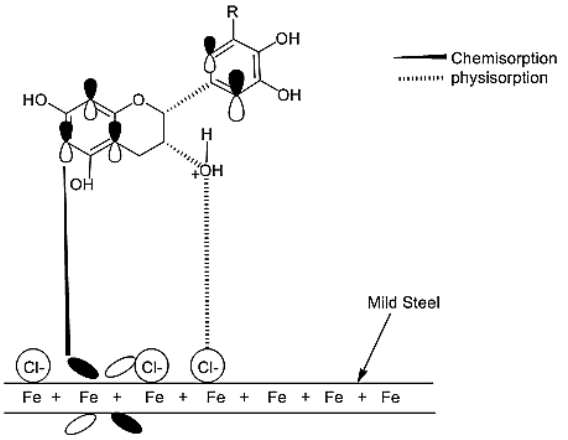

Figure 10. Schematic corrosion inhibition mechanism of TWE adsorption on the mild steel surface

3.9 Surface investigations

Surface analysis on the influence of inhibitors on corrosion substrate at the metal/solution interface was examined by SEM analysis. The surface micrographs of the mild steel substrate exposed to 0.5 M HCl solutions with and without TWE for 24 h were studied by scanning electron microscope (Figure 11). Figure 11a displays a rough damaged mild steel sample dipped in 0.5 M HCl solution, which resulted in the decrease in iron and carbon content as presented in Table 5. The inhibitor adsorption on the mild steel surface caused the rate of decrease in steel deterioration and subsequent lesser surface roughness [7, 9, 12, 31].

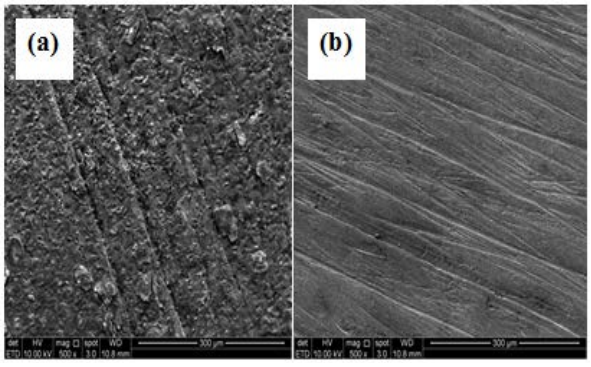

Figure 11. SEM micrographs of mild steel after 24 h immersion in 0.5 M HCl solution (a) mild steel without inhibitor (b) mild steel with 1000 ppm TWE

Table 5. The percentage of an element for the bare mild steel, 0.5M HCl treated and 1000 ppm TWE acquired using EDX analysis

Mild steel	Element (%)			
	Fe	C	O	Cl
Polished	84.83	13.30	1.87	-
0.5M HCl treated	31.52	4,46	61.69	2.33
1000 ppm TWE	71.93	18.05	9.42	-

4. Conclusion

The inhibition efficiency of mild steel in 0.5 M HCl solution considerably increased by the increase in concentration of TWE extract. Inhibition efficiency up to 83.57% has been attained using 1000 ppm at 30 ± 2°C. Potentiodynamic polarization studies revealed that TWE performed as a mixed-type inhibitor. Impedance measurements of mild steel displayed that the charge transfer resistance increased with the increase in concentration of TWE. SEM analyses presented the creation of thin layer comprising TWE molecules on the surface of the mild steel, which inhibits it against severe destruction and deterioration. Adsorption of the inhibitor molecules on the mild steel surface was established to follow a Langmuir adsorption isotherm.

Acknowledgments

The author would like to acknowledge Universiti Sains Malaysia for providing a short term Grant (304/PKIMIA/6315100). And Hassan Usman Katsina Polytechnic, Nigeria for the PhD sponsorship.

References

1. Finšgar M , Jackson J . Application of corrosion inhibitors for steels in acidic me- dia for the oil and gas industry: a review. Corrosin Science 2014;86:17–41 .
2. Deng S , Li X . Inhibition by Ginkgo leaves extract of the corrosion of steel in HCl and H 2 SO 4 solutions. Corrosion Science 2012;55:407–15 .
3. Ji G , Anjum S , Sundaram S , Prakash R . Musa paradisica peel extract as green corrosion inhibitor for mild steel in HCl solution. Corrosion Science 2015;90:107–17 .
4. Odewunmi NA , Umoren SA , Gasem ZM . Utilization of watermelon rind extract as a green corrosion inhibitor for mild steel in acidic media. J Ind Eng Chem 2015;21:239–47.
5. Hooshmand Zaferani S , SharifiM , Zaarei D , Reza Shishesaz M . Application of eco-

friendly products as corrosion inhibitors for metals in acid pickling pro- cesses –A review. Journal of Environmental Chemical Engineering 2013;1(4):652–7 .
6. Abiola OK , James AO . The effects of Aloe vera extract on corrosion and kinetics of corrosion process of zinc in HCl solution. Corrosion Science 2010;52(2):661–4 .
7. Mourya P , Banerjee S , Singh MM . Corrosion inhibition of mild steel in acidic solution by Tagetes erecta (Marigold flower) extract as a green inhibitor. Corrosion Science 2014;85:352–63 .
8. Ostovari A , Hoseinieh SM , Peikari M , Shadizadeh SR , Hashemi SJ . Corrosion inhibition of mild steel in 1 M HCl solution by henna extract: A comparative study of the inhibition by henna and its constituents (Lawsone, Gallic acid, α- d-Glucose and Tannic acid). Corrosion Science 2009;51(9):1935–49 .
9. Li X , Deng S , Fu H . Inhibition of the corrosion of steel in HCl, H2SO4 solutions by bamboo leaf extract. Corrosion Science 2012;62:163–75 .
10. Odewunmi NA , Umoren SA , Gasem ZM . Watermelon waste products as green corrosion inhibitors for mild steel in HCl solution. Journal of Environmental Chemical Engineering 2015;3(1):286–96 .
11. Odewunmi NA , Umoren SA , Gasem ZM , Ganiyu SA . Qamaruddin Muhammadl-Citrulline: an active corrosion inhibitor component of watermelon rind extract for mild steel in HCl medium. Journal Taiwan Institute of Chemical Engineering 2015;51:177–85 .
12. Satapathy AK , Gunasekaran G , Sahoo SC , Amit K , Rodrigues PV . Corrosion inhi- bition by Justicia gendarussa plant extract in hydrochloric acid solution. Corrosion Science 2009;51(12):2848–56 .
13. Kumar KPV , Pillai MSN , Thusnavis GR . Seed Extract of Psidium guajava as ecofriendly corrosion inhibitor for carbon steel in hydrochloric acid medium. Journal of Material Science and Technology 2011;27(12):1143–9
14. Doughari, J. H. (2006). "Antimicrobial Activity of Tamarindus indica". Tropical Journal of Pharmaceutical Research. **5** (2): 597–603.
15. Adur, A. J., Nandini, N., Mayachar, K. S., (2019). Antibacterial Activity of Biosynthesized Nanoparticles using Tamarind Shell Extract JETIR, 6 (5), 665-673.
16. Saad, H., Khoukh, A., Ayed, N., Charrier, B., & Charrier-El Bouhtoury, F. (2014). Characterization of Tunisian Aleppo pine tannins for a potential use in wood adhesive formulation. Industrial crops and products, 61, 517-525.
17. Ricci, A., Olejar, K. J., Parpinello, G. P., Kilmartin, P. A., & Versari, A. (2015). Application of Fourier transform infrared (FTIR) spectroscopy in the characterization of tannins. Applied Spectroscopy Reviews, 50(5), 407-442.
18. Umoren, S. A., & Solomon, M. M. (2015). Effect of halide ions on the corrosion inhibition efficiency of different organic species–A review. Journal of Industrial and Engineering Chemistry, 21, 81-100
19. Ping, L., Pizzi, A., Guo, Z. D., & Brosse, N. (2012). Condensed tannins from grape pomace: characterization by FTIR and MALDI TOF and production of environment friendly wood adhesive. Industrial Crops and Products, 40, 13-20.
20. Martinez, S. (2003). Inhibitory mechanism of mimosa tannin using molecular modeling and substitutional adsorption isotherms.
21. Chupin, L., Motillon, C., Charrier-El Bouhtoury, F., Pizzi, A., & Charrier, B. (2013). Characterisation of maritime pine (Pinus pinaster) bark tannins extracted under different conditions by spectroscopic methods, FTIR and HPLC. Industrial Crops and Products, 49, 897-903.
22. Fu, C., Loo, A. E. K., Chia, F. P. P., Huang, D. (2007). Oligomeric proanthocyanidins from mangosteen pericarps. Journal of Agricultural and Food Chemistry 55(19), 7689-7694.
23. Zhang, L. L., Lin, Y. M. (2008). HPLC, NMR and MALDI-TOF MS analysis of condensed tannins from Lithocarpus glaber leaves with potent free radical scavenging activity Molecules 13(12), 2986-2997.
24. Zhang, L. L., Lin, Y.. M., Zhou, H..C., Wei, S..D., Chen, J..H. (2010). Condensed tannins from mangrove species Kandelia candel and Rhizophora mangle and their antioxidant activity Molecules 15 (1) 420-431.
25. Kiatgrajai, P., Wellons, J. D., Gollob, L., & White, J. D. (1982). Kinetics of epimerization of (+)-catechin and its rearrangement to catechinic acid. The Journal of Organic Chemistry, 47(15), 2910-2912.
26. Pantoja-Castro, M. A., & González-Rodríguez, H. (2011). Study by infrared spectroscopy and thermogravimetric analysis

of tannins and tannic acid. Revista latinoamericana de química, 39(3), 107-112.
27. Klapper, H. S., Goellner, J., & Heyn, A. (2010). The influence of the cathodic process on the interpretation of electrochemical noise signals arising from pitting corrosion of stainless steels. Corrosion Science, 52(4), 1362-1372.
28. Samiento-Bustos, E., Rodriguez, J. G., Uruchurtu, J., Dominguez-Patiño, G., & Salinas-Bravo, V. M. (2008). Effect of inorganic inhibitors on the corrosion behavior of 1018 carbon steel in the LiBr+ ethylene glycol+ H2O mixture. Corrosion Science, 50(8), 2296-2303.
29. Hu, K., Zhuang, J., Zheng, C., Ma, Z., Yan, L., Gu, H., ... & Ding, J. (2016). Effect of novel cytosine-l-alanine derivative based corrosion inhibitor on steel surface in acidic solution. Journal of Molecular Liquids, 222, 109-117.
30. Daoud, D., Douadi, T., Issaadi, S., Chafaa, S., (2014). Adsorption and corrosion inhibition of new synthesized thiophene Schiff base on mild steel X52 in HCl and H2SO4 solutions Corrosion Science. 79, 50–58.
31. Jokar, M. Shahrabi T. Farahani, Ramezanzadeh. B. "Electrochemical and surface characterizations of morus alba pendula leaves extract (MAPLE) as a green corrosion inhibitor for steel in 1M HCl", Journal of the Taiwan Institute of Chemical Engineers, 2016

Immobilized chitinase as an effective biocatalytic platform for producing bioactive chitobiose from biomass-derived chitin

Ailada Charoenpol[1], Daniel Crespy[2], Albert Schulte[3], and Wipa Suginta[4]*

[1]*School of Biomolecular Science and Engineering (BSE), Vidyasirimedhi Institute of Science and Technology (VISTEC), 555 Moo 1, Payupnai, Wangchan, Rayong 21210, Thailand*
[2]*Department of Materials Science and Engineering, School of Molecular Science and Engineering (MSE) Vidyasirimedhi Institute of Science and Technology (VISTEC), 555 Moo 1, Payupnai, Wangchan, Rayong 21210, Thailand*
[3]*School of Biomolecular Science and Engineering (BSE), Vidyasirimedhi Institute of Science and Technology (VISTEC), 555 Moo 1, Payupnai, Wangchan, Rayong 21210, Thailand*
[4]*School of Biomolecular Science and Engineering (BSE), Vidyasirimedhi Institute of Science and Technology (VISTEC), 555 Moo 1, Payupnai, Wangchan, Rayong 21210, Thailand*

**E-mail: wipa.s@vistec.ac.th*

Abstract:

This study describes the development of chitinase immobilization using magnetic nanoparticles (MNPs) as a biocompatible support for chitobiose production from chitin food wastes. The success of chitinase immobilization was validated by transmission electron microscopy (TEM), Fourier transform infrared spectroscopy (FTIR) and thermal gravimetry analysis (TGA). The immobilized *Vh*ChiA exhibited an immobilization yield of 89 ± 2% with 98 ± 2% retention of activity and showed improved thermostability and storage stability compared to the free enzyme. The immobilized enzyme retained 49% of its activity after 16 reaction cycles and could be readily separated from the reaction mixture. Our system showed higher catalytic activity than the free enzyme in converting shrimp shell and squid pen chitins into chitobiose in a single-step reaction. The final yield of the purified compound was 37% from shrimp chitin and 61% from squid-pen chitin. In conclusion, we developed an efficient MNPs-based chitinase immobilization system that can be further tailored for large-scale production.

1. Introduction

Chitin is the most abundant polysaccharide available in marine ecology. It serves as a structural component of crustaceans, such as crabs, shrimps, krill, lobsters and diatoms.[1, 2] It has been estimated that more than one billion metric tons of chitin is produced annually in the oceans,[3] making it an attractive biomaterial for industrial uses. Recently, biodegradation of chitin to chitooligosaccharides (CHOs) has received much attention because of their bioactivity and biocompatibility. Short-chain CHOs are used in biomedicine, pharmaceuticals, biotechnology, in coatings and in agriculture.[4-7] In general, CHOs can be produced either physically, chemically, or through enzymatic degradation of chitin.[8] However, the use of physical and chemical treatments has some limitations, including non-selective degradation, which leads to the production of a mixture of CHOs of different sizes and the generation of residual acids such as hydrochloric acid, sulfuric acid and nitrous acid, which are highly toxic to the environment.[9] In nature, CHOs are produced by the enzymatic hydrolysis of chitin by chitinases[10-14] which offer a more controllable and sustainable method for CHOs production.[15,16] However, the enzymatic hydrolysis of chitin by chitinases in solution also has some limitations, owing to the poor stability, non-reusability and difficulty of separating the enzyme from the reaction products. To overcome such drawbacks, immobilization can be used to improve the enzyme's properties and offers some advantages over enzymes in solution, including enhanced productivity, increased thermostability and retention of catalytic activity during prolonged reaction times.[17,18] In addition, immobilization enables the separation from the reaction mixture, permitting the use of flow bioreactors for continuous operation.

Chitinases are chitin degrading enzymes, produced by various organisms from microbes, fungi and plants.[19-21] These enzymes have great potential for use in CHO production through either hydrolytic or transglycosylation reactions.[22,23] In previous studies, chitinase A (*Vh*ChiA) from the marine bacterium *Vibrio campbellii* (formerly classified as *V. harveyi*), of glycosyl hydrolase family 18, which catalyzes the breakdown of chitin polysaccharide, was shown to yield chitobiose, $(GlcNAc)_2$, as a major product.[16,24,25] We recently reviewed different immobilization systems for chitinases, including adsorption, entrapment and covalent bonding.[26] Reported immobilization carriers were chitosan beads, hydroxypropyl

methylcellulose acetate succinate, carrageenan/alginate beads, carrageenan/guar gum gel beads, silica nanoparticles, polyurethane/nano CuO sheet, polyurethane/nano ZnO sheets and magnetic nanoparticles. Another chitinase from *Trichoderma harzianum* (Chit42) was immobilized on magnetic nanoparticles (MNPs) and chitosan beads using glutaraldehyde (GA) and genepin (GP) as crosslinkers, with immobilization and recovery activity yields of 62-86% and 62-66%, respectively.[27] The immobilized chitinase showed chitin hydrolytic activity that was larger than that of the free enzyme, however, the reusability was low, with only 30% of the initial activity remaining after 5 cycles. Recently, immobilization of chitinase from *Streptomyces albolongus* ATCC 27414 (*Sa*ChiA4) on ultrafiltration membranes was reported.[28] *Sa*ChiA4 was adsorbed on cellulose membranes in the *Sa*ChiA4 membrane bioreactor with an immobilization efficiency of 99.5% and activity retention of 85.6%. The product yields of GlcNAc and $(GlcNAc)_2$ from chitin hydrolysis were 14.4% and 75.6%, respectively. In another report, magnetic nanoparticles (MNPs) were used for immobilization of fungal Chit42.[27]

Our research aim is to develop an efficient biocatalytic chitinase immobilization system for the production of bioactive chitobiose from chitin wastes. We recently employed an in-house produced chitinase, *Vh*ChiA from the marine bacterium *Vibrio campbellii* (formerly *V. harveyi*), to produce chitobiose from shrimp shells, crab shells and squid pens through a single-step reaction.[16] However, only a low yield (25%) was obtained from an incomplete reaction since the enzyme had short-lived activity. An additional drawback was difficulty in removing the enzyme from the reaction product, causing a huge reduction of the final yield during the enzyme removal step. In this present study, we established a thermostable immobilized chitinase system using magnetic nanoparticles in the single-step production of chitobiose from crustacean chitins. The concept relies on the functionalization of magnetic nanoparticles as recyclable support with a high surface area, followed by the efficient immobilization of chitinase. In our particular case, the enzyme has to be immobilized on the surface of the nanoparticles and not inside mesoporous nanoparticles or nanocapsules,[29] because the substrate has a relatively high molecular weight and hence high accessibility to the enzyme is necessary. The overall scheme of the newly developed system is illustrated in Figure 1.

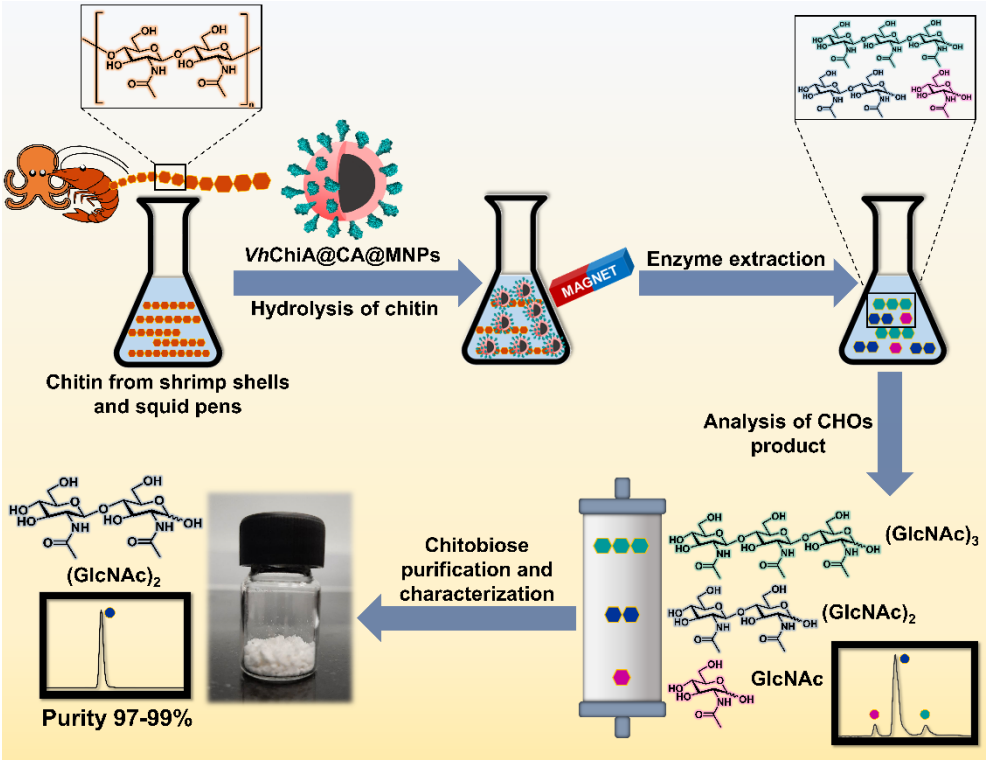

Figure 1. A schematic representation of the development of *Vh*ChiA@CA@MNPs immobilization for chitobiose production from crustacean chitins.

2. Materials and Methods

2.1 Materials

Iron (II) sulfate heptahydrate ($FeSO_4 \cdot 7H_2O$) ≥99%, iron (III) chloride hexahydrate ($FeCl_3 \cdot 6H_2O$) ≥99%, citric acid (CA) 99.5%, sodium acetate (NaOAc) 99%, monobasic ($NaH_2PO_4 \cdot H_2O$) 98% and dibasic (Na_2HPO_4) ≥99% sodium phosphate and 37% hydrochloric acid (HCl) were purchased from CARLO ERBA. 4-Morpholinoethanesulfonic acid (MES) ≥99% and *N*-hydroxysuccinimide (NHS) ≥98% were purchased from Acros Organics. Sodium carbonate (Na_2CO_3) ≥99.9% was purchased from Merck. 1-(3-dimethylaminopropyl)-3-ethylcarbodiimide hydrochloride (EDC) >98% was purchased from TCI. *N*-Acetyl-D-glucosamine ≥95% was purchased from SigmaAldrich. 4-nitrophenyl-*N*,*N*′-diacetyl-β-chitobioside (*p*NP-$(GlcNAc)_2$) >98%, diacetyl-chitobiose ($(GlcNAc)_2$) >95% and triacetyl-chitotriose ($(GlcNAc)_3$) >95% were purchased from Megazyme.

2.2 Synthesis of citric acid-coated magnetic nanoparticles (CA@MNPs)

Citric acid-coated magnetic nanoparticles (CA@MNPs) were prepared by a co-precipitation method described earlier, with some modifications.[30] Briefly, 25 mL of an aqueous solution of 0.64 M $FeSO_4$, 1.28 M $FeCl_3$ and 1.28 M citric acid was vigorously stirred at 80 ºC for 20 min, then 250 mL of 1 M NaOH solution in water was added dropwise, and the mixture was stirred continuously at 80 ºC for 1 h. After the reaction was completed, the dispersion was cooled to room temperature (25 ºC). Then, CA@MNPs were removed by an external magnet and extracted several times with 100 mL of DI water, once with 100 mL of ethanol and finally with 100 mL of DI water again. The extracted CA@MNPs were then freeze-dried to obtain a powder.

2.3 Preparation and purification of chitinase

The *chiA* gene, encoding chitinase A from *Vibrio harveyi* (*Vh*ChiA), was cloned into the expression vector pQE60 and overexpressed in *E. coli* M15 cells as previously described.[23] The transformed cells were cultured at 37 °C in LB medium containing 100 μg·mL^{-1} ampicillin and 50 μg·mL^{-1} kanamycin until the OD_{600} of the cell culture reached 0.6-0.8 for recombinant expression. After that, the cell culture was chilled on ice followed by the addition of isopropyl thio-β-D-galactoside (IPTG) to a final concentration of 0.2 mM to activate chitinase expression. Cell growth was maintained at 25 °C for 18 hours, after which the cell pellet was recovered by centrifugation at 4,500 rpm, 4 °C for 30 minutes. The pellet was resuspended in freshly prepared lysis buffer (20 mM Tris-HCl, pH 8.0, 150 mM NaCl, 1 mM PMSF, and 1 mg·mL^{-1} egg white lysozyme), then lysed on ice with an ultrasonic processor (Cole-Parmer, Vernon Hills, Illinois, USA) with a 1-cm diameter probe (Amp: 30 %, Pulse ON: 20 sec, OFF: 40 sec, Timer: 40 minutes). Unbroken cells and cell debris were eliminated by centrifugation at 12,000 rpm, 4 °C, for 45 minutes. The supernatant was immediately applied to a Ni-charged Resin affinity column (GenScript USA, Inc. Piscataway, NJ08854, USA), and chromatography was performed under gravity at 4 °C. After loading, weakly bound impurities were washed off with buffer containing 20 mM Tris-HCl, pH 8.0, 150 mM NaCl, and 20 mM imidazole. The tightly bound proteins were eluted with 150 mM imidazole in the same buffer and eluted fractions were collected. To validate the purity, 20 μL of each fraction were tested by 12% SDS-PAGE. The fractions with chitinase activity were pooled and subjected to repeated rounds of dialysis (Snake Skin™ Dialysis Tubing, 3.5 K MWCO, 35-mm dry I.D, Thermoscientific, Meridian Rd, Rockford, U.S.A) in the same buffer to remove imidazole. The purified *Vh*ChiA was concentrated using a centrifugal filter unit (Amicon Ultra-15 centrifugal filter unit, 30 K-cut off (Merck Millipore, Tullagreen, Cork, Ireland) and stored at -80 °C until used.

2.4 Preparation of colloidal chitin

Chitin flakes were prepared from shrimp shells and squid pens (Marine Bio Resources Co., Ltd., Thailand). Colloidal chitin was prepared by modifying the protocol as previously described.[31] In a 1000-mL beaker, 20 g of chitin flakes were weighed and treated with 150 mL of concentrated (12 M) HCl, progressively added at 25 °C followed by continuous stirring for 24 h. The HCl-containing supernatant was then removed by centrifugation at 4,500 rpm, 4 °C for 30 min, the pellet was extracted with ice-cold distilled water (DI) and the process was repeated until the pH value of the washing solution reached 7.0. In the final step, chitin pellet was freeze-dried, and was then used as the substrate in the production of chitobiose.

2.5 Immobilization of chitinase (*Vh*ChiA)

Chitinase (*Vh*ChiA) was covalently immobilized on the CA@MNPs using a general 1-(3-dimethylaminopropyl)-3-ethyl carbodiimide/*N*-hydroxysuccinimide (EDC-NHS) activation method. Dried CA@MNPs powder (50 mg) was dispersed in 5 mL MES buffer (10 mM, pH 6.0) for

20 min using an ultrasonicator. The CA@MNPs were then separated using an external magnet and the MES buffer solution was removed, followed by the addition of 5 mL of a solution containing 100 mg·mL^{-1}1-(3-dimethylaminopropyl)-3-ethylcarbodiimide hydrochloride (EDC) and 100 mg·mL^{-1} *N*-hydroxysuccinimide (NHS) in MES buffer (10 mM, pH 6.0). The reaction was incubated with gentle shaking at room temperature (25 °C) for 3 h. After this, the activated CA@MNPs were extracted 10 times with 50 mL of sodium acetate buffer (100 mM, pH 5.5). Various concentrations of EDC/NHS-activated CA@MNPs (0.625, 1.25, 2.5, 5, and 10 mg·mL^{-1}) were used to immobilize 250 µg of *Vh*ChiA in 2 mL of 100 mM sodium acetate buffer at pH 5.5. The immobilized solution was incubated by rocking at 4 ºC for 2 h, then the immobilized chitinase (*Vh*ChiA@CA@MNPs) was extracted 3 times with 6 mL of 100 mM sodium acetate buffer at pH 5.5 and kept at 4 ºC until used. The concentration of the immobilized enzyme was determined from the initial and final concentration of chitinase in the immobilization medium, using the absorbance at 280 nm.

2.6 Characterization of the immobilized enzyme

2.6.1 Transmission electron microscopy (TEM)

Morphology and sizes of CA@MNPs and *Vh*ChiA@CA@MNPs were visualized by transmission electron microscopy (TEM, JEM-ARM200F, JEOL, Tokyo, Japan). Dried CA@MNPs and *Vh*ChiA@CA@MNPs samples (2.5 mg) were dispersed in 1 mL of ethanol and sonicated for 30-40 min, then a single drop of sample suspension was deposited on the carbon-coated copper grid (300 mesh) specimen holder and allowed to dry for 30 to 45 min at room temperature (25 ºC) before being placed under vacuum for TEM imaging. The average sizes of CA@MNPs and *Vh*ChiA@CA@MNPs particles were calculated from counting diameters of approx. 100 particles using the ImageJ 1.52a software and a TEM histogram was plotted by the Origin 2021b SR2 program.

2.6.2 Fourier transform infrared spectroscopy (FTIR)

The major characteristic functional groups of CA@MNPs, EDC/NHS activated CA@MNPs and *Vh*ChiA@CA@MNPs were analyzed by using Fourier Transform Infrared Spectroscopy (FTIR, PerkinElmer, Beaconsfield, UK) with Attenuated Total Reflectance (ATR) measurement. For sample measurements, freeze dried sample powder (approx. 20 mg) was placed on a universal diamond ATR top-plate and the FTIR spectra were recorded over the range 400 – 4000 cm^{-1}.

2.6.3 Thermal gravimetry analysis (TGA)

Thermal decomposition of *Vh*ChiA and weight loss in CA@MNPs and *Vh*ChiA@CA@MNPs were investigated by thermal gravimetry analysis (TGA, STA PT1600, Linseis, Selb, Germany). For sample preparation, freeze dried sample powder (10 mg) was weighed in the sample pan. Then, the sample was heated in the furnace tube and the weight loss of each sample was measured under air over a temperature range of 25 ºC - 700 ºC with a heating rate of 10 ºC·min^{-1}.

2.6.4 X-ray diffraction (XRD)

The crystallographic characteristics of CA@MNPs and *Vh*ChiA@CA@MNPs were investigated using an X-ray powder diffractometer (D8 Advance (XRD), Bruker, Massachusetts, USA). For the sample preparation, the freeze-dried sample powder was filled on a plastic sample holder. Then, a glass slide was used to gently push the sample powder with the sample holder, followed by carefully inserting the sample into the XRD slot. The XRD pattern was measured with Cu $K_{\alpha-1}$ radiation operated at 40 kV and 40 mA (k = 1.5406 Å, with data collection between 2θ values of 20° to 70°, in steps of 0.01°).

2.7 Chitinase activity assay

Chitinase activity was determined by a colorimetric assay using 4-nitrophenyl-*N*,*N*′-diacetyl-β-chitobioside or *p*NP-$(GlcNAc)_2$ as substrate.[25] The reaction was carried out in a 96-well microplate reader, with a reaction mixture (100 µL) containing 0.25 mM *p*NP-$(GlcNAc)_2$, 1 µg of *Vh*ChiA, and 100 mM phosphate buffer, pH 6.5 (optimal pH for free *Vh*ChiA) and pH 7.0 (optimal pH for immobilized *Vh*ChiA). The reaction mixture was incubated at 30 °C, with shaking at 180 rpm for 10 min, and then the reaction was terminated by the addition of 100 µL of 3 M sodium carbonate. The liberation of *p*-nitrophenol (*p*NP) was determined by measuring the absorbance at 405 nm (A_{405}) in a microtiter plate reader (ThermoFisher scientific, Ratastie 2, Finland). The *p*NP standard curve was constructed with a range of 0-50 nmol. One unit (U) of the enzyme activity is defined as the amount of enzyme that liberated 1 nmol of *p*NP per minute under the assay condition. All the assay reactions were carried out in triplicate.

2.8 Determination of immobilization yield and activity recovery

The immobilization yield (%) was calculated from the starting amount of chitinase

($mg \cdot mL^{-1}$) and the amount of unbound chitinase ($mg \cdot mL^{-1}$) in the washing buffer, and the activity recovery from the activity of chitinase immobilized, the activity of chitinase added and the activity of unbound chitinase in the washing buffer after immobilization.

2.9 Effect of pH on the chitinase activity

The effect of pH on the chitinase activity of the immobilized/free enzymes was determined by *p*NP-$(GlcNAc)_2$ assays at different pH values in a 96-well microplate reader. Typically, 0.25 mM *p*NP-$(GlcNAc)_2$ was added to the universal buffer (Britton–Robinson buffer: 0.04 M boric acid, 0.04 M phosphoric acid and 0.04 M acetic acid) at different pH values ranging from pH 3.0-9.0, and 1 µg of *Vh*ChiA was then added. The reaction mixture was incubated with shaking at 180 rpm, 30 °C for 10 min, and the reaction was terminated by the addition of 100 µL of 3 M sodium carbonate. The amount of *p*-nitrophenol liberated was determined by measuring the absorbance at 405 nm, and the activity was calculated using standard p-nitrophenol solutions (0 – 50 nmol). The highest activity was taken as 100%.

2.10 Determination of chitinase stability

To evaluate their pH stability, immobilized or free chitinase were pre-incubated in the universal buffer (Britton–Robinson buffer: 0.04 M boric acid, 0.04 M phosphoric acid and 0.04 M acetic acid) over pH range 3.0 – 9.0 for 30 min, and the chitinase activity was then determined as mentioned above. The starting activity prior to incubation was taken as 100%. Thermostability of immobilized and free chitinase was further evaluated by pre-incubation for 30 min at different temperatures, from 25 ºC to 60 ºC. Afterwards, the residual chitinase activity was determined under optimal conditions. The effect of incubation time on the enzyme stability was investigated by incubating the enzyme at 30 ºC at 0.5, 2, 5, 10, and 24 h. At the end of the incubation time, the residual activity of the chitinase was determined as described above. The chitinase activity at 0 min of the assayed incubation was taken as 100%. Storage stability was evaluated by storing free or immobilized enzyme at 4 °C for 5 weeks, and the residual activity was determined as mentioned above. The chitinase activity on the first day of storage was taken as 100%.

2.11 Reusability of immobilized chitinase

The reusability of the *Vh*ChiA@CA@MNPs was evaluated over 16 repeated cycles. After each reaction cycle (as described above) in a 96-well microplate reader the immobilized enzyme was separated from the reaction mixture using an external magnet. The recovered chitinase was washed with 100 mM sodium phosphate buffer, pH 7.0, followed by the addition of the *p*NP-$(GlcNAc)_2$ substrate to perform the next reaction cycle.

2.12 Chitobiose production and product analysis by thin layer chromatography (TLC)

The efficiency of the immobilized chitinase in chitin hydrolysis was analyzed by thin later chromatography (TLC). The reaction mixture (20 mL) contained 100 mg of dried colloidal chitin from shrimp shells/squid pens and *Vh*ChiA (600 U) in 100 mM phosphate buffer, pH 7.0. The reaction was carried out at 30 ºC for 96 h. Aliquots of 120 µL of the reaction mixture were withdrawn after different time intervals (0, 2, 5, 10, 24, 48, 72 and 96 h) and the reaction was stopped by boiling at 98°C for 5 min in a heating block, followed by centrifugation at 4°C, 27,950 x g for 20 min and the hydrolysis products were then analyzed by TLC. A control reaction was performed with no addition of the enzyme. For product analysis, the TLC silica plate was pre-heated at 60 °C prior to sample application and each reaction solution was applied three times (2 µL each time) to a silica-coated plate and chromatographed four times with a mobile phase containing butanol: methanol: ammonia solution 28% (v/v): water (10:8:4:2) in a TLC chamber, followed by spraying with aniline-diphenylamine reagent and heating until the sugar spots were visible.

2.13 Product analysis by quantitative high-performance liquid chromatography (HPLC)

The quantification of chitobiose from chitin hydrolysis by free/immobilized chitinase was performed by high-performance liquid chromatography (HPLC). The reaction products were analyzed by injecting 20 µL of the sugar aliquots obtained from the reaction sample of various time intervals into the HPLC system (Shimadzu, High Performance Liquid Chromatography Prominence – I LC – 2030 series, Nexera -I LC 2040 series) (Shimadzu Bara Scientific Co., LTD, Bangkok Thailand). The column used to detect the CHO products was TSK Gel Amide-80 (size 4.6 mm (ID) × 25 cm (L)), operated in an isocratic system using acetonitrile: deionized water (75:25) as the mobile phase at a flow rate of 0.7 $mL \cdot min^{-1}$ and a temperature of 25 °C. The CHO products were monitored at 200 nm (Photodiode array detector). The concentrations of the hydrolytic products were estimated from calibration curves constructed from peak areas of the standard CHOs GlcNAc, $(GlcNAc)_2$ and $(GlcNAc)_3$ (0 to 10 mM).

2.14 Purification of chitobiose by preparative HPLC

Total chitobiose generated from 100 mg chitin by free/immobilized chitinase was further purified by preparative HPLC. The reaction product (30 µL) was aliquoted and injected multiple times into an Asahipak NH 2P-50 10E preparative column (10.0 mm × 250 mm, Shodex China Co., Ltd) connected to a Shimadzu HPLC system. A gradient of acetonitrile:water (70:30 v:v) was used as the mobile phase for the HPLC separation, which was carried out at 25 °C, 2000 psi and a flow rate of 1.0 mL·min^{-1}. A PDA detector was used to find the separated products at 200 nm. Finally, the eluted fractions containing chitobiose were collected, concentrated and freeze dried to obtain the purified chitobiose powder.

2.15 Analysis of the purified chitobiose by mass spectrometry

Quadrupole-time-of-flight mass spectrometry (QTOF-MS) (Bruker Biospin AG, Bangkok, Thailand) with source type Electrospray Ionization (ESI) was used to confirm the mass of chitobiose. The purified chitobiose dissolved in methanol (5 mg·mL^{-1}, 200 µL) was injected directly into the ESI-QTOF-MS in the positive ionization mode and capillary and charging voltages of 4500 V and 2000 V, respectively. The m/z data were acquired at a selected mass range of 50–1000 m/z.

3. Results & Discussion

3.1 Characterization of functionalized magnetic nanoparticles (MNPs)

Citric acid (CA)-coated magnetic nanoparticles (CA@MNPs) were synthesized in a one-pot reaction using the co-precipitation of Fe^{2+} and Fe^{3+} aqueous solutions with citric acid.[30] The -COOH groups of the synthesized CA@MNPs were further activated with EDC followed by NHS, then linked with *Vh*ChiA through the formation of amide bonds, as shown in Figure 2A. The CA@MNPs were well dispersed in aqueous solution (Figure 2B, left) and could be separated from the solution with the external magnetic field from a permanent magnet (Figure 2B, right). Transmission Electron Microscopy (TEM) was used to analyze the morphology and sizes of CA@MNPs before and after immobilization. The uncoated CA@MNPs displayed a roughly spherical shape (Figure 2C) with an average diameter of 7 nm ± 2 nm (Figure 2D). After immobilization, there was no observable difference between the sizes of uncoated CA@MNPs (Figure 2D) and CA@MNPs coated with *Vh*ChiA (Figure 2F), meaning that the average size of the *Vh*ChiA@CA@MNP was 7 nm ± 2 nm. This indicates that the nanoparticles were colloidally stable, even after functionalization with the enzymes.

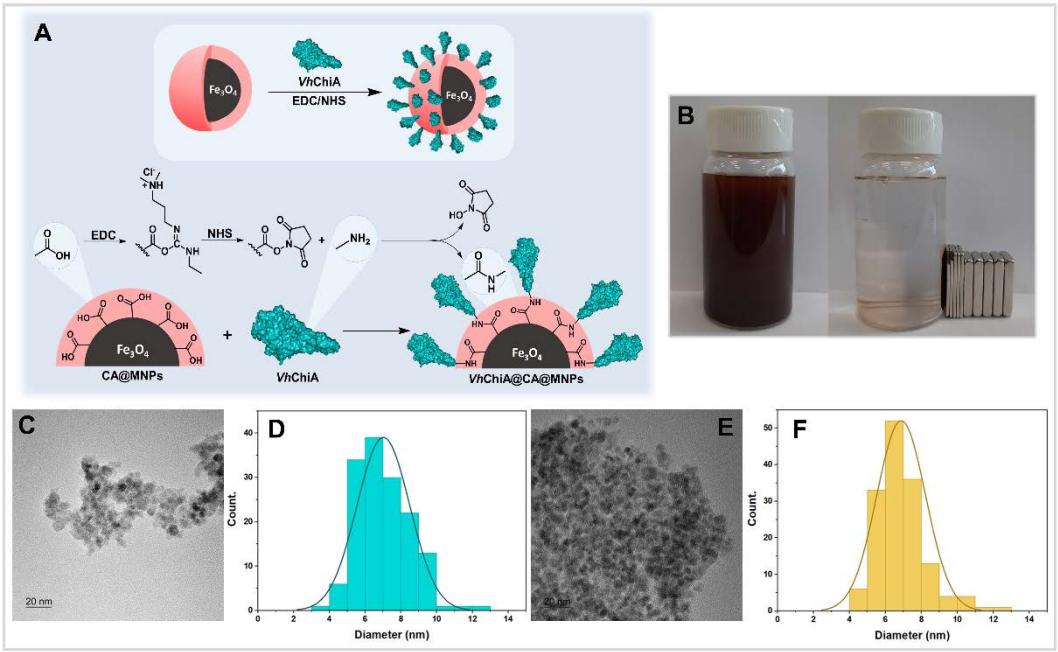

Figure 2. Schematic illustration of the preparation of (A) *Vh*ChiA@CA@MNPs; (B) CA@MNPs dispersed in aqueous solution (left) and extracted with an external magnet (right); Transmission electron microscopy (TEM) images of (C) CA@MNPs and (E) *Vh*ChiA@CA@MNPs; TEM histograms for the particle size distribution of (D) CA@MNPs and (F) *Vh*ChiA@CA@MNPs.

The functionalization of CA on the surface of MNPs was confirmed by FTIR spectroscopy. The results showed characteristic infrared bands for MNPs.[30] Figure 3A shows the FTIR spectra of CA@MNPs (blue trace). The vibration of the Fe-O bonds in the crystal lattice of magnetite is represented by the band at 542 cm^{-1}. The symmetrical and asymmetrical stretching of C=O and C-O vibrations of the carboxylic groups (-COOH) were observed at 1632 cm^{-1} and 1393 cm^{-1}, respectively. The -OH groups were observed by the intense band at 3368 cm^{-1}. Such vibrational stretching confirmed the presence of free -OH groups of citric acid and water traces.[30] From the FTIR analysis, it was clear that citric acid was successfully chemisorbed by the MNP surface. For the CA@MNPs activated with EDC/NHS (orange trace), the bands at 3367, 1598, 1416 and 1261 cm^{-1} represented the vibrations of -OH, O=C-O, C-N-C and C-N of the NHS-ester, respectively.[32,33] The FTIR spectrum of the immobilized chitinase (*Vh*ChiA@CA@MNPs) (red trace) contained additional bands at 1645, 1538, and 1399 and 1262 cm^{-1}, which corresponded to amide I, II and III vibrations, respectively.[32,34] The additional band at 3298 cm^{-1}, representing -OH and N-H vibrations, demonstrated that the chitinase was successfully immobilized on the CA@MNPs.

The crystalline structures of CA@MNPs and *Vh*ChiA@CA@MNPs were characterized by XRD. As illustrated in Figure 3B, the CA@MNPs (black) showed six characteristic XRD peaks at 2θ = 220, 311, 400, 422, 511 and 440, indicating the presence of magnetite.[35] Because citric acid formed only a very thin coating on the surface of MNPs, no changes in the structure or crystallinity of magnetite nanoparticles were observed. After immobilization, the characteristic XRD peaks of CA@MNPs were not changed (red), which confirmed that the covalent attachment of the chitinase on the CA@MNPs surface did not alter the crystalline structure of the activated MNPs.

Thermogravimetric analysis (TGA) was performed to determine the amounts of organic compounds on the MNPs. The total weight loss of the three samples, CA@MNPs, *Vh*ChiA@CA@MNPs, and *Vh*ChiA were calculated to be 11%, 16% and 97%, respectively. By subtracting the weight loss due to the presence of water, it is estimated that the MNPs contained ~5 wt% immobilized enzyme, which is significant given that the density of magnetite is much larger than that of the enzyme.

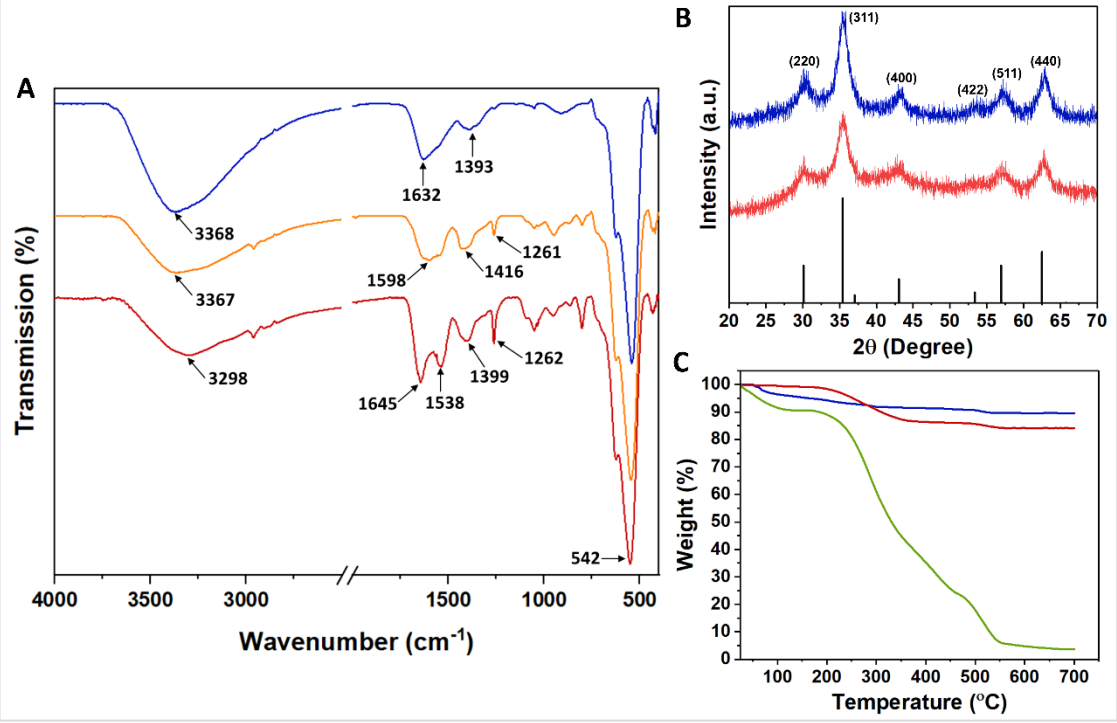

Figure 3. (A) FTIR spectra, (B) XRD patterns (standard XRD data for magnetite (black); JCPDS no. 00-019-0629), and (C) TGA curves of CA@MNPs (blue), EDC/NHS activated CA@MNPs (orange), *Vh*ChiA@CA@MNPs (red) and *Vh*ChiA (green).

The various concentrations of CA@MNPs dispersions (0.625 to 10 mg·mL^{-1}) used as support were further optimized to maximize the enzyme's performance. The immobilization yield increased as the concentration of the CA@MNPs increased. A CA@MNP concentration of 10 mg·mL^{-1} provided the highest immobilization yield (91.4 ± 2.1%), but only a moderate recovery (66.6 ± 5.7%). At a CA@MNP concentration of 2.5 mg·mL^{-1}, the highest activity recovery (98 ± 1.0%) was obtained. The yield and recovery of the catalyst *Vh*ChiA@CA@MNPs measured in this study were higher than for fungal Chit42 immobilized on GA-activated MNPs, which provided 62.3% immobilization yield and 66.7% activity recovery.[27] Taking into account the values of immobilization yield and activity recovery, the optimal concentration of CA@MNPs was 2.5 mg·mL^{-1}. With this concentration, the enzyme loading of CA@MNPs was 47 ± 0.6 mg·g^{-1} CA@MNPs. Reduction of activity recovery at high concentrations of CA@MNPs (5.0 and 10.0 mg·mL^{-1}) was probably due to a loss of structural flexibility, attributed to multiple conjugations between the -NH_2 groups of the enzyme and -COOH groups on CA@MNPs, which resulted in a change of enzyme conformation and dynamic movement of enzyme, and led to a decrease in enzyme activity.[36]

3.2 Effects of MNP-based immobilization on the biochemical properties and stability of *Vh*ChiA

We examined the optimum pH for catalytic activity, stability at various pH value, temperature stability and stability during storage. Figure 4A shows the activity/pH profiles, showing that the optimum pH value for activity of the immobilized *Vh*ChiA was slightly higher (pH 7.0) than for the free enzyme (pH 6.5). A slight shift in the optimum pH value is typically caused by changes in charge distributions on the active site residues, caused by the covalent linkage between the enzyme molecule and the supporting material.[37,38] Shifts in the optimum pH were also previously observed for the co-immobilization of chitinase/NAGase on ZnO/PU sheets,[39] the immobilization of α-amylase on calcium alginate beads,[40] the immobilization of lactoperoxidase on graphene oxide nanosheets[41] and the immobilization of protease on graphene oxide (GO) nanosheets.[42]

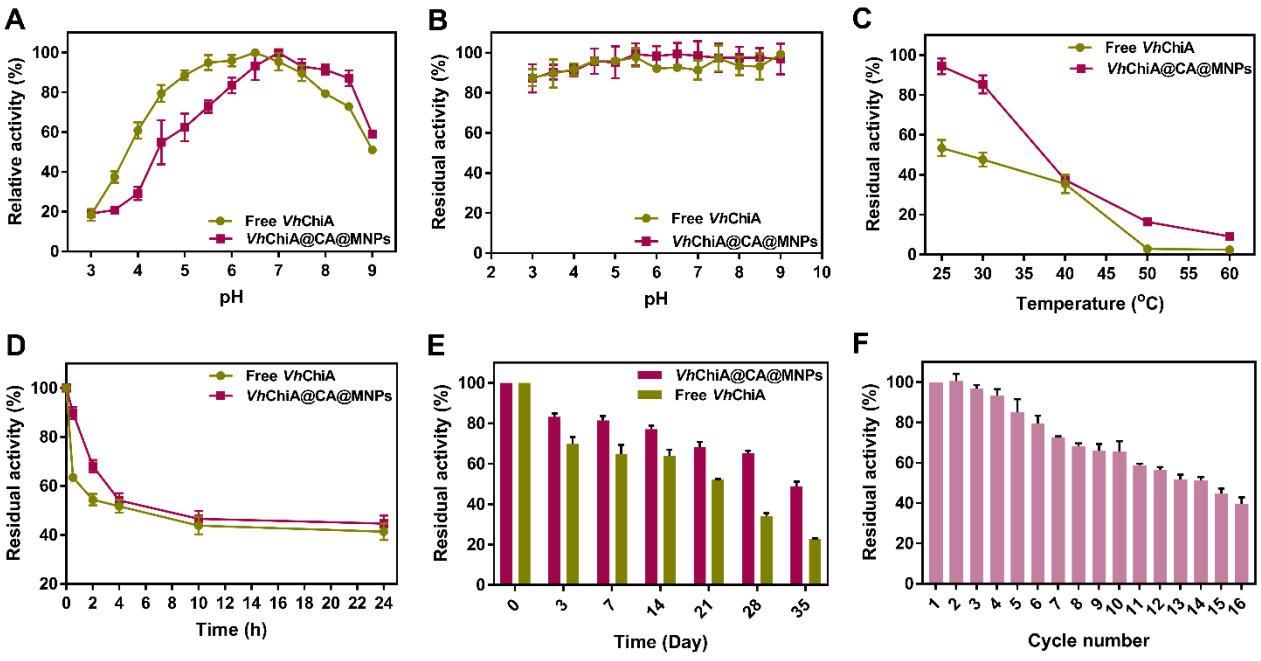

Figure 4. (A) Effect of pH on the activity of free *Vh*ChiA (green) and *Vh*ChiA@CA@MNPs (red); (B) pH stability of free *Vh*ChiA (green) and *Vh*ChiA@CA@MNPs (red); (C) thermal stability of free *Vh*ChiA (green) and *Vh*ChiA@CA@MNPs (red); (D) stability of free *Vh*ChiA (green) and *Vh*ChiA@CA@MNPs (red) at 30 °C; (E) storage stability of free *Vh*ChiA (green) and *Vh*ChiA@CA@MNPs (red) at 4 °C; (F) reusability of *Vh*ChiA@CA@MNPs.

In CA@MNPs the enzyme remained stable over a broad pH range of 3 – 9 (Figure 4B). Moreover, the immobilized *Vh*ChiA exhibited a better stability than the free *Vh*ChiA over a temperature range of 25 – 60 ºC, especially at temperatures below 40 °C (Figure 4C). After incubation for 30 min at 25 ºC, the residual activity of the immobilized *Vh*ChiA was 95%, while that of the free enzyme was only 53%. When the incubation temperature was raised to 60 ºC, immobilized *Vh*ChiA retained 9.1 % of its activity, while the activity of free *Vh*ChiA was completely lost. Figure 4D shows the operational stability of the immobilized enzyme at various times (0.5, 2, 4, 10, and 24 h) of incubation at 30 ºC. The immobilized *Vh*ChiA showed higher activity than the free enzyme at the initial time of incubation. At this incubation time, the activity retaining of the immobilized enzyme was about 70% while the retained activity of the free enzyme was 57%. After 2 h of incubation, the residual activity of the immobilized enzyme was similar to that of the free enzyme until 24 h of incubation (~ 50%).

The effect of chitinase immobilization on CA@MNPs during long-term storage was examined. When the enzyme was stored for various periods (0, 3, 7, 14, 21, 28, 35 days) at 4 ºC, the activity of immobilized *Vh*ChiA slowly decreased, while still retaining a high enzyme activity over a long storage time (Figure 4E). After 35 days of storage, 50% residual activity of the immobilized enzyme was detected, while that of free enzyme was only 20%.

We further examined the performance of the immobilized *Vh*ChiA after multiple cycles of reactions. The initial chitinase activity remained during 2 reaction cycles (see Figure 4F), then gradually decreased and after 14 cycles, the immobilized chitinase had a residual activity of >50%; after 16 cycles, 40% of the enzyme activity remained. The immobilized *Vh*ChiA showed an improved performance compared with previously reported systems. For example, 20% residual enzyme activity after 10 reaction cycles was reported for chitinase from Chit36 immobilized on alginate/sepiolite beads,[43] while 49% activity remained after 7 reaction cycles with *Sa*ChiA4 immobilized on ultrafiltration membrane[28] and 30% of the activity remained after 5 reaction cycles with Chit42 immobilized on GA activated MNPs.[27]

3.3 Chitobiose or $(GlcNAc)_2$ production from chitin conversion of the immobilized chitinase

We further tested the ability of the immobilized *Vh*ChiA to produce chitobiose or $(GlcNAc)_2$ from chitin. Figure 5A shows the TLC analysis of the reaction products derived from the hydrolysis of shrimp chitin at different time intervals from 2 to 96 h. Throughout the reaction *Vh*ChiA hydrolyzed chitin, generating $(GlcNAc)_2$ as the main product, while GlcNAc and $(GlcNAc)_3$ were minor products. Figure 5B shows more intense bands of all three products being generated from squid-pen chitin under the same reaction conditions as for shrimp chitin, indicating that the enzyme preferred squid-pen chitin as substrate. Figures 5C and 5D represent the HPLC quantification of the reaction products from hydrolysis of shrimp shell chitin and squid-pen chitin, respectively. As observed by TLC analysis, $(GlcNAc)_2$ was the dominant product, along with small amounts of GlcNAc and $(GlcNAc)_3$. With both substrates, the product $(GlcNAc)_2$ increased over the course of the reaction and was highest after 96 h.

When comparing the total yields obtained in a one-step reaction, the immobilized enzyme produced larger yields of all three products, GlcNAc, $(GlcNAc)_2$ and $(GlcNAc)_3$, than did the free enzyme. $(GlcNAc)_2$ was the main product throughout the duration of the reaction. The highest yield of all three products was obtained from squid-pen chitin (81.9 mg), with a final $(GlcNAc)_2$ production of 67.4 ± 0.6 mg. The individual yields and the total yields obtained from hydrolysis of two chitin sources are summarized in Table 1.

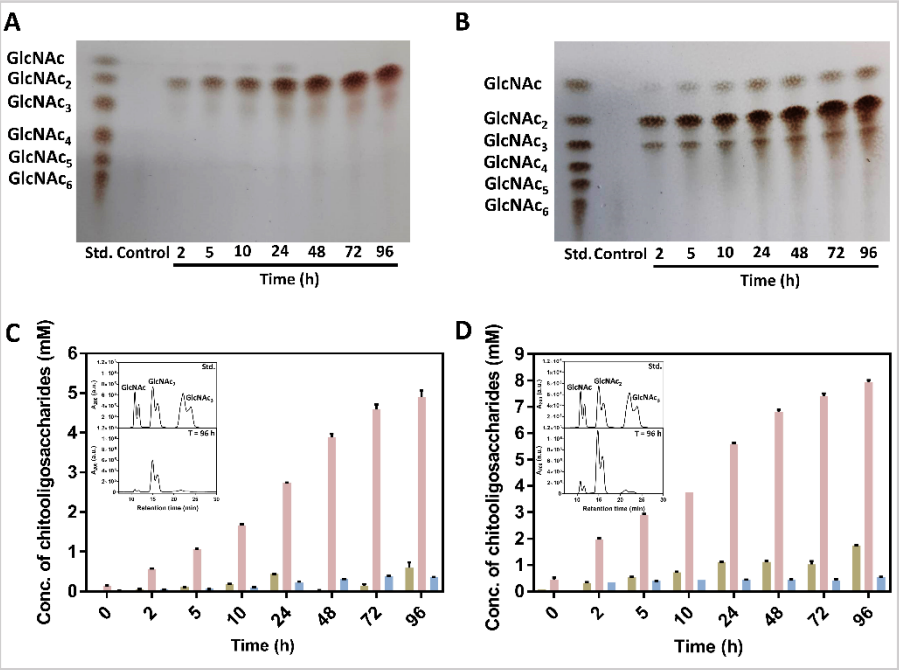

Figure 5. Chitobiose production using immobilized chitinase. Colloidal chitin (100 mg) prepared from (A) shrimp and (B) squid-pen was hydrolyzed by *Vh*ChiA@CA@MNPs. (C) products generated from shrimp and (D) from squid-pen chitin using *Vh*ChiA@CA@MNPs. HPLC chromatograms of the standard chitosugars GlcNAc, $(GlcNAc)_2$ and $(GlcNAc)_3$ (top panel) and the reaction products (bottom) are shown as insets: GlcNAc (green), $(GlcNAc)_2$ (pink), and $(GlcNAc)_3$ (blue). The reaction products obtained from the immobilized enzyme were analyzed on a TSK Gel Amide-80 column (∅ 4.6 mm (ID) × 25 cm (L)) connected to an HPLC system (Shimadzu, Thailand) as described in Methods.

In the final step, the main product $(GlcNAc)_2$ was purified by HPLC. Figure 6A represents the HPLC chromatogram profile of the standard CHOs products $(GlcNAc)_{1-3}$, and chromatograms of the products from shrimp shell and squid pen chitins are shown in Figure 6B and 6C, respectively. The final yields of $(GlcNAc)_2$ obtained after purification were 37.0 ± 1.2 mg (97% purity) from shrimp shell chitin and 61.1 ± 0.5 mg (99% purity) from squid pen chitin and the HPLC chromatogram profile of the purified chitobiose obtained from the hydrolysis of chitin were shown in the Figure 6D, F, H, J. Lower yields of purified $(GlcNAc)_2$ from both chitin sources (31.0 ± 0 mg from shrimp and 48.1 ± 0.2 mg from squid pen) were observed with the reaction catalysed by the free enzyme.

The mass of the purified $(GlcNAc)_2$ was further analyzed by QTOF-MS. The most abundant peak with m/z of 447.2 belonging to the ionized mass of $(GlcNAc)_2 + Na^+$ was identified, confirming that the purified product was $(GlcNAc)_2$ (Figure 6E, G, I and K).

Table 1. Yields obtained from the breakdown of 100 mg of shrimp and squid-pen chitins by free and immobilized *Vh*ChiA.

Chitin substrate	Enzyme	Yield of each product (mg)			Total yield (mg)
		GlcNAc	$(GlcNAc)_2$	$(GlcNAc)_3$	
Shrimp shell	Free *Vh*ChiA	1.7 ± 0.1	37.4 ± 0.4	4.7 ± 0.4	43.8
	*Vh*ChiA@CA@MNPs	2.6 ± 0.6	41.6 ± 1.4	4.5 ± 0.1	48.7
Squid pen	Free *Vh*ChiA	3.4 ± 0.3	53.1 ± 0.2	6.6 ± 0.0	63.1
	*Vh*ChiA@CA@MNPs	7.7 ± 0.1	67.4 ± 0.6	6.8 ± 0.1	81.9

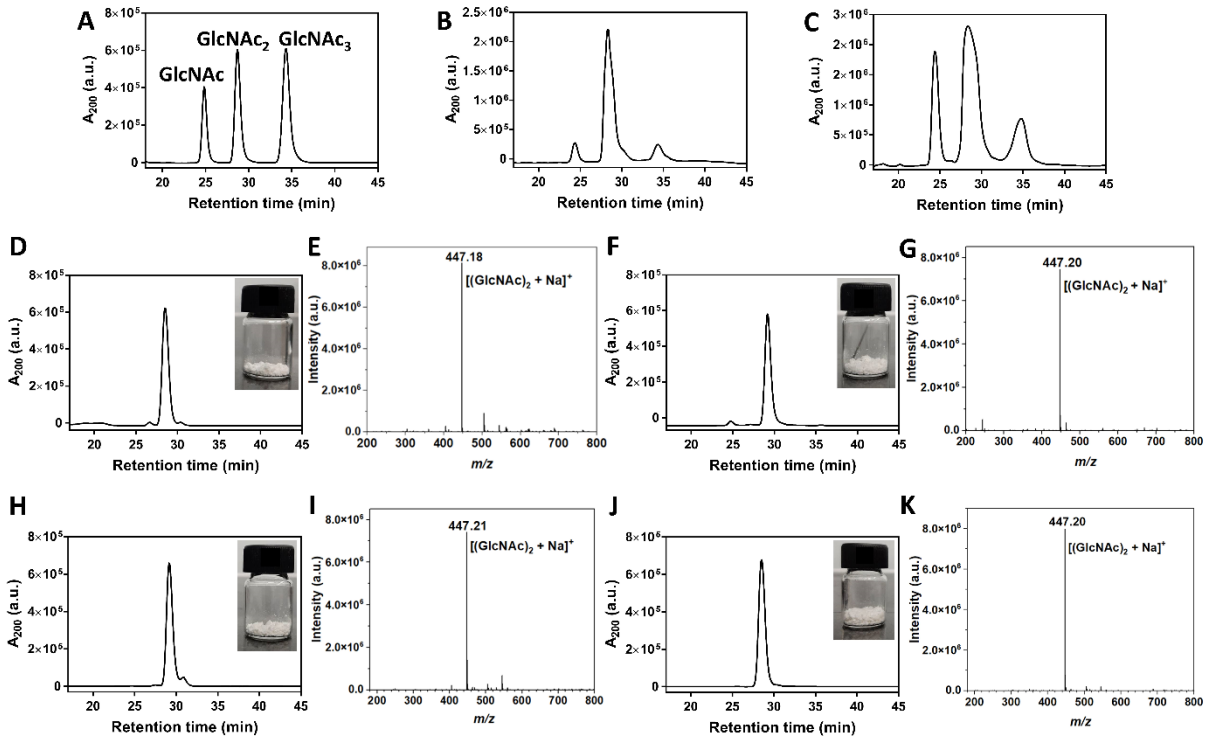

Figure 6. HPLC chromatograms of (A) standard $(GlcNAc)_{1-3}$; (B) chitobiose production from shrimp shell chitin; (C) chitobiose production from squid pen chitin. The purified $(GlcNAc)_2$ from shrimp shell chitin conversion using (D) free *Vh*ChiA and (F) immobilized *Vh*ChiA. Purified $(GlcNAc)_2$ from squid pen chitin conversion using (H) free *Vh*ChiA and (J) immobilized *Vh*ChiA. Mass spectra of purified $(GlcNAc)_2$ from shrimp shell chitin conversion using (E) free *Vh*ChiA and (G) *Vh*ChiA@CA@MNPs; mass spectra of purified $(GlcNAc)_2$ from squid pen chitin conversion using (I) free *Vh*ChiA and (K) immobilized *Vh*ChiA. QTOF-MS was operated with the source type Electrospray Ionization (ESI) under the positive ionization mode with the capillary and charging voltages set at 4500 V and 2000 V, respectively. The m/z data were acquired at a selected mass range of 50–1000.

In Table 2 the yields and purity of $(GlcNAc)_2$ obtained in this study are compared with values from the literature. Most previous studies used the free enzyme system for chitobiose production, with much more chitin as starting material (1.0 – 1.5 g) but relatively low yields of product (1.4 – 20%). Our previous studies[16] used free *Vh*ChiA to hydrolyze shrimp shell chitin, and the maximal yield obtained was 200 mg $(GlcNAc)_2$ from 1 g chitin, corresponding to a 20% yield with 99% purity. The low yield was caused by the loss of the enzyme activity when the reaction was conducted for longer than 48 h, resulting in an incomplete reaction, as well as the large loss of the final product during the enzyme removal step. For the immobilized enzyme system, Li and Mao reported using fungal chitinase (*Sa*ChiA4) adsorbed on a UF membrane to hydrolyze 100 mg of ionic liquid/ultrasound-pretreated chitin. The obtained yield was approximately 64 mg of the product mixture, and no purification of $(GlcNAc)_2$ was documented.[28]

Table 2. Summary of the yield and purity of chitobiose produced from chitin by different chitinases.

Substrate	Source of chitinase	System	Scale	Yield $(GlcNAc)_2$ (mg)	Yield $(GlcNAc)_2$ (%)	Purity (%)	Analytical method	Reference
Colloidal chitin (Crab shells)	*Paenicibacillus barengoltz*	Free chitinase	1.5 g	21.6	1.4	99	TLC and HPLC	44
Colloidal chitin (Shrimp shells)	*Thermomyces lanuginosus*	Free chitinase	1 g	100	10	n.d.[a]	TLC and HPLC	45
Colloidal chitin Shrimp shells)	*Vibrio campbellii* ATCC® BAA 1116	Free *Vh*ChiA	1 g	200	20	>99	TLC, HPLC and Q-TOF–MS	16
Ionic liquid/ultrasound -pretreated chitin	*Streptomyces albolongus* ITCC 8895	*Sa*ChiA4@ UF membrane	100 mg	~64	~64	n.d. [a]	HPLC	28
Colloidal chitin (Shrimp shells)	*Vibrio campbellii* ATCC® BAA 1116	*Vh*ChiA@CA@MNPs	100 mg	37	37	97	TLC, HPLC and Q-TOF–MS	This study
Colloidal chitin (Squid pens)	*Vibrio campbellii* ATCC® BAA 1116	*Vh*ChiA@CA@MNPs	100 mg	61	61	99	TLC, HPLC and Q-TOF–MS	This study

[a] n.d. represents no data on the purity of the final yields were reported.

4. Conclusions

In this research, we developed an efficient system for the biocatalytic production of chitobiose by immobilized chitinase. The in-house produced enzyme (*Vh*ChiA) was attached to the surface of magnetic nanoparticles coated with citric acid, using EDC/NHS coupling. TEM, FTIR and TGA measurements confirmed that the enzyme was successfully immobilized on the MNP carrier. The activity remained stable, with an immobilization yield of 89 ± 1.6% and retained activity of 98 ± 1.2%. The immobilized *Vh*ChiA showed a slight change in the optimum pH for activity, and a significant improvement in thermostability and storage stability compared to those of the free enzyme system. In addition, approximately 50% of the activity of immobilized *Vh*ChiA remained after 16 reaction cycles and magnetic removal from the reaction system, resulting in significant improvement in the final yield of the chitobiose product, compared to that from the free enzyme system. Our chitinase immobilization system could be further tailored for cost-effective, larger-scale production of bioactive chitobiose and longer chain chitooligosaccharides, and our study also demonstrates the employment of an in-house produced chitinase as an effective biocatalyst for a green, sustainable chitin waste management.

Acknowledgements

A.C. received a full-time Ph.D. scholarship from Vidyasirimedhi Institute of Science and Technology (VISTEC) for financial support to this research. W.S. also thanks Program Management Unit for Human Resources & Institutional Development (PMU-B) for funding on sugar production platform (B22WIS-TRS010). We would like to thank Dr. David Apps, Edinburgh Medical School, Edinburgh, Scotland for his critical manuscript reading and language improvements.

References

1. Durkin, C. A.; Mock, T.; Armbrust, E. V. *Eukaryot Cell.* **2009,** *8* (7), 1038-50.
2. Ravi Kumar, M. N. V. *React. Funct Polym.* **2000,** *46* (1), 1-27.
3. Souza, C. P.; Almeida, B. C.; Colwell, R. R.; Rivera, I. N. *Mar Biotechnol (NY).* **2011,** *13* (5), 823-30.
4. He, W.; Parowatkin, M.; Mailänder, V.; Flechtner-Mors, M.; Graf, R.; Best, A.; Koynov, K.; Mohr, K.; Ziener, U.; Landfester, K.; Crespy, D. *Biomacromolecules.* **2015,** *16* (8), 2282-2287.

5. Lodhi, G.; Kim, Y.-S.; Hwang, J.-W.; Kim, S.-K.; Jeon, Y.-J.; Je, J.-Y.; Ahn, C.-B.; Moon, S.-H.; Jeon, B.-T.; Park, P.-J. *BioMed Res. Int.* **2014,** *2014*, 654913.
6. Pitakchatwong, C.; Schlegel, I.; Landfester, K.; Crespy, D.; Chirachanchai, S. *Part. Part. Syst. Charact.* **2018,** *35* (7), 1800086.
7. Tabassum, N.; Ahmed, S.; Ali, M. A. *Carbohydr. Polym.* **2021,** *261*, 117882.
8. Arnold, N. D.; Brück, W. M.; Garbe, D.; Brück, T. B. *Mar Drugs.* **2020,** *18* (2), 93.
9. Kaczmarek, M. B.; Struszczyk-Swita, K.; Li, X.; Szczęsna-Antczak, M.; Daroch, M. *Front. Bioeng. Biotechnol.* **2019,** *7*.
10. Sasaki, C.; Yokoyama, A.; Itoh, Y.; Hashimoto, M.; Watanabe, T.; Fukamizo, T. *J. Biochem.* **2002,** *131* (4), 557-64.
11. Suginta, W.; Robertson, P. A. W.; Austin, B.; Fry, S. C.; Fothergill-Gilmore, L. A. *J. Appl. Microbiol.* **2000,** *89* (1), 76-84.
12. Suzuki, K.; Sugawara, N.; Suzuki, M.; Uchiyama, T.; Katouno, F.; Nikaidou, N.; Watanabe, T. *Biosci. Biotechnol. Biochem.* **2002,** *66* (5), 1075-83.
13. Suzuki, K.; Taiyoji, M.; Sugawara, N.; Nikaidou, N.; Henrissat, B.; Watanabe, T. *Biochem. J.* **1999,** *343* (Pt 3), 587-96.
14. Watanabe, T.; Oyanagi, W.; Suzuki, K.; Tanaka, H. *J. Bacteriol.* **1990,** *172* (7), 4017-22.
15. Poria, V.; Rana, A.; Kumari, A.; Grewal, J.; Pranaw, K.; Singh, S. *Biolog.* **2021,** *10* (12), 1319.
16. Thomas, R.; Fukamizo, T.; Suginta, W. *Bioresour. Bioprocess.* **2022,** *9* (1), 86.
17. Basso, A.; Serban, S. *Mol. Catal.* **2019,** *479*, 110607.
18. Sheldon, R. A.; Basso, A.; Brady, D. *Chem. Soc. Rev.* **2021,** *50* (10), 5850-5862.
19. Bhattacharya, D.; Nagpure, A.; Gupta, R. K. *Crit. Rev. Biotechnol.* **2007,** *27* (1), 21-28.
20. Duo-Chuan, L. *Mycopathologia.* **2006,** *161* (6), 345-360.
21. Grover, A. *Crit. Rev. Plant Sci.* **2012,** *31* (1), 57-73.
22. Madhuprakash, J.; Tanneeru, K.; Purushotham, P.; Guruprasad, L.; Podile, A. R. *J. Biol. Chem.* **2012,** *287* (53), 44619-44627.
23. Suginta, W.; Vongsuwan, A.; Songsiriritthigul, C.; Prinz, H.; Estibeiro, P.; Duncan, R. R.; Svasti, J.; Fothergill-Gilmore, L. A. *Arch. Biochem. Biophys.* **2004,** *424* (2), 171-180.
24. Songsiriritthigul, C.; Pantoom, S.; Aguda, A. H.; Robinson, R. C.; Suginta, W. *J. Struct. Biol.* **2008,** *162* (3), 491-499.
25. Suginta, W.; Vongsuwan, A.; Songsiriritthigul, C.; Svasti, J.; Prinz, H. *FEBS J.* **2005,** *272* (13), 3376-3386.
26. Charoenpol, A.; Crespy, D.; Schulte, A.; Suginta, W. *Green Chem.* **2023,** *25* (2), 467-489.
27. Kidibule, P. E.; Costa, J.; Atrei, A.; Plou, F. J.; Fernandez-Lobato, M.; Pogni, R. *RSC Adv.* **2021,** *11* (10), 5529-5536.
28. Li, J.; Mao, X. *ACS Sustain. Chemi. Eng.* **2022,** *10* (23), 7536-7544.
29. Gonçalves, J. P.; Promlok, D.; Ivanov, T.; Tao, S.; Rheinberger, T.; Jo, S. M.; Yu, Y.; Graf, R.; Wagner, M.; Crespy, D.; Wurm, F. R.; Caire da Silva, L.; Jiang, S.; Landfester, K. *Angew Chem Int Ed Engl.* **2023,** *62* (11), e202216966.
30. Petrinic, I.; Stergar, J.; Bukšek, H.; Drofenik, M.; Gyergyek, S.; Hélix-Nielsen, C.; Ban, I. *Nanomaterials.* **2021,** *11* (11), 2965.
31. Murthy, N.; Bleakley, B. H. *Internet J. Microbiol.* **2012,** *10*.
32. Kong, J.; Yu, S. *Acta Biochim Biophys Sin (Shanghai).* **2007,** *39* (8), 549-59.
33. Mauchauffé, R.; Moreno-Couranjou, M.; Boscher, N. D.; Van De Weerdt, C.; Duwez, A.-S.; Choquet, P. *J. Mater. Chem. B.* **2014,** *2* (32), 5168-5177.
34. Parikh, S. J.; Chorover, J. *Langmuir.* **2006,** *22* (20), 8492-8500.
35. Hardiansyah, A.; Huang, L.-Y.; Yang, M.-C.; Liu, T.-Y.; Tsai, S.-C.; Yang, C.-Y.; Kuo, C.-Y.; Chan, T.-Y.; Zou, H.-M.; Lian, W.-N.; Lin, C.-H. *Nanoscale Res. Lett.* **2014,** *9* (1), 497.
36. Secundo, F. *Chem. Soc. Rev.* **2013,** *42* (15), 6250-6261.
37. Kahraman, M. V.; Bayramoğlu, G.; Kayaman-Apohan, N.; Güngör, A. *Food Chem.* **2007,** *104* (4), 1385-1392.
38. Mazlan, S. Z.; Hanifah, S. A. *Int. J. Polym. Sci.* **2017,** *2017*, 5657271.

39. Preety; Hooda, V. *Int. J. Biol. Macromol.* **2018,** *106*, 1173-1183.
40. Talekar, S.; Chavare, S. *Recent Research in Science and Technology*. **2012,** *4*, 01-05.
41. Shariat, S. Z. A. S.; Borzouee, F.; Mofid, M. R.; Varshosaz, J. *Biotechnol. Lett.* **2018,** *40* (9), 1343-1353.
42. Su, R.; Shi, P.; Zhu, M.; Hong, F.; Li, D. *Bioresour. Technol.* **2012,** *115*, 136-140.
43. Mohammadzadeh, R.; Agheshlouie, M.; Mahdavinia, G. R. *Int. J. Biol. Macromol.* **2017,** *104*, 1664-1671.
44. Yang, S.; Fu, X.; Yan, Q.; Guo, Y.; Liu, Z.; Jiang, Z. *Food Chem.* **2016,** *192*, 1041-1048.
45. Kumar, M.; Madhuprakash, J.; Balan, V.; Kumar Singh, A.; Vivekanand, V.; Pareek, N. *Bioresour. Technol.* **2021,** *337*, 125399.

Selection of the membrane for centrifugal ultrafiltration and protein profile analysis of human primary keratinocyte secretome

Natthakit Bunkam and Kwanchanok Viravaidya-Pasuwat*

Department of Chemical Engineering, Faculty of Engineering, King Mongkut's University of Technology Thonburi, Bangkok, Thailand

**E-mail*: *kwanchanok.vir@kmutt.ac.th*

Abstract:

The potential of keratinocyte secretome as a cell-free regenerative medicine for wound healing necessitates the optimization of its concentration. This study aimed to select an appropriate molecular weight cutoff (MWCO) membrane for centrifugal ultrafiltration of the conditioned medium from human primary keratinocyte cell culture. Three membranes with MWCOs of 3, 10, and 30 kDa were tested at centrifugation speeds of 4,000×g and 14,000×g. The 30 kDa membrane proved unsuitable as all the solution permeated, leaving no retentate. At the lower centrifugation speed, protein loss due to adsorption to the membrane was significant, resulting in suboptimal concentrations. In contrast, using the 10 kDa membrane at 14,000×g achieved a near two-fold increase in protein concentration. The concentrated secretome extracellular vesicles ranged between 20 - 200 nm. The protein profile analysis using mass spectrometry confirmed the presence of essential growth factors for wound healing, including vascular endothelial growth factors (VEGF), fibroblast growth factors (FGF), and epidermal growth factors (EGF). Our findings demonstrate that a 10 kDa membrane is optimal for obtaining a concentrated secretome rich in vital wound-healing components. This membrane will be used for further study of the large-scale production of the keratinocyte secretome using tangential flow filtration.

1. Introduction

Recently, cell secretomes have been proposed as a promising alternative to cell-based therapies, which are often subject to stringent regulatory constraints. Cell secretome refers to the complex mixture of growth factors, cytokines, and extracellular vesicles that are secreted by cells into their culture medium[1]. These bioactive molecules have been increasingly recognized for their essential role in promoting wound healing processes, offering a novel approach in regenerative medicine[2].

The current challenge in utilizing cell secretomes for clinical applications is that the growth factors and cytokines in cell secretomes are present at concentrations too low to achieve the desired therapeutic efficacy. This suboptimal concentration could significantly limit the clinical potential of cell-secretome-based treatments. Therefore, it is essential to develop an effective pre-concentration strategy to increase the concentrations of these key bioactive components to achieve therapeutic impacts.

Centrifugal ultrafiltration is a widely used technique for the separation and pre-concentration of proteins, especially in small volume samples. The technique provides rapid processing and high efficiency with minimal protein damage. Centrifugal ultrafiltration relies on high-speed centrifugal forces to separate components based on their density[3] while ultrafiltration utilizes membranes for size exclusion. Therefore, the centrifuge ultrafiltration could concentrate the cell secretome by retaining larger molecules and reducing the volume of the retentate[4].

In this study, our objective was to select the most effective molecular weight cutoff (MWCO) membrane to optimally concentrate keratinocyte conditioned medium. The MWCO membranes tested were 3, 10, and 30 kDa. The total protein content, protein profiles, extracellular vesicle particle size were analyzed.

2. Materials and Methods

2.1 Preparation of Keratinocyte conditioned-medium

Keratinocyte cell culture medium, consisting of Dulbecco's Modified Eagle Medium (DMEM) (Invitrogen) and Ham's F'12 (Invitrogen), at a 3:1 ratio was collected and filtered using a 0.22 μm filter to remove cell debris.

2.2 Centrifugal ultrafiltration

The keratinocyte conditioned medium was concentrated using Amicon Ultra-0.5 filter units with 3, 10, and 30 kDa MWCO by centrifugation at 4,000×g and 14,000×g, for 15 min at 4 °C. Phosphate buffer saline (PBS) was employed to pre-washing membrane.

2.3 Secretome characterization

2.3.1 Total protein concentration

The micro-BCA Protein Assay Kit (Thermo Fisher Scientific) was used to quantify the total protein content in the cell secretome samples before and after centrifugal ultrafiltration, following the manufacture's instructions. The protein concentrations were determined by measuring the absorbance of the samples and comparing these to a standard curve generated with bovine serum albumin (BSA).

2.3.2 Dot blot analysis

Dot blot analysis was conducted to detect key growth factors in the cell secretome, specifically fibroblast growth factor (FGF), vascular endothelial growth factor (VEGF), and epidermal growth factor (EGF), in cell secretome samples. Briefly, 5 µl of the cell secretome sample was spotted onto a nitrocellulose membrane. This membrane was blocked using 5% nonfat dry milk in Tris-buffered saline (TBS) for 1 hour. Subsequently, it was then incubated with primary antibodies against h/prVEGF (1:500), bFGF (1:2,000) and hEFG (1:500), in TBS containing 2.5% of nonfat dry milk for 1 hour, followed by an hour incubation with a diluted secondary Mouse IgG antibody (1:5,000) for 1 hour. After washing with TBST (0.1% Tween 20), the membrane was visualized by enhanced chemiluminescence.

2.3.3 Extracellular vesicles (EV) particle size determination

The particle sizes of EVs in the keratinocyte cell secretome after purification were measured using a nano particle analyzer (SZ-100V2). EVs typically range in size from exosomes (30 – 150 nm), microvesicles (MVs) (100 – 1,000 nm) and apoptotic bodies (≥ 1,000 nm)[5]. For accurate particle size analysis, the refractive indices (RI) of Dulbecco's Modified Eagle Medium (DMEM) at 0.731 and EVs ranging from 1.33 – 1.40[6] were used to calculate the hydrodynamic diameters of the EVs.

2.3.4 Protein profile analysis

Protein profile analysis was conducted on retentate samples of the keratinocyte cell secretome obtained from centrifugal ultrafiltration using 3 and 10 kDa MWCO membranes at 14,000×g. These samples underwent in-solution digestion using dithiothreitol (DTT) and were subsequently subjected to dimethyl labeling for differentiation; specifically, the retentate from the 3 kDa membrane was labeled with light dimethyl labeling, while the retentate from the 10 kDa membrane received heavy dimethyl labeling. Following digestion and labeling, the samples were analyzed using LC-MS/MS, employing an EASY nano-LC 1000 system coupled to a Q-Exactive™ Quadrupole-Orbitrap instrument. Protein identification and quantification within the secretome were achieved by matching the LC-MS/MS spectra against the *Homo sapiens* UniProt database (2023).

3. Results & Discussion

3.1 Total protein concentration

The centrifugal ultrafiltration technique used relative centrifugal force (RCF) as a primary diving force of the purification process. We selected RCFs of 4,000 × g and 14,000 × g for 15 minutes at 4 °C to represent low and high forces, respectively. At 14,000 × g, a significant portion of the solution was driven through the membrane, resulting in a substantial reduction of the initial volume in the retentate (Table 1). This volume reduction in the retentate would correspondingly result in an increase in protein concentration. Interestingly, when employing the 30 kDa membrane, no cell secretome was retained in the retentate even at low centrifugal force of 4,000 × g (data not shown). This is because the very low protein concentration in the secretome mostly consisted of a solution, which possibly allowed particles to pass through the 30 kDa membrane. Therefore, leading to the decision to exclude this MWCO membrane from subsequent experiments.

Table 1. Secretome volume after centrifugal ultrafiltration

RCF (× g)	MWCO (kDa)		Volume (µl)
4,000	3	retentate	360
		permeate	90
	10	retentate	200
		permeate	260
1,4000	3	retentate	96
		permeate	396
	10	retentate	35
		permeate	450

Table 2 presents the total protein concentrations and the amount of protein in the keratinocyte-conditioned medium before and after centrifugal ultrafiltration. At low centrifugal force, the protein concentrations in the retentates from both membranes did not significantly differ from the initial concentration in the medium, despite the observed reduction in retentate volume. On the other hand, at a high centrifugal force, protein

concentrations in the retentates were effectively doubled. This increase in protein concentration at a higher centrifugal force was possibly a result of the significant volume reduction, as shown in Table 1. In addition, undesirable protein adsorption on the membrane, due to non-specific binding[7], could influence these results. Methods to mitigate non-specific binding of proteins include pre-treating the regenerated cellulose membrane with PBS[8] or increasing the relative centrifugal force.

Table 2. Total protein concentrations and amounts in the retentate before and after centrifugal ultrafiltration

RCF (× g)	MWCO (kDa)	Concentration (µg/ml)	Total protein (µg)
Before centrifugal ultrafiltration		720 ± 36.96	359.97
4,000	3	682 ± 61.23	245.54
	10	767.6 ± 7.80	153.53
1,4000	3	1,228.1 ± 97.23	117.89
	10	1,484.5 ± 26.10	51.95

3.2 The presence of growth factors associated with wound healing

The presence of VEGF, FGF, and EGF in the retentates obtained through centrifugal ultrafiltration using 3 and 10 kDa MWCO membranes at 14,000 × g, analyzed using a dot blot method were illustrated in Figure 1. All three growth factors were detected in the retentates of both membranes. However, higher chemiluminescence intensities of these proteins were observed when the 10 kDa membrane was used, suggesting higher concentrations of these proteins in the retentate.

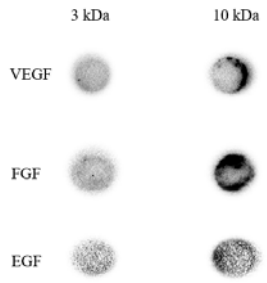

Figure 1. Dot blot results of proteins in the retentate from 3 and 10 kDa centrifugal ultrafiltration. VEGF = vascular endothelial growth factor, FGF = fibroblast growth factor, and EGF = epidermal growth factor.

It is important to note that the molecular weights of these growth factors are significantly higher than the molecular weight cutoffs of the membranes used in this study. In theory, the concentrations of these proteins should have been equivalent for both 3 and 10 kDa membranes. However, it is possible that the 3 kDa membrane possesses a relatively low porosity, resulting in a larger surface area for non-specific protein adsorption[9]. Consequently, more proteins might be lost due to non-specific binding when using the 3 kDa membrane in comparison to the 10 kDa membrane. This observation is consistent with the findings in the previous section regarding the total protein content.

3.3 Extracellular vesicle size

Figure 2 illustrates the vesicle size distribution in the retentates obtained through centrifugal ultrafiltration using 3 and 10 kDa MWCO membranes at both 4,000×g and 14,000×g. Vesicles in all samples were below 150 nm, aligning with the typical size range of extracellular vesicles (EVs)[5].

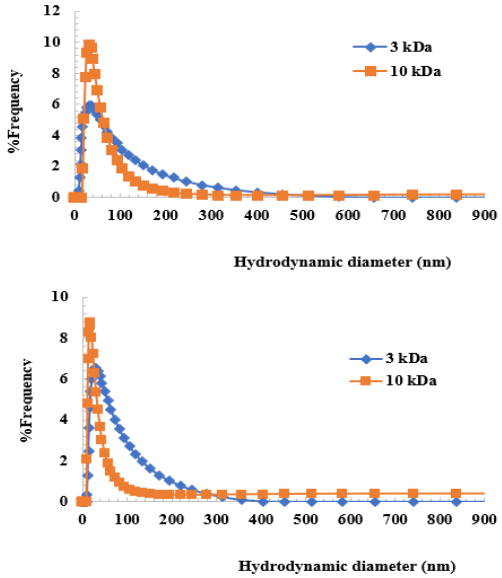

Figure 2. Size distribution of vesicles in the retentates obtained through centrifugal ultrafiltration using 3 and 10 kDa MWCO membranes at (A) 4,000 × g and (B) 14,000 × g.

At 4,000×g, the peak vesicle sizes were 62.4 nm for the 3 kDa membrane and 49.8 nm for the 10 kDa membrane. Their distribution profiles were similar. More importantly, the 10 kDa membrane retained a higher yield of EVs. At the increased speed of 14,000×g, both membranes yielded smaller peak sizes, indicating a shift towards smaller vesicles. This was accompanied by lower overall vesicle yields and narrower vesicle

distribution profiles, suggesting that the higher centrifugal force may lead to more vesicles passing through the membranes. However, the 10 kDa membrane consistently retained more vesicles than the 3 kDa membrane at this higher speed, with peak sizes of 51.1 nm and 28.9 nm, respectively. The presence of vesicles smaller than 50 nm, which include small exosomes, high-density lipoproteins (HDL), low-density lipoproteins (LDL), and intermediate-density lipoproteins (IDL), indicates a diversity in the composition of growth factors derived from keratinocyte cells[9]. Future studies should investigate the biological properties of these various exosome populations to better understand their potential roles in wound healing.

3.4 Protein profiles

In the analysis of protein profiles within the retentates, a total of 122 proteins were identified. Of these, 3 and 34 proteins were exclusively detected in the retentate from the 3 and 10 kDa membranes, respectively. The remaining 85 proteins were commonly identified in both groups. Although, total proteins in 10 kDa was retained lower than 3 kDa membranes as shown in Table 2, in 10 kDa could be high abundance of wound healing-related proteins.

Table 3. Wound healing-related proteins in the retentates

Description	MWCO (kDa)	Abundance Ratio (10kDa) / (3kDa)
Thrombospondin-1	129.3	1.85
Keratin, type II cytoskeletal 1	66	1.85
Keratin, type I cytoskeletal 17	48.1	0.57
Insulin-like growth factor factor-binding protein 7	29.1	1.65
Progranulin	63.5	1.76
Insulin	12	0.89
Metalloproteinase	23.2	1.86
Annexin A1	38.7	100
Fibronectin	272.2	1.68
Laminin	366.4	2.25
Keratin, type II cytoskeletal 5	62.3	1.21
Insulin-like growth factor-binding protein 2	34.8	100
SPARC	34.6	1.32
Filamin-A	280.6	2.29
Keratin, type I cytoskeletal 14	51.5	0.74
Isoform 4 of Extracellular matrix protein 1	63.5	1.46
Antileukoproteinase	14.3	1.41
Plasminogen activator inhibitor 1	45	2.73
CD44 antigen	81.5	1.3
Transforming growth factor-beta-induced protein ig-h3	74.6	100
Keratin, type I cytoskeletal 16	51.2	0.65
Interleukin-1 receptor type 2	45.4	100

Table 3 shows the presence of wound healing-related proteins in the retentates, including thrombospondin-1, several types of keratin, insulin-like growth factor, transforming growth factor, and components of extracellular matrix. A greater abundance of these proteins was found in the retentate from the 10 kDa membrane compared to that of the 3 kDa membrane. This finding suggests that a 10 kDa membrane is more effective in pre-concentrating keratinocyte secretome for wound healing applications.

Our analysis also identified the presence protease in the retentate samples. Protease could degrade proteins into smaller peptide chains[10], which could then pass through a membrane into permeate, resulting in protein loss. Therefore, it is important to consider a method to inhibit protease in the conditioned medium to prevent such degradation.

4. Conclusion

Our study successfully demonstrated the potential use of a 10 kDa MWCO membrane in centrifugal ultrafiltration in concentrating the keratinocyte secretome. Compared to the 3 kDa membrane, the 10 kDa option exhibited superior performance, as evidenced by its higher total protein concentration, more exosome yield, and a greater abundance of essential wound healing proteins.

Acknowledgements

This work was financially supported by Thailand Science Research and Innovation (TSRI) Basic Research Fund: Fiscal year 2024, under project number FRB640008/27703.

References

1. Kratz, G., et al., *Br. J. Dermatol* **1995**, 133(6), 842-846.
2. Md Fadilah, N.I., et al., *J. Tissue Eng*. **2022**, 13, 4-20.
3. Majekodunmi, S.O., Am. J. Biomed. Eng. **2015**, 5(2), 67-78.
4. Ratnaningsih, E., et al., Applied sciences 2021. **11**(3): p. 1078.
5. Stephen J.G, *J. Extracell. Vesicles* **2013**, 2.
6. Hoang, V.T., et al., *Appl. Sci.* **2019**, 9(6).
7. Tai C. Kwong, *Clin. Chim. Acta* **1985**, 151(3), 193-216.
8. Lee, K-J., et al., *Pharm. Res.* **2003**, 20, 1-7.
9. Mathieu, M., et al., *Nat. Cell Bio.* **2019**. 21(1), 9-17.
10. Nakamura, K., et al., *J-Stage* **1989** 33, 28.

Antibacterial effects of *Syzygium aromaticum* essential oil (clove oil) against normal flora on the skin

Nitchakarn Phimthong[1,2], Jomkhwan Meerak[3], Churdsak Jaikang[4], Nitwara Wikan[1], Wutigri Nimlamoon[1] and Saranyapin Potikanond[1,*]

[1]*Department of Pharmacology, Faculty of Medicine, Chiang Mai University, Chiang Mai, 50200, Thailand*
[2]*Graduate School, Chiang Mai University, Chiang Mai,*
[3]*Department of Biology, Faculty of Science, Chiang Mai University*
[4]*Department of Forensic Medicine, Faculty of Medicine, Chiang Mai University, Chiang Mai, 50200, Thailand*

**E-mail: saranyapin.p@cmu.ac.th*

Abstract:

Central line associated bloodstream infection (CLABSI) is an infection that occurs after the insertion of central line into patients. Most two common microorganisms caused CLABSI are *Staphylococcus aureus* and *S. epidermidis* which represent as normal flora on human skin. To prevent this event, chlorhexidine gluconate (CHG) is used to inhibit the growth of normal flora bacteria around the insertion site. However, some patients are allergic to CHG, and cause rash and itching. Therefore, changing an antiseptic agent in the dressing from CHG to other antibacterial agents can be beneficial to patients who have an allergy to CHG. Clove oil is an essential oil from clove bud (*Syzygium aromaticum* (L.) Merr. & L.M. Perry) and has been reported about its antimicrobial activity. This research aimed to evaluate the antibacterial activity of clove oil against *S. aureus* ATCC 25923 and *S. epidermidis* ATCC 12228. Clove oil was obtained by hydrodistillation, and major composition was determined by using gas chromatography coupled with mass spectrometry. From the chromatogram, eugenol was found as major component (40% v/v) Antibacterial activity was observed by using Kirby-Bauer disc diffusion assay, minimum inhibitory concentration (MIC) and minimum bactericidal concentration (MBC) determination. Clove oil demonstrated MIC value against *S. aureus* and *S. epidermidis* as 1% and 0.5% v/v, respectively. For MBC value against *S. aureus* ATCC 25923 and *S. epidermidis* ATCC 12228 is 1% v/v. Time-kill analysis showed that there was a reduction after an exposure to clove oil at least 5 minutes. In conclusion, clove oil demonstrated the strong antibacterial activity against the normal flora. This result might be developed as antibacterial patch using clove oil as disinfectant agent.

1. Introduction

Central line-Associated Blood stream infection (CLABSI) is an infection that develops within 48 hours of the central line replacement. 40%-80% of CLABSI cases are caused by gram-positive bacteria (coagulase-negative staphylococci 34.1%, enterococci 16% and *Staphylococcus aureus* 9.9%).[1] Even though most of these pathogens are normal flora on human skin, they can cause both local and systemic severe infection. Thus, to prevent CLABSI or other infections that caused by normal flora is an efficient elimination of those bacteria on the site of the central line placement. Many antiseptic agents such as chlorhexidine gluconate and povidone iodine, are used for skin preparation to prevent the infection. Furthermore, after finishing the insertion of medical device into patient's body, physicians normally prevent the infection that might occur after the operation by using antibacterial dressing to cover the site of the insertion. Chlorhexidine gluconate is a widely used disinfectant which apply as an antiseptic agent in the gel pad of the dressing. There are many manufacturers which produce these products such as 3M Tegaderm™, BD and GuardIVa™. Although it is an effective agent to get rid of bacteria, some patients' skin cannot tolerate chlorhexidine due to an allergy. The severity of chlorhexidine allergy can range from mild such as rash and itching to severe symptoms including anaphylaxis. Therefore, changing an antiseptic agent in the dressing from chlorhexidine gluconate to other antibacterial agents can be benefit to patients who have an allergy to chlorhexidine gluconate. There are many herbal plants which possess antibacterial activity such as cinnamon (*Cinnamomum verum*), clove (*Syzygium aromaticum*), Citruses and rosemary (*Salvia rosmarinus*).[2] Using herbal plants as antibacterial agents may add value and support agriculturist. In addition, herbal plants also have other medical properties, for example, antifungal effect, local anesthesia, antioxidant activities, and anti-inflammation. *Syzygium aromaticum* L. or clove can be called as "Kan-plu" in Thai. This plant is originated in Malaysia, but it can grow well in Thailand due to the similar climate. Clove bud

contains a high amount of volatile oil and up to 18% of essential oil can be found in clove buds.[3] Clove essential oil composes a eugenol as its major components, and followed by tannins, flavonoids, triterpenes etc.[4] Nowadays, clove oil is widely used as a composition in toothpaste. So, this study is aimed to evaluate efficacy of clove oil against normal flora bacteria on human skin. Furthermore, results from this study will be used to develop the antibacterial patch for use in patients.

2. Materials and Methods

2.1 Extraction of clove essential oil

Dried clove buds were purchased from local Thai herbal shop in Chiang Mai province. Five hundred grams of cloves were grounded into coarse powder by using grinder. The powder and 3 liters of water were added to round bottom flask and subjected to hydrodistillation for 6-8 hours. After that let the oil cool down at room temperature until the oil became clear and showed no turbidity. The oil was collected, and anhydrous sodium sulfate was added to dehydrate residual water. Clove oil was kept at room temperature and protected from sunlight.

2.2 Quantification of eugenol in clove oil

According to previous reports, eugenol is the main component found in clove oil, therefore gas chromatography and mass spectrometry (GC-MS) analysis was performed to quantify eugenol content in the clove oil extract. Eugenol standard was purchased from Sigma Aldrich® (USA).

2.3 Bacterial growth conditions

Bacterial strains used in this study were obtained from ATCC. *S. aureus* ATCC 25923 and *S. epidemidis* ATCC 12228 were cultured in Mueller Hinton Broth (MHB) at 37°C for 16-18 hours. Every experiment uses this condition to observe the growth of bacteria after exposure to clove oil.

2.4 Screening antibacterial activity of clove oil

Sterile cotton swab was impregnated with 10^8 CFU/mL of bacteria and streaked on Mueller Hinton Agar (MHA). Subsequently, 6-mm filter paper discs were applied on the media. Fifteen microliters of clove oil in different concentration were dropped on the discs. The plates were inverted and incubated at optimal condition.

2.5 Determination of minimum inhibitory concentration (MIC) and minimum bactericidal concentration (MBC)

Clove oil was prepared as 16% v/v in 10% ethanol and filled in 96 well plate. Serial two-fold dilution was performed, and bacterial culture was added to the oil in each well (final inoculation = 10^5 CFU). 2% chlorhexidine gluconate and 10% ethanol were used as positive and negative control respectively. The plate was incubated with shaking at 37 °C for 16-18 hours. MIC is defined as the lowest concentration that shows no visible growth when observed by naked eyes. However, due to the turbidity of clove oil, we observed the turbidity by measuring light absorbance at 600 nm, after that, pipetted 20 µL of the suspension from each well and dropped on MHA, and waited until the droplets dried. MHA plates were inverted and incubated at optimal condition. MBC value was defined as the lowest concentration that showed no growth on the media after the incubation.

2.6. Time-kill analysis

Clove oil was prepared into concentration 0.3125%, 0.625% 1.25% and 2.5% v/v at 150 µL. Bacterial culture 50 µL was added to expose with the oil. The tubes were incubated at 37 °C for 0, 5, 10, 15, 30, 45 and 60 minutes. After that, the content in the tubes at 20 µL was pipetted to spread on MHA plates. The plates were inverted and incubated at 37 °C for 16-18 hours. The amount of bacterial colony that grown on media was collected.

3. Results & Discussion

3.1 Extraction and qualification of clove oil by GC-MS and disc diffusion method

Cove oil was extracted into 3 lots. Every lot of clove oil was determined for the eugenol content and its antimicrobial activity against *S. aureus and S. epidermidis*. Eugenol contents are presented as mg% (mg in 100 mL). The results showed that average percentage yield of clove oil was 6.8%. GC-MS also showed that each lot of clove oil contained about 0.27 mg% of eugenol. Previous reports about percent yield of clove oil were 10-20 mg%.[5] However, there are many factors that affected the quantity of eugenol. Eugenol quantity in clove oil can be different depending on the method used for extraction, plant genetics, climate, soil and cultivation techniques.[6] The average yield of clove oil from hydrodistillation method is 11.5%. In this study we used hydrodistillation method to extract clove oil. Antimicrobial activity of extracted clove oil also was screened, and the results are represented in Table 2 and Figure 1. Figure 1 represents inhibition zone produced by clove oil at various concentration against *S. aureus* (a) and *S. epidemidis* (b). Positive control (2% CHG) showed highest inhibition zone (24.5 mm with *S. aureus* and 27.5 mm with *S. epidermidis*). Negative control (10% ethanol) showed no antibacterial activity. Standard eugenol has similar

inhibition zones to positive control. Clove oil at 100%, 50%, 25% v/v have inhibition zone of *S. aureus* ranged from 12.5 to 19.5 mm. Clove oil at 6.25% and 3.125% v/v did not show inhibition zone of *S. aureus.* Clove oil at all concentrations has higher inhibition zone with *S. epidermidis* than that with *S. aureus* and almost all concentrations of clove oil were able to inhibit *S. epidermidis.* Every lot of clove oils has similar antimicrobial profile ($p > 0.05$) (Table 3). The size of inhibition zone is affected by the amount of eugenol. For eugenol standard also showed inhibition zone against two bacterial strains. It can be implied that eugenol is active component for antibacterial activity of clove oil. Clove oil is able to inhibit growth of *S. epidermidis* more than that of *S. aureus.* This could be due to its virulent property which *S. aureus* are more virulent and is a hemolytic bacterium while *S. epidermidis* is a non-hemolytic bacterium. According to many previous studies, clove oil has been reported to exhibit broad-spectrum antimicrobial effects. The antimicrobial effects of clove oil have been showed against bacteria, fungi and viruses.[7]

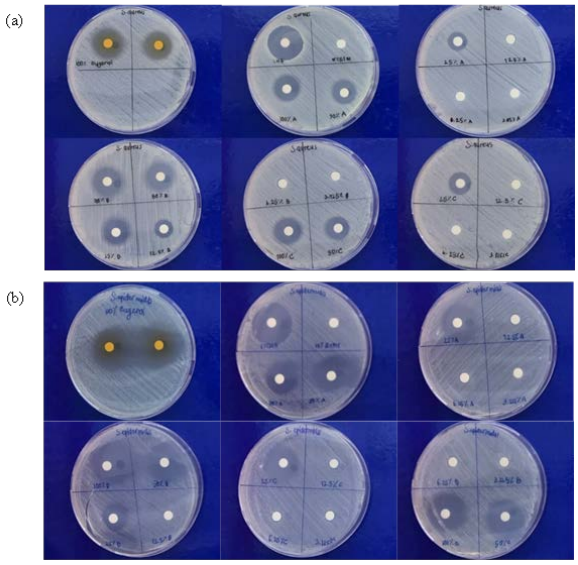

Figure 1. Antimicrobial activities of clove oil against *S. aureus* ATCC 25923 and *S. epidermidis* ATCC 12228

3.2 MIC and MBC value of clove oil

MIC value of clove oil in this study was obtained by measuring the optical density at 600 nm and compared with growth control, positive control (2% w/v CHG) and negative control (10% v/v ethanol). The results are presented in Table 1. Clove oil, at a concentration 0.5% v/v yielded an OD_{600} value of 0.051 which closely resembles the value of the positive control (0.043). Therefore, the MIC value of clove oil against *S. aureus* is determined to be 0.5% v/v. For *S. epidermidis*, at a concentration of 0.25% v/v showed the turbidity absorbance value of 0.049, and the positive control showed at 0.04, so MIC value of clove oil against *S. epidermidis* is 0.25% v/v. For MBC value, the lowest concentration that showed no visible growth of *S. aureus* and *S. epidermidis* on media is 1% v/v (Figure 2). Furthermore, when converting the OD_{600} to percentage of bacterial growth (Figure 3), the IC_{50} values of clove oil against *S. aureus* and *S. epidermidis* are 0.03% and 0.08% respectively. Previous studies also reported the MIC and MBC values of clove oil against *Streptococcus suis* as 0.1% v/v,[8] *Salmonella* typhi 0.0125% v/v (MIC) and 0.25% v/v (MBC).[9]

Table 1. OD_{600} measurement

Substances	*S. aureus*	*S. epidermidis*
2% CHG	0.043	0.040
10%EtOH	0.175	0.165
GC	0.550	0.544
16% CO	0.065	0.067
8% CO	0.054	0.057
4% CO	0.048	0.054
2% CO	0.050	0.049
1% CO	0.049	0.047
0.5% CO	0.051	0.044
0.25% CO	0.090	0.049
0.125% CO	0.168	0.244
0.0625% CO	0.195	0.337

Note: CHG= chlorhexidine gluconate, CO= clove oil

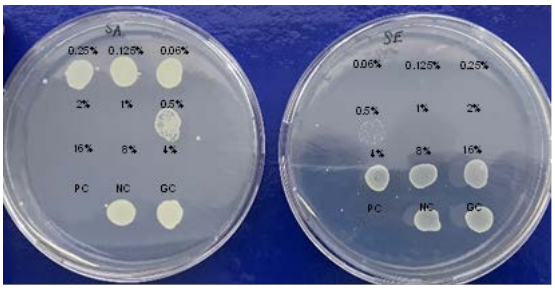

Figure 2. Bacterial growth on MHA after expose to CO at various concentrations

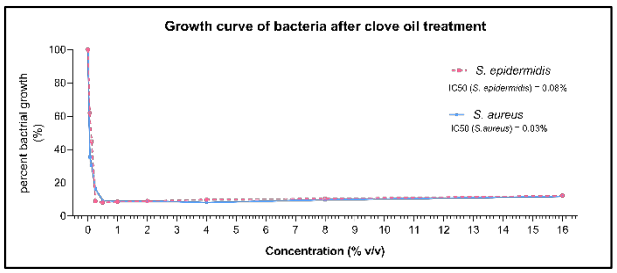

Figure 3. Bacterial growth curve after exposure to CO

3.3 Time-kill analysis

The result from time-kill analysis showed that CO possesses potential antimicrobial activity against *S. aureus* and *S. epidermidis*. CO at concentration 2.5% v/v is able to inhibit *S. aureus* and *S. epidermidis* when they were exposed to the oil for 15 minutes and 5 minutes consecutively (Figure 4). Especially, *S. epidemidis* can be killed as soon as they exposed to the oil. Mechanism of bactericidal of eugenol is disrupting the cell membrane and inhibit virulence factor, inhibit adhesion and migration of bacteria and can also inhibit the biofilm formation.[10]

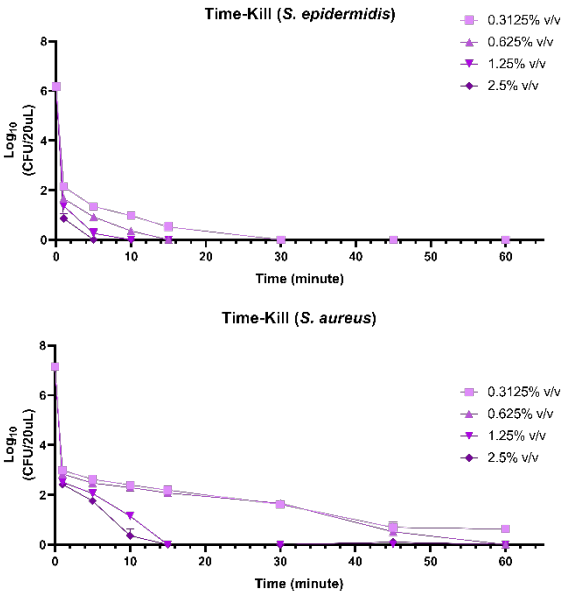

Figure 4 Time-kill analysis of clove oil against (a) *S. epidermidis*, (b) *S. aureus*

4. Conclusion

In conclusion, CO demonstrates strong antibacterial effect against the most common normal flora on skin which is *S. aureus* and *S. epidermidis* with the low MIC and MBC values. This result can be used for developing an antibacterial patch for patient who allergy to CHG. However, irritation study is needed when CO is going to be applied on the skin.

Table 2. Inhibition zone of extracted COs against *S. aureus* ATCC 25923 and *S. epidermidis* ATCC 12228

	Inhibition zone (mm)	
Substances	*S. aureus*	*S. epidermidis*
2% CHG	24.5	27.5
10% ethanol	0	0
Eugenol standard	19.75	28
100% CO		
Lot 1	17	22
Lot 2	19.5	28.5
Lot 3	18	27
50% CO		
Lot 1	16.5	23.5
Lot 2	18.5	27.5
Lot 3	16	25
25% CO		
Lot 1	12.5	22.5
Lot 2	16.5	18
Lot 3	15	23
12.5% CO		
Lot 1	7	8
Lot 2	12.5	8
Lot 3	0	9
6.25% CO		
Lot 1	0	7.5
Lot 2	0	7.5
Lot 3	0	8
3.125% CO		
Lot 1	0	0
Lot 2	0	6.5
Lot 3	0	7

Table 3. Statistical analysis of antibacterial activity of extracted CO (Sidak's multiple comparison test)

Sidak's multiple comparisons test	95.00% CI of diff.	Significant?	Summary	Adjusted P Value
Lot 1 vs. Lot 2	-15.65 to 10.98	No	ns	0.9551
Lot 1 vs. Lot 3	-12.65 to 13.98	No	ns	0.9988
Lot 2 vs. Lot 3	-10.31 to 16.31	No	ns	0.9114

Acknowledgements

This work was supported by Department of Pharmacology, Faculty of medicine, Chiang Mai University.

References

1. Haddadin, Y.; Annamaraju, P.; Regunath, H. Central Line Associated Blood Stream Infections. In *StatPearls*, StatPearls Publishing Copyright © 2022, StatPearls Publishing LLC., 2022.
2. Prabuseenivasan, S.; Jayakumar, M.; Ignacimuthu, S. *BMC Complement. Altern. Med.* **2006**, *6* (1), 39.
3. Cortés-Rojas, D. F.; de Souza, C. R.; Oliveira, W. P. *Asian Pac. J. Trop. Biomed.* **2014**, *4* (2), 90-96.
4. Health, M. o. P. *Thai Herbal Pharmacopeia 2021*. 2021. (accesse December 14, 2023).
5. Alfikri, F. N.; Pujiarti, R.; Wibisono, M. G.; Hardiyanto, E. B. *Scientifica (Cairo)* **2020**, *2020*, 9701701.
6. District, M. M. W. *Heribicide Risk Assessment Chapter 6 Eugenol*; 2010.
7. Nuñez, L.; Aquino, M. D. *Braz. J. Microbiol.* **2012**, *43* (4), 1255-1260.
8. Wongsawan, K.; Chaisri, W.; Tangtrongsup, S.; Mektrirat, R. *Pathogens* **2019**, *9* (1).
9. Devi, K. P.; Nisha, S. A.; Sakthivel, R.; Pandian, S. K. *J. Ethnopharmacol.* **2010**, *130* (1), 107-115.
10. Hu, Q.; Zhou, M.; wei, S. *J. Food Sci.* **2018**, *83* (6), 1476-1483.

Live-cell imaging of intracellular esterases using a rhodol-based fluorescent ester surrogate substrate

Tanatorn Boonklang * and Palangpon Kongsaeree *

Department of Chemistry, Center of Excellence for Innovation in Chemistry (PERCH-CIC), and Centre for Excellence in Protein and Enzyme Technology (CPET), Faculty of Science, Mahidol University, Rama VI Road, Bangkok 10400, Thailand.

**E-mail: tanatorn.boo@student.mahidol.ac.th and palangpon.kon@mahidol.ac.th*

Abstract:

Efforts to develop stable acyl-masked fluorescent probes for esterases are highly significant due to the susceptibility of ester linkages to spontaneous hydrolysis, which competes with enzyme activity. Previous reports have demonstrated that introducing a chlorine atom (–Cl) into phenolic fluorophores can insulate the acyl masking group from that of hydrolysis, making ester profluorophores suitable for practical applications. In this study, we present chlorinated rhodol butyrate (**CRB**) as a stable ester surrogate substrate for detecting esterase activity *in vitro* and *in cellulo*. Our results indicate that the interjection of the –Cl atom into the rhodol fluorophore, along with the hydrophobicity of the butyryl pendant, has enhanced the hydrolytic stability of **CRB**. Unmasking of **CRB** by porcine liver esterase occurs rapidly, with kinetic constants of $k_{cat}/K_M \approx 1.85 \times 10^3\ M^{-1}{\cdot}s^{-1}$ and $K_M \approx 66.55\ \mu M$. Under microscopy, the diffuse yellow cytosolic fluorescence staining observed in unwashed HepG2 and HK-2 cells confirms both the cellular internalization of **CRB** and its subsequent activation by intracellular esterases. This work illustrates the utility of **CRB** for further basic research, including the identification of functional esterases from bioresources and the detection of mammalian cell viability.

1. Introduction

Masked fluorogenic probes are essential in biochemical research, serving as surrogate substrates for studying enzymatic activity *in vitro* and *in cellulo*.[1–9] These probes or profluorophores feature a masking unit that quenches an intrinsic fluorescence of the fluorophore and mimics a site of enzymatic cleavage. Upon cellular entry, intracellular enzymes unmask them, thereby restoring their fluorescence. Effective fluorescent probes for enzymes must be hydrolytically stable to prevent spontaneous hydrolysis that could interfere with enzyme activity. In the case of fluorescent probes for esterases, instability of ester bonds in aqueous medium is a common issue, especially in profluorophores based on fluorophores with lower phenolic pK_a, such as fluorescein and rhodol.[10,11] To address this challenge, two approaches have been developed: self-immolative linkers to raise the overall pK_a values of the profluorophores[12–17] and a linker-free method using an electronic interaction of a chlorine atom (–Cl) to reduce ester reactivity.[18] Incorporating the –Cl group shows promise for stable ester profluorophores. Remarkably, 2′,7′–dichlorofluorescein diisobutyrate benefits from this linker-free strategy, with –Cl atoms shielding ester carbonyl groups on one face ($n_{Cl} \rightarrow \pi^*_{C=O}$) and providing protection against H_2O attack.[18]

In light of these considerations, our research objectives involve synthesizing a monochlorinated rhodol fluorophore (**Cl–Rhodol**) and optimizing the masking group for stable ester surrogate substrates (**CRA**, **CRB**, and **CRC**).

2. Materials and Methods

2.1 Synthesis and characterizations

Reagents were used as commercially sourced. Unless otherwise stated, all experiments were conducted using oven-dried glassware equipped with an N_2 inlet or using a scintillation vial sealed with a screw polypropylene cap in ambient air. Silica gel (60 Å SiO_2, 70–230 Mesh; ASTM, E. Merck) was used for column chromatography, and thin-layer chromatography (60 Å SiO_2, F_{254} precoated on 0.2 mm aluminum plate, E. Merck) monitored reactions and isolations. Solvent and volatiles were removed by rotavapor under water aspirator pressure (<20 torr), with residual solvents evaporated under high vacuum pressure (<0.1 torr). NMR spectra (^{1}H: 400 MHz, ^{13}C: 100 MHz) were acquired on a Bruker Ascend™ 400 spectrometer, referencing chemical shifts (δ) to deuterated solvents (Merck KgaA, Darmstadt, Germany). HRMS spectra were acquired using a Bruker ESI-micrOTOF, FT-IR spectra with a Bruker FT-IR Spectrometer Model ALPHA, and melting point with a Buchi Digital Melting Point M-565 apparatus.

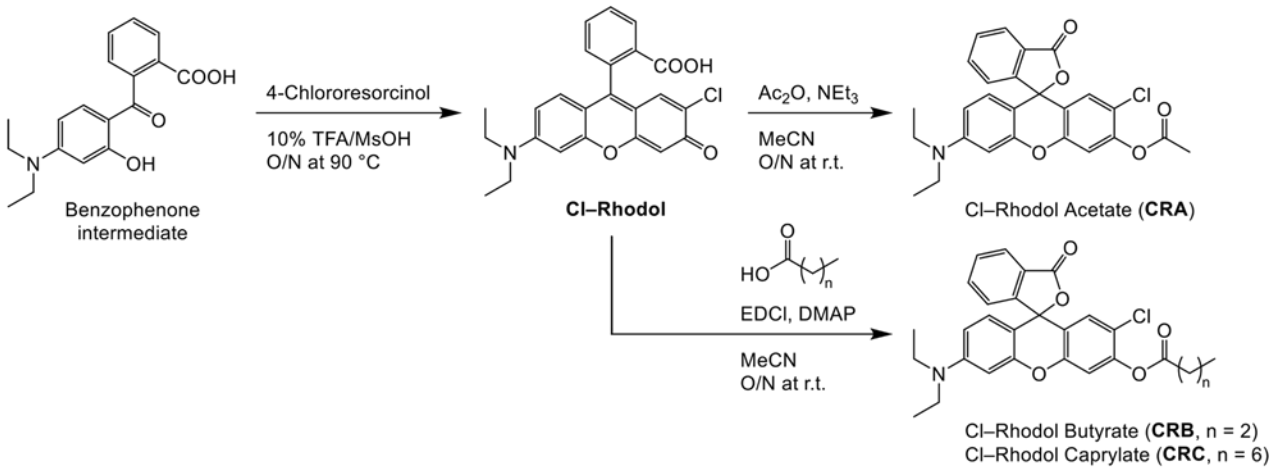

Figure 1. A synthetic route to afford the benzophenone intermediate, **Cl–Rhodol** fluorophore, and three ester profluorophores (**CRA**, **CRB**, and **CRC**).

Synthesis of **Cl–Rhodol** fluorophore and its profluorophores followed established methods[19,20] (**Figure 1**). A benzophenone intermediate was prepared by refluxing of 3–(diethylamino)phenol and phthalic anhydride in toluene overnight. A pale-yellow product was then obtained from recrystallization at –20 °C using methylated spirits. Next, Friedel-Craft acylation was carried out by reacting a 10 mmol equimolar mixture of the given benzophenone and 4-chlororesorcinol in 10% v/v TFA/MsOH (10.0 mL) at 90 °C overnight. The resultant red solution was mixed with $HClO_4$ (10% v/v, 100.0 mL) and a dark red precipitate was then collected using sintered filter funnel. Purification *via* column chromatography (SiO_2; isocratic 25% v/v EtOAc/hexane, then 50% v/v Me_2CO/EtOAc) afforded **Cl–Rhodol**.

Profluorophores were synthesized in a 20.0 mL scintillation vial equipped with a magnetic stirring bar. For acetylation, a solution of **Cl–Rhodol** (1.0 mmol) and NEt_3 (280 µL, 2.0 mmol) in MeCN (15.0 mL) was mixed with Ac_2O (140 µL, 1.5 mmol). For Steglich esterification, butyric or caprylic acid (1.2 mmol) in MeCN (10.0 mL) was reacted with EDCl (1.2 mmol) and DMAP (0.15 mmol) before adding a solution of **Cl–Rhodol** (1.0 mmol) in MeCN (10.0 mL). After 24 h, volatiles were removed *in vacuo* to obtain an oily product. Each crude profluorophore was purified by column chromatography using an isocratic elution of 20% v/v EtOAc/hexane and recrystallized in *n*-heptane at –20 °C.

2′–Chloro–6′–(N,N′–diethylamino)rhodol (**Cl–Rhodol**), maroon solid (3.28 g, 77.9%). **^{1}H NMR** (400 MHz, 10% v/v D_2O in $(CD_3)_2SO$) δ (ppm): 8.01 (d, J = 7.6 Hz, 2H), 7.77 (t, J = 7.1 Hz, 2H), 7.70 (t, J = 7.2 Hz, 2H), 7.24 (d, J = 7.5 Hz, 2H), 6.75 (s, 2H), 6.64 (s, 2H), 6.50 (d, J = 7.6 Hz, 6H), 3.34 (q, J = 6.7 Hz, 4H), 1.05 (t, J = 7.0 Hz, 6H). **^{13}C NMR** (100 MHz, 10% D_2O in $(CD_3)_2SO$) δ (ppm): 169.09, 153.51, 153.03, 150.86, 135.34, 130.78, 129.48, 128.53, 126.84, 126.02, 111.98, 110.07, 106.20, 104.16, 97.08, 44.59, 12.78. **HRMS** (ESI–micrOTOF positive) m/z: calcd for $[M+H]^+$ 422.1154, found 422.1149 (^{35}Cl, 100 %); 424.1128 (^{37}Cl, 33.3 %).

2′–Chloro–6′–(N,N′–diethylamino)rhodol acetate (**CRA**), pale-pink solid (348 mg, 75.4%). **MP**: 198.6–199.5 °C. **IR** (neat, cm^{-1}) ν_{max}: 2982, 1762, 1629, 1611, 1555, 1521, 1486, 1467, 1409, 1255, 1191, 1154, 1104, 1084, 870, 699. **^{1}H NMR** (400 MHz, $(CD_3)_2CO$), δ (ppm): 8.01 (d, J = 7.6 Hz, 1H), 7.84 (t, J = 7.5 Hz, 1H), 7.77 (t, J = 7.4 Hz, 1H), 7.38 (d, J = 7.6 Hz, 1H), 7.30 (s, 1H), 6.97 (s, 1H), 6.59 (d, J = 8.7 Hz, 1H), 6.55–6.49 (m, 2H), 3.44 (q, J = 7.0 Hz, 4H), 2.34 (s, 3H), 1.16 (t, J = 7.0 Hz, 6H). **^{13}C NMR** (100 MHz, $(CD_3)_2CO$), δ (ppm): 169.21, 168.54, 153.30, 153.20, 151.79, 150.77, 149.24, 136.26, 131.08, 129.62, 127.86, 125.64, 125.02, 122.09, 120.21, 113.68, 110.00, 105.44, 98.06, 83.05, 44.98, 20.47, 12.71. **HRMS** (ESI–micrOTOF positive) *m/z*: calcd for $[M+H]^+$ 464.1260, found 464.1257 (^{35}Cl, 100%) and 466.1231 (^{37}Cl, 32.5%).

2′–Chloro–6′–(N,N′–diethylamino)rhodol butyrate (**CRA**), pale-pink solid (296 mg, 60.5%). **MP**: 162.1–164.6 °C. **IR** (neat, cm^{-1}) ν_{max}: 2965, 2929, 2871, 1759, 1626, 1609, 1553, 1520, 1484, 1468, 1407, 1261, 1204, 1158, 1104, 1080, 862, 694. **^{1}H NMR** (400 MHz, $(CD_3)_2CO$), δ (ppm): 8.01 (d, J = 7.6 Hz, 1H), 7.84 (t, J = 7.5 Hz, 1H), 7.77 (t, J = 7.4 Hz, 1H), 7.38 (d, J = 7.6 Hz, 1H), 7.29 (s, 1H), 6.97 (s, 1H), 6.59 (d, J = 8.8 Hz, 1H),

6.56–6.48 (m, 2H), 3.44 (q, *J* = 7.0 Hz, 4H), 2.64 (t, *J* = 7.3 Hz, 2H), 1.77 (h, *J* = 7.4 Hz, 2H), 1.16 (t, *J* = 7.0 Hz, 6H), 1.03 (t, *J* = 7.4 Hz, 3H). **^{13}C NMR** (100 MHz, $(CD_3)_2CO$), *δ* (ppm): 171.17, 169.21, 153.31, 153.21, 151.80, 150.77, 149.25, 136.26, 131.08, 129.62, 127.86, 125.64, 125.02, 122.09, 120.17, 113.69, 110.00, 105.45, 98.06, 83.06, 44.98, 36.08, 18.94, 13.78, 12.71. **HRMS** (ESI–micrOTOF positive) *m/z*: calcd for $[M+H]^+$ 492.1573, found 492.1574 (^{35}Cl, 100%) and 494.1556 (^{37}Cl, 34.3%).

2′–Chloro–6′–(N,N′–diethylamino)rhodol caprylate (**CRC**)**,** off-white solid (235 mg, 43.0%). **MP**: 171.0–173.1 °C. **IR** (neat, cm^{-1}) ν_{max}: 2972, 2926, 2855, 1754, 1631, 1611, 1555, 1521, 1484, 1467, 1407, 1252, 1209, 1156, 1100, 1083, 891, 696. **^{1}H NMR** (400 MHz, $(CD_3)_2CO$), *δ* (ppm): 8.01 (d, *J* = 7.6 Hz, 1H), 7.84 (t, *J* = 7.6 Hz, 1H), 7.77 (t, *J* = 7.2 Hz, 1H), 7.38 (d, *J* = 7.6 Hz, 1H), 7.29 (s, 1H), 6.97 (s, 1H), 6.59 (d, *J* = 8.8 Hz, 1H), 6.56–6.48 (m, 2H), 3.43 (q, *J* = 7.0 Hz, 4H), 2.66 (t, *J* = 7.4 Hz, 2H), 1.79–1.71 (m, 2H), 1.48–1.30 (m, 8H), 1.16 (t, *J* = 7.0 Hz, 6H), 0.88 (t, *J* = 6.8 Hz, 3H). **^{13}C NMR** (100 MHz, $(CD_3)_2CO$), *δ* (ppm): 171.33, 169.24, 153.30, 153.20, 151.79, 150.75, 149.24, 136.27, 131.08, 129.61, 127.83, 125.64, 125.01, 122.08, 120.14, 113.69, 109.99, 105.41, 98.04, 83.07, 44.97, 34.25, 32.40, 25.48, 23.24, 14.31, 12.70. **HRMS** (ESI–micrOTOF positive) *m/z*: calcd for $[M+H]^+$ 548.2199, found 548.2198 (^{35}Cl, 100%) and 550.2176 (^{37}Cl, 34.6%).

2.2 Optimization for detecting conditions

Fluorescence emission was measured with a Cary Eclipse spectrometer, temperature-controlled by a Pelletier system. Spectra were obtained with an excitation wavelength of λ_{525} and a bandwidth (d_{ex}/d_{em}) of 5/5 nm. Samples were held in quartz cuvettes (700 µL, 10.0 mm pathlength). The data represents the mean±SD (n = 3), with outliers excluded from five parallel measurements.

MeCN was used as a solvent instead of DMSO, with a concentration not exceeding 1.0% v/v, to maintain the non-fluorescent "closed" lactone form of the profluorophores.[21] Aqueous solutions were prepared using ASTM type II water (Ω = 5.0 MQ–cm^{-1}) from a Milli-Q® water purification system. Reagents, such as HEPES free acid, Dulbecco's Modified Eagle Medium plus Nutrient Mixture F–12 (DMEM), and fetal bovine serum (FBS), were purchased from Invitrogen.

The following hydrolases were sourced from Sigma–Aldrich: esterase from porcine liver (SLCG4787, PLE), lipase from porcine pancreas (115K0681, PPL), acylase I from porcine kidney (SLBX8505, ACY1), α-chymotripsin from bovine pancreas (054K7680, α-CHY), β-glucosidase from almonds (079K4160, β-GLU), β-lactamase from Enterobactor cloacae (053M4119V, β-LAC), and albumin from bovine serum (58H0456, BSA). Enzymes and BSA were prepared in HEPES–NaOH buffer (10 mM, pH 7.3) using Eppendorf protein LoBind® tubes.

To investigate pH stability, **CRA**, **CRB**, and **CRC** (10.0 µM, 1.0% v/v MeCN) were exposed to pH buffer solutions (50 mM, pH 5–10, 0.05% w/v Tx–100) and incubated for 60 min. Subsequently, these profluorophores (10.0 µM, 1.0% v/v MeCN) were incubated with hydrolases and BSA (10 µg·mL^{-1}) in HEPES–NaOH buffer (10 mM, pH 7.3 + 0.05% w/v Tx–100) for 30 min to examine PLE responsiveness. For long-term stability studies, **CRB** (10.0 µM, 1.0% v/v MeCN) was incubated in different media: i) HEPES–NaOH buffer (10 mM, pH 7.3 + 0.05% w/v Tx–100); ii) DMEM with 10% v/v FBS; and iii) FBS-free DMEM. Time-course spontaneous hydrolysis was monitored at 25±2 °C for 48 h.

2.3 Unmasking kinetics

The concentration-dependent fluorescence emission (λ_{558}) of **CRB** (0–100 µM, 1.0% v/v MeCN), unmasked by PLE (10.0 µg·mL^{-1}), was recorded at 25±2 °C in HEPES–NaOH buffer (10 mM, pH 7.3 + 0.05% w/v Tx–100). Initial rates (V_0) were determined using a standard calibration curve of **Cl–Rhodol** fluorophore. Accordingly, kinetic parameters, including V_{max} (the maximum unmasking rate at saturating [**CRB**]), K_M (the Michaelis constant), and K_{cat}/K_M (specificity constant) were calculated on Microsoft Excel using the hyperbolic Michaelis–Menten equation: $V_0 = (V_{max} \cdot [S]) \div (K_M + [S])$.

2.4 Cell culture and live-cell imaging

In cell culture, HepG2 and HK-2 cell lines were cultured in DMEM supplemented with 10% v/v FBS, 10^2 units·mL^{-1} penicillin, and 10^2 µg·mL^{-1} streptomycin. The cell suspension was maintained in a 5% CO_2 humidified atmosphere at 37 °C for 24 h to obtain adhered cells.

For the cytotoxicity assay, adherent cells were exposed overnight to **CRB** (1.0, 5.0, and 10.0 µM) with a negative control, followed by treatment with the MTT labelling reagent (500 µg·mL^{-1}) for 4 h. The samples were then analyzed for absorbance at λ_{570} nm using an EnVision® multilabel plate reader (PerkinElmer, Inc., Germany).

In live-cell imaging experiments, adherent cells maintained in FBS-free DMEM were pretreated

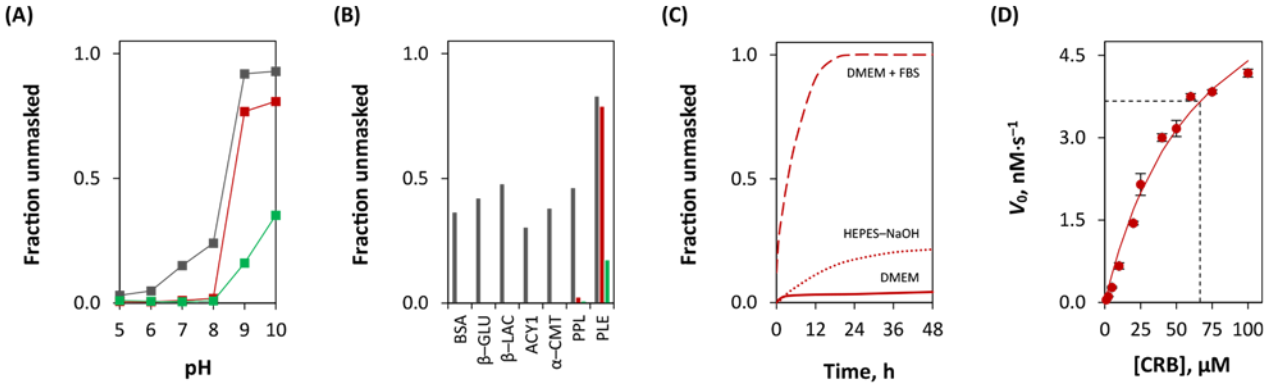

Figure 2. Fraction unmasked values of ester profluorophores (**CRA**, ■; **CRB**, ■; and **CRC**, ■) as measured by fluorescence generation at λ_{558} at 25±2 °C, *t* min or h. (**A**) pH-influenced hydrolysis at *t* = 60 min in pH buffer solutions. (**B**) Screening with hydrolytic enzymes and BSA at *t* = 30 min. (**C**) Time-course for spontaneous hydrolysis in HEPES–NaOH (dotted line) and FBS-supplemented DMEM (dashed line) compared to serum-free medium (solid line) at *t* = 0 to 48 h. (**D**) Michaelis–Menten plots for unmasking of **CRB** by PLE.

with Hoechst 33342 (10.0 µM) for 60 min and subsequently incubated with **CRB** (1.0 and 5.0 µM) for 10 min. Imaging was conducted without washing using an Operetta high-content imaging system from Perkin-Elmer, equipped with a 40× objective lens and Harmony® software. Cytosolic fluorescence of **CRB** was imaged at the wavelength of $\lambda_{550–575}$ with the excitation range of 520–530 nm, while Hoechst-counterstained nuclei were captured at the wavelength of $\lambda_{410–480}$ upon excitation in the range of 360–400 nm.

3. Results & Discussion

3.1 pH stability and PLE specificity

Profluorophores bearing different short-chain fatty acyl groups were subjected to an assessment of their susceptibility to spontaneous hydrolysis and specific unmasking by PLE *in vitro*. Following incubation in a range of pH buffers from pH 5 to 10, profluorophores with methylene (–CH_2) in the chain longer than the acetyl group displayed insensitivity within the physiological pH range (**Figure 2A**).

The specificity of these ester surrogates to PLE was confirmed through screening with a panel of commercially available hydrolases and the plasma protein, BSA. The results revealed that **CRA** and **CRB** exhibited a rapid and distinctive fluorogenic response to PLE, indicative of higher sensitivity to PLE compared to **CRC** (**Figure 2B**).

This stability and specificity can be attributed to the steric and hydrophobic components of acyl pendants. Esterases, in general, tend to exhibit their optimal activity with water-soluble short-chain acyl groups. However, **CRA** exhibited instability under physiological pH and susceptibility to non-specific hydrolysis by other hydrolases. In the case of **CRC**, a poor combination of increased stability and reduced responsiveness to PLE rendered it unsuitable for *in vitro* esterase assay. As a result, **CRB** merely emerged as the preferred candidate for further investigations.

3.2 Spontaneous probe hydrolysis

In long-term stability studies, fluorescence liberation from **CRB** was monitored over time in HEPES–NaOH buffer, FBS-free DMEM, and FBS-supplemented DMEM (DMEM–FBS). **CRB** demonstrated high stability in HEPES-buffered solution and serum-free medium but proceeded spontaneous hydrolysis in DMEM–FBS (**Figure 2C**). This substantial increase in signal within DMEM–FBS might be attributed to the presence of BSA and esterases in FBS.[22] Therefore, conducting *in cellulo* experiments with **CRB** under serum-free conditions is highly recommended.

3.3 PLE-unmasking kinetics

To assess esterase unmasking activity *in vitro*, PLE was used owing to its sequence similarity (>75%) to human liver carboxylesterase and its adherence to Michaelis–Menten kinetics.[23,24] Preliminary kinetic traces suggested that a single-step hydrolysis of the **CRB**'s butyrate pendant resulted in the full manifestation of fluorescence, indicative of single-hit kinetics. From Michaelis–Menten plots, **CRB** exhibited kinetic constants of $k_{cat}/K_M \approx 1.85 \times 10^3$ $M^{-1}{\cdot}s^{-1}$, $K_M \approx 66.55$ µM, and $V_{max} \approx 7.33$ nM·s^{-1} (**Figure 2D**).

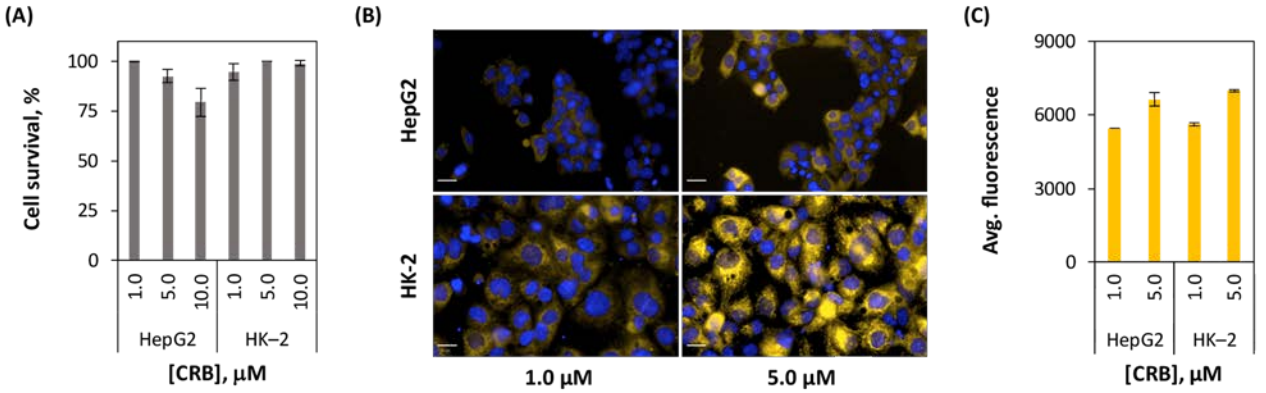

Figure 3. Cell viability and confocal fluorescence imaging in HepG2 and HK-2 cells, acquired after incubation at 37 °C for *t* min. (**A**) *In vitro* MTT assay of HepG2 and HK-2 cells in the presence of **CRB** at *t* = 24 h. (**B**) Confocal images of **CRB**'s hydrolysis in cells, counterstained with Hoechst 33342 at *t* = 10 min. Scale bars: 20 µm. (**C**) Average fluorescence intensities of **CRB** from cell images at *t* = 10 min.

3.4 Live-cell imaging of intracellular esterases

Having optimized for desirable properties, the utility of **CRB** was finally assessed in live HepG2 and HK-2 cells to examine whether it could be unmasked by intracellular esterases. An MTT assay confirmed the probe's applicability with no adverse effects on cell viability at concentrations suitable for confocal imaging (**Figure 3A**). Furthermore, the chemical stability of **CRB** in serum-free DMEM eliminated the need for a wash step prior to the imaging.

Within a short timeframe, both cells manifested diffuse yellow cytosolic fluorescence staining, while nuclear compartments and extracellular regions remained non-fluorescent (**Figure 3B**). Hoechst-counterstained nuclei further affirmed subcellular localization of **Cl–Rhodol**, indicating efficient **CRB** internalization and unmasking by endogenous esterases. In addition, the observed *in vitro* kinetic trends showed a direct parallel in cytoplasmic fluorescence, which supported that *in cellulo* hydrolyses are indeed concentration-dependent (**Figure 3C**).

4. Conclusion

CRB, a stable butyrate ester of **Cl–Rhodol** with ideal characteristics for assessing esterase activity, was successfully devised and optimized. It offers a remarkable combination of increased hydrolytic stability, rapid unmasking by PLE, and reduced non-specific hydrolysis, making it well-suited for applications *in vitro* and *in cellulo*. **CRB** is an innocuous, membrane-permeable ester surrogate substrate for fluorescence imaging of intracellular esterases, as evident in living HepG2 and HK-2 cells. Overall, **CRB** has demonstrated its potential as a promising tool for advancing basic research, such as the evaluation of mammalian cell viability, and the investigation of functional esterases in diverse biological specimens.

Acknowledgements

We gratefully acknowledge the support received from the Scholarship for Master and Doctoral Students' Competency in Academic Presentations, Faculty of Graduate Studies, Mahidol University; and the Department of Chemistry, Center of Excellence for Innovation in Chemistry (PERCH–CIC), Center for Excellence in Protein and Enzyme Technology (CPET), and Central Instrument Facility (CIF), Faculty of Science, Mahidol University. Additionally, portions of this work were done in collaboration with the Excellence Center for Drug Discovery (ECDD), Faculty of Science, Mahidol University.

References

1. Liu, H. W.; Chen, L.; Xu, C.; Li, Z.; Zhang, H.; Zhang, X. B.; Tan, W. *Chem. Soc. Rev.* **2018**, *47*, 7140–7180.
2. Singh, H.; Tiwari, K.; Tiwari, R.; Pramanik, S. K.; Das, A. *Chem. Rev.* **2019**, *119* (22), 11718–11760.
3. Zhang, J.; Chai, X.; He, X. P.; Kim, H. J.; Yoon, J.; Tiana, H. *Chem. Soc. Rev.* **2019**, *48*, 683–722.
4. Chyan, W.; Raines, R. T. *ACS Chem. Biol.* **2018**, *13* (7), 1810–1823.
5. Tallman, K. R.; Levine, S. R.; Beatty, K. E. *ACS Chem. Biol.* **2016**, *11* (7), 1810–1815.
6. Tallman, K. R.; Levine, S. R.; Beatty, K. E. *ACS Infect. Dis.* **2016**, *2* (12), 936–944.
7. White, A.; Koelper, A.; Russell, A.; Larsen, E. M.; Kim, C.; Lavis, L. D.; Hoops, G. C.;

Johnson, R. J. *J. Biol. Chem.* **2018**, *293* (36), 13851–13862.
8. Bassett, B.; Waibel, B.; White, A.; Hansen, H.; Stephens, D.; Koelper, A.; Larsen, E. M.; Kim, C.; Glanzer, A.; Lavis, L. D.; Hoops, G. C.; Johnson, R. J. *ACS Infect. Dis.* **2018**, *4* (6), 904–911.
9. Tian, L.; Yang, Y.; Wysocki, L. M.; Arnold, A. C.; Hu, A.; Ravichandran, B.; Sternson, S. M.; Looger, L. L.; Lavis, L. D. *PNAS.* **2012**, *109* (13), 4756-4761.
10. Lavis, L. D.; Rutkoski, T. J.; Raines, R. T. *Anal. Chem.* **2007**, *79* (17), 6775–6782.
11. Sun, W. C.; Gee, K. R.; Haugland, R. P. *Bioorg. Med. Chem. Lett.* **1998**, *8* (22), 3107–3110.
12. Chandran, S. S.; Dickson, K. A.; Raines, R. T. *J. Am. Chem. Soc.* **2005**, *127* (6), 1652–1653.
13. Lavis, L. D.; Chao, T. Y.; Raines, R. T. *ACS Chem. Biol.* **2006**, *1* (4), 252–260.
14. Lavis, L. D.; Chao, T. Y.; Raines, R. T. *ChemBioChem.* **2006**, *7* (8), 1151–1154.
15. Lavis, L. D.; Chao, T. Y.; Raines, R. T. *Chem. Sci.* **2011**, *2*, 521–530.
16. Hakamata, W.; Tamura, S.; Hirano, T.; Nishio, T. *ACS Med. Chem. Lett.* **2014**, *5* (4), 321–325.
17. Nakamura, N.; Uchinomiya, S.; Inoue, K.; Ojida A. *Molecules.* **2020**, *25* (9), 2153.
18. Chyan, W.; Kilgore, H. R.; Gold, B.; Raines, R. T. *J. Org. Chem.* **2017**, *82* (8), 4297–4304.
19. Li, X. M.; Ding, C. F.; Tian, B. Q.; Liu, Q.; Zhang, S. S.; Xu, H.; Ouyang, P. K. *Chem. Pap.* **2006**, *60*, 220–223.
20. Dickinson, B. C.; Huynh, C.; Chang, C. J. *J. Am. Chem. Soc.* **2010**, *132* (16), 5906–5915.
21. Tokutake, S.; Kasai, K.; Tomikura, T.; Yamaji, N.; Kato, M. *Chem. Pharm. Bull.* **1990**, *38* (12), 3466–3470.
22. Córdova, J.; Ryan, J. D.; Boonyaratanakornkit, B. B.; Clark, D. S. *Enzyme Microb.* 2008, 42 (3), 278–283.
23. Barton, P.; Laws, A. P.; Page, M. I. *J. Chem. Soc., Perkin Trans. 2*, **1994**, 2021–2029.
24. Satoh, T.; Hosokawa, M. *Chem. Biol. Interact.* **2006**, *162* (3), 195–211.

Bacterial cellulose for wound dressing with preventing infection with mangosteen peel (*Garcinia mangostana*) and Pa Thalai Chon (*Andrographis paniculate*) extracts

Jiratchaya Threerodjanataworn [1#], Pattarawadee Hongthong [1#], and Passawuth Nopphakunwong [1#]
Thirawatthana Pharamat[2]* and Chanan Phonprapai[2]

[1]*SCIUS TU, Faculty of Science and Technology,*
Thammasat University, Pathum Thani 12120,
Thailand
[2]*Biotechnology, Faculty of Science and Technology,*
Thammasat University, Pathum Thani 12120,
Thailand
**E-mail:* ptmong@gmail.com

[#]*These authors contributed equally*

Abstract:

Wound dressings are primarily used for covering to keep the wound hydrated and prevent infection from microorganisms. The ideal multifunctional wound dressings need to prevent bacterial infection, provide a moist wound environment for the wound, and promote wound healing and skin recovery. Bacterial cellulose is a biopolymer synthesis by some bacteria. It has several unique properties such as high surface area, flexibility, biocompatibility, high absorption capacity and high porosity, permeability to liquid and gases. This study aims to develop wound dressing using bacterial cellulose supplemented with extracts from mangosteen peel (*Garcinia mangostana*) and Pa Thalai Chon (*Andrographis paniculata*) to prevent infections. Mangosteen peel extract contains xanthones that inhibit the growth of bacteria and tannins which aid in wound healing. Pa Thalai Chon extract also contains Andrographolides, known for their anti-inflammatory effects. Bacterial cellulose was produced from *Acetobacter xylinum* in coconut water medium containing 5% sucrose 0.5% $(NH_4)_2SO4$ and was adjusted to pH 4 using acetic acid to develop a wound dressing. The substances extracted from mangosteen peel and Pa Thalai Chon were added to the wound dressing along with alginate and glycerol in bacterial cellulose to form the wound dressing. This study aims to develop wound dressing using bacterial cellulose supplemented with extracts from mangosteen peel (*Garcinia mangostana*) and Pa Thalai Chon (*Andrographis paniculata*) to prevent infections. The antimicrobial activity determination of mangosteen peel extract and Pa Thalai Chon extract effectively inhibited the growth of *Staphylococcus aureus* with inhibition zones ranging from 9.00 to 16 mm. The results obtained indicated that mangosteen peel extract and Pa Thalai Chon extract were potentially applied in wound dressing. In this study, formation of Bacterial cellulose wound dressing 2 formations, by mixed bacterial cellulose, alginate and glycerol at a ratio of 7:3:1 (w/w) as Formula1 and 7:7:2.5 (w/w) as Formula2. The absorption property of cellulose wound dressing was evaluated by soaking in phosphate buffer saline (PBS) and weighing at 1, 2, 3, 4, 6, 12 and 24 hours. The result of absorption activity in formula 1 has absorption for 12 hours, in formula 2 has absorption for 2 hours. From the results, bacterial cellulose wound dressing combined with antimicrobial substance could have a potential to inhibit the growth of bacteria and prevent infection.

1. Introduction

When a fresh wound occurs and is not properly cleaned, bacteria can enter the skin, leading to infection. Wound healing has a variety of treatment techniques, for example alcohol has been used to wipe around the wound and cover it with gauze. But these techniques need to repeat wound dressing, when we peel off the gauze, often makes the wound open and easily leads to bleeding. Therefore, using wound dressing patch is more comfortable than using gauze. Furthermore, the ideal multifunctional wound dressing patch should prevent bacterial infection and induce skin repair that necessary develop. Bacterial cellulose is a polymer that is produced by bacteria called *Acetobacter xylinum*.[1] It has several unique properties such as high surface area, flexibility, biocompatibility, high absorption capacity and high porosity, permeability to liquid and gases.[2] They tested by soaking bacterial cellulose with fusidic acid, it has been shown to be able to resist *Staphylococcus aureus*. This has shown that bacterial cellulose could absorb substances well. Consequently, bacterial cellulose can be developed into medical wound dressing by adding antimicrobial substances and improving to be a composite that can inhibit bacteria. The biological antimicrobial substances in this study are Mangosteen (*Garcinia mangostana*) peel extract and Pa Thalai Chon (*Andrographis paniculata*) leaves extract. Mangosteen peel has several phytochemicals, such as xanthones, flavonoids, saponins and tannins. Xanthones have biological and pharmaceutical activities including antibacterial, antifungal, antiviral and anti-inflammatory properties.[3] Pa Thalai Chon has substance called "Andrographolide"[4] which has a report of discovery In Indian journals since 1951, most of the research Published in journals from India and China. There is research in as andrographolide extract that has the effect of inhibiting viruses various types for more than 10 years, including research to find the dosage and side effects.[5]

2. Materials and Methods

2.1 Extraction of plant materials

Mangosteen peels and Pa Thalai Chon leaves were collected, chopped, and dried at 50°C. The dried samples were ground to powder. Extraction was performed based on maceration method using ethanol 95% for 7 days at room temperature and then put into sonicater.

The obtained filtrates were evaporated under evaporator, the ethanol crude extract of Mangosteen peel and Pa Thalai chon were obtained, 547.5 g and 22.50 g, respectively.

2.2 Test the antibacterial activity of the extracts

The antibacterial activity of Mangosteen peel and Pa Thalai chon crude extract was evaluated against *Staphylococcus aureus* by using paper-disc diffusion method. The plain filter paper discs (6 mm diameter) were impregnated with extract solutions and placed on inoculated plates. Vancomycin (30µg/disc) was used as positive controls. 95% ethanol was used as a negative control. The paper disc was air dried and placed on *S. aureus* inoculated plates incubated at 37°C for 24 h and measured the inhibition zones in millimeters.

2.3 Production of bacterial cellulose from *Acetobacter xylinum*

Bacterial cellulose were obtained from cultivation of *Acetobacter xylinum* in coconut water medium (containing coconut juice 1000 ml, sucrose 5% (w/v), $(NH_4)_2SO_4$ 0.5% (w/v) and adjusted pH to 4 with acetic acid and then esterized) for 10 days at room temperature (35-37°C).

2.4 Wound dressing forming

The purified bacterial celluloses were soaked in distilled water at a ratio of 1:1 and blended for 5 minutes. Bacterial cellulose was dried by a hot air oven at 50 °C for 24 hours. Bacterial cellulose wound dressing was formation by mixed bacterial cellulose, alginate and glycerol at a ratio of 7:3:1 (w/w, Formula1) and 7:7:2.5 (w/w, Formula2), added crude extracts at 10 mg/ml, and then mixed well by magnetic stirrer and pour into chamber, after that dried at 50 °C for 24 hours. The wound dressing was soaked in 20 ml of 5% CaCl2 % (w/w) 20 ml for 1 hour and soaked in 20 ml of distilled water for 15 minutes. Wound dressings were measured the thickness and kept it with silica gel.

2.5 Testing the absorption activity of wound dressing

The wound dressing was soaked in phosphate buffer saline (PBS) and used filter paper to blot out the PBS. Weigh the wound dressing at 1, 2, 3, 4, 6, 12 and 24 hours.

2.6 Testing the antibacterial activity of wound dressing

The antibacterial activity of wound dressing was evaluated against *Staphylococcus aureus* by using paper-disc diffusion method. Put wound dressing on agar plate at 37°C for 24 h and measured the inhibition zones in millimeters.

3. Results & Discussion

3.1 The antibacterial activity of the extracts

The antimicrobial activity of Mangosteen peel crude extract and Pa Thalai Chon crude extract against S. aureus at concentrations of 6, 8, and 10 mg/disc by disc diffusion method and using the antibiotic standard, vancomycin as a positive control. The results showed that both extracts exhibited against *S. aureus* with inhibition zone ranging from 9-16 mm (Table 1).

Table 1. Antibacterial activity of Mangosteen peel extract and Pa Thalai Chon against *S. Aureus*

Extract	Inhibition zone (mm)		
	6 mg/disc	8 mg/disc	10 mg/disc
Mangosteen peel	9.33±0.94	9.67±0.47	16.67±3.86
Pa Thalai Chon	9.00±1.00	9.00±1.00	10.67±0.58
Vancomycin (30µg/disc)	16.33±0.58		

3.2 Wound dressing forming

The result in Formula 1 the skin cover of the wound dressing is flexible and smooth but unevenly because blends BC not thoroughly.

The result in formula 2 the skin cover of wound dressing is very flexible but not smooth because the blend BC is not thoroughly.

3.3 Absorption activity of wound dressing

Test for absorption with phosphate buffer saline (PBS) and weigh at 1, 2, 3, 4, 6, 12 and 24 hours. The results are as shown in Table 2.

Table 2. The result of the absorption activity of wound dressing

Wound dressing	Absorption activity (g)								
	Time (hr)	0	1	2	3	4	6	12	24
Formula 1	1	0.53	0.41	0.28	0.18	0.14	0.11	0.02	0
	2	0.52	0.43	0.29	0.18	0.13	0.09	0.02	0
	3	0.55	0.45	0.33	0.19	0.15	0.09	0.01	0
Formula 2	1	1.27	0.37	0.03	0	0	0	0	0
	2	1.18	0.2	0	0	0	0	0	0
	3	1.14	0.4	0.01	0	0	0	0	0

4. Conclusion

Crude extracts of mangosteen peel and Pa Thalai Chon at a concentration of 10 mg/disc have the best inhibitory efficiency and wound dressing formula 1 at a ratio of bacterial cellulose alginate glycerol of 7:3:1 has better inhibition efficiency and absorption than formula 2.

Acknowledgements

The authors would like to gratefully thank SCiUS Program TU-SKR, Faculty of Science Thammasat University for their research grant.

References

1. Lahiri, D.; Nag, M.; Dutta, B.; Dey, A.; Sarkar, T.; Pati, S.; Edinur, H. A.; Kari, Z. A.; Noor, H. M.; Ray, R. R. *Int. J. Mol. Sci.* **2021**, *22*(23), 12984
2. Swingler, S.; Gupta, A.; Gibson, H.; Kowalczuk, M.; Heaselgrave, W.; Radecka, I. *Polymers*. **2021**, *13*, 412.
3. Narasimhan, S.; Maheshwaran, S.; Abu-Yousef, I. A.; Majdalawieh, A. F.; Rethavathi, J.; Das P. E.; Poltronieri, P. *Molecules* **2017**, *22*(2), 275.
4. Mishra, U. S.; Mishra, A.; Kumari, R.; Murthy, P. N.; Naik, B. S. *Indian J. Pharm. Sci.* **2009**, *71*(4), 436–438.
5. Zhang, L.; Bao, M.; Liu, Bin.; Zhao, H.; Zhang, Y.; Ji, X.; Zhao, N.; Zhang, C.; He, X.; Yi, Jianfeng.; Tan, Yong.; Li, L.; Lu, C. *Pharmacology* **2020**, *105*(3-4), 123-134.

Total phenolic content and antioxidant activity of *Brassica napus* var. pabularia (Red Russian Kale)

Sukanya Keawsa-ard and Patcharaporn Saengratwatchara*

Faculty of Pharmacy, Payap University, Chiang Mai 50000, Thailand

**E-mail: p.saengratwatchara@gmail.com*

Abstract:

Kale is a popular leafy vegetable with high contents of health-promoting compounds and used to be a mainstay of the traditional diet. There are a number of reports in the literature that mention about antioxidant and biological activities of *Brassica napus* var. pabularia (Red Russian Kale). The aim of this study was to determine the total phenolic content and antioxidant activity of *B. napus* var. pabularia leaf. The extracts were prepared by continuous maceration technique with different organic solvents namely hexane, dichloromethane, and methanol. Crude extracts were investigated for total phenolic content based on the Folin–Ciocalteu colorimetric assay. Antioxidant activity was studied using 2,2-diphenyl-1-picrylhydrazyl (DPPH) and 2,2'-azino-bis-3-ethylbenzothiazoline-6-sulfonic acid cation (ABTS) radical scavenging capacity assays. The results showed that the methanol extract gave the highest percentage yields (6.10 ± 0.37 %w/w), followed by dichloromethane (1.78 ± 0.02 %w/w) and hexane extracts (0.95 ± 0.04 %w/w). The methanol extract contained the highest total phenolic content of 68.05 ± 0.48 mg GAE/g extract and also showed the highest antioxidant activity on DPPH and ABTS radicals of 32.71 ± 0.74 and 32.47 ± 0.25 mg trolox/g extract, respectively. This study demonstrated that the polar solvent (methanol) extract has a better total phenolic content, DPPH, and ABTS radical scavenging activity than the nonpolar solvent extracts. These results indicate that the methanol extract of *B. napus* var. pabularia leaf may be a potential source of antioxidant agents and serves as an effective free radical scavenger. So, *B. napus* var. pabularia leaf could be developed as a promising and effective pharmaceutical product for several diseases caused by free radicals.

1. Introduction

The Brassicaceae family consists of 350 genera and 3,500 species that includes several genera such as *Camelina*, *Crambe*, *Sinapis*, *Thlaspi*, and *Brassica*. In particular, the genus *Brassica* includes species with worldwide economically importance such as *Brassica oleracea*, *Brassica rapa*, and *Brassica napus*.[1] Brassicaceae vegetables have various pharmacological properties, such as antioxidant, gastroprotective, anti-inflammatory, and anti-obesity activities.[2] *Brassica* species are widely used in traditional medicine, human food, and animal feed.[3] Kale is a leafy vegetable grown worldwide and rich in flavonoids, such as quercetin and kaempferol, which have various biological activities, including antioxidant, anti-inflammatory, antimicrobial, anti-carcinogenic, and anti-diabetic activities. Kale is primarily classified as *Brassica oleracea*, with some cultivars classified as *Brassica napus*.[4] Members of the *Brassica* genus (e.g., broccoli, cabbage, kale, cauliflower, and Brussels sprouts) are among the most health-promoting, widely cultivated, and widely consumed vegetables worldwide.[5]

Brassica napus var. pabularia (Red Russian Kale) belongs to the Brassicaceae family and the *Brassica* genus. It is a perennial vegetable plant with green leaves and purple veins.[4] To the best of our knowledge, there are a few reports in the literature mentioned about antioxidant and biological activities of *B. napus* var. pabularia leaf.[5,6] This study goes through the total phenolic content and antioxidant activities on DPPH and ABTS radicals of *B. napus* var. pabularia leaf.

2. Materials and Methods

2.1 Plant Materials

Fresh leaves of *B. napus* var. pabularia were collected in May 2022 from San Sai District of Chiang Mai Province, Thailand.

2.2 Chemicals and Reagents

Sodium carbonate, gallic acid, DPPH, trolox, ABTS, and potassium peroxydisulfate were procured from Sigma-Aldrich While Folin-Ciocalteu reagent, methanol, ethanol, hexane, and dichloromethane were procured from Merck. All chemicals and solvents used were of analytical grade.

2.3 Preparation of extracts

The leaves of *B. napus* var. pabularia were washed with water, sliced into small pieces, dried in a hot air oven at 50 ºC for 6 hours, and powdered afterward. The dried powder (60 g) was extracted by continuous maceration extraction using hexane

(300 mL) for 5 days at room temperature and then filtered through Whatman no.5 filter paper. The residue was air dried and further extracted with dichloromethane and followed by methanol similar to the procedure carried out for the hexane extraction. Each filtrate was concentrated to dryness in a rotary evaporator (Buchi, Switzerland) under reduced pressure and controlled temperature at 60 °C to give final extracts. The yield of each extract was calculated and was kept at 4 ºC until further use. Triplicate determinations were performed.

2.4 Determination of total phenolic content

The total phenolic content was determined by means of the modified Folin-Ciocalteu colorimetric method.[7] Briefly, a series of concentrations of gallic acid (0-0.06 mg/mL) were prepared in 50% (v/v) methanol and used as standard solutions. Then, 1 mL of each gallic acid solution or extract solution (1 mg/mL) was mixed with 5 mL of 10% (w/v) Folin–Ciocalteu reagent. After 10 minutes, 4.0 mL of sodium carbonate solution (7.5%) was added to the mixture and incubated in the dark at room temperature for 2 hours. The absorbance was measured at 765 nm using a UV-Vis spectrophotometer. The results were expressed as mg gallic acid equivalents per gram of dry extract (mg GAE/g). All analyses were carried out in triplicate.

2.5 Antioxidant activity

ABTS assay

The ABTS radical scavenging activity of the extracts was adopted to measure antioxidant activity using the ABTS method[8] with some modifications. Briefly, the $ABTS^{\bullet+}$ solution was prepared by the reaction between 10 mL of 7 mM ABTS solution and 0.176 mL of 140 mM potassium peroxydisulfate solution in the dark at room temperature for 16 hours and diluted with ethanol to an absorbance of 0.6-0.7 at 734 nm. A series of concentrations of trolox (0-0.02 mg/mL) were prepared in ethanol and used as standard solutions. Then, 1 mL of each trolox solution or extract solution (0.5-1.0 mg/mL) was mixed with 3 mL of $ABTS^{\bullet+}$ solution and incubated for 6 min in the dark at room temperature. The absorbance was measured using a UV-Vis spectrophotometer at 734 nm. Antioxidant activity was expressed as mg trolox equivalents per g dry extract (mg trolox/g). All analysis were carried out in triplicate.

DPPH assay

The DPPH radical scavenging activity of the extracts was adopted to measure antioxidant activity using the DPPH method[8] with some modifications. Briefly, various concentrations of trolox solutions in methanol (0-0.03 mg/mL) were used as standard solutions. Then, 1 mL of each trolox solution or extract solution (1.0 mg/mL) was mixed with 3 mL of 0.004% (w/v) DPPH solution and incubated in the dark at room temperature for 30 minutes. The absorbance was measured at 517 nm using a UV-Vis spectrophotometer. Antioxidant activity was expressed as mg trolox equivalents per g dry extract (mg trolox/g). All analysis were carried out in triplicate.

2.6 Statistical Analysis

All experiments were performed in at least triplicate. The results were presented as the mean of three independent experiments ± standard deviation (SD). Statistic significant were analyzed using SPSS 16.0 software, and the results were considered statistically significant when p was less than 0.05 ($p < 0.05$).

3. Results & Discussion

3.1 Extraction

The leaves of *B. napus* var. pabularia were extracted sequentially with hexane (nonpolar solvent), dichloromethane (semipolar solvent), and methanol (polar solvent). The extracts were filtered and evaporated to dryness under reduced pressure to give the crude extracts. The percentage yields of the crude extracts were calculated based on dry weight. The results are shown in **Table 1**. The methanol extract gave the highest percentage yield of 6.10 ± 0.37% w/w, whereas the hexane extract gave the lowest percentage yield of 0.95 ± 0.04% w/w. Efficient extraction with increased solvent polarity (methanol) was higher yield than that of semipolar (dichloromethane) and non-polar solvents (hexane). The high extract yield obtained with methanol extract could be related to the ability of the solvent to extract compounds of varying polarity. Methanol was identified as the most effective solvent for *B. napus* var. pabularia extraction. It could be that the *B. napus* var. pabularia leaf contains high levels of polar compounds that are soluble in polar solvents such as methanol.

Table 1. The extraction yields of *B. napus* var. pabularia extracts

Extract	% Yield ± S.D.
Hexane extract	0.95 ± 0.04^{c}
Dichloromethane extract	1.78 ± 0.02^{b}
Methanol extract	6.10 ± 0.37^{a}

Results are expressed as mean ± SD (n = 3).
Values in the column followed by a different letter superscript are significantly different at $p < 0.05$.

3.2 Total phenolic content

Total phenolic contents in different extracts of *B. napus* var. pabularia leaf were determined by the Folin-Ciocalteu method using gallic acid as the standard. The total phenolic content of crude extracts was calculated from the regression equation of the calibration curve ($y = 10.468x + 0.0095$, $R^2 = 0.9994$) and expressed as mg gallic acid equivalents per gram of dry extract (mg GAE/g). Results are presented in **Table 2**.

Table 2. Total phenolic contents of *B. napus* var. pabularia extracts

Extract	Total phenolic content (mg GAE/g)
Hexane extract	2.53 ± 0.27^{c}
Dichloromethane extract	28.82 ± 0.80^{b}
Methanol extract	68.05 ± 0.48^{a}

Results are expressed as mean ± SD (n = 3).
Values in the column followed by a different letter superscript are significantly different at $p < 0.05$.

Phenolic compounds are phytochemicals found in most plant tissues, including fruits and vegetables. They are considerable potential from a preventive and therapeutic point of view due to their antioxidant, antibacterial, anti-inflammatory, and anticancer properties.[9,10] This study indicates that different extraction solvents yield different concentrations of phenolic compounds. The methanol extract gave the highest total phenolic content of 68.05±0.48 mg GAE/g, followed by dichloromethane, and hexane extracts, respectively. So, the methanol extract of *B. napus* var. pabularia leaf is expected to exhibit good results in antioxidant activity. The total phenolic content was higher in methanol (polar solvent) extract and weaker in non-polar solvent extracts. This result is in agreement with the report of Phowichit *et al* showing that the highest content of total phenolic compounds in *Z. limonella* was found in methanol extract and the lowest was found in hexane extract.[11] Zazouli *et. al.* also demonstrated that methanol is the most suitable solvent for the extraction of phenolic compounds from *C. europaea*.[12] The highest contents of phenolic compounds were observed in the methanolic extract of *B. napus* var. pabularia leaf, thus resulting in the highest extraction yield of methanolic extract.

3.3 Antioxidant activity

In this study, radical scavenging activity was measured by two methods; DPPH and ABTS methods. The ABTS and DPPH methods are among the most popular methods of determining the antioxidant activities.[13] The results of DPPH and ABTS radical scavenging activity of *B. napus* var. pabularia leaf are presented in **Table 3**.

The methanol extract showed the highest antioxidant activity on DPPH and ABTS methods of 32.71±0.74 and 32.47±0.25 mg trolox/g, respectively. This study illustrated that the high content of total phenolic content from methanol extract is associated with high antioxidant activity on both DPPH and DPPH radicals. The antioxidant activity of the extract highly depends on the solvent polarity. Methanol is the best solvent for extracting antioxidants from *B. napus* var. pabularia leaf. Thus, the methanol extract is an important source of natural antioxidant agents. Additionally, the methanol extract of *B. napus* var. pabularia leaf is an important source of natural antioxidant agents. This result of the total phenolic and antioxidant activity of Kale is different from previous research, the differences may be attributed to different solvents used in extraction, methods, and conditions of extraction, and so on.[14-17]

We performed Pearson's correlation analysis to verify the relationship between the total phenolic content (TPC) and percentage yield or the relationship between TPC and ABTS or DPPH radical scavenging capacity. The strength of the correlation is distributed by correlation coefficient (*r*-value) as follows: $r = 0.000$ to 0.200, indicating an insignificant correlation; $r = 0.210$ to 0.400, indicating a weak correlation; $r = 0.410$ to 0.700, indicating a moderate correlation; $r = 0.710$ to 0.900, indicating a high correlation; and $r = 0.910$ to 1.000, indicating a very strong correlation.[18] The percentage yield, ABTS radical scavenging capacity, and DPPH radical scavenging capacity had a very strong correlation to TPC with *r*-values of 0.9635, 0.9594, and 0.9039, respectively. These results showed that TPC might have a significant to the percentage yield, ABTS radical scavenging capacity, and DPPH radical scavenging capacity.

This preliminary study might be a basis for further study in the potential discovery of new natural bioactive compounds. Further analysis should be performed to measure the content of bioactive compounds in the extract and to isolate the bioactive compounds to uncover their good potential as a natural source of antioxidant agents. Moreover, the higher biological activities in other models such as the cytotoxicity of bioactive compounds in cell lines or other specific biological activities that involve pharmaceutical product utilization in animal models should be determined in the future.

Table 3. Antioxidant activity of *B. napus* var. pabularia leaf extracts

Extract	DPPH (mg trolox/g)	ABTS (mg trolox/g)
Hexane extract	3.64± 0.70^{c}	4.48±0.23^{c}
Dichloromethane extract	22.45± 0.61^{b}	26.72±0.34^{b}
Methanol extract	32.71± 0.74^{a}	32.47±0.25^{a}

Results are expressed as mean ± SD (n = 3).
Values in the column followed by a different letter superscript are significantly different at $p < 0.05$.

4. Conclusion

The leaves of *B. napus* var. pabularia were extracted sequentially with hexane, dichloromethane, and methanol solvents. This study indicated that the methanolic extract contained high total phenolic content and exhibited antioxidant activity on DPPH and ABTS radicals. Therefore, the methanolic extract of *B. napus* var. pabularia leaf may be used as a potential source of antioxidant agents. However, the isolation of bioactive compounds and analysis of other specific biological activities should be investigated to improve their efficacy before developing as a promising and effective pharmaceutical product for several diseases caused by free radicals such as antioxidant gel, antioxidant cream, antioxidant serum, or other treatments, etc.

Acknowledgements

The authors would like to express sincerest gratitude to Faculty of Pharmacy, Payap University, Chiang Mai, Thailand for financial support.

References

1. Raiola, A.; Errico, A.; Petruk, G.; Monti, D.M.; Barone, A.; Rigano, M.M. *Molecules*. **2018**, *23*, 15.
2. Deepa, P.; Sowndhararajan, K.; Park, S.J. *J. Agri. Life Environ. Sci*. **2020**, *32*(3), 321-331.
3. Ayadi, J.; Debouba, M.; Rahmani, R.; Bouajila, J. *Molecules*. **2022**, *27*, 6008.
4. Park, Y.J.; Park, J.; Truong, T.Q.; Koo, S.Y.; Choi, J.; Kim, S.M. *Agronomy*. **2022**, *12*(9), 2138
5. Nawaz, H.; Shad, MA.; Muzaffar, S. *Brassica germplasm-characterization, breeding and utilization.* **2018**;1:7-26.
6. Soengas, P.; Cartea, ME.; Francisco, M.; Sotelo T, Velasco, P. *Food Chem*. **2012**, *134*(2), 725-33.
7. Ortega-Hernández, E.; Camero-Maldonado, A.V.; Acevedo-Pacheco, L.; Jacobo-Velázquez, D.A; Antunes-Ricardo, M. *Foods*. **2023**, *12*, 1-21.
8. McDonald, S.; Prenzler, P.D. *Food Chem*. **2001**, *73(1)*, 73-84.
9. Mahdi-Pour, B.; Jothy, S.L.; Latha, L.Y.; Chen, Y.; Sasidharan, S. *Asian Pac J Trop Biomed*. **2012**, *2*(12), 960-965.
10. Rosa, L.A.; Moreno-Escamilla, J.O.; Rodrigo-García, J.; Alvarez-Parrilla, E. *Postharvest Physiology and Biochemistry of Fruits and Vegetables*. **2019**, 253-271.
11. Franco, W.; Arazo, M.C.R.; Benavides, S. *Marine Phenolic Compounds*. **2023**, 239-264.
12. Phowichit, S.; Ratanachamnong, P.; Matsathit, U. *Research Journal Rajamangala University of Technology Thanyaburi*. **2019**, *18*(1), 25-39.
13. Zazouli, S.; Chigr, M.; Jouaiti, A. *Der Pharma Chemica*. **2016**, *8*(11), 191-196.
14. Wołosiak, R.; Druzynska, B.; Derewiaka, D.; Piecyk, M.; Majewska, E.; Ciecierska, M.; Worobiej, E.; Pakosz, P. *Molecules*. **2022**, *27*, 50, 1-20.
15. Cartea, M.E.; Francisco, M.; Soengas, P.; Velasco, P. *Molecules*. **2011**, *16*, 251-280.
16. Ayaz, F.A.; Hayırlıoglu-Ayaz, S.; Alpay-Karaoglu, S.; Gru´z, J.; Valentova´, K.; Ulrichova´, J.; Strnad, M.; *Food Chem*. **2018**, *107*, 19-25.
17. Sikora, E.; Bodziarczyk, I. *Acta Sci. Pol., Technol. Aliment*. **2012**, *11(3)*, 239-248.
18. Chaikhong, K.; Chumpolphant, S., Rangsinth, P.; Sillapachaiyaporn, C.; Chuchawankul, S.; Tencomnao, T.; and Prasansuklab, A. *Plants*. **2022**. *12*(65), 1-17.

A novel organic fluorescent molecule for protease enzyme detection

Kittiporn Nakprasit and Anawat Ajavakom*

Department of Chemistry, Faculty of Science, Chulalongkorn University, Bangkok, Thailand

**E-mail: anawat.a@chula.ac.th*

Abstract:

Cysteine proteases, typically found in all organisms, are generally and primarily involved in peptide bond breaking within numerous cellular and extracellular systems in various biological processes. They play important roles in cellular functions and implicate disease pathways such as cancer, neurodegenerative disorders, and diabetes. Furthermore, parasitic, and pathogenic infections can also release proteases into host cells, which can cause diseases like AIDs, malaria, and immune-related diseases. Therefore, the tools for detecting or visualizing these cysteine proteases are valuable for better understanding the enzymatic activity and their relevance to any disease. In this study, we applied our synthetically developed fluorescent molecule, 1,4-dihydropyridine derivative, as a biosensor for detecting protease enzymes, particularly, cysteine protease. The common cysteine proteases papain and bromelain were tested to demonstrate the peptide bond cleaving concept. The hydrolytic activity was measured by assessing the relative fluorescence enhancement using a fluorometer. The selectivity of the fluorescent biosensor towards the specific cysteine proteases will also be compared with similar function enzymes *in vitro*.

1. Introduction

Proteases are enzymes that can break down the peptide bond. They play a crucial role in many biological functions and can be found in all organisms.[1] Cysteine proteases involve in many biological functions such as enzyme secretion from parasitic or pathogenic infection, programmed cell death, and immune-related diseases.[2] For example, one of cysteine protease plays a key role in immune-related diseases, called caspases, which require aspartic acid being a recognition site on the caspase substrates for amide hydrolysis.[3] Therefore, cysteine proteases detection methods are valuable. The traditional methods for protein and enzyme assays, such as immunofluorescence, still have limitations such as time-consuming, required expensive agents, complicated operation process and not applicable for high-throughput screening (HTS).[4, 5] A fluorescent biosensor for enzymatic detection provides many benefits including highly selective, sensitive, non-invasive, and suitable for HTS and real-time analysis.[5] Many types of fluorescence modes can be used for protease detection or visualization, for instance, fluorescence energy transfer (FRET)[6, 7], near-infrared fluorescence (NIRF) probe[6, 8], aggregate induced emission (AIE)[9], chemiluminescence[10] and bioluminescence.[11]

Dihydropyridine (DHP) has been synthetically developed in our lab.[12] The DHP and its derivatives were mainly applied as a heavy metal sensing such as Hg^{2+}, and Au^{3+}.[13, 14] In this study, we utilized a new derivative on our design as a fluorophore for fluorescent sensing of cysteine protease by using a new DHP analog, called **DHP-NH_2**, coupling with aspartic acid to get the designd probe, **Asp-DHP**. We aim to utilize this probe with cysteine protease that requires aspartic acid to be a recognition motif for doing a catalytic function.

2. Materials and Methods

2.1 Materials

Synthetic reagents were purchased from TCI. Column chromatography was conducted using silica gel (SiliaFlash® F60, from SiliCycle Inc.). All chemicals and organic solvents were from TCI. The synthetic products were characterized by ^{1}H NMR spectroscopy (500 MHz, JEOL, Japan) and Dart-TOF mass spectrometry (JEOL the AccuTOF LC-plus JMS-T100LP, Japan). The photophysical properties were characterized by UV-Vis spectrophotometer, fluorometer, and microplate reader.

2.2 Synthesis of *tert*-butyl hydrazinecarboxylate

The hydrazine monohydrate (500 µL, 1 eq.) was suspended in CH_2Cl_2 (10 mL), and then di-*tert*-butyl decarbonate (2,463 µL, 1 eq.) was added. The resulting solution was stirred at room temperature for 18 h. The solution was concentrated *in vacuo*. The crude product was purified by silica gel column chromatography using 3% MeOH/CH_2Cl_2 to obtain a colorless oil in 30% yield. ^{1}H NMR (500 MHz, CD_3CN) δ 6.46 (s, 1H), 3.67 (s, 2H), 1.41 (s, 11H).

2.3 Synthesis of dihydropyridine derivative (DHP-NH_2)

Synthesis of **DHP-NH_2** has followed the synthetically developed protocol of Hu and co-workers.[15] The product was obtained as a yellow oil in 16% yield. ^{1}H NMR (500 MHz, $CDCl_3$) δ 7.38 – 7.35 (m, 5H), 7.18 (s, 2H), 5.18 (s, 2H), 4.15 (t, 1H), 3.72 (s, 6H), 3.59 (s, 3H), 2.53 (d, 2H); ^{13}C NMR (126 MHz, $CDCl_3$) δ 172.18, 166.48, 155.20, 141.62, 135.03, 128.81, 107.32, 68.53, 51.75, 51.58, 39.91, 29.34.

2.4 Synthesis of dimethyl 1-(2-((((9*H*-fluoren-9-yl)methoxy)carbonyl)amino)-4-(*tert*-butoxy)-4-oxobutanamido)-4-(2-methoxy-2-oxoethyl)-1,4-dihydropyridine-3,5-dicarboxylate (Asp-DHP)

A mixture of Fmoc-Asp(OtBu)/**DHP-NH_2**/HBTU/HOBt/DIPEA (1.5 eq: 1 eq: 2 eq: 2 eq: 4 eq) was dissolved in 2 mL dry CH_2Cl_2. The reaction mixture was stirred at room temperature for 18 h. The completed reaction was quenched with H_2O and then extracted 2 times with CH_2Cl_2. The organic layers were combined. The solution was dried with anhydrous $NaSO_4$ and concentrated *in vacuo*. The crude product was purified by column chromatography (0-40% EtOAc/hexanes) to obtain colorless oil in 44% yield. ^{1}H NMR (500 MHz, $CDCl_3$) δ 8.96 (s, 1H), 7.77 (d, *J* = 7.5 Hz, 2H), 7.61 – 7.55 (m, 2H), 7.40 (t, *J* = 7.5 Hz, 1H), 7.37 – 7.25 (m, 1H), 7.05 (d, *J* = 15.3 Hz, 2H), 5.83 (d, *J* = 8.8 Hz, 1H), 4.59 (dd, *J* = 10.8, 6.4 Hz, 1H), 4.56 – 4.44 (m, 2H), 4.21 (t, *J* = 6.3 Hz, 1H), 4.16 (t, *J* = 5.2 Hz, 1H), 3.70 (s, 3H), 3.69 (s, 3H), 3.60 (s, 3H), 2.92 (dd, *J* = 17.4, 4.6 Hz, 1H), 2.63 (dd, *J* = 17.3, 5.9 Hz, 1H), 2.54 (d, *J* = 5.2 Hz, 2H), 1.43 (s, 11H); ^{13}C NMR (126 MHz, $CDCl_3$) δ 172.27, 170.47, 166.48, 156.26, 143.56, 141.40, 128.04, 127.24, 124.99, 120.23, 107.05, 82.67, 67.28, 51.64, 50.17, 47.28, 39.80, 36.97, 29.41, 28.08.

2.5 Determination of absorption and emission spectrum of DHP-NH_2

The measurement was conducted by preparing a solution in aqueous solution. The concentration of the DHP-NH_2 was diluted to 100 µM from 20 mM stock solution that was dissolved in DMSO.

2.6 Solvatochromic effects

The DHP-NH_2 was diluted from 20 mM stock solution to 10 µM in various solvents. The measurement was conducted using a fluorometer.

2.7 enzymatic screening

Asp-DHP was diluted from 20 mM to obtain 20 µM in 25 mM Tris-HCl pH 7.2 containing 5 mM $CaCl_2$. The corresponding enzyme (10 µg/ml final concentration) was then added, and incubated at 37°C for 18 h. the results were measured using a microplate reader.

2.8 Mass determination of the probe

The solutions from the enzyme screening were subsequently utilized for mass analysis. Cold CH_3OH (1 mL) was added to the solution and filtered through a 0.45 µM microfilter. The filtrate was extracted with CH_2Cl_2. The organic phase was collected and dried *in vacuo*. The mass measurement using Dart-TOF mass spectrometry (JEOL the AccuTOF LC-plus JMS-T100LP.

3. Results & Discussion

3.1 Synthesis of target probe (Asp-DHP)

The **Asp-DHP** was successfully synthesized in 3-step. Firstly, hydrazine monohydrate was protected with Boc_2O to obtain monoprotected hydrazine. The obtained product continually reacted with methyl propiolate through a one-pot reaction, in which the Boc group was also removed to obtain **DHP-NH_2**. Finally, the target (**Asp-DHP**) was synthesized by using an amide coupling reaction, shown in **Scheme 1**.

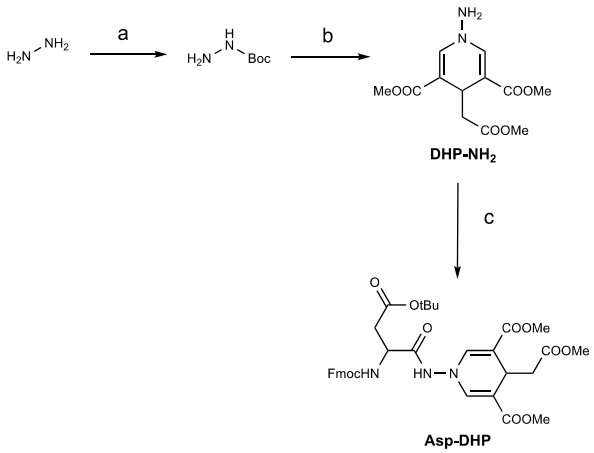

Scheme 1. The synthetic scheme of **Asp-DHP**, a) Boc_2O, CH_2Cl_2, rt, 18h, b) TMSCl, piperazine, DMSO/H_2O, 120°C, 24h, and c) Fmoc-Asp(O^{t}Bu), HBTU, HOBt, DIPEA, CH_2Cl_2, rt, 18h.

3.2 Photophysical properties of DHP-NH_2

DHP-NH_2 displayed absorption and emission spectra at 350 and 450 nm, respectively, in aqueous solution, as shown in **Figure 1b**. It appears as a blue fluorescence in the solution phase, but it emitted a yellow fluorescence in the solid state when monitored under the UV lamp at 365 nm. According to the studies of the solvatochromic effect studies, interestingly, protic solvents like H_2O and MeOH result in emission at 450 nm. In contrast, aprotic solvents, such as

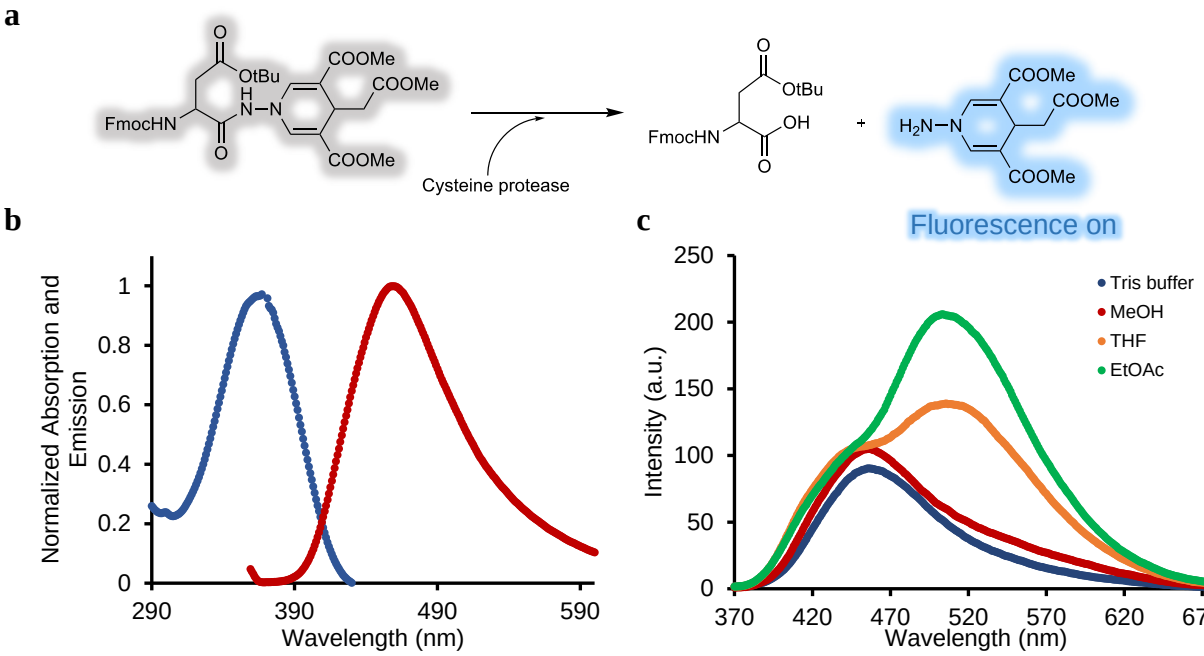

Figure 1. a) The schematic representation of the fluorescence detection of the enzyme, b) The absorption (blue) and the emission (red) spectra of **DHP-NH$_2$**, and c) The solvatochromic effects of **DHP-NH$_2$**

tetrahydrofuran (THF) and ethyl acetate (EtOAc) provided an emission at 520 nm as shown in **Figure 1c**.

3.3 Enzymatic activity of cysteine protease and their similar enzymatic functions

The concept of detection was demonstrated in **Figure 1a**. Upon enzymatic cleavage, the resulting **DHP-NH$_2$** could provide a fluorescence signal. The designed probe was tested with common cysteine proteases—papain and bromelain—and non-cysteine proteases enzymes such as BSA, lysozyme, and lipase. After treating with enzymes, the probe resulted in a relative fluorescence enhancement. Most of the enzymes exhibited a higher signal than that of the control, which is **Asp-DHP** probe in Tris buffer. Only papain did not show enhancement in fluorescent intensity. Interestingly, BSA, without the enzymatic property, did unexpectedly exhibit an increase in fluorescence signal as shown in **Figure 2**. Therefore, we further determine whether or not the fluorescence signal was generated due to the amide hydrolytic process using mass spectroscopy analysis.

3.4 Mass analysis

The mass spectrum of each has not shown the exact molecular ion peak of the expected **DHP-NH$_2$**. However, some of the fractions were found in the spectrum that can represent the structure before ionization occurs. The m/z around 604.5099 indicated that **Asp-DHP** has lost the tertiary butoxy group as well as the peak around 268.6072 indicated the N-N bond breaking of **Asp-DHP** which this peak was not found in mass spectrum of **DHP-NH$_2$**. Therefore, these two characteristic peaks were shown in all spectra, which belonged to the structure of **Asp-DHP**.

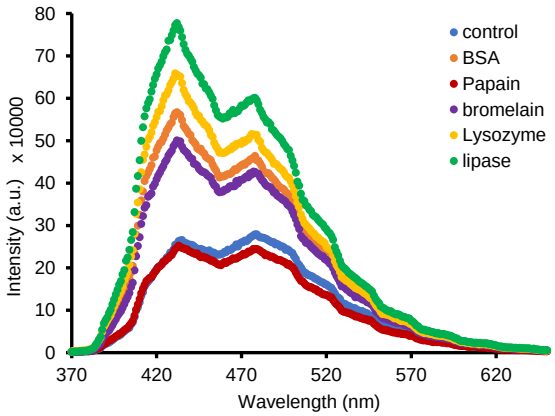

Figure 2. The fluorescence spectra of **Asp-DHP** with and without treated with the proteins.

Especially, the expected cysteine protease, bromelain, should provide the hydrolytic product, DHP-NH$_2$, as well as the non-enzymatic protein (BSA) should not obtain the hydrolytic product, but both of these provided a fluorescence enhancement, which the signals belonged to **Asp-DHP** as described the mass data above. The results are shown in **Figure 3**. According to these data, it can be guaranteed that the fluorescence enhancement was not due to hydrolytic cleavage.

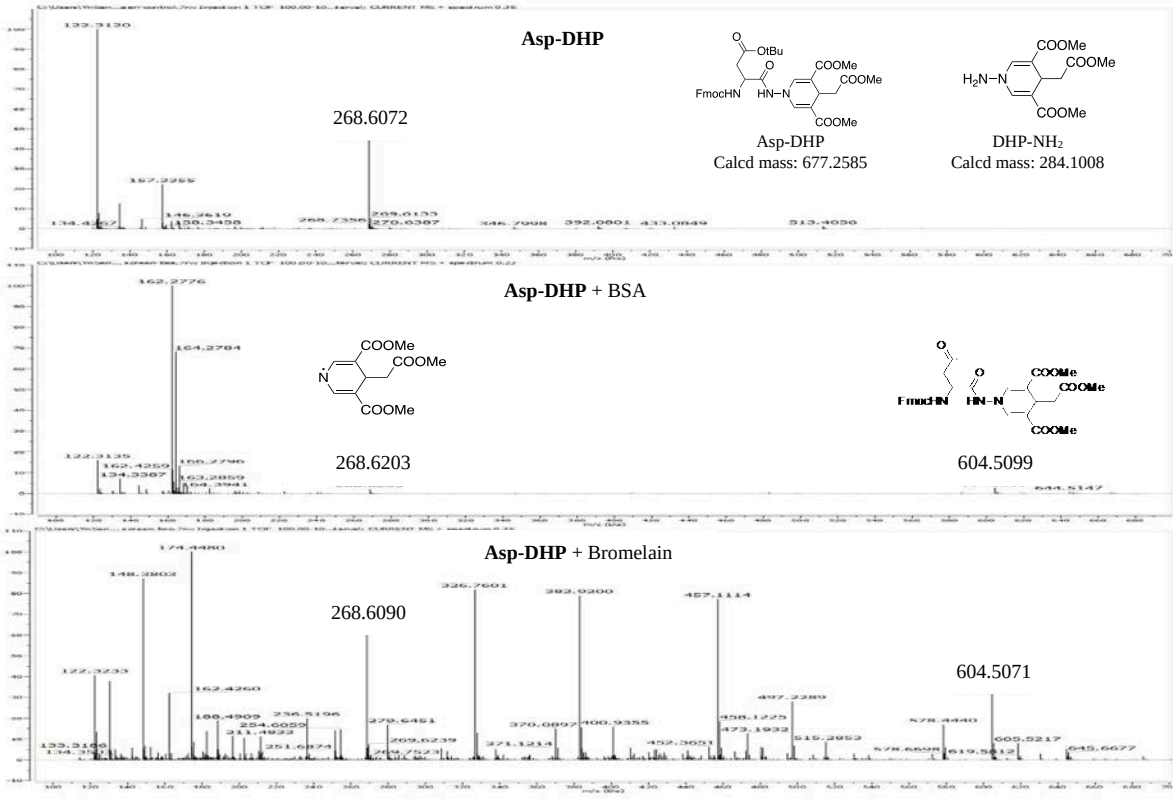

Figure 3. The mass spectra of **Asp-DHP** without enzyme, **Asp-DHP** with BSA, and **Asp-DHP** with bromelain enzyme.

4. Conclusion

The amide hydrolysis of the **Asp-DHP** with cysteine proteases was not successfully detected. Even though fluorescence enhancement was found in most enzymes including BSA, it was not due to the amide bond cleavage. According to the mass analysis, only fragmentation of **Asp-DHP** was observed confirming the absence of amide hydrolytic activity. It could be indirectly assumed that the increase in fluorescence signal might be induced by the interaction of **Asp-DHP** with the protein or enzyme.

Acknowledgments

This project is funded by the National Research Council of Thailand (NRCT, N42A661000).

References

1. López-Otín, C.; Bond, J. S. *J. Biol. Chem.* **2008**, *283* (45), 30433-30437.
2. Yang, N.; Matthew, M. A.; Yao, C. *Microorganisms* **2023**, *11* (6), 1397.
3. Puccini, J.; Kumar, S. *The Caspase Family of Proteases. In Encyclopedia of Cell Biology* (Second Edition), Bradshaw, R. A., Hart, G. W., Stahl, P. D. Eds.; Academic Press, 2023; pp 165-177.
4. Yoon, H. K.; Jung, S. T.; Kim, J. H.; Yoo, T. H. *Biotechnol. Bioprocess Eng.* **2012**, *17* (6), 1113-1119.
5. Rai, P.; Hoba, S. N.; Buchmann, C.; Subirana-Slotos, R. J.; Kersten, C.; Schirmeister, T.; Endres, K.; Bufe, B.; Tarasov, A. *Biosens. Bioelectron.* **2024**, *244*, 115788.
6. Neefjes, J.; Dantuma, N. P. *Nat. Rev. Drug Discov.* **2004**, *3* (1), 58-69.
7. Porubský, M.; Řezníčková, E.; Křupková, S.; Kryštof, V.; Hlaváč, J. *Bioorg. Chem.* **2022**, *129*, 106151.
8. Ren, X.; Tao, M.; Liu, X.; Zhang, L.; Li, M.; Hai, Z. *Biosens. Bioelectron.* **2023**, *219*, 114812.
9. Lin, H.; Yang, H.; Huang, S.; Wang, F.; Wang, D. M.; Liu, B.; Tang, Y. D.; Zhang, C. J. *ACS Appl. Mater. Interfaces* **2018**, *10* (15), 12173-12180.
10. Wu, Y.; Nie, F. *Sens. Actuators B Chem.* **2015**, *220*, 481-484.
11. O'Brien, M.; Moehring, D.; Muñoz-Planillo, R.; Núñez, G.; Callaway, J.; Ting, J.; Scurria, M.; Ugo, T.; Bernad, L.; Cali, J.; Lazar, D. *J. Immunol. Methods* **2017**, *447*, 1-13.
12. Sirijindalert, T.; Hansuthirakul, K.; Rashatasakhon, P.; Sukwattanasinitt, M.; Ajavakom, A. *Tetrahedron* **2010**, *66* (27), 5161-5167.

13. Homraruen, D.; Sirijindalert, T.; Dubas, L.; Sukwattanasinitt, M.; Ajavakom, A. *Tetrahedron* **2013**, *69* (5), 1617-1621.
14. Paisuwan, W.; Sukwattanasinitt, M.; Tobisu, M.; Ajavakom, A. *Sensors (Basel)* **2022**, *23* (1).
15. Hu, D.; Liu, Y.; Wan, J.-P. *Tetrahedron* **2015**, *71* (36), 6094-6098.

New chromone from the stems of *Harrisonia perforata*

Thawatchai Sriwongsa, Waraluck Chaichompoo, Wachirachai Pabuprapap, and Apichart Suksamrarn*

Department of Chemistry and Center of Excellence for Innovation in Chemistry, Faculty of Science, Ramkhamhaeng University, Bangkok, 10240, Thailand

**E-mail: asuksamrarn@yahoo.com*

Abstract:

Phytochemical investigation of the stems of *Harrisonia perforata* (Blanco) Merr. (Simaroubaceae) led to the isolation of one new chromone, peucenin-5,7-di-*O*-methyl ether (**1**), together with six known chromones, peucenin-7-methyl ether (**2**), alloptaeroxylin (**3**), *O*-methylalloptaeroxylin (**4**), perforatic acid (**5**), perforatic acid methyl ester (**6**), and heteropeucenin-5-methoxy-7-methyl ether (**7**). The structure of the new compound was elucidated by spectroscopic data. The known compounds were identified by comparisons of their spectroscopic data and physical properties with those reported in the literature.

1. Introduction

The genus *Harrisonia* belongs to the Simaroubaceae family, a group of shrub or small trees consisting of three to four species distributed from tropical Africa and Southeast Asia to northern Australia.[1] *Harrisonia perforata* (Blanco) Merr., locally known in Thai as 'Khontha', is native to Southeast Asia and is the only species of this genus in Thailand.[2,3] In China, the roots of this plant are used in traditional medicine for the treatment of malaria and boils.[4] In Thailand, *H. perforata* roots have long been used as a folk medicine; which is one of five different herbs in the famous Thai traditional medicine Benchalokawichian remedy, notified in the List of Medicine Products of the Thailand National List of Essential Drugs A.D. 2006 as an antipyretic agent.[5] Chromones, limonoids and polyketides are reported as the most abundant in the several parts of this plant with their fascinating biological activities, for example, anti-malarial, anti-inflammatory, anti-mycobacterial, anti-plasmodial anti-cancer, and cytotoxic activities.[6–11] In our continuing efforts to investigate structurally diverse and biologically active compounds from Thai medicinal plants, we herein report the isolation and structural characterization of one new chromone (**1**) and six known chromones (**2–7**) from the stems of *H. perforata.*

2. Materials and Methods

2.1 General

IR spectra were recorded on a Perkin-Elmer FT-IR 400 spectrophotometer. ^{1}H and ^{13}C NMR spectra were recorded on Bruker ASCEND 400 FT-NMR spectrometers. High-resolution ESI-TOF mass spectra were obtained using a Bruker micrOTOF-QII mass spectrometer. Unless indicated otherwise, column chromatography and TLC were carried out using Merck Silica gel 60 (particle sizes less than 63 µm and 63–200 µm) and Merck pre-coated silica gel 60 F_{254} plates, respectively. Sephadex LH-20 (GE Healthcare) was used for gel filtration chromatography. Spots on TLC were detected under UV light and by spraying with anisaldehyde-H_2SO_4 reagent followed by heating.

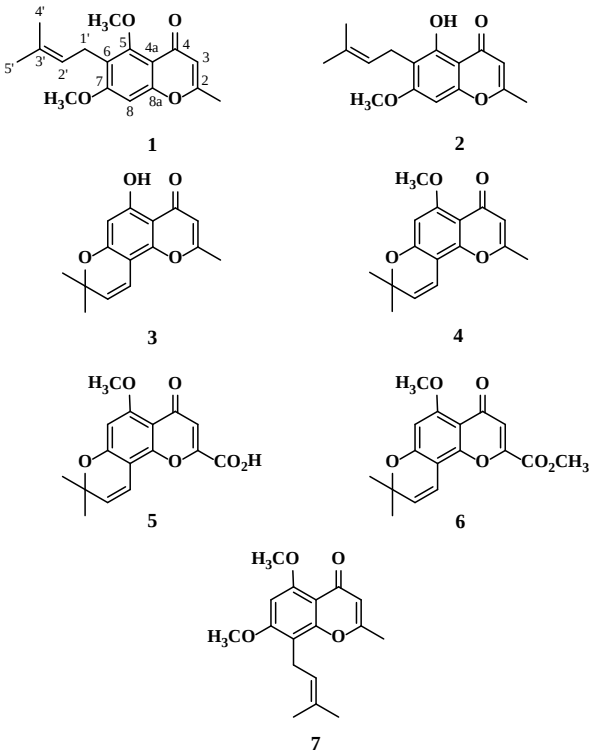

Figure 1. Chemical structures of compounds **1–7**

2.2 Plant Material

The stems of *H. perforata* were collected from Namoungpet subdistrict, Sikao district, Trang, in May 2021, and the plant species was identified by Assoc. Prof. Nopporn Dumrongsiri, Ramkhamhaeng University. A voucher specimen is deposited at the Faculty of Science,

Ramkhamhaeng University (Apichart Suksamrarn, No. 108).

2.3 Extraction and Isolation

The fresh stems of *H. perforata* (5.0 kg) were chopped into small pieces, air-dried, powdered, and macerated successively with *n*-hexane, EtOAc, and MeOH at room temperature (20 L × 3 for each solvent). The filtered solution from each extraction was evaporated to dryness under reduced pressure at 40–45 ºC to give the hexane (83.6 g), EtOAc (119.2 g), and MeOH (157.0 g) extracts.

The *n*-hexane extract (74.2 g, pale brownish yellow viscous oil), upon standing at room temperature, pale yellow solid precipitated, which was filtered and washed with 3% CH_2Cl_2 in *n*-hexane to yield compound **2** (13.86 g).

The EtOAc extract (100.0 g) was fractionated by column chromatography using a gradient solvent system of *n*-hexane, *n*-hexane–EtOAc, EtOAc, EtOAc–MeOH, and MeOH with increasing amounts of the more polar solvent. The eluates were examined by TLC, and ten combined fractions (E1–E10) were obtained. Fraction E4 (18.2 g) was chromatographed on a silica gel column eluting with *n*-hexane to give four subfractions (E4.1–E4.4). Subfraction E4.3 (1.2 g) was recrystallized from CH_2Cl_2–*n*-hexane to afford compound **3** (20.1 mg). Fraction E5 (29.6 g) was purified by crystallization in EtOAc–*n*-hexane to provide compound **4** (3.9 g), and the mother liquor was column chromatographed using 20% CH_2Cl_2 in *n*-hexane as eluent to give four subfractions (E5.1–E5.4). Subfraction E5.2 (2.7 g) was purified by Sephadex LH-20 column eluting with 40% CH_2Cl_2 in MeOH to yield compound **5** (834.2 mg). Fraction E8 (20.2 g) was chromatographed using EtOAc as an eluent to give five subfractions (E8.1–E8.5). Subfraction E8.2 (824 mg) was chromatographed on a Sephadex LH-20 column eluting with 30% CH_2Cl_2 in MeOH to obtain compound **1** (32.0 mg). Subfraction E8.4 (1.6 g) was repeatedly column chromatographed using 30% *n*-hexane in EtOAc as eluent to provide compound **7** (235.8 mg).

The MeOH extract (140.3 g) was fractionated by column chromatography using a gradient solvent system of EtOAc, EtOAc–MeOH, and MeOH with increasing amounts of the more polar solvent. The eluates were examined by TLC to give eight combined fractions (M1–M8). Fraction M4 (5.3 g) was chromatographed on Sephadex LH-20 column eluting with MeOH to yield compound **6** (13.7 mg). The solid, which was obtained from fraction M6 (46.7 g), was filtered and washed with MeOH to give compound **5** (6.4 g).

2.3.1 Peucenin-5,7-di-*O*-methyl ether (1)

Colorless crystals; m.p. 152–155 °C; IR (ATR) ν_{max} 3068, 2926, 2842, 1653, 1627, 1596, 1443, 1322, 1090, 841 cm^{-1}; ^1H and ^{13}C NMR data ($CDCl_3$), see Table 1; HR-TOFMS (ESI^+) *m/z* 311.1260 $[M + Na]^+$ (calcd. for $C_{17}H_{20}O_4Na$, 311.1254).

Table 1. ^1H (400 MHz) and ^{13}C (100 MHz) NMR data of compound **1** in $CDCl_3$

Position	δ_H (*J* in Hz)	δ_C	HMBC
2	-	163.4	-
3	6.01, *s*	111.1	C-4a, 2-CH_3
4	-	178.2	-
4a	-	108.3	-
5	-	156.7	-
6	-	109.7	-
7	-	160.9	-
8	6.35, *s*	91.6	C-4, C-4a, C-6, C-7, C-8a, C-1′
8a	-	159.2	-
1′	3.38, *d* (7.3)	21.8	C-5, C-6, C-7, C-2′, C-3′, C-5′
2′	5.12, *br t* (7.3)	121.9	C-6, C-1′, C-4′, C-5′
3′	-	131.7	-
4′	1.76, *s*	17.8	C-6, C-2′, C-3′, C-5′
5′	1.64, *s*	25.7	C-6, C-2′, C-3′, C-4′
2-CH_3	2.27, *s*	19.9	C-2, C-3
5-OCH_3	3.93, *s*	56.3	C-5
7-OCH_3	3.91, *s*	55.8	C-7, C-8

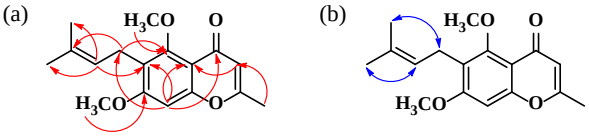

Figure 2. (a) Selected HMBC correlations and (b) key NOE correlations of compound **1**

2.3.2 Peucenin-7-methyl ether (2)

Yellow needles; m.p. 156-157 °C; IR (ATR) ν_{max} 3328, 3074, 2997, 2914, 2848, 1660, 1617, 1592, 1414, 1327, 1076, 854 cm^{-1}; ^1H NMR ($CDCl_3$, 400 MHz) δ_H 12.74 (1H, *s*, 5-OH), 6.32 (1H, *s*, H-8), 5.96 (1H, *s*, H-3), 5.11 (1H, *br t*, *J* = 7.3 Hz, H-2′), 3.84 (3H, *s*, 7-OCH_3), 3.33 (2H, *d*, *J* = 7.2 Hz, H-1′), 2.32 (3H, *s*, 2-CH_3), 1.75 (3H, *s*, CH_3-4′), 1.63 (3H, *br s*, CH_3-5′); ^{13}C NMR ($CDCl_3$, 100 MHz): δ_C 182.9 (C-4), 166.6 (C-2), 162.7 (C-7), 160.3 (C-8a), 154.5 (C-5), 131.5

(C-3′), 121.9 (C-2′), 108.1 (C-3), 107.5 (C-6), 104.5 (C-4a), 94.8 (C-8), 55.8 (7-OCH_3), 25.6 (C-5′), 21.4 (C-1′), 20.5 (2-CH_3), 17.6 (C-4′); HR-TOFMS (ESI^+) *m/z* 297.1111 $[M + Na]^+$ (calcd. for $C_{16}H_{18}O_4Na$, 297.1097).

2.3.3 Alloptaeroxylin (3)

Yellow needles; m.p. 234-236 °C; IR (ATR) ν_{max} 3267, 2942, 1661, 1575, 1428, 1338, 1276, 1121, 839 cm^{-1}; ^1H NMR ($CDCl_3$, 400 MHz) δ_H 12.73 (1H, *br*, 5-OH), 6.62 (1H, *d*, *J* = 10.0 Hz, H-1′), 6.20 (1H, *s*, H-6), 5.99 (1H, *s*, H-3), 5.53 (1H, *d*, *J* = 10.0 Hz, H-2′), 2.33 (3H, *s*, 2-CH_3), 1.43 (6H, *s*, CH_3-4′, CH_3-5′); ^{13}C NMR ($CDCl_3$, 100 MHz) δ_C 182.5 (C-4), 166.3 (C-2), 161.6 (C-5), 159.2 (C-7), 152.3 (C-8a), 127.3 (C-2′), 114.7 (C-1′), 108.7 (C-3), 104.9 (C-4a), 101.0 (C-8), 100.1 (C-6), 77.8 (C-3′), 28.1 (C-4′, C-5′), 20.3 (2-CH_3); HR-TOFMS (ESI^+) *m/z* 281.0787 $[M + Na]^+$ (calcd. for $C_{15}H_{14}O_4Na$, 281.0784).

2.3.4 *O*-methylalloptaeroxylin (4)

Yellow needles; m.p. 225-226 °C; IR (ATR) ν_{max} 3019, 2976, 1658, 1598, 1567, 1463, 1388, 1335, 1269, 1119, 1083, 829 cm^{-1}; ^1H NMR ($CDCl_3$, 400 MHz) δ_H 6.66 (1H, *d*, *J* = 10.0 Hz, H-1′), 6.25 (1H, *s*, H-6), 5.97 (1H, *s*, H-3), 5.53 (1H, *d*, *J* = 10.0 Hz, H-2′), 3.88 (3H, *s*, 5-OCH_3), 2.26 (3H, *s*, 2-CH_3), 1.44 (6H, *s*, CH_3-4′, CH_3-5′); ^{13}C NMR ($CDCl_3$, 100 MHz) δ_C 177.6 (C-4), 162.5 (C-2), 160.5 (C-5), 157.5 (C-7), 154.2 (C-8a), 127.2 (C-2′), 115.2 (C-1′), 111.8 (C-3), 108.4 (C-4a), 102.3 (C-8), 96.3 (C-6), 77.9 (C-3′), 56.3 (5-OCH_3), 28.1 (C-4′, C-5′), 19.7 (2-CH_3); HR-TOFMS (ESI^-) *m/z* 271.0967 $[M - H]^-$ (calcd. for $C_{16}H_{15}O_4$, 271.0975).

2.3.5 Perforatic acid (5)

White amorphous solid; IR (ATR) ν_{max} 3234, 3085, 2947, 1608 (very broad), 1542, 1468, 1390, 1331, 1269, 1115, 1060, 812, 757 cm^{-1}; ^1H NMR (CD_3OD, 400 MHz) δ_H 7.06 (1H, *d*, *J* = 10.0 Hz, H-1′), 6.79 (1H, *s*, H-3), 6.44 (1H, *s*, H-6), 5.69 (1H, *d*, *J* = 10.0 Hz, H-2′), 3.88 (3H, *s*, 5-OCH_3), 1.47 (6H, *s*, CH_3-4′, CH_3-5′); ^{13}C NMR (CD_3OD, 100 MHz) δ_C 181.3 (C-4), 166.3 (2-CO_2H), 161.8 (C-5), 160.3 (C-8a), 159.0 (C-2), 155.7 (C-7), 128.8 (C-2′), 116.5 (C-1′), 114.0 (C-3), 109.9 (C-4a), 104.5 (C-8), 98.1 (C-6), 79.7 (C-3′), 56.8 (5-OCH_3), 28.6 (C-4′, C-5′); HR-TOFMS (ESI^+) *m/z* 325.0684 $[M + Na]^+$ (calcd. for $C_{16}H_{14}O_6Na$, 325.0682).

2.3.6 Perforatic acid methyl ester (6)

Yellow needles; m.p. 228-229 °C; IR (ATR) ν_{max} 3012, 2928, 2853, 1740, 1648, 1597, 1568, 1456, 1397, 1248, 1198, 1129, 771 cm^{-1}; ^1H NMR ($CDCl_3$, 400 MHz) δ_H 6.91 (1H, *s*, H-3), 6.80 (1H, *d*, *J* = 10.0 Hz, H-1′), 6.31 (1H, *s*, H-6), 5.58 (1H, *d*, *J* = 10.0 Hz, H-2′), 3.95 (3H, *s*, 2-CO_2CH_3), 3.91 (3H, *s*, 5-OCH_3), 1.47 (6H, *s*, C-4′, C-5′); ^{13}C NMR ($CDCl_3$, 100 MHz) δ_C 177.0 (C-4), 161.1 (2-$\underline{C}O_2CH_3$), 160.6 (C-5), 158.7 (C-7), 153.7 (C-8a), 149.4 (C-2), 127.6 (C-2′), 116.6 (C-3) 115.0 (C-1′), 109.6 (C-4a), 102.8 (C-8), 97.0 (C-6), 78.5 (C-3′), 56.5 (5-OCH_3), 53.3 (2-$CO_2\underline{CH_3}$), 28.3 (C-4′, C-5′); HR-TOFMS (ESI^+) *m/z* 339.0839 $[M + Na]^+$ (calcd. for $C_{17}H_{16}O_6Na$, 339.0811).

2.3.7 Heteropeucenin-5-methoxy-7-methyl ether (7)

Colorless crystals; m.p. 150–153 °C; IR (ATR) ν_{max} 3069, 2925, 1659, 1600, 1457, 1389, 1326, 1176, 1091, 839, 754 cm^{-1}; ^1H NMR ($CDCl_3$, 400 MHz) δ_H 6.37 (1H, *s*, H-6), 6.14 (1H, s, H-3), 5.13 (1H, *t*, *J* = 7.2 Hz, H-2′), 3.94 (3H, *s*, 5-OCH_3), 3.92 (3H, *s*, 7-OCH_3), 3.40 (2H, *d*, *J* = 7.2 Hz, H-1′), 2.30 (3H, *s*, 2-CH_3), 1.78 (3H, *s*, C-4′), 1.65 (3H, *s*, C-5′); ^{13}C NMR ($CDCl_3$, 100 MHz) δ_C 178.2 (C-4), 163.8 (C-2), 161.1 (C-5), 159.3 (C-7), 156.7 (C-8a), 131.8 (C-3′), 121.8 (C-2′), 110.8 (C-3) 109.7 (C-8), 108.0 (C-4a), 91.6 (C-6), 56.4 (5-OCH_3), 55.9 (7-OCH_3), 25.8 (C-5′), 21.8 (C-1′), 20.0 (2-CH_3), 17.8 (C-4′); HR-TOFMS (ESI^+) *m/z* 311.1263 $[M + Na]^+$ (calcd. for $C_{17}H_{20}O_4Na$, 311.1254).

3. Results & Discussion

The investigation of the stems of *H. perforata* resulted in the isolation of a new chromone, peucenin-5,7-di-*O*-methyl ether (**1**), along with six known chromones, which were identified as peucenin-7-methyl ether (**2**),[6] alloptaeroxylin (**3**),[4] *O*-methylalloptaeroxylin (**4**),[6] perforatic acid (**5**),[6] perforatic acid methyl ester (**6**)[6] and heteropeucenin-5-methoxy-7-methyl ether (**7**)[7] (Figure 1). The structures of the known compounds were identified by spectroscopic data (^1H and ^{13}C NMR and HR-TOFMS) comparisons made with the literature.

Compound **1** was obtained as colorless crystals. The HR-TOFMS spectrum gave a sodiated molecular ion peak at *m/z* 311.1260 $[M + Na]^+$ (calcd. for $C_{17}H_{20}O_4Na$, 311.1254), which was consistent with the molecular formula $C_{17}H_{20}O_4$. The IR spectrum exhibited absorption bands corresponding to chromone carbonyl (1653 cm^{-1}), conjugated olefinic (1627 cm^{-1}), and aromatic (3068, 1596, and 1443 cm^{-1}) functionalities. The ^1H NMR data (Table 1) of compound **1** revealed the presence of an olefin

methyl proton at δ_H 2.27 (*s*, 1H, 2-CH_3), a *cis*-olefinic proton at δ_H 6.01 (*s*, 1H, H-3), a singlet aromatic proton at δ_H 6.35 (1H, H-8), two singlet aromatic methoxy protons at δ_H 3.93 and δ_H 3.91 (each 3H, 5-OCH_3 and 7-OCH_3), which indicated a chromone skeleton.[12] The ^{1}H NMR spectrum of **1** also showed signals for a prenyl group at δ_H 3.38 (*d*, 2H, *J* = 7.3 Hz, H-1′), δ_H 5.12 (*br t*, 1H, *J* = 7.3 Hz, H-2′), δ_H 1.76 (*s*, 3H, H-4′) and δ_H 1.64 (*s*, 3H, H-5′). The ^{13}C NMR and DEPT-135 data showed the presence of seventeen carbon resonances attributed to eight quaternary, three methine, one methylene, and five methyl carbons. The location of two methoxy protons was confirmed by the HMBC correlations of the 5-methoxy protons with C-5 (δ_C 56.3) and the 7-methoxy protons with C-7 (δ_C 55.8). Furthermore, the HMBC correlations of H-1′ with C-5 (δ_C 156.7), C-6 (δ_C 109.7), C-7 (δ_C 160.9), C-2′ (δ_C 121.9), C-3′ (δ_C 131.7) and C-5′ (δ_C 25.7) suggested that the prenyl group was connected to C-6 (Figure 2a). The key NOE correlations between H-1′ and C-4′, and H-2′ and C-5′ (Figure 2b) were in agreement with the orientation of methyl groups of a prenyl moiety. The spectroscopic data above led to the identification of compound **1** as peucenin-5,7-di-*O*-methyl ether.

4. Conclusion

In summary, a new chromone (**1**) and six known chromones (**2**–**7**) have been isolated from the stems of *H. perforata*.

Acknowledgments

This work was supported by Ramkhamhaeng University. TS acknowledges financial support from the Center of Excellence for Innovation in Chemistry (PERCH-CIC), Ministry of Higher Education, Science, Research and Innovation.

References

1. Yamamoto, T.; Fijridiyanto, I. A.; Tobe, H. *Bot. J. Linn. Soc.* **2015**, *180*, 386–400.
2. Smitinand, T. Thai Plant Names, rev. ed. Bangkok, Thailand: Office of the Forest Herbarium, Department of Natural Park, Wildlife and Plant Conservation, 2014; p. 286.
3. Sombatsri, A.; Sribuhom, T.; Phusrisom, S.; Kukongviriyapan, V.; Yenjai C. *Phytochem. Lett.* **2021**, *44*, 192–196.
4. Tanaka, T.; Koike, K.; Mitsunaga, K.; Narita, K.; Takano, S.; Kamioka, A.; Sase, E.; Ouyang, Y.; Ohmoto, T. *Phytochemistry* **1995**, *40*, 1787–1790.
5. Singharachai, C.; Palanuvej, C.; Kiyohara, H.; Yamada, H.; Ruangrungsi, N. *Pharmacog. J.* **2011**, *3*, 1–11.
6. Choodej, S.; Sommit, D.; Pudhom, K. *Bioorg. Med. Chem.* **2013**, *23*, 3896–3900.
7. Cheenpracha, S.; Chokchaisiri, R.; Ganranoo, L.; Maneerat, T.; Rujanapun, N.; Charoensup, R.; Laphookhieo, S.; Injan, N.; Nokbin, S. *Phytochem. Lett.* **2022**, *49*, 192–196.
8. Tuntiwachwuttikul, P.; Phansa, P.; Pootaeng-on, Y.; Taylor, W. C. *Chem. Pharm. Bull.* **2006**, *54*, 44–47.
9. Yin, S.; Chen, X.; Su, Z. S.; Yang, S. P.; Fan, C. Q.; Ding, J.; Yue, J. M. *Tetrahedron* **2009**, *65*, 1147–1152.
10. Thadaniti, S.; Archakunakorn, W.; Tuntiwachwuttikul, P.; Bremner, J. B. *J. Sci. Soc. Thailand* **1994**, *20*, 183–187.
11. Li, S.; Yan, Z.; Huang, X.; Song, S. *A. J. Trad. Med.* **2018**, *13*, 20–29.
12. Satake, T.; Kamiya, K.; Saiki, Y.; Hama, T.; Fujimoto, Y.; Endang, H.; Umar, M. *Phytochemistry* **1999**, *50*, 303–306.

Antibiotic resistance progress and challenges among gram-negative and gram-positive pathogens in southern Thailand: A retrospective 10-year study

Phanvasri Saengsuwan[1]*, Narongdet Kositpantawong[2], Soontara Kawila[3], and Wichien Patugkaro[4]

[1]*Department of Biomedical Sciences and Biomedical Engineering, Faculty of Medicine, Prince of Songkla University, Hat Yai, Songkhla, Thailand*

[2]*Department of Internal Medicine, Faculty of Medicine, Prince of Songkla University, Hat Yai, Songkhla, Thailand*

[3]*Microbiology Unit, Department of Pathology, Faculty of Medicine, Prince of Songkla University, Hat Yai, Songkhla, Thailand*

[4]*Microbiology Clinical Pathology Division, Hat Yai Hospital, Hat Yai, Songkhla, Thailand*

**E-mail: sphanvas@medicine.psu.ac.th*

Abstract:

Multidrug-resistant bacteria pose a significant threat worldwide, including in Southern Thailand, where vancomycin-resistant enterococci (VRE) and *Pseudomonas aeruginosa* remain a public health concern. To investigate the epidemiology and antibiotic resistance patterns of these bacteria, a retrospective descriptive study was conducted on VRE and *P. aeruginosa* isolates from tertiary care hospitals, Southern Thailand over a 10-year period. Of the 304 isolates analyzed, 94 (30.9%) and 210 (69.1%) were found to be VRE and *P. aeruginosa*, respectively, with the highest rates of infection in 2014 and 2016. VRE infections were more common in women, while *P. aeruginosa* infections were more common in men. Most of the positive isolates were from sputum and the genitourinary tract, with the highest rates occurring in medical departments (81; 26.6%), followed by emergency room (42; 13.8%), surgical ward (40; 13.2%), and operation room (33; 10.9%). Resistance to commonly used antibiotics was high, particularly for carbapenems in *P. aeruginosa* and beta-lactamase inhibitors in VRE. Multidrug-resistant VRE patterns were found in all isolates, while *P. aeruginosa* showed a range of resistance patterns, with the carbapenem-resistant pattern being the most prevalent (CR; 121, 57.6%), followed by the carbapenem-resistant with multidrug-resistant pattern (CR-MDR; 72, 34.3%), and the multidrug-resistant pattern (MDR; 17, 8.1%). Therefore, it is important to monitor the distribution of bacteria and their antibiotic resistance to revise certain empirical criteria, and control may provide useful insights into disease epidemiology.

1. Introduction

The emergence of multidrug-resistant bacteria is a major public health concern because it limits the effectiveness of antibiotics, which are a cornerstone of modern medicine. Without effective antibiotics, routine medical procedures such as surgery, chemotherapy, and organ transplants become much riskier, and in some cases, impossible. One of the main factors driving the emergence of multidrug-resistant bacteria is the overuse and misuse of antibiotics. When antibiotics are used excessively or inappropriately, bacteria can quickly develop resistance to them. In addition, the lack of new antibiotics being developed is also a concern, as it limits the ability of healthcare professionals to effectively treat infections caused by multidrug-resistant bacteria.[1]

Vancomycin-resistant enterococci and *P. aeruginosa* are common multidrug-resistant organisms that cause infections in hospitals. According to the CDC, VRE causes over 9,000 life-threatening infections and 1,200 deaths per year in the US. Similarly, *P. aeruginosa* is a leading cause of hospital-acquired infections, with mortality rates ranging from 10% to 60%.[2-3]

Because the incidence of these pathogens is increasing among hospitalized patients, managing their prevalence in healthcare units has become a major issue for public health professionals and our hospitals in Southern Thailand. If not, treating them can be challenging because fewer medications are effective against these resistant bacteria. However, there is limited data on the prevalence of multidrug-resistant pathogens like VRE and *P. aeruginosa* in clinical specimens that has not been published in a timely manner. Thus, understanding the epidemiology and resistance patterns, including candidate pathogens, particularly VRE and *P. aeruginosa*, is essential for infection control and the prevention of a growing global health crisis. The goal of the study was to elucidate a retrospective study to update the antibiotic strategy for Gram-negative and Gram-positive isolates in tertiary care hospitals, Southern Thailand.

2. Materials and Methods

2.1 Sample collection

Pathogens were isolated from clinical specimens that were collected from patients who had presented to tertiary hospitals from Southern Thailand during January 2011 to December 2021. A total of 304 Gram-positive (94, 30.9%) and Gram-negative strains (210, 69.1%) were isolated and analyzed retrospectively. Ethical approval was accepted from the Ethics Committees at Faculty of Medicine, Prince of Songkla University (REC58-183-04-8 and REC-63-557-4-7).

2.2 Bacteriological identification and drug sensitivity test

All bacterial strain isolates were grown on tryptic soy agar plates at 37°C overnight to identify species using a routine biochemical test such as catalase testing, oxidase testing, and substrate utilization tests fit under the category of traditional tests.[4] Antimicrobial susceptibility tests were performed using the disc diffusion method according to the Clinical and Laboratory Standards Institute guidelines.[5] Both bacteria characterization and antibiotic susceptibility tests were conducted at Microbiology Unit, Department of Pathology, Faculty of Medicine, Prince of Songkla University and Hat Yai Hospital.

Antimicrobial susceptibility tests for enterococci were performed using the disk diffusion method according to CLSI guidelines (CLSI 2019). Each disk (Becton Dickinson, Heidelberg, Germany) contained ampicillin (AM, 10 µg), cefoperazone-sulbactam (sulperazone) (SPZ, 75/30 µg), cefotaxime (CTX, 30 µg), ceftazidime (CAZ, 30 µg), ceftriaxone (CRO, 30 µg), ciprofloxacin (CIP, 5 µg), colistin (DA, 10 µg), ertapenem (ETP, 10 µg), gentamicin (GM, 10 µg), imipenem (IMP, 10 µg), meropenem (MEM, 10 µg), norfloxacin (NOR, 10 µg), penicillin (P, 10 µg), tazocin (TZP, 100/10 µg), and vancomycin (VA, 30 µg).

Then, drug susceptibility was tested for *Enterobacteriaceae* and interpreted using disk diffusion test according to the 2015 CLSI guidelines.[6] Each disk (Becton Dickinson, Heidelberg, Germany) contained amikacin (AK, 30 µg), ceftazidime (CAZ, 30 µg), ciprofloxacin (CIP, 5 µg), colistin (DA, 10 µg), gentamicin (GM, 10 µg), IMP (10 µg), MEM (10 µg), norfloxacin (NOR, 10 µg), cefoperazone/sulbactam (Sulperazone) (SPZ, 75/30 µg), ceftriaxone (CRO, 30 µg), ertapenem (ERT, 10 µg), levofloxacin (LVX, 5 µg), sitafloxacin (STFX, 5 µg), cefotaxime (CTX, 30 µg), or piperacillin/tazobactam (Tazocin) (TZP, 100 µg).[7]

Drug-resistant categories were defined as follows: multidrug-resistant (MDR) strains were defined as isolates resistant to at least one agent in ≥3 different antimicrobial categories; extensive drug-resistant (XDR) strains were defined as those resistant to at least one agent in all but two or fewer antimicrobial categories; and pan drug-resistant (PDR) strains were defined as those resistant to all classes except colistin.[8]

2.3 Data analysis

Demographic data are reported as counts with percentages or median values. SPSS Statistics, version 23 (SPSS inc., Chicago, IL, USA), was utilized to analyze all statistical data.

3. Results & Discussion

3.1 Characteristics of the study population

A total of 304 patient's data that were enrolled from various clinical specimens was recorded from the year 2011–2021 for assessment of VRE and *P. aeruginosa* infection. The incidence of *P. aeruginosa* and VRE infections was the highest in 2016 (77.1%) and 2014 (28.7%), respectively (Figure 1). *P. aeruginosa* was the predominant isolate found more than 2.5 times as often as VRE isolates. Out of which 161 (53%) were males and 143 (47.0%) were females, whereas the age ranged from 0.08 to 106 years, with mean and median ages of 62 and 63 years, respectively, similar to an earlier study in Japan that showed age at 73 in bacteremia among ICU-admitted patients with severe sepsis.[9] The occurrence of *P. aeruginosa* infection was higher in males than in females, particularly after the age of 65 years. In contrast, the prevalence of VRE infection was higher in females than males. Of these, sputum was the most common specimen (119, 39.1%), followed by urine (67, 15.2%), body fluid (38, 12.5%), and blood (23, 7.6%). The majority of these were detected in medical wards (112, 36.8%), followed by intensive care units (50, 16.4%), emergency room (42, 13.8%), and surgical wards (40, 13.2%). More demographic wdata are presented in Table 1.

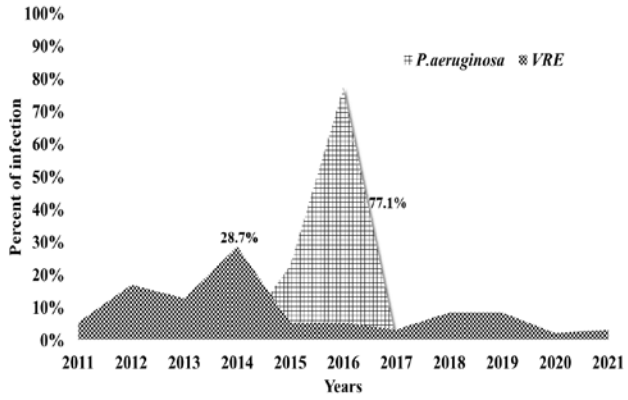

Figure 1. Distribution of multidrug resistant VRE and *P. aeruginosa* isolates among clinical isolates from 2011 to 2021.

Table 1. The Demographic and clinical characteristics of multidrug resistant VRE and *P. aeruginosa* isolates among clinical isolates in tertiary care hospitals, Southern Thailand, 2011–2021.

Variable	No. of infection		Total No. (*n*=304, %)
	P. aeruginosa *n* (%)	VRE *n* (%)	
Gender			
male	122 (58.1)	39 (41.5)	161 (53.0)
female	88 (41.9)	55 (58.5)	143 (47.0)
median age	62	63	
Age (yrs.)			
0-12	24 (11.4)	4 (4.3)	28 (9.2)
13-24	7 (3.3)	6 (6.4)	13 (4.3)
25-64	82 (39.0)	41 (43.6)	123 (40.5)
65 up	97 (46.2)	43 (45.7)	140 (46.1)
Infection sites			
urine	31 (14.8)	36 (38.3)	67 (22.0)
rectal	0	17 (18.1)	17 (5.6)
body fluid (penrose drain, bronchial wash, percutaneous nephrostomy, corneal ulcer, bile, and pleural fluid)	18 (8.6)	20 (21.3)	38 (12.5)
sputum	119 (56.7)	0	119 (39.1)
tissue	16 (7.6)	8 (8.5)	24 (7.9)
pelvic	0	1 (1.1)	1 (0.3)
pus	13 (6.2)	1 (11)	14 (4.6)
blood	12 (5.7)	11 (11.7)	23 (7.6)
corneal	1 (0.5)	0	1 (0.3)
Source of infections			
Medical wards	76 (36.2)	36 (38.3)	112 (36.8)
Gynecology ward	3 (1.4)	8 (8.5)	11 (3.6)
Intensive Care Units	39 (18.6)	11 (11.7)	50 (16.4)
Surgical ward	22 (10.5)	18 (19.1)	40 (13.2)
Operating room	24 (11.4)	9 (9.6)	33 (10.9)
Orthopedic ward	0	2 (2.1)	2 (0.7)
Pediatric ward	10 (4.8)	3 (3.2)	13 (4.3)
Emergency room	35 (16.7)	7 (7.4)	42 (13.8)
Ophthalmology ward	1 (0.5)	0	1 (0.3)

Table 2. Antimicrobial susceptibility profile of VRE and *P. aeruginosa* clinical isolates in tertiary care hospitals, Southern Thailand between 2011-2021 given as numbers and percentages of isolates.

Class	Antimicrobial agents	VRE (*n* = 94)		*P. aeruginosa* (*n* = 210)		Total No. (*n*=304, %)	
		R (%)	S (%)	R (%)	S (%)	R (%)	S (%)
Aminoglycoside	AK, AM, GM	13 (13.8)	81 (86.2)	106 (50.5)	105 (50.0)	119 (39.1)	186 (61.2)
Beta-lactamase inhibitors	P, TZP	72 (76.6)	22 (23.4)	0	105 (50.0)	72 (23.7)	127 (41.8)
Carbapenems	ETP, IMP, MEM	62 (66.0)	32 (34.0)	194 (92.4)	16 (7.6)	256 (84.2)	48 (15.8)
Cephalosporin	CAZ, CRO, CTX, SPZ	13 (13.8)	80 (85.1)	100 (47.6)	110 (52.4)	113 (37.2)	190 (62.5)
Fluoroquinolones	CIP, LVX, NOR	7 (7.4)	87 (92.6)	112 (53.3)	98 (46.7)	119 (39.1)	185 (60.9)
Glycopeptide	VA	94 (100.0)	0	0	0	94 (30.9)	0
Polymicin	DA	4 (4.3)	0	0	0	4 (1.3)	0

Legend: AK: amikacin; AM: ampicilin; CTX: cefotaxime; FOX: cefoxitin; CAZ: ceftazidime; CRO: ceftriaxone; CIP: ciprofloxacin; SXT: trimethoprim-sulfamethoxazole; GM: gentamicin; IPM: imipenem; NOR: norfloxacin; SPZ: sulperazone; MEM: meropenem; TZP: piperacilin/tazobactam; ETP: ertapenem; LVX: levofloxacin; VA: vancomycin; DA: colistin; P: penicillin; R: resistance; S: susceptible.

3.2 Antimicrobial Susceptibility Patterns

Antibiotic resistance patterns of VRE and *P. aeruginosa* isolates are shown in Table 2. Among the VRE isolates, 94 (100%), 72 (76.6%), and 62 (66.0%) were resistant to VA, P/TZP, and ETP/IMP/MEM, respectively. The isolates were mostly susceptible to AK, TZP, and GM (38.4%, 36.3%, and 35.3%, respectively).

The antimicrobial susceptibility testing result showed that *P. aeruginosa* isolates were found to be resistant to aminoglycosides and fluoroquinolones by more than 50%. The lowest antibiotic resistance was recorded against cephalosporin, 100 (47.6%). The carbapenem had almost comparable resistance patterns against both VRE and *P. aeruginosa*, at 256 (84.2%).

However, the antibiotic resistance profiles of multidrug resistant VRE and *P. aeruginosa* isolates from tertiary care hospitals in Southern Thailand were categorized into three patterns: CR, CR-MDR, and MDR pattern, with CR being predominant in *P. aeruginosa* isolates and MDR are predominant in VRE isolates with statistical significance ($P<0.05$) (Figure 2). No PDR isolates were detected.

This is the first report describing a ten-year resistance pattern retrospective analysis of the candidate Gram-positive and Gram-negative pathogens among clinical specimens in tertiary care hospitals, Southern Thailand. The overall number is stable. Due to the alarming system of infectious control in our hospital and nearby hospitals have consequently established stringent

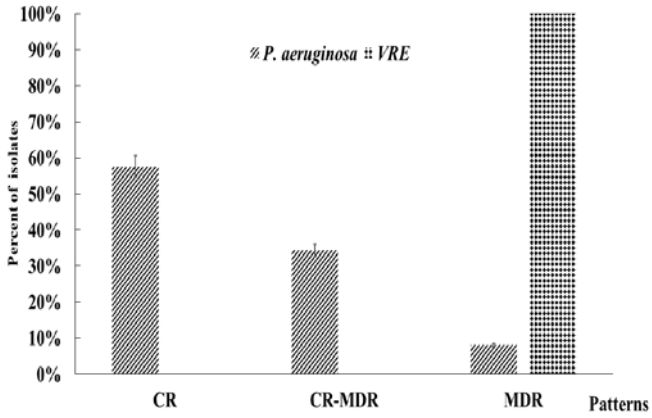

Figure 2. Antibiotic resistance profiles of multidrug resistant VRE and *P. aeruginosa* isolates from tertiary care centers, Southern Thailand over 10 years.
Carbapenem- resistant (CR), carbapenem-resistant with multidrug-resistant (CR-MDR), and multidrug-resistant (MDR).

infectious control measures, particular concerning bacterial infections. A robust alarm system is critical for promptly identifying and managing suspected infections, thus preventing the spread of bacteria throughout the healthcare setting.[10]

The elderly patients (aged >65 years) comprised a majority of the population, which had a higher prevalence than in other age groups, and both Gram-positive and Gram-negative infections were observed, consistent with findings from other studies, in China and elsewhere in the world.[11-12] This finding has implications for treatment

alternative for this age group and severe infections. Moreover, institutions may consider screening this patient population for multidrug-resistant pathogens before admitting them to prevent mortality.[13]

In this study, the prevalence of *P .aeruginosa* infection was the highest in sputum (119, 56.7%) while VRE infection was from urine (36, 38.3%). The findings were similar to the previous study, which was determined in the multiple clinical samples including wound swabs, sputum, and urine.[14-15] This prevalence rate was slightly greater and lower than previous rates at 10.29% and 61.2%, respectively.[16-17]

The distribution of both VRE and *P. aeruginosa* isolates among hospital wards indicated that the majority were from medical wards (112, 36.8%), ICUs (50, 16.4%), and surgical ward (40, 13.2%), respectively. These demonstrated that nosocomial transmission is a key risk factor for subsequent colonization and infection, despite deep cleaning and a strict policy for managing bacteremia infection.[18]

Furthermore, VRE and *P. aeruginosa* are MDR pathogens with limited therapy options; Patients suffer from increased morbidity and mortality.[19-20] The current study revealed resistance to aminoglycosides, fluoroquinolones, and cephalosporin in most of the tested isolates with the highest resistance rate to carbapenems (92.4%) among *P. aeruginosa* isolates, whereas 100% of the VRE isolates were highly resistant to glycopeptide.

For *P. aeruginosa*, the susceptibility rate against cephalosporin, aminoglycosides, and beta-lactamase inhibitors was about 50%, consistent with previous reports from Saudi Arabia, which revealed that aminoglycosides and fluoroquinolones susceptibilities were maintained at 49.3-56.7% and 40.0-43.3%, respectively.[21] Comparable results were found in the United States with ceftazidime (81.0%), meropenem (86.2%), and piperacillin-tazobactam (85.4%).[22]

Once more, the susceptibility to various tested fluoroquinolones, cephalosporin, and aminoglycosides accounted in 85.1–92.6% of the total VRE isolates which consist of the finding from Uganda.[23] These could be owing to variances in the type of infection, as well as various risk factors.[24]

The increase in drug resistance in MDR VRE not only complicates the diagnosis and management of patients infected with *Enterococcus faecium*, but also has implications for drug resistance and *P. aeruginosa*. This could be due to the vancomycin resistance gene being common in plasmid transposons and virulent *P. aeruginosa* isolates, causing a shift to the more virulent. [25-26] This serves as a reminder that, while some strains have a significant impact on patient outcomes, the medication resistance condition of other strains should not be dismissed.

4. Conclusion

A high percentage of CR-MDR among *P. aeruginosa* isolates and MDR VRE isolates are prevalent in Southern Thailand. Therefore, it is crucial to closely monitor changes in antibiotic resistance across various species. Despite this, it is important to note that *P. aeruginosa* infections still respond well to cephalosporins, while VRE infections remain susceptible to fluoroquinolones. Our findings offer up-to-date antimicrobial resistance profiles and valuable insights into the epidemiology of these diseases, aiding in the control of multidrug resistance in our region. Nonetheless, the effectiveness of future antimicrobial treatments hinges on a combination of both novel and existing agents to combat these multidrug-resistant pathogens. Addressing issues related to misuse and overuse of antibiotics, along with implementing molecular research monitoring for early detection, are also critical elements for success.

Acknowledgements

This study was supported by a grant from the Research and Development Office and the Faculty of Medicine, Prince of Songkla University, with a grant number of MED601339S and REC58-183-04-8, respectively.

References

1. Spellberg, B.; Bartlett, J. G.; Gilbert, D. N. *N. Engl. J. Med.* **2013**, *368* (4), 299-302.
2. Reynolds, D.; Kollef, M. *Drugs* **2021**, *81* (18), 2117-2131.
3. Levitus M, R. A., Perera TB. Vancomycin-Resistant *Enterococci*. (accessed Jul 17, 2023).
4. Cheesbrough, M., District laboratory practice in tropical countries, part 2. Cambridge university press: **2005**.
5. Clinical and Laboratory Standards Institute W, PA. Methods for dilution antimicrobial susceptibility tests for bacteria that grow aerobically; approved standard, 31st ed. CLSI document M100: Wayne, PA; **2021**. 2021.
6. Clinical and Laboratory Standards Institute (CLSI). 2015. Clinical and Laboratory Standards Institute, W., PA., Methods for dilution antimicrobial susceptibility tests for bacteria that grow aerobically; approved

standard, 10th ed. CLSI document M07-A10. Wayne, PA: **2015**.
7. Harrington, S.; Stock, F.; Kominski, A.; Campbell, J.; Hormazabal, J.; Livio, S.; Rao, L.; Kotloff, K.; Sow, S.; Murray, P. *J. Clin. Microbiol*. **2007**, *45* (3), 707-714.
8. Magiorakos, A. P.; Srinivasan, A.; Carey, R. B.; Carmeli, Y.; Falagas, M. E.; Giske, C. G.; Harbarth, S.; Hindler, J. F.; Kahlmeter, G.; Olsson-Liljequist, B.; Paterson, D. L.; Rice, L. B.; Stelling, J.; Struelens, M. J.; Vatopoulos, A.; Weber, J. T.; Monnet, D. L. *Clin. Microbiol. Infect*. **2012**, *18* (3), 268-281.
9. Komori, A.; Abe, T.; Kushimoto, S.; Ogura, H.; Shiraishi, A.; Saitoh, D.; Fujishima, S. *et al*. *Sci. Rep*. **2020**, *10* (1), 2983.
10. Morris, S.; Cerceo, E. *Antibiotics* **2020,** *9* (4), 196.
11. Hu, Y. Y.; Cao, J. M.; Yang, Q.; Chen, S.; Lv, H. Y.; Zhou, H. W.; Wu, Z.; Zhang, R. *China. Emerg. Infect. Dis.* **2019**, *25* (10), 1861-1867.
12. Esme, M.; Topeli, A.; Yavuz, B. B.; Akova, M. *Front. Med*. **2019**, *6*, 118.
13. Giacomini, E.; Perrone, V.; Alesandrini, D.; Paoli, D.; Nappi, C.; Degli Esposti, L. *Infect. Drug Resist*. **2021**, *14*, 849-858.
14. Chaudhari, V.; Gunjal, S.; Mehta, M. *India. Int. J. Med. Sci. Public Health* **2013**, *2* (2), 386-9.
15. Saengsuwan, P.; Kositpantawong, N.; Ingviya, N.; Singkhamanan, K. *Southeast Asian J. Trop. Med. Public Health* **2020**, *51* (6), 803-814.
16. Maharjan, N. *J. Nepal. Med. Assoc.* **2022**, *60* (252), 676-680.
17. Azzam, A.; Elkafas, H.; Khaled, H.; Ashraf, A.; Yousef, M.; Elkashef, A. A. *J. Egypt Public Health Assoc.* **2023**, *98* (1), 8.
18. Sumpradit, N.; Wongkongkathep, S.; Malathum, K.; Janejai, N.; Paveenkittiporn, W.; Yingyong, T.; Chuxnum, T. *et al. Bull World Health Organ* **2021**, *99* (9), 661-673.
19. Buetti, N.; Wassilew, N.; Rion, V.; Senn, L.; Gardiol, C.; Widmer, A.; Marschall, J. *Antimicrob. Resist. Infect. Control* **2019**, *8*, 16.
20. Zalipour, M.; Esfahani, B. N.; Havaei, S. A. *BMC Res. Notes* **2019**, *12* (1), 292.
21. Alnimr, A. M.; Alamri, A. M. *J. Taibah Univ. Medical Sci*. **2020**, *15* (3), 203-210.
22. Sader, H. S.; Huband, M. D.; Castanheira, M.; Flamm, R. K. *Antimicrob. Agents. Chemother*. **2017**, *61* (3).
23. Kateete, D. P.; Edolu, M.; Kigozi, E.; Kisukye, J.; Baluku, H.; Mwiine, F. N.; Najjuka, C. F., *BMC Infect. Dis.* **2019**, *19* (1), 486.
24. Bassetti, M.; Vena, A.; Croxatto, A.; Righi, E.; Guery, B. *Drugs Context*. **2018**, *7*, 212527.
25. Arredondo-Alonso, S.; Top, J.; Corander, J.; Willems, R. J. L.; Schürch, A. C. *Genome Med.* **2021**, *13* (1), 9.
26. Hassuna, N. A.; Mandour, S. A.; Mohamed, E. S. *Infect. Drug. Resist.* **2020**, *13*, 587-595.

Inhibition of *Staphylococcus aureus* biofilm formation by natural coumarins

Nattaruja Raksasat[1], Suphat Chantawarin[1], Natthapat Sawektreeratana[1], Sakchai Hongthong[2], Chutima Kuhakarn[1], and Chutima Jiarpinitnun[1,*]

[1]*Department of Chemistry and Center for Innovation in Chemistry (PERCH-CIC), Faculty of Science, Mahidol University, Rama VI Road, Bangkok, 10400, Thailand*
[2]*Division of Chemistry, Faculty of Science and Technology, Rajabhat Rajanagarindra University, Chachoengsao, 24000, Thailand*

**E-mail: chutima.jia@mahidol.ac.th*

Abstract:

Antibiotic resistance development in bacteria raise concerns worldwide. One of the most recognized pathogens that rapidly develop drug resistance is Gram-positive bacterium *Staphylococcus aureus* (*S. aureus*). The ability to form extracellular matrix called biofilm has been reported to strongly associate with drug resistance in *S. aureus*. Biofilm could shield bacteria from host's immune response and antibiotic treatment; therefore, a higher concentration of antibiotic is required to eradicate bacteria under biofilm state. This may attribute to drug resistance development. Here in, we searched for natural products that could inhibit *S. aureus* biofilm formation. Scopoletin and isofraxidin were isolated from *Mallotus spodocarpus* (Euphorbiaceae) plant. These coumarin adducts were first determined their ability to inhibit *S. aureus* growth using Kirby-Bauer disk diffusion susceptibility assay. The results indicated that these compounds could not interfere with bacterial growth. We further investigated their ability to inhibit *S. aureus* biofilm formation. Scopoletin and isofraxidin at concentration ranging from 0.5 to 500 µg/mL were tested. The biofilm developed by *S. aureus* ATCC 25923 in the presence of 1% sucrose was used as the positive control while the negative control was media without bacteria. Scopoletin and isofraxidin exhibited moderate potency with IC_{50} of 130 µg/mL and 52 µg/mL, respectively.

1. Introduction

Bacterial resistance to antibiotic is a major health problem and raise concerns worldwide. Researchers have been attempting to discover new therapeutic strategies to overcome bacterial resistance.[1] One of the most recognized pathogens that rapidly develop resistance to drugs is Gram-positive bacterium *Staphylococcus aureus* (*S. aureus*).

Similar to other bacteria, *S. aureus* can produce extracellular matrix called "biofilm" for communication, nutrients exchange, and protecting themselves from environment exchange and immune response. Biofilm has been suggested to be responsible for antibiotic resistance and pervasiveness.[2] The main function of biofilm is to provide the protection, shielding the microorganism from environmental changes such as fluctuation of pH, osmolarity, nutrients, as well as preventing the microorganism from antibiotics and host's immune response. Therefore, under biofilm state, higher concentration of antibiotic is required to eradicate the bacteria. For instance, to diminish *S. aureus* under biofilm state, it required significantly higher amount of vancomycin (100 times) than the minimum bactericidal concentration (MBC) of planktonic state.[3] In addition, when the planktonic β-lactamase-negative strain of *Klebsiella pneumoniae* was subjected to susceptibility testing, minimum inhibitory concentration (MIC) of 2 µg/mL was required for growth inhibition. However, under the biofilm state, it displayed remarkable resistance. Approximately 66% of the bacteria survived a 4-hour exposure to 5000 µg/mL ampicillin, suggesting that the susceptibility to antibiotic was significantly reduced.[4] These results suggested that biofilm formation attributes significantly to the development of antibiotic resistance.

Our group is interested in development of small molecules for combating with bacterial resistance. In collaboration with Prof. Chutima Kuhakarn and her team, we discovered several potent phenyl vinyl sulfones that could inhibit growth of *S. aureus* and MRSA as well as interfere with bacterial adhesion.[5] The α, β unsaturated region of the phenyl vinyl sulfones was suggested to be crucial for antibacterial activities.

Recently, our collaborative efforts have focused on natural compounds isolated from *Mallotus spodocarpus* (*M. spodocarpus*). *M. spodocarpus* Airy Shaw is a small plant belong in the family euphorbiaceae. It is considered an endemic plant, often found in the central, northern, northeastern and southwestern parts of Thailand. Traditionally, the powdered roots have been used for skin whitening. Isolation of leaves and twigs,

stems and roots *M. spodocarpus* led to complex cylic heptapeptides, mallotumides A-C, along with diterpenes and coumarin derivatives, namely scopoletin and isofraxidin.[6] Due to high solubility in aqueous and the α,β unsaturated moiety in the core structures, we are particularly interested in scopoletin and isofraxidin. The isolated scopoletin and isofraxidin from *M. spodocarpus* was subjected to susceptibility testing in Gram-positive pathogenic *S. aureus* and *Streptococcus mutans* (*S. mutans*). In addition, we also investigated their potentials in the inhibition of biofilm formation.

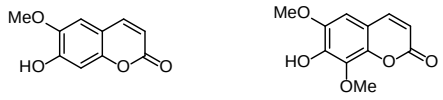

Scopoletin (1) Isofraxidin (2)

Figure 1. Structures of scopoletin and isofraxidin

2. Materials and Methods

2.1 Materials

Tryptic Soy Broth (TSB), Bacto Agar and Mueller Hinton Broth (MHB) were from BD (Sparks, MD). With regards to the bacteria used in this study, *S. aureus* ATCC 25923 was obtained from Assoc. Prof. Soraya Chaturongakul, Institute of Molecular Biosciences, Mahidol University, Thailand. *S. mutans* (ATCC 25175) provided by Assoc. Prof. Nuttawee Niamsiri, Department of Biotechnology, Faculty of Science, Mahidol University, Thailand.

2.2 Extraction and purification of compound

The air-dried and finely ground roots of *M. spodocarpus* (74.3 kg) were extracted with chloroform ($CHCl_3$) for 7 days 9 times at room temperature. Crude $CHCl_3$ extract (448.9 g) was obtained by rotary evaporation to remove solvent under reduced pressure followed by freeze-drying. A part of the $CHCl_3$ extract was purified by column chromatography (CC) on Silica gel with gradient solvent system. Hexane was used as the starting point for elution, followed by gradients of acetone and hexane, methanol (MeOH) and acetone, and 100% MeOH. Fractions were combined on the basis of TLC characteristics to give 21 fractions (F1–F21). Scopoletin (**1**, 589.7 mg) was isolated as yellow needles by recrystallization from MeOH. Isofraxidin (**2**, 126.9 mg) was isolated as an amber rod by recrystallization from dichloromethane/ n-hexane mixture.

The characterizations of compounds were previously reported.[7]

2.3 Spectroscopic measurement

Scopoletin (**1**): ^{1}H-NMR (300 MHz, DMSO-d_6) 10.06 (1H, *br*), 7.62 (1H, *d*, *J*=9.4 Hz), 6.87 (1H, *s*), 6.70 (1H, *s*), 6.05 (1H, *d*, *J*=9.4 Hz), 3.80 (3H, *s*).^{13}C-NMR (75 MHz, DMSO-d_6) 161.1, 151.1, 149.7, 145.2, 143.9, 111.6, 110.5, 108.7, 102.9, 55.9. EI mass spectrum cal. 192, found 192.

Isofraxidin (**2**): ^{1}H-NMR (300 MHz, $CDCl_3$) 7.60 (1H, *d*, *J*=9.5 Hz), 6.66 (1H, *s*), 6.48 (1H, *br*), 6.23 (1H, *d*, *J*=9.5 Hz), 4.06 (3H, *s*), 3.92 (3H, *s*). ^{13}C-NMR (75 MHz, $CDCl_3$) 160.8, 144.6, 143.9, 143.0, 142.6, 134.4, 113.2, 111.1, 103.2, 61.5, 56.4. High resolution mass spectrum cal. 222.0528, found 222.0527.

2.4 Disk Diffusion Method

We performed disk diffusion assay (Kirby-Bauer method) based on the protocol recommended by Clinical and laboratory Standards Institute (CLSI).[8] Muller-Hinton agar plate was used for *S. aureus*. The freshly prepared inoculum of bacteria with inoculum density equivalent to 0.5 McFarland (150 µL) were spread on the plate. The inoculated plate was placed with a sterilized filter paper disk (6 mm). The test compounds (30 µg) were diluted in dimethyl sulfoxide (DMSO) and transferred onto each filter paper disk. The plate was incubated at 37°C for 16-18 hours. Then, the diameter of the inhibition zones was measured. The experiments were repeated at least three times. The standard errors were reported.

2.5 Biofilm inhibition assay

The biofilm assay using crystal violet staining solution was performed based on the previously reported protocol.[9] *S. aureus* ATCC 25923 was used in this assay. The tested compounds were diluted in TSB supplemented with 1% sucrose. An aliquot of 100 µL of serial dilution was added to a sterilized 96-well plate. The bacterial was inoculated in 5 mL of TSB at 37°C for 16-18 hours. The overnight cultures of bacteria were diluted in PBS to obtain inoculum concentration of approximately 2 x 10^7 CFU/mL. Then, 100 µL of freshly diluted bacteria were added to each well. The plate was incubated for 24 hours at 37°C. After incubation, the planktonic bacteria were removed and washed twice with PBS. The biofilm was stained with 0.1% crystal violet solution and let stand for 30 minutes at room

Table 1. Susceptibility and anti-biofilm activity of curcumin and their synthetic derivatives determined by disk diffusion[a] and biofilm inhibition assay

Compound Structure	Compound concentration	Diameter of inhibition zone (mm)	
		S. aureus	*S. mutans*
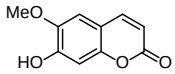 Scopoletin (1)	30 µg	6*	6*
	1000 µg	6*	6*
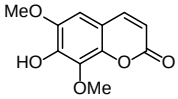 Isofraxidin (2)	30 µg	6*	6*
	1000 µg	6*	6*

[a] 30 µg and 1000 µg in 25 µL of test compound in DMSO were used for disk diffusion testing.
* Whatman disk has diameter of 6 mm. therefore, average inhibition zone of 6 mm indicates inability to inhibit growth

temperature. The excess dye was removed and washed with PBS. Then, 33% acetic acid was added to detach the biofilm. The optical density (OD) was measured at 595 nm using the microplate reader (TECAN Spark 10M). The experiment was repeated at least three times.

3. Results and Discussion

Scopoletin (**1**) and isofraxidin (**2**) were previously isolated from the air-dried and finely ground roots of *M. spodocarpus*. Scopoletin (**1**) was purified by recrystallization from MeOH, resulting in yellow needles. Its characterization was described in section 2.3. ^{1}H-NMR (300 MHz, DMSO-d_6) spectrum exhibited the presence of phenolic hydroxyl group at δ = 10.06 (1H, *br*), two aromatic protons at 6.87 (1H, s) and 6.70 (1H, s), two olefinic protons at δ = 7.62 (1H, d, *J* = 9.4 Hz) and δ = 6.05 (1H, d, *J* = 9.4 Hz). The ^{13}C-NMR (75 MHz) showed 10 signals for 10 carbons. Meanwhile, isofraxidin (**2**) was also subjected for NMR spectroscopy for characterization. Isofraxidin (**2**) was isolated as an amber rod by recrystallization from dichloromethane/n-hexane mixture. The ^{1}H-NMR (300 MHz) of isofraxidin (**2**) in $CDCl_3$ showed the presence of two olefinic protons of AB quartet at δ = 7.60 (1H, d, *J* = 9.5 Hz) and δ = 6.23 (1H, d, *J* = 9.5 Hz), one proton of aromatic ring at δ = 6.66 (1H, s) and a phenolic hydroxy group at δ = 6.48 (1H, br). The ^{13}C-NMR (75 MHz) of isofraxidin (**2**) in $CDCl_3$ exhibited 11 signals for 11 carbons. The structure of scopoletin (**1**) and isofraxidin (**2**) were deduced on the basis of ^{1}H-NMR and ^{13}C-NMR spectrum together with ^{13}C-^{1}H correlations via long-range coupling (HMBC) and NOE experiments as previously reported.[7]

In this study, scopoletin (**1**) and isofraxidin (**2**) were subjected to disk diffusion assay to quantitatively screen for their ability to inhibit growth of Gram-positive bacteria *S. aureus* and *S. mutans*. The compounds were tested at standard amount of 30 µg. This experiment was performed at least 3 times. The disk diffusion results showed that these isolated coumarin derivatives from *M. spodocarpus* did not inhibit growth of both pathogens. We, therefore, further investigated the growth inhibitory activity at significantly higher concentration of 1000 µg. Even at high concentration, both scopoletin (**1**) and isofraxidin (**2**) still did not interfere with growth of *S. aureus* and *S. mutans*. The susceptibility results were shown in Table 1**.**

We further investigated the ability of scopoletin (**1**) and isofraxidin (**2**) in *S. aureus* biofilm inhibition. Since scopoletin (**1**) and isofraxidin (**2**) did not inhibit growth at high concentration, we could explore the biofilm inhibitory activity at wide range of concentrations—from 0.5-500 µM. This experiment repeated 6 times. The results were summarized in Figure 2. Both scopoletin (**1**) and isofraxidin (**2**) showed moderate anti-biofilm activity. At high concentration, both scopoletin (**1**) and isofraxidin (**2**) could reduce biofilm to only

20-30%. The IC_{50} of these natural coumarins were calculated. In biofilm inhibition assay, scopoletin showed IC_{50} of 130 µg/mL while isofraxidin inhibited S. aureus biofilm at more effectively, with IC_{50} of 52 µg/mL. When comparing results of these two compounds, addition of methoxy group may slightly enhance biofilm inhibitory activity. We are currently investigating the susceptibility and anti-biofilm activity of more synthetic derivatives based on coumarin pharmacophore. The results will be reported in due course.

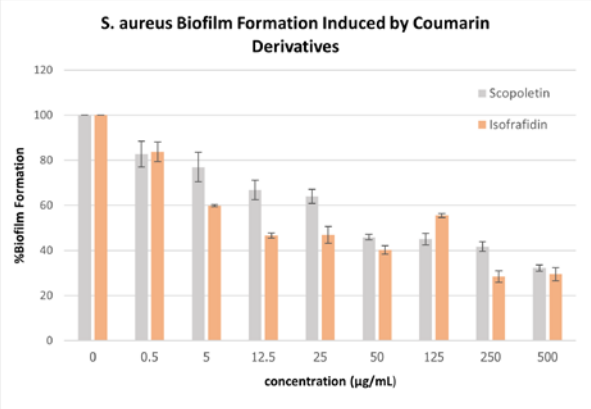

Figure 2. Biofilm inhibition induced by scopoletin and isofraxidin

4. Conclusion

Scopoletin and isofraxidin were previously isolated from *Mallotus spodocarpus*. Susceptibility testing via disk diffusion assay indicated that these courmarin derivatives could not interfere with growth of *S. aureus* and *S. mutans*. The biofilm formation assay was also performed to investigate their potentials as anti-biofilm agents. The results showed that they could moderately inhibit *S. aureus* biofilm formation with the IC_{50} roughly estimated to be in the micromolar range.

Acknowledgements

The authors are grateful to the financial supports provided in part by NSRF through the Program Management unit for Human Resources & Institutional Development, Research and Innovation (B16F640120), the Center of Excellence for Innovation in Chemistry (PERCH-CIC), and Development and Promotion of Science and Technology Talents Project (DPST).

References

1. Prestinaci, F.; Pezzotti, P.; Pantosti, A. *Pathog. Glob. Health* **2015**, *109* (7), 309–318.
2. Mirghani, R.; Saba, T.; Khaliq, H.; Mitchell, J.; Do, L.; Chambi, L.; Diaz, K.; Kennedy, T.; Alkassab, K.; Huynh, T.; Elmi, M.; Martinez, J.; Sawan, S.; Rijal, G. *AIMS Microbiol.* **2022**, *8* (3), 239–277.
3. Williams, I.; Venables, W. A.; Lloyd, D.; Paul, F.; Critchley, I. *Microbiology* **1997**, *143* (7): 2407–2413.
4. Anderl, J. N.; Franklin, M. J.; Stewart, P. S. Antimicrob. Agents Chemother. **2000**, *44* (7), 1818–1824.
5. Vorasin, O.; Momphanao, K.; Katrun, P.; Kuhakarn, C.; Jiarpinitnun, C. *Bioorg. Med. Chem. Lett.* **2022**, *63*, 128652.
6. Sawektreeratana, N.; Krachangchaeng, C.; Pittayanurak, P.; Betterley, N. M.; Chairoungdua, A.; Wongpan, A.; Panvongsa, W.; Janthakit, P.; Nalaoh, P.; Promarak, V.; Nuntasaen, N.; Reutrakul, V.; Kuhakarn, C.; Hongthong, S. *Org. Lett.* **2023**, *25* (46), 8183–8187.
7. Ph.D. Thesis (Faculty of Graduate Studies, Mahidol University): Chongkon Krachangchaeng, 2002.
8. Clinical and Laboratory Standards Institute: Performance Standards for Antimicrobial Susceptibility Testing; Twenty-Second Informational Supplement. Wayne. **2012**; *32*(3)*:* 126-150.
9. Merritt, J. H.; Kadouri, D. E.; O'Toole, G. A. *Curr. Protoc. Microbiol.* **2005**, *00* (1).

Syntheses of curcumin derivatives and their biological activity against *Staphylococcus aureus*

Krit Ruechai and Chutima Jiarpinitnun*

Department of Chemistry and Center for Innovation in Chemistry (PERCH-CIC), Faculty of science, Mahidol University, Rama VI Road, Bangkok, 10400, Thailand

**E-mail: chutima.jia@mahidol.ac.th*

Abstract:

Biofilm formation is considered one of the most serious health concerns. It could lead to an infection that could be lethal. In the biofilm state, biofilm provide a shelter to protect bacteria from being eradicated by antibiotics, leading to drug resistance development. Several anti-biofilm-forming strategies were established. Disruption of bacterial adhesion is one of the alternative methods to avoid biofilm formation at the beginning step, particularly during the initial step that planktonic cells need to attach to a surface. In this work, we investigate the antibacterial activity of curcumin and derivatives against *Staphylococcus aureus*, which has a cysteine transpeptidase enzyme that plays a significant role in the bacterial adhesion, formation and maintenance of biofilms. Due to the Michael addition of enone functional group of curcumin and derivatives that possibly irreversible covalent bond with sulfhydryl group of cysteine, our hypothesis was that these substances might have antimicrobial properties. A total of four curcumin derivatives and one non-conjugated derivative were subjected to susceptibility assays and biofilm formation against *S. aureus*. We discovered that curcumin could inhibit bacterial growth activity against *S. aureus*, which shows a clear inhibition zone of 8.64 ± 0.18 mm. Moreover, these derivatives exhibited anti-biofilm activities in micromolar range. Among these derivatives, compound **2B** was the most potent anti-biofilm agent, with IC_{50} of 41.12 µM.

1. Introduction

Antibiotic resistance is considered as one of the major health concerns worldwide. The widespread and inappropriate use of antibiotics has led to a concerning increase in the rate of antibiotic resistance. Managing infections caused by these pathogens is challenging due to the limited availability of effective antibiotics.

Staphylococcus aureus (*S. aureus*) is a Gram-positive pathogenic bacterium known for its ability to rapidly develop resistance towards antibiotics. *S. aureus* infection could lead to wide range of symptoms, from skin and soft tissue infections to life-threatening diseases such as encephalitis, meningitis, and sepsis.[1] One of leading antibiotic resistant bacteria that impact global healthcare problems is methicillin-resistant *S. aureus* or MRSA.[2]

Bacterial biofilm significantly contributes to antibiotic resistance. Biofilms refer to the community of microorganisms embedded in extracellular matrix that consists of a number of long chained polymeric molecules.[3] The common composition of these polymers are exopolysaccharides and lipopolysaccharides as main polymers.[4] Biofilm functions as a shelter protecting bacteria from the immune response and antibiotics. During the biofilm formation, the genes responsible for porin or efflux pump proteins are also up regulated, allowing bacteria to pump out antibiotics from the cells.[5] Therefore, the biofilm mode of growth could decrease the susceptibility of bacteria to the antibiotics, leading to the increase of antibiotic.[6] Preventing biofilm formation would, as the consequence, reduce chance for the antibiotic resistance development.

Surface proteins in *S. aureus* play a significant role in the formation and maintenance of biofilms, particularly during the initial step that planktonic cells need to attach on a surface. Given the crucial function of cell surface proteins in enabling bacteria to initiate infections, the protein anchoring process is, thereby, our therapeutic target.

In Gram-positive bacteria, including *S. aureus*, the covalent assembly of surface proteins to cell walls is catalyzed by thiol-containing transpeptidase enzyme called sortase A (SrtA). We envisioned that interfering with SrtA catalytic activity could result in inhibition of biofilm. Based on previous reports, natural products and small molecules have recently been reported to inhibit SrtA.[7] These molecules showed various pharmacophores. For example, curcumin, isolated from commonly used natural plant *Curcuma longa* (turmeric), was reported as a potent inhibitor of SrtA, with an IC_{50} value of 13.8 µg/mL.[8] Structurally analogue *trans*-chalcone was recently investigated and discovered that it could inhibit *Streptococcus mutans* SrtA.[9] Mass spectrometry study indicated that the SrtA-chalcone adduct was

formed *via* Michael addition, suggesting that α,β-unsaturated system of *trans*-chalcone was key to binding to *Streptococcus mutans* SrtA. In addition, treatment of *trans*-chalcone at 250 μM could decrease the biofilm formation in *Streptococcus mutans.*

Herein, we synthesize curcuminoids analogues with various substituents on aromatic ring. Their antibacterial and antibiofilm activities in *S. aureus* were investigated. The structure-activity relationships were evaluated.

2. Materials and Methods

2.1 Materials

(i) Chemistry

All chemicals were purchased from commercial suppliers and used without further purification. The reactions were conducted under an inert atmosphere of nitrogen. ^{1}H-NMR and ^{13}C-NMR spectra were performed on a Bruker Advance-400 spectrometer. High-resolution mass spectra (HRMS) were obtained by using Bruker micro TOF spectrometer (ESI mode)

(ii) Microbiology

S. aureus ATCC 25923 were obtained from Assoc. Prof. Soraya Chaturongakul, Institute of Molecular Biosciences, Mahidol University, Thailand. Tryptic soy broth (TSB), Bacto Agar and Mueller Hinton Broth (MHB) were from BD (Spark, MD), Phosphate buffer saline (PBS) was purchased from Sigma-Aldrich (USA). The diameter of inhibitory zones was measured by sliding calipers. The turbidity was measured using Microplate Reader-TECAN (Spark 10M).

2.2 Synthesis of curcumin derivatives

2.2.1 Synthesis of tetrahydrocurcumin (2A)

To a solution of commercially available curcumin (2.1 mmol), a mixture of 15 mL ethyl acetate (EtOAc) and 20 mL methanol (MeOH), 10% palladium on charcoal (0.08 g) was added. The reaction mixture was stirred under hydrogen for 2 hours at room temperature. The palladium on charcoal catalyst was removed by filtration and the solvent was evaporated. The crude product was purified by column chromatography.[10]

2.2.2 General syntheses curcumin derivatives (2B-2E)

Commercially available 2,4-pentanedione (1.0 eq) was mixed with boric anhydride (B_2O_3) (0.7 eq) and added to a solution of tributyl borate (3 mL). The reaction mixture was stirred for 30 minutes at 90°C. Subsequently, the reaction was cooled down to 60°C. To the reaction mixture, substituted benzaldehyde (2.0 eq) was added, followed by addition of tributyl borate (2 mL). Solution of *n*-butylamine (0.7 mL) in tributyl borate (1 mL) was prepared and add to the reaction mixture dropwise. The reaction was heated to 100°C and stirred for 1.5 hours. After cool down reaction, HCl (0.4 M) was slowly added dropwise to adjust the pH to 3-4. Then, the reaction mixture was extracted with EtOAc (3 times). The combined organic layers were washed with saturated NaCl solution and dried over anhydrous sodium sulfate (Na_2SO_4). The solvent was removed by rotary evaporator. The crude product was purified by column chromatograph.[11]

2.3 Spectroscopic data

Compound **2A:** ^{1}H-NMR (400 MHz, $CDCl_3$) 15.50 (s, 1H), 6.81 (s, 2H), 6.81 (s, 4H), 5.66 (s, 2H), 5.43 (s, 1H), 3.84 (s, 6H), 2.84 (t, J = 7.5 Hz, 4H), 2.55 (t, J = 8.1 Hz, 4H). ^{13}C-NMR (100 MHz, $CDCl_3$) 203.6, 193.4, 146.5, 144, 132.6, 120.9, 114.5, 111, 99.9, 55.9, 40.4, 31.4, 29.8, 29.2. ESI-MS cal. For $C_{21}H_{24}O_6$ $[M]^+$: 372.1573, found 372.1572

Compound **2B:** ^{1}H-NMR (400 MHz, $CDCl_3$) 7.62 (d, J = 15.8 Hz, 2H), 7.30 (dd, J = 7.8, 7.9 Hz, 2H), 7.14 (d, J = 7.6 Hz, 2H), 7.06 (s, 1H), 6.92 (d, J = 8.1 Hz, 2H), 6.60 (d, J = 15.8 Hz, 2H), 5.83 (s, 1H), 3.82 (s, 6H) , ^{13}C-NMR (100 MHz, $CDCl_3$) 183.3, 159.9, 140.6, 136.4, 129.9, 124.4, 120.8, 115.9, 113.1, 101.9. ESI-MS cal. For $C_{21}H_{20}O_4$ $[M+H^+]^+$: 337.1434, found 337.1432

Compound **2C:** ^{1}H-NMR (400 MHz, $CDCl_3$) 7.61 (d, J = 15.7 Hz, 2H), 7.49 (d, J = 8.6 Hz, 4H), 6.91 (d, J = 8.6 Hz, 4H), 6.49 (d, J = 15.8 Hz, 2H), 5.77 (s, 1H), 3.83 (s, 6H). ^{13}C-NMR (100 MHz, $CDCl_3$) 183.5, 161.4, 140.3, 129.9, 127.9, 121.9, 114.5, 101.5, 55.5, 36.7, 24.8 ESI-MS cal. For $C_{21}H_{20}O_4$ $[M+H^+]^+$: 337.1432, found 334.1427

Compound **2D:** ^{1}H-NMR (400 MHz, $CDCl_3$) 7.53 (d, J = 15.8 Hz, 2H), 7.40(d, J = 8.6 Hz, 4H), 6.80 (d, J = 8.5 Hz, 4H), 6.44 (d, J = 15.8 Hz, 2H), 5.77 (s, 1H). ^{13}C-NMR (100 MHz, $CDCl_3$) 183.1, 159.2, 140.6, 129.9, 126.5, 120.7, 115.8 ESI-MS cal. For $C_{19}H_{16}O_4$ $[M+H^+]^+$: 309.1121, found 309.1112

Compound **2E:** ^{1}H-NMR (400 MHz, $CDCl_3$) 7.68 (d, J = 15.8 Hz, 2H), 7.56 (d, J = 7.4 Hz, 4H), 7.39 (m, 6H), 6.64 (d, J = 15.8 Hz, 2H), 5.86 (s, 1H). ^{13}C-NMR (100 MHz, $CDCl_3$) 183.3, 140.7, 135, 130.1, 129, 128.2, 124.1, 101.8. ESI-MS cal. For $C_{19}H_{16}O_2$ $[M+H^+]^+$: 278.1257 , found 278.2453

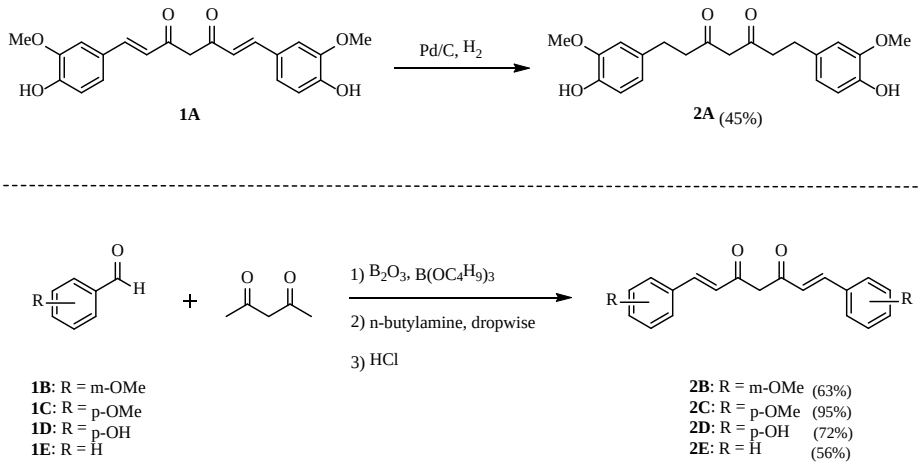

Scheme 1. Syntheses of curcumin derivatives

2.4 Qualitative disk diffusion assay

Disk diffusion assay (Kirby-Bauer method) was performed based on the standard protocol suggested by the Clinical and Laboratory Standards Institute (CLSI).[12] Methicillin susceptible *S. aureus* ATCC 25923 was used as a model *S. aureus* strain for this study. In brief, Muller-Hinton Agar (MHA) plate was prepared by pouring MHB broth supplemented with bacto agar into the petri dish to yield a 4-mm thickness. The plate was let stand to solidify. The freshly prepared inoculum of *S. aureus* ATCC 25923 (at the concentration of $4x10^7$ CFU/mL) was spread on the plate. Then, the sterilized filter paper disks (6 mm) were placed on bacterial spread agar. The test compounds (30 µg) in DMSO were transferred on each paper disk. The plate was incubated at 37 °C for 18 hours. The diameter of inhibition zone was measured using a digital Vernier caliper. . The disk diffusion assay was repeated three times. The average zone with the standard error was reported.

2.5 Biofilm formation assay

The biofilm assay using crystal violet staining solution was conducted based on the previously reported protocol.[13] In brief, *S. aureus* ATCC 25923 overnight culture was diluted with PBS to obtain inoculum concentration of approximately 2 x 10^7 CFU/mL. The test compounds were diluted in TSB supplemented with 1% sucrose. To a sterilized 96-well plate, 100 µL of bacteria is added. The inoculum was added with 100 µL of test compounds at various concentrations. The plate was incubated for 24 hours at 37 °C, allowing biofilm to form. After incubation, the planktonic bacteria were removed. The plate was washed 2 times with PBS. The biofilm was stained by adding 100 µL of 0.1% crystal violet solution. The plate was in let stand for 30 minutes at room temperature. An excess dye was removed, then each well was washed twice with PBS. Subsequently, 33% acetic acid was added to detach the biofilm. The resulting biofilm formed was determined by measuring the optical density (OD) of each well at 595 nm using microplate reader. The amount of biofilm formed is represented by the OD values.

3. Results and Discussion

3.1 Syntheses of curcumin derivatives

Total of five curcumin derivatives were successfully synthesized from inexpensive commercially available materials. Curcumin (**2A**) was simply prepared by hydrogenation using palladium on charcoal. The curcumin derivatives **2B-2E** was synthesized by aldol condensation of substituted benzaldehyde with 2,4-pentanedione. Moderate to high yield were achieved.

3.2 Susceptibility of curcumin derivatives

Curcumin and their derivatives were subjected to the susceptibility testing against *S. aureus*. To determine the ability of the synthetic derivatives to inhibit growth of *S. aureus*, we employed qualitative disk diffusion assay (Kirby-Bauer method). The result was illustrated in **Table 1**. Ampicillin was used as reference antibiotic in order to qualitatively verified to CLSI standard. Ampicillin showed complete inhibition zone of 30.16 mm when tested against *S. aureus* ATCC 25923. The zone diameter was within range as suggested by CLSI.

Table 1. Susceptibility and anti-biofilm activity of curcumin and their synthetic derivatives determined by disk diffusion[a] and biofilm inhibition assay

Entry	Compound Structure	Diameter of inhibition zone (mm) *S. aureus*	IC_{50} (μM) biofilm formation
1	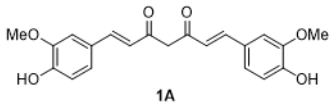 1A	8.64±0.18	74.25
2	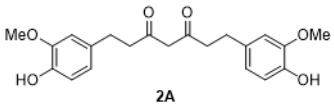 2A	6*	65.40
3	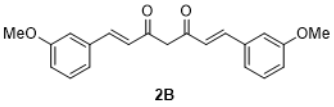 2B	incomplete	41.12
4	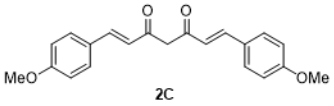 2C	incomplete	70.57
5	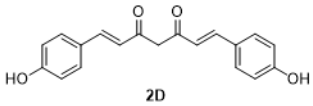 2D	8.55±0.06	103.6
6	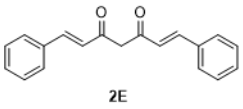 2E	incomplete	147.0
7	ampicillin	31.95±0.03	N/A

[a] 30 μg in 25 μL of test compound in DMSO were used for disk diffusion testing.
* Whatman disk has diameter of 6 mm. therefore, average inhibition zone of 6 mm indicates inability to inhibit growth

The hydrogenated derivative, tetrahydrocurcumin (**2A**) did not show inhibition zone, indicating that the α,β-unsaturated is important for growth inhibition. With regards to the substituents on the phenyl ring, we observed that the lack of hydroxyl group could reduce the susceptibility of the curcumin analogues. As illustrated in the growth inhibitory activity results of *m*-methoxy derivative (**2B**), *p*-methoxy derivative (**2C**), and benzene derivative (**2E**), we observed incomplete zones. In addition, *p*-hydroxyl derivatives (**2D**), which retained the hydroxyl group but lacking methoxy substituents, exhibited complete inhibition zone at 8.55±0.06 mm, comparable to curcumin (8.64±0.18 mm) and possible inhibit growth of *S. aureus*.

3.2 Biofilm inhibition ability

We further evaluated the ability of curcumin derivatives **2A**-**2E** to inhibit *S. aureus* biofilm formation and compared with natural

product curcumin (**1A**). The results are summarized in **Table 1**. Due to the weak growth inhibition, we tested the biofilm inhibition assay in the presence of curcumin derivatives at the concentrations ranging from 0 to 512 µM. The results demonstrated that curcumin and its derivatives could interfere with the ability of *S. aureus* to form biofilm in concentration dependent manner. Curcumin could inhibit *S. aureus* biofilm with IC_{50} value of 74.25 µM. The structure-activity relationship based on the antibiofilm activity results of our small collection of curcuminoid derivatives suggest the importance of methoxy group at the *meta*-position. Compound **2B** (entry 3) showed good antibiofilm activity with an IC_{50} value of 41.12 µM. This derivative retained the *m*-OMe substituents but lacking hydroxyl groups. In addition, when replacing the *m*-OMe with hydrogen and retained hydroxyl group (entry 5, **2D**), the inhibitory activity significantly reduced. The unsubstituted **2E** also showed decrease in potency. Interestingly, the comparable inhibitory activity of **2A** in comparison to curcumin **1A** implicated that the α,β-unsaturated region may not involve in antibiofilm activity observed. We are currently investigating the mode of action underlying biofilm inhibition as well as the ability of these curcumin derivatives to interfere with SrtA and bacterial adhesion. The results will be reported in due course.

4. Conclusion

Total of five curcuminoids were synthesized using inexpensive commercially available starting materials. The reactions were simple and mild condition. The synthesized curcumin derivatives were subjected to susceptibility testing using disk diffusion and found that these could weakly inhibit growth of bacteria. We further explored the potential of these compounds as antibiofilm agents. The results of biofilm formation assay against *S. aureus* showed that curcumin and its derivatives could inhibit *S. aureus* biofilm formation in concentration-dependent manner. The most potent compound was *m*-methoxy derivative **2B** with the IC_{50} value of 41.12 µM. The structure-activity analysis suggested the importance of methoxy substituent at the *meta*-position. This information could be further exploited in the design of antibiofilm agents against *S. aureus*.

Acknowledgements

The authors are grateful to the financial supports provided in part by Department of Chemistry and Center for Innovation in Chemistry (PERCH-CIC), Faculty of Science, Mahidol University.

References

1. Tong, S. Y. C.; Davis, J. S.; Eichelberger, E.; Holland, T. L.; Fowler, V. G. *Clin. Microbiol. Rev.* **2015**, *28* (3), 603–661.
2. Ali Alghamdi, B.; Al-Johani, I.; Al-Shamrani, J. M.; Musamed Alshamrani, H.; Al-Otaibi, B. G.; Almazmomi, K.; Yusnoraini Yusof, N. *Saudi J. Biol. Sci.* **2023**, *30* (4), 103604.
3. Schulze, A.; Mitterer, F.; Pombo, J. P.; Schild, S. *Microbial Cell* **2021**, *8* (2), 28–56.
4. Donlan, R. M. *Emerg. Infect. Dis.* **2002**, *8* (9), 881–890.
5. Hajiagha, M. N.; Kafil, H. S. *Infect. Genet. Evol.* **2023**, *112*, 105459.
6. Sharma, D.; Misba, L.; Khan, A. U. *Antimicrob. Resist. Infect. Control* **2019**, *8* (1).
7. Sapra, R.; Rajora, A. K.; Kumar, P.; Maurya, G. P.; Pant, N.; Haridas, V. *J. Med. Chem.* **2021**, *64* (18), 13097–13130.
8. Park, B.-S.; Kim, J.-G.; Kim, M.-R.; Lee, S.-E.; Takeoka, G. R.; Oh, K.-B.; Kim, J.-H. *J. Agric. Food Chem.* **2005**, *53* (23), 9005–9009.
9. Wallock-Richards, D. J.; Marles-Wright, J.; Clarke, D. J.; Maitra, A.; Dodds, M.; Hanley, B.;Campopiano, D. J. *Chem. Comm.* **2015**, *51* (52), 10483–10485.
10. Portes, E.; Gardrat, C.; Castellan, A. *Tetrahedron* **2007**, *63* (37), 9092–9099.
11. Li, Y.; Gu, Z.; Zhang, C.; Li, S.; hang, L.; Zhou, G.; Wang, S.; Zhang, J. *Eur. J. Med. Chem.* **2018**, *144*, 662–671.
12. Clinical and Laboratory Standards Institute: Performance Standards for Antimicrobial Susceptibility Testing; Twenty-sixth Informational Supplement M100S. Wayne, PA, USA, **2016**.
13. Merritt, J. H.; Kadouri, D. E.; O'Toole, G. A. *Curr. Protoc. Microbiol.* **2011**, *22* (1), 1B.1.1–1B.1.18.

LC-ESI-MS based structural elucidation of major chemical compounds in *Boesenbergia rotunda* (L.) Mansf. ethanolic extract and its antioxidant activity

Laksana Charoenchai* and Thaniya Wannakup

Drug and herbal product research and development center, College of Pharmacy, Rangsit University, Pathum Thani province 12000, Thailand

**E-mail: Laksana.c@rsu.ac.th*

Abstract:

The study aimed to examine chemical compositions and antioxidant activity of the ethanolic extract of *Boesenbergia rotunda* (L.) Mansf., commonly called fingerroot. The powder root of *B. rotunda* was extracted with ethanol using sonication. The chemical compositions of the extract were determined by using liquid chromatography and mass spectrometry. Flavones and prenylated flavonoids have been studied and evaluated. The major compounds which are alpinetin, pinocembrin, pinostrobin and panduratin A were identified by using the information from electrospray ionization mass spectrometry (ESI-MS) comparing with known compounds previously reported in the literature. Mass spectra showed that molecular ions were corresponded to these major compounds. MS/MS fragmentations were also studied to investigate the compounds. In addition, the antioxidant activity was determined using 2,2-diphenyl-1-picrylhydrazyl (DPPH) assay. The extract showed moderate activity with the IC_{50} of 588.89 ± 51.86 μg/mL comparing with gallic acid (IC_{50} = 3.10 ± 0.38 μg/mL) and rutin (IC_{50} = 36.42 ± 7.03 μg/mL).

1. Introduction

Boesenbergia rotunda (L.) Mansf. or fingerroot called in Thai as Kra-chai was found in South East Asia; Thailand, Laos, Myanmar, and Indonesia. Fingerroot has been used in traditional medicine as anti-flatulent and tonic. It was a composition in medicinal recipe to relieve menstrual pain, stomachache, mouth ulcer and enhance appetizer.[1] Previous studies, anti-bacterial activity against oral pathogens i.e., *Streptococcus pyrogens, S. mutans, Porpyrogymonas gingivalis*[2] and antiviral against SARS Co-V2 virus[3] have been reported.

Chemical compositions of fingerroot were chalcones, flavones, and flavanones. Thin layer chromatography and high-performance liquid chromatography have been studied for compound identification.[4] Anti-oxidant assays both *in vitro* and cellular based was screening for the activity.[5] This study focused on compound characterization using LC-ESI-MS. Anti-oxidant test, DPPH radical scavenging on TLC and *in vitro* assay were studied.

2. Materials and Methods

2.1 Materials

Fingerroot powder was purchased from Chonburi, Thailand. 2,2 Diphenyl-1-picrylhydrazyl (DPPH) was bought from Sigma, Aldrich. Dichloromethane and methanol AR grade was bought from Honeywell, Thailand. 95%Ethanol commercial grade was bought from Samchai Chemical, Thailand. Methanol HPLC grade was purchased from Fisher chemical, Korea.

2.2 TLC and DPPH detection

The ethanolic extract of fingerroot powder was applied on a silica gel $G_{60}F_{254}$ for 5 μL using Linomat 5 application (Camag Switzerland). The mobile phase was dichloromethane : methanol (70 : 1) and observed under 254 and 366 nm. DPPH (60 mM) solution was sprayed and kept for 10 minutes before detection under white light. The R_f value was compared with that of Thai Herbal Pharmacopoeia (THP).[6]

2.3 Chromatographic analysis

Fingerroot powder was identified and examined the physical properties (n=3) according to THP.

Fingerroot powder (0.2 g) was extracted with 95% ethanol (20 mL) by sonication for 30 minutes in ultrasonic bath. The extract was filtered through syringe filter (0.45 μ) and injected into HPLC (10 μL). The analytical method was performed on HPLC 1260 [Agilent] with a Zorbax Eclipse XDB C_{18} (4.6 x 250 mm i.d., 5 μm) column. The mobile phase was water (A) and methanol (B) with a gradient elution and a flow rate of 1 mL/min.[7] Methanol was started at 25-70% (0-15 min), 70-100% (15-50 min), 100% (50-55 min), 100-25% (55-60 min), and stayed at 25% for 10 min. The chromatogram was monitored at a wavelength of 290 nm and the total run time was 70 minutes.

LC-ESI-MS was performed on the Ultimate 3000, Dionex HPLC system and Amazon SL, Bruker mass spectrometer. The sample was injected and analyzed on a Poroshell EC C_{18}

column (3 x 150 mm i.d., 2.7 µm). The mobile phase composition was water (A) and acetonitrile (B) gradient. The gradient elution was the same as HPLC chromatographic method. The flowrate was 0.2 mL/min and the injection volume was 3 µL. ESI MS was equipped with quadrupole ion trap. Capillary voltage was set at 4,500 V, nebulizer gas was set at 2 bars, and drying gas temperature was 250 °C with a flow rate of 7.0 L/min. MS evaluation was performed in negative mode and scanned at the mass range of m/z 70-1,000 amu. Chromelon and Hystar were used for controlling the system. The MRM was performed with collision energy 70% of the maximum. The precursor ions were set at mass of 256, 269, 270, 282, 406. The isolation width of the precursor ions of m/z 1.0 and the default value was used for the other parameters.

2.4 DPPH anti-oxidant assay

The DPPH inhibition was determined according to the modified procedure.[8] Fingerroot powder was extracted with 95%ethanol by shaking for 8 hours. The extract was diluted to a final concentration of 125-4,000 µg/mL. Gallic acid and rutin were prepared in methanol with a final concentration of 3.125-100 µg/mL. The sample and standard solution (100 µL) were added into 96 well plate in triplicate. Then 100 µL of 60 mM DPPH solution was added. The plate was stored in dark for 30 minutes. Then the plate was measured the absorbance at the wavelength of 520 nm using a microplate reader [Biorad]. Percent inhibition and IC_{50} were calculated.

3. Results & Discussion

3.1 Physical properties of *B. rotunda*

The physical properties of fingerroot powder were within the acceptance criteria (Table 1). However, there was no volatile oil content in fingerroot powder which might be lost during drying process.

Table 1. Physical properties of fingerroot powder

Parameters	Acceptance criteria	Mean±SD*
Water content (%v/w)	NMT 9	8.5 ± 1.4
Total ash (%w/w)	NMT 8	5.8 ± 0.0
Acid insoluble ash (%w/w)	NMT 2	1.5 ± 0.1
Ethanol soluble extractive (%w/w)	NLT 8	12.3 ± 0.0
Water soluble extractive (%w/w)	NLT 12	15.1 ± 0.0

[a]NMT = not more than
[b]NLT = not less than
* n=3

3.2 Anti-oxidant activity of *B. rotunda* ethanolic extract by DPPH assay

Fingerroot powder were bought from commercials. The ethanolic extracts showed moderate anti-oxidant activity by DPPH assay (Table 2). Gallic acid and rutin were positive control and showed relatively high antioxidant activity.

Table 2. Inhibition concentration (IC_{50}) of fingerroot powder

Samples	IC_{50} (µg/mL)
Gallic acid	3.10 ± 0.38
Rutin	36.42 ± 7.03
Fingerroot extract	588.89 ± 51.86

3.3 Anti-oxidant activity detected by TLC

TLC-DPPH was a fast screening of compounds for the presence of biologically active free radical scavengers. The TLC profile showed chemical compositions eluted and pinostrobin was eluted at R_f = 0.79 (Figure 1). The R_f value of pinostrobin was slightly lower than that of reported in THP (R_f = 0.90). The bands which were eluted at R_f 0.04, 0.06, 0.12, and 0.56 showed quenching after being sprayed with DPPH. Rutin was applied at track 1 as a representative compound that showed antioxidant activity. Panduratin A was eluted at R_f 0.56, which showed intense band after being spray with DPPH solution. TLC-DPPH analysis can provide more information related to some compounds which might be responsible for this activity.

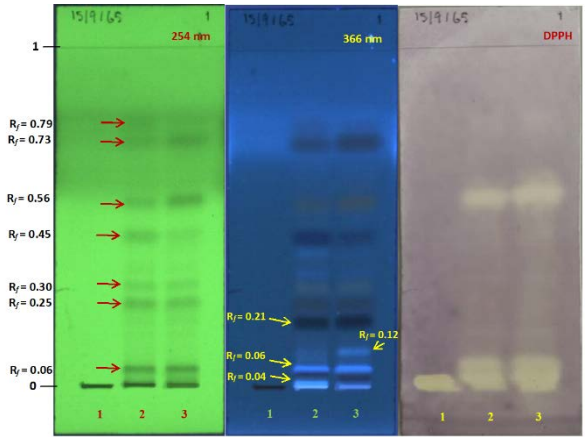

Figure 1. TLC profile of fingerroot powder
Track 1 = Rutin
Track 2 and 3 = fingerroot extract

3.4 Chemical compositions of *B. rotunda*

Fingerroot extract showed that the main compounds eluted in HPLC were tentatively identified as alpinetin, pinocembrin, pinostrobin,

and panduratin A. The retention times were comparable with those of reported by Adhikari and et, al.[7] HPLC chromatogram showed similar elution profile. Alpinetin was eluted first, then pinocembrin, pinostrobin and panduratin A, respectively. These flavone and flavanone share common chemical functional groups. Some compounds have the same molecular weight; therefore, MS/MS fragmentation were required to characterize them. HPLC chromatogram was shown in Figure 2. Panduratin A, which had more than one isomer, cannot clearly separate in this analysis condition.

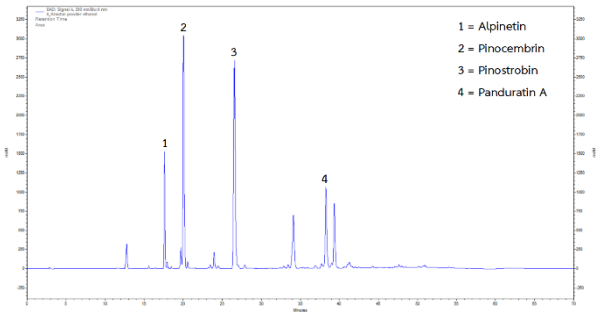

Figure 2. HPLC chromatogram of the ethanolic extract of the fingerroot powder

The eluted peaks were identified using ESI-MS and MSMS fragmentation. Alpinetin, pinostrobin, and cardamonin were the same molecular weight (270.28). Some flavanones found in fingerroot were found in other plants also; i.e., cardamonin, pinocembrin, and pinostrobin. Pinostrobin has been found in *Linderae Reflexae* Radix.[9] Alpinetin, pinostrobin and pinocembrin have been found in eucalyptus also.[10] Previous studies by others reported structure elucidation of compounds identified from *B. rotunda* using GC-MS and LC-MS.[11, 12] For LC-MS it was studied with FAB-MS and QTOF and most of them were in positive mode. In this study HPLC coupled to electrospray ion trap mass spectrometry was developed to separate and identify some compounds from fingerroot. MS/MS spectra in negative mode were obtained by multiple reaction monitoring (MRM) to form fragment ions. Although in negative mode resulted in limited fragmentation, it was selected because it appeared more selective, clearly and less interference. Mass spectra recorded in negative mode provided intense adduct from the mobile phase also.

The characterization of these compounds was based on their retention times and verified the maximal absorption spectra of each eluted peak. ESI-MS was performed in positive and negative modes. MS^2 experiment in the negative mode was then studied using multiple reaction monitoring (MRM). The negative ion mode was more selective and more sensitive than the positive mode although some fragment ion was low intensity. MS/MS fragmentation helped to elucidate some which had the same molecular weight. Nevertheless, nuclear magnetic resonance (NMR) was the technique to confirm the chemical structure.

ESI-MS/MS product ions obtained from $[M-H]^-$ ions of flavones. These fragmentations were supported by MS^2 spectra of fragment ions. MS^2 spectra of the precursor ion $[M-H]^-$ 269 resulted mass spectra of product ions; 245.7, 218.1, and 154.7, which were corresponded to loss of B ring, CO, and the cleavage of C-C in C ring suggesting alpinetin (Figure 3A). These fragment ions are sodium adducts (include mass 23 of sodium ions). Less quantity compounds; i.e. 5,7-dimethoxyflavone (the precursor ion = 282), which was similar structure to pinocembrin (5,7-dihydroxyflavone, M.W. = 256) showed product ions $[M-OCH_3-Na^+]^-$ = 273.6 in Figure 3B. The precursor ion (271) yielded the product ions $[M-OCH_3-Na^+]^-$ = 261.1 suggested pinostrobin (Figure 3C). These fragment ions were common for diagnostic fragment of flavonoid identification.[13] Panduratin A (M.W. = 406.50) and boesenbergin A (M.W. = 404.50) were similar molecular weights. The mass spectra of the fragment ions were showed in Figure 3D suggesting the panduratin A. The purpose fragment ions required either highly accurate mass spectrometer or using undergo MS^n experiments to verify. Although the band indicating panduratin A showed intense band in TLC-DPPH, the eluted peak in HPLC showed small intensity.

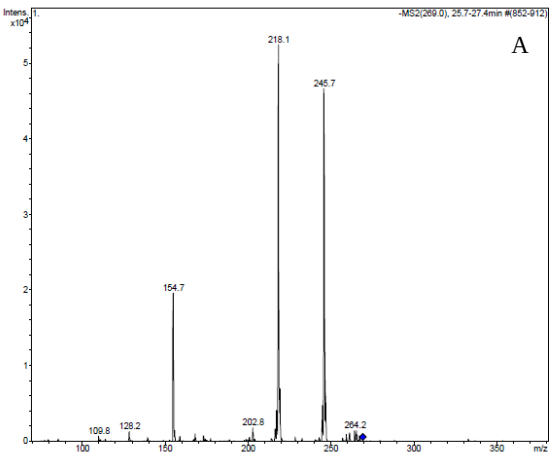

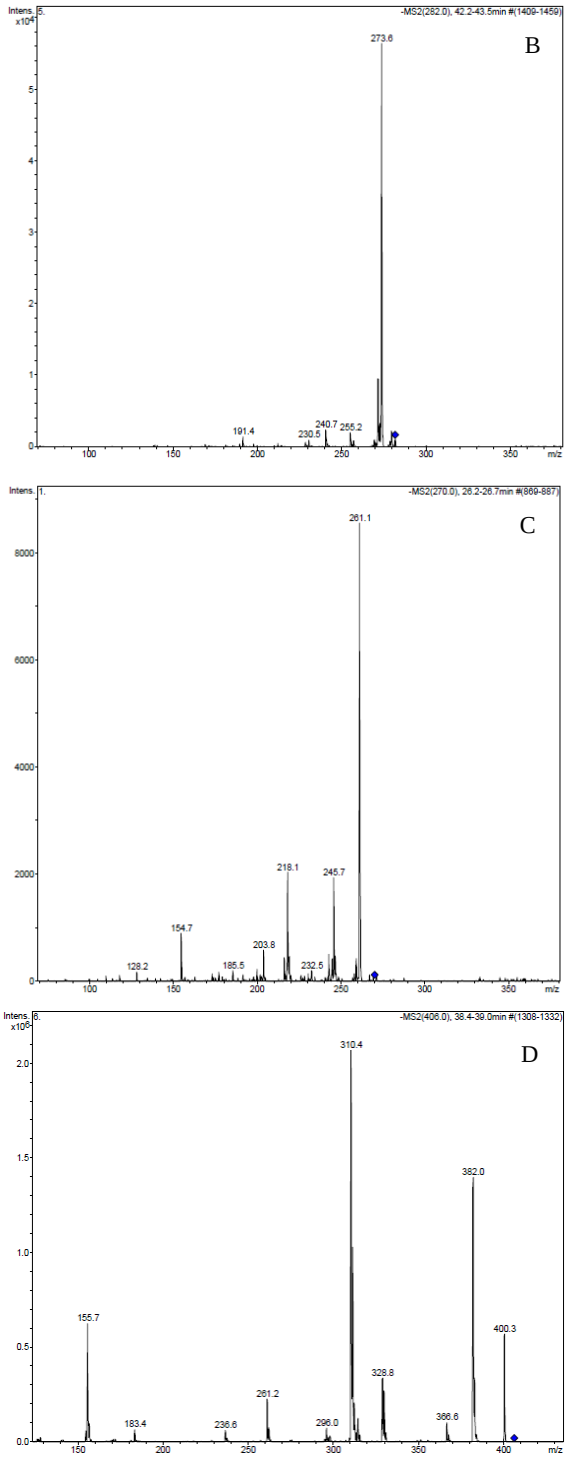

Figure 3. Negative ESI-MS/MS spectra obtained for A. Alpinetin
B. 5,7-dimethoxyflavone
C. Pinostrobin
D. Panduratin A

4. Conclusion

Fingerroot powder from commercials in this study showed good physical characteristics. The ethanolic extract exhibited antioxidant activity in DPPH assay. Panduratin A may be mostly responsible for the antioxidant activity from TLC-DPPH. Four main compounds were identified in HPLC mobile phase system in comparison to previously publications by others. ESI-MS/MS in negative mode showed fragment ions with sodium adducts. The fragmentation profile gave the structural information of those of chalcone, flavone, and flavanone aglycone of flavonoids. However, other components of fingerroot extract needed to be reconfirmed by other MS techniques and NMR.

Acknowledgements

The authors thank College of Pharmacy, Rangsit University for laboratory instruments. The authors greatly appreciate the efforts of professional students in the academic year 2022 who involved in this study.

References

1. Mamak, C.; Duangdamrong, J.; Phayakkhawisai. T.; Trakoolsilp, B.; Jamparngernthaweesri, K.; Sukcharoen, P.; Seeloopmok, P.; Akarasereenont, P.; Lumlerdkij, N. *Siriraj Med. Bull*. **2021**, *14*(2), 61-72.
2. Park, K-M.; Choo, JH.; Sohn, J-H.; Lee, S-H.; Hwang, J-K. *Food Sci. Biotech.* **2005**, *14*(2), 286-289.
3. Kanjanasirirat, P.; Suksatu, A.; Manopwisedjaroen, S.; Munyoo, B.; Tuchinda, P.; Jeerawuttanakul, K.; Seemakhan, S.; Charoensutthivarakul, S.; Wongtrakoongate, P.; Rangkasenee, N.; Pitiporn, S.; Waranuch, N.; Chabang, N.; Khemawoot, P.; Sa-ngiamsuntorn, K.; Pewkliang, Y.; Thongsri, P.; Chutipongtanate, S.; Hongeng, S.; Borwornpinyo, S.; Thitithanyanont, A. *Sci. Rep*. **2020**, *10*, 19963.
4. Sueree, L. & Ruangrungsri, N. Pharmacognostic specification and pinocembrin content of *Boesenbergia rotunda* root. RSU International Research Conference. **2016**, 74-80.
5. Jitrakiattikul, Y.; Rithichai, P.; Prachai, R.; Itharat, A. *Agr. Nat. Resour*. **2021**, *55*, 456-463.
6. Krachai Monograph. Department of Medical Sciences, Ministry of Public Health, Thai Herbal Pharmacopoeia. **2019**. Volume I. Nonthaburi: The Agricultural Co-operative Federation of Thailand, Ltd.
7. Adhikari, D.; Gong, D-S.; Oh, SH.; Sung, EH.; Lee, SO.; Kim, D-W.; Oak, M-H.; Kim, HJ. *Plants*. **2020**, *9*, 1688, 1-13.

8. Brand-Williams, W.; Cuvelier, M.E.; Berset, C.L.W.T. *LWT-Food Science and Technology*. **1995**. *28*, 25-30.
9. Wang, L-L.; Zhang, Y-b.; Sun, X-y.; Chen S-q. *J. Liq. Chromatogr. Relat. Technolo*. **2016**. 39(8), 422-427.
10. Saraf, I.; Marsh, K.J.; Vir, S.; Foley, W.J.; Singh, IP. **2017**. *12*(*11*), 1695-1699.
11. He, Y-q.; Yang, L.; Liu, Y.; Zhang, J-W.; Tang, J.; Su, J.; Li, Y-y.; Lu, Y-l.; Wang, C-h.; Yang, L.; Wang, Z-t. *Acta Pharmacol. Sin*. **2009**. *30*, 1462-1470.
12. Kim, M.; Choi, S.; Noh, K.; Kim, C.; Kim, E.; Hwang, J-K.; Kang W. *J. Pharm & Biomed Anal*. **2017**. 137, 151-154.
13. Fabre, N.; Rustan, I.; Hoffmann, Ed.; Quetin-Leclercq, J. *J. Am Soc Mass Spectrum*. **2001**. 12, 707-715.

Inhibition effect of cytochrome P4502A6 enzyme mutant alleles 7 (CYP2A6*7) activity by luteolin

Weeraphat Hassa[1], Supattra Boonruang[1,2], and Songklod Sarapusit[1,2,3]*

[1]*Department of Biochemistry, Faculty of Science, Burapha University, 169 Long-Hard Bangsaen Rd., Muang, Chonburi 20131, Thailand.*
[2]*Center of Excellence for Innovation in Chemistry, Faculty of Science, Burapha University, Chonburi, 20131, Thailand*
[3]*Research Unit of Natural Bioactive compounds for Healthcare Product Development, Faculty of Science, Burapha University, Chonburi, 20131, Thailand*

**E-mail: songklod@go.buu.ac.th*

Abstract:

Nicotine, one of the major substances in cigarette smoke, has been previously reported as a key compound responsible for smoking addiction. Inhaled nicotine passes to the brain and stimulates dopamine secretion, resulting in pleasure feeling. Nicotine is metabolized by liver-specific cytochrome P4502A6 (CYP2A6) enzyme. This nicotine clearance mechanism, however, could lead to cigarette craving and smoking more frequently in order to maintain nicotine levels in the bloodstream. Thus, maintaining blood-nicotine level by inhibiting the CYP2A6 activity is an alternative approach to decrease cigarette smoking. Luteolin has been previously reported as one of flavonoid compounds that could effectively inhibit the wild-type CYP2A6 (wt-CYP2A6) mediated coumarin 7-hydroxylation activity *in vitro*. This study aims to determine the inhibitory effect of Luteolin against the polymorphic cytochrome P450 2A6 mutant 7 (CYP2A6*7) that has been report in Thai population. 7-hydroxy coumarin hydroxylation was measured. The results indicated that Luteolin could inhibit wt-CYP2A6 and CYP2A6*7 with IC_{50} values of 1.93 ± 0.08 μM and 4.81 ± 0.43 μM, respectively. The molecular docking experiment indicated that wt-CYP2A6 and CYP2A6*7 were bound to Luteolin with different non-covalent interactions.

1. Introduction

The nicotine detoxification pathway by liver-specific Cytochrome P4502A6 (CYP2A6) has been reported to metabolize 80-90% of uptaken nicotine and is considered as an important route for nicotine metabolism. As nicotine is responsible for tobacco addiction, lowering the blood-nicotine level by this pathway could trigger the nicotine craving, resulting in continued smoking for maintaining blood-nicotine level.[1,2] Interestingly, the genetic polymorphism of *cyp2a6* genes has been reported to be associated with smoking behavior and the number of cigarettes smoking per day.[3] The low-metabolizing allele smokers (LM) who carry inefficient *cyp2a6* alleles or lack *cyp2a6* genes could prolong blood-nicotine level for long period of time, resulting in lower number of cigarettes smoking per day. Thus, specific inhibition of CYP2A6 enzyme, mimicking low activity of CYP2A6 enzyme in LM, has been proposed to as an alternative smoking cessation therapy.[1,2]

The 8-methoxypsoralen (8-MOP), a specific mechanism-based inhibitor (MBI) of wild-type CYP2A6 enzyme (wt-CP2A6), had been characterized and used for smoking cessation[4]. Although 8-MOP could effectively decrease the amount of cigarette smoke per day, it could also cause various side effects such as itching of skin and nausea. Therefore, alternative CYP2A6 inhibitors are still looked for. Numerous medicinal plants were screened and searched for natural-derived specific CYP2A6 inhibitors.[1,2] In Thailand, some commonly used medicinal plants were previously screened for their CYP2A6 inhibitory activity by using fluorescence-based method. Various candidate compounds from *Rhinacanthus nasutus*, *Vernonia cinerea*, and *Pluchea indica* were identified and characterized.[5-8] Among isolated active constituents, Luteolin, a flavonoid isolated from *V cinerea* and *P. indica*, exhibited high inhibitory activity against CYP2A6 enzyme with IC_{50} value of 1.38 ± 0.18 μM. Hence, Luteolin is one of the candidate compounds that could be used as an alternative agent for safety-smoking cessation.[8]

In Thailand, *cyp2a6* genetic polymorphism has been reported. Among low-metabolizing variance alleles that had previously reported to decrease in coumarin 7-hydroxylation activity, the allele frequency of *cyp2a6*7* allele (I471T) is relatively high in smoking population compared to *cyp2a6*8*, and *cyp2a6*10* (6.4, 1.1, and 2.7%, respectively).[9] Due to the association of variation in CYP2A6 activity from genetic polymorphism with smoking behavior, tobacco-related lung cancer risk, and smoking cessation, the investigation of the effect of this polymorphism on enzymatic activity is clinically important for

personalized medication.[10] This study aims to investigate the inhibition effected of luteolin on recombinant CYP2A6*7 enzyme. This knowledge may be a beneficial for further application of CYP2A6 inhibitor for smoking cessation on variances *cyp2a6* allele smoker.

2. Materials and Methods

2.1 Materials

Nicotinamide adenosine diphosphate reduced from (NADPH), 8-MOP, luteolin, coumarin, 1,2-didodecanoyl-rac-glycerol-3-phosphocholine (DLPC), and δ- aminolevulinic acid (δ-ALA) were purchased from Sigma-Aldrich (USA), Phenylmethyl sulfonyl fluoride (PMSF) and Isopropyl-β-D-thiogalacto-pyranoside (IPTG) were purchased from Fisher Scientific (UK) and US Biological (USA), respectively. Quick change mutagenesis kit and Ni-NTA affinity column were purchase from Stratagene (USA) and Qiagen (Germany), respectively.

2.2 Expression and Purification of wt-CYP2A6 and NADPH-cytochrome P450 reductase

The human wt-CYP2A6 and rat CPR, a P450s redox partner, were expressed and purified as previously described.[5-8] Briefly, the N-terminal truncation of wt-CYP2A6 in expression plasmid pTrc99A (*pTrc-ΔwtCYP2A6*) was transformed into *E. coli* XL-1 blue cells for expression. A culture was grown in TB media and 100 mg/mL ampicillin at 37 °C to an OD_{600} of 0.4–0.6 when protein expression was induced by addition of 0.5 mM IPTG and 0.005 mg/mL δ-aminolevulinic acid (δ-ALA) to induce the expression and facilitate synthesis of heme porphyrin ring, respectively. The cells were grown at 30 °C and 180 rpm for 48 hour and harvested by centrifugation at 5000 xg for 30 min. Cell pellets were resuspend in lysis buffer (200 mM phosphate buffer pH 7.4, 10% glycerol, 0.2 mM PMSF and 0.1% Triton-X-100) and lysed by sonication. The lysate was centrifuged at 30,000 xg at 4 °C for 1 hour. The supernatant was applied to a Ni-NTA affinity column chromatography previously equilibrated with equilibrating buffer (100 mM phosphate buffer pH 7.4, 200 mM NaCl, 20% glycerol, 0.2% triton X-100 and 0.5 mM PMSF). The column was washed with lysis buffer followed by the same buffer containing 20 mM imidazole. The protein was eluted with 30 to 50 mM imidazole. Purification of the wt-CYP2A6 protein was monitored by analysis of fractions by SDS–PAGE analysis.

The rat NADPH-Cytochrome P450 reductase (CPR) in the pINIII plasmid (*pINIII fl-rat CPR*) was transformed to *E. coli* C41 (DE3) cells. A culture was grown in TB media containing 100 µg/mL ampicillin at 37°C, 250 rpm. After the OD_{600} value reached 0.4-0.6, 0.2 mM IPTG was added to induce expression. The cells were grown at 30 °C and 180 rpm for 48 hour and harvested by centrifugation at 5,000 xg for 30 min. Cell pellets were resuspended in 50 ml lysis buffer (50 mM Tris-HCl pH 7.4, 20 mM NaCl, 10% glycerol, 0.1% triton X-100 and 0.2 mM PMSF) and subjected to sonication. The lysate was further incubated with 0.3% Triton X-100 for 30 min, the clear supernatant was collected after centrifugation at 30,000 xg for 1 hour. The clear supernatant was applied to Ni-NTA affinity column chromatography previously equilibrated with lysis buffer containing 5 mM imidazole. The column was extensively washed with the same buffer with lysis buffer containing 10 mM and 20 mM imidazole. The CPR protein was eluded with 100 mM imidazole in lysis buffer. Purification of the CPR protein was monitored by analysis of fractions by SDS–PAGE analysis.

2.3 Construction, Expression and Purification of CYP2A6*7 enzyme

Mutagenesis of the wtCYP2A6 was performed to produce the I471T mutation (*cyp2a6*7*) using the Quickchange PCR mutagenesis kit. The primer pair is 5′-ACCTAAGGACACTGACGTGTCC CC-3′ and 5′- GGGGACACGTCAGTGTCCTTA GGTG -3′. The constructs were verified by DNA sequencing (*pTrc-ΔCYP2A6*7*) and transformed into XL-1 blue cells. The CYP2A6*7 protein was expressed and purified using the same protocol developed for the wt-CYP2A6 enzyme.

2.4 Cytochrome P450 CYP2A6s activity assay

Either wt-CYP2A6 or CYP2A6*7 enzyme was then used for P450-reconstitution enzymatic assay with CPR enzyme. The enzymatic activity of CYP2A6 to metabolize fluorescence coumarin substrate was determined.[5-8] Briefly, the purified CYP2A6s (wtCYP2A6 or CYP2A6*7) was pre-incubated with rat CPR in 50 mM Tris-Cl buffer for 5 min at room temperature, followed by incubation with coumarin substrate. To determine inhibition activity, various concentrations of luteolin and coumarin substrate (~ the K_m value) were co-incubated with enzyme mixture for 5 min before starting reaction by addition of NADPH. Production of 7-hydroxycoumarin metabolite was measured in real time at excitation 355 nm and emission 460 nm. The IC_{50} values for inhibition were calculated using Graph-Pad Prism software, version 5 (La Jolla, CA). 8-MOP, a known inhibitor of CYP2A6, was used as control in the inhibition assays.

2.5 Molecular Docking

The structure of wtCYP2A6 complexed with 4,4'-dipyridyl disulfide (PDB 2FDY)[11], an CYP2A6 inhibitor was sketched in Discovery Studio 2016 client (BIOVIA, USA). Protein without ligand and luteolin were analyzed protein-ligand interaction by using AutoDockTools-1.5.6 (Molecular Graphic Laboratory, USA) program as previously described.[12,13] The structure of CYP2A6*7 was obtained by inputting DNA sequence with correspond mutation site into SWISS-MODEL (expasy.org).

3. Results & Discussion

3.1 Inhibition of Luteolin against wtCYP2A6 and CYP2A6*7 enzymes

The CPR protein was successfully expressed in *E. coli* strain C41 (DE3) and purified with Ni-NTA affinity column. An estimated molecular weight was at 78 kDa (Figure 1). In addition, the wtCYP2A6 and CPY2A6*7 enzymes were also successfully expressed in *E.coli* strain XL-1 blue and purified by Ni-NTA affinity column chromatography with the calculated molecular weight around 55 kDa (Figure 1).

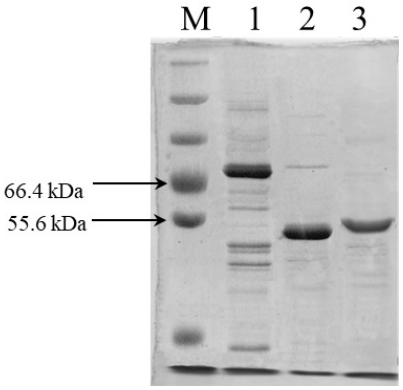

Figure 1. SDS-PAGE of purified CPR, wtCPY2A6 and CYP2A13. Lane includes M, protein marker; 1, CPR; 2, wtCYP2A6, and 3, CYP2A6*7.

The decrease in enzymatic activity of CYP2A6*7 had been previously reported in both individuals who carry either *CYP2A6*7/*7* or *CYP2A6*4/*7* genotype. An individual who contains the *7 allele demonstrated significantly lower plasma levels of nicotine and higher levels of cotinine compared to homozygous wild-type genotype (*CYP2A6*1/*1*).[14] Thus, the kinetic parameter of both CYP2A6s was determined by reconstituted enzyme system containing wtCYP2A6 or CYP2A6*7, CPR as a redox partner and DLPC in Tris-HCL buffer pH 7.4. To access enzymatic activity of CYP2A6, we employed cytochrome P450 CYP2A6s activity assay and monitor metabolization of fluorescence coumarin substrate. The rate of 7-hydroxycoumarin product formation was measured by spectrofluorometer and analyzed and the results showed no significant difference in V_{max} values between wtCYP2A6 and CYP2A6*7 enzymes. However, CYP2A6*7 enzyme exhibited slightly higher K_m value for coumarin 7-hydroxylation compared to the wtCYP2A6 enzyme (Table 1). The kinetic constants for wtCYP2A6 enzyme were comparable to those previously report.[7,8,13] This result suggested that the change from Ile to Thr at position 471 in CYP2A6*7 not mainly affects the catalytic turnover rate of the enzyme but the substrate binding affinity *in vitro*.

Table 1. Kinetic constants from steady state kinetic of coumarin 7-hydroxylation activity.

	K_m (μM)[a]	K_{cat} (s^{-1}) [a]
wtCYP2A6	1.54 ± 0.09 [b]	1.02 ± 0.06
CYP2A6*7	2.31 ± 0.11[b]	0.95 ± 0.19

[a] Each value represent mean ± SD of triplicate experiments

[b] Significant difference between wtCYP2A6 and CYP2A6*7 at $p < 0.05$

The results from inhibition assay, as summarized in Table 2, showed that luteolin could inhibit wtCYP2A6 with high affinity (IC_{50} value of 1.93 ± 0.08 μM). This IC_{50} value was comparable to previously reported at 1.38 ± 0.18 mM.[8] In contrast, luteolin showed less inhibitory activity against CYP2A6*7 with IC_{50} value of 4.81 ± 0.43 μM (Table 2).

Table 2. IC_{50} values of wtCYP2A6 and CYP2A6*7

	Luteolin (μM)[a]	8-MOP (μM) [a]
wtCYP2A6	1.93 ± 0.08[b]	0.90 ± 0.04 [b]
CYP2A6*7	4.81 ± 0.43[b]	1.52 ± 0.11 [b]

[a]Each value represent mean ± SD of triplicate experiment

[b] Significant difference between wtCYP2A6 and CYP2A6*7 at $p < 0.05$

3.2 Molecular docking of Luteolin with wtCYP2A6 and CYP2A6*7 enzymes

The inhibitory activity of flavonoids was slightly different based on the presence of substitution group at either ring B or ring C on the flavonoid structure.[12,15] Recently, it had been reported that the presence of hydroxyl group on flavonoids structures, including apigenin, quercetin, luteolin, kaempferol, and myricetin, could affect the inhibitory activity against

CYP2A6 enzyme. Apigenin, the lowest number of OH-group, could potently inhibit CYP2A6 enzyme with lowest IC_{50} value while Myricetin which contain six hydroxyl groups resulted in the least effective CYP2A6 inhibitor.[12,13] In this study, molecular docking was performed to understand the molecular interaction of Luteolin (Figure 3) with these CYP2A6s enzymes.

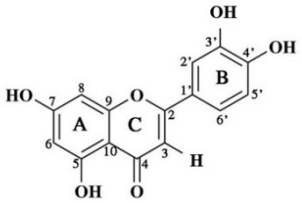

Figure 3. Chemical structures of luteolin. Chemical structure was produced using ChemDraw Professional 8.

As previously reported with wtCYP2A6 enzyme[13], the ring B of luteolin was hydrophobically aligned between the Ile208 and Ile300 with the H-bonding between the hydroxyl-group at C3' with Met205. Similarly, ring C hydrophobically interacted with Phe408 while ring A hydrophobic aligned with Val117 and Leu370. These interactions pointed the C6 position of ring A toward the CYP2A6-catalytic center (Figure 4A). The binding of luteolin to CYP2A6*7 enzyme was slightly different, the ring B hydrophobically interacted with Ile300 and H-bonding with Asn297. Several hydrophobic interactions of ring C with Phe107, Val117, Ile300, Gly301 and Leu366 were observed. Ring A exhibited hydrophobic interactions with Ile366 and Leu370 (Figure.4B). The result suggested that the conformational change due to the mutation from Ile 471 to Thr in Helix L′ of CYP2A6 enzyme might alter the binding interaction in the active site, leading to the loss of binding interactions in the case of coumarin probe substrate (in crease K_m value) as well as that of luteolin inhibitor (higher IC_{50} value) in CYP2A6*7.

4. Conclusion

Previous reports suggested that inhibition of CYP2A6 could be associated with quitting smoking.[1,2] Among various plant constituents, flavonoids are a very potent natural-derived CYP2A6 inhibitor and categorized as one of the promising chemical types for further smoking cessation application. However, the effectiveness of inhibition may be different in each CYP2A6 allele variance. In this study, the *CYP2A6*7* allele variances were successfully constructed, expressed, and purified using bacterial expression system. The enzyme kinetic parameter and inhibition effect of luteolin was determined compared to the wtCYP2A6 enzyme. The results showed that the mutation I471T in CYP2A6*7 enzyme affects the inhibition efficiency of luteolin and 8-MOP, a specific CYP2A6 inhibitor. Thus, the variation of *cyp2a6* allele in smoker should be determined for the effectiveness use of CYP2A6 inhibitor for further smoking cessation application.

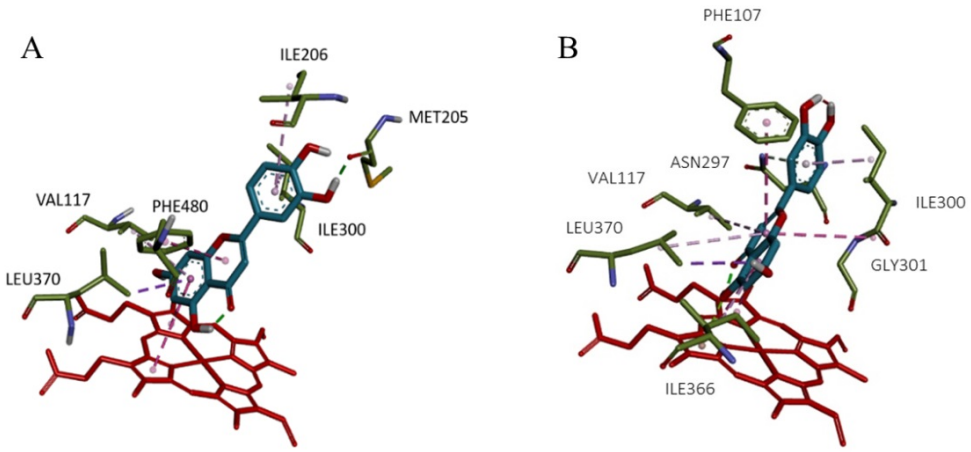

Figure 4. Docking of Luteolin with wtCYP2A6 (A), and CYP2A6*7 enzymes (B).

Acknowledgements

This work was supported by a Research Grant from Burapha University through the National Research Council of Thailand [grant No. 37.4/2562] and the Research Unit of Natural Bioactive Compounds for Healthcare Products Development (S.S).

References

1. Di, Y.M., Chow, V.D., Yang, L.P., Zhou, S.F. *Curr. Drug. Metab.* **2009**, *10*, 754-780.
2. Hukkanen, J.P. Benowitz, N.L. *Pharmacol. Rev.* **2005,** *57*, 79-115.
3. Fujieda, M., Yamazaki, H., Saito, T., Kiyotani, K., Gyamfi, M.A., Sakurai, M., Dosaka-Akita, H., Sawamura, Y., Yokota, J., Kunitoh, H., Kamataki, T. *Carcinog.* **2004,** *25*(12), 2451–2458.
4. Sellers, E.M., Tyndale, R.F., Fernandes, L.C. *Drug Discov Today*. **2003,** *8*, 487–493.
5. Thongjam, S., Rongnoparut, P., Sarapusit, S. Inhibition of The Human Cytochrome P450 2A6, The Nicotine Metabolising Enzyme by *Pluchea indic*a Extract. In *The 5th Science Research Conference.*, Phitsanulok., **2012**, BIO214-217.
6. Anantakul, J., Thongjam, S., Rongnoparut, P., Sarapusit, S. *Burapha Science Journal*. **2014,** *16* (3), 185-190.
7. Pouyfung, P., Prasopthum, A., Sarapusit, S., Srisook, E., Rongnoparut, P. *Drug. Metab. Pharmacok.* **2014,** *29* (1), 75-82.
8. Prasopthum, A., Pouyfung, P., Sarapusit, S., Srisook, E., Rongnoparut, P. *Drug. Metab. Pharmacok.* **2015,** *30*, 174-181
9. Mahavorasirikul, W., Tassaneeyakul, W., Satarug, S., Reungweerayut, R., Na-Bangchang, C., Na-Bangchang, K. *Eur. J. Clin. Pharmacol*. **2009,** *65*, 377–384.
10. Tanner, J-A., Tyndale, R.F. *J. Pers. Med.* **2017**, *7*, 18; doi:10.3390/jpm7040018
11. Yano, J. K., Denton, T. T., Cerny, M. A., Zhang, X., Johnson, E. F., Cashman, J. R. *J. Med. Chem.* **2006**, *49*(24), 6987-7001.
12. Kakimoto, K., Murayama, N., Takenaka, S., Nagayoshi, H., Lim, Y. R., Kim, V., Kim, D., Yamazaki, H., Komori, M., Guengerich, F. P., Shimada, T. *Xenobiotica*. **2019**, *49*(2), 131-142.
13. Boonruang, S., Prakobsri, K., Pouyfung, P., Prasopthum, A., Rongnoparut, P., Sarapusit, S. *Xenobiotica*. **2020**, *50*(6), 630-639.
14. Xu, C., Rao, Y. S., Xu, B., Hoffmann, E., Jones, J., Sellers, E.M., Tyndale, R.F. *Biochem. Biophys. Res. Commun.* **2002**, *290*, 318–324.
15. Hodek, P., Trefil, P., Stiborová, M. *Chem. Biol. Interact.* **2002**, *139*(1), 1-21.

Bioactive substances in the peel of immature *Dictyophora indusiata* mushrooms expressed antioxidant and anti-tyrosinase properties

Sebrian Yusbani[1], Wuttisak Kunu[2], and Supawadee Patathananone[1]*

[1]*Department of Chemistry Faculty of Science and Technology, Rajamangala University of Technology Thanyaburi, Pathum Thani 12110, Thailand*

[2]*Program of Veterinary Technology and Veterinary Nursing, Faculty of Agricultural Technology, Rajabhat Maha Sarakham University, Maha Sarakham 44000, Thailand*

**E-mail: Supawadee_P@rmutt.ac.th*

Abstract:

Bioactive agents in natural resources have been developed for foods, functional foods, pharmaceuticals, and traditional medicine. This study aims to extract the biomolecules from the peel of immature *D. indusiata* mushrooms to determine antioxidant and anti-tyrosinase activity and analyze the types of biomolecules. Raw materials were collected, and the extracts were used at different temperatures and solvents. All extracts were determined for antioxidant and anti-tyrosinase activities, including comparing total phenolics, flavonoids, and terpenoids contents. The results showed that the O-A1-01-80W represented the potential of antioxidant activity at an IC_{50} value of 0.230 mg/mL and FRAP value of 212.46 ± 0.20 mM Fe^{2+}/g extract. The total phenolics, total flavonoids, and total terpenoids contents expressed 26.98 ± 0.34 mg GAE/g, 14.49 ± 0.25 mg QE/g, and 98.93 ± 1.02 mg MT/g O-A1-01-80W extract, respectively. L-A1-02-80W extract expressed high efficacy in terms of anti-tyrosinase activity and an IC_{50} value of 0.430 mg/mL. Therefore, the biological potential represented in the extracts could develop as a functional food ingredient to prevent the risk of non-communicable diseases (NCDs).

1. Introduction

Non-communicable diseases (NCDs) are health problems that are currently of concern to national and global governments. The World Health Organization (WHO) data for 2023 showed that 47 million deaths occur yearly, or the equivalent of 74% caused by NCDs. In countries with low to middle economic levels, 17 million deaths occurring in people aged less than 70 years are caused by NCDs. NCDs have become one of the WHO's priorities in overcoming the current situation. NCDs are the most significant cause of death in the world.[1] Lifestyle and environment influence many risk factors, both external and internal, associated with these diseases. The risk factors for these diseases are associated with free radicals, which can attack human body cells and cause oxidative damage.

Various efforts have been made to overcome this condition, including using antioxidants.[2] Usually, the human body can produce antioxidants. Sometimes, the need for antioxidants cannot be met. It requires an external intake of antioxidants. The antioxidant intake can be met through food supplies or supplements.[3] The various types of plants, especially mushrooms, have good natural antioxidants. Mushrooms contain many bioactive compounds, such as carbohydrates, proteins, lipids, fatty acids, amino acids, vitamins, minerals, and others.[4,5] It is also alleged that mushrooms can be used to treat various diseases such as antitumor, anticancer, antioxidative, antiallergic, antifungal, antiviral, anti-inflammatory, immunomodulatory, and others.[6–8] Generally, the peel of an embryonic mushroom (egg stage) plays a significant role in shielding the interior compartments from the environments, worms, and insects. Consequently, substances with a variety of biological roles may be present in the peels of juvenile mushrooms. Previous reports explained that the 95% ethanoic extract of peel and green mixture of *Dictyophora indusiata* comprehends antioxidants, including polyphenols, flavonoids, and other bioactive compounds.[9] However, no research publications are based only on the analysis of the *D. indusiata* peel extracts. Therefore, this study aims to extract the bioactive components in immature *D. indusiata* peel using hot and cold solvents, combining mechanical methods to investigate and compare the extract's biological activities, total phenolic, flavonoid, and terpenoid contents. The data of this work may promote immature *D. indusiata* peel as the natural source for collecting the bioactive compounds that could be developed for functional food and pharmaceutical applications, healthcare products to become an alternative for preventing the risk of NCDs caused by the activity of free radicals that attack the human body.

2. Materials and Methods

2.1 Raw material preparations

D. indusiata grows in the bamboo forest in the local area of Sa Kaeo province, Thailand. The components of the immature stage were collected, and an ID label was created as A1: peel (Figure 1). In this study, the A1 part was dried in two ways: L-A1-02 was prepared using freeze-dry (at -24 ˚C for 27 h), while O-A1-01 was dried in a hot air oven at 60 ˚C for 24 h.

2.2 Extraction process

This extraction procedure was performed in two significant ways: the first factor was temperature (4 and 80 ˚C), and the second was the extracted solvents (deionized water, methanol, and ethanol). The % yield, qualitative, and quantitative of biological components and properties were compared, associating both factors. The dried raw materials L-A1-02 and O-A1-01 were balanced for 10 g and placed into extracted chambers. Deionized water (DI), methanol, and ethanol were incubated at 4 ˚C and 80 ˚C. These solvents were subjected to the extracted chambers in a ratio of 1:20 (w/v) and then incubated at different temperatures (4 ˚C and 80 ˚C) for 1 h. Afterward, chambers were placed in an ultrasonic machine according to the temperature conditions and then extracted continuously by 35 kHz of ultrasonic three times for 1 h. The supernatant of each condition was collected using 160 nm of mesh. The clear supernatant was prepared using centrifugation at 5,000 rpm for 5 min. The extracts that used water as a solvent were dried by a freeze dryer, while the evaporator concentrated the methanol and ethanol extracts. All extracts were balanced, yields calculated, and then stored at -20 ˚C.

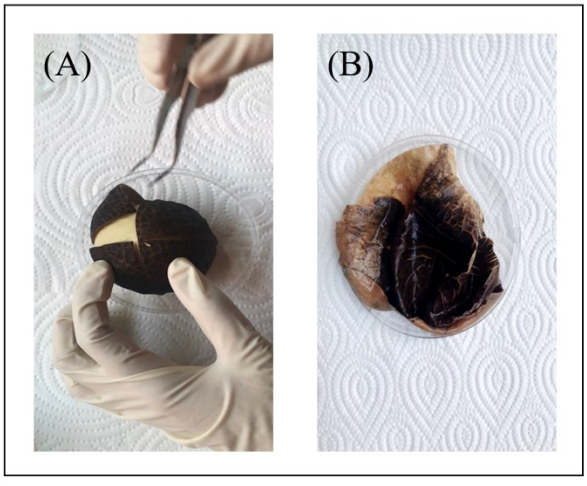

Figure 1. (A) Immature of *D. indusiata*; (B) A1: peel

2.3 DPPH radical scavenging assay

All extracts were dissolved and prepared at different concentrations using two flow dilution techniques. L-ascorbic acid is used as a positive control for antioxidants. The reaction was performed on a 96-well plate. In the order of the test condition, 190 µL of 0.1014 mM DPPH radical solution (0.1014 mM of DPPH in ethanol) was placed into each well. The 10 µL of different concentrations for each extract were incubated with the DPPH radical solution, mixed gently, and incubated at 37 ˚C in the dark for 1 h. The absorbance values were measured at 515 nm using the microplate reader. The percentage of DPPH radical scavenging activity was analyzed as previously described by.[10]

2.4 Ferric reducing antioxidant power (FRAP) assay

The total antioxidants in foods have been investigated wildly by FRAP assay.[11] Iron [III]-2,4,6-tripyridyl-S-triazine (Fe^{3+}—TPTZ) is reduced to ferrous-tripyridyl triazine (Fe^{2+}—TPTZ) by setting with an antioxidant chemical in the FRAP assay reaction. This reaction produces a striking blue hue. For the initial step, 1 mL of 10 mM of 2,4,6-tri(2-pyridyl)-s-triazine (TPTZ) in 40 mM of hydrochloric acid was mixed with 1 mL of 20 mM ferric chloride and 10 mL of 300 mM acetate buffer (pH 3.6), according to the ratio 10:1:1 (v/v), and then incubated at 37 ˚C for 1 min. The working solution of the freshly prepared FRAP reagent was diluted with 40 mM of hydrochloric acid. The reaction was performed by mixing 2.6 mL of FRAP reagent, 100 µL of sample extracts, and 300 µL of deionized water. In addition, α-tocopherol was used as a positive control. The reaction of each tube was incubated at 37 ˚C for 30 min. The absorbance values were measured using a UV-Vis spectrophotometer at 593 nm. Furthermore, ferrous sulfate ($FeSO_4$) with concentrations of 0.07875, 0.1575, 0.315, 0.629, and 1.258 mM was used to prepare a standard curve. The value of antioxidant content can be calculated using the FRAP value equation in mM Fe^{2+}/g extract using the formula $y = 5.1142x + 1.2293$, $R^2 = 0.9973$.

2.5 Anti-tyrosinase activity assay

The anti-tyrosinase test was carried out by weighing a sample of 0.01 g dissolved in 1 mL of deionized water. Then, the sample solution was filtered through a 0.45 nm filter membrane, and the sample was diluted with a double dilution system using 50 mM phosphate buffer pH 6.8 until the solution reached six-fold dilutions. The experimental procedure was analyzed on 96

microplates (96-well plates). In the initiation step, 100 µL of 250 units/mL mushroom tyrosinase was incubated with 10 µL of different concentrations of the extract samples. Then, 70 µL of 50 mM phosphate buffer pH 6.8 was added and mixed gently. The reaction was incubated at 37 ˚C for 10 min. Furthermore, 20 µL of 20 mM L-Dopa in DMSO was placed, mixed, and incubated at 37 ˚C for 30 min. Kojic acid was used as a positive control, and anti-tyrosinase activity was investigated using the same method. The absorbance values were measured at a wavelength of 495 nm. The percentage of anti-tyrosinase activity was analyzed as previously described by.[10]

2.6 Total phenolic content

The modified Folin-Ciocalteu method was carried out by.[11] The Folin-Ciocalteu was diluted ten-fold before being put into the test tube. A total of 100 µL of each sample was taken and put into ethanol. 400 µL of each dilution of Folin-Ciocalteu reagent was added, and 7.5% sodium carbonate solution was added into a 2 mL test tube and allowed to stand for 3 min. The volume of the solution was increased to 7.5 mL with the addition of deionized water and incubated at 37 ˚C for 1 h. A UV-Vis-spectrophotometer measured the wavelength with an absorbance value of 750 nm. The gallic acid standard curve equation is $y = 9.3779x + 0.096$, $R^2 = 0.9946$. It was used to calculate the total phenolic content in the extracted samples. Data are presented in mg GAE/g dry extract.

2.7 Total flavonoid content

The total flavonoid content was determined using a colorimetric method involving modified aluminum chloride ($AlCl_3$).[12,13] Pipette 50 µL (10 mg/mL) of each sample, 1 mL of methanol, 4 mL of deionized water, and 0.3 mL of 5% $NaNO_2$, then mix until the standard solution (Quercetin) becomes 5.0 mg in 1 mL of methanol. Then 0.3 mL of a solution of aluminum chloride ($AlCl_3$ 10%) and 2 mL of mol/L NaOH and water were added to 10 mL of deionized water, followed by distilled water. For 15 min, the mixture was incubated at 37 ˚C. A UV-Vis-spectrophotometer was used to measure the absorbance three times at a wavelength of 510 nm. The total flavonoid content was calculated as mg QE/g dry extract using the equation $y = 1.1305x + 0.0407$, $R^2 = 0.9991$.

2.8 Total terpenoid content

The total terpenoid content of the extract was determined by the method of Truong.[14] The method uses menthol, a standard terpenoid compound. The chloroform solution of as much as 2 mL was added to 10 mg/mL of the sample. Then, the sample mixture was shaken until evenly mixed and left for 3 minutes. After that, 200 µL of concentrated sulfuric acid (H_2SO_4) was added to the mixture, and the solution was then incubated at 37 ˚C for 30 min. During the incubation process, a reddish-brown precipitate will form in the solution. The supernatant was then carefully poured without disturbing the precipitation, and then 3 mL of absolute methanol was added to the precipitate and shaken until well mixed. A UV-Vis spectrophotometer was used to measure the absorbance at 538 nm. The menthol standard curve equation is $y = 0.4269x + 0.091$, $R^2 = 0.9986$. It was used to calculate the total terpenoid content in the extracted samples. Data are presented in mg MT/g extract.

2.9 Statistical data analysis

Statistical analysis was conducted by investigating the ANOVA variance test to see if there was a difference in the value concentration of the sample test using Duncan's at an alpha subset rate of 5%. The value concentrations are analyzed using the software.

3. Results & Discussion

3.1 Raw material yield of the extracts

Preparing raw materials is the first step and is a priority in identifying the bioactive compounds contained therein. Temperature is the reference to see the comparison of biological properties found in natural products. This research used mushrooms from the species *D. indusiata*, which were collected and dried using two methods such as (1) lyophilizing with a performance at 4 ˚C (L-A1-02) and (2) a hot air oven controlled at 60 ˚C (O-A1-01). The differences in temperature and solvent during extraction may relate to the collection of raw materials.

The two raw materials are dissolved using deionized water, methanol, and ethanol solvents for the extraction system. Furthermore, it was pre-incubated with ice-cold solvent (4 ˚C) and hot solvent (80 ˚C), and the extraction was carried out using an ultrasonic instrument at the same temperature conditions as the temperature of each sample solvent.

The results showed that most of the enormous yields were found in extraction using water solvents compared to methanol and ethanol solvents. This condition also showed that the % yield at higher temperatures is better than at low temperatures. This condition can be seen in Table 1. The results indicated that, according to the goal target, the value of higher yield using water solvent is the extraction process economically and safely

(low cost and safety). Therefore, the data relation will be used to determine biological activities.

3.2 DPPH radical scavenging activity

The results showed that the highest antioxidant content from the peel of *D. indusiata* was shown in O-A1-01-80W (80.00%) and L-A1-02-80W (72.21%) with the same extract concentration and temperature. The details can be shown in Figure 2. Higher-temperature treatment can produce excellent antioxidant quality. On the other hand, the water solvents also showed the perfect choice to demonstrate antioxidant power compared to methanol and ethanol solvents. Economically, the water solvents do not require expensive costs. It is easy to choose the application of the product that will be used. Based on previous reports it also explains that *D. indusiata* mushrooms have good antioxidants.[15,16] Another report explains that using of the ultrasonic-assisted extraction method with DI water produces the highest antioxidant activity when compared to others.[17] There are similarities between this research and previous reports. The excellent antioxidant value has many benefits for applications in the health sector. The benefits of antioxidants as an antidote to free radicals. Additionally, it can protect the body from exposure to harmful free radicals, which can damage normal cell function. The impact of free radicals can be oxidative damage, which causes oxidative stress and is associated with NCDs. Furthermore, antioxidants are needed to overcome this problem. Fulfilling the daily supply of antioxidants through food or supplements will help the body prevent various diseases, especially NCDs.

Table 1. Extraction yields, total phenolic, flavonoid, and terpenoid

ID Samples	Extraction yields (%)	Total phenolic (mg GAE/g)	Total flavonoid (mg QE/g)	Total terpenoid (mg MT/g)
O-A1-01-4W	$8.24 \pm 0.04^{a,b}$	15.53 ± 0.41^{c}	8.42 ± 0.13^{d}	82.76 ± 1.76^{a}
O-A1-01-4ME	7.97 ± 0.02^{b}	10.56 ± 0.16^{f}	7.43 ± 0.18^{e}	68.58 ± 1.02^{d}
O-A1-01-4ET	5.19 ± 0.01^{c}	6.23 ± 0.25^{g}	6.61 ± 0.17^{f}	57.28 ± 1.67^{b}
L-A1-02-4W	$8.37 \pm 0.02^{a,b}$	12.83 ± 0.16^{e}	7.88 ± 0.08^{e}	63.48 ± 1.76^{b}
L-A1-02-4ME	2.91 ± 0.01^{d}	9.47 ± 0.34^{f}	6.07 ± 0.18^{f}	52.40 ± 1.02^{e}
L-A1-02-4ET	2.92 ± 0.01^{d}	4.29 ± 0.25^{h}	5.68 ± 0.22^{g}	42.65 ± 1.38^{g}
O-A1-01-80W	9.21 ± 0.05^{a}	26.98 ± 0.34^{a}	14.49 ± 0.25^{a}	98.93 ± 1.02^{c}
O-A1-01-80ME	$8.77 \pm 0.04^{a,b}$	17.47 ± 0.25^{b}	12.54 ± 0.09^{b}	82.98 ± 1.38^{a}
O-A1-01-80ET	5.16 ± 0.02^{c}	12.33 ± 0.32^{e}	10.00 ± 0.25^{c}	70.35 ± 1.67^{a}
L-A1-02-80W	$8.85 \pm 0.08^{a,b}$	18.66 ± 0.11^{b}	11.61 ± 0.09^{c}	92.11 ± 1.43^{c}
L-A1-02-80ME	5.25 ± 0.18^{c}	14.96 ± 0.06^{d}	10.23 ± 0.05^{c}	78.63 ± 1.58^{d}
L-A1-02-80ET	2.99 ± 0.07^{d}	12.44 ± 0.06^{e}	8.25 ± 0.09^{d}	65.83 ± 0.69^{b}

GAE: gallic acid equivalent; QE: quercetin equivalent; MT: menthol equivalent; values followed by different superscript letters (a–h) in the same column are significantly different ($p < 0.05$)

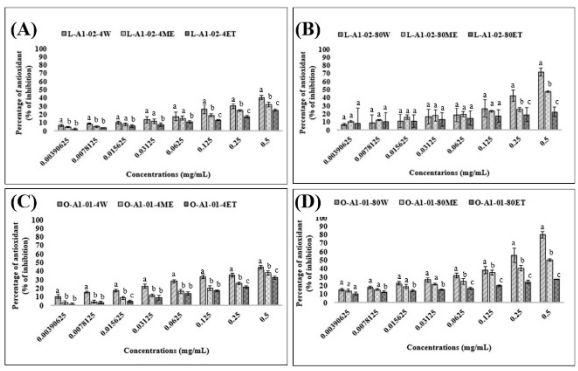

Figure 2. DPPH radical scavenging activity (A) the treatment extracts as L-A1-02-4W, L-A1-02-4ME, L-A1-02-4ET; (B) L-A1-02-80W, L-A1-02-80ME, L-A1-02-80ET; (C) O-A1-01-4W, O-A1-01-4ME, O-A1-01-4ET; (D) O-A1-01-80W, O-A1-01-80ME, O-A1-01-80ET

The determination of antiradical activity is carried out by calculating the inhibitory concentration (IC_{50}). The highest IC_{50} value is the smallest of the antioxidant activity; conversely, the smallest IC_{50} value is the strongest. The IC_{50} value is calculated using the linear curve value of each sample tested, which can be seen in Table 2. The data showed that perfect IC_{50} values are shown in the extracts O-A1-01-80W (0.230 mg/mL), L-A1-02-80W (0.317 mg/mL), O-A1-01-4W (0.552 mg/mL), and L-A1-02-4W (0.588 mg/mL), respectively. The results of the antioxidant activity test also showed that the mushroom peel extract has antioxidant activity. This is probably due to its terpenoid, phenolic, and flavonoid content. The antioxidant mechanism of terpenoid, phenolic, and flavonoid compounds is based on oxidation-reduction reactions, where these compounds will act as reducing agents to reduce the free (reactive)

radicals formed into species that are no longer reactive—the reaction between DPPH radicals and terpenoid, phenolic, and flavonoid compounds in the mushroom peel.

Table 2. Antioxidant contents and IC_{50} value

ID Samples	FRAP value (mM Fe^{2+}/g)	IC_{50} value (mg/mL)
O-A1-01-4W	141.48 ± 0.39[a]	0.552[f]
O-A1-01-4ME	102.34 ± 0.49[e]	0.589[e]
O-A1-01-4ET	75.45 ± 0.63[f]	0.618[d]
L-A1-02-4W	120.49 ± 0.30[b]	0.588[e]
L-A1-02-4ME	75.84 ± 0.74[f]	0.628[c]
L-A1-02-4ET	49.97 ± 0.41[h]	0.693[a]
O-A1-01-80W	212.46 ± 0.20[c]	0.230[i]
O-A1-01-80ME	141.87 ± 0.52[a]	0.496[g]
O-A1-01-80ET	100.86 ± 0.63[i]	0.628[c]
L-A1-02-80W	159.95 ± 0.12[d]	0.317[h]
L-A1-02-80ME	126.45 ± 0.21[g]	0.614[d]
L-A1-02-80ET	88.84 ± 0.12[j]	0.660[b]

The values followed by different superscript letters (a–j) in the same column are significantly different ($p < 0.05$)

3.3 Ferric reducing antioxidant power (FRAP) value

The FRAP value represented the antioxidant efficacy of the biomolecules in each extract. The data is shown in Table 1. The FRAP values of O-A1-01-80W and L-A1-02-80W extracts presented approximately 212.46 ± 0.20 and 159.95 ± 0.12 mM of Fe^{2+}/g extract, respectively, and were different and significant. The results show a correlation between the FRAP value test and the test using DPPH radical scavenging and that temperature treatment affects the results. The results showed that high temperatures produce a better total FRAP value than low temperatures. In addition, the use of water solvents is better than methanol and ethanol solvents, as can be seen in Table 1. The action of antioxidants has many benefits for the health sector. The antioxidants can be used for prevention and treatment in medicine. Antioxidant activity can reduce biomolecule degradation related to the risk of NCDs.

3.4 Anti-tyrosinase activity

Tyrosinase is an oxidoreductase that is very important in medicine and cosmetics because of its ability to produce melanin, which plays a role in the hyperpigmentation process. Tyrosinase is a crucial enzyme for melanin biosynthesis, catalyzing the oxidation of L-tyrosine to L-dopaquinone. Tyrosinase inhibition is a practical approach to controlling hyperpigmentation of the skin. The results of the tyrosinase inhibition test on the peel of *D. indusiata* extract showed an IC_{50} value of 0.430 mg/mL of L-A1-02-80W extract. The results and details are shown in Figure 3. This study is similar to previous reports, which explained that *D. indusiata* showed a significant inhibitor of L-Dopa oxidation.[18] Another report, research conducted by Theeraraksakul,[17] explained that using water as a solvent resulted in significant inhibition of tyrosinase, which indicates similarities with this research. It is possible for mushroom extract to inhibit melanin production. Melanin is responsible for skin color and essential in protecting against UV rays that cause skin damage.[19] Melanin is the primary pigment in skin, hair, and eye color. Melanin can form excessively when exposed to chronic sun exposure, melasma, or other hyperpigmentation diseases.[20] The presence of tyrosinase inhibitors will inhibit the browning reaction or melanin formation. Many cosmetic ingredients, including ascorbic acid, arbutin, kojic acid, mercury, and hydroquinone, have used tyrosinase inhibitors to prevent hyperpigmentation. Of these compounds, kojic acid has the most excellent inhibitory effect and stability in cosmetic products; however, kojic acid is carcinogenic.[21] As a natural compound, mushrooms have no side effects, and their mass production in the future can be developed as functional food and cosmetic products. Further, the action of the peel mushrooms on tyrosinase activity may indicate in at least one of the pharmacological actions of *D. indusiata*.

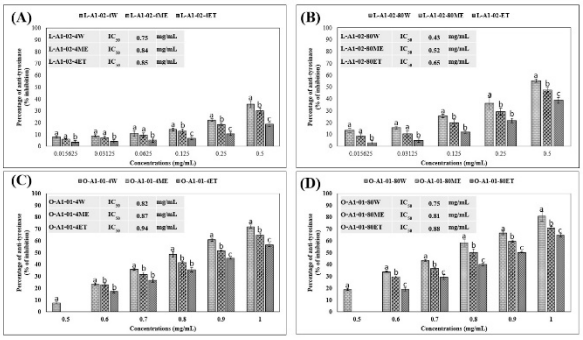

Figure 3. Anti-tyrosinase activity of the extracts (A) L-A1-02-4W, L-A1-02-4ME, L-A1-02-4ET; (B) L-A1-02-80W, L-A1-02-80ME, L-A1-02-80ET; (C) O-A1-01-4W, O-A1-01-4ME, O-A1-01-4ET; (D) O-A1-01-80W, O-A1-01-80ME, O-A1-01-80ET

3.5 Total phenolic content

The results of the total phenolic content are shown in Table. 1. The results show perfect total phenolic content in the extracts O-A1-01-80W (26.98 ± 0.34 mg GAE/g), L-A1-02-80W (18.66 ± 0.11 mg GAE/g), O-A1-01-4W (15.53 ±

0.41 mg GAE/g), and L-A1-02-4W (12.83 ± 0.16 mg GAE/g), respectively. The water-based solvents and high-temperature treatments produce better total phenolic levels compared to water-based solvents and low-temperature treatments. This situation also applies to solvents based on methanol and ethanol. Overall, the water solvents are the best option. Based on previous reports, the peel of *D. indusiata* contains total phenolics from extraction using water-based solvents.[22] This indicates that previous reports have similarities to this research. Phenolic compounds are one type of antioxidant compound. Phenolic compounds are also secondary metabolites found in fruits and plants, including all types of mushrooms, which have benefits against various types of diseases when consumed for human dietary needs. There are many types of phenolic compounds, all functioning as free radical scavengers. Phenolic compounds can suppress damage caused by free radicals. The damage caused by oxidative damage can be prevented and overcome. Phenolic compounds also have various other benefits that have been widely applied in the pharmaceutical industry. Nowadays, consuming natural products has become a tendency to consume safe and healthy products. In the food industry, isolated phenolic compounds from plant sources are used as natural antioxidant supplements in various food products.

3.6 Total flavonoid content

Flavonoid compounds are a subclass of polyphenolic compounds, secondary metabolites with antioxidant activity. The results showed that the best flavonoid levels were shown in the extracts O-A1-01-80W (14.49 ± 0.25 mg QE/g) and L-A1-02-80W (11.61 ± 0.09 mg QE/g), respectively, when compared with the extraction using methanol and ethanol solvents. Meanwhile, the extraction of O-A1-01-4W (8.42 ± 0.13 mg QE/g) and L-A1-02-4W (7.88 ± 0.08 mg QE/g) represented the lower temperature tendency for total flavonoid compounds compared to the higher temperature. According to the findings, extractions conducted at low temperatures yield lower levels of total flavonoid contents than those conducted at high temperatures. The results can be seen in Table 1. Flavonoids, like phenolic compounds, are found in many fruits and plants, especially mushrooms. However, previous reports showed mushrooms have flavonoids.[8] Consuming foods that contain natural compounds is highly recommended for preventing various diseases and improving health promotion.[23,24]

3.7 Total terpenoid content

The results of the research showed that the peel of *D. indusiata* extract contained terpenoids, as shown in Table 1. The highest total terpenoid content was found in the extracts of O-A1-01-80W (98.93 ± 1.02 mg MT/g) and L-A1-02-80W (92.11 ± 1.43 mg MT/g), followed by other extracts such as O-A1-01-4W (82.76 ± 1.76 mg MT/g) and L-A1-02-4W (63.48 ± 1.76 mg MT/g), respectively. Similar to the value of total phenolics and flavonoids, the type of solvent and temperature influence the results obtained. A previous report also explained that *D. indusiata* contains terpenoids from the monoterpenoids and sesterterpenoids, which come from the fruiting body.[25] The types of terpenoids in this study may come from the same type of terpenoid. Terpenoids have effects such as antioxidant, anticancer, antitumor, anti-inflammatory, antimalarial, antibacterial, antiparasitic, prevention and treatment of cardiovascular diseases, hypoglycemic, anti-hyperglycemic, and others.[26–28] Additionally, the high antioxidant properties of plants are due to the presence of large amounts of terpenoids.[29] This aligns with the results from this work, which showed that the total terpenoid content has the most significant value compared to other bioactive compounds.

4. Conclusion

The peel extracts of *D. indusiata* exhibit a variety of biological activities, such as antioxidant and anti-tyrosinase. They also display other biological properties that can be applied as active ingredients in functional foods and pharmaceutical products.

Acknowledgments

This research was supported by The Science, Research, and Innovation Promotion Funding (TSRI) (Granted No. FR64E0619). This research block grant was managed under the Rajamangala University of Technology Thanyaburi (Granted No. FRB640013).

References

1. WHO. *Noncommunicable diseases*. https://www.who.int/news-room/fact-sheets/detail/noncommunicable-diseases (accessed 2023-12-16).
2. Seyedsadjadi, N.; Grant, R. *Antioxidants* **2020**, *10* (1), 15.
3. Ayoka, T. O.; Ezema, B. O.; Eze, C. N.; Nnadi, C. O. *J. Explor. Res. Pharmacol.* **2022**, *7* (3), 178–188.
4. Yadav, D.; Negi, P. S. *Food Res. Int.* **2021**, *148*, 110599.

5. Sande, D.; Oliveira, G. P. D.; Moura, M. A. F. E.; Martins, B. D. A.; Lima, M. T. N. S.; Takahashi, J. A. *Food Res. Int.* **2019**, *125*, 108524.
6. Maity, P.; Sen, I. K.; Chakraborty, I.; Mondal, S.; Bar, H.; Bhanja, S. K.; Mandal, S.; Maity, G. N. *Int. J. Biol. Macromol.* **2021**, *172*, 408–417.
7. Venturella, G.; Ferraro, V.; Cirlincione, F.; Gargano, M. L. *Int. J. Mol. Sci.* **2021**, *22* (2), 634.
8. Lu, H.; Lou, H.; Hu, J.; Liu, Z.; Chen, Q. *Compr. Rev. Food Sci. Food Saf.* **2020**, *19* (5), 2333–2356.
9. Ruksiriwanich, W.; Khantham, C.; Linsaenkart, P.; Chaitep, T.; Rachtanapun, P.; Jantanasakulwong, K.; Phimolsiripol, Y.; Jambrak, A. R.; Nazir, Y.; Yooin, W.; Sommano, S. R.; Jantrawut, P.; Sainakham, M.; Tocharus, J.; Mingmalairak, S.; Sringarm, K. *Int. J. Food Sci. Technol.* **2022**, *57*, 110–122.
10. Patathananone, S.; Daduang, J.; Koraneekij, A.; Li, C.-Y. *Orient. J. Chem.* **2019**, *35* (3), 916–926.
11. Kelman, D.; Posner, E. K.; McDermid, K. J.; Tabandera, N. K.; Wright, P. R.; Wright, A. D. *Mar. Drugs* **2012**, *10* (12), 403–416.
12. Aryal, S.; Baniya, M. K.; Danekhu, K.; Kunwar, P.; Gurung, R.; Koirala, N. *Plants* **2019**, *8* (4), 96.
13. Baba, S. A.; Malik, S. A. Determination of *J. Taibah Univ. Sci.* **2015**, *9* (4), 449–454. https://doi.org/10.1016/j.jtusci.2014.11.001.
14. Truong, D.; Ta, N. T. A.; Pham, T. V.; Huynh, T. D.; Do, Q. T. G.; Dinh, N. C. G.; Dang, C. D.; Nguyen, T. K. C.; Bui, A. V. *Food Sci. Nutr.* **2021**, *9* (3), 1720–1735.
15. Zhang, Y.; Lei, Y.; Qi, S.; Fan, M.; Zheng, S.; Huang, Q.; Lu, X. *Ultrason. Sonochem.* **2023**, *95*, 106356.
16. Bai, X.; Bai, X. *J. Indian Chem. Soc.* **2021**, *98* (10), 100146.
17. Theeraraksakul, K.; Jaengwang, K.; Choowongkomon, K.; Tabtimmai, L. *Cosmetics* **2023**, *10* (5), 121.
18. Sharma, V. K.; Choi, J.; Sharma, N.; Choi, M.; Seo, S. *Phytother. Res.* **2004**, *18* (10), 841–844.
19. Min Chang, T. *J. Biocatal. Biotransformation* **2012**, *01* (02).
20. Briganti, S.; Camera, E.; Picardo, M. *Pigment Cell Res.* **2003**, *16* (2), 101–110.
21. Miyazawa, M.; Tamura, N. *Biol. Pharm. Bull.* **2007**, *30* (3), 595–597.
22. Nazir, Y.; Linsaenkart, P.; Khantham, C.; Chaitep, T.; Jantrawut, P.; Chittasupho, C.; Rachtanapun, P.; Jantanasakulwong, K.; Phimolsiripol, Y.; Sommano, S. R.; Tocharus, J.; Mingmalairak, S.; Wongsa, A.; Arjin, C.; Sringarm, K.; Berrada, H.; Barba, F. J.; Ruksiriwanich, W. *J. Fungi* **2021**, *7* (12), 1100.
23. Chen, L.; Cao, H.; Huang, Q.; Xiao, J.; Teng, H. *Crit. Rev. Food Sci. Nutr.* **2022**, *62* (28), 7730–7742.
24. Ullah, A.; Munir, S.; Badshah, S. L.; Khan, N.; Ghani, L.; Poulson, B. G.; Emwas, A.-H.; Jaremko, M. *Molecules* **2020**, *25*, 1–39.
25. Habtemariam, S. *Biomedicines* **2019**, *7* (98), 1–21.
26. Jahangeer, M.; Fatima, R.; Ashiq, M.; Basharat, A.; Qamar, S. A.; Bilal, M.; Iqbal, H. M. N. *J. Pure Appl. Microbiol.* **2021**, *15* (2), 471–483..
27. Yang; Chen, X.; Li, Y.; Guo, S.; Wang, Z.; Yu, X. *Nat. Prod. Commun.* **2020**, *15* (3), 1-13.
28. Vergara-Jimenez, M.; Almatrafi, M.; Fernandez, M. *Antioxidants* **2017**, *6* (4), 91.
29. Mohandas, G. G.; Kumaraswamy, M. *Pharmacogn. J.* **2018**, *10* (4), 645–649.

Extraction, preliminary phytochemical screening and antioxidant properties of ethanolic crude extract of Madan (*Garcinia schomburgkiana* Pierre)

Supranee Pimpila, Worawat Chanmin, Irawan Cheunangul, and Winai Oungpipat *

Health Science and Aesthetic Program, Department of Science, Faculty of Science and Technology, Rajamangala University of Technology Krungthep, 2 Nang Linchi Road, Sathron, Bangkok 10120, Thailand

**E-mail: winai.o@mail.rmutk.ac.th*

Abstract:

Madan (*Garcinia schomburgkiana* Pierre) is an edible perennial fruit belonging to the Guttiferae family. Local people consumed it fresh and fermented. Madan leaves, root and fruit are also traditionally used as an expectorant, improvement of menstrual blood quality, treatment of coughs, treatment of diabetes and as a laxative. The aim of the present study was to explore the phytochemical constituents, to evaluate the total phenolic and total flavonoid contents and antioxidant activity of the crude fruits and leaves of *G. schomburgkiana* Pierre extracts. The extraction process was performed using 50 g each of the dried powder of *G. schomburgkiana* fruits and leaves soaked in 250 ml of ethanol and macerated for 7 days at room temperature. The crude extract yields obtained were 23.13±3.17 g and 6.46±2.64 g for fruit and leaf extracts, respectively. The phytochemical screening of the Madan fruit extracts revealed the presence of flavonoids, tannins and saponins, while the Madan leaf extracts were found to contain flavonoid, steroids, tannins, glycosides, sterols, and saponins. The total phenolic contents in Madan fruit and leaf extracts using Folin–Ciocalteu method were estimated to be 22.0±1.47 and 10±5.28 mg gallic acid equivalent per 1 g of extract, respectively. Total flavonoid contents of Madan fruit and leaf extracts using aluminum chloride colorimetric method were found to be 0.4083±0.034 and 92.1486±0.614 mg quercetin equivalent per 1 g of extract, respectively. The antioxidant activity of fruit and leaf extracts and standard gallic acid using 2,2-diphenyl-1-picrylhydrazyl (DPPH) assay showed the IC_{50} values of 1694.42±39.50, 275.55±2.78 and 140.68±14.70 mg/ml, respectively.

1. Introduction

During the process of cellular oxidation, reactive oxygen species and nitrogen species in human body such as singlet oxygen, hydrogen peroxide, superoxides, hydroxyl anions, peroxynitrite, nitric oxide and hypochlorous acid are generated. These highly unstable and reactive radicals can damage DNA of human cells and lead to oxidation of lipids and proteins in cells, causing some chronic and degenerative diseases, including atherosclerosis, arthritis, ischemia and reperfusion injury of many tissues, central nervous system injury, gastritis, cellular aging, heart disease, diabetes mellitus type 2, Alzheimer's disease and cancer.[1,2,3,4,5] High levels of reactive free radicals and oxygen species create oxidative stress.

Antioxidants, molecules capable of slowing or preventing the oxidation of other molecules, play an important role in protecting health from these free radicals and reactive oxygen species. They act as radical scavengers; inhibit lipid peroxidation and other free radical-mediated processes. Antioxidants occur naturally and through synthetic chemical processes. In the human body has many endogenous enzymatic antioxidant defenses that protect the cells against oxidative damage. However, most human cells do not generate adequate amounts of antioxidants to protect them against oxidative reactions of the produced free radicals.[6] Synthetic antioxidants such as butylated hydroxy anisole (BHA), butylated hydroxy toluene (BHT), tertiary butylhydroquinone (TBHQ) and propyl gallate are known to have toxic and carcinogenic effects on human health, therefore their application have been limited.[7,8] Therefore, there is a need to look for more dietary sources of antioxidants to decrease the risk of these free radicals.[9]

Plants in nature are rich sources of bioactive secondary metabolites, such as flavonoids, glycosides, saponins, terpenes, sterols, tannins, alkaloids and other metabolites.[10] It has been reported that the most of these groups have antioxidant activity. Therefore, currently, attention is focused to the phytochemical screening and antioxidant activity of the various plant extracts.

Madan *(Garcinia schomburgkiana* Pierre) is an edible perennial fruit belonging to the Guttiferae family. This plant is widely distributed in the central and southern areas of evergreen forests in Thailand, particularly in Nakorn Nayok province. It is a sour-tasting fruit. Local people consumed it fresh and fermented. Madan's leaves, root and fruit are traditionally used as an

expectorant, treatment of coughs, improvement of menstrual blood quality, treatment of diabetes and as a laxative. Leaf and fruit are macerated with saline water and drank as expectorant or mucolytic to relieve cough and treat abnormal menstruation. Stem extract is used for accelerating lochia discharge.[11,12]

The objectives of this study were to perform the phytochemical screening, to determine the total phenolic and flavonoid contents as well as antioxidant activities of *G. schomburgkiana* Pierre extracts from the fruits and leaves.

2. Materials and Methods

2.1. Plant materials

The fruits and leaves of Madan (Figure 1) used in this research is the Kieow Song La variety, which was collected from Nakhon Nayok Province. The fruits are obliquely ellipsoid to ellipsoid-oblong, 4-5 cm long, and 12-13 cm wide, glossy green ripening yellow. The leaves are elliptic-lanceolate or elliptic-ovate, 2-3 cm wide, 5-9 cm long, apex subacute, base cuneate, margin entire, glossy dark green. Fresh fruits and leaves were sliced and dried under sunlight for 7 days. The dried pulps were further heated in a hot air oven at 60 ^{o}C for 6 hours and ground into power. The powder was kept at room temperature for further use.

Figure 1. Madan fruit and leaf

2.2 Reagents

DPPH (2,2-diphenyl-1-picrylhydrazyl), Folin-Ciocalteu reagent, Dragendorff reagent, gallic acid, quercetin, iron (III) chloride, aluminium trichloride, sodium carbonate, hydrochloric acid, sulphuric acid, chloroform, potassium hydroxide and magnesium ribbon were purchased from Sigma–Aldrich (St. Louis, USA). Ethanol was supplied from Merck (Darmstadt, Germany). All reagents were prepared using ultrapure water (Milli-Q, USA) in all experiments.

2.3 Preparation of crude extracts

Extraction of *G. schomburgkiana* Pierre fruits and leaves were conducted by maceration using an electric stirrer. Fifty grams each of the dried powder of *G. schomburgkiana* Pierre fruits and leaves were soaked in 250 ml of ethanol and macerated for 7 days at room temperature. The extracts were filtered and evaporated using rotary evaporator (40 ^{o}C) under reduced pressure to obtain the crude extracts. These crude extracts were used for the phytochemical analysis, total phenolic and flavonoid contents and antioxidant activity.

2.4 Phytochemical screening

Preliminary phytochemical screening was carried out from the fruit and leaf extracts of *G. schomburgkiana* Pierre to determine the phytochemical constituents in the extracts. The qualitative assay consisted of tests for flavonoids, tannins, steroids, alkaloids, glycoside, sterols, lignins quinones, and sponins using the previously reported methods with some modifications.[13,14,15] Control negative containing no *G. schomburgkiana* Pierre extract was performed in each test to ensure that the coloration change in the test was caused by *G. schomburgkiana* Pierre extract. Each test, along with negative control, was replicated three times.

2.4.1 Test for flavonoids

Shinoda test was used to detect for flavonoids.[13] About 0.2 g of the extract was dissolved in 1 ml of ethanol, warmed and then filtered. Three pieces of magnesium ribbon was then added to the filtrate followed by few drops of concentrated hydrochloric acid. Presence of pink, orange, or red to purple coloration indicates the presence of flavonoids.

2.4.2 Test for tannins

Ferric chloride test was used to detect for tannins.[13] About 0.2 g of the extract was stirred with about 1 ml of distilled water and then filtered. Few drops of 1% ferric chloride solution were added to the filtrate, occurrence of a blue-black, green or blue-green precipitate indicates the presence of tannins.

2.4.3 Test for steroids

Liebermann Burchard test was used to detect steroids.[14] About 0.2 g of plant extract was dissolved in 2 ml of acetic acid and a drop of conc. H_2SO_4 was added. The appearance of green color indicates the presence of steroids.

2.4.4 Test for alkaloids

Dragendorff test was used to detect for alkaloids.[15] Two milliliters of the extract and 0.2 ml of dilute hydrochloric acid were taken in a

test tube. After adding 1 ml of Dragendroff's reagent (potassium bismuth iodide solution), presence of orange brown precipitate indicates the presence of alkaloids.

$FeCl_3$ test was also used to detect alkaloids.[15] One drop of ferric chloride solution was added to the extract. Formation of yellow precipitate shows the presence of alkaloids.

2.4.5 Test for glycosides

Glycosides were detected by using Salkowski test.[15] 2.0 ml of the concentrated sulphuric acid were added to the extract. Reddish brown color formed indicates the presence of steroidal aglycone part of the glycoside.

2.4.6 Test for sterols

Salkowski test was used to detect for sterols.[15] Few drops of concentrated sulphuric acid were added to the extract in chloroform. Appearance of red color at the lower layer indicates the presence of sterols.

2.4.7 Tests for lignins

Lignins were detected by using Labat test.[15] Gallic acid was added to the extract, the formation of olive green color shows the presence of flavonoids.

2.4.8 Tests for quinones

Alcoholic KOH test was used to test for quinones.[15] When alcoholic KOH was added to the test samples, the appearance of red to blue color indicates the presence of quinones.

2.4.9 Test for Saponins

Foam test was used to detect for saponins.[15] One gram of the extract was boiled with 5 ml of distilled water, filtered. To the filtrate, about 3 ml of distilled water was further added and shaken vigorously for about 5 mins. Frothing which persisted on warming is taken as an evidence for the presence of saponins.

2.5 Determination of total phenolic content

The total phenolic content was determined with Folin-Ciocalteu method according to the method of Zhou, K. et al. with some modifications.[16] In brief, 0.1 ml of the extract (0.01 g/mL) or standard solution of gallic acid was mixed with 1.5 ml of 20% w/v sodium carbonate, 0.25 ml of Foline–Ciocalteu reagent and 1.15 ml of pure water, the mixture was left in the dark for 10 min at room temperature. The absorbance was measured at 765 nm using a spectrophotometer (Jasco V-730 spectrophotometer, Japan). The analysis was performed in triplicate. The concentration of phenolic compounds was expressed as mg of gallic acid equivalents per gram of extract (mgGAE/g) by comparison with standard curve of gallic acid.

2.6 Determination of total flavonoid content

The total flavonoid content was determined according to the method of Ramamoorthy et.al with some modifications.[17] 0.15 ml of 5% sodium nitrite was mixed with 0.7 ml of the extract (0.01 g/ml) or standard solution of quercetin. After 5 min, 0.15 ml of 2% $AlCl_3$ was added. Immediately, the mixture was diluted by adding 2.3 ml of pure water and mixed thoroughly. The mixture was incubated for 10 min at room temperature. The absorbance was measured using a spectrophotometer (Jasco V-730 spectrophotometer, Japan) at 510 nm against a prepared reagent blank. The analysis was performed in triplicate. Total flavonoid content was expressed as quercetin equivalent per gram of the extract (mg QE/g).

2.7 Determination of antioxidant activity by DPPH radical scavenging assay

Free radical scavenging capacity of the extracts was determined by using the scavenging of the stable 2,2-diphenyl-1-picryhydrazyl (DPPH) free radical according to the method of Mensor, L.L. et al. with some modifications.[18] One milliliter of each sample was added to 2 ml of DPPH in ethanol (0.1 mM). After incubation for 30 min in the dark, the absorbance of each sample was measured at 514 nm spectrophotometrically (Jasco V-730 spectrophotometer, Japan). The DPPH solution was used as a negative control. Gallic acid was used as the reference standard. Triplicate determinations were performed. The percentage of DPPH scavenging activity was calculated using the following formula:

$$\% \text{ inhibition of DPPH radical} = [(A_c - A_s)/ A_c] \times 100$$

where A_c is the absorbance of the control and A_s is the absorbance of the sample. The IC_{50} values denote the concentration of the sample which is required to scavenge 50% of DPPH free radical.

2.8 Statistical analysis

All work was done in triplicates and the data presented are means ± S.D. of three independent determinations. Significance was accepted at $p>0.05$.

3. Results & Discussion

3.1 Percentage yield of extracts

Previous research reports have shown that ethanol was the suitable solvent for the extraction of antioxidant compounds, including phenolic compounds by maceration method.[19] In addition, it

was found that the extraction yield of ethanolic extracts was quite high due to the ability of ethanol to extract a wide range of compounds. Therefore, ethanol was chosen to use as the extraction solvent in this study.

Fruits and leaves of Madan were extracted separately using ethanol as solvent. The weights and percentage yields reported by the ratio of crude extract and weight of the sample (w/w) were presented in Table 1.

Table 1. The percentage yield of crude extracts obtained from different plant parts of *G. schomburgkiana* Pierre.

Extracts	Weight (g)	Percent yield
Fruits	23.13±3.17	46.25±6.34
Leaves	3.13±0.54	1.92±5.27

As shown in Table 1, the fruit extracts gave a percentage of crude extract approximately 23 times higher than the leaf extracts. In fact, leaf extracts gave a percentage of crude extract of 46.25±6.34, while leaf extracts yield 1.92±5.27. The higher extraction yield of the fruit extracts may be described to the development of better hydrogen bonds between polyphenols' hydroxyl groups and the electronegative oxygen of ethanol.[12]

3.2 Phytochemical screening

Preliminary phytochemical analysis of the fruit and leaf extracts of *G. schomburgkiana* Pierre is presented in Table 2.

Table 2. Preliminary phytochemical screening of fruit and leaf extracts of *G. schomburgkiana* Pierre.

Phytochemical tested	Test methods	Results	
		Fruits	Leaves
Flavonoids	Shinoda test	+	+
Tannins	Ferric chloride test	+	+
Steroids	Liebermann Burchard test	-	+
Alkaloids	Dragendorff test	-	-
	Ferric chloride test	-	-
Glycosides	Salkowski test	-	+
Sterols	Salkowski test	-	+
Lignins	Labat test	-	-
Quinones	Alcoholic KOH test	-	-
Saponins	Foam test	+	+

+ = Present, − = Absent

The results of phytochemical screening revealed the presence of bioactive components such as flavonoids, tannins, saponins in the fruit extracts while flavonoids, tannins, steroids, glycosides, sterols and saponins were found in the leaf extracts. Each phytochemical showed potency towards some biological action. Flavonoids have antiviral, antibacterial, and antioxidant, properties. They also control gene expression and modulate enzymatic action.[20] Tannins are reported to have antimicrobial properties and can inhibit the growth of fungi, yeasts, bacteria, and viruses. They can also accelerate blood clotting, lower blood pressure, reduce serum lipid levels, produce liver necrosis, and modulate immune responses.[21] Steroids help reduce redness and swelling (inflammation), which can help treat inflammatory conditions such as asthma and eczema. Steroids also decrease the function of the immune system, which is the body's natural defense against illness and infection.[22] Cardiac glycosides have been used to treat congestive heart failure and cardiac arrhythmia.[23] Plant sterols are known to have blood cholesterol-lowering effect through partial inhibition of cholesterol absorption in the intestinal. Other purported benefits of phytosterols include possible anti-atherogenic effects, immune stimulating and anti-inflammatory activities. There is also emerging evidence suggesting that particularly plant sterols may have beneficial effects against the development of various types of cancer, including colorectal, breast and prostate cancers.[24,25,26,27] Saponins may help reduce cholesterol levels, kill disease-causing bacteria, scavenge oxidative stress and inhibit tumor growth. According to the latest research, they improve lipid metabolism and may help prevent and treat obesity.[28]

3.3 Total phenolic and flavonoid contents

The total phenolic and flavonoid contents of the crude extracts of the fruits and leaves of *G. schomburgkiana* Pierre are shown in Table 3.

Table 3. Total phenolic acid and flavonoid contents of the extracts of *G. schomburgkiana* Pierre.

Extracts	Total phenolic content (mgGAE /g extract)	Total flavonoid content (mgQE/g extract)
Fruits	22.01±1.47	0.41±0.04
Leaves	101.00±5.28	92.15±0.75

Values are written as means±SD of three experiments

Phenolic compounds are important plant constituents with redox properties that play antioxidant roles.[29] The hydroxyl groups in plant extracts are responsible for facilitating scavenging of free radicals. Phenolic content was determined using the Folin–Ciocalteu reagent. The results were derived from a calibration curve of gallic acid and expressed in gallic acid equivalents (GAE) per gram dry extract weight. The analysis of the fruit and leave extracts of *G. schomburgkiana* Pierre revealed the total phenolic content of 22.01±1.47 and 101.00±5.28 mgGAE/g extract, respectively.

Flavonoids are secondary metabolites that have antioxidant activity. Its potency depends on their molecular structures, the position of the hydroxyl group and other features in its chemical structure. They are abundantly found in plants in the form of glycoside.[30] The flavonoid contents in the plant extracts were determined using aluminium chloride in a colorimetric method. The results were derived from the calibration curve of quercetin and expressed in quercetin equivalents (QE) per gram dry extract weight. The analysis of the fruit and leave extracts of *G. pedunculata* Pierre showed the total flavonoid content of 0.41±0.04 and 92.15±0.75 mgQE/g extract, respectively.

3.4 Antioxidant activities

Antioxidant activities of the fruit and leaf extracts of *G. schomburgkiana* Pierre were assessed to identify potential sources of substances possibly useful against the effects of free radicals by DPPH method.

DPPH is a stable free radical at room temperature, which produces a violet solution in ethanol. The DPPH test is based on the ability of the stable DPPH free radical to react with hydrogen donors. The DPPH• radical shows an intense UV-VIS absorption spectrum. In this test, a solution of radical is decolorized after reduction with an antioxidant (AH) or a radical (R•) according to the following scheme:

$$DPPH\bullet + AH \rightarrow DPPH\bullet\text{-}H + A\bullet,$$
$$DPPH\bullet + R\bullet \rightarrow DPPH\bullet\text{-}R.$$

The results of inhibition study in the form of the half-maximal inhibitory concentration (IC_{50}) values and the equation formulars for the plant extracts and standard gallic acid are presented in Table 4.

Table 4. DPPH Inhibitory concentration (IC_{50}, µg/ml) of the extracts of *G. schomburgkiana* Pierre.

Extracts	IC_{50} (µg/mL)	Linear equation
Fruits	1694.43±39.50	y = 0.0105x + 32.670
Leaves	275.55±2.78	y = 0.0723x + 30.306
Gallic acid	140.68±14.70	y = 0.3221x + 0.0479

Values are written as means±SD of three experiments

The fruit and leaf extracts of *G. schomburgkiana* Pierre showed antioxidant potential with IC_{50} values of 1694.43±39.50 and 275.55±2.78 µg/mL, respectively. The standard gallic acid possesses IC_{50} of 140.68±14.70 µg/mL. These indicated that the DPPH free radicals were scavenged by the fruit and leaf extracts of *G. schomburgkiana* Pierre and gallic acid with different capacities. Antioxidant potential is inversely proportional to inhibitory concentration (IC_{50}) value which was calculated from the linear regression of the percentage inhibition versus extract concentration. Hence, standard gallic acid showed higher antioxidant potential than the fruit and leaf extracts of *G. schomburgkiana* Pierre. In addition, it was found that the DPPH free radical scavenging was antioxidant concentration dependent. Table 5 shows example data of this dependency characteristic. The percentage of antioxidant activity increased from 43.06±0.95 to 82.69±1.34 (when the extract concentration increased from 1000 to 5000 µg/mL) and 36.08±0.81 to 66.03±0.79 (when the extract concentration increased from 100 to 500 µg/mL) for the fruit and leaf extracts of *G. schomburgkiana* Pierre, respectively.

Table 5. Antioxidant concentration dependent on DPPH free radical scavenging.

Extracts	concentration (µg/mL)	%inhibition
Fruits	1000	43.06±0.95
	2000	53.56±1.19
	3000	61.46±2.61
	4000	74.41±2.70
	5000	82.69±1.34
Leaves	100	36.08±0.81
	200	45.61±0.63
	300	50.98±1.19
	400	60.42±0.14
	500	66.03±0.79

Table 6. Correlations (R and R^2) between antioxidant activity of plant extracts by DPPH assay and total phenolics, total flavonoids.

	Antioxidant activity, Total phenolics	Antioxidant activity, Total flavonoids
Fruits	R=0.9928 R^2=0.9857	R=0.9941, R^2=0.9882
Leaves	R=0.9297, R^2=0.8644	R=0.8346, R^2=0.6965

The correlation between the total phenolic and flavonoid contents, and the antioxidant activity were determined. The results are shown in Table 6. High and positive correlations between antioxidant activity and total phenols and total flavonoids were observed at a 95% confidence level. By comparing the correlation coefficients (R-values), it is possible to suggest that phenolic and flavonoid groups are responsible for the antioxidant activity of the selected plant extracts.

4. Conclusion

The results of this study revealed that the ethanolic extracts of *G. schomburgkiana* Pierre fruits and leaves is the primary antioxidants, which neutralizes free radicals and thus inhibits free radical-mediated reactions. For this reason, *G. schomburgkiana* Pierre, a fruit commonly found in the central and southern areas Thailand, specifically in Nakhon Nayok Province may help prevent or slow the progression of various oxidative stress-related diseases and can be used as an easily accessible source of natural antioxidant. However, further investigation on isolation, characterisation and identification of individual bioactive compounds responsible for bioactivities and possible synergy amongst them need to be studied and established.

Acknowledgements

The authors would like to thank the Faculty of Science and Technology, Rajamangala University of Technology Krungthep for instrument facilities.

References

1. Aktumsek, A.; Zengin, G.; Guler, G.O.; Cakmak, Y.S.; Duran, A. *Food Chem. Toxicol.* **2013**, 55, 290– 296.
2. Phaniendra, A.; Jestadi, D.B.; Periyasam, L. *Indian J. Clin. Biochem.* **2015,** *30*(1), 11–26.
3. Panchawat S.; Rathore K.S.; Sisodia S.S.; *Int J.Pharma Tech Research*, **2010**, *2*(1), 232-239.
4. Sharma, S.K.; Singh, L.; Singh, S. *Indian J. Res. Pharm. Biotechnol.* **2013**, *3*, 404-409.
5. Li, S.; Tan, H.Y.; Wang, N.; Zhang, Z.J.; Lao, L.; Wong, C.W.; Feng, Y. *Int. J. Mol. Sci.* **2015**, *16*, 26087–26124.
6. Pisoschi, A.M.; Cheregi, M.C.; Danet, A.F. *Molecules* **2009**, *14*, 480 - 493.
7. Sultana, B.; Anwar, F.; Przybylski, R. *Food Chem.* **2007**, 104, 1106-1114.
8. Cesoniene, L.; Daubaras, R.; Viskelis, P.; Sarkinas, A. *Plant Foods Hum. Nutr.* **2012**, *67*, 256-261.
9. Liu, R.H. *Am. J. Clin. Nutr.* **2003**, 200378 (suppl), 517S - 20S.
10. De Fatima, A.; Modolo, L.V.; Conegero, L.S.; Pilli R.A.; Ferreira, C.V. *Curr Med Chem* **2006,** *13*, 3371-3384.
11. Lim, T.K. *Edible Medicinal and Non Medicinal plants Volume 2*; Springer: Netherlands, 2012; pp. 123-124.
12. Thummajitsakul, S.; Boonburapong, B.; Silprasit. K *J. Trop. Agric. Sci.* **2019**, *42*, 45-60.
13. Trease, G.E.; Evans, W.C. *Trease and Evan's Textbook of Pharmacognosy*, 13th ed.; Cambridge University Press, 1989.
14. Alamzeb, M.; Khan, M.R.; Ali, S.; Shah, S.Q.; Mamoon, U.R. *Bangladesh J. Pharmacol.*, **2013**, *8*(2), 107-109.
15. Rajinikanth, M.; Samatha, T.; Srinivas, P.; Shyamsundarachary, R.; Rama, S.N. *Int. J. Pharm. Sci. Rev. Res.*, **2013,** *20*(1), 134-139.
16. Zhou, K.; Yu, L. *LWT* **2006**, *39*, 1155–1162.
17. Ramamoorthy, P.K.; Bono, A. *J. Eng. Sci. Technol*. **2007**, *2*(1), 70-80.
18. Mensor, L.L.; Menezes, F.S.; Leitao, G.G.; Reis, A.S.; Santos, T. S.; Coube, C.S. *Phytother. Res.* **2001,** *15*, 127–130.
19. António, J.Q.; Mota, F.L.; Pinho, S.P.;
3. Macedo, E.A. *J. Phys. Chem. B* **2009**, *113*(11), 3469–3476.
20. Aleksandra, K.; Dorota, S.W. *Rocz Panstw Zakl Hig*. **2014**, *65*(2), 79-85.
21. Chung , K. T.; Wong, T. Y.; Wei, C. I.; Huang, Y. W.; Lin, Y. *Crit Rev Food Sci Nutr*. **1998**, *38*(6), 421-464.
22. Coutinho, A. E.; Chapman, K. E. *Mol Cell Endocrinol.* **2011**, *335*(1), 2–13.
23. Kren, V.; Martínková, L. *Curr. Med. Chem.* **2001**, *8*(11), 1303-1328.
24. Bradford, P.G.; Awad, A.B. *Mol. Nutr. Food Res*. **2007**, *51*, 161-170.
25. Bouic, P.J. *Drug Discov Today*. **2002**, *7*, 775-778.
26. Jones, P.J.; Ntanios, F.Y. Raeini-Sarjaz, M.; VANSTONE, C.A. *Am J Clin Nutr*. **1999**, *69*, 1144-1150.
27. Navarro, A.; De Las Heras B.; Villar A. *Clem. Biol Pharm Bull*. **2001**, *24*, 470-473.

28. Andra, P. What Are the Health Benefits of Saponins? https://www.weekand.com/healthy-living/article/health-benefits-saponins-18012376.php (accessed November 30, 2023)
29. Soobrattee, M.A.; Neergheen, V.S.; Luximon-Ramma, A.; Aruoma, O.I.; Bahorun, T. *Mutat. Res.-Fund. Mol. Mutagen.* **2005**, *579*, 200–213.
30. Rajanandh, M.G.; Kavitha, J. *Int. J. Pharm Tech Res.* **2010,** *2*, 1409-1414.

Comparation synthesis of picric acid from phenol and salicylic acid for crystallization of mitragynine as picrate salt at difference percent purity

Suntisuk Sinthunakorn and Muhammad Niyomdecha*

Department of Chemistry, Faculty of Science, Silpakorn University, Nakhonpathom 73000 Thailand

**E-mail: momoniyom@yahoo.com*

Abstract:

Kratom, or Mitragyna *Speciosa Korth*, contains several alkaloids, one of which is mitragynine. However, a significant number of impurities, including wax and other undesirable alkaloid-derived substances, were included in the mitragynine that was obtained via the extraction method. For this reason, picric acid was used to crystallize mitragynine from a crude extraction. Picric acid is a highly explosive material that can't be bought without authority, so we have to synthesize it on our own and must be extremely cautious when using it due to its properties to form complexes with other compounds like creatinine and metals. These properties were applied to the crystallization of mitragynine. Upon crystallization, the mitragyne became a mitragynine picrate. We are eager to compare the formation of mitragynine picrate from picric acid, which was produced using phenol and salicylic acid as substrates, to study whether different substrates will affect the formation of a mitragynine complex. In this study, we employ a 36.90% and 61.35% crude mitragynine extract for crystallization with picric acid to compare the result.

1. Introduction

Kratom or Mitragyna *Speciosa Korth*, which belongs to the Rubiaceae family, is endemic to the tropics of Southeast Asia, primarily found in the southern region of Thailand (Figure 1).[1] The leaf of kratom has been used to alleviate the fatigue of workers laboring in the scorching heat. Additionally, kratom's pharmacokinetics have been investigated, and the findings indicate that kratom leaves contain more than 25 alkaloids which mitragynine, patnantheine, speciogynine, spacioceleitine and 7-hydroxymitragynine respectively. These alkaloids were mostly found in kratom leaves. The process of producing these alkaloids is quite costly due to its difficulty in separation and purification. Mitragynine has biological activity on neurons similar to opium in that it is ten times weaker moreover, 7-hydroxymitragynine exhibits 17 times greater biological activity than morphine in pain relief.[2] In Thailand, people have been using kratom as medicine for a long time. However, overdosing on consuming kratom leaves can cause paranoia and a fast heart rate.[3] In order to obtain pure mitragynine for use as a standard in forensic sciences, especially as a substrate for the synthesis of 7-hydroxymitragynine, it is necessary to determine the best extraction technique for mitragynine as a complex crystal and then decomplex. Here we report the practical extraction technique complex forming and decomplex method **Figure 1.**

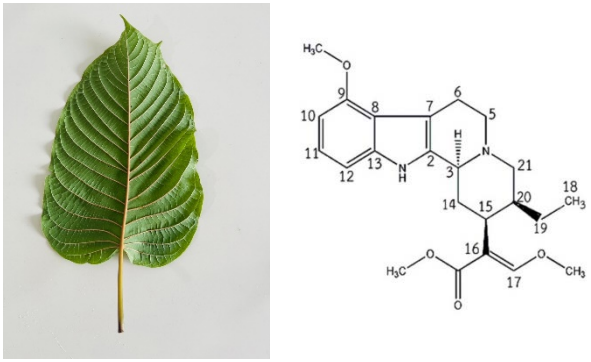

Figure 1. The red vein kratom leaves and mitragynine structure[4]

2. Materials and Methods

2.1 Materials

Dichloromethane, ethanol 50% v/v and citric acid were purchased from Lab-Scan. Hexane, ethyl acetate and sodium sulfate anhydrous were purchased from Sigma-Aldrich. Acetone, ammonium hydroxide and basic laboratory glassware were purchased from Merck. Analytical thin-layer chromatography (TLC) was conducted using Merck precoated with silica gel 60 F254 on aluminum sheet. The solvent was evaporated by Buchi Rotavapor R-114 Rotary Evaporator. The purified mitragynine from the crude ethanolic and crude purified by quick column chromatography showed a single chromatographic peak upon spectroscopic analysis by HPLC in the ACE C_{18}, Mobile phase are 5mM of ammonium acetate /

acetonitrile (40:60), flow rate = 1.000 mL / min and a wavelength = 220 nm. The proton and carbon nuclear magnetic resonance (NMR) spectra were recorded from a Bruker Avance-300 spectrometer.

2.2 Preparation of crude extracts from kratom leaves

The red vein kratom leaves obtained from Ratchaburi province, Thailand, were preliminary examined by means of identifying kratom leaves in the control group by using kratom leaves from the same source. After that, the experiment was carried out when the initial identity was checked, starting with cleaning the kratom leaves with clean water, then drying them at 30 °C until completely dry (weighing until the weight was stable), and grinding them thoroughly. The extraction was done by weighing 20 grams of dried kratom powder, soaking it in 200 mL of 50 % v/v ethanol, adding some citric acid, and leaving it for 24 hours. Then it was filtered via a vacuum filter, basified with ammonium hydroxide, and extracted with dichloromethane, which evaporated until dried with a rotary evaporator. The crude extract from ethanolic extract 2.0 grams was purified by quick column chromatography. The crude extract was analyzed using TLC to compute an R_f value, and its purity was assessed using HPLC and ^{1}H-NMR characterization.

2.3 Synthesis of picric acid

In this section, we synthesized picric acid with two different substrates, which are phenol and salicylic acid. The synthesis was carried out by weighing 20 grams of phenol into a round-bottom flask, adding 12 mL of concentrated sulfuric acid, and stirring at 110 °C for half an hour. The reaction flask was cooling down with an ice bath until the temperature reached 0 °C, then dropwise iced cold, concentrating 125 mL of nitric acid into the flask and stirring for 30 minutes. The reaction flask was removed from an ice bath and heated up to 100 °C for 3 hours. After 3 hours, the reaction flask was cooling down to room temperature. Add 300 mL of cold distilled water to the reaction flask, and the yellow crystal of picric acid will precipitate and be filtered by vacuum filtration. The recrystallization was done by dissolved picric acid in hot distilled water, then hot filtrated through cotton. For the salicylic acid, the synthesis of picric acid was done by the same procedure with the same amount of substrate. As shown in **Figure 2.**

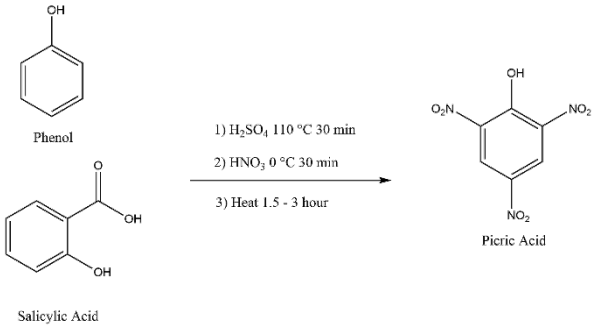

Figure 2. Synthesis of picric acid

2.4 Crystallization with picric acid or formation of a mitragynine complex

0.8 gram of crude mitragynine extract before quick column chromatography dissolved in methanol then dropwise saturated picric acid (synthesized from phenol) in methanol and cooled in freezer 20 minutes and filtered by vacuum filtration. Repeat the same procedure but use picric acid that was synthesize from salicylic acid instead then compare then result. Run another same experiment with 0.8 gram of crude mitragynine by quick column chromatography and then compare the result as shown in **Figure 3.**

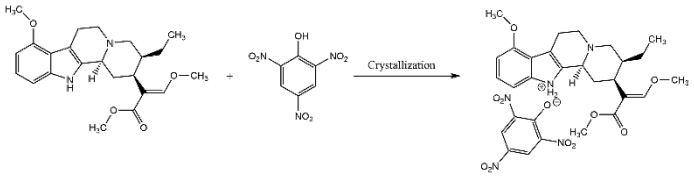

Figure 3. Mitragynine complex formation

2.5 Decomplex of mitragynine

The mitragynine complex was dissolved in 10 mL of saturated acetone, then dropped into an excess 25% ammonia solution as shown in **Figure 4,** extracted with diethyl ether three times, and evaporated until dried. The product was characterized with ^{1}H-NMR.

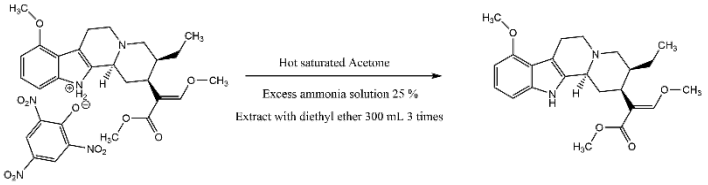

Figure 4. Decomplex of mitragynine

3. Results & Discussion

Mitragynine was extracted by ethanolic citrate from dried kratom powder and given a brownish-green crude extract and then drude extract was purified by quick column chromatography to provide the brownish precipitate. The purity of crude extract was analyzed with HPLC. The characterization of crude mitragynine was done by ^{1}H-NMR. The crystallization with picric acid or the formation of a mitragynine complex and decomplex of mitragynine gave a satisfactory result for purifying mitragynine from crude extract at different percent purity. Although the crystallization process was done with picric acid, the result was different when using picric acid that was synthesized with phenol and salicylic acid. Picric acid that was synthesized from salicylic acid tends to be more effective for purifying mitragynine from crude extract.

3.1 Crude extract purity analysis and characterization

From the 20 gram of red vein kratom powder extract was given 2.3 gram a green for the extraction. The green crude extract 2.0 grams was purified by quick column chromatography was afforded a brownish 1.2 gram as shown in **Table 1**.

Table 1. Weight and percent yield of crude extracts from ethanolic extraction and quick column chromatography

Entries	Crude extract	
	Weight (g)	% Yield
Ethanol 50% / citric acid	2.3	11.5
Quick column chromatography	1.2	60.0

The ethanolic extract and purifying compound by quick column chromatography were analyzed using TLC to compute an R_f value, the system for determination mitragynine with thin layer chromatography (TLC) using the mobile phase of ethylacetate : hexane (1:1), the band of mitragynine on TLC plates at the R_f of mitragynine can be predicted as shown in **Figure 5.**

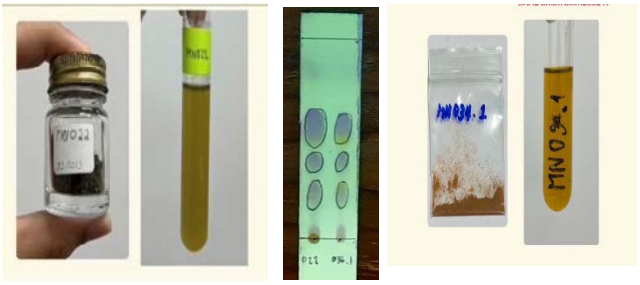

Figure 5. Ethanolic extract (left) and purifying compound by quick column chromatography TLC (right)

The mitragynine and purified mitragynine were analysis with HPLC in the TR = 8.5 min (ACE C_{18} column, 4 : 6 ammonium acetate : acetonitrile, 1000 mL/min and a wavelength = 200 nm) as shown in Figure 6 (36.90 % top) and Figure 7 (61.35 % bottom)

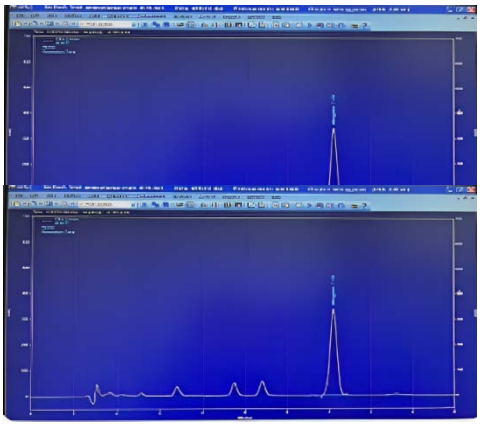

3.2 The synthesis of picric acid from different substrate

In the synthesis of picric acid with two different substrates, which are phenol and salicylic acid. The synthesis was carried out by weighing 20 grams of phenol' concentrated sulfuric acid, and nitic acid as shown in the table 2.

Table 2. Synthesis of picric acid from phenol and salicylic acid

Entries	Product	
	Substrate	% Yield
1	Phenol	68
2	Salicylic acid	77

The allow crystal of picric acid was precipitate and ^{1}H-NMR and ^{13}C-NMR were giving different peaks of picric acid from phenol and salicylic acid' is was found that data that could be confirmed as picric acid from phenol were in the

position of δ-shift 8.943 (m, 6H, =CH-), 5.067 (S, 3H, -OCO-CH_3), and ^{13}C-NMR at δ-shift 171 (=CH-NO_2), 161 (=CH-NO_2), 139 (=CH-NO_2), 131 (=CH-), 127 (=CH-) and 117 (=CH-OH). Similarly' picric acid from salicylic acid was used to prove the structure using nuclear magnetic resonance (NMR; ^{1}H-NMR and ^{13}C-NMR) the position of δ-shift 8.931 (m, 6H, =CH-), 5.065 (s, 3H, -OCO-CH_3), and ^{13}C-NMR at δ-shift 171 (=CH-NO_2), 161 (=CH-NO_2), 139 (=CH-NO_2), 131 (=CH-), 127 (=CH-) and 117 (=CH-OH). Techniques to confirm of the substrate as shown in Figure 6 (Phenol as a substrate) and Figure 7 (Salicylic acid as a substrate)

3.3 The extraction of mitragynine and comparison of the effects of mitragynine complex formation and decomplexation with picric acid at the different percent purity

From the synthesis of picric acid with phenol and salicylic acid, the picric acid that was synthesized from salicylic acid gave a higher yield and a cleaner ^{1}H-NMR and ^{13}C-NMR spectrum. So we decide to use picric acid from salicylic acid to form complexes with mitragynine and purify them by decomplexing 36.90% (achieved from ethanol 50% and citric crude extract) and 61.35% (achieved by quick column chromatography of ethanol 50% and citric crude extracted) purity of mitragynine, as shown in Figure 8 (36.90%) and Figure 9 (61.35%). The 36.90% mitragynine after decomplex was identified by ^{1}H-NMR (300MHz' $CDCl_3$) of complex; (δ, ppm) 7.43 (1H, s, -NH), 7.33 (1H, s, ^{17}CH), 6.98 (1H, dd, ^{11}CH), 6.87 (1H, d, ^{12}CH), 6.44 (1H, d, ^{10}CH), 3.89 (3H, s, -O^9CH_3), 3.73 (3H, s, -O^{17}CH_3), 3.70 (3H, s, -O^{22}CH_3), 3.15 (1H, d, ^{3}CH), 3.10 (2H, m, ^{5}CH_2 and ^{6}CH_2), 3.01 (1H, dd, ^{15}CH), 2.99 (2H, dd, ^{6}CH_2 and ^{21}CH_2), 2.50 (2H, m, ^{14}CH_2 and ^{21}CH_2), 1.78 (2H, m, ^{14}CH_2 and ^{19}CH_2), 1.65 (1H, m, ^{20}CH_2), 1.25 (1H, m, -CH_2 and ^{19}CH_2) and similarly for mitragynine 61.35% as shown in Figure 10 (36.90 %) and Figure 11 (61.35 %).

*** For some figures, you could see supporting information

4. Conclusion

The purification of mitragynine from crude extract by crystallization with picric acid or formation of a mitragynine complex and then decomplex was a practical method and cheaper than conventional purification by column chromatography because this method uses only a small amount of picric acid and a small amount of organic solvent for purification, unlike column chromatography. For this reason, this method is considered to be more environmentally friendly than column chromatography. The substrate that was used to synthesize picric acid affected the properties of picric acid when forming complexes with mitragynine, which differed slightly, causing the difference in the H-NMR peak. Although picric acid is a highly explosive material, it has the potential to purify mitragynine. With this knowledge, we might be able to develop a safer and more complexing agent in the future

Acknowledgements

The researcher would like to thank the research subsidies for the publication of research results in academic journals from the innovation and creativity research support fund of the department of chemistry, faculty of science, Silpakorn University.

References

1. (กระท่อม (Kratom) – กองควบคุมวัตถุเสพติด. https://mnfda.fda.moph.go.th/narcotic/?p=6063.
2. (Watanabe K, YanoS, Horie S,Yamamoto LT (1997). Inhibitory effect of mitragynine, an alkaloid with analgesic effect from Thai medicinal plant Mitragyna specinosa, on electrically stimulated contracteion of isolated guinea-pig ileum thrugh the opioid receptor. Life science 60(12):933-42)
3. การใช้ประโยชน์จากองค์ความรู้ชุมชน และงานวิจัยเกี่ยวกับพืชกระท่อม. งานประชุมวิชาการพืชกระท่อมแห่งประเทศไทยครั้งที่1. https://kratom.sci.psu.ac.th/knowledge/interdisciplinary/3187/ (accessed 2023-12-24).
4. Takayama, H. (2004). Chemistry and Pharmacology of Analgesic Indole Alkaloids from the Rubiaceous Plant, Mitragyna speciosa. Chem. Pharm.Bull, 52(8), 916-928. https://doi.org/10.1248/cpb.52.916
5. Beng, G. T.; Hamdan, M. R.; Siddiqui, M. J.; Mordi, M. N.; Mansor, S. M. A simple and cost effective isolation and purification protocol of mitragynine from mitragyna speciosa korth (ketum) leaves (Satu Protokol Pengasingan Mitragina daripada Daun Mitragyna speciosa Korth (Ketum) yang Mudah dan Kos Efektif). Semantic Scholar. https://www.semanticscholar.org/paper/A-SIMPLE-AND-COST-EFFECTIVE-ISO

Synthesis and evaluation of chrysin derivatives as histone deacetylase inhibitors

Thitiporn Kamloon[1], Narissara Namwan [2], Thanaset Senawong[2], Pakit Kumboonma[3], Somying Leelasubcharoen[1], and Chanokbhorn Phaosiri[1]

[1]*Natural Products Research Unit, Center of Excellence for Innovation in Chemistry, Ministry of Higher Education, Science, Research, and Innovation (Implementation Unit- IU, Khon Kaen University), Department of Chemistry, Faculty of Science, Khon Kaen University, Khon Kaen 40002, Thailand*

[2]*Department of Biochemistry, Faculty of Science, Khon Kaen University, Khon Kaen 40002, Thailand*

[3]*Department of Applied Chemistry, Faculty of Science and Liberal Arts, Rajamangala University of Technology Isan, Nakhon Ratchasima, 30000 Thailand*

**E-mail: thitip.ka@kkumail.com*

Abstract:

Four bromo derivatives of chrysin (**3**) were synthesized via nucleophilic substitution reaction. All synthesized derivatives were gained in 78-84% yield and were characterized by spectroscopy techniques (IR, ^{1}H NMR, and ^{13}C NMR). Biological activity of the obtained compounds against histone deacetylases (HDACs) was tested *in vitro* using trichostatin A (TSA, **2**) as a positive control (91 % inhibition at 25 µM). The preliminary findings showed that bromo compounds had the moderate inhibitory effect against HDACs with 33–43 % inhibition at 100 µM. HDAC inhibitory activity of the investigated compounds demonstrated that 7-(2-bromoethoxy)-5-hydroxy-2-phenyl-4H-chromen-4-one (**4**, 78% yield) possessed the highest inhibitory activity, with a value of 43 % inhibition when compared to the lead compound (chrysin, (**3**) 51 % inhibition). Moreover, molecular docking of the synthesized compounds with class I HDACs was studied. The results showed that compound **4** had the most selectivity against HDAC8 with the ΔG value as -8.76 kcal/mol compared to chrysin (**3**, ΔG = -8.08 kcal/mol). The side-chain alkyl bromo of compound **4** strongly interacted with Phe207 and aromatic region chelated the HDAC cofactor, zinc ion.

1. Introduction

Cancer is one of the most mortal diseases in the world. This is a disease that can affect every organ in the body, caused by abnormalities in the activity of several enzymes, such as histone deacetylases (HDACs). The equilibrium between histone acetylation and deacetylation is an epigenetic layer with a key role in the regulation of gene expression. Histone acetylation is related to transcriptional activation and stimulated by histone acetyl transferases (HATs), whereas histone deacetylation is related to transcriptional repression and is activated by HDACs.[1] HDAC inhibitors (HDACis) have been shown to significantly suppress cell proliferation, angiogenesis, and metastasis through multiple mechanisms. Thus, HDAC inhibitors are promising in the development of anti-cancer drugs.

Human HDACs can be classified into four groups. They consist of class I (HDACs 1−3 and 8), class IIa (HDACs 4, 5, 7 and 9), class IIb (HDACs 6 and 10) and class IV (HDAC11) which are Zn^{2+}-dependent enzymes. Class III HDACs, on the other hand, are NAD^{+}-dependent enzymes. In addition, numerous studies have shown that class I HDACs play a crucial role in the control of tumor growth such as maturation and apoptosis.[2] HDAC8 is an important "epigenetic player" in cancer and has been associated with abnormal expression or interacting with transcription factors essential for tumor development.[3]

Vorinostat (Zolinza®, 1) is a modified form of trichostatin A (TSA, 2), as shown in Figure 1. It is currently approved by the USFDA as HDACi for the treatment of cutaneous T-cell lymphoma (CTCL), peripheral T-cell lymphoma (PTCL) or multiple myeloma (MM).[4] The HDACis consist of three common domains of the pharmacophore, including the surface recognition for aromatic amides (CAP group), the zinc binding group (ZBG) and a linker part that connects CAP and ZBG.[5]

The class of HDACis known as hydroxamates is the most commonly used. Although they are highly potent, but all hydroxamate HDACis have poor selectivity and toxicity.[6] Moreover, its clinical use is further limited by poor pharmacokinetic properties, such as rapid clearance, but this can be tolerated in life-threatening conditions.[7] When comparing between non-hydroxamates and hydroxamates, the non-hydroxamates are often less effective. However, they may be more selective for certain isoforms and less toxic, which can lead to long-term therapeutic use in other non-life-threatening conditions.[6] Therefore, finding non-hydroxamate

HDACis especially from natural compounds with high selectivity is of interest.

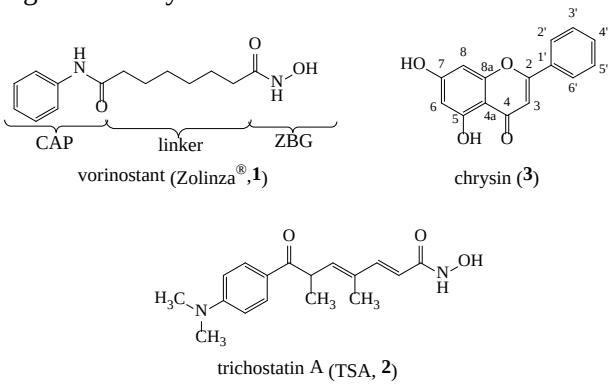

Figure 1. Structures of vorinostat (Zolinza®,**1**) trichostatin A (TSA, **2**) and chrysin (**3**)

Chrysin (**3**) is a natural phenolic compound which can be found in several plants, mushrooms, and honeycomb. This constituent is broadly used in herbal medicine in Asia. Its biological activities have been identified in various studies, such as anticancer, anti-oxidant and anti-inflammatory.[8] Therefore, in this work we focused on the structural modification of chrysin with non-hydroxamic structure to further explore their HDAC inhibitory activity against class I HDACs.

2. Materials and Methods

2.1 Materials

Reagents were purchased from commercial sources and used without further purification. Analytical thin layer chromatography (TLC) was conducted on pre-coated TLC plate using silica gel 60F-254 **(**E. Merck, Darmstadt, Germany). Silica gel for column chromatography was carried out on silica gel 60 (230–400 Mesh ASTM, Merck). NMR spectra were recorded on a Bruker AM400 and operated at 400 MHz (^{1}H) or 100 MHz (^{13}C). When $CDCl_3$ was used as a solvent, the 77.00 ppm (center line) signal was the reference for ^{13}C NMR, and residual $CDCl_3$ (^{1}H NMR, 7.26 ppm) was used as an internal standard. IR spectra were recorded on FT-IR Spectrometer: BRUKER TENSOR 27.

2.2 Structural modification

To a solution of chrysin (0.25 g, 0.98 mmol) in acetone (20 mL), potassium carbonate (1.63 g, 1.18 mmol), and the corresponding dibromoalkanes including 1,2-dibromoethane, 1,3-dibromopropane, 1,4-dibromobutane or 1,5-dibromopentane (1.18 mmol) were added. The reaction was refluxed for 6 h and monitored by TLC. After cooling, the precipitate was washed with acetone (20 mL) and the solvent was removed under reduced pressure to give compounds which were further purified by column chromatography with 20 % EtOAc : Hexane.

7-(2-bromoethoxy)-5-hydroxy-2-phenyl-*4H*-chromen-4-one (**4**) yellow solid (yield = 78%) Rf = 0.37 (20% EtOAc : Hexane). IR ν_{max} (cm^{-1}) = 3067 (C-H aromatic ring), 1610 (C=O), 1099 (C-O), 616 (C-Br). ^{1}H NMR (400 MHz, $CDCl_3$) δ 12.72 (s, 1H, OH), 7.87 (d, *J* = 7.3 Hz, 2H, H-2', 6'), 7.56 – 7.48 (m, 3H, H-3', 4', 5'), 6.66 (s, 1H, H-8), 6.50 (s, 1H, H-3), 6.36 (s, 1H, H-6), 4.34 (t, *J* = 6.3 Hz, 2H, H-1"), 3.65 (t, *J* = 6.2 Hz, 2H, H-2"). ^{13}C NMR (100 MHz, $CDCl_3$) δ 182.43 (C-4), 164.07 (C-7), 163.85 (C-2), 162.29 (C-5), 157.69 (C-8a), 131.89 (C-1'), 131.17 (C-4'), 129.08 (C-3', 5'), 126.26 (C-2', 6'), 106.03 (C-3) 105.86 (C-4a), 98.52 (C-6), 93.28 (C-8), 68.07 (C-1"), 28.25 (C-2").

7-(3-bromopropoxy)-5-hydroxy-2-phenyl-*4H*-chromen-4-one (**5**) yellow solid (yield = 82%) Rf = 0.30 (20% EtOAc : Hexane). IR ν_{max} (cm^{-1}) = 3077 (C-H aromatic ring), 1606 (C=O), 1099 (C-O), 616 (C-Br). ^{1}H NMR (400 MHz, $CDCl_3$) δ 12.69 (s, 1H, OH), 7.86 (d, *J* = 7.3 Hz, 2H, H-2', 6'), 7.56 – 7.45 (m, 3H, H-3', 4', 5'), 6.64 (s, 1H, H-8), 6.49 (s, 1H, H-3), 6.35 (s, 1H, H-6), 4.17 (t, *J* = 6.3 Hz, 2H, H-1"), 3.59 (t, *J* = 6.4 Hz, 2H, H-3"), 2.34 (p, *J* = 6.0 Hz, 2H, H-2"). ^{13}C NMR (100 MHz, $CDCl_3$) δ 182.44 (C-4), 164.59 (C-7), 163.98 (C-2), 162.16 (C-5), 157.75 (C-8a), 131.83 (C-1'), 131.25 (C-4'), 129.07 (C-3', 5'), 126.26 (C-2', 6'), 106.02 (C-3), 105.83 (C-4a), 98.63 (C-6), 93.04 (C-8), 65.90 (C-1"), 31.91 (C-3"), 29.54 (C-2").

7-(4-bromobutoxy)-5-hydroxy-2-phenyl-*4H*-chromen-4-one (**6**) yellow solid (yield = 87%) Rf = 0.34 (20% EtOAc : Hexane) IR ν_{max} (cm^{-1}) = 3076 (C-H aromatic ring), 1609 (C=O), 1099 (C-O), 619 (C-Br). ^{1}H NMR (400 MHz, $CDCl_3$) δ 12.68 (s, 1H, OH), 7.85 (d, *J* = 7.5 Hz, 2H, H-2', 6'), 7.57 – 7.44 (m, 3H, H-3', 4', 5'), 6.63 (s, 1H, H-8), 6.46 (s, 1H, H-3), 6.33 (s, 1H, H-6), 4.05 (t, *J* = 6.0 Hz, 2H, H-1"), 3.48 (t, *J* = 6.5 Hz, 2H, H-4"), 2.02 – 1.99 (m, 4H, H-2", 3"). ^{13}C NMR (100 MHz, $CDCl_3$) 182.56 (C-4), 164.94 (C-7), 164.08 (C-2), 162.29 (C-5), 157.88 (C-8a), 131.96 (C-1'), 131.41 (C-4'), 129.21 (C-3', 5'), 126.39 (C-2', 6'), 105.98 (C-4a), 105.31 (C-3), 98.67 (C-6), 93.18 (C-8), 67.65 (C-1"), 33.32 (C-4"), 29.39 (C-3"), 27.73 (C-2").

7-((5-bromopentyl)oxy)-5-hydroxy-2-phenyl-*4H*-chromen-4-one (**7**) yellow solid (yield = 84%) Rf = 0.34 (20% EtOAc : Hexane). IR ν_{max} (cm^{-1}) = 3071 (C-H aromatic ring), 1607 (C=O), 1110 (C-O), 641 (C-Br). ^{1}H NMR (400 MHz, $CDCl_3$) δ 12.67 (s, 1H, OH), 7.84 (d, *J* = 7.0 Hz,

2H, H-2', 6'), 7.57 – 7.44 (m, 3H, H-3', 4', 5'), 6.63 (s, 1H, H-8), 6.45 (s, 1H, H-3), 6.32 (s, 1H, H-6), 4.02 (t, *J* = 6.4 Hz, 2H, H-1"), 3.43 (t, *J* = 6.7 Hz, 2H, H-5"), 1.99 – 1.78 (m, 4H, H-2",4"), 1.67 – 1.60 (m, 2H, H-3"). ^{13}C NMR (100 MHz, $CDCl_3$) δ 182.40 (C-4), 164.83 (C-7), 163.92 (C-2), 162.13 (C-5), 157.73 (C-8a), 131.80 (C-1'), 131.25 (C-4'), 129.05 (C-3', 5'), 126.23 (C-2', 6'), 105.82 (C-3), 105.68 (C-4a), 98.51 (C-6), 93.02 (C-8), 67.50 (C-1"), 33.17 (C-5"), 32.49 (C-4"), 29.23 (C-2"), 27.57 (C-3").

3. Results & Discussion

3.1 Semi-synthesis

The selective mono-nucleophilic substitution could only occur on C-7, because there was less steric hindrance than C-5. Thus, the derivatives can only undergo mono-substitution at C-7 of chrysin (**3**). Semi-synthetic derivatives of compound **3** are shown in Scheme 1. Briefly, dissolving chrysin and potassium carbonate in acetone, followed by dibromoalkanes including 1,2-dibromoethane, 1,3-dibromopropane, 1,4-dibromobutane and 1,5-dibromopentane to give compounds **4**–**7**, respectively. All synthesized derivatives were gained in 78– 84% yield and were characterized by spectroscopy techniques (IR, ^{1}H NMR, and ^{13}C NMR). The data were in agreement with the earlier reports.[9-10]

Table 1. ClogP and *in vitro* HDAC inhibitory activity of compounds at 100 µM

Compounds	ClogP	%HDAC inhibition
TSA[a]	1.93	91
chrysin	3.56	51
4	4.88	44
5	5.21	39
6	5.59	34
7	6.12	42

[a]A positive control at 25 µM

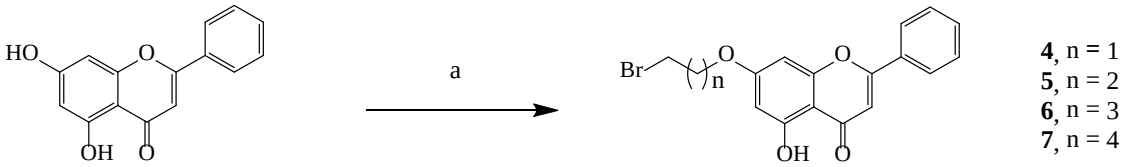

chrysin (**3**)

4-7

4, n = 1
5, n = 2
6, n = 3
7, n = 4

Scheme 1. Semi-synthesis of chrysin (**3**) derivatives. Reagents and conditions: (a) dibromoalkyl halides, K_2CO_3, acetone, reflux, 6h.

3.2 ClogP and *in vitro* HDACs inhibitory activity

Theoretical logP (ClogP) of the synthesized derivatives were calculated using ChemDraw Professional 15.1. The ClogP value is an important factor for membrane permeability.[11] The results demonstrated that all derivatives had ClogP values in the range of 4.88–6.12 (Table 2). Therefore, compound **4**-**6** contained the acceptable parameter for human use.

In addition, fluor-de-Lys HDAC activity test kit was used to screen all derivatives at a concentration of 100 µM. The total HDAC inhibitory activity in the HeLa nuclear extract, which contained several HDAC isoforms, was measured. Trichostatin A (TSA) was used as a positive control with a value of 91 % HDAC inhibition at 25 µM. The results are shown in Table 1. Chrysin (**3**) showed only 51% inhibition against HADCs. Although the chrysin derivatives, compounds **4**–**7**, were not comparable to TSA (91% HDAC inhibition), they illustrated a moderate HDAC inhibition value (34–44% HDAC inhibition) against HDACs compared to the parent compound (**3**). Among the synthesized derivatives, compounds **4** possessed the best % HDAC inhibition value of 44 %. It may be due to the substitution on C-7 of chrysin with bromo ethyl group, which is the shortest side chain when compared to the other synthesized compounds. It could inhibit HDAC in a manner comparable to the lead compound. Compound **4** was further selected to dock into the catalytic pockets of the class I HDACs in order to explain the *in vitro* results and investigate the potential of being HDAC isoform-selective inhibitors.

3.3 Molecular Docking

Class I HDACs have been discovered to play important roles in several tissues, including the control of differentiation, proliferation, cell cycle progression and apoptosis.[12] Therefore, class I HDACs were selected for molecular docking study. The synthesized compound **4** showed the strongest inhibition against HDAC8 with a ΔG value of -8.76 kcal/mol, which is more selective than the lead compound (**3**) (ΔG = -8.08 kcal/mol).

In addition, the selectivity ratio was calculated to confirm the selectivity of the compound for class I HDACs. The results showed that compound **4** was the most selective for HDAC8, as the selectivity ratio of HDAC8 was more than 1 over other HDACs, especially for HDAC3 with a value of 1.17 (HDAC8:HDAC3). It may illustrate that compound **4** was selective for HDAC8. Moreover, the interactions between compound **4** and class I HDACs were summarized in Table 3. Although the results show that compound **4** had more interaction with HDAC1 than the others, the derivative compound **4** showed more π-π interaction towards HDAC8 than HDAC1. This could indicate that compound **4** was selective for HDAC8.[15]

Table 2. *In silico* HDAC inhibitory activity profile of compound **4**.

Compounds	HDAC1		HDAC2		HDAC3		HDAC8	
	ΔG (kcal/mol)	*Ki* (μM)	ΔG (kcal/mol)	*Ki* (μM)	ΔG (kcal/mol)	*Ki* (μM)	ΔG (kcal/mol)	*Ki* (μM)
TSA[a]	-8.12	1.12	-8.75	0.39	-8.23	0.93	-8.85	0.03
chrysin[a]	-7.10	6.20	-8.55	0.54	-8.34	0.77	-8.08	1.17
4	-8.06	1.24	-7.98	1.41	-7.46	3.40	-8.76	0.38
Selectivity ratio	HDAC1		HDAC2		HDAC3		HDAC8	
/HDAC1	1.00[b]		0.99		0.93		1.09	
/HDAC2	1.01[b]		1		0.93		1.10	
/HDAC3	1.08[b]		1.07		1		1.17	
/HDAC8	0.92[b]		0.91		0.85		1	

[a]Previous work.[13]

[b]Selectivity ratio calculated by using ΔG value of HDAC1 divided by ΔG value of HDAC1, 2, 3 and 8.[14] For another column the same calculation was applied.

As can be seen in Figure 2, the synthesized compound (**4**) interacts with Gly151 and Phe208, which are amino residues found in the tunnel wall of the active site of HDAC8.[16] Moreover, the hydroxyl moiety on compound **4** is allowed to interact with Asp101 and Gly151 by hydrogen bonding. In addition, the benzene ring of synthesized compound **4** had π-π interaction with His180, His181 and Trp141, and located near cofactor, Zn^{2+} ion. The results indicated that aromatic region might play an important role to enhance the interaction between compound **4** and HDAC8. The side-chain alkyl bromo strongly interacted with Phe207 via forming an alkyl halide–π interaction,[17] which remarked that the short alkyl bromo side-chain could insert into the active site pocket of the target enzyme.

4. Conclusion

Consequently, it could be concluded that compound **4** which consisted of only two main pharmacophores, including the cap group and the linker showed the best HDAC inhibition both *in vitro* and *in silico*. However, the aromatic regions of **4** could also play an important role in chelation with Zn^{2+} ion which led to better inhibitor-enzyme binding with HDAC8 than lead compound (**3**).

Acknowledgements

This research was supported by the Khon Kaen University (FF2566) and Center of Excellence for Innovation in Chemistry, Ministry of Higher Education, Science, Research, and Innovation (Implementation Unit- IU, Khon Kaen University).

Table 3. Interactions of compound **4** with class I HDACs

	H-bond	π – π interaction	RX – π interaction	π – σ interaction
HDAC1	Asp99 His178 Gly149	Try204 His178	Tyr303 His141	Phe150 His178
HDAC2	Asp104 His183 Phe155	Lue276 Tyr209	His145 His146	-
HDAC3	Phe199 Leu266	His172 Phe200 Phe144	-	-
HDAC8	Asp101 Gly151	His180 His181 Trp141	Phe207	Phe208

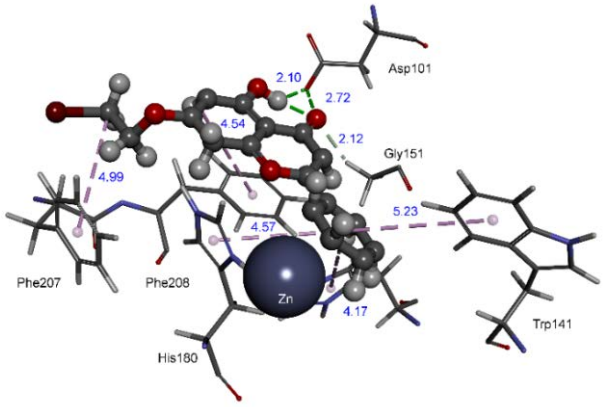

Figure 2. The binding modes of compound **4** into the active site of HDAC8

References

1. Chen, H.; Zhao, Y.; Zhao, T. *Crit. Rev*. **2015**, 20 (1–2), 35–47.
2. Yang, F.; Shan, P.; Zhao, N.; Ge, D.; Zhu, K.; Jiang, C; Li, P.; Zhang, H. *Bioorganic Med. Chem. Lett*. **2019**, 29, 15–21.
3. Chakrabarti, A.; Oehme, I.; Witt. O; Oliverira, G.; Sippl, W.; Romier, C.; Pirece, J. R.; Jung M. *Trends Pharmacol. Sci*. **2015**, 36, 7.
4. Xu, Y.; Tang, H.; Xu, Y.; Guo, J.; Zhao, X.; Meng, Q.; Xiao, J. *Molecules*. **2022**, 27, 3335.
5. Al-Hamashi, A.; Abdulhadi, S.; Ali, R. *Egypt. J. Chem*. **2023**, 66, 215–221.
6. Frühauf, A.; Meyer-Almes, F. *Molecules*. **2021**, 26, 5151.
7. Geurs, S.; Clarisse, D.; Bosscher, K.; D'hooghe, M. *J. Med. Chem*. **2023**, 66, 7698−7729.
8. Al-Oudat, B. A.; Alqudah, M. A.; Audat, S. A.; Al-Balas, Q. A.; El-Elimat, T.; Hassan, M. A.; Frhat, I. N.; Azaizeh, M. M. *Drug Des Devel Ther*. **2019**, 13, 423–433.
9. Abdelkarim, H.; Neelarapu, R.; Madriaga, A.; Vaidya, S. A.; Kastrat, I.; Wang, Y.; Taha, Y., T.; Thatcher, R. J. G.; Frasor, J.; Petukhov, A. P. *ChemMedChem*. **2017**, 12(24), 2030–2043.
10. Hu, K.; Wang, W.; Cheng, H.; Pan, S.; Ren, J. *Med Chem Res*. **2011**, 20, 838-846.
11. Abdizadeh, T; Kalani, R, M; Abnous, K; Tayarani-Najaran, Z; Khashyarmanesh, Z, B; Abdizadeh, R; Ghodsi, R; Hadizadeh, F.
12. Reichert, N; Choukrallah, M; Matthias, P. *Cell. Mol. Life Sci*. **2012**, 69, 2173–2187.
13. Somsakeesit, L.; Senawong, T.; Senawong, G.; Kumboonma, P.; Samankul, A.; Namwan, N.; Yenjai, C.; Phaosiri, C. *J. Nat. Med*. **2023**. (doi: 10.1007/s11418-023-01758-y)
14. Valdez-Calderón, A.; González-Montiel, S.; Martínez-Otero, D.; Martínez-Torres, A.; Vásquez-Pérez, M. J.; Molina-Vera, C.; Torres-Valencia, M. J.; Alvarado-Rodríguez, G. J.; Cruz-Borbolla, J. *J. Mol. Struct*. **2016**, 162–207.
15. Ortore, G; Colo, D, F; Martinelli, A. *J. Chem. Inf. Model*. **2009**, 49, 2774–2785
16. Bannejee, S; Adhikari, N; Amin, A, S; Jha, T. *Eur. J. Med. Chem*. **2019**, 164, 214–240.
17. Braffman, R, N; Ruskoski, B, T; Davis, M, K; Glasser, R, N; Johnson, C; Boal, K, A; Balskus, P, E. *eLife*. **2022**, 11, 75761.

Structural simplification of maytansine and synthesis efficiency for antitumor activity

Tomomi Uchida[1], Mayuka Fujimoto[2], Maina Minamino[2], and Masaki Kuse[1,2]*

[1]*Graduate School of Agricultural Science, Kobe University, Japan*
[2]*Faculty of Agriculture, Kobe University, Japan*

**E-mail: kuse@eagle.kobe-u.ac.jp*

Abstract:

This study shows again the importance of the chemical synthesis of maytansine despite the decline in research following semi-synthetic advances in the 1980s. The renewed interest is due to the use of maytansine derivatives in antibody-drug conjugates (ADCs), particularly in trastuzumab emtansine (Kadcyla®), highlighting its clinical potential despite initial limitations caused by the potent cytotoxicity of maytansine. The binding site of maytansine differs from other anti-tumor agents; thus, we focused on this specificity. Based on the binding structure, the focus was on rational design, targeting non-critical moieties—specifically the dienyl structure and methoxy group—to be replaced with a simpler methylene chain. Computational simulations confirmed the stability of the designed analog, implying comparable activity to maytansine. The provided retrosynthetic analysis outlined a synthetic roadmap involving strategic transformations and critical steps such as aldol condensation. This study furthers the maytansine's binding mechanism and suggests a more efficient synthesis route for maytansine derivatives. The findings will offer potential advancements in ADC development, promoting maytansine's broader application in treating cancers and fostering improved clinical effectiveness.

1. Introduction

Maytansine (Fig 1), an anti-tumor agent, was isolated from *Maytenus ovatus* in 1972 and structurally determined by Kupchan et al.[1] Its structure is a 19-member-ansa macrolide with multiple stereocenters. Due to its significant biological activity and unique chemical structure, total synthesis research was intensively developed worldwide in the 1970s and 1980s.

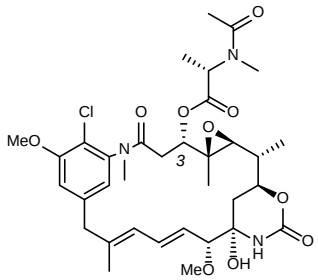

Figure 1. Structure of maytansine.

For example, the total syntheses of maytansinoids, including maytansine, were reported by several groups, such as Meyers (1980),[2] Corey (1980),[3] Isobe (1982),[4] and others.[5-7] On the other hand, at about the same time when the total syntheses were achieved, semi-synthesis using microbial fermentation was reported by Takeda Chemical Industries, Ltd.,[8] and gradually, chemical synthesis research went into decline. However, this study dares to focus again on the importance of chemical synthesis studies of maytansine. This is because maytansine derivatives have been used as payload compounds in antibody-drug conjugates (ADCs) in recent years, demonstrating the utility of maytansine in clinical use.[9] Originally, maytansine was recognized for its potent cytotoxicity, which was 10-1,000 times more cytotoxic than other anti-tumor agents such as taxanes, vincristine, and vinblastine.[10] It was expected to be used for the treatment of breast and liver cancers, etc., but it had limited medical use because of its drawbacks. It only worked in a small dose range and could harm the digestive and nervous systems.[11] However, in 2013, the EMA and FDA approved an ADC drug, trastuzumab emtansine (Kadcyla®), whose payload was a derivative of maytansine.[9] Therefore, maytansine is now being actively investigated for further applications in ADC. Maytansine inhibits tubulin polymerization, which prevents microtubules from forming and inhibits mitosis.[12] The X-ray crystal structure of maytansine in complex with tubulin has already been reported,[13] and it binds a region in tubulin that is distinct from the binding regions of other anti-tumor agents: vinca alkaloid, taxane, colchicine, and laulimalide.[14] This study focuses on how maytansine binds to tubulin, intending to simplify the structure of maytansine while retaining its anti-tumor activity and achieving a more straightforward total synthesis than previously accomplished.

2. Materials and Methods

2.1 General procedures

Unless stated otherwise, anhydrous reactions were conducted in flame-dried glassware

under the atmosphere of argon using commercially available anhydrous solvents. Thin-layer chromatography (TLC) was conducted with silica gel 60 F254 pre-coated plates (0.25 mm) and visualized using a combination of UV and molybdatophosphoric acid staining. Silica gel 60N (neutral, sphere, particle size 0.063-0.210 mm) was used for column chromatography. ^{1}H NMR spectra were recorded on a JNM-ECZ400 (400 MHz) or a Bruker Avance 500 (500 MHz) spectrometer. Data for ^{1}H spectra are reported as follows: chemical shift (δ ppm), multiplicity, coupling constant (J) (Hz), and integration, and are referenced to the residual solvent peak 7.26 ppm for $CDCl_3$. ^{13}C NMR spectra were reported regarding chemical shift (at 100 MHz) and referenced to the residual solvent peak 77.0 ppm for $CDCl_3$. Commercially available chemicals were purchased and used without further purification.

2.2 Analysis of X-ray crystal structure

The crystal structure of maytansine bound to tubulin (PDB: 4TV8) was analyzed using PyMol Version 2.5.5 (Schrödinger, 2023).

2.3 DFT calculations

Stable conformation of the maytansine analog was obtained through the DFT calculations using the geometry calculations with a 6-31G(d) basis set implemented in the Gaussian09W (Frisch et al., 2009).

2.4 Synthesis of Compound 9 ((*R*)-2-((*S*)-1-(benzyloxy)propan-2-yl)oxirane) (East fragment)

Based on the reported procedures,[15-18] we prepared compound **8**, and the spectral data matched the reference data.

To a solution of tosylate **8** (15 mg, 0.040 mmol) in THF (1 mL) was added NaH (10 mg, 0.25 mmol) under an Ar atmosphere. The reaction mixture was stirred at room temperature for 1 h, quenched with a saturated solution of NH_4Cl (3 mL) at 0 °C, and extracted with Et_2O (3 × 3 mL). The combined organic layer was washed with brine, dried over Na_2SO_4, and concentrated by evaporation. The crude material (24 mg) was purified by column chromatography (EtOAc/hexane=1/4) to give **9** (4.90 mg, 64%). ^{1}H NMR (400 MHz, $CDCl_3$): δ 7.28-7.37 (m, 5H), 4.52 (s, 2H), 3.44 (q, J = 9.4 Hz, 1H), 3.44 (dd, J = 9.4, 6.6 Hz, 1H), 2.88 (m, 1H), 2.77 (t, J = 4.6 Hz, 1H), 2.62 (dd, J = 5.0, 2.7 Hz, 1H), 1.73 (m, 1H), 1.03 (d, J = 6.9 Hz, 3H). The Spectral data was matched with the reference.[19]

2.5 Synthesis of Compound 18 (West fragment)

2.5.1 Compound 13 (*tert*-butyl (2-chloro-5-(hydroxymethyl)-3-methoxyphenyl)carbamate)

Compound **13** was prepared in a five-step reaction from methyl vanillate as outlined in the previous study[7] to afford **13**, and the spectral data were matched with the reference data. There were new compounds from **14** to **17**. Compound **18** (West fragment) was identical to the reference data.[20]

2.5.2 Compound 14 (*tert*-butyl (5-(((*tert*-butyldimethylsilyl)oxy)methyl)-2-chloro-3-methoxyphenyl)carbamate)

To a solution of alcohol **13**[21] (119 mg, 0.420 mmol) in THF (5 mL) was added NaH (33.2 mg, 0.830 mmol) and TBSCl (128 mg, 0.830 mmol) at 0 °C. The resulting solution was refluxed for 4 h under an Ar atmosphere. The reaction mixture was cooled to room temperature and then quenched with a solution of sat. NH_4Cl (10 mL). The aqueous layer was extracted with EtOAc (3 ×10 mL). The combined organic layer was washed with water and brine. After drying over Na_2SO_4, the extract was concentrated by evaporation. The crude **14** (145 mg) was obtained in 87% yield, which was employed in the following reaction without further purification ^{1}H NMR (400 MHz, $CDCl_3$): δ 7.71 (s, 1H), 7.08 (s, 1H), 6.78 (s, 1H), 4.72 (s, 2H), 3.90 (s, 3H), 1.52 (s, 9H), 0.94 (s, 9H), 0.10 (s, 6H).

2.5.3 Compound 15 (*tert*-butyl (5-(((*tert*-butyldimethylsilyl)oxy)methyl)-2-chloro-3-methoxyphenyl)(methyl)carbamate)

To a cooled solution of silyl ether **14**[22] (2.00 g, 4.98 mmol) in anhydrous DMF (60 mL) at 0 °C was added NaH (249 mg, 6.22 mmol) in six portions over 1 h. The solution was stirred vigorously for 2 h at 0 °C, then CH_3I (356 µL, 5.72 mmol) was added dropwise at 0 °C for 30 min. The reaction mixture was warmed to room temperature and stirred for 30 min under an Ar atmosphere. The solution was quenched with ice and a solution of sat. NH_4Cl (30 mL). The aqueous layer was extracted with Et_2O (3 × 30 mL). The organic layer was washed with a solution of sat. $NaHCO_3$ and brine. After drying over Na_2SO_4, the extract was concentrated by evaporation. The crude **15** (1.69 g) was obtained in 82% yield and employed in the next reaction without further purification. ^{1}H NMR (500 MHz, $CDCl_3$): δ 6.89 (s, 1H), 6.79 (s, 1H), 4.71 (s, 2H), 3.90 (s, 3H), 3.14 (s, 3H), 1.34 (s, 9H), 0.95 (s, 9H), 0.10 (s, 6H).

2.5.4 Compound 16 (5-(((*tert*-butyldimethylsilyl)oxy)methyl)-2-chloro-3-methoxy-*N*-methylaniline)

To a cooled solution of mono *N*-Boc compound **15**[23] (208 mg, 0.500 mmol) in DCM (5 mL) at 0 °C was and Et_3N (279 µL, 2.00 mmol) and TMSOTf (369 µL, 2.00 mmol) at 0 °C for 20 min.

The reaction mixture was warmed to room temperature and stirred for 2.5 h under an Ar atmosphere. The reaction mixture was cooled to 0 °C and quenched with an ice-cold solution of sat. NH_4Cl (15 mL). The aqueous layer was extracted with Et_2O (2 × 30 mL). The combined organic layer was washed with a solution of sat. $NaHCO_3$ and brine. After drying over Na_2SO_4, the extract was concentrated by evaporation. The crude **16** (154 mg) was obtained in 98% yield and employed in the following reaction without further purification. ^{1}H NMR (500 MHz, $CDCl_3$): δ 6.36 (d, J = 1.6 Hz, 1H), 6.32 (brs, 1H), 4.69 (s, 2H), 3.87 (s, 3H), 2.90 (s, 3H: *Two singlet signals were observed as rotatory isomers derived from *N*-Methyl group), 1.26 (s, 1H), 0.95 (s, 9H), 0.12 (s, 6H).

2.5.5 Compound 17 (*N*-(2-chloro-5-(hydroxymethyl)-3-methoxyphenyl)-*N*-methylacetamide)

To a solution of amine **16** (193 mg, 0.610 mmol) in pyridine (5 mL) was added Ac_2O (5 mL), and the solution was stirred at room temperature under an Ar atmosphere for 6.5 h. To the resulting solution was added toluene (10 mL), and the solution was azeotropically evaporated to remove the remaining volatile compounds. The crude material (200 mg) was purified by column chromatography (SiO_2: 5 g, EtOAc/hexane = 1/4, then 1/1) to give **17a** (155 mg, 71%). ^{1}H NMR (400 MHz, $CDCl_3$): δ 6.98 (d, J = 0.9 Hz, 1H), 6.84 (d, J = 1.3 Hz, 1H), 4.72 (s, 2H), 3.94 (s, 3H), 3.18 (s, 3H), 1.82 (s, 3H), 0.95 (s, 9H), 0.12 (s, 6H).

Amide **17a** [24] (107 mg, 0.300 mmol) was acid hydrolyzed in a solution of AcOH-THF-water=3/1/1 (15 mL) at room temperature under Ar atmosphere. After 18 h, the resulting solution was added to sat. aqueous $NaHCO_3$ (30 mL) and stirred for 30 min. The aqueous layer was extracted with EtOAc (3 × 30 mL), and the combined organic layer was washed with brine. After drying over Na_2SO_4, the extract was concentrated by evaporation. The crude material (78.3 mg) was purified by preparative thin layer chromatography (PTLC) (EtOAc/hexane = 4/1) to give **17** (49.1 mg, 67%). ^{1}H NMR (400 MHz, $CDCl_3$): δ 7.02 (d, J = 1.8 Hz, 1H), 6.90 (d, J = 1.8 Hz, 1H), 4.73 (s, 2H), 3.96 (s, 3H), 3.18 (s, 3H), 2.51 (s, 1H), 1.82 (s, 3H).

2.5.6 Compound 18 (*N*-(5-(bromomethyl)-2-chloro-3-methoxyphenyl)-*N*-methylacetamide) (West fragment)

To a solution of alcohol **17** [7] (24.2 mg, 0.100 mmol) in dehydrated DCM (1 mL) was added CBr_4 (32.9 mg, 0.100 mmol) and PPh_3 (26.0 mg, 0.100 mmol) at 0 °C, and the reaction mixture was stirred at room temperature for 5 h. The reaction mixture was quenched with the solution of sat. NH_4Cl (3 mL). The aqueous layer was extracted with EtOAc (3 × 5 mL). The combined organic layer was washed with sat. aqueous $NaHCO_3$ and brine. After drying over Na_2SO_4, the extract was concentrated by evaporation. The crude material (58.1 mg) was purified by PTLC (EtOAc/hexane = 4/1) to give bromide **18** (14.5 mg, 48 %). ^{1}H NMR (400 MHz, $CDCl_3$): δ 6.99 (d, J = 1.8 Hz, 1H), 6.95 (d, J = 1.8 Hz, 1H), 4.56 (d, J = 1.4 Hz, 2H), 3.97 (s, 3H), 3.19 (s, 3H), 1.83 (s, 3H). ^{13}C NMR (100 MHz, $CDCl_3$): δ 170.5, 156.5, 143.0, 138.3, 121.8, 121.6, 112.2, 56.7, 35.6, 32.0, 21.9. These data were identical to the reported data.[20]

3. Results & Discussion

3.1 Design of the simplified maytansine analog

On closer examination of the X-ray crystal structure of the maytansine-tubulin complex (Fig. 2), it was thought that the binding site of the maytansine was an important structure for expressing its anti-tumor activity.

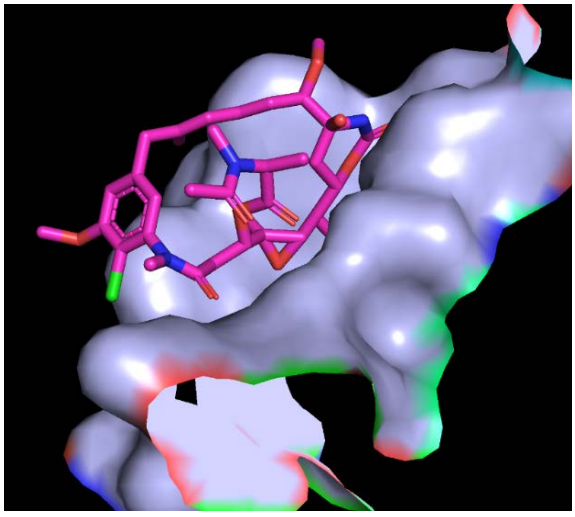

Figure 2. Closer looks at the binding pocket of tubulin. Maytansine is colored purple, and the surface of tubulin is colored gray (PDB: 4TV8).

On the other hand, some moieties would not affect its activity. Specifically, the dienyl structure and methoxy group, located away from the critical binding site, offered the potential for more superficial structures. In addition, they were not conjugated to the aromatic ring, which could destabilize the overall structure and cause difficulties in stereoselective synthesis. Indeed, it was also introduced in a review as one of the difficulties in synthesis.[5] This study selected these structures as the parts to be simplified and replaced by the most straightforward methylene chain. In this way, a novel artificial molecule was designed as a simplified maytansine analog (Fig. 3).

Previous studies have shown that the side chain of the C-3 in maytansine was necessary for its activity.[1b] Since synthesizing this ester moiety is considered easy; the simplified maytansine analog was designed as the alcohol form in this study.

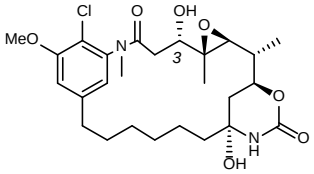

Figure 3. Simplified maytansine analog.

3.2 DFT calculations

We calculated the difference between the conformations of maytansine analogs and maytansine. The stable conformation of the maytansine analog was obtained using DFT calculation (6-31G(d) basis set). The resulting conformation showed little difference (Fig. 4). Therefore, we expected this analog to show the same activity as maytansine. We calculated the maytansine and the maytansine analog with an ester side chain at C-3.

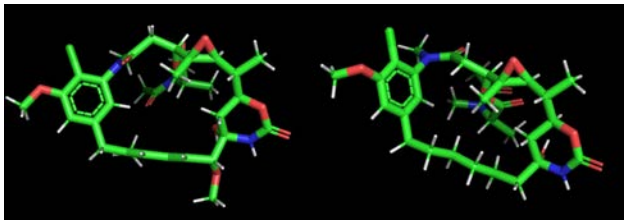

Figure 4. Calculated conformations of maytansine (left) and the simplified analog of maytansine (right).

3.3 Retrosynthetic analysis

Inspired by the previous research,[5] the retrosynthetic analysis of the simplified maytansine analog was illustrated in Scheme 1. It consists of four fragments –North, South, East, and West–. Aldol condensation and cyanohydrin chemistry would serve as the critical steps for this synthesis.

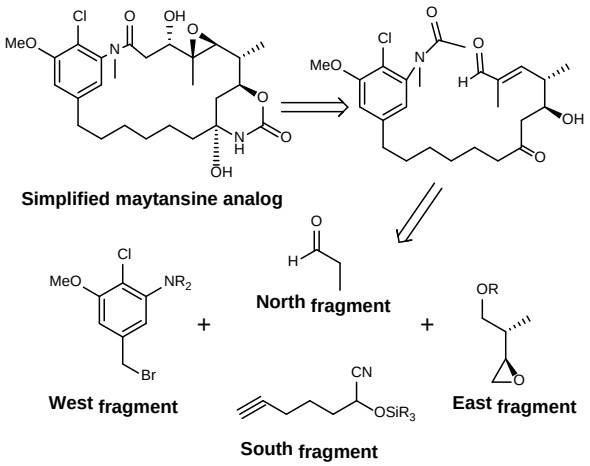

Scheme 1. Retrosynthetic analysis of the simplified maytansine analog.

3.4 The synthesis of the East fragment (9)

Following Corey's approach[15] and Elliott's approach,[16] the synthesis commenced with cis-but-2-ene-1,4-diol (**1**) transformation to make epoxide **9**. In the processes, the conditions for synthesizing epoxide **3** and the deprotection of acetonide with an ion exchange resin to afford the diol **7** were adapted from other literature.[17,18] The resulting diol **7** was converted to the epoxide **9** (East fragment) over two steps. (Scheme 2).

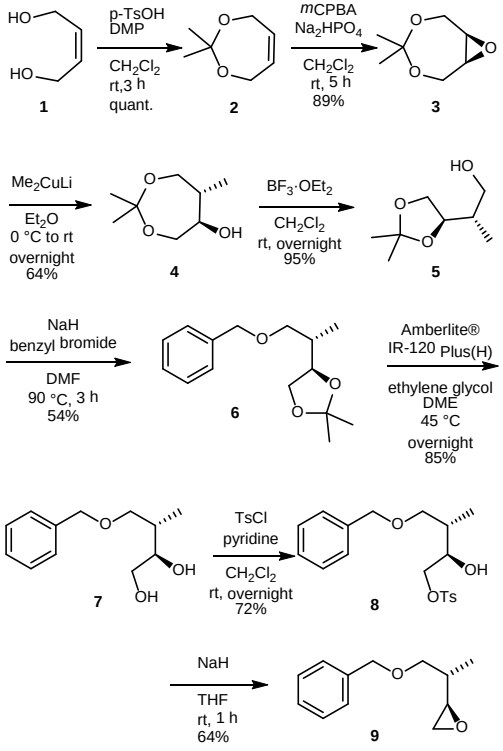

Scheme 2. Synthesis of the East fragment (**9**) starting from (*Z*)-but-2-ene-1,4-diol (**1**). DMP: 2,2-dimethoxypropane, DME: 1,2-dimethoxyethane.

3.5 The synthesis of the West fragment (18)

Following Wang's approach,[7] methyl vanillate (**10**) was converted to compound **13** over five steps. In this sequence, nitrobenzene **11** was reduced to aniline with H_2 using Pt/C catalyst "STAF-1M", which specifically prevented dehalogenation. The amino group was protected with Boc to obtain compound **12**.

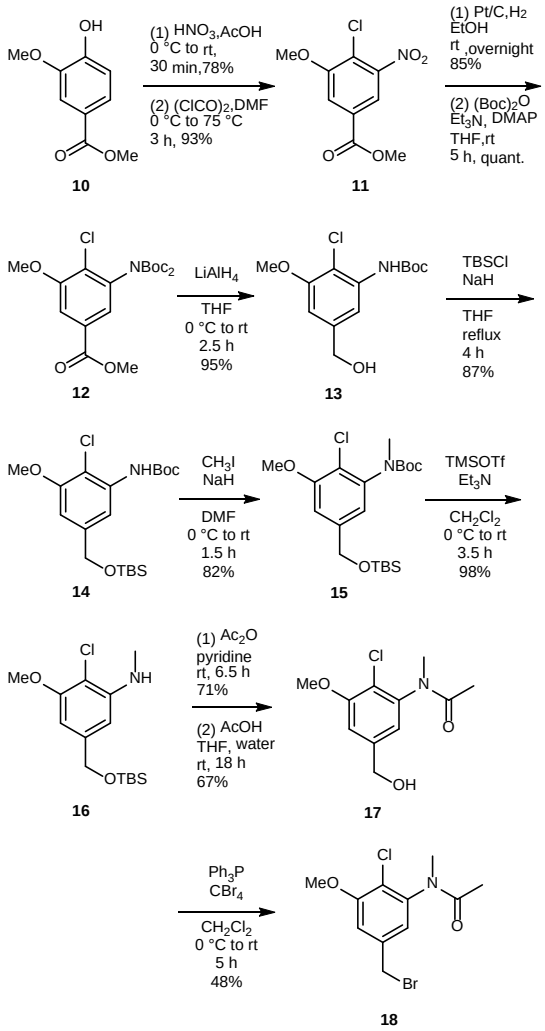

Scheme 3. Synthesis of the West fragment (**18**) starting from methyl vanillate (**10**).

Before proceeding further reactions, attempts were made to convert the *N*-Boc group to the *N*-Me group and to reduce the methoxycarbonyl moiety to alcohol at the same time.[25] However, this step proved challenging since treatment of *N*-Boc and methyl ester groups of **12** with $LiAlH_4$ in refluxing THF only resulted in an additional chloride reduction. Therefore, *N*-methylation and ester reduction had to be carried out independently. After obtaining compound **13** with $LiAlH_4$ reduction at ambient temperature, the hydroxy group of **13** was protected as a silyl ether, followed by *N*-methylation to afford **15**. Since the silyl ether was sensitive to acid conditions, regarding the TMSOTf/2,6-lutidine condition,[18] the cleavage of *N*-Boc was carried out using Et_3N instead of 2,6-lutidine. Treatment of **15** with TMSOTf/Et_3N afforded **16**, remaining in the protected hydroxy group. To obtain **18**, **16** was acetylated, followed by cleavage of the silyl ether protection. Alcohol **17** underwent Appel reaction to give the bromide **18** (West fragment) (Scheme 3).

4. Conclusion

In conclusion, this study has explored the crucial area of binding of maytansine to tubulin and its structural simplification while retaining its anti-tumor activity. A simplified maytansine analog was conceived through careful analysis of the X-ray crystal structure of the maytansine–tubulin complex and subsequent strategic design. The design targeted specific structural elements—such as the dienyl structure and the methoxy group—considered dispensable for the compound's anti-tumor activity, replacing them with simple methylene structures. This approach aimed to streamline the synthesis process and enhance the compound's potential utility. Moreover, DFT calculations were used to confirm the stability of the designed analog. The results indicated a similarity in conformation to maytansine, which supported the presumption of analogous anti-tumor activity. We synthesized the crucial fragments—East and West—necessary to assemble the simplified analog. The east fragment was synthesized in 8 steps with a total yield of 11%, and the West fragment was synthesized in 11 steps with a total yield of 9%. The synthetic strategies presented here were adapted from established procedures and modifications. This study advances the understanding of maytansine's binding mechanism and contributes to the prospect of achieving a more straightforward total synthesis of maytansine derivatives. This could potentially facilitate their broader application in ADCs for enhanced clinical efficacy.

Acknowledgments

The authors are grateful to the Research Facility Center for Science and Technology, Kobe University, for instrumental analyses.

References

1. (a) Kupchan, S. M.; Komoda, Y.; Court, W. A.; Thomas, G. J.; Smith, R. M.; Karim, A.; Gilmore, C. J.; Haltiwanger, R. C.; Bryan, R. F. *J. Am. Chem. Soc.* **1972**, *94*, 1354–1356. (b) Kupchan, S. M.; Komoda, Y.; Branfman, A.

R.; Dailey. Jr., R. G.; Zimmerly, V. A. *J. Am. Chem. Soc.* **1974**, *96*, 3706–3708.
2. Meyers, A. I.; Reider, P. J.; Campbell, A. L. *J. Am. Chem. Soc.* **1980**, *102*, 6597–6598.
3. Corey, E. J.; Weigel, L. O.; Chamberlin, A. R.; Cho, H.; Hua, D. H. *J. Am. Chem. Soc.* **1980**, *102*, 6613–6615.
4. Isobe, M.; Kitamura, M.; Goto, T. *J. Am. Chem. Soc.* **1982**, *104*, 4997–4999.
5. Kirschning, A.; Harmrolfs, K.; Knobloch, T.; *C. R. Chim.* **2008**, *11*, 1523–1543.
6. Huang, Y. Y.; Chen, L.; Ma, G. X.; Xu, X. D.; Jia, X. G.; Deng, F. S.; Li, X. J.; Yuan, J. Q. *Molecules* **2021**, *26*, 4563 (pp 1–41).
7. Wang, L.; Gong, J.; Deng, L.; Xiang, Z.; Chen, Z.; Wang, Y.; Chen, J.; Yang, Z. *Org. Lett.* **2009**, *11*, 1809–1812.
8. (a) Asai, M.; Mizuta, E.; Izawa, M.; Haibara, K.; Kishi, T. *Tetrahedron* **1979**, *35*, 1079–1085. (b) Nakahama, K.; Izawa, M.; Asai, M.; Kida, M.; Kishi, T. *J. Antibiot.* **1981**, *34*, 1581–1586.
9. Baah, S.; Laws, M.; Rahman, K.M. *Molecules* **2021**, *26*, 2943 (pp 1–19).
10. Zhang, Q. Y.; Yu, Q. L.; Luan, W. J.; Li, T. F.; Xiao, Y. N.; Zhang, L.; Li, Y.; Rong, R.; Ren, C.G. *RSC Adv.* **2023**, *13*, 10840–10846.
11. Zafar, S.; Armaghan, M.; Khan, K.; Hassan, N.; Sharifi-Rad, J.; Habtemariam, S.; Kieliszek, M.; Butnariu, M.; Bagiu, I. C.; Bagiu, R. V.; Cho, W. C. *Biomed. Pharmacother.* **2023**, *165*, 115039 (pp 1–16).
12. Issell, B. F.; Crooke, S. T. *Cancer. Treat. Rev.* **1978**, *5*, 199–207.
13. Prota, A. E.; Bargsten, K.; Diaz, J. F.; Marsh, M.; Cuevas, C.; Liniger, M.; Neuhaus, C.; Andreu, J. M.; Altmann, K. H.; Steinmetz, M. O. *Proc. Natl. Acad. Sci. U.S.A.* **2014**, *111*, 13817–13821.
14. Steinmetz, M. O.; Prota, A. E. *Trends. Cell. Biol.* **2018**, *28*, 776–792.
15. Corey, E. J.; Bock, M. G. *Tetrahedron Lett.* **1975**, *31*, 2643–2646.
16. Elliott, W. J.; Fried, J. *J. Org. Chem.* **1976**, *14*, 2469–2475.
17. Szpera, R.; Kovalenko, N.; Natarajan, K.; Paillard, N.; Linclau, B. *Beilstein J. Org. Chem.* **2017**, *13*, 2883–2887.
18. Nicolaou, K. C.; Papahatjis, D. P.; Claremon, D. A.; Magolda, R. L.; Dolle, R. E. *J. Org. Chem.* **1985**, *50*, 1440–1456.
19. Mori, Y.; Asai, M.; Okumura, A.; Furukawa, H. *Tetrahedron* **1995**, *51*, 5299–5314.
20. Foy, J. E.; Ganem, B. *Tetrahedron Lett.* **1977**, *18*, 775–776.
21. Meng, Z.; Fürstner, A. *J. Am. Chem. Soc.* **2022**, *144*, 1528–1533.
22. Krein, D. M.; Lowary, T. L. *J. Org. Chem.* **2002**, *67*, 4965–4967.
23. Bastiaans, H. M. M.; van der Baan, J. L.; Ottenheijm, H. C. J. *J. Org. Chem.* **1997**, *62*, 3880–3889.
24. Corey, E. J.; Venkateswarlu, A. *J. Am. Chem. Soc.* **1972**, *94*, 6190–6191.
25. Huo, H. H.; Zhang, H. K.; Xia, X. E.; Huang, P. Q. *Org. Lett.* **2012**, *14*, 4834–4837.

Syntheses and mechanistic investigations of formamides, formamidines, and formimidates

Chhorvy Kong[1]*, Piyabutr Wanichpongpan[2], Vannapa Luckanawat[1], and Kittichai Chaiseeda[1]

[1]*Organic Synthesis, Electrochemistry and Natural Product Research Unit (OSEN), Department of Chemistry, Faculty of Science, King Mongkut's University of Technology Thonburi, Bangkok 10140, Thailand*
[2]*Department of Chemical Engineering, King Mongkut's University of Technology Thonburi, Bangkok 10140, Thailand*

**E-mail: kong.chho@mail.kmutt.ac.th*

Abstract:

Formamide, formamidine, and formimidate compounds are the organic compounds that have been used in the synthesis of pharmaceutically active compounds and in various industries. This work presents convenient and efficient methods for preparing 3 kinds of products: formamidine, formimidate, and formamide from an amine and triethyl orthoformate (TEOF) under different reaction conditions. Aniline was chosen as a model compound. Various experimental parameters were varied including type of solvent, mole ratio, reaction time, and reaction temperature. It was found that to obtain formamidine, using ethanol as a solvent and 1 equivalent of TEOF at 60 °C in 2 h produced the desired product at 91% yield. The highly efficient protocol for formimidate was carried out under solvent-free condition using 5 equivalents of TEOF at 60 °C and the formimidate product was obtained at 98% yield within 24 h. To produce formamide, 24 equivalents of TEOF in deionized water at 70 °C were used to achieve 97% yield in 24 h. These methods are highly favorable because they are catalyst-free, low-cost, easy, and fast and provide excellent yields.

1. Introduction

Organic compounds containing formamide, formamidine, and formimidate scaffold have been studied extensively because of their significant applications as a valuable intermediate in the production of synthetic compounds[1] and in pharmaceutical industry.[2] For example, a formamide is used as an intermediate in a pharmaceutical process to produce benfotiamine, which is used to treat diabetic neuropathy.[3] Other compounds with formamide included leucovorin, used to treat the toxic effects of methotrexate and pyrimethamine;[4] vincristine, used to treat cancer;[5] and fursultiamine, a medication and vitamin used to treat thiamine deficiency[6]. In addition, formamidine is a significant class of compounds that have garnered much interest thanks to the many different ways they can be used in different industries such as pharmaceuticals, agrochemicals, materials science, and its N=C−N core pattern is a class of chemical biological activity that have been used to synthesize imidazole alkaloids, imidazolium, histidine, optoelectric, and NHC carbene compound.[7] Moreover, the formimidate is the most important compound for the synthesis of pyrimidines[8] which have been demonstrated to engage in a wide variety of different biological activities, including antimicrobial,[9] antioxidant,[10] and anticancer[11] properties, and they can also improve cognitive function, which makes them useful for the treatment of neurodegenerative diseases.[12] Because of the significance of their applications, numerous scientists have created several effective strategies for synthesis them. However, they face similar issues, including inconvenient conditions, extended reaction times, low yields, harsh environments, toxicity, costly catalyst systems, and limited product outcomes. Consequently, these procedures are generally considered less acceptable and desirable.

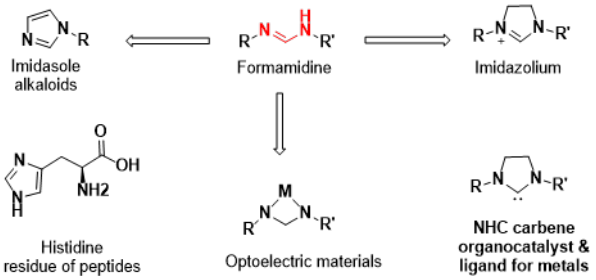

J. Org. Chem. 2022, 87, 13564−13572

Figure 1. Structures of some drugs that use formamidine

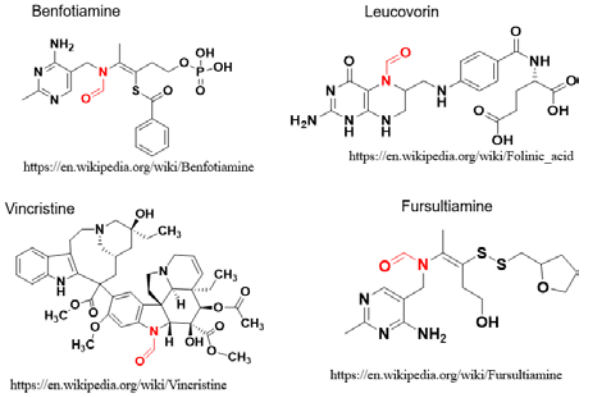

Figure 2. Structures of some drugs that use formamide

Pyrano[2,3-d]pyrimidine

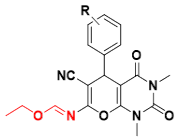

Res Chem Intermed (2016) 42:3763–3774

Figure 3. Structures of compound that use formimidate.

In this work, we describe a convenient method that can be used to produce high yields of three kinds of products, formamides, formamidines, and formimidate, from aniline and triethyl orthoformate (TEOF) by just changing the reaction conditions. We also investigated the mechanical pathway of the reactions.

2. Materials and Methods

2.1 Materials

All chemicals including diethyl ether (99.5%, Thomas Baker), toluene (99.5%, Thomas Baker), ethanol (99.9%, QReC), dimethyl sulfoxide (99.5%, Thomas Baker), DI water, acetone (99.5%, RCI Labscan), acetonitrile (100%, QReC), hexane (99%, QReC), ethyl acetate (99.5%, QReC), dimethylformamide (99.8%, QReC), dichloromethane (97%, RCI Labscan), methanol (≥99.8, RCI Labscan), aniline (99.5%, Thomas Baker), formanilide (>99.0%, TCI Chemicals), *N*,*N*'-diphenylformamidine (>98.0%, TCI Chemicals), triethyl orthoformate (>98.0%, TCI Chemicals), ethyl *N*-phenylformimidate (>98.0%, TCI Chemicals) and naphthalene (>99%, HiMedia aboratories) were used as received without prior purification.

2.2 Methodology

2.2.1 General procedure

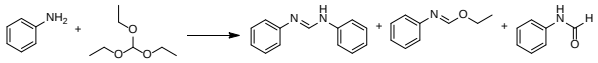

Aniline (1 mmol) with a specified amount of TEOF was added in the presence of an appropriate amount of solvent (or no solvent) to a 4 mL vial and the reaction mixture was stirred at the specified temperature for a specified period. Then the mixture was diluted with 2 mL CH_2Cl_2, and 50 mg of naphthalene, an internal standard, was added to prepare the GC sample. The products from the reactions were identified by compared with commercial standards. The amount of aniline and products were determined using a Shimadzu Nexis GC-2030 gas chromatograph equipped with a Shimadzu SH-I-5MS column.

3. Results & Discussion

3.1 Effect of the amount of TEOF

The amount of triethyl orthoformate was first varied. In the reaction using 1 mmol aniline with 1-5 mmol TEOF at 60 °C for 2 h (Figure 1), the result showed that increasing the amount of triethyl orthoformate resulted in a decreasing amount of *N*,*N*'-diphenylformamidine, while the amount of ethyl *N*-phenylformimidate increased. The amount of formanilide product remained about 2-3% despite varying amount of triethyl orthoformate. Therefore, if *N*,*N*'-diphenylformamidine is the desired product, then 1 mmol of triethyl orthoformate should be sufficient.

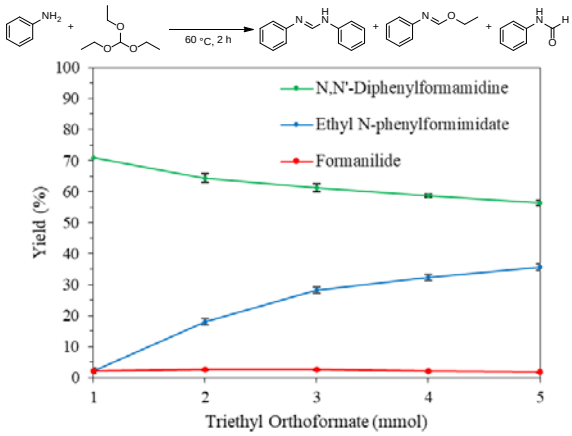

Figure 4. Effect of the amount of TEOF.

Reaction conditions: 1 mmol aniline, 60 °C for 2 h. Yields were determined by GC using naphthalene as an internal standard.

3.2 Effect of reaction time on *N*,*N*'-diphenylfor-mamidine production

To try to increase the yield of *N*,*N*'-diphenylformamidine, the reaction time were varied from 5 min (0.08 h) to 24 h. The reactions were performed with 1 mmol aniline, 1 mmol triethyl orthoformate without solvent and catalyst at 60 °C for the period shown in Figure 2. The result revealed that the reaction for 5 min, 15 min, 30 min, and 1 h give only 9.7, 18.5, 26.4 and 34.1% of *N*,*N*'-diphenylformamidine, respectively. When the reactions were performed at 2 to 24 h, the yields were about 65.3-73.5%. Therefore, 2 h should be enough for this reaction if the goal is to obtain *N*,*N*'-diphenylformamidine.

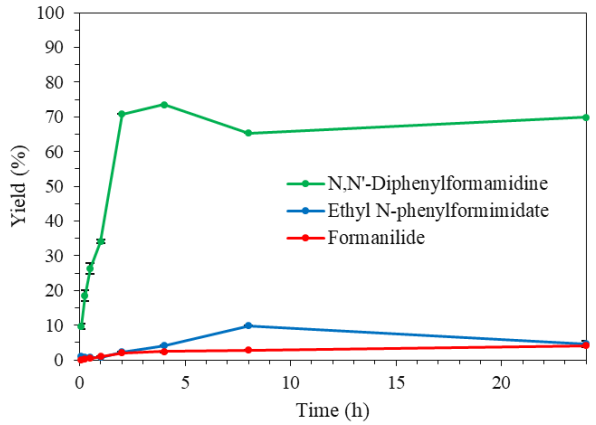

Figure 5. Effect of reaction time on *N*,*N*'-diphenylformamidine production

Reaction conditions: 1 mmol aniline, 1 mmol TEOF, 60 °C. Yields were determined by GC using naphthalene as an internal standard.

3.3 Effect of temperature on *N*,*N*'-diphenylformamidine production

The mixture was stirred for 2 h at the temperature shown in Figure 3. The reaction at room temperature (37 °C) gave only 9.1% of the product (entry 1). At 60 °C, the yields of *N*,*N*'-diphenylformamidine was 70.8% with 2.3% of ethyl *N*-phenylformimidate and formanilide each. When the temperature was increased to 90 and 120 °C, the yields of *N*,*N*'-diphenylformamidine slightly decreased to 57.8% and 47.3% and the yields of ethyl *N*-phenylformimidate increased to 36.4% and 49.6%, respectively, while the yields of formanilide still remained low. These results indicated that increasing the temperature will cause *N*,*N*'-diphenylformamidine to be converted to ethyl *N*-phenylformimidate. Therefore, to obtain *N*,*N*'-diphenylformamidine, the reaction should be performed at 60 °C.

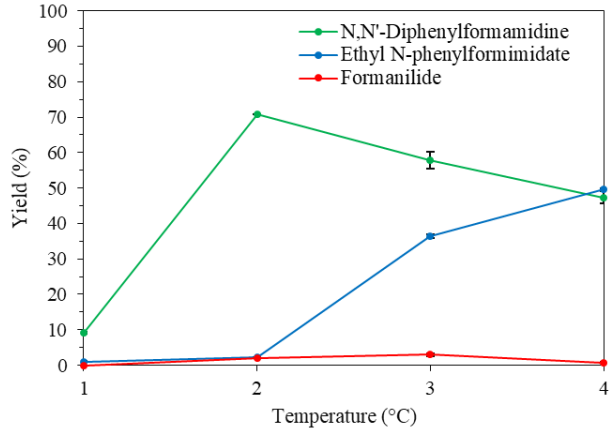

Figure 6. Effect of temperature on *N*,*N*'-diphenylformamidine production

Reaction conditions: 1 mmol aniline, 1 mmol TEOF, 2 h. Yields were determined by GC using naphthalene as an internal standard.

3.4 Effect of solvent on *N*,*N*'-diphenylformamidine production

Various solvents were investigated to identify the best solvents for this reaction (Table 1). Therefore, many results were for 1 mmol of triethyl orthoformate. The results showed that without solvent the yields of *N*,*N*'-diphenylformamidine, ethyl *N*-phenylformimidate, and formanilide were 70.8%, 2.3%, and 2.1%, respectively (entry 1). When ethanol, which is a polar solvent, was used, the yields of *N*, *N*'-diphenyl formamidine, ethyl *N*-phenylformimidate, and formamide were 91.2%, 1.0%, and 8.0%, respectively (entry 2). For ethanol, increasing the reaction time to 4 h made the selectivity worse as the yields were 56.0% *N*,*N*'-diphenylformamidine, 12.0% ethyl *N*-phenylformimidate, and 19.0% formanilide (entry 3). When other polar solvents such as dimethylformamide, acetonitrile, dimethyl sulfoxide, ethyl acetate, dichloromethane, methanol, and acetone were used, the yield of *N*,*N*'-diphenylformamidine were 52.0, 45.8, 43.0, 34.3, 30.0, 30.0%, and 30.4%, ethyl *N*-phenylformimidate were 4.4, 17.8, 1.0, 2.1, 10.7, 0.3, and 2.4%, and formanilide were 8.7, 6.9, 6.3, 25.9, 4.5, 18.9, and 8.0% respectively (entries 4-10). For the remaining nonpolar solvents, including diethyl ether, toluene, hexane, and highly polar solvent that is water, the yields of *N*,*N*'-diphenylformamidine were not as good as when using ethanol (entries 11-14). Note that for methanol there was an additional unidentified peak in GC chromatogram.

Based on these results, if the desired product is *N*,*N*'-diphenylformamidine, the reaction should be performed in ethanol using 1 mmol triethyl orthoformate at 60 °C for 2 h. In addition, the results also suggest that when the amount of triethyl orthoformate increases or the reaction time is longer, the yields of ethyl *N*-phenylformimidate also increases. The amount of triethyl orthoformate was already varied as in Figure 1 and the yields of ethyl *N*-phenylformimidate seem to stop increasing at 5 mmol of triethyl ortho formate. Therefore, the reaction time when using 5 mmol of triethyl orthoformate will be varied next.

Table 1. Effect of solvent on *N*,*N*'-diphenylformamidine production

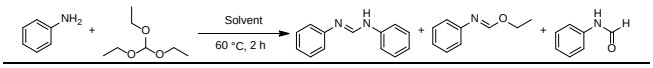

Entry	Solvents	% Yield[a]		
1	No solvent	70.8 ± 0.0	2.3 ± 0.1	2.1 ± 0.2
2	Ethanol	91.2 ± 0.8	1.0 ± 0.6	8.0 ± 0.6
3[b]	Ethanol	56.0 ± 0.5	12.0 ± 0.9	19.0 ± 1.0
4	Dimethylformamide	52.0 ± 0.7	4.4 ± 0.2	8.7 ± 0.6
5	Acetonitrile	45.8 ± 0.3	17.8 ± 0.3	6.9 ± 0.5
6	Dimethyl sulfoxide	43.0 ± 0.8	1.0 ± 0.5	6.3 ± 0.1
7	Ethyl acetate	34.3 ± 0.6	2.1 ± 0.1	25.9 ± 0.1
8	Dichloromethane	30.0 ± 0.2	10.7 ± 0.6	4.5 ± 0.1
9	Methanol	30.0 ± 0.7	0.3 ± 0.2	18.8 ± 0.4
10	Acetone	30.4 ± 0.4	2.4 ± 0.2	8.0 ± 0.3
11	Diethyl ether	42.0 ± 0.3	16.0 ± 0.2	14.1 ± 0.1
12	Toluene	41.2 ± 0.7	2.3 ± 0.6	11.7 ± 0.7
13	Hexane	35.9 ± 1.0	4.2 ± 0.0	12.0 ± 1.6
14	Water	0.0 ± 0.0	0.0 ± 0.0	41.9 ± 0.1

Reaction conditions: 1 mmol aniline, 1 mmol TEOF, 1 mL solvents, 60 °C, 2 h
[a]Determined by GC using naphthalene as an internal standard
[b]Reaction conditions: 1 mmol aniline, 1 mmol TEOF, 1 mL solvents, 60 °C, 4 h

3.5 Effect of reaction time on ethyl *N*-phenylformimidate production

A time-course investigation of the reaction between 1 mmol amine and 5 mmol triethyl orthoformate was performed without solvent at 60 °C (Figure 4). It was found that *N*,*N*'-diphenylformamidine was rapidly produced at the beginning but the yields decreased after about 50 min. Ethyl *N*-phenylformimidate also steadily increased at the beginning and reached 98.1% after 24 h. These results also suggest that *N*,*N*'-diphenylformamidine is converted to ethyl *N*-phenylformimidate over time. Note that the yields of formanilide remained stagnant at 1-3% throughout the 24-hour period.

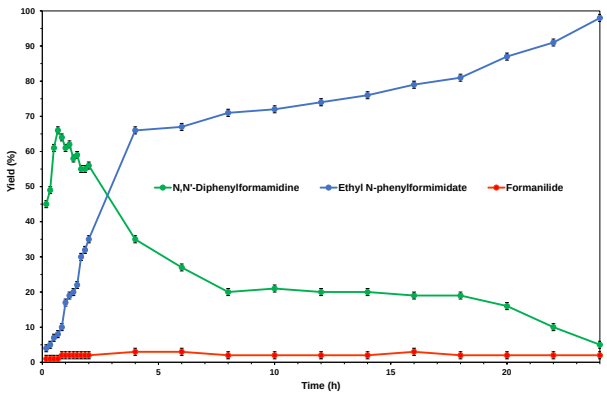

Figure 4. Time-course investigation for ethyl *N*-phenylformimidate production

Reaction conditions: 1 mmol aniline, 5 mmol TEOF, 60 °C. Yields were determined by GC using naphthalene as an internal standard.

3.6 Effect of solvents on *N*-phenylformimidate production

To determine the effect of solvents on the reaction, several solvents, namely dimethyl sulfoxide, water, ethanol, toluene, and diethyl ether, were screened (Table 2) for ethyl *N*-phenylformimidate production. The results reveal that the reactions gave excellent yields (98.1%) with solvent-free conditions (entry 1). When solvents were added, the yields got worse. There was no obvious trend in terms of polarity on the yields of ethyl *N*-phenylformimidate. Dichloromethane, ethanol, acetone, ethyl acetate, acetonitrile, dimethylformamide, and methanol, which are polar, gave a yield of 71.1, 69.0, 65.6, 65.3, 60.8, 60.2, and 0.0% (entries 2-8). While toluene, hexane, are non-polar, gave 61.4, and 55.0% (entries 9-10). The lower polar diethyl ether produced 29.2% ethyl *N*-phenylformimidate (entry 11). Dimethyl sulfoxide, very polar solvent, gave only 57.5% of the product (entry 12) and the highest polar solvent, water, did not produce ethyl *N*-phenylformimidate at all (entry 13). However, it produced formanilide as the sole product. Based on these results, the optimum condition for ethyl *N*-phenylformimidate production is 1 mmol aniline, 5 mmol triethyl orthoformate, no solvent, 60 °C, and 24 h. In addition, further investigation of reaction in water should be performed to obtain higher yields of formanilide.

Table 2. Effect of solvents on ethyl *N*-phenylformimidate production

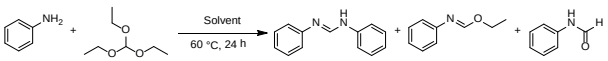

Entry	Solvents	% Yield[a]		
1	No solvent	0.2 ± 0.1	98.1 ± 1.8	1.8 ± 0.0
2	Dichloromethane	25.9 ± 0.7	71.1 ± 0.2	2.6 ± 0.4
3	Ethanol	1.9 ± 0.3	69.0 ± 1.1	1.0 ± 0.4
4	Acetone	20.5 ± 0.2	65.6 ± 0.7	2.7 ± 0.0
5	Ethyl acetate	23.3 ± 2.1	65.3 ± 0.9	5.6 ± 0.3
6	Acetonitrile	27.0 ± 0.8	60.8 ± 0.9	1.3 ± 0.0
7	Dimethylformamide	24.1 ± 0.6	60.2 ± 0.7	1.4 ± 0.2
8	Methanol	30.9 ± 0.7	0.0 ± 0.2	6.8 ± 0.4
9	Toluene	23.8 ± 0.3	61.4 ± 0.7	3.8 ± 0.4
10	Hexane	21.0 ± 0.7	55.0 ± 0.6	3.8 ± 0.3
11	Diethyl ether	0.2 ± 0.8	29.2 ± 2.2	39.3 ± 0.9
12	Dimethyl sulfoxide	24.4 ± 1.0	57.5 ± 0.9	3.6 ± 0.5
13	Water	0.0 ± 0.0	0.1 ± 0.0	72.2 ± 0.7

Reaction conditions: 1 mmol aniline, 5 mmol TEOF, 1 mL solvents, 60 °C, 24 h.
[a]Determined by GC using naphthalene as an internal standard

3.7 Effect of amount of TEOF for formanilide production

The amount of triethyl orthoformate was varied in order to increase the yields of formanilide. In general, the reactions were performed using 1 mmol aniline with triethyl orthoformate in 1 mL of water at 70 °C, slightly increase from previous experiments, for 24 h (Figure 5). The results showed that when the amount of triethyl orthoformate increased, the yields of formanilide also increased and when 24 mmol of triethyl orthoformate was used, the yield of formanilide was 97.0%. Therefore, to produce formanilide, the optimum condition is 1 mmol aniline, 20 mmol triethyl orthoformate in 1 mL of water at 70 °C for 24 h.

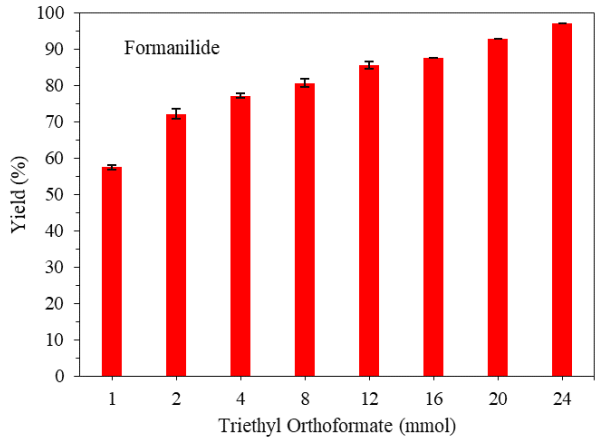

Figure 5. Effect of amount of TEOF for formanilide production
Reaction condition: 1 mmol aniline, water 1 mL, 70 °C, 24 h. Yields were determined by GC using naphthalene as an internal standard.

3.8 Mechanistic investigation

To investigate the mechanism of the reaction, *N*,*N*'-diphenylformamidine, ethyl *N*-phenylformimidate, and formanilide were tested whether they can be converted to one another. *N*,*N*'-diphenylformamidine was first tested (Table 3). When *N*,*N*'-diphenylformamidine was heated at 60 °C in 1 mL water in the presence of 3 mmol triethyl orthoformate, after 2 h, 51% of aniline and 35% of formanilide were produced and when heated for 24 h, nearly all of aniline were converted to formanilide with no *N*,*N*'-diphenylformamidine remaining and 2% of ethyl *N*-phenylformimidate. In ethanol, *N*,*N*'-diphenylformamidine was converted to aniline, ethyl *N*-phenylformimidate, and formanilide at similar amounts after 2 h and significantly much more of formanilide after 24 h. In the reactions without solvent or with other solvents *N*,*N*'-diphenylformamidine seems to be mainly converted to ethyl *N*-phenylformimidate with small amounts of aniline and formanilide produced. These results indicated that *N*,*N*'-diphenylformamidine can be converted back to aniline in water in the presence of triethyl orthoformate. It is then converted to formanilide. In ethanol, methanol, and diethyl ether, *N*,*N*'-diphenylformamidine can be converted back to aniline and also converted to ethyl *N*-phenylformimidate and subsequently formanilide. For the remaining solvents tested, *N*,*N*'-diphenylformamidine is mainly converted to ethyl *N*-phenylformimidate and may require a longer reaction time or higher temperature to be converted to formanilide.

Table 3. Conversion of *N*,*N*'-diphenylformamidine

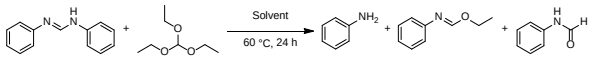

Entry	Solvent	% Yield[a]		
			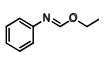	
1[b]	Water	51	0	35
2	Water	6	2	82
3[b]	Ethanol	6	9	12
4	Ethanol	4	10	32
5[b]	No solvent	0	3	2
6	No solvent	0	54	3
7	Acetonitrile	0	74	2
8	Dichloromethane	0	65	4
9	Toluene	0	56	5
10	Ethyl acetate	0	49	7
11	Acetone	0	47	7
12	Dimethylformamide	0	40	2
13	Hexane	0	40	4
14	Diethyl ether	1	36	9
15	Dimethyl sulfoxide	0	17	2
16	Methanol	2	7	3

Reaction conditions: 1 mmol *N*,*N*'-diphenylformamidine, 3 mmol TEOF, 1 mL solvents, 60 °C, 24 h
[b]Reaction conditions: 1 mmol *N*,*N*'-diphenylformamidine, 3 mmol TEOF, 1 mL solvents, 60 °C, 2 h
[a,b]Determined by GC using naphthalene as an internal standard

Ethyl *N*-phenylformimidate was next investigated with similar condition (Table 4). It seems to be quite stable in all solvents, with small amount of *N*,*N*'-diphenylformamidine and formanilide produced, except for highly polar solvent such as water, ethanol, and methanol. In water, ethyl *N*-phenylformimidate is converted back to aniline and also converted to formanilide. In ethanol and methanol, small amount is converted back to aniline, but a lot are converted to *N*,*N*'-diphenylformamidine and some to formanilide.

Table 4. Conversion of ethyl *N*-phenylformimidate

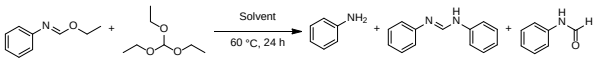

Entry	Solvent	% Yield[a]		
			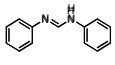	
1[b]	Water	65	0	38
2	Water	5	0	97
3[b]	Ethanol	4	59	12
4	Ethanol	2	52	20
5[b]	No solvent	0	3	0
6	No solvent	0	4	0
7	Acetonitrile	0	4	1
8	Dichloromethane	0	3	1
9	Toluene	0	3	0
10	Ethyl acetate	0	13	1
11	Acetone	0	14	1
12	Dimethylformamide	0	5	1
13	Hexane	0	3	0
14	Diethyl ether	0	7	2
15	Dimethyl sulfoxide	0	4	1
16	Methanol	3	59	4

Reaction conditions: 1 mmol ethyl *N*-phenylformimidate, 3 mmol TEOF, 1 mL solvents, 60 °C, 24 h.

[b]Reaction conditions: 1 mmol ethyl *N*-phenylformimidate, 3 mmol TEOF, 1 mL solvents, 60 °C, 2 h

[a,b]Determined by GC using naphthalene as an internal standard

Formanilide was also tested the same way (Table 5). It was found to be highly stable in all solvents, with minimal amounts converted back to aniline, *N*,*N*'-diphenylformamidine, ethyl *N*-phenylformimidate. Only in water and ethanol that significant amounts of aniline were formed.

Table 5. Conversion of formanilide

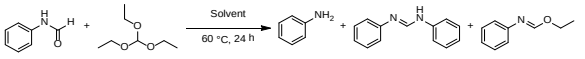

Entry	Solvent	% Yield[a]		
			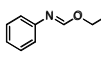	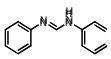
1[b]	Water	2.0	0	0
2	Water	5.8	0.0	0.0
3[b]	Ethanol	1	0	0
4	Ethanol	2.3	0.0	0.0
5[b]	No solvent	0	0	0
6	No solvent	0.0	0.5	0.0
7	Acetonitrile	0.1	0.2	0.0
8	Dichloromethane	0.0	0.3	0.0
9	Toluene	0.4	0.3	0.0
10	Ethyl acetate	0.0	0.3	0.0
11	Acetone	0.0	0.3	0.0
12	Dimethylformamide	0.0	0.1	0.0
13	Hexane	0.0	0.5	0.0
14	Diethyl ether	0.3	1.3	0.1
15	Dimethyl sulfoxide	0.1	0.1	0.0
16	Methanol	0.2	0.4	0.3

Reaction conditions: 1 mmol formanilide, 3 mmol TEOF, 1 mL solvents, 60 °C, 24 h

[b]Reaction conditions: 1 mmol formanilide, 3 mmol TEOF, 1 mL solvents, 60 °C, 2 h

[a,b]Determined by GC using naphthalene as an internal standard

4. Conclusion

This study describes easy and effective ways to produce formamidine, formimidate, and formamide from an amine and TEOF just simply by varying the reaction conditions without using any catalyst. Using ethanol as a solvent and 1 equivalent of TEOF at 60 °C for 2 h yielded 91% of formamidine. Formimidate was produced at 98% yield in 24 h using 5 equivalents of TEOF at 60 °C in a solvent-free procedure. Formamide was produced in 24 h with 24 equivalents of TEOF in deionized water at 70 °C with 97% yield. These compounds' behavior and attributes were studied mechanistically to propose a reaction process to make these three chemicals. The current method is beneficial because of its catalyst-free, low-cost, facile reaction, short reaction time, eco-friendly, and high yields.

Acknowledgments

C.K. would like to thank the Greater Mekong Sub-region Country Scholarship (GMS). This research was supported by a research grant from the Faculty of Science, King Mongkut's University of Technology Thonburi, fiscal year 2022.

References

1. Thauer, R. K. *Microbiology* **1998**, *144*, 9, 2377-2406.
2. Gerack, C. J. and McElwee-White, L. *Molecules* **2014**, *19*, 6, 7689-7713.
3. Wada, T.; Takagi, H.; Minakami, H.; Hamanaka, W.; Okamoto, K.; Ito, A.; Sahashi, Y. *Science* **1961**, *134*, 3473, 195-196.
4. Forsch, R. A.; Rosowsky, A. *J. Org. Chem.* **1985**, *50*, 14, 2582-2583.
5. Ravina, E., The Evolution of Drug Discovery: From Traditional Medicines to Modern Drugs; John Wiley & Sons; Hoboken, NJ, 2011.
6. Lonsdale, D. *Med. Sci. Monit.* **2004**, *10*, 9, RA199-203.
7. Si, Y.-X.; Feng, C.-C.; Zhang, S.-L. *J. Org. Chem.* **2022**, *87*, 21, 13564-13572.
8. Yalagala, K.; Maddila, S.; Rana, S.; Maddila, S. N.; Kalva, S.; Skelton, A. A.; Jonnalagadda, S. B. *Res. Chem. Intermed.* **2016**, *42*, 4, 3763-3774.
9. Maddila, S.; Jonnalagadda, S. B. *Arch. Pharm. Pharm. Med. Chem.* **2012**, *345*, 2, 163-168.
10. Maddila, S.; S. Kumar, A.; Gorle, S.; Singh, M.; Lavanya, P.; Jonnalagadda, S.B. *Lett. Drug Des. Discov.* **2013**, *10*, 2, 186-193.
11. Paliwal, P. K.; Jetti, S. R.; Jain, S. *Med. Chem. Res.* **2013**, *22*, 6, 2984-2990.
12. Riley, T. N.; Rankin, G. O. *J. Med. Chem.* **1976**, *19*, 2, 334-336.

Development of visible-light-induced hydrogen atom transfer (HAT) process as a tool for C–H functionalization of indole derivatives

Prakansi Naksing, Rungroj Saruengkhanphasit, and Worawat Niwetmarin*

Program in Chemical Sciences, Chulabhorn Graduate Institute, Bangkok 10210, Thailand

**E-mail: worawat@cgi.ac.th*

Abstract:

Indole is a core structure commonly found in alkaloids and is a valuable pharmacophore in numerous medicinal drugs. These indole-containing biologically active compounds exhibit various activities, including anticancer, antifungal, anti-HIV, antitubercular, *etc.* To extensively study these bioactivities, a fast and practical methodology, used for generating a library of the compounds, is crucial. This study develops a new synthetic route to access indole derivatives using the photoinduced hydrogen atom transfer (HAT) process, which is a simple way to generate radical intermediates and has a unique potential for green and sustainable synthesis. To study the improvement of the reaction efficiency, the intramolecular reaction and model substrates (indoles and *N*-methyl-2-pyrrolidinone) were subjected to optimization by the treatment of HAT reagent, *e.g.* diacetyl, under blue LEDs irradiation. By the treatment of diacetyl and $K_2S_2O_8$, the reaction of 1-phenylindole and *N*-methyl-2-pyrrolidinone provided the C3-alkylated product in 72% isolated yield with a high regioselectivity. We expected that this strategy could be used to prepare pyrrolo- or piperidoindole derivatives in an intramolecular manner, which are similar to the core structures of natural products, such as harmacine, cuscutamine, *etc*.

1. Introduction

Indoles are one of the most common heterocycles found in natural products. Some indole derivatives are known to have a key role in human and animal essential activity. As shown in Figure 1, tryptophan, a basic amino acid, participates in a variety of important biological activities.[1] Tryptamine is a biogenic amine. Serotonin, also known as 5-hydroxytryptamine (5-HT), is a neurotransmitter that is produced biochemically from tryptophan. It is found in all bilateral vertebrates,[2] and melatonin is a hormone found in plants and animals.[3]

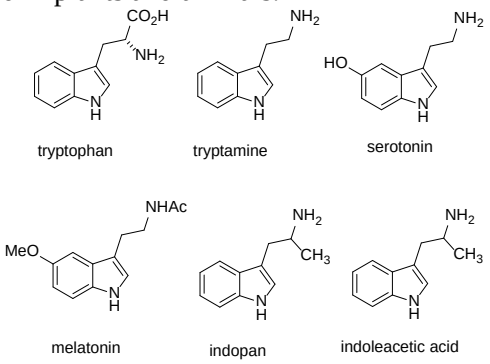

Figure 1. Examples of indole derivatives.

Photocatalysis encompasses an ever-increasing number of generic activation modes in which photonic energy is selectively directed to a specifically designed photon-absorbing catalyst (a photocatalyst) that, upon excitation, can induce an accompanying substrate, reagent, or secondary catalyst to participate in previously unattainable reaction pathways under thermal control. This approach is based on the ability of metal complexes and organic dyes to engage in single-electron-transfer (SET) reactions with substrates after being photoexcited with visible light.[4]

The C–H functionalization is the transformation of carbon-hydrogen bonds into carbon-carbon or carbon-heteroatom bonds.[5] Unlike any previously existed functionalization which prerequisites C–H activation, these strategies enable a rapid transformation and installation of desired substituents on a molecule. Thus, it is particularly effective for reducing the number of steps syntheses, which are utilized in drug development.[6]

Herein, our research group is interested in the investigation of green photochemistry as a potential tool for the efficient synthesis of indole derivatives *via* an intermolecular *α*-amidoalkylation driven by a visible-light-mediated HAT process.[7-11]

2. Materials and Methods

2.1 Materials

All photoredox reactions were performed in a Schlenk tube under an Ar atmosphere at ambient temperature. Chemicals were commercially available from chemical suppliers and were utilized without purification. Merck silica gel (70-230 mesh) thin layer chromatography (TLC) was used to monitor the reactions, and UV light was used for observing. SiliCycle silica gel (230-400 mesh) was used for silica gel column

chromatography. A Bruker AVANCE III HD 300MHz spectrometer was used to collect ^{1}H and ^{13}C NMR spectra. A Thermo Scientific orbitrap Q Exactive Focus mass spectrometer was used to obtain high resolution mass spectra (HRMS) utilizing electrospray ionization (ESI) or atmospheric pressure chemical ionization (APCI). As light sources, a Kessil PR160L–456NM blue LEDs was employed.

2.2 Preparation of 1-tosyl-1*H*-indole starting material

To a solution of 1*H*-indole (**1a**) (586 mg, 5.00 mmol) in 30 mL of acetonitrile at 0 °C, was added NaH (168 mg, 7.00 mmol, 60% in mineral oil). After stirring at 0 °C for 10 min, TsCl (1.05 g, 5.50 mmol) was added portionwise. The reaction mixture was warmed to room temperature and stirred for 4 h. Water (20 mL) was added and the aqueous phase was extracted by EtOAc (3 x 30 mL). The combined organic phase was washed with brine, dried over Na_2SO_4 anhydrous, filtered, and concentrated *in vacuo*. The crude was purified by flash column chromatography using 20% EtOAc:hexanes to give **1d** (554 mg, 41%) as a brown solid (Scheme 1).

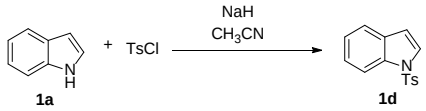

Scheme 1. Synthesis of 1-tosyl-1*H*-indole **1d**.

2.3 Preparation of 1-phenyl-1*H*-indole derivative starting materials

2.3.1 A Schlenk tube was charged with 1*H*-indole (**1a**) (984 mg, 8.40 mmol), iodobenzene (1.22 g, 6.00 mmol), CuI (228 mg, 1.20 mmol), and Cs_2CO_3 (3.91 g, 12.00 mmol) in DMF (12 mL). The reaction mixture was stirred at 120 °C under Ar atmosphere for 16 h (Scheme 2). After cooling to room temperature, EtOAc (20 mL) and water (20 mL) were added. The aqueous phase was extracted with EtOAc (3 x 30 mL). The combined organic phase was washed with brine, dried over Na_2SO_4, filtered, and concentrate *in vacuo*. The crude was purified by flash column chromatography using 100% hexanes to give **1d** (1.03 g, 90%) as a yellow oil (Scheme 2a).

2.3.2 Following the procedure for **1e**, **1f** was prepared from 3-methyl-1*H*-indole (**1b**) (1.31 g, 10 mmol) and obtained as a colorless oil (2.04 g, 98%) (Scheme 2b).

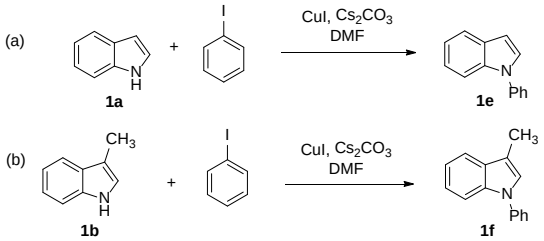

Scheme 2. Preparation of *N*-phenylindoles.

2.4 General procedure for visible-light-induced HAT reaction of indole derivatives

To a solution of indole derivatives in appropriate solvent, were added HAT reagent and NMP (if necessary). The reaction mixture was irradiated with visible light for an overnight in the ventilated fume hood (at approximately 30–35 °C). After work-up with appropriate method, the crude was purified by flash column chromatography to afford the corresponding indole derivatives (Scheme 3)

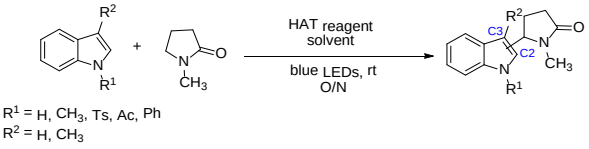

Scheme 3. Preparation of α-amidoalkylation of indole derivatives *via* intermolecular HAT.

2.5 Spectroscopic data

2.5.1 1-Tosyl-1*H*-indole (1d)

^{1}H NMR (300 MHz, $CDCl_3$) δ 7.99 (d, J = 8.3, 1H), 7.76 (d, J = 8.4 Hz, 2H), 7.56 (d, J = 3.7 Hz, 1H), 7.52 (d, J = 7.8 Hz, 1H), 7.30 (td, J = 8.4, 7.2, 1.4 Hz, 1H), 7.21 (m, 3H), 6.65 (d, J = 3.7 Hz, 1H), 2.32 (s, 3H). ^{13}C NMR (75 MHz, $CDCl_3$) δ 144.74, 135.1, 134.6, 130.6, 129.7, 126.6, 126.2, 124.4, 123.1, 121.2, 113.4, 108.8, 21.4. HRMS (ESI) m/z: $[M + Na]^+$ calcd. for $C_{15}H_{13}O_2NNaS$, 294.0559; found, 294.0559.

2.5.2 1-Phenyl-1*H*-indole (1e)

^{1}H NMR (300 MHz, $CDCl_3$) δ 7.72 – 7.63 (m, 1H), 7.55 (d, J = 8.4 Hz, 1H), 7.46 (d, J = 4.3 Hz, 4H), 7.36 – 7.27 (m, 2H), 7.24 – 7.11 (m, 2H), 6.66 (d, J = 3.2 Hz, 1H). ^{13}C NMR (75 MHz, $CDCl_3$) δ 139.8, 135.8, 129.6, 129.3, 127.9, 126.4, 124.3, 122.3, 121.1, 120.3, 110.5, 103.5. HRMS (ESI) m/z: $[M + H]^+$ calcd. for $C_{14}H_{12}N$, 194.0964; found, 194.0966.

2.5.3 3-Methyl-1-phenyl-1*H*-indole (1f)

^{1}H NMR (300 MHz, $CDCl_3$) δ 7.66 – 7.59 (m, 1H), 7.59 – 7.52 (m, 1H), 7.51 – 7.43 (m, 4H), 7.36 – 7.26 (m, 1H), 7.26 – 7.15 (m, 2H), 7.13 (s, 1H), 2.39 (d, J = 1.1 Hz, 3H). ^{13}C NMR (75 MHz, $CDCl_3$) δ 140.0, 135.9, 129.8, 129.5, 125.8, 125.4, 123.9, 122.3, 119.7, 119.2, 112.8, 110.3. HRMS

(ESI) m/z: $(M + H)^+$ calcd. for $C_{15}H_{14}N$, 208.1126; found, 208.1123.

2.5.4 5-(1*H*-indol-3-yl)-1-methylpyrrolidin-2-one (6a)

Colorless oil (3 mg, 7%). ^{1}H NMR (600 MHz, $CDCl_3$) δ 8.13 (s, 1H), 7.54 (d, J = 8.0 Hz, 1H), 7.41 (d, J = 8.2 Hz, 1H), 7.25 – 7.22 (m, 1H), 7.17 – 7.11 (m, 2H), 4.87 (t, J = 7.2 Hz, 1H), 2.71 (s, 3H), 2.68 – 2.60 (m, 1H), 2.56 – 2.43 (m, 2H), 2.25 – 2.18 (m, 1H). ^{13}C NMR (150 MHz, $CDCl_3$) δ 175.1, 136.8, 125.3, 122.7, 122.30, 120.1, 119.0, 115.7, 111.5, 57.8, 30.7, 28.0, 27.0. HRMS (ESI) m/z: $(M + H)^+$ calcd. for $C_{13}H_{15}ON_2$, 215.1179; found, 215.1182.

2.5.5 1-Methyl-5-(3-methyl-1*H*-indol-2-yl)pyrrolidin-2-one (6b)

Yellow oil (6.9 mg, 15%).^{1}H NMR (400 MHz, $CDCl_3$) δ 8.72 (s, 1H), 7.54 (d, J = 7.8 Hz, 1H), 7.35 (d, J = 8.0 Hz, 1H), 7.19 (t, J = 7.5 Hz, 1H), 7.12 (t, J = 7.4 Hz, 1H), 4.91 (t, J = 7.4 Hz, 1H), 2.66 (s, 3H), 2.64 – 2.41 (m, 3H), 2.32 (s, 3H), 2.20 – 2.07 (m, 1H). ^{13}C NMR (100 MHz, $CDCl_3$) δ 175.4, 136.1, 132.1, 128.8, 122.5, 119.3, 118.7, 111.0, 110.07, 56.2, 30.5, 28.2, 26.0, 8.3. HRMS (ESI) m/z: $(M + H)^+$ calcd. for $C_{14}H_{17}ON_2$, 229.1335; found, 229.1339.

2.5.6 1-Methyl-5-(1-methyl-1*H*-indol-3-yl)pyrrolidin-2-one (6c)

Yellow oil (5 mg, 11%).^{1}H NMR (400 MHz, $CDCl_3$) δ 7.52 (d, J = 8.0 Hz, 1H), 7.34 (d, J = 8.3 Hz, 1H), 7.31 – 7.22 (m, 1H), 7.16 – 7.08 (m, 1H), 6.98 (s, 1H), 4.84 (t, J = 7.2 Hz, 1H), 3.78 (s, 3H), 2.70 (s, 3H), 2.66 – 2.12 (m, 4H). ^{13}C NMR (100 MHz, $CDCl_3$) δ 175.2, 137.7, 127.0, 125.8, 122.2, 119.6, 119.0, 114.0, 109.7, 57.8, 32.8, 30.7, 28.1, 27.3. HRMS (ESI) m/z: $(M + H)^+$ calcd. for $C_{14}H_{17}ON_2$, 229.1335; found, 229.1338.

2.5.7 1-Methyl-5-(1-phenyl-1*H*-indol -3 yl)pyrrolidin-2-one (6e)

Yellow oil (41.8 mg, 72%).^{1}H NMR (300 MHz, $CDCl_3$) δ 7.62 – 7.45 (m, 6H), 7.41 – 7.33 (m, 1H), 7.30 – 7.13 (m, 3H), 4.91 (t, J = 7.3 Hz, 1H), 2.77 (s, 3H), 2.68 – 2.41 (m, 3H), 2.33 – 2.17 (m, 1H). ^{13}C NMR (75 MHz, $CDCl_3$) δ 175.2, 139.3, 136.8, 129.7, 126.8, 126.6, 126.0, 124.3, 123.0, 120.7, 119.2, 116.4, 111.0, 57.7, 30.6, 28.2, 27.0. HRMS (ESI) m/z: $(M + H)^+$ calcd. for $C_{19}H_{19}ON_2$, 291.1492; found, 291.1492.

3. Results & Discussion

For the preliminary study, 1-phenylindole **1e** and *N*-methyl-2-pyrrolidinone (NMP) (**4**) were chosen as the model substrates. The model reaction was then carried out in MeCN with diacetyl and potassium persulfate under blue LEDs at room temperature (Table 1). Various wavelengths of light sources were attempted *e.g.* 456 nm, 440 nm, 390 nm, 11 W CFL, and 8 W household blue LEDs. The blue LEDs 456 nm can generate the C3-alkylated product **6e** with the highest yield of 72% (Table 1, Entry 1), while the other light sources significantly provided decreases in yields of **6e** (Table 1, Entries 2–5) with other oxidants were carried out (Table 1, Entries 6–13). The persulfate oxidants (such as $Na_2S_2O_8$, $(NH_4)_2S_2O_8$, Oxone®) did not improve the yield of **6e**, which gave 18%, 10%, and 32% NMR yield, respectively (Table 1, entries 6–8). Peroxides (DTBP, *t*-BuOOH, $(BzO)_{2)}$, and dicumyl peroxide) were employed, but there were traces or no formation of the targeted product (Table 1, entries 9–12). The formation of **6e** was subsided when carried out the reaction under open air (Table 1, Entries 13, and 23). This suggests that oxygen in air could not paritcipate in the reaction conditions as an oxidant. Different solvents were attempted, such as MeCN:H_2O, DMSO, DCM, DCE, MeOH, EtOH, EtOAc, and acetone (Table 1, Entries 14–21) and the formation of product **6e** was not enhanced. Control experiments were investigated (Entries 22–29). The reaction without additional solvent under Ar atmosphere was conducted, and it gave a good yield of the product (Table 1, Entry 22). The results from entries 24–29 confirmed the importance of $K_2S_2O_8$, diacetyl, blue LEDs, and amount of diacetyl and NMP to form **6e** in high yield.

Indole derivatives with substitutions at N and C3 position were investigated as substrates with optimal reaction conditions (Table 2). 1*H*-Indole and 3-methyl-1*H*-indole provided decreased yields of desired products (Table 2, Entries 1-2). These results indicate that the reaction requires a protecting group at nitrogen atom and C3-methyl group also prohibits a subsequent alkylation. Using *N*-methyl and *N*-Ts substituents as substrates (Table 2, Entry 1). Lastly, there was no product observed from the reaction of indole **1f** (Table 2, Entry 5).

To confirm the absorption properties of the reaction mixture for blue light irradiation, UV−vis spectra of diacetyl and 3-methyl indole were determined. In MeCN, diacetyl exhibits a maximum absorption peak at 420 nm (λ_{max}), while 3-methylindole absorbs only in the midrange UV region (approximately 300–310 nm). Notably, the mixture of these two substances showed no significant change in the blue region (Scheme 4). This observation confirms that blue LEDs are the most suitable light source for this reaction.

Table 1. The optimization of reaction conditions of the α-amidoalkylation of indole derivatives via intermolecular HAT.

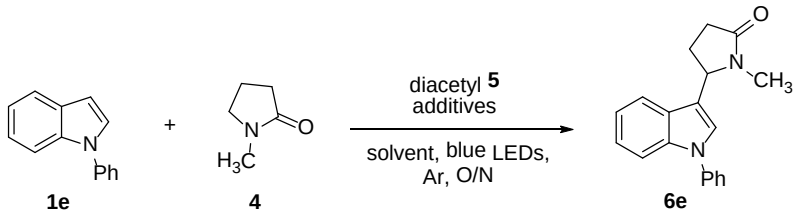

Entry	Additive	Solvent	Light source	Yield (%)[a]
1	$K_2S_2O_8$	MeCN	456 nm	72
2	$K_2S_2O_8$	MeCN	440 nm	57
3	$K_2S_2O_8$	MeCN	390 nm	43
4	$K_2S_2O_8$	MeCN	11 W CFL	12[b]
5	$K_2S_2O_8$	MeCN	8 W blue LEDs	38
6	$Na_2S_2O_8$	MeCN	456 nm	18[b]
7	$(NH_4)_2S_2O_8$	MeCN	456 nm	10[b]
8	Oxone®	MeCN	456 nm	25
9	DTBP	MeCN	456 nm	NP
10	*t*-BuOOH	MeCN	456 nm	NP
11	$(BzO)_2$	MeCN	456 nm	NP
12	dicumyl peroxide	MeCN	456 nm	traces
13[c]	-	MeCN	456 nm	NP
14	$K_2S_2O_8$	MeCN:H_2O (1:1)	456 nm	12[b]
15	$K_2S_2O_8$	DMSO	456 nm	NP
16	$K_2S_2O_8$	DCM	456 nm	48
17	$K_2S_2O_8$	DCE	456 nm	42
18	$K_2S_2O_8$	MeOH	456 nm	8[b]
19	$K_2S_2O_8$	EtOH	456 nm	11[b]
20	$K_2S_2O_8$	EtOAc	456 nm	39
21	$K_2S_2O_8$	acetone	456 nm	47
22	$K_2S_2O_8$	-	456 nm	64
23[d]	$K_2S_2O_8$	MeCN	456 nm	NP
24	-	MeCN	456 nm	NP
25[e]	$K_2S_2O_8$	MeCN	456 nm	NP
26	$K_2S_2O_8$	MeCN	-	NP
27[f]	$K_2S_2O_8$	MeCN	456 nm	45
28[g]	$K_2S_2O_8$	MeCN	456 nm	38
29[h]	$K_2S_2O_8$	MeCN	456 nm	20

Reaction conditions: **1e** (0.20 mmol), **4** (2.10 mmol, 0.2 mL), **5** (11.5 mmol, 0.2 mL), additives (4.0 equiv.) in solvent (0.4 mL) under blue LEDs irradiation under Ar atmosphere.
[a]Isolated yield, NP = no product.
[b]NMR yield were determined by ^{1}H NMR spectroscopy with 1,1,2,2-tetrachloroethane as an internal standard.
[c]The reaction was performed without $K_2S_2O_8$ under air.
[d]The reaction was performed with $K_2S_2O_8$ under air.
[e]The reaction was performed without diacetyl under Ar.
[f]The reaction was performed with $K_2S_2O_8$ (2.0 equiv.) under Ar.
[g]The reaction was performed with diacetyl (0.1 mL) under Ar.
[h]The reaction was performed with NMP (0.1 mL) under Ar.

Table 2. Synthesis of the *α*-amidoalkylation of indole derivatives *via* intermolecular HAT.

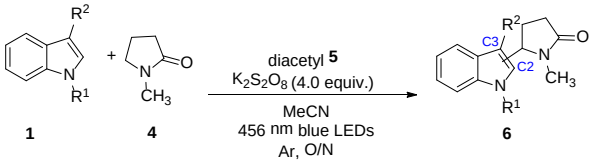

Entry	Substrates	Products	Isolated yield (%)
1	**1a** 	**6a** 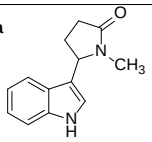	7
2	**1b** 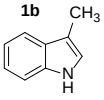	**6b** 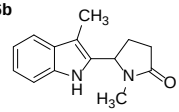	11
3	**1c** 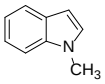	**6c** 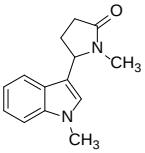	15
4	**1d** 	**6d** 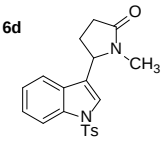	NP
5	**1f** 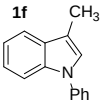	**6f** 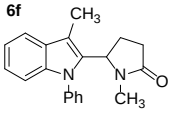	NP

Reaction conditions: **1** (0.20 mmol), **4** (2.10 mmol, 0.2 mL), **5** (11.5 mmol, 0.2 mL), $K_2S_2O_8$ (4.0 equiv.) in MeCN (0.4 mL) under blue LEDs irradiation under Ar atmosphere, NP = no product.

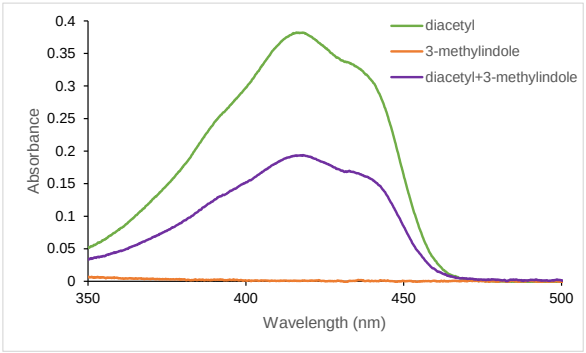

Scheme 4. Absorption spectra of diacetyl, 3-methylindole, and their mixture in MeCN.

3.1 Plausible mechanism

According to the related previous literatures,[10] the plausible mechanism for this reaction was depicted as shown in Scheme 5. Diacetyl was excited by blue LEDs irradiation to generate excited species (**5-I**) (Scheme 5, left). For the reaction with persulfate ($K_2S_2O_8$), **5-I** can undergo an energy transfer to persulfate anion, which is then fragmentated to two sulfate radical anions. HAT process between sulfate radical anions and NMP is occurred and generates an *α*-amidoalkyl radical. After that, the coupling between alkyl radical and indole derivatives at C3 position gives adduct radical, which then further oxidizes by sulfate radical anions to afford the desired product **6e**. However, photoexcited diacetyl **5-I** can also act as HAT reagent under the reaction conditions either with or without persulfate (Scheme 5, right). This process results in the formation of acetoin as a by-product.

4. Conclusion

The synthesis of α-amidoalkylation was successfully developed *via* intermolecular HAT process of indole derivatives by diacetyl and $K_2S_2O_8$ approach under blue LEDs irradiation. Substrate scope will be explored to generate a library of structurally diverse indole derivatives. With this strategy, the structurally diverse indole derivatives could be generated in a highly effective and selective manner, and readily to be used as a compound library for further screening of biological activities. We anticipate that this rapid and transition-metal-free approach will benefit the synthesis of small molecules used in the area of medicinal chemistry. Further investigations into the full potential of this chemistry are ongoing.

Acknowledgements

This research project is supported by Thailand Science Research and Innovation (FRB660044/0240 Project code 180850 and FRB660044/0240 Project code 180874), and Chulabhorn Graduate Institute, Chulabhorn Royal Academy (grant code: CGS (2022)/13).

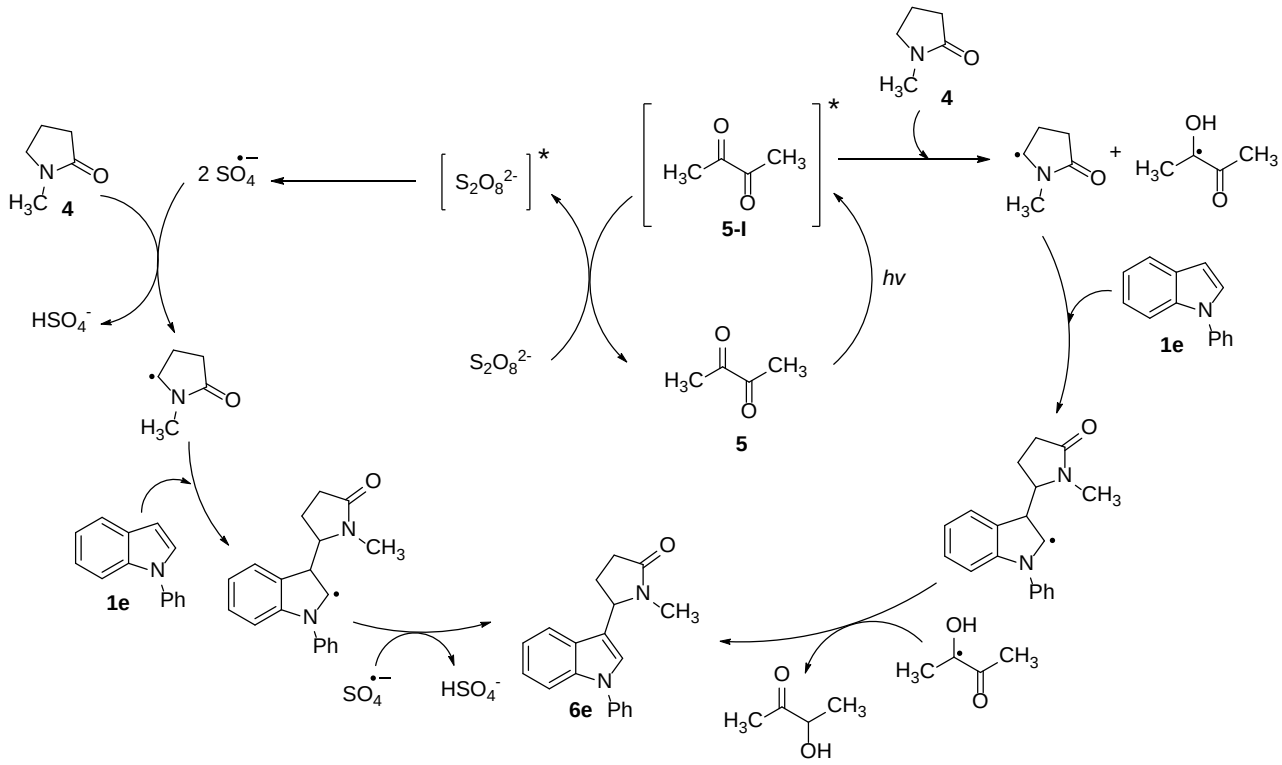

Scheme 5. Proposed mechanism.

References

1. Abele, E.; Abele, R.; Dzenitis, O.; Lukevics, E. Indole and Isatin Oximes: Synthesis, Reactions, and Biological Activity. (Review). *Chem. Heterocycl. Compd.* **2003**, *39*, 3-35.
2. King, M. V.; Marsden, C. A.; Fone, K. C. A role for the 5-HT(1A), 5-HT4 and 5-HT6 receptors in learning and memory. *Trends. Pharmacol. Sci.* **2008**, *29*, 482-492.
3. Arnao, M. B.; Hernández-Ruiz, J. The physiological function of melatonin in plants. *Plant. Signal. Behav.* **2006**, *1*, 89-95.
4. Romero, N. A.; Nicewicz, D. A. Organic photoredox catalysis. *Chem. Rev.* **2016**, *116*, 10075-10166.
5. Wang, X.; Xu, Q.; Li, M.; Shen, S.; Wang, X.; Wang, Y.; Feng, Z.; Shi, J.; Han, H.; Li, C. photocatalytic overall water splitting promoted by an α–β phase Junction on Ga_2O_3. *Angew. Chem., Int. Ed.* **2012**, *51*, 13089-13092.
6. Bergman, R. G. C–H activation. *Nature* **2007**, *446*, 391-393.
7. Dai, C.; Meschini, F.; Narayanam, J. M. R.; Stephenson, C. R. J. Friedel–Crafts Amidoalkylation *via* thermolysis and oxidative photocatalysis. *J. Org. Chem.* **2012**, *77*, 4425-4431.
8. Weng, J.-Q.; Xu, W.-X.; Dai, X.-Q.; Zhang, J.-H.; Liu, X.-H. Alkylation reactions of benzothiazoles with *N*,*N*-dimethylamides catalyzed by the two-component system under visible light. *Tetrahedron Lett.* **2019**, *60*, 390-396.
9. Dantas, J. A.; Echemendía, R.; Santos, M. S.; Paixão, M. W.; Ferreira, M. A. B.; Corrêa, A. G. Green approach for visible-light-induced direct functionalization of 2-methylquinolines. *J. Org. Chem.* **2020**, *85*, 11663-11678.
10. Huang, C.-Y.; Li, J.; Liu, W.; Li, C.-J. Diacetyl as a “traceless” visible light photosensitizer in metal-free cross-dehydrogenative coupling reactions. *Chem. Sci.* **2019**, *10*, 5018-5024.
11. Zhou, J.; Ren, Q.; Xu, N.; Wang, C.; Song, S.; Chen, Z.; Li, J. $K_2S_2O_8$-catalyzed highly regioselective amidoalkylation of diverse *N*-heteroaromatics in water under visible light irradiation. *Green Chem.* **2021**, *23*, 5753-5758.

Applications of methyl itaconate-anthracene adducts as chiral resolving agents for binaphthol derivatives

Wichai Saema,[1,2] Puracheth Rithchumpon,[1,3] Nopawit Khamto,[1,2] and Puttinan Meepowpan[1,4]*

[1]*Department of Chemistry, Faculty of Science, Chiang Mai University, Chiang Mai, 50200 Thailand*
[2]*Multidisciplinary and Interdisciplinary School, Chiang Mai University, Chiang Mai, 50200 Thailand*
[3]*Office of Research Administration, Chiang Mai University, Chiang Mai, 50200 Thailand*
[4]*Center of Excellence of Material Sciences, Chiang Mai University, Chiang Mai, 50200 Thailand*

**E-mail: puttinan.m@cmu.ac.th*

Abstract:

Chiral BINOL derivatives have several applications such as asymmetric synthesis, circularly polarized luminescence (CPL) dyes and charge transfer host system. There are several methods for enantiopure BINOLs preparation which are asymmetric synthesis from 2-naphthol, enzymatic resolution, and chiral resolution by crystallization or chromatography. Herein, we applied the latter method using methyl itaconate–anthracene adducts (MIAs) as chiral auxiliaries. Diastereomeric pairs of MIAs and BINOLs were prepared through esterification reaction and obtained with moderate yield. Spectroscopic analysis was applied for the structural characterization and confirmation. Chiral resolution was further investigated using thin layer chromatographic (TLC) technique. The difference of retention factor (ΔR_f) values between (*S*)-MIA-(*S*)-BINOL and (*S*)-MIA-(*R*)-BINOL was determined to be 0.11. For other BINOL derivatives, H_8-BINOL and BINAM were selected to validate the efficiency of MIA. The results demonstrated the effectiveness of MIA in chiral resolution process of BINOL and its derivatives, as indicated by significant differences in ΔR_f values. Surprisingly, both diastereomers of BINOL and H_8-BINOL with (*S*,*R*)-configuration exhibited a distinct characteristic on TLC, appearing at a higher position compared to the (*S*,*S*)-configuration. In contrast, BINAM diastereomers displayed the opposite pattern. Diastereomers of BINOL were investigated to study methanolysis for deriving enantiopure forms of BINOL with high optical purity.

1. Introduction

1,1′-Bi-2-naphthols or BINOLs and their derivatives: axially chiral compounds, which refer to stereoisomerism resulting from the nonplanar arrangement of four groups in pairs about a chirality axis.[1] They have been explored for various applications for a long time. Interestingly, BINOL configurations significantly impact the configuration and purity of enantioselective products,[2, 3] especially, in asymmetric synthesis of alcohols, anti-*β*-aminoesters, *α*-hydroxy- and aminophosphonates, and 1-alkoxy-2,2,2-trifluoroethanol derivatives occurs *via* reduction, oxidation, aldol reaction, Mannich reaction, or Diels-Alder reaction.[4, 5] In addition, chiral BINOL derivatives are also applied in pharmaceuticals,[6] charge-transfer host systems,[7] and circularly polarized luminescence (CPL) dyes.[8] Regarding to the applications, it is crucial to use enantiomerically pure BINOLs, which are capable of providing enantioselective or affording products of interest. In contrast, racemic BINOLs are completely ineffective. This aspect poses challenges for chemists in devising synthetic strategies to yield the enantiomerically pure BINOLs. The synthetic strategies include the asymmetric oxidative coupling of 2-naphthol, enzymatic chiral resolution, and chemical chiral resolution.[9, 10] Among these strategies, chemical chiral resolution is an efficient method which resolves racemic BINOL to enantiopure BINOLs in good yield and high enantioselectivity. Chemical chiral resolution is assisted by chiral auxiliary, which is the chiral molecule reacts with BINOLs to generate diastereomeric pairs. The differences in physical properties of diastereomers are examined to facilitate resolution, including crystallization technique which applied the differences in solubility and chromatographic techniques which applied the differences in dipole moment. Chromatographic techniques offer some advantages over crystallization since they do not require crystalline materials and can obtain both enantiomers of BINOLs in optically pure forms.[11] Chromatographic techniques, including the column liquid chromatography and gas chromatography are widely employed techniques for achieving chiral resolution. However, thin-layer chromatography (TLC) is the most readily available approach for the direct resolution of racemates and enantiomeric purity control because it offers various desired characteristics, such as simplicity, flexibility, and low cost.[12] TLC proves to be an effective separation technology, demonstrating excellent performance in isolating analytes from mixtures.

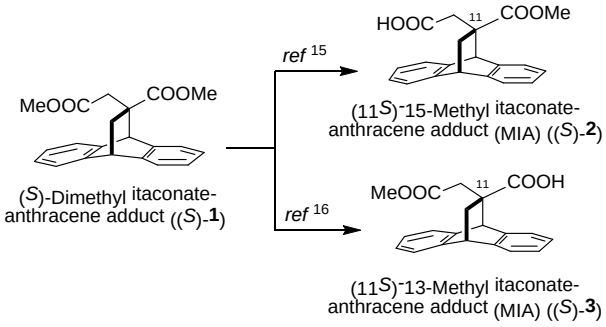

Scheme 1. Preparation of MIA using as the chiral auxiliaries

TLC applied the different inherent polarities of the components in the mixture, which depend on the adsorption capacity of each component in the mixture, for separation process.[13] The position of the analytes on the TLC plate is represented by the retardant factor (R_f) value which was produced by diastereomeric pairs of chiral auxiliaries and BINOL derivatives. Herein, we improved the preparation methods of BINOL derivatives using methyl itaconate-anthracene adducts (MIAs) as new chiral auxiliaries. MIAs can be prepared easily from the method outlined belong with high overall yield.[14-16] Then TLC was studied to investigate their significant differences, expressed as R_f values.

2. Materials and Methods

2.1 Materials

Chiral BINOLs and 5,5',6,6',7,7',8,8'-octahydro-1,1'-bi-2-naphthols (H_8-BINOLs) were purchased from Tokyo Chemical Industry (TCI). 1,1'-binaphthyl-2,2'-diamines (BINAMs), *N*,*N*′-dicyclohexylcarbodiimide (DCC). 4-dimethylaminopyridine (DMAP), lithium hydroxide, oxalyl chloride $(COCl)_2$, and triethylamine (NEt_3) were purchased from Sigma-Aldrich.

2.2 General procedures

All reactions were carried out under nitrogen. Unless otherwise noted, materials were obtained from commercial suppliers and used without further purification. The high-resolution mass spectra (HRMS, *m*/*z* value) were obtained from a MS/MS Agilent 6540 UHD QTOF mass spectrometer. Specific rotations were measured in $CHCl_3$ or toluene with a Rudolph Research Analytical Autopol I Automatic Polarimeter. Melting points were determined by using a Gallenkamp Electrothermal apparatus and were uncorrected. The ^{1}H NMR spectra were recorded on Bruker Neo^{TM} 500 MHz spectrometers and chemical shifts were given in ppm downfield from tetramethylsilane (TMS). NMR spectra were measured in $CDCl_3$ or toluene-d_8 and chemical shifts were reported as δ-values in parts per million (ppm) relative to residue internal reference (^{1}H, $CHCl_3$: δ 7.26 and toluene : δ 2.08) and coupling constants (J values) were reported in hertz (Hz). Peak multiplicities are indicated as follows: s (singlet), d (doublet), t (triplet), dd (doublet of doublets), dt (doublet of triplets), td (triplet of doublets), ddd (doublet of doublet of doublets), and m (multiplet). Flash column chromatography was performed employing Merck silica gel 60 and Merck silica gel 60H. Preparative thin layer chromatography (PLC) plates were carried out using Merck silica gel 60 PF_{254}. Analytical thin layer chromatography was conducted with Merck silica gel 60 F_{254} aluminum plates. DCM were dried over CaH_2 and distilled before used. Triethylamine was distilled over CaH_2 and stored under nitrogen.

2.2.1 The preparation of chiral methyl itaconate-anthracene adducts ((*S*)-2 and (*S*)-3)

A racemic mixture of dimethyl itaconate-anthracene adducts (**1**), obtained from Diels-Alders reaction between anthracene and dimethyl itaconate, underwent the hydrolysis, esterification with (–)-menthol for chiral resolution, and transmethylation to provide (*R*)- and (*S*)-**1** following procedures previously published.[14] Then, the enantiomeric pure form of **1** was applied to prepare (*R*)- and (*S*)-**2** through a hydrolysis reaction according to the previous published article.[14-16] Furthermore, in the synthesis of (*R*)- and (*S*)-**3**, each chiral adduct of **1** underwent full hydrolysis, and selective methylation following the identical procedure outlined in the references.[15, 16] Then, the chiral (*S*)-**2** and (*S*)-**3** were chosen to further investigate their efficiency in being chiral resolving agents of chiral BINOL and BINAM derivatives.

2.2.2 General procedure in preparation of diastereomeric BINOL- and H_8-BINOL-esters (5-6 and 8-9) Chiral BINOL derivatives, **4** and **7** (1.0 eq.), MIAs (1.5 eq.), DCC (1.5 eq.), and DMAP (0.15 eq.) were added to rounded-bottom flask with the magnetic stirrer apparatus. Then, DCM (5 mL) was introduced into the reaction flask under the N_2 atmosphere at 0 °C. The reaction mixture was further stirred at 0 °C for 5 hours. When the reaction finished, the mixture was evaporated and then purified using flash column chromatography.

(+)-(11*S*,1′*R*)-11-[(Carbo-1′,1′′-bi-2-napthoxy)-(carbomethoxymethyl)]-9,10-dihydro-9,10-ethanoanthracene ((+)-(11*S*,1′*R*)-5): 53% yield; pale yellow solid; $[\alpha]_{589}^{26.0}$ = +250.04

(*c* 0.10, $CHCl_3$); R_f (25% EtOAc/hexane) 0.53; δ_H (500 MHz, $CDCl_3$) 1.30 (dd, *J* = 2.7, 13.0 Hz, 1H), 1.68 (d, *J* = 16.8 Hz, 3H), 2.39 (d, *J* = 16.8 Hz, 1H), 2.43 (dd, *J* = 2.9, 13.1 Hz, 1H), 3.41 (s, 3H), 3.55 (s, 1H), 4.13 (t, *J* = 2.7 Hz, 1H), 6.65 (dd, *J* = 1.4, 7.2 Hz, 1H), 6.92 (dd, *J* = 1.8, 6.9 Hz, 1H), 6.96 (td, *J* = 1.4, 7.5 Hz, 1H), 6.98–7.09 (m, 3H), 7.10–7.18 (m, 3H), 7.29 (ddd, *J* = 1.4, 6.8, 8.2 Hz, 2H), 7.32–7.39 (m, 3H), 7.41 (ddd, *J* = 1.2, 6.8, 8.1 Hz, 1H), 7.44 (d, *J* = 8.9 Hz, 1H), 7.49 (dt, *J* = 3.9, 8.1 Hz, 1H), 7.90–8.00 (m, 3H), 8.00 (d, *J* = 9.0 Hz, 1H) ; HRMS (ESI) calcd for $C_{40}H_{31}O_5$ $[M+H]^+$ *m/z* 591.2171 found 591.2174.

(+)-(11*S*,1′*S*)-11-[(Carbo-1′,1′′-bi-2-napthoxy)-(carbomethoxymethyl)]-9,10-dihydro-9,10-ethanoanthracene ((+)-(11*S*,1′*S*)-6): 56% yield; white solid; $[\alpha]_{589}^{25.1}$ = +90.02 (*c* 0.10, $CHCl_3$); R_f (25% EtOAc/hexane) 0.42; δ_H (500 MHz, $CDCl_3$) 1.33 (dd, *J* = 2.7, 13.1 Hz, 1H), 1.78 (d, *J* = 16.5 Hz, 1H), 2.31 (d, *J* = 16.5 Hz, 1H), 2.43 (dd, *J* = 3.0, 13.2 Hz, 1H), 3.46 (s, 4H), 3.86 (s, 1H), 4.15 (t, *J* = 2.7 Hz, 1H), 6.37 (dd, *J* = 1.1, 7.4 Hz, 1H), 6.77 (td, *J* = 1.2, 7.5 Hz, 1H), 7.01 (td, *J* = 1.2, 7.5 Hz, 1H), 7.03–7.10 (m, 2H), 7.12 (dd, *J* = 1.0, 8.5 Hz, 1H), 7.14–7.20 (m, 1H), 7.28 (dd, *J* = 1.2, 8.4 Hz, 1H), 7.31–7.36 (m, 3H), 7.41 (ddd, *J* = 1.2, 6.7, 8.1 Hz, 1H), 7.45 (d, *J* = 9.0 Hz, 1H), 7.48 (ddd, *J* = 1.4, 6.7, 8.2 Hz, 1H), 7.88–7.97 (m, 2H), 7.99 (d, *J* = 8.9 Hz, 1H); HRMS (ESI) calcd for $C_{40}H_{31}O_5$ $[M+H]^+$ *m/z* 591.2171 found 591.2179.

(+)-(11*S*,1′*R*)-11-[(Carbo-1′,1′′-5′,5′′,6′,6′′,7′,7′′,8′,8′′-octahydro-bi-2-napthoxy)-(carbomethoxymethyl)]-9,10-dihydro-9,10-ethanoanthracene ((+)-(11*S*,1′*R*)-8): 62% yield; white solid; $[\alpha]_{589}^{25.3}$ = +110.02 (*c* 0.10, $CHCl_3$); R_f (20% EtOAc/hexane) 0.51; δ_H (500 MHz, $CDCl_3$) 1.47 (dd, *J* = 2.7, 13.1 Hz, 1H), 1.66 – 1.84 (m, 8H), 1.86 (s, 1H), 2.01–2.10 (m, 1H), 2.15–2.30 (m, 2H), 2.39–2.47 (m, 1H), 2.50 (dd, *J* = 2.9, 13.1 Hz, 1H), 2.56 (d, *J* = 16.8 Hz, 1H), 2.80 (t, *J* = 6.3 Hz, 2H), 2.85 (t, *J* = 6.2 Hz, 2H), 3.96 (s, 1H), 4.25 (t, *J* = 2.7 Hz, 1H), 6.86 (d, *J* = 8.4 Hz, 1H), 6.90 (d, *J* = 8.4 Hz, 1H), 7.00–7.06 (m, 2H), 7.07–7.16 (m, 6H), 7.21–7.26 (m, 2H); HRMS (ESI) calcd for $C_{40}H_{39}O_5$ $[M+H]^+$ *m/z* 599.2797 found 599.2791.

(−)-(11*S*,1′*S*)-11-[(Carbo-1′,1′′-5′,5′′,6′,6′′,7′,7′′,8′,8′′-octahydro-bi-2-napthoxy)-(carbomethoxymethyl)]-9,10-dihydro-9,10-ethanoanthracene ((+)-(11*S*,1′*R*)-9): 63% yield; white solid; $[\alpha]_{589}^{25.5}$ = -20.00 (*c* 0.10, $CHCl_3$); R_f (20% EtOAc/hexane) 0.38; δ_H (500 MHz, $CDCl_3$) 1.33 (dd, *J* = 2.6, 13.1 Hz, 1H), 1.53–1.74 (m, 8H), 1.91 (d, *J* = 16.2 Hz, 1H), 1.97–2.08 (m, 2H), 2.17–2.34 (m, 4H), 2.56–2.78 (m, 4H), 3.41 (s, 3H), 4.09 (t, *J* = 2.7 Hz, 1H), 4.21 (s, 1H), 6.56 (d, *J* = 8.2 Hz, 1H), 6.83 (d, *J* = 8.4 Hz, 1H), 6.88 (d, *J* = 8.2 Hz, 1H), 6.94–7.07 (m, 6H), 7.10–7.14 (m, 3H); HRMS (ESI) calcd for $C_{40}H_{39}O_5$ $[M+H]^+$ *m/z* 599.2797 found 599.2819.

2.2.3 General procedure in preparation of diastereomeric BINAM-amides (11-12) To a solution of MIAs (1.5 eq.) in DCM in rounded-bottom flask fitted with the magnetic stirrer apparatus with a Claisen head, $(COCl)_2$ (2.0 eq.) was added, following by 2-3 drops of NEt_3 *via* syringe. The solution was stirred at ambient temperature for 4 hours under nitrogen atmosphere. Then, the reaction mixture was evaporated to remove residual $(COCl)_2$. The crude product was dissolved in DCM, and then BINAM, **10** (1.0 eq.) in the presence of NEt_3 base was added *via* syringe under nitrogen atmosphere. After the reaction finished, the crude solution was extracted with DCM/H_2O 3 times, followed by purification with column chromatography.

(+)-(11*S*,1′*R*)-11-[(Carbo-1′,1′′-bi-2-napthanamide)-(carbomethoxymethyl)]-9,10-dihydro-9,10-ethanoanthracene ((+)-(11*S*,1′*R*)-11): 40% yield; pale yellow solid; $[\alpha]_{589}^{30.4}$ = -227.31 (*c* 0.11, toluene); R_f (10% EtOAc 40% DCM/hexane) 0.55; δ_H (500 MHz, Toluene-d_8) 1.46 (dd, *J* = 2.5, 14.3 Hz, 1H), 1.74 (d, *J* = 16.6 Hz, 1H), 2.08–2.12 (m, 1H), 2.85 (d, *J* = 16.8 Hz, 1H), 3.11 (s, 3H), 3.68 (t, *J* = 2.7 Hz, 1H), 4.24 (s, 1H), 6.30–6.42 (m, 2H), 6.64 (td, *J* = 1.7, 7.2 Hz, 1H), 6.69 (dd, *J* = 1.0, 8.5 Hz, 1H), 6.73 (d, *J* = 8.7 Hz, 1H), 6.83–6.89 (m, 3H), 6.89–6.98 (m, 4H), 6.99–7.03 (m, 1H), 7.06–7.15 (m, 2H), 7.19 (dd, *J* = 1.1, 8.5 Hz, 1H), 7.58 (dt, *J* = 0.9, 8.2 Hz, 1H), 7.60–7.70 (m, 3H), 8.87 (d, *J* = 9.0 Hz, 1H); HRMS (ESI) calcd for $C_{40}H_{33}O_3N_2$ $[M+H]^+$ *m/z* 589.2486 found 589.2509.

(+)-(11*S*,1′*S*)-11-[(Carbo-1′,1′′-bi-2-napthanamide)-(carbomethoxymethyl)]-9,10-dihydro-9,10-ethanoanthracene ((+)-(11*S*,1′*S*)-12): 41% yield; pale yellow solid; $[\alpha]_{589}^{31.0}$ = -18.19 (*c* 0.11, toluene); (10% EtOAc 40% DCM/hexane) 0.63; δ_H (500 MHz, Toluene-d_8) 1.31 (dd, *J* = 2.7, 13.5 Hz, 1H), 1.90 (d, *J* = 16.2 Hz, 1H), 2.04–2.12 (m, 1H), 2.36 (d, *J* = 16.2 Hz, 1H), 3.09 (s, 3H), 3.74 (t, *J* = 2.8 Hz, 1H), 4.22 (s, 1H), 6.59 (td, *J* = 1.3, 7.4 Hz, 1H), 6.63 (dd, *J* = 1.4, 7.4 Hz, 1H), 6.69–6.78 (m, 2H), 6.80–6.91 (m, 4H), 6.91–6.99

(m, 2H), 6.99–7.05 (m, 2H), 7.05–7.11 (m, 1H), 7.13 (ddd, J = 1.4, 6.8, 8.2 Hz, 1H), 7.29 (d, J = 8.4 Hz, 1H), 7.45 (s, 1H), 7.59 (d, J = 8.1 Hz, 1H), 7.62–7.71 (m, 3H), 8.77 (d, J = 9.0 Hz, 1H); HRMS (ESI) calcd for $C_{40}H_{33}O_3N_2$ $[M+H]^+$ m/z 589.2486 found 589.2455.

2.2.4 General procedure for methanolysis

The diastereomeric esters **5** and **6** were chosen to investigate the capability in methanolysis to obtain pure form of (*R*)- and (*S*)-BINOL, respectively. To a solution of each ester **5** and **6** (1.0 eq.) dissolved in methanol, $LiOH{\cdot}H_2O$ (2.0 eq.) was added. The reaction mixture was then stirred at room temperature for 24 hours. Finally, the solution was extracted with DCM/H_2O 3 times and purified with preparative chromatography to obtain enantiopure forms of BINOLs.

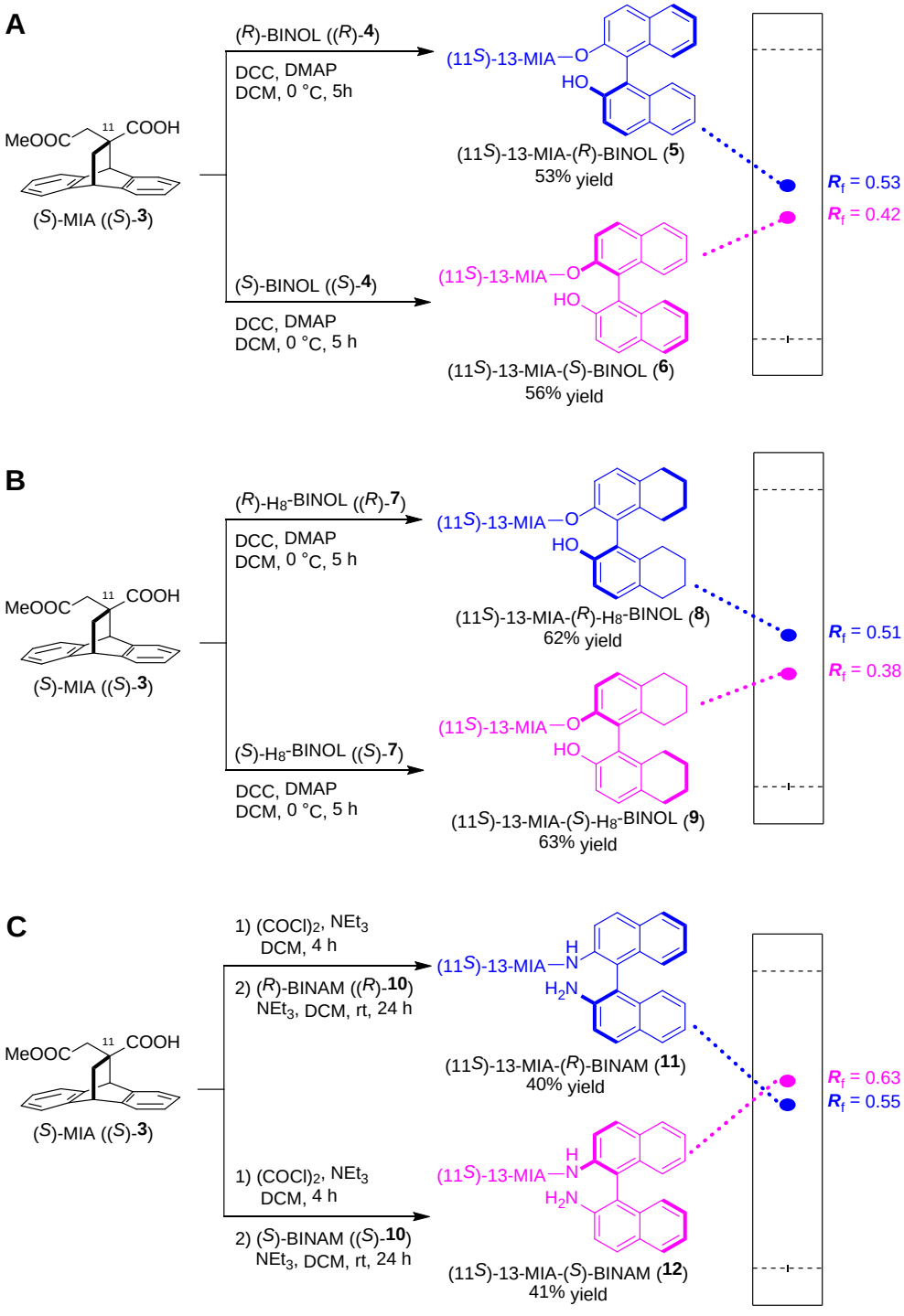

Scheme 2. Synthesis of diastereomeric pairs of BINOL and BINAM derivatives and their comparison of the derived R_f values, **A**: adducts **5** and **6**, **B**: adducts **8** and **9**, and **C**: adducts **11** and **12**

3. Results & Discussion

3.1 Synthesis and characterization of MIA-BINOL esters and MIA-BINOL amides

All diastereomers were synthesized under mild conditions by using enantiopure BINOL derivatives as starting materials. Diastereomeric pairs **5** and **6** were synthesized using the DCC reagent in the presence of the DMAP catalyst at 0 °C, yielding excellent products. Under identical conditions, BINOL diastereomers **5** and **6** were produced with yields of 50% and 46%, respectively. Additionally, H_8-BINOL diastereomers **8** and **9** were achieved with yields of 62% and 63% using this method. On the other hands, due to their inability to undergo conversion under DCC conditions, diastereomeric pairs of BINAM **11** and **12** were synthesized through $(COCl)_2$ in a triethylamine base, yielding 40%. It's noteworthy that the primary byproduct was an anhydride compound resulting from the self-condensation of MIA.

The ^{1}H-NMR characterization of BINOLs and H_8-BINOL diastereomers in $CDCl_3$ revealed interesting information in the significantly different chemical shift on MIA ((*S*)-**3**), particularly for the H_y proton. In most cases, this proton is shielded by anisotropic effect of naphthalene moiety. Notably, (*S*,*R*)-configuration were affected more than (*S*,*S*)- configuration, which exhibited the lower chemical shift. Despite H_y being shielded in BINOL and H_8-BINOL diastereomers, BINAM was not observed. BINAM diastereomers also have some protons which are shielded and deshielded. However, these protons are bulky and complex, making them challenging to identify analytically.

3.2 Efficiency of MIAs to resolve BINOL derivatives by TLC

To study the efficiency of MIAs in the resolution of diastereomeric pairs of BINOL derivatives, several solvents were applied as eluents. However, we cannot find the optimal system to resolve diastereomeric pairs **5** and **6** which obtained from (*S*)-**2**. Therefore, we assume that (*S*)-**2** is not appropriate to resolve BINOL derivatives. In the case of (*S*)-**3**, BINOL and H_8-BINOL diastereomers were resolved by ethyl acetate/hexane as the eluents. This combination provided excellent resolution for diastereomeric pairs **5** and **6** with ΔR_f 0.11 (25% ethyl acetate/hexane) and diastereomeric pairs **8** and **9** with ΔR_f 0.13 (20% EtOAc/hexane). Furthermore, (*S*)-**3** also separated diastereomeric pairs of BINAM with ΔR_f 0.08 (10% EtOAc 40% DCM/hexane), albeit in the opposite trend.

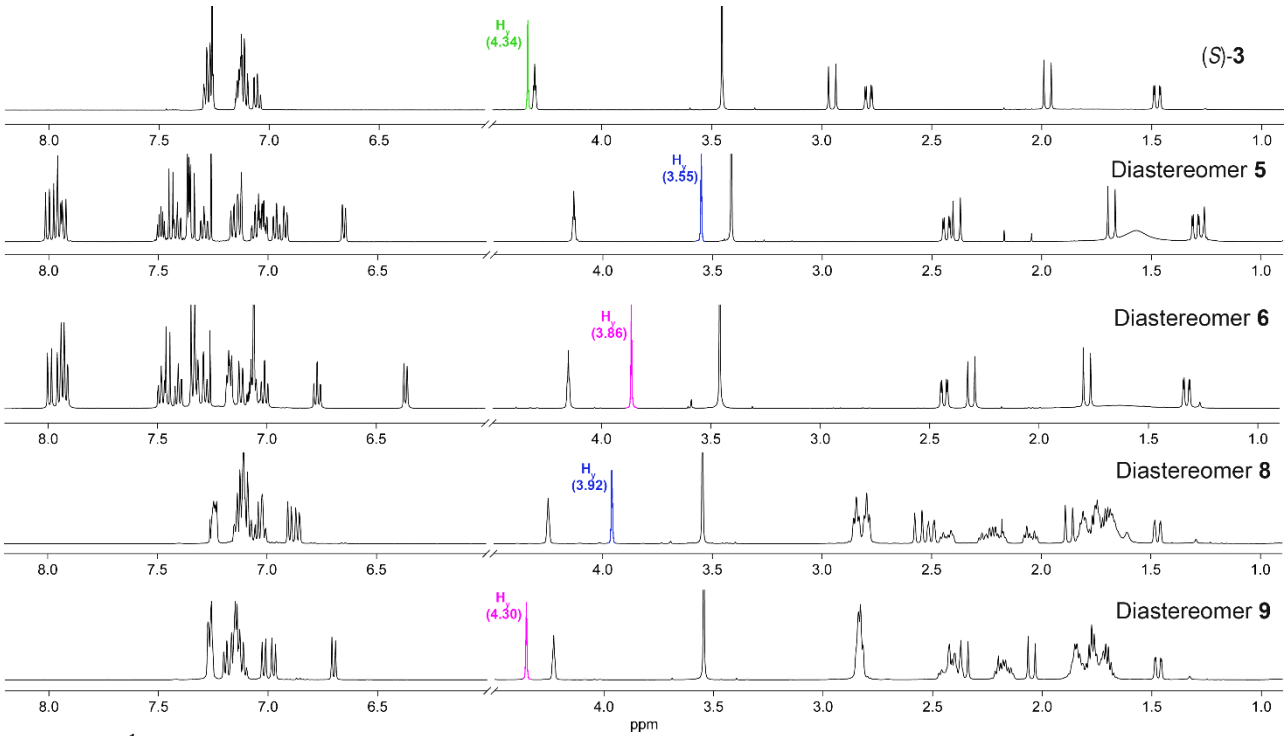

Figure 1. ^{1}H-NMR (500 MHz, $CDCl_3$) of BINOLs and H_8-BINOLs diastereomers which are compared H_y proton (*S*,*R*- configuration : blue color, *S*,*S*- configuration : pink color) with (*S*)-**3** (green color)

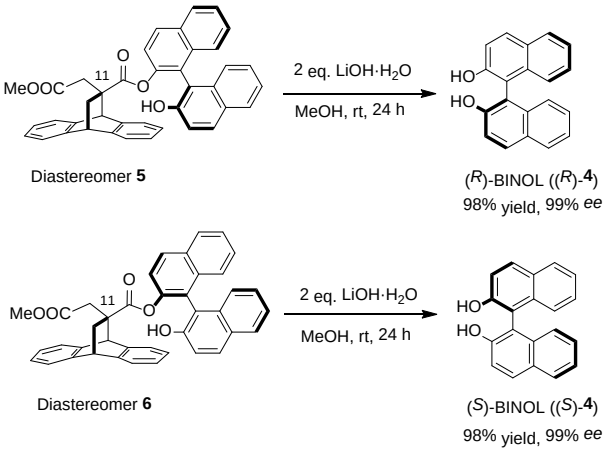

Scheme 3. Methanolysis of BINOL diastereomers

3.3 Methanolysis of BINOL diastereomers

To obtain enantiopure BINOLs after the resolution process, LiOH in MeOH was employed as reagents. We introduced diastereomers of BINOLs for study. The diastereomer **5** was methanolysis, yielding enantiopure (*R*)-BINOL with a 98% yield 99 %*ee*. Similarly, diastereomer **6** resulted in enantiopure (*S*)-BINOL with a 98% yield and 99% *ee* (% *ee* according to the specific rotation of BINOLs from methanolysis compared with its enantiopure forms:

$$\%ee = \frac{\text{observed specific rotation}}{\text{specific rotation of enantiopure form}} \times 100).$$

Additionally, we obtained the dimethyl itaconate-anthracene adduct (*S*)-**1**, a compound in the synthetic route of MIAs, as another product with 78% yield (Scheme 3).

4. Conclusion

MIA ((*S*)-**3**) demonstrates efficiency in resolving racemic BINOL derivatives through esterification reactions. It is noteworthy that BINOLs and H_8-BINOLs exhibit similar characteristics on TLC, in contrast to BINAM. This similarity is associated with the H_y proton, which is shielded by the naphthalene moiety. Enantiopure forms can be achieved with high purity after methanolysis.

Acknowledgements

This work was supported by the Mid-career Research Grant (NRCT5-RSA63004-17), provided by the National Research Council of Thailand (NRCT) (grant numbers N41A650086) for NK. In addition, we would like to thank the Development and Promotion of Science and Technology, the Ministry of Higher Education, Science, Research and Innovation for the support provided to WS. Finally, we would gratefully thank the Department of Chemistry, Faculty of Science, Chiang Mai University for facilities and Central Science Laboratory, Faculty of Science, Chiang Mai University for NMR instrumental supports.

References

1. Wang, Y. B.; Tan, B. *Acc. Chem. Res.* **2018**, *51*, 534-547.
2. Noyori, R.; Tomino, I.; Tanimoto, Y.; Nishizawa, M. *J. Am. Chem. Soc.* **1984**, *106*, 6709-6716.
3. Kobayashi, S.; Ishitani, H. *J. Am. Chem. Soc.* **1994**, *116*, 4083-4084.
4. Brunel, J. M. *Chem. Rev.* **2007**, *107*, PR1-PR45.
5. McCarthy, M.; Guiry, P. J. *Tetrahedron* **2001**, *57*, 3809-3844.
6. Wang, J.; Zhao, C.; Wang, J. *ACS Catal.* **2021**, *11*, 12520-12531.
7. Imai, Y.; Kamon, K.; Kinuta, T.; Tajima, N.; Sato, T.; Kuroda, R.; Matsubara, Y. *Tetrahedron* **2007**, *63*, 11928-11932.
8. Takaishi, K.; Murakami, S.; Yoshinami, F.; Ema, T. *Angew. Chemie - Int. Ed.* **2022**, *61*.
9. Narute, S.; Parnes, R.; Toste, F. D.; Pappo, D. *J. Am. Chem. Soc.* **2016**, *138*, 16553-16560.
10. Ayad, S.; Posey, V.; Das, A.; Montgomery, J. M.; Hanson, K. *Chem. Commun.* **2019**, *55*, 1263-1266.
11. Panchal, B. M.; Einhorn, C.; Einhorn, J. *Tetrahedron Lett.* **2002**, *43*, 9245-9248.
12. Del Bubba, M.; Checchini, L.; Lepri, L. *Anal. Bioanal. Chem.* **2013**, *405*, 533-554.
13. Zhang, M.; Yu, Q.; Guo, J.; Wu, B.; Kong, X. *Biosensors* **2022**, *12*.
14. Kongsaeree, P.; Meepowpan, P.; Theptharanont, Y. *Tetrahedron: Asymmetry* **2001**, *12*, 1913-1922.
15. Intakaew, N.; Rithchumpon, P.; Prommin, C.; Yimklan, S.; Kungwan, N.; Thavornyutikarn, P.; Meepowpan, P. *Org. Biomol. Chem.* **2019**, *17*, 541-554.
16. Rithchumpon, P.; Intakaew, N.; Khamto, N.; Yimklan, S.; Nimmanpipug, P.; Thavornyutikarn, P.; Meepowpan, P. *Org. Biomol. Chem.* **2021**, *19*, 8955-8967.

The synthesis of benzazepine analogs via intramolecular ritter-type reaction

Suthimon Boonmee[1], Gunniga Tanomsiri[1], Jumreang Tummatorn[1, 3]*, Charnsak Thongsornkleeb[1, 2], and Somsak Ruchirawat[1, 3]

[1]*Program on Organic Chemistry, Chulabhorn Graduate Institute, Center of Excellence on Environmental Health and Toxicology (EHT), OPS, MHESI, 54 Kamphaeng Phet 6, Laksi, Bangkok, 10210, Thailand*

[2]*Laboratory of Medicinal Chemistry, Chulabhorn Research Institute, 54 Kamphaeng Phet 6, Laksi, Bangkok, 10210, Thailand*

[3]*Laboratory of Medicinal Chemistry, Chulabhorn Research Institute, 54 Kamphaeng Phet 6, Laksi, Bangkok 10210, Thailand*

**E-mail: jumreang@cri.or.th*

Abstract:

The benzazepine moiety has garnered significant attention from researchers globally owing to its noteworthy biological and pharmacological activities. Consequently, our research group aims to devise a novel approach for synthesizing benzazepine analogs utilizing an intramolecular Ritter reaction with the aid of bismuth(III) trifluoromethanesulfonate ($BiOTf_3$) and *p*-toluenesulfonic acid. $Bi(OTf)_3$ is recognized as one of the highly efficient catalysts for transforming benzylic alcohol into benzylic cations. Therefore, we incorporated this catalyst into our procedure which could provide the desired products in moderate to good yields.

1. Introduction

The benzazepine, characterized by its seven-membered ring, is part of an important group of heterocyclic compounds. This core structure exhibits various biological and pharmacological effects, such as anticancer, antidepressant, and anti-diabetic properties. Moreover, natural products also feature this fundamental structure. Currently, there is considerable focus on this compound class. Figure 1 illustrates examples of bioactive compounds that incorporate the benzazepine moiety.[8] Numerous methods have been documented for the synthesis of benzazepine derivatives,[1-7] incorporating variations in the positions of nitrogen and aryl rings. The conventional techniques for producing benzazepine derivatives, with a particular emphasis on integrating nitrogen and aryl rings, are versatile and can be applied in both intermolecular and intramolecular reactions.

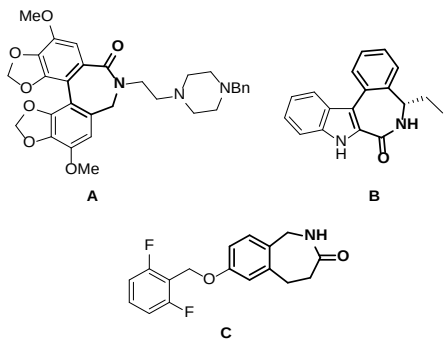

Figure 1. Bioactive benzazepine analogs.

Our research group is actively working on developing a novel method for synthesizing benzazepine analogs through an intramolecular Ritter-Type reaction, employing bismuth(III) trifluoromethanesulfonate ($Bi(OTf)_3$) and *para*-toluenesulfonic acid as catalysts. The pivotal starting material for this transformation is 1,1'-biphenyl]-2-carbonitrile alcohol, which can be synthesized *via* a Suzuki cross-coupling reaction between 2-bromobenzaldehydes and *ortho*-cyanophenyl boronic acid, followed by Grignard addition. Drawing on previous research findings,[9] $BiOTf_3$ stands out as one of the most effective catalysts for converting benzylic alcohol into benzylic cations. Our novel devised approach insides on the creation of 7-membered rings, taking into consideration the associated ring strain. Consequently, we hypothesize that the synthesis of benzazepine could be achieved through a Ritter-Type reaction, which has not been documented previously. Hence, we have incorporated this catalyst into our procedure for the synthesis of benzazepines via Ritter-Type reaction. We are optimistic that the synthesis of benzazepine libraries will yield novel bioactive compounds, presenting promising avenues for further exploration.

2. Materials and Methods

2.1 Materials

The reagents and solvents were used in their as-received state directly from the suppliers unless otherwise specified. ^{1}H NMR, ^{13}C NMR, ^{19}F

NMR and 1D NOE NMR spectra were recorded in $CDCl_3$ with Bruker 300 MHz, 400 MHz or 600 MHz NMR spectrometers. Chemical shifts for ^1H and ^{13}C NMR spectra were reported in part per million (ppm), relative to tetramethylsilane (TMS) (δ = 0 ppm). Coupling constants (J) were reported in Hertz (Hz). Infrared spectra were measured using an FT-IR spectrometer and were reported in cm^{-1}. High-resolution mass spectra (HRMS) were measured on an Agilent mass spectrometer.

2.2 Preparation of 1-(2-Bromophenyl) ketone starting material

A round-bottomed flask containing a magnetic stir bar and 2-bromobenzaldehyde derivatives in anhydrous tetrahydrofuran (THF) was added with methylmagnesium chloride at 0°C to room temperature under argon and the reaction was stirred for 3 h. After completion, the reaction mixture was diluted with saturated aqueous NH_4Cl and extracted with EtOAc. The combined organic phases were washed with saturated aqueous NaCl, dried over anhydrous Na_2SO_4, filtered and concentrated in vacuo to give a crude material. Then, this product was oxidized using pyridinium chlorochromate (PCC) and Celite in CH_2Cl_2 (DCM) at room temperature for overnight. Then, the reaction mixture was filtered through Celite and concentrated under reduced pressure to give a crude material. The crude material was purified by SiO_2 column chromatography eluting with 10% EtOAc-hexane to give the desired product as a yellow oil.

Similar procedures were performed to prepare other 1-(2-bromophenyl) ethan-1-one products starting from appropriate 2-bromobenzaldehyde derivatives.

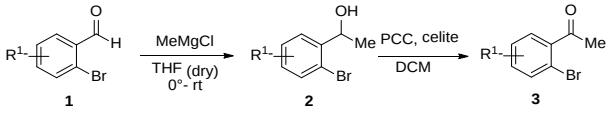

Scheme 1. The synthesis of 1-(2-bromophenyl) ketone derivatives.

2.3 Preparation of [1,1'-Biphenyl]-2-carbonitrile ketone derivatives

A solution mixture of 1-(2-bromophenyl) ketone (1.0 equv) in THF was added with (2-cyanophenyl) boronic acid (1.4 equiv), $PdCl_2(PPh_3)_2$ (0.05 equiv), K_2CO_3 (5.0 equiv) and THF at room temperature. The reaction mixture was allowed to stir at 85°C for overnight. After the reaction was complete, the reaction mixture was diluted with saturated aqueous NH_4Cl and the separated aqueous layer was extracted with EtOAc. Combined organic phases were washed with saturated aqueous NaCl, dried over anhydrous Na_2SO_4, filtered and concentrated in vacuo to give a crude material. The crude material was purified by SiO_2 column chromatography eluting with 20% EtOAc-hexane to give the desired product as a yellow oil.

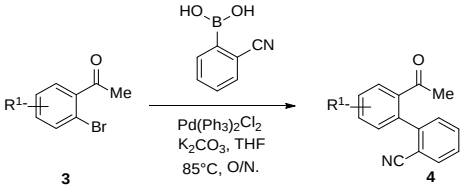

Scheme 2. The synthesis of [1,1'-biphenyl]-2-carbonitrile ketone derivatives.

2.4 Preparation of [1,1'-Biphenyl]-2-carbonitrile alcohol derivatives

A round-bottomed flask containing a magnetic stir bar and [1,1'-biphenyl]-2-carbonitrile ketone was added with $NaBH_4$ and MeOH. The reaction mixture was allowed to stir at room temperature under argon for 2 h. After the reaction was complete, the reaction mixture was diluted with saturated aqueous NH_4Cl and the separated aqueous layer was extracted with EtOAc. Combined organic phases were washed with saturated aqueous NaCl, dried over anhydrous Na_2SO_4, filtered and concentrated in vacuo to give a crude material. The crude material was purified by SiO_2 column chromatography eluting with 30% EtOAc-hexane to give the desired product as a white solid.

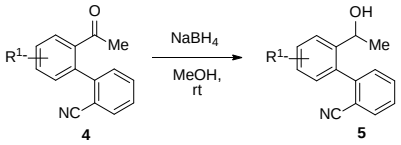

Scheme 3. The synthesis of [1,1'-biphenyl]-2-carbonitrile alcohol derivatives.

2.5 Preparation of Benzazepine derivatives

A mixture of [1,1'-biphenyl]-2-carbonitrile alcohol was placed in round-bottomed flask containing a magnetic stir bar and DCE. Then, the reaction mixture was added with $Bi(OTf)_3$ (0.05 equiv), and *p*-toluenesulfonic acid (5.0 equiv). The reaction mixture was allowed to stir at 150°C for overnight. After the reaction was complete, the reaction mixture was diluted with saturated aqueous NH_4Cl and the separated aqueous layer was extracted with CH_2Cl_2. Combined organic phases were washed with

saturated aqueous NaCl, dried over anhydrous Na_2SO_4, filtered and concentrated in vacuo to give a crude material. The crude material was purified by SiO_2 column chromatography eluting with 40% EtOAc-hexane to give the desired product as a white solid.

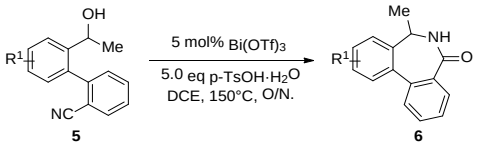

Scheme 4. The synthesis of benzazepine derivatives.

3. Results & Discussion

The optimization studies of reaction conditions were conducted as shown in Table 1. Initially, entry 1, 3.0 equiv acid of *p*-TsOH·H_2O and add 5 mol% of Lewis acid ($Bi(OTf)_3$) were used at 85°C for overnight which gave the desired product in 38% yield. In entries 2 and 3, the reactions were varied the reaction temperature 100 °C and 150 °C which could obtain the corresponding products in slightly higher yields. Then the equivalents of acid were investigated employing 5.0 and 7.0 equivalents as shown in entries 4 and 5. The desired product was obtained in 78% and 49%, respectively. Next, other acids including CSA, TFA and saccharin were employed to give the product in lower yields (entries 6-8). The Lewis acids were also investigated as shown entries 9-11 which could provide the desired product in good yields (55-72%) which were lower than entry 4. Then, we also tried to reduce the reaction concentration in entry 12 and used 5 mol% of $Bi(OTf)_3$ and 5 equiv of *p*-toluenesulfonic acid in DCE (1 mL) at 150 °C for overnight, is the best condition for the synthesis of benzazepine products.

In this work, benzazepine derivatives could be prepared from [1,1'-biphenyl]-2-carbonitrile alcohol. The reaction mechanism is proposed into two pathways. First, nitrile moiety is hydrolyzed to amide, followed by intramolecular cyclization to afford the desired product. In the second proposed pathway, lone pair electron on nitrogen atom of nitrile activates benzylic alcohol to form nitrilium ion intermediate which is hydrolyzed to form seven membered ring benzazepine product as shown in Figure 2.

The result revealed that the second pathway is more favorable because we could monitor and isolate amide intermediate which is a good evidence to support the proposed mechanism.

Table 1. The optimization studies.

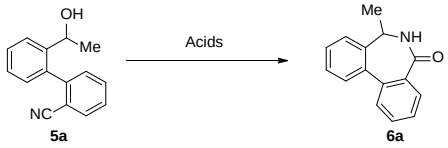

Entries	Acid	Lewis acid	Temp.	Time	%Yield
1	3.0 equiv *p*-TsOH·H_2O	5 mol% $Bi(OTf)_3$	85	O/N	38
2	3.0 equiv *p*-TsOH·H_2O	5 mol% $Bi(OTf)_3$	100	O/N	47
3	3.0 equiv *p*-TsOH·H_2O	5 mol% $Bi(OTf)_3$	150	O/N	55
4	5.0 equiv *p*-TsOH·H_2O	5 mol% $Bi(OTf)_3$	150	O/N	78
5	7.0 equiv *p*-TsOH·H_2O	5 mol% $Bi(OTf)_3$	150	O/N	49
6	5.0 equiv CSA	5 mol% $Bi(OTf)_3$	150	O/N	45
7	5.0 equiv TFA	5 mol% $Bi(OTf)_3$	150	O/N	23
8	5.0 equiv saccharin	5 mol% $Bi(OTf)_3$	150	O/N	19
9	5.0 equiv *p*-TsOH·H_2O	5 mol% $Ln(OTf)_3$	150	O/N	71
10	5.0 equiv *p*-TsOH·H_2O	5 mol% $Sc(OTf)_3$	150	O/N	55
11	5.0 equiv *p*-TsOH·H_2O	5 mol% $Cu(OTf)_3$	150	O/N	72
12	5.0 equiv *p*-TsOH·H_2O	5 mol% $Bi(OTf)_3$	150	O/N	91
13	5.0 equiv *p*-TsOH·H_2O	1 mol% $Bi(OTf)_3$	150	O/N	63
14	5.0 equiv *p*-TsOH·H_2O	Not added	150	O/N	65

[a]Reaction condition: **5a** (1.0eq, 0.035M), DCE (6.4mL); [b]isolated yield; [e]Reaction condition: **5a** (1.0 equiv, 0.3 M)

We then applied the optimal conditions to various substrate as shown in Table 2. When substrate **5a**, the reaction could provide the corresponding product in 91% yield. Substrate **5b** containing *ortho*-fluorine atom also give the desired product **6b** in 91% yield. Surprisingly,

when the substrate **5c** containing *para*-methyl group, the product **6c** was obtained in only 50% yield while compound **5d** also gave the desired product in low yield (14%) possibly due to the decomposition of styrene intermediate under acidic and high temperature conditions. In the case of compound **5e**, the reaction could not provide the desired product possibly due to the generation of *para*-quinonemethide intermediate leading to the decomposition reaction.

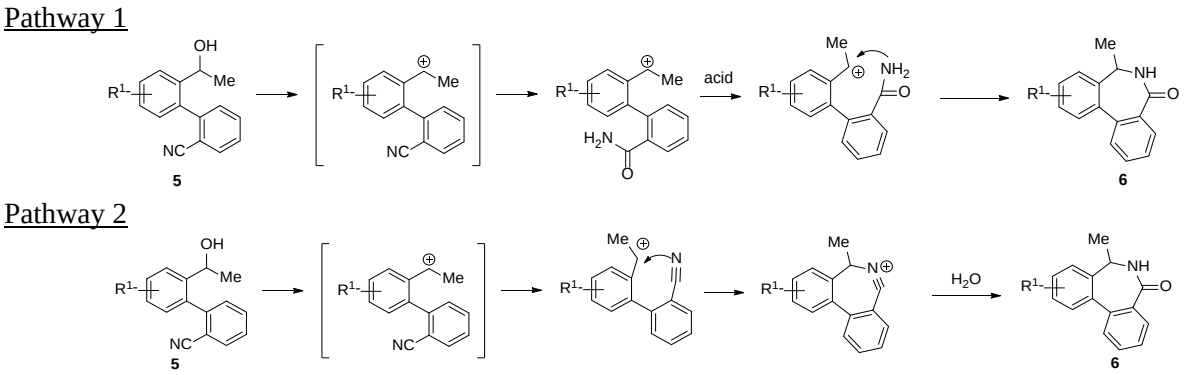

Figure 2. The proposed mechanism for the formation of benzazepines.

Table 2. The synthesis of benzazepine derivatives.

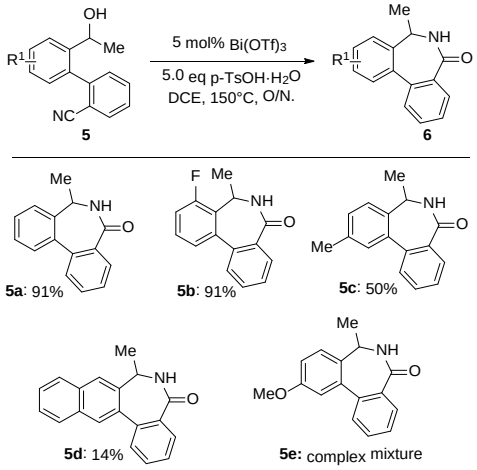

4. Conclusion

In conclusion, we demonstrated the novel method for the synthesis of benzazepine analogs using Ritter-Type reaction. This method could be useful for the synthesis of this core structure to create several libraries of compounds. We can prepare the desired product in 4 steps by using the above mention method. Therefore, our studied would be useful for synthesis methods for benzazepine analogs for drug discovery and development.

2'-(1-hydroxyethyl)-[1,1'-biphenyl]-2-carbonitrile (5a). Yield 680.0 mg (94%, major : minor 1: 0.71, white solid); mp 77.8-78.0 °C; IR (neat) vmax: 3413, 3062, 3029, 2973, 2928, 2226, 1595, 1473 cm^{-1} ; ^{1}H NMR (600 MHz, $CDCl_3$) δ 7.76 (t, 2.13H, J = 6.8 Hz, minor), 7.72-7.42, (m, 2.13H, minor), 7.57-7.42 (m, 4.71H, major + minor), 7.40-7.34, (m, 3H, major), 7.20 (d, 0.71H, J = 7.5 Hz, minor), 7.15 (d, 1H, J = 7.6 Hz, major), 4.82-4.68 (m, 1.71H, major + minor), 2.25 (br s, 1H, major), 1.68 (br s, 0.71, minor), 1.42 (d, 2.13H, J = 6.4, minor), 1.32 (d, 3H, J = 6.4, major), $^{13}C\{1H\}$ NMR (150 MHz, CDCl3) δ 145.0 (major), 144.8 (minor), 144.0 (major), 142.9 (minor), 136.4 (minor), 135.8 (major), 132.9 (minor), 132.8 (major), 132.6 (minor), 132.3 (minor), 130.7 (major), 130.5 (minor), 129.7, 129.6, 129.54, 129.49, 127.9 (minor), 127.8 (major), 127.52 (major), 127.49 (minor), 126.2 (major), 125.6 (minor), 118.7 (major), 117.9 (minor), 113.3 (minor), 112.6 (major), 66.8 (minor), 66.6 (major), 24.7 (major), 24.5 (minor) ; HRMS (ESI-Orbitrap) m/z: calcd for $C_{15}H_{13}ON_{23}Na$ $[M + Na]^+$ 246.0889; found 246.0888.

7-methyl-6,7-dihydro-5H-dibenzo[c,e]azepin-5-one (6a). Yield 73 mg (91 %, white solid); mp 100.4-101; IR (neat) vmax: 3284, 3175, 3057, 2979, 2890, 1648, 1600 cm^{-1} ; ^{1}H NMR (600 MHz, CDCl3) δ 8.00 (dd, *1*H, J = 7.8, 1.0 Hz), 7.62-7.54 (m,3H), 7.53-7.48 (m, 1H), 7.46-7.41 (m,2H), 7.40-7.37 (m,1H), 6.37 (br s, 1H), 4.40 (q, 1H, J = 6.8 Hz), 1.70 (d, 3H, J = 6.9 Hz); $^{13}C\{1H\}$ NMR (150 MHz, CDCl3) δ 169.7, 141.9, 138.8, 137.8, 133.8, 131.3, 129.9, 129.7, 129.2, 128.2, 128.1, 128.0, 122.0, 47.6, 16.5; HRMS (ESI-Orbitrap) m/z: calcd for $C_{15}H_{12}ON$ $[M + H]^+$ 222.0913; found 222.0912.

Acknowledgements

This research work was supported by Thailand Science Research and Innovation (TSRI), Chulabhorn Research Institute (Grant Numbers 36824/4274394 and 36827/4274407), Chulabhorn Graduate Institute, Chulabhorn Royal Academy

(FRB660044/0240 Project Codes 180874 and 180850). S.B. was grateful for a scholarship from Chulabhorn Graduate Institute, Chulabhorn Royal Academy (grant code: CGS(2021)/14).

References

1. Ek, F.; Wistrand, L.-G.; Frejd, T. Aromatic Allylation via Diazotization: Variation of the Allylic Moiety and a Short Route to a Benzazepine Derivative. The Journal of Organic Chemistry. **2003**. *68(5)*, 1911-1918.
2. Singer, R. A.; McKinley, J. D.; Barbe, G.; Farlow, R. A. Preparation of 1,5-Methano-2,3,4,5- tetrahydro-1H-3-benzazepine via Pd-Catalyzed Cyclization. Organic letters. **2004**. *6(14)*, 2357-2360.
3. So, M.; Kotake, T.; Matsuura, K.; Inui, M.; Kamimura, A. Concise Synthesis of 2-Benzazepine Derivatives and Their Biological Activity. The Journal of Organic Chemistry. **2012**. *77*, 4017-4028.
4. Katritzky, A. R.; Maimait, R.; Xu, Y.-J.; Akhmedova, R. G. A New Synthesis of 2-Benzazepines. Synthesis 2002. **2002**. *5*, 601-604.
5. Li, D.; Park, Y.; Yoon, W.; Yun, H.; Yun, J. Asymmetric Synthesis of 1-Benzazepine Derivatives via Copper-Catalyzed Intramolecular Reductive Cyclization. Organic letters. **2019**. *21(23)*, 9699-9703.
6. Donets, P. A.; Van der Eycken, E. V. Efficient Synthesis of the 3-Benzazepine Framework via Intramolecular Heck Reductive Cyclization. Organic letters. **2007**. *9(16)*, 3017-3020.
7. Kamimura, A.; Taguchi, Y.; Omata, Y.; Hagihara, M. Convenient Synthesis of 2-Benzazepines via Radical Cyclization. The Journal of Organic Chemistry. **2003**. *68(12)*, *4996-4998*.
8. Zhang, Y., Liu, Y., Hu, L., Zhang, X., Yin, Q. Asymmetric Reductive Amination/Ring-Closing Cascade: Direct Synthesis of Enantioenriched Biaryl-Bridged NH Lactams. Organic letters. **2020**. *22*. 6479-6483.
9. Tummatorn, J., Thongsornkleeb, C., Ruchirawat, S., Thongaram, P., Kaewmee, B. Convenient and Direct Azidation of sec-Benzyl Alcohols by Trimethylsilyl Azide with Bismuth(III) Triflate Catalyst. Synthesis. **2015**. *47(03)*. 323-329.

Phospha-1,4-addition promoted highly regioselective cyclization of *N*-propargyl azlactone: Unprecedented synthesis of benzopyrroloazepine

Papitchaya Patangwasa[1], Takumi minami[1,2], Naiyana Saesian[1], Rattana Worayuthakarn[2], Somsak Ruchirawat[1,3,4], and Nopporn Thasana[1,3,4]*

[1]*Program in Chemical Sciences, Chulabhorn Graduate Institute, Bangkok 10210, Thailand*
[2]*The Graduate School of Pharmaceutical Sciences, Chiba University, Chiba, Japan*
[3]*Laboratory of Medicinal Chemistry, Chulabhorn Research Institute, Bangkok 10210, Thailand*
[4]*Center of Excellence on Environmental Health and Toxicology (EHT), OPS, Ministry of Education, Science, Research and Innovation, Bangkok, 10400, Thailand*

**E-mail: nopporn@cri.or.th*

Abstract:

Phosphorylated heterocycles have significant value in both chemical and biological properties. Despite their importance, there are relatively few reports on these compounds. Therefore, the development of efficient methods for synthesizing heterocyclic compounds bearing a phosphonate group on the ring is of great interest. In this study, we successfully employed a highly regioselective approach to synthesize benzopyrroloazepine characterized by 6/7/5 ring systems containing a phosphorus atom, resulting in moderate yield. Our approach involves *N*-propargyl azlactone and diphenylphosphine oxide (DPPO) as precursors in a Pd-catalyzed cascade cyclization. The reaction encompasses phospha-1,4-addition, 7-*exo-dig* cyclization, ring-opening of the oxazolone, and the construction of a 5-membered pyrrole ring, respectively. This sequence leads to the formation of both C-P and two C-C bonds of benzopyrroloazepine. Additionally, a minor product, benzooxazaninylbenzamide, was also obtained through 9-*exo-dig* cyclization.

1. Introduction

Medium-sized rings composed of benzo-fused *N*-heterocycles with seven- and five-membered have been obtained in natural products with biological properties and play a vital role in drug discovery. For example, asperazepanone B, isolated from the coral-derived *Aspergillus candidus* fungus, displayed promising potential an anti-inflammatory drug.[1] Marinoazepinone B, isolated from the strain *Mooreia alkaloidigena*, showed antibacterial activity (Figure 1).[2]

Organophosphorus has attracted intense attention of chemists due to their wide applications in the fields of material science, medicinal chemistry, and organic synthesis. The phosphorus-substituted heterocycles are important scaffolds for bioactive compounds and valuable applications (Figure 1).[3,4] Thus, the topic of phosphorylated heterocycles has attracted interest. The majority of research on synthetic phosphorylated heterocycles investigates with five- and six-membered rings. However, the synthesis of medium-sized rings with phosphorylated heterocycles presents considerable challenges, and very few strategies have so far been reported.

Due to the attractive qualities of benzo-fused *N*-heterocycles with seven- and five-membered and organophosphorus derivatives, these are of great interest. In this study, the synthesis of benzopyrroloazepine containing a phosphorus atom was explored.

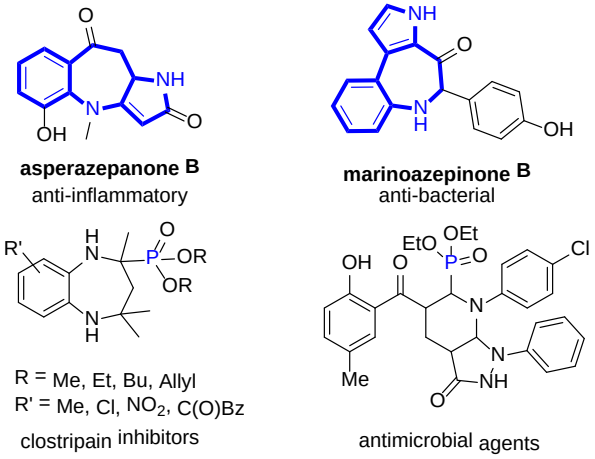

Figure 1. Examples of benzo-fused *N*-heterocycles with seven- and five-membered rings and bioactives phosphorylated heterocycles.

2. Materials and Methods

2.1 Materials

All chemicals utilized in this work were purchased from commercial supplies. The reactions were monitored by Merck silica gel (70-230 mesh) thin layer chromatography (TLC) and visualized using UV light. Silica gel column chromatography was performed on SiliCycle silica gel (230-400 mesh). ^{1}H NMR spectra were carried out on a Bruker AVANCE 300, 400 and 600 MHz spectrometers. High-resolution mass spectra

(HRMS) were observed using a Bruker Daltonics MicroTOF instrument ESI mode.

2.2 Synthesis of *N*-propargyl azlactone starting materials 6

On the basis of our group hypothesis, benzopyrroloazepine **7a** could be efficiently synthesized from *N*-propargyl azlactone **6a** diphenylphosphine oxide (DPPO) *via* phospha-1,4-addition and intramolecular cyclization (Table 1). A set of **6** were prepared in simple 4 steps, including the *N*-sulfonylation, *N*-alkylation, oxidation and Erlenmeyer–Plöchl azlactone synthesis, respectively, as show in Scheme 1.

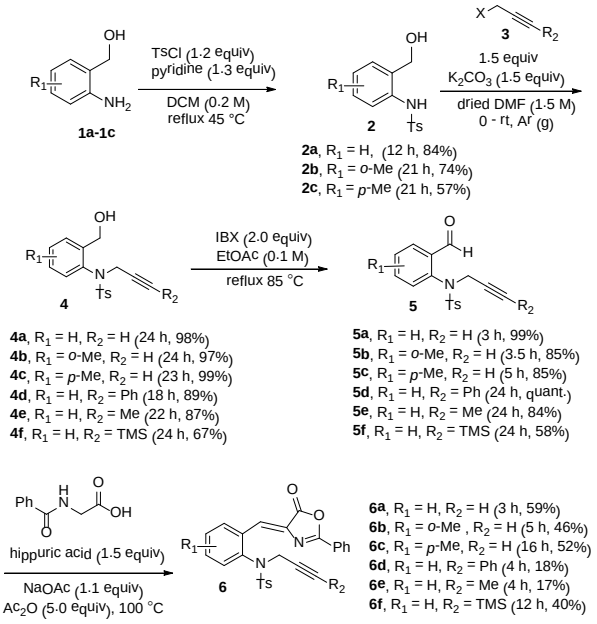

Scheme 1. Preparation of *N*-propargyl azlactone derivatives 6a-6f

2.2.1 *N*-Sulfonylation of aniline 1

A suspension 2-Aminobenzyl alcohol derivatives **1** (1.0, equiv) in DCM (0.2 M) was added with pyridine (1.3 equiv), *p*-toluenesulfonyl chloride (TsCl) (1.2 equiv) and refluxed at 45 °C for 12-21 h. The resulting mixture was allowed to cool to room temperature and washed with diluted hydrochloric acid (50 mL, 1 M), brine (3 x 50 mL) and dried over anhydrous Na_2SO_4. After remove of the solvent, the residue was purified by dry-loaded column chromatography on silica gel (*n*-Hexane/EtOAc) to obtain compounds **2** as a white solid in moderate to good yields.

2.2.2 *N*-Alkylation of 2

A solution of propargyl halides **3** (1.5 equiv) was added dropwise to *N*-Ts-aminobenzyl alcohol derivatives **2** (1.0 equiv) and K_2CO_3 in dried DMF (1.5 M) at 0 °C. The suspension was stirred at room temperature for 18-24 h. The resulting mixture was quenched and extracted with EtOAc and water (3 x 100 mL). The combined organic layer was dried over anhydrous Na_2SO_4 and then concentrated under reduced pressure. The residue was purified through flash column chromatography on silica gel (*n*-Hexane/EtOAc) providing *N*-alkylation compounds **4** as a yellow viscous (67 – 99% yield).

2.2.3 Oxidation of 4

The primary alcohol compound **4** (1.0 equiv) was performed an oxidation reaction using 2-iodoxybenzoic acid (IBX) (2.0 equiv) dissolved in EtOAc (0.1 M). The solution was refluxed at 85 °C for 3-24 h. After the reaction completed, the resulting mixture was filtered through a short-pad silica gel using ethyl acetate as an eluent, and then solution was extracted with saturated aqueous $NaHCO_3$ to remove the residue of IBX, followed by washing the organic layer with brine and over anhydrous Na_2SO_4. The crude product was concentrated under reduced pressure. The residue was purified by flash column chromatography on silica gel (*n*-Hexane/EtOAc) to obtain aldehyde **5** as yellow solid in moderate to good yields.

2.2.4 Erlenmeyer–Plöchl azlactone synthesis of 5

The condensation reaction of aldehyde derivative **5** (1.0 equiv), hippuric acid (1.5 equiv), NaOAc (1.1 equiv) and Ac_2O (5.0 equiv) were stirred in round-bottomed flask at 100 °C for 3-12h. After the reaction completed, the reaction mixture was cooled to room temperature. Then the reaction was quenched and washed with cold EtOH, filter out of yellow solid to afford *N*-propargyl azlactones **6** in poor to moderate yields.

***(Z)-4-Methyl-N-(2-((5-oxo-2-phenyloxazol-4(5H)-ylidene)methyl)phenyl)-N-(prop-2-yn-1-yl)benzenesulfonamide* (6a)**

^{1}H NMR (300 MHz, $CDCl_3$) δ 8.94 (dd, *J* = 8.0, 1.5 Hz, 1H), 8.19–8.15 (m, 2H), 7.66–7.60 (m, 3H), 7.56–7.50 (m, 3H), 7.47 (s, 1H), 7.40 (td, *J* = 7.9, 1.6 Hz, 1H), 7.28 (s, 1H), 7.25 (s, 1H) 7.17 (dd, *J* = 8.0, 1.1 Hz, 1H), 4.46 (d, *J* = 24.9 Hz, 2H), 2.40 (s, 3H), 2.22 (t, *J* = 2.4 Hz, 1H). HRMS (ESI) *m/z*: $(M+H)^+$ for $C_{26}H_{21}N_2O_4S$, 457.1222; found 457.1222.

***(Z)-4-Methyl-N-(2-methyl-6-((5-oxo-2-phenyloxazol-4(5H)-ylidene)methyl)phenyl)-N-(prop-2-yn-1-yl)benzenesulfonamide* (6b)**

^{1}H NMR (300 MHz, $CDCl_3$) δ 8.68 (t, *J* = 4.4 Hz, 1H), 8.15 (dt, *J* = 6.2, 1.2 Hz, 2H), 7.68 (dd, *J* = 6.6, 1.7 Hz, 2H), 7.61 (dt, *J* = 6.4, 1.4 Hz, 1H), 7.53 (td, *J* = 6.2, 1.3 Hz, 2H), 7.43 (d, *J* = 0.8 Hz, 1H), 7.42 (s, 1H), 7.24 (s, 2H) 6.95 (s, 1H), 4.77 (dd, *J* = 17.9, 2.5 Hz, 1H), 4.28 (dd, *J* = 17.9, 2.5 Hz, 1H), 2.45 (s, 3H), 2.40 (s, 3H), 2.31 (t, *J* =

2.5 Hz, 1H). HRMS (ESI) *m/z*: $(M+Na)^+$ for $C_{27}H_{22}N_2NaO_4S$, 493.1188; found 493.1198.

***(Z)-4-Methyl-N-(4-methyl-2-((5-oxo-2-phenyloxazol-4(5H)-ylidene)methyl)phenyl)-N-(prop-2-yn-1-yl)benzenesulfonamide* (6c)**

^{1}H NMR (300 MHz, $CDCl_3$) δ 8.72 (d, J = 1.6 Hz, 1H), 8.16 (dt, J = 6.2, 1.2 Hz, 2H), 7.66 – 7.52 (m, 5H), 7.43 (s, 1H), 7.30 (s,1H), 7.27 (s, 1H), 7.23 (dd, J = 8.1, 1.6 Hz, 1H), 7.05 (d, J = 8.1 Hz, 1H), 4.49 (s, 1H), 4.41 (s, 1H), 2.48 (s, 3H), 2.39 (s, 3H), 2.21 (t, J = 2.3 Hz, 1H). HRMS (ESI) *m/z*: $(M+Na)^+$ for $C_{27}H_{22}N_2NaO_4S$, 493.1189; found 493.1198.

***(Z)-4-Methyl-N-(2-((5-oxo-2-phenyloxazol-4(5H)-ylidene)methyl)phenyl)-N-(3-phenylprop-2-yn-1-yl)benzenesulfonamide* (6d)**

^{1}H NMR (300 MHz, $CDCl_3$) δ 8.98 (dd, J = 8.0 Hz, 1H), 8.18 (d, J = 7.5 Hz, 2H), 7.72-7.52 (m, 8H), 7.42 (t, J = 8.0 Hz, 1H), 7.29-7.21 (m, 7H), 4.78 (t, J = 9.6 Hz, 1H), 4.63 (t, J = 10.5 Hz, 1H), 2.41 (s, 3H). HRMS (ESI) *m/z*: $(M+H)^+$ for $C_{32}H_{25}N_2O_4S$, 532.1457; found 533.1538.

***(Z)-N-(But-2-yn-1-yl)-4-methyl-N-(2-((5-oxo-2-phenyloxazol-4(5H)-ylidene)methyl) phenyl)benzenesulfonamide* (6e)**

^{1}H NMR (300 MHz, $CDCl_3$) δ 8.96 (dd, J = 8.0, 1.7 Hz, 1H), 8.21-8.18 (m, 2H), 7.66-7.51 (m, 7H), 7.42 (td, J = 7.8, 1.7 Hz, 1H), 7.30-7.27 (m, 1H), 7.18 (dd, J = 7.9, 1.2 Hz, 1H), 4.43 (d, J = 1.7 Hz, 2H) 2.42 (s, 3H), 1.67 (t, J = 2.5 Hz 3H). HRMS (ESI) *m/z*: $(M+H)^+$ for $C_{27}H_{22}N_2O_4S$, 470.1300; found 470.1372.

***(Z)-4-Methyl-N-(2-((5-oxo-2-phenyloxazol-4(5H)-ylidene)methyl)phenyl)-N-(3-(trimethylsilyl)prop-2-yn-1-yl) benzenesulfonamide* (6f)**

^{1}H NMR (300 MHz, $CDCl_3$) δ 8.93 (dd, J = 7.9, 1.5 Hz, 1H), 8.7 (dt, J = 6.2, 1.2 Hz, 2H), 7.65-7.51 (m, 8H), 7.36 (td, J = 7.9, 1.6 Hz, 1H), 7.27 (s, 1H), 7.11 (dd, J = 8.0, 1.2 Hz, 1H), 4.56 (d, J = 16.4 Hz, 1H), 4.37 (d, J = 16.4 Hz, 1H), 2.39 (s, 3H), 0.00 (s, 9H). HRMS (ESI) *m/z*: $(M+H)^+$ for $C_{29}H_{29}N_2O_4SSi$, 529.1610; found 529.1617.

2.2.5 Synthesis of phosphorylated benzopyrroloazepine 7

In glove box, a sealed tube was charged with *N*-propargyl azlactones **6** (1.0 equiv), $Pd(OAc)_2$ and BHT, DPPO and 1,4-dioxane (0.1 M). The reaction mixture was stirred at 80 °C for 24 h. The solution was quenched by filtration through Celite and used DCM as an elution. Purification by PTLC (DCM/EtOAc). The product **7** was obtained as a pale-yellow solid in moderate yields.

***(R)-Diphenyl(2-phenyl-5-tosyl-1,4,5,10-tetrahydrobenzo[b]pyrrolo[2,3-e]azepin-10-yl)phosphine oxide* (7a)**

^{1}H NMR (300 MHz, DMSO-d6) δ 10.18 (s, 1H), 7.88 (t, J = 8.3 Hz, 2H), 7.68-7.62 (m, 2H), 7.60-7.58 (m, 3H), 7.52 (d, J = 8.0 Hz, 2H), 7.48-7.40 (m, 2H), 7.34-7.24 (m, 5H), 7.19 (d, J = 7.4 Hz, 2H), 7.11 (dd, J = 11.5, 7.4 Hz, 3H), 6.96 (t, J = 7.5 Hz, 1H), 6.72 (d, J = 8.1, 1H), 6.18 (d, J = 2.4 Hz, 1H), 5.17 (d, J = 13.0 Hz, 1H), 4.99 (d, J = 16.6 Hz, 1H), 4.43 (d, J = 15.5 Hz, 1H), 2.26 (s, 3H). HRMS (ESI) *m/z*: $(M+H)^+$ for $C_{37}H_{32}N_2O_3PS$, 615.1871; found 615.1874.

***(R)-(6-Methyl-2-phenyl-5-tosyl-1,4,5,10-tetrahydrobenzo[b]pyrrolo[2,3-e]azepin-10-yl)diphenylphosphine oxide* (7b)**

^{1}H NMR (300 MHz, $CDCl_3$) δ 10.10 (s, 1H), 7.88-7.69 (m, 6H), 7.47-7.23 (m, 13H), 7.14-7.09 (m, 1H), 6.97-6.87 (m, 2H), 6.24 (d, J = 12.3 Hz, 1H), 6.08 (d, J = 1.5 Hz, 1H), 5.42 (d, J = 15.9 Hz, 1H), 4.21 (d, J = 16.5 Hz, 1H), 2.43 (s, 3H), 1.97 (s, 3H). HRMS (ESI) *m/z*: $(M+Na)^+$ for $C_{38}H_{33}N_2NaO_3PS$, 651.1840; found 651.1847.

***(R)-(8-Methyl-2-phenyl-5-tosyl-1,4,5,10-tetrahydrobenzo[b]pyrrolo[2,3-e]azepin-10-yl)diphenylphosphine oxide* (7c)**

^{1}H NMR (300 MHz, $CDCl_3$) δ 10.09 (s, 1H), 8.02-7.86 (m, 6H), 7.46-7.25 (m, 13H), 7.13 (t, J = 7.3 Hz, 1H), 6.89-6.81 (m, 2H), 6.15 (d, J = 2.1 Hz, 1H), 5.81 (d, J = 8.4 Hz, 1H), 5.28 (s, 1H), 4.33 (d, J = 13.2 Hz, 1H), 2.43 (s, 3H), 2.01 (s, 3H). HRMS (ESI) *m/z*: $(M+H)^+$ for $C_{38}H_{34}N_2O_3PS$, 629.2021; found 629.2028.

***N-((7R)-7-(Diphenylphosphoryl)-3-methylene-5-oxo-1-tosyl-1,2,3,5,6,7-hexahydrobenzo[e][1,4]oxazonin-6-yl)benzamide* (8a)**

^{1}H NMR (400 MHz, $CDCl_3$) δ 9.00 (s, 1H), 8.64 (d, J = 8.0 Hz, 1H), 8.12 (dd, J = 10.4, 8.0 Hz, 2H), 7.99 (t, J = 8.0 Hz, 4H), 7.61 (t, J = 7.2 Hz, 3H), 7.54-7.40 (m, 4H), 7.38-7.20 (m, 7H), 7.01 (t, J = 7.6 Hz, 1H), 6.15 (d, J = 8.0 Hz, 1H), 5.50 (dd, J = 10.4, 4.0 Hz, 1H), 4.94 (s, 1H), 4.85 (s, 1H), 4.80 (s, 1H), 4.68 (d, J = 15.6 Hz, 1H), 4.07 (d, J = 16.4 Hz, 1H), 2.43 (s, 3H). HRMS (ESI) *m/z*: $(M+H)^+$ for $C_{38}H_{34}N_2O_6PS$, 677.1863; found 677.1875.

***(4S,5R)-3-((Z)-Benzylidene)-5-(diphenylphosphoryl)-2'-phenyl-1-tosyl-1,2,3,5-tetrahydro-5'H-spiro[benzo[b]azepine-4,4'-oxazol]-5'-one* (9d)**

^{1}H NMR (600 MHz, $CDCl_3$) δ 8.25 (d, J = 7.6 Hz, 1H), 7.93 (d, J = 8.3 Hz, 2H), 7.57-7.19 (m, 20H), 6.84 (t, J = 7.3 Hz, 2H), 6.68 (dd, J = 14.5, 7.2 Hz, 1H) 6.52 (s, 1H), 6.40 (d, J = 7.7 Hz, 2H), 5.33 (d, J = 11.3 Hz, 1H), 4.70 (d, J = 10.1 Hz, 1H),

3.94 (d, *J* = 11.6 Hz, 1H), 2.45 (s, 3H). (ESI) *m/z*: $(M+H)^+$ for $C_{44}H_{36}N_2O_5PS$, 735.2066; found 735.2083.

3. Results and Discussion

3.1 Optimization

Based on our group hypothesis, benzopyrroloazepine **7a** could be synthesized efficiently from the *N*-propargyl azlactone **6a** using diphenylphosphine oxide (DPPO) through phospha-1,4-addition and palladium-catalyzed cascade intramolecular cyclization.[5,6] The optimal reaction conditions were explored as shown in Table 1.

Initially, benzopyrroloazepine **7a** was obtained in 33% yield using $Pd(OAc)_2$ at 2.5 mol%, BHT (0.5 equiv), DPPO (1.5 equiv) in 1,4-dioxane at 80 °C for the first 24 h, followed by an additional 2.5 mol% of $Pd(OAc)_2$ for a total reaction time of 48 h (entry 1). The reaction was used CuI as co-catalyst resulted in decrease yield (entry 2). Increasing temperature conditions (100 and 120 °C) with 5 mol% of $Pd(OAc)_2$ led to a lower yield (entries 3-5). Interestingly, entry 4 resulted in the minor product, benzooxazoninyl benzamide **8** with a 3% yield. Further increasing the concentration to 10 mol% of $Pd(OAc)_2$ showed a lower yield and product decomposition (entries 6-7). Notably, entries 8 and 9 achieved a 41 and 42% yields of compound **7a**, respectively. Investigating the reaction with 5 mol% of $Pd(OAc)_2$ for 24 h (entry 10) furnished **7a** in 37% yield along with the minor product **8** at 3% yield. Conducting the reaction without a Pd-catalyst resulted in mere 16% yield of **7a** (entry 11).

We chose the conditions in entry 8, which yielded **7a** at 41% yield, for further investigation into the solvent and the amount of DPPO effects. Screening with alternative solvents, including DCM, DCE, CH_3CN, DMF, THF and Toluene (entries 12-17), did not lead to an improvement in the yield of product **7a**. The impact of varying amount of DPPO was explored by increasing to 3.0 and 5.0 equiv instead of 1.5 equiv (entries 18-19). The results indicated that 5.0 equiv of DPPO giving a significant improvement of the yield **7a** up to 50% yield.

Table 1. Optimization of reaction conditions.[a]

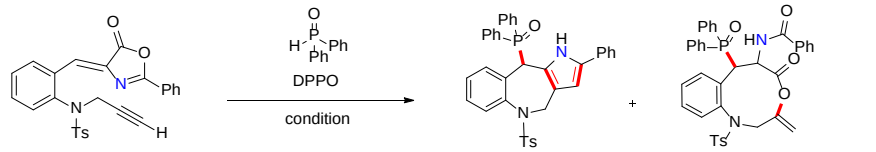

N-propargyl azlactone, **6a**

Benzopyrroloazepine, 7a *via 7-exo-dig cyclization* (C-P/2 C-C bond formation)

Benzooxazaninylbenzamide, 8a *via 9-exo-dig cyclization* (C-P/C-O bond formation)

Entries	Catalyst (mol%)	BHT (equiv)	DPPO (equiv)	Solvent (M)	Temp (°C)	Time (h)	Yield (%)		
							7a	**8a**	RSM[b]
1	$Pd(OAc)_2$ (2.5+2.5)	0.5	1.5	1,4-dioxane	80	48	33	-	8
2	$Pd(OAc)_2$ (2.5) CuI (2.5)	0.5	1.5	1,4-dioxane	80	48	29	-	-
3	$Pd(OAc)_2$ (5)	0.5	1.5	1,4-dioxane	80	48	6	-	-
4	$Pd(OAc)_2$ (5)	0.5	1.5	1,4-dioxane	100	48	9	3	trace
5	$Pd(OAc)_2$ (5)	0.5	1.5	1,4-dioxane	120	48	19	-	-
6	$Pd(OAc)_2$ (10)	0.5	1.5	1,4-dioxane	100	48	3	-	trace
7[c]	$Pd(OAc)_2$ (10)	0.5	1.5	1,4-dioxane	120	48	-	-	-
8	$Pd(OAc)_2$ (5)	0.5	1.5	1,4-dioxane	80	24	41	3	24
9	$Pd(OAc)_2$ (10)	0.5	1.5	1,4-dioxane	80	24	42	2	5
10	$Pd(OAc)_2$ (5)	0.5	1.5	1,4-dioxane	100	24	37	3	trace
11	-	0.5	1.5	1,4-dioxane	100	24	16	8	trace
12	$Pd(OAc)_2$ (5)	0.5	1.5	DCM	80	24	8	-	46
13	$Pd(OAc)_2$ (5)	0.5	1.5	DCE	80	24	13	7	19
14	$Pd(OAc)_2$ (5)	0.5	1.5	CH_3CN	80	24	22	4	18
15	$Pd(OAc)_2$ (5)	0.5	1.5	DMF	80	24	29	2	3
16	$Pd(OAc)_2$ (5)	0.5	1.5	THF	80	24	33	3	3
17	$Pd(OAc)_2$ (5)	0.5	1.5	Toluene	80	24	37	-	8
18	$Pd(OAc)_2$ (5)	0.5	3.0	1,4-dioxane	80	24	14	4	N/D[d]
19	**$Pd(OAc)_2$ (5)**	**0.5**	**5.0**	**1,4-dioxane**	**80**	**24**	**50**	**3**	**N/D[d]**

[a]Reaction were performed using with azlactones **6a** (0.2 mmol, 1 equiv), butylated hydroxytoluene (BHT) (0.5 equiv), diphenylphosphine oxide (1.5-5.0 equiv), $Pd(OAc)_2$ (2.5+2.5-10 mol%), solvent (0.1 M) at 80-120 °C for 24 or 48 h.
[b]RSM = Recovered starting material.
[c]Decomposition of staring material.
[d]N/D = not determined.

Consequently, the optimal conditions were identified when the reaction was conducted with *N*-propargyl azlactone (0.2 mmol, 1 equiv), BHT (0.5 equiv), DPPO (5.0 equiv), $Pd(OAc)_2$ (5 mol%) in 1,4-dioxane (0.1 M) at 80 °C for 24 h (entry 19) and further used in the scope of substrates.

3.2 Scope of Substrates

With the optimal conditions in hand, the substrate scopes of phospha-1,4-addition and Pd-catalyzed intramolecular cyclization involving substituents on R_1 and R_2 of *N*-propargyl azlactones **6** were then explored as shown in Scheme 2. The reaction of **6b** containing methyl group at *ortho*-position on R_1 with *N*-tosyl group gave **7b** in a modest yield of 29%. Conversely, the methyl group at *para*-position of product **7c** yielded poor result. Further exploration with a diverse range of the R_2 position, including phenyl, methyl and tetramethylsilane were investigated under the optimal condition. Unfortunately, no reactions were observed, and anticipated corresponding products **7d-7f** did not materialize. However, we could obtained a potential intermediate **9d** in 43% yield and recovered starting material **6d** in 40% yield. Notably that disubstituted alkynyl group of substrate **6d**, the construction of a 7-membered ring azaheterocycle *via* 7-*exo-dig* cyclization did not lead to the formation of a 5-membered ring pyrrole might be due to electronic effects. Investigation into the interaction between the phenyl group of azlactone and the phenyl group at the R_2 position revealed a π-π stacking interaction.[5] Furthermore, reactions involving R_2 positions with methyl and tetramethylsilane resulted in the acquisition of starting materials **6e** and **6f**.

3.3 Proposed Mechanism

The reaction mechanism was proposed as show in Scheme 3. Initially, the phospha-1,4-addition of *H*-phosphine oxide (DPPO) reacts with *N*-propargyl azlactone **6a**, giving rise to intermediate **I**.[6] Then, intramolecular cyclization of intermediate **I** into intermediate **II** *via* 7-*exo-dig* cyclization, subsequently, hydrogen atom transfer by BHT resulted in intermediate **III**, as depicted compound **9d**. Ring opening of azlactone **III** is facilitated using H_2O to give intermediate **IV**. $Pd(OAc)_2$ coordinates with carbonyl group of amide and alkene, followed by oxidative decarboxylation to yield intermediate **V**. Further progression involves C-C bond formation and reductive elimination ultimately yielding the desired product benzopyrroloazepine **7a**.

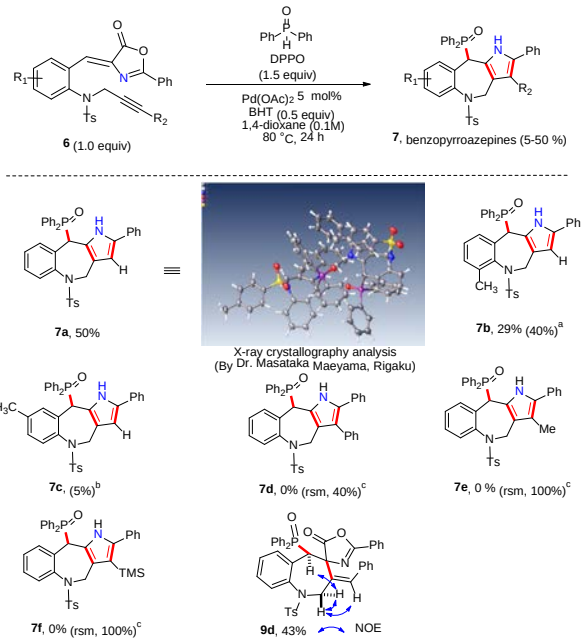

[a]Using 15.6 equiv DPPO instead of 5 equiv
[b]Using 3.0 equiv DPPO instead of 5 equiv
[c]Recovered starting material

Scheme 2. Scope of Substrates

4. Conclusion

A facile method for synthesizing benzo-pyrroloazepine characterized by 6/7/5 ring systems containing a phosphorus atom has been successfully developed, albeit in poor to moderate yields. This synthesis involves the phospha-1,4-addition and palladium-catalyzed cascade intramolecular cyclization of *N*-propargyl azlactones.

Acknowledgement

This work was supported by Chulabhorn Graduate Institute and Chulabhorn Graduate Scholarship (CGS(2022)/12), the Thailand Research and Innovation (TSRI), Grant Number FRB660044/0204 Project code 180874 for Chulabhorn Royal Academy and Grant Number 48296/4691996 for Chulabhorn Research Institute. The authors would like to thank Center of Excellence on Environment Health and Toxicology (EHT), OPS, Ministry of Higher Education, Science, Research and Innovation for their excellent technical support.

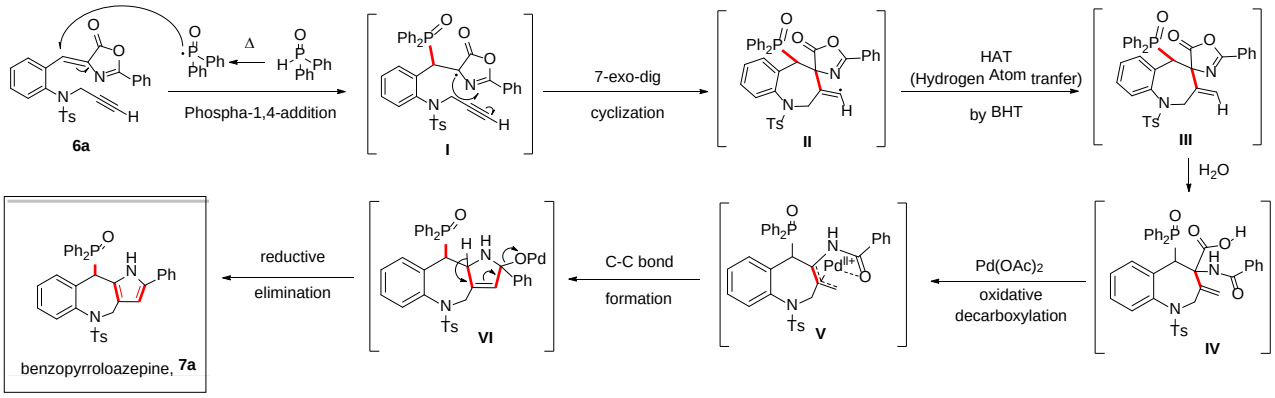

Scheme 3. Proposed Mechanism

References

1. Xu, L.; Guo, F. W.; Zhang, X. Q.; Zhou, T. Y.; Wang, C. J.; Wei, M. Y.; Gu, Y. C.; Wang, C. Y.; Shao, C. *Commun. Chem.* **2022**, *5*, 80.
2. Choi, E. J.; Nam, S. J.; Paul, L.; Beatty, D.; Kauffman, C. A.; Jensen, P. R.; Fenical, W. *Chem. Biol*. **2015**, *22*, 1270-1279.
3. Bhattacharya, A. K.; Rana, K. C.; Raut, D. S.; Mhaindarkar, V. P., Khan, M. I. *Org. Biomol. Chem.* **2011**, *9*, 5407-5413.
4. Chen, L., Liu, X. Y. and Zou, Y. X. *Adv. Synth. Catal.* **2020**, *362*, 1724−1818.
5. Worayuthakarn, R.; Deesiri, S.; Chainok, K.; Wannarit, N.; Ruchirawat, S.; Thasana, N. *J. Org. Chem.* **2021,** *86*, 9360-9383.
6. Worayuthakarn, R.; Boontan, K.; Chainok, K.; Ruchirawat, S.; Thasana, N. *J. Org. Chem.* **2023**, *88*, 16520-16538.

The synthesis of phenanthrene-9-ols *via* palladium-catalyzed annulation

Kamonlak Chatrangsan,[1] Phornphan Yongpanich,[1] Charnsak Thongsornkleeb,[1,2] Jumreang Tummatorn[1, 2]*, and Somsak Ruchirawat [1,2]

[1]*Program on Chemical Sciences, Chulabhorn Graduate Institute, Center of Excellence on Environmental Health and Toxicology (EHT), OPS, MHESI,* 54 *Kamphaeng Phet* 6, *Laksi, Bangkok, 10210, Thailand*
[2]*Laboratory of Medicinal Chemistry, Chulabhorn Research Institute, 54 Kamphaeng Phet* 6, *Laksi, Bangkok, 10210, Thailand*

**E-mail: Jumreang@cgi.ac.th*

Abstract:

Phenanthrene is a crucial component of many chemical compounds that exhibit intriguing biological properties such as antimalarial, anticancer, and antibacterial properties. As this core structure shows several biological activities which draws our attention to develop a novel method for the synthesis of phenanthrene-9-ols using palladium-catalyzed cascade annulation, *via* Suzuki cross-coupling reaction/Heck reaction, followed by Michael addition to produce the desired products in low to good yields. The chemoselectivity of sequential reaction is controlled by concentration, solvent and temperature of the reactions.

1. Introduction

Phenanthrenes is a polycyclic aromatic hydrocarbon. There structure demonstrated several biological activities.[1] Interesting biological feature have been reported for a number of compounds with phenanthrene and 9-phenanthrol core structures. Therefore, these core structures have been used as the substrates for the functionalization to create libraries of compounds which could be useful for drug discovery and development (Figure 1).[2]

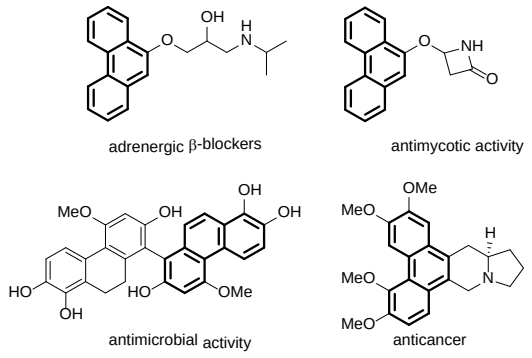

Figure 1. Examples of bioactive phenanthrene and 9-phenanthrol analogs.

In addition, researchers have developed several new methods for synthesizing phenanthrene and phenanthrol derivatives. In 2017, Nishihara group reported the synthesis of phenanthrenes *via* three-component coupling reaction under the present of alkynes, aryl bromides, *o*-bromobenzyl alcohol, palladium catalyst and phosphene ligand.[3] Another method is [4+2] benzannulation reaction was reported in 2011 by Nakamura using alkynes and 2-alkenylpheny Grignard reagent under the present of iron catalyst.[4] Moreover, radical cyclization under photoirradiation was reported by Shin group in 2022 using *N*-enoxybenzotriazole as a substrate to synthesize 9-phenanthrol derivatives.[5]

This work, we focused on the development of new methods for synthesizing 9-phenanthrol derivatives using palladium-catalyzed *via* Suzuki cross-coupling reaction/Heck reaction and Michael addition in one-pot protocol.

2. Materials and Methods

2.1 Materials

The characterization of the products was performed using ^{1}H-NMR, ^{13}C-NMR, ^{19}F-NMR spectra were recorded in $CDCl_3$ with Bruker 300 MHz, 400 MHz or 600 MHz NMR spectrometers. Infrared spectra were measured using an FT-IR spectrometer. High-resolution mass spectra (HRMS) were measured on an Agilent mass spectrometer.

2.2 Preparation of 2-bromochalcone derivatives starting material

A mixture of 2-bromoacetone (0.5 mL, 3.74 mmol, 1.0 equiv), NaOH (0.23 g, 5.61 mmol, 1.5 equiv), MeOH (1.0 mL) in round bottom flask and the solution was stirred at room- temperature for 5 min. Then, aldehyde (0.50 g, 4.12 mmol, 1.1 equiv) was added in the reaction and the reaction was stirred at room temperature for 4 h. After completion, the reaction was diluted by water (15 mL) and the mixture was extracted with EtOAc (3×20 mL). The combined organic layers were dried over anhydrous Na_2SO_4 and filtered. After solvent removal under reduced pressure, the crude product was obtained which was purified by

column chromatography (5%EtOAc/Hexane) to yield the desired product (Scheme 1).

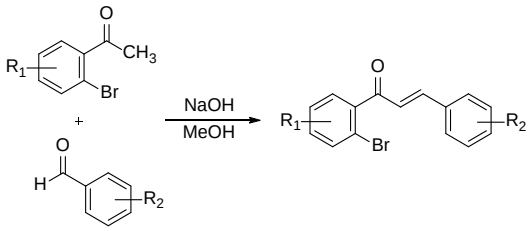

Scheme 1. Synthesis of 2-bromochalcone

2.3 Preparation of 9-phenanthrol derivatives

A round-bottomed flask containing a magnetic stir bar, 2-bromochalcone (186.8 mg, 0.59 mmol, 1.5 equiv), boronic acid (78.7 mg, 0.39 mmol, 1.0 equiv). $PdCl_2(PPh_3)_2$ (5.4 mg, 7.83 µmol, 2 mol%) and $NaHCO_3$ (65.8 mg, 0.78 mmol, 2,0 equiv) were dissolved in EtOH (39.0 mL, 0.01 M) and water (0.2 mL). The solution was stirred at 100 ˚C for 6-7 h. Then, the mixture was concentrated under reduced pressure. After that, the crude product was purified by column chromatography (1% EtOAc/Hexane) to yield the desired product (Scheme 2).

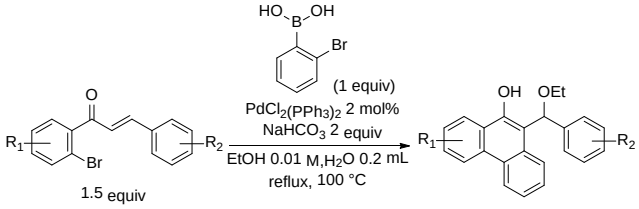

Scheme 2. Synthesis of 9-phenanthrol derivatives

2.4 The optimization conditions by varying concentration reactions for synthesizing 9-phenantrol

A round-bottomed flask containing a magnetic stir bar, 2-bromochalcone (1.5 equiv), boronic acid (1.0 equiv) and was added $PdCl_2(PPh_3)_2$ (2 mol%) and $NaHCO_3$ (2.0 equiv) were dissolved in EtOH (see table 1) and water (0.2 mL). The solution was stirred at 100 ˚C for 6-7 h. Then, the mixture was concentrated under reduced pressure. After that, the crude product was purified by column chromatography (1% EtOAc/Hexane) to yield the desired product (Scheme3).

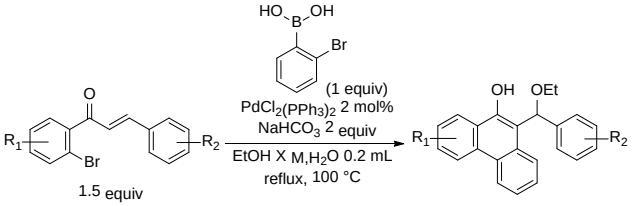

Scheme 3. The optimization experiments for the synthesis of 9-phenanthrol derivatives

2.5 The optimization conditions by varying bases for synthesizing 9-phenantrol

A round-bottomed flask containing a magnetic stir bar, 2-bromochalcone (1.5 equiv), boronic acid (1.0 equiv) and was added $PdCl_2(PPh_3)_2$ (2 mol%) and base (see Table 1) were dissolved in EtOH (0.01 M) and water (0.2 mL). The solution was stirred at 100 ˚C for 6-7 h. Then, the mixture was concentrated under reduced pressure. After that, the crude product was purified by column chromatography (1% EtOAc/Hexane) to yield the desired product (Scheme4).

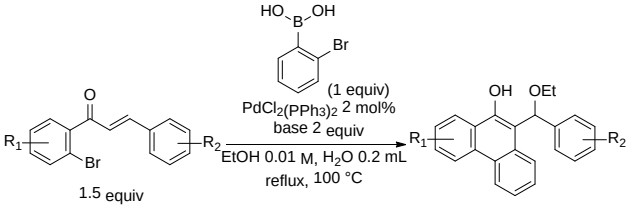

Scheme 4. The optimization experiments for the synthesis of 9-phenanthrol derivatives

3. Results & Discussion

The optimization studies of reaction conditions using 2-bromochalcone as a substrate to synthesize 9-phenanthrene derivatives were shown in Table 1. In entry 1, the reaction was conducted at the concentration of EtOH 0.005 M and the desired product was obtained in 69% yield. After we increased the concentration, we observed 9-phenanthrol in 71% yield (entry 2). However, we found that increasing concentration from 0.01 M to 0.03 and 0.1 M could obtain the desired product in lower yields, 48% and 47%, respectively, possibly due to homocoupling of 2-bromophenyl boronic acid. After that, we tried to vary bases including K_2CO_3, Na_2CO_3, Cs_2CO_3 (entry5-7). The result showed that when Na_2CO_3 was employed to provide 9-phenanthrol in highest yield. Therefore, we employed the conditions in entry 6 as the optimal conditions for synthesizing 9-phenanthrol derivatives.

Next, we investigated the scope of our method by varying 2-bromochalcones (Table 2). The electronic properties of R^1 and R^2 on 2-

bromochalcone **1a**-**1c** have no effect on the reactions giving the corresponding 9-phananthrol in good yields. However, when R^1 was varied in enties 4-5. The result showed that substrate containing electron withdrawing group (F) (entry 4) gave the desired product in good yield (70%) while electron donating group (OMe) at *para*-position (entry 5) provided the corresponding product in only 28% yield. We suspected that the delocalization of electron of *para*-OMe could reduce electrophilicity of ketone which resulted in the decreasing of the ability of Michael acceptor leading decomposition of the intermediate. The proposed synthetic method for the synthesis of 9-phenanthrol shown in **Scheme 5**.

Table 1. The optimization studies by varying mol% of catalyst and concentration of solvent to synthesize 9-phenanthrol derivatives

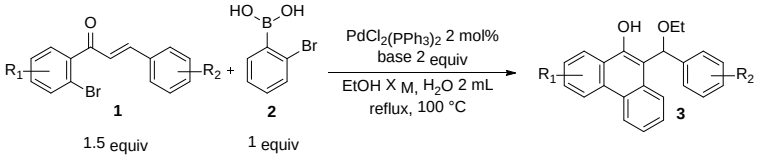

Entry	EtOH (M)	Base (2 equiv)	yield[a]
1	0.005	$NaHCO_3$	69
2	0.01	$NaHCO_3$	71
3	0.03	$NaHCO_3$	48
4	0.10	$NaHCO_3$	47
5	0.01	K_2CO_3	37
6	0.01	Na_2CO_3	74
7	0.01	Cs_2CO_3	30

[a] Isolated yields

Table 2. Scope of 2-bromochalcone in Reactions with boronic acid

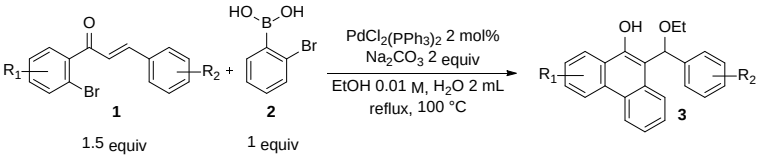

entry	2-bromochalcone (**1**)	9-phenanthrols (**3**)	yield[a]
1	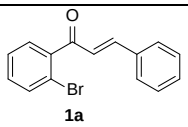 **1a**	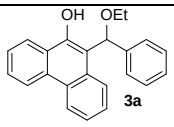 **3a**	68%
2	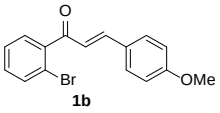 **1b**	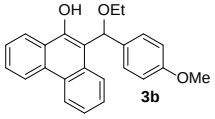 **3b**	73%
3	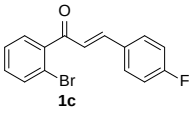 **1c**	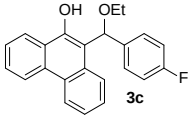 **3c**	73%
4	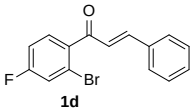 **1d**	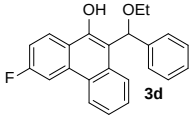 **3d**	70%
5	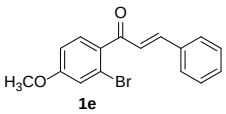 **1e**	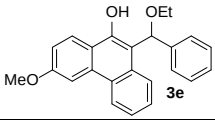 **3e**	28%

[a] Isolated yields

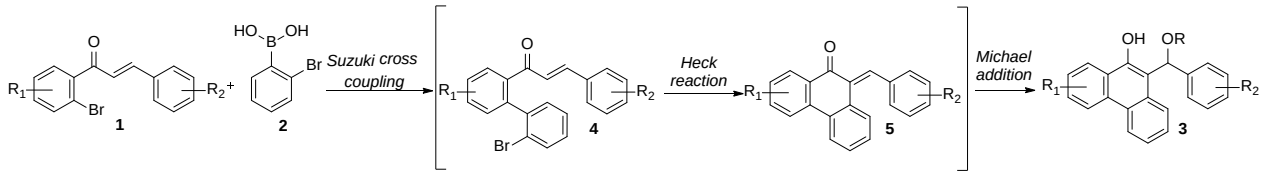

Scheme 5. The proposed synthetic method for the synthesis of 9-phenanthrol derivatives

4. Conclusion

In conclusion, we have developed new method for synthesizing 9-phenanthrol derivatives from 2-bromochalcone derivatives *via* Suzuki cross-coupling reaction/Heck reaction and Michael addition in one-pot protocol under the present of palladium catalyst to produce the desired products in low to good yields. We hope this method will be useful for future drug discovery and development.

Acknowledgements

This research work was supported by Thailand Science Research and Innovation (TSRI), Chulabhorn Research Institute (Grant Numbers 36824/4274394 and 36827/4274407), Chulabhorn Graduate Institute, Chulabhorn Royal Academy (FRB660044/0240 Project Codes 180874 and 180850). K.C. was grateful for a scholarship from Chulabhorn Graduate Institute, Chulabhorn Royal Academy (grant code: CGS(2022)/10).

References

1. Kovacs, A.; Vasas, A.; Hohmann, J. Natural phenanthrenes and their biological activity. *Phytochem.* **2008,** *69*, 1084-110.
2. Ling, H. B.; Chen, Z. S.; Yang, F.; Xu, B.; Gao, J. M.; Ji, K. Gold-Catalyzed Oxidation Terminal Alkyne: An Approach to Synthesize Substituted Dihydronaphthalen-2(1H)-ones and Phenanthrenols. *J. Org. Chem.* **2017,** *82*, 7070-7076.
3. Iwasaki, M.; Araki, Y.; Nishihara, Y. Phenanthrene Synthesis by Palladium-Catalyzed Benzannulation with o-Bromobenzyl Alcohols through Multiple Carbon-Carbon Bond Formations. *J. Org. Chem.* **2017,** *82*, 6242-6258.
4. Matsumoto, A.; Ilies, L.; Nakamura, E. Phenanthrene Synthesis by Iron-Catalyzed [4 + 2] Benzannulation between Alkyne and Biaryl or 2-Alkenylphenyl Grignard Reagent. *J. Am. Chem. Soc.* **2011,** *133*, 6557-6559.
5. Nguyen, Q. H.; Um, T. W.; Shin, S. alpha-Carbonyl Radicals from N-Enoxybenzotriazoles: De Novo Synthesis of 9-Phenanthrols. *Org. Lett.* **2022,** *24*, 8337-8342.

Development of the cobra antivenom production efficiency by using radioactive tracer techniques

Wiranee Sriwiang*, Nantanat Chailanggar, Piriya Kaeopookum, Sarinya Wongsanit, and Wanpen Rangsawai

Thailand Institute of Nuclear Technology, Ongkarak, Nakornnayok, 26120, Thailand

**E-mail: wiranee@tint.or.th*

Abstract:

Antivenom production of Thai cobra (*Naja kaouthia*) has proved to be the most cumbersome, as a low antibody titer was observed. In order to enhance the antivenom production capability, a radioactive tracer technique is used. Iodine-131 (^{131}I) was chosen as a radionuclide due to its high energy gamma rays, low cost, and easy to radiolabel on phenolic group of tyrosine via electrophilic substitution (ES) reaction. Cobratoxin, which contains a tyrosine residue, was radiolabeled with ^{131}I using the Iodogen method *via* the ES reaction. A high radiochemical yield of 85-95% was achieved. The radiolabeled cobratoxin could be used without further purification, and could be divided into three parts; without addition of adjuvant, mixing with Freund's incomplete adjuvant (FIA), and using Alum as additives. To investigate the means of ^{131}I-cobratoxin within hosts, biodistribution profiles in circulatory system and internal organs as well as dynamic whole-body scans had been acquired. The mixture of radiolabeled cobratoxin with FIA delivered promising results as it effectively extended the duration of cobratoxin in rats, while the effect of Alum or without adjuvant could not be notably detected.

1. Introduction

Snake envenomation belongs to a challenging problem of Thai public health. In 2017, the World Health Organization (WHO) has announced the snake envenomation as a neglected tropical disease, which results in death and injury worldwide, especially in agricultural and countryside regions.[1] The Ministry of Public Health of Thailand has monitored snakebite cases worldwide and found that from 5.4 million cases existed yearly, around 40-50% of which were bitten by venomous snakes. One tenth of them lost their lives and one third experienced to amputation of limbs.[2] In Thailand, a number of 7,000-10,000 snakebites was to be expected in a year. This number and victim's deaths has been increasing since 2009. Mostly, the victims are men with the age of over 45 years old, laborer, and living in the northern or southern parts of Thailand. Moreover, the incidents usually occur at the end of the summer and last throughout rainy season.

Queen Saovabha Memorial Institute (QSMI), a part of Thai Red Cross Society, is responsible for the production of antivenoms. Commercially available are seven monovalent antivenoms against seven most encountered venomous snakes in Thailand, and two polyvalent antivenoms, which categorized after the affected locality. Cobra, King Cobra, Banded Krait, and Malayan Krait have in general neurological effects, while Malayan Pit Viper, Russell's Viper, and Green Pit Viper possess hematological effects. The polyvalent antivenoms facilitate the use of antivenoms in case that the patient could not distinguish or identify the type of the snake, but a doctor can roughly estimate from the onset, backgrounds of the patient including occupation, location where the incident occurred, and eventually blood test to find out which system, *i.e.* nervous or circulation system, was affected. As a result, the according antivenom could be applied.

Despite the convenience of utilizing polyvalent antivenoms to treat snake envenomation, their efficacies are rather low, which are a problem during antivenom production step. A low potency could lead to an excess use of antivenom, and induce some allergies after applying the antivenom.[3,4]

Venom of the Thai cobra comprises of several proteins, which have a variety of biological effects, including enzymes, neurotoxins, and other non-toxic molecules. Neurotoxins of Thai cobras (*Naja kaouthia)*, accounted for around 10% of total venom's weight, is the most potent among cobra species.[5] In the production of antivenom against cobratoxin, horses are injected with cobratoxin in a series. After the series has ended, antibody titer is measured. A low antibody titer is usually observed in comparison with those exposed to toxins from other snakes. Only 0-70% of horses stimulated with cobratoxin exceed the titer threshold, while a percentage of 80-100 is achieved using other snake's toxins. It means, only little amount of cobratoxin antivenom can be obtained in each production, which in turn, limits supplier to hospitals or local health centers, and user must carry high treatment course.[3] Efforts to maximize the yield of cobratoxin antivenom production have

been made *via* the use of adjuvants. Two adjuvants are generally exploited in a series of immunization program, namely, Freund's adjuvant and Alum. Freund's adjuvant is a water-in-oil emulsion, in which an antigenic substance dissolved in water phase is dispersed in oily adjuvant phase. The emulsion is believed to decelerate the release of antigenic substance from the site of injection, thus prolong the retention time of the antigen to stimulate the immune system and generate corresponding antibody. While Alum consisted of colloidal aluminium salts, to which the antigenic protein is attached at the surface. The mechanism to trigger the immune system lies on a higher surface area to react with the immune response.[6,7] However, the mechanisms of both adjuvants are still complexed and a proof can be conducted with the help of radiotracer technique.

Labeling cobratoxin with radioisotope can not only trace a path of cobratoxin within a host but also manifest the effects of adjuvants, allowing us to optimize the immunization program for higher antivenom production efficiency. The radioisotope used in this study is I-131, with the energy of its emitted gamma rays of 364 keV. It can be detected with a gamma camera, providing a diagnostic property, and the relatively easy labeling procedure *via* electrophilic substitution (ES) reaction on phenolic group of tyrosine residue promotes its use in radiopharmaceutical.[8]

In this study, we labeled cobratoxin with ^{131}I *via* ES reaction. The radiolabeled product was either mixed with Freund's Incomplete Adjuvant (FIA), or Alum, or without any adjuvant. Results were obtained as time-activity curves, biodistributions and dynamic gamma scans, which illustrated the means of radiolabeled cobratoxin in rats and the effect of adjuvants.

2. Materials and Methods

2.1 Materials

Lyophilized cobratoxin and ^{131}I were provided by QSMI and Radioisotope Department of Thailand Institute of Nuclear Technology (TINT), respectively. Pierce™ Iodination Reagent (1,3,4,6-tetrachloro-3α,6α-diphenyl-glycoluril) (Iodogen), and dichloromethane (DCM) were purchased from Sigma Aldrich. Phosphate buffer (PB) 0.15 M pH 7.0 was prepared by Radioisotope Department of TINT. Imject® Alum, Imject™ Freund's Incomplete Adjuvant were provided by QSMI.

2.2 Radiolabeling

Iodogen dissolved in DCM at a concentration of 0.01 μg/μL was freshly prepared by coating on an inner side of a 1.5 mL glass vial wall. Subsequently, the solvent was slowly flushed with nitrogen gas until it completely dried out. Directly before radiolabeling, the Iodogen coated tube was rinsed with 100 mL 0.15 M PB pH 7.0 and the solvent was discarded. To the Iodogen tube was added the solution of cobratoxin in 0.15 M PB pH 7.0, the solution of ^{131}I in 0.15 M PB pH7.0, and adjusted total volume with 0.15 M PB pH 7.0. The mixture was incubated and occasionally shaken at room temperature. To terminate the reaction, the solution was transferred to another glass vial. The radiolabeling efficiency was measured with iTLC using a mobile phase of 85%methanol and 15%saline. Radiochemical purity could be obtained by radioHPLC. The product was used without further purification only when the radiolabeling reached at least 90%. The radiolabeled product was afterwards subjected into 3 groups: without adding any adjuvant (no adjuvant), mixing with FIA, and mixing with Alum.

2.3 Animal experiments

Fifteen male Sprague Dawley rats, aged between 6-8 weeks, with weights between 150-200 g, were divided into 3 groups, each group consists of 5 rats. Each group was injected with ^{131}I-cobratoxin with 1. no adjuvant, 2. FIA, and 3. Alum, separately. Radioactivity in syringes was measured before and after each injection. Immediately after injection and at each blood collection time, two rats from each group were imaged with gamma camera. Bloods from other three rats were collected at 1h, 2h, 3h, 4h, 8h, 24h, and every day until 14 days post injection (pi). After 7 days and 14 days pi, rats from each group were terminated and their organs (thyroid, blood, lung, heart, liver, kidney, stomach, muscle, spleen, and injected area called muscle inject) were dissected. Accumulated activities in blood samples and organs were *ex vivo* measured *via* gamma counter.

3. Results & Discussion

3.1 Radiolabeling

To optimize radiolabeling conditions, six factors (cobratoxin amount, activity of ^{131}I, Iodogen amount, reaction volume, reaction time, and pH) were varied. In table 1, the Iodogen amount, reaction time, and pH were beforehand examined and set at 20 mg, 10 minutes, and around 7.0-7.4, respectively. Considering entries 1, 3, 6, when only the activity of ^{131}I was differed, a higher activity did not deliver a higher %radiolabeling. The reason could be attributed to the amount Iodogen, as Iodogen oxidized I^- to I^+, which further underwent electrophilic substitution (ES) reaction

and substituted a hydrogen atom at α-carbon of phenolic group of tyrosine in cobratoxin. An insufficient amount of Iodogen or a too thick Iodogen film, as resulting from a too concentrated Iodogen solution, could discourage the radiolabeling process. As the oxidation step only occurred on the surface of Iodogen film. Additionally, higher activity levels might also require a longer reaction time to effectively convert I- to I+ and let the ES reaction to take place. To promote the oxidation reaction, pH of the reaction must not exceed 7.4. As presented hydroxide ions would shift the reaction to facilitate the establishment of I^- as shown in the equations below:[9,10]

$$I^- + 4H^+ + O_2 \rightarrow 2I_2 + 2H_2O \quad (1)$$

$$I_2 + H_2O \rightarrow H^+ + I^- + H_2O \quad (2)$$

(1) Iodide ions are oxidized in acidic solution in the presence of oxygen.
(2) Hydrolysis of established iodine.

In contrast, low pH solution seemed to support the radiolabeling, as iodide ions will be oxidized in acidic environment (Equation 1). However, iodine as a product of oxidation reaction of iodide is highly volatile and difficult to handle.[11] Since stock ^{131}I had been previously prepared in basic solution preventing volatility of I_2, phosphate buffer pH 7.0 was administered to adjust pH of the reaction and allow for dispensing. Giving that other factors were optimized, %radiolabeling tended to depend on the concentration of cobratoxin, as lower %radiolabeling was achieved when using lower cobratoxin concentration.
The optimal condition so far was 0.3 μg/μL cobratoxin. The Iodogen amount depended on the ^{131}I activity, with higher activity requiring more Iodogen, and a longer reaction time, and pH ranged between 7.0-7.4. Following these factors, radiolabeling of 86-90% could be achieved.

Table 1. Radiolabeling conditions and their %radiolabeling

Entry	Cobratoxin (μg)	^{131}I (mCi)	Cobratoxin : ^{131}I	Reaction volume (μL)	Cobratoxin conc. (μg/μL)	Radiolabeling (%)
1	200	8.6	1 : 43	600	0.33	90.32
2	100	9.87	1 : 98.7	600	0.17	86.64
3	200	25.9	1 : 129.5	600	0.33	89.37
4	50	15.2	1 : 304	525	0.10	86.95
5	20	9.6	1 : 480	310	0.06	81.53
6	200	48.2	1 : 241	600	0.33	22.75

3.2 Animal experiments

Activities distributed in bloods were illustrated as time-activity curve. Three groups of rats injected with ^{131}I-cobratoxin in different mixture (no adjuvant, FIA, Alum) showed similar trends. Within hours (ranging between 1-4 hours) after subcutaneous injections at the back of the rats, the highest uptake of activity in blood was observed. Then, the activity significantly decreased within several days and reached its lowest point at around 4 days pi, except for the FIA group (Fig. 1). Activities in blood samples of rats in FIA group fluctuated over a time, which proved to be the effect of FIA in gradually releasing ^{131}I-cobratoxin from the injection site to circulatory system and other organs, subsequently. As a result, a small amount of activity could still be detected at 14 days pi. To investigate in which organ the activity had accumulated, the biodistribution has been used. Ten organs suspected to be target organs for either free ^{131}I or ^{131}I-cobratoxin were brought to study. After 7d pi, most of the activity accumulated in rat's thyroid, followed by kidney and stomach (Fig. 2, left). Kidney is an organ in the excretory system, through which both ^{131}I and cobratoxin are excreted from the body. In thyroid and stomach, there is sodium/iodide symporter (NIS), which serves as a passage for transporting iodide in and out from cells. Therefore, free ^{131}I cleaved from metabolic processes or unbound ^{131}I left from the radiolabeling steps, could accumulate in these organs. Similar results were observed in the biodistribution of 14 days pi (Fig. 2, right). The highest activity was observed in thyroid, followed by stomach, lung, spleen, and the injected area, respectively. The spleen, being part of the immune system, which is responsible for an immune response against cobratoxin, showed activity detection, serving as evidence that ^{131}I-cobratoxin reached the spleen and maintained as radiolabeled product up to 14 days pi. The long-lasting retainment of activity at the injected site, when using FIA as an adjuvant, repeatedly confirmed the effect that FIA retarded releasing of ^{131}I-cobratoxin to other organs and could prolong the retention of cobratoxin within hosts.

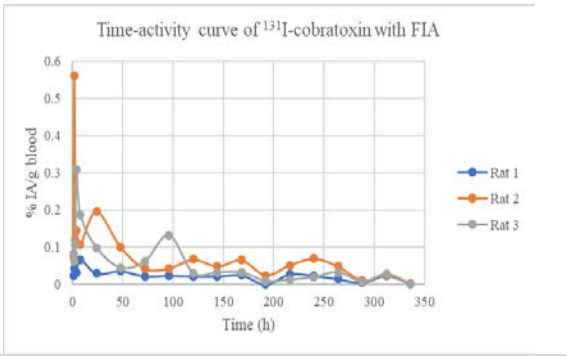

Figure 1. Time-activity curve derived from three rats injected with ^{131}I-cobratoxin mixed with FIA.

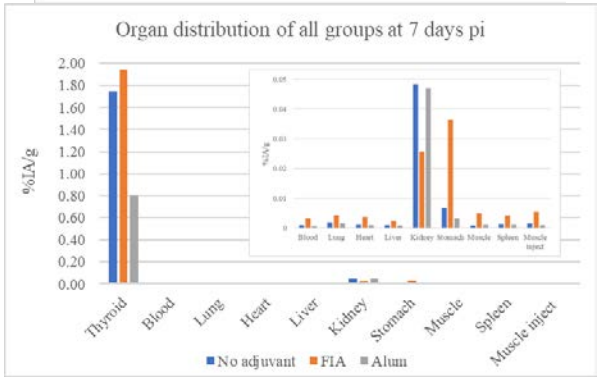

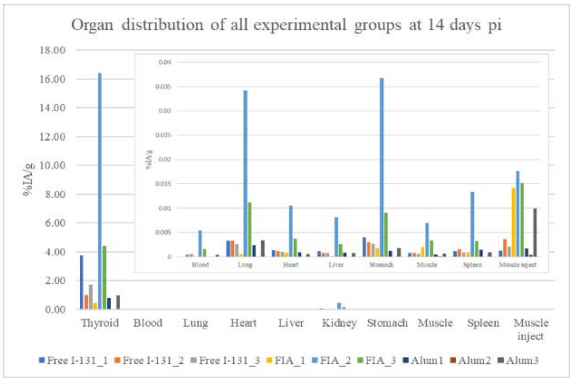

Figure 2. Organ distribution of three groups of rats at 7 days (left) and 14 days (right) post injection.

Blood collections delivered, *via* time-activity curve, activities in blood hour- and daily. Biodistribution profiles provided the accumulated activities in organs after 7- and 14-days pi. The hour- and daily distributed activities in organs could be compensated by dynamic gamma camera scans (Fig. 3). At time of injection (0 h), activities were immediately visualized in all groups of rats, but gamma intensity varied extensively according to the injected activity. A few hours after injection, higher activities (intensities) were observed in all groups and there was an allocation of activity from the injected site to other organs, except for FIA group. In accordance with rat's anatomy, the allocated activities migrated to abdominal organs and supposedly bladder.

However, it was not possible to visibly distinguish the actual target organs of apportioned activities, given the small and compact internal organs of rats. Even the injected activities in the no adjuvant and the Alum groups were higher than the FIA group, the activity in the FIA group retained obviously longer in rat, which was in good agreement with the time-activity and biodistribution results.

4. Conclusion

FIA has proved its properties of prolonging the retention time of ^{131}I-cobratoxin within hosts, as evident in the time-activity curves and the biodistributions in organs. The extended retention time is anticipated to enhance the horse's capability in producing cobra antivenom. However, other indicators ensuring the antivenom production and antivenom efficacy like antibody titer, ED_{50} must be further investigated.

Acknowledgements

This project has been funded by National Research Council of Thailand (NRCT) (Contract No. N12E660077).

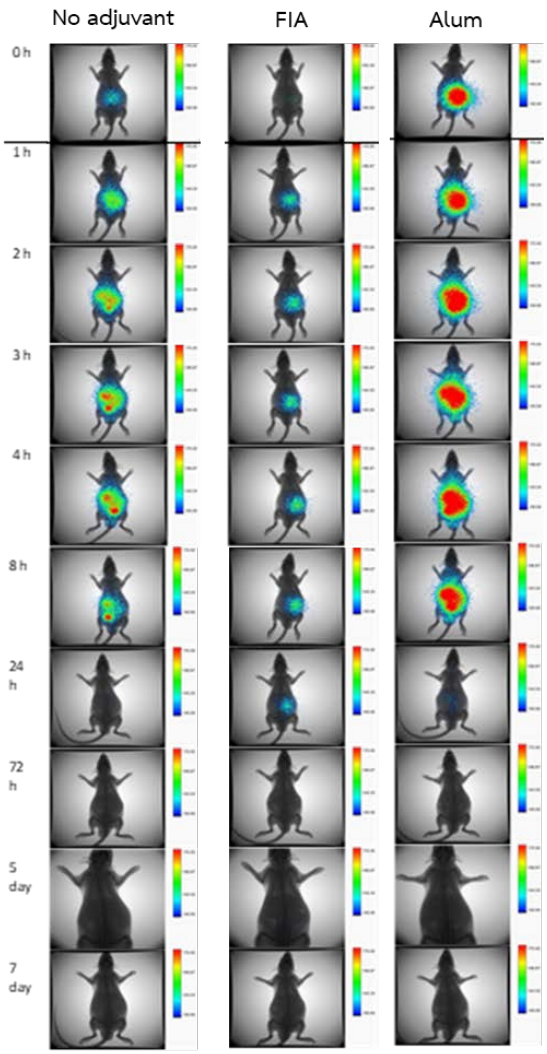

Figure 3. Dynamic gamma camera scans of three groups of rats from time of injection (0 h) to 7-day pi. The color distribution varied from red to blue refers to high to low accumulation of activity.

References

1. Chippaux, J.-P. Snakebite Envenomation Turns Again into a Neglected Tropical Disease! *J Venom Anim Toxins Incl Trop Dis* **2017**, *23*, 38. https://doi.org/10.1186/s40409-017-0127-6.
2. *Snakebite envenoming*. https://www.who.int/news-room/fact-sheets/detail/snakebite-envenoming (accessed 2023-09-12).
3. Leong, P. K.; Fung, S. Y.; Tan, C. H.; Sim, S. M.; Tan, N. H. Immunological Cross-Reactivity and Neutralization of the Principal Toxins of Naja Sumatrana and Related Cobra Venoms by a Thai Polyvalent Antivenom (Neuro Polyvalent Snake Antivenom). *Acta Trop* **2015**, *149*, 86–93. https://doi.org/10.1016/j.actatropica.2015.05.020.
4. Ratanabanangkoon, K. Polyvalent Snake Antivenoms: Production Strategy and Their Therapeutic Benefits. *Toxins*. Multidisciplinary Digital Publishing Institute (MDPI) September 1, 2023. https://doi.org/10.3390/toxins15090517.
5. Sriprapat, S.; Aeksowan, S.; Sapsutthipas, S.; Chotwiwatthanakun, C.; Suttijitpaisal, P.; Pratanaphon, R.; Khow, O.; Sitprija, V.; Ratanabanangkoon, K. *The Impact of a Low Dose, Low Volume, Multi-Site Immunization on the Production of Therapeutic Antivenoms in Thailand*. www.elsevier.com/locate/toxicon.
6. Facciolà, A.; Visalli, G.; Laganà, A.; Di Pietro, A. An Overview of Vaccine Adjuvants: Current Evidence and Future Perspectives. *Vaccines*. MDPI May 1, 2022.
7. Arguedas, M.; Umaña, D.; Moscoso, E.; García, A.; Pereira, C.; Sánchez, A.; Durán, G.; Cordero, D.; Sánchez, A.; Segura, Á.; Vargas, M.; Herrera, M.; Villalta, M.; Gómez, A.; Salas, C.; Díaz, C.; María Gutiérrez, J.; León, G. Comparison of Adjuvant Emulsions for Their Safety and Ability to Enhance the Antibody Response in Horses Immunized with African Snake Venoms. *Vaccine X* **2022**, *12*. https://doi.org/10.1016/j.jvacx.2022.100233.
8. Kumar, K.; Ghosh, A. Radiochemistry, Production Processes, Labeling Methods, and ImmunoPET Imaging Pharmaceuticals of Iodine-124. *Molecules* **2021**, *26* (2). https://doi.org/10.3390/molecules26020414.
9. Lin, C. C.; Chao, J. H. Radiochemistry of Iodine: Relevance to Health and Disease. *Comprehensive Handbook of Iodine: Nutritional, Biochemical, Pathological and Therapeutic Aspects* **2009**, 171–182. https://doi.org/10.1016/B978-0-12-374135-6.00017-0.
10. Schmitz, G. Inorganic Reactions of Iodine(+1) in Acidic Solutions. *Int J Chem Kinet* **2004**, *36* (9), 480–493. https://doi.org/10.1002/kin.20020.
11. Cook, M. K.; Dial, A. R.; Hendy, I. L. Iodine Stability as a Function of PH and Its Implications for Simultaneous Multi-Element ICP-MS Analysis of Marine Carbonates for Paleoenvironmental Reconstructions. *Mar Chem* **2022**, *245*, 104148. https://doi.org/10.1016/J.MARCHEM.2022.104148.

Design, synthesis, and biological activity evaluation of novel colchicine derivative as anticancer agents

Gbenga Olorunmodimu, Takorn Chow, and Tanatorn Khotavivattana*

Center of Excellence in Natural Product Chemistry, Department of Chemistry, Faculty of Science, Chulalongkorn University, Bangkok, 10330, Thailand

**E-mail: tanatorn.k@chula.ac.th*

Abstract:

Colchicine has been identified as a potential anticancer agent due to its ability to inhibit the formation of microtubules by interacting with β-tubulin at the 'colchicine binding site'. However, it exhibits high systemic toxicity and lacks selectivity, leading to various side effects. Several structural modifications of the colchicine scaffold, specifically at the C7, and C10 positions have been reported with significant improvement to its potential in cancer treatment. Notably, replacing the C7-acetamide with long-chain amides significantly increased the activity due to the interaction of alkyl moieties with the hydrophobic groove of α-tubulin. In this work, we designed a novel structure of colchicine derivative with a 4-bromophenyl ring linked to the C7 via an aliphatic linker and the replacement of C10-OMe with NHMe. The synthesis was performed by the substitution of the C10-OMe of an ester-protected colchicine with methylamine. A newly optimized hydrolysis of the C7-acetamide gave the amino-colchicine, which was then coupled with our pre-synthesized linker via amide coupling to give the 4-bromophenyl-linked colchicine derivative in good yield over six steps. In vitro testing of derivatives against Mia Paca-2 and HCT cell lines demonstrated potent anticancer activity with IC_{50} values of 6.77 ± 0.40 nM and 0.71 ± 0.14 nM respectively.

1. Introduction

Every nation of the world has cancer as one of the primary causes of mortality and a major obstacle to raising life expectancy.[1] The problem of cancer drug resistance due to the overexpression of p-gp in tumor cells has also contributed to the difficulties experienced in cancer treatment. Furthermore, the toxic side effects that accompany the usage of anticancer drugs have contributed to the intricacies of cancer treatment.[2]

The mitotic spindle, which controls every step of cell proliferation and segregation of chromosomes, is primarily made up of microtubules.[3] Microtubules, composed mostly of α and β tubulin, are present in all eukaryotic cells and are highly conserved [4]. Scientists have identified inhibition of microtubule dynamics as a viable approach to cancer treatment and drug development due to their importance in cell proliferation.

Colchicine is a tricyclic alkaloid extracted from *Colchicum autumnale*. It is the first agent found to destabilize tubulin.[5] The anticancer activity of colchicine stems from its ability to bind to α-β tubulin heterodimers which bind to the ends of microtubules and inhibit the elongation of microtubules through polymerization.[6] Although colchicine exhibits potent anticancer activity, it has a high system toxicity, limiting its use. It has been reported that colchicine causes severe gastrointestinal disorders, multiorgan failure, and sepsis.[7]

Despite these limitations, it is believed that the derivatization of colchicine could yield new analogues with improved biological activity.[8] One factor that could also support the interest in colchicine modification could be due to its simple structure and the ease of derivatizing it. Although potent, Vinca alkaloids and taxanes (Fig. 1) are poorly bioavailable and possess complex structural architecture, making them complicated to synthesize.[9-10]. Many cancer agents including microtubule-binding agents (MTAs) like vinca drugs, paclitaxel, and docetaxel (**Fig. 1**) have been severely limited by drug resistance in cancerous cells after a period of efficacy. [11]

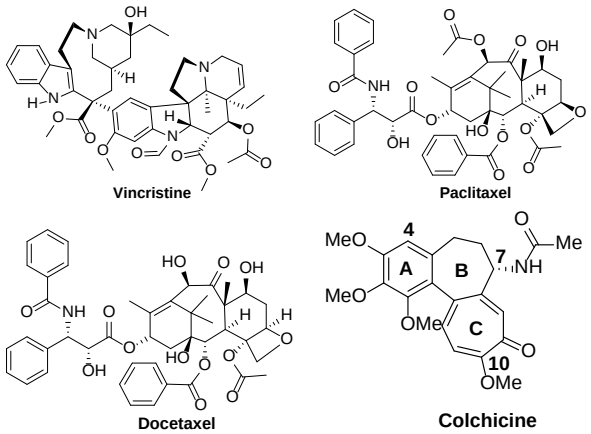

Figure 1. Microtubule binding agents.

The modification of colchicine can be carried out on the three rings. The methoxy groups on ring A are crucial to its binding at the colchicine

binding site. The demethylation of the methoxy groups on ring A has been reported to drastically reduce the antimitotic activity of colchicine.[5, 12]

Modification of colchicine (**Fig. 1**) at C7 is tolerated since it is not required by the molecule to bind, but can improve the general biological activity of the compound as reported by Marzomas *et al*. in 2017.[13] In that study, the *N*-acyl group was replaced by a long chain at C7 (**Fig. 2**) and homologs with a carbon chain between nine to eleven carbons were reported to exhibit the best cytotoxicity against HT-29 and MCF-7 cancer cell lines which was attributed to the hydrophobic interaction of extended carbon side chains of the homologs with α-tubulin binding pocket. Initiating other interactions between C7 side chains and α-tubulin could induce other interesting biological properties in the anticancer evaluation of colchicine against cancer cells. Other modifications of colchicine at C7 include the replacement of the *N*-acyl group with triazole analogs[7] (**Fig. 2**), carbamate[5], and urea analogs.[14] However, most of these derivatives have narrow therapeutic indexes when assessed against four cancer cells although they have impressive IC_{50} in the nanomolar range.

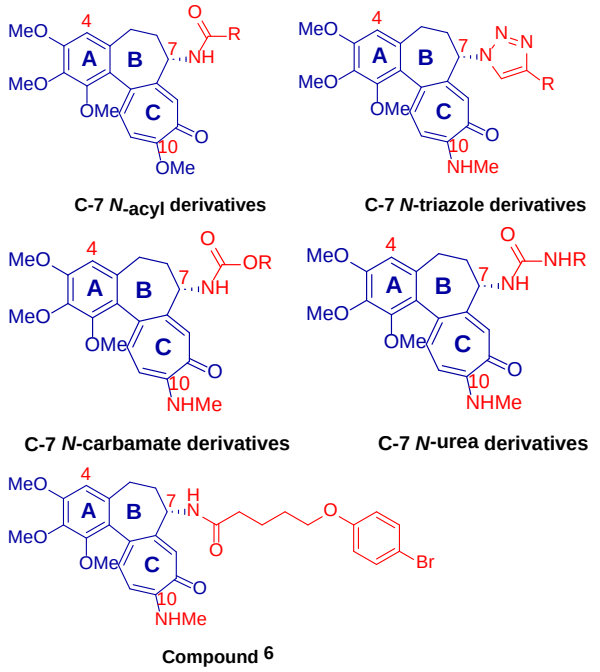

Figure 2. Colchicine derivatives

The methoxy group at C10 (**6**, **Fig. 2**) is important to the molecule's binding at the colchicine binding site. The replacement of OMe at C10 with NHMe has been reported by Krzywik *et al*. in 2020 to improve the activity of colchicine by multiple folds and allow the hydrolysis of colchicine in a single step using harsher conditions without the risk of isomerization to isocolchicine [15].

Herein, we report the synthesis of our new colchicine derivative **6** (**Fig. 2**) as well as the biological evaluation with Mia Paca and HCT cancer cell lines. The methoxy group at C10 was replaced with NHMe to improve the binding and activity of colchicine. The acetamide moiety at C7 was substituted with an amide that bears a four-carbon chain length linker whose end is fitted with an oxygen atom, connected to bromophenyl. With this modification, the structural plan is to have our derivative extend the C7 side chain to α-tubulin which could be made possible by the linker chain and phenyl ring in the structure as the methoxy groups on ring A bind to colchicine binding site at β-tubulin. The oxygen at the end of the linker and the phenyl π-system could encourage hydrogen bond, dipole, and π interactions, while the Bromo group could enhance halogen interaction with the amino group components at α-tubulin. Furthermore, we also report a new optimized protocol for the successful hydrolysis of colchicine at C7.

2. Materials and Methods

2.1 Materials

Reagents and solvents were purchased from Sigma-Aldrich (St. Louis, MO, USA), and TCI chemicals (Tokyo Japan). The Merck aluminium TLC plates coated with silica gel 60 F254 were for monitoring the reactions. Silica gels 60 (0.063-0.200 mm, 70-230 mesh ASTM, Merck, Darmstadt, Germany) was used in carrying out column chromatography. Structural characterization was done using proton and carbon nuclear magnetic resonance (^{1}H and ^{13}C NMR) was conducted using JEOL JNM-ECZ500/SI (500 MHZ). The high-resolution mass spectrometer was obtained using Bruker micro-TOF mass spectrometer.

2.2 Chemical Synthesis

2.2.1 5-(4-Bromophenoxy)pentanoic acid (3)

To a solution of 5-bromopentanoic acid (2.0 g, 11 mmol) in MeOH (20 mL) was added *p*-toluenesulfonic acid (948 mg, 5.5 mmol). The mixture was stirred under reflux conditions for 2 hours and concentrated in *vacuo*. Then, sat. $NaHCO_3$ (30 mL) was added and the resulting mixture was followed by extraction using DCM (3×10 mL). The combined organic layers were dried over $MgSO_4$ and then concentrated *in vacuo* to obtain methyl 5-bromopentanoate (**1**, 1.6 g, 82%) as a colorless oil. To the crude residue, **1** (286 mg, 1.47 mmol) in dry acetone (10 mL) was added 4-bromophenol (256 mg, 1.48 mmol), and anh. K_2CO_3 (608 mg, 4.4 mmol). The mixture was stirred under reflux conditions for 2 days. After the

reaction was quenched with 1M HCl (10 mL), the resulting mixture was extracted with EtOAc (3×10 mL). The combined organic layers were washed with brine, dried over $MgSO_4$, filtered, then concentrated *in vacuo*. The crude was purified by silica gel column chromatography (eluent: EtOAc/hexane 1:16 v/v) to obtain methyl 5-(4-bromophenoxy)pentanoate (**2**, 297 mg, 70% yield) as a colorless oil. To **2** (208 mg, 0.72 mmol) in 1:1 v/v of MeOH/H_2O (10 mL) was added KOH pellets (163 mg, 2.90 mmol). The mixture was stirred under reflux conditions for 4 hours and quenched with 1M HCl (10 mL). The resulting mixture was extracted with EtOAc (3×10 mL). The combined organic layers were washed with brine, dried over $MgSO_4$, filtered, and concentrated *in vacuo* to obtain **3** (146 mg, 74% yield) as a white oily solid.

2.2.2 10-Methylaminocolchicine (4)

To colchicine (1.0 g, 2.5 mmol) in MeOH (20 mL) was added methylamine solution (40% in MeOH, 2.0 ml, 25 mmol). The mixture was stirred under reflux conditions for 24 hours. The resulting mixture was concentrated *in vacuo* to obtain **4** (990 mg, 99% yield) as a yellow solid.

2.2.3 7-Amino-10-methylaminocolchicine (5)

To **4** (500 mg, 1.26 mmol) in dioxane (4 mL) was added 4M HCl (3.2 ml, 12.6 mmol). The mixture was stirred at 70 ºC for 2 days and quenched with 4M (10 mL) NaOH. The resulting mixture was extracted with EtOAc (4×10 mL). The combined organic layers were washed with water and brine, dried over $MgSO_4$, and concentrated *in vacuo* to obtain **5** (374 mg, 83% yield) as a yellow solid.

2.2.4 *N*-(5-(4-Bromophenoxy)pentanoyl)-7-amino-10-methylaminocolchicine (6)

To **3** (41 mg, 0.13 mmol) in dry DMF (1.0 mL) was added HATU (49 mg, 0.17 mmol) and triethylamine (55 µL, 0.39 mmol). **5** (45 mg, 0.13 mmol) was added to the mixture, and the reaction was stirred at room temperature overnight. The mixture was quenched with 2N HCl (8 mL) and extracted with EtOAc (4×10 mL). The combined organic layers were washed with sat. $NaHCO_3$ (20 mL), filtered and concentrated in *vacuo*. The crude was purified by silica gel column chromatography (eluent: 3% MeOH:EtOAc v/v) to obtain **6** (48 mg, 62%) as a yellow solid.

2.3 Spectroscopic Data

2.3.1 Methyl-5-bromopentanoate (1)

^{1}H NMR (500 MHz, $CDCl_3$) δ 3.66 (s, 2H), 3.40 (t, *J* = 6.6 Hz, 2H), 2.34 (t, *J* = 7.3 Hz, 2H), 1.89 (dd, *J* = 15.1, 6.9 Hz, 2H), 1.83 – 1.74 (m, 2H).

2.3.2 Methyl-5-(4-bromophenoxy)pentanoate (2)

^{1}H NMR (500 MHz, $CDCl_3$) δ 7.36 (d, *J* = 8.9 Hz, 2H), 6.76 (d, *J* = 9.0 Hz, 2H), 3.94 – 3.92 (t, 3H), 3.67 (s, 3H), 2.41 – 2.38 (m, 2H), 1.86 – 1.76 (m, 2H).

2.3.3 5-(4-Bromophenoxy)pentanoic acid (3)

^{1}H NMR (500 MHz, $CDCl_3$) δ 7.36 (d, *J* = 8.8 Hz, 2H), 6.76 (d, *J* = 8.9 Hz, 2H), 3.94 (t, *J* = 5.6 Hz, 2H), 2.50 – 2.38 (m, 2H), 1.89 – 1.77 (m, 2H).

2.3.4 10-(Methylamino)colchicine (4)

^{1}H NMR (500 MHz, $CDCl_3$) δ 7.53 (s, 1H), 7.46 (d, *J* = 6.1 Hz, 1H), 7.44 (s, 1H), 6.57 (d, *J* = 11.5 Hz, 1H), 6.53 (s, 2H), 3.94 (s, 3H), 3.89 (s, 3H), 3.62 (s, 3H), 3.09 (d, *J* = 5.4 Hz, 3H), 2.48 (dd, *J* = 13.4, 6.3 Hz, 1H), 2.37 (td, *J* = 13.0, 6.8 Hz, 1H), 2.26 (dq, *J* = 12.4, 6.3 Hz, 1H), 1.98 (s, 3H), 1.96 – 1.87 (m, 1H).

2.3.5 7-Amino-10-(methylamino)colchicine (5)

^{1}H NMR (500 MHz, $CDCl_3$) δ 7.62 (s, 1H), 7.35 (d, *J* = 21.1 Hz, 2H), 6.51 (d, *J* = 11.7 Hz, 2H), 3.88 (s, 6H), 3.73 (s, 1H), 3.60 (s, 3H), 3.16 – 2.94 (d, 3H), 2.45 – 2.39 (m, 1H), 2.34 – 2.26 (m, 2H), 1.66 – 1.62 (m, 1H).

2.3.6 *N*-(5-(4-Bromophenoxy)pentanoyl)-7-amino-10-(methylamino)colchicine (6)

^{1}H NMR (500 MHz, Methanol-d_4) δ 7.47 (d, *J* = 11.2 Hz, 1H), 7.36 (d, *J* = 7.2 Hz, 1H), 7.33 (d, *J* = 9.0 Hz, 2H), 7.24 (s, 1H), 6.79 (d, *J* = 6.7 Hz, 2H), 6.76 (s, 1H), 6.72 (s, 1H), 4.52 (dd, *J* = 12.2, 6.4 Hz, 1H), 3.93 (t, *J* = 5.1 Hz, 2H), 3.89 (s, 3H), 3.88 (s, 3H), 3.56 (s, 3H), 3.08 (s, 3H), 2.57 (dd, *J* = 19.0, 5.6 Hz, 1H), 2.34 (t, *J* = 6.4 Hz, 2H), 2.31 – 2.26 (m, 1H), 2.17 (dq, *J* = 12.8, 6.4 Hz, 1H), 2.01 – 1.91 (m, 1H), 1.82 – 1.75 (m, 4H). ^{13}C NMR (126 MHz, methanol-d_4) δ 176.4 173.7 157.9, 155.2, 152.6, 151.4, 141.8, 139.7, 136.8, 131.8, 129.1, 125.7. 122.7, 118.8, 113.9, 108.7, 106.2, 66.7, 61.4 56.4, 53.0, 37.7, 35.0, 31.6, 28.4, 28.3, 23.2 HRMS (ESI$^+$): m/z calcd for $C_{31}H_{36}BrN_2O_6$, $[M+H]^+$ 611.1757, found 611.1693.

2.3.7 7-Amino-10-hydroxycolchicine (5a)

^{1}H NMR (500 MHz, $CDCl_3$) δ 7.58 (d, *J* = 11.6 Hz, 1H), 7.53 (s, 1H), 7.31 (d, *J* = 11.7 Hz, 1H), 6.55 (s, 1H), 4.67–4.64 (m, 1H), 3.94 (s, 3H), 3.90 (s, 3H), 3.63 (s, 3H), 2.55–2.49 (m, 2H), 2.33 (d, *J* = 11.8 Hz, 2H). ^{13}C NMR (126 MHz, $CDCl_3$) δ 171.0, 169.8, 169.3, 153.7, 151.0, 150.6, 141.8, 141.6, 136.9, 134.4, 127.0, 124.0, 119.9, 108.7, 61.5, 56.2, 53.5, 52.8, 39.0, 31.9, 24.9

2.4 Evaluation of the inhibitory activity against Mia Paca-2 and HCT cell lines.

Pathogenic cells namely Mia Paca-2 (pancreatic cancer epithelial cell line) and HCT (colon cancer cell line) were used in the study. Compound **6** was diluted using the three-fold dilution method in 96-well plates at varying concentrations and was added to pre-incubated cancer cells in cell culture plates. These cell culture plates were incubated for 72 hrs. Prepared MTT dye was added to the cell culture plates and incubated for 3 hours to measure cell viability. After the incubation period, liquids in the plate were vacuumed out and DMSO was added to each well. The absorbance of samples was measured using a UV/Visible spectrophotometer at 560-570 nm.

3. Results and Discussion

3.1 Chemical Synthesis

The synthesis of colchicine analog **6** follows a 6-step synthetic process as shown in **Figure 3**. The protocol for the synthesis of the four-carbon linker intermediate **3** was adapted from Nishiyama *et al* (2015) and modified.[16] 5-Bromopentanoic acid was esterified with MeOH in the presence of *p*-toluenesulfonic acid under reflux conditions to give the corresponding ester **1**. Next, **1** was refluxed with 4-bromophenol using anh. K_2CO_3 in acetone for 2 days to form the ether **2** which was isolated using column chromatography. The long reaction time was required to get as much yield of a product as possible due to the poor yield of this reaction. Ester hydrolysis of **2** with KOH yielded the carboxylic acid linker **3** in good yield, which is now ready for amide coupling in the final step.

In the next step, colchicine was converted to 10-aminocolchicine **4** by refluxing with methylamine in MeOH for 24 hours which gave the expected product in excellent yield. The replacement of OMe with NHMe at C10 is aided by the resonance contribution of the carbonyl group at C9. The following acid hydrolysis of **4** was attempted according to the previously reported protocol,[7] using 2M HCl in dioxane under reflux conditions for 24 hours (the exact reaction time was not reported in the previous protocol). However, we observed a decomposition of the starting material with no desirable product. Therefore, we attempted to optimize this step as summarized in **Table 1**. Since the original protocol using reflux temperature was unsuccessful (**Table 1**, entry 1), the temperature was reduced to 80 ºC while increasing the concentration of HCl to 6M. However, the decomposed product remained observed (**Table 1**, entry 2). We then adjusted the temperature to 60 ºC while still maintaining 6M HCl for the hydrolysis; however, a partially hydrolyzed product was observed (**Table 1**, entry 3). Due to prior unsuccessful hydrolytic attempts of colchicine, we proceeded to try base hydrolysis. Hydrolysis of **4** using ten equivalents of KOH, NaOH, and LiOH in dioxane yielded a hydrolyzed by-product **5a** in which NHMe has been replaced with OH (**Table 1**, entries 4-6). Attempting the hydrolysis of **4** with 10 equivalents of K_2CO_3 in dioxane gave no reaction (**Table 1**, entry 7). Finally, we achieved the successful hydrolysis of amino colchicine by using ten equivalents of 4M HCl at 70 ºC for 44 hours in dioxane which gave the expected product **5** in a good yield of 86% (**Table 1**, entry 8).

In the final synthetic step, we performed an amide coupling reaction between **3** and **5** using HATU as a coupling agent and TEA as a base in dry DMF which was stirred at room temperature overnight to obtain **6** a yellow solid in good yield of 83%.

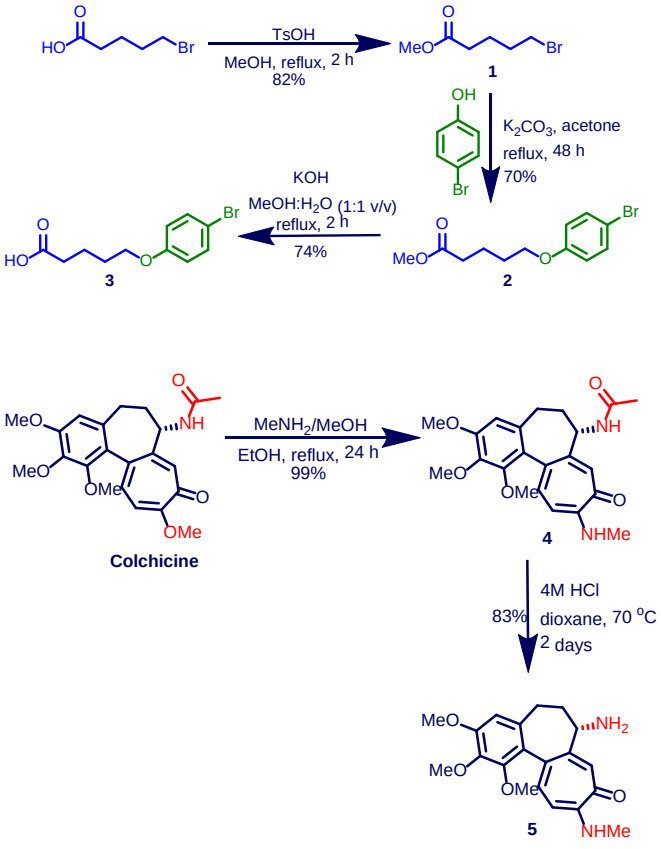

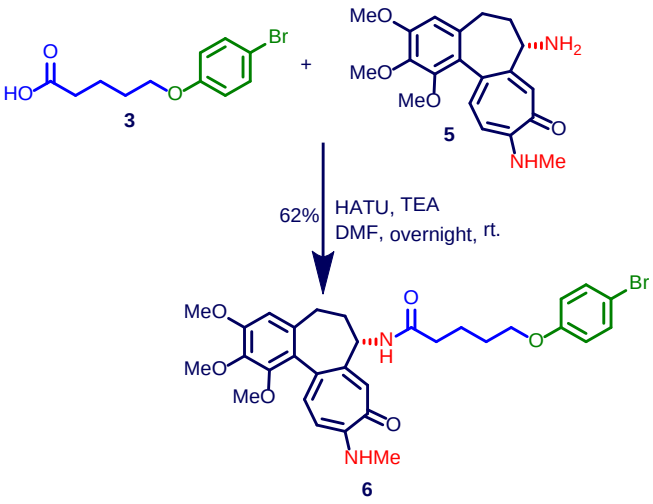

Figure 3: Synthesis of colchicine derivative

Table 1: Optimization attempts for the hydrolysis of colchicine

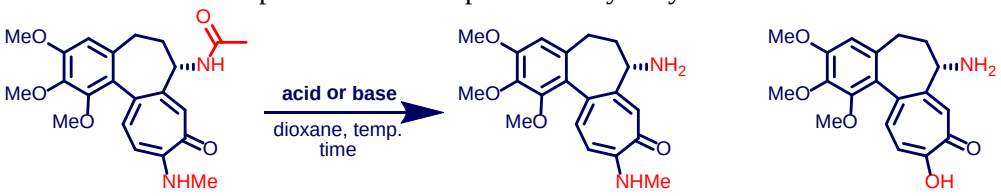

4 — Desired product (5) — By-product (5a)

Entries	Reagent	Equivalent	Temperature (^{0}C)	Time	Outcome
1	2M HCl	10	100	24 hours	Decomposed product
2	6M HCl	10	80	24 hours	Decomposed product
3	6M HCl	10	60	24 hours	Incomplete reaction
4	NaOH pellets	20	70	7 days	By-product **5a**
5	KOH pellets	20	70	7days	By-product **5a**
6	LiOH pellets	20	70	7 days	By-product **5a**
7	K_2CO_3 pellets	20	70	7 days	No reaction
8	4M HCl	10	70	44 hours	Desired product **5**

3.3 Anticancer Activity

A cytotoxicity study of the final compound was carried out using Mia Paca-2 and HCT cell lines (**Table 2**). The IC_{50} values of **6** against tested cancer cells were observed to be in the nanomolar range. Mia Paca-2 cells which are one of the pancreatic ductal adenocarcinoma (PDAC) cell lines exhibit drug and radiotherapy resistance,[17] which makes it important in the in vitro studies of pancreatic cancer. Compound **6** exhibited good activity against Mia Paca-2 cancer cells recorded an IC_{50} value of 6.77 ± 0.40 nM which is more potent than the reported activity of colchicine against Mia Paca-2 cells with an IC_{50} value of 55 ± 5 nM[18] (**Table 2**). The potency of **6** against the Mia Paca-2 cell line at low concentration could signify safer treatment due to low dosage. Against the HCT cell line, an impressive IC_{50} value of 0.71 ± 0.14 nM was observed. This value demonstrates that **6** is more potent than the reported colchicine's IC_{50} value of 50 ± 5 nM against HCT.[19] The improved activity of **6** against HCT-116 could be mainly due to inherent apoptosis caused by intensified antimitotic activity as reported for colchicine activity against HCT-116.[20]

Table 2: Anticancer activity of colchicine derivative against Mia Paca-2 and HCT cells.

Compound	Mia Paca-2 IC_{50} (nM)	HCT IC_{50} (nM)
6	6.77 ± 0.40	0.71 ± 0.14
colchicine	55 ± 5[a]	50 ± 5[b]

[a b] Literature reported value.[20, 21]

4. Conclusion

We have synthesized a novel colchicine derivative (**6**) with key alterations at C7 and C10 on the colchicine core. This synthesis was achieved in six key steps. Furthermore, we also detailed our optimization efforts in the hydrolysis of amino colchicine in a single step. Finally, we have reported the anticancer activity of **6** against Mia Paca-2 and HCT cells which showed good activity in the nanomolar range. Notably, the activity of **6** was found to be much higher than that of colchicine against both Mia Paca-2 and HCT cells

when compared with previously reported values. In our future derivatization attempts, we plan to make some other interesting alterations to the colchicine core architecture in the hope of obtaining derivatives with desirable therapeutic qualities.

Acknowledgments

We acknowledge the Thailand and Innovation Fund Chulalongkorn University (HEA662300079) and the Chulalongkorn University graduate scholarship for ASEAN and non-ASEAN countries whose funding made this research work possible.

References

1. Bray, F.; Laversanne, M.; Weiderpass, E.; Soerjomataram, I. The ever-increasing importance of cancer as a leading cause of premature death worldwide. *Cancer* **2021**, *127*, 3029-3030.
2. Zhang, X.; Kong, Y.; Zhang, J.; Su, J.; Zhou, Y.; Zang, Y.; Li, Y.; Chen, Y.; Fang, Y.; Zhang, X.; Lu W. Design, synthesis and biological evaluation of colchicine derivatives as novel tubulin and histone deacetylase dual inhibitors. *Eur. J. Med Chem.* **2015**, *95*, 129-135.
3. Cirrilo, L.; Gotta M.; Meraldi, P. The Elephant in the Room; The role of microtubules in cancer. *Adv. Exp. Med. Biol.* **2017**, *1002*, 93-124.
4. Schummel, P.; Gao, M.; Winter, R.; Modulation of the polymerization kinetics of alpha/beta-tubulin by osmolytes and macromolecular crowding. *Chemphyschem*, **2017**, 18, 189-197.
5. Krzywik, J.; Aminpour, M.; Janczak, J.; Maj, E.; Moshari, M.; Mozga, W.; Wietrzyk, J.; Tuszyński, J.; Huczyński, A. An insight into the anticancer potential of carbamates and thiocarbamates of 10-demethoxy-10-methylaminocolchicine. *Eur. J. Med. Chem.* **2021**, *215*, 113282.
6. Albert, I.; Albert, W.; Thomas J. A New perspective on the pharmacoeconomics of colchicine. *Curr. Med. Res. Opin.*, **2011**, 27, 931-937.
7. Krzywik, J.; Nasulewicz-Goldeman, A.; Mozga, W.; Wietrzyik, J.; Huczyncki, A. Novel double-modified colchicine derivatives bearing 1,2,3-triazole: Design, synthesis, and biological activity evaluation. *ACS OMEGA* **2021**, *6*, 26583-26600.
8. Wardle, N.; Kalber, T.; Bell, J.; Annie Bligh, S. Synthesis and characterization of a novel tubulin-directed DO3A-colchicine with potential theranostic features. *Bioorg. Med. Chem. Lett*. **2011**, *21*, 3346-3348.
9. Tischer, J.; Gergely, F., Anti-mitotic therapies in cancer. *J. Cell. Biol*. **2019**, 218 (1), 10-11.
10. Yin, S.; Bhattacharya, R.; Cabral, F., Human mutations that confer paclitaxel resistance. Molecular cancer therapeutics **2010**, 9 (2), 327-335.
11. Henriquez, F.; Ingram, P.; Muench, S.; Rice, D.; Roberts, C. Molecular basis for resistance of Acanthamoeba tubulins to all major classes of antitubulin compounds. *Antimicrob. Agents Chemother.* **2008**, 52 (3), 1133-1135.
12. 12 Ghawanmeh, A.; Al-Bajalan, H.; Mackeen, M.; Alali, F.; Chong, K. Recent developments on (−)-colchicine derivatives: Synthesis and structure-activity relationship. *Eur. J. Med. Chem.* **2019**, 185, 111788.
13. Marzo-Mas, A.; Barbier, P.; Breuzard, G.; Allegro, D.; Falomir, E.; Murga, J.; Carda, M.; Peyrot, V.; Marco, J. Interactions of long-chain homologues of colchicine with tubulin, *Eur. J. Med. Chem.* **2017**, 126, 526-535.
14. Krzywik, J.; Maj, E.; Nasulewicz-Goldeman, A.; Mozga, W.; Wietrzyk, J.; Huczyncki, A. Synthesis and antiproliferative screening of doubly modified colchicines containing urea, thiourea and guanidine moieties. *Bioorg. Med. Chem. Lett.*, **2021**, 47, 128197.
15. Krzywik, J.; Mozga, W.; Aminpour, M.; Janczak, J.; Maj, E.; Wietrzyk, J.; Tuszynski, J.A.; Huczynski, A. Synthesis, antiproliferative activity and molecular docking studies of novel doubly modified colchicine amides and sulfonamides as anticancer agents. *Molecules***, 2020**, 25, 1789.
16. Nishiyama, J.; Makita, Y.; Kihara, N. The cyclopentyl group, as a small but bulky terminal group, allows rapid and efficient active transport. *Org. Lett*., **2015**, 17, 138-141.
17. Yamaguchi M and Murata T: Suppressive effects of exogenous regucalcin on the proliferation of human pancreatic cancer mia paca-2 cells in vitro. *Int J Mol Med*., **2015**, 35, 1773–1778.
18. Kumar A, Singh B, Mahajan G, Sharma PR, Bharate SB, Mintoo MJ, Mondhe DM. A novel colchicine-based microtubule inhibitor exhibits potent antitumor activity by inducing mitochondrial mediated apoptosis in MIA PaCa-2 pancreatic cancer cells. *Tumour Biol.*, **2016**, 37, 13121-13136.
19. Kumar, A.; Singh, B.; Sharma, P.; Bharate, S.; Saxena, A.; Mondhe, D. A novel microtubule depolymerizing colchicine analogue triggers

apoptosis and autophagy in HCT-116 colon cancer cells. *Cell Biochem Funct*. **2016**, 34, 69-81.

20. AbouAitah, K.; Hassan, H.; Swiderska-Sroda, A.; Gohar, L.; Shaker, O.; Wojnarowicz, J.; Opalinska A, Smalc-Koziorowska J, Gierlotka S, Lojkowski, W. Targeted nano-drug delivery of colchicine against colon cancer cells by means of mesoporous silica nanoparticles. *cancers*., **2020** 12, 144.

Development of a PSMA-11 lyophilized kit for convenient radiolabeling with ^{68}Ga

Boon-Uma Jowanaridhi*, Thidarat Kohud, Kanyapat Lumyong, Suppamat Makjan, Chonticha Phaophang, and Sudkanung Phumkem

Radioisotope Center, Thailand Institute of Nuclear Technology (Public Organization), Nakhon Nayok, Thailand

**E-mail: boonuma@tint.or.th*

Abstract:

Prostate specific membrane antigen (PSMA) targeting ligands labeled with various types of radionuclides have been developed and used for diagnosis of prostate cancer. The positron-emitting radionuclide gallium-68 (^{68}Ga) produced from a ^{68}Ge/^{68}Ga generator has an excellent advantage in terms of on-site synthesis. It is similar in principle to ^{99}Mo/^{99m}Tc generator which makes the cold kits for ^{99m}Tc radiolabeling become widely used in medical imaging. ^{68}Ga-PSMA-11 has been increasingly used in Thailand since 2017. This radiopharmaceutical is often produced by commercial synthesis modules which have high consumable costs and require hot cell facilities. While the kit-based production has advantages of lower cost, shorter preparation time and easier to operate. The aim of this work was to develop the PSMA-11 kit in a form of lyophilized powder to be ready for radiolabel with ^{68}Ga. The lyophilization process was performed under sterile conditions. The kit could be radiolabeled with 5–20 mCi of ^{68}Ga at room temperature in 15 min. The radiopharmaceutical ^{68}Ga-PSMA-11 produced from the kit had high radiochemical purity without purification and was stable for at least 4 h. The biological quality control showed that the lyophilized product was a sterile, nonpyrogenic kit. It could be said that, by using the PSMA-11 kit, the production of ^{68}Ga-PSMA-11 was relatively easy, cost effective and radiologically safe.

1. Introduction

Prostate cancer is a serious disease. According to the American Cancer Society, about 1 man in 8 will be diagnosed and 1 man in 41 will die. It is the most common cancer diagnosed in men in 2023 and its incidence rate has risen by approximately 3% per year[1]. The survival rate is based on the stages of cancer. For example, the survival rate of the localized cancer stage, which is the stage that the cancer has not spread outside the prostate, is around 99%. While the survival rate of the distant cancer stage, which is the stage that the cancer has spread to parts of the body farther from the prostate such as lungs, liver, or bones, is less than 32%. Therefore, the accurate diagnosis in the early stage is an essential key to design a treatment plan and to increase the survival rate. There are several methods used for prostate cancer diagnosis. The prostate cancer screening tests are typically blood test and rectal examination. Biopsy is a standard diagnostic test for prostate cancer. Small samples of suspicious tissues from the prostate are removed and examined under a microscope. Some patients may have an uncomfortable experience during the biopsy procedure. Magnetic Resonance Imaging (MRI) is an imaging technique used to localize the cancer; however, patients with metallic implants have a limitation for this test. Positron Emission Tomography (PET) scan is another powerful imaging technique and has been widely used for clinical routine diagnostics. The detection of radioactivity levels from the imaging agent administered into the patient reveals the function of organs and the location of diseases. ^{68}Ga-PSMA-11 is one of the most important imaging agents for diagnosis of prostate cancer[2] and has been approved by the US FDA since 2020[3]. The structures of PSMA-11 and ^{68}Ga-PSMA-11 are shown in Figure 1.

The aim of this research was to formulate PSMA-11 in a form of lyophilized kit for radiolabeling with ^{68}Ga.

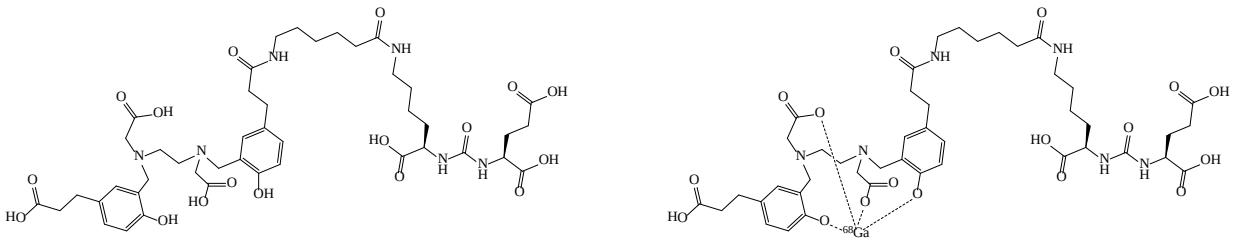

PSMA-11 ^{68}Ga-PSMA-11

Figure 1. Structures of PSMA-11 and ^{68}Ga-PSMA-11.

2. Materials and Methods

2.1 Materials

PSMA-11 was purchased from ABX. The radionuclide ^{68}Ga as gallium chloride ($^{68}GaCl_3$) solution in 0.1 M HCl was eluted from a commercial ^{68}Ge/^{68}Ga generator model IGG100 from Eckert & Ziegler. Solvents used for high performance liquid chromatography (HPLC) were HPLC grade and purchased from Merck, Germany. All other chemicals were analytical grade.

2.2 PSMA-11 kit formulation

The kit was formulated under sterile conditions with laminar flow. A 1-mL mixture solution of 20 µg of PSMA-11, 45 mg of sodium acetate trihydrate and 1 mg of ascorbic acid, was filtered through a 0.22 µm membrane filter. The lyophilization process was performed for 48 h and the kit was filled with N_2 in the final step.

2.3 Radiolabeling

The radionuclide ^{68}Ga in a form of $^{68}GaCl_3$ solution was eluted from a ^{68}Ge/^{68}Ga generator by using 0.1 M HCl. A fraction containing 5–20 mCi in a total volume of 2–2.5 mL was collected and added into a PSMA-11 lyophilized kit. The mixture was incubated at room temperature for 15 min.

2.4 Radiochemical purity and stability

The radiochemical purity (RCP) was analyzed by thin layer chromatography (TLC). By using a glass microfiber chromatography paper impregnate with silica gel (iTLC-SG) and a mixture of 1 M sodium acetate (CH_3COONa) and methanol (MeOH) (1:1 v/v) as a mobile phase, the impurities stayed at the origin while the radiolabeled compound ^{68}Ga-PSMA-11 moved to the solvent front (R_f 0.8–1.0). The TLC strips were measured by Raytest radio-TLC scanner equipped with Bismuth Germanium Oxide (BGO) detector. The RCP of the radiopharmaceutical was monitored for 4 h.

2.5 Peptide content in PSMA-11 kit

The peptide content in kit was analyzed by HPLC using a BDS Hypersil^{TM} C18 column, 150 mm x 3 mm, 3 µm, 130Å. Eluent A contained 0.1% TFA in water and eluent B was acetonitrile. It was carried out with a gradient of 5% B to 40% B at t = 0.5–10 min, and stayed at 40% B for 2 min with the flow rate of 0.6 mL/min. Radiation detection was measured by a 2”x2” NaI detector. A serial dilution and the standard curve of PSMA-11 solutions were generated.

2.6 Moisture content in PSMA-11 kit

Moisture content in the lyophilized kit was analyzed by the volumetric Karl Fischer titrator V30S. Dry methanol was used as a solvent and CombiTitrant 5 was used as a titrant.

2.7 Container closer integrity test

Tracer liquid submersion method was chosen and a solution of 10 mg/mL methylene blue was used as a liquid tracer. The kit vials were submerged by the liquid tracer in an evacuation chamber and subjected to vacuum at -0.8 bar for 30 min. After the vacuum released, the kit vials were checked for evidence of tracer ingress.

2.8 Sterility and bacterial endotoxin test

The test for sterility was carried out by a direct inoculation method using 2 types of culture media. Soyabean Casein Digest Medium (SCDM) was used for the detection of aerobic bacteria and fungi. Fluid Thioglycollate Medium (FTM) was used for the detection of anaerobic bacteria. The kits were dissolved in 2 mL of water for injection (WFI) and added directly into the required media. The samples were incubated for 14 days at 20–25^{o}C for SCDM and at 30–35^{o}C for FTM. Blank and control samples were performed as a negative control. Bacterial endotoxin test was detected by the LAL (Limulus Amoebocyte Lysate) reagent test.

3. Results & Discussion

3.1 PSMA-11 kit formulation

The lyophilization process was applied as an important technique for preservation of the active ingredients. There were 3 main stages; freezing stage, primary drying stage, and secondary drying stage. The sample was first frozen in the freezing stage at the temperature of approximately -40^{o}C for 7 h and became a frozen solution. In the primary stage, the reducing of pressure to 0.13 mBar and the gradual increasing of temperature over 36 h were applied to create the sublimation. More than 95% of water was removed in this stage. While the residual water in a form of unfrozen water molecule was removed in the secondary stage at 25^{o}C for 5 h. The lyophilized product in a 10-mL glass vial was kept under N_2 atmosphere, stored at 2–8^{o}C, and ready to be radiolabeled with ^{68}Ga, see Figure 2. The process of the lyophilization is shown in Figure 3.

Figure 2. Lyophilized PSMA-11 kits.

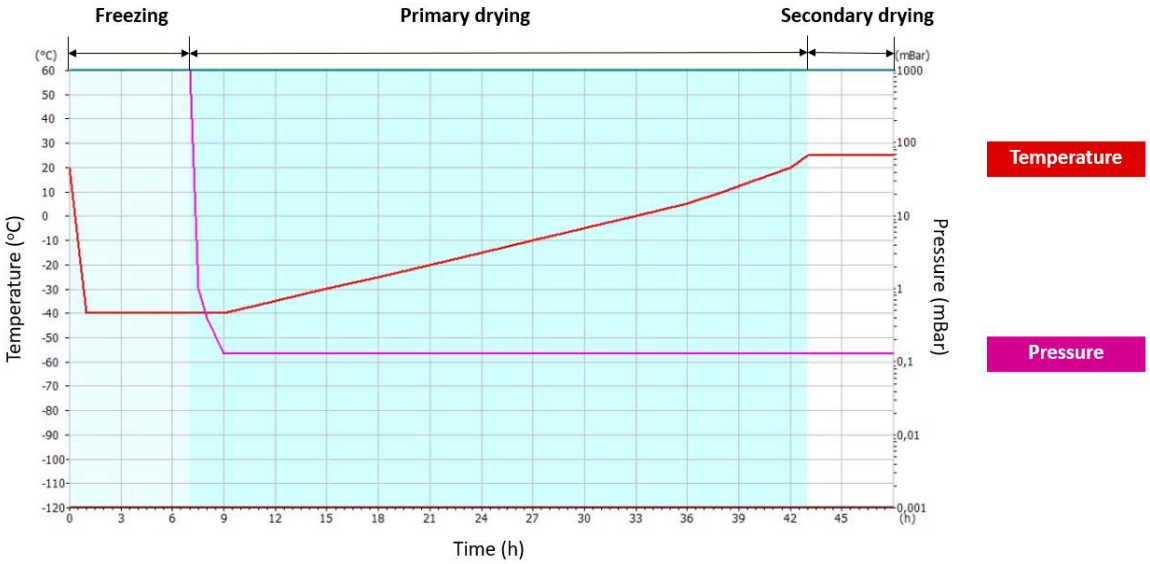

Figure 3. Lyophilization process of the PSMA-11 kit.

3.2 Radiolabeling

A simple, rapid, and efficient method for radiolabeling of PSMA-11 with ^{68}Ga was developed[4,5]. The labeling was carried out under ambient temperature in 15 min. The procedure for the preparation of ^{68}Ga-PSMA-11 is shown in Figure 4. The radiolabeling without a purification process is required for the preparation of short-half-life radiopharmaceuticals especially ^{68}Ga-PSMA-11. In addition, it was reported that ascorbic acid, which is the well known ingredient to reduce the effects of radiolysis[6], was removed when using a C18 solid phase extraction to purify the radiolabeled peptide ^{177}Lu-DOTATATE[7].

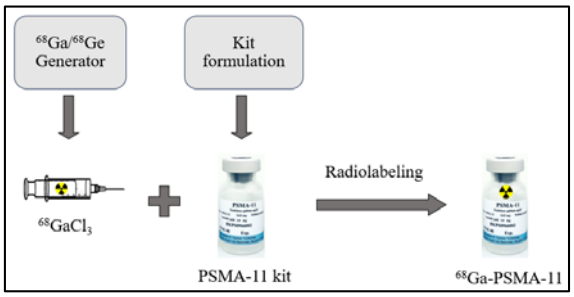

Figure 4. Procedure for the preparation of ^{68}Ga-PSMA-11.

3.3 Radiochemical purity and stability

The RCP is the ratio of ^{68}Ga-PSMA-11 to the total radioactivity in the sample. Measurement of RCP is important to avoid undesired radiochemical forms such as unbound ^{68}Ga and ^{68}Ga colloidal which lead to create low-quality images and interfere with the interpretation. The RCP of the product obtained by TLC was found to be greater than 95% without purification as shown in Figure 5. The radiopharmaceutical ^{68}Ga-PSMA-11 was stable for at least 4 h.

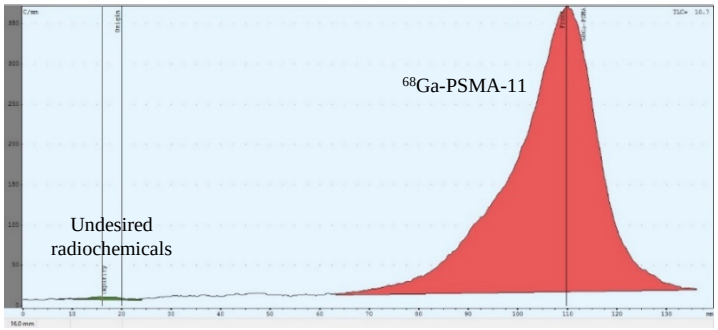

Figure 5. Radio-chromatogram of ^{68}Ga-PSMA-11 produced from PSMA-11 lyophilized kit.

3.4 Peptide content in PSMA-11 kit

According to the European Pharmacopoeia, peptide content in the radiopharmaceutical ^{68}Ga-PSMA-11 must not more than 30 µg per injection. The standard curve was created and used to determine the amount of PSMA-11 in kit. The results obtained by HPLC showed that the amount of PSMA-11 was 19.3±0.3 µg as shown in Figure 6. It could be stated that PSMA-11 kit is safe for a clinical use.

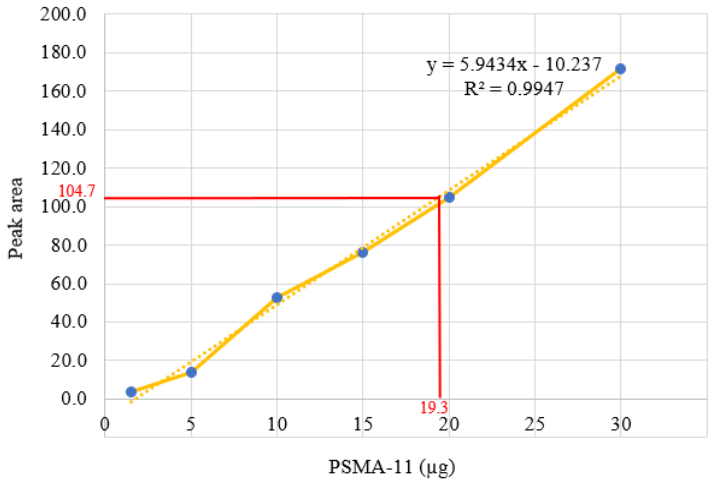

Figure 6. Standard curve of PSMA-11 contents and PSMA-11 amount in the lyophilized kit.

3.5 Moisture content in PSMA-11 kit

The recommendation of moisture content in radiopharmaceutical cold kits by the International Atomic Energy Agency (IAEA) guideline is not more than 3%[8]. The residual humidity can affect the present of antioxidants or radical scavengers including ascorbic acid in cold kits. The degradation of ascorbic acid is the major reason for the radiopharmaceutical stability. The results obtained by volumetric Karl Fischer titration showed that the moisture content in the kit was 1.9±0.4%.

3.6 Container closer integrity test

It is important to ensure that the container has the ability to maintain the quality of the sterile drug product. The container that allows penetration of air and microorganisms is unsuitable for a sterile product. The defects that cause a sterile vial to leak are unable to detect by visual inspection. This test method is described in USP41 <1207.2>. It is a destructive test for packages that can tolerate wetting. A test vessel equipped with vacuum pump and pressure monitor is set up as shown in Figure 7. All test parameters; submersion time during and after pressure application, holding time between tracer liquid challenge and final inspection, and various hold sizes of positive control samples, were validated.

Figure 7. Container closer integrity instrument.

The results showed that there was no evidence of the tracer liquid in the pharmaceutical kit vials as shown in Figure 8.

Figure 8. The kit vials (A) before the integrity test and (B) after the integrity test.

3.7 Summary of quality control

The preparation of lyophilized kits was successful. The radiolabeling method was simple, reliable, and radiologically safe. The results of quality control are divided into 2 parts; lyophilized kit and kit after radiolabeling with ^{68}Ga, and are summarized in Table 1. Sterility and bacterial endotoxin tests were investigated in both the lyophilized kit and the radiolabeled product. It was found that all tests met the requirements stated in the European Pharmacopoeia.

Table 1. Summary of quality control results.

Test	Specification	Method	Result
Lyophilized kit			
PSMA content	≤ 30 µg	HPLC	19.3±0.3 µg
Moisture content	≤ 3%	Karl Fischer titration	1.9±0.4%
Sterility			
- Bacterial contamination	Bacterial absence	Inoculation in FTM	Conforms
- Fungi contamination	Fungi absence	Inoculation in SCDM	Conforms
Bacterial endotoxins	< 35 EU/mL	LAL test	Conforms
Kit after radiolabeling with ^{68}Ga			
Appearance	Clear colorless solution	Visual inspection	Conforms
Radiochemical purity	≥ 95.0% as ^{68}Ga-PSMA-11	TLC	≥ 95.0%
Radiochemical identification	R_f 0.8–1.0 as ^{68}Ga-PSMA-11	TLC	Conforms
pH	4.0–8.0	pH paper	4.0–5.0
Sterility			
- Bacterial contamination	Bacterial absence	Inoculation in FTM	Conforms
- Fungi contamination	Fungi absence	Inoculation in SCDM	Conforms
Bacterial endotoxins	< 35 EU/mL	LAL test	Conforms

4. Conclusion

This study presented the PSMA-11 kit formulation. The kit was a sterile product and suitable for radiolabeling with ^{68}Ga. The convenient labeling process benefits the operators in terms of operating time, hot cell facilities and radiation safety. The quality control results showed that the radiopharmaceutical had high radiochemical purity and stability. It also met the other quality requirements of European Pharmacopoeia. The promising results indicated that this kit formulation could be further developed for commercial production. Moreover, the radiopharmaceutical preparation by using the kit could be applied in hospitals far from a cyclotron facility. For future work, peptide stabilizers should be considered in order to extend the drug shelf-life.

Acknowledgements

This research is financially supported by Thailand Science Research and Innovation (Fundamental fund: fiscal year 2023, project no. 181058).

References

1. Siegel, R. L.; Miller, K. D.; Wagle, N. S.; Jemal, A. *CA. Cancer J. Clin.* **2023**, *73* (1), 17–48.
2. Chen, H.; Cai, P.; Feng, Y.; Sun, Z.; Wang, Y.; Chen, Y.; Zhang, W.; Liu, N.; Zhou, Z. *Sci. Rep.* **2021**, *11* (1), 19122.
3. Hennrich, U.; Eder, M. *Pharm. Basel Switz.* **2021**, *14* (8).
4. Wichmann, C. W.; Ackermann, U.; Poniger, S.; Young, K.; Nguyen, B.; Chan, G.; Sachinidis, J.; Scott, A. M. *J. Label. Compd. Radiopharm.* **2021**, *64* (3), 140–146.
5. Calderoni, L.; Farolfi, A.; Pianori, D.; Maietti, E.; Cabitza, V.; Lambertini, A.; Ricci, G.; Telo, S.; Lodi, F.; Castellucci, P.; Fanti, S. *J. Nucl. Med. Off. Publ. Soc. Nucl. Med.* **2020**, *61* (5), 716–722.
6. Liu, S.; Ellars, C. E.; Edwards, D. S. *Bioconjug. Chem.* **2003**, *14* (5), 1052–1056.
7. Maus, S.; Blois, E.; Ament, S.-J.; Schreckenberger, M.; P., W. *Int. J. Diagn. Imaging* **2014**, *1*, 5.
8. *Technetium-99m Radiopharmaceuticals: Manufacture of Kits*; Technical Reports Series; International Atomic Energy Agency: Vienna, 2008.

The modified formula of aggregated human albumin in lyophilization form (MAA-Cold kit) by adding human albumin solution

Thidarat Kohud*, Wanpen Rangsawa, Sanguansak hykunya, Boon-Uma Jowanaridhi, Krittika Somruedee, Kanyapat Lumyong, Suppamat Makjan, Chotiwid Wiriyachailerd, Sudkanung Phumkem, Siriwat Thida, and Chonticha Phaophang

Radioisotope Center, Thailand Institute of Nuclear Technology (Public Organization), Bangkok, Thailand

**E-mail: thidarat@tint.or.th*

Abstract:

Macro aggregated human albumin (MAA) are labelled with Tc-99m for lung perfusion imaging. However, the MAA kit in-house formula was adsorbed on plastic syringe after labelled by Tc-99m. To solve this problem, a modified formula of the MAA-cold kit was studied by adding surfactant. The human albumin solution (HSA) was used as surfactant of aggregated particles by themselves. The preparation of MAA-cold kit was modified by varying the amount of HSA surfactant added [0.75 mg/vial (0.75AS) and 1.50 mg/vial (1.5AS)]. Radiochemical purity (%RCP), percent of MAA adsorbed on plastic syringe (%adsorb), particles size distribution, and water content were determined for both preparation. The radiochemical purity (%RCP) of 0.75AS and 1.50AS formula were 96.54 and 96.43 respectively. The both formula had similarly the particles size distribution. Moreover, the water determination of 0.75AS and 1.50AS formula were 4.28% and 3.22% respectively. Percent of MAA adsorbed on plastic syringe of original formula, 0.75AS and 1.50AS formula were 38.45, 11.90 and 9.56 respectively. The results reveal that MAA adsorbed 0.75AS and 1.50AS formula decrease form original formula, therefore the both formula can solve this problem.

1. Introduction

Macro aggregated albumin (MAA) is labeled with Tc-99m to form 99mTc-MAA which is the first choice for pulmonary thrombosis diagnosis. Assuming that a sufficient number of radioactive particles have been used, uniform perfusion will produce a uniform image. Labeled macro aggregated albumin was located in lungs and the particles are trapped in pulmonary arterioles and capillaries. The MAA particle size suitable for imaging is 10 – 90 µm in order to be loaded on capillary bed after intravenous administration.[1-3]

Radiopharmaceutical MAA kit was prepared by heating the solution of albumin and stannous chloride in acetate buffer.[4] The particles size of macro aggregated albumin was controlled by optimum heating process to give the suitable size of 10 – 90 µm.[1, 5]

The aggregated albumin adsorbed on plastic syringe was previously reported by measuring the radioactivity remaining on the syringe. Both PVP-30 and Tween 80 were surfactant that used to solve this problem, however the results showed that the addition of both surfactant reduced shelf-life of MAA kit.[3]

There are reports that use albumin solution as surfactant in MAA kit.[2] Generally, albumin solution is used as a stabilizing agent for formulations containing proteins, moreover it has also been used as a cryoprotectant during lyophilization and to prevent the adsorption of other proteins to surfaces.[7]

The aim of this study was to compare the effect of the amount of albumin on percent adsorbed of 99mTc-MAA on plastic syringe.

2. Materials and Methods

2.1 Materials

Albumin solution human 30% concentration was purchased from Sigma-Aldrich Ltd. Stannous chloride dihydrate was obtained from Merck Ltd. 99mTc-pertechnetate generator was supplied by Monrol Ltd. Other chemicals were purchased from Sigma-Aldrich Ltd.

2.2 Formulation of MAA kit

0.25 mL of 30% human albumin solution was dissolved to 1.875 mg/mL in 40 mL sterile water for injection then 1.5 mL of 15 mg/mL stannous chloride dihydrate solution was added. The pH of solution was adjusted to 2.5 and 14 mL of acetate buffer was added to solution., The solution was purged with nitrogen gas thoroughly. Aggregated albumin was formed by heating in water bath at 75°C. Non aggregated was removed, after that HSA at 0.75 mg/mL and 1.50 mg/mL of final volume was added. The solution volume was adjusted to 100 mL by acetate buffer and sterile water for injection. Composition of solution was shown in Table 1. The final bulk solution was dispensed to 1 mL aliquot. The suspension in the vials was lyophilized by Epsilon 2-10D LSC plus model, Martin Christ, Germany.

Table 1. Composition of formulations.

Type of sample	Composition	Concentration
Original Kit	Aggregated albumin	0.75 mg/mL
	Stannous chloride dihydrate	0.2 mg/mL
	Albumin solution human	0 mg/mL
AA0.75AS0.75	Aggregated albumin	0.75 mg/mL
	Stannous chloride dihydrate	0.2 mg/mL
	Albumin solution human	0.75 mg/mL
AA0.75AS1.50	Aggregated albumin	0.75 mg/mL
	Stannous chloride dihydrate	0.2 mg/mL
	Albumin solution human	1.50 mg/mL

2.3 Radiochemical purity

MAA kit was labeled with 30 mCi/ 5mL $Na^{99m}TcO_4$. Radiochemical purity was determined by filtration. Polycarbonate membrane filter and suitable holder were purchased from Merck Ltd. The 0.2 mL of ^{99m}Tc-MAA was placed on the filter, and then was flushed with 20 mL normal saline. The radioactivity remaining on the membrane was measured.

2.4 Percent of MAA adsorbed on plastic syringe

MAA kit was labeled with ^{99m}Tc at calculated activity and volume. One syringe contained 1 mL suspension of 5 mCi of 200,000 particles of aggregated albumin. The 18G x 1/2" hypodemic needle was used. The suspension inside syringe was stand for 10 min and 20 min. The radioactivity remaining on syringe and needle were measured, then the amount adsorbed on syringe was determined.

2.5 Particles size distribution

MAA kit was resuspended in 2 mL sterile water for injection. A syringe fitted with 18G x 1/2" hypodemic needle was used, placed a suitable volume on haemocytometer, and then the number and size of particles were analyzed using microscope (Olympus Ltd.).

2.6 Water content

Water content in MAA kit was determined by Karl Fischer titrator (DL 38 model, Mettler Toledo Ltd.)

3. Results & Discussion

3.1 Radiochemical purity

Radiochemical purity (RCP) of both formulae at month 1 were 96.54 ± 0.21%, and 95.42 ± 0.13% for AA0.75AS0.75 and AA0.75AS1.50, respectively. At month 4, RCP of AA0.75AS0.75 and AA0.75AS1.50 were 94.93 ± 0.17% and 89.35 ± 8.80%, respectively. At month 5, RCP of AA0.75AS0.75 and AA0.75AS1.50 were 94.77 ± 1.49% and 85.04 ± 2.91%, respectively, as shown in Table 2. At month 4 and 5, RCP of AA0.75AS1.50 was less than 90% RCP. Therefore, it could be observed that the amount of albumin solution added as surfactant up to 1.50 mg/mL decreased the RCP.

Table 2. Radiochemical purity of AA0.75AS0.75 and AA0.75AS1.50 at 1, 4, and 5 months after manufacturing.

Formula	Limit	Radiochemical purity (%)		
		Month 1	Month 4	Month 5
AA0.75ASS0.75	90%	96.54±0.21	94.93±0.17	94.77±1.49
AA0.75ASS1.50		95.42±0.13	89.35±8.80	85.04±2.91

3.2 Percent of MAA adsorbed on plastic syringe

Percent of $Na^{99m}TcO_4$ adsorbed on plastic syringe after let stand for 10 min and 20 min were 10.42 ± 0.42 and 9.56 ± 0.87, respectively. While percent of radioactivity of original MAA kit adsorbed on plastic syringe which stood for 10 min and 20 min were 38.45 ± 8.56 and 36.10 ± 8.12, respectively. Moreover, percent adsorbed of AA0.75AS0.75 and AA0.75AS1.50 on plastic syringe were comparable to that of $Na^{99m}TcO_4$ when let stand for 10 min and 20 min, respectively, as seen in Figure 1. As mentioned in previous report that the addition of albumin solution could prevent protein adsorption on the surface.[7] It could

be concluded that both formulae can solve the issue involving the absorption of aggregated proteins on syringe.

However, radiochemical purity (RCP) of AA0.75AS0.75 was shown to be more than limit of RCP (≥90%RCP) for more than 5 months, but that of AA0.75AS1.50 failed to meet criteria after 4 months after manufacturing. Therefore, the AA0.75AS0.75 formula was selected for further study.

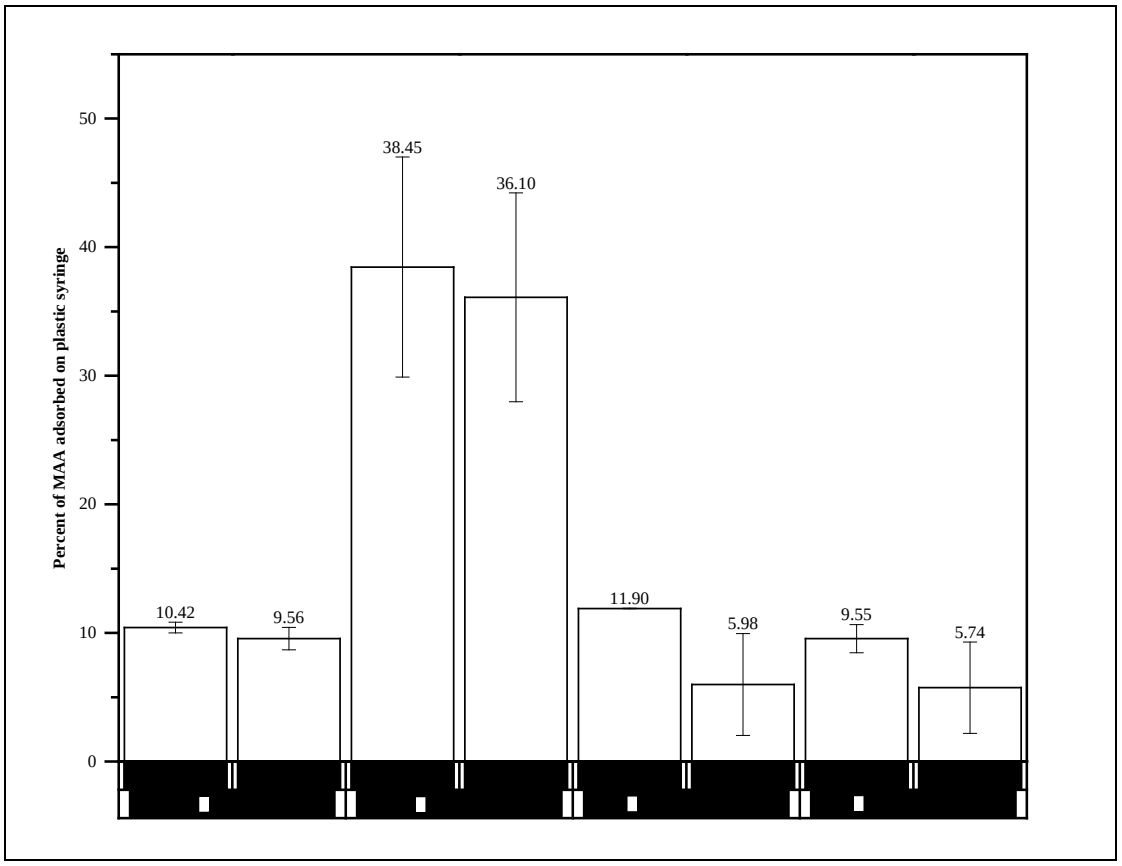

Figure 1. Percent of MAA adsorbed on plastic syringe of $Na^{99m}TcO_4$, original MAA kit, AA0.75AS0.75, and AA0.75AS1.50.

3.3 Particles size distribution

Morphology and particles size distribution of AA0.75AS0.75 and AA0.75AS1.50 were shown in Figure 2. The AA0.75AS0.75 and AA0.75AS1.50 formulae showed similar morphology. Particles size of AA0.75AS0.75 and AA0.75AS1.50 in the range of 10 – 90 μm were 93% and 96% respectively. There was no particle larger 150 μm in both formulae. The mean particle size of AA0.75AS0.75 and AA0.75AS1.50 were 62.81 ± 18.16 μm and 61.50 ± 18.03 μm respectively. Maximum particles size of AA0.75AS0.75 and AA0.75AS1.50 was 133.72 μm and 111.30 μm.

Addition of albumin solution as surfactant in MAA kit showed no effect on morphology and particle size distribution of aggregated albumin.

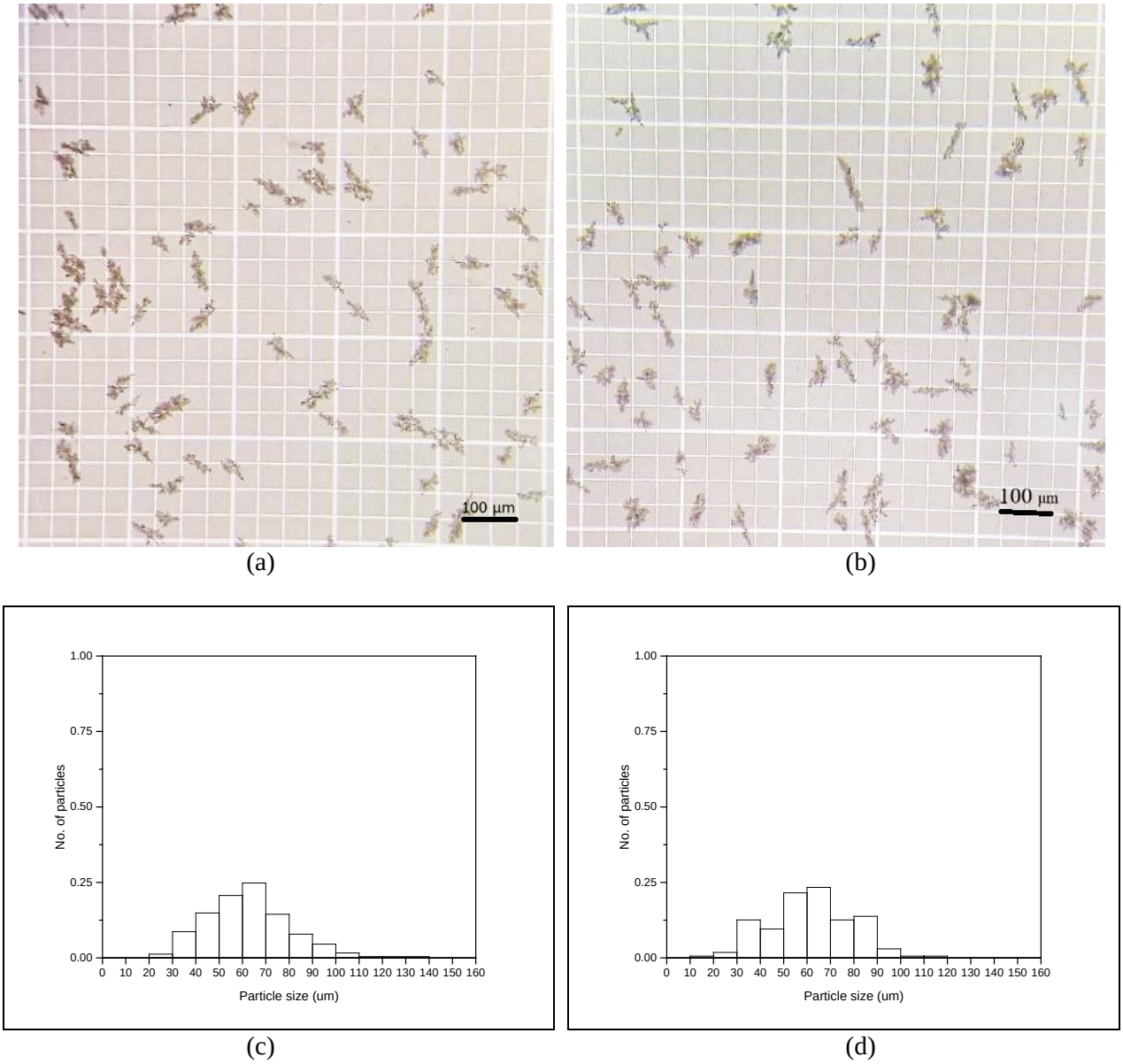

Figure 2. Particle size distribution of AA0.75AS0.75 and AA0.75AS1.50 (a) aggregated albumin on haemocytometer of AA0.75AS0.75 (b) aggregated albumin on haemocytometer of AA0.75AS1.50 (c) particles size distribution of AA0.75AS0.75 and (d) particles size distribution of AA0.75AS1.50

3.4 Water content

Water content of original MAA kit, AA0.75AS0.75, and AA0.75AS1.50 were 4.01 ± 1.01%, 3.62 ± 0.57%, and 4.98 ± 0.98%, respectively. Water content of added surfactant formula was similar to that of the original MAA one.

4. Conclusion

The AA0.75AS0.75 and AA0.75AS1.50 formulation can reduce the aggregated albumin adsorbed on syringe. Both formulations revealed similar properties including morphology, size distribution, and water content. However, the AA0.75AS0.75 formulation showed promising results in terms of %RCP and stability. Therefore, the AA0.75AS0.75 formula was selected for further study.

Acknowledgements

The authors gratefully acknowledge the Thailand Science Research and Innovation (TRSI) for grant no. 2567190612029.

References

1. Kowalsky, R. J.; Falen, S. W., Lung. In *Radiopharmaceuticals in Nuclear Pharmacy & Nuclear Medicine*, second ed.; Landis, N. T., Ed. American Pharmacists Association: Washington DC, 2004; pp 561-587.
2. Hunt, A. P.; Frier, M.; Johnson, R. A.; Berezenko, S.; Perkins, A. C., Preparation of

Tc-99m-macroaggregated albumin from recombinant human albumin for lung perfusion imaging. *European Journal of Pharmaceutics and Biopharmaceutics* **2006,** *62* (1), 26-31.

3. Ilyas, M.; Haider, K. H.; Saeeda, A.; Javed, M.; Shams, Z.; Sameera, C., In-House Preparation and Characterization of Ready-To-Use TC99m-Sn-Macroaggregated Albumin Kit for Lung Perfusion Studies. *Medical Journal of Islamic World Academy of Sciences* **1998,** *11* (4), 131-138.
4. Lyster, D.; Scott, J.; Mincey, E.; Morrison, R., Preparation of a 99mTc-Sn-MAA Kit for Use in Nuclear Medicine. *Journal of nuclear medicine : official publication, Society of Nuclear Medicine* **1974,** *15*, 198-199.
5. Saha, G. B., Radiopharmaceuticals and General Methods of Radiolabeling. In *Fundamentals of Nuclear Pharmacy*, Saha, G. B., Ed. Springer International Publishing: Cham, 2018; pp 93-121.
6. Berit, A. J.; Meta, B. G.; Brita, N. Å., Adsorption of Some Technetium-99m Radiopharmaceuticals onto Disposable Plastic Syringes. *Journal of Nuclear Medicine Technology* **1998,** *26* (3), 196.
7. Rowe;, R. C.; Sheskey;, P. J.; Quinn, M. E., Albumin. In *Handbook of Pharmaceutical Excipients*, 6 ed.; Pharmaceutical Press and American Pharmacists Association: USA, 2009; pp 14-16.

Production and quality control of ^{177}Lu-PSMA for prostate cancer treatment

Suppamat Makjan*, Kanyapat Lumyong, Chotiwid Wiriyachailerd, Sudkanung Phumkem, Boon-Uma Jowanaridhi, and Thanete Duangta

Radioisotope Center, Thailand Institute of Nuclear Technology (Public Organization), Bangkok, Thailand

**E-mail: suppamat@tint.or.th*

Abstract:

Prostate Specific Membrane Antigen (PSMA) is an important target in nuclear medicine owing to its overexpression in metastatic castration-resistant prostate cancer. ^{177}Lu-PSMA is a targeted radionuclide therapy that is currently an alternative for prostate cancer treatment. The aim of this research was to study the preparation and quality control of ^{177}Lu-PSMA-617 and ^{177}Lu-PSMA-I&T. The radiochemical purity (RCP) evaluation was carried out by high-performance liquid chromatography (HPLC) and thin-layer chromatography (TLC). The results of ^{177}Lu-PSMA-617 and ^{177}Lu-PSMA-I&T prepared in this study revealed that the RCP was >95.0% at room temperature, pH 5. The two radiopharmaceuticals remained stable in saline up to 48 h after radiolabeling and bacterial endotoxins complied with the endotoxin limit for parenteral drugs. In conclusion, both ^{177}Lu-PSMA-617 and ^{177}Lu-PSMA-I&T are highly stable radiolabeled compounds. The combination of HPLC and TLC provides a reliable quality control method for ^{177}Lu-PSMA-617 and ^{177}Lu-PSMA-I&T.

1. Introduction

Prostate cancer is the second most common cancer and the fifth leading cause of cancer death in men worldwide. In 2020, there were an estimated 1,414,000 new cancer cases and 375,304 deaths.[1] Although there are several treatment options such as prostectomy, orchidectomy, chemotherapy and radiation therapy to treat prostate cancer.[2] Targeted radionuclide therapy is an effective treatment option to treat patients having metastatic castration-resistant prostate cancer (mCRPC).

Prostate specific membrane antigen (PSMA) is a type II membrane glycoprotein overexpressed in prostate cancer cell.[3] This makes PSMA an excellent target for prostate cancer imaging and therapy using gallium-68 (^{68}Ga) and lutetium-177 (^{177}Lu) labeled ligands.[4]

Currently, ^{177}Lu-labeled PSMA ligand such as ^{177}Lu-PSMA-617 and ^{177}Lu-PSMA-I&T, are therapeutic radiopharmaceuticals in the clinical management of prostate cancer.[5] ^{177}Lu-PSMA-617 has been approved by the FDA for the treatment of prostate cancer patients.[6] ^{177}Lu-PSMA-I&T has proven high efficiency and safety in treating patients with metastatic castration-resistant prostate cancer.[7] The structure of ^{177}Lu-PSMA-617 and ^{177}Lu-PSMA-I&T are shown in Figure 1.

Lutetium-177 (^{177}Lu) can be obtained via two different routes. Non-carrier added (NCA) ^{177}Lu is produced by indirect production route and carrier added (CA) ^{177}Lu is produced by direct production route. NCA ^{177}Lu has high specific activity and longer shelf-life.[8] Therefore, NCA ^{177}Lu was used in this study.

The aim of this research was to study the preparation and quality control of ^{177}Lu-PSMA-617 and ^{177}Lu-PSMA-I&T.

2. Materials and Methods

2.1 Materials

PSMA-617 peptide was purchased from Center of Molecular Research (CMR) (Russia), PSMA-I&T peptide was purchased from ABX advanced biochemical compounds (Germany), ammonium acetate and sodium L-ascorbate was purchased from Sigma-Aldrich (USA).

Lutetium chloride ($LuCl_3$, ^{177}Lu) was purchased from ITM Medical Isotopes (Germany) and Eczacıbaşı – Monrol (İstanbul). ^{177}Lu having a specific activity ≥3000 GBq/mg and radioactive concentration in the range of 36-44 GBq/mL.

All radioactivity measurements were done using Capintec CRC-55tR dose calibrator.

2.2 Preparation of reagents

One mg of PSMA was dissolved in 500 µL of 10% ethanol and aliquots of 75 µL and 100 µL were dispensed in 1 mL Eppendorf tubes and frozen at -20°C. 1.0 M ammonium acetate buffer was prepared by weighing 19.27 g and dissolved in 250 mL of Sterile Water for Injection (SWI), 5.5 mL of glacial acetic acid (HOAc) was added to this solution to give a final pH ~5.0. Ascorbate solution was prepared by dissolving sodium L-ascorbate 200 mg in 2 mL of 1.0 M ammonium acetate buffer.

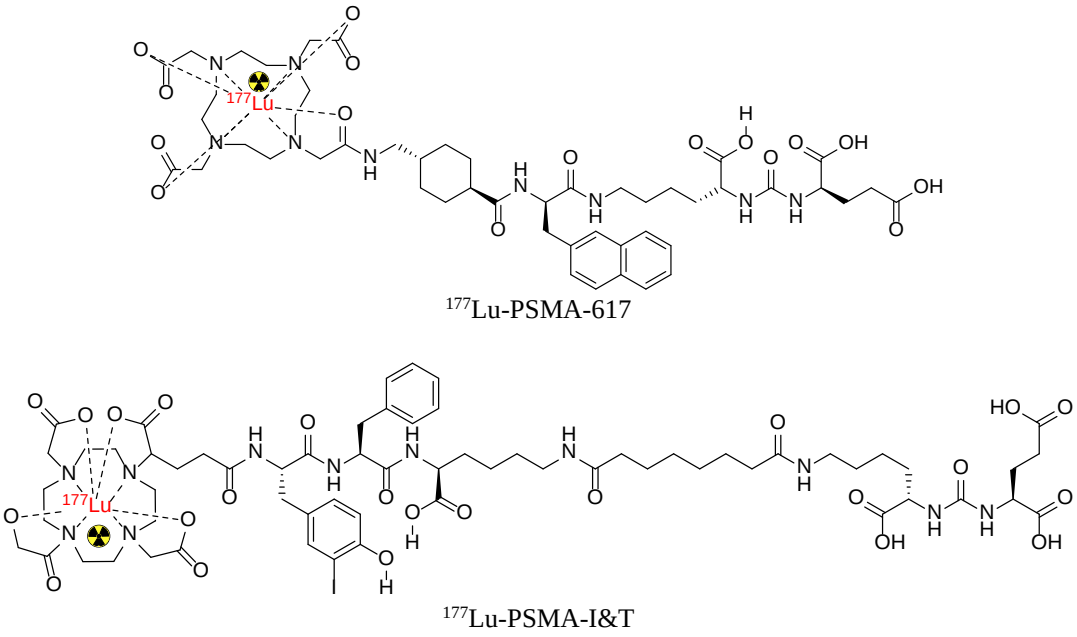

^{177}Lu-PSMA-617

^{177}Lu-PSMA-I&T

Figure 1. The structure of ^{177}Lu-PSMA-617 and ^{177}Lu-PSMA-I&T.

2.3 Preparation of ^{177}Lu-PSMA

^{177}Lu-PSMA-617

^{177}Lu-PSMA-617 was prepared by addition of $LuCl_3$ solution (41 GBq/ml) and ascorbate solution 0.7 mL into 10 mL sterile vacuum vial (reaction vial). The mixture of PSMA-617 with 0.3 mL ascorbate solution was added into the reaction vial. The pH of the solution was confirmed to be 4.5-5.0. The reaction mixture was heated at 95°C for 30 min in a dry block heater. After cooling down of the reaction vial to room temperature the volume was added 5 mL of ascorbate solution (20 mg/mL in saline). After sterile filtration (0.22 µm) of this preparation to a sterile vial the volume was completed to 20 mL with sterile saline under aseptic conditions.

^{177}Lu-PSMA-I&T

^{177}Lu-PSMA-I&T was prepared similar to the preparation of ^{177}Lu-PSMA-617 but after cooling down of the reaction vial, 5 mL of ascorbate solution (40 mg/mL in saline) was added, the volume was diluted with sterile saline solution, and the preparation was filter-sterilized (0.22 µm).

The radiochemical purity (RCP) of the radiopharmaceutical was determined immediately after radiolabeling by thin layer chromatography (TLC) and high-performance liquid chromatography (HPLC). The radionuclidic purity (RNP), sterility, and bacterial endotoxins were also evaluated.

2.4 Quality control

Quality control studies involving the determination of radiochemical purity of ^{177}Lu-PSMA were carried out by TLC and HPLC. TLC was performed using 0.1 M sodium citrate buffer pH 5 (System A) and methanol : 1 M ammonium acetate (1:1) (System B). HPLC was performed using Ultremex C18 5µm, 80 Å, 4.6 x 250 mm as the stationary phase and 0.1% tri-fluoro acetic acid (TFA) in water (Solvent A) and acetonitrile (Solvent B) as the mobile phase. The gradient solvent system of HPLC was shown in Table 1.

Table 1. Reverse-phase HPLC was performed using a gradient solvent system comprising 0.1% TFA (A) and acetonitrile (B) as the mobile phase

Time (min)	Solvent A (%)	Solvent B (%)
0 - 3	100	0
3 – 5	40	60
5 – 15	40	60
15 – 18	100	0
18 – 23	100	0

The flow rate of the eluting solvent mixture was maintained at 1 mL/min, and the elution profile was monitored by detecting the radioactivity signal related with the eluting solvent.

The radionuclidic purity was determined in gamma spectroscopy using a high-purity germanium (HPGe) detector in combination with a multi-channel analyzer (MCA).

Stability of ^{177}Lu-PSMA was analyzed by HPLC and TLC method at 0 and 48 h after radiolabeling. A sample of ^{177}Lu-PSMA solution was kept at room temperature for up to 48 h.

Sterility and endotoxin assays were performed according to United States

Pharmacopeia (USP). In the sterility test, a sample of ^{177}Lu-PSMA was incubated in fluid thioglycollate medium (FTM) and soybean casein digest medium (SCDM) at 30 – 35 ºC and 20 – 25 ºC, respectively, for 14 days. The bacterial endotoxin test was performed using LAL Test (Limulus Amebocyte lysate Test). A sample of ^{177}Lu-PSMA was added into a tube of LAL with 0.2 mL. The tube was incubated at 37 ± 1 ºC for 60 ± 2 minutes.

3. Results & Discussion

3.1 Preparation of ^{177}Lu-PSMA

Process validation was carried out by producing six different batches of ^{177}Lu-PSMA-617 and ^{177}Lu-PSMA-I&T in the same conditions set for representative routine preparations. Each batch was prepared according to the validation protocol, with the purpose to verify that the product meets the acceptance criteria as for all the established quality parameters. The results were summarized in Table 2.

Table 2. Details of the preparation of ^{177}Lu-PSMA-617 and ^{177}Lu-PSMA-I&T

	Activity of $LuCl_3$ (mCi)	Amount of PSMA (µg)	RCY (%)	RCP (%)	pH
^{177}Lu-PSMA-617					
1st batch	184.0	150	99.62	99.84	5.0
2nd batch	186.7	150	95.61	98.80	5.0
3rd batch	239.0	200	100.00	99.66	5.0
^{177}Lu-PSMA-I&T					
1st batch	221.0	200	91.40	99.67	5.0
2nd batch	246.0	200	99.59	99.03	5.0
3rd batch	247.0	200	97.57	95.23	5.0

For ^{177}Lu-PSMA-617, the first batch was prepared with 184.0 mCi (6.81 GBq) of $^{177}LuCl_3$ and 150 µg of PSMA peptide. The radiochemical yield at the end of preparation was 99.62%. In the second batch, 186.7 mCi (6.91 GBq) of $^{177}LuCl_3$ was used with 150 µg of PSMA peptide and a radiochemical yield of 95.61% could be obtained. The third batch was prepared with 239.0 mCi (8.84 GBq) of activity and 200 µg of PSMA peptide, radiochemical yield was 100%.

For ^{177}Lu-PSMA-I&T. The first, second and third batch were prepared with 211 mCi (7.81 GBq), 246 mCi (9.10 GBq) and 247 mCi (9.14 GBq) of $^{177}LuCl_3$ and 200 µg of PSMA peptide, respectively. The radiochemical yields were 91.40%, 99.59% and 97.57%, respectively.

The radiochemical yield and radiochemical purity of all products was >91.4% and >95.23%, respectively at room temperature and pH 5. The products were done without purification.

3.2 Quality control

Radiochemical purity (RCP)

Thin-Layer Chromatography (TLC) was performed using a silica gel 60 (Merck, Germany). In TLC, carried out using 0.1 M sodium citrate buffer pH 5 (System A) as the mobile phase, ^{177}Lu-PSMA-617 moved towards the solvent front (R_f = 0.9-1.0), while ^{177}Lu-colloid remained at point of spotting (R_f = 0.0-0.1) under identical conditions. On the other hand, TLC was carried out using methanol : 1 M ammonium acetate (1:1) (System B), ^{177}Lu-PSMA-617 remained at the spotting (R_f = 0.0-0.1), while free ^{177}Lu moved to the solvent front (R_f = 0.9-1.0). Analyses of TLC data showed that ^{177}Lu-PSMA-617 could be obtained with >98.80% radiochemical purity. TLC profiles of free $^{177}LuCl_3$ with ^{177}Lu-PSMA-617 and ^{177}Lucolloid with ^{177}Lu-PSMA-617 were shown in Figures 2(a) and 2(b), respectively. Correspondingly, TLC patterns of ^{177}Lu-PSMA-I&T were shown in Figures 3(a) and 3(b). The radiochemical purity of ^{177}Lu-PSMA-I&T was >95.23%. The TLC data indicated that ^{177}Lu-PSMA-617 and ^{177}Lu-PSMA-I&T gave similar results under identical conditions. Thus, TLC method with two solvent systems suggested that System A was achieved to separate ^{177}Lu-PSMA from ^{177}Lu-colloid, and System B also separated ^{177}Lu-PSMA from free ^{177}Lu.

High Performance Liquid Chromatography (HPLC) was performed on Waters 600 system equipped by a UV detector coupled with a radiometric detector. The column was an Phenomenex Ultremex C18, 5 µm, 80 Å, 250 x 4.6 mm with guard column C18. A multi-step gradient was applied using 0.1% TFA in water (Solvent A) and acetonitrile (Solvent B). The radiochemical purity of the ^{177}Lu-PSMA was further confirmed by HPLC studies, where ^{177}Lu-PSMA revealed a retention time of approximately 13.0 min while free $^{177}LuCl_3$ eluted with a retention time of approximately 3.0 min. HPLC studies also exhibited that ^{177}Lu-PSMA-617 and ^{177}Lu-PSMA-

I&T could be obtained with radiochemical purity of 99.59 ± 1.0% and 99.71 ± 1.0%, respectively. HPLC profiles of ^{177}Lu-PSMA-617 and ^{177}Lu-PSMA-I&T were shown in Figure 4(a) and 4(b).

Radionuclidic purity (RNP)

Gamma spectroscopy was used for the measurement of the radionuclidic purity of radiopharmaceuticals. The result presented that the two radiopharmaceuticals were 100% radionuclidic purity. High purity germanium detectors are required to detect impurities of less than 0.1%. For identification, the same method was used to compare γ energies lines characteristics of the radionuclide. *Stability*

The radiopharmaceuticals remained stable in saline up to 48 h after radiolabeling at room temperature. The radiochemical purity at 48 h was found >99.01% for ^{177}Lu-PSMA-617 and 95.00% for ^{177}Lu-PSMA-I&T. The stability data were shown in Table 3 and 4. The analysis of the radiochemical purity was carried out by HPLC and TLC because the TLC method was used to detect the presence of ^{177}Lu-colloid that was not detectable with HPLC analysis. The sterility and bacterial endotoxins complied with the endotoxin limit for parenteral drugs.

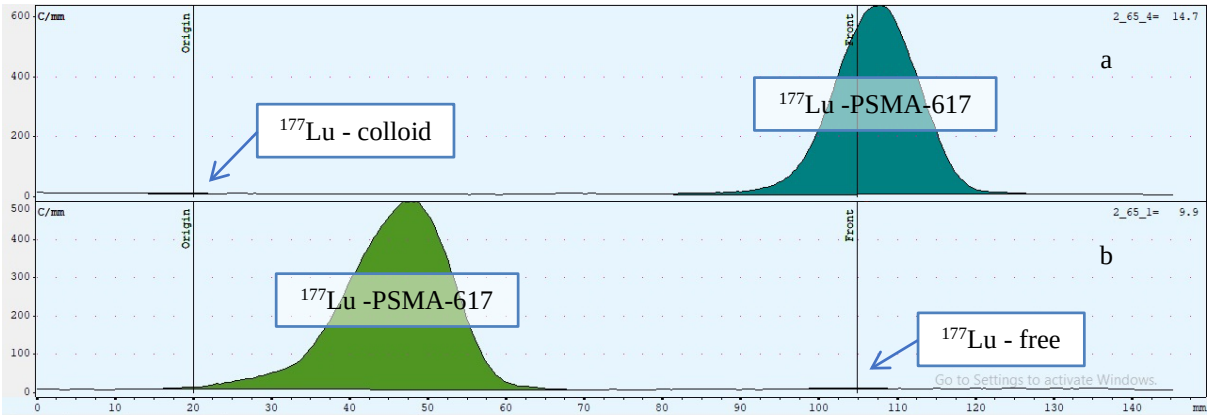

Figure 2. TLC patterns of free ^{177}Lu and ^{177}Lu-PSMA-617 obtained using (a) 0.1 M sodium citrate buffer pH 5 (System A) and (b) methanol : 1 M ammonium acetate (1:1) (System B).

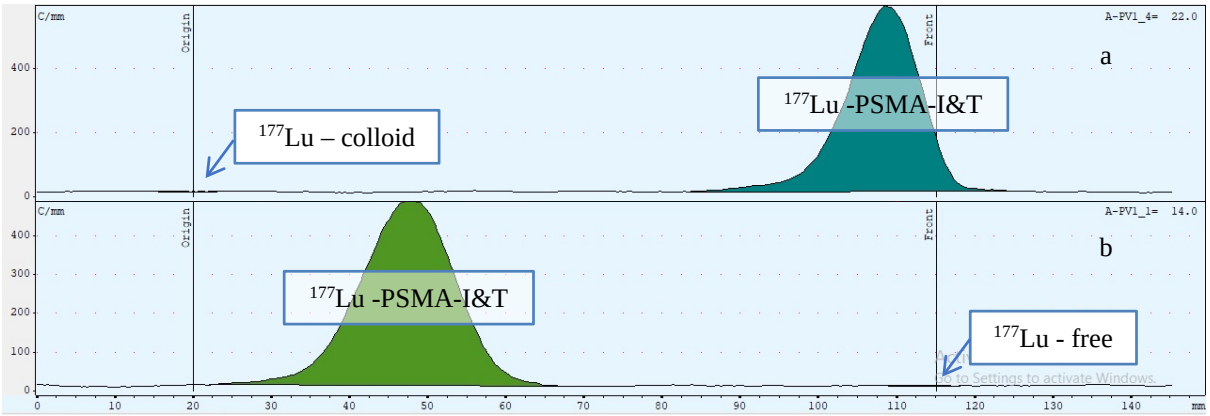

Figure 3. TLC patterns of free ^{177}Lu and ^{177}Lu-PSMA-I&T obtained using (a) 0.1 M sodium citrate buffer pH 5 (System A) and (b) methanol : 1 M ammonium acetate (1:1) (System B).

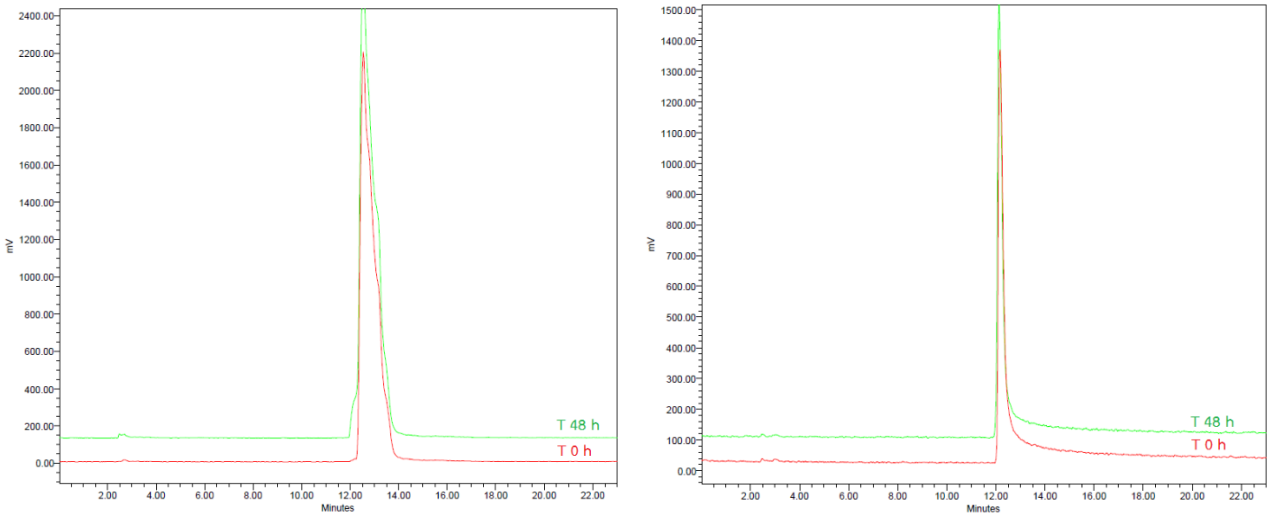

Figure 4. HPLC profiles of (a) ^{177}Lu-PSMA-617 and (b) ^{177}Lu-PSMA-I&T

Table 3. Stability data of ^{177}Lu-PSMA-617 at T0 and after 48 h at room temperature.

Parameter	Acceptance Criteria	1st batch	2nd batch	3rd batch
Appearance	Clear colorless to light amber solution	Complies	Complies	Complies
pH	4.0 – 6.0	5.0	5.0	5.0
Radionuclide identification	Major photopeak at 0.113 MeV and 0.208 MeV	Complies	Complies	Complies
%RNP	Lu-177 ≥ 99.9%	100.0	100.0	100.0
%RCP at T0	^{177}Lu-PSMA-617 ≥ 95.0%	99.84	98.80	99.66
%RCP at T48	^{177}Lu-PSMA-617 ≥ 95.0%	99.01	98.10	99.31
Sterility test	Bacterial & Fungi absence (-ve)	Complies	Complies	Complies
Bacterial endotoxin	< 8.75 EU/mL (Maximum volume = 20 mL)	Complies	Complies	Complies

Table 4. Stability data of ^{177}Lu-PSMA-I&T at T0 and after 48 h at room temperature.

Parameter	Acceptance Criteria	1st batch	2nd batch	3rd batch
Appearance	Clear colorless to light amber solution	Complies	Complies	Complies
pH	4.0 – 6.0	5.0	5.0	5.0
Radionuclide identification	Major photopeak at 0.113 MeV and 0.208 MeV	Complies	Complies	Complies
%RNP	Lu-177 ≥ 99.9%	100.0	100.0	100.0
%RCP at T0	^{177}Lu-PSMA-I&T ≥ 95.0%	99.67	99.03	95.23
%RCP at T48	^{177}Lu-PSMA-I&T ≥ 95.0%	99.54	99.35	95.00
Sterility test	Bacterial & Fungi absence (-ve)	Complies	Complies	Complies
Bacterial endotoxin	< 8.75 EU/mL (Maximum volume = 20 mL)	Complies	Complies	Complies

The most significant quality problem in preparation of ^{177}Lu-PSMA-I&T was the poor stability of the finished product when diluted with saline to a final volume of 20 mL. ^{177}Lu-PSMA-I&T was found to be instable in saline solution (<95% radiochemical purity after 48 h), while ^{177}Lu-PSMA-617 was stable in saline. This result could be described to ^{177}Lu-PSMA-617 and ^{177}Lu-PSMA-I&T having different linkers that were affected differently by radiolysis.

The two molecules (PSMA-617 and PSMA-I&T) showed slight differences in solubility characteristics. However, they were not require significant changes in the buffer solutions. In regard to quality parameters, the experimental results from the six batches of ^{177}Lu-PSMA-617 and ^{177}Lu-PSMA-I&T satisfied the specifications.

Additionally, the radiolabeling conditions always led to a high radiochemical yield. To prevent radiolysis of the radiopharmaceutical, the radiolabeling was carried out in presence of ascorbate.

4. Conclusion

In conclusion, ^{177}Lu-PSMA-617 and ^{177}Lu-PSMA-I&T can be prepared as radiopharmaceuticals suitable for prostate cancer treatment. They were highly stable radiolabeled compounds under established preparation. However, adding ascorbic acid to the preparation solution was importance because ^{177}Lu-PSMA-I&T was quickly undergone degradation, especially if stored at room temperature. The combination of HPLC and TLC provided a reliable quality control method for ^{177}Lu-PSMA-617 and ^{177}Lu-PSMA-I&T.

References

1. Sung, H.; Ferlay, J.; Siegel, R. L.; Laversanne, M.; Soerjomataram, I.; Jemal, A.; Bray, F. Global Cancer Statistics 2020: GLOBOCAN Estimates of Incidence and Mortality Worldwide for 36 Cancers in 185 Countries. *CA: a Cancer Journal for Clinicians* **2021**, 71 (3), 209–249.
2. Nanabala, R.; Sasikumar, A.; Joy, A.; Pillai, M. Preparation of [177Lu]PSMA-617 Using Carrier Added (CA) 177Lu for Radionuclide Therapy of Prostate Cancer. *Journal of Nuclear Medicine & Radiation Therapy* **2016**, 7 (5).
3. Chakravarty, R.; Chakraborty, S. A Review of Advances in the Last Decade on Targeted Cancer Therapy Using 177Lu: Focusing on 177Lu Produced by the Direct Neutron Activation Route. *American Journal of Nuclear Medicine and Molecular Imaging* **2021**, 11 (6), 443–475.
4. Kabasakal, L.; Toklu, T.; Yeyin, N.; Demirci, E.; Abuqbeitah, M.; Ocak, M.; Aygün, A.; Karayel, E.; Pehlivanoğlu, H.; Alan Selçuk, N. Lu-177-PSMA-617 Prostate-Specific Membrane Antigen Inhibitor Therapy in Patients with Castration-Resistant Prostate Cancer: Stability, Bio-Distribution and Dosimetry. *Malecular Imaging and Radionuclide Therapy* **2017**, 26 (2), 62–68.
5. Eline; Nicole van Vliet; Dalm, S. U.; Erik de Blois; Gent, van; Haeck, J.; Corrina de Ridder; Stuurman, D.; Konijnenberg, M.; Weerden, van; Marion de Jong; Nonnekens, J. Extensive Preclinical Evaluation of Lutetium-177-Labeled PSMA-Specific Tracers for Prostate Cancer Radionuclide Therapy. *European Journal of Nuclear Medicine and Molecular Imaging* **2020**, 48 (5), 1339–1350.
6. Hennrich, U.; Eder, M. [177Lu]Lu-PSMA-617 (PluvictoTM): The First FDA-Approved Radiotherapeutical for Treatment of Prostate Cancer. *Pharmaceuticals* **2022**, 15 (10), 1292.
7. Bu, T.; Zhang, L.; Yu, F.; Yao, X.; Wu, W.; Zhang, P.; Shi, L.; Zang, S.; Meng, Q.; Ni, Y.; Shao, G.; Qiu, X.; Ai, S.; Jia, R.; Guo, H.; Wang, R. 177Lu-PSMA-I&T Radioligand Therapy for Treating Metastatic Castration-Resistant Prostate Cancer: A Single-Centre Study in East Asians. *Frontiers in Oncology* **2022**, 12.
8. Dash, A.; Pillai, M. R. A.; Knapp, F. F. Production of 177Lu for Targeted Radionuclide Therapy: Available Options. *Nuclear Medicine and Molecular Imaging* **2015**, 49 (2), 85–107.

Radiolabeling of DFO-NCS and DFO*-NCS siderophore chelator with zirconium-89 radiometal

Kanyapat Lumyong[1]*, Thidarat Kohud[1], Suppamat Makjan[1], Thanete Duangta[1], Boon-Uma Jowanaridhi[1], Chotiwid Wiriyachailerd[1], Sudkanung Phumkem[1], Siriwat Thida[1], Wiranee Sriwiang[2], and Piriya Kaeopookum[2]

[1]*Radioisotope Center, Thailand Institute of Nuclear Technology (Public Organization), Nakorn Nayok 26120, Thailand*
[2]*Nuclear Technology Research and Development Center, Thailand Institute of Nuclear Technology (Public Organization), Nakorn Nayok 26120, Thailand*

**E-mail: kanyapat@tint.or.th*

Abstract:

Over the past few years, zirconium-89 (^{89}Zr) labeled with monoclonal antibodies (mAbs) has emerged as a crucial diagnostic tool for a wide range of cancer types, for example, [^{89}Zr]Zr-J591 is used to identify PSMA-expressing tumors in patients with prostate cancer, and [^{89}Zr]Zr-trastuzumab is used to detect breast cancer. Chelation agents play the important roles for the radiometal ^{89}Zr to compound and attach to the mAbs. Although desferrioxamine (DFO) is now widely employed in clinical purposes, it has been demonstrated that in many of these cases, the [^{89}Zr]Zr-DFO complex has low stability and can release the radiometal ^{89}Zr, resulting in unnecessary bone uptake. In order to increase the stability of the [^{89}Zr]Zr-DFO complex, DFO derivatives have been developed. The aim of this research was to compare the radiolabeling yield of DFO*-NCS octadentate chelator and DFO-NCS hexadentate chelator labeled with ^{89}Zr. The results have shown that the [^{89}Zr]Zr-DFO-NCS had a high radiochemical yield of up to >99% in 30 minutes at room temperature and pH 7.5. On the contrary, [^{89}Zr]Zr-DFO*-NCS had a high radiochemical yield of up to >99% in 1 hour at the same conditions. But after 90 minutes, the radiochemical purity of [^{89}Zr]Zr-DFO-NCS slightly declined to 98%, whereas [^{89}Zr]Zr-DFO*-NCS continued to have a high radiochemical yield of up to >99% throughout the same period. In conclusion, as a comparison, DFO*-NCS was more stable than DFO-NCS throughout the same duration, although the DFO-NCS chelator connected to the ^{89}Zr more rapidly. This investigation is intended to be preliminary exploration for the development of Zr-89 radiopharmaceuticals.

1. Introduction

Molecular imaging aims to study the biological characteristics of tumors in order to uncover their phenotype, which assists in the identification of the most suitable targeted cancer treatments and the monitoring of tumor response to therapy.[1] Positron emission tomography (PET) is one of the most delicate technologies for medical imaging. ^{89}Zr-immuno-PET is a noninvasive imaging technology that is utilized to identify the level of interaction between therapeutic antibodies (or mAb conjugates) and their targets in the body.[2] Potential future uses of this clinical tool include the identification of monoclonal antibodies (mAbs) for drug development and the selection of patients who are expected to respond well to therapy.

In the past ten years, there has been a significant rise in the application of ^{89}Zr-labelled monoclonal antibodies (mAbs) in clinical research. This growth serves as strong evidence for the significance of immuno-positron emission tomography (PET) imaging, particularly in the field of cancer.[3] Having a half-life of 78.4 hours, ^{89}Zr is ideal for investigating the kinetics of compounds that have relatively prolonged plasma half-lives. At present, most ^{89}Zr immuno-PET investigations utilize desferrioxamine B (DFO). DFO is commonly employed as a chelator for the purpose of labeling ^{89}Zr. Nevertheless, there are limitations when it comes to DFO use as a chelator for ^{89}Zr. The ^{89}Zr-DFO complex has a tendency to disintegrate *in vivo*, leading to the buildup of unbound $^{89}Zr^{4+}$ in the bones and joints.[4] Consequently, this leads to an increasing level of noise in the PET image and unnecessary radiation exposure to patients. These issues have led to the creation of many octadentate chelators for ^{89}Zr, which are expected to enhance the stability of the ^{89}Zr complexes. The novel chelator, DFO*-NCS octadentate chelator, which is derived from DFO, has shown initial enhancements in performance *in vitro* and *in vivo* when compared to DFO.[5] These chelators are now being evaluated for potential therapeutic use.

The objective of this study was to evaluate the radiolabeling efficiency and stability of DFO*-NCS octadentate chelator and DFO-NCS hexadentate chelator labeled with ^{89}Zr. The stability was examined at 37 °C in both serum and formulation solution. This research project aims to be utilized as an initial exploration for the future development of Zr-89 radiopharmaceuticals.

2. Materials and Methods

2.1 Materials

All chemicals were purchased from Sigma Aldrich® (USA) (DMSO, Na_2CO_3, oxalic acid, gentisic acid and 1 M HEPES). Zirconium-89 in 1 mol/L oxalic acid was obtained from Revvity Ltd. (USA). Ultrapure water produced by a Barnstead™ Smart2Pure™ Water Purification System from Thermofisher scientific (USA) was used throughout (18.2 MΩ cm). *p*-SCN-Bn-deferoxamine (B-705), also known as DFO-NCS, was acquired from Macrocyclics Inc. (Dallas, TX, USA). DFO*-NCS was obtained from ABX advanced biochemical compounds GmbH (Germany). Instant Thin Layer Chromatography Medium (iTLC) with binderless, glass microfiber chromatography paper impregnated with silica gel (SG) was purchased from Agilent (USA).

2.2 Preparation of chelators

To prepare stock solutions of the chelators at a concentration of 1 mM, dissolve 7.5 mg of DFO-NCS and 5 mg of DFO*-NCS in DMSO. Both chelator solutions were thoroughly sonicated in order to encourage complete dissolution.

2.3 Synthesis of ^{89}Zr-labelled compounds

Approximately 15 MBq of ^{89}Zr-oxalate was transferred into a low-protein binding Eppendorf tube and diluted with 0.1 M oxalic acid (pH 1) to a total volume of 200 µL. Subsequently, a 90 µL of 2 M sodium carbonate solution was added into the mixture, which was then allowed to incubate for 3 min at room temperature (pH 6–7). 50 µL of DFO-NCS and DFO*-NCS stock solutions (50 nmol) were diluted with water to a volume of 200 µL and added to the ^{89}Zr solution. A 0.5 M HEPES buffer with a pH of 7.4 was added to obtain a final volume of 1 mL, resulting in precursor concentrations of 50 µM.

2.4 In vitro stability

The in vitro stability was assessed using two sets of studies. The initial tests involved formulating the [^{89}Zr]Zr-DFO-NCS and [^{89}Zr]Zr-DFO*-NCS (Figure 1) complexes according to the procedure described in Section 2.3. These complexes were subsequently stored at room temperature in a formulation solution with a pH range of 7.0–7.5. The samples were tested for radiochemical purity at time intervals of 15 minutes, 30 minutes, 60 minutes, 90 minutes, 24 hours, 48 hours, 72 hours, and 120 hours using radio-iTLC with iTLC-SG.

In a subsequent trial, the [^{89}Zr]Zr-DFO-NCS and [^{89}Zr]Zr-DFO*-NCS compounds were incubated in the presence of fetal bovine serum (FBS). Each of the complexes in the formulation buffer, adjusted to pH = 7 with 2 M Na_2CO_3, was incubated with 100 microliters in 900 µL of FBS serum. The samples were incubated for 5 days at a temperature of 37 °C in an incubator. The starting pH of the solution remained steady at 7 throughout the incubation time, with observed values ranging from 7.0 to 7.3. The radiochemical purity was assessed by radio-iTLC with iTLC-SG at various times.

2.5 Quality Controls

The radiochemical purity of [^{89}Zr]Zr-DFO-NCS and [^{89}Zr]Zr-DFO*-NCS complexes was assessed using Radio-iTLC with iTLC-SG. Each sample was prepared twice. In order to choose an appropriate solvent system for analyzing radiochemical purity, a comparison was made between two systems: 0.1 M Citrate buffer with a pH of 4.0, and 50 mM diethylenetriamine-pentaacetic acid (DTPA) solution.

Radio-iTLC evaluated the stability of [^{89}Zr]Zr-DFO-NCS and [^{89}Zr]Zr-DFO*-NCS complexes at various time intervals: 15 minutes, 30 minutes, 60 minutes, 90 minutes, 24 hours, 48 hours, 72 hours, and 120 hours after radiolabeling in formulation solution at room temperature and in fetal bovine serum (FBS) at 37 °C at 15 minutes, 3 hours, 6 hours, 24 hours, 48 hours.

The radionuclidic purity was assessed using gamma spectroscopy utilizing a high-purity germanium (HPGe) detector combined with a multi-channel analyzer (MCA).

3. Results & Discussion

Radiolabeling [^{89}Zr]Zr-DFO-NCS and [^{89}Zr]Zr-DFO*-NCS complexes was examined utilizing Radio-iTLC using Instant Thin Layer Chromatography Medium including binderless, glass microfibre chromatography paper soaked with silica gel (iTLC-SG) at certain time periods.

In this investigation, we compared two solvent systems: a 0.1 M Citrate buffer with a pH of 4.0, and a 50 mM DTPA solution, as the mobile phase. The purpose was to determine the most suitable solvent system for evaluating radio-chemical purity at time intervals that varied from 15 to 120 minutes.

The initial experiment involved assessing the radiochemical purity of complexes using

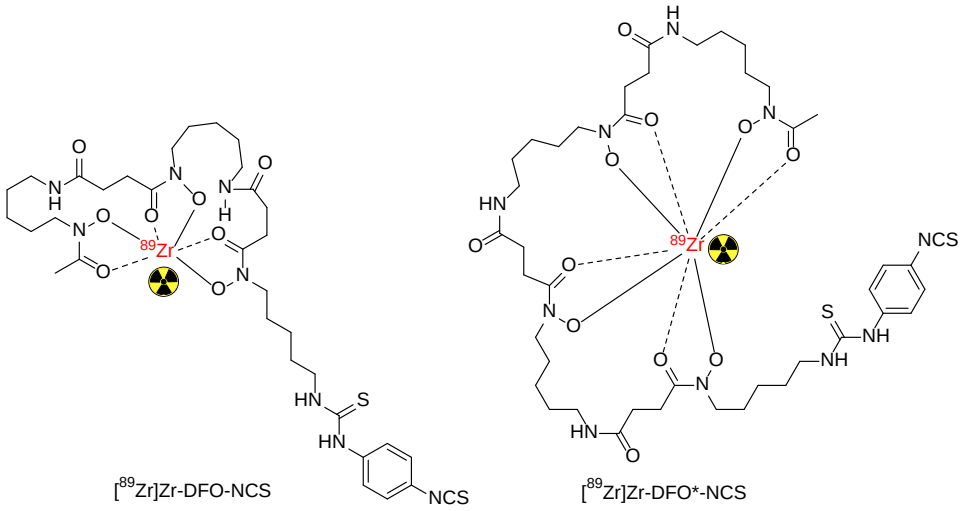

Figure 1. Structures of [^{89}Zr]Zr-DFO-NCS (A) and [^{89}Zr]Zr-DFO*-NCS (B).

iTLC-SG. A 50 mM DTPA solution was used as the mobile phase. The complexes [^{89}Zr]Zr-DFO-NCS and [^{89}Zr]Zr-DFO*-NCS were found to remain at the origin spotting, with a retention factor (Rf) value of 0.1-0.2. On the other hand, unbound ^{89}Zr migrated to the solvent front, with an Rf value of 1.0-1.1.

In another trial, the similar approach was employed with the exception that a 0.1 M Citrate buffer with a pH of 4.0 was utilized as the mobile phase.

Table 1 shows the percentages of radiochemical purity (%RCP) of [^{89}Zr]Zr-DFO-NCS and [^{89}Zr]Zr-DFO*-NCS in two different solvent systems. Figure 2A and 2B depict radio-thin-layer chromatography (radio-TLC) chromatograms of [^{89}Zr]Zr-DFO*-NCS running in 50 mM DTPA and 0.1 M citrate buffer (pH 4.0), respectively.

Based on the analysis of the Radio-TLC chromatograms and %RCP, there was not a significant deviation in the results obtained from the two solvent systems. Therefore, any of the two systems, particularly 50 mM DTPA and 0.1 M Citrate buffer (pH 4.0), could potentially be utilized appropriately for quality control of both Zr-89 complexes.

For our subsequent study, we examined the stability of [^{89}Zr]Zr-DFO-NCS and [^{89}Zr]Zr-DFO*-NCS in a formulation solution at room temperature and in fetal bovine serum (FBS) at 37 $^{\circ}$C. The outcomes are displayed in Table 2 and 3.

Table 1. Percentage of radiochemical purity of [^{89}Zr]Zr-DFO-NCS and [^{89}Zr]Zr-DFO*-NCS in various solvent systems

Time (min)	Percentage of radiochemical purity (%RCP)			
	[^{89}Zr]Zr-DFO-NCS		[^{89}Zr]Zr-DFO*-NCS	
	50 mM DTPA	0.1 M Citrate buffer (pH 4.0)	50 mM DTPA	0.1 M Citrate Buffer (pH 4.0)
15	98.24	97.92	97.06	95.81
30	99.14	99.10	98.70	99.04
60	98.90	98.84	99.54	99.61
90	98.53	98.55	99.19	99.18
120	98.41	98.47	99.50	99.51

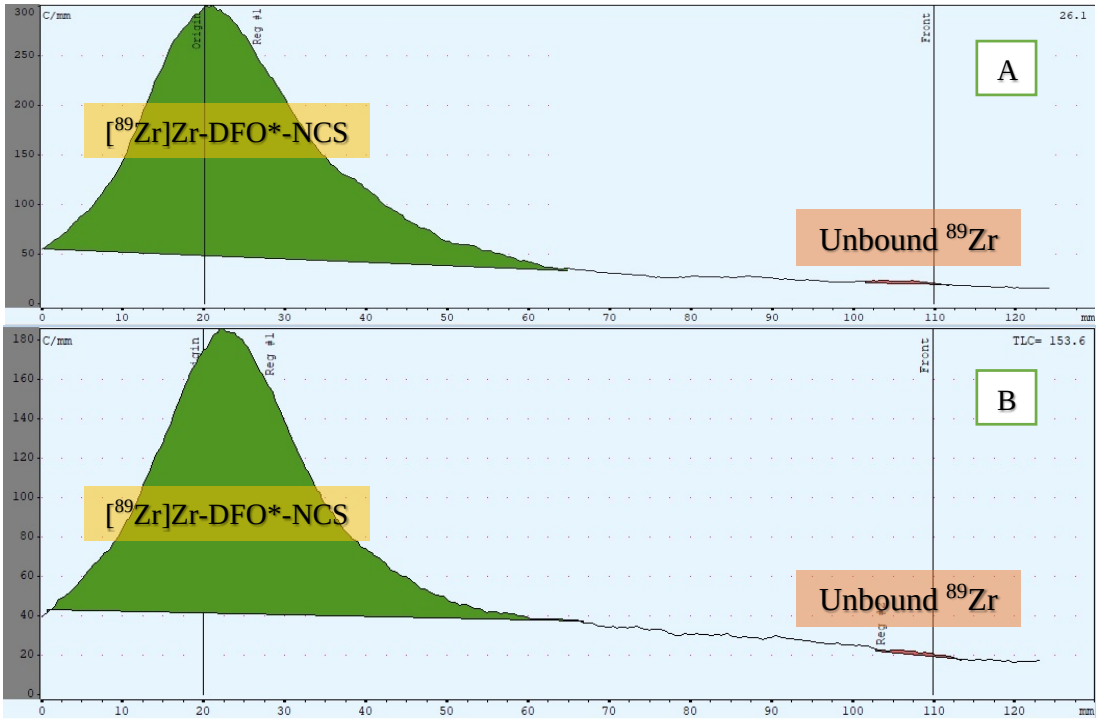

Figure 2. The radio-TLC chromatograms showing the pattern of [^{89}Zr]Zr-DFO*-NCS and unbound ^{89}Zr, which were analyzed using solvent systems 50 mM DTPA (A) and 0.1 M citrate buffer at pH 4 (B)

According to the data provided in Table 2, the percentage of %RCP for [^{89}Zr]Zr-DFO-NCS and [^{89}Zr]Zr-DFO*-NCS was 98.44% and 98.08%, respectively, after the first 15 minutes. However, [^{89}Zr]Zr-DFO-NCS reached over 99% after 30 minutes, while [^{89}Zr]Zr-DFO*-NCS reached over 99% at 60 minutes. It is evident that the formation of [^{89}Zr]Zr-DFO-NCS occurs slightly more rapidly than that of [^{89}Zr]Zr-DFO*-NCS.

Both complexes maintained their stability in the formulation solution for a period of 120 hours after radiolabeling at room temperature. The radiochemical purity for each of [^{89}Zr]Zr-DFO-NCS and [^{89}Zr]Zr-DFO*-NCS at 120 hours was determined to be over 98%.

Table 2. Stability of [^{89}Zr]Zr-DFO-NCS and [^{89}Zr]Zr-DFO*-NCS in formulation solution at RT

Time (min)	Percentage of radiochemical purity (%RCP)	
	[^{89}Zr]Zr-DFO-NCS	[^{89}Zr]Zr-DFO*-NCS
15	98.44	98.08
30	98.89	98.91
60	99.35	99.35
90	98.66	99.33
120	98.51	99.22
1440 (24 h.)	98.52	99.01
2880 (48 h.)	98.45	99.38
4320 (72 h.)	98.41	99.41
7200 (120 h.)	98.34	99.62

Table 3. Stability data of [^{89}Zr]Zr-DFO-NCS and [^{89}Zr]Zr-DFO*-NCS in fetal bovine serum (FBS) at 37 °C

Time (min)	Percentage of radiochemical purity (%RCP)	
	[^{89}Zr]Zr-DFO-NCS	[^{89}Zr]Zr-DFO*-NCS
15	98.16	98.82
180	98.78	99.02
360	98.86	99.60
1440 (24 h.)	98.31	99.55
2880 (48 h.)	98.16	99.23
4320 (72 h.)	98.25	99.29
7200 (120 h.)	81.92	99.43

Stability experiments were conducted on [^{89}Zr]Zr-DFO-NCS and [^{89}Zr]Zr-DFO*-NCS in fetal bovine serum (FBS) at 37 °C to mimic the human body environment. Over a period of 15 minutes to 72 hours, the radiochemical purity of both complexes appeared to be similar to stability studies conducted in a formulation solution. Nevertheless, after 120 hours, the radiochemical purity of [^{89}Zr]Zr-DFO-NCS decreased to 81.92%, but the radiochemical purity of [^{89}Zr]Zr-DFO*-NCS remained at 99%. The outcome can be clarified using density functional theory (DFT) to determine the different coordination isomers of ^{89}Zr, as reported by Holland et al.[6] The experiments revealed that [^{89}Zr]Zr-DFO*-NCS possesses eight-coordinate isomers, whereas [^{89}Zr]Zr-DFO-NCS only has six-coordinate isomers. Consequently, the DFO*-NCS chelator demonstrated superior stability in comparison to the DFO chelator.

To evaluate the radionuclidic purity, the [^{89}Zr]zirconium oxalate solution underwent testing for radionuclidic identity and purity with a high purity germanium (HPGe) detector. The investigation revealed the existence of peaks at energy levels of 909 and 511 keV. No further presence of radioactive contamination was observed. The experiments revealed that the radionuclidic purity of ^{89}Zr was obtained >99.9%.

4. Conclusion

During the investigation of a potential chelator for the further development of ^{89}Zr-immunoPET, DFO*-NCS showed a superior stability in formulation solution and in simulated human environment trials compared to the current clinical gold standard, DFO-NCS. The stability of [^{89}Zr]Zr-DFO* complex could reduce the issue of ^{89}Zr accumulation in bones, which causing misdiagnosis in situations of bone metastases. Therefore, DFO*-NCS is a highly promising novel chelator for use in clinical diagnostics.

Acknowledgements

The authors gratefully acknowledge the Thailand Science Research and Innovation (TRSI) for grant no. 2567190612029.

References

1. Higgins, L. J.; Pomper, M. G. The evolution of imaging in cancer: current state and future challenges. In *Seminars in oncology*, 2011; Elsevier: Vol. 38, pp 3-15.
2. Jauw, Y. W.; O'Donoghue, J. A.; Zijlstra, J. M.; Hoekstra, O. S.; Menke-Van Der Houven, C. W.; Morschhauser, F.; Carrasquillo, J. A.; Zweegman, S.; Pandit-Taskar, N.; Lammertsma, A. A. 89Zr-Immuno-PET: toward a noninvasive clinical tool to measure target engagement of therapeutic antibodies in vivo. *Journal of Nuclear Medicine* **2019**, *60* (12), 1825-1832.
3. van Dongen, G. A.; Beaino, W.; Windhorst, A. D.; Zwezerijnen, G. J.; Oprea-Lager, D. E.; Hendrikse, N. H.; van Kuijk, C.; Boellaard, R.; Huisman, M. C.; Vugts, D. J. The role of ^{89}Zr-immuno-PET in navigating and derisking the development of biopharmaceuticals. *Journal of Nuclear Medicine* **2021**, *62* (4), 438-445.
4. Abou, D. S.; Ku, T.; Smith-Jones, P. M. In vivo biodistribution and accumulation of ^{89}Zr in mice. *Nuclear Medicine and Biology* **2011**, *38* (5), 675-681.
5. Vugts, D. J.; Klaver, C.; Sewing, C.; Poot, A. J.; Adamzek, K.; Huegli, S.; Mari, C.; Visser, G. W.; Valverde, I. E.; Gasser, G. Comparison of the octadentate bifunctional chelator DFO*-p Phe-NCS and the clinically used hexadentate bifunctional chelator DFO-p Phe-NCS for ^{89}Zr-immuno-PET. *European Journal of Nuclear Medicine and Molecular Imaging* **2017**, *44*, 286-295.
6. Holland, J. P. Predicting the thermodynamic stability of zirconium radiotracers. *Inorganic Chemistry* **2020**, *59* (3), 2070-2082.

The development of new azobenzene derivatives within three-colors range absorption for biological applications

Waraporn Pimboonma, Chanikan Wongkaew, Tonman Lim-o-pas Phannoudej, Nuttakorn Jewyean, and Nopporn Ruangsupapichat*

Department of Chemistry, Mahidol University, Rama VI Road, Ratchathewi, Bangkok 10400, Thailand

**E-mail: nopporn.rua@mahidol.ac.th*

Abstract:

Azobenzene is one of the molecular photoswitches that can undergo reversible isomerization between *cis*- and *trans*-isomers when exposed to light (normally UV-light). In the present, azobenzene that can be activated via visible light has gained significant interest. With good rational design, we can synthesize azobenzene derivatives (**AZ1, AZ2**) by using a push-pull substituent on the phenyl group of azobenzene, which includes attaching the donor and acceptor group to the azobenzene moiety. As a result, the energy gap between the ground state and the excited state is small, resulting in an increase of red shift adsorption. These two molecules can be light-activated by blue and green light (visible light) to switch between cis-trans isomers. In this study, we include a new azobenzene (**AZ3**) that can absorb light in a longer wavelength (550–650 nm) than previous molecules (**AZ1** and **AZ2**). Furthermore, all compounds showed faster thermal relaxation (*cis*- back to *trans-)* than classic azobenzene, which will be further useful for biological and medical applications such as 11-*cis*-retinal in rhodopsin with a half-life of 80 milliseconds (thermal isomerization).

1. Introduction

Azobenzene is a molecular photoswitch with *N=N* substituents on the double bond that was developed in the 1880s and initially employed as a coloring agent in the industry due to its ease of manufacturing and low cost. Later, in the 1930s, *cis*-azobenzene was discovered using absorbance measurements under light irradiation, becoming azobenzene the best-known photoswitch molecules. Since then, azobenzene has been the most closely associated with scientists, particularly when it comes to biological molecules.[1] The *trans*-azobenzene can be converted to *cis*-azobenzene by 340 nm UV-irradiation, and *cis*-azobenzene can be converted back to *trans*-azobenzene at room temperature in the dark or 450 nm Vis-irradiation.[2]

Because azobenzene is water-soluble, non-toxic, and stable in the presence of many biological environment reaction, such as hydrolysis, reduction, and photobleaching[1], it has been widely used in biological systems such as protein probes,[3] molecular machines,[4] surface-modified materials,[5] nonlinear optical,[6] photorefractive material,[7] optical poling, holographic memory storage devices, and reversible optical wave guides.[8] In addition, the substitution group on the phenyl group of azobenzene has an important effect on its absorbance, emission, photochemical properties, and thermal relaxation of the *cis*-isomer to the *trans*-isomer.[9]

The push-pull group was chosen as azobenzene replacements for the phenyl group, resulting in a small energy gap, creating a red shift and the highest visible light absorption. Furthermore, the push-pull substituent on the phenyl ring not only affects the absorption spectra but also thermal *cis* to *trans* relaxation with an increase in the dipole moment character, which can decrease the activation barrier for thermal relaxation.[10-12] In this study, we developed and synthesized three azobenzenes **(AZ1-AZ3)** by substituting a push-pull group on the phenyl group of an azobenzene that can employ visible light (blue, green, and red) to regulate *cis-trans* isomerization and rapid thermal relaxation, as shown in **Figure 1**.

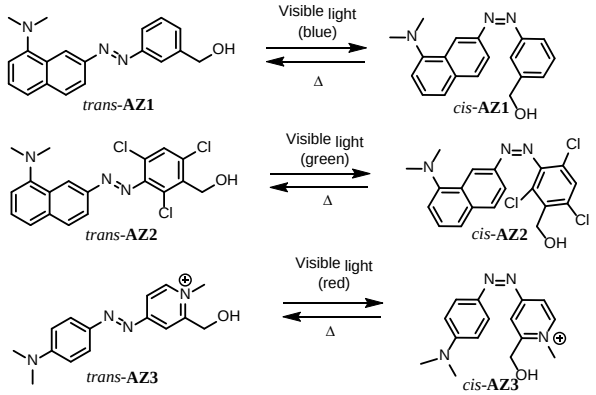

Figure 1. New azobenzene derivatives can undergo photoisomerization using visible light (blue,green, and red)

2. Materials and Methods

2.1 Materials

All commercially available chemicals were purchased from Sigma Aldrich, TCI, and Merk chemical companies and used without

additional purification. TLC was performed on alumina sheets pre-coated with Merck silica gel 60 F254 plate, and compounds were observed under UV light. Column chromatography was performed with Merk silica gel 60H. ^{1}H and ^{13}C NMR spectra were obtained using 400 MHz Bruker apparatus in $CDCl_3$ and Acetone-d_6 solution where chemical shift (δ) are recorded in ppm relative to TMS as the internal reference. Mass spectra (ESI-TOF MS) were determined on a Bruker microTOF in the ESI mode. The absorption spectra of compounds were measured on PerkinElmer LAMBDA 1050 + UV/Vis/NIR spectrophotometer in HPLC-grade solvent. UV/Vis absorptions were changed at different LED flashlight 3.7 V under ambient conditions.

2.2 Synthesis and characterization

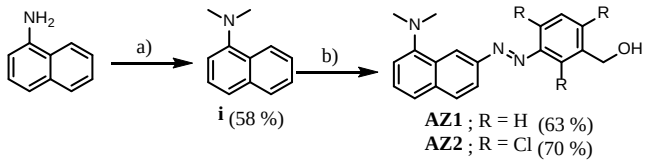

Scheme 1. Synthesis of compound **AZ1**-**AZ2**. a) MeI, KOH, DMSO, reflux, 24 h; b) From **i** to **AZ1**: 1) 4N HCl, $NaNO_2$, 0 °C 2)3-aminobenzyl alcohol, 0 °C ,3 h; From **i** to **AZ2**: 1) 4N HCl, $NaNO_2$, 0 °C 2) compound **ii**, 0 °C ,3 h.

2.2.1. Synthesis of *N,N*-dimethylnaphthalen-1-amine (i)

A mixture of naphthalen-1-amine (2.00 g, 13.97 mmol) and KOH (1.56 g, 27.96 mmol) was dissolved in DMSO (25 mL). Then, methyl iodide (3.97 g, 27.96 mmol) was added to the solution. The reaction was stirred at 50 °C for 12 h. The reaction mixture was then extracted with EtOAc (4x50 mL), and the combined organic extracts were dried over Na_2SO_4, filtered, and concentrated to dryness. Normal phase column chromatography (EtOAc: Hexane = 1:4) yields the product (i) (1.38 g, 58 %) as a dark red liquid. ^{1}H NMR (400 MHz, $CDCl_3$) δ 8.24 (d, J = 7.6 Hz, 1H), 7.83 (d, 1H), 7.56 – 7.44 (m, 2H), 7.40 (t, J = 7.8 Hz, 1H), 7.08 (d, J = 7.4 Hz, 1H), 2.91 (s, 6H). HRMS $[M+H]^+$ $C_{12}H_{14}N$ calculated for 172.1126, found 172.1128.

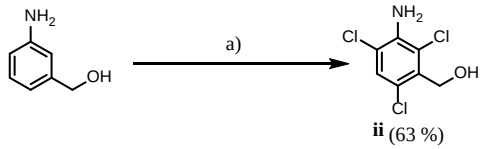

Scheme 2. Synthesis of compound **ii** a) NCS, THF, 0 °C to RT, overnight.

2.2.2. Synthesis of (3-Amino-2,4,6-trichlorophenyl)methanol (ii)

A solution of 3-aminobenzyl alcohol (1.00 g, 8.12 mmol) in THF was added NCS (3.25 g, 24.36 mmol) at 0 °C. The reaction mixture was stirred at room temperature for 12 h. Then, the crude mixture was extracted with EtOAc (4x50 mL), and the combined organic layers were dried over Na_2SO_4, filtered and concentrated to dryness. Normal phase column chromatography (EtOAc: Hexane = 3:7) yields the compound (ii) (1.15 g, 63%) as a brown solid. ^{1}H NMR (400 MHz, Acetone-d_6) δ 7.34 (s, 1H), 5.31 (s, 2H), 4.81 (d, J = 5.3 Hz, 2H). ^{13}C NMR (101 MHz, $CDCl_3$) δ 139.8, 134.7, 128.3, 123.0, 120.8, 119.5, 60.7. HRMS $[M+H]^+$ $C_7H_7Cl_3NO$ calculated for 225.9593, found 225.9590.

2.2.3. Synthesis of *N,N*-dimethylnaphthalen-1-amine (AZ1)

A Compound AZ1 was prepared with dissolving 3-aminobenzyl alcohol (1.00 g, 8.13 mmol) in 4N HCl and then cooled to 0-5°C. Then, the previously cooled solution was added with a cold solution of $NaNO_2$ (0.56 g, 8.13) at 0 °C. After 15 minutes, compound (i) (1.39 g, 8.13 mmol) was added dropwise to the reaction mixture and stirred for 3 hours. The reaction mixture was quenched with a CH_3COONa solution, which was then allowed to warm to room temperature. The crude mixture was extracted with EtOAc (4x50 mL), and the resulting organic extracts were dried over Na_2SO_4, filtered, and concentrated to dryness. The orange solid product (AZ1) (1.85 g, 63%) was obtained by normal phase column chromatography (EtOAc: Hexane = 3:7). ^{1}H NMR (400 MHz, Acetone-d_6) δ 9.05 – 9.02 (m, 1H), 8.29 (dt, J = 8.4, 1.1 Hz, 1H), 8.05 (d, J = 2.0 Hz, 1H), 7.91 (dd, J = 7.9, 3.6 Hz, 2H), 7.69 (ddd, J = 8.4, 6.7, 1.4 Hz, 1H), 7.62 (ddd, J = 8.3, 6.7, 1.5 Hz, 1H), 7.59 – 7.51 (m, 2H), 7.22 (d, J = 8.3 Hz, 1H), 4.80 (d, J = 5.9 Hz, 2H), 3.02 (s, 6H). HRMS $[M+H]^+$ $C_{19}H_{20}N_3O$ calculated for 306.1606, found 306.1596.

2.2.4. Synthesis of (*E*)-(2,4,6-trichloro-3-((8-(dimethylamino)naphthalen-2-yl)diazenyl)phenyl)methanol (AZ2)

A compound (AZ2) was prepared by diazotization of compound (ii) with $NaNO_2$. Then, the mixture reaction was coupling with compound (i) by the same method and stoichiometry of reagent employed in AZ1. ^{1}H NMR (400 MHz, Acetone-d_6) δ 8.87 – 8.80 (m, 1H), 8.30 (dd, J = 7.9, 1.3 Hz, 1H), 7.98 (d, J = 8.4 Hz, 1H), 7.76 – 7.60 (m, 3H), 7.24 (d, J = 8.4 Hz, 1H), 4.99 (d, J = 6.0 Hz, 2H), 3.10 (s, 6H). HRMS $[M+H]^+$ $C_{19}H_{17}Cl_3N_3O$ calculated for 408.0497, found 408.0436

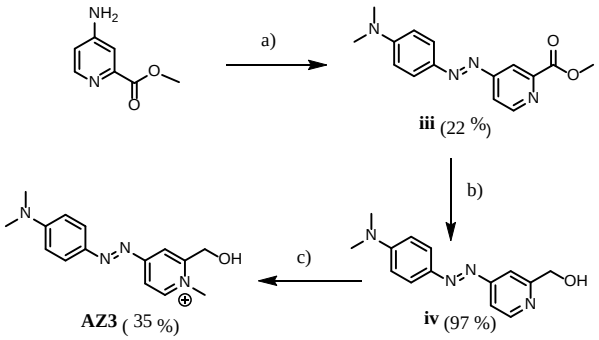

Scheme 3. Synthesis of compound **AZ3**. a) 1) H_2SO_4, $NaNO_2$, 0 °C 2) dimethylaniline, 0 °C ,15 min; b) $LiAlH_4$, THF, -78 °C, 3h; c) MeI, acetone, rt, 24 h.

2.2.5. Synthesis of Methyl (E)-4-((4-(dimethylamino)phenyl)diazenyl)picolinate (iii).

A Methyl 4-Aminopyridine carboxylate (100.00 mg, 0.65 mmol) in an H_2SO_4 solution was mixed with a cold $NaNO_2$ solution (79.50 mg, 0.65 mmol, 2 mL water) and stirred at 0 °C for 3 minutes. Then, the reaction mixture was added dimethylaniline (49.86 mg, 0.72 mmol) and agitated for 3 minutes at 0 °C. The reaction mixture was quenched with a concentrated sodium hydroxide solution, extracted with EtOAc (4x50mL), and dried with $NaSO_4$. The crude product was purified using column chromatography (EtOAc: Hexane = 3; 7) to yield a 22% orange solid. ^{1}H NMR (400 MHz, $CDCl_3$) δ 8.81 (d, *J* = 5.2 Hz,1H), 8.46 (d, *J* = 1.9 Hz, 1H), 7.94 – 7.90 (m, 2H), 7.80 (dd, *J* = 5.2, 1.9 Hz, 1H), 6.77 – 6.73 (m, 2H), 4.03 (s, 3H), 3.13 (s, 6H).

2.2.6. Synthesis of (E)-(4-((4-(dimethylamino) phenyl)diazenyl)pyridin-2-yl)methanol (iv).

A Compound iii (54.3 mg, 0.19 mmol) in dry THF (15 mL) was added $LiAlH_4$ (0.3822 mmol) at -78 °C under a nitrogen atmosphere. The reaction mixture was stirred for 3 hours at room temperature. Then, the reaction mixture was poured into cool saturated aqueous NH4Cl, extracted with EtOAc (3 x 50 mL), and dried with sodium sulfate ($NaSO_4$). The crude product was purified by flash chromatography (EtOAc: Hexane = 1: 1) to give an orange solid (iv) in 97% 1H NMR (400 MHz, $CDCl_3$) δ 8.67 (d, *J* = 5.1 Hz, 1H), 8.36 – 8.34 (m, 1H), 7.66 – 7.62 (m, 3H), 6.81 – 6.78 (m, 2H), 4.04 (d, *J* = 1.1 Hz, 2H), 3.04 (s, 6H).

2.2.7. Synthesis of (E)-4-((4-(dimethylamino)phenyl)diazenyl)-2-(hydroxymethyl)-1-methylpyridin-1-ium (AZ3).

Compound iv (50 mg, 0.20 mmol) in acetone (5 mL) was added with methyl iodide (0.25 g, 1.8 mmol). The mixture reaction was stirred at room temperature for 17 hr. Then, the mixture reaction was filtered and washed with hexane. The product was dried under vacuum and gave compound AZ3. ^{1}H NMR (400 MHz, Chloroform-d) δ 8.36 (s, 1H), 8.07 (dd, *J* = 10.9, 6.3 Hz, 1H), 7.97 (dd, *J* = 9.2, 4.4 Hz, 2H), 7.88 – 7.82 (m, 1H), 6.79 (dd, *J* = 9.1, 6.3 Hz, 2H), 5.30 (s, 3H), 4.44 (s, 2H), 3.24 (d, *J* = 10.3 Hz, 6H).

2.3 Spectroscopic measurement

The compound **AZ1-AZ3** stock solution was produced in acetonitrile at room temperature with a concentration of 6 x 10^{-5} M. All photochemical experiments can absorb in blue and green range leading to using an LED flashlight 3.7 V at 405 nm and 520 nm for irradiation. UV/Vis spectra were used to monitor composition changes over time to identify photostationary states.

2.4 Kinetic measurement

Thermal isomerization kinetics were studied using UV/Vis spectroscopy at four distinct temperatures (-5, 0, 5, and 10°C). The temperature was controlled by CoolSpeK UV USP-203. The rate constants (k) for the computation of $\Delta^{\ddagger}H$, $\Delta^{\ddagger}S°$, $\Delta^{\ddagger}G$, and $t_{1/2}$ were determined from the information obtained.

2.4.1. The rate constants

The rate constants for each temperature were calculated using the exponential decay function provided by equation (1).

$$A(t) = (A_0 - A_i)e^{-\frac{t}{\tau}} + A_i \quad (1)$$

Where τ is the reciprocal of the rate constants of thermal isomerization process, A_0 is the absorbance of *cis*-isomer after irradiation, A_i is the absorbance of cis-isomer before irradiation, and *A*(t) is the time evolution of absorbance after irradiation.

2.4.2. The enthalpy of activation and the entropy of activation

The enthalpy of activation and the entropy of activation were calculated by a linear relationship using the Erying equation (2).

$$\ln\left(\frac{k}{T}\right) = -\frac{\Delta H^{\ddagger}}{RT} + ln\left[\frac{kB}{h}\right] + \frac{\Delta S^{\ddagger}}{R} \quad (2)$$

Where k is the rate constant, T is the temperature (K), R is the universal gas constant (8.31 J/mol K), kB is Boltzmann's constant (1.38 x 10^{-23} m^2 kg $s^{-1}K^{-1}$), h is Planck's constant (6.63 x 10^{-34} m^2 kg s^{-1}), $\Delta H^{\ddagger}$ is the enthalpy of activation (kJ/mol), and $\Delta S^{\ddagger}$ is the entropy of activation (J/mol).

The plot of ln(k/T) versus 1/T was a linear plot in which -(H)/R represents the slope and ln[kB/h] + (S)/R represents the intercept.

2.4.3. The Gibbs free energy of activation

The Gibbs free energy was estimated by Gibb free energy equation (3).

$$\Delta G^{\ddagger} = \Delta H^{\ddagger} - T\Delta S^{\ddagger} \quad (3)$$

Where $\Delta G^{\ddagger}$ is the Gibbs free energy of activation.

2.4.4. The half life

The half-life was calculated by half-life equation for first-order reaction (4).

$$t_{1/2} = \frac{ln2}{k} \quad (4)$$

Where $t_{1/2}$ is the half-life

3. Results & Discussion

3.1 Molecular design

The azobenzene that can be activated by visible light must have its structure design changed to provide a higher redshift wavelength. As a result, all the synthesized compounds used an amino group as an the electron donor. Furthermore, the other benzene rings of compounds **AZ1** and **AZ2** were formed up of three hydrogen and chlorines, as seen in Figure **1.** In addition, compound **AZ3** has pyridinium salt as a strong electron acceptor. The **AZ1-AZ2** compounds were synthesized by azo coupling aniline and *N,N*-dimethylnaphthalen-1-amine in 4N hydrochloric acid using sodium nitrile in excellent yield, as illustrated in Scheme **1**. The compound **AZ3** was produced in three steps, beginning with azo coupling between methyl 4-aminopicolinate and dimethylaniline, followed by a reduction reaction with $LiAlH_4$ to obtain compound **iv**. Compound **iv** was finally treated with methyl iodide to generate azopyridium salts (AZ3) (35% yield) shown in Scheme **3**. ^{1}H-NMR, ^{13}C-NMR spectroscopy, and mass spectrometry were used to confirm the structure of compounds **AZ1-AZ3.**

3.2 Photochemical isomerization

The photoisomerization of **AZ1** was studied by UV-Vis spectroscopy in acetonitrile ($6x10^{-5}$ mol/L) at -5 °C and irradiated with blue light (405 nm), as shown in Figure **2a**. The maximum absorption of **AZ1** was observed at 425 nm, from ^{1}H NMR suggesting that it is a *trans*-isomer. When *trans*-**AZ1** was irradiated under blue light (405 nm), the maximum absorption peak at 425 nm was gradually reduced in a range of one minute, indicating that the *cis*-isomer was obtained. Later, the *trans*- **AZ1** was recovered when the room temperature incresed, as presented by the red line of Figure **2a**.

The photoisomerization of **AZ2** was studied by UV-Vis spectroscopy in acetonitrile ($6x10^{-5}$ mol/L) at -5 °C after being irradiated by green light (520 nm). Compound **AZ2** showed its maximum absorption at 435 nm, which indicated as a *trans*-isomer as similar to compound **AZ1** by ^{1}H NMR spectrum. The maximum absorption peak at 435 nm was then decreased when irradiated with 520 nm of green light, showing that the *cis*-isomer was formed in a photostationary state (PSS) within 1 minute. The *trans*-isomer of **AZ2** was recovered using a thermal process of increased temperature, as illustrated by the red line in Figure **2b**.

The absorption spectra of **AZ2** were more redshifted than **AZ1** due to the effect of the substituent on the ortho-positions of **AZ2**. Because the ortho-chlorine of **AZ2** is facing the nitrogen lone pair, their repulsive interaction destabilizes the n molecular orbital, lowering the energy gap of the π^* molecular orbital.

3.3 The kinetic of thermal process

The kinetics of the thermal process (*cis*-back to *trans*-isomer) were studied using UV/Vis spectroscopy. The change of absorption peak at 450 nm of **AZ1** was measured in acetonitrile ($6x10^{-5}$ mol/L) at different temperatures (-5, 0, 5, and 10 °C) after 1 minute of 405 nm irradiation. In Figure **3a**, the exponential decay of each temperature were plotted and showed the different rate constant. As illustrated in Figure **3c**, an Erying plot was generated using the different rate constants, to calculate the half-life and Gibbs free energy of activation. The half-life at room temperature was determined to be 3.08 seconds ($\Delta^{\ddagger}G°$ = 76.68 kJ/mol), suggesting that thermal isomerization from *cis*-isomer to *trans*-isomer proceeds in 3.08 seconds in the dark at 298 K.

On the other hand, the kinetics of thermal process **AZ2** were studied using green light (520 nm) and monitored in acetonitrile at various temperatures (-5, 0, 5 and 10 °C) (6×10^{-5} M). The rate constant of each temperature was obtained using an exponential decay plot, as illustrated in Figure **3b**. Then, the Erying plot was used to determine the half-life and Gibbs free energy of activation (Figure **3d**.). These finding indicated the half-life at room temperature was calculated to be 30 seconds and the Gibbs free energy of activation ($\Delta\ddagger G°$) was determined to be 81.67 kJ/mol. The thermal relaxation of **AZ2** were slower than **AZ1** due to electronic effect of ortho-chlorine **AZ2**.

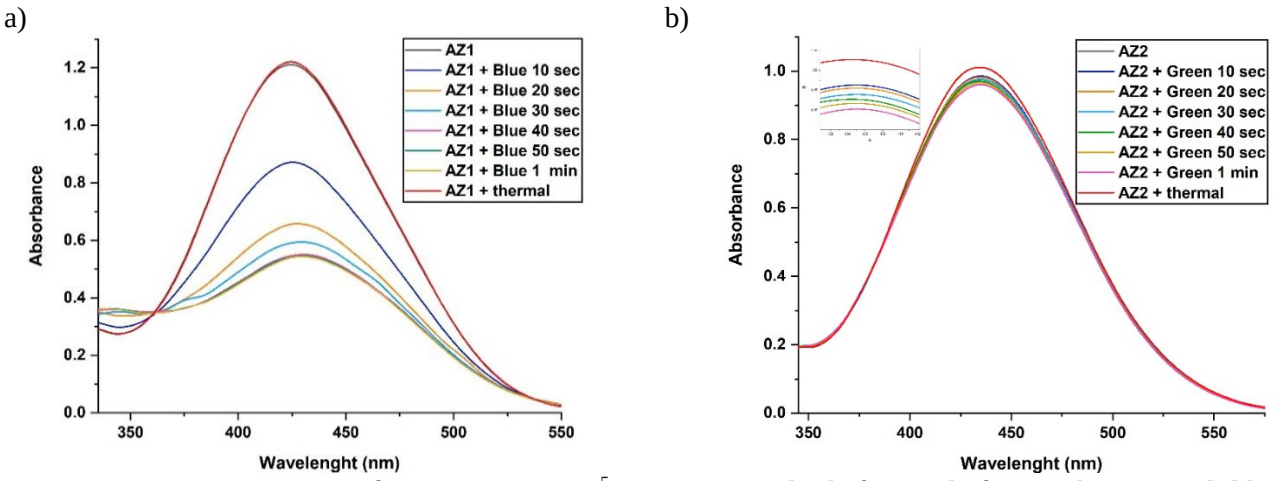

Figure 2. a) UV-Vis spectra of *trans*-**AZ1** ($6x10^{-5}$M in acetonitrile) before and after irradiation with blue light (405 nm) to form *cis*-**AZ2** and b) UV-Vis spectra of *trans*-**AZ2** ($6x10^{-5}$M in acetonitrile) before and after irradiation with green light (520 nm) to form *cis*-**AZ2**.

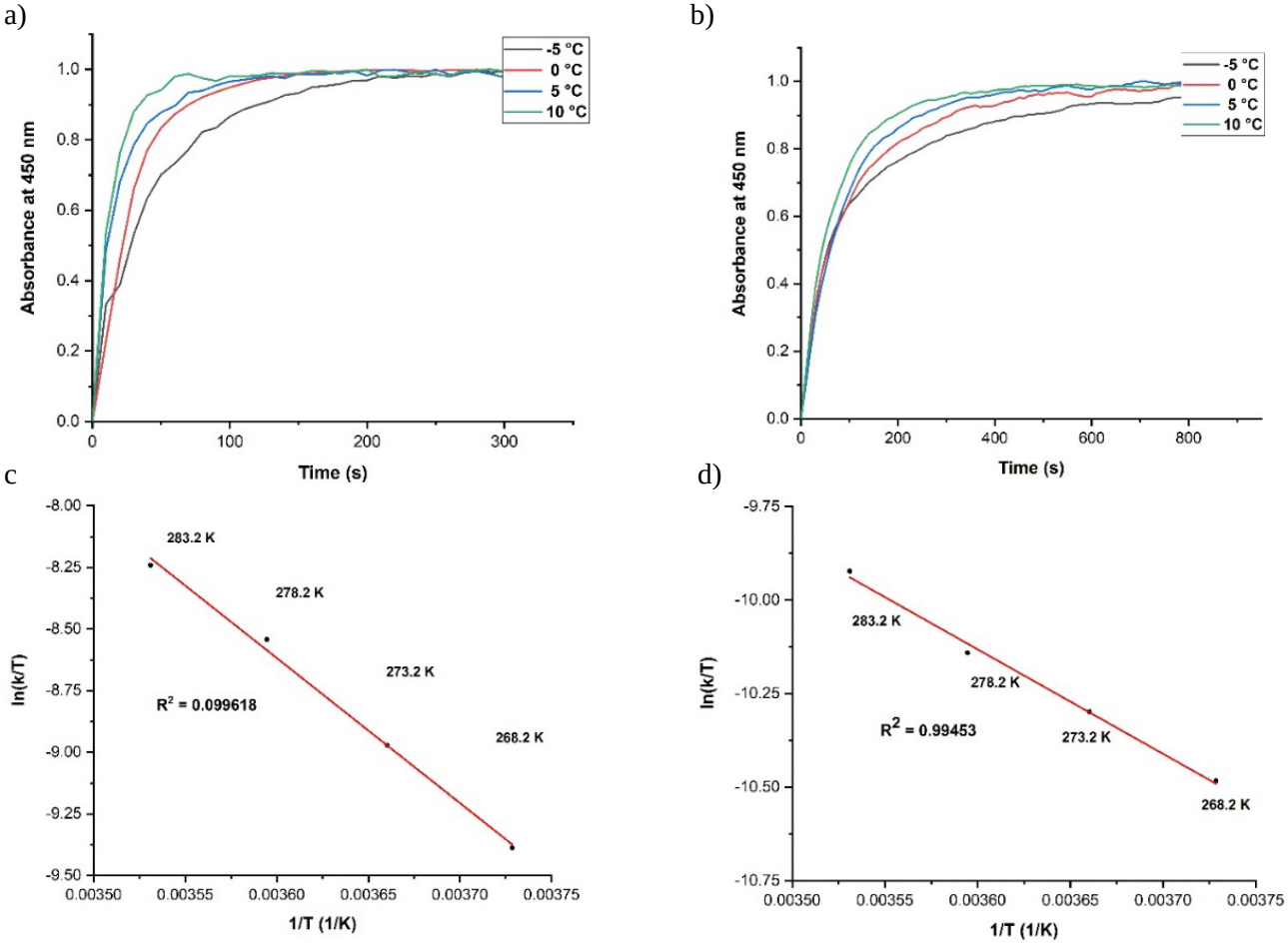

Figure 3. a) The thermal decay kinetics at 450 nm of **AZ1** from *cis*-isomer to *trans*-isomer at different temperature (-5, 0, 5, and 10 °C) after irradiated with blue light (405 nm)**,** b) The thermal decay kinetics at 450 nm of **AZ2** from *cis*-isomer to *trans*-isomer at different temperature (-5, 0, 5, and 10 °C) after irradiated with green light (520 nm), c) Erying plot of **AZ1** for thermal process of *cis*-isomer back to *trans*-isomer after irradiated with blue light (405 nm**)**, and d) Erying plot of **AZ2** for thermal process of *cis*-isomer back to *trans*-isomer after irradiated with green light (520 nm)

4. Conclusion

In conclusion, we designed and synthesized new azobenzene (**AZ1-AZ3**) that can absorb in the visible region. In this work, we study the photoisomerization of compound **AZ1** and **AZ2**. Both compounds can absorb light at around 400-450 nm, with a more-red shift than usual azobenzene. In addition, compound **AZ1** and **AZ2** can change their configuration from *trans*- to *cis*-isomer by blue and green light stimulation, respectively. In addition, they can convert back to trans-isomer in darkness at room temperature. Furthermore, compound **AZ1-AZ2** show fast thermal relaxation, which is supported by the short half-life of the cis-isomer. As a result, compound **AZ1-AZ2** can later be applied in biological application.

Acknowledgements

This work is supported by Professor. Dr. Makoto Ogawa (VISTEC) for supporting the equipment of UV-Vis spectrometer measurements at low temperatures, Thailand Graduate Institute of Science and Technology Scholarship, and the Faculty of Science, Mahidol University. We appreciate Dr. Kamonnart Imwiset's assistance in providing instruction and setting up an LED setup for UV-Vis measurements.

References

1. Beharry, A. A.; Woolley, G. A., *Chem. Soc. Rev.* **2011**, *40*, 4422.
2. Marturano, V.; Ambrogi, V.; Bandeira, N. A. G.; Tylkowski, B.; Giamberini, M.; Cerruti, P., *Physical Sciences Reviews* **2017,** *2*
3. Nuti, F.; Gellini, C.; Larregola, M.; Squillantini, L.; Chelli, R.; Salvi, P. R.; Lequin, O.; Pietraperzia, G.; Papini, A. M., *Front. Chem*. **2019**, *180*.
4. Choi, Y.-J.; Kim, J.-T.; Yoon, W.-J.; Kang, D.-G.; Park, M.; Kim, D.-Y.; Lee, M.-H.; Ahn, S.-k.; Jeong, K.-U., *ACS Macro Lett.* **2018**, *7*, 576.
5. Ferri, V.; Elbing, M.; Pace, G.; Dickey, M. D.; Zharnikov, M.; Samorì, P.; Mayor, M.; Rampi, M. A., Angew. *Chem. Int. Ed*. **2008**, *47*, 3407.
6. Dudek, M.; Kaczmarek-Kędziera, A.; Deska, R.; Trojnar, J.; Jasik, P.; Młynarz, P.; Samoć, M.; Matczyszyn, K., J. *Phys. Chem. B.* **2022**, *126*, 6063.
7. Fang, H.; Li, M., *Journal of Wuhan University of Technology-Mater. Sci. Ed*. **2014,** *29*, 1290.
8. He, J.; Kovach, A.; Chen, D.; Saris, P. J. G.; Yu, R.; Armani, A. M., *Opt. Express* **2020**, *28*, 22462
9. Bandara, H. M. D.; Burdette, S. C., *Chem. Soc. Rev*. **2012,** *41*, 1809
10. Noell, W. K.; Walker, V. S.; Kang, B. S.; Berman, S., *Invest. Ophthalmol.* **1966**, *5*, 450.
11. Aleotti, F.; Nenov, A.; Salvigni, L.; Bonfanti, M.; El-Tahawy, M. M.; Giunchi, A.; Gentile, M.; Spallacci, C.; Ventimiglia, A.; Cirillo, G.; Montali, L.; Scurti, S.; Garavelli, M.; Conti, I., J. *Phys. Chem. A*. **2020**, *124*, 9513.
12. Garcia-Amoros, J.; Diaz-Lobo, M.; Nonell, S.; Velasco, D., Angew. *Chem., Int. Ed*. **2012**, *51*, 12820.

Synthesis and α-glucosidase inhibitory activity of bis-coumarin derivatives

Tipanan Wisarutwanit, Sorachat Tharamak, and Wanchai Pluempanupat*

Department of Chemistry and Center of Excellence for Innovation in Chemistry, Special Research Unit for Advanced Magnetic Resonance, Faculty of Science, Kasetsart University, Bangkok 10900, Thailand

**E-mail: fsciwcp@ku.ac.th*

Abstract:

Diabetes is the most common type of chronic metabolic disease that affects a large number of elderly people. α-Glucosidase inhibitors, such as acarbose, nojirimycin, voglibose, and miglitol, display an essential role in the treatment of diabetes by inhibiting the digesting α-glucosidase. However, new and more efficient compounds are still necessary as an alternative approach for treating this enzyme. In the present study, bis-coumarin derivatives were synthesized from the condensation of 4-hydroxycoumarin with various aldehydes under environmentally friendly conditions. Under optimized conditions, aromatic aldehydes could be transformed into the corresponding products in high to excellent yields, whereas the products produced from aliphatic aldehydes were obtained in moderate yields. All synthesized bis-coumarin derivatives were further evaluated for their α-glucosidase inhibitory activity. The results found that compound **8** was the most potent inhibitor, with an IC_{50} value of 7.03 ± 0.57 µM. This compound could be developed into a new potential antidiabetic drug.

1. Introduction

Chronic metabolic disease known as diabetes mellitus (DM) is the third leading cause of death worldwide. Type-II diabetes, which is prevalent among many senior citizens, constitutes ninety percent of diabetes cases.[1] Primary factors include inadequate insulin production by the pancreas and the development of insulin resistance. This resistance leads to hyperglycemia, causing elevated blood sugar levels and potentially resulting in various complications.[2] One therapeutic approach to diabetes mellitus involves reducing postprandial hyperglycemia by inhibiting digestive enzymes such as α-glucosidase, thereby slowing the conversion of carbohydrates into simple sugars.[3] Nowadays, there are several α-glucosidase inhibitors, such as acarbose, voglibose, miglitol, *N*-butyldeoxynojirimycin, and nojirimycin, that are clinically used for the treatment of type-II diabetes mellitus.[4-7] However, these drugs were later discovered to be associated with side effects, such as diarrhea, bloating, and stomach pain.[8] Hence, it is necessary to discover compounds that can efficiently inhibit the enzyme for diabetes treatment while minimizing toxicity.

Dicoumarol, a naturally occurring chemical found in fungi and plants, is a coumarin derivative synthesized from 4-hydroxycoumarin and formaldehyde. Recognized as an anticoagulant for its structural resemblance to vitamin K, dicoumarol inhibits prothrombin production by interfering with vitamin K.[9] Additionally, dicoumarol and its derivatives showcase antibacterial, antifungal, antiviral, anticancer, anti-inflammatory, and antioxidant activities.[10-14] Moreover, they have been reported inhibitory activities on enzymes such as acetylcholinesterase and α-glucosidase.[15-16]

Given the efficiency and properties of dicoumarol mentioned above, the present study focused on modifying natural dicoumarol compounds to create a wider range of bis-coumarin derivatives. The synthesis process is designed to be environmentally friendly, minimizing the use of hazardous chemicals.[13,17-19] The investigation could explore the correlation between the compound's structures and their inhibitory activity against α-glucosidase, aiming to develop as a candidate for DM treatment.

2. Materials and Methods

2.1 Materials

All reagent-grade chemicals and solvents were purchased from Sigma-Aldrich (St. Louis, MO, USA), Acros Organics™ (Geel, Belgium) and TCI (Tokyo, Japan). All synthesized compounds were analyzed for their structure using spectroscopy techniques. The ^{1}H and ^{13}C NMR spectra were performed in deuterated dimethyl sulfoxide (DMSO-d_6) and recorded on a Bruker 400 MHz AVANCE III HD spectrometer operating at 400 MHz (^{1}H) and 100 MHz (^{13}C). The high-resolution mass spectra were recorded on Bruker microtof-Q III instrument (Karlsruhe, Germany). Spectrophotometric analysis were performed using a microplate reader (MPR, Spark™ 10M. The α-glucosidase from *Saccharomyces cerevisiae* (EC 3.2.1.20) was purchased from Sigma-Aldrich. *p*-Nitrophenyl-α-D-glucopyranoside (PNP-G) and acarbose were supplied by TCI.

2.2 General procedure for the synthesis of bis-coumarin derivatives (1-12)

The mixture of 4-hydroxycoumarin (1 eq) and aldehydes (1 eq) in water-ethanol (2:1, 0.25 M) was prepared in a round-bottom flask and refluxed in an oil bath for 1.5 hours. The reaction was followed by TLC. After the completion of the reaction, the mixture was cooled to room temperature, filtered, washed with cold water and ethanol, and dried to yield the desired products **1-12**.

3,3'-(Ethane-1,1-diyl)bis(4-hydroxy-2*H*-chromen-2-one) (**1**). White solid; yield 60%; ^{1}H NMR (400 MHz, DMSO-d_6) δ 7.93 (d, *J* = 7.9 Hz, 2H), 7.57 (t, *J* = 7.7 Hz, 2H), 7.36 – 7.28 (m, 4H), 4.98 (q, *J* = 7.5 Hz, 1H), 1.60 (d, *J* = 7.5 Hz, 3H); ^{13}C NMR (100 MHz, DMSO-d_6) δ 164.6 (x2), 163.7 (x2), 151.9 (x2), 131.9 (x2), 124.0 (x2), 123.7 (x2), 117.5 (x2), 116.0 (x2), 106.8 (x2), 26.4, 16.4; HRMS (ESI) calcd for $C_{20}H_{14}NaO_6$ ([M+Na]$^+$) 373.0688, found 373.0686.

3,3'-(Butane-1,1-diyl)bis(4-hydroxy-2*H*-chromen-2-one) (**2**). White solid; yield 78%; ^{1}H NMR (400 MHz, DMSO-d_6) δ 7.85 (dd, *J* = 7.8, 1.7 Hz, 2H), 7.45 (ddd, *J* = 8.6, 7.3, 1.7 Hz, 2H), 7.25–7.14 (m, 4H), 4.87 (t, *J* = 8.4 Hz, 1H), 2.01 (sex, *J* = 7.2 Hz, 2H), 1.14 (q, *J* = 7.6 Hz, 2H), 0.82 (t, *J* = 7.4 Hz, 3H); ^{13}C NMR (100 MHz, DMSO-d_6) δ 167.1 (x2), 164.3 (x2), 152.3 (x2), 130.5 (x2), 123.9 (x2), 122.7 (x2), 120.1 (x2), 115.2 (x2), 104.2 (x2), 31.9, 31.3, 21.0, 14.0; HRMS (ESI) calcd for $C_{22}H_{18}NaO_6$ ([M+Na]$^+$) 401.1001, found 401.0998.

3,3'-(Phenylmethylene)bis(4-hydroxy-2*H*-chromen-2-one) (**3**). Off white solid; yield 100%; ^{1}H NMR (400 MHz, DMSO-d_6) δ 7.89 (dd, *J* = 8.0, 1.6 Hz, 2H), 7.58 (ddd, *J* = 9.8, 7.5, 1.6 Hz, 2H), 7.35 (d, *J* = 8.2 Hz, 2H), 7.31 (t, *J* = 7.6 Hz, 2H), 7.26–7.17 (m, 2H), 7.17–7.09 (m, 3H), 6.35 (s, 1H); ^{13}C NMR (100 MHz, DMSO-d_6) δ 166.2 (x2), 165.2 (x2), 152.5 (x2), 140.5, 132.1 (x2), 128.3 (x2), 126.9 (x2), 125.8, 124.2 (x2), 124.0 (x2), 118.5 (x2), 116.1 (x2), 104.2 (x2), 36.2; HRMS (ESI) calcd for $C_{25}H_{16}NaO_6$ ([M+Na]$^+$) 435.0845, found 435.0839.

3,3'-(*p*-Tolylmethylene)bis(4-hydroxy-2*H*-chromen-2-one) (**4**). White solid; yield 96%; ^{1}H NMR (400 MHz, DMSO-d_6) δ 7.90 (dd, *J* = 7.9, 1.6 Hz, 2H), 7.59 (ddd, *J* = 8.6, 7.2, 1.6 Hz, 2H), 7.36 (dd, *J* = 8.3, 1.1 Hz, 2H), 7.32 (ddd, *J* = 8.1, 7.3, 1.1 Hz, 2H), 7.03 (s, 4H), 6.31 (s, 1H), 2.24 (s, 3H); ^{13}C NMR (100 MHz, DMSO-d_6) δ 165.2 (x2), 164.9 (x2), 152.2 (x2), 136.7, 134.5, 131.9 (x2), 128.7 (x2), 126.7 (x2), 123.9 (x2), 123.8 (x2), 117.9 (x2), 116.0 (x2), 104.3 (x2), 35.6, 20.5; HRMS (ESI) calcd for $C_{26}H_{18}NaO_6$ ([M+Na]$^+$) 449.1001, found 449.0996

3,3'-((4-Methoxyphenyl)methylene)bis(4-hydroxy-2*H*-chromen-2-one) (**5**). Off white solid; yield 92%; ^{1}H NMR (400 MHz, DMSO-d_6) δ 7.90 (d, *J* = 7.9 Hz, 2H), 7.59 (t, *J* = 7.7 Hz, 2H), 7.36 (d, *J* = 8.3 Hz, 2H), 7.32 (t, *J* = 7.5 Hz, 2H), 7.05 (d, *J* = 8.3 Hz, 2H), 6.80 (d, *J* = 8.1 Hz, 2H), 6.29 (s, 1H), 3.69 (s, 3H); ^{13}C NMR (100 MHz, DMSO-d_6) δ 165.2 (x2), 165.0 (x2), 157.5, 152.3 (x2), 132.1 (x2), 131.4, 127.9 (x2), 124.0 (4C), 117.9 (x2), 116.1 (x2), 113.7 (x2), 104.5 (x2), 55.1, 35.4; HRMS (ESI)calcd for $C_{26}H_{18}NaO_7$ ([M+Na]$^+$) 465.0950, found 465.0945.

3,3'-((4-Hydroxyphenyl)methylene)bis(4-hydroxy-2*H*-chromen-2-one) (**6**); Off white solid; yield 93%; ^{1}H NMR (400 MHz, DMSO-d_6) δ 7.92 (dd, *J* = 7.9, 1.6 Hz, 2H), 7.61 (ddd, *J* = 8.6, 7.3, 1.6 Hz, 2H), 7.38 (d, *J* = 8.2 Hz, 2H), 7.34 (t, *J* = 7.4 Hz, 2H), 6.95 (d, *J* = 8.2 Hz, 2H), 6.65 (d, *J* = 8.6 Hz, 2H), 6.26 (s, 1H); ^{13}C NMR (100 MHz, DMSO-d_6) δ 164.9 (x2), 164.7 (x2), 155.4, 152.1 (x2), 132.0 (x2), 129.1, 127.7 (x2), 123.9 (x2), 123.9 (x2), 117.6 (x2), 116.0 (x2), 115.0 (x2), 104.6 (x2), 35.2; HRMS (ESI) calcd for $C_{25}H_{16}NaO_7$ ([M+Na]$^+$) 451.0794, found 451.0786.

4-(Bis(4-hydroxy-2-oxo-2*H*-chromen-3-yl)methyl)benzonitrile (**7**); White solid; yield 96%; ^{1}H NMR (400 MHz, DMSO-d_6) δ 7.87 (dd, *J* = 7.9, 1.6 Hz, 2H), 7.67 (d, *J* = 8.5 Hz, 2H), 7.57 (ddd, *J* = 8.6, 7.2, 1.7 Hz, 2H), 7.34 (dd, *J* = 7.8, 3.7 Hz, 4H), 7.29 (td, *J* = 8.9, 7.3, 0.8 Hz, 2H), 6.36 (d, *J* = 1.3 Hz, 1H); ^{13}C NMR (100 MHz, DMSO-d_6) δ 166.5 (x2), 164.5 (x2), 152.4 (x2), 147.8, 131.9 (x2), 131.7 (x2), 127.9 (x2), 124.1 (x2), 123.5 (x2), 119.2 (x2), 118.6, 115.9 (x2), 108.1, 103.2 (x2), 36.7; HRMS (ESI) calcd for $C_{26}H_{15}NNaO_6$ ([M+Na]$^+$) 460.0797, found 460.0792.

3,3'-((4-Nitrophenyl)methylene)bis(4-hydroxy-2*H*-chromen-2-one) (**8**); Off white solid; yield 85%; ^{1}H NMR (400 MHz, DMSO-d_6) δ 8.08 (d, *J* = 8.9 Hz, 2H), 7.87 (dd, *J* = 7.9, 1.6 Hz, 2H), 7.57 (ddd, *J* = 8.6, 7.2, 1.7 Hz, 2H), 7.41 (d, *J* = 7.8 Hz, 2H), 7.33 (d, *J* = 7.3 Hz, 2H), 7.29 (t, *J* = 7.6 Hz, 2H), 6.39 (s, 1H); ^{13}C NMR (100 MHz, DMSO-d_6) δ 166.6 (x2), 164.4 (x2), 152.5 (x2), 150.3, 145.5, 131.7 (x2), 128.1 (x2), 124.1 (x2), 123.5 (x2), 123.2 (x2), 118.7 (x2), 115.9 (x2), 103.3 (x2), 36.7; HRMS (ESI) calcd for $C_{25}H_{15}NNaO_8$ ([M+Na]$^+$) 480.0695, found 480.0691.

3,3'-((4-Fluorophenyl)methylene)bis(4-hydroxy-2*H*-chromen-2-one) (**9**); White solid; yield 93%; ^{1}H NMR (400 MHz, DMSO-d_6) δ 7.90 (dd, *J* = 7.9, 1.6 Hz, 2H), 7.59 (ddd, *J* = 8.6, 7.2, 1.6 Hz, 2H), 7.36 (dd, *J* = 8.3, 1.1 Hz, 2H), 7.32

(ddd, J = 8.2, 7.3, 1.1 Hz, 2H), 7.22 – 7.13 (m, 3H), 7.03 (t, J = 8.9 Hz, 2H), 6.33 (s, 1H); ^{13}C NMR (100 MHz, DMSO-d_6) δ 165.5 (x2), 164.7 (x2), 161.7, 159.3 (x2), 152.3 (x2), 136.2, 131.9 (x2), 128.6 (d, J = 7.8 Hz, 2C), 123.8 (d, J = 23.6 Hz, 2C), 118.1 (x2), 116.0 (x2), 114.7 (d, J = 21.2 Hz, 2C), 104.1 (x2), 35.5; HRMS (ESI) calcd for $C_{25}H_{15}FNaO_6$ ($[M+Na]^+$) 453.0750, found 453.0746.

Table 1. Optimum conditions for the synthesis of bis-coumarin derivative **3**

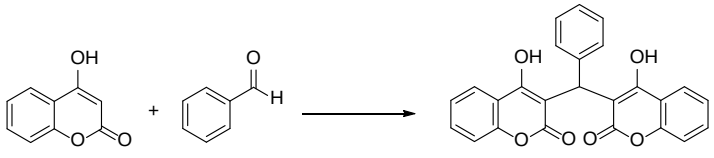

3

Entry	Ratio of 4-hydroxy coumarin:aldehyde	Solvent	Catalyst	Temp. (°C)	Time (h)	Yield[a,b] (%)
1	1:1	H_2O	-	RT	8	97
2	2:1	H_2O	Ceric ammonium nitrate (20 mol%)	RT	6	50
3	2:1	EtOH	Piperidine (0.2 mol%)	RT	8	Quant
4	2:1	H_2O-EtOH (2:1)	-	Reflux	1.5	92
5	1:1	H_2O-EtOH (2:1)	-	Reflux	1.5	Quant

[a]Isolated yield.
[b]Based on 4-hydroxycoumarin.

Table 2. The synthesis of bis-coumarin derivatives **1-12**

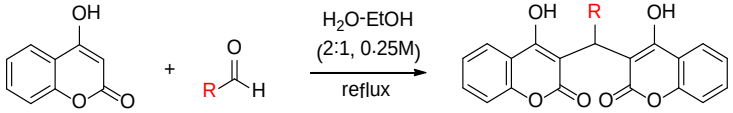

1 eq 1 eq **1-12**

Compound	R	Time (h)	Yield[a,b] (%)
1	-CH$_3$	28	60, 30[c]
2	-(CH$_2$)$_2$CH$_3$	31	78
3		1.5	Quant
4		1.5	96
5		1.5	92
6		3	93
7		1.5	96
8		1.5	85
9		1.5	93
10		2	79
11		2	N.D.[d]
12		3.5	91

[a]Isolated yield.
[b]Based on 4-hydroxycoumarin.
[c]Ratio of 4-hydroxycoumarin:aldehyde was 2:1
[d]Compound **11a** was obtained in 93% yield.

3,3'-((4-Bromophenyl)methylene)bis(4-hydroxy-2*H*-chromen-2-one) (**10**); White solid; yield 79%; ^{1}H NMR (400 MHz, DMSO-d_6) δ 7.89 (dd, *J* = 7.9, 1.6 Hz, 2H), 7.58 (ddd, *J* = 8.6, 7.2, 1.6 Hz, 2H), 7.39 (d, *J* = 8.8 Hz, 2H), 7.35 (d, *J* = 8.3 Hz, 2H), 7.31 (t, *J* = 7.6 Hz, 2H), 7.11 (dd, *J* = 8.5, 1.2 Hz, 2H), 6.29 (s, 1H) ; ^{13}C NMR (100 MHz, DMSO-d_6) δ 165.8 (x2), 164.7 (x2), 152.3 (x2), 140.1, 131.9 (x2), 130.8 (x2), 129.2 (x2), 124.0 (x2), 123.7 (x2), 118.5, 118.3 (x2), 115.9 (x2), 103.8 (x2), 35.8; HRMS (ESI) calcd for $C_{25}H_{15}BrNaO_6$ ([M+Na]$^+$) 512.9950, found 512.9944.

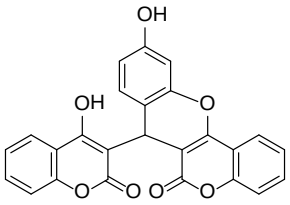

11a

Figure 1. Chemical structure of compound **11a**

10-Hydroxy-7-(4-hydroxy-2-oxo-2H-chromen-3-yl)chromeno[4,3-b]chromen-6(7H)-one (**11a**); Light pink solid; yield 93%; ^{1}H NMR (400 MHz, DMSO-d_6); δ 8.07 (d, *J* = 7.8 Hz, 2H), 7.68 (t, *J* = 7.9 Hz, 1H), 7.58 (t, *J* = 7.8 Hz, 1H), 7.50 – 7.39 (m, 2H), 7.39 – 7.26 (m, 2H), 6.99 (d, *J* = 8.3 Hz, 1H), 6.71 (s, 1H), 6.58 (dd, *J* = 8.3, 2.5 Hz, 1H) , 5.62 (s, 1H); ^{13}C NMR (100 MHz, DMSO-d_6) δ 160.6 (x2), 157.4 (x2), 152.2, 152.0 (x2), 132.5 (x2), 132.2, 129.2, 124.6 (x2), 124.0, 122.7, 116.5 (x2), 116.2 (x2), 113.9 (x2), 113.1, 102.8 (x2), 28.2; HRMS (ESI) calcd for $C_{25}H_{14}NaO_7$ ([M+Na]$^+$) 449.0637, found 449.0635.

3,3'-((4-Hydroxy-3-methoxyphenyl) methylene)bis(4-hydroxy-2*H*-chromen-2-one) (**12**). Off white solid; yield 91%; ^{1}H NMR (400 MHz, DMSO-d_6) δ 7.92 (d, *J* = 8.3 Hz, 2H), 7.61 (t, *J* = 7.3 Hz, 2H), 7.38 (d, *J* = 8.3 Hz, 2H), 7.34 (t, *J* = 7.6 Hz, 2H), 6.74 – 6.63 (m, 2H), 6.57 (d, *J* = 7.4 Hz, 2H), 6.27 (s, 1H), 3.59 (s, 3H); ^{13}C NMR (100 MHz, DMSO-d_6) δ 165.0 (x2), 164.8 (x2), 152.3 (x2), 147.7, 145.1, 132.2 (x2), 130.1, 124.1 (x2), 124.0 (x2), 119.4 (x2), 117.7, 116.2 (x2), 115.4, 111.9, 104.9 (x2), 56.0, 35.8; HRMS (ESI) calcd for $C_{26}H_{18}NaO_8$ ([M+Na]$^+$) 481.0899, found 481.0895

Table 3. *α*-Glucosidase inhibitory activity of bis-coumarin derivatives

Compound	R	% Inhibition[a]	IC_{50} (μM)[b]
Dicoumarol		85.90 ± 0.86	-
1		71.43 ± 1.50	-
2	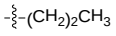	96.80 ± 0.16	9.14 ± 1.44
3		96.31 ± 0.44	18.29 ± 3.13
4	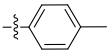	93.26 ± 0.37	8.09 ± 1.37
5	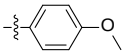	96.56 ± 0.13	9.88 ± 1.75
6	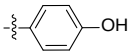	91.33 ± 0.57	10.05 ± 3.29
7	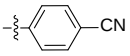	96.46 ± 0.40	15.33 ± 1.28
8	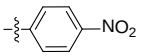	98.84 ± 0.08	7.03 ± 0.57
9	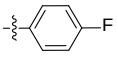	93.81 ± 0.03	12.76 ± 2.80
10	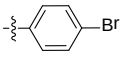	92.32 ± 0.51	11.56 ± 2.31
11a	-	96.26 ± 0.51	10.00 ± 1.22
12	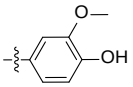	84.88 ± 1.31	-
Acarbose	-	-	147.30 ± 11.55

[a]% Inhibition at a concentration of 100 μM
[b]IC_{50} values displayed as mean ± SD

3. Results & Discussion

3.1 Synthesis of bis-coumarin derivatives

The optimization of conditions was initially explored using the synthesis of 3,3'-(phenylmethylene)bis(4-hydroxy-2*H*-chromen-2-one, **3**) as a model through the reaction of 4-hydroxycoumarin with benzaldehyde. The yield of the desired compound **3** is presented in Table 1. Compound **3** was successfully synthesized at room temperature in an aqueous medium with a 1:1 reactant ratio and without a catalyst, resulting in high yield (entry 1). Conversely, the yield was halved when the reactant ratio was 2:1 in the presence of ceric ammonium nitrate (CAN) as the catalyst (entry 2). The use of piperidine as a catalyst in ethanol produced the desired product in quantitative yield (entry 3). However, the yield was not different from the condition without a catalyst (entry 1). Hence, a catalyst is dispensable for this reaction. Moreover, increasing the temperature from room temperature (8 h, entry 1) to reflux (1.5 h, entries 4-5) significantly reduced the reaction time. The suitable condition (entry 5) was chosen for future synthesis due to their advantages, including a short reaction time, low cost, high yield, and environmental friendliness.

Twelve bis-coumarin derivatives were synthesized by reacting 4-hydroxycoumarin with various aliphatic and aromatic aldehydes. The corresponding reaction times and yields are tabulated in Table 2. The results indicated that aliphatic aldehydes produced products in moderate amounts, while aromatic aldehydes could be transformed into the corresponding products in high to excellent yields. One exception was the use of 2,4-dihydroxybenzaldehyde which did not proceed to yield compound **11** (entry 11). However, cyclized product **11a** (Figure 1) was obtained with 93% yield. Despite changing the substituent on the aromatic aldehydes, the product yield remained high, showcasing the efficiency and simplicity of this reaction.

3.2 *α*-Glucosidase inhibitory activity of bis-coumarin derivatives

Bis-coumarin derivatives **1-10**, **11a** and **12** were preliminarily screened for their *α*-glucosidase inhibitory activity at a concentration of 100 µM. The results found that the inhibition percentages of all synthesized compounds were above 70%, as shown in Table 3.

Additionally, it assessed the IC_{50} values for compounds with *α*-glucosidase inhibitory activity exceeding 90%. The presence of the R group as an aliphatic chain in compounds **1** and **2** showed a correlation, indicating that an increase in chain length could enhance the efficacy of *α*-glucosidase inhibition. Furthermore, compounds **3-10**, derived from aromatic aldehydes, showed a simultaneous increase in the inhibitory efficiency. Presenting a substituent group, such as CH_3, OCH_3, OH, CN, NO_2, F, or Br, at the para position significantly enhanced the efficiency of *α*-glucosidase inhibition. The presence of a NO_2 group (Compound **8**) exhibited the highest potent inhibitory activity with an IC_{50} value of 7.03 ± 0.57 µM. Notably, almost synthesized bis-coumarin derivatives were more potent than acarbose (IC_{50} = 147.30 ± 11.55 µM), which serves as a positive control. Therefore, these target compounds could be used to develop anti-diabetic candidates in the future.

4. Conclusion

In summary, a series of 12 bis-coumarin derivatives, utilizing various aliphatic and aromatic aldehydes, was successfully synthesized under green conditions, exhibiting medium to excellent yields. Furthermore, the evaluation of *α*-glucosidase inhibitory activity revealed that all synthesized bis-coumarin derivatives displayed notable efficacy. Compound **8** was first reported to inhibit *α*-glucosidase 21-fold more efficiently than acarbose. It is possible to develop a novel antidiabetic medication using this compound.

Acknowledgements

This work was supported by the Center of Excellence for Innovation in Chemistry (PERCH-CIC), Ministry of Higher Education, Science, Research and Innovation; the Kasetsart University Research and Development Institute (KURDI); the Department of Chemistry, Faculty of Science, Kasetsart University.

References

1. Maurya, A. K.; Mulpuru, V.; Mishra, N. *ACS Omega* **2020**, *5* (50), 32234-32249.
2. Liebl, A.; Mata, M.; Eschwège, E. *Diabetologia* **2002**, *45* (1), S23-S28.
3. Baron, A. D. *Diabetes Res. Clin. Pract.* **1998**, *40*, S51-S55.
4. Oboh, G.; Ogunsuyi, O. B.; Ogunbadejo, M. D.; Adefegha, S. A. *J. Food. Drug. Anal.* **2016**, *24* (3), 627-634.
5. Dash, R. P.; Babu, R. J.; Srinivas, N. R. *Xenobiotica* **2018**, *48* (1), 89-108.
6. Fischer, P. B.; Collin, M.; Karlsson, G. B.; James, W.; Butters, T. D.; Davis, S. J.; Gordon, S.; Dwek, R. A.; Platt, F. M. *J. Virol.* **1995**, *69* (9), 5791-5797.

7. Chambers, J. P.; Elbein, A. D.; Williams, J. C. *Biochem. Biophys. Res. Commu.* **1982**, *107* (4), 1490-1496.
8. Ghosh, S.; Collier, A. *Churchill's Pocketbook of Diabetes (Second Edition)*. **2012**, 83-125.
9. Timson, D. J. *Curr. Drug Targets* **2017**, *18* (5), 500-510.
10. Mansi; Khanna, P.; Gupta, D.; Yadav, S.; Khanna, L. *J. Biomol. Struct. Dyn.* **2023**, *41* (19), 9651-9665.
11. Mnasri, A.; Amri, N.; Ghalla, H.; Gatri, R.; Hamdi, N. *ACS Omega* **2023**, *8* (17), 14926-14943.
12. Silva, V. L. M.; Silva-Reis, R.; Moreira-Pais, A.; Ferreira, T.; Oliveira, P. A.; Ferreira, R.; Cardoso, S. M.; Sharifi-Rad, J.; Butnariu, M.; Costea, M. A.; et al. *Chin. Med.* **2022**, *17* (1), 145.
13. Banday, S.; Showkat, M.; Khan, K. *Asian J. Pharm.* **2019**, *5*.
14. Al-Hazmy, S. M.; Bensalah, D.; Dlala, N. A.; Bouazizi, Y.; Ghalla, H.; Hamdi, N. *Green Chem. Lett. Rev.* **2023**, *16* (1), 2151323.
15. Baruah, P.; Basumatary, G.; Yesylevskyy, S. O.; Aguan, K.; Bez, G.; Mitra, S. *J. Biomol. Struct. Dyn.* **2019**, *37* (7), 1750-1765.
16. Khan, K. M.; Rahim, F.; Wadood, A.; Kosar, N.; Taha, M.; Lalani, S.; Khan, A.; Fakhri, M. I.; Junaid, M.; Rehman, W.; et al. *Eur. J. Med. Chem.* **2014**, *81*, 245-252.
17. Khan, K. M.; Iqbal, S.; Lodhi, M. A.; Maharvi, G. M.; Ullah, Z.; Choudhary, M. I.; Rahman, A.-u.; Perveen, S. *Bioorg. Med. Chem.* **2004**, *12* (8), 1963-1968.
18. Brahmachari, G.; Begam, S. *ChemistrySelect* **2019**, *4* (19), 5415-5420,
19. Liu, Z.; Yin, S.; Zhang, R.; Zhu, W.; Fu, P. *ACS Sustain. Chem. Eng.* **2022**, *10* (1), 655-661.
20. Pluempanupat, W.; Adisakwattana, S.; Yibchok-Anun, S.; Chavasiri, W. *Arch. Pharm. Res.* **2007**, *30* (12), 1501-1506.

A study of pre-vulcanization time affected on the nano-porous structure preservation in silica aerogel/natural rubber composite

Chayanan Boonrawd[1]*, Thutiyaporn Thiwawong[2], Ittipol Jangchud[3], and Darapond Triampo[4]

[1]*College of Materials Innovation and Technology, King Mongkut's Institute of Technology Ladkrabang, Bangkok 10520, Thailand*
[2]*Electronics and Control Systems for Nanodevices Research Laboratory, College of Materials Innovation and Technology, King Mongkut's Institute of Technology Ladkrabang, Bangkok 10520, Thailand*
[3]*Department of Chemistry, Faculty of Science, King Mongkut's Institute of Technology Ladkrabang, Bangkok, 10520, Thailand*
[4]*Department of Chemistry and Center of Excellence for Innovation in Chemistry, Faculty of Science, Mahidol University, Nakhon Pathom 73170, Thailand*

**E-mail: chayanan.bo@hmitl.ac.th*

Abstract:

This study investigated the effectiveness of pre-vulcanized natural rubber latex (PVNRL) in maintaining the nano-pores of silica aerogel (SA). Different pre-vulcanization times of natural rubber (NR) were employed to prepare SA/NR composites. The crosslink density test was employed to assess the reduction in performance of the free-moving chains with varying pre-vulcanization times. The nano-porous structure of SA was examined using Field Emission Scanning Electron Microscopy (FESEM). The results indicated that the SA/NR composite prepared with an 8-day pre-vulcanization time exhibited high potential performance in preserving the porous structure of SA in the composite. This is attributed to the highest crosslink density value, signifying a lower number of free-moving NR chains with reduced potential to fill the SA pores. The porous structure of the pre-SA/NR composites suggests that the amount of filled SA pores depends on the pre-vulcanization time of PVNRL, indicating decreased penetration of free-moving NR chains with longer pre-vulcanization times. In conclusion, the pre-vulcanization time of NRL plays an important role in maintaining the nanoporous structures of SA in composites, offering a promising approach to enhance the expression of SA properties in polymer composites.

1. Introduction

Silica aerogels (SAs) are porous materials consisting of the nano-spherical particles in the structure agglomerate to form larger necklace-like formations. The interweaving of these necklaces creates numerous open nanometric pores with sizes ranging from a few to several tens of nanometers.[1] Because of their structure, SA possesses distinctive characteristics, including a notably high specific surface area and porosity ranging from 75% to 99%. These features result in an exceptionally low density and the lowest thermal conductivity, falling within the range of 0.01 to 0.03 W mK^{-1}.[2-6] Therefore, the main applications of SA are the thermal insulation materials because the entrapment of nanometric air within the aerogel pores, forming chambers that minimize heat exchange between gas molecules. Consequently, this inhibits air convection and reduces the thermal conductivity of the gas phase.[1] Moreover, the notable application of a superhydrophobic surface is attributed to the significant surface area featuring hydrophobic functional groups. These groups are produced through cost-effective surface modification steps in the synthesis of SA. Hence, the presence of a porous structure plays a crucial role in manifesting the exceptional properties of SAs in various applications such as absorbent materials, and especially thermal insulation materials in buildings, and aerospace.[2-5]

Because of the high porosity structure of SAs, the limitations of their monoliths are brittleness and fragility, one solution to address these drawbacks is to create a composite with polymers.[7, 8] Several SA/polymer composites were investigated to enhance the mechanical properties and provide the synergistic polymer properties. For example, the thermosetting polymer as the epoxy was applied to be composite with SA to improve the temperature range using composite.[9] Polyimide is a high heat-resistance polymer that was used as the polymer matrix in polyimide/SA composite to support the mechanical property of SA and then obtained a high heat-resistance composite.[10] Normally, The polymers were mixed with SA via solution and melt stage, leading to the pores of SA impregned with those polymers and then reduction of the composite performance eventually.[11] Thus, the attempts to preserve SA pores in the polymer composite have been continued by researchers.[12, 13] The one interesting method to limit the polymer movement during the mixing process is to crosslink the polymer chains before contacting the SA pores.

It was reported that the pre-vulcanization process of natural rubber latex (NRL) causes the reduction of the free-moving chain between natural rubber particles (RPs) during film formation and post-vulcanization.[14] In addition, NRL is a milky colloid consisting of RPs dispersed in the water. NRL is the biopolymer (poly(1,4-cis-isoprene)) produced naturally by the rubber tree (*Hevea brasiliensis* tree).[15, 16] The colloidal structure of NRL refers to the conformation of the polymer chains compacted to be the particle. From the properties of NRL, it could be beneficial to the preservation of SA's pores as follows, (i) NRL can pre-vulcanize and still obtain the liquid-like solution, (ii) it is the compacted chain conformation. For both reasons, the free-moving chains are limited by the crosslink of each chain in the liquid form, thus the potential of the polymer chains to move and fill the porous structure of SA during the mixing and drying process is reduced.

In this work, the performance of pre-vulcanized NRL (PVNRL) to preserve the nano-pore of SA was studied through the preparation of SA/NR composite with different pre-vulcanization times of NRL. The crosslink density test was utilized to indicate the reduction performance of the free-moving chains by different pre-vulcanization times. The nano-porous structure of SA was investigated by FESEM images. Then, the correlation between the crosslink density and the existence of SA porous structure depending on the pre-vulcanization times was analyzed and answered the hypothesis of this work.

2. Materials and Methods

2.1 Materials

60% High ammonia-NRL was acquired from Thai Rubber Latex Corporation (Thailand) Public Company Limited. SA was sourced from RAGEL-P/REM TECH Co., Ltd. Ammonia buffer solution with a pH of 10, polyethylene glycol sorbitan monolaurate ($C_{58}H_{114}O_{26}$) or Tween 20 were procured from Sigma Aldrich. Potassium hydroxide (KOH) was obtained from Suksapanpanit. Toluene was bought from Merck, and vulcanizing agents were supplied by Lucky Four Company Limited. These agents comprised 60% sulfur dispersion, 50% zinc oxide (ZnO) dispersion, 50% zinc diethyldithiocarbamate (ZDEC) dispersion, and 50% LOWINOX™ CPL (CPL).

2.2 Pre-vulcanization of NRL

The initial step in pre-vulcanizing NRL involved blending it with a KOH solution to ensure uniform dispersion in latex form. Sulfur dispersion, serving as a curing agent, was then added to the mixture, followed by stirring using a magnetic stirrer at 250 rpm for 5 min. Subsequently, a ZnO suspension, acting as an activator, was introduced, and stirred for an additional 5 min at the same speed. Next, ZDEC as an additional accelerator, along with CPL as an antioxidant were combined. The compounded NRL underwent stirring for 30 min at room temperature, with the ingredient proportions detailed in Table 1. The obtained PVNRL was maturated as 0, 2, 4, 6, and 8 days at room temperature prior to utilizing in preparation of SA/NR composites and the control sample onward.

Table 1. Formulation of PVNRL compounding

Ingredients	Formulation (phr)
60 wt% NRL	100
10 wt% KOH	0.30
60 wt% Sulfur	0.50
50 wt% ZnO	0.25
50 wt% ZDEC	0.75
50 wt% CPL	0.50
8.20 wt% SA dispersion	20

2.3 Preparation of SA dispersion

To prepare the stock solution of SA dispersion, 100.00 g of deionized (DI) water served as the aqueous medium. A surfactant, 0.40 g of Tween 20, was pre-mixed with DI water using a magnetic stirrer at 250 rpm for 15 min to enhance compatibility between water and the hydrophobic surface of SA. Subsequently, the resulting DI water was re-mixed with a 1500 W blender for 1 min to ensure better homogenization of the components. 9.00 g of SA powder was added to the DI water and carefully blended using the same blender. The mixture underwent vigorous blending for 1 min, followed by a 2-minute pause to allow any scattered SA to settle from the blender's cavity onto the mixture's surface before commencing the next blending cycle. This blending pattern was repeated five times. The stock of SA dispersion in DI water was then adjusted to pH 7 using 0.25 g of a 10 wt%-KOH solution. The resulting SA dispersion was indicated the certain concentration by investigating the total solid content prior to composite preparation.

2.4. SA/NR composite preparation

The SA/NR composites were created by maintaining SA contents at 20 parts per hundred of rubber (phr). PVNRL was mixed with 0.6 wt% of pH 10-ammonia buffer and stirred at 250 rpm for 5 min. Following this, the resulting PVNRL with varying pre-vulcanization periods was introduced into the SA dispersion with magnetic stirring at 250 rpm. The mixtures underwent continuous stirring for 30 min, and the resulting mixtures in

termed of slurries were left at room temperature for 1 h to allow the release of bubbles. Subsequently, these slurries were applied onto a 0.05-mm-thick glass plate and air-dried at room temperature for 2 days, resulting in the pre-vulcanized SA/NR film composite, labeled as pre-SA/NR, along with control samples (without SA), labeled as pre-NR. The dried films obtained were then divided for the continuation of the post-vulcanization process by placing the samples in an oven at 100 ℃ for 2 h, labeled as post-SA/NR, and post-NR for the control sample.

2.5 Crosslink density test

SA/NR films and control samples, prepared through PVNRL with various pre-vulcanization times, were precisely weighed (0.05 g) and placed in dried toluene (5 mL) within a glass bottle. These samples were maintained at 40 ± 3 °C for 48 h, with a toluene change after 24 h. Upon reaching equilibrium, the swollen samples were removed and the excess toluene was eliminated using filter paper. The samples were then weighed in a capped weighing bottle. The crosslink density (ν) for each composite and control film was determined using the Flory–Rehner equation (Equation (1))

$$\nu = -(\ln(1-V_r^0)+V_r^0+\chi V_r^{0^2})/2\rho_r V_0(V_r^{0^{1/3}}-V_r^0/2) \quad (1)$$

where V_r^0 represents the volume fraction of the vulcanized rubber, χ is the Huggins interaction constant, and V_0 is the molar volume of the solvent used. The V_r^0 value was obtained using Equation (2).

$$V_r^0 = 1/(\rho_r/\rho_s)\cdot((W_s-W_u)/W_u)+1 \quad (2)$$

where W_u and W_s are the weights of the unswollen and swollen rubber samples at equilibrium, respectively. The densities of toluene (ρ_s) and NR (ρ_r) are 0.886 and 0.930 g cm^{-3}, respectively. The V_0 of toluene is 106.9 cm^3 mol^{-1}, and the χ constant for gum NR with toluene is 0.39.[17]

3. Results & Discussion

3.1 Crosslink density

The crosslink density of vulcanized NR is indicative of the number of crosslink points between NR chains. This parameter can be examined through swelling in toluene until equilibrium is achieved. Figure 1 illustrates the crosslink density of the pre-vulcanized SA/NR film (pre-SA/NR), post-vulcanized SA/NR film (post-SA/NR), and control samples without SA (pre-NR and post-NR) in relation to the pre-vulcanization period at room temperature.

The crosslink density of post-SA/NR films exhibited a gradual increase with pre-vulcanization time until fourth day, followed by a significant escalation from fourth day to sixth day, reaching a plateau at sixth day and eighth day. A similar trend was observed for pre-SA/NR, indicating that pre-vulcanization time influenced crosslink density and facilitated efficient post-vulcanization.

In comparison to NR film, the pre-SA/NR film demonstrated a higher crosslink density than pre-NR, whereas only a slight difference was observed between post-vulcanized films. This suggests that the presence of SA minimally affected crosslink density during post-vulcanization but played a significant role in the pre-vulcanization process. Notably, the crosslink density of post-vulcanized films was over 2.35 times greater in SA/NR films and 4.31 times greater in NR films than that of pre-vulcanized films. This implies that SA influenced the efficiency of crosslinking in the NR chain. It can be described that the similar hydrophobic surfaces of SA and NR brought about the physical crosslinking via filler-rubber interaction. These networks took part in the reduction of the toluene swelling parameters and the increase in the total crosslink density of the bulk composite.

The significance of pre-vulcanization was emphasized in the study by C. C. Ho and M. C. Khew, who investigated film formation of PVNRL with varying pre-vulcanization times.[14] Their findings indicated that increased crosslinking through pre-vulcanization of NRL resulted in the retardation of free-flowing chains during post-vulcanization, leading to smoother film formation. Therefore, considering the preservation of the nanoporous structure of SA within the polymer matrix chains, pre-vulcanized NRL at day 8 could potentially maintain the nanoporous structure of SA in the composite efficiently. The remaining nanopores of SA will be explored further in the morphology section.

3.2 Morphology

The morphologies of the SA/NR composites were studied to inform the bulk composite structure and analyze the existence of the porous structure of SA in the composite by the FESEM image as shown in Figure 2. To confirm the qualitative components of the SA/NR composite, the appearance of the smooth cross-section surface of NR-film is presented in the FESEM image (Figure 2a). On the other hand, the morphology of SA (Figure 2b.) showed a powder-like and puffy structure consisting of particle sizes of about 10-20 μm, and the tiny particles less than 1 μm that may be generated from the fracture down

of the larger particle because of fragile structure characteristics of SA. The porous structure of a pristine SA is shown in Figure 2c, a higher magnification image assisted to be obvious pores between the agglomeration of the tiny particles in less than a micron-size, which referred to the characteristic structure of SA.

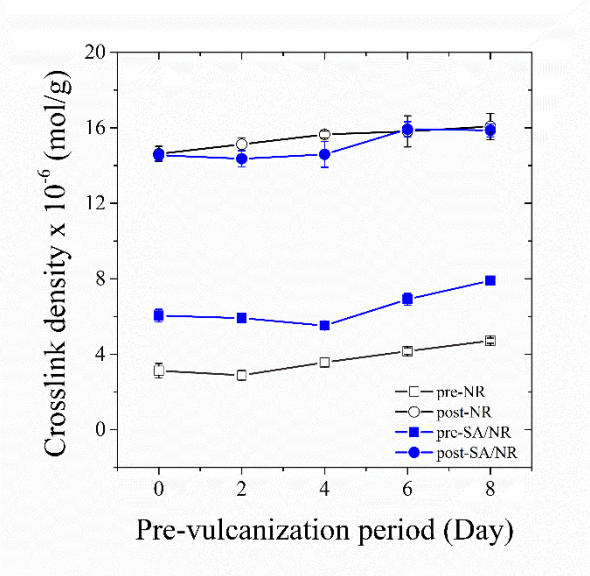

Figure 1. Crosslink density of the pre-vulcanized film (pre-NR), the pre-vulcanized film (pre-NR) with the continuing post-vulcanization process (post-NR), the SA/NR film (pre-SA/NR), and the SA/NR film with the continuing post-vulcanization process (post-SA/NR) as a function of the pre-vulcanization period at room temperature

The presence of the NR and SA structures appeared in the cross-section surface of the SA/NR composite as shown in Figure 2d-2g and 2d1-2g1 (the higher magnification images). The appearance of the pre-SA/NR, prepared with 0-day (Figure 2d) and 8-day (Figure 2e) PVNRL, presented the porous structure consisting of the empty pores (white arrow) and the filled pores (orange arrow). This structure may refer to the structure preservation of the micelle droplets of SA in the dispersion until the composite was dried. These droplets were generated by SA dispersion with a surfactant, the micelle became more stable until presented in the dried composite. It was because of the super-hydrophobic surface of SA.

The empty pores of pre-SA/NR with 0-day pre-vulcanization time were more than the amount of the filled pores, whereas the filled pores seemed more than the empty pores in the pre-SA/NR with 8-day pre-vulcanization time. In the higher magnification images, both pre-SA/NR with 0-day and pre-SA/NR with 8-day pre-vulcanization time showed the merging structure of the NR and SA (Figure 2d1) and the filled pores showing the SA structure inside the pore (Figure 2e1). The lower crosslink density due to short pre-vulcanization time caused more moving chains of NR during the film formation (drying process) leading to higher NR chains penetrating through the SA porous structure and simultaneously destroying the droplet of SA. Eventually, it left the mixing structure between SA and NR and an empty pore structure in the bulk morphology.

On the other hand, higher crosslink density, initiated by longer pre-vulcanization time, brought about high chain networks or lower movable chains resulting in lower penetrating of NR chains through the SA's porous structure and filled pores structure by SA generating in the bulk morphology. It may be concluded that the increase in the pre-vulcanization time provided a higher performance to preserve pores of SA by the reduction of free-moving NR chains in NRL before the preparation of SA/NR composite.

The post-SA/NR composites (Figure 2f-2g) seemed to appear the similar morphology presenting the agglomeration of SA particles linked to each other by the NR and destroyed porous structure. It can be described that the free-moving chains grew with the increase in temperatures during the post-vulcanization process leading to the extreme penetrating of NR's chains to SA porous structure and obtaining almost full embedded SA in NR matrix. It supported the slight changes in crosslink density with the increase in pre-vulcanization times. To analyze the SA porous structure precisely, the high magnification FESEM images present the morphology of the post-SA/NR with 0-day and 8-day pre-vulcanization time as shown in Figure 2f1 and 2g1, respectively. Although a major part of the morphology of the post-SA/NR composite illustrated the merged structure of SA and NR, the remaining porous structures of SA were observed in post-SA with 8-day pre-vulcanization. These results correlated with the higher crosslink density with the pre-vulcanization time bringing about the lower ratio of the free movable chains of NR in the film formation stage and post-vulcanization process and resulting in the lower potential penetrating NR chain through the porous structure of SA. Therefore, the increase in pre-vulcanization time of NRL before mixing with SA had a high potential to preserve the porous structure of SA.

4. Conclusion

The effect of the pre-vulcanization time of NRL on the performance to preserve nanoporous structures was studied through the preparation of

the SA/NR composite with different pre-vulcanization times. The SA/NR composite prepared by 8-day pre-vulcanization time presented a high performance to preserve the porous structure of SA in the composite due to the highest crosslink density value which referred to the lower number of free-moving chains of NR leading to lower potential to fill in the SA pores. The porous structure of the pre-SA/NR composites appeared and consisted of the embedded SA pores The amount of filled SA pore seemed to depend on the pre-vulcanization time of PVNRL, suggesting reduced penetration of free-moving NR chains as the pre-vulcanization time increased. Additionally, the post-SA/NR composite highlighted the influence of the pre-vulcanization time by the remaining SA porous structure in the bulk composite morphology. In summary, the pre-vulcanization time of NRL plays a crucial role in preserving nanoporous structures of SA in composites. This observation might be a beneficial idea to enhance the original properties of SAs in the polymer composites.

Acknowledgments

The authors would like to acknowledge the laboratory equipment support from College of Materials Innovation and Technology (CMIT), and Nanotechnology and Materials Analytical Instrument Service Unit (NMIS) of College of Materials Innovation and Technology, King Mongkut Institute of Technology Ladkrabang. Furthermore, special thanks to Prime nanotechnology co., ltd. for the measurements of the field emission scanning electron microscope (FESEM).

References

1. Tang, G. H.; Bi, C.; Zhao, Y.; Tao, W. Q., *Energy* **2015,** *90*, 701-721.
2. Hüsing, N.; Schubert, U., *Angew. Chem. Int. Ed.* **1998,** *37* (1-2), 22-45.
3. Wang, X.-D.; Sun, D.; Duan, Y.-Y.; Hu, Z.-J., *J. Non. Cryst. Solids.* **2013,** *375*, 31-39.
4. Xie, T.; He, Y.-L., *Int. J. Heat Mass Transf.* **2016,** *95*, 621-635.
5. Yan, J.; Choi, H. Y.; Hong, Y. K.; Jeong, Y. G., *Fibers Polym.* **2018,** *19*, 854-860.
6. Lee, C. J.; Kim, G. S.; Hyun, S. H., *J. Mater. Sci.* **2002,** *37* (11), 2237-2241.
7. Boday, D. J.; Keng, P. Y.; Muriithi, B.; Pyun, J.; Loy, D. A., *J. Mater. Chem.* **2010,** *20* (33), 6863-6865.
8. Ge, D.; Yang, L.; Li, Y.; Zhao, J., *J. Non. Cryst. Solids.* **2009,** *355* (52-54), 2610-2615.
9. Kim, H. M.; Kim, H. S.; Kim, S. Y.; Youn, J. R., *e-Polymers*. **2015,** *15* (2), 111-117.

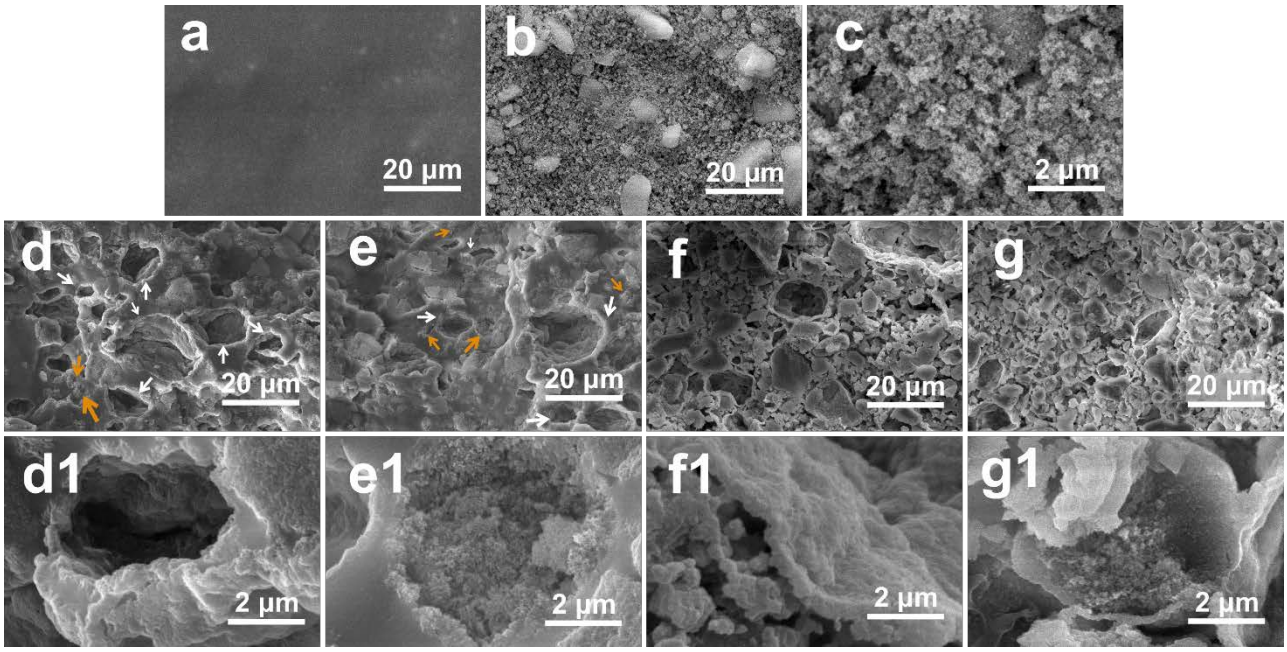

Figure 2. Cross-section FESEM images of pre-vulcanized NR film (a), SA with different magnifications as ×5K (b) and ×50K (c), and SA/NR composite films prepared by different conditions as using 0-day PVNRL in different magnifications as ×5K (d) and ×50K (d1), using 8-day PVNRL in different magnifications as ×5K (e) and ×50K (e1), using 0-day PVNRL with following by post-vulcanization in different magnifications as ×5K (f) and ×50K (f1), and using 8-day PVNRL with following by post-vulcanization in different magnifications as ×5K (g) and ×50K (g1)

10. Kim, S. Y.; Noh, Y. J.; Lim, J.; You, N.-H., *Macromol. Res.* **2014,** *22* (1), 108-111.
11. Kim, G.; Hyun, S., *J. Mater. Sci.* **2003,** *38*, 1961-1966.
12. Kim, H. M.; Noh, Y. J.; Yu, J.; Kim, S. Y.; Youn, J. R., *Compos. - A: Appl. Sci.* **2015,** *75*, 39-45.
13. Lee, H.; Lee, D.; Cho, J.; Kim, Y.-O.; Lim, S.; Youn, S.; Jung, Y. C.; Kim, S. Y.; Seong, D. G., *Compos. - A: Appl. Sci.* **2019,** *123*, 108-113.
14. Ho, C. C.; Khew, M. C., *Langmuir* **1999,** *15* (19), 6208-6219.
15. Nawamawat, K.; Sakdapipanich, J. T.; Ho, C. C.; Ma, Y.; Song, J.; Vancso, J. G., *Colloids Surf. A Physicochem. Eng. Asp.* **2011,** *390* (1), 157-166.
16. Sansatsadeekul, J.; Sakdapipanich, J.; Rojruthai, P., *JBB* **2011,** *111* (6), 628-634.
17. Sriring, M.; Nimpaiboon, A.; Dechnarong, N.; Kumarn, S.; Higaki, Y.; Kojio, K.; Takahara, A.; Ho, C. C.; Sakdapipanich, J., *Macromol Mater Eng.* **2019,** *304* (9), 1900283.

Production and characterization of cellulose powders from brewery' spent grain

Kawalee Kumpangnil and Sasithorn Kongruang*

Department of Biotechnology, Faculty of Applied Science, King Mongkut's University of Technology North Bangkok, Bangkok, Thailand

**E-mail: sasithorn.k@sci.kmutnb.ac.th*

Abstract:

Brewery Spent Grain (BSG) is a byproduct of the brewing industry, primarily consisting of cellulose, hemicellulose, lignin, and protein sourced from malted barley. Although often discarded as waste, BSG holds untapped potential as animal feed and contains valuable cellulose, which is applicable across various industries like food, pharmaceuticals, and cosmetics. This study aims to optimize the extraction process to produce cellulose from BSG. We used the Box-Behnken Design to find the best combination of three important factors to get the most cellulose: temperature (90–100 °C), alkaline concentration (1–2% w/v NaOH), and extracting time (1-3 h). The extracted cellulose samples were then bleached with H2O2 at 70 °C for 40 min, followed by washing and drying to obtain pure cellulose powders. The result found that the cellulose yield was 10.89 with 60.32% crystallinity under 1.69% w/v alkaline concentration at 100 °C and 1 hour of extracting time. The assessment of the structural features and bonds, with a particular emphasis on eliminating undesirable components of lignin and hemicellulose via Fourier transform infrared (FT-IR) analysis, It was revealed that a strong, sharp lignin stretching vibration positioned at 1633 cm^{-1} (C=stretching) of lignin was reduced by 34.70% compared with the untreated BSG. 11% reductions of lignin (aromatic skeletal vibration) and hemicellulose (COO-stretching) were also observed. These purified cellulose powders were further analyzed using X-ray diffraction (XRD) to determine crystallinity and obtained 59.22% cellulose purity, while the cellulose powder standard gained 65.85% of crystallinity. This research contributes to the value-added of BSG and its potential integration into the wider food industry, opening new possibilities for its use beyond traditional waste disposal.

1. Introduction

Brewery's Spent Grain (BSG) is a byproduct generated in the brewery business. Raw barley grains go through the malting process to produce BSG. One of the waste products generated by industrial plants during beer manufacture and available at affordable costs Despite its abundance throughout the year, malt residue can be utilized as animal feed because of its protein, dietary fiber, and calorie content, which make it suitable for various animal species (Mussatto et al., 2006). Nevertheless, its utilization as animal fodder is of minimal worth. Malt residue, aside from its application as animal feed, contains additional constituents such as cellulose that can be effectively utilized, hence enhancing the usefulness of industrial waste (Mussatto et al., 2008). Cellulose and its derivatives are currently utilized in a wide range of industries, encompassing food, pharmaceuticals, cosmetics, detergents, paper production, textiles, polymers, oil extraction, ceramics, pesticides, adhesives, and paints, among others. Due to the growth and expansion of the industrial sector, Thailand lacks domestic production of cellulose and its derivatives, necessitating the country to depend on imports from foreign sources (Pimchan et al., 2018). It results in numerous consequences, particularly in the economic sphere, leading to significant financial losses for the country because of the expenditure on designating unprocessed resources. Additionally, it exerts influence on the capacity for production, particularly within the pharmaceutical sector, resulting in constraints on drug manufacturing.

Cellulose and its derivatives serve as pharmacological additives, namely as excipients, predominantly in tablet form, which is the prevailing method of illness treatment in contemporary medicine (Dusadi et al., 2014). According to a study by Tita et al. (2014), cellulose has the ability to absorb carcinogens. It inhibits the absorption of carcinogens and prevents the reabsorption of sugar by the body. There are two variants available for consumption: microcrystalline cellulose and cellulose powder. The cellulose powder variant is a colorless powder devoid of any scent or flavor and acts as a viscosity stabilizer and texture quality enhancer (Tita et al., 2014). Also, it is employed as a food bulking agent. Cellulose powder has been utilized as an ingredient in health foods in both Europe and America. Additionally, it is utilized in several food items, including cakes, cookies, margarine, pasta, soup, and meat products. Particularly in the freezing sector, cellulose serves as a cryoprotectant for pharmaceutical purposes (Yoon et al., 1990).

Cellulose molecules exhibit variations in both particle size and moisture content. In pharmaceutical applications, it also possesses a voluminous aspect, exhibits limited permeability and flowability, yet demonstrates compressive characteristics, rendering it suitable as a direct compression filler (Yun et al., 2020). Consequently, the objective of this study is to quantify cellulose powder with alkaline extraction for design experts. The Box-Behnken Design (BBD) was employed to determine the optimum production for cellulose, determine optimal conditions for production, and convert it into a powdered form. The qualities of the cellulose were subsequently examined.

2. Materials and Methods

2.1 Processing of Brewery Spent Grain (BSG)

The malt residue produced during the beer manufacturing process was collected. The dehydrate process of the malt pulp was subjected to a hot air oven at 50 °C for a duration of 12 hours, followed by a thorough blending. Subsequently, the size was segregated using a sieve with a mesh aperture of 500 micrometers in order to facilitate analysis and experimentation in the subsequent stage.

2.2 Cellulose extraction from BSG

2.2.1 the digestion process with Alkaline

The mixture of malt pulp was introduced into a sodium hydroxide solution with concentrations of 1%, 1.5%, and 2% in a total volume of 100 mL. Subsequently, the sample was subjected to high-pressure sterilization (autoclave) at temperatures of 90, 95, and 100 °C for 60, 120, and 180 min. sample were then separated into solid and liquid components by centrifugation at 4,000 rpm for 20 min. The cellulose component was rinsed with 100 mL of distilled water to eliminate any residual lignin present in the cellulose.

2.2.2 Bleaching process

Samples were bleached by adding 16.7 mL of 5% w/v of concentrated hydrogen peroxide (H2O2) solution in 100 mL of distillation water after alkaline treatment, then applying heat using a high-pressure sterilizer (autoclave) at 70 °C for 40 min. Afterward, the solid was separated from the liquid by centrifugation at 4,000 rpm for 10 min.

2.2.3 Washing process

The cellulose residues were further neutralized by using 0.01% w/v hydrochloric acid. The mixture was stirred for 30 min, then subjected to centrifugation at 4,000 rpm for 10 min. A neutral pH was achieved by cleaning with 100 mL of distilled water. The samples were filtrated and transferred to a 50 °C hot air oven for 12 hours.

2.3 Analysis of the physicochemical composition

2.3.1 Quantification of cellulose functional groups by Fourier Transform Infrared spectrometer

FTIR (Invenio-s, Bruker,Germany) with an ATR sampling accessory was used to assess the structural composition and functional groups of isolated cellulose from malt pulp. The spectra were recorded and studied in the range of 400 to 4000 cm^{-1}.

2.3.2 Crystallinity analysis of cellulose derived from BSG

The X-ray diffractometer (XRD) was used to assess the crystallinity of cellulose obtained from extracted cellulose powder. The samples were scanned in the range of $2q=5\text{-}60^0$ with a scanning rate of 0.020/min using Ni-filtered Cu Kα radiation at room temperature. The crystallinity index was calculated using the equation CI = (I002-Iam)/I002, where I002 is the maximum intensity of the peak (200) at $2q=22.5^0$ and Iam is the minimum intensity at the valley between planes (110) and (200) at $2q=18.6^0$.

2.4 BBD criteria for BSG cellulose powder manufacturing.

BBD methodology using the Design Expert program version 12 was used to design the experimental run from the chosen parameters with 3 factors and 3 levels, as shown in Table 1.

Table 1. Factors and levels parameters for BBD

Factors	Level of factors		
	-1	0	+1
NaOH(%w/v)	1	1.5	2
Temperature (°C)	90	95	100
Time (h)	1	2	3

3. Results & Discussion

3.1 Functional group analysis of cellulose

The results of the chemical structure of isolated cellulose power after alkaline treatment were assessed by FTIR, and the results of the spectra are presented in Fig 1. The spectra of treated cellulose samples contained a broad peak in the region of 3500–4000 cm^{-1}. Results found a substantial reduction of 34.70% in the intense and distinct lignin stretching vibrations at 1633 cm^{-1} (C = stretching) compared to untreated BSG, showing a significant elimination of unwanted elements of lignin and hemicellulose out of the cellulose component. The study revealed that approximately 11% reductions in lignin (aromatic skeletal vibration) and hemicellulose (COO stretching) were found in Fig 1. Furthermore, the

absorption bands around 1100 cm^{-1} showed the C-O anti-symmetric bridge stretching, and 900 cm^{-1}, originated from the glycoside C-H deformation with the ring vibration.

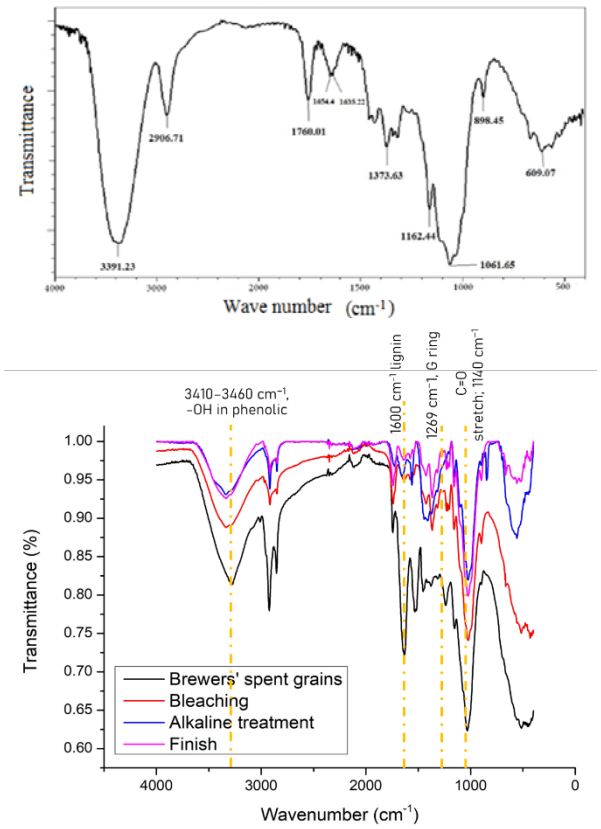

Figure 1. FTIR spectra of the commercial cellulose and isolated cellulose from BSG through alkaline treatment.

3.2 Cellulose crystallinity analysis

Table 2. The yield and crystallinity obtained from isolated cellulose powder.

Sample	Crystallinity (%)	Yield (%)
cellulose powders	65.85	0.0
2% 90°C 2h	59.41	9.4
2% 95°C 1h	66.56	11.3
2% 95°C 3h	59.68	8.7
2% 100°C 2h	59.10	9.0
1.5% 90°C 1h	55.66	12.2
1.5% 90°C 3h	57.98	11.4
1.5% 95°C 2h	55.73	10.5
1.5% 100°C 1h	58.60	11.1
1.5% 100°C 3h	58.84	12.7
1.5% 95°C 2h (1)	61.63	12.5
1.5% 95°C 2h (2)	60.47	11.5
1.5% 95°C 2h (3)	62.56	12.0
1.5% 95°C 2h (4)	60.80	13.7
1% 90°C 2h	58.09	9.7
1% 95°C 1h	61.53	7.2
1% 95°C 3h	58.34	8.7
1% 100°C 2h	55.56	12.1

The yield and crystallinity of cellulose powder at each condition are shown in Table 2, where 1.5% 95 °C 2h was repeated for a total of 4 replicates. The analysis revealed that the isolated cellulose powder had a crystallization rate of approximately 55–65% While the standard cellulose powder had a crystallinity of 65.85%, X-ray diffraction (XRD) analysis of the cellulose powder samples obtained revealed crystallinity values that closely matched typical cellulose values. The acceptable range for the degree of crystallinity of cellulose is generally between 40% and 60% (Table 2).

3.3 Optimization of cellulose powder production

ANOVA results of the quadratic model evaluation are presented in Table 3. Results found the concentration of NaOH, treatment temperature and time did not significantly affect the yield and crystallinity of the isolated cellulose powder of BSG. An extensive examination of the composite tests utilizing the BBD approach, conducted using the Design Expert tool, revealed that the most favorable conditions in all 17 trials. The maximum yield was 12.1 % under the alkaline treatment at 1.45% at 96 °C for 2 h. The illustration of the response surface methodology of the relationship between the concentration of sodium hydroxide and the test variable were constructed. The response surface graphs of the isolated cellulose yield were depicted in Fig. 2 a–c and in terms of the crystallinity in Fig. 2d–f.

Table 3. Analyzing the variation of experimental outcomes for cellulose manufacturing in terms of yield and crystallinity.

Source	Sum of Squares	df	Mean Square	F-value	P-value
Model	35.95	9	3.99	2.07	0.1752
A-NaOH	0.0613	1	0.0613	0.0317	0.8637
B-Temp	0.6050	1	0.6050	0.3133	0.5931
C- Time	0.0113	1	0.0113	0.0058	0.9413
AB	1.96	1	1.96	1.01	0.3473
AC	4.20	1	4.20	2.18	0.1837
BC	1.44	1	1.44	0.7456	0.4165
A2	24.91	1	24.91	12.90	0.0088
B2	0.8244	1	0.8244	0.4269	0.5344
C2	1.68	1	1.68	0.8722	0.3814
Residual	13.52	7	1.93		
Lack of Fit	7.89	3	2.63	1.87	0.2759
Pure Error	5.63	4	1.41		
Cor Total	49.47	16			

Source	Sum of Squares	df	Mean Square	F-value	P-value
Model	22.93	3	7.64	1.00	0.4227
A-NaOH	15.76	1	15.76	2.07	0.1740
B-Temp	0.1152	1	0.1152	0.0151	0.9040
C- Time	7.05	1	7.05	0.9250	0.3537
Residual	99.08	13	7.62		
Lack of Fit	71.06	9	7.90	1.13	0.4908
Pure Error	28.02	4	7.01		
Cor Total	122.01	16			

4. Conclusion

In this investigation of cellulose extraction through alkaline treatment from BSG through BBD, The optimal conditions from 17 experiments found that the maximum cellulose power yield of 12.1% was achieved at a NaOH concentration of 1.45% at 96 °C over 2 h. The cellulose powder had 59.22% crystallinity, which was close to the 65.85% found in the cellulose powder standard. The experiment showed that lignin was removed during the cellulose extraction of BSG through alkaline hydrolysis, as shown by FTIR analysis.

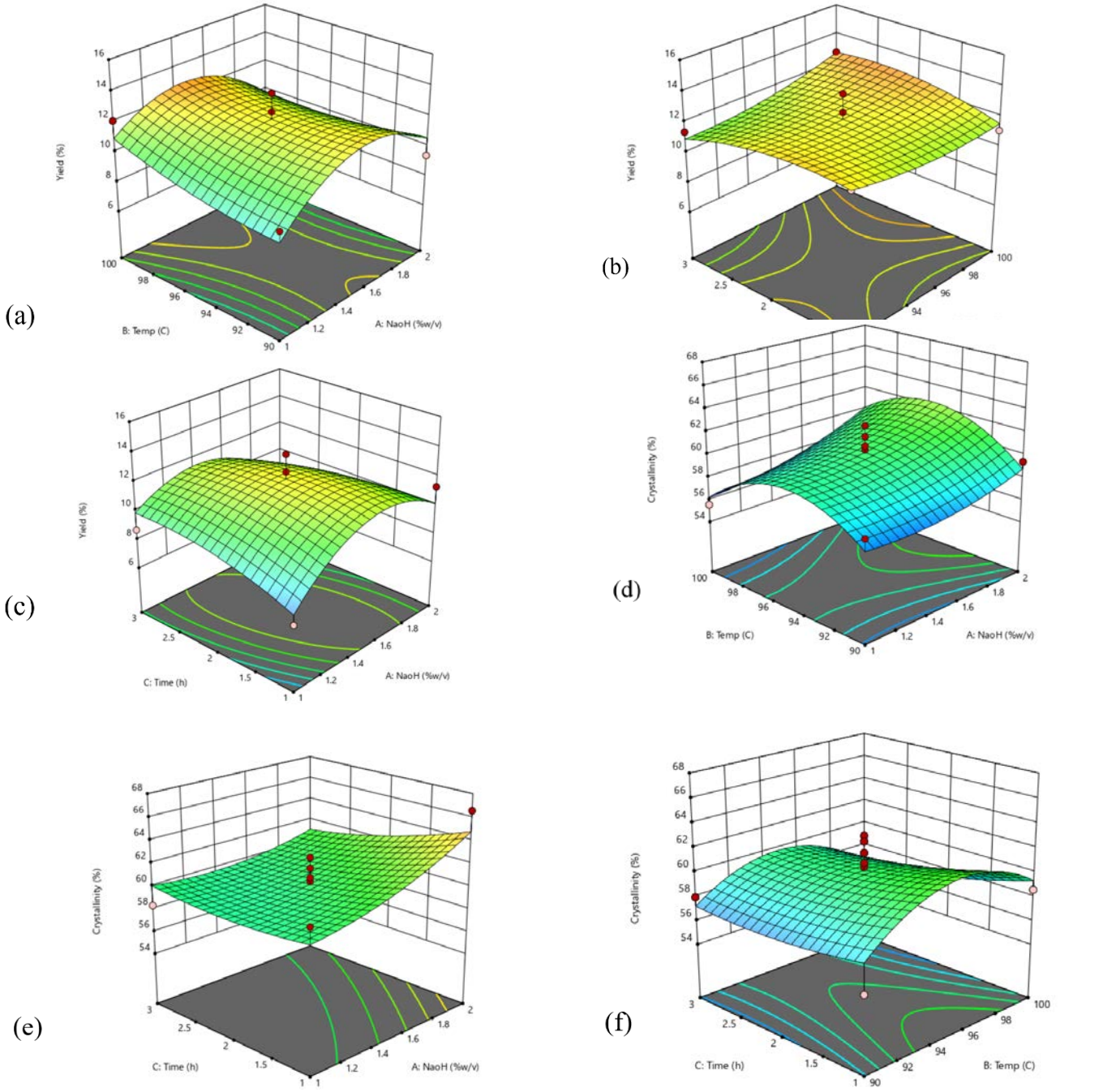

Figure 2. Effect of interaction of influential factors on yield (a-c) and crystallinity (d-f) The quadratic model was chosen to fit the experimental data.

The relationships between cellulose yield and crystallinity on concentration of alkaline, hydrolysis temperature, and hydrolysis time are listed in Tables 4 and 5.

Table 4. Final Equation in Terms of Actual Factors (Yield)

Yield	=	R^2
+118.70		0.73
+60.07	*NaOH	
-3.13	*Temp	
-5.83	*Time	
-0.28	*NaOH*Temp	
-2.05	*NaOH*Time	
+0.12	*Temp*Time	
-9.73	$*NaOH^2$	
+0.02	$*Temp^2$	
-0.63	$*Time^2$	

Table 5. Final Equation in Terms of Actual Factors (Crystallinity)

Crystallinity	=	R^2
-1003.95		0.56
-23.95	*NaOH	
+22.53	*Temp	
+9.67	*Time	
+0.22	*NaOH*Temp	
-1.85	*NaOH*Time	
-0.10	*Temp*Time	
+3.12	$*NaOH^2$	
-0.12	$*Temp^2$	
+0.51	$*Time^2$	

Acknowledgements

This research was supported by Will program through the cooperation with King Mongkut's University of Technology North Bangkok.

References

1. Duwadee, S. Extraction and Characterization of Cellulose from Bagasse, Water Hyacinth, and Cattail. (2014).
2. Thita, E.; Atchara, P.; Patchara, O.; Weera, H. Effects of Extraction Methods on the Properties of Cellulose Extracts from Moringa Seed Meal. J. Food Health Bioenv. Sci. 2014, 7 (2), 43–56.
3. Mussatto, S. I.; Dragone, G.; Roberto, I. C. Brewers' Spent Grain: Generation, Characteristics, and Potential Applications. J. Cereal Sci. 2006, 43 (1), 1–14.
4. Mussatto, S. I.; Rocha, G. J.; Roberto, I. C. Hydrogen Peroxide Bleaching of Cellulose Pulps Obtained from Brewer's Spent Grain. Cellulose 2008, 15, 641–649.
5. Pimchan, P.; Phongthai, S.; Boonta, P.; Utai, K. Cellulose Extraction from Cyperus Corymbosus Rottb. L. for Dietary Fiber. J. Sci. Technol. Rajabhat Maha Sarakham Univ. 2018, 1 (1), 19–25.
6. Yan, G.; Chen, B.; Zeng, X.; Sun, Y.; Tang, X.; Lin, L. Recent Advances on Sustainable Cellulosic Materials for Pharmaceutical Carrier Applications. Carbohydr. Polym. 2020, 244, 116492.
7. Yoon, K. S.; Lee, C. M. Effect of Powdered Cellulose on the Texture and Freeze-Thaw Stability of Surimi-Based Shellfish Analog Products. J. Food Sci. 1990, 55 (1), 87–91.

Development and characterization of amidated pectin-PVA hydrogels for enhanced drug delivery and antimicrobial properties

Supatcha Suankhem, Woranart Jonglertjunya, Warangkana pornputtapitak, and Suthida Boonsith*

Department of Chemical Engineering, Faculty of Engineering, Mahidol University, Nakhon Pathom 73170, Thailand

**E-mail: suthida.bos@mahidol.edu*

Abstract:

Hydrogel-based drug delivery systems have gained significant attention due to their unique properties and applications. In this study, hydrogels were prepared from polyvinyl alcohol (PVA), pectin (Pec)-PVA, and amidated pectin (AMDP)-PVA for potential drug delivery and antimicrobial applications. Pectin was extracted from pomelo peel through acid extraction, and amidation was carried out using ethanolamine. The hydrogels were created using a freeze-thaw (FT) cycle, with varying freezing times of 24, 48, and 72 hours. The FT cycle duration had a significant impact on the hydrogels' properties. The swelling behavior of the hydrogel at different FT cycles and types was thoroughly investigated. Furthermore, loading and release studies were conducted by using Chlorhexidine as a model drug, revealing that AMDP-PVA hydrogels exhibited superior loading and release profiles compared to PVA and Pec-PVA hydrogels. These findings emphasized the potential of amidated pectin as a valuable component for controlled drug delivery systems. To assess their suitability for biomedical applications, the antimicrobial properties of these hydrogels were evaluated against *E. coli* and *S. aureus*. This study emphasized the importance of modifying hydrogel characteristics by selecting appropriate constituents and processing conditions for drug delivery applications and the potential of amidated pectin-PVA hydrogels in the field of pharmaceutical and medical research.

1. Introduction

The development of drug delivery systems is a critical aspect of modern pharmaceutical research, aimed at enhancing the therapeutic efficacy of pharmaceutical agents while minimizing potential side effects. Hydrogels have emerged as promising candidates for controlled drug release applications due to their unique characteristics, such as high water content and the ability to encapsulate and release drugs in a controlled manner.[1] This study delves into the characterization and performance evaluation of pectin-based hydrogels loaded with Chlorhexidine (CHX) for potential use in drug delivery.

Pectin, a natural polysaccharide found in various plant materials, offers attractive properties for hydrogel formulations, including biocompatibility, biodegradability, and pH sensitivity.[2] By incorporating pectin into hydrogel matrices, we aimed to harness its distinct attributes for effective drug delivery. This investigation involves the analysis of different types of pectin-based hydrogels, including pomelo pectin, amidated pectin, and pectin-modified hydrogels. These hydrogel systems were characterized using various analytical techniques, and their drug-loading and release behaviors were systematically assessed.

2. Materials and Methods

2.1 Pectin extraction

Pomelo powder 10 g was weighed therefrom acidified with 1 M citric acid solution (1:29 (w/v)). The mixture was stirred at 70 °C for 2 hours and cooled to room temperature. Then, 95% (v/v) ethanol solution was added to precipitate pectin (the pectin solution/alcohol ratio was 1:3 (v/v)) for overnight. The precipitated pectin was filtered through cheesecloth, dialyzed against deionized water at room temperature for 48 hours using Spectra-Por® 3 dialysis membrane (3,500-Da MWCO), and freeze-dried. The purified pectin was stored in a desiccator until further use.

2.2 Preparation of amidated pectin

Ethanolamine (0.13 mol) was dissolved in methanol (6 ml) and the solution was gradually added into the flask of pectin solution containing pectin (0.02 mol, 0.25 g) and 40 mL of methanol. The reaction mixture was maintained at 5°C for 12 hours with continuous stirring. After that, the product was obtained by centrifugation and washed twice with chloroform to remove the excess amine. Thereafter, the free carboxylic group of the sample was converted into a protonated form by treating it with 0.1 M HCl in ethanol-water (1:1 ratio, v/v). Finally, the product was washed several times with 40% (v/v) ethanol until it displayed (colorless) a negative reaction to chloride, washed with 80% (v/v) ethanol, and freeze-dried.

2.3 Hydrogel preparation

Polyvinyl alcohol (PVA), Pectin-Polyvinyl alco-hol (Pec-PVA), and Amidated Pectin- Polyvinyl alcohol (AMDP-PVA) hydrogel were prepared by the freeze-thaw method. First PVA, pectin, and/or amidated pectin powders were

weighed according to the ratio outlined in Table 1. PVA was gradually dissolved in distilled water and heated to 60-75 °C with stirring. When PVA became a clear solution, pectin/amidated pectin and glycerol were gradu-ally added and stirred until a homogeneous solu-tion was observed. The solution was subsequently transferred into a mold and the mold was subjected to a freeze and thaw cycle, where it was frozen at -18 °C (24, 48, and 72 h freeze time) and thawed at room temperature for 1 h. The freeze and thaw (F/T) were prepared at different cycles. The obtained hydrogels were characterized by Fourier Transform Infrared Spectroscopy (FTIR), Thermo Gravimetric Analysis (TGA), and Scanning Elec-tron Microscope (SEM).

Table 1. Polyvinyl alcohol, pectin and amidated pectin hydrogel synthesized at different material ratios

Samples	PVA (%w/v)	Pectin (%w/v)	AMDP (%w/v)	Glycerol (%v/v)
PVA	5	-	-	1.5
Pec-PVA	2.5	2.5	-	1.5
AMDP-PVA	2.5	1.25	1.25	1.5

2.4 Physicochemical Analyses

2.4.1 Pectin yield

The pectin yield is the ratio of the dry weight of pectin to the dry weight of pomelo powder and was calculated using Eq. (1)

$$\text{yield (\%)} = \frac{W_{\text{dried pectin (g)}}}{W_{\text{dried pomelo peel (powder)(g)}}} x100 \quad (1)$$

2.4.2 Degree of esterification

Purified pectin was further characterized using FTIR spectroscopy. Briefly, Infrared spectra (4000 -400 cm^{-1}) of the samples were measured on Nico-
let 6700 FTIR spectrometer (Thermo Scientific, USA); 64 scans were acquired per sample and integrated to obtain spectra mean values. The Degree of esterification (DE) of products was calculated from Eq. (2)

$$\text{DE (\%)} = \frac{A_{(C=O)}}{A_{(C=O)} + A_{(COO^-)}} x100 \quad (2)$$

where $A_{(C=O)}$ is the areas of the separate peaks at 1710-1760 cm^{-1} and $A_{(COO-)}$ is the areas of the separate peaks at 1600-1630 cm^{-1}

2.4.3 Degree of amidation

The elemental analyses of all the samples were performed in duplicate using CHNS/O Analyzer (Thermo Scientific TM FLASH 2000) with Gaseous products freed by pyrolysis in high-purity oxygen and was chromatographically separated by elution development with quantitatively detected by thermal conductivity detector. The degree of amidation (DA) of the products were calculated from the elemental composition according to the formula[3]:

$$M_R = M_N \times \frac{12}{14} \times \frac{K}{I}, \quad (3)$$

$$M_{CP} = M_C - M_{CR}, \quad (4)$$

$$DA = \frac{M_{CR}}{M_{CP}} \times \frac{6}{K} \times 100, \quad (5)$$

In the part of Eq. (3), (4) and (5), M_N and M_C are contents of nitrogen and carbon (%), M_{CR} and M_{CP} are contents of carbon (%), respectively, in amine substituents and pectin, 12/14 is the ratio of carbon to the nitrogen atomic mass, 6 is the sum of carbons in the galacturonic unit of pectin, K and I are the sum of carbons and nitrogens in the amine molecule, respectively.

2.5 Swelling

A pre-weighed hydrogel sample was immersed in distilled water at 25±2 °C. After specifying time intervals as 1, 2, 3, 4, 5, and 6 h, the samples were taken out of the weighed distilled water. The samples were examined in triplicate and the average and the standard deviation were calculated. The swelling percentage of the hydrogels was calculated according to Eq. (6)

$$\text{Swelling (\%)} = \frac{W_t}{W_0} \times 100 \quad (6)$$

where W_t was the weight of the swollen sample at a predetermined time and W_0 was the initial weight.

2.6 Drug loading and release studies

Drug loading was divided into 2 methods: (A) soaking in CHX solution 0.5 mg/mL, 10 mL for 1 h and (B) CHX pre-load 1 mg/g hydrogel. Hydrogels were immersed in phosphate buffered saline solution (PBS) pH 5.5 containing CHX for 1 h and the drug loading was calculated (A). The CHX was weighed and added to the hydrogel solution at the preparation stage (B). The release study was performed by suspending hydrogels in PBS solution at 37 °C for 6 h. 1 mL of sample solution was withdrawn every hour for further analysis and replaced with an equal volume of fresh PBS. The drug concentration was calculated using UV-VIS spectrophotometer at 280 nm (UV-1800 Shimadzu, double beam) against a standard curve. The percentage of drug release was calculated by Eq. (7). All samples proceeded in triplicate and the standard deviation were calculated.

$$\text{Release (\%)} = \frac{\text{Conc.}_{\text{drug release at certained time}}}{\text{Conc.}_{\text{drug loading}}} \times 100 \quad (7)$$

2.7 Antimicrobial activity

The antimicrobial activity of the hydrogels was tested against *Staphylococcus aureus* (*S. aureus*) (ATCC 6538; a Gram-positive bacterium) and *Escherichia coli* (*E. coli*) (ATCC 8739; a Gram-negative bacterium) according to a disc diffusion method. During the antimicrobial test, the hydrogels were each placed in Petri dishes that were streaked by aforementioned pathogens and covered with the lid of the Petri dish to prevent drying. The Petri dishes were subsequently placed in an incubator (at 37 ± 1 ^{o}C for 24 ± 1 h). After the contact time (24 h), the inhibition zone was measured.

3. Results & Discussion

3.1 Pectin Yield and DE values

Typically, pectin is classified into two main types based on the degree of esterification, high and low methoxyl pectin. The pectin extracted from pomelo peel, with a yield of 55.11% under the same conditions of citric acid extraction, has a degree of esterification (DE) of 60.45% classified as high methoxyl pectin. High methoxyl pectin is characterized by a higher content of methyl ester groups. These pectins are often used in applications where gelling properties are desirable.[4, 5] The high degree of esterification allows for the formation of a gel structure under specific conditions, contributing to the textural properties of the final product.[6]

3.2 Elemental Analysis

The composition of modified pectin was confirmed by Elemental analysis. The results in Table 2 indicated nominal value of nitrogen in pectin but the nitrogen content (M_N) increased after amidation reaction from ethanolamine.

Table 2 Results of elemental analysis and degree of amidation (DA) of pectins

Sample	M_C (%)	M_N (%)	M_{CR}	M_{CP}	DA (%)
Pectin	40.09	0.24	0.41	39.68	-
AMDP	40.19	3.18	5.45	34.74	47.07

3.3 Characterization

3.3.1 FTIR Analysis

The FTIR spectrum of pomelo pectin, and amidated pectin were taken in the range of 4000-400 cm^{-1} as KBr pellet with the help of an FTIR spectrophotometer (JASCO, Model: FTIR-6800). Figure 1A, the pectin spectrum has 3415 cm^{-1} due to the stretching of -OH groups, 2935 cm^{-1} due to C-H stretching vibration, 1743 cm^{-1} due to -C=O stretching vibration peak, 1636 cm^{-1} suggested COO^-, 1445 and 1347 cm^{-1} could be assigned to -CH_2 scissoring and -OH bending vibration peak respectively, and 1021 cm^{-1} suggested -CH-O-CH- stretching. The peak at 1146 cm^{-1} suggested the presence of secondary alcohol (characteristic of -CH-OH in aliphatic cyclic alcohol C-O stretch). The AMDP spectrum shows the acid form of the modified pectin as two important bands at 1634 cm^{-1} (amide I) and 1548 cm^{-1} (amide II) and the absence of carboxylate stretching. The peak at 2925 cm^{-1} indicated the presence of symmetric C-H stretching vibrations of methylene groups. This can be accounted to the increase of C-H bond content after the amidation reaction.

In FTIR spectrum of PVA powder (Figure 1B), the broad peak around 3391 cm^{-1} is attributable to the OH stretching vibration from the intermolecular and intramolecular hydrogen bonds. The vibration band between 2917 cm^{-1} refers to the stretching C–H group. The peak at 1645 cm^{-1} was assigned as C=O symmetric stretching. The two peaks of 1420 and 1322 cm^{-1} are attributed to the coupling of the secondary O-H in-plane bending and the C-H wagging vibrations. Absorption at 1111 cm^{-1} was produced by C-O stretching vibration. Evidently, the AMDP-PVA Hydrogel spectra were similar to those of PVA and AMDP. The hydrogel from blending of PVA with AMDP caused the O-H stretching peak of higher wavenumbers: 3295-3465 cm^{-1} and the C-O stretching shifted to 1115-1034 cm^{-1}. Moreover, the C=O stretching shifted to 1676-1615 cm^{-1}.

3.3.2 TGA Analysis

Figure 2 shows the TGA/DTG curves of Pec, AMDP, and AMDP-PVA Hydrogel samples. The weight loss of the Pec and AMDP are different. For pectin, the distinct stages can be observed from their TGA curves. For pectin and AMDP, the first stage is in the range of 30–150 ^{o}C. In this stage, the mass loss was contributed by the absorbed water and volatile compounds. Their weight loss of pectin and AMDP are around 7% and 4.5% respectively, indicating that it retained more of its mass and was less affected by the removal of water and volatile components. This suggested that AMDP has better resistance to moisture-related degradation at lower temperatures. AMDP shows a lower weight loss at the first stage, suggesting a later onset of thermal degradation compared to pure pectin. The second stage is in the range of 220–350 ^{o}C, the initial degradation of the pectin samples. The weight loss (around 64%) observed at this temperature can be attributed to pyrolytic

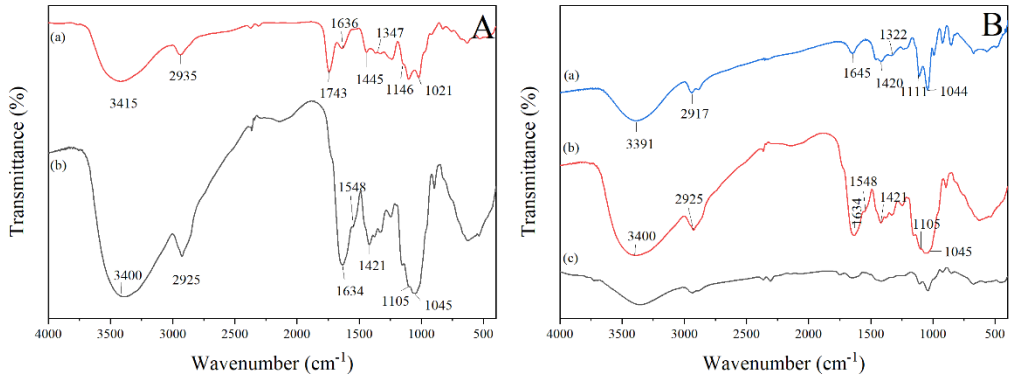

Figure 1. FTIR spectrum of (a) Pectin (b) AMDP (left) and FTIR spectrum of (a) PVA (b) AMDP (c) AMDP-PVA Hydrogel (right)

decomposition initially, while the subsequent portion was a result of the decarboxylation of the acid side group and carbon within the pectin ring. Meanwhile, the weight loss of the AMDP sample is approximately 56%. When comparing Pec and AMDP, it becomes evident that AMDP exhibits greater thermal stability than Pec within the temperature range below 350°C. Clearly, our method of hydrogel fabrication yields thermally stable crosslinked matrices of pectin.

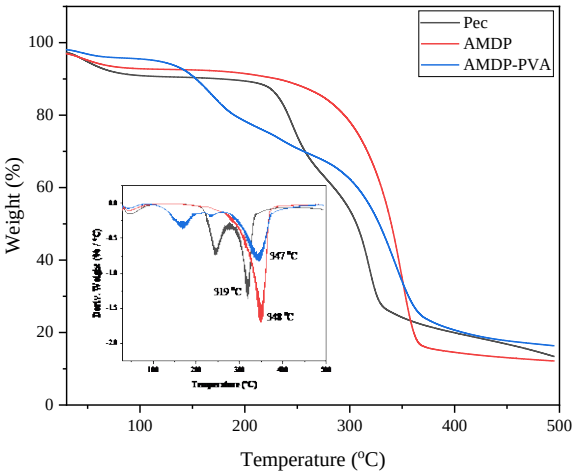

Figure 2. TGA/DTG curves of Pec, AMDP, and AMDP-PVA Hydrogel

3.3.3 SEM Analysis

In the absence of drug loading, pure PVA hydrogel exhibited a more homogeneous structure (Figure 3a). The hydrogel's surface appeared smoother and less porous because there were no drug particles or aggregates within the hydrogel. In soaking, it was introduced drugs into the hydrogel after the hydrogel had already been formed, resulting in the
drug being absorbed into the existing hydrogel matrix. The drug molecules diffused into the hydrogel led to the relatively uniform and smooth matrix (Figure 3b). Figure 3c shows drug distribution within the hydrogel, with drug particles dispersed throughout the hydrogel structure. There was a noticeable change in porosity and surface roughness compared to the drug-free hydrogel. When the drug was loaded into the hydrogel during the preparation stage, it was mixed with the hydrogel solution before the hydrogel was formed. This method allowed for a more uniform distribution of the drug within the hydrogel, as it was incorporated into the hydrogel matrix during the formation process. The surface of AMDP-PVA hydrogel loaded with CHX displayed slight differences depending on the loading method. The AMDP-PVA hydrogel with pre-load tended to feature a slighter uniform appearance (Figures 3d-3f) as the CHX was more evenly distributed within the hydrogel matrix during the preparation process.

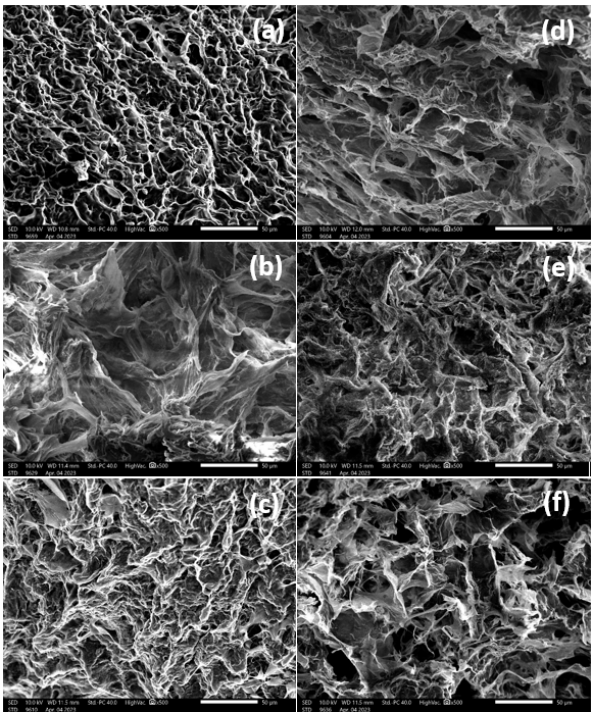

Figure 3. PVA Hydrogel (a) no load (b) soaking CHX 0.5 mg/mL (c) CHX load-in 1 mg/g and

AMDP-PVA Hydrogel (d) no load (e) soaking CHX 0.5 mg/mL (f) CHX load-in 1 mg/g

The 24-FT Pec-PVA hydrogel revealed a relatively uniform and fine-grained structure (Figures 4a and 4d). This structure could be characterized by a porous network with small, regularly shaped pores distributed throughout the matrix. In contrast, the 48-FT Pec-PVA hydrogel presented a more complex and irregular structure (Figures 4b and 4e). The surface texture was rougher, showing more variations and irregularities. The 72-FT Pec-PVA hydrogel displayed an even more intricate and porous structure. These hydrogels have the highest porosity of the three, with the largest and most irregularly shaped pores (Figures 4c and 4f). Pec-PVA hydrogels with pre-load show a smoother and more uniform appearance without distinct drug-related voids.

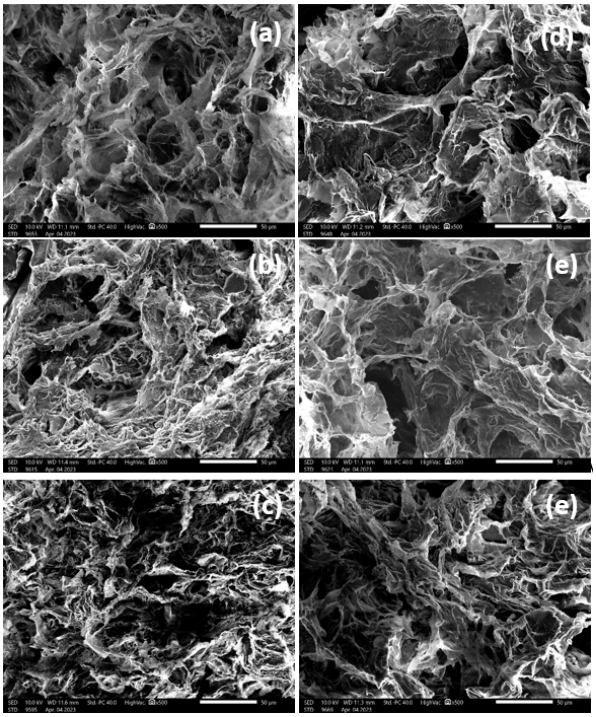

Figure 4. Pec-PVA Hydrogel at FT cycle (a) 24 hours (b) 48 hours (c) 72 hours after soaking CHX 0.5 mg/mL and (d) 24 hours (e) 48 hours (f) 72 hours CHX load-in 1 mg/g

Pectin-PVA hydrogel shows a complex and porous network with various pore sizes and shapes because of pectin's complex polysaccharide structure, while PVA hydrogel has a smoother surface with smaller, more uniformly distributed pores due to its synthetic composition. The smoother surface observed in AMDP-PVA involves introducing amide functional groups into the pectin polymer chain, replacing some of the hydroxyl (-OH) groups. This chemical alteration induces several structural changes in the hydrogel, resulting in a smoother surface.[7] These changes included reduced hydrophilicity, which means it has a lower affinity for water, leading to less water absorption and, consequently, a smoother surface. Moreover, amidation can affect the cross-linking density of the hydrogel, possibly resulting in a more uniform and controlled cross-linking structure.[8]

3.4 Swelling

The swelling behavior of hydrogels is a critical parameter that directly influences their functio-nality, particularly in drug delivery applications. Figure 7 illustrates the %swelling of various hydrogel formulations. To prepare the hydrogel pieces, fixed ratios of pure PVA, Pec-PVA, and AMDP-PVA hydrogels were utilized. The freeze-thaw method with a twice 72-FT cycle time was employed in the hydrogel synthesis.

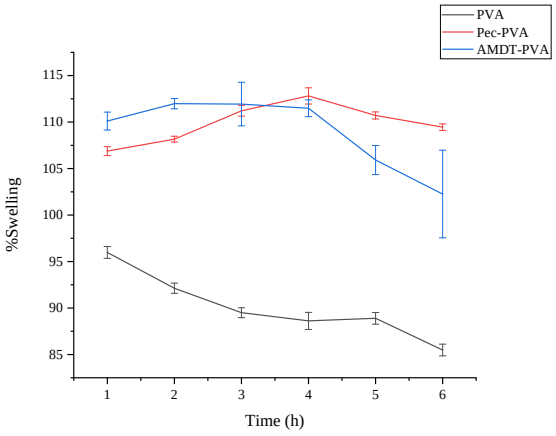

Figure 7. %Swelling of PVA, Pec-PVA, and AMDP-PVA Hydrogel

The observed differences in %swelling can be attributed to the distinct morphologies and structures of the hydrogels. PVA hydrogel exhibited the lowest %swelling, consistent with its smallest pore size structure (Figure 3). The %swelling of PVA hydrogel is the lowest compared to all hydrogels at all measured time points. This suggested that the addition of pectin led to increased swelling in the hydrogel. Pec-PVA hydrogels displayed a more irregular and rougher surface with larger pore sizes, resulting in a higher %swelling. Modifying pectin through amidation could indeed lead to a higher crosslinking density in the hydrogel and decrease hydrophilicity of the hydrogels potentially resulting in a slightly lower %swelling. Higher crosslinking density generally leads to a more compact and less porous hydrogel structure. The presence of more crosslinks restricts the movement of polymer chains reduces the available space for buffer absorption[9] and influences the overall swelling behavior.[10]

Increasing the number of freeze-thaw cycles significantly affected the swelling behavior of hydrogels. This process crucially shaped the hydrogel's structure and porosity, consequently impacting its swelling properties[6]. Generally, for each time point, there was a trend of increased swelling with longer freeze-thaw cycle times: 72>48>24 (Figure 8). This observed trend suggested that prolonged freeze-thaw cycles likely result in a more porous hydrogel structure, enhancing swelling due to the increased available space for buffer absorption. However, excessive cycles could overly crosslink the structure, potentially limiting swelling due to reduced available space for liquid absorption. The balance between these factors was vital in determining the hydrogel's overall swelling behavior. [7]

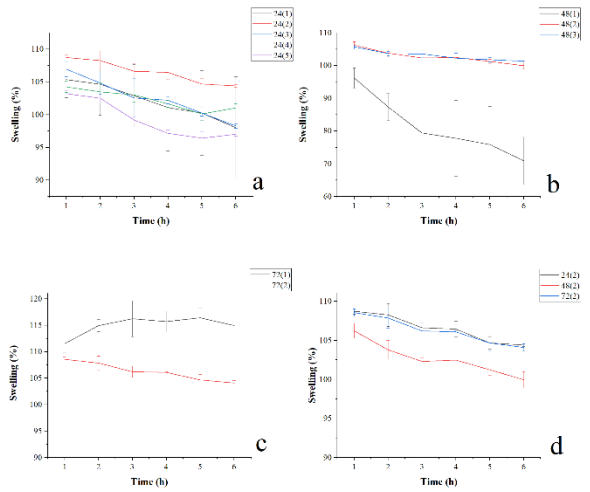

Figure 8. Effect of Freeze-thaw cycle time on swelling of Pec-PVA hydrogel (a) 24 hours (1-5 cycles) (b) 48 hours (1-3 cycles) (c) 72 hours (1-2 cycles) (d) 24(2),48(2), and 72(2)

3.5 Drug Loading and Release

As shown in Figure 9a, the loading capacity of Pec-PVA hydrogels increased with the freezing time during the soaking method (A). The loading capacities for 24(A), 48(A), and 72(A) were 0.783, 0.816, and 0.912 mg/g hydrogel, respectively. The swelling percentage of Pec-PVA hydrogels also showed a trend with freezing time that was consistent with the loading capacity result. The loading capacity generally increased with freezing time, likely due to the increased porosity of the hydrogels at longer freeze-thaw durations. For pre-loading method (B), it was evident that the 48(B) resulted in the highest loading capacity (0.964 mg/g hydrogel), followed by the 72(B), which is only slightly lower at 0.923 mg/g hydrogel. The 24(B) had a slightly lower loading capacity at 0.840 mg/g hydrogel. The result suggested that a longer freezing time during the preparation of Pec-PVA hydrogels may lead to an increased loading capacity for CHX. This could be due to the formation of a hydrogel structure and porosity that can accommodate more of the drug. The 48(A) hydrogel exhibited the fastest cumulative release (Figure 9b), followed by 24(A) and 72(A), which had similar release profiles. The faster release from the 48(A) hydrogel might be attributed to its unique structural properties, such as larger and less uniform pores, which could provide a greater surface area for initial drug release. The freezing time during hydrogel preparation appeared to have a significant impact on the release profile of CHX. Longer freezing times (48 and 72 hours) resulted in a more controlled and sustained release, while the 24- FT exhibited a relatively faster release. These findings highlight the importance of optimizing parameters to achieve the desired drug release characteristics.
Among the hydrogels in the soaking method, AMDP-PVA exhibited the highest loading capacity with a value of approximately 1.107 mg/g of hydrogel (Figure 9d). PVA also showed a good loading capacity, although slightly lower than AMDP-PVA, with a loading capacity of around 0.982 mg/g. Pec-PVA has the lowest loading capacity in soaking, with a value of about 0.912 mg/g. Among the three types of hydrogels, AMDP-PVA in the pre-loading method (B) has the highest loading capacity at 1.099 mg/g hydrogel. Pec-PVA (B) followed closely with a loading capacity of 0.906 mg/g hydrogel and PVA (B) has the lowest loading capacity at 0.765 mg/g hydrogel, suggesting that the modification of pectin through amidation significantly improved the hydrogel's ability to load CHX. This could be due to the enhanced interaction between the modified pectin and the drug, allowing for more efficient drug loading.[11] PVA (B) had the lowest loading capacity, likely because it lacked the modifications and natural properties that promote drug binding and retention.
In terms of drug release profiles, when comparing the three hydrogels, AMDP-PVA stood out for its relatively slow and controlled release behavior with the soaking loading method (Figure 9e). It began with a modest 16.38% release in the first hour and gradually increased to about 24.69% by the 6th hour. This indicated a sustained and controlled release of the loaded drug over time.

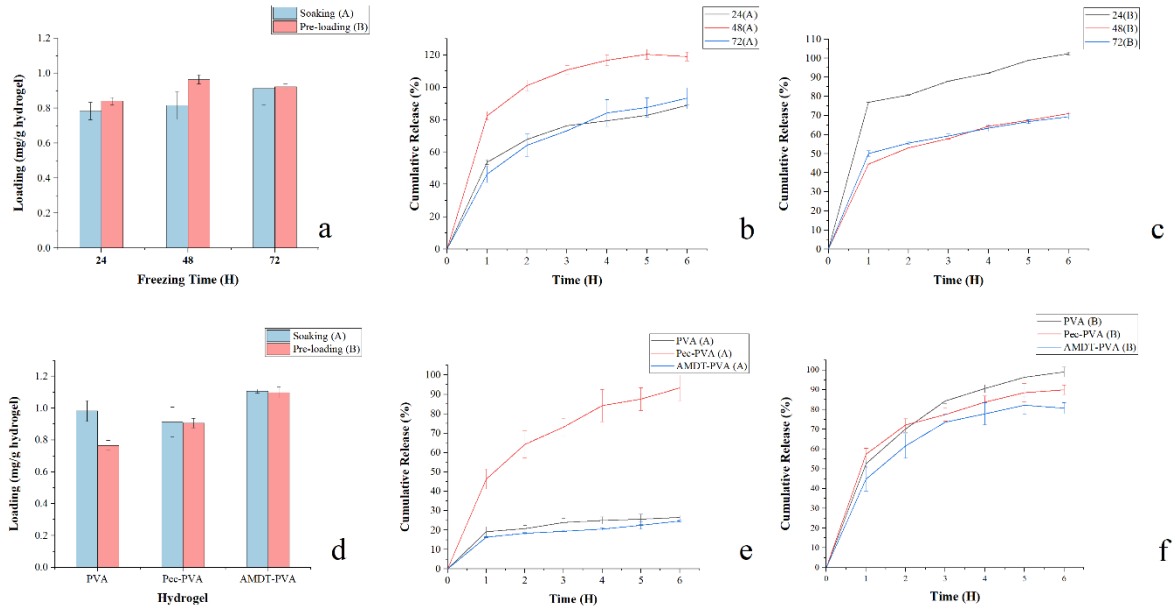

Figure 9. Loading capacity and Release of the hydrogels at different formula (a-c) and freezing time (d-f) with CHX soaking and load-in as drug loading method

On the other hand, Pec-PVA hydrogel demonstrated a significantly faster drug release profile, starting at 46.31% in the first hour and reaching 93.32% by the 6th hour, indicating a relatively rapid release rate. PVA hydrogel fell in between the other two, with a slow-release profile starting at 19.19% and reaching 26.55% by the 6th hour. PVA (B) demonstrated a gradual and controlled release of CHX over the 6 hours, starting at 52.57% and increasing to 98.99% (Figure 9f). Pec-PVA (B) followed a similar release pattern to PVA (B) but with a slightly lower cumulative release. It started at 57.38% and reached to 89.95%. AMDP-PVA (B) demonstrated a relatively lower cumulative release compared to the other two hydrogels (B). It started at 44.81% and reached to 80.68%. AMDP-PVA hydrogel appeared to offer a more sustained and controlled release of CHX. This could be due to the structural properties and modification of pectin in AMDP-PVA, which affected the interaction with CHX and the hydrogel's release kinetics.

3.6 Antimicrobial assay

In the case of *E.coli*, the findings revealed varying degrees of effectiveness among the hydrogel types and loading methods. Notably, pre-loading appeared to be more efficient in inhibiting *E.coli*

Table 3 Antimicrobial Effect of Different Hydrogel Formulations Against *E. coli* and *S. aureus*

Hydrogel	Real Loading (mg/g)	%Cum. Release$_{6\text{-}h}$	Clear zone$_{avg}$ (mm)	
			E.coli	*S.aureus*
PVA (A)	0.98	27%	7.72±0.25	5.90±0.22
PEC-PVA (A)	0.91	93%	9.58±0.07	7.53±0.40
AMDP-PVA (A)	1.11	25%	6.90±0.56	5.12±0.22
PVA (B)	0.77	99%	9.91±0.40	8.02±0.33
PEC-PVA (B)	0.91	90%	9.59±0.08	7.60±0.19
AMDP-PVA (B)	1.10	81%	8.80±0.13	6.59±0.05
24:PEC-PVA (B)	0.84	102%	9.26±0.48	7.44±0.12
48:PEC-PVA (B)	0.96	71%	9.39±0.43	6.80±0.14
72:PEC-PVA (B)	0.92	69%	9.59±0.08	7.60±0.19

*Hydrogel diameter = 30 ±3 mm

**Example of antimicrobial effect of hydrogel samples (Right)

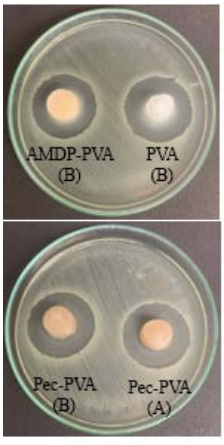

growth for PVA and AMDP-PVA hydrogels. In contrast, for Pec-PVA hydrogels, both loading methods exhibited similar levels of effectiveness against *E.coli*. For *S.aureus*, a similar trend was observed. In terms of different freezing time hydrogels, there is no clearly difference in inhibiting *E.coli* and *S.aureus* growth. Overall, the data suggested that for both *E.coli* and *S.aureus*, the pre-loading method was generally more effective in enhancing the antimicrobial properties of these hydrogels compared to the soaking method.

4. Conclusion

In conclusion, the findings from this study clarified the potential of pectin-based hydrogels for controlled drug delivery applications. The characterization results, including FTIR, TGA, and SEM analyses, provided essential insights into the structural properties of the hydrogels, highlighting differences between the various formulations. Notably, AMDP hydrogels exhibited a smoother and more uniform surface, indicating the impact of chemical modification on hydrogel structure. These modifications not only influenced the physical characteristics but also enhanced drug-loading capacity and drug-release profiles. Longer freezing times led to increased loading capacity, mainly attributed to higher porosity and larger pores in the hydrogel structures. AMDP-PVA hydrogels consistently displayed the highest loading capacity, suggesting the significance of pectin modification in improving drug absorption. The release profiles of different hydrogel formulations showed interesting insights. AMDP hydrogels exhibited controlled and sustained drug release behavior, making them a promising candidate for prolonged drug delivery applications. Nevertheless, the pre-drug loading method employed during the preparation stage allows for more efficient and precise control of drug loading and release compared to the soaking-based loading approach. These findings contribute to the expanding field of hydrogel-based drug delivery, offering insights that can be further explored and optimized for specific pharmaceutical applications.

Acknowledgments

This research project is supported by the Mahidol University. We also appreciate Mahidol University-Frontier Research Facility (MU-FRF) and the Department of Chemical Engineering, Mahidol University for instrument support.

References

1. Thang, N. H.; Chien, T. B.; Cuong, D. X. Polymer-based hydrogels applied in drug delivery: An overview. *Gels* **2023**, *9* (7), 523.
2. Fan, Z.; Cheng, P.; Chu, L.; Han, J. Exploring the Rheological and Structural Characteristics of Novel Pectin-Salecan Gels. *Polymers* **2022**, *14* (21), 4619.
3. Šimkovic, I.; Synytsya, A.; Uhliariková, I.; Čopíková, J. Amidated pectin derivatives with n-propyl-, 3-aminopropyl-, 3-propanol-or 7-aminoheptyl-substituents. Carbohydrate poly mers **2009**, 76 (4), 602-606.
4. Matta, E.; Bertola, N. Development and characterization of high methoxyl pectin film by using isomalt as plasticizer. *Journal of Food Processing and Preservation* **2020**, *44* (8), e14568.
5. Abdel Hamid, E. M.; Muawad, A. M.; Hassan, H. A.; Ragaa, M. A.; El-Kader, A.; Abd El-Meged, M.; El-Latef, A.; Farid, M.; Ibrahim, M. E.; El-Fatah, A. Production and Characte-rization of Pectin by Acid Extraction Method from Orange Peels Waste Using Response Surface Methodology (RSM). *International Journal of Industry and Sustainable Development* **2022**, *3* (1), 34-45.
6. Liang, W.-l.; Liao, J.-s.; Qi, J.-R.; Jiang, W.-x.; Yang, X.-q. Physicochemical characteristics and functional properties of high methoxyl pectin with different degree of esterification. *Food Chemistry* **2022**, *375*, 131806.
7. Islam, M. R.; Tanveer, S.; Chen, C.-C. Modeling swelling behavior of hydrogels in aqueous organic solvents. *Chemical Engineering Science* **2021**, *242*, 116744.
8. Sutar, P. B.; Mishra, R. K.; Pal, K.; Banthia, A. K. Development of pH sensitive polyacry-lamide grafted pectin hydrogel for controlled drug delivery system. *Journal of Materials Science: Materials in Medicine* **2008**, *19*, 2247-2253.
9. Khurana, A.; Kumar, A.; Sharma, A. K.; Jogle-kar, M. M. Effect of polymer chains entan-glements, crosslinks and finite extensibility on the nonlinear dynamic oscillations of dielectric viscoelastomer actuators. *Nonlinear Dynamics* **2021**, *104* (2), 1227-1251.
10. Ahmad, N.; Khan, M.; Ma, X.; Ul-Haq, N. The influence of cross-linking/chain extension structures on mechanical properties of HTPB-based polyurethane elastomers. *Arabian Journal for Science and Engineering* **2014**, *39*, 43-51.

Comparison properties of hybrid carbon-based nanocomposites between engineering-thermoplastic Acrylonitrile-Butadiene-Styrene and commodity-thermoplastic polypropylene for electrical and thermal application

Sorawit Duangsripat*, Pajaera Patanathabutr, and Nattakarn Hongsriphan

Department of Materials Science and Engineering, Faculty of Engineering and Industrial Technology, Silpakorn University, Nakhon Pathom 73000, Phone +66 3424 1708, Fax +66 3424 1708

**E-mail: Duangsripatsorawit@gmail.com*

Abstract:

Electronic based industry has become one of the highest growth industries in the world, which electrostatic discharge (ESD) could be a serious problem associated for a specific application. Due to the low price and availability of pristine graphite in large quantities, graphene nanoplatelets (GNPs) is considered an ideal choice as conductive fillers to replace carbon nanotube (CNTs) or mix them to produce hybrid conductive fillers. Accordingly, this report was focused on using suitable oxygen-gas modified hybrid fillers in amorphous Acrylonitrile-Butadiene-Styrene (ABS) and semi-crystalline polypropylene (PP), which they are mainly used for electronic packaging. Nanocomposites were successfully prepared using a twin-screw extruder, which ABS/nanofiller or PP/nanofiller masterbatch was mixed with neat polymer to the desired concentrations of nanofillers (2, 4, 6, and 8 wt%). Based on static dissipative range of surface electrical resistivity, the suitable ratio of nanofiller (80:20 of O_2-CNTs:O_2-GNPs) and critical amount of nanofiller loading on mechanical properties was found to be 2.0 wt%. ABS reinforced with 2.0 wt% of nanofiller resulted in an increase of Young's modulus 27% and of tensile strength 24%, with a reduction of elongation at break 75%. PP reinforced with 2.0 wt% of nanofiller resulted in an increase of Young's modulus 12% and of tensile strength 6%, with a reduction of elongation at break 71%. The surface electrical resistivity and thermal conductivity of nanocomposites were sharply decreased from 10^{16} to 10^{6} ohm/square and increased from 0.208 to 0.349 W/m.K, respectively, which could be designated as a static dissipative material.

1. Introduction

Electrostatic discharge (ESD) is mostly created by the contact and separation of two materials. When the two materials come in contact and then separate, electron is transferred between the two materials. One of the materials that loss electron results in a positive charge on the surface and the other that gains electron, a negative charge. As a result, electric potentials of the two materials are different expressing as electrostatic voltage. Level of the electrostatic voltage depends on material type, speed of contact and separation, humidity and several other factors. To eliminate the electrostatic voltage, the positive charge is transferred to the negative charge the different electrical potentials. This charge transfer is known as EDS. However, if the level of electrostatic voltage is high enough, a great many charges carrying energy is rapidly transferred to the sensitive material. Hence, the sensitive material is suddenly destroyed by ESD attack.[1] In the electronics industry, ESD can be occurred on the devices throughout touch of charged human bodies to the devices, move of devices across machine surfaces, slide of devices in packages, or induction of electrostatic fields, etc. Occurred ESD can easily damage the sensitive devices in the form of an arc or spark at the sufficiently difference potentials. Accordingly, the ensitive device fails immediately or loss their electrical characteristics. Furthermore, reduction of device sizes to increase speed and decrease power consumption today cause increment of their sensitivity to ESD damage at very low electrostatic voltages. Consequently, static safe techniques such as grounding, ionization, and the use of conductive packaging materials have been developed to products from ESD.

One of the static safe techniques that can directly protect the devices from ESD charges is the use of conductive packaging materials. When surface of the conductive packaging becomes charged by rubbing between the device and the packaging, the charges are allowed to dissipate across its surface or through its volume and then transfer to ground or another nearly conductive object in order to reduce the electrostatic voltage to the low level. As a result, ESD event is not violent enough to damage the device. Accordingly, the conductive packaging materials can safely protect the devices from ESD event by limiting the passage of ESD current and reducing the energy that causes from ESD. Moreover, they can shield the electrostatic fields which induce charges to accumulate on the devices and create ESD. Typically, the material's ability to prevent ESD

damage is measured by surface resistivity. Conductive compounds which have surface resistivity values in a range of 10^3-10^9 ohm/square can be used to directly protect from ESD event.[2]

Electronic packaging materials are most commonly made from conductive compounds which compose of thermoplastic resins and conductive fillers. The common antistatic agents or conducting fillers are carbon black (CB), carbon nanotube (CNTs) or expended graphite, and form of amorphous carbon with intrinsic conductivity. The main drawback of these conductive fillers is their intrinsic black color and the tendency to generate particles. The CNTs can substantially increase the electrical conductivity of polymer nanocomposites at low loading (0.1vol%)[3], but it is expensive. As for cheap carbon black, higher loading is usually required to make the polymer conductive. It has been found that these CB-filled single polymer compounds normally require high CB loading (~10-20 wt%)[3] to reach the percolation threshold. It is well known that disadvantages of using high content of carbon black are relatively high cost, difficult processing, sloughing (peeling off of CB from product surfaces), and inferior mechanical properties. Thus, several authors[4-6] have been studying to enhance the electrically conductivity and reduce critical CB content in CB-filled single polymer system through studying the effect of processing conditions, such as processing temperature and mixing speed. It has been noted that increasing processing temperature or decreasing mixing speed in mixing process of CB-filled single polymer system can reduce the surface resistivity and percolation threshold of the system because both of them promote the enhancement of network quality of the CB-filled single polymer systems. Due to the low price and availability of pristine graphite in large quantities, a graphene nanoplatelet (GNP) is considered an ideal choice as conductive fillers in the preparation of conductive polymer nanocomposites. In general, GNP gives a much lower percolation threshold (0.3 vol %) than graphite (3.0 vol %).[2] The current trend is to decrease the size and structures of electronic components with highly concern regarding the global environment is needed. Accordingly, this research was focused on the study of using CNTs:GNPs hybrid as nanofiller in Acrylonitrile-Butadiene-Styrene (ABS) and polypropylene (PP), which is aimed to be applied mainly for IC shipping tray and packaging for electronic parts.

2. Materials and Methods

2.1 Materials

Acrylonitrile-Butadiene-Styrene (ABS, GA800, injection molding grade, MFI of 20 (10 kg/220°C)) was kindly provided by IRPC Public Company Limited, Thailand. It was designated to represent an amorphous polymer. Polypropylene (PP, PP2500TC, injection molding grade, a density of 0.90 g/cm^3, MFI of 45 (2.16 kg/230°C) was also kindly provided by IRPC Public Company Limited, Thailand. It was designated to represent a semi-crystalline polymer. These polymer types are commonly applied in the electrical/electronic applications.

Two types of nanofillers were used; oxygen functionalized graphene (O_2-GNPs) and oxygen functionalized carbon nanotube (O_2-CNTs). They were mixed in a fixed ratio as the hybrid nanofiller. They were kindly supported by Haydale Technologies Co. Ltd., Thailand. The fixed weight ratio was recommended[7] from the company's experimental results.

2.2 Masterbatch preparation

The ABS and PP-based masterbatches were prepared using an internal mixer (Thermo Scientific Haake model Rheomax OS) at 200°C and a rotor speed of 60 rpm for 12 min. The nanofiller content was 10 phr (part per hundred of resin) in the masterbatch, which the blend ratio of the hybrid carbon-based nanofiller was fixed at O_2-CNTs 80 wt% and O_2-GNPs 20 wt%.

2.3 Compounding of nanocomposites

The ABS and PP-based nanocomposites were prepared by diluting the masterbatch, which the final concentrations of the O_2-CNTs:O_2-GNPs nanofiller was 1.0, 2.0, 4.0 and 8.0 wt%. The melt compounding was performed using a twin-screw extruder (CT model CTE-D22L32, Chareon Tut Co., Ltd, Thailand) with the temperature profile of 200, 210, 220, 230, 240, and 240°C and a screw speed of 80 rpm. The extrudate was water cooled and then pelletized by a pelletizer. For the PP-based nanocomposites, PP-g-MA of 10 wt% was added as a compatibilizer.

2.4 Fabrication of specimens

Prior to fabrication, the ABS and PP-based composite pellets were dried in an air-circulating oven at 70°C overnight. The composite pellets were hydraulically pressed using a hot-pressing machine (LabTech model LP-S-20, Thailand) at 210°C to prepared electrical/thermal conductivity testing specimens in a square shape. For tensile testing, the dogbone-shaped specimens were injection molded using an injection molding machine (Battenfeld model BA250CDC, Austria).

The injection molding temperature profile were set at 180, 190, 200 and 200°C. The mold temperature was 50°C.

2.5 Surface electrical resistivity testing

Surface electrical resistivity measurement was performed according to the ASTM D257 using a silver paint electrode. The hot-pressed specimens with a square shape (20.0 x 20.0 x 3.0 mm) were conditioned at 23°C and 50% relative humidity for 48 hrs. The DC voltage of 500 Volt was applied to the testing specimens for 1 minute, then the current was readout, and the surface electrical resistivity was determined. One specimen of each composite concentration was tested by measuring the resistivity five times, and the results were averaged from five readouts to obtain the average value.

2.6 Thermal conductivity testing

Thermal conductivity of the composite sample was measured using a thermal constants analyzer (Model TCA TA-01). The hot-pressed specimens with a square shape (20.0 x 20.0 x 10.0 mm) were conditioned at 23°C and 50% relative humidity for 48 hrs. The disk sensor was placed between two pieces of the sample, and then heated by a constant electrical current for a short period of time. The generated heat dissipated from the sensor into the surrounding sample material, causing a rise in temperature of the sensor and the surrounding sample material. The average transient temperature increased of the sensor, of the order 0.5 - 5 K, was simultaneously measured by monitoring the change in electrical resistance. The Temperature Coefficient of Resistivity of the sensor material correlated the change in resistivity with the corresponding change in temperature.

2.7 Tensile testing

The injection molded specimens were measured tensile properties in accordance to ASTM-D638 (type V) using Tinius Olsen instrument model H50KS. The load cell was 10 kN, and the crosshead speed was set at 50 mm/min. For each composite composition, five specimens were tested, which the averages and the standard deviations were reported.

3. Results & Discussion

3.1 Surface electrical resistivity of PP/nanofiller and ABS/nanofiller nanocomposites

The plots of the surface electrical resistivity of the ABS and PP/nanofiller nanocomposites versus nanofiller concentration are shown in Figure 1 (a) and (b), respectively. Unfilled ABS and PP have the surface electrical resistivity value of ~10^{14} and ~10^{16} Ohm/square, respectively which could be classified as an insulating material for having the resistivity greater than 10^{12} Ohm/square. It should be noticed that hydrophilic ABS allows the electron charge to flow better than hydrophobic PP. The incorporation of hybrid nanofiller into both polymers resulted in the alteration of the surface electrical resistivity of the nanocomposites. At low hybrid nanofiller loading, nanocomposite showed surface electrical resistivity value of ~10^{11} Ohm/square which was still in the insulating range. When the hybrid nanofiller loading was increased up to 2 wt%, the surface electrical resistivity of both nanocomposites was sharply decreased to ~10^{6} Ohm/square which could be designated as a static dissipative material. Based on this result, it can be stated that the rapid drop of the resistivity represented the drastic transition of the nanocomposite from insulative to conductive material. In addition, this result suggested that ABS and PP/nanofiller nanocomposite reached the percolation threshold[8] at O_2-CNTs:O_2-GNPs loading of 2 wt%.

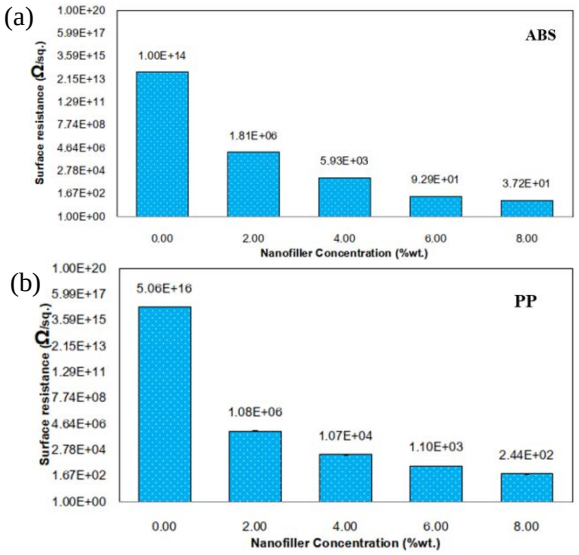

Figure 1. The effect of O_2-modified nanofillers content on surface electrical resistivity of ABS/nanofiller nanocomposite (a), and PP/ nanofiller nanocomposite (b).

Based on the result, it can be stated that the rapid drop of the resistivity with the addition of nanofiller above 2 wt% can be explained by the percolation theory.[9] The conduction through the bulk of the compound is controlled by a number of paths (the aggregate chains). As the number of particles increases, the number of continuous chain or conductive path through the compound increase. The total resistance for any chain consisted of the sum of individual resistance at each point of contact. Above the critical content of hybrid

nanofiller, the surface electrical resistivity of the ABS and PP nanocomposites were successively decreased to ~10^1 and ~10^2 Ohm/square, respectively, which could be designated as a conductive nanocomposite when the hybrid nanofiller loading increased up to 8 wt%.

3.2 Thermal conductivity of ABS/nanofiller and PP/nanofiller nanocomposites

The plots of thermal conductivity of the ABS and PP/nanofiller nanocomposites versus nanofiller concentrations are shown in Figure 2 (a) and (b), respectively. Unfilled PP had the thermal conductivity value of 0.239 W/m.K, while ABS had the thermal conductivity value of 0.208 W/m.K. This indicated that heat could pass through a semi-crystalline polymer better through the crystalline region similarly to the graphite structure. According to the work of Shen Xu *et al.*[10], the thermal conductivity (k) of the polymeric matrix can be improved by increasing the crystallinity level of the material since the crystalline structure has a k value much higher than that of the amorphous region.

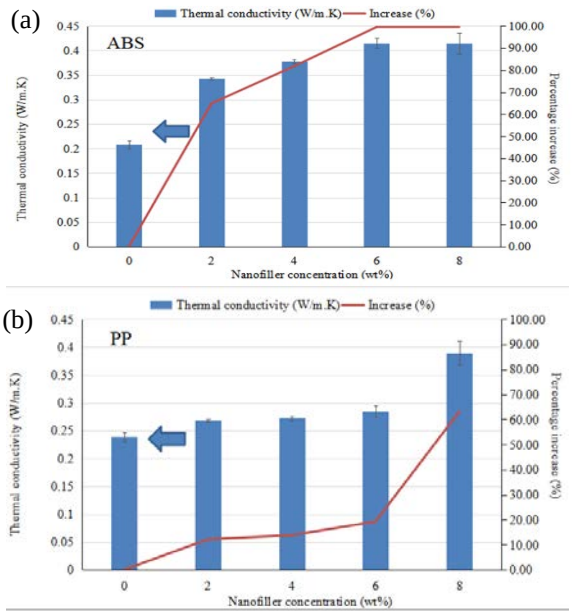

Figure 2. The effect of O_2-modified nanofillers content on thermal conductivity of (a) ABS/ nanofiller nanocomposite, and (b) PP/nanofiller nanocomposite.

When adding the hybrid nanofiller of 2 wt%, the thermal conductivity of the ABS-based nanocomposite was sharply increased to be 65% higher than the unfilled ABS. Meanwhile, the increase of the thermal conductivity value was just 12% for the PP-based nanocomposite adding the same hybrid nanofiller loading. This implied good dispersion of the oxygen-modified nanofillers in the amorphous ABS matrix having polar groups in the polymer matrix. Since the hybrid nanofillers were functionalized with oxygen via plasma treatment resulting them to obtain the carbonyl and the hydroxyl groups onto the surface, these added hydrophilic groups could interact physically via secondary bonding with the lone-paired electrons of the acrylonitrile units.

Increasing the hybrid nanofiller further enhanced thermal conductivity of the ABS-based nanocomposites which the k value was doubled when incorporating the hybrid nanofiller loading of 8 wt%. For the PP-based nanocomposite, thermal conductivity was sharply increased to be 60% higher than the unfilled one only when adding the hybrid nanofiller up to 8 wt%. These results suggested that ABS and PP/nanofiller nanocomposite reached the percolation threshold at nanofiller loading of 2 and 8 wt%, respectively. The sharpy increase in thermal conductivity of the nanocomposites can be explained by the percolation theory[11] as same as the surface electrical resistivity of the nanocomposites.

3.3 Tensile properties of PP/nanofiller and ABS/nanofiller nanocomposites

Figure 3 and 4 (a), (b), and (c) show the effects of nanofiller content on tensile modulus, tensile strength, and elongation at break of the ABS and PP/nanofiller nanocomposite, respectively. As presented in Figure 3 (a) and (b), it was observed that tensile modulus and tensile strength of the ABS-based nanocomposite was increased linearly with the hybrid nanofiller concentration. This agrees with the rule of mixture for the polymeric composite. It confirms good dispersion of the oxygen-modified carbon-based nanofillers in the hydrophilic polymer matrix, which the percolation threshold reached at the nanofiller loading of 2 wt%.

In contrast, tensile modulus of the PP-based nanocomposite was slightly increased in a linear fashion with the hybrid nanofiller concentration between 2-6 wt% and then increased moderately when the nanofiller loading reaching the percolation threshold. However, tensile strength of the PP-based nanocomposite did not show a clear trend as a function of the hybrid nanofiller concentration. This implied the poor interfacial adhesion between the PP matrix and the O_2-CNTs:O_2-GNPs although the 10 wt% PP-g-MA compatibilizer was added to improve the dispersion. The suitable weight ratio between the nanofiller volume and the compatibilizer should be further studied.

ABS reinforced with 2.0 wt% of hybrid nanofiller resulted in an increase of Young's modulus 27% and of tensile strength 24%, with a reduction of elongation at break 75%. PP reinforced with 2.0 wt% of hybrid nanofiller resulted in an increase of Young's modulus 12% and of tensile strength 6%, with a reduction of elongation at break 71%. As shown in Figure 3 and 4(c), it was obvious that elongation at break of the nanocomposites was decreased when the content of nanofiller increased. This result might be associated with the impediment effect of nanofiller to reduce the deformability[10] of matrix (at the higher nanofiller loading).

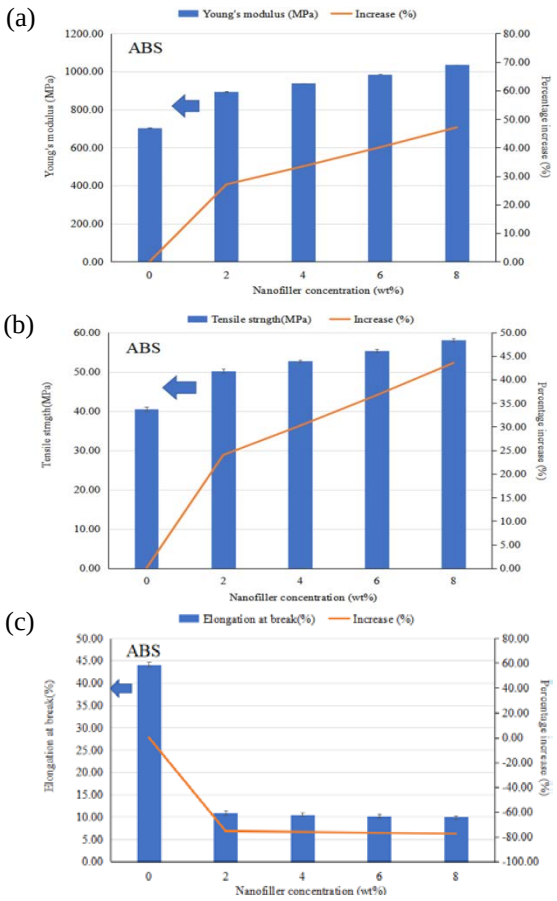

Figure 3. Tensile modulus (a), tensile strength (b), and elongation at break (c) of ABS/nanofiller nanocomposite.

4. Conclusion

ABS and PP/nanofiller nanocomposites were successfully prepared by the melt blending method and diluting the PP and ABS/nanofiller masterbatch with the neat polymer to the desired concentrations of nanofiller. There was presence of a critical amount of nanofiller loading on the mechanical properties. The suitable ratio of nanofiller was found to be 80:20, and the critical

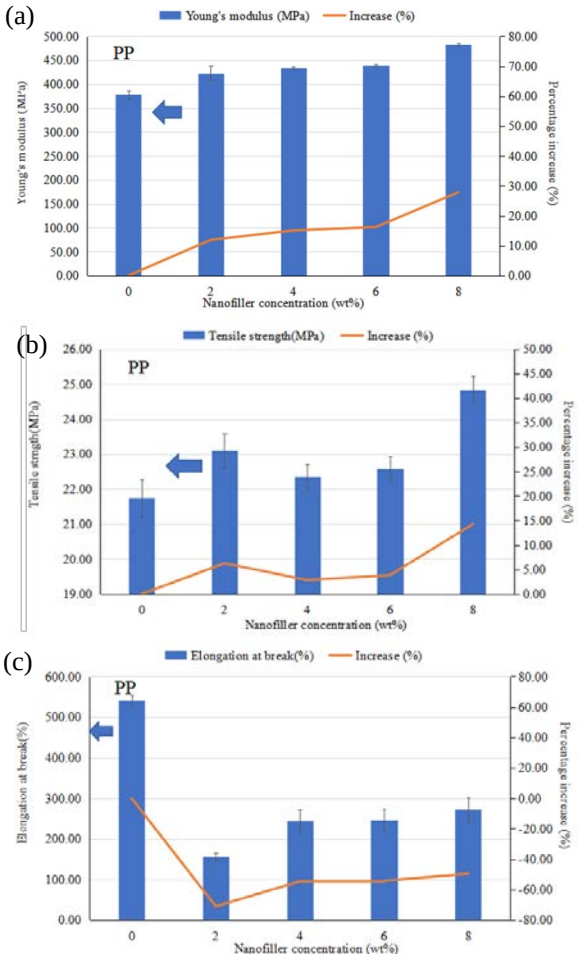

Figure 4. Tensile modulus (a), tensile strength (b), and elongation at break (c) of PP/nanofiller nanocomposite.

amount of nanofiller loading was found to be 2.0%wt. PP and ABS reinforced with 2.0%wt of 80:20(CNT: GNP). ABS reinforced with 2.0 wt% of nanofiller resulted in an increase of Young's modulus 27% and of tensile strength 24%, with a reduction of elongation at break 75%. PP reinforced with 2.0 wt% of nanofiller resulted in an increase of Young's modulus 12% and of tensile strength 6%, with a reduction of elongation at break 71%.There was presence of a critical amount of nanofiller loading on the thermal and electrical properties. The suitable critical amount of nanofiller loading was found to be 2.0%wt. The PP and ABS reinforced with 2.0%wt of 80:20 nanofiller resulted in the resistivity was sharply decreased to 10^6 Ohm/square and increased from 0.208 to 0.415 W/m.K, respectively which could be designated as a static dissipative nanocomposite. High thermal and electrical conductivity polymer nanocomposites can be obtained by using a hybrid mixture of nanofiller. In general, thermal, and electrical conductivity values increase as the filler volume fraction increases.

Acknowledgements

The authors would like to thank the IRPC Public Co., Ltd and Haydale Technologies Co. Ltd. for their materials support. The Department of Materials Science and Engineering, Faculty of Engineering and Industrial Technology, Silpakorn University, is appreciated for the author's assistant teaching scholarship funding. In addition, the Faculty of Engineering and Technology King Mongkut's University of Technology North Bangkok, Rayong campus, is appreciated for locations and tools for research during the covid pandemic situation.

References

1. Saravanan, N., et al. Graphene and modified graphene-based polymer nanocomposites – A review. *J. Reinf. Plast. Compos.* **2014**, *33* (12), 1158–1170.
2. Jones, W. E., Jr.,; Chiguma, J.; Johnson, E.; Pachamuthu, A.; Santos, D. Electrically and thermally conducting nanocomposites for electronic applications. *Materials* **2010**, 1478-1496.
3. Alberto, C. Toward Greener Chemistry Methods for Preparation of Hybrid Polymer Materials Based on Carbon Nanotubes. under CC BY 3.0 license, 2016. 2016.
4. Zhang, Q.; Wang, J.; Zhang, B.-Y.; Guo, B.-H.; Yu, J.; Guo, Z.-X. Improved electrical conductivity of polymer/carbon black composites by simultaneous dispersion and interaction-induced network assembly. *Compos. Sci. Technol.* **2019**, *179*, 106-114.
5. Kuester, S.; Merlini, C.; Barra, G. M. O.; Jr., J. C. F.; Lucas, A.; Souza, A. C. d.; Soares, B. G. Processing and characterization of conductive composites based on poly(styrene-b-ethylene-ran-butylene-b-styrene) (SEBS) and carbon additives: A comparative study of expanded graphite and carbon black. *Compos. B. Eng.* **2016**, *84*, 236-247.
6. Ibarrola JMA, L. S., Santiago EV, Alaniz-Pérez J, Pérez-Valverde MI. Experimental study of the processing parameters of polymer conductive semicrystalline polymer composites with carbon black: Optimizations and reproducibility. *J. Thermoplast. Compos. Mater.* **2015**, *28* (4), 574-590.
7. Hongsriphan, N.; Thaisa, N.; Yuenyong, W.; Pruekchat, S.; Duangsripat, S. Influence of internal mixing condition on properties of conductive biocomposites between poly(lactic acid) and hybrid graphene. *Key Eng. Mater.* **2021**, *889*, 38-43.
8. Marsden, A. J.; Papageorgiou, D. G.; Vallés, C.; Liscio, A.; Palermo, V.; Bissett, M. A.; Young, R. J.; Kinloch, I. A. Electrical percolation in graphene–polymer composites. *2D Mater.* **2018**, *5*, 032003.
9. Spahr, M. E.; Gilardi, R.; Bonacchi, D. *Carbon black for electrically conductive polymer applications*; Springer, Cham, 2017. DOI: 10.1007/978-3-319-28117-9_32.
10. Xu, S.; Liu, J.; Wang, X. Thermal conductivity enhancement of polymers via structure tailoring. *J. Enhanc. Heat Transf.* **2020**, *27* (5), 463-489.
11. Wieme, T.; Duan, L.; Mys, N.; Cardon, L.; D'hooge, D. R. Effect of matrix and graphite filler on thermal conductivity of industrially feasible injection molded thermoplastic composites. *Polymers* **2019**, *11*, 87.

Preparation and properties of poly(vinyl chloride) composites recycled from used peritoneal dialysis solution containers and reinforced with silane-treated pineapple leaf fibers

Bongkodporn Khonpet[1] and Nonsee Nimitsiriwat [2]*

[1]*Department of Chemical Engineering Faculty of Engineering, KMUTT, Bangkok 10140, Thailand*
[2]*Chemical Engineering Practice School, Pilot Plant Development and Training Institute, KMUTT, Bangkok 10140, Thailand*

**E-mail: nonsee.nim@kmutt.ac.th*

Abstract:

In response to growing environmental concerns related to the accumulation of plastic wastes, this research study aimed to recycle medical-grade PVC plastic from used peritoneal dialysis solution containers (PDCs) by incorporating them into PVC composites reinforced with 3-aminopropyltriethoxysilane-treated pineapple leaf fibers (APS-PALF). The investigation focused on varying the APS-PALF content (10-40 phr) to examine its influence on the mechanical and thermal properties of the PVC composites. PALF underwent alkaline and silane treatments, and the APS-PALF/PVC composites, mainly consisting of the mixed PVC (neat PVC:used PDCs = 50:50 phr) and APS-PALF, were fabricated by internal mixing, two-roll milling and compression molding. Characterization through ATR-FTIR and SEM techniques confirmed successful fiber treatments, and revealed interfacial compatibility in the APS-PALF/PVC composites. Mechanical property tests indicated the superior tensile and flexural strengths of the 40 phr APS-PALF/PVC composite while the 10 phr APS-PALF/PVC composite demonstrated the highest impact strength. Moreover, the TGA results indicated that the incorporation of APS-PALF led to higher thermal stability.

1. Introduction

Chronic kidney disease (CKD) hinders efficient waste removal by the kidneys, leading to waste accumulation in the blood and the potential progression to end-stage renal disease (ESRD). In Thailand, there are over 170,000 CKD patients, with an annual increase of 15-20% [1]. Peritoneal dialysis, conducted 4-5 times daily, generates 0.8 kg of used peritoneal dialysis solution containers (PDCs) as poly(vinyl chloride) (PVC) waste per person daily. PVC, non-biodegradable plastic, is typically managed through environmentally harmful methods like burning and landfilling. To address this issue, recycling PVC waste into composites is proposed.

PVC composites, commonly employed in construction and furniture, can be improved by incorporating natural fibers. Pineapple leaf fiber (PALF) is selected for its strength and abundance in Thailand. PALF, however, encounters challenges such as high moisture absorption, low processing temperature, and poor interfacial adhesion with the polymer matrix [2]. To enhance its compatibility, surface treatments such as alkaline treatment and silane treatment are explored [3].

The process of alkaline treatment entails submerging fibers in a solution, typically composed of NaOH, for a specified duration. This method is understood to enhance the surface roughness of the fibers, thereby improving mechanical bonding [4]. Additionally, it facilitates the exposure of more cellulose on the fiber surface, enabling potential chemical bonding with the matrix material [4]. Through mechanical behavior assessments, encompassing tensile, flexural, and impact analyses, M. Mokhtar et al. reported that the optimal fiber loading for achieving the best performance is at 30 wt% in NaOH-treated PALF/PP composites [5].

Silane treatment involves immersing fibers in a diluted silane solution within a water/alcohol mixture, causing the silane compound to break down into silanol [6]. This process leads to the formation of stable covalent bonds between silanol and the OH groups of cellulose in natural fibers, enhancing cross-linking in the interface region and increasing the fiber surface area for stronger bonding with the polymer matrix [6]. In a study by O. M. L. Asumani et al. [3], PP composites with 30% kenaf fiber, treated using alkaline-silane treatment (5% NaOH solution and 5% APS solution), exhibited the highest tensile and flexural strength.

Therefore, this research aimed to recycle medical-grade PVC plastic from used PDCs by incorporating them into PVC composites reinforced with silane-treated PALF. The study investigated the impact of the loading content of silane-treated PALF in the mixed PVC (neat PVC:PDCs = 50:50 phr) on the mechanical and thermal properties of the PVC composites. The surface chemical structure of the silane-treated

PALF as well as the morphology and interfacial adhesion between the silane-treated PALF and the polymer matrix were examined.

2. Materials and Methods

2.1 Materials

Used peritoneal dialysis solution containers (PDCs) were provided from Tam Tong Recycle Company and the Kidney Friends Association of Thailand. Poly(vinyl chloride) resin SG660, referred to as PVC660 or SCG 660, was obtained from SCG Chemicals Co., Ltd. Pineapple leaf fiber (PALF) was purchased from the Pineapple Farmer Group of Ban Kha (Ratchaburi). Sodium hydroxide (NaOH) and acetic acid were purchased from Merck. 3-aminopropyltriethoxysilane (APS) was purchased from Alfa Aesar. Stearic acid was obtained from Fisher Chemical. Ethanol (99.99%, commercial grade) was obtained from RCI Labscan Ltd. Ca/Zn thermal stabilizer (Commercial grade) was obtained from Siam Stabilizer and Chemicals Co. Ltd. All chemicals were analytical grade unless stated otherwise.

2.2 Preparation of APS-PALF

PALF was cleaned and cut into 4-6 mm lengths, referred to as untreated PALF (UT-PALF). UT-PALF was subjected to alkaline treatment using a 5 wt% NaOH solution for 1 h, followed by multiple washes with tap water and DI water, and dried at 80°C overnight to obtain NaOH-treated PALF (NaOH-PALF). In order to enhance fiber dispersion in the silane treatment step, NaOH-PALF was soaked with ethanol and DI water (50/50 v/v), separated, and dried at 80°C overnight. NaOH-PALF was subjected to treatment with a 0.1 M APS solution for 4 h, followed by washing with ethanol and air-drying. To complete the silane treatment, the silane treated PALF was heated at 100°C for 1.5 h to obtain APS-treated PALF (APS-PALF).

2.3 APS-PALF/PVC composite fabrication

The composite fabrication employed the mixed PVC containing neat PVC and used PDCs with the weight ratio of 50:50, referred to as 50PDC, and APS-PALF with different loading contents, ranging from 10-40 phr of the polymer matrix while maintaining Ca/Zn and stearic acid at 5 and 2 phr, respectively. For composite compounding, the procedure involved internal melt mixing at 175°C, with a speed of 70 rpm for 15 min. Subsequently, the resulting compound underwent rolling using a two-roll mill at 90°C and with a speed of 20 rpm, followed by the formation of the desired specimen shape. The conditions for achieving the composites through compression molding were at 175°C under a pressure of 80 psi, requiring 2, 4.5 and 5 min for pre-forming, hot compression, and cooling, respectively.

2.4 Characterization

The chemical properties of all PALF and composites samples were examined using ATR-FTIR spectroscopy (NICOLET iS5, Thermo Scientific) recorded in a range of 400–4000 cm^{-1} The morphologies of all PALF (untreated and treated) and APS-PALF/PVC composites samples were analyzed using SEM (JSM 6610-LV Series, JEOL) at an accelerating voltage of 10 kV. The mechanical properties of the APS-PALF/PVC composites were examined using a universal testing machine (LLOYD INSTRUMENTS™, LR50K), following ASTM standards D638 [7] and D790 [8] for tensile and flexural properties. Impact property was tested using an impact testing machine (YASUDA) in accordance with ASTM D265 [9]. For all mechanical testing, all specimens were kept at 23 ± 2°C and 50 ± 5% humidity for 24 h. For tensile testing, the specimens were prepared in a dog-bone-shape with a 3.2 mm thickness and the test was conducted at a crosshead speed of 5 mm/min. For flexural testing, the specimens was cut into 127x13x3.2 mm^3 with applying a crosshead speed of 1.3 mm/min and a 50 mm span. For impact strength testing, the specimens was cut into 65 × 13 × 3.2 mm^3 with applying a 1 J pendulum impact at a height of 160°. The thermal stability of the PALF, polymer, and composites were assessed using TGA (Q50 model with Module TGA InstSerial 0050-1507, TA Instrument) from 20-750°C at a heating rate of 10°C/min, maintained under a continuous nitrogen flow of 50 ml/min.

3. Results & Discussion

3.1 Morphology of untreated PALF and treated PALF

To start, SEM images were used to determine the average diameter of UT-PALF, NaOH-PALF, and APS-PALF, resulting in the following outcomes also with standard deviation. SEM analysis of UT-PALF reveals a rough surface with an approximate diameter of 151.3 (±67.8) μm, notably larger than the treated PALFs. This size difference raised concerns about suboptimal distribution within the polymer phase, as substances on the cellulose surface hindered adhesion, compromising strength transfer in composites.[10] Alkaline treatment of PALF resulted in a reduced diameter to approximately 83.9 (±38.7) μm by removing coatings and hemicellulose, leading to improved surface area

and enhanced adhesion between fibers and the polymer phase. Surface treatment with APS further reduced the diameter to approximately 17.3 (±16.5) µm. This transformation highlighted the positive effects of the APS-PALF surface on interfacial interactions between the fiber phase and the polymer phase within the composite. All SEM images of untreated PALF and treated PALF are shown in Figure 1.

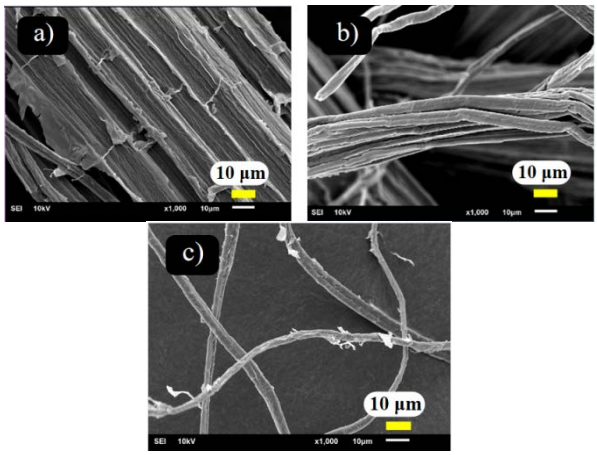

Figure 1. SEM images of (a) UT-PALF, (b) NaOH-PALF and (c) APS-PALF

3.2 Chemical structures of untreated PALF and treated PALF

Chemical structure variations among UT-PALF, NaOH-PALF, and APS-PALF were analyzed through ATR-FTIR spectroscopy, as shown in Figure. 2. The FTIR spectrum of UT-PALF displayed the characteristic peaks at 1250 cm^{-1} and 1750 cm^{-1} signifying the presence of C-O stretching and C=O stretching from hemicellulose and cellulose structures. [12], [13]

Furthermore, the peak observed at 3000 cm^{-1} to 3700 cm^{-1} indicated hydrogen-bonded (-OH) vibrations within the cellulosic structure. [14]

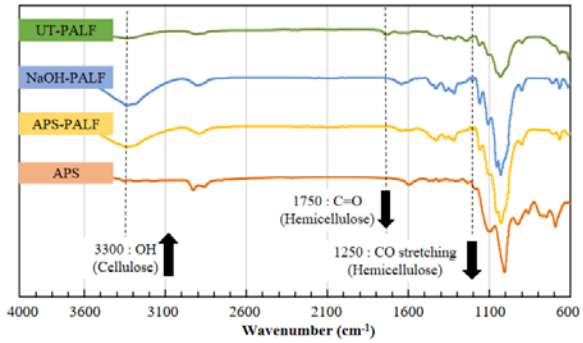

Figure 2. FTIR spectra of UT-PALF, NaOH-PALF, APS-PALF and APS

In the case of NaOH-PALF, the selective removal of hemicellulose led to increasing the proportion of cellulose through NaOH treatment, as evident in the reduced peaks at 1250 and 1750 cm^{-1} (hemicellulose, cellulose) and the increased band at 3300 (cellulose), emphasizing the effectiveness of NaOH treatment in modifying both fiber structure and composition.

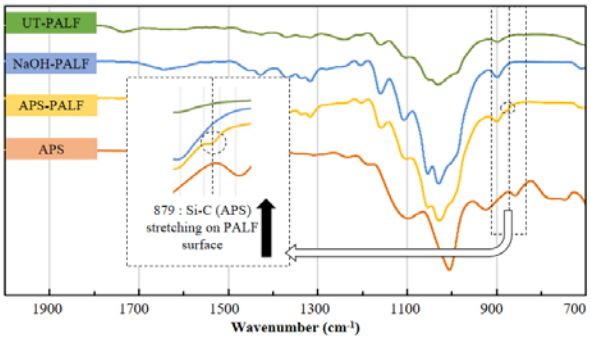

Figure 3. FTIR spectra of UT-PALF, NaOH-PALF, APS-PALF and APS

The APS treatment introduces Si-C bond, as evident in a distinctive peak at approximately 879 cm^{-1} (Figure. 3), indicating a successful linkage of APS onto the cellulose molecule. [11]

Table 1. Detailed FTIR data with wavenumbers and corresponding functional groups

Wave number.	Functional group	Reference
3300-3400	OH (cellulose)	[14]
2917, 2915	CH, CH_2 (hemicellulose, cellulose)	[12]
2949, 2863	CH_2, CH_3	[11]
2867, 2925	CH_2, CH_3 (silane coupling agent) long chain strong peak	[16]
1745	C=O stretching vibration of carboxylic acid and ester groups of hemicellulose	[13]
1735	C=O (hemicellulose, cellulose)	[12]
1637	Absorbed water H_2O bending	[17]
1566-1650	C=C stretching (polyene conjugate structure)	[18]
1597	N (APS) replacing Cl (PVC)	[18]
1429,1371	C-H bending (cellulose)	[17]
1245	C-O (hemicellulose, cellulose)	[12]
1159-1109	C-O stretch ester (cellulose)	[17]
1059	C-O stretching alcohol °1, °2.	[17]
879	Si-C (APS-cellulose linkage)	[11]

Table 2. Mechanical properties of the APS-PALF/PVC composites with different APS-PALF contents

Mechanical properties	Unit	APS-PALF/PVC composites				
		50PDC	10APS-PALF/ 50PDC	20APS-PALF/ 50PDC	30APS-PALF/ 50PDC	40APS-PALF/ 50PDC
Tensile strength (TS)	MPa	13 (±3)	17 (±2)	19 (±1)	21 (±1)	17 (±3)
Tensile modulus (TM)	MPa	208 (±51)	492 (±46)	656 (±61)	565 (±540)	1,284 (±82)
%Elongation	%	116 (±42)	13 (±2)	7 (±1)	5 (±2)	6 (±6)
Flexural strength (FS)	MPa	18 (±1)	7 (±2)	11 (±2)	13 (±1)	42 (±3)
Flexural modulus (FM)	MPa	1,074 (±409)	178 (±150)	402 (±183)	556 (±98)	2,743 (±222)
Impact strength (IS)	J	3.02 (±1.44)	0.26 (±0.03)	0.19 (±0.03)	0.19 (±0.01)	1.77 (±0.09)

This enhancement in chemical composition and surface characteristics in APS-PALF indicated significant implications for the compatibility and interactions between the fiber phase and the polymer phase in the composite materials. Detailed FTIR data with wavenumbers and corresponding functional groups are provided in Table 1.

3.3 Mechanical properties of APS-PALF/PVC composites

The study reveals a strong correlation between the incorporation of varying amounts of APS-PALF and the enhanced load-bearing capacity of the APS-PALF/PVC composites, particularly in terms of tensile and flexural properties. The internal melt mixer plays a crucial role in achieving optimal fiber dispersion within the polymer phase while surface modification using APS contributes significantly to chemical bonding, improving adhesion between APS-PALF fibers and Cl atoms from PVC and used PDC. Table 2 illustrates the tensile, flexural and impact properties of all APS-PALF/PVC composites. Higher APS-PALF content was associated with enhanced force transmission, resulting in the increased tensile strength and modulus values. Among the APS-PALF/PVC composites, the 40 phr APS-PALF/PVC composite demonstrated the highest tensile strength at 23 MPa and modulus at 1193 MPa. Similarly, in terms of flexural strength and modulus, the 40 phr APS-PALF/PVC composite exhibited the highest values at 19 MPa and 611 MPa, respectively. Nevertheless, maintaining a balance in the fiber content is essential to prevent concerns like agglomeration and pull out. [3] The % elongation value, which signifies the material flexibility and ductility, decreased as the APS-PALF content increased due to chemical bonding, rendering the material more brittle. There was an inverse correlation between the APS-PALF content and the impact strength value; lower impact strength value at higher APS-PALF content was due to increased rigidity and reduced flexibility. This underscores the significance of exploring alternative composites, such as composite foam, to enhance impact resistance.

3.4 Morphology of APS-PALF/PVC composites

SEM images of 40 phr APS-PALF/PVC composite reveals the favorable morphology, emphasizing good compatibility, minimal fiber agglomeration and the lower occurrence of fiber pull-out. Figure. 4 illustrates the good dispersion of APS-PALF, contributing to an increased surface area that enhanced interaction with the polymer phase. This expanded surface area, coupled with the chemical reaction initiated by APS, plays a crucial role in strengthening the composite. The smaller APS-PALF diameter further enhanced the fiber surface area, fostering chemical reactions with the polymer phase and improving interfacial interaction and adhesion between the phases. As a result, the APS-PALF/PVC composite exhibited the lowest occurrence of fiber pull-out**,** imparting superior mechanical properties. These findings underscore the critical importance of both surface treatment and morphological considerations in optimizing composite materials for enhancing overall performance.

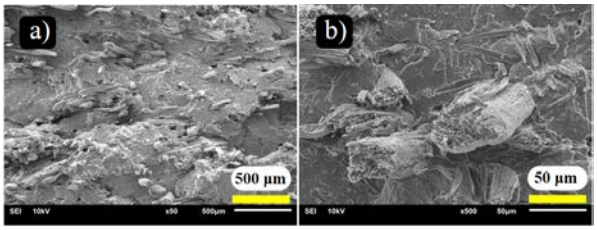

Figure 4. SEM images of the 40 phr APS-PALF/PVC composite

3.5 Chemical structures of APS-PALF/PVC composites

To clarify the successful reaction between APS-PALF and Cl atoms from neat PVC and used PDC, Figure 5 illustrates the FTIR spectra of the PVC composite with 40 phr APS-PALF and the mixed PVC (50PDC without APS-PALF) in the range of 1550 to 1610 cm^{-1}. In this range, the peak at 1597 cm^{-1} not only indicated water absorption (H_2O bending at 1635 cm^{-1}) [17] and polymer degradation to form polyene (C=C stretching 1566-1650 cm^{-1}) [18] but was also associated with the substitution reaction that replaced Cl atoms in neat PVC and used PDCs with N atoms from APS [15].

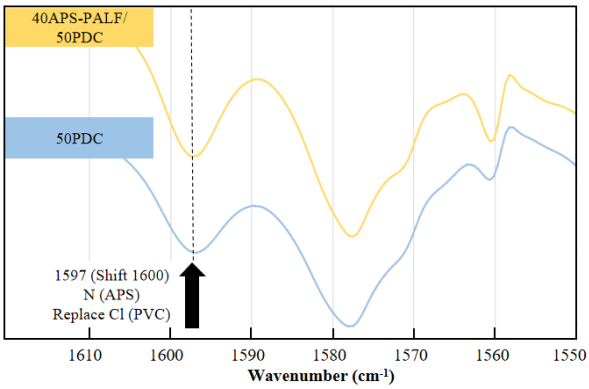

Figure 5. FTIR spectra of the mixed PVC (50PDC) and the 40 phr APS-PALF/PVC composite

3.5 Thermal properties

Figure 6 depicts TGA analysis results revealing thermal decomposition behaviors of neat PVC, used PDCs, and APS-PALF/PVC composites. Used PDCs, the PVC-based polymer, showed dual-stage decomposition at 286°C and 457°C while neat PVC displayed dual-stage decomposition at 311°C and 449°C. These stages corresponded to dehydrochlorination and polyene chain cleavage, respectively. Additives in used PDCs, i.e., plasticizers, lowered the first stage temperature compared to neat PVC. Untreated PALF (UT-PALF) and treated PALF (NaOH-PALF and APS-PALF) exhibited singular decomposition processes. APS-PALF, notably, showed improved thermal degradation due to higher cellulose content from chemical treatment. The 40 phr APS-PALF/PVC composite demonstrated higher T_{max} in the first decomposition stage, indicating the increased heat susceptibility during fabrication compared to neat PVC and used PDCs. However, it exhibited the highest %residual value, suggesting the crosslinking reactions through polyene conjugation. Table 3 summarizes decomposition behaviors of all components and 40 phr APS-PALF/PVC composite.

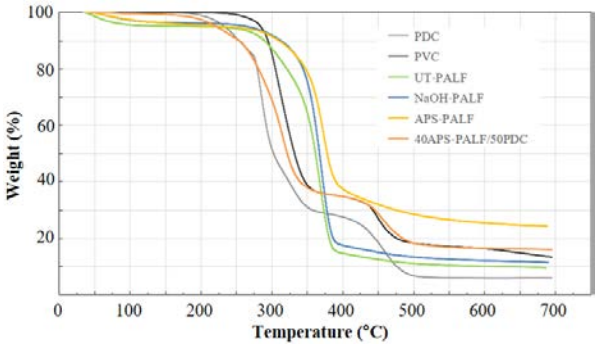

Figure 6. TGA thermograms of neat PVC, used PDCs, UT-PALF, NaOH-PALF, APS-PALF and 40 phr APS-PALF/PVC composite

4. Conclusion

In conclusion, this study aimed to recycle used PDCs, PVC-based medical plastic waste, by using them as polymer matrix to fabricate silane-treated PALF/PVC composites. The investigation focused on evaluating the effect of the APS-PALF content (10-40 phr) on the mechanical and thermal properties of the APS-PALF/PVC composites. SEM and ATR-FTIR spectrometry were utilized to analyze morphology and chemical structure,

Table 3. Thermal degradation from TGA

Materials	1st stage		2nd stage		Residue at 700 °C (%)
	T_{max} (°C)	Weight loss (%)	T_{max} (°C)	Weight loss (%)	
UT-PALF	369	84	-	-	9
Na-PALF	370	84	-	-	11
APS-PALF	373	71	-	-	24
PVC	311	65	449	21	14
Used PDC	286	71	457	23	6
40 phr APS-PALF/PVC composite	316	64	456	19	16

respectively. Mechanical properties were assessed according to ASTM D638, D790, and D256 standards for tensile, flexural, and impact properties, respectively. The results revealed that an increase in the APS-PALF content improved the tensile and flexural strengths and modulus but decreased ductility and impact strength. NaOH and silane treatments reduced the PALF diameter, enhancing interfacial interaction surface area. Successful APS treatment on PALF resulted in chemical bonding and interfacial interaction between the polymer and reinforcement phases, confirmed by FTIR and SEM. The 40 phr APS-PALF/PVC composite exhibited the best tensile and flexural properties while 10 phr APS-PALF/PVC composite demonstrated superior impact properties. Moreover, the 40 phr APS-PALF/PVC composite exhibited higher thermal stability compared to neat PVC and used PDCs.

Acknowledgements

The authors express their sincere gratitude to all individuals who contributed to this research work. Special thanks are extended to Kidney Friends Association of Thailand, Tam Tong Recycle Company, SCG Chemical, and Pineapple Farmer Group of Ban Kha (Ratchaburi) for their generosity.

References

1. Thailand renal replacement therapy (TRT), Thailand renal replacement therapy year 2020, 2020, The Nephrology Society of Thailand, pp 8
2. Hao, L. C.; Sapuan, S. M.; Hassan, M. R.; Sheltami, R. M. Natural Fiber Reinforced Vinyl Polymer Composites. In Elsevier eBooks; 2018; pp 27–70.
3. Asumani, O.M.L.; Reid, R. G.; Paskaramoorthy, R. The Effects of Alkali–Silane Treatment on the Tensile and Flexural Properties of Short Fibre Non-Woven Kenaf Reinforced Polypropylene Composites. Composites Part A: Applied Science and Manufacturing 2012, 43 (9), 1431–1440.
4. Li, X.; Tabil, L. G.; Panigrahi, S. Chemical Treatments of Natural Fiber for Use in Natural Fiber-Reinforced Composites: A Review. Journal of Polymers and the Environment 2007, 15 (1), 25–33.
5. Mokhtar, M.; Hassan, A.; Rahmat, A. R.; Samat, S. A. Characterization and Treatments of Pineapple Leaf Fibre Thermoplastic Composite for Construction Application. ResearchGate 2005.
6. Xie, Y.; Hill, C. a. S.; Xiao, Z.; Militz, H.; Mai, C. Silane Coupling Agents Used for Natural Fiber/Polymer Composites: A Review. Composites Part A: Applied Science and Manufacturing 2010, 41 (7), 806–819.
7. Test Method for Tensile Properties of Plastics. ASTM 2015.
8. Test Methods for Flexural Properties of Unreinforced and Reinforced Plastics and Electrical Insulating Materials. ASTM 2017.
9. Test Methods for Determining the Izod Pendulum Impact Resistance of Plastics. ASTM 2018.
10. Stokke, D. D.; Wu, Q.; Han, G. Introduction to Wood and Natural Fiber Composites; 2013. pp 19-34
11. Ghouti, H. A.; Zegaoui, A.; Derradji, M.; Zu, L.; Cai, W.; Wang, J.; Dayo, A. Q.; Liu, W. Structural and Mechanical Characteristics of Silane-Modified PIPD/Basalt Hybrid Fiber-Reinforced Polybenzoxazine Composites. Materials Chemistry and Physics 2019, 237, 121850.
12. Liu, Y.; Lv, X.; Bao, J.; Xie, J.; Xu, T.; Che, J.; Ma, Y.; Jin, T. Characterization of Silane Treated and Untreated Natural Cellulosic Fibre from Corn Stalk Waste as Potential Reinforcement in Polymer Composites. Carbohydrate Polymers 2019, 218, 179–187.
13. Sabarinathan, P.; Rajkumar, K.; Annamalai, V. E.; Vishal, K. Characterization on Chemical and Mechanical Properties of Silane Treated Fish Tail Palm Fibres. International Journal of Biological Macromolecules 2020, 163, 2457–2464.
14. Asim, M.; Jawaid, M.; Abdan, K.; Ishak, M. R. Effect of Alkali and Silane Treatments on Mechanical and Fibre-Matrix Bond Strength of Kenaf and Pineapple Leaf Fibres. Journal of Bionic Engineering 2016, 13 (3), 426–435.
15. Yu, S.; Oh, K.; Hong, S. H. Enhancement of the Mechanical Properties of Basalt Fiber-Reinforced Polyamide 6,6 Composites by Improving Interfacial Bonding Strength through Plasma-Polymerization. Composites Science and Technology 2019, 182, 107756.
16. Yu, S.; Oh, K.; Hwang, J. Y.; Hong, S. H. The Effect of Amino-Silane Coupling Agents Having Different Molecular Structures on the Mechanical Properties of Basalt Fiber-Reinforced Polyamide 6,6 Composites. Composites Part B: Engineering 2019, 163, 511–521.
17. Hivechi, A.; Bahrami, S. H.; Siegel, R. A.; Milan, P. B.; Amoupour, M. In Vitro and in Vivo Studies of Biaxially Electrospun

Poly(Caprolactone)/Gelatin Nanofibers, Reinforced with Cellulose Nanocrystals, for Wound Healing Applications. Cellulose 2020, 27 (9), 5179–5196.

18. Team, H. FTIR Functional Group Database Table with Search - InstaNANO. InstaNANO. https://instanano.com/all/characterization/ftir/ftir-functional-group-search/.

Dyeing silk fabric with natural dyes from Garcinia Dulcis (Roxb.) Kurz bark

Napawan Martjarern[1], Pacharapol Sirisoontorn[1], Pornpen Atorngitjawat[2], and Kanitta Watcharaporn[1]*

[1]*Department of Textile Science, Faculty of Agro-Industry, Kasetsart University, Bangkok 10900, Thailand*
[2]*Department of Chemistry, Faculty of Science, Burapha University, Chonburi 20131, Thailand*

**E-mail: kanitta.a@ku.th*

Abstract:

Natural dyes extracted from Garcinia Dulcis (Roxb.) Kurz bark (GD) were applied to a silk fabric by an exhaustion dyeing process. Silk fabrics were conducted with and without metallic salt mordants, using three types of mordants: aluminum potassium sulfate, copper sulfate and ferrous sulfate. The dyed fabric was investigated in terms of the CIELAB (L*, a* and b*) and K/S values. The color fastness to washing and colorfastness to light of the GD dyes were investigated. It was found, silk fabrics dyed with GD extraction showed a pale-yellow shade. Silk fabric mordanted with aluminum potassium sulfate and copper sulfate appeared more yellow, while that mordanted with ferrous sulfate turned darker brown. The results showed that meta-mordanting was the optimal dyeing conditions to yield dark yellow on dyed fabric with K/S change from 4.32 to 15.95. The colorfastness to washing was better; from level of (1-2) to (4-5). However, the colorfastness to light was lower; from level of (4-5) to (3-4). It can be concluded that GD extraction can be used for silk dyeing to obtain high color intensity as well as good colorfastness.

1. Introduction

Nowadays, Natural dyes have been growing rapidly. Because during the last few years, the use of synthetic dyes is gradually decreasing due to an increase of environmental awareness as well as harmful effects of degraded products[1]. So natural dyes get more and more interesting because it plays as alternated sources for the synthetic dyes.

Natural dyes can be obtained from plants and minerals. The natural dyes from plants can be extracted from roots, bark, leaves as well as wood. Biodiversity of plants in Thailand made many varieties of natural dyes colors, such as yellow, red, blue, brown etc.[2]. They are non-toxic as well as obtained mostly from renewable resources. Those dyes are used for natural fiber such as cotton, linen, silk and wool. Although natural dyes have the advantageous but their drawbacks were founded; for example, low dye uptake, low color fastness and poor light fastness. However, there are many ways to improve those drawbacks of natural dyes. It was reported on controlling of dyeing conditions and using metal ions mordants in dyeing natural dyes process which were possible approach to improve the dye uptake and color fastness of natural dyes [3] Garcinia Dulcis (Roxb.) Kurz bark, also called “Maphut” in Thailand [4]. It is from the genus Garcinia (Clusiaceae). They are founded in the tropical rainforest area of the world and found in some areas of Thailand [5] as well as in other country in Southeast Asia. Garcinia Dulcis (Roxb.) Kurz bark.gives very bright yellow colors. The main chemical component of Garcinia Dulcis (Roxb.) Kurz bark is Garcigerrin A, which is a structure of Xanthones that shows in Fig.1[6]. It was reported that Xanthones functioned as chromophores or chemicals that gives color in natural yellow dyes[7]. However, the yellow natural dyes showed poor colorfastness either in wash fastness or lightfastness[8]. In order to optimize colorfastness of the Garcinia Dulcis (Roxb.) Kurz bark dyes, mordant dyeing with aluminum potassium sulfate, copper sulfate and ferrous sulfate solution were used to study on dyeing with Thai silk fabric

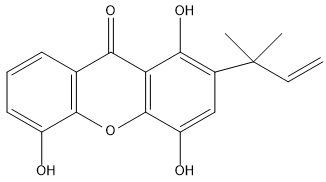

Figure 1. Chemical structures of Garcigerrin A, which is a major component of Garcinia Dulcis (Roxb.) Kurz bark.

2. Materials and Methods

2.1. Materials and Methods

Plain weave 100% silk fabric with ready Desized and scoured (density 55.44 g/m^2) was collected from commercial grade Thai silk fabric. Garcinia Dulcis (Roxb.) Kurz bark was collected from Chaiyaphum province, Thailand. Three different mordants, i.e. aluminum potassium sulfate ($AlK(SO_4)_2).{}_{12}H_2O$), copper sulfate ($CuSO_4.{}_5H_2O$), ferrous sulfate ($FeSO_4.{}_7H_2O$) were laboratory grade and purchased from Loba Chemie Pvt. Ltd. (Thailand)

2.2. Extraction of dyes solution.

Firstly, Garcinia Dulcis (Roxb.) Kurz bark was dried in sunlight and later crushed to small pieces before being used for dyes extraction. The dyes extraction was performed by mixing the bark material and deionized water in the weight ratio of 1:5 and boiling for 1 hour. After that, the extracting solution was filtered to remove the residue for using in the next experiment

2.3 Mordanting and dyeing

a) Mordanting

Silk fabric were dyed in 75% (v/v). Using three types of mordants (aluminum potassium sulfate, copper sulfate, ferrous sulfate) with concentration of the mordants 2 g/L [9]. Three different mordanting methods were employed, i.e. pre-mordanting, simultaneous mordanting or meta-mordanting and post-mordanting in order to study the optimum intensity on silk fabric.

b) Dyeing process

Silk fabrics were dyed at a liquor ratio of 1:50, at 90°C for 60 min. For the pre-mordanting method, silk fabric was impregnated in a mordanting solution at a liquor ratio of 1:50, at room temperature for 15 min before dyeing. Then, dyeing using dye solution at a liquor ratio of 1:50 at 90°C for 60 min. In the meta-mordanting, the mordant was added to a bath containing dye solution. Silk fabric were dyed at a liquor ratio of 1:50, at 90°C for 60 min. And in the post-mordanting method, silk fabric was impregnated in a mordanting solution at a liquor ratio of 1:50, at room temperature for 15 min after dyeing at a liquor ratio of 1:50, at 90°C for 60 min. After dyeing, the dyed samples were rinsed with cold water. Then it washed with non-ionic soap, and finally rinsed with water and air-dried.

2.4 Measurements

a) Color strength.

The color strength values and CIELAB color parameters (L^*, a^*, b^*) were evaluated using a Datacolor 550 Spectrophotometer. The spectral reflectance of silk fabrics in the wavelength range from 400 to 700 nm under illuminant D_{65} and 10° observer. The color strength (*K/S* value) was calculated from the reflectance value using the Kubelka–Munk equation.[10]

$$K/S = \frac{(1-R)^2}{2R}$$

(1) Where R is the reflectance of the dyed sample.

b) Color fastness

The color fastness of dyed silk fabrics were evaluate. The color fastness to washing was evaluated using standard method of AATCC Test Method 61-2010 and the color fastness to light was evaluated using standard method of ISO 105-B02:1994.

3. Results and Discussion

3.1. Effect of dyeing condition

Influence of mordant in dyeing extracted from Garcinia Dulcis (Roxb.) Kurz bark on silk fabric is show in Table 1. The results showed that mordants had a significant effect on the color of the dyed silk fabrics. The effects of mordants not only caused the color changes but also significantly improved the color strength (*K/S* value). It can be noticed from Table 1, for pre-mordanting method with $FeSO_4$ mordanting, showed the highest color strength (*K/S* value) followed by $AlK(SO_4)_2$ and $CuSO_4$ mordanting. In meta-mordanting methods with $FeSO_4$ mordanting, showed the highest color strength (*K/S* value) followed by $AlK(SO_4)_2$ and $CuSO_4$ mordanting. For post-mordanting methods with $FeSO_4$ mordanting, also showed the highest color strength (*K/S* value) followed by $CuSO_4$ and $AlK(SO_4)_2$ mordanting, same as those two methods before. In all cases, adding mordant on silk fabric help dyeing get darker shade and show differences in color shade compared to the fabric dyed with only natural dyed extraction. This is reported that the metal ion in a mordant can form a complex with the conjugate structure of the natural dyes which it has been affected more or less depend on attraction ability of the metal ion for the π-electron Ferrous sulfate is mordant yielded the highest K/S values in all methods, and shows a color change to a darker shade.

However, the color appearance shows in Table 1 shows that $FeSO_4$ mordanting make color change toward dark brown which is not a target of improving on yellow shade. With However $AlK(SO_4)_2$ mordanting, the dyeing of silk fabric from Garcinia Dulcis (Roxb.) Kurz bark showed the improving on the color change to darker yellow. has effective. Next section the color fastness of the dyed fabric with $AlK(SO_4)_2$ were evaluated

3.2. Fastness properties of dyed silk fabric

The performance of the extracted natural dyes on the dyeing of silk fabric mordanting with $AlK(SO_4)_2$ was evaluated by testing the color fastness of the dyed silk fabrics. Table 2 shows the color fastness to washing and the color fastness to light of silk fabric dyed with Garcinia Dulcis (Roxb.) Kurz bark extraction using different

methods, with or without $AlK(SO_4)_2$ mordant. The ratings achieved for wash fastness were in the range of fair to excellent (3 to 4-5), except for the non-mordanted fabric, whose rating was poor (2). The meta mordant dyed silk fabric showed best results of the color fastness to washing.

The color fastness to light of the dyed fabric mordant with $AlK(SO_4)_2$ was lower showing that the light fastness ratings were lower with mordant for the meta method. The result of the meta mordant that showed the best color fastness was rating of (4-5).

The CIELAB values show the highest b* values from $AlK(SO_4)_2$ in the meta method, with B values affecting the yellow color hue.

Table 1. Effect of dyeing method and dyed silk fabric using various mordants of Garcinia Dulcis (Roxb.) Kurz bark.

Mordant	Method	CIE Lab				
		*L**	*a**	*b**	*K/S*	*Color obtained*
-	No mordant	85.41	- 0.38	27.73	4.32	
$AIK(SO_4)_2$	Pre-mordant	78.53	- 2.05	46.64	11.69	
	Meta-mordant	76.69	1.10	65.86	15.95	
	Post-mordant	81.23	- 1.37	59.86	10.82	
$CuSO_4$	Pre-mordant	69.32	- 1.14	40.19	11.59	
	Meta-mordant	60.87	4.64	43.09	14.36	
	Post-mordant	71.06	- 3.25	50.97	12.65	
$FeSO_4$	Pre-mordant	33.27	4.71	15.89	16.69	
	Meta-mordant	27.55	3.92	10.24	16.68	
	Post-mordant	42.62	1.91	19.79	13.31	

Table 2. Washing and light fastness values of dyed silk fabric with Garcinia Dulcis (Roxb.) Kurz bark.

Mordant	Dyeing method	Color fastness to washing	Color fastness to light
		Color change	*Color change*
		rating	*rating*
No mordant	-	1-2	4-5
$AlK(SO_4)_2$	Pre-mordant	3-4	4
	Meta-mordant	4-5	3-4
	Post-mordant	4	4

4. Conclusion

Silk fabric can be successfully dyed with Garcinia Dulcis (Roxb.) Kurz bark extraction by meta-mordanted dyed method with aluminum potassium sulfate for mordant. The results of dyed silk fabric showed the color change to darkest yellow and good color fastness to washing. However, the dyed silk fabric showed low color fastness to light. Therefore, dyeing is suitable for products used indoor. Do not exposed to sunlight directly. The lmax is 400nm.s

Acknowledgements

This project was financially supported by Kasetsart University Research and Development Institute (KURDI).

References

1. Chowdhury, A. K. R., Eco-friendly dyes and dyeing. *Advanced Materials and Technologies for Environmental Applications*, 2(1) 2018, 145-176.
2. Mansour, R., Natural Dyes and Pigments: Extraction and Applications.*Materials for Coloration and Finishing.* 2018, 75-102.
3. B. U. Banna, R. M., K. S. Tanni, N. Sultana, A. M. Shamim, R. K. Turzo, M. Tanjil, Effectiveness of dyeing with dye extracted from mango leaves on different fabrics by using various mordants. *North American Academic Research*, 2(10) 2019, 123-143.
4. R. Mongkholrattansit, N. R., N. Tubtimthai, N. Sasivatchutikool, & N. Punrattanasin., Natural Dye from Garcinia dulcis (Roxb.) Kurz Bark and Application on Silk Fabric by Using Pad-Batch Dyeing: A Study on Mordant Concentrations Efficiency. *Advanced Materials Research*, 884-885 2014, 216-219.
5. P. Thepthong, S. P., Anthony R. Carroll, S. P. Voravuthikunchai, & W. Mahabusarakam. , Prenylated xanthones from the stem bark of Garcinia dulcis. *Phytochemistry Letters*, 21 2017, 32-37.
6. Tamhid, H. A., Chemical compounds and antibacterial activity of Garcinia dulcis (Roxb) kurz. 2019, 71-85.
7. Daniel., M., Useful Herbs of Planet Earth. Inddia: Scientific Publisher. 2013.
8. C. Wang, C. X., Anli Tian, Shaohai Fu, & C. Wang., Extraction of natural dyes from Alpinia blepharocalyx K. Schum. for dyeing of silk fabric. *Coloration Technology*, 129 2012, 32-38.
9. Y. Zhou, R.-C. T., Modification of curcumin with a reactive UV absorber and its dyeing and functional properties for silk. *Dyes and Pigments*, 134 2016, 203-211.
10. C. K. Jha, R. K., V. Kumar S, & D. Rajeswari , Extraction of natural dye from marigold flower (Tagetes erecta.) and dyeing of fabric and yarns: A focus on colorimetric analysis and fastness properties. *Scholars Research Library*, 7(1) 2015, 185-195.

Comparison of natural and synthetic fibers on the properties of fiber cements

Piyalak Ngernchuklin*, Wuttinai kokkamhang, and Suwatchai Thongnoi

Expert Centre of Innovative Materials, Thailand Institute of Scientific and Technological Research (TISTR), 35 Mu 3 Khlong Ha, Khlong Luang, Pathum Thani, 12120, Thailand

**E-mail: piyalak@tistr.or.th*

Abstract:

Nowadays fiber cement (FC) is drawn much attention for construction applications such as ceiling, wall, roof, and floor due to its functionalized and modernized designs. Their manufacturing processes are also improved for better mechanical properties and lifetime. Fiber cement is composed of Portland cement, fine sand, and water in a majority with adding of filler including minerals (asbestos), natural fibers and synthetic fibers, etc. Due to the hazard of asbestos in fiber cement to respiration system during prolong period of usage, several alternative fibers have been replaced. Therefore, the objective of this study was to compare the properties of fiber cement from natural waste plant fibers (banana; B and water hyacinth; WHC) and synthetic fiber (glass reinforced concrete; GRC) fabricated by mimic hatschek process. The type of fiber, method of fiber treatment and degradation of fiber cement were studied in terms of microstructure, flexural strength, flexural strain, and degradation, respectively. The results demonstrated that all fiber cement samples showed flexural strength in a range of 8-10 MPa in which pass the requirement of the Thai standard (TIS no. 1472-2561). FCs (B-NaOH, WHC-NaOH, GRC) possess deformation behavior observed by non-linear S-E curve. The degradation of FC-WHC-NaOH and GRC was found to be 10 and 12 percent, respectively. It could be concluded that the fiber cements with NaOH treated-natural waste plant fibers demonstrated comparable properties to those of synthetic glass fiber. Thus, such natural waste plant fibers have a potential to act as the filler in fiber cement application.

1. Introduction

Nowadays, construction products are not consideration for a function but also for a design. Fiber cement is one of the prototypes that has been developed to meet such requirements. Its major compositions are composed of portland cement, fine sand, water and some fiber/mineral. Due to the hazard of asbestos in fiber cement to respiration system during long period of usage, substitution of fibers has been proposed[1]. Synthetic fibers were studied to improve fiber cement properties such as polyvinyl alcohol fiber (PVA) due to their high strength and toughness[2], PVA grafted SiO_2 to improve interfacial bonding strength[3]. In addition, natural fibers from agricultural waste also drawn much attraction to construction products including banana fiber in concrete beams[4], nanofibril from fique fiber[5], bio-chars from sugarcane bagasse[6], coconut coir and oil palm fibers[7,8], jute fibers[9] , wood pined mixed PVA[10], tobacco stalk pulp[11]. Furthermore, the method of fiber treatments to obtain pure fiber for better bonding strength and good interface have been conducted including chemical and mechanical treated oil palm fibers[12], chemical treated bagasse fiber by alkali, acetylated, enzyme and silane[13] and physical, chemical and mixed treatments in plant biomass[14]. Therefore, the objective of this study was to compare the properties of natural and synthetic fibers. The local plants, for example, banana stem, water hyacinth and fiber glass acted as fiber reinforced in cement. Fiber treatment methods physical-mechanical-properties relation was studied to confirm the use of such fibres.

2. Materials and Methods

2.1 Fiber preparation

In this experiment, three types of fibers including banana fiber, water hyacinth fiber and glass reinforced cement were used as filler in cement matrix. Natural fibers were prepared with two different methods. Firstly, banana stem was milled with high speed mixer designated as B-HS. Others, raw banana stem and water hyacinth stem were rolled to obtain 2-3 feet-long fiber shown in Figure 1. Then, they were cut into 2-3 centimeters and soaked in 5 percent of hot sodium hydroxide solution for 2 hrs. Brownish solution from wax, hemicellulose, lignin and others was drained and fiber was cleaned with water until neutral designated as B-NaOH and WHC-NaOH. Glass reinforced cement was in white and 2-centimeter length designated for GRC. All types of fibers were observed the microstructure before and after treatment by Scanning Electron Microscope (SEM, JSM-5410LV, JEOL, Japan). The fiber diameter was measured from fiber width at different locations through fiber length by

Scanning Electron Microscope (SEM) and stereo microscope (Zeiss, Stemi SV11, Geramany) together with ZEN blue EOS 850D software. The fiber diameter was not determined from cross-sectional part of fiber due to a very small size of fiber in micrometer range and not much enough strength to align the fiber straight.

2.2 Fiber cement preparation

In this experiment, Portland cement type I, fine sand (90 percent pass 200 mesh sieve) water and fiber were used in the formula of fiber cement. The water to cement ratio (W/C) and cement to sand ratio (C/S) were kept constant at 0.85 and 1.5, respectively, and the amount of fiber at 1 percent of cement and sand were assigned. Firstly, cement, sand and fiber were put into mixer to avoid a chunk of fiber and then followed by water to homogenously mix. The obtained cement slurry with high concentration of solid was poured to pressing mold (20-cm length by 7.5-cm width) connected with vacuum pump used to drain out of water during pressing a 10-mm thick sheet of fiber cement. The fiber cement samples were set for 2-3 hours and cured in moist condition for 7 days and then dried at 60 ^{o}C for 24 hours. The physical properties such as microstructure, bulk density, porosity and water absorption of all samples were tested by Archimedes method. The mechanical properties and S-E graph were observed by Instron universal testing machine. For the application propose, the degradation (percent of difference in flexural strengths) of all fiber cements was studied by alternatively 1-day soaking in water (30 ^{o}C) and 1-day drying in oven (60 ^{o}C) for 15 cycles.

Figure 1. Natural fibers (banana and water hyacinth) before treatment and synthetic fiber (glass reinforced cement).

3. Results & Discussion

3.1 Physical properties of fibers.

Figure 2 demonstrated microstructures and average diameter of all six fibers prepared by different conditions of banana (B), water hyacinth (WHC) and glass reinforced cement (GRC). Original banana and original water hyacinth fibers were no treatment fibers and when treatment with sodium hydroxide solution called B-NaOH and

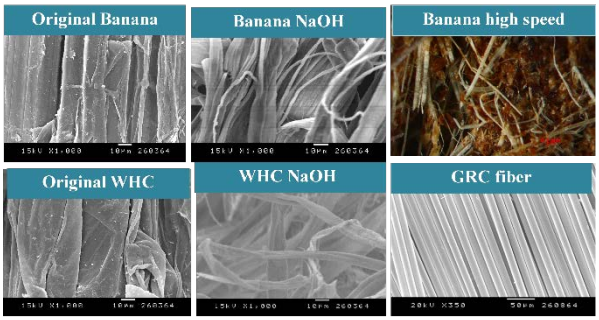

Figure 2. Microstructures of natural fibers (with various treatment conditions) and synthetic fiber.

WHC-NaOH. Banana stem was subjected to high speed mixer called B-HS. From micrograph, original banana and original water hyacinth fibers were about 200 microns in diameter as the same size of B-HS while B-NaOH and WHC-NaOH fibers could be reduced the size down to 10-20 microns. This was because wax, hemicellulose and other impurities were dissolved by strong base NaOH solution. Treated B-NaOH, WHC-NaOH and GRC fibers were almost the same size (width) in a range of 10-30 microns. Obviously observed impurities of banana stem with 200-microns-width fiber after high speed milling B-HS.

3.2 Physical, mechanical properties and degradation of fiber cement.

Table 2 showed physical properties of fiber cements (FCs) with various treatment conditions compared to conventional cement (CC). Homogenously mixed fiber was found in FC-B-NaOH and FC- GRC unlike FC-B-HS and FC-WHC-NaOH. Bulk density of FCs was a bit lower than CC due to lightweight fiber. Porosity and water absorption of FCs were a little higher than CC thanks to high degree of absorption (swelling) from fiber.

Table 2 Physical properties of fiber cements compared to conventional cement.

Sample	Bulk density (g/cm^3)	Porosity (%)	Water absorption (%)
Conventional Cement (CC.)	1.90±0.02	20.14±0.45	10.61±0.35
FC-B-NaOH	1.84±0.01	19.75±0.27	10.74±0.23
FC-WHC-NaOH	1.79±0.04	21.70±1.48	12.13±1.10
FC-B-HS	1.82±0.02	21.17±0.60	11.61±0.48
FC-GRC	1.80±0.04	21.07±0.55	11.71±0.56

Figure 3 was flexural stress results of fiber cements with various treatment conditions com-pared to conventional cement. Flexural stress of all samples were about 8-11 MPa. All FCs yielded flexural stress close to CC but higher extension. Moreover, the highest flexure extension obtained from FC-GRC, FC-B-NaOH, FC-WHC-NaOH (1 and 0.85 mm, respectively) and the lowest one was FC-B-HS (0.5 mm) as shown in Figure 4. These results were corresponded to fiber behavior in Figure 1 in which GRC were separately in each single fiber while B-HS was fiber chunk with impurities (lignin, wax, hemicellulose and others). With the fiber morphology, they gave an effect on fiber cement extension.

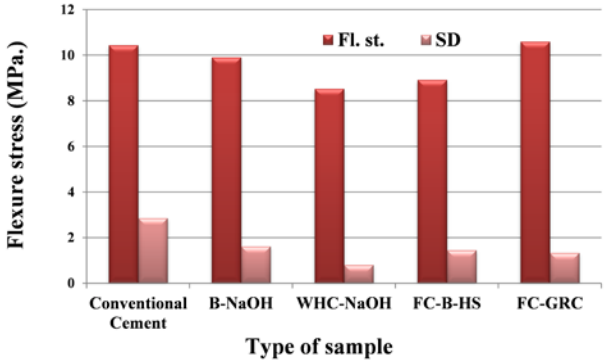

Figure 3. Flexural stress of fiber cements with various treatment conditions compared to conventional cement.

Figure 5 was the stress-extension curve of fiber cements with various treatment conditions compared to conventional cement. It was found that FCs (B-NaOH, WHC-NaOH, GRC) were non-linear S-E curves and gave rise to more deformation behavior as a result of reinforced fibers while keep flexure stress still.

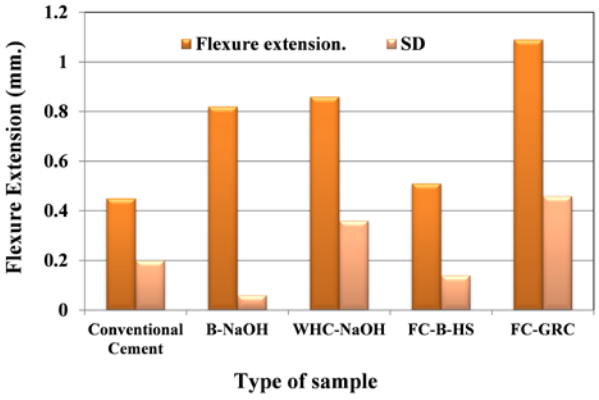

Figure 4. Flexural extension of fiber cements with various treatment conditions compared to conventional cement.

In case of CC and FC-B-HS showed linear S-E curve from the brittle cement matrix. FC-B-HS was not benefit to improve cement properties.

In general, Portland cement is one type of calcium aluminosilicate compound that consists of CaO 60-70%, SiO_2 18-22%, Al_2O_3 4-6% and Fe_2O_3 2-4%. All four type mineral compounds mentioned have chemical cross- linking to form tricalcium silicate (C_3S) 55-56%, dicalcium silicate (C_2S) 15-25%, tricalcium aluminate (C_3A) 8-14 % and tetracalcium aluminoferrite (C_4AF) 8-12%. Such compounds are the majority phases to give the strength of cement after combining with water and hydration reaction occurred. The majority parameters that control the strength of cement are the amount of cement and water, cement and water ratio and curing condition (method of curing, time and temperature). The requirement of high strength of cement is needed to serve better function in any applications but the drawback of high strength material like cement is easily brittle during operation construction. So, search of fiber type and fiber structure mixed with cement matrix as a composite compound are required. This can show dominant properties of the two materials of high strength property by Portland cement and high flexibility from fiber. From these results, it could be concluded that fiber needed chemical treatment to obtain pure cellulose and gave rise to high deformation and reinforcement as obtained in FCs (B-NaOH, WHC-NaOH). Normally chemical treatment is an important process because natural fiber is composed of cellulose, hemicellulose, lignin and wax. Both hemicellulose and lignin are not required in fiber cement because they obstruct the hydration process of cement as a result of lower strength of fiber cement. Also, hemicellulose is a type of low molecular polymer where its micro fibril cell wall is located between cellulose and lignin. Lignin is an aromatic compound. They are quite hard to separate to obtain pure cellulose by milling, soaking in water or boiling. Therefore, chemical treatment by NaOH, KOH, and etc., are normally used to extract cellulose. That benefits fiber cement including good bonding of cement-fiber interface, less porosity and low water absorption. All properties can prolong shelf life of fiber cement during application. Pure cellulose will enhance the flexibility and good deformation of fiber cement while high strength obtained from cement matrix. The possible interaction between natural fiber and cement and synthetic fiber and cement could be explained that an important role of fiber in cement matrix was in the bridging effect resulting in enhancing post-cracking strength and giving more flexible properties in cement/concrete

products[15]. As shown in Figure 5, obviously observed the characteristic of brittle material (high strength but easily crack) with small flexure extension (average of 0.4 millimeter) in CC and FC-B-HS. When adding the banana and water hyacinth treated with NaOH (B-NaOH and WHC-NaOH), it was found that they improved fiber cement samples more extension with average 1 millimeter before cracking. And, the last one by mixing glass reinforced cement (GRC), obtained the highest ductility from fiberglass to 1.1 millimeter with higher elongation characteristic without a point of fracture observed from stress-extension curve (green curve). In the last two cases, it could be explained by the interaction between fiber and cement that natural fiber and synthetic fiber possessed flexible properties in nature which can absorb more energy from stress applied and gave a result of delay crack or rupture. This would bring the cement/concrete more ductile and benefit to tensile force applications.

The degradation testing is a crucial property that represents efficiency of application. Figure 6 was the flexural strength values of all five type samples before (in blue) and after soaking in water at 30 °C and drying in the oven at 60 °C for 1 day each cycle (in red). The degradation test (in green) was performed for 15 cycles (30 days). The results showed that natural fibers (B and WHC) treated with NaOH were degraded to synthetic fiber (GRC). The flexural strength differences were 10-14 percent lower than that of CC (21 percent). FC-B-HS exhibited the highest degradation (31 percent) due to no treatment and more impurities (lignin, wax, hemicellulose and others) that were incompatible between fiber and cement matrix. This may cause higher porosity in such samples.

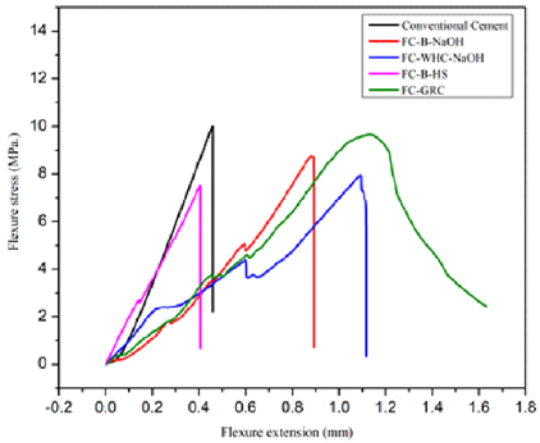

Figure 5. Stress-extension curve of fiber cements with various treatment conditions compared to conventional cement.

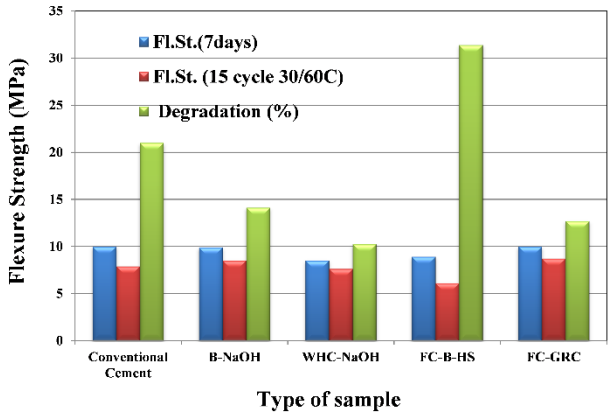

Figure 6. Flexural strength after degradation testing of fiber cements with various treatment conditions compared to conventional cement.

4. Conclusion

Natural fibers (banana and water hyacinth) were treated with NaOH to get rid of wax, hemicellulose and lignin resulting in smaller the size from 200 to 30 microns. This was in the same range as synthetic fiber (glass reinforced cement). Two treatments for banana fibers, high speed milling and NaOH solution, were applied. Better physical and chemical properties of NaOH-B fiber were obtained. No significant change in physical properties of fiber cements compared to conventional cement. The highest extension obtained from FC-GRC followed by FC-NaOH-WHC and FC-NaOH-B, respectively. Flexure stress-flexural extension curves in fiber cements were deformation dominated from fibers. The poor properties were found in FC-B-HS both in deformation and degradation. From the results, it could be drawn the summarization that FC-GRC dominated in deformation properties to FC-NaOH-WHC and FC-NaOH-B.

Acknowledgements

This project was funded by National Research Council of Thailand.

References

1. Seung-Hyun, P. *Safety and Health at Work.* **2018**, *9*, 360-364.
2. Paknahad, A.; Petre, D. G.; Sander, C.G.; Leeuwenburgh and Lambertus, J.S. *Acta Biomater.* **2019**, *96*, 582–593.
3. Zhang, W.; Zou, X.; Wei, F.; Wanga, H.; Zhanga, G.; Hua, Y.; Zhang, Y. *Compos. B. Eng*. **2019**, *162*, 500–507.
4. Elbehiry, A.; Elnawawy, O.; Kassem, M.; Zaher, A.; Uddin, N.; Mostafa, M. *Constr. Mater*. **2020**, *13*, e00361.

5. Hoyos, C. G.; Zuluaga, R.; Ganan, P.; Pique, T.M. *J. Clean. Prod.* **2019**, *235*, 1540-1548.
6. Rodier, L.; Biba, K.; Onessippe, C.; Arsene, M.A. *Ind Crops Prod*. **2019**, *141*, 111731.
7. Lertwattanaruk, P.; Suntijitto, A. *Constr Build Mater*. **2015**, *94*, 664-669.
8. Kochova, K.; Gauvin, F.; Schollbach, K.; Brouwers, H.J.H. *Constr Build Mater*. **2020**, *231*, 117121.
9. Fonseca, C. S.; Silva, M. F.; Mendes, R. F.; Hein, P. R. G.; Zangiacomo, A. L.; Tonoli. G. H. D. *Constr Build Mater*. **2019**, *211*, 517–527.
10. Schabowicz, K.; Jóźwiak-Niedźwiedzka, D.; Ranachowski, Z.; Kudela, S. Jr.; Dvorak, T. *Arch. Civ. Mech*. **2018**, *18*, 1068-1078,
11. Wasanapiarnpong, T.; Nilpairach, S.; Siraleartmukul, K.; Charoenvai, O.; Aungatichart, O.; Laoharungpisit, N. *Key. Eng. Mater*. **2015**, *659*, 102-105. .
12. Bonnet-Masimbert, P.-A.; Gauvin, F.; Brouwers, H.J.H.; Amziane, S. *Results Eng*. **2020**, *7*, 100150.
13. Huerta-Cardoso, O.; Durazo-Cardenas, I.; Marchante-Rodriguez, V.; Longhurst, P.; Coulon, F.; Encinas-Oropesa, A. *Results Mater.* **2020**, *8*, 100158.
14. Loan T.T.V.; Navard, P. *Constr Build Mater*. **2016**, *121*, 161–176.
15. Khan M.S.; Fuzail Hashmi A.;Sharia M.; Ibrahim S.M. *Mat. Tod. Proc.* **2023**, https://doi.org/10.1016/j.matpr.2023.05.106.

Bacterial cellulose from Kombucha for water and oil separation

Sira Amatsaena, Supak Suksawat, Chananthon Chanawit, Phoom Sangsuwan*, and Kamonchanok Phoonsawat*

KOSEN-KMUTT, Engineering Science Classroom, King Mongkut's University of Technology Thonburi, Bangkok, 10140, Thailand

**E-mail: Phoom.san@kmutt.ac.th and Kamonchanok.phoon@kmutt.ac.th*

Abstract:

Kombucha has well-known as a beverage consumed worldwide. Kombucha fermentation process produces symbiotic culture of bacteria and yeast (SCOBY) as a byproduct, that is currently considered of little value. The SCOBY possesses highly porous structure of bacterial cellulose (BC) fiber, which is a non-toxic and biodegradable biopolymer. High porosity of SCOBY has potentials as adsorbent materials. In this work, initially hydrophilic BC was modified with methyltrimethoxysilane (MTMS) to increase hydrophobicity for oil absorption application. The BC aerogel was obtained from freeze-drying of SCOBY hydrogel and was treated with MTMS via chemical vapor deposition (CVD) under mild condition and short deposit time to yield oleophilic aerogel. Hydrophobic property of the resulting aerogel was confirmed by contact-angle measurement and oil-water separation test. This work presents a method to prepare environmental-friendly aerogels and its potential in oil adsorption, making it highly suitable for solving oil leakage problem.

1. Introduction

Oily sewage comes from a wide range of sources, including oil leakages (oil exploitation, transportation, etc.), industries (petrochemical, etc.) and domestic sewage (cooking oil, etc.) and other various sources. The oily sewage can pollute natural water resources, endanger aquatic organisms and human health. The common oil-water separation technologies mainly include biological oxidation methods, chemical methods, *in situ* combustion methods and adsorption methods. Among them, adsorption method is the most potential development direction at present, because it has many advantages, such as recyclable adsorbent and low secondary pollution to the environment.[1, 2] Traditional adsorbents for oil absorption are mainly porous materials, such as activated carbon, coal adsorbents, expanded graphite, zeolite, and porous materials prepared from polymers, such as PP, PVDF, etc.[3, 4]

Cellulose is an exopolysaccharide and insoluble biopolymer, consisting of β-1,4-linked D-glucose units.[5, 6] It is the basic component of eukaryotic plants and also known as to be synthesized by marine animals, Protista, bacteria, algae, fungi and cell free systems.[7-9] Bacterial cellulose (BC) is cellulose produced by bacteria via fermentation process to protect bacteria from UV rays, provide an oxygen-rich environment, protect undesirable environmental conditions such as low water content or extreme pH, and protect bacteria from pathogenic microorganisms.[10-12]

BC has many advantages over plant-based cellulose. One of them is that BC does not require extra treatment procedures before its use since it does not contain lignin, hemicellulose, pectin, arabinose and other plant-derived elements.[13-15] BC also has higher water holding capacity, hydrophilicity and porosity.[16] These properties allow cellulose to be used as a drug delivery system, wound dress, tissue engineering agent and stabilizer. Another advantage of BC is that, depending on the type of fermentation, the culture media and additives used, the produced BC can have different properties.[17]

Kombucha is a beverage which has been traditionally obtained from a fermentation of sweetened black and green tea leaves, which results in a product with a slightly acid, sweet flavor and high sensory acceptance.[18] The starter culture of Kombucha fermentation is known as symbiotic culture of bacteria and yeast (SCOBY), in which BC is formed.[19]

Due to fibrous nature, high porosity,[4] and varieties from different methods of fermentation, BC had been widely studied as substrate for absorbent. However, due to its hydrophobicity, BC must be modified to use as oil absorbent. There were multiple efforts to increase hydrophobicity of BC[4, 20, 21]. However, to the best of our knowledge, there was no study of using SCOBY from kombucha fermentation as oil absorbent. Since BC has high water holding capacity, hydrophilicity, porosity,[4] and their structure varies depending on source of BC, the objective of this research was to synthesis an oil absorbent using a new kombucha consortium which had not studied been together before in the literature.

2. Materials and Methods

2.1 Materials and Instruments

A symbiotic culture of bacteria and yeast (SCOBY) from the Kombucha fermentation process. Tea leaves was purchased from local grocery store. NaOH and NH_4OH (28%) were purchased from Quality Reagent Chemical. Methyltrimethoxysilane (MTMS, 97%) was purchased from Alfa Aesar.

2.2 Preparation of bacterial cellulose from the Kombucha fermentation

Bacterial cellulose was prepared from the Kombucha fermentation. First, tea leaves and sugar were added to hot water and allowed to cool to 37 ºC. After that, SCOBY was added and kept at room temperature for 10 days. After the fermentation process, a cellulose film forms on the solution surface. Next, the bacterial cellulose was purified by washing it in deionized water. Then immersed in 1.0 M NaOH solution at 60 °C for 4 h. and washed repeatedly with deionized water every 2 h. until the solution was neutral.

2.3 Preparation of BC aerogel

The pure BC aerogels were prepared directly via freeze-drying according to a procedure previously published[4]. The bacterial cellulose from Kombucha fermentation process was washed with deionized water followed by soaking in 10% NaOH at 80 °C for 6 h. After that they were washed repeatedly with deionized water at 80 °C for 4 h. Then, the hydrogel was freeze-dried to produce BC aerogel while preserve the web-like structure of the bacterial cellulose fiber in dry state.

2.4 Hydrophobic modification of aerogel via chemical vapor deposition (CVD) of methyltrimethoxysilane (MTMS)

Modification of aerogel to hydrophobic by CVD was conducted with slight modification from the reported method[4]. A 25 mL beaker were charged with 5 mL of MTMS and 7 mL of NH_4OH solution. Then, BC aerogel was placed on a beaker, then another beaker was spliced together and sealing the joint with a parafilm to prevent the escape of gases and vapors. Subsequently, the assembly was heated to 60 ºC for durations of 5 and 10 minutes. After the dismantling of the assembly, the bacterial cellulose aerogel was moved to a hot air oven, which maintaining a temperature of 60 ºC for 15 minutes to allow for thorough drying. The CVD process was repeated with only either of reagents at 10 minutes deposit time to confirm the cause of hydrophilicity. The method was repeated in milder condition with 5 minutes deposit time at room temperature, followed with drying at 60 °C.

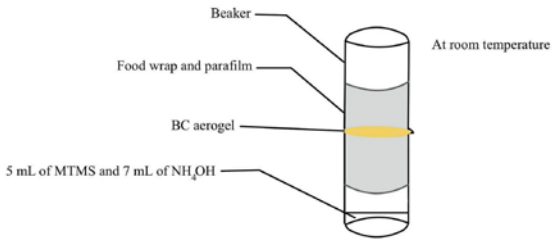

Figure 1. Equipment for hydrophobicity modification of aerogel via chemical vapor deposition (CVD) of methyltrimethoxysilane (MTMS) at room temperature.

2.5 Contact angle measurement

Contact angle measurements were carried out using a smartphone application. The contact angle value was measured 5 minutes after the water and oil drops contacted the surface of the BC aerogel.

2.6 Oil/water separation

Used cooking oil of equal weight with hydrophobic aerogel was added to beaker containing excess DI water. The aerogel was dropped over the floating oil drop and removed from the beaker after 10 minutes and weight of aerogel and absorbed oil was measured. The reusability was tested by squeezing to remove the absorbed oil, followed by cleaning of remaining oil from the aerogel with water and tissue paper, then drying in oven and weighted again after cooling.

3. Results & Discussion

3.1. Hydrophobic modification of aerogel via chemical vapor deposition (CVD)

Chemical vapor deposition of NH_4OH and MTMS was conducted at 60 °C for 10 minutes, followed by drying at 60 °C until the aerogel was completely dried, which double as time for reaction between both reagents. The modified aerogel exhibited hydrophobicity as desired. The hydrophobicity was result of heterogenous surface caused by formation of microscopic silane coating from base-catalyzed sol-gel reaction of MTMS.[22] This surface exhibit lotus effect as predicted by Cassie model. Reaction between reagents is required for this surface modification, as CVD of single reagent did not alter hydrophilic surface of BC aerogel. These experiments confirmed that the hydrophobic surface did not cause by deposition of hydrophobic reagent.

The temperature and deposit time was lower than reported method in literature[4], which is advantages in manufacturing of materials. This advantage is likely due to volatility of both

reagents and high porosity of BC aerogel, facilitating the gas-phase modification. The CVD process was attempted at even shorter time and at room temperature, which successfully achieved hydrophobicity with similar contact angle as longer deposit time.

3.2 Contact angle measurements

The high hydrophobicity and porosity of BC aerogel determine the absorption of water droplets during the contact angle measurements, and the short time between the droplet release and image recording is necessary. It is expected that the aerogels will become more water-resistant after treatment, causing droplets to remain on their surface for longer periods. Conditions were applied for contact angle measurements in the modified and non-modified aerogel cases, meaning that photos were captured five minutes after the droplet touched the aerogel surface for comparison. In these conditions, the non-modified aerogels displayed a contact angle value of about 30º (Figure 2). Significantly higher contact angle values—58° for modified aerogels and 13° for non-modified aerogels—were found for the functionalized BC aerogels, indicating an improved hydrophobic nature. Because the modified aerogels were hydrophobic, they displayed a higher contact angle value. For every type of BC aerogel, the droplet images used to calculate contact angles are also provided in Figure 2. The contact angle value of the aerogels modified with MTMS is 22.4% higher than that of the aerogels without modification.

3.3 Oil/water separation test

The BC aerogel have hydrophobic and oleophilic properties that endow them with an excellent selectivity for oil adsorption from water. The hydrophobic BC aerogel, weighing 0.04 grams, has the capability to absorb approximately 40-50% of equal weight oil drop from water. The mechanical property of the aerogel allows it to be squeezed without compromising its structure, resulted in ability to remove absorbed oil with squeezing and washing residue oil with water. After drying, the aerogel returned to its original weight and can be used to removing oil drop from water again with similar approximate 40-50% weight of equal weight oil drop.

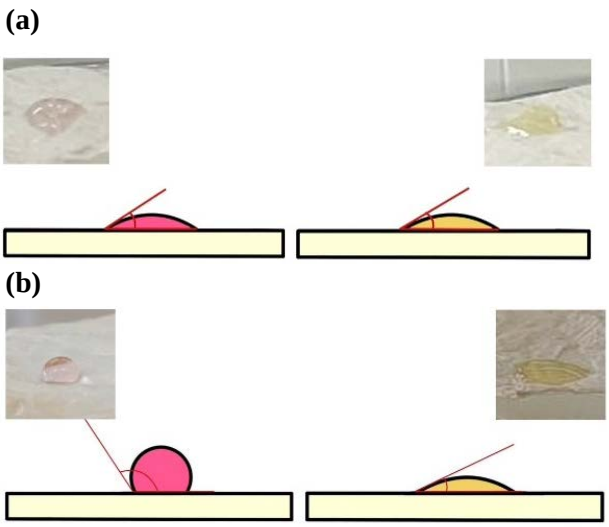

Figure. 2 Contact angle images for droplets water and oil on (a) non-modified BC aerogels and (b) MTMS modified BC aerogels.

4. Conclusion

In summary, hydrophobic BC aerogel was prepared from treatment of pellicle of Kombucha fermentation with freeze-drying and CVD of MTMS and ammonium hydroxide. The deposit time could be shortened only 5 minutes at room temperature. The increase in hydrophobicity was confirmed by contact angle measurements after the silane treatments. The resulted aerogel shows potential as oil absorbent materials. Overall, the BC coated with silanes is an eco-friendly, effective method to obtain aerogels with increased hydrophobicity for applications.

Acknowledgements

This project was supported by KOSEN institute of King Mongkut's University of Technology Thonburi, Thailand.

References

1. Atoufi, Z.; Reid, M. S.; Larsson, P. A.; Wågberg, L. Surface tailoring of cellulose aerogel-like structures with ultrathin coatings using molecular layer-by-layer assembly. *Carbohydrate Polymers* **2022**, *282*, 119098.
2. Wang, Q.; Wang, D.; Cheng, W.; Huang, J.; Cao, M.; Niu, Z.; Zhao, Y.; Yue, Y.; Han, G. Spider-web-inspired membrane reinforced with sulfhydryl-functionalized cellulose nanocrystals for oil/water separation. *Carbohydrate Polymers* **2022**, *282*, 119049.
3. Hu, X.; Yang, B.; Hao, M.; Chen, Z.; Liu, Y.; Ramakrishna, S.; Wang, X.; Yao, J. Preparation of high elastic bacterial cellulose aerogel through thermochemical vapor deposition catalyzed by solid acid for oil-water

separation. *Carbohydrate Polymers* **2023**, *305*, 120538.
4. Yan, Z.; Zhu, K.; Li, X.; Wu, X. Recyclable bacterial cellulose aerogel for oil and water separation. *Journal of Polymers and the Environment* **2022**, *30* (7), 2774-2784.
5. Adebayo-Tayo, B.; Akintunde, M.; Alao, S. Comparative effect of agrowastes on bacterial cellulose production by Acinetobacter sp. BAN1 and Acetobacter pasteurianus PW1. *Turkish J Agric Nat Sci* **2017**, *4* (2), 145-154.
6. Islam, M. U.; Ullah, M. W.; Khan, S.; Shah, N.; Park, J. K. Strategies for cost-effective and enhanced production of bacterial cellulose. *International journal of biological macromolecules* **2017**, *102*, 1166-1173.
7. Molina-Ramírez, C.; Castro, M.; Osorio, M.; Torres-Taborda, M.; Gómez, B.; Zuluaga, R.; Gómez, C.; Gañán, P.; Rojas, O. J.; Castro, C. Effect of different carbon sources on bacterial nanocellulose production and structure using the low pH resistant strain Komagataeibacter medellinensis. *Materials* **2017**, *10* (6), 639.
8. Du, R.; Zhao, F.; Peng, Q.; Zhou, Z.; Han, Y. Production and characterization of bacterial cellulose produced by Gluconacetobacter xylinus isolated from Chinese persimmon vinegar. *Carbohydrate polymers* **2018**, *194*, 200-207.
9. Dórame-Miranda, R.; Gámez-Meza, N.; Medina-Juárez, L.; Ezquerra-Brauer, J.; Ovando-Martínez, M.; Lizardi-Mendoza, J. Bacterial cellulose production by Gluconacetobacter entanii using pecan nutshell as carbon source and its chemical functionalization. *Carbohydrate polymers* **2019**, *207*, 91-99.
10. Gopu, G.; Govindan, S. Production of bacterial cellulose from Komagataeibacter saccharivorans strain BC1 isolated from rotten green grapes. *Preparative Biochemistry and Biotechnology* **2018**, *48* (9), 842-852.
11. Machado, R. T.; Meneguin, A. B.; Sábio, R. M.; Franco, D. F.; Antonio, S. G.; Gutierrez, J.; Tercjak, A.; Berretta, A. A.; Ribeiro, S. J.; Lazarini, S. C. Komagataeibacter rhaeticus grown in sugarcane molasses-supplemented culture medium as a strategy for enhancing bacterial cellulose production. *Industrial Crops and Products* **2018**, *122*, 637-646.
12. Güzel, M.; Akpınar, Ö. Production and characterization of bacterial cellulose from citrus peels. *Waste and Biomass Valorization* **2019**, *10*, 2165-2175.
13. AL-Kalifawi, E. J.; Hassan, I. A. Factors Influence on the yield of bacterial cellulose of Kombucha (Khubdat Humza). *Baghdad Science Journal* **2014**, *11* (3), 1420-1428.
14. Suwanposri, A.; Yukphan, P.; Yamada, Y.; Ochaikul, D. Statistical optimisation of culture conditions for biocellulose production by Komagataeibacter sp. PAP1 using soya bean whey. *Maejo International Journal of Science and Technology* **2014**, *8* (1), 1.
15. Machado, R. T.; Gutierrez, J.; Tercjak, A.; Trovatti, E.; Uahib, F. G.; de Padua Moreno, G.; Nascimento, A. P.; Berreta, A. A.; Ribeiro, S. J.; Barud, H. S. Komagataeibacter rhaeticus as an alternative bacteria for cellulose production. *Carbohydrate polymers* **2016**, *152*, 841-849.
16. Al-Shamary, E. E.; Al-Darwash, A. K. Influence of fermentation condition and alkali treatment on the porosity and thickness of bacterial cellulose membranes. *Tojsat* **2013**, *3* (2), 194-203.
17. Petrosian, A. Production of bacterial cellulose from kombucha SCOBY: optimization of the bioprocess and industrial application. Instituto Politecnico de Braganca (Portugal), 2022.
18. Jayabalan, R.; Waisundara, V. Y. Kombucha as a functional beverage. In *Functional and medicinal beverages*, Elsevier, 2019; pp 413-446.
19. Soares, M. G.; de Lima, M.; Schmidt, V. C. R. Technological aspects of kombucha, its applications and the symbiotic culture (SCOBY), and extraction of compounds of interest: A literature review. *Trends in Food Science & Technology* **2021**, *110*, 539-550.
20. Sai, H.; Fu, R.; Xing, L.; Xiang, J.; Li, Z.; Li, F.; Zhang, T. Surface Modification of Bacterial Cellulose Aerogels' Web-like Skeleton for Oil/Water Separation. *ACS Applied Materials & Interfaces* **2015**, *7* (13), 7373-7381.
21. Wahid, F.; Zhao, X.-J.; Duan, Y.-X.; Zhao, X.-Q.; Jia, S.-R.; Zhong, C. Designing of bacterial cellulose-based superhydrophilic/underwater superoleophobic membrane for oil/water separation. *Carbohydrate Polymers* **2021**, *257*, 117611.
22. (22) Jin, W.; Jianjun, C.; Zhipeng, J.; Xiaoli, G.; Ruizhi, Z.; Jing, H.; Guoqiang, L. Fabrication and Performances of MTMS/TMCS Bilayer Transparent Superhydrophobic Silica Coating. In *Proceedings of the 2nd International Conference on Civil, Materials and Environmental Sciences*, 2015/04, 2015; Atlantis Press: pp 651-653.

Simulated gastrointestinal digestion of microencapsulated *Lactobacillus salivarius* culture in biopolymer

Kiattisak Kaewkaenkhun, Thitinun Pradubsang, and Sasithorn Kongruang*

Department of Biotechnology, Faculty of Applied Science, King Mongkut's University of Technology North Bangkok, Bangkok, Thailand, [2]Enserv Holding Co., Ltd, Bangkok, Thailand

**E-mail: sasithorn.k@sci.kmutnb.ac.th*

Abstract:

Lactobacillus salivarius assumes a crucial role as a probiotic organism, significantly contributing to bacteriocin production and both innate and acquired immunity. This study evaluated the survival of encapsulated *L. salivarius* TISTR 1112 under simulated gastrointestinal conditions using a 5-L batch fermentation in de Man-Rogosa-Sharpe broth over 7 days of cultivation time. The microencapsulation technique was applied to entrap the freeze-dried cell with the single biopolymer alginate (A) and alginate mixed octenyl succinic anhydride modified starch (A+O) and the dual biopolymer alginate coated with chitosan (A+C) and alginate mixed octenyl succinic anhydride modified starch coated with chitosan (A+O+C). The results showed that in all treatments, encapsulation efficiency reached 95%. To simulate the replete and fasting states of humans, only the pH was altered in each section of the intestinal tract. The pH of the simulated gastrointestinal fluid (SGIF) was regulated throughout the procedure. The results found that both the release and viability of probiotics in the SGIF were pH-dependent; at the end, the pH of the caecum showed that a biopolymer coated with chitosan provided superior protection for probiotics when exposed to gastrointestinal fluid, A+O+C, A+C, A+O, and A, respectively. The findings indicate that all heteropolysaccharides have the potential to serve as a promising material for microencapsulation in functional foods.

1. Introduction

Probiotics are living microorganisms that enhance digestive function by enhancing the quantity and equilibrium of advantageous bacteria while decreasing detrimental bacteria. Additionally, it reduces inflammation and improves the immune system. Prebiotics, as non-digestible elements of food, support the growth of probiotics by establishing favorable conditions in the digestive system and serving as nourishment for probiotics. Modern health food items frequently incorporate synbiotics, which are nutritional supplements that combine probiotics and prebiotics. In order to optimize effectiveness, it is crucial to incorporate suitable probiotics and prebiotics within the same food composition. The medical community is increasingly utilizing synbiotics as supplementary therapeutic alternatives. This is because it has the potential to effectively combat diseases like cancer, which is a prominent contributor to mortality in many cultures (Pandey et al., 2015).

Encapsulation of probiotics is a method employed in the fields of food technology and biotechnology to protect probiotic bacteria. Probiotics are live bacteria that, when given in sufficient quantities, provide a health advantage to the host. Nevertheless, these advantageous microorganisms are frequently sensitive to environmental parameters such as pH, temperature, humidity, oxygen levels, and other variables (Sarao & Arora, 2017). The current techniques for microencapsulation include freezing drying, spray drying, prilling, and extrusion (Al-Muzafar & Amin, 2017). The microgels are typically constructed from biopolymers that are carefully selected for their biocompatibility and non-toxicity towards cells. Polysaccharides, including gum acacia, pectin, and alginate, as well as proteins like gelatin and whey protein, are the most often employed biopolymers for encapsulating microorganisms. The process of encapsulating probiotics within alginate microgels has been established to decrease their susceptibility to the surrounding conditions (Yeung, Arroyo-Maya, et al., 2016). Octenyl succinic anhydride-modified starch (OSA-modified starch) is produced by chemically modifying native starch molecules through esterification. This modified starch shows effectiveness in several applications such as emulsification, encapsulation, film and coating production, and gel formation (Ettelaie, Holmes, Chen, & Farshchi, 2016). The study by D'Orazio et al. (2015) demonstrated that chitosan-coated alginate microgels improve the survival and functional properties of probiotic formulations designed for administration to the gastrointestinal tract. While it is possible to use single biopolymers to create microgels in certain situations, it is often more beneficial to combine many biopolymers to improve their effectiveness.

Lactobacillus salivarius subsp. *salivarius* TISTR 1112 is a Gram-positive, rod-shaped bacterium typically observed as single cells or in short chains. The cells are generally elongated, measuring around 0.5 to 1.0 µm in width and 2.0 to 4.0 µm in length. As a non-motile species, it lacks flagella and does not form spores, a characteristic trait of many lactobacilli. The thick peptidoglycan layer in its cell wall, evident from its gram-positive nature, plays a crucial role in its structural integrity and interaction with the surrounding environment. This morphology is significant for its role as a probiotic, especially in its adherence to the gut lining and interaction with the host's immune system. The study aims to encapsulate *L. salivarius* subsp. *salivarius* TISTR 1112 using a biopolymer for the purpose of targeted delivery to the gut microbiota. Both single biopolymers (alginate) and combined biopolymers (alginate-OSA-modified starch) are coated with chitosan. This study aims to gather significant information on enhancing the viability of encapsulated *L. salivarius* subsp. *salivarius* TISTR 1112 in simulated gastrointestinal conditions through a 5-L batch fermentation process.

2. Materials and Methods

2.1 Materials

Alginate, chitosan and de Man-Rogosa-Sharpe broth (MRS broth) was purchased from CTi & science co., Ltd., Thailand. OSA-modified starch derived from Chanjao Longevity Co., Ltd., Thailand. All other reagents were of food grade.

2.2 Production of *Lactobacillus salivarius* subsp. *salivarius* TISTR 1112 in bioreactor

Lactobacillus salivarius subsp. *salivarius* TISTR 1112, obtained from the Thailand Institute of Scientific and Technological Research in Pathum Thani, Thailand, was inoculated into sterile test tubes containing 5 mL of De Man's Sharpe and Rogosa Broth (MRS broth) medium. The culture was placed in an incubator at a temperature of 37 ºC and stirred at a speed of 200 rpm for a duration of 72 hours. Subsequently, the cultivation broth was transferred to Erlenmeyer flasks with volumes of 50 mL and 500 mL, respectively, before being transferred into a bioreactor (BioFlo 120, Eppendorf) with a total volume of 5 L of MRS medium. The temperature was regulated at 37 °C while the agitation speed was upheld at 250 rpm. The pH of the experiment was maintained at 6.0 using a pH controller, which controlled the addition of 3.0 M HCl and 3.0 M NaOH through an acid and base peristaltic pump. Consecutively, samples of fermentation were taken at 24-hour intervals to analyze the kinetics of growth, substrate concentration and lactic acid production. Finally, the mixture was subjected to centrifugation in order to separate and collect cell material. This collected material can then be dried using the freeze-drying technique.

2.3 Preparation of emulsion

The experiment involved combining 1 gram of *L.salivarius* subsp. *salivarius* TISTR 1112 cell mass with a mixture of 2% alginate and 2% OSA-modified starch. The experiment was designed with four distinct treatments. Treatment 1 consisted of 1 gram of cell production and 2% alginate (A). Treatment 2 involves combining 1 gram of cell mass with a mixture of 2% alginate and 2% OSA-modified starch (A+O). Blend until the mixture becomes a uniform and consistent texture. The encapsulation process involved using a Büchi B-390 encapsulator from Flawil, Switzerland, which had a nozzle size of 450 µm and operated at a frequency of 350 Hz. The encapsulation was carried out under an electrode potential of 1000 V and a pressure of 420 bar. Crosslinking was achieved by treating the encapsulated material with a 0.1 mol/L solution of $CaCl_2$ for 1 hour. Afterward, the encapsulated material was washed with sterile distilled water and coated with a 2% chitosan solution for 1 hour. Treatment 3 involves the use of a solution containing 2% alginate, which is then coated with chitosan (A+ C). Treatment 4 involved the use of a mixture containing 2% alginate and 2% modified starch, which was then coated with sterile chitosan (A+O+C). The percentage of encapsulation efficiency (%EE) was subsequently calculated using all treatments.

2.4 *In vitro* release and viability assays in the gastrointestinal tract model

In order to simulate the process of digestion in the human body, phosphate buffer saline (PBS) was utilized as a simulated gastrointestinal fluid (SGIF). The pH at the beginning was 6.5. The experiment involved using four different encapsulated polymer treatments: A, A+O, A+C, A+O+C and free cell controlled. Each treatment consisted of 1 gram of polymer encapsulated in a 500 mL solution. The temperature was controlled at 37 °C. The pH was initially adjusted to 1.8, simulating the stomach's acidity, using concentrated hydrochloric acid. The mixture was then incubated for 2 hours to simulate gastric conditions. Following that, the pH was gradually adjusted to 4 using 10 mol/L sodium hydroxide to mimic the small intestine's pH in the

duodenum for 0.25 hours. The pH was then adjusted to 6 to maintain the pH range of the jejunum for 3 hours. Subsequently, the pH was set to 7 to simulate the pH of the ileum for 4 hours. Finally, the pH was maintained at 7 for 1 hour to simulate the conditions in the caecum. Following each period of incubation, a volume of 1 mL of SGIF was collected for sampling. The sample was diluted using a serial dilution technique, where 9 mL of a solution containing 9 g/L of sodium chloride was added. Then, 0.1 mL of the diluted sample was put onto a Petri dish with MRS agar. The Petri dish was incubated at a temperature of 37 °C for a duration of 48 hours. After incubation, the number of colony-forming units (cfu) per grams was counted, as described by Gildas K. G. and Vandamme, T. in 2012.

3. Results & Discussion

3.1 Kinetic production *Lactobacillus salivarius* subsp. *Salivarius* TISTR 1112

The study involved the cultivation of *L. salivarius* subsp. *Salivarius* TISTR 1112 in a bioreactor. The highest level of growth was observed 48 hours after fermentation, resulting in an increase in dry weight from 1.20 to 1.80 g/L. Additionally, there was a modest decrease in glucose concentration from 10.84 to 8.65 g/L. The maximal cell dry weight (2.95 g/L) was attained following the fermentation period. The maximum amount of lactic acid produced by *L. salivarius* was determined to be 3.66 g/L, as shown in table 1. The highest lactic acid yield ($Y_{p/s}$) and productivity were found to be 0.04g/g of consumed glucose and 0.004 g/L/h, respectively, after 120 hours of cultivation.

3.2 The quantity of cells trapped and the efficacy of encapsulation in microcapsules

The results for encapsulation efficiency of A, A+O, A+C, and A+O+C are shown in Table 3. The highest encapsulation efficiencies are 96.73, 96.32, 95.99, and 95.07 of A+O+C, A+C, A+O, and A, respectively.

3.3 Stability of the encapsulation beads at different pH conditions

After being incubated in the SGIF at pH values of 1.8 and 4.0, the beads remained present in the SGIF for 2 and 0.25 hours, respectively. The free cells, on the other hand, decreased from 7.46 + 0.09 logcfu/g to 2.03 + 0.12 logcfu/g for STO (pH = 1.8) and remained at 1.80 logcfu/g for DUO (pH = 4). This suggests that the bacteria were not released from the beads. Consequently, the beads remained intact. As the pH values were adjusted from 6.0 to 7.0, the beads began to break apart and slowly dissolve into the SGIF as the incubation time increased. The encapsulated bacteria were partially released either in the jejunum at a pH of 6.0 or in the ileum at a pH of 7.0. While, the free cells still continue to decrease. The bacteria encapsulated within the beads were completely released into the simulated gastrointestinal fluid (SGIF) when the pH was 7.0, indicating that the release was both effective and dependent on pH (Fig. 1). However, free cells did not survive in the same conditions. The pH of the caecum showed that a biopolymer coated with chitosan offered better protection for probiotics when exposed to gastrointestinal fluid, specifically in combinations A+O+C, A+C, A+O, and A, respectively. This work utilized a singular medium for the SGIF, allowing the pH values to accurately represent various situations within the human digestive tract. pH has a crucial role in the division of the digestive system into compartments.

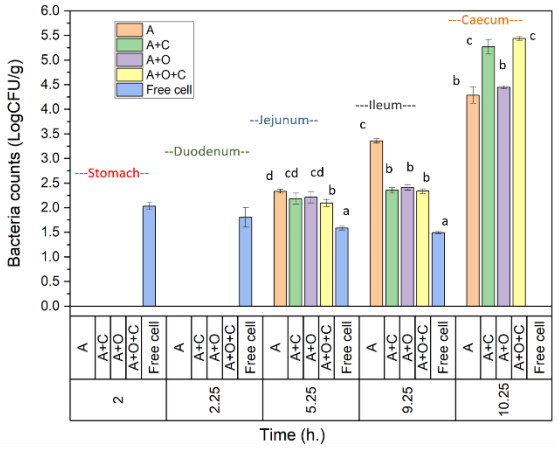

Figure 1. Figure show investigates the impact of pH on the release and survival of bacteria that are encapsulated in alginate (A), mixture of 2% alginate and 2% OSA-modified starch (A+O), 2% alginate, coated with chitosan (A+ C), mixture containing 2% alginate and 2% modified starch, coated with sterile chitosan (A+O+C) beads. The data presented are the average values along with their standard deviations, obtained from tree replications conducted on Petri dishes. The abbreviations are as follows: STO for stomach, DUO for duodenum, JEJ for jejunum, IL for ileum, and CC for caecum.

Table 1. Effect of fermentation time on utilization of glucose during lactic acid production by *L. salivarius* subsp. *salivarius* TISTR 1112

Fermentation time (h)	Absorbance 600 nm	C_x (g cell/L)	C_s (g glucose/L)	Lactic acid concentration (g/L)
0	0.821	0.30	17.70	3.20
24	0.856	0.80	11.93	3.66
48	0.870	1.20	10.84	3.66
72	0.876	1.80	8.65	3.66
96	0.889	2.28	7.82	3.66
120	0.892	2.95	7.13	3.66

Table 2. Growth kinetics parameter of *L. salivarius* subsp. *salivarius* TISTR 1112 from bioreactor fermentation

μ_{max} (h^{-1})	T_D (h)	$Y_{x/s}$ (g cell / g glucose)	$Y_{p/s}$ (g lactic acid / g glucose)	**Productivity** (g/L/h)
0.0174	144.75	0.05	0.04	0.004

Table 3. The quantity of trapped cells and the efficacy of encapsulation in microcapsules after encapsulation

Microcapsule type	Initial cell (logcfu/g)	Encapsulated cell (logcfu/g)	EE (%)
A	7.44 ± 0.15	7.07 ± 0.10	95.07
A+C	7.48 ± 0.12	7.13 ± 0.14	96.32
A+O	7.42 ± 0.08	7.12 ± 0.08	95.99
A+O+C	7.38 ± 0.07	7.14 ± 0.04	96.73

4. Conclusion

The study's findings show that the pH level affected the release of biopolymer-encapsulated *Lactobacillus salivarius* subsp. *salivarius* TISTR 1112. The release was observed in various encapsulation forms, including alginate alone (A), a mixture of 2% alginate and 2% OSA-modified starch (A+O), alginate coated with chitosan (A+C), and a mixture of 2% alginate and 2% modified starch coated with sterile chitosan (A+O+C). The encapsulated bacteria remained viable during incubation in the simulated gastrointestinal fluid (SGIF) that simulated the stomach and duodenum compartments. The bacteria were released into the SGIF at a pH of 6.0 in the jejunum region. The efficacy of encapsulation in providing protection varied depending on the bacterial strains and the harsh conditions to which they were subjected. When the probiotics were exposed to digestive fluid, a biopolymer coated with chitosan protected them better than the other combinations tested, which were A+O+C, A+C, A+O, and A. The *in vitro* model employed in this investigation had the benefit of being uncomplicated. The entrapped procedure can be replicated in any laboratory and applied to maintain the effectiveness of an easier-oxidized bioactive compound. The approach has the potential to be generally implemented in order to simplify comparisons between studies.

Acknowledgements

This research was support by Sweet D international company limited under Enserv Holding CO., LTD.

References

1. Pandey, K. R.; Naik, S. R.; Vakil, B. V. Probiotics, Prebiotics and Synbiotics- a Review. J. Food Sci. Technol. 2015, 52 (12),

7577–7587. https://doi.org/10.1007/s13197-015-1921-1.
2. Sarao, L. K.; Arora, M. Probiotics, Prebiotics, and Microencapsulation: A Review. Crit. Rev. Food Sci. Nutr. 2017, 57 (2), 344–371. https://doi.org/10.1080/10408398.2014.887055.
3. Al-Muzafar, H. M.; Amin, K. A. Probiotic Mixture Improves Fatty Liver Disease by Virtue of Its Action on Lipid Profiles, Leptin, and Inflammatory Biomarkers. BMC Complement. Altern. Med. 2017, 17 (1), 43. https://doi.org/10.1186/s12906-016-1540-z.
4. Yeung, T. W.; Arroyo-Maya, I. J.; McClements, D. J.; Sela, D. A. Correction: Microencapsulation of Probiotics in Hydrogel Particles: Enhancing *Lactococcus Lactis* Subsp. *Cremoris* LM0230 Viability Using Calcium Alginate Beads. Food Funct. 2016, 7 (6), 2909–2909. https://doi.org/10.1039/c6fo90021f.
5. Ettelaie, R.; Holmes, M.; Chen, J.; Farshchi, A. Steric Stabilising Properties of Hydrophobically Modified Starch: Amylose vs. Amylopectin. Food Hydrocoll. 2016, 58, 364–377. https://doi.org/10.1016/j.foodhyd.2016.03.004.
6. D'Orazio, G.; Di Gennaro, P.; Boccarusso, M.; Presti, I.; Bizzaro, G.; Giardina, S.; Michelotti, A.; Labra, M.; La Ferla, B. Microencapsulation of New Probiotic Formulations for Gastrointestinal Delivery: In Vitro Study to Assess Viability and Biological Properties. Appl. Microbiol. Biotechnol. 2015, 99 (22), 9779–9789. https://doi.org/10.1007/s00253-015-6853-1.
7. Gbassi, G. K.; Vandamme, T. Probiotic Encapsulation Technology: From Microencapsulation to Release into the Gut. Pharmaceutics 2012, 4 (1), 149–163. https://doi.org/10.3390/pharmaceutics4010149.

Chitosan coated on magnetic nanoparticles for a simple *Escherichia coil* detection

Kamonluck Witthayasutthaphon[1], Piyaporn Na Nongkhai [1,2]*, and Thanida Trakulsujaritchok[1]*

[1]*Department of Chemistry and Center of Excellence for Innovation in Chemistry, Faculty of Science, Burapha University, Chonburi, 20131, Thailand*
[2]*Research Unit for Sensor Innovation (RUSI), Burapha University, Chon Buri 20131, Thailand*

**E-mail: thanida@buu.ac.th, piyapornn@buu.ac.th*

Abstract:

The rapid and high-efficiency measurement of *Escherichia coli* (*E. coli*) can help prevent diseases caused by food. In this research, a simple method for *Escherichia coli* detection was designed using an integrated approach under chitosan coated magnetic nanoparticles and portable glucose meter (PGMs). Magnetic nanoparticles (MNPs) were synthesized using the co-precipitation of Fe^{2+} and Fe^{3+} in the presence of NH_4OH. To increase particle stability, citric acid was added after MNPs formation. The MNPs are subsequently coated with chitosan polymer. ATR-FTIR spectrum confirmed the effectiveness of chitosan-coated MNPs. Zeta-potential analysis also confirmed this success in which the surface charge of MNPs changes from a negative to a positive upon chitosan coating. Chitosan coated magnetic nanoparticles (MNPs-CH) demonstrated strong capture capability for *Escherichia coli* through electrostatic adsorption between the positively charged MNPs-CH and the negatively charged bacteria. MNPs-CH demonstrated a 98.22% efficiency in capturing *E. coli*. Subsequently, the captured *E. coli* was detected using PGMs in the presence of LB broth and glucose. A decrease in glucose concentration was observed upon the introduction of *E. coli*. By measuring the glucose consumption by *E. coli*, this method can achieve simple and cost-effective detection of *E. coli* in food samples, water, and other samples.

1. Introduction

Foodborne pathogens contamination is one of the main sources of food safety problems. According to the World Health Organization (WHO) estimated that food contamination has affected more than 600 million people worldwide with 420,000 deaths. Considering the seriousness of bacterial contamination, a simple, rapid, reliable, sensitive, and early screening method to detect bacteria is critically important to conduct early diagnosis as well as timely treatment to effectively prevent and cure the disease [1]. *Escherichia coli* (*E. coli*) bacteria are found in the environment, foods, and intestines of people and animals. Some can cause diarrhea, while others cause urinary tract infections, respiratory illness pneumonia, and other illnesses. At present, various techniques can be used for bacteria detection, including the plate colony counting method [2], the polymerase chain reaction (PCR) [3], and enzyme-linked immunosorbent assay (ELISA) [4]. These methods have drawbacks, including the need for expensive instruments, prolonged detection time, specialized staff, and an inability to provide on-site bacterial detection.

Magnetic nanoparticles (MNPs) have demonstrated significant utility in bacterial enrichment, attributed to their ease of control under external magnetic fields, high surface area, and facile surface modification. In previous research, amino-modified MNPs such as Fe_3O_4@SiO_2-NH_2, CS-MNPs and Fe_3O_4@Polydopamine@Poly-ethyleneimine were successfully employed to capture pathogenic bacteria from sample solutions [5-7]. Even though the positive charge of amino-modified magnetic nanoparticles had an outstanding effect in electrostatic interactions with the negatively charged bacterial membrane, the detection process remains complex and requires specialized instruments. There is a need for a simple, rapid, sensitive, and reliable screening method for effective disease prevention and treatment.

The objective of this research was to synthesize and modify MNPs with positively charged polymer chitosan (MNPs-CH). These MNPs-CH were employed to capture and concentrate *E. coli* bacteria. Additionally, a simple and instrument-free method for *E. coli* detection was developed. The method involves capturing and detecting bacteria using portable glucose meters (PGMs), based on the concept of glucose consumption by the captured bacteria. As bacteria consume the glucose, a noticeable alteration in the glucose concentration within the sample occurs, which can be detected by the PGM (Scheme 1.).

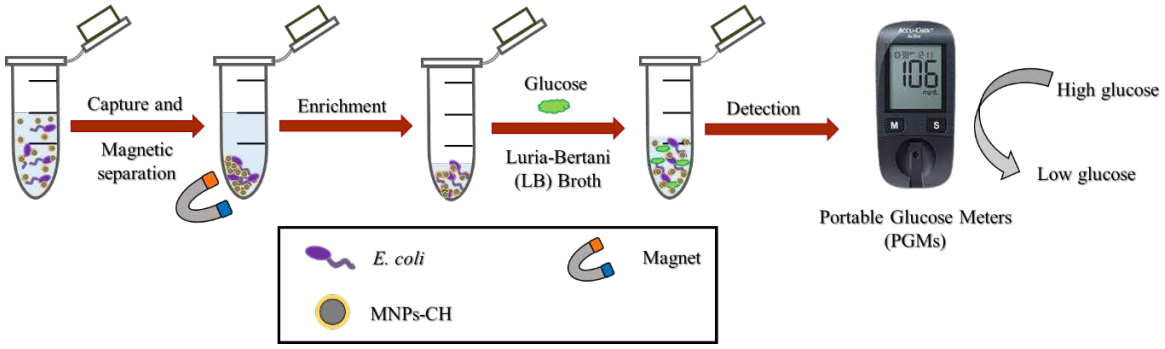

Scheme 1. The proposed portable glucose meters (PGMs) for *E. coli* detection.

2. Materials and Methods

2.1 Materials

Iron (II) chloride tetrahydrate; $FeCl_2 \cdot 4H_2O$, (Sigma-Aldrich, USA), Iron (III) chloride tetrahydrate; $FeCl_3 \cdot 6H_2O$ (Sigma-Aldrich, USA), 28%w/v Ammonia solution; NH_3OH, (QREC, New Zealand), Citric Acid Anhydrous 99.5%; $C_6H_8O_7$, (QReC™, New Zealand), Phosphate buffer saline; PBS (Sigma-Aldrich, USA), Chitosan (poly-D-glucosamine), medium molecular weight, (Sigma-Aldrich, USA), Acetic acid; CH_3COOH, (QReC™, New Zealand). All solutions were prepared with deionized water purified. Portable glucose meters (PGMs) are Accu-Chek Active.

2.2 Synthesis of magnetite nanoparticle (MNPs)

Magnetite nanoparticles (MNPs) were synthesized by the chemical co-precipitation method (Figure 1). A solution of $FeCl_2$ and $FeCl_3$ salts in the dissolving of deionized water. Subsequently, the mixed solution was added to a three-neck flask under a N_2 gas atmosphere, and the flask was heated to 60°C with high-speed stirring (750 rpm) for 30 minutes. A total of 36 mL of 28% (w/v) ammonia solution was slowly added to the solution, and the mixture was stirred for 2 hours until the color changed from yellow-orange to black. To stabilize the MNPs, citric acid (0.1 M) was added and stirred for 1 hour. The mixture was then cooled down to room temperature. The citric stabilized MNPs were thoroughly washed multiple times with deionized water to eliminate any remaining unreacted chemicals, continuing until a neutral pH was achieved. The citric stabilized MNPs were then redispersed in deionized water and stored at room temperature until they were used.

2.3 Synthesis of Chitosan modified MNPs (MNPs-CH)

MNP surfaces were coated with chitosan through electrostatic interaction between the positively charged chitosan and the negatively charged citric-stabilized MNPs [8]. The procedure involved washing the citric-stabilized MNPs (500 mg) with PBS buffer (20 mM, pH 7.4), followed by redispersion in 100 mL of PBS buffer (20 mM, pH 7.4). The chitosan solution was prepared by dissolving chitosan with different amounts (62.5, 125 and 250 mg) in 100 mL of 2%v/v acetic acid and stirred overnight at room temperature. The chitosan solutions were added to the MNPs dispersion and agitated with shaker at 300 rpm for 16 hours. The resulting MNPs-CH were collected by magnetic separation and washed with deionized (DI) to remove free chitosan. Finally, the MNPs-CH were resuspended in DI water and stored at room temperature.

2.4 Bacterial culture

The *E. coli* was cultured in Nutrient Broth medium at 37°C for 16 h. The optical density (OD_{600nm}) was measured by a UV spectrometer to estimate bacterial concentration. Every experiment was conducted using fresh *E. coli* at OD = 0.7 (approximately ~$7.0x10^8$ cfu/mL).

2.5 Separation of bacteria with MNPs-CH

1.0 mL of bacterial suspension in 0.85% NaCl (OD = 0.7) was mixed with MNPs-CH and incubated at room temperature under gentle shaking. The mixture was separated magnetically and 250 µL of the clear supernatant was collected. The optical density (OD) of the collected supernatant was measured at 600 nm to calculate the capture efficiency (%CE) using equation (1):

$$\%CE = \frac{C_0 - C_e}{C_0} \times 100 \qquad (1)$$

C_0 is the OD of bacteria suspension before capturing
C_e is the OD of bacteria suspension after capturing

2.6 Detection of bacteria

The captured bacteria were detected using portable glucose meters (PGMs). A 5.0 mL of bacterial suspension in 0.85% NaCl (approximately OD600nm = 0.5, ~1.0 x 10^8 cfu/mL) was mixed with MNPs-CH and incubated at room temperature with gentle shaking. The MNPs-CH-bacteria complex was magnetically separated, and the clear supernatant was discarded. The complex was then washed with PBS to remove unbound bacteria. Then 0.1 mL of Luria-Bertani broth (LB) containing glucose was added. The mixture was incubated with shaking at 37 °C. A drop of the solution was placed on the PGM strip, and the concentration of glucose was measured every 30 min.

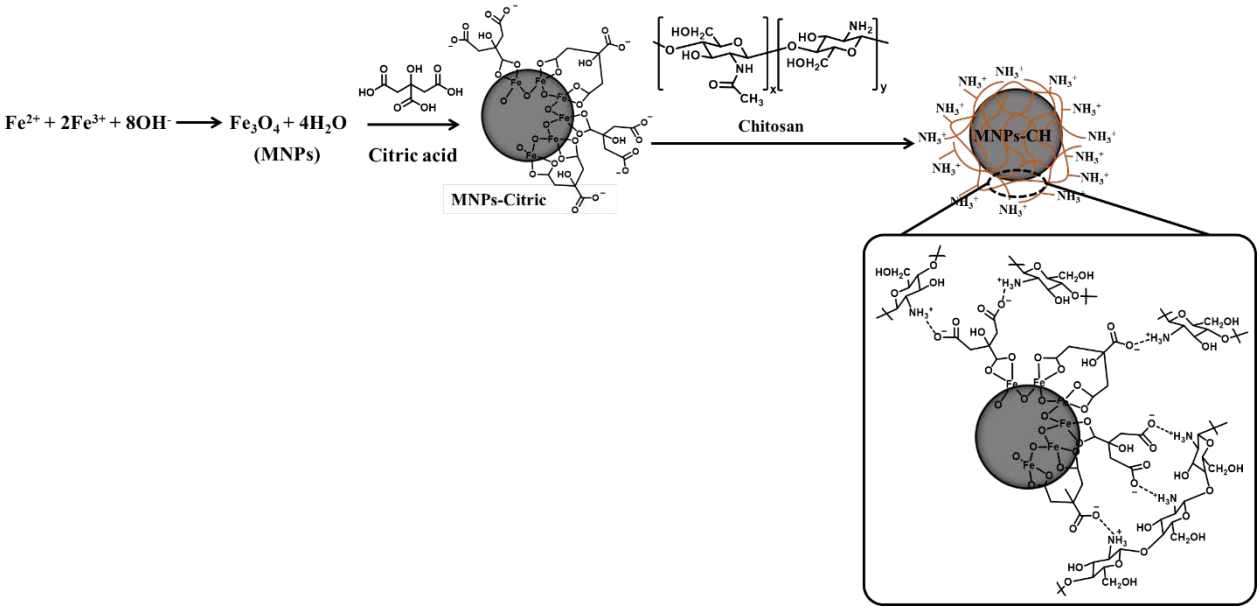

Figure 1. Schematic illustration of chitosan modified magnetic nanoparticles (MNPs-CH).

3. Results & Discussion

3.1 Characterization of MNPs-CH

To prove their successful synthesis, it is necessary to characterize the synthesized MNPs-CH. The results of the hydrodynamic diameters are displayed in Figure 2A, where the average diameter of the citric-stabilized MNPs is about 454.0 nm. With the modification of chitosan on its surface, the diameter of MNPs-CH increases to 638.3, 690.8 and 628.9 nm for 62.5, 125, and 250 mg of chitosan, respectively, which also proves the successful synthesis of MNPs-CH. The MNPs, whose surfaces are coated with chitosan, may form clusters, resulting in an increase in size. However, when the amount of chitosan exceeds 125 mg, the excess chitosan may begin to hinder the coating process, resulting in a decrease in size. Their zeta potentials (Figure 3B) were measured, and the potential of citric-stabilized MNPs was -4.8 mV. When chitosan coated MNPs, its potential changed to positive value, which was due to the increase of positively charged chitosan. With the addition of the chitosan concentration, its zeta potential further increased and was maximized at 250 mg of chitosan. The morphology of citric-stabilized MNPs and MNPs-CH were observed using TEM. Next, as shown in Figure 2C, ATR-FTIR spectrum demonstrated the characteristic absorption peak located at 539 cm^{-1} belongs to Fe-O bond in MNPs. The absorption peak located at 1597 cm^{-1} and 1380 cm^{-1} are formed by the symmetric and asymmetric C-O stretching of COO^- group in citric acid. The characteristic peak located at 1066 cm^{-1} was from the stretching vibration of C-O-C stretching vibration of polysaccharide backbone in chitosan. These results indicated that chitosan has been successfully modified on MNPs. Figure 3 illustrates that the single crystal of citric-stabilized MNPs exhibited an almost spherical shape with a diameter of approximately 30 nm. After chitosan coating, MNPs-CH appear to form a larger nanocluster with irregular shape.

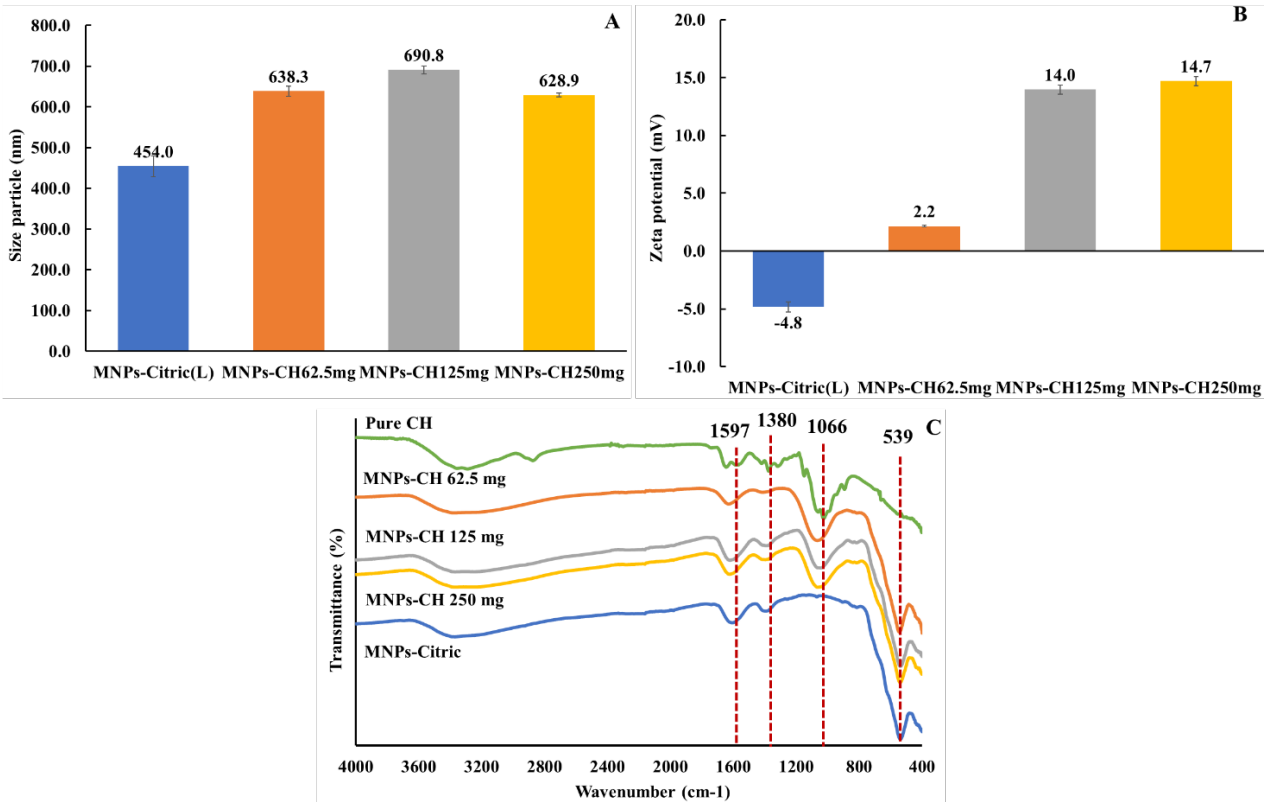

Figure 2. The hydrodynamic diameter (**A**), Zeta potential analysis (**B**) and ATR-FTIR spectra (**C**) of citric stabilized MNPs and MNPs-CH.

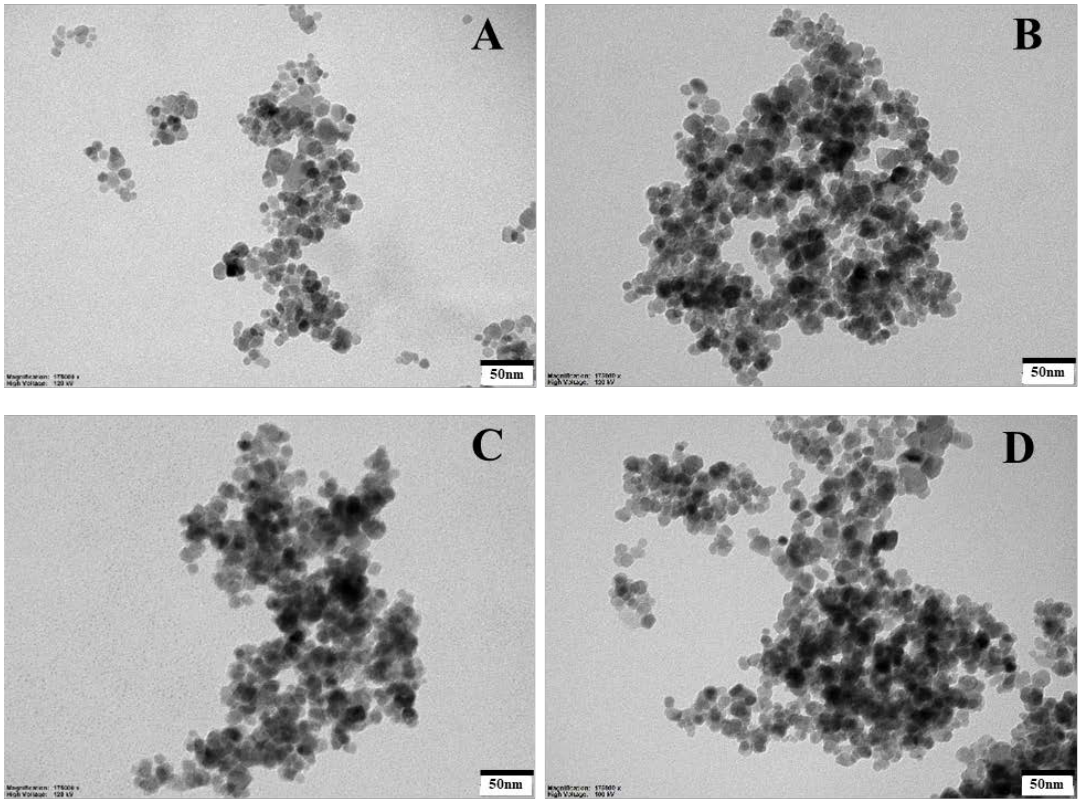

Figure 3. TEM image of MNPs-Citric (**A**), MNPs-CH 62.5 (**B**), MNPs-CH 125 (**C**), MNPs-CH 250 (**D**)

3.2 The separation of bacteria with MNPs-CH

Figure 4 showed the capture efficiency (%) of MNPs-CH at different amounts of chitosan (62.5, 125 and 250 mg). The results showed that MNPs-CH125 and MNPs-CH250 performed well in separating *E. coli*, reaching nearly 100% efficiency.

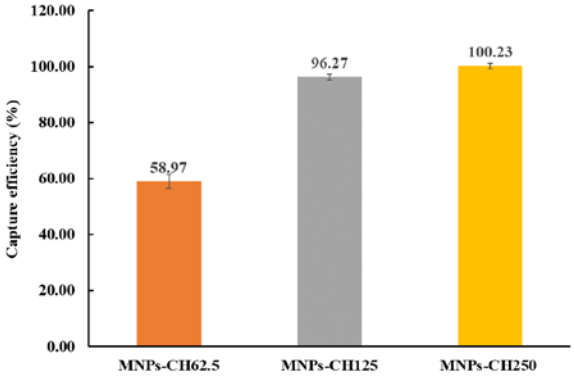

Figure 4. *E. coli* capture efficiency of MNPs-CH62.5, MNPs-CH125 and MNPs-CH250.

3.3 Detection of *E. coli*

The *E. coli* detection procedure was developed employing an integrated approach, involving the separation of bacteria with MNPs-CH250 and the monitoring of glucose consumption by bacteria using a PGM. Initially, *E. coli* was captured with MNPs-CH250, and the captured bacteria were subsequently incubated in LB broth (LB) containing known quantities of glucose. The decrease in glucose levels was then monitored using a PGM every 30 min. Figure 5A illustrates the decline in glucose concentrations over time and displays the characteristic curve of the PGM, demonstrating the reduction in glucose levels for specific *E. coli* concentrations. It can be observed that there is no drop in glucose concentrations for samples without *E. coli* (control). The decrease in glucose concentrations occurs more rapidly (within 1 hour) for samples with very high *E. coli* concentrations (4.3×10^7 CFU/mL) and is slower for samples with extremely low concentrations of *E. coli* (4.3×10^2 CFU/mL). Figure 5B presents a comparison of the time required to observe a significant drop in glucose concentrations for various concentrations of *E. coli*. The results reveal the linearity range of the time required to observe a significant drop and the corresponding *E. coli* concentrations.

4. Conclusion

In summary, MNPs were successfully synthesized and modified with positively charged polymer chitosan (MNPs-CH). The positively charged MNPs-CH showed outstanding *E. coli* capture ability (> 96 %) through electrostatic interaction. The captured *E. coli* demonstrated the ability for glucose consumption, with the decrease in glucose concentration detectable using a portable glucose meter (PGM). The *E. coli* detection showed a good linear correlation between the time needed to detect a significant decrease in glucose concentrations and *E. coli* concentration. The established *E. coli* detection procedure demonstrated a simple and low-cost detection method based on remarkable bacteria separation and glucose consumption.

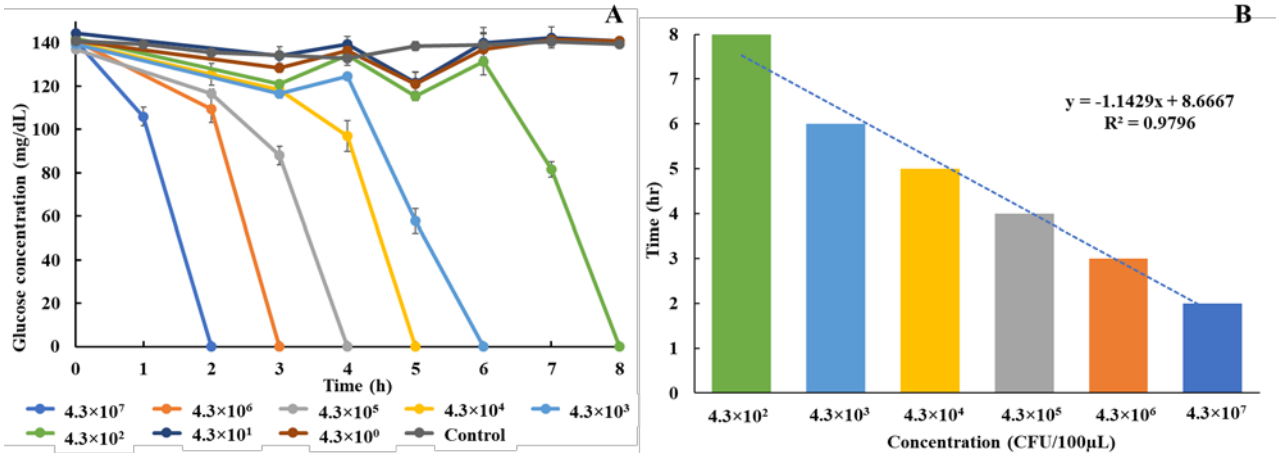

Figure 5. Decrease in glucose concentration over time of glucose consumption by *E. coli* (**A**) and time needed to detect a significant decrease in glucose concentrations at various concentrations of *E. coli.* (**B**).

Acknowledgements

This research was financially supported by (i) Burapha University (BUU), (ii) Thailand Science Research and Innovation (TSRI), (iii) National Science Research and Innovation (NSRF) (Fundamental Fund: Grant no.30/2566), and (iv) the Center of Excellence for Innovation in Chemistry (PERCH-CIC). The authors acknowledge the technical support provided by Faculty of Science, Burapha University, Thailand.

References

1. Agyarkwa, M. A., et al. Surveillance of WHO Priority Gram-Negative Pathogenic Bacteria in Effluents from Two Seafood Processing Facilities in Tema, Ghana, 2021 and 2022: A Descriptive Study. *International Journal of Environmental Research and Public Health*, **2022**, *19*(17), 10823.
2. Wen, C. Y., et al. Efficient enrichment and analyses of bacteria at ultralow concentration with quick-response magnetic nanospheres. *ACS Applied Materials & Interfaces*, **2017**, *9*(11), *9416-9425*.
3. Sun, J., Huang, J., Li, Y., Lv, J., & Ding, X. A simple and rapid colorimetric bacteria detection method based on bacterial inhibition of glucose oxidase-catalyzed reaction. *Talanta*. **2019**, *197*, 304-309.
4. Kumar, H., et al. Detection of Bacterial Pathogens and Antibiotic Residues in Chicken Meat: A Review. *Foods*, **2020**, *9*(10), 1504.
5. Che, Y., Xu, Y., Wang, R., & Chen, L. Rapid fluorescence detection of pathogenic bacteria using magnetic enrichment technique combined with magnetophoretic chromatography. *Analytical and bioanalytical chemistry*, **2017**,*409*, 4709-4718.
6. Le, T. N., Tran, T. D., & Kim, M. I., A convenient colorimetric bacteria detection method utilizing chitosan-coated magnetic nanoparticles. *Nanomaterials*, **2020**, *10*(1), 92.
7. Zhang, Y., et al. Fe_3O_4@PDA@PEI Core-Shell Microspheres as a Novel Magnetic Sorbent for the Rapid and Broad-Spectrum Separation of Bacteria in Liquid Phase. *Materials (Basel)*, **2022**, *15*(6) 2039.
8. Altun, T., Ecevit, H., & Çiftçi, B. Production of chitosan coated, citric acid modified almond, and hazelnut shell adsorbents for Cr (VI) removal and investigation of equilibrium, kinetics, and thermodynamics of adsorption. *Arabian Journal of Geosciences*, **2021**, *14*(6), 439.

Preparation of carboxymethylcellulose (CMC)-polyethylene glycol (PEG) hydrogel for the growth of plants

Pattrawadee Toprangkobsin

Faculty of Science and Technology. University of Phra Nakhon Sri Ayutthaya Rajabhat

E-mail: tpks.pattrawadee@gmail.com

Abstract:

Hydrogels are three-dimensional polymeric networks prepared from chemical crosslinks. Their outstanding properties are the capability of swelling and retaining water within their structure without dissolving in water. These properties are interesting therefore the hydrogel was applied to mix within cultivated soil for moisture control and plant growth. This research was to study the preparation of hydrogel film from carboxymethylcellulose (CMC)-polyethylene glycol (PEG) using citric acid as a non-toxic crosslinking agent. The hydrogel films were measured by solid-state using an FTIR spectrophotometer to confirm the formation of ester crosslinks between CMC and PEG. The intensity of the carbonyl peak of the ester crosslink was found to increase, as the amount of PEG was increased. Corresponding with the amount of ester crosslinked hydrogels increased, the carboxyl content of hydrogel film using acid-base titration and swelling behavior were increased also. Therefore, the maximum content of PEG (CP3) was the appropriate hydrogel that studied the plant-grown. The cultivated soil, mixing 50% hydrogel was suitable for glowing plants because of the highest stem and root for 40 days.

1. Introduction

Hydrogels are water-insoluble, three-dimensional polymeric network structures. Their structure can absorb water with hydrophilic functional groups attached to a polymeric backbone, which presents a cross-link between the network chain making their properties resistant to dissolving water [1]. The presence of void spaces or pores within their three-dimensional structure is referred to as the porosity of a hydrogel [2]. Porous hydrogels have a network of interconnected voids, and these pores can be of different sizes and shapes depending on the method of fabrication and the intended use of the hydrogel. This property is particularly valuable in applications where moisture retention is essential, such as wound dressings, contact lenses, and agricultural soil amendment [3].

Hydrogels are prepared from physical or chemical crosslinking to create a three-dimensional network of polymer chains. Crosslinking creates a structure that allows the hydrogel to absorb and retain water while maintaining its integrity. However, chemical crosslinking often provides a stable and permanent network, contributing to the hydrogel's mechanical strength and long-term stability [4].

Cellulose is a polysaccharide composed of repeating glucose units linked together by β1,4-glycosidic bonds. Each glucose unit in the cellulose chain has three hydroxyl groups attached to carbon atoms. The numerous hydroxyl groups along the cellulose chain create a large number of potential sites for hydrogen bonding with water. This abundance of hydrophilic sites increases the water-holding capacity of cellulose and enhances its ability to form hydrogels that absorb and retain water [5]. Carboxymethylcellulose (CMC) is a cellulose derivative, and its structure is modified through a chemical process known as carboxymethylation. This modification involves the introduction of carboxymethyl groups onto the hydroxyl groups of the cellulose molecule which made the structure of the hydrophilic polymer increase [6]. Therefore, CMC is interested in basing hydrogel because it is biocompatible, biodegradable, non-toxic, and cheap.

Citric acid (CA) is a crosslinking agent due to its non-toxic nature, biocompatibility, and ability to form ester linkage with hydroxyl and carboxyl groups on CMC. CA crosslinked CMC is a biocompatible and environmentally friendly hydrogel [7]. However, CA crosslinked CMC showed less swelling in water. In research by Vishwajeet Sampatrao Ghorpade et al in 2018 fabricated CA crosslinked CMC-PEG (polyethylene glycol) hydrogel for retained soluble drugs more than CA crosslinked CMC [8].

In this research, we fabricated CA crosslinked CMC-PEG hydrogel as a cheap and environmental alternative to mix within cultivated soil for moisture control and plant growth.

2. Materials and Methods

2.1 Materials

CMC was purchased from Chemipan Corporation Co. Ltd., Bangkok, Thailand. Citric acid monohydrate (Grade AR) was purchased by Qchemical Co. Ltd., Bangkok, Thailand. PEG was purchased from Ajax Finechem Pty Ltd., Australia.

2.2 Preparation of CMC-PEG hydrogel

CMC (2% w/v) was prepared in distilled water using a magnetic stirrer bar at 900 rpm (90° C) for 1 h until the solution of CMC was clear. Citric acid and PEG were added to this solution followed by uniform stirring to dissolve them completely for 30 min. The percent weight of the component is presented in Table 1. The air bubbles in the solution were removed by keeping them undisturbed for 24 h. The bubble-free solution was poured into the petri dish (90×15 mm) and placed in a hot air oven to remove water at 90° C for 12 h. Then, the obtained polymers were cured at 145° C for 5 min so the crosslink reaction was complete. Hydrogel films were stored in a desiccator before analysis to test the properties of hydrogel.

Table 1. The percent component of CMC-PEG hydrogel

Component	Batch			
	CP0	CP1	CP2	CP3
CMC (%)	2	2	2	2
CA (%)	0.4	0.4	0.4	0.4
PEG (%)	-	0.2	0.4	0.6

2.3 Characterization of CMC-PEG hydrogel using FTIR spectrophotometer

The infrared spectra of CMC, PEG, CA, and hydrogel film (CP0-CP3) were acquired using an FTIR spectrophotometer (Perkin-Elmer, L1600412 Spectrum TWO DTGS, Llantrisant, United Kingdom). The samples were scanned in a wavenumber range of 550-4000 cm^{-1}.

2.4 Determination of carboxyl content

The total carboxyl content (TCC) of the hydrogel films was determined by acid-base titration as reported previously with slight modification [9]. 0.1 g of hydrogel film (W_H) was added to 0.1M NaOH (25 ml) and stirred on a magnetic stirrer at 900 rpm for 2 h. The ester crosslinks broke in the NaOH solution and the film dissolved completely. After that, the excess of 0.1M NaOH was titrated against 0.1M HCl (C_{HCl}) using phenolphthalein as an indicator (Endpoint: pink to colorless). The titrations were recorded at the volume of 0.1M HCl (ml) used for titration in the sample (V_1) and blank (V_2), respectively. The TCC of the hydrogen film was determined using the following Eq. (1):

$$\mathrm{TCC}\left(\frac{\mathrm{mmol}}{100\mathrm{g}}\right) = \frac{(V_2 - V_1) \times C_{HCl} \times 100}{W_H} \quad (1)$$

2.5 Swelling study

Each hydrogel film stored in a desiccator was weighed about 0.2 ± 0.03 g (W_d) and placed in DI water (pH 5.4-6.2) at 35 ± 2°C. After that, we studied the swelling time of hydrogel to absorb water for 1, 5, 10, 20, 40, 60, and 1,440 min. The swollen hydrogels were taken out of the DI water, removed the excess water from the surface with filter paper, and weighed (W_s). the swelling ratio was determined by using Eq. (2):

$$\text{Swelling ratio}\left(\frac{\mathrm{g}}{\mathrm{g}}\right) = \frac{W_s - W_d}{W_d} \quad (2)$$

2.6 Effect of hydrogels on plant growth

The experiment studied the growth of *Coriandrum sativum L.* (Coriander) from seeds to the mature plant stage. The height of the root and stem were measured and recorded at 10, 20, 30, and 40 d (at the end of the vegetative growth period). The objective of this test was to determine the effect of the hydrogel on moisture control and plant growth. Therefore, the experiment provides three study groups: 25% HG (25% hydrogels; cultivated soil from mixing of soil and hydrogel with a weight ratio 3:1), 50% HG (50% hydrogels; cultivated soil from mixing of soil and hydrogel with a weight ratio 1:1), 75% HG (75% hydrogels; cultivated soil from mixing of soil and hydrogel with a weight ratio 1:3), and no hydrogel (100% cultivated soil: the mixture of 1:1 by weight of peat moss and vermicompost) was a control group.

The condition was set up in an atmosphere at a temperature of 38±2°C for 40 d. The plastic pots (diameter 16 cm, height 8 cm) were filled with cultivated soil at 5 cm (control group), and then 20 seeds were sowed on the surface after that seeds were covered with cultivated soil about 0.5 cm in each group. For 25% HG, we prepared the cultivated soil from the height of hydrogels 1.25 cm on the bottom and filled soils 3.75 cm and then sowed 20 seeds on the surface and covered it with cultivated soil 0.5 cm. Each study group set the total cultivated soil at a height of 5 cm but the amount of hydrogel was different. The sample test (three study groups and one control group) was placed on a tray (50×35×8 cm). The sample test was repeated for 3 times.

3. Results & Discussion

3.1 Preparation of CMC-PEG hydrogel

The hydrogel films were prepared by the esterification crosslinking method, using CA as a crosslinking agent. At a temperature of 90°C, CA forms cyclic anhydride which esterifies the reactive hydroxyl groups of CMC or PEG polymer chains. This leads to the formation of ester crosslinks. This experiment referred to Vishwajeet Sampatrao Ghorpade et al [8] research on the obtained hydrogel which has good swelling properties and matrix integrity [10]. It used a suitable curing time and the curing temperature was 5 min, and 145°C, respectively. The characteristics of the obtained hydrogel films are shown in Figure 1. That showed a photograph of a non-crosslinked CMC, CA crosslinked CMC, and CA crosslinked CMC-PEG with three different concentrations of PEG. It is clear that the visual turbidity of hydrogel films increases as the PEG concentration increases, indicating a higher crosslinking density [11]. The shape of the hydrogel film is non-integrity when crosslinking density increases. The porosity of crosslinked hydrogels were larger sizes than non-crosslinking when the solvents were removed, and chains of polymers were rearranged to be the contracted shape. However, the application of hydrogels didn't use film form. They are soaked in water to swell hydrogel and retain water.

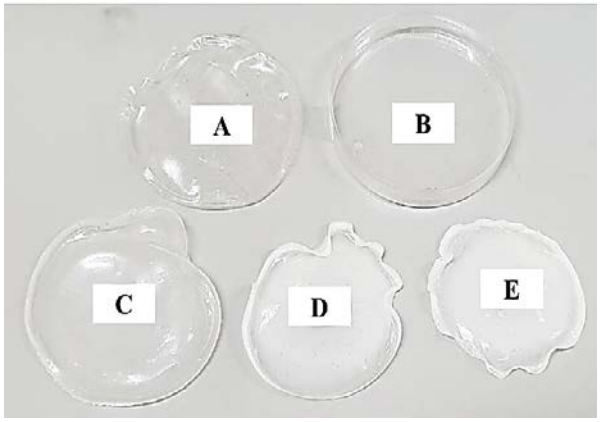

Figure 1. A photograph illustrating the difference in visual turbidity between; non-crosslinked (A), CP0: CA crosslinked CMC (B), and CP1-3: CA crosslinked CMC-PEG 10, 20, and 30% of PEG in total polymer, respectively.

3.2 Characterization of CMC-PEG hydrogel using FTIR spectrophotometer

Figure 2a shows FTIR spectra of CMC, PEG, and hydrogel films. The characteristic IR peaks of CMC were observed at 3643 cm^{-1} and 1502 cm^{-1} corresponding to O-H stretching and carboxylate C=O stretching. The spectrum of PEG exhibited peaks at 3599 cm^{-1} (O-H stretching), 1966 cm^{-1} (C-H stretching), 1413 cm^{-1} (C-H bending), 1266 cm^{-1} (C-H bending), and 1099 cm^{-1} (C-O stretching). The spectrum of CA showed a board peak at 3502 cm^{-1} due to O-H stretching and peaks at 1757 cm^{-1} and 1689 cm^{-1} representing C=O stretching of carboxylic acid.

In the spectra of all the crosslink hydrogel films, the carbonyl peak of CA at 1689 cm^{-1} was found to be shifted to 1725 cm^{-1}, indicating the existence of an ester bond along with free carboxylic acid [12]. The peak at 1587 cm^{-1} responded to C=O stretching of the carboxylated group of CMC. The ester and acid carbonyl peak overlapped with the peak at 1650 cm^{-1} which may be the reason behind its shift towards lower frequency. As the concentration of PEG was increased (CP0 to CP3), the intensity of the carbonyl peak of carboxylic acid, and ester was found to increase as seen in Figure 2b. This indicates that the addition of PEG increases the carboxyl content and improves the cross-linking in the hydrogel films. However, the intensity of the carbonyl peak of the carboxylate group of CMC didn't show a trend when the concentration of PEG increased but CP3 showed the highest intensity and sharp peak.

3.3 Determination of carboxyl content

Crosslinking reaction, the carboxylic acid of CA creates covalent intermolecular di ester linkage with the hydroxyl groups of CMC [12]. On the other hand, CA was sufficient for the formation of an adequate number of interpolymer crosslinks, interaction of CA and CMC presented weak electrostatic repulsion. When PEG is added to the reaction, the CA is ineffective in crosslinking. CMC can form a bonding with PEG in the formation of CMC-PEG, CMC-PEG-CMC linkage by carboxylate and hydroxyl groups of CMC and PEG, respectively. Therefore, CP0 showed the least carboxyl content, and CP1-3 which increased the concentration of PEG presented the carboxyl content increase shown in Table 2. Adding PEG causes an increase in the carboxyl content of hydrogel indicating the higher-order crosslink.

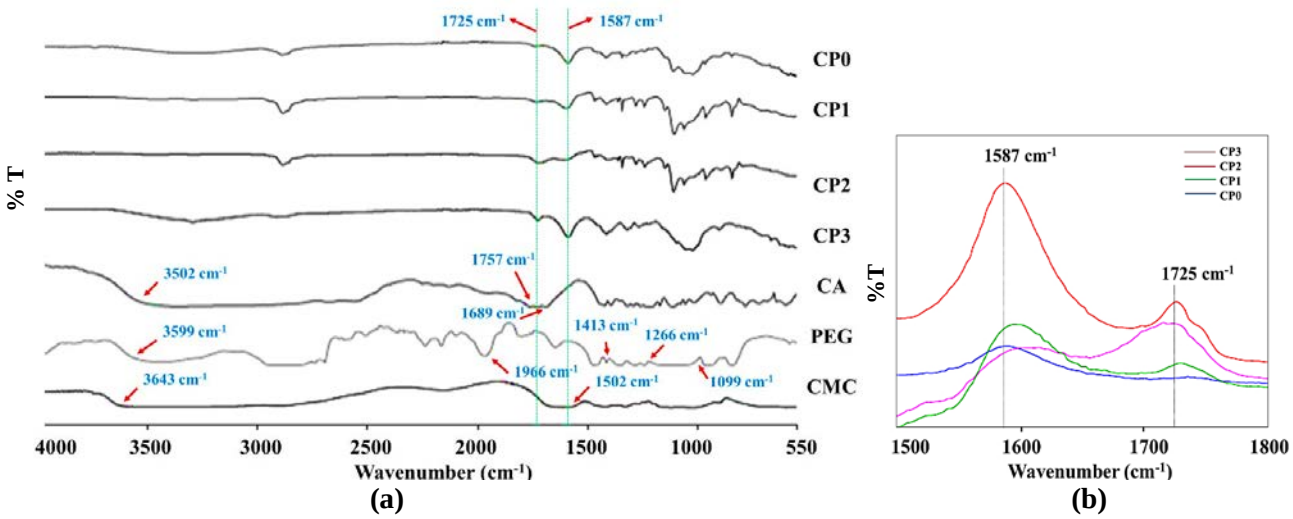

Figure 2. FTIR spectra of CMC, PEG, CA, and crosslinked hydrogel films (a) and baseline corrected spectra of hydrogel films in between 1587 cm^{-1} and 1725 cm^{-1}.

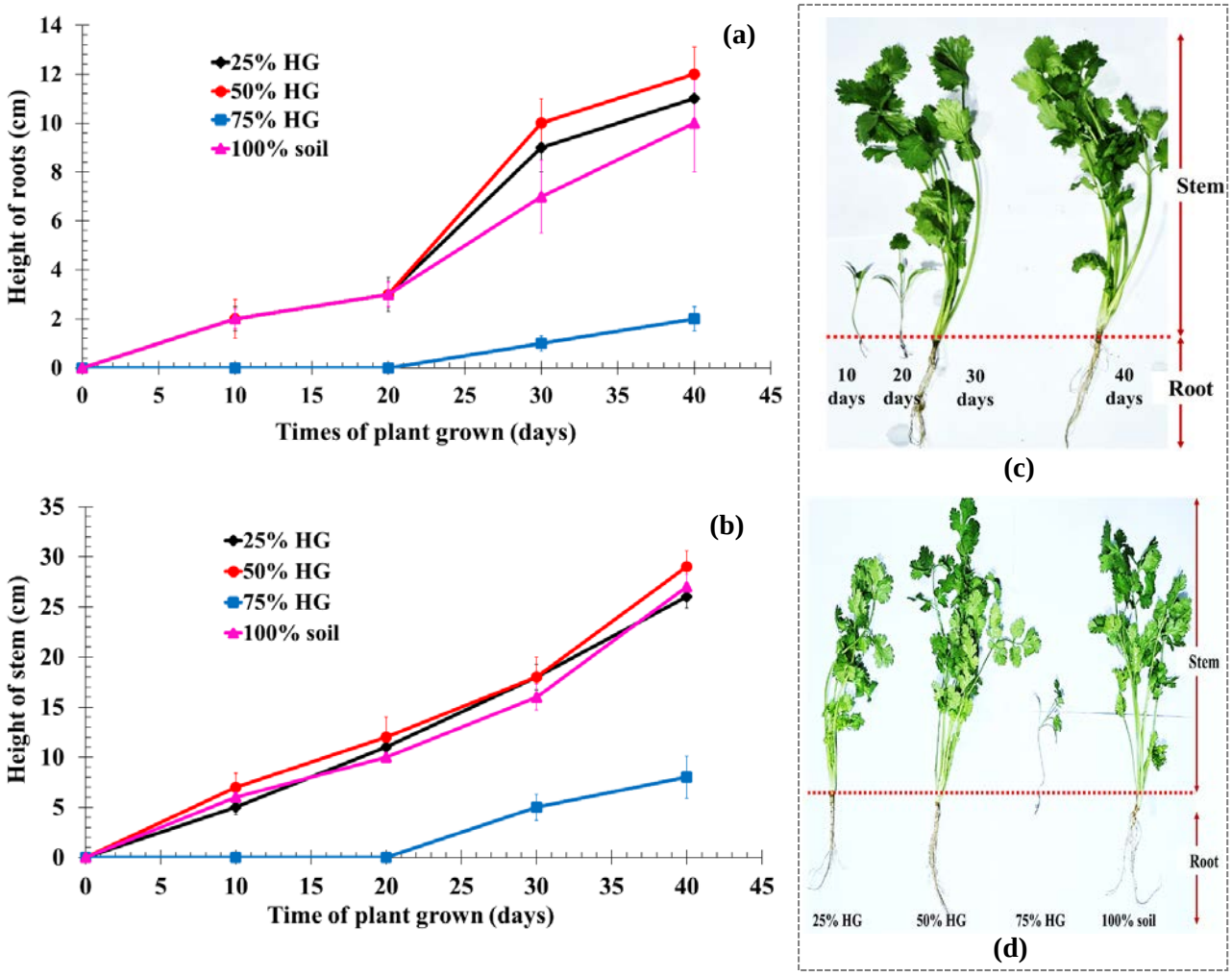

Figure 4. Metric indicators of *Coriandrum sativum L.* seeding growth: (a) the growth stage of roots, (b) the growth stage of the stem, (c) a photograph of the *Coriander* growth stage with the cultivated soil from mixing 50% hydrogel, and (d) a photograph of the *Coriander* growth in 40 d that apply a different cultivated soil, mixing 25% HG, 50%HG, 75%HG, and 100% soil, respectively.

Table 2. Carboxyl content of the crosslinked hydrogel film

Batch	TCC (mmol/ 100g of hydrogel films)
CP0	157.22
CP1	260.71
CP2	359.04
CP3	487.60

3.4 Swelling study

Figure 3 illustrates the swelling behavior of the crosslink hydrogels in DI water. All the hydrogel showed a rapid increase in the swelling ratio, after 60 mins they slowly increased to equilibrium at 1440 mins. The hydrogel of CP3 (maximum PEG) presented the highest swelling ratio at 1440 min and the lowest swelling ratio was presented on the hydrogel of CP0 (without PEG). It was because the addition of PEG and the increased number of free OH groups in hydrogel enhanced the hydrophilicity of hydrogels [13]. Furthermore, the increase in swelling of CP1-3 may be an introduction of highly hydrophilic carboxylic groups due to an increase in the number of crosslinks. These free carboxylic groups play an important role in the formation of a polyelectrolyte network within the hydrogel and improve water sorption [14]. The CP3 presented the highest number of crosslinks and can be able to absorb maximum water. Therefore, CP3 was the appropriate hydrogel for further study of the plant-grown.

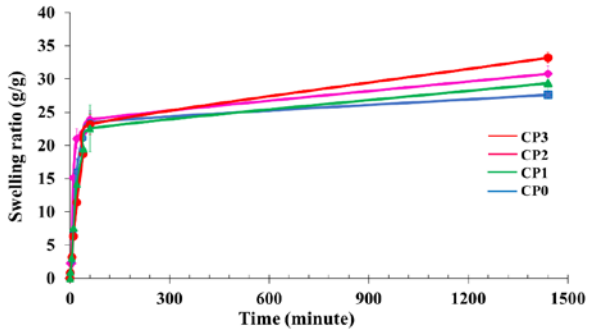

Figure 3. Swelling behavior of crosslinked hydrogels: CA crosslinked CMC (blue line), and CA crosslinked CMC-PEG 10% (green line), 20% (pink line), and 30% (red line) of PEG in total polymer.

3.5 Effect of hydrogel on a plant grown

Coriandrum sativum L. (Coriander) was studied in this work because all parts of them are edible, especially the stem and roots are the parts that are most traditionally used in cooking and the grown stage of the plants are short-time around 40-45 d.

The experiment selected the swelled hydrogel of CP3 to test the plant growth that mixed with cultivated soil in the ratio 3:1 (25%HG), 1:1 (50%HG), and 1:3 (75%HG), compared with 100% soil (without hydrogel). For a 40-day plant growth assessment, it was observed that Coriander can thrive in all types of cultivated soil in the experiment, indicating that CP3-hydrogel is safe for plant growth. In Figure 4a, the root length of the Coriander on cultivated soil mixing 50% HG was higher than 25% HG and 100% soil, while the cultivated soil mixing 75% HG presented the root length as the lowest. Furthermore, the stem length on the cultivated soil mixing 50% HG showed the highest as shown in Figure 4b. It was confirmed that the cultivated soil with mixing 50% HG was appropriate to improve the growth of plants. The hydrogel can retain water and control moisture well. However, 75% HG slows down the plant growth as shown in Figure 4d because of the high capacity of water. It made excess moisture in cultivated soils.

4 Conclusion

The CA-crosslinked CMC and CA-crosslinked CMC-PEG hydrogels were formed due to esterification crosslinking. The increase in PEG amount led to an increase in carboxyl content and hydrogel swellability and the solid-stage FTIR analysis confirmed the formation of ester crosslinks. CP3-hydrogel mixing the cultivated soil with a ratio of 1:1 exhibited good moisture control and retained water by metric indicators of stem and root length that were the highest in all test groups for 40 d.

Acknowledgment

The author would like to thank, Faculty of Science and Technology fund from the University of Phra Nakhon Sri Ayutthaya Rajabhat.

References

1. Hoare, T. R.; Kohane, D. S. Hydrogels in drug delivery: progress and challenges. *Polym.* **2018**, *49*, 1993-2007.
2. Thang, N. H.; Chien, T. B.; Cuong, D. X. Polymer-Based Hydrogels Applied in Drug Delivery: An Overview. *Gels*. **2023**, *9(7)*, 523-561.
3. Ali, F.; Khan, I.; Chan, J.; Akhtar, K.; Bakhsh, E. M.; Khan, S. B. Emerging Fabrication Strategies of Hydrogels and Its Applications. *Gels*. **2022**, *8(4)*, 205-244.
4. Revete, A.; Aparicio, A.; Cisterna, B. A.; Revete, J.; Luis, L. Advancement in the Use of hydrogels for Regenerative Medicine:

Properties and Biomedical Applications. *Int. J. Biomater*. **2022**, *2022*, 3606765-3606780.
5. Manal, A.; Sheikh, E. A novel photo-grafting of acrylamide onto carboxymethyl starch. 1. Utilization of CMS-g-PAAm in easy-care finishing of cotton fabrics. *Carbohydr. Polym.* **2016**, *152*, 105-118.
6. Rahman, S.; Hasan, S.; Nital, A. S.; Nam, S.; Karmakar, A. K. Recent Developments of Carboxymethyl Cellulose. *Polym.* **2021**, *13*, 1345-1393.
7. Sharmin, N.; Rosnes, J. T.; Prabhu, L.; Bocker, U.; Sivertsvik, M. Effect of Citric acid Cross-Linking on the Mechanical, Rheological, and Barrier Properties of Chitosan. *Molecules*. **2022**, *16*, 5118-5134.
8. Ghorpade, V. S.; Yadav, A. V.; Dias, R. J.; Mali, K. K.; Pargaonkar, S. S. Citric acid crosslinked carboxymethylcellulose-poly (ethylene glycol) hydrogel films for delivery of poorly soluble drugs. *Int. J. Biol. Macromol.* **2018**, *118*, 783-791.
9. Salam, A.; Brothers, G. P. Incorporation of carboxyl groups into xylan for improved absorbency. *Cellul*. **2011**, *18*, 1033-1041.
10. Capanema, N. S. V.; Mansur, A. A. P.; Jesus, A. C.; Carvalho, S. M.; Mansur, H. S.; Olivera, L. C. Superabsorbent crosslinked carboxymethyl cellulose-PEG hydrogels for potential wound dressing applications, *Int. J. Biol. Macromol*. **2018**, *106*, 1218–1234.
11. Elzoghby, A. O.; Helmy, M. W.; Samy, W. M.; Elgindy, N. A. Novel ionically crosslinked casein nanoparticles for flutamide delivery: formulation, characterization, and in vivo pharmacokinetics. *Tnt. J. Nanomedicine*. **2013**, *8*, 1721-1732.
12. Reddy, N.; Yang, Y. Citric acid cross-linking of starch films. *Food Chem*. **2010**, *118*, 702-711.
13. Wang, S.; Gunasekaran, S. State of water in chitosan-PVA hydrogel. *J. Appl. Polym*. **2016**, *101*, 3227-3232.
14. Demitri, C.; Sole, R. D.; Scalera, F.; Sannino, A.; Vasapollo, G.; Maffezzoli, A.; Nicolais, L. Novel superabsorbent cellulose-based hydrogels crosslinked with citric acid. *J. Appl. Polym. Sci*. **2008**, *110*, 2453-2460.

Mechanical properties of hybrid fibers paper sheet from pineapple leaf fiber and banana fiber for packaging

Borwon Narupai*, Arisa Jaiyu, Malinee Leekrajang, Nattaporn Chutichairattanaphum, Teerakorn Kongkaew, Julaluk Phunnoi, Niphaporn Yawongsa, and Passakorn Sueprasit

Expert Centre of Innovative Materials, Thailand Institute of Scientific and Technological Research, Khlong Luang, Pathumthani, 12120, Thailand

**E-mail: borwon@tistr.or.th*

Abstract:

Agricultural waste of pineapple leaves and leaf sheaves of banana trees, which are eco-friendly, are abundantly found in Thailand. The natural fibers also have good mechanical properties. The pineapple leaf fibers (PLF) have high stiffness while the toughness of banana fibers (BF) is good. This study aimed to investigate the mechanical properties of hybrid fibers paper sheet from PLF and BF for packaging. The PLF and BF were treated with 5 wt% KOH alkali solutions at 80 °C for 5 h and subsequently 2 wt% H_2O_2 solutions at 80 °C for 3 h to remove lignin and the other contaminants. The PLF and BF were then beaten to mix in the following PLF:BF ratios of 80:20, 60:40, 40:60, and 20:80, respectively. The findings indicated that increasing BF contents exhibited the continuous increase in tensile, tear, and burst indices in the hybrid fibers sheet. The SEM analysis revealed that PLF and BF occurred a partial adhesion. As a result, the optimal condition produced for the hybrid fibers paper sheet for packing comprising PLF:BF with a 20:80 ratio is the highest of all mechanical properties.

1. Introduction

Plastic is commonly used in various industries, such as packaging, aerospace, marine, and automobiles, due to its lightweight, inexpensive manufacture, corrosion resistance, and excellent mechanical properties.[1] However, most plastics are not naturally degradable. Therefore, researchers are exploring alternatives to plastic packaging by utilizing sustainable, renewable, and biodegradable materials as a solution to these challenges. Paper packaging is an attractive alternative to traditional packaging materials like plastic because it is inexpensive and environmentally friendly. Developing alternate sources of fiber for paper manufacture has also become necessary due to increasing environmental concerns and the demand for sustainable materials. Utilizing natural fiber from agricultural waste, such as coir, pineapple, kenaf, banana, and hemp fiber, has attracted much attention.[2-6] Natural fibers are suitable for composites, textiles, pulp, and paper production due to their composition, properties, and structure. Considering that natural fiber is more biodegradable than synthetic fiber, it will be critical to improve its potential sources and enhance the efficacy of the fiber extraction process in the developing green economy.

Pineapple leaf fiber (PLF), is one of the waste products produced by the agricultural industry. It is a smooth, glossy fiber, and has a high tensile strength. It also contains a high cellulosic content (70–82%), hemicelluloses (18.8%), and lignin (5–12.7%).[7] Asim. M. et al. studied pineapple and its composites, containing the most significant percentage of cellulose content nearly 80%. Pineapple fibers have extremely high tensile strength and Young's modulus values.[7] Another natural material useful for producing paper is banana fiber (BF).[8] Banana fiber is a waste product of banana cultivation and contains cellulose and lignin in the range of 44-54% and 11-22%, respectively.[9] The use of natural banana fiber is becoming increasingly popular due to its versatility in various applications. For instance, banana fiber can be used to create lightweight automobile interior parts thanks to its high specific strength and flexural strength.[10] It is also used to reinforce concrete, which results in improved compression, split, and flexural strength.[11–13] A study conducted by Ghosh et al.[14] found that composites made from banana fiber reinforced with vinyl ester resin had an ultimate tensile strength 67% higher than pure resin.

Research on the manufacturing of paper has primarily concentrated on hybrid natural fibers, which are typically created by combining waste fibers from agriculture with other natural or synthetic fibers. This combination aims to combine the special properties of each type of fiber to produce hybrids with enhanced mechanical strength, durability, and other desired attributes. Maries Idicula et al.[15] reported improvements in the flexural and tensile modulus based on dynamic investigations of the mechanical properties of randomly mixed sisal and banana fibers. Sahu et al.[16] The sisal and pineapple fiber hybrid

composites were fabricated, and several experiments were conducted, including tensile, bending, and impact tests. According to test results, the hybrid weight ratio of 50/50 exhibited the highest impact strength of 47.2 N/mm^2. This hybrid also showed good tensile and bending stress values.

This research aims to develop a novel hybrid fiber for paper sheet packaging using inexpensive and eco-friendly natural fibers. As a result, this study investigated paper sheets made from a mixture of PLF and BF in various composition ratios. The mechanical properties of PLF/BF papers were examined by analyzing their ability to tensile, tear, burst index, and partial adhesion using SEM.

2. Materials and Methods

2.1 Materials

Pineapple leaf fibers (PLF) and banana fibers (BF) were purchased from community enterprise groups in Thailand. The appearance of these two fibers is depicted in Figure 1. All the reagents and chemicals used in this research were analytical reagent grades. Potassium hydroxide (KOH) was obtained from Ajax-Finechem, and hydrogen peroxide (H_2O_2) solution was provided by Chem-Supply.

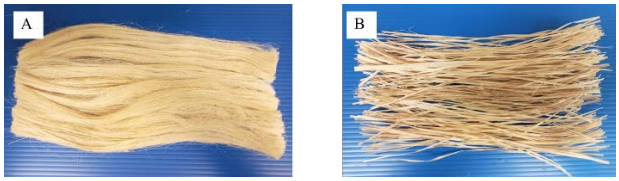

Figure 1. (A) Pineapple leaf fibers (PLF) and (B) banana fibers (BF)

2.2 Methods

To begin with, PLF and BF were cut into approximately 1-inch pieces. Subsequently, they were treated with 5 wt% KOH alkali solutions at 80 °C for 5h. Following the alkali treatment, PLF and BF underwent bleaching using 2 wt% H_2O_2 solutions at 80 °C for 3 h. After alkali treatment and bleaching, PLF and BF were then beaten to create a pulp mixture in a pulp beater machine at room temperature for 30 min, following a different composition outlined in Table 1.

Table 1. The composition of the hybrid fibers paper sheet

Sample	PLF (%)	BF (%)
1	80	20
2	60	40
3	40	60
4	20	80

Hybrid pulps resulting from the combination of PLF and BF were formed and subsequently placed in an oven at 70 °C overnight for drying. Finally, it became the hybrid fibers paper sheet product illustrated in Figure 2.

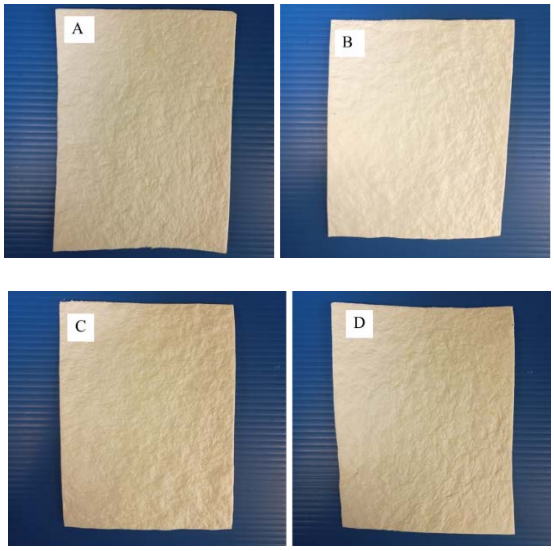

Figure 2. Hybrid fibers paper sheet from PLF:BF; (A) 80:20, (B) 60:40, (C) 40:60, and (D) 20:80.

2.3 Characterization of the hybrid fibers paper sheet

The tensile index of the hybrid fibers paper sheet was analyzed according to ISO 1924-2:2008. The tear index of samples was tested following ISO 1974:1990. The burst index of the hybrid fibers paper sheet was evaluated according to ISO 2758-2201. The morphology of the surface hybrid fibers paper sheet was observed by using Thermo Fisher Scientific Prisma E SEM equipment at an accelerating voltage of 10 kV. Before microscopic observation, the samples were placed on an aluminum stub and coated with a thin layer.

3. Results & Discussion

3.1 Tensile index of the hybrid fibers paper sheet

The tensile index is an important parameter in evaluating the quality of paper, as it provides information about the paper's strength and durability. The results of the tensile index of the hybrid fibers paper sheet following PLF:BF at ratios of 80:20, 60:40, 40:60, and 20:80 are shown in Figure 3. The tensile index of the hybrid fibers paper sheet was found to continuously increase when the composition of BF rose from 20% to 60%. After that, there was a dramatic increase in the tensile index of the hybrid fibers paper sheet to 41.8 Nm/g at PLF:BF ratio of 20:80. This result may be due to some fibers forming as flattened

objects spreading in parts of the paper structure, as observed in the SEM image.

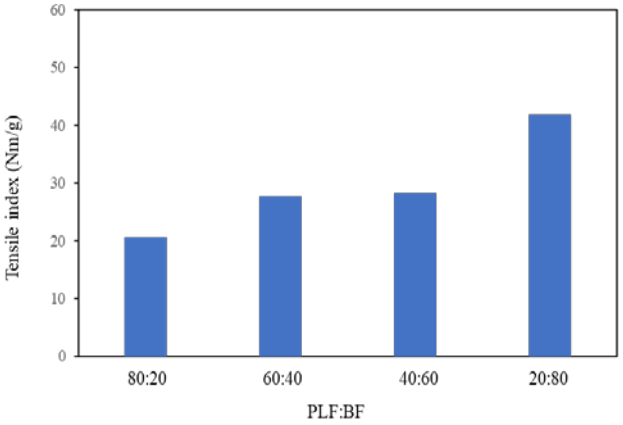

Figure 3. The tensile index of the hybrid fibers paper sheet

3.2 Tear index of the hybrid fibers paper sheet

The tear index indicates the resistance of the paper subjected to a tearing force. The tear index of the hybrid fibers paper produced at varying composition ratios of PLF and BF is illustrated in Figure 4. The tear index of the hybrid fibers paper sheet presents a steady growth from 33.95 mNm^2/g to 39.58 mNm^2/g with increasing BF composition from 30 to 60%. The tear index of the hybrid fibers paper sheet then is the highest at 66.58 mNm^2/g as the composition of BF increases up to 80%. It can be observed that the testing results of the tear index exhibit a similar trend to the tensile index because paper products with high tensile index values are generally strong and less likely to tear or fail under stress.

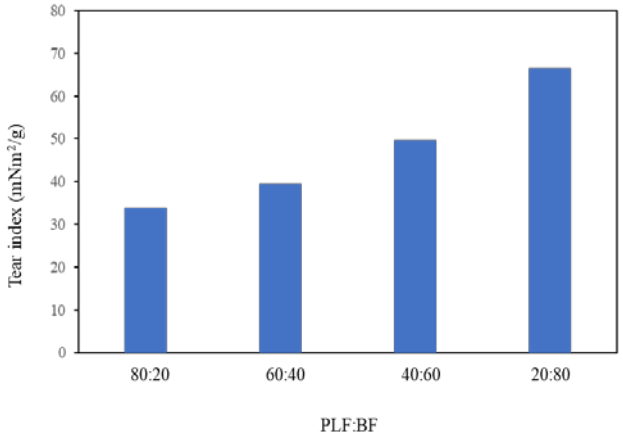

Figure 4. The tear index of the hybrid fibers paper sheet

3.3 Burst index of the hybrid fibers paper sheet

The burst index is a property used in the paper and packaging industry to evaluate the strength and durability of paper. It measures the resistance of a paper sheet to bursting forces. Figure 5 shows the burst index of the hybrid fibers at various composition ratios of PLF and BF. The burst index of the hybrid fibers paper sheet slightly rose as BF composition increased from 20 to 40%. Then, the burst index was followed by a considerable rise in the hybrid fibers paper sheet when the ratio of PLF:BF stood at 40:60 and 20:80. The ratio of PLF:BF at 20:80 was the highest value of the burst index, reaching 3.50 $kPa.m^2/g$. It was generally acknowledged that papers with a well-organized and uniform structure often exhibit good resistance to bursting.

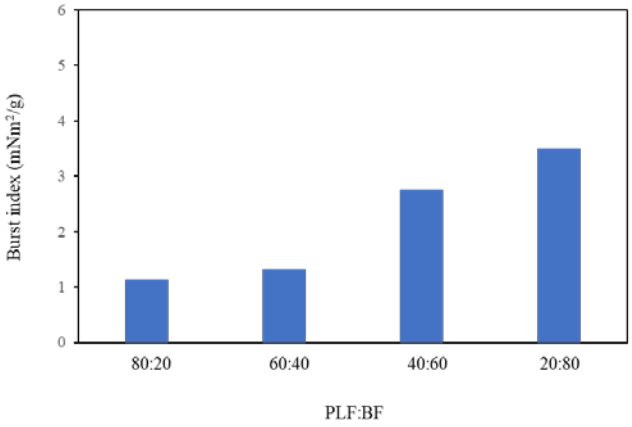

Figure 5. The burst index of the hybrid fibers paper sheet

3.4 SEM micrograph of the hybrid fibers paper sheet

The surface morphology of the hybrid fibers paper sheet between PLF and BF at 80:20, 60:40, 40:60, and 20:80 was observed under a scanning electron microscope presented in Figure 6. The SEM images of the surface hybrid fiber paper sheet depicted variations in fiber shape: straight or flattened fibers, the presence of curls and kinks, entanglements, and the formation of some fibers becoming flattened objects. It can be observed that there was a higher level of adhesion of fibers when the composition of BF increased. This is because some fibers form a larger number of flattened objects, distributing in some parts of the hybrid fiber paper sheet at a PLF to BF ratio of 20:80. As a result, it caused the higher mechanical properties of the hybrid fiber paper sheet. This corresponded with the testing results in the tensile index, tear index, and burst index.

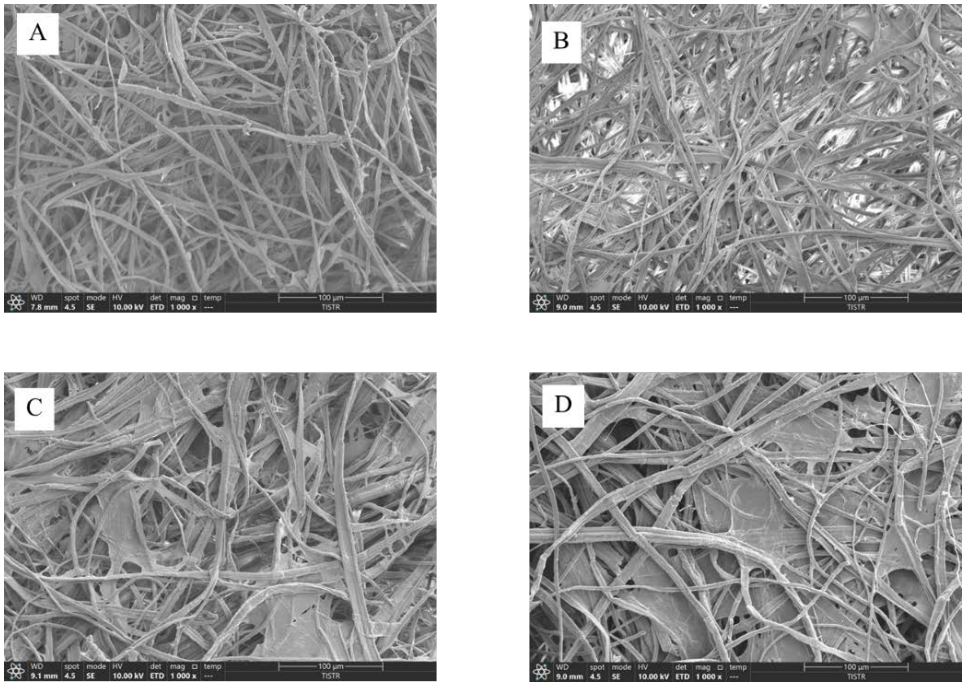

Figure 6. The SEM micrograph of hybrid fibers paper sheet from PLF:BF; (A) 80:20, (B) 60:40, (C) 40:60, and (D) 20:80.

4. Conclusion

The hybrid fibers paper sheet was produced from PLF:BF at ratios of 80:20, 60:40, 40:60, and 20:80. The tensile, tear, and burst index of the hybrid fibers paper sheet continuously increased with the growing proportion of BF, resulting from higher fiber entanglement as shown in the SEM micrograph. Therefore, the highest mechanical properties are observed at PLF:BF ratios of 20:80 in the hybrid fiber paper sheet, which can be applied to produce packaging.

Acknowledgements

The authors gratefully acknowledge the Thailand Institute of Scientific and Technological Research (TISTR) for financial, material, and instrument support.

References

1. Chen, Y.; Awasthi, A.K.; Wei, F.; Tan, Q.Y.; Li, J.H. Single-use plastics: Production, usage, disposal, and adverse impacts. *Sci. Total Environ.* **2021**, 752, 141772.
2. Jayavani, S.; Deka, H.; Varghese, T. O.; Nayak, S. K. Recent Development and Future Trends in Coir Fiber-Reinforced Green Polymer Composites: *Review and Evaluation. Polymer Composites* **2015**, 37 (11), 3296–3309.
3. Asim, M.; Abdan, K.; Jawaid, M.; Nasir, M.; Dashtizadeh, Z.; Ishak, M. R.; Hoque, M. E. A Review on Pineapple Leaves Fibre and Its Composites. *International Journal of Polymer Science* **2015**, 1–16.
4. Akil, H. M.; Omar, M. F.; Mazuki, A. A. M.; Safiee, S.; Ishak, Z. a. M.; Bakar, A. Kenaf Fiber Reinforced Composites: *A Review. Materials in Engineering* **2011**, 32 (8–9), 4107–4121.
5. Kavitha, V.; Aparna, G. A Review on Banana Fiber and Its Properties. *Asian Journal of Pharmaceutical Research and Development* **2021**, 9 (3), 118–121.
6. Mohammed, L.; Ansari, M. N. M.; Pua, G.; Jawaid, M.; Islam, S. A Review on Natural Fiber Reinforced Polymer Composite and Its Applications. *International Journal of Polymer Science* **2015**, *2015*, 1–15.
7. Asim, M.; Abdan, K.; Jawaid, M.; Nasir, M.; Dashtizadeh, Z.; Ishak, M. R.; Hoque, M. E. A Review on Pineapple Leaves Fibre and Its Composites. *International Journal of Polymer Science* **2015**, *2015*, 1–16.
8. Arafat, K. M. Y.; Nayeem, J.; Quadery, A.; Quaiyyum, M. A.; Jahan, M. S. Handmade Paper from Waste Banana Fibre. *Bangladesh Journal of Scientific and Industrial Research* **2018**, *53* (2), 83–88.

9. Jayaprabha, J. S.; Brahmakumar, M.; Manilal, V. B. Banana Pseudostem Characterization and Its Fiber Property Evaluation on Physical and Bioextraction. *Journal of Natural Fibers* **2011**, *8* (3), 149–160.
10. Subba Reddy D, Thyagaraj N, Manjunatha.K.N, Evaluation of Mechanical Properties in Banana Fiber Reinforced Polymer Composites, *Iconic Research And Engineering Journal* (2017).
11. Kesavraman, S. Studies on metakaolin based banana fibre reinforced concrete. *Int. J. Civ. Eng. Technol*. **2017**, 8, 532–543.
12. Sakthivel, S.S.S.; Parameswari, R.; Gomathi, M. Experimental Investigation on Concrete with Banana Fiber and Partial Replacement of Cement By Banana Leaf Ash. *Int. Res. J. Eng. Technol*. **2019**, 6, 3914–3919.
13. Akinwande, A.A.; Adediran, A.A.; Balogun, O.A.; Olusoju, O.S.; Adesina, O.S. Influence of alkaline modification on selected properties of banana fiber paperbricks. *Sci. Rep.* 2021, 11, 5793.d
14. R. Ghosh, K.V. Narasimham, M. Pydi Kalyan, in: S. Pujari, S. Srikiran, S. Subramonian (Eds.), Recent Advances in Material Sciences, *Springer*, Singapore, 2019, pp. 375–382.
15. Idicula, M.; Malhotra, S. K.; Joseph, K.; Thomas, S. Dynamic Mechanical Analysis of Randomly Oriented Intimately Mixed Short Banana/Sisal Hybrid Fibre Reinforced Polyester Composites. *Composites Science and Technology* **2005**, *65* (7–8), 1077–1087.
16. Sahu V, Bisen KS, Krishna M. Mechanical properties of sisal and pineapple fiber hybrid composites reinforced with epoxy resin. *Int. J. Mod. Eng. Res*. IJMER. **2015**;1(5):32-8.

Preparation of microcrystalline cellulose from corn cob and synthesis of microcrystalline cellulose-derived polyol for polyurethane foam

Sudarat Kulabphet, Chanchai Thongpin, and Sudsiri Hemsri*

Department of Materials Science and Engineering, Faculty of Engineering and Industrial Technology, Silpakorn University, Sanam Chandra Palace Campus, Nakhon Pathom 73000, Thailand

**E-mail: sudsirihemsri@yahoo.com*

Abstract:

Corn cob is an agricultural waste that is available in large quantities and can be used as renewable materials. In this study, corn cob was converted into microcrystalline cellulose (MCC) by chemical treatments. The corn cob was treated with an alkaline solution, followed by sodium chlorite ($NaClO_2$) solution as a bleaching agent, and then treated with hydrogen peroxide to obtain MCC. The morphology, crystallinity, and thermal stability of the prepared MCC were analyzed. The results revealed that the MCC showed a porous fibrous structure with an average diameter size and porous size of 13.73 and 1.08 μm, respectively. The crystallinity of the corn cob-derived MCC investigated by X-ray diffraction was 35.19 %. Moreover, it was found that the thermal stability of the MCC was higher than the untreated corn cob. Furthermore, the polyol was synthesized from the corn cob-derived MCC by reacting with glycidol in water. The obtained polyol was characterized by FT-IR, ^{1}H-NMR, and gel permeation chromatography (GPC). The FT-IR and ^{1}H-NMR results confirmed the presence of ether bonds formed in the synthesized polyol due to the reaction between hydroxy groups of MCC and epoxide rings of glycidol. The number average and weight average molecular weight of polyol were 213 and 304, respectively with a polydispersity index (PDI, Mw/Mn) of 1.4. The synthesized polyol is expected that be used as a component for the preparation of polyurethane foam in our further research.

1. Introduction

Polyurethane foam (PU) is a versatile material that features lightweight, high strength, and good cushioning, as well as excellent thermal and sound insulation properties. Therefore, polyurethane foam has been widely used in industry, packaging, transportation, construction, and agriculture. Polyurethanes are synthesized by a reaction between polyols and diisocyanates that is accompanied by surfactants, catalysts, and foaming agents. Polyol is one of the important factors in the properties of polyurethane foam. This is because the polyols are derived from non-renewable petrochemical resources and are being depleted. Thus, there have been many researchers trying to study and develop alternative resources as raw materials.[1,2]

Nowadays, more environmentally friendly alternatives are being developed for the synthesis of polyols as precursors in the preparation of polyurethane foams. Various renewable resources, especially natural oils such as soybean, castor, and cotton seeds oils, as well as cellulose, are used as precursors for the synthesis of polyols.[1,3,4]

However, to the best of our knowledge in the available literature, no work has been studied related to the synthesis of polyols from cellulose derived from agricultural waste materials. Thus, in this research, we are interested in extracting microcrystalline cellulose (MCC) from corn cobs and synthesizing polyol from the corn cob-derived MCC.

2. Materials and Methods

2.1 Materials

Dried corn cobs obtained from Pakornwan Co., Ltd. (Thailand). Sodium hydroxide (NaOH, 99%) was received from Merck KGaA. (Germany). Sodium chlorite ($NaClO_2$, 80%) was purchased from DC Fine Chemicals SLU. (Spain). Hydrogen peroxide (H_2O_2, 35%) was supplied from QRëC (New Zealand). Glycidol (GL, 96%) was obtained from Thermo Fisher Scientific Co., Ltd. (Japan).

2.2 Preparation of microcrystalline cellulose (MCC) from corn cob

The corn cobs were washed with water to remove dust, followed by treatment with 15%wt NaOH at 70°C for 12 hr. The fiber was again treated with 5%wt NaOH at 70°C for 6 hr., followed by fiber bleached in 1.4% $NaClO_2$ at 70°C for 5 hr. The fibers after treatment in each step were washed with Reverse Osmosis water and dried in an oven at 60°C overnight. Then the dried fiber was treated with 35%wt H_2O_2 at 80°C for 6, 12, and 24 hr. The fibers were washed with distilled water several times until neutral pH, and the fiber was dried in an oven at 40°C for 24 hr. to obtain MCC.

2.3 Synthesis of polyol from the corn cob-derived MCC

Polyol was synthesized by liquefying MCC with glycidol (GL). The polyol synthesis was modified from the method of Szpiłyk, M. et al.[2] Water (7 g) and GL (35 g) were mixed in a three-neck reaction flask equipped with a stirrer and a reflux condenser at room temperature for 5 min. The corn cob-derived MCC (4 g) was added into the GL solution and the mixture was heated at 100°C for 50 hr. The mixture was vacuum filtered, and after that water in the filtrate was removed by a rotary evaporator to obtain the polyol. The scheme of synthesis of polyol is shown in scheme 1.

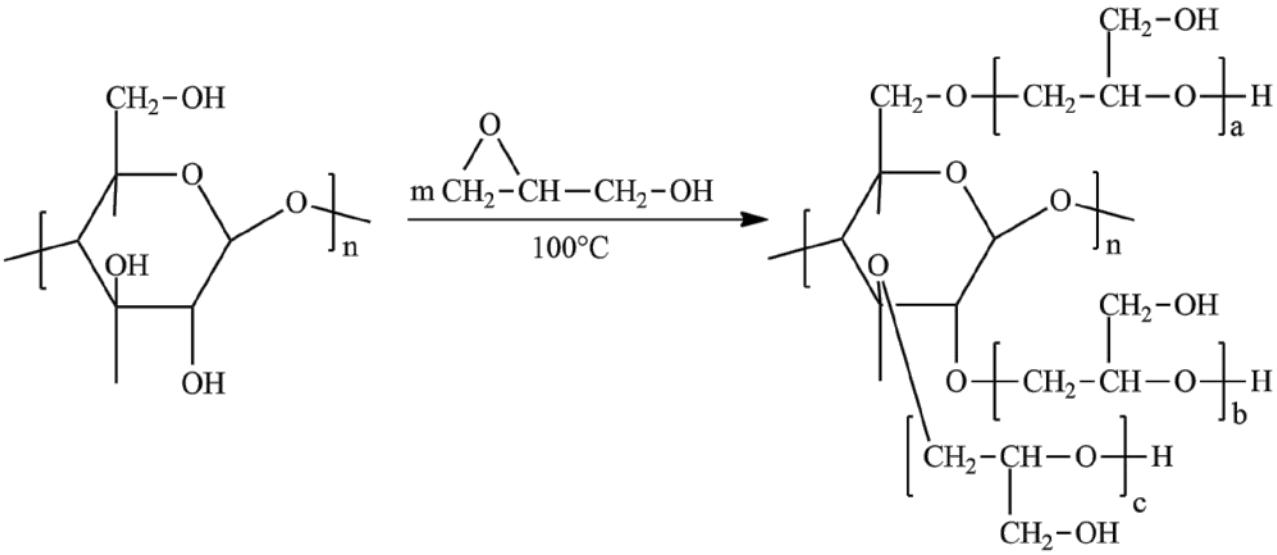

Scheme 1. Synthesis of polyol from microcrystalline cellulose. where: n (a + b + c) = m.

2.4 Characterization

2.4.1 The corn cob-derived MCC

The morphology, average diameter size, and porous size of the corn cob before and after chemical treatments were obtained through a scanning electron microscope (SEM, TM3030, Hitachi). The samples were sputter-coated with gold before testing. The functional groups were studied using a Fourier transform infrared spectroscopy (FTIR, VERTEX 70v, Bruker). The scanned range was 4,000 to 400 cm^{-1}. The crystallinity of the samples was analyzed using an X-ray diffractometer (XRD, XRD-6100, Shimadzu) with 2θ range from 5° to 40°. The Thermal stability of the samples before and after treatment were studied using a Thermogravimetric analyzer (TGA, TGA2, Mettler Toledo) with a temperature range of 50 to 700°C at a heating rate of 10°C/min under an N_2 atmosphere with flow rate of 30 mL/min.

2.4.2 The polyol from corn cob-derived MCC

Fourier transform infrared spectroscopy analysis was performed to determine the structure of the obtained polyol. The scanned range was 4,000 to 400 cm^{-1}. The ^{1}H-NMR spectra of polyol were recorded at 300 MHz using Nuclear Magnetic Resonance Spectroscopy (NMR, AVANCE III HD, Bruker) and using DMSO-d6 as a solution. The hydroxyl number (OH number) of polyol was determined by reflux phthalation with phthalic anhydride in pyridine according to standard ASTM D4274-Test method C. The hydroxyl number of polyols directly affects the number of urethane linkages, significantly impacting the properties of the polyurethane product. The number average molecular weight, weight average molecular weight, and polydispersity index (PDI, Mw/Mn) of polyol were determined using a gel permeation chromatography (GPC, HPLC 10Avp, Shimadzu) using water as solvent.

3. Results & Discussion

3.1 The corn cob-derived MCC

The corn cob was treated with an alkaline solution, followed by sodium chlorite solution as a bleaching agent, and then treated with hydrogen peroxide to obtain MCC, contributing to the yield of 21.63 %

The physical appearance and morphology analysis of raw corn cob and treated corn cob was shown in Figures 1 and 2. The original color of the corn cob was brown (Figure 1a) and the surface was reticular with a smooth surface with an average fiber diameter of around 109.72 µm (Figure 2a). After alkali treatment, the fibers became brighter yellow and brown (Figure 1b), and appeared the pores on the surface (Figure 2b). After bleaching (Figure 1c), the color of cellulose became cream. After being treated with hydrogen

peroxide, the color of MCC for 6 and 12 hr. turned to off-white (Figure 1d and 1e). Then treated with hydrogen peroxide at 24 h., the color of MCC changed to white (Figure 1f). This indicated that the main component is cellulose. The whiteness of them was attributed to partial elimination of lignin and hemicellulose. The treated corn cob has more porous, meaning that the surface area of cellulose has increased (Figure 2f).[5] Moreover, after chemical treatment, MCC had a smaller diameter with an average size of 13.73 µm and an average pore size of 1.08 µm. The porous on the treated corn cob was showed in figure 2d, e, and f with white circles.

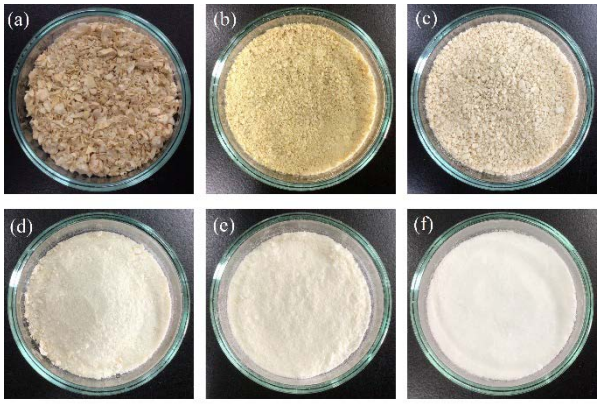

Figure 1. The Physical appearance of corn cob (a) raw corn cob, (b) alkali-treated corn cob, (c) bleached corn cob and hydrogen peroxide treated corn cob for (d) 6, (e) 12, (f) 24 hr.

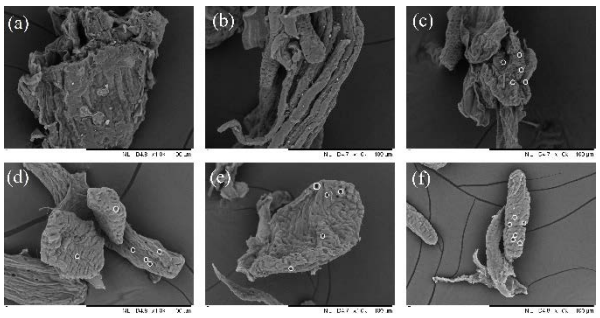

Figure 2. SEM images of (a) raw corn cob, (b) alkali-treated corn cob, (c) bleached corn cob, and hydrogen peroxide treated corn cob for (d) 6, (e) 12, (f) 24 hr. The images were recorded at the magnification of 1,000×

Figure 3 showed the FT-IR spectra of raw corn cob and corn cob after passed various treatments. Corn cob showed characteristic bands of cellulose at 3410, 2900, 1030, and 890 cm^{-1}, corresponding to O–H stretching, C–H stretching, C–O–C pyranose ring stretching, and C-O stretching at the β-glycosidic linkage, respectively.[6,7] The peak at 1730 and 1510 cm^{-1} corresponded to the C-O stretching vibrations of hemicellulose, and the C=C vibrations of lignin in raw corn cob. After alkali treatment, the spectrum of hemicellulose at 1730 cm^{-1} disappeared. Moreover, the spectrum of hemicellulose and lignin at 1730 and 1510 cm^{-1} completely disappeared due to its removal after hydrogen peroxide treatment. The peak at 890 cm^{-1} was the crystalline band of cellulose.[8]

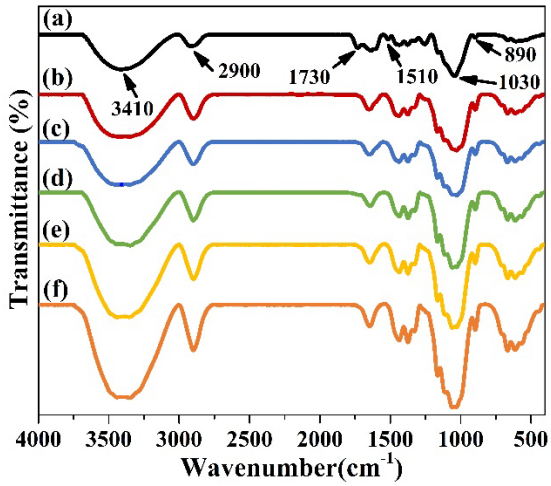

Figure 3. FT-IR spectra of (a) raw corn cob, (b) alkali-treated corn cob, (c) bleached corn cob and hydrogen peroxide treated corn cob for (d) 6, (e) 12, (f) 24 hr.

The XRD spectra of raw corn cob and corn cob after passed various treatments was shown in Figure 4 and the calculated crystallinity index represented in Table 1. As shown in Figure 4, The major diffraction peaks appeared at 2θ of 16°, 22.1°, and 34.5°, and a shoulder in the region of 20°. These results indicated that the cellulose I type.[5,7] After chemical treatments, the peak at 22.1° became sharper, indicating the removal of hemicellulose and lignin[5,7,8]. This was consistent with the FT-IR results, showing that hemicellulose and other amorphous components were partially degraded after treatment. The crystallinity index (CI) of the samples were calculated following equation:

$$CI(\%) = \left(\frac{I_{crystalline} - I_{amorphous}}{I_{crystalline}} \right) \times 100$$

where Icrystalline is the peak intensity of crystalline at 2θ of 22.1° for the all samples and Iamorphous is the peak intensity of amorphous cellulose at 2θ of 18°. The corn cob after treatment resulted in the crystallinity index increasing from 20.02 to 35.19%. The crystallinity of MCC after treated with bleaching process was less than other research because the concentration of bleaching agent was lower than other research.

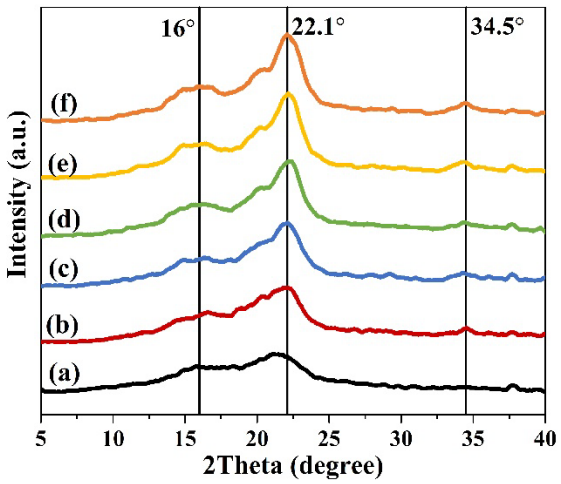

Figure 4. XRD spectra of (a) raw corn cob, (b) alkali-treated corn cob, (c) bleached corn cob and hydrogen peroxide treated corn cob for (d) 6, (e) 12, (f) 24 hr.

Table 1. Crystallinity index (CI)

Samples	CI (%)
raw corn cob	20.02
Alkali-treated corn cob	28.17
bleached corn cob	28.84
H_2O_2 treated corn cob for 6 hr.	30.80
H_2O_2 treated corn cob for 12 hr.	34.05
H_2O_2 treated corn cob for 24 hr.	35.19

Thermogravimetric (TG) of corn cob before and after chemical treatments were investigated by TGA and DTG curves which was showed in Figures 5 and 6. It could be seen that corn cob shows three main weight loss stages. The initial weight loss in the range of 50–120 °C could be due to evaporation of moisture for all the samples. The pyrolysis of hemicellulose and cellulose appeared in the range of 220–315 and 315–390 °C, respectively. Lignin did not show a decomposition peak due to lignin decomposes over a broad temperature range (200–500 °C)[5,7]. The hemicellulose peak in the range of 220–315 was absent upon pretreatment, indicating that hemicellulose was removed. In addition, the removal of hemicellulose, lignin, and increased crystallinity results in higher thermal stability. This was in agreement with the XRD analysis which showed an increase in crystallinity of corn cob after chemical treatments. From Figure 5, the corn cobs after chemical treatment provided single-step decomposition in the temperature range of 320–370 °C, indicating the main decomposition of cellulose without hemicellulose. This was supported by the DTG graph, which showed a single peak of the corn cob after chemical treatment.

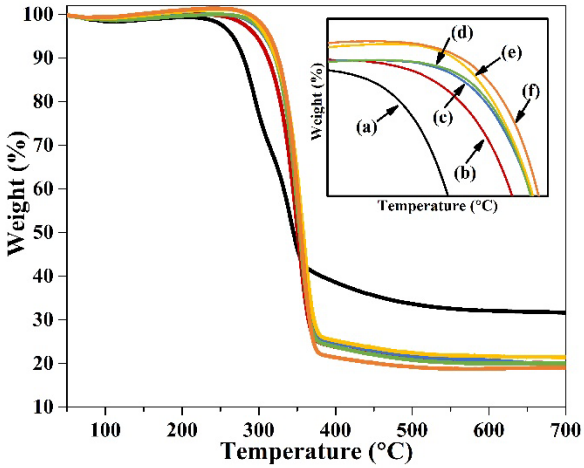

Figure 5. Thermogravimetry Analysis (TGA) curves of (a) raw corn cob, (b) alkali-treated corn cob, (c) bleached corn cob and hydrogen peroxide treated corn cob for (d) 6, (e) 12, (f) 24 hr.

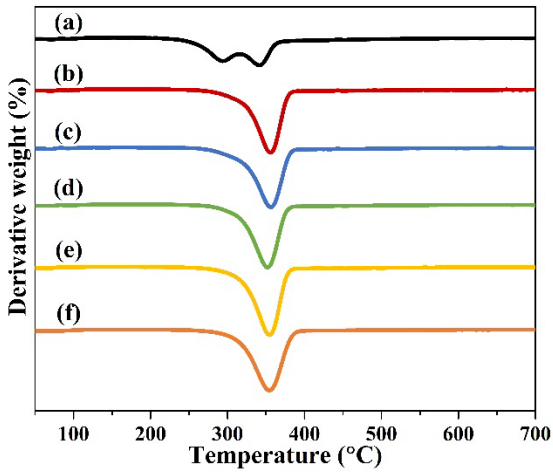

Figure 6. Derivative thermogravimetry (DTG) curves of (a) raw corn cob, (b) alkali-treated corn cob, (c) bleached corn cob and hydrogen peroxide treated corn cob for (d) 6, (e) 12, (f) 24 hr.

3.2 The polyol from corn cob-derived MCC

The typical properties of the MCC-derived polyol are represented in Table 2 including hydroxy number, Mn, Mw, Polydispersity index, and color.

Table 2. Typical Properties of Polyol

Properties	Polyol
OH number, mg KOH/ g	204
Number–average molecular weight (M_n, g/mol)	213
Weight-average molecular weight (M_w, g/mol)	304
Polydispersity index (PI)	1.4
Color	Yellow

FT-IR spectroscopy could identify the functional groups and chemical changes that occurred in the reaction of MCC with GL, as shown in Fig. 7. For the polyol (Figure 7b), the OH-stretching vibrations band showed at 3450 cm^{-1}. The peak at 2,935–2,880 cm^{-1} was associated with symmetric and asymmetric CH stretching vibrations caused by CH_2 groups present in aliphatic chains and CH_3 groups. The absorption bands at 1460–1340 cm^{-1} were related to the CH_2 and H-O-C in-plane bending vibrations. The characteristic for C–O–C ether group vibrations could be spotted in the range of 1130-930 cm^{-1}. The other signals at 930-850 cm^{-1} could be attributed to C=C and C–H bonds in aromatic rings present in the cellulose structure.[3,4]

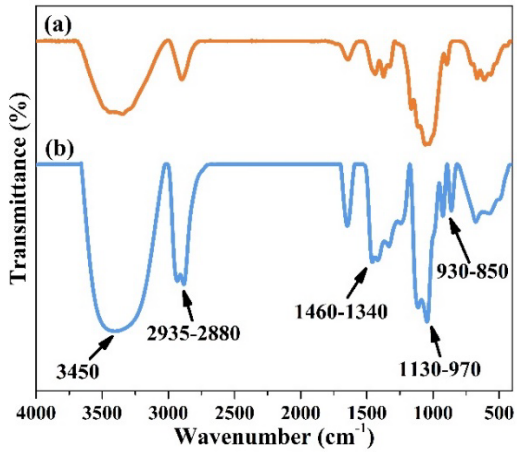

Figure 7. FT-IR spectra of (a) the corn cob-derived MCC and (b) the polyol.

In the ^{1}H-NMR spectrum of the polyol (Figure 8), the resonances in the 3.2–3.7 ppm region were attributed to the ring opening of hydroxy alkylating agents of GL. The hydroxyl group proton resonances corresponding to primary and secondary groups were observed in the region of 4.4–4.8 ppm region.[2] This was consistent with the FT-IR results, which confirmed that an ether bond was formed in the synthesized polyol due to the reaction between hydroxy groups of MCC and epoxide rings of glycidol.

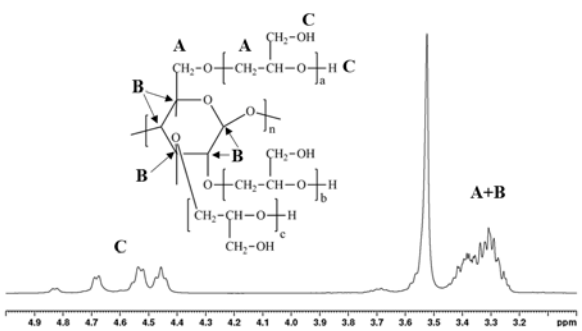

Figure 8. NMR spectra of the polyol.

4. Conclusion

Preparation of MCC from corn cob as an agricultural waste by chemical treatments has been successfully carried out with yields of 21.63 %. Based on the SEM analysis showed MCC had a smaller diameter than corn cob from 109.72 µm to 13.73 µm and an average pore size of 1.08 µm. FT-IR analysis showed that hemicellulose and lignin could be removed sequentially by this method. Moreover, the spectral intensity of the cellulose was well preserved throughout the process. The degree of MCC crystallinity of cellulose is 35.19 %. The thermal stability of cellulose increased with treatment time due to increased crystallinity.

Moreover, in this research, the corn cob-derived MCC was converted into bio-based polyols, a value-added product as a component for the preparation of polyurethane foam. The bio-based polyol was synthesized via cellulose hydroxy alkylation with glycidol. The obtained polyol was characterized by the hydroxyl number of 204 mg KOH/g. The FT-IR and ^{1}H-NMR results confirmed the presence of ether bonds formed in the synthesized polyol due to the reaction between hydroxy groups of MCC and epoxide rings of glycidol. GPC analysis showed that the number average and weight average molecular weight of polyol were 213 and 304, respectively with a PDI of 1.4.

Molecular weight of polyols affects the molecular structure and mechanical properties of polyurethanes. Polyurethanes consist of soft and hard segments. The soft chain segment is usually polyols, polyethers or polyesters providing flexibility, where as the hard segment is composed of diisocyanates and chain extenders contributing strength and rigidity. The low molecular weight polyols leads to more highly crosslinked polyurethane with improved modulus, tensile strength, hardness, but with reduced elasticity. Thus, the low molecular weight polyols are suitable for preparation of ridged polyurethane foam.

Acknowledgments

This work is supported by the Department of Materials Science and Engineering, Faculty of Engineering and Industrial Technology, Silpakorn University.

References

1. Liao, J.; Luan, P.; Zhang, Y.; Chen, L.; Huang, L.; Mo, L.; Li, J.; Xiong, O., A light weight, biodegradable, and recyclable cellulose-based bio-foam with good

mechanical strength and water stability. Journal of Environmental Chemical Engineering. **2022**, 10, 107788.
2. Szpiłyk, M.; Lubczak, R.; Lubczak, J., The biodegradable cellulose-derived polyol and polyurethane foam. Polymer Testing. **2021**, 100, 107250.
3. Kosmela, P.; Hejna, A.; Formela, K.; Haponiuk, J. T.; Piszczyk, Ł., Biopolyols obtained via crude glycerol-based liquefaction of cellulose: their structural, rheological and thermal characterization. Cellulose. **2016**, 23, 2929–2942
4. Olszewski, A.; Kosmela, P.; Mielewczyk-Gryn, A.; Piszczyk, Ł., Bio-Based Polyurethane Composites and Hybrid Composites Containing a New Type of Bio-Polyol and Addition of Natural and Synthetic Fibers. Materials. **2020**,13, 2028.
5. Romruen, O.; Shiekh; K. S.; Rawdkuen, S.; Karbowiak, Th.; Tongdeesoontorn; W., Extraction and Characterization of Cellulose from Agricultural By-Products of Chiang Rai Province, Thailand. Polymers. **2022**, 14, 1830.
6. Singh, H.K.; Patil, T.; Vineeth, S.K.; Das, S.; Pramanik, A.; Mhaske, S.T., Isolation of microcrystalline cellulose from corn stover with emphasis on its constituents: Corn cover and corn cob. Materials Today: Proceedings. **2020**, 27, 589-594.
7. Zhang, S.; Zhang, F.; Jin, L.; Liu, B.; Mao, Y.; Liu, Y.; Huang, J., Preparation of spherical nanocellulose from waste paper by aqueous NaOH/thiourea. Cellulose. **2019**, 26, 5177–5185.
8. Sartika, D.; Firmansyah, A. P.; Junais, I.; Arnata, I. W.; Fahma, F.; Firmanda, A., High yield production of nanocrystalline cellulose from corn cob through a chemical-mechanical treatment under mild conditions. International Journal of Biological Macromolecules. **2023**, 240, 124327.

Hybrid interpenetrating polymer networks of κ-carrageenan/poly(vinyl alcohol) films

Kamonwan Kanphai, Anan Athipornchai, and Thanida Trakulsujaritchok*

Department of Chemistry and Center of Excellence for Innovation in Chemistry, Faculty of Science, Burapha University, Chonburi, 20131, Thailand
**Email: thanida@buu.ac.th*

Abstract:

In this work, interpenetrating polymer networks (IPNs) of κ-carrageenan/poly(vinyl alcohol) films were developed. In order to improve physical properties of the films, the crosslinking contents and the compositions between both homopolymers were optimized with κ-carrageenan/poly(vinyl alcohol) ratios of 40:60, 50:50 and 60:40. The sol-gel process involving hydrolysis and polycondensation reactions and the solution casting were used to fabricate the hybrid films. The results obtained from ATR-FTIR, SEM-EDX, swelling test and thermal analysis confirmed that the crosslinked films containing covalent coupling between organic and inorganic hybrid networks were successfully formed. The hybridization resulted in enhancement of mechanical properties and dimensional stability in aqueous swollen state. The films were colorless and transparent. Their homogeneous microstructure morphology was confirmed by SEM micrographs indicating compatibility between both homopolymers. The combination of their physical properties, mechanical strength as well as simplicity of fabrication process made these IPNs films promising for packaging application.

1. Introduction

In recent years, investigations on natural polymer-based materials have been widely explored in various fields due to their environmentally friendly nature and numerous properties. However, the poor mechanical properties have restricted their application in certain [1]. Various approaches have been established to solve this problem, including fabrication of polymer blends [2-4]. Interpenetrating polymer networks (IPNs) are crosslinked polymers comprising two or more polymeric components that are interlaced on a molecular scale. IPNs are a good choice for approach in improving the properties of natural polymers [5].

Carrageenan is a linear sulfated polysaccharide mostly derived from marine red algae and can be mainly classified as κ-carrageenan that have one sulfate per disaccharide, ι- carrageenan with two sulfates per disaccharide, and λ-carrageenan containing three sulfates per disaccharide. κ-carrageenan can form reversible gels and films and mainly used in food, pharmaceutical and biomedical materials. However, its drawbacks are the hydrophilicity, low dimensional stability and low mechanical strength which limit its utilization in several applications especially as a packaging material. In general, the poor properties of biopolymers can be enhanced by blending with other polymers [2, 4]. For this purpose, poly(vinyl alcohol) is one of the promising synthetic polymers and an interesting choice for the formulation of IPNs due of its water solubility, biocompatibility, non-toxicity, elastic nature, mechanical strength, and excellent film-forming properties [7].

In our previous work, we reported the enhancement in mechanical properties and dimensional stability of polymeric material by sol-gel fabrication of hybrid organic-inorganic crosslinked polymer [8]. The process provides advantages of mild condition, ease of the procedure and possibility to control the crosslink degree by altering the organic-inorganic ratio together with the reaction parameters.

The aim of this study was to prepare films from the κ-carrageenan/poly(vinyl alcohol) blends containing different homopolymer ratios and optimize their physicochemical properties through a sol-gel approach. The final κ-carrageenan /poly(vinyl alcohol) IPNs of three-dimensional networks containing siloxane crosslinking between the organic polymer and the inorganic siloxane linkage were fabricated in the form of thin films by solution casting. In addition, characteristics of the films including morphology, swelling, moisture content, mechanical strength and thermal property were also analyzed.

2. Materials and Methods

2.1 Materials

κ-Carrageenan (CAS number 11114-20-8) was obtained from the Tokyo Chemical Industry. Poly(vinyl alcohol) (MW 60,000 g/mol, degree of hydrolysis 98%, CAS number 9002-89-5) was purchased from Merck. Tetraethyl orthosilicate (TEOS, CAS number 78-10-4) was obtained from Acros Organics. Ethanol and other chemicals were purchased from CT chemical.

2.2 Preparation of κ-carrageenan/poly(vinyl alcohol) (KC/PV) films

A series of KC/PV films were fabricated by mixing the solutions of κ-carrageenan and poly(vinyl alcohol) under stirring at 80 °C for 2 h. The clear and homogeneous solutions were cast onto petri dishes and dried at 60 °C for 20 h. The obtained films comprising different ratios between κ-carrageenan and poly(vinyl alcohol) were named 40KC/60PV, 50KC/60PV IPNs.

A series of crosslinked 40KC/60PV IPNs films was developed by mixing both homopolymer solutions under the same procedure as mentioned above. After bringing the temperature down to 60 °C, ethanol and tetraethyl orthosilicate (TEOS: 45, 90, 135 and 180 µL or 5, 10, 15 and 20% of the polymer content, respectively) were added to the solutions. The sol-gel reaction was allowed to proceed by stirring the mixtures for 20 h at 60 °C. Finally, the obtained solutions were cast into films on petri dishes at 60 °C for 20 h. The crosslinked films of 40KC/60PV-T45, 40KC/60PV-T90, 40KC/60PV-T135 and 40KC/60PV-T180 IPNs were obtained.

2.3 Characterization of the films

2.3.1 ATR-FTIR spectroscopy

Functional analysis of the films was performed using an ATR–FTIR spectrometer (Frontier, Perkin Elmer) at a scan range of 400-4000 cm^{-1} and a resolution of 4 cm^{-1}, with 16 scans per sample.

2.3.2 Morphology

Surface morphology of the films was analyzed using a scanning electron microscope (LEO 1450 VP, Carl Zeiss).

2.3.3 Percentage of moisture content

The films were cut into 2cm × 2cm pieces, weighed, kept in a hot air oven at 110 °C for 20 minutes, allowed to cool down in a desiccator and weighed. The difference in weights of each film before and after moisture adsorption in ambient condition was used to calculate the moisture content.

2.3.4 Swelling and solubility

The films (2cm × 2cm) were weighed and immersed in 30 mL of deionized water. At certain time intervals, the swollen films were taken out of the medium and reweighed. Swelling ratio of the films was calculated using the following equation.

$$\text{Swelling ratio (g/g)} = (W_F - W_O)/W_O$$

where W_O and W_F were the sample weights before and after swelling test, respectively.

After 360 min of swelling test, the swollen films were taken out of deionized water, oven dried (110 °C, 2 h) and weighed (W_S). %Solubility was calculated using the following equation.

$$\text{Solubility (\%)} = [(W_O - W_S)W_O] \times 100$$

2.3.5 Mechanical properties

Mechanical strength of the films was determined using a texture analyzer (TA.XT plus, Stable Micro Systems). Five specimens with the size of 1cm × 5cm were tested with a crosshead speed of 1.0 mm/sec and a grip separation of 30 mm. The tensile strength, %elongation at break and modulus at 1% elongation of the films were reported.

2.3.6 Thermal analysis

Thermal properties of the films were examined by thermogravimetric analysis (TGA). The samples were heated from 35 to 700 °C with 10 °C/min heating rate under nitrogen atmosphere.

3. Results and Discussion

3.1 Properties of the KC/PV films

The blend films of κ-carrageenan/poly(vinyl alcohol) at the weight ratios of 40/60, 50/50 and 60/40 were fabricated. They were smooth, colorless, transparent and homogeneous as shown in Figure 1, indicating compatibility between both homopolymers.

Figure 1. Digital photographs of KC/PV films at different homopolymer ratios

3.1.1 ATR-FTIR analysis

The ATR-FTIR analysis of the homopolymers and the blend films was carried out and the spectra are shown in Figure 2. κ-carrageenan and poly(vinyl alcohol) showed both common and specific absorption peaks. The two samples presented broad bands around 3330 cm^{-1} and 2900 cm^{-1} that indicated vibrational stretching of hydroxyl groups and stretching frequency of C-H bonding (Figure 2a). For the κ-carrageenan film, the characteristic peaks observed at 1225, 1120 with a shoulder, 927 and 842 cm^{-1} could be attributed to the ester sulfate asymmetric stretching, C-O stretching, 3, 6-anhydrogalactose and D-galactose-4-sulfate stretching, respectively [2, 9]. The ATR-FTIR spectrum of poly(vinyl alcohol) showed important bands at 1720, 1450, 1320 and 1018 cm^{-1} that could be assigned to the

C=O stretching of non-hydrolyzed vinyl acetate groups, C-H bending, O-H bending and C-O stretching, respectively [2, 8]. The KC/PV blend films (Figure 2b) resulted in absorption bands inherited from their homopolymers with small shifting on the intensities due to the interactions between both polymers.

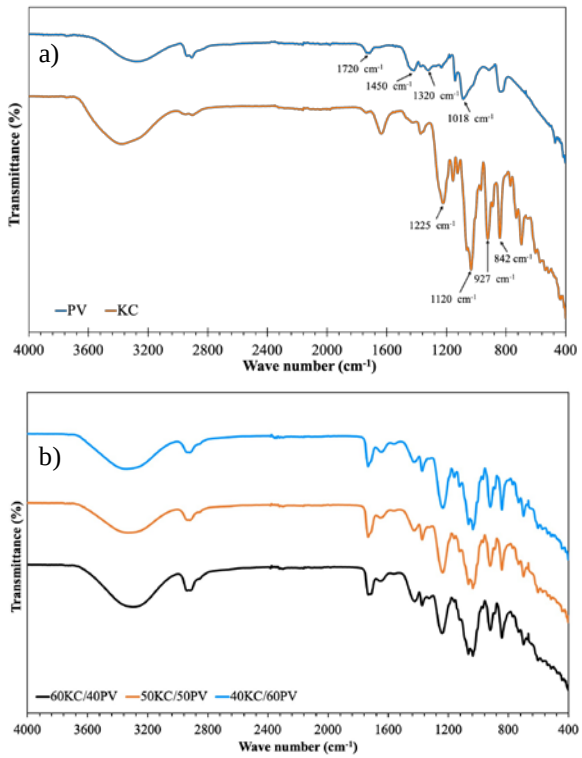

Figure 2. FITR spectra of films a) both homopolymers and b) the blends containing different homopolymer ratios.

3.1.2 Moisture content

The moisture contents of KC/PV films comprising different homopolymer ratios are shown in Figure 3. Among the three blend films, the 60KC/40PV showed its highest moisture content (11.31 and 15.52% at 3 and 24 h, respectively) as compared to the lowest values obtained from the 40KC/60PV (2.16 and 7.14 % at 3 and 24 h, respectively). Moisture absorption character of the blends was significantly influenced by their κ-carrageenan component. Increasing the content of κ-carrageenan led to an increase in %moisture adsorbed into the samples which could be explained by hydrophilicity of κ-carrageenan that facilitated the intermolecular interactions between water molecules and the polymeric film [10].

3.1.3 Swelling ratio and %solubility

The swelling ratio and solubility in aqueous medium of the KC/PV films are demonstrated in Figure 4. Comparing with their homopolymers which were completely dissolved after the tests, it was observed that the blends showed more water resistance due to the macromolecular interactions between their polymeric constituents such as hydrogen bonding and chain entanglement. Both swelling ratio and %solubility increased with increasing in κ-carrageenan component. The swelling ratios obtained from 40KC/60PV, 50KC/50PV and 60KC/40PV films at 30 min of the test were 8.6, 12.0 and 14.6 g/g, respectively. %Solubility of the films after 360 min immersion in distilled water were 54.0, 60.2, and 69.1% for the 40KC/60PV, 50KC/50PV and 60KC/40PV, respectively. The results correspond with those of moisture content in which the hydrophilicity of κ-carrageenan had strong influence on the blend and governed their water resistance.

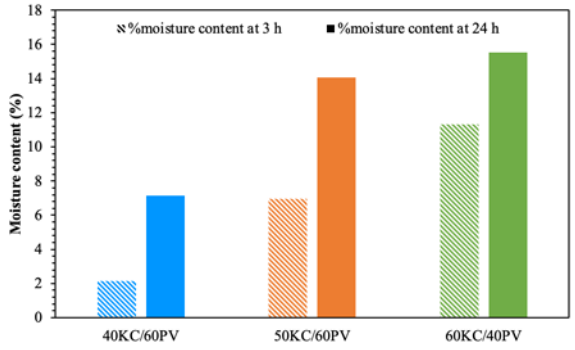

Figure 3. %Moisture content of the KC/PV films.

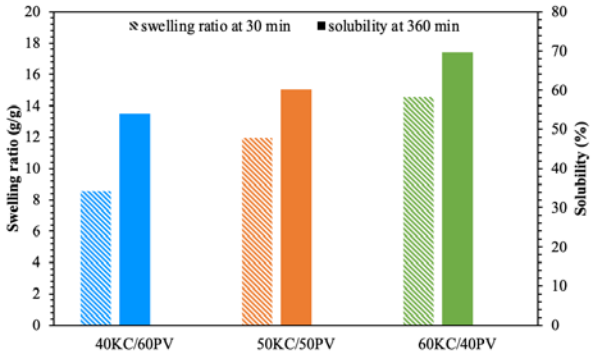

Figure 4. Swelling ratio and %solubility of the KC/PV blend films.

3.1.4 Mechanical properties

Tensile properties of the KC/PV films were investigated and the results are reported in Table 1. It was confirmed that incorporation of poly(vinyl alcohol) into κ-carrageenan matrix was a practical method to enhance both tensile strength and flexibility of the blends. Similar results have been reported in the literature [11]. Among the three compositions, the 40KC/60PV exhibited ultimate values of mechanical strength with tensile strength of 24.68 MPa, elongation at break of 3.55% and Young's modulus of 8.67 MPa.

Considering the mechanical strength and water resistance character of the samples, the 40KC/60PV blend was chosen for further investigation on the effects of hybrid organic-inorganic crosslinking on the physico-chemical properties in next section.

Table 1. Mechanical properties of the KC/PV films

Samples	Tensile strength (MPa)	Elongation at break (%)	Young's Modulus* (MPa)
40KC/60PV	24.68	3.55	8.67
50KC/50PV	18.65	2.97	3.48
60KC/40PV	11.04	1.60	2.91

*Young's modulus at 1% elongation

3.2 Properties of the crosslinked KC/PV-T films

In this work, chemical crosslinking was used to enhance the properties of 40KC/60PV film. The sol-gel process involving two reactions, hydrolysis and condensation, was applied for the development of hybrid organic-inorganic crosslinked films (Figure 5).

Hydrolysis:

$Si\text{-}(OR)_4 + H_2O \rightarrow HO\text{-}Si\text{-}(OR)_3 + ROH$

Polycondensation:

$(RO)_3\text{-}Si\text{-}OH + HO\text{-}Si\text{-}(OR)_3 \rightarrow (RO)_3\text{-}Si\text{-}O\text{-}Si\text{-}(OR)_3 + H_2O$

$(RO)_3\text{-}Si\text{-}OH + RO\text{-}Si\text{-}(OR)_3 \rightarrow (RO)_3\text{-}Si\text{-}O\text{-}Si\text{-}(OR)_3 + ROH$

and/or

$(RO)_3\text{-}Si\text{-}OH + HO\text{-}[polymer] \rightarrow (RO)_3\text{-}Si\text{-}O\text{-}[polymer] + H_2O$

R : alkyl group

During the hydrolysis, the ethoxysilane groups of an inorganic precursor, tetraethyl orthosilicate (TEOS), were hydrolyzed forming -Si-OH pendants. Then, the polycondensation proceeded resulting in formation of -Si-O-Si- covalent crosslinking of the organic-inorganic hybridized networks polymer chains [8]. The obtained crosslinked films, 40KC/60PV-T45, 40KC/60PV-T90, 40KC/60PV-T135, and 40KC/60PV-T180, were colorless and transparent, making it promising for packaging applications.

3.2.1 ATR-FTIR analysis

The success of sol-gel synthesis and the occurrence of organic-inorganic crosslinking in the hybrid KC/PV-T films was formed through the Si-O-Si linkage that could be confirmed by FTIR spectroscopy. The ATR-FTIR spectra ranging from 1600 to 400 cm^{-1} of the sol-gel crosslinked film, 40KC/60PV-T180, comparing with its linear blend, 40KC/60PV, are shown in Figure 6. The new bands of C-H bending (TEOS ethoxy groups) at 1330 cm^{-1} and those of the siloxane linkage formation in the 40KC/60PV-T180 were observed at 1140, 1080 and 820 cm^{-1} corresponding to the asymmetric stretching bands and symmetric stretching band of Si-O-Si, respectively [8].

3.2.2 Morphology and elemental compositions

Surface morphology of the films was examined by a scanning electron microscope and the results are shown in Figure 7. From the SEM micrographs, surface of the blend before sol-gel synthesis (40KC/60PV) was smooth and homogeneous. The surfaces of crosslinked IPNs (40KC/60PV-T45, 40KC/60PV-T90, 40KC/60PV -T135 and 40KC/60PV-T180) exhibited slightly coarse morphology due the formation of hybrid organic-inorganic network which was confirmed by their EDX elemental compositions. All crosslinked samples showed Si-elemental content in accordance with the amount of TEOS crosslinking agent added into the reaction. The highest Si-percentage was detected from the 40KC/60PV-T180.

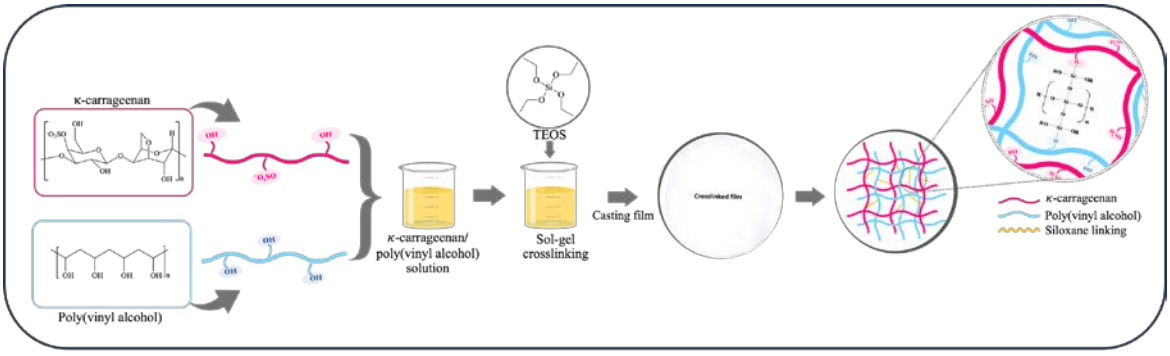

Figure 5. Preparation scheme for sol-gel crosslinking of the hybrid KC/PV-T films.

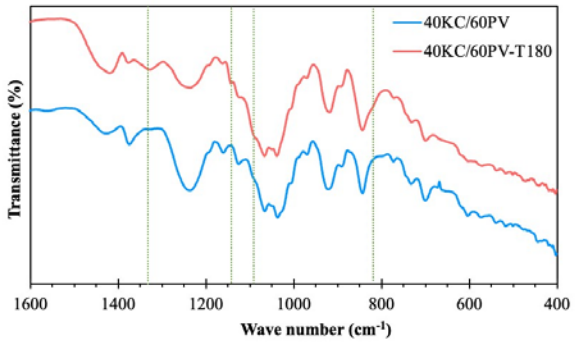

Figure 6. ATR-FTIR spectra of the linear blend (40KC/60PV) and the crosslinked blend (40KC/60PV-T180) films.

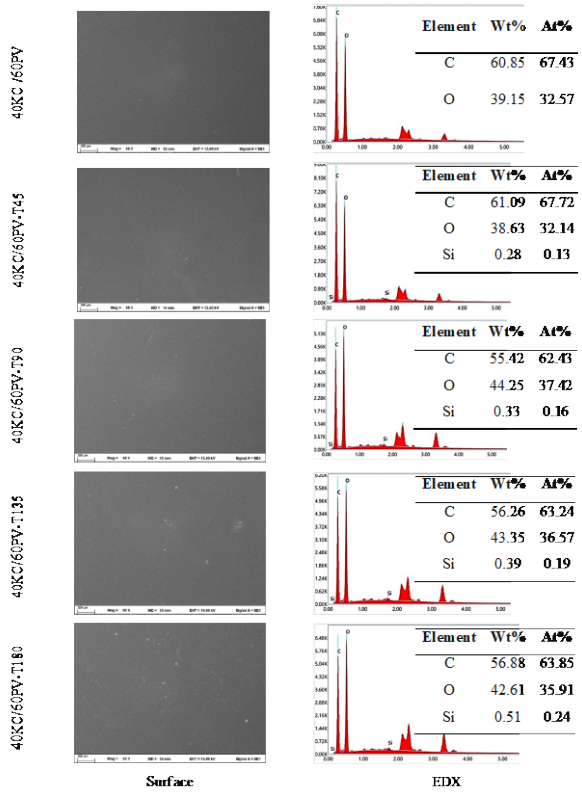

Figure 7. SEM-EDX analysis of the crosslinked films fabricated with different crosslinking degrees

3.2.3 Mechanical properties

In order to investigate the effects of sol-gel crosslinking on mechanical properties of the 40KC/60PV-T IPNs, the tensile strength at break, elongation and Young's modulus were determined and the results are summarized in Table 2. Comparing with the 40KC/60PV film without an addition of sol-gel precursor, the hybrid IPNs possessed significantly higher mechanical properties. The ultimate values observed from the 40KC/60PV-T45 were 43.20 MPa, 11.94 MPa and 7.47% for tensile strength, modulus and elongation at break, respectively. The hybrid IPNs fabricated with increasing TEOS content from 40KC/60PV-T45 to 40KC/60PV-T135 showed an enhancement in tensile properties in comparison to that of the 40KC/60PV. However, further increase in TEOS concentration caused a decrease in tensile strength at break, suggesting the detrimental effect of excessive crosslinking and brittleness of the film.

Table 2. Mechanical properties of the hybrid IPNs containing different degrees of crosslinking.

Samples	Tensile strength (MPa)	Elongation at break (%)	Young's Modulus* (MPa)
40KC/60PV	24.68	3.55	8.67
40KC/60PV-T45	43.20	7.47	11.94
40KC/60PV-T90	42.31	6.78	10.93
40KC/60PV-T135	35.85	5.12	7.66
40KC/60PV-T180	21.04	3.67	7.90

*Young's modulus at 1% elongation

3.2.4 Thermal analysis of the KC/PV films

Thermogravimetric analysis (TGA) was conducted to evaluate the effect of hybrid crosslinking on thermal stability of the films and the thermograms are shown in Figure 8. Both samples exhibited two major stages of thermal degradation. The first stage of weight loss below 230 °C could be ascribed to moisture evaporation and elimination of small molecules. The second stage in the range of 230-480 °C was probably caused by chain scission and decomposition of linkage polymeric networks [12-14]. Compare with the 40KC/60PV, enhanced thermal stability of the crosslinked 40KC/60PV-T45 IPNs was observed with the higher weight retention over the ranges of degradation. At 700 °C, the residue weight of the 40KC/60PV-T45 IPNs was slightly higher than that of the 40KC/60PV due to the organic-inorganic crosslink networks.

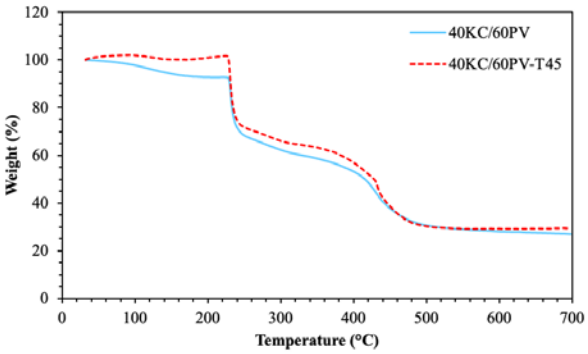

Figure 8. Thermal stability of the linear blend and the crosslinked films.

4. Conclusion

The hybrid interpenetrating polymer networks (IPNs) of κ-carrageenan/poly(vinyl alcohol) films were developed by a solution casting procedure. The incorporation of poly(vinyl

alcohol) into biopolymeric κ-carrageenan and the sol-gel synthesis were successfully used to fabricate the hybrid organic-inorganic films with siloxane crosslink networks. The hybrid covalent linkage exhibited primary impact on improvement in mechanical and thermal properties of the κ-carrageenan/poly(vinyl alcohol) IPNs with the 40KC/60PV-T45 possessing strong potential application as a packaging material. These results also contributed to the establishment of a procedure to optimize the biopolymeric based film for several applications.

Acknowledgements

This work was financially supported by (i) Burapha University (BUU), (ii) Thailand Science Research and Innovation (TSRI), and (iii) National Science Research and Innovation Fund (NSRF) (Fundamental Fund : Grant no.17/2567). Financial support from the Center of Excellence for Innovation in Chemistry (PERCH-ICI), Ministry of Higher Education, Science, Research and Innovation is gratefully acknowledged. This work was supported by Science Innovation Facility, Faculty of Science, Burapha University.

References

1. Dai, Q.; Huang, X.; Jia, R.; Fang, Y.; Qin, Z. *J. Food Eng.* **2022**, *330*, 111106.
2. Sukhlaaied, W.; Riyajan, S. A. *Carbohyd. Polym*. **2013**, 98(1), 677-685.
3. Athipornchai, A.; Pabunrueang, P.; Trakulsujaritchok, T. *Food Hydrocoll*. **2024**, *147*, 109394.
4. Forghani, S.; Zeynali, F.; Almasi, H.; Hamishehkar, H. *Food Chem.* **2022**, *388*, 133057.
5. Naseri, N.; Deepa, B.; Mathew, A. P.; Oksman, K.; Girandon, L. *Biomacromolecules*. **2016**, *17* (11), 3714-3723.
6. Sani, M. A.; Tavassoli, M.; Salim, S. A.; Azizi-lalabadi, M.; McClements, D. J. *Food Hydrocoll*. **2022**, *124*, 107324.
7. Panpinit, S.; Pongsomboon, S. A.; Keawin, T.; Saengsuwan, S. *React. Funct. Polym.* **2020**, *156*, 104739.
8. Pipattanawarothai, A.; Trakulsujaritchok, T. *Dyes Pigm.* **2020**, *173*, 107946.
9. Lapwanit, S.; Sooksimuang, T.; Trakulsujaritchok, T. *J. Environ. Chem. Eng.* **2018**, 6(5), 6221-6230.
10. Qin, Y.; Liu, Y., Zhang, X.; Liu, J. *Food Hydrocoll.* **2020**, *100*, 105410.
11. Liu, Y.; Qin, Y.; Bai, R.; Zhang, X.; Yuan, L.; Liu, J. *Int. J. Biol. Macromol.* **2019**, *134*, 993-1001.
12. Sabbagh, F.; Khatir, N. M.; Kiarostami, K. *Polym.* **2023**, *15*(2), 272.
13. Forghani, S.; Zeynali, F.; Almasi, H.; Hamishehkar, H. *Food Chem.* **2022**, *388*, 133057.
14. de Jesus, G. A.; Berton, S. B.; Simões, B. M.; Zola, R. S.; Monteiro, J. P.; Martins, A. F.; Bonafé, E. G. *Inter. J. Bio. Macromol.* **2023**, *253*, 127087.

Investigation of mechanical properties on TPS/PLA bio-plastic composite with oil palm fiber

Busarin Noikaew*, Punthinee Somwongsa, Saengdoen Doungdaw, Sureeporn Kumneadklang, and Siriporn Larpkiattaworn

Expert Centre of Innovative Materials, Thailand Institute of Scientific and Technological Research, Khlong Luang, Pathum Thani, 12120, Thailand

**E-mail: busarin@tistr.or.th*

Abstract:

Environmental pollution problems from burning of agricultural waste and plastic waste from petroleum-based plastic which cannot be degraded in nature are recently considered on global problem. The utilization of agricultural residue from oil palm fiber and bio-plastic composite might solve this global issue and lead to Bio-Circular-Green Economy (BCG) model. In this research, thermoplastic starch (TPS) and polylactic acid (PLA) blend were chosen for biodegradable plastic composite with and without oil palm fiber. The amount of palm oil fibers was added from 0 wt% to 5 wt% of TPS. The ratios of TPS/PLA as 40 : 60 and 70 : 30 with and without oil palm fiber were compared to pure PLA. The TPS/PLA composite were prepared by using a twin-screw extruder. After that, the melt-flowable characteristic of TPS/PLA composite pellets was investigated. Mechanical properties of TPS/PLA with and without oil palm fiber compared to pure PLA were also investigated. The results revealed that the addition of oil palm fiber decreased the melt flow rate of TPS/PLA composite. In addition, the tensile strength of TPS/PLA composite increased with increasing the amount of oil palm fibers, however, increasing oil palm fibers up to 5 wt% caused a reducing in tensile strength. Thus, the results indicated that the optimum tensile strength of TPS/PLA composite with 1 wt% oil palm fiber could reinforce the bio-plastic composite.

1. Introduction

The widespread use of plastics due to their beneficial properties such as weathering resistance, lightness, transparency and low maintenance requirements. Conventional plastics such as polyethylene (PE), polypropylene (PP) and polystyrene (PS) and polyvinylchloride (PVC) find application in various sectors like agriculture, commerce, and industry due to these advantageous features.[1-3] However, despite their advantages, plastics pose significant challenges of their non-degradability. Most plastics take centuries to decompose fully, leading to a global issue of plastic waste accumulation in the environment. Furthermore, the conventional methods of producing plastics involve monomers derived from fossil hydrocarbons like propylene and ethylene exhibit resistance to microbial degradation, hindering the development of enzymes capable of breaking down these common polymers. Addressing these challenges requires innovative solutions to mitigate plastic pollution and develop more eco-friendly alternatives or recycling methods.[4-5] The development and utilization of biodegradable "green" composites have emerged as a potential solution. These composites offer advantages not only from an environmental perspective but also economically, particularly during periods of rising oil prices. Green composites are created by incorporating natural fibers into biodegradable polymers such as starch, chitin, chitosan, cellulose, and protein. The addition of natural fibers enhances the water resistance, as well as the mechanical and thermal properties of these polymers, making them more viable alternatives to conventional plastics.[6-8] Various types of natural fibers had been used as reinforcement in polymer composites, including corn, water hyacinth, coir, ginger, cotton, kenaf, sugarcane, flax, ramie, hemp, kapok, sisal, wood, oil palm, banana as well as sugar palm.[9] Oil palm fiber is a well-known lignocellulosic fiber with a high cellulose content and high toughness. Natural fibers can be blended with biopolymers as polyvinyl alcohol (PVA), polyhydroxyalkanoate (PHA), polylactic acid (PLA) and polyethylene glycol (PEG) to create more useable bio-plastic composites and biomaterials for good mechanical, physical, electrical, thermal and biodegradation characteristics. For bio-plastic composite, thermoplastic starch is becoming more popular biodegradable plastic due to their non-toxic, cheap and globally available raw material by mixing with plasticizers under high temperature and shear. However, TPS had high moisture absorption and poor mechanical strength material. Then, it could be blended with other bioplastics such as PLA which have good mechanical properties, hydrophobic and processability, but it has brittle and expensive compared with conventional petroleum-based plastics.[10-12]

In this research, TPS and PLA were chosen for blending, both with and without oil

palm fiber. These bio-plastic composites were tested for their mechanical properties compared to pure PLA.

2. Materials and Methods

2.1 Materials

Bio-polymer compounds can be classified into two types: thermoplastic starch (TPS) and polylactic acid (PLA). In this research, TPS compounding was prepared by blending various ingredients, including native cassava starch obtained from a general grocery store, plasticizer (glycerol), citric acid, and oil palm fiber, in a high-speed mixer. Subsequently, PLA purchased from Zhejiang Hisun Biomaterials Co., Ltd., was combined with the TPS compounding.

2.2 Preparation of oil palm fiber

The raw material for oil palm fiber sourced from a local oil palm plantation underwent processing steps. Initially, the raw material was chipped into small pieces using a chipper shredder and then dried at 100°C for 24 h in an oven. For alkaline treatment, the dried fiber was subjected to 5% sodium hydroxide (NaOH) with a liquor to raw material ratio of 10 : 1 in a 10-liter vertical rotating pulp digester under pressure at 5 bar. The optimum treatment temperature was set at 150°C for a duration of 1 h, aimed at removing undesirable components such as lignin, pectin, hemicellulose, and cellulose. Following the alkaline treatment, the fiber underwent a 15 min beating process with tap water. Subsequently, the fiber was washed repeatedly until reaching a neutral pH value. Finally, the pulp was dried in a hot air oven at 60°C for 24 h. The quantity of utilized oil palm fibers in this research varied, ranging from 0 wt%, 1 wt%, 3 wt% to 5 wt% of TPS.

2.3 The TPS/PLA compounding process

The preparation of TPS/PLA, with and without oil palm fiber involved two steps prior to extrusion. Firstly, TPS compound was prepared using native cassava starch, glycerol, citric acid and oil palm fiber by varying weights ranging from 0 wt% to 5 wt%. All ingredients were mixed together in a high-speed mixer. Secondly, the obtained TPS compound was further blended with pure PLA. Finally, TPS/PLA compounds were processed in a twin-screw extruder and the resulting extrudates of TPS/PLA bio-plastic composite were cut using a pelletizer.

The ratio of TPS/PLA, with and without oil palm fiber, was varied as 70 : 30 with oil palm fiber content at 0 wt%, 1 wt%, 3 wt%, and 5 wt%, and 40 : 60 with 1 wt% oil palm fiber compared to pure PLA. The mixing of TPS/PLA, with and without oil palm fiber, was carried out in a twin-screw extruder with a length/diameter (L/D) ratio of 40 and a screw diameter of 26 mm. The extrusion process was performed at a barrel temperature profile ranging from 50 to 150°C (from hopper to die) with a screw speed of approximately 40 rpm. Subsequently, the extrudates of the TPS/PLA bioplastic composite were cut into 2.5-mm-long pellets using a pelletizer.

The bioplastic composite pellets of TPS/PLA were molded into a dumbbell shape for tensile testing using an injection molding machine (TR80EH2, Sodick Plustech). The machine operated within a temperature range of 150-170°C, with an injection rate of 110 cm^3/s, a screw diameter of 32 mm, and a plunger diameter of 32 mm.

2.3 Characterization of TPS/PLA bio-plastic composite

The morphological characteristics of oil palm fiber were determined using a pulp morphology analyzer (Techpap, Morfi Neo) through optical microscope measurements with analyzer software. The analysis such as fiber length, fiber width, fibrillation index, hard wood, and soft wood, following ISO 160652 standards.

The TPS/PLA bioplastic composite, with and without oil palm fiber, as well as pure PLA, underwent characterization using the melt flow indexer (MFI) (MP1200, Tinius Olsen) in accordance with ASTM D1238. Additionally, tensile strength and elongation properties of the samples were tested using a universal testing machine (AG-X plus, Shimadzu) according to ISO 527-2, with a load cell of 10 kN. Each sample was tested with at least five specimens. Furthermore, the moisture content of TPS/PLA bioplastic composite pellets was also examined.

3. Results & Discussion

3.1 Properties of oil palm fiber

The raw materials for oil palm fiber were processed into oil palm pulp. This oil palm pulp was then blended into fine particles. The selection of fine oil palm pulp for compounding with TPS ranged from 0 wt% to 5 wt%. The appearance of oil palm fiber before and after alkaline treatment can be observed in Figure 1.

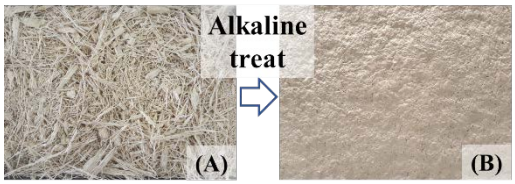

Figure 1. The appearance of oil palm fiber (A) before and (B) after alkaline treatment.

The properties of oil palm fiber, including fiber length, fiber width, fibrillation index, hard wood, and soft wood were assessed using a software analyzer and the results are presented in Table 1. According to the analysis, oil palm fiber exhibits a combination of wide and long fibers with dimensions of 17.8 µm in width and 1,124 µm in length. Additionally, the fibrillation index, hard wood and soft wood content were determined to be 1.1%, 16.5% and 83.5%, respectively.[13] These findings suggest that oil palm fiber possesses an optimal fiber length and a significant proportion of soft wood, making it well-suited for use in reinforced bio-plastic composites. The combination of these properties contributes to the overall quality and effectiveness of the fiber in enhancing the properties of the bio-plastic composite.

Table 1. Properties of oil palm fiber.

Fiber	Fiber length (µm)	Fiber width (µm)	Fibrillation index (%)	Hard wood (%)	Soft wood (%)
Oil palm	1,124.0	17.8	1.1	16.5	83.5

3.2 Properties of TPS/PLA compounds

The conditions of the bio-plastic composite with and without oil palm fiber are detailed in Table 2. Additionally, the appearances of the bioplastic composite pellets are illustrated in Figure 3. In the case of TPS/PLA bioplastic pellets without oil palm fiber, a white color is observed.

Table 2. Conditions of bio-plastic composites with and without oil palm fiber.

Sample name	TPS/PLA	Oil palm fiber (wt%)
PLA	0 : 100	0
TP01	40 : 60	1
TP02	70 : 30	0
TP03	70 : 30	1
TP04	70 : 30	3
TP05	70 : 30	5

Figure 3. The appearance of bio-plastic pellets with and without oil palm fiber.

For TPS/PLA with ratios of 40 : 60 and 70 : 30, the color changes from light to dark brown in correspondence with the amount of oil palm fiber ranging from 1 wt% to 5 wt% when compared to pure PLA.

3.3 Moisture content of TPS/PLA compounds

The moisture content of TPS/PLA bio-plastic composite and pure PLA was determined by weighing the initial bioplastic weight. Subsequently, all samples were dried at 105°C in an oven for 24 h. After the drying process, all samples were reweighed. The moisture content in TPS/PLA bioplastic and pure PLA was calculated using the following equation,[14] where w represents the initial weight of the bioplastic pellet and d is the final or dry weight of the bioplastic pellet.

$$Moisture\ content\ (\%) = \frac{(w-d)}{w} \times 100$$

The moisture contents of TPS/PLA bio-plastic composite and pure PLA are presented in Table 3. It is evident that the moisture content of TPS/PLA in the ratio of 40 : 60 is lower than that of TPS/PLA of 70 : 30 with the same 1 wt% oil palm fiber due to the lower amount of TPS. As the amount of oil palm fibers increased from 0 wt% to 5 wt%, the moisture content also increased. Conversely, the moisture content of pure PLA exhibited the lowest value when compared to the bio-plastic composites. This is because PLA is a less hydrophilic polymer than TPS when no additional fiber content is present.[15] When increasing the TPS compound with oil palm fiber in the TPS/PLA blend, there is a subsequent increase in moisture absorption. This is due to the fibers slowly absorbing or desorbing moisture from the surrounding environment until they reach an equilibrium moisture content. This behavior can be explained by the higher hydrophilic character of the fibers compared to pure PLA.[16]

Table 3. Moisture content of bio-plastic composites with and without oil palm fiber.

Sample	Moisture content (%)
PLA	0.08
TP01	0.32
TP02	0.64
TP03	0.80
TP04	0.81
TP05	0.85

3.4 Melt flow index of TPS/PLA compounds

The Melt Flow Index (MFI) is a particularly valuable method for identifying the rheological properties of polymers. MFI is defined as the weight of the polymer that melts and flows through a die with a certain diameter and length for 10 min at a constant temperature.[17] In this research, MFI was employed to characterize the melt-flowable characteristics of thermoplastic-based materials, measured at 190°C with a load cell of 3.8 kg. The MFI values of TPS/PLA, with and without oil palm fiber are presented in Table 4 and the trends in melt flowability are clearly illustrated in Table 4. The obtained MFI values indicate that pure PLA had the lowest MFI value. The ratio of TPS/PLA at 40 : 60 exhibited a lower MFI value than the ratio of TPS/PLA at 70 : 30 with the same 1 wt% oil palm fiber resulting in a decrease in the viscosity of the TPS/PLA blend when the PLA ratio exceeds that of TPS. For the ratio of TPS/PLA at 70 : 30 with an increasing amount of oil palm fiber from 0 wt% to 5 wt%, the MFI value decreased indicating a reduction in the viscosity of TPS/PLA due to a higher amount of oil palm fiber. This result suggests that the MFI value of TPS/PLA can be adjusted by varying the amount of oil palm fiber.

Table 4. Melt flow index of bio-plastic composites with and without oil palm fiber.

Sample	Melt flow index (g/10 minutes)
PLA	15.4±1.65
TP01	24.8±1.45
TP02	33.2±1.11
TP03	31.6±1.79
TP04	30.4±1.83
TP05	25.4±1.81

3.5 Tensile strength and elongation at break of TPS/PLA bio-plastic composites

The mechanical properties of TPS/PLA bio-plastic composites were characterized by tensile strength and elongation at break and the results are summarized in Table 4.

Table 4. Mechanical properties of bio-plastic composites with and without oil palm fiber.

Sample	Tensile strength (MPa)	Elongation at break (%)	Dumbbell shape
PLA	48.56±2.22	4.80±0.77	
TP01	36.76±0.71	1.78±0.04	
TP02	12.93±1.23	0.48±0.11	
TP03	20.83±0.80	0.83±0.02	
TP04	20.36±0.75	0.67±0.03	
TP05	19.45±2.72	0.54±0.09	

The findings reveal that pure PLA exhibited the highest mechanical properties in term of both tensile strength and elongation at break. For the TPS/PLA ratio at 40 : 60, the tensile strength and elongation at break were higher than those for TPS/PLA at 70 : 30 with the same 1 wt% oil palm fiber as 36.76 MPa and 1.78%, respectively. In the case of the TPS/PLA ratio at 70 : 30, with an increase in oil palm fiber from 0 wt% to 5 wt%, there was a significant difference observed in the mechanical properties, indicating that the presence of oil palm fibers had a substantial impact on bio-plastic composites. TPS/PLA blend without oil palm fiber showed the lowest mechanical properties in term of both tensile strength and elongation at break. It can be concluded that the increasing oil palm fiber in the TPS/PLA blend leads to reinforce in the mechanical properties of the bioplastic composite. However, an increase in oil palm fibers up to 5 wt% led to a reduction in both tensile strength and elongation at break compared to the weight of oil palm fiber as 1 wt% and 3 wt%. This result suggests that a higher amount of oil palm fibers might contribute to agglomeration in the TPS/PLA blend, leading to lower melt flowability. Additionally, TPS/PLA with 1 wt% and 3 wt% exhibited no significant differences in mechanical properties. Although

TPS/PLA bio-plastic composites exhibited a slight decrease in mechanical properties when compared to pure PLA, they played a crucial role in reducing the overall amount of pure PLA in the process.

4. Conclusion

Blending TPS into PLA reduce the tensile strength and elongation at break of PLA. Agricultural residue from oil palm fiber was incorporated into the composite, ranging from 0 wt% to 5 wt% of TPS. The addition of oil palm fiber in the TPS/PLA at 70 : 30 blend tended to decrease melt flowability and increase moisture content, while appropriate amount of fiber enhanced the mechanical properties. The optimal mechanical properties were achieved in TPS/PLA composites with a ratio of 40 : 60 and 1 wt% oil palm fiber, acting as reinforcement for bio-plastic composites. Thus, the obtained TPS/PLA bio-plastic composites represent promising alternative materials for renewable, biodegradable, and environmentally friendly products.

Acknowledgements

The authors are sincerely grateful to Program Management Unit for Competitiveness (PMUC) and Seesan 56 Co.,Ltd for their financial support. Additionally, the authors extend their sincere gratitude to The Expert Centre of Innovative Materials, Thailand Institute of Scientific and Technological Research (TISTR).

References

1. Ali, S. S.; Elsamahy, T.; Koutra, E.; Kornaros, M.; El-Sheekh, M.; Abdelkarim, E. A.; Zhu, D.; Sun, J. *J. Sci. Total Environ.* **2021**, 771, 144719.
2. Jefferson, A. J.; Dhakal, H. N. *J. Compos. C: Open Access.* **2022**, 7, 100220.
3. Ludwiczak, J.; Dmitruk, A.; Skwarski, M.; Kaczyński, P.; Makuła, P. *Int. J. Polym. Anal.* **2023**, 28(4), 366–382.
4. Amobonye, A.; Bhagwat, P.; Singh, S.; Pillai, S. *J. Sci. Total Environ.* **2021**, 759, 143536.
5. Dimassi, S. N.; Hahladakis, J. N.; Yahia, M. N. D.; Ahmad, M. I.; Sayadi, S.; Al-Ghouti, M. A. *J. Chem*. **2022**, 15, 104262.
6. Hahladakis, A. J.; Velis, C. A.; Weber, R.; Iacovidou, E.; Purnell, P. *J. Hazard. Mater.* **2018**, 344, 179–99.
7. Xie, Q.; Li, F.; Li, J.; Wang, L.; Li, Y.; Zhang, C.; Xu, J.; Chen, S. *J. Carbohydr. Polym.* **2018**, 189, 56–64.
8. Whitacre, R.; Amiri, A.; Ulven, C. *J. Ind Crops Prod*. **2015**, 77, 232–238.
9. Ahmad, M. N.; Ishak, M. R.; Taha, M. M.; Mustapha, F; Leman, Z; Irianto. *J. Polym. Test.* **2023**, 120, 107972.
10. Chotiprayon, P.; Chaisawad, B.; Yoksan, R. *Int. J. Biol. Macromol.* **2020**, 156, 960-968.
11. Shanmugam, V.; Mensah, R. A.; Försth, M.; Sas, G.; Restás, A.; Addy, C.; Xu, Q.; Jiang, L.; Neisiany, R. E.; Singha, S.; George, G.; Jose, E. T.; Berto, F.; Hedenqvist, M. S.; Das, O.; Ramakrishna, S. *J. Compos. C: Open Access*. **2021**, 5, 100138.
12. Dang, K. M.; Yoksan, R. *Int. J. Biol. Macromol.* **2021**, 188, 290-299.
13. Noikaew, B.; Kumneadklang, S.; Pumwongpitak, P.; Wangmooklang, L.; Daungdaw, S.; Larpkiattaworn, S. In *Frontiers in Chemical Sciences for Health, Energy, and Sustainability, Proceedings of the 2022 Pure and Applied Chemistry International Conference*. **2022**, 678-682.
14. Mohammad Azmin, S. N. H.; Mohd Hayat, N. A. B.; Mat Nor, M. S. *J. Bioresour. Bioprod.* **2020**, 5, 248-255.
15. Aranda-García, F. J.; González-Núñez, R.; Jasso-Gastinel, C. F.; Mendizábal, E. *Int. J. Polym. Sci.* **2015**, 1-8.
16. Wang, J.; Gardner, D. J.; Stark, N. M.; Bousfield, D. W.; Tajvidi, M.; Cai, Z.; 2018. *J. Chem. Eng.* **2018**, 6, 49-70.
17. Dewi, R.; Sylvia, N.; Zulnazri; Riza, M. *J. Mater. Today: Proc.* **2023**, 87, 396-400.

Enhancing the mechanical properties of pineapple leaf fiber paper sheets with a dispersing agent

Malinee Leekrajang*, Nattaporn Chutichairattanaphum, Borwon Narupai, and Teerakorn Kongkaew

Expert Centre of Innovative Materials, Thailand Institute of Scientific and Technological Research, Khlong Luang, Pathumthani, 12120, Thailand

**E-mail: malinee@tistr.or.th*

Abstract:

Pineapple leaf fiber (PALF) is an agricultural waste material valued for its abundant cellulose content and eco-friendly characteristics. This research aimed to investigate the mechanical properties of PALF paper. To enhance its quality, PALF paper underwent a process that involved the removal of lignin and other components through treatment with a NaOH alkali solution, followed by bleaching with an H_2O_2 solution. Additionally, dispersing agents at various concentrations (0, 1, 3, 5, 7 and 9 g/l) were incorporated into the PALF paper to aid in the paper formation process. The outcomes demonstrated that the inclusion of a dispersing agent led to significantly improve in the properties of PALF papers, particularly in terms of enhanced bursting and tearing strength. To gain a deeper insight into the structural transformations, scanning electron microscopy (SEM) was employed to examine the surface morphology of the PALF papers. The SEM images revealed the arrangement of dispersing agent and fibers within the PALF papers.

1. Introduction

In recent years, there has been a significant increase in research aimed at using sustainable and eco-friendly biomaterials. One of the world's most abundant and renewable natural biopolymers is cellulose, and there is great interest in using agricultural waste residues as the primary source.[1] Natural fibers, known as lignocellulosic fibers, consist of cellulose, hemicellulose, lignin, pectin, wax, and water-soluble substances.[2,3] These fibers have several advantages, such as low cost, eco-friendliness, high strength-to-weight ratios, recyclability, and biodegradability, which have made them the subject of academic and industrial research in several fields, including packaging, automotive, textile, and construction.[4,5] Pineapple leaf fibers (PALF) are agricultural waste products that can be used as renewable materials in various industries and research. PALF is a low-cost and easily accessible option due to its high cellulose content, which ranges from 70% to 82%. This is different from other natural fibers like banana stem fibers, CF, and hemp.[6] PALF's high cellulose content and reduced microfibrillar angle improve the mechanical and physical strength of the materials. PALF is used as a raw material in several products and processes, including the extraction of nanofiber and cellulose fibers, as well as the creation of composites, paper, and textiles.[7-10] PALF is used in the production of polymer-reinforced biocomposites,[4] polyester composites,[11] low-density polyethylene (LDPE) composites,[12] and biodegradable plastic composites.[13]

Fiber properties can be enhanced and customized to varying degrees through various treatments, such as chemical, physical, and biological modifications. These treatments have been used to improve the properties of natural fibers.[14] Many chemicals are used in these treatments, including sodium hydroxide,[15] peroxide,[16] silane,[17] anhydrides,[18] and organic and inorganic acids.[2] Recently, significant studies have been conducted to exploit PALF for extracting cellulose using surface modification methods. To obtain pure cellulose, the raw material must undergo pulping (alkali) and bleaching treatments to remove lignin and hemicellulose. This chemical treatment breaks intermolecular and intramolecular hydrogen bonding between the hydroxyl groups, increasing the accessibility of cellulose.[19] Lopattananon *et al*. studied PALF and treated it with NaOH solutions of varying concentrations (1%w/v, 3%w/v, 5% w/v, and 7%w/v). They found that the treatment with 5% NaOH improved composite strength compared to untreated fiber.[20] For pulp production, several chemicals act as pulp-dispersing agents, such as Acramine 3187[21] and polyethylene oxide (PEO)[22]. These agents help the fibers distribute evenly in the frame and increase the strength of the paper by causing the fibers to be arranged neatly while stacking sheets.

This study aims to enhance the mechanical properties of PALF paper by utilizing chemical treatment with NaOH alkali solution and bleaching with H_2O_2 solution. Furthermore, several concentrations of dispersing agents for Acramine 3187 were prepared. The mechanical properties of

PALF papers were evaluated by conducting burst and tear testing, whereas surface morphology was analyzed through SEM.

2. Materials and Methods

2.1 Materials

The raw materials of smooth cayenne pineapple leaves were obtained from a Thai market in Pathum Thani province. The leaves with 60-70 cm long were chosen from pineapple plants at the age between 12-14 months. The process of preparing pineapple leaf fibers includes utilizing a pineapple leaf decorticator, a machine specifically designed for separating fibers from the leaves. This results in green-colored fibers, which is then washed before being dried. The fibers obtained through this process exhibit high mechanical strength. Furthermore, the leaves were cut into lengths of 10-15 cm and stored at room temperature to reduce water content. All reagents and chemicals employed in our study were of analytical reagent grades, including sodium hydroxide, hydrogen peroxide, sodium silicate and other relevant chemicals. The dispersing agent is Acramine 3187 as a polymer emulsion.

2.2 Chemical treatment

The pineapple leaf fibers, cut into small pieces approximately 10 centimeters in length, are soaked in a 4% sodium hydroxide (NaOH) solution overnight. The process involved treating pineapple leaves with an alkali solution for a duration of 2 hours at 70 °C, followed by multiple washes with distilled water. Subsequent to the alkali treatment, a bleaching process was conducted to eliminate lignin, utilizing hydrogen peroxide at 80 °C for 2 hours. The resulting fiber pulp was then subjected to drying in an oven for a period of 12 hours at 80 °C.

2.3 Preparation of sheets

The PALF papers were fabricated following the ISO 5269-1 procedure. The fiber pulps were soaked in water overnight to induce swelling, and then mechanically disintegrated using a customized blender. Polymer dispersing agent (Acramine 3187) was added at concentrations of 0, 1, 3, 5, and 7 incorporated into the PALF paper preparation. The fiber pulp is blended with Acramine 3187 by pulp disintegrator at the rate period time of 10 minutes. Subsequently, the dispersed pulp was formed into sheets using a wooden frame. The wet sheet was then dried in an oven at 60 °C to remove moisture until the pulp was completely dried.

2.4 Characterization of pineapple leaf fiber paper sheets

The bursting and tearing strengths of PALF paper sheets were evaluated in accordance with the ISO 2758:2001 and ISO 1974:1990 methods, respectively, employing a testometric machine with clamp movement set at 1 mm/min. Each sample was replicated with more than five specimens. The surface morphology of PALF paper sheets at different concentrations of dispersing agent was analyzed using scanning electron microscopy (SEM) with a Jeol JSM-6400 scanning electron microscope.

3. Results & Discussion

3.1 Sheet formation

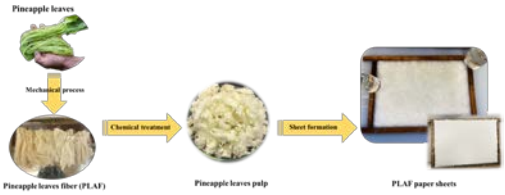

Figure 1. The fabrication of PLAF paper sheets with dispersing agent.

Preparation of paper sheets from pineapple leaf fibers for mechanical property testing using Acramine 3187 as a dispersing agent in the paper sheet formation process. The study investigated the concentration of dispersing agent at 0, 1, 3, 5, 7 and 9 g/l. The mechanical properties testing of pineapple leaf fiber paper sheets includes tear resistance according to ISO 1974 standards and burst strength according to ISO 2758 standards. Furthermore, the evaluation of the mechanical properties of five paper sheets revealed an average weight of 80±5 g/m², an average density of 0.438±7 g/m^3, and an average thickness of 0.18±6 mm.

3.2 Bursting strength properties

Bursting strength is the ability of paper to resist pressure applied on a test specimen at a consistently increasing rate until the paper bursts. The ISO 2758: 2001 method is employed to evaluate the durability and toughness of the paper. In general, the bursting strength value depends on the type, proportion, fiber preparation, and total fiber content, including the content of substances in the paper sheet. Figure 2 displays the bursting strength outcomes of PLAF paper sheets at different concentrations of a dispersing agent, specifically at 0, 1, 3, 5, 7 and 9 g/l for formation of paper sheets.

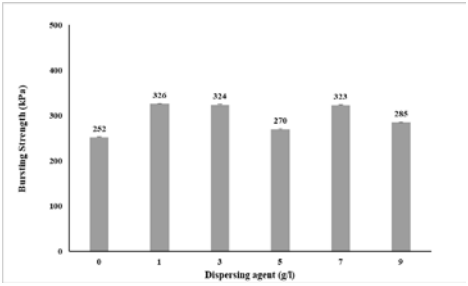

Figure 2. Effect of dispersing agent concentration on the bursting strength.

The bursting strength of the PLAF paper sheets increased with the addition of the dispersing agent. For sample without dispersing agent, the bursting strength was the lowest, indicating a weaker paper sheet. The PLAF paper with the dispersing agent shows no significant difference in bursting strength. However, it leads to an increase in tearing strength. Moreover, as the dispersing agent was added, the fibers became more uniformly distributed, leading to smoother paper and helping to prevent the agglomerates of pulp. The dispersing agent can be attributed to the improved dispersion and bonding of the fibers, which ultimately led to enhance overall sheet strength.

3.3 Tearing strength properties

The tearing strength is a quantitative measure of a paper's resistance to the force required for tearing, as specified by the guidelines outlined in ISO 1974:1990. The tearing strength of PLAF paper sheets, formed under different concentrations of dispersing agent ranging from 0 to 9 g/l, is depicted in Figure 3. The results show a clear trend of increasing tearing strength with increasing concentration of dispersing agent. At a concentration of 0 g/l, the tearing strength is relatively low, indicating poor inter-fiber bonding. However, as the concentration of dispersing agent increases, the tearing strength improves significantly. The highest tearing strength of 3780 mN was obtained at a dispersing agent concentration of 7 g/l, indicating strong inter-fiber bonding and enhanced paper strength. These findings suggest that the addition of dispersing agent can greatly improve the tearing strength of PLAF paper sheets. The dispersing agent played a crucial role in improving the strength and quality of the paper sheets during formation. The tearing strength value decreased at a dispersing agent concentration of 9 g/l due to an excess of dispersing agent, causing the fibers to become excessively slippery. This resulted in a weaker bond between the fibers, leading to a decrease in tearing strength. The dispersing agent at a concentration of 7 g/L exhibits a maximum tearing strength and a bursting strength of 323 kPa. Therefore, this concentration is selected as the appropriate strength for paper sheet formation.

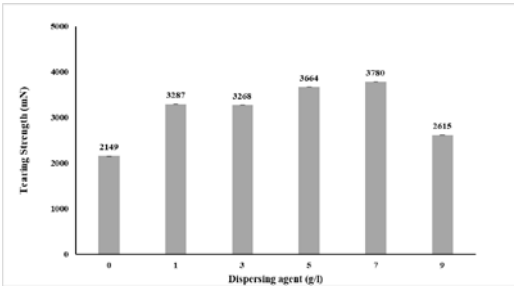

Figure 3. Effect of dispersing agent concentration on the tearing strength.

3.4 Surface morphology

The effect of dispersing agent concentration on the morphology of PLAF paper sheets was revealed by SEM analysis. Figure 4A revealed that the PLAF paper sheets had a highly fibrous structure with a uniform distribution of fibers throughout the sheet. In contrast, Figures 4B-F indicated that the dispersing agents were responsible for filling the gaps between the pineapple fibers, resulting in a more interconnected network.

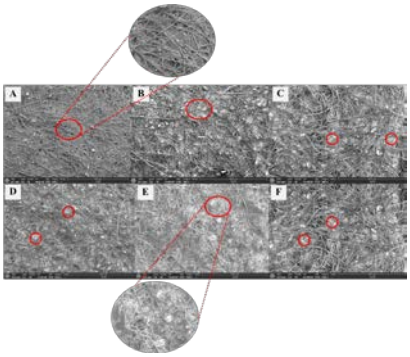

Figure 4. Surface structures of PLAF paper sheets at various dispersing agent concentrations: 0 g/l (A), 1 g/l (B), 3 g/l (C), 5 g/l (D), 7 g/l (E), and 9 g/l (F).

In the PLAF paper sheet forming process, a dispersing agent helps the pulp disperse well in water, preventing fibers from aggregating. Moreover, the dispersing agent not only enhances the surface strength but also helps to improve the uniformity and smoothness of the paper surface, as shown in Figure 5.

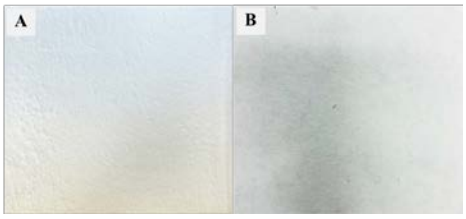

Figure 5. (A) PLAF paper sheets without dispersing agent and (B) PLAF paper sheets at dispersing agent concentrations of 7 g/l.

4. Conclusion

The PLAF paper sheets were formed by adding dispersing agent at 0-9 g/l. The bursting and tearing strengths were characterized in compliance with ISO 2758:2001 and ISO 1974:1990 methods. The results showed that the addition of the dispersing agent had a significant impact on the mechanical properties of the PALF paper. The addition of dispersing agent is known to improve the fiber dispersion and the coordination of fibers during the paper formation process. The morphology of the PLAF paper sheets was revealed by scanning electron microscopy (SEM) analysis. The analysis demonstrated that the arrangement of fibers with dispersing agent in the PLAF paper sheets significantly contributed to their elevated mechanical strength and durability.

Acknowledgements

The financial support for this project was provided by National Research Council of Thailand (NRCT) and Thailand Institute of Scientific and Technological Research (TISTR).

References (In ACS style)

1. Zugenmaier, P. *Prog. Polym. Sci.* **2001**, *26* (9), 1341–1417.
2. Li, X.; Tabil, L. G.; Panigrahi, S. *J. Polym. Environ.* **2007**, *15* (1), 25–33.
3. Faruk, O.; Bledzki, A. K.; Fink, H.-P.; Sain, M. *Prog. Polym. Sci.* **2012**, *37* (11), 1552–1596.
4. Sedan, D.; Pagnoux, C.; Smith, A.; Chotard, T. *J. Eur. Ceram. Soc.* **2008**, *28* (1), 183–192.
5. Majeed, K.; Jawaid, M.; Hassan, A.; Abu Bakar, A.; Abdul Khalil, H. P. S.; Salema, A. A.; Inuwa, I. *Mater. & Des.* **2013**, *46*, 391–410.
6. Petchwattana, N.; Covavisaruch, S. *J. Bionic Eng.* **2014**, *11* (4), 630–637.
7. Kengkhetkit, N.; Amornsakchai, T. *Ind. Crop. Prod.* **2012**, *40*, 55–61.
8. Chollakup, R.; Tantatherdtam, R.; Ujjin, S.; Sriroth, K. *J. Appl. Polym. Sci.* **2010**, *119* (4), 1952–1960.
9. Mishra, S.; Mohanty, A. K.; Drzal, L. T.; Misra, M.; Hinrichsen, G. *Macromol. Mater. Eng.* **2004**, *289* (11), 955–974.
10. Threepopnatkul, P.; Kaerkitcha, N.; Athipongarporn, N. *CompositesB* **2009**, *40* (7), 628–632.
11. Mishra, S.; Misra, M.; Tripathy, S. S.; Nayak, S. K.; Mohanty, A. K. *J. Reinf. Plast. Compos.* **2001**, *20* (4), 321–334.
12. George, J.; Bhagawan, S. S.; Prabhakaran, N.; Thomas, S. *J. Appl. Polym. Sci.* **1995**, *57* (7), 843–854.
13. Liu, W.; Misra, M.; Askeland, P.; Drzal, L. T.; Mohanty, A. K. *Polymer* **2005**, *46* (8), 2710–2721.
14. Kabir, M. M.; Wang, H.; Lau, K. T.; Cardona, F. *CompositesB* **2012**, *43* (7), 2883–2892.
15. Yan, L.; Chouw, N.; Yuan, X. *J. Reinf. Plast. Compos.* **2012**, *31* (6), 425–437.
16. Wang, B.; Panigrahi, S.; Tabil, L.; Crerar, W. *J. Reinf. Plast. Compos.* **2007**, *26* (5), 447–463.
17. Asim, M.; Jawaid, M.; Abdan, K.; Ishak, M. R. *J. Bionic Eng.* **2016**, *13* (3), 426–435.
18. Tserki, V.; Zafeiropoulos, N. E.; Simon, F.; Panayiotou, C. *CompositesA* **2005**, *36* (8), 1110–1118.
19. Ariffin, A.; Yusof, Y. *MATEC Web Conf.* **2017**, *135*, 00042.
20. Lopattananon, N.; Panawarangkul, K.; Sahakaro, K.; Ellis, B. *J. Appl. Polym. Sci.* **2006**, *102* (2), 1974–1984.
21. Leupong, K., Sasithorn, N., & Manarungwit, K. *RMUTP sci.J.* **2017**, 11(1): 15-22.
22. Jayaramudu, T.; Ko, H.-U.; Kim, H. C.; Kim, J. W.; Choi, E. S.; Kim, J. *CompositesB* **2019**, *156*, 43–50.

Developing hydrophobic cellulose fibers for oil absorption from pineapple leaves

Nattaporn Chutichairattanaphum*, Malinee Leekrajang, and Borwon Narupai

Expert Centre of Innovative Materials, Thailand Institute of Scientific and Technological Research, Khlong Luang, Pathumthani, 12120, Thailand

**E-mail: nattaporn@tistr.or.th*

Abstract:

The process of developing hydrophobic cellulose fibers from pineapple leaves for oil absorption involves several key steps. Initially, raw pineapple leaf fibers are treated with a sodium hydroxide solution to remove hemicellulose, a component that attracts water. Subsequently, these fibers are coated with a gel solution and a surfactant to make them hydrophobic. This transformation is achieved through a gelation process and surface modification, resulting in cellulose fibers with hydrophobic properties. The experimental results reveal that these treated fibers exhibit outstanding water repellency and oil absorption capabilities. The combination of surface coating with a surfactant and the fiber preparation process directly affects the interaction between the surfactant and the hydroxyl groups on cellulose molecules, leading to improved fiber strength. This is evident from the increased contact angle of water droplets on the fiber surface, which falls within the range of 145.3° to 144.6°, signifying enhanced water resistance. Regarding their performance in oil absorption, the treated fibers prove to be highly effective. They demonstrate oil absorption efficiencies ranging from 93.42% to 91.40% after the first use and 87.44% to 85.65% after five uses, highlighting their sustained effectiveness over multiple applications.

1. Introduction

The significant increase in oil spills, estimated to be around 100 million gallons per year, poses a crucial environmental problem linked to the extensive utilization and transportation of oil and its derivatives1. This ecological threat spreads throughout ecosystems, affecting species, disturbing oxygen levels, and introducing extremely poisonous elements. The repercussions have a far-reaching impact on human food sources, as oil pollutants directly contaminate the food chain, depriving animals and plants of essential nutrients and wasting energy resources[2,3]. Given these obstacles, it is crucial to prioritize the development of novel materials that can swiftly and efficiently eliminate oil spills. These materials are crucial in reducing negative effects on ecosystems and human health. Commercial oil absorbents have advantageous effects on ecosystems, including expediting the effective remediation of oil spills, reducing pollution, alleviating environmental damage, and supporting restoration efforts. However, it is essential to consider negative outcomes such as harmful chemical composition, disruption of natural processes, additional pollution caused by improper disposal, impact on wildlife, and alteration of habitat structure. To successfully market these products, it is crucial to highlight their exceptional cleaning capabilities and their dedication to environmental safety. Moreover, providing explicit guidelines about the utilization and proper disposal of the products, along with endorsing investigations on sustainable resources, might allure environmentally-aware customers. A wide range of techniques, including mechanical, chemical, physicochemical, and biological approaches, have been developed for the purpose of removing oil. Among these, sorbents have shown great potential as a promising solution. Although several methods are used in the cleanup of oil spills, there are ongoing difficulties that exist. These obstacles include limited effectiveness in separating oil from water, expensive operations, vulnerability to environmental factors, lengthy cleanup periods, disturbances to ecosystems, and the creation of additional pollutants. Adsorption is a highly successful and diverse approach for controlling oil spills in this setting. It showcases efficiency, cost-effectiveness, simplicity, ease of operation, longevity, and reusability. Nevertheless, chemically synthesized sorbents such as melamine sponges, polyethylene, and polypropylene, despite their high sorption effectiveness, have challenges such as expensive costs, complex manufacturing methods, and lack of biodegradability, which limit their sustainable use. Therefore, it is crucial to develop novel materials that enable rapid and effective oil spill cleanup, while also limiting negative effects on ecosystems and human well-being. Natural materials, which are known for being inexpensive, abundant, and environmentally beneficial, frequently have lower sorption effectiveness compared to synthetic materials because they inherently lack the ability to attract and repel oil and water. [4-6] To overcome this

constraint, it is necessary to make alterations to sorbents via mechanical, thermal, and chemical techniques. Coupling agents are used to improve the adhesion between the fiber and polymer phases by creating a chemical link between them. During this process, the coupling agent undergoes a reaction with the surface of the fiber, specifically at the hydroxyl group. Simultaneously, the other end of the coupling agent forms connections with the functional group of the polymer matrix through different interactions, such as covalent bonds, hydrogen bonds, acid-base interactions, and chain entanglement. The nature of the interaction varies depending on the specific polymer in question.[7-9] Silanes and isocyanates are the predominant coupling agents utilized in natural fiber-reinforced polymer composites.[10-12] During the process of silane treatment, the hydroxyl groups present on the fiber participate in the creation of a covalent link with silanol groups. Similarly, during the isocyanate treatment, a chemical bond called a urethane linkage is formed between the hydroxyl groups of the natural fiber and the isocyanate groups[12]. Furthermore, a prominent strategy involves altering cellulose I, a common constituent found in natural fibers. The hydrophilic characteristic of cellulosic fibers can be reduced by altering or eliminating their hydrophilic or hydrophobic groups using different chemical treatments. This improves the mechanical strength and dimensional stability, especially in composites made of natural fibers and polymers. This study focuses on examining the effects of chemical treatment on pineapple leaf fibers in order to impart hydrophobic characteristics for the purpose of oil spill remediation. The leaf sections of pineapple plants include highly cellulose fiber components that are known for their exceptional strength and stiffness. The cellulose concentration in pineapple leaf fiber is remarkably high, measuring 81.27%. It is followed by hemicellulose at 12.31% and lignin at 3.46%.[13] The reduced lignin content in pineapple leaf fibers provides a beneficial characteristic for chemical extraction, as lignin functions as a binding agent that holds together cellulose and hemicellulose. The research aims to augment the mechanical characteristics, raise water resistance, and diminish water absorption in pineapple leaf fibers by means of chemical treatment. The study aims to enhance the development of efficient and long-lasting methods for cleaning up oil spills, focusing on environmental preservation and optimizing material usage.

2. Materials and Methods

2.1 Materials

The pineapple leaves were obtained from the Community Enterprise Network: Pineapple Cultivation Group located in Ao Noi Subdistrict, Mueang District, Prachuap Khiri Khan Province. All reagents and substances used in this study were of analytical reagent grades. The sodium hydroxide (NaOH) and 2-Propanol were obtained from KEAMUS. Trichloro(octadecyl) silane and Octadecyltrichlorosilane (OTS) were acquired from Sigma, whereas hydrogen peroxide (H_2O_2) solutions were supplied by Q RëC™. Toluene and Ammonia were provided by RCI Labscan™, while Ethanol was obtained via RCL Labscan.

2.2 Methods

2.2.1 Preparation of Absorbent Material from Pineapple Leaves

Prepare absorbent materials from dried pineapple leaf fibers by immersing the fibers in a 4% NaOH solution with a fiber-to-solution ratio of 1:10 for 12 hours.

2.2.2 Modification of Pineapple Leaf Fibers

In a 4% NaOH solution, submerge dry pineapple leaves in a fiber-to-solution ratio of 1:10. As the solution's temperature rises to 80°C, maintain the leaves submerged for a duration of two hours, monitoring for the initiation of delamination. Subsequently, rinse the leaves meticulously with distilled water until a neutral pH of 7 is achieved. The leaves should then be desiccated for 24 hours at 105°C in an oven, as illustrated in Figures 1 (A), (B), and (C).

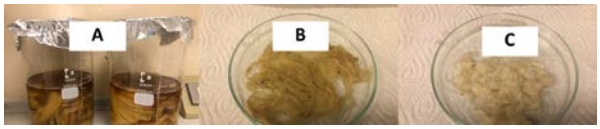

Figure 1. Pineapple leaves (A) before, (B, C) Fiber after soaking for 12 hours treatment with NaOH.

2.2.3 Hydrogen Peroxide Bleaching of Fibers

Commence the procedure by cutting the fibers into tiny strands, then measure the weight of a single fiber to be 120 g. A solution is formed by combining 3,600 ml of deionized water (DI water), 18 g of 30% hydrogen peroxide (H_2O_2), 5.4 g of sodium silicate, and 21.6 g of NaOH. To bleach the fibers, immerse them in the prepared solution and heat them at a temperature of 80°C for one hour. Thoroughly wash the fibers in distilled water, repeating the procedure five to ten times, or until the pH reaches a stable neutral level of seven. Retain these samples in order to assess their

hydrophobicity using silane (Si), as illustrated in Figure 2.

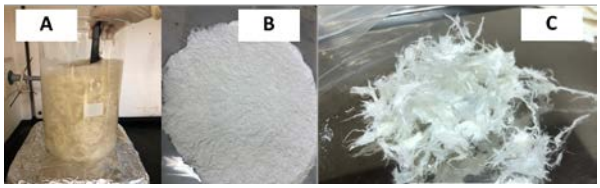

Figure 2. Pineapple Fiber Before (A) and (B, C) After Bleaching.

Then, oven-dry the fibers at 105°C for 24 hours. Following that, the hydrogen peroxide-bleached fibers are meticulously mechanically treated to enhance their surface area and so improve their absorption capabilities.

2.2.4 Preparing the Fiber Surface Before Hydrophobic Coating

Weigh 10 g of NaOH-modified fibers. Subsequently, soak the fibers in a solution of Ammonia: Isopropyl alcohol: H_2O in the following ratios: 63:400:220. Then, add tetraethyl orthosilicate (TEOS) to the solution mixture and stir for 10 minutes. After that, soak the fibers for 5 hours in a row. Following the immersion period, rinse the fibers with distilled water 5-10 times, or until the pH hits 7. Finally, oven-dry the fibers for 24 hours at 105 ˚C.

2.2.5 Surface Modification of Pineapple Leaf Fibers for Hydrophobicity

In order to apply the coupling agent toluene, immerse 1 g of pineapple fibers that have been surface-modified (4% NaOH) in a solution consisting of 50 ml of toluene and 1 g of OTS (as depicted in Figure 3A). After 5 mins of blending, the fibers are extracted from the solution and transferred to a receptacle containing 100 ml of ethanol. Follow an ultrasonic apparatus to promote agitation for a duration of 1 min. This period serves as the preliminary purification stage, intentionally removing any remaining reaction by-products. After two additional rinsing cycles, transfer the fibers to a receptacle containing 100 ml of ethanol per cycle and agitate for 1 min. (defined 3B) Following the last rinse, dehydrate the fibers at 60˚C for 1 hr. in accordance with the composition listed in Table 1. The subsequent samples are as follows: FIB_Si demonstrated the fiber coated with silane; FiB_H_2O_2Si demonstrated the fiber subsequent to breaching and coating with silane; and FiB_GelSi demonstrated the fiber subsequent to solgel followed by coating with silane.

Figure 3. Coating pineapple fiber with a hydrophobic substance A) . Submerge the fiber in a silane-containing solution. B) Dry FiB_H_2O_2 fiber based on Si.

Table 1. The composition of the hybrid fibers paper

Sample	Composition
FiB_Si	Treated Fiber with NaOH + Si
FiB_H_2O_2Si	Treated Fiber with NaOH + H_2O_2+Si
FiB_GelSi	Treated Fiber with NaOH + Coated Gel + Si

2.3 Characterization of Pineapple Fiber

This research represents the thorough examination of significant functional groups through the utilization of Fourier Transform Infrared Spectrometry (FT-IR). The FTIR analysis is performed utilizing a Shimadzu IRPrestige-21 instrument in Attenuated Total Reflectance (ATR) mode. The spectra of the samples were obtained over a period of 45 images, spanning from 750 to 4000 cm^{-3}, with a resolution of 4 cm^{-3}. Furthermore, a comprehensive analysis of the morphological properties of pineapple fibers, both prior to and following modification, is performed utilizing a scanning electron microscope (SEM) in this research. Moreover, by measuring the contact angle, the wetting properties of liquid droplets on a solid surface can be ascertained. The value of this angle is determined by the equilibrium between the surface forces of the object and the internal forces of the liquid at the point of intersection between the liquid droplet and the surface of the object in contact. A contact angle in proximity to 0˚ signifies extensive liquid dispersion across the surface, which is suggestive of a high capacity for wetting. On the contrary, a contact angle approaching 180˚ indicates that the water droplet has a low wettability and will float without expanding. A number of variables affect this angle, including the surface tension of the liquid, the surface energy of the substance, and the surface roughness. The contact angle measurement is also utilized to provide valuable insights into the hydration capabilities of the material when assessing the water absorption properties of fibers in accordance with ASTM D 281.

2.3.1 Oil absorption testing (ASTM D 281)

The experiment involved testing fibers that had been conditioned and exhibited good water resistance for their ability to absorb oil and water according to ASTM D 281 standards as follow;

Set up by placing absorbent grains on a glass dish or soft rock, weighing 0.2 g. Then, using a dropper, add the oil drop by drop, stirring thoroughly with a spatula, as illustrated in Figure 4. The test is finished when enough oil has been absorbed and combined with the absorbent fibers. Weigh and compute the difference in weight of the utilized oil. After that, weigh a 50 ml beaker and record its empty weight. After that, take a beaker of hexane and submerge the oil-absorbed fibers in it. Raise the fibers to enable the hexane to drain, then collect the hexane mixture that has gone through the fibers in the beaker. When the hexane has entirely evaporated, weigh the leftover oil and subtract it from the original beaker weight. Figures 4A and 4B show the fiber following oil and water absorption tests. The determination of absorbency capacity (%WC) involves the calculation outlined in Equation 1.

$$\%WC = \frac{Wt_{After} - Wt_{Before}}{Wt_{After}} \times 100 \qquad (1)$$

When, (%WC) denotes the absorbency capacity of the material. Wt_{Before} represents the initial mass of the substance prior to absorption, whereas Wt_{After} indicates the mass of the substance after it reaches saturation.

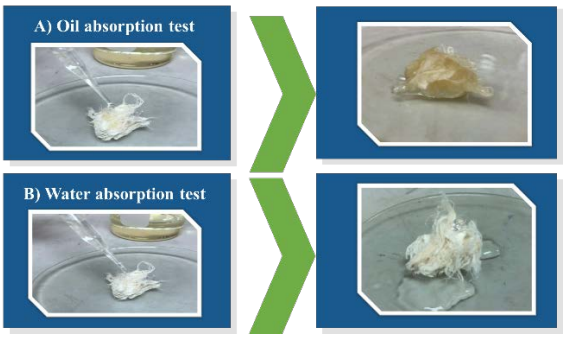

Figure 4. An investigation of the fibers' oil and water absorption capacities. The fiber absorbs oil test (A). B) A fiber water absorption test.

3. Results & Discussion

3.1 Analysis of functional groups using a Fourier Transform Infrared Spectrometer (FT-IR).

The results of the analysis of important functional groups in pineapple fibers before surface modification using FTIR in the wavelength range of 4,000-500 cm^{-1} revealed specific peaks. In Figure 5, a peak at 3,331 cm^{-1} indicates the vibration of the O-H stretch, suggesting the presence of lignin and cellulose. Another peak at 2,916 cm^{-1} represents the C-H stretch, while a peak at 1,728 cm^{-1} corresponds to the C=O stretch in ester and acetyl groups within hemicellulose or carbonyl groups in ferulic and p-coumaric acids of lignin. After surface modification with NaOH, the peak at 1,728 cm^{-1} disappeared, indicating the removal of carbonyl groups. However, a peak at 1,643 cm^{-1} persisted, indicating the presence of the C=C functional group in the aromatic ring of lignin and absorbed water. When the fibers were further treated and coated with a silane compound, the Si-O-Si peak at 1049 cm^{-1} indicated successful attachment.

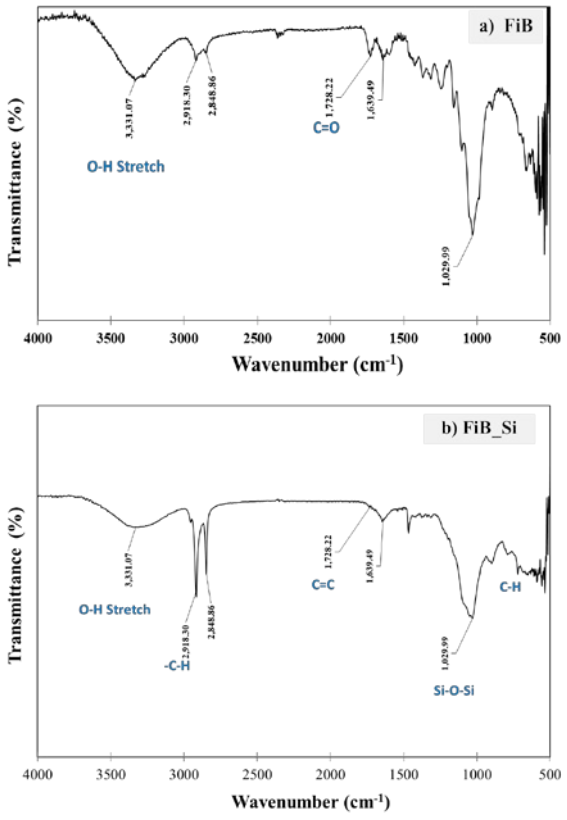

Figure 5. FTIR study of pineapple fibers a) before and b) after treatment with Silane.

3.2 Analysis of Wetting Properties through Contact Angle Measurement.

In this research, contact angle measurement is employed to demonstrate surface energy related to wetting behavior, which depends on the interplay between adhesion and cohesion forces. Surface classification according to the contact angle θ of a water droplet is as follows: superhydrophilic at θ = 0°, hydrophilic at θ< 90°,

and hydrophobic at θ > 90°.[14] Analyzing the relationship between fiber modification methods and contact angles from the results table, it is observed that the fiber treated with silane maintains high water wettability, as illustrated in Figure 6

This is due to the inability to measure the angle directly when water is dropped onto the fiber surface, as water rapidly penetrates the fibers. When fibers treated with NaOH and coated with a single layer of TEOS are tested, the results show that the fibers still exhibit high water affinity, with contact angle measurements in the range of approximately 90°. Furthermore, upon enhancing fiber surface coating with a silane compound or OTS, it is evident that the fibers become more water-resistant, with contact angle values ranging from 145.3° to 144.6°, as illustrated in Figure 7.

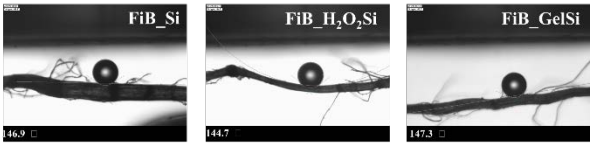

Figure 6. The Contact Angle of Water Droplets on Different Pineapple Fiber Samples Varies According to Sample Preparation Steps.

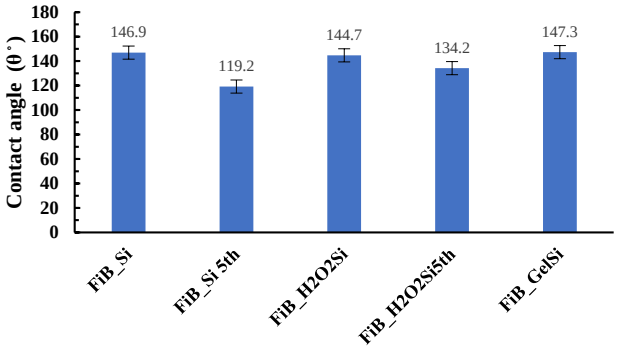

Figure 7 The Effects of Pineapple Fiber Modification Methods on the Contact Angle of Water Droplets on Fibers.

Table 3 An analysis of pineapple fibers subjected to various surface modifications revealed that fibers that underwent sizing to induce hydrophobicity retained the capacity to absorb oil repeatedly. Table 3 displays the absorption capability (%WC), which serves as an indication of the reusability of the fibers. When subjected to five cycles of testing, pineapple fibers treated with NaOH and coated with sizing demonstrated the capacity to absorb oil on multiple occasions. The initial absorption of oil was 93.42 percent; subsequent cycles witnessed a reduction of approximately 6 to 7 percent. This underscores the substantial impact that sizing has on augmenting the hydrophobicity of the surface of the pineapple fiber, thereby facilitating recurrent oil absorption capabilities.

Table 3. Illustrates the performance of fiber absorbency.

Sample	%WC
FiB_Si	93.42
FiB_Si ^{5th}	87.44
FiB_H_2O_2Si	91.4
FiB_$H_2O_2Si^{5th}$	85.65
FiB_GelSi	92.0
FiB_$GelSi^{5th}$	86.33

3.3 Study of the morphological characteristics of pineapple fibers using a Scanning Electron Microscope (SEM).

The SEM investigation on pineapple fibers showed structural alterations after surface modification with a gel coating. Before surface modification, the fiber surface shows minor imperfections, suggesting an unequal distribution. After surface modification, shown in Figures 7B, 7C, and 7D, there is a significant increase in surface roughness. A thicker layer of coating is obvious especially when treated with hydrogen peroxide or gel coating. Applying gel coating greatly improves surface evenness. The fiber surface is covered with a protective coating layer, demonstrating the uniform dispersion of the coating material. The surface alteration of the pineapple fibers does not affect their structural integrity. The fibers retain their quality without any cracks or losses. This study highlights how surface modification via gel coating may enhance the uniformity and maintain the structure of pineapple fibers without compromising their natural quality, as illustrated in Figure 8.

4. Conclusion

In summary, the project of producing a cellulose material derived from pineapple leaves that possesses improved resistance to oil has been effective. The methodology incorporates the utilization of both fresh and desiccated fibers derived from pineapple leaves, which are conditioned using a solution of sodium hydroxide. As a consequence, newly harvested fibers exhibit a more malleable consistency, whereas desiccated fibers demonstrate a nuanced enhancement in suppleness while maintaining their fibrous attributes.

Additional purification with a solution of hydrogen peroxide not only improves the color but also the softness of the fibers. The fibers that are treated with the hydrophobic properties imparted by the ensuing coating process are exceptionally oil-absorbent and water-repellent. This prosperous endeavor exhibits potential for applications in which efficient oil repellency is essential.

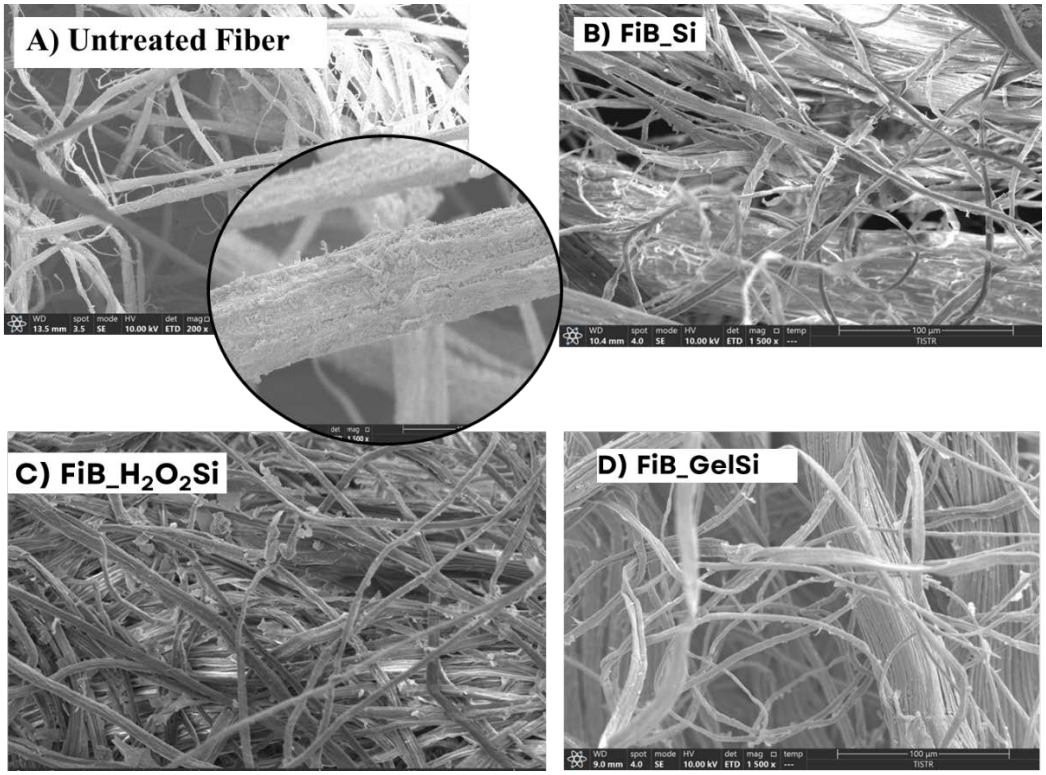

Figure 8. Scanning Electron Microscope (SEM) images before and after surface modification with Silane treatment.

Acknowledgements

The authors gratefully acknowledge the Thailand Institute of Scientific and Technological Research (TISTR) for financial, material, and instrument support.

References

1. Tran, Y. D. T.; Zenitova, L. A. Effective Treatment of Oil Spills by Adsorbent Formed from Chitin and Polyurethane Foam. *Current Applied Science and Technology*. **2020**, 20, 2 (May-August 2020).
2. Zunaira, A.; Zhi, C.; Chunjiang, A.; Jinxin D. Environmental Impacts and Challenges Associated with Oil Spills on Shorelines. *J. Mar. Sci. Eng*. **2022**, 10, 762.
3. Chughtai, R.; Asif, Z. Study fate of pollutants due to oil spill in sea water through multimedia environmental modeling. *Int. J. Environ. Sci. Technol*. **2021**, 18, 761–770.
4. Zhiyong, L.; Mengyao, C.; Che, L.; Fuying, L.; John, T. A.; Jiahui, H.; Gang Z., Zipeng Q., Xiaowang, Z.; Weijie, Z.; Dinggui, C.; Xiangfang, P.; Tingjie, C. Solar-assisted high-efficient cleanup of viscous crude oil spill using an ink-modified plant fiber sponge. *J. Hazard. Mater.***2022**,432.
5. Egle, A.; Vaidotas, V. Natural oil sorbents modification methods for hydrophobicity improvement. *Energy Procedia*. **2018**, 147, 295-300.
6. Pungpai, P.; Watankornsiri, A.; & Kangkun, N. Comparison of Absorptive Efficiency of Oil Spill Dispersants Using Naturally Nano-technologically Porous Materials. *Koch Cha Sarn Journal of Science*. **2018**, 40 (1) January-June 2018.
7. Sergiu, C.; Gabriela, B.; Lidija, F. Z.; Jasna, S. S.; Per, T. L.; Simona, S.; Tatjana, K.; Ali, N.; Tom, L. One-shot carboxylation of microcrystalline cellulose in the presence of nitroxyl radicals and sodium periodate. *RSC Adv*. **2015**, 5, 85889.
8. Max, J. H. W.; Cameron, J. S.; Louisa J. E.; Jonathan A. C.; Christopher, T.; Gibson, S. K. L.; Yanting, Y.; Nicholas, A. L.; Jason R. G.; Inês, S. A.; Joseph, G. S.; Gunther, G. A.; David, A. L.; Gonçalo, J. L. B.; Justin, M. C. Sustainable Polysulfides for Oil Spill Remediation: Repurposing Industrial Waste

for Environmental Benefit. *Adv. Sustainable Syst*. **2018**, 2, 1800024.

9. Orratai, W.; Rinradee, N.; Panjai, S.; Jittima P. Adsorption of Suspended Oil Using Bagasse and Modified Bagasse. *J Sci Technol MSU*. **2012**, 31, 4, July-August 2012.
10. Stefan, C.; Anna, M. Superiority of Cellulose Non-Solvent Chemical Modification over Solvent-Involving Treatment: Application in Polymer Composite (part II). *Materials* **2020**, 13, 290.
11. Potjanart, S.; Thiranan, T.; Wirasak, S.; Rungsima, C. Modification of pineapple leaf fiber surfaces with silane and isocyanate for reinforcing thermoplastic. *Journal of Thermoplastic Composite Materials*. Downloaded from jtc.sagepub.com at FLORIDA INTERNATIONAL UNIV on March 16, 2016.
12. Chinnappa, A.; Gandarvakottai, S. A.; Ashok, G.; Sarojadevi, M. M. Water Absorption Properties of Short Banana Fiber/Unsaturated Polyester/Molecular Sieves + ZnO Nanorod HybridNanobiocomposites. *ACS Omega* **2021**, 6, 35256−35271.
13. Cherian, B.M.; Leão, A.L.; de Souza, S.F.; Thomas, S.; Pothan, L.A.; Kottaisamy, M. Isolation of nanocellulose from pineapple leaf fibres by steam explosion. Carbohydr. Polym. **2010**, 81, 720–725.
14. Arun, K. Kota.; Gibum Kwon; Anish T. The design and applications of superomniphobicsurfaces. NPG Asia Materials **2014** 6.

Synthesis of conjugated network polymers from thieno[3,4-b]pyrazine derivatives

Prapassorn Ongjaroon[1], Worawan Bhanthumnavin[2], and Yongsak Sritana-Anant[2]*

[1]*Program in Petrochemistry and Polymer Science, Faculty of Science, Chulalongkorn University, Bangkok,10330, Thailand*
[2]*Department of Chemistry, Faculty of Science, Chulalongkorn University, Bangkok 10300, Thailand*

**E-mail: yongsak.s@chula.ac.th*

Abstract:

Conjugated polymers have been widely used in many applications such as organic field effect transistors, organic light-emitting diodes (OLEDs), sensors, and organic photovoltaic (OPV) cells. They consist of π–conjugated system with alternating single and double bonds along the main chain. The naturally rotating linking single bonds can decrease the efficiency of π–delocalization on the main chain and limit the conjugated properties of the polymer. Conjugated network polymers (CNPs), derived from monomers joined together in more than 2 directions, could block such rotations, and flatten the polymer plane, hence improving the efficiency of electron delocalization. Derivatives of thienopyrazine have been reported to be excellent precursors for delivering visible-NIR absorbed low bandgap conjugated polymer. In this research, we use 2,3-di-(bromomethyl)thieno[3,4-b]pyrazine as a monomer with 4 connection sites to form novel CNPs through solid-state polymerizations (SSPs), oxidative polymerizations and substitutions. Poly(2,3-di-(bromomethyl)thieno[3,4-b]pyrazine) had been prepared, characterized by solid UV and IR, exhibited broad absorption in the visible regions extending into the near-infrared. The facile synthesis of these materials could expand the scope of their applications in organic devices.

1. Introduction

Polymers are formed from several monomer molecules joined together, usually with only two reactive sites, resulting in a usual two-dimensional chain-like polymeric form. If monomers have more than two functional groups or reactive sites that can connect with other molecules in more than two directions, crosslinked polymers with potentially extended into a network structure would be obtained. Network polymers consist of two main components: the main chain and the junctions. Their properties can be controlled by the proportions and types of the junctions, the types of main chains, the forms of the network and the conditions of polymerization reactions.[1,2] Network polymers tend to have unique and distinct properties such as flexibility, porosity, solidity, expandability and other mechanical properties.[3,4] They have been applied in many areas such as drug delivery systems,[5] tissue engineering,[6] gas storage,[7] catalysts,[7] and electronic devices.[8]

Conjugated polymers are polymers that have semi-conducting properties. The main structure of conjugated polymers has an alternating arrangement of single and double bonds throughout the main chain structure, called π conjugate system. When the polymers are stimulated by external energy, the electrons in the π orbitals can move through the π–conjugated system, resulting in their ability to conduct electricity. The magnitude of this special property depends on the difference in the energy levels between the HOMO (valence band) and the LUMO (conduction band) or band gap (E_g) of the polymer. The narrow difference of these energy levels or low E_g value is preferred to allow the valence electrons to be easily excited with low external energy and initiate the desired conductivity and other electroactive related properties. Derivatives of thieno[3,4-*b*]pyrazine (TP) are examples of aromatic monomeric units that have been incorporated as part of some conjugated polymers and reported to exhibit excellent properties such as optical absorption in visible-NIR region, a representative character of low bandgap polymers.[9] A general method to synthesize the TP structure is by condensing 3,4-diaminothiophene with selected α-dione derivatives (**Figure 1**). Different side chains can be attached to the TP core unit via modification of α-diones.[10]

Apart from using an appropriate π-monomeric unit to construct the conjugated polymer, a process of chain twisting that disrupt the conjugated system of the polymer is another factor of concern. The presence of naturally rotating linking single bonds along the main chain inevitably decrease the efficiency of π–delocalization on the main chain and limit the conjugated properties of the polymer. Herein, we are interested in developing the synthesis of conjugated polymers of TP into network form that potentially block bond rotations, flatten the

π–conjugated system of the polymer plane, and hence improving the efficiency of electron delocalization. (**Figure 2**). Our targeted network conjugated polymer is proposed to use 2,3-di-(bromomethyl)thieno[3,4-*b*]pyrazine as the main monomeric core unit, in which 4 sites of possible connections are present. The synthesized network conjugated polymers are new and have never been reported. This research will focus on the scope of the synthesis method of the required monomers and processes to polymerize into the network conjugated polymers with improved electrical and optical performance.

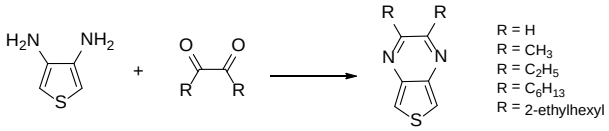

Figure 1. Synthesis of thieno[3,4-b]pyrazine (TP) derivatives.

2. Materials and Methods

2.1 Materials

All chemicals and organic solvents were purchased from various commercial sources and used directly without further purification. The solvents for column chromatography were distilled from commercial grade prior to use. Thin layer chromatography (TLC) was conducted using Merck (0.2 mm layer thickness of silica gel 60 F-254) and visualized by ultraviolet lamp. Flash column chromatography was carried out using Silicycle silica gel 40-63 μm (230-400 mesh).

2.2 Spectroscopic measurement

Infrared (IR) spectra were recorded on a Nicolet iS50 spectrometer. UV-Visible spectra were obtained using absorption mode on Aglilent 8453 spectrophotometer for solution samples and reflection mode on Shimadzu UV-2600i spectrophotometer for solid samples using $BaSO_4$ as a matrix. Melting points were determined on a Stuart Scientific Melting Point SMP20. ^1H NMR (500 MHz) and ^{13}C NMR(125 MHz) spectra were obtained in $CDCl_3$ with JEOL JNM-ECZ500R/S1 NMR spectrometer.

2.3 Synthesis of monomers

2,5-Dibromo-3,4-dinitrothiophene, DBDNT (1): Fuming HNO_3 (7 mL) and concentrated H_2SO_4 (30 mL) were combined in a round bottom flask, cooled in an ice bath for 15 minutes. 2,5-Dibromothiophene (1.13 mL, 10.0 mmol) was added dropwise to keep the temperature around 20-25 °C, stirred at room temperature for an additional 3 h and then was work up the reaction by pouring on ice. The solid residue was recovered by vacuum filtration to give a light-yellow solid (2.189 g, 6.59 mmol, 65.8%). Mp 137.0-139.0 °C [lit. 135.0-137.0 °C];[11] ^{13}C NMR ($CDCl_3$): δ (ppm) 139.2, 113.8 [lit. 159.7, 113.7].[11]

3,4-Diaminothiophene (2): Compound **1** (1.992 g, 6.00 mmol) and concentrated HCl (24 mL) were combined in a round bottom flask, cooled in an ice bath. Tin powder (4.274 g, 36.0 mmol) was added slowly to keep the temperature below 16-20°C,

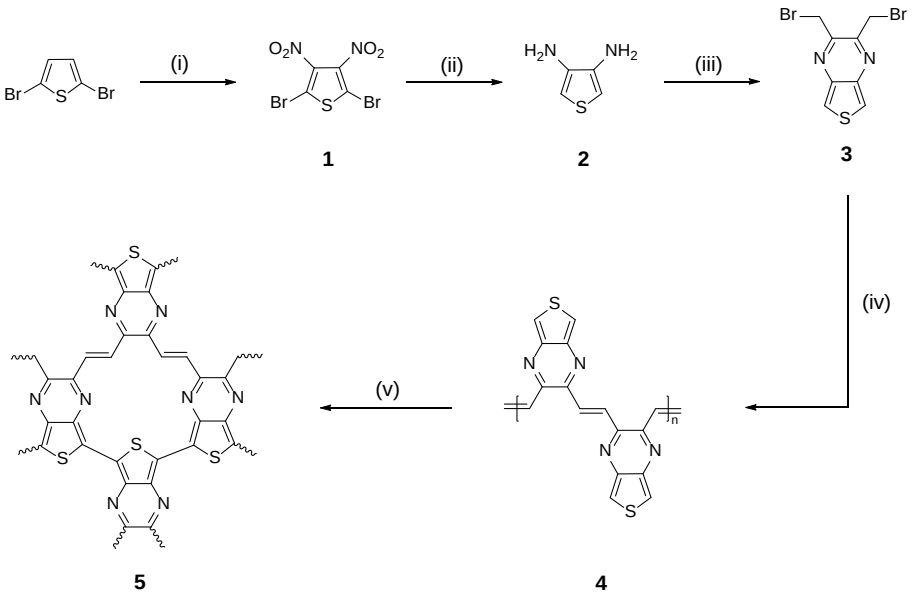

Figure 2. Synthesis of Network Poly(2,3-dimethinethieno[3,4-b] pyrazine); *Reagents and conditions*: (i) fuming HNO_3, conc. H_2SO_4; (ii) Sn, conc. HCl; (iii) 1,4-dibromobutane-2,3-dione, EtOAc; (iv) potassium *tert*-butoxide, 18-crown-6, dry toluene; (v) $FeCl_3$, $CHCl_3$.

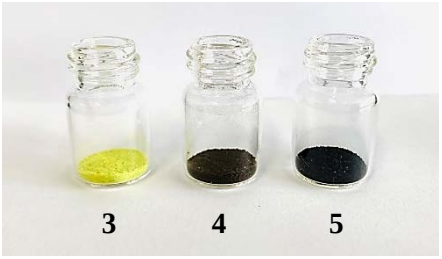

Figure 3. Solid appearance of 2,3-Bis(bromo-methyl)-thieno[3,4-b]pyrazine (**3**), Poly(2,3-di-methine-thieno[3,4-b]pyrazine) (**4**) and Polymer network of Poly(2,3-dimethine-thieno[3,4-b] pyrazine) (**5**), respectively.

stirred at room temperature for an additional 3 h and then placed in a freezer (-20 °C) overnight. The solid residue was recovered by vacuum filtration and washed with acetonitrile until the wash was colorless, giving 1.948 g of diammonium salt. The salt was dissolved in water, cooled with an ice bath, and aqueous KOH (0.89 M) was added slowly until the pH reached 7-8. And then the solution was extracted with ethyl acetate, dried with anhydrous Na_2SO_4, and concentrated by rotary evaporation at room temperature to give 0.331 g (48%) of a light brown solid of **2**. Mp 95.5-96.8 °C [lit. 95.5-96.9 °C];[11] ^{1}H NMR ($CDCl_3$): δ (ppm) 6.17(s,2H), 3.35(br,4H) [lit. 6.16, 3.36][11]; ^{13}C NMR ($CDCl_3$): δ (ppm) 139.2, 113.8 [lit. 137.2, 101.7].[11]

2,3-Bis(bromomethyl)thieno[3,4-b]pyrazine (3): 3,4-Diaminothiophene **2** (0.325 g, 2.85 mmol), 1,4-dibromobutane-2,3-dione (1.039 g, 4.28 mmol) and ethyl acetate (20 mL) were combined in a round bottom flask, stirred at 0°C for 3 h. The product was purified by column chromatography (1:9 ethyl acetate/hexane) to obtain the greenish-yellow solid of the **3** (0.539 g, 1.67 mmol, 58.3%). Product **3** decomposes above 115 °C; ^{1}H NMR ($CDCl_3$): δ (ppm) 8.01(s,1H), 4.85(s,2H); ^{13}C NMR ($CDCl_3$): δ (ppm) 150.1, 141.5, 118.7, 31.2; IR(cm^{-1}): 3107, 3072, 3031, 1432, 1298, 1218, 1173, 1095, 770, 549.

2.4 Synthesis of polymer Poly(2,3-dimethine-thieno[3,4-b]pyrazine) (4): The monomer **3** (0.322 g, 1 mmol) and 18-crown-6 (0.02 g) were combined in dry toluene (50 mL) under nitrogen atmosphere. And then, potassium *tert*-butoxide (0.67 g, 6 mmol) in dry toluene (50 mL) was added. Allow the mixture to heat at reflux for 3 h and cool to room temperature. The brown insoluble polymer **4** was purified by washing with water and methanol, and then vacuum-dried at room temperature for 2-3 h to yield 0.432 g of the product (>100%). IR(cm^{-1}): broad signals around 3500-3100, 1581, 1403, 1108, 615; UV-vis (solid): broad band 200-1200 nm with λ_{max} 330 and 370 nm, λ_{onset} 916 nm, E_g 1.354 eV.

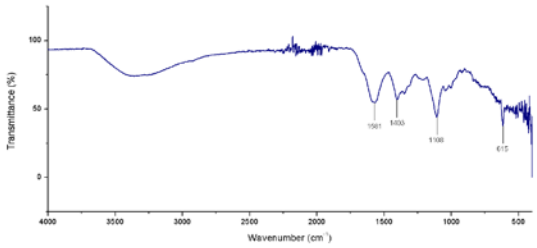

Figure 4. FT-IR spectra of polymer **4**

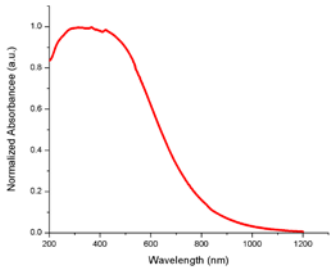

Figure 5. UV spectrum of polymer **4**

Polymer network of Poly(2,3-dimethine-thieno[3,4-b] pyrazine) (5): $FeCl_3$ (0.454 g, 2.8 mmol) and chloroform (20 mL) were combined in a round bottom flask, stirred for 3-5 min. After that polymer **4** (0.046 g, 0.4 mmol) was added at room temperature. The mixture was stirred for 24 h. The black insoluble polymer **5** was purified by washing with water and methanol, and then vacuum-dried at room temperature for 2-3 h to yield 0.013 g of the product (23%). IR(cm^{-1}): broad signals 1059, 981, 599; UV-vis (solid): broad band 200-1,200 nm with λ_{max} 241 nm, λ_{onset} 1181 nm, E_g 1.05 eV.

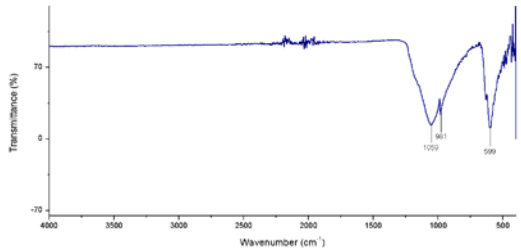

Figure 6. FT-IR spectra of polymer **5**

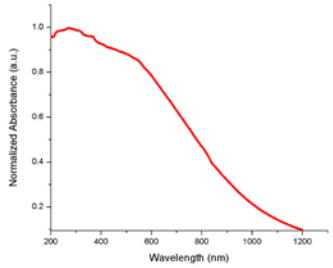

Figure 7. UV spectrum of polymer **5**

3. Results & Discussion

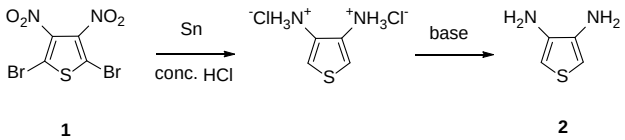

Figure 8. Synthesis of 3,4-Diaminothiophene (**2**)

Compounds **1** and **2** were synthesized by using the previously reported procedure,[11] starting from the nitration of commercially available 2,5-dibromothiophene to obtain DBDNT **1**,[13]C NMR spectrum confirm the structure of **1** and conform to the data from the literature. [11] After that, compound **1** was reduced to give diammonium salts of **2,** and then the diammonium salts were neutralized by KOH to obtain amine form of **2** (**Figure 8**), in this process should be careful to air and high temperature. All thiophene compounds, especially 3,4-diaminothiophene **2**, tend to decompose easily through air oxidation and high temperature, turning from light brown to brown-black solids. We can confirm the structure of **2** by ^{1}H and ^{13}C NMR, the results confirm to the data from the literature.[11] Compound **3**, as monomer, was synthesized via condensation with 1,4-dibromobutane-2,3-dione. The reaction must be kept at low temperature to minimize possible nucleophilic attacks on the dione. We obtained the greenish-yellow solid of **3**. ^{1}H NMR spectrum exhibited singlet signal at δ 4.85 and 8.01 ppm, which referred to the methyl protons and α-protons on thiophene ring respectively. ^{13}C NMR spectrum exhibited signal at δ 31.21 ppm of methyl carbon and three characteristic signals of thienopyrazine at 118.67, 141.45 and 150.11 ppm.

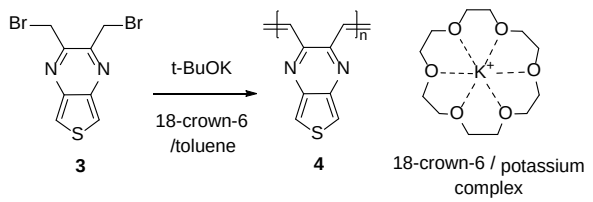

Figure 9. Synthesis of Poly(2,3-dimethine-thieno[3,4-b]pyrazine) (**4**)

The first two-dimensional polymerization to get Poly(2,3-dimethine-thieno[3,4-b]pyrazine) (**4**) was successful to obtain a brown insoluble polymer from monomer **3** through polydehydro-halogenation in the presence of potassium *tert*-butoxide as a base, and 18-crown-6 as an initiator (**Figure 9**). The polymer structure was identified by IR broad absorption bands of C=C stretching at 1581 cm^{-1}, and the disappearance of C-Br stretching at 549 cm^{-1} of the monomer **3.** The solid UV-visible spectroscopy appeared as an overly broad band with unclear maximum wavelength (λ_{max}) at around 400 nm and extended into visible region up to 1000 nm approximately, indicating the moderate π–conjugated system of polymer **4**.

Polymer **4** was then oxidative polymerized using $FeCl_3$ to give black insoluble network polymer **5**, though only in small yield. The solid UV-visible spectroscopy of polymer **5** showed an even broader band in visible region, with possible regional maxima at around 500 nm and extended as tail absorption further beyond 1200 nm. The limit of the instrument and small amount of insoluble sample make it difficult to get a clear and conclusive character of the final polymer and its properties. Nevertheless, the solid UV-visible absorption spectra of **4** and **5** were used to estimate the absorption onset of the lowest energy transition (λ_{onset}) and calculate the optical band gaps (E_g) of the polymers by Planck's equation:

$$E = \frac{hc}{\lambda}$$

where *h* describes the Planck's constant (4.1357 x 10^{-15} eV·s); *c* describes speed of light (29979 x 10^{8} m/s) and λ describes to λ_{onset} which determined by extrapolation of the steepest slope of the far end of visible absorption band that intersects with the spectral baseline.[12] Polymer **4**, the two-dimensional conjugated polymer of vinylic TP already showed relatively high λ_{onset} that translated to low band gap values at about 1.35 eV, supporting the role of TP as an excellent electron carrier in conjugated polymer. Polymer **5**, the network conjugated polymer already showed relatively higher λ_{onset} than polymer **4** that translated to lower band gap values at about 1.05 eV, supporting the role of network structure that potentially block bond rotations, flatten the π–conjugated system of the polymer plane, and hence improving the efficiency of electron delocalization. However, absorption was not yet leveled down to baseline beyond 1200 nm, reflecting the limit of the instrument. Optimization of the synthesis of this polymer to get appreciable

amounts of the product and use of more relevant instruments such as NIR spectrometer are under current investigation.

4. Conclusion

The main monomer, 2,3-Bis(bromomethyl) thieno[3,4-b]pyrazine could be obtained in three steps from 2,5-dibromothiophene in good yield. It was successfully polymerized into a two-dimensional conjugated polymer **4** through polydehydrohalogenation in the presence of potassium *tert*-butoxide and 18-crown-6. Its absorption, though mainly in early visible region, extended far closer to almost reach NIR region with relatively high λ_{onset}, supporting the excellent electronic property of TP as part of the conjugated units. Unfortunately, its network polymer **5** was obtained in very low amount and its full characteristics are still incomplete, although show some promising sign of expected results.

Acknowledgements

Prapassorn Ongjaroon would like to thank Petrochemistry and Polymer Science program, Faculty of Science, Chulalongkorn University for a M.Sc. scholarship.

References

1 Gao, H.; Matyjaszewski, K. Synthesis of functional polymers with controlled architecture by CRP of monomers in the presence of cross-linkers: From stars to gels. *Progress in Polymer Science* **2009**, 34 (4), 317-350.

2 Gu, Y.; Schauenburg, D.; Bode, J. W.; Johnson, J. A. Leaving groups as traceless topological modifiers for the synthesis of topologically isomeric polymer networks. *Journal of the American Chemical Society* **2018**, 140 (43), 14033-14037.

3 Kamata, H.; Akagi, Y.; Kayasuga-Kariya, Y.; Chung, U.-i.; Sakai, T. "Nonswellable" hydrogel without mechanical hysteresis. *Science* **2014**, 343 (6173), 873-875.

4 Spontak, R. J.; Patel, N. P. Thermoplastic elastomers: fundamentals and applications. *Current opinion in colloid & interface science* **2000**, 5 (5-6), 333-340.

5 Li, J.; Mooney, D. J. Designing hydrogels for controlled drug delivery. *Nature Reviews Materials* **2016**, 1 (12), 1-17.

6 Lee, K. Y.; Mooney, D. J. Hydrogels for tissue engineering. *Chemical reviews* **2001**, 101 (7), 1869-1880.

7 McKeown, N. B.; Budd, P. M. Polymers of intrinsic microporosity (PIMs): organic materials for membrane separations, heterogeneous catalysis and hydrogen storage. *Chemical Society Reviews* **2006**, 35 (8), 675-683.

8 Rogers, J. A.; Someya, T.; Huang, Y. Materials and mechanics for stretchable electronics. *Science* **2010**, 327 (5973), 1603-1607.

9 Rasmussen, S. C.; Schwiderski, R. L.; Mulholland, M. E. Thieno [3, 4-b] pyrazines and their applications to low band gap organic materials. *Chemical Communications* **2011**, 47 (41), 11394-11410.

10 Wen, L.; Nietfeld, J. P.; Amb, C. M.; Rasmussen, S. C. Synthesis and Characterization of New 2,3-Disubstituted Thieno[3,4-b]pyrazines: Tunable Building Blocks for Low Band Gap Conjugated Materials. *The Journal of Organic Chemistry* **2008**, 73 (21), 8529-8536.

11 Kenning, D. D.; Mitchell, K. A.; Calhoun, T. R.; Funfar, M. R.; Sattler, D. J.; Rasmussen, S. C. Thieno[3,4-b]pyrazines: Synthesis, Structure, and Reactivity. *The Journal of Organic Chemistry* **2002**, 67 (25), 9073-9076.

12 Wallace, A. M.; Curiac, C.; Delcamp, J. H.; Fortenberry, R. C. Accurate determination of the onset wavelength (λ_{onset}) in optical spectroscopy. *Journal of Quantitative Spectroscopy and Radiative Transfer* **2021**, *265*, 107544.

Volatile organic compound absorption and photocatalytic degradation of natural rubber foam with modified TiO_2 composites

Sassawat Mailaeeiad[1], Siriluk Chiarakorn[2], and Yeampon Nakaramontri[1]*

[1]*Sustainable Polymer & Innovative Composites Material Research Group, Department of Chemistry, Faculty of Science, King Mongkut's University of Technology Thonburi, Bangkok, Thailand*
[2]*Environmental Technology Program, School of Energy, Environment and Materials, King Mongkut's University of Technology Thonburi, Bangkok, Thailand*

**E-mail: yeampon.nak@kmutt.ac.th*

Abstract:

The present work aims to study the effects of modified titanium dioxide (TiO_2) with zinc oxide on mechanical properties and volatile organic compounds (VOC) absorption of the natural rubber (NR) foam composites filled with ZnO-TiO_2 at different concentration. It was found that the values of 100% modulus, tensile strength, hardness and density increased with varying the ZnO-TiO_2 concentration. Absorption and photodegradation of methylene blue (MB) solution were the composition determination indicator increased significantly due to the photocatalytic mechanism. This mechanism leads to the rapid generation of reactive hydroxyl radicals, which react with the methyl and methylene groups on the methylene blue molecule with increasing the irradiation time under lighting conditions compared to dark conditions especially NR with the addition of modified ZnO-TiO_2 at 5 phr. In terms of the relationship between absorption and volume change under benzene gas condition (BZ-95), it was found that natural rubber (NR) composite foam filled with ZnO-TiO_2 can absorb benzene gas higher and longer than natural rubber composite foam without added ZnO-TiO_2

1. Introduction

Titanium dioxide (TiO_2) is widely recognized as one of the key additives in the rubber industry, commonly employed as a color enhancer or brightener in colored products. It falls under the category of semi-reinforced fillers.[1] Contributing to improved mechanical properties and enhanced resistance to UV rays.[2,3] Moreover, the incorporation of such fillers imparts photocatalytic properties to rubber, a notable advantage not shared by other fillers like silica, soot, clay, and calcium carbonate. Natural rubber (NR), being a prominent biological resource among various rubber types, is extensively used in the industry. This presents an opportunity to add value to rubber and a challenge in rubber technology. To address these aspects, the application of rubber foam, in conjunction with modified TiO_2, is explored as an interesting initiative to tackle air pollution.

2. Materials and Methods

2.1 Materials

Natural latex with high ammonia concentration (HA-NR) with a dry rubber content (DRC) of 60% Produced by Nam Rubber and Latex Company Limited. (Trang, Thailand). Potassium oleate (K-oleate), Sulfur, Zinc 2-mercaptobenzothiazone (ZMBT), Zinc diethylthiocarbonate (ZDEC), Lowinox CPL (butylate reaction product of paracresol and dicyclopentadiene), zinc oxide (ZnO), diphenylguanidine (DPG) and buy sodium silicofluoride (SSF) from Thanadom Trading Co., Ltd. (Bangkok, Thailand) modified TiO_2 with ZnO ratio 80:20 (ZnO-TiO_2) supplied by Global Chemical Co., Ltd. (Samut Prakan, Thailand)

2.2 Preparation of NR composite foams

Prepare sponge rubber using the dunlop process by using natural latex dispersion agents for soap, sulfur, accelerators, and metal oxide modified titanium nanoparticles. According to the quantities shown in Table 1 , mixed into the rubber foaming machine. Adjust the spinning speed to low at 80 rpm, then increase the speed to 180 rpm until the desired volume of rubber sponge is obtained. Then reduce the speed to break down the bubbles into smaller sizes. Use the lowest speed of 80 rpm to break down the bubbles thoroughly. When the desired resolution is achieved, zinc oxide and additional gelling agent are added, followed by the main gelling agent. Then pour it into the mold. When the sponge is completely gelled put it in a steam bath for 45-60 minutes, then rinse it with water to get rid of any residual chemicals and dried at 70 ^{o}C for 24 hours.

2.3 Mechanical properties

Tensile properties of the foams were measured using a low force electromechanical universal testing machine (model 3365, Instron® Inc., Massachusetts,USA). The dumbbell shape specimens were prepared according to ISO 37

Type 2, and the load was varied at a crosshead speed of 500 mm/min. Modulus at 100% elongation, tensile strength, and elongation at break of the foam were reported.[4]

2.4 Hardness

Hardness of the NR composite foams was measured by using shore OO Durometer according to ASTM 2240. A digital durometer (Digi test, Bareiss, Oberdischingen, Germany) was employed to measure the hardness of the specimen in five positions, and the average value was then reported.

2.5 Foam density

Densities of natural rubber composite foams filled with modified TiO_2 were determined by calculation from the mass (M) per volume (V) of the specimen.[5]

2.6 Photocatalytic properties

The photocatalytic activity of NR/ZnO-TiO_2 composites was carried out by photoreduction of MB solution at a concentration of 5×10^{-5} M under fluorescent irradiation (20 W fluorescent), Samples of 2.0 × 2.0 × 0.2 cm^3 were immersed in 60 ml of MB solution under dark condition at room temperature until the absorption reaches equilibrium. 2 mL of MB solution was taken and measured the absorbance by using UV-visible spectrophotometer (Shimadzu, UV2100, Kyoto, Japan). The photocatalytic activity of composite foams was observed from the reduction of maximum wavelength (λmax) of MB at 664 nm and efficiency of a photocatalytic degradation of MB was calculated.[6] By using Equation (1): C_0 and C_t are the MB concentration at the initial time and measuring time, respectively.

$$\text{Photocatalytic degradation} = \left[\frac{C_0 - C_t}{C_0}\right] \times 100\% \quad (1)$$

2.7 Vapor absorption and change volume under benzene gas (BZ-95) conditions

Natural rubber composite foam filled with modified TiO_2 was by preparing a sample size of 2.0×2.0×0.2 cm^3, baking it at 50 ± 2°C for 24 hours, then letting it cool for 30 minutes, and then weighing the sample. Weigh with a 4-position precision scale and find the volume of composite rubber foam and record it. It was then tested for vapor absorption under the dark for 24 hours. The sample was then weighed after vapor absorption and the volume of the composite rubber foam was measured. Continue for 5 days to find the peak. (stored in a closed container filled with benzene so that the rubber foam absorbs vapors from benzene at a concentration of 7.5 million ppm). The percentage of volatile substance adsorption and the change in volume increase of composite rubber foam can be calculated from Equations (3) and (4):

$$\text{vapor absorption}\,(\%) = \frac{Wet\ weight}{Dry\ weight} \times 100 \quad (3)$$

$$\text{change volume}\,(\%) = \frac{V_b - V_a}{V_b} \times 100 \quad (4)$$

where V_b is the volume before change (cm^3), V_a is the volume after change (cm^3).

3. Results & Discussion

3.1 Photocatalytic degradation of MB

Figure 1 illustrates the photodegradation of a methylene blue solution in natural rubber composite foam without (Gum NR) and with different concentrations of ZnO-TiO_2 (5, 15, and 20 phr). When electrons in the valence band gap absorb energy and move to the conduction band, electron-hole pairs are simultaneously generated in the semiconductor material. Meanwhile, in the valence band, the loss of electrons results in the formation of holes (h^+). These electron-hole pairs formed on the surface of titanium dioxide (TiO_2) initiate redox reactions with water or moisture in the air, producing hydroxyl radicals ($OH^\bullet$). At the same time, electrons in the conduction band react with oxygen to form superoxide anions ($^\bullet O^{2-}$), which then react with H^+ (from water dissociation) to produce $OH^\bullet$. This mechanism is known as photocatalytic reaction or photocatalysis, where the generated hydroxyl radicals ($OH^\bullet$) exhibit strong oxidative properties and contribute to the degradation of methylene blue's molecular structure.[10]

As the concentration of ZnO-TiO_2 increases, the absorption capacity of the methylene blue solution intensifies in the dark. Upon turning on the light, the photocatalytic reaction occurs in both the natural rubber foam composite with varying concentrations and without concentrations. A decreasing trend in the concentration of the methylene blue solution is observed over the duration of the photocatalytic reaction, further reducing the concentration compared to the dark condition. It was also observed that at a concentration of 5 phr in the photocatalytic reaction, the most significant decrease in the concentration of the methylene blue solution occurred compared to concentrations at 15 and 20 phr. This excess amount proved more than sufficient, causing the filler to agglomerate on the rubber surface and obstruct the access of light for the reaction, consequently diminishing the degradability of the methylene blue solution.[7]

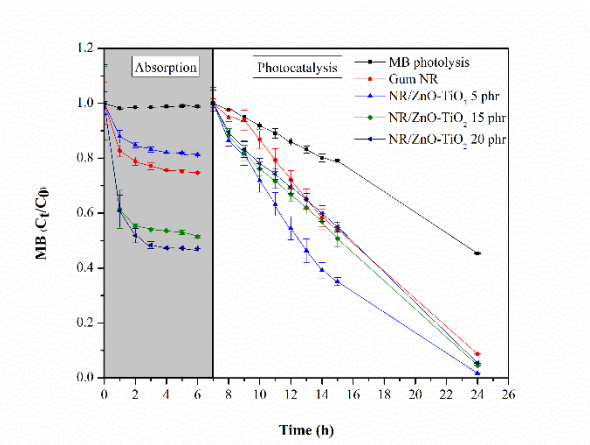

Figure 1. absorption and photocatalytic degradation of MB solution under fluorescent irradiationby natural rubber composite foam at various concentration of ZnO-TiO_2

3.2 Vapor absorption and change volume under benzene gas (BZ-95) conditions.

The test for vapor absorption and volume change was conducted on composite rubber foam without filler and with concentrations of 5, 15, and 20 phr of titanium modified with zinc oxide (ZnO-TiO_2). Figure 2 depicts an increase in absorption value with the adsorption time, reaching a maximum after 3 days. By varying the concentration of ZnO-TiO_2, the composite exhibited high vapor absorption and a prolonged vapor adsorption threshold. After reaching the peak, there is a tendency for absorption to decrease, albeit less than in natural rubber foam without added fillers. The absorption was most effective at a concentration of 5 phr, followed by 15 phr, while the concentration of ZnO-TiO_2 at 20 phr showed the least adsorption compared to the substance-free condition.

The addition and variation in concentration at 5, 15 phr and when increased to 20 phr (maximum concentration) resulted in an excess amounts, leading to reduced vapor absorption. This is attributed to the gas absorption mechanism occurring between two states of the substance, namely gas and solid. Gas is absorbed or trapped on the surface of the porous solid composite rubber foam and then moves into the pores of the composite rubber foam. This is closely tied to the uniformity within the composite rubber foam cell. An increase in filler amount results in reduced absorption surface of the rubber foam structure due to filler agglomeration, which may hinder the movement of adsorbed vapors across the surface of the composite rubber foam.[8]

Additionally, the absorption effect is linked to the volume change within the rubber foam over the experiment's duration. As shown in Figure 3, during vapor absorption, the pores in the composite rubber foam expand. Consequently, the adsorption surface decreases after the 3 day peak. It was also observed that as the concentration of ZnO-TiO_2 increased, particularly at 20 phr, the composite rubber foam exhibited increased solidity, facilitating easier return to its original state compared to scenarios without added filler or with lower concentrations.

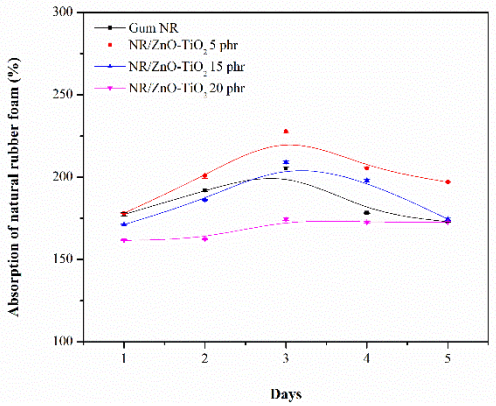

Figure 2. Vapor absorption of natural rubber foam without filler and various concentration of ZnO-TiO_2 over a period of 5 days

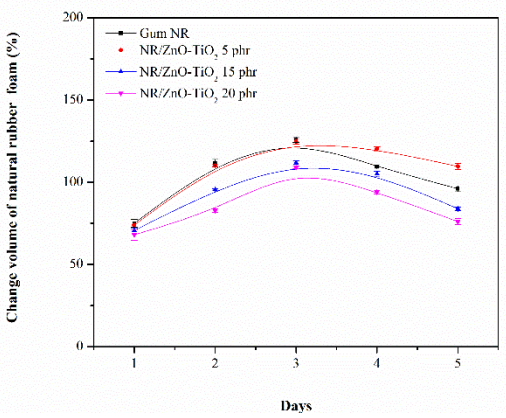

Figure 3. change volume of natural rubber foam without filler and various concentration of ZnO-TiO2 over a period of 5 days.

Table 1. Formulation for the preparation of natural rubber foam with modified TiO_2 composites

Ingredients	Contents (phr[a])
60% HA-NR latex	100
20% Potassium oleate	1.5
50% Sulfur	2
50% ZMBT	1
50% ZDEC	1
50% ZnO	3
50% Lowinox CPL	1
50% DPG	1
20% SSF	1
25% ZnO-TiO_2	5, 15 and 20

[a] phr = part per hundred rubber

3.3 Properties of natural rubber foam

The results of preparing rubber foam from natural latex without adding fillers (Gum NR) and incorporating titanium modified with zinc oxide (NR/ZnO-TiO_2) at varying concentrations of 5, 15, and 20 phr, including modulus, tensile strength, elongation at break, density, and hardness, are presented in Table 2. The fillers were found to enhance the modulus, tensile strength, elongation at break, density, and hardness, together with its densities after the addition of the ZnO-TiO_2. With the addition and increasing of the ZnO-TiO_2 to the NR composites foams, the modulus, tensile strength and elongation at break had reached the optimal situation at 5 phr. This correlates with the absorption efficiency of the foam owing to the state of dispersion and distribution of ZnO-TiO_2 throughout the NR matrix. However, when the amount was increased to more than sufficient, specifically at 20 phr, it was observed that the tensile strength and elongation at break decreased. This decline is attributed to the agglomeration of the filler within the natural rubber matrix, resulting in poor interaction and diminishing the reinforcing effect of the filler.[9]

Table 2. Properties of natural rubber foam without adding fillers (Gum NR) and adding titanium modified with zinc oxide (NR/ZnO-TiO_2) at varying concentrations of 5, 15, and 20 phr

Tests	Natural rubber foam			
	Gum NR	5 phr	15 phr	20 phr
100% Modulus	0.20 ±0.00	0.21 ±0.01	0.23 ±0.01	0.23 ±0.01
Tensile strength (MPa)	0.41 ±0.02	0.58 ±0.06	0.61 ±0.05	0.51 ±0.50
Elongation at break (%)	338 ±11	464 ±22	413 ±30	362 ±33
Density (g/cm^3)	0.1390 ±0.0	0.1480 ±0.0	0.2149 ±0.0	0.2579 ±0.0
Hardness Shore OO	49 ±0.6	55 ±0.6	59 ±0.6	62 ±0.6

4. Conclusion

The objective of this research is to investigate natural rubber foam for the absorption of volatile organic compounds and photocatalytic reactions. As the concentration of ZnO-TiO_2 increased to 5 phr, it demonstrated the capability to adsorb benzene vapors and exhibited the most effective decomposition of methylene blue solution. Additionally, it enhanced the properties of natural rubber foam, leading to increased modulus, tensile strength, elongation at break, density, and hardness compared to the scenario without added fillers. Consequently, natural rubber foam with a concentration of 5 phr is deemed suitable for application. In addition, the researchers observed that the addition of ZnO-TiO_2 had an effect on the morphology and pore size of the rubber foam.

Acknowledgements

The authors gratefully acknowledge the financial support from the King Mongkut's University of Technology Thonburi (KMUTT), Bangkok, in the form of KMUTT Research Fund for the financial support and equipment.

References

1. Leblanc, J. L. *Progress in polymer science.* **2002**, *27*(4), 627-687.
2. Seentrakoon, B.; Junhasavasdikul, B.; Chavasiri, W. *Polymer degradation and stability*. **2013**, *98*(2), 566-578.
3. Toh-ae, P. *Photocatalytic properties of nano-titanium dioxide on NR and NBR compounds*. PhD Thesis: Prince of Songkla University, **2017.**
4. Krainoi, A.; Prasert, W.; Kesakomol, P.; Thongdee, P.; Nitchaphanit, S.; Sungsirin, N.; Nakaramontri, Y. *Materials Today Communications*. **2023**, *35*, 105601.
5. Roslim, R.; Hashim, M. A.; Augurio, P. T. *J. Eng. Sci*. **2012**, *8*, 15-27.
6. Sirivallop, A.; Areerob, T.; Chiarakorn, S. *Catalysts*. **2020**, *10*(2), 251.
7. Demeestere, K.; Dewulf, J.; De Witte, B.; Beeldens, A.; Van Langenhove, H. *Building and environment*. **2008**, *43*(4), 406-414.
8. BETZ, W. R.; MAPOLDO, S. G.; WACHOB, G. D.; FIRTH, M. C. *American Industrial Hygiene Association Journal*. **1989**, *50*(4), 181-187.
9. Phomrak, S.; Nimpaiboon, A.; Newby, B. M. Z.; Phisalaphong, M. *Polymers*. **2020**, *12*(9), 1959.
10. Zhang, T.; Oyama, T.; Aoshima, A.; Hidaka, H.; Zhao, J.; Serpone, N. *Journal of Photochemistry and Photobiology A: Chemistry*. **2001**, *140*(2), 163-172.

Effects of plasticizers on light transmission of silk fibroin films

Sitthichai Audtoom and Supranee Kaewpirom*

Department of Chemistry, Faculty of Science, Burapha University, Chonburi 20131, Thailand
**E-mail: kaewpiro@go.buu.ac.th*

Abstract:

Silk fibroin was extracted from white silk cocoons using Na_2CO_3 solution. The recovery percentages for silk fibroin and silk sericin were determined to be 64.81± 0.01 % w/w and 35.19± 0.01 % w/w, respectively. Subsequently, a silk fibroin solution was formulated through the dissolution of degummed silk fibroin in a mixture of $CaCl_2/C_2H_5OH/H_2O$, with a molar ratio of 1:2:8. This solution was further refined through dialysis against distilled water. The concentration of the silk fibroin solution after dialysis was 4.56 ± 0.01 %w/v. Following this, a silk fibroin film was fabricated using a solution casting method. The resulting silk fibroin film exhibited notable transparency within the visible spectrum and demonstrated distinctive UV absorption properties. The impact of various plasticizers, specifically glycerol (Gly), sorbitol (Sor), and maltitol (Mal), on the light transmission of silk fibroin films was examined through UV-VIS spectroscopy. The experimental findings indicated that the light transmission percentage of the films varied based on the type of plasticizers used. The UV transmission at a wavelength of 250 nm increased in correlation with the number of carbon atoms in the plasticizers. Conversely, the light transmittance at 600 nm in the films decreased with an increasing number of carbon atoms. Nonetheless, the values fell within the range of 86-90%, signifying the films' exceptional transparency.

1. Introduction

Silk is a natural protein fiber obtained from silkworms. Silk consists of two important proteins fibroin represents approximately 70-75 % weight, it is a protein that is insoluble in water. Two silk fibers have a diameter of approximately 10-25 micrometers, coated with the silk glue protein called sericin. Silk glue is water soluble and exist at approximately 25-30 percent by weight of silk cocoons.[1] To our knowledge, silk has been used for a long time, initially for medical application such as suturing. It is also commonly used in the weaving industry, cosmetics industry as well as medical material industry.

Silk is a natural fiber that gain popularity in the textile and clothing industry. This is due to its high strength, good flexibility, good mechanical properties, and beautiful luster making it different from other types of textile fibers. As mentioned above, silk fibroin protein is used in cosmeceuticals, including skin cleansing cream, foundation cream, makeup cream, and shampoo. In addition, silk fibroin protein has also been used as a medical material, tissue engineering, including threads for sutures, wound dressings, contact lenses, and artificial skin.

Because silk fibroin protein is a biopolymer that is biocompatible with good mechanical properties and can be naturally biodegraded, many researchers have paid attentions to tailor its properties to suit their specific application. One of the easy methods to alter silk fibroin properties is adding a plasticizer.

Glycerol is an organic compound with the chemical formula $C_3H_8O_3$. Glycerol is a viscous, colorless, odorless, and sweet-tasting liquid with a molecular weight of 92.1 g/mol. Glycerol contains 3 hydroxyl groups, making it well soluble both in water and alcohol such as methanol, ethanol and isomers of propanol, etc. With its hygroscopic property, glycerol is applied as an additive for many industries, such as the pharmaceutical, food, and cosmetic industries, etc.[2]

Sorbitol is a hexahydric alcohol with a structural formula of $C_6H_{14}O_6$ and a molecular weight of 182.17 g mol^{-1}. Sorbitol consists of a straight chain of 6 carbon atoms and 6 hydroxyl groups.[3] Sorbitol is a white solid crystals, non-volatile, and is well-soluble in water, methanol, isopropanol, butanol, cyclohexanol, phenol, acetone, acetic acid, pyridine, and acetamide. Sorbitol is widely used in pharmaceutical manufacturing industry, cosmetic industry, and food industry.

Maltitol is obtained from the sugar maltose, classified as disaccharide sugar. Maltitol has a structural formula of $C_{12}H_{24}O_{11}$, consisting of 12 carbon atoms and 9 hydroxyl groups. Maltitol is freely soluble in water: 200 g of maltitol is soluble in 100 mL of water at 37 °C.[4]

In this present study, silk fibroin was extracted from white silk cocoons using sodium

carbonate solution. The pure silk fibroin solution was then prepared via dialysis. Then silk fibroin films with various formulations were prepared from purified silk fibroin solutions by means of solution casting method. The effect of plasticizers with different chemical structures, namely glycerol, sorbitol, and maltitol on optical property of the silk film was investigated.

2. Materials and Methods

2.1 Materials

White silk cocoons (J-1) were from Udon Thani Province, Thailand. Glycerol; 99.5% purity, sodium carbonate, analytical reagent, and calcium chloride; laboratory reagent, were purchased from Ajax Finechem.

2.2 Extraction of silk fibroin from silk cocoons

Extraction of silk fibroin from silk cocoons was achieved by degumming process. After distilled water (1.8 L) was brought to boil, 3.6 g of sodium carbonate was added into. After complete dissolution of sodium carbonate, chopped silk cocoons (5.0 g) was added into the solution and the boiling was continued for 30 min with occasional stirring. The degummed silk fibroin was then obtained and washed thoroughly with distilled water until neutral, followed by drying in a hot air oven at 60 °C for 24 hours or until constant weight. Finally, the recovery percentage (%Recovery) was calculated using equation (1).

$$\%\text{Recovery} = \frac{W_{SF}}{W_S} \times 100 \qquad (1),$$

where WSF and WS are the weights of degummed silk fibroin and silk cocoon, respectively.

2.3 Preparation of silk fibroin solution

The degummed silk fibroin was solubilized in $CaCl_2/C_2H_5OH/H_2O$ solution (mole ratio of 1:2:8) for 1 h at 110 °C. $CaCl_2$ was subsequently removed through dialysis against deionized water at room temperature (30±2°C) for a total of 72 h, using cellulose dialysis bag with molecular cut-off (MWCO) of 12-14 KDa (Cellu Sep®). The deionized water was replaced every 4–6 h. The purification of resulting silk fibroin suspension was carried out twice by centrifugation at 2200 rpm for 10 min at room temperature. The final concentration of a homogeneous SF solution, determined by gravimetric method, was 4.56 ± 0.01 %w/v. For tailoring the properties of silk films, after preparing the initial silk fibroin solution, each additional plasticizer (glycerol, sorbitol, or maltitol) was added to the purified silk fibroin solution at the concentration of 30%w/v, with respect to dry weight of silk fibroin film, before processing silk fibroin film.

2.4 Preparation of silk fibroin films

Various SF films were casted by pouring SF solution (5%w/v), without and with the addition of a plasticizer at weight ratios of 30%w/v, into polyethylene terephthalate molds and let to dry at room temperature for 48 h. Further drying was carried out in a vacuum oven at room temperature for another 4 h to remove the residue water molecules. The SF films with altered properties were obtained with the thickness in the range 30−55 micron. Names of silk fibroin films are exhibited in WSF+xxx, where WSF stands for white silk films and the letters followed by WSF stand for the names of plasticizers (Gly, Mal, Sor, for glycerol, maltitol, and sorbitol, respectively).

2.5 UV/vis measurement

Transmittance of silk fibroin films (2.54 cm × 2.54 cm) were examined over the range 200 nm to 900 nm, using UV-Visible spectrophotometer (Shimadzu 2600). The baseline measurement was accomplished automatically by the spectrophotometer with air as a reference.

3. Results & Discussion

3.1 Recovery percentage

After extracting silk fibroin from silk cocoons, the degummed silk fibroin was weighed and the recovery percentage was calculated. It was found that silk sericin glue was successfully separated from silk fibroin by the simple degumming process. Digital images of white silk cocoons and degummed silk fibroin are showed in Fig. 1. The recovery percentages for silk fibroin and silk sericin were determined to be 64.81± 0.01 % w/w and 35.19± 0.01 % w/w, respectively. The results are consistent with the results proposed by Lu et al.[5]. Therefore, it can be seen that the method of removing silk glue with sodium carbonate solution is the appropriate method.

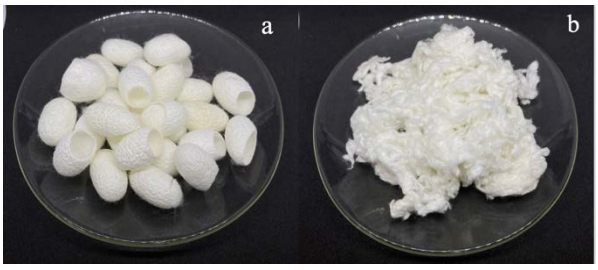

Figure 1. Digital images of (a) white silk cocoons and (b) degummed silk fibroin.

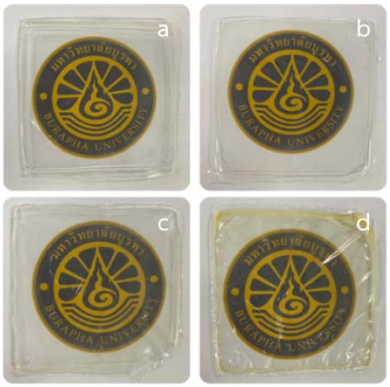

Figure 2. Digital images of silk fibroin films (a) WSF, (b) WSF + Gly, (c) WSF + Sor, (d) WSF + Mal

3.2 The light transmission of silk fibroin films

Fig. 2 represents that the resulting silk fibroin films exhibited notable transparency within the visible spectrum.

The impact of various plasticizers, specifically glycerol (Gly), sorbitol (Sor), and maltitol (Mal), on the light transmission of silk fibroin films was examined in details through UV-VIS spectroscopy and the UV/vis spectra are given in Fig. 3. It was found from the figure that all the silk fibroin films exhibited notable transparency within the visible spectrum. and demonstrated distinctive UV absorption properties. Interestingly, the films can absorb UV light in the spectral range of 200–300 nm. This implies that all the silk fibroin films displayed an excellent UV-shield property and have potential to preserve the intrinsic optical property of the substrate onto which it may be mounted, if apply as coatings. The principal chromophores such as the aromatic amino acids, tyrosine, phenylalanine and tryptophan, presented in silk structure, are believed to be responsible for the UV absorbing property of the films.[6] Furthermore, the results reveal that all the silk fibroin films revealed excellent transmission from 350 nm to 900 nm (visible range), where the percentage transmittance within the range of 86-90% was observed.

It's interesting to note that the light transmission percentage of the films varied based on the type of plasticizers used. The change in %T at 600 nm and 250 nm was normalized by dividing the %T measured by that of a reference %T at 230 nm. Figure 4. illustrates the percent transmittance ratio obtained from UV/vis spectra for the silk fibroin films both without and with the addition of plasticizers. It was found that the light transmittance at 600 nm of the silk fibroin films decreased with an increasing number of carbon atoms of the added plasticizer. This may be due to some degree of phase separation between silk fibroin and plasticizer rich phase.[1] It was expected that the plasticizer with higher numbers of C atom and OH groups could produce more hydrogen-bonding interactions between plasticizer and silk molecules as well as among plasticizer molecules themselves, resulting in higher degree of phase separation. Nonetheless, the values fell within the range of 86-90%, signifying the films' extraordinary transparency. Contrariwise, the UV transmission at a wavelength of 250 nm increased in correlation with the number of carbon atoms in the plasticizers. As mention earlier, when a large amount of plasticizer is added to a protein matrix, the plasticizer molecules are likely to form hydrogen bonds with silk peptides as well as with other plasticizer molecules, resulting in phase separation.[7] Consequently, UV-light could travel through local plasticizer-rich domains in the silk fibroin structure, resulting in higher UV transmission.

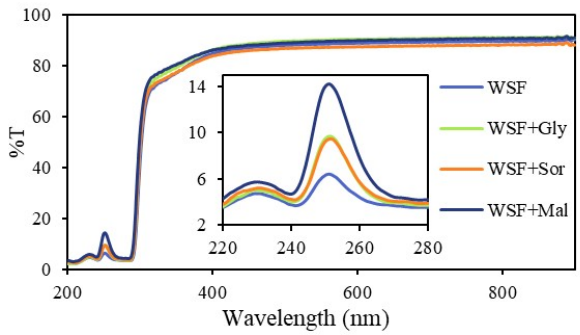

Figure 3. UV-Vis spectrum of silk fibroin films in diverse compositions in the UV range of 200–900 nm.

4. Conclusion

Silk fibroin films with adjustable optical property were successfully fabricated from white silk cocoons. Glycerol, sorbitol, and maltitol were applied as plasticizers. The films exhibited notable transparency within the visible spectrum and demonstrated distinctive UV absorption properties. The light transmission percentage of the films varied based on the type of plasticizers used. The UV transmission at a wavelength of 250 nm increased in correlation with the number of carbon atoms in the plasticizers. On the contrary, the light transmittance at 600 nm in the films decreased with an increasing number of carbon atoms. However, the values are in the range of 86-90%, signifying the excellent transparency of silk fibroin films.

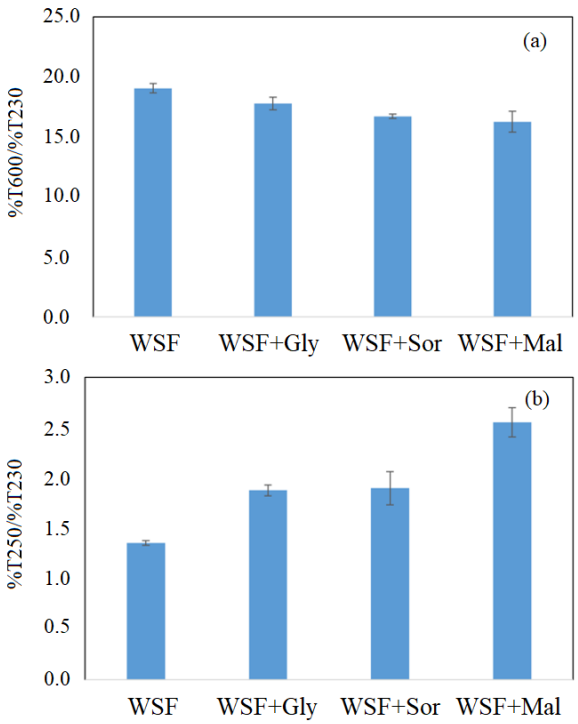

Figure 4. The percent transmittance ratio obtained from UV/vis spectra (a) %Transmittance at 600 nm to %Transmittance at 230 nm ratio and (b) %Transmittance at 250 nm to %Transmittance at 230 nm ratio for the silk fibroin films.

Acknowledgements

This study was partially supported by the Science Innovation Facility, Faculty of Science, Burapha University (SIF-IN-55300056).

References

1. Kaewpirom, S.; Boonang, S. *Adv. Mater. Interfaces*. **2022**, *9*(9), 2102072, doi.org/10.1002/admi.202102072.
2. Pirzadi, Z.; Meshkani, F. *Fuel*. **2022**, *329*: 125044. doi.org/10.1016/j.fuel.2022.125044.
3. Mohamad, R.; Aki, T.; Yakashimada, Y.; Okamura. Y.; Tajima, T.; Matsumura, Y. *J. Jpn. Pet. Inst.* **2016**, *59*(4),149-154.
4. Saraiva, A.; Carrascosa, C.; Raheem, D.; Ramos, F.; Raposo, A. *Inter. J. Environ. Res. Public. Health.*, **2020**, *17*(14):5227. doi: 10.3390/ijerph17145227.
5. Lu, S., Tang, X., Lu, Q., Huang, J., You, X., & Zhang, F. *Mater. Today Commun.* **2021**, *27*, 102369. doi.org/10.1016/j.mtcomm.2021.102369.
6. Kaewpiom, S.; Boonsang, S. *RSC Adv.* **2020**, *10*, 15913–15923.
7. Brown, J. E., Davidowski, S. K.; Xu, D.; Cebe, P.; Onofrei, D.; Holland, G. P.; Kaplan, D. L. *Biomacromolecules.* **2016**, *17*,(12), 3911-3921.

Preparation of levan from *B. subtilis* under different cultivation conditions

Pornpun Aramsangtienchai[1]* and Warisara Raksachue[2]

[1]*Research unit of natural bioactive compounds for healthcare products development, Department of Biochemistry, Faculty of Science, Burapha University, Chonburi, 20131, Thailand*
[2]*Department of Biochemistry, Faculty of Science, Burapha University, Chonburi, 20131, Thailand*

**E-mail: Pornpun.ar@go.buu.ac.th*

Abstract:

Levan is a fructan biopolymer consisting of fructose molecules linked via beta-2, 6 glycosidic bond. It is typically synthesized through the catalysis levansucrase, secreted from certain microorganisms. Interestingly, variations in the molecular weight (MW) of levan have been associated with different levels of biological activities, including anti-bacterial and antitumor effects. However, the preparation of different MW of microbial levan is still challenging. Herein, we investigated the MW of levan produced from *Bacillus subtilis* under different cultivation conditions. Our findings revealed that the MW of levan from *B. subtilis* cultured in minimal medium was 1.8 x 10^4 Da. It was higher than the MW of levan from cells in a complete medium, which was 9 x 10^3 Da. Additionally, shaking speed (Round Per Minute, RPM) also impacted the levan MW. Specifically, the levan MW of 1.7 x 10^4 Da and 9.8 x 10^3 Da were detected at the shaking speed of 100 and 180 RPM, respectively. The results of this study thus provided cultivation conditions for preparing levan with different MWs from *B. subtilis*. Also, it will facilitate further investigation of biological activities associated with levan of varying MW.

1. Introduction

Levan constitutes a homopolymer of fructose molecules. Owing to its remarkable properties such as film-forming capabilities, low viscosity, robust adhesion properties, and effective emulsification characteristics, levan is regarded as a highly promising exopolysaccharide with potential applications in food, feed, and cosmetics industries[1]. Furthermore, levan has been reported for its various bioactivities, such as antioxidant, antimicrobial, antitumor, hypocholesterolemic, and prebiotic effects[2]. Levan thus becomes known as a prospective polysaccharide for functional foods and pharmaceutical products. The structural characteristics of microbial levan exhibit variation in terms of branching and polymerization degree, or molecular weight (MW). The MW of levan can be found as low as 2 Da, up to 100 x 10^6 Da[3].

Interestingly, previous studies indicated that alterations in levan MW could influence its biological activities[4, 5]. For example, the low MW of levan (5x10^4 Da) from *Zymomonas mobilis* demonstrated a more potent antibacterial effect, compared to its higher one (3x10^6 Da). Consequently, applying low MW levan as a sweetener in bread was proposed to reduce bacterial contamination, particularly from foodborne pathogens[6]. Nevertheless, producing microbial levan in various MW remains an ongoing challenge; thereby, exploring the effect of MW on biological activities is still quite limited. The structure and yield of levan produced by bacteria are highly dependent on its cultivation conditions[7]. Therefore, we investigated the MW of levan generated from *B. subtilis* under different media and shaking speeds. The crude levan was fractionated and detected for its MW by Gel permeation chromatography (GPC). The results from this research would provide the cultivation conditions to obtain different sizes of levan for further exploring its biological activities.

2. Materials and Methods

2.1 Bacterial cultivation

B. subtilis (TBRC573) was procured from Thailand Bioresource Research Center, Pathum Thani, Thailand. A single colony of *B. subtilis* was initially grown in a starter medium (5 g/L peptone, 5 g/L NaCl 1.5 g/L meat extract and 1.5 g/L yeast extract). The bacterial culture was incubated at 37 °C, 180 rpm for 24 h, and subsequently transferred into different media as follows.

(1) Minimal medium was composed of 3 g/L Na_2HPO_4, 3 g/L NaH_2PO_4, 0.5 g/L $MgSO_4 \cdot 7H_2O$ and 150 g/L sucrose.

(2) Complete medium was composed of 2 g/L yeast extract, 3 g/L K_2HPO_4, 0.2 g/L $MgSO_4 \cdot 7H_2O$ and 150 g/L sucrose.

The bacterial cultures were further incubated at 37 °C, at different agitation speeds, 100 and 180 RPM, for 55 h. After that, the supernatant was collected and obtained by centrifugation at 3,500 × *g* for 15 min.

2.2 Precipitation of levan

The supernatant was concentrated by evaporating at 65 °C until the volume was reduced

by half. The clear supernatant was obtained after centrifugation at 7,800 × *g* for 45 min. To precipitate levan, 95% (v/v) cold ethanol was added into the supernatant at a ratio of 1:2 (v/v) (supernatant : ethanol), and left at -20 °C for 3 h. Then, the crude levan was collected through centrifugation at 3,500 × *g* for 20 min. The crude levan was subsequently washed twice with 80% (v/v) cold ethanol.

2.2 Fractionation of levan and TLC

To separate levan by its size, the crude levan was dissolved in water and loaded onto Sephacryl S-300 HR column (GE Health care, 150 x 2.5 cm) using 50 mM NaCl as a mobile phase with a flow rate of 0.5 mL/min. To determine polysaccharide-contained fractions, the modified phenol-sulfuric assay was performed[8]. Briefly, 10 microliter of each fraction was added into 96-well plate, followed by 120 microliter of sulfuric acid and 30 microliter of 5%(v/v) phenol and subsequently incubated at 80 °C for 10 min. The 96-well plate was measured at the absorbance of 490 nm.

Each fraction was also verified as a fructan by thin layer chromatography (TLC)[9]. In short, each sample including standard sugars such as fructose, sucrose, and levan were spotted on TLC plate (Silica gel 60F254, Merck Millipore). The TLC plate was then developed in a solvent system of butanol, acetic acid and water in a ratio of 5: 3: 1.5. To detect compounds containing fructose, the plate was treated with a urea solution in HCl and then incubated at 120 °C for 10 min.

2.3 Gel permeation chromatography (GPC)

To estimate the average MW of levan, GPC-HPLC (Waters 600) with an RI-detector (Waters 2414) using water as a mobile phase with a flow rate of 1 mL/min, was employed. Various MW of pullulans (0.2, 0.5, 6.2, 10, 48.8, 113, 348 kDa) were used as a standard curve.

3. Results & Discussion

B. subtilis was grown in minimal and complete media, as described in material and methods. The supernatant was collected, and precipitated for crude levan. After that, the crude levan was separated by its size on Sephacryl S-300 HR column and each fraction was detected for carbohydrate-containing compounds by phenol-sulfuric assay. The gel filtration chromatogram of levan from *B. subtilis* cultured in minimal and complete media were demonstrated in Fig 1(A) and 1(C), respectively. Each fraction was also verified as a fructan by TLC as shown in Fig 1(B) and 1(D), respectively. It was found that most of levan from *B. subtilis* grown in the minimum medium were eluted out earlier than those of the complete medium, suggesting the higher MW of levan.

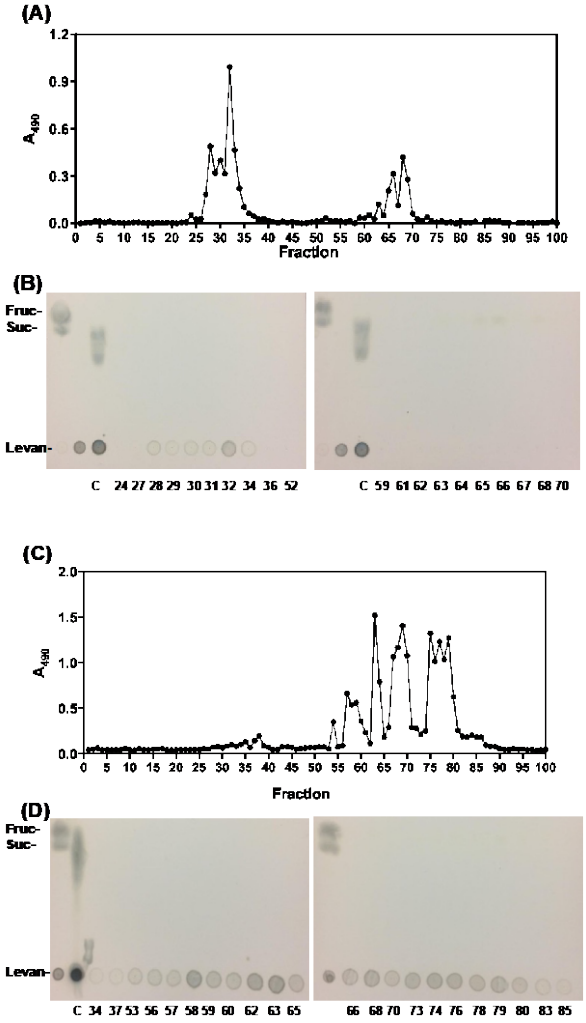

Figure 1. Gel filtration chromatogram of levan on Sephacryl S-300 HR column (90 x 1.5 cm, with a flow rate of 1 mL/min). Levan production from *B. subtilis* under minimum medium (A) and complete medium (C). The eluted fractions were monitored by phenol-sulfuric assay with the absorbance of 490 nm. Also, TLC chromatograms of standard sugars and fractions collected from Sephacryl S-300 HR columns, from minimum medium (B) and complete medium (D), were analyzed, respectively. Fruc and Suc represent fructose, and sucrose. C represents the crude levan before loading onto the column.

Moreover, the effect of different shaking speed (100 and 180 RPM) on the MW of levan were investigated. As shown in Fig 2(A)-(D), the size of levan were more broadly distributed in the culture with 180 RPM when compared to that of 100 RPM. Certain peaks of these fractions were pooled and freeze dried for further MW analysis.

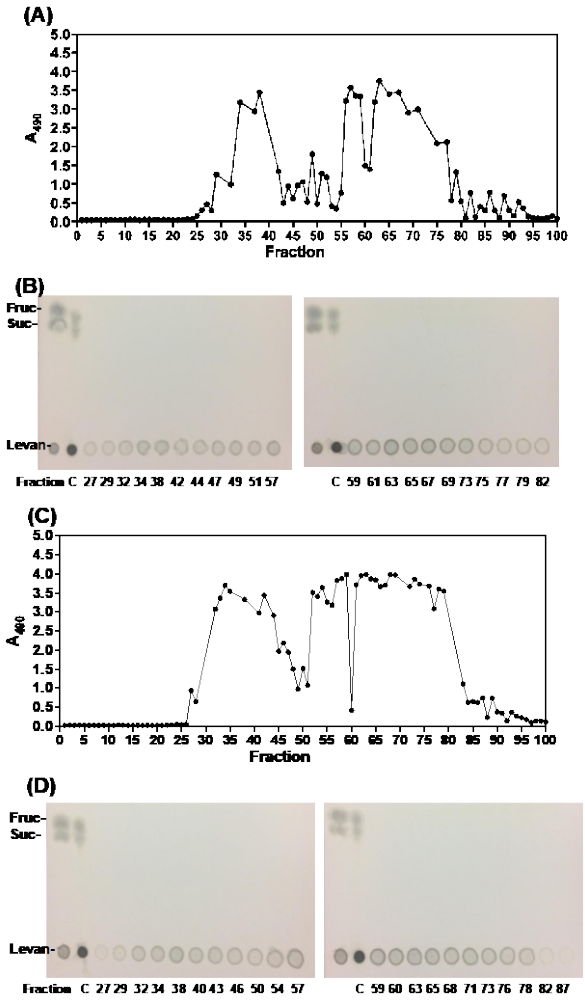

Figure 2. Gel filtration chromatogram of levan on Sephacryl S-300 HR column (90 x 1.5 cm, with a flow rate of 1 mL/min). Levan production from *B. subtilis* grown under a complete medium with shaking speed of 100 RPM (A) and 180 RPM (C), respectively. The eluted fractions were monitored by phenol-sulfuric assay with the absorbance of 490 nm. Also, TLC chromatograms of standard sugars and fractions collected from Sephacryl S-300 HR columns, with the shaking speed of 100 RPM (B) and 180 RPM (D), were analyzed, respectively. Fruc and Suc represent fructose, and sucrose. C represents the crude levan before loading onto column. The average MW of levan from different conditions were further analyzed by GPC and the results were demonstrated in Table 1. The average MW of levan from *B. subtilis* cultivated under minimal medium was 1.9 x 10^4 Da while the smaller MW, 4.6 x 10^3 and 9.0 x 10^3 Da were detected from those grown under complete medium. Thus, the medium composition affected the size of levan produced by *B. subtilis*. However, the yield of levan from minimum medium was lower than that of the complete medium. In addition, the influence of shaking speed was explored. Levan with the average MW of 1.7 x 10^4 and 6.2 x 10^3 Da, and the smaller average MW of 6.5 x 10^3 and 9.8 x 10^3 Da were detected from using shaking speed of 100 and 180 RPM, respectively. Therefore, the low rotation speed could result in a higher MW of levan compared to using high rotation speed. Also, using 10% and 15% sucrose under the complete medium with 180 RPM produced the different MW of levan. These results suggested the effect of sucrose concentration on transfructosylation activity of levansucrase, leading to the production of levan with different MW.

Table 1. The average MW of levan from *B. subtilis* under different conditions

Cultural conditions			Pooled fraction number	MW (Da)
Medium	Minimal medium	with 15% sucrose, 180 RPM	27-35	18,696 (91%), >805,000 (8%)
	Complete medium	with 15% sucrose, 180 RPM	65-70	9,002
			73-80	4,611
Shaking speed	100 RPM	with 10% sucrose in complete medium	27-49	>805,000 (7%), 17,475 (93%)
			62-80	6,278
	180 RPM	with 10% sucrose in complete medium	27-49	9,898 (90%), >805,000 (10%)
			61-84	6,596

4. Conclusion

In this study, we investigated the MW of levan prepared from *B. subtilis* under different cultivation conditions such as media and shaking speed. The results revealed that growing *B. subtilis* in the minimum medium could generate levan with the MW of 1.9 x 10^4 Da, while that of complete media produce levan with the smaller MW, 4.6 x 10^3 and 9.0 x 10^3 Da. Furthermore, varying the shaking speed for *B. subtilis* led to differences in levan MW. Lower RPM could yield higher MW compared to the higher RPM. The findings of this study demonstrated the influence of cultivation parameters on levan MW. This information could be useful for producing levan in various sizes for future testing of its bioactivities.

Acknowledgements

This research was financially supported by the Research and Development Fund, Burapha University (Grant no. 12/2562 & 10/2565); the Science Innovation Facility, Faculty of Science, Burapha University (SIF-IN-60300003) and the Center of Excellence for Innovation in Chemistry (PERCH-CIC), the Commission on Higher Education, Ministry of Education, Thailand.

References

1. Ateş, O.; Oner, E. T., Microbial Xanthan, Levan, Gellan, and Curdlan as Food Additives. In *Microbial Functional Foods and Nutraceuticals*, 2017; pp 149-173.
2. Oner, E. T.; Hernandez, L.; Combie, J., Review of Levan polysaccharide: From a century of past experiences to future prospects. *Biotechnol Adv* **2016,** *34* (5), 827-844.
3. Srikanth, R.; Reddy, C. H.; Siddartha, G.; Ramaiah, M. J.; Uppuluri, K. B., Review on production, characterization and applications of microbial levan. *Carbohydr Polym* **2015,** *120*, 102-14.
4. Calazans, G. M. T.; Lima, R. C.; de Franca, F. P.; Lopes, C. E., Molecular weight and antitumour activity of *Zymomonas mobilis* levans. *Int J Biol Macromol* **2000,** *27* (4), 245-7.
5. Yoo, S. H.; Yoon, E. J.; Cha, J.; Lee, H. G., Antitumor activity of levan polysaccharides from selected microorganisms. *Int J Biol Macromol* **2004,** *34* (1-2), 37-41.
6. Byun, B. Y.; Lee, S.-J.; Mah, J.-H., Antipathogenic activity and preservative effect of levan (β-2,6-fructan), a multifunctional polysaccharide. *Int J Food Sci* **2014,** *49*, 238-245.
7. Wu, F.-C.; Chou, S.-Z.; Shih, I.-L., Factors affecting the production and molecular weight of levan of *Bacillus subtilis* natto in batch and fed-batch culture in fermenter. *Journal of the Taiwan Institute of Chemical Engineers* **2013,** *44* (6), 846-853.
8. DuBois, M.; Gilles, K. A.; Hamilton, J. K.; Rebers, P. A.; Smith, F., Colorimetric Method for Determination of Sugars and Related Substances. *Analytical Chemistry* **1956,** *28* (3), 350-356.
9. Aramsangtienchai, P.; Kongmon, T.; Pechroj, S.; Srisook, K., Enhanced production and immunomodulatory activity of levan from the acetic acid bacterium, *Tanticharoenia sakaeratensis*. *International Journal of Biological Macromolecules* **2020,** *163*, 574-581.

Production of nanocellulose from freshwater green algae

Anurak Khiewchaon[1], Kanitta Watcharaporn[2], and Pornpen Atorngitjawat[1]*

[1]*Department of Chemistry, Faculty of Science, Burapha University, Chonburi 20131, Thailand*
[2]*Department of Textile Science, Faculty of Agro-Industry, Kasetsart University, Bangkok 10900, Thailand*

**E-mail: pornpena@go.buu.ac.th*

Abstract:

Green algae are the most common algae found in freshwater sources in Thailand. In this research, nanocellulose was prepared from green algae. Cellulose was extracted with sodium hydroxide solution and nanocellulose was produced via acid hydrolysis. The optimum conditions for cellulose extraction and nanocellulose production were studied. The chemical structure of cellulose was determined with Fourier transform infrared spectroscopy. The morphology and size of produced nanocellulose were obtained using transmission electron microscope. The results show that concentrations of sodium hydroxide solutions (0.5, 1.0 and 1.5 M) and temperatures (30 and 60 °C) did not affect the percentage yield of extracted cellulose fibers. Nanocellulose was hydrolyzed with sulfuric acid at 50, 60 and 80 °C, respectively, for 3 h. The results from Transmission electron microscope analysis displayed that the average diameter of nanocellulose fibers was 18.54, 18.37 and 18.30 nm, respectively, which has no significant difference. The shortest length of nanocellulose fibers was observed with an average length of 675.52 nm when hydrolysis at 80 °C.

1. Introduction

Nowadays, cellulose and nanocellulose gain more attraction for wide utilizations. They have been extracted from a variety of agricultural wastes such as rubberwoods, rice husks, sugarcane bagasse, coconut pulps and coirs.[1-5] Cellulose is classified as the most abundant natural polymers because it is the main component of wood and plant cell walls. The major constituents of cell walls are lignocellulose, cellulose, hemicellulose, and lignin. A molecular formula of cellulose is $(C_6H_{10}O_5)_n$, a polysaccharide of glucose units which contain hydroxyl groups connected by glycosidic bonds at beta 1,4 positions (β (1→4) glycosidic bond), called cellobiose [7-8] as seen in Figure 1.

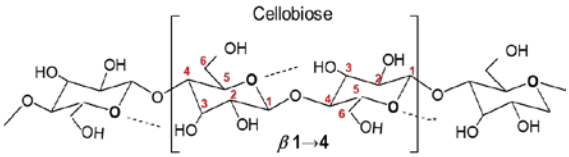

Figure 1. Chemical structure of cellulose.

Typically, nanocellulose can be prepared from extracted cellulose via mechanical treatment, enzymatic hydrolysis, and acid hydrolysis.[9] The rod-like or whisker shaped nanoparticles are observed after acid hydrolysis process (see Figure 2) with the diameter and length in the range of 3-20 nm and 100-800 nm, respectively.[10]

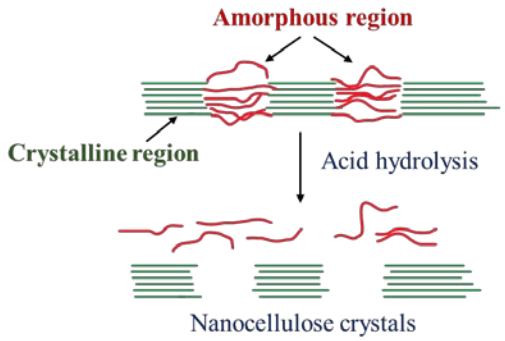

Figure 2. Nanocellulose crystals from acid hydrolysis process.

Algae are low-class organisms without roots, stems, and leaves. Their size ranges vary from a tiny to meter size (unicellular to multicellular). Green algae belong to the group of photosynthetic organisms called chlorophytes, which are green in color due to the presence of chlorophyll. These algae can be found in seawater and freshwater ecosystems. Green algae (genus *Spirogyra or charophytes*) are found in freshwater environments consisting of thin unbranched chains of cylindrical cells. Their nuclei are suspended by fine strands of cytoplasm. Green algae are generally composed of carbohydrates, lipids, and protein. Their cell walls mainly consist of an inner layer of cellulose and hemicellulose, and an outer layer of pectin, responsible for the greasy texture of the green algae. Compared to wood celluloses, green algal celluloses provide a higher crystallinity, pore volume and larger surface area.[11-12] Therefore the aim of this research is to preliminary study the optimal condition for preparing nanocellulose from freshwater green algae and reduce the unwanted blooming algae.

In this article, the extraction of cellulose and nanocellulose from freshwater green algae was performed by alkali treatment and strong acid hydrolysis, respectively. The structure of extracted cellulose and nanocellulose was characterized using Fourier-transform infrared spectroscopy (FTIR). The morphology and size of nanocellulose were examined by transmission electron microscopy (TEM).

2. Materials and Methods

2.1 Materials

Green algae were obtained from several ponds in Chonburi province, Thailand. Methanol, sodium hydroxide (NaOH), hydrochloric acid (HCl), sulfuric acid (H_2SO_4) and sodium hypochlorite (NaClO) were purchased from QRëCTM.

2.2 Cellulose extraction

Green algae were washed with water several times (see Figure 3a) until they were clean and left dry at room temperatures. For defatting, the dried algae were soaked in methanol for a period of eight days at a room temperature, four days of each cycle. The defatted algae were filtered and dried at 60 °C for 24 h. The dried defatted algae were cut and ground with a blender (see Figure 3b). Dried algal powder was weighted and soaked into 0.5 M of NaOH with the sample ratio to sodium hydroxide of 1:100 (w/v) at 30 °C for 24 h (repeated at 60 °C). The sample was filtered and rinsed with distilled waters until it reached a neutral pH. The cellulose sample was dried at 60 °C for 24 h, and then bleached with 3 %w/w of NaClO for 3 h at 60 °C. The sample was filtered and rinsed with distilled water until it reached a neutral pH and dried at 60 °C for 24 h. The concentration of NaOH was changed to 1.0 and 1.5 M. The % recovery of extracted cellulose was estimated from equation:

$$\%\ recovery = \frac{final\ weigth\ of\ product}{original\ weight\ of\ product} \times 100$$

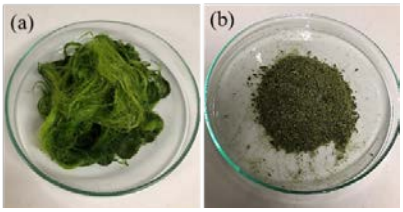

Figure 3. The figure of (a) raw green algae and (b) defatted green algae.

2.3 Nanocellulose preparation

Cellulose was added into 49 % w/w of H_2SO_4, with the sample ratio to H_2SO_4 of 1: 100 at 50 °C (60 and 80 °C) for 3 h, in an ultrasonic bath. The excess of sulfuric acids was removed by centrifugation at a speed of 3000 rpm for 10 min, followed by centrifugation with distilled waters until getting neutral water. After centrifugation, the light-yellow suspension of nanocellulose was observed.

2.4 Characterization

The structure characterization of cellulose and nanocellulose was examined by using a PerkinElmer system, Frontier FT-IR spectrometer in a range of 400 to 4,000 cm^{-1}, signal accumulation 4 scans at a resolution of 4 cm^{-1}.
The characteristics and size of nanocellulose were examined by transmission electron microscopy (TEM), Tecnai 20 Phillips model with high voltage 120 KV and magnification of 89000x.The diameter and length of the nanocellulose crystals were measured from TEM photographs by an ImageJ program.

3. Results & Discussion

3.1 Recovery of cellulose

The light yellow flaky of extracted cellulose was obtained after bleaching for all conditions. The average recovery of cellulose extracted with 0.5, 1.0 and 1.5 M of NaOH at 30 °C was 58.5, 59.1, and 58.8 %, respectively. The % recovery of cellulose extracted with 0.5 M of NaOH at 60 °C was 57.3 as presented in Figure 4. There is no significant difference in the percentage recovery of extracted cellulose at any condition.

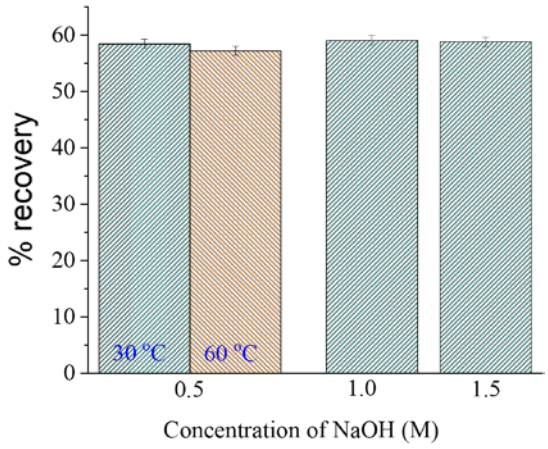

Figure 4. The recovery of extracted cellulose at various NaOH concentrations at 30 and 60 °C.

3.2 Structure characteristics

FTIR spectra of beached celluloses extracted with 0.5, 1.0, and 1.5 M of NaOH were displayed in Figure 5. FTIR spectra of raw green algae, bleached cellulose and nanocellulose in the range of 4000-750 cm^{-1} and 2000-750 cm^{-1} were shown in Figure 6. As seen in Figure 6a, the bands around 3340 and 2897 cm^{-1} contributed to O-H and C-H stretching, respectively. As shown in Figure 6b, the peak at 1740-1637 cm^{-1} has been clearly observed for raw green algae and assigned to C=O stretching of hemicellulose, lipid, and pectin. The peaks at 1370 and 1232 cm^{-1} were attributed to the plane bending of C-O vibration. The bands range 1000-1062 cm^{-1} were due to the vibration of C-O-C and C-OH stretching.[11-14]

As seen in Figure 5 and 6, compared to raw green algae, a peak at 1740 cm^{-1} disappeared for all cellulose extracted with NaOH. This indicated that NaOH solutions can isolate some lipid, pectin, and hemicelluloses. Nanocellulose contained the main structure of cellulose.

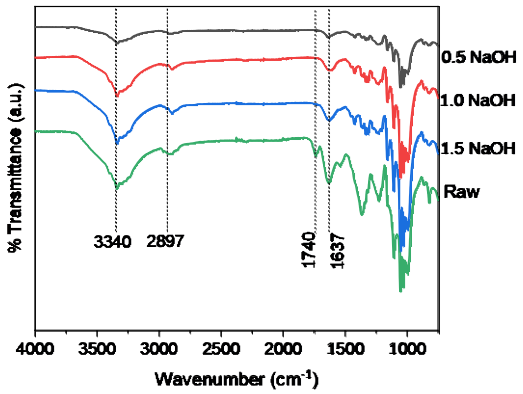

Figure 5. FTIR spectra of raw green algae and bleached celluloses extracted with 0.5, 1.0, 1.5 M of NaOH

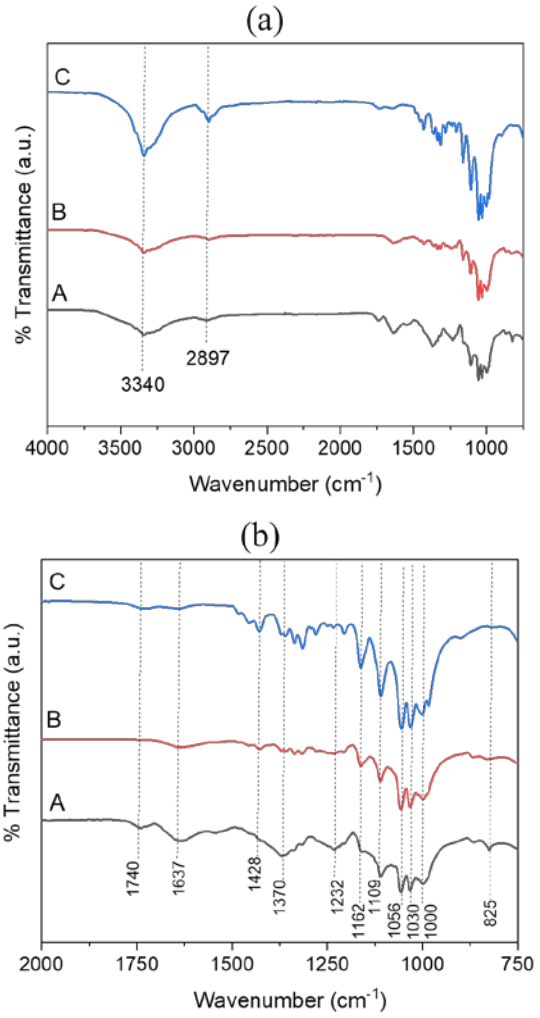

Figure 6. FTIR spectra of raw green algae (A), bleached cellulose (B) and nanocellulose (C) in the region of (a) 4000-750 and (b) 2000-750 cm^{-1}.

3.3 Size and morphology

Figure 6 displayed TEM images of nanocellulose prepared at 50, 60, and 80 °C. The morphology of nanocellulose obtained for all conditions are straight rods. But at 80 °C, the smallest size of straight rod was observed, compared to other prepared temperatures. The length of nanocellulose prepared at 50, 60, and 80 °C was 1190 ±395.43 nm, 791.94 ±247.80 nm and 675.52 ±307.86 nm, respectively and diameters of 18.54 ±2.39 nm, 18.37 ±2.71 nm, and 18.30 ±2.60 nm, respectively. The deviations of lengths of the nanocellulose are quite large. This might be due to the dried algal powder was not grounded perfectly before extraction with NaOH. In addition, the length of nanocellulose fibers reduced with increasing temperatures.

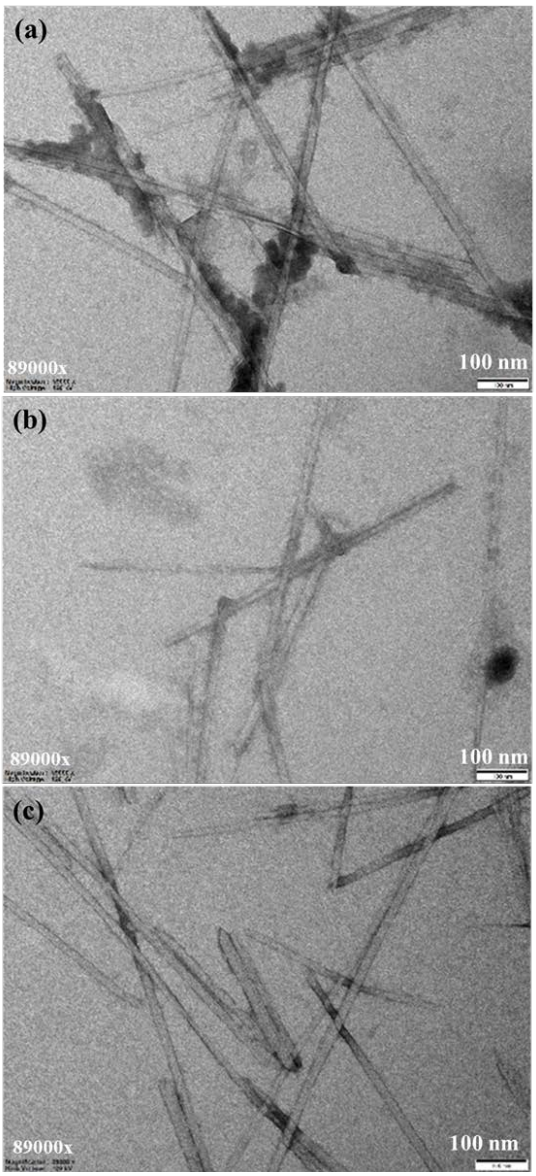

Figure 6. TEM images of nanocellulose prepared at (a) 50, (b) 60 and (c) 80 ^{o}C.

4. Conclusion

The investigation of optimal conditions for the extraction and production of cellulose and nanocellulose from freshwater green algae showed that the extracted temperature and concentration of NaOH had no significant effected on percentage of cellulose recovery. The chemical structure of cellulose and nanocellulose were similar for all prepared conditions. There are no significant changes of diameter of cellulose nanocrystal at different prepared temperatures, which was about 18.30 nm. The length of nanocellulose fibers reduced with increasing temperatures, which the shortest length was obtained when prepared at 80 ^{o}C, about 676 nm.

Acknowledgements

This work was supported by project funding from the Chemistry Department, Faculty of Science, Burapha University.

References

1. Abraham, E.; Deepa, B.; Pothen, L.A.; Cintil, J.; Thomas, S.; John, M.J.; Anandjiwala, R.; Narine, S.S. *Carbohydr. Polym*. **2013**, *92*, 1477-1483.
2. Johar, N.; Ahmad, I.; Dufresne, A. Ind. *Crops Prod*. **2012**, *37*, 97-99.
3. Jonoobi, M.; Khazaeian, A.; Tahir, P.M.; Azry, S.S.; Oksman, K. *Cellulose*. **2011**, *18*, 1085-1095.
4. Nascimento, D.M.; Almeida, J.S.; Vale, M.S.; Leitão, R.C.; Muniz, C.R.; Figueirêdo, M.C.; Morais, J.P.S.; Rosa, M.F. *Ind. Crops Prod*. **2016**, *93*, 66-75.
5. Pavalaydon, K.; Ramasawmy, H.; Surroop, D. *Environ Dev Sustain*. **2022**, *24*, 9963-9984.
6. Phanthong, P.; Reubroycharoen, P.; Hao, X.; Xu, G.; Abudula, A.; Guan, G. *Carbon Resour. Convers*. **2018**, *1*, 32-43.
7. Gilbert, R.D.; Kadla, J.F. Polysaccharides–cellulose. In Biopolymers from Renewable Resources; Kaplan D.L., Ed.; Springer, Berlin, 1998; pp 47-95.
8. Klemm, D.;Heublein, B.; Fink, H.P.; Bohn, A. *Angew. Chem. Int. Ed.* **2005**, *44*, 3358-3393.
9. Rebouillat, S.; Pla, F. *J. biomater. nanobiotechnol*. **2013**, *4*, 165-188.
10. Peng, B.L.; Dhar, N.; Liu, H.L.; Tam, K.C. *Can. J. Chem. Eng*. **2011**, *89*, 1191-1206.
11. Sucaldito, M.R.; Camacho, D.H. *Carbohydr. Polym*. **2017**, *169*, 315-323.
12. Zabed, H.M.; Akter, S.; Yun, J.; Zhang, G.; Awad, F.N.; Qi, X.; Sahu, J.N. *Renew. Sust. Energ. Rev*. **2019**, *105*, 105-128.
13. Du, L.; Wang, J.; Zhang, Y.; Qi, C.; Wolcott, M.P.; Yu, Z. *Nanomaterials*. **2017**, *7*, 1-12.
14. AS, S.; Teixeira, C.M.; Silva, P.R.M.; Cunha, V.S. *Res. Dev. Material Sci*. **2019**, *10*, 000744-12.

Silk yarn dyeing with extracted dye from spent coffee grounds using a moka pot

Wanrudee Kaewmesri[1*], Nattida Pinjai[2], Manat Jaimasith[1], and Sorachai Khamsan[1]

[1]*Division of Chemistry, School of Science, University of Phayao, Phayao, 56000 Thailand*
[2]*Division of Materials Science, School of Science, University of Phayao, Phayao, 56000 Thailand*

**E-mail: wanrudee.ka@up.ac.th*

Abstract:

In this investigation, a sustainable Moka pot extraction method is utilized to extract dye from coffee grounds, eliminating the necessity for harmful solvents. Before silk dyeing, the silk undergoes surface treatment, and the derived coffee dye is employed to dye silk yarn with varying times (1.0, 1.5, 2.0, and 3.0 h) and temperatures (85 °C and 120 °C), using a pressure cooker at 120 °C. UV-vis spectrometry gauges the absorptivity of dye solutions before and after dyeing under diverse conditions. The dark brown hue in the dyeing liquors, post-pressure cooker usage, is attributed to residue removal during pressurization, potentially enhancing dye affinity on the silk surface. CIELAB parameters (L*, a*, and b*) measure the color of dyed silk yarn, exhibiting a natural brown shade. Although bleaching marginally impacts tensile strength, dyed silk yarn provides higher elongation than pristine. FT-IR analysis distinguished coffee-extracted dye, dyed silk yarn under various conditions, and untreated yarn. This innovative approach highlights the potential of utilizing coffee remnants as an environmentally sustainable dye for silk yarn, offering conscientious alternatives in the textile sector. The research emphasizes efficient coffee ground utilization and eco-conscious dyeing practices for sustainable textile production.

1. Introduction

Textile processing is a major environmental polluter due to wastewater. Green chemistry aims to reduce hazardous substances. There's a rising demand for sustainable extraction of valuable natural substances on an industrial scale. Natural dyes were replaced by synthetic ones due to cost and colorfastness advantages. However, they're now making a comeback, especially in eco-friendly textile production, driven by environmental awareness and concerns about toxic synthetic dyes. They're commonly used on natural substrates like leather, wool, silk, and cotton in artisan and small-scale, high-value textile fabrication globally. The expansion of industrial applications for natural dyes necessitates a simultaneous commitment to environmental sustainability and minimizing quality variations. Key considerations include water-based extraction methods for dyestuff content and optimizing existing textile dye house equipment without substantial additions. Natural dyes fall into three categories: substantive, vat, and mordant dyes. Most require mordants like metal oxides to enhance fiber affinity, and their effectiveness on animal or vegetable fibers depends on the dye's nature. They work best on natural fibers such as wool, cotton, linen, silk, sisal, and jute, with wool being the most receptive, followed by cotton, linen, silk, and coarse fibers[1,2,3]. Coffee is the world's most consumed luxury table beverage and the second most traded commodity globally, following petroleum. Recent growth in coffee value sales is attributed to the out-of-home sector. However, the substantial amount of spent coffee grounds, constituting 45-50% of total coffee bean mass, poses environmental concerns despite some reuse practices. Over 6 million tons of dried spent coffee grounds are generated annually worldwide, contributing to landfill issues[4,5]. Spent coffee grounds boast high concentrations of functional compounds, including phenolic compounds, terpenes, caffeine, and Maillard reaction products. While caffeine is prevalent, melanoidin and chlorogenic acids exhibit antioxidant, antimicrobial, and anti-inflammatory properties[6,7]. Melanoidins, resulting from the Maillard reaction, constitute about 16% of spent coffee grounds, appearing brown with a browning index measured by absorbance at 420 nm (ranging from 0.090 to 0.160). The browning index varies across brewing methods, with filter coffee extracts from Arabica and Robusta displaying 3-5 times higher indices than espresso and plunger coffeemakers[8]. Aqueous extracts of soluble spent coffee grounds exhibit a lower browning index (0.271) compared to roasted coffee brews (0.305)[9,10,11,12]. Instead of conventional disposal, prioritizing sustainable recycling of spent coffee grounds can offer an environmentally friendly solution while harnessing the functional compounds for potential uses, including antioxidant properties, and utilizing the appealing brown color as a dyeing agent in the textile industry[13,14]. Silk, a natural

protein fiber produced by silkworms, is composed of 75% fibroin, 21% sericin, and 4% impurities. Fibroin, insoluble in weak alkalis and soap, forms the silk fiber and has a polypeptide chain structure. Sericin, strengthening the silk but dulling its luster, requires degumming before dyeing. Known for water absorption and a smooth texture, silk finds applications in fabrics, tire linings, artificial blood vessels, and surgical sutures. Despite its unique properties, silk's surface may need modification to enhance crease recovery, dyeability, and colorfastness. Dyeing silk relies on phenolic groups with accessible -OH, free amino, and carboxyl groups. Although acid dyes have drawbacks like low dyeability and wastewater discharge, their brilliance, color variety, high wet fastness, and convenient usage make them suitable for silk[15,16,17].

The purpose of this study was to investigate whether dye extracted from spent coffee grounds could be used as a dyeing agent for silk yarn using a simple extraction method with a Moka pot. The dyeing time (1.0, 1.5, 2.0, and 3.0 h) and temperature (85 °C and 120 °C) were varied to determine the optimal dyeing conditions. The absorptivity of the extracted dye from spent coffee grounds, and that of the dyeing solution after the various dyeing conditions, was measured using a UV-vis spectrometer. FT-IR analysis was used for the chemical identification of coffee-extracted dye, dyed silk yarn, and undyed yarn. Tensile testing was conducted to evaluate the effect of utilizing a bleaching agent in the surface treatment of the dyed silk yarn compared to the pristine.

2. Materials and Methods

2.1 Collection of Spent Coffee Grounds

Because of the increased consumption of coffee beverages in coffee shops and convenience stores, we chose brewed coffee grounds as a raw material to prepare the dye solution. To prevent microorganism growth, the coffee grounds were dehydrated by drying them in a hot air oven at 65 °C for 8 h. Then they were stored in a ziplock bag and placed in a desiccator.

2.2 Extraction of Coffee Solution

A Moka pot was used to make hot brewed coffee (BLU SASTA 6 Italian cups). The brewing process began by filling the base of a Moka pot with 300 ml of DI water for 24 g of coffee grounds and then inserting the funnel. Place a filter paper before loosely packing the grounds to prevent residue from rising into a collector chamber. After assembling the collecting chamber and base, ensure that the rim is properly fitted to maintain pressure during the brewing process. The Moka pot was then put on the hot plate, and after 2 minutes the coffee started to flow until all the water had moved up. The coffee-extracted solution was collected for use as a dyestuff.

2.3 Dyeing of Silk Yarn

Before dyeing, the natural silk yarn was carefully cleaned to degum. A 20% (w/v) wetting agent solution was applied at 60°C for 1 h, followed by rinsing and multiple water washes (4-5 times) to remove impurities. After cleaning, the yarn underwent bleaching by immersing it in a 0.4%w/v sodium hydroxide solution for 1 h at room temperature. The yarn was then rinsed until achieving a neutral pH, indicating complete removal of the alkaline solution. Finally, the yarn was air-dried naturally, and each batch was given a unique code for tracking purposes. Silk yarn dyeing was conducted based on Kasozi (2011) and Janani (2013) methods[14,15] with minor adjustments. Bleached silk yarn groups were immersed in a dyeing agent at a ratio of 1 g per 100 ml and gradually heated to 85°C for 1 h. Additional yarn groups underwent dyeing at the same temperature with varied durations (1.5 h, 2.0 h, and 3.0 h). The dyed yarns were then rinsed until no further color change was observed in the cleaning water and air-dried at room temperature. Another group of yarn was dyed in a pressure cooker at 120°C. Within the pressure cooker, subgroups experienced different dyeing durations (1.0 h, 1.5 h, 2.0 h, and 3.0 h). Following pressure-infused dyeing, thorough rinsing was performed, and the samples were dried at room temperature.

2.4 Color Measurement of Dyed Silk Yarns

The color of dyed silk yarns was measured using a portable color reader (Konica Minolta, Model CR-10) that measured CIELAB values (L*, a*, and b*). The Commission Internationale de L'Eclairage (CIE) has developed a Mathematical method for describing color, widely used in research[19]. This system looks at color in terms of lightness (L*), redness-greenness (a*), and blueness-yellowness (b*). To compare the color of dyed silk yarn with its original sample, we calculated the differences in color values (ΔL*, Δa*, and Δb*), and then a single value (ΔE*) represented the overall color difference, A ΔE* value zero indicates that the two colors are identical, while larger values indicate a greater difference in color[20].

$$\Delta E^* = \sqrt{(\Delta L^*)^2 + (\Delta a^*)^2 + (\Delta b^*)^2}$$

2.5 UV-vis Absorption of Coffee-Extracted Dyes

In the conducted research, the determination of absorptivity for dyes extracted from browning coffee was executed utilizing a Jasco V-530 UV/VIS Spectrophotometer. Absorbance measurements were taken at 420 nm according to the maximum absorbance of the brown compounds[12]. The experimentation involved assessing the absorbance of coffee-extracted dyes at diverse extraction temperatures (85 °C and 120 °C) both before and following the dyeing process.

2.6 FT-IR Analysis

Fourier transforms infrared (FT-IR) spectrometry was performed using a Thermo Scientific Nicolet iS5 FT-IR spectrometer with a resolution of 4 cm^{-1} in the range of 400-4000 cm^{-1} at room temperature in the transmittance mode. The FT-IR measurements were carried out using an attenuated total reflectance (ATR) technique. This study also identifies and characterizes the peak changes of silk yarns dyed with coffee-extracted dye.

2.7 Tensile Testing of Silk Yarns

In this investigation, the tensile properties of various silk yarns were investigated across 10 samples for each type to ascertain the mean values of their tensile strength, second modulus, and percentage of elongation. The mechanical attributes of the silk yarns were evaluated within a 25 mm gauge length, employing a test speed of 300 mm/min and a load cell of 100 N on a Universal Testing Machine (UTM) manufactured by Comtech. Tensile tests are performed on ASTM D3822[21,22].

Table 1. Color and CIELAB of pristine, bleached silk yarn, and dyed silk yarn at 85 °C

	Types of Yarns		Yarns with various dyeing times (h)			
	Pristine	Bleached	1.0	1.5	2.0	3.0
CIELAB parameters						
L*	82.7667	83.4000	74.2667	70.5000	70.4667	67.6667
a*	-2.4000	-3.1000	0.6000	1.9000	1.8667	2.3000
b*	16.4000	14.1333	19.0333	19.7333	19.800	19.4333
ΔE*	-	2.4779	9.3813	13.4413	13.4662	16.0965

Table 2. Color and CIELAB of pristine, bleached silk yarn, and dyed silk yarn at 120 °C

	Types of Yarns		Yarns with various dyeing times (h)			
	Pristine	Bleached	1.0	1.5	2.0	3.0
CIELAB parameters						
L*	82.7667	83.4000	75.5667	72.0667	72.8667	69.6667
a*	-2.4000	-3.1000	0.5000	1.2333	0.8333	1.5333
b*	16.4000	14.1333	18.3333	19.1333	18.5333	18.5333
ΔE*	-	2.4779	8.0886	11.6534	10.6614	13.8808

3. Results & Discussion

3.1 The Color Magnitude of the Dyed Silk Yarn

The magnitude of the color parameter ΔE* is commonly used to represent the perception of color differences between two samples. If ΔE* ≤ 1.0, a normal observer cannot detect a color difference, while an experienced observer can recognize the difference for 8 < ΔE* < 16, there is a clear color difference. Colors are considered different if the ΔE* is greater than 5[20]. The result from the bleaching process shows a normal perception of color difference between the pristine silk and the bleached sample as ΔE* equal to 2.48. While ΔE* values of dyed samples (at 85 °C and 120 °C) have differed from the pristine as the results in Tables 1 and 2, respectively. It has been proposed that achieving a more vibrant and intense color absorption during the dyeing process depends on the duration, even when employing a pressure cooker. Interestingly, there is minimal distinction between dyeing temperatures. Nonetheless, at a slightly lower temperature, ΔE*

values appear to be higher compared to dyeing the yarn at 120 °C using a pressure cooker. The ΔE* values for silk yarns dyed at 120°C exhibit distinct variations compared to those dyed at 85°C, as indicated by the respective values for various dyeing durations (1.4799, 1.8053, 2.9039, and 1.1823). The resulting-colored silk yarns exhibit distinct brown and dark brown shades, signifying the impact of the dyeing process. Further research is warranted to optimize pressure cooker dyeing parameters and explore its broader applicability in silk yarn coloration.

3.2 Absorptivity of Coffee-Extracted Dyes

The maximum wavelength (λ_{max}= 420 nm) for brown compounds extracted from spent coffee observed in these experiments was quite like those reported by Clarke and Macrae (1985)[9]. Table 3 shows the absorptivity of the dyes before and after dying at various temperatures and times. The absorptivity of the dyes after dyeing shows a slight decreasing[20].

Table 3. Absorptivity of the coffee-extracted dye and the dye liquors after dyeing at 85 °C and 120 °C

Dyeing time (h)	% Absorptivity of all dyes		
	Before	After dyeing	
	Extracted dye	Dyeing temperature	
		85 °C	120 °C
1.0	41.02	36.75	35.30
1.5		34.60	34.32
2.0		32.20	30.33
3.0		31.25	29.95

3.3 FT-IR spectra of silk yarns dyed with coffee-extracted dyes

The FT-IR spectra presented in Figure 1 depict a comparison among the silk yarns before dyeing step, silk yarns treated with spent coffee extract, and the resultant coffee-extracted dye. Silk yarns consist of diverse components, including 76 % fibroin, 1.5% wax, 1.5% salt, and 0.5% mineral salt. Fibroin, an insoluble protein in weak alkalis and soap, forms a chain molecule through amino acids, constituting a polypeptide chain with the molecular formula $NH_2CHRCOOH$[15,16,17]. The dyeability of silk is influenced by the presence of various functional groups, particularly those with an accessible (-OH) group, along with free amino and carboxyl groups. peptide backbone (-gly-gly- and gly-ala-). Notably, peaks corresponding to the (-OH) stretch are observed in the range of 3200-3800 cm^{-1}. Consequently, silk can be effectively dyed using anionic dyes such as acid dyes. Anionic dyestuffs like spent coffee dyes exhibit a strong affinity for the amino and carboxyl groups on the silk surface. As a result, all dyed silk yarns exhibit characteristic peaks at 1634 cm^{-1} (amide I), 1512 cm^{-1} (amide II), and 1229 cm^{-1} (amide III). The peaks (1400 cm^{-1}) prove the existence of sericin protein. The presence of sericin coating seems to mask two distinctive fibroin bands at lower wavenumbers such as 994 cm^{-1} and 971 cm^{-1}. These bands are the characteristic features of the Additionally, bands at 3283 cm^{-1} and 2873 cm^{-1} correspond to N-H and O-H bonds, as well as (-CH_2) bonds, respectively[18].

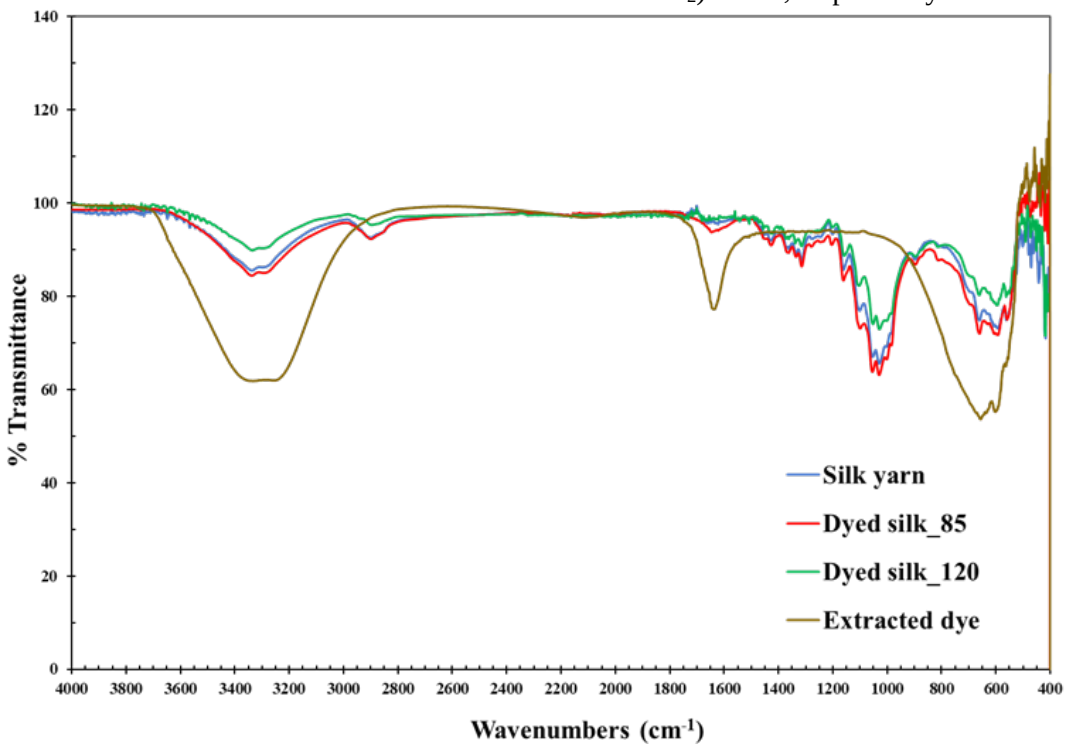

Figure 1. FT-IR spectra of coffee-extracted dye, dyed silk yarn, and pristine.

3.4 Tensile Properties of Silk Yarns

Natural silk is impressive because it's strong, flexible, and stretchy, making it tough and versatile. It's even tougher than Kevlar, a well-known high-performance material. Silk's ability to handle stress when stretched is crucial, especially for things that need to absorb energy. Because silk yarns are strong and tough, they find uses in various applications[15,23]. Structurally, silk fibers have two fibroin filaments coated with sericin proteins, forming a thread with a diameter of 10-25 mm. This thread consists of two core fibroin fibers, each measuring 5-10 mm in diameter. Fibroin is rich in amino acids like alanine, glycine, and serine, and others with acidic side chains. These components work together to give silk its unique mechanical properties, including high strength, stretchiness, and compressibility[15,22]. The results depicted in Figures 2 and 3 indicate a slight reduction in the tensile strength and moduli of silk yarns dyed with coffee extract compared to untreated yarns. This decline is attributed to the removal of sericin layers through degumming methods, such as washing with solutions like sodium hydroxide, soap, and hot water[9,15,16]. When dyeing silk yarns at 120°C in a pressure cooker, a marginal decrease in tensile properties (strength and moduli) is observed compared to dyeing at 85°C. Furthermore, the decrease in strength and moduli at higher temperatures is influenced by the duration of the dyeing process. The dyed silk yarns exhibit tensile strength ranging from 288-384 N/mm^2 and moduli ranging from 668-819 N/mm^2. Nevertheless, the coffee-extracted dyes show a notable attraction to the amino and carboxyl groups on the surface of silk, leading to a modest increase in the percentage of elongation in dyed silk yarns (14-48%), as illustrated in Figure 4, in comparison to the untreated sample.

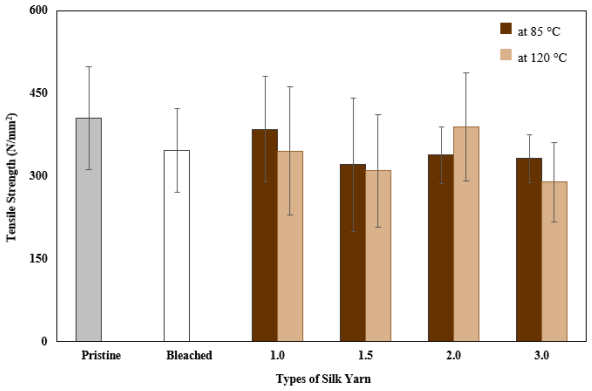

Figure 2. Tensile strength of silk yarns at various conditions.

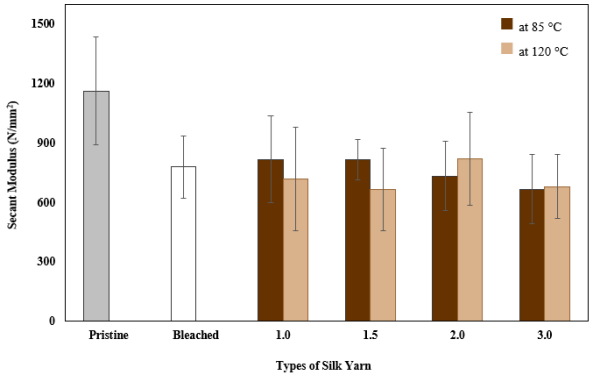

Figure 3. Secant moduli of silk yarns at various conditions.

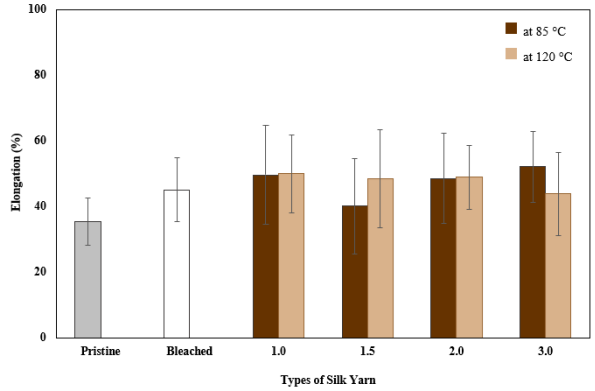

Figure 4. %Elongation of silk yarns at various conditions.

4. Conclusion

In summary, the study explored the viability of using a moka pot to extract natural dye from discarded coffee grounds for dyeing bleached-silk yarns. Dyeing was conducted conventionally at 85°C and in a pressure cooker at 120°C with varying durations, resulting in natural brown shades, lighter tones at higher temperatures, and distinctive E* value variations. FT-IR spectra confirmed dye presence on all yarns, despite potential tensile strength impact from bleaching. The research aimed for mordant-free dyeing using eco-friendly methods and simple equipment[14,24]. The approach not only produced diverse browning shades but also hinted at self-surface cleaning potential at higher temperatures, emphasizing enhanced dyestuff affinity with silk surface functional groups[24].

Acknowledgments

The authors gratefully acknowledge the invaluable contribution of Shinawatra Thai Silk, San Kamphaeng, Chiang Mai, for supplying the essential silk yarns used in this study. Their partnership was crucial to the research's success.

References

1. Ali, S.; Hussain, T.; Nawaz, R. Optimization of alkaline extraction of natural dye from Henna leaves and its dyeing on cotton by exhaust method. *J. Cleaner Prod.* **2009**, *17*, 61-66.
2. Guesmi, A.; Hamadi, N. B.; Ladhari, N.; Sakli, F. Dyeing properties and colour fastness of wool dyed with indicaxanthin natural dye. *Ind. Crops Prod.* **2012**, *37*, 493-499.
3. Manley, J. B.; Anastas, P. T.; Cue, B. W. Frontiers in Green Chemistry: meeting the grand challenges for sustainability in R&D and manufacturing. *J. Cleaner Prod.* **2008**, *16*, 743-750.
4. Jung, Y. Koreans fascinated by coffee: The coffee market reached its first level of 10 trillion won last year. *Yonhap News* **2018**. Available online: http://m.news.naver.com/read.nhn?mode=LSD&sid1=101&sid2=310&oid=001&aid=0009899801.
5. Jo, J.; Kim, S.; Min, B.; Jung, H.; Han, Y.; Kim, J. Optimization of hot-water extraction condition of bioactive compounds from coffee residue extracts. *Korean Chem. Eng. Res.* **2017**, *55*(3), 358–362.
6. Mussatto, S. I.; Ballesterols, L. F.; Martins, S.; Teixeira, J. A. Extraction of antioxidant phenolic compounds from spent coffee grounds. *Sep. Purif. Technol.* **2011**, *83*, 173–179. https://doi.org/10.9713/kcer.2017.55.3.358
7. Xu, H.; Wang, W.; Liu, X.; Yuan, F.; Gao, Y. Antioxidative phenolics obtained from spent coffee grounds (*Coffea arabica* L.) by subcritical water extraction. *Ind. Crops Prod.* **2015**, *76*, 946–954. https://doi.org/10.1016/j.indcrop.2015.07.054.
8. Koca, N.; Burdurlu, H. S.; Karadenus, F. Kinetics of nonenzymatic browning reaction in citrus juice concentrates during storage. *Turk. J. Agric. For.* **2003**, *27*, 907–916.
9. Clarke, R. J.; Macrae, R. Coffee Chemistry; Vol. 1; Elsevier Applied Science: Amsterdam, **1985**; pp. 124–125.
10. Rufián-Henares, J. A.; de la Cueva, S. P. Antimicrobial activity of coffee melanoidins—a study of their metal chelating properties. *J. Agric. Food Chem.* **2009**, *57*(2), 432–438. https://doi.org/10.1021/jf8027842.
11. Moreira, A. S. P.; Nunes, F. M.; Dominguesa, M. R.; Coimbra, M. A. Coffee melanoidins: Structures, mechanisms of formation and potential health impacts. *Food Funct.* **2012**, *3*, 903–915.
12. Bravo, J.; Monente, C.; Ju aniz, I.; De Pena, M. P.; Cid, C. Influence of extraction process on antioxidant capacity of spent coffee. *Food Res. Int.* **2013**, *50*(2), 610–616.
13. Heine, E.; Hoecker, H. Bioprocessing for Smart Textiles and Clothing. *Smart Fibres, Fabr. Cloth.* **2001**, 254–277.
14. Janani, L.; Winifred, D. Suitability of Dyes from Mulberry and Coffee Leaves on Silk Fabrics using Eco-Friendly Mordants. *Int. J. Sci. Res. Pub.* **2013**, 3(11), 1-4.
15. Kasozi, J. Government of Uganda to Revamp Silk Business. *Short Communication* **2011**.
16. Ester, K. S.; Adhi, K. *J. Teknobuga* **2008**, *Vol. 1*, (1), 22-27.
17. Kongkachuchai, P.; Shitangkoon, A.; Chiwongamoin, N. *Sci. Asia* **2002**, *Vol. 28*, 161-166.
18. Lee, J.; Kang, M. H.; Lee, K. B.; Lee, Y. Characterization of natural dyes and traditional Korean silk fabric by surface analytical techniques. *Materials* **2013**, *6*(5), 2007–2025. https://doi.org/10.3390/ma6052007.
19. Pavia, D. L.; Lampman, G. M.; Kriz, G. S. *Introduction to Spectroscopy*; Harcourt Brace College Publishers: Florida, **1996**; Chapter 2.
20. Wojciech, M.; Maciej, T. Color Difference Delta E - A Survey. *Mach. Graph. Vis.* **2011**, *20*, 383–411.
21. Ahmad, J.; Zhou, Z. Mechanical Properties of Natural as Well as Synthetic Fiber Reinforced Concrete: A Review. *Constr. Build. Mater.* **2022**, *333*, 127353.
22. American Society for Testing and Materials. "ASTM D3822-01: Standard Test Method for Tensile Properties of Single Textile Fibers." *pp.* 1-6, **2001**.
23. Ranakoti, L.; Gangil, B.; Rajesh, P. K.; Singh, T.; Sharma, S.; Li, C.; Ilyas, R. A.; Mahmoud, O. Effect of Surface Treatment and Fiber Loading on the Physical, Mechanical, Sliding Wear, and Morphological Characteristics of Tasar Silk Fiber Waste-Epoxy Composites for Multifaceted Biomedical and Engineering Applications: Fabrication and Characterization. *J. Mater. Res. Technol.* **2022**, *19*, 2863–2876.
24. Bae, J.; Hong, K. H. Optimized dyeing process for enhancing the functionalities of spent coffee dyed wool fabrics using a facile extraction process. *Polymers* **2019**, *11*(4), 574. https://doi.org/10.3390/polym11040574.

Utilization of silk sericin as an ingredient in acne hydrogels: Inhibitory effect against *Staphylococcus aureus*

Patchareeya Khaopenyai, Waraporn Phokka, and Supranee Kaewpirom*

Department of Chemistry, Faculty of Science, Burapha University, Chonburi 20131, Thailand.

**E-mail: kaewpiro@go.buu.ac.th*

Abstract:

Silk sericin, a naturally occurring polymer, is synthesized by the silkworm Bombyx mori. The cosmetic industry can benefit from the extended application of sericin due to its antioxidant activity. In this study, silk sericin was extracted from white silk cocoons using distilled water at 100 °C. The resulting silk sericin solution with the concentration of 0.52 %w/v was obtained. Acne hydrogel was prepared from carbomer with the addition of the sericin solution, glycerol and tea tree oil at different concentrations. The chemical structure of the acne hydrogel was analyzed using Fourier transform infrared spectroscopy (FT-IR). The inhibitory effect of the acne hydrogel was also tested against *Staphylococcus aureus (S. aureus)*. The results showed that tea tree oil was effective in inhibiting the infection, and the effectiveness increased with increasing tea tree oil concentration. Acne hydrogels containing 10, 12.5 and 15%w/v of tea tree oil inhibited the growth of *Staphylococcus aureus*, with the mean inhibition zone diameters of 7.33±0.57, 8.66±0.28 and 10.66±1.60 mm, respectively. In the absence of tea tree oil supplementation, the hydrogel exhibited no inhibitory effects on the growth of *Staphylococcus aureus*, with recorded mean inhibition zone diameters of 0 mm. Additionally, the skin irritation test showed that the acne hydrogel did not irritate human skin.

1. Introduction

Currently, the studies of silk properties and its quality improvement are widely conducted to explore its versatility and specific applications. Silk is a natural protein that is biocompatible and biodegradable. Silk also shows promise as an eco-friendly biomaterial with high strength, heat resistance, and transparency.[1] Silk production is widespread in Thailand, especially in the Northeast region. However, the production is frequently undertaken on a part-time basis to complement farmers' income. This leads to discontinuous production. Another factor is that the prices of raw cocoons and raw silk are relatively uncertain and mostly low, which does not motivate farmers to produce silk as their main occupation. Moreover, the use of silk is still limited to the textile industry. Recent research on silk properties has led to its use in other industries, increasing the value and demand for silk. For example, silk can be used in cosmetics, food, and pharmaceuticals.[2] Silk has been processed into powder, meltable silk, and film, which can be pure silk or mixed with other substances to obtain the desired properties.

Silk is a natural protein composed of 70-80% fibroin and 20-30% sericin.[3] Sericin is produced by the middle pituitary gland of silkworms and is secreted to coat the silk core to form a fiber. It is also known as silk glue. Sericin is composed of important amino acids such as serine, aspartic acid, glutamic acid, arginine, threonine, and lysine. Sericin has antibacterial, antioxidant, anti-tyrosinase enzyme, UV protection, and water absorption properties. It is therefore used as an ingredient in cosmetics such as soap, shampoo, creams, and lotions. In cosmetics, it can be mixed with various extracts, such as mangosteen peel extract or tea tree oil, to develop anti-acne hydrogels.

Tea tree oil is an essential oil extracted from the leaves of Melaleuca alternifolia. It is composed of a variety of monoterpenes, with terpinen-4-ol being the most abundant compound, accounting for at least 30% of the oil.[4] Terpinen-4-ol is a potent antibacterial agent that can inhibit the growth of *Propionibacterium acnes* and *Staphylococcus aureus*, which are two of the main causes of acne.[5] Therefore, in this study, the preparation of hydrogel with antibacterial activity against acne-causing bacteria was investigated. Silk glue sericin, glycerol and tea tree oil extracts at different concentrations were applied as additives. The hydrogels were tested for their chemical properties, as well as their efficacy in inhibiting the growth of *Staphylococcus aureus* and their skin irritation potential.

2. Materials and Methods

2.1 Materials

White silk cocoons (J-1) were from Ubon Ratchathani Province, Thailand. Tea tree oil (TTO), Triethanolamine (TEA) and carbomer 940 were cosmetic grade and purchased from Chemipan Co. Lth., Thailand. Glycerol (99.5%), sodium carbonate (analytical reagent), and calcium

chloride (laboratory reagent) were from Ajax Finechem.

2.2 Preparation of silk sericin solution

Silk cocoons (2 g) were cut into small pieces before adding into 200 mL of boiling distilled water. After 2-h boiling, water from which the silk fibroin was removed was centrifuged at a speed of 2,000 rpm for 20 minutes. The clear liquid of silk sericin solution was then obtained.

2.3 Preparation of anti-acne hydrogel

Into the beaker, 10.0 mL of distilled water was warmed to 50°C. Accurately weighed carbomer (0.05 g) was slowly sprinkled onto the surface of the heated water. The mixture was continuously stirred by means of magnetic bar for 15 minutes to ensure complete dispersion. The mixture was then allowed to cool to room temperature before desired volume of sericin silk solution and glycerol (30% v/v) were added into the mixture and the mixture was stirred until homogenous. The same procedure was repeated with the addition of desired volume of tea tree oil extract. Finally, the pH of the mixture was adjusted to the desired range by adding triethanolamine dropwise while stirring continuously to stabilize the gel.

2.4 Fourier-transform infrared spectroscopy (FTIR)

Functional group analysis of hydrogel samples was carried out through FT-IR at wave numbers 400-4000 cm^{-1}. The resolution for data collection is 4 cm^{-1} with 18 scans by analyzing each sample 3 times.

2.5 Disc diffusion method

A sterile cotton swab was dipped into a *S. aureus* culture tube and spread on the surface of the Mueller Hinton agar (MHA) medium. The surface of the medium was allowed to dry for 5-10 minutes. A paper disk with 6-mm diameter was packed with the TTO extract (20 µl) at different concentrations and with the antibiotic gentamycin, concentration 10 µg/plate. The plates were dried in a sterile container and then placed on the surface of the spread culture medium as described above. The plates were incubated at 37 °C for 24 h, and the results were recorded by measuring the diameter of the apparent inhibition zone.

2.6 Skin irritation test

A total of 30 healthy people were selected to test for their skin irritation when 10 of each sample, namely WSS/TTO10/G30, WSS/TTO12.5/G30 and WSS/TTO15/G30 were applied on their skin. The inside of the upper arm was cleaned with a cotton swab, soaked with 70% v/v alcohol and left to dry. Then 0.1 mL of anti-acne hydrogel product was applied to the tested area of the skin with a diameter of 6.6 cm until the gel was absorbed into the skin. The tested area was covered with a bandage, as shown in Figure 4 and left it for 24 hours. When the time had elapsed, the bandage was removed and waited approximately 15 minutes before recording the skin irritation.

3. Results & Discussion

3.1 Determination of the concentration of silk sericin

The experiment was carried out by pipetting 1.00 mL of silk sericin solution into a weighed polypropylene plastic mold. It was then allowed to dry at room temperature for 24 hours, followed by drying in a vacuum oven at 50°C for 4 hours or until the weight stabilized. The polypropylene plastic mold was then reweighed. The concentration of silk sericin solution (%w/v) was calculated. From the experimental results, it was found that the concentration of silk sericin was 0.52 %w/v, which was close to the value reported by Joe and Um.[6] Therefore, the method of peeling silk glue with hot water was an effective method and was used in this study.

3.2 Physical characteristics of anti-acne hydrogel

The digital pictures of anti-acne hydrogel products prepared using carbomer (a gelling agent), silk sericin (an antioxidant agent), glycerol (a moisturizing agent), tea tree oil extracts (an antibacterial agent), at different concentrations, and triethanolamine (a stabilizing agent) were shown in Fig 1. The physical characteristics of WSS/TTO hydrogels with different TTO concentrations were investigated. The hydrogel with 5% v/v TTO was homogeneous with no precipitates and slightly turbid (Fig. 1(a)). On the other hand, the samples with high concentrations of TTO, namely WSS/TTO10/G30, WSS/TTO12.5/G30 and WSS/TTO15/G30 showed the gel texture with turbidness.

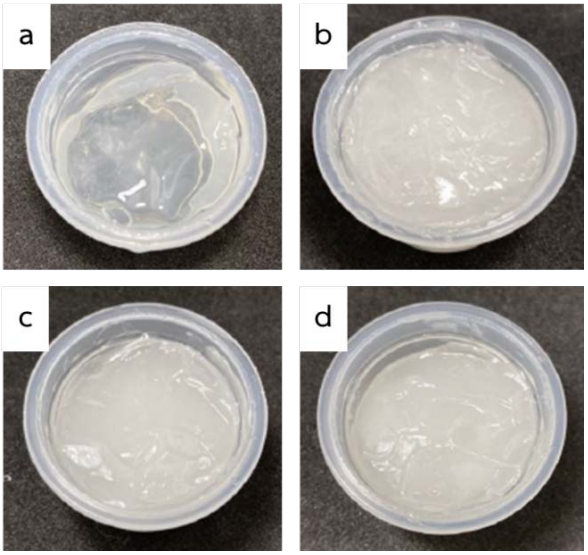

Figure 1. Digital photographs of acne-fighting hydrogels. (a) WSS/TTO5/G30, (b) WSS/TTO10/G30, (c) WSS/TTO12.5/G30 and (d) WSS/TTO15/G30. The results showed that the samples with low concentrations of TTO 5% were homogeneous. However, the samples with high concentrations of TTO (10%, 12.5%, and 15%) were very turbid.

3.3 Analysis of the chemical structure of anti-acne hydrogels

Fig 2 displayed FT-IR spectra of anti-acne hydrogel products. Functional groups found in silk sericin solution (WSS) included OH stretching at 3290 cm^{-1} and Amide I at 1635 cm^{-1}. This is consistent with the results reported by Teramoto et al.,[7] confirming the Amide 1 position of silk sericin at 1,647 cm^{-1}. Glycerol showed a peak of O-H stretching at 3290 cm^{-1} and C-O at 1040 cm^{-1}, which is consistent with the result proposed by Brown et al.[8] TTO showed O-H stretching at 3343 cm^{-1}, C-H stretching at 2962 cm^{-1}, C-H at 1450 cm^{-1}, and C-O at 1,000 cm^{-1}. The WSS/TTO/G30 hydrogel showed OH stretching at 3290 cm^{-1}, Amide I at 1635 cm^{-1} and C-O at 1,030 cm^{-1}. These observed spectral signatures are indicative of the presence of both silk sericin and glycerol within the hydrogel matrix. It can be concluded from the results that the addition of glycerol and silk sericin as a moisturizing agent and antioxidant agent, respectfully, did not cause any reaction with other ingredients found in the hydrogel.

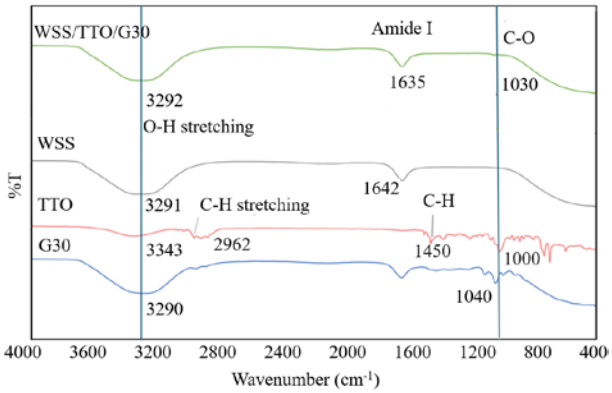

Figure 2. Functional group analysis of anti-acne hydrogel products using FT-IR.

3.4 The efficiency in inhibiting the growth of bacteria

The effect of TTO in inhibiting the growth of *S. aureus* of the anti-acne hydrogel was carried out using the standard disc diffusion method. The results showed that TTO (control) had an average diameter of the inhibition zone of 17.33±1.25 mm (Fig 3 (a)). This is consistent with the results reported by Risa Dittanoi and colleagues.[9] The hydrogel with low concentration of TTO (WSS/TTO5/G30) had no effect on inhibiting growth of *S. aureus* bacteria (Fig 3 (b)). With increased tea tree oil concentration (10, 12.5, and 15 %v/v), WSS/TTO10/G30, WSS/TTO12.5/G30 and WSS/TTO15/G30 showed their ability in inhibiting the growth of *S. aureus* bacteria. The average diameter of the inhibition zone increased with increasing tea tree oil concentration: 7.33, 8.66 and 10.66 mm, respectively (Fig 3 (c), (d) and (e)).

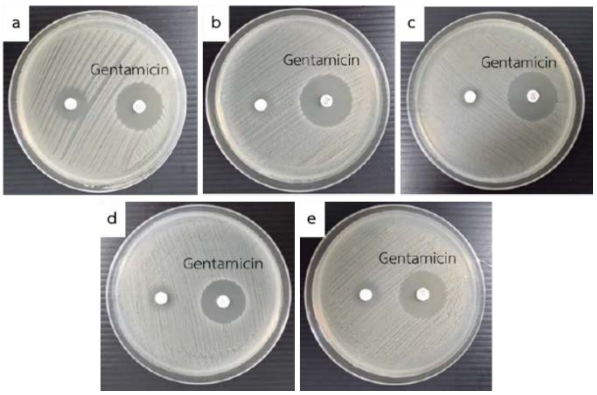

Figure 3. The inhibition zone against the growth of *Staphylococcus aureus* ATCC 25923 for (a) TTO (control), (b) WSS/TTO5/G30, (c) WSS/TTO10/G30, (d) WSS/TTO12.5/G30 and (e) WSS/TTO15/G30

3.5 Skin irritation test

With their effectiveness in inhibiting the growth of *Staphylococcus aureus*, WSS/TTO10/G30, WSS/TTO12.5 and WSS/TTO15/G30 were chosen to test for skin irritation. A patch test is a widely recognized diagnostic technique employed to identify the particular substances that trigger allergic inflammation on a patient's skin. Skin irritation test of 10 volunteers per hydrogel formula, both men and women, aged between 20-24 years. revealed that none of the volunteers had an allergic reaction to the hydrogels. This implies that the anti-acne hydrogel prepared in our study are safe for the users.

Figure 4. Skin irritation testing

4. Conclusion

Anti-acne hydrogels prepared in this study showed the effect of inhibiting acne-causing bacteria. Silk sericin, glycerol and TTO can be successfully used as additives without causing skin irritation. With high concentration of tea tree oil (10, 12.5, and 15 %v/v), the anti-acne hydrogels showed their ability in inhibiting the growth of *S. aureus* bacteria.

Acknowledgements

This study was partially supported by the Science Innovation Facility, Faculty of Science, Burapha University (SIF-IN-40100054).

References

1. Hou, T. C.; Jeng, S. C. *ACS Appl. Bio Mater.* **2020**, *3*(12), 8575–8580.
2. Sutheerawattananond, M: *Method development of fibroin films for medical products*: Nakhon Ratchasima, 2006; pp 3-6.
3. Kansingh, S.; Pomtong, B.; Chuluk, S.; Chankhangram, W. *KKU Sci. J.* **2017**, *45*(1), 128-137.
4. Shi, C.; Zhang, X.; Guo, N. *Microb. Pathog.* **2018**, *125*, 262-271.
5. Mazzarello, V.; Donadu, M. G.; Ferrari, M.; Piga, G.; Usai, D.; Zanetti, S.; Sotgiu, M. A. *Adv. Appl.* **2018**, *10*, 175-181.
6. Jo, Y. N.; Um, I. C. *Int. J. Biol. Macromol.* **2015**, *78*, 287-295.
7. Teramoto, H.; Nakajima, K. I.; Takabayashi, C. *Biosci. Biotechnol. Biochem.* **2005**, *69*(4), 845-847.
8. Brown, J. E.; Davidowski, S. K.; Xu, D.; Cebe, P.; Onofrei, D.; Holland, G. P.; Kaplan, D. L. *Biomacromolecules.* **2016**, *17*(12), 3911-3921.
9. Ditnoi, R.; Sukatta, U.; Winitchai, S.; Chantarapanont, W. in Proceedings of 50th Kasetsart University Annual Conference: Agro-Industry. Bangkok, Thailand, Jan 31 - Feb 2, 2012.

Influence of functionalized graphene on short-glass fiber reinforced polyamide12 composites

Nattakarn Hongsriphan* and Pajaera Patanathabutr

Department of Materials Science and Engineering, Faculty of Engineering and Industrial Technology, Silpakorn University, Nakhon Pathom 73000, Phone +66 3424 1708, Fax +66 3424 1708

**E-mail: Hongsriphan_N@silpakorn.edu*

Abstract:

Polyamide12 (PA12) composites reinforced with short glass fibers (GF) of 12.6-13.0 μm diameter and 6 mm length in the weight ratio of 2, 4, and 6 wt% were compounded using a twin-screw extruder. The influence of functionalized graphene (Gr-O2) was investigated by incorporating Gr-O2 of 0.3 and 0.5 wt% into the composites. As characterized by the supplier, these Gr-O2 were plasma functionalized by oxygen to obtain the carbonyl and the hydroxyl groups onto the surface. Mechanical, thermal and morphological properties of the injection molded composites were evaluated. It was found that Young's modulus and the ultimate tensile strength of the PA12-based composites increased linearly with respect to the GF concentration. Incorporating Gr-O2 of 0.3 wt% further increased both modulus and ultimate tensile strength of the PA12-based composites, which the highest ultimate tensile strength was achieved when adding GF of 6 wt% and Gr-O2 of 0.3 wt%. Due to plasticizing effect by the Gr-O2, the energy at break of the GF-reinforced PA12 composites was higher when incorporating Gr-O2 of 0.3-0.5 wt%. However, these Gr-O2 did not dissipate the shock loading well enough to improve the impact resistance. Two crystal melting temperatures of the PA12 were observed after annealing, and the merging of them occurred with the presence of Gr-O2 implying the physical interaction between the PA12 molecules and the nanoplatelets. SEM micrographs indicated the interfacial adhesion between the PA12 matrix and the GFs was improved due to the inclusion of Gr-O2 nanoplatelets that provided chemical compatibility via the functionalized groups.

1. Introduction

Polyamide12 (PA12)[1], also known as nylon12, is a type of aliphatic polyamide with a repeating unit of $[(CH_2)_{11}C(O)NH]_n$. This polymer provides mechanical properties between commercially-available short chain aliphatic nylons (e.g., nylon6 and nylon6,6) and polyolefins. Compared to nylon6, PA12 has low moisture absorption due to long hydrocarbon chain that resembles olefin-like structure. In addition, it is chemical resistant and insensitive to stress cracking. PA12 is injection molded to produce parts in automotive, electric and electronic, industrial and sport applications. Mechanical properties of PA12 are improved by reinforcing with glass fibers.[2]

Graphene and graphene derivatives have been interesting materials for researchers because they enhance better mechanical properties when compounding into polymers[3]. Graphene nano-platelets (GNPs) are small particles of graphene containing nanoplatelets, which could be plasma treated to modify the surface of the nanomaterials for enhancements in applications. The plasma treatment imparts chemical species onto the surface of the GNPs which improves the compatibility with various polymer matrix. Plasma surface modifications do not penetrate into the bulk of these materials, and therefore does not damage the structural integrity and related properties.

In this research, the PA12-based composites were melt compounded using short glass fibers (GFs) in the weight ratio of 2, 4 and 6 wt%, which the influence of functionalized GNPs was investigated by incorporating GNPs of 0.3 and 0.5 wt% into the composites. The GFs were aimed to be the main reinforcement which was less expensive and widely available, while graphene could be complemented for mechanical enhancement. Mechanical properties of the injection molded composites were evaluated by means of tensile and impact testing. Thermal and morphological properties of the composites were studied via differential scanning calorimetry (DSC), and scanning electron microscopy (SEM), respectively. Surface electrical resistivity of the PA12-based composites was also measured.

2. Materials and Methods

2.1 Materials

Polyamide 12 (PA12, Rilsamid® AMNO TLD, injection molding grade, density of 1.02 g/cm^3, melting temperature of 178°C) was purchased from Arkema Innovative Chemistry, France. It had a melt flow index of 57 cm^3/10 min (ISO1133). Short glass fibers (GF) with average diameter of 12.6-13.0 μm and an average length of 6 mm were provided by the Concrete Composite Co., Thailand. Functionalized graphene nano-platelets (Gr-O2, HDPlas®GNP-O2-STD, Batch No.18209) were kindly supplied by Haydale

Technologies Co. Ltd., Thailand. These GNPs were plasma functionalized by oxygen to obtain the carbonyl [C=O] and the hydroxyl [OH] onto the surface of the GNPs. The basic properties[4] provided by the supplier are a bulk density of about 2.15 g/cm^3, a specific surface area of about ~25 m^2/g, a typical GNP planar size of 0.3-5 µm (SEM) and a typical GNP thickness of less than 50 nm (SEM).

2.2 Melt compounding

Prior to melt compounding, PA12 pellets, GF fibers and Gr-O2 were dried thoroughly in an air-circulating oven at 90°C (12 hours), 120°C (12 hours), and 120°C (12 hours), respectively. The composition of the composites is shown in Table 1. Dried GF fibers and Gr-O2 were premixed by mixing and shaking together in a small polyethylene (PE) bag. Then, they were poured into a PE bag of warm PA12 pellets and shaking. This mixing procedure helped Gr-O2 to be wetted evenly onto pellet surface.

The melt compounding was performed in a twin-screw extruder (SHJ-25, Nanjing Youngteng Chemical Equipment, China) using a processing temperature profile of 190-220°C and a screw speed of 75-80 rpm. Each composition in Table 1 was fed through a controlled-velocity screw-type feeder at the same feed rate. The extrudate was water cooled and pelletized by a pelletizer.

Table 1. Abbreviations and compositions of neat PA12 and PA12-based composites.

Abbreviations	PA12 (wt%)	GF (wt%)	Gr-O2 (wt%)
PA12	100.0	0.0	0.0
PA12GF2_Gr0	98.0	2.0	0.0
PA12GF4_Gr0	96.0	4.0	0.0
PA12GF6_Gr0	94.0	6.0	0.0
PA12GF2_Gr03	97.7	2.0	0.3
PA12GF4_Gr03	95.7	4.0	0.3
PA12GF6_Gr03	93.7	6.0	0.3
PA12GF2_Gr05	97.5	2.0	0.5
PA12GF4_Gr05	95.5	4.0	0.5
PA12GF6_Gr05	93.5	6.0	0.5

2.3 Injection molding of specimens

The extruded PA12 and PA12-based composite pellets were dried in an air-circulating oven at 100°C for at least 12 hours. The specimens were injection molded using an injection molding machine (SmartPower 35/210 UNILOG B8, Wittmann Battenfeld, Thailand). Three zones of barrel temperature were set at 200, 220, and 230°C, and the nozzle temperature was set at 240°C. The injection velocity, the packing/holding pressure, and the packing/holding time were set constant. The mold temperature was set constant at 50°C (T_g of PA12 was 48.8°C), and the cooling time was set constant for 30 second.

2.4 Tensile and impact properties

The molded specimens were measured their tensile properties in accordance to ASTM-D638 using a universal testing machine (Instron 5969, Instron Engineering Corporation, USA). The load cell was 5 kN, and the crosshead speed was set at 50.8 mm/min. Ten specimens of each composition were tested, which the averages and the standard deviations were reported. The molded specimens were measured their impact properties using a pendulum impact tester (Instron Ceast9050, Instron Engineering Corporation, USA) in accordance to ASTM-D256 (notched Izod). The specimens were notched using a notch cutter. Ten specimens of each composition were tested using a pendulum of 1 Joule, which the averages and the standard deviations were reported.

2.5 Thermal properties by DSC

The molded specimens of each composition were cut into small pieces (14-15 mg) at the center of an impact specimen for thermal property analysis by a differential scanning calorimeter (DSC Pyris 1, Perkin Elmer, USA). The tests were performed in a heat-cool-reheat mode from 25 to 220°C with a heating/cooling rate of 5°C/min under nitrogen atmosphere. The crystal melting temperature (T_m), the crystallization temperature (T_c), and the degree of crystallinity (X_c) were reported. The X_c was calculated as the following:

$$\%x_c = \frac{\Delta H_m}{\Delta H_f^o} \times \frac{100}{w}$$

where ΔH_m was melting enthalpy of crystallinity (J/g), ΔH_f^o was melting enthalpy of 100% crystalline of PA12 (209.3 J/g)[5], and w was weight fraction of PA12 in composites.

2.6 Morphology by SEM

Cross-sectional surface of impact-fractured specimens was examined using a scanning electron microscope (SEM) (Tabletop microscopeTM3030, Hitachi, Japan). The surface was platinum-gold coated prior to inspection to avoid electrostatic charging.

2.7 Electrical surface resistivity measurement

Electrical surface resistivity of neat PA12 and PA12-based composites was measured using a surface electrical resistance meter (BFN-TR1380, Thailand). Five molded specimens were measured

and the averages were reported. The electrical surface resistivity of neat low-density polyethylene molded specimen was also measured as a reference.

3. Results & Discussion

3.1 Tensile properties

Figure 1 presents Young's modulus of the PA12 and PA12-based composites, which the percentage increase compared with the modulus of PA12 is also shown in the figure. The Young's modulus of the PA12-based composites increased linearly with respect to the GF concentration. Adding GF of 2, 4, and 6 wt% increased the modulus 12.55, 34.88, and 54.89%, respectively. Adding Gr-O2 of 0.3 wt% further increased the modulus of the composites, however, the reinforcement of the GF was interfered when adding Gr-O2 of 0.5 wt%. This could be attributed to the plasticizing effect[6] of the Gr-O2 nanoplatelets that the nanoplatelets slipped from each other for energy dissipation.

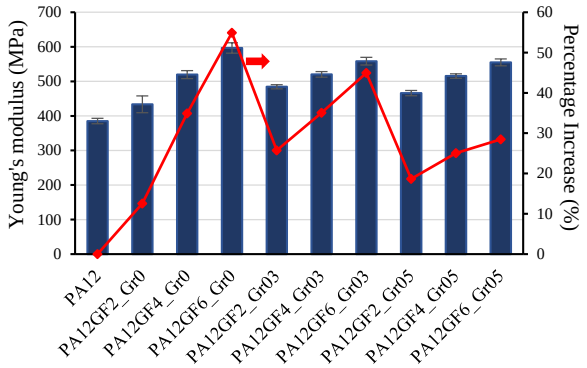

Figure 1. Young's modulus of PA12 and PA12-based composites.

Figure 2 presents ultimate tensile strength of the PA12 and PA12-based composites, which the percentage increase compared with the ultimate tensile strength of PA12 is also shown in the figure. It should be noted that the ultimate tensile strength of these composites occurred at yielding similarly to neat PA12. Identically to Young's modulus, the ultimate tensile strength of the PA12-based composites increased linearly with respect to the GF concentration. When the Gr-O2 of 0.3 wt% was incorporated into the composites, the ultimate tensile strength was further enhanced, which the highest ultimate tensile strength was achieved when adding GF of 6 wt% and Gr-O2 of 0.3 wt%. This was attributed to the nanoscale reinforcing effect that these Gr-O2 nanoplatelets reinforced the polyamide molecules while they were extended beyond the elastic region.

Figure 3 presents energy at break of the PA12 and PA12-based composites. The energy at break of the neat PA12 was about 122 J, and they were impact broken in ductile behaviour. Adding short GF of 2-6 wt% caused the PA12-based composites to be broken toward brittle behaviour with significant lower energy to break. This was attributed to the untreated GF fibers became the stress concentrator after the yielding. Interestingly, the GF-reinforced PA12 composites had higher energy at break when incorporating Gr-O2 of 0.3-0.5 wt%. This was attributed to the plasticizing effect of the nanoplatelets that increased the extension at break of the composites.

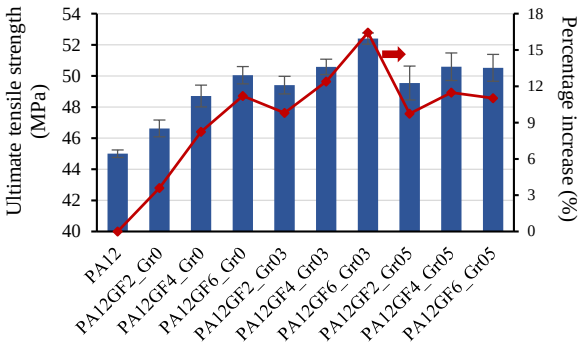

Figure 2. Ultimate tensile strength of PA12 and PA12-based composites.

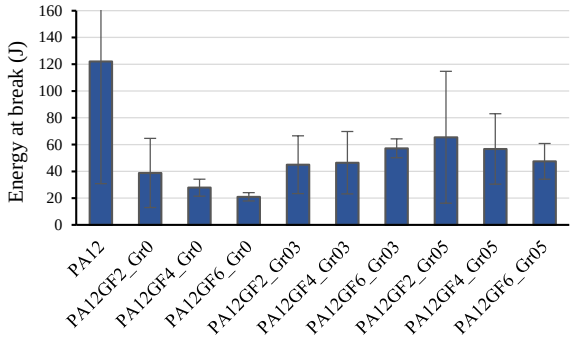

Figure 3. Energy at break of PA12 and PA12-based composites.

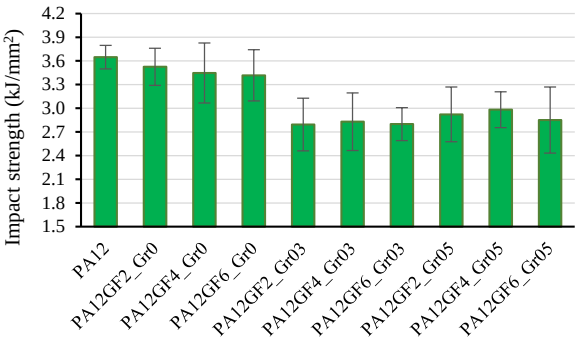

Figure 4. Impact strength of PA12 and PA12-based composites.

3.2 Impact properties

Figure 4 shows impact strength of the PA12 and the PA12-based composites. Due to lack of GF treatment, the average values of impact strength decreased linearly with the presence of the GF, and all specimens were broken completely under the pendulum of 1 Joule. Incorporating Gr-O2 of 0.3 wt% further reduced the impact resistance although the energy to break of the PA12-based composites with Gr-O2 was higher than the composites without Gr-O2. This indicates the brittleness of the PA12-based composites with the reinforcement of inorganic fillers when being subjected to a high-speed loading.

3.3 Thermal properties by DSC

Figure 5 shows DSC thermograms of the PA12 and the PA12-based composites from the 1st and 2nd heating scans. The heating and the cooling rate of the DSC testing were set constant at 5°C/min. It is seen that the crystal meting temperature (T_m) of the PA12 matrix was a single peak in the 1st heating scan, and it was split into double peaks in the 2nd heating scan. With the presence of the Gr-O2, the merging of these two T_m occurred implying the physical interaction between the PA12 molecules and the Gr-O2 nanoplatelets.

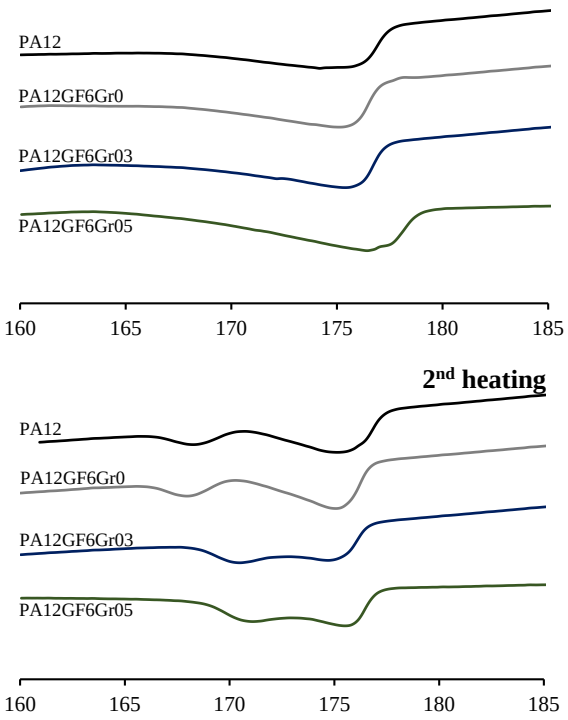

Figure 5. Thermograms of the PA12 matrix from the 1st and the 2nd heating scans.

PA12 has two crystal forms[7], namely α and γ form depending on the arrangement of the polymer chains. In the γ-form, the polymer chains are aligned parallel and the full hydrogen bonding requires some twisting of the chains. The extended CH_2 zigzags of each chain are in the plane of a molecular sheet, while the amide plane is twisted out of the polyethylene plane by about 60°. In the α-form, the molecular chains are antiparallel, and the full hydrogen bonding between extended chains can be easily attained. Figure 6 shows crystallization temperature (T_c) thermograms of the PA12 and the PA12-based composites. It is clearly shown that the Gr-O2 acted as the nucleating agents of the crystallization resulting the shifting of T_c from about 152°C to 155-156°C.

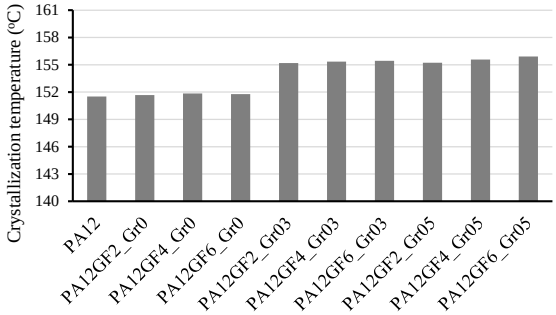

Figure 6. Crystallization temperatures (T_c) of the PA12 matrix from the cooling scan.

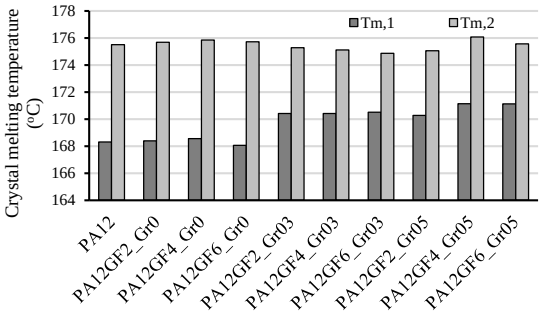

Figure 7. Crystal melting temperatures (T_m) of the PA12 matrix from the 2nd heating scans.

Figure 7 presents the crystal melting temperatures (T_m) of the PA12 matrix from the 2nd heating scan. $T_{m,1}$ and $T_{m,2}$ are assigned for the first and the second melting peak of the 2nd heating scan, respectively. It is seen that PA12 has the $T_{m,1}$ at about 175.5°C and the $T_{m,2}$ at about 168°C. This finding is similarly to the research work by Ma *et al.*[7] They reported that the α-form crystals of PA12 exhibited double melting peaks at 168.5 and 177°C, indicating the existence of either a mixed crystal structure or a process related to melting-recrystallization during heating. With the presence of the Gr-O2, the $T_{m,1}$ was shifted toward higher melting temperature at about 171°C. This implied the influence of Gr-O2 on the crystallization of the better stable γ-form crystals, which possessed higher mechanical property than those of α-form crystals.[8] The slow cooling condition in the DSC

testing allowed the PA12 to form the α-form crystal. Dai *et al.*[9] explained that the antiparallel arrangement of the α-form crystal provided the easy arrangement to achieve the hydrogen bonded surfaces between the extended chains. Since the DSC thermogram in the 1st heating scan was a single peak, this suggests that the PA12 and their composites only had the γ-form crystals with different lamella thickness after being cooled down by the cooling condition in the injection molding process.

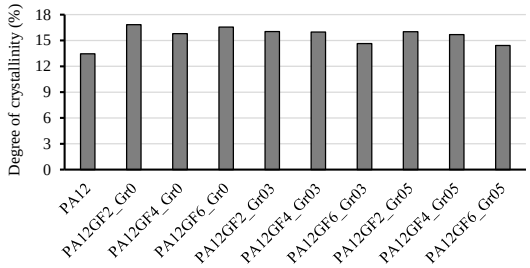

Figure 8. Degree of crystallinity (X_c) of the PA12 matrix from the 1st heating scan.

Figure 8 presents the degree of crystallinity (X_c) of the PA12 matrix from the 1st heating scan that is the percentage of crystals forming at the cooling condition of the injection molding process. The mold temperature was set constant at 50°C which was higher than the T_g of PA12 was 48.8°C. The single melting peak at 175-176°C was attributed to the γ-form crystals of the PA12 matrix. It has been known that incorporating the fillers into the PA12 matrix increased the X_c due to the nucleating effect of both the GF and the Gr-O2. Moreover, the influence of Gr-O2 favored the γ-form crystals that had higher mechanical properties.

3.4 Morphology by SEM

SEM micrographs of the PA12 and the PA12-based composites are presented in Figure 9 and 10. Under the magnification of 60X, the short glass fibers were found to be evenly distributed and embedded in the PA12 matrix. The distribution of GFs did not differ significantly in the PA12 matrix with the presence of Gr-O2. The impact fractured surface of the PA12 shows ripples with hill-like pattern attributed to the ductility of the matrix. These ripples became scattered chasm due to high concentration of short glass fibers, while adding high concentration of Gr-O2 caused brittle cracks resulting the appearance of deep valleys.
Using the magnification of 600X, the ripples of neat PA12 matrix are clearly visualized. Adding these inorganic fillers into the ductile PA12 matrix changed failure from ductile to brittle behaviour, therefore, the ripple edges became shallower. Since these short GF were not surface treated, voids were observed randomly indicating the pull-out of untreated short glass fibers.

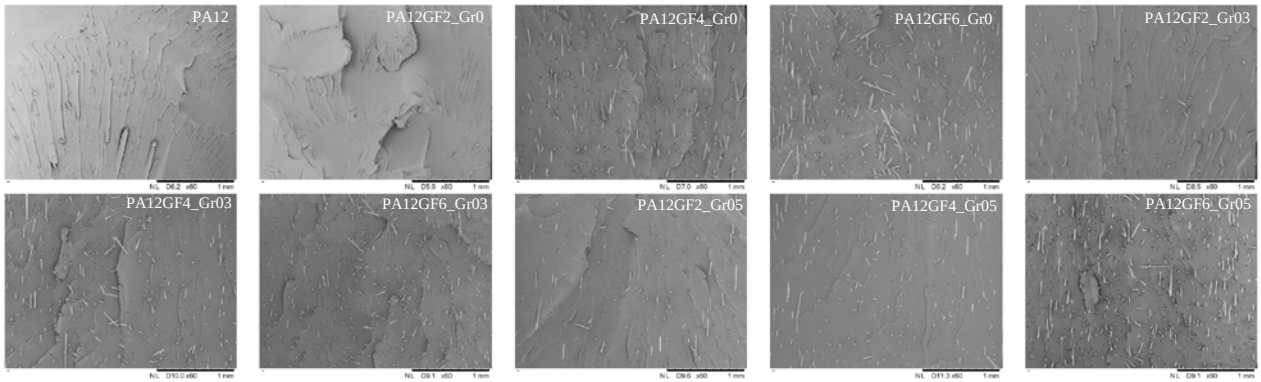

Figure 9. SEM micrographs (magnification of 60X) of PA12 and PA12-based composites.

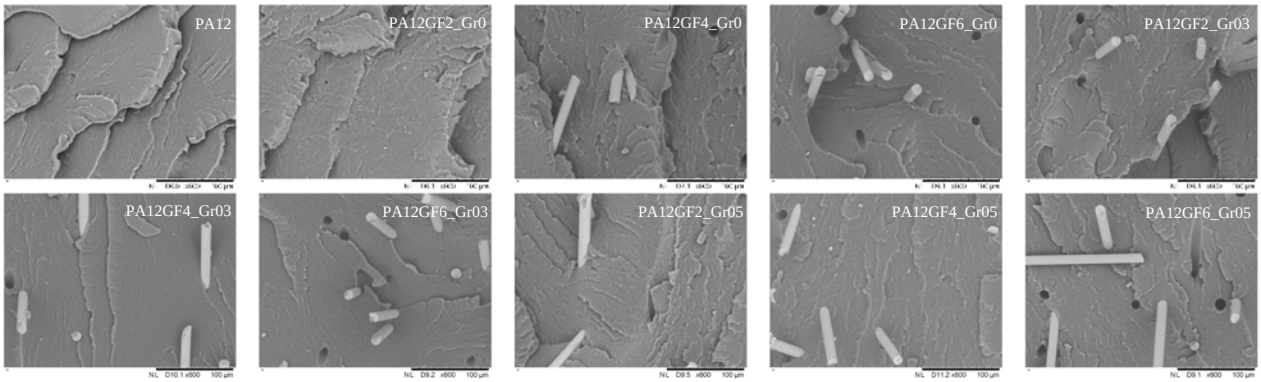

Figure 10. SEM micrographs (magnification of 600X) of PA12 and PA12-based composites.

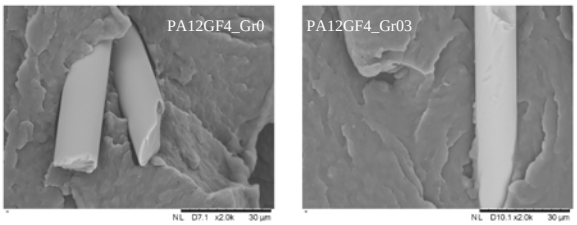

Figure 11. SEM micrographs (magnification of 2000X) of PA12-based composites with and without Gr-O2.

Figure 11 compares interfacial adhesion between the PA12 matrix and the short GFs with or without the presence of Gr-O2. It is seen that there is gap between the PA12 and the GFs, while the wetting of PA12 matrix onto the glass fibers is clearly observed for the composite adding Gr-O2. Mederic *et al.*[10] compounded PA12 with polar graphene nanoplatelets (oxygen percentage of 4%) and studied morphology of the nanocomposites with TEM. They reported there was the presence of some graphene aggregates exhibiting a micrometric length and thickness of a few hundreds of nanometers inside the PA12 matrix. In this research, these GNPs or Gr-O2 were plasma functionalized by oxygen to obtain the carbonyl and the hydroxyl groups onto their surface. These functionalized groups could interact physically via secondary bonding with the hydroxyl groups of the chain ends or the carbonyl groups on the PA12 backbones. Moreover, they could interact with the hydroxyl groups on the short GFs and became the bridge between the PA12 matrix and the short GFs.

3.5 Electrical surface resistivity measurement

It was found that the electrical surface resistivity of PA12 and PA12-based composites of this research was the same with the value of about 10^{12} ohm/sq. To be used as a reference, the electrical surface resistivity of low-density polyethylene specimens was measured using the same meter, and found that it was 10^{13} ohm/sq. Thus, incorporating Gr-O2 of up to 0.5 wt% did not affect the electrical surface resistivity of the PA12 significantly.

4. Conclusion

Young's modulus and the ultimate tensile strength of the PA12-based composites increased linearly with respect to the short GFs and Gr-O2 concentration. The composite with the best mechanical properties was PA12/GF6wt%/Gr-O2 0.3wt% considering from the highest ultimate tensile strength. SEM micrographs indicated the interfacial adhesion between the PA12 matrix and the GF was improved with the presence of Gr-O2.

Acknowledgement

This research was financial supported by the Department of Materials Science and Engineering, Faculty of Engineering and Industrial Technology, Silpakorn University.

References

1. Griehl, W.; Ruestem, D. Nylon-12-Preparation, Properties, and Applications. *Ind. amp; Eng. Chem.* **1970**, *62* (3), 16-22.
2. Thomason, J. L. Glass fibre sizing: A review. *Compos. Part A Appl. Sci. Manuf.* **2019**, *27*, 105619.
3. Wang, J.; Jin, X.; Li, C.; Wang, W.; Wu, H.; S. Guo. Graphene and graphene derivatives toughening polymers: Toward high toughness and strength. *Chemical Engineering Journal* **2019**, *370*, 831-854.
4. Haydale. *HDPlas™ GNPs Plasma Functionalised Graphene NanoPlatelets*. 2013. https://www.graphene-info.com/files/graphene/HDPlas-GNP-Technical-Sheet-2.03.pdf (accessed August 8, 2023).
5. Hou, Y.; Gao, M.; An, R.; Tey, W. S.; Li, B.; Chen, J.; Zhao, L.; Zhou, K. Surface modification of oriented glass fibers for improving the mechanical properties and flame retardancy of polyamide 12 composites printed by powder bed fusion. *Addit. Manuf.* **2023**, *62*, 103195.
6. Gao, X.-F.; Yu, W.-G.; Han, N.; Zhang, X.-X. Fabrication of super-strength PA66/graphene nanocomposite fibers reinforced with small lateral-sized graphene and graphene oxide nanosheets. *J. Mater. Sci.* **2022**, *57*, 14297–14309.
7. Ma, N.; Liu, W.; Ma, L.; He, S.; Liu, H.; Zhang, Z.; Sun, A.; Huang, M.; Zhu, C. Crystal transition and thermal behavior of Nylon 12. *E-Polym.* **2020**, *20* (1), 346-351.
8. Dencheva, N.; Denchev, Z.; Oliveira, M. J.; Nunes, T. G.; Funari, S. S. Relationship between the crystalline structure and mechanical behavior in isotropic and oriented polyamide 12. *J. Appl. Polym. Sci.* **2008**, *109* (1), 288-302.
9. Ruixin Dai, M. H., Lili Ma, Wentao Liu, Suqin He, Hao Liu, Chengshen Zhu, Yujie Wang, Zhenya Zhang & Aihua Sun. Study on crystal structure and phase transitions of polyamide 12 via wide-angle X-ray diffraction with variable temperature. *Adv. Compos. Hybrid Mater.* **2020**, *3*, 522-529.
10. Mederic, P.; Rahmaoui, F. E. Z.; Hocine, N. A. Properties of clay/graphene/thermoplastic nano composites in relation to their composition: Synergetic effect of hybrid nanofillers and role of matrix. *Appl. Clay Sci.* **2022**, *228*, 106659.

Investigation of physicochemical properties of pomegranate extract loaded nanoliposome for cosmetic application

Punyaporn Thongprasert, Thanyaluck Thanyacharoen, Piyachat Chuysinuan* and Supanna Techasakul*

Laboratory of Organic Synthesis, Chulabhorn Research Institute, 54, Kamphaeng Phet 6, Talat Bang Khen, Lak Si, Bangkok, 10210, Thailand

**E-mails: piyachat@cri.or.th*

Abstract:

Pomegranate extract (PE) contains phenolic compounds which are very sensitive to light and heat. In order to improve the stability of PE, nanoliposomes (NLPs) are an efficient way to encapsulate the compounds and controlled release. Therefore, the aim of this study was to produce pomegranate extract loaded nanoliposomes (PE-NLPs) by thin-film hydration method, using phosphatidylcholine as phospholipids and tween 80 and span 80 as surfactants. The studied variables were different concentrations of PE (0, 1, 10 mg/mL). Then, the morphology, physicochemical properties, encapsulation efficiency, antioxidant activity, *in vitro* release study and stability studies of PE-NLPs were investigated. The prepared PE-NLPs spherical or nearly spherical shape and the FTIR analysis demonstrated the successful encapsulation of PE in the NLPs. An average size and zeta potential were in the range of 205 to 1703 nm and -8 to -10 mV, respectively. The encapsulation efficiency of PE-NLPs was 81 to 86%. The antioxidant activities ranged from 0.8 to 86%. In addition, the maximum cumulative release of PE-NLPs was 88 to 99% at 1440 min. Stability studies revealed that PE-NLPs was stable after 21 days under 4°C storage. Consequently, result showed potential of PE-NLPs would be an option in innovative development of natural products for cosmetic application.

1. Introduction

In the present, development of delivery system for pharmaceutical and cosmetics applications, which can be used to encapsulate active ingredient and carry drugs into the body. Pomegranate is well known for its richness in phenolic compounds [1], which composed of gallic acid, ellagic acid, punicalin, quercetin, punicalagin, catechin, chlorogenic acid, vanillic, epicatechin, caffeic acid, ferulic acid, delphinidin, and rutin [2]. This compound has potent antioxidant. These previous results indicate that the phenolics compound of the PE could be used as multipurpose bioactive ingredient. Therefore, there is research to bring pomegranate can be integrated into cosmetic products that help in brightening skin and reducing wrinkles [3]. However, phenolic compounds are not stable, which sensitive to light and heat [4]. Compounds are more stable when they are through microencapsulation whereby the phenolics are enclosed in a wall material [5]. However, pomegranate showed low water solubility and poor bioavailability restricts for therapeutic use. Therefore, the selection of a suitable deliver carrier need to be used in order to overcome the solubility and improve the therapeutic activity.

Liposomes are the most commonly used delivery system because it consists phospholipid bilayers are non-toxic, biologically degradable and biocompatibility [6]. Generally, liposomes structures, they can be divided into four categories depending on size and lamellarity are small unilamellar vesicles (SUV; 20-100 nm), large unilamellar vesicles (LUV; >100 nm), multilamellar vesicle (MLV; >500 nm), and multivesicular vesicles (MVV; >1000 nm) [7-8]. The technique for liposome preparation, e.g., thin-film hydration, high pressure homogenization, solvent injection, reverse-phase evaporation, and extrusion methods [7,9]. Especially, the thin-film hydration is one of the most commonly and simple method for preparation, which was developed by making a thin lipid film in a round bottom flask by the evaporation of organic solvent [7]. Afterwards, A thin film was rehydrated with water or phosphate buffer solution (PBS) when phospholipids were dispersed in an aqueous solution to form liposomes [10].

The main objective of this study was pomegranate extract loaded nanoliposomes (PE-NLPs) by thin-film hydration method, which enables more effective stability of antioxidants in pomegranate extract (PE). Then, the morphology, physicochemical properties (average size, zeta potential and polydispersity index), encapsulation efficiency (EE), antioxidant activity, in vitro release study, Fourier transform infrared spectroscopy (FTIR) and stability of PE-NLPs were investigated.

2. Materials and Methods

2.1 Materials

Pomegranate extract (PE) was acquired from Colossal international, Co., Ltd. (Thailand). Phosphatidylcholine with ~ 90% purity from soy lecithin was purchased from Chanjao Longevity, Co., Ltd. (Thailand). Methanol and ethanol were purchased from Labscan Asia, Co., Ltd. (Thailand). Polysorbate 80 (Tween 80), Sorbitan Oleate 80 (span 80), Phosphate buffered saline (PBS) and 2,2-diphenyl-1-picrylhydrazyl (DPPH) were purchased from Sigma Aldrich Co., Ltd. (USA). Deionized (DI) water was used throughout this study.

2.2 Preparation of pomegranate extract loaded nanoliposomes (PE-NLPs)

Nanoliposomes (NLPs) were prepared by thin-film hydration method. Firstly, phosphatidylcholine (900 mg) and surfactants such as span 80 (80 mg) and tween 80 (20 mg), which making NLPs more flexible and smaller vesicle [11], were dissolved in 100 mL of ethanol in a round bottom flask. The ethanol was evaporated using a rotary evaporator under vacuum, at 50°C, 60 rpm to form a thin film in the round bottom flask. Afterwards, A thin film was rehydrated with 50 mL of PE solution (0, 1 and 10 mg/mL) to form a nanoliposomes (NLPs). The PE was dissolved in DI water. The PE-NLPs were sonicated by sonication for 15 min [6] at 25 °C and 35 kHz.

2.3 Morphology analysis

The morphology of PE-NLPs was observed by transmission electron microscopy (TEM) [6]. The PE-NLPs were deposited onto a carbon-coated copper grid. Then the samples were air dried and were imaged using a TEM system with an accelerating voltage of 300 kV.

2.4 Encapsulation efficiency (EE%)

Encapsulation efficiency (EE%) of the PE-NLPs was determined by analyzing free polyphenol of the supernatant after centrifugation. Firstly, the PE-NLPs was transferred into Amicon®Ultra-4 Centrifugal Filters (molecular weight cut off 100 kDa, Millipore, UK) and centrifuged with 10,000 rpm at 4 °C for 10 min. Then, the passed solution through the filter was separated as non-encapsulated PE [6,12-13]. The absorbance of the separated solution was measured at 364 nm using a microplate reader. After that, the absorbance value was put into the regression equations of the standard curve of PE ($y = 0.5624x+0.0813$, $R^2 = 0.99$). Finally, the EE value was calculated using Eq. (1) as follows:

$$EE\ (\%) = [(E-N)/E] \times 100 \quad (1)$$

where E denotes the total PE weight used in NLPs formulation, and N stands for the non-encapsulated PE.

2.5 Antioxidant activity by 2,2-diphenyl-1-picrylhydrazyl (DPPH) assay

The DPPH assay was determined according to the method described by Thanyacharoen et al [14] with some modifications. Firstly, the PE-NLPs were mixed with 0.3 mM DPPH reagent in a ratio of 1:3 (sample:DPPH reagent) and mixture was incubated for 25 min in the dark at ambient temperature, and centrifuged at 4000 rpm for 5 min [13]. Then, the absorbance of the samples was measured at 517 nm using microplate reader. Radical scavenging activity (%) was calculated using Eq. (2) as follows:

$$\%\ \text{Radical scavenging} = [(Abs_{blank} - Abs_{sample}) / Abs_{blank}] \times 100 \quad (2)$$

where Abs_{blank} is the absorbance of the DPPH solution without the sample; and Abs_{sample} is the absorbance of the sample

2.6 *In vitro* release study

The release of PE-NLPs with different PE concentrations was evaluated by the cumulative release method. The 5 mL of PE-NLPs were put into a dialysis bag (molecular weight cut off 12-14 kDa). Then, the bag was immersed into 15 mL of PBS at 37°C, under orbital shaker. 1 mL of the releasing media was removed at predetermined intervals (10, 20, 30, 40, 50, 60, 120, 180, 240, 300, 360, 420, 480, 1,440 min), and the same amount of PBS was added [15]. The released PE was quantified with a UV/Vis spectrophotometer at λ = 364 nm at regular intervals. The cumulative percentage of PE released was calculated by comparing with the standard curve ($y = 0.5624x+0.0813$, $R^2 = 0.99$). The measurements were analyzed in triplicate (n=3).

2.7 Fourier transform infrared spectroscopy

FTIR analysis of the freeze-dried samples was measured using a FTIR spectrophotometer (Perkin Elmer Spectrum One). Spectra were recorded at the wavenumber range from 4000 to 650 cm^{-1} with a resolution of ± 4 cm^{-1} for 32 scans at room temperature

2.8 Stability studies

The PE-NLPs and PE solution stability were studied over a period of 21 days. The samples were kept at two different temperatures (4 and 25°C) [16] and were collected at 0, 1, 3, 5, 7, 14

and 21 days to evaluate antioxidant activity. The antioxidant activity was determined by DPPH assay according to the method described above.

2.9 Average size, polydispersity index (PDI) and zeta potential (ZP) measurements

In order to evaluate of average size, PDI and ZP of PE-NLPs were measured by dynamic light scattering (DLS) method using a Malvern Zetasizer Nano ZS instrument. This test was conducted at a dispersant refractive index of 1.33 and a scattering angle of 173° at 25°C. All measurements were performed in triplicate.

3. Results & Discussion

3.1 Morphology analysis

The morphology of PE-NLPs was observed by transmission electron microscopy (TEM). TEM method was used to obtain the visual information concerning the morphology of nanoliposome. TEM images showed in Figure 1. PE-NLPs 0 mg/mL, PE-NLPs 1 mg/mL and PE-NLPs 10 mg/mL were spherical or nearly spherical shape.

3.2 Encapsulation efficiency (EE)

The EE% is a key indicator to assess the potency for nanocarriers of bioactive compounds, which EE% of the PE-NLPs was determined by analyzing free polyphenol of the supernatant after centrifugation and the results were reported in Figure 2. The results showed that the PE concentrations had influence on the EE% of PE-NLPs. After increasing the concentration from 1 to 10 mg/mL. The EE% of PE-NLPs increased from 81.26 ± 0.41% to 85.96 ± 0.32%, respectively. The PE-NLPs 10 mg/mL achieved the maximum EE value of 85.96 ± 0.32%. Generally, raising the loading concentration of extract caused the raise of EE% [17-18]. Similarly, the results of Upputuri et al [19], who reported that encapsulation of green tea polyphenols (GTP) to liposomal nanoparticles using phosphatidylcholine and cholesterol. In this study, EE% of the GTP from liposomal nanoparticles were studied with different concentrations of the GTP (1, 2.5, 5, and 10 mg/mL) were found that raising the loading concentration of GTP into nanoliposomes caused the raise of EE%,

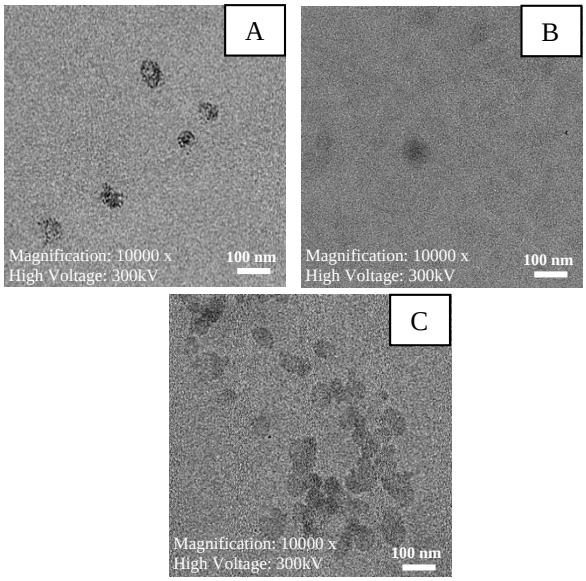

Figure 1. TEM images of PE-NLPs 0 mg/mL (A), PE-NLPs 1 mg/mL (B) and PE-NLPs 10 mg/mL (C)

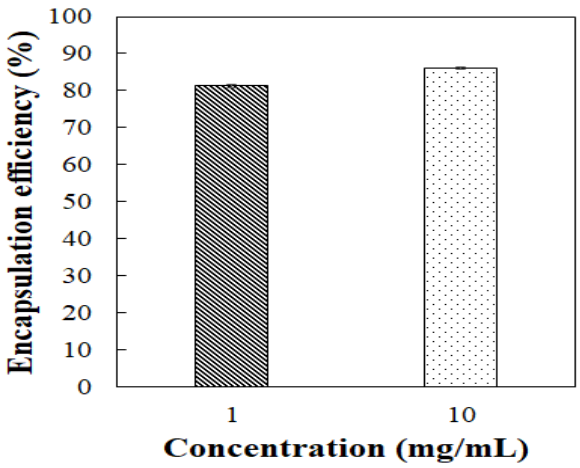

Figure 2. Encapsulation efficiency of PE-NLPs. # indicates no encapsulation detected. Data are represented as the mean ± SD (n = 3).

3.3 Antioxidant activity by 2,2-diphenyl-1-picrylhydrazyl (DPPH) assay

The antioxidant activity of PE-NLPs 0, 1 and 10 mg/mL determined by the DPPH assay are shown in Figure 3. It can be observed that the 0, 1 and 10 mg/mL presented antioxidant activities of 0.75 ± 2.18%, 83.71 ± 2.00% and 85.59 ± 0.27%, respectively. The results showed that 1 and 10 mg/mL PE-NLPs had antioxidant activity when compared to those of 0 mg/mL PE-NLPs. An enhance of PE rose the antioxidant activity of the compound, perhaps due to the rise of phenolic compounds in the PE. Similarly, the results of Dundar et al [20], who study the antioxidant activity of pomegranate peel extract loaded nanophytosomes. The results showed that the DPPH free radical scavenging activities of

pomegranate peel extract loaded nanophytosomes were increased when increasing concentration of pomegranate peel extract (1, 1.5, and 3 g). When compared those of phosphatidylcholine.

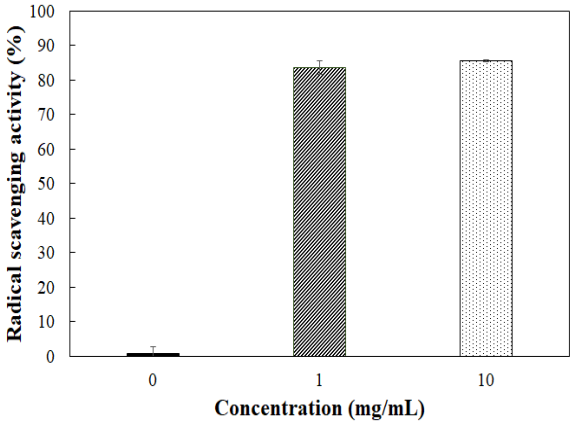

Figure 3. Antioxidant activity of PE-NLPs. Data are represented as the mean ± SD (n = 3).

3.4 *In vitro* release study

In vitro release model was used to evaluate the release characteristics of PE-NLPs using the dialysis bag diffusion technique, which is an important on the application potential of nanoliposomes as nanocarriers. The studies were performed to evaluate the release of PE from the two concentrations of 1 and 10 mg/mL. Figure 4. shows the release rate of PE from nanoliposome with a both concentrations of 1 and 10 mg/mL, which showed a burst release at 100 min after submersion. Then, the release was steady from 600 min to 1440 min. The maximum cumulative amounts of release of PE from NLPs containing 1 and 10 mg/mL PE were 99% and 88% at 1440 min, respectively.

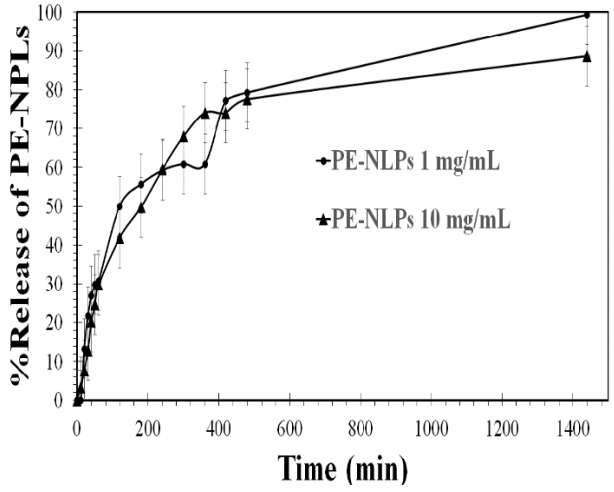

Figure 4. In vitro release studies of PE-NLPs in PBS at 37°C. Data are represented as the mean ± SD (n = 3).

3.5 Fourier transform infrared spectroscopy

FTIR spectra of PE-NLPs 0 mg/mL, PE-NLPs 1 mg/mL, PE-NLPs 10 mg/mL, PE and Phosphatidylcholine were shown in Figure 5. The several spectral changes were noticed in the wave range of 4000-650 cm^{-1}. Generally, the phenolic compounds of PE. The peak values of PE were found in a characteristic peak ~3400 cm^{-1} (O-H stretch), ~1720 cm^{-1} (C=O stretch) and ~1,060 cm^{-1} is due to the C-OH stretching vibration, maybe from phenolics compounds [21]. Furthermore, the choline head of phosphatidylcholine can easily form hydrogen bond with the –OH groups of polyphenols and the fatty acid chain of phosphatidylcholine can then envelop the polyphenolic molecules [22]. The results showed that the wide peak at 3431 cm^{-1} in PE-NLPs 0 mg/mL displays of O-H stretch, which was deflected to 3328 cm^{-1}, after loading PE in nanoliposome. The results demonstrated that the increased intensity of O-H stretch should be a result of adding more PE, which contains phenolic compounds. Moreover, the C=O group of the PE (1715 cm^{-1}) shifted to a higher intensity peak at 1737 cm^{-1} of PE-NLPs 10 mg/mL that it indicates the confirmation of PE into nanoliposome. The prominent change observed was the expansion of peak at 1051 cm^{-1} indicating the C-O-P stretching resulting from interaction between OH groups and phosphate groups, similar to studies reported by Wickramasinghe [18].

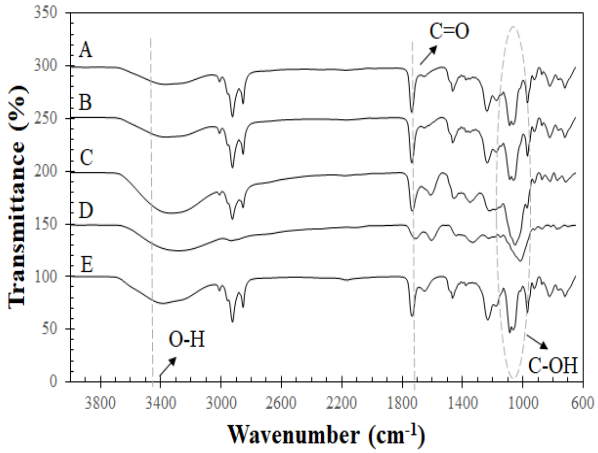

Figure 5. FTIR spectra of PE-NLPs 0 mg/mL (A), PE-NLPs 1 mg/mL (B), PE-NLPs 10 mg/mL (C), PE (D) and Phosphatidylcholine (E)

3.6 Stability studies

The antioxidant activities of 1 and 10 mg/mL of PE solution and PE-NLPs at day 21 are almost the same level, with only 2-3% change from day 0 at 4°C and 25°C, which, the results were reported in Figure 6 (B-C). On the other hand, the

physical characteristics of samples storage at 25°C showed the color changed Figure 6 (A) when compared with those of the samples storage at 4°C [16]. The color of PE became browner at higher temperatures [23]. The Figure 6 (A) shows the color of PE-NLPs 1 mg/mL and PE-NLPs 10 mg/mL. The result was observed for PE-NLPs 1 mg/mL at 25 °C on day 21 exhibited a color change, while PE-NLPs 10 mg/mL at 25°C on day 21 showed little to on color change. This observation consistent with the data presented in EE%. The PE-NLPs 10 mg/mL has EE% higher than PE-NLPs 1 mg/mL. Consequently, PE-NLPs 1 mg/mL is less stable than PE-NLPs 10 mg/mL. Therefore, the results confirmed that PE solution and PE-NLPs were stable during 21 days of storage at 4°C.

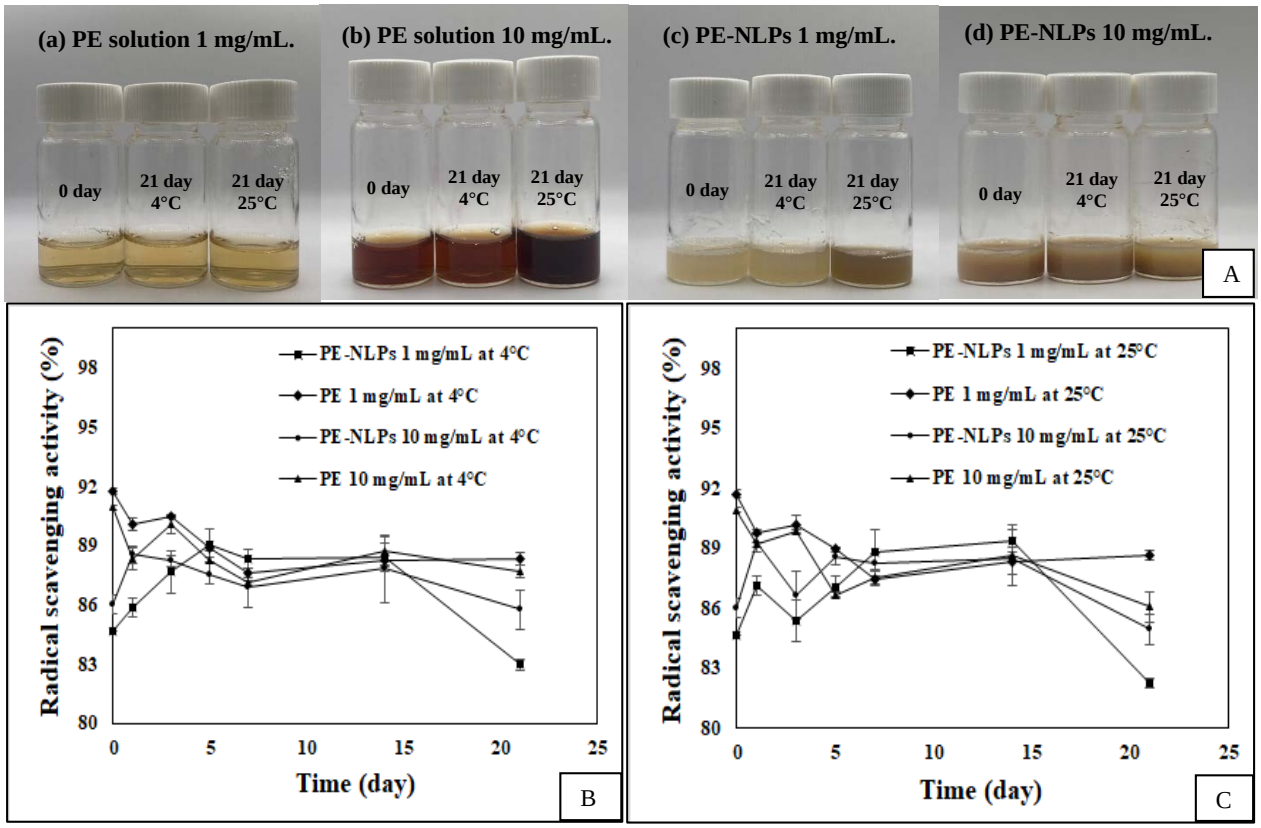

Figure 6. Physical characteristics of samples (A), Stability of samples were determined by the DPPH assay at 4°C (B), Stability of samples were determined by the DPPH assay at 25°C (C)

3.7 Average size, polydispersity index (PDI) and zeta potential (ZP) measurements

The average size, PDI and ZP of PE-NLPs prepared with different amounts of PE are shown in Table 1. The size of particles increases at high PE concentrations. The increase in particle size by increasing PE content might be due to the incorporation of bioactive material may increase the size of particles [10,20]. Generally, the size of liposomes ranges from 50 nm to 100 µm [24] and the size of liposome is reduced to a nanometer scale as increasing their water solubility, bioavailability and delivery properties [10]. All the samples displayed particle size in nanoscale, which can be beneficial for cellular delivery particularly for endocytotic uptake (particles <500 nm) [25], except for PE-NLPs 10 mg/mL had 1.7 µm particle size. In addition, The PDI of PE-NLPs 0, 1, 10 mg/mL were 0.79 ± 0.05, 0.54 ± 0.03 and 0.62 ± 0.01, respective. The ZP can predict the stability of colloidal suspensions and information about the agglomeration of nanoliposomes [26]. The zeta potential of PE-NLPs 0, 1, 10 mg/mL were -16.17 ± 1.16, -7.95 ± 0.22 and -12.13 ± 0.31 mV respective, repelling each other to prevent aggregation [27]. The negative charge on the particles was mostly contributed by the phosphate group of the phosphatidylcholine [28]. Similarly, ZP of turmeric extract loaded nanoliposomes was prepared by the thin-film hydration method coupled with homogenization and sonication, using phosphatidylcholine was −11.2 ± 0.1 mV [24].

Table 1. Average size, PDI and ZP of PE-NLPs with increasing concentrations of PE

	Average size (nm)	PDI	ZP (mV)
PE-NLPs 0 mg/mL	204.70 ± 2.89	0.79 ± 0.05	-16.17 ± 1.16
PE-NLPs 1 mg/mL	304.53 ± 14.90	0.54 ± 0.03	-7.95 ± 0.22
PE-NLPs 10 mg/mL	1703.33 ± 177.27	0.62 ± 0.01	-12.13 ± 0.31

4. Conclusion

In this study, PE-NLPs by thin-film hydration method, using phosphatidylcholine as phospholipids and tween 80 and span 80 as surfactants with different concentrations of PE was done. TEM images showed samples were spherical or nearly spherical shape. Evaluation of chemical structure by FTIR indicates the confirmation of PE into NLPs. Furthermore, the results demonstrated that the PE concentration affected the average size, EE% and antioxidant activities of samples which, average size, EE% and antioxidant activities were increased with an increase in the PE concentration. In addition, the release rate of PE from nanoliposome was rapid within 100 min, and samples steady from 600 min to 1440 min. The maximum cumulative release of PE-NLPs (1 and 10 mg/mL) was showed 99% and 88% at 1440 min, respectively. Finally, stability studies of samples were found that samples were stable after 21 days of storage at 4°C which, achieving optimal conditions for PE stabilization. Therefore, the potential of PE-NLPs would be an option in innovative development of natural products for cosmetic application.

Acknowledgements

This work was supported by the Thailand Science Research and Innovation and the Chulabhorn Research Institute (Grant Nos. 48295/4691988 and 48297/4692002).

References

1. Swilam, N, Nematallah, K.A. *Sci. Rep.* **2020**, *10*, 14851.
2. Teniente, S.L.; Flores-Gallegos, A.C.; Esparza-González, S.C.; Campos-Múzquiz, L.G.; Nery-Flores, S.D. *Antioxidants* **2023,** *12*, 127.
3. Ko, K.; Dadmohammadi, Y.; Abbaspourrad, A. *Foods* **2021**, *10*, 657.
4. Figueroa-Robles, A.; Antunes-Ricardo, M.; Guajardo-Flores, D. *Int. J. Pharm.* **2021,** *593*, 120125.
5. Kaderides, K.; Mourtzinos, I.; Goula, A.M. *Food Chem.* **2020**, *310*, 125849.
6. Han, S.B.; Won, B.; Yang, S. C.; Kim, D. H. *J. Ind. Eng. Chem.* **2021**, *98*, 289-297.
7. Nsairat, H.; Khater, D.; Sayed, U.; Odeh, F.; Al Bawab, A.; Alshaer, W. *Heliyon.* **2022**
8. Maja, L.; Željko, K.; Mateja, P. *J. Supercrit. Fluids* **2020,** *165*, 104984.
9. Lu, Q.; Lu, P.M.; Piao, J.H.; Xu, X.L.; Chen, J.; Zhu, L.; Jiang, J.G. *LWT - Food Sci Technol* **2014,** *57*,686-695
10. Nahr, F.K.; Ghanbarzadeh, B.; Hamishehkar, H.; Kafil, H.S.; Hoseini, M.; Moghadam, B.E. *LWT.* **2019**, *105*, 282-289.
11. Khan, I.; Needham, R.; Yousaf, S.; Houacine, C.; Islam, Y.; Bnyan, R.; Sadozai, S. K.; Elrayess, M. A.; Elhissi, A. *J. Drug. Deliv. Sci. Technol.* **2021,** *66*, 102822.
12. Souri, J.; Almasi, H.; Hamishehkar, H.; Amjadi, S. *LWT.* **2021**, *151*, 112174.
13. Sarabandi, K.; Mahoonak, A. S.; Hamishehkar, H.; Ghorbani, M.; Jafari, S. M. *J. Food Eng.* **2019**, *251*, 19-28.
14. Thanyacharoen, T.; Chuysinuan, P.; Techasakul, S.; Noenplab, ANL.; Ummartyotin, S. *J. Mol. Liq.* **2017,** *248*, 1065-1070.
15. Pan, L.; Wang, H.; Gu, K. *Molecules.* **2018**, *23*, 2822.
16. Yang, C.; Gong, L.; Li, X.; Li, W.; Meng, X.; Liu, B. *Food Chem.* **2023,** *404*, 134526.
17. Azari, A.; Ghaboos, S. H. H.; Moghadam, V. E.; Jafari, S. M. *Algal Res.* **2023,** *72*, 103120.
18. Wickramasinghe, A. S. D.; Attanayake, A. P.; Kalansuriya, P. *J. Pharm. Sci.* **2023,** *112*, 2538-2551.
19. Upputuri, R. T. P.; Mandal, A. K. A. *Iran. J. Biotechnol.* **2017,** *15*, 277.
20. Dundar, A. N.; Ozdemir, S.; Uzuner, K.; Parlak, M. E.; Sahin, O. I.; Dagdelen, A. F.; Saricaoglu, F. T. *Food Chem.* **2023,** *398*, 133921.
21. Rafi, M.; Wulansari, L.; Septaningsih, D. A.; Purnomo, T. F.; Auliatifani, R.; Ilmiawati, A.; Yulianti, W.; Nengsih, N. K.; Suparto, I. H.; Kusuma, W. A. *J. Trop. Life Sci.* **2021,** *11*, 375-382.
22. Vora, A.; Londhe, V.; Pandita, N. *J. Funct. Foods* **2015,** *12*, 540-548.
23. Alighourchi, H.; Barzegar, M. *J. Food Eng.* **2009,** *90*, 179-185.

24. Karimi, N.; Ghanbarzadeh, B.; Hajibonabi, F.; Hojabri, Z.; Ganbarov, K.; Kafil, H. S.; Hamishehkar, H.; Yousef, M.; Mokarram, R. R.; Kamounah, F. S.; Yousef, B.; Moaddab, S. R. *Food Biosci.* **2019**, *29*, 110-117.
25. Shishir, M. R. I.; Karim, N.; Xu, Y.; Xie, J.; Chen, W. *Food Chem.* **2021,** *337*, 127654.
26. Feng, Y.; Zarei, V.; Mousavipour, N. *LWT.* **2023,** *175*, 114194.
27. Dutta, D.; Dutta, D. *Process Biochem.* **2024**
28. Sharma, K.; Nilsuwan, K.; Ma, L.; Benjakul, S. *Foods* **2023**, *12*, 761.

Effect of kappa-carrageenan concentration on encapsulating and releasing vitamin C

Kunlaya Chanachai and Nophawan Paradee*

Sustainable Polymer & Innovative Composite Materials Research Group, Department of chemistry, Faculty of Science, King Mongkut's University of Technology Thonburi, Bangkok Thailand 10140

**E-mail address: nophawan.par@kmutt.ac.th*

Abstract:

Benefits of vitamin C (VC) include boosting the body's immune system, strengthening collagen, and making the skin smoother and more radiant. However, VC can be broken down by heat, air, or acids, so there needs to be a proper way to release VC into the body. At present, the mask has been developed in the form of a hydrogel sheet to deliver the active ingredients through the skin because it can retain more moisture and does not cause irritation to the skin. Thus, this study aims to fabricate the hydrogel for loading and releasing VC from kappa-carrageenan (k-CAR). The k-CAR hydrogel was prepared by the solvent casting method based on the effect of k-CAR concentrations of 2-5% w/v. The VC was encapsulated into the k-CAR hydrogel by soaking the hydrogel in the VC solution. The amount of VC loaded in the k-CAR hydrogel was 2.1 mg. The amount of VC release decreased with increasing k-CAR concentration, which was consistent with decreasing swelling behavior. The amount of VC release from k-CAR hydrogel was more than 50% of the amount of VC loading within 20 min.

1. Introduction

Nowadays, the health care comes together with getting vitamins into the body. The advantages of vitamins include strengthening the immune system, improving body performance, and being antioxidants. Vitamin C (VC), or ascorbic acid, is a hydrophilic compound with six carbon atoms in its structure has been widely studied by food and pharmaceutical researchers due to its important health properties and great antioxidant functions. However, the limitation of using VC is an instability under exposed to heat, light, moisture, oxygen and metal ions, accompanied by color changes.[1] A transdermal patch is another interesting method to deliver the active ingredients through the skin into the body.[2] Currently, the transdermal patch is being applied as a facial mask to deliver skincare substances and vitamins to the skin such as aloe vera, VC, and artificial scents, etc.[3] The mask has been developed in the form of a hydrogel sheet for moisture-retaining capabilities and non-irritating properties.[3] The hydrogel is produced by natural polymers such as chitosan, alginate, fibrin, gelatin and hyaluronic acid, etc., as well as synthetic polymers such as polyethylene glycol and polyvinyl alcohol.[4] The structure of hydrogel enables effective water absorption, storage, biocompatibility and flexibility.[5] Previously, the VC studied the transdermal release behavior from the biopolymer hydrogel matrix namely hyaluronic acid[6] and salecan/chitosan.[7] The VC was released within 90 min and 10 h from hyaluronic acid and salecan/chitosan, respectively.

Thus, the aim of this work is to fabricate the hydrogel patch from biopolymer namely kappa-carrageenan for a faster release VC within 1 h. Kappa-carrageenan (k-CAR) is a sulfated galactan polysaccharide extracted from red algae, Its chemical structure consists of 1,3-linked-β-d-galactopyranose-4-sulfate and 1,4-linked-3,6-anhydro-α-d-galactose. The k-CAR is widely used as a thickening agent and gelling agent in the food and pharmaceutical industries. The general property of carrageenan hydrogels is a high swelling rate. Therefore, it has been used as a material for delivering active substances[8-10] The samples of VC-loaded carrageenan hydrogel was investigated by FTIR to study the interaction between VC and carrageenan, the swelling behavior and amount of VC loading and release based on the effect of carrageenan concentrations.

2. Materials and Methods

2.1 Materials

Kappa-carrageenan (k-CAR) from Sigma-Aldrich Co., Ltd., potassium dihydrogen phosphate, di-potassium hydrogen phosphate, sodium ascorbyl phosphate (vitamin C; VC) and distilled water.

2.2 Preparation of kappa-carrageenan hydrogel

The k-CAR hydrogel at various concentrations of 2, 3, 4 and 5% w/v (sample code for k-CAR2, k-CAR3, k-CAR4 and k-CAR5, respectively) was prepared by dissolving the k-CAR in DI water at a temperature of 80 °C under continuous stirring for 45 min. The 10 mL of k-CAR solution was poured into a plate (diameter of 9 cm) before being stored in the refrigerator for 48 h to obtain the k-CAR hydrogel.

2.3 Swelling analysis

The k-CAR hydrogel sample (diameter of 1.6 cm) was soaked in the PBS buffer solution (100 mL) at pH 5.5 for 2 h The sample was weighted at different times to determine the swelling behavior and calculate the degree of swelling by Eq. (1).[11]

$$\text{Degree of swelling} = \frac{M_s - M_i}{M_i} \times 100 \quad (1)$$

where M_i is dry weight; and M_s is swelled weight.

2.4 Scanning Electron Microscopy (SEM) analysis

The morphology of k-CAR hydrogel at various k-CAR concentrations of 3 and 4% w/v was observed via a scanning electron microscope at an applied potential of 5 kV. The samples were prepared by immersing hydrogel in a DI water for 30 min then freeze in a liquid N_2 and lyophilizing at −80 °C for 24 h The samples ware coated with gold for 120 seconds before measurement.

2.5 In vitro VC release studies

2.5.1 Preparation of VC loading into kappa-carrageenan hydrogel (k-CAR-loaded-VC)

The hydrogel was soaked in a VC solution (10 mL) at a concentration of 1% w/v for 15 min, then the sample loaded VC was washed with DI water to remove the excess VC and stored at 5-7 °C. The actual amount of VC content in the carrageenan hydrogel was studied by dissolved the k-CAR-loaded-VC hydrogel (in the diameter of 1.6 cm) in DMSO for 1 day. Then, the solution was sampling to determine the amount of VC by using the UV-Visible spectrophotometer at the maximum wavelength of 258 nm as shown in Figure 1. After, the absorbance was converted to mass of VC by using a calibration curve (VC concentration rang of 5-200 ppm) under the linear equation of y = 0.0062x+0.0288 at the R^2 of 0.994.

2.5.2 Structural analysis

A FTIR spectrometer was used to investigate the presence of functional groups on hydrogel samples with and without VC loading. The ATR mode was used to study at a scan rate of 256 scans with a resolution of 16 cm^{-1}.

2.5.3 In vitro VC release studies

The VC release behavior was studied by using a modified Franz diffusion cell in a PBS buffer solution of pH 5.5 containing in the receptor chamber at 37 °C. The k-CAR -loaded-VC with a diameter of 1.6 cm was placed on the receptor chamber. The PBS buffer solution was collected from the sampling port at various times until 90 min. The collected solution was determined the amount of VC released by using UV-Vis spectroscopy as same as 2.5.1

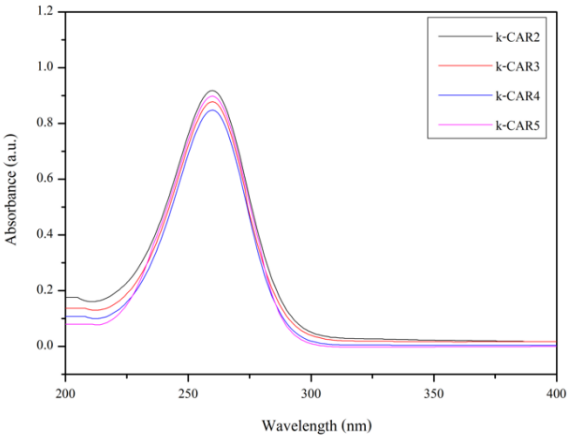

Figure 1. UV-Vis absorption spectra of VC-loaded k-CAR hydrogel at various k-CAR concentrations of 2, 3, 4 and 5% w/v.

3. Results & Discussion

3.1 Preparation of kappa-carrageenan hydrogel

Table 1 shows the k-CAR hydrogel before and after soaking in VC solution to load VC into the hydrogel. The color of k-CAR hydrogel after soaking in VC was clearer than that of before loading VC. Moreover, the k-CAR-loaded VC hydrogel was thicker than that of before loading VC which referred to the swelling behavior of hydrogel for encapsulation the medium solution as a VC solution into the hydrogel matrix.

3.2 Structural analysis

The FTIR spectra of k-CAR hydrogel at various k-CAR concentrations with and without VC loading are shown in Figure 2 to indicate the existence of the VC in a hydrogel. The functional groups of k-CAR hydrogel were the significant peaks of -OH at the wavenumber of 3330 cm^{-1}, the H_2O deformation band at the wavenumber of 1640 cm^{-1}, O=S=O at the wavenumber of 1250 cm^{-1}, C-O-C vibration at the wavenumber of 928 $cm^{-1}$and -O-S at the wavenumber of 846 cm^{-1}.[12-14] The functional groups of pure VC were the significant peaks of -OH appearing at the wavenumber of 3152 cm^{-1}, C=O stretching vibration at the wavenumber of 1720 cm^{-1}, C=C stretching vibration at the wavenumber of 1581 cm^{-1}, C-H stretching at the wavenumber of 1414 cm^{-1}, and C-O-C stretching vibration at the wavenumber of 1115 cm^{-1}. The deformation of phosphate group occurred in the wavenumbers of 840-1120 cm^{-1} and 790-900 cm^{-1}, for the complexation of phosphate and sodium of VC, respectively.[15] For k-CAR-loaded-VC hydrogel showed the peak of C=O stretching, C-H stretching

and C-O-C stretching vibration of VC at the same position with pure VC. Thus, The FTIR spectra confirmed that the VC was completely loaded into the k-CAR hydrogel and the sodium ascorbyl phosphate (SAP) in solution has the potential to undergo degradation into ascorbic acid through hydrolysis. This hydrolysis process is triggered by the presence of water or hydrogen ions, ultimately resulting in the removal of the phosphate group from SAP.[16-18] As a result, no peaks were found in the 790-900 cm^{-1}.

Table 1. Images before and after loading VC of 1 %w/v at various k-CAR concentrations of 2, 3, 4 and 5% w/v.

Sample	Before loading VC	After loading VC
k-CAR2	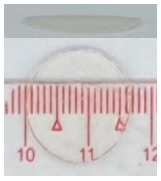	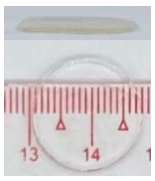
Thickness	0.62 ± 0.01	1.20 ± 0.01
Width	1.6	1.80 ± 0.01
k-CAR3	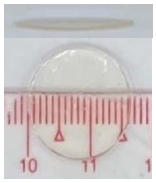	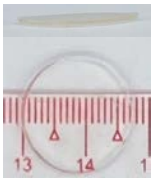
Thickness	0.64 ± 0.01	1.11 ± 0.01
Width	1.6	1.76 ± 0.03
k-CAR4	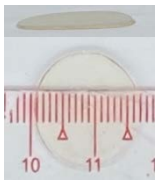	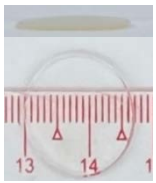
Thickness	0.61 ± 0.01	0.93 ± 0.01
Width	1.6	1.69 ± 0.01
k-CAR5		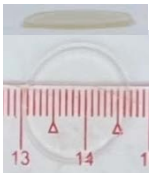
Thickness	0.64 ± 0.02	0.78 ±0.01
Width	1.6	1.64 ± 0.01

3.3 Swelling

The swelling behavior of k-CAR hydrogel without loaded VC is shown in Figure 3 and Table 1. The degree of swelling increased with time until it reached equilibrium after 30 min. In addition, the swelling behavior depended on the k-CAR concentration. The degree of swelling was 77.26, 71.41, 68.56 and 60.02% for 2, 3, 4 and 5% w/v of k-CAR concentration, respectively.

The swelling's degree of the samples decreased with increasing k-CAR concentration because the increasing k-CAR concentration provided more hydrogen bonding interaction between the k-CAR chain with resulting in more chain entanglement and a smaller pore size.[19-21] as corresponding to the SEM images in Figure 4. The pore size of k-CAR4 was a little bit smaller than that of k-CAR3 under increasing k-CAR concentration. This is the causes to reduce the penetration of the solution into the hydrogel and decrease the degree of swelling.

3.4 In vitro VC release

3.4.1 Amount of vitamin c loading

The amount of VC loading into the k-CAR hydrogel is shown in Table 2. The amount of VC contained in the K-CAR hydrogel in a diameter of 1.6 cm was 2.10, 2.05, 2.03 and 2.08 mg for 2, 3, 4 and 5% w/v of k-CAR, respectively.

3.4.2 In vitro vitamin c release studies

Figure 5 shows the amount of VC release from k-CAR hydrogel at various k-CAR concentrations. The amount of VC released increased with increasing the release time within 20 min after that, the amount of VC was closed to equilibrium. Moreover, the amount of VC released depended
on the k-CAR concentration. The amount of VC release was 80.85, 72.17, 68.02 and 61.34% for k-CAR concentrations of 2, 3, 4 and 5% w/v, respectively, as seen in Table 2. According to the release results, when increasing the k-CAR concentration, the amount of VC release decreased due to more chain entanglement and reducing the pore size of the k-CAR hydrogel, corresponding to a swelling result.[19- 21]

4. Conclusion

The k-CAR hydrogel was fabricated for loading and releasing VC as the transdermal patch. The k-CAR hydrogel was prepared by solution casting method at various k-CAR concentrations. The swelling behavior of k-CAR hydrogel was decreased with increasing k-CAR concentration. The VC was loaded into the k-CAR hydrogel by soaked k-CAR hydrogel in the VC solution. The amount of VC loading was about 2.1 mg per area of 2 cm^2. The amount of VC release was increased with decreasing k-CAR concentration. The 2% w/v of k-CAR examined the highest amount of VC release at 80.85%.

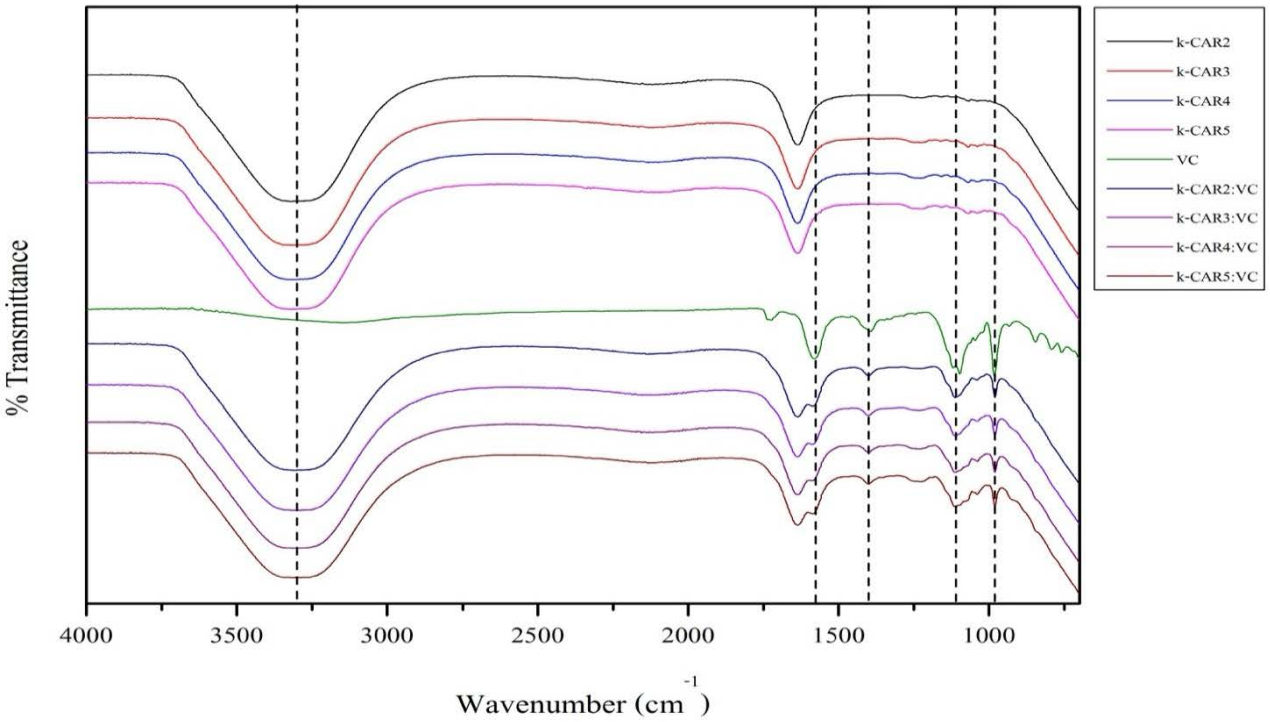

Figure 2. FTIR spectra of k-CAR hydrogel at various k-CAR concentrations of 2, 3, 4 and 5% w/v with and without VC loading.

Table 2. The degree of swelling, amount of VC loading into the hydrogel, and amount of VC release at various k-CAR concentrations.

Sample	Swelling (%)	Amount of VC loading (mg)	Amount of VC release		Time to equilibrium (min)
			mg	%	
k-CAR2	77.26	2.10	1.69	80.85	15
k-CAR3	71.41	2.05	1.48	72.17	18
k-CAR4	68.56	2.03	1.38	68.02	18
k-CAR5	60.02	2.08	1.27	61.34	18

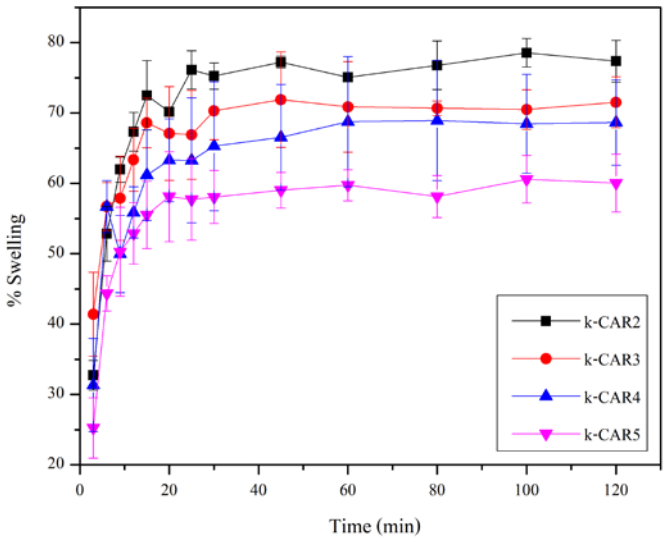

Figure 3. Degree of swelling of k-CAR hydrogel at various k-CAR concentrations of 2, 3, 4 and 5% w/v.

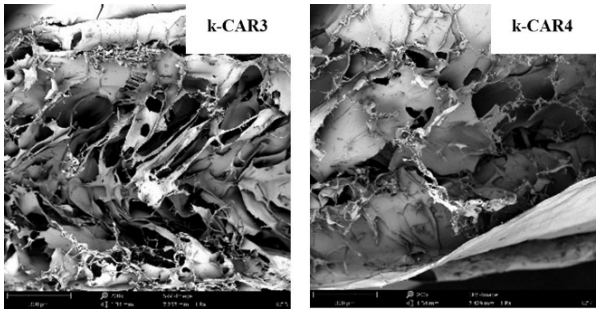

Figure 4. SEM images (magnification 200x) of k-CAR hydrogel at various k-CAR concentrations of 3 and 4 % w/v.

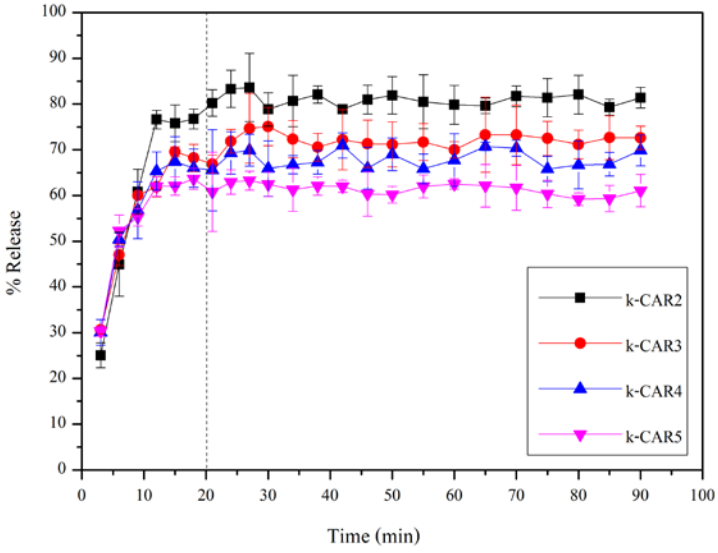

Figure 5. The amount of VC release from k-CAR hydrogel at various k-CAR concentrations of 2, 3, 4 and 5% w/v.

Acknowledgement

This research project is supported by King Mongkut's University of Technology Thonburi (KMUTT), Thailand Science Research and Innovation (TSRI), and National Science, Research and Innovation Fund (NSRF) Fiscal year 2024 and KMUTT Research Center of Excellence Project.

References

1. Poiroux-Gonord, F.; Bidel, L. P. R.; Fanciullino, A. L.; Gautier, H.; Lauri-Lopez, F.; &Urban, L. J. Agric. Food Chem. 2010, 58, 12065-12082.
2. Anjali, V. P.; Biren, N. Int J Pharm *Sci Res*. 2018, 9, 378-390.
3. Nilforoushzadeh, M. A.; Amirkhani, M. A.; Zarrintaj, P. J. Cosmet. Dermatol. 2018, 1–10.
4. Vigata, M.; Meinert, C.; Hutmacher, D. W.; Nathalie, B. Int J Pharm, 2020, 12, 1188.
5. Ahsan, A.; Tian, W. X.; Farooq, M.; Asim, Khan, D. H. Int. J. Polym. Mater. 2020, 70, 1-11.
6. Fallacara, A.; Busato, L.; Pozzoli, M.; Ghadiri, M.; Ong, H. X.; Young, P. M.; Traini, D. Eur. j. pharm. sci. 2018, 120, 96-106.
7. Liu, X.; Chen, T.; Wang, L. Carbohydr. Polym., 2020, 234, 115920.
8. Daniel-da-Silva, A. L.; Ferreira, L.; Gil, A. M.; Trindade, T. J. Colloid Interface Sci. 2011, 355, 512-517.
9. Joy, R.; Vigneshkumar, P.N.; John, F.; George, J. Plant and Algal Hydrogels for Drug Delivery and Regenerative Medicine. 2021, 293-325.
10. Roberts, M. A.; Queener, B. Trends Food Sci Technol, 1999, 10, 169-181.
11. Haima, J. S.; Nair, S. N.; Juliet, S.; Nisha, A. R.; Dhanushkrishna, B.N J. Pharmacognosy Phytother. 2021, 10, 1, 459-463.
12. Kacurakova, M.; Wilson, R.H. Carbohydr. Polym. 2011, 44, 291-303.
13. Tranquilan-Aranilla, C.; Nagasawa, N.; Bayquen, A.; Dela Rosa, A. Carbohydr. Polym. 2012, 87, 1810-1816.
14. Cerqueira, M. A.; Souza, B. W. S.; Simões, J.; Teixeira, J. A.; Domingues, M. R. M.; Coimbra, M. A.; Vicente, A. A. Carbohydr. Polym. 2011, 83, 179-185.
15. Yang, H.; Irudayaraj, J. J. Pharm. Pharmacol. 2002, 54, 1247-1255.
16. Dewhirst, R.A.; Fry, S.C. Biochem. J. 2018, 475, 3451-3470.

17. Sawamura, M.; Takemoto, K.; Matsuzaki, Y.; Ukeda, H.; Kusunose, H. 1994, 42, 1200-1203.
18. Shephard, S.C.; Nichols, A.; Braithwaite, A. 1999, 48, 585-593.
19. Chen, S. C.; Wu, Y. C.; Mi, F. L.; Lin, Y. H.; Yu, L. C.; Sung, H.-W. J. Control. Release. 2004, 96, 285-300
20. Francis, S.; Kumar, M.; Varshney, L. Radiat. Phys. Chem. 2004, 69, 481-486.
21. Weng, L.; Gouldstone, A.; Wu, Y.; Chen, W. Biomater. 2008, 29, 2153-2163.

Roles of reactants for Suzuki C-C cross-coupling reaction using molecular volcano plot

Kwanchanok Kaewkwan[1], Vudhichai Parasuk[2], and Boodsarin Sawatlon[1]*

[1]*Department of Chemistry, Faculty of Science, Chulalongkorn University, Pathumwan, Bangkok, 10330, Thailand*
[2]*Center of Excellence in Computational Chemistry (CECC), Department of Chemistry, Faculty of Science, Chulalongkorn University, Pathumwan, Bangkok, 10330, Thailand*

**E-mail: Boodsarin.s@chula.ac.th*

Abstract:

Suzuki-Miyaura C-C cross-coupling reaction is a powerful and well-known reaction to construct C-C bond due to its easily accessibility of organoboron reactants and its non-harmful condition reaction. However, this reaction does not always exhibit excellent efficiency especially when changing reactants, and the reasons behind its behavior are still unclear. To understand a more complete picture of the Suzuki C-C cross-coupling reaction, we have investigated the effects of both electrophile (R_1-Br) and nucleophile (R_2-$B(OH)_2$) reactants when catalyzed by $Pd(PMe_3)_2$ using Density Functional Theory (DFT) calculations and molecular volcano plots. Among five selected different substituents on R_1 and R_2 (furan, pyridine, phenyl, styrene and vinyl), we found that the reactions involving 2-bromofuran, when paired with any of boronic acid proceed the lowest energy barrier in the rate-determining step compared to others. Molecular volcano plots also illustrate that the feasible reaction with 2-bromofuran reactant is resulted from the balance of interaction between reactants and $Pd(PMe_3)_2$ catalyst, leading to the effortless oxidative addition and reductive elimination processes. The order of the interaction between each reactant and catalyst, ranking from strongest to weakest, is furan, pyridine, styrene, phenyl and vinyl, where furan is locating at the most balanced point (volcano top) of interaction.

1. Introduction

C-C cross-coupling reaction is a reaction in which the organohalide (R_1-X), serving as an electrophile, reacting with coupling partner (R_2-Y), acting as a nucleophile, to produce a R_1-R_2 product that creating C-C bond, which come from both electrophile and nucleophile fragments. In this category of reactions, Suzuki-Miyaura C-C cross-coupling[1] is a commonly employed due to its mild condition, stability toward air, and a variety of commercial boronic acid reactants. The reaction is usually catalyzed by palladium-phosphines catalyst. Generally, it proceeds through three main steps: (i) oxidative addition, binding the organohalide fragments to the metal complex; (ii) transmetalation, replacing halide position on the metal center with organoboron fragment; and (iii) reductive elimination, coupling the two organofragments together to release the R_1-R_2 product and regenerate the starting catalyst (Figure 1).

However, the reaction does not always reach high efficiency when substituents of the reactant are altered, and the cause of this behavior remains unclear. To obtain a more comprehensive overview of this reaction, one of the tools that can compare reactivity when varying factors (for example, substituent group) in the reaction is molecular volcano plot.[2] This tool was first introduced to homogeneous catalysis by the group of Corminboeuf[2] in 2015, deriving from volcano plots that are previously used to find a potential catalyst in heterogeneous[3] and surface reaction.[4] This approach is based on the Sabatier's principle[5] stating that the interaction between reactant and substrate should be neither too strong (points located on the left slope of the plot) nor too weak (points located on the right slope). Consequently, the ideal catalyst should be located on or near the volcano's top or plateau.

Earlier works have proven that the molecular volcano plot can predict promising catalysts having the most energetic reactivity as well as figure out the most energetic reaction step in a catalytic cycle.[6-8] Uniquely molecular volcano plots can deal with enormous data, illustrating and comparing reactivity between each single catalytic cycle. However, some of the prior works had investigated the reactivity by considering only intermediates, no inclusion of transition states, which may lead to incorrect summation especially when the kinetic energy profiles play important roles in the catalytic reactions. Therefore, in order to understand a completed picture of this reaction, we constructed molecular volcano plots (based on linear free-energy scaling relationships and the energetic valuables from DFT calculation) to investigate the effects of different substitution groups (furan, pyridine, phenyl, styrene and vinyl) on both electrophile (R_1-Br) and nucle-

ophile (R_2-$B(OH)_2$) reactants toward the reactivity in Suzuki-Miyaura C-C cross-coupling reaction catalyzed by $Pd(PMe_3)_2$.

2. Computational details

All DFT calculations were performed using Gaussian16 program.[9] The optimization and frequencies calculation were executed at PBE0[10]/6-31+G(d)[11] (SDD[12] effective core potential for Pd, 6-31G(d) for Br) level of theory. All complexes were confirmed by the imaginary frequency in which the intermediate has zero and transition state has single imaginary frequency that corresponds to the reaction pathway. The "ultrafine" integration grid was used to prevent an error on the computed free energies.[13] Optimized structures were then proceed the single point calculation at the M06[14]/6-31++G(d,p) (SDD for Pd, 6-311G(d) for Br) level of theory in THF using SMD solvation model.[15] The linear scaling relationship as well as the molecular volcano plots were constructed using in-house python script based on the published instruction.[2]

3. Results & Discussion

3.1 Choice of reactants

In this work, the calculation of Suzuki-Miyaura C-C cross-coupling reaction between electrophile R_1-Br and nucleophile R_2-$B(OH)_2$ catalyzed by $Pd(PMe_3)_2$ has been carried out using various choices of substituents, which are vinyl (Vi), styrene (St), phenyl (Ph), furan (fu), and pyridine (py) (Figure 1). Note that the choices of reactants were chosen to enable a comparison of reactivity when the functional and properties of substituent are changed.

The detailed mechanism of our studied reaction starts from the oxidative addition on intermediate **1** through a transition state **TSOA** yielding **2**. Subsequently, an anion exchange occurs, where OH^- base is added to metal complex **3**, replacing the bromide ligand. Transmetalation then exchanges the OH^- moiety with R_2 substituent on organoboron compound via transition state **TST** to produce **5**. Finally, the reaction moves forward to reductive elimination progressing from **5** to **1** via **TSRE** to complete a catalytic cycle and releasing R_1-R_2 product.

For the purpose of building molecular volcano plots, firstly, we need to define the descriptor, which is a variable that can linearly describe the relative free energies (ΔG_{RRS}) of all structures within the catalytic cycle. The ΔG_{RRS}(A) is defined as the free energy of intermediate/transition state A relative to the first step of the reaction (intermediate **1** reacting with R_1-Br). The appropriate descriptor in our work should be the intermediate that has both R_1 and R_2 substituents bind to the metal center (intermediate **4** or **5**). Therefore, we choose ΔG_{RRS}(**5**) (defined in equation (1))

$$\Delta G_{RRS}(\mathbf{5}) = G(\mathbf{5}) - G(\mathbf{1}) \qquad (1)$$

as our descriptor due to its strong correlation with other structures when plotting the linear free energy scaling relationship.

With the descriptor defined, we further constructed linear free energy scaling relationships (details in section 3.2). These relationships represent the correlation between the ΔG_{RRS} of each step in catalytic cycle (y-axis) and the energy descriptor (x-axis), presented in the form of mathematical equations. Subsequently, these equations are used to created molecular volcano plots (details in section 3.3).

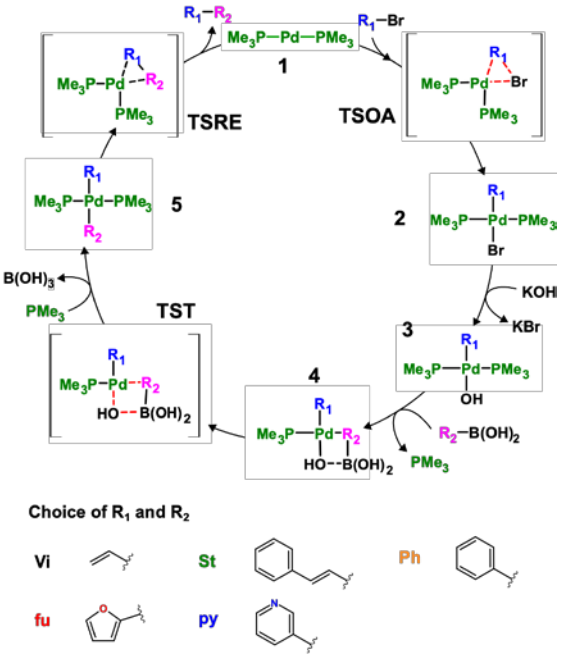

Figure 1. Mechanism of the catalytic cycle and choice of R_1 and R_2 used in this work.

3.2 Linear free energy scaling relationship

Linear free energy scaling relationships are plots between the relative free energy of intermediates/transition states and the energy of the descriptor ΔG_{RRS}(**5**). Due to a remarkable linearity trends between our descriptor and

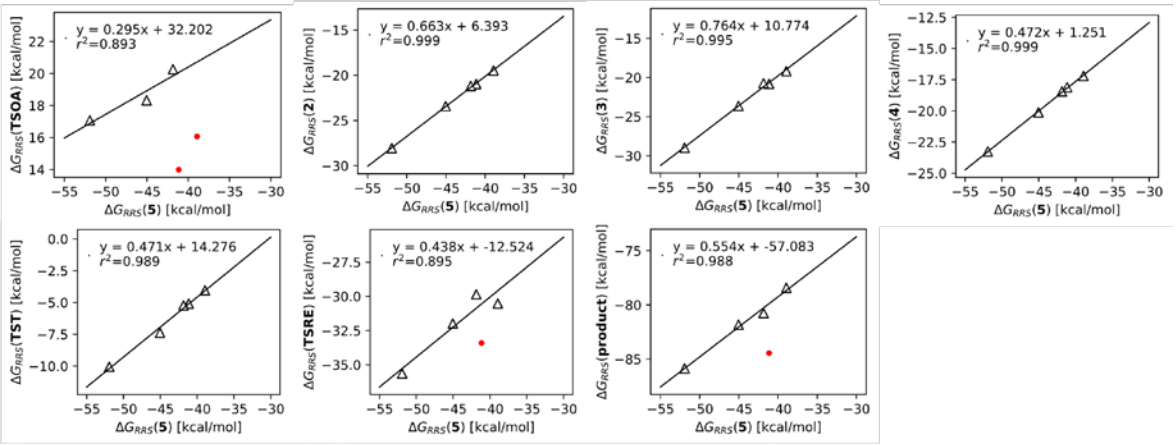

Figure 2. Linear scaling relationship of ΔG_{RRS} of the descriptor against ΔG_{RRS} relative to structure **1** of the intermediates and transition states of the reaction having R_2 as vinyl group. Red dot referred to outlier according to Grubbs' statistical test.

other structures when plotting the identical R_2 with five various R_1, we have a total number of five scaling systems (i.e., the system when R_2 is vinyl, styrene, phenyl, furan, and pyridine). In each plot corresponding to each system, we vary electrophile (R_1-Br) reactant, resulting in five points in each plot.

The linear regression between ΔG_{RRS}(**5**) against ΔG_{RRS} of intermediates and transition states have calculated while keeping the R_2 group fixed. The results found that most of the structures follow the linearity; as shown in Figure 2 for the case of R_2 = vinyl. The energy of ΔG_{RRS}(**5**) is well correlated with others, especially the relationship between ΔG_{RRS}(**2**) and ΔG_{RRS}(**4**) that has the coefficient of determination (r^2) of 0.99. The linear equations and r^2 values of other R_2 systems is shown in Table 1. All scaling plots exhibit a similarity in point distribution, equation, with acceptable r^2. Consequently, with this relationship in hand, we can write the free energy relative to resting state of every structure in term of ΔG_{RRS}(**5**), which is used to construct the molecular volcano plots later on.

3.3 Molecular volcano plots

The ΔG of each reaction step in the catalytic cycle (ΔG_{Rxn}) can be expressed in terms of ΔG_{RRS}(**5**) by subtracting the mathematical equations of corresponding intermediates or transition states. For example, the ΔG_{Rxn} of the oxidative addition (from **1** to **TSOA**) can be calculated using equation (2),

Table 1. Linear scaling relationship equation obtained from linear regression between the x-axis, ΔG_{RRS}(**5**) [kcal/mol], and the y-axis, ΔG_{RRS} of other structures [kcal/mol].

y-axis [kcal/mol]	**R_2**				
	Vinyl	**Styrene**	**Phenyl**	**Furan**	**Pyridine**
ΔG_{RRS}(**TSOA**)	y=0.30x+32.20 r^2=0.893	y=0.29x+30.57 r^2=0.871	y=0.25x+29.39 r^2=0.931	y=0.42x+38.41 r^2=0.922	y=0.27x+30.65 r^2=0.822
ΔG_{RRS}(**2**)	y=0.66x+6.39 r^2=0.999	y=0.67x+3.72 r^2=0.998	y=0.64x+3.84 r^2=0.964	y=0.90x+18.82 r^2=0.996	y=0.70x+7.62 r^2=0.979
ΔG_{RRS}(**3**)	y=0.76x+10.77 r^2=0.995	y=0.77x+7.70 r^2=0.995	y=0.74x+8.09 r^2=0.977	y=1.04x+25.10 r^2=0.993	y=0.82x+12.28 r^2=0.981
ΔG_{RRS}(**4**)	y=0.47x+1.25 r^2=0.999	y=0.52x+5.76 r^2=0.953	y=0.38x+3.40 r^2=0.943	y=0.52x+7.78 r^2=0.993	y=0.40x+4.74 r^2=0.947
ΔG_{RRS}(**TST**)	y=0.47x+14.28 r^2=0.989	y=0.58x+19.26 r^2=0.993	y=0.48x+16.38 r^2=0.929	y=0.75x+24.00 r^2=0.941	y=0.52x+17.92 r^2=0.950
ΔG_{RRS}(**TSRE**)	y=0.44-12.52 r^2=0.895	y=0.48x-9.51 r^2=0.889	y=0.57x-3.76 r^2=0.992	y=0.95x+14.88 r^2=0.976	y=0.64x-0.41 r^2=0.984
ΔG_{RRS}(**product**)	y=0.55x-57.08 r^2=0.998	y=0.52x-60.04 r^2=0.889	y=0.55x-56.47 r^2=0.951	y=0.53x-54.34 r^2=0.943	y=0.58x-53.37 r^2=0.988

$$\Delta G_{Rxn}(\mathbf{1}\rightarrow\mathbf{TSOA}) = \Delta G_{RRS}(\mathbf{TSOA}) - \Delta G_{RRS}(\mathbf{1}) \quad (2)$$

where ΔG_{RRS}(**TSOA**) and ΔG_{RRS}(**1**) are replaced by linear scaling equations obtained in Table 1. Subsequently, we have plotted the negative of relative energies of each reaction step ($-\Delta G_{Rxn}$) against the descriptor, ΔG_{RRS}(**5**). The plot for R_2 = vinyl system is depicted in Figure 3. As the values in y-axis is the negative of energy required for corresponding reaction step, a lower position in y-axis indicates the higher energy requirement for completing that reaction. In Figure 3,the lowest line when ΔG_{RRS}(**5**) is small (being the left slope) is the line of **5→TSRE** reaction, which is the reductive elimination. On the right slope, the lowest line is the step of **1→TSOA** (oxidative addition), specifically when the ΔG_{RRS}(**5**) > -53 kcal/mol. These lines represent the slope in the molecular volcano plot since they have the most negative y-value, indicating the most energetic reaction step. Hence, in the Suzuki-Miyaura C-C cross-coupling reaction we have studied, the rate-determining step should be either reductive elimination or oxidative addition, depending on the magnitude of ΔG_{RRS}(**5**).Interestingly, similar trends emerged in both the left and right slopes of volcano plots when R_2 was changed to other substituent groups, only the volcano peak was shifted. Molecular volcano plots of the reaction with varying R_1 for all R_2 systems are illustrated in Figure 4. The plots demonstrate that the points using furan group as R_1 always lie on or near the peak of the molecular volcanoes despite of changing R_2 to any substituents group. This can be indicated that the easiest reaction to carry out is when the electrophile reactant (R_1-Br) is 2-bromofuran (red triangle in Figure 4) since it has the lowest free energy barrier among other R_1 groups, followed by 3-bromopyridine (blue triangle in Figure 4), which clearly lies below the furan, but still above vinyl, styrene, and phenyl group, meaning that its reaction requires lower energy than those who lie below.

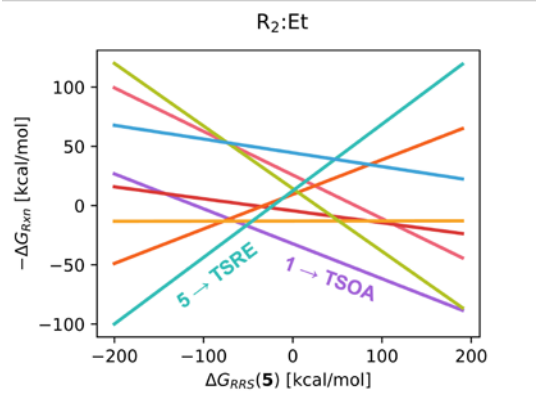

Figure 3. Overlapping line of the reactions within catalytic cycle when the R_2 is vinyl.

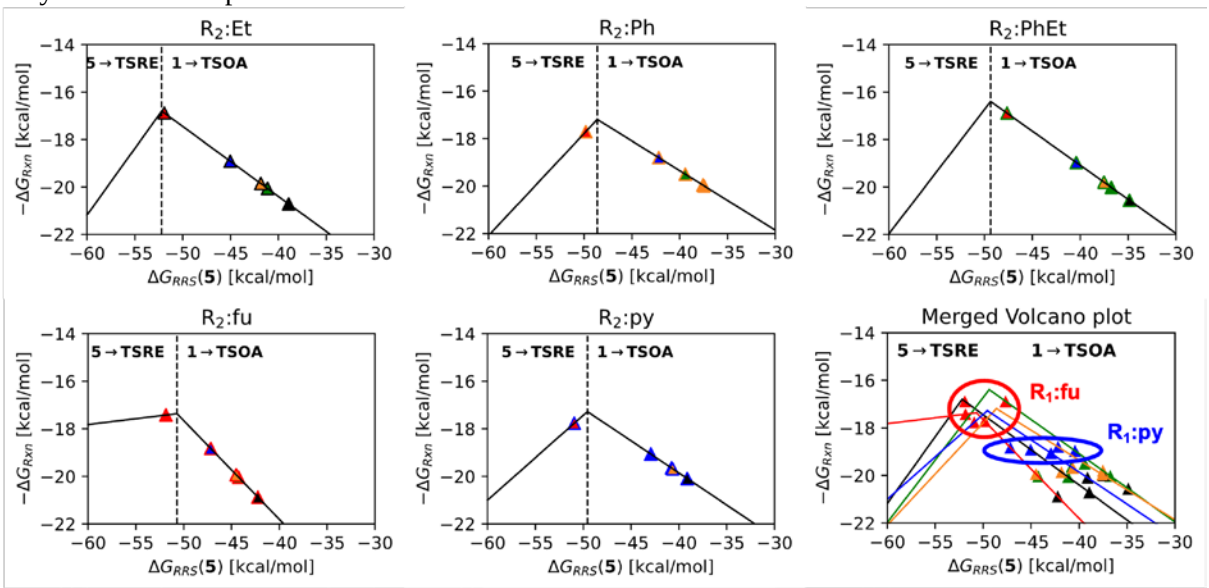

Figure 4. Molecular volcano plot of the catalytic cycle with R_2 (a) vinyl (b) phenyl (c) styrene (d) furan (e) pyridine, and (f) the merged molecular volcano plot. Left slope and right slope indicates the energy of reductive elimination going from intermediate **5** to **TSRE** and oxidative addition going from intermediate **1** to **TSOA** described as ΔG_{RRS}(5).

The molecular volcano plots also clarify the rate-determining step of the reaction. For each individual catalytic cycle, the rate-determining step is determined by projecting the $\Delta G_{RRS}(5)$ of the cycle onto the volcano slope corresponding to either reductive elimination (left slope) or oxidative addition (right slope). It is noteworthy that the lines in the plot represent the most energetic reaction step for all individual cycle in the system depending on magnitude of $\Delta G_{RRS}(5)$. The location of most of the points are on the right side of volcano slope, indicating that the rate-determining step is the oxidative addition process (Figure 4). Except a few systems having furan group as R_1 that located on the reductive elimination zone.

The heteroatom, particularly the electron-withdrawing atoms, in the electrophile (R_1-Br) reactants play a significant role in enhancing interaction between reactant and catalyst. This is evident from the plot that the points corresponding to heterocyclic atom shift to the left, indicating a stronger interaction, compared to the points associated with homocyclic atoms. Furthermore, the presence of aromaticity (e.g., pyridine, styrene and phenyl) on R_1 group also make a stronger interaction. As shown in the Figure 4, the interaction order between reactant and catalyst follows the sequence: furan, pyridine, styrene, phenyl, and vinyl. The order is affected by electronic properties from heteroatom in the ring and aromaticity of the substituents. Considering the position of volcano peak, furan has the most balanced interaction between reactants and catalyst $Pd(PMe_3)_2$, as it lies closely around the peak of the volcano plot.

4. Conclusion

The effect of electrophile and nucleophile reactants on the reactivity of the Suzuki-Miyaura C-C cross-coupling reaction has been investigated, revealing that aromaticity and the presence of electronegative atom can drive the reaction to the top of volcano as most points lies on the right side. Utilizing 2-bromofuran as electrophile renders the easiest reaction process due to its highest position on the volcano plots, requiring less energy than others. The rate-determining step in most cases is the oxidative addition process, which also corresponds to the experimental known.

Acknowledgements

This work was financially supported by Office of the Permanent Secretary, Ministry of Higher Education (Grant No. RGNS 65-009). KK would like to acknowledge financial support from Development and Promotion of Science and Technology Talents Projects (DPST).

References

1. Miyaura, N.; Suzuki, A. Palladium-Catalyzed Cross-Coupling Reactions of Organoboron Compounds. *Chemical Reviews* **1995**, *95* (7), 2457-2483.
2. Busch, M.; Wodrich, M. D.; Corminboeuf, C. Linear Scaling Relationships and Volcano Plots in Homogeneous Catalysis - Revisiting the Suzuki Reaction. *Chemical Science* **2015**, *6* (12), 6754-6761.
3. Cheng, J.; Hu, P.; Ellis, P.; French, S.; Kelly, G.; Lok, C. M. Brønsted-Evans-Polanyi Relation of Multistep Reactions and Volcano Curve in Heterogeneous Catalysis. *The Journal of Physical Chemistry C* **2008**, *112* (5), 1308-1311.
4. Exner, K. S. Recent Advancements Towards Closing the Gap between Electrocatalysis and Battery Science Communities: The Computational Lithium Electrode and Activity–Stability Volcano Plots. *ChemSusChem* **2019**, *12* (11), 2330-2344.
5. Sabatier, P. Hydrogénations et déshydrogénations par catalyse. *Berichte der deutschen chemischen Gesellschaft* **1911**, *44* (3), 1984-2001.
6. Busch, M.; Wodrich, M. D.; Corminboeuf, C. Improving the Thermodynamic Profiles of Prospective Suzuki-Miyaura Cross-Coupling Catalysts by Altering the Electrophilic Coupling Component. *ChemCatChem* **2018**, *10* (7), 1592-1597.
7. Sawatlon, B.; Wodrich, M. D.; Corminboeuf, C. Probing Substrate Scope with Molecular Volcanoes. *Organic Letters* **2020**, *22* (20), 7936-7941.
8. Wodrich, M. D.; Sawatlon, B.; Busch, M.; Corminboeuf, C. On the Generality of Molecular Volcano Plots. *ChemCatChem* **2018**, *10* (7), 1586-1591.
9. *Gaussian 16 Rev. C.01*; Wallingford, CT, 2016.
10. Adamo, C.; Barone, V. Toward Reliable Density Functional Methods Without Adjustable Parameters: The PBE0 Model. *The Journal of Chemical Physics* **1999**, *110* (13), 6158-6170.
11. Hehre, W. J.; Ditchfield, R.; Pople, J. A. Self–Consistent Molecular Orbital Methods. XII. Further Extensions of Gaussian–Type Basis Sets for Use in Molecular Orbital Studies of

Organic Molecules. *The Journal of Chemical Physics* **2003**, *56* (5), 2257-2261.
12. Andrae, D.; Häußermann, U.; Dolg, M.; Stoll, H.; Preuß, H. Energy-Adjustedab Initio Pseudopotentials For the Second and Third Row Transition Elements. *Theoretica chimica acta* **1990**, *77* (2), 123-141.
13. Bootsma, A. N.; Wheeler, S. Popular Integration Grids Can Result in Large Errors in DFT Computed Free Energies. **2019**.
14. Zhao, Y.; Truhlar, D. G. The M06 Suite of Density Functionals for Main Group Thermochemistry, Thermochemical Kinetics, Noncovalent Interactions, Excited States, and Transition Elements: Two New Functionals and Systematic Testing of Four M06-Class Functionals and 12 Other Functionals. *Theoretical Chemistry Accounts* **2007**, *120* (1-3), 215-241.
15. Marenich, A. V.; Cramer, C. J.; Truhlar, D. G. Universal Solvation Model Based on Solute Electron Density and on a Continuum Model of the Solvent Defined by the Bulk Dielectric Constant and Atomic Surface Tensions. *The Journal of Physical Chemistry B* **2009**, *113* (18), 6378-6396.

Molecular docking and dynamic simulations of anti-apoptotic Bcl-2 proteins as targets for bioactive compounds in *Durio zibethinus* for anti-cancer activity

Ayomi Vidana Pathiranage[1], Kulpavee Jitapunkul[2], Anotai Suksangpanomrung[3], Pisanu Toochinda[1], and Luckhana Lawtrakul[1]*

[1]*School of Bio-Chemical Engineering and Technology, Sirindhorn International Institute of Technology, Thammasat University, Pathum Thani 12120, Thailand*
[2]*Department of Chemical Engineering, Faculty of Engineering, Kasetsart University, Bangkok 10900, Thailand*
[3]*Department of Mechanical Engineering, Academic Division, Chulachomklao Royal Military Academy, Nakhon Nayok 26001, Thailand*

**E-mail: luckhana@siit.tu.ac.th*

Abstract:

Different extracts of *Durio Zibethinus* showcase multiple cancer activities, from antioxidant and anti-inflammatory to cytotoxic in different cancer models. Many cancers are occurred due to the overexpression of antiapoptotic protein B-Cell Lymphoma 2 (Bcl-2), which impedes programmed cell death and contributes to uncontrolled cell differentiation. The BH3 domain in Bcl-2 is crucial for suppressing its expression, making BH3 mimetics essential in promoting apoptosis in malignant cells. However, mutations in the BH3 domain can confer resistance to existing BH3 mimetics, prompting ongoing efforts to develop more effective Bcl-2 inhibitors. This study explores the binding interactions between five bioactive compounds from Durio Zibethinus with both wild-type (WT) Bcl-2 and mutant Bcl-2G101V protein, with a focus on their BH3 mimetic potential. Flexible receptor docking revealed procyanidin B2 as a standout candidate, demonstrating good binding with docking scores of -8.30 and -8.80 kcal/mol for Bcl-2WT and Bcl-2G101V, respectively. The stability and structural parameters of the Bcl-2/Procyanidin B2 complexes were further analyzed using molecular dynamic simulations. Procyanidin B2 exhibits significant potential as a Bcl-2 inhibitor, displaying a good affinity for binding within the hydrophobic groove of Bcl-2.

1. Introduction

Durio zibethinus, a plant belonging to the Bombacaceae family, contains bioactive compounds that demonstrate a promising inhibitory profile against various types of cancer cell, including human leukemia (HL-60) and Abelson murine leukemia virus-induced tumors [1,2]. Higher concentrations of durian fruit extracts notably reduced the cell viability of HL-60 cells by a significant margin 30% - 70% [1], while durian peel and seed extracts exhibited substantial cytotoxic effects on Abelson murine leukemia virus-induced tumors (RAW 264.7 cells) [2]. Furthermore, several studies reported that durian peel extracts showed pronounced nitric oxide (NO) inhibitory activity against RAW 264.7 cells [3]. Most cancers arise due to the over expression of antiapoptotic protein B-Cell Lymphoma 2 (Bcl-2), which hinders the programmed cell death and lead to uncontrolled cell differentiation [4,5].

The BH3 domain in Bcl-2 plays a crucial role in suppressing Bcl-2 expression, making BH3 mimetics essential in cancer treatments by promoting apoptosis in malignant cells [6–9]. BH3 mimetics play a vital role in cancer treatment by promoting apoptosis in malignant cells. BH3 mimetics are compounds that compete with proapoptotic proteins for the hydrophobic groove of antiapoptotic proteins, inhibiting their function. Several small molecules, including Venetoclax, Obatoclax, ABT-737, and Navitoclax, have been developed as BH3 mimetics, specifically targeting Bcl-2 antiapoptotic proteins. However, challenges such as mutations in the BH3 domain (G101V) and side effects like cytotoxicity and thrombocytopenia have limited the therapeutic potential of BH3 mimetics. Despite these challenges, ongoing efforts aim to develop BH3 mimetics for use in monotherapy or combinatorial therapy as potential Bcl-2 inhibitors.

A structure-based computational approach is employed to investigate the effectiveness of bioactive compounds obtained from durian as BH3 mimetics. This work is interested in studying the potential of five polyphenolic compounds derived from *Durio zibethinus* as inhibitors of the antiapoptotic Bcl-2 protein, comparing with clinically available drug, Venetoclax. These compounds categorized under different chemical groups known to have anticancer and antiproliferative activity on different cancer cells and have ability induce apoptosis by downregulating the expression of Bcl-2 [10, 11–13].

In this regard, we hypothesized that the bioactive compounds could bind within the BH3 binding pocket of either Bcl-2 wild type (WT) or Bcl-2 G101V mutation and could act as BH3-mimetics. Molecular docking studies were

employed to investigate the compound with highest binding energy (ΔG) and to investigate its structural interactions inside the BH3 binding pocket of WT and mutant Bcl-2 proteins. The complex structures which show the highest binding affinity towards Bcl-2 protein in molecular docking calculations are further evaluated using molecular dynamics (MD) simulations.

2. Materials and Methods

2.1 Molecular construction

The 3D structures of bioactive compounds were taken from PubChem Database, as shown in **Table 1**. The compound, 5'-methoxy-7'-epi-jatrorin A was constructed and its energy was minimized using Chem3D 16.0 via MM2 method. The crystal structures of Bcl-2WT (PDB ID: 6O0K) and Bcl-2G101V (PDB ID: 6O0L) were downloaded from RCSB Protein Data Bank.

Table 1. Ligands used in this study.

Compound	Chemical formula	PubChem ID
Hesperetin	$C_{16}H_{14}O_6$	72281
Quercetin	$C_{15}H_{10}O_7$	5280343
Cleomiscosin B	$C_{20}H_{18}O_8$	156875
5'-Methoxy-7'-epi-jatrorin A	$C_{20}H_{18}O_9$	-
Procyanidin B2	$C_{30}H_{26}O_{12}$	122738
Venetoclax	$C_{45}H_{50}ClN_7O_7S$	49846579

2.2 Molecular docking

The ADFRsuite 1.0 software package [14] was utilized to conduct flexible receptor docking of ligands with both WT and mutant Bcl-2 protein. Prior to docking procedure important amino acid residues were investigated using rigid receptor docking and made four amino acids flexible in this docking. The target file was generated by selecting the cluster which has higher affinity points via AutoSite 1.0 [15] available in ADFRsuite 1.0. Affinity maps were analyzed for every atom type. The ligands were docked to receptors with 100 independent searchers each using up to 2 500 000 evaluations of the scoring function. WindowsPyMol version 2.5.5 [16] were utilized to investigate the binding interactions between protein-ligand complexes. The binding pockets of bioactive compounds were investigated compared to Venetoclax.

2.3 Molecular dynamics simulation

MD of Bcl-2 WT, and mutant Bcl-2 complexed with Procyanidin B2 were performed in AMBER20 program package [17]. The force field parameters for the Procyanidin B2 molecule were generated using [17] "antechamber" with AM1-BCC charge method. Both receptor-ligand complexes were then solvated in the periodic truncated octahedral box while the TIP3P water molecules were randomly distributed along with neutralized ion (Na+) throughout the box cavity [18]. The buffer distance between the receptor-ligand complex and the box boundaries has been set to be 10 Å. The recently developed AMBER-FB15 force field [19] and general AMBER force field were adopted to simulate the dynamic of Bcl-2 and Procyanidin B2, respectively, for the whole MD simulations. The energy minimization was initially performed with 1000 cycles of steepest descent, followed by 1000 cycles of the conjugate gradient. Afterward, solvated receptor-ligand complexes were gradually heated from 273.15 K (0 °C) to 298.15 K (25 °C) via a two steps heating procedure while the volume held constant, to prevent protein degradation due to abrupt heating. The molecular dynamics equilibration of solvated protein-ligand complexes was performed for 100 ns with 2 fs time step. The isothermal-isobaric ensemble (NPT) at ambient conditions: 1 atm and 25 °C. The SHAKE algorithm was applied to provide constraints for bonds which connected to hydrogen atoms. The MD trajectories were collected, and the stability of receptor-ligand complex can be determined by observation of system energies and atomic root-mean-squared-deviation (RMSD) for both receptor and ligand. Generalized Born surface area continuum solvation (MM/GBSA) is an economical method to calculate free binding energy between small molecules and biological macromolecules.

3. Results and discussion

3.1 Molecular docking analysis

Table 2 presents the binding pockets of Venetoclax in Bcl-2WT and G101V which were obtained from x-ray structures, PDB ID:6O0K and 6O0L, respectively. It was observed that Venetoclax interacts with N143 and G145 via hydrogen bond interactions with Bcl-2 WT. In contrast, with Bcl-2 G101V, Venetoclax interacts with D103, G145 and Y202 via hydrogen bonds. However, in both cases most amino acids are interacting with hydrophobic interactions.

Table 2. Binding motifs of Venetoclax with Bcl-2 WT (6O0K) and Bcl-2 G101V (6O0L).

Protein	H-bonds	Hydrophobic interactions
WT	N143, G145	A100, G101, D103, F104, S105, Y108, D111, F112, M115, V133, E136, L137, N143, G145, V148, A149, F153, V156, F198, Y202
G101V	D103, G145, Y202	A100, V101, D103, F104, S105, Y108, D111, F112, M115, V133, V134, E136, L137, N143, G145, R146, V148, A149, F153, V156, F198, Y202

Table 3. The binding energy (ΔG) in kcal/mol observed in flexible receptor docking calculations.

Ligands	ΔG	
	WT	G101V
Venetoclax	-14.90	-13.90
Hesperetin	-7.50	-7.70
Quercetin	-7.70	-7.60
Cleomiscosin B	-7.30	-8.10
5'-methoxy-7'-epi-jatrorin A	-8.30	-7.40
Procyanidin B2	-8.30	-8.80

The molecular docking binding energies of bioactive compounds indicate a range of -7.30 to -8.30 kcal/mol during interactions with Bcl-2WT and -7.40 to -8.80 kcal/mol when engaging with Bcl-2G101V, as shown in **Table 3**. Notably, Procyanidin B2 exhibits favorable docking potential with both Bcl-2WT and Bcl-2G101V.

Hence, the stability of complexes was further analysed using MD simulation. Protein-ligand analysis of Venetoclax and procyanidin B2 demonstrated that procyanidin B2 can bind with the studied Bcl-2 protein like Venetoclax by sharing same amino acids. Procyanidin B2 mainly bind with P2 binding pocket of Bcl-2 protein while Venetoclax binds with both P2 and P4 binding pockets as shown in **Figure 1 (a)** and **(c)**.

Venetoclax and Procyanidin B2 were found to share similar amino acid residues, including D111, F112, M115, V133, E136, L137, and F153, in their interactions with Bcl-2WT **Figure 1 (b)**. With Bcl-2G101V, the observed residues were F104, Y108, D111, F112, M115, V133, E136, L137, R146, A149, E152, and V156 **Figure 1 (d)**. These findings establish that Procyanidin B2 can engage with Bcl-2, akin to Venetoclax, as they exhibit similar amino acid residues. However, Procyanidin B2 only binds with P2 while Venetoclax interacts with both P2 and P4 pockets. This distinction is attributed to the smaller size of Procyanidin B2 compared to Venetoclax.

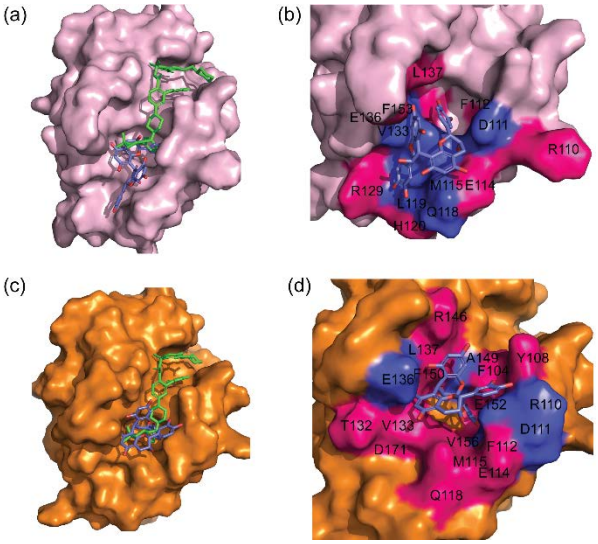

Figure 1. Binding mode of Venetoclax and Procyanidin B2 with (a) Bcl-2 WT (b) Bcl-2 G101V. The amino acid residues interacting with Procyanidin B2 (c) Bcl-2 WT (d) Bcl-2 G101V

3.2 Molecular dynamics simulation analysis

System energies and RMSD profiles of Procyanidin B2 complex with WT and mutated Bcl-2 are presented in **Figure 2 (a)-(d)**. The blue, red, and black line refer to kinetic energy, potential energy, and total energy profile. The enlarged xy-axis scale subplots with light cyan background represent the total energy profile of selected stable interval from 90 to 100 ns. The total system energies are averagely stable through 100 ns at -49,000 kcal/mol and -43,000 kcal/mol for WT and mutated Bcl-2, respectively. Hence, the negative total energies for both systems indicate that they are fully equilibrated under isothermal-isobaric conditions. The larger negative value of system energy from Procyanidin B2 complexed with Bcl-2WT directly referred to the higher stability of complexation compared to the mutated species. In **Figure 2 (c)** and **(d)** present the RMSD of Procyanidin B2 and Bcl-2, the blue and black line refer to all-atom RMSD of Procyanidin B2 and alpha-carbon RMSD of Bcl-2, respectively. The enlarged x-axis scale subplots with pale yellow background represent the RMSD profiles of selected stable interval from 90 to 100 ns. The motion of Procyanidin B2 bounded to Bcl-2 WT is stable after 30 ns, the RMSD is steady fluctuated between 0.5 to 1.0 Å. The motion of Bcl-2 backbone carbons is stable after 30 ns as well, fluctuation is between 1.5 to 2.0 Å. On the other hand, the motion of Procyanidin B2 bound to mutated Bcl-2 is highly fluctuated for the first 60 ns, then, it starts to stabilize. The all-atom RMSD of Procyanidin B2 fluctuates between 1.5 to 2.5 Å during the 60 to 100 ns time frame. Dynamics of mutated Bcl-2 backbone is rigorous through the

first 50 ns and stabilized afterwards, which is like behavior of bound Procyanidin B2. The alpha-carbon RMSD of mutated Bcl-2 fluctuates between 2.0 to 2.5 Å during the 50 to 100 ns time frame. Therefore, these observed dynamics directly confirm our prior discussion that the binding between Procyanidin B2 and Bcl-2WT holds superior stability. To facilitate the binding strength and binding modes analysis, a stable interval of 90 to 100 ns is selected for free binding energy calculation and binding modes visualization.

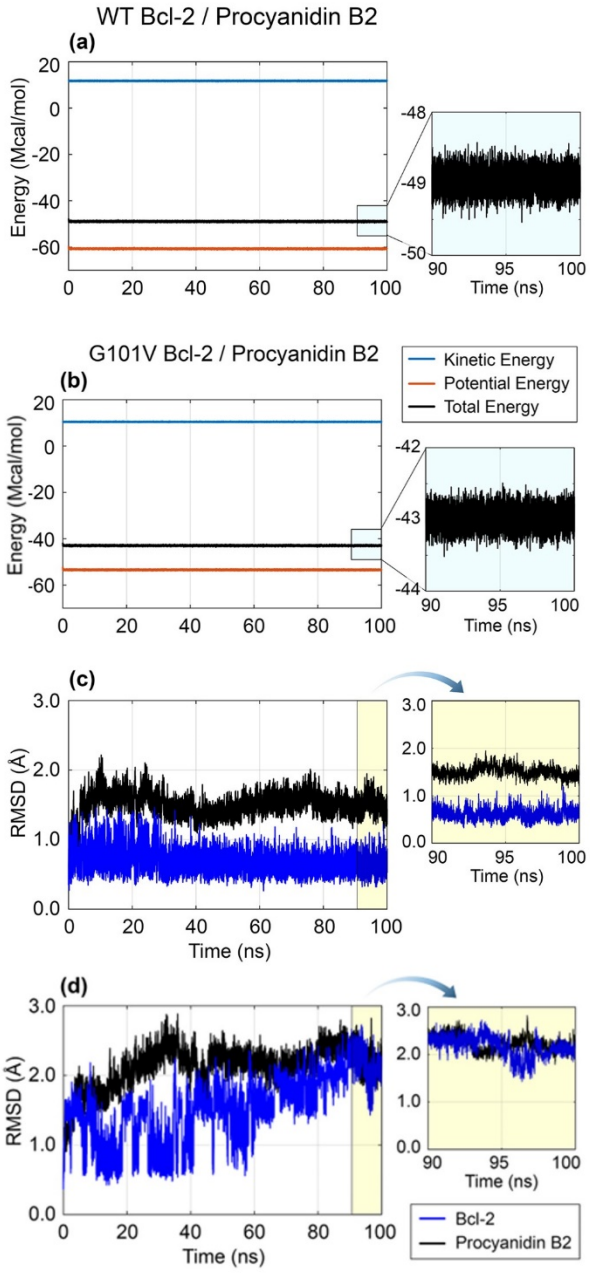

Figure 2. System energies and RMSD profiles of Procyanidin B2 complex with WT and mutated Bcl-2.

Table 4. MM/GBSA binding energies (ΔG in kcal/mol) of WT and mutated Bcl-2/Procyanidin B2 complexes

Component	WT	G101V
ΔG_{gas}	-61.13 ± 9.76	-70.02 ± 11.17
ΔG_{sol}	36.34 ± 8.73	52.88 ± 9.68
ΔG	-24.79 ± 3.11	-17.15 ± 3.43

From **Table 4**, the highly negative interaction energy in gas phase (ΔG_{gas}) diluted the positive solvation free energies (ΔG_{sol}) for both complex systems. Thus, the total energy different (ΔG) for both systems turned out to be negative values which imply the favorable protein-ligand binding. However, the binding between Procyanidin B2 and Bcl-2WT showed higher strength than the binding with mutated species which in contrast to the calculation from the molecular docking. This may be the effect of water molecules which result in different dynamic of protein structure under solvated space. **Figure 3** presents the hydrogen bonding lifetime profile for Procyanidin B2 complexes with WT and mutated Bcl-2. The horizontal bar plot presents the frequency of hydrogen bonding between atoms of Procyanidin B2 and major amino acid residues of Bcl-2. The frequency for both plots is represented by shade of the bar color, high frequency presents as darker shade while low frequency presents as lighter shade.

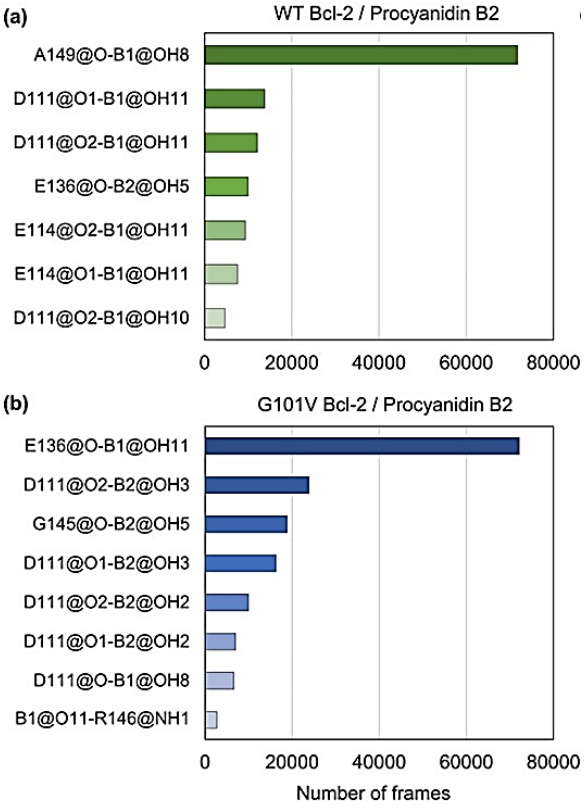

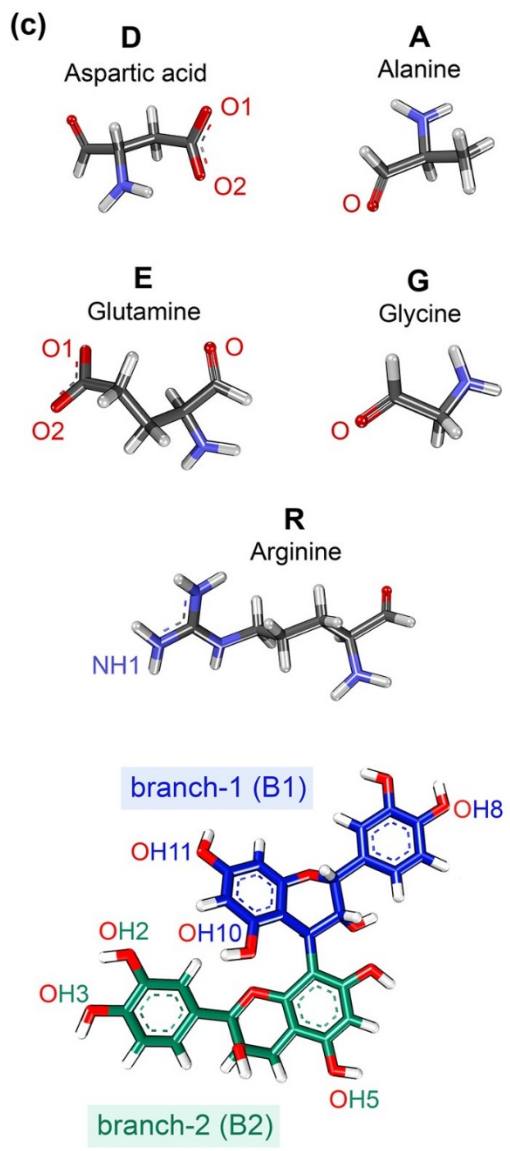

Figure 3. Hydrogen bonding lifetime profile for Procyanidin B2 complexes with (a) WT, and (b) mutated Bcl-2, (c) molecular structure and the atomic labelled of Procyanidin B2 and major amino acid residues that involve hydrogen bonds formation.

The overall frequency of hydrogen bonds formation between Procyanidin B2 with mutated Bcl-2 is higher than the Bcl-2WT. Since the alignment of branch-1 and branch-2 of Procyanidin B2 within binding cleft of WT and mutated Bcl-2 is different. Thus, the hydrogen bonding is dominantly formed with branch-1 of Procyanidin B2 for Bcl-2WT. In contrast, the hydrogen bonding is dominantly formed with branch-2 of Procyanidin B2 for mutated Bcl-2. Four amino acid residues are the major residues for hydrogen bond formation with Procyanidin B2 in both complex systems. For Bcl-2 WT, D111, E114, E136, and A149 are the major residues. For mutated Bcl-2, D111, E136, G145, and R146. The frequent hydrogen bonding found here is mainly involved with hydroxyl groups of Procyanidin B2, oxygen atoms of aspartic acid, alanine, glutamine, glycine, and amino group of arginine as illustrated in **Figure 3 (c)**. Among those reported major amino acid residues, only a single amino acid residue has higher frequency over half of MD simulation time (50,000 frames) for both complex systems. We shall call these residues dominant residues that promote hydrogen bonding which are A149 and E136 for WT and mutated Bcl-2, respectively. Both dominant residues and most of major residues are the members of P2 pockets. Thus, this may imply the role of P2 binding pocket as an important site for hydrogen bonds formation.

4. Conclusion

The results can provide insight on the binding of Procyanidin B2 with WT and mutated Bcl-2. We found that this bioactive compound has superior ability to tightly bind to hydrophobic groove of WT Bcl-2 over the mutated species. Since the mutated residue in BH3 motif may significantly induce the structural change of targeted hydrophobic cleft. Thus, allowing the hydrophobic cavity to be widened which may prone to interference by surrounded water molecules and eventually weaken the protein-ligand interaction. However, Procyanidin B2 can be considered as promising natural BH3 mimetics because it has ability to occupied similar binding sites as Venetoclax which is commercial BH3-mimetics. Lastly, we also found that both hydrophobic interaction and electrostatic forces in form of hydrogen bonding are playing crucial roles in binding of Procyanidin B2, but not equally. The hydrophobic interaction tends to promote tighter binding and facilitate the embedding of compound inside hydrophobic cavity of Bcl-2. While the electrostatic forces can promote both interaction with amino acid residues and surrounding water which may increase the chance of ligand migration from the binding cavity.

Acknowledgements

This work was supported by the Thammasat University Research Fund, Contract No. TUFT 84/2566. The author, Ayomi Vidana Pathiranage, gratefully acknowledges the financial support received from the Excellent Foreign Students (EFS) scholarship program of Sirindhorn International Institute of Technology (SIIT), Thammasat University.

References

1. Sitheek, M.; Kanakarajan, S.; Selvaraj, R.; Kamalanathan, A. Anti-proliferative effect of durian fruit (*Durio Zibethinus*) against hl-60 cells and its phytochemical analysis. *IJASRD* **2020**, *11*, 174–181.
2. Charoenphun, N.; Klangbud, W. K. Antioxidant and Anti-Inflammatory Activities of Durian (Durio Zibethinus Murr.) Pulp, Seed and Peel Flour. *PeerJ* **2022**, *10*, e12933–e12933.
3. Feng, J.; Wang, Y.; Yi, X.; Yang, W.; He, X. Phenolics from Durian Exert Pronounced NO Inhibitory and Antioxidant Activities. *J Agric Food Chem* **2016**, *64* (21), 4273–4279.
4. Pfeffer, C. M.; Singh, A. T. K. Apoptosis: A Target for Anticancer Therapy. *Int J Mol Sci* **2018**, *19* (2), 448.
5. Lopez, J.; Tait, S. W. Mitochondrial Apoptosis: Killing Cancer Using the Enemy Within. *Br J Cancer* **2015**, *112* (6), 957–962.
6. McBride, A.; Houtmann, S.; Wilde, L.; Vigil, C.; Eischen, C. M.; Kasner, M.; Palmisiano, N. The Role of Inhibition of Apoptosis in Acute Leukemias and Myelodysplastic Syndrome. *Front Oncol* **2019**, *9*, 192.
7. Kale, J.; Osterlund, E. J.; Andrews, D. W. BCL-2 Family Proteins: Changing Partners in the Dance towards Death. *Cell Death Differ* **2018**, *25* (1), 65–80.
8. Campbell, K. J.; Tait, S. W. G. Targeting BCL-2 Regulated Apoptosis in Cancer. *Open Biol* **2018**, *8* (5).
9. Shamas-Din, A.; Kale, J.; Leber, B.; Andrews, D. W. Mechanisms of Action of Bcl-2 Family Proteins. *Cold Spring Harb Perspect Biol* **2013**, *5* (4), a008714–a008714.
10. Alshatwi, A. A.; Ramesh, E.; Periasamy, V. S.; Subash-Babu, P. The Apoptotic Effect of Hesperetin on Human Cervical Cancer Cells Is Mediated through Cell Cycle Arrest, Death Receptor, and Mitochondrial Pathways. *Fundam Clin Pharmacol* **2013**, *27* (6), 581–592.
11. Primikyri, A.; Chatziathanasiadou, M. V; Karali, E.; Kostaras, E.; Mantzaris, M. D.; Hatzimichael, E.; Shin, J. S.; Chi, S. W.; Briasoulis, E.; Kolettas, E.; Gerothanassis, I. P.; Tzakos, A. G. Direct Binding of Bcl-2 Family Proteins by Quercetin Triggers Its pro-Apoptotic Activity. *ACS Chem Biol* **2014**, *9* (12), 2737–2741.
12. Song, D. Q.; Liu, J.; Wang, F.; Li, X. F.; Liu, M. H.; Zhang, Z.; Cao, S. S.; Jiang, X. Procyanidin B2 Inhibits Lipopolysaccharide-induced Apoptosis by Suppressing the Bcl-2/Bax and NF-κB Signalling Pathways in Human Umbilical Vein Endothelial Cells. *Mol Med Rep* **2021**, *23* (4).
13. Omid, G. Cytotoxicity and Apoptosis Induction by Coumarins in CLL. In *Cytotoxicity*; Tülay Aşkin, Ç., Ed.; IntechOpen: Rijeka, 2018; p Ch. 6.
14. Ravindranath, P. A.; Forli, S.; Goodsell, D. S.; Olson, A. J.; Sanner, M. F. AutoDockFR: Advances in Protein-Ligand Docking with Explicitly Specified Binding Site Flexibility. *PLoS Comput Biol* **2015**, *11* (12), e1004586.
15. Ravindranath, P. A.; Sanner, M. F. AutoSite: An Automated Approach for Pseudo-Ligands Prediction-from Ligand-Binding Sites Identification to Predicting Key Ligand Atoms. *Bioinformatics* **2016**, *32* (20), 3142–3149.
16. Schrödinger, L. L. C. and W. D. *PyMOL*. Version 1.2r3pre. http://www.pymol.org/pymol.
17. Case, D.; Aktulga, H. M.; Belfon, K.; Ben-Shalom, I.; Brozell, S.; Cerutti, D.; Cheatham, T.; Cruzeiro, V.; Darden, T.; Duke, R.; Giambasu, G.; Gilson, M.; Gohlke, H.; Götz, A.; Harris, R.; Izadi, S.; Izmailov, S.; Jin, C.; Kasavajhala, K.; Kollman, P. *Amber 2021*; 2021.
18. Linse, J. B.; Hub, J. S. Three- and Four-Site Models for Heavy Water: SPC/E-HW, TIP3P-HW, and TIP4P/2005-HW. *J Chem Phys* **2021**, *154* (19), 194501.
19. Wang, L.-P.; McKiernan, K. A.; Gomes, J.; Beauchamp, K. A.; Head-Gordon, T.; Rice, J. E.; Swope, W. C.; Martínez, T. J.; Pande, V. S. Building a More Predictive Protein Force Field: A Systematic and Reproducible Route to AMBER-FB15. *J Phys Chem B* **2017**, *121* (16), 4023–4039.
20. Lomonosova, E.; Chinnadurai, G. BH3-Only Proteins in Apoptosis and beyond: An Overview. *Oncogene* **2008**, *27* (1), S2–S19.

Structural investigation on chiral recognition of dapoxetine enantiomers with methylated cyclodextrins

Arthiwath Anyamaneearmornrath, Chetsada Thanin, Potcharadanai Pitakannop, Nat Triamchaisri, and Luckhana Lawtrakul*

School of Bio-Chemical Engineering and Technology, Sirindhorn International Institute of Technology (SIIT), Thammasat University, Pathum Thani 12120, Thailand

**E-mail: Luckhana@siit.tu.ac.th*

Abstract:

Dapoxetine (Dpx), a premature ejaculation drug, exhibits varying potency between its enantiomers, with (*S*)-Dpx proving 3.5 times more potent than (*R*)-Dpx. Enantiomeric purity of pharmaceutical preparation is necessary to be controlled. Chiral selection of cyclodextrin (CyD) is one of the most used methods. Molecular docking and semi-empirical PM6 calculations were performed to predict the conformations and the interaction of inclusion complexes between Dpx enantiomers and β-CyD, γ-CyD, heptakis-(2,3,6-tri-O-methyl)-β-CyD or TRIMEB, and octakis-(2,3,6-tri-O-methyl)-γ-CyD or TRIMEG. The calculated complexation energies showed (*R*)-Dpx forms more stable inclusion complexes with all CyDs than (*S*)-Dpx, agreeing well with experimental data as (*R*)-Dpx have more negative values of complexation energies compared to (*S*)-Dpx. The energy difference of the most favorable inclusion complex of (*R*)- and (*S*)-Dpx in each of CyD system provide the information relate to their ability for chiral recognition as follow: TRIMEB > TRIMEG > γ-CyD > β-CyD. This insight enhances our understanding of the interaction dynamics and the stability of Dpx enantiomers within different CyDs, crucial for optimizing pharmaceutical formulations.

1. Introduction

The efficacy of pharmaceutical formulations often relies on the precise control of enantiomeric purity, particularly in the case of drugs with chiral centers. **Figure 1** represents the chemical structure of dapoxetine (Dpx), a drug designed for the treatment of premature ejaculation, exemplifies this challenge, as its eutomer, (*S*)-Dpx, has been reported to be 3.5 times more potent than its enantiomer, (*R*)-Dpx [1]. Achieving and maintaining enantiomeric purity is crucial for ensuring the therapeutic effectiveness and safety of Dpx-containing pharmaceutical preparations.

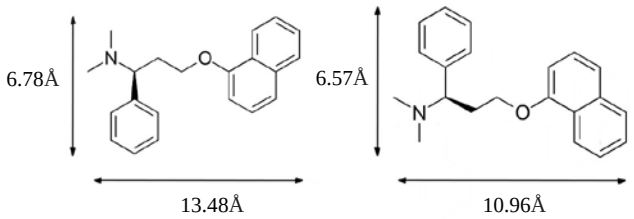

(a) (b)

Figure 1. Schematic representation of size of PM6 optimized structures (a) (*S*)-Dpx and (b) (*R*)-Dpx.

Chiral selection using cyclodextrin (CyD) which is consisting of a ring of glucose subunits, is a widely used method of achieving enantioresolution of racemic compounds. Two natural cyclodextrins (β-CyD, and γ-CyD) and their methylated derivatives were use in capillary electrophoresis to separate Dpx enantiomers. The diameter of CyDs as presented in **Figure 2** suggests the 1:1 molecular ratio of host:guest CyD/Dpx inclusion complexes.

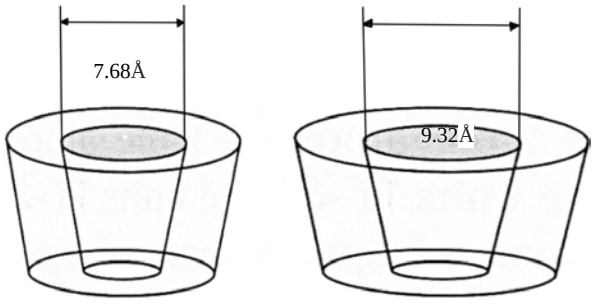

(a) (b)

Figure 2. Schematic representation of the wider rim diameter of the PM6 optimized structures (a) β-CyD which consisting of seven glucose units and (b) γ-CyD which consisting of eight glucose units.

Despite the success in enantioresolution, a critical knowledge gap exists concerning the conformation of inclusion complexes and the molecular interactions between Dpx and CyD [2]. Understanding these aspects is fundamental for the comprehensive assessment of the inclusion mechanism of Dpx encapsulated with CyD, a key factor in the development of pharmaceutical production processes.

To address this gap, the present study employs molecular docking and semi-empirical PM6 calculations. These computational methods are utilized to predict the conformations and interactions within inclusion complexes formed between Dpx enantiomers and various CyD derivatives, including β-CyD, γ-CyD, heptakis-(2,3,6-tri-O-methyl)-β-CyD (TRIMEB), and octakis-(2,3,6-tri-O-methyl)-γ-CyD (TRIMEG). The results reveal the potential formation processes of 1:1 host-guest ratio complexes with two orientations. Moreover, the complexation energies of the selected structure are quantitatively determined through density functional theorem calculations [3].

This study not only contributes to filling the existing knowledge gap but also lays the foundation for a deeper understanding of the molecular-level interactions driving the formation of inclusion complexes. The findings have implications for the advancement of pharmaceutical production processes, where precise control over enantiomeric purity is a critical factor in ensuring the safety and efficacy of DpX-based medications.

2. Materials and Methods

2.1 Molecular structure construction

The molecular structure of γ-CyD, β-CyD, TRIMEB, TRIMEG, and (*S*)-Dpx were prepared by downloading the molecular structure of all related molecules from the Cambridge Crystallographic Data Centre (CCDC) with deposition numbers 1126610, 2255693, 112114, 118818 and 2183908 respectively. (*R*)-Dpx is modified from (*S*)-Dpx in viewer 16.0. Furthermore, modified each structure using Discovery Studio to eliminate an undesired atom. Then prepare both host and guest molecules in AutoDock as grid and docking parameters.

2.2 Inclusion complex formation

The Inclusion complexes between various types of cyclodextrin and (*S*)-Dpx were constructed by molecular docking calculation using AutoDock software packages with the Lamarckian GA. Preparation of the host (γ-CyD, β-CyD, TRIMEB, and TRIMEG) and the guest (DpX) using AutoDockTools. The charge of the non-polar hydrogens was merged with the carbon atom. Type of atom, donors, and acceptors of hydrogen bonds. The grid maps were computed using AutoGrid, with a 1:1 grid with the size of 48 x 48 x 48 was set at the center of host molecule. Applied Command Prompt (cmd) to run grid and docking parameters. At this step, an enormous number of calculations were conducted. After docking simulation finished, it represents the binding energy and cluster for each conformation which can also represent the lowest energy form of all possible conformations [4].

2.3 Complexation energy calculation

Full geometry optimization was performed on the monomers and the 1:1 host-guest stoichiometry inclusion complex structure using the semiempirical PM6 utilizing the Gaussian 16 molecular modeling program [4-6]. The interaction between the host and the guest in the ideal geometries in Equation can be measured using the complexation energy (ΔE):

$$\Delta E = E_{complex}^{opt} - (E_{host}^{opt} + E_{guest}^{opt})$$

Where $E_{complex}^{opt}$, E_{host}^{opt}, E_{guest}^{opt} are the optimized energy of inclusion complex. The more negative complexation energy, the more stability of inclusion complex.

The energy difference of the most favorable inclusion complex of (*R*)- and (*S*)-Dpx ($|\mathbf{\Delta E}_R\text{-}\mathbf{\Delta E}_S|$) can show the relationship between complexation energy and retention time in enantiomer separation. As more differences in energy, the more retention time in enantiomer separation which makes these enantiomers easier to separate in higher retention time.

3. Results & Discussion

3.1 Inclusion complex formation analysis

Molecular docking is used to determine the possibility of conformation occurring in the inclusion complex by fixing the host molecule and varies guest molecule which allows Dpx to move freely inside the host's cavity [5]. Then all inclusion complexes were further fully optimized at PM6 method. The calculations represented two possible inclusion complex conformations in 1:1 host-guest ratio in between Dpx enantiomers and two native β-CyD and γ-CyD, as shown in **Figure 3** [10]. In conformation I (**Figure 3 (a)**), both of Dpx's phenyl and naphthalene aromatic rings were entrapped near the wider rim of CyD while the amine group stayed outside the CyD's cavity. In conformation II (**Figure 3 (b)**), Dpx's amine group and its phenyl ring located inside the CyD's cavity close to narrow rim while the naphthalene ring stayed outside the cavity near the wider rim of CyD. However, some conformations could not be found in the inclusion complexes between Dpx enantiomers with methylated derivatives TRIMEB and TRIMEG, as reported in **Table 1.**

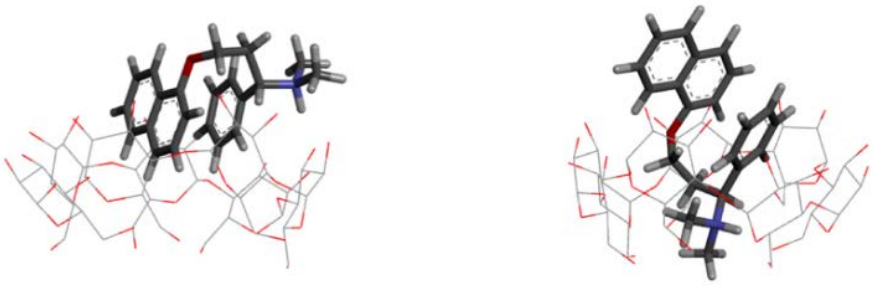

(a) (b)

Figure 3. PM6 energy-optimized structure of 1:1 inclusion complex between Dpx and β-CyD: (a) Conformation I and (b) Conformation II.

Table 1. The optimized energy (E), complexation energy (ΔE), HOMO and LUMO energies and their gap (Δ|HOMO-LUMO|) of 1:1 inclusion complex calculated by PM6 method. 1 hartree = 627.51 kcal/mol

	Conf.	HOMO (eV)	LUMO (eV)	|HOMO- LUMO| (eV)	E (hartree)	ΔE (kcal/mol)	$\|\Delta E_R-\Delta E_S\|$ (kcal/mol)
β-CyD		-0.44	-0.14	0.30	-2.16		
γ-CyD		-0.43	-0.16	0.27	-2.56		
TRIMEB		-0.40	-0.13	0.27	-2.08		
TRIMEG		0.40	-0.11	0.28	-2.41		
(*S*)-Dpx		-0.40	-0.14	0.26	0.25		
(*R*)-Dpx		-0.39	-0.15	0.24	0.25		
β-CyD/(*S*)-Dpx	I	-0.40	-0.12	0.28	-2.26	-218.54	6.35
	II	**-0.40**	**-0.09**	**0.30**	**-2.28**	**-230.23**	
β-CyD/(*R*)-Dpx	I	-0.39	-0.11	0.28	-2.28	-234.79	
	II	**-0.41**	**-0.11**	**0.30**	**-2.28**	**-236.58**	
γ-CyD/(*S*)-Dpx	I	-0.40	-0.11	0.28	-2.62	-194.96	8.41
	II	**-0.38**	**-0.10**	**0.28**	**-2.66**	**-217.30**	
γ-CyD/(*R*)-Dpx	**I**	**-0.37**	**-0.10**	**0.27**	**-2.66**	**-225.71**	
	II	-0.40	-0.11	0.28	-2.63	-203.78	
TRIMEB/(*S*)-Dpx	I	-0.37	-0.11	0.26	-2.14	-191.98	11.45
	II	**-0.39**	**-0.09**	**0.30**	**-2.16**	**-202.38**	
TRIMEB/(*R*)-Dpx	**I**	**-0.37**	**-0.08**	**0.29**	**-2.17**	**-213.83**	
	II	-0.37	-0.07	0.30	-2.15	-202.63	
TRIMEG/(*S*)-Dpx	**I**	**-0.38**	**-0.09**	**0.29**	**-2.50**	**-214.70**	9.71
	II	-0.38	-0.10	0.28	-2.50	-213.40	
TRIMEG/(*R*)-Dpx	I	-0.37	-0.09	0.28	-2.49	-209.65	
	II	**-0.38**	**-0.12**	**0.27**	**-2.51**	**-224.41**	

Note: the bold letters indicate the most favorable inclusion complex.

The HOMO-LUMO gap (Δ|HOMO-LUMO|) represents the energy variance between the Highest Occupied Molecular Orbital (HOMO) and Lowest Unoccupied Molecular Orbital (LUMO). This disparity serves as a predictive measure for robustness and endurance inclusion complexes. Generally, a compound with a larger HOMO-LUMO gap tends to exhibit increased stability [9]. The values of Δ|HOMO-LUMO| in **Table 1** indicated that all inclusion complexes are as chemically stable as the free Dpx and CyD molecules. Complexation energy (ΔE) also has an important role in determining the stability of the inclusion complex as lower in ΔE will have more stability in the inclusion complex [11,12]. The ΔE of all host-guest systems are negative which also support that Dpx enantiomers can form stable inclusion complexes with all four CyDs in this study. The (*R*)-Dpx has a strong binding affinity with CyDs, which correspond to the binding constants (*K*) of the complexes from experimental data[1] that $K_R > K_S$. The energy difference of the most favorable inclusion complex of (*R*)- and (*S*)-Dpx ($|\Delta E_R-\Delta E_S|$) in each of CyD system provide the information relate to their ability for chiral recognition as follow: TRIMEB > TRIMEG > γ-

CyD > β-CyD. The methylation in CyDs significantly affects the chiral recognition ability of molecules.

The interaction between host and guest components in the inclusion complex are further determined by M062X/6-31G(d,p) calculations. The results indicated that TRIMEB/(*R*)-Dpx form the more stable inclusion complex with lower binding energy 23.48 kcal/mol than TRIMEB/(*S*)-Dpx.

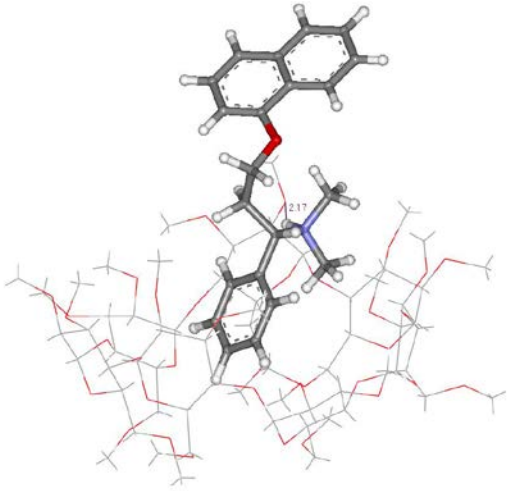

(a) TRIMEB/(*S*)-Dpx

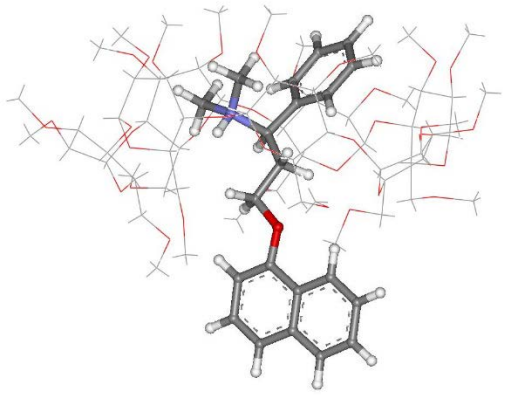

(b) TRIMEB/(*R*)-Dpx

Figure 4. M062X/6-31G(d,p) structures of Dpx enantiomers with TRIMEB in 1:1 inclusion complex.

As depicted in **Figure 4**, both the (*S*)-Dpx and (*R*)-Dpx enantiomers exhibit the insertion of their phenyl amine groups into the cavity of TRIMEB. However, the orientation of their naphthalene rings is opposite to each other. A hydrogen bond (H-bond) forms between the hydrogen atom of (*S*)-Dpx's amine group and O2 at the broader rim of TRIMEB, with a distance of 2.17 Å. This H-bond may hinder the deep penetration of the (*S*)-Dpx molecule compared to the TRIMEB/(R)-Dpx complex, where the hydrocarbon segments are more effectively enclosed within the cavity.

4. Conclusion

Employing molecular docking and PM6 calculations, we predicted the conformations and interactions of inclusion complexes between Dpx enantiomers and various CyDs, including β-CyD, γ-CyD, TRIMEB, and TRIMEG. The computed complexation energies provided valuable insights, indicating that (*R*)-Dpx forms more stable inclusion complexes with all CyDs compared to (*S*)-Dpx, agreeing very well with experimental observations. Furthermore, the energy differences of the most favorable inclusion complexes in each CyD system shed light on the chiral recognition ability of (*R*)- and (*S*)-Dpx, with the order of TRIMEB > TRIMEG > γ-CyD > β-CyD. The methylation in CyDs significantly affects the chiral recognition ability of molecules.

Acknowledgements

This work was supported by the Thammasat University Research Fund, Contract No. TUFT 84/2566. We are grateful for computational resources supported by NSTDA Supercomputer center (ThaiSC) and the National e-Science Infrastructure Consortium for their support of computing facilities for this work.

References

1. Neumajer, G.; Sohajda, T.; Darcsi, A.; Tóth, G.; Szente, L.; Noszál, B.; Béni, S. Chiral Recognition of Dapoxetine Enantiomers with Methylated-Gamma-Cyclodextrin: A Validated Capillary Electrophoresis Method. *Journal of Pharmaceutical and Biomedical Analysis* **2012**, 62, 42–47.
2. Periasamy,R.; Kothainayaki, S.; Sivakumar, K. Host-Guest Inclusion Complex of β-Cyclodextrin and 4,4′-(1,4-Phenylenediisopropylidene)Bisaniline: Spectral, Structural and Molecular Modeling Studies. *Journal of Molecular Structure* **2021**, 1224, 129050.
3. Antony, J.; Sure, R.; Grimme, S. Using Dispersion-Corrected Density Functional Theory to Understand Supramolecular Binding Thermodynamics. *Chemical Communications* **2015**, 51 (10), 1764–1774.
4. Triamchaisri, N.; Toochinda, P.; Lawtrakul, L. Structural Investigation of Beta Cyclodextrin Complexes with Cannabidiol and Delta-9-Tetrahydrocannabinol in 1:1 and 2:1 Host-Guest Stoichiometry: Molecular Docking and Density Functional Calculations. *International Journal of Molecular Sciences* **2023**, 24 (2), 1525.

5. Sorrawee Chulurks; Kulpavee Jitapunkul; Sasimas Katanyutanon; Pisanu Toochinda; Luckhana Lawtrakul. Stability Enhancement and Skin Permeation Application of Nicotine by Forming Inclusion Complex with β-Cyclodextrin and Methyl-β-Cyclodextrin. *Scientia Pharmaceutica* **2021**, 89 (4), 43–43.
6. Zhao, Y.; Truhlar, D. G. The M06 Suite of Density Functionals for Main Group Thermochemistry, Thermochemical Kinetics, Noncovalent Interactions, Excited States, and Transition Elements: Two New Functionals and Systematic Testing of Four M06-Class Functionals and 12 Other Functionals. *Theoretical Chemistry Accounts* **2007**, 120 (1-3), 215–241.
7. Uria-Canseco, E.; Perez-Casas, S.; Navarrete Vázquez, G. Thermodynamic Characterization of the Inclusion Complexes Formation between Antidiabetic New Drugs and Cyclodextrins. *The Journal of Chemical Thermodynamics* **2019**, 129, 55–60.
8. Raff, L. M. Spontaneity and Equilibrium II: Multireaction Systems. *Journal of Chemical Education* **2014**, 91 (6), 839–847.
9. Griffith, J. S.; Orgel, L. E. Ligand-Field Theory. *Quarterly Reviews, Chemical Society* **1957**, 11 (4), 381.
10. Darcsi, A. Chemical and Structural Characterization of Dapoxetine and Its Cyclodextrin Complexes. Ph.D. Thesis, Semmelweis University, Budapest, 2017.
11. Mittlefehldt, D. W.; Wilson, T. Quantum effects in cosmochemistry: complexation energy and Van der Waals radii. https://ntrs.nasa.gov/api/citations/20070009930/downloads/20070009930.pdf (accessed December 29, 2023).
12. Rahim, M.; Madi, F.; Nouar, L.; Haiahem, S.; Fateh, D.; Khatmi, D. Chapter 14 – β-Cyclodextrin Interaction with Edaravone: Molecular Modeling Study. ScienceDirect. https://www.sciencedirect.com/science/article /abs/pii/B9780128005361000149 (accessed December 29, 2023).

Chiral recognition of terbutaline enantiomers with β-cyclodextrin and its three methylated derivatives: Molecular modeling approaches

Yodfa Jantam, Sasicha Namkeaw, Nat Triamchaisri, and Luckhana Lawtrakul*

School of Bio-Chemical Engineering and Technology, Sirindhorn International Institute of Technology (SIIT), Thammasat University, Pathum Thani 12120, Thailand

**E-mail: Luckhana@siit.tu.ac.th*

Abstract:

The study explored the interactions between terbutaline (TBT) enantiomers and β-cyclodextrin (BCD) along with its derivatives: heptakis(2-O-methyl)-β-cyclodextrin (2-MEB), heptakis(6-O-methyl)-β-cyclodextrin (6-MEB), and heptakis(2,6-di-O-methyl)-β-cyclodextrin (2,6-DIMEB) using molecular docking and AM1 calculations. Results suggested three distinct TBT orientations within cyclodextrin's cavity, forming stable 1:1 inclusion complex with both (*R*)-TBT and (*S*)-TBT for all cyclodextrins. However, the AM1 complexation energies for TBT enantiomers with BCD, 2-MEB, and 6-MEB were comparable (0.68 to 1.53 kcal/mol), suggesting an inability to distinguish TBT chirality. In contrast, 2,6-DIMEB exhibited a significant energy difference (7.29 kcal/mol), indicating its ability to recognize TBT enantiomeric chirality. M06-2X/6-31G(d,p) calculations supported the superior binding affinity of (*R*)-TBT/2,6-DIMEB over (*S*)-TBT/2,6-DIMEB, with a noteworthy energy difference of 39.88 kcal/mol. These insights enhance our understanding of the selective recognition of TBT enantiomers by cyclodextrin derivatives.

1. Introduction

Terbutaline (TBT), 5-[2-(tert-butylamino)-1-hydroxyethyl] benzene-1,3-diol, a crucial β2-adrenoceptor agonist with two enantiomers, (*R*)- and (*S*)-TBT enantiomer, the treatment of asthma and chronic obstructive pulmonary disease as shown in **Figure 1**. (*R*)-TBT stimulates the activity of β2-adrenergic agonist receptors, generating a therapeutic effect, whereas (*S*)-TBT shows side effects[1–3]. Its presence in the market is still in racemic form owing to technical, commercial, and economic reasons. There was prevailing assumption that the (*S*)-TBT of racemic could potentially lead to a reduction in airway hyperreactivity, cardiac disorders, and be a contributing factor to an elevated risk of fatalities associated with asthma[4].

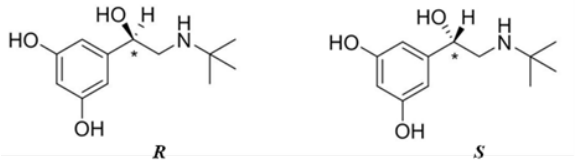

Figure 1. Chemical structure of terbutaline enantiomers.

Previous efforts to resolve the enantiomeric forms of TBT have utilized various approaches, including absolute asymmetric synthesis and the use of chiral selectors such as β-cyclodextrin (BCD) which is cyclic oligosaccharide with seven D-glucose units 1,4 linkages and its derivatives[5–8]. In 2014, Venkatesh et al.,[9] studied inclusion complexes of Orciprenaline (ORC) and Terbutaline (TBT) with native and 2-hydroxypropylated cyclodextrins, assessing solubility and spectral properties via absorption, fluorescence, and molecular modeling. They identified aliphatic chain insertion, negative Gibbs free energy, and complexation energy driven by favorable host-guest interactions, vital for stability comprehension. However, In 2019, Varga and the colleagues[10] mentioned that its methylated derivatives, including heptakis(2-O-methyl)-β-cyclodextrin (2-MEB), heptakis(6-O-methyl)-β-cyclodextrin (6-MEB), and heptakis(2,6-di-O-methyl)-β-cyclodextrin (2,6-DIMEB) had the ability on chiral recognition with terbutaline but they didn't specify that (*R*)- or (*S*)-TBT can separate by BCD which and its three methylated derivatives. Moreover, no energetic data, such as binding energy and complexation energy on 2-MEB, 6-MEB, and 2,6-DIMEB have been reported yet. In 2021, Dou et al.,[11] probed enantiomer separation mechanisms of BCD and heptakis(2,3-di-O-acetyl) β-cyclodextrin (HAD-β-CD) towards (*R*)- and (*S*)-TBT using MD, QM, and CSM methods, aiming to improve chiral separation efficiency computationally. Therefore, in this study shows for a detailed exploration of the molecular interactions and chiral recognition mechanisms underlying the enantiomeric forms of TBT when interacting with native β-cyclodextrin (BCD) and its derivatives (2-MEB, 6-MEB, 2,6-DIMEB). This study employs molecular docking and AM1 calculations to elucidate the enantiomeric recognition of (*R*)-TBT and (*S*)-TBT, unveiling two distinct orientations of TBT within the cyclodextrin's cavity with a 1:1 molecular ratio.

Furthermore, the investigation extends to explore the complexation energy and electronic properties through Density Functional Theory calculations (DFT). This research aims to fill the existing knowledge gap, providing crucial insights into the molecular-level interactions that influence the chiral recognition of TBT enantiomers. These insights are vital for the development of targeted pharmaceutical interventions, offering improved therapeutic outcomes and minimizing undesirable side effects associated with certain TBT enantiomers.

2. Materials and Methods

2.1 Molecular structure construction

The geometric crystal structures of TBT, BCD, and 2,6-DIMEB were downloaded from the Cambridge Crystallographic Data Centre with deposit numbers of 126278, 2255693, and 2022888, respectively. 2-MEB, 6-MEB, and the chirality of TBT were modified by using Discovery Studio 2020 Client (DSC) program as shown in **Figure 2**.

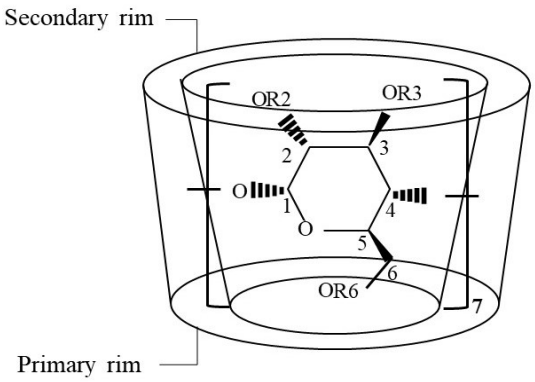

	R2	R3	R6
BCD	H	H	H
2-MEB	CH_3	H	H
6-MEB	H	H	CH_3
2,6-DIMEB	CH_3	H	CH_3

Figure 2. Schematic representation of the chemical structures of BCD and its three methylated derivatives.

2.2 Molecular docking calculation

The molecular docking techniques were constructed to address the inclusion complexes of host, BCD, 2-MEB, 6-MEB and 2,6-DIMEB and guest, (*R*)-TBT and (*S*)-TBT using AutoDockTools 1.5.7 and AutoDock 4.2 software packages with the Lamarckian genetic algorithm (LGA)[12]. AutoDockTools was used for file preparation of the host and guest. The host is fixed with flexible guest and the grid map was defined as grid spacing of 0.375 Å with grid size, 48 Å × 48 Å × 48 Å for each atom type present in the guest being docked. The grid center was set at the center of the host molecules for a 1:1 host-guest ratio in complex systems. Besides, a docking host-guest complexes of hundred runs were performed then investigated and classified groups of related conformations. The Gibbs free energy of binding (ΔG) and information of clusters for each docked were in result files. The lowest binding energy or higher negative values were selected for full geometry optimization[13-15].

2.3 Complexation energy calculation

The full geometry of the 1:1 host-guest inclusion complex with semi-empirical AM1 method was performed to optimize the inclusion complexes and verify the molecular interaction between host and guest molecules by using the GaussianView 6.0 and Gaussian 16 software packages [16]. To calculate the complexation energy (ΔE), illustrate on equation 1.

$$\Delta E = E^{opt}_{complex} - \left(E^{opt}_{host} + E^{opt}_{guest}\right) \qquad (1)$$

$E^{opt}_{complex}$ is the optimized energy of the inclusion complex, E^{opt}_{host} is optimized energy of the isolated host molecules (BCD, 2-MEB, 6-MEB and 2,6-DIMEB) and E^{opt}_{guest} is optimized energy of the isolated guest (*R*)-TBT and (*S*)-TBT. The inclusion complex conformations of cyclodextrin with the best performance of chiral recognition of terbutaline enantiomers from AM1 calculations are further investigated by M06-2X method using 6-31G(d,p) basis set.

3. Results & Discussion

3.1 Molecular docking calculation analysis

The results of the binding energy (ΔG) were negative values indicated that their formations were entropy favorable[17]. Docking calculations suggested three distinct conformations (Conf. I, II, and III), as shown in **Figure 3** and **Table 1**. Conformation I (**Figure 3 (a)**) demonstrated the aromatic ring of TBT entrapped within the cavity deep down to the BCD's primary rim, with the aliphatic chain elongated to the secondary rim. Conformation II (**Figure 3 (b)**) the aliphatic chain deep inside the cavity while the aromatic ring is located at the secondary rim. Conformation III (**Figure 3 (c)**) depicted a bent U-shaped orientation of both the aromatic ring and aliphatic chain located at the secondary rim while its hydroxyethyl group was within the cavity.

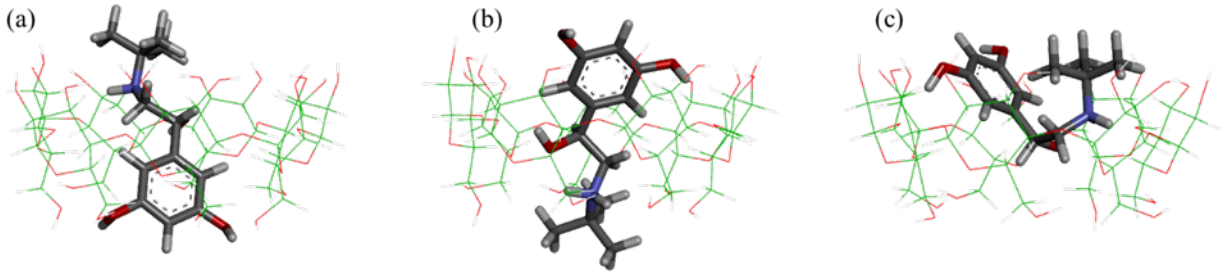

Figure 3. Schematic representations of the conformations of 1:1 inclusion complex: (a) Conformation I, (b) Conformation II, and (c) Conformation III.

Table 1. The Gibbs free energy of binding (ΔG) of inclusion complex and the percent frequency of conformations (Conf.) in a cluster obtained from molecular docking calculations.

Inclusion complex	Conf.	%	ΔG (kcal/mol)	
			Lowest	Average
(*R*)-TBT/ BCD	II	86	-5.42	-5.10
	III	11	-4.94	-4.76
	I	3	-4.35	-4.35
(*S*)-TBT/ BCD	II	78	-5.36	-5.03
	III	15	-5.03	-4.76
	I	7	-4.78	-4.53
(*R*)-TBT/2-MEB	II	59	-5.74	-5.31
	III	40	-5.73	-5.38
	I	1	-4.72	-4.72
(*S*)-TBT/2-MEB	III	53	-5.78	-5.27
	II	36	-5.61	-5.37
	I	11	-5.43	-4.97
(*R*)-TBT/6-MEB	III	77	-5.38	-5.06
	I	15	-5.16	-4.86
	II	8	-5.14	-4.92
(*S*)-TBT/6-MEB	III	78	-5.74	-5.46
	II	8	-5.30	-5.04
	I	14	-5.10	-4.89
(*R*)-TBT/2,6-DIMEB	III	78	-6.30	-6.01
	I	18	-5.64	-5.38
	II	4	-5.20	-5.17
(*S*)-TBT/2,6-DIMEB	III	93	-6.18	-5.87
	II	1	-5.41	-5.41
	I	6	-5.24	-5.24

In molecular docking, due to the rigidity of BCD, 2-MEB, 6-MEB, and 2,6-DIMEB were not feasible, and their presence was neglected. Therefore, the inclusion complexes of (*R*)- and (*S*)-TBT with BCD, 2-MEB, 6-MEB, and 2,6-DIMEB were further fully optimized using semi-empirical AM1 method.

3.2 AM1 complexation energy calculation

Table 2. presents complexation (ΔE), and HOMO and LUMO energies of 1:1 inclusion complex calculated by AM1 of monomers and inclusion complexes with BCD, 2-MEB, 6-MEB, and 2,6-DIMEB. A Δ|HOMO-LUMO| gap with larger values for all inclusion complexes tends to increase the stability and chemical properties of both the free host and guest molecules 11,15. Therefore, molecules with a larger energy gap should be less reactive than those with a smaller energy gap. According to the energy gap of (*R*)- and (*S*)-TBT (7.38 and 6.92 kcal/mol, respectively) is not much differed with their favorable inclusion complexes (7.38 and 7.61 kcal/mol, **Table 2** bold letter). The property of TBT does not alter when insertion inside the cavity of cyclodextrins, no chemical reaction occurs. The energy gap of cyclodextrins decrease around 2-3 kcal/mol shows they are less reactive after they form inclusion complex with TBT.

The complexation energy (ΔE) is important to determine the stability of 1:1 inclusion complex between host and guest molecules. The more negative ΔE is the more favorable to form the stable inclusion complex.

The lowest complexation energies obtained from AM1 calculations for each of TBT enantiomers with BCD, 2-MEB, and 6-MEB are favorable to form in Conformation II (**Table 2,** bold letters). The different in ΔE of the inclusion complex between (*R*)- and (*S*)-TBT are 0.68 to 1.53 kcal/mol, suggesting an inability to distinguish TBT chirality of these three cyclodextrins.

In contrast, 2,6-DIMEB exhibited a significant energy difference when form complex with TBT enantiomers (7.29 kcal/mol), indicating its ability to recognize TBT enantiomeric chirality. Conformation I is the most favorable inclusion complex form of (*R*)-TBT/2,6-DIMEB while (*S*)-TBT/2,6-DIMEB prefer to occur in Conformation II. The interaction between host and guest components in the inclusion complex are further determined by M06-2X/6-31G(d,p) calculations.

Table 2. The optimized energy (E), complexation energy (ΔE), HOMO and LUMO energies and their gap (Δ|HOMO-LUMO|) of 1:1 inclusion complex calculated by AM1 method (in kcal/mol).

Conformation		HOMO	LUMO	Δ|HOMO-LUMO|	E	ΔE
BCD		-8.99	1.15	10.15	-1650.37	
2-MEB		-8.76	1.38	10.15	-1603.65	
6-MEB		-8.76	1.38	10.15	-1609.96	
2,6 DIMEB		-8.53	1.61	10.38	-1560.64	
(*R*)-TBT		-10.61	-3.23	7.38	13.41	
(*S*)-TBT		-10.15	-3.00	6.92	10.51	
(*R*)-TBT/BCD	I	-9.69	-2.08	7.61	-1661.45	-24.49
	II	**-9.92**	**-2.31**	**7.38**	**-1664.91**	**-27.95**
	III	-9.69	-2.31	7.38	-1656.82	-19.87
(*S*)-TBT/BCD	I	-9.46	-2.08	7.38	-1664.45	-24.60
	II	**-9.69**	**-2.31**	**7.38**	**-1669.34**	**-29.49**
	III	-9.92	-2.31	7.61	-1655.43	-15.58
(R)-TBT/2-MEB	I	-9.46	-2.31	7.15	-1614.68	-24.45
	II	**-9.69**	**-2.08**	**7.38**	**-1623.33**	**-33.10**
	III	-9.69	-2.08	7.61	-1614.66	-24.43
(*S*)-TBT/2-MEB	I	-9.46	-2.08	7.38	-1617.20	-24.07
	II	**-9.46**	**-2.08**	**7.38**	**-1624.89**	**-31.75**
	III	-9.46	-1.84	7.61	-1614.37	-21.24
(*R*)-TBT/6-MEB	I	-9.46	-1.84	7.38	-1622.65	-26.10
	II	**-9.46**	**-2.08**	**7.38**	**-1624.08**	**-27.53**
	III	-9.46	-1.84	7.61	-1622.18	-25.63
(*S*)-TBT/6-MEB	I	-9.46	-2.08	7.15	-1623.93	-24.48
	II	**-9.69**	**-2.08**	**7.61**	**-1626.30**	**-26.85**
	III	-9.69	-2.08	7.61	-1620.97	-21.52
(*R*)-TBT/2,6-DIMEB	**I**	**-9.22**	**-2.08**	**7.38**	**-1581.93**	**-34.71**
	II	-9.46	-1.84	7.61	-1576.83	-29.61
	III	-9.46	-1.84	7.61	-1578.62	-31.40
(*S*)-TBT/2,6-DIMEB	I	-9.46	-1.84	7.61	-1576.00	-25.88
	II	**-9.46**	**-1.84**	**7.61**	**-1577.54**	**-27.42**
	III	-9.22	-1.84	7.61	-1574.79	-24.67

Note: the bold letters indicate the most favorable inclusion complex.

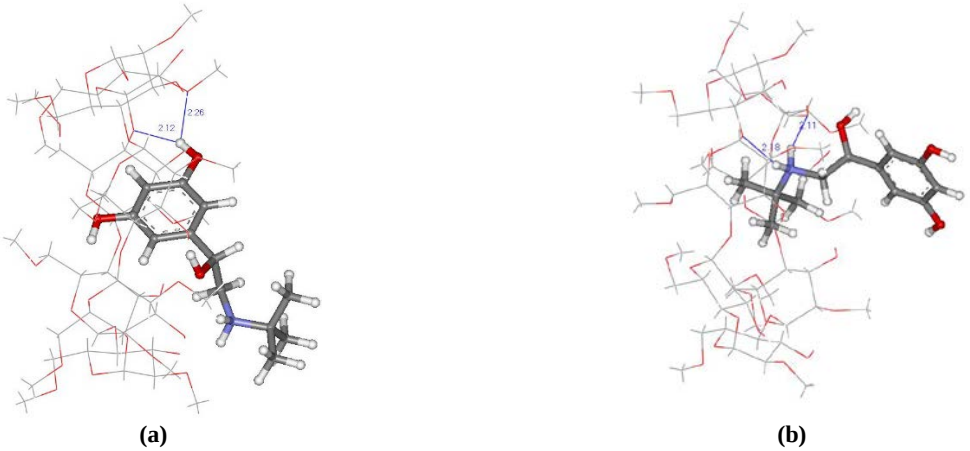

(a) **(b)**

Figure 4. M06-2X/6-31G(d,p) structure of (a) (*R*)-TBT/2,6-DIMEB Conformation I and (b) (*S*)-TBT/2,6-DIMEB Conformation II

In the configuration labeled Conformation I of (*R*)-TBT bound to 2,6-DIMEB, two crucial intermolecular hydrogen bonds (H-bonds) are evident, as depicted in **Figure 4(a)**. The initial bond is established between an ether-like anomeric oxygen atom in the n glucose unit of 2,6-DIMEB and a hydrogen atom from the hydroxyl group on the benzene ring of (*R*)-TBT, with a distance of

2.12 Å. Simultaneously, this hydrogen atom forms a second H-bond with an oxygen atom from the secondary hydroxyl group at O2 in the same n glucose unit of 2,6-DIMEB, maintaining a distance of 2.26 Å.

In **Figure 4(b)**, the H-bonds in (*S*)-TBT/2,6-DIMEB Conformation II involve one hydrogen atom from the amino group of (*S*)-TBT, forming a bond with an ether-like anomeric oxygen atom in the n glucose unit of 2,6-DIMEB at 2.18 Å. Another hydrogen atom from the amino group establishes a second H-bond with O3 in the n+1 glucose unit of 2,6-DIMEB, maintaining 2.11 Å. These H-bond interactions within the investigated complex conformation play a pivotal role in stabilizing the orientation of TBT within the 2,6-DIMEB cavity.

The computational analysis using M06-2X/6-31G(d,p) indicated a significant preference for the binding of (*R*)-TBT with 2,6-DIMEB over (*S*)-TBT, showcasing a substantial energy difference of 39.88 kcal/mol. This finding contributes valuable insights into the specific recognition of TBT enantiomers by cyclodextrin derivatives. Notably, the methyl substitutions at O2 and O6 positions of BCD play a crucial role in facilitating TBT chiral recognition. However, it was observed that the introduction of a methyl group solely at O2 in 2-MEB or O6 in 6-MEB did not alter the binding affinity between TBT enantiomers and these cyclodextrins. This highlights the distinct impact of methyl substitutions at specific positions within the cyclodextrin structure on their ability to selectively recognize TBT enantiomers.

4. Conclusion

We investigated the molecular interactions between TBT enantiomers and BCD, 2-MEB, 6-MEB, and 2,6-DIMEB, employing molecular docking and AM1 calculations. The results showed a significant ability of all cyclodextrins to form stable 1:1 inclusion complex with both (*R*)-TBT and (*S*)-TBT, characterized by distinct TBT orientations within the cyclodextrin cavity. While BCD, 2-MEB, and 6-MEB demonstrated comparable AM1 complexation energies, indicative of their inability to distinguish TBT chirality effectively, 2,6-DIMEB exhibited a significant energy difference, suggesting a pronounced capability to recognize TBT enantiomeric chirality. The M06-2X/6-31G(d,p) calculations further substantiated these findings, highlighting the higher binding affinity of (*R*)-TBT with 2,6-DIMEB over its (*S*)-TBT counterpart which indicates the potential of 2,6-DIMEB as a chiral selector for TBT enantiomers. These insights into the molecular interactions and chiral recognition properties of cyclodextrins contribute valuable information to the field of molecular host-guest interactions and may have implications in the design of chiral separation systems or drug delivery applications. Further research can build upon these findings, exploring the practical applications and expanding the understanding of chiral recognition mechanisms in similar molecular systems.

Acknowledgements

This work was supported by the Thammasat University Research Fund, Contract No. TUFT 84/2566. We are grateful for computational resources supported by NSTDA Supercomputer center (ThaiSC) and the National e-Science Infrastructure Consortium for their support of computing facilities for this work.

References

1. Beng, H., Zhang, H., Jayachandra, R., Li, J., Wu, J., & Tan, W. (2018). Enantioselective resolution of Rac-terbutaline and evaluation of optically pure R-terbutaline hydrochloride as an efficient anti-asthmatic drug. *Chirality*, *30*(6), 759–768.
2. Aboushady, D., Parr, M. K., & Hanafi, R. S. (2020). Quality-by-design is a tool for quality assurance in the assessment of enantioseparation of a model active pharmaceutical ingredient. *Pharmaceuticals*, *13*(11), 1–17.
3. Aboushady, D., Hanafi, R. S., & Parr, M. K. (2022). Quality by design approach for enantioseparation of terbutaline and its sulfate conjugate metabolite for bioanalytical application using supercritical fluid chromatography. *Journal of Chromatography A*, *1676*.
4. Fan, Z., Lin, W., Lv, N., Ye, Y., & Tan, W. (2016). R- and S-terbutaline activate large conductance and Ca2 + dependent K+ (BKCa) channel through interacting with β2 and M receptor respectively. *Biochimica et Biophysica Acta - Biomembranes*, *1858*(11), 2745–2752.
5. Poulson, B. G., Alsulami, Q. A., Sharfalddin, A., El Agammy, Emam. F., Mouffouk, F., Emwas, A.-H., Jaremko, L., & Jaremko, M. (2021). Cyclodextrins: Structural, Chemical, and Physical Properties, and Applications. *Polysaccharides*, *3*(1), 1–31.
6. Scriba, G. K. E., Konjaria, M., & Krait, S. (2023). Cyclodextrins. In *Chiral Separations*

and Stereochemical Elucidation (pp. 273–323). Wiley.

7. Gogolashvili, A., Tatunashvili, E., Chankvetadze, L., Sohajda, T., Szeman, J., Gumustas, M., Ozkan, S. A., Salgado, A., & Chankvetadze, B. (2018). Separation of terbutaline enantiomers in capillary electrophoresis with cyclodextrin-type chiral selectors and investigation of structure of selector-selectand complexes. *Journal of Chromatography A*, *1571*, 231–239.
8. Sandilya, A. A., Natarajan, U., & Priya, M. H. (2020). Molecular View into the Cyclodextrin Cavity: Structure and Hydration. *ACS Omega*, *5*(40), 25655–25667.
9. Venkatesh, G., Thulasidhasan, J., & Rajendiran, N. (2014). A spectroscopic and molecular modeling studies of the inclusion complexes of orciprenaline and terbutaline drugs with native and modified cyclodextrins. *Journal of Inclusion Phenomena and Macrocyclic Chemistry*, *78*(1–4), 225–237.
10. Varga, E., Benkovics, G., Darcsi, A., Várnai, B., Sohajda, T., Malanga, M., & Béni, S. (2019). Comparative analysis of the full set of methylated β-cyclodextrins as chiral selectors in capillary electrophoresis. *Electrophoresis*, *40*(21), 2789–2798.
11. Dou, R., Chen, K., Chi, G., Luo, J., Wong, C. F., & Zhou, B. (2021). Why heptakis (2, 3-di-O-acetyl)-β-cyclodextrin can separate terbutaline enantiomers better than β-cyclodextrin: Nonbonding and hydrophobic interactions. *Journal of Inclusion Phenomena and Macrocyclic Chemistry*, *100*, 189-195.
12. Wiley, E. A., MacDonald, M., Lambropoulos, A., Harriman, D. J., & Deslongchamps, G. (2006). LGA-Dock/EM-Dock - Exploring Lamarckian genetic algorithms and energy-based local search for ligand-receptor docking. *Canadian Journal of Chemistry*, *84*(3), 384–391.
13. Triamchaisri, N., Toochinda, P., & Lawtrakul, L. (2023). Structural Investigation of Beta-Cyclodextrin Complexes with Cannabidiol and Delta-9-Tetrahydrocannabinol in 1:1 and 2:1 Host-Guest Stoichiometry: Molecular Docking and Density Functional Calculations. *International Journal of Molecular Sciences*, *24*(2).
14. Papezhuk, M. V., Volynkin, V. A., Stroganova, T. A., Krapivin, G. D., Usacheva, T. R., & Thi, L. P. (2020). Theoretical and experimental study of inclusion complex formation of β-cyclodextrin with some 1,4-diazepine derivatives. *Macroheterocycles*, *13*(1), 64–73.
15. Dermawan, D., Prabowo, B. A., & Rakhmadina, C. A. (2021). In silico study of medicinal plants with cyclodextrin inclusion complex as the potential inhibitors against SARS-CoV-2 main protease (Mpro) and spike (S) receptor. *Informatics in Medicine Unlocked*, *25*.
16. Gaussian 16, Frisch, M. J., Trucks, G. W., Schlegel, H. B., Scuseria, G. E., Robb, M. A., Cheeseman, J. R., Scalmani, G., Barone, V., Petersson, G. A., Nakatsuji, H., Li, X., Caricato, M., Marenich, A. V., Bloino, J., Janesko, B. G., Gomperts, R., Mennucci, B., Hratchian, H. P., Ortiz, J. V., Izmaylov, A. F., Sonnenberg, J. L., Williams-Young, D., Ding, F., Lipparini, F., Egidi, F., Goings, J., Peng, B., Petrone, A., Henderson, T., Ranasinghe, D., Zakrzewski, V. G., Gao, J., Rega, N., Zheng, G., Liang, W., Hada, M., Ehara, M., Toyota, K., Fukuda, R., Hasegawa, J., Ishida, M., Nakajima, T., Honda, Y., Kitao, O., Nakai, H., Vreven, T., Throssell, K., Montgomery, J. A., Jr., Peralta, J. E., Ogliaro, F., Bearpark, M. J., Heyd, J. J., Brothers, E. N., Kudin, K. N., Staroverov, V. N., Keith, T. A., Kobayashi, R., Normand, J., Raghavachari, K., Rendell, A. P., Burant, J. C., Iyengar, S. S., Tomasi, J., Cossi, M., Millam, J. M., Klene, M., Adamo, C., Cammi, R., Ochterski, J. W., Martin, R. L., Morokuma, K., Farkas, O., Foresman, J. B., Fox, D. J. Gaussian, Inc., Wallingford CT, 2016.
17. Sancho, M. I., Andujar, S., Porasso, R. D., & Enriz, R. D. (2016). Theoretical and Experimental Study of Inclusion Complexes of β-Cyclodextrins with Chalcone and 2′,4′-Dihydroxychalcone. *Journal of Physical Chemistry B*, *120*(12), 3000–3011.

Transient luminescence studies for excited-state kinetics of organic indoline dyes adsorbed on nanocrystalline TiO_2 and ZrO_2 films

Kanon Ie, Rina Watanabe, and Koichiro Mitsuke*

Josai University, Graduate School of Science, Department of Material Science, Keyakidai 1-1, Sakado, Saitama, 350-0295 Japan

**E-mail: mitsuke@josai.ac.jp*

Abstract:

Time-correlated single photon counting has been employed to study the primary photovoltaic process of dye sensitized solar cells, namely electron injection from photoexcited dye molecules to a mesoporous metal oxide film on the anode. Indoline dyes D149 and D205 were made to adsorb on thin films of TiO_2 and ZrO_2, which allowed us to make a comparison between the fluorescence decay curves, respectively, with and without electron injection. Absorption of a 470 nm photon produces the S_1 state excited locally with ground state minimum geometry hereafter denoted as S_1(LE). From transient fluorescence we have determined the rate constants for the following deexcitation processes: (a) intramolecular relaxation of S_1(LE) to the twisted intramolecular charge transfer TICT state, (b) non-radiative internal conversion of TICT to the S_0 state mainly due to photoisomerization, and (c) electron injection from S_1(LE) and TICT to the conduction band of TiO_2. In data analyses the radiative lifetimes of respective dyes in the TICT state were derived from the fluorescence lifetimes and quantum yield for D149 and D205 dissolved in chloroform. Moreover, we found that the rate constant for the transformation from S_1(LE) to TICT can be evaluated from the ratio between the integrated fluorescence intensity from the dye adsorbed to ZrO_2 and that from the dye adsorbed to TiO_2.

1. Introduction

The anodes of dye sensitized solar cells (DSSCs) are made of sensitizer dye and mesoporous oxides such as nanoparticles of titanium dioxide TiO_2.[1] The primary photovoltaic process is electron injection from photoexcited dye molecules to the conduction band of TiO_2. This process may compete with other intramolecular decay pathways involving radiative and nonradiative transitions. High-efficient photon-to-electron conversion can be realized at the anodes under condition that the rate of the electron injection is much larger than that of radiative decay of the sensitizer.[2-4]

We have chosen indoline dyes D149 and D205 as the sensitizer for the anodes of DSSCs (see Fig. 1) whose solar light conversion efficiencies are comparable to those of the Ru complexes (D149, η = 9.0%; D205 η = 9.5%).[5] These dyes incorporate an electron donor unit (D), a bridging unit (Π), and an electron-acceptor unit (A) to form a push-pull type D-Π-A system. The electron density is mostly localized on the D moiety in the ground S_0 state. Photoexcitation to the S_1 state causes an intramolecular charge transfer which induces charge shifting from the D to A units and localization of the electron density on the A unit. If the D-Π-A dyes are adsorbed on TiO_2 surface, electron injection across the dye-TiO_2 interface is considered to proceed in parallel with such a charge shifting, because the time scale of electron injection encompasses several orders of magnitude.

It has been generally accepted that ultrafast transient absorption spectroscopy is required for monitoring the decay of the dye excited state and determining the relevant rate constants. Recently, an alternative method of transient fluorescence technique based on time correlated single photon counting (TCSPC) has attracted considerable attention as this method is less laborious and less costly technique.[6]

In the present study we investigate the kinetics of intramolecular deactivation and electron injection of indoline dyes on the TiO_2 surface by using TCSPC. Fully commercial TCSPC apparatus, together with well characterized control samples, proves to be powerful tool for studying decay mechanism of photoexcited D-Π-A dyes and for improving the photon-to-electron conversion efficiency at the anodes.

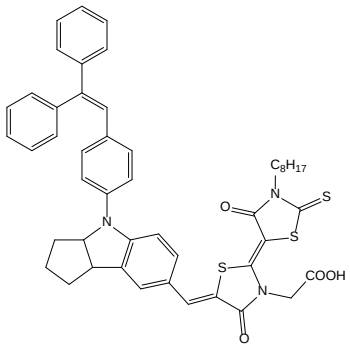

Figure 1. Molecular structure of D205 dye (Ref. 5). The C_8H_{17} chain is replaced by C_2H_5 in D149.

2. Experimental Methods

2.1 Fabrication of the anode of DSSC

A control sample consists of a ZrO_2 film to which no electron is injected from the excited state dye, since the conduction band edge of ZrO_2 lies high enough to prevent electron injection. Commercial nanoparticles of TiO_2 or ZrO_2 (P25 or VR from Degussa) were mixed with acetic acid as dispersant, α-terpineol as surfactant, and ethylcellulose as viscosity control. Each paste was applied on an FTO conductive glass by doctor blading method. The FTO glass coated with TiO_2 or ZrO_2 was sintered at 500 °C and immersed into the dye solution for overnight. The dye powder D149 and D205 were used as received from Mitsubishi Paper Mills, Japan, and dissolved in the mixed solvent of acetonitrile and t-butyl alcohol.

2.2 Spectroscopic measurement

The fluorescence lifetime of the electrode thus prepared was measured by a fluorescence spectrometer (Hamamatsu, C11367) at the excitation and emission wavelengths of λ_{ex} = 470 and 660 ± 10 nm, respectively. The instrumental response function (IRF) was obtained by using a scatter aqueous solution of silica (Ludox). The observed fluorescence signals were deconvoluted with the IRF, and a decay curve was obtained as a single (A_2=0) or double (A_1≠0, A_2≠0) exponential function

$$G(t) = A_1 \exp\left(-\frac{t}{\tau_1}\right) + A_2 \exp\left(-\frac{t}{\tau_2}\right) \qquad (1)$$

where A_i and τ_i represent the amplitude and decay time for each term, respectively. We can thereby determine decay time constants with a resolution of ≈ 60 ps.

3. Data analyses

3.1 Deexcitation pathways from the S_1 state

The absorption spectrum of D149 in chloroform $CHCl_3$ in Figure 2 shows two peaks centered at 390 nm and 550 nm, respectively, which have been identified as resulting from the $S_0 \rightarrow S_2$ and $S_0 \rightarrow S_1$ transitions.[7,8] Apparently the 470 nm photo-excitation in the present study gives rise to the S_1(LE) state, that is Franck-Condon locally excited state with ground state minimum geometry of D149. This is also the case for D205.

On the TiO_2 surface an excited electron of S_1(LE) is promptly injected into the conduction band of titania in a time scale of sub-picosecond (D149: τ_{inj}^{LE} = 0.45 ps and k_{inj}^{LE} = 2.2 × 10^{12} s^{-1}; D205: τ_{inj}^{LE} = 0.32 ps and k_{inj}^{LE} = 3.1 × 10^{12} s^{-1}).[9]

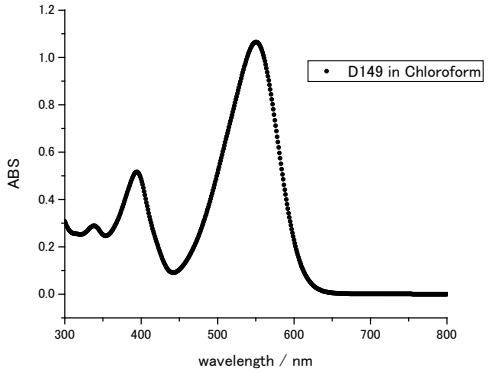

Figure 2. Absorption spectrum of D149.

El-Zohry et al. have proposed that the S_1(LE) states of D149 and D205 on TiO_2 undergo transformation to the twisted intramolecular charge transfer TICT state (rate constant of k_{TICT}).[9,10] The TICT state arises from twisting of a single bond in the S_1 state which decouples the π-conjugate system of the D and A units. They explained[9] an additional slow electron injection process in picosecond timescale in terms of TICT. Referring to their argument, we expect that the TICT state may decay by three competing processes: fluorescence emission (k_f) to S_0, non-radiative internal conversion to the vibrationally hot S_0 (k_{nr}), and electron injection into TiO_2 (k_{inj}) forming radical dye cation Dye^+, as illustrated by the scheme:

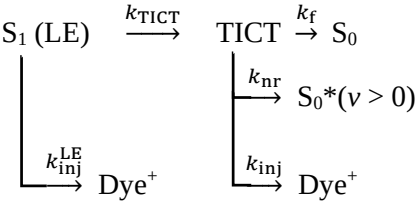

3.2 Expressions of fluorescence signal decay

We assume the relation between five rate constants

$$k_{inj}^{LE} > k_{TICT} > k_{inj} > k_f + k_{nr} \qquad (2)$$

for the following three reasons.

(1) We observed the fluorescence signal count ratio $\mathcal{I}_F(ZrO_2)/\mathcal{I}_F(TiO_2)$ of at most 12.5, which suggests the relation of $k_{TICT} > (12.5–1)^{-1} \times k_{inj}^{LE}$ = 1.9 × 10^{11} s^{-1}. Here, $\mathcal{I}_F(ZrO_2)$ and $\mathcal{I}_F(TiO_2)$ represent the fluorescence intensity integrated over the decay time and emission wavelength for the dye on ZrO_2 and TiO_2 electrodes, respectively.

(2) k_{inj} of the above scheme appears to correspond to the slower component of the lifetime for D149 on TiO_2, viz. k_{inj} = (3.1 – 3.3) × 10^{10} s^{-1} by El-Zohry et al.,[9,11] or 7.1 × 10^9 s^{-1} by Sobus et al.[12] and 3.0 × 10^9 s^{-1} by Snaith et al.[13]

(3) Fluorescence lifetimes of D149 and D205 on the ZrO_2 surface are reported by many authors to be several hundreds picoseconds to ~ 2 ns.[11,14]

Assuming eq. (2) one can express the fluorescence decay $I_F(t)$ from the TiO_2 electrode as an approximate form of the kinetics of pseudo-first order reaction

$$I_F(t) = k_f\,[\mathrm{TICT}] = [S_1(\mathrm{LE})]_0 \frac{k_{\mathrm{TICT}} k_f}{k_{\mathrm{TICT}} + k_{\mathrm{inj}}^{\mathrm{LE}} - k_{\mathrm{nr}} - k_{\mathrm{inj}} - k_f} \times \left[e^{-(k_f+k_{\mathrm{inj}}+k_{\mathrm{nr}})t} - e^{-\left(k_{\mathrm{TICT}}+k_{\mathrm{inj}}^{\mathrm{LE}}\right)t}\right] \approx [S_1(\mathrm{LE})]_0 \frac{k_{\mathrm{TICT}} k_f}{k_{\mathrm{inj}}^{\mathrm{LE}}} e^{-k_{\mathrm{inj}}t} \quad (3)$$

Here, $[S_1(\mathrm{LE})]_0$ is the primary concentration of $S_1(\mathrm{LE})$ at t = 0 produced by photoexcitation; its value differs from D149 to D204, from electrodes to solution, and from TiO_2 to ZrO_2 surfaces.

Due to absence of electron injection the fluorescence decay in the $CHCl_3$ solution or dye on ZrO_2 can be approximated as

$$I_F(t) = k_f\,[\mathrm{TICT}] = [S_1(\mathrm{LE})]_0 \times \frac{k_{\mathrm{TICT}} k_f}{k_{\mathrm{TICT}} - k_{\mathrm{nr}} - k_f}\left[e^{-(k_f+k_{\mathrm{nr}})t} - e^{-k_{\mathrm{TICT}}\,t}\right] \approx [S_1(\mathrm{LE})]_0\; k_f\, e^{-(k_f+k_{nr})t} \quad (4)$$

The S_1 state of D149 is subject to deexcitation by solvation in methanol (< 11.9 ps) and to deactivation in collision with solvents in tetrahydrofuran THF (< 30 ps).[8] We will dismiss a participation of similar processes in $CHCl_3$ solution, because $CHCl_3$ does not act as a protic solvent, and because such rapid solvation dynamics was indiscernible[7] at the S_1 emission band in ultrafast up-conversion spectroscopy. Hence, it is likely that the solvation has no influence on the time dependence of eq. (4).

3.3 Estimates of the rate constants

Using eq. (3) the k_{inj} value was derived from the transient signals for the dye on TiO_2. Rate constants k_f and k_{nr} are calculated from the fluorescence quantum yield,

$$\Phi(CHCl_3) \approx \Phi(ZrO_2) = \frac{k_f}{k_f+k_{\mathrm{nr}}} = \tau_f k_f \quad (5)$$

by using the fluorescence lifetime τ_f of the dye on the ZrO_2 surface, or $(k_f+k_{\mathrm{nr}})^{-1}$ in eq. (4).

We measured $\Phi(CHCl_3)$ by employing an integral sphere. The resultant values of 0.118 and 0.133 from the D149 and D205 solution, respectively, agree well with Φ = 0.10 for both the dyes in $CHCl_3$,[15] and Φ = 0.140 for D149 in THF.[8]

On the other hand, k_{TICT} can be evaluated from the other four rate constants, $\mathcal{I}_F(ZrO_2)/\mathcal{I}_F(TiO_2)$, and the ratio of the photoabsorption signal counts $A(TiO_2)/A(ZrO_2)$.

$$\frac{\mathcal{I}_F(ZrO_2)}{\mathcal{I}_F(TiO_2)}\frac{A(TiO_2)}{A(ZrO_2)} = \left(1+\frac{k_{\mathrm{inj}}}{k_f+k_{\mathrm{nr}}}\right)\left(1+\frac{k_{\mathrm{inj}}^{\mathrm{LE}}}{k_{\mathrm{TICT}}}\right) \quad (6)$$

Here, $A(ZrO_2)$ and $A(TiO_2)$ denote the photoabsorbance of the dye on the ZrO_2 and TiO_2 surfaces, respectively, at 470 nm.

4. Results & Discussion

4.1 Fluorescence decay curves of D149

Figure 3 shows the results of TCSPC measured at 470 nm photoexcitation, that is, fluorescence decay signals of D149 on TiO_2 (red circle) and on ZrO_2 (blue triangle), as well as the curve of D149 dissolved in $CHCl_3$ (black square).

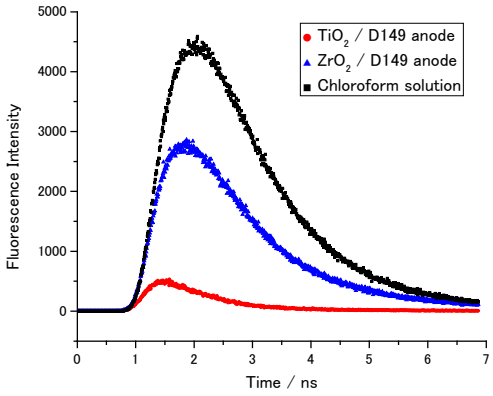

Figure 3. Fluorescence decay curves of D149.

If an approximate relation of eq. (2) holds, the red TiO_2/D149 curve should arise from the convolution of IRF with $I_F(t)$ of eq. (3). Thus τ_{inj} of D149 on TiO_2 can be estimated by deconvolution of this curve with IRF. The resultant τ_{inj} is 255 ± 60 ps, corresponding to k_{inj} of 3.9 × 10^9 s^{-1}.

Deconvolution of the blue ZrO_2/D149 curve with IRF provides τ_f = 920 ps for D149 adsorbed on ZrO_2 film, in good agreement with τ_f = 960 ps of $CHCl_3$ solution. Namely, apparent lifetimes become 3.6 times as long on ZrO_2 as on TiO_2. This confirms the absence of electron injection from D149 to ZrO_2 which has a conduction band lying higher by 0.85 eV than TiO_2.[6]

Eq. (4) gives $k_f + k_{\mathrm{nr}} = \tau_f^{-1}$ = 1.09 × 10^9 s^{-1}. Individual rate constants were evaluated from eq. (5) and $\Phi(CHCl_3)$ = 0.118 to be k_f = 1.28 × 10^8 s^{-1} and k_{nr} = 9.57 × 10^8 s^{-1}. Moreover, eq. (6) yields the rate constant of k_{TICT} = 1.24 × 10^{12} s^{-1} or the corresponding lifetime of 0.81 ps for transformation from S_1(LE) to TICT.

Table 1. Decay parameters of D149 photoexcited to S_1(LE) at wavelength λ_{ex}.

solution or metal oxide surface	τ_1 (ps) [a]	Other works. τ_1 and τ_2 in ps; with λ_{ex}
$CHCl_3$ solution	960	800; 484 nm [Ref.8] 900; 470 nm [Ref.15] 700; 405 nm [Ref.16,17]
TiO_2	255	1.3 / 8.6; 400 nm [Ref.18] 0.45[b] / 30; 410 nm [Ref.9] 47 / 287; 405 nm [Ref.11] 7.6 / 140; 425 nm [Ref.12] – /200; 407 nm [Ref.13]
ZrO_2	920	260 / 1053; 405 nm [Ref.11] 700 / 2300; 405 nm [Ref.14]

[a] This study with λ_{ex} = 470 nm. By assuming eq. (1).
[b] Corresponding to the electron injection from S_1(LE).

Decay parameters derived from deconvolution of TCSPC curves are listed in Table 1. Moreover, the rate constants obtained from concomitant analyses are summarized in Table 2.

4.2 Reliability in extracting τ_1 from the fluorescence decay curves

In this section we will demonstrate the accuracy of τ_{inj} = 255 ps for the TiO_2/D149 anode system. Figure 4 shows three theoretical single exponential decays with lifetimes of 150, 250, and 350 ps, together with the scatter plot of experimental TiO_2/D149 data (red) in Figure 3. These theoretical curves are synthesized by convolution of the IRF with a single exponential decay function, $\exp(-\frac{t}{\tau})$.

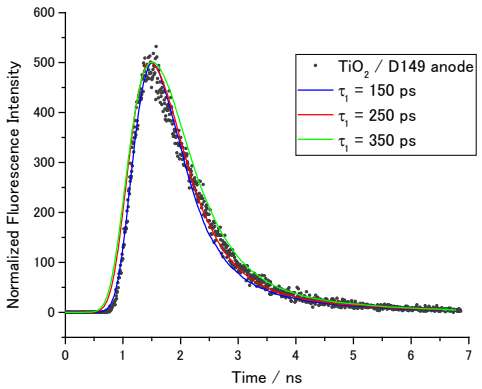

Figure 4. Decay curves of D149 synthesized by convolution of the IRF with single exponential functions with three different time constants.

In Figure 4 the data points lie around the synthesized function of τ = 250 ps, rather than around those of 150 and 350 ps. Such a separation of scatter plot data from the functions of 150 and 350 ps is the clear manifestation of the resolving power in the present deconvolution procedure.

A closer inspection of Figure 4 clarifies a noticeable deviation of the data points from the synthesized curves below ~2 ns. This deviation can be interpreted as that the observed decay of the TiO_2/D149 system should be simulated by a convolution of the IRF with a single stretched exponential function of a form

$$G(t) = A_0 \exp\left[-(\frac{t}{\tau})^{\beta}\right] \qquad (7)$$

in place of double exponential decays [see eq. (1)]. Here, τ and β are free fitting parameters, and the amplitude A_0 of the stretched exponential should be set to the deconvoluted amplitude of the control non-injecting TCSPC trace of the ZrO_2/dye anode system. Many authors have ascertained that this stretched exponential function is consistent with a reasonable microscopic model of electron injection into the conduction band of a metal oxide surface based on an inhomogeneous distribution of injection energetics.[6,19,20]

4.3 Fluorescence decay curves of D205

The TCSPC data of D205 are illustrated in Figure 5. These decay curves allow us to calculate the rate constants in a manner similar to that described in Sec. 4.1. First, τ_{inj} and k_{inj} of D205 on the TiO_2 film were estimated to be 261 ± 60 ps and 3.8 × 10^9 s^{-1}, respectively, by deconvoluting the TiO_2/D205 curve with the IRF. Second, deconvolution of the ZrO_2/D205 curve gives τ_f = 971 ps for D205 adsorbed on ZrO_2 film. Then applying eq. (5) to $k_f + k_{nr} = \tau_f^{-1}$ and $\Phi(CHCl_3)$ = 0.133 results in k_f = 1.37 × 10^8 and k_{nr} = 8.93 × 10^8 s^{-1}. Third, k_{TICT} = 2.1 × 10^{12} s^{-1} was obtainable from eq. (6).

Table 2. Summary of the rate constants of D149 and D205 photoexcited to S_1(LE) at wavelength λ_{ex}.

Dyes	k_f, 10^8 s^{-1}	k_{nr}, 10^9 s^{-1}	k_{inj}, 10^{10} s^{-1}	k_{TICT}, 10^{12} s^{-1}	k_{inj} for DSSCs, 10^{10} s^{-1}
D149	1.28 [a] 1.1 [Ref.15] 1.75 Φ=0.14 [Ref.8] 3.1 [Ref.21]	0.957 [a] 1.0 [Ref.15] 1.1 Φ=0.14 [Ref.8]	0.39 [a] 3.3 [Ref.9] 12 [Ref.18]	1.24 [a]	0.71 [Ref.12] 0.3 [Ref.13]
D205	1.37 [a] 1.1 [Ref.15]	0.893 [a] 0.95 [Ref.15]	0.38 [a] 11 [Ref.9]	2.1 [a]	

[a] This study with λ_{ex}= 470 nm.

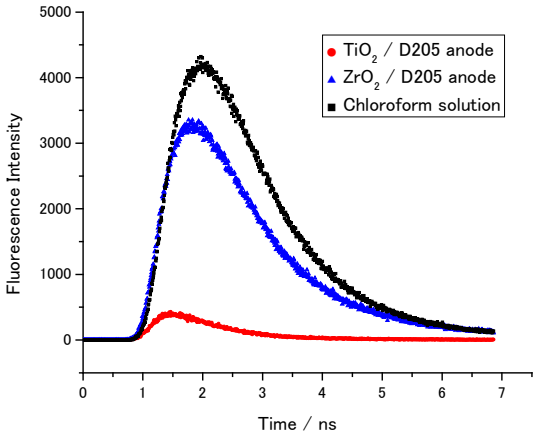

Figure 5. Fluorescence decay curves of D205.

Table 3. Decay parameters of D205 photoexcited to S_1(LE) at wavelength λ_{ex}.

solution or metal oxide surface	τ_1 (ps) [a]	Other works. τ_1 and τ_2 in ps, with λ_{ex}
$CHCl_3$ solution	868	950; 470 nm Ref.15 900; 405 nm Ref.17
TiO_2	261	0.32 / 9.1; 410 nm Ref.9
ZrO_2	971	350 / 1370; 405 nm Ref.17

[a] This study with λ_{ex} = 470 nm. By assuming eq. (1).

Tables 2 and 3 show, respectively, the rate constants and decay parameters of D205 in various environments.

4.4 Mechanisms and kinetics for electron injection

The present deexcitation scheme suggests that electron injection to the conduction band of TiO_2 takes place either from the locally excited S_1(LE) or from the TICT state (see Sec. 3.1). The electron injection via TICT proceeds three orders of magnitude slower than that from S_1(LE). This is because the energy level of TICT is close to or below the conduction band edge of TiO_2. Consequently the electrons injected from TICT are transferred to the trap states of TiO_2 which are localized near the formed Dye^+. Most of such electrons are considered to suffer from relatively rapid recombination with Dye^+ and make no contribution to the short circuit current of DSSCs.

The k_{inj} values $(0.38 – 0.39) \times 10^{10}$ s^{-1} in Table 2 are in fair agreement with the corresponding data in the literature for indoline dyes on the TiO_2 surface. Those are 0.71×10^{10} and 0.3×10^{10} s^{-1} measured by TCSPC of D149 on TiO_2 in complete DSSCs.[12,13] Much larger k_{inj} values of 3.3×10^{10} s^{-1} and 1.2×10^{11} s^{-1} have been reported for the anodes, respectively, by femtosecond visible-IR transient absorption[9] and femtosecond up-conversion measurements.[18]

We can calculate a quantum yield φ_{inj} for electron injection with the help of the rate constants in Table 2 and k_{inj}^{LE}. The resultant φ_{inj}'s are 0.92 for D149 and 0.91 for D205. These values can be compared with the electron injection efficiency evaluated by Sobuś et al.[12] who employed transient femtosecond emission measured with up-conversion setup at λ_{ex} = 570 nm with 300 fs resolution. The averaged decay times were 7.6 ps and 47 ps for the TiO_2/D149 sample and Al_2O_3/D149 control, respectively, giving 84 % electron injection efficiency.[12] This value appears to be consistent with our φ_{inj}.

5. Conclusion

We have studied the electron injection mechanisms and kinetics of indoline dyes adsorbed on the metal oxide surface by using TCSPC technique at λ_{ex} = 470 nm with 60 fs resolution. This temporal resolution is sufficient to discuss the decay dynamics of the TICT state occurring in several hundreds picoseconds or longer. Transient fluorescence detection in TCSPC has a beneficial feature of being sensitive only to the excited states of the dye molecules. This superiority is much more emphasized in the study of working solar cells, because the rate of electron injection becomes markedly slower in the complete cells than in the photovoltaic anode, as is often the case with DSSCs filled with electrolyte containing various ingredients.[22]

Acknowledgements

We are grateful to Prof. Mitsuru Ishikawa and Prof. Masashi Hashimoto for valuable support and helpful discussions. This work has been supported by Grants-in-Aid for Scientific Research (Grant No. 17K05760) from the ministry of Education, Culture, Sports, Science and Technology, Japan.

References

1. O'Regan, B.C.; Grätzel, M. *Nature* **1991,** *353*, 000737−740.
2. Tachibana, Y.; Haque, S.A.; Mercer, I.P.; Moser, J.E.; Klug, D.R.; Durrant, J.R. *J. Phys. Chem. B* **2001**, *105*, 7424–7431.
3. Durrant, J.R. *J. Photochem. Photobiol. A*: Chemistry **2002,** *148*, 5–10.
4. Haque, S.A.; Palomares, E.; Cho, B.M.; Green, A.N.M.; Hirata, N.; Klug, D.R.; Durrant, J.R. *J. Am. Chem. Soc.* **2005**, *127*, 3456–3462.

5. Ito, S.; Miura, H.; Uchida, S.; Takata, M.; Sumioka, K.; Liska, P.; Comte, P.; Pechy, P.; Grätzel, M. *Chem. Commun.* (J. Chem. Soc. Sec.D) **2008,** *41*, 5194−5196.
6. Koops, S.E.; Durrant, J.R. *Inorg. Chim. Acta* **2008,** *361*, 663–670.
7. Fakis, M.; Hrobárik, P.; Stathatos, E.; Giannetas, V.; Persephonis, P. *Dyes and Pigments* **2013,** *96*, 304–312.
8. Lohse, P.W.; Kuhnt, J.; Druzhinin, I.; Scholz, M.; Ekiomova, M.; Oekermann, T.; Lenzer, T.; Oum, K. *Phys. Chem. Chem. Phys.* **2011,** *13*, 19632–19640.
9. El-Zohry A.M. *Dyes and Pigments* **2019,** *160*, 671–674.
10. El-Zohry, A.M.; Roca-Sanjuán, D.; Zietz, B. *J. Phys. Chem. C* **2015**, *119*, 2249–2259.
11. El-Zohry, A.M.; Zietz, B. *J. Phys. Chem. C* **2020**, *124*, 16300–16307.
12. Sobuś, J.; Burdziński, G.; Karolczak, J.; Idigoras, J.; Anta, J.A.; Ziółek, M. *Langmuir* **2014,** *30*, 2505−2512.
13. Snaith, H.J.; Petrozza, A.; Ito, S.; Miura, H.; Grätzel, M. *Adv. Funct. Mater.* **2009,** *19*, 1810–1818.
14. El-Zohry, A.M.; Orthaber, A.; Zietz, B. *J. Phys. Chem. C* **2012**, *116*, 26144–26153.
15. Matsui, M.; Aoki, R.; Nishiwaki, D.; Kubota, Y.; Funabiki, K.; Jin, J.; Yoshida, T.; Higashijima, S.; Miura, H. *RSC Adv.* **2015,** *5*, 57721–57724.
16. El-Zohry, A.M.; Zietz, B. *J. Phys. Chem. C* **2013**, *117*, 6544–6553.
17. El-Zohry, A.M.; Agrawal, S.; Angelis, F.D.; Pastore, M.; Zietz, B. *J. Phys. Chem. C* **2020**, *124*, 21346–21356.
18. Fakis, M.; Stathatos, E.; Tsigaridas, G.; Giannetas, V.; Persephonis, P. *J. Phys. Chem. C* **2011**, *115*, 13429–13437.
19. Tachibana, Y.; Rubtsov, I.V.; Montanari, I.; Yoshihara, K.; Klug, D.R.; Durrant, J.R. *J. Photochem. Photobiol. A*: Chemistry **2001,** *142*, 215–220.
20. Koops, S.E.; O'Regan, B.C.; Barnes, P.R.F.; Durrant, J.R. *J. Am. Chem. Soc.* **2009**, *131*, 4808–4818.
21. Le Bahers, T.; Pauporte, T.; Scalmani, G.; Adamo, C.; Ciofini, I. *Phys. Chem. Chem. Phys.* **2009,** *11*, 11276–11284.
22. Long, H.; Zhou, D.; Zhang, M.; Peng, C.; Uchida, S.; Wang, P. *J. Phys. Chem. C* **2011**, *115*, 14408–14414.

Theoretical study on butylone inclusion complexes with β-cyclodextrin and its three methylated derivatives

Waraitip Laosangprateep, Watanyuta Jantarose, Nat Triamchaisri, and Luckhana Lawtrakul*

School of Bio-Chemical Engineering and Technology, Sirindhorn International Institute of Technology (SIIT), Thammasat University, Pathum Thani 12120, Thailand

**E-mail: Luckhana@siit.tu.ac.th*

Abstract:

Butylone (BTL), or β-keto-N-methylbenzodioxolylbutanamine, is a class of psychoactive substances with a chiral center, so it may exist as two stereoisomers with different biological activities. Molecular docking and PM6 calculation are used to study the enantiomeric recognition of *(R)*- and *(S)*-BTL of β-cyclodextrin (BCD), heptakis(2-O-methyl)-β-cyclodextrin (2MEB), heptakis(2,6-di-O-methyl)-β-cyclodextrin (DIMEB), and heptakis(2,3,6-tri-O-methyl)-β-cyclodextrin (TRIMEB). The results indicate two distinct orientations of butylone within cyclodextrin's cavity, with a 1:1 molecular ratio. According to the complexation energy results, the *(S)*-butylone/BCD system at the M062X/6-31G(d,p) level, Conformation II exhibits a lower complexation energy (-16.52 kcal/mol) compared to Conformation I. This suggests that Conformation II is more favorable.

1. Introduction

Butylone (BTL), also known as β-keto-N-methylbenzodioxolylbutanamine (**Figure 1**), falls under the category of psychoactive substances characterized by a chiral center, which means it can exist in two stereoisomeric forms with distinct biological activities. The separation of these enantiomers is a complex process due to their inherent difficulty in being distinguished from one another. In the case of butylone, both enantiomers (*R* and *S*) are typically pharmacologically active, collectively influencing the drug's effects. Typically, the substance is commercially available as a racemic mixture, containing equal proportions of both enantiomers. However, there's potential for enhancing the drug's efficacy using the pure enantiomeric form.

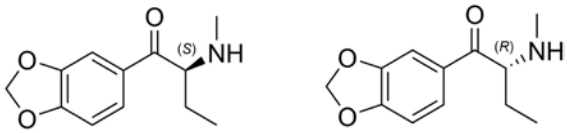

Figure 1. Butylone enantiomer structures.

Cyclodextrins (CDs), cyclic oligosaccharides featuring a central hydrophobic cavity, play a crucial role in this study. CDs are widely employed as chiral selectors due to their diverse cavity sizes, side-chain variations, degree of substitution, and charge. CDs' hydrophobic cavity promotes the replication of inclusion complexes with enantiomers, wherein one enantiomer exhibits a higher binding affinity than the other. The research specifically explores the utilization of β-cyclodextrin (BCD) and its derivatives (**Figure 2**) —namely heptakis(2-O-methyl)-β-cyclodextrin (2MEB), heptakis(2,6-di-O-methyl)- β-cyclodextrin (DIMEB), and heptakis(2,3,6-tri-O-methyl)-β-cyclodextrin (TRIMEB)—for the enantiomeric recognition and separation of *(R)*-BTL and *(S)*-BTL. Molecular docking and PM6 calculations are employed in the study to find the binding affinities and structural aspects of the BTL/CD complexes. The results of this study have the potential to support the research and development of efficient methods for separating the butylone enantiomers.

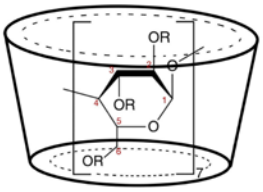

Figure 2. Schematic representation of BCD (R=H) and its methylated derivatives (R= H or CH_3).

2. Materials and Methods

2.1. Molecular structure construction

β-Cyclodextrin (BCD) and butylone (BTL), were obtained from the Cambridge Crystallographic Data Centre with the respective deposition numbers 1107192 [1] and 1504572 [2]. The Discovery Studio was employed to make structural modifications to BCD, involving atom deletion and addition. Additionally, DSC was used to manipulate and reposition both BTL and BCD molecules, facilitating the incorporation of butylone into BCD.

2.2. Molecular docking calculation

Molecular docking computations were performed using AutoDock 4.2.6 [3] software along with the Lamarckian genetic algorithm [4]. These calculations aimed to generate potential conformations of the butylone/BCD complexes and their derivatives. The process began by preparing coordinate files for the host (BCD) and guests (BTL) using AutoDock. Non-polar hydrogens were combined with carbon atoms to determine properties such as the atom types of the guest molecules, hydrogen bond donors and recipients, aliphatic and aromatic carbon atoms, and bonds that rotate. Autogrid was employed to create a three-dimensional grid around the host, which facilitated the calculation of molecular descriptors. These descriptors offered insights into the spatial distribution of properties around the host molecule. Using Autogrid, grid maps were generated for each atom in the docked guest (typically carbon, oxygen, and hydrogen atoms). The systems were examined within a volume partitioned into numerous grid boxes with a 0.375Å spacing of the grid, and the center of the grid was positioned in the center of the host molecules (48Å × 48Å × 48Å for 1:1 host-guest stoichiometry complexes).

Subsequently, each host-guest complex underwent a hundred docking calculations. Following the simulation, the results were analyzed to identify the most favorable binding poses and assess the stability of the inclusion complex. Discovery Studio software was employed for visualizing the docked complexes and analyzing their intermolecular interactions or clusters. The result files recorded energy of binding (ΔG), data of clustering, and coordinates for each docked conformation. Consistent with prior research [5-8] the conformations of docking with the lowest energy were selected for thorough geometry optimization.

2.3. Complexation Energy Calculation

Using the Gaussian molecular modeling program, we conducted full geometry optimization on the 1:1 host-guest stoichiometry inclusion complex structures employing the PM6 calculations. The complexation energy (ΔE) was calculated using Equation (1):

$$\Delta E = E^{opt}_{complex} - (E^{opt}_{host} + E^{opt}_{guest}) \quad (1)$$

This equation quantifies in the optimal geometry the interaction between the host and the guest. In the equation, $E^{opt}_{complex}$ represents the inclusion complex optimized energy between the host and guest, E^{opt}_{guest} is the optimized energy of the BTL molecule, and E^{opt}_{host} is the optimized energy of the host or BCD and its three derivatives. The stability of the inclusion complex is indicated by a lower value of complexation energy.

3. Results & Discussion

Molecular docking is used to determine the possibility of the inclusion complex's conformation by fixing the host molecule and flexing the guest molecule, allowing BTL to move freely inside the host's cavity. The PM6 method was then used to fully optimize all inclusion complexes. As shown in **Figure 3**, the calculations represented two possible inclusion complex configurations in a 1:1 host-guest stoichiometry ratio between BTL enantiomers and BCD and its three methylated derivatives. In Conformation I (**Figure 3(a)**), both benzodioxolyl ring and methylamino group of BTL are located near the wider rim of BCD while its butanone part is located inside the cavity point to the narrow rim of BCD. Whereas in Conformation II (**Figure 3(b)**), the benzodioxolyl ring of BTL is entrapped inside the BCD cavity located near the narrow rim of BCD.

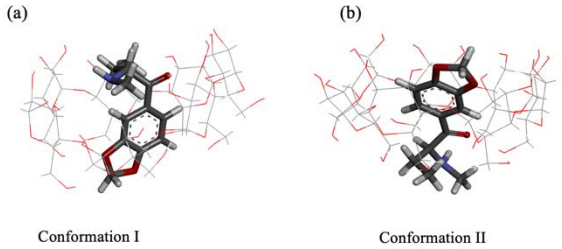

Figure 3. Schematic representations of the conformations of 1:1 inclusion complex (a) Conformation I and (b) Conformation II

Table 1. The free energy of binding (ΔG) of 1:1 inclusion complex and the % frequency of conformations (Conf.) from molecular docking.

Inclusion complex	Conf.	%	ΔG (kcal/mol)	
			Average	Lowest
BCD/*(R)*-BTL	I	97	-4.82	-4.91
	II	3	-4.73	-4.66
BCD/*(S)*-BTL	I	95	-4.98	-4.80
	II	5	-4.43	-4.52
2MEB/*(R)*-BTL	I	74	-5.17	-5.41
	II	26	-5.42	-5.43
2MEB/*(S)*-BTL	I	75	-5.16	-5.26
	II	25	-5.17	-5.42
DIMEB/*(R)*-BTL	I	98	-5.79	-5.47
	II	2	-5.32	-5.27
DIMEB/*(S)*-BTL	I	33	-5.46	-5.65
	II	67	-5.08	-5.76
TRIMEB/*(R)*-BTL	I	100	-6.23	-6.65
TRIMEB/*(S)*-BTL	I	100	-6.53	-6.64

Table 2. The optimized energy (E), complexation energy (ΔE), HOMO and LUMO energies and their gap (Δ|HOMO-LUMO|) of 1:1 inclusion complex calculated by PM6 method. 1 hartree = 627.51 kcal/mol

	Conf.	HOMO (eV)	LUMO (eV)	|HOMO- LUMO| (eV)	E (hartree)	ΔE (kcal/mol)	$\|\Delta E_R-\Delta E_S\|$ (kcal/mol)
BCD		-0.38	0.01	0.39	-2.16		
2MEB		-0.37	0.01	0.37	-2.15		
DIMEB		-0.41	-0.17	0.25	-2.12		
TRIMEB		-0.35	0.03	0.38	-2.07		
(*R*)-BTL		-0.43	-0.16	0.28	0.09		
(*S*)-BTL		-0.43	-0.16	0.28	0.09		
BCD/(*R*)-BTL	I	-0.41	-0.20	0.21	-2.34	-172.57	135.04
	II	**-0.42**	**-0.13**	**0.29**	**-2.39**	**-206.70**	
BCD/(*S*)-BTL	I	-0.32	-0.05	0.27	-2.60	-232.56	
	II	**-0.32**	**-0.03**	**0.29**	**-2.61**	**-341.74**	
2MEB/(*R*)-BTL	I	-0.42	-0.15	0.30	-2.41	-218.50	15.75
	II	**-0.43**	**-0.14**	**0.28**	**-2.44**	**-238.83**	
2MEB/(*S*)-BTL	I	-0.40	-0.11	0.24	-2.41	-218.37	
	II	**-0.42**	**-0.14**	**0.28**	**-2.42**	**-223.08**	
DIMEB/(*R*)-BTL	I	-0.41	-0.13	0.28	-2.34	-203.44	2.45
	II	**-0.41**	**-0.13**	**0.28**	**-2.35**	**-206.89**	
DIMEB/(*S*)-BTL	I	-0.41	-0.12	0.30	-2.34	-202.18	
	II	**-0.41**	**-0.12**	**0.29**	**-2.36**	**-209.34**	
TRIMEB/*(R)*-BTL	**I**	**-0.41**	**-0.12**	**0.29**	**-2.31**	**-208.40**	2.94
TRIMEB/*(S)*-BTL	**I**	**-0.41**	**-0.13**	**0.28**	**-2.31**	**-210.34**	

Note: the bold letters indicate the most favorable inclusion complex.

From molecular docking results, two orientations were found in BCD, 2MEB, and DIMEB inclusion complex with BTL enantiomers, while only the Conformation I was found in TRIMEB/BTL inclusion complex, as presented in **Table 1**.

All inclusion complexes have negative complexation energy (ΔE) values **Table 2**, indicating that their formation is energetically favorable. The Highest Occupied Molecular Orbital (HOMO) is the highest energy molecular orbital with electrons, while the Lowest Unoccupied Molecular Orbital (LUMO) is the next highest energy orbital with no electrons. The energy difference between HOMO and LUMO is represented by (|HOMO-LUMO|) gap with larger values for all inclusion complexes tend to higher the stability as the free host and guest molecules [11]. The energy different of the most favorable inclusion complex of (*R*)- and (*S*)-BTL ($|\mathbf{E}_R-\mathbf{E}_S|$) in each of the CD's system provide the information relate to their ability for chiral recognition as follow: BCD >> 2MEB > TRIMEB, DIMEB.

The lowest complexation energies obtained from PM6 calculations for each of BTL enantiomers with BCD, 2-MEB, and DIMEB are favorable to form in Conformation II (Table 2, bold letters). Whereas the methylated substituted at all three-hydroxyl group of all glucose units in TRIMEB indicated only the Conformation I of inclusion complex is possible for both BTL enantiomers.

BCD itself could distinguish the chirality of (*R*)-BTL or (*S*)-BTL much better than its three methylated derivatives (2MEB, DIMEB, and TRIMEB). Conformation II is the most favorable inclusion complex form of BCD/(*R*)-BTL and BCD/(*S*)-BTL.

According to the complexation energy results for the *(S)*-BTL /BCD system at the M062X/6-31G(d,p) level, Conformation I exhibits a lower complexation energy (-16.52 kcal/mol) compared to Conformation I. This suggests that Conformation II is more favorable.

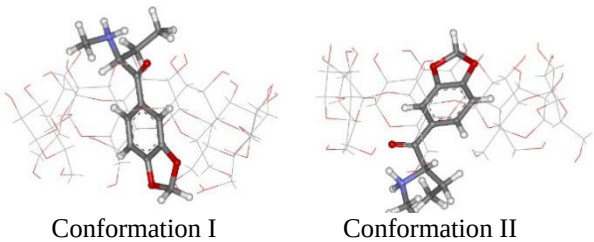

Conformation I Conformation II

Figure 4. The M062X/6-31G(d,p) structure of (*S*)butylone/BCD inclusion complexes.

4. Conclusion

Employing molecular docking and PM6 calculations, we predicted the conformations and interactions of inclusion complexes between BTL enantiomers and various cyclodextrins, including BCD, 2-MEB, DIMEB, and TRIMEB. The computed complexation energies indicating that both (*R*)-BTL and (*S*)-BTL, form the 1:1 energetically comparable inclusion complex with all methylated substituted cyclodextrins. However, the energy differences of the most favorable inclusion complexes in BCD/BTL systems shed light on the chiral recognition ability between (*R*)- and (*S*)-BTL of BCD molecule. This information enhances our understanding of the intricate interaction dynamics and stability of BTL enantiomers within BCD, crucial for the optimization of pharmaceutical formulations.

Acknowledgements

This work was supported by the Thammasat University Research Fund, Contract No. TUFT 84/2566. We are grateful for computational resources supported by NSTDA Supercomputer center (ThaiSC) and the National e-Science Infrastructure Consortium for their support of computing facilities for this work.

References

1. Steiner, T., & Koellner, G. (1994). Crystalline β-Cyclodextrin Hydrate at Various Humidities: Fast, Continuous, and Reversible Dehydration Studied by X-ray Diffraction. *Journal of the American Chemical Society*, 116(12), 5122–5128.
2. Wood, M. R., Bernal, I., & Lalancette, R. A. (2017). The Hydrochloride Hydrates of Pentylone and Dibutylone and the Hydrochloride Salt of Ephylone: The Structures of Three Novel Designer Cathinones. *Structural Chemistry*, 28(5), 1369–1376.
3. Morris, G.M., Huey, R., Lindstrom, W., Sanner, M.F., Belew, R.K., Goodsell, D.S., & Olson, A.J. (2009), AutoDock4 and AutoDockTools4: Automated docking with selective receptor flexibility. *Journal of Computational Chemistry*, 30(16), 2785–2791.
4. Morris, G.M., Goodsell, D.S., Halliday, R.S., Huey, R., Hart, W.E., Belew, R.K., & Olson, A.J. (1998), Automated docking using a Lamarckian genetic algorithm and an empirical binding free energy function. *Journal of Computational Chemistry*, 19(14), 1639–1662.
5. Sueishi, Y., Matsumoto, Y., Sohama, J., Osawa, Y., & Okamoto, H. (2019). Distinctive effects on fluorescence quantum yields of 4-substituted N-methylphthalimides by inclusion complexation with β-cyclodextrins. *Journal of Inclusion Phenomena and Macrocyclic Chemistry*, 93, 275–281.
6. Jitapunkul, K., Toochinda, P., & Lawtrakul, L. (2021). Molecular Dynamic Simulation Analysis on the Inclusion Complexation of Plumbagin with β-Cyclodextrin Derivatives in Aqueous Solution. *Molecules*, 26 (22), art. no. 6784.
7. Chulurks, S., Jitapunkul, K., Katanyutanon, S., Toochinda, P., & Lawtrakul, L. (2021). Stability Enhancement and Skin Permeation Application of Nicotine by Forming Inclusion Complex with β-Cyclodextrin and Methyl-β-Cyclodextrin. *Scientia Pharmaceutica*, 89 (4), art. no. 43.
8. Srihakulung, O., Maezono, R., Toochinda, P., Kongprawechnon, W., Intarapanich, A., & Lawtrakul, L. (2018). Host-Guest Interactions of Plumbagin with β-Cyclodextrin, Dimethyl-β-Cyclodextrin and Hydroxypropyl-β-Cyclodextrin: Semi-Empirical Quantum Mechanical PM6 and PM7 Methods. *Scientia Pharmaceutica*, 86 (2), art. no. 20.
9. Zhao, Y., & Truhlar, D. G. (2008). The M06 Suite of Density Functionals for Main Group Thermochemistry, Thermochemical Kinetics, Noncovalent Interactions, Excited States, and Transition Elements: Two New Functionals and Systematic Testing of Four M06-Class Functionals and 12 Other Functionals. *Theoretical Chemistry Accounts*, 120(1), 215–241.
10. Gaussian 16, Frisch, M. J., Trucks, G. W., Schlegel, H. B., Scuseria, G. E., Robb, M. A., Cheeseman, J. R., Scalmani, G., Barone, V., Petersson, G. A., Nakatsuji, H., Li, X., Caricato, M., Marenich, A. V., Bloino, J., Janesko, B. G., Gomperts, R., Mennucci, B., Hratchian, H. P., Ortiz, J. V., Izmaylov, A. F.,

Sonnenberg, J. L., Williams-Young, D., Ding, F., Lipparini, F., Egidi, F., Goings, J., Peng, B., Petrone, A., Henderson, T., Ranasinghe, D., Zakrzewski, V. G., Gao, J., Rega, N., Zheng, G., Liang, W., Hada, M., Ehara, M., Toyota, K., Fukuda, R., Hasegawa, J., Ishida, M., Nakajima, T., Honda, Y., Kitao, O., Nakai, H., Vreven, T., Throssell, K., Montgomery, J. A., Jr., Peralta, J. E., Ogliaro, F., Bearpark, M. J., Heyd, J. J., Brothers, E. N., Kudin, K. N., Staroverov, V. N., Keith, T. A., Kobayashi, R., Normand, J., Raghavachari, K., Rendell, A. P., Burant, J. C., Iyengar, S. S., Tomasi, J., Cossi, M., Millam, J. M., Klene, M., Adamo, C., Cammi, R., Ochterski, J. W., Martin, R. L., Morokuma, K., Farkas, O., Foresman, J. B., Fox, D. J. Gaussian, Inc., Wallingford CT, 2016.

11. Ding, L. P., Zhang, F. H., Zhu, Y. S., Lu, C., Kuang, X. Y., Lv, J., & Shao, P. (2015). Understanding the Structural Transformation, Stability of Medium-Sized Neutral and Charged Silicon Clusters. *Scientific Reports*, 5, 15951.

Improving hydrophobicity in 3D printing of resin inks with porogen additives and micro-pillar structures

Bantita Chomdee, Natthawut Butphom, Kanoksak Saelee, Supranee Kaewpirom, and Teeranan Nongnual*

Department of Chemistry, Faculty of Science, Burapha University, Chonburi, Thailand 20131

**E-mail: teeranan.no@buu.ac.th*

Abstract:

The study of hydrophobicity is significant for applications such as self-cleaning, anti-fouling, and water-repellency in materials. It has recently gained particular interest for enhancing 3D printed surfaces. Common methods to achieve hydrophobicity include coatings, the use of inherently water-repellent additives, or surface texture modifications. However, coatings often suffer from mechanical instability and limited durability. This study aimed to enhance the resin inks used in stereolithographic LCD 3D printing by introducing specific additives that could interfere with polymerization. Porous agents, or porogens, containing different long-chain alcohols (PP, BT, PT, CH, and DD), were blended into commercial resin inks (AA, AB, AH, and JS) and solidified using a 405-nm curing machine. The results showed that the AB:CH mixture with a ratio of 60:40 significantly increased the water contact angle from 53.5 to 77.3 degrees. The hydrophobic properties were attributed to the nanoscale roughness of inherent pores observed via scanning electron microscopy. This modification likely affected material hardness, reducing the shore D hardness from 87.7 to 63.7. Additionally, an array of micro conical pillars, each 800 µm in height and 150 µm in width, was designed and printed using the developed resin ink with a commercial LCD 3D printer. The capillary pressure from the pillars further improved the material hdrophobicity, achieving a water contact angle higher than 109.9 degrees. These results present a promising strategy for enhancing hydrophobicity in 3D printed materials, potentially benefiting fields such as medicine, automotive, and electronics.

1. Introduction

Additive manufacturing, also known as 3D printing, has remarkable advanced in recent years, enabling the creation of objects with intricate shapes and unique properties.[1] These properties encompass characteristics like hardness, tensile strength, durability, viscoelasticity (how materials deform and return to shape), reactivity, melting point, and conductivity. This technology has revolutionized various industries, from aerospace to healthcare, by providing precise control over complex designs. One notable 3D printing technique is Liquid Crystal Display (LCD) 3D printing, known for its high resolution, which can reach as low as a few to tens microns, allowing for the fabrication of detailed and precise objects.

LCD 3D printing operates on the principle of stereolithography, a widely used 3D printing method. Stereolithography involves the selective curing of liquid resin layer by layer using a light source, usually an ultraviolet (UV) laser or projector. The key feature of LCD 3D printing is its high-resolution display, where an array of liquid crystal pixels, each corresponding to a voxel (a 3D pixel), controls the passage of UV light. This precise control enables the formation of intricate structures with fine details, making it a preferred choice for applications where high-resolution objects are essential.

Hydrophobicity simply refers to a material ability to resist water. This property holds significant value across different fields. For example, in self-cleaning surfaces, materials with hydrophobic properties enable water droplets to roll off effortlessly, preventing dirt and contaminants from adhering. In anti-fouling applications, hydrophobic materials discourage the attachment of microorganisms, making them valuable in marine coatings and medical devices. Additionally, in electronics, hydrophobic surfaces protect sensitive components from moisture-related damage.

Achieving and enhancing hydrophobicity in 3D printed objects presents various challenges with different approaches.[2–5] Common monomers used in LCD 3D printing include acrylates and epoxy resins. When these monomers polymerize, they typically yield cured polymers with hydrophilic properties. Therefore, modifying these materials to become hydrophobic becomes a critical endeavor.

One innovative approach involves the intrinsic construction of materials with inherent hydrophobic properties by introducing special additives known as "porogens" or porous agents.[6,7] Porogens are carefully selected substances added to the 3D printing resin. During the LCD 3D printing process, they create tiny holes or pores within the material structure. Once the 3D object is

complete, these porogens are removed, leaving behind a porous structure that contributes to the material hydrophobicity.

In the context of this research, the primary objective is to enhance the hydrophobicity of 3D printed objects using LCD technology by incorporating specific porogens into the resin ink. This method involves blending porogens with different commercial resin inks. These mixtures are then solidified using a 405-nm curing machine. The research aims to find the best combination of porogens and resin inks that not only improves hydrophobicity but also considers other important properties like material hardness. Furthermore, an additional aspect of this research involves introducing an array of micro pillars to further enhance the hydrophobicity of the inherently porous 3D-printed object. These micro pillars are designed and printed using the developed resin ink with a commercial LCD 3D printer.

By investigating the interaction between porogens, microstructures, and LCD 3D printing materials, this study seeks to provide a comprehensive and innovative approach for achieving superior hydrophobicity in 3D printed objects. This method has the potential to overcome the limitations of traditional coatings while expanding our understanding of material design and manipulation, leading to innovative applications across various industries.

2. Materials and Methods

2.1 Materials. Four commercial resin inks which are popular among 3D modelers and artists were purchased from a local authorized dealer. Those brands - formula include the Anycubic - ABS-Like Resin Plus (**AA**) with ρ = 1.1543 g·cm^{-3}, the Anycubic - Basic Rigid Resin (**AB**) with ρ = 1.1560 g·cm^{-3}, the Anycubic - High Clear Resin (**AH**) with ρ = 1.1276 g·cm^{-3}, and the Jamg He - Standard Plus Resin (**JS**) with ρ = 1.1631 g·cm^{-3}. The reported density was measured by using a 25-mL pycnometer. These resin inks are colorless with common main ingredients of acrylate monomers including phenolic epoxy resin and methylene diacrylate derivatives. A photoinitiator such as photocure 184 and benzoyl phosphine oxide was pre-mixed in the formula, which was made for specific 3D printer with the excitation wavelength of 405 nm.

Solvents used as porous agents including isopropanol (**PP**), 1-butanol (**BT**), pentanol (**PT**), cyclohexanol (**CH**), and 1-dodecanol (**DD**) were purchased from QReC and used as received. Orange 13 or Fast Orange - Disazo Pyrazolone (**O13**) was purchased from Sarkotet, Thailand.

2.2 Polymerization of resin inks with porogens. Contact angle and hardness measurements. The porogens were blended into each commercial resin in a 1-cm typical polystyrene cuvette with a concentration up to 50 %w. 3 mL of the mixture was cured by using a curing machine 3D Resin Wash & Cure Station UW-01 (Creality, China) for 2 minutes with an illumination intensity at 405 nm of about 10 mW/cm^2 measured by using a power and energy meter console PM100D (Thorlabs, USA). The cuvette was rotated during the curing at the speed of about 12 rpm. It was noted that the exposure time and excitation intensity were tuned to reduce the over-heating caused by the exothermic polymerization reaction. After the solidified content was removed from the cuvette, it was washed by using IPA and air dried for an hour. To evaporate the solvent trapped in the material, it was then dried by using a freeze dryer Buchi Lyovapor L-200 (Buchi, Switzerland) at –55 °C for 1.5 hours.

The contact angle was measured by using a drop shape analyzer DSA-30 (Kruss, Germany). The camera Stingray F046B IRF was operated at a camera framerate of 25 frames per second by using the DSA-4 software. A camera angle with a bow of about 5 degrees related to the sample plane was chosen. The contrast and brightness were pre-adjusted to enhance the difference between bright and dark areas. The corresponding contact angle will be determined by using our custom computational scripts written in MATLAB.

The hardness of the material was estimated by using a Shore hardness test gauge LX-D-2 with a test stand LD-J (Shahe, China). This could measure in Shore D zone compatible with a cured polymer in this work. Adding the porogens in resin ink could increase the contact angle caused by the roughness but decrease the hardness.

2.3 FTIR spectroscopy and transparency measurements. FTIR spectra of the resin ink, the porogens, and the cured mixture were acquired on a Frontier Fourier Transform Infrared Spectrometer (PerkinElmer, USA) using a single reflection. ZnSe attenuated total reflection (ATR) in the range of 4000 – 400 cm^{-1} was used for the background and sample measurement.

A thick film with about 0.9 mm thickness was made to analyze its transparency. The UV-Vis spectrum was recorded using a UV-Vis spectrophotometer (Agilent Cary 3500, USA). The transparency was estimated by the absorbance in between 400 – 800 nm. In addition, the image of

selected materials was taken by a typical smartphone to compare the transparent visibility.

2.4 Polymerization process. The kinetics was studied by estimating the weight of solidified content with different exposure time. Curing was performed by using an LCD 3D printer Photon Mono M5s (Anycubic, China) with the excitation intensity at 405 nm of 1.8 mW·cm^{-2}. The resin ink was filled in a vat that was masked by a UV shield cloth with a 35-mm hole for curing zone. The presence of porogen could have a minor effect on the curing while the photoblocker O13 could significantly decrease the polymerization rate.

2.5 Graphic design and 3D printing of micro pillars. To enhance the hydrophobicity of printed object, an array of micro pillars with the dimension of 800 µm in height and 150 µm in width, was printed. The printing resolution was adjusted at the maximum of 10 µm in z-axis and 19×24 µm^2 pixel size.

3. Results & Discussion

3.1 Wettability and hardness measurements. The contact angle measurements were used to scan the optimum ratio of various porogens in the commercial resin inks as shown in **Figure 1**. The results showed that adding an amount of alcohol porogen could increase the contact angle of resin ink by about 30 degrees. It was found that the ink with porogen of AA:PT (60:40), AB:CH (60:40), and JS:CH (80:20) significantly improved the hydrophobicity compared to the pristine ink. It might be caused by the high solubility of the alcohols in the monomer solution. These porogens will evaporate by the heat from exothermic polymerization reaction.

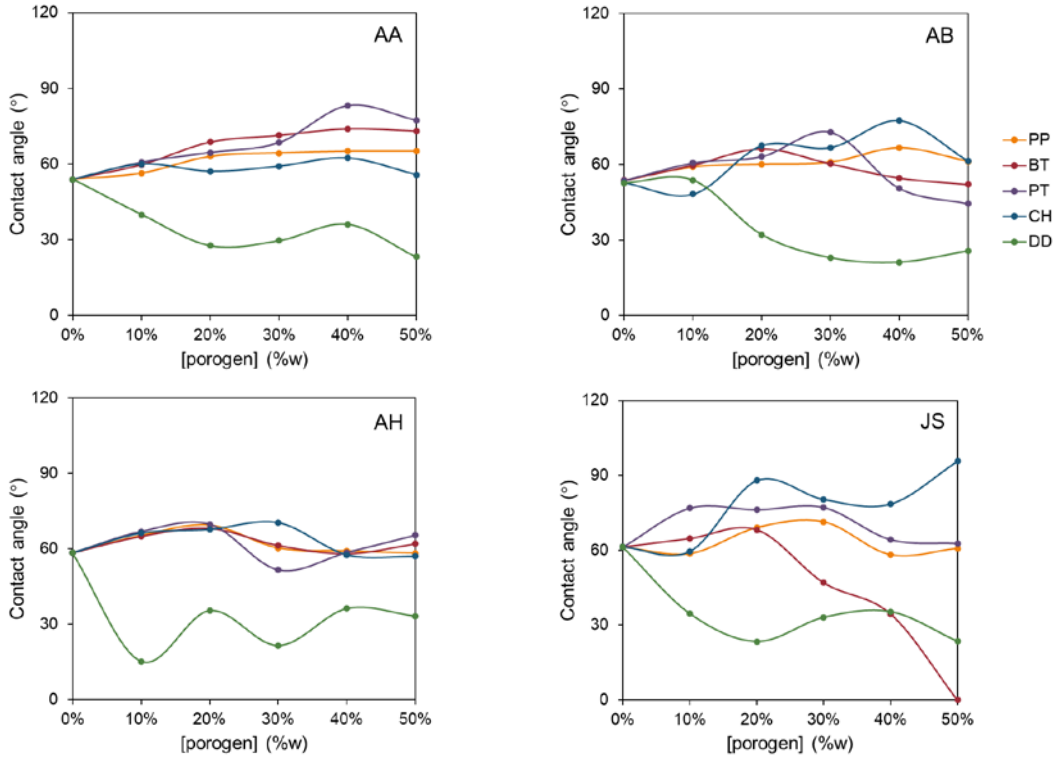

Figure 1. The contact angle of cured commercial resin inks mixed with different porous agents or porogens at the concentrations up to 50 %w.

Table 1. Hydrophobicity of cured commercial resin inks mixed with different porogens presents in contact angle (CA) and sliding angle (SA). The hardness is reported in Shore D.

Resin ink : Porogen	%w/w	Air dried			Freeze dried		
		CA (°)	SA (°)	Shore D	CA (°)	SA (°)	Shore D
AA	100	56.6 (1.7)	28.7 (7.7)	89.0 (2.6)	76.3 (5.2)	21.7 (0.9)	89.0 (1.0)
AA:PT	60:40	83.2 (4.7)	24.6 (8.7)	60.5 (1.3)	59.0 (0.3)	20.7 (0.6)	42.3 (0.6)
AB	100	53.5 (0.6)	26.3 (5.2)	87.7 (1.0)	65.6 (4.1)	22.4 (1.0)	89.2 (1.0)
AB:CH	60:40	77.3 (3.4)	29.6 (2.5)	63.7 (0.6)	72.7 (2.1)	18.3 (0.1)	59.0 (1.0)
JS	100	62.3 (1.1)	27.7 (9.0)	82.2 (1.2)	80.7 (1.9)	- [a]	83.0 (1.0)
JS:CH	80:20	87.9 (3.4)	30.1 (2.0)	55.3 (3.5)	80.7 (1.3)	23.4 (3.5)	54.7 (0.6)

[a] SA was not applicable due to strong adherence to the surface.

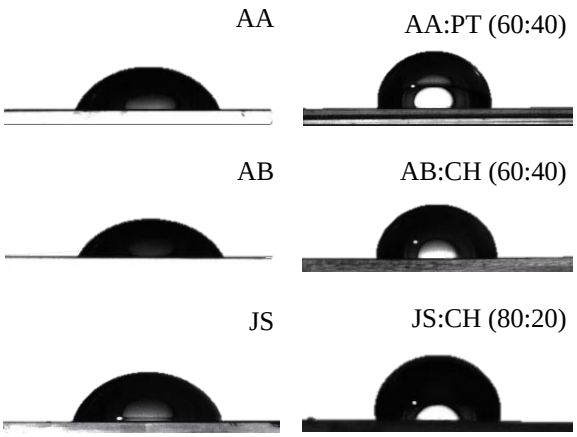

Figure 2. Drop shape image of pristine cured resin inks and their mixture with porogens.

The hydrophobicity and hardness of selected pristine resin inks and their combination with porogens were presented in **Table 1**. The corresponding drop shape images are shown in **Figure 2**. The result showed that the contact angle of air dried solid was improved after adding the porogens by about 20 degrees. Surface roughness and micro pores might be generated during curing process resulting consequent hydrophobic surface. To further improve the hydrophobicity, the cured polymer was freeze dried at –55 °C for 1.5 hours. This resulted in the improvement of water repellency, which was showed in the decreasing of sliding angle to as low as 18.3 degrees of AB:CH (60:40).

Adding porogen to resin ink has been known to create porous structure in materials, thus lowering the solid hardness. The results showed that the shore D hardness was slightly decreased after adding 40% of porogens into resin inks, AA and AB. Whereas the hardness of JS:CH (80:20) was significantly lower than pristine JS. This might be caused by the larger amount of porous structure was created by the higher exothermic reaction. The porogen was quickly released from the material driven by the heat. This should be noted that although the higher emitting heat could create larger amounts of porous structures, it might be causing a problem to the screen of LCD 3D printer.

3.2 Characterization and transparency of cured resin ink with porogen. The FTIR spectrum of cured resin ink before and after adding porogen is shown in **Figure 3**. The cured resins show a wide band aromatic protons of the epoxy resin at 3500 and 2925 cm^{-1}. The band at 1725 cm^{-1} is assigned to the vibrations of the aldehyde groups of diacrylates. Meanwhile, the porogens show a wide band of O-H bond at 3300 cm^{-1} and C-H at 2900

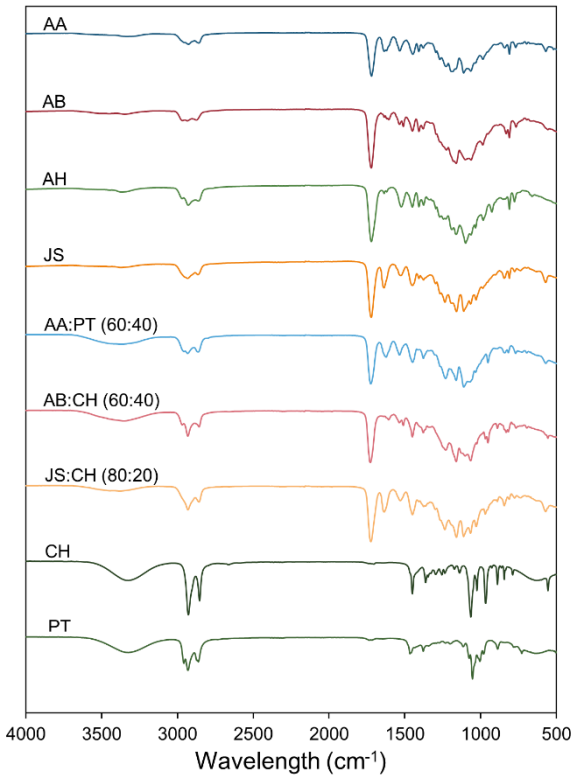

Figure 3. FTIR spectrum of cured pristine commercial resin inks, liquid porogens, and solidified mixtures.

(a)

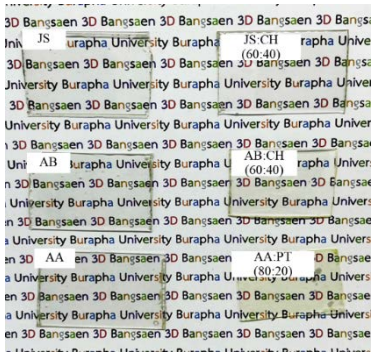

(b)

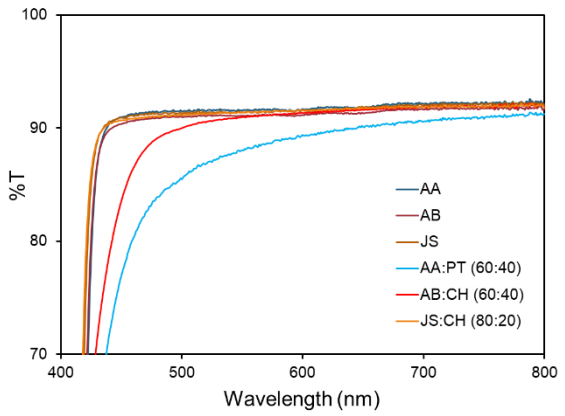

Figure 4. (a) Image of cured resin inks and the mixture with porogens corresponding to (b) their transmittance spectrum.

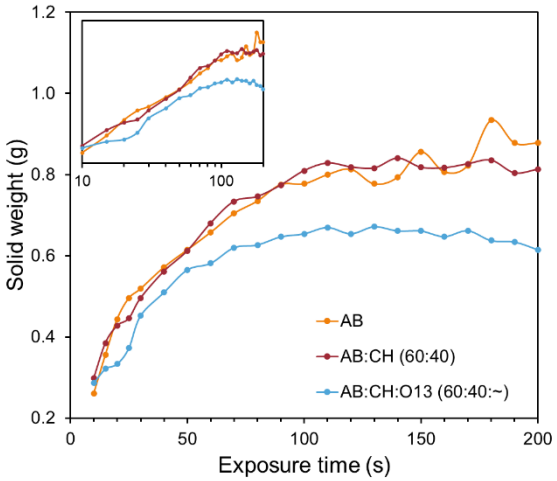

Figure 5. Weight of solidified content against exposure time of resin ink AB, with porogen CH, and with O13 photoblocker. The inset shows the *x* axis in logarithmic scale.

and 1400 cm^{-1}. The spectrum of the blended solution is exactly the combination of resin ink and its porogen, thus no chemical reaction occurred from the mixing. In addition, there was a small amount of porogen trapped in the material.

The transparency and transmittance of the material are shown in **Figure 4 (a-b)**. All solids seem highly transparent but the AA:PT (60:40) and AB:CH (60:40) are slightly yellowish. This agrees well with the transmittance spectrum showing that there was noticeably unchanged at remaining 90 %T from 420 – 800 nm. The slight decrease of those two mixtures likely caused the yellowish in materials. These results suggested that the cured solid in this work is more transparent than previous studies, thus our formulate could be a competing alternate.

3.3 Polymerization kinetics of resin ink. The weight of solidified content against exposure time is shown in **Figure 5**. The results showed that the initial rate of pristine AB and porogen-added AB:CH (60:40) yielded fast polymerization of 13.1 and 9.1 $mg{\cdot}s^{-1}$, respectively. According to the polymerization area of 35 mm and excitation flux of 1.8 $mW{\cdot}cm^{-2}$, the polymerization rates could be expressed by the polymerization conversion at 0.76 and 0.53 $g{\cdot}J^{-1}$, respectively. By adding photoblocker O13 to increase 3D printing resolution, the initial conversion was decreased to 0.45 $g{\cdot}J^{-1}$. After the exposure of about 100 s, the material thickness played an important role shielding the illumination, resulting in a flat profile. In addition, the photoblocker in AB:CH:O13 (60:40:~) could efficiently absorb the excitation wavelength thus decreasing the maximum thickness by about 25% compared to pristine ink. These results showed that the porogen did not interfere with the kinetics, while the dye could reduce the solid thickness enhancing printing resolution.

Figure 6. Drop shape image of the cured porogen-added resin ink AB:CH (60:40) with modified surface roughness of 3D-printed micro pillars.

3.4 Micro pillar array printed on surface. An array of micro-scale pillars was designed and printed on the surface of AB:CH (60:40). A capillary pressure between the pillars could reduce the adhesion of water thus increasing the water contact angle as shown in **Figure 6**. The hydrophobicity was significantly increased with a contact angle of 109.9 degrees. The combination of porogen addition and precisely printed micro pillar array could be a simple approach that enhances the hydrophobicity of 3D printed materials.

4. Conclusion

The enhancement of hydrophobic properties in 3D printed resin structures through the incorporation of porogen additives and the implementation of micro-pillar arrays was studied. Our findings demonstrate a significant improvement in the water contact angle, a key indicator of hydrophobicity. A resin ink AB, initially exhibiting a contact angle of 53.5 degrees, showed a marked increase to 77.3 degrees with the addition of porogen at a ratio of AB:CH (60:40). The integration of micro-pillar arrays further amplified this effect, elevating the contact angle to 109.9 degrees. Our research not only highlights the potential of porogens and micro-structures in manipulating surface properties but also opens new avenues for application-specific optimizations in 3D printing technologies for diverse industrial applications.

Acknowledgements

The authors gratefully acknowledged the use of services, facilities, and research grants from the Department of Chemistry, Faculty of Science, Burapha University. This research was supported by a basic/fundamental research fund from the Thailand Science Research and Innovation (Grant number 2472757/2022 and 4367233/2023).

References

1. Ligon, S. C.; Liska, R.; Stampfl, J.; Gurr, M.; Mülhaupt, R. Polymers for 3D Printing and Customized Additive Manufacturing. *Chem Rev* **2017**, *117* (15), 10212–10290.
2. Liu, H.; Zhang, Z.; Wu, C.; Su, K.; Kan, X. Biomimetic Superhydrophobic Materials through 3D Printing: Progress and Challenges. *Micromachines (Basel)* **2023**, *14* (6).
3. Li, X.; Yu, J.; Hu, D.; Li, Q.; Chen, X. Freezing of Nanofluid Droplets on Superhydrophobic Surfaces. *Langmuir* **2020**, *36* (43), 13034–13040.
4. Kaur, G.; Marmur, A.; Magdassi, S. Fabrication of Superhydrophobic 3D Objects by Digital Light Processing. *Addit Manuf* **2020**, *36* (October), 101669.
5. Barraza, B.; Olate-Moya, F.; Montecinos, G.; Ortega, J. H.; Rosenkranz, A.; Tamburrino, A.; Palza, H. Superhydrophobic SLA 3D Printed Materials Modified with Nanoparticles Biomimicking the Hierarchical Structure of a Rice Leaf. *Sci Technol Adv Mater* **2022**, *23* (1), 300–321.
6. Dong, Z.; Cui, H.; Zhang, H.; Wang, F.; Zhan, X.; Mayer, F.; Nestler, B.; Wegener, M.; Levkin, P. A. 3D Printing of Inherently Nanoporous Polymers via Polymerization-Induced Phase Separation. *Nat Commun* **2021**, *12* (1), 1–12.
7. Dong, Z.; Vuckovac, M.; Cui, W.; Zhou, Q.; Ras, R. H. A.; Levkin, P. A. 3D Printing of Superhydrophobic Objects with Bulk Nanostructure. *Advanced Materials* **2021**, *33* (45).

Incorporating organic pigments as photoblockers in commercial resin inks to improve micro-scale resolution in 3D printing

Sudarat Dokmaihom, Chonthicha Chotsanthia, Pagapon Phooka, Natthawut Butphom, Kanoksak Saelee, and Teeranan Nongnual*

Department of Chemistry, Faculty of Science, Burapha University, Chonburi, Thailand 20131

**E-mail address: teeranan.no@buu.ac.th*

Abstract

In recent years, 3D printing has undergone rapid development, enabling the creation of objects ranging from microscale components to large-scale structures. LCD 3D printing, a popular and inexpensive method, employs an LCD screen to project an illumination pattern that solidifies liquid resin into 3D objects. However, this process often encounters challenges like shrinkage, warping, and limited resolution, potentially leading to defects in the final product. This study investigated the polymerization kinetics of four commercial colorless resin inks (AA, AB, AH, and JS). The polymerization reaction was initiated using a blueish 405-nm excitation wavelength with a mind illumination intensity of 6.2 mW/cm² generated by a curing machine. Among the tested resins, JS exhibited the highest polymerization depth rate at 63.32 µm/s. This research then explored the effect of eleven commercial pigments as a photoblocker or an excitation absorber on polymerization depth rate and printing resolution. The addition of 0.01% w/v orange O13 coloring agent to JS significantly reduced the polymerization rate by a factor of three. This could improve lateral resolution to 15.3 µm in a 12K-LCD 3D printer, while maintaining a high-speed printing rate of under 2.5 seconds per layer. These findings suggest the feasibility of developing new resin inks tailored for LCD 3D printing, capable of achieving high-resolution results. Such advancements have the potential to drive the creation of innovative commercial products requiring exceptional precision.

1. Introduction

In additive layer manufacturing known as 3D printing techniques, LCD 3D printing, a derivative of Stereolithography Apparatus (SLA) technology, has significantly improved the production of structures ranging from intricate micro-architectures to large macroscopic entities. This method, achieving resolutions in the range of 25-100 microns, uses an LCD screen to precisely control UV light exposure, starting the polymerization of resin inks layer by layer.[1–4] These inks usually consist of a formulation that includes acrylates like Methyl Methacrylate (MMA) and Ethyl Methacrylate (EMA), chosen for their fast polymerization characteristics, as well as epoxy species such as Bisphenol A epoxy resin and Novolac epoxy resin, which are added for their durability and thermal resistance.[5,6] Despite the advancements in resolution, LCD printing faces the ongoing issue of light leakage or 'photo leaking,' especially when using clear or colorless resin inks, leading to accidental over-curing and thus affecting the intended resolution.

To address this challenge, the use of photoblockers has been recognized as an effective strategy, for example, Sudan Orange G, Benetex OB+, Avo D, Sudan I, and Sudan IV.[7,8] These compounds, skilled at absorbing or blocking stray excitation light emitted by the 3D printer, successfully reduce the occurrence of over-polymerization within the resin vat. By finely adjusting the light penetration, photoblockers significantly improve the resolution of LCD 3D printing, resulting in better detail and clarity of the printed objects, which is essential for applications that rely on precision.[9]

This study performs a thorough analysis of the polymerization kinetics of four commercially available colorless resin inks under a controlled 405-nm excitation wavelength. It also explores the impact of eleven commercial pigments as photoblockers, evaluating their effect on the polymerization depth rate and the resulting printing resolution. The research aims to carefully determine the ideal balance between enhancing resolution and maintaining printing efficiency, thereby guiding the creation of new resin formulations specifically made for LCD 3D printing. The results indicate a hopeful direction towards achieving higher resolution, signaling the potential for producing innovative commercial products that require exceptional precision. This investigation not only reveals the potential of photoblockers in improving LCD printing capabilities but also adds to the broad understanding of additive manufacturing processes and materials.

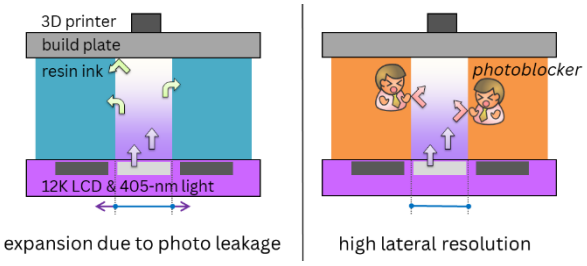

Figure 1. Schematic illustration of the resin ink polymerization by using an LCD 3D printer during the UV excitation without (left) and with (right) the photoblocker.

2. Materials and Methods

2.1 Materials. Four commercial resin inks which are popular among 3D modelers and artists were purchased from a local authorized dealer. Those brands - formula include the Anycubic - ABS-Like Resin Plus (**AA**), the Anycubic - Basic Rigid Resin (**AB**), the Anycubic - High Clear Resin (**AH**), and the Jamg He - Standard Plus Resin (**JS**). These resin inks are colorless with common main ingredients of acrylate monomers including phenolic epoxy resin and methylene diacrylate derivatives. A photoinitiator such as photocure 184 and benzoyl phosphine oxide was pre-mixed in the formula, which was made for specific 3D printer with the excitation wavelength of 405 nm.

The organic dyes, inorganic powders, and blended pearly powders were purchased from Sarkotet, Thailand. Different commercial coloring agents with their abbreviations and some known chemical compounds stated elsewhere including Blue 15.0 - Phthalocyanine (**B15**), Green G7 or Fast Green G-Y - Phthalocyanine (**G7**), Yellow 12 or Fast Yellow GK - Benzidine (**Y12**), Orange 13 or Fast Orange - Disazo Pyrazolone (**O13**), Red FGR or Red 112 - Naphthol Azo (**R112**), Iron Oxide Red 130 - Fe_2O_3 (**IR130**), Zinc Oxide (**ZnO**), Titanium dioxide (**TiO_2**), Gold KW-300 (**GLD**), Silver KW-100 (**SLV**), and Bronze 7000 (**BRZ**) were used as a photoblocker. Solvents cyclohexanol (Sigma-Aldrich) and iso-propyl alcohol (QReC) were used as received.

2.2 Polymerization Kinetics. A volume of 3 mL of each resin ink was added to a typical polystyrene cuvette with the size of 1×1×4 cm^3. The monomer was solidified by using a curing machine 3D Resin Wash & Cure Station UW-01 (Creality, China) with an illumination intensity at 405 nm of about 6.2 mW/cm^2 measured by using a power and energy meter console PM100D (Thorlabs, USA). The cuvette was rotated during the curing at the speed of about 12 rpm. The illumination time varied from 30 to 800 seconds and the non-polymerized liquid resin was then rinsed off. These resulted in different partial polymerizations; thus, polymerization kinetics was discussed in the weight percent of total solidified content or solid content against the original liquid resin ink.

2.3 UV-Vis and FTIR Spectroscopy. An amount of each photoblockers was dissolved in cyclohexanol with the concentration of 0.003 - 0.050 %w/v. The UV-Vis spectrum was recorded using a UV-Vis spectrophotometer (Agilent Cary 3500, USA). The mass absorption coefficient in $L \cdot g^{-1} \cdot cm^{-1}$ was calculated by the Beer's law, $\varepsilon_m = A / bc$, where A is the absorbance, b is path length in cm, and c is the concentration in $g \cdot L^{-1}$. The mass absorption coefficient in the UV zone (ε_m^*) was also calculated from the average absorbance in between 380 – 430 nm to discuss the absorption efficiency of the 405-nm excitation.

FTIR spectra of the resin ink with the fastest polymerization kinetics and a superior photoblocker were acquired on a Frontier Fourier Transform Infrared Spectrometer (PerkinElmer, USA) using a single reflection. ZnSe attenuated total reflection (ATR) in the range of 4000 – 400 cm^{-1} was used for the background and sample measurement.

2.4 Photoblock Efficiency. The photoblocker was added to the resin ink JS at the concentration of 0.01 – 0.05 %w/v to investigate the photoblock efficiency. The experiments are similar to the kinetics with some modifications. The cuvette containing 3 mL of the solution was illuminated for 180 s only on one side. The solid thickness was then calculated by the solid content with the maximum of 1 cm of the cuvette width.

2.5 3D Printing Resolution. To estimate the printing resolution of the colored resin ink, 3D models were designed by computer graphic software, Blender. A rectangular prism of 1×1×0.5 cm^3 was cut through by a group of isosceles triangles with the vertex angle of 30 degrees and the height of 2 mm. Whereas, a sharp cone with the apex angle of 30 degrees was constructed on the side of another rectangular prism. These models were printed by using an LCD 3D printer Photon Mono M5s (Anycubic, China) with the smallest z-axis accuracy of 10 µm and the excitation intensity at 405 nm of 1.8 mW/cm^2. The printed models were imaged by using a scanning electron microscope LEO1450VP (Carl Zeiss AG, Germany). The length, area, and angle were analyzed by using ImageJ software.

In addition, a rectangular prism of 0.1×5×1 cm^3 was printed with the same setups. The thickness was then measured by using a

micrometer to analyze the expansion of the resin ink with and without the photoblocker. The effective photoblocker could adsorb the excitation leakage to adjacent pixels, thus reducing the solid expansion due to over-polymerization.

3. Results & Discussion

3.1 Polymerization Kinetics of Commercial Resin Inks. The commercial resin inks contain different species and amounts of acrylate and epoxy monomers depending on each specific formulate. A monomer with shorter chain could polymerize at a faster rate but the exothermic reaction could cause a problem with the printer. **Figure 2** showed the solid content of the resin inks in a 1-cm cuvette under a strong UV excitation which clearly demonstrates the polymerization kinetics. It was found that the JS resin ink yielded the fastest polymerization rate with a slope at 0 – 150 second of 0.63 % solid content per second. This refers to the polymerization depth rate of the JS 63.32 µm/s which equals to the polymerization depth rate per excitation flux at 10.2 mm·$(J/cm^2)^{-1}$.

Among the four commercial resin inks, the polymerization reaction of the JS was completed in only 180 seconds which is 2 – 3 times faster than others. In addition, this could be noted that the JS released the largest amount of heat during the polymerization, thus the apparatus must be air vented during printing to decrease the temperature and protect the screen. Owing to the outstanding polymerization rate, the JS resin ink was selected to study the effect of the kinetics and the 3D printing resolution by adding different colors.

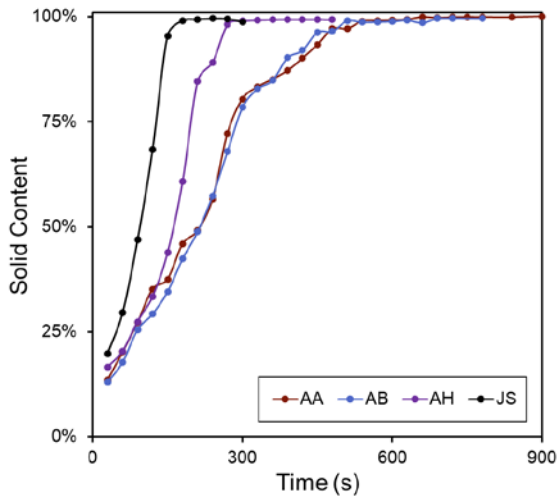

Figure 2. Polymerization kinetics of commercial resin inks presenting in total solidified content against excitation exposure time. This was performed by using a curing machine with an illumination intensity of 6.2 mW/cm^2.

3.2 UV-Vis Spectroscopy and Fourier Transform Infrared (FTIR) Spectroscopy. The relative UV-Vis spectrum of coloring agents divided by their concentration are shown in **Figure 3(a)** in the logarithmic scale. The absorbance peaks were built up by multiple functional groups in each dye yielding different present colors. According to the wavelength of the 3D printer excitation at 405 nm, the A/c graph was considered in the range of 380 – 430 nm as highlighted in blue color. The O13 and TiO_2 provided the highest absorbance in this zone, thus suitable for mixing in the JS as an effective photoblocker.

The FTIR spectrum of the JS ink, O13 dye, and their mixture are shown in **Figure 3(b)**. The organic dye showed the C=O stretching at 1650 cm cm^{-1}, conjugated C=C stretching at 1550-1500 cm^{-1}, and C-N stretching at 1150 cm^{-1}. Meanwhile the cured JS shows a wide band aromatic protons of the epoxy resin at 3500 and 2925 cm^{-1}. The band

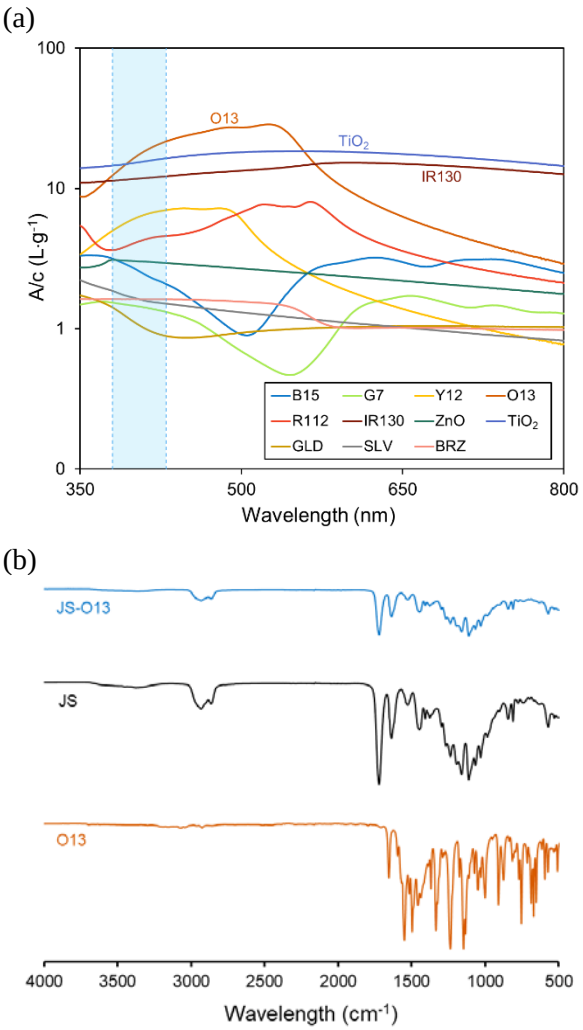

Figure 3. (a) UV-Vis spectrum of coloring agents relative to their concentration. (b) FTIR spectrum of JS resin ink, O13 organic pigment, and the mixture.

Table 1. The λ_{max} of commercial coloring agents with the mass absorption coefficient.

Coloring agent	Code	Group	λ_{max} (nm)	ε_m	ε_m*
Blue 15.0	B15	Organic dye	360	3.57	2.83
Green G7	G7	Organic dye	658	1.56	1.08
Yellow 12	Y12	Organic dye	444	7.60	6.54
Orange 13	O13	Organic dye	522	26.79	16.45
Red FGR (112)	R112	Organic dye	563	7.32	3.63
Iron Oxide Red 130	IR130	Inorganic powder	602	9.59	7.40
Zinc oxide	ZnO	Inorganic powder	380	3.10	3.00
Titanium dioxide	TiO_2	Inorganic powder	372	12.75	12.04
Gold KW-300	GLD	Pearly powder	350[a]	1.68	0.91
Silver KW-100	SLV	Pearly powder	350[a]	2.13	1.17
Bronze 7000	BRZ	Pearly powder	350[a]	1.61	1.26

The mass absorption coefficients in the units of $L \cdot g^{-1} \cdot cm^{-1}$; ε_m and ε_m* were calculated from the absorbance at the λ_{max} and the average absorbance in between 380 – 430 nm, respectively. [a]The pearly powders contain large particle polymers scattering the entire wavelength resulting in a broad spectrum.

at 1725 cm^{-1} is assigned to the vibrations of the aldehyde groups of diacrylates. In addition, there was no difference in the resin spectrum after mixing with a small amount of the dye.

To block the wavelength at 405 nm, the near-IR emission colors such as yellow, orange, and red were predicted to efficiently absorb the UV excitation. The λ_{max} and mass absorption coefficient of the commercial coloring agents is shown in **Table 1**. The O13 with the λ_{max} at 522 nm yielded the outstanding ε_m of 26.79 $L \cdot g^{-1} \cdot cm^{-1}$. The TiO_2, IR130, Y12, and R112 could be alternatives with about 3 folds lower than O13. Furthermore, the ε_m* was calculated from the average absorbance in 380 – 430 nm to evaluate the absorption efficiency of the UV light. It was found that the O13 and TiO_2 remained effective to absorb UV light with the ε_m* of 16.45 and 12.04 $L \cdot g^{-1} \cdot cm^{-1}$, respectively. The results suggested that O13 and TiO_2 could be a promising photoblocker which could increase the 3D printing resolution.

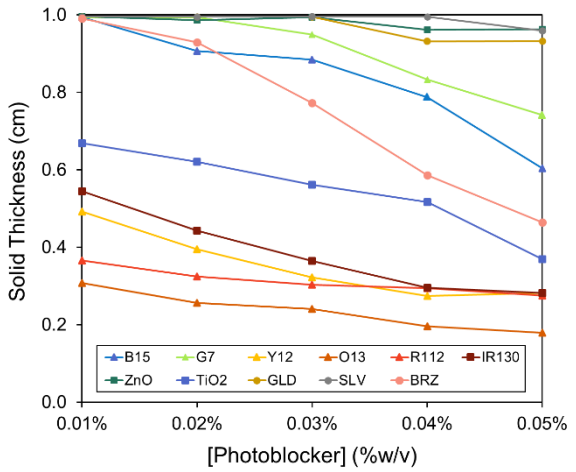

Figure 4. The photoblocker concentration in the JS resin ink against the thickness of solidified content that cured in a typical polystyrene cuvette.

3.3 Coloring Agents as a Photoblocker. The effect of photoblocker on the polymerization of the JS was studied by estimating the thickness of solidified contents as shown in **Figure 4**. The results shown that O13, R112, Y12, IR130, and TiO_2 lowered the polymerization by 2 – 5 times compared to the pristine ink, which agreed well with the ε_m* described above. In addition, the JS with O13 of 0.01 %w/v was solidified by the curing machine resulting in a solid content of 0.3 cm thick.

According to the polymerization depth rate per excitation flux of the JS and the illumination intensity of the 3D printer, a fast speed printing at 2.5 seconds per layer could solidify the JS-O13 resin at 10.2 $mm \cdot (J/cm^2)^{-1} \times 1.8\ mW/cm^2 \times 2.5\ s \times (1/3) = 15.3\ \mu m$/layer. This could advise that, at this printing speed, the *z*-axis step should be at the smallest *z* resolution unless the ink will not be cured at the build plate. The results suggested that the photoblocker could suppress the photo leakage during the printing process resulting in higher *xy* resolution, but the *z*-axis step should be taken into account.

3.4 3D Printing and Lateral Resolution.

3D graphical models of isosceles triangular holes and conical pillars were designed and printed with the JS ink and selected photoblockers. The SEM images are shown in **Figure 5**. The triangle holes of JS appeared to be less shaper in all apex angles compared to those with the photoblockers. Meanwhile, its conical pillar seemed to be larger than others. This might be caused by the photo leakage during the printing process; thus, making the cured JS pristine broader in lateral coordinates. In addition, adding TiO_2 micro particle to the ink significantly increased the roughness of the material, which might be causing the brittleness. The precise length, angle, and area

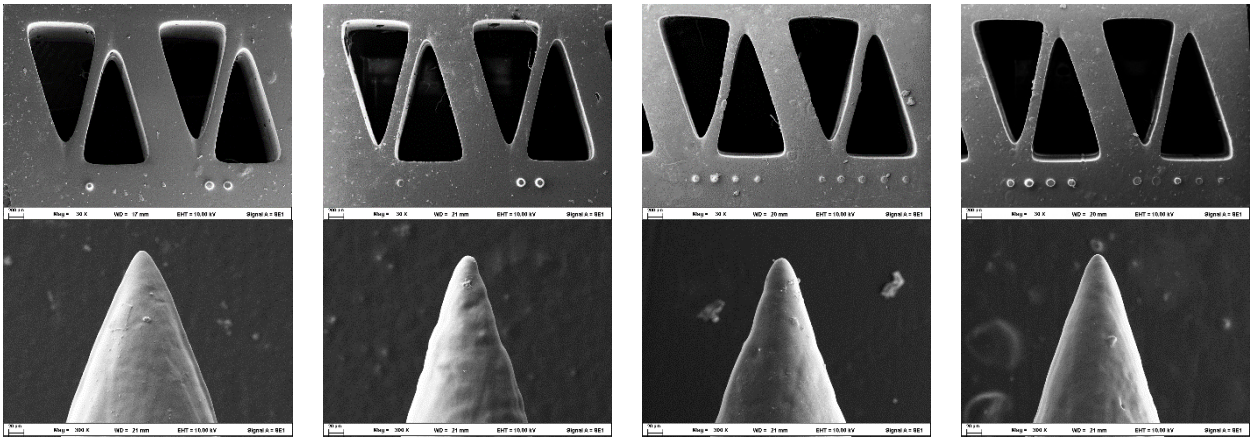

JS JS-O13 JS-TiO_2 JS-O13-TiO_2

Figure 5. SEM images of the 3D-printed isosceles triangular holes and conical pillars from the JS resin inks mixed with the photoblockers, O13 and TiO_2.

Table 2. Geometrical analysis of 3D-printed microscale isosceles triangular holes and conical pillars, and millimeter-scale rectangular prism.

Resin ink (-Photoblockers)	Printed triangle[a]		Apex angle of cone (°)[b]	Lateral expansion (μm)[c]	
	Relative area	Smallest gap (μm)		2.5 s	5 s
JS	0.691 (0.108)	180.5 (18.5)	+5.14 (0.64)	+34 (37)	+162 (72)
JS-O13	0.759 (0.088)	155.2 (21.5)	+3.53 (0.71)	+8 (20)	+119 (56)
JS-TiO_2	0.954 (0.044)	131.0 (28.1)	+3.96 (0.85)	+29 (29)	+120 (59)
JS-O13-TiO_2	0.845 (0.106)	132.4 (25.7)	+3.04 (0.77)	-7 (22)	+111 (77)

The mean (S.D.) is calculated from [a]40, [b]10, and [c]10 measurements.

of these shapes were then measured by using ImageJ software to discuss in lateral resolution.

The geometrical measurements of the 3D-printed JS ink with photoblockers are shown in **Table 2**. The estimated relative area of the hole made by the ink with photoblockers was closer to the original design than the pristine ink, especially the JS-TiO_2 with the value of 0.954. Their smallest gap at the vertex was also shorter by about 50 μm thus the phoblocker-added ink is likely suitable for printing a 3D model with sharp vacancies.

The conical pillars were printed with the original apex angle of 30°. The expansion was observed in the pristine JS ink due to the photo leakage yielding an average apex angle of +5.14°. The photoblocker lowered the expansion of the cone resulting in a 2° sharper than the naked JS. These results suggested that the photoblocker could effectively enhance the lateral resolution in 3D printing of microscale model.

A one-millimeter rectangular prism was printed with two different exposure times. Longer illumination time obviously increased the lateral expansion. With shorter and proper exposure time, the 3D printing of JS-O13 and JS-O13-TiO_2 inks suppressed the lateral expansion to only +8 and -7 μm, respectively. This also confirmed the improved printing lateral resolution of the resin ink by adding an effective photoblocker.

4. Conclusion

The polymerization kinetic rate of commercial resin inks was determined by the total solidified content after curing. The JS ink yielded the fastest polymerization depth rate at 10.2 $mm \cdot (J/cm^2)^{-1}$ likely due to its reactive short monomer constituents. Coloring agent was added into the ink to improve the printing resolution. O13 and TiO_2 could strongly absorb the UV light with ε_m* of 16.45 and 12.04 $L \cdot g^{-1} \cdot cm^{-1}$, respectively, blocking the photo leakage to adjacent pixels during 3D printing. This enhanced the printing resolution of micron-scale isosceles triangular holes and conical pillars with the open gap of about 130 μm and the apex angle deviated by +3 degrees. The lateral expansion was also decreased by a factor of five compared to the pristine ink. Thus, the photoblocker-added resin ink could increase the sharpness of the LCD 3D printing, suitable for micro-resolution materials.

Acknowledgements

The authors gratefully acknowledged the use of services, facilities, and research grants from the Department of Chemistry, Faculty of Science, Burapha University. This research was supported by a basic/fundamental research fund from the Thailand Science Research and Innovation (Grant number 2472757/2022 and 4367233/2023).

References

1. de Beer, M. P.; van der Laan, H. L.; Cole, M. A.; Whelan, R. J.; Burns, M. A.; Scott, T. F. Rapid, Continuous Additive Manufacturing by Volumetric Polymerization Inhibition Patterning. *Sci Adv* **2019**, *5* (1).
2. Zhu, G.; Hou, Y.; Xiang, J.; Xu, J.; Zhao, N. Digital Light Processing 3D Printing of Healable and Recyclable Polymers with Tailorable Mechanical Properties. *ACS Appl Mater Interfaces* **2021**, *13* (29), 34954–34961.
3. Kowsari, K.; Akbari, S.; Wang, D.; Fang, N. X.; Ge, Q. High-Efficiency High-Resolution Multimaterial Fabrication for Digital Light Processing-Based Three-Dimensional Printing. *3D Print Addit Manuf* **2018**, *5* (3), 185–193.
4. Mauriello, J.; Maury, R.; Guillaneuf, Y.; Gigmes, D. 3D/4D Printing of Polyurethanes by Vat Photopolymerization. *Adv Mater Technol* **2023**, *8* (23).
5. Bagheri, A.; Jin, J. Photopolymerization in 3D Printing. *ACS Appl Polym Mater* **2019**, *1* (4), 593–611.
6. Xu, W.; Jambhulkar, S.; Zhu, Y.; Ravichandran, D.; Kakarla, M.; Vernon, B.; Lott, D. G.; Cornella, J. L.; Shefi, O.; Miquelard-Garnier, G.; Yang, Y.; Song, K. 3D Printing for Polymer/Particle-Based Processing: A Review. *Compos B Eng* **2021**, *223*, 109102.
7. Shahzadi, L.; Maya, F.; Breadmore, M. C.; Thickett, S. C. Functional Materials for DLP-SLA 3D Printing Using Thiol-Acrylate Chemistry: Resin Design and Postprint Applications. *ACS Appl Polym Mater* **2022**.
8. Ahn, D.; Stevens, L. M.; Zhou, K.; Page, Z. A. Rapid High-Resolution Visible Light 3D Printing. *ACS Cent Sci* **2020**, *6* (9), 1555–1563.
9. Zhu, G.; Zhang, J.; Huang, J.; Yu, X.; Cheng, J.; Shang, Q.; Hu, Y.; Liu, C.; Zhang, M.; Hu, L.; Zhou, Y. Self-Healing, Antibacterial, and 3D-Printable Polymerizable Deep Eutectic Solvents Derived from Tannic Acid. *ACS Sustain Chem Eng* **2022**, *10* (24), 7954–7964.

Utilization of *Dialium Cochinchinensis* shell: Preparation and characterization of composite beads activated carbon

Fareeda Hayeeye[1]*, Memoon Sattar[2], and Aeesoh Benhawan[3]

[1]*Department of Science, Faculty of Science and Technology, Prince of Songkla University, Pattani Campus, Thailand*
[2]*Faculty of Sports and Health Science, Thailand National Sports University, Yala Campus, Thailand*
[3]*Department of Chemistry, Faculty of Science Technology and Agriculture, Yala Rajabhat University*

**E-mail: Corresponding Author fareeda.ha@psu.ac.th*

Abstract:

Dialium cochinchinense shell (DS), an abundant agricultural waste in Pattani, was used as a feedstock to produce activated carbon (DAC) and then fabricated into composite bead adsorbents with gelatin and polylactic acid (GE-DAC and PLA-DAC, respectively). The activated carbon prepared at a carbonization temperature of 400 °C for 180 min and KOH activation (1: 1.5) at 450 °C has a specific surface area of 359.65 $m^2 g^{-1}$ for 60 min. The SEM image showed that GE-DAC had less porosity than PLA-DAC. The GE-DAC and PLA-DAC had a specific surface area of 80.96 and 184.65 $m^2 g^{-1}$, respectively. The composite bead adsorbents could provide an alternative and effective granular adsorbent for the adsorption process.

1. Introduction

At present, the adsorption methods were employed for the removal of contaminants from water. The adsorbents include activated carbon (AC) and nanocomposite materials [1 - 2]. AC has a high surface area and is porous which makes it an excellent adsorbent [3]. The material is derived from carbonaceous sources. In previous works, the preparation of activated carbon used many agricultural waste materials such as bagasse, potato peelings, pericarp of rubber fruits, and almond shells [4 – 7].

In the Yarang district of Pattani province, velvet tamarind, *Dialium cochinchinense (DS)*, a species of flowering plant in the family of legumes, is abundant in the community and has edible sweet pulp similar to tamarind. Thus, it is considered a local economic crop. However, its shells are usually discarded. By this utilizing DS in the production of activated carbon (DAC) can be added value to agricultural waste. However, the dispersion of powdered activated carbon makes it inconvenient to use. In this research, two adsorbents were prepared—a composite material consisting of activated carbon with natural and synthetic polymers. The selected polymer materials included natural polymers like gelatin (GE) and synthetic polymers like polylactic acid (PLA), which are biodegradable polymers [8 - 9]. The composites of gelatin/DS (GE-DAC) and polylactic acid/DS (PLA-DAC) were prepared. The composite bead could serve as an alternative to granular adsorbents to enhance environmental sustainability.

2. Materials and Methods

2.1 Materials

Dialium cochinchinensis shell was kept from Yarung, Pattani province. Potassium hydroxide; KOH was purchased from Sigma-Aldrich. Sodium hydroxide; NaOH and hydrochloric acid; HCl used for pH adjustment were purchased from Labscan Ireland and Merck, respectively. The GE, PLA, and NMP were purchased from Ajax Finechem Pty. Ltd., NatureWorks (USA), and RCI Labscan Limited (Thailand), respectively.

2.2 Preparation of adsorbents

2.2.1 DAC

Dialium cochinchinensis shell (DS) was washed and dried in the oven at 120 °C then it was carbonized in a muffle furnace at a temperature of 400 °C for 180 min under normal air. Then, the mixing of the char with 20% wt/wt KOH which is activating agents at the char: KOH ratio of 1:1.5 conducted at 450 and 500 °C for 30, 60, and 120 min. The obtained activated carbon was then washed with distilled water until a neutral pH value. Finally, it was dried in the oven at 110°C for 24 h and was kept in a desiccator [10].

2.2.2 GE-DAC

A homogeneous solution containing 30% wt. of GE was created and DAC (6-10% wt./wt.) was added to the GE solution. The resulting suspension was stirred at room temperature for 30 minutes and then added dropwise to cold water, leading to the gelling of the gelatin. The formed GE-DAC beads were filtered, and immersed in a 1% v/v glutaraldehyde aqueous solution overnight to induce crosslinking in the gel and stabilize it. The GE-DAC beads were dried at 60°C for 6 h [8].

2.2.3 PLA-DAC

The 10% PLA solution was prepared in NMP, and the DAC (1-5wt%) was added to the PLA solution. The mixture was stirred for 24 h at room temperature. The bead formation step utilized the phase inversion method, where the homogeneous solution was dropped into a non-solvent (distilled water), resulting in the immediate formation of beads. Finally, the PLA-DAC beads were thoroughly washed multiple times with double-distilled water and then dried in an oven for 6 h at 60 °C [9].

2.3 Characterization of adsorbents

The DAC products were characterized by iodine number, BET surface area (Model Autosorb 1 MP Quantachrome Instruments, FL, USA), scanning electron microscopy (SEM–Quanta 400), FT-IR spectrum in ATR mode (Spectrum GX, Perkin Elmer, USA), and point of zero charge (pH_{pzc}).

The procedure for determination of iodine number defined by ASTM D4607-94 [11-12] is as follows: 0.1 g of adsorbents was added with 10 mL of 5% HCl swirled in a conical flask until the entire adsorbent was wetted. The wetted solution was then boiled for exactly 30 s and the solution was cooled to room temperature. Then 100 mL of standard 0.05 M iodine solutions was added to the contents of the conical flask. This solution was filtered using a Whatman 2V filter paper and 50ml of this filtrate was then titrated with 0.10 N sodium thiosulphate until the yellow color had almost disappeared. 1 mL of starch indicator was added and the titration was continued until the blue color just disappeared. The procedure was repeated with each adsorbent. The equilibrium concentration is determined by calculation using the amount of sodium thiosulphate used in the titration from equation (1) and the amount of iodine adsorption determination in equation (2).

$$C = \frac{N_1}{50 \times S} \qquad (1)$$

$$\frac{x}{m} = \frac{A - (DF \times B \times S)}{M} \qquad (2)$$

Where C is the residual concentration of iodine solution (N), N_1 is the concentration of sodium thiosulphate (N), S is the volume of sodium thiosulphate solution, N_2 is the concentration of iodine solution (N), x/m is the amount of iodine adsorption (mg g^{-1}), A = N_2 × 12693, B = N_1× 126.93 and M is the weight of adsorbent (g).

Scanning electron microscopy (SEM– Quanta 400) was used for morphological investigation.

The surface area was specified from nitrogen adsorption/desorption isotherm utilizing model autosorb 1 MP quantachrome instruments. They were performed by the Scientific Equipment Center, Prince of Songkla University.

The point of zero charge was determined using the pH drift method [13] as follows: 50 mL of the pH of 0.1 M NaCl solution was adjusted between 2 and 10 by using 0.1 M HCl or 0.1 M NaOH equilibrated for 24 h. and plotted between initial pH and the final pH at which the curve crossed the line $pH_f = pH_0$ was taken as the pH_{pzc} of the adsorbents (GE-DAC and PLA-DAC).

3. Results & Discussion

From Table 1, the influence of the activation process of DAC which activated with KOH at different times (30, 60, 120 min) and temperatures (450 and 500 °C) resulted in the DAC with 450 °C at 60 min having a high iodine number (603.61 mg g^{-1}) and specific surface area (359.65 m^2 g^{-1}). It can be attributed to the more extensive reaction of KOH and surface carbon [14]. The quantity of iodine absorbed by 1 g of carbon at the mg level is the iodine number, which measures the porosity of the AC [15]. However, the iodine number slightly decreased at 500 °C with 575.12 mg g^{-1}. This could be attributed to the higher reaction rate of carbon and KOH, leading to the release of more volatile components, while simultaneously improving the textural characteristics and carbon burn-off [16]. The iodine numbers showed similar trends of increasing surface area and porosity with the activation time but the values are largely different. Thus, the DAC of activation at 450 °C, 60 min was selected for the preparation of GE-DAC and PLA-DAC. The high iodine number and specific surface area can also be attributed to the high adsorption capacity.

Table 2 shows the optimal weight ratio for forming beads. The results represented the formation of GE-DAC to obtain DAC of 10% wt. and immersed in 1% v/v of GA. It is a suitable condition to maintain GE-DAC granules in bead form. For forming PLA-DAC beads, the optimal weight ratio of PLA: DAC is 5% wt. by phase inversion technique.

Table 1. Influence of activation process of DAC at 450 and 500 °C

Physical properties	Time of activation (450 °C)			Time of activation (500 °C)		
	30	60	120	30	60	120
% yield	45.67	42.78	41.45	39.67	37.65	36.56
Iodine number (mg g^{-1})	497.94	603.61	546.76	436.32	575.12	503.63
Specific Surface area (m^2 g^{-1})	312.89	359.65	360.56	300.76	315.87	319.72

Table 2. Influence of percentage of DAC content affected bead form
Note: × *not bead form* ✓ *bead form*

GE Solution (% wt./wt.)	Percentage of DAC content					
	2%	4%	6%	8%	10%	12%
30	×	×	×	×	✓	×
PLA solution (%wt./wt.)	Percentage of DAC content					
	1%	2%	3%	4%	5%	6%
10	✓	✓	✓	✓	✓	×

Table 3 Physical properties of GE-DAC and PLA-DAC

Physical properties	Iodine number (mg g^{-1})	Specific Surface area (m^2 g^{-1})	Total pore volume (cm^3 g^{-1})	Micropore volume (cm^3 g^{-1})	Average pore size (nm)	pH_{pzc}
GE-DAC	412.02	80.96	0.234	0.021	7.23	5.5
PLA-DAC	576.54	184.65	0.376	0.053	8.49	6.5

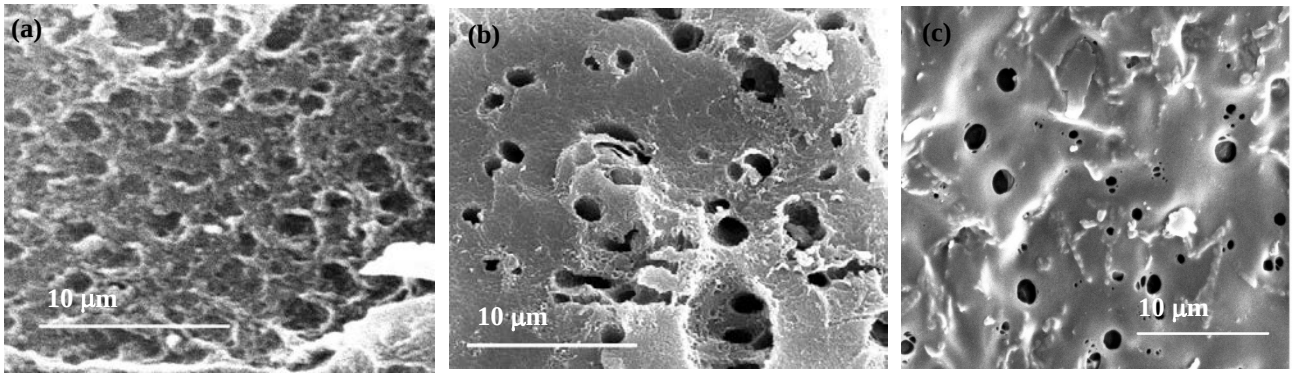

Figure 1. The SEM images of the external surface structures of DAC (a), GE-DAC(b), and PLA-DAC (c) (×5000)

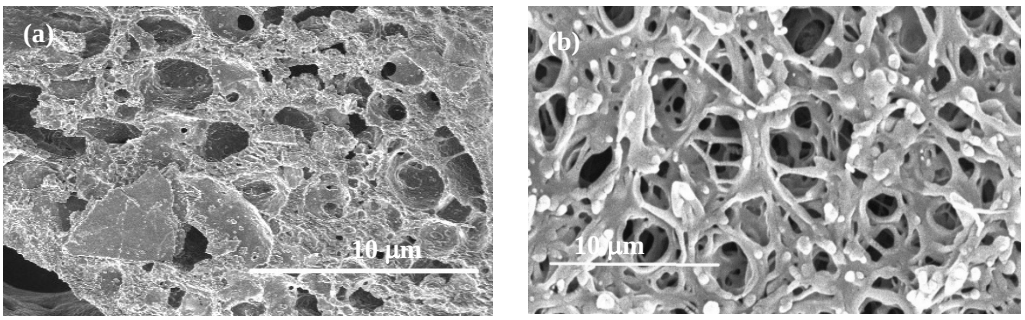

Figure 2. SEM images of the internal surface structures of GE-DAC (a) and PLA-DAC (b) (×5000)

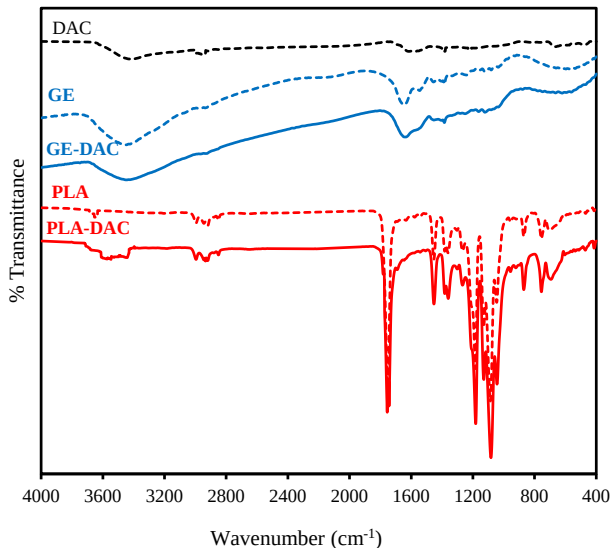

Figure 3. FT-IR spectra of DAC, GE, GE-DAC, PLA, and PLA-DAC

The morphology of DAC, GE-DAC, and PLA-DAC is shown in Figure 1. It can be clearly seen that porosity was strongly affected by the characteristics of the starting materials. DAC surface appears to be a rough surface covered with finely textured carbon structures and with random pore openings. GE-DAC and PLA-DAC showed dense and smooth surfaces, this is probably due to the presence of GE and PLA additives. In addition, the pores of PLA-DAC presented a highly interconnected structure in the internal surface structure (see also Figure 2). It's related to the values of BET surface area and total pore volume of GE-DAC and PLA-DAC were determined by using the model Brunauer-Emmett-Teller (BET) [17], as shown in Table 3. The results indicated that the GE-DAC had a BET surface area value less than PLA-DAC. In comparison to other adsorbents in the literature. The BET surface area values of GE-DAC and PLA-DAC were 80.96 and 184.65 m^2 g^{-1}, respectively, which were significantly higher than those of other granular activated carbon [18 - 20]. The BET results strongly support the fact that the GE-DAC and PLA-DAC beads have a porous structure and this is consistent with the observations from the SEM image. The average pore diameter of GE-DAC and PLA-DAC were 7.23 and 8.49 nm, respectively, called mesopores [21]. The functional groups in DAC, GE-DAC, and PLA-DAC were assessed from the FT - IR spectrum (Figure 3). The band at about 3,300 - 3,500 cm^{-1} was assigned to the O-H stretching vibrations. Moreover, the band at 1,750 cm^{-1} was assigned to the C=O stretching of keto-

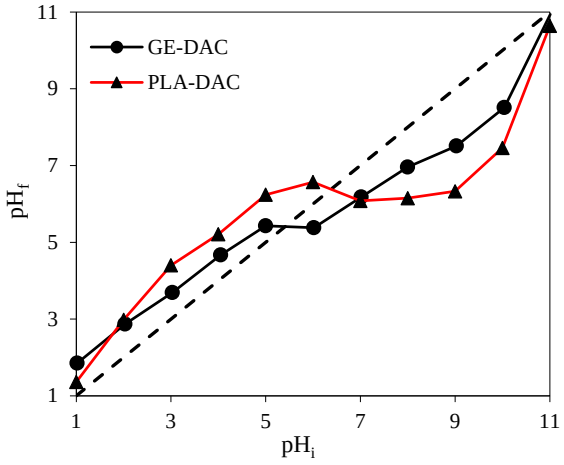

Figure 4. The pH_{pzc} of GE-DAC and PLA-DAC

carbonyl groups [22]. The functional groups on DAC, GE-DAC, and PLA-DAC did not change the functional groups of GE and PLA. However, the FT - IR spectrum of PLA-AC and GE-DAC shows that the O-H band and the N-H band are blue-shifted compared to pure PLA, GE, and DAC, respectively. This could indicate the presence of DAC in the PLA and GE spheres.

The point of zero charges (pH_{pzc}) was calculated by the pH drift method which plotted between the pH_f and the pH_i (Figure 4). The GE-DAC and PLA-DAC had values of pH_{pzc} 5.5 and 6.5, respectively, the surface of the beads was negatively charged, and when pH was below pH_{pzc}, the surface was positively charged. The GE-DAC and PLA-DAC had a positive charge that caused electrostatic repulsion with the positive charge of the cationic adsorbate [23].

4. Conclusion

The GE-DAC and PLA-DAC were successfully prepared in bead form. The PLA-DAC has higher a specific surface area and porosity than the GE-DAC. The average pore size was classified as mesopore. The point of zero charge of GE-DAC and PLA-DAC indicates the surface of both adsorbent beads is positively charged. Thus, the GE-DAC and PLA-DAC could be convenient, eco-friendly, biocompatible, and effective. They have the potential to serve in industrial wastewater treatment applications.

Acknowledgment

The authors gratefully the research grant of Prince of Songkla University, Pattani campus (Grant no. SAT6603018S) for the financial support. The authors are grateful to the Department of Science, Faculty of Science and Technology, Prince of Songkla University, Pattani Campus, Thailand.

References

1. Zhou, R.; Zhou, R.; Zhang, X.; Bazaka, K.; and Ostrikov, K. *Front. Chem. Sci. Eng.* **2019**, *13(2)*, 340- 349.
2. Rahnama, S.; Shariati, S. and Divsar, F. *Combi. Chem. High Through. Screen*. **2018**, *21(8)*, 583 – 593.
3. Krishnamoorthy, R.; Govindan, B.; Banat, F.; Sagadevan, V.; Purushothaman, M. and LokeShow, P. *J. Biosci. Bioengineer.,* **2019**, *128(1)*, 88 - 97.
4. Hayeeye, F. and Sattar, M. *Desal. Water Treat.* **2020**, *202*, 420–434.
5. Lairini, S.; Mahtal, K.; Miyah, Y.; Tanji, K. Guissi, S.; Boumchita, S. and Zerrouq, F. *J. Mater. Envir. Sci.*, **2013,** *8(9)*, 3252-3261.
6. Hayeeye, F.; Sattar, M.; Tekasakul, S. and Sirichote, O. *Songklanakarin J. Sci. Technol.*, **2014**, *36 (2)*, 177-187.
7. Saeed, K.; Ishaq, M.; Sultan, S. and Admad, I. *Desal. Water Treat.*, **2016**, *57(29*), 13484-13493.
8. Hayeeye, F.; Sattar, M.; Chinpa, W. and Sirichote, O. *Colloid & Sur. A: Physico.& Eng. Aspects.*, **2017**, *513*, 259–266.
9. Sattar, M.; Hayeeye, F.; Chinpa, W. and Sirichote, O. *J. Environ. Chem. Eng.*, **2017**, *5*, 3780–3791.
10. Benhawan, A.; Hayeeeye, F. and Sattar, M. *YRU. J. Sci Tech.* **2022**, *7(1)*, 48-56.
11. Philadelphia. P.A. Standard test method for determination of iodine number of activated carbon, ASTM D4607 – 94, United States of America, **2011**.
12. Pornsawan, A.; Natthanon. P. and Amornrat, M. *Rattanakosin J. Sci. Technol.*, **2021**, *3(2)*, 36 – 44.
13. Hayeeye, F.; Benhawan, A. and Sattar, M. *Des. Water Treat.* **2022**, *269*, 200–211.
14. Deng, H.; Li, G.; Yang, H.; Tang, J. and Tang, *J. Chem. Eng. J.*, **2010**, *163(3)*, 373–381.
15. Mopoung, S.; Moonsri, P.; Palas, W. and Khumpai, S. *Sci. World J.*, 2015, 1-9.
16. Saka, C., *J. Anal. Appl. Pyrol.*, **2012**, 95, 21–24.
17. Brunauer, S.; Skalny, J. and. Bodor, E.E, J. *Colloid Interface Sci.*, **1969**, *30*, 546–552.
18. Wenqiang, Luo.; Zhishan, B. and Yong, Zhu. *RSC Adv.*, **2018**, *8*, 13370–13387.
19. Setthamongkol, P. and Salaenoi, *J. Inter. Sch. Sci. Res. Inno.* **2012**, *6(9)*, 155-160.
20. Rajeswari, A.; Amalraj, A. and Pius, A. *J. Water Pro.Eng.*, **2016**, *9*, 123-134.
21. Kuila, U. and Prasad, M. *Geophys. Prospect.*, **2013**, *62*, 341–362.
22. Stuart,B. Infrared Spectroscopy: Fundamentals and Applications, John Wiley & Sons Ltd., University of Technology, Sydney, Australia, **2004**, 56-67.
23. Agarwal, G.; Bhuptawat, H. and Chaudhari, S. *Biores. Technol.*, **2006**, *97(7)*, 949–956.

Computational investigation of hydrogen storage on boron nitrogen four-membered ring structure

Patcharaporn Supho, Natcha Temnuch, Thinnaphat Poonsawat, and Ekasith Somsook*

NANOCAST Laboratory, Center for Catalysis Science and Technology (CAST), Department of Chemistry and Center of Excellence for Innovation in Chemistry, Faculty of Science, Mahidol University, 272 Rama VI Road, Ratchathewi, Bangkok 10400, Thailand

**E-mail: ekasith.som@mahidol.ac.th*

Abstract

Clean and sustainable energy is refining the role of decisive attraction based on renewable fuels. A new platform of boron nitrogen heterocyclic ring is in charge demonstration on Lithium-ion batteries (LIBs) and hydrogen (H_2) storage systems. In this work, the possible boron nitrogen four-membered structure was particularly investigated regarding the capacity of lithium (Li) atom and H_2 molecule *via* Density Function Theory (DFT) calculations by second-order Møller-Plesset perturbation theory (MP2) utilized in a def2-TZVP basis set with the Gaussian 16 package. The results showed the promising storage performance of the four Li-decorated B_2N_2 structure ($B_2N_2Li_4$) with the possible maximum hydrogen (H_2) adsorption up to 12 molecules related to Li atoms. This calculation has a potential to develop boron nitrogen materials for exploration in short- and long-term hydrogen technology.

1. Introduction

Currently, routine activities in human life utilize fossil fuels in various application such as agriculture, transportation, and so forth. Non-renewable resources including coal, oil and natural gases has the vast impact to generate waste energy and released carbon dioxide (CO_2) into the atmosphere that affects to the climate change.[1] The disadvantages of CO_2 that are released from the use of fuel make the troubling issues to environment. A clean energy revolution is taking place to solve the steady expansion of these problems with the responsible energy resources as solar, wind, water, geothermal, bioenergy, nuclear, and hydrogen.[2] Fuel cells based on material-based system for chemical storage of H_2 molecule offer a flexible technology with highly efficient to produce power and release zero emissions.[3] Particularly, chemical adsorption of H_2 gas is stored in three main materials consisting of sorbents, metal hydrides, and chemical hydrides. The development of hydrogen storage has received attention due to its unique properties of non-toxic and high gravimetric energy density.[4] However, storing hydrogen is quite difficult and challenging because most of this gas on Earth exists in the form of water structures (H_2O) with the greatest quantities. Nowadays, the U.S. Department of Energy (DOE) establish a goal to discover new material storages with a variety of research.[5-6] H_2 storage materials have a variety of properties which include high density of hydrogen, thermodynamic characteristics, rapid reaction kinetics, simple to control, and unlimited source at low cost.[7] The broad research scope of storing H_2 with various materials such as metal hydrides,[8] clathrates,[9] inorganic nanotubes,[10] organic materials,[11] porous polymer,[12] zeolites,[13] alanates,[14] carbon-based nanomaterials,[15] and boron-based material,[16] etc. The suggestion of H_2 absorption materials is metal organic frameworks (MOFs) for satisfactory adsorption-desorption standards.[17] Gas storage utilizes lightweight of Li-doped clusters as a sorbent with the promising properties to adsorb and to desorb H_2.[18-19] Li atom could be polarized the H_2 molecules.[20] The Li-doped lightweight MOFs appeared to have more H_2 storage in MOFs than bare MOFs.[21] Diborane ($B_2H_4Li_2$) and diboryne ($B_2H_2Li_2$) could uptake a maximum of six H_2 molecules.[22] $Be_2(NLi)_2$ clusters show the capacity of this unique cluster for H_2 adsorption and desorption. Quantum chemical calculations reveal that the beryllium cluster could take up to 8 H_2 molecule.[23] Furthermore, the gravimetric system of H_2 storage is increased by the characteristics of pyridine–lithium to 1:1 complex.[24] Due to the heteropolar nature of the B and N atoms' binding, BN-based materials have been regarded as promising candidates for hydrogen storage,[25] and in order to store hydrogen up to 2.6 wt.%, BN nanotubes must be both thermally and chemically stable.[26] However, the BN cluster that contains a Li atom is attractive in improving the H_2 storage efficiently.

In this work, we report the possibility of devising a new proposed structure related to the

boron-nitrogen (BN) materials involving the attachment of lithium atoms to increase the adsorption potential of hydrogen gas. The smallest cluster of boron nitrogen four-membered ring structure is used as a basis for determining gas retention in the structure of carbon materials that have been modified with boron and nitrogen atoms. Computational details on the structural BNLi cluster investigated the chemisorption and physisorption in term of binding energy.

2.Computational details

All calculations were carried out using the Gaussian 16 computational chemistry package and GaussView 6 software.[27] All optimization of study clusters that were weak non-covalent interactions were used the Coupled-Cluster Singles and Doubles (CCSD) model with cc-pVTZ basis set and the second-order Møller–Plesset (MP2)[28] level with def2-TZVP basis set.

The calculating of adsorption energy with DFT method (E_{ads}) that is the energy of H_2 storage as binding energy calculation used Equation 1 and for average adsorption energy ($\bar{E}_{ads}$) was calculated by $(BN)_2Li_2$ cluster using Equation 2 as follows.

Equation 1

$$\Delta E_{ads} = [\{E\big((BN)_2Li_x - nH_2\big)\} - \{E\big(BN)_2Li_x - (n-1)\big)H_2 + H_2\}]$$

Equation 2

$$\Delta \bar{E}_{ads} = [\{E\big((BN)_2Li_x - nH_2\big)\} - \{E(BN)_2Li_x + E(nH_2)\}]/n$$

Where x is a verify Li-dope based on N atoms in the BN cluster, and $E((BN)_2Li_2)$, $E((BN)_2Li_2\text{-}nH_2)$, $E(nH_2)$ are total energy of BNLi cluster, H_2 storage on BNLi cluster, and H_2 molecule, respectively.

3. Result & Discussion

The proposed structures of the boron nitrogen four-membered ring with different Li atoms are shown in Figure 1. The four proposed boron-nitrogen clusters were arranged through the possibility of 4 atoms to understand the coordination of lithium atoms. The computational results depicted the total energy after theoretical calculation using the Coupled-Cluster Singles and Doubles (CCSD) model with cc-pVTZ basis set of $BBBNLi_4$, $BNNNLi_4$, $BNBNLi_4$ and $BBNNLi_4$ that were -359,186, -261,734, -118,448 and -118,392 kcal/mol, respectively. Optimized structure of $BNBNLi_4$ revealed the probability of hydrogen access occurring around lithium atoms due to the appropriate distance.

Cluster	Proposed structure	Optimized structure
$BBBNLi_4$	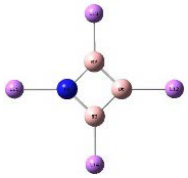	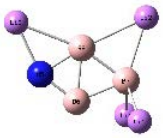
Total energy = -359,186 kcal/mol		
$BNNNLi_4$	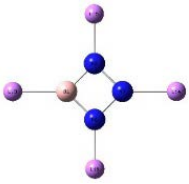	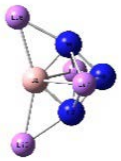
Total energy = -261,734 kcal/mol		
$BNBNLi_4$	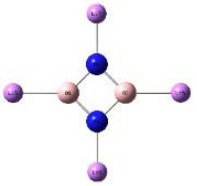	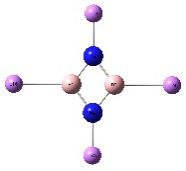
Total energy = -118,448 kcal/mol		
$BBNNLi_4$	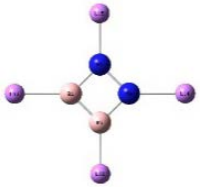	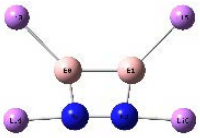
Total energy = -118,392 kcal/mol		

Figure 1. Proposed and optimized structures of $B_xN_yLi_4$ clusters using the Coupled-Cluster Singles and Doubles (CCSD) model with cc-pVTZ basis set.

According to a preliminary study to compare between proposed and optimized structures of boron-nitrogen four membered ring, the $B_2N_2Li_4$ was chosen to be a model to further investigate the application of hydrogen storage. The optimized structure of B_2N_2Li clusters was demonstrated using MP2/def2-TZVP theoretical level with various Li atoms. All geometries are shown in Figure 2 to explain the structure on bear B_2N_2 and B_2N_2Li clusters with 3 proposed structures that related to $B_2N_2H_4$, $B_2N_2LiH_3$, and $B_2N_2Li_2H_2$. The results of optimized structures showed the distance between B

and N atom that was 1.454 Å, 1.451 Å, and 1.465 Å for $B_2N_2H_4$, $B_2N_2LiH_3$, and $B_2N_2Li_2H_2$, respectively. In addition, the distance of H–BN clusters show 1.189 (Å) for H–B and 1.004 (Å) for H–N on $B_2N_2H_4$ structure, 1.200 (Å) for H–B and 1.010 (Å) for H–N on $B_2N_2LiH_3$ structure, and 1.213 (Å) for H–N on $B_2N_2Li_2H_2$ structure, and distance between BN clusters and Li atoms are 1.779 (Å) of $B_2N_2LiH_3$ and 1.762 (Å) of $B_2N_2Li_2H_2$.

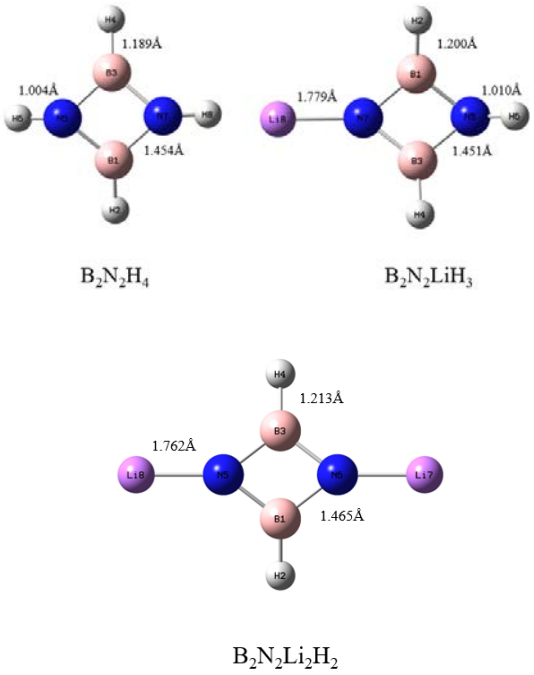

$B_2N_2H_4$ $B_2N_2LiH_3$

$B_2N_2Li_2H_2$

Figure 2. the B_2N_2 clusters with various Li atoms for H_2 adsorption with MP2/def2-TZVP level

The optimization of BN clusters with various Li atoms which increase a Li atom from bare BN cluster to two atoms on structural geometries of BN ring by MP2/def2-TZVP level for H_2 adsorbed complexes is shown on Figure 3. The bare BN cluster is unabsorbed for any H_2 molecule because BN ring system has high stability. Nevertheless, increasing a Li atom on BN cluster effects an increasing electron density and electron donating for Li center, and H_2 absorption on the cluster appears a pair of H_2 molecules for storge. The BN cluster with two Li atoms absorb maximum storage for four H_2 molecules, and ratio of 1:n (where is n = 0, 1, 2, 3, and 4) that is clustered : H_2 molecules is on trend the increasing Li atom that increase storage of H_2 molecules except $B_2N_2Li_2H_6$, there is ratio of 1:2, which is unstable in MP2/def2-TZVP theorical level. The H_2 addition on adsorbed complexes has the normal H–H distance of 0.744 Å on BNLi clusters and the range of Li–H distance from 2.155 Å.

Table 1. The calculating of adsorption energy (E_{ads}), average adsorption energy ($\bar{E}_{ads}$), and H–H stretching frequency in free H_2 molecule with MP2/def2-TZVP level of theoretical.

molecule	ΔE_{ads} (eV)	$\Delta \bar{E}_{ads}$ (eV)	υ_{H-H} (cm^{-1})
$B_2N_2LiH_5$	0.12	0.12	4495.99
$B_2N_2Li_2H_4$	0.14	0.14	4497.58
$B_2N_2Li_2H_6$	0.27	0.21	4447.88
$B_2N_2Li_2H_8$	0.27	0.23	4462.99
$B_2N_2Li_2H_{10}$	0.14	0.21	4497.59

The Table 1. shown the calculation of H_2 molecule storage on BN structures which had B_2N_2 clusters with a Li atom for $B_2N_2LiH_5$ and B_2N_2 clusters with two Li atoms for $B_2N_2Li_2H_4$, $B_2N_2Li_2H_6$, $B_2N_2Li_2H_8$, and $B_2N_2Li_2H_{10}$ at MP2/def2-TZVP level of theoretical. The adsorption energy appeared between physisorption and chemisorption at 0.15-0.31 eV[30] of $B_2N_2Li_Z$ structures which had similar values in the range. The calculated average adsorption energy obtained a range of 0.14-0.21 eV. Addition, H–H stretching frequency in free H_2 molecules on these cluster exhibited B_2N_2Li for 4,495.99 cm^{-1} and $B_2N_2Li_2$ for average 4476.51 cm^{-1} in the H_2 storage.

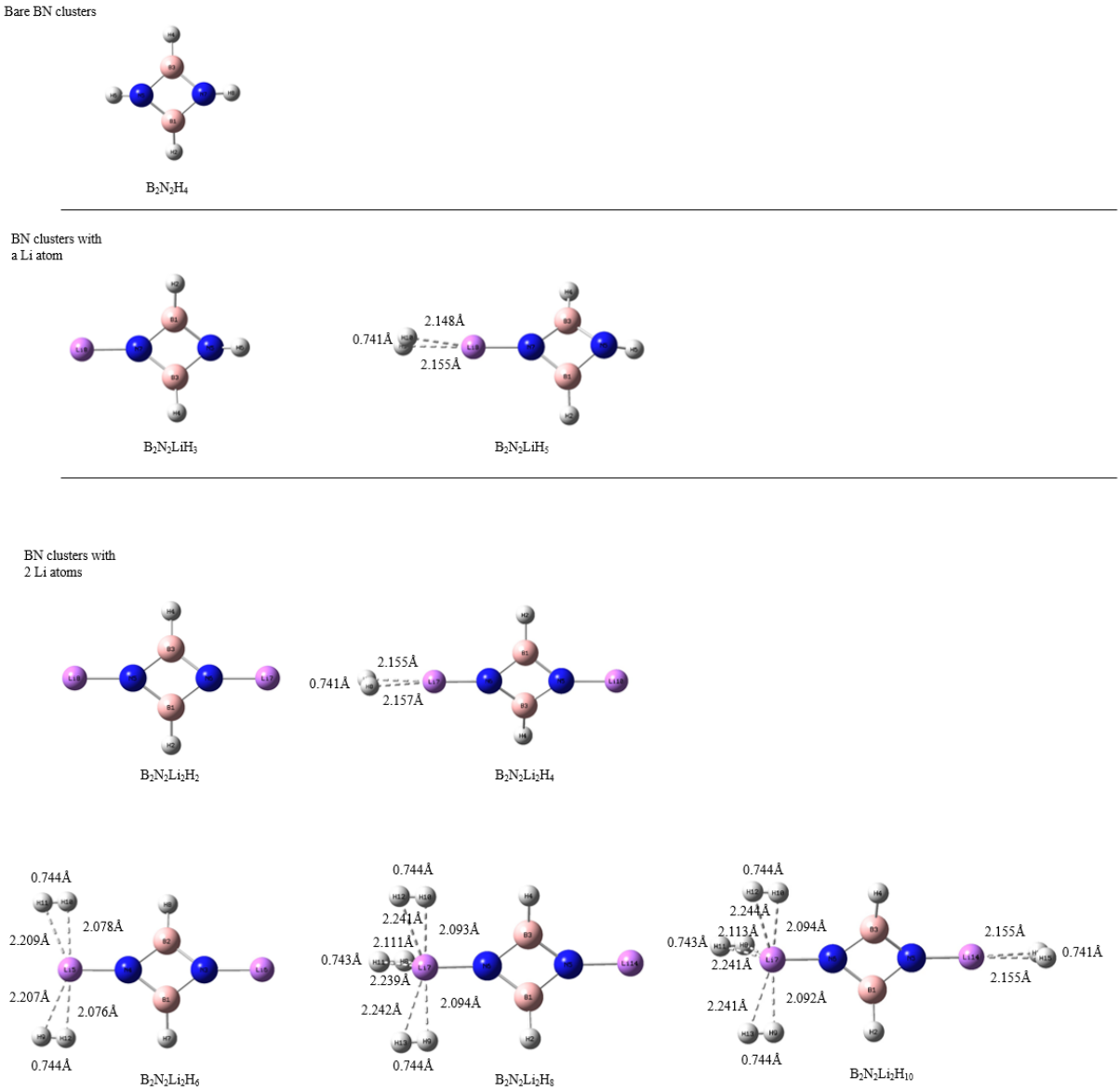

Figure 3. calculation optimized geometries of BN clusters with various Li atoms by MP2/def2-TZVP for 1:n (n=1, 1-3, and 1-6, respectively) complexes.

Conclusions

The Li–doped boron-nitrogen structure was successfully investigated of optimization structure of four membered-ring by MP2/def2-TZVP level to study bond length of B–N, Li–BN clusters, H_2–BNLi system rings for finding the possibility of hydrogen storage in the molecules. The proper structure storage of hydrogen molecules has been BNBN cluster due to lower energy for optimization and symmetry electron arrangement at CCSD/cc-pVTZ basis set. These B-N structures added Li were potential dihydrogen at Li surrounding BN clusters and $B_2N_2Li_2H_{10}$ appears the highest absorption for four H_2 molecule. The addition of Li molecules affects potential ability to increase the binding H_2 molecules.

Acknowledgements

The authors gratefully acknowledge financial support from the Center of Excellence for Innovation in Chemistry (PERCH-CIC) and NANOCAST Laboratory.

References

1. Friedlingstein, P.; O'Sullivan, M.; Jones, M. W.; Andrew, R. M.; Hauck, J.; Olsen, A.; Peters, G. P.; Peters, W.; Pongratz, J.; Sitch, S.; et al.

Global Carbon Budget 2020. *Earth Syst. Sci. Data* **2020**, *12* (4), 3269-3340.
2. Rowsell, J. L.; Yaghi, O. M. Strategies for hydrogen storage in metal--organic frameworks. *Angew Chem Int Ed Engl* **2005**, *44* (30), 4670-4679.
3. Sartbaeva, A.; Kuznetsov, V. L.; Wells, S. A.; Edwards, P. P. Hydrogen nexus in a sustainable energy future. *Energy Environ Sci* **2008**, *1* (1), 79-85.
4. İzgi, M.; Baytar, O.; Şahin, Ö.; Horoz, S. Studies on catalytic behavior of Co–Cr–B/Al_2O_3 in hydrogen generation by hydrolysis of nabh4. *Dig. J. Nanomater. Biostructures* **2019**, *14*, 1005-1012.
5. Hassmann, K.; Kühne, H. M. Primary energy sources for hydrogen production. *Int. J. Hydrogen Energy*. **1993**, *18* (8), 635-640.
6. ENERGY, O. o. E. E. R. DOE Technical Targets for Onboard Hydrogen Storage for Light-Duty Vehicles. n.d.
7. Kojima, Y.; Miyaoka, H.; Ichikawa, T. Chapter 5 - Hydrogen Storage Materials. In *New and Future Developments in Catalysis*, Suib, S. L. Ed.; Elsevier, 2013; pp 99-136.
8. Sakintuna, B.; Lamari-Darkrim, F.; Hirscher, M. Metal hydride materials for solid hydrogen storage: A review. *Int. J. Hydrogen Energy*. **2007**, *32* (9), 1121-1140.
9. Struzhkin, V. V.; Militzer, B.; Mao, W. L.; Mao, H. K.; Hemley, R. J. Hydrogen storage in molecular clathrates. *Chem Rev* **2007**, *107* (10), 4133-4151.
10. Cheng, F.; Chen, J. Storage of hydrogen and lithium in inorganic nanotubes and nanowires. *J. Mater. Sci. Res.* **2006**, *21* (11), 2744-2757.
11. McKeown, N. B.; Budd, P. M. Polymers of intrinsic microporosity (PIMs): organic materials for membrane separations, heterogeneous catalysis and hydrogen storage. *Chem. Soc. Rev.* **2006**, *35* (8), 675-683.
12. McKeown, N. B.; Gahnem, B.; Msayib, K. J.; Budd, P. M.; Tattershall, C. E.; Mahmood, K.; Tan, S.; Book, D.; Langmi, H. W.; Walton, A. Towards polymer-based hydrogen storage materials: engineering ultramicroporous cavities within polymers of intrinsic microporosity. *Angew Chem Int Ed Engl* **2006**, *45* (11), 1804-1807.
13. Nijkamp, M. G.; Raaymakers, J. E. M. J.; van Dillen, A. J.; de Jong, K. P. Hydrogen storage using physisorption – materials demands. *Appl. Phys. A* **2001**, *72* (5), 619-623.
14. Baldé, C. P.; Hereijgers, B. P. C.; Bitter, J. H.; de Jong, K. P. Facilitated Hydrogen Storage in NaAlH4 Supported on Carbon Nanofibers. *Angew. Chem. Int. Ed.* **2006**, *45* (21), 3501-3503.
15. Lee, H.; Lee, J.-W.; Kim, D. Y.; Park, J.; Seo, Y.-T.; Zeng, H.; Moudrakovski, I. L.; Ratcliffe, C. I.; Ripmeester, J. A. Tuning clathrate hydrates for hydrogen storage. *Nat.* **2005**, *434* (7034), 743-746.
16. Fakioğlu, E.; Yürüm, Y.; Veziroğlu, T. N. A review of hydrogen storage systems based on boron and its compounds. *Int. J. Hydrogen Energy* **2004**, *29* (13), 1371-1376.
17. Rosi, N. L.; Eckert, J.; Eddaoudi, M.; Vodak, D. T.; Kim, J.; O'Keeffe, M.; Yaghi, O. M. Hydrogen storage in microporous metal-organic frameworks. *Science* **2003**, *300* (5622), 1127-1129.
18. Srinivasu, K.; Ghosh, S. K.; Das, R.; Giri, S.; Chattaraj, P. K. Theoretical investigation of hydrogen adsorption in all-metal aromatic clusters. *RSC Advances* **2012**, *2* (7), 2914-2922.
19. Du, J.; Sun, X.; Zhang, L.; Zhang, C.; Jiang, G. Hydrogen storage of Li4&B36 cluster. *Sci. Rep.* **2018**, *8* (1), 1-7.
20. Ataca, C.; Aktürk, E.; Ciraci, S.; Ustunel, H. High-capacity hydrogen storage by metallized graphene. *Appl. Phys. Lett.* **2008**, *93* (4), 043123.
21. Blomqvist, A.; Araújo, C. M.; Srepusharawoot, P.; Ahuja, R. Li-decorated metal-organic framework 5: a route to achieving a suitable hydrogen storage medium. *Proc Natl Acad Sci U S A* **2007**, *104* (51), 20173-20176.
22. Srinivasu, K.; Ghosh, S. K. Theoretical studies on hydrogen adsorption properties of lithium decorated diborene (B2H4Li2) and diboryne (B2H2Li2). *Int. J. Hydrogen Energy* **2011**, *36* (24), 15681-15688.
23. Sarmah, K.; Kalita, A. J.; Konwar, D.; Guha, A. K. Hydrogen storage capacity of Be2 (NLi) 2 cluster with ultra-short beryllium–beryllium distance. *J. Comput. Chem.* **2022**, *43* (26), 1764-1770.
24. Chattaraj, S.; Srinivasu, K.; Mondal, S.; Ghosh, S. K. Hydrogen trapping ability of the pyridine–lithium+ (1: 1) complex. *J. Phys. Chem. A* **2015**, *119* (12), 3056-3063.

25. Mpourmpakis, G.; Froudakis, G. E. Why boron nitride nanotubes are preferable to carbon nanotubes for hydrogen storage?: An ab initio theoretical study. *Catal. Today* **2007**, *120* (3-4), 341-345.
26. Ma, R.; Bando, Y.; Zhu, H.; Sato, T.; Xu, C.; Wu, D. Hydrogen uptake in boron nitride nanotubes at room temperature. *J. Am. Chem. Soc.* **2002**, *124* (26), 7672-7673.
27. Frisch, M.; Trucks, G.; Schlegel, H.; Scuseria, G.; Robb, M.; Cheeseman, J.; Scalmani, G.; Barone, V.; Petersson, G.; Nakatsuji, H. Gaussian 16, Revision C. 01. Gaussian, Inc., Wallingford CT. 2016. *Google Scholar There is no corresponding record for this reference* **2020**.
28. Møller, C.; Plesset, M. S. Note on an approximation treatment for many-electron systems. *Phys. Rev.* **1934**, *46* (7), 618.
29. Reed, A. E.; Curtiss, L. A.; Weinhold, F. Intermolecular interactions from a natural bond orbital, donor-acceptor viewpoint. *Chem. Rev.* **1988**, *88* (6), 899-926.
30. Guo, C.; Wang, C. Computational investigation of hydrogen storage on B_6Ti^{3+}. *Int. J. Hydrogen Energy*. **2018**, 43(3), 1658-1666.

Role of trace elements affecting coloration in blue, yellow, and green synthetic corundum

Davis Muhummud[1], Wiwat Wongkokua[2], Chatree Saiyasombat[3], and Natthapong Monarumit[1]*

[1] *Department of Earth Sciences, Faculty of Science, Kasetsart University, Bangkok 10900, Thailand*
[2] *Department of Physics, Faculty of Science, Kasetsart University, Bangkok 10900, Thailand*
[3] *Synchrotron Light Research Institute (Public Organization), Nakhon Ratchasima, 30000, Thailand*

**E–mail: natthapong.mon@ku.th*

Abstract:

Although we have a general knowledge of the factors that give corundum its color, the underlying mechanism for each color variety is still being debated and is a topic of controversy to this day. Green corundum is one color for which there has yet to be a dedicated study focused on its color mechanism. To determine the underlying color mechanism and construct energy band models, blue, green, and yellow synthetic corundum were analyzed using colorimeter, EDXRF, UV–Vis–NIR, and XAS. Energy band gap calculations for synthetic corundum resulted in values of 4.30 eV for blue, 4.01 eV for green, and 3.62 eV for yellow. The energy band model for synthetic blue corundum incorporates the Fe^{3+}/Ti^{4+} mixed acceptor state while the model for synthetic yellow corundum utilizes Cr^{3+} neutral state with XANES showing interference signal from metallic iron and a possibility of Fe^{3+} neutral state. Synthetic green corundum, on the other hand, employs both Ni^{2+} donor states and Fe^{3+}/Fe^{3+} neutral state to explain its energy band model.

1. Introduction

Corundum, commonly known as sapphire except for the red variety known as ruby, in its purest form is comprised of only Al_2O_3 and is colorless. As an allochromatic gem, it can produce various shades of color when d–orbital transition metal inclusions are introduced to its crystal structure. Commonly known variations of this are Cr^{3+} impurities which produce ruby and pink sapphire while yellow is caused by Fe^{3+} with either a single Fe ion with oxygen-metal charge transfer or a pair of Fe in a crystal field.[1] Additionally, yellow in corundum may also be caused by Ni, structural defect color centers induced by radiation, natural occurring color centers[2] as well as Be-heat treated sapphires[3] and Mg-trap hole color centers.[4] In the case of blue corundum, it was believed to be the product of Fe^{2+}–Ti^{4+} pair Intervalence Charge Transfer (IVCT).[1]Although, with more recent findings using X–ray Absorption Near Edge Spectroscopy (XANES),[5] the oxidation state of iron in blue sapphire was proven to be Fe^{3+} rather than Fe^{2+} as previously stated in IVCT. Thus, the study suggested the use of an energy band model with Fe^{3+}/Ti^{4+} mixed acceptor states to describe the color phenomena in blue sapphire. Less commonly known varieties such as green sapphire, have not been narrowed down to a single transition metal or transition metal pair. Hughes (1990) pointed to the color of natural green sapphires occurring through electronic transition by Fe^{2+} inclusions while synthetic green sapphires are caused similarly by electronic transition but with cobalt (Co), vanadium (V), and/or nickel (Ni).[1] More modern theories suggest that green sapphires are caused by a combination of both yellow and blue sapphire mechanisms that give the sapphire its green color.[6] This assumption is corroborated by BGY sapphires which are sapphires that display three colors including: blue, green, and yellow.

Despite the various theories, there have been no dedicated studies, nor has it been definitively determined with more modern equipment, what color mechanisms govern the green color in corundum due to the fact that green sapphire is not quite a commodity in the gem market thus not generating much interest in research. However, as sapphire is a precious gemstone and the green color in green sapphire, albeit not as intense a green as emeralds, have a subtle beauty in their olive to teal green, as such they can also produce value as fancy sapphires.

This research is interested in defining the exact mechanisms and elements that give green sapphire their beautiful hue by comparing the spectroscopic and chemical properties of synthetic blue, green, and yellow sapphires. Through our better understanding of the mechanisms that give green sapphires their color, we may be able to improve the quality or develop a more cost–efficient gem enhancement or gem synthesis method for green sapphires.

2. Materials and Methods

2.1 Materials

A total of three flame fusion (verneuil) synthetic sapphires of different colors were acquired from the same manufacturer, including blue, green, and yellow. The samples were cut into

slab sections with an average thickness of 3 mm to 4 mm before being polished down to 2 mm for spectroscopic analysis.

2.2 Spectroscopic measurement

The Avantes AvaSpec–2048 fiber optic spectrometer at the Department of Physics, Kasetsart University, was used as a colorimeter to accurately measure the color of the samples which are then plotted in CIELAB color space.

Chemical composition along with Ultraviolet–Visible–Near Infrared Spectroscopy (UV–Vis–NIR) were measured at the Gem and Jewelry Institute of Thailand (GIT) using the EDAX Eagle III Energy Dispersive X-ray Fluorescence (EDXRF) and PerkinElmer Lambda 1050 UV–Vis–NIR Spectrophotometer, respectively. EDXRF analysis was focused on the oxide percentage of Al_2O_3, Fe_2O_3, TiO_2, Cr_2O_3, and V_2O_5. UV–Vis–NIR spectra acquisition range was set at 250 nm to 1000 nm.

X–ray Absorption Spectroscopy (XAS) measurements were conducted at beamline 7.2W, employing the Siam Photon Source (SPS) 1.2 GeV synchrotron light source located at the Synchrotron Light Research Institute (SLRI), Thailand. Samples were secured to sample holders with Kapton tape and placed at 45° in respect to light source and detector. Data acquisition was conducted in fluorescence mode for 2 scans per sample. Data processing was completed using Demeter's Athena XAS data processing program which is then put into Larch's Larix: X-ray Visualization and Analysis for pre-edge fitting.

2.3 Energy band model

Energy band models for each sample are simulated using the following Tauc's equation to calculate the energy band gap (E_g):

$$(\alpha h\nu) = A\,(h\nu - E_g)^p \qquad (1)$$

where α is the optical absorption coefficient, h is Plank's constant, ν is the frequency, A is a constant dependent on transition probability, and p characterizes whether the optical absorption process is indirect or direct, with it being equal to 2 or ½, respectively.[7]

Plank's equation is also applied to calculate the energy state that represents the position in which the photon energy is absorbed.

Lastly, data visualizations were conducted under the performance of an R programming (R Core Team).[8]

3. Results & Discussion

3.1 CIELAB plot

Color analyses on all samples are displayed in CIELAB color plot as seen in Figure 1. The synthetic blue, green, and yellow sapphires display a* values of +1.11, -23.09, and -1.45, and b* values of -10.98, +1.30, and +24.98, respectively. All sample colors are well within their respective color designations with minimal to negligible deviation to their respective colors.

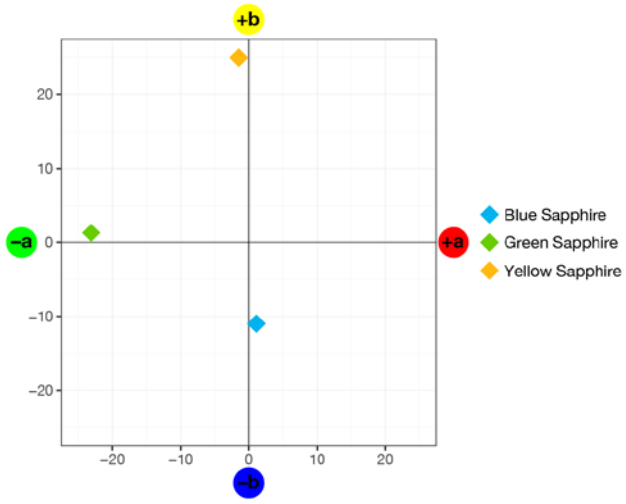

Figure 1. CIELAB color plot of all three synthetic sapphire samples.

3.2 Chemical composition

Chemical composition analysis results completed by the EDAX-EAGLE III are displayed in Table 1. All samples show high percentages of Al_2O_3 which coincide with corundum as the major element. Fe_2O_3 concentrations are over twice as high in the blue sample than the green and triple that of the yellow sample. TiO_2 quantities are close in all samples with green being the highest followed by yellow then blue. Similarly, Cr_2O_3 also has close values but with the highest concentration in yellow and lowest in blue. Finally, V_2O_5 quantities are close between blue and green while the outlier, green, has less than twice the amount of the aforementioned two.

Table 1. Semi-quantitative chemical analyses in oxide percentage of synthetic sapphire samples. Scale bars are 1 cm.

Sample		Al_2O_3	Fe_2O_3	TiO_2	Cr_2O_3	V_2O_5
Blue sapphire		99.928	0.030	0.012	0.007	0.013
Green sapphire		99.949	0.012	0.016	0.007	0.007
Yellow sapphire		99.943	0.010	0.014	0.009	0.014

3.3 UV–Vis–NIR result

The UV-Vis-NIR results are shown in Figure 2. The blue sapphire shows a generally unchanging absorption range with distinct absorption peaks at 405 nm, 580 nm, and 710 nm. The peaks correspond to absorptions by Cr^{3+} ion at 405 nm,[9] and Fe^{3+}/Ti^{4+} at 580 nm and 710 nm.[5,10] Absorption spectrum for green sapphire displays three distinct peaks at 450 nm, 580 nm, and 640 nm which coincide with Fe^{3+}/Fe^{3+} pair at 450 nm,[10] and Ni^{2+} at 580 nm and 640 nm.[11] Lastly, the yellow sapphire displays absorbance at 405 nm which is influenced by a Cr^{3+}.

Tauc plot calculations for all three samples are presented as inserts of each spectrum in Figure 2. The E_g results for the blue, green, and yellow samples are 4.30 eV, 4.01 eV, and 3.62 eV, respectively. Generally, a wider band gap relates to a paler sample while a narrow band gap corresponds to a darker sample. Although, it is shown that the samples display the opposite in this study as the blue and green sapphires have larger E_g than the yellow sapphire. It is possible that this could be caused by the difference in sample thickness as well as the shape of the samples. Additionally, the turbidity of the yellow sapphire may also be a factor impacting its decreased E_g.

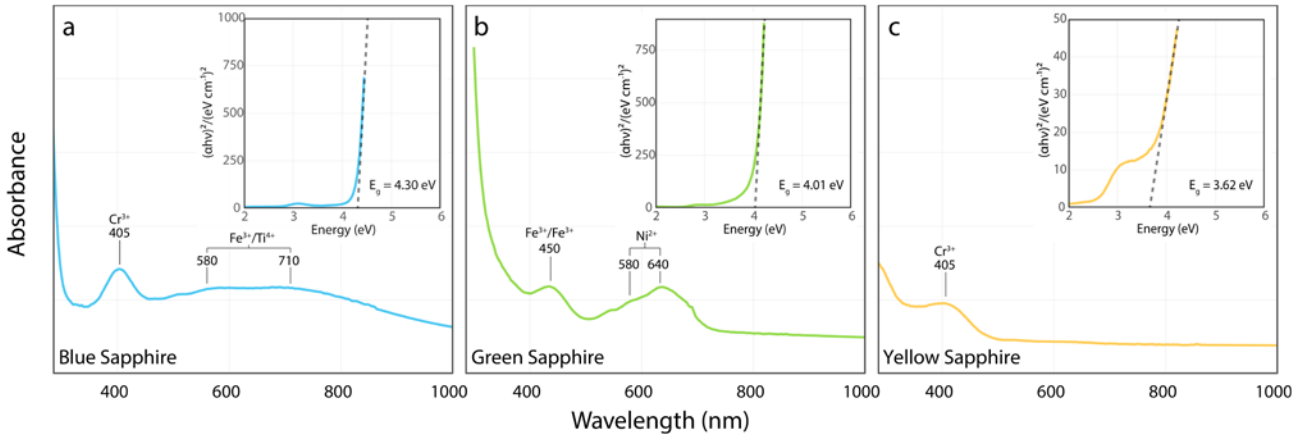

Figure 2. UV-Vis-NIR spectrum including inserts of Tauc plot calculations of synthetic blue sapphire (a) synthetic green sapphire (b) and synthetic yellow sapphire (c).

3.4 XAS result

Table 2. LCF value of all three synthetic sapphires with reference to Fe^0, Fe^{2+}, and Fe^{3+}.

Samples	Fe foil, Fe^0	FeO, Fe^{2+}	Fe_2O_3, Fe^{3+}
Blue sapphire	0.17±0.04	0.00±0.04	0.83±0.06
Green sapphire	0.53±0.02	0.02±0.02	0.46±0.03
Yellow sapphire	0.92±0.01	0.000±0.01	0.08±0.01

XAS measurements were analyzed in X-ray Absorption Near Edge Structure (XANES) region to determine the oxidation and coordination of the Fe within the sample's crystal structure with binding energy (E_0) of metallic iron (Fe^0) calibrated to 7112 eV. E_0 for the synthetic blue sapphire was revealed to be 7123.56 eV while pre-edge fitting resulted in a fit centroid of 7114.28 eV and an integrated intensity of 0.10. The results point toward mainly Fe^{3+} in octahedral site.[12,13] As for the green and yellow sapphire samples there was an issue in their spectra showing interference patterns from the absorption edge of metallic iron. The interference made interpretations of XANES spectra and pre-edge fitting for green and yellow samples difficult to produce but some features may still be identified. As seen in Figure 3a the XANES spectra of yellow displays near identical features to metallic iron (Fe foil) which can also be seen in Figure 3b. Linear Combination Fitting (LCF) was completed in Athena for all samples in Table 2 to compensate for the lack of pre-edge fitting. LCF was done in respect to Fe^0, Fe^{2+}, and Fe^{3+} due to the low iron content in samples though it is a moderate approximation.

The results show high metallic iron in both green and yellow sapphire with a small amount found in the synthetic blue sapphire as well. Additionally, a 35% Fe foil subtracted synthetic green sapphire XAS spectrum was created for pre-edge fitting to provide supplementary data. LCF Fe^{2+} to Fe^{3+} ratio leaned heavily towards Fe^{3+} with Fe^{2+} being close to zero in all samples and Fe^{3+} being predominant in all three samples if metallic iron is excluded from the green and yellow samples. Pre-edge fit for green sapphire with 35% Fe foil subtracted spectrum revealed E-E_0 of 2.77 eV which is close to Fe^{3+}.[12,13] It is to be noted however that even with the subtracted spectrum, the influence of Fe^0 is still present as seen with the unusually high integrated intensity of 0.28. Yellow sapphire shows major presence of Fe^0 which is supported by the XAS spectrum when compared to the metallic iron spectrum in Figure 3. This shows that without the interference, the iron in the synthetic green sapphire should be predominantly Fe^{3+} with no Fe^{2+} contrasting with literature.[14] While the majority of iron in yellow sapphire is in the form of metallic iron with a minor portion being Fe^{3+} and a lack of Fe^{2+} presence according to LCF.

In respect to the metallic iron absorption edge interference, the interference of Fe^0 from the equipment can be dismissed as the same pattern does not occur in the blue sapphire sample which was measured in the same environment although small amounts of metallic iron were detected in respect to the data. It is possible that during the process of synthesizing the sapphires, either metallic iron was added alongside or instead of iron oxide perhaps with the intent to conceal the manufacturing process, or the environment supported reduction of the iron oxide that was added to induce color within the verneuil, resulting in Fe^0 signals coming from the XAS measurements. The blue sample did not display such abnormality even though a small amount of metallic iron was detected, probably due to how the beam position was placed on the sample. As the synthetic blue sapphire was nonhomogeneous in its color, the beam was placed near the outer rim of the verneuil to more focus on the blue color of the sample in question. The green and yellow sapphires were more homogeneous, and emphasis on the beam position was thus not considered.

3.5 Energy band modelling

After E_g calculations using tauc plot method,[15] we then apply Plank's equation to the significant UV-Vis-NIR absorption peaks to generate energy states for each sample which are then used to create the energy band model. The energy band model for the synthetic blue sapphire as seen in Figure 4a exhibits a large E_g of 4.30 eV with energy states at 3.06 eV, 2.14 eV and 1.75 eV corresponding to absorption peaks at 405 nm, 580 nm and 710 nm, respectively. The replacement of Al^{3+} pair by the Fe^{3+}/Ti^{4+} pair is charged imbalance as the total oxidation number of the original pair is 6+ while the replacing ion pair is of 7+. The charge must then be supplemented by an excited electron from the valence band making the energy state where the electron is excited towards to be an acceptor state. Although, as we have currently no definitive way of determining which energy state between 2.13 eV or 1.75 eV, nor the ion that the electron would be excited to, Wongrawang et al. (2016) thus suggests that it is an Fe^{3+}/Ti^{4+} mixed acceptor states[5] unlike Fe^{2+}/Ti^{4+} IVCT.[16]

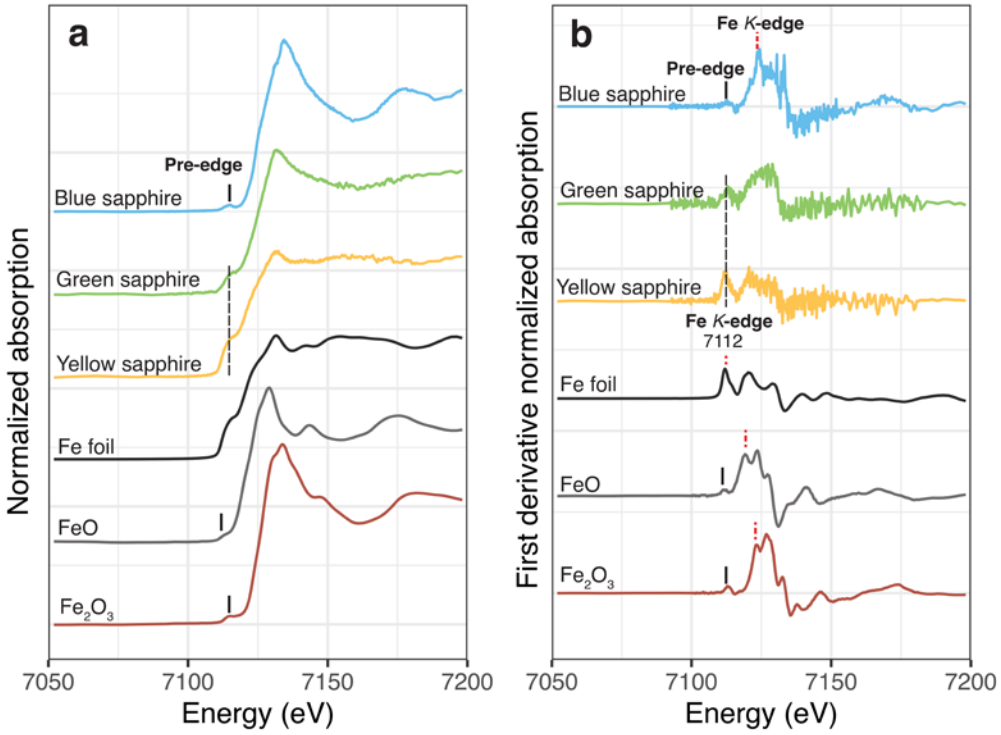

Figure 3. XANES spectra of synthetic blue, green, and yellow sapphire samples as well as Fe foil, FeO, and Fe_2O_3 (a) including the associated first derivative spectra (b). The solid lines represent the pre-edge position, the red dashed lines represent Fe *K*-edge, and the black dashed lines show a mixed feature of ionic iron pre-edge and metallic iron K-edge.

The green sapphire model has an E_g of 4.01 eV. As seen in Figure 4b, green sapphire displays energy states at 2.76 eV, 2.14 eV, and 1.94 eV which are generated from the absorption peaks at 450 nm, 580 nm, and 640 nm, respectively. The energy state at 2.76 eV is a neutral state corresponding to absorption by Fe^{3+}/Fe^{3+} pair.[5] The energy state at 2.14 eV and 1.94 eV are modified from the absorption edge at 580 nm and 640 nm. These two energy states correspond to Ni^{2+} ion[11,17] which to balance out the charge, e^- is excited to the conduction band and thus, the energy states of Ni are that of donor states.

Energy band model for yellow as seen in Figure 4c, is modelled with the absorbance peak of 405 which results in a neutral state of 3.06 eV related to the absorbance of Cr^{3+} in the crystal field.[18] E_g for the model is 3.62 eV.

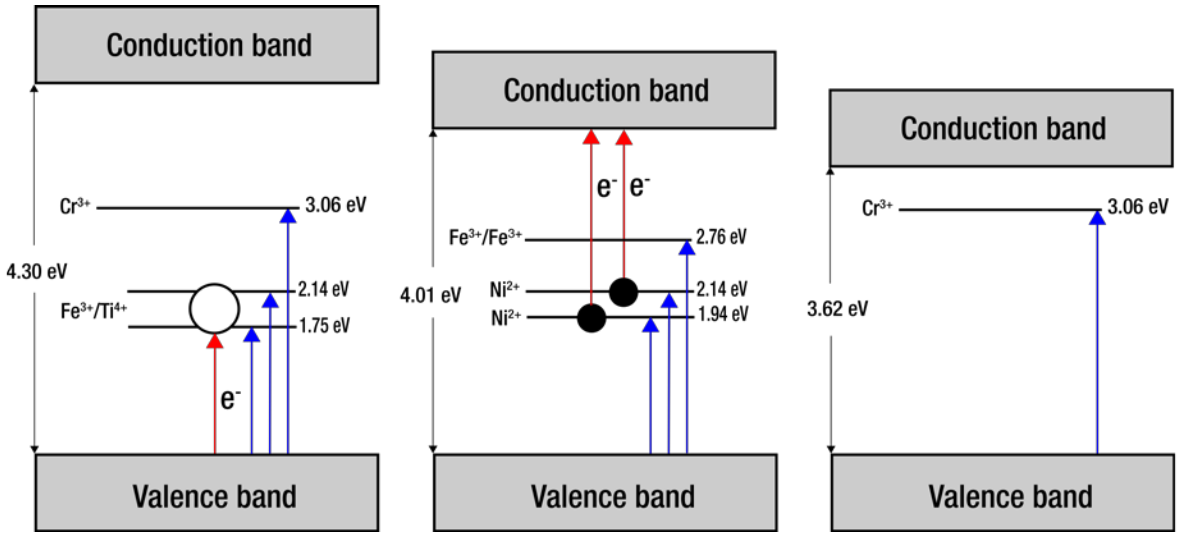

Figure 4. Energy band model of all three synthetic sapphires. From left to right, synthetic blue sapphire, synthetic green sapphire, and synthetic yellow sapphire. The blue arrow represents the energy absorbed by each energy state when excited. The red arrow shows the migration of electrons when excited.

The energy band gap of all three samples i.e. synthetic blue, green, and yellow are clearly different at 4.30 eV, 4.01 eV, and 3.62 eV, despite the similar chemical composition apart from Fe_2O_3. This anomaly may be caused by band gap engineering in the synthesis process by chemical doping or by the increased turbidity caused by the dispersed metallic iron in the crystal material as revealed from the XAS results. The role of trace elements found in this study contradict with other chromophore studies.[19,20] Future studies should aim to find correlation between band gap and its effect on color in corundum.

4. Conclusion

Synthetic green corundum energy band model is proposed to be Ni^{2+} donor states with a Fe^{3+}/Fe^{3+} pair neutral state. The synthetic blue corundum is caused by the diffusion of Fe^{3+}/Ti^{4+} mixed acceptor states while the synthetic yellow corundum is caused by Cr^{3+} neutral state. Oxidation states of Fe that gives the samples their color is Fe^{3+} which is supported by LCF and XANES pre-edge fitting of the synthetic blue and green corundum, ignoring the presence of Fe^0 as it does not interact with the crystal structure therefore does not influence the color of corundum. Our future study will aim to compare natural as well as synthetic sapphires including the presence of Fe^0, an anomaly that should be investigated in depth.

Acknowledgements

We express our gratitude to the Synchrotron Light Research Institute (Public Organization) for providing access to beamline 7.2W as well as the Gem and Jewelry Institute of Thailand (Public Organization) in allowing access to their equipment. To Nopparat Anantaprayoon, we give our thanks for his insight and knowledge on data visualization. Lastly, to Arissara Aramrueng that assisted in the data collection.

References

1. Hughes, R. *Ruby & Sapphire*. White Lotus Co. Ltd., Bangkok, 1992.
2. Nassau, K.; Valente, G. K. *Gems Gemol*. **1987**, 23, 222–231.
3. Monarumit, N.; Lhuaamporn, T.; Wathanakul, P.; Saiyasombat, C.; Wongkokua, W. *Radiat. Phys. Chem*. **2023**, 206, 110756.
4. Pisutha-Arnond, V.; Häger, T.; Atichat, W.; Wathanakul, P. *J. Gemmol*. **2006**, 30(3/4), 131–143.
5. Wongrawang, P.; Monarumit, N.; Thammajak, N.; Wathanakul, P.; Wongkokua, W. *Mater. Res. Express* **2016**, 3, 026201.
6. Mogmued, J.; Monarumit, N.; Won-in, K.; Satitkune, S. *IOP Conf. Ser.: J. Phys.: Conf. Ser*. **2017**, 901, 012075.
7. Kusuma, H. H.; Ibrahim, Z.; Saidin, M. K. *J. Appl. Sci*. **2011**, 11(5), 888–891.
8. R Core Team. R: A Language and Environment for Statistical Computing. R Foundation for Statistical Computing: Vienna, Austria, 2022. URL https://www.R-project.org/.
9. Monarumit, N.; Lhuaamporn, T.; Satitkune, S.; Wongkokua, W. *J. Appl. Spectrosc*. **2019**, 86(3), 486–492.
10. Monarumit, N.; Lhuaamporn, T.; Sakkaravej, S.; Wathanakul, P.; Wongkokua, W. *J. Phys. Commun*. **2020**, 4, 105018.
11. Thomas, V. G.; Mashkovtsev, R. I.; Smirnov, S. Z.; Maltsev, V. S. *Gems Gemol*. **1997**, 33(3), 188–202.
12. Wilke, M.; Farges, F.; Petit, P.-E.; Brown, G. E. Jr.; Martin, F. *Am. Mineral*. **2001**, 86, 714–730.
13. Bunnag, N.; Kasri, B.; Setwong, W.; Sirisurawong, E.; Chotsawat, M.; Chirawatkul, P.; Saiyasombat, C. *Radiat. Phys. Chem*. **2020**, 177, 109107.
14. Ferguson, J.; Fielding, P. E *Aust. J. Chem*. **1972**, 25, 1371–1385.
15. Klein, J.; Kampermann, L.; Mockenhaupt, B.; Behrens, M.; Strunk, J.; Bacher, G. *Adv. Funct. Mater*. **2023**, 2304523.
16. Amphon, R.; Chankhantha, C.; Thammajak, N.; Intarasiri, S.; Shen, A. H. *Cryst. Res. Technol*. **2022**, 2200152.
17. Winotai, P.; Saiseng, S.; Sudyoadsuk, T. *Mod. Phys. Lett. B* **2001**, 15(20), 873–882.
18. Yamchuti, O. *Oxidation states of trace elements in synthetic corundum*. Chulalongkorn University Theses and Dissertations, 2019.
19. Dubinsky, E. V.; Stone-Sundberg, J.; Emmett, J. L. *Gems Gemol*. **2020**, 56(1), 2-28.
20. Emmett, J. L.; Atikarnsakul, U.; Stone-Sundberg, J.; Sangsawong, S. *Gem. Gemol*. **2023**, 59(3), 268–297

Evaluation of the aromaticity of two star[3]calicene isomers

Thawalrat Ratanadachanakin[1]* and Willard E. Collier[2]*

[1]*Faculty of Science, Maejo University, Sansai, Chiang Mai, 50290, Thailand*
[2]*Department of Chemistry, Tuskegee University, Tuskegee, AL 36088, USA*

**E-mail: thawalrat4@gmail.com, wcollier@tuskegee.edu*

Abstract:

Polycalicenes are an essentially unexplored region of chemical space. Polycalicenes are polymers of the monomer calicene, also known as triapentafulvalene. One provocative feature of polycalicenes is that even though calicene has never been synthesized, a few polycalicenes have been synthesized and shown to be aromatic. Polycalicenes encompass a vast region of chemical space as it is easy to envision different polycalicene families by changing the bonding motif between the calicene monomers. In previous studies, we have investigated several polycalicene families. This study explores the aromaticity of two isomers of a new polycalicene family, star[3]calicene isomers **1-2** (Figure 2), using density functional theory (DFT). Star[N]calicenes have a star shape where [N] indicates the number of calicene monomers. The aromaticities of the two star[3]calicene isomers **1** and **2** were evaluated using Schleyer's nucleus independent chemical shift (NICS). All geometries, vibrational frequencies, and properties (dipoles, NMR, etc.) of all molecules are reported at the B3LYP/6-31+G(d,p) level of theory. Calicene, benzene, cyclopentadienyl anion, and cyclopropenyl cation are reported as references.

1. Introduction

Aromaticity is a foundational concept of organic chemistry that has yet to be definitively defined and is vigorously debated even after almost 160 years of investigation [1-3]. No one ultimate criterion of aromaticity has been accepted out of the many criteria of aromaticity proposed through the years including chemical reactivity, aromatic stabilization energy (ASE), bond length equalization, and various magnetic properties such as 1H chemical shifts [4-6]. Non-benzenoid aromatic compounds are intriguing molecules that extend our understanding of aromaticity beyond the benzenoid paradigm.

Polycalicenes, polymers, of calicene (Figure 1), are a vast region of chemical space with an untold number of non-benzenoid aromatic molecules. Our research has focused on the computational investigation of the aromaticity of some polycalicene families [7-13] that are made possible by changing the bonding motif between the calicene monomers. Yoshida et al [14] synthesized bicalicene and experimentally determined it to be aromatic [15-16], but in the over forty years since Yoshida's success, little has been done either synthetically or theoretically to explore polycalicene chemical space.

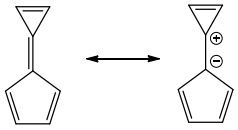

Figure 1. Resonance structure of calicene.

This work investigates the aromaticity of two isomers of the simplest star[N]calicenes where N is the number of calicene monomers. The aromaticities of the star[3]calicene isomers **1-2** (Figure 2) were evaluated using Schleyer's nucleus independent chemical shifts (NICS) [17]. The NICS values of calicene **3**, bicalicene **4**, cyclopropenyl cation **5**, cyclopentadienyl anion **6** and benzene **7** (Figure 4) were calculated as references.

2. Materials and Methods

To evaluate the aromaticity of the two star[3]calicene isomers **1** and **2** (Figure 2), both molecules were fully optimized using the B3LYP functional [18-19] and 6-31+G(d,p) basis set [20]. Harmonic vibrational frequency calculations at the same level of theory confirmed minima.

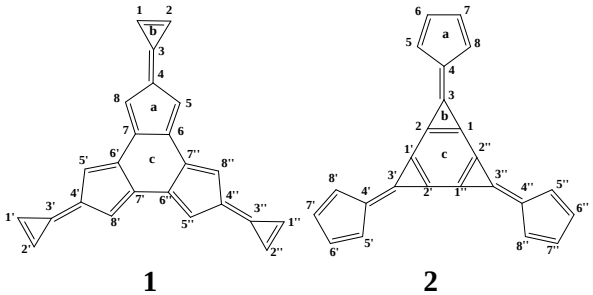

1 **2**

Figure 2. Structure and numbering system of star[3]calicene isomers **1** and **2**.

Nucleus independent chemical shifts (NICS), defined as the negative of the calculated isotropic shielding [21-22], were evaluated at

selected points (Figure 3). The NICS(0) values (z=0) were calculated at points located at the center (non-weighted average of ring atom coordinates) and in the plane of the three-membered rings (b), five-membered rings (a) and six-membered rings (c). The NICS(1) values (z=+1) and NICS(-1) values (z=-1) were calculated at 1 Å above and below their respective NICS(0) point, respectively. All reference molecules, including calicene **3**, bicalicene **4**, cyclopropenyl cation **5**, cyclopentadienyl anion **6**, and benzene **7** (Figure 4), were optimized at the same level of theory and their respective NICS(0), NICS(1) and NICS(-1) values were calculated for comparison with the NICS results of star[3]calicenes **1** and **2**. Bond lengths are reported in angstroms (Å) and NICS values in ppm. All calculations were carried out using the Gaussian 16 suite of quantum mechanical programs [23].

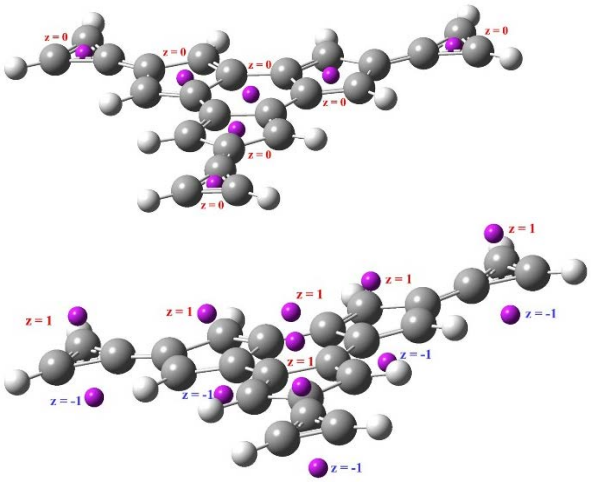

Figure 3. Location of NICS points, z=0, z=+1 and z=-1, illustrated using star[3]calicene **1**.

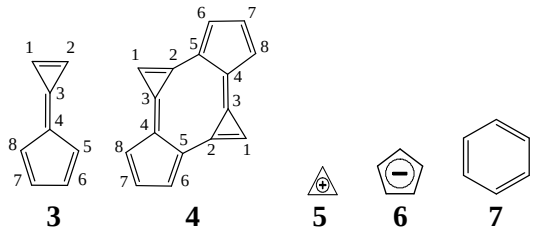

Figure 4. Reference molecules used in this study.

3. Results & Discussion

The aromaticities of star[3]calicenes **1** and **2**, are evaluated and compared in the discussion below using bond lengths and NICS values.

3.1 Bond Lengths

Structures and numbering of star[3]calicenes **1** and **2** are shown in Figure 2. Bond lengths of molecules **1-2** (Table 1) are discussed and compared with reference molecules **3-7** as shown in Table 1. Bond lengths in molecules **1-2** are discussed and compared in two groupings or systems.

The first system is the calicene system or monomers that have been bonded to other calicenes to yield star[3] calicenes **1** and **2**. The bonds of interest are (1) C_1-C_2, (2) C_3-C_4, (3) C_4-C_5, (4) C_4-C_8, (5) C_5-C_6, (6) C_6-C_7, and (7) C_7-C_8.

The second system is the 6-membered ring formed by bonding of the calicenes with two bonds of interest in molecule **1**: (1) C_6-C_7 and C_6-$C_{7''}$, and two in molecule **2**: (1) C_1-C_2 and (2) C_1-$C_{2''}$.

The first system, the calicene monomer:

The C_1-C_2 bond length in molecule **1** is 1.328 Å, equal to the respective bond length of calicene **3**. These bond lengths are shorter than the respective bond length of the cyclopropenyl cation **5** (1.367 Å). The C_3-C_4 bond length in molecule **1** is 1.357 Å, almost equal to the respective bond length of calicene **3** (1.356 Å). The C_4-C_5 bond lengths (1.455 Å) of molecule **1** is also almost equal to the respective bond length of calicene **3** (1.459 Å). But these bond lengths are longer than the respective bond length of the cyclopentadienyl anion **6** (1.418 Å). Molecule **1** has a C_5-C_6 bond length, 1.375 Å, slightly longer than the respective bond length of calicene **3** (1.369 Å). Both bond lengths are shorter than the respective bond length of of the cyclopentadienyl anion **6** (1.418 Å). The bond length of C_6-C_7 in molecule **1,** 1.478 Å is longer than the respective bond lengths of calicene **3** (1.456 Å) and the cyclopentadienyl anion **6** (1.418 Å). These data suggest the calicene system in the star[3]calicene **1** is very similar to the calicene monomer.

Molecule **2** has a C_1-C_2 bond length of 1.411 Å, much longer than the respective bond lengths of calicene **3** (1.328 Å) and the cyclopropenyl cation **5** (1.367 Å). The C_1-C_2 bond length is almost equal to benzene **7** (1.398 Å). The C_3-C_4 bond length of molecule **2**, 1.353 Å, is almost equal to the respective bond length of calicene **3** (1.356 Å). Molecule **2** has a C_4-C_5 bond length of 1.464 Å just slightly longer than the respective bond length of calicene **3** (1.459 Å), but significantly longer than the respective bond length of the cyclopentadienyl anion **6** (1.418 Å). The C_5-C_6 bond length of molecule **2** is 1.362 Å, slightly shorter than the respective bond length of calicene **3** (1.369 Å). Both those bond lengths are shorter than the respective bond length of the cyclopentadienyl anion **6** (1.418 Å). Molecule **2** has a C_6-C_7 bond length of 1.469 Å, longer than the respective bond length of calicene **3** (1.456 Å) and

much longer than the respective bond length of the cyclopentadienyl anion **6** (1.418 Å). These results indicate that the calicene system in star[3]calicene **2** is distinctly different from the calicene monomer.

The second system, six-membered ring:

Molecule **1** has a C_6-$C_{7''}$ bond length of 1.450 Å and a C_6-C_7 bond length of 1.478 Å, both much longer than the respective bond length of benzene **7** (1.398 Å). These longer bond lengths indicate greater single bond character. Therefore, the six-membered ring in molecule **1** is not expected to be aromatic like benzene.

In sharp contrast, molecule **2** has a C_1-$C_{2''}$ bond length of 1.375 Å that is shorter than the respective bond length of benzene **7** (1.398 Å) but much longer than the respective bond length of calicene **3** (1.328 Å). The C_1-C_2 bond length of molecule **2** is 1.411Å longer than the respective bond length of benzene **7** (1.398 Å). Unlike molecule **1** where both bonds of the six-membered ring are much longer than the respective bond in benzene, the bond lengths of the six-membered ring in molecule **2** average to almost exactly the benzene bond length. Thus, the six-membered ring in molecule **2** should be more aromatic than the six-membered ring in molecule **1**.

Table 1. Bond lengths (Å) of **1-7** at B3LYP/6-31+G(d,p).

Molecule	1	2	3	4	4**	5	6	7
Bond								
C_1-C_2	1.328	1.411	1.328	1.375	1.365	1.367		
C_3-C_4	1.357	1.353	1.356	1.394	1.394			
C_4-C_5	1.455	1.464	1.459	1.458	1.433		1.418	
C_4-C_8	1.455	1.464	1.459	1.414	1.406		1.418	
C_5-C_6	1.375	1.362	1.369	1.414	1.401		1.418	
C_6-C_7	1.478	1.469	1.456	1.406	1.391		1.418	
C_7-C_8	1.375	1.362	1.369	1.406	1.410		1.418	
C_6-$C_{7''}$	1.450							1.398
C_1-$C_{2''}$		1.375						1.398

* Numbering of bond lengths are illustrated in Figure 2.
****** Results from the experiment [15-16].

3.3 Nucleus Independent Chemical Shifts (NICS)

NICS(0) and NICS(1) values, considered together, are a reliable and simple method of assessing aromaticity. Because NICS values are dependent on ring size and electron density, reference molecules that are like the molecules under evaluation are critical to accurately assessing aromaticity. The NICS(0) values (z=0) were calculated at points located at the center and in the plane of the three-membered rings (**b**), five-membered rings (**a**), and the six-membered ring (**c**). The NICS(1) values (z=1) were calculated at 1 Å above their respective NICS(0) point. In this study, the NICS(0) and NICS(1) values of reference molecules **3-7** are compared to star[3]calicene isomers **1-2** (see Table 2).

*Star[3]calicene **1***:

The NICS(0) values for the **a** ring and **b** ring of star[3]calicene **1** are -3.5 ppm and -19.7 ppm, respectively. The NICS(0) values of **1** for both the **a** ring has a higher NICS value compared to the respective NICS(0) values of calicene **3** and cyclopentadienyl anion **6**, -4.5 ppm and -12.8 ppm, respectively. The NICS(0) value of the **b** ring in **1** also has a higher NICS value compared to the respective NICS(0) values of calicene **3** and cyclopropenyl cation **5**, -20.5 ppm and -22.4 ppm, respectively. The **c** ring of **1** has a positive NICS(0) value (2.9 ppm) in contrast to the negative NICS(0) value for rings **a** and **b**.

The positive NICS(0), indicating antiaromatic character, for **c** while both **a** and **b** are negative, indicating aromatic character, is an excellent example of the need to distinguish global vs. local aromaticity in larger molecules. Another factor is NICS(0) values are known to be sensitive to the σ electron density. Often, NICS(1) values will indicate aromaticity (negative values) while the NICS(0) values indicate antiaromaticity (positive values).

NICS(1) values for the **a** ring and **b** ring of star[3]calicene **1** are -4.4 ppm and -6.0 ppm, respectively. The NICS(1) value (-4.4 ppm) of the **a** ring of **1** has a higher NICS value compared to the respective NICS(1) values of calicene **3** and cyclopentadienyl anion **6**, -5.1 ppm, and -9.6 ppm. The NICS(1) value (-6.0 ppm) of the **b** ring in **1**

has a higher NICS value compared to the NICS(1) values of calicene **3** and cyclopropenyl cation **5**, -6.9 ppm, and -14.5 ppm, respectively. The **c** ring of **1** has a higher NICS(1) value (-0.1 ppm) compared to the respective NICS values of benzene **7** (-10.2 ppm).

The NICS results indicate star[3]calicene **1** can be considered an aromatic molecule.

*Star[3]calicene isomer **2**:*

The NICS(0) values for the **a** ring and **b** ring of star[3]calicene isomer **2** are 1.3 ppm and -11.4 ppm, respectively. The NICS(0) value for isomer **2** of the **c** ring is -2.7 ppm. The NICS(0) value for the **b** ring of isomer **2** is a higher than the NICS(0) values of calicene **3** and cyclopropenyl cation **5**, -20.5 ppm, and -22.4 ppm, respectively.

The NICS(1) value for the **a** ring and **b** ring of isomer **2** are -1.2 ppm and -5.4 ppm, respectively. The NICS(1) value of the **a** ring of **2** has a higher NICS value compared to the respective NICS(1) values of calicene **3** and the cyclopentadienyl anion **6**, -5.1 ppm, and -9.6 ppm, respectively. The NICS(1) value of the **b** ring of isomer **2** also has a higher NICS value than the respective NICS values of calicene **3** and cyclopropenyl cation **5**, -6.9 ppm, and -14.5 ppm, respectively. The **c** ring NICS(1) value of **2** has a higher NICS value compared to the respective NICS value of benzene **7** (-10.2 ppm).

All NICS(1) values for star[3]calicene **2** are negative indicating that the molecule is aromatic. While it is reasonable to consider both star[3]calicene isomers **1** and **2** to be aromatic, it would be difficult to rank them in order of aromaticity with any confidence from this limited study. More detailed investigations are planned on the star[N[calicene family.

Table 2. NICS(z=0) and NICS(z=1) values (ppm) of star[3]calicene isomers **1-2** and references **3-7** at B3LYP/6-31+G(d,p).

	a ring					b ring					c ring		
Molecule	**1**	**2**	**3**	**4**	**6**	**1**	**2**	**3**	**4**	**5**	**1**	**2**	**7**
z = 0	-3.5	1.3	-4.5	-4.7	-12.8	-19.6	-11.4	-20.5	-23.3	-22.4	2.9	-2.7	-8.1
z = 1	-4.4	-1.2	-5.1	-5.7	-9.6	-6.0	-5.4	-6.9	-7.5	-14.5	-0.1	-7.5	-10.2

*Ring locations are illustrated in Figure 2.

4. Conclusion

The NICS data indicate that both star[3]calicene isomers **1** and **2** are aromatic.

Acknowledgements

The computer time for this research was provided by the Alabama Center for Superconducting Research.

References

1. Lloyd, D. “What is aromaticity?”, *J. Chem. Inf. Comput. Sci.*, **1996**, *36*, 442-447.
2. von Rague Schleyer, P. and Jiao, H. “What is aromaticity?”, *Pure Appl. Chem.*, **1996**, *68*, 209 218.
3. Balaban, A. T. “Is aromaticity outmoded?”, *Pure Appl. Chem.*, **1980**, *52*, 1409-1429.
4. Cyranski, M. K.; Krygowski, T. M.; Katritzky, A. R.; Schleyer, P. V. R. “To what extent can aromaticity be defined uniquely?”, *J. Org. Chem.*, **2002**, *67*, 1333-1338.
5. Krygowski, T. M.; Cyranski, M. K.; Czarnocki, Z.; Häfelinger, G.; Katritzky, A. R. “Aromaticity: A theoretical concept of immense pratical importance”, *Tetrahedron*, **2000**, *56(13)*, 1783-1796.
6. Minkin, V. I.; Glukhovtsev, M. N.; Simkin, B. “Aromaticity and Antiaromaticity: Electronic and Structural Aspects”, John Wiley and Sons, New York, **1994**.
7. Collier, W. E. A Computational Investigation of Some Polycalicenes as Novel Nonbenzenoid Aromatic Molecules and the Strange Case of the Cyclopropenyl Anion. Ph.D. Dissertation, Mississippi State University, Mississippi State, MS, USA. **2009**.
8. Collier, W. E.; Ratanadachanakin, T. The Potential of Bandcalicenes as carbon dioxide
9. Hosts. J. Interdiscipl. Networks, **2013**, 2(Sp. Iss.1), 112-117.
10. Ratanadachanakin, T.; Collier, W. E. A Theoretical Investigation of the Push-Pull Effect on the Aromaticity of Some Poly-2,7-[2]calicene Derivatives. *Proceedings of PACCON 2014*, **2014**, 235-238.
11. Ratanadachanakin, T.; Collier, W. E. Aromaticity of a series of poly-2,7-[N]calicenes. *Maejo Int. J. Sci. Techno*, **2015**, *9(01)*, 21-31.
12. Ratanadachanakin, T.; Collier, W. E. The Effect of Reversing the Location of Donor and Acceptor Groups on the Aromaticity and

Electronic Structure of a Series of Substituted Poly-2,7-[2]calicenes. *Proceedings of PACCON 2015*, **2015**, 287-290.
13. Ratanadachanakin, T.; Collier, W. E. A Density Functional Investigation of the Push-Pull Effect in Some Poly-2,7′,1′,6″-[3]calicenes: Towards Novel Molecular Wires. *Proceedings of The 2nd International and National Conference on Multidisciplinary for Innovation Development in 21st Century*, **2021**, A331-A339.
14. Yoshida, Z. I. Novel pi systems possessing cyclopropenylidene moiety. *Pure & Appl. Chem*. **1982**, *54*, 1059-1074.
15. Yonedo, S.; Shibata, M.; Kida, S.; Yoshida, Z. I.; Kai, Y.; Miki, K.; Kasai, N. A Novel Aromatic Hydrocarbon with 16π-Electron Periphery:“Cyclic Bicalicene”. Angewandte Chemie International Edition in English, **1984**, *23(1)*, 63-64.
16. Oziminski, W. P.; Palusiak, M.; Dominikowska, J.; Krygowski, T. M.; Havenith, R. W. A.; Gibson, C. M.; Fowler, P. W. Capturing the elusive aromaticity of bicalicene. *Phys. Chem. Chem. Phys.*, **2013**, 15(9), 3286-3293.
17. Schleyer, P. V. R.; Maerker, C.; Dransfeld, A.; Jiao, H.; van Eikema Hommes, N. J. Nucleus-independent chemical shifts: a simple and efficient aromaticity probe. *J. Am. Chem. Soc.*, **1996**, *118(26)*, 6317-6318.
18. Lee, C.; Yang, W.; Parr, R.G. Development of the Colle-Salvetti correlation-energy formula into a functional of the electron density. *Phys. Rev.* **1988**, *B* 37. 785-789. doi.org/10.1103/PhysRevB.37.785
19. Becke, A.D. Density-functional thermo-chemistry. III. The role of exact exchange. *J. Chem. Phys.* **1993**, 98. 5648-5652. doi.org/10.1063/1.464913
20. Clark, T.; Chandrasekhar, J.; Spitznagel, G. W.; Schleyer, P. v. R. Efficient diffuse function-augmented basis-sets for anion calculations. 3. The 3-21+G basis set for 1st-row elements, Li-F. *J. Comp. Chem.*, **1983**, *4* 294-301. doi.org/10.1002/jcc.540040303
21. Schleyer, P. V. R.; Jiao, H. What is aromaticity? *Pure & Appl. Chem.* **1996**, *68(2)*. 209-218. dx.doi.org/10.1351/pac199668020209
22. Schleyer, P. v. R.; Maerker, C.; Dransfeld, A.; Jiao, H.; Hommes, N. J. R. v. E. Nucleus-Independent Chemical Shifts: A Simple and Efficient Aromaticity Probe. *J. Am. Chem. Soc.* **1996**, *118(26)*, 6317-6318. doi.org/10.1021/ja960582d
23. Frisch, M. J.; Trucks, G. W.; Schlegel, H. B.; Scuseria, G. E.; Robb, M. A.; Cheeseman, J. R.; Scalmani, G.; Barone, V.; Petersson, G. A.; Nakatsuji, H.; Li, X.; Caricato, M.; Marenich, A. V.; Bloino, J.; Janesko, B. G.; Gomperts, R.; Mennucci, B.; Hratchian, H. P.; Ortiz, J. V.; Izmaylov, A. F.; Sonnenberg, J. L.; Williams-Young, D.; Ding, F., Lipparini, F.; Egidi, F.; Goings, J.; Peng, B.; Petrone, A.; Henderson, T.; Ranasinghe, D.; Zakrzewski, V. G.; Gao, J.; Rega, N.; Zheng, G.; Liang, W.; Hada, M.; Ehara, M.; Toyota, K.; Fukuda, R.; Hasegawa, J.; Ishida, M.; Nakajima, T.; Honda, Y.; Kitao, O.; Nakai, H.; Vreven, T.; Throssell, K.; Montgomery, J. A.; Jr., Peralta, J. E.; Ogliaro, F.; Bearpark, M. J.; Heyd, J. J.; Brothers, E. N.; Kudin, K. N.; Staroverov, V. N.; Keith, T. A.; Kobayashi, R.; Normand, J.; Raghavachari, K.; Rendell, A. P.; Burant, J. C.; Iyengar, S. S.; Tomasi, J.; Cossi, M., Millam, J. M.; Klene, M.; Adamo, C.; Cammi, R.; Ochterski, J. W.; Martin, R. L.; Morokuma, K.; Farkas, O.; Foresman, J. B.; Fox, D. J. *Gaussian 16, revision C. 01*. Wallingford: Gaussian. **2016**.

Chemistry for Bio-Circular-Green Economy

www.paccon2024.kasetsart.org